

T. Pradeep

Publications 2025

Contents

1. Publications	**10 - 956**
2. Editorials	**957 - 961**
3. Patents	**962 - 963**
4. Selected media reports	**964 - 966**

Journal papers in 2025

Publications from our group

1. Understanding the kinetics of CO2 hydrate formation in dry water for carbon capture and storage: X-ray diffraction and in-situ Raman studies, Gaurav Vishwakarma, Vikas Dhamu, M Fahed Qureshi, Gaurav Bhattacharjee, Thalappil Pradeep and Praveen Linga, ACS Appl. Mater. Interfaces. (2025) (DOI: 10.1021/acsami.4c17727)

2. Nanomechanical investigations of crystals of copper nanocluster isomorphs: enhanced hardness of the low-density analogue, Amoghavarsha Ramachandra Kini, Sanghamitra Debta, Arijit Jana, C. Aparna, Vivek Yadav, Nataliia Kusiak, Tomas Base, Umesh Waghmare, Pijush Ghosh and Thalappil Pradeep, Chem. Mat. (2025) (DOI: 10.1021/acs.chemmater.4c03265)

3. Cellulose-derived nanomaterials for affordable and rapid remediation of uranium in water, Tanmayaa Nayak, Sritama Mukherjee, Amoghavarsha Ramachandra Kini, Md Rabiul Islam, Ankit Nagar, Sonali Seth and Thalappil Pradeep, ACS Sustain. Chem. Eng. (2025) (DOI: 10.1021/acssuschemeng.4c10246)

4. Structural changes in atomically precise Ag29 nanoclusters upon sequential attachment and detachment of secondary ligands, Jayoti Roy, Amitabha Das, Arijit Jana, Papri Chakraborty, Marco Neumaier, Horst Hahn, Biswarup Pathak, Manfred Kappes and Thalappil Pradeep, ACS Nano. (2025) (DOI: 10.1021/acsnano.4c16413)

5. Site-specific substitution in atomically precise carboranethiol-protected nanoclusters and concomitant changes in electronic properties, Vivek Yadav, Arijit Jana, Swetashree Acharya, Sami Malola, Harshita Nagar, Ankit Sharma, Amoghavarsha Ramachandra Kini, Sudhadevi Antarjanam, Jan Machacek, Kumaran Nair Valsala Devi Adarsh, Tomas Base, Hannu Hakkinen and Thalappil Pradeep, Nat. Commun. (2025) (DOI: 10.1038/s41467-025-56385-w)

6. Nanosheet-to-nanoparticle transformation in charged water microdroplets: A pathway for 2D to 0D materials, B. K. Spoorthi, Angshuman Ray Chowdhuri, Biswajit Mondal, Sujan Manna, Anubhav Mahapatra, Amoghavarsha Ramachandra Kini, Thalappil Pradeep, Chem. Commun. (2025). (DOI: 10.1039/D4CC06697A)

7. Ultraviolet photoactivation perturbs the metal–ligand interface of atomically precise nanoclusters, Anagha Jose, Jada N. Walker, Maya Khatun, Sami Malola, B. S. Sooraj,

Hannu Häkkinen, Jennifer S. Brodbelt, and Thalappil Pradeep, Chem. Commun. (2025) (DOI: 10.1039/D5CC00757G)

8. Morphology-preserved alloying in anisotropic gold nanoparticles using atomically precise nanoclusters, Amrita Chakraborty, Sujan Manna, Biswajit Mondal, Mohammad Bodiuzzaman, Ankit Nagar, Soham Chowdhury, Tanmayaa Nayak, Nonappa and Thalappil Pradeep, Small (2025) (DOI: 10.1002/smll.202410784)

9. Composition-dependent formation and dissociation of structure I and structure II clathrate hydrates of trimethylene oxide in ultrahigh vacuum, Soham Chowdhury, Bijesh Malla, Gaurav Vishwakarma, Anupriya Nyayban and Thalappil Pradeep, J. Phys. Chem. C. (2025) (DOI: 10.1021/acs.jpcc.5c01603)

10. Ultraviolet photolysis of CO2 clathrate hydrate and H2O–CO2 mixed ice under ultrahigh vacuum, Gaurav Vishwakarma, Bijesh Malla, Soham Chowdhury, Jyotirmoy Ghosh, Rabin Rajan J. Methikkalam, Rajnish Kumar and Thalappil Pradeep, PCCP. (2025) (DOI: 10.1039/D5CP00620A)

11. Solvent-modulated luminescent spheroidal assemblies of Cu8 nanocluster for volatile amine sensing, Subrata Duary, Arijit Jana, Amitabha Das, Ankit Sharma, Biswarup Pathak, Kumaran Nair Valsala Devi Adarsh and Thalappil Pradeep, Inorg. Chem. (2025) (DOI: 10.1021/acs.inorgchem.5c01082)

12. Accelerated synthesis of pyrazoles mediated by water microdroplets, Manish Jana, Keerthana Unni, Thalappil Pradeep and R. Graham Cooks, ACS Sustain. Chem. Eng. (2025) (DOI: 10.1021/acssuschemeng.5c03026)

13. Dissociation and reformation of CO2 clathrate hydrate cages in amorphous ice thin film under ultrahigh vacuum, Bijesh Malla, Soham Chowdhury, Gaurav Vishwakarma, Rajnish Kumar and Thalappil Pradeep, J. Phys. Chem. Lett. (2025) (DOI: 10.1021/acs.jpclett.5c00393)

14. Bimetallic nanocluster-based light-emitting diodes with high external quantum efficiency and saturated red emission, Jose V. Rival, Savita Chand, Arijit Jana, Nonappa, Vasudevanpillai Biju, Thalappil Pradeep, Pachaiyappan Rajamalli, and Edakkattuparambil Sidharth Shibu, Adv. Mater. (2025) (DOI: 10.1002/adma.202507893)

15. Cluster versus coordination: The chemistry of cyclopentadienyl titanium and vanadium complexes with B- and C-functionalized carborane-thiols, [C2B10H12-n(SH)n] (n = 2 or 3), Subhash Bairagi, Deepak Kumar Patel, Debipada Chatterjee, Monika Kučeráková, Jan Macháček, Tomas Base, Thalappil Pradeep and Sundargopal Ghosh, Chem. Sci. (2025) (DOI: 10.1039/D5SC03562G)

16. Mechanochromic luminescence in copper nanoclusters: Resolving structural transitions through microcrystal electron diffraction, Harshita Nagar, Subrata Duary, Vivek Yadav, Amoghavarsha Ramachandra Kini, Sudhadevi Antharjanam, Tomas Base, Anirban Som, Brent Lane Nannenga and Thalappil Pradeep, Chem. Comm. (2025) (DOI: 10.1039/D5CC02594J)

17. A silver-chalcogenide nanomaterial enveloped with a carborane-thiolate shell for the electroreduction of CO2 to CO, Arijit Jana, Zhengyuan Li, Amoghavarsha Ramachandra Kini, Vivek Yadav, Akhil S. Nair, Astrid Campos Mata, Jingjie Wu, Jan Macháček, Tomas Base, Biswarup Pathak, Soumyabrata Roy and Thalappil Pradeep, ACS Appl. Nano Mater. (2025) (DOI: 10.1021/acsanm.5c01918)

18. Charging of ligand protected gold nanoparticles in electrospray ionization: probing ligand bond strength by charge detection mass spectrometry, B. S. Sooraj, Sylvain Maclot, Anagha Jose, Clothilde Comby-Zerbino, Tessa Reinert, Keerthana Unni, Rodolphe Antoine, and Thalappil Pradeep, J. Phys. Chem. Lett. (2025) (DOI: 10.1021/acs.jpclett.5c01075)

19. Enhanced U(VI) removal from groundwater using amide-functionalized biopolymer-based adsorbent for a practical solution, Sonali Seth, Md Rabiul Islam, Tanmayaa Nayak, Amoghavarsha Ramachandra Kini, Sujan Manna, Bijesh K. Malla, Ankit Nagar and Thalappil Pradeep, ACS Sustain. Chem. Eng. (2025) (DOI: 10.1021/acssuschemeng.5c03058)

20. From micro-to-nano in charged water microdroplets: Unveiling steps in the weathering of minerals, Anubhav Mahapatra, Anirban Som, B. K. Spoorthi, Depanjan Sarkar and Thalappil Pradeep, Chem. Comm. (2025) (DOI: 10.1039/D5CC02952J)

21. Recent advances in the recycling of precious metals using sustainable chemistry, Abhijit Nag, Ahsanulhaq Qurashi, Carole A. Morrison, Kasper Moth-Poulsen, Thalappil Pradeep and Jason B. Love, Coord. Chem. Rev. (2025) (DOI: 10.1016/j.ccr.2025.217186)

22. $[Ag_{62}S_{12}(CBT)_{32}]^{4+}$: A 2.2 nm two-electron superatomic carborane-thiolated silver nanocluster exhibiting multilayer charge separation, Arijit Jana, Vivek Yadav, Monika Kucerakova, Sami Malola, Amoghavarsha Ramachandra Kini, Swetashree Acharya, Ajay K. Poonia, Jan Machacek, Kumaran Nair Valsala Devi Adarsh, Hannu Häkkinen, Tomas Base and Thalappil Pradeep, ACS Nano (2025) (DOI: 10.1021/acsnano.5c11836)

23. Precision at the nanoscale: An 'ionic' view of composition, structure and properties, Anagha Jose, B. S. Sooraj, and Thalappil Pradeep, Nanoscale (2025) (DOI: 10.1039/D5NR03845F)

24. CO_2 Electroreduction to CO over silver nanoclussters: The impact of nuclearity on synergistic activity modulation, Parvathy Jayan, Arijit Jana, Zhengyuan Li, Rahul Kumar

Sharma, Vivek Yadav, Astrid Campos Mata, Ming-Husan Li, Ali Shayesteh Zeraati, Tomas Base, Sung-Fu Hung, Jingjie Wu, Biswarup Pathak, Thalappil Pradeep and Soumyabrata Roy, Small (2025) (DOI: 10.1002/smll.202505305)

25. A holey 2D MoS2-based membrane with Mo-rich edges for water desalination, Biswajit Mondal, Sudhin Rathnakumaran, Amrita Chakraborty, Pragin Chettiyankandy, Pillalamarri Srikrishnarka, Md Rabiul Islam, Jenifer Shantha Kumar, Ramesh Kumar, Sandeep Bose, Sooraj Kunnikuruvan and Thalappil Pradeep, ACS Appl. Nano Mater. (2025) (DOI: 10.1021/acsanm.5c05244)

26. Secondary guest-driven nucleation of N2O clathrate hydrate in amorphous ice mixture under ultrahigh vacuum, Bijesh Malla, Soham Chowdhury, Samir Nayak, Sofia Baji, Teena Mathew, Rabin Methikkalam, S. R. K. C. Sharma Yamijala, Rajnish Kumar and Thalappil Pradeep, J. Phys. Chem. Lett. (2025) (DOI: 10.1021/acs.jpclett.5c02778)

27. Microdroplet mechanochemistry, Thalappil Pradeep, ACS Sustain Chem Eng (2025) (DOI: 10.1021/acssuschemeng.5c12102)

Publications from other groups

28. Enhancement of photoluminescence quantum yield of silver clusters by heavy atom effect, Aoi Akiyama, Sakiat Hossain, Yoshiki Niihori, Kazutaka Oiwa, Jayoti Roy, Tokuhisa Kawawaki, Thalappil Pradeep, and Yuichi Negishi, Small 21 (2025) 2500700. (DOI: 10.1002/smll.202500700)

29. Association of urine heavy metals with prevalence of type 1 diabetes and poor glycaemic control, Samrat Ashok Vasudevan, Srinidhi Narayani Seenivasan, Avinash Kumar Raghupathy, Dinakaran Vasudevan, Parthasarathy Ayothi, Tanmayaa Nayak, Buvaneswari Gajendran, Karthika Durairaj, Divya Shree Sathish, Srilaxmi Balaji, Abisheak Kandasamy, P. Amaravathy, Sundaresan Mohanraj, Shankar Dhandapani, Thalappil Pradeep, Krishnan Swaminathan and Ganesan Velmurugan, Biol. Trace Elem. Res. (2025) (DOI: 10.1007/s12011-025-04903-8)

30. Cooperative borane activation by tuning hemilability of different Os-κ^2–N,Se-chelated complexes, Faneesha Assanar, Sourav Gayen, Deepak Kumar Patel, Thalappil Pradeep and Sundargopal Ghosh, Chem. Sci. (2025) (DOI: 10.1039/D5SC06346A)

Editorials

31. The ACS sustainable family–complementary yet distinct: Some evolving thoughts from the editors' desks, Thalappil Pradeep, Michael K. C. Tam, Danielle Julie Carrier, Jingwen Chen, Bing Joe Hwang, Michael Meier, Bala Subramaniam, Rowan S. Brower and Peter Licence, ACS Sustain. Chem. Eng. 13 (2025) 14675–14676. (DOI: 10.1021/acssuschemeng.5c08629) PDF File, also in ACS Sustainable Resour. Manage. 2 (2025) 1618−1619 (DOI: 10.1021/acssusresmgt.5c00410)

Journal papers

Publications from our group

ACS APPLIED MATERIALS & INTERFACES

www.acsami.org Research Article

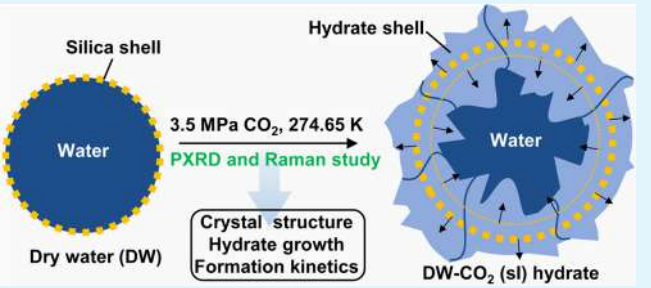
Understanding the Kinetics of CO_2 Hydrate Formation in Dry Water for Carbon Capture and Storage: X-ray Diffraction and In Situ Raman Studies

Gaurav Vishwakarma,[‖] Vikas Dhamu,[‖] M. Fahed Qureshi, Gaurav Bhattacharjee, Thalappil Pradeep,* and Praveen Linga*

Cite This: *ACS Appl. Mater. Interfaces* 2025, 17, 4865−4874 Read Online

ACCESS | Metrics & More | Article Recommendations | Supporting Information

ABSTRACT: Hydrate-based carbon capture and storage (HBCS) is a sustainable and promising approach to combating global warming by utilizing water, which is a ubiquitous resource. Here, we report a comprehensive study of CO_2 hydrate formation in dry water (DW), a water-in-air dispersion confined in silica particles, for improving the kinetics of hydrate growth. Utilizing a combination of a home-built high-pressure reactor, in situ Raman spectroscopy, and powder X-ray diffraction (PXRD), we elucidate the crystal structure, growth dynamics, and morphology of CO_2 hydrates formed in DW, with and without the kinetic hydrate promoter, L-tryptophan. Our analysis reveals that CO_2 forms structure I (sI) hydrate in DW, with hydrate growth occurring both on and beneath the silica shell. This results in a substantial increase in CO_2 uptake—approximately 2.8 times higher than that observed in pure water (∼134 v/v compared to ∼48 v/v). Moreover, incorporation of L-tryptophan in DW formation markedly accelerates the DW-CO_2 hydrate formation process, reducing both the induction time and the time required to achieve 90% gas uptake at 274.65 K. These findings offer crucial insights into the formation of CO_2 hydrate in DW, highlighting its potential to improve the efficiency and scalability of HBCS technologies.



KEYWORDS: *CO_2 hydrates, dry water, carbon capture and storage, Raman spectroscopy, X-ray diffraction*

Downloaded via INDIAN INST OF TECH MADRAS on December 30, 2025 at 05:33:47 (UTC).
See https://pubs.acs.org/sharingguidelines for options on how to legitimately share published articles.

1. INTRODUCTION

Excess CO_2 emissions in the atmosphere are considered a primary source of global warming. A 50% reduction in CO_2 emissions by 2030 is required to obtain a zero-carbon economy by 2050.[1] To restrict global temperature from rising more than 2 °C and limit CO_2 emissions to 1100 gigatons (2011−2050), it is essential to use carbon capture and storage (CCS) techniques, along with other renewable technologies.[2−4] Using gas hydrates for CCS is one of the potential techniques, as they offer a high theoretical storage capacity of about 180 v/v (volume of gas at STP/volume of hydrate).[5,6] Gas hydrates are crystalline, nonstoichiometric host−guest compounds that form when guest molecules are encapsulated within hydrogen-bonded water cages under high-pressure and low-temperature conditions.[7] Moreover, gas hydrates have been widely studied across diverse experimental conditions[8−14] and through computational approaches.[15−17] Gas hydrates naturally exist in permafrost zones[18,19] and are speculated to exist in interstellar medium and within the solar system.[20−22] These compounds are often classified into three distinct structures: structure I (sI, cubic, two small 5^{12}, and six large $5^{12}6^2$ cages per unit cell), structure II (sII, cubic, 16 small 5^{12}, and eight large $5^{12}6^4$ cages per unit cell), and structure H (sH, hexagonal).[23,24] Analogous to natural gas hydrates, researchers are investigating the possibility of storing industrial CO_2 emissions in the form of CO_2 hydrates.[25−27] However, this faces several challenges, including the sluggish rate of CO_2 hydrate formation and low water-to-hydrate conversion.[28−31]

To enhance clathrate hydrate formation kinetics, increasing the contact between liquid (water) and gas (guest) is the key.[7] Methods to achieve this include the use of high pressures, vigorous mixing, ice particles, surfactants, amino acids, dry water (DW), etc.[32] Among these, DW, a powder made from blending water, air, and hydrophobic nanosilica particles, is noted for its high gas storage capacity and faster formation rates.[32,33] DW consists of minuscule water droplets, called water pools, enclosed by a hydrophobic nanosilica layer that prevents the droplets from merging.[34] The enhanced storage capacity in DW-gas hydrates can be attributed to its higher

Received: October 15, 2024
Revised: December 1, 2024
Accepted: December 31, 2024
Published: January 9, 2025



© 2025 American Chemical Society

https://doi.org/10.1021/acsami.4c17727
ACS Appl. Mater. Interfaces 2025, 17, 4865−4874



Figure 1. DW Preparation: 5 g of hydrophobic nanosilica was blended with 95 g of water at 24,000 rpm for 90 s to produce DW powder. The figure shows an illustration of the blender, a photograph of the prepared DW, and an optical micrograph of DW (scale bar = 50 μm). Inset provides a schematic representation of DW, where water is depicted in blue and silica particles in yellow. The micrograph was captured using an Olympus SZX16 microscope.

surface-to-volume ratio than bulk water.[32,35] Recent studies show that DW significantly accelerated the hydrate formation kinetics of several gases (e.g., CH_4, CO_2, Kr, C_2H_6, etc.) and should be further explored as a potential medium for synthesizing bulk CH_4 and CO_2 hydrates for storage and transportation applications.[32,33,36−40] Wang et al., in one of the initial reports, found that DW-CH_4 hydrate can store about ∼175 v/v of CH_4 at 273.2 K.[32] Carter et al. found that DW can speed up the formation of CO_2 and Kr hydrates.[33] They observed that CO_2 could be stored up to ∼150 v/v in DW at 273.2 K, while the theoretical maximum storage capacity of sI hydrates is ∼180 v/v (STP). The lower CO_2 storage capacity in DW-gas hydrates, according to Carter et al., might be due to the incomplete filling of the sI hydrate cages or the cocrystallization of both sII and sI hydrates. Thus, although several studies have examined gas hydrate formation and growth dynamics in DW, critical aspects of DW and DW-CO_2 hydrates are yet to be fully understood.

Wang et al. identified the potential of using second guest molecules (thermodynamic promoters) to form DW-gas hydrates at pressures much lower than their typical formation pressures.[32] However, attempts to achieve this using thermodynamic promoters such as tetrahydrofuran and tetrabutylammonium bromide were met with limited success, as these compounds disrupted the integrity of DW. In contrast, recent research highlights the potential of using amino acids as kinetic hydrate promoters.[41,42] For instance, Khandelwal et al. showed that L-tryptophan (L-trp) significantly enhances both the formation rate and CO_2 uptake in hydrates, achieving up to a 3-fold increase compared to systems without the promoter. These findings point to the importance of exploring the combined use of eco-friendly amino acids like L-trp with DW, to further enhance CO_2 uptake kinetics above the freezing point.[43,44]

Despite the volume of research on DW-CO_2 hydrates, several fundamental aspects remain unclear, such as the crystal structure, hydrate growth dynamics, combined effect of kinetic hydrate promoters, morphology, and the stability of DW when additives are introduced.[45−48] In other words, comprehensive studies on CO_2 uptake kinetics in DW-gas hydrates are still limited, highlighting the need for further macro- and microscale study to evaluate DW's reusability and commercial potential. The present work examines the CO_2 hydrate formation kinetics in DW with L-trp (0−1000 ppm) at 3.5 MPa and 274.65 K. We found that DW prepared using 500 and 1000 ppm L-trp solution was stable over a few months. The formation kinetics and morphology at the macroscale were investigated using a high-pressure reactor. The crystal structure and hydrate growth dynamics were analyzed at the microscale with powder X-ray diffraction (PXRD) and in situ Raman spectroscopy.

2. EXPERIMENTAL SECTION

2.1. Materials. Hydrophobic nanosilica particles (HDK grade H18, 5−30 nm) and L-tryptophan (L-trp, >99% purity) were supplied by Wacker Chemie and Sigma-Aldrich, respectively. CO_2 gas (>purity 99.9%) was obtained from Air Liquide Singapore Pvt. Ltd. The deionized water was collected from the in-house Merck Millipore Direct-Q 3 UV system, which was used for all experimental trials and for preparing DW.

2.2. Preparation of DW. The deionized water (95 g) was poured into a blender (Vitamix, glass jug blender, 2 L), and 5 g of nanosilica particles were added to it. Mixing was carried out at the highest speed setting (average speed of ∼24,000 rpm) for 90 s, divided into three 30 s bursts. The air/water/silica volume ratio was constant for each DW preparation. The material was produced as a free-flowing, dry, white powder that could be easily transferred between vessels without leaving a residue, indicating the formation of water droplets encapsulated by a silica shell. For visual confirmation, Figure S1 presents a photograph illustrating the transfer of DW from a blender jar to a storage bottle. DW containing L-trp was prepared in the same way using solutions of appropriate concentrations. The DW prepared with a solution containing L-trp was stable over a few months. It should be noted that thermodynamic promoters like tetrahydrofuran and tetrabutylammonium bromide were reported to destabilize the DW.[32] A schematic of the DW preparation is shown in Figure 1.

2.3. Equipment. *2.3.1. High-Pressure Reactor.* A high-pressure reactor (made of SS316) with an internal volume of about 150 mL was used for all macro-kinetics experiments (a schematic diagram of the setup is shown in the Supporting Information, Figure S2). Two acrylic viewing windows, each with a diameter of 3 cm, were installed in the reactor's front and back to monitor the morphology of CO_2 hydrate formation in DW and pure water.[49] To regulate the reactor's temperature, coolant from an external chiller bath was circulated in the cooling jacket of the reactor vessel. Throughout the experiments, the temperature within the system was continuously monitored by using a thermocouple placed at the gas−liquid/DW interface. The pressure inside the crystallizer chamber was monitored with a pressure transducer (PT) with an uncertainty of ±0.1% in the pressure range of 0−3.5 MPa. A data acquisition (DAQ) device linked to the thermocouple and the pressure sensors was used to record the

https://doi.org/10.1021/acsami.4c17727
ACS Appl. Mater. Interfaces 2025, 17, 4865−4874

temperature and pressure data at regular intervals of 10 s. The HD camera was installed at the front window to closely monitor the CO_2 hydrate formation morphology in water/DW.

2.3.2. In Situ Raman Spectroscopy. The in situ Raman spectroscopy analysis was performed using a dispersive laser Raman spectrometer (Model: SRaman-532). The jacketed high-pressure reactor is constructed of stainless steel with an internal volume of about 230 mL (a schematic diagram of the setup is shown in Figure S3). The Raman probe inside the reactor vessel has two optical fibers that transmit the laser to the reactor and the resulting signals back to the spectrometer. Raman experiments were performed with an Nd:Yag laser source (wavelength = 532 nm) with a laser power of ∼42 mW. The acquired spectra span from 150 to 4490 cm^{-1}, with a resolution of 2.8 cm^{-1}/pixel at 2200 cm^{-1}. The procedure for hydrate formation in the in situ Raman analysis was identical to that in macroscale kinetic experiments. The Raman spectra were obtained during the hydrate formation at 30 or 60 min intervals, with an integration time of 1.0 s.

2.3.3. Powder X-ray Diffraction Analysis. The crystal structure of synthesized CO_2 hydrate in DW was determined by using PXRD, a widely accepted method for analyzing hydrate samples. First, a typical CO_2 hydrate formation experiment was performed with DW at 274.65 K and 3.5 MPa without Trp. Once hydrate formation was complete, the residual pressure inside the reactor was quickly vented, the reactor flange was removed, and the synthesized hydrates were instantly quenched with liquid nitrogen (∼77 K). Quenching allowed the sample collection of the hydrates, which were then crushed into a roughly uniform powder with a mortar and pestle in a liquid nitrogen environment. The liquid nitrogen helped to keep the synthesized hydrates stable while operating under atmospheric conditions. Finally, the hydrate powder was transferred to the in-house PXRD unit for characterization. The PXRD measurements were performed by using a BRUKER D8 advanced diffractometer (40 kV, 30 mA). The Cu Kα radiation (λ = 1.542 Å) was utilized as the X-ray. The PXRD patterns were collected in the 2θ range of 10−40°, with a 0.02° step size. Further details on the procedure used to calculate the lattice parameter of the synthesized hydrate crystals are given in the Supporting Information.[50]

2.4. Experimental Procedure. Before each experiment, the reactor was thoroughly cleaned and rinsed three times before adding water/DW. The reactor was then purged with CO_2 gas and vented three times to eliminate any remaining air. All experiments were conducted at a constant temperature within a closed system. The reactor was loaded with 40 g of pure water (density ∼1000 kg/m^3), 20 g of pure DW (density ∼500 kg/m^3), or 20 g of DW + 500/1000 ppm L-trp (density ∼500 kg/m^3).[32] Then, the system was allowed to cool to a temperature of 274.65 K. No agitation was employed in trials with pure water or DW. During the formation step, a pressure of 3.5 MPa was exerted on the system by introducing pure CO_2 gas into the reactor. The experimental conditions of 3.5 MPa and 274.65 K were selected to maximize the thermodynamic driving force for CO_2 hydrate formation, while ensuring that water in the DW system remained in the liquid state. The temperature of 274.65 K was chosen to prevent the freezing of water in DW, enabling clear observation of DW's kinetic promotion effects on hydrate formation with and without a kinetic promoter. Frozen water would obscure these effects. Upon pressurizing the system at a temperature of 274.65 K, CO_2 hydrate formation was detected by a sudden increase in system temperature and a subsequent pressure drop. The rise in temperature phenomenon can be attributed to hydrate formation releasing heat, which is an exothermic process. The front camera recorded the complete process of hydrate formation. To ensure the reproducibility of the results, each experiment was conducted at least twice. Trails with pure water are labeled A1 and A2; those with DW are labeled B1 and B2. Trails with DW + 500 ppm L-trp are labeled C1 and C2, and those with DW + 1000 ppm L-trp are labeled D1 and D2.

2.5. Calculation Procedure. The overall CO_2 uptake and the total amount of water transformed into CO_2 hydrate were estimated using the following equations.[4,51] Equation 1 was used to estimate the number of moles of CO_2 captured by CO_2 dissolving in the aqueous solution and solid hydrate phases at any given time.

$$\Delta n_t = \left[\frac{PV}{zRT}\right]_{t=0} - \left[\frac{PV}{zRT}\right]_t \text{ (mol)} \quad (1)$$

The P and T represent the pressure and temperature (recorded during the experiments), respectively; R is the universal gas constant, and t is any time during the experiment. Pitzer correlation[52] was used to calculate the compressibility factor z; P and T are measured at "0" (start of the experiment) and "t" (any time throughout the experiment) and V denotes the volume of the gas phase within the reactor.

By dividing the gas uptake from eq 1 by the moles of water in the system, one may determine the normalized gas uptake (mol of gas consumed per mole of water, mol/mol). Then, the normalized molar gas uptake (mol/mol) was converted into volumetric gas storage capacity (volume of gas (STP)/volume of hydrate) using the following equation[50]

$$\text{volumetric } CO_2 \text{ storage capacity}\left(\frac{\text{vol of gas (STP)}}{\text{vol of hydrate}}\right) = k\left(\frac{\Delta n_t}{n_w^o}\times 1000\right) \quad (2)$$

$$k = \frac{v}{M_{CO_2\text{hydrate}}/(\rho_{CO_2\text{hydrate}} \times 5.75)} \quad (3)$$

where the v,$M_{CO_2\text{hydrate}}$ and $\rho_{CO_2\text{hydrate}}$ stand for the volume of gas at STP (22.4 cm^3/mmol), the molar mass of CO_2 hydrate (1180 g) and density of CO_2 hydrate (1.1 g/cm^3).[26,53] Further, eq 4 was used to determine the fraction of water converted to gas hydrates.

$$\text{water conversion } (\%n_w^t) = \frac{5.75 \times \Delta n_t}{n_w^o} \times 100 \quad (4)$$

Here, n_w° (t = 0) is the total mole of water, and 5.75 is the hydration number derived from the literature.[46]

3. RESULTS AND DISCUSSION

3.1. Crystal Structure of DW-CO_2 Hydrate. Wang et al.[33] suggested that the reduced CO_2 uptake in DW-gas hydrates (∼150 v/v, compared to the theoretical capacity of sI hydrates, ∼180 v/v) could result from incomplete occupancy of the sI hydrate cages or the cocrystallization of sII with the sI phase. To the best of our knowledge, no studies have yet reported the structures of DW-CO_2 hydrates. Therefore, it is crucial to examine the crystal structure of DW-CO_2 hydrate using PXRD and in situ Raman spectroscopy (Figures 2 and 3).

For PXRD analysis, DW-CO_2 hydrate was prepared in the high-pressure reactor at initial conditions of 3.5 MPa and 274.65 K. Then, the hydrate sample was quenched and harvested at a liquid N_2 temperature (∼77 K). For data collection, the sample was prepared at ∼77 K to prevent hydrate dissociation under atmospheric pressure. Figure 2 presents the XRD pattern of pure hydrophobic nanosilica particles and the DW + CO_2 sample. The XRD pattern (black trace) depicted in Figure 2 exhibits a precise correspondence with the standard patterns of sI hydrates reported in the literature.[54,55] The calculated lattice parameter in the current study was 12.010 (±0.005) Å, closely matching the reported value of 12.070 Å.[56] This strong agreement provides compelling evidence that only sI hydrates were produced. Details of the calculation of the lattice parameter are given in the Supporting Information. During PXRD analysis, unreacted

https://doi.org/10.1021/acsami.4c17727
ACS Appl. Mater. Interfaces 2025, 17, 4865−4874

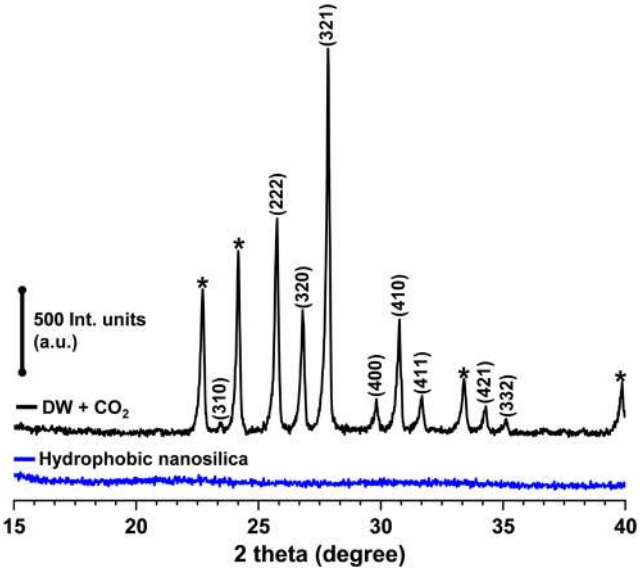


Figure 2. PXRD pattern of the DW + CO_2 sample (black trace) and of pure hydrophobic nanosilica particles (blue trace). After hydrate formation under initial conditions of 3.5 MPa and 274.65 K, DW-CO_2 hydrate was harvested at ~77 K for PXRD analysis. The peaks corresponding to the sI hydrate are marked by their corresponding (*hkl*) values, while the asterisks indicate the presence of ice Ih. Hydrophobic nanosilica was featureless in the 2θ range of 15−40°.

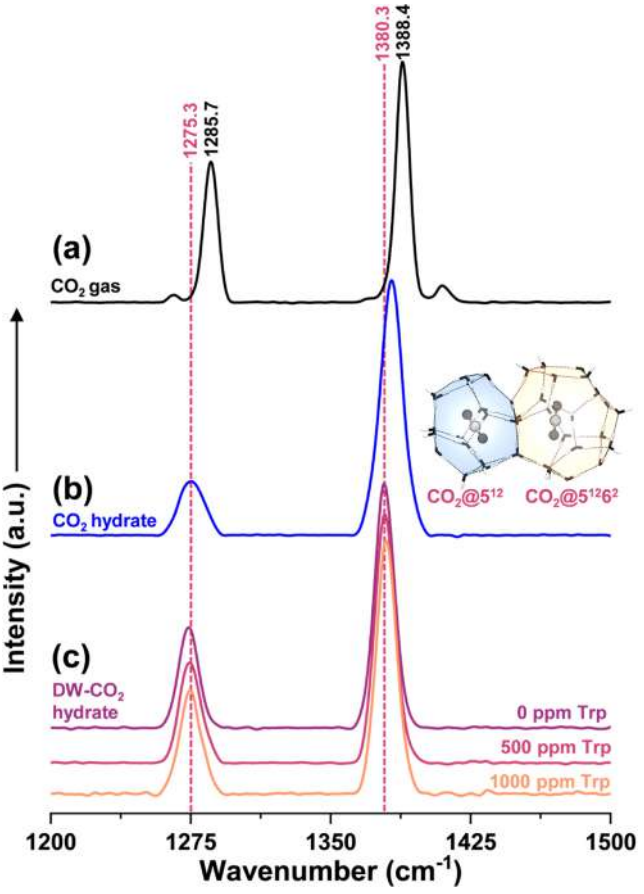


Figure 3. In situ Raman spectra of (a) CO_2 gas, (b) CO_2 hydrate prepared with pure water, and (c) CO_2 hydrate prepared with DW (0−1000 ppm L-trp). CO_2 hydrate, in all cases, was achieved at 3.5 MPa and 274.65 K.

water appeared as hexagonal ice, ice Ih (marked by asterisks), due to the sample being recovered at ~77 K (Figure 2). Moreover, hydrophobic nanosilica was featureless in the 2θ range of 15−40° (blue trace in Figure 2).

Further, using in situ Raman spectroscopy (a schematic diagram of the setup is shown in Figure S3), we independently analyzed the CO_2 hydrate formation in pure water and DW systems on a microscale under similar experimental conditions (3.5 MPa and 274.65 K). Figure 3 presents the Raman spectra for (a) pure CO_2 gas, (b) the CO_2 hydrate formed in pure water, and (c) the CO_2 hydrate formed in DW with and without Trp in the CO_2 Fermi dyad region. The obtained spectra for CO_2 hydrates formed in pure water and in DW (with or without L-trp) align perfectly with the Raman peaks of sI hydrates (Figure 3).[57,58] Time-dependent Raman spectra in the CO_2 Fermi dyad and the O−H stretching regions, showing the evolution of CO_2 hydrates, are detailed in Figure S4.

The identification of sI hydrates was determined by the presence of two Fermi dyad peaks at ~1380.3 and 1275.3 cm^{-1}, as established in the literature.[57−59] This confirms the formation of exclusively sI hydrates in the CO_2-DW systems under the experimental conditions of 3.5 MPa and 274.65 K. Thus, the current work provides the first-ever comprehensive in situ Raman and PXRD analysis for the formation of DW-CO_2 hydrate. So, the reduced CO_2 uptake in DW systems may primarily be due to incomplete occupancy of the hydrate cages, given that CO_2 forms only sI hydrates in these systems. The incomplete occupancies or reduced gas uptake may also be linked to the decreasing pH of the water content in DW, which results from the dissolution of CO_2 over time. However, this hypothesis must be confirmed by further research.

3.2. CO_2 Hydrate Growth Dynamics in DW. DW is a water-in-air dispersion primarily composed of water and stabilized by hydrophobic nanosilica particles (Figure 1). DW accelerates hydrate formation compared to bulk water by increasing the surface area for gas−water contact, which enhances gas dissolution and promotes the formation of hydrate nuclei and water-guest clusters.[32,60] According to Li et al.,[37] gas hydrate formation in DW involves two consecutive steps. Initially, the guest gas permeates a hydrophobic silica shell and enters the water core, and then the interaction between the guest gas and water molecules results in the formation of a gas hydrate.

However, there are conflicting reports about whether hydrate shells form on or beneath the silica shell (Figure 4).[35,48,61] To understand the hydrate growth dynamics in DW, Zhang et al.[61] used a modified shrinking core model by incorporating the effects of dissolved gas, capillary effects of the porous hydrate shell, and the volume change from water to hydrate. They found that the hydrate film initially forms on the outer surface of water droplets beneath the silica shell, where the gas concentration is the highest. Then, as gas diffuses through the hydrate shell, the hydrate grows inward at the hydrate−water interface. Additionally, due to water moving outward through capillaries (because of volume expansion upon hydrate formation), hydrates grow on the outer surface of the preformed hydrate shell (at the hydrate−gas interface) within the silica shell, causing the outer radius of DW to grow continuously (Figure 4a). Conversely, Park et al. utilized PXRD and Raman spectroscopy to conclude that the hydrate shell forms on the surface of DW above the silica shell.[35] They attributed this to the chemical potential difference between water molecules in hydrate cages and free water molecules in

https://doi.org/10.1021/acsami.4c17727
ACS Appl. Mater. Interfaces 2025, 17, 4865−4874

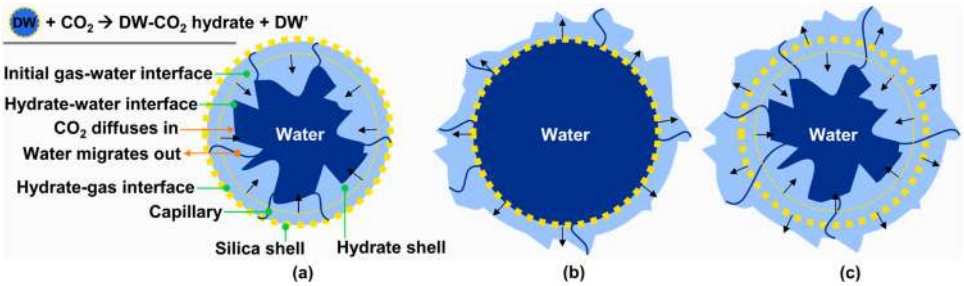


Figure 4. Physical model of the hydrate growth dynamics in DW systems. The top left corner displays the reaction scheme for the interaction between the guest gas and DW. Schematic (a) depicts the modified shrinking core model, indicating hydrate formation beneath the silica shell. Schematic (b) illustrates hydrate growth on the surface of DW particle. Schematic (c), based on PXRD and Raman analysis from the current work, demonstrates hydrate growth both on and beneath the silica shell. Key components of DW and DW-gas hydrates are labeled in (a). According to the shrinking core model, CO_2 diffuses through a porous hydrate shell in the water core and forms a hydrate at the hydrate−water interface, while water migrates out through capillaries and forms a hydrate at the hydrate−gas interface.

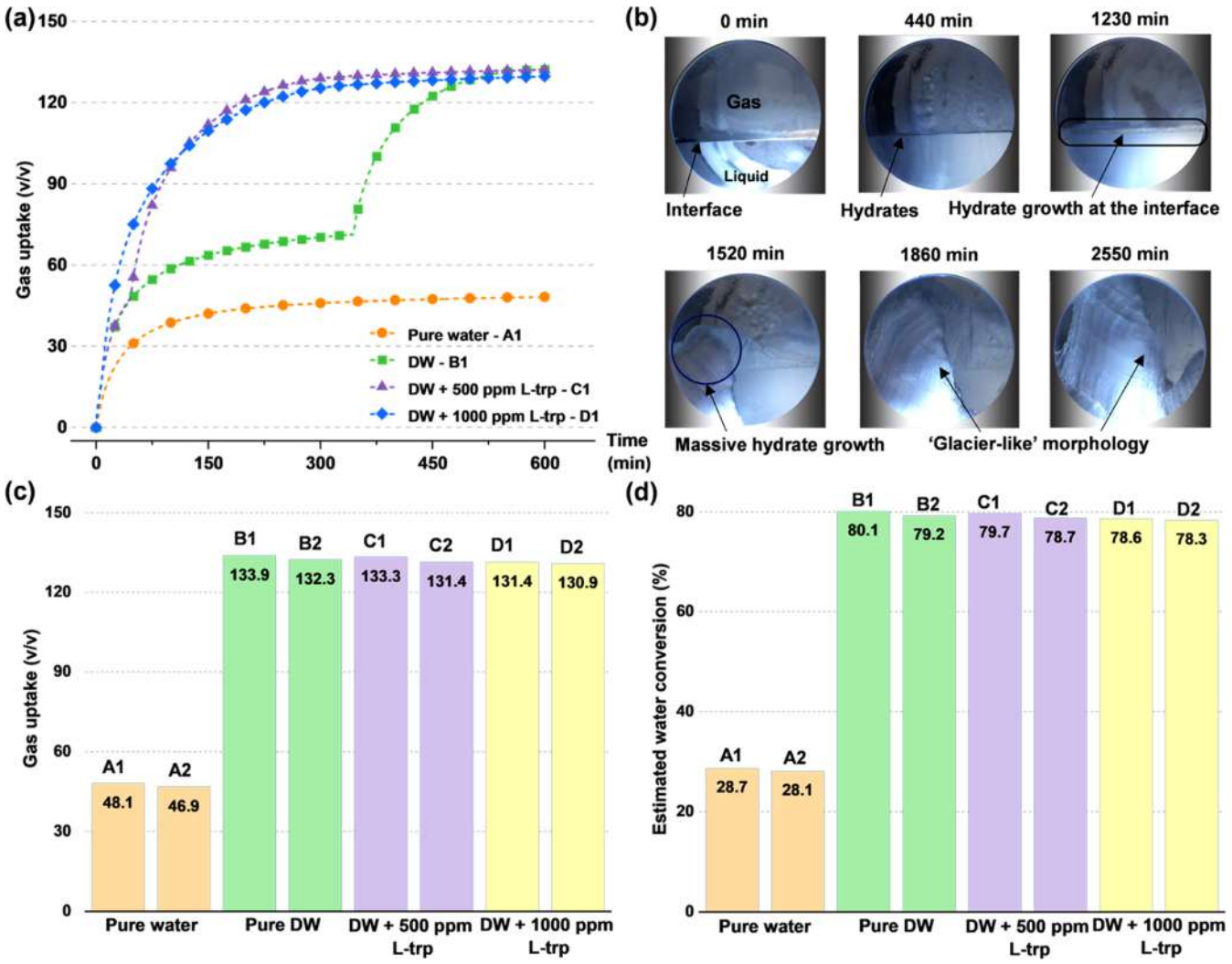


Figure 5. (a) Normalized CO_2 uptake achieved in trails A1 (pure water and orange trace), B1 (DW, green trace), C1 (DW + 500 ppm L-trp, violet trace), and D1 (DW + 1000 ppm L-trp, blue trace). CO_2 uptake in each case was estimated based on the experimentally observed changes in temperature and pressure, starting from initial conditions of 3.5 MPa and 274.65 K. Normalized gas uptake is depicted in volumetric gas storage capacity (volume of gas (STP)/volume of hydrate, v/v). (b) Morphology of CO_2 hydrate formation in pure water without L-trp and without mechanical agitation at 3.5 MPa and 274.65 K. Comparison of the (c) CO_2 uptakes and (d) water-to-hydrate conversions obtained for pure water (trails A1, and A2), DW (trails B1, and B2), DW + 500 ppm L-trp (trails C1, and C2), and DW + 1000 ppm L-trp (trails D1, and D2). In each experiment, the results from both trials were consistent, ensuring reliability.

DW particles, causing water to migrate out and form an external hydrate shell (Figure 4b). However, our current work reveals a different scenario. We found that the CO_2 hydrate in DW forms both on and beneath the silica shell. Unlike Park et

https://doi.org/10.1021/acsami.4c17727
ACS Appl. Mater. Interfaces 2025, 17, 4865−4874

Table 1. Estimated Water Conversion, Gas Uptake, Induction Time, and t_{90}, for Each Trial

system	trails	estimated water conversion (%)	estimated gas uptake (volume of gas at STP/volume of hydrate)	induction time (min)	t_{90} (min)
pure water	A1	28.7	48.1	212.5	164.3
	A2	28.1	46.9	714.3	295.3
DW + 0 ppm L-trp	B1	80.1	133.9	64.2	439.2
	B2	79.2	132.3	85.4	1085.2
DW + 500 ppm L-trp	C1	79.7	133.3	48.8	192.7
	C2	78.7	131.4	52.5	175.7
DW + 1000 ppm L-trp	D1	78.6	131.4	7.8	209.7
	D2	78.3	130.9	4.3	192.7

al., who did not observe a broad signal from silica particles in the 2θ range of 10−15° in their PXRD analysis—interpreting this as evidence of a hydrate shell covering DW particles. We observed a broad signal in our PXRD pattern (Figure S5a), indicating hydrate formation within the silica shell of DW. Additionally, the reduction in peak intensity of the Si−O−Si stretching band in Raman spectra (Figure S5b) suggests that a small fraction of the hydrates was also formed above the silica shell (Figure 4c). However, Park et al. noted a complete disappearance of the Si−O−Si stretching band in the Raman spectra after hydrate formation. This PXRD and Raman analysis confirms our findings and provides a nuanced understanding of hydrate formation in the CO_2-DW systems. All three scenarios of hydrate growth dynamics in DW are depicted in Figure 4(a−c).

Previously, DW-gas hydrates have been tested for reusability through multiple hydrate formation-dissociation cycles.[33,35] Notably, the hydrate shells that form on DW will convert to free water upon dissociation and will not re-enter DW without high-speed reblending. Park et al.[35] observed that in the first formation-dissociation cycle, approximately 80% of the water was converted to hydrate covering the silica shell, meaning this 80% will become free water after dissociation. This indicates that only about 20% of the water remains inside the DW for the second cycle. However, in their second cycle with the same sample, they found that around 50% of the water converted to hydrate, which cannot be explained by the hypothesis that hydrate shells form solely above the silica shells. Our hypothesis provides a more comprehensive explanation: hydrates can grow on and beneath the silica shell, and only the fraction of hydrates formed above the silica shell converts to free water, while the remaining water stays inside DW. This means that during hydrate dissociation, while the hydrate formed above the silica shell accounts for the free water, the hydrate formed beneath the silica shell retains water within the silica shell, ensuring the stability and reusability of DW. This dual hydrate growth dynamics—hydrates forming both on and beneath the silica shell—explains the observed reusability and water retention in DW, offering a better understanding of the hydrate formation-dissociation processes.

3.3. Formation Kinetics and Morphology of CO_2 Hydrates in Pure Water, DW, and DW + L-trp.

Understanding the kinetic characteristics of hydrate formation is crucial for evaluating the potential of hydrate-based carbon capture and storage (HBCS) technology. This study investigates the CO_2 hydrate formation kinetics and morphology in three systems: pure water, DW, and DW with 500 and 1000 ppm of L-trp. Here, L-trp is used as a kinetic hydrate promoter. All experiments were conducted with an initial temperature of 274.65 K and a pressure of 3.5 MPa, and each was repeated twice to ensure reliable results. From the recorded temperature and pressure data, we estimated the CO_2 uptake, water-to-hydrate conversion, induction time, and time required to reach 90% gas uptake (t_{90}) for all systems, providing a comprehensive comparison of their kinetic performance. To establish a baseline for CO_2 hydrate formation kinetics, initial experiments were conducted using pure water. Changes in the pressure and temperature during the hydrate formation process are shown in Figure S6a. The CO_2 gas uptake kinetics for pure water are presented in Figure 5a (orange trace), while the morphology of hydrate formation is illustrated in Figure 5b. In two experimental trials with pure water, normalized gas uptake was 48.1 v/v with a 28.75% water-to-hydrate conversion in trial A1 and 46.9 v/v with a 28.11% conversion in trial A2 (Figure 5c,d). Induction time and t_{90} are detailed in Table 1.

Figure 5b reveals the morphology of the CO_2 hydrate formed in pure water. We observed that initially, as CO_2 dissolves, the solution turns from translucent to milky white. After ∼420 min, a thin hydrate film forms at the gas−water interface and grows slowly until ∼1200 min. At this stage, a branch-like crystal emerges from the reactor's edge, causing the thin film to rupture due to volume expansion. This rupture triggers spontaneous, rapid hydrate formation throughout the reactor aided by enhanced CO_2 diffusion. By 1800 min, bulk hydrates with a "glacier-like appearance" are visible (Figure 5b and Video S1). This overall process occurs in three stages: nucleation, film formation, and film breakup with bulk hydrate growth.[13,53] While, Dhamu et al.[13] reported different types of CO_2 hydrate morphologies, which included fine caladium-like crystalline growth, hydrate dendrites, hydrate glaciers, and atrichous-hydrate branchlets. In the present case, we observed an atrichous-hydrate branchlet at ∼1500 min and a glacier-like morphology at ∼1800 min.[27]

The next set of experiments was conducted by using DW and DW + L-trp. The changes in pressure and temperature during CO_2 hydrate formation in these systems are shown in Figure S6b−d. Figure 5a,c,d presents the CO_2 gas uptakes and water conversions achieved with DW + (0−1000 ppm) L-trp. The CO_2 uptake in DW was estimated to be 133.9 v/v with a water-to-hydrate conversion of 80.1% for trail B1 and 132.3 v/v with a water-to-hydrate conversion of 79.2% for trail B2 (Figure 5c,d). Hence, the CO_2 gas uptake in DW was about ∼2.8 times higher than that of pure water (∼48 v/v).

To optimize the DW-CO_2 hydrate formation kinetics above the freezing point, L-trp was used as a kinetic promoter in DW. L-trp concentrations of 500 and 1000 ppm were tested, and DW prepared with L-trp-doped solutions remained stable for over 1 month. The CO_2 uptake and water-to-hydrate conversion in DW with 500 ppm L-trp (C1 and C2) and

https://doi.org/10.1021/acsami.4c17727
ACS Appl. Mater. Interfaces 2025, 17, 4865−4874

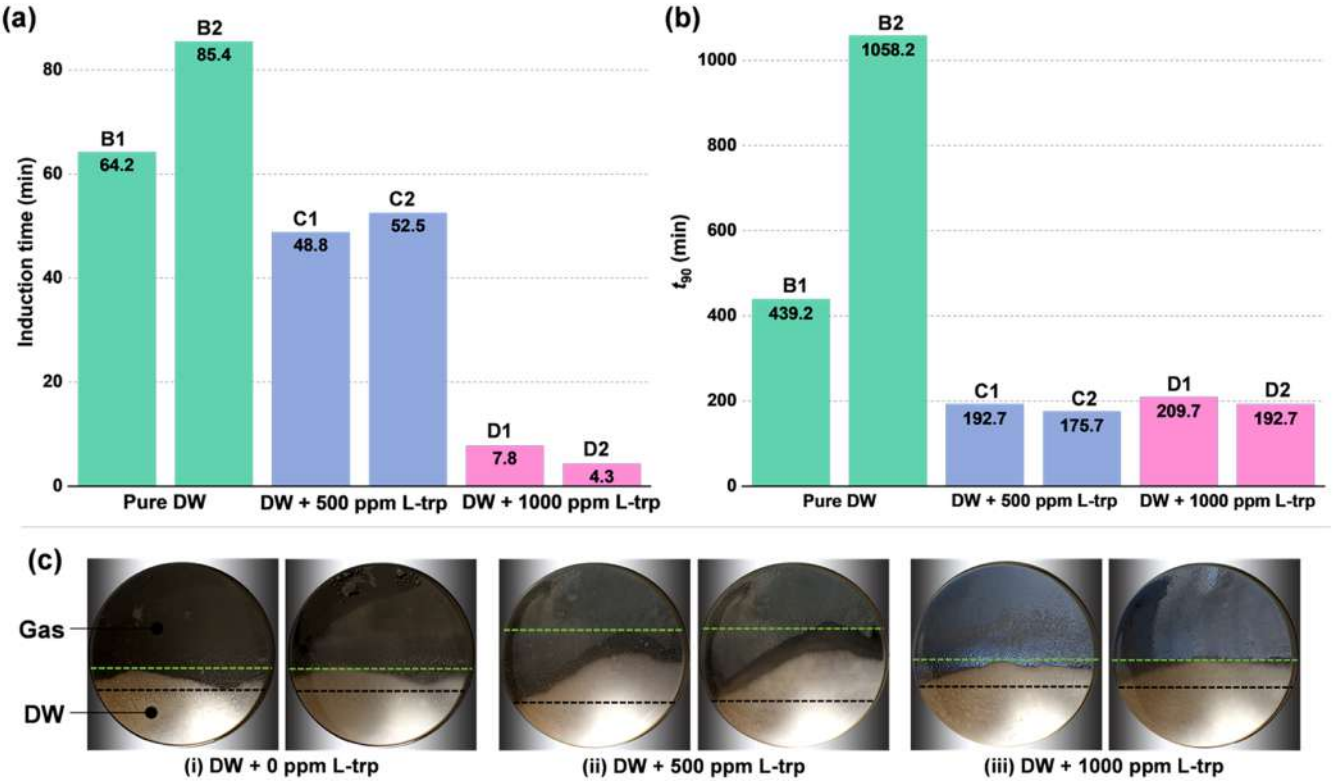


Figure 6. Comparison of the (a) induction time, and (b) the time required to reach 90% completion of gas uptake (t_{90}) for DW (trails B1, and B2), DW + 500 ppm L-trp (trails C1, and C2), and DW + 1000 ppm L-trp (trails D1, and D2). (C) Comparison of the DW-CO_2 hydrate morphology before (initial) and after (final) the hydrate formation in (i) DW, (ii) DW + 500 ppm L-trp, and (iii) DW + 1000 ppm L-trp systems at 3.5 MPa and 274.65 K. Changes in DW can be visualized between the black and green dotted lines, drawn at the lowest and highest heights of the initial morphology, respectively. During hydrate formation, an increase in the height of the DW column was observed with a simultaneous change in the temperature and pressure. During pressurization, the initial arrangements of DW change, unlike in liquid water.

1000 ppm L-trp (D1 and D2) were comparable to those observed in pure DW, as presented in Table 1 and Figure 5c,d. This demonstrates that both L-trp-doped and pure DW exhibit high CO_2 uptake and rapid hydrate formation compared with pure water. Further, Figure 6a,6b present the induction time and t_{90} for CO_2 hydrate formation in DW with and without L-trp. We observed that the addition of L-trp leads to a roughly linear decrease in induction time with increasing L-trp concentration (Figure 6a). Although L-trp doping in DW significantly reduces t_{90}, the values for 500 and 1000 ppm of L-trp are similar (Figure 6b). Furthermore, the nucleation and growth of CO_2 hydrates in pure DW at 274.65 K exhibited stochastic behavior (Figure 6a,b), meaning that the process was less predictable and highly variable, similar to hydrate formation in pure water. While the variability is not fully understood, incorporating additives like L-trp (as observed in this study) or lowering the formation temperature[33] can reduce this stochastic behavior. Future studies will focus on understanding the behavior of pure DW at higher temperatures. Table 1 summarizes the CO_2 uptake, water-to-hydrate conversion, induction time, and t_{90} values for each experimental trial.

The morphology of the CO_2 hydrate formation in DW + (0−1000 ppm) L-trp is shown in Figure 6c. The initial arrangement of the DW particles inside the high-pressure reactor changes slightly during the CO_2 pressurization, as evidenced by the column heights for different trials shown in Figure 6c. During the formation of the CO_2 hydrate in DW, detected by a simultaneous rise in temperature and drop in pressure, a slight change in DW arrangement or increase in the height of the DW column was observed (Figure 6c, Videos S2, S3, and S4). The change in the DW arrangement before and after hydrate formation can be realized by seeing between black and green dotted lines in Figure 6c. However, compared to pure water, the morphological growth pattern of CO_2 hydrates in DW is difficult to observe as both DW-CO_2 hydrate and DW have a similar white appearance.

From the foregoing, we understand that DW offers clear advantages for CO_2 storage in hydrates by eliminating the need for mechanical stirring or additional promoters. Our findings indicate that incorporating L-trp into DW significantly accelerates hydrate formation, reducing both induction time and t_{90} at 274.65 K. L-trp, well-established for its kinetic promotion of CO_2/CH_4 hydrate formation in liquid water, operates through its amphiphilic structure, which (i) lowers interfacial tension, (ii) facilitates gas transfer, and (iii) arranges water molecules to accelerate nucleation and stabilize hydrate structures.[41] Since the current set of DW experiments were conducted above freezing point (274.65 K, water inside silica shell will remain in liquid phase), we anticipate similar promotion effects of L-trp in DW as observed in liquid water systems. Previous studies, like the one by Khandelwal et al.,[43] reported a maximum CO_2 uptake of approximately 116 v/v in water doped with L-trp. In contrast, our study demonstrates that pure DW achieves a CO_2 uptake of about 134 v/v. This distinction is critical for assessing the commercial potential of DW in CO_2 storage applications. Our future research will focus on screening new thermodynamic promoters for enhancing

https://doi.org/10.1021/acsami.4c17727
ACS Appl. Mater. Interfaces 2025, 17, 4865−4874

DW stability to improve hydrate formation kinetics further at lower pressures and ambient temperatures.

4. CONCLUSIONS

We conducted a detailed experimental investigation into the formation of CO_2 hydrates in both pure water and DW doped with L-trp (0−1000 ppm) under conditions of 3.5 MPa and 274.65 K, without mechanical agitation. Through a comprehensive analysis employing a high-pressure reactor, PXRD, and in situ Raman spectroscopy, we explored critical aspects of DW-CO_2 hydrate, including crystal structure, hydrate growth dynamics, morphology, and gas uptake kinetics. The PXRD and Raman spectroscopy data unequivocally confirm the formation of sI hydrate in DW, revealing the incomplete occupancy of hydrate cages, which could be one of the reasons for the reduction in CO_2 uptake in DW systems. Our findings notably demonstrate the existence of hydrate shells both on and beneath the silica shell. This insight into hydrate growth dynamics is crucial for understanding the reusability of DW. Moreover, kinetic studies demonstrated that the CO_2 gas uptake in DW is approximately three times higher than in pure water, highlighting the suitability of DW for CCS. Our findings also indicate that doping DW with L-trp does not significantly enhance CO_2 uptake, though it effectively reduces stochasticity, induction time and t_{90}. These characteristics emphasize DW's potential as an energy-efficient and suitable solution for CO_2 storage, with significant implications for large-scale deployment.

■ ASSOCIATED CONTENT

Supporting Information

The Supporting Information is available free of charge at https://pubs.acs.org/doi/10.1021/acsami.4c17727.

Additional experimental details, schematics of experimental setups, Raman spectra, and P-T plots (PDF)

CO_2 hydrate formation morphology in pure water (Video S1) (MP4)

CO_2 hydrate formation morphology in dry water (Video S2) (MP4)

CO_2 hydrate formation morphology in dry water +500 ppm L-trp (Video S3) (MP4)

CO_2 hydrate formation morphology in dry water +1000 ppm L-trp (Video S4) (MP4)

■ AUTHOR INFORMATION

Corresponding Authors

Thalappil Pradeep − *DST Unit of Nanoscience (DST UNS) and Thematic Unit of Excellence (TUE), Department of Chemistry, Indian Institute of Technology Madras, Chennai 600036, India; International Centre for Clean Water, IIT Madras Research Park, Chennai 600113, India;* orcid.org/0000-0003-3174-534X; Email: pradeep@iitm.ac.in

Praveen Linga − *Department of Chemical and Biomolecular Engineering, National University of Singapore, Singapore 117580, Singapore;* orcid.org/0000-0002-1466-038X; Email: praveen.linga@nus.edu.sg

Authors

Gaurav Vishwakarma − *Department of Chemical and Biomolecular Engineering, National University of Singapore, Singapore 117580, Singapore; DST Unit of Nanoscience (DST UNS) and Thematic Unit of Excellence (TUE), Department of Chemistry, Indian Institute of Technology Madras, Chennai 600036, India;* orcid.org/0009-0002-6076-3299

Vikas Dhamu − *Department of Chemical and Biomolecular Engineering, National University of Singapore, Singapore 117580, Singapore*

M. Fahed Qureshi − *Department of Chemical and Biomolecular Engineering, National University of Singapore, Singapore 117580, Singapore*

Gaurav Bhattacharjee − *Department of Chemical and Biomolecular Engineering, National University of Singapore, Singapore 117580, Singapore;* orcid.org/0000-0001-5284-2785

Complete contact information is available at: https://pubs.acs.org/10.1021/acsami.4c17727

Author Contributions

‖G.V. and V.D. contributed equally to this work. P.L. and T.P. supervised the project. P.L., T.P., G.V., V.D., M.F.Q., and G. B. conceptualized the work and designed the experiments. G.V. and V.D. carried out the experiments and data analytics. All authors contributed to writing the manuscript, reviewed the final draft, and approved its submission.

Notes

The authors declare no competing financial interest.

■ ACKNOWLEDGMENTS

P.L. acknowledges the funding support from the Agency of Science, Technology and Research (A*STAR) under the Low-Carbon Energy Research (LCER) Funding Initiatives (Project U2102d2010). T.P. acknowledges funding from the Centre of Excellence on Molecular Materials and Functions under the Institution of Eminence scheme of IIT Madras. G.V. thanks IIT Madras for providing the research fellowship and the International Immersion Experience (IIE) travel grant.

■ REFERENCES

(1) Meinshausen, M.; Jeffery, L.; Guetschow, J.; Robiou du Pont, Y.; Rogelj, J.; Schaeffer, M.; Höhne, N.; den Elzen, M.; Oberthür, S.; Meinshausen, N. National post-2020 greenhouse gas targets and diversity-aware leadership. *Nat. Clim. Change* **2015**, *5* (12), 1098−1106.

(2) Staniaszek, Z.; Griffiths, P. T.; Folberth, G. A.; O'Connor, F. M.; Abraham, N. L.; Archibald, A. T. The role of future anthropogenic methane emissions in air quality and climate. *npj Clim. Atmos. Sci.* **2022**, *5* (1), No. 21.

(3) Qureshi, M. F.; Zheng, J.; Khandelwal, H.; Venkataraman, P.; Usadi, A.; Barckholtz, T. A.; Mhadeshwar, A. B.; Linga, P. Laboratory demonstration of the stability of CO2 hydrates in deep-oceanic sediments. *Chem. Eng. J.* **2022**, *432*, No. 134290.

(4) Qureshi, M. F.; Khandelwal, H.; Usadi, A.; Barckholtz, T. A.; Mhadeshwar, A. B.; Linga, P. CO2 hydrate stability in oceanic sediments under brine conditions. *Energy* **2022**, *256*, No. 124625.

(5) Lee, H.; Lee, J.-w.; Kim, D. Y.; Park, J.; Seo, Y.-T.; Zeng, H.; Moudrakovski, I. L.; Ratcliffe, C. I.; Ripmeester, J. A. Tuning clathrate hydrates for hydrogen storage. *Nature* **2005**, *434* (7034), 743−746.

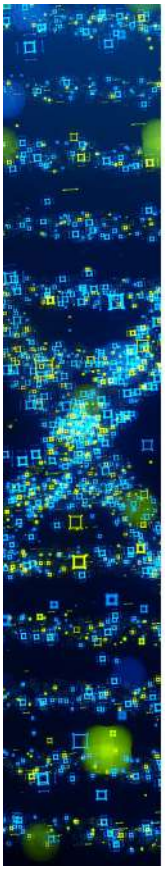
(6) Zheng, J.; Chong, Z. R.; Qureshi, M. F.; Linga, P. Carbon Dioxide Sequestration via Gas Hydrates: A Potential Pathway toward Decarbonization. *Energy Fuels* **2020**, *34* (9), 10529−10546.

(7) Sloan, E. D. Fundamental principles and applications of natural gas hydrates. *Nature* **2003**, *426* (6964), 353−359.

(8) Berni, S.; Scelta, D.; Romi, S.; Fanetti, S.; Alabarse, F.; Pagliai, M.; Bini, R. Exploring High-Pressure Polymorphism in Carbonic Acid

through Direct Synthesis from Carbon Dioxide Clathrate Hydrate. *Angew. Chem., Int. Ed.* **2024**, No. e202403953.
(9) Ghosh, J.; Vishwakarma, G.; Kumar, R.; Pradeep, T. Formation and Transformation of Clathrate Hydrates under Interstellar Conditions. *Acc. Chem. Res.* **2023**, *56* (16), 2241−2252.
(10) Vishwakarma, G.; Malla, B. K.; Reddy, K. S. S. V. P.; Ghosh, J.; Chowdhury, S.; Yamijala, S. S. R. K. C.; Reddy, S. K.; Kumar, R.; Pradeep, T. Induced Migration of CO2 from Hydrate Cages to Amorphous Solid Water under Ultrahigh Vacuum and Cryogenic Conditions. *J. Phys. Chem. Lett.* **2023**, *14* (11), 2823−2829.
(11) Vishwakarma, G.; Malla, B. K.; Kumar, R.; Pradeep, T. Partitioning photochemically formed CO2 into clathrate hydrate under interstellar conditions. *Phys. Chem. Chem. Phys.* **2024**, *26* (22), 16008−16016.
(12) Dhamu, V.; Mengqi, X.; Qureshi, M. F.; Yin, Z.; Jana, A. K.; Linga, P. Evaluating CO2 hydrate kinetics in multi-layered sediments using experimental and machine learning approach: Applicable to CO2 sequestration. *Energy* **2024**, *290*, No. 129947.
(13) Dhamu, V.; Qureshi, M. F.; Abubakar, S.; Usadi, A.; Barckholtz, T. A.; Mhadeshwar, A. B.; Linga, P. Investigating High-Pressure Liquid CO2 Hydrate Formation, Dissociation Kinetics, and Morphology in Brine and Freshwater Static Systems. *Energy Fuels* **2023**, *37* (12), 8406−8420.
(14) Ren, M.; Sevilla, M.; Fuertes, A. B.; Mokaya, R.; Tour, J. M.; Jalilov, A. S. Pore Characteristics for Efficient CO2 Storage in Hydrated Carbons. *ACS Appl. Mater. Interfaces* **2019**, *11* (47), 44390−44398.
(15) Cao, P.; Ning, F.; Wu, J.; Cao, B.; Li, T.; Sveinsson, H. A.; Liu, Z.; Vlugt, T. J. H.; Hyodo, M. Mechanical Response of Nanocrystalline Ice-Contained Methane Hydrates: Key Role of Water Ice. *ACS Appl. Mater. Interfaces* **2020**, *12* (12), 14016−14028.
(16) Cao, P.; Li, T.; Ning, F.; Wu, J. Mechanical Instability of Methane Hydrate−Mineral Interface Systems. *ACS Appl. Mater. Interfaces* **2021**, *13* (38), 46043−46054.
(17) Phan, A.; Stamatakis, M.; Koh, C. A.; Striolo, A. Correlating Antiagglomerant Performance with Gas Hydrate Cohesion. *ACS Appl. Mater. Interfaces* **2021**, *13* (33), 40002−40012.
(18) Kim, B.; Zhang, Y. G. Methane hydrate dissociation across the Oligocene−Miocene boundary. *Nat. Geosci.* **2022**, *15* (3), 203−209.
(19) Liang, M.; Chen, G.; Sun, C.; Yan, L.; Liu, J.; Ma, Q. Experimental and modeling study on decomposition kinetics of methane hydrates in different media. *J. Phys. Chem. B* **2005**, *109* (40), 19034−19041.
(20) Ghosh, J.; Bhuin, R. G.; Vishwakarma, G.; Pradeep, T. Formation of Cubic Ice via Clathrate Hydrate, Prepared in Ultrahigh Vacuum under Cryogenic Conditions. *J. Phys. Chem. Lett.* **2020**, *11* (1), 26−32.
(21) Ghosh, J.; Vishwakarma, G.; Das, S.; Pradeep, T. Facile Crystallization of Ice Ih via Formaldehyde Hydrate in Ultrahigh Vacuum under Cryogenic Conditions. *J. Phys. Chem. C* **2021**, *125* (8), 4532−4539.
(22) Vishwakarma, G.; Malla, B. K.; Chowdhury, S.; Khandare, S. P.; Pradeep, T. Existence of Acetaldehyde Clathrate Hydrate and Its Dissociation Leading to Cubic Ice under Ultrahigh Vacuum and Cryogenic Conditions. *J. Phys. Chem. Lett.* **2023**, *14* (23), 5328−5334.
(23) Aminnaji, M.; Qureshi, M. F.; Dashti, H.; Hase, A.; Mosalanejad, A.; Jahanbakhsh, A.; Babaei, M.; Amiri, A.; Maroto-Valer, M. CO2 gas hydrate for carbon capture and storage applications − Part 2. *Energy* **2024**, *300*, No. 131580.
(24) Aminnaji, M.; Qureshi, M. F.; Dashti, H.; Hase, A.; Mosalanejad, A.; Jahanbakhsh, A.; Babaei, M.; Amiri, A.; Maroto-Valer, M. CO2 Gas hydrate for carbon capture and storage applications − Part 1. *Energy* **2024**, *300*, No. 131579.
(25) Davies, R. J.; Yang, J.; Ireland, M. T.; Berndt, C.; Maqueda, M. Á. M.; Huuse, M. Long-distance migration and venting of methane from the base of the hydrate stability zone. *Nat. Geosci.* **2024**, *17* (1), 32−37.
(26) Dhamu, V.; Qureshi, M. F.; Barckholtz, T. A.; Mhadeshwar, A. B.; Linga, P. Evaluating liquid CO2 hydrate formation kinetics, morphology, and stability in oceanic sediments on a lab scale using top injection. *Chem. Eng. J.* **2023**, *478*, No. 147200.
(27) Dhamu, V.; Xiao, M.; Qureshi, M. F.; Linga, P. Deciphering the CO2 hydrates formation dynamics in brine-saturated oceanic sediments using experimental and machine learning modelling approach. *Energy* **2024**, *313*, No. 133802.
(28) Veluswamy, H. P. Energy Storage in Hydrates: Status, Recent Trends, and Future Prospects. *ACS Appl. Energy Mater.* **2024**, *7*, 11497−11515.
(29) Burla, S. K.; Pagar, E.; Veluswamy, H. P. Synergistic CH4 Recovery and CO2 Sequestration through Amino Acid-Assisted Injection in Methane Hydrate Sediments. *Energy* **2024**, *304*, No. 132089.
(30) Alhejaili, A.; Babu, P.; Daraboina, N. Impact of chloride salts on TBAB/Methane and TBAB/Carbon dioxide semiclathrate hydrates: Application to desalination. *Fluid Phase Equilib.* **2024**, *583*, No. 114128.
(31) Babu, P.; Alhejaili, A.; Bollineni, C.; Daraboina, N. Phase Equilibrium of Carbon Dioxide/Tetra-n-butyl Ammonium Bromide Mixed Hydrate in the Presence of Produced Water. *J. Chem. Eng. Data* **2024**, *69* (3), 1307−1313.
(32) Wang, W.; Bray, C. L.; Adams, D. J.; Cooper, A. I. Methane Storage in Dry Water Gas Hydrates. *J. Am. Chem. Soc.* **2008**, *130* (35), 11608−11609.
(33) Carter, B. O.; Wang, W.; Adams, D. J.; Cooper, A. I. Gas Storage in "Dry Water" and "Dry Gel" Clathrates. *Langmuir* **2010**, *26* (5), 3186−3193.
(34) Binks, B. P.; Murakami, R. Phase inversion of particle-stabilized materials from foams to dry water. *Nat. Mater.* **2006**, *5* (11), 865−869.
(35) Park, J.; Shin, K.; Kim, J.; Lee, H.; Seo, Y.; Maeda, N.; Tian, W.; Wood, C. D. Effect of hydrate shell formation on the stability of dry water. *J. Phys. Chem. C* **2015**, *119* (4), 1690−1699.
(36) Hu, G.; Ye, Y.; Liu, C.; Meng, Q.; Zhang, J.; Diao, S. Direct measurement of formation and dissociation rate and storage capacity of dry water methane hydrates. *Fuel Process. Technol.* **2011**, *92* (8), 1617−1622.
(37) Li, Y.; Zhang, D.; Bai, D.; Li, S.; Wang, X.; Zhou, W. Size Effect of Silica Shell on Gas Uptake Kinetics in Dry Water. *Langmuir* **2016**, *32* (29), 7365−7371.
(38) Podenko, L. S.; Drachuk, A. O.; Molokitina, N. S.; Nesterov, A. N. Effect of Silica Nanoparticles on Dry Water Gas Hydrate Formation and Self-Preservation Efficiency. *Russ. J. Phys. Chem. A* **2018**, *92* (2), 255−261.
(39) Podenko, L. S.; Nesterov, A. N.; Drachuk, A. O.; Molokitina, N. S.; Reshetnikov, A. M. Formation of propane hydrates in Frozed dry water. *Russ. J. Appl. Chem.* **2013**, *86* (10), 1509−1514.
(40) Golkhou, F.; Haghtalab, A. Kinetic and thermodynamic study of CO2 storage in reversible gellan gum supported dry water clathrates. *J. Taiwan Inst. Chem. Eng.* **2020**, *115*, 79−95.
(41) Bhattacharjee, G.; Linga, P. Amino Acids as Kinetic Promoters for Gas Hydrate Applications: A Mini Review. *Energy Fuels* **2021**, *35* (9), 7553−7571.
(42) Qureshi, M. F.; Khraisheh, M.; AlMomani, F. Probing the effect of various water fractions on methane (CH4) hydrate phase equilibria and hydrate inhibition performance of amino acid L-proline. *J. Mol. Liq.* **2021**, *333*, No. 115888.
(43) Khandelwal, H.; Qureshi, M. F.; Zheng, J.; Venkataraman, P.; Barckholtz, T. A.; Mhadeshwar, A. B.; Linga, P. Effect of l-Tryptophan in Promoting the Kinetics of Carbon Dioxide Hydrate Formation. *Energy Fuels* **2021**, *35* (1), 649−658.
(44) Jeenmuang, K.; Pornaroontham, P.; Qureshi, M. F.; Linga, P.; Rangsunvigit, P. Micro kinetic analysis of the CO2 hydrate formation and dissociation with L-tryptophan in brine via high pressure in situ Raman spectroscopy for CO2 sequestration. *Chem. Eng. J.* **2024**, *479*, No. 147691.
(45) Zebardast, S.; Haghtalab, A. Thermodynamic modeling and measurement of CO2 clathrate equilibrium conditions with a

hydrophobic surface − An application in dry water hydrate. *Chem. Eng. Sci.* **2022**, *251*, No. 117486.
(46) Wei, Y.; Maeda, N. Kinetic promotion of gas hydrate formations using dispersions. *Chem. Eng. Sci.* **2024**, *286*, No. 119673.
(47) Farhang, F.; Nguyen, A. V.; Sewell, K. B. Fundamental Investigation of the Effects of Hydrophobic Fumed Silica on the Formation of Carbon Dioxide Gas Hydrates. *Energy Fuels* **2014**, *28* (11), 7025−7037.
(48) Shi, B.-H.; Fan, S.-S.; Lou, X. Application of the shrinking-core model to the kinetics of repeated formation of methane hydrates in a system of mixed dry-water and porous hydrogel particulates. *Chem. Eng. Sci.* **2014**, *109*, 315−325.
(49) Altamash, T.; Khraisheh, M.; Qureshi, M. F. Investigating the effects of mixing ionic liquids on their density, decomposition temperature, and gas absorption. *Chem. Eng. Res. Des.* **2019**, *148*, 251−259.
(50) Bhattacharjee, G.; Goh, M. N.; Arumuganainar, S. E.; Zhang, Y.; Linga, P. Ultra-rapid uptake and the highly stable storage of methane as combustible ice. *Energy Environ. Sci.* **2020**, *13* (12), 4946−4961.
(51) Dhamu, V.; Thakre, N.; Jana, A. K. Structure-H hydrate of mixed gases: Phase equilibrium modeling and experimental validation. *J. Mol. Liq.* **2021**, *343*, No. 117605.
(52) Zheng, J.; Zhang, B.-Y.; Wu, Q.; Linga, P. Kinetic Evaluation of Cyclopentane as a Promoter for CO2 Capture via a Clathrate Process Employing Different Contact Modes. *ACS Sustainable Chem. Eng.* **2018**, *6* (9), 11913−11921.
(53) Dhamu, V.; Qureshi, M. F.; Selvaraj, N.; Yuanmin, L. J.; Guo, I. T.; Linga, P. Dual Promotional Effect of l-Tryptophan and 1,3-Dioxane on CO2 Hydrate Kinetics in Seawater under Static/Unstatic Conditions for Carbon Capture and Storage Application. *Energy Fuels* **2024**, *38*, 11980−11993.
(54) Kumar, A.; Daraboina, N.; Linga, P.; Kumar, R.; Ripmeester, J. A. Experimental study on hydrate structure transition using an in situ high-pressure powder X-ray diffractometer: application in CO2 capture. *ACS Sustainable Chem. Eng.* **2022**, *10* (35), 11473−11482.
(55) Jin, Y.; Kida, M.; Nagao, J. Clathrate Hydrates Coexisting Thiazole: Two Roles of Structure II Hydrate Former and Structure I Thermodynamic Inhibitor. *Energy Fuels* **2023**, *37* (3), 2467−2474.
(56) Koh, C. A.; Savidge, J. L.; Tang, C. C. Time-Resolved in-Situ Experiments on the Crystallization of Natural Gas Hydrates. *J. Phys. Chem. A* **1996**, *100* (16), 6412−6414.
(57) Qin, J.; Kuhs, W. F. Quantitative analysis of gas hydrates using Raman spectroscopy. *AlChE J.* **2013**, *59* (6), 2155−2167.
(58) Chen, L.; Lu, H.; Ripmeester, J. A. Raman spectroscopic study of CO2 in hydrate cages. *Chem. Eng. Sci.* **2015**, *138*, 706−711.
(59) Li, Y.; Gambelli, A. M.; Rossi, F.; Mei, S. Effect of promoters on CO2 hydrate formation: Thermodynamic assessment and microscale Raman spectroscopy/hydrate crystal morphology characterization analysis. *Fluid Phase Equilib.* **2021**, *550*, No. 113218.
(60) Forny, L.; Pezron, I.; Saleh, K.; Guigon, P.; Komunjer, L. Storing water in powder form by self-assembling hydrophobic silica nanoparticles. *Powder Technol.* **2007**, *171* (1), 15−24.
(61) Zhang, F.; Wang, X.; Wang, B.; Lou, X.; Lipiński, W. Experimental and numerical analysis of CO2 and CH4 hydrate formation kinetics in microparticles: A comparative study based on shrinking core model. *Chem. Eng. J.* **2022**, *446*, No. 137247.


CAS BIOFINDER DISCOVERY PLATFORM™
STOP DIGGING THROUGH DATA —START MAKING DISCOVERIES
CAS BioFinder helps you find the right biological insights in seconds
Start your search
CAS
A division of the American Chemical Society

https://doi.org/10.1021/acsami.4c17727
ACS Appl. Mater. Interfaces 2025, 17, 4865−4874

Supporting Information

Understanding the Kinetics of CO_2 Hydrate Formation in Dry Water for Carbon Capture and Storage: X-Ray Diffraction and In Situ Raman Studies

Gaurav Vishwakarma[1,2,#], Vikas Dhamu[1,#], M. Fahed Qureshi[1], Gaurav Bhattacharjee[1], Thalappil Pradeep[2,3] and Praveen Linga[1*]*

[1]Department of Chemical and Biomolecular Engineering, National University of Singapore, Singapore 117580

[2]DST Unit of Nanoscience (DST UNS) and Thematic Unit of Excellence (TUE), Department of Chemistry, Indian Institute of Technology Madras, Chennai 600036, India

[3]International Centre for Clean Water, IIT Madras Research Park, Chennai 600113, India

*Corresponding authors

pradeep@iitm.ac.in, praveen.linga@nus.edu.sg

#G.V. and V.D. contributed equally.

Morphology Videos S1-S4

Figures S1-S6 (pages S2-S8)

Calculation of the Lattice Parameter (S5)

References (page S9)

Videos

Video S1- CO_2 hydrates morphology in pure water

Video S2- CO_2 hydrates morphology in dry water

Video S3- CO_2 hydrates morphology in dry water + 500 ppm L-trp

Video S4- CO_2 hydrates morphology in dry water + 1000 ppm L-trp

Supporting Information 1

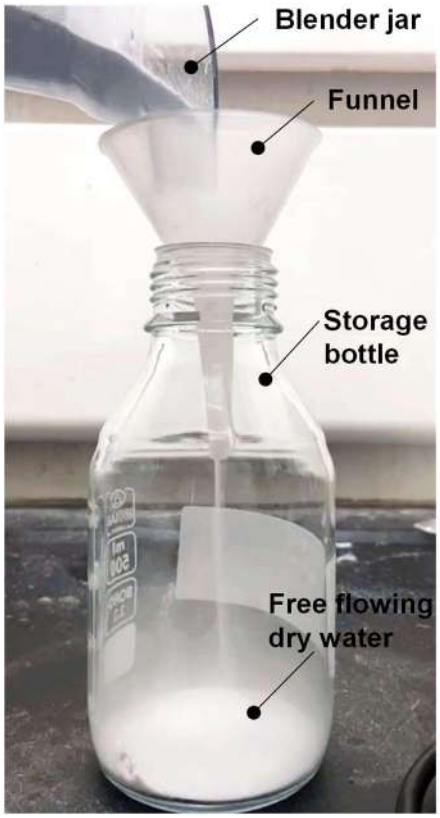


Figure S1. Photograph showing the transfer of dry water (DW) from a blender jar to a storage bottle. DW was prepared by blending 95 g of deionized water with 5 g of nanosilica particles at ~24,000 rpm for 90 seconds (in three 30-second bursts). The resulting free-flowing white powder transferred easily without leaving residue.

Supporting Information 2

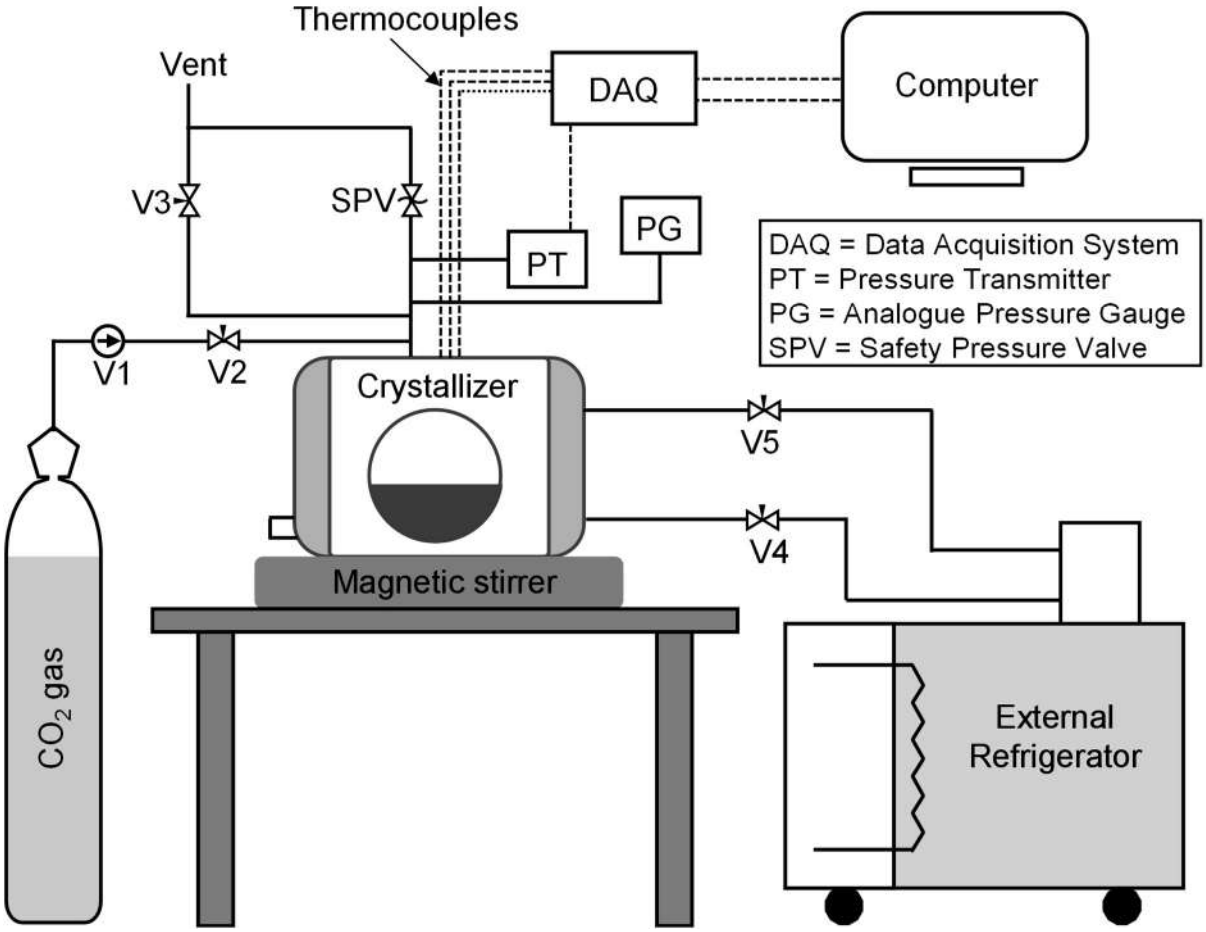


Figure S2. Experimental setup for studying CO_2 hydrate formation kinetics and morphology, as well as for sample preparation for PXRD analysis. The setup includes a high-pressure crystallizer chamber, external refrigerator, gas inlet, and data acquisition system.

Supporting Information 3

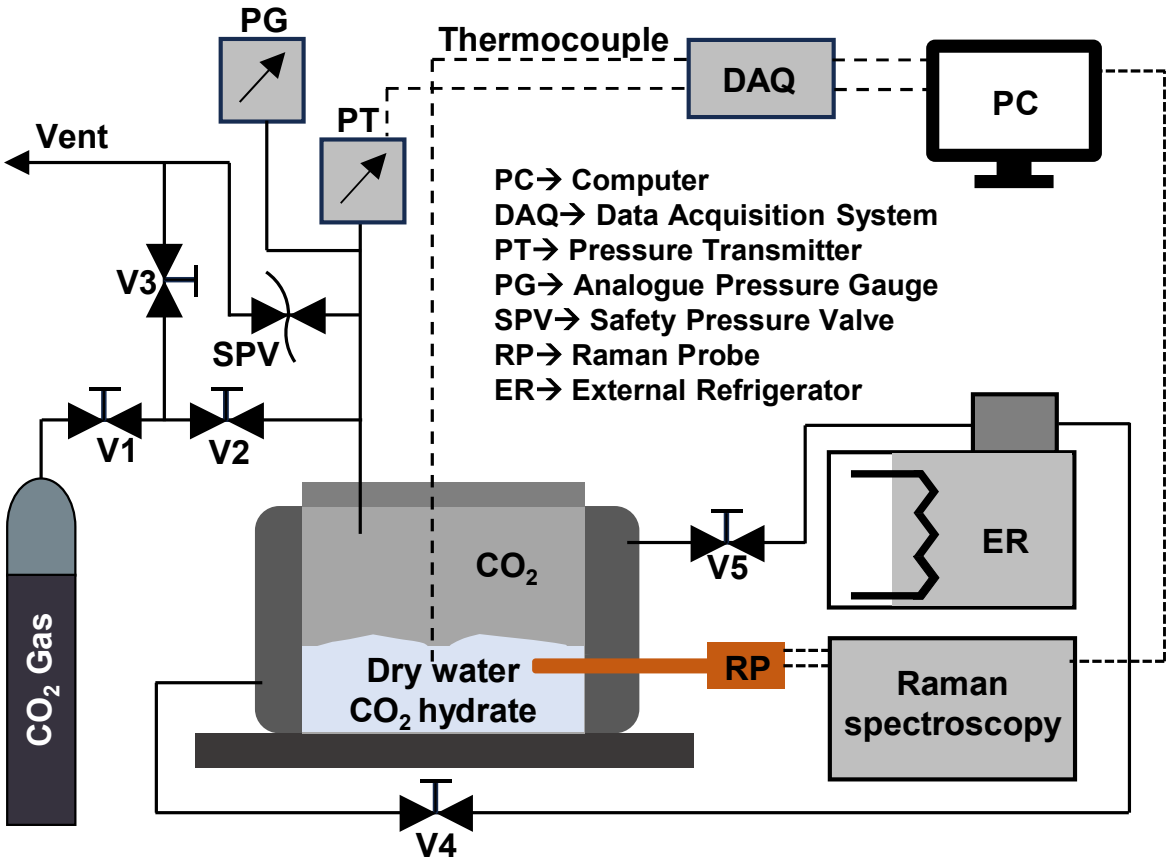


Figure S3. Schematic of the in situ Raman setup coupled with high-pressure reactor. The setup consists of a high-pressure crystallizer chamber, Raman spectrometer, external refrigerator, gas inlet, and data acquisition systems.

Calculation of the Lattice Parameter of the CO_2 (sI) Hydrate Using the Observed PXRD Data

Two equations were employed to determine the lattice parameter (*a*) of DW-CO_2 (sI) hydrate. The procedure is outlined as follows:

Initially, eqn. (S1) utilizes Bragg's law to calculate "*d*," which denotes the interplanar spacing of the crystal:

$$n\lambda = 2d \sin\Theta \quad \text{(S1)}$$

Here, "λ" denotes the wavelength of the incident X-ray (1.542 Å in this case), and "Θ" is the incident angle (the angle between the incident ray and the scattering plane) obtained from the PXRD peak position. "*n*" is set to 1 for the first order of diffraction.

Subsequently, the p-XRD pattern is indexed against the standard sI hydrate PXRD pattern.[1, 2] At least three peaks with known Miller Indices (*"hkl"*) are selected. For cubic crystals, the interplanar spacing *"d"* between adjacent (*hkl*) lattice planes is described by eqn. (S2):

$$\frac{1}{d^2} = \frac{h^2+k^2+l^2}{a^2} \quad \text{(S2)}$$

Given the other known parameters, solving eqn. (S2) yields the lattice parameter "*a*" for the cubic unit cell of the sI hydrate.

Supporting Information 4

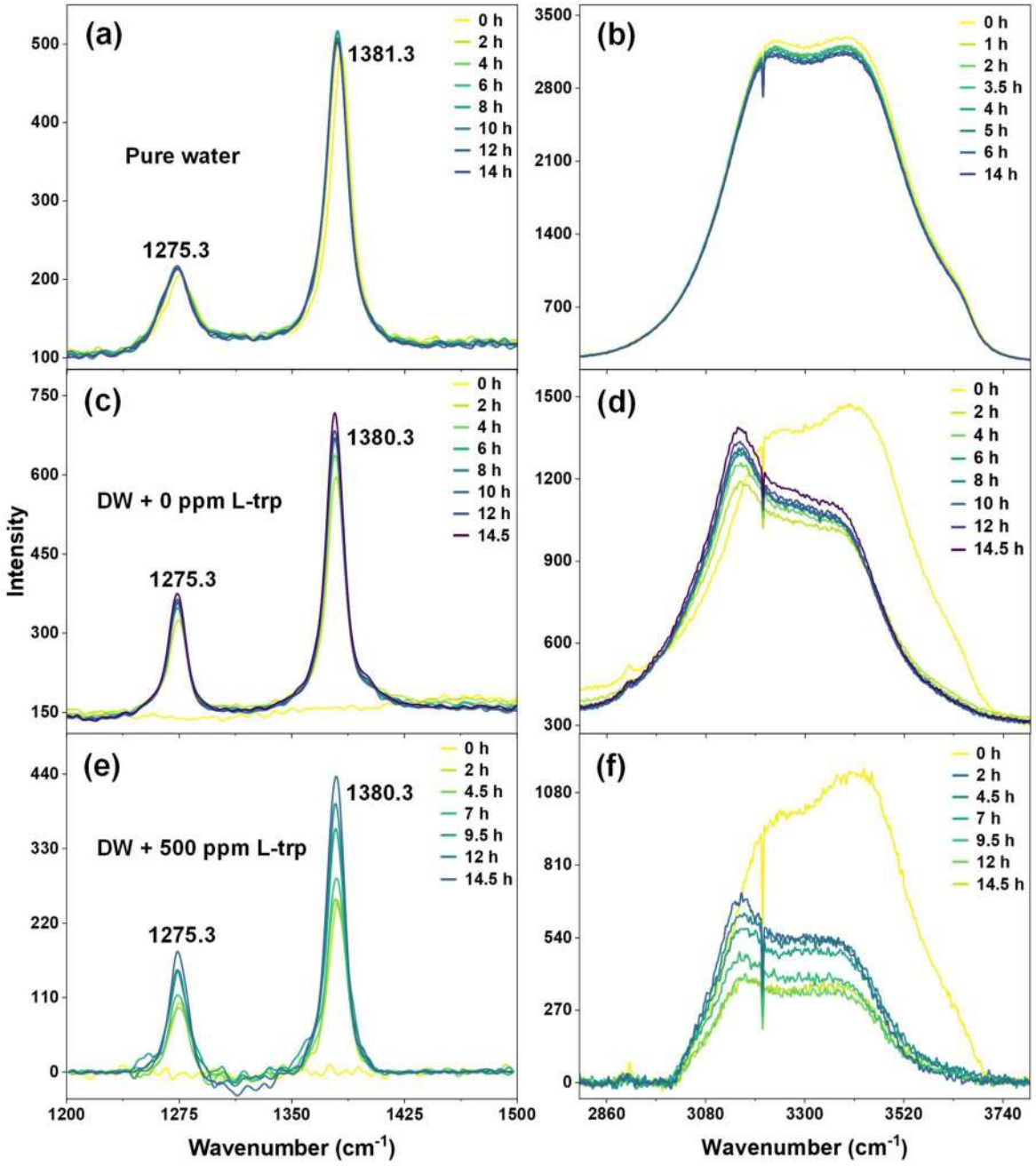


Figure S4. Time-dependent in situ Raman spectra for CO_2 hydrate formation in (a, b) pure water, (c, d) DW, and (e, f) DW + 500 ppm L-trp. Here, the first and second columns present Raman spectra for the CO_2 Fermi dyad, and O-H stretching bands, respectively. In all cases, CO_2 hydrate formation was achieved at 3.5 MPa and 274.65 K. While the presence of two Fermi dyad peaks at ~1380.3 and 1275.3 cm^{-1} confirms the formation of CO_2 hydrates, the O-H stretching suggests that the water molecules are forming the hydrate cages.

Supporting Information 5

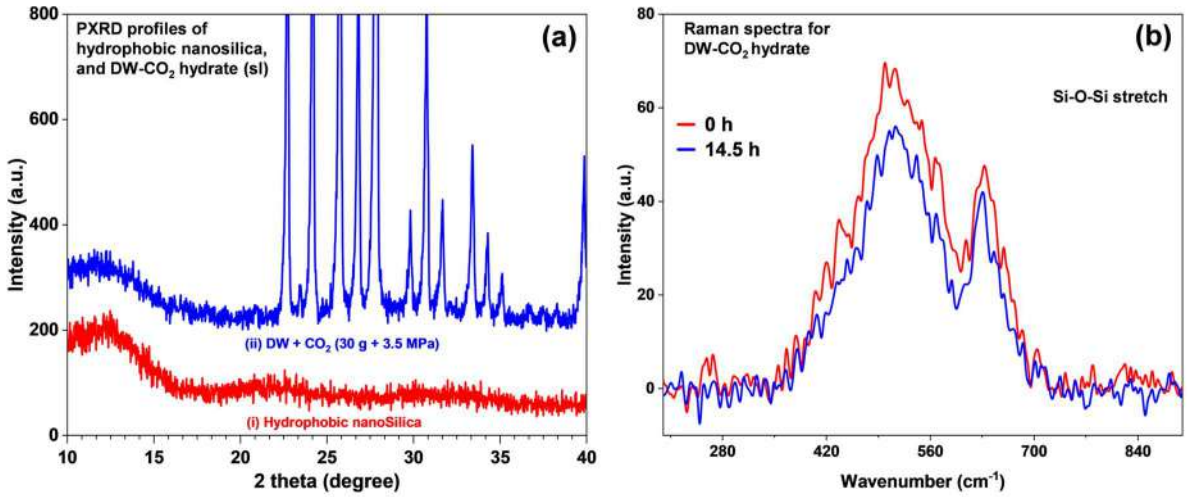


Figure S5. (a) PXRD pattern of the (i) hydrophobic nanosilica, and (ii) DW-CO_2 hydrate formed at 3.5 MPa and 274.65 K (initial conditions). A broad PXRD pattern in the 2θ range of 10-15° corresponding to silica particles can be seen in both systems. (b) In situ Raman spectra before and after DW-CO_2 hydrate formation in the Si-O-Si stretching region of silica. The reduced peak intensity after hydrate formation suggests that a small fraction of CO_2 hydrates formed above the silica shell.

Supporting Information 6

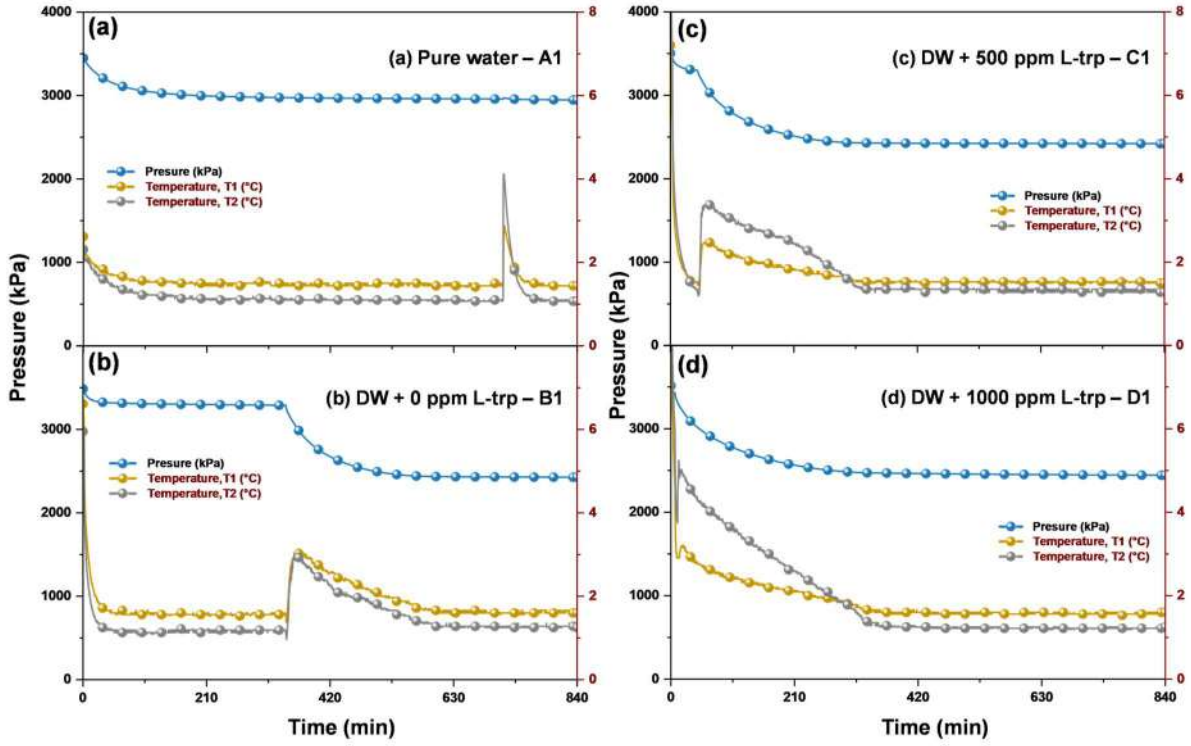


Figure S6. Changes in the *P-T* with respect to time during CO_2 hydrate formation in (a) pure water, (b) DW without L-trp, (c) DW with 500 ppm L-trp, and (d) DW with 100 ppm L-trp at 3.5 MPa. The onset of hydrate formation is realized by observing a sudden drop in pressure and an increase in temperature.

References

(1) Kumar, A.; Daraboina, N.; Linga, P.; Kumar, R.; Ripmeester, J. A. Experimental study on hydrate structure transition using an in situ high-pressure powder X-ray diffractometer: application in CO2 capture. *ACS Sustainable Chemistry & Engineering* **2022**, *10* (35), 11473-11482.
(2) Jin, Y.; Kida, M.; Nagao, J. Clathrate Hydrates Coexisting Thiazole: Two Roles of Structure II Hydrate Former and Structure I Thermodynamic Inhibitor. *Energy & Fuels* **2023**, *37* (3), 2467-2474.

CHEMISTRY OF MATERIALS

pubs.acs.org/cm

Article

Nanomechanical Investigations of Crystals of Copper Nanocluster Isomorphs: Enhanced Hardness of the Low-Density Analogue

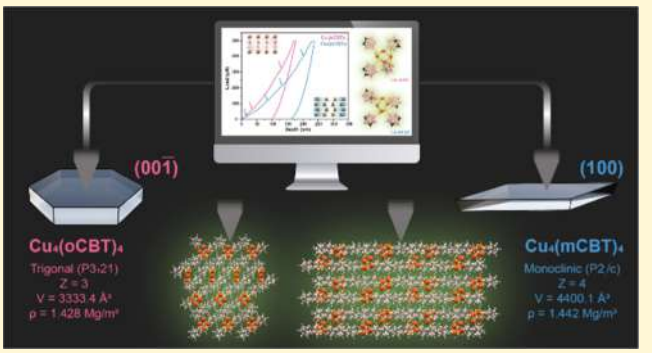
Amoghavarsha Ramachandra Kini,[#] Sanghamitra Debta,[#] Arijit Jana,[#] C. Aparna, Vivek Yadav, Nataliia Kusiak, Tomas Base,* Umesh V. Waghmare,* Pijush Ghosh,* and Thalappil Pradeep*

Cite This: *Chem. Mater.* 2025, 37, 1284−1296

Read Online

ACCESS | Metrics & More | Article Recommendations | Supporting Information

ABSTRACT: Atomically precise cluster crystals, with constituent units composed of tens to hundreds of atoms, are important for the construction of miniaturized solid-state devices. Understanding the mechanical characteristics of such crystals is crucial for these applications. In this study, we focused on the nanomechanical properties of crystals of two isomorphic copper nanoclusters (Cu_4L_4), protected by *ortho*-carborane-9-thiol, $Cu_4(o\text{CBT})_4$, and *meta*-carborane-9-thiol, $Cu_4(m\text{CBT})_4$. These two clusters possess identical square planar Cu_4 cores embedded in butterfly-shaped Cu_4S_4 staples. Load−displacement measurements indicated that the crystals of $Cu_4(o\text{CBT})_4$ (hardness of ∼534.31 MPa) were harder than those of $Cu_4(m\text{CBT})_4$ (hardness of ∼335.49 MPa). Despite their lower density, crystals of $Cu_4(o\text{CBT})_4$ demonstrated increased hardness, owing to the presence of locked slanted layers that efficiently interacted with each other through various short contact supramolecular interactions. During indentation studies, multiple "pop-in" events were observed for the crystals of both clusters, suggesting the dislocation of molecular layers within the crystal lattice. Dynamic mechanical analysis conducted at different loading frequencies indicated that crystals of $Cu_4(o\text{CBT})_4$ have a higher storage modulus than $Cu_4(m\text{CBT})_4$. Both the crystals are thermally robust, as evident from thermogravimetric analysis and attenuated total reflection-IR analysis. Using density functional theory, we calculated Young's modulus (E_r) for both crystals at 1 and 2% strain and found that the high-density isomorph had a lower E_r, consistent with experimental data showing E_r of $Cu_4(o\text{CBT})_4$ and $Cu_4(m\text{CBT})_4$ to be 9.79 and 8.54 GPa, respectively. These findings highlight the significant role of subtle structural differences in governing the nanomechanical behavior of isomorphic cluster crystals, paving the way for their rational design in advanced solid-state device applications.

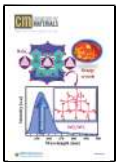


INTRODUCTION

Atomically precise metal nanoclusters, particularly those composed of coinage metals, are a fascinating class of nanomaterials, well-known for their unique and finely tunable properties at the atomic scale.[1−3] These nanoclusters exhibit quantum behavior, manifested by discrete electron energy levels and size-dependent optical properties, similar to molecules, due to their small size and precise atomic structure.[4] Nanoclusters, typically made up of a few to several tens of atoms, display unique electrical,[5−8] optical,[9,10] magnetic,[11−13] and catalytic[14−16] properties that significantly distinguish them from both bulk materials and larger nanoparticles. These properties of nanoclusters make them ideal for various applications, ranging from highly efficient catalysts for chemical reactions to ultrasensitive sensors[17] and novel electronic devices.[18] Furthermore, atomically precise nanoclusters offer tunability in structure and properties that are hard to achieve with larger nanoparticles and/or bulk materials.

Nanoclusters can be synthesized by mixing metal salts and ligands in precise molar ratios, followed by the reduction of metal ions using appropriate reducing agents in compatible solvents.[19−21] By precisely controlling the number and nature of atoms within the nanoclusters, we can fine-tune their properties for specific applications. Ligands play an essential role in defining the properties of nanoclusters, and several types of ligands have been used to synthesize metal nanoclusters, such as phosphines,[22,23] organic thiols,[24,25] alkynes,[26,27] proteins,[28,29] and carboranethiols.[30−32] Carboranethiol-protected metal clusters exhibit exceptional stability due to the thermally and chemically robust nature of carborane scaffolds. Structural stability is an essential characteristic for clusters to be used in nanodevices, and copper nanoclusters protected by carboranethiols represent one of the suitable

Received: November 28, 2024
Revised: January 10, 2025
Accepted: January 14, 2025
Published: January 23, 2025



Downloaded via INDIAN INST OF TECH MADRAS on December 29, 2025 at 03:07:13 (UTC).
See https://pubs.acs.org/sharingguidelines for options on how to legitimately share published articles.

© 2025 American Chemical Society

materials for electronics and other applications owing to their unique optical and catalytic properties and stability when exposed to elevated temperatures.[33]

The physical, chemical, and mechanical properties of molecular crystals are intricately linked to their crystal structures, intermolecular interactions, and molecular orientations in the crystal.[34−40] To study the mechanical properties of molecular materials, such as active pharmaceutical ingredients,[35,41] metal−organic frameworks (MOFs),[42−44] and perovskites,[45,46] depth-sensing techniques are commonly employed. Molecular crystals tend to be very soft or prone to fracturing under stress, necessitating extremely small loads to study their mechanical properties. Therefore, nanoindentation is the most appropriate technique for investigating the mechanical behavior of such materials.[35] In nanoindentation, a sharp indenter tip is pressed into the surface of the material, leading to localized deformation, while the material's response to the applied load is recorded. Nanoclusters can act as building blocks for self-assembled solids, which can be precisely tuned at the atomic level by modifying the nanoclusters that constitute these structures. These self-assembled solids can be classified as molecular crystals, characterized by an ordered arrangement of nanoclusters with molecule-like properties.[47] Understanding the mechanical properties of nanocluster crystals is paramount for their use in nanoelectronic devices, although such studies are rare. Previous investigations have employed nanoindentation to explore the mechanical properties of Ag_{29} and $Ag_{40/46}$ nanocluster crystals.[47,48] Nanoindentation experiments provide valuable insights into the hardness, elastic modulus, stiffness, and plastic deformation traits of the investigated material. These insights are instrumental in establishing structure−property relationships in nanoclusters.[34−36]

Here, we present the nanoindentation studies of crystals of Cu_4 nanoclusters protected by *ortho*-carborane-9-thiol (*o*CBT) and *meta*-carborane-9-thiol (*m*CBT) to understand their mechanical properties under different static and dynamic loading conditions. The exceptional thermal stability and unique optical properties of Cu_4 nanoclusters prompted us to study their mechanical properties to find possible applications.[33] We performed various tests under load-controlled and displacement-controlled conditions and performed dynamical mechanical analyses, which are discussed in detail in subsequent sections. Our results suggest that Cu_4 nanoclusters protected by carboranethiol ligands have hardness and elastic modulus comparable to MOFs and organic crystals, making them more suitable for solid-state nanodevices and various other applications.

EXPERIMENTAL METHODS

Chemicals. The *o*CBT and *m*CBT were synthesized following the established procedures described in the literature.[49,50] Copper iodide (CuI) and sodium borohydride ($NaBH_4$, 98%) were obtained from Aldrich Chemicals. 1,2-Bis(diphenylphosphino)ethane (DPPE) was purchased from Rankem Chemicals. Solvent-grade dichloromethane (DCM), acetone, acetonitrile, and methanol were procured from Rankem and Finar India. All chemicals used in this study were commercially available and used without further purification.

Synthesis of $[Cu_{18}(DPPE)_6H_{16}]^{2+}$ Nanocluster. The $[Cu_{18}(DPPE)_6H_{16}]^{2+}$ cluster, denoted as (Cu_{18}), was synthesized following the established procedure described in the literature.[51] Initially, a mixture of 95 mg (0.49 mM) of CuI and 120 mg (0.03 mM) of DPPE was prepared under an argon atmosphere and dissolved in 15 mL of acetonitrile. After a reaction time of 30 min, the resulting white complex was subjected to reduction by the direct addition of 180−185 mg of $NaBH_4$ powder. The reduction process was allowed to proceed for an additional 1 h with stirring at 750 rpm and room temperature. Subsequently, an orange-colored precipitate was observed, indicating the successful formation of the Cu_{18} cluster. The reaction mixture was stirred for 6 h to isolate the desired product. Following this, the mixture was subjected to centrifugation, which resulted in the formation of an orange solid. The solid was washed three times using 5 mL of acetonitrile and methanol to remove any residual starting materials. Finally, the Cu_{18} cluster, appearing as a dark orange-colored compound, was extracted using dichloromethane (DCM) for subsequent use in the LEIST reaction. The yield of the Cu_{18} cluster was approximately 75% relative to that of the corresponding copper precursor.

Synthesis of $Cu_4(oCBT)_4$ and $Cu_4(mCBT)_4$ Clusters. *$Cu_4(oCBT)_4$.* The synthesis was done precisely as described in the literature.[33] Briefly, ∼50 mg of the purified Cu_{18} nanocluster was dissolved in 15 mL of dichloromethane (DCM) and reacted with 40 mg of *o*CBT at room temperature. After a reaction time of 2 h, the solution, initially yellowish in color, transformed, forming white precipitates. These white precipitates exhibited a vibrant green emission when subjected to a 365 nm UV lamp. The reaction was allowed to proceed for 5 h until completion. Subsequently, the microcrystalline white precipitates were thoroughly washed multiple times with methanol and DCM to eliminate any unreacted ligands present in excess. This white precipitate was soluble in acetone and was further purified by crystallization.

$Cu_4(mCBT)_4$. The synthesis of $Cu_4(mCBT)_4$ followed the same steps as above, but the ligand used was *m*CBT. The as-formed $Cu_4(mCBT)_4$ clusters were soluble in DCM. The reaction solvents were removed using rotavapor, and the solid white product that formed showed a green luminescence under a 365 nm UV lamp.

Crystallization of $Cu_4(oCBT)_4$ and $Cu_4(mCBT)_4$. *$Cu_4(oCBT)_4$.* The $Cu_4(oCBT)_4$ cluster is soluble only in acetone. Around 40 mg of the as-prepared cluster was dissolved in 2 mL of acetone. 2 mL of DCM (antisolvent) was added and mixed well with the cluster solution. A glass slide was kept to provide a substrate for crystallization. The solution was kept undisturbed in a 4 °C fridge. After 5−7 days, hexagonal crystals of $Cu_4(oCBT)_4$ were obtained, characterized by single-crystal X-ray diffraction (SC-XRD).

$Cu_4(mCBT)_4$. Around 40 mg of the as-prepared $Cu_4(mCBT)_4$ cluster was dissolved in 2 mL of DCM, and 1.5:1 (v/v) acetone and toluene (antisolvent) were mixed. A glass slide was kept to provide a substrate for crystallization. The solution was kept undisturbed in a 4 °C fridge. After 5−7 days, hundreds of parallelepiped crystals of $Cu_4(mCBT)_4$ were obtained, characterized by SC-XRD.

The crystals grown on the glass slides were directly used for nanoindentation experiments without any additional treatment.

Characterization. *UV−Visible Spectroscopy.* UV−vis absorption spectra of the clusters in their respective solution were recorded using a PerkinElmer Lambda 25 spectrophotometer in the 200−1100 nm wavelength range. The slit width used for the measurement is 1 nm. The cuvettes used had a thickness of 10 mm (path length). Measurements were conducted using solutions of $Cu_4(oCBT)_4$ in acetone and $Cu_4(mCBT)_4$ in dichloromethane.

SC-XRD (Face Indexing). SC-XRD data collection of Cu_4 clusters was performed with a Bruker D8 VENTURE single-crystal X-ray diffractometer equipped with a graphite monochromatic Mo (Kα) (λ = 0.71073 Å) radiation and a PHOTON 100 CMOS detector. The data collection for both crystals was performed at 296 K. Face indexing was carried out by capturing a video of the crystals on the goniometer, and the faces were indexed using APEX software.

We did not conduct postindentation crystal structure analysis for crystals **1** and **2** because of the highly localized nature of the deformation caused by nanoindentation, which has minimal impact on the overall crystal structure. The indentation process can alter the structure in a small region at the indentation tip, known as the plastic zone, but probing this tiny volume would require specialized in situ

https://doi.org/10.1021/acs.chemmater.4c03265
Chem. Mater. 2025, 37, 1284−1296

SC-XRD facilities. Instead, we investigated structural changes within the plastic region through computational studies.

Photoluminescence Spectroscopy. Photoluminescence spectra were measured using Horiba Jobin Nanolog spectrometer by applying a 3 nm bandpass filter having a resolution bandwidth of 5 nm. The Nanolog instrument has a 450 W xenon-arc lamp source, double monochromator with gratings, associated reflective optics, and a CCD detector. Solid samples were used for photoluminescence measurements as the samples show crystallization-induced luminescence.

X-ray Photoelectron Spectroscopy. X-ray photoelectron spectroscopy (XPS) was conducted using an Omicron Nanotechnology ESCA probe TPD spectrometer equipped with a polychromatic dual X-ray source of Mg Kα ($h\nu$ = 1253.6 eV) and Al Kα ($h\nu$ = 1486.6 eV). Al Kα was used for the measurements of both crystals, which were drop-cast onto sample grids. The binding energies of all spectral regions were calibrated relative to the C 1s peak at 284.8 eV. The survey spectrum was acquired by using a pass energy of 50 eV with a step size of 0.5 eV. High-resolution scans for all elements were recorded at a pass energy of 20 eV and a step size of 0.08 eV to ensure precise peak resolution. Additionally, Cu LMM Auger spectra were collected for both samples to determine the oxidation state of copper in the nanocluster. These spectra were obtained by using a pass energy of 20 eV and a step size of 0.08 eV.

Attenuated Total Reflectance Infrared Spectroscopy. A PerkinElmer attenuated total reflectance infrared (ATR-IR) spectrometer was used to analyze the crystalline samples. Temperature-dependent chemical stability was assessed on heat-treated crystals that were heated to 150 °C. Measurements were taken just after heating the crystals at 30, 50, 80, 100, and 150 °C.

Thermogravimetric Analysis. Thermogravimetric measurements of about 5 mg of cluster sample in an alumina crucible were performed using NETZSCH STA 449 F3 Jupiter instruments equipped with Proteus-6.1.0 software. The measurements for both samples were performed under a nitrogen atmosphere at a flow rate of 20 mL/min in the temperature range of 30−700 °C with a heating rate of 10 °C/min.

Optical Microscopic Images. Optical microscopic images of the crystal were collected at different magnifications using a LEICA optical microscope equipped with LAS V4.8 software. A UV light (365 nm) was used to record luminescence images of the crystals.

Nanoindentation Measurements. The nanoindentation experiments were performed by using a Hysitron TI Premier nanomechanical testing instrument. We used a Berkovich indenter with a radius of 150 nm for nanomechanical measurements. Before the measurements, the nanoindenter was calibrated using a quartz crystal with a hardness value of 9.25 GPa. Indentation loads of 500, 1000, and 5000 μN were used with a trapezoidal load function. Among several different load functions used commonly in nanoindentation measurements, the trapezoidal load function is used commonly because of the linear loading segment, which ensures that the force is applied at a controlled rate. Also, molecular crystals can exhibit time-dependent behavior due to their softer and more ductile nature compared to metal and ceramic materials. The hold period in the trapezoidal load function allows time for any creep or time-dependent deformations to stabilize. This ensures that the unloading segment reflects only the elastic recovery, which leads to more accurate measurements of the hardness and elastic modulus. The unloading phase in the trapezoidal function is used to extract the elastic properties of the material by using gradual unloading of the nanoindenter from the sample. This gives an accurate load−displacement curve, which is important for analyzing the material's elastic modulus. All of these points also ensure that the data obtained are reproducible across multiple tests, making comparisons more reliable.[52,53]

In situ scanning probe microscopy (SPM) was used to examine the surface topographies before and after indentation. The E_r and H were calculated by applying the Oliver and Pharr method, which used the initial part of the unloading segment of the load−displacement curve. Five crystals were indented in each sample. All measurements were performed at 25 ± 2 °C in a temperature-controlled room maintained by air conditioning.

Nano Dynamic Mechanical Analysis Measurements. Dynamic mechanical analysis (DMA) was conducted in a load-controlled frequency sweep mode. An oscillating dynamic load of 10 μN was applied on top of a static load of 500 μN over a frequency range of 10−200 Hz. The storage modulus, loss modulus, and damping factors were determined by applying a sinusoidal force signal and recording the resulting displacement response.

Computational Details. First-principles density functional theory calculations were performed using the Vienna Ab initio Simulation Package (VASP)[54−57] to study the mechanical properties of carboranethiol-protected nanoclusters $Cu_4(o\text{CBT})_4$ and $Cu_4(m\text{CBT})_4$. The interaction between the core and valence electrons was modeled using a projected augmented wave (PAW)[58,59] potential, and exchange and correlation energy was treated using the Perdew−Burke−Ernzerhof (PBE) functional for a generalized gradient approximation (GGA).[60] Grimme's DFT-D3 scheme was employed to account for the effect of dispersion interactions.[61] The energy cutoff for the plane wave basis was set to 520 eV, and a 1 × 1 × 1 k-point grid centered at the Γ point was used in sampling Brillouin zone integration. A Fermi−Dirac function of width k_BT = 0.05 eV was employed to smear the discontinuity in occupation numbers of states near the Fermi level. The crystal structures of $Cu_4(o\text{CBT})_4$ and $Cu_4(m\text{CBT})_4$ are hexagonal and monoclinic, and they belong to the space groups $P3_121$ and $P2_1/c$, respectively. Structural optimization was carried out with the convergence threshold of energy and forces set to 10^{-8} eV and 10^{-3} eV/Å, respectively. Our estimates of lattice parameters and their experimental values are tabulated in Table S2. It is observed that they are less than the experimental values by 1−4%, which is in contrast to the expected trend from using GGA. This is attributed to the presence of solvents such as DCM, toluene, and acetone in the experimental samples. Since we plan to compare the properties of these two systems, these errors (being similar for both) will introduce systematic errors. However, the comparative trend should be reliable.

RESULTS AND DISCUSSION

Synthesis and Characterization of Cu_4 Nanoclusters.

Isomorphic Cu_4 nanoclusters protected by *ortho* and *meta*-carborane-9-thiol were synthesized according to our previously published study,[33] and herein, we discuss some essential structural features relevant to this investigation. Figure 1a shows a schematic of the synthesis of Cu_4 nanoclusters using the ligand-exchange-induced structural transformation (LEIST) method. A detailed LEIST synthesis procedure is provided in the Experimental Methods. $Cu_4(o\text{CBT})_4$ crystallizes as transparent hexagon-shaped crystals (referred to as **1**), while $Cu_4(m\text{CBT})_4$ crystallizes as parallelepiped crystals (referred to as **2**). Figure 1b,c shows optical microscopic images of the respective crystals under daylight and ultraviolet light.

The UV−vis optical absorption spectra of both nanoclusters exhibited a single absorption band around 275 nm (Figure S1). Emission spectra revealed characteristic emission bands peaking at 520 nm for $Cu_4(o\text{CBT})_4$ (**1**) and 532 nm for $Cu_4(m\text{CBT})_4$ (**2**) (Figure S2). Both nanoclusters displayed green photoluminescence under ultraviolet light, as shown in Figure 1b,c. The chemical purity of the samples was confirmed by using X-ray photoelectron spectroscopy (XPS) and ATR-IR spectroscopy. XPS survey spectra for **1** and **2** (Figures S3 and S4, respectively) confirmed the presence of the expected elements. High-resolution XPS scans were conducted for all of the key elements in both samples. In each case, the sulfur (S) peak corresponds to the metal-bound thiolate state. The Cu $2p_{3/2}$ peak appeared at 931.6 eV for nanocluster **1** and at 931.3

https://doi.org/10.1021/acs.chemmater.4c03265
Chem. Mater. 2025, 37, 1284−1296

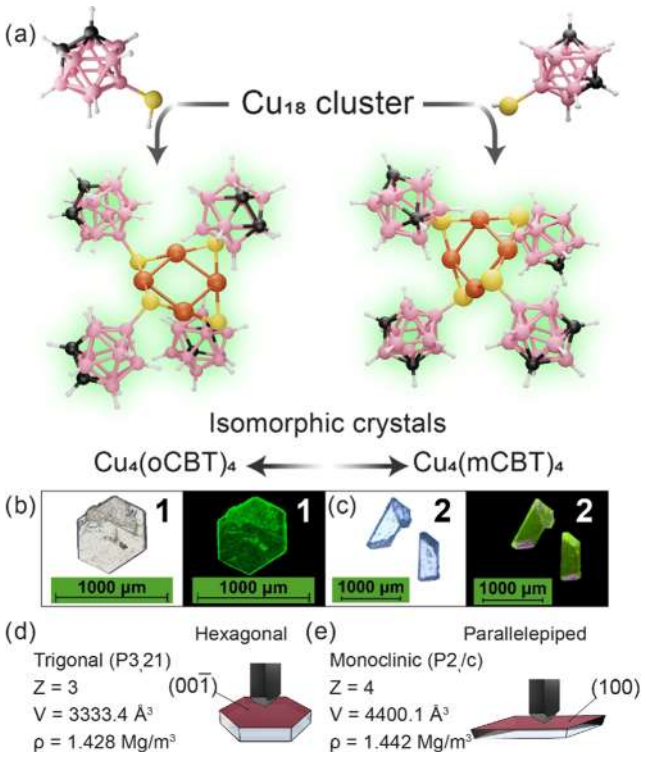


Figure 1. (a) Schematic representation of the synthesis of $Cu_4(oCBT)_4$ and $Cu_4(mCBT)_4$ from the Cu_{18} nanocluster through a LEIST reaction. Microscopic images of (b) $Cu_4(oCBT)_4$ and (c) $Cu_4(mCBT)_4$ single crystals under daylight and UV light. Labels **1** and **2** indicate the crystals of $Cu_4(oCBT)_4$ and $Cu_4(mCBT)_4$, respectively. The indented planes in these crystals are facing the reader. Scale bar: 1000 μm. Crystal parameters and the indented surfaces of the crystals of (d) $Cu_4(oCBT)_4$ and (e) $Cu_4(mCBT)_4$. Color codes: orange: copper, yellow: sulfur, pink: boron, black: carbon, and white: hydrogen.

eV for nanocluster **2**. The absence of satellite peaks indicates that copper is in the +1 or 0 oxidation state. The oxidation state of Cu was further verified via a high-resolution scan of the Cu LMM Auger peak (Figures S3 and S4, insets), with peaks centered at approximately 915.5 and 915.4 eV for nanoclusters **1** and **2**, respectively, consistent with the Cu^{1+} oxidation state.[62]

The thermal stability of the nanoclusters was assessed using TGA, and these have been discussed previously.[33] Clusters **1** and **2** are stable up to 380 and 370 °C, respectively. As an example, we present the data corresponding to cluster **2** in Supporting Figure S5. The mass loss of ~65.59% at 371.3 °C is assigned to the desorption of two carboranethiolate units and two carborane units, leaving behind Cu_2S as the residue. The decomposition pathway of nanocluster **1** remains unclear, potentially due to the hypergolic activity of *o*-carborane moieties,[30] preventing the determination of the decomposition products. However, as the present study is independent of the nature of the decomposition products and high-temperature events, we did not pursue this aspect further. To further assess chemical stability at elevated temperatures, ATR-IR spectroscopy was performed on both samples. Spectra were recorded at 30, 50, 80, 100, and 150 °C to monitor any potential structural changes. No significant variations in the IR spectra were detected across this temperature range, confirming that both the nanoclusters retain their structural integrity under thermal treatment (Supporting Figures S6 and S7). These results underline the resilience of the nanoclusters under controlled heating conditions and provide insights into their potential applications in thermally demanding environments.

Structural Features of Cu_4 Nanoclusters. SC-XRD reveals that both clusters have nearly square planar cores of four Cu atoms with the average Cu−Cu distance of 2.6 Å. The carboranethiols are attached to the square planar metal core through μ_2 sulfide linkages. The face indexing of the crystals was performed to identify the exposed planes of the crystals available for indentation. Finely shaped crystals were selected for face indexing. The indices of all of the crystal faces of **1** and **2** are shown in Figures S8 and S9, respectively. The indentation experiments were carried out on (00$\bar{1}$) and (100) surfaces of **1** and **2**, respectively (marked in Figure 1d,e).

Figure 2a,b represents the extended packing configurations of nanoclusters **1** and **2** as viewed along the *a*- and *b*-axes, respectively. These figures also highlight the crystallographic planes where nanoindentation measurements were conducted. Figures 2a and S10 show that, in the extended packing structure of nanocluster **1**, the clusters are arranged in slanted layers. The metallic cores are aligned linearly along a plane; however, the intercluster interactions predominantly occur along the slanted planes. Notably, each cluster is rotated by 120° along the *c*-axis (as observed from the *a*-axis perspective), compared to the cluster in the layer immediately above it, as shown in Figure S10a. Furthermore, the precise orientation of the cluster in the initial layer repeats in the fourth layer, demonstrating that nanocluster **1** exhibits an ···ABCABC··· arrangement, as shown in Figures 2a and S10b.

In contrast, nanocluster **2** showcases a configuration where the clusters are organized in straight, parallel planes with intercluster interactions predominantly in the same plane, as shown in Figure 2b. Each cluster is rotated 180° along the *b*-axis (as viewed from the *b*-axis perspective) relative to the cluster in the layer above it, as illustrated in Figure S11a. When inspected from the *b*-axis, the exact orientation of the cluster in the first layer reappears in the third layer, following a complete

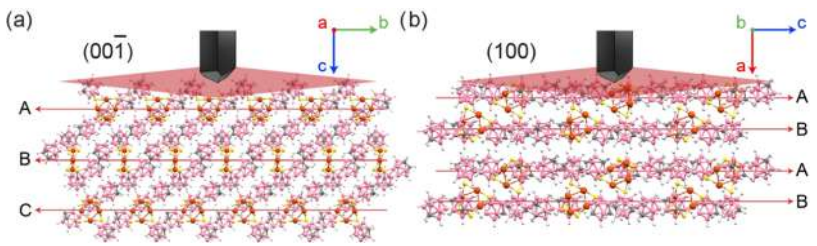


Figure 2. Extended supramolecular packing of (a) $Cu_4(oCBT)_4$ (**1**) and (b) $Cu_4(mCBT)_4$ (**2**) along the marked indentation planes. The ···ABCABC··· and ···ABAB··· packings of **1** and **2** are shown.

https://doi.org/10.1021/acs.chemmater.4c03265
Chem. Mater. 2025, 37, 1284−1296

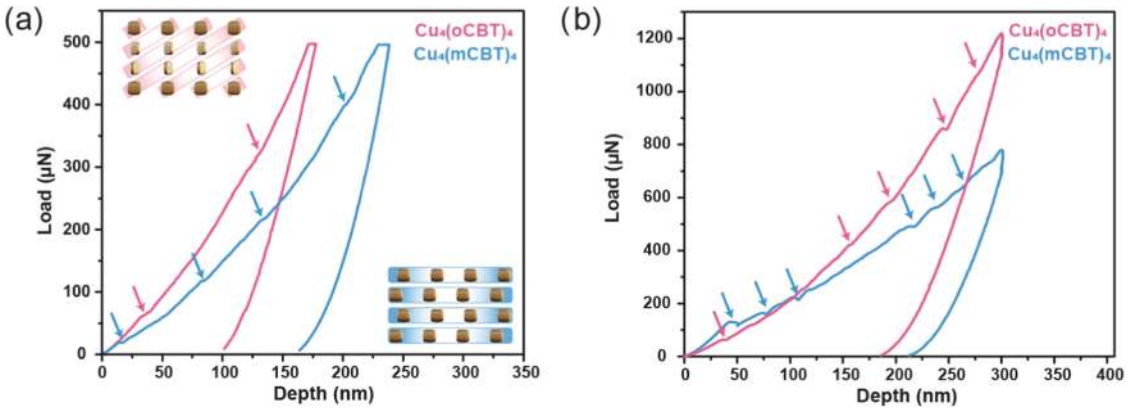


Figure 3. (a) Load−displacement curves of both crystals under a fixed load of 500 μN using a load function of 5−10−5 s. The inset shows the schematic packing diagram of $Cu_4(o\text{CBT})_4$ (top) and $Cu_4(m\text{CBT})_4$ (bottom). The differently oriented rectangles represent the clusters. (b) Load−displacement curves with a fixed displacement of 300 nm. Arrows indicate pop-in events occurring during nanoindentation experiments.

360° rotation. This pattern indicates that nanocluster **2** is arranged in an ···ABAB··· fashion within its crystal lattice, as depicted in Figures 2b and S11b. Remarkably, the adjacent clusters exhibit a mirror-image symmetry when observed along the *a*-axis (Figure S11c,d).

Nanoindentation Studies on Crystals of Cu_4 Nanoclusters. The mechanical properties of the Cu_4 crystals were investigated by using a Hysitron TI 950 Triboindenter equipped with a 150 nm Berkovich tip. Before the measurements, the nanoindenter was calibrated using a quartz crystal with a hardness value of 9.25 GPa. Crystals **1** and **2** were directly grown onto a glass slide, and nanoindentation was performed on the single crystals as-prepared, i.e., without any additional treatment. While the literature suggests cleaving of the crystals before indentation measurements to reduce surface roughness, it was not feasible for this study due to the small size of the crystals. Moreover, the crystals were not subjected to solvent washing to avoid increasing surface roughness.[39] Indentation was performed on the $(00\bar{1})$ plane for cluster **1** and on the (100) plane for cluster **2**. These specific planes were chosen since they are naturally exposed after crystal growth, while other planes remained inaccessible due to the dimensions of the crystals. Five crystals were indented for each sample with five indentations per crystal, to ensure a reproducible load−displacement response.

Quasi-static measurements were performed initially where the indenter is loaded onto the crystals smoothly without any frequency, while the dynamic measurements were done with frequency changes from 10 to 220 Hz. Load-controlled nanoindentation measurements were conducted by using loads of 500, 1000, and 5000 μN to assess the durability of the material under stress. Different loads were chosen to gain insight into the elastic properties of the material as a function of the load. A trapezoidal load function was employed for all measurements, characterized by varying loading rates. This was achieved by adjusting the loading−holding−unloading times to 5−10−5, 20−10−20, and 50−20−50 s, respectively. Similarly, displacement-controlled experiments were performed at 100, 300, and 500 nm depths, with displacement functions of 20−10−20 s. Stress relaxation, creep behavior, and dynamic mechanical analysis were performed to understand the time-dependent mechanical behavior of the crystals, which is discussed in more detail in the next section.

Mechanical Properties of Cu_4 Nanoclusters. At first, load-controlled nanoindentation studies were performed on both crystals at a fixed load of 500 μN with a trapezoidal load function of 5−10−5 s. The load−displacement curve (shown in Figure 3a) illustrates that the crystals of **1** and **2** exhibit displacements of approximately 175 and 225 nm, respectively, for the applied load of 500 μN. The difference in displacements suggests that the crystals of **2** are less stiff than those of **1**. Crystals **1** and **2** also show residual displacements (strain present in the system after the removal of stress) of 100 and 170 nm, respectively. The load-controlled indentation measurements, with a load of 500 μN, were also performed at different load functions of 20−10−20 and 50−20−50, presented in Figure S12a,b, respectively. The load-controlled indentations were also carried out at higher loads of 1000 and 5000 μN at three different load functions of 5−10−5, 20−10−20, and 50−20−50, as shown in Figure S13. These measurements consistently indicate that crystal **2** is undergoing a larger displacement than crystal **1** for a given maximum load.

Similarly, displacement-controlled nanoindentation studies were performed at fixed displacements of 100, 300, and 500 nm. Figure 3b indicates the load−displacement curve obtained for a 300 nm constant displacement, and it indicates that the crystals of **1** need a higher load of 1200 μN, while crystals of **2** require only 700 μN to attain the same displacement. Figure S14 presents the load−displacement curves for 100 and 500 nm constant displacements, showing similar results. The difference in response between these two types of crystals can be attributed to the different arrangements of molecular planes in the crystals, shown in Figure 2a,b. In the case of **2**, the planes are arranged perpendicular to the indentation direction, making them more susceptible to plastic deformation. Conversely, the planes of **1** are slanted relative to the indentation direction, and the clusters may be packed more effectively at the local deformation scale, rendering them more resistant to deformation.[35] Similarly, the molecular arrangement-dependent mechanical response was also observed in crystals of omeprazole,[63] Ag_{29} nanocluster,[47] and in the cocrystals of glutaric acid and caffeine.[64]

We observed significant kinks in the measured load−displacement curves of both crystals, represented by arrows in Figure 3a,b. These kinks are called "pop-ins" and are characteristic of molecular crystals. They occur due to the slipping or breaking of crystal planes. Among the two crystals,

https://doi.org/10.1021/acs.chemmater.4c03265
Chem. Mater. 2025, 37, 1284−1296

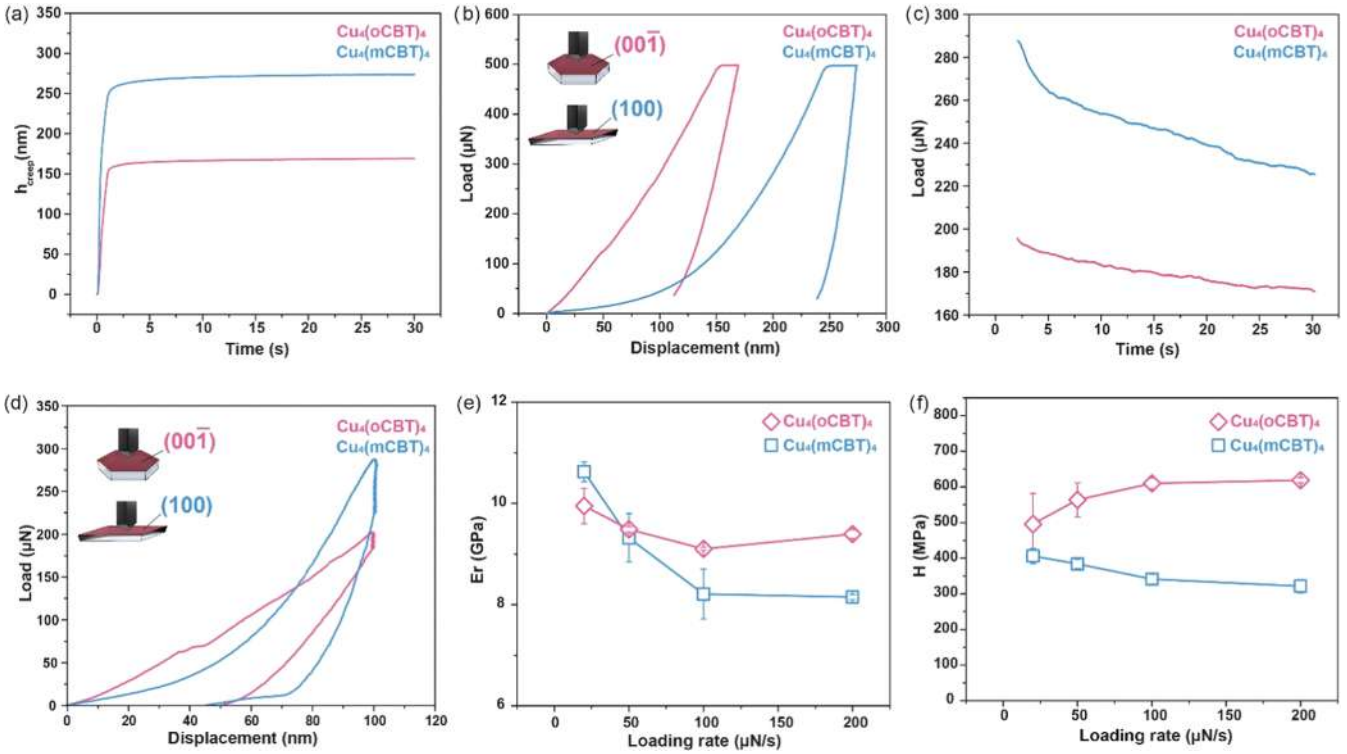


Figure 4. (a) Creep behavior as a function of time and (b) their corresponding load−displacement curves of $Cu_4(oCBT)_4$ and $Cu_4(mCBT)_4$ crystals with an applied load of 500 μN. (c) Stress relaxation curves and (d) their corresponding load−displacement curves for $Cu_4(oCBT)_4$ and $Cu_4(mCBT)_4$ crystals with a fixed displacement of 100 nm. Variation of (e) Young's modulus (E_r) and (f) hardness (H) at different loading rates for $Cu_4(oCBT)_4$ and $Cu_4(mCBT)_4$ crystals. Insets in panels (b, c) show the plane of indentation in both the crystals.

2 shows more of these pop-ins than **1**. The molecular planes of **2** tend to easily break or slip as they are perpendicular to the indentation direction, leading to "pop-in" events, while the slanted molecular planes of **1** are resistant to pop-ins as they can slide reasonably smoothly in the direction of indentation. Anisotropic molecular crystals exhibit similar direction-dependent mechanical behavior due to the arrangement of lattice planes.[40,64] However, we could not access other crystal planes for our studies due to the difficulty of manipulating tiny crystals.

While most organic crystals can be characterized by their structural and optical properties, certain molecular crystals exhibit additional rheological characteristics such as creep, stress relaxation, and viscoelasticity, depending on the specific molecular structure and the applied load. Understanding these rheological properties is essential for their application in polymer science, materials engineering, and pharmaceuticals.[47,48] Therefore, a comprehensive set of load and displacement-controlled tests were conducted to probe the rheological behavior of both the crystals. In order to study the creep behavior, the load was increased from 0 to 500 μN in 1 s and then held for another 30 s, and the displacement was measured. Figure 4a indicates the displacement vs time curve (creep behavior) of crystals **1** and **2**. When a force of 500 μN was applied to crystals **1** and **2** in 1 s, they showed the characteristic displacement of 150 and 250 nm, respectively. In typical creep measurements, the initial prominent displacement peak represents the occurrence of primary creep, followed by secondary and tertiary creeps. The primary creep starts rapidly and slows with time, while secondary creep shows a uniform increase in displacement while holding the load. Tertiary creep has an increased creep rate and sets in when the material breaks or ruptures. The secondary and tertiary creeps are usually found in materials like polymers, ceramics, concrete, and construction materials, especially at elevated temperatures.[65,66] Both crystals show primary creep with large initial displacement, as indicated in Figure 4a. However, there are no signs of secondary or tertiary creeps as the displacement remains constant for the entire time the indenter tip is held in position. This indicates that the crystals resist continuous deformation and are stable under stress.

Similarly, stress relaxation tests were also performed to investigate the relaxation behavior of the crystals. In these tests, a displacement of 100 nm was applied in 1 second and held for another 30 s. The resulting change in the stress over time was measured. Figure 4c represents the stress relaxation curve, where both crystals showed a decrease in load with time, indicating that the clusters rearrange in the crystal structure to gradually reduce their internal stress over time under a constant applied load. These provide insights into the time-dependent mechanical behavior of crystals **1** and **2**. The load−displacement plots obtained from creep and stress relaxation tests (Figure 4b,d) demonstrated a higher residual displacement in the case of crystal **2**, which provided evidence for the reduced hardness of **2** compared to that of **1**. The insets in Figure 4b,d indicate the planes on which the indentations were carried out.

Multiple indentation tests were performed on the crystals of both nanoclusters to accurately assess their nanomechanical behavior. The load−displacement curves collected at various indentation loads, as shown in Figure S15, demonstrate reproducibility across the tests. These curves were subsequently used to determine the reduced modulus (E_r) and hardness (H) of the crystals. Figures S16 and S17 present a

https://doi.org/10.1021/acs.chemmater.4c03265
Chem. Mater. 2025, 37, 1284−1296

Table 1. Measured Hardness and Young's Modulus in Single Crystals of Isomorphic Cu_4 Nanoclusters along with Other Nanoclusters Studied to Date[1]

cluster	crystal system	ρ (g cm^{-3})	H (MPa)	E_r (GPa)	ref
$[Ag_{46}(2,5\text{-DMBT})_{24}(PPh_3)_8]^{2+}$	trigonal	1.322	168.10 ± 25.52	2.27 ± 0.25	47
cocrystals of $[Ag_{46}(2,5\text{-DMBT})_{24}(PPh_3)_8]^{2+}$and $[Ag_{40}(2,4\text{-DMBT})_{24}(PPh_3)_8]^{3+}$	monoclinic	1.497	166.70 ± 28.02	2.73 ± 0.51	47
$[Ag_{29}(1,3\text{-BDT})_{12}(PPh_3)_4]^{3-}$	cubic	2.11	282.19 ± 53.33	5.66 ± 0.44	48
$[Ag_{29}(1,3\text{-BDT})_{12}(PPh_3)_4]^{3-}$	trigonal	2.04	498.15 ± 23.61	7.53 ± 0.41	48
$Cu_4(o\text{CBT})_4$	trigonal	1.428	534.31 ± 82.48	9.79 ± 0.98	this work
$Cu_4(m\text{CBT})_4$	monoclinic	1.442	335.49 ± 68.68	8.54 ± 0.73	this work

[1](Abbreviations: 2,5-DMBT—2,5-dimethylbenzenethiol, 2,4-DMBT—2,4-dimethylbenzenethiol, 1,3-BDT—1,3-benzenedithiol, and PPh_3—triphenylphosphine).

statistical analysis of the data for clusters **1** and **2**, respectively. The mean E_r values were 9.79 ± 0.98 GPa for cluster **1** and 8.54 ± 0.73 GPa for cluster **2**, while the corresponding hardness values were 534.31 ± 82.48 and 335.49 ± 68.68 MPa, respectively. The histograms illustrate the distribution of E_r and H values for the crystals, with overlaid Gaussian fits that suggest a normal distribution pattern. This Gaussian distribution supports the reliability and consistency of the measurements, validating the reproducibility of the nanomechanical properties observed across the data set. We have compiled the E_r and H values of various nanoclusters studied to date, in Table 1, to illustrate the range of these mechanical properties across different nanoclusters.

Both crystals, like viscoelastic materials, manifest stress relaxation behavior over a holding time (Figure 4c). However, this behavior was not very pronounced in the creep vs time plot (Figure 4a), indicating that the material gradually released its internal stresses when exposed to a constant applied load while avoiding significant and continuous deformation. Materials such as elastomers and thermosetting polymers display this behavior characterized by stress relaxation without significant creep. Elastomers quickly adapt to deformed states and revert to their original form upon removal of the deforming force, thus exhibiting stress relaxation. Similarly, thermosetting polymers resist flow and permanent deformation under sustained loads due to their rigid cross-linked network, allowing them to demonstrate stress relaxation while preventing significant creep.[67−69]

Stress reduction in molecular crystals can have various mechanisms, such as readjustment or rearrangement within the crystal lattices through molecular rotations and acoustic vibrations, leading to decreased overall stress.[47,70,71] As for viscoelastic materials, the stress is proportional to the strain rate. Hence, indentation tests were performed at different loading rates to quantify the relationship between stress and the loading rate on the crystals (Figures S12−S14). The values of E_r and H at various loading rates are depicted in Figure 4e,f. It is noted from Figure 4e that for both **1** and **2**, the value of Young's modulus (E_r) decreases with an increase in the loading rate until 100 μN/s and remains constant after that. An interesting behavior was observed for the crystals of **2** at lower loading rates, where the E_r value was initially higher than that of **1**. This behavior can be explained by analyzing the stress relaxation plot. At lower loading rates, the crystals undergo gradual deformation, allowing the clusters within the crystal to reorganize and adjust their orientations to relieve the stress faster, as evident in the stress relaxation plot (Figure 4c). This results in a higher apparent E_r. However, as the loading rate increases, the available time for molecular or structural reorganization within the lattice decreases. Consequently, the crystal's ability to fully adapt to the applied stress is limited, leading to a reduced apparent E_r.

Figure 4f represents the variation of hardness with loading rate and measures plastic deformation occurring in the crystal. The crystals of **2** show a gradual decrease in hardness with an increase in loading rate. However, crystals of **1** show an increase in hardness with respect to the loading rate, which can be explained by the favorable arrangement/orientation of crystal planes to resist plastic deformation. As presented in Figure 2a,b, the crystal planes are arranged slanting in **1** while perpendicular to the indentation direction in the case of **2**. In the crystals of **2**, with an increase in loading rate, the hardness decreases as the clusters have less time to relax and resist the incoming stress at a higher loading rate. However, in the case of **1**, the planes must slide along the adjacent planes, possibly leading to friction due to intercluster interactions, which increases as the loading rate increases. Hence, the indenter experiences more resistance from the crystal as the loading rate increases.

To understand the strain-hardening effect of the crystals, we indented the same region four times. Figure S18 shows the indentation-induced hardness in the crystals of both compounds **1** and **2**. Initial indentations on crystals can induce stresses in the material, and these stresses may undergo relaxation and redistribution with each subsequent indentation, leading to variations in the measured indentation depth.[47] Figure S18a shows the behavior of the crystals of **1**, and Figure S18b shows the behavior of the crystals of **2** under repeated indentations. The crystals of cluster **1** show an increase in hardness with repeated indentations, which is typically observed for molecular crystals that exhibit strain-hardening effects. In the case of **2**, the hardness increases with repeated indentation, but in the fourth indentation, we observed that the hardness dropped suddenly and was almost equal to that of the first indentation, as it traces the first curve closely, indicating that **2** (observed to be softer among the isomorphs) exhibits a gradual degradation effect. In contrast, **1** (harder among the isomorphs) shows a sudden change in hardness, suggesting that crystals of **1** become harder under stress, while there is a gradual increase in hardness of crystals of **2**, along with a sudden decrease in hardness, which may be due to sudden failure of molecular layers due to previous indentations.

Figures S19 and S20 illustrate the atomic force microscopy topography and surface features of samples **1** and **2**, respectively, after indentation. In crystal **1** (Figure S19), three triangular indentations are visible within a 10.000 μm scan with height variations from 0 to 157.9 nm. The lateral and vertical distances across indentation 2 are 1.47975 μm and 2.74226 nm, with roughness values of R_a = 29.5845 nm and R_q = 33.7117 nm. In crystal **2** (Figure S20), five indentations were

https://doi.org/10.1021/acs.chemmater.4c03265
Chem. Mater. 2025, 37, 1284−1296

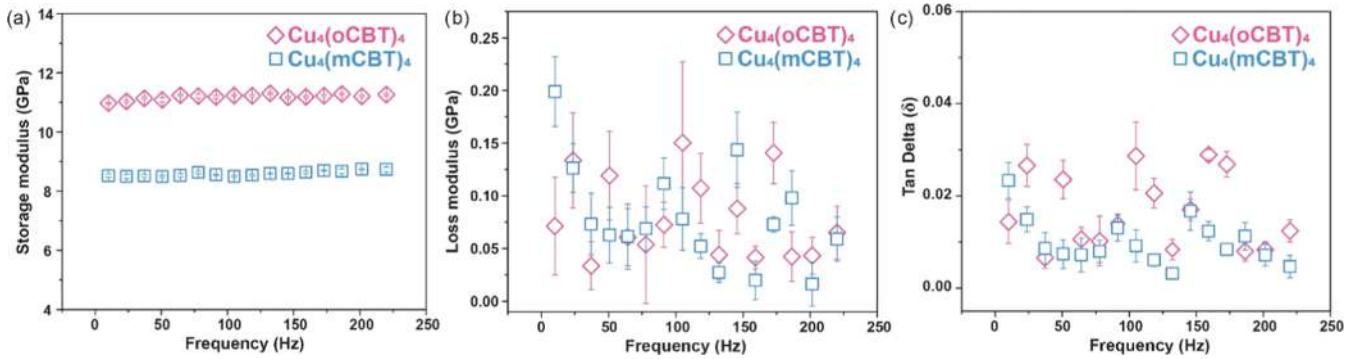


Figure 5. Frequency-dependent variations of (a) storage modulus, (b) loss modulus, and (c) tan delta (δ) observed through dynamic mechanical measurements of $Cu_4(oCBT)_4$ and $Cu_4(mCBT)_4$ crystals.

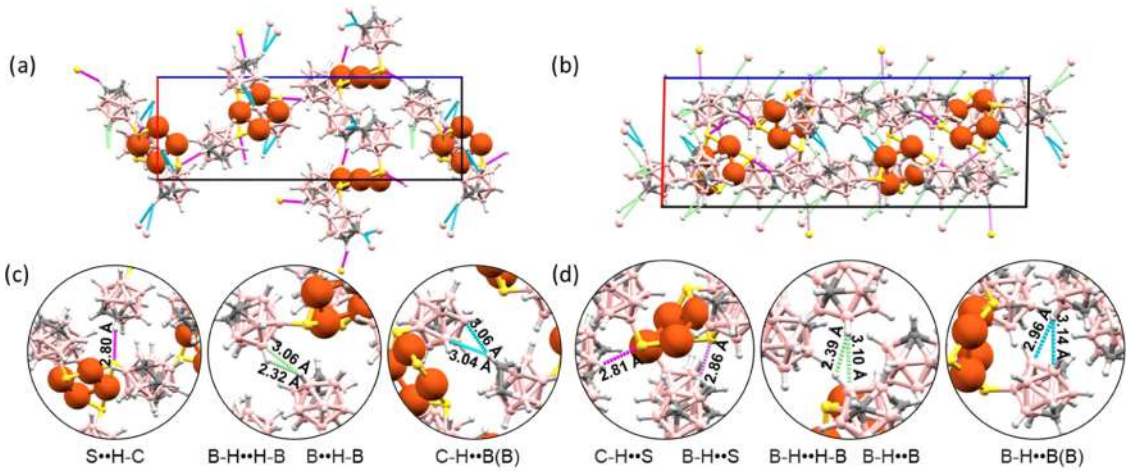


Figure 6. Unit cell supramolecular packing (as viewed along the *b*-axis) of (a) $Cu_4(oCBT)_4$ and (b) $Cu_4(mCBT)_4$ crystals along the *b*-axis. Different short contact intermolecular interactions of (c) $Cu_4(oCBT)_4$ and (d) $Cu_4(mCBT)_4$ clusters along with their interatomic distances. The colored dotted lines indicate intercluster interactions as follows: pink: S···H−C interaction, green: B−H···H−B and B···H, B interactions, blue: C−H···B(B) and B−H···B(B) interactions.

performed within a 20.000 μm scan, with height variations from 0 to 1029.2 nm. The profile across indentation 1 has lateral and vertical distances of 3.51379 and 23.0089 nm and roughness values of R_a = 90.8734 nm and R_q = 106.799 nm, respectively. These findings suggest that crystal **2** has a rougher surface and potentially more variable indentation response, indicating differences in surface resilience and mechanical properties between the two crystal samples.

Dynamic Mechanical Analysis (DMA) of Isomorphic Cu_4 Nanoclusters. From the results of the quasi-static nanoindentation experiments, such as creep and stress relaxation behaviors discussed in the previous sections, it can be inferred that the crystals possess time-dependent properties. These results prompted us to conduct dynamic mechanical analysis tests at the same length scale. The different viscoelastic properties like storage modulus (G'), loss modulus (G''), and tan δ are plotted as a function of frequency, as shown in Figure 5a−c, respectively. The storage modulus quantifies the energy stored within the system, while the loss modulus characterizes the energy dissipated or lost. tan δ (Damping or loss factor) represents the phase shift between the applied stress and the resulting displacement and is the ratio between the loss and storage moduli. Figure 5a shows that the storage modulus for both crystals has no apparent frequency dependency, as the storage modulus values remain almost constant at all of the frequencies measured and are consistent with the higher mean value of modulus obtained from quasi-static indentation. The loss modulus plot, Figure 5b, on the other hand, shows that the softer crystal **2** is more sensitive to frequency change than is **1**.

Similarly, the low or almost negligible values of tan δ, as shown in Figure 5c, confirm that the crystals of both **1** and **2** exhibit very low energy dissipation and minimal phase lag between the applied stress and resulting strain. In other words, the crystals are highly elastic. These crystals can be used for applications like crystal optics, precision measurement instruments and machinery, mechanical resonators, and nanomechanical instruments, where damping of vibrations is essential.[72,73]

Structural Features Leading to Observed Mechanical Response. In our study, we find that crystals of **1** are harder than those of **2**, even though **2** has a density (1.442 g/cm^3) higher than that of **1** (1.428 g/cm^3). So, the mechanical properties of the nanocluster crystals are governed by other factors like the arrangement of clusters in the crystal with respect to indentation direction, interactions between the nanoclusters in the crystal, the relaxation modes of the clusters under stress, the characteristics of the ligands protecting the metal nanoclusters, and so on.

We examined the intercluster interactions within cluster crystals to elucidate their mechanical properties. Unlike Sugi et al.'s findings, our crystals lacked $\pi\cdots\pi$ interactions.[47] Instead, the interactions in crystals **1** and **2** include S···H−C, B−H···

https://doi.org/10.1021/acs.chemmater.4c03265
Chem. Mater. 2025, 37, 1284−1296

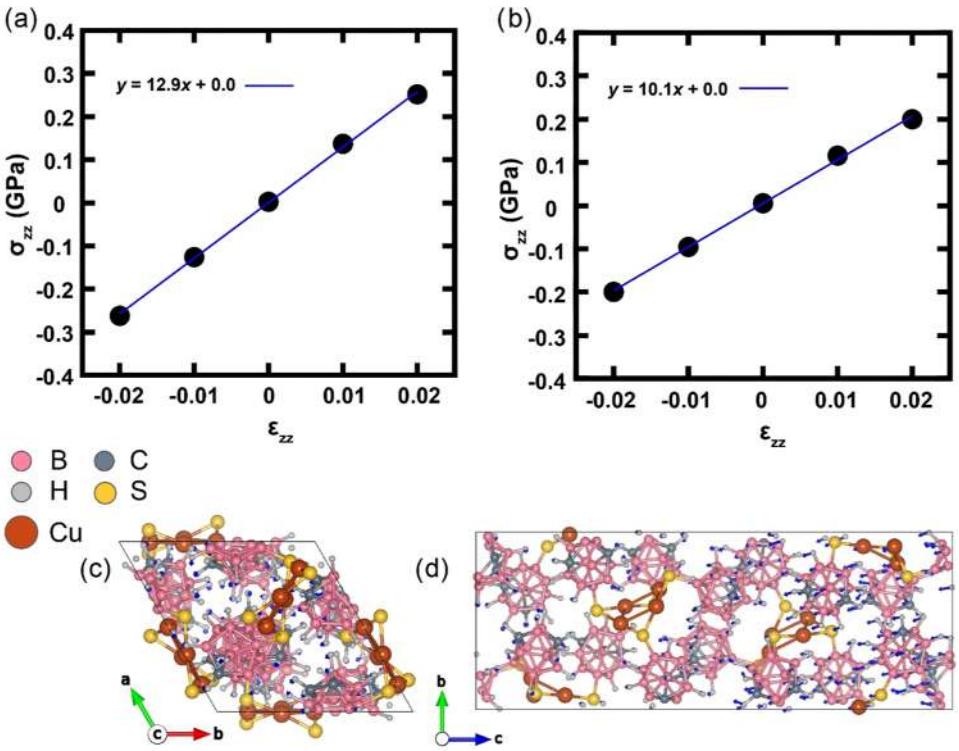


Figure 7. Stress vs strain curve is plotted for (a) $Cu_4(oCBT)_4$ and (b) $Cu_4(mCBT)_4$. Stress varies linearly with strain, and the slope of the curve gives the value of Young's modulus. Atomic rearrangement inside the lattice during structural optimization in (c) $Cu_4(oCBT)_4$ and (d) $Cu_4(mCBT)_4$. All displacements greater than 0.01 Å were incorporated and scaled up by a factor of 10 for better visualization.

H−B, C−H···B(B), and C−H···S, B−H···S, B−H···H−B, B−H···B, B−H···B(B), as shown in Figure 6a,b, respectively. These interactions contribute to the distinct mechanical responses of each crystal. The distances of each interaction are shown in the insets of Figure 6 as well as tabulated in Table S1 in the Supporting Information. These interactions are very weak interaction but still are responsible for the mechanical properties observed in both the crystals. In **1**, the interactions are along the slant planes of the crystal, which slides along smoothly when indentation is carried out at lower loading rates while providing friction as the loading rate increases. However, the interactions in **2** are along the crystal planes and are perpendicular to the indentation direction. These planes cannot slide upon each other and hence have lesser stiffness than **1**.

Further, DFT calculations were conducted to understand the response of the crystals to the applied stress. Specific details of the calculations are summarized in the Experimental Methods. Young's modulus (E_r) of **1** along $[hkl] = [00\bar{1}]$ and **2** along [100] were estimated using the stress−strain method. Initially, a set of four distorted configurations corresponding to strains of ±1 and ±2% along the *c*-axis (which lies along $\hat{Z}$) of **1** was generated. Clamping the structure along the strained direction, atomic positions, and the rest of the lattice parameters were allowed to relax. The stress σ_{zz} developed in the optimized structures was calculated, and its variation with strain ε_{zz} was used to estimate Young's modulus, E_{001}. This exercise was repeated for **2**, but with a strain applied along the *a*-axis (which lies along $\hat{x}$), and E_{100} was estimated from σ_{xx} and ε_{xx} (Figure 7a,b). The linear nature of the plots in Figure 7a,b, indicates elastic behavior of the material within the applied strain range. The slopes of the linear fits represent the material's elastic moduli, and our estimates of E_{001} and E_{100} are summarized in Table S3. It is clear that the E_{100} of **2** is lower than the E_{001} of **1**, despite **2** having a higher density, aligning with our experimental findings. However, the bare elastic moduli calculated from stresses in the unrelaxed strained structures exhibit the opposite trend, as expected from their relative densities (Table S3). This suggests that the atomic rearrangement in **2** occurs at a larger scale than in **1** during structural optimization.

We trace the movement of atoms during optimization of structures corresponding to 1% applied strain for both crystals (Figure 7c,d). In $Cu_4(oCBT)_4$, the H atoms attached to the CBT cage exhibit weak displacements toward the voids (Figure 7c). The square planar Cu_4 nanoclusters inside the crystal are arranged nearly perpendicular to the *ab* plane and lie along the direction of applied strain (Figure S21a). Examination of an isolated unit of $Cu_4(oCBT)_4$ reveals that during structural optimization, this arrangement causes two of the *o*CBTs attached to adjacent vertices of the Cu nanocluster to roll inward and two others to roll outward. This effectively leads to the motion shown in Figure S21b. It is found that the degree of internal rearrangement in $Cu_4(mCBT)_4$ is higher than that in $Cu_4(oCBT)_4$. Besides this, we observe the directional and collective translational motion of atoms in the *bc* plane of $Cu_4(mCBT)_4$ in some regions at different scales (Figure 7d). A cross section taken along the *a*-axis in the system shows that this is possible due to the nearly linear arrangement of *m*CBT attached to the Cu nanoclusters along the *a* direction (Figure S22), with gaps between them along both *c* and *b* directions, which allow for easy movement under strain. Our results explain the unexpected trend in Young's modulus observed in experiments and uncover the structural mechanisms of the mechanical response of these crystals. They suggest that these crystals are highly flexible,[74] somewhat akin to MOFs.

https://doi.org/10.1021/acs.chemmater.4c03265
Chem. Mater. 2025, 37, 1284−1296

Additional investigations of these systems are underway in our laboratory.

Our previous work on the mechanical characteristics of nanocluster crystals has been expanded upon in this article. Together, these investigations demonstrate the distinct mechanical properties of nanocluster crystals and emphasize their enormous potential for a wide range of applications. These discoveries could be used to investigate the effects of ligands, dopant atoms, and environmental variables, such as temperature, on the mechanical properties of other relevant nanocluster materials. We successfully conducted nanoindentation studies on a specific plane for both the crystals. Attempts to explore additional planes were unsuccessful.

CONCLUSIONS

In conclusion, this study has provided valuable insights into the mechanical behavior of isomorphic crystals composed of tetranuclear copper clusters protected by isomeric carboranethiol ligands as investigated through nanoindentation experiments. Despite their closely related molecular structures, Cu_4 nanoclusters protected by *ortho*-carboranethiol exhibit superior rigidity and hardness compared to their *meta*-carboranethiol isomeric analogue. Notably, multiple "pop-in" events, particularly observed for the $Cu_4(m\text{CBT})_4$ cluster, suggest the translocation of lattice planes within the crystals upon loading. Additionally, dynamic mechanical studies have shed light on the storage moduli of these crystals. DFT calculations provide insights into the atomic dynamics under external stresses, elucidating the relaxation pathways governing the enhanced hardness observed within the low-density isomorph. Our findings indicate the critical role played by the orientation of lattice planes relative to the direction of the applied load and the interactions among clusters in determining the observed mechanical properties. These insights emphasize the precision in atomic arrangement within this class of copper clusters, characterized by exceptional stability, well-defined structures, and unprecedented control over their properties. These materials have the potential to significantly contribute to the forefront of modern materials science and nanotechnology, thus presenting a promising avenue for a broad range of applications.

ASSOCIATED CONTENT

Supporting Information

The Supporting Information is available free of charge at https://pubs.acs.org/doi/10.1021/acs.chemmater.4c03265.

Intercluster interactions, comparison of lattice parameters, computational calculations of E_r, UV−vis spectroscopy, PL spectroscopy, XPS, TGA, ATR-IR, face indexing, arrangement of clusters in crystal, load−displacement plots, statistical analysis, and SPM images (PDF)

AUTHOR INFORMATION

Corresponding Authors

Tomas Base − *Department of Syntheses, Institute of Inorganic Chemistry, The Czech Academy of Sciences 1001, Husinec-Rez 25068, Czech Republic;* orcid.org/0000-0003-2533-8705; Email: tbase@iic.acs.cz

Umesh V. Waghmare − *Theoretical Sciences Unit and School of Advanced Materials (SAMat), Jawaharlal Nehru Centre for Advanced Scientific Research, Bengaluru 560064 Karnataka, India;* orcid.org/0000-0002-9378-155X; Email: waghmare@jncasr.ac.in

Pijush Ghosh − *Department of Applied Mechanics and Biomedical Engg., Indian Institute of Technology Madras, Chennai 600036, India;* orcid.org/0000-0002-6077-6498; Email: pijush@iitm.ac.in

Thalappil Pradeep − *Department of Chemistry, DST Unit of Nanoscience (DST UNS) and Thematic Unit of Excellence (TUE), Indian Institute of Technology Madras, Chennai 600036, India;* orcid.org/0000-0003-3174-534X; Email: pradeep@iitm.ac.in

Authors

Amoghavarsha Ramachandra Kini − *Department of Chemistry, DST Unit of Nanoscience (DST UNS) and Thematic Unit of Excellence (TUE), Indian Institute of Technology Madras, Chennai 600036, India;* orcid.org/0009-0003-6863-7729

Sanghamitra Debta − *Department of Applied Mechanics and Biomedical Engg., Indian Institute of Technology Madras, Chennai 600036, India;* orcid.org/0009-0003-6675-6783

Arijit Jana − *Department of Chemistry, DST Unit of Nanoscience (DST UNS) and Thematic Unit of Excellence (TUE), Indian Institute of Technology Madras, Chennai 600036, India*

C. Aparna − *Theoretical Sciences Unit, Jawaharlal Nehru Centre for Advanced Scientific Research, Bengaluru 560064 Karnataka, India*

Vivek Yadav − *Department of Chemistry, DST Unit of Nanoscience (DST UNS) and Thematic Unit of Excellence (TUE), Indian Institute of Technology Madras, Chennai 600036, India*

Nataliia Kusiak − *Department of Syntheses, Institute of Inorganic Chemistry, The Czech Academy of Sciences 1001, Husinec-Rez 25068, Czech Republic*

Complete contact information is available at: https://pubs.acs.org/10.1021/acs.chemmater.4c03265

Author Contributions

#A.R.K., S.D., and A.J. have contributed equally to this work. A.J., P.G., and T.P. suggested the idea. A.R.K., A.J., and V.Y. synthesized and characterized the materials. S.D. performed nanomechanical studies, and S.D. and A.R.K. performed the data analysis. N.K. and T.B. are responsible for the ligands used in this work. C.A. and U.V.W. carried out the computational studies. A.R.K. wrote the first draft of the manuscript with inputs from A.J. and S.D., and all of the authors finalized the manuscript. T.P., U.V.W., and P.G. conceptualized the project and finalized the manuscript.

Notes

The authors declare no competing financial interest.

ACKNOWLEDGMENTS

The authors acknowledge the support of the Science and Engineering Research Board (SERB), Department of Science and Technology (DST), and Government of India. T.P. acknowledges funding from the Centre of Excellence on Molecular Materials and Functions under the Institution of Eminence scheme of IIT Madras. T.P. thanks the Science and Engineering Research Board (SERB), India, for funding through the SPR/2021/000439 research grant. The authors

thank the Sophisticated Analytical Instruments Facility, IIT Madras, and Sudhadevi Antharjanam for the SC-XRD measurements. A.R.K. thanks the Council of Scientific and Industrial Research (CSIR) for his research fellowship. A.J. thanks IITM for his research fellowship. U.V.W. and T.P. acknowledge funding through their JC Bose Fellowships. C.A. acknowledges support from IKST, Bengaluru. V.Y. thanks the Ministry of Education for his Prime Minister's Research Fellowship.

DEDICATION

This article is dedicated to the Chemical Research Society of India in celebration of its 25th anniversary.

REFERENCES

(1) Jin, R.; Zeng, C.; Zhou, M.; Chen, Y. Atomically Precise Colloidal Metal Nanoclusters and Nanoparticles: Fundamentals and Opportunities. *Chem. Rev.* **2016**, *116* (18), 10346−10413.
(2) Chakraborty, I.; Pradeep, T. Atomically Precise Clusters of Noble Metals: Emerging Link between Atoms and Nanoparticles. *Chem. Rev.* **2017**, *117* (12), 8208−8271.
(3) Kang, X.; Li, Y.; Zhu, M.; Jin, R. Atomically Precise Alloy Nanoclusters: Syntheses, Structures, and Properties. *Chem. Soc. Rev.* **2020**, *49* (17), 6443−6514.
(4) Jana, A.; Kini, A. R.; Pradeep, T. Atomically Precise Clusters: Chemical Evolution of Molecular Matter at the Nanoscale. *AsiaChem Mag.* **2023**, *3* (1), 56−65, DOI: 10.51167/acm00040.
(5) Reato, M.; Dainese, T.; Antonello, S.; Maran, F. Electron Transfer in Films of Atomically Precise Gold Nanoclusters. *Chem. Mater.* **2021**, *33* (11), 4177−4187.
(6) Feng, A.; Hou, S.; Yan, J.; Wu, Q.; Tang, Y.; Yang, Y.; Shi, J.; Xiao, Z.-Y.; Lambert, C. J.; Zheng, N.; Hong, W. Conductance Growth of Single-Cluster Junctions with Increasing Sizes. *J. Am. Chem. Soc.* **2022**, *144* (34), 15680−15688.
(7) Higaki, T.; Russell, J. C.; Paley, D. W.; Roy, X.; Jin, R. Electron Transport through Supercrystals of Atomically Precise Gold Nanoclusters: A Thermal Bi-Stability Effect. *Chem. Sci.* **2023**, *14*, 13191−13197.
(8) Ji, S.; Peng, D.; Sun, F.; You, Q.; Wang, R.; Yan, N.; Zhou, Y.; Wang, W.; Tang, Q.; Xia, N.; Zeng, Z.; Wu, Z. Coexistent, Competing Tunnelling, and Hopping Charge Transport in Compressed Metal Nanocluster Crystals. *J. Am. Chem. Soc.* **2023**, *145* (44), 24012−24020.
(9) Jin, R. Atomically Precise Metal Nanoclusters: Stable Sizes and Optical Properties. *Nanoscale* **2015**, *7* (5), 1549−1565.
(10) Aikens, C. M. Electronic and Geometric Structure, Optical Properties, and Excited State Behavior in Atomically Precise Thiolate-Stabilized Noble Metal Nanoclusters. *Acc. Chem. Res.* **2018**, *51* (12), 3065−3073.
(11) De Nardi, M.; Antonello, S.; Jiang, D.; Pan, F.; Rissanen, K.; Ruzzi, M.; Venzo, A.; Zoleo, A.; Maran, F. Gold Nanowired: A Linear $(Au_{25})_n$ Polymer from Au_{25} Molecular Clusters. *ACS Nano* **2014**, *8* (8), 8505−8512.
(12) Agrachev, M.; Antonello, S.; Dainese, T.; Ruzzi, M.; Zoleo, A.; Aprà, E.; Govind, N.; Fortunelli, A.; Sementa, L.; Maran, F. Magnetic Ordering in Gold Nanoclusters. *ACS Omega* **2017**, *2* (6), 2607−2617.
(13) Tian, S.; Liao, L.; Yuan, J.; Yao, C.; Chen, J.; Yang, J.; Wu, Z. Structures and Magnetism of Mono-Palladium and Mono-Platinum Doped $Au_{25}(PET)_{18}$ Nanoclusters. *Chem. Commun.* **2016**, *52* (64), 9873−9876.
(14) Du, Y.; Sheng, H.; Astruc, D.; Zhu, M. Atomically Precise Noble Metal Nanoclusters as Efficient Catalysts: A Bridge between Structure and Properties. *Chem. Rev.* **2020**, *120* (2), 526−622.
(15) Jin, R.; Li, G.; Sharma, S.; Li, Y.; Du, X. Toward Active-Site Tailoring in Heterogeneous Catalysis by Atomically Precise Metal Nanoclusters with Crystallographic Structures. *Chem. Rev.* **2021**, *121* (2), 567−648.
(16) Du, X.; Jin, R. Atomically Precise Metal Nanoclusters for Catalysis. *ACS Nano* **2019**, *13* (7), 7383−7387.
(17) Jana, A.; Spoorthi, B. K.; Nair, A. S.; Nagar, A.; Pathak, B.; Base, T.; Pradeep, T. A Luminescent Cu_4 Cluster Film Grown by Electrospray Deposition: A Nitroaromatic Vapour Sensor. *Nanoscale* **2023**, *15* (18), 8141−8147.
(18) Yuan, P.; Zhang, R.; Selenius, E.; Ruan, P.; Yao, Y.; Zhou, Y.; Malola, S.; Häkkinen, H.; Teo, B. K.; Cao, Y.; Zheng, N. Solvent-Mediated Assembly of Atom-Precise Gold−Silver Nanoclusters to Semiconducting One-Dimensional Materials. *Nat. Commun.* **2020**, *11* (1), No. 2229.
(19) Khatun, E.; Pradeep, T. New Routes for Multicomponent Atomically Precise Metal Nanoclusters. *ACS Omega* **2021**, *6* (1), 1−16.
(20) Kini, A. R.; Pradeep, T. Chapter 8 - Synthesis of Atomically Precise Clusters. In *Atomically Precise Metal Nanoclusters*; Pradeep, T., Ed.; Elsevier, 2023; pp 157−176.
(21) Yao, Q.; Cao, Y.; Chen, T.; Xie, J. Total Synthesis of Thiolate-Protected Noble Metal Nanoclusters. In *Atomically Precise Nanochemistry*; John Wiley & Sons, Ltd, 2023; pp 57−85.
(22) Bootharaju, M. S.; Dey, R.; Gevers, L. E.; Hedhili, M. N.; Basset, J.-M.; Bakr, O. M. A New Class of Atomically Precise, Hydride-Rich Silver Nanoclusters Co-Protected by Phosphines. *J. Am. Chem. Soc.* **2016**, *138* (42), 13770−13773.
(23) Yuan, S.-F.; Li, J.-J.; Guan, Z.-J.; Lei, Z.; Wang, Q.-M. Ultrastable Hydrido Gold Nanoclusters with the Protection of Phosphines. *Chem. Commun.* **2020**, *56* (51), 7037−7040.
(24) Jin, R.; Zhao, S.; Xing, Y.; Jin, R. All-Thiolate-Protected Silver and Silver-Rich Alloy Nanoclusters with Atomic Precision: Stable Sizes, Structural Characterization and Optical Properties. *CrystEngComm* **2016**, *18* (22), 3996−4005.
(25) Joshi, C. P.; Bootharaju, M. S.; Alhilaly, M. J.; Bakr, O. M. $[Ag_{25}(SR)_{18}]^-$: The "Golden" Silver Nanoparticle. *J. Am. Chem. Soc.* **2015**, *137* (36), 11578−11581.
(26) Guan, Z.-J.; Hu, F.; Li, J.-J.; Liu, Z.-R.; Wang, Q.-M. Homoleptic Alkynyl-Protected Gold Nanoclusters with Unusual Compositions and Structures. *Nanoscale* **2020**, *12* (25), 13346−13350.
(27) Ma, X.; Xiong, L.; Qin, L.; Tang, Y.; Ma, G.; Pei, Y.; Tang, Z. A Homoleptic Alkynyl-Protected $[Ag_9Cu_6(^tBuC{\equiv}C)_{12}]^+$ Superatom with Free Electrons: Synthesis, Structure Analysis, and Different Properties Compared with the Au_7Ag_8 Cluster in the M_{15}^+ Series. *Chem. Sci.* **2021**, *12* (38), 12819−12826.
(28) Meng, X.; Zare, I.; Yan, X.; Fan, K. Protein-Protected Metal Nanoclusters: An Emerging Ultra-Small Nanozyme. *Wiley Interdiscip. Rev.:Nanomed. Nanobiotechnol.* **2020**, *12* (3), No. e1602.
(29) Chen, X.; Ren, X.; Gao, X. Peptide or Protein-Protected Metal Nanoclusters for Therapeutic Application. *Chin. J. Chem.* **2022**, *40* (2), 267−274.
(30) Wang, Q.-Y.; Wang, J.; Wang, S.; Wang, Z.-Y.; Cao, M.; He, C.-L.; Yang, J.-Q.; Zang, S.-Q.; Mak, T. C. W. *O* -Carborane-Based and Atomically Precise Metal Clusters as Hypergolic Materials. *J. Am. Chem. Soc.* **2020**, *142* (28), 12010−12014.
(31) Jana, A.; Unnikrishnan, P. M.; Poonia, A. K.; Roy, J.; Jash, M.; Paramasivam, G.; Machacek, J.; Adarsh, K. N. V. D.; Base, T.; Pradeep, T. Carboranethiol-Protected Propeller-Shaped Photoresponsive Silver Nanomolecule. *Inorg. Chem.* **2022**, *61* (23), 8593−8603.
(32) Jana, A.; Jash, M.; Poonia, A. K.; Paramasivam, G.; Islam, M. R.; Chakraborty, P.; Antharjanam, S.; Machacek, J.; Ghosh, S.; Adarsh, K. N. V. D.; Base, T.; Pradeep, T. Light-Activated Intercluster Conversion of an Atomically Precise Silver Nanocluster. *ACS Nano* **2021**, *15*, 15781−15793.
(33) Jana, A.; Jash, M.; Dar, W. A.; Roy, J.; Chakraborty, P.; Paramasivam, G.; Lebedkin, S.; Kirakci, K.; Manna, S.; Antharjanam, S.; Machacek, J.; Kucerakova, M.; Ghosh, S.; Lang, K.; Kappes, M. M.; Base, T.; Pradeep, T. Carborane-Thiol Protected Copper Nanoclusters: Stimuli-Responsive Materials with Tunable Phosphorescence. *Chem. Sci.* **2023**, *14* (6), 1613−1626.

(34) Reddy, C. M.; Rama Krishna, G.; Ghosh, S. Mechanical Properties of Molecular Crystals—Applications to Crystal Engineering. *CrystEngComm* **2010**, *12* (8), 2296.
(35) Varughese, S.; Kiran, M. S. R. N.; Ramamurty, U.; Desiraju, G. R. Nanoindentation in Crystal Engineering: Quantifying Mechanical Properties of Molecular Crystals. *Angew. Chem., Int. Ed.* **2013**, *52* (10), 2701−2712.
(36) Ramamurty, U.; Jang, J. Nanoindentation for Probing the Mechanical Behavior of Molecular Crystals−a Review of the Technique and How to Use It. *CrystEngComm* **2014**, *16* (1), 12−23.
(37) Saha, S.; Mishra, M. K.; Reddy, C. M.; Desiraju, G. R. From Molecules to Interactions to Crystal Engineering: Mechanical Properties of Organic Solids. *Acc. Chem. Res.* **2018**, *51* (11), 2957−2967.
(38) Gabriele, B. P. A.; Williams, C. J.; Lauer, M. E.; Derby, B.; Cruz-Cabeza, A. J. Isomechanical Groups in Molecular Crystals and Role of Aromatic Interactions. *Cryst. Growth Des.* **2020**, *20* (11), 7516−7525.
(39) Gabriele, B. P. A.; Williams, C. J.; Lauer, M. E.; Derby, B.; Cruz-Cabeza, A. J. Nanoindentation of Molecular Crystals: Lessons Learned from Aspirin. *Cryst. Growth Des.* **2020**, *20* (9), 5956−5966.
(40) Gabriele, B. P. A.; Williams, C. J.; Lauer, M. E.; Derby, B.; Cruz-Cabeza, A. J. Impact of Polymorphism on Mechanical Properties of Molecular Crystals: A Study of *p* -Amino and *p* -Nitro Benzoic Acid with Nanoindentation. *CrystEngComm* **2021**, *23* (10), 2027−2033.
(41) Mishra, M. K.; Varughese, S.; Ramamurty, U.; Desiraju, G. R. Odd−Even Effect in the Elastic Modulii of α,ω-Alkanedicarboxylic Acids. *J. Am. Chem. Soc.* **2013**, *135* (22), 8121−8124.
(42) Spencer, E. C.; Kiran, M. S. R. N.; Li, W.; Ramamurty, U.; Ross, N. L.; Cheetham, A. K. Pressure-Induced Bond Rearrangement and Reversible Phase Transformation in a Metal−Organic Framework. *Angew. Chem., Int. Ed.* **2014**, *53* (22), 5583−5586.
(43) Tan, J. C.; Bennett, T. D.; Cheetham, A. K. Chemical Structure, Network Topology, and Porosity Effects on the Mechanical Properties of Zeolitic Imidazolate Frameworks. *Proc. Natl. Acad. Sci. U.S.A.* **2010**, *107* (22), 9938−9943.
(44) Kanoo, P.; Mishra, M. K.; Hazra, A. Probing Time Dependent Phase Transformation in a Flexible Metal−Organic Framework with Nanoindentation. *Dalton Trans.* **2021**, *50* (33), 11380−11384.
(45) Ma, L.; Li, W.; Yang, K.; Bi, J.; Feng, J.; Zhang, J.; Yan, Z.; Zhou, X.; Liu, C.; Ji, Y.; Huang, J. C.; Han, X. *A* - or *X* -Site Mixture on Mechanical Properties of *A* Pb X_3 Perovskite Single Crystals. *APL Mater.* **2021**, *9* (4), No. 041112.
(46) Rosenhek-Goldian, I.; Cahen, D.; Cohen, S. R. Measuring and Understanding the Nanomechanical Properties of Halide Perovskites and Their Correlation to Structure—A Perspective. *J. Vac. Sci. Technol. B* **2023**, *41* (5), No. 058501.
(47) Sugi, K. S.; Bandyopadhyay, P.; Bodiuzzaman, M.; Nag, A.; Hridya, M.; Dar, W. A.; Ghosh, P.; Pradeep, T. Manifestation of Structural Differences of Atomically Precise Cluster-Assembled Solids in Their Mechanical Properties. *Chem. Mater.* **2020**, *32* (18), 7973−7984.
(48) Sugi, K. S.; Mallikarjunachari, G.; Som, A.; Ghosh, P.; Pradeep, T. Probing the Mechanical Response of Luminescent Dithiol-Protected Ag29(BDT)12(TPP)4 Cluster Crystals. *ChemNanoMat* **2018**, *4* (4), 401−408.
(49) Plešek, J.; Janoušek, Z.; Heřmánek, S. Chemistry of 9-Mercapto-1,7-Dicarba-*Closo*-Dodecaborane. *Collect. Czech. Chem. Commun.* **1978**, *43* (5), 1332−1338.
(50) Plešek, J.; Heřmánek, S. Syntheses and Properties of Substituted Icosahedral Carborane Thiols. *Collect. Czech. Chem. Commun.* **1981**, *46* (3), 687−692.
(51) Li, J.; Ma, H. Z.; Reid, G. E.; Edwards, A. J.; Hong, Y.; White, J. M.; Mulder, R. J.; O'Hair, R. A. J. Synthesis and X-Ray Crystallographic Characterisation of Frustum-Shaped Ligated [Cu18H16(DPPE)6]2+ and [Cu16H14(DPPA)6]2+ Nanoclusters and Studies on Their H2 Evolution Reactions. *Chem. − Eur. J.* **2018**, *24* (9), 2070−2074.
(52) Briscoe, B. J.; Fiori, L.; Pelillo, E. Nano-Indentation of Polymeric Surfaces. *J. Phys. D: Appl. Phys.* **1998**, *31* (19), 2395.
(53) Klapperich, C.; Komvopoulos, K.; Pruitt, L. Nanomechanical Properties of Polymers Determined From Nanoindentation Experiments. *J. Tribol.* **2001**, *123* (3), 624−631.
(54) Kresse, G.; Hafner, J. *Ab Initio* Molecular Dynamics for Liquid Metals. *Phys. Rev. B* **1993**, *47* (1), 558−561.
(55) Kresse, G.; Hafner, J. *Ab Initio* Molecular-Dynamics Simulation of the Liquid-Metal−Amorphous-Semiconductor Transition in Germanium. *Phys. Rev. B* **1994**, *49* (20), 14251−14269.
(56) Kresse, G.; Furthmüller, J. Efficient Iterative Schemes for *Ab Initio* Total-Energy Calculations Using a Plane-Wave Basis Set. *Phys. Rev. B* **1996**, *54* (16), 11169−11186.
(57) Kresse, G.; Furthmüller, J. Efficiency of Ab-Initio Total Energy Calculations for Metals and Semiconductors Using a Plane-Wave Basis Set. *Comput. Mater. Sci.* **1996**, *6* (1), 15−50.
(58) Blöchl, P. E. Projector Augmented-Wave Method. *Phys. Rev. B* **1994**, *50* (24), 17953−17979.
(59) Kresse, G.; Joubert, D. From Ultrasoft Pseudopotentials to the Projector Augmented-Wave Method. *Phys. Rev. B* **1999**, *59* (3), 1758−1775.
(60) Perdew, J. P.; Burke, K.; Ernzerhof, M. Generalized Gradient Approximation Made Simple. *Phys. Rev. Lett.* **1996**, *77* (18), 3865−3868.
(61) Grimme, S.; Antony, J.; Ehrlich, S.; Krieg, H. A Consistent and Accurate Ab Initio Parametrization of Density Functional Dispersion Correction (DFT-D) for the 94 Elements H-Pu. *J. Chem. Phys.* **2010**, *132* (15), No. 154104.
(62) Biesinger, M. C. Advanced Analysis of Copper X-ray Photoelectron Spectra. *Surface Interface Anal.* **2017**, *49* (13), 1325−1334.
(63) Mishra, M. K.; Ramamurty, U.; Desiraju, G. R. Solid Solution Hardening of Molecular Crystals: Tautomeric Polymorphs of Omeprazole. *J. Am. Chem. Soc.* **2015**, *137* (5), 1794−1797.
(64) Mishra, M. K.; Mishra, K.; Narayan, A.; Reddy, C. M.; Vangala, V. R. Structural Basis for Mechanical Anisotropy in Polymorphs of a Caffeine−Glutaric Acid Cocrystal. *Cryst. Growth Des.* **2020**, *20* (10), 6306−6315.
(65) Duan, X.; Yuan, H.; Tang, W.; He, J.; Guan, X. A Phenomenological Primary−Secondary−Tertiary Creep Model for Polymer-Bonded Composite Materials. *Polymers* **2021**, *13* (14), 2353.
(66) Wu, D.; Huang, X.; Duan, X.; Jiang, Y.; Shi, D.; Chang, L.; Zhang, L.; He, J. Static and Time-Dependent Plasticity of Monolithic Metal−Organic Frameworks. *J. Phys. Chem. C* **2023**, *127* (9), 4749−4758.
(67) Lin, C.-Y.; Chen, Y.-C.; Lin, C.-H.; Chang, K.-V. Constitutive Equations for Analyzing Stress Relaxation and Creep of Viscoelastic Materials Based on Standard Linear Solid Model Derived with Finite Loading Rate. *Polymers* **2022**, *14* (10), 2124.
(68) Sahu, R.; Patra, K.; Szpunar, J. Experimental Study and Numerical Modelling of Creep and Stress Relaxation of Dielectric Elastomers. *Strain* **2015**, *51* (1), 43−54.
(69) Yamaguchi, K.; Thomas, A. G.; Busfield, J. J. C. Stress Relaxation, Creep and Set Recovery of Elastomers. *Int. J. Nonlinear Mech.* **2015**, *68*, 66−70.
(70) Yu, K.; Jiang, Y.; Wright, C.; Hartland, G. V. Energy Dissipation for Nanometer Sized Acoustic Oscillators. *J. Phys. Chem. C* **2022**, *126* (8), 3811−3819.
(71) Das, S.; Mondal, A.; Reddy, C. M. Harnessing Molecular Rotations in Plastic Crystals: A Holistic View for Crystal Engineering of Adaptive Soft Materials. *Chem. Soc. Rev.* **2020**, *49* (24), 8878−8896.
(72) Wang, W.; Zhao, D.; Yang, J.; Nishi, T.; Ito, K.; Zhao, X.; Zhang, L. Novel Slide-Ring Material/Natural Rubber Composites with High Damping Property. *Sci. Rep.* **2016**, *6* (1), No. 22810.
(73) Pelton, M.; Sader, J. E.; Burgin, J.; Liu, M.; Guyot-Sionnest, P.; Gosztola, D. Damping of Acoustic Vibrations in Gold Nanoparticles. *Nat. Nanotechnol.* **2009**, *4* (8), 492−495.

(74) Bhogra, M.; Goodwin, A. L.; Cheetham, A. K.; Waghmare, U. V. Quantifying the Intrinsic Mechanical Flexibility of Crystalline Materials. *Phys. Rev. B* **2023**, *108* (21), No. 214106.



https://doi.org/10.1021/acs.chemmater.4c03265
Chem. Mater. 2025, 37, 1284−1296

Supporting Information

Nanomechanical Investigations of Crystals of Copper Nanocluster Isomorphs: Enhanced Hardness of the Low-Density Analogue

Amoghavarsha Ramachandra Kini,[a$] Sanghamitra Debta,[b$] Arijit Jana,[a$] C. Aparna,[c] Vivek Yadav,[a] Nataliia Kusiak,[d] Tomas Base,[d] Umesh V. Waghmare,*[e] Pijush Ghosh,*[b] and Thalappil Pradeep*[a]*

[a] *Department of Chemistry, DST Unit of Nanoscience (DST UNS) and Thematic Unit of Excellence (TUE), Indian Institute of Technology Madras, Chennai 600036, India. E-mail: pradeep@iitm.ac.in*

[b] *Department of Applied Mechanics & Biomedical Engg., Indian Institute of Technology Madras, Chennai 600036, India. E-mail: pijush@iitm.ac.in*

[c] *Theoretical Sciences Unit, Jawaharlal Nehru Centre for Advanced Scientific Research, Bengaluru, Karnataka 560064, India. E-mail: waghmare@jncasr.ac.in*

[d] *Department of Synthesis, Institute of Inorganic Chemistry, The Czech Academy of Science 1001, Husinec – Rez, 25068, Czech Republic. E-mail: tbase@iic.acs.cz*

[e] *Theoretical Sciences Unit and School of Advanced Materials (SAMat), Jawaharlal Nehru Centre for Advanced Scientific Research, Bengaluru, Karnataka 560064, India. E-mail: waghmare@jncasr.ac.in*

[$] *These authors contributed equally to this work.*

Table of contents:

Items	Contents	Page No
Table S1	Intercluster interactions present in the crystals of $Cu_4(oCBT)_4$ and $Cu_4(mCBT)_4$ with their distances.	4
Table S2	A comparison of lattice parameters and density obtained from DFT calculations and experiments.	4
Table S3	Estimates of effective and bare Young's moduli of $Cu_4(oCBT)_4$ and $Cu_4(mCBT)_4$, compared with experiments.	5

Figure S1	UV-visible absorption spectra of $Cu_4(oCBT)_4$ and $Cu_4(mCBT)_4$	5
Figure S2	Photoluminescence excitation and emission spectra of $Cu_4(oCBT)_4$ and $Cu_4(mCBT)_4$ crystals	6
Figure S3	XPS spectrum of $Cu_4(oCBT)_4$ nanocluster showing the chemical purity of the sample.	7
Figure S4	XPS spectrum of $Cu_4(mCBT)_4$ nanocluster showing the chemical purity of the sample.	8
Figure S5	Thermogravimetric analysis of $Cu_4(mCBT)_4$ crystals showing the thermal stability of the nanocluster.	9
Figure S6	ATR- IR spectra of heat treated $Cu_4(oCBT)_4$ crystals showing the chemical stability of the samples up to 150°C.	10
Figure S7	ATR- IR spectra of heat treated $Cu_4(mCBT)_4$ crystals showing the chemical stability of the samples up to 150°C.	11
Figure S8	Face indexing of hexagonal $Cu_4(oCBT)_4$ single crystal from two different orientations.	12
Figure S9	Face indexing of hexagonal $Cu_4(mCBT)_4$ single crystal from two different orientations.	12
Figure S10	Arrangement of $Cu_4(oCBT)_4$ clusters in the crystal.	13
Figure S11	Arrangement of $Cu_4(mCBT)_4$ clusters in the crystal.	14
Figure S12	Load-controlled load-displacement curves at a load of 500 µN at different load functions.	15
Figure S13	Load-controlled load-displacement curves at loads of 1000 µN and 5000 µN at different load functions.	15
Figure S14	Displacement-controlled load-displacement curves at displacements of 100 and 500 nm.	16
Figure S15	. Load-displacement curves of all the indentation measurements for $Cu_4(oCBT)_4$ and $Cu_4(mCBT)_4$ at different loads.	16
Figure S16	Statistical analysis of all the indentation data collected for $Cu_4(oCBT)_4$ nanocluster crystal.	17
Figure S17	Statistical analysis of all the indentation data collected for $Cu_4(mCBT)_4$ nanocluster crystal.	17

Figure S18	Load-displacement curves representing indentation induced hardness.	18
Figure S19	SPM images, surface roughness and height profile of $Cu_4(oCBT)_4$ nanocluster crystal surface after nanoindentation.	19
Figure S20	SPM images, surface roughness and height profile of $Cu_4(mCBT)_4$ nanocluster crystal surface after nanoindentation.	20
Figure S21	Arrangement of Cu_4 nanoclusters and CBTs in the ab plane of $Cu_4(oCBT)_4$.	21
Figure S22	Arrangement of Cu_4 nanoclusters and CBTs in the ab plane of $Cu_4(mCBT)_4$.	21

Table S1. Intercluster interactions present in the crystals of $Cu_4(oCBT)_4$ and $Cu_4(mCBT)_4$ with their distances.

$Cu_4(oCBT)_4$		$Cu_4(mCBT)_4$	
Interactions	**Distance**	**Interactions**	**Distance**
S••H-C	2.80 Å	C-H••S	2.81 Å
B-H••H-B	2.32 Å	B-H••S	2.86 Å
B••H-B	3.06 Å	B-H••H-B	2.39 Å
C-H••B(B)	3.04 Å (3.06 Å)	B-H••B	3.10 Å
		B-H••B(B)	2.96 Å (3.14) Å

Table S2. A comparison of lattice parameters and density obtained from DFT calculations and experiments.

Lattice parameters	$Cu_4(oCBT)_4$			$Cu_4(mCBT)_4$		
	DFT value	**Experimental**	**Deviation (%)**	**DFT value**	**Experimental**	**Deviation (%)**
a (Å)	11.23	11.43	-1.75	11.29	11.40	-0.96
b (Å)	11.23	11.43	-1.75	11.61	11.95	-2.85
c (Å)	28.73	29.44	-2.41	31.15	32.31	-3.59
α	90°	90°	0	90°	90°	0
β	90°	90°	0	89.61°	91.20°	-1.74
γ	120°	120°	0	90°	90°	0
Density (g/cm^3)	1.52	1.428	6.44	1.55	1.442	7.49

Table S3. Estimates of effective and bare Young's moduli of $Cu_4(oCBT)_4$ and $Cu_4(mCBT)_4$, compared with experiments.

Parameters	$Cu_4(oCBT)_4$	$Cu_4(mCBT)_4$
E_{bare}	232 GPa	234 GPa
$E_{elastic}$	12.9 GPa	10.1 GPa
$E_{experimental}$	9.79 GPa	8.54 GPa
Density (DFT)	1.52 g/cm^3	1.55 g/cm^3

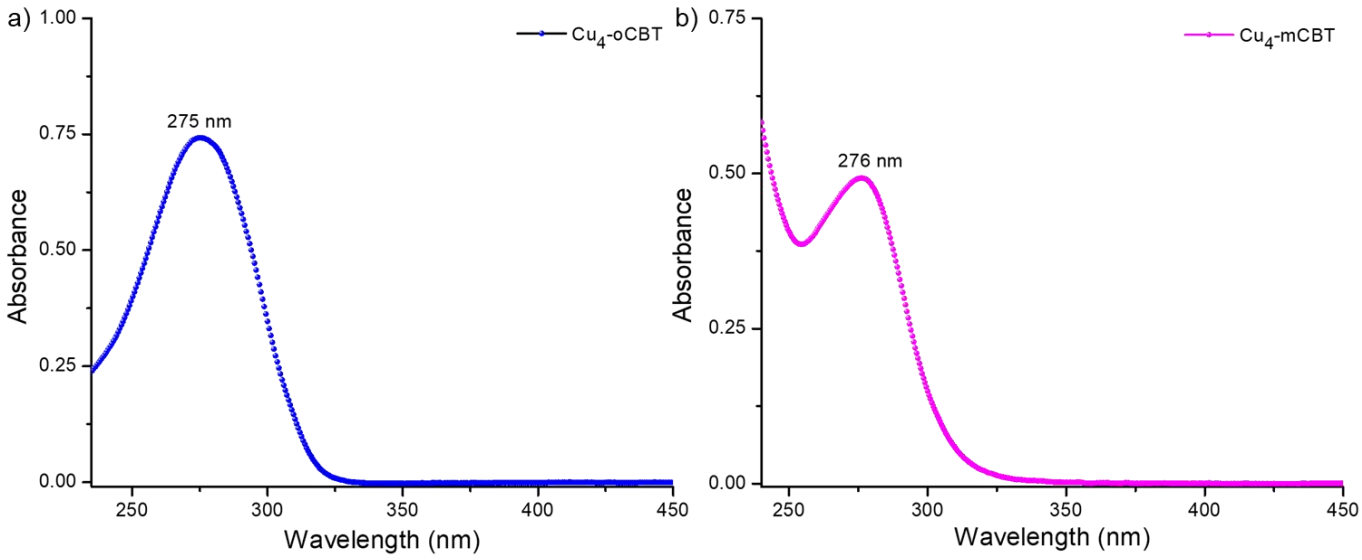


Figure S1. UV-visible absorption spectra of $Cu_4(oCBT)_4$ and $Cu_4(mCBT)_4$ in acetonitrile upon dissolving a few crystals.

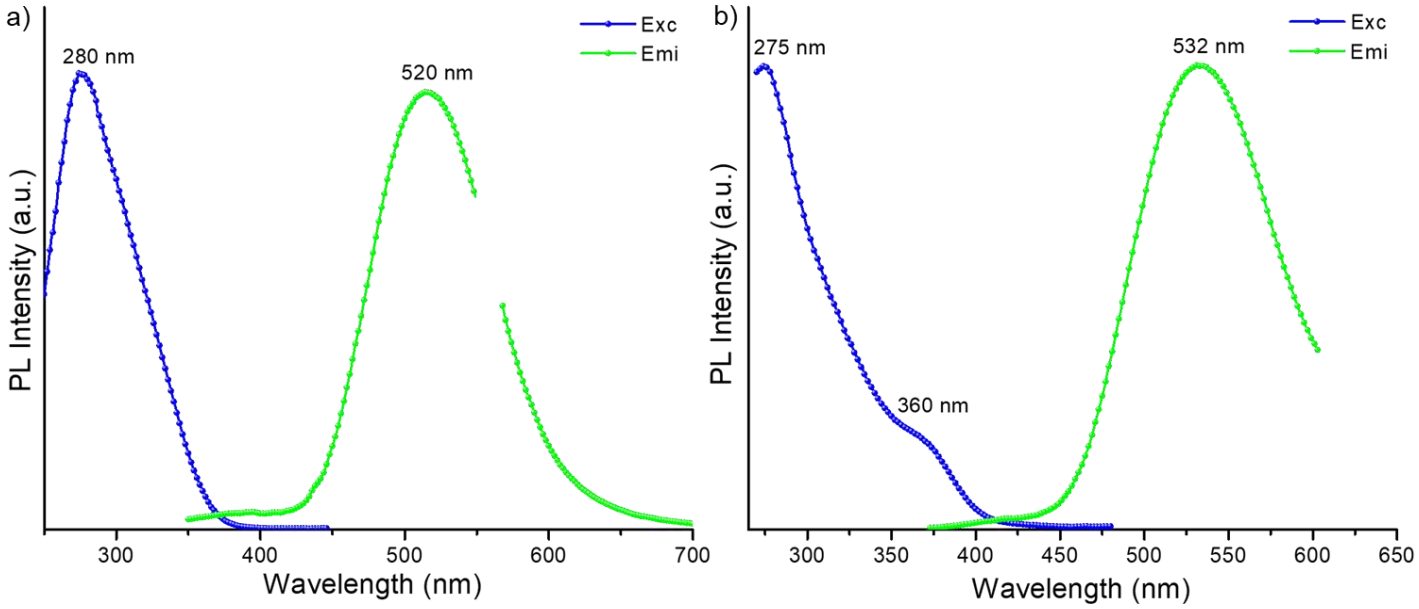


Figure S2. Solid state photoluminescence excitation and emission spectra of $Cu_4(oCBT)_4$ and $Cu_4(mCBT)_4$ crystals.

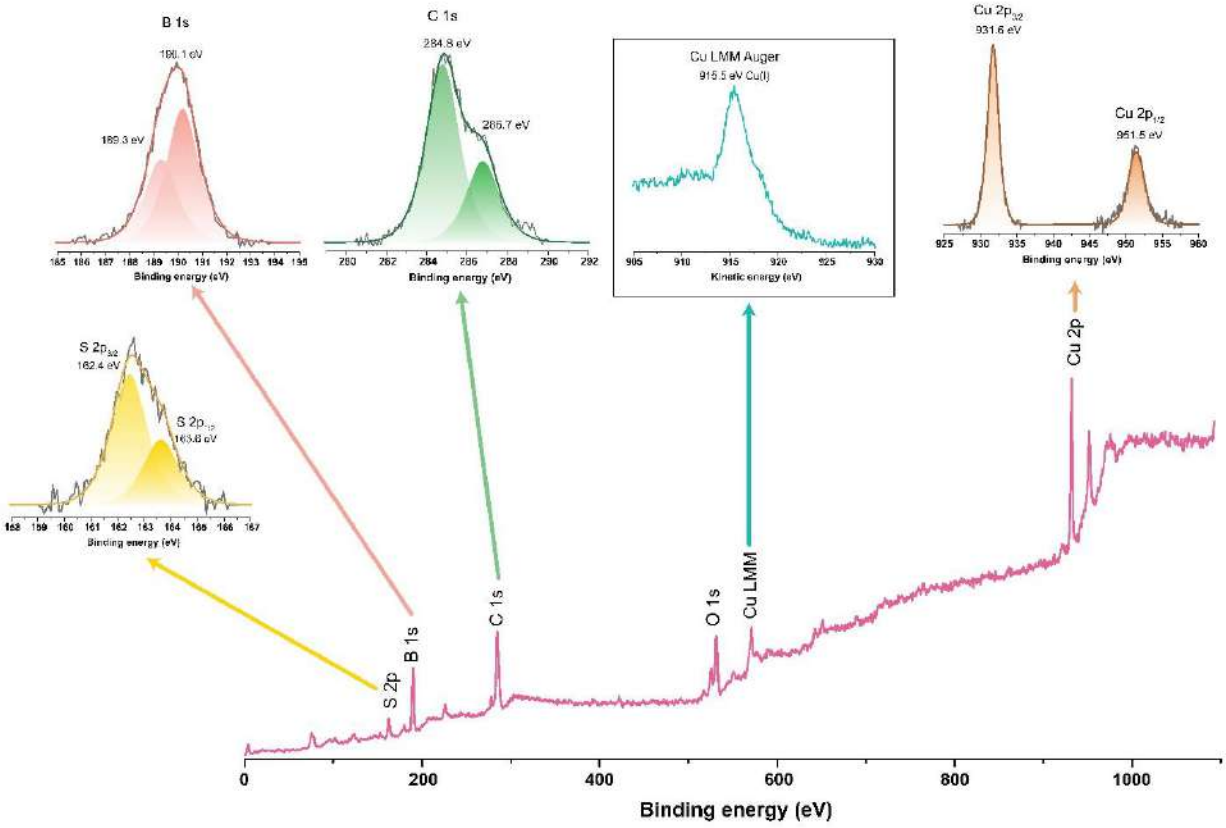


Figure S3. XPS spectra of $Cu_4(oCBT)_4$ crystals. Survey spectra showing the presence of respective elements of the cluster along with detailed spectra of C 1s (green), B 1s (pink), S 2p (yellow) and Cu 2p (orange). The Cu LMM Auger peak is shown within the box. Note that the x-axis is Kinetic Energy.

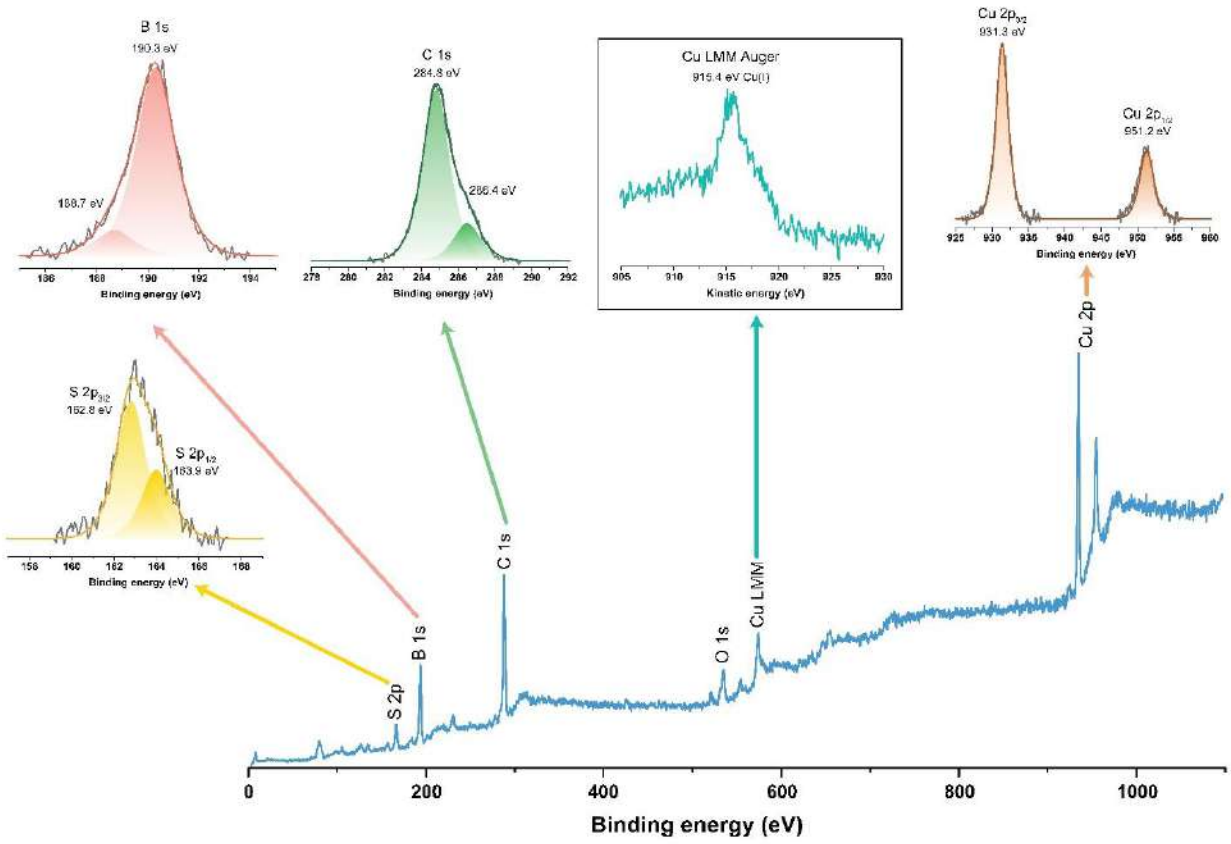


Figure S4. XPS spectra of $Cu_4(mCBT)_4$ crystals. Survey spectra showing the presence of respective elements of the cluster along with detailed spectra of C 1s (green), B 1s (pink), S 2p (yellow) and Cu 2p (orange). The Cu LMM Auger peak is shown within the box. Note that the x-axis is Kinetic Energy.

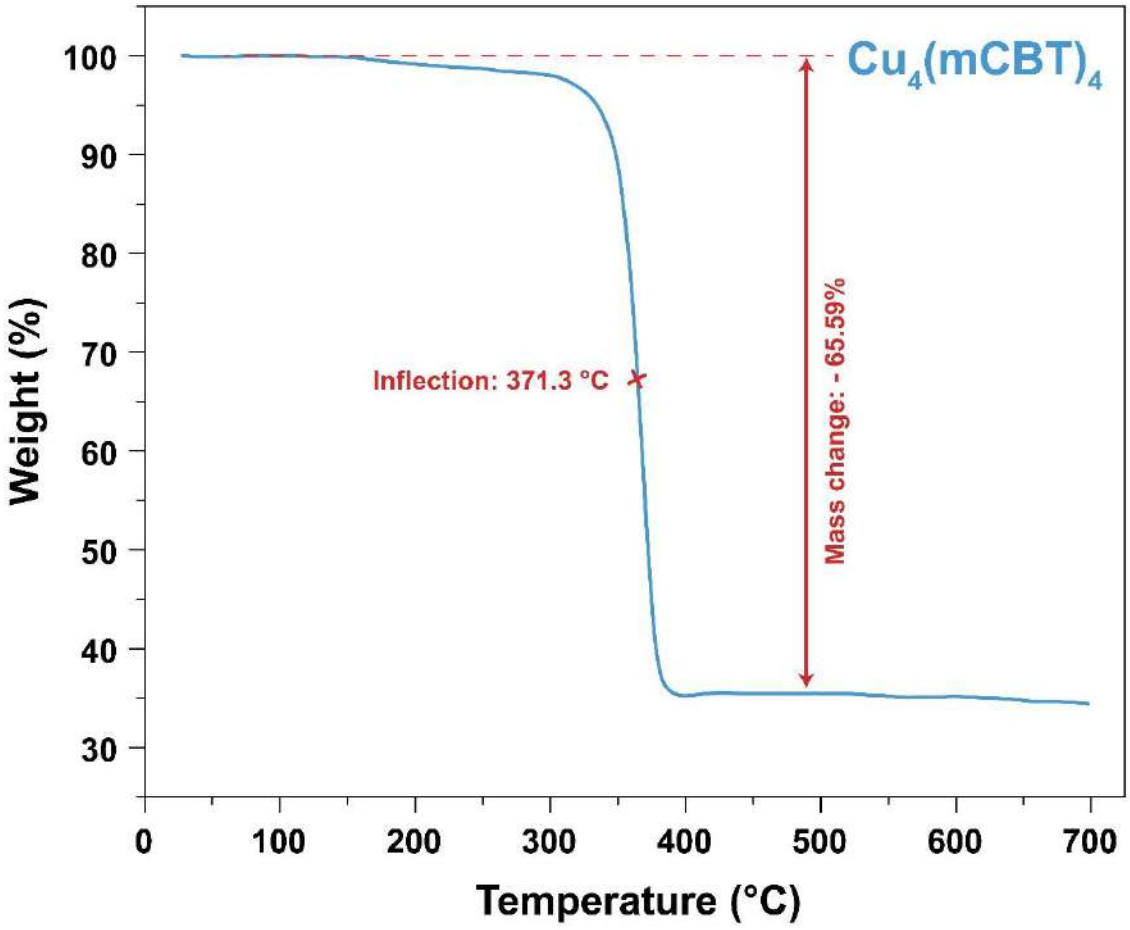


Figure S5. Thermogravimetric analysis of $Cu_4(mCBT)_4$ crystals showing thermal stability up to 370 °C. The cluster $Cu_4(oCBT)_4$ is stable up to 380 °C. Data corresponding to $Cu_4(mCBT)_4$ crystals alone are presented as these have been discussed previously.[1]

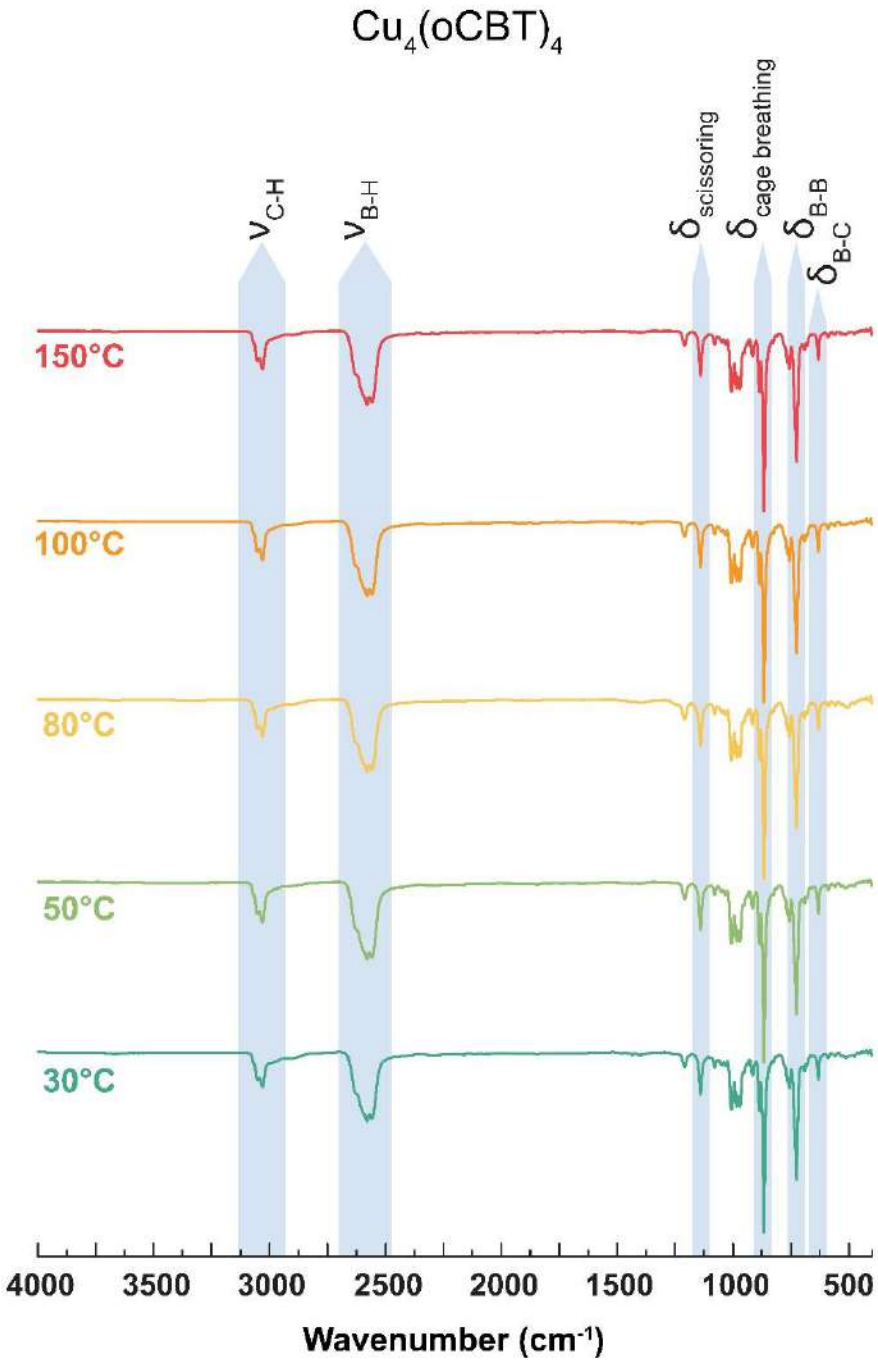


Figure S6. ATR- IR spectra of heat treated $Cu_4(oCBT)_4$ crystals showing the chemical stability of the samples up to 150°C.

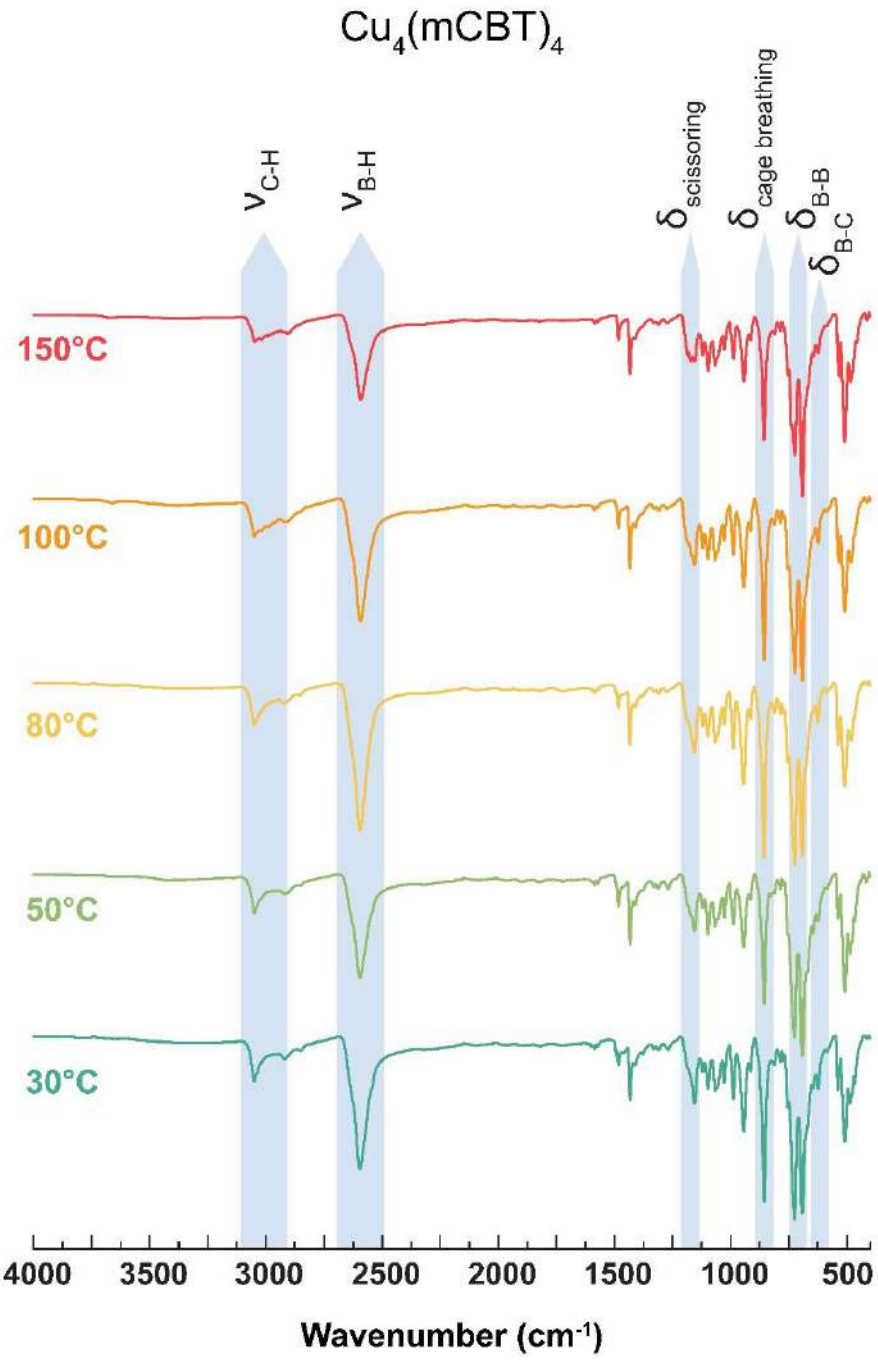


Figure S7. ATR- IR spectra of heat treated $Cu_4(mCBT)_4$ crystals showing the chemical stability of the samples up to 150°C

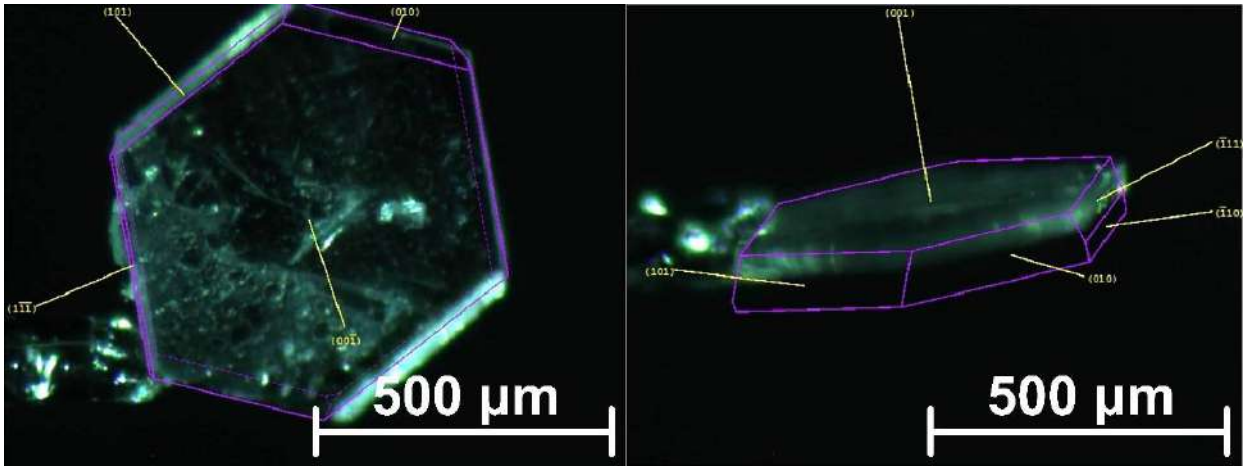


Figure S8. Face indexing of hexagonal $Cu_4(oCBT)_4$ single crystal from two different orientations.

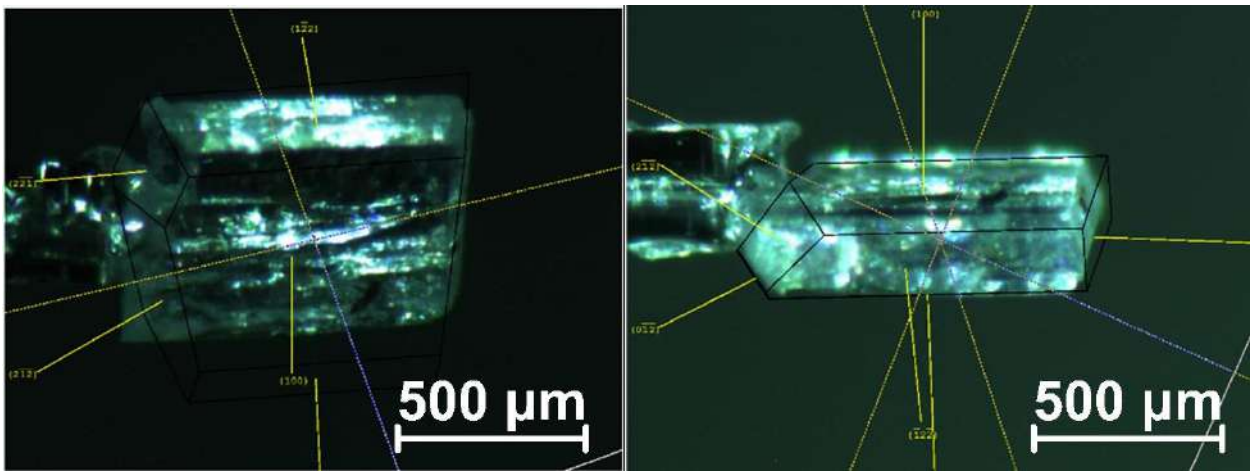


Figure S9. Face indexing of parallelepiped $Cu_4(mCBT)_4$ single crystal from two different orientations.

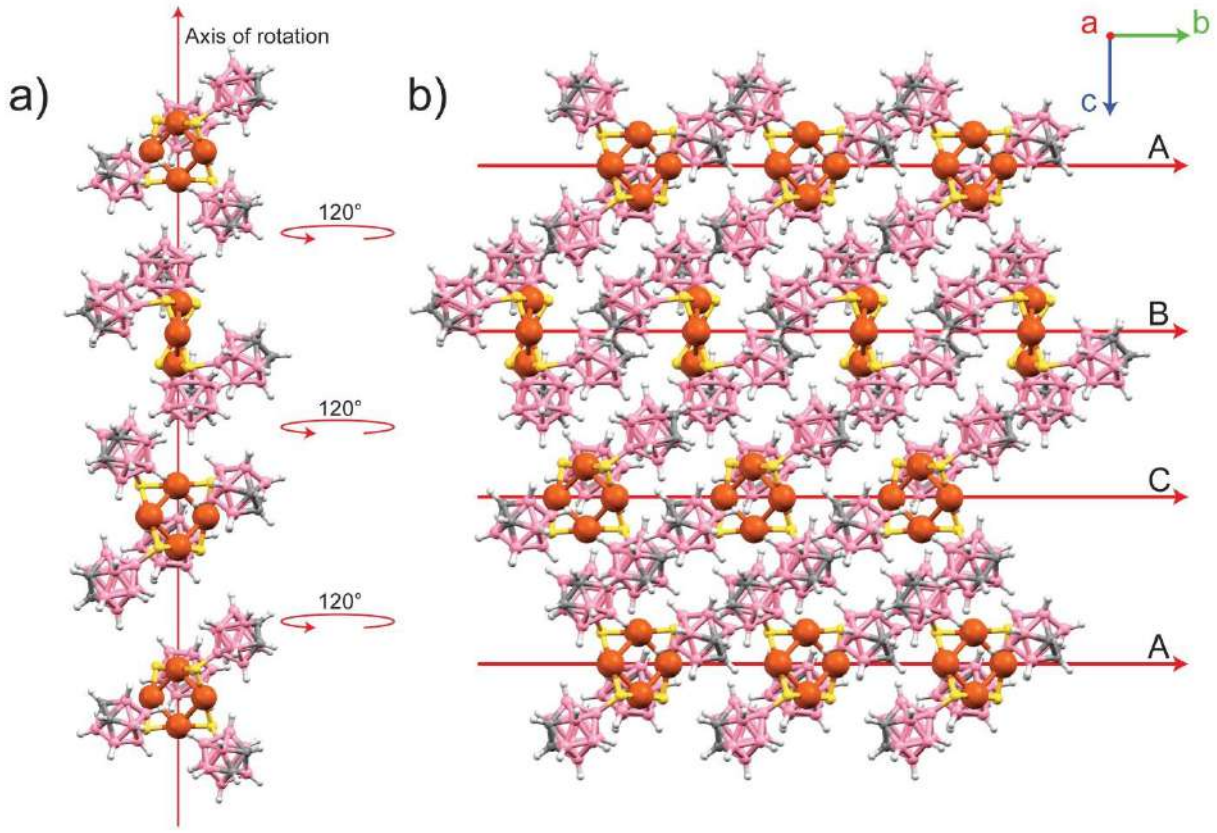


Figure S10. a) Orientation of each cluster with respect to the cluster in its upper layer showing 120° rotation along the axis of rotation. b) Extended packing structure of $Cu_4(oCBT)_4$ nanoclusters showing …ABCA… packing.

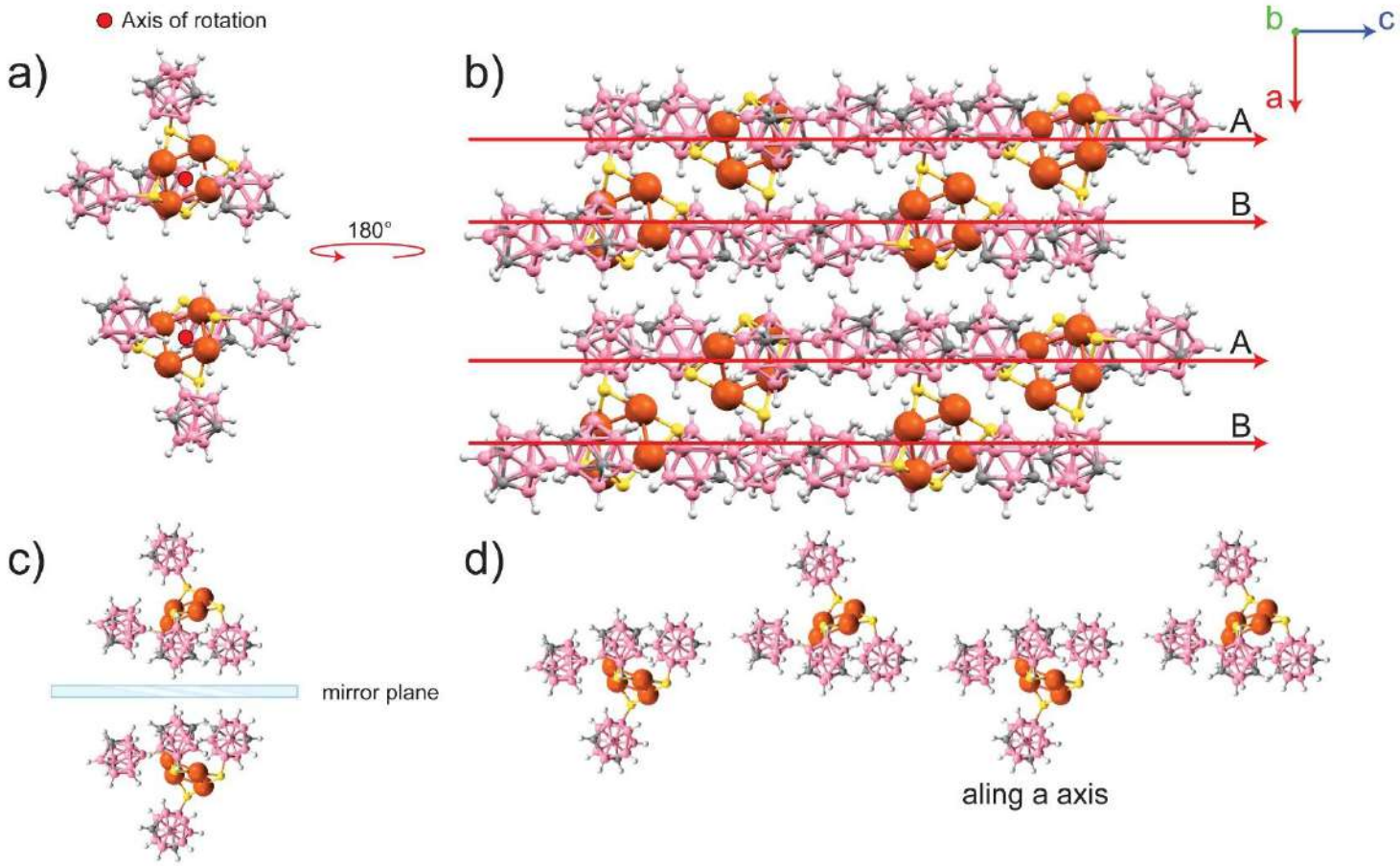


Figure S11. a) Orientation of each cluster with respect to the cluster in its upper layer showing 180° rotation along the axis of rotation. (Axis of rotation is perpendicular to the visible plane). b) Extended packing structure of $Cu_4(mCBT)_4$ nanoclusters showing …ABAB… packing. c) Shows the orientation of adjacent clusters as non-superimposable mirror images. An imaginary mirror plane is also shown. d) Adjacent clusters as observed along the *a* axis showing arrangement of clusters which are mirror images of each other.

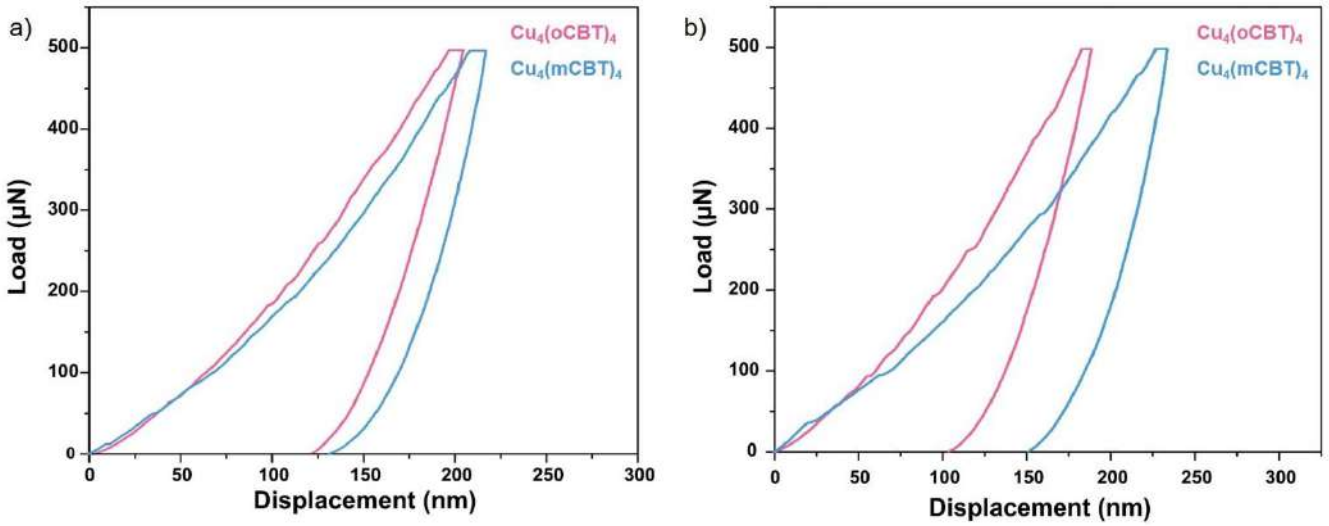


Figure S12. Load-controlled load-displacement curves of $Cu_4(oCBT)_4$ and $Cu_4(mCBT)_4$ crystals for a load of 500 μN with load functions a) 20_10_20 and b) 50_20_50.

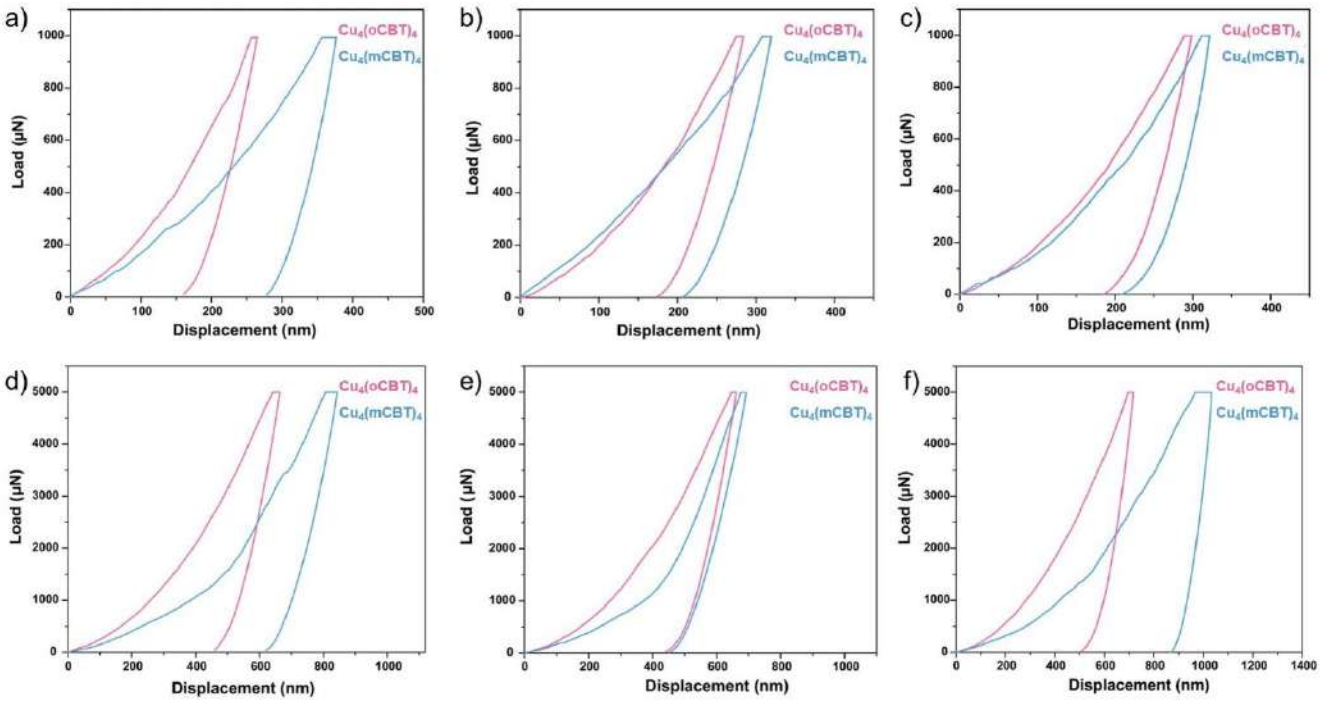


Figure S13. Load-controlled load-displacement curves of $Cu_4(oCBT)_4$ and $Cu_4(mCBT)_4$ crystals for a load of 1000 μN for a), b) and c) and a load of 5000 μN for d), e) and f) with load functions 5_10_5, 20_10_20 and 50_20_50, respectively.

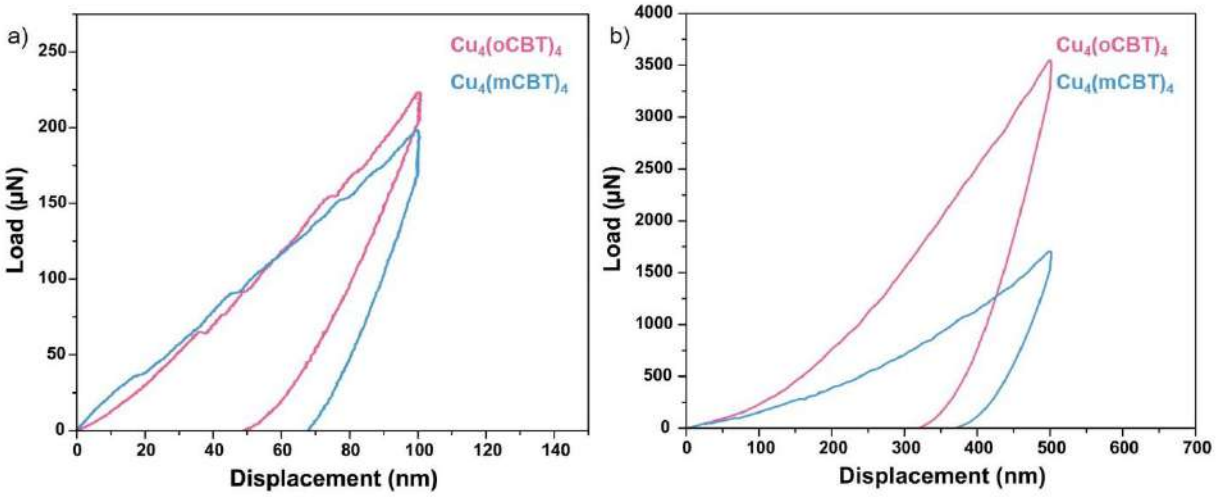


Figure S14. Displacement controlled load-displacement curves for $Cu_4(oCBT)_4$ and $Cu_4(mCBT)_4$ crystals with a fixed displacement of a) 100 nm and b) 500 nm.

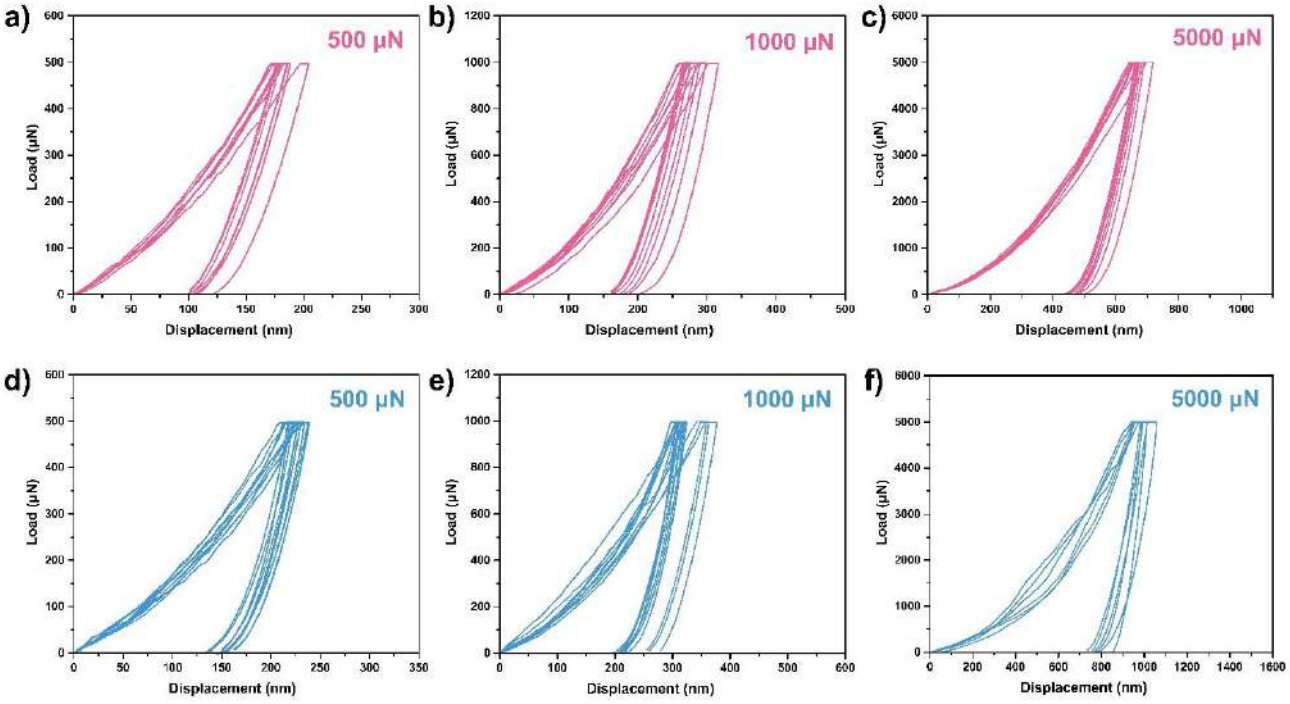


Figure S15. All the indentation measurements for $Cu_4(oCBT)_4$ (pink traces) and $Cu_4(mCBT)_4$ (blue traces) at varying loads; 500 μN (a and d), 1000 μN (b and e) and 5000 μN (c and f) plotted together to show the reproducibility for the measurements.

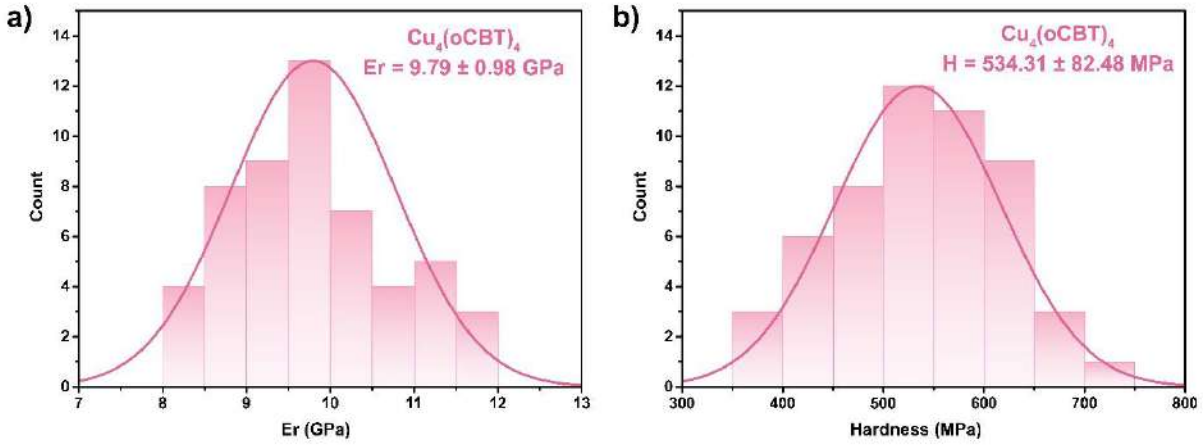


Figure S16. Statistical analysis of all the indentation data collected for $Cu_4(oCBT)_4$ nanocluster crystal. a) The distribution of the Young's modulus, Er, among the data sets collected. b) The distribution of Hardness, H, among the data sets collected.

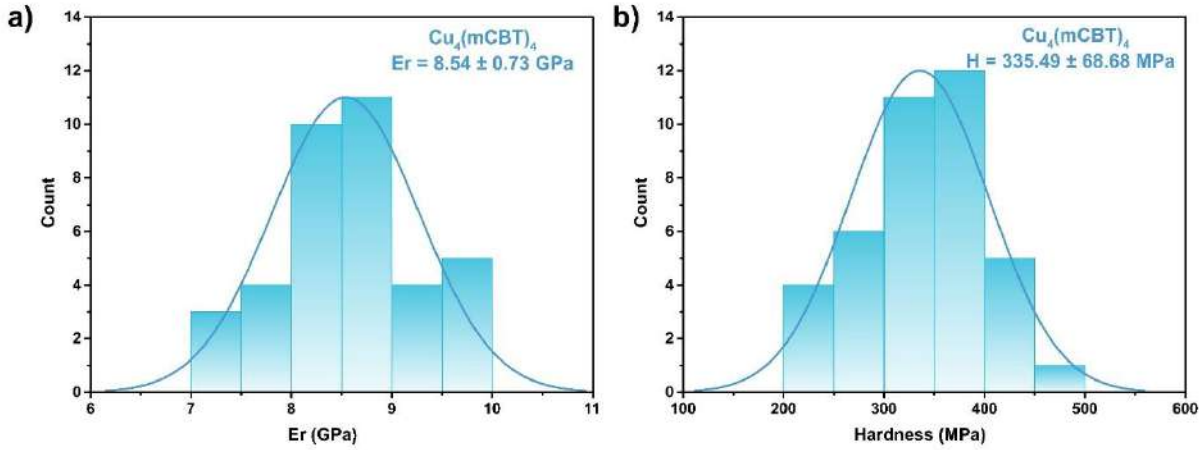


Figure S17. Statistical analysis of all the indentation data collected for $Cu_4(mCBT)_4$ nanocluster crystal. a) The distribution of the Young's modulus, Er, among the data sets collected. b) The distribution of Hardness, H, among the data sets collected.

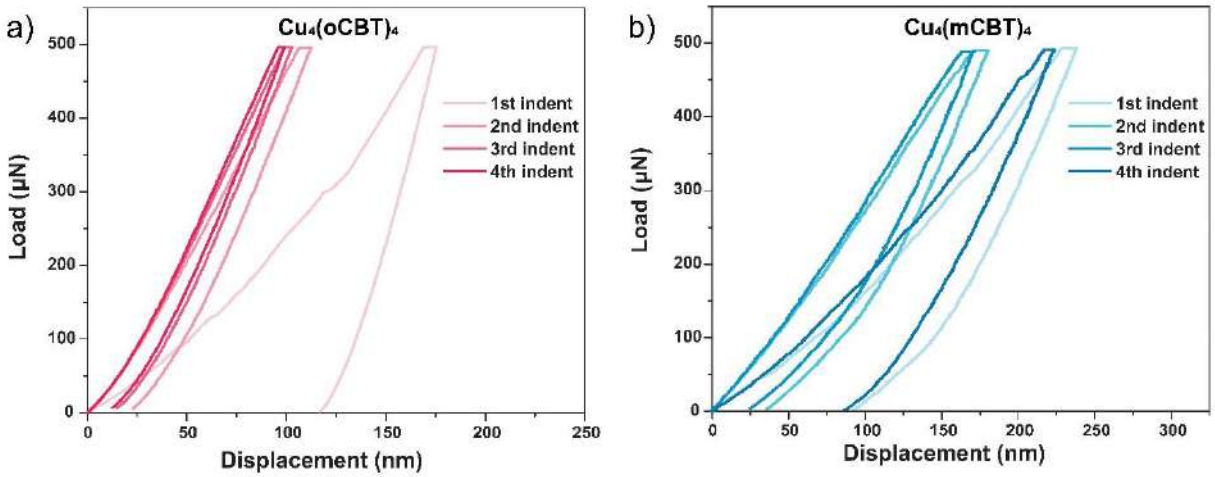


Figure S18. Load-displacement curves obtained by repeated indentations in the same place for a) Cu_4(o-CBT)$_4$ and b) Cu_4(m-CBT)$_4$, showing the indentation induced hardness in the crystals of the nanoclusters.

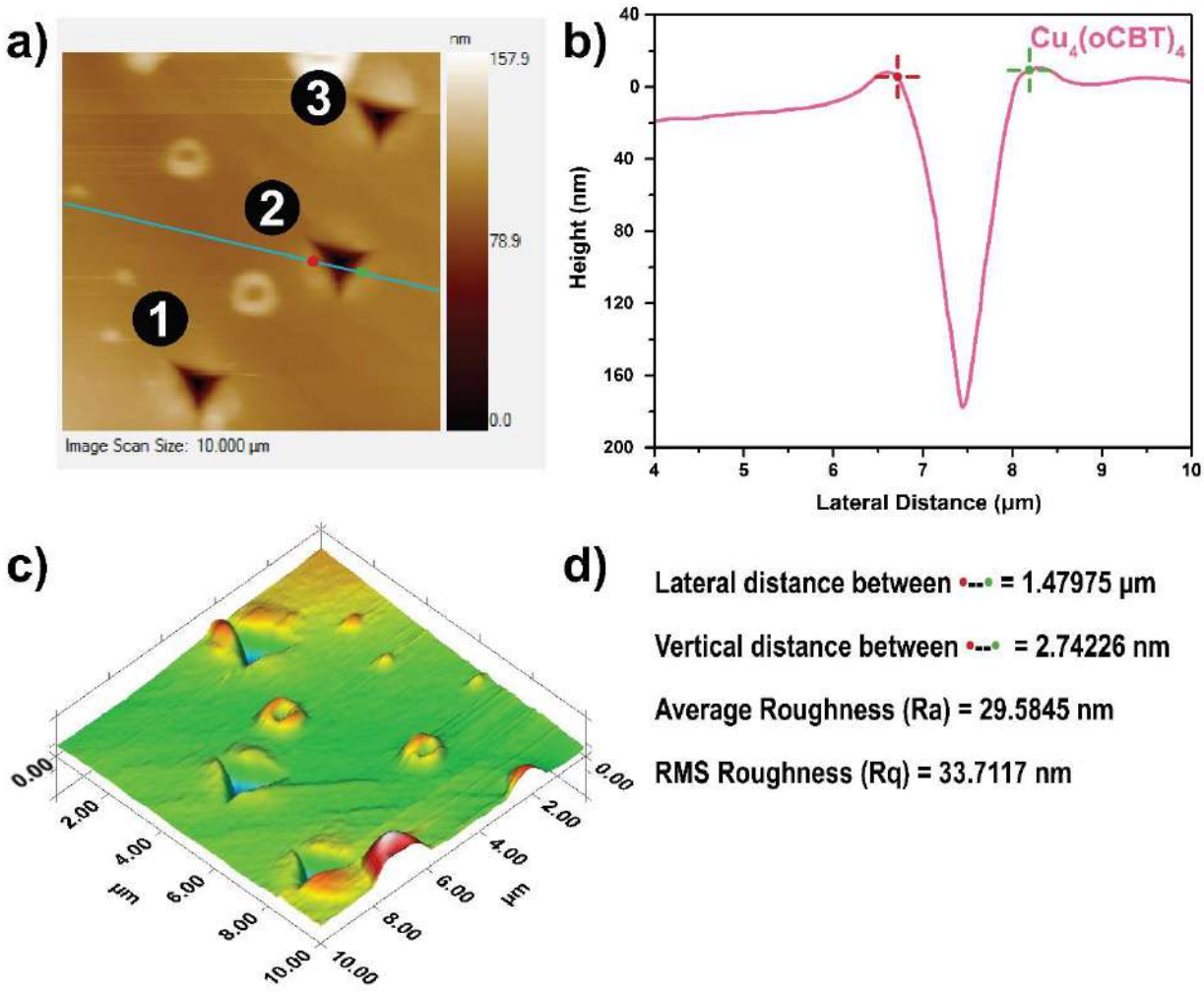


Figure S19. a) Scanning probe microscopy image of the surface of $Cu_4(oCBT)_4$ crystal after three indentations showing residual imprints on the surface with an applied load of 500 µN. b) Height profile of indentation **2** along the blue line. c) 3D projection of scanning probe microscopy image. d) Distance and roughness data between the red and green points shown in images a) and b).

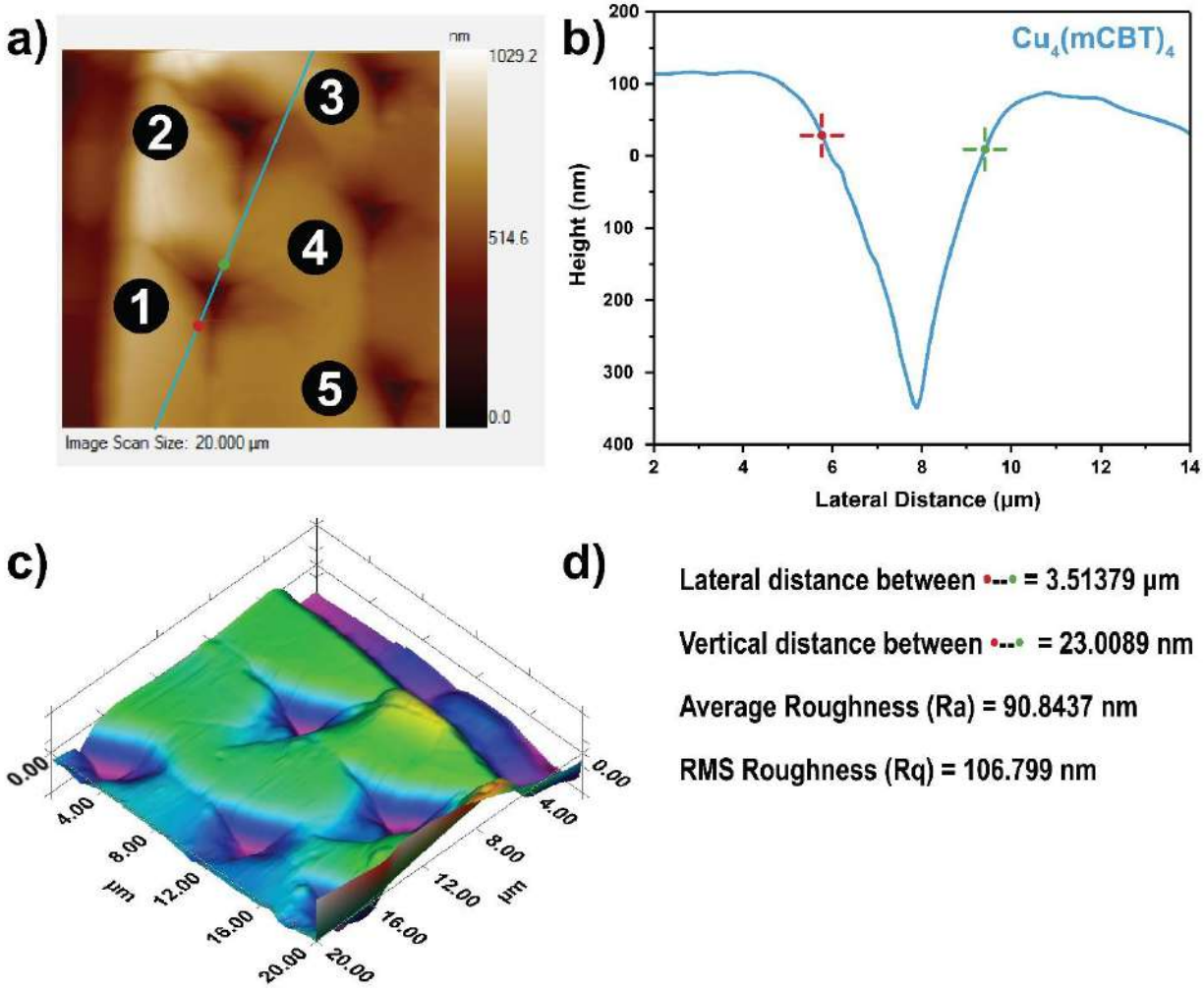


Figure S20. a) Scanning probe microscopy image of the surface of $Cu_4(mCBT)_4$ crystal after five indentations showing residual imprints on the surface with an applied load of 500 µN. b) Height profile of indentation **1** along the blue line. c) 3D projection of scanning probe microscopy image. d) Distance and roughness data between the red and green points shown in images a) and b).

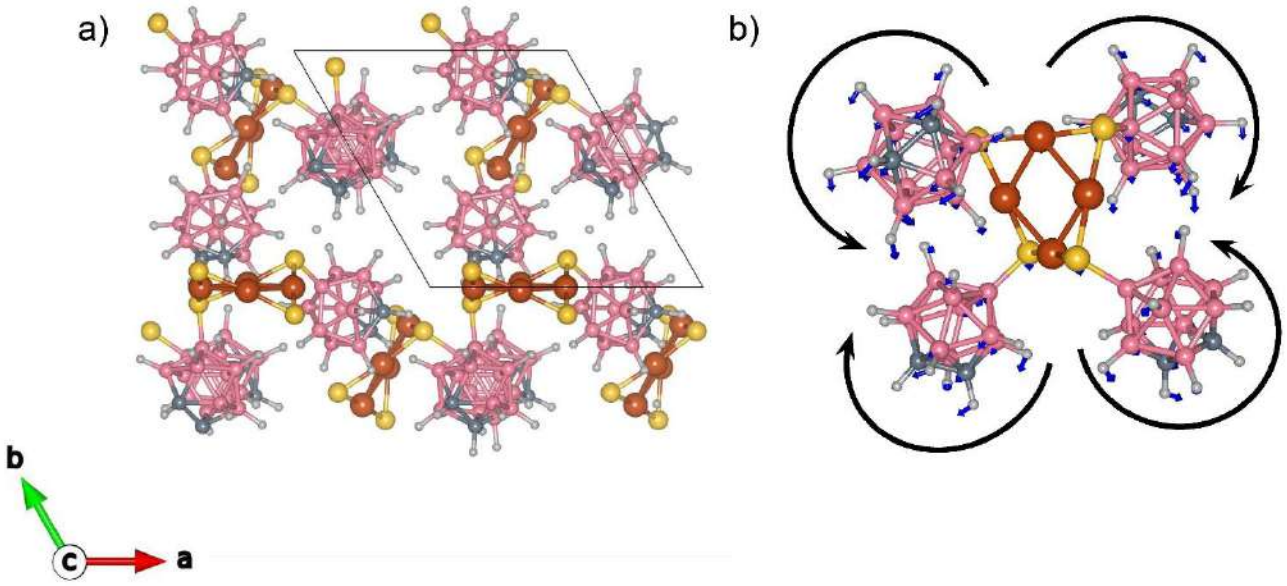


Figure S21. a) Arrangement of Cu_4 nanoclusters and ligands in the *ab* plane of $Cu_4(oCBT)_4$. The square planar Cu_4 clusters lie perpendicular to the plane, in the vacant space between oCBTs. b) Motion of various atoms in an isolated $Cu_4(oCBT)_4$ unit.

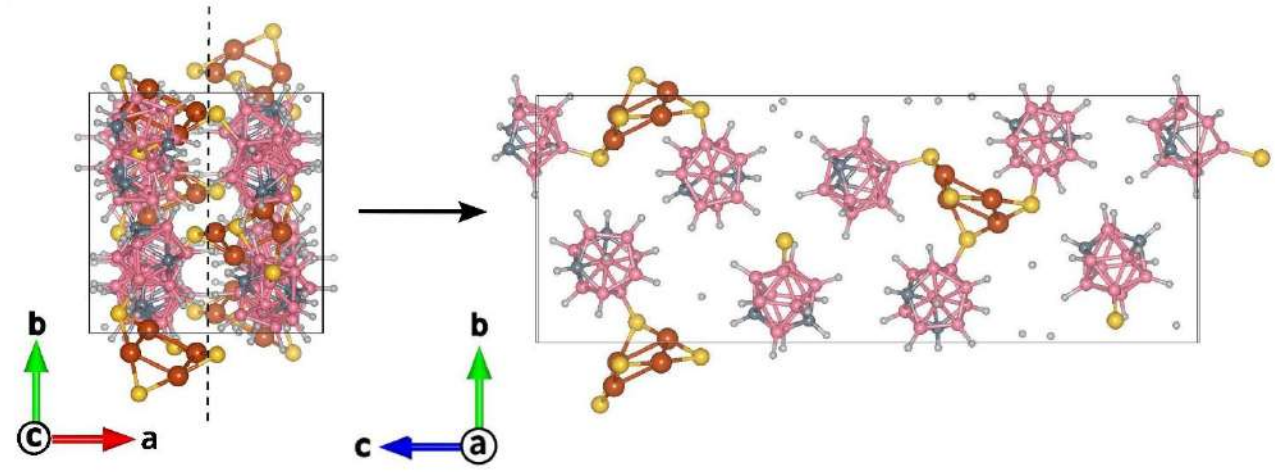


Figure S22. A transverse section of $Cu_4(mCBT)_4$ taken along the *a* axis reveals loosely packed CBT molecules attached to Cu_4 clusters.

Reference:

(1) Jana, A.; Jash, M.; Dar, W. A.; Roy, J.; Chakraborty, P.; Paramasivam, G.; Lebedkin, S.; Kirakci, K.; Manna, S.; Antharjanam, S.; Machacek, J.; Kucerakova, M.; Ghosh, S.; Lang, K.; Kappes, M. M.; Base, T.; Pradeep, T. Carborane-Thiol Protected Copper Nanoclusters: Stimuli-Responsive Materials with Tunable Phosphorescence. *Chem. Sci.* **2023**, *14* (6), 1613–1626. https://doi.org/10.1039/D2SC06578A.

ACS Sustainable Chemistry & Engineering

pubs.acs.org/journal/ascecg

Research Article

Cellulose-Derived Nanomaterials for Affordable and Rapid Remediation of Uranium in Water

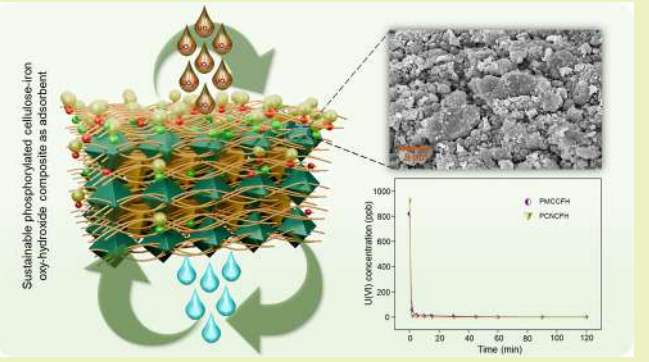
Tanmayaa Nayak, Sritama Mukherjee, Amoghavarsha Ramachandra Kini, Md Rabiul Islam, Ankit Nagar, Sonali Seth, and Thalappil Pradeep*

Cite This: *ACS Sustainable Chem. Eng.* 2025, 13, 1838−1850

Read Online

ACCESS | Metrics & More | Article Recommendations | Supporting Information

ABSTRACT: Due to its long half-life of 4.5 billion years and inherent toxicity, uranium is an important radioactive pollutant, necessitating effective methods for its removal from water, although its chemical toxicity is more significant. Adsorption using advanced materials is emerging as an affordable and sustainable approach for the removal of soluble uranium, principally in the form of UO_2^{2+}, a major concern in several water sources in India and other parts of the world. This study is a comparative investigation of the adsorption capabilities of two phosphorylated cellulose-reinforced iron oxyhydroxide composites, namely, nano- and microstructures and their potential use in removing UO_2^{2+} from water. Results indicate that cellulose nanostructures exhibit superior efficiency compared to the corresponding microstructures for UO_2^{2+} adsorption, with equilibrium achieved within 2 min of exposure. Green synthesis of the composite produces particulate media with excellent structural integrity. Furthermore, it exhibits rapid adsorption dynamics despite the presence of competing ions in water. It also exhibits high uranium extraction efficiency over a broad pH range and exhibits outstanding regeneration performance. Various analytical techniques, including XRD, SEM, HRTEM, XPS, TGA, and FT-IR, were employed to investigate the structure of the composites and their interactions with uranium. We find that UO_2^{2+} binds through oxygen and phosphorus functional groups of the material. We evaluated various sustainability metrics to assess the ecological impact of the composite and its synthesis process. We demonstrate the potential of the developed adsorbent as a highly efficient and sustainable method for uranium removal from water.



KEYWORDS: *cellulose nanocrystal, cellulose microcrystalline, uranium, adsorption, sustainability metrics, water treatment, Langmuir isotherm*

Downloaded via INDIAN INST OF TECH MADRAS on December 29, 2025 at 03:07:41 (UTC).
See https://pubs.acs.org/sharingguidelines for options on how to legitimately share published articles.

INTRODUCTION

Uranium (U), a dense, silvery actinide, is chemically and radiologically toxic, with chemical toxicity posing a greater health risk.[1,2] Naturally occurring uranium, present in the earth's crust (3 ppm) and seawater (3 ppb), consists of three isotopes: ^{238}U (99.274%), ^{235}U (0.7%), and ^{234}U (0.0055%).[3,4] It exhibits multiple oxidation states ranging from 2+ to 6+, but it predominantly occurs in its hexavalent (uranyl) and tetravalent (uranous) forms in nature, with the hexavalent form occurring predominantly as the uranyl ion (UO_2^{2+}).[5] Uranium has been mobilized into groundwater due to anthropogenic activities like nuclear power, mining, and fertilizers as well as natural processes like weathering and volcanic eruptions.[6] Its solubility in groundwater is influenced by pH, conductivity, redox potential, temperature, and the presence of specific ions such as carbonates, nitrates, and sulfates, with acidic, oxidizing conditions enhancing dissolution.[7−10] Many complexes of uranium exist at a specific pH of the solution. For example, at a pH range of 5−7, cationic species such as $(UO_2)_3(OH)^{5+}$ and UO_2OH^+ as well as anionic species like $UO_2(CO_3)^{4-}$ and $(UO_2)_2CO_3(OH)^{3-}$ are present.[11]

Uranium can accumulate in organs, increasing the risk of cancer, blood disorders, kidney damage and affecting the neurological, reproductive, and circulatory systems.[12−14] According to a survey conducted by the Ministry of Jal Shakti of India in 2020, 151 districts in 18 states of India are partly affected by high concentrations (>30 ppb, which is the WHO threshold limit for uranium in drinking water) of uranium in groundwater, highlighting the critical need for efficient and cost-effective removal methods.[15] Chemical methods for

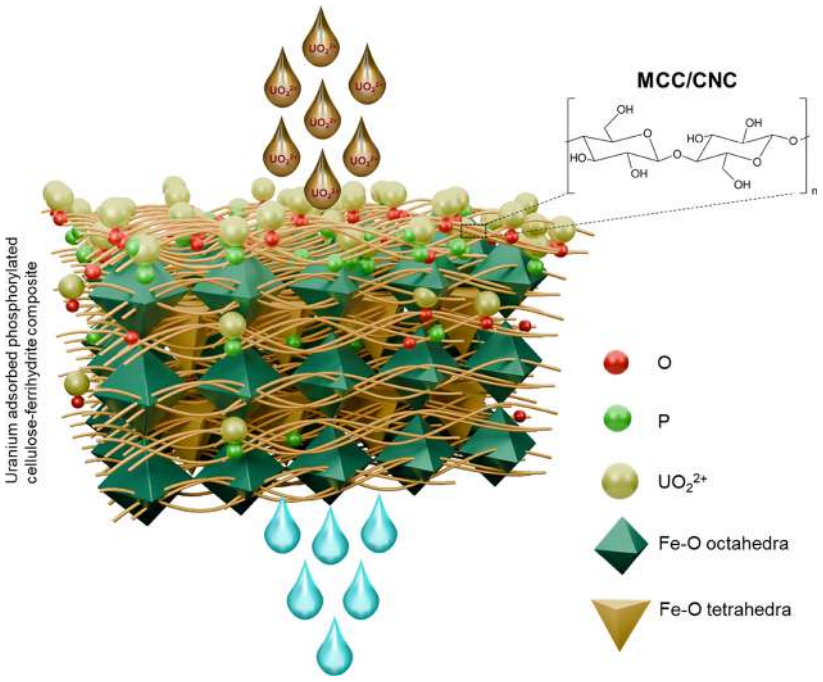
Received: December 7, 2024
Revised: January 13, 2025
Accepted: January 14, 2025
Published: January 24, 2025



ACS Publications

© 2025 American Chemical Society

Scheme 1. Schematic Diagram of the Application of Phosphorylated Cellulose-Ferrihydrite Composite Material for Cost-Effective Removal of Uranium from Water



uranium extraction frequently implemented include ion exchange, membrane processes, precipitation, solvent extraction, adsorption, and electrochemical/photochemical techniques.[16−23] Among these, adsorption is the most favorable in terms of design, cost and operational flexibility, effectiveness, and efficiency.[24] Many adsorbents such as zeolites, biosorbents, activated carbon, carbon nanotubes, clays, metal oxides, and metal−organic frameworks (MOFs) have been reported for uranium extraction from water.[25−33] However, carbon-based adsorbents and MOFs exhibit insufficient adsorption capacity and selectivity for uranium, while their complex synthesis, high cost, and potential ecotoxicity hinder practical water treatment applications. The development of sustainable and efficient adsorbent materials plays a vital role in addressing environmental and resource challenges. Recent advancements, such as the utilization of molten pyrolysis to synthesize high-value carbon materials from abundant sources, as reported by Zhang et al., exemplify innovative approaches that combine environmental compatibility with high performance.[34] Wang et al. synthesized titanium-doped zirconium-based MOFs for uranium extraction, exhibiting high sorption capacity across a broad pH range but showing reduced efficiency in the presence of competing anions such as CO_3^{2-} and PO_4^{3-}.[35] On the other hand, nanoscale metal oxides, like Al_2O_3, TiO_2, MgO, Fe_2O_3, and ZrO_2, are effective adsorbents for heavy metals due to their high surface area, porosity, and stability across various pH conditions and high ionic concentrations, making them ideal for water treatment applications.[36] Among these, iron oxides, including forms like magnetite (Fe_3O_4), hematite (α-Fe_2O_3), maghemite (γ-Fe_2O_3), iron oxyhydroxide (FeOOH), and metallic zerovalent iron are widely used for their low cost, easy synthesis, and efficacy in removing metals such as As, Cd, Hg, and Sb across various oxidation states.[37−39]

Compared with other adsorption processes, biosorption offers several advantages, including cost-effectiveness, high efficiency, reusability, and potential for metal recovery. Chitosan, a biopolymer with hydroxyl and amine groups that exhibit a strong affinity for uranium ions, has been used for uranium adsorption.[40] But we cannot ignore that chitosan is environmentally less stable and expensive due to its origin from crustacean exoskeletons and degrades at 254.6 °C. In this context, cellulose, a naturally occurring polysaccharide found in plant cell walls, is more thermally stable, with degradation beginning at 312.9 °C, making it suitable for harsh conditions.[41] Microcrystalline cellulose (MCC) and cellulose nanocrystals (CNCs) have been explored for pollutant removal, including uranium, with differing adsorption capabilities due to their structural properties.[42,43] MCC, derived via acid hydrolysis, has a crystalline structure with particle sizes of 2−50 μm in diameter and 100−1000 μm in length. CNCs, on the other hand, obtained through acid hydrolysis and homogenization, are smaller, with particle sizes of 5−20 nm in diameter and 100−500 nm in length, offering higher surface area and crystallinity. The phosphorus-, oxygen-, and nitrogen-based additional functional groups act as chelating agents, enhancing the binding of uranyl species. In a study, researchers synthesized phosphorylated cellulose nanofibers to improve uranium adsorption capacity.[44] Phosphorylated carboxy methyl cellulose and chitosan composites have also been studied for the same.[45] Although both the composites are showing high uptake capacity, their adsorption efficiency decreases after certain pH. To the best of our knowledge, there are no reports on the removal of U(VI) using iron oxyhydroxide-incorporated phosphorylated cellulose. This low-cost material notably overcomes the limitations of most of the previously reported adsorbents such as slow kinetics, reduced adsorption efficiency in the presence of coexisting ions, and performance across a wide pH range, making it suitable for industrial applications.

Incorporating sustainability into the synthesis of adsorbents for contaminant removal from water ensures environmental protection, cost-effectiveness, safety, and regulatory compliance and promotes resource efficiency and longevity. Here, in

https://doi.org/10.1021/acssuschemeng.4c10246
ACS Sustainable Chem. Eng. 2025, 13, 1838−1850

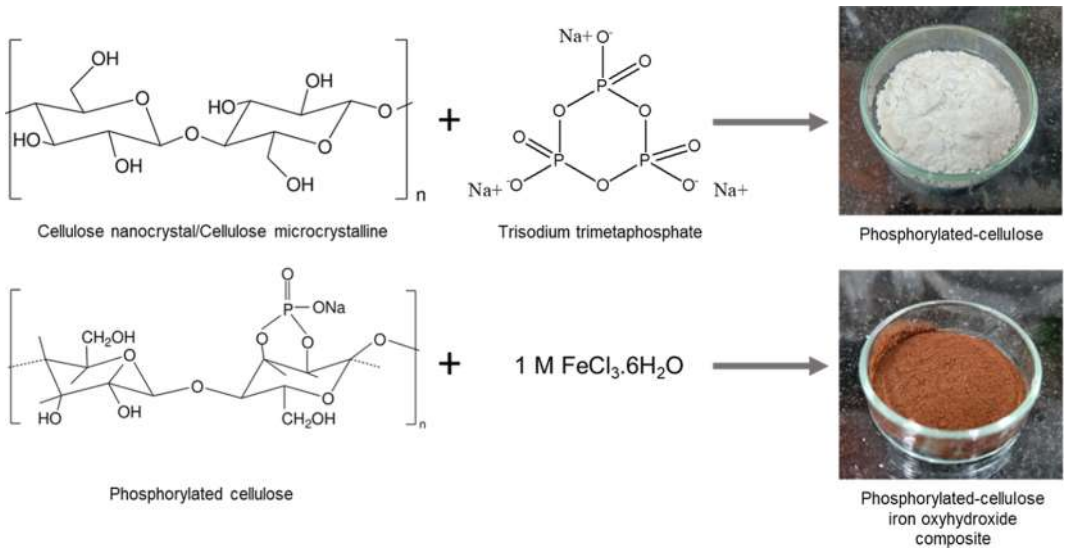


Figure 1. Schematic diagrams illustrating the synthetic procedures and molecular structures of CNC/MCC and synthesized phosphorylated cellulose. Photographs of PCNC and PCNCFH are also shown. PMCC and PMCCFH are also similar to PCNC and PCNCFH, respectively, in terms of physical appearance.

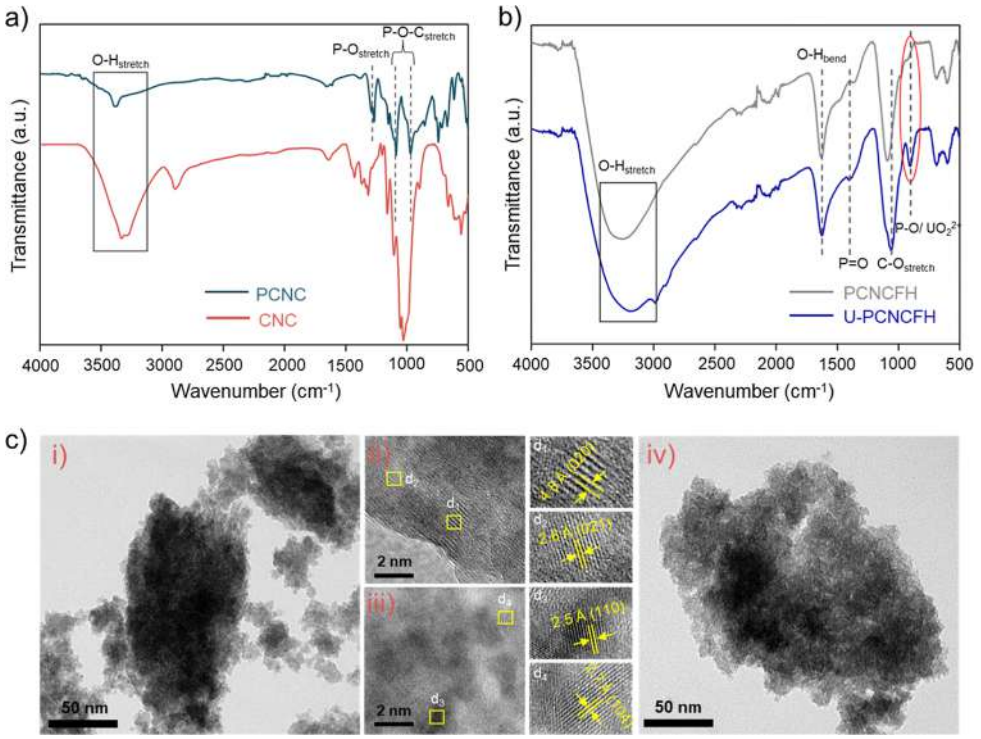


Figure 2. (a) FTIR spectra of blank CNC and PCNC. (b) FTIR spectra of PCNCFH and U−PCNCFH. (c) HRTEM image: (i) PCNCFH and (ii,iii) beam-induced crystallization of PCNCFH and (iv) U−PCNCFH.

this study, we successfully synthesized phosphorylated cellulose-iron oxyhydroxide materials for uranium removal from water with a comprehensive evaluation of relevant sustainability metrics. The cellulose precursors were functionalized with phosphorus groups to enhance adsorption efficiency as uranium, a "hard" Lewis acid, preferentially forms stable complexes with "hard" Lewis bases such as phosphate, carboxyl, and amino ligands.[45,46] Incorporation of iron oxyhydroxide produced novel and structurally robust nanocomposites, addressing the stability and recovery limitations of phosphorylated cellulose, which exhibited a partial water solubility. Additionally, we compared the uranium uptake performance of phosphorylated cellulose-incorporated iron oxyhydroxide nanocomposites by taking two different cellulose precursors MCC and CNC (Scheme 1). Although previous research indicated that MCC-based composites performed better than CNC-based composites for arsenic removal, our findings showed a different trend for uranium removal. Specifically, the CNC-based nanocomposite exhibited superior adsorption capacity for uranium due to its smaller particle size and higher surface area of CNC, which was confirmed from BET. In this work, the uptake capacity and

https://doi.org/10.1021/acssuschemeng.4c10246
ACS Sustainable Chem. Eng. 2025, 13, 1838−1850

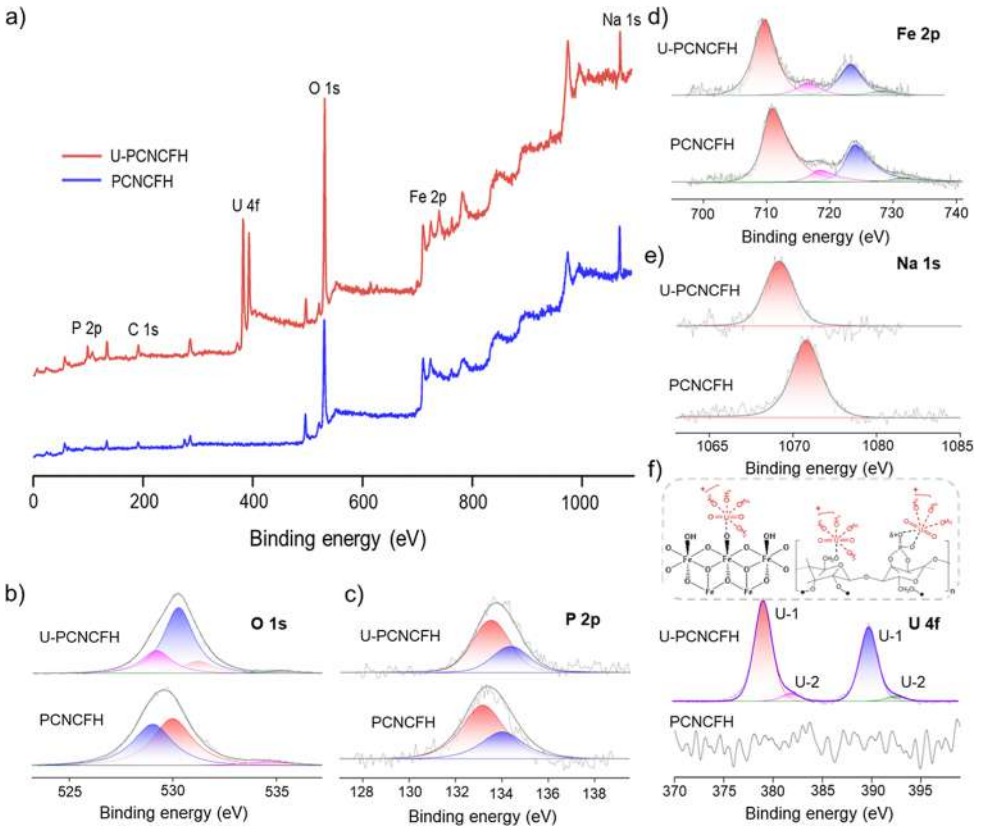


Figure 3. (a) XPS of PCNCFH and U−PCNCFH. High-resolution XPS spectra in the (b) O 1s, (c) P 2p, (d) Fe 2p, (e) Na 1s, and (f) U 4f regions of PCNCFH and U−PCNCFH (U-1 = U−O, U-2 = U−O−P). The structures in the inset of (f) show the possible mechanism of U(VI) adsorption on iron oxy-hydroxide and phosphorylated cellulose. Spectra in the expanded regions have been fitted using Casa XPS software.[50] Conditions: T = 293 K, pH = 7, initial concentration of uranium = 1000 mg/L.

comparative affinity of both composites for uranium were thoroughly investigated in the context of a variety of environmental factors, such as the pH of the solution and coexisting heavy metal ions of relevance. Both the composites exhibited rapid adsorption kinetics and maintained high performance across a broad pH range and even in the presence of coexisting ions. Further, the morphology of the composite and the mechanism of uranium uptake were thoroughly investigated by several microscopic (SEM and TEM) and spectroscopic techniques (XPS and FTIR).

EXPERIMENTAL SECTION

The materials used, protocol of synthesis, experimental methodology adopted for characterizations, and evaluation of adsorption are presented in Supporting Information. Essentially, synthesis involved functionalizing CNC and MCC with trisodium trimetaphosphate (STMP) resulting in phosphorylated materials, which are used to create appropriate iron oxyhydroxide composites. They were characterized by XRD, SEM, HRTEM, XPS, TGA, and FT-IR techniques, and these materials were used for evaluating adsorption by established methods. Materials after adsorption were also studied using various diverse techniques. Suspended media were evaluated for toxicity characteristic leaching protocol (TCLP). Kinetics of the adsorption were fitted with various adsorption models.

RESULTS AND DISCUSSION

The schematic diagram of material of Figure 1 represents the chemical structures of CNC, MCC, and synthesized phosphorylated cellulose and photographs of phosphorylated-cellulose nanocrystal (PCNC) and phosphorylated-cellulose nanocrystal ferrihydrite (PCNCFH). Phosphorylated-microcrystalline cellulose (PMCC) and phosphorylated-microcrystalline cellulose ferrihydrite (PMCCFH) exhibit similar physical appearance to PCNC and PCNCFH. A green synthesis approach was used to prepare phosphorylated cellulose-ferrihydrite nanocomposites in two steps: phosphorylation of cellulose using STMP, followed by the incorporation of ferric chloride to form a stable composite. The final product, a dark brown crystalline material, was obtained through pH-controlled reactions and thorough washing, yielding approximately 3.68 g of nanocomposite.

Characterization of PCNCFH, before and after Uranium Uptake. The FTIR spectra of CNC and phosphorylated CNC (PCNC) are compared in Figure 2a. For PCNC, there is a broad band at 3378 cm^{-1} corresponding to the −OH stretching mode in cellulose. The phosphorylation of cellulose is indicated by the disappearance of the −OH group bending vibration at 1323 cm^{-1} and the emergence of a distinct peak at 1277 cm^{-1}, characteristic of the free P−O stretching vibration. Additionally, the stretching vibration at 1025 cm^{-1} corresponding to the C−O bond of cellulose disappears, while two sharp peaks emerge at 1083 cm^{-1} and at 973 cm^{-1} corresponding to the out-of-plane P−O−C and in-plane P−O−C stretching, respectively. These spectral changes confirm the phosphorylation of hydroxyl groups in the cellulose matrix. Figure 2b represents the FTIR spectra of PCNCFH before and after uranium adsorption [samples after adsorption are labeled as (U−PCNCFH)]. The iron oxide content within the composite was confirmed using infrared

https://doi.org/10.1021/acssuschemeng.4c10246
ACS Sustainable Chem. Eng. 2025, 13, 1838−1850

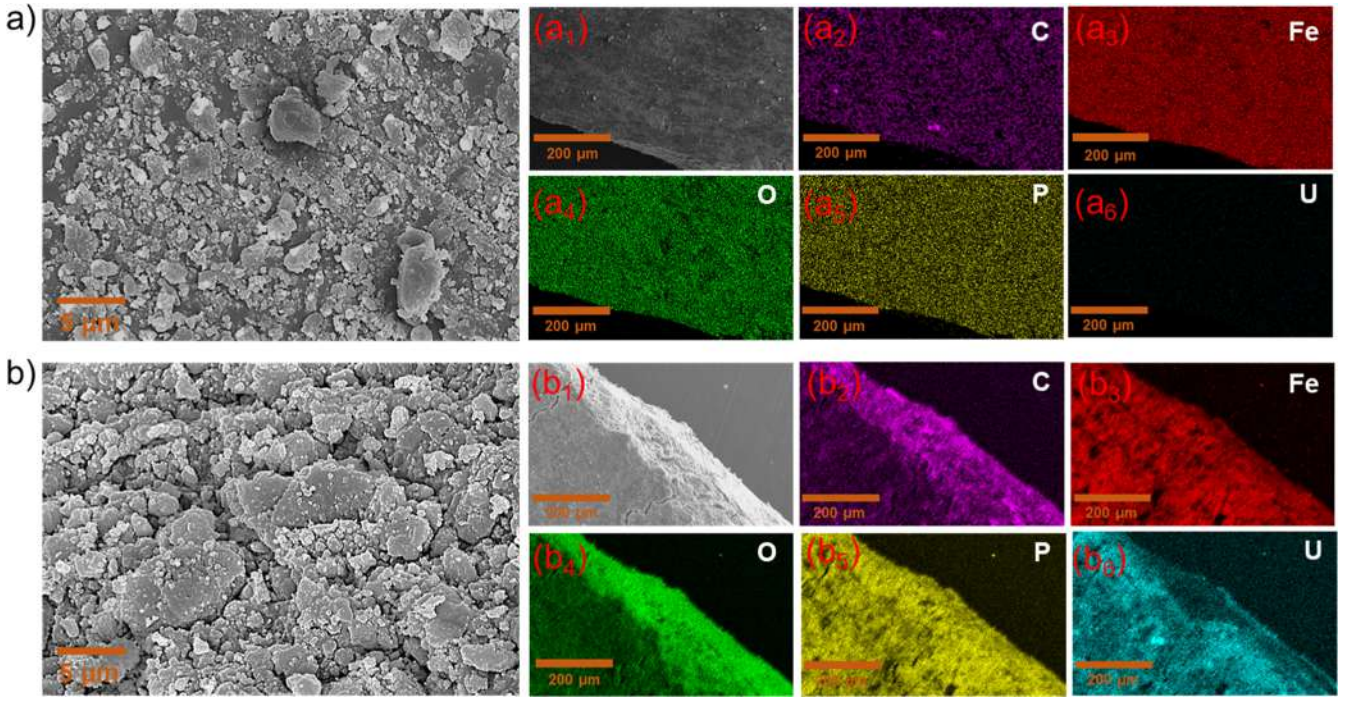


Figure 4. (a) SEM image of PCNCFH and corresponding EDS elemental mapping (a_1–a_6), and (b) SEM image of U–PCNCFH and corresponding EDS elemental mapping (b_1–b_6).

spectroscopy, revealing Fe–O vibrations within the range of 600–700 cm^{-1}. A prominent and intense absorption peak of the O–U–O bond overlaps with the weak P–O stretching vibration at 905 cm^{-1}.[45] The peak observed at 905 cm^{-1} corresponds to the asymmetric stretching vibration of the O–U–O bond, confirming the successful adsorption of uranyl ions onto the ferrihydrite surface.[5] Similar spectra were obtained for PMCC and PMCCFH [Figure S1(a,b)]. Figure 2c(i,iv) represents the high-resolution transmission electron microscopy (HRTEM) images of the PCNCFH and U–PCNCFH, respectively. From Figure 2c, it is confirmed that the iron oxyhydroxide nanoparticles were embedded within the cellulosic matrix, thereby confirming the formation of a composite.[47] This analysis is further supported by surface area measurements using the BET isotherm via N_2 adsorption. The specific surface area of the parent CNC was found to be 3.51 m^2/g, while the composite exhibited 299.89 m^2/g. This substantial increase in surface area may be attributed to the incorporation of nanoscale iron oxyhydroxide particles within the cellulose matrix, which also enhances U(VI) removal efficiency of the composite. Both the structures exhibit a predominantly amorphous nature. The amorphous nature of PCNCFH was further supported by the comparative powder XRD data (Figure S2), which reveal two broad peaks characteristic of amorphous or poorly crystalline phases. Specifically, the broad peaks observed at 25.08° and 63.4° correspond to the (110) and (221) planes, respectively, of goethite (α-FeOOH).[48] The phase remains stable under ambient conditions but progressively transforms into more stable forms of hematite and goethite upon exposure to electron beam irradiation for 25–30 min [Figure 2c(ii,iii)]. High-resolution lattice images of these phases are presented in insets d_1, d_2, d_3, and d_4. The phases were confirmed by the lattice planes of goethite (d_1, d_2) and hematite (d_3, d_4).[49]

Figure 3a presents the X-ray photoelectron spectroscopy (XPS) data of PCNCFH and U–PCNCFH. Figure 3b–f shows the deconvoluted spectra in the O 1s, P 2p, Fe 2p, Na 1s, and U 4f, regions, respectively. High-resolution C 1s spectra (Figure S3) reveal three characteristic peaks corresponding to 291.8 eV for the C–C bond, 286.1 eV for the C–OH and C–O–P bonds, and 284.7 eV for the–CH_2 bond. Shift can be observed in the case of the O 1s spectra (Figure 3b) of U–PCNCFH. Here, the O 1s peak of the parent PCNCFH composed of Fe–O, P–O, and C–O (C–OH, C–O–P, and O–C–O) shows peaks at 528.99, 529.98, and 534.6 eV, respectively. In U–PCNCFH, we can see a characteristic peak at 530.22 eV corresponding to the U–O bond. The P 2p spectrum of U–PCNCFH (Figure 3c) exhibits a blue shift compared to that of the pristine PCNCFH. It suggests that the phosphate groups play a crucial role in uranium removal. The Fe 2p spectra (Figure 3d) show a peak at 711.2 eV for $2p_{3/2}$ core level and a broad satellite feature at 718.4 eV, which is characteristic of Fe (III) species in iron oxyhydroxides.[51] The Fe 2p spectrum of U–PCNCFH shows a slight shift toward lower binding energy. This observation could be attributed to changes in the chemical environment of the adjacent oxygen atoms due to interaction with uranium. In the case of the Na 1s spectrum (Figure 3e) of U–PCNCFH, area under the peak is less as compared to the pristine PCNCFH. This is due to the replacement of some Na^+ of STMP with UO_2^{2+} after adsorption. The U 4f spectrum (Figure 3f) reveals two distinct interactions following adsorption: a U $4f_{7/2}$ peak at 379.0 eV, corresponding to the U–O bond (U-1), and a U $4f_{7/2}$ peak at 381.0 eV (U-2), corresponding to U–O–P. These two features appear in a 9:1 ratio, respectively. We interpret this observation in terms of two distinct kinds of interactions experienced by the hydrated uranyl species. The species $UO_2(H_2O)_5^{2+}$ can interact with the phosphorylated cellulose, hydroxyl groups of cellulose, as well as iron-oxyhydroxide, as

https://doi.org/10.1021/acssuschemeng.4c10246
ACS Sustainable Chem. Eng. 2025, 13, 1838–1850

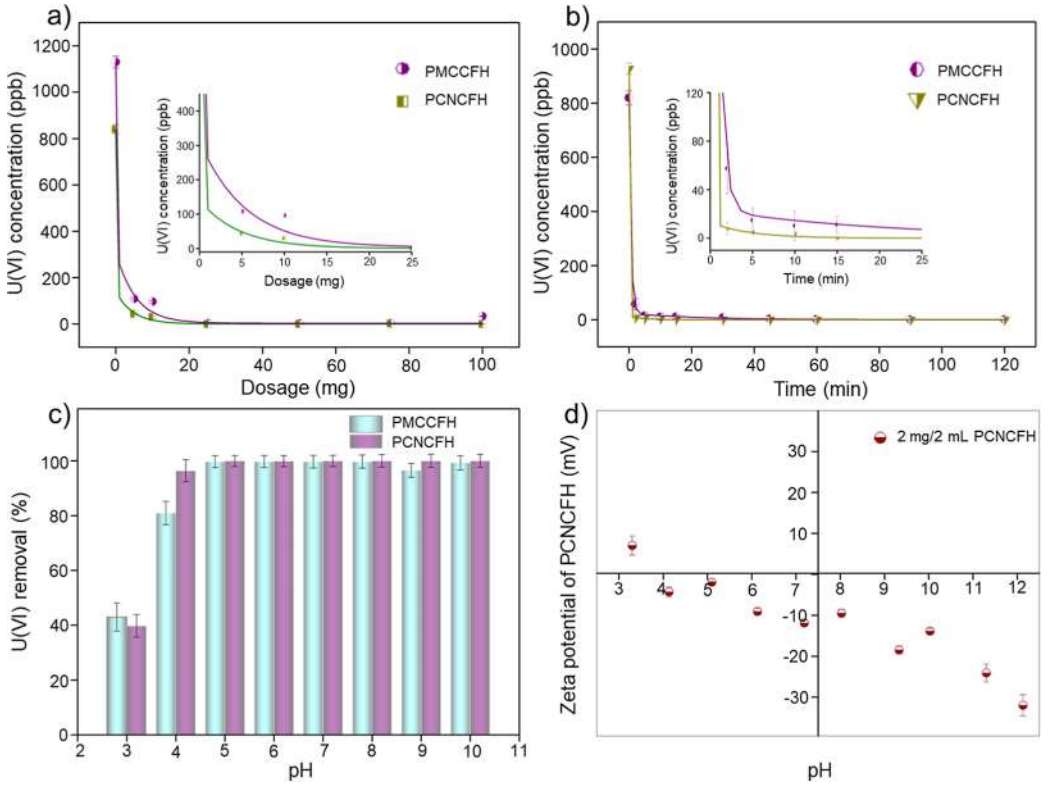


Figure 5. Batch study comparing the uranium removal performance of the composites, PMCCFH and PCNCFH. (a) Residual uranium concentrations as a function of composite dosage. (b) Residual uranium concentrations in relation to the contact time with the composites. (c) Performance of composites made of MCC and CNC toward uranium removal over a pH window of 3−10. (d) Zeta potential as a function of pH (range 3−11) for PCNCFH particles in water (2 mg in 2 mL). Insets in a,b show magnified images in the low concentration region, for clarity.

shown in the inset of Figure 3f. Latter two types of interactions are more common as these species are available in plenty and all the hydroxyl species are electron rich. Therefore, these contribute to the lower binding energy feature at 379.0 eV. The phosphine oxide binding, in contrast, reduces the electron density slightly at uranium, making it a higher binding energy feature at 381.0 eV. From the intensity, it is apparent that the available phosphorus sites are far too few in comparison to the hydroxyl groups.

The adsorption mechanism of U(VI) on PCNCFH is attributed to inner-sphere surface complexation, where uranium forms stable bonds with oxygen and phosphorus containing functional groups. These groups generate an electron-rich environment that enhances the U(VI) binding. Recent studies have emphasized the critical role of an electron-dense environment in U(VI) adsorption. For instance, Meng et al. (2024) developed an all-polymer-based 0*D*/2D C_4N/C_6N_7 material designed to efficiently separate charges, which helps create an electron-rich surface for better U(VI) removal. This material achieved >97% uranium removal under acidic conditions and maintained high efficiency even under radiation exposure.[52] Recent studies have demonstrated the role of secondary metal ions such as alkaline earth metals (e.g., Ca^{2+} and Mg^{2+}), transition metals (e.g., Fe^{3+} and Pb^{2+}), and lanthanides (e.g., Ce^{4+}, Th^{4+}) in stabilizing reduced uranium species during the electrochemical reduction processes, emphasizing the significance of strong binding interactions.[53] The combination of cellulose and Fe enhances the U(VI) sorption efficiency of PCNCFH. Cellulose provides hydroxyl and carboxyl groups for adsorption and complexation along with structural stability. Fe contributes additional active sites through coordination and facilitates the binding of U(VI). Furthermore, the nanostructured morphology of CNCs ensures a uniform dispersion of Fe, improving the accessibility of active sites and enabling efficient uranium removal through multiple mechanisms.

The SEM images of pristine PCNCFH and U−PCNCFH are shown in Figure 4a,b, respectively. Exposure to high concentration of uranium solution did not lead to any alterations in the particle morphology, indicating that the interaction mechanism is likely to be adsorption. EDS elemental mappings of PCNCFH and U−PCNCFH are presented in a_1−a_6 and b_1−b_6, respectively. From the EDS elemental mapping, it is confirmed that uranyl is evenly adsorbed and homogeneously distributed on PCNCFH. To support this, the EDS analysis of U−PCNCFH is depicted in Figure S4, with the weight percentages of each element.

Batch Adsorption Studies of Uranium Adsorption on Cellulosic Composites. Figure 5 shows the comparative batch adsorption performance of PCNCFH and PMCCFH toward uranium uptake from water. As illustrated in Figure 5a, it is evident that both of the composites demonstrate exceptional performance upon treating 100 mL of water spiked with 1.1 mg/L uranium using various dosages of adsorbent composites, ranging from 5 to 100 mg. For both the composites, within 2 h of exposure, uranium concentrations drop to less than 15 μg/L upon adding just 25 mg of the composite. Figure 5b illustrates the rapid uptake kinetics of the composites, where the initial uranium concentration of 950 μg/L was quickly reduced to less than 10 μg/L within 2 min of incubation due to the abundance of available free surface sites. The residual uranium concentration decreased even further at

https://doi.org/10.1021/acssuschemeng.4c10246
ACS Sustainable Chem. Eng. 2025, 13, 1838−1850

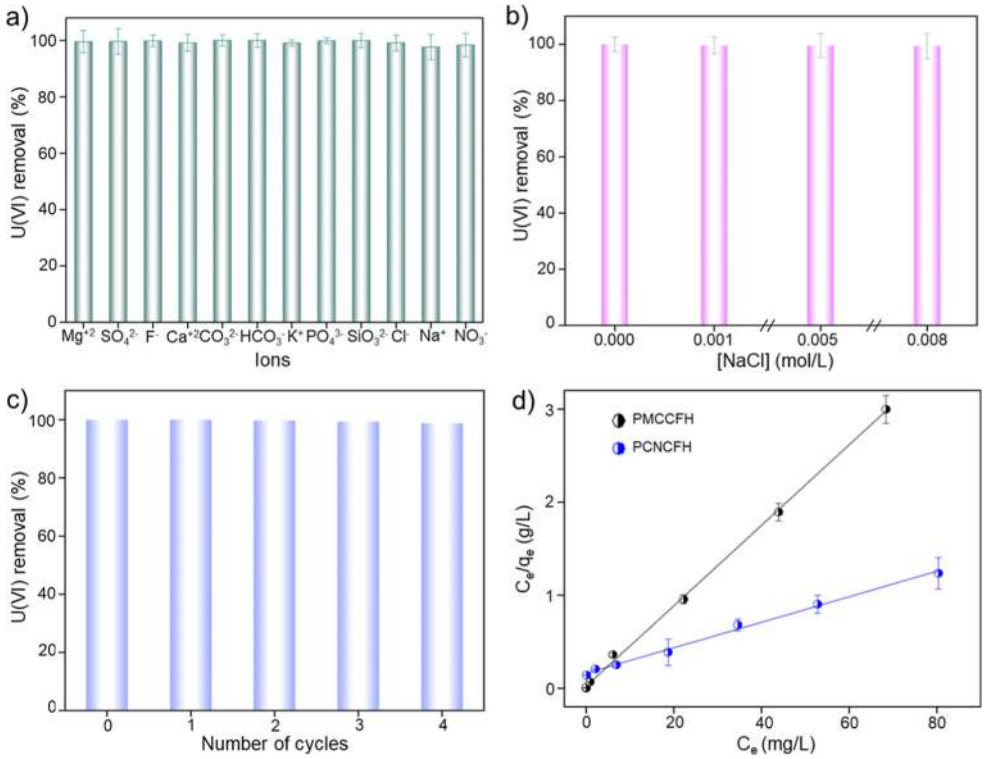


Figure 6. (a) Adsorption selectivity of PCNCFH for uranium in the presence of multiple metals, at concentrations of relevance to tap water. (b) Effect of ionic strength for the uranium adsorption capacity. (c) Regeneration performance of PCNCFH toward uranium adsorption using 0.01 M HNO_3. (d) Langmuir adsorption isotherms of the composites for comparing the maximum uptake capacities of uranium.

the end of 2 h, following slower kinetics. It is clear that the PCNCFH is more effective in uranium removal.

To better understand the system, data from the kinetics study were initially evaluated using a reaction model named Ho's pseudo-second-order model (Figure S5). The plots illustrating the relationship between t/q_t [where q_t is the amount of adsorbate adsorbed at time t (mg/g)] against time (for the adsorption of uranium) followed the pseudo-second-order model. The correlation coefficients approached unity (>0.9999), indicating that the availability of surface sites significantly impacted the adsorption process, thus playing a major role in determining the overall rate. From this, it was calculated that q_e (the amount of adsorbate adsorbed at equilibrium) is 3711.95 mg/g and k_2 (the rate constant of pseudo-second-order adsorption) is 0.01939 g/mg min. This also suggests that the primary mechanism for the removal of uranium by PCNCFH could be the complexation of phosphorus and oxygen containing groups with uranium. The following complexation equations could also contribute to the overall adsorption rate.

$$\equiv FeOH + UO_2^{2+} \leftrightarrow FeOUO_2^{+} + H^{+} \quad \text{(i)}$$

$$\equiv FeOH + UO_2^{2+} + H_2O \leftrightarrow FeOUO_2(OH)^0 + 2H^{+} \quad \text{(ii)}$$

where ≡ denotes the reactive sites on the surface of the solid adsorbent.

In an open environment, the adsorbed species of uranium on iron oxyhydroxides consisted of $\equiv FeOUO_2^{+}$ at pH below 4.5 and $\equiv FeOUO_2(OH)^0$ at pH above 4.5.[54,55] In contrast to the photochemical generation of studtite ($(UO_2)(O_2).4H_2O$) nanodots facilitated by H_2O_2 on imine-based covalent organic framework photocatalysts, uranium adsorption on PCNCFH proceeds through the formation of inner-sphere surface complexes with oxygen-donating functional groups such as hydroxyl and phosphorus groups, as evidenced by XPS and FTIR analyses.[56] The sorption capacity of both PCNCFH and PMCCFH toward uranium was also examined under different pH conditions. As illustrated in Figure 5c, all of the composites demonstrated outstanding effectiveness within a wide pH range of pH 4−10. We find that PCNCFH performs better than PMCCFH due to its larger specific surface area, attributed to its distinctive nanostructure. The BET analysis revealed that the surface area of PCNCFH was 299.89 m^2/g, whereas that of PMCCFH exhibited a surface area of 276.71 m^2/g. Figure 5d represents the zeta potential of PCNCFH in aqueous solutions, which explains their pH-dependent sorption behavior. As we can see from the figure, sorption efficiency of both the composites is very high in basic pH as compared to that in acidic pH. As the pH level was changed from acidic to alkaline conditions, the zeta potential exhibited a transition from a positive value of +7.01 mV at pH 3 to a negative value of −32 mV at pH 12. At a low pH level (pH 3), $Fe^{3+}-O^{2-}$ (from ferrihydrite) and C−OH (from cellulose) groups of nanocomposites would undergo protonation, resulting in the formation of $Fe^{3+}-$ OH and $C-OH_2^{+}$ species. This would cause the composite to carry a positive charge below pH 4.0. The positively charged adsorbent would repel UO_2^{2+} electrostatically, which is the dominant species below pH 5.0. Electrostatic repulsion between the adsorbent and adsorbate led to a decreased efficiency of adsorption. As the pH increases, the sorbent becomes more negatively charged and shows a strong attraction to uranium species that are dominant in alkaline conditions, such as $[(UO_2)_3(OH)_5^{+}]$ and $[(UO_2)_2(OH)_2^{2+}]$.[57] Furthermore, to gain deeper insights into the mechanism, diverse isotherm models such as

https://doi.org/10.1021/acssuschemeng.4c10246
ACS Sustainable Chem. Eng. 2025, 13, 1838−1850

Freundlich and Langmuir were assessed.[58,59] The Freundlich isotherm yielded a correlation coefficient (R^2) of 0.949, which is inferior to the R^2 = 0.994 value acquired from the Langmuir fit (Figures S6 and 6d). This indicates a prevalent chemisorption pathway for the UO_2^{2+} species.

Since natural groundwater typically contains a variety of other ions, it is crucial to assess the impact of these coexisting ions on the adsorption of UO_2^{2+} by PCNCFH. Figure 6a represents the uranium uptake performance of PCNCFH in the presence of ions such as Mg^{2+}, SO_4^{2-}, F^-, Ca^{2+}, CO_3^{2-}, HCO_3^-, K^+, PO_4^{3-}, SiO_3^{2-}, Cl^-, Na^+, and NO_3^- with concentrations relevant to tap water. PCNCFH maintains a uranium removal effectiveness of >98% in the presence of all other anions, except for sodium. It may be due to increase of ionic strength of the solution due to high concentration of sodium, in agreement with the Na^+ release mentioned in the section on XPS. To further understand the influence of ionic strength on uranium adsorption by PCNCFH in detail, we have conducted ionic strength experiment by varying the concentration of NaCl from 0.001 to 0.008 M, representing the maximum TDS levels permissible in groundwater or drinking water. As shown in Figure 6b, uranium removal efficiency remains consistently above 99% even at 0.008 M NaCl, indicating no significant reduction in performance compared with a pristine U(VI) solution. This observation suggests that uranium uptake capacity of PCNCFH in groundwater level is unaffected by ionic strength, affirming that the adsorption process predominantly involves inner-sphere surface complexation rather than outer-sphere interactions.[60] We evaluated the uranium uptake performance of PCNCFH in a multi-ion solution containing major heavy metals such as Cu(II), Cd(II), Al(III), Zn(II), Mn(II), Mg(II), Cr(III), Li(I), Co(II), and Ni(II) with concentrations up to 1 ppm (Figure S7). Metal ion removal percentage is calculated using the equation mentioned (Supporting Information, eq i). Despite the existence of several interfering cations, PCNCFH shows a uranium removal efficiency of >88%. Al(III) and Cr(III) are two main competitors for adsorption. Notably, it has the added advantage of simultaneously removing uranium with toxic contaminants such as chromium, highlighting its versatile remediation potential. The concurrent removal of chromium and aluminum, alongside uranium by iron oxide-based materials can be attributed to the speciation of these ions at specific pH. In the pH range of 5−7, Cr(III) and Al(III) predominantly exist as hydroxylated species such as $Cr(OH)^{2+}$, $Cr(OH)_2^+$ and $Al(OH)_2^+$, $Al(OH)_3$, which exhibit stronger affinities for oxygen-donating functional groups (e.g., hydroxyl, phosphate).[61−63] Conversely, the adsorption of Zn(II), Mn(II), Li(I), Co(II), and Ni(II) is significantly lower, likely due to their lower charge density compared to those of Cr(III), Al(III), and U(VI). This result demonstrates that PCNCFH adsorbent possesses good selectivity for uranium in water with a significant number of relevant ions. Considering that V(V) and U(VI) have similar properties for binding to oxygen-containing functional groups, U(VI) adsorption experiments were carried out in the presence of V(V), with concentrations of both the metals being nearly equal (Figure S8). The results indicate that the presence of V(V) does not adversely affect the U(VI) removal efficiency of PCNCFH, but it can also remove V(V) up to 85%. However, it is worth noting that V(V) concentrations are negligible in uranium-contaminated groundwater regions of India.[64] Figure 6c shows the regeneration of PCNCFH up to four cycles toward uranium adsorption. The reusability of sorbents is a crucial characteristic that impacts their environmental sustainability and economic viability.[65] Here, 0.01 M HNO_3 was used as the eluent, and the continuous adsorption−desorption cycle revealed that regeneration efficiency of the sorbent is above 99% even after four continuous cycles. HNO_3 is a good eluting agent as regeneration happens within 90 min of the reaction. This can be attributed to the protonation of the negatively charged surface groups such as hydroxyl groups on PCNCFH in acidic solutions. This reduces the electrostatic attraction between the surface and adsorbed uranium species (often in the form of uranyl ions, UO_2^{2+}).[54] Adsorbed uranyl cations on the adsorbent can form water-soluble uranyl nitrate complexes such as $UO_2(NO_3)_2$. Formation of these soluble complexes facilitates the desorption of uranium from the adsorbent surface into the solution. The adsorption isotherm of both the composites (PCNCFH and PMCCFH) at neutral pH and room temperature was examined using the Langmuir equation to obtain a better understanding of the adsorption mechanism and efficiency. The plots of C_e/q_e against C_e exhibit linear relationships when utilizing the linearized form of the Langmuir eq (Supporting Information, eqs S3 and S4) for both the composites, as illustrated in Figure 6d. A linear relationship observed in the plot of C_e/q_e against C_e, coupled with a high correlation coefficient value exceeding 0.99 in each instance, suggests that the mechanism was monolayer adsorption. PCNCFH exhibited a higher adsorption capacity compared to PMCCFH.

The differences in U(VI) sorption performance between PMCCFH and PCNCFH, as seen in Figure 5 and Table 1, can be attributed to the experimental conditions and material structure. In Figure 5, adsorption studies were performed with an initial uranium concentration of 1 ppm, consistent with typical uranium levels in Indian groundwater, showing minimal differences in U(VI) removal efficiency at this lower concentration. However, the maximum adsorption capacity, calculated from the Langmuir isotherms in Table 1 with uranium concentrations up to 150 ppm, shows a substantially higher sorption capacity for PCNCFH. This is due to the nanostructure of PCNCFH, which provides a larger surface

Table 1. Comparison of the Adsorption Capacity of PCNCFH with Other Reported Cellulose-Based Adsorbents from the Literature

adsorbents	q_{max} (mg/g)	pH and temperature	refs
amidoximated cellulose	52.88	5.0	66
cellulose microspheres modified by *n*-aminotrizole, *n* = 3 *n* = 4	98.90 (*n* = 3) and 72.20 (*n* = 4)	5.0	67
plasma-light-amidoxime-cellulose	101.15	6 and 303 K	68
PGTDC−COOH	99.4	6	69
Poly(B2MEP)-*g*-cellulose	79.9		70
PCNCFH	100	neutral	this work
PMCCFH	25	neutral	this work
cellulose p-toluidine	80	10.5	71
Fe_2O_3-impregnated cellulose beads	7.6	7	72
phosphate-functionalized bacterial cellulose	50.65	4.0−8.0	73
graphene oxide-cellulose (GOC)	101.01		74

https://doi.org/10.1021/acssuschemeng.4c10246
ACS Sustainable Chem. Eng. 2025, 13, 1838−1850

area and more accessible active sites compared to the microstructure of PMCCFH. At higher concentrations, these features enable PCNCFH to achieve much greater uranium removal efficiency. This highlights the critical role of nanostructure in enhancing sorption performance.

The thermal stability of PCNCFH was assessed through thermogravimetric analysis (TGA) conducted under both nitrogen and air atmospheres (Figure S8). The composite experiences weight losses of 25.66% and 28.61% as it was heated from room temperature to 1000 °C in nitrogen and air atmospheres, respectively. The composite initially releases loosely bound water from both its interior and exterior surfaces up to 100 °C, accounting for the initial weight loss. Subsequently, significant thermal degradation of the cellulosic framework occurs as the temperature reaches 250−300 °C.

Preliminary Sustainability Evaluation. Water treatment processes often require substantial energy consumption and have numerous economic, environmental, and social implications. Consequently, for a technology to be sustainable, it must address the three core aspects of sustainability: environmental, economic, and societal.[75] To evaluate these parameters, it is essential to first determine the extent of its "greenness" by assessing some relevant sustainability parameters.[76−78] The formulas used to compute the sustainability metrics are detailed as eqs 4−8 in Supporting Information

Resource Efficiency. One of the primary raw materials is cellulose, which is both biodegradable and renewable. CNCs are derived from cellulose and are abundantly available from renewable sources such as wood pulp, waste materials, and agricultural residues. This makes CNCs a sustainable alternative to nonrenewable materials. Alkali and iron salts were utilized in minimal amounts, both of which are not considered toxic. Additionally, water was used as the solvent in the process. The mass intensity (excluding water) was determined to be 3.11, while the water intensity was measured as 22.28. The reaction mass efficiency was calculated to be 32.08%. Enhancing the reaction mass efficiency can be accomplished by further optimizing the quantities of reactants and minimizing the use of surplus reagents.

Energy Use. Electricity was employed for the purposes of stirring, vacuum filtration, and drying. There will be no consumption of energy in the operation of the technology. The energy intensity, determined through the lab-scale synthesis setup, was 2.63 kW·h/kg of the composite. Mukherjee et al. reported the energy use of 2.3 kW h/kg for cellulose-ferrihydrite composite, which is comparable with the above-mentioned value.[59]

Emission. No deleterious solvents or fumes or secondary products were emitted during the synthesis of the composite. The E-factor was 0.11, signifying minimal release of harmful byproducts.

Similar calculations were also performed for PCNC (Table S2).

Toxicity potential of the reagents In toxicology analysis, LD_{50} (Lethal Dose 50) values are important because they provide a standardized measure of the acute toxicity of a substance. LD_{50} represents the dose of a substance required to cause death in 50% of a population of test animals (typically rodents) within a specified time period. The lower the value of LD_{50}, the more toxic the substance is. The LD_{50} values for some common phosphorylated reagents are presented in Table 2. Here, STMP is used as the phosphorylating agent for cellulose. STMP is less toxic than other phosphorylating agents such as phosphoric acid, phosphorus acid, and diphosphorus pentoxide.

Table 2. Comparison of LD_{50} Values of Different Phosphorylating Agents

phosphorylating agent	route	organism	dose (mg/kg)
STMP	oral	rat	3650
phosphoric acid	oral	rat	1530
phosphorous acid	oral	rat	1560−1580
diphosphorus pentoxide	oral	rat	200

Furthermore, according to the European Chemicals Agency (ECHA), $FeCl_3$ (ferric chloride) has been categorized as a skin irritant, while NaOH (sodium hydroxide) has been classified as corrosive. Despite these classifications, both substances exhibit nonflammable properties and remain stable at ambient temperature.

Waste Management. Uranium-loaded composites underwent repeated regeneration processes through acidic treatments to facilitate subsequent adsorption cycles. They can be disposed of by methods such as encapsulation in cementitious materials, incorporation into ceramic waste forms, deep geological disposal, and incineration followed by immobilization.

Societal Approval. The social acceptability of a technology based on adsorption depends on various factors, including its perceived benefits, potential risks, and alignment with societal values and norms. The PCNCFH-based technology is environmentally sustainable, straightforward, and economically efficient and does not entail excessive operational expenses. Therefore, it is anticipated that the project will garner significant acceptance from the impacted communities.

The TCLP studies, following the USEPA standard SW-846 Test Method 1311, were performed on saturated composite PCNCFH to evaluate the potential leaching of adsorbed uranium. The analysis indicated a leaching concentration of 2.41 mg/L, which is below the permissible limits. We have taken the limit of leaching as that of arsenic as no limit for TCLP is mentioned for uranium.[79] Note that limit of arsenic in drinking water (10 ppb) is below that of uranium (30 ppb), and so, using the arsenic limit in TCLP is justified.

By considering the maximum adsorption capacity of PCNCFH as 100 mg/g, we have theoretically assessed the cost of this technology, including both material and electricity expenses. It is estimated that this method can deliver uranium-free water at a cost of less than rupee 14.60 per 1000 L of clean water ($0.17 per 1000 L).

CONCLUSIONS

We employed a sustainable and cost-effective method to synthesize a phosphorylated cellulose ferrihydrite composite for uranium removal from water. The composite, PCNCFH, exhibited superior performance over PMCCFH in adsorbing uranium. Both the oxygen and phosphorus groups on the composite surface serve as the binding sites for uranium adsorption. The enhanced capacity of PCNCFH is found to be due to the enhanced specific surface area of the adsorbent. Equilibrium was reached within 2 min of the reaction (at C_o = 1 ppm, adsorbent dose, 25 mg). Utilizing the Langmuir model, the highest adsorption capacity of PCNCFH for uranium was determined to be 100 mg/g at room temperature and neutral pH. Furthermore, the composite demonstrated effectiveness across a wide pH range and in the presence of various

https://doi.org/10.1021/acssuschemeng.4c10246
ACS Sustainable Chem. Eng. 2025, 13, 1838−1850

interfering ions. SEM, HRTEM, XPS, and IR analyses confirmed that the surface morphology of both the composites remained unchanged even after saturation with uranium, while TCLP results indicated negligible leaching of uranium from PCNCFH. PCNCFH displayed efficient reusability for up to 4 cycles with a minimal decrease in adsorption efficiency. Assessing the sustainability metrics further offered deeper insights into the socioeconomic benefits and environmental impact of the manufacturing process of nanocomposites. Due to its high uranium extraction capacity, affordability, and rapid adsorption rate, PCNCFH emerged as a promising bio-adsorbent for uranium extraction from water.

■ ASSOCIATED CONTENT

Supporting Information

The Supporting Information is available free of charge at https://pubs.acs.org/doi/10.1021/acssuschemeng.4c10246.

Instrumentation; materials, synthesis, and batch adsorption studies; comparative FTIR spectra of phosphorylated MCC and blank MCC; powder XRD patterns of blank cellulose nanocrystal (CNC), phosphorylated CNC, and PCNCFH; deconvoluted XPS spectra of C 1s of PCNCFH before and after U(VI) adsorption; SEM-EDS of PCNCFH after U(VI) adsorption with weight percentage of elements; pseudo-second-order reaction kinetics plot for the adsorption of uranium on PCNCFH; Freundlich adsorption isotherm model showing the correlation coefficient for uranium adsorption on PCNCFH; selectivity of adsorption of PCNCFH for multiple metals; effect of V(V) on U(VI) adsorption on PCNCFH; thermogravimetric analysis (TGA) of PCNCFH at air and nitrogen atmospheres from room temperature to 900 °C with 10 min scan rates; equations used in the main text; composition of synthetic tap water; and sustainability metrics evaluation for the synthesis of PCNC (PDF)

■ AUTHOR INFORMATION

Corresponding Author

Thalappil Pradeep − *DST Unit of Nanoscience (DST UNS) and Thematic Unit of Excellence (TUE), Department of Chemistry, Indian Institute of Technology Madras, Chennai 600036, India;* orcid.org/0000-0003-3174-534X; Email: pradeep@iitm.ac.in

Authors

Tanmayaa Nayak − *DST Unit of Nanoscience (DST UNS) and Thematic Unit of Excellence (TUE), Department of Chemistry, Indian Institute of Technology Madras, Chennai 600036, India*

Sritama Mukherjee − *DST Unit of Nanoscience (DST UNS) and Thematic Unit of Excellence (TUE), Department of Chemistry, Indian Institute of Technology Madras, Chennai 600036, India;* orcid.org/0000-0002-3204-3043

Amoghavarsha Ramachandra Kini − *DST Unit of Nanoscience (DST UNS) and Thematic Unit of Excellence (TUE), Department of Chemistry, Indian Institute of Technology Madras, Chennai 600036, India;* orcid.org/0009-0003-6863-7729

Md Rabiul Islam − *DST Unit of Nanoscience (DST UNS) and Thematic Unit of Excellence (TUE), Department of Chemistry, Indian Institute of Technology Madras, Chennai 600036, India;* orcid.org/0000-0001-6454-4013

Ankit Nagar − *DST Unit of Nanoscience (DST UNS) and Thematic Unit of Excellence (TUE), Department of Chemistry, Indian Institute of Technology Madras, Chennai 600036, India*

Sonali Seth − *DST Unit of Nanoscience (DST UNS) and Thematic Unit of Excellence (TUE), Department of Chemistry, Indian Institute of Technology Madras, Chennai 600036, India*

Complete contact information is available at: https://pubs.acs.org/10.1021/acssuschemeng.4c10246

Notes

The authors declare no competing financial interest.

■ ACKNOWLEDGMENTS

Authors thank B. K. Spoorthi and S. Banupriya for TEM measurements. The authors also thank the Common facility, Department of Chemistry, IIT Madras, and Sophisticated Analytical Instrument Facility at IIT Madras for XRD and TGA measurements, respectively. T.P. acknowledges financial support of SERB SUPRA (Grant SPR/2021/000439) and funding from the Centre of Excellence on Molecular Materials and Functions under the Institution of Eminence scheme of IIT Madras. T.N. thanks the Ministry of Human Resource Development, Government of India, for a senior research fellowship. A.R.K. thanks CSIR for his research fellowship. The authors also acknowledge the Department of Science and Technology, Government of India, for supporting our research program on nanomaterials.

■ REFERENCES

(1) Liddle, S. T. The Renaissance of Non-Aqueous Uranium Chemistry. *AngewandteReviews* **2015**, *54* (30), 8604−8641.

(2) Chen, L.; Liu, J.; Zhang, W.; Zhou, J.; Luo, D.; Li, Z. Uranium (U) Source, Speciation, Uptake, Toxicity and Bioremediation Strategies in Soil-Plant System: A Review. *J. Hazard. Mater.* **2021**, *413*, 125319.

(3) Skierszkan, E. K.; Schoepfer, V. A.; Fellwock, M.; Lindsay, M. B. J. Uranium Speciation and Mobilization in Thawing Permafrost. *Environ. Sci. Technol.* **2024**, *58*, 17058.

(4) Zhang, D.; Fang, L.; Liu, L.; Zhao, B.; Hu, B.; Yu, S.; Wang, X. Uranium Extraction from Seawater by Novel Materials: A Review. *Sep. Purif. Technol.* **2023**, *320*, 124204.

(5) Lu, G.; Haes, A. J.; Forbes, T. Z. Detection and Identification of Solids, Surfaces, and Solutions of Uranium Using Vibrational Spectroscopy. *Coord. Chem. Rev.* **2018**, *374*, 314−344.

(6) Rani, N.; Singh, P.; Kumar, S.; Kumar, P.; Bhankar, V.; Kamra, N.; Kumar, K. Recent Advancement in Nanomaterials for the Detection and Removal of Uranium: A Review. *Environ. Res.* **2023**, *234*, 116536.

(7) Chaudhari, U.; Mehta, M.; Sahoo, P. K.; Mittal, S.; Tiwari, R. P. Co-Occurrence of Geogenic Uranium and Fluoride in a Semiarid Belt of the Punjab Plains, India. *Groundw. Sustain. Dev.* **2023**, *23*, 101019.

(8) Nolan, J.; Weber, K. A. Natural Uranium Contamination in Major U.S. Aquifers Linked to Nitrate. *Environ. Sci. Technol. Lett.* **2015**, *2* (8), 215−220.

(9) Coyte, R. M.; Jain, R. C.; Srivastava, S. K.; Sharma, K. C.; Khalil, A.; Ma, L.; Vengosh, A. Large-Scale Uranium Contamination of Groundwater Resources in India. *Environ. Sci. Technol. Lett.* **2018**, *5* (6), 341−347.

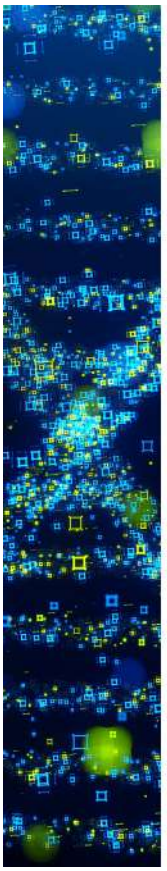
(10) Coyte, R. M.; Vengosh, A. Factors Controlling the Risks of Co-Occurrence of the Redox-Sensitive Elements of Arsenic, Chromium,

Vanadium, and Uranium in Groundwater from the Eastern United States. *Environ. Sci. Technol.* **2020**, *54* (7), 4367−4375.
(11) Hassan, A.; Mollah, M. M. R.; Jayashree, R.; Jain, A.; Das, S.; Das, N. Ultrafast Removal of Thorium and Uranium from Radioactive Waste and Groundwater Using Highly Efficient and Radiation-Resistant Functionalized Triptycene-Based Porous Organic Polymers. *ACS Appl. Mater. Interfaces* **2024**, *16* (19), 24547−24561.
(12) Orloff, K. G.; Mistry, K.; Charp, P.; Metcalf, S.; Marino, R.; Shelly, T.; Melaro, E.; Donohoe, A. M.; Jones, R. L. Human Exposure to Uranium in Groundwater. *Environ. Res.* **2004**, *94* (3), 319−326.
(13) Kurttio, P.; Komulainen, H.; Leino, A.; Salonen, L.; Auvinen, A.; Saha, H. Bone as a Possible Target of Chemical Toxicity of Natural Uranium in Drinking Water. *Environ. Health Perspect.* **2005**, *113* (1), 68−72.
(14) Canu, I. G.; Ellis, E. D.; Tirmarche, M. Cancer Risk In Nuclear Workers Occupationally Exposed To Uranium—Emphasis On Internal Exposure. *Health Phys.* **2008**, *94* (1), 1−17.
(15) *Uranium Occurrence In Shallow Aquifer In India*, 2020. https://www.cgwb.gov.in/old_website/WQ/URANIUM_REPORT_2019-20.pdf (accessed 2024−07−27).
(16) Meng, C.; Du, M.; Zhang, Z.; Liu, Q.; Yan, C.; Li, Z.; Dong, Z.; Luo, J.; Ma, J.; Liu, Y.; Wang, X. Open-Framework Vanadate as Efficient Ion Exchanger for Uranyl Removal. *Environ. Sci. Technol.* **2024**, *58* (21), 9456−9465.
(17) Liu, T.; Li, Z.; Zhang, X.; Tan, H.; Chen, Z.; Wu, J.; Chen, J.; Qiu, H. Metal−Organic Framework-Intercalated Graphene Oxide Membranes for Selective Separation of Uranium. *Anal. Chem.* **2021**, *93* (48), 16175−16183.
(18) Zarrougui, R.; Ferhi, N.; Raouafi, N.; Hamzaoui, A. H.; Messaoudi, S. Advanced Uranium Removal with Pure, Nonfluorinated Ionic Liquids: Fine-Tuning Hydrophilic and Hydrophobic Properties for Enhanced Selectivity. *Inorg. Chem.* **2024**, *63* (18), 8059−8069.
(19) Wang, S.; Yang, X.; Xu, L.; Miao, Y.; Yang, X.; Xiao, C. Selective Extraction of Uranium(VI) from Thorium(IV) Using New Unsymmetrical Acidic Phenanthroline Carboxamide Ligands. *Ind. Eng. Chem. Res.* **2023**, *62* (38), 15613−15624.
(20) Lin, T.; Chen, T.; Jiao, C.; Zhang, H.; Hou, K.; Jin, H.; Liu, Y.; Zhu, W.; He, R. Ion Pair Sites for Efficient Electrochemical Extraction of Uranium in Real Nuclear Wastewater. *Nat. Commun.* **2024**, *15* (1), 4149.
(21) Li, Y.; Wang, S.; Wang, X. Highly Selective Removal of U(VI) from Aqueous Solutions by Porous Nanomaterials. *EcoEnergy* **2024**, *2* (2), 205−219.
(22) Ma, X.; Meihaus, K. R.; Yang, Y.; Zheng, Y.; Cui, F.; Li, J.; Zhao, Y.; Jiang, B.; Yuan, Y.; Long, J. R.; Zhu, G. Photocatalytic Extraction of Uranium from Seawater Using Covalent Organic Framework Nanowires. *J. Am. Chem. Soc.* **2024**, *146* (33), 23566−23573.
(23) Balakrishnan, A.; Kunnel, E. S.; Sasidharan, R.; Chinthala, M.; Kumar, A. Tailored Citric Acid-Functionalized Carbon Nitride Homojunction-Immobilized Carboxymethyl Cellulose 3D Photocatalytic Hydrogels: A Multifaceted Approach toward Environmental Remediation. *ACS Sustain. Chem. Eng.* **2024**, *12* (13), 5169−5185.
(24) Bolisetty, S.; Peydayesh, M.; Mezzenga, R. Sustainable Technologies for Water Purification from Heavy Metals: Review and Analysis. *Chem. Soc. Rev.* **2019**, *48* (2), 463−487.
(25) Tuo, K.; Li, J.; Li, Y.; Liang, C.; Shao, C.; Hou, W.; Li, Z.; Pu, S.; Deng, C. Construction of Hierarchical Porous and Polydopamine/Salicylaldoxime Functionalized Zeolitic Imidazolate Framework-8 *via* Controlled Etching for Uranium Adsorption. *Mater. Horiz.* **2024**, *11* (14), 3364−3374.
(26) Zhang, N.; Li, J.; Tian, B.; Li, T.; Zhang, J.; Wang, Q.; Zhao, H. RIGP-Induced Surface Modification of Cellulose for the Preparation of Amidoxime-Modified Cellulose/Graphite Oxide Composites with Enhanced Uranium Adsorption. *Ind. Eng. Chem. Res.* **2024**, *63* (5), 2337−2346.
(27) Liao, J.; Ding, C.; Shi, J.; Jiang, L.; Wang, Q.; Wang, L. Efficient Separation of Uranium(VI) by $CaCO_3$-Doped Chitosan with PO_4^{3-} Modification: Adsorption Behaviors and Mechanism Study. *ACS Appl. Polym. Mater.* **2024**, *6*, 4885−4895.
(28) Ji, D.; Wang, Y.; Liu, Y.; Hao, S.; Yang, J.; Yan, Y.; Lu, C.; Guan, S.; Gao, Q.; Wu, H. Efficient Capture of Uranium by a Hydroxyapatite-Modified Polyethyleneimine@carbon Nanotube Composite from Radioactive Nuclear Waste. *Dalton Trans.* **2023**, *52* (29), 10136−10144.
(29) Wall, N. A.; Maulden, E.; Gager, E. J.; Ta, A. T.; Ullberg, R. S.; Zeng, G.; Nava-Farias, L.; Sims, A. P.; Nino, J. C.; Phillpot, S. R.; Szecsody, J. E.; Pearce, C. I. Functionalized Clays for Radionuclide Sequestration: A Review. *ACS Earth Space Chem.* **2022**, *6* (11), 2552−2574.
(30) Zhao, M.; Cui, Z.; Pan, D.; Fan, F.; Tang, J.; Hu, Y.; Xu, Y.; Zhang, P.; Li, P.; Kong, X.-Y.; Wu, W. An Efficient Uranium Adsorption Magnetic Platform Based on Amidoxime-Functionalized Flower-like Fe_3O_4@TiO_2 Core−Shell Microspheres. *ACS Appl. Mater. Interfaces* **2021**, *13* (15), 17931−17939.
(31) Gandhi, T. P.; Sampath, P. V.; Maliyekkal, S. M. A Critical Review of Uranium Contamination in Groundwater: Treatment and Sludge Disposal. *Sci. Total Environ.* **2022**, *825*, 153947.
(32) Xie, Y.; Yu, L.; Chen, L.; Chen, C.; Wang, L.; Liu, F.; Liao, Y.; Zhang, P.; Chen, T.; Yuan, Y.; Lu, Y.; Huang, B.; Yang, H.; Wang, S.; Wang, S.; Ma, L.; Luo, F.; Liu, Y.; Hu, B.; Wang, H.; Pan, D.; Zhu, W.; Wang, N.; Wang, Z.; Mao, L.; Ma, S.; Wang, X. Recent Progress of Radionuclides Separation by Porous Materials. *Sci. China Chem.* **2024**, *67* (11), 3515−3577.
(33) Hao, M.; Liu, Y.; Wu, W.; Wang, S.; Yang, X.; Chen, Z.; Tang, Z.; Huang, Q.; Wang, S.; Yang, H.; Wang, X. Advanced Porous Adsorbents for Radionuclides Elimination. *EnergyChem.* **2023**, *5* (4), 100101.
(34) Zhang, K. H.; Huang, Z.; Yang, M.; Liu, M.; Zhou, Y.; Zhan, J.; Zhou, Y. Recent Progress in Melt Pyrolysis: Fabrication and Applications of High-Value Carbon Materials from Abundant Sources. *Susmat* **2023**, *3* (5), 558−580.
(35) Wang, X.; Xiao, C.; Qi, J.; Guo, X.; Qi, L.; Zhou, Y.; Zhu, Z.; Yang, Y.; Li, J. Enhancing Uranium Removal with a Titanium-Incorporated Zirconium-Based Metal−Organic Framework. *Langmuir* **2023**, *39* (48), 17366−17377.
(36) Wang, L.; Shi, C.; Wang, L.; Pan, L.; Zhang, X.; Zou, J.-J. Rational Design, Synthesis, Adsorption Principles and Applications of Metal Oxide Adsorbents: A Review. *Nanoscale* **2020**, *12* (8), 4790−4815.
(37) Aragaw, T. A.; Bogale, F. M.; Aragaw, B. A. Iron-Based Nanoparticles in Wastewater Treatment: A Review on Synthesis Methods, Applications, and Removal Mechanisms. *J. Saudi Chem. Soc.* **2021**, *25* (8), 101280.
(38) Li, Q.; Li, R.; Ma, X.; Sarkar, B.; Sun, X.; Bolan, N. Comparative Removal of As(V) and Sb(V) from Aqueous Solution by Sulfide-Modified α-FeOOH. *Environ. Pollut.* **2020**, *267*, 115658.
(39) Mohamed, A.; Atta, R. R.; Kotp, A. A.; Abo El-Ela, F. I.; Abd El-Raheem, H.; Farghali, A.; Alkhalifah, D. H. M.; Hozzein, W. N.; Mahmoud, R. Green Synthesis and Characterization of Iron Oxide Nanoparticles for the Removal of Heavy Metals (Cd2+ and Ni2+) from Aqueous Solutions with Antimicrobial Investigation. *Sci. Rep.* **2023**, *13* (1), 7227.
(40) Jabbar, A. A.; Hussain, D. H.; Latif, K. H.; Jasim, A. K.; Al-aqbi, Z. T.; Alghannami, H. S.; Albishri, A. High-Efficiency Adsorption of Uranium from Wastewater Using Graphene Oxide/Graphene Oxide Nanoribbons/Chitosan Nanocomposite Aerogels. *ACS Omega* **2024**, *9* (25), 27260−27268.
(41) Arora, S.; Lal, S.; Kumar, S.; Kumar, M.; Kumar, M. Comparative Degradation Kinetic Studies of Three Biopolymers: Chitin, Chitosan and Cellulose. *Arch. Appl. Sci. Res.* **2011**, *3* (3), 188−201.
(42) Garba, Z. N.; Lawan, I.; Zhou, W.; Zhang, M.; Wang, L.; Yuan, Z. Microcrystalline Cellulose (MCC) Based Materials as Emerging Adsorbents for the Removal of Dyes and Heavy Metals − A Review. *Sci. Total Environ.* **2020**, *717*, 135070.

(43) Kurniawan, T. W.; Sulistyarti, H.; Rumhayati, B.; Sabarudin, A. Cellulose Nanocrystals (CNCs) and Cellulose Nanofibers (CNFs) as Adsorbents of Heavy Metal Ions. *J. Chem.* **2023**, *2023*, 1−36.
(44) Lehtonen, J.; Hassinen, J.; Kumar, A. A.; Johansson, L.-S.; Mäenpää, R.; Pahimanolis, N.; Pradeep, T.; Ikkala, O.; Rojas, O. J. Phosphorylated Cellulose Nanofibers Exhibit Exceptional Capacity for Uranium Capture. *Cellulose* **2020**, *27* (18), 10719−10732.
(45) Cai, Y.; Chen, L.; Yang, S.; Xu, L.; Qin, H.; Liu, Z.; Chen, L.; Wang, X.; Wang, S. Rational Synthesis of Novel Phosphorylated Chitosan-Carboxymethyl Cellulose Composite for Highly Effective Decontamination of U(VI). *ACS Sustain. Chem. Eng.* **2019**, *7* (5), 5393−5403.
(46) Wang, C.-Z.; Lan, J.-H.; Wu, Q.-Y.; Luo, Q.; Zhao, Y.-L.; Wang, X.-K.; Chai, Z.-F.; Shi, W.-Q. Theoretical Insights on the Interaction of Uranium with Amidoxime and Carboxyl Groups. *Inorg. Chem.* **2014**, *53* (18), 9466−9476.
(47) Mukherjee, S.; Ramireddy, H.; Baidya, A.; Amala, A. K.; Sudhakar, C.; Mondal, B.; Philip, L.; Pradeep, T. Nanocellulose-Reinforced Organo-Inorganic Nanocomposite for Synergistic and Affordable Defluoridation of Water and an Evaluation of Its Sustainability Metrics. *ACS Sustain. Chem. Eng.* **2020**, *8* (1), 139−147.
(48) Ghosh, M. K.; Poinern, G. E. J.; Issa, T. B.; Singh, P. Arsenic Adsorption on Goethite Nanoparticles Produced through Hydrazine Sulfate Assisted Synthesis Method. *Korean J. Chem. Eng.* **2012**, *29* (1), 95−102.
(49) Chernova, E.; Botvin, V.; Galstenkova, M.; Mukhortova, Y.; Wagner, D.; Gerasimov, E.; Surmeneva, M.; Kholkin, A.; Surmenev, R. A Comprehensive Study of Synthesis and Analysis of Anisotropic Iron Oxide and Oxyhydroxide Nanoparticles. *Nanomaterials* **2022**, *12* (23), 4321.
(50) Fairley, N.; Fernandez, V.; Richard-Plouet, M.; Guillot-Deudon, C.; Walton, J.; Smith, E.; Flahaut, D.; Greiner, M.; Biesinger, M.; Tougaard, S.; Morgan, D.; Baltrusaitis, J. Systematic and Collaborative Approach to Problem Solving Using X-Ray Photoelectron Spectroscopy. *Appl. Surf. Sci. Adv.* **2021**, *5*, 100112.
(51) Mallet, M.; Barthélémy, K.; Ruby, C.; Renard, A.; Naille, S. Investigation of Phosphate Adsorption onto Ferrihydrite by X-Ray Photoelectron Spectroscopy. *J. Colloid Interface Sci.* **2013**, *407*, 95−101.
(52) Meng, Q.; Wu, L.; Chen, T.; Xiong, Y.; Duan, T.; Wang, X. Constructing the Electron-Rich Microenvironment of an All-Polymer-Based S-Scheme Homostructure for Accelerating Uranium Capture from Nuclear Wastewater. *Environ. Sci. Technol.* **2024**, *58*, 15333.
(53) Liu, X.; Xie, Y.; Hao, M.; Li, Y.; Chen, Z.; Yang, H.; Waterhouse, G. I. N.; Wang, X.; Ma, S. Secondary Metal Ion-Induced Electrochemical Reduction of U(VI) to U(IV) Solids. *Nat. Commun.* **2024**, *15* (1), 7736.
(54) Ping, L.; Zhuoxin, Y.; Jianfeng, L.; Qiang, J.; Yaofang, D.; Qiaohui, F.; Wangsuo, W. The Immobilization of U(vi) on Iron Oxyhydroxides under Various Physicochemical Conditions. *Env. Sci. Process. Impacts* **2014**, *16* (10), 2278−2287.
(55) Wang, Y.; Wang, J.; Li, P.; Qin, H.; Liang, J.; Fan, Q. The Adsorption of U(VI) on Magnetite, Ferrihydrite and Goethite. *Environ. Technol. Innov.* **2021**, *23*, 101615.
(56) Gao, P.; Hu, Y.; Shen, Z.; Zhao, G.; Cai, R.; Chu, F.; Ji, Z.; Wang, X.; Huang, X. Ultra-Highly Efficient Enrichment of Uranium from Seawater via Studtite Nanodots Growth-Elution Cycle. *Nat. Commun.* **2024**, *15* (1), 6700.
(57) Lu, G.; Forbes, T. Z.; Haes, A. J. Evaluating Best Practices in Raman Spectral Analysis for Uranium Speciation and Relative Abundance in Aqueous Solutions. *Anal. Chem.* **2016**, *88* (1), 773−780.
(58) Manjunath, S. V.; Kumar, M. Evaluation of Single-Component and Multi-Component Adsorption of Metronidazole, Phosphate and Nitrate on Activated Carbon from Prosopis Juliflora. *Chem. Eng. J.* **2018**, *346*, 525−534.
(59) Mukherjee, S.; Kumar, A. A.; Sudhakar, C.; Kumar, R.; Ahuja, T.; Mondal, B.; Srikrishnarka, P.; Philip, L.; Pradeep, T. Sustainable and Affordable Composites Built Using Microstructures Performing Better than Nanostructures for Arsenic Removal. *ACS Sustain. Chem. Eng.* **2019**, *7* (3), 3222−3233.
(60) Mei, D.; Li, H.; Liu, L.; Jiang, L.; Zhang, C.; Wu, X.; Dong, H.; Ma, F. Efficient Uranium Adsorbent with Antimicrobial Function: Oxime Functionalized ZIF-90. *Chem. Eng. J.* **2021**, *425*, 130468.
(61) Gupta, V. K.; Agarwal, S.; Saleh, T. A. Chromium Removal by Combining the Magnetic Properties of Iron Oxide with Adsorption Properties of Carbon Nanotubes. *Water Res.* **2011**, *45* (6), 2207−2212.
(62) Botté, A.; Zaidi, M.; Guery, J.; Fichet, D.; Leignel, V. Aluminium in Aquatic Environments: Abundance and Ecotoxicological Impacts. *Aquat. Ecol.* **2022**, *56* (3), 751−773.
(63) Asrarian, R.; Jadidian, R.; Parham, H.; Haghtalab, S. Removal of Aluminum from Water and Wastewater Using Magnetic Iron Oxide Nanoparticles. *Adv. Mater. Res.* **2013**, *829*, 752−756.
(64) Mouttoucomarassamy, S.; Virk, H. S.; Dharmalingam, S. N. Evaluation and Health Risk Assessment of Arsenic and Potentially Toxic Elements Pollution in Groundwater of Majha Belt, Punjab, India. *Environ. Geochem. Health* **2024**, *46* (6), 208.
(65) Xu, M.; Zhou, L.; Zhang, L.; Zhang, S.; Chen, F.; Zhou, R.; Hua, D. Two-Dimensional Imprinting Strategy to Create Specific Nanotrap for Selective Uranium Adsorption with Ultrahigh Capacity. *ACS Appl. Mater. Interfaces* **2022**, *14* (7), 9408−9417.
(66) Wang, Y.; Zhang, Y.; Li, Q.; Li, Y.; Cao, L.; Li, W. Amidoximated Cellulose Fiber Membrane for Uranium Extraction from Simulated Seawater. *Carbohydr. Polym.* **2020**, *245*, 116627.
(67) Wen, D.; Dong, Z.; Ao, Y.; Xie, K.; Zhai, M.; Zhao, L. Aminotriazole Isomers Modified Cellulose Microspheres for Selective Adsorption of U(VI): Performance and Mechanism Investigation. *Carbohydr. Polym.* **2021**, *257*, 117666.
(68) Yu, S.; Sun, C.; Fang, S.; Wang, C.; Alharbi, N. S.; Chen, C. Preparation of Cellulose@amidoxime by Plasma-Induced Grafting Technology and Its Potential Application for Uranium Extraction. *Appl. Surf. Sci.* **2023**, *637*, 157883.
(69) Anirudhan, T. S.; Sreekumari, S. S. Synthesis and Characterization of a Functionalized Graft Copolymer of Densified Cellulose for the Extraction of Uranium(VI) from Aqueous Solutions. *Colloids Surf. Physicochem. Eng. Asp.* **2010**, *361* (1−3), 180−186.
(70) Misra, N.; Rawat, S.; Kumar Goel, N.; Shelkar, S. A.; Mallavarapu, A.; Tiwari, M.; Kumar, V. C.U. S. CellUSorb: A high-performance, radiation functionalized cellulose based adsorbent for Uranium (VI) remediation in ground water. *Sep. Purif. Technol.* **2023**, *322*, 124215.
(71) Dacrory, S.; Haggag, E. S. A.; Masoud, A. M.; Abdo, S. M.; Eliwa, A. A.; Kamel, S. Innovative Synthesis of Modified Cellulose Derivative as a Uranium Adsorbent from Carbonate Solutions of Radioactive Deposits. *Cellulose* **2020**, *27* (12), 7093−7108.
(72) Rule, P.; K, B.; Gonte, R. R. Uranium(VI) Remediation from Aqueous Environment Using Impregnated Cellulose Beads. *J. Environ. Radioact.* **2014**, *136*, 22−29.
(73) Zhuang, S.; Wang, J. Removal of U(VI) from Aqueous Solution Using Phosphate Functionalized Bacterial Cellulose as Efficient Adsorbent. *Radiochim. Acta* **2019**, *107* (6), 459−467.
(74) Yang, A.; Wu, J.; Huang, C. P. Graphene Oxide-Cellulose Composite for the Adsorption of Uranium(VI) from Dilute Aqueous Solutions. *J. Hazard. Toxic Radioact. Waste* **2018**, *22* (2), 04017029.
(75) Mukherjee, S.; Nayak, T.; Pradeep Chapter 17 - Evaluating Sustainability for Water and Wastewater Treatment Technologies. In *Technological Solutions for Water Sustainability: Challenges and Prospects*; Philip, L., Pradeep, T., Bhallamudi, S. M., Eds.; IWA Publishing, 2023; pp 191−199..
(76) Curzons, A. D.; Mortimer, D. N.; Constable, D. J. C.; Cunningham, V. L. So You Think Your Process Is Green, How Do You Know?−Using Principles of Sustainability to Determine What Is Green − a Corporate Perspective. *Green Chem.* **2001**, *3* (1), 1−6.
(77) Jiménez-González, C.; Constable, D. J. C.; Ponder, C. S. Evaluating the "Greenness" of Chemical Processes and Products in the Pharmaceutical Industry—a Green Metrics Primer. *Chem. Soc. Rev.* **2012**, *41* (4), 1485−1498.

https://doi.org/10.1021/acssuschemeng.4c10246
ACS Sustainable Chem. Eng. 2025, 13, 1838−1850

(78) Sheldon, R. A. Metrics of Green Chemistry and Sustainability: Past, Present, and Future. *ACS Sustain. Chem. Eng.* **2018**, *6* (1), 32−48.
(79) *Toxicity Characteristic Leaching Procedure (TCLP) for VOCs, SVOCs, Chlorinated Pesticides and Herbicides, and Metals by SW-846 Method 1311 and Analysis*. 2017. https://19january2017snapshot.epa.gov/sites/production/files/2015-06/documents/tclp.pdf (accessed 2024−09−16).


CAS BIOFINDER DISCOVERY PLATFORM™
STOP DIGGING THROUGH DATA —START MAKING DISCOVERIES
CAS BioFinder helps you find the right biological insights in seconds
Start your search
CAS
A division of the American Chemical Society

https://doi.org/10.1021/acssuschemeng.4c10246
ACS Sustainable Chem. Eng. 2025, 13, 1838−1850

Cellulose-Derived Nanomaterials for Affordable and Rapid Remediation of Uranium in Water

Tanmayaa Nayak Sritama Mukherjee, Amoghavarsha Ramachandra Kini, Md Rabiul Islam, Ankit Nagar, Sonali Seth and Thalappil Pradeep*

DST Unit of Nanoscience (DST UNS) and Thematic Unit of Excellence (TUE), Department of Chemistry, Indian Institute of Technology Madras, Chennai 600 036, India

*Email: pradeep@iitm.ac.in

Tel.: +91-44 2257 4208; Fax: +91-44 2257 0545/0509

Contents

Total number of pages: 14

Total number of figures: 9

Total number of tables: 2

Total number of equations: 8

Table of Contents

Items	Title	Page No.
	Instrumentation	S2-S4
	Materials, synthesis and batch adsorption studies	S4-S6
Figure S1	Comparative FTIR spectra of phosphorylated MCC and blank MCC	S6
Figure S2	Powder XRD patterns of blank cellulose nanocrystal (CNC), Phosphorylated CNC and PCNCFH	S6
Figure S3	Deconvoluted XPS spectra of C 1s of PCNCFH before and after U(VI) adsorption	S7
Figure S4	SEM-EDS of PCNCFH after U(VI) adsorption with weight percentage of elements	S7
Figure S5	Pseudo second-order reaction kinetics plot for adsorption of uranium on PCNCFH	S8
Figure S6	Freundlich adsorption isotherm model showing the correlation coefficient for uranium adsorption on PCNCFH	S9
Figure S7	Selectivity of adsorption of PCNCFH for multiple metals.	S9
Figure S8	Effect of V(V) on U(VI) adsorption on PCNCFH.	S10
Figure S9	Thermogravimetric analysis (TGA) of PCNCFH at air and nitrogen atmospheres from room temperature to 900°C with 10 mins scan rates	S11
Equations used	Equations used in the main text	S12-S13
Table S1	Composition of synthetic tap water	S13
Table S2	Sustainability metrics evaluation for the synthesis of PCNC	S14

Instrumentation:

High resolution transmission electron microscopy (HRTEM): - TEM images were obtained using a JEOL 3010 instrument fitted with an ultra-high resolution (UHR) polepiece, operating at an accelerating voltage of 200 kV. For high-resolution TEM (HRTEM) analysis, the nanocomposite was first dispersed in water, and the suspension was subsequently drop-cast onto carbon-coated copper grids. The prepared grids were left to dry under ambient conditions at room temperature for imaging.

Infrared (IR) – IR spectra are collected using PerkinElmer IR instrument within the range of 400-4000 cm^{-1}.

Powder XRD – Measurements was performed by using a D8 Advance Bruker instrument, using Cu Kα as the X-ray source.

X-ray photoelectron spectroscopy (XPS) - XPS measurements were carried out using an ESCA probe TPD spectrometer from Omicron Nanotechnology. A polychromatic Al Kα source (hν = 1486.6 eV) was employed as the X-ray source. Samples were prepared as drop-cast films on a sample stub for analysis. A constant analyser energy of 20 eV was applied during data acquisition. The binding energy values were referenced to the C 1s peak at 284.8 eV. All XPS spectra were deconvoluted using CasaXPS software for detailed analysis.

Scanning electron microscope (SEM) – The surface morphology, elemental distribution, and composition were investigated using SEM coupled with energy dispersive X-ray spectroscopy (EDS) on an FEI Quanta 200 system. Samples were mounted on carbon adhesive tape, which was affixed to an aluminium sample holder for analysis.

Inductively coupled plasma mass spectrometry (ICP-MS)- Quantitative determination of uranium and other metal concentrations was conducted using a NexION 300X ICP-MS calibrated with appropriate reference standards. The ICP-MS system is equipped with an electron multiplier detector, which converts the flux of ionized analyte species into electrical signals. The intensity of these signals is directly proportional to the concentration of analyte ions present in the sample, enabling precise quantification.

Thermogravimetric analysis (TGA)- Thermogravimetric (TG) analysis was conducted on approximately 3.5 mg of the nanocomposite using a NETZSCH STA 449 F3 Jupiter system, controlled by Proteus-6.1.0 software. The experiment was carried out in a nitrogen atmosphere, with a gas flow rate of 20 mL/min. The temperature was ramped from 30°C to 900°C at a constant heating rate of 10°C/min. The sample was placed in an alumina crucible for the measurements.

Zeta potential- Zeta potential measurements were performed using a Malvern Zetasizer Nano ZSP. The surface charge of particles in suspension was determined via laser Doppler electrophoresis, with a measurable zeta potential range of -200 to +200 mV. The instrument required approximately 100 µl of sample for analysis within an electrode cell, with temperature control maintained between 1°C and 70°C during measurements.

Brunauer-Emmett-Teller (BET)- The BET surface area was determined using a Micromeritics Tri Star II. Prior to analysis, the samples were degassed under vacuum at 100°C for 6 hours and then analyzed at 77 K using ultrahigh-purity nitrogen gas.

Materials

Two distinct cellulose types, MCC and CNC were purchased from SRL Pvt. Ltd. (India) and BioPlus, respectively. NaOH, $FeCl_3 \cdot 6H_2O$, and Na_2SO_4 were obtained from RANKEM Glasswares and Chemicals Pvt. Ltd., India. Uranyl nitrate hexahydrate salt and trisodium trimetaphosphate (STMP) were procured from Thomas Baker (Chemicals) Ltd. and Sigma Aldrich, respectively. All chemicals were of laboratory grade and were utilized without additional purification. Deionized (DI) water was used for all the experiments, unless noted.

Synthesis of phosphorylated-microcrystalline cellulose ferrihydrite (PMCCFH) and phosphorylated- cellulose nanocrystal ferrihydrite (PCNCFH) composites

A green synthetic method was employed to synthesize phosphorylated cellulose-ferrihydrite nanocomposites. The synthesis process was conducted in two stages. In the initial stage, the phosphorylation of cellulose was carried out by STMP. Later, iron oxide was incorporated into phosphorylated cellulose to synthesize a mechanically stable composite by reacting it with ferric chloride hexahydrate. Phosphorylated cellulose was synthesized using a method with slight modifications from that reported by Yawen Cai et.al.[45] The synthesis of phosphorylated cellulose (PCNC/PMCC) involved the utilization of STMP as the phosphating agent. The phosphorylation process depended on the cross-linking reaction between the ring-opened STMP and the hydroxyl (-OH) groups of cellulose in 1% NaOH solution. Using alkaline water with a pH of 12, adjusted with 2.0 M NaOH solution, a 25 mL solution containing 0.25 g of cellulose (CNC or MCC) was prepared. Subsequently, 6.25 mL of a 60% (w/v) STMP solution was added to activate the hydroxyl groups in the disaccharide units. The mixture, with its pH maintained at approximately 12.0 was gently stirred at 25 °C for 2 hours, then vigorously stirred at 65 °C for 5 hours. The resulting product was dried at 45 °C. To prepare a homogeneous dispersion, approximately 0.2 g of phosphorylated cellulose was dissolved in 40 mL of water and subjected to sonication for approximately 10 minutes. The pH of the solution was adjusted to 9 using 0.2 M NaOH. After 5 minutes of stirring, 2 g of Na_2SO_4 was incorporated, followed by an additional 5 minutes of

incubation. Subsequently, 21.6 mL of 1 M $FeCl_3 \cdot 6H_2O$ was introduced to the mixture. The resulting mixture was precipitated, and its pH was adjusted to 8 by dropwise addition of 2 M NaOH. The final reaction mixture was incubated for approximately 12 hours at room temperature. The resulting precipitate was washed with water to eliminate soluble salts and dried at ambient temperature (around 30 °C). The final composite material appeared as dark brown shiny crystals. The total weight of the product obtained was approximately 3.68 g.

Batch Adsorption Studies

To prepare 1000 mg/L uranium metal ion solutions, $UO_2(NO_3)_2 \cdot 6H_2O$ was dissolved in deionized water, and diluted to different concentrations. In a standard batch adsorption test, 25 mg of the material was mixed with 100 mL of distilled water spiked with uranium at a concentration of 1 mg/L. The water sample was subsequently collected at various time intervals to measure the concentration of remaining uranium in the solution using Inductively Coupled Plasma Mass Spectrometry (ICP-MS). Prior to analysis, the samples were acidified with 5% HNO_3 and filtered through 0.22-micron filter paper.

To investigate the impact of pH on adsorption of uranium, 25 mg of the composite was introduced to 100 mL of water, spiked with uranium. The pH of the solution was adjusted to the required level using 1 M HCl or 1 M NaOH, and the mixture was shaken for a duration of 2 hours. After following this sample preparation protocol, the treated water sample was analysed using ICP-MS.

To evaluate the impact of interfering ions on uranium adsorption, a series of heavy metal ions such as Cu(II), Cd(II), Al(III), Zn(II), Mn(II), Mg(II), Cr(III), Li(I), Co(II) and Ni(II) were taken into consideration. In one conical flask, all cations were added to 100 mL of distilled water, spiked with uranium at a concentration of 1 mg/L. On the other hand, in separate conical flasks, individual ions which are generally present in ground water such as Mg^{2+}, SO_4^{2-}, F^-, Ca^{2+}, CO_3^{2-}, HCO_3^-, K^+, PO_4^{3-}, SiO_3^{2-}, Cl^-, Na^+, and NO_3^- were introduced separately into 100 mL of water with concentrations relevant to ground water (Table S1). Input uranium concentration was 1.1 mg/L. Subsequently, the water samples were treated with 25 mg of the composite for a duration of 2 hours, followed by ICP-MS measurements.

Regeneration of adsorbent

The regeneration of the adsorbent holds paramount importance for any cost-effective technology. In this study, 25 mg of adsorbent were introduced into a 20 mL solution containing 1 ppm of uranium (VI). Adsorption was followed by desorption conducted with varying concentrations of

HNO_3 solution, while maintaining a constant volume of solution, namely 20 mL. Optimal desorption outcomes were observed with 0.01 M HNO_3, within 90 minutes of agitation. Quantitative assessment of uranium uptake was conducted by ICP-MS. Subsequently, the uranium removal percentage was calculated, and the experiment was repeated up to four cycles.

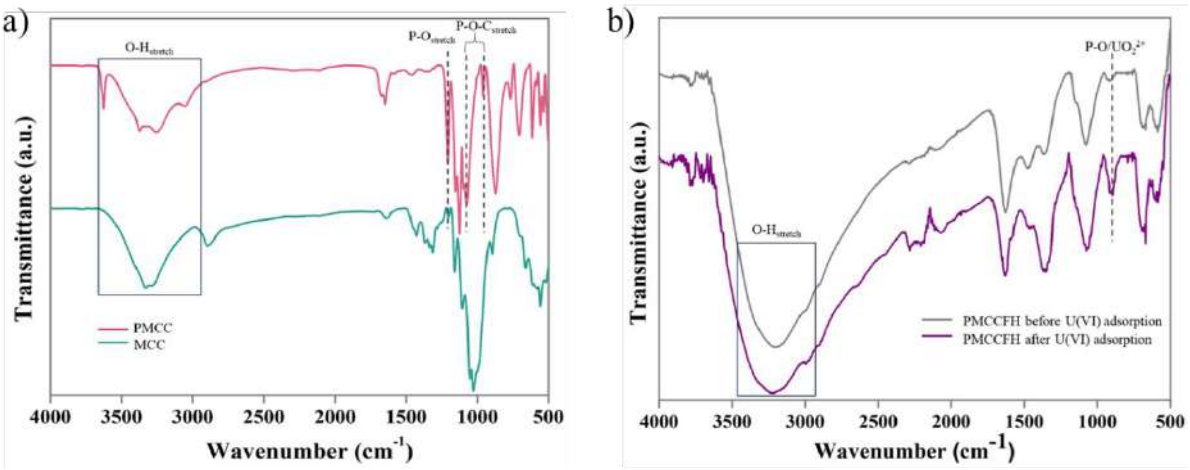


Figure S1. (a) Comparative FTIR spectra of phosphorylated MCC and blank MCC. (b) FTIR spectra of PCNCFH before and after U(VI) adsorption.

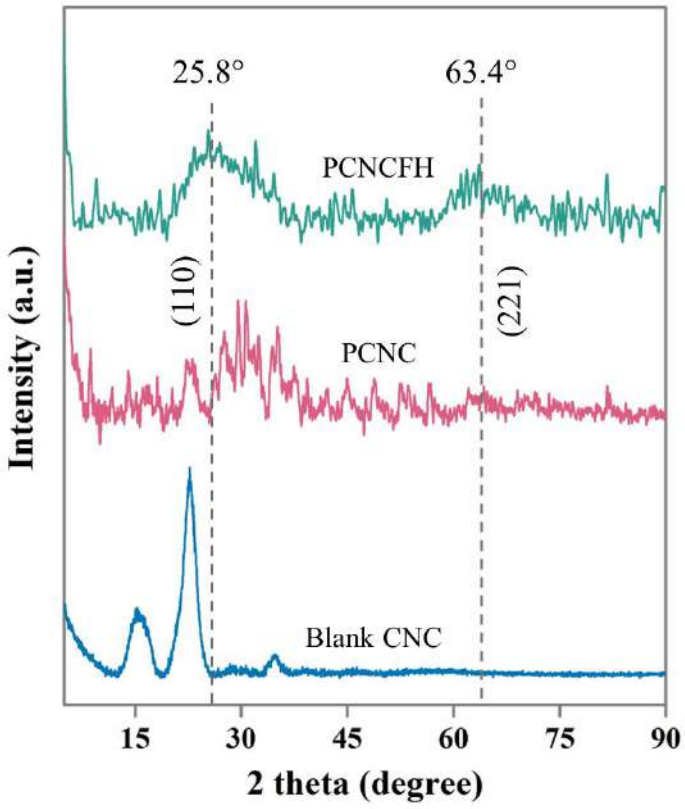


Figure S2. Powder XRD patterns of blank cellulose nanocrystal (CNC), Phosphorylated CNC and PCNCFH.

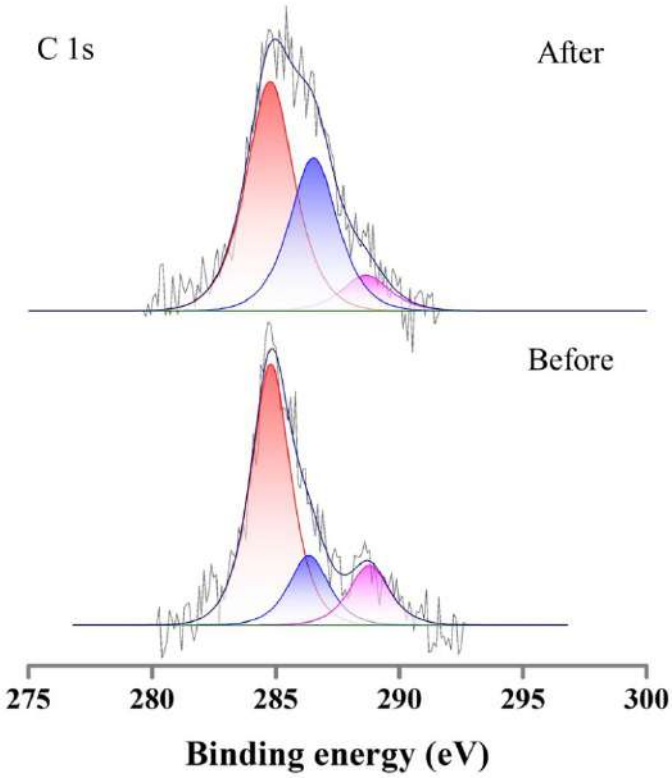
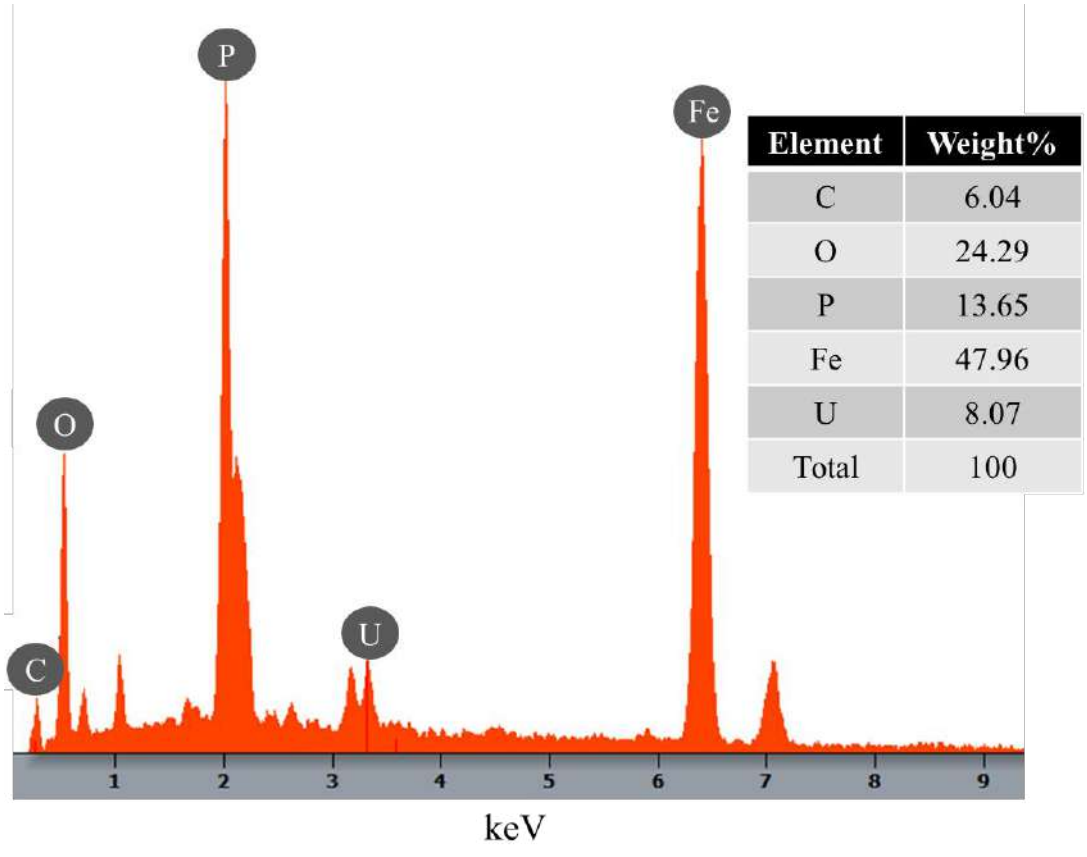


Figure S3. Deconvoluted XPS spectra of C 1s of PCNCFH before and after U(VI) adsorption.



Element	Weight%
C	6.04
O	24.29
P	13.65
Fe	47.96
U	8.07
Total	100

Figure S4. SEM-EDS of PCNCFH after U(VI) adsorption with weight percentage of elements.

Ho's pseudo-second-order model:

$$\frac{t}{q_t} = \frac{1}{k_2 q_e^2} + \frac{1}{q_e} t$$

q_t (mg/g) and q_e (mg/g) are the amount of adsorbed uranium at particular time t and equilibrium, respectively.

k_2 (g mg^{-1} min^{-1}) is the adsorption rate constant.

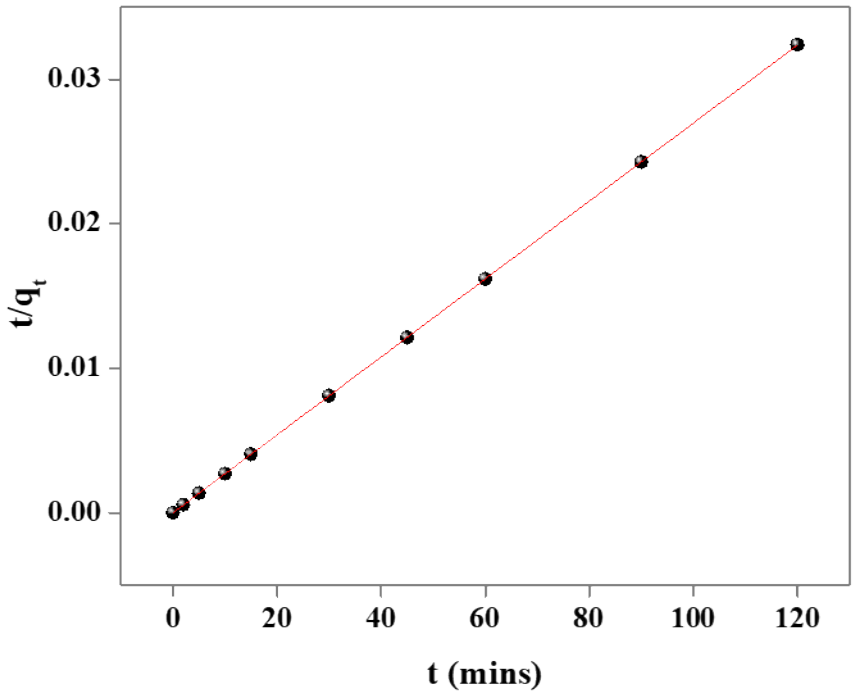


Figure S5. Pseudo second-order reaction kinetics plot for adsorption of uranium on PCNCFH.

Freundlich adsorption isotherm:

The Freundlich isotherm model can be expressed as follows:

$$\text{Log } Q_e = \text{Log } K_F + (1/n) \log C_e$$

where Q_e is the experimental adsorption capacity (mg/g), C_e is the equilibrium concentration (mg/L); K_F represents the equilibrium constant in Freundlich equation (L/mg), n signifies the Freundlich constant associated with adsorption intensity.

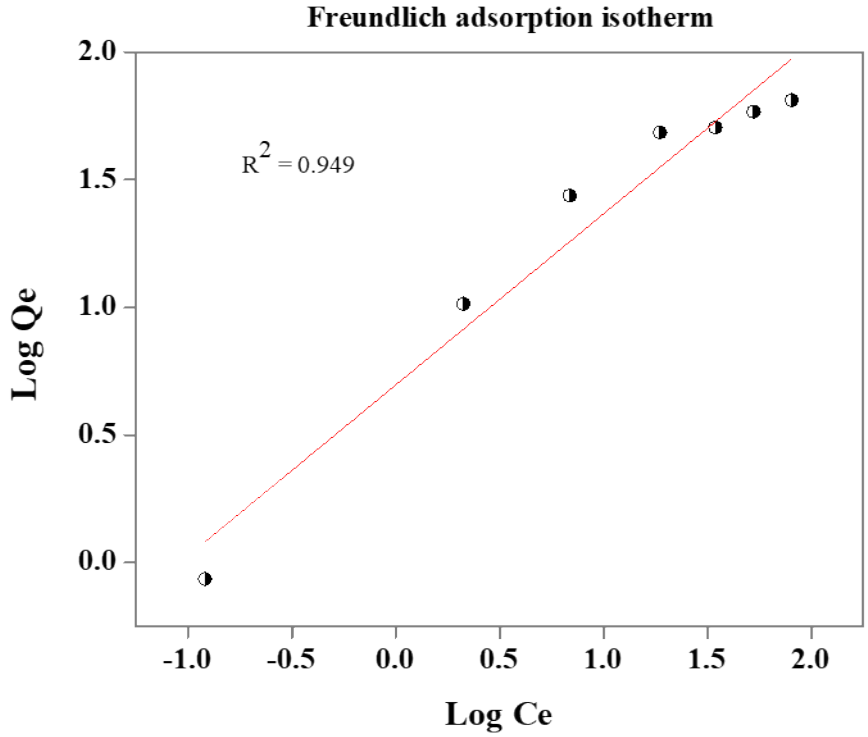


Figure S6. Freundlich adsorption isotherm model showing the correlation coefficient for uranium adsorption on PCNCFH.

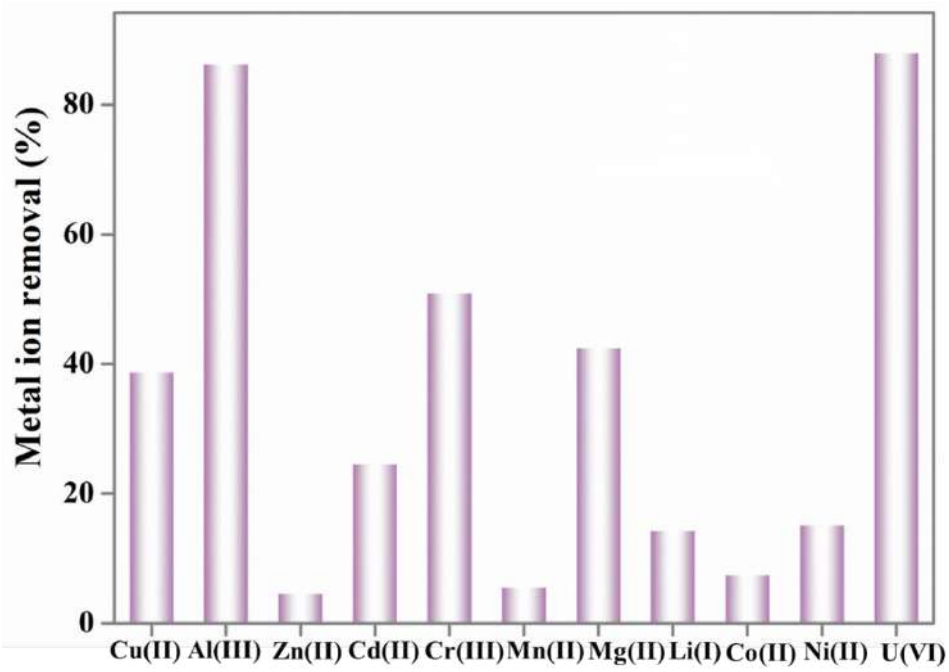


Figure S7. Selectivity of adsorption of PCNCFH for multiple metals.

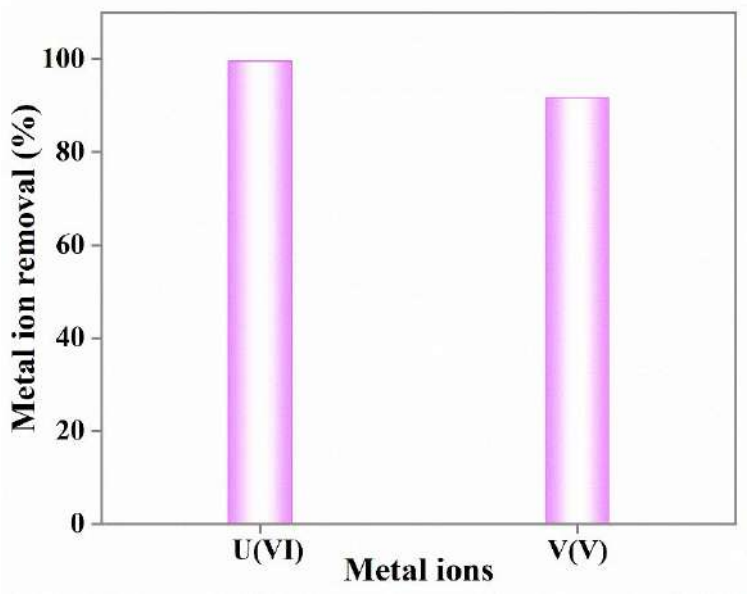


Figure S8. Effect of V(V) on U(VI) adsorption on PCNCFH.

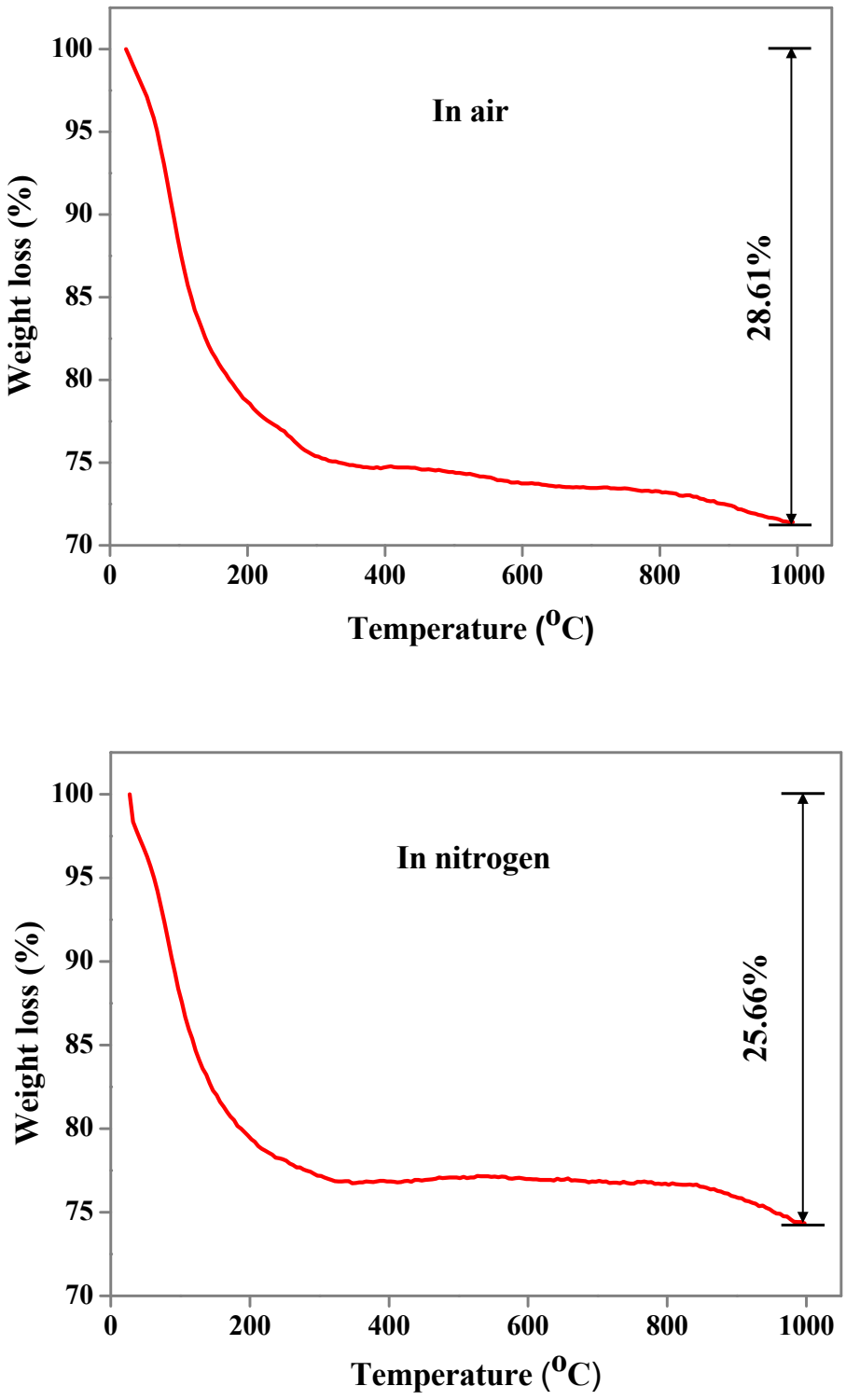


Figure S9. Thermogravimetric analysis (TGA) of PCNCFH at air and nitrogen atmospheres from room temperature to 900^0C with 10 mins scan rates.

Equations used

Equation (1): The removal percentage of uranium is calculated using the equation mentioned below:

$$\text{Removal \%} = [(C_o\text{-}C_e)/C_o] * 100$$

where C_o and C_e represent the initial and equilibrium concentrations of the metal ions, respectively.

Equation (2): The maximum uptake of uranium (q_e) by nanocomposites was determined using the following equation:

$$q_e = (C_o\text{-}C_e) * V/m$$

where q_e represents the amount of U(VI) adsorbed per gram of adsorbent at equilibrium (mg/g), C_e is the equilibrium concentration of uranium in the bulk solution (mg/L), C_o is the initial concentration of uranium (mg/L), V is the volume of the solution (L), and m is the mass of the adsorbent (g).

Equation (3): The linearized form of Langmuir equation used in this work is defined as,

$$C_e/q_e = C_e/q_{max} + 1/bq_{max}$$

where q_e is the amount of adsorption at the surface of the adsorbent (mg/g), C_e is the equilibrium concentration of the solution (mg/L), q_{max} is the maximum surface density at monolayer coverage and b is the Langmuir adsorption constant (L/mg) related to the free energy of adsorption and $1/q_{max}$ and $1/bq_{max}$ are the Langmuir constants.

Equations used for evaluating sustainability metrics

Equation (4):

$$\text{Mass intensity, or process mass intensity} = \frac{\text{Total mass used in a process excluidng water}}{\text{Mass of product}} \text{ (kg/kg)}$$

Equation (5):

$$\text{Water intensity} = \frac{\text{Mass of all water used in a process}}{\text{Mass of product}} \text{(kg/kg)}$$

Equation (6):

$$\text{Reaction mass efficiency} = \text{For a particular reaction A+B} \longrightarrow \text{C,}$$

$$\frac{\text{Mass (C)}}{\text{Mass (A)} + \text{Mass (B)}} * 100\%$$

Equation (7):

$$\text{Energy intensity} = \frac{\text{Total process energy}}{\text{Mass of the final product}} \text{ KW.h/kg}$$

Equation (8):

$$\text{E factor} = \frac{[\text{kg(raw materials)} - \text{kg(desired product)}]}{\text{kg(total product including water)}}$$

Table S1. Composition of synthetic tap water.

Types of ions	Concentration of ion used in ppm
Mg^{2+}	15
SO_4^{2-}	33
F^-	0.6
Ca^{2+}	29
CO_3^{2-}	100
HCO_3^-	100
K^+	2.5
PO_4^{3-}	55.83
SiO_3^{2-}	16
Cl^-	87
Na^+	53.74
NO_3^-	1.9

Table S2.

Sustainability metrics evaluation for the synthesis of PCNC.

Material	Mass intensity (MI) (kg/kg)	Solvent intensity (SI) (kg/kg)	Reaction mass efficiency (RME) %	E - factor
PCNC	1.42	10.72	70.40	0.03

ACS NANO

www.acsnano.org

ARTICLE

Structural Changes in Atomically Precise Ag_{29} Nanoclusters upon Sequential Attachment and Detachment of Secondary Ligands

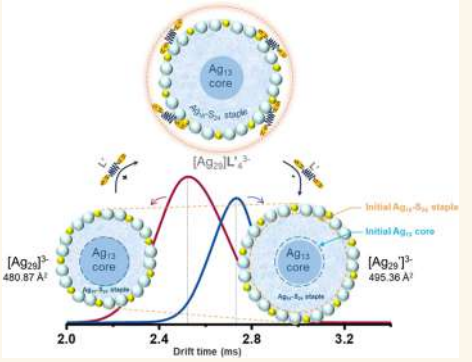
Jayoti Roy, Amitabha Das, Arijit Jana, Papri Chakraborty, Marco Neumaier, Horst Hahn, Biswarup Pathak,* Manfred M. Kappes,* and Thalappil Pradeep*

Cite This: *ACS Nano* 2025, 19, 5727−5738

Read Online

ACCESS | Metrics & More | Article Recommendations | Supporting Information

ABSTRACT: **Elucidating the structural dynamics of ligand-stabilized noble metal nanoclusters (NCs) is critical for understanding their properties and for developing applications. Ligand rearrangement at NC surfaces is an important contributor to structural change. In this study, we investigate the dynamic behavior of ligand-protected $[Ag_{29}(L)_{12}]^{3-}$ NC's (L = 1,3-benzenedithiol) interacting with secondary ligand 2,2′-[1,4-phenylenebis (methylidynenitrilo)] bis[benzenethiol] (referred to as L′). We specifically focus on the structural characteristics of NC-based adducts $[Ag_{29}(L)_{12}]L'_n{}^{3-}$ where n ranges from 1 to 4. This is probed experimentally by using a combination of ultraviolet−visible (UV−vis) spectroscopy, high-resolution electrospray ionization mass spectrometry (ESI MS), and ion mobility mass spectrometry (IM MS) coupled with collision-induced dissociation (MS^2 IMS). Density functional theory (DFT) calculations infer comparatively weak noncovalent interactions between the NCs and attached secondary ligands consistent with the fragmentation behavior and experimentally determined collision cross-sections (CCSs), which show a monotonic CCS increase of $[Ag_{29}(L)_{12}]L'_n{}^{3-}$ with an increasing number of L′ (n = 1−4). From a detailed analysis of the predicted structures, we infer progressive expansion of the Ag−S staple framework of the precursor NC as secondary ligands are added. Interestingly, detachment of L′ from gas-phase $[Ag_{29}(L)_{12}]L'_n{}^{3-}$ by collisional heating yields structures which retain "footprints" of the detached secondary ligands on a millisecond time scale.**



KEYWORDS: *atomically precise noble metal nanoclusters, Ag_{29} nanocluster, structural isomerism, supramolecular interactions, secondary ligand interaction, ion mobility mass spectrometry, DFT calculation*

INTRODUCTION

Atomically precise, ligand-protected, noble metal nanoclusters (NCs) are an exceptional class of ultrasmall nanoparticles that are composed of metal atoms and organic ligands.[1−3] These metallic nanostructures have potential applications as catalysts,[4,5] agents for biological imaging and sensing,[6,7] and tunable nanomaterials for diagnostics and therapeutics.[8] The properties of these materials depend strongly on their size due to their distinct molecular electronic levels.[9−11]

Determination of the molecular structures of NCs by single-crystal X-ray diffraction (SCXRD) has been a major driver of progress in this area.[12,13] Numerous structures have been resolved since the first reported crystal structure of a thiolate-protected gold NC, $Au_{102}(pMBA)_{44}$ (where pMBA = *p*-mercaptobenzoic acid).[14] Later, structures of Au and Ag NCs and, to a limited extent, Cu and other metal alloy NCs protected by various ligands such as thiolates, phosphines, alkynyls, or N-heterocyclic carbenes and carboranes have been solved.[3,15−22] Although SCXRD is a proven technique to determine the structure of monolayer-protected coinage metal NCs in the solid state, it is still challenging to characterize NC structures in solution and gas phases.[23,24] NCs can become quite dynamic when freed from their crystalline lattice. For example, it has been shown that $[Au_{25}(PET)_{18}]$ NC ions can exist in dimeric and trimeric aggregate states in the gas phase, whereas a chiral NC, such as $Au_{38}(PET)_{24}$ (PET = phenylethanethiolate), can even invert its handedness in solution.[25,26] Such dynamic phenomena are known to depend strongly on the nature of the surface layer of NC. In thiolate-

Received: November 15, 2024
Revised: January 15, 2025
Accepted: January 15, 2025
Published: January 28, 2025



Downloaded via INDIAN INST OF TECH MADRAS on December 29, 2025 at 03:08:12 (UTC).
See https://pubs.acs.org/sharingguidelines for options on how to legitimately share published articles.

© 2025 American Chemical Society

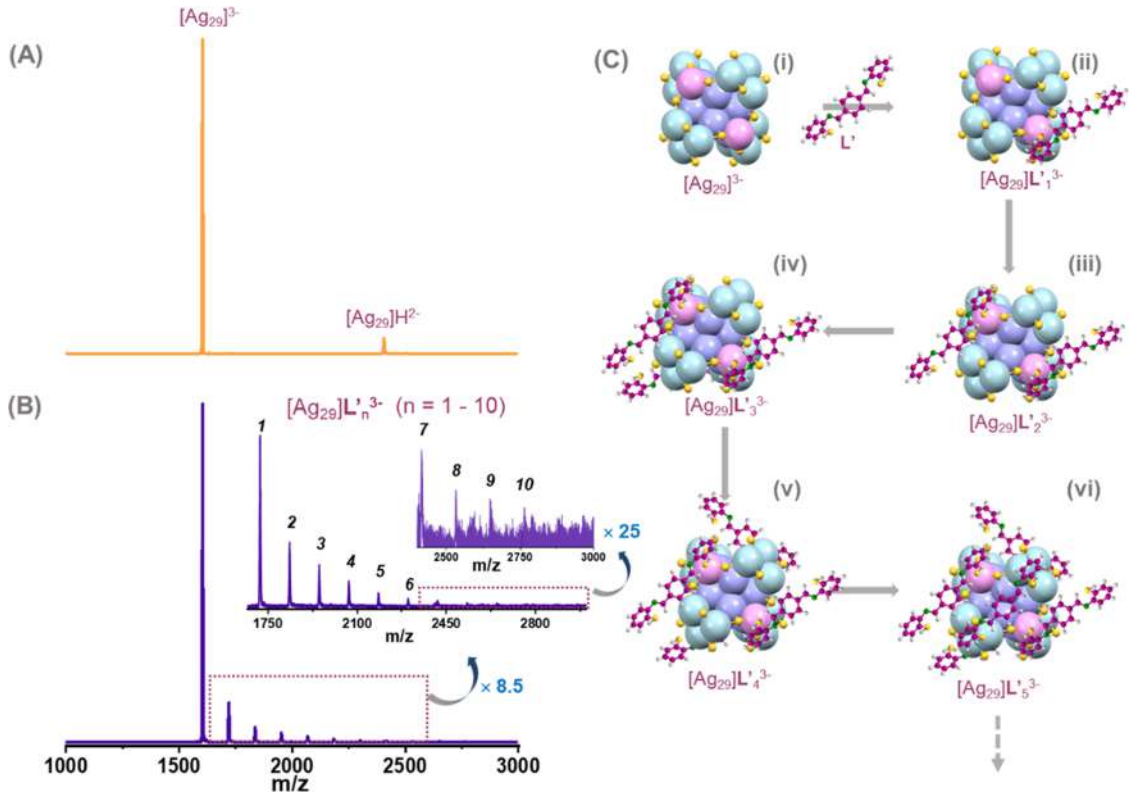


Figure 1. Partial ESI MS of (A) precursor $[Ag_{29}]^{3-}$ NC solution and (B) precursor NC solution with L′ added (in the DMF solvent). (C) Schematic of the proposed reaction sequence generating $[Ag_{29}]L'_n{}^{3-}$ NCs by sequential addition of L′. Color code: Ag, purple, pink, and cyan blue; S, yellow; C, dark magenta; H, light gray; and N, dark green.

protected coinage metal NCs, for example, the ligands are covalently attached to metal−thiolate staples, which together constrain the metallic cluster core. One of the conceptually simplest solution reactions of such a system involves the interaction of the NC thiolate surface layer with a secondary ligand. Surprisingly though, the secondary ligand-induced chemical properties of NCs have only been explored to a limited extent.[27−30] Contributing effects include (i) host−guest interactions with the primary ligands,[23] (ii) rearrangement of the metal−thiolate interface,[33−35] (iii) modulation of the primary ligand binding affinity by incoming molecules,[36−38] and (iv) flexibility of the metal(I)-thiolate staples.[31,34,39] All of these processes are likely to involve multiple intermediates, i.e., isomeric structures. However, there are few experimental data on isomers formed during the interaction of the metal−thiolate framework with foreign molecules.

Understanding the structural dynamics of NC structures therefore has also been greatly profited from computational modeling, in addition to experiments.[40,41] For example, Matus et al. explored the possibilities of isomerism in the Au_{13} core of $[Au_{25}(SR)_{18}]$ NCs using MD and density functional theory (DFT) studies. The MD-simulated Au_{13} core was shown to differ structurally from that known in the crystal by a low-barrier collective rotation.[42] This study revealed that topological isomers of isolated $[Au_{25}(SR)_{18}]^{-}$ have distinctly different collision cross-sections (CCS) as compared to the known solid-state structures, emphasizing the need and importance of gas-phase ion mobility-mass spectrometry (IM MS) studies to better elucidate structural dynamics, which is also relevant in the solution phase.

IM MS, in combination with theoretical calculations, has been used extensively to assign gas-phase structures of large biomolecular ions, NCs, proteins, etc.[43−45] Also, the combination of IM MS with collisional fragmentation (MS^2 IMS) has become an indispensable tool for identifying structural changes.[46−53] This approach has been applied recently to explore possible isomeric structures of coinage metal NCs in the gas phase and to follow their structural changes during chemical reactions.[39,48,54,55] Often, the results from high-resolution IM MS have been validated by SCXRD. For NCs, the reliability of IM MS-based structural assignment has been evidenced in the literature by comparing such results with known X-ray structures.[56] Soleilhac et al. used IM MS to determine the CCSs of a series of gold NCs protected by glutathione and demonstrated that the relative changes in CCSs in the gas phase were consistent with the results from powder XRD in the solid phase and time-resolved fluorescence anisotropy in the liquid phase.[40] Advanced IM MS techniques, such as high-resolution trapped ion mobility spectrometry (TIMS) MS, in combination with DFT, were used to resolve smaller changes in the CCS resulting from Cu doping in different positions of the $[Ag_{29}(L)_{12}]^{3-}$ NC (L = 1,3-benzenedithiol).[56] Notably, structures of several NCs, such as $[Au_7(PPh_3)_7H_5]^{2+}$ and $[Au_8(PPh_3)_7]^{2+}$, have even been assigned purely based on the agreement between the experimental and calculated CCS values.[57]

In this study, we use electrospray ionization MS (ESI MS) and IM MS to explore structural dynamics and isomerism associated with the interaction of the $[Ag_{29}(L)_{12}]^{3-}$ silver-thiolate NC model system (where L corresponds to 1,3-benzene-dithiol) with the secondary ligand, 2,2′-[1,4-phenyl-

https://doi.org/10.1021/acsnano.4c16413
ACS Nano 2025, 19, 5727−5738

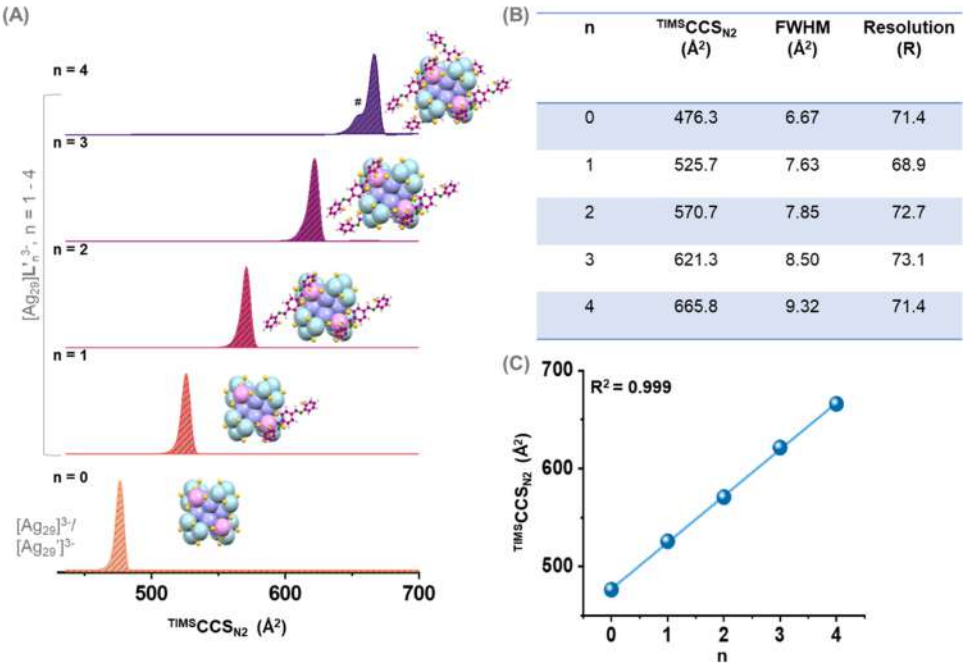


Figure 2. (A) Mobilograms of individual $[Ag_{29}]L'_n{}^{3-}$ (n = 0−4) ions showing increasing CCS with an increasing number of L′-adducts to $[Ag_{29}]^{3-}$ NCs. (B) Table showing the $^{TIMS}CCS_{N2}$, FWHM, and resolution (R) values corresponding to the number of L′-ligands (n) attached to parent $[Ag_{29}]^{3-}$ NCs. (C) Linear correlation plot of $^{TIMS}CCS_{N2}$ versus n. Color code: Ag, purple, pink, and cyan blue; S, yellow; C, dark magenta; H, light gray; and N, dark green. # marks that the ions of lower CCS than $[Ag_{29}]L'_4{}^{3-}$ could be attributed to either fragmentation or artifact during elution from the TIMS tunnel of timsTOF.

enebis (methylidynenitrilo)]bis[benzenethiol] (denoted as **L′**). Mixing **L′** with $[Ag_{29}(L)_{12}]^{3-}$ NC solution leads to the formation of weakly bound adduct ions $[Ag_{29}(L)_{12}]\mathbf{L}'_n{}^{3-}$ (n = 1−4). This is associated with a monotonic increase in their overall size as **L′** is added. Collisional dissociation (CID) of these adducts leads to the sequential detachment of (neutral) **L′** as the lowest-energy fragmentation channel. Surprisingly, the resulting fragment ions have larger collision cross-sections than the corresponding (unfragmented) equi-m/z ions directly electrosprayed from solution. DFT calculations[58] as well as trajectory method simulations of CCS values for plausible model structures[59] provide insights into the underlying structure changes and show that they reflect specific noncovalent interactions between secondary ligands and NC. These results are described in detail in the following where we will abbreviate $[Ag_{29}(L)_{12}]^{3-}$ as $[Ag_{29}]^{3-}$ and $[Ag_{29}(L)_{12}]\mathbf{L}'_n{}^{3-}$ as $[Ag_{29}]\mathbf{L}'_n{}^{3-}$, respectively.

RESULTS AND DISCUSSION

The $[Ag_{29}](TPP)_4{}^{3-}$ NC solid with counterions (TPP is triphenylphosphine) and secondary ligand, **L′**, were synthesized using reported protocols (see the Experimental Section in the Supporting Information) and characterized by high-resolution ESI MS (Figure S1), ultraviolet−visible (UV−vis) absorption spectroscopy, and photoluminescence spectroscopy (Figure S2).[60] The negative ion ESI mass spectrum of a $[Ag_{29}](TPP)_4{}^{3-}$ solution displays two NC-derived ion signals in two different charge states, predominantly 3- (as $[Ag_{29}]^{3-}$) and also some 2- (as $[Ag_{29}]H^{2-}$). Each forms after losing four weakly bound neutral TPP ligands (Figure S1). Under our ESI MS conditions, the relative dianionic intensity was less than 5% of the total ion count. The expanded isotopic distribution of the major peak (i.e., trianionic) in the mass spectrum is in agreement with the calculated isotopic distribution, as shown in Figure S1C, thus demonstrating sample purity. Upon introduction of **L′** (0.026 mM) into a ∼ 50 μM DMF−methanol solution of $[Ag_{29}]^{3-}$ at room temperature (∼298 K), $[Ag_{29}]\mathbf{L}'_n{}^{3-}$ adducts (n = 1−10) were observed to form faster than 30 s after mixing (corresponding to the apparatus dead time before ESI MS detection) as shown in Figure 1B(i−ii). The concentrations of **L′** and $[Ag_{29}]^{3-}$ NC were fixed at an optimal concentration, which was arrived at by concentration-dependent measurements. At higher concentrations of **L′**, larger aggregates were formed and a study of the same will be reported in the future.

Many other studies have shown that ESI MS can yield a good relative measure of the composition of solutions of charged, atomically precise NCs. On the basis of the ratio of mass spectral peak intensity for $[Ag_{29}]^{3-}$ to the sum of $[Ag_{29}]\mathbf{L}'_n{}^{3-}$ signals, we infer that roughly 15% of the parent ions form adducts in solution (or during ESI). Accurate mass measurements confirmed that adduct ions were separated by ∼ m/z 116, corresponding to the addition of **L′** (mass of **L′** is 348, i.e., 116 × 3). Therefore, structural integrity of **L′** appears maintained upon binding to the NC (i.e., no loss of small fragments such as H or H_2). This is consistent with a comparison of the UV−vis spectrum of the mixed solution with that of pure $[Ag_{29}](TPP)_4{}^{3-}$ NC and the pure secondary ligand, **L′**. The spectrum changes additively upon mixing. Similar changes were observed during photoluminescence studies upon luminating the solution at 445 nm. Upon increasing the concentration of **L′** to the NC solution, no apparent shift in the photoluminescence spectrum of $[Ag_{29}](TPP)_4{}^{3-}$ (at 660 nm) was observed.

Under the ESI conditions used to study the mixed solutions (after adding **L′**), the relative dianionic intensity was below the detection limit (peak intensity of $[Ag_{29}]H^{2-}$ (m/z 2405) was masked by the isotopic distribution of $[Ag_{29}]\mathbf{L}'_7{}^{3-}$, m/z 2415).

https://doi.org/10.1021/acsnano.4c16413
ACS Nano 2025, 19, 5727−5738

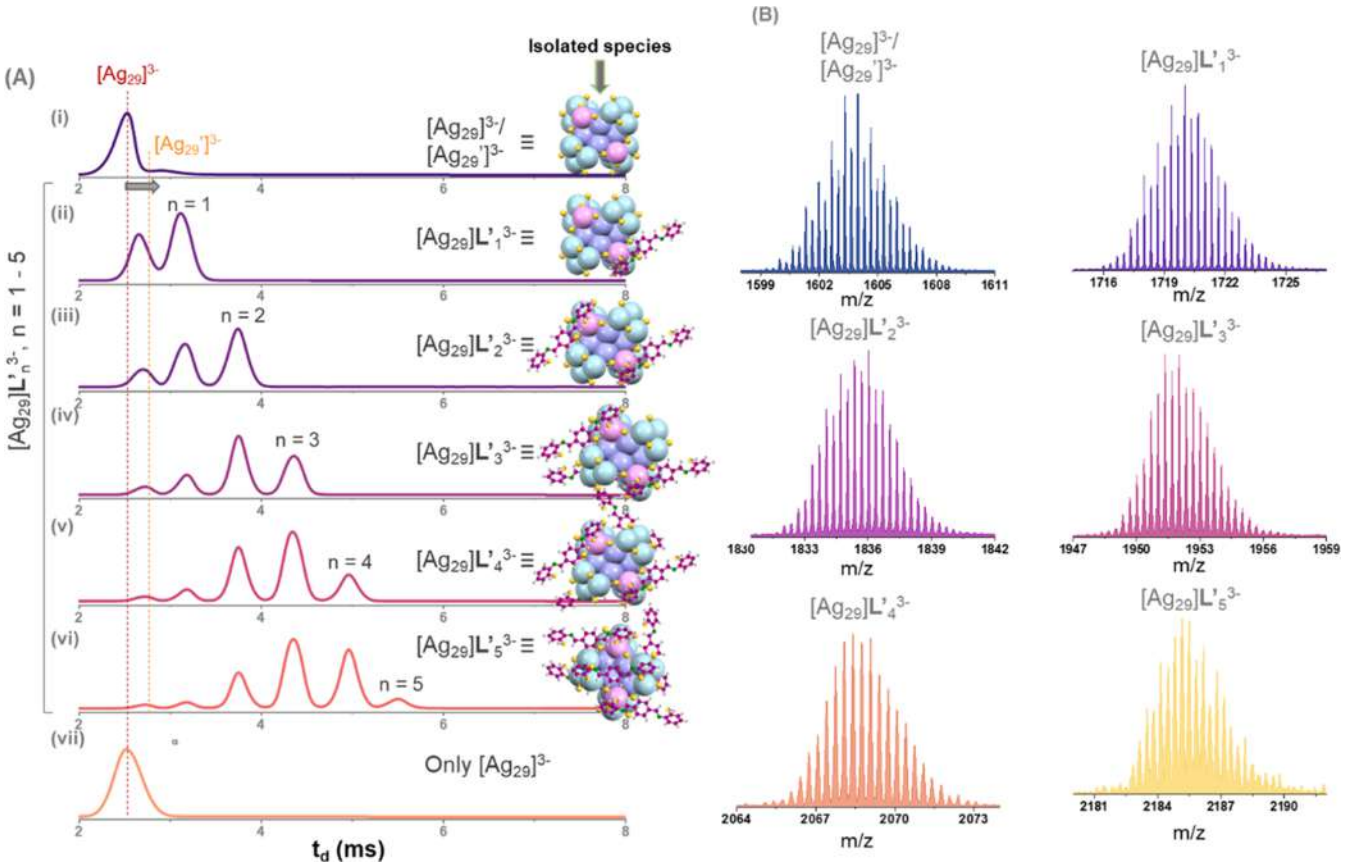


Figure 3. (A) (i–vi) Drift time measurements of mass-selected NC (complex) ions, $[Ag_{29}]L'_n{}^{3-}$ (n = 0–5) as sprayed from a solution of $[Ag_{29}]^{3-}$ and L′; (vii) reference drift time measurement for $[Ag_{29}]^{3-}$ sprayed from a pure $[Ag_{29}]^{3-}$ NC solution. Dotted lines indicate the shift in drift time from $[Ag_{29}]^{3-}$ toward a higher value for $[Ag_{29}']^{3-}$ (see text and Figure S4). (B) Extracted MS for individual peaks in the ATDs of $[Ag_{29}]L'_n{}^{3-}$ allowing the indicated assignment of the corresponding t_d values to specific parents and fragments (as also checked by comparing experimental and simulated isotopic distributions).

We therefore confine further discussion below to the trianions. The mass spectrum is consistent with the sequential addition of L′ to $[Ag_{29}]^{3-}$ NC as schematically depicted in Figure 1C. While signals of $[Ag_{29}]L'_n{}^{3-}$, $n \leq 4$, were quite stable, the intensity of ions with $n \geq 5$ decreased over time, suggesting a secondary process leading to a shift in solution equilibrium favoring smaller complexes. Therefore, only $[Ag_{29}]L'_n{}^{3-}$ complexes with n values from 1 to 4 are considered here (see Figure 1B(ii)).

IM MS was next employed to characterize the structure of the $[Ag_{29}]L'_n{}^{3-}$ complexes as well as to examine the influence of complexation on the NC precursor by using both timsTOF and Synapt IMS mass spectrometers.

Experimental CCS of $[Ag_{29}]^{3-}$ and $[Ag_{29}]L'_n{}^{3-}$ Ions. *TimsTOF Measurements.* $[Ag_{29}]^{3-}$ and $[Ag_{29}]L'_n{}^{3-}$ NC ions were monitored with high-resolution trapped ion mobility spectrometry in nitrogen collision gas (IMS MS) using procedures which we have described previously.[61−63] This results in calibrated collision cross-sections, which we denote as $^{TIMS}CCS_{N2}$. Figure 2A shows typical mobilograms (detected ion intensity versus $^{TIMS}CCS_{N2}$). The small peak labeled with # could be attributed to either fragmentation or artifact due to the nature of these weak adducts. $^{TIMS}CCS_{N2}$, full width at half maximum (FWHM, Å^2), and resolution (R) of individual ions are listed in Figure 2B and plotted versus n in Figure 2C. From this, we see that (i) within the CCS resolution obtainable, there is only one peak in each case (i.e., only one resolvable $[Ag_{29}]L'_n{}^{3-}$ isomer) and (ii) $^{TIMS}CCS_{N2}$ values increase linearly with the number of L′ added. The relative deviation in $^{TIMS}CCS_{N2}$ values of the NCs was <0.2% upon repeated measurements with the same instrumental conditions.[62]

Synapt Measurements. To further explore the dynamics of structural transformations upon reaction with secondary ligands, we performed systematic MS^2 IMS experiments on all isolated $[Ag_{29}]L'_n{}^{3-}$ (n = 0–5) using the Synapt instrumental platform.

The Synapt platform ensures that ions can be m/z-selected before the IMS measurement, thus also allowing for IMS studies of fragment ions. Fragments can be controllably formed during injection of m/z-selected species into the traveling wave ion mobility (TWIMS) cell with a selected collision energy (CE).[64,65] A TOF MS subsequently (re)analyzes the ions transmitted through the TWIMS, and as a result, tandem MS measurements combined with IMS analysis can be carried out: MS^2 IMS. Specifically, we applied a CE setting of 10 V to the trap cell, which leads only to the sequential loss of neutral secondary ligands from mass-selected $[Ag_{29}]L'_n{}^{3-}$ without causing additional fragmentation of the component NC, reaction 1.

https://doi.org/10.1021/acsnano.4c16413
ACS Nano 2025, 19, 5727−5738

Table 1. $^{TW}CCS_{N2}$ of Parent Ions ($[Ag_{29}]^{3-}$ and $[Ag_{29}]L'_n{}^{3-}$) and Fragment Ions Corresponding to Loss of m L′ Secondary Ligands ($[Ag_{29}]L'_{n-m}{}^{3-}$)—as Generated by Collisions Upon Injection of Parent Ions into the Triwave Sector of the Synapt IMS MS (See Text for Details)

Gas phase fragment ions ↓ / Selected ions →	$[Ag_{29}]^{3-}$ $^{TW}CCS_{N2}$ (Å²)	$[Ag_{29}]L'_1{}^{3-}$ $^{TW}CCS_{N2}$ (Å²)	$[Ag_{29}]L'_2{}^{3-}$ $^{TW}CCS_{N2}$ (Å²)	$[Ag_{29}]L'_3{}^{3-}$ $^{TW}CCS_{N2}$ (Å²)	$[Ag_{29}]L'_4{}^{3-}$ $^{TW}CCS_{N2}$ (Å²)	$[Ag_{29}]L'_5{}^{3-}$ $^{TW}CCS_{N2}$ (Å²)
$[Ag_{29}']^{3-}$	480.9	488.6	492.8	494.7	494.8	495.4
$[Ag_{29}]L'_1{}^{3-}$	-	536.6	540.5	542.4	542.9	542.6
$[Ag_{29}]L'_2{}^{3-}$	-	-	597.2	598.3	598.1	598.3
$[Ag_{29}]L'_3{}^{3-}$	-	-	-	652.9	651.8	652.5
$[Ag_{29}]L'_4{}^{3-}$	-	-	-	-	704.7	705.0
$[Ag_{29}]L'_5{}^{3-}$	-	-	-	-	-	748.7

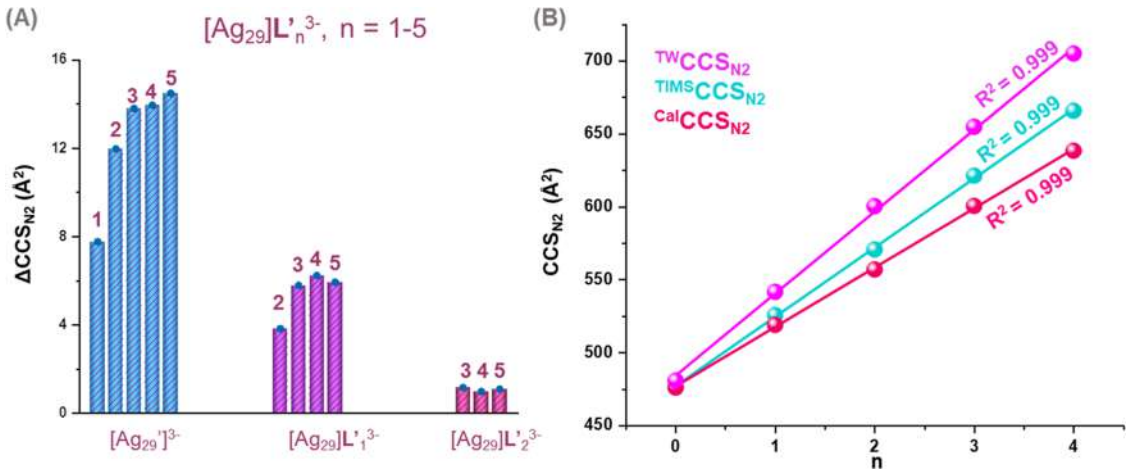


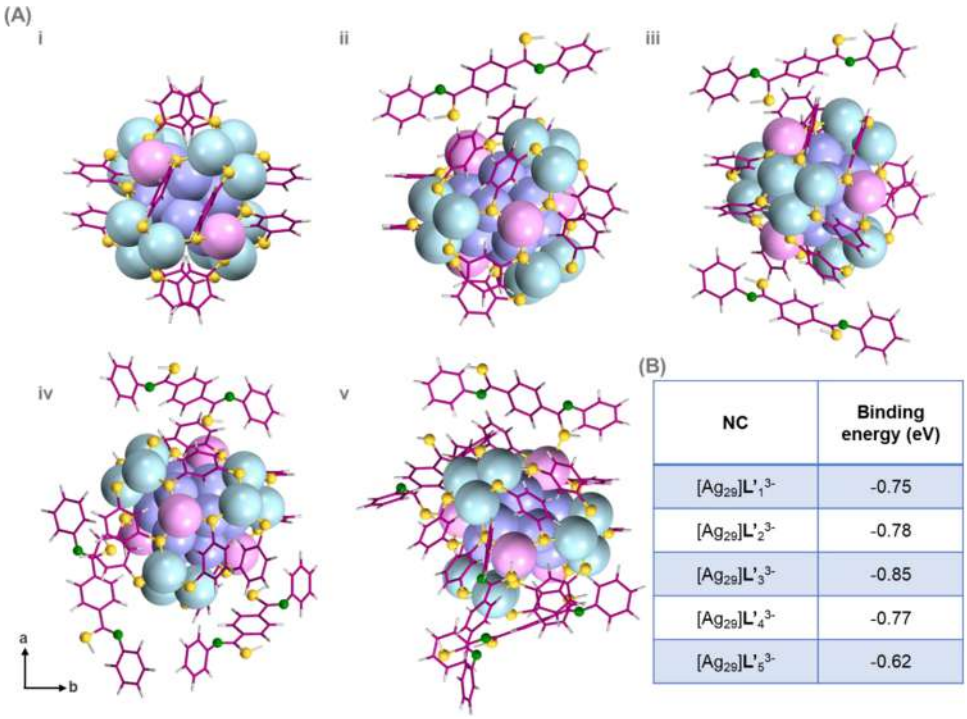
Figure 4. (A) Trend of ΔCCS values, calculated as the difference between the $^{TW}CCS_{N2}$ of parent ions and the $^{TW}CCS_{N2}$ of equi-m/z fragment species generated from higher adducts. (B) Theoretical ($^{Cal}CCS_{N2}$) and experimental CCS_{N2} ($^{TIMS}CCS_{N2}$ and $^{TW}CCS_{N2}$) of the parent and ligand added NC ions ($[Ag_{29}]^{3-}$, $[Ag_{29}']^{3-}$, and $[Ag_{29}]L'_n{}^{3-}$, n = 1−4) at ∼300 K. Note that while there is a linear dependence of CCS on n for both $^{TW}CCS_{N2}$ and $^{TIMS}CCS_{N2}$, slopes differ because of different calibration procedures.

$$[Ag_{29}]\mathbf{L}'_n{}^{3-*} \rightarrow [Ag_{29}]\mathbf{L}'_{n-1}{}^{3-} + \mathbf{L}' \rightarrow [Ag_{29}]\mathbf{L}'_{n-2}{}^{3-} + \mathbf{L}'\text{... so on (*represents the energetically excited } [Ag_{29}]\mathbf{L}'_n{}^{3-}\text{ions)} \quad (1)$$

Figure 3A, (i)−(vii), shows the resulting stacked mobilograms. This plot (overall injected ion signal intensity versus drift times, t_d) for all mass-selected $[Ag_{29}]\mathbf{L}'_n{}^{3-}$ was obtained after spraying from solution mixtures of $[Ag_{29}]^{3-}$ + L′ in comparison to the mobilogram of $[Ag_{29}]^{3-}$ recorded for a pure NC solution under the same instrumental settings. Drift times of features resolved in the heatmaps were correlated with the subsequent TOF mass analysis to yield "extracted MS". This allows to distinguish parent from fragment ions formed upon injection into the TWIMS cell. Figure 3B documents these extracted MS, which allowed us to assign the t_d features as labeled in (i)−(vi). From these, we have inferred that in the CE range probing all $[Ag_{29}]\mathbf{L}'_n{}^{3-}$ ($n > 0$) fragments according to reaction 1, i.e., there is no retention of thiol H atoms on the fragment multianions.

Interestingly, significant shifts in t_d between equi-m/z fragments (resulting from $[Ag_{29}]\mathbf{L}'_{n-m}{}^{3-}$ where m ranges up to 4) and unfragmented $[Ag_{29}]\mathbf{L}'_n{}^{3-}$ species indicate that the fragment ions have changed their structure. They are on average larger. This effect is further highlighted in the "heatmaps" shown in Figure S4A,B (ion signals versus t_d in milliseconds (ms), recorded for an m/z range around 1603 corresponding to $[Ag_{29}]^{3-}$ before and after introducing L′ to the solution). The peaks labeled with $[Ag_{29}]^{3-}$ in Figure S4A,B have essentially the same t_d value and can be attributed to the (unchanged) $[Ag_{29}]^{3-}$ parent ion. Introducing L′ into the solution leads to an additional peak in the heat map. This we interpret as a structural isomer of $[Ag_{29}]^{3-}$ generated through some gas-phase fragmentation of $[Ag_{29}]\mathbf{L}'_n{}^{3-}$ ($n > 0$) adducts

https://doi.org/10.1021/acsnano.4c16413
ACS Nano 2025, 19, 5727−5738



NC	Binding energy (eV)
$[Ag_{29}]L'_1{}^{3-}$	-0.75
$[Ag_{29}]L'_2{}^{3-}$	-0.78
$[Ag_{29}]L'_3{}^{3-}$	-0.85
$[Ag_{29}]L'_4{}^{3-}$	-0.77
$[Ag_{29}]L'_5{}^{3-}$	-0.62

Figure 5. (A) DFT-optimized structures of $[Ag_{29}]^{3-}$ NC (i) and its L′ complex ions $[Ag_{29}]L'_n{}^{3-}$ ions (n = 1−5; (ii) − (v)). (B) Table showing the calculated binding energy (per L′ attachment, in eV) of Color code: Ag, purple, pink, and cyan blue; S, yellow; C, dark magenta; H, light gray; and N, dark green.

by way of **L′** loss already prior to the initial mass selection. Again, this peak appears at a higher t_d (~2.9 ms) than the parent, suggesting significantly expanded structural isomers which we denote as $[Ag_{29}']^{3-}$ for further discussion below.

Thus, we infer an overall three-step process: (i) **L′** attachment to $[Ag_{29}]^{3-}$ in solution (or during ESI) to form $[Ag_{29}]L'_n{}^{3-}$ ($n > 0$) adducts, (ii) isolation of these adducts in the gas phase, and then (iii) soft collision-induced detachment of secondary ligands **L′** upon initiating the ion mobility measurement. Each ion mobility measurement was multiply repeated to confirm the reproducibility of the measured t_d values, and from these, the corresponding (calibrated) $^{TW}CCS_{N2}$ values were determined, which will be discussed next.

Table 1 shows the experimental $^{TW}CCS_{N2}$ values of the parent and fragment ions as determined by MS^2 IMS measurements (calibrated using reported methods).[66,67] The $^{TW}CCS_{N2}$ values were found to be stable across a range of activation conditions, indicating the structural stability of the ions (which are rapidly thermalized back down to room temperature at the beginning of their passage through the TWIMS cell). Specifically, the $^{TW}CCS_{N2}$ value for parent $[Ag_{29}]^{3-}$ was 480.9 Å^2, aligning closely with recently reported values.[56,66,67] Table 1 reveals a progressive increase in $^{TW}CCS_{N2}$ from left to right for the m/z ratio corresponding to $[Ag_{29}]^{3-}$ and $[Ag_{29}']^{3-}$ ($^{TW}CCS_{N2}$ (Å^2): 480.9 < 488.6 < 492.8 < 494.7 < 494.8 < 495.4), indicating progressive structural changes in $[Ag_{29}]^{3-}$ isomers formed by fragmentation of $[Ag_{29}]L'_n{}^{3-}$ (n = 1−5).

The detachment of **L′** ligands due to collisional excitation of $[Ag_{29}]L'_n{}^{3-}$ ($n > 0$) ions generally resulted in increased $^{TW}CCS_{N2}$ values relative to the unfragmented reference mass, independent of the $[Ag_{29}]L'_{n-m}{}^{3-}$ species formed as Figure 4A illustrates. This shows the extent of $^{TW}CCS_{N2}$ changes for fragment masses $[Ag_{29}']^{3-}$, $[Ag_{29}]L'_1{}^{3-}$, and $[Ag_{29}]L'_2{}^{3-}$, compared to the number of secondary ligands previously detached to generate them, e.g., a deviation of 1.7% is observed for $[Ag_{29}']^{3-}$ resulting from $[Ag_{29}]L'_1{}^{3-}$ (relative to the $^{TW}CCS_{N2}$ of the parent $[Ag_{29}]^{3-}$). Deviations become larger as more secondary ligands are lost to generate the fragment in question. Analogous but smaller effects are seen when analyzing the $[Ag_{29}]L'_1{}^{3-}$ or $[Ag_{29}]L'_2{}^{3-}$ fragment formation.

To put the impact of secondary **L′** ligands on the structural dynamics of the $[Ag_{29}]^{3-}$ NC into a wider context, analogous IMS MS experiments were also attempted with two other foreign ligands, namely 2-pyreneiminethiol (referred to as **L″**) and 1,6-hexanedithiol (denoted as **L‴**), separately. These two ligands (for structures, see Figure S5) were chosen because **L″** has a terminal group similar to **L′**, and **L‴** is a dithiol similar to **L′**. **L″** and **L‴** ligands were introduced separately into the $[Ag_{29}](TPP)_4{}^{3-}$ NC solution, followed by ESI MS and subsequent IMS MS measurements (see Figure S6). No additional peaks related to foreign ligand incorporation were observed in ESI MS for either case. Furthermore, IMS MS results showed no significant changes in the drift time (t_d) of the parent NC, indicating minimal impact on its structure (see Figure S6).

Density Functional Theory (DFT) and CCS Calculations by the Trajectory Method (TM). The interaction of secondary **L′** ligands with the $[Ag_{29}]^{3-}$ NC was studied computationally using DFT. First, structural optimization of the isolated $[Ag_{29}]^{3-}$ NC was performed starting from the previously reported crystal structure.[60] The calculated CCS for $[Ag_{29}]^{3-}$ NC was found to be 476.04 Å^2, which is comparable with our experimentally determined $^{TIMS}CCS_{N2}$ and $^{TW}CCS_{N2}$ values (those are 476.3 and 480.9 Å^2, respectively). The small difference can be rationalized by Ag not being specifically parametrized in IMoS (a general default setting is used

https://doi.org/10.1021/acsnano.4c16413
ACS Nano 2025, 19, 5727−5738

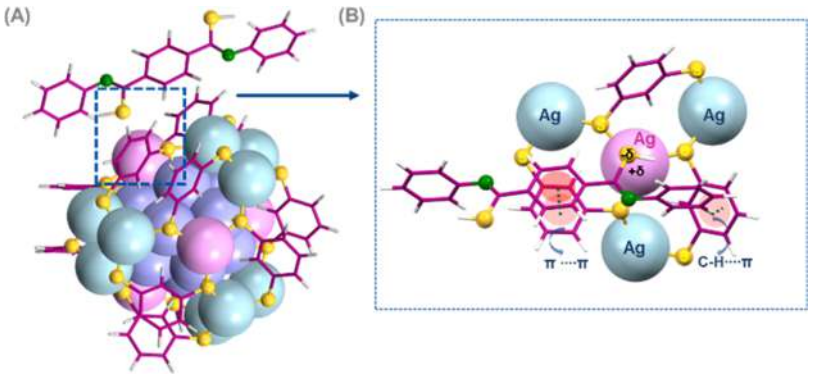


Figure 6. (A) DFT-optimized lowest-energy structure of $[Ag_{29}]L'_1{}^{3-}$ NC, highlighting the interaction of L′ ligand at the Ag atom at crown site. (B) Enlarged view of the staples around the crown Ag atom and peripheral tetrahedral Ag-L showing how three proximal L ligands (and associated Ag−S bonds) of the $[Ag_{29}]^{3-}$ NC are influenced by ionic, $\pi\cdots\pi$, and CH$\cdots\pi$ interactions with the attached L′ ligand. The partial ionic character associated with $[Ag_{29}]^{3-}$-L′ complexation is denoted by $\delta+$ / $\delta-$. Color code: Ag, purple, pink, and cyan blue; S, yellow; C, dark magenta, H, light gray; and N, dark green.

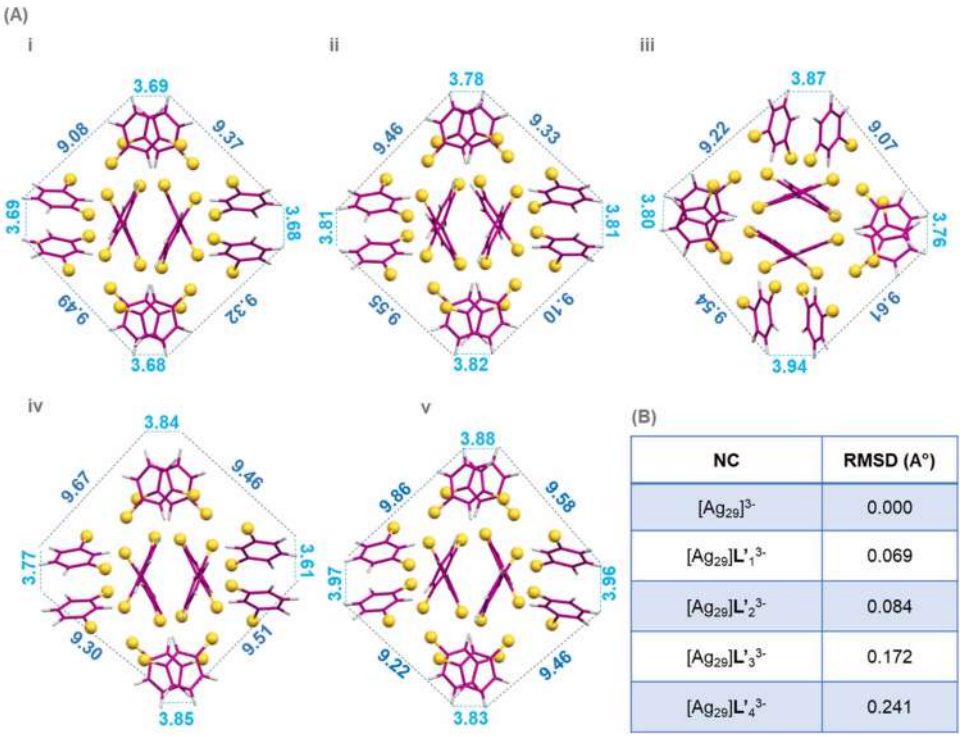
instead). This optimized $[Ag_{29}]^{3-}$ structure was then used as a starting point to model the secondary ligand addition (Figure 5A(i)). To rationally correlate plausible DFT-derived structural models, their corresponding $^{Cal}CCS_{N2}$ values were then calculated by using the trajectory method (TM) and compared to experimentally observed $^{TW}CCS_{N2}$ values of $[Ag_{29}]L'_n{}^{3-}$. Due to the large size of the system, we have not considered zero-point energy corrections for structural optimization.

Before the results are described, it is useful at this stage to further familiarize the reader with the structure of $[Ag_{29}]^{3-}$. The DFT-derived-optimized structure is very similar to the crystal structure, which manifests four distinct types of Ag atoms. These types encompass (see Figure S3) the central Ag atom positioned within the replete icosahedral core, the residual set of 12 Ag atoms constituting the icosahedral framework (icosahedral Ag), another 12 atoms directly bonded to the S atoms of the L ligands forming the NC thiolate shell (tetrahedral Ag (4 × 3)), and 4 undercoordinated Ag atoms (crown Ag) to each of which a PPh_3 ligand is bound in the solid (these are lost in the gas phase).[60] The 12 L ligands coordinate to 12 tetrahedral Ag atoms as bidentate thiols constituting the shell of the NC. Pairs of L ligands coexist on the surface of the NC due to the $\pi\cdots\pi$ interactions between parallel phenyl rings of Ls.

Both the regular ESI MS pattern of $[Ag_{29}]L'_n{}^{3-}$ adducts and the low CE threshold for **L′** detachment are consistent with comparatively weak supramolecular interactions between the secondary ligands and $[Ag_{29}]^{3-}$ NC. We therefore explored many possible noncovalent adducts of **L′**. We optimized the **L′** ligand in both its *cis* and trans forms using DFT in TURBOMOLE[68] with the B3-LYP functional[69−73] and the def2-TZVP[74] (valence triple-ζ polarization) basis set and accounting for dispersion at the D3(BJ)[75,76] level. We found a negligible relative energy difference between *cis*-**L′** and trans-**L′** of 0.0005 eV in favor of the trans-isomer (see Figure S7). Preliminary DFT calculations indicate a low rotational barrier (∼0.08 eV) and an easy interconversion between the two isomers at room temperature using the wB97X-V/def2-TZVP basis set with the r^{2}SCAN-3c method and the conductor-like polarizable continuum model (CPCM)-like implicit solvation model, which will be discussed in more detail in a future publication. Note that the ligand contains both nitrogen (N) and sulfur (S) atoms. Interestingly, both show enhanced interactions with specific silver (Ag) atoms on the $[Ag_{29}]^{3-}$ NC when **L′** is positioned to allow this (see Figure S8). The strongest interaction found (ca. 0.75 eV overall binding energy, see Figure 5) occurs when the secondary ligand is oriented *tangentially* to the ligand shell of $[Ag_{29}]^{3-}$ NC such that an S atom in the terminal SH group of the **L′** ligand can optimally interact with a tetrahedral Ag site on the NC (by contrast, radial attachment or partial radial insertion into the preexisting L ligand shell is found to be highly unfavorable; see Figure S8). This configuration is schematically shown in Figure 5A(ii) and depicted in more detail in Figures S7 and S8. Note that tangential binding of **L′** to undercoordinated Ag atoms at crown sites was found to be less favorable than to tetrahedral sites. Binding of **L′** to tetrahedral Ag sites allows the additional $\pi\cdots\pi$ stacking interaction between **L′** and L ligands (see Figure 6). A related noncovalent interaction between a fullerene secondary ligand and $[Ag_{29}]^{3-}$ was observed in a previous report.[32] Based on the optimal **L′** bonding orientation found for $[Ag_{29}]L'^{3-}$, we also constructed structural models for $[Ag_{29}]L'_{2-4}{}^{3-}$ (addition of further **L′** ligands tangentially and keeping them as far apart as possible). CCS_{N2} values simulated on the basis of these models (using DFT + TM; Figure 5A(ii−v),5B) show a linear increase with the number of **L′** added as plotted in Figure 4B—in good qualitative agreement with the experiment. Predicted $^{Cal}CCS_{N2}$ values were however found to depend quite sensitively on the (relative) orientations of **L′**. Furthergoing studies (also including systematic docking simulations of higher numbers of secondary ligands onto $[Ag_{29}]^{3-}$ NC) will be reported elsewhere.

Beyond the predicted linear increase in $^{Cal}CCS_{N2}$ with the number of secondary ligands added, it is also instructive to examine the changes to the precursor $[Ag_{29}]^{3-}$ NC structure upon **L′** attachment. Figures 6, S9, and S10 provide the corresponding details of the DFT-optimized structures (including calculated root-mean-square displacement (RMSD) values). The $Ag_{core} - Ag_{ico}$ bond length of ∼2.83 Å in the $[Ag_{29}]^{3-}$ NC remains essentially the same at ∼2.81 Å in $[Ag_{29}]L'_4{}^{3-}$. By contrast, the average $Ag_{core} - Ag_{crown}$ bond length in $[Ag_{29}]^{3-}$ NC is significantly increased during **L′**-attachments (∼4.64 Å), compared to the $[Ag_{29}]^{3-}$ (∼4.52 Å). Changes in Ag−Ag atomic distances (Å) in $[Ag_{29}]L'_4{}^{3-}$ as a function of bond index (i.e., variation of individual $Ag_{ico/crown} - Ag_{core}$ bond lengths of the NC before and after the **L′** incorporation) and the distances between L ligands are shown in Figure S10 and Figure 7, respectively.

https://doi.org/10.1021/acsnano.4c16413
ACS Nano 2025, 19, 5727−5738



NC	RMSD (A°)
$[Ag_{29}]^{3-}$	0.000
$[Ag_{29}]L'_1{}^{3-}$	0.069
$[Ag_{29}]L'_2{}^{3-}$	0.084
$[Ag_{29}]L'_3{}^{3-}$	0.172
$[Ag_{29}]L'_4{}^{3-}$	0.241

Figure 7. Reduced representations of DFT-derived minimum energy structures for $[Ag_{29}]L'_n{}^{3-}$ NC, n = 0−4 (i−v) depicted in Figure 5 (here, the Ag_{29} core and the L′ ligands have been removed from the $[Ag_{29}]L'_n{}^{3-}$ structures for clarity). This representation highlights changes to the Ag−S staple and ligand L orientation upon incorporation of L′ into the parent $[Ag_{29}]^{3-}$. Shown are (A) distances between different L ligands attached to Ag−S staples in the DFT-optimized structure of $[Ag_{29}]L'_n{}^{3-}$ NC, n = 0−4 (i−v). Color codes: light blue denotes the distance measured between two pairs of parallel Ls; dark blue denotes the distance between terminal Hs of two parallel Ls. All distances are given in Å. (B) Root-mean-square displacement (RMSD) of silver atoms in L′-$[Ag_{29}]^{3-}$ adduct ions from the parent $[Ag_{29}]^{3-}$ ion calculated as indicated in the text. Color code: S, yellow; C, dark magenta; and H, light gray. Overall, L′ complexation leads to the expansion of Ag−S staples and to associated changes in positions/extensions of the 12 L ligands.



Figure 8. Schematic structures of (A) L′, (B) L″, and (C) L‴. Color code: S, yellow; C, dark magenta; and H, light gray.

We infer that upon attachment of **L′**, the proximal Ag−S staple framework of the NC precursor expands, and correspondingly, the distance between adjacent L-pairs increases (see Figure 6 for further details). Compared to the parent $[Ag_{29}]^{3-}$ NC, $[Ag_{29}]L'_n{}^{3-}$ ions not only have larger ${}^{Cal}CCS_{N2}$ because of the added secondary ligands, they are also larger because **L′** complexation causes the $[Ag_{29}]^{3-}$ NC precursor to noticeably expand. This ultimately reflects an enhanced $\pi\cdots\pi$ stacking[77] interaction between **L′** and L ligands as well an ionic contribution resulting from charge transfer between terminal SH and axial Ag atoms on the NC as the detail in Figure 6 shows.

In analogous calculations of adducts of the $[Ag_{29}]^{3-}$ NC with the other two structurally similar secondary ligands screened in this study (**L″** and **L‴**, see Figure 8), we found no significant structural changes of the central $[Ag_{29}]^{3-}$ NC consistent with no detectable adduct formation in the experiment (see Figure S11). The calculated binding energies of **L″** and **L‴** ligands on $[Ag_{29}]^{3-}$ NC were −0.58 and −0.71 eV, respectively. This observation highlights the highly specific interaction of **L′** with the $[Ag_{29}]^{3-}$ NC, which leads to a significant restructuring of its surface.

CONCLUSIONS

We have studied the interaction between the secondary dithiol ligand **L′** = 2,2′-[1,4-phenylenebis(methylidynenitrilo)] bis-[benzenethiol] and the atomically precise silver cluster $[Ag_{29}(L)_{12}]^{3-}$ (L = 1,3-benzene-dithiol). Our results imply a specific interaction between the secondary ligand and $[Ag_{29}]^{3-}$ NC, leading to facile formation of a series of noncovalently bound adducts $[Ag_{29}]L'_n{}^{3-}$. DFT calculations indicate that this is also associated with a progressive volume expansion of the $[Ag_{29}]^{3-}$ precursor as secondary ligands are added. Our ion mobility measurements (IMS MS and MS^2 IMS) provide further support for this interpretation. Upon electrospray ionization, $[Ag_{29}]L'_n{}^{3-}$, can be transferred intactly into the gas phase and subsequently collisionally dissociated. In the studies of adducts with n ≤ 4, we found loss of neutral **L′** to be the primary (and lowest energy) fragmentation channel, consistent with DFT-computed secondary ligand binding energies of < 1 eV (see Figure 7B). In all cases, $[Ag_{29}]L'_{n-m}{}^{3-}$ fragments

https://doi.org/10.1021/acsnano.4c16413
ACS Nano 2025, 19, 5727−5738

(thermalized to room temperature after having lost m **L′** secondary ligands) were found to have *larger* ^{TW}CCS than equi-mass ions, which had not undergone fragmentation. Apparently, these "footprints" of previously bound **L′** can survive in the gas phase on the time scale of the ion mobility measurement (ca. 1 ms). Perhaps, this time is too short to allow these isomers to return to their parent structure.

Although our study was centered around secondary ligand-induced structural distortion of $[Ag_{29}]^{3-}$ NCs, our methods and results are applicable to extremely fast ligand interactions of metal NCs in general. In this system, we have recently looked at higher **L′** coverages and interlinked dimers and will report the results in a separate contribution.

EXPERIMENTAL SECTION

ESI MS and IM MS Measurements. High-resolution ESI MS, IMS MS, and MS^2 IMS measurements were performed using two different ion mobility mass spectrometers, namely, a Synapt G2-Si HDMS (Waters, Manchester, U.K.) at IIT Madras and a timsTOF (Bruker Daltonics, Bremen, Germany) at KIT. The timsTOF was used to obtain high-resolution mobility data for the parent ions directly sprayed from solution (IMS MS), whereas the Synapt allowed us to also study charged fragments but at somewhat reduced mobility resolution (MS^2 IMS). The Synapt instrumental platform comprises a combination of quadrupole mass filter, TWIMS, and time-of-flight mass spectrometer, which allow separation of ions according to their CCS ($^{TW}CCS_{N2}$; with a resolution of ~40 ($^{TW}CCS_{N2}/\Delta\ ^{TW}CCS_{N2}$) in terms of full width at half maximum, FWHM) and mass-to-charge ratio, m/z. The trap and transfer were filled with argon (Ar) with a flow rate of 3 mL/min (p = ~0.006 mbar),[78] whereas the TWIMS cell was filled with N_2 (40 mL/min).[79] All samples were measured in negative electrospray ionization mode. The mass scale of the instrument was calibrated by using NaI cluster ions. Typical experimental parameters were as follows: desolvation gas temperature: 150 °C, source temperature: 100 °C, desolvation gas flow: 400 L/h, capillary voltage: 3 kV, sample cone: 10−20 V, source offset: 0−20 V, trap collision energy: 2−30 V, trap gas flow: 2 mL/min, helium cell gas flow: 90−150 mL/min, IMS gas flow: 60−80 mL/min, trap DC bias: 28−45 V; IMS wave height: 38 V, and IMS wave velocity: 550 m/s. The collision voltage in the trap cell was raised until fragmentation of the selected ion was initiated (typically CE = 2−30 V). The sample concentration was 1 μg/mL (in DMF−methanol solvent mixture) and infused at a flow rate of 20 μL/min. Polyalanine ions were used for calibrating the $^{TW}CCS_{N2}$ values (correcting for charge state) and were measured under the same experimental conditions as $[Ag_{29}]^{3-}$ ions. The $^{TW}CCS_{N2}$ value of the $[Ag_{29}]^{3-}$ NC was consistent with the previous literature determination (see also below).[39] Data processing was conducted by using Waters Masslynx 4.1 and DriftScope 2.1.

The timsTOF platform was used to determine ion mobilities with a particularly high accuracy and resolution. In timsTOF, electrosprayed ions are separated according to their $^{TIMS}CCS_{N2}$ in a trapped ion mobility cell (typical resolution: ~200 ($^{TIMS}CCS_{N2}/\Delta^{TIMS}CCS_{N2}$)) followed by mass separation in a time-of-flight mass spectrometer (i.e., no mass selection prior to the IMS separation). ESI MS and IMS MS measurements in timsTOF were recorded in negative ion mode under the following experimental conditions. ESI flow rate: 100 μL/h, capillary voltage: 5 kV, end plate offset: 2200 V, nebulizer gas flow: 0.3 bar, dry gas: 3 L/min, dry temperature: 200 °C, and TIMS delta values (Δ1 − Δ6): 100, 100, −80, −50, 5, and −100 V. Other parameters and CCS_{N2} calibration procedures were as described previously.[80]

Despite the different ESI sources and spray conditions used, mass spectra were in qualitative agreement across the two different instrumental platforms.

Computational Details. All DFT-based calculations were carried out using the projector augmented wave (PAW) method as implemented in the Vienna *Ab initio* Simulation Package (VASP).[81] The electronic exchange and correlation interactions have been integrated utilizing the generalized gradient approximation of Perdew−Burke−Ernzerhof (GGA-PBE) functional.[82] The conjugate gradient algorithm has been considered for ionic relaxation with electronic energy and force criteria set to 10^{-4} eV and 0.05 eV/Å (Hellmann−Feynman forces on atoms), respectively. The plane wave cutoff energy has been set to 470 eV to enlarge the electronic wave function. $A \sim 8$ Å vacuum was set along all directions to avoid possible interactions between periodic images. As the unit cells of the compounds were rather large, we sampled the Brillouin zone at the 1 × 1 × 1 Γ k-point mesh.

CCS Calculations. The CCS was calculated for DFT-derived structural models using the trajectory method (TM) as implemented in IMoS 1.10.[32,83] For each structure considered, we typically ran 4,500,000 trajectories.[39] In order to investigate changes in Ag−Ag bond distances as a result of **L′** addition to $[Ag_{29}]^{3-}$ NC, the resulting RMSD of the 16 staple Ag atoms from the central Ag atom of NC ions was calculated following the equation[84]

$$\mathrm{RMSD} = \sqrt{\frac{1}{N}\sum_{j=1,m}(da_j - db_j)^2}$$

where da_j and db_j are the distances between the staple Ag atom (j = m) and central Ag atom (j = 1) in $[Ag_{29}]^{3-}$ and $[Ag_{29}]\mathbf{L'}_n^{3-}$ NC ions, respectively.

ASSOCIATED CONTENT

Supporting Information

The Supporting Information is available free of charge at https://pubs.acs.org/doi/10.1021/acsnano.4c16413.

Reagents and materials; synthesis; concentration calculation; UV−vis study; ESI MS study; ESI IM MS study; CID MS study; DFT-optimized structures; and bond length calculation (PDF)

AUTHOR INFORMATION

Corresponding Authors

Biswarup Pathak − *Department of Chemistry, Indian Institute of Technology Indore, Indore 453552, India;* orcid.org/0000-0002-9972-9947; Email: biswarup@iiti.ac.in

Manfred M. Kappes − *Institute of Nanotechnology, Karlsruhe Institute of Technology (KIT), 76131 Karlsruhe, Germany; Institute of Physical Chemistry, Karlsruhe Institute of Technology (KIT), 76131 Karlsruhe, Germany;* orcid.org/0000-0002-1199-1730; Email: manfred.kappes@kit.edu

Thalappil Pradeep − *DST Unit of Nanoscience (DST UNS) & Thematic Unit of Excellence (TUE), Department of Chemistry, Indian Institute of Technology Madras, Chennai 600036, India; International Centre for Clean Water, Chennai 600113, India;* orcid.org/0000-0003-3174-534X; Email: pradeep@iitm.ac.in; Fax: 91-44-2257-0545/0509

Authors

Jayoti Roy − *DST Unit of Nanoscience (DST UNS) & Thematic Unit of Excellence (TUE), Department of Chemistry, Indian Institute of Technology Madras, Chennai 600036, India*

Amitabha Das − *Department of Chemistry, Indian Institute of Technology Indore, Indore 453552, India;* orcid.org/0000-0002-5000-4451

Arijit Jana − *DST Unit of Nanoscience (DST UNS) & Thematic Unit of Excellence (TUE), Department of*

https://doi.org/10.1021/acsnano.4c16413
ACS Nano 2025, 19, 5727−5738

Chemistry, Indian Institute of Technology Madras, Chennai 600036, India

Papri Chakraborty − *Institute of Nanotechnology, Karlsruhe Institute of Technology (KIT), 76131 Karlsruhe, Germany; Institute of Physical Chemistry, Karlsruhe Institute of Technology (KIT), 76131 Karlsruhe, Germany;* orcid.org/0000-0002-1353-7734

Marco Neumaier − *Institute of Nanotechnology, Karlsruhe Institute of Technology (KIT), 76131 Karlsruhe, Germany; Institute of Physical Chemistry, Karlsruhe Institute of Technology (KIT), 76131 Karlsruhe, Germany;* orcid.org/0000-0002-3810-3377

Horst Hahn − *Institute of Nanotechnology, Karlsruhe Institute of Technology (KIT), 76131 Karlsruhe, Germany; School of Sustainable Chemical, Biological and Materials Engineering, The University of Oklahoma, Norman 73019-1004 Oklahoma, United States*

Complete contact information is available at: https://pubs.acs.org/10.1021/acsnano.4c16413

Notes

The authors declare no competing financial interest.

ACKNOWLEDGMENTS

The authors thank the Department of Science and Technology (DST), Government of India, for constantly supporting our research program. J.R. and A.J. thank IIT Madras for an institute doctoral fellowship. J.R. also acknowledges partial support by the Gunther-Schroff Foundation. T.P. acknowledges funding from the Centre of Excellence on Molecular Materials and Functions under the Institution of Eminence scheme of IIT Madras. T.P. also acknowledges the Science and Engineering Research Board (SERB) for a J.C. Bose Fellowship (CHY1516331DSTXTPRA) and a Scientific and Useful Profound Research Advancement research grant (SP22230413CYSERB002505). He also thanks the DST for a research grant from the Indo-German Collaborative Activities in Chemistry and Physics scheme (SP20210994CYDSTX002505). M.K. and H.H. thank the German Science Foundation (DFG) for support of a DFG-DST collaborative project under KA 972/11-1 and HA 1344/47-1.

REFERENCES

(1) Pradeep, T. *Atomically Precise Metal Nanoclusters*, 1st ed.; Elsevier, 2023.

(2) Kang, X.; Chong, H.; Zhu, M. $Au_{25}(SR)_{18}$: The Captain of the Great Nanocluster Ship. *Nanoscale* **2018**, *10*, 10758−10834.

(3) Kang, X.; Zhu, M. Transformation of Atomically Precise Nanoclusters by Ligand-Exchange. *Chem. Mater.* **2019**, *31* (24), 9939−9969.

(4) Du, Y.; Sheng, H.; Astruc, D.; Zhu, M. Atomically Precise Noble Metal Nanoclusters as Efficient Catalysts: A Bridge between Structure and Properties. *Chem. Commun.* **2020**, *120* (2), 526−622.

(5) Cai, J.; Javed, R.; Ye, D.; Zhao, H.; Zhang, J. Recent Progress in Noble Metal Nanocluster and Single Atom Electrocatalysts for the Hydrogen Evolution Reaction. *J. Mater. Chem. A* **2020**, *8* (43), 22467−22487.

(6) Zhang, L.; Wang, E.; Wang, E. ScienceDirect Metal Nanoclusters: New Fluorescent Probes for Sensors and Bioimaging. *Nano Today* **2014**, *9*, 132−157.

(7) Bergamaschi, G.; Metrangolo, P.; Dichiarante, V. Photoluminescent Nanocluster-Based Probes for Bioimaging Applications. *Photochem. Photobiol. Sci.* **2022**, *21* (5), 787−801.

(8) Yang, G.; Wang, Z.; Du, F.; Jiang, F.; Yuan, X.; Ying, J. Y. Ultrasmall Coinage Metal Nanoclusters as Promising Theranostic Probes for Biomedical Applications. *J. Am. Chem. Soc.* **2023**, *145*, 11879−11898.

(9) Negishi, Y.; Takasugi, Y.; Sato, S.; Yao, H.; Kimura, K.; Tsukuda, T. Magic-Numbered Au_n Clusters Protected by Glutathione Monolayers (n = 18, 21, 25, 28, 32, 39): Isolation and Spectroscopic Characterization. *J. Am. Chem. Soc.* **2004**, *126* (21), 6518−6519.

(10) Qian, J.; Yang, Z.; Lyu, J.; Yao, Q.; Xie, J. Molecular Interactions in Atomically Precise Metal Nanoclusters. *Precis. Chem.* **2024**, *2* (10), 495−517.

(11) Gholipour-Ranjbar, H.; Sertse, L.; Forbes, D.; Laskin, J. Effect of Ligands on the Reactivity of the Undercoordinated Fragment Ions of $Co_6S_8(PEt_{3-X}Ph_x)_6^+$ (x = 0−3) Clusters on Surfaces. *J. Phys. Chem. C* **2024**, *128* (20), 8232−8238.

(12) Fei, W.; Antonello, S.; Dainese, T.; Dolmella, A.; Lahtinen, M.; Rissanen, K.; Venzo, A.; Maran, F. Metal Doping of $Au_{25}(SR)_{18}^-$ Clusters: Insights and Hindsights. *J. Am. Chem. Soc.* **2019**, *141* (40), 16033−16045.

(13) Kang, X.; Wei, X.; Jin, S.; Yuan, Q.; Luan, X.; Pei, Y.; Wang, S.; Zhu, M.; Jin, R. Rational Construction of a Library of M_{29} Nanoclusters from Monometallic to Tetrametallic. *Proc. Natl. Acad. Sci. U.S.A.* **2019**, *116* (38), 18834−18840.

(14) Jadzinsky, P. D.; Calero, G.; Ackerson, C. J.; Bushnell, D. A.; Kornberg, R. D. Structure of a Thiol Monolayer-Protected Gold Nanoparticle at 1.1 Å Resolution. *Science* **2007**, *318* (5849), 430−433.

(15) Yang, H.; Wang, Y.; Chen, X.; Zhao, X.; Gu, L.; Huang, H.; Yan, J.; Xu, C.; Li, G.; Wu, J.; Edwards, A. J.; Dittrich, B.; Tang, Z.; Wang, D.; Lehtovaara, L.; Häkkinen, H.; Zheng, N. Plasmonic Twinned Silver Nanoparticles with Molecular Precision. *Nat. Commun.* **2016**, *7*, No. 12809.

(16) Mondal, B.; Jana, A.; Roy, J.; Mata, A. C.; Nair, A. S.; Mahendranath, A.; Roy, S.; Pathak, B.; Ajayan, P. M.; Pradeep, T. Structure and Electrocatalytic Performance of Cocrystallized Ternary Molybdenum Oxosulfide Clusters for Efficient Water Splitting. *ACS Mater. Lett.* **2023**, *5* (12), 3306−3315.

(17) Wei, X.; Chu, K.; Adsetts, J. R.; Li, H.; Kang, X.; Ding, Z.; Zhu, M. Nanocluster Transformation Induced by SbF6-Anions toward Boosting Photochemical Activities. *J. Am. Chem. Soc.* **2022**, *144* (44), 20421−20433.

(18) Song, Y.; Lambright, K.; Zhou, M.; Kirschbaum, K.; Xiang, J.; Xia, A.; Zhu, M.; Jin, R. Large-Scale Synthesis, Crystal Structure, and Optical Properties of the $Ag_{146}Br_2(SR)_{80}$ Nanocluster. *ACS Nano* **2018**, *12* (9), 9318−9325.

(19) Roy, J.; Mondal, B.; Vishwakarma, G.; Nonappa; Sridharan, N. V.; Krishnamurthi, P.; Pradeep, T. Dissociative Reactions of $[Au_{25}(SR)_{18}]^-$ at Copper Oxide Nanoparticles and Formation of Aggregated Nanostructures. *Nanoscale* **2023**, *15* (18), 8225−8234.

(20) Wei, X.; Kang, X.; Jin, S.; Wang, S.; Zhu, M. Aggregation of Surface Structure Induced Photoluminescence Enhancement in Atomically Precise Nanoclusters. *CCS Chem.* **2021**, *3* (7), 1929−1939.

(21) Jana, A.; Jash, M.; Dar, W. A.; Roy, J.; Chakraborty, P.; Paramasivam, G.; Lebedkin, S.; Kirakci, K.; Manna, S.; Antharjanam, S.; Machacek, J.; Kucerakova, M.; Ghosh, S.; Lang, K.; Kappes, M. M.; Base, T.; Pradeep, T. Carborane-Thiol Protected Copper Nanoclusters: Stimuli-Responsive Materials with Tunable Phosphorescence. *Chem. Sci.* **2023**, *14* (6), 1613−1626.

(22) Jadzinsky, P. D.; Calero, G.; Ackerson, C. J.; Bushnell, D. A.; Kornberg, R. D. Structure of a Thiol Monolayer-Protected Gold Nanoparticle at 1.1 Å Resolution. *Science* **2007**, *318* (5849), 430−433.

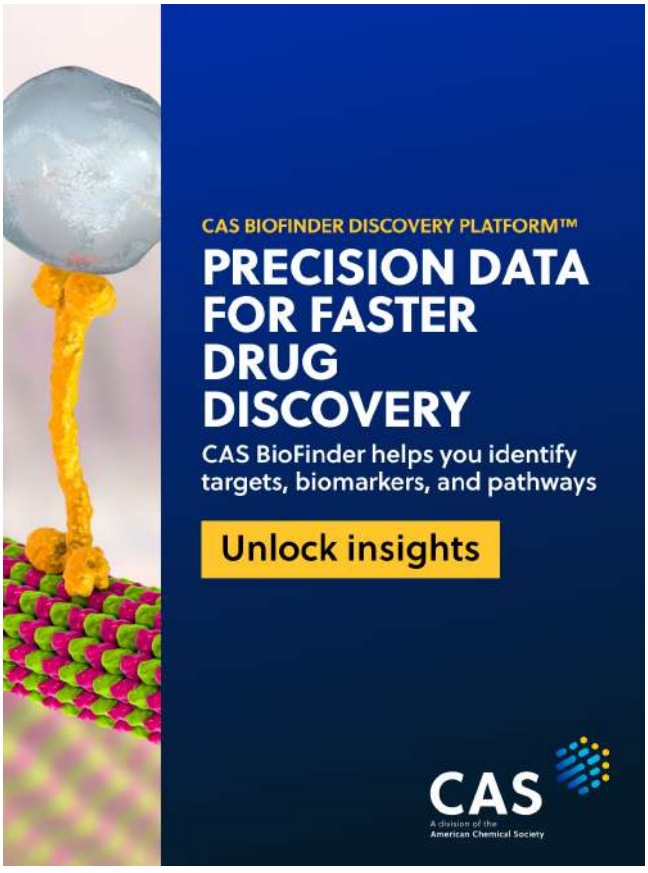
(23) Guo, J.; Kumar, S.; Bolan, M.; Desireddy, A.; Bigioni, T. P.; Griffith, W. P. Mass Spectrometric Identification of Silver Nanoparticles: The Case of $Ag_{32}(SG)_{19}$. *Anal. Chem.* **2012**, *84* (12), 5304−5308.

(24) Hirata, K.; Chakraborty, P.; Nag, A.; Takano, S.; Koyasu, K.; Pradeep, T.; Tsukuda, T. Interconversions of Structural Isomers of $[PdAu_8(PPh_3)_8]^{2+}$ and $[Au_9(PPh_3)_8]^{3+}$ Revealed by Ion Mobility Mass Spectrometry. *J. Phys. Chem. C* **2018**, *122* (40), 23123−23128.

(25) Baksi, A.; Chakraborty, P.; Bhat, S.; Natarajan, G.; Pradeep, T. [Au25(SR)18]22−: A Noble Metal Cluster Dimer in the Gas Phase. *Chem. Commun.* **2016**, *52*, 8397−8400.
(26) Wang, Y.; Nieto-Ortega, B.; Bürgi, T. Amplification of Enantiomeric Excess by Dynamic Inversion of Enantiomers in Deracemization of Au_{38} Clusters. *Nat. Commun.* **2020**, *11*, No. 4562.
(27) Ligare, M. R.; Reveles, J. U.; Govind, N.; Johnson, G. E.; Laskin, J. Influence of Interligand Interactions and Core-Charge Distribution on Gold Cluster Stability: Enthalpy Versus Entropy. *J. Phys. Chem. C* **2019**, *123* (40), 24899−24911.
(28) Krishnadas, K. R.; Baksi, A.; Ghosh, A.; Natarajan, G.; Pradeep, T. Manifestation of Geometric and Electronic Shell Structures of Metal Clusters in Intercluster Reactions. *ACS Nano* **2017**, *11*, 6015−6023.
(29) Salassa, G.; Krishnadas, K. R.; Pupier, M.; Viger-Gravel, J.; Bürgi, T. Role of Intercluster and Interligand Dynamics of $[Ag_{25}(DMBT)_{18}]^-$ Nanoclusters by Multinuclear Magnetic Resonance Spectroscopy. *J. Phys. Chem. C* **2021**, *125* (4), 2524−2530.
(30) Ligare, M. R.; Baker, E. S.; Laskin, J.; Johnson, G. E. Ligand Induced Structural Isomerism in Phosphine Coordinated Gold Clusters Revealed by Ion Mobility Mass Spectrometry. *Chem. Commun.* **2017**, *53*, 7389−7392.
(31) Nag, A.; Pradeep, T. Assembling Atomically Precise Noble Metal Nanoclusters Using Supramolecular Interactions. *ACS Nanosci. Au* **2022**, *2* (3), 160−178.
(32) Chakraborty, P.; Nag, A.; Paramasivam, G.; Natarajan, G.; Pradeep, T. Fullerene-Functionalized Monolayer-Protected Silver Clusters: $[Ag_{29}(BDT)_{12}(C_{60})_n]^{3-}$ (n = 1−9). *ACS Nano* **2018**, *12* (3), 2415−2425.
(33) Knoppe, S.; Bürgi, T. The Fate of Au25(SR)18 Clusters upon Ligand Exchange with Binaphthyl-Dithiol: Interstaple Binding vs. Decomposition. *Phys. Chem. Chem. Phys.* **2013**, *15* (38), 15816−15820.
(34) Malola, S.; Häkkinen, H. Chiral Inversion of Thiolate-Protected Gold Nanoclusters via Core Reconstruction without Breaking a Au−S Bond. *J. Am. Chem. Soc.* **2019**, *141* (14), 6006−6012.
(35) Wang, Y.; Bürgi, T. Ligand Exchange Reactions on Thiolate-Protected Gold Nanoclusters. *Nanoscale Adv.* **2021**, *3* (10), 2710−2727.
(36) Ghosh, A.; Ghosh, D.; Khatun, E.; Chakraborty, P.; Pradeep, T. Unusual Reactivity of Dithiol Protected Clusters in Comparison to Monothiol Protected Clusters: Studies Using $Ag_{51}(BDT)_{19}(TPP)_3$ and $Ag_{29}(BDT)_{12}(TPP)_4$. *Nanoscale* **2017**, *9* (3), 1068−1077.
(37) Tang, L.; Kang, X.; Wang, X.; Zhang, X.; Yuan, X.; Wang, S. Dynamic Metal Exchange between a Metalloid Silver Cluster and Silver(I) Thiolate. *Inorg. Chem.* **2021**, *60*, 3037−3045.
(38) Bootharaju, M. S.; Kozlov, S. M.; Cao, Z.; Harb, M.; Parida, M. R.; Hedhili, M. N.; Mohammed, O. F.; Bakr, O. M.; Cavallo, L.; Basset, J.-M. Direct versus Ligand-Exchange Synthesis of $[PtAg_{28}(BDT)_{12}(TPP)_4]^{4-}$ Nanoclusters: Effect of a Single-Atom Dopant on the Optoelectronic and Chemical Properties †. *Nanoscale* **2017**, *9*, 9529−9536, DOI: 10.1039/c7nr02844j.
(39) Zeng, Y.; Havenridge, S.; Gharib, M.; Baksi, A.; Weerawardene, K. L. D. M.; Ziefuß, A. R.; Strelow, C.; Rehbock, C.; Mews, A.; Barcikowski, S.; Kappes, M. M.; Parak, W. J.; Aikens, C. M.; Chakraborty, I. Impact of Ligands on Structural and Optical Properties of Ag_{29} Nanoclusters. *J. Am. Chem. Soc.* **2021**, *143* (25), 9405−9414.
(40) Matus, M. F.; Häkkinen, H. Understanding Ligand-Protected Noble Metal Nanoclusters at Work. *Nat. Rev. Mater.* **2023**, *8* (6), 372−389.
(41) Hazer, M. S. A.; Malola, S.; Häkkinen, H. Isomer Dynamics of the $[Au_6(NHC\text{-}S)_4]^{2+}$ Nanocluster. *Chem. Commun.* **2022**, *58* (19), 3218−3221.
(42) Matus, M. F.; Malola, S.; Bonilla, E. K.; Barngrover, B. M.; Aikens, C. M.; Häkkinen, H. A Topological Isomer of the $Au_{25}(SR)_{18}^-$ Nanocluster. *Chem. Commun.* **2020**, *56* (58), 8087−8090.
(43) Christofi, E.; Barran, P. Ion Mobility Mass Spectrometry (IM-MS) for Structural Biology: Insights Gained by Measuring Mass, Charge, and Collision Cross Section. *Chem. Rev.* **2023**, *123*, 2902−2949.
(44) Zhong, Y.; Hyung, S.-J.; Ruotolo, B. T. Ion Mobility−Mass Spectrometry for Structural Proteomics. *Expert Rev. Proteomics* **2012**, *9* (1), 47−58.
(45) Donor, M. T.; Mroz, A. M.; Prell, J. S. Experimental and Theoretical Investigation of Overall Energy Deposition in Surface-Induced Unfolding of Protein Ions. *Chem. Sci.* **2019**, *10* (14), 4097−4106.
(46) Vicent, C.; Martinez-Agramunt, V.; Gandhi, V.; Larriba-Andaluz, C.; Gusev, D. G.; Peris, E. Ion Mobility Mass Spectrometry Uncovers Guest-Induced Distortions in a Supramolecular Organometallic Metallosquare. *Angew. Chem., Int. Ed.* **2021**, *60* (28), 15412−15417.
(47) Gholipour-Ranjbar, H.; Deepika; Jena, P.; Laskin, J. Gas-Phase Fragmentation of Single Heteroatom-Incorporated Co5MS8(PEt3)6+ (M = Mn, Fe, Co, Ni) Nanoclusters. *Commun. Chem.* **2022**, *5* (1), No. 130.
(48) Baksi, A.; Schneider, E. K.; Weis, P.; Krishnadas, K. R.; Ghosh, D.; Hahn, H.; Pradeep, T.; Kappes, M. M. Nanogymnastics: Visualization of Intercluster Reactions by High-Resolution Trapped Ion Mobility Mass Spectrometry. *J. Phys. Chem. C* **2019**, *123* (46), 28477−28485.
(49) Wu, R.; Metternich, J. B.; Tiwari, P.; Benzenberg, L. R.; Harrison, J. A.; Liu, Q.; Zenobi, R. Structural Studies of a Stapled Peptide with Native Ion Mobility-Mass Spectrometry and Transition Metal Ion Förster Resonance Energy Transfer in the Gas Phase. *J. Am. Chem. Soc.* **2022**, *144* (32), 14441−14445.
(50) Zhou, M.; Huang, C.; Wysocki, V. H. Surface-Induced Dissociation of Ion Mobility-Separated Noncovalent Complexes in a Quadrupole/Time-of-Flight Mass Spectrometer. *Anal. Chem.* **2012**, *84* (14), 6016−6023.
(51) Masike, K.; Stander, M. A.; de Villiers, A. Recent Applications of Ion Mobility Spectrometry in Natural Product Research. *J. Pharm. Biomed. Anal.* **2021**, *195*, No. 113846.
(52) Mu, Y.; Schulz, B.; Ferro, V. Applications of Ion Mobility-Mass Spectrometry in Carbohydrate Chemistry and Glycobiology. *Molecules* **2018**, *23* (10), No. 2557.
(53) Kang, X.; Zhu, M. Structural Isomerism in Atomically Precise Nanoclusters. *Chem. Mater.* **2021**, *33* (1), 39−62.
(54) Chakraborty, P.; Baksi, A.; Mudedla, S. K.; Nag, A.; Paramasivam, G.; Subramanian, V.; Pradeep, T. Understanding Proton Capture and Cation-Induced Dimerization of $[Ag_{29}(BDT)_{12}]^{3-}$ Clusters by Ion Mobility Mass Spectrometry. *Phys. Chem. Chem. Phys.* **2018**, *20*, 7593−7603.
(55) Baksi, A.; Ghosh, A.; Mudedla, S. K.; Chakraborty, P.; Bhat, S.; Mondal, B.; Krishnadas, K. R.; Subramanian, V.; Pradeep, T. Isomerism in Monolayer Protected Silver Cluster Ions: An Ion Mobility-Mass Spectrometry Approach. *J. Phys. Chem. C* **2017**, *121* (24), 13421−13427.
(56) Baksi, A.; Schneider, E. K.; Weis, P.; Chakraborty, I.; Fuhr, O.; Lebedkin, S.; Parak, W. J.; Kappes, M. M. Linear Size Contraction of Ligand Protected Ag_{29} Clusters by Substituting Ag with Cu. *ACS Nano* **2020**, *14* (11), 15064−15070.
(57) Ligare, M. R.; Morrison, K. A.; Hewitt, M. A.; Reveles, J. U.; Govind, N.; Hernandez, H.; Baker, E. S.; Clowers, B. H.; Laskin, J.; Johnson, G. E. Ion Mobility Spectrometry Characterization of the Intermediate Hydrogen-Containing Gold Cluster $Au_7(PPh_3)_7H_5^{2+}$. *J. Phys. Chem. Lett.* **2021**, *12* (10), 2502−2508.
(58) Hossain, S.; Imai, Y.; Suzuki, D.; Choi, W.; Chen, Z.; Suzuki, T.; Yoshioka, M.; Kawawaki, T.; Lee, D.; Negishi, Y. Elucidating Ligand Effects in Thiolate-Protected Metal Clusters Using $Au_{24}Pt(TBBT)_{18}$ as a Model Cluster. *Nanoscale* **2019**, *11* (45), 22089−22098.
(59) Gabelica, V.; Marklund, E. Fundamentals of Ion Mobility Spectrometry. *Curr. Opin. Chem. Biol.* **2018**, *42*, 51−59.

https://doi.org/10.1021/acsnano.4c16413
ACS Nano 2025, 19, 5727−5738

(60) AbdulHalim, L. G.; Bootharaju, M. S.; Tang, Q.; Del Gobbo, S.; AbdulHalim, R. G.; Eddaoudi, M.; Jiang, D.; Bakr, O. M. $Ag_{29}(BDT)_{12}(TPP)_4$: A Tetravalent Nanocluster. *J. Am. Chem. Soc.* **2015**, *137* (37), 11970−11975.
(61) Hennrich, F.; Ito, S.; Weis, P.; Neumaier, M.; Takano, S.; Tsukuda, T.; Kappes, M. M. Cyclic Ion Mobility of Doped $[MAu_{24}L_{18}]^{2-}$ Superatoms and Their Fragments (M = Ni, Pd and Pt; L = Alkynyl). *Phys. Chem. Chem. Phys.* **2024**, *26* (10), 8408−8418.
(62) Chakraborty, P.; Malola, S.; Weis, P.; Neumaier, M.; Schneider, E. K.; Häkkinen, H.; Kappes, M. M. Tailoring Vacancy Defects in Isolated Atomically Precise Silver Clusters through Mercury-Doped Intermediates. *J. Phys. Chem. Lett.* **2023**, *14* (51), 11659−11664.
(63) Baksi, A.; Schneider, E. K.; Weis, P.; Chakraborty, I.; Fuhr, O.; Lebedkin, S.; Parak, W. J.; Kappes, M. M. Linear Size Contraction of Ligand Protected Ag_{29} Clusters by Substituting AG with Cu. *ACS Nano* **2020**, *14* (11), 15064−15070.
(64) Sarbu, M.; Clemmer, D. E.; Zamfir, A. D. Ion Mobility Mass Spectrometry of Human Melanoma Gangliosides. *Biochimie* **2020**, *177* (8), 226−237.
(65) Baksi, A.; Chakraborty, P.; Bhat, S.; Natarajan, G.; Pradeep, T. $[Au_{25}(SR)_{18}]_2^{2-}$: A Noble Metal Cluster Dimer in the Gas Phase. *Chem. Commun.* **2016**, *52* (54), 8397−8400.
(66) Chakraborty, P.; Malola, S.; Neumaier, M.; Weis, P.; Häkkinen, H.; Kappes, M. M. Elucidating the Structures of Intermediate Fragments during Stepwise Dissociation of Monolayer-Protected Silver Clusters. *Angew. Chem., Int. Ed.* **2023**, *62*, No. e202305836, DOI: 10.1002/anie.202305836.
(67) Zeng, Y.; Havenridge, S.; Gharib, M.; Baksi, A.; Weerawardene, K. L. D. M.; Ziefuß, A. R.; Strelow, C.; Rehbock, C.; Mews, A.; Barcikowski, S.; Kappes, M. M.; Parak, W. J.; Aikens, C. M.; Chakraborty, I. Impact of Ligands on Structural and Optical Properties of Ag29 Nanoclusters. *J. Am. Chem. Soc.* **2021**, *143* (25), 9405−9414.
(68) Ahlrichs, R.; Bär, M.; Häser, M.; Horn, H.; Kölmel, C. Electronic Structure Calculations on Workstation Computers: The Program System Turbomole. *Chem. Phys. Lett.* **1989**, *162* (3), 165−169.
(69) Vosko, S. H.; Wilk, L.; Nusair, M. Accurate Spin-Dependent Electron Liquid Correlation Energies for Local Spin Density Calculations: A Critical Analysis. *Can. J. Phys.* **1980**, *58* (8), 1200−1211.
(70) Lecklider, T. Maintainng a Heathy Rhythm. *Endeavor Bus. Media LLC* **2011**, *50* (1), 36−39.
(71) Becke, A. D. Density-Functional Thermochemistry. III. The Role of Exact Exchange. *J. Chem. Phys.* **1993**, *98* (7), 5648−5652.
(72) Dirac, P. A. M. Quantum Mechanics of Many-Electron Systems. *Proc. R. Soc. London, Ser. A* **1929**, *123* (792), 714−733.
(73) Slater, J. C. A Simplification of the Hartree-Fock Method. *Phys. Rev.* **1951**, *81* (3), No. 385.
(74) Weigend, F.; Ahlrichs, R. Balanced Basis Sets of Split Valence, Triple Zeta Valence and Quadruple Zeta Valence Quality for H to Rn: Design and Assessment of Accuracy. *Phys. Chem. Chem. Phys.* **2005**, *7* (18), 3297−3305.
(75) Grimme, S.; Ehrlich, S.; Goerigk, L. Effect of the Damping Function in Dispersion Corrected Density Functional Theory. *J. Comput. Chem.* **2011**, *32* (7), 1456−1465.
(76) Grimme, S.; Antony, J.; Ehrlich, S.; Krieg, H. A Consistent and Accurate Ab Initio Parametrization of Density Functional Dispersion Correction (DFT-D) for the 94 Elements H-Pu. *J. Chem. Phys.* **2010**, *132* (15), No. 154104.
(77) Shen, H.; Xu, J.; Fu, Z.; Wei, X.; Kang, X.; Shi, W.; Zhu, M. Photoluminescence Quenching of Hydrophobic Ag_{29} Nanoclusters Caused by Molecular Decoupling during Aqueous Phase Transfer and EmissionRecovery through Supramolecular Recoupling. *Angew. Chem., Int. Ed.* **2024**, *63* (12), No. e202317995, DOI: 10.1002/ANIE.202317995.
(78) Roy, J.; Chakraborty, P.; Paramasivam, G.; Natarajan, G.; Pradeep, T. Gas Phase Ion Chemistry of Titanium−Oxofullerene with Ligated Solvents. *Phys. Chem. Chem. Phys.* **2022**, *24* (4), 2332−2343.
(79) May, J. C.; McLean, J. A. Ion Mobility-Mass Spectrometry: Time-Dispersive Instrumentation. *Anal. Chem.* **2015**, *87* (3), 1422−1436.
(80) Chakraborty, P.; Malola, S.; Weis, P.; Neumaier, M.; Schneider, E. K.; Häkkinen, H.; Kappes, M. M. Tailoring Vacancy Defects in Isolated Atomically Precise Silver Clusters through Mercury-Doped Intermediates. *J. Phys. Chem. Lett.* **2023**, *14* (51), 11659−11664.
(81) Hafner, J. Ab-Initio Simulations of Materials Using VASP: Density-Functional Theory and Beyond. *J. Comput. Chem.* **2008**, *29* (13), 2044−2078.
(82) Perdew, J. P.; Burke, K.; Ernzerhof, M. Generalized Gradient Approximation Made Simple. *Phys. Rev. Lett.* **1996**, *77* (18), No. 3865.
(83) Nag, A.; Chakraborty, P.; Paramasivam, G.; Bodiuzzaman, M.; Natarajan, G.; Pradeep, T. Isomerism in Supramolecular Adducts of Atomically Precise Nanoparticles. *J. Am. Chem. Soc.* **2018**, *140* (42), 13590−13593.
(84) Fang, K. C.; Weng, C. I. An Investigation into the Melting of Silicon Nanoclusters Using Molecular Dynamics Simulations. *Nanotechnology* **2005**, *16* (2), 250−256.



Supporting information

Structural Changes in Atomically Precise Ag_{29} Nanoclusters upon Sequential Attachment and Detachment of Secondary Ligands

Jayoti Roy,[†] *Amitabha Das,*[‡] *Arijit Jana,*[†] *Papri Chakraborty,*[§,∥] *Marco Neumaier,*[§,∥] *Horst Hahn,*[§,⊥] *Biswarup Pathak,*[*,‡] *Manfred M. Kappes,*[*,§,∥] and *Thalappil Pradeep*[*,‡,#]

[†]DST Unit of Nanoscience (DST UNS) & Thematic Unit of Excellence (TUE), Department of Chemistry, Indian Institute of Technology Madras, Chennai 600036, India

[‡]Department of Chemistry, Indian Institute of Technology Indore, Indore 453552, India

[§]Institute of Nanotechnology, Karlsruhe Institute of Technology (KIT), Kaiserstr. 12, 76131 Karlsruhe, Germany

[∥]Institute of Physical Chemistry, Karlsruhe Institute of Technology (KIT), Kaiserstr. 12, 76131 Karlsruhe, Germany

[⊥]School of Sustainable Chemical, Biological and Materials Engineering, The University of Oklahoma, Norman 73019-1004, Oklahoma, United States

[#]International Centre for Clean Water, 2nd Floor, B-Block, IIT Madras Research Park, Kanagam Road, Taramani, Chennai 600113, India

*Email: biswarup@iiti.ac.in.

*Email: manfred.kappes@kit.edu.

*Email: pradeep@iitm.ac.in. Fax: 91-44-2257-0545/0509.

Table of contents

Name	Description	Page no.
SI1	Chemicals	**S3**
SI2	Synthesis	**S3**
SI3	Concentration of stock solution	**S4**
Figure S1	ESI MS and structure of $[Ag_{29}]^{3-}$ NCs	**S5**
Figure S2	UV-vis absorbance and photoluminescence studies	**S5**
Figure S3	Full range ESI MS	**S6**
Figure S4	Structural elucidation of $[Ag_{29}]^{3-}$ NCs	**S6**
Figure S5	Drift time "heat-maps" of $[Ag_{29}]^{3-}$	**S7**
Figure S6	CID MS of **L'**	**S7**
Figure S7	Drift time and extracted MS of **L"** and **L'"** added to $[Ag_{29}]^{3-}$	**S8**
Figure S8	Cis - and trans - **L'**	**S9**
Figure S9	Lowest energy DFT-optimized structures	**S9**
Figure S10	Comparison of bond length changes	**S10**
Figure S11	DFT structure of $[Ag_{29}]$**L"**$_1^{3-}$ and $[Ag_{29}]$**L'"**$_1^{3-}$	**S10**

Experimental Section

SI1. Reagents and Materials

All the chemicals except NCs and **L'** were commercially available and used without further purification. Silver nitrate ($AgNO_3$, 99.9%) was purchased from Rankem, India. Sodium borohydride ($NaBH_4$), 1,3-benzene dithiol (L), benzene-1,4-dicarbaldehyde, and ortho-aminothiophenol were purchased from Sigma-Aldrich. 1,6-Hexanedithiol was purchased directly from Sigma-Aldrich and used without further purification. Triphenylphosphine (TPP) was purchased from Spectrochem, India. All the solvents, methanol (MeOH), dichloromethane (DCM), dimethylformamide (DMF), acetonitrile (ACN), and ethanol (EtOH) were of HPLC grade (≥ 99.9%) and used without further purification.

SI2. Synthesis

SI2.1 Synthesis of $[Ag_{29}](TPP)_4^{3-}$ NC. $[Ag_{29}](TPP)_4^{3-}$ NC was synthesized following the reported method with little modification.[1] About 20 mg of $AgNO_3$ was dissolved in a mixture of 5 mL MeOH and 7 mL of DCM. About 13.5 µL of L ligand was then added to the reaction mixture. Due to the formation of Ag-S complex upon the addition of the dithiol, the color of the solution turned yellow, immediately. The mixture was kept under stirring conditions, and shortly after this, 200 mg of PPH_3 dissolved in 1 mL of DCM was added. Soon after the addition of PPH_3, the solution turned colorless, indicating the formation of Ag-S-P complexes. After ~15 min, 10.5 mg of $NaBH_4$ in 0.5 mL of ice-cold water was added. After the addition of $NaBH_4$, an immediate dark-brown color was observed, which turned orange gradually, indicating the formation of the NCs. The entire reaction was carried out under dark conditions to avoid the oxidation of silver. After 4 h of continuous stirring in the dark, the reaction mixture was centrifuged, and the supernatant was discarded. The dark brown precipitate was washed repeatedly with methanol to remove all of the unreacted compounds and complexes to get purified NC. The NC were obtained as the dark brown precipitate. The precipitate was dissolved in DMF for further studies. The solution was characterized by UV-vis and ESI MS, which confirmed the formation of $[Ag_{29}]^{3-}$ NCs. However, as the NC was synthesized without the TPP ligands, they were only stable for a few hours as stated in the literature.[1,2]

SI2.2 Synthesis of secondary ligand 2,2′-[1,4-Phenylenebis(methylidynenitrilo)] bis[benzenethiol] (L'). The **L'** secondary ligand was synthesized through an thermal condensation reaction following an earlier report.[3] In brief, ~500 mg (3.5 mM) of benzene-1,4-dicarbaldehyde was dissolved in EtOH. ~1.125 g (~9 mM) ortho-aminothiophenol was also dissolved in MeOH-EtOH (2:1, v/v) solvent mixture. It was added dropwise to the solution at inert argon closed condition, which resulted in some yellow precipitates. As-synthesized yellow precipitates are kept for 1 day under reflux conditions. Recrystallized sample from hot DCM/hexane mixture was used for further studies. The yield of the product is 85 %. The product was soluble in various organic solvents such as DMF, DCM, MeOH, ACN.

SI2.3 Synthesis of 2-Pyreneiminethiol ligand (L"). The ligand was synthesized by using a reported condensation method.[4] ~1000 mg (~4.35 mM) of pyrene aldehyde was mixed with 762 mg (~6.09 mM, 1.4 eq) of 2-aminothiophenol in an argon atmosphere. After 20 min of solid-state mixing, 20 ml MeOH and 10 ml of EtOH were added into the reaction mixture. The

solution was kept for 4 hours of reflux at 60℃. After the reaction, the yellow-colored compound was filtered using Whatman 42 filter paper and washed several times with excess MeOH-EtOH (1:1, v/v) solvent mixture to remove the excess precursor materials and other byproducts. The formation of the product was confirmed by SCXRD and ESI MS study.

SI3. Calculation of concentration of L'/ml.

Molecular weight of **L'** (M): 348 gm/mL

Amount of **L'** taken to prepare 1 mL (V_1) stock solution (m): 3.00 mg

Amount of solvent in the reaction mixture (V_2): 8 mL

Concentration of stock solution (S_1):

1000 ml 1 (M) **L'** ≡ 348 gm of **L'**

3 mg of **L'**: $\left(\frac{3}{0.348}\right)$ (mM) of **L'** in 1 mL stock

= 8.6 (mM) of **L'** in 1 mL stock

Amount of stock used: 0.025 mL

The final concentration (S_2) of **L'** in the reaction: $V_1*S_1 = V_2*S_2$

(8.6 mM * 0.025 ml) = (S2 * 8 mL)

$S_2 \approx 0.026$ (mM)

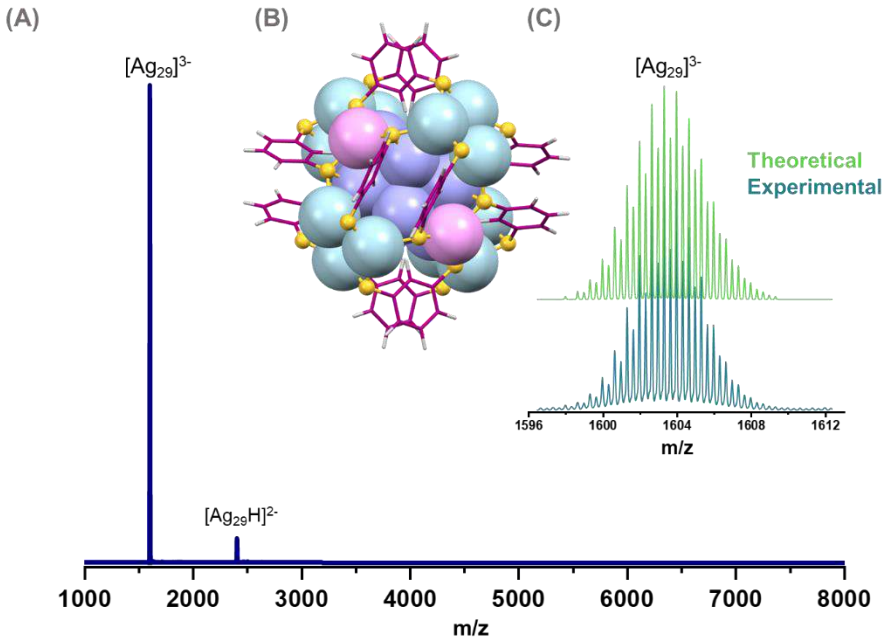


Figure S1. (A) Partial range negative ion ESI MS obtained upon dissolving as prepared $[Ag_{29}](TPP)_4^{3-}$ NC solid with counterion (see synthesis in SI2) in DMF. The MS manifests a dominant $[Ag_{29}]^{3-}$ and a weak $[Ag_{29}\mathbf{H}]^{2-}$ multianion signal (i.e. in both cases all four TPP ligands have been detached either prior to or during ESI). Throughout the paper this is referred to simply as a $[Ag_{29}]^{3-}$ NC solution. (B) DFT optimized structure of $[Ag_{29}]^{3-}$ NCs and (C) experimental and calculated isotope patterns of the most abundant, $[Ag_{29}]^{3-}$ cluster ions.

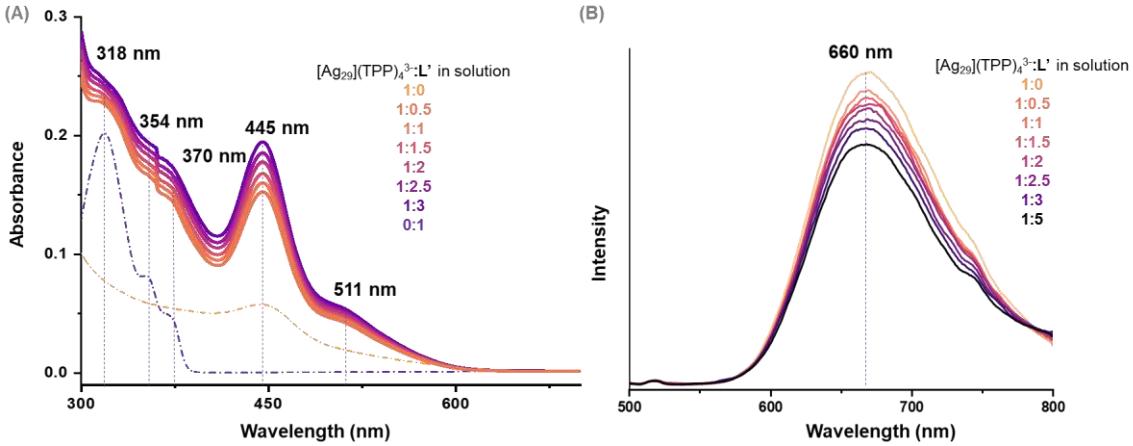


Figure S2. Sequential monitoring of (A) the UV-vis absorption spectra of $[Ag_{29}](TPP)_4^{3-}$ NCs, **L'** ligand, at a variable molar ratios of $[Ag_{29}](TPP)_4^{3-}$:**L'** in DMF-methanol solvent. The dash-dotted spectra represent the UV-vis absorption of pure solutions of $[Ag_{29}](TPP)_4^{3-}$ NC and **L'** , respectively. (B) Photoluminescence spectra of $[Ag_{29}](TPP)_4^{3-}$ NCs and after adding **L'** to $[Ag_{29}](TPP)_4^{3-}$ NC solution at variable molar ratios upon exciting the solution at 445 nm.

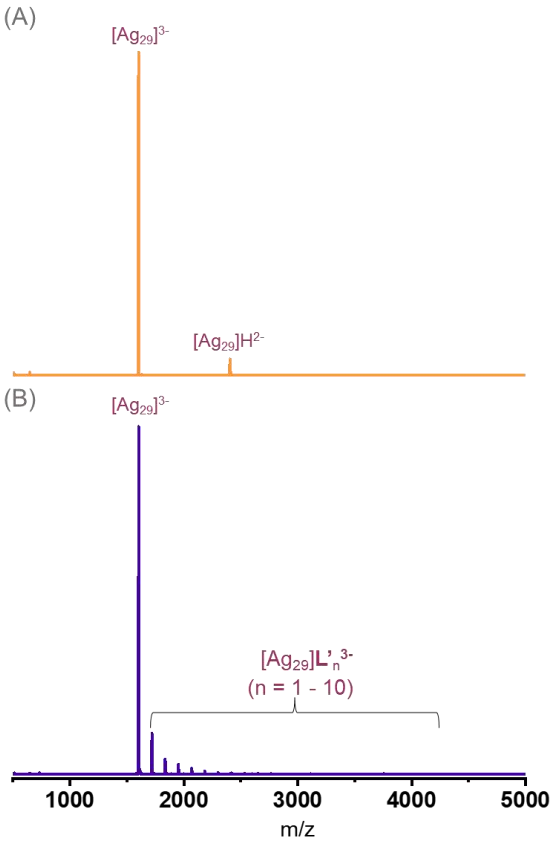


Figure S3. Full range ESI MS of m/z 500-5000 range of (A) precursor $[Ag_{29}]^{3-}$ NC, and(B) after addition of **L'** ligand to NC solution (in DMF solvent).

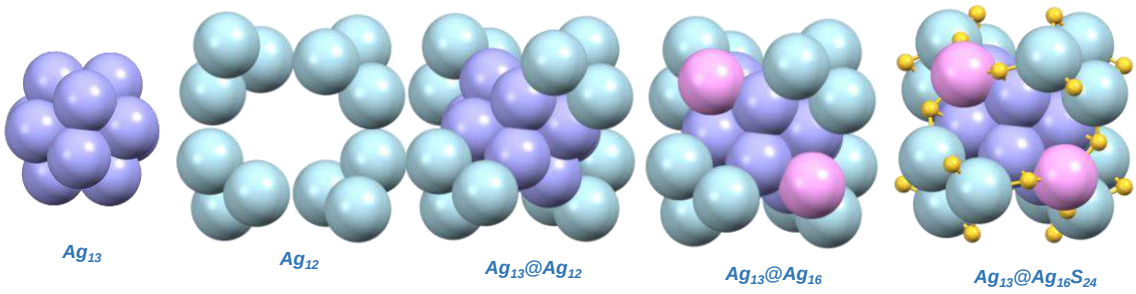


Figure S4. Schematic deconstruction of $[Ag_{29}]^{3-}$ NCs to highlight the different types of Ag atoms present in the molecule. Color code: icosahedron Ag, purple; crown Ag, pink; tetrahedral Ag, cyan blue; and sulfur (S), yellow.

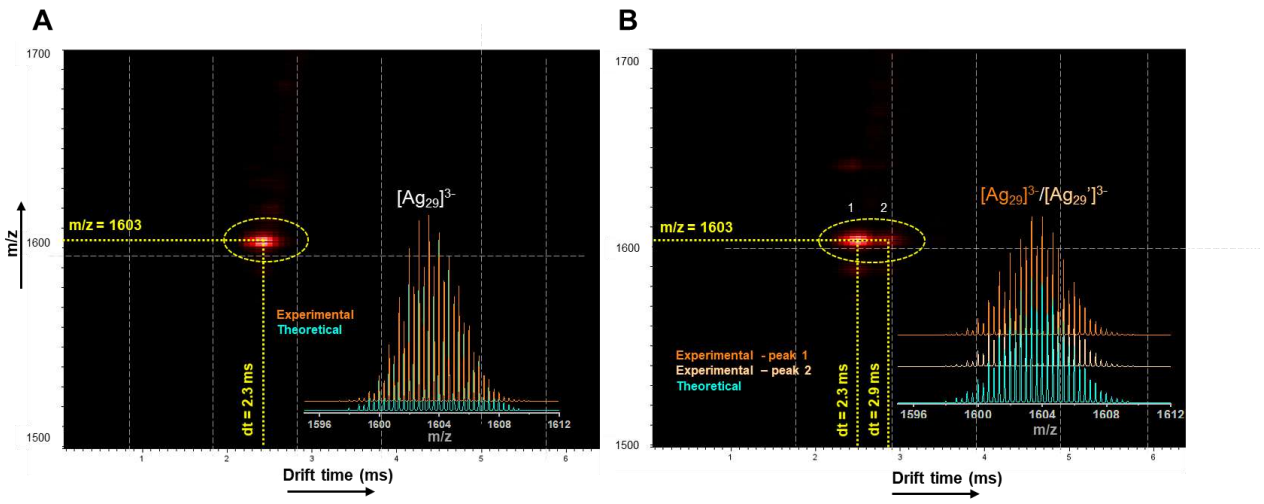


Figure S5. "Heat-map" plots recorded on the Synapt platform showing drift time (t_d) versus selected m/z recorded over the mass range of $[Ag_{29}]^{3-}$ as obtained upon electrospray of (A) a $[Ag_{29}]^{3-}$ NC solution before and (B) after adding the **L'** secondary ligand to it. Note that (B) shows two features at m/z = 1603. The extracted MS (and their simulated isotope patterns) shown in the insets confirm that the ions corresponding to both features have transited the TWIMS without (further) fragmentation. We assign them as the $[Ag_{29}]^{3-}$ parent isomer and as a larger equi-m/z isomeric $[Ag_{29}']^{3-}$ species formed by collisional detachment of **L'** from $[Ag_{29}(L)_{12}]\mathbf{L'}_n^{3-}$ upstream of the primary quadrupole mass selection.

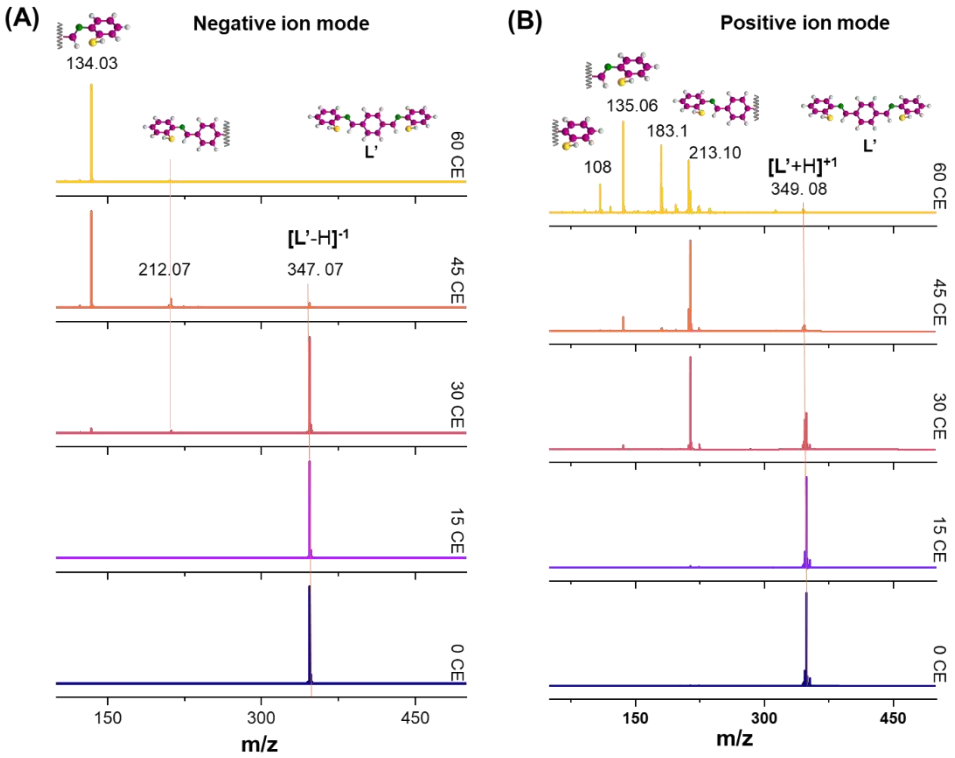
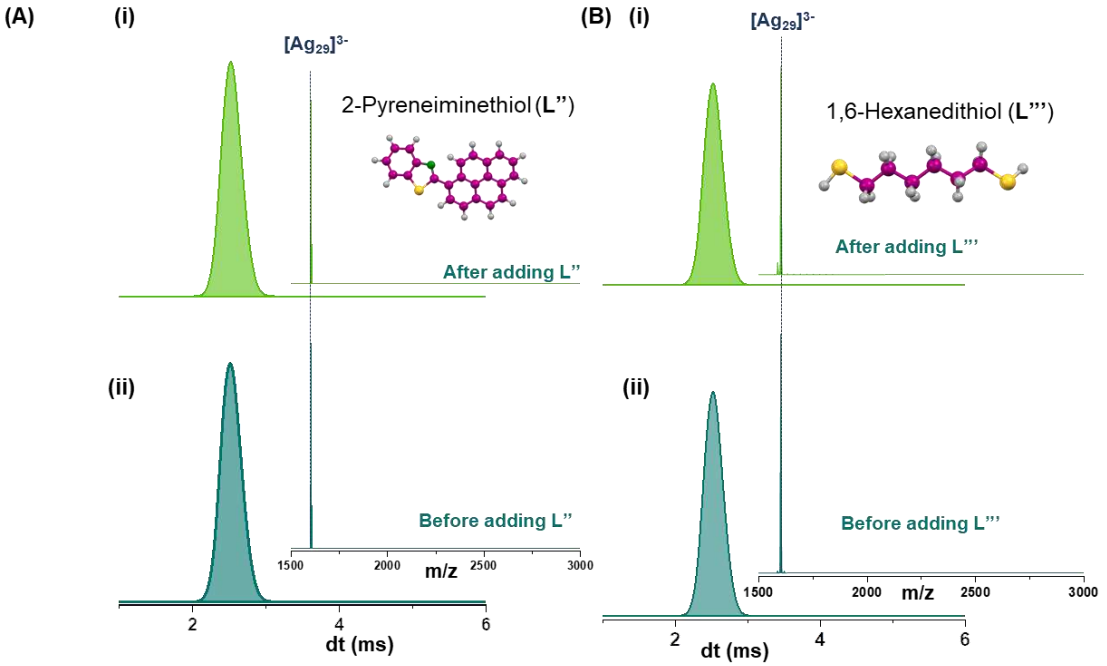


Figure S6. CID MS study to assess relative stability of **L'**$^{-/+}$ ligand. (A) Probed as deprotonated [**L'**-H]$^-$ in negative ion mode and (B) as protonated [**L'**+H]$^+$ in positive ion mode as a function of collision energy (CE). Color code: S, yellow; C, dark magenta, H, light grey; N, dark green. The mass peaks generated during CID are identified with the fragment ion structures and the jagged lines also shown indicate the position of cleavage from the rest of the **L'** structure. Note that fragmentation of **L'** sets in above 15 CE and therefore does not contribute in CE 10 measurements of $[Ag_{29}(L)_{12}]\mathbf{L'}_n^{3-}$.



(C)

S. no.	Ligand	Before	After
1.	2-Pyreneiminethiol (**L"**)	$^{TW}CCS[Ag_{29}]^{3-}{}_{N2}$ = 478.8 Å^2	$^{TW}CCS[Ag_{29}]^{3-}{}_{N2}$ = 477.8 Å^2
2.	1,6-Hexanedithiol (**L"'**)	$^{TW}CCS[Ag_{29}]^{3-}{}_{N2}$ = 478.8 Å^2	$^{TW}CCS[Ag_{29}]^{3-}{}_{N2}$ = 476.9 Å^2

Figure S7. Drift time plots, and extracted MS of $[Ag_{29}]^{3-}$ NC solutions (i) before and (ii) after the addition of (A) **L"** ligand, and (B) **L'"** ligands. (C) Table showing the experimental $^{TW}CCS_{N2}$ of the $[Ag_{29}]^{3-}$ NC mass signal before and after the addition of the foreign ligands. No significant change is observed in either case. (Also, no adducts are observed in the corresponding ESI mass spectra).

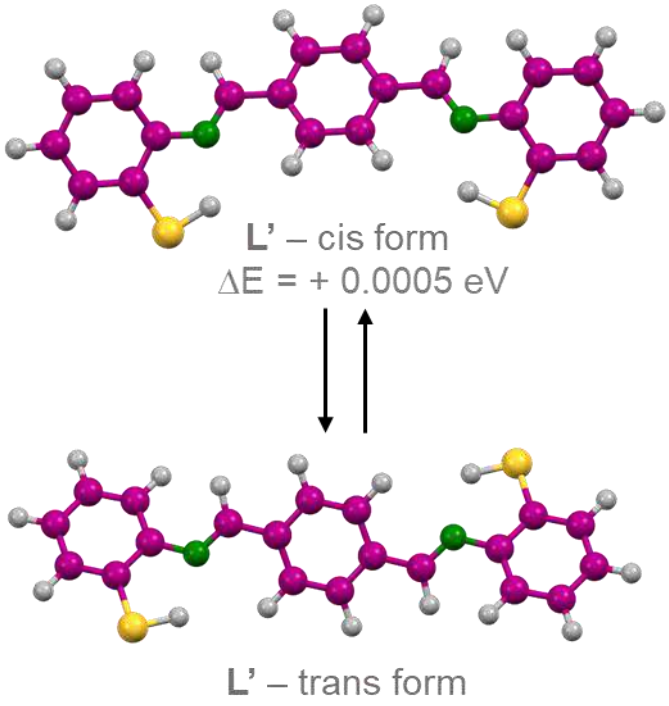


Figure S8. Optimized **L'** structure in cis as well as in trans form. ΔE is the relative energy difference between the cis- and the trans-**L'**.

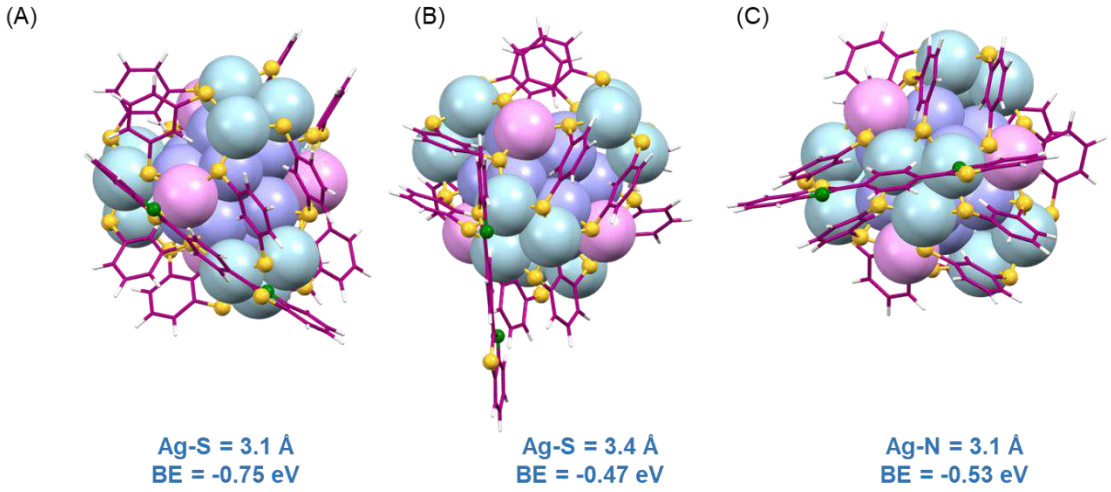


Figure S9. Lowest energy DFT-optimized structures and corresponding ligand binding energies in eV for $[Ag_{29}]\mathbf{L'}_1^{3-}$: (A) sulfur atom of **L'** interacts strongly with tetrahedral Ag atom, (B) sulfur of **L'** interacts strongly with a crown Ag atom, (C) N of **L'** interacts strongly with a tetrahedral Ag atom of the NC. Color code: icosahedron Ag, purple; crown Ag, pink; tetrahedral Ag, cyan blue; and sulfur, yellow.

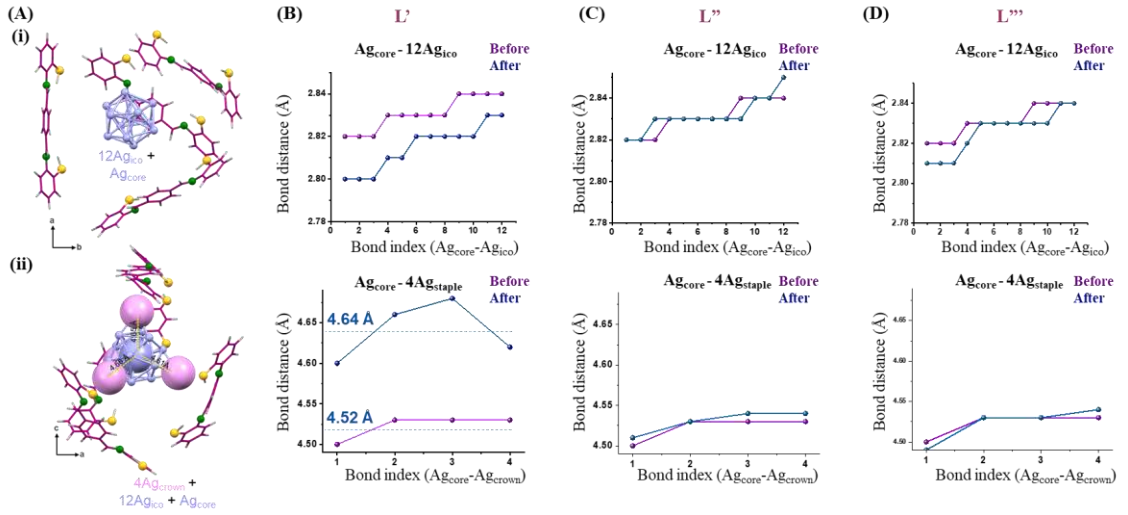


Figure S10. (A)(i) and (A)(ii) show the position of Ag_{ico}, Ag_{core}, Ag_{crown}, with respect to **L'** in the optimized $[Ag_{29}]$**L'**$_4^{3-}$ structure. Tetrahedral Ag and L ligands are omitted for clarity. Comparison of bond length change between (B) $[Ag_{29}]$**L'**$^{3-}$, (C) $[Ag_{29}]$**L"**$^{3-}$, and (D) $[Ag_{29}]$**L"'**$^{3-}$ before and after foreign ligand incorporation. Whereas **L"** and **L"'** cause little structural change the specific interaction with **L'** leads to significant volume expansion.

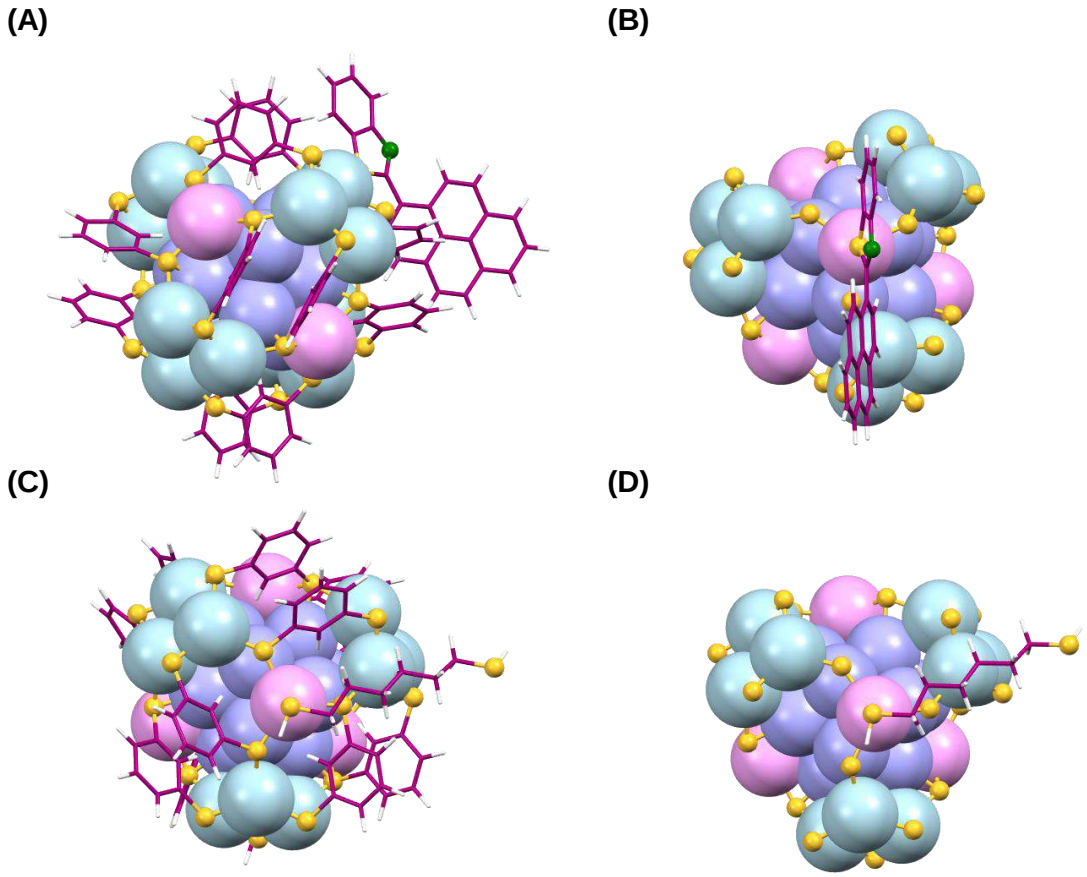


Figure S11. DFT-optimized lowest energy structures of $[Ag_{29}]^{3-}$ NC with **L"** (A) and **L"'** (C). For clarity, we also show the optimized structures with the phenyl ring of L removed – for **L"** (B) and **L"'** (D), respectively. Color code: Ag, purple, pink, and cyan blue; S, yellow; C, dark magenta, H, light grey; N, dark green.

References

(1) G. AbdulHalim, L.; S. Bootharaju, M.; Tang, Q.; Del Gobbo, S.; G. AbdulHalim, R.; Eddaoudi, M.; Jiang, D.; M. Bakr, O.; AbdulHalim, L. G.; Bootharaju, M. S.; Tang, Q.; Gobbo, S. Del; AbdulHalim, R. G.; Eddaoudi, M.; Jiang, D.; Bakr, O. M. $Ag_{29}(BDT)_{12}(TPP)_4$: A Tetravalent Nanocluster. *J. Am. Chem. Soc.* **2015**, *137* (37), 11970–11975. https://doi.org/10.1021/JACS.5B04547.

(2) Nag, A.; Chakraborty, P.; Paramasivam, G.; Bodiuzzaman, M.; Natarajan, G.; Pradeep, T. Isomerism in Supramolecular Adducts of Atomically Precise Nanoparticles. *J. Am. Chem. Soc.* **2018**, *140* (42), 13590–13593. https://doi.org/10.1021/jacs.8b08767.

(3) Wang, X.; Li, G.; Li, X.; Zhu, D.; Shen, R. One-Pot Three-Component Reaction of p-Quinone Monoacetals, L-Proline and Naphthols to Afford N-Aryl-2-Arylpyrrolidines. *Org. Chem. Front.* **2021**, *8* (2), 297–303. https://doi.org/10.1039/D0QO01294G.

(4) Jana, A.; Chakraborty, P.; Dar, W. A.; Chandra, S.; Khatun, E.; Kannan, M. P.; Ras, R. H. A.; Pradeep, T. Dual Emitting Ag35 Nanocluster Protected by 2-Pyrene Imine Thiol. *Chem. comm.* **2020**, *56* (83), 12550–12553. https://doi.org/10.1039/D0CC03983G.

nature communications

Article

https://doi.org/10.1038/s41467-025-56385-w

Site-specific substitution in atomically precise carboranethiol-protected nanoclusters and concomitant changes in electronic properties

Received: 24 July 2024

Accepted: 16 January 2025

Published online: 30 January 2025

Check for updates

Vivek Yadav[1], Arijit Jana[1], Swetashree Acharya[1], Sami Malola[2], Harshita Nagar[1], Ankit Sharma[3], Amoghavarsha Ramachandra Kini[1], Sudhadevi Antharjanam[4], Jan Machacek[5], Kumaran Nair Valsala Devi Adarsh[3] ✉, Tomas Base[5] ✉, Hannu Häkkinen[2] ✉ & Thalappil Pradeep[1] ✉

We report the synthesis of $[Ag_{17}(o_1\text{-CBT})_{12}]^{3-}$ abbreviated as Ag_{17}, a stable $8e^-$ anionic cluster with a unique $Ag@Ag_{12}@Ag_4$ core-shell structure, where o_1-CBT is *ortho*-carborane-1-thiol. By substituting Ag atoms with Au and/or Cu at specific sites we created isostructural clusters $[AuAg_{16}(o_1\text{-CBT})_{12}]^{3-}$ ($AuAg_{16}$), $[Ag_{13}Cu_4(o_1\text{-CBT})_{12}]^{3-}$ ($Ag_{13}Cu_4$) and $[AuAg_{12}Cu_4(o_1\text{-CBT})_{12}]^{3-}$ ($AuAg_{12}Cu_4$). These substitutions make systematic modulation of their structural and electronic properties. We show that Au preferentially occupies the core, while Cu localizes in the tetrahedral shell, influencing stability and structural diversity of the clusters. The band gap expands systematically (2.09 eV for Ag_{17} to 2.28 eV for $AuAg_{12}Cu_4$), altering optical absorption and emission. Ultrafast optical measurements reveal longer excited-state lifetimes for Cu-containing clusters, highlighting the effect of heteroatom incorporation. These results demonstrate a tunable platform for designing nanoclusters with tailored electronic properties, with implications for optoelectronics and catalysis.

Atomically precise nanoclusters (NCs) of coinage metals (Au, Ag and Cu), protected by various organic ligands, represent an intensely active category of functional nanomaterials, capturing significant attention of materials science and nanotechnology[1–4]. With diameters ranging typically between 1 and 3 nm, these NCs resemble molecules with electronic energy states transitioning from quasi-continuous bands to discrete orbitals[5]. This transition, a consequence of quantum confinement, endows NCs with distinctive chemical, photophysical and optical properties[1,6–9]. Notably, the monodisperse character of these NCs, with a precise structure and composition and the ability to adopt various atomic arrangements offer unprecedented insights into their structure-property relationships[10,11]. These NCs possess intriguing optical properties attributed to multiple optical absorption bands, luminescence, and X-ray radioluminescence, which find applications across diverse fields of optics, sensors, nonlinear optics, X-ray scintillation, biomolecular imaging and solar cells[12–20]. Coinage metals have a strong affinity for various protecting ligands including thiolates, selenolates, phosphines, hydrides, halides, and alkynes[21–25]. The selection and combination of these ligands play crucial roles in determining the structure, size and composition of the resulting NCs[26–28]. Thiolate

[1]DST Unit of Nanoscience (DST UNS) and Thematic Unit of Excellence (TUE), Department of Chemistry, Indian Institute of Technology, Madras, Chennai 600036, India. [2]Department of Physics and Chemistry, Nanoscience Center, University of Jyväskylä, FI 40014 Jyväskylä, Finland. [3]Department of Physics, Indian Institute of Science Education and Research Bhopal, Bhopal 462066, India. [4]Sophisticated Analytical Instruments Facility (SAIF), Indian Institute of Technology, Madras, Chennai 600036, India. [5]Department of Synthesis, Institute of Inorganic Chemistry, The Czech Academy of Science, Rez 25068, Czech Republic. ✉e-mail: adarsh@iiserb.ac.in; tbase@iic.acs.cz; hannu.j.hakkinen@jyu.fi; pradeep@iitm.ac.in

ligands form stable metal NCs due to strong binding via the metal-thiolate (sulfide) interface[1].

In comparison to the conventional organo-thiols, carborane-thiols have emerged as an interesting group of ligands with structurally robust backbone. Metal NCs with carborane ligands have been reported as sensors of nitro-aromatic vapors[29] and as materials exhibiting hypergolic activity[30,31]. Similar type of activity was not observed for organo-thiolate-stabilized metal clusters. Carboranes, more precisely dicarba-*closo*-dodecaboranes of general formula, $C_2B_{10}H_{12}$, with their 12-vertex nearly icosahedral structure, offer promising prospects for synthesizing metal NCs with tunable properties as they can be derivatized by almost any organic functional group (thiol, selenol, phosphine, alkyne, etc.) commonly used in metal NCs[32–35]. In general, carboranes are characterized by rigid, robust, three-dimensional architectures, with superior chemical and thermal stability, having distinct electronic structures, making them valuable for applications ranging from luminescent polymer materials to catalysts, drug synthesis, energy storage materials, and molecular nanomachines[36–39]. Carboranes possess tunable electronic properties influenced by their dipole moment and 3D pseudoaromatic character, distinguishing them from other organic compounds[40,41]. While there are reports on carborane-thiol stabilized metal clusters with luminescence properties, challenges remain in synthesizing tunable multimetallic clusters with precise positioning of heteroatoms in the shell[32–35,42].

Incorporating a precise number of hetero-metal atoms into NCs through alloying represents a promising approach for introducing synergistic effects aimed at enhancing ambient stability, catalytic activity, and other key properties[43–49]. Heteroatoms like Pt, Pd, Au and Cu have been effectively incorporated into various Ag-based NCs via co-reduction of metal ions, galvanic and antigalvanic exchange, and post-synthetic modifications[43,50–56]. The selection of metal components and ligands plays a critical role in regulating the quantity and distribution of dopant atoms, and influencing the overall atomicity and consequently the electronic structure of the NCs[26,54,57–59]. Precise spatial arrangement of metal dopants and the formation of heteronuclear bimetallic bonds influence the properties of NCs, particularly their optical characteristics. Furthermore, adding different metals to single-metal nanohybrid systems has been shown to enhance their nonlinear optical properties[60–62]. Synthesizing silver NCs of specific nuclearity, site-specific incorporation of other metals and high purity of the resulting systems pose persistent challenges. Several factors, such as acidity, solvent, temperature, light, metal precursor, and ligand of choice, profoundly influence the nuclearity, shape, and surface activity of these NCs[1,32,63,64]. In addition to conventional co-reduction methods yielding NCs with metal-thiolate interfaces, unconventional synthetic strategies such as solid-state gel-based synthesis, mechanical grinding, microwave irradiation, and metal exchange-induced size focusing have been employed. Furthermore, fast purification techniques utilizing desalting columns have been used to scale up the production of high-purity NCs[65–68]. An Ag_{17} core protected with 4-*tert*-butylbenzene-thiol was predicted commputationally[69], in view of the difficulties associated with crystallization, and upon Au incorporation, the structure was solved by single crystal X-ray diffraction (SC-XRD)[70].

Herein, we present a systematic study of incorporation of gold and copper heteroatoms into a carborane-thiol protected M_{17} NCs, starting from monometallic Ag_{17} to bimetallic $AuAg_{16}$ and $Ag_{13}Cu_4$ to trimetallic $AuAg_{12}Cu_4$ clusters. The X-ray crystal structure of Ag_{17} revealed two different positions in the metal kernel which were substituted with Au and Cu, resulting in significant changes in the luminescence properties of the resulting clusters. Comparative photophysical studies show that the inner metallic skeleton determines the emissive band gap and excited state carriers. Density-functional theory (DFT) calculations provided insights into the molecular orbitals responsible for their electronic transitions. Additionally, femtosecond and nanosecond transient absorption (fs-ns TA) measurements were employed to further explore the excited state charge transfer and relaxation dynamics of the NCs. This work manifests an interesting class of isostructural NCs with site-specific optical properties and establishes that specific ligands allow the creation of a range of compositionally diverse clusters of the same nuclearity, with distinctly different properties.

Results and discussion

Synthesis and crystallization

The Ag_{17} cluster was synthesized through a single-step chemical reduction of mixed precursors composed of silver nitrate ($AgNO_3$), 1,2-bis(diphenylphosphino)ethane (DPPE) and *ortho*-carborane-1-thiol (o_1-CBT) in dichloromethane (DCM):methanol (MeOH) (9:5, v/v) solvent mixture using sodium borohydride ($NaBH_4$) as a reducing agent. The bimetallic $AuAg_{16}$ and $Ag_{13}Cu_4$ clusters were synthesized with chloroauric acid ($HAuCl_4$) and copper(I) chloride (CuCl) as metal sources. Trimetallic $AuAg_{12}Cu_4$ NC was synthesized using the mixture of all three starting precursors: $AgNO_3$, $HAuCl_4$, and CuCl. Other synthetic conditions remained identical as for the synthesis of Ag_{17}. Specific details of the synthetic procedures are presented in the Methods. Incorporation of Cu at the shell by precisely alloying all the four positions was much challenging for $Ag_{13}Cu_4$ and $AuAg_{12}Cu_4$. Initially, in the synthesis of Cu incorporated Ag_{17}, multiple peaks in ESI-MS corresponding to $Ag_{17-x}Cu_x$ (x = 0-4) were observed as shown in Supplementary Fig. 1 which was later overcome leading to pure $Ag_{13}Cu_4$ NC by optimising the quantities of precursors. Similarly, crude sample of the trimetallic cluster showed multiple peaks in ESI-MS as shown in Supplementary Fig. 2 where the final cluster was isolated by crystallization. The formation of these NCs was monitored using time dependent UV-Vis absorption spectroscopy, which showed the prominent absorption peak at 400 nm for Ag_{17} and $Ag_{13}Cu_4$ as well as 385 nm for $AuAg_{16}$ and $AuAg_{12}Cu_4$ after 15 h of reduction (Supplementary Figs. 3–6). Although DPPE did not constitute the outer ligand shell of these NCs, it played a significant role in the synthesis as neither of the products were observed in the absence of it (Supplementary Fig. 7). DPPE also played an important role in making counterions in the crystallization of the bimetallic $AuAg_{16}$ and $Ag_{13}Cu_4$ NCs. The formation of metal clusters assisted by phosphine has also been observed in refs. 71,72 We performed synthesis by replacing DPPE with PPh_4Br and $n$$Bu_4NF$ as stabilizing counter cations in which no NCs were observed. Single-crystals suitable for X-ray diffraction were obtained by slow diffusion of hexane (either from vapors or from an overlayer) into the concentrated DCM or DCM- acetonitrile (ACN) /chloroform ($CHCl_3$) mixture solutions of the clusters (Ag_{17}, $AuAg_{16}$ and $Ag_{13}Cu_4$) and slow evaporation of the DCM-MeOH solution, at 4 °C in the case of $AuAg_{12}Cu_4$. Optical microscopy images demonstrated hexagonal, cuboidal, rod-like, and polyhedral crystals of Ag_{17}, $AuAg_{16}$, $Ag_{13}Cu_4$ and $AuAg_{12}Cu_4$ clusters (Supplementary Fig. 8), respectively. Surface morphology of each crystal was further investigated using field emission scanning electron microscopy (FE-SEM), and elemental composition was analyzed by EDS (see Supplementary Figs. 9–12).

Structural details resolved through SC-XRD

The SC-XRD analysis identifies the crystal system and space groups of the clusters. The Ag_{17} and $Ag_{13}Cu_4$ clusters were crystallized in orthorhombic and triclinic crystal systems in space groups Pbcn and P-1, respectively. $AuAg_{16}$ and $AuAg_{12}Cu_4$ clusters crystallized in trigonal and cubic crystal systems of space groups R-3 and Fd-3, respectively (crystallographic details are presented in Supplementary Tables 2–6). Optical anisotropy was also observed when the crystals were placed between cross-polarizing filters in the optical microscope where Ag_{17}, $AuAg_{16}$ and $Ag_{13}Cu_4$ show distinct change in color whereas $AuAg_{12}Cu_4$, being cubic, does not show any polarization (Supplementary Fig. 8).

The crystal structure of Ag_{17} reveals a metal core featuring three distinct positions, with a central atom surrounded by twelve Ag atoms

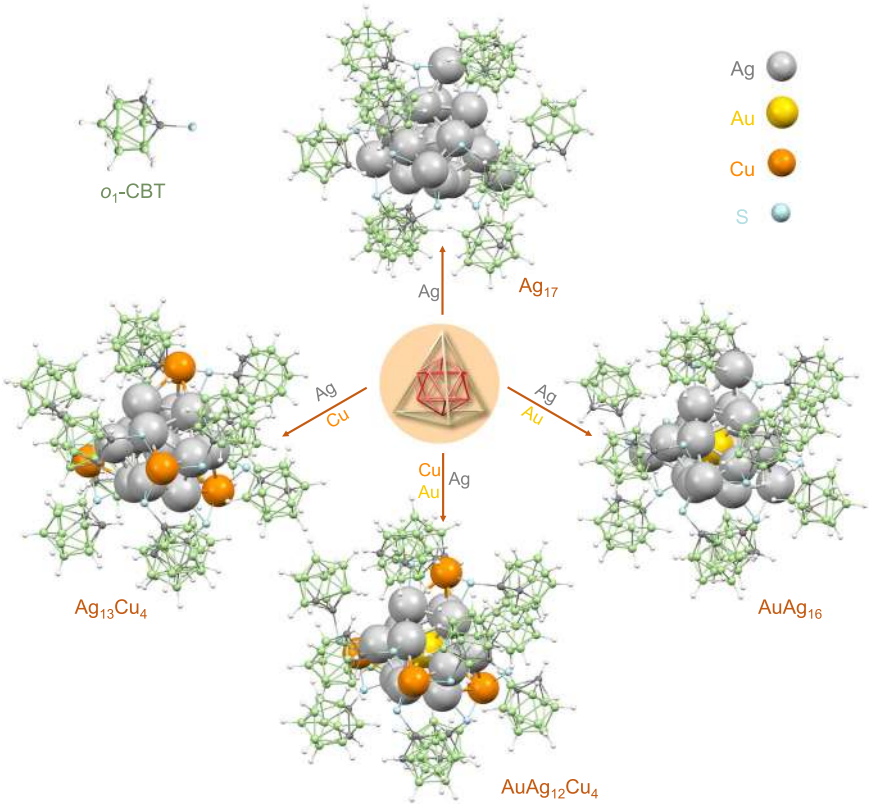


Fig. 1 | Elucidation of systematic synthesis and molecular architectures of isostructural Ag_{17}, $AuAg_{16}$, $Ag_{13}Cu_4$ and $AuAg_{12}Cu_4$ clusters shielded by o_1-CBT ligands. Systematic synthesis and molecular structures of isostructural Ag_{17}, $AuAg_{16}$, $Ag_{13}Cu_4$ and $AuAg_{12}Cu_4$ clusters, protected by twelve o_1-CBT ligands (metallic gray: silver, yellow: gold, reddish orange: copper, cyan: sulphur, green: boron, dark grey: carbon and white: hydrogen). The tetrahedral framework, built on an icosahedron is shown at the center.

forming an icosahedron and capped with four Ag atoms in a tetrahedral fashion (as depicted in Supplementary Fig. 13). Strong intermetallic bonding having an average Ag-Ag distances of 2.930 Å was observed in the metallic kernel. We note that the Ag-Ag distance in bulk silver metal is 2.89 Å. The structure offers three distinct positions for Ag within the Ag_{17} NC, simply understood as $Ag@Ag_{12}@Ag_4$, making it possible for the synthesis of bimetallic and trimetallic NCs. Introduction of Au in the reaction vessel results in $AuAg_{16}$, where Au occupies the central position ($Au@Ag_{12}@Ag_4$), while introduction of Cu results in $Ag_{13}Cu_4$, where the tetrahedral positions are occupied by Cu ($Ag@Ag_{12}@Cu_4$). In the case of trimetallic $AuAg_{12}Cu_4$ NC, both Au and Cu occupy their respective positions as central atom and outer tetrahedral positions, while Ag occupies the icosahedral positions ($Au@Ag_{12}@Cu_4$), as illustrated in Fig. 1.

All the four NCs are enveloped by twelve o_1-CBT ligands, where each carborane is connected with tetrahedral and icosahedral metal atoms through μ_2 sulfide linkages with an average metal-S distance of 2.495, 2.515, 2.385 and 2.339 Å for Ag_{17}, $AuAg_{16}$, $Ag_{13}Cu_4$ and $AuAg_{12}Cu_4$ clusters, respectively (Supplementary Fig. 14). The average intermetallic distances of the central icosahedral M_{13} inner kernel was 2.938 Å for Ag_{17}; 2.931 and 2.930 Å for $AuAg_{16}$ and $Ag_{13}Cu_4$, respectively; and 2.902 Å for $AuAg_{12}Cu_4$, as presented in Supplementary Fig. 14. Contraction of the icosahedral core of Ag_{17} was observed for $AuAg_{16}$ and $Ag_{13}Cu_4$, which was further contracted for $AuAg_{12}Cu_4$ making it the highest symmetrical structure. The centred icosahedral Ag_{13} kernel of $M_{17}S_{12}$ atomic arrangement resembles the seven or eight Ag(I) ions capping of the Ag_{13} kernel, forming the M_{20} and M_{21} clusters. Comparison of different dopped systems of M_{20} or M_{21} with M_{17} systems shows site specificity of the M_{17} system where the nuclearity, type of ligands as well as the definite composition remain intact for the bimetallic as well as trimetallic clusters (Supplementary Fig. 15)[73–77].

The unit cell molecular packing of $AuAg_{16}$ and $Ag_{13}Cu_4$ as presented in Supplementary Fig. 16 reveals that certain fragments, namely, $[Au(DPPE)_2]^+$ and $[Cu(DPPE)_2]^+$, were crystallized along with the NCs. The distance of $[Au(DPPE)_2]^+$ and $[Cu(DPPE)_2]^+$ fragments from the respective central metal atom of NC is ≈13 Å (Supplementary Fig. 16). The existence of non-covalent interactions such as, C-H…π and B-H…π, between the fragments and NCs are the key features in the crystal lattice of $AuAg_{16}$ and $Ag_{13}Cu_4$ which assist in holding the molecules together in their crystal lattice (Supplementary Fig. 17). Additionally, B-H…π interactions between the carboranes gives stabilization to the crystal lattice of all the NCs. Figure 2 and Supplementary Fig. 18 indicating lamellar packing of the NCs within the lattice. The cluster $AuAg_{12}Cu_4$ crystallizes in the cubic system which also shows pores but the void size and porosity are not well defined as the counter ions are not evident in the SC-XRD structure as shown in Supplementary Fig. 19.

Mass spectrometric investigations

High-resolution electrospray ionization mass spectrometric (HR-ESI-MS) studies were performed to verify the molecular compositions of these clusters. Negative ion mode ESI-MS spectrum of Ag_{17}, $AuAg_{16}$, $Ag_{13}Cu_4$ and $AuAg_{12}Cu_4$ clusters showed prominent peaks at m/z 1312.42, 1342.11, 1253.48, and 1283.15, respectively (Fig. 3a). All these peaks have (3-) charge making the overall masses as 3937.26, 4026.33, 3760.44, and 3849.45 amu, which correspond to the Ag_{17}, $AuAg_{16}$, $Ag_{13}Cu_4$ and $AuAg_{12}Cu_4$ clusters, respectively, with their ligands showing exact mass differences between the respective NCs. The isotopic distribution of the experimental peak matches well with the simulated spectrum (inset of Fig. 3a). The initially synthesised crude samples of $Ag_{13}Cu_4$ and $AuAg_{12}Cu_4$ NCs showed multiple peaks in the negative mode ESI-MS (Supplementary Figs. 1, 2) which were later

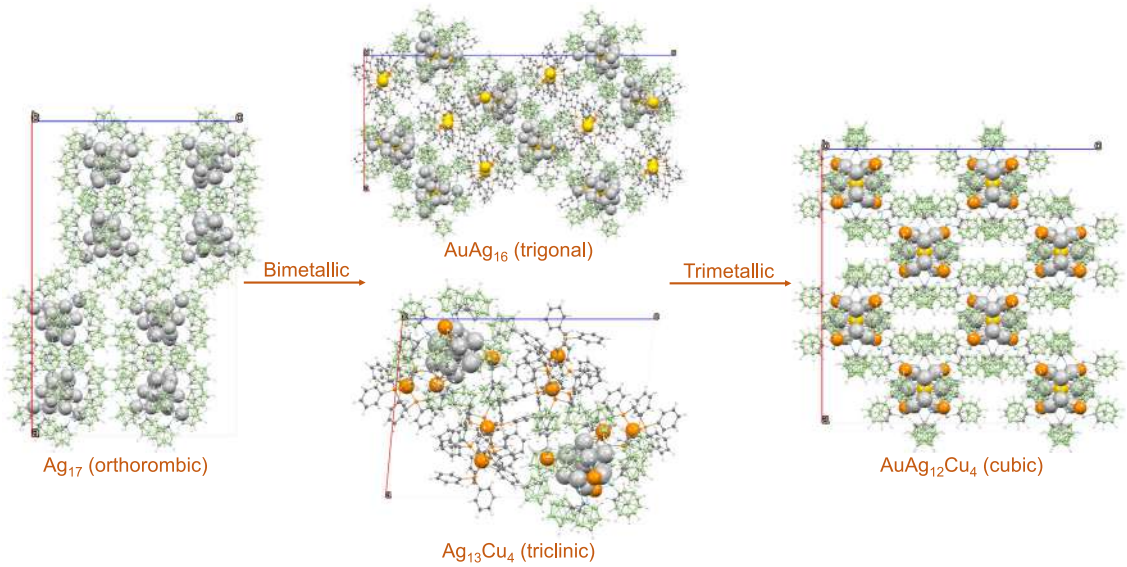


Fig. 2 | Supramolecular packing of the monometallic Ag_{17}, bimetallic $AuAg_{16}$ and $Ag_{13}Cu_4$, and trimetallic $AuAg_{12}Cu_4$. Ag_{17} are packed in an orthorhombic system. When Au and Cu are incorporated, the resulting bimetallic clusters $AuAg_{16}$ and $Ag_{13}Cu_4$ are packed in trigonal and triclinic systems, respectively. The trimetallic $AuAg_{12}Cu_4$ cluster, packed in a cubic system, exhibits the most symmetrical packing (metallic gray: silver, yellow: gold, reddish orange: copper, cyan: sulphur, green: boron, dark grey: carbon, orange: phosphorous and white: hydrogen).

eliminated by optimising precursor quantities and crystallization, respectively. Collision energy dependent MS/MS fragmentation of the selected molecular ion peaks were performed to get additional molecular insights of the clusters. The selected peak at *m/z* 1312.42 for the Ag_{17} cluster reveals that by incrementally increasing the collision energy (CE) from 0 to 15 (in instrumental units), two additional peaks emerge at *m/z* 1740.04 and 458.17, attributed to $[Ag_{16}L_{10}]^{2-}$ and $[AgL_2]^-$ species (as depicted in Supplementary Fig. 20). In the case of $AuAg_{16}$, at a CE of 15, the appearance of two new peaks at *m/z* 1784.06 and 458.17 implies the generation of $[AuAg_{15}L_{10}]^{2-}$ and $[AgL_2]^-$ fragments, respectively (Supplementary Fig. 21). Upon increasing the CE to 25, two peaks were detected at *m/z* 1672.72 and 414.27, due to $[Ag_{13}Cu_3L_{10}]^{2-}$ and $[CuL_2]^-$ species, respectively (Supplementary Fig. 22). Similarly, for the trimetallic $AuAg_{12}Cu_4$ cluster, peaks appeared at *m/z* 1717.28 and 414.27 at CE 25 due to $[AuAg_{12}Cu_3L_{10}]^{2-}$ and $[CuL_2]^-$, respectively (Supplementary Fig. 23). The emergence of $[ML_2]^-$ fragments with M representing either Ag in Ag_{17} and $AuAg_{16}$ or Cu in $Ag_{13}Cu_4$ and $AuAg_{12}Cu_4$, distinctly illustrates the peripheral environments characteristic of these clusters (Fig. 3b, Supplementary Figs. 20–23). In our earlier reports, comparable patterns of systematic fragmentation of surface carborane and carborane-thiolates were noted in Ag_{42} and Ag_{21} clusters[32,35]. The clusters did not show features in the positive-ion mode. However, the characteristic ion peak at *m/z* 993.24 and 859.20 in positive-ion mode confirms the presence of $[Au(DPPE)_2]^+$ and $[Cu(DPPE)_2]^+$ as counterions in the crystals of $AuAg_{16}$ and $Ag_{13}Cu_4$, respectively. However, both the ions were seen in the mass spectrum of the as synthesized crude of $AuAg_{12}Cu_4$ but detailed analysis of the crystal structure and the positive mode ESI-MS of the crystals confirmed their absence in the crystals (Supplementary Figs. 24, 25). Such complex counter cations like $[Ag(DPPE)_2]^+$, $[Au(DPPE)_2]^+$ and $[Cu(DPPE)_2]^+$ were not observed in the case of Ag_{17} and $AuAg_{12}Cu_4$ in the SC-XRD as well as in the ESI-MS measurements and we propose that Na^+ derived from $NaBH_4$ could be the plausible counterion. Therefore, the complete compositions have been identified as $[Na^+]_3[Ag_{17}(o_1\text{-CBT})_{12}]^{3-}$, $[[Au(DPPE)_2]^+]_3[AuAg_{16}(o_1\text{-CBT})_{12}]^{3-}$, $[[Cu(DPPE)_2]^+]_3[Ag_{13}Cu_4(o_1\text{-CBT})_{12}]^{3-}$ and $[Na^+]_3[AuAg_{12}Cu_4(o_1\text{-CBT})_{12}]^{3-}$ for Ag_{17}, $AuAg_{16}$, $Ag_{13}Cu_4$ and $AuAg_{12}Cu_4$, respectively. Crystallization of the NCs using PPh_4^+ and $n Bu_4N^+$ as counter cations was also tried where the clusters degraded and eventually no crystals were formed.

Additional characterization

The UV-Vis absorption spectra of the NCs in DCM show distinct characteristic features (Fig. 3c–f). Strong and relatively sharp absorption bands were observed: Ag_{17} exhibits bands at 400, 312, 269, and 241 nm; $AuAg_{16}$ at 385, 288, and 271 nm; $Ag_{13}Cu_4$ at 475, 400, and 307 nm; and $AuAg_{12}Cu_4$ at 385, 303, and 265 nm. These features signify the closely-spaced molecule-like electronic states within these NCs. The major absorption bands centered at 400 nm for Ag_{17} and $Ag_{13}Cu_4$ shift to 385 nm for $AuAg_{16}$ and $AuAg_{12}Cu_4$, attributed to the electronic perturbation of the cluster upon single Au atom substitution in the center of the icosahedral framework. Stability over 2 months of the clusters in the solution was observed, which is demonstrated by identical UV-Vis absorption features (Supplementary Fig. 26).To further explore the thermal stability, UV-Vis spectra as well as the real time ESI-MS were collected after subjecting microcrystalline powder samples (8–10 mg) to heating at various temperatures for 90 min. All characteristic absorption features (Supplementary Figs. 27–30) remained without any change, which indicates high structural robustness of these clusters. They were stable up to 125, 150, 175, and 100 °C for Ag_{17}, $AuAg_{16}$, $Ag_{13}Cu_4$, and $AuAg_{12}Cu_4$, respectively. We see stability enhancement from Ag_{17} to bimetallic $AuAg_{16}$ and $Ag_{13}Cu_4$ but not in the trimetallic $AuAg_{12}Cu_4$. Thermogravimetric analysis (TGA) (Supplementary Figs. 31–34) revealed no discernible weight loss up to 125 °C for the clusters. As previously observed, carborane-thiol ligands have once again provided remarkable stability to the NCs. The exceptional stability of NCs with site-specific alloying protected by carborane-thiols aligns well with earlier reports, reinforcing their effectiveness in stabilizing these systems[35,78].

The X-ray photoelectron spectra of the four clusters, depicting peaks corresponding to all the anticipated elements, are presented in Supplementary Fig. 35. A more detailed examination of the metallic components within the NCs is presented in Supplementary Fig. 36. Specifically, the detailed spectra of Ag 3 *d* reveal the existence of silver in two distinct oxidation states within Ag_{17}, $AuAg_{16}$ and $Ag_{13}Cu_4$. However, in the case of the $AuAg_{12}Cu_4$ NC, Ag is in zero oxidation state with a binding energy of 368.26 eV. Furthermore, the central Au atom is in its zero oxidation state in both $AuAg_{16}$ and $AuAg_{12}Cu_4$. Cu is detected in the clusters, $Ag_{13}Cu_4$ and $AuAg_{12}Cu_4$ (931.3 eV) in the oxidation state close to 1+. Notably, all the NCs exhibit sulfur in the

https://doi.org/10.1038/s41467-025-56385-w

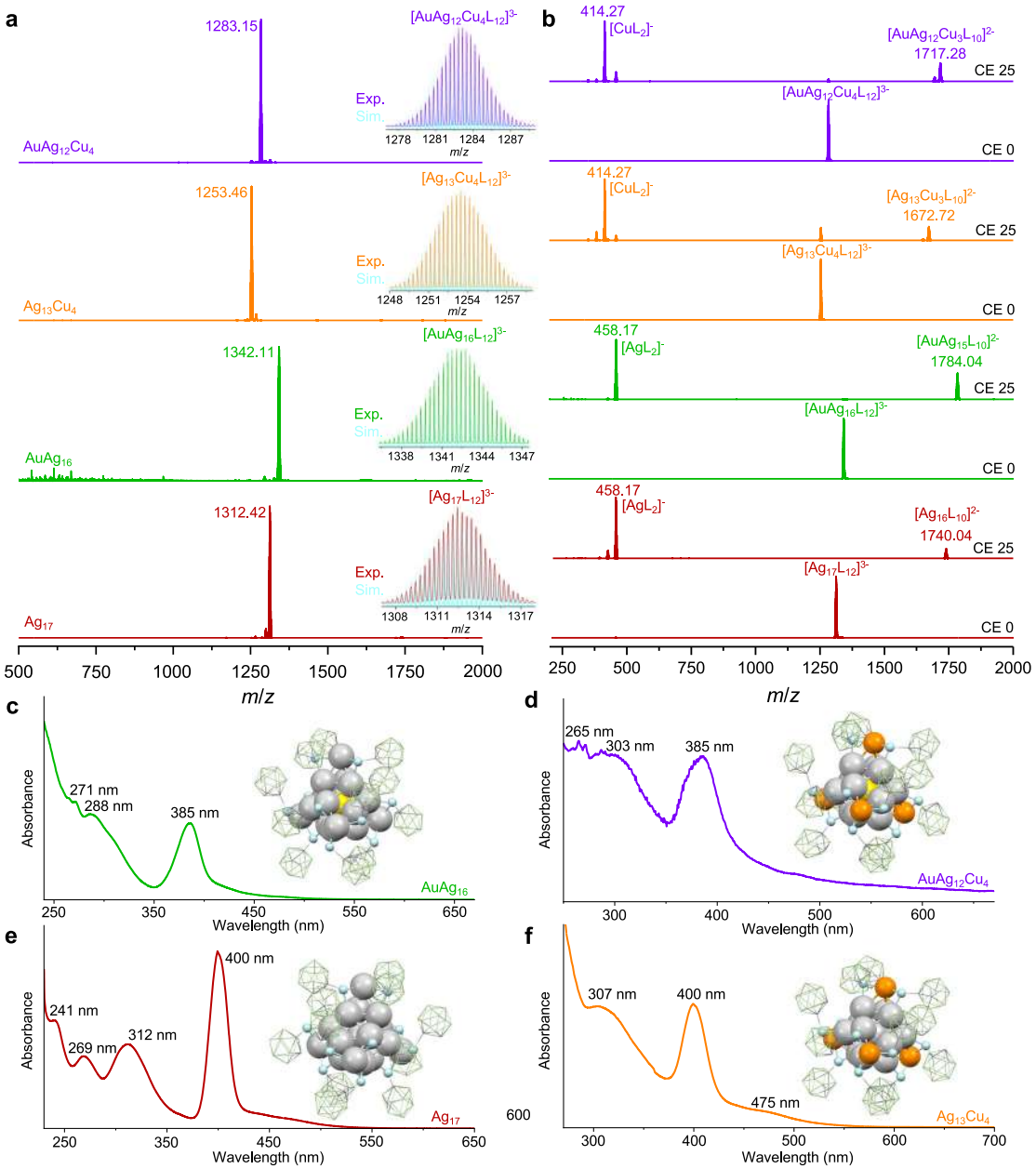


Fig. 3 | Comprehensive characterization of Ag_{17}, $AuAg_{16}$, $Ag_{13}Cu_4$ and $AuAg_{12}Cu_4$ clusters showing the comparative mass spectrometry, MS/MS fragmentation and UV-Vis absorption spectra. a Full range mass spectrum of all the four clusters. Inset shows the exact matching of the isotopic distributions of the experimental and simulated spectra (all simulated spectra are in cyan colour). **b** MS/MS fragmentation of the respective clusters at CE 0 and 25 showing the dissociation of surface ML_2 fragments (L: o_1-CBT). UV-Vis absorption spectra of **e** Ag_{17} and **c** $AuAg_{16}$, **f** $Ag_{13}Cu_4$ and **d** $AuAg_{12}Cu_4$ clusters measured in DCM. Insets of **c**–**f** show the structures of the respective clusters (metallic gray: silver, yellow: gold, reddish orange: copper, cyan: sulphur, green: boron and dark grey: carbon).

thiolate form, along with two types of boron, originating from the carborane ligands (Supplementary Fig. 37).

To further investigate the ligand shell, FT-IR spectra of all the NCs were compared with that of the free o_1-CBT ligand (Supplementary Fig. 38). Typical vibration bands were observed in all the spectra confirming the presence of carboranes with their terminal BH bonds in the NCs. Two BH stretching vibration bands in free o_1-CBT at 2601 and 2573 cm^{-1} were shifted to a single band at a lower frequency of 2561 cm^{-1} upon binding to the NCs. This shift in the spectra of the NC-bound o_1-CBT ligand can be assigned to the effect of heavy substrate atoms, the molecule is anchored to, and to the general effect of space restriction within the packed surface, both of which affect the vibrational modes. The observed lower wavenumber of the ν_{BH} band in the NCs thus matches with the formation of chemically bound thiolate moieties.

DFT investigations of substitution

DFT calculations were used to study the energetics of different sites for Au and Cu to get insights into the relative stability of the experimentally crystallized structures (for details, see the Methods). We investigated the cluster system with single Au and Cu substitutions using experimentally determined structure of the Ag_{17} cluster. Heteroatoms were added in all the symmetrically different metal atom positions. Optimized structures and their relative energies are presented in Supplementary Fig. 39. Based on energies, Au favors the central site of the icosahedral metal core by 0.34–0.37 eV, in comparison to the

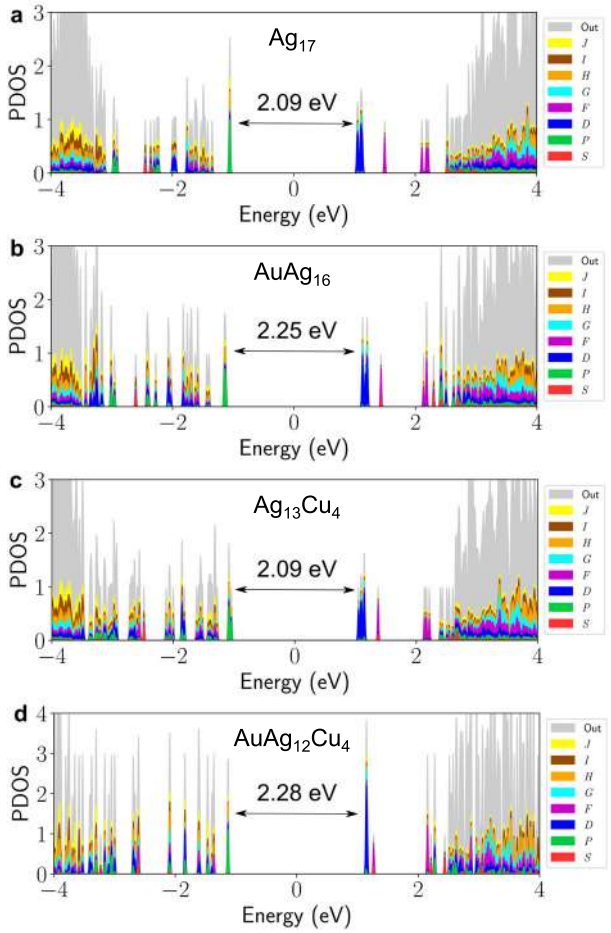


Fig. 4 | Comparative projected electronic density of states (PDOS) of the clusters. a–d The HOMO-LUMO energy gap of each cluster is centered around zero and the magnitude of the gap is presented. The Au-incorporated clusters, $AuAg_{16}$ and $AuAg_{12}Cu_4$, manifest the most substantial HOMO-LUMO gaps, measuring 2.25 and 2.28 eV respectively whereas the Ag_{17} and $Ag_{13}Cu_4$ clusters display band gaps of 2.09 eV.

capping sites of the outer kernel. Positions at the outermost metal layer, i.e., at the metal-thiolate interface, are the most unstable ones with 0.71 eV higher energy compared to the cluster with a gold atom in the center. The most stable cluster also seems to maximize the HOMO-LUMO gap (2.19 eV) from all the calculated systems, being ≈0.1 eV larger than for the other model structures. This structural and electronic stability, in comparison to the other sites, confirm the experimental observation of single Au-dopant in the center of the cluster.

Copper shows the opposite behavior than gold, i.e., energetically preferred sites are in the outermost metal-ligand interface, within the Cu-$(SR)_3$ surface motifs as presented in Supplementary Fig. 40. The rest of the possible sites in the metal core are 0.38–0.40 eV higher in energy. Considering the symmetry of the metal-ligand interface, there are exactly four energetically favorable sites in the metal-ligand interface which follow tetrahedral arrangement. This matches well with the experimental observation of exactly four Cu-dopants crystallized in the bi- and trimetallic clusters. The energetically stable Cu-substituted cluster model, similarly to the one with a Au atom in the center, has slightly larger (increase of 0.05–0.08 eV) HOMO-LUMO gap (2.05 eV) compared to the other calculated cluster models. This means that in both the cases the energetically stable structure is also electronically stable. Seemingly, the calculated energy difference is large enough to affect selectively the molecular composition and structure of the final cluster products. Similar behaviour of the electronically preferred position of copper and gold was also observed for the MAg_{20} system having an icosahedral core[79].

DFT calculations of optical absorption properties

The electronic structures of these clusters were analyzed by projecting the density of states to spherical harmonic functions centered at the center of mass of the cluster which reveals the positions and symmetries of the superatom states. The results of this analysis are presented in Fig. 4. All clusters show the $8e^-$-superatom characteristics, the highest occupied states being of *P*-symmetry and the lowest unoccupied states of *D*-symmetry. Au-incorporated clusters, $AuAg_{16}$ and $AuAg_{12}Cu_4$ have the largest HOMO-LUMO gaps of 2.25 and 2.28 eV, whereas Ag_{17} and $Ag_{13}Cu_4$ clusters have 2.09 eV as the band gap. Distribution of the states vary slightly below the *P*-symmetric states between −1.5 and −3.5 eV, which is the region for metal-ligand interface states. Analysis of the electronic structure primarily suggests that the optical gap and dipole-allowed first transitions between HOMO *P*-states and LUMO *D*-states are potentially located similarly in Ag_{17} and $Ag_{13}Cu_4$, and would be found at slightly shorter wavelengths for $AuAg_{16}$ and $AuAg_{12}Cu_4$. The experimental band gap was estimated using differential pulse voltammetry (Supplementary Fig. 41) and the Tauc plot method. The Tauc plot analysis reveals experimental band gaps of 2.12, 2.25, 2.08, and 2.26 eV for Ag_{17}, $AuAg_{16}$, $Ag_{13}Cu_4$, and $AuAg_{12}Cu_4$, respectively (Supplementary Fig. 42), closely matching the theoretical values.

Theoretical UV-Vis absorption spectra of the clusters were calculated using the linear response time-dependent density-functional theory (LR-TDDFT). A comparison of the calculated and experimental UV-Vis spectra for all the clusters is presented in Fig. 5. More detailed comparison of the band positions is presented in Supplementary Table 1. For all these clusters, the first feature in the spectrum has relatively low intensity compared to the most prominent second band. Both experimental and computational spectra of Ag_{17} and $AuAg_{16}$ clusters are in good agreement across the measured spectrum. In the calculated spectra, the main bands are at 396 and 391 nm for Ag_{17} and $AuAg_{16}$, respectively while the corresponding experimental positions are 400 and 385 nm. A blueshift upon Au incorporation was observed in both experimental and theorical spectra. The two lowest energy bands in the spectra of $Ag_{13}Cu_4$ and $AuAg_{12}Cu_4$ are also present, but the calculated main peaks at 428 and 423 nm seem to be red-shifted by ≈0.2 eV, compared to the experiments. The first peak determining the optical gap is in agreement with the HOMO-LUMO gap. For Ag_{17} and $Ag_{13}Cu_4$, the first peak appears at 492 and 499 nm, respectively, whereas for the Au-incorporated clusters $AuAg_{16}$ and $AuAg_{12}Cu_4$, the peaks are at slightly lower wavelengths, 458 and 477 nm. This coincides with the corresponding HOMO-LUMO gap. The overall shape of the calculated spectra of Cu substituted clusters at lower wavelengths is however richer and more pronounced than the measured spectra. The trend with respect to incorporation of the cluster with Au-atom remains the same: the main peak is observed at a lower wavelength for the clusters with Au than without it, i.e., Ag_{17} compared to $AuAg_{16}$ and $Ag_{13}Cu_4$ compared to $AuAg_{12}Cu_4$. The clusters shown in Fig. 5c, d exhibit numerous “place-isomers” in solution due to mixing of metals at various core positions, driven by entropy. Calculations based solely on a single, “frozen” crystal structure may not fully capture the spectral properties observed experimentally in solution, leading to deviations between calculated and measured spectra in Fig. 5c, d. The excitations of all clusters create an oscillating electron density (as visualized in Fig. 5 insets) at the metal core and at the metal-ligand interface, but they does not reach the carborane ligands.

To analyze the spectral features, we calculated the dipole transition contribution maps (DTCMs) that show the strengthening and screening contributions in Kohn-Sham basis at the energy of the selected absorption band. The analysis is based on the perturbation time-dependent density-functional theory and was done for the Ag_{17}

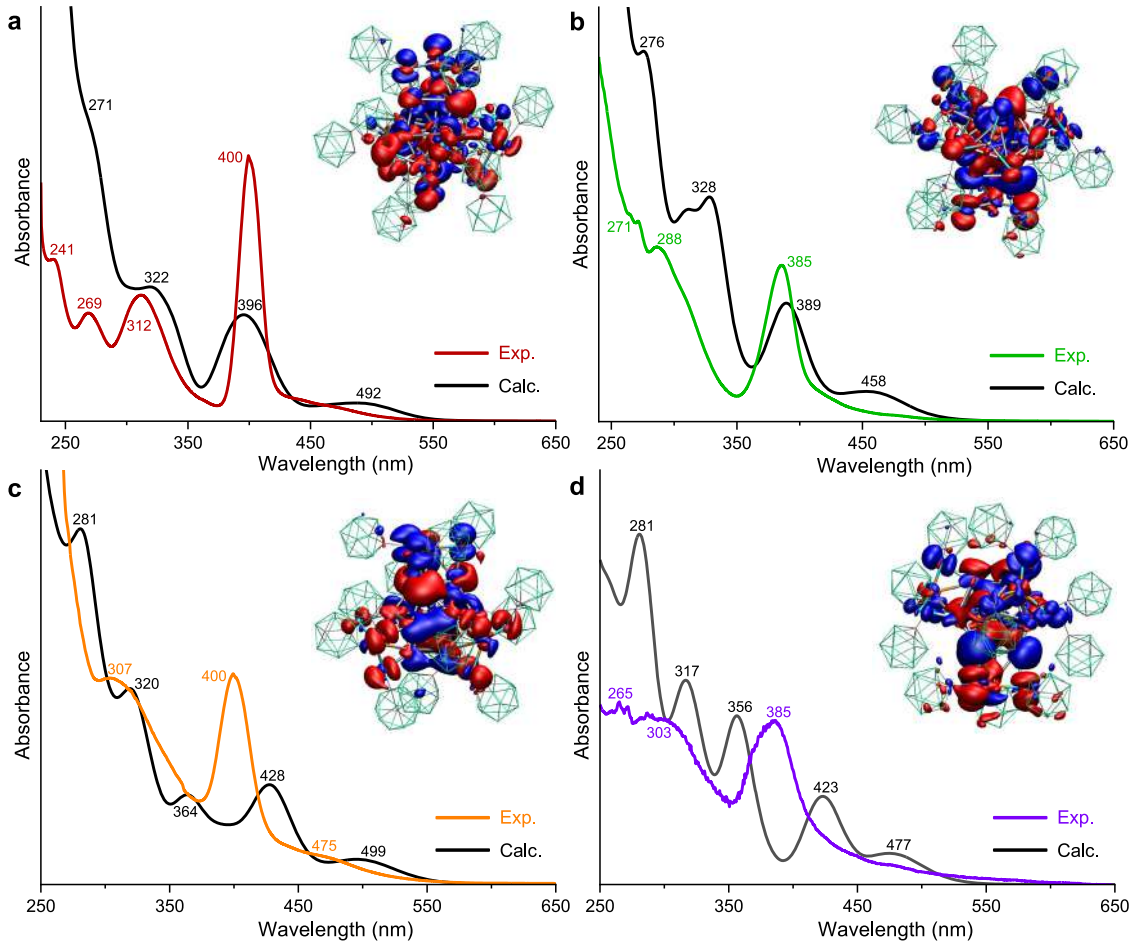


Fig. 5 | Comparison of calculated and experimental UV-Vis spectra with induced density inset for Ag_{17}, $AuAg_{16}$, $Ag_{13}Cu_4$ and $AuAg_{12}Cu_4$ clusters. Comparison of calculated and experimental UV-Vis spectra for **a** Ag_{17}, **b** $AuAg_{16}$, **c** $Ag_{13}Cu_4$, and **d** $AuAg_{12}Cu_4$. As two spectra are compared, absorbance is plotted in arbitrary units. Major peak positions are marked. Inset figures show the induced density (i.e., electron density oscillations, where red and blue are the positive and negative isosurfaces, respectively) for the excitations related to the peaks at **a** Ag_{17}: 396 nm, **b** $AuAg_{16}$: 389 nm, **c** $Ag_{13}Cu_4$: 428 nm and **d** $AuAg_{12}Cu_4$: 423 nm.

cluster as a reference system. The results are presented in Supplementary Fig. 43 and they confirm that the dipole-allowed transitions between superatom states *P* and *D* are mainly controlling the first two features in the spectrum. The highest wavelength peak is purely $P \rightarrow D$ transitions, while for the second main peak, the $P \rightarrow D$ transitions have been coupled with metal-ligand interface $\rightarrow D$-state type transitions. At even lower wavelengths, the bands change due to new transitions. These include transitions from superatom *P* states to higher unoccupied states (2.5–3.0 eV) and from states in the metal *d*-band region to unoccupied superatom *D* states. This analysis shows that superatom *P* and *D* states play a crucial role in the optical response, appearing throughout the wavelength range as starting or target states. For Cu-incorporated clusters, the red shift in the main peaks compared to Ag_{17} and $AuAg_{16}$ clusters is due to differences in the coupling between $P \rightarrow D$ transitions and metal-ligand interface $\rightarrow D$ transitions.

Photoluminescence properties

The photoluminescence (PL) properties of these clusters are studied in solution (in DCM) and solid states. Ag_{17} and $AuAg_{16}$ clusters emit weak luminescence in solution (insets of Fig. 6a, b). However, $Ag_{13}Cu_4$ and trimetallic $AuAg_{12}Cu_4$ clusters emit bright red and yellowish-orange emissions in solution (insets of Fig. 6c, d respectively). PL spectral measurement of Ag_{17} shows a very weak emission band at 650 nm upon a characteristic excitation centered at ≈400 nm. For centrally Au incorporated cluster, we observed a week emission band in the visible region (at 610 nm) and a prominent NIR emission band at ≈815 nm. The absolute quantum yields of $Ag_{13}Cu_4$ and trimetallic $AuAg_{12}Cu_4$ clusters in DCM (using an excitation wavelength of 380 nm) were 5.80% and 4.37%, respectively. Quantum yields were below 0.1% for weekly emissive Ag_{17} and $AuAg_{16}$ clusters. We also observed significant emission enhancement upon cooling the Ag_{17} and $AuAg_{16}$ cluster samples to 77 K due to the rigidification-induced structural modification as presented in Fig. 6e, f. Bright luminescence was observed for Ag_{17} and $AuAg_{16}$ upon crystallization as well (Supplementary Fig. 44). Detailed structural analyses revealed robust intermolecular noncovalent interactions, specifically BH···BH, CH···BH, and BH···π interactions, within Ag_{17} and $AuAg_{16}$ crystals (Supplementary Fig. 17). These interactions create rigid order in the crystals giving rise to a crystallization-induced emission. Enhanced emission by crystallization and lowering the temperature was reported for gold, silver and their alloy clusters[27,80,81]. $Ag_{13}Cu_4$ and $AuAg_{12}Cu_4$ exhibit emission bands at 650 and 610 nm, respectively, in solution (Fig. 6c, d). These clusters showed broad excitations ranging from 380-470 nm with a peak at 380 nm (Supplementary Figs. 45, 46). Bright luminescence was observed for the crystals of $Ag_{13}Cu_4$ and $AuAg_{12}Cu_4$ (Supplementary Fig. 47). Au incorporation in the core ($AuAg_{16}$) did not intensify the luminescence in solution, however the incorporation of Cu (for $Ag_{13}Cu_4$ cluster) in the outer shell significantly enhanced the luminescence intensity in solution. Similarly, the trimetallic $AuAg_{12}Cu_4$ cluster with both the core and the shell incorporation showed strong emission in solution. The emission behaviour of Ag_{17} NCs upon heteroatom doping can be compared with $Ag_{29}(S\text{-Adm})_{18}(PPh_3)_4$ (where *S*-Adm is the adamantane

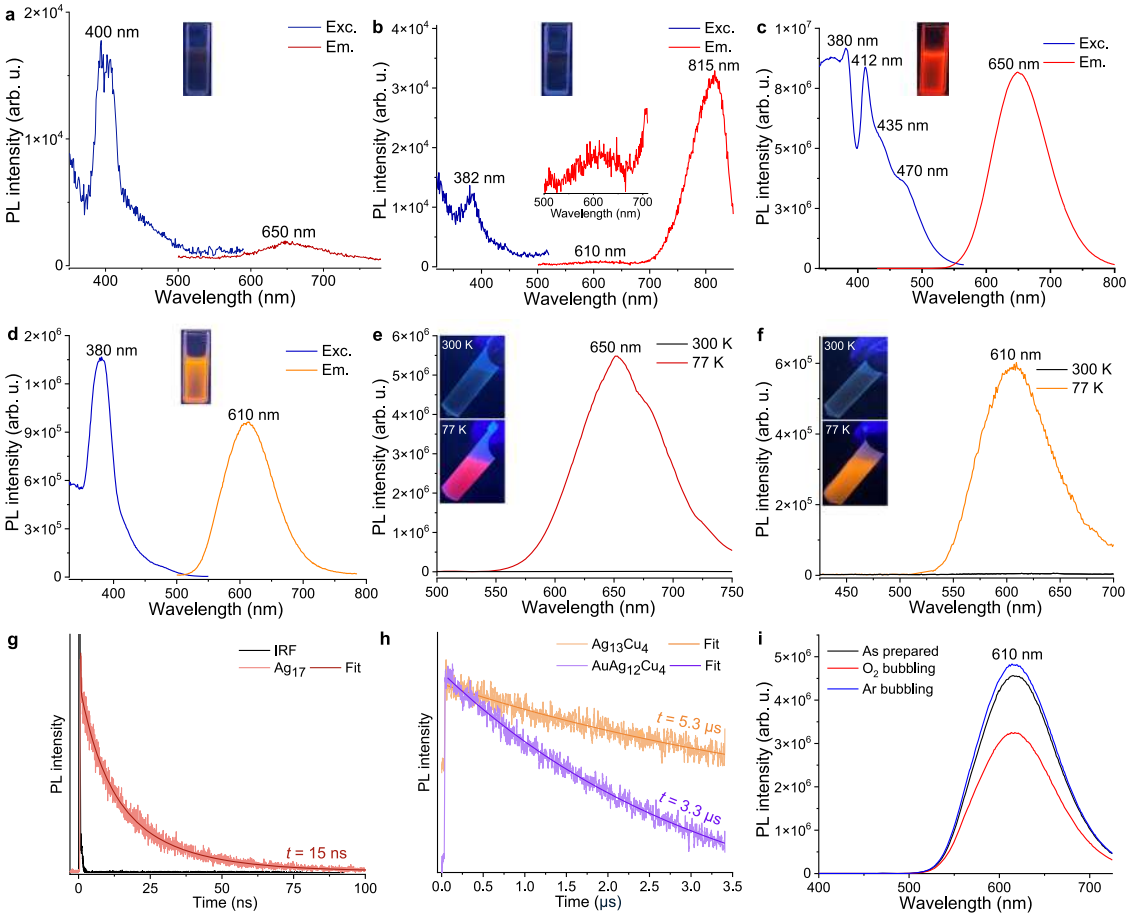


Fig. 6 | Photoluminescence spectra, emission enhancements, and decay profiles of Ag_{17}, $AuAg_{16}$, $Ag_{13}Cu_4$ and $AuAg_{12}Cu_4$ clusters. Photoluminescence excitation and emission spectra of **a** Ag_{17}, **b** $AuAg_{16}$, **c** $Ag_{13}Cu_4$ and **d** $AuAg_{12}Cu_4$ in DCM solution. Each inset shows the photograph of the respective cluster solution under a UV lamp at 365 nm. Solidification-induced emission enhancement of **e** Ag_{17} and **f** $AuAg_{16}$ clusters achieved by cooling the solution to 77 K. Inset shows the respective photographs of the solution at different temperatures. Luminescence decay profiles of **g** Ag_{17}, **h** $Ag_{13}Cu_4$ and $AuAg_{12}Cu_4$ clusters with average lifetimes. **i** PL intensity of $AuAg_{12}Cu_4$ cluster after exposure to oxygen and argon in DCM solution.

mercaptan) NCs, where luminescence was modulated based on the dopant type and its specific atomic position. In Ag_{29}, Au doping enhances luminescence, while Cu incorporation reduced it. However, in Ag_{17}, Cu doping at the shell ($Ag_{13}Cu_4$ and $AuAg_{12}Cu_4$) significantly increased the luminescence. These effects highlight the complex role of heteroatom positioning in modulating optical properties[82].

To understand the nature of the emissive excited states, luminescence decay measurements were performed. TCSPC measurement showed three component decay for Ag_{17} in DCM solution, having an average lifetime of 15 ns. Such decay is associated with a singlet excited state (Fig. 6g). On the other hand, Au and Cu incorporation significantly enhances the emissive lifetime (0.64 μs for $AuAg_{16}$ with two component decay and 5.3 μs for $Ag_{13}Cu_4$ with one component decay, see Supplementary Fig. 48 and Fig. 6h, respectively). Such a microsecond lifetime indicates phosphorescence emission, originating from the triplet states. Trimetallic $AuAg_{12}Cu_4$ cluster also showed phosphorescence emission with an average lifetime of 3.3 μs with one component decay (Fig. 6h). To further understand, oxygenation studies were performed upon exposing the cluster to oxygen gas. We observed significant quenching of luminescence intensity for $Ag_{13}Cu_4$ and trimetallic clusters after oxygen bubbling as depicted in Supplementary Fig. 49 and Fig. 6i, which further proved the presence of triplet excited states. Quenching of the emission intensity upon oxygen exposure confirmed the presence of triplet excited state for metal clusters[78].

Photophysics from TA spectroscopy

To understand the effect of heteroatoms on carrier dynamics of NCs, we performed fs TA spectroscopy on all the four NCs. We recorded the TA spectra (ΔA) of these NCs across the range of 440–650 nm at various pump-probe delay times, utilizing a 400 nm pump excitation with a pulse duration of 120 fs and a fluence of 350 μJ cm^{-2}. The results are presented in Fig. 7a–h. The TA spectrum of Ag_{17} (Fig. 7a) shows a broad featureless photoinduced absorption spanning from 440 to 640 nm, which grows continuously up to ≈1 ps before saturating and then starts to decay (Fig. 7b). This photoinduced absorption feature that shows a decay is not predicted by our theoretical calculations or observed in the optical absorption spectrum, suggesting its origin to the excited state absorption (ESA) of the NCs. ≈50% of 600 nm and ≈20% of 490 nm of ESA decays within 1 ns (Fig. 7b), indicating a differential relaxation process in Ag_{17}. In contrast, bimetallic $AuAg_{16}$ reached ESA saturation at ≈0.5 ps, and displayed a slower decay than Ag_{17} (Fig. 7c, d).

In contrast, the ESA of $Ag_{13}Cu_4$ shows continuous growth by many orders of magnitude compared to Ag_{17} and $AuAg_{16}$ without any observable saturation up to 1.5 ns (Fig. 7e, f), which is the limit of our experiment. This response starkly differs in the trimetallic $AuAg_{12}Cu_4$, which demonstrates a growth pattern up to 10 ps followed by a slower decay, providing a mixed response between the bimetallic $AuAg_{16}$ and $Ag_{13}Cu_4$ (Fig. 7g, h). To probe further into nanosecond timescales, flash photolysis experiments were conducted using a 355 nm, 7 ns pump excitation. Decay kinetics at 400 nm were best described by a single

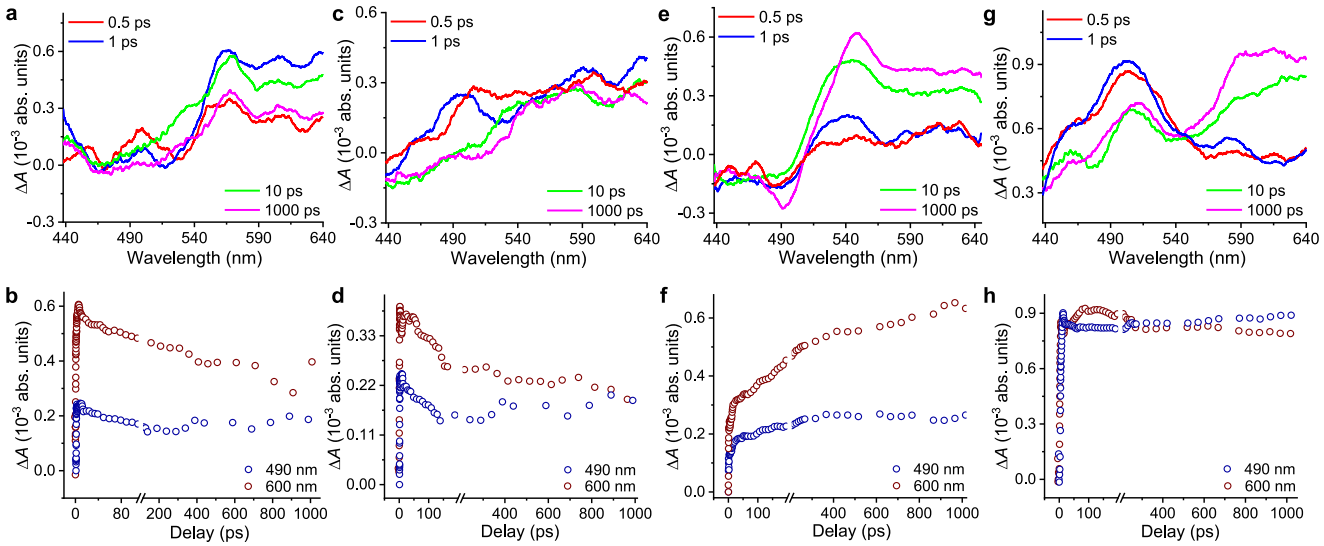


Fig. 7 | Fs TA spectra and decay kinetics of Ag_{17}, $AuAg_{16}$, $Ag_{13}Cu_4$ and $AuAg_{12}Cu_4$ clusters. Fs TA of the NCs at a fluence of 350 μJ cm^{-2}, at a 120 fs duration pump at 400 nm and different pump-probe delay times. The TA spectrum of **a** Ag_{17}, **c** $AuAg_{16}$, **e** $Ag_{13}Cu_4$, and **g** $AuAg_{12}Cu_4$. Decay kinetics at selected wavelengths for **b** Ag_{17}, **d** $AuAg_{16}$, **f** $Ag_{13}Cu_4$, and **h** $AuAg_{12}Cu_4$.

exponential function with a decay constant of ≈11 μs, indicating longer stability of the photo-excited carriers (Supplementary Fig. 50a). At 560 nm, the decay was too fast to capture, suggesting faster dynamics at this wavelength. TA decay profiles for $AuAg_{12}Cu_4$ demonstrated the short lifetime of carriers that is also described with single exponential decay kinetics having a decay constant of ≈6 ns (Supplementary Fig. 50b). The obtained lifetime of excited carriers follow the pattern similar to the PL lifetime, where also we saw the long lifetime of carriers upon introduction of the Cu atoms in the NCs. Comprehensively, the PL enhancement in bi and tri-metallic NCs appeared due to increased heteronuclearity and polarizability of metal-metal bonds[60,83]. The doping of Cu and Au into the Ag_{17} cluster is likely to introduces relativistic effects where Au produces more pronounced effects compared to Cu in the electronic structure[84]. These relativistic effects are likely to alter orbital energies and electronic configurations, which can modulate the electronic states and optical characteristics of the NCs. This modulation may create more favorable conditions for intersystem crossing[85], ultimately leading to the observed extended decay lifetimes and enhanced phosphorescence in our Cu and Au-doped NCs.

Discussion

In this study, we explored the synergy of different metal atoms within atomically precise M_{17} NCs, with a $M@M_{12}@M_4$ structure, exhibiting unique photophysical properties, protected with *ortho*-carborane-1-thiol (o_1-CBT). The parent Ag_{17} cluster has a central icosahedral (Ag_{13}) core encapsulated by four capped Ag atoms. For bimetallic clusters, Au atoms occupies the central position of the icosahedron and resulted in the centrally Au incorporated $Au@Ag_{16}$, while four Cu atoms prefer the outer tetrahedral positions, and thus resulted in $Ag_{13}@Cu_4$. Incorporation of both Au and Cu atoms at their respective preferred positions lead to the formation of the trimetallic $Au@Ag_{12}@Cu_4$. All these clusters were stabilized by twelve carborane-thiol ligands. Molecular composition and structure of these clusters were revealed by mass spectrometry and SC-XRD structural analysis. Site-specific incorporation of Au and Cu in the M_{17} NCs was supported by theoretical calculations. Alloying stabilizes the bimetallic clusters, rigidifies the cluster core, which was supported by computations and it leads to the opening up of the HOMO-LUMO gap. The Ag_{17} displays fluorescence emission. Au incorporation provides slight stabilization to the emissive excited state, whereas Cu incorporation significantly enhances the decay lifetimes and resulted in phosphorescence emission. Theoretical calculations revealed that the central atom incorporation of the cluster with a Au expands the HOMO-LUMO band gap in both $AuAg_{16}$ and $AuAg_{12}Cu_4$, whereas Cu incorporation to the outer capping region enhances photoluminescence emission in $Ag_{13}Cu_4$ and $AuAg_{12}Cu_4$. Fs TA showed structure specific relaxation of the excited state carriers. Altogether, this work explores the systematic site specific alloying leading to the synthesis of a carborane-thiol-protected trimetallic NC. It can also play a role to prepare diverse types of atomically precise photoemitters upon specific placement of a selective metal atom. Outer kernel substituted with Cu, bright luminescence and the packing pores of the trimetallic cluster in the solid state may lead to new catalysts, sensors and nano traps, especially considering the stability of these clusters.

Methods

Chemicals

Silver nitrate ($AgNO_3$, 99.0%) was purchased from Rankem Chemicals, while copper(I) chloride (CuCl, 97.0%), chloroauric acid ($HAuCl_4$, 98.0%), sodium borohydride ($NaBH_4$, 98.0%), 1,2-bis(diphenylphosphino)ethane (DPPE, 98.0%), and triphenylphosphine (TPP, 98.0%) were purchased from Sigma Aldrich. *Ortho*-carborane-1-thiol (o_1-CBT) was synthesized from *ortho*-carborane derivative, purchased from Katchem, Czech Republic. Crystalline o_1-CBT ligands (98.9%) were used for the NC synthesis. High-performance liquid chromatography (HPLC)-grade solvents, including dichloromethane (DCM, 99.8%), chloroform ($CHCl_3$, 99.4%), *n*-hexane (99.0%), acetonitrile (ACN, 99.8%), and methanol (MeOH, 99.5%), were sourced from Rankem Chemicals and Finar, India. Milli-Q water was used for cluster synthesis and purification. All the chemicals were commercially available and used without further purification.

Synthesis of Ag_{17}

The Ag_{17} was synthesized at ice cold condition (≈ 0 °C) using a DPPE-assisted silver-thiolate co-reduction reaction. In brief, 20 mg $AgNO_3$ was dissolved in 5 mL of MeOH. 10 mg of o_1-CBT ligand was dissolved in 9 mL DCM, which was added in stirring condition. After 5 min of the reaction, 10 mg of DPPE, dissolved in 1 mL DCM was added to the reaction mixture. After 15 min of reaction, 20 mg $NaBH_4$, dissolved in 1 mL water, was added. A brownish solution was formed, which eventually converted to a dark brown solution after overnight reaction. After 18 h of reaction, the mixture was thoroughly washed with MeOH/H_2O followed by complete solvent evaporation. Then the cluster was

extracted using DCM and dried on a rotavapor. The yield of the product is 78% in terms of silver. Hexagonal single crystals were grown after 10 days at 4 °C through hexane vapor diffusion into the concentrated DCM solution (20 mg mL^{-1}) of the cluster.

Synthesis of bimetallic $AuAg_{16}$ and $Ag_{13}Cu_4$

To synthesize the bimetallic NCs $AuAg_{16}$ and $Ag_{13}Cu_4$, a similar synthetic procedure was employed. For the $AuAg_{16}$, a starting reagent consisting of 20 mg $AgNO_3$ and 5 mg of $HAuCl_4$ was utilized. On the other hand, for $Ag_{13}Cu_4$, a starting reagent containing 20 mg $AgNO_3$ and 20 mg of CuCl was used. Following a reaction time of 18 h, the resulting $AuAg_{16}$ NC exhibited a greenish-brown solution in DCM. On the other hand, $Ag_{13}Cu_4$ cluster gave an orange-brown color. Both the clusters were purified by thoroughly washing with MeOH/H_2O followed by complete solvent evaporation with final extraction in DCM. The yield of $AuAg_{16}$ and $Ag_{13}Cu_4$, measured in terms of silver content, was 65% and 72%, respectively. Rod-shaped yellowish-orange $Ag_{13}Cu_4$ crystals were grown by allowing hexane vapor diffusion into a concentrated solution in DCM/$CHCl_3$ mixture (1:1). After multiple efforts, cuboid crystals of $AuAg_{16}$ were grown in the DCM/ACN mixture (4:1), layered with hexane.

Synthesis of trimetallic $AuAg_{12}Cu_4$

The synthesis of the $AuAg_{12}Cu_4$ with three different metals was carried out using a similar procedure. To conduct the synthesis, a mixture consisting of 20 mg of $AgNO_3$, 5 mg of $HAuCl_4$, and 20 mg of CuCl was employed. The reaction took place for 18 h at 0 °C, followed by overnight standing at 4 °C. Formation of the trimetallic NC had a low yield of 35%-40% (measured in terms of silver). By allowing the as-synthesized mixture in a solution of DCM and MeOH to slowly evaporate at 4 °C, beautiful orange-colored polyhedral trimetallic crystals were obtained. The resulting trimetallic $AuAg_{12}Cu_4$ from the crystallization process was utilized for further studies.

Characterisations

All UV-vis absorption data were obtained on a Perkin Elmer Lambda 365 spectrophotometer at room temperature. The SC-XRD data was measured at temperatures (T = 173 or 296 K), using a Bruker D8 VENTURE diffractometer equipped with Cu K_α (λ = 1.54178 Å) radiation source and PHOTON II detector. The structure was solved by SHELXT-2018 and refined by full-matrix least squares techniques using SHELXL-2018 or 2019 software packages incorporated in WingX suite. High-resolution mass spectrometry employed a Waters Synapt G2-Si instrument for electrospray ionization and collision-induced dissociation studies. Photoluminescence properties of the nanoclusters in DCM/MeOH were recorded by a Horiba Jobin Yvon Nanolog, using a 450 W xenon-arc lamp source. TA spectrometer generate 120 fs pulses centered at 800 nm by Spectra physics Mai-Tai oscillator which are sent to Spectra physics Spitfire amplifier to generate high energy (4 mJ $pulse^{-1}$) 120 fs pulses with a repetition rate of 1 kHz. Differential pulse voltammetry measured a 2.04 eV band gap for Ag_{17} clusters, aligning closely with theoretical predictions, though carborane-thiol protection caused electrode fouling, limiting further experiments.

DFT calculations. The DFT calculations were done using the GPAW software. The Kohn-Sham problem was solved by using real-space grids with 0.2 Å grid spacing. The electron-electron exchange-correlation interaction was approximated using the Perdew-Burke-Ernzerhof functional. Structure optimization started from the resolved crystal structures for each cluster type, and we used 0.05 eV/$Å^{-1}$ maximum force limit for convergence. Symmetries of the frontier orbitals were analyzed using projections to spherical harmonics with respect to cluster's center of mass with 12.0 Å cutoff. LR-TDDFT was used for absorption spectra, dipole transition contribution map (DTCM) was used for analyzing the origin of the absorption peaks, and electron density oscillations of the peaks were visualized by using induced densities.

Data availability

The data that support the findings of this study are available from the corresponding authors upon request. Crystallographic data for the structures reported in this article have been deposited at the Cambridge Crystallographic Data Centre (CCDC), under deposition numbers CCDC 2356804 (Ag_{17}), 2356806 ($AuAg_{16}$), 2356807 ($Ag_{13}Cu_4$) and 2356892 ($AuAg_{12}Cu_4$).

References

1. Chakraborty, I. & Pradeep, T. Atomically Precise Clusters of Noble Metals: Emerging Link between Atoms and Nanoparticles. *Chem. Rev.* **117**, 8208–8271 (2017).
2. Takano, S. & Tsukuda, T. Chemically Modified Gold/Silver Superatoms as Artificial Elements at Nanoscale: Design Principles and Synthesis Challenges. *J. Am. Chem. Soc.* **143**, 1683–1698 (2021).
3. Lee, S. et al. [Pt2Cu34(PET)22Cl4]2–: An Atomically Precise, 10-Electron PtCu Bimetal Nanocluster with a Direct Pt–Pt Bond. *J. Am. Chem. Soc.* **143**, 12100–12107 (2021).
4. Jin, R., Zeng, C., Zhou, M. & Chen, Y. Atomically Precise Colloidal Metal Nanoclusters and Nanoparticles: Fundamentals and Opportunities. *Chem. Rev.* **116**, 10346–10413 (2016).
5. Desireddy, A. et al. Ultrastable silver nanoparticles. *Nature* **501**, 399–402 (2013).
6. Gan, Z., Xia, N. & Wu, Z. Discovery, Mechanism, and Application of Antigalvanic Reaction. *Acc. Chem. Res.* **51**, 2774–2783 (2018).
7. Bootharaju, M. S., Joshi, C. P., Parida, M. R., Mohammed, O. F. & Bakr, O. M. Templated Atom-Precise Galvanic Synthesis and Structure Elucidation of a [Ag24Au(SR)18]– Nanocluster. *Angew. Chem. Int. Ed* **55**, 922–926 (2016).
8. Takano, S., Ito, S. & Tsukuda, T. Efficient and Selective Conversion of Phosphine-Protected (MAu8)2+ (M = Pd, Pt) Superatoms to Thiolate-Protected (MAu12)6+ or Alkynyl-Protected (MAu12)4+ Superatoms via Hydride Doping. *J. Am. Chem. Soc.* **141**, 15994–16002 (2019).
9. Fan, X. et al. Structural Isomerization in Cu(I) Clusters: Tracing the Cu Thermal Migration Paths and Unveiling the Structure-Dependent Photoluminescence. *CCS Chem*. https://doi.org/10.31635/ccschem.022.202101741 (2023).
10. Han, B.-L. et al. Polymorphism in Atomically Precise Cu23 Nanocluster Incorporating Tetrahedral [Cu4]0 Kernel. *J. Am. Chem. Soc.* **142**, 5834–5841 (2020).
11. Sakthivel, N. A. & Dass, A. Aromatic Thiolate-Protected Series of Gold Nanomolecules and a Contrary Structural Trend in Size Evolution. *Acc. Chem. Res.* **51**, 1774–1783 (2018).
12. Gell, L., Lehtovaara, L. & Häkkinen, H. Superatomic S2 Silver Clusters Stabilized by a Thiolate–Phosphine Monolayer: Insight into Electronic and Optical Properties of Ag14(SC6H3F2)12(PPh3)8 and Ag16(SC6H3F2)14(DPPE)4. *J. Phys. Chem. A* **118**, 8351–8355 (2014).
13. Kang, X. & Zhu, M. Tailoring the photoluminescence of atomically precise nanoclusters. *Chem. Soc. Rev.* **48**, 2422–2457 (2019).
14. Abbas, M. A., Kamat, P. V. & Bang, J. H. Thiolated Gold Nanoclusters for Light Energy Conversion. *ACS Energy Lett* **3**, 840–854 (2018).
15. Huang, R.-W. et al. Radioluminescent Cu–Au Metal Nanoclusters: Synthesis and Self-Assembly for Efficient X-ray Scintillation and Imaging. *J. Am. Chem. Soc.* **145**, 13816–13827 (2023).
16. Russier-Antoine, I. et al. Ligand-core NLO-phores: a combined experimental and theoretical approach to the two-photon absorption and two-photon excited emission properties of small-ligated silver nanoclusters. *Nanoscale* **9**, 1221–1228 (2017).
17. Zhang, C., Si, W.-D., Wang, Z., Tung, C.-H. & Sun, D. Chiral Ligand-Concentration Mediating Asymmetric Transformations of Silver Nanoclusters: NIR-II Circularly Polarized Phosphorescence Lighting. *Angew. Chem. Int. Ed.* **63**, e202404545 (2024).
18. Zhang, M.-M. et al. Chiral Hydride Cu18 Clusters Transform to Superatomic Cu15Ag4 Clusters: Circularly Polarized Luminescence Lighting. *J. Am. Chem. Soc.* **145**, 22310–22316 (2023).

19. Qian, S. et al. Engineering luminescent metal nanoclusters for sensing applications. *Coord. Chem. Rev.* **451**, 214268 (2022).
20. Liu, C. et al. Chiral Ag23 nanocluster with open shell electronic structure and helical face-centered cubic framework. *Nat. Commun.* **9**, 744 (2018).
21. Nguyen, T.-A. D. et al. A Cu25 Nanocluster with Partial Cu(0) Character. *J. Am. Chem. Soc.* **137**, 13319–13324 (2015).
22. Chiu, T.-H. et al. Homoleptic Platinum/Silver Superatoms Protected by Dithiolates: Linear Assemblies of Two and Three Centered Icosahedra Isolobal to Ne2 and I3. *J. Am. Chem. Soc.* **141**, 12957–12961 (2019).
23. Bootharaju, M. S. et al. Cd12Ag32(SePh)36: Non-Noble Metal Doped Silver Nanoclusters. *J. Am. Chem. Soc.* **141**, 8422–8425 (2019).
24. Dhayal, R. S., van Zyl, W. E. & Liu, C. W. Polyhydrido Copper Clusters: Synthetic Advances, Structural Diversity, and Nanocluster-to-Nanoparticle Conversion. *Acc. Chem. Res.* **49**, 86–95 (2016).
25. Qu, M. et al. Observation of Non-FCC Copper in Alkynyl-Protected Cu53 Nanoclusters. *Angew. Chem. Int. Ed.* **59**, 6507–6512 (2020).
26. Kang, X., Li, Y., Zhu, M. & Jin, R. Atomically precise alloy nanoclusters: syntheses, structures, and properties. *Chem. Soc. Rev.* **49**, 6443–6514 (2020).
27. Khatun, E. et al. Confining an Ag10 Core in an Ag12 Shell: A Four-Electron Superatom with Enhanced Photoluminescence upon Crystallization. *ACS Nano* **13**, 5753–5759 (2019).
28. Nguyen, T.-A. D. et al. Ligand-Exchange-Induced Growth of an Atomically Precise Cu29 Nanocluster from a Smaller Cluster. *Chem. Mater.* **28**, 8385–8390 (2016).
29. Jana, A. et al. A luminescent Cu 4 cluster film grown by electrospray deposition: a nitroaromatic vapour sensor. *Nanoscale* **15**, 8141–8147 (2023).
30. Wang, Q.-Y. et al. o-Carborane-Based and Atomically Precise Metal Clusters as Hypergolic Materials. *J. Am. Chem. Soc.* **142**, 12010–12014 (2020).
31. Huang, J.-H., Ji, A.-Q., Wang, Z.-Y., Wang, Q.-Y. & Zang, S.-Q. Boosting 2000-Fold Hypergolic Ignition Rate of Carborane by Substitutes Migration in Metal Clusters. *Adv. Sci.* **11**, 2401861 (2024).
32. Jana, A. et al. Light-Activated Intercluster Conversion of an Atomically Precise Silver Nanocluster. *ACS Nano* **15**, 15781–15793 (2021).
33. Wang, J., Wang, Z.-Y., Li, S.-J., Zang, S.-Q. & Mak, T. C. W. Carboranealkynyl-Protected Gold Nanoclusters: Size Conversion and UV/Vis–NIR Optical Properties. *Angew. Chem.* **133**, 6024–6029 (2021).
34. Wang, J., Xu, F., Wang, Z.-Y., Zang, S.-Q. & Mak, T. C. W. Ligand-Shell Engineering of a Au28 Nanocluster Boosts Electrocatalytic CO2 Reduction. *Angew. Chem. Int. Ed.* **61**, e202207492 (2022).
35. Jana, A. et al. Carboranethiol-Protected Propeller-Shaped Photoresponsive Silver Nanomolecule. *Inorg. Chem.* **61**, 8593–8603 (2022).
36. Morin, J.-F., Shirai, Y. & Tour, J. M. En Route to a Motorized Nanocar. *Org. Lett.* **8**, 1713–1716 (2006).
37. Goronzy, D. P. et al. Influence of Terminal Carboxyl Groups on the Structure and Reactivity of Functionalized m-Carboranethiolate Self-Assembled Monolayers. *Chem. Mater.* **32**, 6800–6809 (2020).
38. Wang, J. et al. Carborane Derivative Conjugated with Gold Nanoclusters for Targeted Cancer Cell Imaging. *Biomacromolecules* **18**, 1466–1472 (2017).
39. Fisher, S. P. et al. Nonclassical Applications of closo-Carborane Anions: From Main Group Chemistry and Catalysis to Energy Storage. *Chem. Rev.* **119**, 8262–8290 (2019).
40. Poater, J. et al. Too Persistent to Give Up: Aromaticity in Boron Clusters Survives Radical Structural Changes. *J. Am. Chem. Soc.* **142**, 9396–9407 (2020).
41. White, K. E. et al. Competing Intermolecular and Molecule–Surface Interactions: Dipole–Dipole-Driven Patterns in Mixed Carborane Self-Assembled Monolayers. *Chem. Mater.* **36**, 2085–2095 (2024).
42. Huang, J.-H., Wang, Z.-Y., Zang, S.-Q. & Mak, T. C. W. Spontaneous Resolution of Chiral Multi-Thiolate-Protected Ag30 Nanoclusters. *ACS Cent. Sci.* **6**, 1971–1976 (2020).
43. Ghosh, A., Mohammed, O. F. & Bakr, O. M. Atomic-Level Doping of Metal Clusters. *Acc. Chem. Res.* **51**, 3094–3103 (2018).
44. Kim, M. et al. Dopant-Dependent Electronic Structures Observed for M2Au36(SC6H13)24 Clusters (M = Pt, Pd). *J. Phys. Chem. Lett.* **9**, 982–989 (2018).
45. Choi, W. et al. Effects of Metal-Doping on Hydrogen Evolution Reaction Catalyzed by MAu24 and M2Au36 Nanoclusters (M = Pt, Pd). *ACS Appl. Mater. Interf.* **10**, 44645–44653 (2018).
46. Xie, S., Tsunoyama, H., Kurashige, W., Negishi, Y. & Tsukuda, T. Enhancement in Aerobic Alcohol Oxidation Catalysis of Au25 Clusters by Single Pd Atom Doping. *ACS Catal* **2**, 1519–1523 (2012).
47. Chakrahari, K. K. et al. Synthesis of Bimetallic Copper-Rich Nanoclusters Encapsulating a Linear Palladium Dihydride Unit. *Angew. Chem. Int. Ed.* **58**, 4943–4947 (2019).
48. Bootharaju, M. S. et al. Atom-Precise Heteroatom Core-Tailoring of Nanoclusters for Enhanced Solar Hydrogen Generation. *Adv. Mater.* **35**, 2207765 (2023).
49. Masuda, S., Sakamoto, K. & Tsukuda, T. Atomically precise Au and Ag nanoclusters doped with a single atom as model alloy catalysts. *Nanoscale* **16**, 4514–4528 (2024).
50. Chen, S. et al. Assembly of the Thiolated [Au1Ag22(S-Adm)12]3+ Superatom Complex into a Framework Material through Direct Linkage by SbF6− Anions.*Angew. Chem.* **132**, 7612–7617 (2020).
51. Du, W. et al. Ag50(Dppm)6(SR)30 and Its Homologue AuxAg50−x(Dppm)6(SR)30 Alloy Nanocluster: Seeded Growth, Structure Determination, and Differences in Properties. *J. Am. Chem. Soc.* **139**, 1618–1624 (2017).
52. Chai, J. et al. Chiral Inversion and Conservation of Clusters: A Case Study of Racemic Ag32Cu12 Nanocluster. *Inorg. Chem.* **60**, 9050–9056 (2021).
53. Kim, M. et al. Insights into the Metal-Exchange Synthesis of MAg24(SR)18 (M = Ni, Pd, Pt) Nanoclusters. *Chem. Mater.* **32**, 10216–10226 (2020).
54. Khatun, E. & Pradeep, T. New Routes for Multicomponent Atomically Precise Metal Nanoclusters. *ACS Omega* **6**, 1–16 (2021).
55. Yan, J. et al. Total Structure and Electronic Structure Analysis of Doped Thiolated Silver [MAg24(SR)18]2− (M = Pd, Pt) Clusters. *J. Am. Chem. Soc.* **137**, 11880–11883 (2015).
56. Yang, Y. et al. An All-Alkynyl Protected 74-Nuclei Silver(I)–Copper(I)-Oxo Nanocluster: Oxo-Induced Hierarchical Bimetal Aggregation and Anisotropic Surface Ligand Orientation. *Angew. Chem. Int. Ed.* **58**, 12280–12285 (2019).
57. He, L. et al. Kernel Tuning and Nonuniform Influence on Optical and Electrochemical Gaps of Bimetal Nanoclusters. *J. Am. Chem. Soc.* **140**, 3487–3490 (2018).
58. Hossain, S. et al. Thiolate-Protected Trimetallic Au~20Ag~4Pd and Au~20Ag~4Pt Alloy Clusters with Controlled Chemical Composition and Metal Positions. *J. Phys. Chem. Lett.* **9**, 2590–2594 (2018).
59. Han, B.-L. et al. Precise Implantation of an Archimedean Ag@Cu12 Cuboctahedron into a Platonic Cu4Bis(diphenylphosphino)hexane6 Tetrahedron. *ACS Nano* **15**, 8733–8741 (2021).
60. Xie, X.-Y. et al. The Origin of the Photoluminescence Enhancement of Gold-Doped Silver Nanoclusters: The Importance of Relativistic Effects and Heteronuclear Gold–Silver Bonds. *Angew. Chem. Int. Ed.* **57**, 9965–9969 (2018).
61. Hirai, H. et al. Doping-Mediated Energy-Level Engineering of M@Au12 Superatoms (M=Pd, Pt, Rh, Ir) for Efficient Photoluminescence and Photocatalysis. *Angew. Chem. Int. Ed.* **61**, e202207290 (2022).

62. Fakhouri, H. et al. Effects of Single Platinum Atom Doping on Stability and Nonlinear Optical Properties of Ag29 Nanoclusters. *J. Phys. Chem. C* **126**, 21094–21100 (2022).
63. Yuan, S.-F., Guan, Z.-J., Liu, W.-D. & Wang, Q.-M. Solvent-triggered reversible interconversion of all-nitrogen-donor-protected silver nanoclusters and their responsive optical properties. *Nat. Commun.* **10**, 4032 (2019).
64. Chevrier, D. M. et al. Interactions between Ultrastable Na4Ag44(SR)30 Nanoclusters and Coordinating Solvents: Uncovering the Atomic-Scale Mechanism. *ACS Nano* **14**, 8433–8441 (2020).
65. Udayabhaskararao, T. & Pradeep, T. New Protocols for the Synthesis of Stable Ag and Au Nanocluster Molecules. *J. Phys. Chem. Lett.* **4**, 1553–1564 (2013).
66. Manno, R. et al. Continuous Microwave-Assisted Synthesis of Silver Nanoclusters Confined in Mesoporous SBA-15: Application in Alkyne Cyclizations. *Chem. Mater.* **32**, 2874–2883 (2020).
67. Bootharaju, M. S. et al. Reversible Size Control of Silver Nanoclusters via Ligand-Exchange. *Chem. Mater.* **27**, 4289–4297 (2015).
68. Yuan, X. et al. Traveling through the Desalting Column Spontaneously Transforms Thiolated Ag Nanoclusters from Non-luminescent to Highly Luminescent. *J. Phys. Chem. Lett.* **4**, 1811–1815 (2013).
69. Wickramasinghe, S. et al. M3Ag17(SPh)12 Nanoparticles and Their Structure Prediction. *J. Am. Chem. Soc.* **137**, 11550–11553 (2015).
70. Conn, B. E. et al. Confirmation of a de novo structure prediction for an atomically precise monolayer-coated silver nanoparticle. *Sci. Adv.* **2**, e1601609 (2016).
71. Jana, A. et al. Photoconversion of Ag31 to Ag42 Initiated by Solvated Electrons. *Chem. Mater.* **35**, 7020–7031 (2023).
72. Qu, M. et al. Bidentate Phosphine-Assisted Synthesis of an All-Alkynyl-Protected Ag74 Nanocluster. *J. Am. Chem. Soc.* **139**, 12346–12349 (2017).
73. Dhayal, R. S. et al. Ag21S2P(OiPr)212]+: An Eight-Electron Superatom. *Angew. Chem. Int. Ed.* **54**, 3702–3706 (2015).
74. Chang, W.-T. et al. Eight-Electron Silver and Mixed Gold/Silver Nanoclusters Stabilized by Selenium Donor Ligands. *Angew. Chem. Int. Ed.* **56**, 10178–10182 (2017).
75. Dhayal, R. S. et al. [Ag20S2P(OR)212]: A Superatom Complex with a Chiral Metallic Core and High Potential for Isomerism. *Chem. – Eur. J* **22**, 9943–9947 (2016).
76. Yen, W.-J., Liao, J.-H., Chiu, T.-H., Wen, Y.-S. & Liu, C. W. Homoleptic Silver-Rich Trimetallic M20 Nanocluster. *Inorg. Chem.* **61**, 6695–6700 (2022).
77. Zhong, Y.-J. et al. Doping effect on the structure and properties of eight-electron silver nanoclusters. *J. Chem. Phys.* **155**, 034304 (2021).
78. Jana, A. et al. Carborane-thiol protected copper nanoclusters: stimuli-responsive materials with tunable phosphorescence. *Chem. Sci.* **14**, 1613–1626 (2023).
79. Gam, F. et al. Alloying dichalcogenolate-protected Ag21 eight-electron nanoclusters: a DFT investigation. *Nanoscale* **14**, 196–203 (2021).
80. Liu, D. et al. [Au14(2-SAdm)9(Dppe)2]+: a gold nanocluster with a crystallization-induced emission enhancement phenomenon. *Chem. Commun.* **60**, 1337–1340 (2024).
81. Kang, X., Wang, S. & Zhu, M. Observation of a new type of aggregation-induced emission in nanoclusters. *Chem. Sci.* **9**, 3062–3068 (2018).
82. Kang, X. et al. Rational construction of a library of M29 nanoclusters from monometallic to tetrametallic. *Proc. Natl. Acad. Sci.* **116**, 18834–18840 (2019).
83. Galassi, R. et al. Cupriphication of gold to sensitize d10–d10 metal–metal bonds and near-unity phosphorescence quantum yields. *Proc. Natl. Acad. Sci.* **114**, E5042–E5051 (2017).
84. Häkkinen, H., Moseler, M. & Landman, U. Bonding in Cu, Ag, and Au Clusters: Relativistic Effects, Trends, and Surprises. *Phys. Rev. Lett.* **89**, 033401 (2002).
85. Song, Y. et al. Ultrabright Au@Cu14 nanoclusters: 71.3% phosphorescence quantum yield in non-degassed solution at room temperature. *Sci. Adv.* **7**, eabd2091 (2021).

Acknowledgements

The authors acknowledge the support of Department of Science and Technology (DST), Government of India for the support of instrumentation used in this work. T. P. acknowledges funding from the Centre of Excellence on Molecular Materials and Functions under the Institution of Eminence scheme of IIT Madras. T. P. thanks the Science and Engineering Research Board (SERB), India, for funding through the SPR/2021/000439 research grant. The authors thank the Sophisticated Analytical Instrumental Facility, Indian Institute of Technology Madras (SAIF-IITM) for SC-XRD and TGA measurements. The computational work at University of Jyväskylä was supported by the Academy of Finland and the computations were performed at the Finnish National Supercomputing Center CSC. K.N.V.D.A. gratefully acknowledges the Science and Engineering Research Board (Project No. CRG/2023/003013) and the Department of Science and Technology (DST/NM/TUE/QM-8/2019(G)/1). VY thank IIC, Czech Republic for funding his short duration stay. VY and SA thank the Ministry of Education for their Prime Minister's Research Fellowships. H. N., A. S. and A. R. K. thank CSIR-UGC for their research fellowships. T. P. acknowledges funding through a JC Bose Fellowship.

Author contributions

V.Y. performed the synthesis, crystallization, and most of the experimental studies. A.J. and V.Y. performed structural characterization and photophysical studies. S.Ac. performed mass spectrometric studies. H.N. assisted V.Y. for synthetic scaleup. A.R.K. conducted electron microscopic and XPS measurements. All the fs–ns time-resolved studies were conducted by A.S. in the laboratory of K.N.V.D.A. S.M. and H.H. performed computational studies. J.M. and T.B. synthesized the carborane thiols used in this work and conducted all the work relating to those systems. Single-crystal X-ray structure refinement was done by S.An. The first draft of the manuscript was written by V.Y., and all the authors contributed to improving it. T.P. suggested the problem, supervised the project, and finalized the manuscript. This work is a part of longer-term collaboration aimed at unlocking the potential of materials produced by combining metal NCs and carborane ligands initiated by T.P. and T.B.

Competing interests

The authors declare no competing interests.

Additional information

Supplementary information The online version contains supplementary material available at https://doi.org/10.1038/s41467-025-56385-w.

Correspondence and requests for materials should be addressed to Kumaran Nair Valsala Devi Adarsh, Tomas Base, Hannu Häkkinen or Thalappil Pradeep.

Peer review information *Nature Communications* thanks the anonymous reviewers for their contribution to the peer review of this work. A peer review file is available.

Reprints and permissions information is available at http://www.nature.com/reprints

Publisher's note Springer Nature remains neutral with regard to jurisdictional claims in published maps and institutional affiliations.

Open Access This article is licensed under a Creative Commons Attribution-NonCommercial-NoDerivatives 4.0 International License, which permits any non-commercial use, sharing, distribution and reproduction in any medium or format, as long as you give appropriate credit to the original author(s) and the source, provide a link to the Creative Commons licence, and indicate if you modified the licensed material. You do not have permission under this licence to share adapted material derived from this article or parts of it. The images or other third party material in this article are included in the article's Creative Commons licence, unless indicated otherwise in a credit line to the material. If material is not included in the article's Creative Commons licence and your intended use is not permitted by statutory regulation or exceeds the permitted use, you will need to obtain permission directly from the copyright holder. To view a copy of this licence, visit http://creativecommons.org/licenses/by-nc-nd/4.0/.

© The Author(s) 2025

Supplementary Information

Site-specific substitution in atomically precise carboranethiol-protected nanoclusters and concomitant changes in electronic properties

Vivek Yadav[1], Arijit Jana[1], Swetashree Acharya[1], Sami Malola[2], Harshita Nagar[1], Ankit Sharma[3], Amoghavarsha R. Kini[1], Sudhadevi Antharjanam[4], Jan Machacek[5], Kumaran Nair Valsala Devi Adarsh[* 3], Tomas Base[* 5], Hannu Häkkinen[*2], and Thalappil Pradeep[* 1]

1 DST Unit of Nanoscience (DST UNS) and Thematic Unit of Excellence (TUE), Department of Chemistry, Indian Institute of Technology, Madras, Chennai – 600036, India

2 Department of Physics and Chemistry, Nanoscience Center, University of Jyväskylä, FI 40014 Jyväskylä, Finland

3 Department of Physics, Indian Institute of Science Education, and Research Bhopal, Bhopal-462066, India

4 Sophisticated Analytical Instruments Facility (SAIF), Indian Institute of Technology, Madras, Chennai – 600036, India

5 Department of Synthesis, Institute of Inorganic Chemistry, The Czech Academy of Science, 1001 Husinec-Rez, 25068, Czech Republic

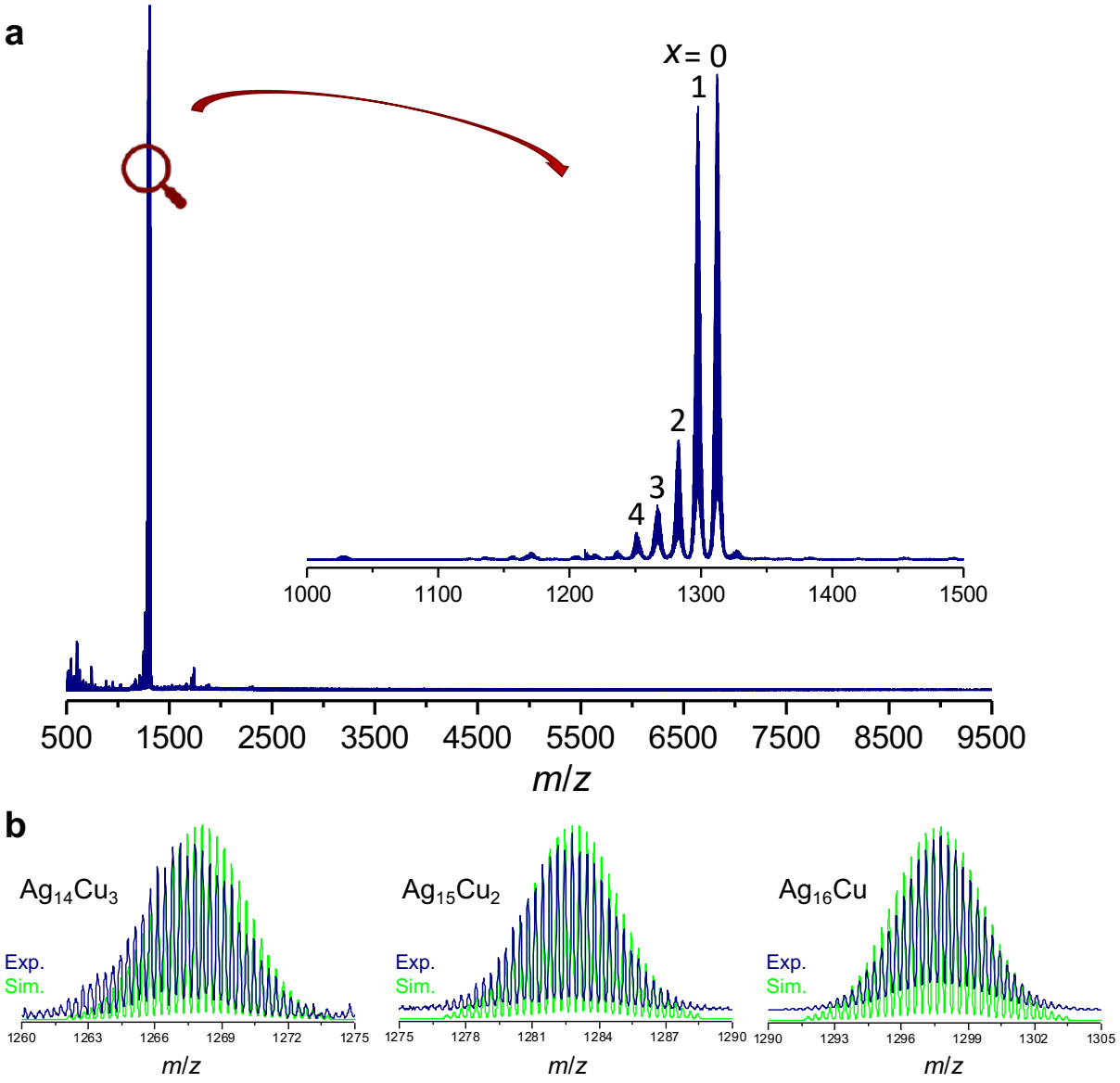
*Corresponding authors email: pradeep@iitm.ac.in, hannu.j.hakkinen@jyu.fi, tbase@iic.acs.cz, adarsh@iiserb.ac.in

Table of Contents

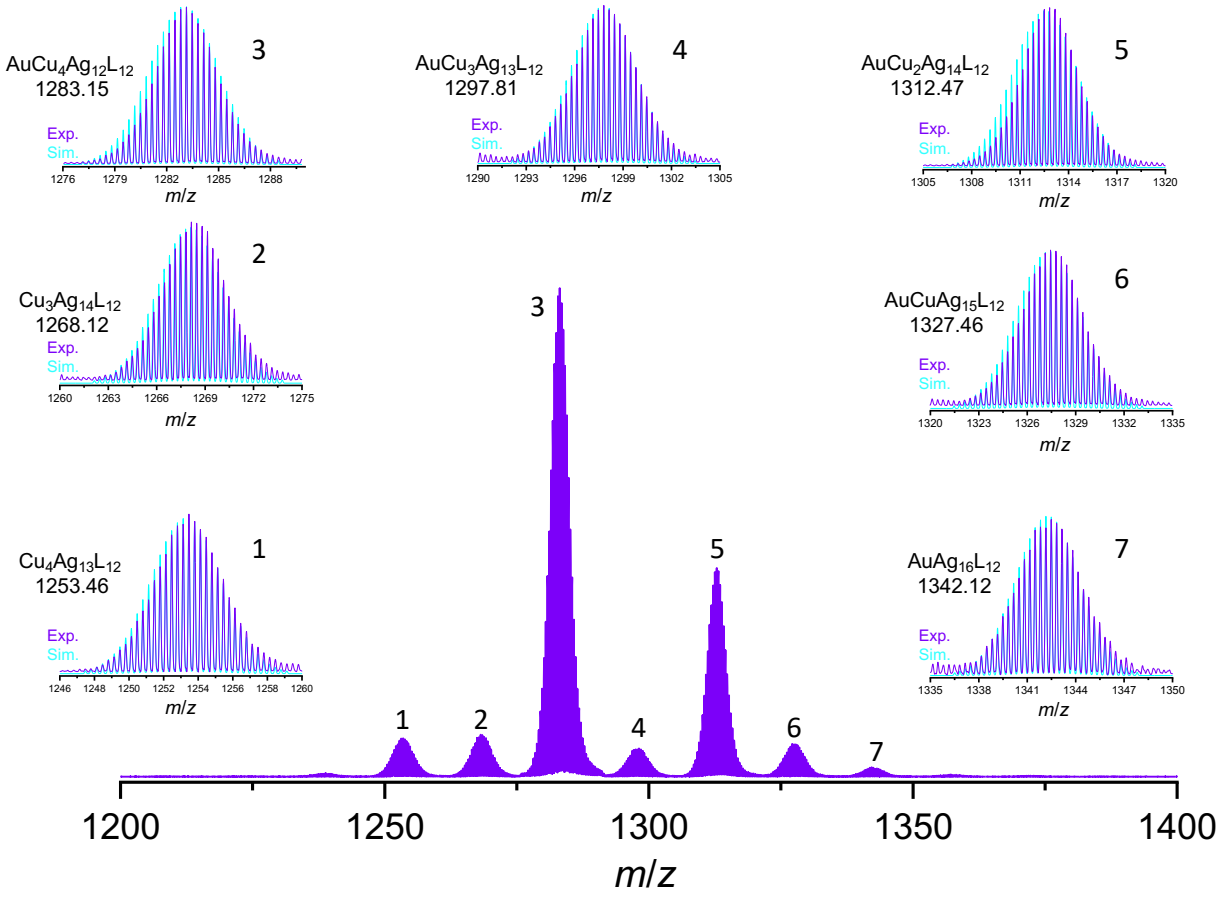
Supplementary Figures S2-S42

Supplementary Tables S43-S66

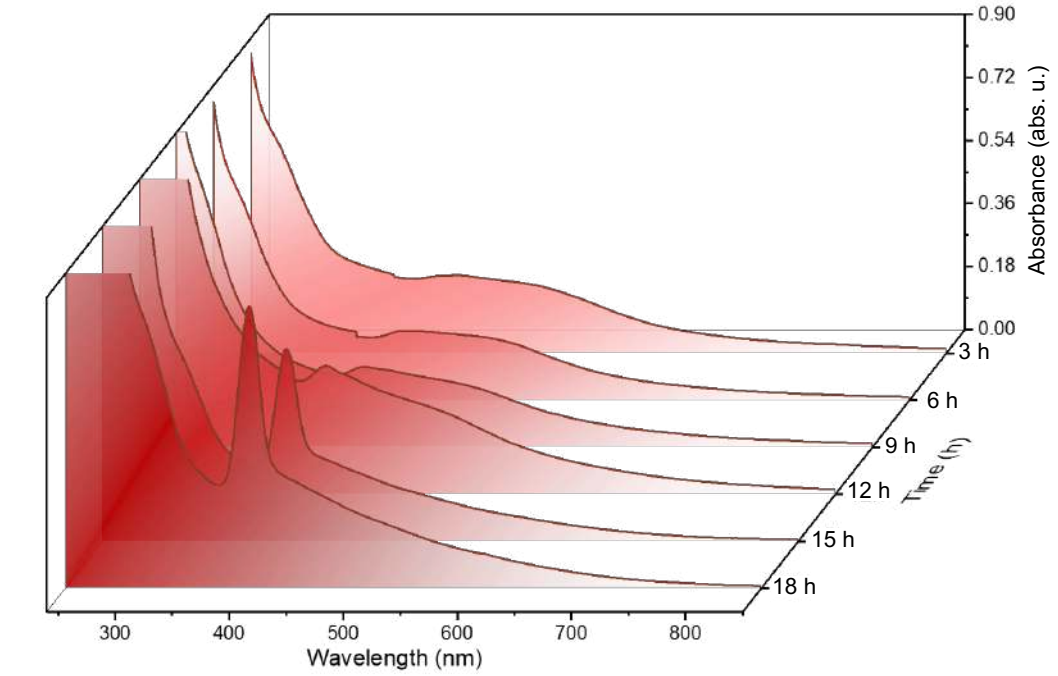
Supplementary Figures



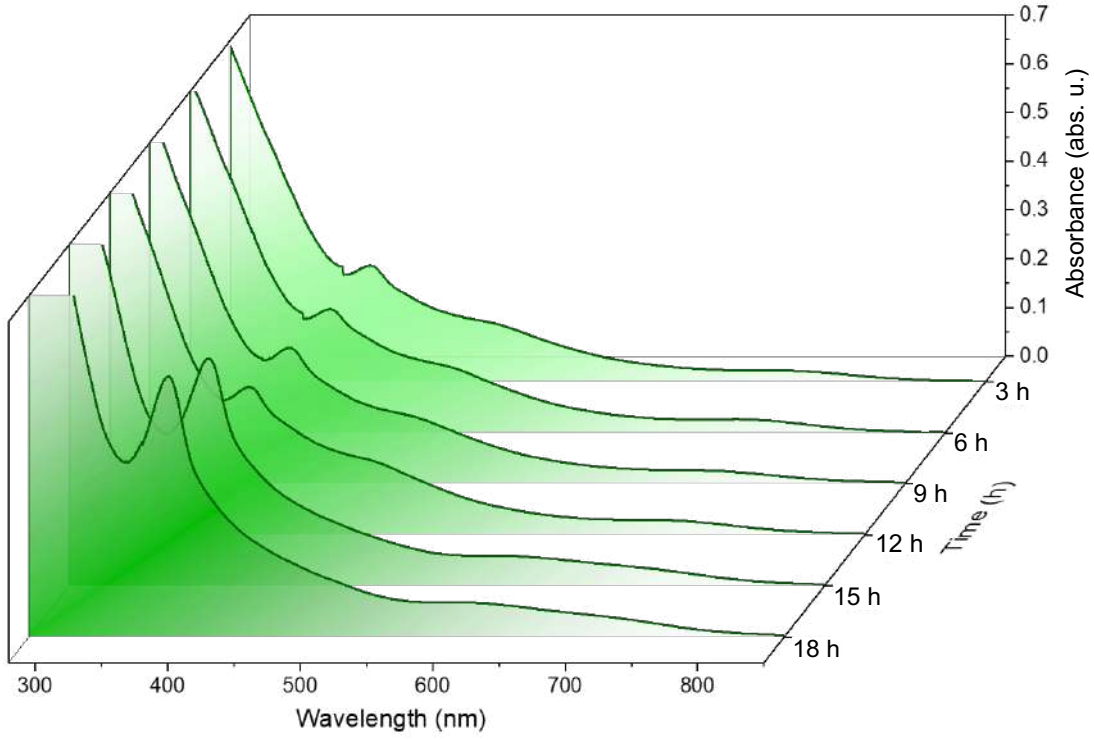
Supplementary Fig. 1 | a Mass Spectrum of the initial synthesis trial for incorporating Cu in Ag_{17} NC showing a mixture of products as $Ag_{17-x}Cu_x$ (x= 0-4). **b** Exact matching of the isotopic distributions of the experimental (dark blue) and simulated spectra (light green) of $Ag_{14}Cu_3$, $Ag_{15}Cu_2$ and $Ag_{16}Cu$ NCs.



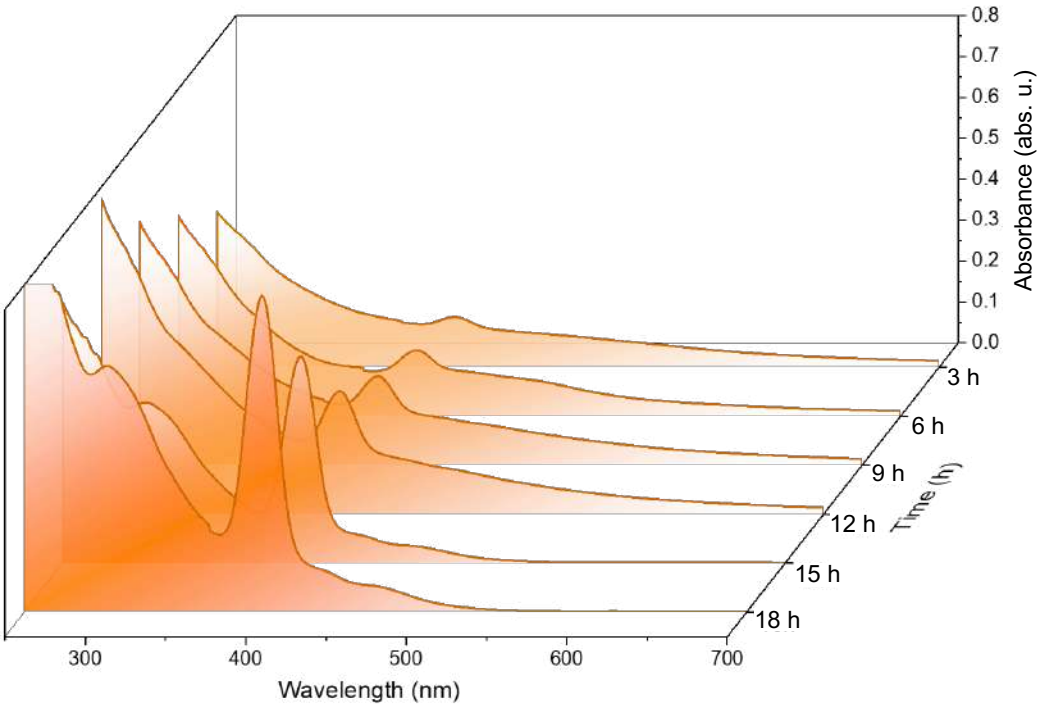
Supplementary Fig. 2 | Mass spectrum of $AuAg_{12}Cu_4$ showing multiple peaks assigned and their exact matching of the isotopic distributions of the experimental (deep purple) and simulated (cyan) spectra.



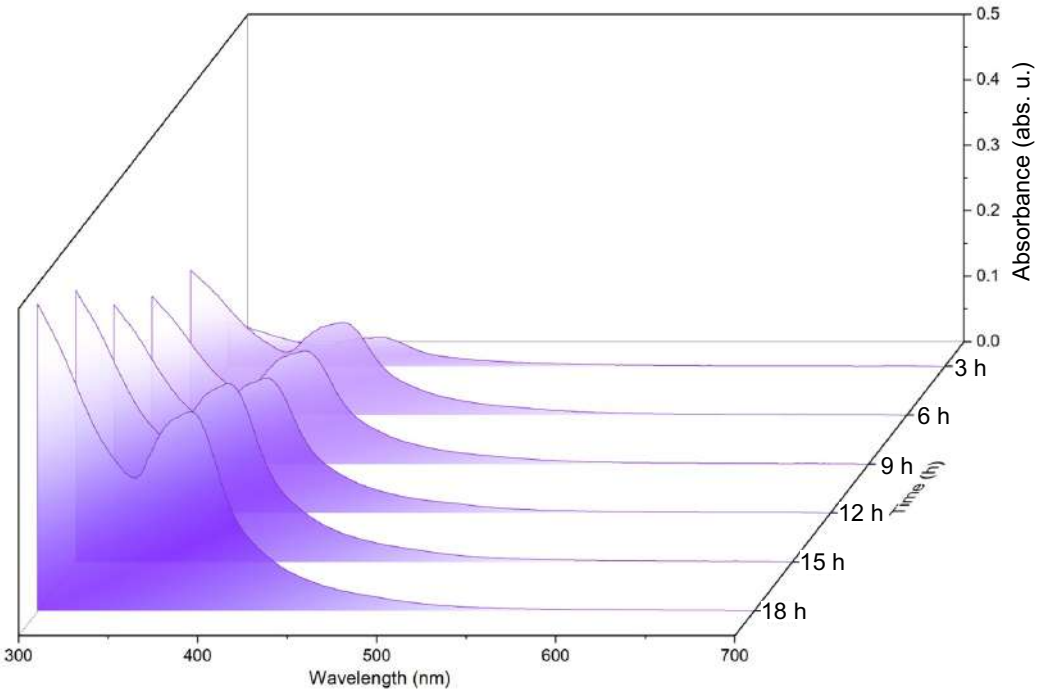
Supplementary Fig. 3 | Time dependent UV-Vis absorption spectra of the Ag_{17}, after the addition of $NaBH_4$ during the synthesis. The cluster Ag_{17} started forming after 15 h of reaction.



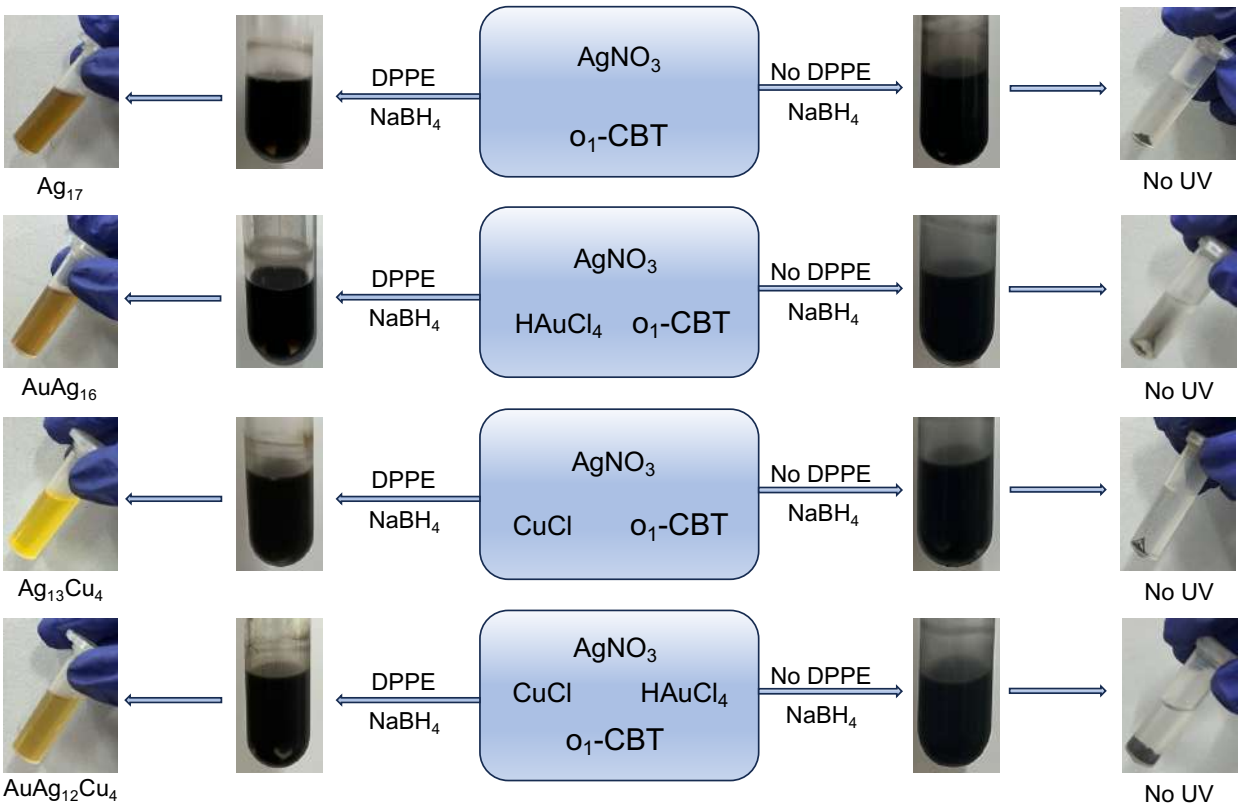
Supplementary Fig. 4 | Time sequence UV-Vis absorption spectra of the $AuAg_{16}$, after the addition of $NaBH_4$ during the synthesis. The $AuAg_{16}$ started forming after 15 h of reaction.



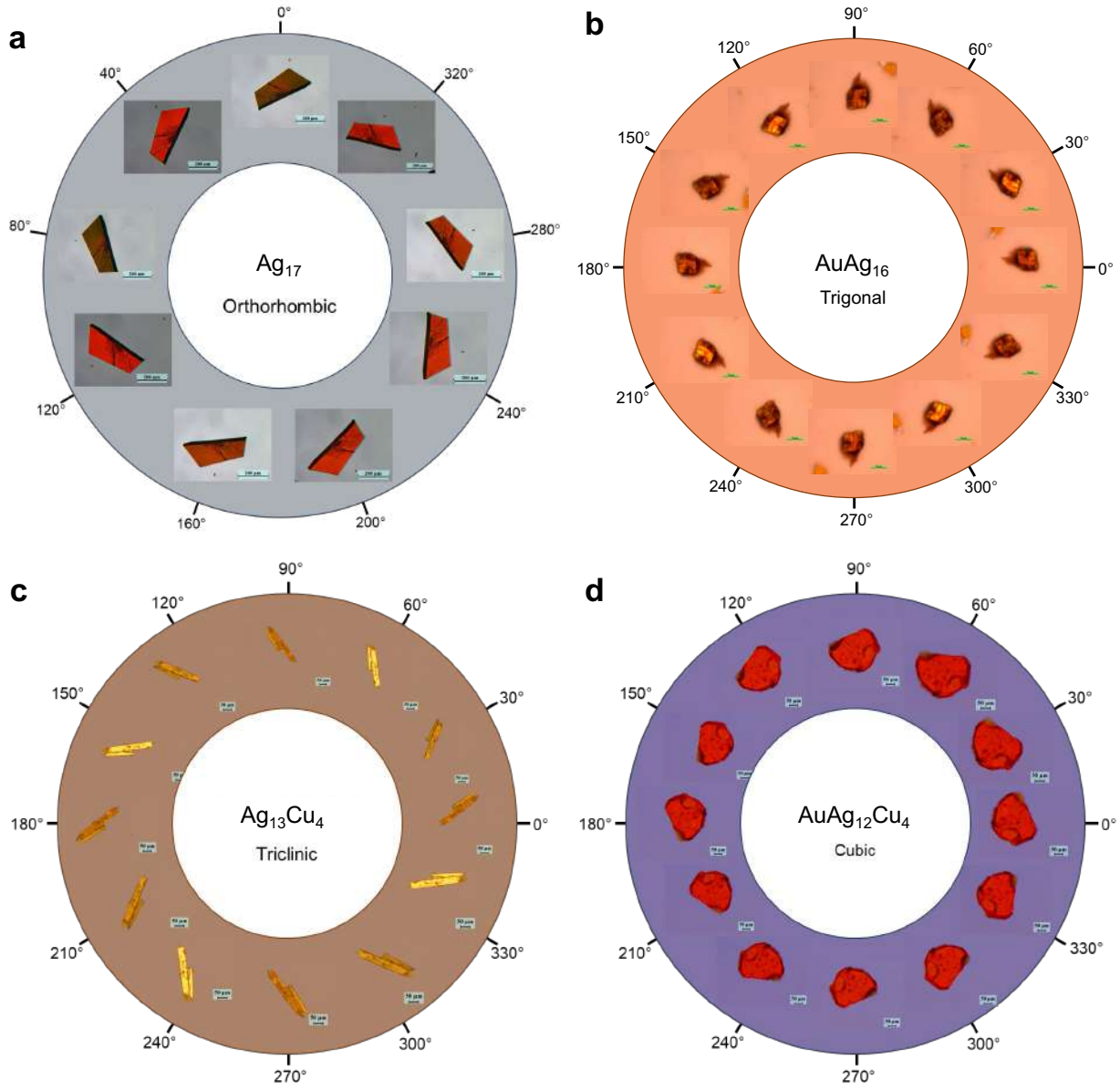
Supplementary Fig. 5 | Time dependent UV-Vis absorption spectra of $Ag_{13}Cu_4$, after the addition of $NaBH_4$ during the synthesis. The $Ag_{13}Cu_4$ started forming after 12 h of reaction.



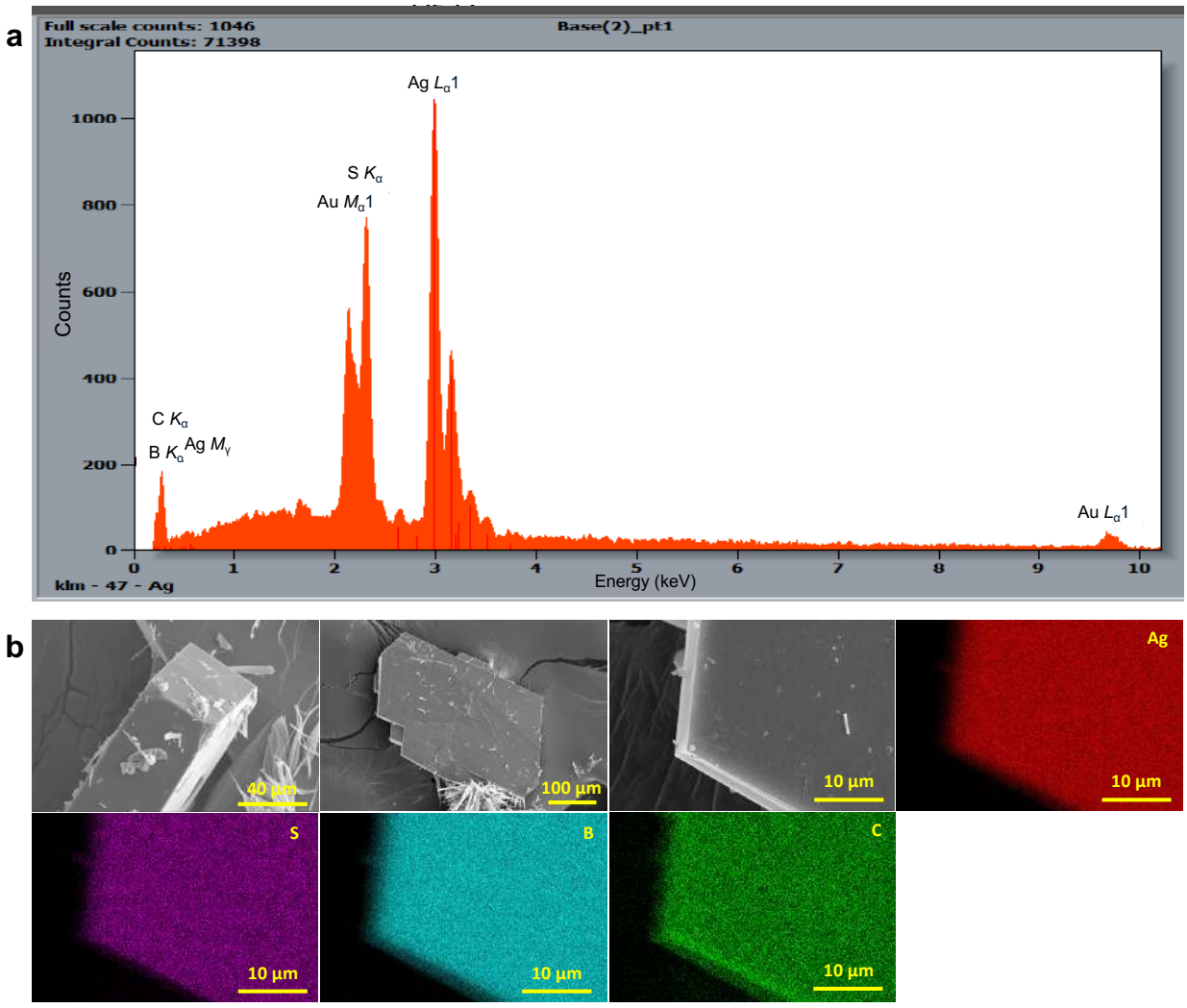
Supplementary Fig. 6 | Time sequence UV-Vis absorption spectra of $AuAg_{12}Cu_4$, after the addition of $NaBH_4$ during the synthesis. The $AuAg_{12}Cu_4$ started forming after 12 h of reaction.



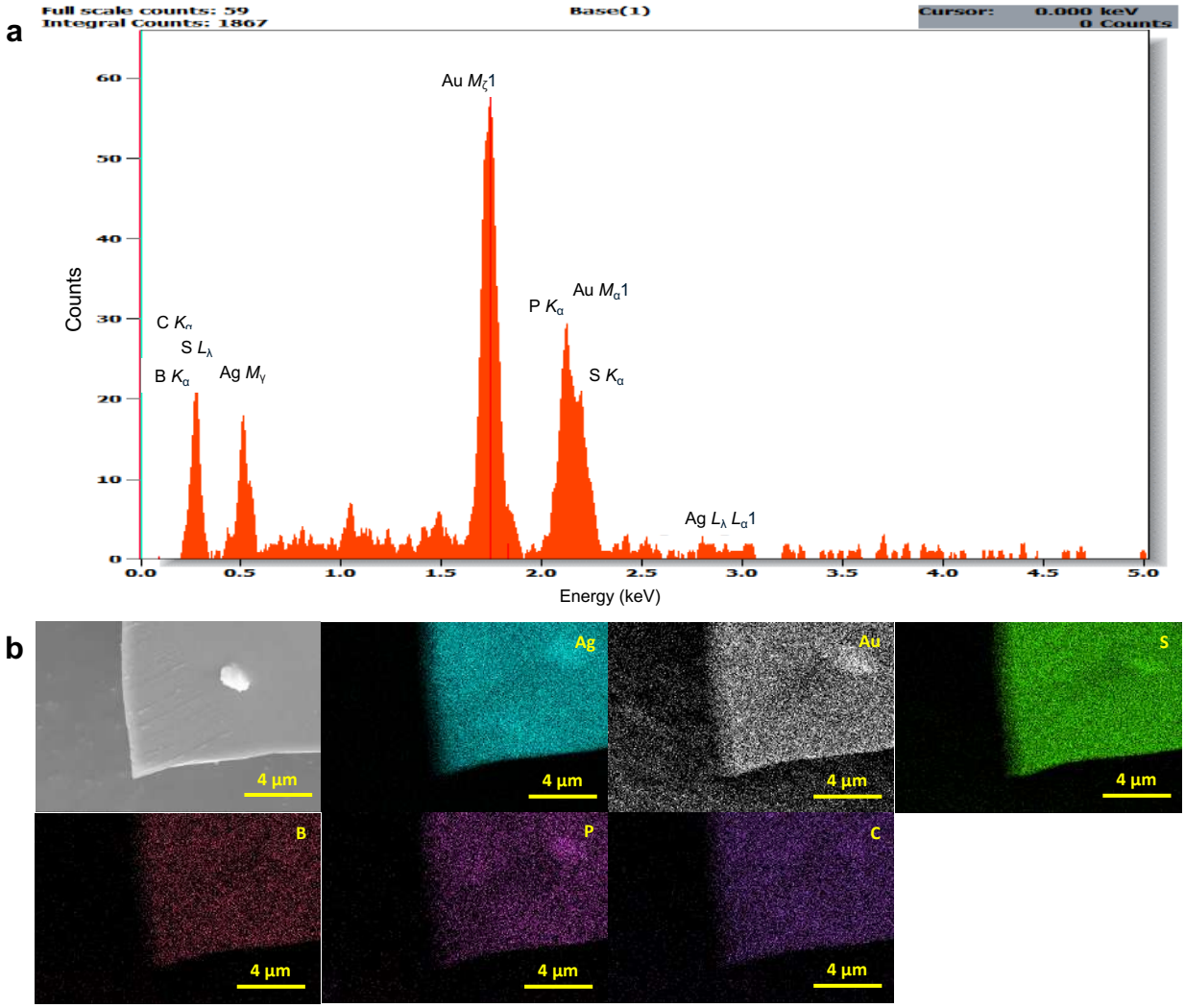
Supplementary Fig. 7 | Photographic images of the different synthetic steps of all the four clusters with and without DPPE. No product was formed without DPPE as a supporting ligand.



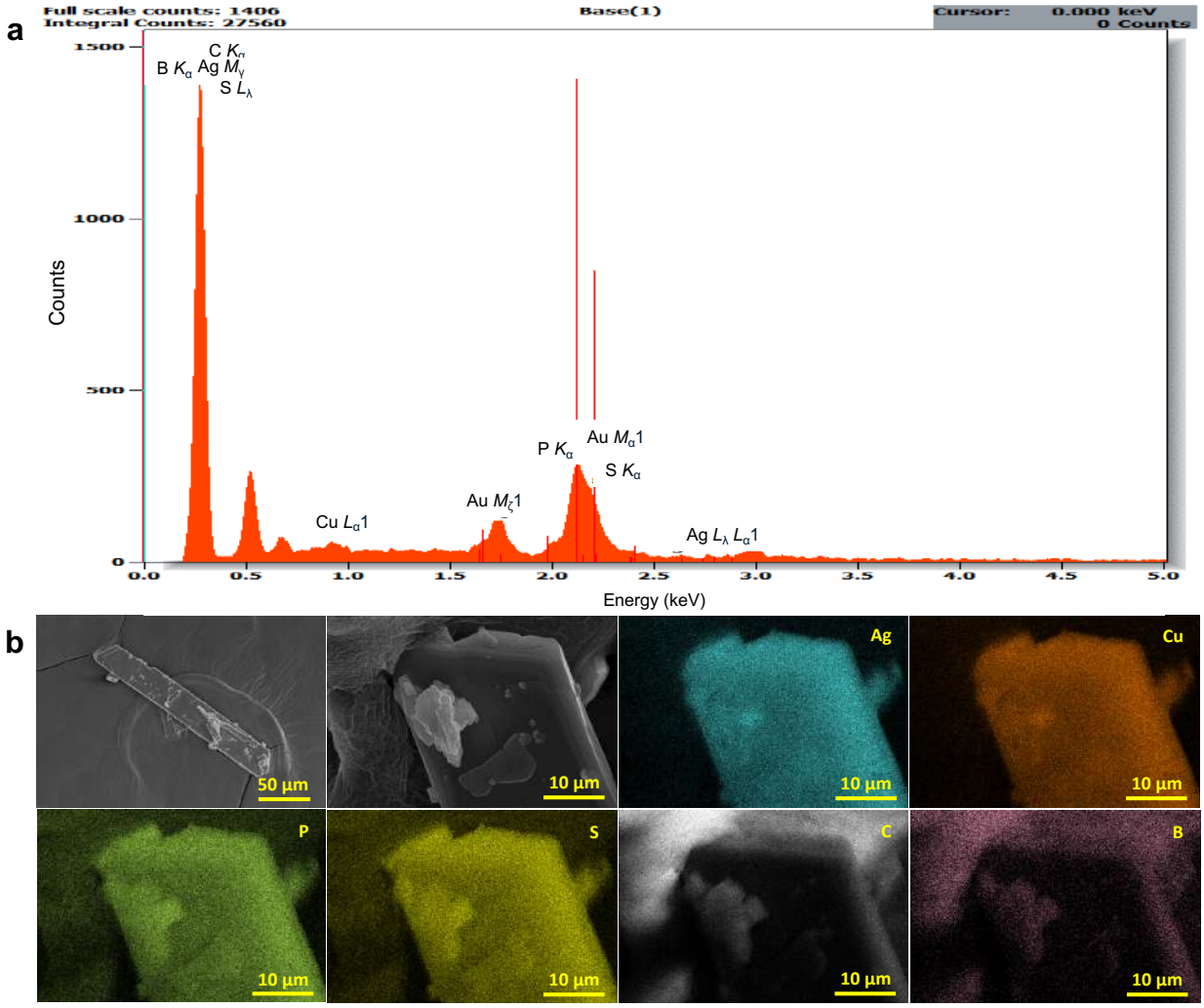
Supplementary Fig. 8 | Optical microscopic images of **a** Ag_{17}, (Scale bar: 200 μm) **b** $AuAg_{16}$, (Scale bar: 50 μm) **c** $Ag_{13}Cu_4$ (Scale bar: 50 μm) and **d** $AuCu_4Ag_{12}$ (Scale bar: 50 μm) single crystal under the polarizer at various rotation. Distinct optical polarization was observed for Ag_{17}, $AuAg_{16}$ and $Ag_{13}Cu_4$ cluster crystals. Such polarization was absent for trimetallic $AuCu_4Ag_{12}$ cluster.



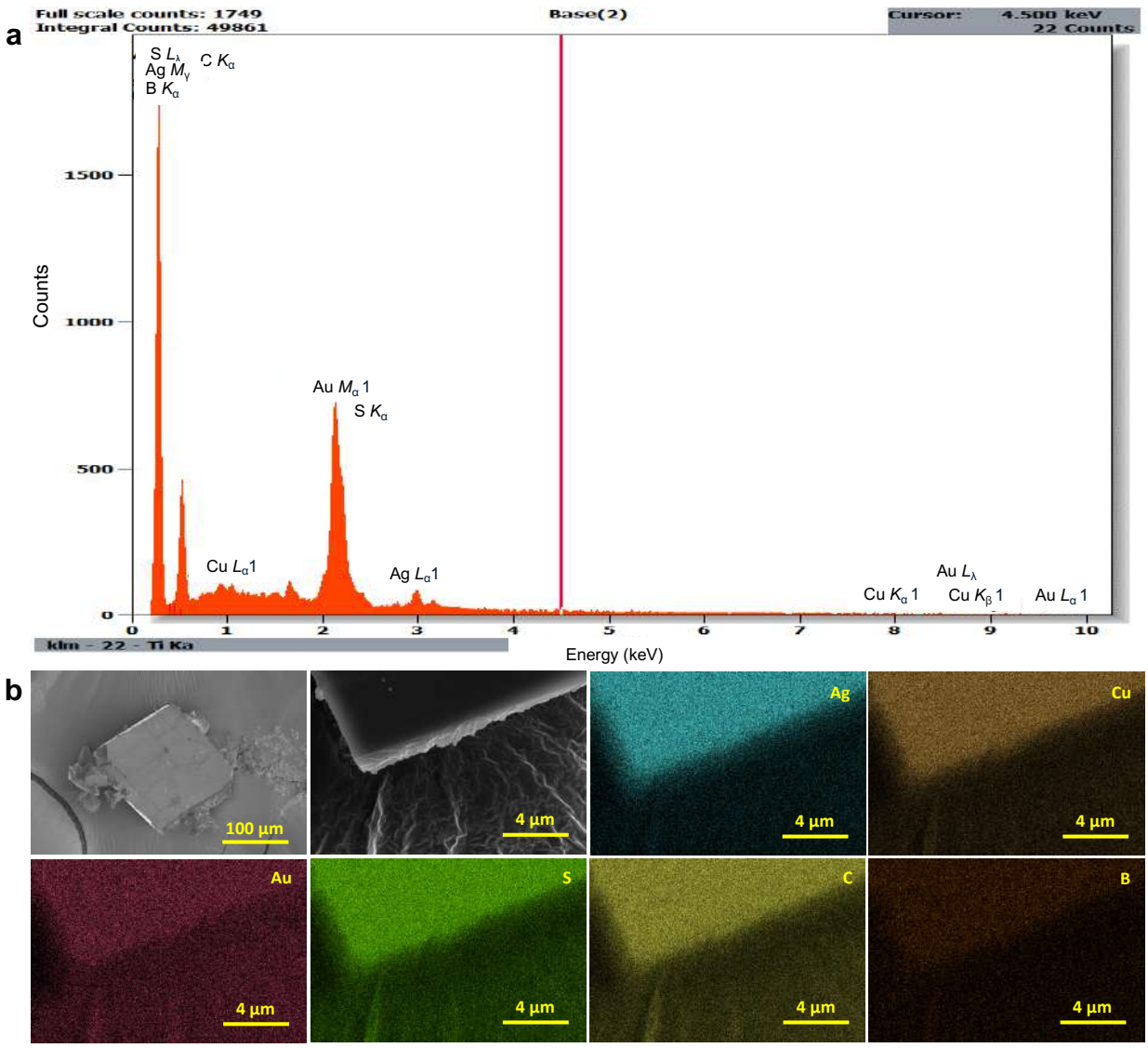
Supplementary Fig. 9 | FESEM images of the crystals and EDS mapping of Ag_{17}. a The EDS spectrum indicates the presence of respective elements. **b** The FESEM image of a single crystal and the collected EDS elemental mapping of the same crystal, showing Ag, S, C and B elements.



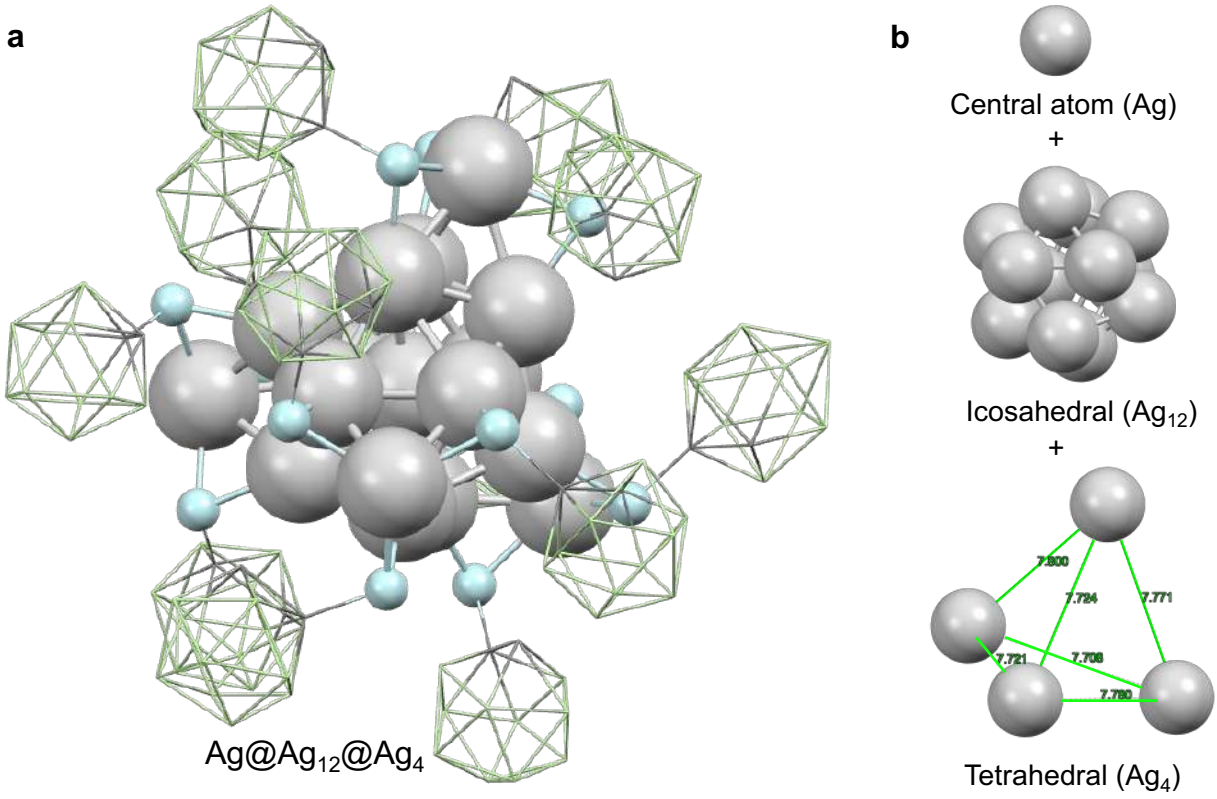
Supplementary Fig. 10 | FESEM images of the crystals and EDS mapping of $AuAg_{16}$. a The EDS spectrum indicates the presence of respective elements. **b** The FESEM image of a single crystal and the collected EDS elemental mapping of the same crystal, showing Ag, Au, S, P, C and B elements.



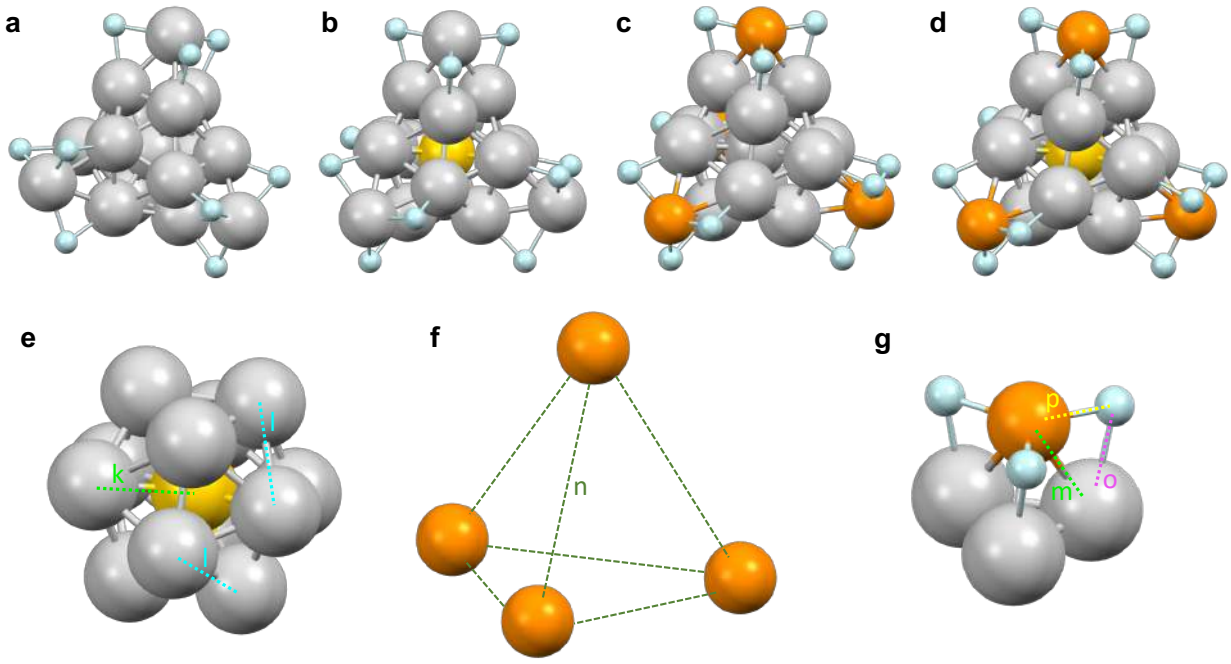
Supplementary Fig. 11 | FESEM images of the crystals and EDS mapping of $Ag_{13}Cu_4$. a The EDS spectrum indicates the presence of respective elements. **b** The FESEM image of a single crystal and the collected EDS elemental mapping of the same crystal, showing Ag, Cu, S, P, C and B elements.



Supplementary Fig. 12 | FESEM images of the crystals and EDS mapping of $AuAg_{12}Cu_4$. a The EDS spectrum indicates the presence of respective elements. **b** The FESEM image of a single crystal and the collected EDS elemental mapping of the same crystal, showing Ag, Cu, Au, S, C and B elements.

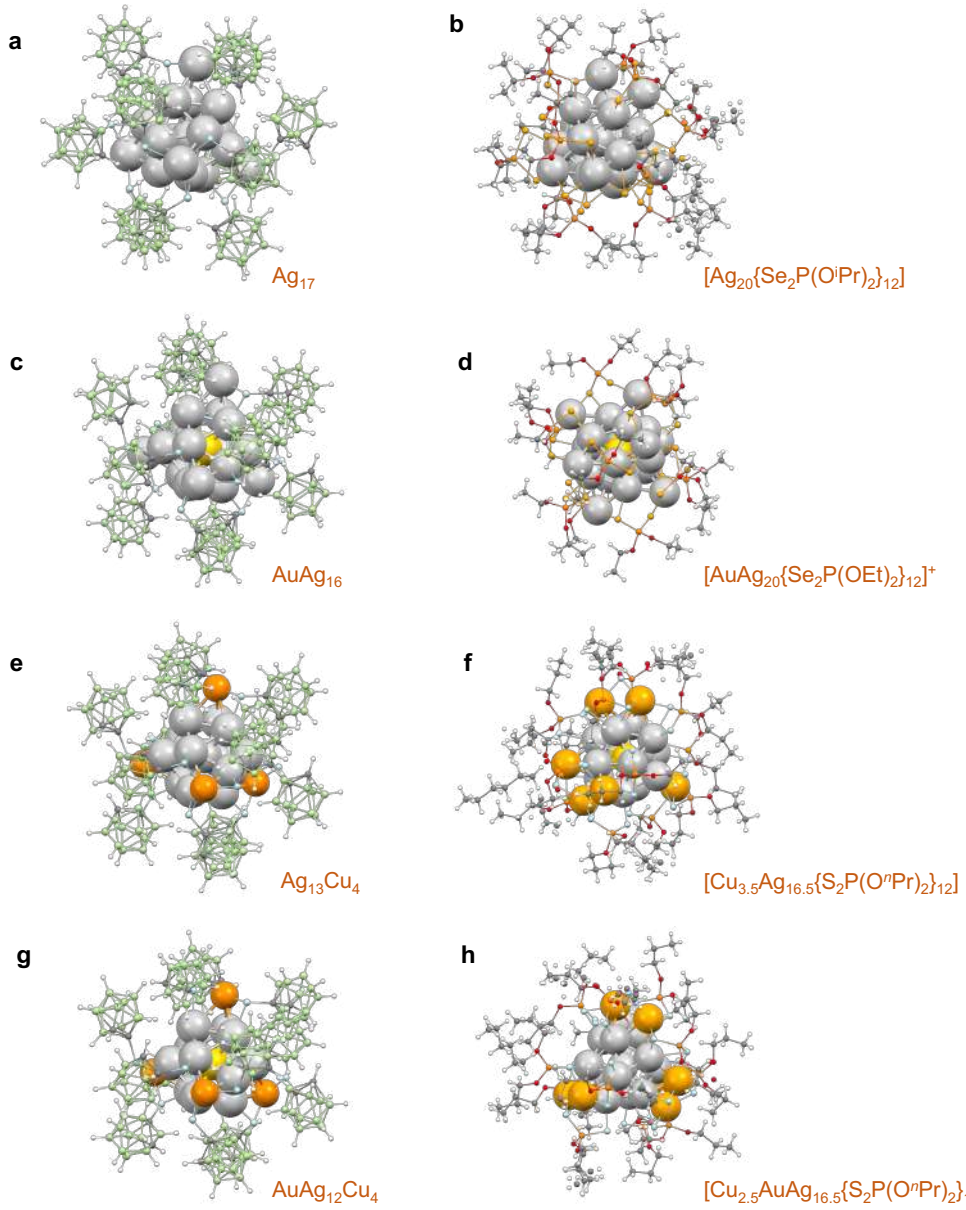


Supplementary Fig. 13 | Structural composition of the Ag_{17}. a Full structure of Ag_{17} shows the 17-silver core binded with sulphur of o_1-CBT (Hydrogen has been removed for clarity). **b** Composition of silver core with central atom (Ag) covered with an icosahedral (Ag_{12}) capped with tetrahedral (Ag_4) for overall core to become $Ag@Ag_{12}@Ag_4$. Color codes: metallic gray: silver, cyan: sulphur, green: boron and dark grey: carbon.

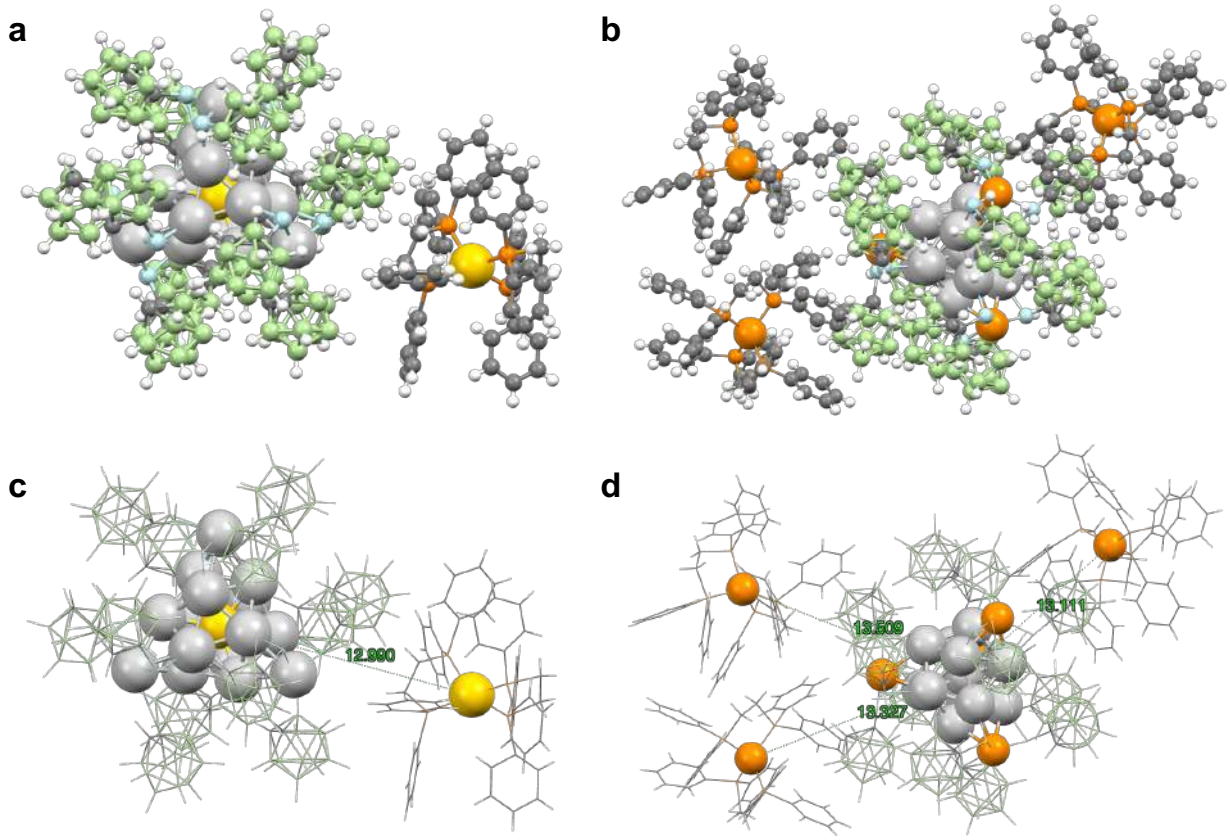


Nanocluster	Average distance (Å) between central atom to Icosahedral atoms (k)	Average distance (Å) among the bonds of Icosahedral atoms (l)	Average distance (Å) between capped tetrahedral metal atom to Icosahedral atoms (m)	Average distance (Å) among capped tetrahedral atoms (n)	Average distance (Å) between Sulphur of ligand to Icosahedral atoms (o)	Average distance (Å) between Sulphur of ligand to capped tetrahedral atoms (p)
Ag_{17}	2.792	2.938	3.061	7.750	2.492	2.498
$AuAg_{16}$	2.785	2.931	3.054	7.776	2.481	2.548
$Ag_{13}Cu_4$	2.785	2.930	2.986	7.611	2.493	2.277
$AuAg_{12}Cu_4$	2.759	2.902	2.958	7.580	2.491	2.186

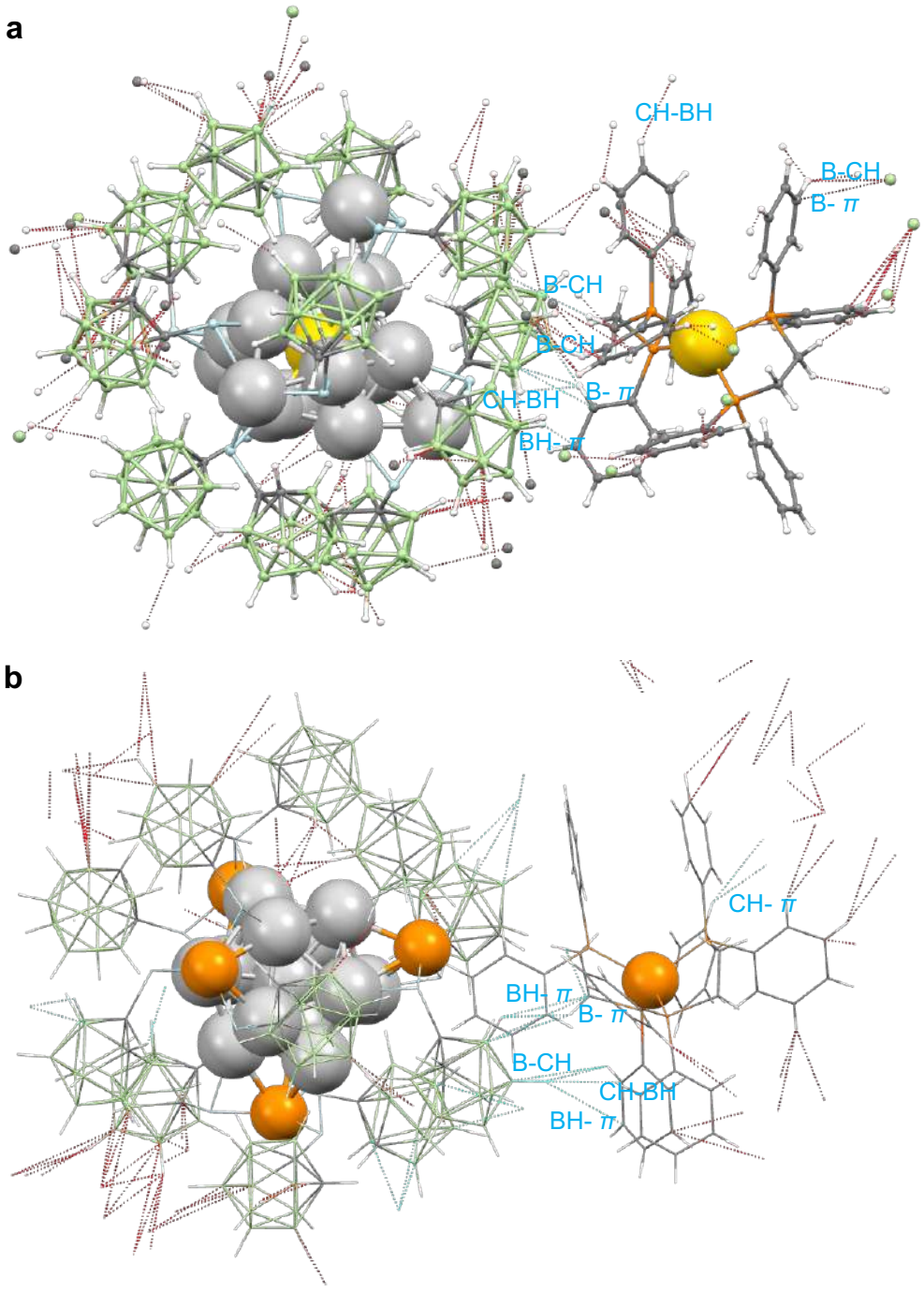
Supplementary Fig. 14 | Metal sulphur core of **a** Ag_{17}, **b** $AuAg_{16}$, **c** $Ag_{13}Cu_4$ and **d** $AuAg_{12}Cu_4$ shows the site-specific doping of Au and Cu in the desired NCs. **e,f** shows the inner icosahedral core and the capped tetrahedral units i.e. M_{13} having two different metal sites (Central M_1 and icosahedral M_{12}) and M_4 respectively. **g** shows the binding of S with the metal core. Table shows all the average bond distances associated with the NCs.



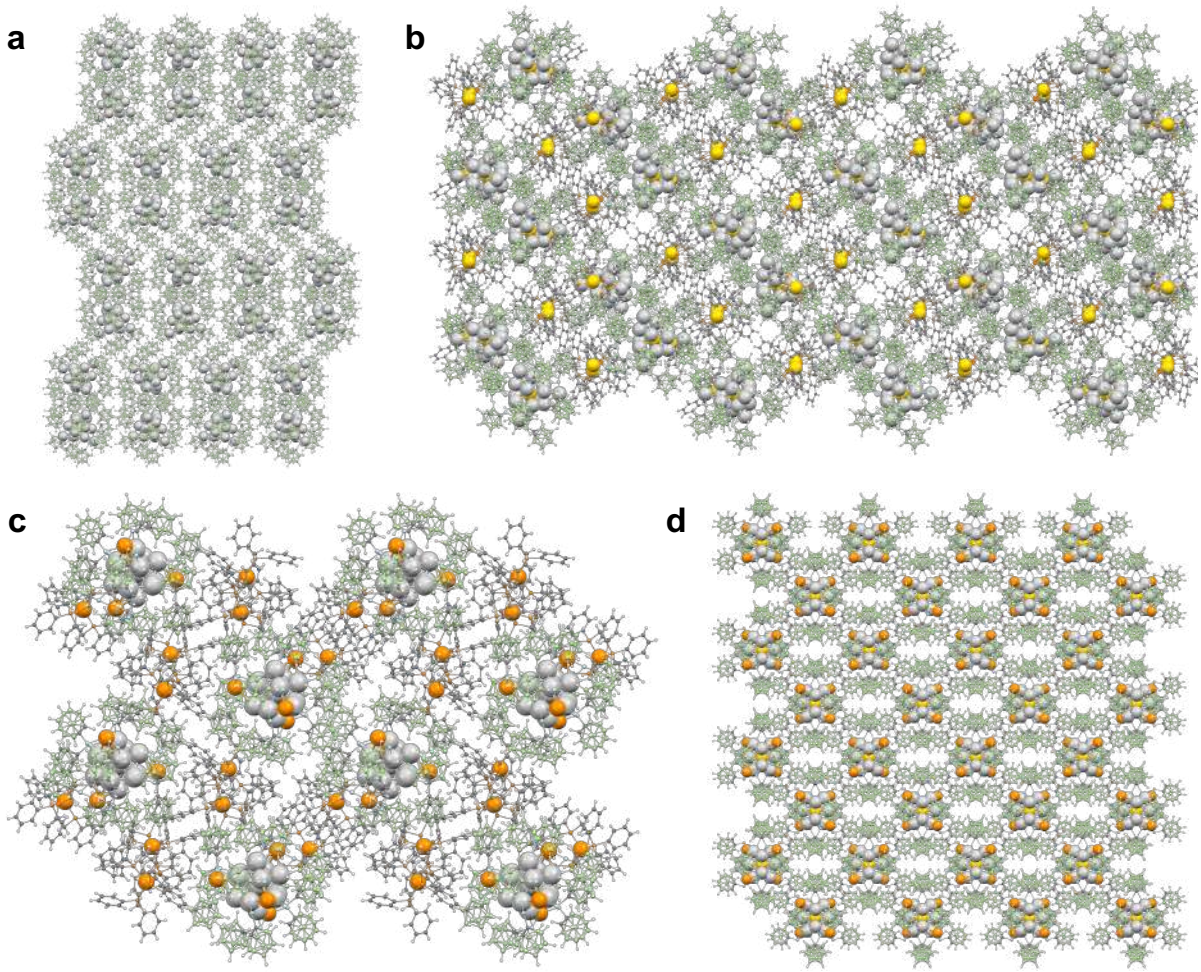
Supplementary Fig. 15 | Structural comparison of different doped systems of M_{20} and M_{21} with M_{17} systems showing site specificity of the M_{17} system. Structures **a,b** represent the similar icosahedra-centred structures of Ag_{17} and $[Ag_{20}\{Se_2P(O^iPr)_2\}_{12}]$. Structures **c,d** represent $AuAg_{16}$ and $[AuAg_{20}\{Se_2P(OEt)_2\}_{12}]^+$ clusters where the incorporation of Au is possible with the selenium based ligand, increasing the nuclearity to M_{21}. Structures **e,f** show $Ag_{13}Cu_4$ and $[Cu_{3.5}Ag_{16.5}\{S_2P(O^nPr)_2\}_{12}]$ clusters where the position of Cu is fixed at the four peripheral sites for $Ag_{13}Cu_4$ whereas it is randomly distributed at the capping positions for $[Cu_{3.5}Ag_{16.5}\{S_2P(O^nPr)_2\}_{12}]$. Structures **g,h** show the trimetallic $AuAg_{12}Cu_4$ and $[Cu_{2.5}AuAg_{16.5}\{S_2P(O^nPr)_2\}_{12}]$ clusters where the position of Cu is not definite for the M_{20} system.



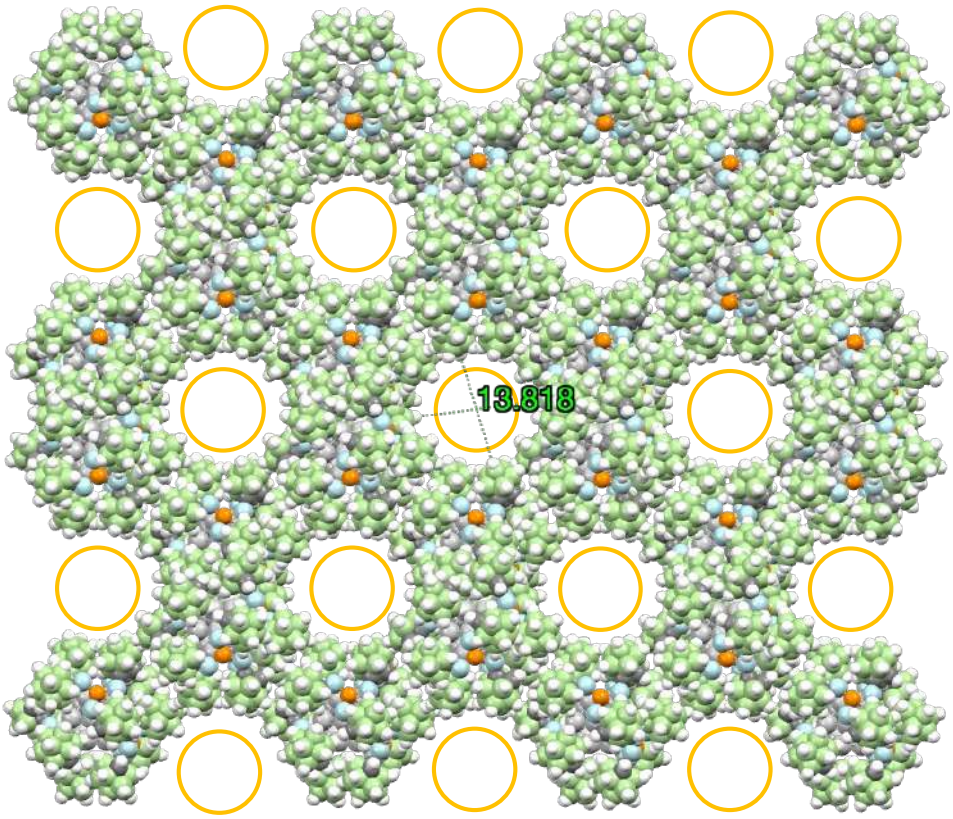
Supplementary Fig. 16 | Structure of **a** $AuAg_{16}$ and **b** $Ag_{13}Cu_4$ show $[Au(DPPE)_2]^+$ and $[Cu(DPPE)_2]^+$ units surrounding the $AuAg_{16}$ and $Ag_{13}Cu_4$ NC respectively; **c,d** show the distance of $[Au(DPPE)_2]^+$ and $[Cu(DPPE)_2]^+$ units from the centre of $AuAg_{16}$ and $Ag_{13}Cu_4$ respectively.



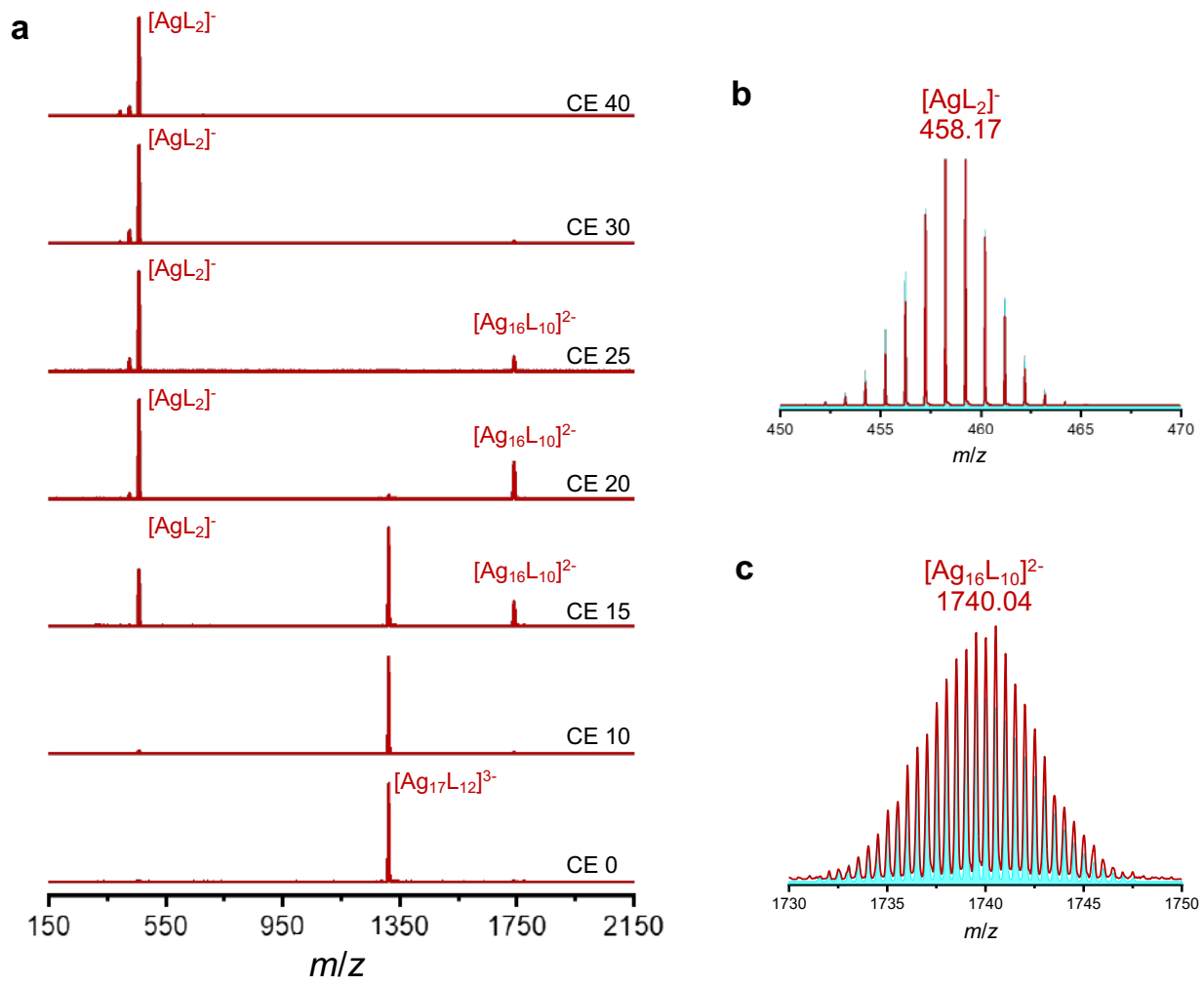
Supplementary Fig. 17 | Intermolecular interaction such as CH-π, BH- π, B-CH, BH-CH, CH-CH, B-π of **a** $AuAg_{16}$ with $[Au(DPPE)_2]^+$ and **b** $Ag_{13}Cu_4$ with $[Cu(DPPE)_2]^+$ units.



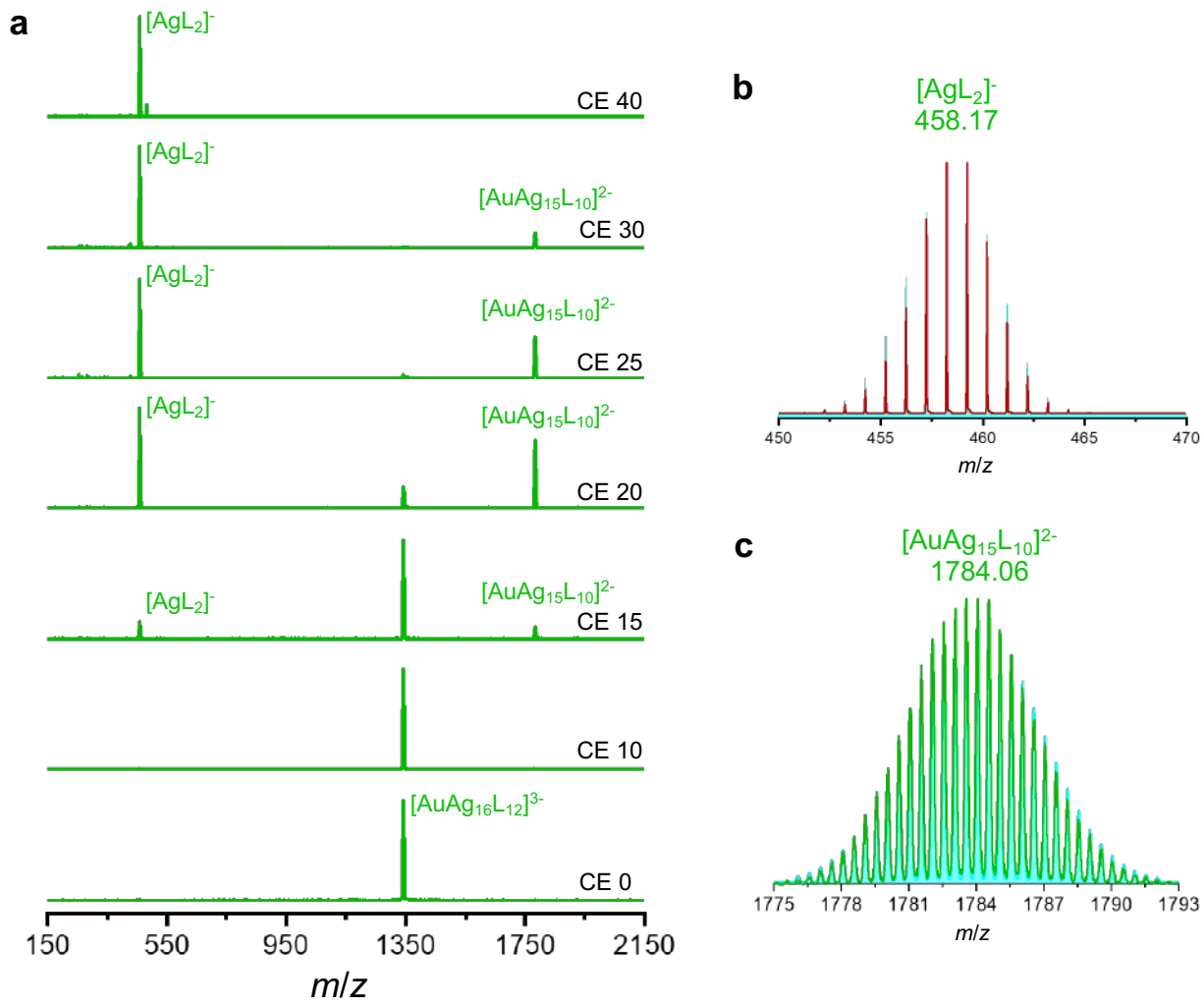
Supplementary Fig. 18 | Extended molecular packing of **a** Ag_{17}, **b** $AuAg_{16}$ along with $[Au(DPPE)_2]^+$ units, **c** $Ag_{13}Cu_4$ along with $[Cu(DPPE)_2]^+$ units and **d** $AuAg_{12}Cu_4$ NCs.



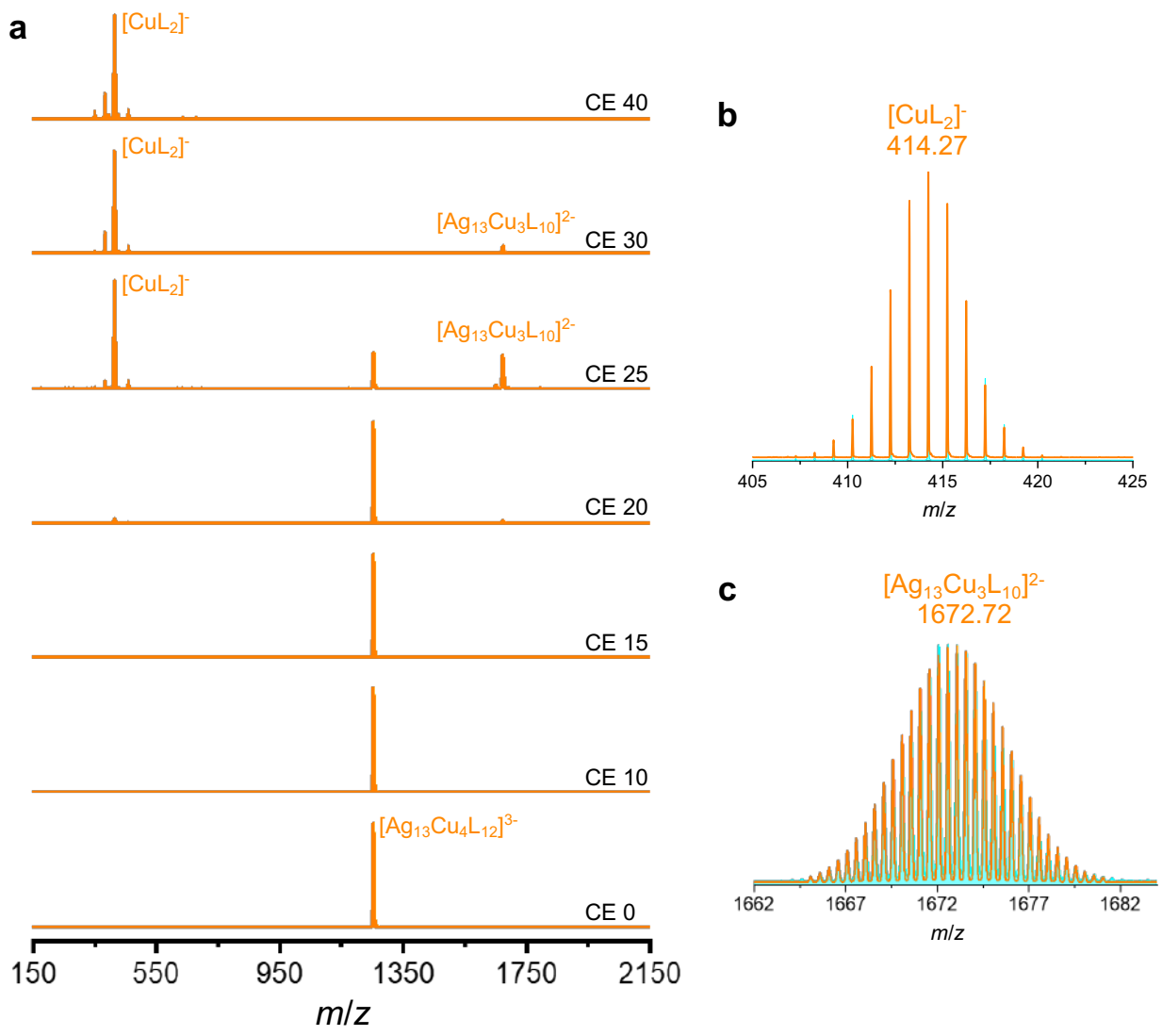
Supplementary Fig. 19 | The space-filled molecular packing of $AuAg_{12}Cu_4$, highlighting its (011) plane, reveals packing pores represented by saffron circles. However, due to the unresolved counter ions and the diffuse electron densities likely to be originating from solvent molecules (which were squeezed out during analysis), the void size (13.818 Å) and porosity of the region marked by saffron circles remain undefined.



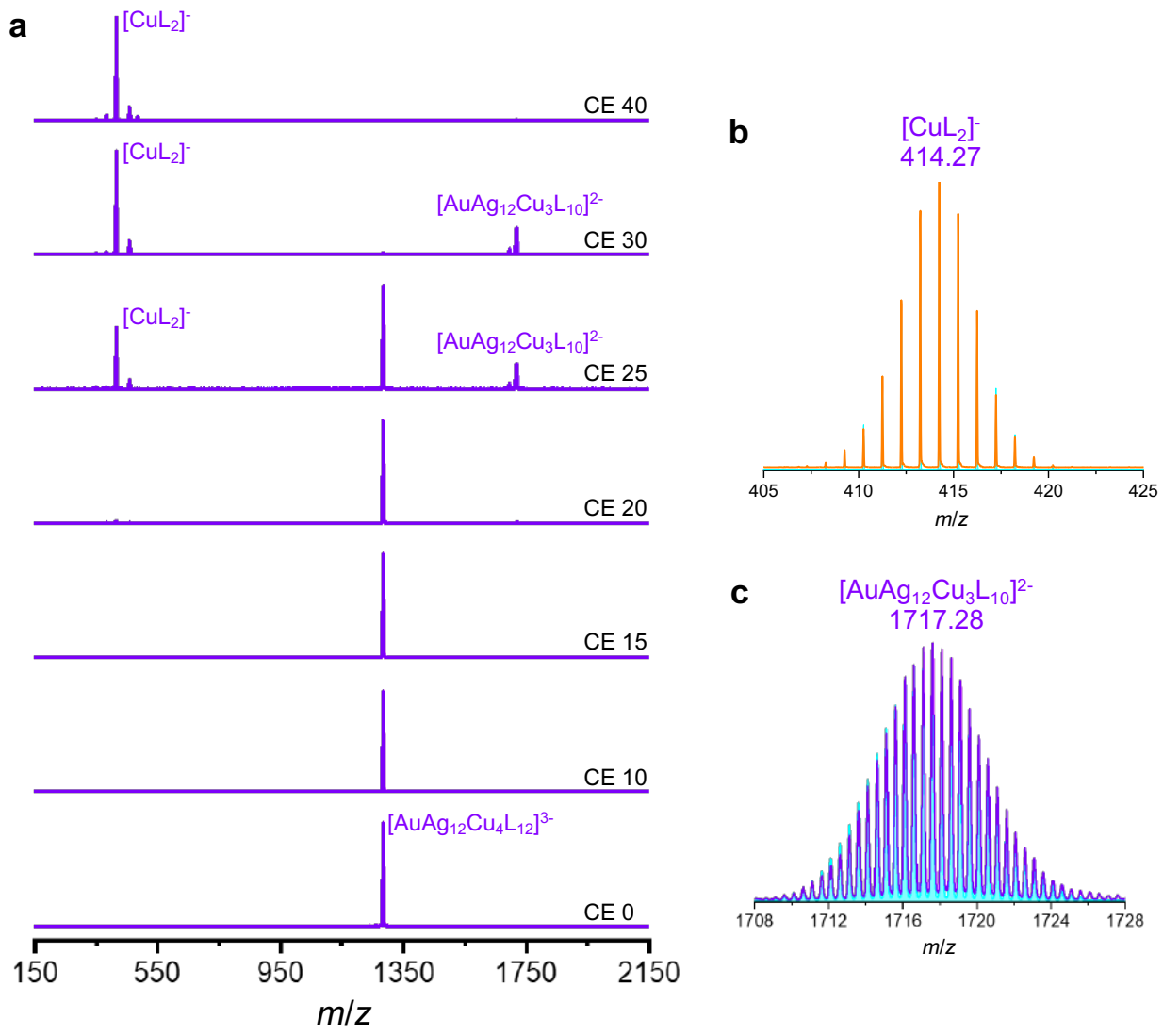
Supplementary Fig. 20 | a Collision energy dependent MS/MS fragmentation spectra of Ag_{17} (L: o_1-CBT). Fragmentation studies were performed upon selecting the molecular ion peak at 1312.42, having a charge state of 3-. **b,c** Comparative isotopic distribution of the experimental and simulated (Cyan) peaks for **b** $[AgL_2]^-$ and **c** $[Ag_{16}L_{10}]^{2-}$ fragments.



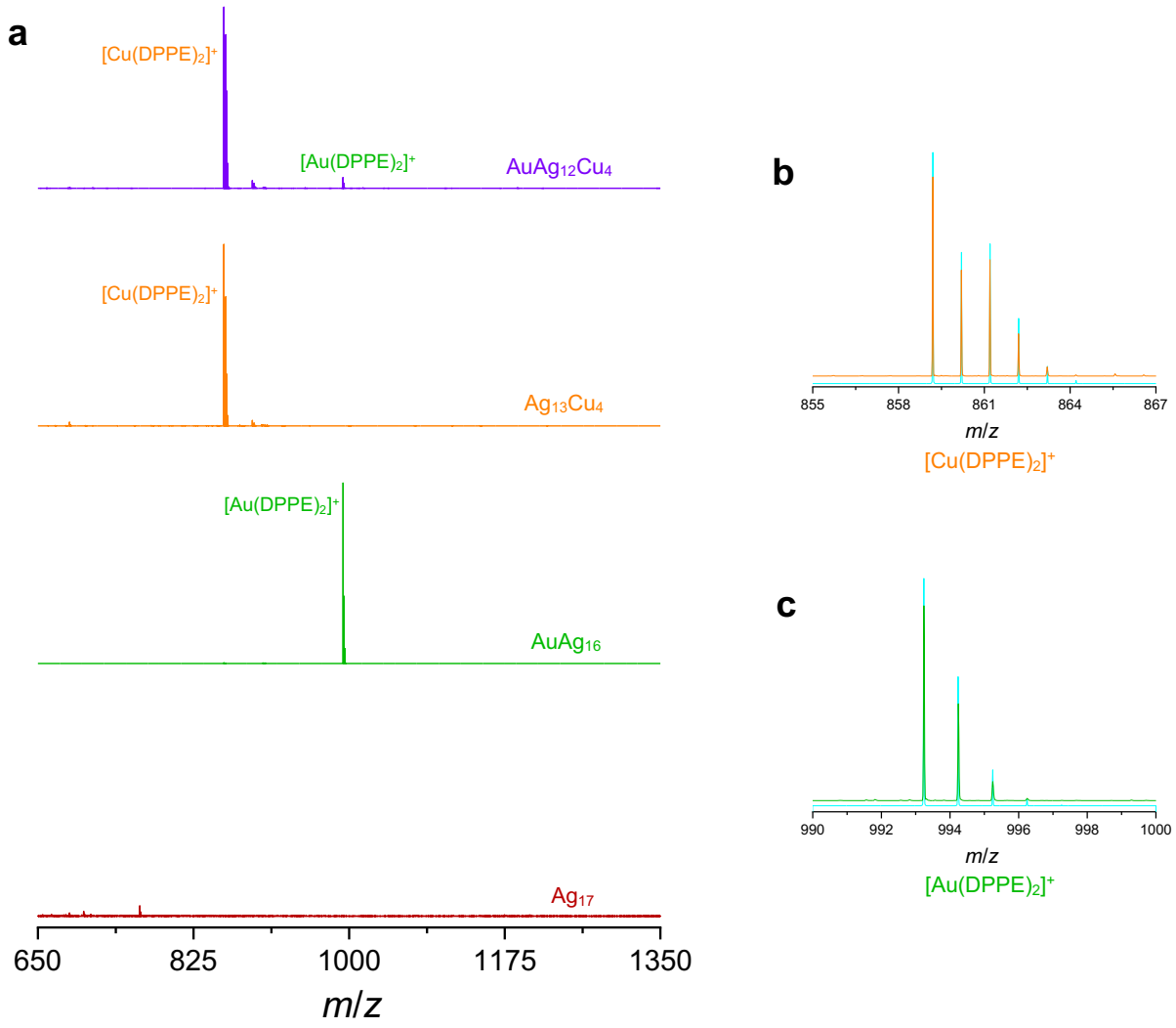
Supplementary Fig. 21 | a Collision energy dependent MS/MS fragmentation spectra of $AuAg_{16}$ (L: o_1-CBT). Fragmentation studies were performed upon selecting the molecular ion peak at 1342.11, having a charge state of 3-. **b,c** Comparative isotopic distribution of the experimental and simulated (Cyan) peaks for **b** $[AgL_2]^-$ and **c** $[AuAg_{15}L_{10}]^{2-}$ fragments.



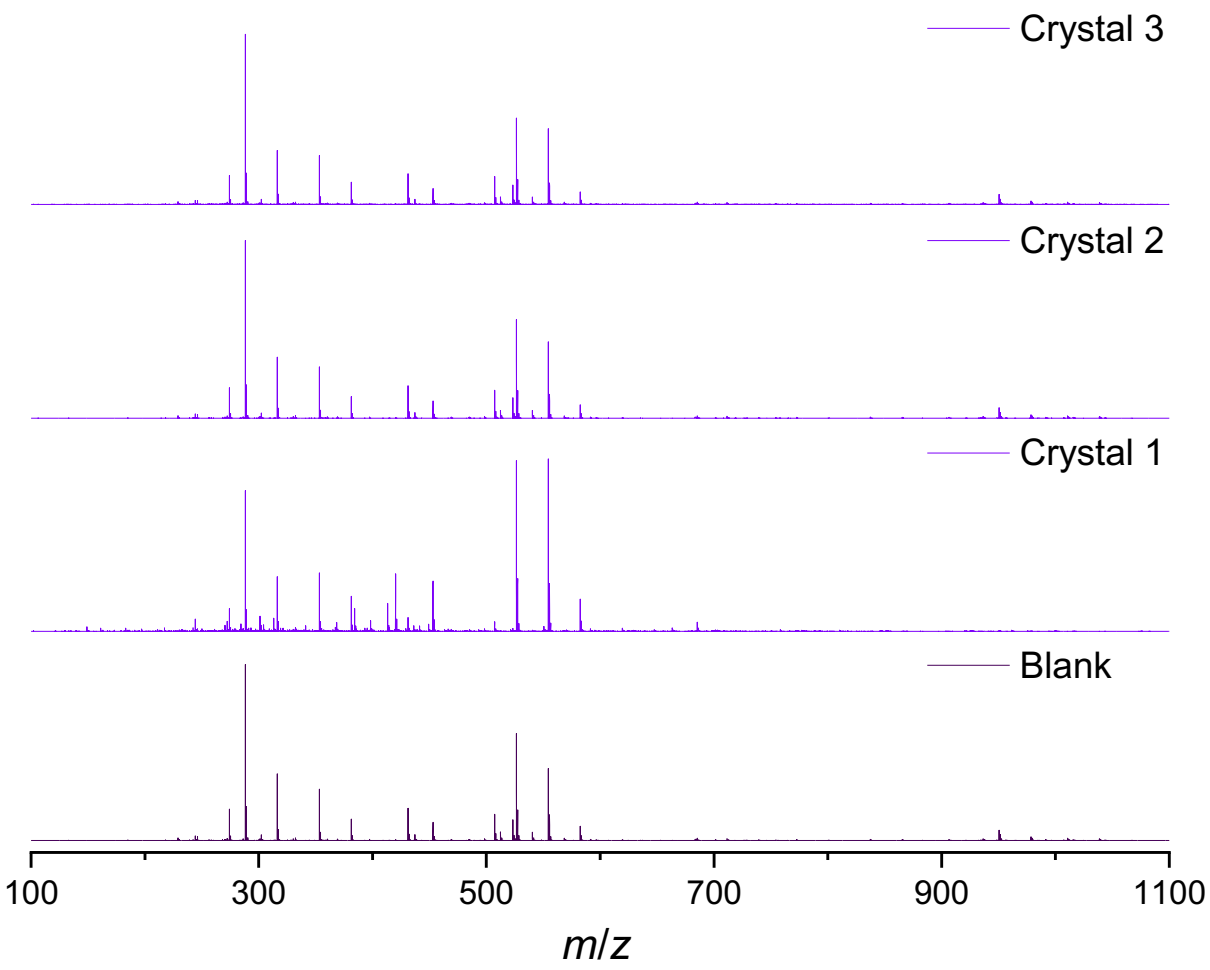
Supplementary Fig. 22 | a Collision energy dependent MS/MS fragmentation spectra of $Ag_{13}Cu_4$ (L: o_1-CBT). Fragmentation studies were performed upon selecting the molecular ion peak at 1253.46, having a charge state of 3-. **b,c** Comparative isotopic distribution of the experimental and simulated (Cyan) peaks for **b** $[CuL_2]^-$ and **c** $[Ag_{13}Cu_3L_{10}]^{2-}$ fragments.



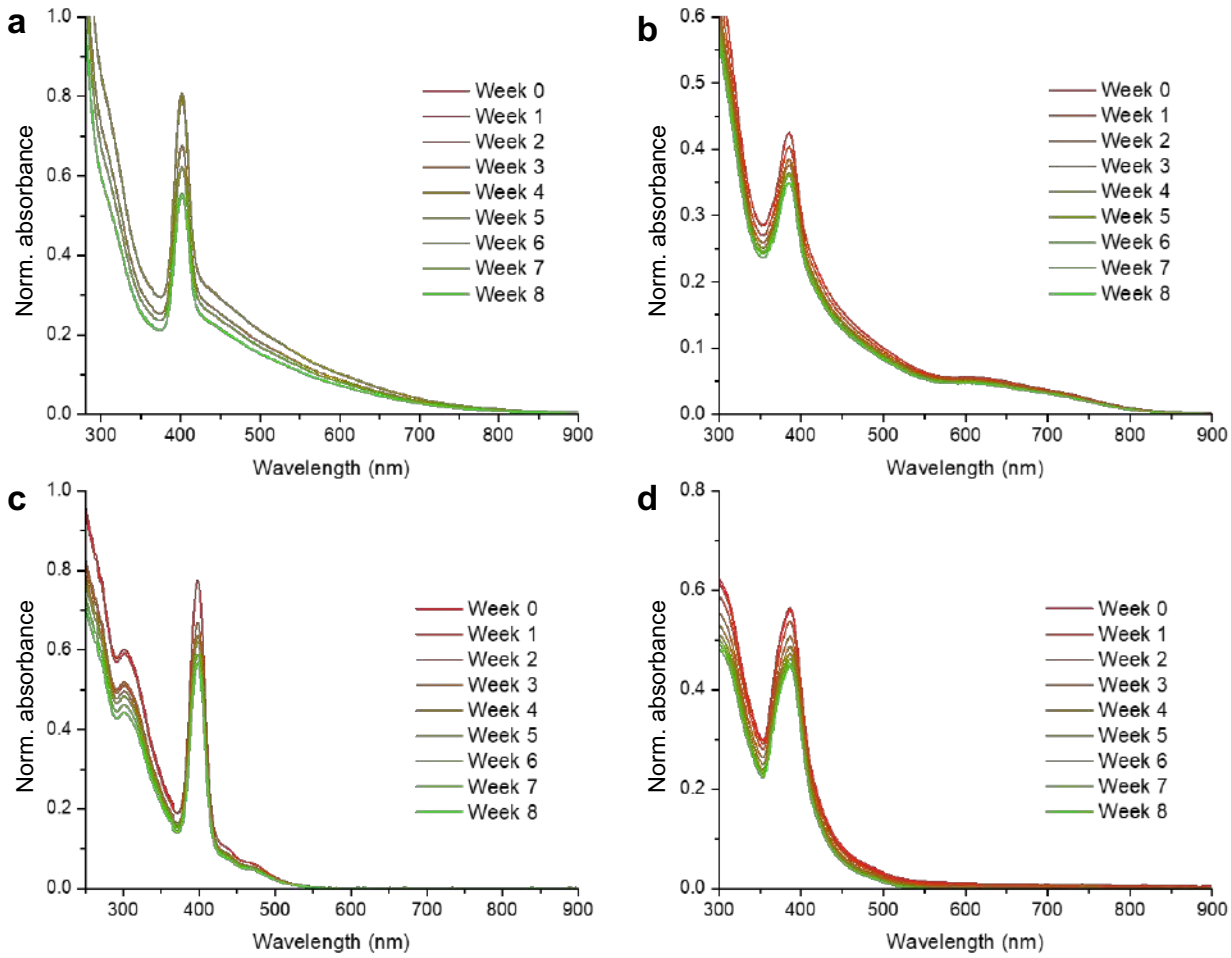
Supplementary Fig. 23 | a Collision energy dependent MS/MS fragmentation spectra of $AuAg_{12}Cu_4$ (L: *o*$_1$-CBT). Fragmentation studies were performed upon selecting the molecular ion peak at 1283.15, having a charge state of 3-. **b,c** Comparative isotopic distribution of the experimental and simulated (Cyan) peaks for **b** $[CuL_2]^-$ and **c** $[AuAg_{12}Cu_3L_{10}]^{2-}$ fragments.



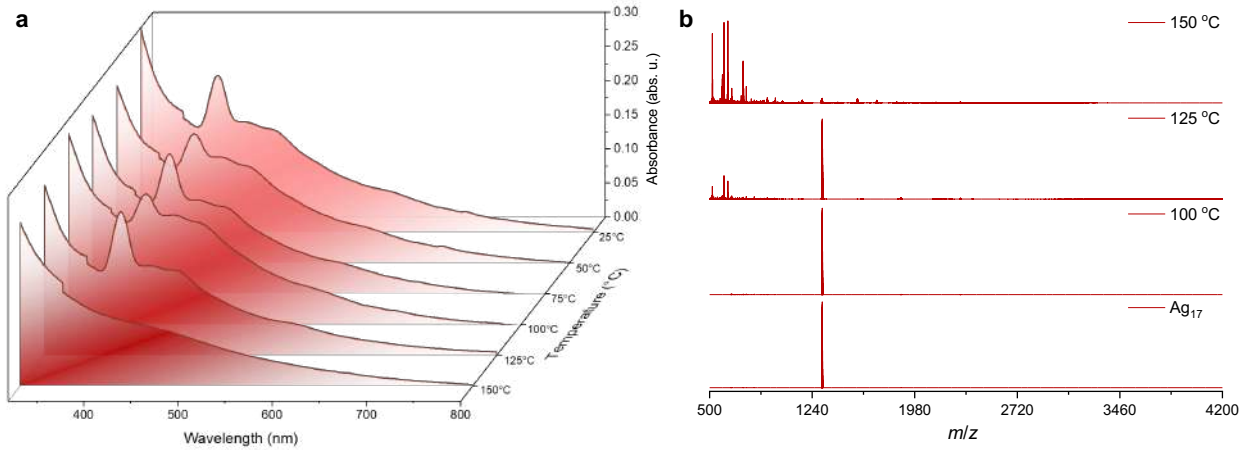
Supplementary Fig. 24 | a Positive ion mode ESI-MS spectrum of the as synthesized crude of Ag_{17}, $AuAg_{16}$, $Ag_{13}Cu_4$ and $AuAg_{12}Cu_4$. Ag_{17}, didn't show the any peaks with DPPE whereas $AuAg_{16}$, showed $[Au(DPPE)_2]^+$ peak, $Ag_{13}Cu_4$ showed $[Cu(DPPE)_2]^+$ peak and $AuAg_{12}Cu_4$ showed both $[Au(DPPE)_2]^+$ and $[Cu(DPPE)_2]^+$ peaks in the crude sample. **b,c** Comparative isotopic distribution of the experimental and simulated (Cyan) peaks for **b** $[Cu(DPPE)_2]^+$ and **c** $[Au(DPPE)_2]^+$ peaks.



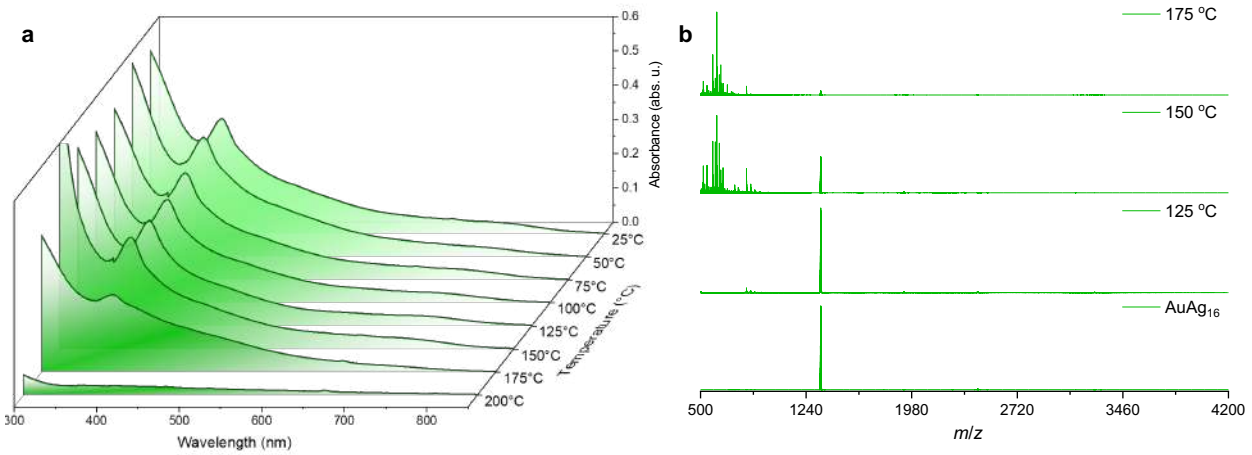
Supplementary Fig. 25 | Positive ion mode ESI-MS spectrum of different crystals of $AuAg_{12}Cu_4$. ESI-MS of the crystals of $AuAg_{12}Cu_4$ did not show any peaks corresponding to $[Au(DPPE)_2]^+$ and $[Cu(DPPE)_2]^+$ expected at *m*/*z* 993.24 and 859.20, respectively.



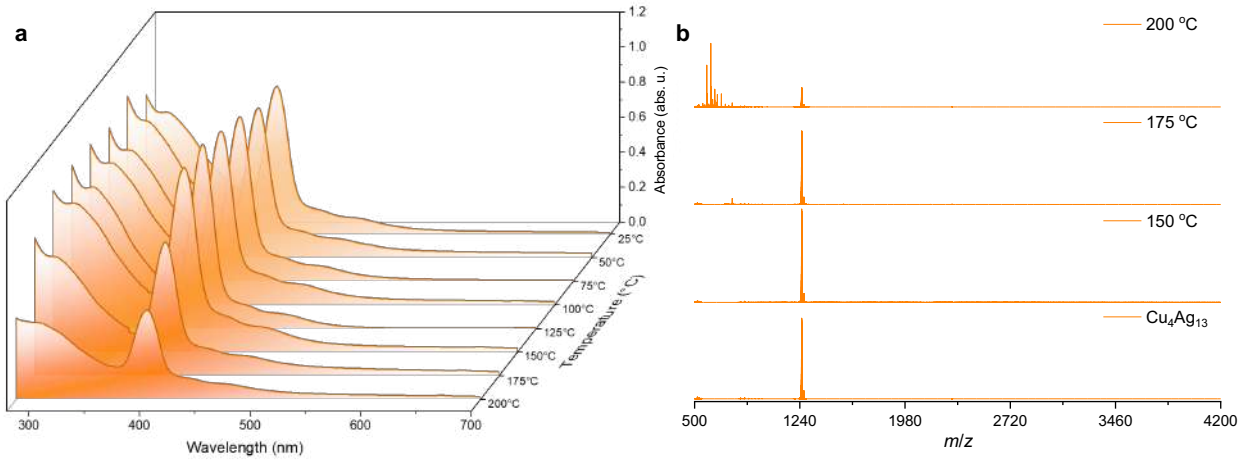
Supplementary Fig. 26 | Time dependent stability UV-Vis absorption spectra of **a** Ag_{17}, **b** $AuAg_{16}$, **c** $Ag_{13}Cu_4$ and **d** $AuAg_{12}Cu_4$ in DCM solution. During this study, clusters are saved in a closed Eppendorf vial in dark condition at 4 °C.



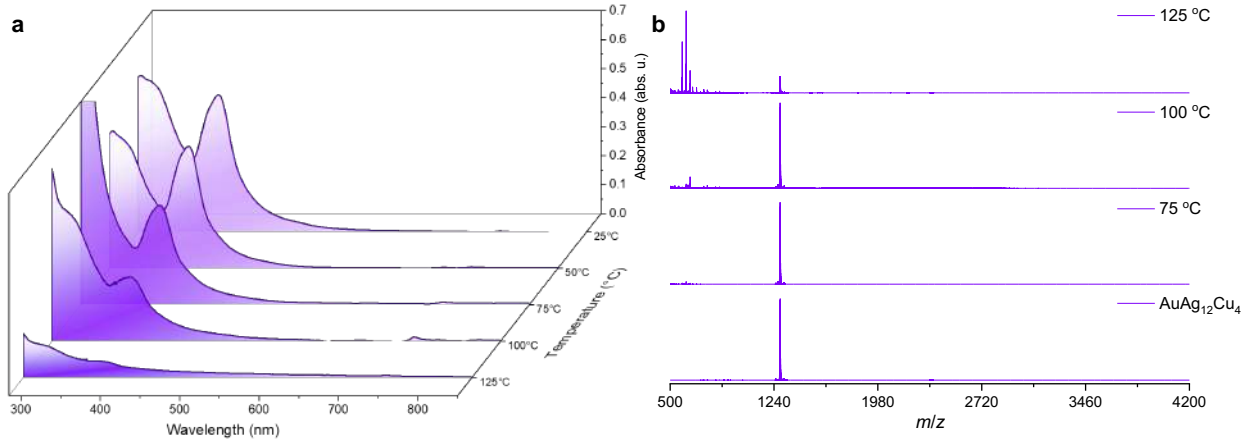
Supplementary Fig. 27 | Thermal Stability of Ag_{17} NC at different temperatures. Comparative **a** UV-Vis absorption spectra and **b** ESI-MS data of Ag_{17} after heating the cluster at different temperatures. After 90 min of heating, the powder sample was dissolved in DCM for UV-Vis and ESI-MS measurements.



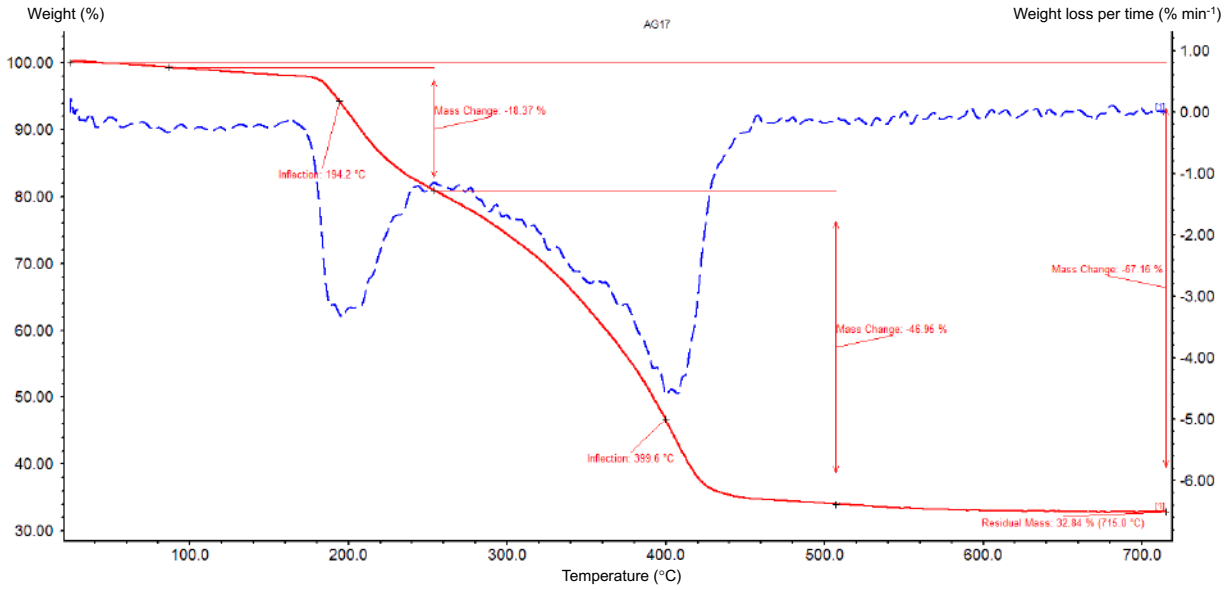
Supplementary Fig. 28 | Thermal Stability of $AuAg_{16}$ NC at different temperatures. Comparative **a** UV-Vis absorption spectra and **b** ESI-MS data of $AuAg_{16}$ after heating the cluster at different temperatures. After 90 min of heating, the powder sample was dissolved in DCM for UV-Vis and ESI-MS measurements.



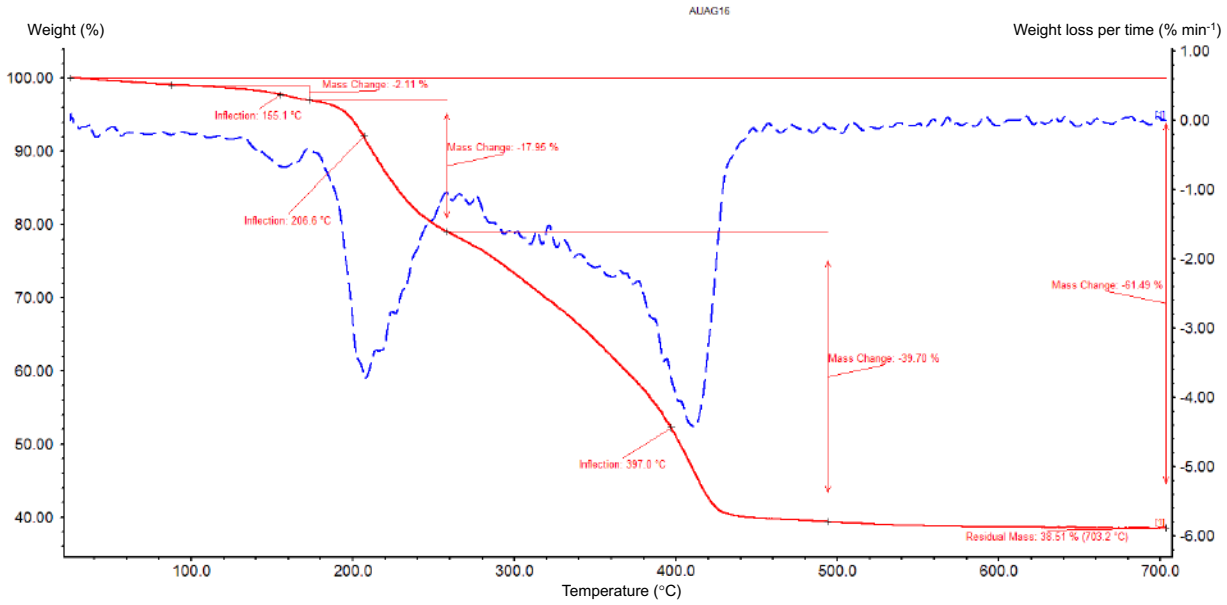
Supplementary Fig. 29 | Thermal Stability of $Ag_{13}Cu_4$ NC at different temperatures. Comparative **a** UV-Vis absorption spectra and **b** ESI-MS data of $Ag_{13}Cu_4$ after heating the cluster at different temperatures. After 90 min of heating, after 90 min of heating, the powder sample was dissolved in DCM for UV-Vis and ESI-MS measurements.



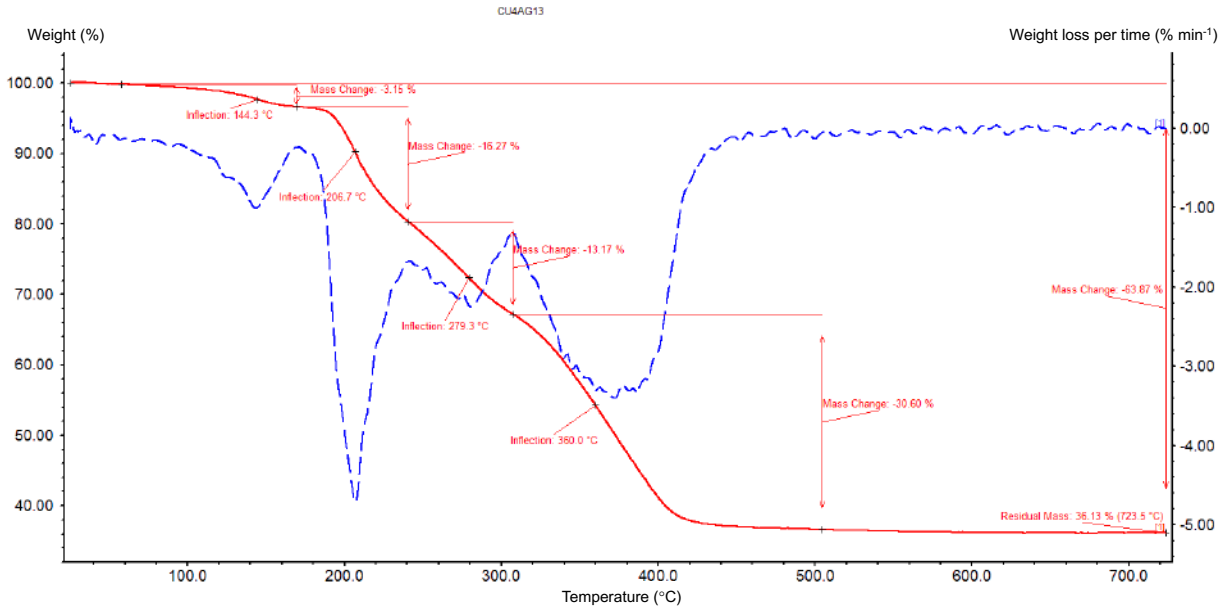
Supplementary Fig. 30 | Thermal Stability of $AuAg_{12}Cu_4$ NC at different temperatures. Comparative **a** UV-Vis absorption spectra and **b** ESI-MS data of $AuAg_{12}Cu_4$ after heating the cluster at different temperatures. After 90 min of heating, the powder sample was dissolved in DCM for UV-Vis and ESI-MS measurements.



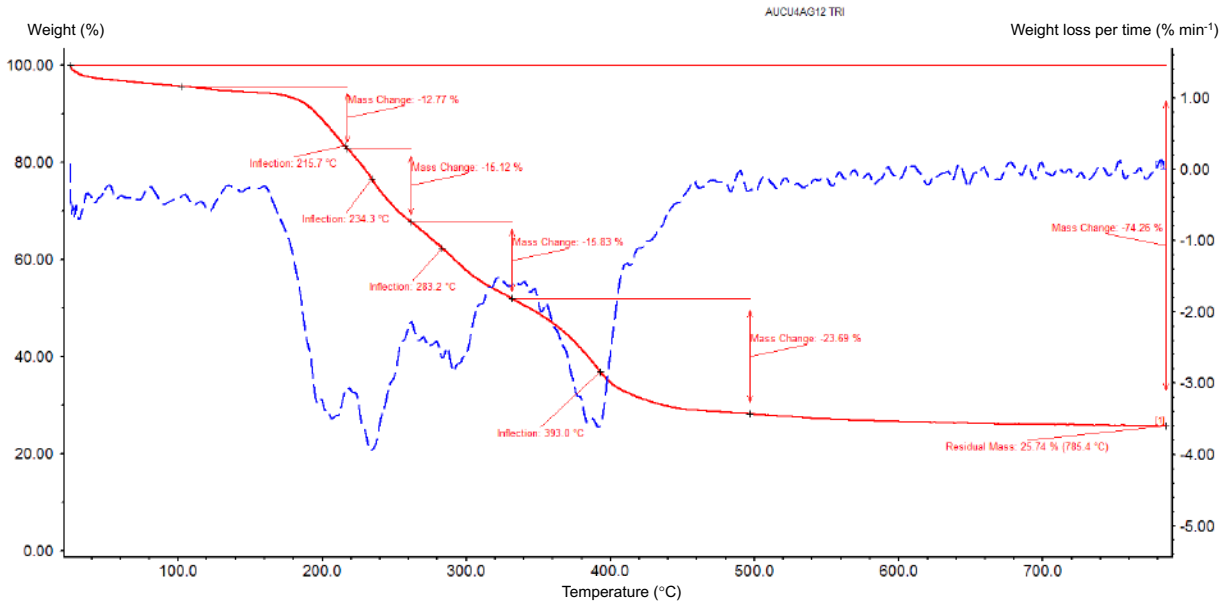
Supplementary Fig. 31 | TG and DTG plots of microcrystalline Ag_{17} solids.



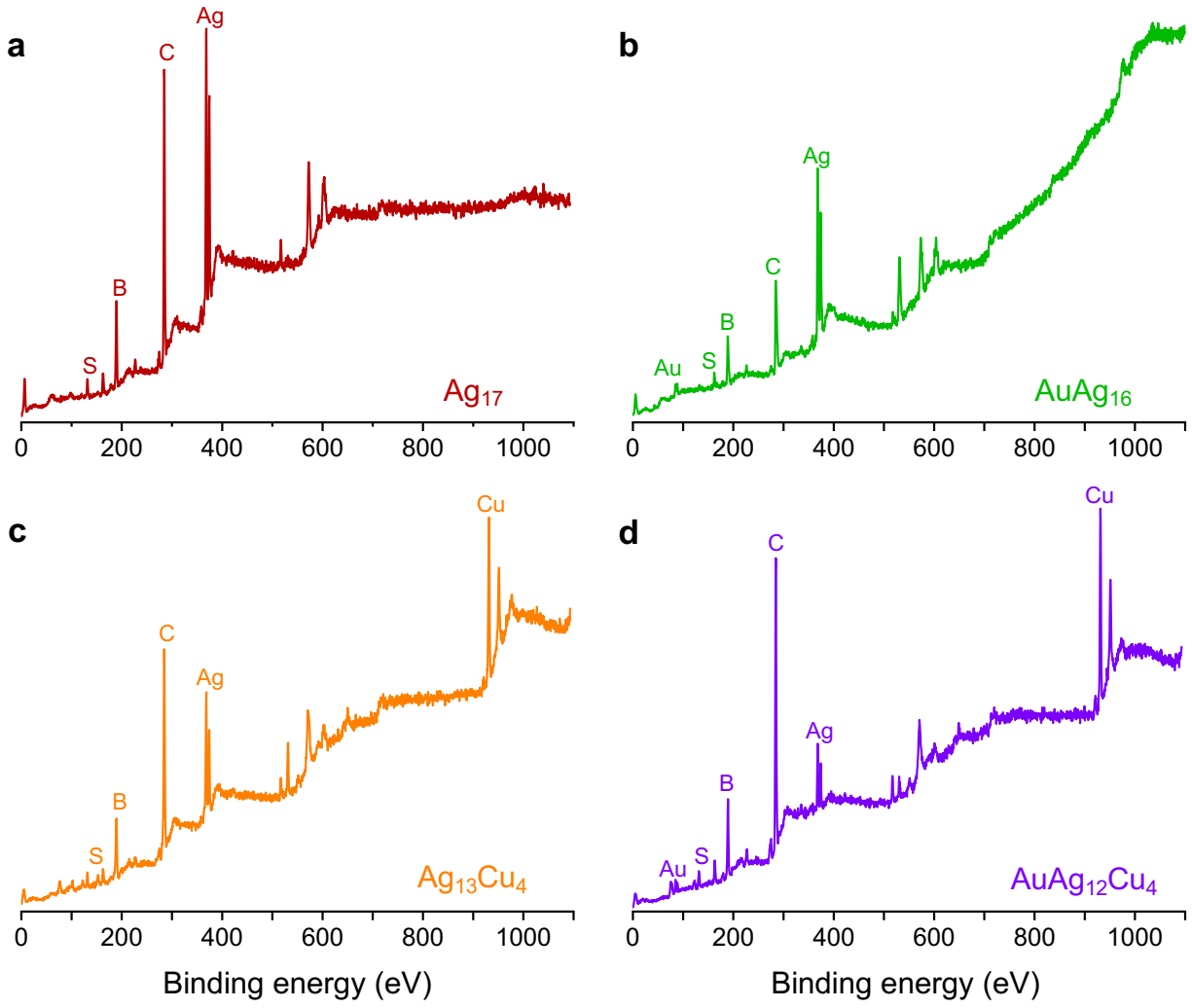
Supplementary Fig. 32 | TG and DTG plots of microcrystalline $AuAg_{16}$ solids.



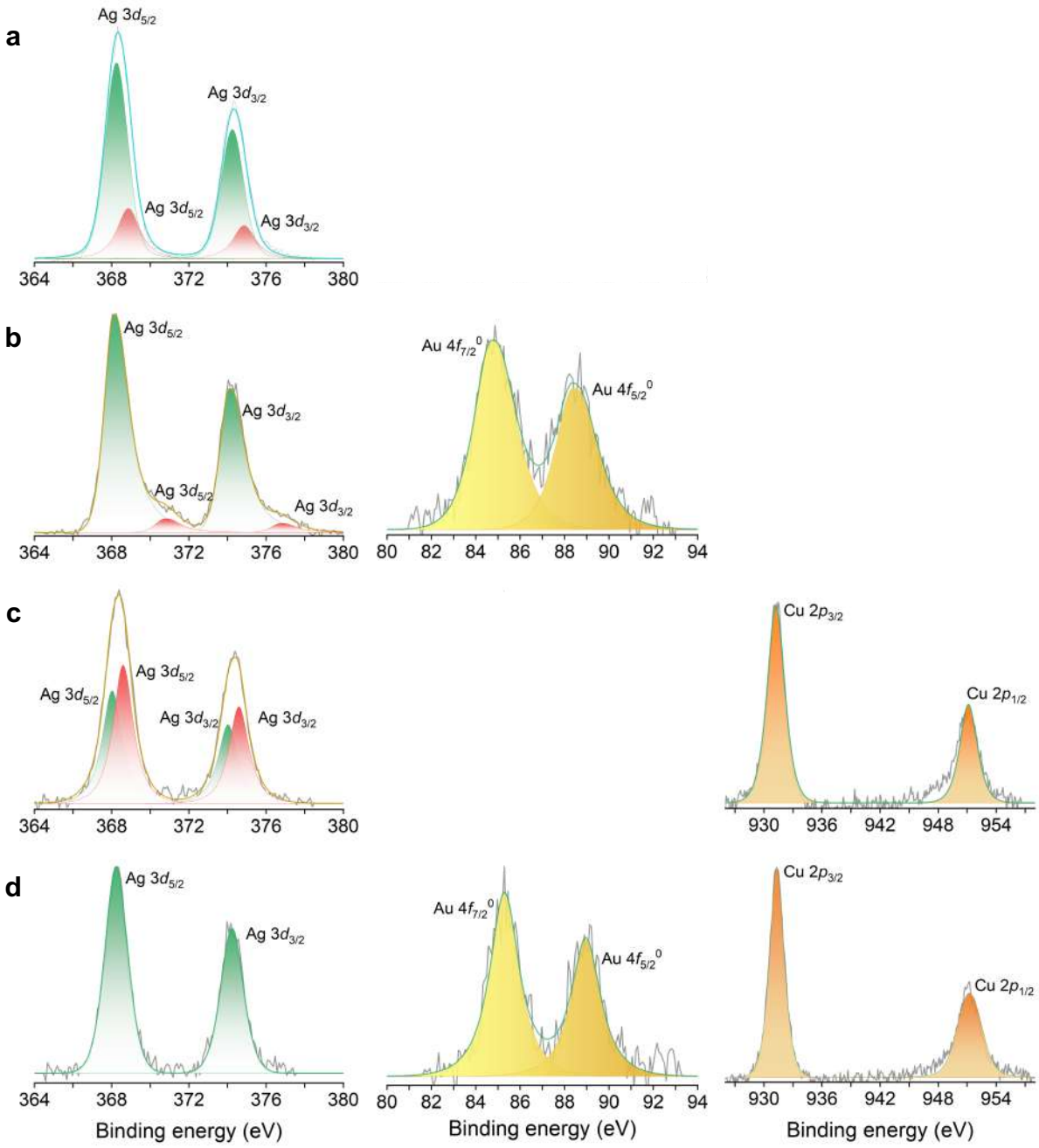
Supplementary Fig. 33 | TG and DTG plots of microcrystalline $Ag_{13}Cu_4$ solids.



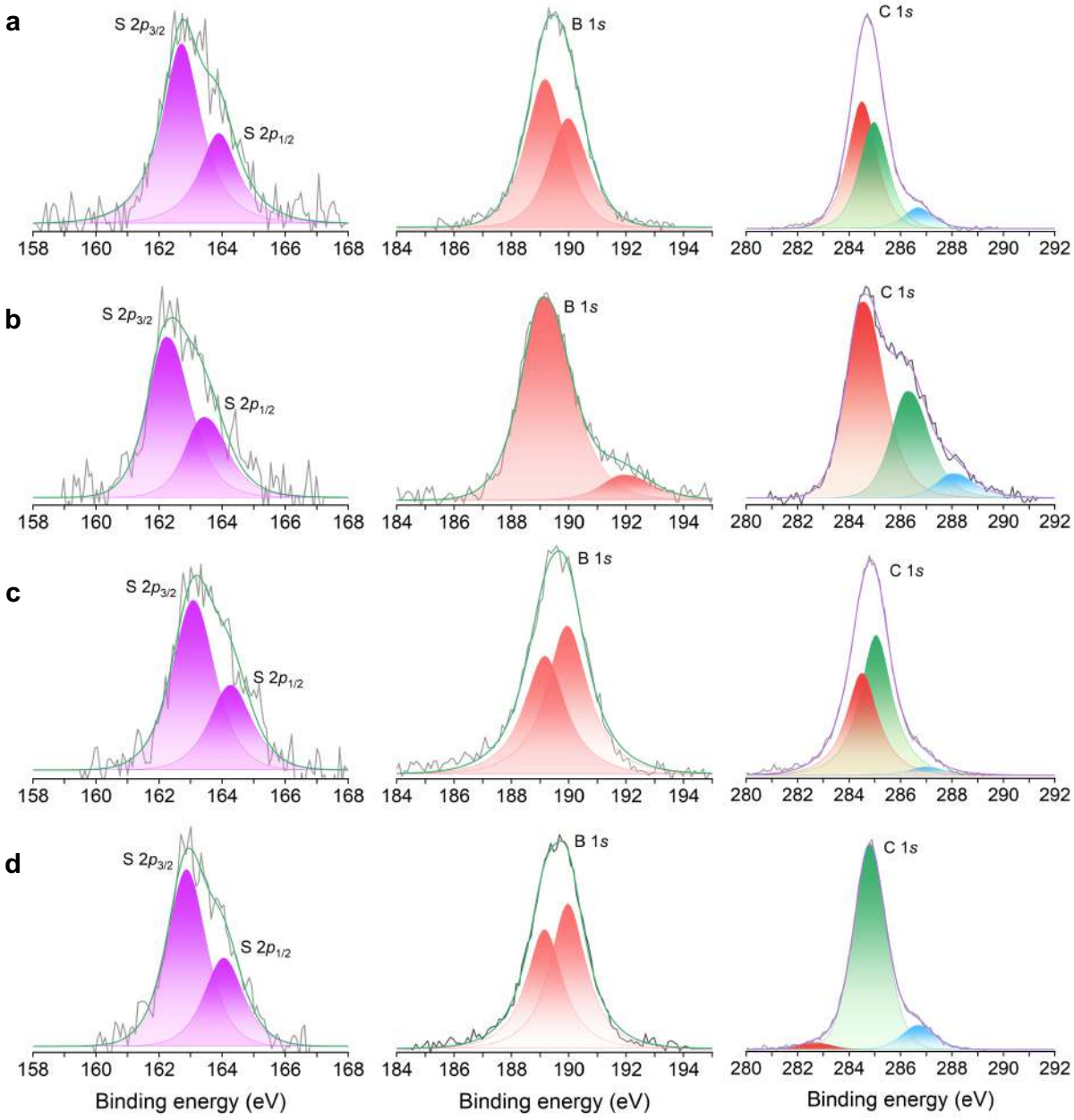
Supplementary Fig. 34 | TG and DTG plots of microcrystalline $AuAg_{12}Cu_4$ solids.



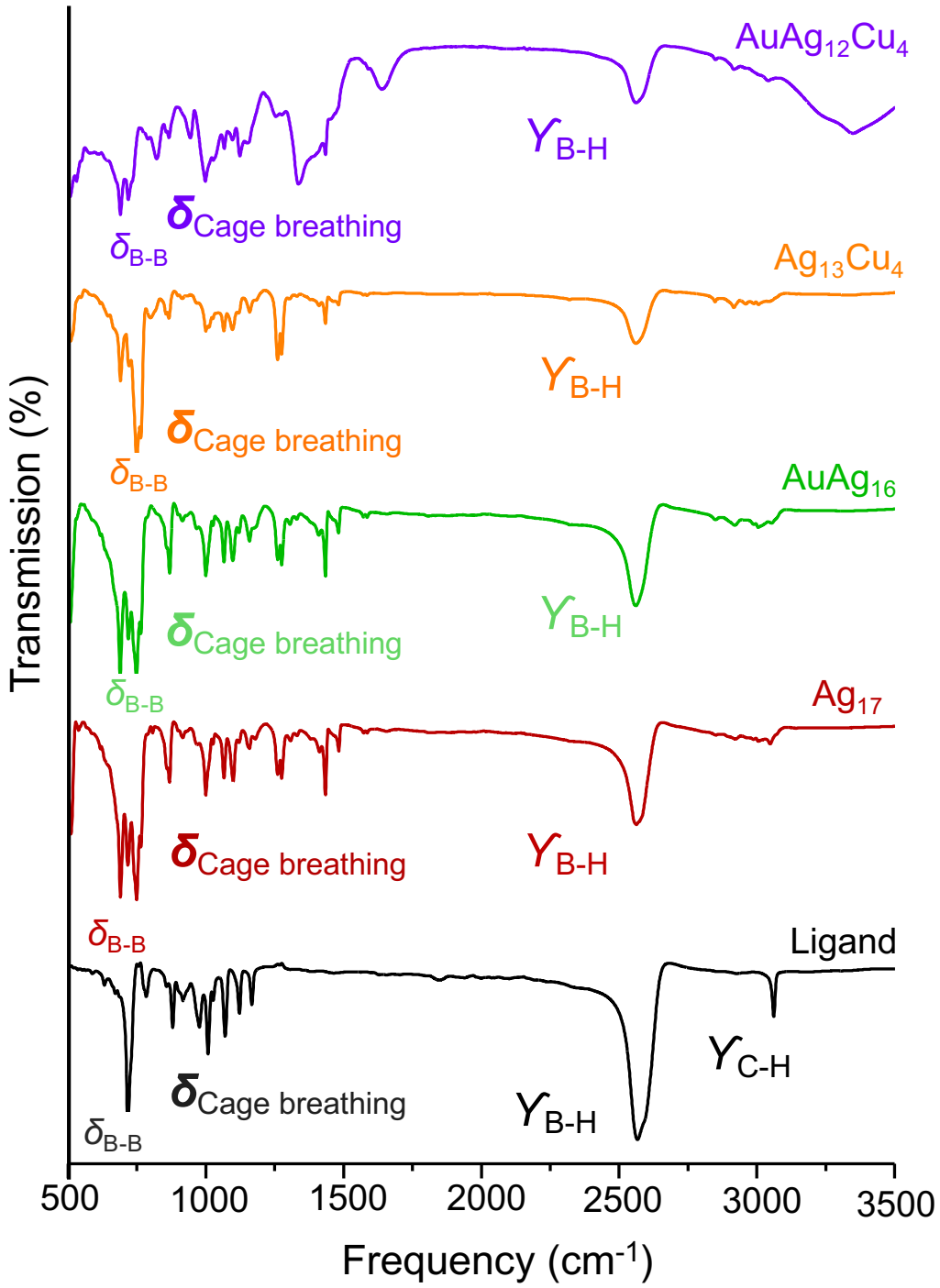
Supplementary Fig. 35 | XPS survey scan of **a** Ag_{17}, **b** $AuAg_{16}$, **c** $Ag_{13}Cu_4$ and **d** $AuAg_{12}Cu_4$. Binding energy of the respective elements are marked here.



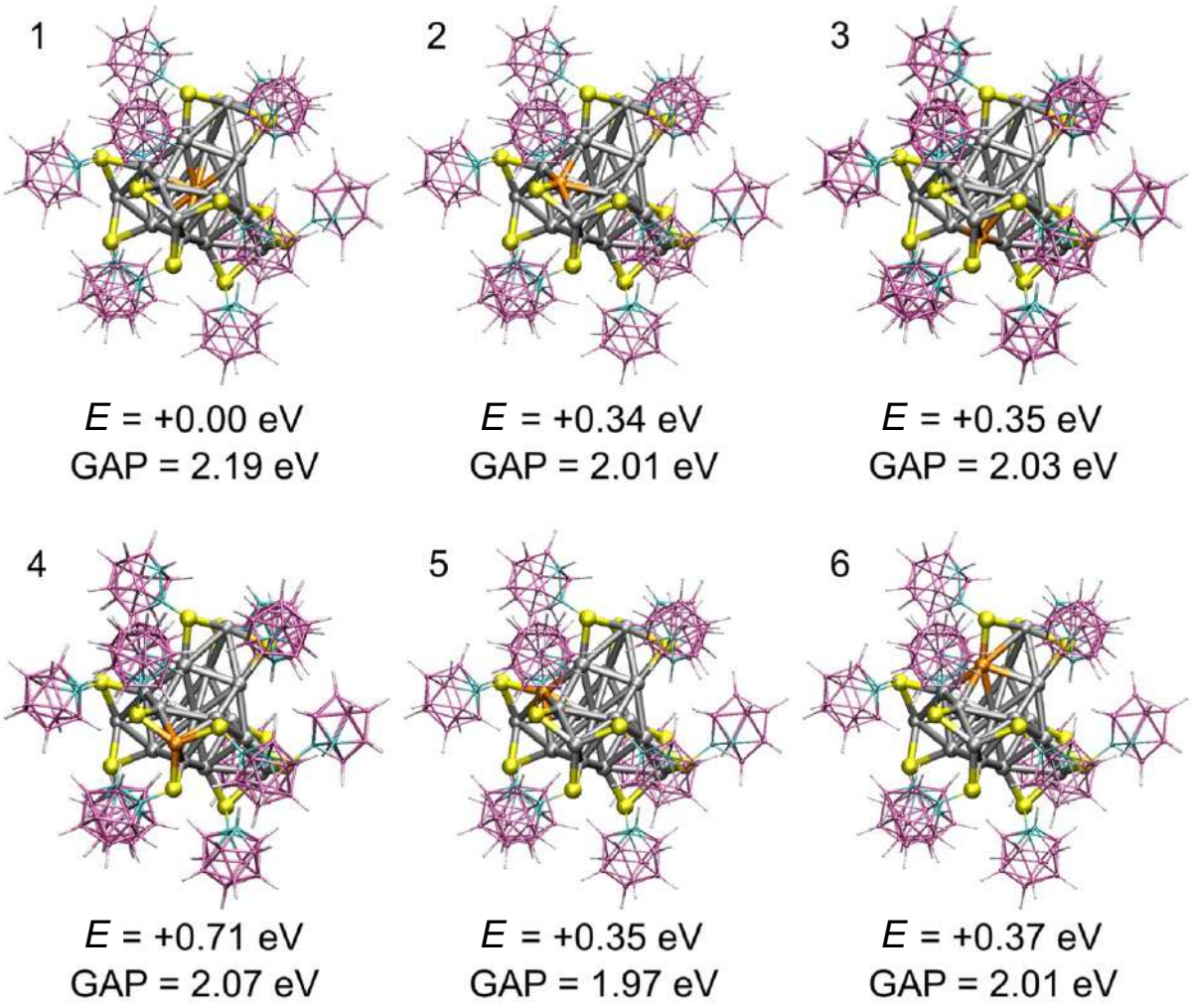
Supplementary Fig. 36 | Selected scan with respective peak fittings of **a** Ag_{17}, **b** $AuAg_{16}$, **c** $Ag_{13}Cu_4$ and **d** $AuAg_{12}Cu_4$.



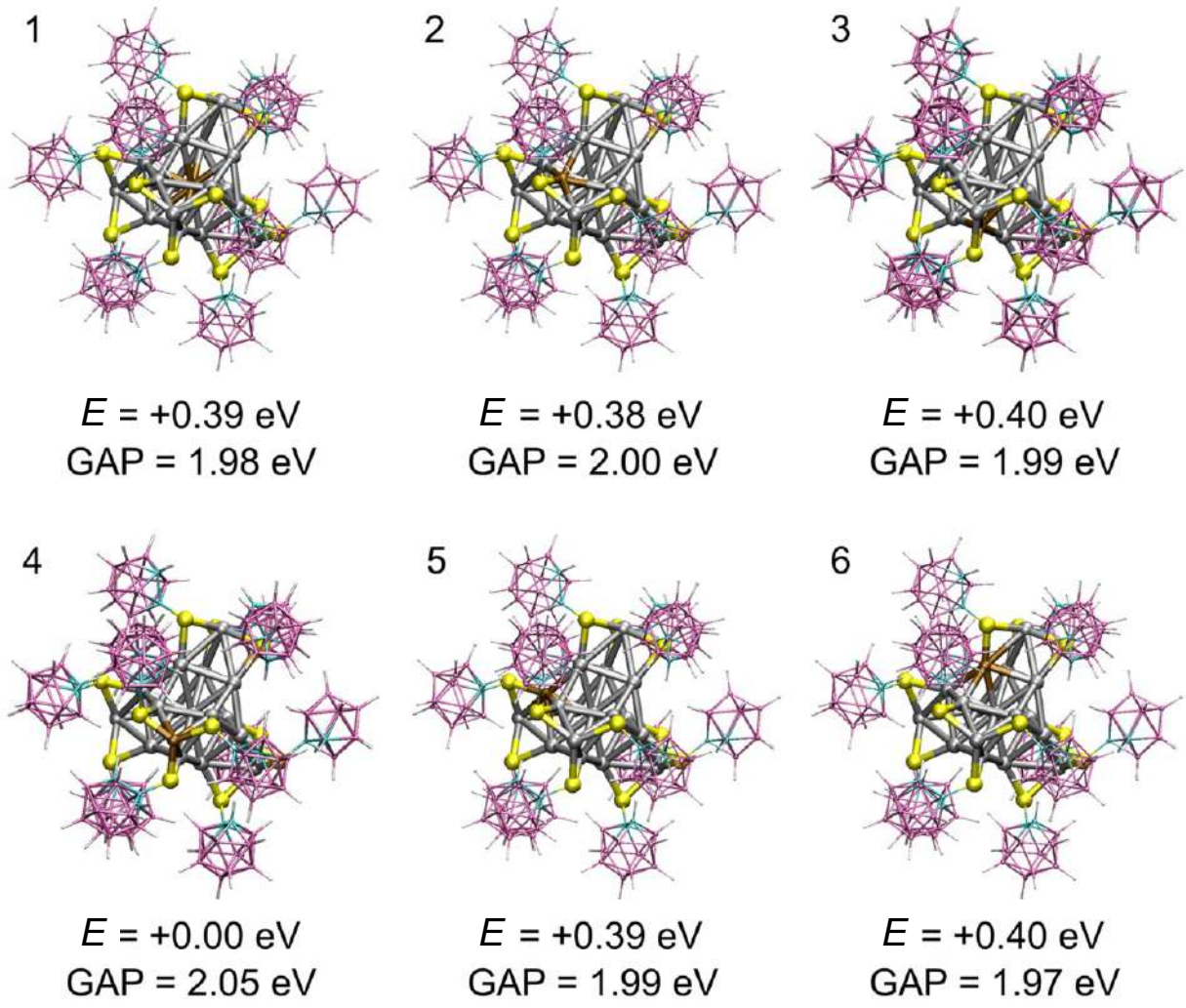
Supplementary Fig. 37 | Selected scan with respective peaks i.e., S 2*p*, B 1*s* and C 1*s* of **a** Ag_{17}, **b** $AuAg_{16}$, **c** $Ag_{13}Cu_4$ and **d** $AuAg_{12}Cu_4$.



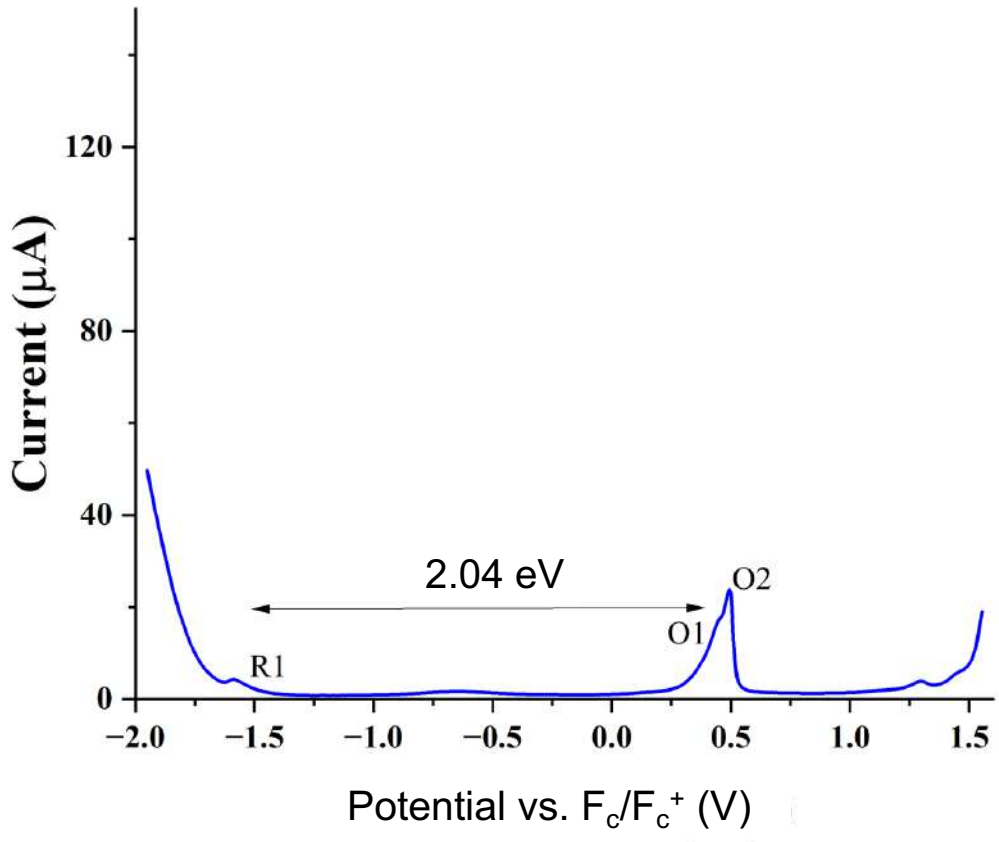
Supplementary Fig. 38 | Combined FT-IR spectra of the *o*1-CBT ligand, Ag_{17}, $AuAg_{16}$, $Ag_{13}Cu_4$ and $AuAg_{12}Cu_4$.



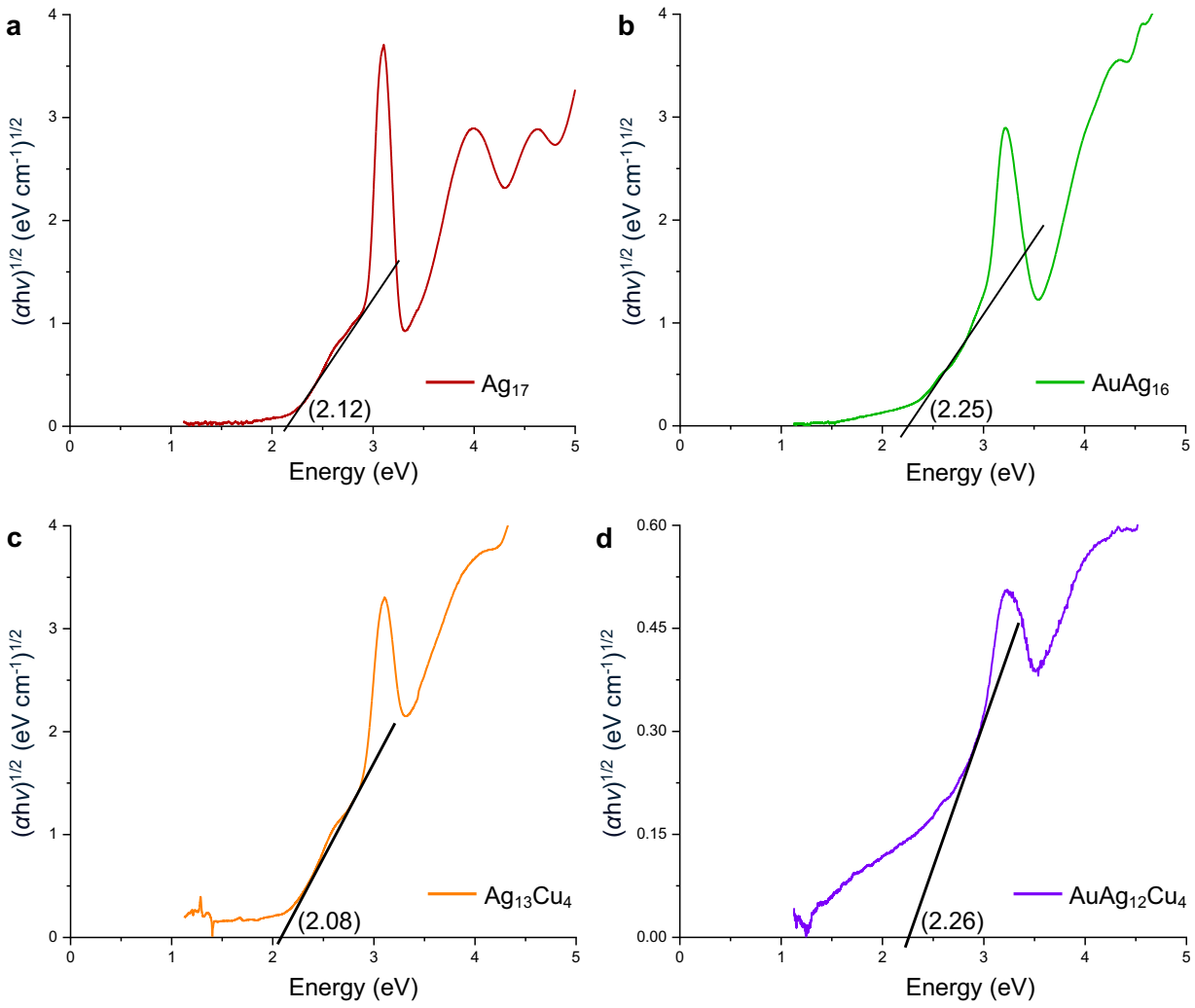
Supplementary Fig. 39 | Optimized structures and relative energies of cluster when Au is added in all symmetrically different metal atom positions.



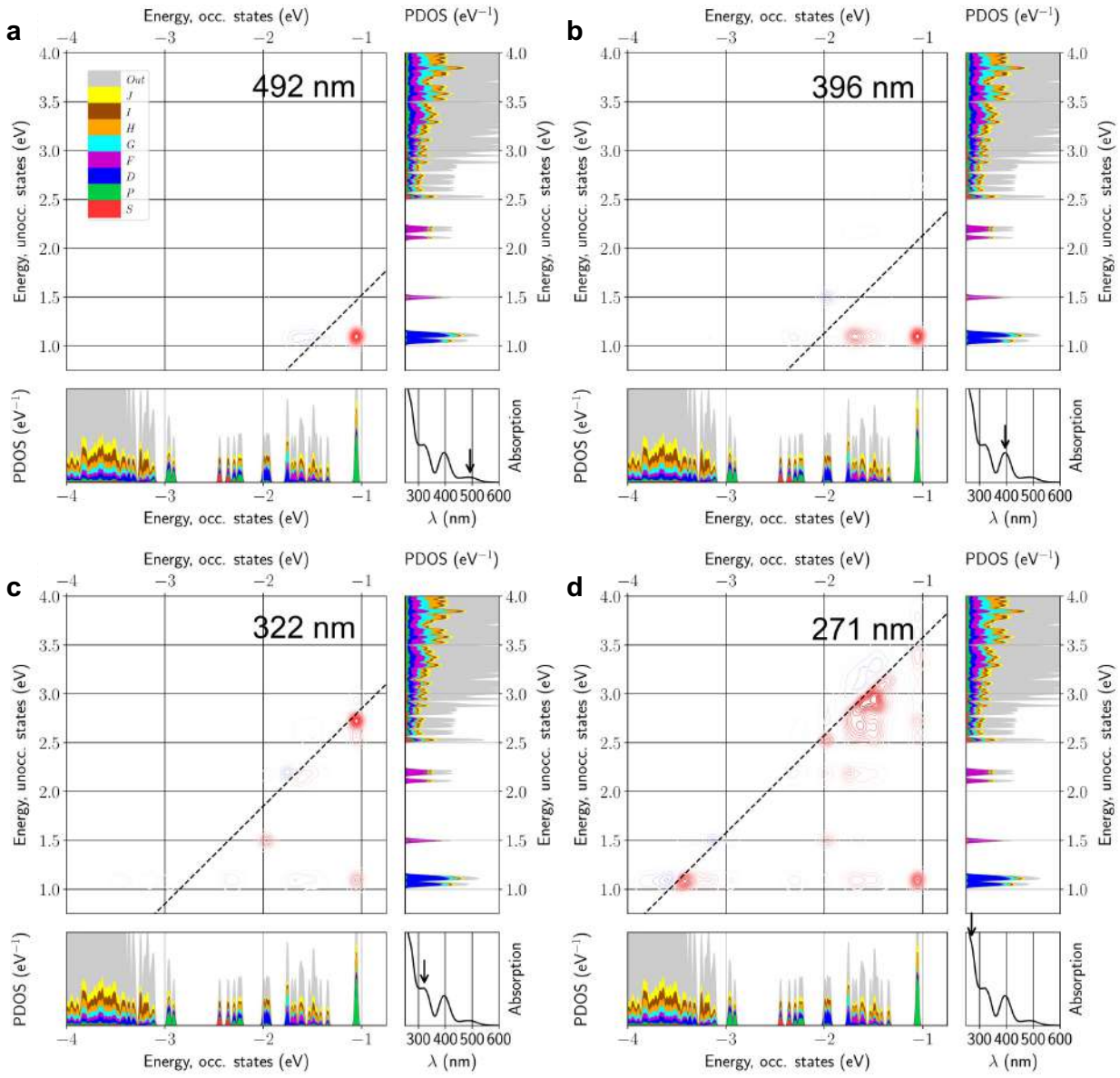
Supplementary Fig. 40 | Optimized structures and relative energies of cluster when Cu is added in all symmetrically different metal atom positions.



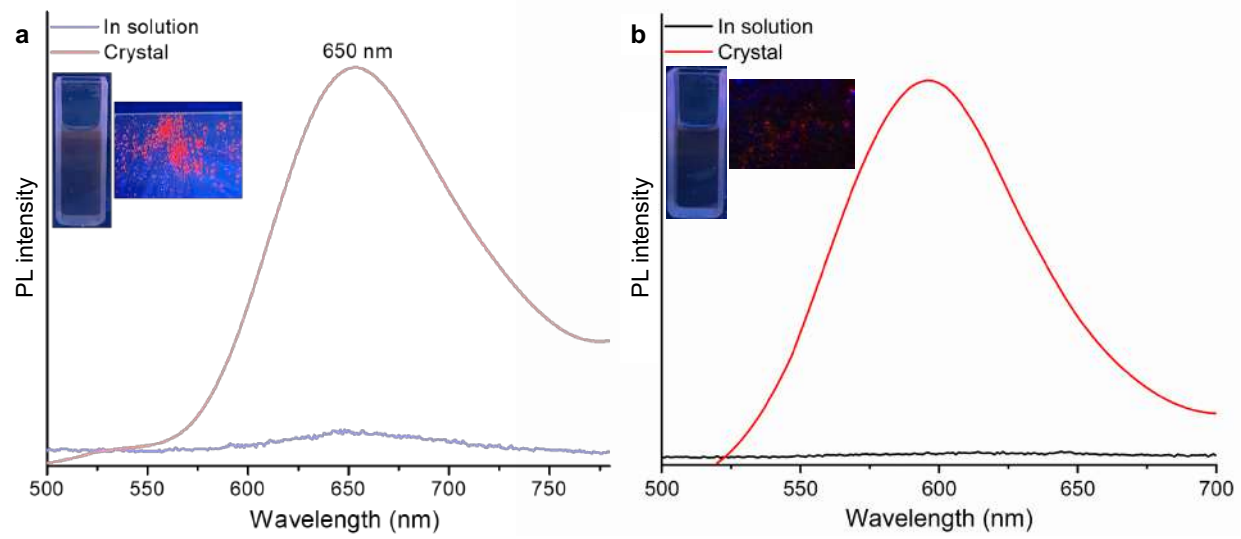
Supplementary Fig. 41 | DPV studies with Ag_{17} NC showing the experimental band gap of 2.04 eV.



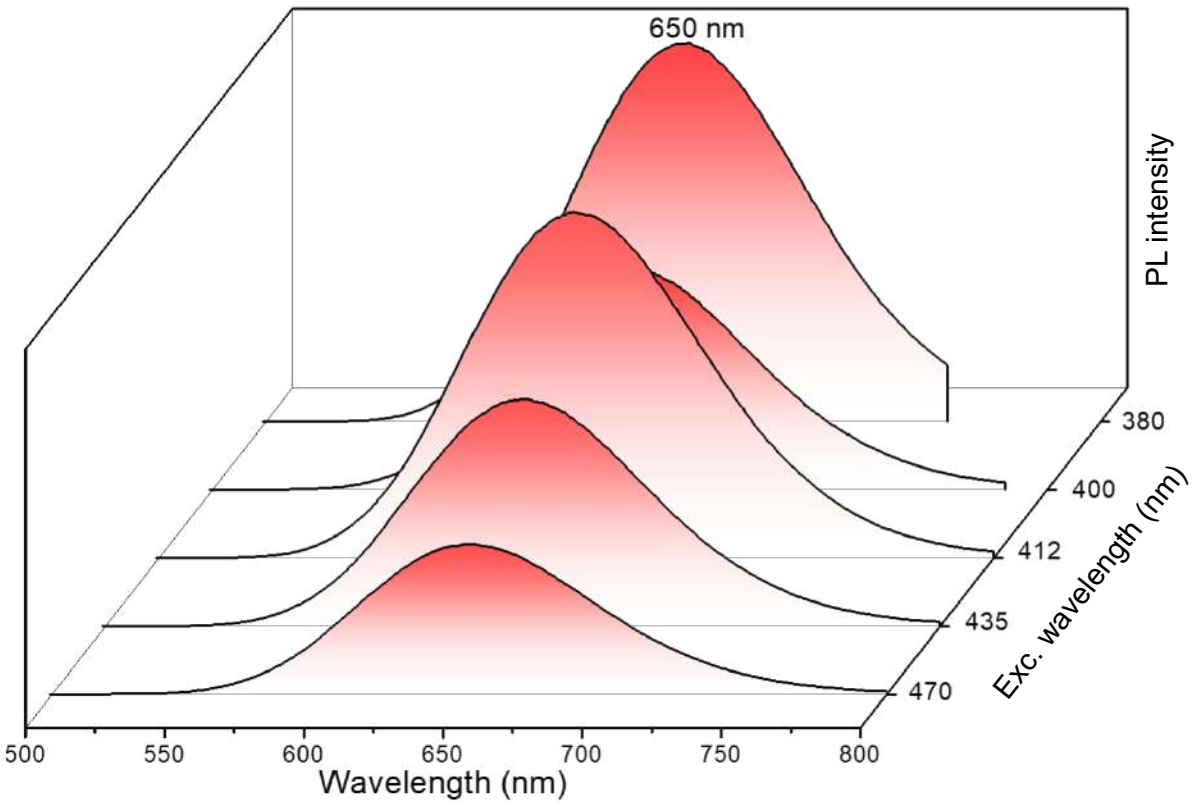
Supplementary Fig. 42 | Tauc's plots for the energy band gap of the **a** Ag_{17}, **b** $AuAg_{16}$, **c** $Ag_{13}Cu_4$ and **d** $AuAg_{12}Cu_4$ nanoclusters.



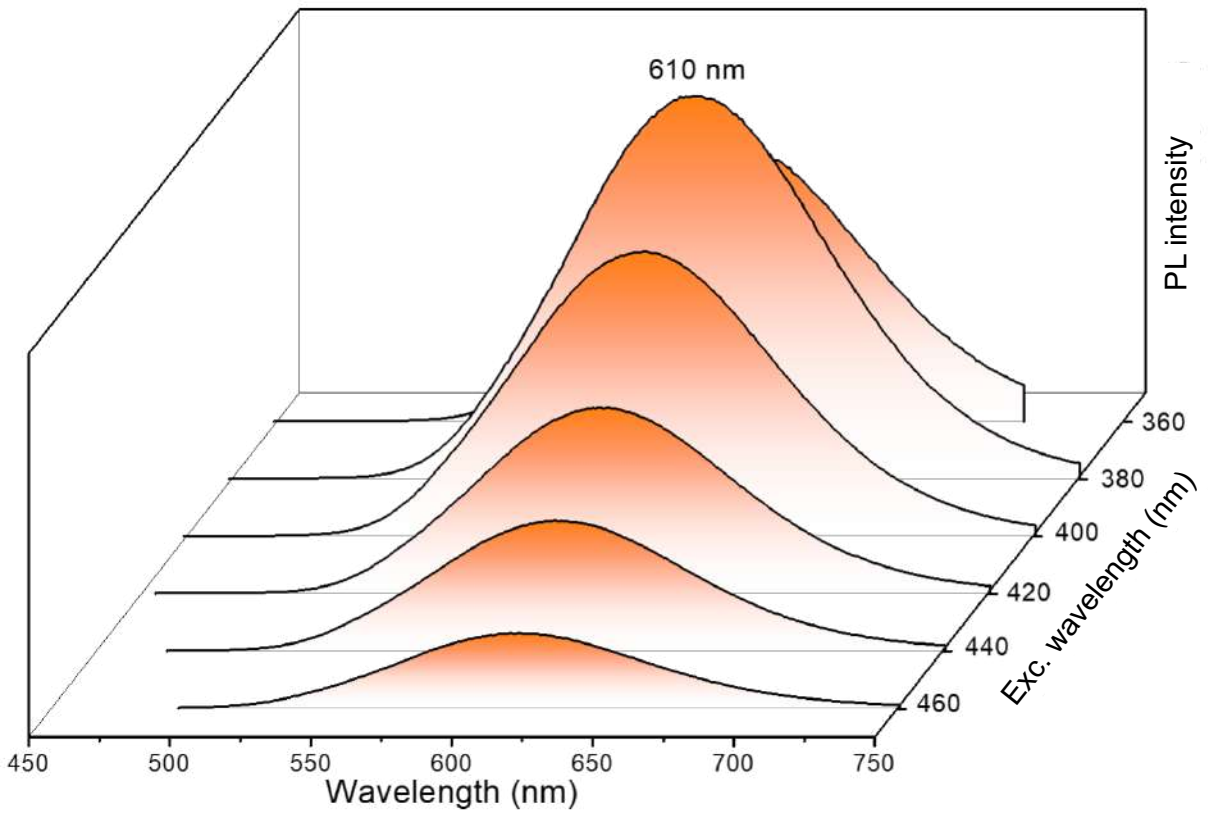
Supplementary Fig. 43 | Dipole transition contribution maps (DTCMs) showing the strengthening and screening contributions in Kohn-Sham basis for Ag_{17} at the energy of **a** 492 nm **b** 396 nm **c** 322 nm **d** 271 nm absorption peaks.



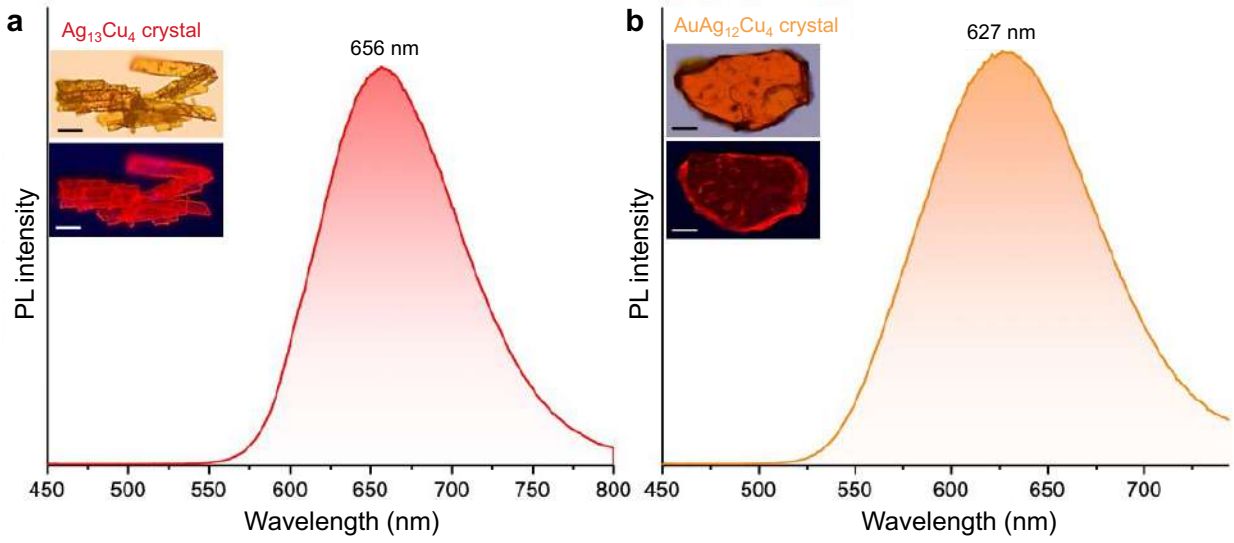
Supplementary Fig. 44 | Crystallization induced emission (CIE) behavior of **a** Ag_{17} and **b** $AuAg_{16}$. Inset shows the photographs of the respective cluster under UV light in solution and crystals.



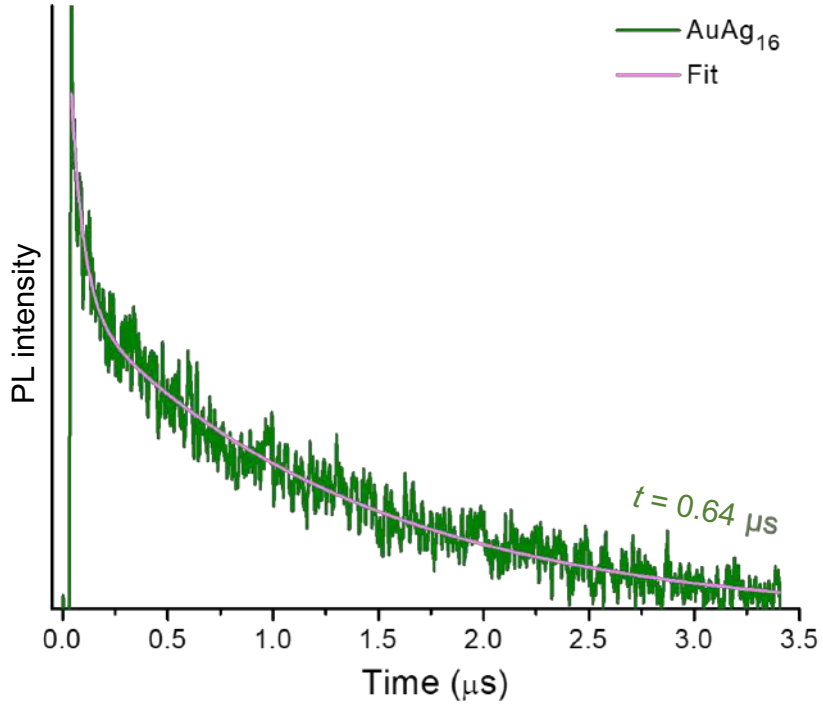
Supplementary Fig. 45 | Excitation-dependent emission spectra of $Ag_{13}Cu_4$ in DCM solution.



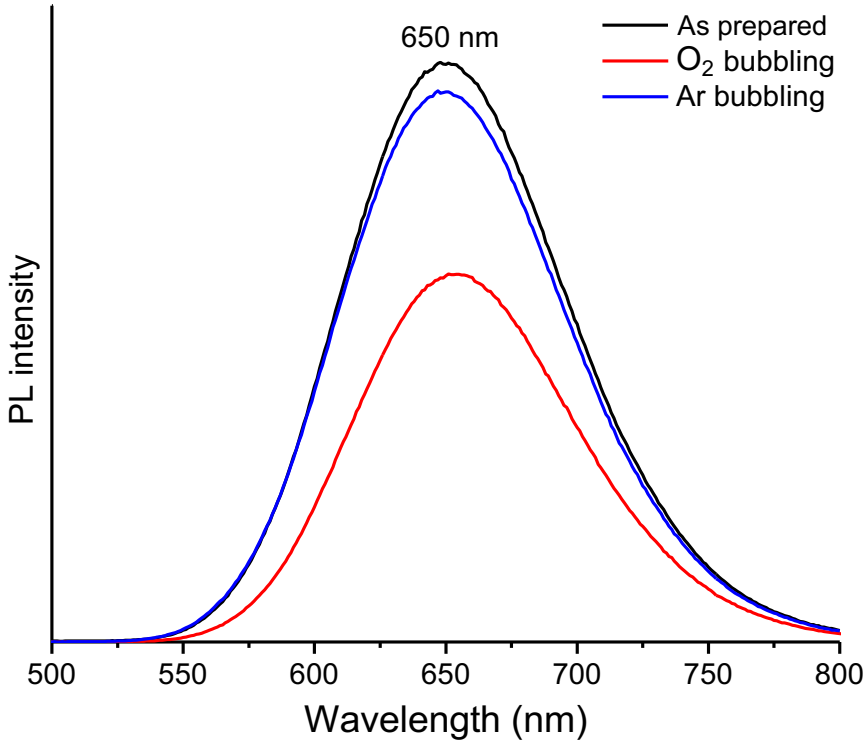
Supplementary Fig. 46 | Excitation-dependent emission spectra of $AuAg_{12}Cu_4$ in DCM solution.



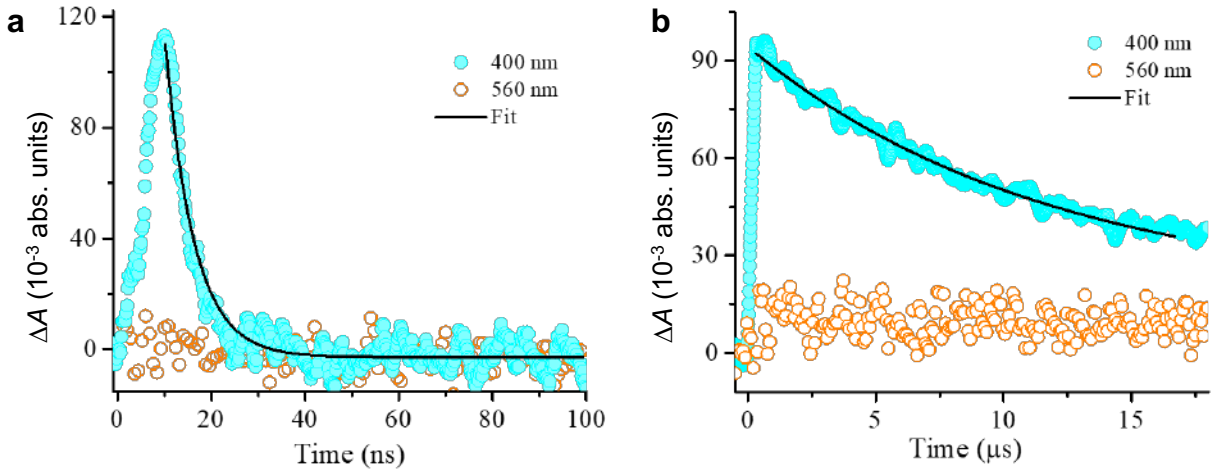
Supplementary Fig. 47 | Photoluminescence emission spectra of **a** $Ag_{13}Cu_4$ and **b** trimetallic $AuAg_{12}Cu_4$ crystals. Inset shows the optical micrographs of the respective crystals. Top: daylight, down: UV light. Scale bar 50 μm.



Supplementary Fig. 48 | Photoluminescence decay profile of $AuAg_{16}$.



Supplementary Fig. 49 | Photoluminescence emission spectra of $Ag_{13}Cu_4$ in DCM solution after oxygen and argon bubbling indicating phosphorescence emission originating from triplet state. Excitation wavelength was 412 nm.



Supplementary Fig. 50 | Nanosecond transient absorption decay kinetics for **a** $Ag_{13}Cu_4$ and **b** $AuAg_{12}Cu_4$. The solid line in the figures represents the single exponential fit.

Supplementary Tables

Supplementary Table 1 | Peak positions of the experimental and calculated absorption spectra. Possible additional non-assigned peaks are given in parenthesis at the next closest assigned peak.

Cluster	Absorption peak positions (nm)				
Ag_{17}, exp.	-	400	312	269	241
Ag_{17}, calc.	492	396	322	271	-
$AuAg_{16}$, exp.	-	385	288	271	-
$AuAg_{16}$, calc.	458	389	328	276	-
$Ag_{13}Cu_4$, exp.	475	400	307	-	-
$Ag_{13}Cu_4$, calc.	499	428	320 (364)	281	-
$AuAg_{12}Cu_4$, exp.	-	385	303	265	-
$AuAg_{12}Cu_4$, calc.	477	423	317 (356)	281	-

Supplementary Table 2 | Crystallographic information of Ag_{17}, $AuAg_{16}$, $Ag_{13}Cu_4$ and $AuAg_{12}Cu_4$ cluster crystals.

	Ag_{17}	**$AuAg_{16}$**	**$Ag_{13}Cu_4$**	**$AuAg_{12}Cu_4$**
Chemical formula	C_{24} H_{132} Ag_{17} B_{120} S_{12}	C_{180} H_{276} Ag_{16} Au_4 B_{120} P_{12} S_{12}	C_{180} H_{276} Ag_{13} B_{120} Cu_7 P_{12} S_{12}	C_{24} H_{132} Ag_{12} Au B_{120} Cu_4 S_{12}
Formula weight	3937.00	7007.34	6340.64	3848.77
Temperature	173(2) K	296(2) K	273(2) K	129(2) K
Crystal system	Orthorhombic	Trigonal	Triclinic	Cubic
Space group	Pbcn	R -3	P-1	F d -3
Crystal Size (mm^3)	0.178 x 0.115 x 0.078	0.121 x 0.092 x 0.017	0.261 x 0.115 x 0.088	0.090 x 0.095 x 0.075
a (Å)	51.188(2)	30.0358(11)	22.4896(10)	38.364(17)
b (Å)	21.0030(9)	30.0358(11)	23.7297(12)	38.364(17)
c (Å)	33.3626(18)	59.198(4)	30.8515(14)	38.364(17)
α (°)	90	90	94.853(3)	90
β (°)	90	90	94.104(2)	90

γ (°)	90	120	103.94(3)	90
V (Å)^3	35868(2)	46250(5)	15850.2(13)	56464(8)
Z	8	6	2	8
Density calc. (mg m^{-3})	1.458	1.510	1.329	0.905
Absorption coefficient	15.976 mm^{-1}	13.055 mm^{-1}	8.359 mm^{-1}	8.700 mm^{-1}
F(000)	14936	20376	6284	14616
Theta range for data collection	1.726 to 51.241°.	1.855 to 44.408°.	2.285 to 66.000°.	1.995 to 65.909°
Index ranges	-51<=h<=47, -11<=k<=20, -33<=l<=32	-21<=h<=25, -25<=k<=27, -29<=l<=53	-26<=h<=26, -28<=k<=28, -36<=l<=36	-44<=h<=45, -42<=k<=44, -43<=l<=40
Reflections collected	148451	29799	361230	96882
Independent reflections	18940 [R(int) = 0.1631]	7828 [R(int) = 0.1333]	53869 [R(int) = 0.1469]	4113 [R(int) = 0.0805]
Completeness to theta	97.5 %	97.1 %	97.5	100.0 %
Max. and min. transmission	0.3030 and 0.0912	0.5041 and 0.1731	0.5210 and 0.2208	0.5872 and 0.3571
Data / restraints / parameters	18940 / 3142 / 1558	7828 / 1899 / 937	53869 / 2009 / 3074	4113 / 0 / 131
Goodness-of-fit on F^2	1.030	1.481	1.036	1.085
Final R indices [I>2sigma(I)]	R1 = 0.0949, wR2 = 0.2658	R1 = 0.1726, wR2 = 0.4085	R1 = 0.0765, wR2 = 0.2069	R1 = 0.0782, wR2 = 0.2469
R indices (all data)	R1 = 0.1989, wR2 = 0.3665	R1 = 0.3348, wR2 = 0.5357	R1 = 0.1787, wR2 = 0.3161	R1 = 0.1015, wR2 = 0.2895

Largest diff. peak and hole	1.515 and -0.642 e Å^{-3}	4.161 and -0.930 e Å^{-3}	1.131 and -1.276 e Å^{-3}	2.445 and -0.764 e Å^{-3}
CCDC No.	2356804	2356806	2356807	2356892

Supplementary Table 3 | Atomic coordinates (x 10^4) and equivalent isotropic displacement parameters (Å^{2}x 10^3) for Ag_{17} cluster. *U*(eq) is defined as one third of the trace of the orthogonalized U^{ij} tensor. Check CIF justifications of level A and level B alerts.

	x	*y*	*z*	*U*(eq)
Ag(1)	6338(1)	7418(1)	6317(1)	140(1)
Ag(2)	6354(1)	8608(1)	6696(1)	151(1)
Ag(3)	6767(1)	7640(1)	6814(1)	150(1)
Ag(4)	6562(1)	6393(1)	6715(1)	152(1)
Ag(5)	6925(1)	9043(1)	6728(1)	159(1)
Ag(6)	6298(1)	6240(1)	5930(1)	156(1)
Ag(7)	6709(1)	8266(1)	6024(1)	153(1)
Ag(8)	5881(1)	7934(1)	6639(1)	153(1)
Ag(9)	6277(1)	7309(1)	7150(1)	151(1)
Ag(10)	6800(1)	6941(1)	5983(1)	155(1)
Ag(11)	6801(1)	5491(1)	6093(1)	169(1)
Ag(12)	6115(1)	8470(1)	5942(1)	155(1)
Ag(13)	5964(1)	6544(1)	6579(1)	155(1)
Ag(14)	6419(1)	7510(1)	5486(1)	158(1)
Ag(15)	5904(1)	7170(1)	5838(1)	157(1)
Ag(16)	5704(1)	7067(1)	7336(1)	163(1)
Ag(17)	5930(1)	8054(1)	5109(1)	175(1)
C(1)	6995(5)	8351(13)	7693(10)	157(4)
C(2)	6683(5)	8589(13)	7791(10)	167(6)
B(1)	6690(8)	9057(18)	8235(12)	176(7)
B(2)	6826(8)	8637(17)	8630(13)	182(7)
B(3)	6818(6)	7803(17)	7946(12)	161(6)
B(4)	6935(7)	9073(17)	7838(13)	169(6)
B(5)	7129(7)	7913(17)	8080(12)	167(5)

B(6)	7217(8)	8697(17)	8004(12)	173(6)
B(7)	6619(8)	8234(17)	8286(12)	172(7)
B(8)	6888(8)	7847(18)	8460(13)	181(7)
B(9)	7012(8)	9191(19)	8329(12)	183(8)
B(10)	7147(8)	8353(18)	8473(13)	185(7)
C(3)	7366(5)	8671(12)	5947(10)	166(5)
C(4)	7413(6)	7972(14)	5684(11)	189(7)
B(11)	7701(8)	8021(19)	5479(15)	196(8)
B(12)	7653(7)	7556(18)	5895(14)	190(8)
B(13)	7448(7)	8006(16)	6236(14)	176(7)
B(14)	7863(7)	8732(17)	5591(14)	189(8)
B(15)	7770(7)	7977(19)	6306(14)	188(7)
B(16)	7921(8)	7947(17)	5856(14)	185(8)
B(17)	7882(7)	8705(18)	6101(14)	186(8)
B(18)	7586(6)	8682(17)	6345(14)	175(6)
B(19)	7510(8)	8673(18)	5449(14)	191(7)
B(20)	7645(7)	9120(18)	5922(12)	178(7)
C(5)	7294(5)	6262(13)	6824(11)	179(6)
C(6)	7130(5)	5650(13)	7014(11)	164(5)
B(21)	7503(7)	5317(17)	7548(14)	185(7)
B(22)	7655(7)	5317(17)	7091(13)	183(8)
B(23)	7327(6)	5028(17)	7184(12)	172(7)
B(24)	7179(7)	5544(16)	7477(14)	173(6)
B(25)	7160(7)	6297(16)	7296(13)	175(6)
B(26)	7496(7)	6604(18)	7229(13)	193(8)
B(27)	7642(7)	6062(17)	6873(15)	189(8)
B(28)	7704(8)	5980(18)	7402(15)	199(9)
B(29)	7415(7)	6137(17)	7676(14)	192(8)
B(30)	7399(6)	5440(17)	6778(13)	174(6)
C(7)	6488(6)	10154(14)	6100(11)	182(6)
C(8)	6456(5)	10240(13)	6609(11)	166(6)
B(31)	6272(8)	10640(18)	5846(15)	198(8)
B(32)	6175(7)	10271(17)	6320(13)	182(7)
B(33)	6233(7)	10833(17)	6724(15)	191(7)
B(34)	6558(8)	10987(16)	6733(15)	197(8)
B(35)	6702(7)	10589(17)	6345(14)	187(7)

B(36)	6583(7)	10827(17)	5887(15)	195(7)
B(37)	6629(8)	11375(18)	6259(15)	207(9)
B(38)	6349(7)	11464(18)	5975(16)	201(9)
B(39)	6331(8)	11517(19)	6508(17)	215(9)
B(40)	6099(8)	11076(18)	6278(15)	200(8)
C(9)	5548(6)	9184(15)	5641(11)	179(6)
C(10)	5353(6)	9635(18)	5316(12)	219(9)
B(41)	5492(8)	9311(18)	6084(14)	185(7)
B(42)	5469(8)	9940(20)	5813(14)	202(8)
B(43)	5135(8)	10040(30)	5706(16)	236(10)
B(44)	5242(8)	9860(20)	6171(16)	224(10)
B(45)	5308(7)	8810(20)	5381(14)	205(8)
B(46)	5375(7)	8610(20)	5864(13)	188(8)
B(47)	5186(8)	9010(20)	6225(15)	211(9)
B(48)	5047(8)	8680(30)	5732(15)	223(10)
B(49)	4951(9)	9430(20)	5902(15)	232(10)
B(50)	5023(8)	9350(30)	5417(16)	241(10)
C(11)	5760(6)	9340(14)	7327(11)	191(7)
C(12)	5596(5)	8696(14)	7438(11)	172(6)
B(51)	5633(8)	9990(20)	7608(16)	217(9)
B(52)	5650(6)	8520(20)	7917(13)	185(6)
B(53)	5369(7)	8883(18)	7802(13)	181(7)
B(54)	5421(7)	9395(18)	7404(14)	189(7)
B(55)	5901(7)	8800(20)	7608(13)	186(7)
B(56)	5851(8)	9070(20)	8098(15)	211(9)
B(57)	5522(8)	9090(20)	8232(15)	210(8)
B(58)	5400(8)	9650(20)	7899(14)	202(8)
B(59)	5930(8)	9610(20)	7715(15)	213(9)
B(60)	5697(8)	9790(20)	8106(16)	226(11)
C(13)	5307(6)	6174(16)	6690(10)	174(6)
C(14)	5238(6)	6922(16)	6459(10)	183(7)
B(61)	4889(7)	7080(20)	6470(13)	203(8)
B(62)	5075(7)	6710(20)	6887(14)	183(7)
B(63)	5029(7)	5870(20)	6910(13)	190(7)
B(64)	5179(8)	5540(20)	6448(12)	194(7)
B(65)	5298(8)	6230(20)	6207(13)	189(7)

B(66)	5030(8)	6720(20)	6032(14)	201(8)
B(67)	4754(8)	6430(20)	6767(14)	214(9)
B(68)	4722(9)	6400(30)	6222(15)	225(10)
B(69)	4826(8)	5700(20)	6481(14)	220(9)
B(70)	4963(9)	5870(20)	6040(15)	217(10)
C(15)	6296(7)	3789(14)	5934(12)	210(8)
C(16)	6229(6)	4596(14)	6056(12)	180(6)
B(71)	6370(8)	4183(17)	6391(14)	193(7)
B(72)	5899(8)	4684(19)	6171(14)	203(8)
B(73)	6168(8)	4741(18)	6492(14)	190(7)
B(74)	6250(9)	3470(19)	6439(16)	216(9)
B(75)	5980(9)	4110(20)	5808(17)	217(9)
B(76)	5784(10)	3930(20)	6147(17)	235(10)
B(77)	5868(9)	4282(19)	6629(17)	222(9)
B(78)	6170(9)	4021(19)	6803(17)	213(8)
B(79)	5936(9)	3490(20)	6547(18)	235(10)
B(80)	6007(10)	3350(20)	6045(18)	246(11)
C(17)	6159(5)	6290(14)	7974(10)	168(5)
C(18)	6470(6)	5964(14)	7842(10)	185(7)
B(81)	6414(8)	5165(18)	7825(13)	186(7)
B(82)	6191(7)	5684(17)	7631(13)	175(6)
B(83)	5940(7)	5715(18)	7974(12)	171(7)
B(84)	6028(7)	6060(20)	8392(13)	181(7)
B(85)	6362(7)	6210(20)	8385(13)	191(7)
B(86)	6536(8)	5470(20)	8312(13)	196(8)
B(87)	6261(7)	5500(20)	8608(14)	195(8)
B(88)	6266(7)	4870(20)	8259(13)	188(8)
B(89)	5982(7)	5200(20)	8345(13)	186(8)
B(90)	6079(7)	4997(19)	7872(13)	183(8)
C(19)	6525(7)	8487(15)	4653(11)	191(6)
C(20)	6824(6)	8710(15)	4863(12)	198(7)
B(91)	6560(7)	9134(16)	4992(14)	183(7)
B(92)	6569(8)	9870(20)	4765(14)	204(9)
B(93)	6787(9)	8460(20)	4381(15)	215(8)
B(94)	7016(9)	9090(20)	4469(15)	222(10)
B(95)	6800(10)	9150(20)	4033(16)	231(10)

B(96)	6876(9)	9790(20)	4360(14)	221(10)
B(97)	6525(9)	9730(20)	4264(15)	220(10)
B(98)	6353(9)	9260(19)	4578(13)	200(8)
B(99)	6868(8)	9512(19)	4901(14)	200(9)
B(100)	6513(10)	8760(20)	4155(15)	217(9)
C(21)	5648(6)	6549(16)	4965(11)	189(6)
C(22)	5399(8)	6415(19)	4623(11)	226(8)
B(101)	5892(10)	5430(20)	4770(15)	218(9)
B(102)	5692(11)	5190(30)	4390(17)	265(14)
B(103)	5441(9)	5930(20)	5029(15)	210(8)
B(104)	5744(8)	5829(18)	5201(15)	197(8)
B(105)	5941(9)	6191(19)	4886(14)	199(8)
B(106)	5913(11)	5860(20)	4376(17)	236(10)
B(107)	5584(10)	5250(20)	4938(16)	231(10)
B(108)	5389(11)	5580(30)	4552(17)	260(12)
B(109)	5610(12)	6000(30)	4179(17)	261(12)
B(110)	5750(9)	6560(20)	4463(15)	219(8)
C(23)	7105(6)	6072(12)	5245(11)	168(6)
B(113)	7021(8)	6672(19)	4927(13)	191(8)
B(111)	6829(9)	6023(19)	4972(14)	194(7)
B(112)	6898(11)	6380(20)	4503(15)	231(10)
C(24)	7337(7)	6414(17)	4929(11)	209(8)
B(114)	7186(11)	6500(30)	4449(16)	230(10)
B(115)	7395(12)	5900(20)	4519(15)	248(11)
B(116)	7160(13)	5320(30)	4588(17)	267(12)
B(117)	7114(13)	5880(30)	4160(19)	286(15)
B(118)	7346(10)	5620(20)	5034(15)	220(9)
B(119)	6990(10)	5370(19)	5006(15)	214(9)
B(120)	6872(13)	5540(30)	4556(17)	261(12)
S(1)	7061(1)	9082(3)	6011(3)	158(2)
S(2)	6078(1)	7083(4)	7818(3)	160(2)
S(3)	7111(1)	8222(3)	7195(3)	155(2)
S(4)	6814(1)	5401(3)	6839(3)	162(2)
S(5)	6530(1)	9636(3)	6960(3)	162(2)
S(6)	5882(2)	9124(4)	5440(3)	164(2)
S(7)	5504(1)	8097(4)	7102(3)	162(2)

S(8)	6405(2)	5126(4)	5718(3)	176(3)
S(9)	5600(2)	6065(4)	6971(3)	170(3)
S(10)	6348(2)	7793(4)	4772(3)	174(2)
S(11)	7136(2)	6158(4)	5751(3)	165(3)
S(12)	5590(2)	7247(4)	5269(3)	172(2)

checkCIF/PLATON report (justification)

Alert level A

THETM01_ALERT_3_A The value of sine(theta_max)/wavelength is less than 0.550

Calculated sin(theta_max)/wavelength = 0.5058

Response: The crystal was not diffracting at higher Brag angles.

Hence a resolution cut was made during data integration in order to omit

weak higher reflections.

Alert level B

PLAT084_ALERT_3_B High wR2 Value (i.e. > 0.25) ..... 0.37 Report

Response: Due to weak higher angle reflections. Also, the carborane

moieties disordered in the lattice. This contributes high wR2 values.

PLAT342_ALERT_3_B Low Bond Precision on C-C Bonds ..... 0.04556 Ang.

Response: Due to poor resolution of the crystal, the accuracies of C-C bonds are low.

Supplementary Table 4 | Atomic coordinates (x 10^4) and equivalent isotropic displacement parameters (Å^{2}x 10^3) for $Ag_{13}Cu_4$ cluster. U(eq) is defined as one third of the trace of the orthogonalized U^{ij} tensor. Check CIF justifications of level A and level B alerts.

	x	*y*	*z*	*U*(eq)
Ag(1)	8144(1)	2594(1)	7794(1)	82(1)
Ag(2)	7346(1)	3291(1)	8006(1)	90(1)
Ag(3)	8577(1)	3376(1)	8537(1)	91(1)
Ag(4)	7573(1)	2405(1)	8561(1)	91(1)
Ag(5)	8464(1)	3779(1)	7668(1)	92(1)
Ag(6)	7511(1)	2979(1)	7123(1)	91(1)
Ag(7)	6901(1)	2041(1)	7684(1)	90(1)
Ag(8)	9396(1)	3132(1)	7882(1)	94(1)
Ag(9)	7685(1)	1787(1)	7056(1)	93(1)
Ag(10)	8770(1)	2235(1)	8485(1)	94(1)

Ag(11)	8749(1)	2797(1)	7045(1)	94(1)
Ag(12)	8975(1)	1942(1)	7574(1)	96(1)
Ag(13)	7788(1)	1410(1)	7902(1)	94(1)
Cu(1)	6300(1)	2563(1)	8397(1)	84(1)
Cu(2)	9563(1)	4350(1)	8285(1)	89(1)
Cu(3)	7805(1)	2431(1)	6276(1)	89(1)
Cu(4)	8898(1)	1030(1)	8216(1)	95(1)
C(1)	5928(6)	3557(6)	7752(4)	86(3)
C(2)	5239(7)	3095(8)	7604(5)	114(4)
C(3)	6959(6)	3040(6)	9443(4)	89(3)
C(4)	6595(7)	3579(7)	9440(6)	109(3)
C(5)	6520(6)	1320(6)	6189(4)	92(3)
C(6)	6129(7)	588(7)	6136(5)	113(4)
C(7)	7647(7)	3817(7)	6252(4)	96(3)
C(8)	7246(8)	4322(8)	6231(6)	127(4)
C(9)	5743(6)	1099(6)	8106(5)	92(3)
C(10)	6174(8)	628(7)	7961(5)	111(3)
C(11)	9207(6)	2173(6)	6123(4)	87(3)
C(12)	9400(7)	2138(7)	5602(5)	106(3)
C(13)	9808(6)	3963(6)	9298(4)	85(3)
C(14)	10138(7)	3438(7)	9113(5)	108(4)
C(15)	10545(7)	4176(7)	7533(5)	103(3)
C(16)	10555(8)	4874(8)	7417(6)	119(4)
C(17)	8582(6)	5212(6)	8108(5)	92(3)
C(18)	8280(9)	5674(9)	7833(6)	137(4)
C(19)	10334(7)	1563(7)	7890(5)	109(4)
C(20)	10702(9)	2211(9)	7748(7)	147(4)
C(21)	7868(7)	19(6)	7512(5)	97(3)
C(22)	7210(8)	-482(8)	7346(6)	130(4)
C(23)	8705(7)	1318(6)	9296(5)	97(3)
C(24)	8352(9)	598(8)	9338(7)	140(5)
S(1)	6378(2)	3503(2)	8248(1)	92(1)
S(2)	6729(2)	2404(2)	9052(1)	92(1)
S(3)	7349(2)	1470(2)	6258(1)	96(1)
S(4)	7233(2)	3101(2)	6348(1)	93(1)
S(5)	5829(2)	1792(2)	7895(1)	93(1)

S(6)	8834(2)	2748(2)	6245(1)	93(1)
S(7)	9273(2)	4239(2)	8972(1)	94(1)
S(8)	10330(2)	3957(2)	8049(1)	101(1)
S(9)	9053(2)	4818(2)	7828(1)	97(1)
S(10)	9563(2)	1199(2)	7686(1)	102(1)
S(11)	7947(2)	427(2)	8037(1)	101(1)
S(12)	9210(2)	1536(2)	8886(1)	103(1)
B(1)	5287(8)	3795(9)	7805(7)	108(4)
B(2)	4752(9)	3487(10)	7361(7)	123(5)
B(3)	5130(8)	3042(10)	7030(6)	112(4)
B(4)	5869(8)	3078(8)	7296(5)	96(4)
B(5)	5936(9)	4236(8)	7639(6)	105(4)
B(6)	5215(10)	4201(11)	7371(7)	132(5)
B(7)	5127(9)	3724(11)	6895(7)	128(5)
B(8)	5778(8)	3476(9)	6849(6)	107(4)
B(9)	6272(8)	3778(8)	7314(6)	97(4)
B(10)	5838(10)	4201(10)	7064(7)	125(5)
B(11)	6491(10)	3101(9)	9834(6)	109(4)
B(12)	7196(10)	2938(9)	9948(6)	114(4)
B(13)	7731(9)	3324(9)	9610(7)	112(4)
B(14)	7332(9)	3707(8)	9307(7)	103(4)
B(15)	7103(9)	4233(9)	9636(7)	118(4)
B(16)	7829(10)	4085(9)	9742(7)	120(5)
B(17)	7735(11)	3628(10)	10162(7)	138(5)
B(18)	6952(12)	3467(10)	10305(7)	140(6)
B(19)	6576(11)	3872(10)	9968(8)	134(5)
B(20)	7370(11)	4171(10)	10169(7)	134(5)
B(21)	6159(8)	1710(9)	5876(6)	106(4)
B(22)	6183(8)	1014(8)	5687(6)	105(4)
B(23)	6115(8)	1742(9)	6433(6)	103(4)
B(24)	6105(8)	1084(9)	6600(6)	106(4)
B(25)	5416(8)	1283(9)	6544(7)	112(4)
B(26)	5416(8)	560(9)	6344(7)	112(4)
B(27)	5459(9)	553(9)	5782(7)	120(5)
B(28)	5481(9)	1250(9)	5631(7)	118(5)
B(29)	5469(8)	1717(9)	6100(7)	114(4)

B(30)	5027(9)	990(8)	6032(6)	109(4)
B(31)	7796(10)	4365(8)	6660(7)	110(4)
B(32)	8395(8)	4136(9)	6443(7)	107(4)
B(33)	8194(9)	3920(10)	5893(7)	118(4)
B(34)	7450(10)	4010(11)	5755(7)	129(5)
B(35)	7559(12)	4770(12)	5811(9)	165(7)
B(36)	8150(13)	4533(12)	5637(8)	156(6)
B(37)	8709(11)	4588(10)	6060(7)	125(5)
B(38)	8467(10)	4873(10)	6531(7)	121(5)
B(39)	7757(10)	5000(10)	6406(9)	138(5)
B(40)	8309(11)	5119(11)	6037(8)	140(5)
B(41)	5384(9)	482(8)	7781(6)	105(4)
B(42)	5017(9)	755(9)	8204(6)	108(4)
B(43)	5583(8)	1038(8)	8618(6)	97(3)
B(44)	6278(8)	977(8)	8485(6)	101(4)
B(45)	6258(9)	226(8)	8402(6)	103(4)
B(46)	5701(9)	-83(9)	7959(7)	114(4)
B(47)	4999(9)	-1(9)	8124(7)	121(5)
B(48)	5092(9)	352(9)	8660(7)	115(4)
B(49)	5894(9)	508(9)	8829(7)	110(4)
B(50)	5523(9)	-159(9)	8512(7)	114(4)
B(51)	9715(8)	2013(8)	6496(6)	97(4)
B(52)	9002(8)	1502(8)	6310(6)	94(3)
B(53)	8862(8)	1573(8)	5770(5)	94(3)
B(54)	9956(7)	2378(9)	6049(6)	95(3)
B(55)	9683(9)	1267(9)	6356(7)	108(4)
B(56)	10282(9)	1818(9)	6181(6)	112(4)
B(57)	10104(9)	1904(9)	5628(7)	110(4)
B(58)	9391(8)	1392(9)	5453(6)	110(4)
B(59)	9142(9)	1020(9)	5895(6)	106(4)
B(60)	9931(9)	1189(9)	5828(6)	112(4)
B(61)	10561(8)	4147(8)	9234(6)	96(3)
B(62)	10299(7)	4452(9)	9660(5)	96(4)
B(63)	9704(9)	3943(9)	9838(6)	106(4)
B(64)	9619(9)	3287(9)	9482(6)	108(4)
B(65)	10048(10)	3394(11)	10015(7)	126(5)

B(66)	10309(9)	3076(10)	9551(6)	111(4)
B(67)	10905(9)	3602(9)	9377(7)	115(4)
B(68)	10988(9)	4261(9)	9721(6)	113(4)
B(69)	10466(9)	4131(10)	10117(6)	121(5)
B(70)	10829(9)	3582(9)	9937(6)	118(5)
B(71)	10392(9)	3709(9)	7072(6)	109(4)
B(72)	11137(8)	3963(9)	7324(7)	110(4)
B(73)	11227(9)	4682(9)	7537(7)	117(4)
B(74)	10011(9)	4269(9)	7129(6)	110(4)
B(75)	10305(9)	4141(9)	6645(7)	116(4)
B(76)	10398(10)	4885(10)	6852(7)	125(5)
B(77)	11150(10)	5123(10)	7115(7)	125(5)
B(78)	11533(10)	4555(10)	7058(7)	124(5)
B(79)	11011(10)	3950(10)	6757(7)	123(5)
B(80)	11015(10)	4678(10)	6623(7)	126(5)
B(81)	7804(9)	5048(10)	7999(7)	117(4)
B(82)	7604(12)	5730(11)	8072(7)	140(6)
B(83)	8306(12)	6276(11)	8226(8)	143(5)
B(84)	8923(11)	5942(8)	8230(7)	114(4)
B(85)	8628(10)	6139(9)	8720(7)	122(5)
B(86)	7834(11)	6022(10)	8617(7)	125(5)
B(87)	7532(9)	5252(10)	8495(7)	119(5)
B(88)	8148(7)	4944(8)	8500(6)	96(3)
B(89)	8775(8)	5492(7)	8627(5)	89(3)
B(90)	8168(9)	5534(9)	8887(7)	109(4)
B(91)	10515(9)	2151(10)	8282(7)	126(4)
B(92)	11256(10)	2575(12)	8200(8)	144(4)
B(93)	11486(11)	2207(13)	7739(9)	162(5)
B(94)	10900(10)	1556(12)	7574(9)	151(4)
B(95)	11539(10)	1512(13)	7905(7)	162(4)
B(96)	11756(10)	2094(10)	8277(8)	152(4)
B(97)	11154(10)	2080(10)	8595(8)	140(4)
B(98)	10586(8)	1504(11)	8403(7)	126(4)
B(99)	10814(9)	1107(12)	7981(8)	143(4)
B(100)	11332(8)	1445(9)	8429(7)	152(4)
B(101)	8205(8)	317(9)	7067(6)	100(4)

B(102)	7417(8)	174(9)	7076(6)	107(4)
B(103)	7885(10)	-683(9)	7515(8)	123(4)
B(104)	8465(9)	-193(8)	7321(7)	108(4)
B(105)	7769(9)	-14(9)	6603(7)	114(4)
B(106)	7126(11)	-533(11)	6760(8)	141(6)
B(107)	7412(13)	-1052(10)	7037(8)	148(6)
B(108)	8227(13)	-856(10)	7043(8)	141(5)
B(109)	8426(11)	-221(9)	6773(7)	121(4)
B(110)	7768(12)	-770(10)	6587(8)	139(5)
B(111)	8965(12)	988(11)	9703(7)	133(5)
B(112)	8888(9)	1681(9)	9795(6)	113(4)
B(113)	8296(9)	1773(9)	9486(6)	104(4)
B(114)	7935(9)	1092(9)	9203(7)	116(4)
B(115)	8330(15)	529(12)	9917(10)	175(7)
B(116)	8677(13)	1219(13)	10180(8)	153(6)
B(117)	8249(11)	1724(11)	10043(7)	133(5)
B(118)	7626(11)	1330(10)	9692(7)	127(5)
B(119)	7658(13)	623(11)	9592(9)	153(6)
B(120)	7876(13)	993(12)	10107(9)	153(6)
Cu(5)	3761(1)	2228(1)	10417(1)	97(1)
Cu(6)	7942(1)	262(1)	3685(1)	93(1)
Cu(7)	6087(1)	3616(1)	3785(1)	103(1)
C(25)	3462(8)	908(8)	9692(6)	118(4)
C(26)	3624(9)	472(9)	9462(6)	150(5)
C(27)	3271(11)	160(10)	9097(7)	176(6)
C(28)	2711(11)	257(11)	8963(8)	178(7)
C(29)	2516(9)	676(10)	9194(7)	155(6)
C(30)	2883(8)	1026(8)	9565(6)	131(5)
C(31)	4652(7)	1191(7)	10149(5)	97(4)
C(32)	4837(8)	778(8)	10377(5)	115(5)
C(33)	5439(9)	708(8)	10351(6)	129(6)
C(34)	5836(8)	1045(8)	10080(6)	116(5)
C(35)	5634(8)	1417(7)	9863(5)	108(4)
C(36)	5039(7)	1513(7)	9884(5)	101(4)
C(37)	3570(7)	921(7)	10618(5)	107(4)
C(38)	2928(6)	1012(7)	10701(6)	108(4)

C(39)	3267(11)	1743(10)	11618(7)	162(5)
C(40)	3292(13)	1935(11)	12065(8)	184(6)
C(41)	3046(15)	2355(13)	12213(9)	210(7)
C(42)	2620(15)	2516(12)	11930(9)	212(7)
C(43)	2579(13)	2380(10)	11476(8)	187(6)
C(44)	2912(12)	1963(9)	11324(7)	156(5)
C(45)	2155(9)	1776(9)	10486(7)	181(6)
C(46)	2097(9)	2198(9)	10211(6)	175(6)
C(47)	1527(9)	2197(10)	10002(8)	206(7)
C(48)	1015(10)	1784(11)	10075(10)	234(8)
C(49)	1067(10)	1338(12)	10338(10)	245(8)
C(50)	1641(9)	1332(11)	10553(9)	224(7)
C(51)	4562(8)	3276(7)	11285(5)	109(4)
C(52)	4001(10)	3386(10)	11346(7)	155(8)
C(53)	3944(13)	3835(13)	11641(9)	201(12)
C(54)	4426(16)	4154(14)	11892(10)	204(13)
C(55)	4994(13)	4092(11)	11837(8)	176(9)
C(56)	5085(9)	3623(8)	11533(6)	136(6)
C(57)	5149(8)	2343(7)	11116(6)	117(5)
C(58)	4950(10)	2055(8)	11477(7)	141(6)
C(59)	5318(12)	1731(10)	11671(9)	174(9)
C(60)	5843(14)	1674(13)	11491(11)	196(12)
C(61)	6040(12)	1941(12)	11127(10)	187(10)
C(62)	5679(8)	2287(9)	10931(6)	141(6)
C(63)	5066(7)	3174(7)	10476(5)	102(4)
C(64)	4631(7)	3463(7)	10233(5)	106(4)
C(65)	3429(8)	3379(8)	9820(6)	114(4)
C(66)	3261(9)	3475(9)	9407(7)	148(5)
C(67)	2853(10)	3818(11)	9325(8)	170(6)
C(68)	2614(10)	4067(10)	9647(9)	158(6)
C(69)	2756(9)	3983(9)	10039(8)	144(5)
C(70)	3171(8)	3630(8)	10153(7)	129(5)
C(71)	4186(7)	2694(7)	9430(5)	99(4)
C(72)	3814(11)	2210(8)	9194(6)	147(7)
C(73)	4013(14)	1979(11)	8813(7)	188(11)
C(74)	4550(12)	2259(13)	8661(7)	163(8)

C(75)	4910(10)	2715(13)	8887(7)	179(10)
C(76)	4726(9)	2968(11)	9267(6)	154(8)
C(77)	4761(8)	4204(7)	3832(6)	120(4)
C(78)	4531(9)	3771(9)	4096(8)	151(7)
C(79)	3961(11)	3701(12)	4247(10)	194(10)
C(80)	3586(12)	4059(13)	4097(11)	204(12)
C(81)	3813(11)	4475(12)	3834(11)	204(12)
C(82)	4402(9)	4573(10)	3706(7)	152(7)
C(83)	5855(8)	5043(8)	3688(7)	121(5)
C(84)	5872(9)	5333(9)	4099(7)	139(6)
C(85)	6166(12)	5908(11)	4199(10)	183(10)
C(86)	6426(14)	6206(10)	3904(12)	188(12)
C(87)	6442(12)	5962(12)	3469(10)	186(10)
C(88)	6141(10)	5362(10)	3376(8)	156(7)
C(89)	5317(8)	4093(8)	3031(6)	130(5)
C(90)	5148(7)	3446(8)	2909(6)	121(5)
C(91)	6312(5)	3367(6)	2663(4)	119(4)
C(92)	6782(6)	3875(6)	2753(4)	162(8)
C(93)	7149(6)	4079(6)	2428(5)	198(12)
C(94)	7046(7)	3777(8)	2013(4)	195(11)
C(95)	6576(7)	3270(7)	1922(3)	182(10)
C(96)	6209(6)	3065(5)	2248(4)	157(7)
C(97)	5560(10)	2373(8)	2995(7)	136(5)
C(98)	4982(11)	2059(9)	3020(7)	158(6)
C(99)	4807(12)	1431(10)	3001(8)	170(6)
C(100)	5253(12)	1156(10)	2928(8)	162(6)
C(101)	5832(11)	1428(9)	2876(7)	163(6)
C(102)	5989(10)	2057(9)	2909(7)	155(5)
C(103)	5416(8)	2296(8)	4282(6)	122(4)
C(104)	4803(9)	2191(9)	4185(7)	152(5)
C(105)	4404(10)	1652(9)	4123(8)	170(6)
C(106)	4638(10)	1178(9)	4158(8)	155(6)
C(107)	5262(10)	1231(8)	4243(8)	153(5)
C(108)	5642(9)	1817(8)	4314(7)	139(5)
C(109)	5691(8)	3377(8)	4847(6)	108(4)
C(110)	5764(9)	3967(8)	4905(6)	130(6)

C(111)	5638(12)	4230(10)	5300(6)	160(8)
C(112)	5435(12)	3899(11)	5622(7)	162(9)
C(113)	5365(12)	3336(11)	5573(8)	166(9)
C(114)	5493(9)	3047(9)	5193(6)	131(6)
C(115)	7555(8)	4632(8)	4176(6)	147(5)
C(116)	7441(8)	5073(7)	3944(6)	145(5)
C(117)	7765(8)	5654(8)	4027(7)	159(6)
C(118)	8178(11)	5800(11)	4389(8)	203(7)
C(119)	8397(12)	5363(9)	4582(7)	208(8)
C(120)	8076(10)	4776(9)	4481(7)	197(7)
C(121)	7628(8)	3555(10)	3722(6)	135(5)
C(122)	8255(10)	3783(11)	3719(8)	165(6)
C(123)	8578(11)	3459(12)	3474(9)	179(7)
C(124)	8342(12)	2950(13)	3266(9)	188(7)
C(125)	7747(11)	2711(12)	3281(8)	174(6)
C(126)	7359(10)	2989(10)	3530(7)	151(5)
C(127)	6675(7)	2978(7)	4522(5)	105(4)
C(128)	7138(8)	3568(7)	4560(5)	115(5)
C(129)	6756(4)	-623(4)	2872(3)	95(4)
C(130)	6166(4)	-938(5)	2932(3)	118(5)
C(131)	5926(4)	-1488(5)	2707(4)	137(7)
C(132)	6275(5)	-1723(4)	2421(4)	127(6)
C(133)	6864(5)	-1408(6)	2360(4)	165(9)
C(134)	7105(4)	-858(5)	2586(4)	145(7)
C(135)	7149(7)	568(8)	2747(6)	117(5)
C(136)	7577(9)	1096(8)	2776(6)	131(6)
C(137)	7631(10)	1483(10)	2466(8)	159(8)
C(138)	7251(11)	1346(11)	2082(8)	181(10)
C(139)	6835(11)	781(11)	2025(7)	166(8)
C(140)	6789(8)	428(9)	2348(6)	141(7)
C(141)	6512(6)	246(7)	3493(5)	105(4)
C(142)	6768(7)	806(7)	3812(5)	107(4)
C(143)	7739(7)	1493(7)	4418(5)	100(4)
C(144)	8132(10)	1905(8)	4225(6)	138(6)
C(145)	8381(10)	2478(8)	4414(7)	141(7)
C(146)	8212(9)	2640(9)	4818(7)	131(6)

C(147)	7825(8)	2236(8)	4997(6)	121(5)
C(148)	7560(7)	1678(7)	4823(5)	106(4)
C(149)	7175(7)	333(7)	4592(5)	101(4)
C(150)	7594(8)	247(8)	4919(5)	115(5)
C(151)	7415(9)	-95(8)	5251(6)	125(5)
C(152)	6800(10)	-364(8)	5268(6)	134(6)
C(153)	6376(9)	-295(9)	4941(6)	134(6)
C(154)	6552(7)	77(8)	4613(6)	118(5)
C(155)	8479(7)	-672(7)	4370(5)	95(4)
C(156)	8866(7)	-185(7)	4599(5)	106(4)
C(157)	9185(8)	-186(9)	4994(6)	125(6)
C(158)	9093(8)	-687(9)	5187(6)	127(6)
C(159)	8692(8)	-1184(9)	4982(6)	136(6)
C(160)	8382(7)	-1173(8)	4571(5)	115(5)
C(161)	6940(9)	-1273(9)	3988(7)	145(5)
C(162)	6418(9)	-1737(9)	3973(8)	154(6)
C(163)	6431(10)	-2215(10)	3686(8)	157(6)
C(164)	6885(11)	-2238(9)	3437(7)	155(6)
C(165)	7446(10)	-1779(8)	3497(7)	153(6)
C(166)	7451(8)	-1295(7)	3765(6)	116(4)
C(167)	8621(7)	-753(7)	3465(5)	109(4)
C(168)	9152(7)	-212(7)	3464(5)	111(4)
C(169)	8957(8)	638(8)	2883(6)	111(4)
C(170)	8719(8)	204(9)	2531(6)	132(6)
C(171)	8692(11)	320(12)	2107(7)	166(8)
C(172)	8913(15)	903(15)	2008(9)	207(12)
C(173)	9132(14)	1364(13)	2355(9)	207(12)
C(174)	9155(11)	1202(10)	2779(8)	165(8)
C(175)	9554(7)	1013(7)	3733(5)	100(4)
C(176)	10156(8)	1070(9)	3594(6)	136(7)
C(177)	10657(9)	1479(9)	3803(7)	145(7)
C(178)	10571(9)	1845(9)	4150(7)	139(7)
C(179)	9992(9)	1785(8)	4291(6)	136(6)
C(180)	9490(8)	1363(8)	4081(5)	116(5)
P(1)	3892(2)	1327(2)	10182(1)	98(1)
P(2)	4623(2)	2721(2)	10859(1)	101(1)

P(3)	3948(2)	2938(2)	9955(1)	95(1)
P(4)	2918(2)	1785(2)	10738(2)	115(1)
P(5)	5520(2)	4268(2)	3624(2)	112(1)
P(6)	5813(2)	3159(2)	3089(2)	112(1)
P(7)	7112(2)	3889(2)	4034(1)	108(1)
P(8)	5904(2)	3035(2)	4344(2)	104(1)
P(9)	7455(2)	754(2)	4156(1)	98(1)
P(10)	7111(2)	93(2)	3166(1)	95(1)
P(11)	8901(2)	475(2)	3443(1)	101(1)
P(12)	8077(2)	-623(2)	3855(1)	98(1)

checkCIF/PLATON report (justification)

Alert level B

PLAT342_ALERT_3_B Low Bond Precision on C-C Bonds ..... 0.02913 Ang.

Response: The structure contains disordered phenyl moieties. This

caused low accuracies in C-C bonds

PLAT973_ALERT_2_B Check Calcd Positive Resid. Density on Ag1 1.93 eA-3

Response: These are Fourier truncation ripples around the heavy atoms.

Supplementary Table 5 | Atomic coordinates (x 10^4) and equivalent isotropic displacement parameters (Å^{2}x 10^3) for $AuAg_{16}$ nanocluster. *U*(eq) is defined as one third of the trace of the orthogonalized U^{ij} tensor. Check CIF justifications of level A and level B alerts.

	x	*y*	*z*	*U*(eq)
Au(1)	6667	3333	5573(1)	164(2)
Ag(1)	7283(2)	3818(2)	5951(1)	169(2)
Ag(2)	6783(2)	3929(2)	5195(1)	176(2)
Ag(3)	6980(2)	4364(2)	5650(1)	172(2)
Ag(4)	7690(2)	4070(2)	5505(1)	172(2)

Ag(5)	6667	3333	6374(2)	180(3)
Ag(6)	6440(2)	4707(2)	5308(1)	187(2)
S(1)	7591(6)	4060(6)	6348(3)	182(5)
S(2)	6767(6)	4558(6)	4921(3)	183(5)
S(3)	7092(6)	5227(6)	5613(3)	182(5)
S(4)	8617(6)	4475(6)	5422(3)	189(6)
C(1)	7572(18)	4631(17)	6396(9)	188(9)
C(2)	7660(20)	5098(19)	6206(9)	188(9)
B(1)	8140(20)	5185(18)	6394(11)	188(9)
B(2)	7800(20)	4936(19)	6645(10)	190(9)
B(3)	7190(20)	4656(19)	6603(10)	190(9)
B(4)	7120(20)	4790(20)	6332(11)	189(9)
B(5)	8010(20)	5660(20)	6335(10)	189(10)
B(6)	8120(20)	5583(19)	6598(11)	189(10)
B(7)	7490(20)	5240(19)	6732(9)	191(10)
B(8)	7110(20)	5156(18)	6549(11)	190(9)
B(9)	7380(20)	5430(20)	6300(10)	190(9)
B(10)	7657(19)	5734(18)	6547(9)	191(9)
C(3)	6200(14)	4191(15)	4754(7)	196(9)
C(4)	6363(19)	4261(18)	4479(8)	209(11)
B(11)	5643(17)	3641(15)	4805(7)	197(11)
B(12)	5651(17)	4211(16)	4793(7)	195(10)
B(13)	6081(16)	4589(14)	4591(8)	201(10)
B(14)	5850(20)	3710(20)	4330(10)	212(12)
B(15)	5860(20)	4282(17)	4338(8)	211(12)
B(16)	5440(16)	4262(16)	4535(8)	203(11)
B(17)	5160(13)	3678(16)	4669(8)	200(11)
B(18)	5390(20)	3312(16)	4558(9)	201(12)
B(19)	5300(17)	3719(17)	4387(8)	204(12)
B(20)	6043(19)	3662(16)	4595(9)	204(10)
C(5)	7683(14)	5653(15)	5473(8)	200(10)
C(6)	7840(20)	6263(17)	5406(10)	209(11)
B(21)	7670(30)	5820(20)	5199(8)	208(11)
B(22)	7930(30)	5440(30)	5269(10)	211(11)
B(23)	8210(20)	5600(20)	5529(12)	205(11)
B(24)	8210(20)	6160(20)	5589(12)	208(12)

B(25)	8800(30)	6350(30)	5498(10)	218(13)
B(26)	8470(30)	6640(30)	5410(10)	217(12)
B(28)	8280(30)	5930(20)	5075(12)	217(13)
B(27)	8180(20)	6420(30)	5155(12)	218(12)
B(29)	8550(30)	5860(20)	5315(12)	216(11)
B(30)	8754(16)	6450(20)	5216(9)	221(13)
C(7)	8967(13)	4611(15)	5684(6)	172(9)
C(8)	9173(16)	4189(15)	5728(9)	174(9)
B(31)	8730(20)	4192(18)	5904(9)	172(10)
B(32)	8850(20)	4802(18)	5935(9)	179(9)
B(33)	9368(18)	5216(14)	5781(11)	181(10)
B(34)	9611(13)	4834(16)	5702(13)	179(10)
B(35)	8982(16)	4520(19)	6155(12)	181(11)
B(36)	9420(20)	5128(19)	6068(12)	188(11)
B(37)	9920(20)	5150(18)	5923(11)	187(11)
B(38)	9770(20)	4531(19)	5883(10)	183(10)
B(39)	9170(17)	4165(18)	5998(11)	179(10)
B(40)	9614(15)	4704(17)	6129(7)	189(11)
Au(2)	4924(1)	4733(1)	7277(1)	213(2)
P(1)	4542(7)	4490(7)	6904(4)	219(6)
P(2)	5682(7)	4807(7)	7108(4)	212(7)
P(3)	4822(9)	5337(9)	7503(5)	280(8)
P(4)	4427(8)	4117(8)	7566(4)	254(7)
C(15)	5590(20)	4820(20)	6827(11)	234(16)
C(16)	4990(20)	4370(20)	6809(10)	206(15)
C(9)	5830(20)	4273(14)	7177(11)	256(13)
C(10)	6106(17)	4141(19)	7032(7)	262(15)
C(11)	6125(15)	3690(20)	7069(9)	261(15)
C(12)	5860(20)	3379(12)	7252(11)	281(18)
C(13)	5585(17)	3510(20)	7397(7)	291(17)
C(14)	5566(16)	3960(20)	7359(9)	278(15)
C(17)	6296(14)	5464(16)	7142(10)	256(13)
C(18)	6630(30)	5416(17)	7286(9)	290(17)
C(19)	7100(20)	5850(30)	7346(7)	311(19)
C(20)	7218(13)	6330(20)	7261(10)	320(20)
C(21)	6880(20)	6376(14)	7117(9)	308(19)

C(22)	6418(19)	5940(30)	7057(7)	303(17)
C(23)	4490(20)	4990(20)	6723(9)	243(14)
C(24)	4226(15)	4855(13)	6519(11)	250(15)
C(25)	4257(16)	5230(30)	6374(6)	261(16)
C(26)	4560(20)	5750(20)	6432(9)	269(18)
C(27)	4823(15)	5887(14)	6635(11)	261(17)
C(28)	4792(17)	5510(30)	6781(6)	248(15)
C(29)	3884(12)	3906(14)	6861(8)	216(12)
C(30)	3806(15)	3460(20)	6754(7)	244(16)
C(31)	3310(20)	3040(13)	6735(7)	247(16)
C(32)	2896(11)	3066(15)	6822(8)	247(17)
C(33)	2974(16)	3510(20)	6928(7)	229(16)
C(34)	3470(20)	3932(13)	6948(6)	221(15)
C(35)	3991(10)	3420(11)	7481(7)	272(13)
C(36)	3467(10)	3191(12)	7522(7)	281(17)
C(37)	3126(12)	2736(13)	7413(8)	296(18)
C(38)	3309(17)	2509(13)	7263(7)	310(20)
C(39)	3834(18)	2738(13)	7222(7)	323(19)
C(40)	4175(14)	3193(13)	7330(7)	305(17)
C(41)	4810(30)	4050(30)	7809(6)	304(16)
C(42)	4467(16)	3600(20)	7920(14)	326(19)
C(43)	4590(30)	3496(17)	8133(14)	330(20)
C(44)	5050(30)	3850(30)	8235(6)	330(20)
C(45)	5387(17)	4300(20)	8125(11)	320(20)
C(46)	5270(20)	4403(18)	7912(11)	305(19)
C(47)	4420(30)	5570(30)	7349(7)	290(13)
C(48)	4717(14)	6100(30)	7361(8)	303(16)
C(49)	4560(30)	6411(15)	7252(11)	317(17)
C(50)	4100(30)	6190(30)	7131(8)	308(18)
C(51)	3801(16)	5650(30)	7120(6)	297(17)
C(52)	3960(20)	5347(14)	7228(9)	302(16)
C(53)	5320(20)	5857(16)	7698(10)	322(14)
C(54)	5304(18)	6140(20)	7881(11)	335(18)
C(55)	5750(30)	6464(18)	7998(7)	344(19)
C(56)	6217(19)	6510(19)	7932(12)	360(20)
C(57)	6230(20)	6230(30)	7749(13)	364(19)

C(58)	5790(40)	5900(20)	7632(8)	351(17)
C(59)	4290(30)	4820(30)	7726(13)	305(14)
C(60)	3920(30)	4240(30)	7685(13)	295(14)

---

checkCIF/PLATON report (justification)
Alert level A
THETM01_ALERT_3_A The value of sine(theta_max)/wavelength is less than 0.550
Calculated sin(theta_max)/wavelength = 0.4539
Response: The crystal is very weakly diffracting at higher angles. Even
though data was collected up to 0.82 A resolution, the crystal did not diffract at
higher angles. Hence a resolution cut was applied during data integration. This is
the only crystal that we could obtain after several repeated crystallization.
PLAT084_ALERT_3_A High wR2 Value (i.e. > 0.25) ..... 0.54 Report
Response: The crystal diffracted extremely weakly. Also the
peripheral moieties are highly disordered. Inclusion of very weak reflections
above 35 degrees caused high wR2.
PLAT973_ALERT_2_A Check Calcd Positive Resid. Density on Au1 5.12 eA-3
Response: The electron density is observed near a heavy atom. Due to
poor quality of the data, absorption correction is not adequate.
PLAT973_ALERT_2_A Check Calcd Positive Resid. Density on Au2 3.11 eA-3
Response: The electron density is observed near a heavy atom. Due to
poor quality of the data, absorption correction is not adequate.
PLAT973_ALERT_2_A Check Calcd Positive Resid. Density on Ag1 3.04 eA-3
Response: The electron density is observed near a heavy atom. Due to
poor quality of the data, absorption correction is not adequate.
PLAT973_ALERT_2_A Check Calcd Positive Resid. Density on Ag3 2.92 eA-3
Response: The electron density is observed near a heavy atom. Due to
poor quality of the data, absorption correction is not adequate.PLAT973_ALERT_2_A Check
Calcd Positive Resid. Density on Ag4 2.82 eA-3
Response: The electron density is observed near a heavy atom. Due to
poor quality of the data, absorption correction is not adequate.
PLAT973_ALERT_2_A Check Calcd Positive Resid. Density on Ag2 2.76 eA-3
Response: The electron density is observed near a heavy atom. Due to
poor quality of the data, absorption correction is not adequate.
PLAT973_ALERT_2_A Check Calcd Positive Resid. Density on Ag5 2.60 eA-3

Response: The electron density is observed near a heavy atom. Due to poor quality of the data, absorption correction is not adequate.

PLAT973_ALERT_2_A Check Calcd Positive Resid. Density on Ag6 2.54 eA-3

Response: The electron density is observed near a heavy atom. Due to poor quality of the data, absorption correction is not adequate.

Alert level B

PLAT026_ALERT_3_B Ratio Observed / Unique Reflections (too) Low .. 30% Check

Response: The data quality is very poor due to very weak diffraction of the crystal. Several attempts were made to prepare the crystal during a period of 6-7 months and we could get this crystal specimen only for the data collection. A total of 21 runs performed by an optimized data collection strategy, however only 5 runs contain diffraction spots.

PLAT082_ALERT_2_B High R1 Value ..... 0.17 Report

Response: Data quality is very poor and also the structure contains disordered moieties. All the carborane moieties are refined using DFIX, SIMU and ISOR restraints. Due to poor resolution of the crystal, AFIX 66 was used to generate idealized coordinates for all phenyl moieties All these factors contributed to high R1 values. The data presented here is only used for representation purpose and to show that the molecule has been formed with the support of other experimental observations.

PLAT094_ALERT_2_B Ratio of Maximum / Minimum Residual Density .... 4.47 Report

Response: The residual electron density is observed near a heavy atom. Due to poor quality of the data, absorption correction is not adequate.

PLAT342_ALERT_3_B Low Bond Precision on C-C Bonds ..... 0.08463 Ang.

Response: Due to poor resolution of the crystal and disorder in phenyl moieties, the accuracies in C-C bonds are low.

Supplementary Table 6 | Atomic coordinates (x 10^4) and equivalent isotropic displacement parameters (Å^{2}x 10^3) for $AuAg_{12}Cu_4$ nanocluster. *U*(eq) is defined as one third of the trace of the orthogonalized U^{ij} tensor. Check CIF justifications of level A and level B alerts.

	x	*y*	*z*	*U*(eq)
Cu(1)	6946(1)	1946(1)	6946(1)	82(1)
Ag(1)	6849(1)	1654(1)	6242(1)	66(1)
Au(1)	6250	1250	6250	58(1)
S(1)	7279(1)	2072(1)	6481(1)	88(1)
C(1)	7172(4)	2489(4)	6307(4)	96(4)
C(2)	7042(5)	2820(4)	6573(5)	125(5)
B(1)	7466(8)	2816(6)	6365(8)	160(10)
B(2)	7418(5)	2635(4)	5976(5)	105(5)
B(3)	6994(5)	2525(4)	5899(4)	93(4)
B(4)	6768(5)	2640(4)	6272(4)	95(5)
B(5)	7225(8)	3215(5)	6381(8)	155(10)
B(6)	6811(8)	3105(5)	6308(7)	139(8)
B(7)	6748(6)	2913(4)	5886(5)	112(6)
B(8)	7171(6)	2916(5)	5732(6)	134(8)
B(9)	7441(8)	3097(6)	6017(8)	156(10)
B(10)	7040(7)	3259(5)	5981(7)	143(8)

checkCIF/PLATON report (justification)

Alert level B

PLAT973_ALERT_2_B Check Calcd Positive Resid. Density on Ag1 1.76 eA-3

Response: Residual electron density is found near the metal atoms as expected for heavy atom structures, which are probably due to absorption error or Fourier ripples around the heavy atom.

PLAT973_ALERT_2_B Check Calcd Positive Resid. Density on Au1 1.76 eA-3

Response: Residual electron density is found near the metal atoms as expected for heavy atom structures, which are probably due to absorption error or Fourier ripples around the heavy atom.

ChemComm

COMMUNICATION

View Article Online
View Journal | View Issue

Check for updates

Cite this: *Chem. Commun.*, 2025, **61**, 5577

Received 23rd December 2024,
Accepted 19th February 2025

DOI: 10.1039/d4cc06697a

rsc.li/chemcomm

Published on 26 February 2025. Downloaded on 12/29/2025 3:09:13 AM.

Nanosheet-to-nanoparticle transformation in charged water microdroplets: a pathway for 2D to 0D materials†

B. Krishnamurthy Spoorthi,[a] Angshuman Ray Chowdhuri,[a] Biswajit Mondal,[a] Sujan Manna,[a] Anubhav Mahapatra,[a] Amoghavarsha Ramachandra Kini[a] and Thalappil Pradeep *[ab]

This study explores the electrospray-induced transformation of molybdenum disulfide (MoS_2), graphene oxide (GO), and tungsten disulphide (WS_2) nanosheets of micrometer lateral dimensions into the respective zero-dimensional nanoparticles within the reactive environment of charged water microdroplets. The products characterized by high-resolution transmission electron microscopy (HRTEM) and Raman spectroscopy showcase charged microdroplets as an ambient, scalable medium for the synthesis of nanomaterials with promising applications in catalysis and environmental remediation.

Layered two-dimensional (2D) materials, such as MoS_2, GO, and WS_2, have attracted scientific interest due to their unique structural and electronic properties.[1–3] Their layered configuration provides a large surface area, tuneable electronic properties, and abundant edge sites, making them valuable for catalysis, sensing, and environmental applications.[4,5] The transition from the bulk to 2D enhances their reactivity and electronic characteristics, allowing them to function in ways that are not achievable in the parent form.[6] However, reducing these 2D materials to zero-dimensional (0D) structures, like nanoparticles, offers even greater benefits, including increased reactivity, due to additional quantum confinement effects, an enhanced surface-to-volume ratio, and more active sites for chemical interactions. The transformation from multilayer 2D nanosheets to 0D nanoparticles is challenging as it requires destabilizing the van der Waals forces that hold the layers together, cleavages of chemical bonds within the 2D sheets, and reproducible control of the processes leading to uniform nanoparticles. Traditional methods for achieving this transformation, such as hydrothermal processes, often demand extreme conditions, such as high energy inputs or reactive environments, which can limit scalability and reproducibility.[7] Transformations in charged microdroplets are an innovative approach to effect the same. Electrospray produces charged microdroplets in which strong electric fields, coulombic forces, and associated effects may be used to fragment 2D nanosheets into nanoparticles under ambient conditions. Microdroplets have emerged as a unique reaction environment due to their ability to accelerate chemical reactions[8,9] and drive bond rearrangements that are not feasible in bulk solutions.[10,11] Within microdroplets, high electric fields, rapid solvent evaporation, and interfacial effects create a highly energetic microenvironment that can induce bond polarization, solvation of changes, and mechanical stress. These conditions have been shown to facilitate rapid transformations, such as oxidation, reduction, and nanoparticle assembly, occurring within micro- to milli-seconds.[12–14] The new microdroplet-based electrospray process offers a faster, safer, and more energy-efficient alternative to conventional nanoparticle synthesis. Unlike hydrothermal or chemical reduction methods, it operates under ambient conditions, avoiding high temperatures, harsh reagents, and long reaction times. Building on previous work in microdroplet-based synthesis, including our recent publication on the fragmentation of microparticles of hard minerals such as quartz and ruby into their nanoparticle analogues, *via* charged microdroplets,[15] this study focuses on the transformation of MoS_2, WS_2 and GO nanosheets into uniform nanoparticles. Using pre-prepared nanosheets simplifies transformation, as their exfoliated structure fragments easily in microdroplets. This experiment extends our understanding of microdroplet-induced transformations and explores the potential of electrospray to produce nanostructured MoS_2, GO, and WS_2 with enhanced reactivity and surface properties. By understanding how these materials behave in microdroplet environments, we can unlock new avenues for their applications in catalysis, water purification, and other environmentally focused technologies.

Briefly, to synthesize MoS_2 nanosheets, MoS_2 powder was reacted with *n*-butyllithium in hexane under argon.[16] This intercalation was followed by exfoliation in water, causing rapid H_2 evolution that separated the layers.

[a] *DST Unit of Nanoscience (DST UNS) & Thematic Unit of Excellence (TUE), Department of Chemistry, Indian Institute of Technology Madras (IITM), Chennai 600036, India. E-mail: pradeep@iitm.ac.in*

[b] *International Centre for Clean Water, 2nd Floor, B-Block, IIT Madras Research Park, Kanagam Road, Taramani, Chennai 600113, India*

† Electronic supplementary information (ESI) available. See DOI: https://doi.org/10.1039/d4cc06697a

This journal is © The Royal Society of Chemistry 2025

Published on 26 February 2025. Downloaded on 12/29/2025 3:09:13 AM.

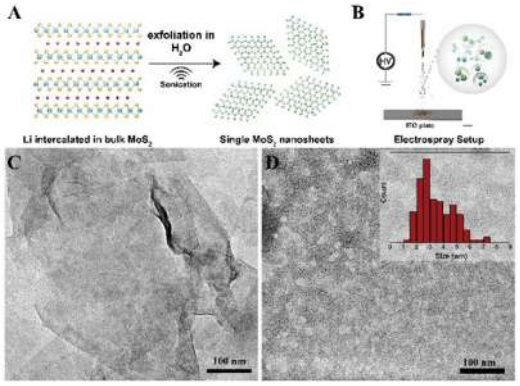


Fig. 1 (A) A schematic of the preparation of MoS_2 nanosheets from bulk MoS_2 through wet chemical synthesis. (B) Schematic of the electrospray set-up. (C) Transmission electron microscopy (TEM) image showing the MoS_2 nanosheets synthesized by wet chemical synthesis. (D) Large area TEM image of MoS_2 nanoparticles formed by ambient electrospray. The inset shows the particle size distribution of electrosprayed MoS_2.

The nanosheets were then purified by centrifugation to isolate single- to few-layer structures (Fig. 1A). The detailed synthesis procedure is outlined in the ESI.† In this experiment, we used a custom-built nanoelectrospray source (Fig. 1B) to generate charged water microdroplets containing a fine dispersion of MoS_2 nanosheets, which were deposited onto a TEM grid positioned on an indium tin oxide (ITO)-coated collector plate. The collector was grounded *via* a picoammeter to measure the deposition current, and a voltage of approximately 3.0 kV was applied to the solution within a glass spray tip using a platinum (Pt) wire electrode. The spray plume emitted from the nanoelectrospray tip was visualized with a laser torch. Additional details of the experiment can be found in the ESI.† The electrospray setup, shown schematically in Fig. 1B, enabled the deposition of charged microdroplets containing MoS_2 nanosheets onto a substrate positioned at a defined distance from the spray tip. During deposition, a dark circular spot appeared on the substrate due to the continuous impact of the spray plume. This process led to the fragmentation of MoS_2 nanosheets into uniformly distributed nanoparticles, underscoring the role of water microdroplets and electrospray parameters in facilitating nanosheet-to-nanoparticle transformation. The nanosheets and the formed nanoparticles were examined using TEM. The TEM image of the MoS_2 nanosheets before electrospray deposition reveals a well-defined, sheet-like morphology with lateral dimensions in the nanometer range (Fig. 1C). These images show a relatively smooth and continuous surface with no observable defects, confirming the high-quality exfoliation of MoS_2 into thin nanosheets. In the TEM image of MoS_2 after electrospray (Fig. 1D), we observe a significant morphological transformation from sheet-like structures to discrete nanoparticles. The original nanosheets, characterized by their extended and layered morphology, have been effectively fragmented into uniformly distributed nanoparticles with a relatively narrow size distribution with an average size of 3.4 ± 1.5 nm (inset, Fig. 1D). These particles appear well-dispersed across the TEM grid, indicating effective breakup and dispersion, facilitated by the electrospray process (Fig. S1, ESI†). The nanoparticles exhibit a consistent size, suggesting that the electrospray's charged microdroplets provide a controlled environment for fragmentation and stabilization. Fig. S2 (ESI†) shows the TEM images of MoS_2 nanoparticles post-electrospray at varying magnifications, indicating a clear morphological transformation. The extended and layered MoS_2 nanosheets now appear as discrete, uniformly distributed nanoparticles. The HRTEM images reveal lattice fringes with a *d*-spacing of 0.27 nm, consistent with the (100) planes of MoS_2, confirming the structural integrity of MoS_2 even after nanosheet fragmentation. This *d*-spacing further validates the transformation of MoS_2 from 2D nanosheets to well-defined 0D nanoparticle structures, retaining characteristics that are crucial for potential catalytic and electronic applications. The morphology of the nanoparticles shows spherical boundaries with minimal aggregation. The observed uniformity in particle size and shape aligns with the rapid, high-energy reactions typical of microdroplet chemistry, where transformations can occur within microseconds to milliseconds as the droplet undergoes rapid evaporation and charge-induced processes (ESI†). In the optimization of electrospray conditions, we tested a range of voltages, emitter-to-collector distances, effect of the solvent, and nebulization pressures to achieve well-dispersed MoS_2 nanoparticles. Based on trials, an optimal applied voltage of 3.0 kV was identified for an emitter-to-collector distance (*d*) of 5 mm. At this distance, uniform MoS_2 nanoparticles were observed. Water was used as a solvent to achieve the transformation. In optimizing the electrospray conditions for MoS_2 nanosheet transformation, the parameter '*d*' was varied systematically (Fig. S3, ESI†). At an optimized distance of 5 mm, uniform and well-dispersed MoS_2 nanoparticles were observed. At shorter distances (<5 mm), aggregation was evident due to limited time for the transformation, resulting in partially fragmented particles. In contrast, at longer distances (>5 mm), there was no transformation, but broken sheets were formed, likely to have been caused by changes in the electric field (ESI†). Instead of applied potential, we used varying nebulization pressures to generate microdroplets containing MoS_2 nanosheets (Fig. S5, ESI†). It is evident that the applied pressures of 10, 15, 20, and 25 psi, typically used in electrospray processes, were insufficient to induce the nanosheet-to-nanoparticle transformation and MoS_2 remained in its original nanosheet morphology. Applied voltage and the electric field strength affect the electrospray process, which can significantly influence the energy imparted to the microdroplets containing MoS_2 nanosheets, thereby affecting disintegration (Fig. S5, ESI†). For applied potentials below 3.0 kV (2.4, 2.6, and 2.8 kV), the electric field strength was insufficient to fully fragment the MoS_2 nanosheets, resulting in partial disintegration where the sheet-like morphology persisted. This limited breakdown is likely to be due to inadequate coulombic forces to overcome the interlayer interactions of the nanosheets and the bond energy within the nanosheets. At a higher potential of 3.2 kV, increased electric field strength led to particle irregularities and polydispersity, as the elevated voltage introduced instability in droplet formation. At a slightly higher potential of 3.5 kV, inorganic fullerene (IF)-like structures were observed (Fig. S6, ESI†), which suggest unique conditions within the microdroplets. In this environment, rapid

This journal is © The Royal Society of Chemistry 2025

Published on 26 February 2025. Downloaded on 12/29/2025 3:09:13 AM.

evaporation and high electric field strength promote significant structural rearrangements. The charged microdroplets are likely to have induced surface stress inducing van der Waals interactions between the MoS_2 layers, encouraging the nanosheets to bend and fold. This self-assembly process minimizes surface energy, resulting in cage-like IF structures. The electric field and confinement within microdroplets provide ideal conditions for MoS_2 to transform into these closed and stable configurations, like the formation mechanisms observed in other fullerene-like structures (ESI†). The choice of solvent greatly affects the dispersion of MoS_2 nanosheets. MoS_2 disperses well in water but tends to stack in methanol-rich environments. Testing various water-to-methanol solvent ratios (Fig. S7, ESI†) showed no disintegration of the nanosheets. Instead, increased methanol content caused the sheets to align into stacked layered structures. This stacking of MoS_2 nanosheets in methanol-rich environments is likely to be a result of methanol's lower polarity, which decreases the solubility of the MoS_2 sheets. While water provides strong dispersive forces that keep MoS_2 sheets separated, the weaker interactions of methanol allow the sheets to restack. Additionally, faster evaporation in methanol-rich droplets increases the local concentration of MoS_2, promoting aggregation. Together, these factors lead to a stacked layered structure, as van der Waals forces between sheets dominate in the less disruptive environment of methanol. The stacked sheets would need more force for fragmentation.

To explore whether GO nanosheets, a 2D material in oxide form, would undergo similar transformations to MoS_2, we electrosprayed a GO dispersion in water (details of synthesis are presented in the ESI†) at 3.5 kV. The results showed a comparable phenomenon, with the GO nanosheets transitioning into nanoparticles through ambient electrospray (Fig. 2). The initial sheet-like morphology of GO (Fig. 2A) was successfully fragmented (Fig. 2B) and formed nano-sized particles. Also, IF-like cages were observed at an applied potential of 4.0 kV (Fig. 2C and D), suggesting that the high electric field and surface stress in the electrospray environment drive self-assembly into closed, spherical structures. These IF-like configurations in GO highlight the role of the electric field in promoting structural rearrangement, as the nanosheets fold and curve to minimize surface energy under appropriate conditions, driven by enhanced van der Waals interactions under the elevated field conditions. This process confirms that the electrospray technique can induce similar transformations in GO and MoS_2, broadening the applicability of this method to oxide-based 2D materials. To analyze the transformation of MoS_2 and GO nanosheets into nanoparticles, we conducted Raman spectroscopy of the samples collected on aluminium substrates post-electrospray (Fig. 3). The spectra provide insights into the structural and vibrational characteristics before and after transformation. The shifts in both E^1_{2g} and A^1_g modes reflect the transition from bulk to 2D and then to 0D forms of MoS_2 (Fig. 3A). A gradual upward shift with reduced dimensionality of the E^1_{2g} mode (in-plane vibration) indicates layer thinning and confinement as nanoparticles.

An initial downshift with nanosheet formation, followed by an upshift in nanoparticles of the A_{1g} mode, is likely to be due to changes in out-of-plane vibrational constraints.[17–19] These changes confirm that the structural changes due to size reduction from the bulk to nanosheet to nanoparticle affect the vibrational properties of MoS_2, reflecting decreased layer interactions and increased phonon confinement in nanoparticles. Raman peaks in Fig. 3B include the D band around 1350 cm^{-1}, associated with structural defects or disorder, and the G band near 1580 cm^{-1}, which corresponds to the graphitic domains. An increase in the D/G intensity ratio after electrospray suggests enhanced disorder, consistent with the fragmentation and reorganization of GO nanosheets into nanoparticles. This observation aligns with previous findings that structural reconfiguration or reduced dimensionality can amplify defect-related signals in the Raman spectra.[20] These results confirm the effectiveness of the electrospray process in inducing transformations in both MoS_2 and GO, yielding nanoparticles that exhibit distinct structural changes observable *via* Raman peak shifts and intensity variations.

To generalize the process, we also electrosprayed WS_2, prepared similarly to the MoS_2 nanosheets as described in the ESI.† This experiment demonstrated that the transformation process is applicable to other 2D materials, following similar synthesis and electrospray conditions. As shown in

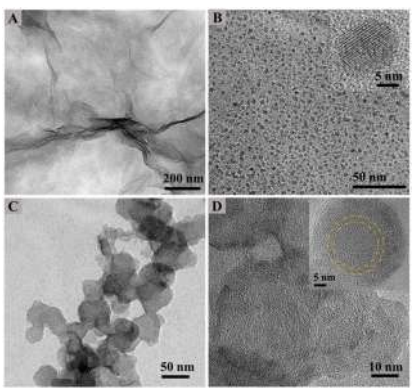


Fig. 2 Process of nanoparticle formation from GO nanosheets. (A) TEM image of the as-prepared GO nanosheet. (B) GO nanoparticles formed through ambient electrospray at 3.5 kV. (C) Formation of IF-like cages at 4.0 kV. (D) Magnified TEM images of IF-like particles. Magnification of a part of the image is presented as an inset to show the concentric stacks of GO sheets.

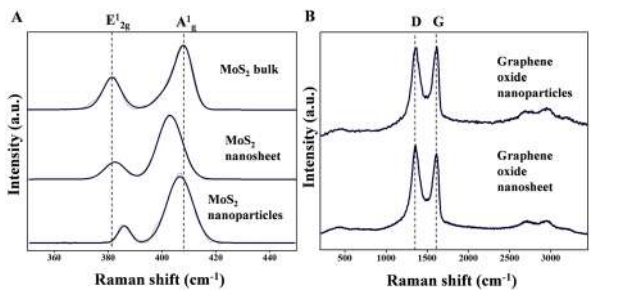


Fig. 3 Raman analysis of (A) MoS_2 bulk, nanosheets, and nanoparticles as well as (B) GO nanosheets and nanoparticles.

Published on 26 February 2025. Downloaded on 12/29/2025 3:09:13 AM.

Fig. S8 (ESI†), WS_2 also underwent a structural transformation at 3.0 kV applied potential, resulting in nanoparticles with uniform morphology and crystallinity. Thus, the electrospray approach outlined is a versatile technique for converting layered 2D materials like MoS_2 and WS_2 into stable, well-dispersed nanoparticles, making it a broadly applicable method for nanoparticle synthesis across various transition metal dichalcogenides. The formation of nanoparticles from nanosheets during the electrospray process can be attributed to several contributing factors that are activated within the charged microdroplets under high electric field conditions. The key factors driving this transformation include coulombic forces, rapid solvent evaporation, confinement effects, and interlayer disruption. The high electric field polarizes the nanosheets, generating surface charges that create strong coulombic repulsion, which disrupts the interlayer van der Waals forces, promoting fragmentation (ESI†). The Coulomb explosion of the droplets results in intense pressure fluctuations within the droplets. The concentration of charges may also destabilize the layered structure enhancing interlayer separation. As the droplet shrinks, confinement within the microdroplets favors surface energy minimization, encouraging the sheets to fold or fragment into stable, spherical nanoparticles, depending on the microenvironment. This reconfiguration often leads to uniform particles or fullerene-like structures, as the nanosheets adapt to minimize energy in response to the unique electrospray conditions. As many of these effects are complex and are also further complicated by the presence of reactive species,[21–23] a consistent mechanism is yet to be developed, as in the case of mineral fragmentation.[15]

In conclusion, this study highlights the transformative potential of electrospray in synthesizing zero-dimensional nanoparticles from two-dimensional nanosheets like MoS_2, GO, and WS_2. By leveraging the unique environment of reactive microdroplets, we demonstrate a controlled and efficient pathway for nanosheet fragmentation under ambient conditions. This electrospray-based method offers a scalable, versatile alternative to conventional high-energy approaches, as shown by our TEM and Raman spectroscopy results, which reveal uniform and stable nanoparticles with enhanced reactivity and structural integrity. These findings underscore the promise of the electrospray method for advancing nanomaterials synthesis, with potential applications in catalysis, environmental remediation, and beyond. This work opens doors to novel applications of microdroplet chemistry in nanotechnology, emphasizing the role of ambient electrospray in precision fabrication with sustainability. However, it needs further validation across additional materials.

The authors thank the Department of Science and Technology, Government of India, for its continuous support of our research program on nanomaterials.

Data availability

The data supporting this article, including all experimental results and analysis, are included in the main article and its ESI.† No additional data have been deposited in external repositories.

Conflicts of interest

There are no conflicts to declare.

Notes and references

1 W. Zhao, R. M. Ribeiro and G. Eda, *Acc. Chem. Res.*, 2015, **48**, 91–99.
2 W. Zhao, J. Pan, Y. Fang, X. Che, D. Wang, K. Bu and F. Huang, *Chem. – Eur. J.*, 2018, **24**, 15942–15954.
3 X. Li, L. Tao, Z. Chen, H. Fang, X. Li, X. Wang, J. Bin Xu and H. Zhu, *Appl. Phys. Rev.*, 2017, **4**, 021306.
4 Z. Wang and B. Mi, *Environ. Sci. Technol.*, 2017, **51**, 8229–8244.
5 B. L. Li, M. I. Setyawati, H. L. Zou, J. X. Dong, H. Q. Luo, N. B. Li and D. T. Leong, *Small*, 2017, **13**, 1–20.
6 M. Chhowalla, H. S. Shin, G. Eda, L. J. Li, K. P. Loh and H. Zhang, *Nat. Chem.*, 2013, **5**, 263–275.
7 D. Pan, J. Zhang, Z. Li and M. Wu, *Adv. Mater.*, 2010, **22**, 734–738.
8 S. Banerjee and R. N. Zare, *Angew. Chem., Int. Ed.*, 2015, **54**, 14795–14799.
9 K. Naveen, V. S. Rawat, R. Verma and E. Gnanamani, *Chem. Commun.*, 2024, **60**, 13263–13266.
10 Z. Wei, Y. Li, R. G. Cooks and X. Yan, *Annu. Rev. Phys. Chem.*, 2020, **71**, 31–51.
11 S. Bose, M. Mofidfar and R. N. Zare, *J. Am. Chem. Soc.*, 2024, **146**, 27964–27971.
12 J. K. Lee, K. L. Walker, H. S. Han, J. Kang, F. B. Prinz, R. M. Waymouth, H. G. Nam and R. N. Zare, *Proc. Natl. Acad. Sci. U. S. A.*, 2019, **116**, 19294–19298.
13 C. Gong, D. Li, X. Li, D. Zhang, D. Xing, L. Zhao, X. Yuan and X. Zhang, *J. Am. Chem. Soc.*, 2022, **144**, 3510–3516.
14 A. Ray Chowdhuri, B. K. Spoorthi, B. Mondal, P. Bose, S. Bose and T. Pradeep, *Chem. Sci.*, 2021, **12**, 6370–6377.
15 B. K. Spoorthi, K. Debnath, P. Basuri, A. Nagar, U. V. Waghmare and T. Pradeep, *Science*, 2024, **384**, 1012–1017.
16 L. Yuwen, H. Yu, X. Yang, J. Zhou, Q. Zhang, Y. Zhang, Z. Luo, S. Su and L. Wang, *Chem. Commun.*, 2016, **52**, 529–532.
17 X. Zhang, W. P. Han, J. B. Wu, S. Milana, Y. Lu, Q. Q. Li, A. C. Ferrari and P. H. Tan, *Phys. Rev. B: Condens. Matter Mater. Phys.*, 2013, **87**, 1–8.
18 A. Berkdemir, H. R. Gutiérrez, A. R. Botello-Méndez, N. Perea-López, A. L. Elías, C. I. Chia, B. Wang, V. H. Crespi, F. López-Urías, J. C. Charlier, H. Terrones and M. Terrones, *Sci. Rep.*, 2013, **3**, 1–8.
19 C. Lee, H. Yan, L. E. Brus, T. F. Heinz, J. Hone and S. Ryu, *ACS Nano*, 2010, **4**, 2695–2700.
20 Å. Björkman, *Schweiz. Z. Hydrol.*, 1969, **31**, 632–645.
21 M. Angelaki, J. D'Erceville, D. J. Donaldson and C. George, *J. Am. Chem. Soc.*, 2024, 2–6.
22 D. Xing, Y. Meng, X. Yuan, S. Jin, X. Song, R. N. Zare and X. Zhang, *Angew. Chem., Int. Ed.*, 2022, **61**, e202207587.
23 L. E. Krushinski and J. E. Dick, *Proc. Natl. Acad. Sci. U. S. A.*, 2024, **121**, e2321064121.

This journal is © The Royal Society of Chemistry 2025

Supplementary Information (SI) for ChemComm.
This journal is © The Royal Society of Chemistry 2025

Electronic Supplementary Information

Nanosheet-to-Nanoparticle Transformation in Charged Water Microdroplets: A Pathway to Zero-Dimensional Materials†

B Krishnamurthy Spoorthi, [a] Angshuman Ray Chowdhuri,[a] Biswajit Mondal,[a] Sujan Manna,[a] Anubhav Mahapatra,[a] Amoghavarsha Ramachandra Kini [a] and Thalappil Pradeep *[ab]

[a]DST Unit of Nanoscience (DST UNS) & Thematic Unit of Excellence (TUE), Department of Chemistry, Indian Institute of Technology Madras, Chennai 600036, India.

[b]International Centre for Clean Water, 2nd Floor, B-Block, IIT Madras Research Park, Kanagam Road, Taramani, Chennai 600113, India.

Table of contents

Name	Description	Page no.
S1	**Synthesis of MoS_2 NS**	S3
S2	**Synthesis of WS_2 nanosheet**	S3
S3	**Synthesis of graphene oxide (GO)**	S4
S4	**Electrospray deposition of MoS_2 NSs**	S4
S5	**Electrospray deposition of WS_2 and GO NSs**	S6
S6	**The charge-induced process**	S6
S7	**The effect of tip-collector distance on the morphology**	S6
S8	**Plausible reasons for the effect of evaporation on observed morphology**	S7
S9	**The confinement effect**	S7
S10	**The effect of surface charge**	S8

Fig. S1	**Comparison of nanosheets before and after electrospray at different magnification**	S10
Fig. S2	**TEM images showing MoS_2 nanoparticles**	S11
Fig. S3	**Effect of distance on the morphology**	S12
Fig. S4	**Nebulization at different gas pressures**	S13
Fig. S5	**Effect of applied potential on the electrosprayed MoS_2**	S14
Fig. S6	**Inorganic fullerene like (IF) MoS_2 nanoparticles**	S15
Fig. S7	**Effect of solvent**	S16
Fig. S8	**Electrospray of WS_2 nanosheets**	S17

S1. Synthesis of MoS_2 NS

Direct electrospraying of MoS_2 powder dispersions is challenging because MoS_2 is inherently hydrophobic and tends to aggregate in water due to strong van der Waals forces between its layers, leading to an unstable dispersion. To overcome this, we synthesized lower-dimensional materials, specifically the nanosheets.

To synthesize MoS_2 nanosheets (NSs), a chemical exfoliation method was applied starting from MoS_2 powder. Initially, 300 mg of MoS_2 powder was placed in a round-bottom flask under an argon atmosphere, and 3 mL of 1.6 M n-butyllithium was introduced. This mixture was stirred continuously for 48 hours under the same conditions. Afterward, the lithium-intercalated product was thoroughly washed with hexane to eliminate any residual reactants, followed by the addition of 100 mL of distilled water. The resulting mixture was then sonicated in a bath sonicator for one hour. To separate unexfoliated MoS_2, the aqueous MoS_2 NSs dispersion was centrifuged at 18,000 rpm. The quality of the synthesized MoS_2 NSs was subsequently assessed using electron microscopy and Raman spectroscopy. 500 µg of MoS_2 was then dispersed in 2 mL of water and used for the electrospray experiments.

S2. Synthesis of WS_2 nanosheet

To synthesize WS_2 nanosheets (NSs), a chemical exfoliation technique was employed starting with WS_2 powder. A total of 300 mg of WS_2 powder was placed in a round-bottom flask under an argon atmosphere, and 3 mL of 1.6 M n-butyllithium was added. The mixture was stirred continuously for 48 hours under the same conditions. Afterward, the lithium-intercalated product was repeatedly washed with hexane to remove any remaining reactants. Then, 100 mL of distilled water was added, and the product was sonicated in a bath sonicator for one hour. The resulting aqueous dispersion of WS_2 NSs was then centrifuged at 18,000 rpm to separate unexfoliated WS_2. 500 µg of WS_2 was then dispersed in 2 mL of water and used for the electrospray experiments.

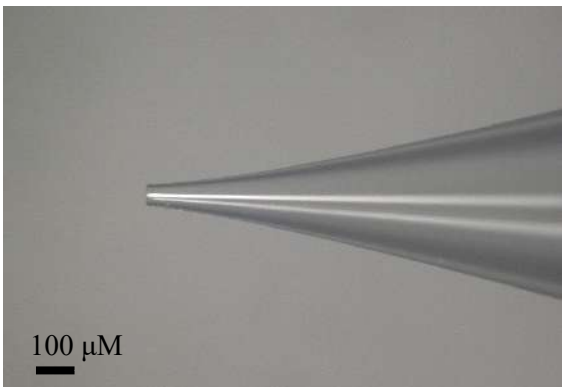
S3. Synthesis of graphene oxide (GO)

Graphene oxide (GO) was synthesized from graphite powder using a modified Hummers' method. Initially, 2 g of graphite powder was oxidized in a hot solution (100°C) containing 25 mL of concentrated sulfuric acid (H_2SO_4), 4 g of potassium persulfate ($K_2S_2O_8$), and 4 g of phosphorus pentoxide (P_2O_5). The resulting dark blue mixture was allowed to cool to room temperature over 6 hours, then diluted to 200 mL with deionized water and filtered. The filtrate was dried overnight at 60°C in a hot air oven. The pre-oxidized graphite powder (2 g) was then added to 92 mL of cold H_2SO_4 (0°C) under continuous stirring in an ice bath. Potassium permanganate ($KMnO_4$, 12 g) was gradually introduced to the mixture with stirring. After 15 minutes, 2 g of sodium nitrate ($NaNO_3$) was added, and the solution was stirred for an additional 2 hours at 35°C. Distilled water (200 mL) was added dropwise during stirring. The reaction was terminated by the simultaneous addition of a mixture of 300 mL distilled water and 10 mL of 30% hydrogen peroxide (H_2O_2). The final product was sequentially washed: first with diluted hydrochloric acid (HCl, 1:10), then with water. The product was suspended in distilled water, resulting in a brown dispersion, which was dialyzed extensively to remove residual metal ions and acids. The dispersion was exfoliated via ultrasonication at 300 W for 2 hours, and unexfoliated graphite oxide was removed by centrifugation at 12,000 rpm for 20 minutes using a KUBOTA centrifuge (Tokyo, Japan).

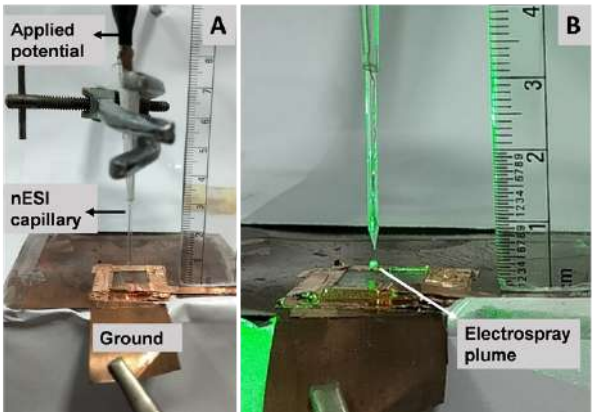
S4. Electrospray deposition of MoS_2 NSs

For electrospray deposition, a custom-built nanoelectrospray ionization (nESI) source was utilized. This nESI source was constructed by pulling a borosilicate glass capillary (0.86 mm inner diameter and 1.5 mm outer diameter) into two segments using a micropipette puller (Sutter Instruments, USA). The tips, after pulling, were examined under an optical microscope to ensure the precision and quality of the cut. Tips with a 50 μm opening were selected for all deposition experiments.

The MoS_2 solution was loaded into the nESI tips using a micro-injector pipette tip, and a platinum (Pt) wire was inserted into the solution to act as an electrode for high-voltage application. For the electrospray deposition of MoS_2 nanosheets (NSs), an aqueous suspension of MoS_2 NSs was prepared, and the spray was directed toward a grounded substrate. The distance between the tip of the nESI source and the surface of the substrate was optimized to 5 mm.



Photograph: nESI source tip used for the electrospray experiment.



Photograph: A) nanoelectrospray set up. B) The spray plume emitted from the nanoelectrospray tip visualized by a laser torch.

For TEM analysis, 20 µL of the precursor was used. For Raman spectroscopy, 500 µL of the precursor was electrosprayed to ensure uniform and reproducible sample deposition.

Nanoparticles can be collected in larger quantities by scaling up the experiment. Increasing the dispersion volume while maintaining optimized electrospray parameters enables large-scale production, making the method suitable for catalytic applications.

S5. Electrospray deposition of WS_2 and GO NSs

Electrospray deposition of WS_2 nanosheets and graphene oxide nanosheets was carried out under similar conditions as described for MoS_2, ensuring consistency in the deposition process.

S6. The charge-induced process

In electrospray occurs due to the interaction of a high electric field with microdroplets containing dispersed nanosheets. The high electric field induces polarization within the nanosheets. This results in fragmentation of the nanosheets into nanoparticles. As the droplets shrink due to rapid solvent evaporation, Coulombic repulsion between like charges on the nanosheets further aids in breaking down the layers. Additionally, confinement effects (in tiny droplets) within the microdroplets create localized stress, promoting uniform nanoparticle formation. This dynamic interplay between electric field strength, solvent evaporation, and confinement effects ensures the reproducible synthesis of nanoparticles with controlled morphology[1].

S7. The effect of tip-collector distance on the morphology

Th optimized distance of 5 mm resulted in uniformly distributed nanoparticles. At shorter distances (<5 mm), the droplets had insufficient time for complete solvent evaporation and nanosheet fragmentation, leading to particle aggregation and partially fragmented nanosheets. Conversely, at longer distances (>5 mm), the electric field strength weakened, resulting in incomplete transformations and the formation of irregular, broken sheets. This behavior can be attributed to two primary factors:

Electric Field Dynamics: The strength of the electric field decreases with increased distance between the emitter and collector, impacting the Coulombic forces responsible for nanosheet disintegration.

Time for Solvent Evaporation: Shorter distances limit the time available for solvent evaporation, preventing complete fragmentation, whereas excessive distances lead to reduced field effects and inefficient particle formation.

S8. Plausible reasons for the effect of evaporation on observed morphology

1. Coulombic Forces and Surface Charge Effects: During the electrospray process, high electric fields induce Coulombic forces and surface charges on the MoS_2 nanosheets. These forces disrupt interlayer van der Waals interactions and create mechanical stress, facilitating nanosheet fragmentation into smaller particles.

2. Localized Confinement and Supersaturation: The rapid solvent evaporation reduces the droplet volume swiftly, leading to confinement effects. This localized confinement increases the concentration of MoS_2 nanosheets within the droplet, enhancing the likelihood of structural rearrangements due to surface energy minimization.

3. Fragmentation and Morphological Changes: The shrinking microdroplet environment, coupled with strong surface tension, promotes bending, folding, and fragmentation of the 2D nanosheets into 0D nanoparticles. The rapid evaporation also provides insufficient time for re-stacking, ensuring uniform nanoparticle formation with narrow size distributions, as confirmed by TEM and Raman spectroscopy in our study.

S9. The confinement effect

Microdroplets are tiny reaction vessels. The confinement effects are embodied in the charged microdroplet environment created during the electrospray process. These effects are discussed and supported by the following observations and findings:

1. Droplet Shrinkage and Concentration Effects: As the solvent rapidly evaporates, the droplet volume decreases, leading to spatial confinement of MoS_2 nanosheets within the microdroplet. This enhances the local concentration of nanosheets and promotes their fragmentation.

2. TEM Evidence of Morphological Transformation: Figure 1 shows the transformation of MoS_2 nanosheets into uniformly distributed nanoparticles with narrow size distributions. This uniformity arises from confinement effects that restrict random aggregation and allow controlled fragmentation.

3. Electric Field and Surface Stress: The manuscript highlights how high electric fields within the charged microdroplets create surface stress and induce structural rearrangements. These effects are amplified by the droplet's shrinking size, as described in the discussion on electrospray parameters and their influence on morphology.

4. Surface Energy Minimization: The confinement effects lead to surface energy minimization, promoting bending, folding, and fragmentation of nanosheets into stable nanoparticles, as explained in the context of TEM and Raman data.

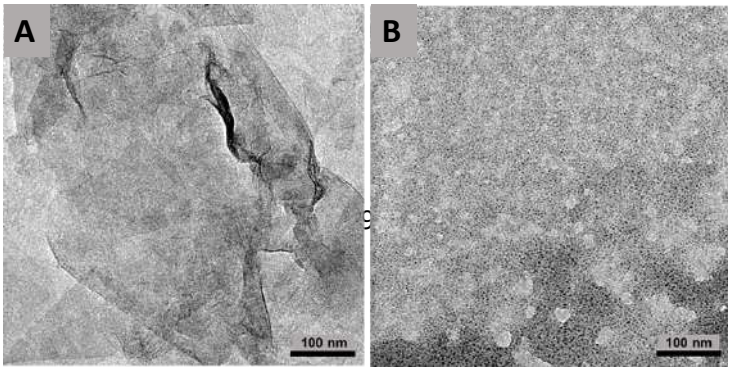
S10. The effect of surface charge

We attribute that the surface charge is formed during the electrospray process due to the high electric field applied to the dispersion. The electrospray process generates charged microdroplets, which undergo fission due to Coulomb repulsion as the solvent evaporates and the charge density increases. From the literature, it is known that at low flow rates (typically ~5 μL min^{-1}), the resulting droplets have a narrow size distribution, with the most abundant droplet radius being ~1.5 μm. Each of these droplets carry a charge of approximately ~10^{-14} C, corresponding to ~60,000 singly charged ions[2]. This process produces smaller tiny droplets via Coulomb fission, leading to high charge densities that polarize the MoS_2 nanosheets. The Coulombic forces induced by this polarization disrupt van der Waals interactions, fragmenting the nanosheets into nanoparticles. These insights highlight the critical role of droplet charge in driving nanosheet-to-nanoparticle transformations, as observed in our study.

Evidence for surface charge: TEM Analysis shows the transformation of nanosheets into uniformly distributed nanoparticles, consistent with Coulombic fragmentation. The shifts in E_{2g}^1 and A_{1g} modes in

the Raman spectroscopy confirm the reduced interlayer coupling due to charge-induced stress. Fragmentation occurs optimally at 3.0 kV, while lower voltages result in incomplete transformation, confirming the role of surface charge.

Supplementary figures



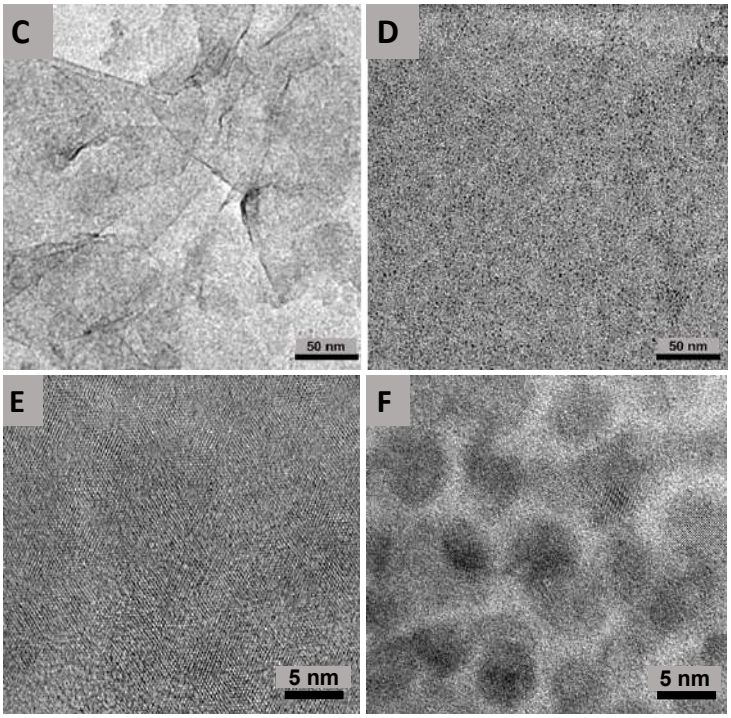


Fig. S1: Comparison of MoS_2 nanosheet before and after electrospray at different magnifications. A, C, E) As synthesised MoS_2 nanosheets before electrospray. B, D, F) MoS_2 nanoparticles formed after the electrospray.

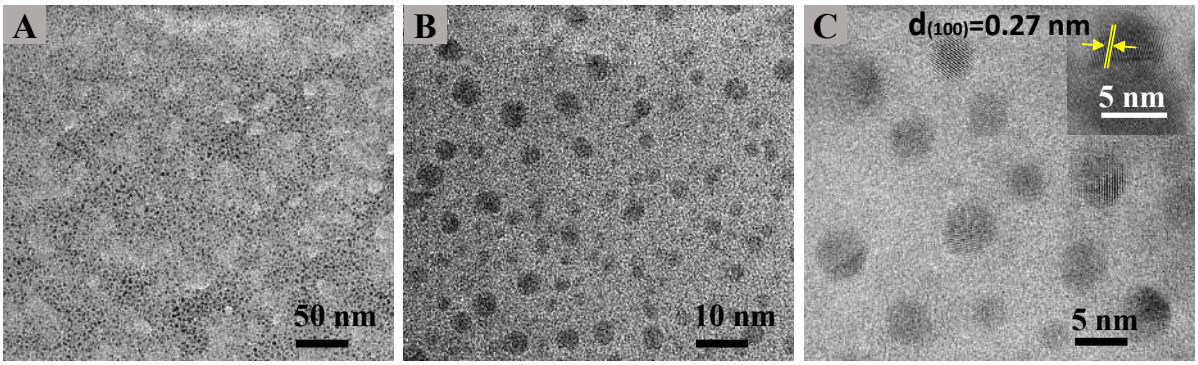


Fig. S2: TEM images showing MoS_2 nanoparticles at various magnifications. High resolution image in C shows the d spacing of (100) MoS_2.

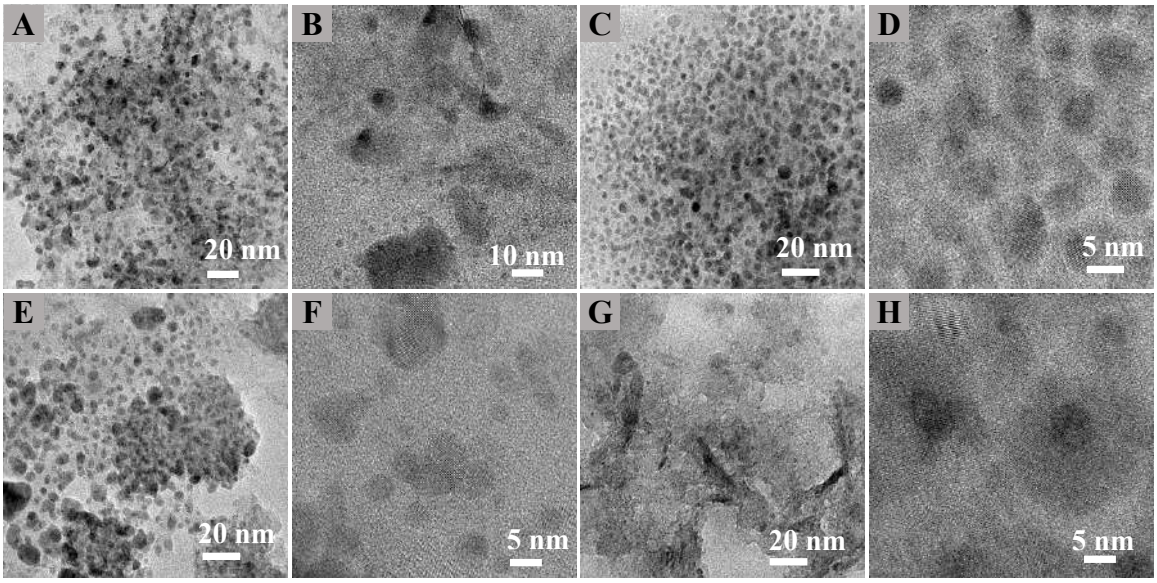


Fig. S3: Effect of distance between the emitter to the collector on the morphology of the electrosprayed MoS_2. A,B) 3 mm, C,D) 7 mm, E,F) 9 mm and G,H) 11 mm.

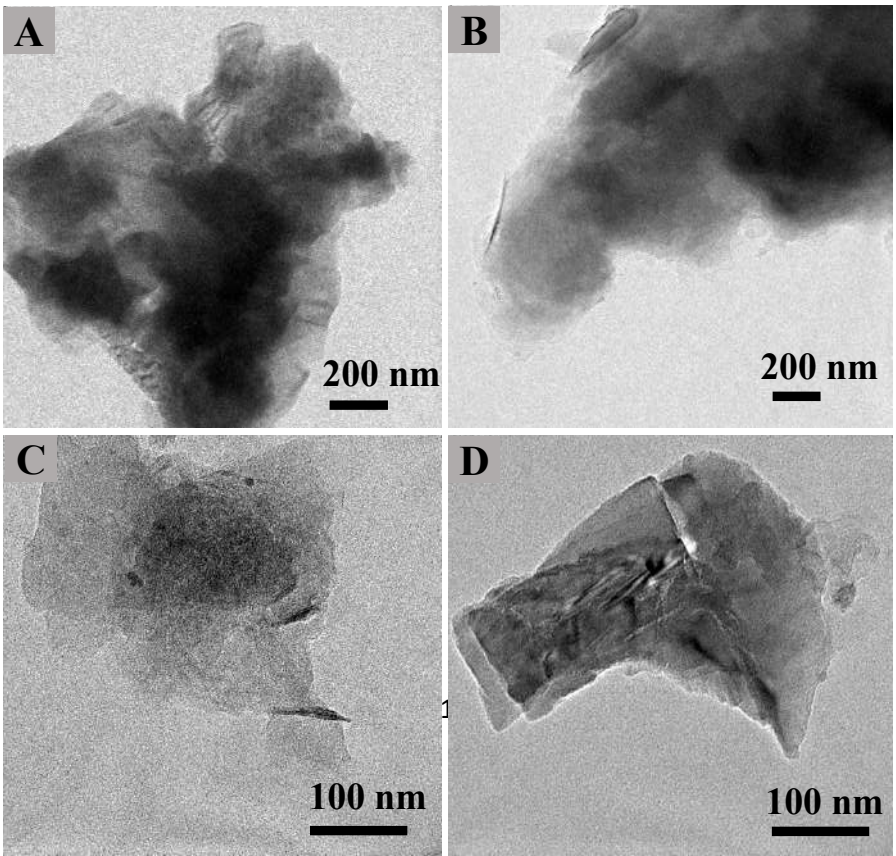


Fig. S4: Nebulization at different gas pressures A) 10 psi, B) 15 psi, C) 20 psi, D) 25 psi.

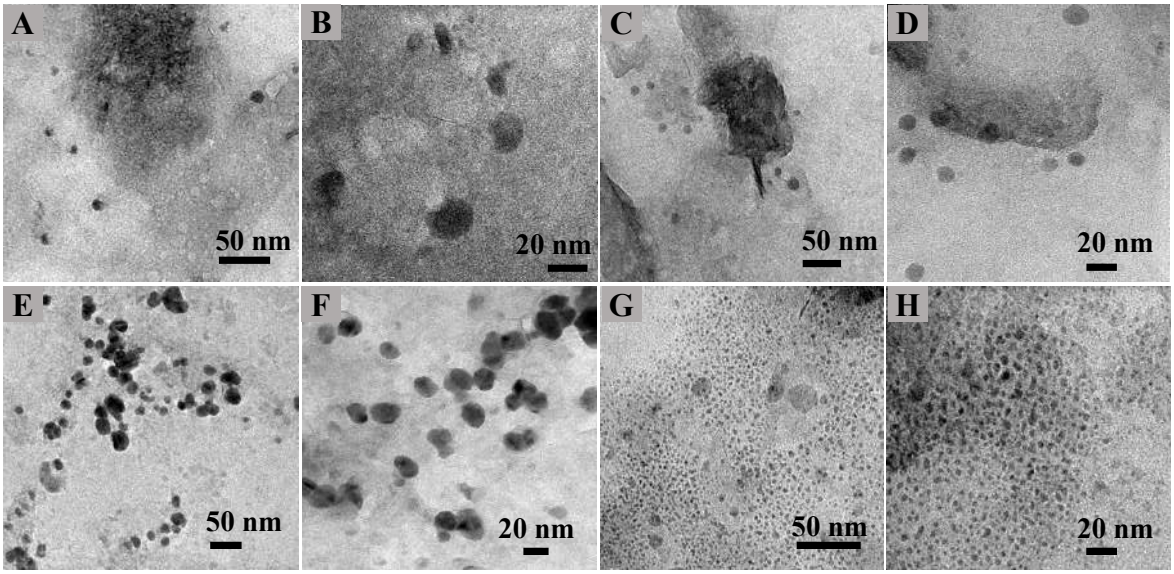


Fig. S5: Effect of applied potential on the electrosprayed MoS_2. A, B) 2.4 kV, C, D) 2.6 kV, E, F) 2.8 kV and G, H) 3.2 kV.

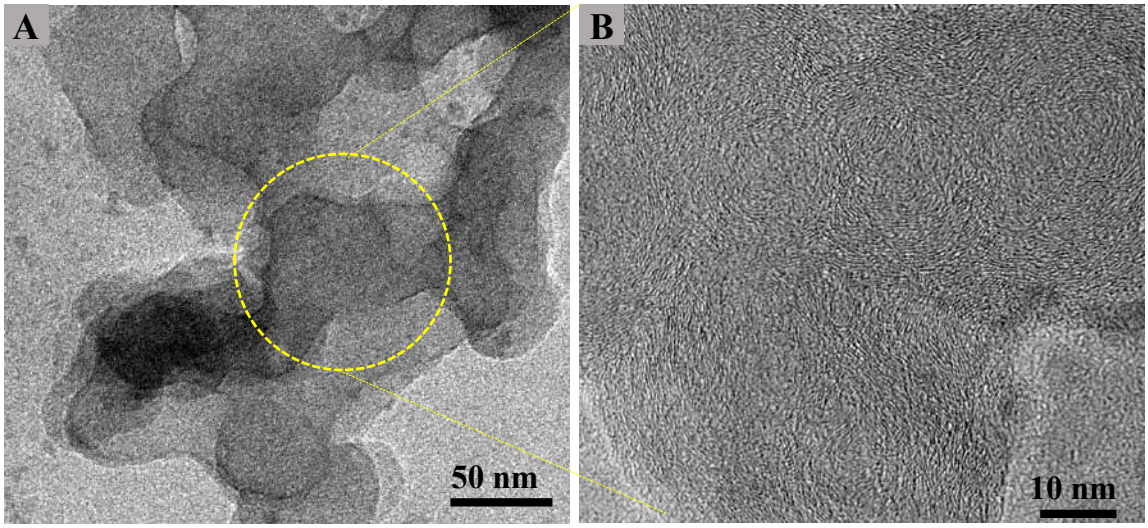


Fig. S6: TEM images showing Inorganic fullerene like (IF) MoS_2 nanoparticles.

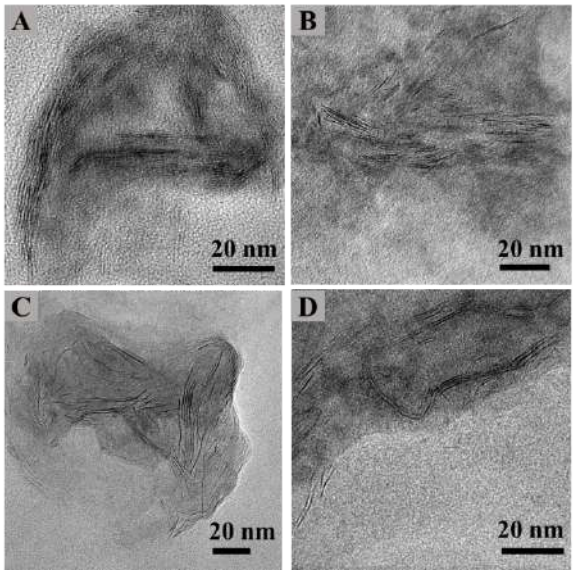


Fig. S7: Effect of solvent on the disintegration process. A) 100% methanol B) 75% methanol C) 50% Methanol D) 25% methanol.

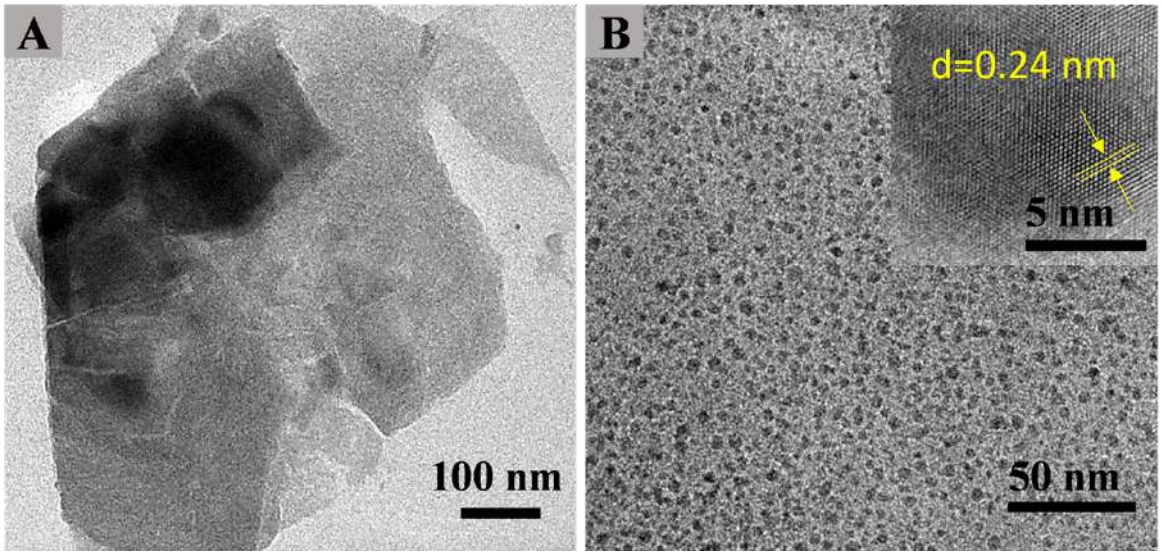

A
100 nm
B
d=0.24 nm
5 nm
50 nm

Fig. S8: Generalization of electrospray process of conversion of 2D materials to 0D materials. A) WS_2 nanosheet before electrospray. B) WS_2 nanoparticles after electrospray. Inset shows the high magnification image of a particle.

References

1 J. K. Lee, K. L. Walker, H. S. Han, J. Kang, F. B. Prinz, R. M. Waymouth, H. G. Nam and R. N. Zare, *Proc. Natl. Acad. Sci. U. S. A.*, 2019, **116**, 19294–19298.

2 S. Banerjee and S. Mazumdar, *Int. J. Anal. Chem.*, 2012, **2012**, 1–40.

ChemComm

COMMUNICATION

View Article Online
View Journal | View Issue

Published on 03 April 2025. Downloaded by Indian Institute of Technology Chennai on 12/29/2025 3:10:02 AM.

Check for updates

Cite this: *Chem. Commun.*, 2025, **61**, 6482

Received 11th February 2025,
Accepted 24th March 2025

DOI: 10.1039/d5cc00757g

rsc.li/chemcomm

Ultraviolet photoactivation perturbs the metal-ligand interface of atomically precise nanoclusters†‡

Anagha Jose, [a] Jada N. Walker, [b] Maya Khatun, [c] Sami Malola, [c] B. S. Sooraj, [a] Hannu Häkkinen, *[c] Jennifer S. Brodbelt *[b] and Thalappil Pradeep *[ad]

This study investigates the use of ultraviolet (UV) photoactivation to structurally characterize atomically precise clusters in the gas phase. UV photoactivation of negatively charged precursor ions generates electron photodetachment species in lower charge states. These ions dissociate through single ligand losses, a mechanism that differs notably from the well known dissociation pathways of 8-electron cluster ions caused by collisional activation with implications to photochemistry. Computations show that the photodetachment induced by UV photoactivation perturbs the metal-ligand interfaces, providing a mechanistic understanding of UV based dissociation processes across different cluster systems.

Atomically precise clusters (APCs) of noble metals protected with ligands are an important family of materials in contemporary science.[1–5] Over 500 APCs are known today, and about 350 of them have crystal structures.[6] The structure of APCs consists of an inner metal core connected by metal–metal bonds, a metal-ligand interface, and an outer ligand shell.[2] The stability of the metal-ligand interface is crucial for the functionality, and tunability of clusters. Additionally, the metal-ligand interface protects the metal core from oxidation and aggregation, and it determines the size, shape, and electronic structure of the APCs. Modulating the surface reactivity, active site accessibility, and charge distribution enhances the catalytic, optical, and sensing properties of APCs.[7–14] The structure and stability of the metal-ligand interface of various APCs have been probed by analytical methods, principally by mass spectrometry.

Individual cluster ions have gained significant attention in the past decade owing to their promising structural properties.[15] For instance, Black *et al.* investigated the application of ultraviolet photodissociation mass spectrometry for analyzing gold nanoclusters, specifically $Au_{25}(p\text{MBA})_{18}$ and $Au_{36}(p\text{MBA})_{24}$, protected with *para*-mercaptobenzoic acid (*p*MBA) ligands.[16,17] UVPD was shown to cause extensive fragmentation of the monolayer-protected cluster (MPC) ions using a single 193 nm UV pulse, uncovering unique structural insights not achieved with conventional methods like collision induced dissociation (CID).

Absorption of UV photons by negatively charged ions in the gas phase can induce electron photodetachment of nanocluster systems.[18] Photodetachment produces ions of reduced charge that can be subsequently mass selected for supplemental collisional activation. Termed activated-electron photodetachment (a-EPD), this dissociation strategy effectively unravels the structural and electronic properties of nanoclusters. Additionally, ions excited by UV photons can produce unique fragment ions that provide further insights into the stability of the metal-ligand interfaces of APCs. Mass-selected photodetachment spectroscopy can also reveal the ionization potentials of cluster ions, providing information on their photophysical properties.[19,20]

In this work, we present the UV photoactivation mass spectrometric investigation of two model APCs, $[Ag_{29}(BDT)_{12}]^{3-}$ and $[PtAg_{24}(DMBT)_{18}]^{2-}$, abbreviated as Ag_{29} and $PtAg_{24}$, revealing a perturbation of their metal-ligand interfaces. Isolation and activation of the charge-reduced precursors generated by UV photoactivation cause the loss of a single ligand, distinctly different from the dissociation channel usually observed upon CID of these superatomic clusters. The computational analysis demonstrates that the metal-ligand interface has perturbed upon photodetachment in both cluster systems.

The clusters Ag_{29} and $PtAg_{24}$ were synthesized in solution, with counter ions, as discussed in the experimental section.[21,22]

[a] *DST Unit of Nanoscience (DST UNS) & Thematic Unit of Excellence (TUE), Department of Chemistry, Indian Institute of Technology Madras (IITM), Chennai 600036, India. E-mail: pradeep@iitm.ac.in*
[b] *Department of Chemistry, University of Texas at Austin, Texas 453552, USA. E-mail: jbrodbelt@cm.utexas.edu*
[c] *Departments of Chemistry and Physics, Nanoscience Center, University of Jyväskylä, FI-40014 Jyväskylä, Finland. E-mail: hannu.j.hakkinen@jyu.fi*
[d] *International Centre for Clean Water, 2nd Floor, B-Block, IIT Madras Research Park, Kanagam Road, Taramani, Chennai 600113, India*

† Dedicated to Prof. G. Ranga Rao on his 65th birthday.

‡ Electronic supplementary information (ESI) available. See DOI: https://doi.org/10.1039/d5cc00757g

This journal is © The Royal Society of Chemistry 2025

Published on 03 April 2025. Downloaded by Indian Institute of Technology Chennai on 12/29/2025 3:10:02 AM.

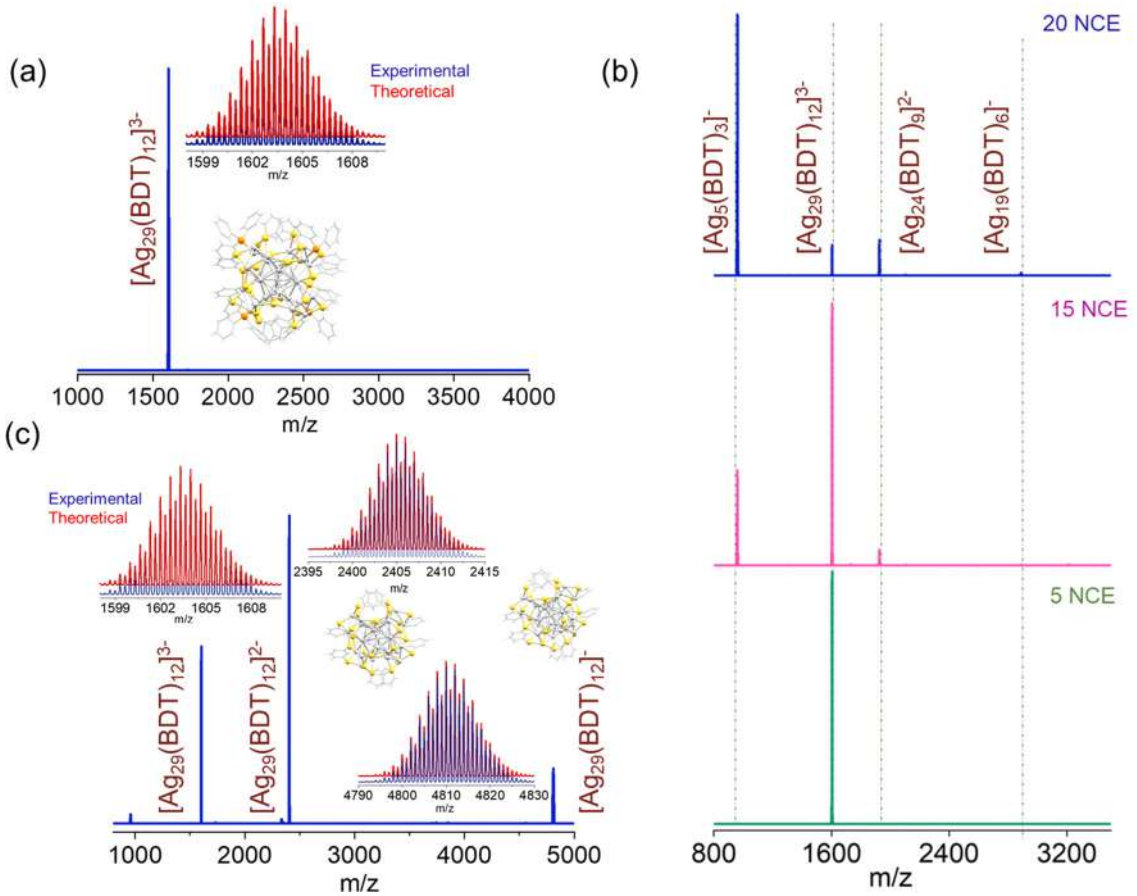


Fig. 1 (a) Electrospray ionization mass spectra (ESI MS) of $[Ag_{29}(BDT)_{12}]^{3-}$. (b) HCD of $[Ag_{29}BDT_{12}]^{3-}$ at NCE 5, NCE 15, and NCE 20. (c) UV photoactivation of $[Ag_{29}BDT_{12}]^{3-}$ at 2 pulses at 2 mJ per pulse. Photodetachment of $[Ag_{29}(BDT)_{12}]^{3-}$ produced $[Ag_{29}(BDT)_{12}]^{2-}$ and $[Ag_{29}(BDT)_{12}]^{1-}$ species. Simulated and experimental isotopic distributions are shown in the inset. The structures of the clusters are represented near their molecular-ion peaks. Gray: Ag, Blue: Pt, yellow: S, orange: P, grey: C, white: H.

The protecting ligands of Ag_{29} and $PtAg_{24}$ are 1,3-benzenedithiol (BDT) and 2,4-dimethylbenzenethiol (DMBT), respectively. These clusters were characterized by various spectroscopic and diffraction studies (presented in ESI‡). The optical absorption spectrum of Ag_{29} exhibited the characteristic features at 447 nm and 513 nm (Fig. S1, ESI‡). Time-dependent optical absorption spectra of Ag_{29} were measured to confirm the stability of the cluster (Fig. S2, ESI‡). High-resolution electrospray ionization mass spectrometry (HRESI-MS) of the cluster generated an ion of *m*/*z* 1603, corresponding to the 3− charge state ($[Ag_{29}(BDT)_{12}]^{3-}$), as shown in Fig. 1a. The cluster exists as $[Ag_{29}(BDT)_{12}]^{3-}$ as the principal charge species under these electrospray conditions. The observed isotopic distribution pattern is in good agreement with the simulated pattern of $[Ag_{29}(BDT)_{12}]^{3-}$, confirming the purity of the synthesized samples. The structure of the cluster determined by single crystal X-ray diffraction (SCXRD) is shown in the inset of Fig. 1a. We compare the higher energy collisional dissociation (HCD) and ultraviolet photoactivation of Ag_{29} at different normalized collision energy (NCE) and pulse energy, respectively. Systematic fragmentation is seen upon collisional activation of $[Ag_{29}(BDT)_{12}]^{3-}$; fragments obtained were assigned as $[Ag_{19}(BDT)_6]^-$ (*m*/*z* 2888), $[Ag_{24}(BDT)_9]^{2-}$ (*m*/*z* 1924), and $[Ag_5(BDT)_3]^-$ (*m*/*z* 960) as reported previously (Fig. 1b).[23] However, upon UV photoactivation of $[Ag_{29}(BDT)_{12}]^{3-}$, we see the emergence of $[Ag_{29}(BDT)_{12}]^{2-}$ and $[Ag_{29}(BDT)_{12}]^{1-}$ species in the mass spectrum (Fig. 1c). Simulated and experimental isotopic distributions are shown as insets in Fig. 1c. DFT calculations have shown the first and second ionization potentials of $[Ag_{29}(BDT)_{12}]^{3-}$ to be 0.46 eV and 2.76 eV, respectively. The 1- and 2-species observed in the mass spectrum are justified, as these energies are lower than the accessible energies generated from a single 193 nm UV photon (6.44 eV). We conducted similar experiments using the same number of laser pulses and different laser energies (*i.e.*, 1 pulse at 1 mJ per pulse, 1 pulse at 2 mJ per pulse, and 1 pulse at 3 mJ per pulse) (Fig. S3a, ESI‡). Also, we performed experiments with different numbers of laser pulses and the same laser energy (*i.e.*, 1 pulse at 2 mJ per pulse, 2 pulses at 2 mJ per pulse, and 3 pulses at 2 mJ per pulse) (Fig. S3b, ESI‡). The abundances of $[Ag_{29}(BDT)_{12}]^{2-}$ and $[Ag_{29}(BDT)_{12}]^{1-}$ species increase with increasing laser pulses and laser energies. Activated-electron photodetachment dissociation (a-EPD) experiments were performed using UV photoactivation (1 pulse at 2 mJ per pulse) to generate

This journal is © The Royal Society of Chemistry 2025

Published on 03 April 2025. Downloaded by Indian Institute of Technology Chennai on 12/29/2025 3:10:02 AM.

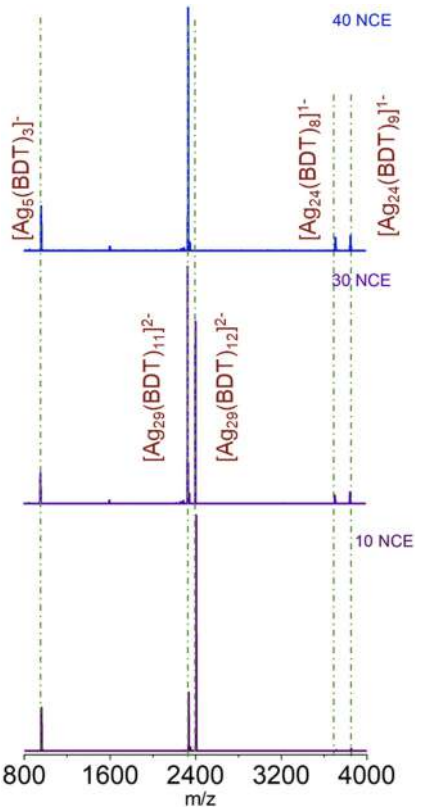


Fig. 2 a-EPD experiments of charge-reduced radical species $[Ag_{29}(BDT)_{12}]^{2-}$ at NCE 10, NCE 30 and NCE 40.

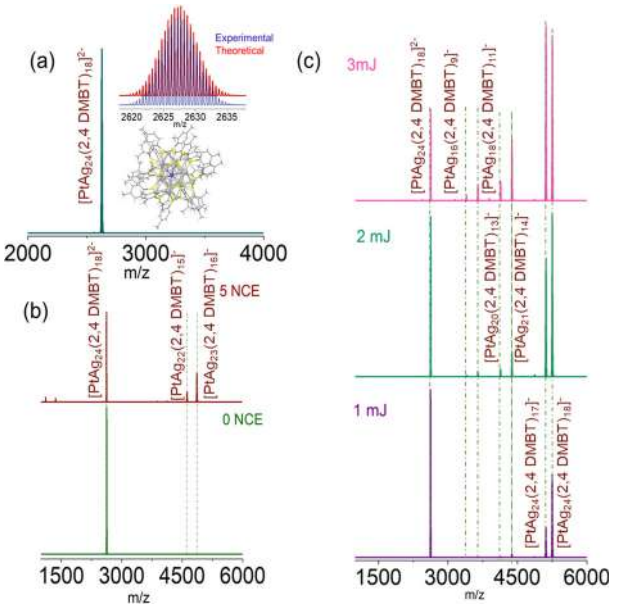


Fig. 3 (a) Electrospray ionization mass spectrum of $[PtAg_{24}(DMBT)_{18}]^{2-}$. Simulated and experimental isotopic distributions of $[PtAg_{24}(DMBT)_{18}]^{2-}$ are shown in the inset. (b) HCD of $[PtAg_{24}(DMBT)_{18}]^{2-}$ at NCE 0 and NCE 5. (c) UV photoactivation of $[PtAg_{24}(2,4\text{-}DMBT)_{18}]^{2-}$ at different energies, 2 pulses at 1 mJ per pulse, 2 pulses at 2 mJ per pulse, and 2 pulses at 3 mJ per pulse.

charge-reduced radical species, followed by isolation and collisional activation of the primary charge-reduced precursor ion, $[Ag_{29}(BDT)_{12}]^{2-}$ (MS^3) (Fig. 2). For a-EPD of $[Ag_{29}(BDT)_{12}]^{2-}$ the fragments observed were $[Ag_{24}(BDT)_9]^-$ (*m*/*z* 3852), $[Ag_{24}(BDT)_8]^-$ (*m*/*z* 3712), $[Ag_{29}(BDT)_{11}]^{2-}$ (*m*/*z* 2336), and $[Ag_5(BDT)_3]^-$ (*m*/*z* 960). We find that the emergence of $[Ag_{29}(BDT)_{11}]^{2-}$, the one ligand loss feature, is increasingly prominent with increasing collisional energy.

This fragmentation pattern is distinctly different from the collisional activation of $[Ag_{29}(BDT)_{12}]^{3-}$, as reported earlier (Fig. 1b).

We also synthesized a bimetallic $PtAg_{24}$ nanocluster using a previously reported protocol,[22] and it exhibited prominent absorption features at 450 and 580 nm (Fig. S4, ESI‡). Time-dependent optical absorption measurements confirmed the stability of the $PtAg_{24}$ cluster (Fig. S5, ESI‡). Fig. 3a presents the ESI MS of $PtAg_{24}$, which exhibits a peak at *m*/*z* 2626 with a 2− charge state corresponding to $[PtAg_{24}(2,4\text{-}DMBT)_{18}]^{2-}$. The inset of Fig. 3a shows the overlay of experimental and simulated isotopic distributions. The structure of $[PtAg_{24}(2,4\text{-}DMBT)_{18}]^{2-}$ was determined by SCXRD, which is shown in the inset (Fig. 3a). Experiments have been conducted on the $PtAg_{24}$ system, which ionizes in the 2− state, and upon UV photoactivation, it produces the $[PtAg_{24}(2,4\text{-}DMBT)_{18}]^-$ species. In Fig. 3b and c, we compare the HCD and UV photoactivation mass spectra of $[PtAg_{24}(2,4\text{-}DMBT)_{18}]^{2-}$ at different collisional and laser pulse energies. The compositions of the fragment ions are assigned in the mass spectra. Systematic fragmentation occurs upon collisional activation, resulting in several fragments, all of which are 8e-species (Fig. 3b).[24] For the UV photoactivation spectra, ions corresponding to $[PtAg_{24}(2,4\text{-}DMBT)_{18}]^-$ and $[PtAg_{24}(2,4\text{-}DMBT)_{17}]^-$ are observed along with other fragments. Photodetachment calculations have shown that the first ionization potential of $[PtAg_{24}(2,4\text{-}DMBT)_{18}]$ is 1.68 eV. The abundance of the ion corresponding to a single ligand loss increases with an increase in the laser energy per pulse.

To understand the difference in the fragmentation process, we performed computational studies on Ag_{29} and $PtAg_{24}$. We have computed the DFT optimized structures of Ag_{29}, with increase in charge, namely $[Ag_{29}(BDT)_{12}]^-$, $[Ag_{29}(BDT)_{12}]^{2-}$, and $[Ag_{29}(BDT)_{12}]^{3-}$ (Fig. S6a–c, ESI‡). While comparing the DFT-optimized structures of $[Ag_{29}(BDT)_{12}]^{3-}$, we observe a slight perturbation of the Ag–S bond in its $[Ag_{29}(BDT)_{12}]^-$, and $[Ag_{29}(BDT)_{12}]^{2-}$ charge states as compared to the $[Ag_{29}(BDT)_{12}]^{3-}$ parent species. The ligand detachment energy (LDE) for one ligand loss was calculated using both optimized and non-optimized structures. The values were 4.66 and 5.55 eV, respectively. Similarly, we have computed the DFT optimized structures of $[PtAg_{24}(2,4\text{-}DMBT)_{18}]^-$, and $[PtAg_{24}(2,4\text{-}DMBT)_{18}]^{2-}$ (Fig. S6d and e, ESI‡). A comparison of the DFT-optimized structures showed slight perturbation of the Ag–S bond in $[PtAg_{24}(2,4\text{-}DMBT)_{18}]^-$ as compared to the $[PtAg_{24}(2,4\text{-}DMBT)_{18}]^{2-}$ parent species. We have considered two possible DMBT ligands based on the symmetry of the metal-ligand interface. The detachment energies for the loss of ligand were calculated as 1.66 and 2.14 eV, for both these

This journal is © The Royal Society of Chemistry 2025

Published on 03 April 2025. Downloaded by Indian Institute of Technology Chennai on 12/29/2025 3:10:02 AM.

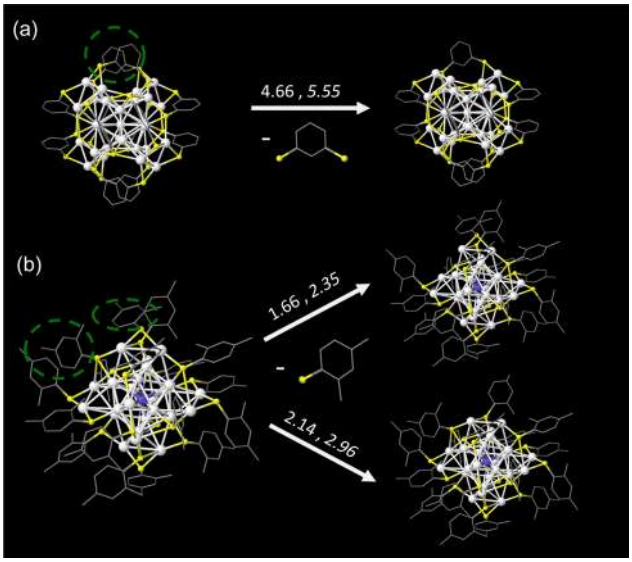


Fig. 4 Ligand detachment energy obtained from the optimization and without optimization (italic) of the dissociated fragments (in eV) (a) $[Ag_{29}(BDT)_{12}]^{2-}$ and it's one ligand loss species $[Ag_{29}(BDT)_{11}]^{2-}$; (b) $[PtAg_{24}(2,4\text{-DMBT})_{18}]^{-}$ and it's one ligand loss species $[PtAg_{24}(2,4\text{-DMBT})_{11}]^{-}$. Atomic colour codes: gray: Ag, Blue: Pt, yellow: S, orange: P, grey: C, Hs are omitted for clarity.

cases using optimized structures. However, the non-optimized structures gave values of 2.35 and 2.96 eV, respectively. The ligand detachment processes of $[Ag_{29}(BDT)_{12}]^{2-}$ and $[PtAg_{24}(2,4\text{-DMBT})_{18}]^{-}$ are shown in Fig. 4. The calculated ligand detachment energies, whether considering optimized or non-optimized dissociation structures for both the clusters were much below the accessible energies of the UV photon used, which was 6.44 eV (193 nm).

In conclusion, we have examined the UV photoactivation of two APCs, $[Ag_{29}(BDT)_{12}]^{3-}$ and $[PtAg_{24}(DMBT)_{18}]^{2-}$ in the gas phase. UV photoactivation results in the formation of the charge-reduced electron-detached species, yielding clusters in 2- and 1-charge states from the 3-precursor. These ions dissociate through single ligand losses, distinctly different from the dissociation channels seen for the same cluster ions using collisional activation. UV photoactivation of $[PtAg_{24}(DMBT)_{18}]^{2-}$ also yielded similar results. This unique pathway suggests a change in the energetics of the metal-ligand interface, as supported by calculations. These insights on the atomically precise clusters will be useful in understanding the behaviour of the clusters in the gas phase. Expanding UV photoactivation analysis into APCs could provide more insights into their structure and bonding. Such studies would help us gain insights into structures of larger nanoparticles, which may resemble proteins, on the latter UV photoactivation studies are performed routinely. These structural insights enable us to understand the behaviour of clusters in the gas phase, which could enhance their utility in catalytic (including photocatalytic) and electrochemical applications.

A. J. acknowledges the MHRD for the PMRF and IIT Madras for the IIE grant. The computational work was supported by the Research Council of Finland and carried out during M. K.'s extended visit to IIT Madras. The simulations were performed at the Finnish National Supercomputing Center CSC. J. S. B. acknowledges funding from the Welch Foundation (F-1155). T. P. thanks the SERB, India, for funding through the research grant, SPR/2021/000439 and through a JC Bose Fellowship. T. P. also acknowledges funding from the Centre of Excellence on Molecular Materials and Functions, through the Institute of Eminence Scheme IIT Madras.

Data availability

Data supporting this article have been included as part of the ESI.‡

Conflicts of interest

There are no conflicts to declare.

References

1 R. Jin, C. Zeng, M. Zhou and Y. Chen, *Chem. Rev.*, 2016, **116**, 10346–10413.
2 I. Chakraborty and T. Pradeep, *Chem. Rev.*, 2017, **117**, 8208–8271.
3 H. Hirai, S. Ito, S. Takano, K. Koyasu and T. Tsukuda, *Chem. Sci.*, 2020, **11**, 12233–12248.
4 J. Xie, Y. Zheng and J. Y. Ying, *J. Am. Chem. Soc.*, 2009, **131**, 888–889.
5 S. Knoppe and T. Burgi, *Acc. Chem. Res.*, 2014, **47**, 1318–1326.
6 A. Pihlajamäki, S. Malola and H. Häkkinen, *ChemRxiv*, 2024, preprint, DOI: **10.26434/chemrxiv-2024-kxjpb**.
7 X. Du and R. Jin, *ACS Nano*, 2019, **13**, 7383–7387.
8 R. Jin, *Nanoscale*, 2015, **7**, 1549–1565.
9 S. Knoppe, M. Vanbel, S. Van Cleuvenbergen, L. Vanpraet, T. Bürgi and T. Verbiest, *J. Phys. Chem. C*, 2015, **119**, 6221–6226.
10 B. N. S. Sooraj and T. Pradeep, *Atomically Precise Metal Nanoclusters*, Elsevier, 2022, pp. 83–101.
11 K. S. Sugi, A. P. Sandra, N. Nonappa, D. Ghosh, J. S. Mohanty, M. Paulthangam Kannan, B. S. Sooraj, P. Srikrishnarka, J. Roy, W. A. Dar and T. Pradeep, *Nanoscale*, 2023, **15**, 11927–11934.
12 Y. Chen, C. Zeng and R. Jin, *Catalysis*, 2016, **28**, 51–85.
13 S. Malola and H. Häkkinen, *Chem. Commun.*, 2019, **55**, 9460–9462.
14 A. Jana, B. K. Spoorthi, A. S. Nair, A. Nagar, B. Pathak, T. Base and T. Pradeep, *Nanoscale*, 2023, **15**, 8141–8147.
15 M. Azubel, A. L. Koh, K. Koyasu, T. Tsukuda and R. D. Kornberg, *ACS Nano*, 2017, **11**, 11866–11871.
16 D. M. Black, C. M. Crittenden, J. S. Brodbelt and R. L. Whetten, *J. Phys. Chem. Lett.*, 2017, **8**, 1283–1289.
17 Y. Zhang, X. Gu, F. K. Busari, S. Barkaoui, Z. K. Han, A. Baiker, Z. Zhao and G. Li, *Nano Res.*, 2024, **17**, 9594–9600.
18 R. Antoine, J. Lemoine and P. Dugourd, *Mass Spectrom. Rev.*, 2014, **33**, 501–522.
19 S. Ito, Y. Tasaka, K. Nakamura, Y. Fujiwara, K. Hirata, K. Koyasu and T. Tsukuda, *J. Phys. Chem. Lett.*, 2022, **13**, 5049–5055.
20 K. Hirata, K. Yamashita, S. Muramatsu, S. Takano, K. Ohshimo, T. Azuma, R. Nakanishi, T. Nagata, S. Yamazoe, K. Koyasu and T. Tsukuda, *Nanoscale*, 2017, **9**, 13409–13412.
21 L. G. AbdulHalim, M. S. Bootharaju, Q. Tang, S. Del Gobbo, R. G. AbdulHalim, M. Eddaoudi, D. E. Jiang and O. M. Bakr, *J. Am. Chem. Soc.*, 2015, **137**, 11970–11975.
22 J. Yan, H. Su, H. Yang, S. Malola, S. Lin, H. Häkkinen and N. Zheng, *J. Am. Chem. Soc.*, 2015, **137**, 11880–11883.
23 P. Chakraborty, S. Malola, M. Neumaier, P. Weis, H. Häkkinen and M. M. Kappes, *Angew. Chem., Int. Ed.*, 2023, **62**, e202305836.
24 J. Yan, H. Su, H. Yang, S. Malola, S. Lin, H. Häkkinen and N. Zheng, *J. Am. Chem. Soc.*, 2015, **137**, 11880–11883.

Supplementary Information (SI) for Chemical Communications.
This journal is © The Royal Society of Chemistry 2025

Supplementary Information

Ultraviolet photoactivation perturbs the metal-ligand interface of atomically precise nanoclusters

Anagha Jose,[a] Jada N. Walker,[b] Maya Khatun,[c] Sami Malola,[c] B. S. Sooraj,[a] Hannu Häkkinen,*[c] Jennifer S. Brodbelt,*[b] and Thalappil Pradeep*[a,d]

[a.] *Department of Chemistry, DST Unit of Nanoscience (DST UNS) and Thematic Unit of Excellence (TUE), Indian Institute of Technology Madras, Chennai 600036, India. E-mail: pradeep@iitm.ac.in*

[b.] *Department of Chemistry, University of Texas at Austin, Texas, 78712 United States of America. Email:jbrodbelt@cm.utexas.edu.*

[c.] *Departments of Chemistry and Physics, Nanoscience Center, University of Jyväskylä, FI-40014 Jyväskylä, Finland. Email: hannu.j.hakkinen@jyu.fi*

[d.] *International Centre for Clean Water, 2nd Floor, B-Block, IIT Madras Research Park, Kanagam Road, Taramani, Chennai 600113, India.*

Table of contents

Title	Description	Page no
1.	Experimental section	2
2.	Instrumentation	3
3.	Computational Studies	3

Fig. S1	UV-Vis absorption spectrum of $[Ag_{29}(BDT)_{12}]^{3-}$	5
Fig. S2	Stability of $[Ag_{29}(BDT)_{12}]^{3-}$ cluster in DMF based on absorbance profiles acquired over several hours.	6
Fig. S3	UVPD of $[Ag_{29}(BDT)_{12}]^{3-}$(a) Different laser energies, and (b) Different number of pulses	7
Fig. S4	UV-Vis absorption spectrum of $[PtAg_{24}(DMBT)_{18}]^{2-}$	8
Fig. S5	Stability of $[PtAg_{24}(DMBT)_{18}]^{2-}$ in DCM based on absorbance profiles acquired over several hours.	8
Fig. S6	DFT optimized structure of (a) $[Ag_{29}(BDT)_{12}]^{-}$, (b) $[Ag_{29}(BDT)_{12}]^{2-}$, (c) $[Ag_{29}(BDT)_{12}]^{3-}$,(d) $[PtAg_{24}(DMBT)_{18}]^{-}$ and (c) $[PtAg_{24}(DMBT)_{18}]^{2-}$	9

1. Experimental Section

Materials. All the materials were commercially available. All chemicals, including silver nitrate ($AgNO_3$), 1,3-benzenedithiol (BDT), sodium borohydride ($NaBH_4$), triphenylphosphine (TPP, 97%), and 2,4-dimethylbenzenethiol (DMBT) were purchased from Sigma-Aldrich. HPLC grade dichloromethane (DCM), dimethylformamide (DMF), and methanol (MeOH) were purchased from Rankem. All solvents and chemicals were used as such without further purification.

Synthesis of $Ag_{29}(BDT)_{12}(PPh_3)_4$ (Ag_{29}). The cluster was synthesized by adopting an already-reported method. First, ∼20 mg of AgNO3 was dissolved in 5 mL of MeOH, and then 9 mL of DCM was added. After a few mins, ∼13.5 μL of BDT (0.5 mL of DCM) was added to the solution. Then, after 5 min of stirring in the dark, ∼200 mg of PPh3 (in 0.5 mL of DCM) was added to the mixture, and next, 0.5 mL of an ice-cold aqueous solution containing ∼11 mg of $NaBH_4$ was added, which immediately changed the color of the solution to dark brown. The reaction was kept for 3 h under dark conditions. Then, the precipitate (red color) was collected by centrifugation, and the concentrated solution was collected by rotary evaporation. The cluster was washed several times with MeOH and then dissolved in DCM. The reddish-orange colored cluster was collected after the removal of unwanted byproducts.

Synthesis of $PtAg_{24}(DMBT)_{18}$ ($PtAg_{24}$). For the synthesis of $PtAg_{24}$, we followed a reported method after some modifications.46 At first, ∼10 mg of AgNO3 was dissolved in MeOH (5 mL) along with ∼10

mg of K_2PtCl_4 (9 mL of DCM). Then, ~10 µL of DMBT in 0.5 mL of DCM was added to the mixture followed by the addition of ~10 mg of PPh_4Br (in 0.5 mL of DCM). After ~20 min, $NaBH_4$ (40 mg in 0.5 mL of ice-cold water) was added, resulting in the reduction of Ag-Pt-phosphine-thiolate to form NCs, and 50 µL of triethylamine was added after 5 min. The solution was kept stirring overnight. The formed cluster solution was evaporated and then washed with MeOH. The clusters were extracted in DCM.

2. Instrumentation

UV-Vis absorption spectra of the cluster in their respective solution were optimized using a PerkinElmer Lambda 25 spectrophotometer in the 200–1100 nm wavelength range. The slit width used for the measurement is 1 nm.

UV Photoactivation -Mass Spectrometry

Static emitters (1.2 mm o.d.) were pulled to a fine tip using a Sutter Instrument P-2000 laser puller (Novato, CA) and coated in an Au/Pd mixture for static electrospray. Emitters were loaded with 5–10 µL of the Ag_{29}(BDT) solution, and a spray voltage of 1.1–1.3 kV was used for direct infusion. Mass spectra were collected in negative mode on a Thermo Scientific Orbitrap Fusion Lumos mass spectrometer (San Jose, CA), modified with a 193 nm Coherent ExciStar excimer laser (Santa Cruz, CA) to perform UVPD in the high-pressure linear ion trap. All data were collected using a maximum injection time of 100 ms, an AGC (automatic gain control) target of 1×10^6, and a resolution of 120,000 at m/z 200. For all spectra, 20 scans were collected and averaged with 1 microscan per scan. Ion activation methods were performed following quadrupole isolation with the isolation width set to 50 m/z. An activation time of 10 ms and q-value of 0.25 were used when performing CID (10–40% NCE) and HCD (5– 25% NCE) at the MS2 and MS3 levels. Activated-electron photodetachment dissociation (a-EPD) experiments were performed using UV photoactivation with various numbers of pulses and laser energies (e.g., 2 pulses at 2 mJ per pulse) to generate charge-reduced radical species (MS2), followed by isolation and collisional activation of the primary charge-reduced precursor ion (MS3).

ESI-MS of $PtAg_{24}$ was performed on a Thermo Scientific Q Exactive HF-X quadrupole-Orbitrap mass spectrometer (Bremen, Germany), which was modified to perform ultraviolet photodissociation (UVPD) with a 500 Hz, 193 nm Coherent ExciStar excimer laser (Santa Cruz, CA) in the higher energy collisional dissociation (HCD) cell as previously described. Ions were generated by nanoelectrospray ionization using Au/Pd-coated borosilicate emitters fabricated in-house and using a spray voltage of 1.2 kV. Mass spectra were collected in negative mode. $PtAg_{24}$ ions were quadrupole-isolated and activated using HCD (1-5% NCE). For the manuscript, experiments involving $PtAg_{24}$ were undertaken using the HF-X mass spectrometer, which does not have the capability to perform a-EPD, which is a

MS^3 experiment. UV photoactivation of $PtAg_{24}$ using the Lumos mass spectrometer resulted in a product ion of *m/z* 5253, corresponding to $[PtAg_{24}(DMBT)_{18}]$-. The high *m/z* value of this ion exceeds the upper *m/z* limit of ion isolation (which is *m/z* 4000). Therefore, this species ($[PtAg_{24}(DMBT)_{18}]$-) could not be isolated and subjected to collisional activation, and thus no results are reported.

No photodetached species were detected without photoactivation. Both the clusters Ag_{29} and $PtAg_{24}$ ionize in the negative mode. No peaks were observed in the positive mode in the ESI-MS before and after photoactivation.

3. Computational Studies

Geometry optimizations and electronic structure calculations were carried out using the projector-augmented wave (PAW) method, as implemented in the GPAW code.[1,2] Real-space grids with a 0.2 Å grid spacing were used for all computations. Electron-electron interactions were described using the Perdew–Burke–Ernzerhof (PBE) exchange-correlation functional[3] in the generalized gradient approximation (GGA). The BFGS (Broyden–Fletcher–Goldfarb–Shanno) method was used in the optimization process to iteratively minimize forces on the atoms. Convergence was reached at a maximum force threshold of 0.05 eV/Å. The initial structure of $[Ag_{29}(BDT)_{12}]^{3-}$ was built using its known crystal structure.[4] Meanwhile, $[PtAg_{24}(DMBT)_{18}]^{2-}$ was designed by modifying the computed structure of $[Ag_{25}(DMBT)_{18}]$,[5] substituting the central Ag atom with a Pt atom, and optimizing the structure for different charge states. The systems studied included $[Ag_{29}(BDT)_{12}]^{3-}$, $[Ag_{29}(BDT)_{12}]^{2-}$, $[Ag_{29}(BDT)_{12}]^{-}$, $[PtAg_{24}(DMBT)_{18}]^{2-}$, and $[PtAg_{24}(DMBT)_{18}]^{-}$ where BDT and DMBT refer to 1,3-benzenedithiol and dimethylbenzenethiol ligands, respectively. To investigate ligand detachment energies, we have computed the energy required to detach one BDT ligand from $[Ag_{29}(BDT)_{12}]^{2-}$ and one DMBT ligand from $[PtAg_{24}(DMBT)_{18}]^{-}$. The ligand detachment energy $E_{detachment}$ was calculated using the following expression:

$$E_{detachment} = E_{fragment1} + E_{fragment2} - E_{cluster}$$

where, $E_{fragment1}$ is the energy of the cluster after detaching single ligand ($[Ag_{29}(BDT)_{11}]^{2-}$ or $[PtAg_{24}(DMBT)_{17}]^{-}$), $E_{fragment2}$ is the energy of the detached ligand (BDT or DMBT), and $E_{cluster}$ is the energy of the intact cluster ($[Ag_{29}(BDT)_{12}]^{2-}$ or $[PtAg_{24}(DMBT)_{18}]^{-}$). All fragments and clusters were optimized as part of this study.

To calculate the ionization potentials (IP1 and IP2) or the energy required to remove one or two electrons, optimizations were done for different charge states of the clusters. The first ionization potential (IP1) was calculated as:

$$IP1 = M_{parent}^{opt+} - M_{parent}^{opt}$$

where, M_{parent}^{opt+} is the energy of the optimized cluster with one electron removed ($[Ag_{29}(BDT)_{12}]^{2-}$ or $[PtAg_{24}(DMBT)_{18}]^{-}$) and M_{parent}^{opt} is the energy of the optimized cluster with the initial charge state ($[Ag_{29}(BDT)_{12}]^{3-}$ or $[PtAg_{24}(DMBT)_{18}]^{2-}$).

The second ionization potential (IP2) was calculated as:

$$IP2 = M_{parent}^{opt++} - M_{parent}^{opt}$$

where, M_{parent}^{opt++} is the energy of the optimized cluster with two electron removed ($[Ag_{29}(BDT)_{12}]^{-}$) from M_{parent}^{opt}.

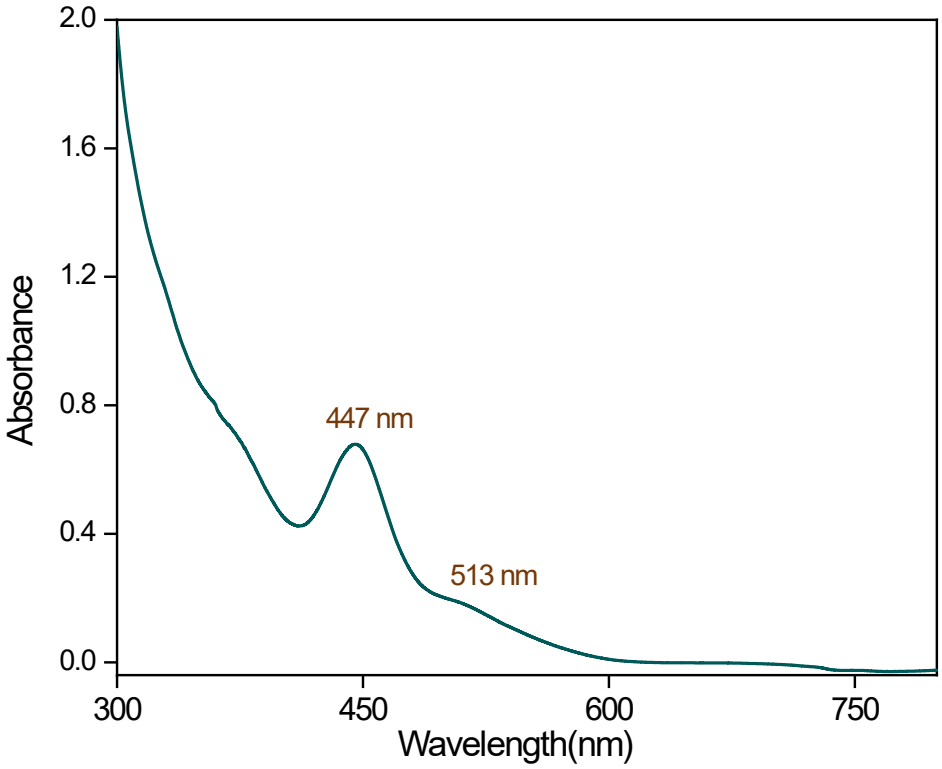


Fig. S1. UV-Vis absorption spectrum of $[Ag_{29}(BDT)_{12}]^{3-}$ cluster in N,N-Dimethylformamide (DMF).

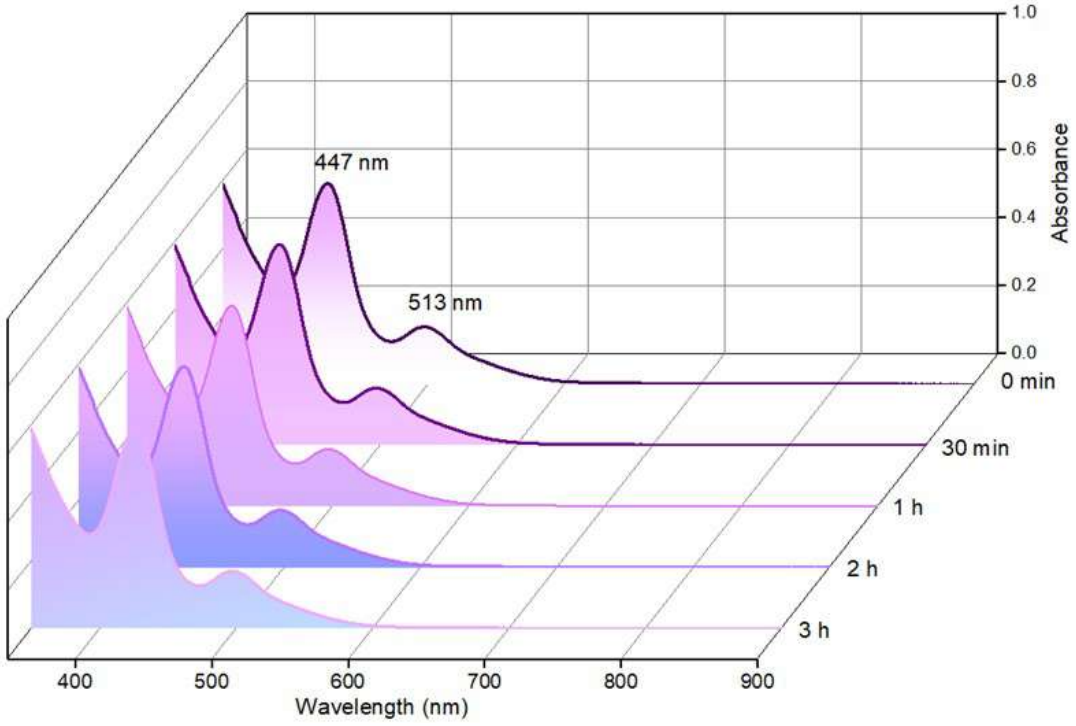


Fig. S2. Stability of $[Ag_{29}(BDT)_{12}]^{3-}$ cluster in DMF based on absorbance profiles acquired over several hours.

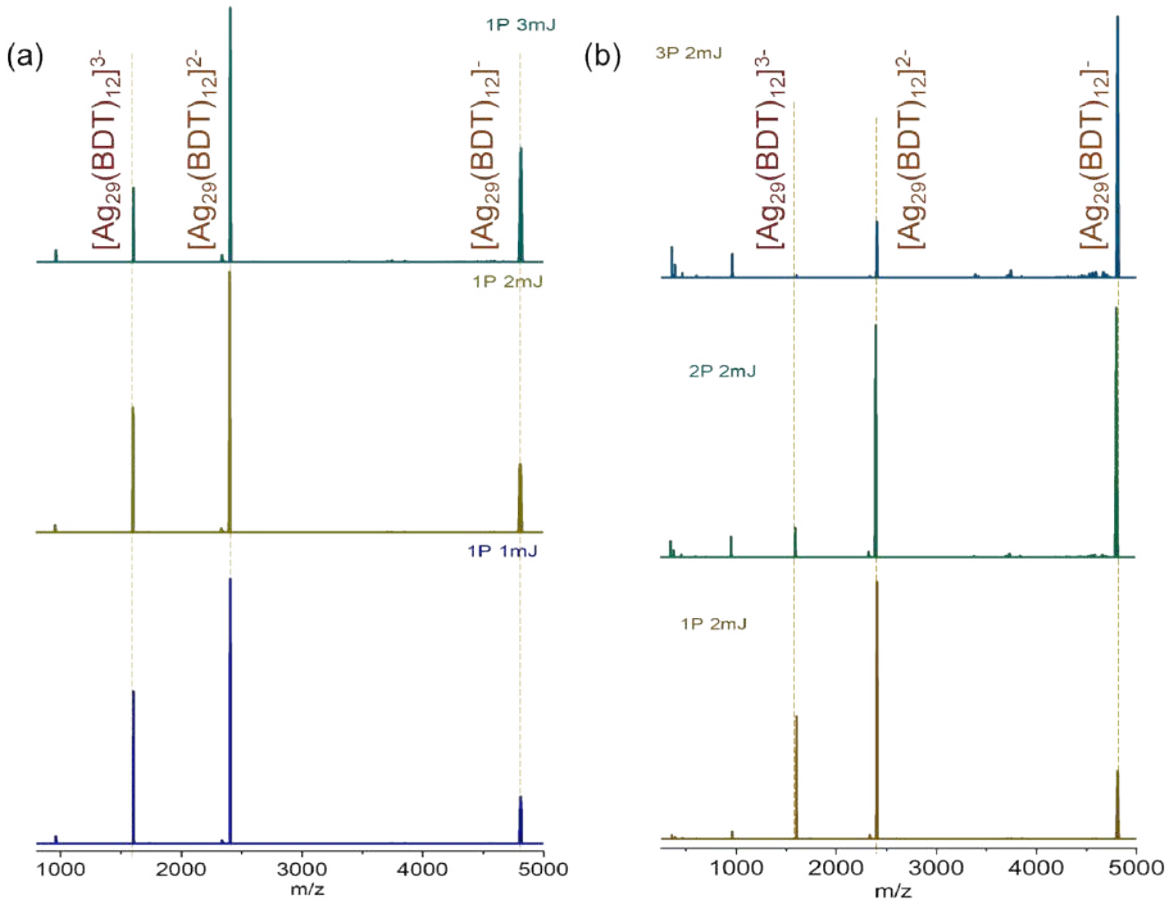
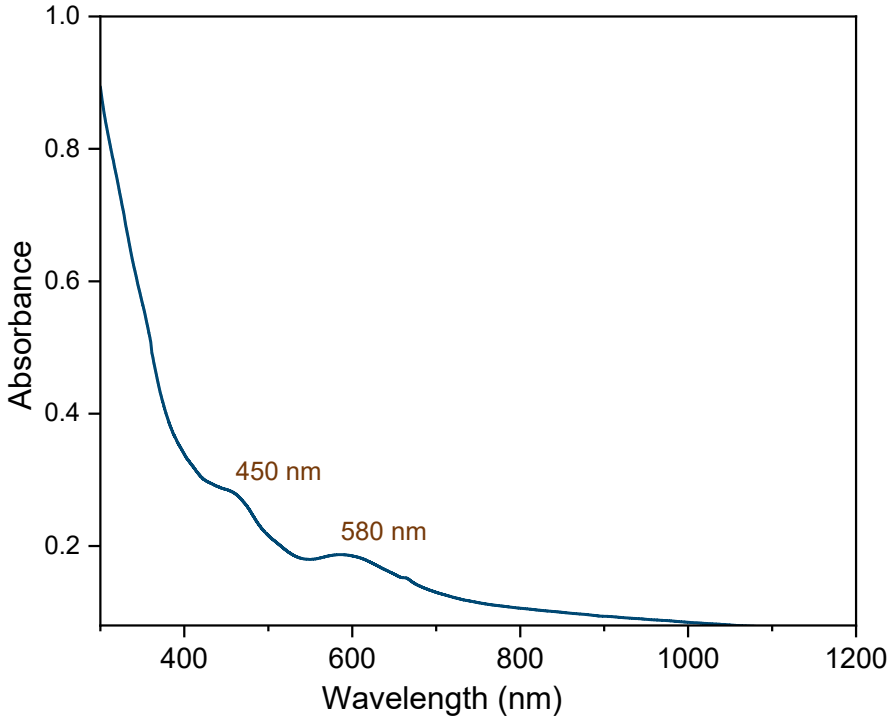


Fig. S3. UV photoactivation of $[Ag_{29}(BDT)_{12}]^{3-}$ obtained us ing (a) Different laser energies, and (b) Different number of laser pulses.



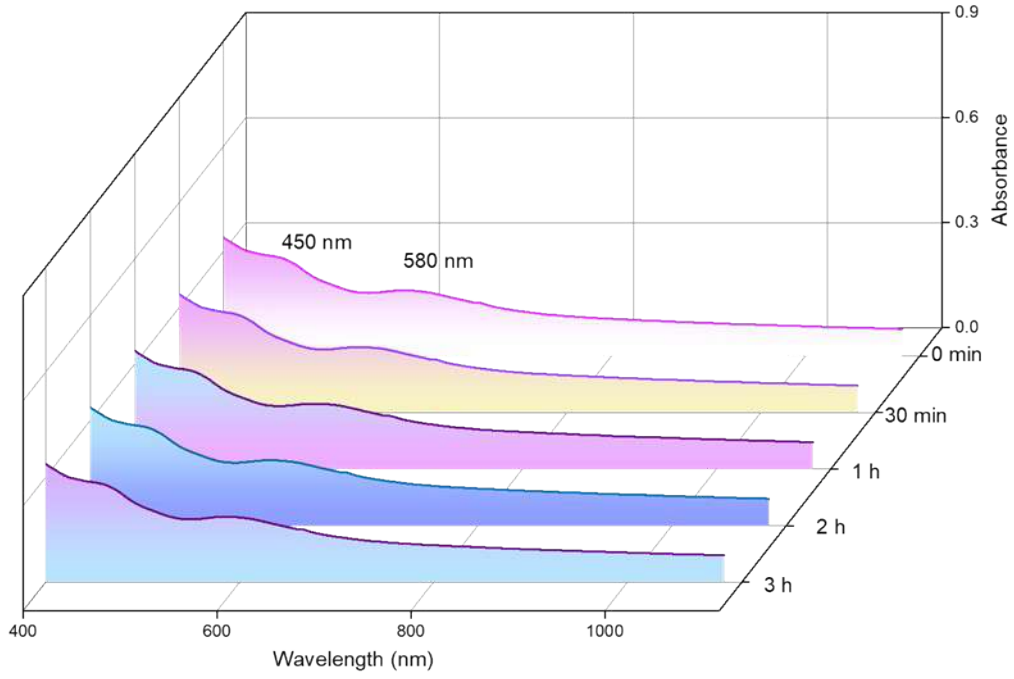


Fig. S4. UV-Vis absorption spectrum of $[PtAg_{24}(DMBT)_{18}]^{2-}$ in dichloromethane (DCM).

Fig. S5. Stability of $[PtAg_{24}(DMBT)_{18}]^{2-}$ in DCM based on absorbance profiles acquired over several

hours.

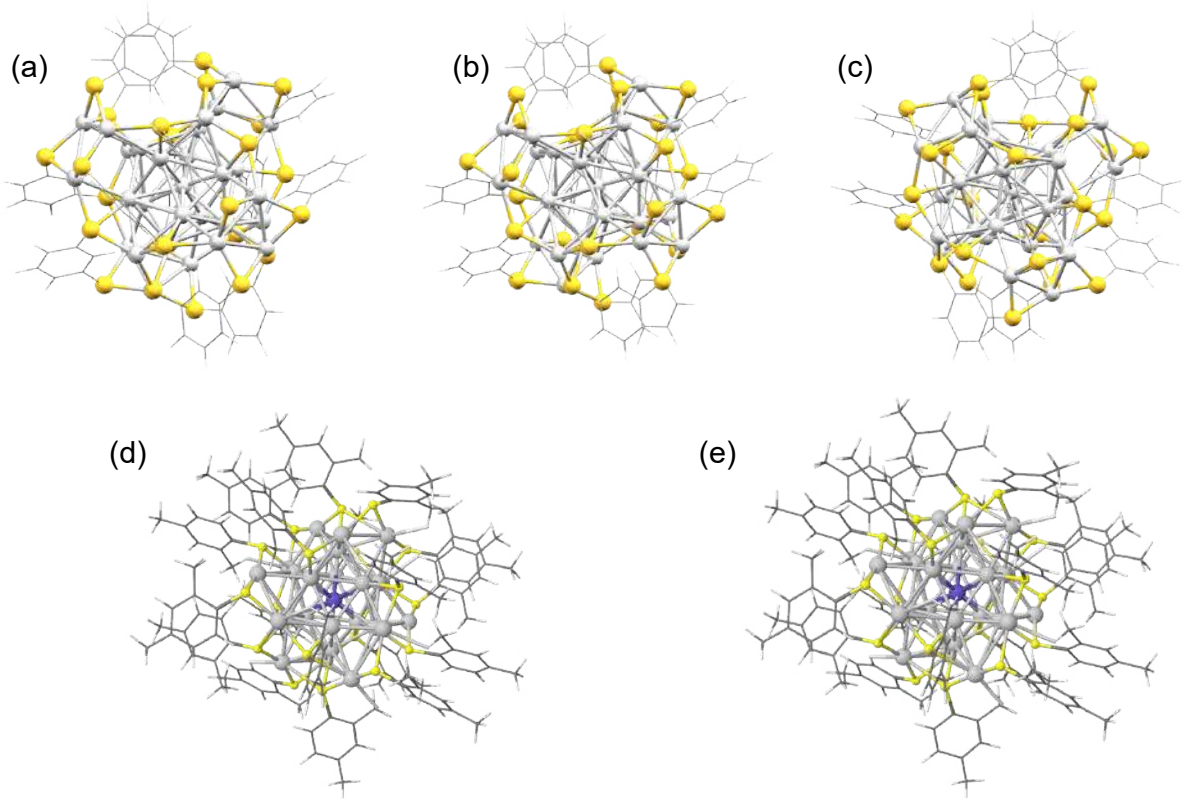


Fig. S6. DFT-optimized structures of (a) $[Ag_{29}(BDT)_{12}]^{-}$, (b) $[Ag_{29}(BDT)_{12}]^{2-}$, (c) $[Ag_{29}(BDT)_{12}]^{3-}$, (d) $[PtAg_{24}(DMBT)_{18}]^{-}$ and ,(c) $[PtAg_{24}(DMBT)_{18}]^{2-}$. Grey: Ag, Blue: Pt, yellow: S, grey: C, white: H.

Coordinates

$Ag_{29}BDT_{12}^{3-}$

173

Ag	15.028012	15.028011	15.028012
Ag	12.582394	14.895607	13.574644
Ag	15.073122	16.55673	12.633689
Ag	13.500071	17.404522	15.18863
Ag	17.47649	14.928692	16.483813
Ag	10.745465	13.224404	11.642769
Ag	12.295271	17.665137	12.466397
Ag	16.685302	18.511054	10.850022
Ag	11.62222	19.226633	16.916808
Ag	18.435767	19.364443	13.243939
Ag	17.669079	17.66908	17.669078

S	15.828985	12.374723	10.568225
S	14.087933	17.829536	10.683036
S	12.194337	19.394556	14.314548
S	19.427366	15.866048	17.778226
S	11.689744	13.000161	9.338203
S	18.206702	17.231623	9.353563
S	16.965626	20.784359	11.836986
S	20.711545	18.373122	12.980928
C	16.319954	13.603427	9.35947
C	16.221632	13.307485	7.991011
H	15.75969	12.375362	7.663128
C	16.731759	14.220059	7.06356
H	16.663376	13.992581	5.99682
C	17.333787	15.411833	7.471539
H	17.738574	16.111648	6.739443
C	17.417307	15.723016	8.840304
C	16.897378	14.810433	9.761322
H	16.957949	15.047953	10.823696
C	13.595037	16.626126	9.454577
C	13.728742	16.938555	8.093847
H	14.2088	17.869305	7.79335
C	13.23836	16.044208	7.138965
H	13.342084	16.284894	6.078178
C	12.622331	14.848739	7.513495
H	12.23851	14.15742	6.761287
C	12.500941	14.519708	8.875561
C	12.996996	15.41838	9.825484
H	12.907138	15.166916	10.883331
C	13.414884	20.62589	13.86992
C	14.58134	20.270559	13.186046
H	14.773687	19.218927	12.972846
C	15.507884	21.227226	12.759835
C	15.24871	22.580492	13.041973
H	15.962193	23.341624	12.724375
C	14.089828	22.938385	13.733043
H	13.906452	23.991222	13.961475
C	13.166151	21.976565	14.151096
H	12.269792	22.259861	14.702466
C	20.638668	16.458972	16.603956
C	20.260431	17.00052	15.37156
H	19.210605	16.976244	15.076873
C	21.190281	17.596459	14.513537
C	22.541615	17.620635	14.905126
H	23.283833	18.080189	14.251358
C	22.924903	17.053899	16.121532
H	23.976735	17.06749	16.414806

C	21.988974	16.47513	16.980739
H	22.290224	16.047256	17.937179
Ag	13.574645	12.582393	14.895606
Ag	12.633689	15.073121	16.556732
Ag	15.18863	13.50007	17.404522
Ag	16.483816	17.476488	14.92869
Ag	11.642773	10.745462	13.224404
Ag	12.466395	12.295273	17.665138
Ag	10.850023	16.685304	18.511053
Ag	16.916809	11.622219	19.226633
Ag	13.243947	18.435765	19.364444
S	10.568225	15.828983	12.374724
S	10.68303	14.087941	17.829541
S	14.314546	12.194339	19.394558
S	17.778228	19.427365	15.866047
S	9.338207	11.689741	13.000162
S	9.353563	18.2067	17.231625
S	11.836985	16.965626	20.784356
S	12.980931	20.711542	18.373119
C	9.35947	16.319952	13.603429
C	7.99101	16.22163	13.307487
H	7.663127	15.759689	12.375364
C	7.063561	16.731757	14.22006
H	5.996821	16.663375	13.992583
C	7.471539	17.333785	15.411835
H	6.739444	17.738572	16.11165
C	8.840305	17.417304	15.723017
C	9.761321	16.897376	14.810434
H	10.823696	16.957949	15.047954
C	9.454578	13.595037	16.626125
C	8.093845	13.72874	16.938553
H	7.793348	14.2088	17.869301
C	7.138967	13.238355	16.044205
H	6.078178	13.342078	16.284891
C	7.513497	12.622325	14.848738
H	6.76129	12.238502	14.15742
C	8.875565	12.500938	14.519708
C	9.825485	12.996995	15.418381
H	10.883332	12.907138	15.166916
C	13.86992	13.414884	20.625891
C	13.186049	14.581341	20.27056
H	12.972846	14.773694	19.218929
C	12.759837	15.507884	21.227229
C	13.041976	15.248709	22.580495
H	12.72438	15.962194	23.341628
C	13.733043	14.089827	22.938388

H	13.961476	13.906449	23.991221
C	14.151094	13.166149	21.976566
H	14.70246	12.26979	22.259859
C	16.603959	20.638667	16.45897
C	15.371564	20.260428	17.000517
H	15.076877	19.210603	16.976241
C	14.51354	21.190278	17.596456
C	14.905129	22.541612	17.620633
H	14.251359	23.283829	18.080188
C	16.121535	22.9249	17.053899
H	16.414808	23.976733	17.067491
C	16.980742	21.988973	16.475129
H	17.937184	22.290224	16.047257
Ag	14.895608	13.574643	12.582393
Ag	16.556733	12.633688	15.073123
Ag	17.404524	15.188628	13.50007
Ag	14.928693	16.483813	17.476489
Ag	13.224407	11.642767	10.745463
Ag	17.66514	12.466396	12.295272
Ag	18.511055	10.850022	16.685305
Ag	19.226636	16.916808	11.622221
Ag	19.364447	13.243945	18.435765
S	12.374726	10.568225	15.828984
S	17.829542	10.683032	14.087939
S	19.394563	14.314545	12.19434
S	15.86605	17.778224	19.427366
S	13.000165	9.3382	11.689742
S	17.231626	9.353563	18.206701
S	20.784359	11.836981	16.965626
S	18.373118	12.980927	20.711544
C	13.60343	9.359471	16.319953
C	13.307489	7.991011	16.221631
H	12.375366	7.663127	15.759689
C	14.220062	7.063561	16.731757
H	13.992586	5.996821	16.663375
C	15.411836	7.471538	17.333786
H	16.111652	6.739444	17.738573
C	15.723019	8.840304	17.417306
C	14.810436	9.761321	16.897378
H	15.047955	10.823696	16.957953
C	16.626129	9.454576	13.595039
C	16.93856	8.093845	13.728743
H	17.869311	7.793351	14.2088
C	16.044214	7.138965	13.23836
H	16.284902	6.078178	13.342084
C	14.848745	7.513492	12.622331

H	14.157426	6.761285	12.23851
C	14.519712	8.875558	12.500941
C	15.418383	9.825481	12.996998
H	15.166917	10.883329	12.90714
C	20.625895	13.86992	13.414886
C	20.270564	13.186048	14.581343
H	19.218932	12.972844	14.773696
C	21.227233	12.759835	15.507885
C	22.580499	13.041974	15.248711
H	23.341632	12.724376	15.962195
C	22.938391	13.733042	14.089829
H	23.991226	13.961474	13.90645
C	21.976569	14.151094	13.166152
H	22.259862	14.702462	12.269794
C	16.458971	16.603956	20.638668
C	17.00052	15.371562	20.26043
H	16.976244	15.076874	19.210604
C	17.596457	14.513537	21.19028
C	17.620635	14.905125	22.541614
H	18.08019	14.251356	23.283831
C	17.0539	16.121531	22.924902
H	17.067493	16.414804	23.976734
C	16.47513	16.980738	21.988975
H	16.047258	17.937179	22.290226

$Ag_{29}BDT_{12}^{2-}$

173

Ag	15.028289	15.028288	15.028289
Ag	12.582858	14.898226	13.575545
Ag	15.068508	16.55596	12.632862
Ag	13.499918	17.404718	15.188258
Ag	17.474978	14.928041	16.481726
Ag	10.745468	13.219828	11.643011
Ag	12.293164	17.66361	12.464453
Ag	16.689187	18.509962	10.851678
Ag	11.622733	19.225419	16.919835
Ag	18.438992	19.366703	13.237902
Ag	17.668742	17.668742	17.668742
S	15.824819	12.373866	10.5652
S	14.094125	17.832057	10.681078
S	12.192185	19.395768	14.31991
S	19.429572	15.859463	17.776957
S	11.695501	13.005915	9.347632
S	18.201653	17.225402	9.362158
S	16.963347	20.781522	11.842287

S	20.705663	18.363985	12.988617
C	16.317707	13.602535	9.360668
C	16.2212	13.30825	7.991773
H	15.761726	12.376485	7.66169
C	16.730643	14.220569	7.064593
H	16.664316	13.992792	5.99826
C	17.331569	15.4123	7.473254
H	17.7397	16.11007	6.740852
C	17.4153	15.718772	8.843362
C	16.894795	14.80825	9.765063
H	16.956956	15.047088	10.827781
C	13.59697	16.627253	9.455373
C	13.730046	16.93842	8.094044
H	14.206385	17.87043	7.792808
C	13.240044	16.044061	7.139037
H	13.341049	16.286412	6.07851
C	12.624683	14.848858	7.514905
H	12.238528	14.160674	6.761238
C	12.504838	14.521998	8.877837
C	12.999143	15.420467	9.828435
H	12.907677	15.16678	10.886152
C	13.412916	20.625122	13.872166
C	14.578616	20.26667	13.188545
H	14.7737	19.215169	12.973485
C	15.505557	21.223909	12.764107
C	15.24934	22.578376	13.044869
H	15.960426	23.340533	12.724752
C	14.091175	22.938069	13.735565
H	13.90554	23.99084	13.961112
C	13.167089	21.976822	14.152893
H	12.269888	22.262177	14.700966
C	20.637113	16.456425	16.604986
C	20.25647	16.995886	15.373633
H	19.20661	16.974522	15.077533
C	21.187229	17.592122	14.518395
C	22.539887	17.616399	14.905439
H	23.281433	18.078415	14.252743
C	22.924225	17.051062	16.121151
H	23.975452	17.068032	16.414886
C	21.988063	16.47365	16.980562
H	22.291384	16.048632	17.936854
Ag	13.575547	12.582857	14.898227
Ag	12.632862	15.068507	16.555962
Ag	15.188259	13.499917	17.404718
Ag	16.481729	17.474977	14.92804
Ag	11.643015	10.745466	13.219828

Ag	12.464452	12.293165	17.663611
Ag	10.85168	16.689193	18.509965
Ag	16.919836	11.622732	19.225419
Ag	13.237912	18.438989	19.366703
S	10.565199	15.824817	12.373866
S	10.681072	14.094132	17.832062
S	14.319908	12.192188	19.39577
S	17.776961	19.42957	15.859461
S	9.347636	11.695498	13.005916
S	9.362158	18.201652	17.225404
S	11.842286	16.963346	20.781518
S	12.988619	20.70566	18.363982
C	9.360669	16.317705	13.602537
C	7.991772	16.221198	13.308252
H	7.66169	15.761724	12.376487
C	7.064594	16.730642	14.220571
H	5.99826	16.664315	13.992793
C	7.473253	17.331567	15.412302
H	6.740852	17.739698	16.110072
C	8.843363	17.415298	15.718773
C	9.765062	16.894793	14.808251
H	10.827781	16.956956	15.047089
C	9.455375	13.596969	16.627252
C	8.094043	13.730044	16.938419
H	7.792806	14.206385	17.870426
C	7.139039	13.240038	16.044058
H	6.078511	13.341044	16.286409
C	7.514907	12.624678	14.848857
H	6.761241	12.238519	14.160674
C	8.877841	12.504836	14.521998
C	9.828435	12.999142	15.420467
H	10.886153	12.907678	15.16678
C	13.872165	13.412918	20.625123
C	13.188547	14.578617	20.266671
H	12.973485	14.773706	19.215171
C	12.764109	15.505557	21.223912
C	13.044872	15.249338	22.578378
H	12.724757	15.960426	23.340537
C	13.735564	14.091173	22.938071
H	13.961112	13.905536	23.990839
C	14.152891	13.167086	21.976822
H	14.700961	12.269886	22.262175
C	16.604989	20.637111	16.456422
C	15.373637	20.256467	16.995883
H	15.077537	19.206608	16.974519
C	14.518399	21.187225	17.59212

C	14.905441	22.539883	17.616397
H	14.252745	23.281427	18.078414
C	16.121154	22.924223	17.051061
H	16.414889	23.975451	17.068034
C	16.980565	21.988061	16.473649
H	17.936858	22.291384	16.048632
Ag	14.898228	13.575545	12.582857
Ag	16.555963	12.632861	15.068509
Ag	17.40472	15.188257	13.499916
Ag	14.928043	16.481726	17.474977
Ag	13.219831	11.643009	10.745467
Ag	17.663613	12.464452	12.293164
Ag	18.509967	10.851679	16.689194
Ag	19.225421	16.919835	11.622734
Ag	19.366706	13.23791	18.43899
S	12.373869	10.5652	15.824818
S	17.832062	10.681075	14.09413
S	19.395776	14.319907	12.192188
S	15.859464	17.776956	19.42957
S	13.005918	9.347628	11.695499
S	17.225405	9.362158	18.201652
S	20.781522	11.842283	16.963345
S	18.363982	12.988614	20.705662
C	13.602538	9.360669	16.317707
C	13.308254	7.991773	16.221199
H	12.376489	7.661691	15.761724
C	14.220573	7.064594	16.730642
H	13.992796	5.998261	16.664315
C	15.412303	7.473254	17.331568
H	16.110073	6.740853	17.739699
C	15.718775	8.843363	17.415299
C	14.808252	9.765062	16.894795
H	15.047091	10.827781	16.95696
C	16.627256	9.455372	13.596972
C	16.938426	8.094042	13.730047
H	17.870436	7.792809	14.206385
C	16.044067	7.139037	13.240044
H	16.28642	6.07851	13.341049
C	14.848864	7.514902	12.624684
H	14.160681	6.761235	12.238528
C	14.522002	8.877835	12.504839
C	15.420469	9.828432	12.999145
H	15.166781	10.886149	12.907679
C	20.625127	13.872165	13.412919
C	20.266675	13.188546	14.57862
H	19.215174	12.973483	14.773709

C	21.223916	12.764108	15.505558
C	22.578382	13.04487	15.24934
H	23.340541	12.724754	15.960427
C	22.938074	13.735563	14.091175
H	23.990843	13.96111	13.905538
C	21.976826	14.152891	13.16709
H	22.262177	14.700962	12.26989
C	16.456425	16.604986	20.637112
C	16.995886	15.373634	20.25647
H	16.974522	15.077534	19.20661
C	17.592121	14.518395	21.187228
C	17.616398	14.905438	22.539885
H	18.078416	14.252741	23.28143
C	17.051063	16.121149	22.924224
H	17.068036	16.414885	23.975453
C	16.47365	16.980561	21.988064
H	16.048634	17.936854	22.291386

$Ag_{29}BDT_{12}^{1-}$

173

Ag	15.026122	15.02612	15.026121
Ag	12.584916	14.901964	13.574422
Ag	15.082743	16.561511	12.630195
Ag	13.50937	17.408223	15.179691
Ag	17.470971	14.930864	16.493393
Ag	10.750389	13.231101	11.644455
Ag	12.310113	17.668071	12.46886
Ag	16.690625	18.534352	10.816364
Ag	11.608329	19.239538	16.933398
Ag	18.445137	19.354144	13.224324
Ag	17.674331	17.67433	17.674332
S	15.82627	12.365529	10.568829
S	14.108569	17.847552	10.680997
S	12.190924	19.39707	14.327009
S	19.432029	15.862173	17.787448
S	11.716411	13.021797	9.371212
S	18.199772	17.22321	9.362196
S	16.963093	20.776811	11.851196
S	20.711453	18.360658	12.994976
C	16.313297	13.599083	9.368895
C	16.221319	13.306614	7.998363
H	15.772529	12.370746	7.664356
C	16.727923	14.221658	7.07229
H	16.667069	13.993334	6.007191

C	17.321417	15.415615	7.4837
H	17.727977	16.115163	6.753604
C	17.400188	15.719995	8.854058
C	16.882284	14.808245	9.776066
H	16.943285	15.04415	10.839034
C	13.611317	16.637995	9.457008
C	13.734778	16.942166	8.092273
H	14.206521	17.874569	7.783184
C	13.240486	16.042004	7.14486
H	13.333424	16.277753	6.082673
C	12.632607	14.846799	7.530998
H	12.244801	14.153267	6.783561
C	12.522464	14.530397	8.897347
C	13.017918	15.433698	9.84018
H	12.926899	15.187621	10.898521
C	13.412937	20.62507	13.876864
C	14.577545	20.26268	13.195277
H	14.76871	19.212018	12.979437
C	15.506229	21.216824	12.771891
C	15.254713	22.573125	13.048733
H	15.966338	23.332115	12.722491
C	14.095564	22.937217	13.735749
H	13.909478	23.989698	13.955539
C	13.169294	21.979327	14.154565
H	12.26972	22.271127	14.696323
C	20.640411	16.451766	16.612533
C	20.257034	16.98641	15.379621
H	19.207107	16.959851	15.086303
C	21.183363	17.584121	14.521773
C	22.537529	17.613547	14.906549
H	23.273836	18.081319	14.252468
C	22.926691	17.053487	16.123613
H	23.978361	17.077053	16.41464
C	21.993051	16.475478	16.986648
H	22.30212	16.061253	17.94645
Ag	13.574423	12.584914	14.901965
Ag	12.630197	15.082743	16.561511
Ag	15.179691	13.509368	17.408223
Ag	16.493394	17.470968	14.930866
Ag	11.644458	10.750388	13.231102
Ag	12.46886	12.310113	17.668074
Ag	10.816366	16.690624	18.534357
Ag	16.933398	11.608327	19.239538
Ag	13.224322	18.445134	19.354148
S	10.568828	15.826267	12.365531
S	10.680999	14.108567	17.84755

S 14.327009 12.190926 19.397071
S 17.78745 19.432026 15.862174
S 9.371215 11.716408 13.021798
S 9.362195 18.199769 17.223213
S 11.85119 16.96309 20.776817
S 12.994979 20.711449 18.360659
C 9.368894 16.313295 13.599085
C 7.998362 16.221318 13.306616
H 7.664354 15.772529 12.370747
C 7.072288 16.727922 14.22166
H 6.00719 16.667068 13.993336
C 7.483698 17.321416 15.415618
H 6.753602 17.727975 16.115166
C 8.854056 17.400187 15.719997
C 9.776064 16.882282 14.808247
H 10.839031 16.943283 15.044152
C 9.457006 13.611317 16.637996
C 8.092271 13.734777 16.942167
H 7.78318 14.206519 17.874571
C 7.14486 13.240482 16.042005
H 6.082673 13.333414 16.277753
C 7.531 12.632605 14.8468
H 6.783566 12.244795 14.153267
C 8.897349 12.522464 14.530397
C 9.84018 13.017919 15.433699
H 10.898522 12.926902 15.187627
C 13.876863 13.41294 20.62507
C 13.195279 14.57755 20.262682
H 12.97944 14.768715 19.21202
C 12.771889 15.506231 21.216827
C 13.048732 15.254713 22.573127
H 12.72249 15.966336 23.332119
C 13.735747 14.095564 22.937219
H 13.955539 13.909476 23.9897
C 14.154562 13.169294 21.979328
H 14.696321 12.269719 22.271127
C 16.612535 20.640409 16.451765
C 15.379623 20.257032 16.986409
H 15.086305 19.207105 16.959848
C 14.521775 21.183361 17.584121
C 14.906551 22.537527 17.613547
H 14.25247 23.273834 18.081318
C 16.123615 22.926688 17.053487
H 16.414643 23.978359 17.077054
C 16.98665 21.993049 16.475478
H 17.946452 22.302118 16.061254

Ag	14.901966	13.574421	12.584915
Ag	16.561514	12.630195	15.082743
Ag	17.408225	15.17969	13.50937
Ag	14.930867	16.493391	17.47097
Ag	13.231103	11.644454	10.750387
Ag	17.668076	12.46886	12.310114
Ag	18.53436	10.816366	16.690623
Ag	19.239541	16.933396	11.608329
Ag	19.354148	13.224319	18.445135
S	12.365533	10.568829	15.826269
S	17.847554	10.680997	14.108568
S	19.397077	14.32701	12.19093
S	15.862173	17.787445	19.432028
S	13.021803	9.371213	11.716409
S	17.223215	9.362195	18.199769
S	20.776822	11.851186	16.963092
S	18.360659	12.994974	20.711451
C	13.599087	9.368894	16.313297
C	13.306618	7.998362	16.221319
H	12.37075	7.664355	15.772529
C	14.221662	7.072288	16.727922
H	13.993338	6.00719	16.667067
C	15.41562	7.483698	17.321417
H	16.115168	6.753602	17.727975
C	15.719999	8.854056	17.400188
C	14.808248	9.776064	16.882286
H	15.044152	10.839032	16.94329
C	16.638	9.457005	13.611319
C	16.942171	8.09227	13.73478
H	17.874576	7.783179	14.206522
C	16.042008	7.144858	13.240488
H	16.277756	6.082671	13.333425
C	14.846803	7.530998	12.632609
H	14.153271	6.783561	12.244802
C	14.530401	8.897346	12.522466
C	15.433703	9.840178	13.017921
H	15.187628	10.898519	12.926904
C	20.625075	13.876863	13.412946
C	20.262686	13.195278	14.577555
H	19.212024	12.979438	14.76872
C	21.216831	12.771887	15.506235
C	22.573132	13.048729	15.254717
H	23.332123	12.722486	15.96634
C	22.937224	13.735746	14.095569
H	23.989705	13.955537	13.90948
C	21.979333	14.154563	13.169301

H 22.271132 14.696321 12.269725
C 16.451765 16.61253 20.640413
C 16.98641 15.379619 20.257035
H 16.95985 15.086302 19.207107
C 17.584122 14.52177 21.183363
C 17.613549 14.906547 22.537529
H 18.081321 14.252465 23.273836
C 17.053488 16.123609 22.926691
H 17.077056 16.414636 23.978362
C 16.475477 16.986645 21.993053
H 16.061253 17.946446 22.302123

$PtAg_{24}DMBT_{18}^{2-}$

349
Ag 15.338793 19.811962 17.273493
Ag 18.097825 20.962818 17.842104
Ag 19.857245 18.425739 18.801524
Ag 17.747447 16.098949 18.953449
Ag 13.831386 18.772406 19.56637
Ag 12.264645 20.865519 17.812253
Ag 13.743635 20.77739 14.998654
Ag 15.334239 17.689424 15.120843
Ag 16.805771 18.808226 19.583549
Ag 15.238087 19.008323 22.246282
Ag 12.160677 17.437615 21.735239
Ag 12.983921 15.995719 18.996981
Ag 15.376126 14.355408 18.537688
Ag 12.639618 13.032944 17.728815
Ag 10.79198 15.913332 17.02201
Ag 12.944924 18.076864 16.802248
Ag 16.807581 15.379898 16.226804
Ag 18.213428 13.248301 17.85327
Ag 17.1352 13.525433 20.772314
Ag 15.391187 16.441684 20.634551
Ag 13.888948 15.350871 16.190212
Ag 15.669501 15.136539 13.284329
Ag 18.335822 16.69739 14.094161
Ag 17.703872 18.155669 16.75156
Pt 15.33466 17.089175 17.894467
S 16.038462 22.249416 17.580419
S 20.489874 20.681779 18.115363
S 20.229485 16.047643 19.212069
S 12.332935 22.474183 15.994943
S 15.301599 19.656259 13.544595
S 11.62767 19.97354 19.976069

S 17.571508 19.601088 21.850027
S 13.096507 18.959057 23.384167
S 10.736779 16.158369 20.229603
S 14.833703 11.97748 17.866126
S 10.312065 13.550747 17.363308
S 10.450421 18.261321 16.452537
S 18.463539 11.756662 19.762324
S 15.631315 14.579001 22.357107
S 18.806918 13.985784 15.597826
S 13.38149 14.582513 13.827958
S 17.798786 15.287563 12.155046
S 19.836428 18.163999 15.369946
C 20.173348 11.845041 20.268093
C 21.1725 12.203866 19.351998
C 20.549835 11.440157 21.572541
C 22.518936 12.174482 19.703903
C 21.912536 11.422202 21.895049
C 19.534441 11.036987 22.603935
C 22.914773 11.786732 20.988425
C 24.364955 11.802461 21.396146
C 14.878572 10.522292 18.902588
C 15.638265 9.445709 18.413914
C 14.213554 10.387976 20.143372
C 15.746088 8.253624 19.128455
C 14.338381 9.174899 20.832894
C 13.393504 11.492786 20.733789
C 15.090832 8.095623 20.354481
C 15.18976 6.818018 21.149507
C 18.486738 12.620332 14.488233
C 17.220191 12.036565 14.360676
C 19.552505 12.141405 13.686509
C 16.992873 10.999354 13.456874
C 19.291716 11.099721 12.788623
C 20.932322 12.734635 13.760341
C 18.027042 10.513989 12.650496
C 17.793028 9.396947 11.663902
C 13.227729 12.861815 13.364903
C 12.928625 12.523701 12.023506
C 13.347737 11.836044 14.310953
C 12.778103 11.169378 11.693135
C 12.77924 13.573115 10.95944
C 13.195183 10.500256 13.953469
C 12.90974 10.139364 12.630937
C 12.779048 8.691986 12.230334
C 9.819892 12.809304 15.8166
C 9.520834 11.426713 15.767546

C 9.63901 13.589315 14.665583
C 9.058421 10.889834 14.559444
C 9.695514 10.539584 16.968153
C 9.176534 13.02655 13.479332
C 8.879148 11.660827 13.404677
C 8.426553 11.034009 12.111558
C 9.866644 18.278834 14.768941
C 8.555036 17.834187 14.472466
C 10.655357 18.810454 13.737992
C 8.106959 17.927636 13.147241
C 7.646754 17.272121 15.530074
C 10.177747 18.90256 12.435362
C 8.890933 18.45173 12.113618
C 8.364051 18.543708 10.705124
C 10.738266 22.498255 15.190429
C 10.61491 23.02613 13.883148
C 9.583797 22.091304 15.876
C 9.334844 23.104286 13.317887
C 11.808071 23.493536 13.098293
C 8.326818 22.185093 15.286483
C 8.179344 22.690837 13.989536
C 6.826167 22.747826 13.329254
C 11.380985 21.330188 21.109287
C 10.134588 21.365231 21.754534
C 12.336721 22.331176 21.395531
C 9.821945 22.372171 22.664346
C 11.989007 23.332752 22.311283
C 13.686277 22.34411 20.752082
C 10.747076 23.381878 22.955779
C 10.416749 24.500473 23.912549
C 17.585001 21.344131 22.244079
C 17.388503 22.325643 21.266574
C 17.853343 21.745889 23.577377
C 17.43911 23.681214 21.582944
C 17.897643 23.115286 23.864528
C 18.093955 20.740236 24.66839
C 17.690473 24.103465 22.891897
C 17.727181 25.567927 23.251053
C 20.986813 21.84153 19.381162
C 20.698795 23.201267 19.172109
C 21.754182 21.4686 20.509302
C 21.145558 24.181461 20.052161
C 22.177832 22.481102 21.382703
C 22.136979 20.045279 20.797429
C 21.890723 23.835121 21.185452
C 22.334769 24.875583 22.181549

C 20.883488 15.922498 20.866054
C 20.057404 15.677992 21.973391
C 22.281913 16.021155 21.059665
C 20.586237 15.538644 23.253324
C 22.782661 15.888461 22.361125
C 23.226766 16.250348 19.913952
C 21.965607 15.6494 23.470644
C 22.55398 15.501603 24.850144
C 16.387426 14.277676 23.952845
C 16.366422 12.951362 24.417171
C 16.946351 15.283478 24.774087
C 16.893533 12.608411 25.659829
C 17.463238 14.905324 26.022443
C 17.000071 16.72026 24.35065
C 17.455051 13.586016 26.490453
C 18.013839 13.245204 27.849211
C 13.398072 18.280202 25.008037
C 13.634738 19.171585 26.082848
C 13.366896 16.900642 25.260116
C 13.835589 18.630914 27.360655
C 13.66584 20.662731 25.888527
C 13.574518 16.395811 26.539922
C 13.813532 17.256186 27.618855
C 14.05805 16.711584 29.003129
C 16.309058 23.341886 16.18952
C 15.72462 24.630918 16.214235
C 17.09862 22.977313 15.087459
C 15.964631 25.492017 15.132383
C 14.865061 25.099994 17.354838
C 17.325622 23.859139 14.034576
C 16.759417 25.141396 14.036639
C 17.004551 26.107413 12.904621
C 20.167462 19.521735 14.256743
C 21.49035 20.024246 14.174255
C 19.180533 20.058796 13.417582
C 21.759132 21.036748 13.244786
C 22.599419 19.495499 15.04146
C 19.485035 21.060167 12.497557
C 20.783639 21.570447 12.393543
C 21.134221 22.647938 11.398688
C 17.650496 16.189065 10.623631
C 18.733776 16.954505 10.126187
C 16.501199 16.045187 9.829569
C 18.588518 17.575509 8.877308
C 20.020393 17.113082 10.88422
C 16.394068 16.662638 8.587354

C	17.436564	17.457442	8.092505
C	17.310985	18.18876	6.780856
C	14.636599	19.991758	11.914787
C	14.874368	21.277541	11.397587
C	13.932456	19.052095	11.130632
C	14.419234	21.643702	10.134129
C	13.489642	19.452882	9.860385
C	13.658483	17.663146	11.616938
C	13.712392	20.731628	9.338117
C	13.230161	21.106814	7.958992
C	9.899416	14.761221	20.962313
C	8.606034	14.509604	20.471009
C	10.412389	13.938928	21.990423
C	7.825405	13.476076	20.977971
C	9.600218	12.903925	22.478524
C	11.773421	14.149142	22.57428
C	8.313104	12.647717	21.997314
C	7.476266	11.534335	22.573766
H	20.882728	12.515147	18.347982
H	23.272173	12.465391	18.967749
H	22.198485	11.112138	22.905147
H	18.881411	10.230865	22.236966
H	18.868177	11.875863	22.863044
H	20.029981	10.696944	23.5238
H	25.027405	11.751731	20.520338
H	24.609369	10.959374	22.05859
H	24.613463	12.727773	21.941242
H	16.157528	9.55721	17.461363
H	16.352613	7.436775	18.728048
H	13.819135	9.075665	21.791818
H	13.998762	12.397685	20.895694
H	12.961493	11.190776	21.696843
H	12.56539	11.786709	20.06585
H	15.680955	6.02066	20.575491
H	14.195621	6.452015	21.448675
H	15.771167	6.963108	22.074114
H	16.40222	12.395547	14.985221
H	15.990476	10.574432	13.37255
H	20.11618	10.740286	12.163064
H	21.339981	12.694091	14.781628
H	20.921499	13.798309	13.4762
H	21.617489	12.201204	13.086635
H	16.769999	9.004157	11.743179
H	18.489949	8.559915	11.829046
H	17.933007	9.737132	10.625712
H	13.579826	12.085703	15.345885

H 12.549795 10.91763 10.652461
H 12.001562 14.304175 11.22869
H 12.522597 13.117013 9.994053
H 13.709959 14.149545 10.834199
H 13.306615 9.72971 14.720676
H 12.331154 8.588928 11.231991
H 12.15674 8.130554 12.943051
H 13.761423 8.192026 12.203416
H 9.88093 14.652423 14.700268
H 8.837506 9.817299 14.524031
H 9.144457 10.926536 17.838305
H 10.752784 10.487715 17.275585
H 9.347684 9.518971 16.756893
H 9.057608 13.660141 12.596574
H 7.787596 10.156507 12.288917
H 9.289156 10.696577 11.513407
H 7.86393 11.751094 11.496204
H 11.662281 19.160425 13.972311
H 7.094719 17.577768 12.918727
H 8.068003 16.358581 15.981813
H 6.664113 17.024478 15.106301
H 7.506502 17.981766 16.359516
H 10.820256 19.326677 11.65989
H 7.408232 18.011022 10.604327
H 9.070328 18.112328 9.979126
H 8.200608 19.591569 10.406329
H 9.679638 21.689775 16.885642
H 9.244513 23.50718 12.304514
H 12.391967 24.238752 13.659235
H 11.49851 23.93135 12.138944
H 12.50314 22.664349 12.884889
H 7.448127 21.851625 15.843374
H 6.806188 23.481095 12.510519
H 6.039006 23.018329 14.049203
H 6.549726 21.768502 12.905076
H 9.408218 20.58226 21.534231
H 8.844376 22.370464 23.152912
H 12.730572 24.108898 22.524089
H 13.612434 22.40914 19.654114
H 14.235093 21.40889 20.956092
H 14.298051 23.182223 21.107282
H 9.555412 24.244265 24.545939
H 10.162157 25.430733 23.376927
H 11.269318 24.729918 24.569431
H 17.194738 22.020626 20.238177
H 17.286463 24.417215 20.790171

H 18.109086 23.418503 24.89506
H 17.213407 20.096826 24.823512
H 18.329952 21.238962 25.618903
H 18.919935 20.06028 24.409256
H 17.735452 26.198495 22.351214
H 18.618738 25.8167 23.847719
H 16.848872 25.860757 23.848856
H 20.112718 23.486492 18.297505
H 20.910088 25.230596 19.854792
H 22.765699 22.188472 22.257619
H 22.719394 19.606612 19.973318
H 21.250904 19.401275 20.929305
H 22.738505 19.982499 21.713917
H 22.505846 25.849732 21.700664
H 23.264509 24.576001 22.685928
H 21.573721 25.027477 22.965092
H 18.979061 15.603147 21.822908
H 19.914484 15.343039 24.092693
H 23.863758 15.975807 22.507024
H 23.160636 15.433074 19.180074
H 24.262503 16.314407 20.273632
H 22.987904 17.174024 19.364228
H 21.986738 16.083976 25.591491
H 23.5974 15.846337 24.874443
H 22.54148 14.452365 25.18549
H 15.932021 12.179882 23.779546
H 16.868768 11.564018 25.981315
H 17.891952 15.688907 26.655861
H 15.989149 17.12918 24.202212
H 17.52712 16.84886 23.395656
H 17.503901 17.33759 25.105548
H 18.239317 12.172812 27.93696
H 17.298709 13.496058 28.650248
H 18.937843 13.804588 28.057171
H 13.19449 16.213854 24.431969
H 14.012835 19.324321 28.18937
H 14.451694 20.968281 25.179172
H 13.838803 21.173646 26.846473
H 12.720496 21.029131 25.460972
H 13.565794 15.314553 26.697916
H 14.127882 17.518234 29.74676
H 14.998446 16.138536 29.044168
H 13.253073 16.03036 29.320067
H 17.541756 21.982642 15.055706
H 15.504181 26.485242 15.155364
H 13.946163 24.499251 17.433664

H	14.575515	26.150139	17.209508
H	15.387271	25.007126	18.31961
H	17.956993	23.537636	13.2027
H	16.482487	27.059933	13.072555
H	16.656291	25.701846	11.941992
H	18.076263	26.330932	12.784036
H	18.156372	19.687161	13.480656
H	22.783306	21.41854	13.180077
H	22.727842	18.410555	14.911412
H	22.380491	19.655865	16.108687
H	23.549871	19.992451	14.799521
H	18.692527	21.440943	11.849289
H	21.747181	23.436215	11.862516
H	20.231445	23.121481	10.987884
H	21.712813	22.246142	10.549423
H	15.678671	15.436449	10.206663
H	19.423619	18.175103	8.50081
H	20.475516	16.138931	11.117742
H	19.867452	17.619153	11.851406
H	20.738957	17.706857	10.303094
H	15.480509	16.534812	8.000989
H	18.295761	18.472343	6.38445
H	16.722073	19.114109	6.896309
H	16.803767	17.578812	6.01839
H	15.415764	21.996181	12.015551
H	14.612186	22.655571	9.76698
H	12.944355	18.722329	9.255152
H	14.599062	17.116958	11.790997
H	13.062849	17.092947	10.891977
H	13.125018	17.65813	12.576538
H	12.873294	22.147016	7.922889
H	12.408549	20.454018	7.630324
H	14.036124	21.018448	7.211752
H	8.22315	15.136306	19.665321
H	6.827929	13.303273	20.566872
H	10.002279	12.266734	23.271732
H	11.847061	15.14368	23.048051
H	12.56375	14.127028	21.811282
H	12.002447	13.388363	23.331686
H	6.887154	11.023104	21.798399
H	6.760889	11.914661	23.321324
H	8.102182	10.781819	23.073992

$PtAg_{24}DMBT_{18}^{1-}$

349

Ag	15.291914	19.785325	17.237743
Ag	18.067586	20.959486	17.806678
Ag	19.811724	18.39808	18.794049
Ag	17.690062	16.025576	18.964507
Ag	13.813106	18.752482	19.571884
Ag	12.215133	20.856664	17.801467
Ag	13.72279	20.770092	14.955794
Ag	15.32585	17.619247	15.071536
Ag	16.76561	18.796149	19.553022
Ag	15.216327	18.991638	22.259011
Ag	12.14181	17.379797	21.771006
Ag	12.985386	15.897262	19.009251
Ag	15.351624	14.312013	18.523036
Ag	12.615021	12.993862	17.706427
Ag	10.819503	15.891664	16.988331
Ag	12.963451	18.12479	16.71702
Ag	16.744938	15.327931	16.175299
Ag	18.180239	13.19257	17.814535
Ag	17.089713	13.482134	20.787864
Ag	15.354219	16.440296	20.638346
Ag	13.835604	15.319258	16.172949
Ag	15.630149	15.102483	13.257576
Ag	18.297787	16.701008	14.060428
Ag	17.646151	18.166052	16.730516
Pt	15.297584	17.054894	17.873132
S	16.000169	22.199964	17.556174
S	20.441623	20.639835	18.087707
S	20.162009	16.025925	19.179871
S	12.315998	22.435857	15.982226
S	15.262086	19.607951	13.528447
S	11.611618	19.925422	19.936897
S	17.532214	19.564795	21.822005
S	13.070352	18.929827	23.363338
S	10.764578	16.124195	20.218337
S	14.801883	11.956114	17.845134
S	10.301607	13.550657	17.347918
S	10.486531	18.225769	16.434076
S	18.425193	11.758648	19.757562
S	15.59118	14.566597	22.32652
S	18.766699	13.97392	15.58388
S	13.349673	14.56432	13.813635
S	17.763846	15.279511	12.156733
S	19.763976	18.142791	15.366331
C	20.13855	11.846969	20.260032
C	21.138959	12.195807	19.341839
C	20.510277	11.437167	21.562939

C 22.485738 12.154744 19.694443
C 21.872274 11.410396 21.885122
C 19.489209 11.026235 22.583513
C 22.878679 11.769255 20.98124
C 24.325999 11.779092 21.39535
C 14.846492 10.508422 18.895701
C 15.60833 9.434748 18.406585
C 14.175627 10.375406 20.132232
C 15.709948 8.243465 19.121022
C 14.300385 9.163316 20.823639
C 13.347143 11.479462 20.709211
C 15.055708 8.085655 20.347582
C 15.166718 6.807419 21.13638
C 18.437015 12.610819 14.470647
C 17.171568 12.02566 14.346752
C 19.504864 12.133754 13.672923
C 16.948603 10.984796 13.445941
C 19.245671 11.090707 12.776707
C 20.882527 12.72897 13.757035
C 17.983089 10.501821 12.639299
C 17.750746 9.389494 11.649765
C 13.200091 12.840528 13.36154
C 12.904149 12.502643 12.019998
C 13.320043 11.817366 14.309286
C 12.755943 11.148797 11.69112
C 12.753345 13.549756 10.954663
C 13.163068 10.481421 13.952273
C 12.882846 10.119419 12.6289
C 12.745209 8.675541 12.224661
C 9.810507 12.811244 15.794201
C 9.508949 11.429509 15.750002
C 9.628146 13.591336 14.643321
C 9.041288 10.892574 14.544536
C 9.678744 10.542034 16.9501
C 9.161834 13.025359 13.459515
C 8.861326 11.659981 13.388601
C 8.405583 11.023035 12.102705
C 9.882995 18.240554 14.753916
C 8.567679 17.799169 14.467563
C 10.661382 18.784232 13.72091
C 8.109622 17.907223 13.14672
C 7.654611 17.237085 15.521166
C 10.173746 18.883974 12.423143
C 8.883951 18.436814 12.110134
C 8.346484 18.5383 10.707879
C 10.720772 22.457556 15.174444

C 10.597146 22.995654 13.872114
C 9.56804 22.042815 15.858239
C 9.31728 23.073089 13.306834
C 11.786606 23.485716 13.097799
C 8.310956 22.139102 15.269396
C 8.162594 22.651604 13.974139
C 6.808474 22.729055 13.319813
C 11.379452 21.293743 21.071331
C 10.129474 21.325392 21.709083
C 12.328506 22.301459 21.353595
C 9.80766 22.336405 22.611213
C 11.96995 23.303802 22.265485
C 13.681566 22.320778 20.715029
C 10.726398 23.349854 22.90575
C 10.390558 24.460753 23.866295
C 17.538538 21.308185 22.227626
C 17.337876 22.287858 21.249223
C 17.801471 21.707711 23.562628
C 17.385558 23.643785 21.565706
C 17.841619 23.077538 23.845627
C 18.035702 20.710315 24.663419
C 17.637651 24.065959 22.873881
C 17.686284 25.526802 23.235685
C 20.934142 21.799118 19.357394
C 20.634538 23.155558 19.145497
C 21.708703 21.431033 20.481365
C 21.083341 24.139086 20.020003
C 22.134062 22.447752 21.348692
C 22.093883 20.009726 20.772783
C 21.84079 23.799534 21.147605
C 22.298368 24.847686 22.12687
C 20.815246 15.918544 20.837567
C 19.991759 15.686721 21.947731
C 22.215674 16.009096 21.020577
C 20.528136 15.547184 23.224465
C 22.721183 15.871434 22.319906
C 23.154516 16.239389 19.869153
C 21.910148 15.637594 23.43492
C 22.505125 15.465883 24.807867
C 16.346029 14.260661 23.92549
C 16.333161 12.929417 24.375771
C 16.895992 15.26244 24.755944
C 16.853366 12.581682 25.620354
C 17.406349 14.878002 26.004031
C 16.952005 16.701694 24.345463
C 17.400262 13.556859 26.463881

C 17.946492 13.21195 27.823996
C 13.375116 18.246275 24.986365
C 13.611764 19.142847 26.054049
C 13.341077 16.867325 25.237912
C 13.813991 18.605959 27.332211
C 13.638289 20.631177 25.845334
C 13.544857 16.368405 26.520595
C 13.789573 17.23288 27.595319
C 14.021543 16.70052 28.984432
C 16.275071 23.293402 16.165566
C 15.699948 24.585076 16.201197
C 17.064705 22.923117 15.065916
C 15.943374 25.447782 15.122214
C 14.843277 25.04828 17.346175
C 17.291733 23.80773 14.015588
C 16.732244 25.092493 14.024263
C 16.968874 26.052559 12.886616
C 20.103806 19.503099 14.252049
C 21.431608 19.990078 14.162608
C 19.117444 20.044254 13.41592
C 21.700503 21.004257 13.234938
C 22.543233 19.447045 15.017102
C 19.424336 21.050334 12.500953
C 20.725209 21.552565 12.393282
C 21.078106 22.628698 11.399437
C 17.612993 16.187671 10.628002
C 18.701284 16.937746 10.12147
C 16.453592 16.052853 9.847885
C 18.551125 17.552286 8.869766
C 19.995365 17.076647 10.870715
C 16.339745 16.670839 8.60701
C 17.389568 17.446011 8.097642
C 17.266458 18.1545 6.774137
C 14.601285 19.941856 11.894527
C 14.842013 21.229636 11.384565
C 13.893697 19.006724 11.110521
C 14.384646 21.601111 10.124176
C 13.452445 19.412786 9.841989
C 13.606055 17.61986 11.594364
C 13.677142 20.692631 9.324704
C 13.199234 21.071131 7.947298
C 9.907805 14.724942 20.93283
C 8.615624 14.489551 20.432833
C 10.401853 13.905629 21.970103
C 7.82066 13.469072 20.943753
C 9.575994 12.88297 22.458952

C 11.754911 14.115424 22.569238
C 8.288502 12.641699 21.972912
C 7.43123 11.544702 22.547932
H 20.851768 12.498373 18.333076
H 23.240267 12.434653 18.955422
H 22.154215 11.088598 22.891285
H 18.845177 10.220773 22.201118
H 18.819 11.860975 22.842074
H 19.976155 10.679529 23.503706
H 24.992562 11.70387 20.526058
H 24.560444 10.950676 22.078329
H 24.575453 12.716031 21.918871
H 16.128421 9.545807 17.453888
H 16.311857 7.425048 18.719568
H 13.778895 9.066337 21.78028
H 13.942381 12.392688 20.857578
H 12.918418 11.186762 21.675402
H 12.515286 11.752443 20.037384
H 15.632704 6.011506 20.541456
H 14.18084 6.448699 21.465251
H 15.777772 6.944981 22.041584
H 16.351766 12.380905 14.972952
H 15.949595 10.552754 13.36766
H 20.070349 10.730265 12.154471
H 21.285371 12.673587 14.77907
H 20.872315 13.79647 13.488455
H 21.572111 12.205837 13.082303
H 16.727662 8.997746 11.723319
H 18.446817 8.553364 11.813929
H 17.897288 9.737412 10.6163
H 13.554193 12.068659 15.344452
H 12.527773 10.894335 10.652403
H 11.974717 14.280565 11.220066
H 12.497934 13.091208 9.990886
H 13.685073 14.123992 10.831227
H 13.267209 9.71207 14.72066
H 12.295283 8.577753 11.227874
H 12.122141 8.115537 12.936297
H 13.72545 8.174132 12.195152
H 9.863099 14.656702 14.677443
H 8.811463 9.823529 14.51144
H 9.118146 10.924774 17.815312
H 10.733075 10.492244 17.2656
H 9.335074 9.522354 16.733295
H 9.037307 13.657545 12.577286
H 7.788846 10.132755 12.288355

H 9.270518 10.699932 11.501899
H 7.821851 11.721204 11.486902
H 11.667614 19.142432 13.950923
H 7.095003 17.563985 12.923167
H 8.062799 16.315041 15.965575
H 6.670694 17.004528 15.093161
H 7.51735 17.943857 16.352422
H 10.806295 19.320904 11.647447
H 7.387779 18.012404 10.611596
H 9.047793 18.102105 9.981676
H 8.189068 19.587767 10.414442
H 9.665702 21.6424 16.86931
H 9.226706 23.486589 12.298658
H 12.341914 24.254353 13.655734
H 11.478796 23.905018 12.131039
H 12.503308 22.672086 12.903036
H 7.433872 21.806829 15.828597
H 6.799572 23.453569 12.494063
H 6.032003 23.020911 14.041644
H 6.512921 21.751641 12.906162
H 9.407403 20.538763 21.486802
H 8.826173 22.332821 23.089769
H 12.706742 24.082428 22.480804
H 13.612904 22.388312 19.616775
H 14.2339 21.389054 20.925247
H 14.286905 23.161876 21.073033
H 9.526536 24.198036 24.491197
H 10.140692 25.393615 23.335898
H 11.239359 24.684052 24.528283
H 17.14258 21.982152 20.220048
H 17.230358 24.378992 20.773817
H 18.049282 23.380618 24.875143
H 17.155405 20.067246 24.819651
H 18.258127 21.221408 25.609657
H 18.866885 20.030276 24.424364
H 17.669948 26.161048 22.339718
H 18.594688 25.769839 23.807121
H 16.82587 25.812814 23.859793
H 20.045823 23.436061 18.270372
H 20.841445 25.186133 19.823367
H 22.729443 22.163355 22.220673
H 22.668948 19.567568 19.946141
H 21.205329 19.373179 20.918253
H 22.702508 19.950509 21.683732
H 22.496619 25.806105 21.627266
H 23.213852 24.535645 22.647813

H 21.529926 25.032828 22.894502
H 18.912368 15.61112 21.798521
H 19.857109 15.358629 24.064382
H 23.802557 15.950277 22.458632
H 23.079172 15.431544 19.126468
H 24.194067 16.293411 20.217704
H 22.916745 17.171346 19.334213
H 21.941599 16.030695 25.563513
H 23.548838 15.804138 24.832847
H 22.495143 14.410351 25.119432
H 15.914893 12.159874 23.723461
H 16.829644 11.535551 25.93325
H 17.830562 15.659111 26.641719
H 15.940016 17.115586 24.220063
H 17.465937 16.83286 23.384112
H 17.472025 17.307407 25.098326
H 18.198266 12.145877 27.899013
H 17.214284 13.431891 28.617068
H 18.850273 13.793229 28.054222
H 13.163769 16.181705 24.408515
H 13.994086 19.299677 28.15781
H 14.419658 20.928075 25.128405
H 13.815107 21.154616 26.793954
H 12.689454 20.989307 25.419977
H 13.521959 15.28904 26.684153
H 14.113361 17.515179 29.714828
H 14.943593 16.100576 29.033324
H 13.196756 16.04826 29.307799
H 17.505756 21.926299 15.03227
H 15.493326 26.444452 15.149303
H 13.915473 24.459807 17.406877
H 14.570488 26.103864 17.220336
H 15.358073 24.926772 18.310963
H 17.919264 23.488905 13.180084
H 16.459381 27.00973 13.061089
H 16.6001 25.643703 11.933098
H 18.040539 26.260854 12.748609
H 18.093099 19.669552 13.475545
H 22.726219 21.376458 13.165883
H 22.671613 18.363961 14.874737
H 22.331124 19.600234 16.086373
H 23.491763 19.945165 14.774052
H 18.631446 21.438918 11.858334
H 21.68852 23.418083 11.861485
H 20.177512 23.098556 10.981792
H 21.661112 22.223156 10.556932

H 15.635427 15.439164 10.227539
H 19.389171 18.138663 8.481924
H 20.43133 16.094646 11.108698
H 19.852954 17.59463 11.832657
H 20.723148 17.649501 10.281783
H 15.421237 16.548021 8.028443
H 18.250228 18.450049 6.387287
H 16.65805 19.068773 6.864603
H 16.782654 17.517656 6.019521
H 15.385091 21.943792 12.006613
H 14.575236 22.614955 9.764418
H 12.90264 18.687367 9.235986
H 14.53934 17.055846 11.749643
H 12.989848 17.065537 10.874343
H 13.085194 17.622611 12.560957
H 12.840506 22.109525 7.916065
H 12.382504 20.416526 7.613625
H 14.009423 20.986744 7.205656
H 8.241551 15.125316 19.629904
H 6.82281 13.314174 20.530324
H 9.966904 12.249916 23.259688
H 11.805496 15.099168 23.068009
H 12.547856 14.122248 21.809753
H 11.987418 13.341403 23.311477
H 6.853203 11.034228 21.7658
H 6.707421 11.942429 23.27686
H 8.03923 10.792124 23.067278

References

[1]. Mortensen, J. J.; Larsen, A. H.; Kuisma, M.; Ivanov, A. V.; Taghizadeh, A.; Peterson, A.; Haldar, A.; Dohn, A. O.; Schäfer, C.; Jónsson, E. Ö.; Hermes, E. D.; Nilsson, F. A.; Kastlunger, G.; Levi, G.; Jónsson, H.; Häkkinen, H.; Fojt, J.; Kangsabanik, J.; Sødequist, J.; Lehtomäki, J.; Heske, J.; Enkovaara, J.; Winther, K. T.; Dulak, M.; Melander, M. M.; Ovesen, M.; Louhivuori, M.; Walter, M.; Gjerding, M.; Lopez-Acevedo, O.; Erhart, P.; Warmbier, R.; Würdemann, R.; Kaappa, S.; Latini, S.; Boland, T. M.; Bligaard, T.; Skovhus, T.; Susi, T.; Maxson, T.; Rossi, T.; Chen, X.; Schmerwitz, Y. L. A.; Schiøtz, J.; Olsen, T.; Jacobsen, K. W.; Thygesen, K. S. GPAW: An Open Python Package for Electronic Structure Calculations. *J. Chem. Phys.* 2024, **160** (9), 092503.

[2]. Enkovaara J; Rostgaard C.; Mortensen J. J.; Chen J.; Dułak M.; Ferrighi L.; Gavnholt J.; Glinsvad C.; Haikola V.; Hansen H. A.; Kristoffersen H. H.; Kuisma M.; Larsen A. H.; Lehtovaara L.; Ljungberg M.; Lopez-Acevedo O.; Moses P. G.; Ojanen J; Olsen T.; Petzold V.; Romero N. A.; Stausholm-Møller J.;

Strange M.; Tritsaris G. A.; Vanin M.; Walter M.; Hammer B.; Häkkinen H.; Madsen G. K. H.; Nieminen R. M.; Nørskov J. K.; Puska M.; Rantala T. T.; Schiøtz J.; Thygesen K. S.; Jacobsen K. W., Electronic structure calculations with GPAW: a real-space implementation of the projector augmented-wave method, *J. Phys. Condens. Matter.* 2010, **22**, 253202.

[3]. Perdew J. P.; Burke K.; Ernzerhof M., Generalized Gradient Approximation Made Simple*, Phys. Rev. Lett.*, 1996, **77**, 3865-3868.

[4]. L. G. AbdulHalim, M. S. Bootharaju, Q. Tang, S. Del Gobbo, R. G. AbdulHalim, M. Eddaoudi, D. E. Jiang and O. M. Bakr, *J. Am. Chem. Soc.*, 2015, **137**, 11970–11975.

[5]. Neumaier, M., Baksi, A., Weis, P., Schneider, E. K., Chakraborty, P., Hahn, H., Pradeep, T. and Kappes, M. M., *J. Am. Chem. Soc.***,** 2021**, 143**, 6969–6980.

Check for updates

NANO · MICRO small
www.small-journal.com

Morphology-Preserved Alloying in Anisotropic Gold Nanoparticles Using Atomically Precise Nanoclusters

*Amrita Chakraborty, Sujan Manna, Biswajit Mondal, Mohammad Bodiuzzaman, Ankit Nagar, Soham Chowdhury, Tanmayaa Nayak, Nonappa, and Thalappil Pradeep**

Noble metal nanoparticles (NPs) exhibit superior plasmonic, catalytic, electronic, and magnetic properties upon alloying with a second metal. However, the synthesis of bimetallic alloy NPs of non-spherical morphologies presents a challenge due to the necessity of concurrently modulating the nucleation and growth kinetics of various metallic constituents. In this study, a simple solution-phase reaction between a phosphine-protected copper nanocluster (NC), namely $[Cu_{18}(DPPE)_6H_{16}]^{2+}$ [DPPE = 1,2-bis(diphenyl phosphino)ethane] (abbreviated as Cu_{18}) and gold nanotriangles (AuNTs) is reported as a straightforward strategy to obtain gold-copper alloy nanotriangles (AuCuNTs) while keeping their sizes and sharp edges intact. Extending this protocol to gold nanorods (AuNRs) and nanocubes (AuNCbs) demonstrates its generality for creating anisotropic AuCu alloy NPs. Auger spectroscopic analyses confirm that Cu(0) is the predominant Cu species in the AuCuNTs, indicating that oxidation of Cu in the resulting nanostructures is prevented. A further interaction of AuCuNTs with $[Ag_{25}(DMBT)_{18}]^-$ [DMBT = 2,-dimethylbenzenethiol] (abbreviated as Ag_{25}) has yielded AuCuAgNTs, offering a facile synthetic route to trimetallic anisotropic NPs. Thus, the current study corroborates atomically precise metal NCs as versatile precursors for tuning the composition of plasmonic anisotropic NPs to meet diverse technological and industrial needs.

1. Introduction

Noble metal nanoparticles (NPs) exhibit unique optical properties that are sensitive to their dimensions, morphologies, compositions, and dielectric environments.[1–3] Due to synergetic interaction between different metals, bi- and trimetallic nanostructures have shown remarkably improved physicochemical properties, making them attractive nanoprobes in Surface-enhanced Raman spectroscopy (SERS)-based sensing,[4] catalysis,[5,6] photothermal therapy,[7] and solar cells.[8] Depending on the reaction mechanism, different metals can combine to form diverse morphologies ranging from crown-jewel, hollow, heterostructure, core-shell, alloyed, and nanosnowmen to porous structures.[9–13] Among noble metals, Au and Cu possess common face-centered cubic (fcc) crystal structures and share similar valences (+1). Moreover, the relatively minor difference in atomic radii (less than 15%) and the modest discrepancy in molar heat of vaporization (merely 11%) between Au and Cu suggests a strong propensity for nanoscale mixing that facilitates the synthesis of Au—Cu alloy nanostructures. Such Au—Cu alloy NPs serve as cost-effective candidates while showing superior catalytic activity, compared to pure Au NPs.[14] More recently, Au_3Cu tetrapod nanocrystals (TPNCs) have shown excellent photothermal performance,[15] while hollow Au—Cu alloy rods exhibited enhanced catalytic activity compared to the solid alloy nanorods and spherical NPs.[16] Highly branched Au—Cu nanostructures have been used for non-enzymatic specific detection of glucose and hydrogen peroxide.[17] These results indicate the relative distribution of different planes, edges, and corners, which makes the non-spherical NPs show optimal performances.[18] Despite the recent advances yielding bimetallic NPs with dilute concentrations of a secondary metal in low-index, and high-index surface facets,[19] the synthesis of anisotropic homogeneous alloy NPs faced great challenges. Different metals often require distinct thermodynamic or kinetic conditions for deposition,[13] making it difficult to achieve precise control over reaction parameters to guide the growth along specific crystallographic directions. Solution phase synthesis of Au—Cu alloy nanocubes,[20] nanorods,[21] nanopentacles,[7] and nanotriangles[22] either necessitated elevated temperatures, use of lasers, or specialized organic solvents, often yielding success specific to a particular shape. Thus, the independent control over both morphology and composition of anisotropic Au—Cu nanostructures is still an unmet need. Considering the availability of diverse shapes of AuNPs

A. Chakraborty, S. Manna, B. Mondal, M. Bodiuzzaman, A. Nagar, S. Chowdhury, T. Nayak, T. Pradeep
Department of Chemistry
DST Unit of Nanoscience (DST UNS) and Thematic Unit of Excellence (TUE)
Indian Institute of Technology Madras
Chennai 600 036, India
E-mail: pradeep@iitm.ac.in
Nonappa
Faculty of Engineering and Natural Sciences
Tampere University
Tampere FI-33720, Finland

The ORCID identification number(s) for the author(s) of this article can be found under https://doi.org/10.1002/smll.202410784

DOI: 10.1002/smll.202410784

 © 2025 Wiley-VCH GmbH

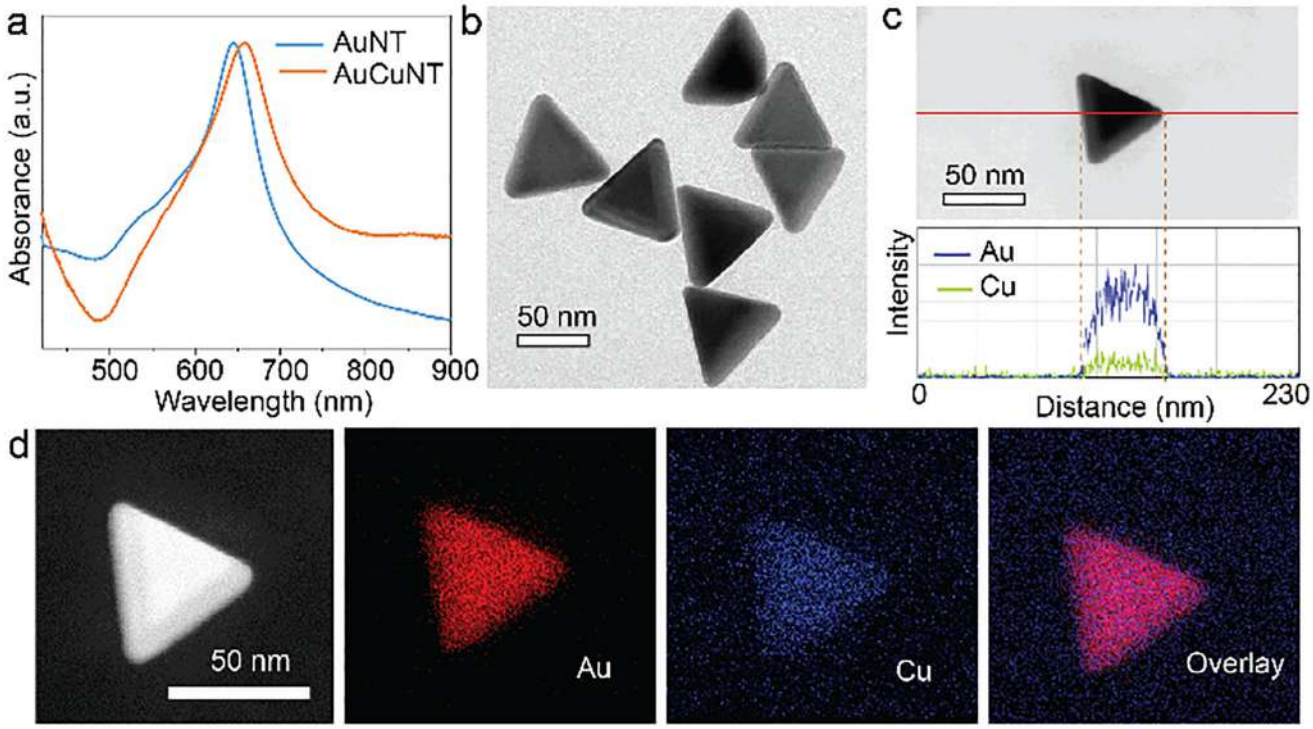


Figure 1. Characterization of AuCuNTs. a) Absorption spectra of parent AuNT and alloy AuCuNTs. b) TEM image of AuCuNTs showing size and shape uniformity. c) Bright-field STEM EDS line profile and d) dark-field STEM image of a single AuCuNT along with corresponding EDS elemental mapping that shows uniform distribution of Au and Cu along the NTs.

in the literature, we envisioned a strategy of doping elemental Cu to these AuNPs, keeping their morphology unaltered as a generic route to synthesize Au—Cu alloy anisotropic NPs of desired morphology and composition. For this, we chose planar gold nanotriangles (AuNTs) as a model anisotropic NP as their sharp edges are highly sensitive toward any morphological changes during the alloy formation. The approach developed has been extended to gold nanorods (AuNRs) and gold nanocubes (AuNCbs).

Since their discovery in the 1960s, atomically precise noble metal nanoclusters (NCs) have garnered significant interest due to their distinctive molecule-like optoelectronic properties,[23,24] as well as their catalytic activities,[25] among other applications. They form colloidal assemblies with anisotropic NPs such as tellurium nanowires,[26] and AuNRs,[27] leading to novel composite materials. Recently, spontaneous solution phase reaction has emerged as a facile route towards doping heteroatom into ultrasmall NCs[28] as well as plasmonic NPs.[29,30] Inspired by these results, we studied the chemical reactivity of $[Cu_{18}(DPPE)_6H_{16}]^{2+}$ where DPPE = 1,2-bis(dipehnylphosphino)ethane (abbreviated herein as Cu_{18}), with AuNTs to demonstrate a unique strategy of alloy formation without altering the morphology of the latter. This approach has been extended to AuNRs and AuNCbs that yielded gold-copper alloy nanorods (AuCuNRs) and alloy nanocubes (AuCuNCbs), respectively, with high size and shape monodispersity. We further extended the protocol to silver NCs to make trimetallic gold-copper-silver (AuCuAg) nanostructures.

2. Results and Discussion

The synthesis of Cu_{18} NC was adapted from the methodology established by Li et al.[31] The emergence of an orange color in the solution and the characteristic UV–vis absorption spectrum suggested the successful formation of Cu_{18} NC, which was further confirmed by the two peaks at m/z 3552 and 1775 in electrospray ionization mass spectrum (ESI MS) (Figure S1, Supporting Information). As a monometallic template, planar AuNTs of ≈75.5 nm edge-length were synthesized via a seed-mediated growth protocol reported by Scarabelli et al.[32] As illustrated in Figure S2 (Supporting Information), the purified AuNTs exhibited a high degree of uniformity in size and shape. These AuNTs were dispersed in *N, N*-Dimethylformamide (DMF), to which, Cu_{18} NC was added under moderate stirring at room temperature. UV–vis absorption spectra of the particles, before and after the reaction, are presented in **Figure** 1a, where the resultant AuCuNTs exhibit a red shift in the localized surface plasmon resonance (LSPR) peak position. Alloying of Cu into Au NPs is known to cause such a red shift along with a broadening of the LSPR band.[33] Transmission electron microscopy (TEM) image of the reacted AuNTs, as shown in Figure 1b and Figure S3a (Supporting Information), confirmed preserving the planar triangular morphology post-reaction. Moreover, a comprehensive analysis of the edge-length distribution of the NTs before and after the reaction shows negligible changes in their sizes (Figure S2c, Supporting Information), suggesting that the observed spectral shift in Figure 1a was attributable to the alloying process.

© 2025 Wiley-VCH GmbH

16136829, 2025, 43, Downloaded from https://onlinelibrary.wiley.com/doi/10.1002/smll.202410784 by Central Library The Librarian, Wiley Online Library on [28/12/2025]. See the Terms and Conditions (https://onlinelibrary.wiley.com/terms-and-conditions) on Wiley Online Library for rules of use; OA articles are governed by the applicable Creative Commons License

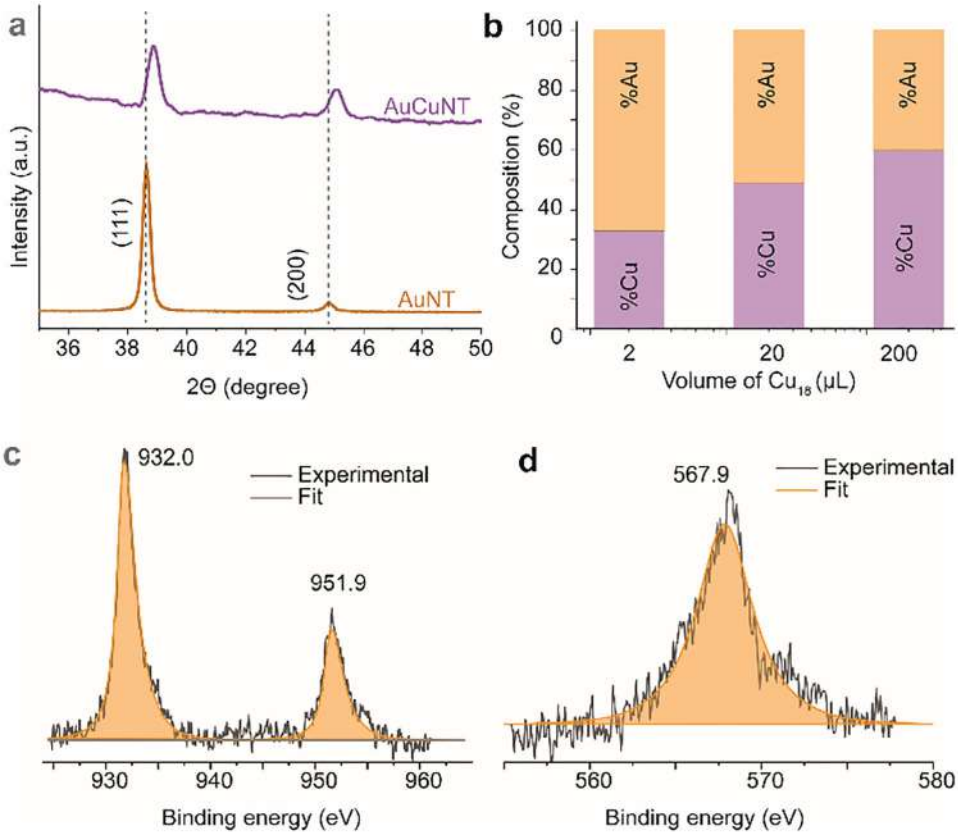


Figure 2. a) Comparative XRD spectra before and after reaction showing increased 2Θ, i.e., decreased lattice spacing in AuCuNT, b) Variation of atomic % of Cu and Au in AuCuNTs as a function of Cu_{18} concentration in the reaction medium, c) Cu 2p X-ray photoelectron spectrum and d) Cu LMM Auger showing the presence of Cu(0) exclusively in AuCuNT.

Scanning transmission electron microscopy (STEM) and corresponding energy-dispersive X-ray spectroscopy (EDS) offer a powerful visual confirmation to distinguish alloy versus core-shell structures.[34] STEM-EDS line scans show that in homogeneous alloys the two metals are equally distributed throughout each particle, whereas a core-shell particle shows a bimodal elemental distribution with one element enriched in the shell.[35,36] Bright-field STEM image of an isolated AuCuNT and the corresponding line scan (Figure 1c) demonstrate a homogeneous distribution of Au and Cu along the NTs, which indicates alloy formation. High-angle annular dark-field STEM (HAADF-STEM) and corresponding EDS mapping were also performed on the NTs. As shown in Figure 1d, they further confirm the integration of Au and Cu within the NTs, keeping their sharp edges and flat faces intact. Figure S3b (Supporting Information) presents EDS line scans of three additional AuCuNTs. Comparable intensities for Au and Cu in all of them confirm the uniform composition of AuCuNTs at the single-particle level. We further conducted inductively coupled plasma mass spectrometry (ICP-MS) on both the parent AuNTs and the AuCuNTs. As summarized in Figure S3c (Supporting Information), the ICP-MS results confirm that the AuCuNTs have an Au:Cu ratio of ≈5.7, which matches closely with the ratio observed in the STEM EDS study (Au:Cu = 5.5).

Powder X-ray diffraction (PXRD) is a reliable technique for determining the structure and the crystallinity of metallic NPs. The comprehensive XRD spectra of AuNTs and AuCuNTs, as depicted in Figure S4 (Supporting Information), show a single-phase face-centered cubic (fcc) pattern. A magnified view of the peaks corresponding to (111) and (200) planes in **Figure 2a** reveals a discernible shift towards higher 2θ values in AuCuNTs, validating the formation of an Au-Cu alloy.[33] According to the calibration curve of lattice parameter based on the XRD peak positions proposed by Chang et al.,[37] lattice parameter of AuNT is calculated to be 4.050 Å, whereas that of AuCuNT is 4.036 Å in our case. This suggests uniform alloying of 88% elemental Au and 12% Cu, over the possibilities of Cu shell formation or surface-limited Cu doping. The observed broadening of XRD peaks in AuCuNTs may be attributed to the uncertainty of composition within the AuCuNTs. Further, the absence of a superlattice peak (110) confirms that the alloy possesses atomic disorder.[38] This finding speaks for the unique reactivity of Cu_{18} NC towards AuNTs. Previously, in the case of a similar reaction between AuNTs and $[Ag_{25}(DMBT)_{18}]^-$ [DMBT = 2,4-dimethylbenzenethiol] (abbreviated as Ag_{25}), the XRD peak positions reflected no shift. Besides, the concentration of the reactant NC, Ag_{25}, had little effect on the low elemental ratio of Ag to Au in the resulting bimetallic NT, indicating that Ag doping was limited to the surface of the AuNTs.[29] As a result, the concentration of the reactant NC, Ag_{25}, had little effect on the composition of the resulting bimetallic NTs. However, varying atomic ratio of the metallic components within alloy

© 2025 Wiley-VCH GmbH

16136829, 2025, 43, Downloaded from https://onlinelibrary.wiley.com/doi/10.1002/smll.202410784 by Central Library The Librarian, Wiley Online Library on [28/12/2025]. See the Terms and Conditions (https://onlinelibrary.wiley.com/terms-and-conditions) on Wiley Online Library for rules of use; OA articles are governed by the applicable Creative Commons License

NPs often alters their photoluminescent properties,[39] catalytic efficiency,[40,41] SERS performance.[42] Therefore, it is beneficial to have the freedom to tune the composition of the NTs without altering their morphology. In this study, the atomic percentage of Cu in the resulting NTs was modulated simply by varying the concentration of Cu_{18} NC in the reaction medium. The Cu content within the AuCuNTs, as obtained from their TEM EDS analysis, is graphically represented against the NC concentration in Figure 2b (NTs of the same sample showed ±3% variation in Cu content). The quantitative correlation indicates that the Cu content of the NTs increased up to 60% upon the addition of 200 µL of 1.35 mg mL^{-1} Cu NC. This observation is consistent with most Au—Cu alloy NPs that exhibit a linear dependency between the alloy's metallic composition and the precursor metal concentration introduced.[43]

A major challenge faced by Cu and Cu-based NPs is their pronounced vulnerability to oxidation.[44] Cu colloids tend to turn yellow or precipitate immediately upon exposure to air in solution, forming copper(I) oxide (Cu_2O) or copper(II) oxide (CuO). Incorporating Au into Cu NPs has been a popular approach for protecting Cu NPs from oxidation.[45] In the case of AuCuNTs, the absence of an additional XRD peak for the (110) plane at 29.60° of Cu_2O indicates the absence of an oxide layer surrounding the NTs.[46] AuCuNTs were further investigated by performing X-ray photoelectron spectroscopy (XPS) and corresponding Auger transitions. The XPS survey spectrum is presented in Figure S5a (Supporting Information). The atomic composition derived from the spectrum indicates 88% elemental Au and 12% elemental Cu. These values rule out the possibility of the formation of a Cu shell on AuNTs, as such configurations would result in a predominant Cu signal in XPS. For example, Sakthisabarimoorthi et al. observed no detectable Cu signal in the XPS analysis of Cu core-Ag shell particles.[47] The Au 4f region (Figure S5b, Supporting Information) contained the two characteristic peaks for metallic Au, whereas, Cu 2p region of the XPS spectrum (Figure 2c) indicates the presence of Cu^0 and/or Cu^+ from the two distinct peaks at 932.0 eV (Cu $2p_{3/2}$) and 951.9 eV (Cu $2p_{1/2}$) along with the absence of Cu^{2+} satellite peaks in between them. Since it is difficult to distinguish between Cu^0 and Cu^+ from their XPS spectrum, the Cu LMM region of the Auger transition is depicted in Figure 2d. A single peak at 567.9 eV in the binding energy axis, i.e., 918.7 eV in terms of kinetic energy (kinetic energy = 1486.6 eV–567.9 eV = 918.7 eV), is the characteristic Auger peak of metallic Cu.[48] Notably, the absence of peaks due to Cu^+ and Cu^{2+} (916.4 and 917.8 eV, respectively) proves that Cu is incorporated in the alloy NTs solely in its metallic form. In core-shell structures, the shell-forming metal is typically found in its oxidized form.[49] Here, the presence of Cu exclusively in Cu(0) state further mitigates the possibility of core-shell morphology. Homogeneous Au—Cu alloying in a highly anisotropic nanoparticle without altering its morphological features is a unique finding and warrants further investigation into the overall reaction mechanism.

Unlike NP-NC reactions reported so far,[29] here the size and shape of the reacted NTs remained unaltered, necessitating additional experiments to assess potential Au etching. At various Cu_{18} concentrations, the reaction mixture was centrifuged to precipitate the AuCuNTs. UV–vis spectroscopy and TEM were employed to confirm the absence of AuNTs in the supernatant prior to performing the ICP-MS to quantify the Au etched out to the reaction mixture. A control experiment was also conducted in which an equivalent volume of DMF, instead of Cu_{18}, was added to maintain the volume constant. The ICP-MS results from three distinct sets of reactions are compiled in Table S1 (Supporting Information). A significant increase in the quantity of Au atoms leached into the reaction medium was observed with the addition of Cu_{18}. This trend approached saturation at higher NC concentrations. This observation, combined with Figure 2b, indicates that with the course of the reaction, the amount of Cu increased in the NTs, and the amount of Au increased in the supernatant, i.e., some of the Au atoms within the AuNTs were replaced by Cu atoms. Additionally, ESI MS analysis of the same supernatant was performed to identify the charge state of etched Au in the dispersion. The MS depicted in Figure S6 (Supporting Information) confirms the presence of $[Au_2(DPPE)_2]^{2+}$ ions in the dispersion. The isotopic distribution pattern of the experimental peak at m/z 595, as shown in the inset, aligns precisely with the theoretical counterpart, which confirms that Au(0) leaches out in the form of $[Au_2(DPPE)_2]^{2+}$ (Statement 1).

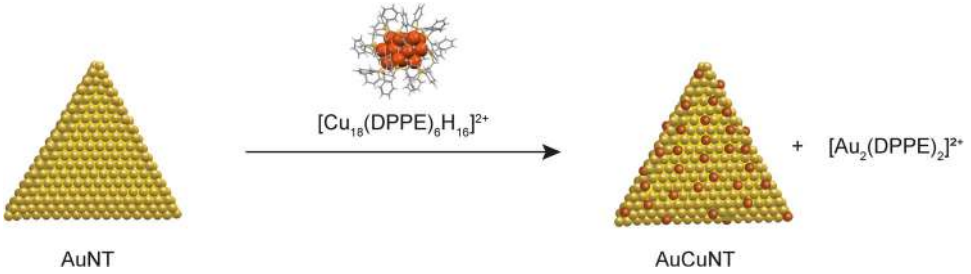
Now, oxidation of Au(0) by Cu^{n+} is not expected when the standard electrode reduction potentials are considered. However, due to the quantum confinement effect, the oxidation potential of metal NPs greatly decreases,[50] As a result, nanoscopic systems, especially those less than 3 nm in diameter often participate in unconventional redox behavior, where Au NPs are known to be oxidized by less noble metal ions.[51–53] Such redox reactions, unexpected based on classical galvanic theory, are referred to as "anti-galvanic" reduction (AGR). Studies on noble metal NCs have reported that AGR is dependent on several factors such as surface ligand, ion precursor, ion dosage, solvent, and so on.[30,53–57] Here, to identify the Cu precursor in the present case, we conducted a control experiment where Cu_{18} NC was treated in an equivalent reaction condition in absence of AuNTs, and the ESI MS was analyzed. As depicted in Figure S8 (Supporting Information), $[Cu_xDPPE_y]^+$ (x = 1, y = 1, 2) complexes were identified. Such Cu-DPPE complexes of varying composition were presumably generated in situ that reacted with the AuNTs (Statement 2).

Ciganda et al. have shown that surface ligands play a crucial role as AuNPs act as electron reservoir redox catalysts.[58] Precisely, ligand-free and surfactant-free gold NPs are known to reduce Ag and Cu ions as the oxidation potential value of bare AuNPs is sufficiently lower, which presumably is the driving force of AGR.[53] Here, although the AuNTs purified by flocculation method ("purified AuNTs") showed characteristic peaks of CTAC in their IR spectrum (Figure S7, Supporting Information), after the removal of excess CTAC by centrifugation (denoted as "clean AuNTs"), no such IR peaks were observed. This can be attributed to the fact that the low propensity of Cl^- for the Au surface causes the CTA^+ micelles to detach from the AuNT leaving a few disordered CTA^+ ions sticking to the surface, as reported by Meena et al.[59] Thus, we believe that unprotected Au atoms coexisted on the AuNT surface along with the CTA^+-protected sites. These bare Au atoms were accessible to any reactant present in the reaction medium and might have acted as the starting points of the AGR reaction (Statement 3).

Here, a complete characterization of the reaction intermediates was not possible, making it difficult to explain the exact reaction mechanism. However, using dispersion correction

© 2025 Wiley-VCH GmbH

16136829, 2025, 43, Downloaded from https://onlinelibrary.wiley.com/doi/10.1002/smll.202410784 by Central Library The Librarian, Wiley Online Library on [28/12/2025]. See the Terms and Conditions (https://onlinelibrary.wiley.com/terms-and-conditions) on Wiley Online Library for rules of use; OA articles are governed by the applicable Creative Commons License



Scheme 1. Schematic representation of the fabrication of AuCuNT.

density functional theory, Peng et al. have demonstrated that foreign metal atoms in the form of ML_2 (M═Ag, Cd, Hg, L = thiolate) can rapidly diffuse to the surface of Au_{25} NC. Later, it can slowly diffuse to the icosahedral core of the NC releasing AuL_2 moieties.[60] We believe that a similar mechanism takes place in the present case where L = DPPE and M═Cu. Here, Cu is first incorporated into the AuNT surface, and later relocated towards the interior, as observed in many AuCu alloy NPs.[61,62] Molecular rearrangements of metal-phosphine complexes on Au NC surface observed by Wang et al. align well with our hypothesis.[63] Au has a larger atomic radius, and such elemental distribution reduces the total number of surface atoms, thereby decreasing the surface energy associated with broken bonds at the surface. Using decahedrons, Guisbiers et al. have shown that at room temperature, the formation energy of a Cu core- Au shell NP is comparable with the thermal energy of clusters of similar dimensions, suggesting the possibility of a uniform distribution of the elements.[61] In the present study, the absence of a Cu_2O shell on the surface, along with the greater atomic percentage of elemental Au (≈88%) than that in the volume of AuCuNTs (≈85%) suggests that Cu atoms migrate into the core of the AuCuNTs without any phase segregation (Statement 4).

The above four statements are based on experimental evidences. Building upon these and previous reports on the unique reactivity of low coordinated surface atoms of larger metallic NPs showing unique/specific reactions towards NCs,[30,64,65] we propose a plausible reaction mechanism between AuNT and Cu_{18} NCs (**Scheme 1**):

1) Cu_{18} was decomposed into $[Cu_xDPPE_y]^+$ (x = 1, y = 1, 2) in the reaction medium.
2) These Cu-DPPE complexes first formed an adduct with the partially unprotected AuNT surface. Although could not be isolated in this case, such adducts are previously identified as intermediates of inter-AgNP-AuNC reaction,[66] as well as AuNT-Ag_{25} NC reaction.[64]
3) Metal-DPPE bond being labile, DPPE moieties freely migrate between neighboring Au and Cu atoms at AuNT surface. As demonstrated by Peng et al.[63] and Wang et al.,[63] $Au_2(DPPE)_2]^{2+}$ moieties were eventually detached from the nanoparticle, Cu atoms taking up the space of Au atoms.
4) Finally, to reduce surface energy, Cu atoms migrated to the core making room for further reaction while keeping the morphology intact.

Motivated by their exceptional efficacy in plasmonic, catalytic, and biomedical applications, significant efforts have been made to fabricate Au—Cu alloy NPs of diverse geometries.[16] However, due to inherent disparities in lattice constants between Au and Cu, minor variations in experimental conditions can significantly alter the reaction kinetics and pathways, especially for complex shapes. Bimetallic phase formation can't be deduced from the intrinsic thermodynamic predictors, like reduction potentials. Rather, it depends on the reaction kinetics (i.e., side reactions) and constantly variable thermodynamics, including ligand exchange, making it complicated. Acknowledging the demand for a generic alloying strategy, we extended our protocol to synthesize Au—Cu alloy NPs of alternative shapes. Among various anisotropic structures, monodisperse cubes are of great interest as building blocks in designing novel hierarchical nanostructures suitable for devices.[67,68] AuCuNCbs of a range of sizes have been synthesized using a one-pot polyol strategy, which still requires elevated temperature.[20] On the other hand, AuNRs, characterized by their high-index surface facets,[69] have been applied across a broad spectrum of fields. Chen et al. have reported that Au—Cu alloy nanorod catalysts show nearly twice the catalytic efficiency compared to their spherical counterparts despite possessing a 4-fold reduced total surface area.[70] Synthetic procedures of high-quality AuNCbs and AuNRs are well documented in the literature. Here, AuNCbs with an approximate edge length of 50 nm and AuNRs with dimensions of roughly 30 nm (length) by 10 nm (width) were synthesized,[71] and subsequently treated with Cu_{18} in a similar manner. According to Meena et al., CTAB forms a layer of distorted cylindrical micelles on AuNR surfaces.[72] Channels among these micelles allow reactants to freely diffuse from the bulk solution to the gold surface facilitating a similar reaction as observed in the case of CTAC protected AuNTs. The resulting products were examined using UV–vis absorption spectra, TEM, and field emission scanning electron microscopy (FESEM) (characterization details are included in **Figure 3**; Figures S8, and S9, Supporting Information). TEM image of the resulting AuCuNCbs, shown in Figure 3a, confirms the preservation of monodispersity in size and shape, including edge sharpness. FESEM image of a single AuCuNCb is presented in Figure 3b. Spot EDS collected from the center of the particle reveals a composition of 36 atomic percent Cu and 64 atomic percent Au. Further, EDS line profiling (Figure 3c) along the yellow line shows a homogeneous distribution of Au and Cu within the reacted AuNCb. Similarly, Figure 3d presents a TEM image of AuCuNRs. FESEM image of them (Figure 3e), along with the simultaneously acquired line scan spectrum (Figure 3f), illustrates an even distribution of both metals along the nanostructure, with spot EDS analysis yielding ≈78% Au and 22% Cu. These findings validate that interaction with Cu_{18} NC converts AuNPs of

© 2025 Wiley-VCH GmbH

16136829, 2025, 43, Downloaded from https://onlinelibrary.wiley.com/doi/10.1002/smll.202410784 by Central Library The Librarian, Wiley Online Library on [28/12/2025]. See the Terms and Conditions (https://onlinelibrary.wiley.com/terms-and-conditions) on Wiley Online Library for rules of use; OA articles are governed by the applicable Creative Commons License

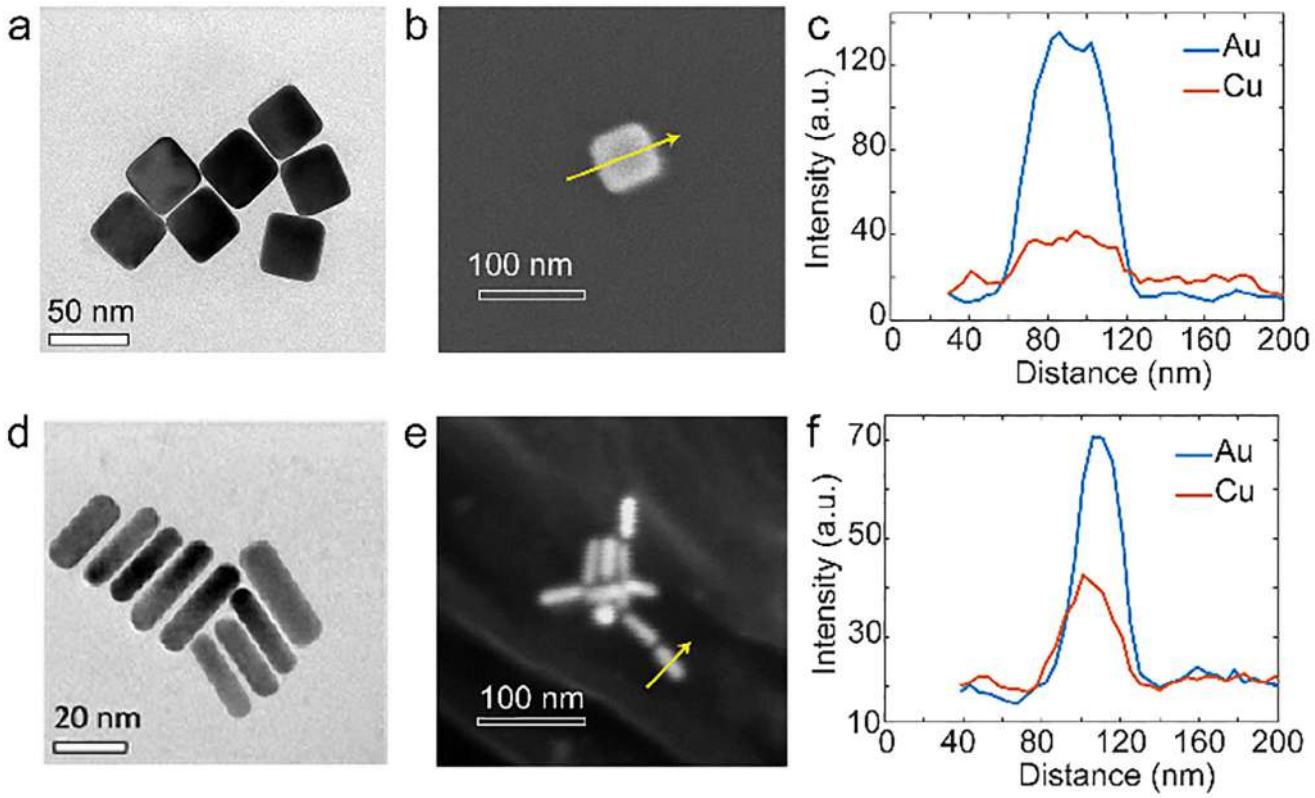


Figure 3. Au—Cu alloying in nanocubes and nanorods. a) TEM image of the AuCuNCbs, b) FESEM image of a single AuCuNCb with point EDS collected from the center, c) FESEM EDS line profile across the AuCuNCb particle along the yellow line, d) TEM image of the AuCuNRs, e) FESEM image of AuCuNRs, f) EDS line profile along the yellow line across the NR at the bottom.

any dimension and transforms them into Au—Cu alloy NPs while maintaining their original morphology, marking the first known shape-independent method for fabricating Au—Cu alloy NPs at room temperature, to the best of our knowledge.

We believe that the challenges associated with the fabrication of trimetallic NPs of desired non-spherical morphology may be overcome by using NCs as precursors. As proof of this concept, the solution-phase reactivity of Ag_{25} NC toward AuCuNTs was explored, and the resultant particles were subjected to comprehensive characterization. **Figure** 4a shows the dark-field STEM image of the NTs post-reaction. Noticeable blunting of the NTs at the tips and edges along with a reduction in edge length (Figure S10, Supporting Information) can be observed which indicates atomic etching at sites with low coordination. The bright-field STEM image of a single particle, along with the corresponding EDS line profile (in Figure 4b), reveals the homogeneous distribution of Au, Ag, and Cu along the NTs. The elemental STEM mapping of the particles, shown in Figure 4c, further supports the transformation of bimetallic AuCuNTs into trimetallic AuCuAgNTs following the interaction with Ag_{25} NC. However, the low atomic percentage of Ag (below 10%) within the AuCuAgNTs and the unaltered XRD peak positions, as compared to parent AuCuNTs (not shown), suggest that the doping of Ag was limited to the surface of the NTs, as opposed to complete alloying. These observations are consistent with the reactivity of Ag_{25} toward pure AuNTs[29] and suggests that the reactivity of different Ag NCs with AuNTs can be extended to alloy AuCuNPs to achieve diverse trimetallic NPs. Thus, our strategy shows the reproducibility and the robust nature of inter-nanoparticle reaction schemes, potentially encouraging the community to explore the reactivity of the other NCs to successfully tune the composition of nanostructures with intricate shapes.

3. Conclusion

In conclusion, we propose a novel strategy to fabricate alloy bimetallic NPs of targeted morphology by using anisotropic AuNPs as scaffolds through their reactivity with Cu_{18} NCs. Specifically, we demonstrated that Cu_{18} NCs serve as a precursor to incorporate Cu(0) into AuNTs, facilitating the formation of uniform AuCuNTs in DMF. This transformation fully conserves the size and shape of the parent nanostructure, occurs at room temperature, and requires no special equipment. The formation of alloys was confirmed from XRD analysis, while their composition was determined from electron microscopic elemental analyses, and ICP MS. Using AuNCbs and AuNRs, the general applicability of the protocol was proven. Finally, leveraging the reactivity of Ag_{25} toward AuCuNTs, trimetallic AuCuAg NTs were successfully synthesized. Thus, the methodology presented herein addresses the challenge of synthesizing multimetallic anisotropic NPs with high shape and size monodispersity. With the wide range of Au NPs and metallic NCs documented in scientific literature, the present study shows enormous potential

© 2025 Wiley-VCH GmbH

16136829, 2025, 43, Downloaded from https://onlinelibrary.wiley.com/doi/10.1002/smll.202410784 by Central Library The Librarian, Wiley Online Library on [28/12/2025]. See the Terms and Conditions (https://onlinelibrary.wiley.com/terms-and-conditions) on Wiley Online Library for rules of use; OA articles are governed by the applicable Creative Commons License

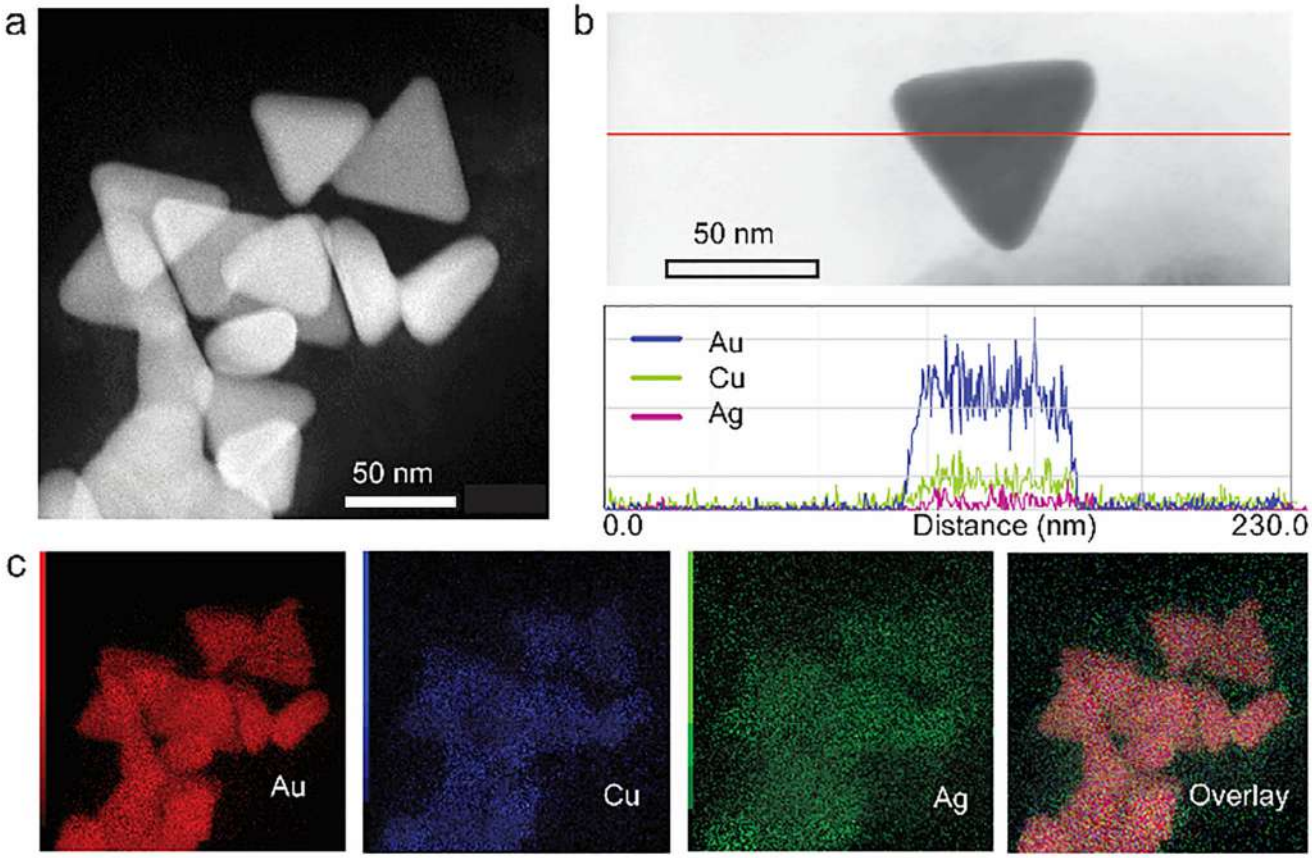


Figure 4. Characterization of AuCuAgNT. a) Dark-field STEM image of AuCuAgNTs, b) STEM EDS line profile of a single AuCuAgNT, c) STEM EDS elemental mapping corresponding to Figure a. Due to their random orientation on the TEM grid, some NTs appear as different shapes in their 2D projections.

in fabricating functional nanomaterials through the strategic selection of reactant pairs.

Supporting Information

Supporting Information is available from the Wiley Online Library or from the author.

Acknowledgements

A.C. and S.M. contributed equally to this work. The authors thank the Department of Science and Technology, the Government of India, and IIT Madras for supporting the research. A.C. and S.M., respectively, thank the Council of Scientific and Industrial Research and UGC for their research fellowships. The authors acknowledge the Research Council of Finland for project funding (No. 352900), Photonics Research and Innovation (PREIN) flagship, and Tampere Microscopy Centre for imaging facilities. T.P. thanks the Science and Engineering Research Board (SERB), India, for funding through the SPR/2021/000439 research grant, SUPRA project, and the JC Bose Fellowship. T.P. acknowledges funding from the Centre of Excellence (CoE) on Molecular Materials and Functions from the Institute of Eminence scheme of IIT Madras. A.C. was responsible for the conception and design of the work. A.C. and S.M. performed the experiments, analyzed the data, and prepared the manuscript. B.M. performed the transmission electron microscopy. M.B. helped with the synthesis of the nanoclusters. A.N. performed scanning electron microscopy. S.C. performed the XPS, T.N. performed the ICP MS, and N. performed the scanning transmission electron microscopy. T.P. supervised the study and helped to improve the manuscript.

Conflict of Interest

The authors declare no conflict of interest.

Data Availability Statement

The data that support the findings of this study are available from the corresponding author upon reasonable request.

Keywords

alloy nanoparticles, copper nanoclusters, morphology-preserved alloying, noble metal nanoparticles, trimetallic nanoparticles

Received: November 15, 2024
Revised: April 3, 2025
Published online: May 2, 2025

© 2025 Wiley-VCH GmbH

16136829, 2025, 43, Downloaded from https://onlinelibrary.wiley.com/doi/10.1002/smll.202410784 by Central Library The Librarian, Wiley Online Library on [28/12/2025]. See the Terms and Conditions (https://onlinelibrary.wiley.com/terms-and-conditions) on Wiley Online Library for rules of use; OA articles are governed by the applicable Creative Commons License

[1] K. L. Kelly, E. Coronado, L. L. Zhao, G. C. Schatz, *J. Phys. Chem. B* **2003**, *107*, 668.
[2] H. Wang, D. W. Brandl, P. Nordlander, N. J. Halas, *Acc. Chem. Res.* **2007**, *40*, 53.
[3] Y. Wang, J. Chen, Y. Zhong, S. Jeong, R. Li, X. Ye, *J. Am. Chem. Soc.* **2022**, *144*, 13538.
[4] J. Reguera, J. Langer, D. J. de Aberasturi, L. M. Liz-Marzán, *Chem. Soc. Rev.* **2017**, *46*, 3866.
[5] C. L. Bracey, P. R. Ellis, G. J. Hutchings, *Chem. Soc. Rev.* **2009**, *38*, 2231.
[6] D. D. Robertson, M. L. Personick, *Chem. Mater.* **2019**, *31*, 1121.
[7] R. He, Y.-C. Wang, X. Wang, Z. Wang, G. Liu, W. Zhou, L. Wen, Q. Li, X. Wang, X. Chen, J. Zeng, J. G. Hou, *Nat. Commun.* **2014**, *5*, 4327.
[8] E. C. Garnett, M. L. Brongersma, Y. Cui, M. D. McGehee, *Annu. Rev. Mater. Res.* **2011**, *41*, 269.
[9] X. Liu, D. Wang, Y. Li, *Nano Today* **2012**, *7*, 448.
[10] R. Borah, S. Verbruggen, *J. Phys. Chem. C* **2020**, *124*, 12081.
[11] A. Loiseau, L. Zhang, D. Hu, M. Salmain, Y. Mazouzi, R. Flack, B. Liedberg, S. Boujday, *ACS Appl. Mater. Interfaces.* **2019**, *11*, 46462.
[12] J.-H. Lee, G.-H. Kim, J.-M. Nam, *J. Am. Chem. Soc.* **2012**, *134*, 5456.
[13] Y. Xia, K. D. Gilroy, H.-C. Peng, X. Xia, *Angew. Chem., Int. Ed.* **2017**, *56*, 60.
[14] Z. D. Pozun, S. E. Rodenbusch, E. Keller, K. Tran, W. Tang, K. J. Stevenson, G. Henkelman, *J. Phys. Chem. C* **2013**, *117*, 7598.
[15] Z. Wang, Y. Ju, S. Tong, H. Zhang, J. Lin, B. Wang, Y. Hou, *Nanoscale Horiz.* **2018**, *3*, 624.
[16] S. Thota, S. Chen, J. Zhao, *Chem. Commun.* **2016**, *52*, 5593.
[17] A. Ngamaroonchote, Y. Sanguansap, T. Wutikhun, K. Karn-orachai, *Microchim. Acta* **2020**, *187*, 559.
[18] A. K. Bentley, S. E. Skrabalak, *J. Chem. Educ.* **2023**, *100*, 3425.
[19] H. Jung, M. E. King, M. L. Personick, *Curr. Opin. Colloid Interface Sci.* **2019**, *40*, 104.
[20] Y. Liu, A. R. H. Walker, *Angew. Chem., Int. Ed.* **2010**, *49*, 6781.
[21] A. Henkel, A. Jakab, G. Brunklaus, C. Sönnichsen, *J. Phys. Chem. C* **2009**, *113*, 2200.
[22] M. Hajfathalian, K. D. Gilroy, A. Yaghoubzade, A. Sundar, T. Tan, R. A. Hughes, S. Neretina, *J. Phys. Chem. C* **2015**, *119*, 17308.
[23] I. Chakraborty, T. Pradeep, *Chem. Rev.* **2017**, *117*, 8208.
[24] T. Pradeep, *Atomically Precise Metal Nanoclusters*, Elsevier, Amsterdam, Netherlands **2022**.
[25] S. Nematulloev, A. Sagadevan, B. Alamer, A. Shkurenko, R. Huang, J. Yin, C. Dong, P. Yuan, K. E. Yorov, A. A. Karluk, W. J. Mir, B. E. Hasanov, M. Nejib Hedhili, N. M. Halappa, M. Eddaoudi, O. F. Mohammed, M. Rueping, O. M. Bakr, *Angew. Chem., Int. Ed.* **2023**, *62*, 202303572.
[26] A. Som, I. Chakraborty, T. A. Maark, S. Bhat, T. Pradeep, *Adv. Mater.* **2016**, *28*, 2827.
[27] A. Chakraborty, A. C. Fernandez, A. Som, B. Mondal, G. Natarajan, G. Paramasivam, T. Lahtinen, H. Häkkinen, T. P. Nonappa, *Angew. Chem., Int. Ed.* **2018**, *57*, 6522.
[28] K. R. Krishnadas, A. Ghosh, A. Baksi, I. Chakraborty, G. Natarajan, T. Pradeep, *J. Am. Chem. Soc.* **2016**, *138*, 140.
[29] A. Chakraborty, M. M. Stanley, B. Mondal, Nonappa, M. B., P. Chakraborty, M. P. Kannan, T. Pradeep, *Nanoscale* **2023**, *15*, 2690.
[30] P. Bose, J. Roy, V. Khokhar, B. Mondal, G. Natarajan, S. Manna, V. Yadav, A. Nyayban, S. S. R. K. C. Yamijala, T. P. Nonappa, *Chem. Mater.* **2024**, *36*, 7581.
[31] J. Li, H. Z. Ma, G. E. Reid, A. J. Edwards, Y. Hong, J. M. White, R. J. Mulder, R. A. J. O'Hair, *Chem. – Eur. J.* **2018**, *24*, 2070.
[32] L. Scarabelli, M. Coronado-Puchau, J. J. Giner-Casares, J. Langer, L. M. Liz-Marzán, *ACS Nano.* **2014**, *8*, 5833.
[33] D. Kim, J. Resasco, Y. Yu, A. M. Asiri, P. Yang, *Nat. Commun.* **2014**, *5*, 4948.
[34] Z. Niu, S. Chen, Y. Yu, T. Lei, A. Dehestani, K. Schierle-Arndt, P. Yang, *Nano Res.* **2020**, *13*, 2564.
[35] S. Alayoglu, P. Zavalij, B. Eichhorn, Q. Wang, A. I. Frenkel, P. Chupas, *ACS Nano.* **2009**, *3*, 3127.
[36] G. Yang, D. Chen, P. Lv, X. Kong, Y. Sun, Z. Wang, Z. Yuan, H. Liu, J. Yang, *Sci. Rep.* **2016**, *6*, 35252.
[37] F. Chang, C. Wang, X. Wu, Y. Liu, J. Wei, Z. Bai, L. Yang, *Materials* **2022**, *15*, 5064.
[38] A. K. Sra, T. D. Ewers, R. E. Schaak, *Chem. Mater.* **2005**, *17*, 758.
[39] C. M. Andolina, A. C. Dewar, A. M. Smith, L. E. Marbella, M. J. Hartmann, J. E. Millstone, *J. Am. Chem. Soc.* **2013**, *135*, 5266.
[40] S. Dai, T.-H. Huang, W.-I. Liu, C.-W. Hsu, S.-W. Lee, T.-Y. Chen, Y.-C. Wang, J.-H. Wang, K.-W. Wang, *Nano Lett.* **2021**, *21*, 9293.
[41] X. Ye, X. He, Y. Lei, J. Tang, Y. Yu, H. Shi, K. Wang, *Chem. Commun.* **2019**, *55*, 2321.
[42] X. T. Van, L. T. Trinh, H. Van Pham, M. T. T. Nguyen, *J. Electron. Mater.* **2022**, *51*, 1857.
[43] B. Shan, Y. Zhao, Y. Li, H. Wang, R. Chen, M. Li, *Chem. Mater.* **2019**, *31*, 9875.
[44] M. B. Gawande, A. Goswami, F.-X. Felpin, T. Asefa, X. Huang, R. Silva, X. Zou, R. Zboril, R. S. Varma, *Chem. Rev.* **2016**, *116*, 3722.
[45] Y. Wang, X. Duan, J. Zheng, H. Lin, Y. Yuan, H. Ariga, S. Takakusagi, K. Asakura, *Catal. Sci. Technol.* **2012**, *2*, 1637.
[46] L. Chen, Y. Zhang, P. Zhu, F. Zhou, W. Zeng, D. D. Lu, R. Sun, C. Wong, *Sci. Rep.* **2015**, *5*, 9672.
[47] A. Sakthisabarimoorthi, M. Jose, S. A. Martin Britto Dhas, S. J. Das, *J. Mater. Sci. Mater. Electron.* **2017**, *28*, 4545.
[48] M. C. Biesinger, *Surf. Interface Anal.* **2017**, *49*, 1325.
[49] S. Alayoglu, P. Zavalij, B. Eichhorn, Q. Wang, A. I. Frenkel, P. Chupas, *ACS Nano.* **2009**, *3*, 3127.
[50] W. J. Plieth, *Surf. Sci.* **1985**, *156*, 530.
[51] Z. Wu, *Angew. Chem.* **2012**, *124*, 2988.
[52] Z. Gan, N. Xia, Z. Wu, *Acc. Chem. Res.* **2018**, *51*, 2774.
[53] M. Wang, Z. Wu, Z. Chu, J. Yang, C. Yao, *Chem. – Asian J.* **2014**, *9*, 1006.
[54] S. Tian, C. Yao, L. Liao, N. Xia, Z. Wu, *Chem. Commun.* **2015**, *51*, 11773.
[55] Z. Wu, M. Wang, J. Yang, X. Zheng, W. Cai, G. Meng, H. Qian, H. Wang, R. Jin, *Small* **2012**, *8*, 2027.
[56] M. Zhu, P. Wang, N. Yan, X. Chai, L. He, Y. Zhao, N. Xia, C. Yao, J. Li, H. Deng, Y. Zhu, Y. Pei, Z. Wu, *Angew. Chem., Int. Ed.* **2018**, *57*, 4500.
[57] C. Yao, J. Chen, M.-B. Li, L. Liu, J. Yang, Z. Wu, *Nano Lett.* **2015**, *15*, 1281.
[58] R. Ciganda, N. Li, C. Deraedt, S. Gatard, P. Zhao, L. Salmon, R. Hernández, J. Ruiz, D. Astruc, *Chem. Commun.* **2014**, *50*, 10126.
[59] S. K. Meena, S. Celiksoy, P. Schäfer, A. Henkel, C. Sönnichsen, M. Sulpizi, *Phys. Chem. Chem. Phys.* **2016**, *18*, 13246.
[60] J. Peng, B. Huang, P. Wang, Y. Pei, *J. Phys. Chem. A* **2022**, *126*, 8910.
[61] G. Guisbiers, S. Mejia-Rosales, S. Khanal, F. Ruiz-Zepeda, R. L. Whetten, M. José-Yacaman, *Nano Lett.* **2014**, *14*, 6718.
[62] S. Jeong, Y. Liu, Y. Zhong, X. Zhan, Y. Li, Y. Wang, P. M. Cha, J. Chen, X. Ye, *Nano Lett.* **2020**, *20*, 7263.
[63] S. Wang, H. Abroshan, C. Liu, T.-Y. Luo, M. Zhu, H. J. Kim, N. L. Rosi, R. Jin, *Nat. Commun.* **2017**, *8*, 848.
[64] A. Chakraborty, M. M. Stanley, B. Mondal, Nonappa, M. B., P. Chakraborty, M. P. Kannan, T. Pradeep, *Nanoscale* **2023**, *15*, 2690.
[65] A. Som, A. K. Samal, T. Udayabhaskararao, M. S. Bootharaju, T. Pradeep, *Chem. Mater.* **2014**, *26*, 3049.
[66] P. Bose, P. Chakraborty, J. S. Mohanty, Nonappa, A. R. C., E. Khatun, T. Ahuja, A. Mahendranath, T. Pradeep, *Nanoscale* **2020**, *12*, 22116.
[67] B. Gao, G. Arya, A. R. Tao, *Nat. Nanotechnol.* **2012**, *7*, 433.

© 2025 Wiley-VCH GmbH

16136829, 2025, 43, Downloaded from https://onlinelibrary.wiley.com/doi/10.1002/smll.202410784 by Central Library The Librarian, Wiley Online Library on [28/12/2025]. See the Terms and Conditions (https://onlinelibrary.wiley.com/terms-and-conditions) on Wiley Online Library for rules of use; OA articles are governed by the applicable Creative Commons License

[68] G. Singh, H. Chan, A. Baskin, E. Gelman, N. Repnin, P. Král, R. Klajn, *Science* **2014**, *345*, 1149.
[69] E. Carbó-Argibay, B. Rodríguez-González, S. Gómez-Graña, A. Guerrero-Martínez, I. Pastoriza-Santos, J. Pérez-Juste, L. M. Liz-Marzán, *Angew. Chem., Int. Ed.* **2010**, *49*, 9397.
[70] S. Chen, S. V. Jenkins, J. Tao, Y. Zhu, J. Chen, *J. Phys. Chem. C* **2013**, *117*, 8924.
[71] A. K. Samal, T. S. Sreeprasad, T. Pradeep, *J. Nanoparticle Res.* **2010**, *12*, 1777.
[72] S. K. Meena, M. Sulpizi, *Langmuir* **2013**, *29*, 14954.

© 2025 Wiley-VCH GmbH

16136829, 2025, 43, Downloaded from https://onlinelibrary.wiley.com/doi/10.1002/smll.202410784 by Central Library The Librarian, Wiley Online Library on [28/12/2025]. See the Terms and Conditions (https://onlinelibrary.wiley.com/terms-and-conditions) on Wiley Online Library for rules of use; OA articles are governed by the applicable Creative Commons License

NANO · MICRO small

Supporting Information

for *Small*, DOI 10.1002/smll.202410784

Morphology-Preserved Alloying in Anisotropic Gold Nanoparticles Using Atomically Precise Nanoclusters

*Amrita Chakraborty, Sujan Manna, Biswajit Mondal, Mohammad Bodiuzzaman, Ankit Nagar, Soham Chowdhury, Tanmayaa Nayak, Nonappa and Thalappil Pradeep**

Supporting Information
©Wiley-VCH 2021
69451 Weinheim, Germany

Morphology-Preserved Alloying in Anisotropic Gold Nanoparticles Using Atomically Precise Nanoclusters

Amrita Chakraborty,[1,‡] Sujan Manna,[1,‡] Biswajit Mondal,[1] Mohammad Bodiuzzaman,[1] Ankit Nagar,[1] Soham Chowdhury,[1] Tanmayaa Nayak,[1] Nonappa,[2] and Thalappil Pradeep[1,*]

[1]Department of Chemistry, DST Unit of Nanoscience (DST UNS) and Thematic Unit of Excellence (TUE), Indian Institute of Technology Madras, Chennai, 600 036, India

[2]Faculty of Engineering and Natural Sciences, Tampere University, Tampere, FI-33720, Finland

E-mail: pradeep@iitm.ac.in

‡ These authors contributed equally to this work

Abstract: Noble metal nanoparticles (NPs) exhibit superior plasmonic, catalytic, electronic, and magnetic properties upon alloying with a second metal. However, the synthesis of bimetallic alloy NPs of non-spherical morphologies presents a challenge due to the necessity of concurrently modulating the nucleation and growth kinetics of various metallic constituents. In this study, a simple solution-phase reaction between a phosphine-protected copper nanocluster (NC), namely $[Cu_{18}(DPPE)_6H_{16}]^{2+}$ [DPPE = 1,2-bis(diphenylphosphino)ethane] (abbreviated as Cu_{18}) and gold nanotriangles (AuNTs) is reported as a straightforward strategy to obtain gold-copper alloy nanotriangles (AuCuNTs) while keeping their sizes and sharp edges intact. Extending this protocol to gold nanorods (AuNRs) and nanocubes (AuNCbs), demonstrates its generality for creating anisotropic Au–Cu alloy NPs. Auger spectroscopic analyses confirm that Cu(0) is the predominant Cu species in the AuCuNTs, indicating that oxidation of Cu in the resulting nanostructures is prevented. A further interaction of AuCuNTs with $[Ag_{25}(DMBT)_{18}]^-$ [DMBT = 2,4-dimethylbenzenethiol] (abbreviated as Ag_{25}) has yielded AuCuAgNTs, offering a facile synthetic route to trimetallic anisotropic NPs. Thus, the current study corroborates atomically precise metal NCs as versatile precursors for tuning the composition of plasmonic anisotropic NPs to meet diverse technological and industrial needs.

SUPPORTING INFORMATION

Table of Contents

Serial no.	Details	Page no.
SI 1	Experimental procedures	3
SI 2	Instrumentation	4
Figure S1	Characterization of Cu_{18} NC	5
Figure S2	Characterization of AuNTs	6
Figure S3	Elemental analysis of AuCuNTs	6
Figure S4	Powder XRD patterns of AuNT and AuCuNT	7
Table S1	The concentration of Au found in the supernatant at different molar ratios of Cu_{18} to AuNT	7
Figure S5	XPS spectra of AuCuNT	8
Figure S6	ESI-MS of the reaction product	9
Figure S7	FT-IR spectra of purified and clean AuNT	9
Figure S8	ESI-MS of Cu_{18} in DMF	10
Figure S9	Characterization of AuNCbs	10
Figure S10	Characterization of AuNRs	11
Figure S11	Size distribution of AuCuAgNTs	11
References	References	11

Experimental procedures:

Chemicals. Tetrachloroauric acid trihydrate ($HAuCl_4$, $3H_2O$), hexadecyltrimethylammonium chloride (CTAC), hexadecyltrimethylammonium bromide (CTAB), sodium borohydride ($NaBH_4$), 2,4-dimethylbenzenethiol (DMBT), 1,2-bis(dipehnylphosphino)ethane (DPPE), sodium iodide (NaI) and ascorbic acid (AA) were purchased from Sigma Aldrich. Silver nitrate ($AgNO_3$) and sodium hydroxide (NaOH) pellets were procured from Rankem, India. All organic solvents, including dimethylformamide (DMF), dichloromethane (DCM) and methanol (MeOH) were purchased from Rankem chemicals in analytical grade quality. These chemicals were utilized without further purification. Glassware was thoroughly cleansed using aqua regia, followed by extensive rinsing with distilled water and subsequent drying under ambient conditions prior to their application.

Synthesis of gold nanotriangles. Trigonal planar nanoparticles with high size and shape monodispersity were synthesized following a method previously reported.[1] The first step of the synthesis was seed preparation, where 4.7 mL 100 mM CTAC was taken in a 20 mL glass vessel. Under mild stirring, 25 µL of 10 mM $HAuCl_4$ was mixed to it followed by the rapid injection of 300 µL 10 mM freshly prepared (in ice-cold water) $NaBH_4$. Vigorous stirring continued for 2 min after the addition of $NaBH_4$ to facilitate the release of hydrogen gas generated in the medium. After this, the brown-colored seed solution was kept undisturbed for 2 hours. Two separate growth solutions were then prepared.

Growth solution I, i.e., G-I. To 1.6 mL of 100 mM CTAC, 8 mL of water, 40 µL of 10 mM $HAuCl_4$, and 15 µL of 10 mM NaI were sequentially added by mild manual mixing.
Growth solution II, i.e., G-II. To 40 mL of 50 mM CTAC, 500 µL of 10 mM $HAuCl_4$ and 300 µL of 10 mM NaI were added, following the same procedure as for **G-I**. The seed solution was subsequently diluted 10 times using 100 mM CTAC. 40 µL and 400 µL of 100 mM AA were added in single shots to **G-I** and **II**, respectively. Immediately after this, 100 µL of the diluted seed was added to **G-I** under gentle manual mixing. Within 1 s of mixing, as the color of the **G-I** turned pink, 3.2 mL of it was transferred to the **G-II**. This was mixed in a similar fashion for 10 s. Within 10 min, the **G-II** turned blue in color.

Purification of AuNTs. As-synthesized AuNTs contained a proportion of gold nanoparticles of non-targeted shapes. To eliminate them, the flocculation method suggested by Scarabelli *et al.* was employed.[1] The synthesized AuNTs were dispersed in 175 mM CTAC by adding a suitable amount of aqueous CTAC stock solution (25 wt%) into growth solution II. The mixture was kept undisturbed for 2 hours at room temperature. As a result of this, AuNTs with high size and shape monodispersities were selectively precipitated, leaving the undesired particles in the supernatant. The supernatant was subsequently decanted, and the sediment was dispersed in DI water with mild sonication, yielding a greenish-blue dispersion. These purified AuNTs were centrifuged twice at 6000 rpm for 5 min and redispersed in DI water before use.

Synthesis of Cu_{18}. The synthesis followed an established procedure[2] with certain modifications. In a Schlenk tube under vacuum, 100 mg copper iodide and 120 mg bis(diphenylphosphino)ethane was taken. 15 mL Acetonitrile was added to it with stirring. After 30 minutes, solid sodium borohydride (180 mg) was added and the reaction mixture was continuously stirred for 4 hours at room temperature. The resulting precipitate was centrifuged and rinsed with DI water to remove unreacted $NaBH_4$, if any. The product was extracted with DCM, filtered and finally dispersed in DMF.

Synthesis of gold nanorods. AuNRs were synthesized following the method described by Samal *et al.*[3] Precisely, 1 mL of 10 mM $HAuCl_4$ was added to 20 mL of 100 mM CTAB with mild stirring. Subsequently, 130 µL of 10 mM $AgNO_3$ and 140 µL of 100 mM AA were added in sequence. Following these additions, 200 µL of 1.67 mM $NaBH_4$ (freshly prepared using cold DI water) was added and the stirring was stopped immediately. The solution was kept undisturbed for at least four hours. Before any further treatment, the AuNR was centrifuged (at 13000 rpm for 15 min, twice), the supernatant containing excess CTAB was discarded, and the precipitated AuNRs were redispersed in DI water.

Synthesis of gold nanocubes (AuNCbs). The synthesis of AuNCbs was executed following a 3 step synthetic protocol proposed by Nam group.[4]

Seed solution: 9.75 mL 100 mM CTAB solution was prepared in a glass vial, to which 250 µL of 10 mM $HAuCl_4$ was added under moderate stirring. Then 600 µL of 10 mM $NaBH_4$ (freshly prepared in ice-cold DI water) was quickly added to the brownish-yellow solution. Stirring was continued for an additional 3 min before the seed was allowed to age at room temperature (27 °C for 3 hours).

Growth solution I. In a separate 10 mL vial, 2 mL of 200 mM CTAC, 1.5 mL of 100 mM AA, and 50 µL of the previously prepared seed solution were mixed sequentially with moderate stirring. The stirring speed was then fixed at 300 rpm, and 2 mL of 0.5 mM $HAuCl_4$ was injected in one shot. Mixing was continued for 15 min at room temperature, followed by centrifugation twice at 13000 rpm for 30 min. Each time the supernatant was decanted to remove unreacted chemicals. The pellet was resuspended in 1 mL DI water and, 1 mL of 20 mM CTAC after the first and second wash, respectively.

Growth solution II. For the final growth solution, in a 20 mL glass vial, 6 mL of 100 mM CTAC was mixed with 30 µL of 13 mM aqueous NaBr solution. The concentration of growth solution I was adjusted such that the optical density (O.D.) was 2; and 6 µL of it was added subsequently. To this, 390 µL of 10 mM AA was added, with thorough mixing at a constant 500 rpm. Finally, 6 mL of 0.5 mM $HAuCl_4$ was added to the vial in a single step, and the mixing continued for 25 min. The final growth solution was centrifuged at 7000 rpm for 12 min followed by resuspension in DI water, twice.

Reaction between AuNT and Cu_{18}. A 2 mL aqueous dispersion of clean AuNTs, exhibiting O.D. ~1 at 640 nm (LSPR peak position), was centrifuged, and redispersed in the same volume of DMF. This suspension was transferred to a 5 mL glass vial. For a typical reaction, the freshly synthesized Cu_{18} NC (concentration 135 mg/mL) was diluted 100 times using DMF, and 20 µL of this Cu_{18} NC was added to the AuNTs under moderate stirring. The stirring continued for at least 3 hours, after which the reaction mixture was centrifuged at 6000 rpm. The pallet was redispersed in either DMF or DI water and used for further experiments or investigation.

Instrumentation:

Absorption spectra in solution were recorded in standard cuvettes using a PerkinElmer Lambda 365 spectrometer in the wavelength range of 200- 800 nm. Mass spectra of all the clusters were measured using the Waters Synapt G2Si High-Definition Mass Spectrometer. XPS Measurements were done using an ESCA Probe TPD spectrometer of Omicron Nanotechnology. Polychromatic Al Kα was used as the X-ray source (hv = 1486.6 eV). The concentration of Au in the reaction mixture was detected using PerkinElmer NexION 300X ICPMS with appropriate standards. XRD patterns were obtained using a Bruker AXS D8 Discover diffractometer with Cu Kα radiation (λ = 1.54 Å). The samples underwent scanning from 5° to 90° in the 2θ range, and the resulting peaks were compared with the Joint Committee on Powder Diffraction Standards (JCPDS) database. Morphology and elemental analyses of AuCuNCbs and AuCuNRs were performed using Verios G4 UC, FEI scanning electron microscope. All TEM images were collected using a JEOL 3010 high-resolution TEM operated at 200 kV. A Gatan multistage CCD camera was used to record the image. The STEM imaging was performed using a JEOL JEM-2800 high throughput electron microscope operated at 200 kV with simultaneous bright field (BF) and dark field (DF) STEM imaging. All electron microscopy samples were prepared by dropcasting 10 µL of sample on 300 mesh Ni grids with ultrathin carbon support film.

Supplementary Figures

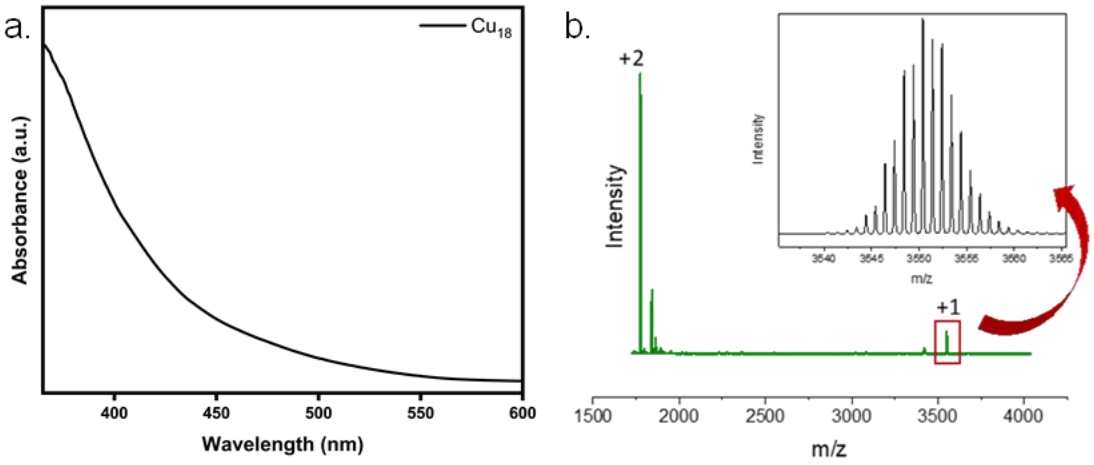


Figure S1. Characterization of Cu_{18} NC. a. UV-vis spectrum of Cu_{18}. b. ESI-MS of Cu_{18} showing molecular ion peak at m/z 3552 and +2 charge state at m/z 1775. The inset shows the distribution of the former peak.

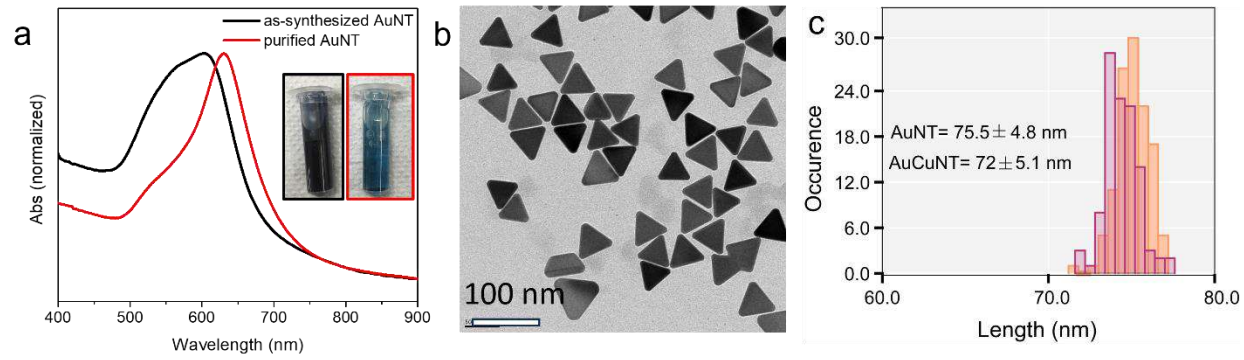
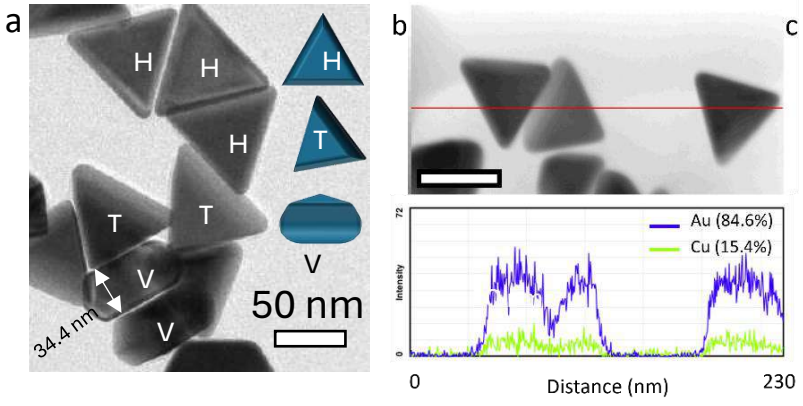


Figure S2. Characterization of AuNTs. (a) UV vis absorption spectra before and after purification by the flocculation method (inset shows the change in color of the dispersion), (b) TEM image of the purified AuNTs, (c) size distribution of AuNT and AuCuNTs (125 particles each).



c

Sample	Au (ppb)	Cu (ppb)
AuNT	1273	0
	1306	0
	1114	0
Mean	1231±103	0
AuCuNT	996	204
	1044	173
	1017	156
Mean	1019±24	178±24.3
Au:Cu in AuCuNT (ICP MS)	5.7:1	
Au:Cu in AuCuNT (STEM EDS)	5.5:1	

Figure S3. (a) TEM image of AuCuNTs including horizontal (H), tilted (T), and vertical (V) orientations of the NTs. Inset shows the cartoon representation of these orientations. (b) Bright field STEM image of three additional AuCuNTs and respective EDS line scans showing uniformity of Cu content in each AuCuNT, (c) ICP MS of parent AuNTs and AuCuNTs showing Au:Cu = 5.7:1. Three separate analyses were done to take an average.

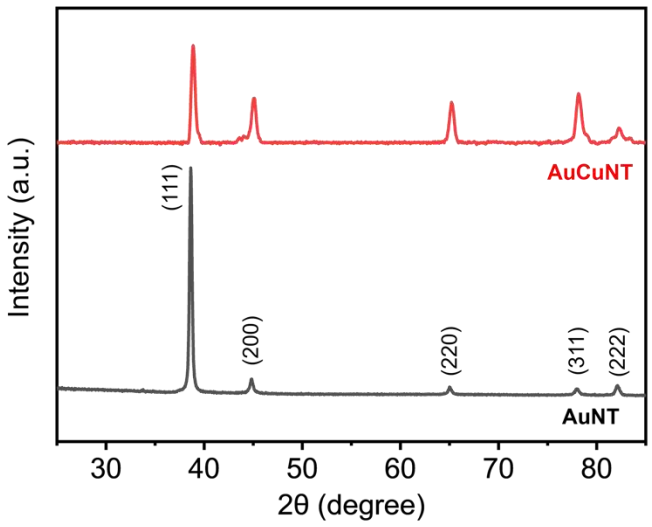


Figure S4. Powder XRD patterns of AuNT and AuCuNT. All the peaks are preserved but shifted upon alloying. No new peaks appeared, which indicates the absence of copper oxide layers in AuCuNTs.

Table S1. The concentration of Au found in the supernatant at different molar ratios of Cu_{18} to AuNT.

O.D. of AuNTs at λ_{max}	1	1	1	1	1
[Cu_{18}] (mg/mL)	0	0.24	1.21	2.42	12.1
[Au(I)] in supernatant (ppb)	96	104	576	776	996
	85	153	617	786	795
	77	158	748	545	642
Average [Au(I)]	86±7.8	138±24	647±73	702±111	811±145

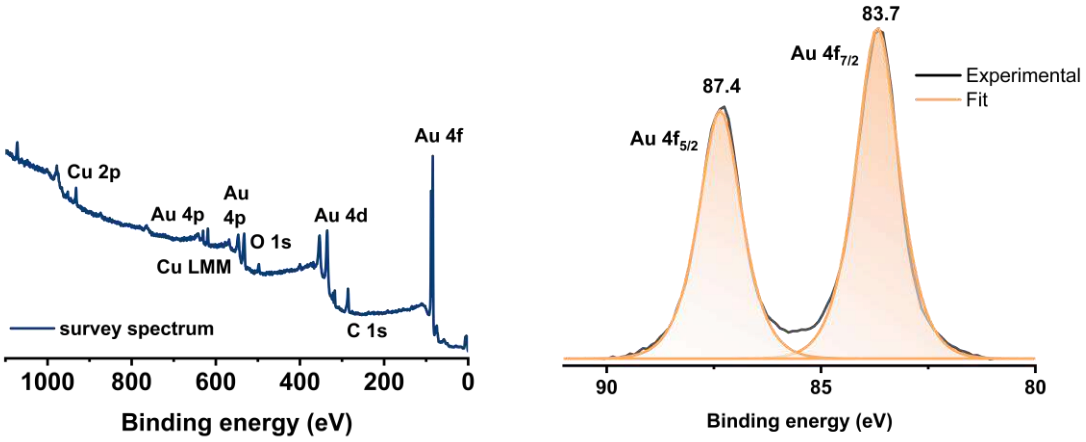


Figure. S5. XPS spectra of AuCuNT: (a) the survey spectrum, b) Au 4f X-ray photoelectron spectrum of AuCuNT.

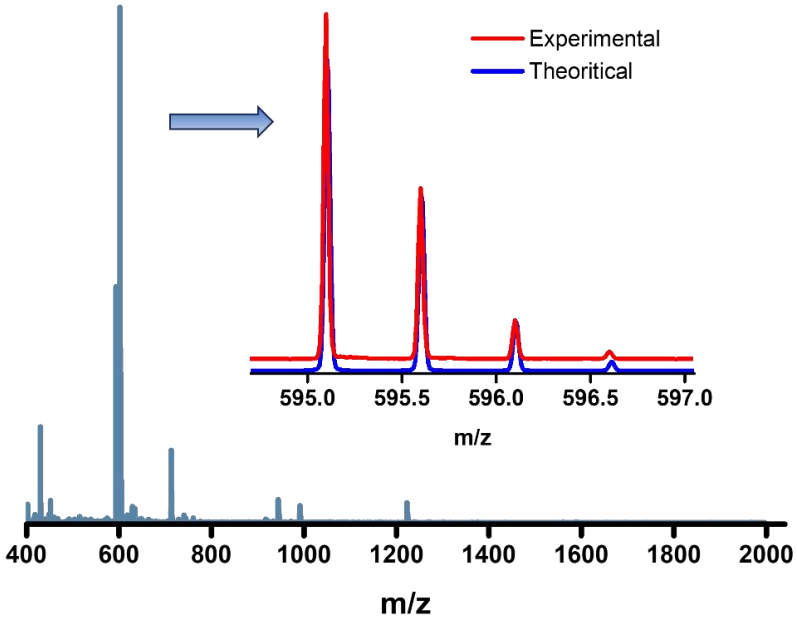


Figure S6. ESI-MS of the supernatant obtained by centrifuging the reaction product. The inset shows the exact matching of the isotopic distribution of the experimental and theoretical spectra of the species $[Au_2(DPPE)_2]^{2+}$ at m/z 595.

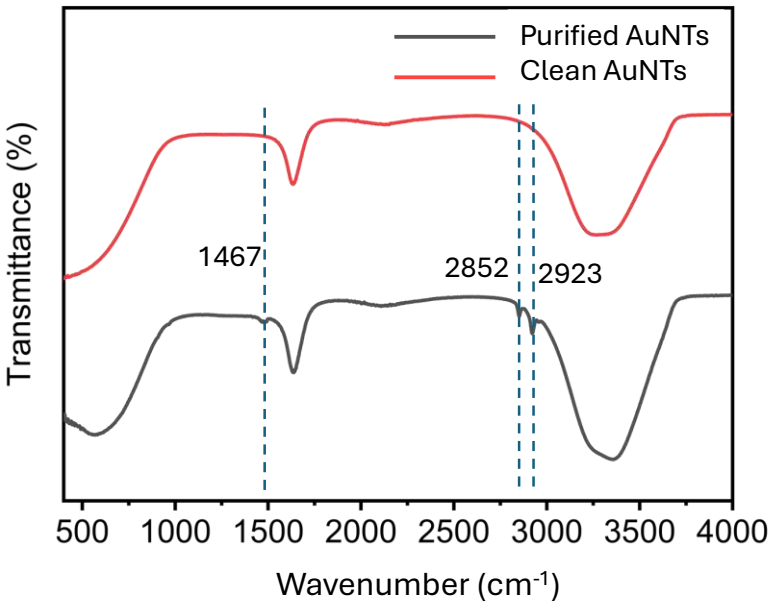


Figure S7. FT-IR spectra of purified AuNTs showing characteristic peaks of CTAC (peaks at 2923 and 2852 cm $^{-1}$ due to the $–CH_2$ stretching of the CTAC chain, at 1467 cm^{-1} results from the deformation vibrations of $–CH_3$ and $-CH_2$ groups),[5] that was absent in clean AuNTs.

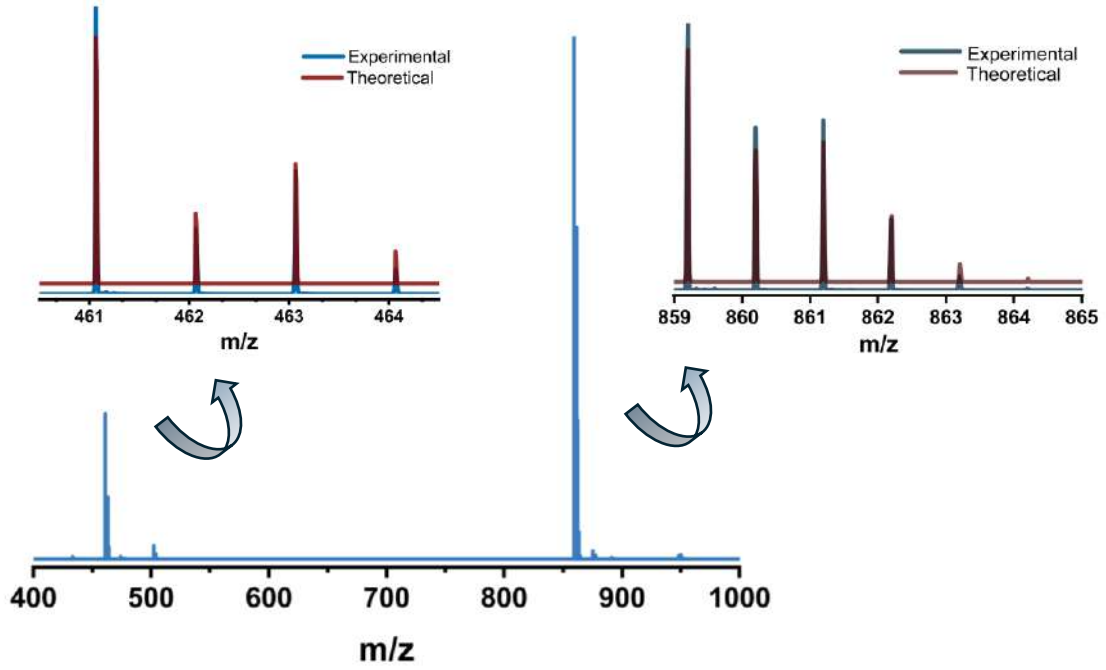


Figure S8. ESI-MS of Cu_{18} in DMF shows peaks at m/z 462 and 860 for $[Cu(DPPE)^{+}$ and $[Cu(DPPE)_2]^{+}$, respectively. Inset shows the isotopic distribution of the peaks with a theoretical match.

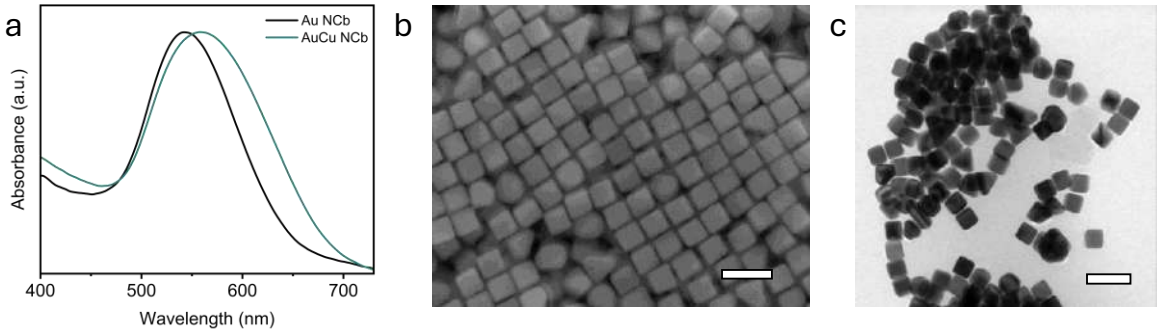


Figure S9. Characterization of AuNCbs: (a) Comparative UV vis absorption spectra of AuNCb and AuCuNCbs showing red shift and broadening of the SPR peak at 540 nm, (b) SEM and (c) TEM image of parent AuNCbs, scale bar 100 nm.

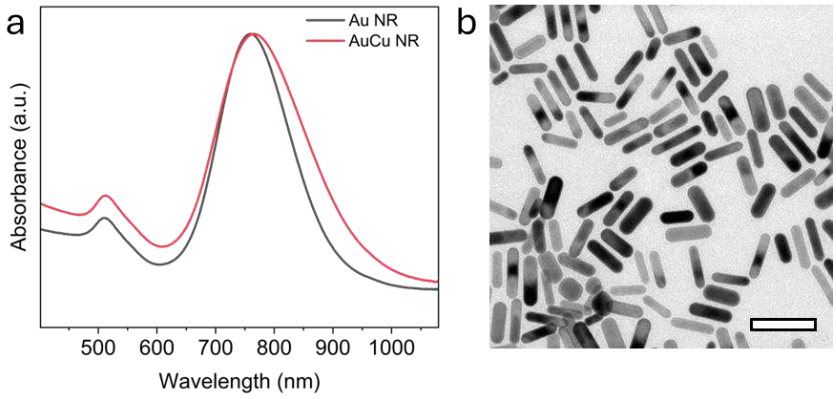


Figure S10. Characterization of AuNRs: (a) Comparative UV vis absorption spectra of AuNR and AuCuNR showing slight red shift and broadening of the SPR peak at 760 nm, (b) TEM image of parent AuNRs, scale bar 50 nm.

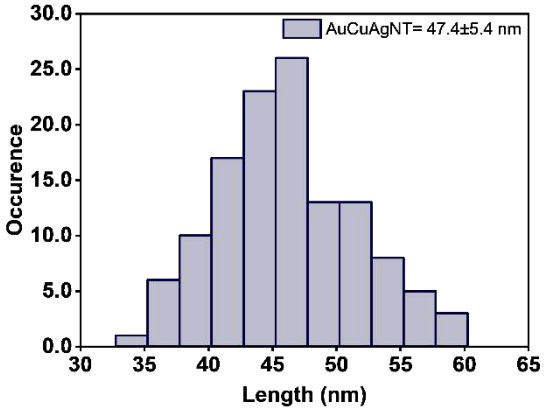


Figure S11. Size distribution of AuCuAgNTs (125 particles).

References:

[1] L. Scarabelli, M. Coronado-Puchau, J. J. Giner-Casares, J. Langer, L. M. Liz-Marzán, *ACS Nano* **2014**, *8*, 5833–5842.
[2] J. Li, H. Z. Ma, G. E. Reid, A. J. Edwards, Y. Hong, J. M. White, R. J. Mulder, R. A. J. O'Hair, *Chem. – Eur. J.* **2018**, *24*, 2070–2074.
[3] A. K. Samal, T. S. Sreeprasad, T. Pradeep, *J. Nanoparticle Res.* **2010**, *12*, 1777–1786.
[4] J.-E. Park, Y. Lee, J.-M. Nam, *Nano Lett.* **2018**, *18*, 6475–6482.
[5] E. Podlesnaia, S. E. Stanca, B. Çinçin, G. Zieger, A. Csáki, W. Fritzsche, *Nanoscale Adv.* **2024**, *6*, 5430–5440.

THE JOURNAL OF PHYSICAL CHEMISTRY C
A JOURNAL OF THE AMERICAN CHEMICAL SOCIETY

pubs.acs.org/JPCC

Article

Composition-Dependent Formation and Dissociation of Structure I and Structure II Clathrate Hydrates of Trimethylene Oxide in Ultrahigh Vacuum

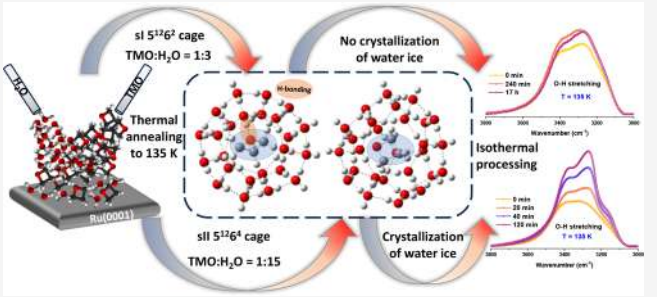
Soham Chowdhury, Bijesh K. Malla, Gaurav Vishwakarma, Anupriya Nyayban, and Thalappil Pradeep*

Cite This: J. Phys. Chem. C 2025, 129, 8937−8945

Read Online

ACCESS | Metrics & More | Article Recommendations | Supporting Information

ABSTRACT: This study reports the formation of structure I (sI) and structure II (sII) clathrate hydrates (CHs) of trimethylene oxide (TMO) at different concentrations of the components under cryogenic conditions in ultrahigh vacuum. We codeposited TMO:H_2O ices of 1:3 and 1:15 ratios at 10 K and thermally annealed them to 135 K. Using reflection−absorption infrared spectroscopy, we observed the formation of distinct CH structures from compositionally varied ices at 135 K. Although TMO occupied the $5^{12}6^2$ cage of sI CH in the 1:3 mixture, in the 1:15 mixture, it occupied the $5^{12}6^4$ cage of sII. The sI TMO CH demonstrated greater thermal stability compared to sII. Interestingly, the dissociation of these CH structures exerts different effects on amorphous solid water (ASW). While the sI CH dissociation does not lead to the expected conversion of ASW to crystalline hexagonal ice, the dissociation of sII CH crystallizes ASW. This observation may be attributed to the relative stability and host−guest hydrogen bonding of the CHs, as supported by density functional theory analysis.



Downloaded via INDIAN INST OF TECH MADRAS on December 29, 2025 at 03:11:05 (UTC).
See https://pubs.acs.org/sharingguidelines for options on how to legitimately share published articles.

INTRODUCTION

Formation of clathrate hydrates (CHs) in laboratory interstellar conditions has been established by several studies using reflection−absorption infrared spectroscopy (RAIRS).[1−5] Subsequently, Tychengulova et al. have reported infrared spectroscopic investigations of the formation of CO_2 CH under simulated interstellar environments.[6] Besides RAIRS, a recent study has shown the formation of tetrahydrofuran and 1,3-dioxolane under ultrahigh vacuum (UHV) and cryogenic conditions by reflection high-energy electron diffraction (RHEED).[7] The chemically diverse interstellar medium (ISM) contains more than 300 species, such as neutral atoms and molecules, cations, anions, and radicals.[8] These species exist in the gas phase or in the solid phase on interstellar ice-dust.[9,10] As the ice matrices are predominantly rich in water, many molecular species may be entrapped in them as CHs, forming different structures. The size of the CH cages depends on the size of the guest molecule, which determines whether the CH will be in structure I (sI) or structure II (sII) or structure H (sH).[11] Temperature and pressure are two crucial parameters to decide the CH structure for a particular guest molecule. Additionally, one structure can be converted to another, either by altering the condition or by introducing other foreign molecules.[12,13] Most of these studies have been conducted under high-pressure conditions, where the guest molecule is forced to occupy the hydrate cage. However, in UHV, this mechanism is different, particularly for nanoscale thin film ices, at cryogenic temperatures. Here, thermal annealing of the mixed ice containing host and guest molecules enables their mobilization, followed by reorientation of the water molecules, resulting in enclathration of the guest, all under UHV.[14]

Trimethylene oxide (TMO), a four-membered cyclic ether, has yet to be detected in space. However, recently its structural isomer, propylene oxide, has been detected in ISM.[15] Ethers are known to form CH; for example, tetrahydrofuran, a five-membered cyclic ether, and dimethyl ether, a noncyclic ether, form $5^{12}6^4$ cages of sII CH in UHV.[3,16] Ethylene oxide, a three-membered cyclic ether analogous to TMO, commonly forms $5^{12}6^2$ cage of sI CH in atmospheric pressure and in vacuum.[17,18] The CH structure and its cage size are largely dictated by the size and chemical nature of the guest molecule. TMO has an intermediate size between ethylene oxide and tetrahydrofuran. Investigating TMO CH structure under UHV is crucial for understanding how molecules behave in a water ice matrix and occupy clathrate cages at cryogenic temperatures (10−135 K).

Received: March 10, 2025
Revised: April 21, 2025
Accepted: April 23, 2025
Published: May 5, 2025



© 2025 American Chemical Society

There are a few reports on the effect of composition in TMO CH formation, where CHs are formed by vapor deposition of guest molecules on crystalline ice nanocrystals.[19−22] However, there is no such study of the formation of TMO CH in amorphous ice under UHV. Also, the consequence of their dissociation affecting the crystallization of ice has hitherto not been observed. The effect of CH dissociation on the crystallization kinetics of amorphous solid water (ASW) provides new insights into the physical transformations of icy bodies in space. Deciphering how guest molecules interact with ASW and contribute to phase transitions enhances our understanding of the stability and structural evolution of materials in extraterrestrial environments.

Here, we report the formation of TMO CHs from amorphous TMO-H_2O mixed ice by thermally annealing the mixtures from 10 to 135 K. We observed the formation of sI and sII CH from 1:3 and 1:15 mixtures of TMO and H_2O, respectively, under identical temperature and pressure conditions. For the first time, we demonstrate the role of composition in CH formation under UHV conditions. The RAIR spectra illustrate the formation of two CHs using two vibrational modes: for sI using the ring puckering mode and for sII using the C−O−C stretching mode. These observations are supported by density functional theory (DFT) analyses, which highlight the influence of host−guest hydrogen bonding and a distorted planar geometry of TMO in the CHs. Interestingly, the dissociation of these two types of CH structures impacts the ASW differently. While the dissociation of sII CH crystallizes ASW into hexagonal ice at 135 K, as expected, the dissociation of sI CH does not induce this phase transition, leaving the amorphous ice intact. This contrasting effect is attributed to the greater stability of sI compared to sII, as evidenced by the RAIR study as well as the DFT analyses.

EXPERIMENTAL SECTION

All experiments were conducted using a UHV chamber maintained at a base pressure of ∼5 × 10^{-10} mbar, illustrated in Figure 1. The apparatus is described in detail elsewhere.[23−25] Briefly, the chamber is equipped with several analytical techniques, including RAIRS, low-energy ion scattering (LEIS), mass spectrometry, secondary ion mass spectrometry (SIMS), temperature-programmed desorption mass spectrometry (TPD-MS), and a vacuum ultraviolet deuterium continuum source. The base pressure of the vacuum chamber is achieved by six turbomolecular pumps, further supported by scroll pumps. A single-crystal Ru(0001) substrate of 1.5 cm in diameter and 1 mm in thickness was used for our experiments to grow nanoscale ice films. This substrate was mounted on a copper holder and placed at the tip of a closed-cycle helium cryostat. The substrate is also equipped with a 25 Ω resistive heater, allowing precise temperature control in the range of 8 to 1000 K. Temperature measurement was achieved using a platinum sensor and a K-type thermocouple, providing a temperature accuracy of 0.5 K. Before each experiment, the Ru(0001) was heated to 400 K repeatedly to ensure cleanliness. It is worth noting that the substrate has no effect in this study due to multilayer deposition.

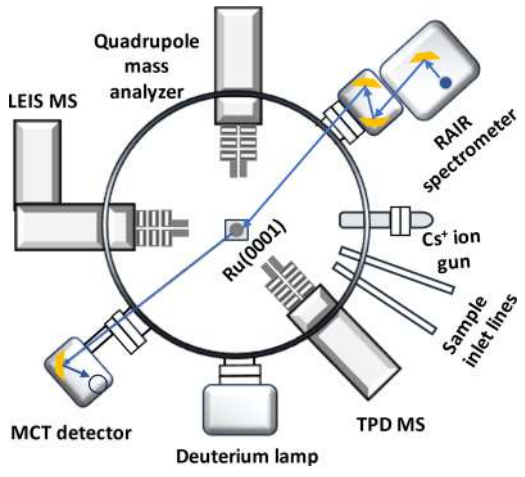


Figure 1. Schematic diagram of the experimental setup. As shown in this representation, the Ru(0001) substrate is oriented to perform the RAIR experiment.

Milli-Q water (H_2O of 18.2 MΩ resistivity) and TMO (99.9%, Sigma-Aldrich) were taken in two separate vacuum-sealed test tubes (with a glass-to-metal seal) and were further purified by several freeze−pump−thaw cycles. TMO and H_2O were connected to the UHV chamber through separate sample inlet lines. Precise control over the deposition of these two samples was achieved by utilizing all-metal leak valves. For quantification purposes, we considered that 1.33 × 10^{-6} mbar exposure for one second, equated to 1 monolayer (ML), was estimated to contain approximately 1.1 × 10^{15} molecules cm^{-2}, assuming an ion gauge sensitivity factor of unity.[26] The ion gauge sensitivity factor of H_2O is ∼1.0, and for TMO, it is considered as ∼3.0 based on the known sensitivity factor for tetrahydrofuran (THF), chemically similar cyclic ether.[27] To deposit 300 ML of ice consisting of a 1:3 ratio of TMO and H_2O mixture, the chamber was backfilled to a total pressure of 5 × 10^{-7} mbar for 10 min with TMO reaching 2.5 × 10^{-7} mbar and the H_2O pressure maintained at 2.5 × 10^{-7} mbar. The other two ratios of TMO and H_2O (1:15 and 1:30) were prepared at 10 K by keeping the total pressure constant and changing the inlet pressure of TMO and H_2O accordingly. During codeposition, the total chamber pressure typically varies between 4.90 × 10^{-7} and 5.10 × 10^{-7} mbar, resulting in a variation of approximately 10−15 ML in total thickness for a 300 ML ice film. For instance, a 1:3 TMO:H_2O mixture is achieved by maintaining the partial pressure of each component at ∼2.50 × 10^{-7} mbar (due to the difference in gauge sensitivity factors). The maximum fluctuation in individual partial pressure is around 0.10 × 10^{-7} mbar, which translates to ∼5−8 ML variation per component in a 300 ML film. As a result, the composition of 1:3 mixed ice can be varied from 1.11:3 to 0.89:3 and from 1:3.11 to 1:2.89. This gives an uncertainty of ±0.11 in the mixing ratio for the 1:3 ice. Throughout the vapor deposition process, mass spectra were continuously obtained to verify both the purity and the ratio of the deposited molecules.

The formation and dissociation of TMO CH were investigated using RAIR spectroscopy. RAIR spectra were recorded in the 4000−550 cm^{-1} range with a spectral resolution of 2 cm^{-1}, using a Bruker Vertex 70 FT-IR spectrometer equipped with a liquid-nitrogen-cooled mercury cadmium telluride (MCT) detector. The IR beam path outside the UHV chamber was continuously purged with dry nitrogen to avoid absorption from atmospheric gases.

Computational Details. All of the electronic structure calculations were performed using the Gaussian 09 software package. At first, the ground-state geometries of the TMO and

https://doi.org/10.1021/acs.jpcc.5c01603
J. Phys. Chem. C 2025, 129, 8937−8945

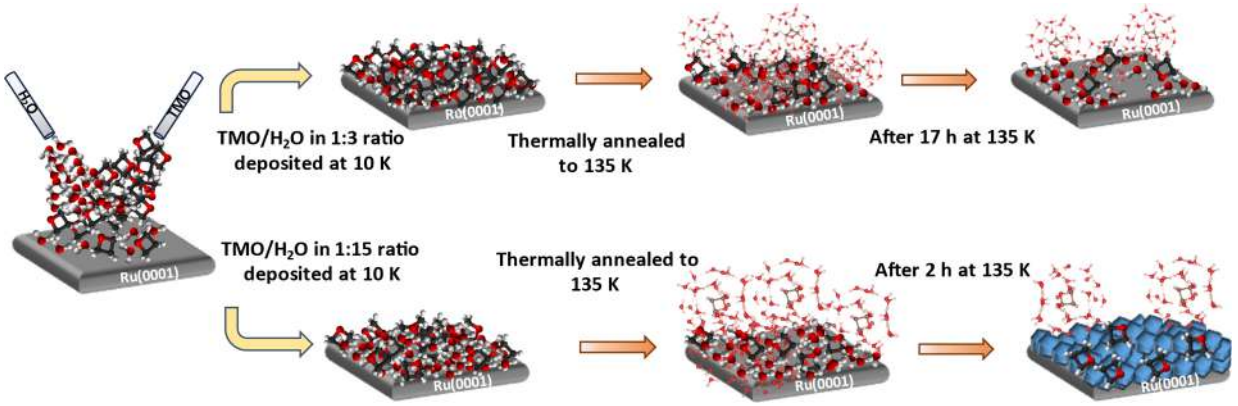


Figure 2. Schematic illustration of TMO CH formation in water ice at 135 K. The vapors of TMO and H_2O were deposited at 1:3 and 1:15 ratios, respectively, and thermally annealed to 135 K. The blue three-dimensional film represents hexagonal water ice.

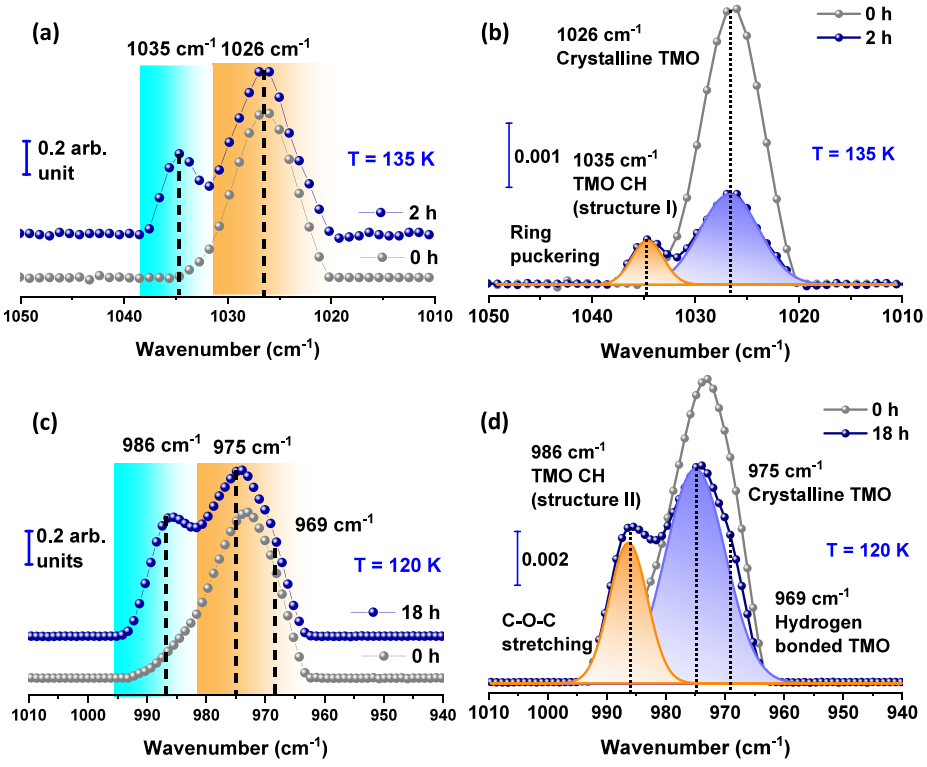


Figure 3. RAIRS study of sI and sII CH of TMO in two spectral regions. (a, b) Time-dependent RAIR spectra of 300 ML of TMO-H_2O of 1:3 composition at 135 K in the ring puckering mode region. (a) Normalized and (b) deconvoluted spectra. (c, d) Time-dependent RAIR spectra of 300 ML of TMO-H_2O of 1:15 composition at 120 K in the C−O−C stretching region. (c) Normalized and (d) deconvoluted spectra. In parts b and d, the intensity loss at 2 and 18 h, respectively, is due to desorption in UHV.

the CH cages (namely, the 5^{12}, $5^{12}6^2$, and $5^{12}6^4$ cages) were optimized using DFT at the B3LYP/6-311++g(d,p) level of theory. Next, the optimized TMO molecule was placed inside the optimized CH cages, and the geometries were reoptimized at the same level of theory. Furthermore, frequency calculations are performed to justify that these geometries are at the minimum of the potential energy surface, and these calculations generate nonimaginary frequencies, confirming that these geometries are in the ground state. The binding energies of sI and sII CHs were obtained by subtracting the ground state energy of optimized TMO and empty CH cages from the optimized TMO CH structures. The dihedral angle of TMO inside $5^{12}6^2$ and $5^{12}6^4$ cages was calculated, and host−guest hydrogen bonding was identified from DFT-optimized CHs.

RESULTS AND DISCUSSION

TMO CHs were prepared by thermally annealing codeposited ice mixtures of TMO and H_2O at two varying compositions (Figure 2). After TMO and H_2O were deposited at 10 K for 300 ML of thickness, the samples were slowly heated to 135 K at a heating rate of 5 K min^{-1}, followed by isothermal processing of ice for an extended period. The experiments were carried out at different compositions of the TMO and H_2O ice. In one experiment, TMO and H_2O mixed ice were created at a 1:3 composition, and in another mixed ice, TMO and H_2O were taken at a 1:15 composition.

https://doi.org/10.1021/acs.jpcc.5c01603
J. Phys. Chem. C 2025, 129, 8937−8945

The RAIR spectrum of 150 ML pure TMO in the ring puckering region is plotted in Figure S1b, showing the 1026 cm^{-1} peak attributed to this mode of crystalline TMO. The TMO-H_2O ice mixture at 135 K for 1:3 composition presents this peak at 0 h in Figure 3a,b. However, upon annealing for 2 h at 135 K, a new peak emerges at 1035 cm^{-1}, indicating a structural change. This peak is attributed to TMO in the large $5^{12}6^2$ cage of sI CH, consistent with the findings by Buch et al. and others.[19−21] The RAIR spectrum was further deconvoluted to assign the crystalline and CH phases of TMO in Figure 3b, and the relative percentages of CH and crystalline fractions of TMO were estimated as 20.72 and 79.28%, respectively.

In a similar manner, the 1:15 ice composite was thermally annealed at 120 K. The RAIR spectra in the C−O−C stretching shown in Figure 3c,d exhibit a peak at 975 cm^{-1}. A comparison with the spectrum of 150 ML TMO in the C−O−C stretching region (Figure S1a) confirms that the peak at 975 cm^{-1} is characteristic of crystalline TMO. After 18 h at 120 K, a new peak appears at 986 cm^{-1} alongside the crystalline TMO feature. This new peak is assigned to TMO in the large $5^{12}6^4$ cage of sII CH.[19−21] Also, a small quantity of TMO forms hydrogen bonds between the hydrogen of H_2O and the ethereal oxygen of TMO, resulting in a red-shifted peak at 969 cm^{-1}, in the C−O−C stretching region.[28] Deconvolution of the RAIR spectrum is shown in Figure 3d, and the relative percentages of CH, crystalline TMO, and hydrogen-bonded TMO are 27.77, 66.98, and 5.25%, respectively.

The C−O−C stretching region of 1:3 composition is plotted in Figure S2a. Here, the sI CH feature is assigned. The deconvoluted spectrum of 1:3 composition in C−O−C stretching reveals peaks at 975, 981, and 989 cm^{-1}. As attributed above, the peak at 975 cm^{-1} corresponds to the crystalline TMO (shown in Figure 3d), whereas the other two blue-shifted peaks indicate the confined state of the TMO in water ice. Ethers are known to form clusters. As Fleyfel et al. suggested, TMO may form clusters in water ice at higher concentrations.[20] The peak at 981 cm^{-1} corresponds to the TMO cluster, while the peak at 989 cm^{-1} is attributed to the $5^{12}6^2$ cage of sI, as its position is 3 cm^{-1} higher than the 986 cm^{-1} peak, associated with sII CH. This is expected for the smaller $5^{12}6^2$ cage of sI, where TMO experiences more confinement than the larger $5^{12}6^4$ cage of sII. The 969 cm^{-1} peak is not observed in the C−O−C stretching of sI CH (Figure S2a). This is because, in a 1:3 ratio, crystalline TMO resides as isolated TMO clusters in ASW. This structural change prevents further interaction between TMO and free water molecules, as evidenced by the absence of the hydrogen-bonded feature (969 cm^{-1}).

Additionally, the ring puckering region of the 1:15 composition plotted in Figure S2b also confirms the presence of sII CH. The 1030 cm^{-1} feature of larger sII CH is 5 cm^{-1} red-shifted than the 1035 cm^{-1} peak of smaller sI CH. The peak at 1026 cm^{-1} is due to crystalline TMO.

We further investigated whether codeposition is a prerequisite for composition-dependent CH formation or if sequential deposition at the same composition would also lead to sI and sII CH. Figures S3 and S4 illustrate this with the formation of CH in sequentially deposited TMO and H_2O ice in 1:3 and 1:15 ratios, respectively, followed by thermal annealing from 10 to 140 K. The temperature-dependent spectra in Figure S3 show that the 1035 cm^{-1} peak emerges at 130 K in 1:3 TMO-H_2O layered ice, confirming the formation of sI CH, whereas the 986 cm^{-1} peak appears in 1:15 TMO-H_2O layered ice, confirming the formation of sII CH (Figure S4).

To understand the effect of composition, the TMO-H_2O mixed ices were prepared at various compositions and isothermally processed at elevated temperatures (Figure S5). Figure S5a,b show that sI CHs are formed at ratios of 2:3 and 5:3 at 135 K, featuring the 1035 cm^{-1} peak. Similarly, the 986 cm^{-1} peak emerges in 1:6 and 1:30 compositions of mixed ices, due to sII CH. Combining the results of Figures 3 and S5, the trend in these compositions is stated as follows. The sI CH is formed at 5:3, 2:3, and 1:3 ratios, whereas the sII CH is formed at 1:6, 1:15, and 1:30 ratios. Here, 1:3 is the limiting composition, as equal or more concentration of TMO than H_2O in mixed ice leads to sI. If the concentration of TMO is slightly less than H_2O in mixed ice, it always leads to sII for all the compositions, ranging from 1:6 to 1:30.

To support our IR results of the formation of large $5^{12}6^2$ and $5^{12}6^4$ cages of sI and sII, we conducted quantum chemical calculations of TMO within these CH cages. The calculations allowed us to compute the infrared frequencies of their vibrational modes. Our calculations reveal a significant shift in the vibrational frequencies between the optimized structures of free TMO and TMO encaged in CH. Figure 4 illustrates the optimized structures of TMO within 5^{12},$5^{12}6^2$, and $5^{12}6^4$ cages. The optimized structure of TMO (Figure 4a) was unstable within the smaller 5^{12} cage (Figure 4b).[29] Higher molecular size with respect to the small cage size leads to instability and cage rapturing. However, in the case of $5^{12}6^2$ and $5^{12}6^4$ cages (Figure 4c,e), the TMO was stable. These results are justifiable as the molecular diameter of TMO across the C−O axis is 6.1 Å, and therefore, it could not be accommodated in a smaller 5^{12} cage, which has a cavity diameter of 5.09 Å. The cavity diameter of the sI $5^{12}6^2$ cage is 5.86 Å, slightly smaller than the size of TMO. The $5^{12}6^4$ cage of sII with 6.6 Å as the cavity diameter, is much larger in size than TMO.[22,30] As a result,

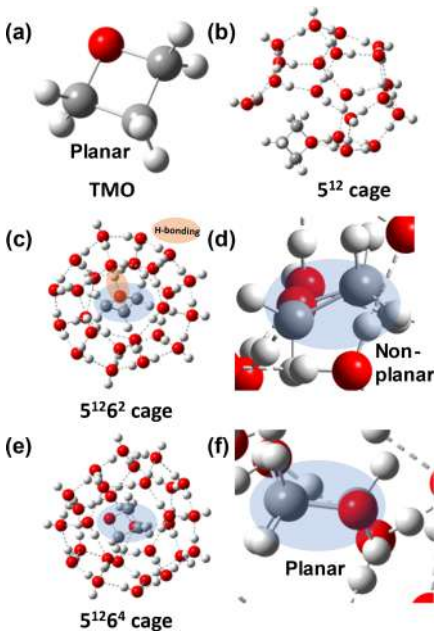


Figure 4. DFT-optimized structures of TMO trapped within various CH cages. (a) Free TMO compared with (b) 5^{12}, (c) $5^{12}6^2$, (d) $5^{12}6^2$ zoomed in, (e) $5^{12}6^4$, and (f) $5^{12}6^4$ zoomed in structures. Color codes used: white, H; red, O; and gray, C.

https://doi.org/10.1021/acs.jpcc.5c01603
J. Phys. Chem. C 2025, 129, 8937−8945

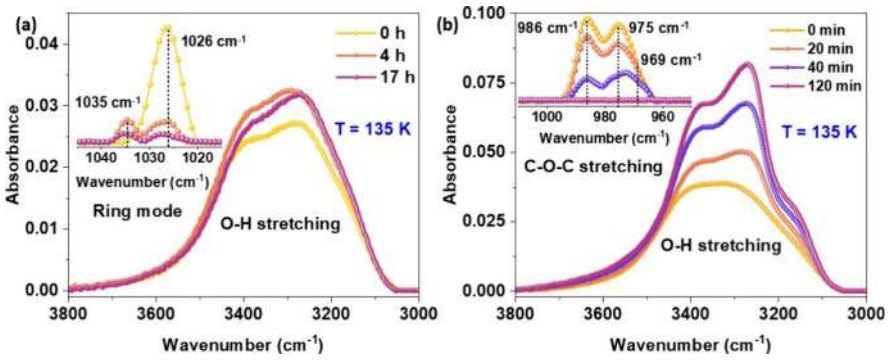


Figure 5. (a) Time-dependent RAIR spectra of 300 ML of a TMO-H_2O ice mixture (1:3) at 135 K in the O−H stretching region. The corresponding RAIR spectra in the ring mode region are shown in the inset. (b) Time-dependent RAIR spectra of 300 ML of a TMO-H_2O ice mixture (1:15) at 135 K in the O−H stretching region. The corresponding RAIR spectra in the C−O−C stretching region are shown in the inset.

TMO is constricted in the $5^{12}6^2$ cage and forces the cage to expand slightly.

The binding energies of TMO CHs are calculated by subtracting the energy of the optimized empty cage + the optimized free TMO from the energy of the optimized TMO CHs. It shows that the binding energy of sI (−2.18 eV) is more negative than that of sII (−2.07 eV), implying the greater stability of sI than sII (Table S2). The DFT-optimized structure depicts the host−guest hydrogen bonding between TMO and H_2O in sI CH, reaffirming the proximity of TMO and H_2O in the $5^{12}6^2$ cages (Figure 4c). Possibly due to hydrogen bonding as well as the steric hindrance in a tightly fitted $5^{12}6^2$ cage, this planar cyclic ether molecule gets distorted and becomes nonplanar (Figure 4d). The dihedral angle of trapped TMO is calculated from the optimized CH structures. The result shows that the dihedral angle of TMO is 9.2° and 1.3° in the $5^{12}6^2$ and $5^{12}6^4$ cages, respectively (Table S2). This implies a distorted nonplanar structure of TMO in the $5^{12}6^2$ cage, which can be attributed to the distortion caused by TMO-H_2O hydrogen bonding. This hydrogen bonding is absent in sII, and TMO remains almost planar (Figure 4f), with a limited deviation from its original structure.

These DFT-optimized structures suggest the reason for identifying the two CHs in two different vibrational modes. The C−O−C stretching mode manifests CH formation in sII, as observed for cyclic ether CHs.[31,32] This is not observed in sI, where the ring puckering mode manifests CH formation. The ring puckering mode is less active for the planar structure and more active for the distorted planar structure. Therefore, in sI, the distorted TMO activates the ring puckering mode strongly, and CH formation is evident in it. In sII, the ring puckering mode is less active, and as a result, the C−O−C stretching mode prominently manifests the CH formation.

Results of theoretical calculations of vibrational frequencies of free TMO and TMO trapped in the ring puckering mode of $5^{12}6^2$ and the C−O−C stretching mode of $5^{12}6^4$ cages are presented in Table S1. The experimental blue-shift for TMO CH is compared theoretical blue-shift. As it is encaged, the steric hindrance hardens the frequencies. A blueshift of 12 cm^{-1} was observed for TMO within the $5^{12}6^2$ cage (ring puckering mode), while a blueshift of 10 cm^{-1} occurred in the $5^{12}6^4$ cage (C−O−C stretching mode). Experimentally, we observed that the crystalline TMO shows peaks at 1026 and 975 cm^{-1} due to ring mode and C−O−C stretching mode, respectively, which shift to 1035 and 986 cm^{-1} with an increase of 9 and 11 cm^{-1}, respectively. It has been reported that the $5^{12}6^2$ cage expands slightly to accommodate the TMO, which may cause this difference in theoretical and experimental observations. Overall, the theoretically calculated positions match well with the experimental data for both $5^{12}6^2$ and $5^{12}6^4$ cages and, thereby, ascertain the formation of sI and sII structures.

The dissociation of metastable CHs leading to the crystallization of ASW is observed in UHV for several CHs as a generic physical phenomenon at cryogenic temperatures.[33,34] During the formation of CH, the amorphous water ice becomes more structurally ordered. As CH dissociates at a higher temperature, the desorption of the enclathrated guest molecule mobilizes the water molecules in the vicinity of the cage, promoting rapid reorientation. This facilitates the conversion of amorphous ice into either hexagonal or cubic ice.[33−35] This phenomenon was particularly evident in the dissociation of sII CH of TMO. It dissociates completely at 135 K within 2 h, and simultaneously, amorphous water was converted to hexagonal ice, as shown in Figure 5b. As dissociation progresses, the broad peak in the O−H stretching region becomes narrower and sharper with time. This continuous transformation in the IR spectra reflects the gradual conversion of amorphous water ice to crystalline ice. Despite this crystallization, water does not desorb from the matrix at 135 K, maintaining a constant concentration. As shown in the inset, the IR peaks at 986, 975, and 969 cm^{-1} decrease rapidly, as shown in the C−O−C stretching region (Figure 5b). This indicates that TMO, previously confined within the CH cages, is desorbed from the ice matrix along with crystalline TMO and hydrogen-bonded TMO in the mixed ice.

The behavior of sI CH at 135 K differs significantly from that of sII CH under the same conditions (Figure 5a). At 135 K, the IR peak at 1035 cm^{-1}, corresponding to sI CH, initially increased for the first 4 h, indicating CH formation. Subsequently, the peak gradually diminishes, reflecting slow dissociation, although a significant amount of CH still persists even after 17 h. Notably, the crystalline TMO peak at 1026 cm^{-1} decreases steadily over time. However, complete desorption is not observed here, even after 17 h, as shown in the ring puckering mode region. The O−H stretching region reveals that with time, water ice becomes increasingly ordered and compact, yet it does not crystallize. After 17 h, the intensity of the O−H band increases slightly, and desorption from the matrix begins, but water does not crystallize. This result contrasts with an isothermal RAIR study of pure

https://doi.org/10.1021/acs.jpcc.5c01603
J. Phys. Chem. C 2025, 129, 8937−8945

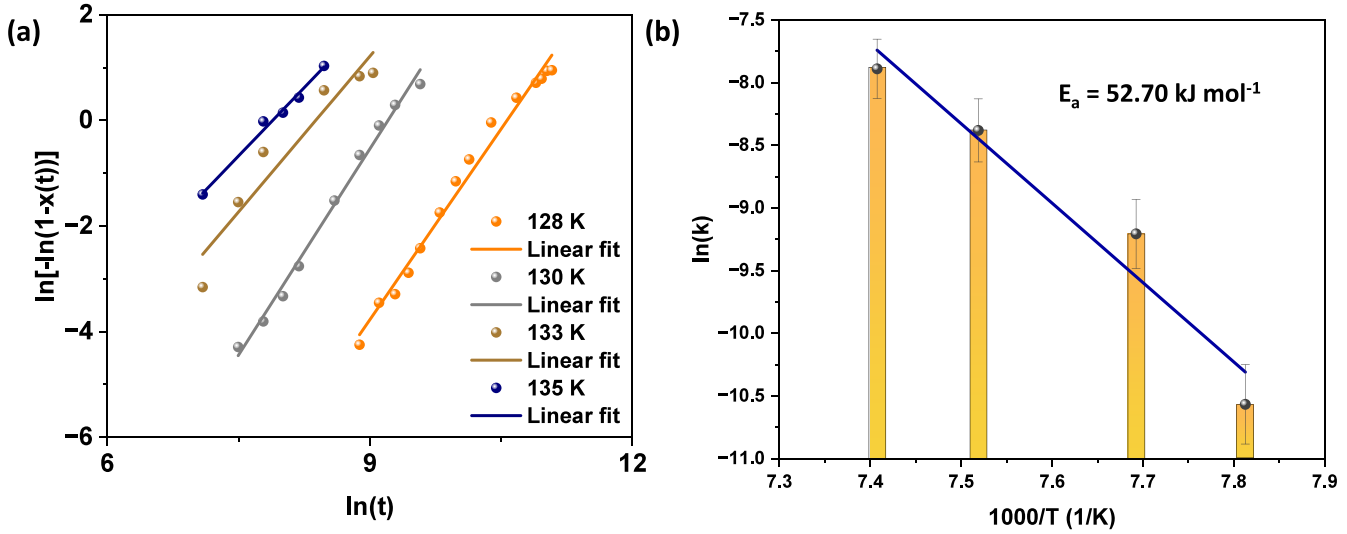


Figure 6. (a) Linear plot of the Avrami equation for ASW crystallization. Plots of $\ln(-\ln - [1 - x])$ versus $\ln(t)$ at 128, 130, 133, and 135 K were evaluated using the O−H stretching modes. The obtained data points were fitted using the Avrami equation. (b) Arrhenius plot of $\ln k$ versus $1/T$, obtained from the analysis of the slope and intercept of the linearly fitted lines of plot (a) for different temperatures. The activation energy (E_a) of ice crystallization was calculated from the slope of the linearly fitted straight line of plot (b).

amorphous water ice at 135 K, where it crystallizes to hexagonal ice in 12 h at 135 K (Figure S8). However, in the presence of sI CH, even after 17 h, water remains in a more ordered state but retains its amorphous nature. Despite the dissociation of sI CH, the anticipated crystallization of water does not occur within the experimental time scale, indicating a significant suppression of crystallization kinetics following the dissociation of sI CH compared to that of pure amorphous water ice. This might be attributed to the TMO-H_2O hydrogen bonding interaction from residual TMO in ASW for sI CH inhibiting crystallization. In sII CH, TMO completely desorbs, and ASW crystallizes in the absence of TMO-H_2O hydrogen bonding. Although this TMO-H_2O hydrogen bonding continuously diminishes as 80% of TMO desorbs within 2 h at 135 K, for sI CH. As a result, while concentration effects are certainly relevant, they do not fully explain the qualitative difference in the behavior of ASW crystallization following sI vs sII CH dissociation observed in our study, highlighting the impact of the sI CH structure in impeding phase transition.

These contrasting effects of the two CH structures of the same TMO guest molecules, namely, sI and sII, in determining the crystallization kinetics of water ice have never been observed hitherto. These differences can be attributed to structural variations between sI and sII CHs, as well as the orientation of TMO and its hydrogen bonding interactions inside the cages. While the crystallization of amorphous water ice following CH dissociation has been well-documented for both sI and sII CHs, in the case of TMO-CH, it is structure-dependent with only sII TMO-CH dissociating to form crystalline ice. Previous reports show that water transforms from amorphous ice to crystalline ice via the dissociation of CO_2 CH (sI) and DME CH (sII), suggesting that dissociation-induced crystallization is generally independent of CH structure.[3,36] This crystallization process occurs through the rapid reorientation of water molecules as they transition from the disordered amorphous phase to the more ordered crystalline phase. When dissociation is initiated at a higher temperature, a significant amount of cages break, releasing the guest molecules within a very short time window. As the hydrogen bonding network of caged water is disrupted, other water molecules in their proximity get reoriented. This combined effect of caged water and the guest molecule mobilizes water, leading to crystallization. Since sI CH is more stable, it dissociates slowly at 135 K, as observed in our study. This gradual dissociation leads to the formation of compact ice but is insufficient to induce crystallization. Additionally, TMO weakly interacts with caged water via hydrogen bonding in sI CH, a feature absent in sII CH. This hydrogen-bonded TMO may restrict caged water from interacting with amorphous ice, further hindering crystallization. As a result, crystallization at 135 K becomes even slower than that of pure water ice, possibly attributed to the stability and host−guest hydrogen bonding interaction in sI CH.

The crystallization kinetics study on the transition from CH to hexagonal ice possesses significant relevance in various scientific fields, including CH chemistry, physical chemistry, astrochemistry, atmospheric chemistry, and planetary science.[37−40] To evaluate the kinetic parameters governing this phase transition, we conducted isothermal time-dependent RAIRS experiments using a 300 ML TMO-H_2O (1:30) film within the temperature range of 128−135 K.

Figure S6 represents time-dependent RAIR spectra in the O−H stretching region at 128, 130, 133, and 135 K. In Figure S6a, the initial spectrum (0 min) displays contributions from water molecules involved in the CH phase, along with remaining ASW. After 80 min, the spectrum reveals the characteristic features of hexagonal crystalline ice, consistent with previous literature (Figure S6a).[33,35,41,42] It is well-known that pure amorphous ice converts to hexagonal ice at elevated temperatures in UHV. To validate this, we formed hexagonal ice from pure amorphous water at 135 K and compared the results to our data (Figure S8). The crystallization fraction at different temperatures versus time is shown in Figure S7 (derived from the RAIR spectra shown in Figure S6). The absorbance intensity at 3260 cm^{-1} was used to obtain the crystallization fraction, $x(t)$, by using eq 1.

https://doi.org/10.1021/acs.jpcc.5c01603
J. Phys. Chem. C 2025, 129, 8937−8945

Table 1. Parameters Estimated Using the Avrami Equation at Various Temperatures

temperature	128 K	130 K	133 K	135 K
n	2.41	2.60	1.96	1.72
rate constant (ks^{-1})	0.26×10^{-4}	1.00×10^{-4}	2.29×10^{-4}	3.75×10^{-4}

$$x(t) = \frac{\Delta A(1)}{\Delta A(2)} \quad (1)$$

$\Delta A(1)$ represents the difference between absorbance at a specific time t and one at time 0, and $\Delta A(2)$ is the corresponding difference in absorbance of a completely crystallized film and that at time 0. The thermodynamics of the dissociation of CH and its impact on the crystallization of water ice can be understood from the crystallization fraction. The transition of the shape of the curve from sigmoidal (occurring at a lower temperature, 128 K) to exponential (evident at a higher temperature, 135 K) (shown in Figure S6) implies a notable increase in the crystallization kinetics with temperature.

The kinetics parameters and activation energy for the CH to hexagonal ice transition were calculated using the Avrami equation.[43,44]

$$x(t) = 1 - \exp(-k.\ t)^n \quad (2)$$

where k is the rate constant, t is the time, and n is a parameter related to the crystallization mechanism.[44] The variable "n" can take values in the range of 1−4, and these values are used to predict the nature of the crystallization process.[45,46] Eq 2 can be rearranged in a linear form.

$$\ln(-\ln[1 - x(t)]) = n\ln(t) + n\ln k \quad (3)$$

Figure 6a shows the plots of $\ln(-\ln[1 - x(t)])$ versus $\ln(t)$ at different temperatures. The values of n and k at different temperatures were obtained using the slope and intercept of linearly fitted lines as shown in Table 1. The value calculated for n is found to be between 1.7 and 2.4, indicating that the nucleation originates from CH and ASW interfaces and progresses in a polyhedral growth pattern within the ice matrix.[4,43] The slope of the linearly fitted line of the Arrhenius plot (Figure 6b) was used to determine the activation energy (E_a) of ice crystallization. The calculated value of E_a for the phase transition from ASW to hexagonal ice is 52.70 kJ mol^{-1}. This aligns with our previous studies, which reported an activation energy of ∼52−58 kJ mol^{-1} for desorption-induced ASW-to-hexagonal ice transition. This suggests that the dissociation of TMO sII CH leads to the facile crystallization of amorphous water ice to hexagonal ice.

CONCLUSIONS

In this work, we succeeded in forming TMO CHs from TMO-H_2O mixed ice under UHV, analogous to interstellar conditions. We have shown that two types of CH structures were formed at different compositions in cryogenic ices within UHV under the same temperature and pressure conditions. The 1:3 ratio of the TMO-H_2O ice mixture leads to sI CH, whereas the 1:15 ratio leads to sII CH. DFT analysis shows the presence of host−guest hydrogen bonding and structurally distorted planar TMO in sI CH, which does not occur in sII CH. While sI CH dissociation does not induce crystallization of ASW, dissociation of sII CH leads to the crystallization of ASW to hexagonal ice. The results suggest that by dissociating a specific structure of CH, the transformation of amorphous water ice to crystalline hexagonal ice can be controlled. The crystallization process accelerates as sII CH dissociates, while, on the contrary, the dissociation of sI CH retards crystallization, slower than that of pure water ice at the same temperature. Our results provide evidence that the same guest molecule creates two different CH and consequently affects ice crystallization differently at two distinct compositions. These observations describe the importance of structural conformers of enclathrated molecules in deciding the phase transition of water ice. This study also suggests the possibility of isolation of structurally hindered conformers in interstellar ices and CHs, contributing to the phase evolution of mixed molecular solids.

ASSOCIATED CONTENT

Supporting Information

The Supporting Information is available free of charge at https://pubs.acs.org/doi/10.1021/acs.jpcc.5c01603.

Temperature and time-dependent RAIR spectra of pure TMO and TMO-H_2O ice mixtures (PDF)

AUTHOR INFORMATION

Corresponding Author

Thalappil Pradeep − *DST Unit of Nanoscience (DST UNS) and Thematic Unit of Excellence (TUE), Department of Chemistry, Indian Institute of Technology Madras, Chennai 600036, India; International Centre for Clean Water, IIT Madras Research Park, Chennai 600113, India;* orcid.org/0000-0003-3174-534X; Email: pradeep@iitm.ac.in

Authors

Soham Chowdhury − *DST Unit of Nanoscience (DST UNS) and Thematic Unit of Excellence (TUE), Department of Chemistry, Indian Institute of Technology Madras, Chennai 600036, India*

Bijesh K. Malla − *DST Unit of Nanoscience (DST UNS) and Thematic Unit of Excellence (TUE), Department of Chemistry, Indian Institute of Technology Madras, Chennai 600036, India*

Gaurav Vishwakarma − *DST Unit of Nanoscience (DST UNS) and Thematic Unit of Excellence (TUE), Department of Chemistry, Indian Institute of Technology Madras, Chennai 600036, India;* orcid.org/0009-0002-6076-3299

Anupriya Nyayban − *DST Unit of Nanoscience (DST UNS) and Thematic Unit of Excellence (TUE), Department of Chemistry, Indian Institute of Technology Madras, Chennai 600036, India*

Complete contact information is available at: https://pubs.acs.org/10.1021/acs.jpcc.5c01603

Author Contributions

T.P. and S.C. designed the experiments, S.C. and B.K.M. performed the experiments, and S.C., B.K.M., and G.V. analyzed the results. T.P. proposed the project and supervised

the progress. A.N. performed the quantum chemical calculations. The manuscript was written with the contributions of all authors.

Notes

The authors declare no competing financial interest.

■ ACKNOWLEDGMENTS

We acknowledge the Science and Engineering Research Board (SERB), Department of Science and Technology (DST), Government of India, for research funding through a CRG grant (CRG/2018/003922) and a Swarnajayanti fellowship. T.P. acknowledges funding from the Centre of Excellence on Molecular Materials and Functions under the Institution of Eminence scheme of IIT Madras. S.C., G.V., and A.N. thank IITM for their research fellowship. B.K.M. thanks the Council of Scientific and Industrial Research (CSIR) for his research fellowship.

■ REFERENCES

(1) Ghosh, J.; Vishwakarma, G.; Kumar, R.; Pradeep, T. Formation and Transformation of Clathrate Hydrates under Interstellar Conditions. *Acc. Chem. Res.* **2023**, *56* (16), 2241−2252.

(2) Malla, B. K.; Vishwakarma, G.; Chowdhury, S.; Selvarajan, P.; Pradeep, T. Formation of Ethane Clathrate Hydrate in Ultrahigh Vacuum by Thermal Annealing. *J. Phys. Chem. C* **2022**, *126* (42), 17983−17989.

(3) Malla, B. K.; Vishwakarma, G.; Chowdhury, S.; Nayak, S. K.; Yamijala, S. S. R. K. C.; Pradeep, T. Formation and Dissociation of Dimethyl Ether Clathrate Hydrate in Interstellar Ice Mimics. *J. Phys. Chem. C* **2024**, *128* (6), 2463−2470.

(4) Vishwakarma, G.; Malla, B. K.; Chowdhury, S.; Khandare, S. P.; Pradeep, T. Existence of Acetaldehyde Clathrate Hydrate and Its Dissociation Leading to Cubic Ice under Ultrahigh Vacuum and Cryogenic Conditions. *J. Phys. Chem. Lett.* **2023**, *14* (23), 5328−5334.

(5) Vishwakarma, G.; Malla, B. K.; Reddy, K. S. S. V. P.; Ghosh, J.; Chowdhury, S.; Yamijala, S. S. R. K. C.; Reddy, S. K.; Kumar, R.; Pradeep, T. Induced Migration of CO2 from Hydrate Cages to Amorphous Solid Water under Ultrahigh Vacuum and Cryogenic Conditions. *J. Phys. Chem. Lett.* **2023**, 2823−2829.

(6) Tychengulova, A.; Katpayeva, K.; Shomshekova, S.; Ibragimova, S.; Golikov, O.; Yerezhep, D.; Sokolov, D.; Aldiyarov, A. Laboratory Studies of the Clathrate Hydrate Formation in the Carbon Dioxide-Water Mixtures at Interstellar Conditions. *ACS Omega* **2025**, *10*, 1237−1248.

(7) Malla, B. K.; Yang, D.-S.; Pradeep, T. Growth of Clathrate Hydrates in Nanoscale Ice Films Observed Using Electron Diffraction and Infrared Spectroscopy. *J. Phys. Chem. Lett.* **2025**, *16*, 365−371.

(8) *Molecules [CDMS classic documentation]*. https://cdms.astro.uni-koeln.de/classic/molecules (accessed January 2025).

(9) Puzzarini, C.; Alessandrini, S. Interstellar Ices: A Factory of the Origin-of-Life Molecules. *ACS Cent. Sci.* **2024**, *10* (1), 13−15.

(10) Blake, D.; Allamandola, L.; Sandford, S.; Hudgins, D.; Freund, F. Clathrate Hydrate Formation in Amorphous Cometary Ice Analogs in Vacuo. *Science* **1979**, *254* (5031), 548−551.

(11) Sloan, E. D. Fundamental Principles and Applications of Natural Gas Hydrates. *Nature 2003 426:6964* **2003**, *426* (6964), 353−359. .

(12) Yeon, S. H.; Seol, J.; Lee, H. Structure Transition and Swapping Pattern of Clathrate Hydrates Driven by External Guest Molecules. *J. Am. Chem. Soc.* **2006**, *128* (38), 12388−12389.

(13) Halpern, Y.; Thieu, V.; Henning, R. W.; Wang, X.; Schultz, A. J. Time-Resolved in Situ Neutron Diffraction Studies of Gas Hydrate: Transformation of Structure II (SII) to Structure I (SI). *J. Am. Chem. Soc.* **2001**, *123* (51), 12826−12831.

(14) Devlin, J. P. Structure, Spectra, and Mobility of Low-Pressure Ices: Ice I, Amorphous Solid Water, and Clathrate Hydrates at T < 150 K. *J. Geophys Res. Planets* **2001**, *106* (E12), 33333−33349.

(15) McGuire, B. A.; Carroll, P. B.; Loomis, R. A.; Finneran, I. A.; Jewell, P. R.; Remijan, A. J.; Blake, G. A. Discovery of the Interstellar Chiral Molecule Propylene Oxide (CH3CHCH2O). *Science* **2016**, *352* (6292), 1449−1452.

(16) Ghosh, J.; Bhuin, R. G.; Ragupathy, G.; Pradeep, T. Spontaneous Formation of Tetrahydrofuran Hydrate in Ultrahigh Vacuum. *J. Phys. Chem. C* **2019**, *123* (26), 16300−16307.

(17) Udachin, K. A.; Ratcliffe, C. I.; Ripmeester, J. A. Structure, Dynamics and Ordering in Structure I Ether Clathrate Hydrates from Single-Crystal X-Ray Diffraction And2H NMR Spectroscopy. *J. Phys. Chem. B* **2007**, *111* (39), 11366−11372.

(18) Maşlakcı, Z.; Devlin, J. P.; Uras-Aytemiz, N. H-Bonding Behavior of Ethylene Oxide within the Clathrate Hydrates Revisited: Experiment and Theory. *Chem. Phys. Lett.* **2020**, *754*, No. 137728.

(19) Buch, V.; Devlin, J. P.; Monreal, I. A.; Jagoda-Cwiklik, B.; Uras-Aytemiz, N.; Cwiklik, L. Clathrate Hydrates with Hydrogen-Bonding Guests. *Phys. Chem. Chem. Phys.* **2009**, *11* (44), 10245−10265.

(20) Fleyfel, F.; Devlin, J. P. Infrared Spectra of Large Clusters Containing Small Ether Molecules: Liquid, Crystalline, and Clathrate-hydrate Cluster Spectra. *J. Chem. Phys.* **1998**, *92* (1), 36.

(21) Subramaniam, S.; Lance, M. J.; Rawn, C. J.; Chakoumakos, B. C.; Rondinone, A. J. Raman Spectroscopic Studies on Structure I and Structure IItrimethylene Oxide Hydrate. *Canadian J. Phys.* **2005**, *83* (9), 941−949.

(22) Rondinone, A. J.; Chakoumakos, B. C.; Rawn, C. J.; Ishii, Y. Neutron Diffraction Study of Structure I and Structure II Trimethylene Oxide Clathrate Deuterate. *J. Phys. Chem. B* **2003**, *107* (25), 6046−6050.

(23) Bag, S.; Bhuin, R. G.; Methikkalam, R. R. J.; Pradeep, T.; Kephart, L.; Walker, J.; Kuchta, K.; Martin, D.; Wei, J. Development of Ultralow Energy (1−10 EV) Ion Scattering Spectrometry Coupled with Reflection Absorption Infrared Spectroscopy and Temperature Programmed Desorption for the Investigation of Molecular Solids. *Rev. Sci. Instrum.* **2014**, *85* (1). .

(24) Malla, B. K.; Vishwakarma, G.; Chowdhury, S.; Pradeep, T. Vacuum Ultraviolet Photolysis of Condensed Methyl Chloride in Interstellar Model Conditions and Trapping of Intermediates at Intergrain Interfaces. *J. Phys. Chem. C* **2023**, *127* (50), 24149−24157.

(25) Malla, B. K.; Chowdhury, S.; Paliwal, D.; Hanoona, K. M.; Vishwakarma, G.; Methikkalam, R. R. J.; Pradeep, T. Simulated Interstellar Photolysis of N2O Ice: Selectivity in Photoproducts. *J. Phys. Chem. C* **2025**, *129*, 1120−1128.

(26) Moon, E. S.; Kang, H.; Oba, Y.; Watanabe, N.; Kouchi, A. DIRECT EVIDENCE FOR AMMONIUM ION FORMATION IN ICE THROUGH ULTRAVIOLET-INDUCED ACID−BASE REACTION OF NH3 WITH H3O+. *Astrophys. J.* **2010**, *713* (2), 906.

(27) Bartmess, J. E.; Georgiadis, R. M. Empirical Methods for Determination of Ionization Gauge Relative Sensitivities for Different Gases. *Vacuum* **1983**, *33* (3), 149−153.

(28) Mizuno, K.; Masuda, Y.; Yamamura, T.; Kitamura, J.; Ogata, H.; Bako, I.; Tamai, Y.; Yagasaki, T. Roles of the Ether Oxygen in Hydration of Tetrahydrofuran Studied by IR, NMR, and DFT Calculation Methods. *J. Phys. Chem. B* **2009**, *113* (4), 906−915.

(29) Mohammadi-Manesh, H.; Ghafari, H.; Alavi, S. Molecular Dynamics Study of Guest-Host Hydrogen Bonding in Ethylene Oxide, Trimethylene Oxide, and Formaldehyde Structure i Clathrate Hydrates. *J. Phys. Chem. C* **2017**, *121* (16), 8832−8840.

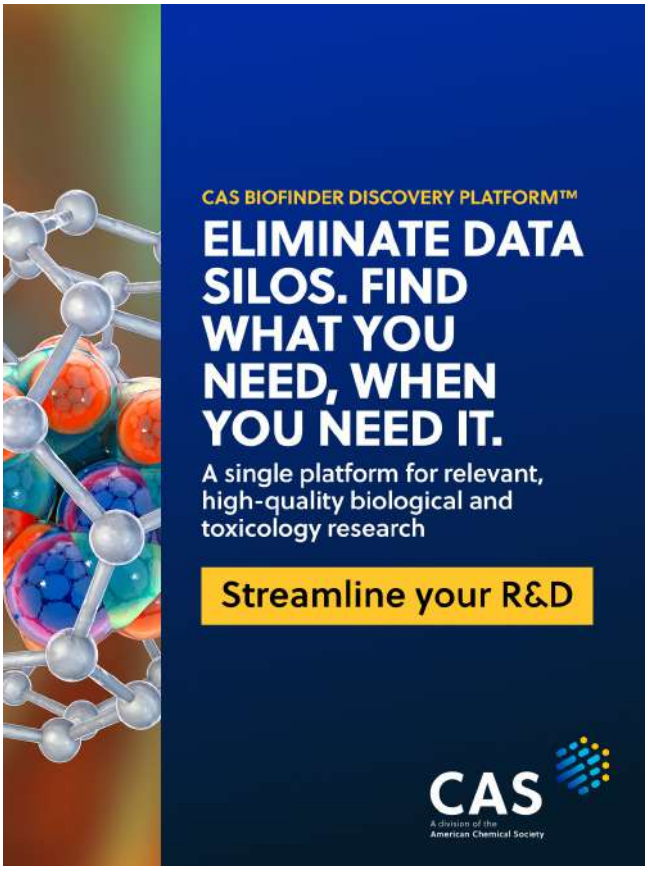
(30) Sloan, E. D., Jr.; Koh, C. A.; Koh, C. A. Clathrate Hydrates of Natural Gases. *Clathrate Hydrates of Natural Gases* **2007**.

(31) Monreal, I. A.; Cwiklik, L.; Jagoda-Cwiklik, B.; Devlin, J. P. Classical to Nonclassical Transition of Ether-HCN Clathrate Hydrates at Low Temperature. *J. Phys. Chem. Lett.* **2010**, *1* (1), 290−294.

(32) Monreal, I. A.; Devlin, J. P.; Maşlakc, Z.; Çiçek, M. B.; Uras-Aytemiz, N. Controlling Nonclassical Content of Clathrate Hydrates through the Choice of Molecular Guests and Temperature. *J. Phys. Chem. A* **2011**, *115* (23), 5822−5832.

(33) Ghosh, J.; Vishwakarma, G.; Das, S.; Pradeep, T. Facile Crystallization of Ice Ihvia Formaldehyde Hydrate in Ultrahigh

Vacuum under Cryogenic Conditions. *J. Phys. Chem. C* **2021**, *125* (8), 4532−4539.
(34) Ghosh, J.; Bhuin, R. G.; Vishwakarma, G.; Pradeep, T. Formation of Cubic Ice via Clathrate Hydrate, Prepared in Ultrahigh Vacuum under Cryogenic Conditions. *J. Phys. Chem. Lett.* **2020**, *11* (1), 26−32.
(35) Vishwakarma, G.; Ghosh, J.; Pradeep, T. Desorption-Induced Evolution of Cubic and Hexagonal Ices in an Ultrahigh Vacuum and Cryogenic Temperatures. *Phys. Chem. Chem. Phys.* **2021**, *23* (41), 24052−24060.
(36) Falenty, A.; Hansen, T. C.; Kuhs, W. F.; Hansen, T. C. *Cubic Ice Formation and Annealing during CO2 Clathrate Hydrate Decomposition at Low Temperatures Cubic Ice Formation and Annealing during CO 2 Clathrate Hydrate Decomposition at Low Temperatures*; Hokkaido University Press, 2011.
(37) Cao, H. S. Formation and Crystallization of Low-Density Amorphous Ice. *J. Phys. D Appl. Phys.* **2021**, *54* (20), 203002.
(38) Takeya, S.; Fujihisa, H.; Alavi, S.; Ohmura, R. Thermally Induced Phase Transition of Cubic Structure II Hydrate: Crystal Structures of Tetrahydropyran-CO2 Binary Hydrate. *J. Phys. Chem. Lett.* **2023**, *14* (7), 1885−1891.
(39) Minissale, M.; Aikawa, Y.; Bergin, E.; Bertin, M.; Brown, W. A.; Cazaux, S.; Charnley, S. B.; Coutens, A.; Cuppen, H. M.; Guzman, V.; Linnartz, H.; McCoustra, M. R. S.; Rimola, A.; Schrauwen, J. G. M.; Toubin, C.; Ugliengo, P.; Watanabe, N.; Wakelam, V.; Dulieu, F. Thermal Desorption of Interstellar Ices: A Review on the Controlling Parameters and Their Implications from Snowlines to Chemical Complexity. *ACS Earth Space Chem.* **2022**, *6* (3), 597−630.
(40) Bartels-Rausch, T.; Bergeron, V.; Cartwright, J. H. E.; Escribano, R.; Finney, J. L.; Grothe, H.; Gutiérrez, P. J.; Haapala, J.; Kuhs, W. F.; Pettersson, J. B. C.; Price, S. D.; Sainz-Díaz, C. I.; Stokes, D. J.; Strazzulla, G.; Thomson, E. S.; Trinks, H.; Uras-Aytemiz, N. Ice Structures, Patterns, and Processes: A View across the Icefields. *Rev. Mod. Phys.* **2012**, *84* (2), 885−944.
(41) Vishwakarma, G.; Malla, B. K.; Methikkalam, R. R. J.; Pradeep, T. Rapid Crystallization of Amorphous Solid Water by Porosity Induction. *Phys. Chem. Chem. Phys.* **2022**, *24* (42), 26200−26210.
(42) Watanabe, N.; Kouchi, A. Ice Surface Reactions: A Key to Chemical Evolution in Space. *Prog. Surf. Sci.* **2008**, *83* (10−12), 439−489.
(43) Avrami, M. Kinetics of Phase Change. II Transformation-Time Relations for Random Distribution of Nuclei. *J. Chem. Phys.* **1940**, *8* (2), 212−224.
(44) Harada, K.; Sugimoto, T.; Kato, F.; Watanabe, K.; Matsumoto, Y. Thickness Dependent Homogeneous Crystallization of Ultrathin Amorphous Solid Water Films. *Phys. Chem. Chem. Phys.* **2020**, *22* (4), 1963−1973.
(45) Hage, W.; Hallbrucker, A.; Mayer, E.; Johari, G. P. Crystallization Kinetics of Water below 150 K. *J. Chem. Phys.* **1998**, *100* (4), 2743.
(46) Lee, D. H.; Kang, H. Acid-Promoted Crystallization of Amorphous Solid Water. *J. Phys. Chem. C* **2018**, *122* (42), 24164−24170.



Composition-Dependent Formation and Dissociation of Structure I and Structure II Clathrate Hydrates of Trimethylene Oxide in Ultrahigh Vacuum

*Soham Chowdhury[1], Bijesh K. Malla[1], Gaurav Vishwakarma[1], Anupriya Nyayban[1], Thalappil Pradeep[1,2]**

[1]DST Unit of Nanoscience (DST UNS) and Thematic Unit of Excellence (TUE), Department of Chemistry, Indian Institute of Technology Madras, Chennai 600036, India

[2]International Centre for Clean Water, IIT Madras Research Park, Chennai 600113, India

Corresponding authors

***Email:** pradeep@iitm.ac.in

This PDF file includes:

Figure S1 to S8 (pages S2-S9)

Table S1, S2 (pages S5, S6)

Supporting information 1:

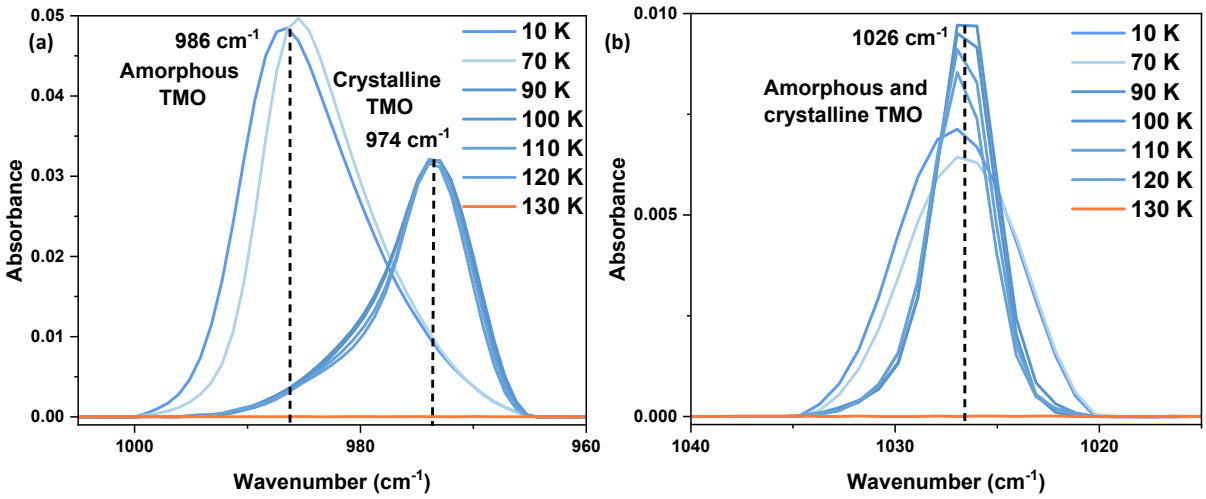


Figure S1. Temperature-dependent RAIR spectra of pure 150 ML TMO in (a) C-O-C stretching and (b) ring puckering mode regions. Pure TMO vapor was deposited on Ru(0001) substrate at 10 K and annealed to 130 K at a rate of 5 K min^{-1}. Vapor-deposited TMO resulted in the amorphous form at 10 K, which crystallized above 90 K and completely desorbed at 130 K.

Supporting information 2:

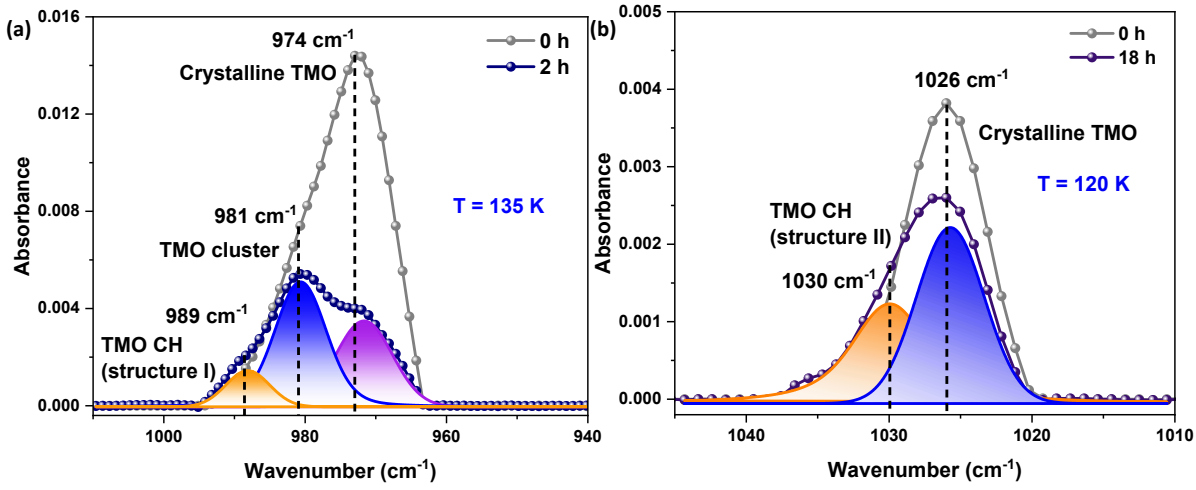


Figure S2. Time-dependent RAIR spectra of 300 ML of TMO-H_2O ice mixture. (a) C-O-C stretching region of TMO-water mixed ice in 1:3 ratio at 135 K after 2 h and (b) ring puckering mode region of TMO-water mixed ice in 1:15 ratio at 120 K after 18 h. TMO and water vapor were co-deposited on Ru(0001) substrate at 10 K and annealed to 135 K in (a) and 120K in (b) at a rate of 5 K min^{-1}.

Supporting information 3:

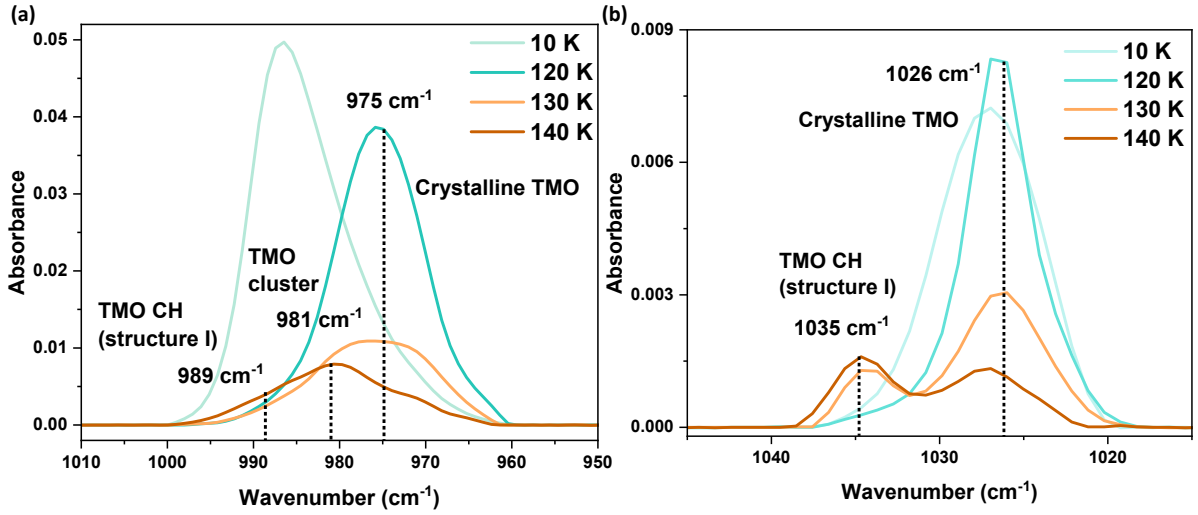


Figure S3. Temperature-dependent RAIR spectra of 300 ML of TMO@H_2O ice mixture of 1:3 ratio in (a) C-O-C stretching and (b) ring puckering mode regions. To prepare 300 ML of (1:3) TMO@H_2O layered ice, 50 ML of TMO were deposited first on Ru(0001) substrate, followed by 150 ML of water vapor were sequentially deposited at 10 K and annealed to 140 K at a rate of 5 K min^{-1}.

Supporting information 4:

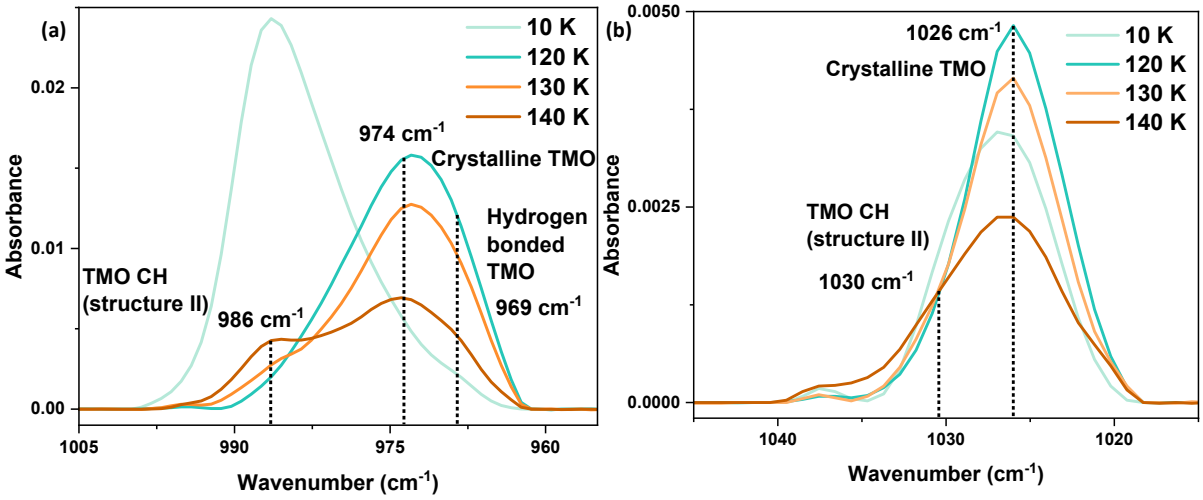


Figure S4. Temperature-dependent RAIR spectra of 300 ML of TMO@H_2O ice mixture of 1:15 ratio in (a) C-O-C stretching and (b) ring puckering mode regions. To prepare 300 ML of (1:15) TMO@H_2O layered ice, 18 ML of TMO were deposited first on Ru(0001) substrate, followed by 250 ML of water vapor were sequentially deposited at 10 K and annealed to 140 K at a rate of 5 K min^{-1}.

Supporting information 5:

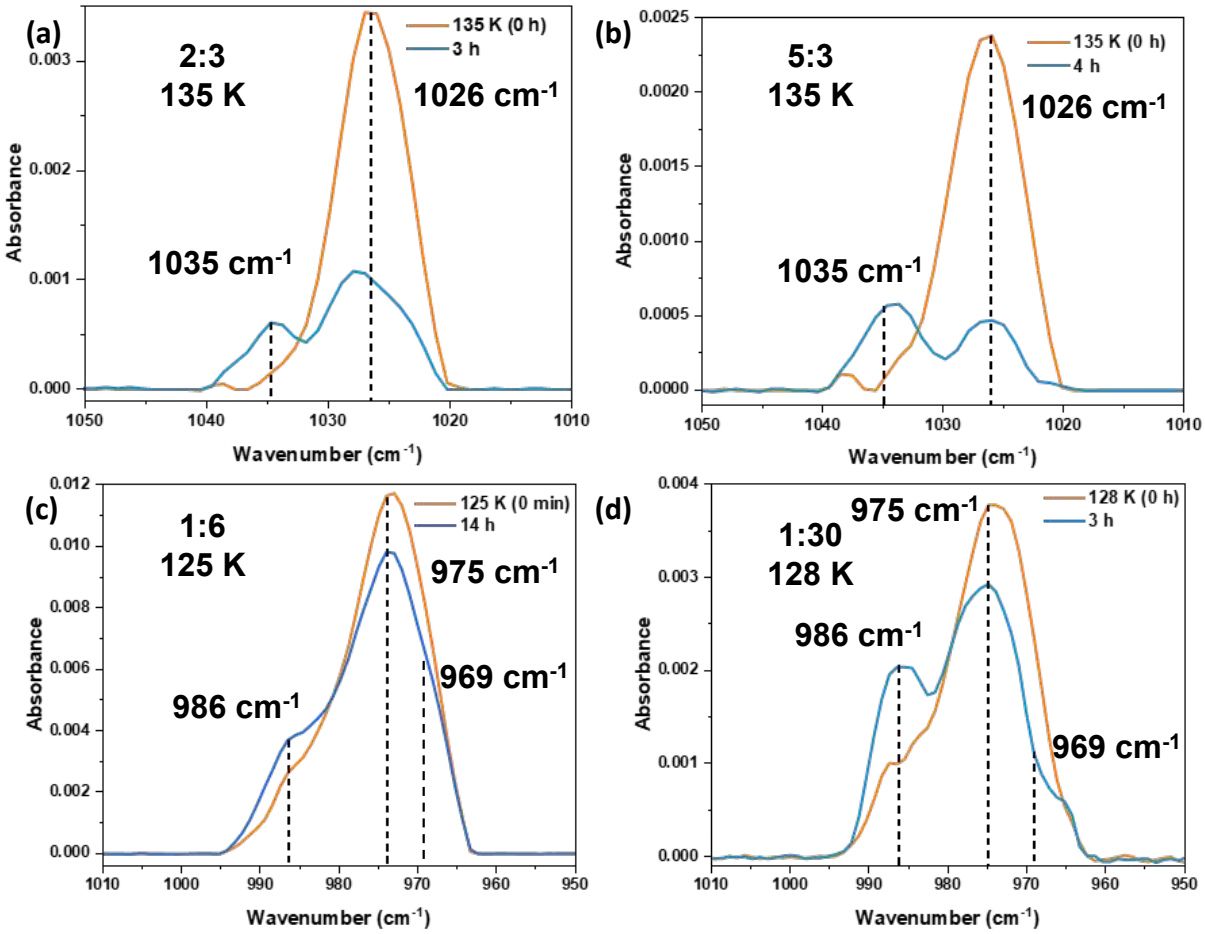


Figure S5. Isothermal time-dependent RAIR spectra of 300 ML of TMO-H_2O ice at different composition. (a) and (b) correspond to the ring puckering vibrational mode of 2:3 and 5:3 composition of mixed ice, at 135 K. (c) and (d) correspond to the C-O-C stretching vibrational mode of 1:6 and 1:30 composition of mixed ice, at 125 K and 128 K respectively.

Supporting information 6:

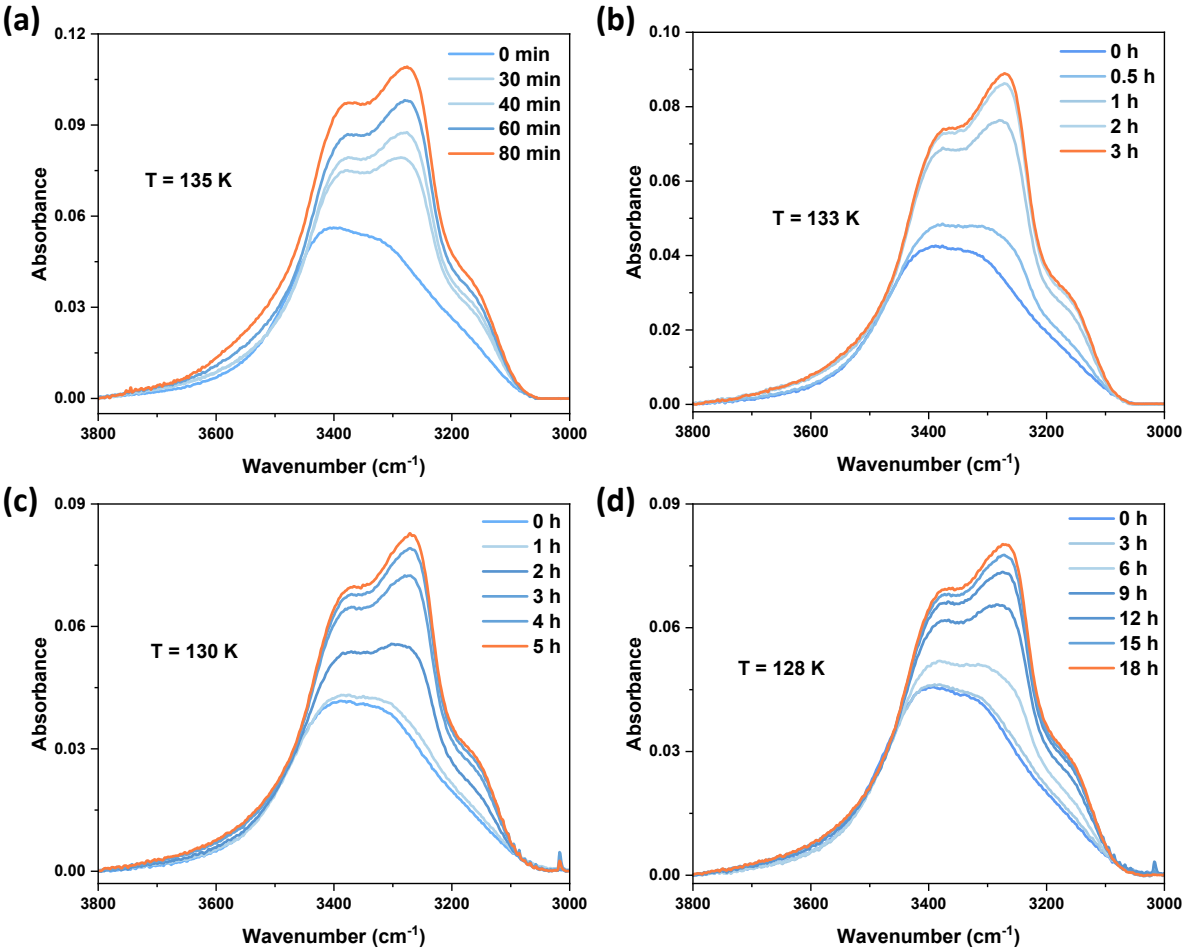


Figure S6. RAIR study of phase transition from amorphous solid water to hexagonal ice through clathrate hydrate dissociation. Isothermal time-dependent RAIR spectra of 300 ML of TMO-H_2O (1:30) in the O-H stretching region at (a) 135 K, (b) 133 K, (c) 130 K, and (d) 128 K. TMO and water vapor were co-deposited on Ru(0001) substrate at 10 K and annealed at a rate of 5 K min^{-1} to the set temperatures.

Supporting information 7:

Table S1. Comparison of the computational and experimental vibrational shifts of TMO CH compared to free TMO in the C-O-C stretching and ring puckering mode region.

		B3LYP/6-311++g(d,p)		**Experimental**	
System	IR stretching mode	IR stretch (cm^{-1})	Shift (cm^{-1})	IR stretch (cm^{-1})	Shift (cm^{-1})
TMO	ring puckering mode	1526	-	1026	-
	C-O-C stretching region	997	-	975	-
$TMO@5^{12}$	ring puckering mode	-	-	-	-
	C-O-C stretching region	-	-	-	-
$TMO@5^{12}6^{2}$	ring puckering mode	1538	+12	1035	+9
	C-O-C stretching region	1018	+21	989	+14
$TMO@5^{12}6^{4}$	ring puckering mode	1540	+14	1030	+4
	C-O-C stretching region	1007	+10	986	+11

Supporting information 8:

Table S2. Computationally calculated binding energy and dihedral angle of TMO CH. Binding energy is calculated as the change in the energy for TMO CH from (free TMO + empty cage). The four dihedral angles of TMO in the $5^{12}6^{2}$ and $5^{12}6^{4}$ cage are obtained and averaged.

System	Binding energy (eV)	Dihedral angle (degree)
TMO@$5^{12}6^{2}$	-2.18	9.2
TMO@$5^{12}6^{4}$	-2.07	1.3

Supporting information 9:

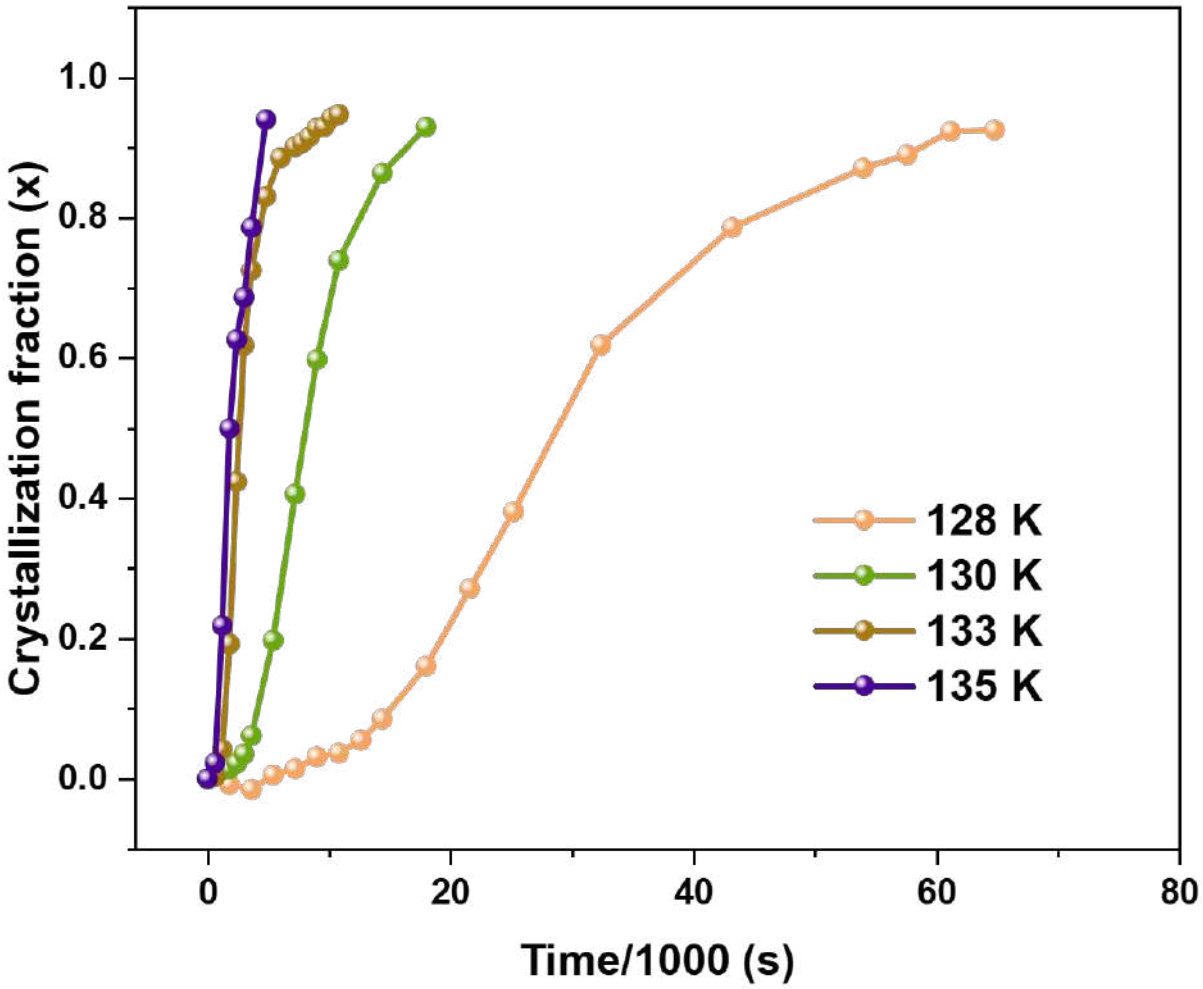


Figure S7. Crystallization fraction of 300 MLs of TMO-water ice mixture obtained from isothermal RAIRS measurements at 135, 133, 130, and 128 K. The crystallization fraction was estimated from the 3260 cm^{-1} peak in the O−H stretching region.

Supporting information 10:

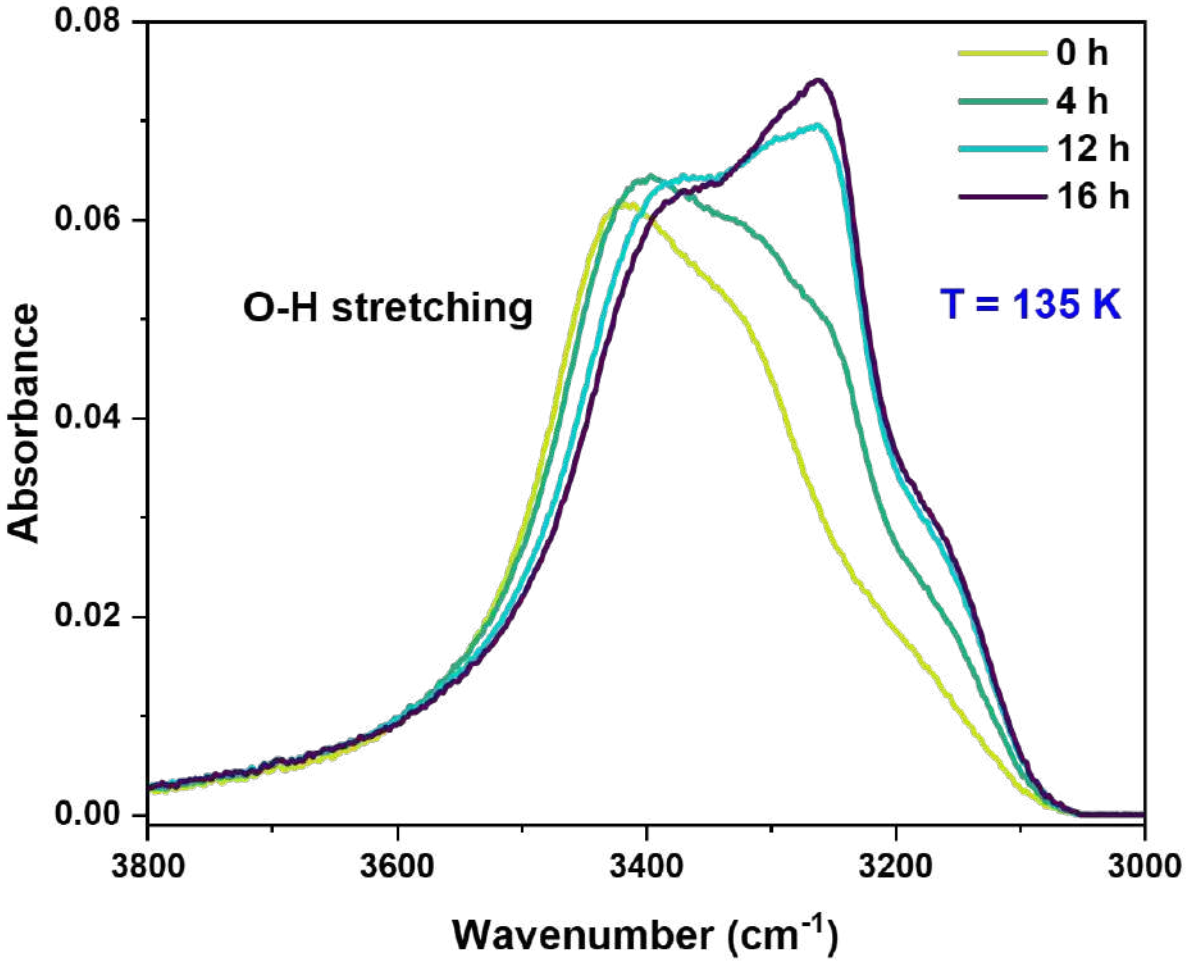


Figure S8. Time-dependent RAIR spectra of hexagonal crystalline ice obtained by thermally annealing pure water at 135 K for 16 h. Water ice exists in amorphous form for 4 h, and crystallizes in 12 h.

Published on 14 May 2025. Downloaded by Indian Institute of Technology Chennai on 12/29/2025 3:11:48 AM.

PCCP

ROYAL SOCIETY OF CHEMISTRY

PAPER

View Article Online
View Journal | View Issue

Check for updates

Cite this: *Phys. Chem. Chem. Phys.*, 2025, **27**, 11025

Ultraviolet photolysis of CO_2 clathrate hydrate and H_2O–CO_2 mixed ice under ultrahigh vacuum†

Gaurav Vishwakarma,[a] Bijesh K. Malla,[a] Soham Chowdhury,[a] Jyotirmoy Ghosh,[b] Rabin Rajan J. Methikkalam,[c] Rajnish Kumar *[de] and Thalappil Pradeep *[ae]

Received 16th February 2025,
Accepted 25th April 2025

DOI: 10.1039/d5cp00620a

rsc.li/pccp

Photolysis of mixed ices, such as H_2O–CO_2, is a key driver of chemical evolution in planetary, cometary, and interstellar environments. Despite their ubiquitous presence, the photolysis of H_2O–CO_2 ices remains underexplored experimentally, largely due to the significant attenuation of vacuum ultraviolet light caused by the intermixing of H_2O and CO_2, which restricts the formation of new species. Here, we demonstrate two previously unknown photolysis pathways for H_2O–CO_2 ices at 10 K under ultrahigh vacuum ($\sim 10^{-10}$ mbar), revealing differences between bulk and surface photochemistry. In bulk, first, we trapped CO_2 within clathrate hydrate (CH) cages to prevent intermixing with H_2O, then subjected it to photolysis and analyzed it *via* reflection absorption infrared spectroscopy. Our results demonstrate that photon-induced destruction of the clathrate cages prompts the free CO_2 to migrate into the ice matrix without producing any new photoproducts. In contrast, a mixed solid formed by the simultaneous deposition of residual H_2O on CO_2 ice produces a variety of photoproducts on the surface, which were detected using Cs^+-based secondary ion mass spectrometry. Photoproducts such as CO, H_2CO_3, and CH_3OH, along with elusive intermediates such as HCO, H_2CO, and HCO_3 were seen on the surface but were not observed in the bulk. These results present a better understanding of the synthesis and chemical evolution of H_2O–CO_2-rich astrophysical environments.

1. Introduction

Ice photochemistry, driven by ultraviolet (UV) irradiation of interstellar and cometary ice analogues, is crucial for understanding the synthesis of complex organic molecules in space.[1] Water (H_2O) and carbon dioxide (CO_2) ices are among the most prevalent in various astrophysical environments, including comets, molecular clouds, icy satellites, and protostellar regions.[2] Consequently, the photolysis of H_2O–CO_2 mixtures has been considerably studied under laboratory conditions, typically at $\sim$10–18 K and vacuum of the order of $\sim 10^{-8}$ mbar.[3–5] These studies, however, face significant challenges in identifying photoproducts due to the strong attenuation of vacuum ultraviolet (VUV) light in H_2O–CO_2 mixtures, which limits UV penetration and the extent of photochemical reactions.[6] For instance, using infrared spectroscopy, Gerakines *et al.*[3] reported the formation of carbonic acid (H_2CO_3), carbon monoxide (CO), and carbon trioxide (CO_3) through VUV (10.20 eV) photolysis of H_2O–CO_2 (1 : 1) mixed ices at 18 K. In contrast, Wu *et al.*[4] observed only H_2CO_3 and CO when using extreme ultraviolet (40.78 eV and 21.23 eV) photolysis on H_2O–CO_2 (4 : 1) mixed ices at 10 K. Extending these findings, Radhakrishnan *et al.*[5] demonstrated that pure CO_2 ice produces molecular and radical species such as CO, CO_3, and ozone (O_3), while their formation is significantly suppressed in an H_2O–CO_2 (1 : 1) mixture, likely due to the trapping of oxygen (O) atoms within the H_2O matrix. They also demonstrated that CO_3 and O_3 form exclusively in pure CO_2 ice, and this finding could be used to infer the coexistence of H_2O–CO_2 ice, with CO_3 indicating pure CO_2 domains and its absence suggesting H_2O–CO_2 mixing. However, the detection of intermediate species like HCO, H_2CO, and HCO_3 has been proven elusive in these studies. Another often overlooked study by Berger *et al.*[7] demonstrated that UV photolysis of CO_2 embedded in amorphous solid water (ASW) on Ru(001) (where CO_2 molecules were initially adsorbed onto the Ru(001) surface prior to water exposure), resulted in the formation of CO, atomic oxygen (O), and H_2CO, tentatively identified as formaldehyde.

[a] *DST Unit of Nanoscience (DST UNS) and Thematic Unit of Excellence (TUE), Department of Chemistry, Indian Institute of Technology Madras, Chennai 600036, India*
[b] *Department of Chemistry, Purdue University, West Lafayette, Indiana 47907, USA*
[c] *Department of Chemistry, Mar Ivanios College, Thiruvananthapuram, Kerala 695015, India*
[d] *Department of Chemical Engineering, Indian Institute of Technology Madras, Chennai 600036, India*
[e] *International Centre for Clean Water, IIT Madras Research Park, Chennai 600113, India*

† Electronic supplementary information (ESI) available: Full range RAIR spectra of photolysis of pure CO_2 and H_2O–CO (5 : 1) ice with and without O_2. See DOI: https://doi.org/10.1039/d5cp00620a

This journal is © the Owner Societies 2025

Published on 14 May 2025. Downloaded by Indian Institute of Technology Chennai on 12/29/2025 3:11:48 AM.

Previously, to avoid VUV attenuation in solid H_2O–CO_2 ices and identify photoproducts through IR analysis, simultaneous condensation and UV photolysis of the H_2O + CO_2 gas mixture was employed.[3,6] In this current study, we report two novel photolysis pathways. In the first pathway, we trapped CO_2 within clathrate hydrate (CH) cages (*via* previously known methods)[8–11] in the bulk of H_2O–CO_2 ice, which prevents CO_2 from mixing with H_2O. We then photolyzed the water ice containing CO_2 CHs. We studied the photolysis of CH of CO_2 also in view of our earlier studies (see below). In the second pathway, rather than co-depositing the H_2O and CO_2 gas mixture, we first created a CO_2 ice film, followed by simultaneous residual water deposition and photolysis. The resulting ices were analyzed using reflection absorption infrared spectroscopy (RAIRS) for bulk composition and Cs^+-based secondary ion mass spectrometry (SIMS) for surface composition.

CHs are inclusion compounds formed by water molecules encasing small guests such as CH_4, CO_2, N_2, and H_2 within H-bonded cages.[12,13] While experimental evidence for CHs in a high vacuum was noted since the 1980s,[8,14–18] our group had recently reported their existence under ultrahigh vacuum (UHV) and cryogenic conditions.[9] This study[9] had generated reactions[19] and they were answered.[20] Subsequently, several other molecules were reported to form CHs under UHV and cryogenic conditions.[11,21–26] The formation of CHs under UHV, observed through RAIRS was subsequently proved by reflection high energy electron diffraction (RHEED).[27] Notably, RHEED has been widely used to study ice nucleation and growth during water vapor deposition as well as the heating of ASW films on substrates like HOPG, Pt(111), Ru(0001), Ni(111), and Si(100)/(111).[22,28–33] However, no reports have yet explored the photolysis of CHs under these conditions. In this study, we report the photolysis of CO_2 CH for the first time. Some studies reported gamma-ray irradiation of CHs, formed under high pressures.[34–36] During irradiation, CHs enabled distinctive hydrogen transfer reactions with radicals. Also, clathrate cages were found to stabilize free radicals within the cages.[37]

Thus, the current study aims to advance our understanding of how H_2O–CO_2 thin ice film changes chemically under VUV light exposure, simulating astrophysical conditions. In the current study, we have carried out VUV photolysis experiments with H_2O–CO_2 model interstellar ice by slicing the thin film to two segments—bulk ice and surface layers—under UHV and cryogenic conditions (10 K and $\sim 10^{-10}$ mbar) using a custom-built UHV setup.[11,38,39] Our findings are expected to contribute to a better understanding of the chemical evolution within H_2O–CO_2-rich astrophysical environments.

2. Experimental

2.1. Experimental setup

Photolysis of H_2O–CO_2 model interstellar ice has been performed under ultrahigh vacuum (UHV) using a custom-built apparatus described elsewhere.[9,11,38] The apparatus mainly comprises a stainless steel UHV chamber with a base pressure of $\sim 5 \times 10^{-10}$ mbar, a gas inlet system, and a metal substrate connected to a closed-cycle He cryostat for sample preparation. The UHV chamber is equipped with several tools such as reflection absorption infrared spectroscopy (RAIRS), temperature-programmed desorption (TPD) mass spectrometry, Cs^+-based secondary ion mass spectrometry (SIMS), low energy ion scattering (LEIS) mass spectrometry, and a vacuum ultraviolet (VUV) lamp.[11] Several turbomolecular pumps backed by oil-free diaphragm pumps were used to maintain the vacuum inside the chamber. The gas inlet system is equipped with two high-precision all-metal leak valves to control the vapor deposition. Whereas the metal substrate is a highly polished single-crystal Ru(0001). The substrate is mounted at the cold end of the He cryostat and fitted with a precision x–y–z–θ sample manipulator. The substrate temperature was monitored and controlled by a temperature controller, Lakeshore, Model 336, and adjusted by using a resistive heater (25 Ω) in the range of 8–1000 K. A K-type thermocouple and a platinum sensor were used to measure the temperature with an accuracy/uncertainty of 0.5 K.

2.2. Materials and reagents

We have used Millipore water (H_2O of 18.2 M Ω resistivity) and CO_2 gas (99.99%) for all the experiments. Millipore water was taken in a vacuum-sealed test tube and further purified *via* several freeze–pump–thaw cycles. Moreover, CO_2 gas was purchased from Indogas and used without further purification.

2.3. Sample preparation

Prior to each sample preparation, the Ru(0001) substrate was heated to 400 K multiple times to ensure that the surface was sufficiently clean. Thin ice films were created on the pre-cooled Ru(0001) substrate by vapor deposition. For this, two gas inlets, one for H_2O and the other for CO_2 exclusively, were used to introduce the vapors to backfill the chamber. The purity of H_2O and CO_2 gas was confirmed during vapor deposition using a residual gas analyzer quadrupole mass spectrometer. The deposition coverage or the thickness of ice samples was expressed in monolayers (ML) with an assumption of 1.33×10^{-6} mbar s = 1 ML, which was estimated to contain $\sim 1.1 \times 10^{15}$ molecules cm^{-2}, as implemented in previous studies.[9,11,40,41] All coverages were >50 ML, and therefore, no substrate effect is expected.

2.4. Experimental protocol

2.4.1. Bulk photochemistry. In the first photolysis pathway, CO_2 was trapped within clathrate hydrate (CH) cages to avoid mixing with H_2O. To form CH of CO_2, the H_2O–CO_2 thin film was prepared by co-depositing H_2O and CO_2 vapors on Ru(0001) at 10 K in a 5 : 1 ratio, as adopted in our previous study.[9] ~100 ML of H_2O–CO_2 (5 : 1) ice was created at a total pressure of $\sim 5 \times 10^{-7}$ mbar for 3 minutes 20 seconds where the inlet pressure of H_2O vapor was $\sim 4 \times 10^{-7}$ mbar and that of CO_2 gas was $\sim 1 \times 10^{-7}$ mbar.

To comprehend the bulk photochemistry of H_2O–CO_2 thin film, two sets of experiments were carried out. In the first (control) set, the as-deposited ~50 ML of pure CO_2 and ~100 ML H_2O–CO_2 (5 : 1) thin films at 10 K were exposed to VUV for 4 h, and

This journal is © the Owner Societies 2025

Published on 14 May 2025. Downloaded by Indian Institute of Technology Chennai on 12/29/2025 3:11:48 AM.

RAIR spectra were collected at regular intervals. In the second set, to form CO_2 CH, the as-prepared ~100 ML H_2O–CO_2 (5 : 1) thin film and ~30 ML O_2@100 ML H_2O–CO_2 (5 : 1) composite ice at 10 K were annealed to 120 K to create CO_2 CH and to get rid of free CO_2 from the ice matrix, as adopted previously.[8,9] It should be noted that heating the H_2O–CO_2 ice sample above the desorption temperature (90 K) of pure CO_2 ice to ~120 K will result in CH formation and desorption of free CO_2.[9–11,42] After preparing CO_2 CH at 120 K, the samples were cooled back to 10 K and exposed to VUV for 2 h, followed by RAIR spectral collection at regular intervals. Further, the photolyzed samples (at 10 K) were heated to 120 K. The ~30 ML O_2@100 ML H_2O–CO_2 (5 : 1) composite ice was prepared by first depositing ~30 ML of pure O_2 on the clean Ru(0001) substrate, followed by a co-deposition of ~100 ML of H_2O–CO_2 thin film in a 5 : 1 ratio over it.

2.4.2. Surface photochemistry. For the second photolysis pathway, we first created a CO_2 ice film, followed by simultaneous residual water deposition and photolysis. Control SIMS experiments were performed on the surface of (i) ~50 ML pure H_2O, (ii) ~50 ML pure CO_2, and (iii) ~50 ML H_2O–CO_2 ice at 10 K before VUV exposure. For ~50 ML H_2O–CO_2 ice, we first prepared ~50 ML pure CO_2 ice on clean substrate and then waited for the adsorption of residual water vapor from the UHV chamber at 10 K. This was done for the fact that in the co-deposition experiments, due to excess H_2O (accumulating on the ice surface through background deposition), detection of other extremely low-abundant species by Cs^+ was challenging. After sample preparation at 10 K, SIMS spectra were collected by colliding Cs^+ at a particular kinetic energy (details are given in the SIMS setup section). For time-dependent experiments, the first SIMS spectrum collected after the deposition of the sample was noted as a time zero spectrum. Then, after 15, 30, and 60 min, spectra were collected subsequently. For temperature-dependent experiments, samples were heated to the set temperatures, 10, 20, 30, 40, and 50 K, at a rate of 5 K min^{-1}, and SIMS spectra were collected at the corresponding temperatures. To minimize the time-dependent effects on the ice sample, the experiment was completed within 20 min. For photolysis and identification of photoproducts on the surface of the H_2O–CO_2 system, H_2O condensation (on CO_2 film) and photolysis were carried out simultaneously for 4 h at 10 K. After photolysis, the resulting ice collided with 80 eV Cs^+ to detect the photoproducts at 10 K.

2.5. VUV lamp

To carry out the photolysis of molecular ices, we have added a VUV lamp to our existing UHV chamber.[11] The UV light source was a deuterium lamp (McPherson, Model 634, with MgF_2 window, 30 W) of VUV range, 115–400 nm. The VUV lamp was attached to the UHV chamber through the MgF_2 window (with a cut-off at ~114 nm (10.87 eV)) and differentially pumped with a turbomolecular pump. The UV lamp flux was determined by applying the widely used ozone method ($O_2 \rightarrow O_3$ conversion).[43,44] The average photon flux reaching the ice sample was estimated to be $\sim 6 \times 10^{12}$ photons cm^{-2} s^{-1}.

2.6. RAIRS setup

RAIR setup was attached to our UHV chamber externally through an IR transparent ZnSe viewport. The setup comprised of a Bruker Vertex 70 FT-IR spectrometer and a liquid nitrogen-cooled mercury cadmium telluride (MCT) detector. RAIR spectra were collected in the 4000–550 cm^{-1} range with a spectral resolution of 2 cm^{-1}. For a better signal-to-noise ratio, each RAIR spectrum was averaged over 512 scans which took 7 min for acquisition. During experiments, the IR beam was focused on the ice sample at an incident angle of $80^\circ \pm 7^\circ$ through ZnSe viewport. The reflected beam from the ice sample was recorded with the MCT detector. The IR beam outside the vacuum chamber was purged with dry nitrogen to avoid absorption from atmospheric gases.

2.7. SIMS setup

Cs^+ with a mass-to-charge ratio (m/z) of 133 is a widely recognized choice as the primary ions in SIMS studies. This technique is highly sensitive only to the topmost layer of the sample. Through a low-energy collision, Cs^+ transforms neutral adsorbate species (X) into gas-phase ions (CsX^+) *via* an association reaction, a phenomenon commonly referred to as reactive ion scattering (RIS). We have conducted ion collision experiments on the H_2O/CO_2/H_2O–CO_2 ice using Cs^+ of 60/80 eV kinetic energy produced from a low-energy alkali ion gun (Kimball Physics Inc.). The resulting scattered ions from the ice sample were analyzed using a quadrupole mass analyzer. We have used the RIS signal intensities corresponding to the complex of Cs^+ with H_2O {such as, m/z = 151, $Cs(H_2O)^+$, m/z = 169, $Cs(H_2O)_2^+$, m/z = 187, $Cs(H_2O)_3^+$, *etc.*}, with CO_2 {such as, m/z = 177, $Cs(CO_2)^+$, m/z = 221, $Cs(CO_2)_2^+$, *etc.*}, and with H_2O–CO_2 complexes {such as, m/z = 195, $Cs((H_2O–CO_2)^+)$, m/z = 213, $Cs((H_2O)_2–CO_2)^+$, m/z = 239, $Cs(H_2O–(CO_2)_2)^+$, *etc.*} to identify the species present on the topmost surface of ice sample. Here, the signal intensities are directly proportional to the surface population of the molecule (or complex) on the ice surface.

3. Results and discussion

The photochemistry of H_2O–CO_2 ices in bulk was investigated *via* RAIRS. To begin with, we photolyzed ~50 ML of pure CO_2 and ~100 ML of a 5 : 1 mixture of H_2O–CO_2 ices at 10 K for 4 h and collected RAIR spectra at regular intervals, as shown in Fig. 1a and b. After 4 h of VUV exposure, pure CO_2 ice was depleted by ~19.5%, forming CO, CO_3, and O_3 (Fig. 1a and Fig. S1, ESI†).[5] In contrast, no photodissociation products were detected in the 5 : 1 H_2O–CO_2 mixed ice (Fig. 1b and Fig. S2, ESI†). Nonetheless, VUV photons did penetrate the ice matrix, albeit with attenuation, as evidenced by changes in the O–H stretching region (Fig. S3a, ESI†). Fig. 1b presents the RAIR spectra of the H_2O–CO_2 (5 : 1) mixed ice in the C═O antisymmetric stretching region of CO_2. Prior to VUV exposure, two peaks at 2346 and 2353 cm^{-1} and two shoulders at 2340 and 2360 cm^{-1} are evident (see deconvoluted peaks in Fig. 1c). After 4 h of VUV exposure (Fig. 1b), no significant depletion was observed in the 2340, 2346, or 2353 cm^{-1} peaks, while the

Published on 14 May 2025. Downloaded by Indian Institute of Technology Chennai on 12/29/2025 3:11:48 AM.

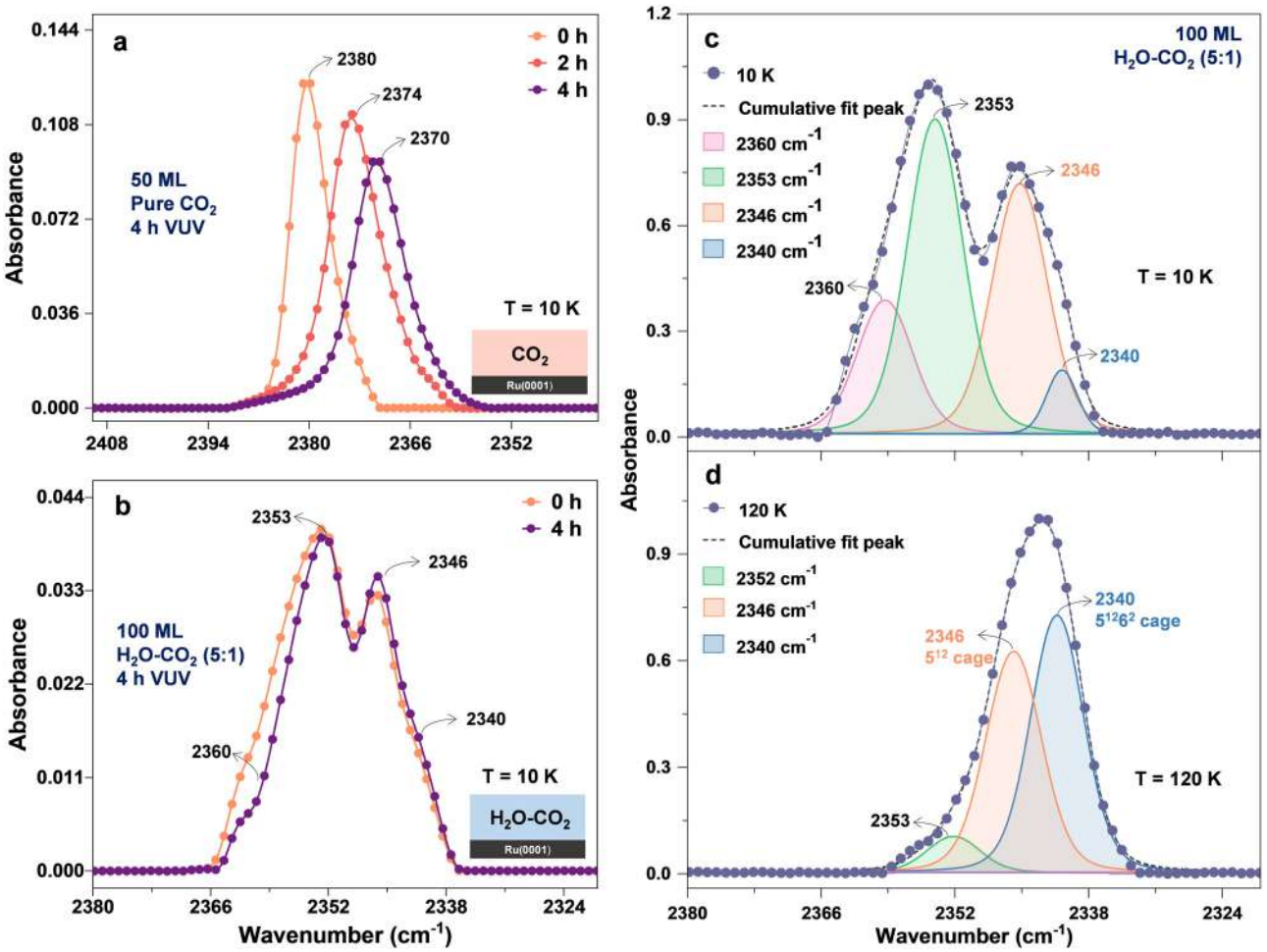


Fig. 1 (a) RAIR spectra of ~50 ML pure CO_2 ice before and after 4 h of VUV photolysis in the C=O antisymmetric stretching region at 10 K. The shift and reduction in the peak intensity of 2380 cm^{-1} is attributed to the decrease in the fraction of pure CO_2 ice, as observed previously.[11,45] (b) RAIR spectra of ~100 ML H_2O–CO_2 (5 : 1) ice before and after 4 h of VUV photolysis in the C=O antisymmetric stretching region of CO_2. No photon-induced products were detected by RAIRS, see Fig. S2. A slight depletion in the 2360 cm^{-1} shoulder may be attributed to the photodesorption of CO_2 molecules with prolonged exposure to VUV. At the right bottom of (a) and (b), the insets show the composition of the initial ice used for the study. Normalized RAIR spectra of ~100 ML H_2O–CO_2 (5 : 1) ice in the C=O antisymmetric stretching region at (c) 10 K and (d) 120 K before VUV photolysis. The ice sample was heated from 10 K to 120 K at a rate of 5 K min^{-1}.

2360 cm^{-1} shoulder showed slight depletion, suggesting photodesorption of adsorbed CO_2. The absence of photodissociation products in the H_2O–CO_2 (5 : 1) mixed ice (Fig. S2, ESI†), in contrast to pure CO_2 ice (Fig. S1, ESI†), is likely due to limited UV transmission in the bulk ice matrix, as previously reported in the literature.[3,4,6]

At 10 K, the absorption band at 2353 cm^{-1} and its accompanying shoulder at 2360 cm^{-1} are attributed to CO_2 present as either bulk ice or isolated molecules in the pores of amorphous solid water (ASW).[9,13] In contrast, the peak at 2346 cm^{-1} and the shoulder at 2340 cm^{-1} are tentatively assigned to CO_2 molecules interacting with H_2O *via* weak van der Waals forces.[9,10,46] Notably, the 2346 cm^{-1} peak has also been associated with CO_2 trapped within the 5^{12} cages of sI CH in previous studies.[8–11,14] To minimize molecular intermixing and enhance VUV penetration, it is essential to remove free CO_2 (present in ASW pores, 2353 and 2360 cm^{-1}) and encapsulate the remaining CO_2 within CH cages. This was achieved by heating the H_2O–CO_2 (5 : 1) ice sample to 120 K (Fig. 1d), beyond the desorption temperature of pure CO_2. This approach aligns with established literature methods.[10,11,14,16] The corresponding changes in water (O–H stretching band) are shown in Fig. S4 (ESI†). Upon heating to 120 K, the 2353 and 2360 cm^{-1} peaks disappeared (Fig. 1d), confirming their assignment to bulk CO_2 or CO_2 in ASW pores, while the 2346 and 2340 cm^{-1} peaks varied in intensity, correlating with changes in the O–H stretching region (shown in Fig. S4, ESI†). The 2346 and 2340 cm^{-1} features have previously been assigned to CO_2 enclosed in the 5^{12} and $5^{12}6^2$ cages of sI CH above 90 K, provided that concurrent changes occur in the O–H stretching region.[10,14,16] It should be noted that above the desorption temperature of CO_2, CO_2 does not exists in an amorphous or crystalline phase within ASW; rather, it may exist as trapped gas or be confined within CH cages. Thus, heating the ice sample to 120 K will result in the desorption of CO_2 present in ASW pores and the persistence of CO_2 trapped in CH cages. After isolating

This journal is © the Owner Societies 2025

Published on 14 May 2025. Downloaded by Indian Institute of Technology Chennai on 12/29/2025 3:11:48 AM.

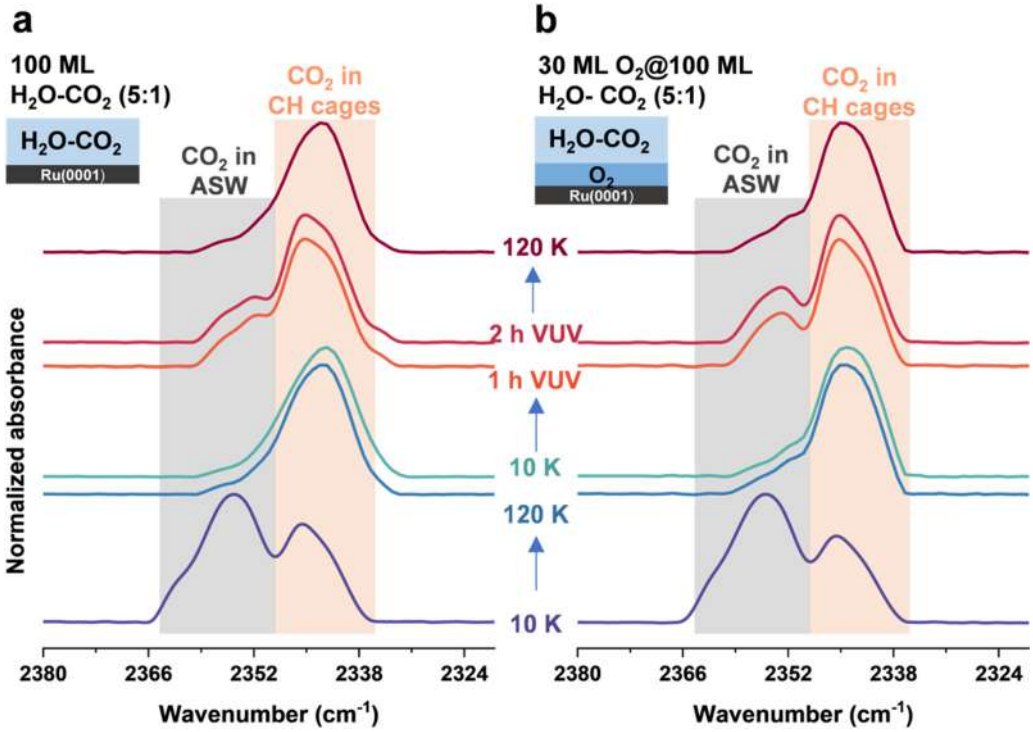


Fig. 2 Normalized RAIRS spectra for ~100 ML H_2O–CO_2 (5 : 1) ice before and after VUV photolysis (a) without O_2 and (b) with 30 ML O_2 film in the C=O antisymmetric stretching region of CO_2. In both systems, the ice samples were prepared at 10 K and then heated to 120 K. Further, the samples were cooled to 10 K and irradiated with VUV for 2 h. Finally, the photolyzed sample was further heated to 120 K. At the top corner of (a) and (b), the insets show the composition of the initial ice used for the study. For simplicity, CO_2 is categorized into two phases: CO_2 in ASW (light grey shade) and CO_2 in CH cages (light orange shade). This is because VUV radiation photodissociates the H_2O molecules in 5^{12} and $5^{12}6^2$ cages without preference.

CO_2 in CH cages at 120 K, the ice sample was cooled to 10 K for photolysis.

Trapping of CO_2 inside cages can effectively prevent the mixing of CO_2 with bulk water ice, which may allow the transmission of photons in the bulk. After creating CO_2 CH in the water matrix at 120 K and cooling it back to 10 K, the ice sample was photolyzed by VUV exposure for a duration of 2 h, as presented in Fig. 2a. For simplicity, we have categorized the CO_2 into two phases: CO_2 in ASW and CO_2 in CHs, as indicated by light grey and orange shades, respectively (a detailed deconvoluted spectra are presented in Fig. 1c and d). This is because, VUV photodissociates the H_2O molecules of 5^{12} and $5^{12}6^2$ cages without preference. A full range (4000–1000 cm^{-1}) RAIR spectrum of the photolyzed sample is shown in Fig. S5a (ESI†), revealing no new photoproducts. However, Fig. 2a shows the reappearance of the 2353 cm^{-1} peak following 1 h of VUV exposure, indicating potential CO_2 migration from clathrate cages to the ice matrix. This phenomenon likely stems from the photon-induced decomposition of the CH structures. Further confirmation of this was sought by examining the O–H stretching band of the same system presented in Fig. S3b and S5a (ESI†). The RAIR traces in Fig. S3b (ESI†) display a notable change in the O–H stretching band. The decrease in the intensity of the O–H stretching band after VUV exposure indicates the decomposition of CH structures and the rearrangement/disordering of ordered H_2O molecules. Notably, upon annealing to 120 K, the H_2O matrix undergoes a process of ordering its molecules.[40,41,47] Furthermore, exposure to UV radiation has been reported to induce disordering (amorphization) in the ordered/crystalline water structures.[29] Thus, the IR study of the VUV photolysis of CO_2 CH at 10 K suggests the decomposition of clathrate cages and subsequent migration of CO_2 to the water matrix without yielding new photoproducts in the bulk of the ice matrix.[11,48] Obviously, VUV does penetrate the clathrate matrix, although with attenuation.

In the current study, we propose that annealing the H_2O–CO_2 (5 : 1) mixed ice to 120 K made the ice sample transparent to VUV transmission. This may primarily be due to the desorption of free CO_2 from the water matrix and confinement of the remaining CO_2 within clathrate cages. This allowed us to study the photolysis of CH of CO_2 for the first time. Fig. 2a reveals that following 1 h of VUV irradiation, even a minute amount of free CO_2 within the water matrix made the system opaque to VUV transmission, limiting further decomposition of CO_2 CH. This can be comprehended by comparing the RAIRS traces of VUV exposed samples of 1 and 2 h in Fig. 2a. This indicates that increased CO_2 migration from clathrate cages to the water matrix or, in other words, an increased fraction of free CO_2 in the water matrix would make the system opaque to VUV, inhibiting further CH decomposition. Finally, the resulting ice after 2 h of VUV irradiation was heated to 120 K (top trace in Fig. 2a) to validate the assignment of the 2353 cm^{-1} peak to free CO_2 within the water matrix and that at 2346 and 2340 cm^{-1} to CO_2 within the CH cages. The vanishing of the 2353 cm^{-1} peak

Published on 14 May 2025. Downloaded by Indian Institute of Technology Chennai on 12/29/2025 3:11:48 AM.

and the persistence of the 2346 and 2340 cm^{-1} peaks served as a confirmation for our assignments.[9,11]

To induce photochemistry or investigate the impact of a third molecule on the decomposition of CO_2 CH during VUV exposure, we incorporated O_2 in the H_2O–CO_2 (5 : 1) mixed ice. In the solid state, O_2 is known to readily dissociate by UV ($\lambda <$ 240 nm) to produce highly reactive atomic O.[49] We created a composite ice film of ~30 ML O_2@100 ML H_2O–CO_2 (5 : 1) at 10 K (see the Experimental section for details of sample preparation). The composite ice underwent treatment using a method similar to that used for Fig. 2a, and the outcomes are displayed in Fig. 2b (a full range RAIR spectra are presented in Fig. S5b, ESI†). The findings illustrated in Fig. 2b suggest that in the presence of O_2, a slightly larger fraction of CO_2 migrated from the clathrate cages, while the overall outcome closely resembles the pattern seen in Fig. 2a. Thus, the presence of foreign molecules can impact the photolysis of CO_2 CH. Faster decomposition of CO_2 CH in the presence of O_2 and CH_3OH is also observed at ambient conditions.[12]

Next, we examined the surface photochemistry of the H_2O–CO_2 ice under VUV exposure. To do this, we employed Cs^+-based SIMS due to its exceptional sensitivity for the first few monolayers of the ice surface. The higher sensitivity of the technique allows species of low abundance on the ice surfaces to be detected.[40,50,51] In the current study, SIMS was used in reactive ion scattering (RIS) mode.[40,51,52] To detect photoproducts on the ice surface by SIMS, we have prepared the samples by the 'condensation and simultaneous photolysis' method. Before performing the photolysis experiment, we analyzed the surface of pure H_2O, pure CO_2, and H_2O–CO_2 ices at 10 K by SIMS, as presented in Fig. 3a, b, and c, respectively. Fig. 3a shows a series of mass peaks for the pickup of n H_2O (m/z = 18) by Cs^+ (m/z = 133), such as, $Cs(H_2O)_n^+$ at m/z = 151 (n = 1), 169 (n = 2), 187 (n = 3), *etc.* Similarly, Fig. 3b shows the pickup of n CO_2, such as, $Cs(CO_2)_n^+$ at m/z = 177 (n = 1), 221 (n = 2), *etc.*, and Fig. 3c shows the pickup of n H_2O, m CO_2 and H_2O–CO_2 complexes from H_2O–CO_2 surface. Notably, three H_2O–CO_2 complexes were detected at m/z = 195, $Cs(H_2O–CO_2)^+$, 213, $Cs((H_2O)_2–CO_2)^+$, and 239, $Cs(H_2O–(CO_2)_2)^+$ at 10 K. Kim *et al.*, in a similar study by SIMS, reported that CO_2 adsorption on a H_2O ice film does not form H_2O–CO_2 complexes at 80 K.[53] However, in the present study, when residual H_2O vapor was allowed to adsorb on CO_2 ice film at 10 K, three H_2O–CO_2 complexes were detected by SIMS. For this, we first prepared ~50 ML CO_2 ice at 10 K and waited for the adsorption of residual water vapor from the UHV chamber. Such weakly bound complexes of CO_2 and H_2O are important in atmospheric systems, planetary bodies, and in the context of cometary and interstellar ices. Consequently, they have attracted considerable theoretical and experimental interest.[54–57] We have further examined the H_2O–CO_2 system by SIMS to monitor the residual deposition of H_2O vapor and the stability of H_2O–CO_2 complexes. Two sets of experiments were performed. The first experiment was a time-dependent SIMS at 10 K for 60 min, as presented in Fig. 4a. We observed that, with time, the fraction of H_2O on the CO_2 ice film was increasing. This can be realized by observing the intensity of m/z 169, 187, and 205. Simultaneously, with time, the fraction of CO_2 at the surface

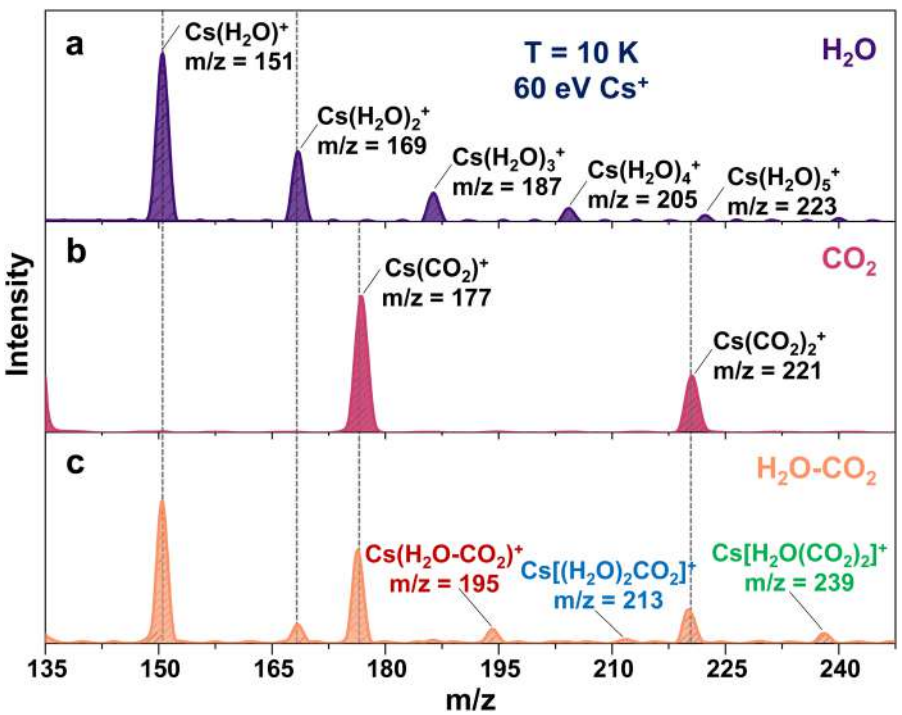


Fig. 3 RIS mass spectra taken from the surface of (a) ~50 ML pure H_2O, (b) ~50 ML pure CO_2, and (c) ~50 ML H_2O–CO_2 ice in the mass range of 135–245 amu. The mass spectrum was obtained by colliding the sample with 60 eV Cs^+ ions at 10 K. The ~50 ML H_2O–CO_2 ice was prepared by creating ~50 ML pure CO_2 ice on clean Ru(0001) and letting the residual water vapor from the UHV chamber adsorb on it over time.

This journal is © the Owner Societies 2025

Published on 14 May 2025. Downloaded by Indian Institute of Technology Chennai on 12/29/2025 3:11:48 AM.

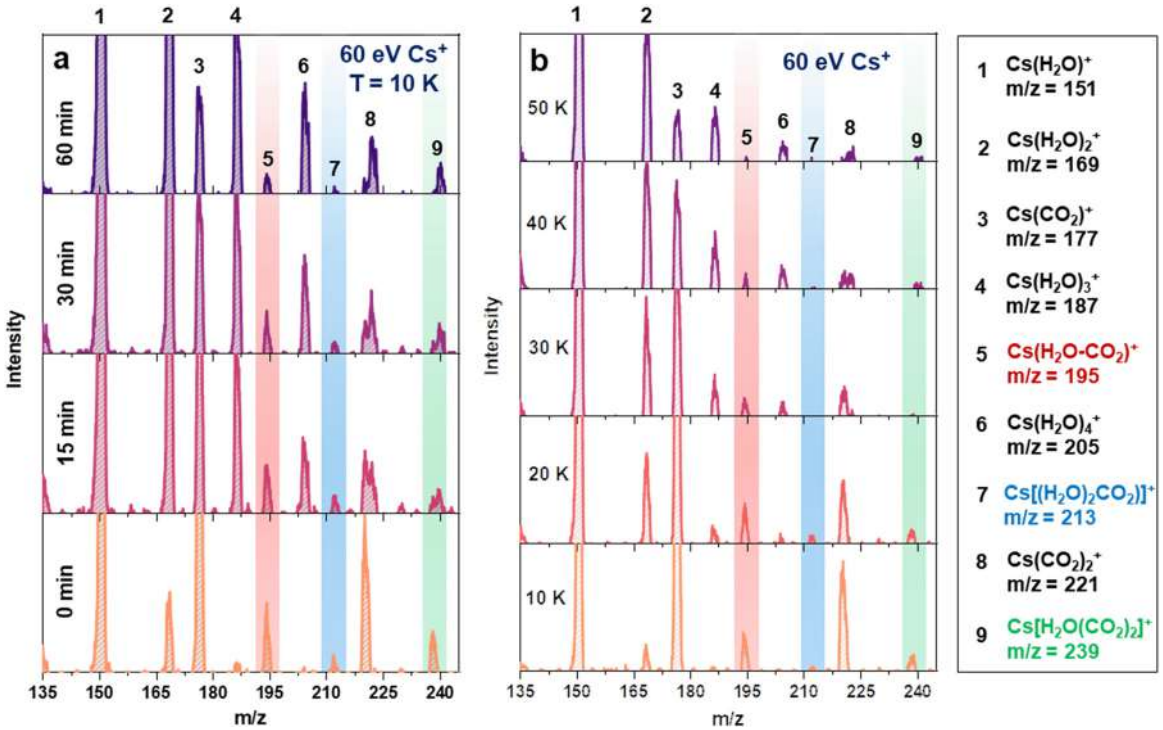
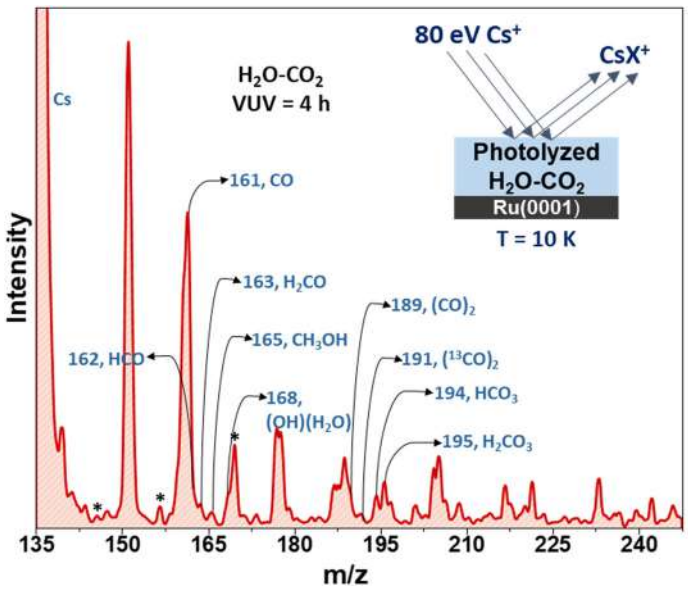


Fig. 4 RIS mass spectra for ~50 ML $H_2O–CO_2$ ice. (a) Time-dependent mass spectra were taken for $H_2O–CO_2$ ice at 10 K for 60 min. After sample preparation, the first spectrum collected was noted as the time zero spectrum. (b) Temperature-dependent mass spectra were taken at 10–50 K. The mass spectrum in the range of 135–245 amu was obtained by colliding the sample with 60 eV Cs^+ ions. The table on the right shows the assignment of mass peaks. In (a) and (b), peaks of $H_2O–CO_2$ complexes were highlighted by red, blue, and green shades.

decreases (see the peaks at *m*/*z* 177 and 221) so, as do the fractions of $H_2O–CO_2$ complexes (*m*/*z* 195, 213, and 239). In the second set, temperature-dependent SIMS experiments were carried out in the range of 10–50 K, and the results are presented in Fig. 4b. This experiment was done to examine the stability of $H_2O–CO_2$ complexes. At 50 K, all three mass peaks corresponding to the $H_2O–CO_2$ complexes disappeared, aligning with the finding of Kim *et al.* of no $H_2O–CO_2$ complexes at 80 K.[53]



Reactants	Photoproducts
151 = $Cs(H_2O)^+$	*157 = $Cs(C_2)^+$
153 = $Cs(H_2{}^{18}O)^+$	161 = $Cs(CO)^+$
169 = $Cs(H_2O)_2^+$	162 = $Cs(HCO)^+$
171 = $Cs(H_2O)(H_2{}^{18}O)^+$	163 = $Cs(H_2CO)^+$
173 = $Cs(H_2{}^{18}O)(H_2{}^{18}O)^+$	165 = $Cs(CH_3OH)^+$
187 = $Cs(H_2O)_3^+$	168 = $Cs(OH)(H_2O)^+$
205 = $Cs(H_2O)_4^+$	189 = $Cs(CO)_2^+$
223 = $Cs(H_2O)_5^+$	191 = $Cs(^{13}CO)_2^+$
177 = $Cs(CO_2)^+$	194 = $Cs(HCO_3)^+$
178 = $Cs(^{13}CO_2)^+$	195 = $Cs(H_2CO_3)^+$
221 = $Cs(CO_2)_2^+$	217 = $Cs(CO)_3^+$

Fig. 5 RIS mass spectra for the photolyzed $H_2O–CO_2$ ice taken at 10 K in the mass range of 135–245 amu. The mass spectrum was obtained by colliding the sample with 80 eV Cs^+ ions at 10 K. Inset figure presents the ice sample and RIS process schematically. The table on the right shows the assignments of mass peaks for both reactants and photoproducts.

Published on 14 May 2025. Downloaded by Indian Institute of Technology Chennai on 12/29/2025 3:11:48 AM.

For the photolysis experiment, we created a ~50 ML CO_2 ice film on Ru(0001) at 10 K. Then, after waiting for 5 minutes, we switched on the VUV lamp, assuming continuous condensation of residual H_2O vapor onto the CO_2 film, as can be inferred from Fig. 4a. In other words, H_2O condensation (on CO_2 film) and photolysis were carried out simultaneously for 4 h. Importantly, our study does not involve a pre-deposited CO_2@ASW mixed film. After photolysis, RAIR detected only CO, CO_3, and O_3 in the bulk ice sample. However, when the resulting ice collided by 80 eV Cs^+, several photoproducts were detected on the sample surface. Fig. 5 presents the mass spectrum of picked-up photoproducts and a table containing the list of detected reactants and photoproducts. Fig. 5 confirms the detection of CO, HCO, H_2CO, CH_3OH, HCO_3, and H_2CO_3 by SIMS, which were previously unidentified using RAIRS. The hydrogen (H) in the detected photoproducts on the H_2O–CO_2 surface comes from the breakdown of residual H_2O through photolysis in both the gas phase and on the CO_2 ice surface. Photolysis of H_2O is known to produce primary and secondary photoproducts such as $H_2O + h\nu \rightarrow$ H, OH, H_2, O, HO_2, HO_3, H_2O_2, O_2, O_3.[58] A few small peaks at (marked by *) m/z 145, 157, and 169, are tentatively assigned to C_1, C_2, and C_3 carbons. However, additional isotope labelling experiments are required to validate this. The earlier H_2O–CO_2 photolysis studies have only reported the identification of CO, CO_3, O_3, and H_2CO_3 by IR analysis.[3,4] They could not positively identify the HCO, H_2CO, HCO_3, and CH_3OH in their study. Thus, this study shows the formation of not only CO, CO_3, O_3, H_2CO_3, and CH_3OH but also the intermediates, HCO, H_2CO, and HCO_3, which have not been detected earlier.

The contrasting photochemistry of H_2O–CO_2 ice was not only observed due to the different experimental approaches but also because of the experimental tool used to detect the photoproducts. When CO_2 was mixed with H_2O ice in bulk, it does not photodissociate likely due to limited VUV photon penetration. However, when CO_2 was confined within clathrate cages in a water matrix, allowing VUV penetration, it underwent decomposition upon photon exposure. This led to the diffusion of CO_2 from CH cages to the water matrix, possibly triggered by VUV photons causing the photodissociation of H_2O molecules within the CH structure (5^{12} and $5^{12}6^2$ cages). However, RAIRS did not observe any photoproducts or chemical changes. In contrast, simultaneous deposition of residual H_2O on CO_2 ice and VUV exposure resulted in the photodissociation of both CO_2 (C, O, CO) and H_2O (H, O, OH) at the ice–vacuum interface, inducing chemical changes with several detectable photoproducts by mass spectrometry.

Our study provides critical insights into the photochemistry of H_2O–CO_2 ices across a broad range of astrophysical and planetary environments, from interstellar ice mantles to cometary nuclei and planetary surfaces. By distinguishing the photochemical behavior of bulk and surface ice, we demonstrate that CO_2 CH act as molecular reservoirs, regulating the release and reactivity of volatiles, whereas surface photolysis leads to the formation of key photoproducts, including CO, H_2CO_3, CH_3OH, and intermediates such as HCO, H_2CO, and HCO_3. These findings have direct implications for planetary processes, including the seasonal evolution of CO_2–H_2O ice deposits on Mars and radiolytic ice chemistry on Europa and Ganymede. Furthermore, our results contribute to a growing understanding of how UV-driven processes in H_2O–CO_2-rich environments facilitate the synthesis of complex organics, which may be relevant to prebiotic chemistry and the organic inventory of planetary atmospheres. This study advances the discussion on the role of CHs in trapping and releasing volatile species, influencing atmospheric compositions and surface chemistry on planetary bodies. By bridging laboratory astrochemistry and planetary science, our work refines perspectives on the molecular evolution of ices in extraterrestrial settings and their potential contributions to the chemical complexity of habitable environments.

4. Conclusions

This study provides experimental insights into the photolysis pathways of H_2O–CO_2 ices under UHV and cryogenic conditions, revealing a distinction between bulk and surface photochemistry. In the bulk, CO_2 molecules trapped within CH cages remain photochemically inert, as photon-induced decomposition of the hydrate structure results solely in CO_2 migration into the surrounding ice matrix without forming new photoproducts. In contrast, photolysis at the surface of the H_2O–CO_2 mixed film leads to the formation of various reaction products, including CO, CH_3OH, H_2CO_3, and crucial intermediates such as HCO, H_2CO, and HCO_3, which were identified using Cs^+-based SIMS. These findings highlight the critical role of ice morphology and molecular confinement in governing photochemical reactivity and provide valuable implications for understanding the synthesis and evolution of H_2O–CO_2-rich astrophysical environments.

Author contributions

T. P. and G. V. designed the research. G. V. and B. K. M. have performed the experiments. T. P. supervised its progress. G. V., B. K. M., S. C., J. G., R. R. J. M., R. K. and T. P. analyzed the results. The first draft of the manuscript was written by G. V. The final version of manuscript was prepared including the contributions of all authors.

Data availability

The data supporting this article have been included as part of the ESI.†

Conflicts of interest

The authors declare no competing financial interests.

This journal is © the Owner Societies 2025

Published on 14 May 2025. Downloaded by Indian Institute of Technology Chennai on 12/29/2025 3:11:48 AM.

Acknowledgements

We acknowledge the Science and Engineering Research Board (SERB), Department of Science and Technology (DST), Government of India for research funding. T. P. and R. K. acknowledge funding from the Centre of Excellence on Molecular Materials and Functions under the Institution of Eminence scheme of IIT Madras. G. V. and S. C. thank IITM for their research fellowships. B. K. M. thanks the Council of Scientific & Industrial Research (CSIR) for his research fellowship.

Notes and references

1 K. I. Öberg, Photochemistry and Astrochemistry: Photochemical Pathways to Interstellar Complex Organic Molecules, *Chem. Rev. Am. Chem. Soc.*, 2016, 9631–9663, DOI: **10.1021/acs.chemrev.5b00694**.

2 A. C. A. C. A. Boogert, P. A. Gerakines and D. C. B. B. Whittet, Observations of the Icy Universe, *Annu. Rev. Astron. Astrophys.*, 2015, **53**(1), 541–581, DOI: **10.1146/annurev-astro-082214-122348**.

3 P. A. Gerakines, M. H. Moore and R. L. Hudson, Carbonic Acid Production in H_2O:CO_2 Ices - UV Photolysis vs. Proton Bombardment, *Astron. Astrophys.*, 2000, **357**(2), 793–800.

4 C. Y. R. Wu, D. L. Judge, B. M. Cheng, T. S. Yih, C. S. Lee and W. H. Ip, Extreme Ultraviolet Photolysis of CO_2-H_2O Mixed Ices at 10 K, *J. Geophys. Res. Planets*, 2003, **108**(4), 5032, DOI: **10.1029/2002je001932**.

5 S. Radhakrishnan, M. S. Gudipati, W. Sander and A. Lignell, Photochemical Processes in CO_2/H_2O Ice Mixtures with Trapped Pyrene, a Model Polycyclic Aromatic Hydrocarbon, *Astrophys. J.*, 2018, **864**(2), 151, DOI: **10.3847/1538-4357/aad4a6**.

6 M. H. Moore, R. L. Hudson and P. A. Gerakines, Mid- and Far-Infrared Spectroscopic Studies of the Influence of Temperature, Ultraviolet Photolysis and Ion Irradiation on Cosmic-Type Ices, *Spectrochim. Acta, Part A*, 2001, **57**(4), 843–858, DOI: **10.1016/S1386-1425(00)00448-0**.

7 R. Berger, Y. Lilach, Y. Ayoub and M. Asscher, Photochemistry of Molecules at Confined Environment: CD3Br/O/Ru(001) and CO_2@Ice, *Isr. J. Chem.*, 2005, **45**(1–2), 97–109, DOI: **10.1560/veyg-4lq8-dtpt-tdu4**.

8 D. Blake, L. Allamandola, S. Sandford, D. Hudgins, D. Blake, L. Allamandola, S. Sandford, D. Hudgins and F. Freund, Clathrate Hydrate Formation in Amorphous Cometary Ice Analogs in Vacuo, *Science*, 1991, **254**(5031), 548–551.

9 J. Ghosh, R. R. J. Methikkalam, R. G. Bhuin, G. Ragupathy, N. Choudhary, R. Kumar and T. Pradeep, Clathrate Hydrates in Interstellar Environment, *Proc. Natl. Acad. Sci. U. S. A.*, 2019, **116**(5), 1526–1531, DOI: **10.1073/pnas.1814293116**.

10 R. Netsu and T. Ikeda-Fukazawa, Formation of Carbon Dioxide Clathrate Hydrate from Amorphous Ice with Warming, *Chem. Phys. Lett.*, 2019, **716**, 22–27, DOI: **10.1016/j.cplett.2018.12.005**.

11 G. Vishwakarma, B. K. Malla, K. S. S. V. P. Reddy, J. Ghosh, S. Chowdhury, S. S. R. K. C. Yamijala, S. K. Reddy, R. Kumar and T. Pradeep, Induced Migration of CO_2 from Hydrate Cages to Amorphous Solid Water under Ultrahigh Vacuum and Cryogenic Conditions, *J. Phys. Chem. Lett.*, 2023, **14**, 2823–2829, DOI: **10.1021/acs.jpclett.3c00373**.

12 E. D. Sloan Jr. and C. A. Koh, *Clathrate Hydrates of Natural Gases*, CRC Press, 2007, DOI: **10.1201/9781420008494**.

13 G. Vishwakarma, V. Dhamu, M. F. Qureshi, G. Bhattacharjee, T. Pradeep and P. Linga, Understanding the Kinetics of CO_2 Hydrate Formation in Dry Water for Carbon Capture and Storage: X-Ray Diffraction and In Situ Raman Studies, *ACS Appl. Mater. Interfaces*, 2025, **17**(3), 4865–4874, DOI: **10.1021/acsami.4c17727**.

14 F. Fleyfel and J. P. Devlin, FT-IR Spectra of 90 K Films of Simple, Mixed, and Double Clathrate Hydrates of Trimethylene Oxide, Methyl Chloride, Carbon Dioxide, Tetrahydrofuran, and Ethylene Oxide Containing Decoupled D_2O, *J. Phys. Chem.*, 1988, **92**(3), 631–635, DOI: **10.1021/j100314a013**.

15 J. E. Bertie and J. P. Devlin, Infrared Spectroscopic Proof of the Formation of the Structure I Hydrate of Oxirane from Annealed Low-Temperature Condensate, *J. Chem. Phys.*, 1983, **78**(10), 6340–6341, DOI: **10.1063/1.444563**.

16 F. Fleyfel and J. P. Devlin, Carbon Dioxide Clathrate Hydrate Epitaxial Growth: Spectroscopic Evidence for Formation of the Simple Type-II Carbon Dioxide Hydrate, *J. Phys. Chem.*, 1991, **95**(9), 3811–3815, DOI: **10.1021/J100162A068**.

17 A. Hallbrucker, A Clathrate Hydrate of Nitric Oxide, *Angew. Chem., Int. Ed. Engl.*, 1994, **33**(6), 691–693, DOI: **10.1002/anie.199406911**.

18 E. Mayer and A. Hallbrucker, Unexpectedly Stable Nitrogen and Oxygen Clathrate Hydrates from Vapour Deposited Amorphous Solid Water, *Chem. Commun.*, 1989, 749–751, DOI: **10.1039/c2cc35637f**.

19 M. Choukroun, T. H. Vu and E. C. Fayolle, No Compelling Evidence for Clathrate Hydrate Formation under Interstellar Medium Conditions over Laboratory Time Scales, *Proc. Natl. Acad. Sci. U. S. A.*, 2019, **116**(29), 14407–14408, DOI: **10.1073/pnas.1902381116**.

20 J. Ghosh, R. R. J. Methikkalam, R. G. Bhuin, G. Ragupathy, N. Choudhary, R. Kumar and T. Pradeep, Reply to Choukroun *et al.* IR and TPD Data Suggest the Formation of Clathrate Hydrates in Laboratory Experiments Simulating ISM, *Proc. Natl. Acad. Sci. U. S. A.*, 2019, **116**(29), 14409–14410, DOI: **10.1073/pnas.1905894116**.

21 J. Ghosh, R. G. Bhuin, G. Ragupathy and T. Pradeep, Spontaneous Formation of Tetrahydrofuran Hydrate in Ultrahigh Vacuum, *J. Phys. Chem. C*, 2019, **123**, 16300–16307, DOI: **10.1021/acs.jpcc.9b04370**.

22 J. Ghosh, R. G. Bhuin, G. Vishwakarma and T. Pradeep, Formation of Cubic Ice via Clathrate Hydrate, Prepared in Ultrahigh Vacuum under Cryogenic Conditions, *J. Phys. Chem. Lett.*, 2020, **11**(1), 26–32, DOI: **10.1021/acs.jpclett.9b03063**.

23 J. Ghosh, G. Vishwakarma, S. Das and T. Pradeep, Facile Crystallization of Ice Ihvia Formaldehyde Hydrate in Ultrahigh Vacuum under Cryogenic Conditions, *J. Phys. Chem. C*, 2021, **125**(8), 4532–4539, DOI: **10.1021/acs.jpcc.0c10367**.

Published on 14 May 2025. Downloaded by Indian Institute of Technology Chennai on 12/29/2025 3:11:48 AM.

24 B. K. Malla, G. Vishwakarma, S. Chowdhury, P. Selvarajan and T. Pradeep, Formation of Ethane Clathrate Hydrate in Ultrahigh Vacuum by Thermal Annealing, *J. Phys. Chem. C*, 2022, **126**(42), 17983–17989, DOI: 10.1021/acs.jpcc.2c06264.
25 G. Vishwakarma, B. K. Malla, S. Chowdhury, S. P. Khandare and T. Pradeep, Existence of Acetaldehyde Clathrate Hydrate and Its Dissociation Leading to Cubic Ice under Ultrahigh Vacuum and Cryogenic Conditions, *J. Phys. Chem. Lett.*, 2023, **14**(23), 5328–5334, DOI: 10.1021/acs.jpclett.3c01181.
26 B. K. Malla, G. Vishwakarma, S. Chowdhury, S. K. Nayak, S. S. R. K. C. Yamijala and T. Pradeep, Formation and Dissociation of Dimethyl Ether Clathrate Hydrate in Interstellar Ice Mimics, *J. Phys. Chem. C*, 2024, **128**(6), 2463–2470, DOI: 10.1021/acs.jpcc.3c07792.
27 B. K. Malla, D. Yang and T. Pradeep, Growth of Clathrate Hydrates in Nanoscale Ice Films Observed Using Electron Diffraction and Infrared Spectroscopy, *J. Phys. Chem. Lett.*, 2025, **16**(1), 365–371, DOI: 10.1021/acs.jpclett.4c03106.
28 R. Souda and T. Aizawa, Reflection High Energy Electron Diffraction (RHEED) Study of Ice Nucleation and Growth on Ni(111): Influences of Adspecies and Electron Irradiation, *Phys. Chem. Chem. Phys.*, 2019, **21**(35), 19585–19593, DOI: 10.1039/C9CP03082D.
29 A. Kouchi and T. Kuroda, Amorphization of Cubic Ice by Ultraviolet Irradiation, *Nature*, 1990, **344**, 134–135.
30 N. D. Lisgarten and M. Blackman, The Cubic Form of Ice, *Nature*, 1956, **178**, 39–40.
31 R. Souda and T. Aizawa, Crystallization Kinetics of Water on Graphite, *Phys. Chem. Chem. Phys.*, 2018, **20**(34), 21856–21863, DOI: 10.1039/c8cp03000f.
32 R. Souda and T. Aizawa, Crystallization Kinetics of Water on Bare, Hydrogenated, and Hydroxylated Si(100) and Si(111) Surfaces Studied by RHEED, TOF-SIMS, and TPD, *J. Phys. Chem. C*, 2019, **123**(33), 20373–20383, DOI: 10.1021/acs.jpcc.9b05348.
33 R. Souda and T. Aizawa, Nucleation and Growth of Water Ice on Ru(0001): Influences of Oxygen and Carbon-Monoxide Adspecies, *Chem. Phys. Lett.*, 2019, **722**(December 2018), 132–139, DOI: 10.1016/j.cplett.2019.03.006.
34 K. Takeya, A. Tani, T. Yada, M. Ikeya and K. Ohgaki, Electron Spin Resonance Study on γ-Ray-Induced Methyl Radicals in Methane Hydrates, *Jpn. J. Appl. Phys.*, 2004, **43**(1), 353–357, DOI: 10.1143/JJAP.43.353.
35 K. Ohgaki, K. Nakatsuji, K. Takeya, A. Tani and T. Sugahara, Hydrogen Transfer from Guest Molecule to Radical in Adjacent Hydrate-Cages, *Phys. Chem. Chem. Phys.*, 2008, **10**(1), 80–82, DOI: 10.1039/B715284A.
36 T. Sugahara, Y. Kobayashi, A. Tani, T. Inoue and K. Ohgaki, Intermolecular Hydrogen Transfer between Guest Species in Small and Large Cages of Methane + Propane Mixed Gas Hydrates, *J. Phys. Chem. A*, 2012, **116**(10), 2405–2408, DOI: 10.1021/jp300814s.
37 P. Goldberg, Free Radicals and Reactive Molecules in Clathrate Cavities, *Science*, 1963, **142**(3590), 378–379, DOI: 10.1126/science.142.3590.378.
38 S. Bag, R. G. Bhuin, R. R. J. Methikkalam, T. Pradeep, L. Kephart, J. Walker, K. Kuchta, D. Martin and J. Wei, Development of Ultralow Energy (1-10 EV) Ion Scattering Spectrometry Coupled with Reflection Absorption Infrared Spectroscopy and Temperature Programmed Desorption for the Investigation of Molecular Solids, *Rev. Sci. Instrum.*, 2014, **85**(1), 14103, DOI: 10.1063/1.4848895.
39 B. K. Malla, G. Vishwakarma, S. Chowdhury and T. Pradeep, Vacuum Ultraviolet Photolysis of Condensed Methyl Chloride in Interstellar Model Conditions and Trapping of Intermediates at Intergrain Interfaces, *J. Phys. Chem. C*, 2023, **127**(50), 24149–24157, DOI: 10.1021/acs.jpcc.3c05889.
40 G. Vishwakarma, B. K. Malla, R. R. J. Methikkalam and T. Pradeep, Rapid Crystallization of Amorphous Solid Water by Porosity Induction, *Phys. Chem. Chem. Phys.*, 2022, **24**(42), 26200–26210, DOI: 10.1039/D2CP02640F.
41 G. Vishwakarma, J. Ghosh and T. Pradeep, Desorption-Induced Evolution of Cubic and Hexagonal Ices in an Ultrahigh Vacuum and Cryogenic Temperatures, *Phys. Chem. Chem. Phys.*, 2021, **23**(41), 24052–24060, DOI: 10.1039/D1CP03872A.
42 H. H. Richardson, P. J. Wooldridge and J. P. Devlin, FT-IR Spectra of Vacuum Deposited Clathrate Hydrates of Oxirane H 2S, THF, and Ethane, *J. Chem. Phys.*, 1985, **83**(9), 4387–4394, DOI: 10.1063/1.449055.
43 A. Schriver, J. M. Coanga, L. Schriver-Mazzuoli and P. Ehrenfreund, FTIR Studies of Ultraviolet Photo-Dissociation at 10 K of Dimethyl-Ether in Argon and Nitrogen Matrices, in the Solid Phase and in Amorphous Water Ice, *Chem. Phys. Lett.*, 2004, **386**(4–6), 377–383, DOI: 10.1016/j.cplett.2004.01.044.
44 G. Leto and G. A. Baratta, Ly-α Photon Induced Amorphization of Lc Water Ice at 16 Kelvin. Effects and Quantitative Comparison with Ion Irradiation, *Astron. Astrophys.*, 2003, **397**(1), 7–13, DOI: 10.1051/0004-6361:20021473.
45 R. M. Escribano, G. M. M. Caro, G. A. Cruz-Diaz, Y. Rodríguez-Lazcano and B. Maté, Crystallization of CO_2 Ice and the Absence of Amorphous CO_2 Ice in Space, *Proc. Natl. Acad. Sci. U. S. A.*, 2013, **110**(32), 12899–12904, DOI: 10.1073/pnas.1222228110.
46 J. L. Edridge, K. Freimann, D. J. Burke and W. A. Brown, Surface Science Investigations of the Role of CO2 in Astrophysical Ices, *Philos. Trans. R. Soc. A Math. Phys. Eng. Sci.*, 1994, **2013**, 371, DOI: 10.1098/rsta.2011.0578.
47 E. H. G. Backus, M. L. Grecea, A. W. Kleyn and M. Bonn, Surface Crystallization of Amorphous Solid Water, *Phys. Rev. Lett.*, 2004, **92**(23), 236101, DOI: 10.1103/PhysRevLett.92.236101.
48 G. Vishwakarma, B. K. Malla, R. Kumar and T. Pradeep, Partitioning Photochemically Formed CO 2 into Clathrate Hydrate under Interstellar Conditions, *Phys. Chem. Chem. Phys.*, 2024, **26**(22), 16008–16016, DOI: 10.1039/D4CP01414F.
49 H. Mokrane, H. Chaabouni, M. Accolla, E. Congiu, F. Dulieu, M. Chehrouri and J. L. Lemaire, Experimental evidence for water formation via ozone hydrogenation on dust grains at 10 K, *Astrophys. J.*, 2009, **705**(2), L195–L198, DOI: 10.1088/0004-637X/705/2/L195.
50 A. Ishibashi, H. Hidaka, Y. Oba, A. Kouchi and N. Watanabe, Efficient Formation Pathway of Methyl Formate: The Role of OH Radicals on Ice Dust, *Astrophys. J. Lett.*, 2021, **921**(1), L13–L13, DOI: 10.3847/2041-8213/ac3005.

This journal is © the Owner Societies 2025

Published on 14 May 2025. Downloaded by Indian Institute of Technology Chennai on 12/29/2025 3:11:48 AM.

51 R. R. J. Methikkalam, R. G. Bhuin, J. Ghosh, B. Sivaraman and T. Pradeep, Interaction of Acetonitrile with Alcohols at Cryogenic Temperatures, *J. Phys. Chem. C*, 2017, **121**(5), 2822–2835, DOI: **10.1021/acs.jpcc.6b11483**.

52 H. Kang, Chemistry of Ice Surfaces. Elementary Reaction Steps on Ice Studied by Reactive Ion Scattering, *Acc. Chem. Res.*, 2005, **38**(12), 893–900, DOI: **10.1021/ar0501471**.

53 Y. K. Kim, S. C. Park, J. H. Kim, C. W. Lee and H. Kang, Interaction of Carbon Dioxide and Hydroxide Ion at the Surface of Ice Films, *J. Phys. Chem. C*, 2008, **112**(46), 18104–18109, DOI: **10.1021/jp806643e**.

54 P. Soulard and B. Tremblay, Vibrational Investigations of CO2-H2O, CO2-(H2O)2, and (CO2)2-H2O Complexes Isolated in Solid Neon, *J. Chem. Phys.*, 2015, **143**(22), 224311, DOI: **10.1063/1.4936913**.

55 K. S. Thanthiriwatte, J. R. Duke, V. E. Jackson, A. R. Felmy and D. A. Dixon, High-Level Ab Initio Predictions of the Energetics of m CO_2(H_2O) n (n = 1-3, m = 1-12) Clusters, *J. Phys. Chem. A*, 2012, **116**(39), 9718–9729, DOI: **10.1021/jp306594h**.

56 G. M. Chaban, M. Bernstein and D. P. Cruikshank, Carbon Dioxide on Planetary Bodies: Theoretical and Experimental Studies of Molecular Complexes, *Icarus*, 2007, **187**(2), 592–599, DOI: **10.1016/j.icarus.2006.10.010**.

57 X. Wang and T. Bürgi, Observation of Carbonic Acid Formation from Interaction between Carbon Dioxide and Ice by Using In Situ Modulation Excitation IR Spectroscopy, *Angew. Chem., Int. Ed.*, 2021, **60**(14), 7860–7865, DOI: **10.1002/anie.202015520**.

58 M. Y. Kulikov, A. M. Feigin and O. Schrems, H_2O_2 Photoproduction inside H_2O and H_2O:O_2 Ices at 20–140 K, *Sci. Rep.*, 2019, **9**(1), 11375, DOI: **10.1038/s41598-019-47915-w**.

Supplementary Information (SI) for Physical Chemistry Chemical Physics.
This journal is © the Owner Societies 2025

Supplementary Information

Ultraviolet Photolysis of CO_2 Clathrate Hydrate and H_2O-CO_2 Mixed Ice under Ultrahigh Vacuum

Gaurav Vishwakarma[a], Bijesh K. Malla[a], Soham Chowdhury[a], Jyotirmoy Ghosh[b], Rabin Rajan J. Methikkalam[c], Rajnish Kumar*[de], and Thalappil Pradeep*[ae]

[a.] DST Unit of Nanoscience (DST UNS) and Thematic Unit of Excellence (TUE), Department of Chemistry, Indian Institute of Technology Madras, Chennai 600036, India

[b.] Department of Chemistry, Purdue University, West Lafayette, Indiana 47907, United States

[c.] Department of Chemistry, Mar Ivanios College, Thiruvananthapuram, Kerala 695015, India

[d.] Department of Chemical Engineering, Indian Institute of Technology Madras, Chennai 600036, India

[e.] International Centre for Clean Water, IIT Madras Research Park, Chennai 600113, India

Corresponding author

***Email:** pradeep@iitm.ac.in, rajnish@iitm.ac.in

This PDF file includes:
Fig. S1 to S5 (pages S2-S6)
References (page S7)

Supplementary Information 1

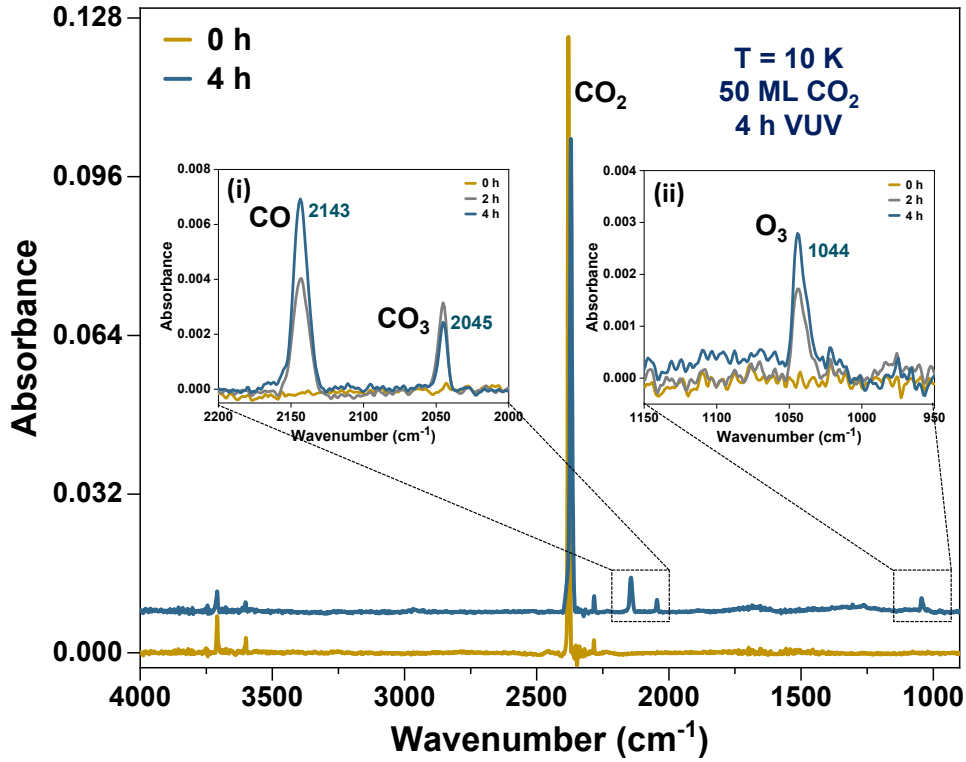


Fig. S1. RAIR spectra recorded before (golden trace) and after 4 h of photolysis (blue trace) of ~50 ML pure CO_2 ice at 10 K. For this, ~50 ML of pure CO_2 ice was prepared by vapor deposition at 10 K and photolyzed by VUV for 4 h. The photon-induced products detected by RAIR were CO (2143 cm^{-1}), CO_3 (2045 cm^{-1}), and O_3 (1044 cm^{-1}). The peak assignments are consistent with previous studies.[1,2] The inset (i) illustrates the evolution of CO and CO_3. CO production steadily increases over time, while CO_3 initially rises before declining. Similarly, inset (ii) shows the production of O_3 which increases with prolonged exposure to VUV. By estimating the area under the curve of 3708 cm^{-1} peak, we calculated the column density of CO_2 (band strength of 3708 cm^{-1} = 1.4 × 10^{-18} cm $molecule^{-1}$)[3] and found that after subjecting the pure CO_2 ice to VUV exposure for 4 h, approximately 19.51% of the total CO_2 was depleted.

Supplementary Information 2

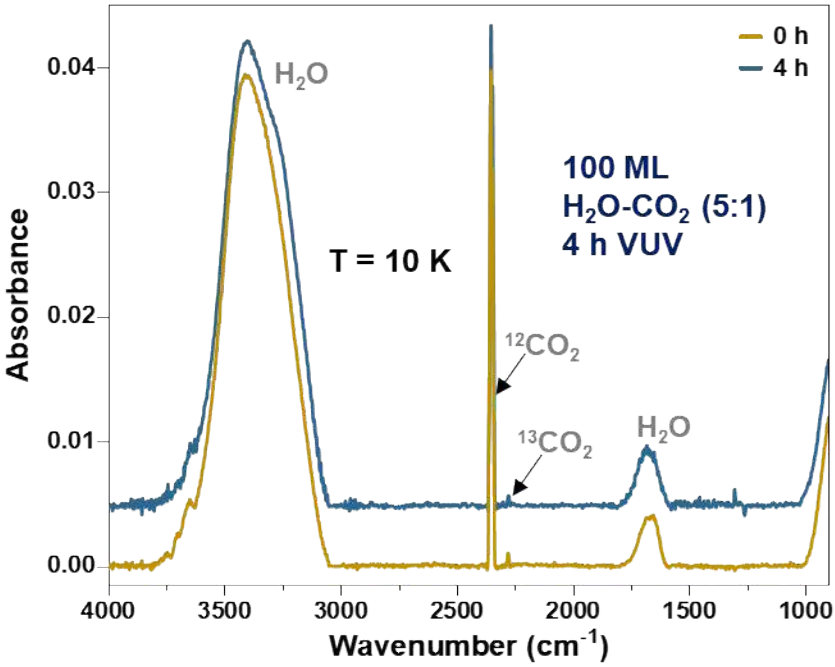


Fig. S2. RAIR spectra of ~100 ML H_2O-CO_2 (5:1) ice before and after VUV exposure in the full range, 4000-1000 cm^{-1}. Ice sample was prepared by vapor deposition at 10 K and photolyzed for 4 h. RAIR spectra were collected at regular intervals. No photon-induced products were detected by RAIRS.

Supplementary Information 3

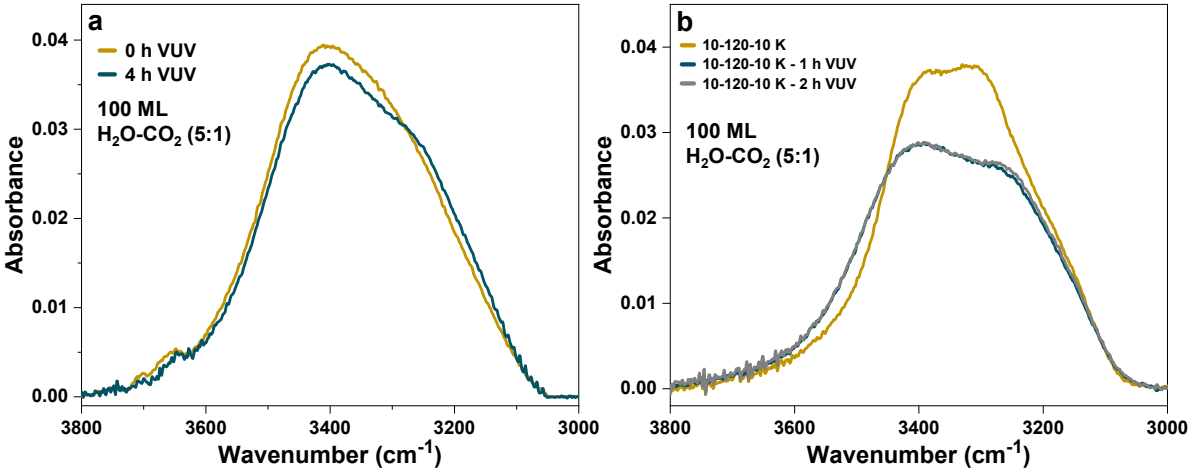


Fig. S3. RAIR spectra of ~100 ML H_2O-CO_2 (5:1) mixed ice in the O-H stretching region: (a) before and after VUV exposure at 10 K, and (b) after annealing to 120 K, cooling back to 10 K, and subsequent 2 h of VUV photolysis at 10 K. The greater intensity decrease in (b) compared to (a) occurs because annealing to 120 K orders H_2O molecules, which then undergo disordering during VUV photolysis.

Supplementary Information 4

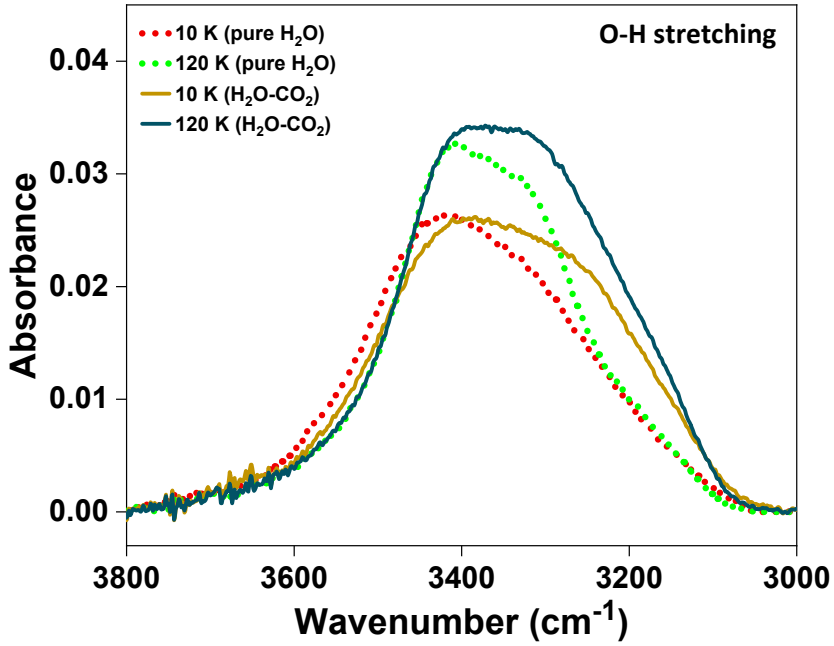


Fig. S4. Comparison of RAIR spectra in the O-H stretching bands of pure water (dotted lines) and H_2O-CO_2 (5:1) mixture (solid lines) at 10 and 120 K. The change in shape and intensity of the O-H stretching band in the presence of CO_2 at 10 and 120 K suggests the formation of CO_2 sI CH.[4]

Supplementary Information 5

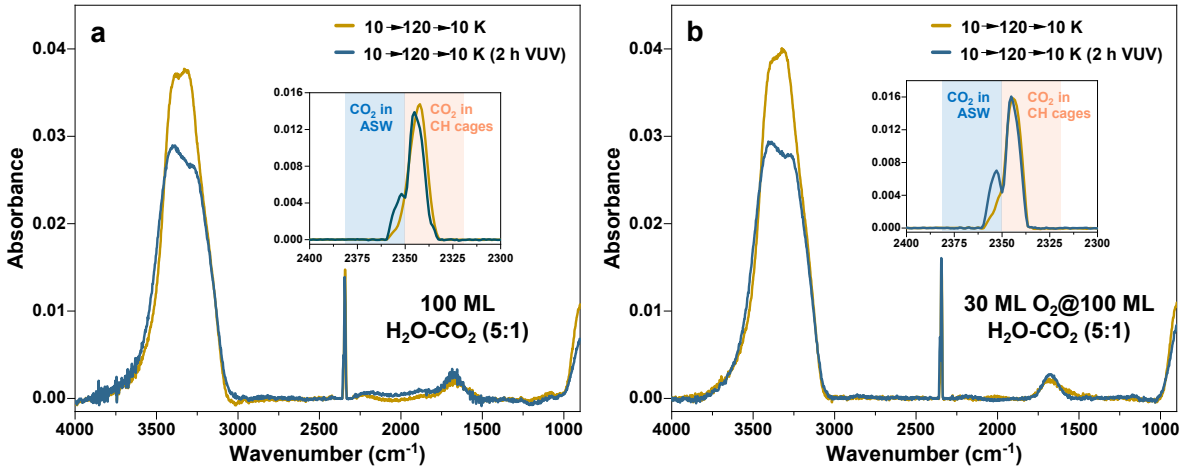


Fig. S5. Full range RAIR spectra of (a) ~100 ML H_2O-CO_2 (5:1) ice, and (b) ~30 ML O_2@100 ML H_2O-CO_2 (5:1) composite film at 10 K before and after VUV exposure. In both cases, sample was prepared by vapor deposition at 10 K. The resulting ice was heated at rate of 5 K min^{-1} to 120 K, and cooled down to 10 K. Then, the ice sample was exposed to VUV for 2 h and RAIR spectra were collected at regular intervals. Insets in both (a) and (b) show the reduction in the area under the curve for CH peaks while increase for CO_2 in ASW, which depicts CH decomposition and migration of CO_2 to the water matrix. For the H_2O-CO_2 (5:1) ice containing a small fraction of O_2, the decomposition of CH was slightly higher, as presented in the inset of (b). For ~100 ML H_2O-CO_2 (5:1) ice, the ice was prepared on Ru(0001) by codeposition of CO_2 gas and H_2O vapor at 10 K. The ~30 ML O_2@100 ML H_2O-CO_2 (5:1) composite film was prepared by first creating 30 ML of O_2 ice on Ru(0001) followed by codeposition of ~100 ML H_2O-CO_2 (5:1) mixture on top of it.

References

(1) Gerakines, P. A.; Moore, M. H.; Hudson, R. L. Carbonic Acid Production in H2O:CO2 Ices - UV Photolysis vs. Proton Bombardment. *Astron. Astrophys.* **2000**, *357* (2), 793–800.

(2) Mifsud, D. V.; Kaňuchová, Z.; Ioppolo, S.; Herczku, P.; Traspas Muiña, A.; Field, T. A.; Hailey, P. A.; Juhász, Z.; Kovács, S. T. S.; Mason, N. J.; McCullough, R. W.; Pavithraa, S.; Rahul, K. K.; Paripás, B.; Sulik, B.; Chou, S.-L.; Lo, J.-I.; Das, A.; Cheng, B.-M.; Rajasekhar, B. N.; Bhardwaj, A.; Sivaraman, B. Mid-IR and VUV Spectroscopic Characterisation of Thermally Processed and Electron Irradiated CO2 Astrophysical Ice Analogues. *J. Mol. Spectrosc.* **2022**, *385*, 111599.

(3) Wu, C. Y. R.; Judge, D. L.; Cheng, B. M.; Yih, T. S.; Lee, C. S.; Ip, W. H. Extreme Ultraviolet Photolysis of CO2-H2O Mixed Ices at 10 K. *J. Geophys. Res. Planets* **2003**, *108* (4), 5032.

(4) Netsu, R.; Ikeda-Fukazawa, T. Formation of Carbon Dioxide Clathrate Hydrate from Amorphous Ice with Warming. *Chem. Phys. Lett.* **2019**, *716*, 22–27.

Inorganic Chemistry

pubs.acs.org/IC Article

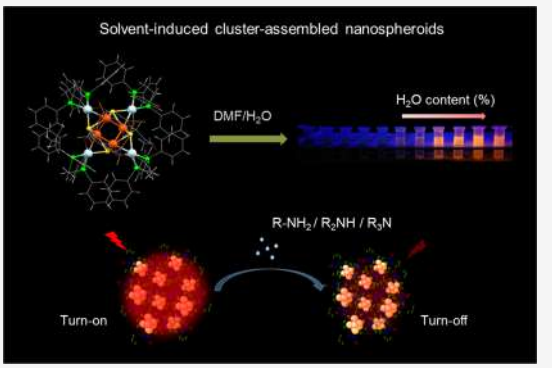
Solvent-Modulated Luminescent Spheroidal Assemblies of Cu_8 Nanocluster for Volatile Amine Sensing

Subrata Duary, Arijit Jana, Amitabha Das, Ankit Sharma, Biswarup Pathak,* Kumaran Nair Valsala Devi Adarsh,* and Thalappil Pradeep*

Cite This: *Inorg. Chem.* 2025, 64, 11001−11011 Read Online

ACCESS | Metrics & More | Article Recommendations | Supporting Information

ABSTRACT: Cluster-assembled luminescent microstructures built with metal nanoclusters (NCs) represent a promising class of nanomaterials with diverse applications in photonics and sensing. In this work, we have designed a strategy to make a photoluminescent material by assembling atom-precise NCs of $[Cu_8(TFMPT)_4(DPPE)_4]$ (abbreviated as Cu_8), where TFMPT is 4-hydroxy-6-(trifluoromethyl) pyrimidine-2-thiolate and DPPE is 1,2-bis(diphenylphosphino)ethane. Single-crystal X-ray diffraction (SC-XRD) reveals a unique tetracapped tetrahedral Cu_8 core structure. Upon gradual addition of water (50−85 vol %) to the visibly nonluminescent dimethylformamide (DMF) solution of the clusters, a strong orange luminescence (emission at 625 nm under ultraviolet (UV) light) was observed. It is due to the formation of spheroidal assemblies of nanometer dimension. The cluster-assembled spheroids (CASs) are formed due to hydrophobic interactions among clusters as the concentration of water increases in the solution. Time-correlated single-photon counting reveals that the lifetime of luminescent aggregates is on a microsecond scale, which suggests phosphorescence. Such phosphorescent CASs show a fast response, high selectivity, and naked-eye detection of volatile amines (VAs). Spectroscopic studies and density functional theory (DFT) calculations provide an in-depth understanding of luminescence quenching of CASs and a mechanistic understanding of ammonia and trimethyl amine sensing. The limits of detection (LoD) of ammonia and trimethyl amine were measured to be 0.568×10^{-7} M (0.001 ppm) and 0.362 0.568×10^{-7} M (0.002 ppm), respectively. Overall, apart from enriching the family of copper clusters, this work additionally introduces a new photoluminescent material for volatile organic amine (VOA) compound sensing of environmental relevance.



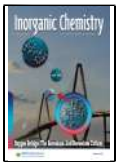
Downloaded via INDIAN INST OF TECH MADRAS on December 29, 2025 at 03:12:09 (UTC).
See https://pubs.acs.org/sharingguidelines for options on how to legitimately share published articles.

INTRODUCTION

Atomically precise noble metal nanoclusters (NCs) of size below ∼3 nm belong to a class of novel nanomaterials, endowed with molecule-like discrete energy levels, photoluminescence, chirality, magnetism, etc.[1] In the last two decades, intense efforts on the synthesis, characterization, and diverse applications of silver and gold NCs have been reported. However, copper NCs have received comparatively less attention due to the easy oxidation of copper under air (E^0 values of Au^+/Au, Ag^+/Ag, and Cu^+/Cu are 1.69, 0.79, and 0.52 V, respectively).[2] Notwithstanding this limitation, Cu NCs need to be explored because of their earth abundance and consequently low cost, nontoxicity, and high catalytic activity. Tuning the synthesis and crystallization methods has been used intensely to obtain the structures of several small and moderately sized copper clusters (e.g., Cu_4, Cu_5, Cu_8, Cu_{12}, Cu_{14}, Cu_{15}, Cu_{23}, Cu_{25}, Cu_{61}, Cu_{81}, Cu_{93}, Cu_{96}, and Cu_{136}) with appropriate ligand protection.[3−10]

Photoluminescence is one of the fascinating properties of ultrasmall noble metal NCs used for applications in nanophotonics and optical sensing. Copper clusters with intense emission, good photostability, and high yield of synthesis make them promising luminescent materials for optoelectronic applications.[11,12] Such luminescent Cu NCs show similar characteristics such as large Stokes shift and long emission lifetimes in comparison to the conventional luminescent materials (organic dyes and semiconductor quantum dots).[13−15] To enhance the photoluminescence of such clusters, researchers have used several approaches such as surface functionalization, alloying, host−guest interaction, and aggregation-induced emission (AIE).[16−21,26] Out of such approaches, AIE occurs very frequently for Cu NCs. In the aggregated state of clusters, metallophilic interactions, restricted motion of ligands, and enhanced radiative relaxation pathways result in enhanced photoluminescence intensity

Received: March 8, 2025
Revised: May 8, 2025
Accepted: May 13, 2025
Published: May 22, 2025



ACS Publications © 2025 American Chemical Society

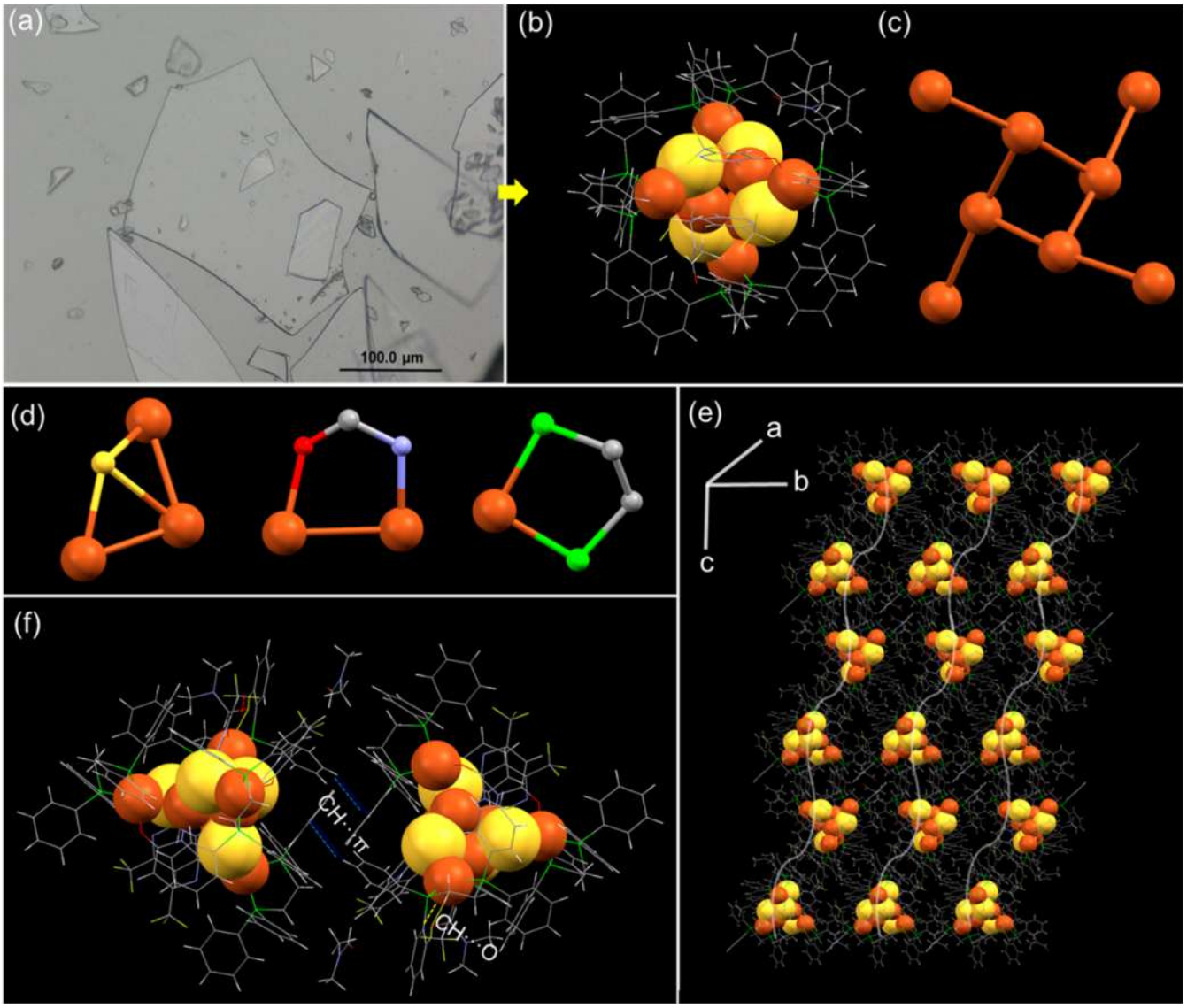


Figure 1. (a) Optical images of single crystals of the Cu_8 nanocluster (scale bar 100 μm). (b) Full structure of ligand-protected Cu_8 cluster (hydrogens are removed for clarity) with crystallized DMF molecules. (c) Cu_8 core structure. (d) Binding sites of ligand part to Cu. (e) Structured packing (3 × 3 × 3) of Cu_8 nanocluster along the *a*-axis. (f) Different noncovalent interactions within ligands and crystallized DMF molecules. Atomic color code: orange = Cu, yellow = S, green = P, gray = C, red = O, blue = N, light green = F, and white = H.

compared with isolated NCs.[26] The aggregation phenomenon is driven by intercluster interactions or electrostatic attractions (dipole−dipole, hydrogen bonding, metallophilic interactions, and hydrophobic interactions) arising through ligands.[22−25] The emission wavelength in such aggregates is highly determined by interatomic distances and compactness of assembled metal NCs.[26] The origin of photoluminescence due to the aggregation and self-assembly of metal NCs is a burgeoning area of research.

Recently, cluster-assembled materials have emerged as promising candidates for various sensing applications, related to environmental contamination and human health.[27−29] Nowadays, environmental contamination due to the release of volatile organic amine (VOA) compounds from industrial fertilizers and biological degradation processes is a matter of concern to public health and water bodies.[30,31] Although there are many analytical techniques available for their detection such as high-performance liquid chromatography, gas chromatography−mass spectrometry, capillary electrophoresis, Raman scattering, and electrochemical methods, new strategies are essential for efficient detection of VOAs.[32] This is made possible by the discovery of highly sensitive materials.

In this work, we have synthesized a copper nanocluster $[Cu_8(TFMPT)_4(DPPE)_4]$ following the strategy of ligand-exchange-induced structural transformation (LEIST), where TFMPT is 4-hydroxy-6-(trifluoromethyl) pyrimidine-2-thiolate and DPPE is 1,2-bis(diphenylphosphino)ethane. The cluster in dimethylformamide (DMF) was crystallized by the slow evaporation of solvent at ambient temperature. The Cu_8 core is composed of a unique tetracapped tetrahedral geometry. Interestingly, the Cu_8 cluster, which remains nonemissive in both solid and solution states, displays intense orange luminescence when mixed with water (vol %, 50−85%). The origin of luminescence is attributed to the formation of cluster-assembled spheroids (CASs). Such CASs exhibit "turn-off" luminescence in the presence of amines (liquid and vapor) due to the binding of such molecules with clusters. Altogether, this work presents an unexplored Cu_8 nanocluster manifesting

https://doi.org/10.1021/acs.inorgchem.5c01082
Inorg. Chem. 2025, 64, 11001−11011

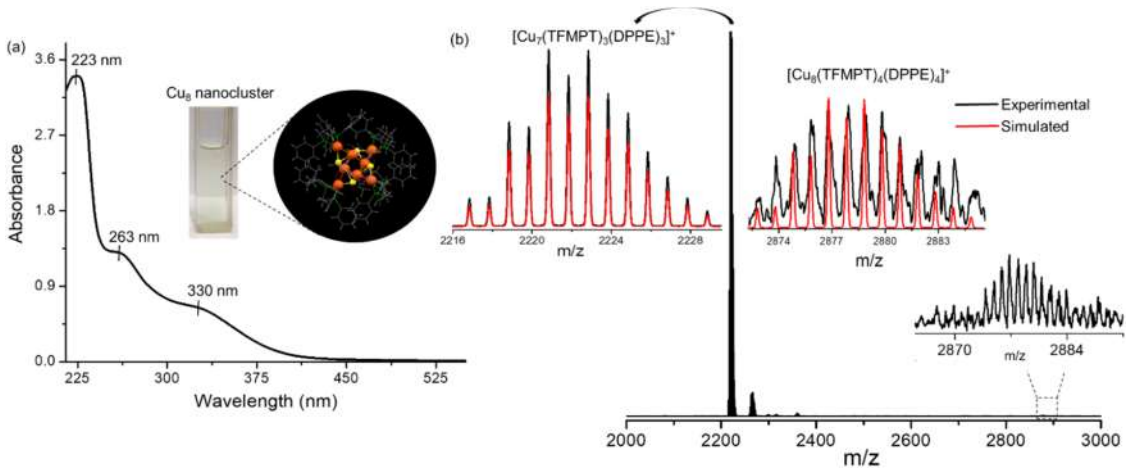


Figure 2. (a) UV−vis absorption spectrum of Cu_8 nanocluster in acetonitrile, inset photographic images of the cluster in acetonitrile and full structure. (b) Full-range high-resolution ESI-MS of Cu_8 nanocluster in positive mode; inset shows exact matching of experimental (black) and simulated (red) spectra. Inset shows the molecular ion peak at low abundance.

solvent-induced aggregation and the use of resulting assemblies for amine sensing.

RESULTS AND DISCUSSION

Synthesis and Characterization. The $[Cu_8(TFMPT)_4(DPPE)_4]$ nanocluster, abbreviated as Cu_8, was synthesized under ambient conditions following the LEIST reaction, starting from the $[Cu_{18}H_{16}(DPPE)_6]^{2+}$ (abbreviated as Cu_{18}) nanocluster. The synthesis protocol is described in the Experimental Section. The precursor Cu_{18} NC was synthesized following an earlier report.[33] Essential characterization of the Cu_{18} NC is covered in Figure S1. Synthesized Cu_8 cluster was crystallized as colorless sheet-like single crystals from the reaction mixture via slow evaporation of the solvent DMF under ambient conditions (Figure 1a).

Single Crystal Structure. The molecular structure of the cluster was determined by single-crystal X-ray diffraction (SC-XRD). The field emission scanning electron microscopy (FESEM) micrograph (gold sputtered on single crystals to reduce charging effect and improve image contrast) further verified the sheet-like surface morphology of the crystals (Figure S2a), and energy dispersive spectroscopy (EDS) elemental mapping shows the atomic composition as Cu (3.22%), S (0.96%), N (2.92%), O (22.08%), P (1.73%), and F (3.99%) (Figure S2d). SC-XRD reveals that Cu_8 was crystallized in a triclinic crystal system with the space group of *P*-1 having a cell volume of 6510.8 $Å^3$ (brief crystallographic details are summarized in Table S1 in SI). The ORTEP representation of the Cu_8 cluster is drawn at the 50% probability level showing the arrangement of copper atoms (Figure S8). The Cu_8 cluster core is composed of two interpenetrating puckered Cu_6S_2 units. Some reports suggest that most of the Cu_8 cluster cores are branched chain, fused tetrahedron, or cubic (summarized in Figure S3).[35−40] We report a tetracapped distorted tetrahedral Cu_8 core structure, distinctly different from those known already (Figure 1b). The entire molecular structure contains a Cu_8 kernel protected by 1:1 thiol (TFMPT-H_2) and phosphine (DPPE). The inner $[Cu_4]_{td}$ is protected by four units of Cu(HTFMP)(DPPE) making a compact Cu_8S_4 core. Each Cu atom of the outer $[Cu_4]_{td}$ is coordinated by one DPPE ligand. Careful analysis of single crystal structure indicates that thiols play a unique role in stabilizing the core structure. The N and O sites of thiol coordinate to inner and outer Cu, respectively, which provides rigidity to the core. The Cu−Cu distance in the inner $[Cu_4]$ unit is 2.572−2.596 Å, which is slightly longer than that in bulk copper. All S atoms are μ_3 bridging and the Cu−S distance is 2.240−2.386 Å (Figure S4e). The Cu−N, Cu−O, and Cu−P bond distances are 1.991−1.998, 2.042−2.078, and 2.235−2.386 Å, respectively (Figure S4f−h). In the Cu_8S_4 framework, copper and sulfur are arranged in tetrahedral units ($[Cu_4]_{inner}@S_4@[Cu_4]_{outer}$). Two molecules are present in each unit cell (Figure S4a). We observed two cocrystallized DMF molecules with one Cu_8 cluster (Figure 2b). In the extended lattice, clusters are packed through noncovalent interactions such as CH···O, CO···F, CH··· π, CH··· F, and CH··· CH with distances of 2.57, 2.98, 6.87, 2.414, and 2.184 Å, respectively (Figure 1f). These interactions contribute to the stabilization and organization of the clusters within the crystal lattice (Figure 1e).

Other Characterization Data. The UV−visible (UV−vis) absorption spectrum of Cu_8 NC in acetonitrile (ACN) shows three absorption peaks at 223, 263, and 330 nm, respectively (Figure 2a). The absorption features of the cluster in ACN show stability for up to 15 days (Figure S5). High-resolution ESI-MS spectrum in the positive ion mode shows a molecular ion peak at *m*/*z* 2878.65 (Figure 2b), which is assigned to $[Cu_8(TFMPT)_4(DPPE)_4]^+$. Another peak was observed at *m*/*z* 2225.53 (1+), which corresponds to the molecular composition, $[Cu_7(TFMPT)_3(DPPE)_3]^+$. The isotopic distributions of the experimental and theoretical spectra agreed well with each other (inset of Figure 2b). Upon an increase in the collision energy (CE), thiol and phosphine losses were observed from $[Cu_7(TFMPT)_3(DPPE)_3]$ (Figure S6). X-ray photoelectron spectroscopy (XPS) analysis shows the presence of all elements in the crystal structure of Cu_8 NC, as described in Figure S7. The spectral regions of Cu $2p_{3/2}$ and $2p_{1/2}$ at 932.5 and 952.4 eV, respectively, suggested the presence of mixed Cu^0 and Cu^I oxidation states, which were also supported by the Cu LMM Auger peak at 570 eV (inset of Figure S7). Such types of oxidation states in copper nanoclusters were also previously reported.[5,34] Fourier transform infrared (FTIR) spectroscopy study indicates the binding of ligand to cluster core (Figure S9). The vibrational signal of −SH (~2565 cm^{-1})

https://doi.org/10.1021/acs.inorgchem.5c01082
Inorg. Chem. 2025, 64, 11001−11011

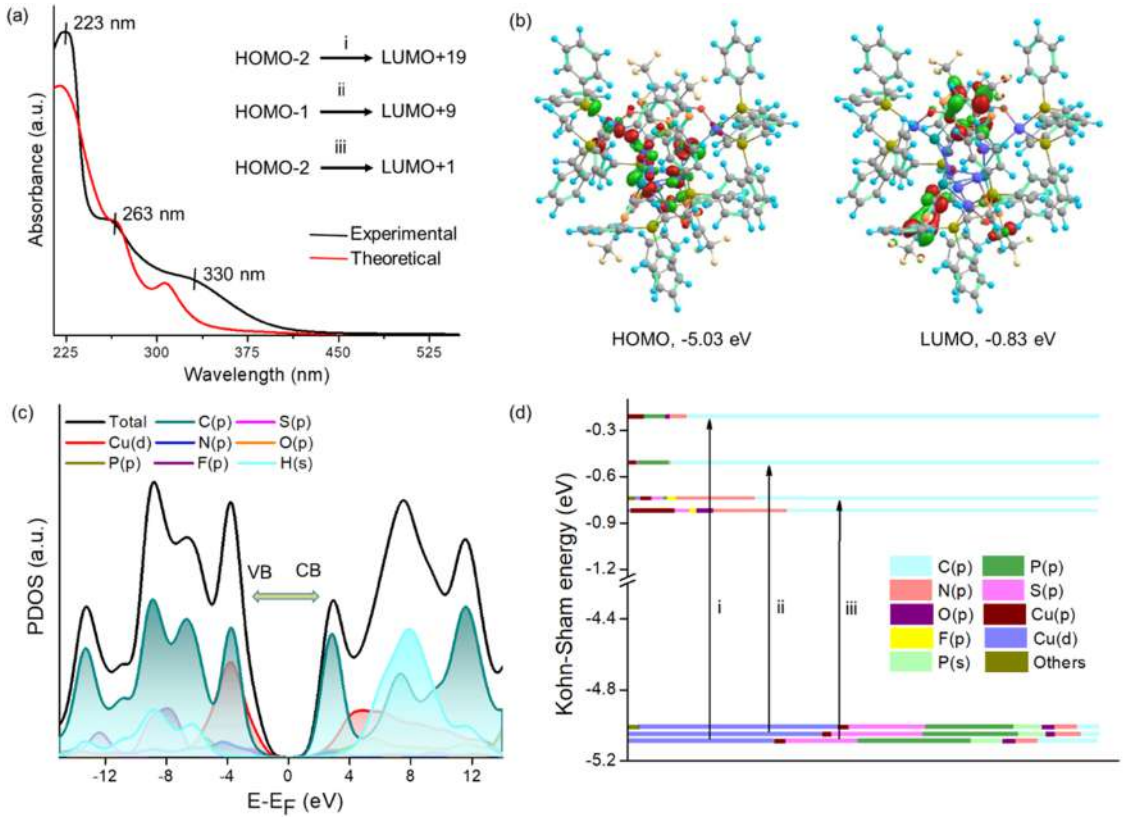


Figure 3. (a) Experimental absorption spectrum (black) of Cu_8 nanocluster and correlation with the theoretical spectrum (red); inset shows electronic transitions associated with the respective absorption features. (b) HOMO and LUMO of Cu_8 nanocluster. (c) Projected density of states of Cu_8 nanocluster with respect to individual atomic orbitals (VB = valence band and CB = conduction band). (d) KS energy diagram of the cluster representing the electronic transitions.

and −OH (~3170 cm^{-1}) peaks was not observed in FTIR of the cluster confirming the thiol bound to the metal core through S and O sites.

Theoretical Understanding of the Electronic Structure. Time-dependent density functional theory (TDDFT) has been carried out using B3LYP and 6−31G* level of theory implemented in the Gaussian 09 package to gain insights into electronic energy levels and associated optical properties of the cluster.[41] The simulated UV−vis spectrum is in good agreement with the experimental spectrum of the cluster dissolved in acetonitrile (Figure 3a). TDDFT reveals three distinct optical absorption peaks (at 223, 263, and 330 nm), which are due to transitions of HOMO − 2 → LUMO + 19 (5.61 eV/221 nm), HOMO − 2 → LUMO + 9 (4.68 eV/265 nm), and HOMO − 2 → LUMO + 1 (3.92 eV/316 nm), respectively, as mentioned in Figure S10. The electron density maps of these molecular orbitals, along with the Kohn−Sham (KS) molecular orbital analysis indicate that the electronic transitions primarily occur from the core d and p orbitals of Cu and S, respectively, to the p orbitals of C and N in the ligand region. To gain better insights into the electronic properties of Cu_8 NC, we have performed a projected density of state (PDOS) analysis using the Vienna Ab initio Simulation Package.[42] The valence band edges are dominated by the Cu(d) state; on the other hand, the conduction band edges are dominated by the states of ligand (specifically C) of the Cu_8 NC. This finding aligns well with the TDDFT analysis and altogether suggests a possibility of core-to-ligand transitions.

Formation of Cluster-Assembled Spheroids and Photophysical Properties. A mixed solvent strategy was used for the preparation of luminescent spheroidal assemblies with a range of nanometric dimensions (Figure 4e). Literature suggests that such an assembly by MNCs is energetically favorable, as shown by molecular dynamics (MD) studies.[43] Cu_8 NCs are stabilized by a combination of hydrophobic and hydrophilic ligands (thiol and phosphine) and are well dispersed in DMF. When water is added to the cluster in DMF, the polarity of the local environment changes, which drives the aggregation of such clusters leading to stable noncovalent interactions (C−H···π, π···π, CH···F, etc.) forming spheroidal assemblies. The formation of such spherical morphology of cluster-assembled structures is possibly due to the minimization of surface energy.[44,45] We have performed additional self-assembly experiments to show the role of other polar protic solvents (methanol/MeOH, ethanol/EtOH, *n*-propanol/*n*-PrOH, *n*-butanol/*n*-BuOH, and *t*-Butanol/*t*-BuOH, 80% volume fraction of solvents). In all cases, we found no assembly formation, which does not result in any emission under UV (Figure S11). Based on these experiments, we anticipated that the polarity of the medium (dielectric constant for water) plays a key role in forming such assembled spheroids. Dynamic light scattering (DLS) measurement shows a larger size of aggregates as the volume % of water is increased up to 80% (Figure S12). FESEM shows the growth and size of such spheroids with different dimensions (Figure S13). Transmission electron microscopy (TEM) image shows the spheroid shape of aggregates (Figure S14). The restriction

https://doi.org/10.1021/acs.inorgchem.5c01082
Inorg. Chem. 2025, 64, 11001−11011

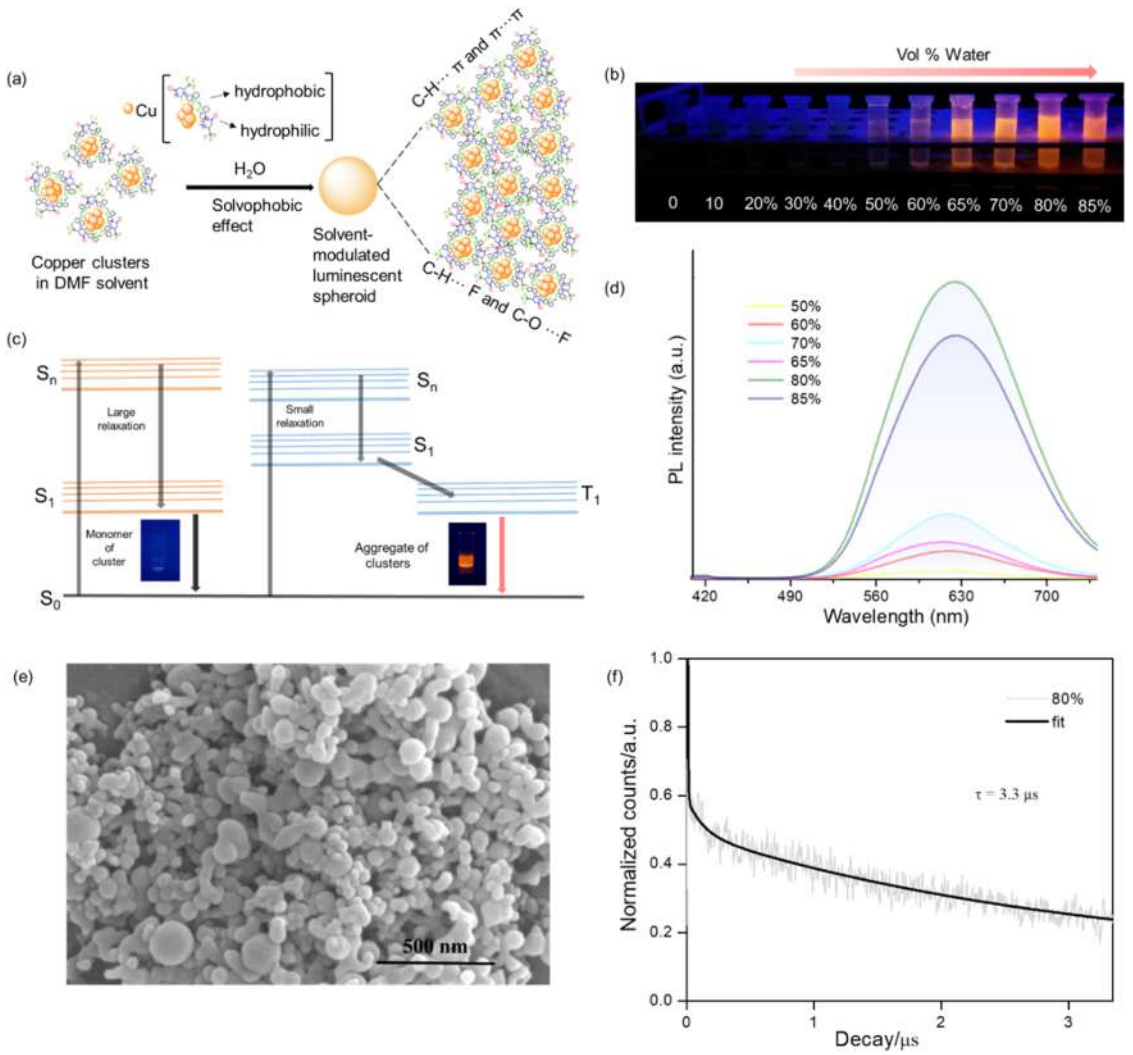


Figure 4. (a) Schematic illustration of the assembly of clusters within the spheroids. (b) A photograph of the samples in volume % of water under UV light exposure, showing the solvent-induced aggregation property of the cluster. (c) A schematic diagram distinguishing PL decay pathways of monomeric clusters and aggregates. (d) PL spectra at different volume % of water. (e) FESEM shows the morphology of as-synthesized spheroids (80% volume fraction of water) and (f) TCSPC decay curve of aggregates (80% volume fraction of water).

of molecular vibrations and rotations within these spheroids enhances their radiative decay, which leads to an orange emission. Generally, the aggregated clusters have different excited states PL and lifetimes compared with monomeric clusters, which enrich their photophysical properties.[46,47] Time-correlated single-photon counting (TCSPC) measurements show that CASs exhibit phosphorescence with lifetimes of τ_{avg} 3.3 μs/80%, τ_{avg} 2.6 μs/85%, τ_{avg} 0.7 μs/60%, and τ_{avg} 0.7 μs/50% (Figure S15), with volume % of water mentioned in each case. The effect of pH on the luminescence of CASs (using an 80% volume fraction of water) was monitored. The as-prepared CASs show pH-switchable orange emission (Figure S16). The emission feature vanished at pH ∼10, which reappeared at pH ∼5 (using sodium hydroxide and acetic acid, respectively). A red shift (∼5 nm) with an increase in PL intensity was observed by changing the pH of the solution from 10 to 5.

The pH-triggered luminescence reversibility was monitored for up to 5 cycles by altering the pH (from 10 to 5, or vice versa) of the solution (Figure S16b). The pH-induced modulation in PL properties is possibly due to the charge transfer phenomenon between metal core and ligand. Upon protonation of free nitrogen site of bipyrimidine moiety at pH ∼5, the charge transfer becomes facile, while deprotonation at pH ∼10 disturbs the charge transfer. The morphology of CASs in pH ∼10 changes, which may be due to the interaction between cluster and base (Figure S16c).[49b] PL decay upon oxygen exposure to the luminescent aggregates supports that their emission occurs from the triplet excited state (Figure S17). Such aggregates retain their emission even for up to 30 days (Figure S18). Temperature-dependent PL was measured from room temperature to 200 °C (Figure S19), and it shows a gradual decrease in emission. The powder X-ray diffraction spectrum of synthesized Cu_8 NC was measured using 30 mg of powder sample showing crystallinity behavior similar as predicted from single crystal structure (Figure S24). Thermogravimetric analysis (TGA) and derivative thermogravimetry (DTG) analysis together show that the initial mass loss is due to solvent molecules, and then the major mass loss is due to bond breakage of the cluster (Figure S25).

Volatile Amine Compound Sensing. To expand the application of such luminescent aggregates, a sensing experiment was performed for the detection of amines. They show "turn-off" luminescence in both liquid and vapor states of

https://doi.org/10.1021/acs.inorgchem.5c01082
Inorg. Chem. 2025, 64, 11001−11011

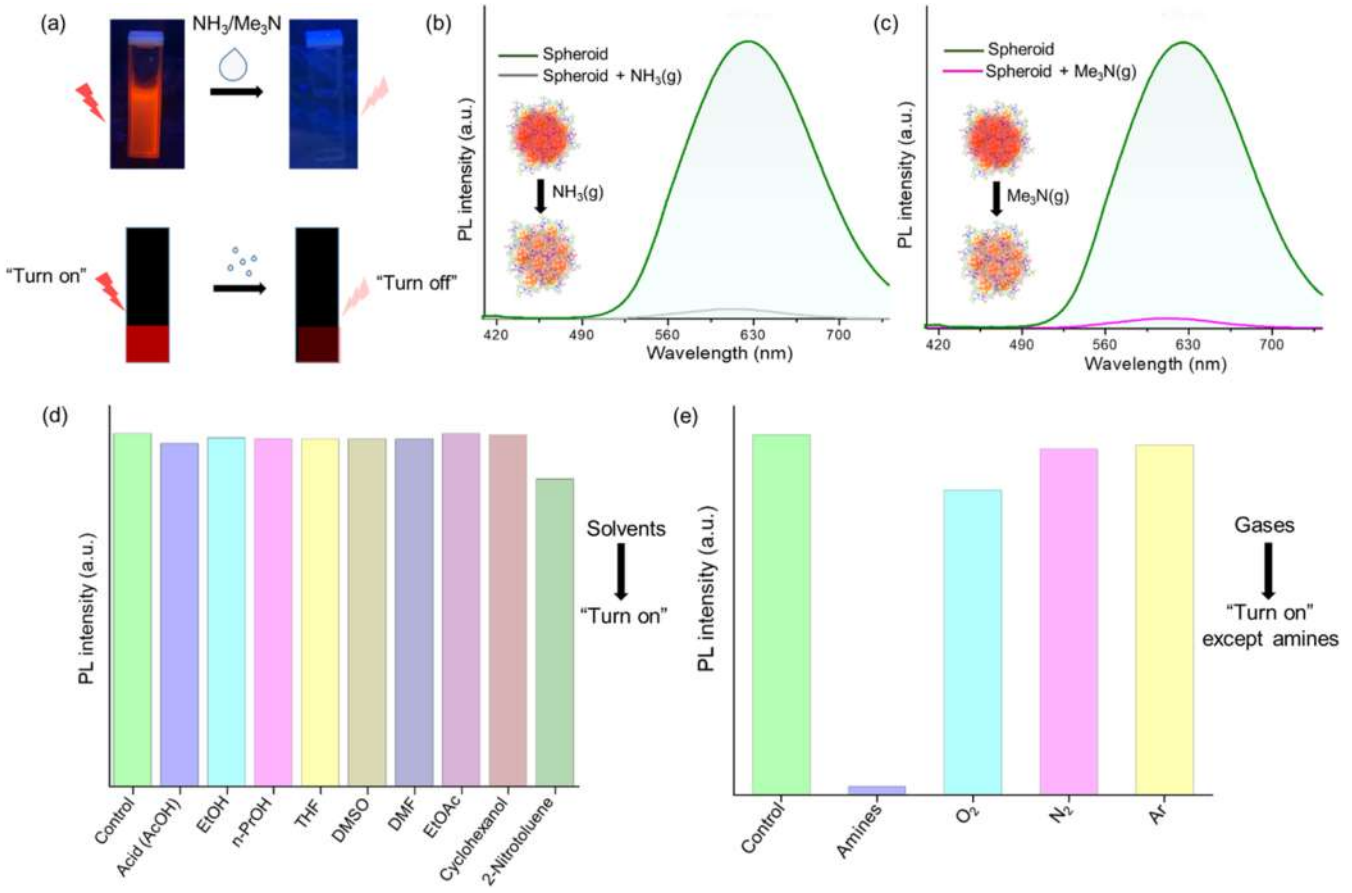


Figure 5. (a) Schematic illustration of luminescence quenching upon ammonia and trimethyl amine (in liquid and vapor) exposure, respectively. (b, c) PL quenching upon amine (NH_3 and NMe_3) exposure, respectively; inset shows representation of spheroids in turn-on and turn-off conditions. (d, e) Bar diagram showing the selectivity to different solvents/acids and other gases, significant quenching was observed for amine vapor.

amines (Figure 5a). To carry out the luminescence quenching experiment, the luminescent aggregates (80% volume fraction of water, ~1.5 mg) were drop cast onto a graphite strip (Experimental Section in SI), and it was dried in an air oven (1 h, 40 °C). After that, the coated strip was exposed to amine vapor (300 μL of ammonia, trimethyl amine, diethyl amine, dimethyl amine, triethyl amine, and ethylene diamine in a closed container of 15 mL). The emission of CASs was quenched spontaneously in all cases (Figures 5b,c and S20). A detailed study of luminescence quenching was performed on NH_3 and NMe_3 due to their relevance to foodstuffs (fish and chicken) spoilage.[48] Experiments were also performed to show the material's usability in realistic samples. The freshly prepared luminescent aggregates (80 vol % fraction of water) were drop casted on a strip and dried in oven (50 °C for 10 min.). Then the strip was exposed to spoiled fish and chicken kept inside the container (SI, page S3), and no emission of aggregates (365 nm UV light) was observed. The rate of decrease in PL intensity upon amine exposure (Figure S21) was recorded, which suggests that luminescence quenching upon NH_3 vapor exposure occurs more rapidly compared with NMe_3 (8 and 12 min, respectively, Figure S21). Such luminescent CASs can detect NH_3 and Me_3N with an ultralow detection limit of 0.568 × 10^{-7} M and 0.362 0.568 × 10^{-7} M (0.001 and 0.002 ppm), respectively (Figure S22), which is better or comparable to previous reports on NH_3 and Me_3N sensing by different materials.[49] UV−vis spectra indicate that the cluster remains stable after amine (NH_3 and Me_3N) sensing experiments (Figure S23). Further, to check the sensitivity of the material, the emission was measured for a broad range of volatile solvents, nitroaromatics, and other gases, which do not show any significant reduction in the emission intensity (Figure 5d,e). DFT calculations were performed to investigate the "turn-off" luminescence of CASs upon amine (NH_3 and NMe_3) exposure. The calculated adsorption energies for NH_3 and NMe_3 were −0.48 and −0.62 eV, respectively (inset of Figure 6a). These values confirm the spontaneous binding of amines to the surface of the cluster. Additionally, charge density difference (CDD) analysis revealed the charge accumulation on the cluster surface due to bound amines (NH_3 and NMe_3) and Cu_8 NC, respectively (Figure 6b,c). Interaction between cluster and amine possibly causes nonradiative decay leading to "turn-off" luminescence.

■ CONCLUSIONS

In summary, we have prepared *a* new Cu_8 nanocluster, primarily protected by a 4-hydroxy-6-(trifluoromethyl) pyrimidine-2-thiol ligand. Copper atoms are arranged in a tetracapped distorted tetrahedral geometry, which makes the core unique over the Cu_8 clusters reported so far. The cluster, as a discrete molecular entity, does not show luminescence in solution and the crystalline state; however, it shows bright luminescence due to the formation of cluster-assembled spheroids upon the addition of water as the antisolvent. The

https://doi.org/10.1021/acs.inorgchem.5c01082
Inorg. Chem. 2025, 64, 11001−11011

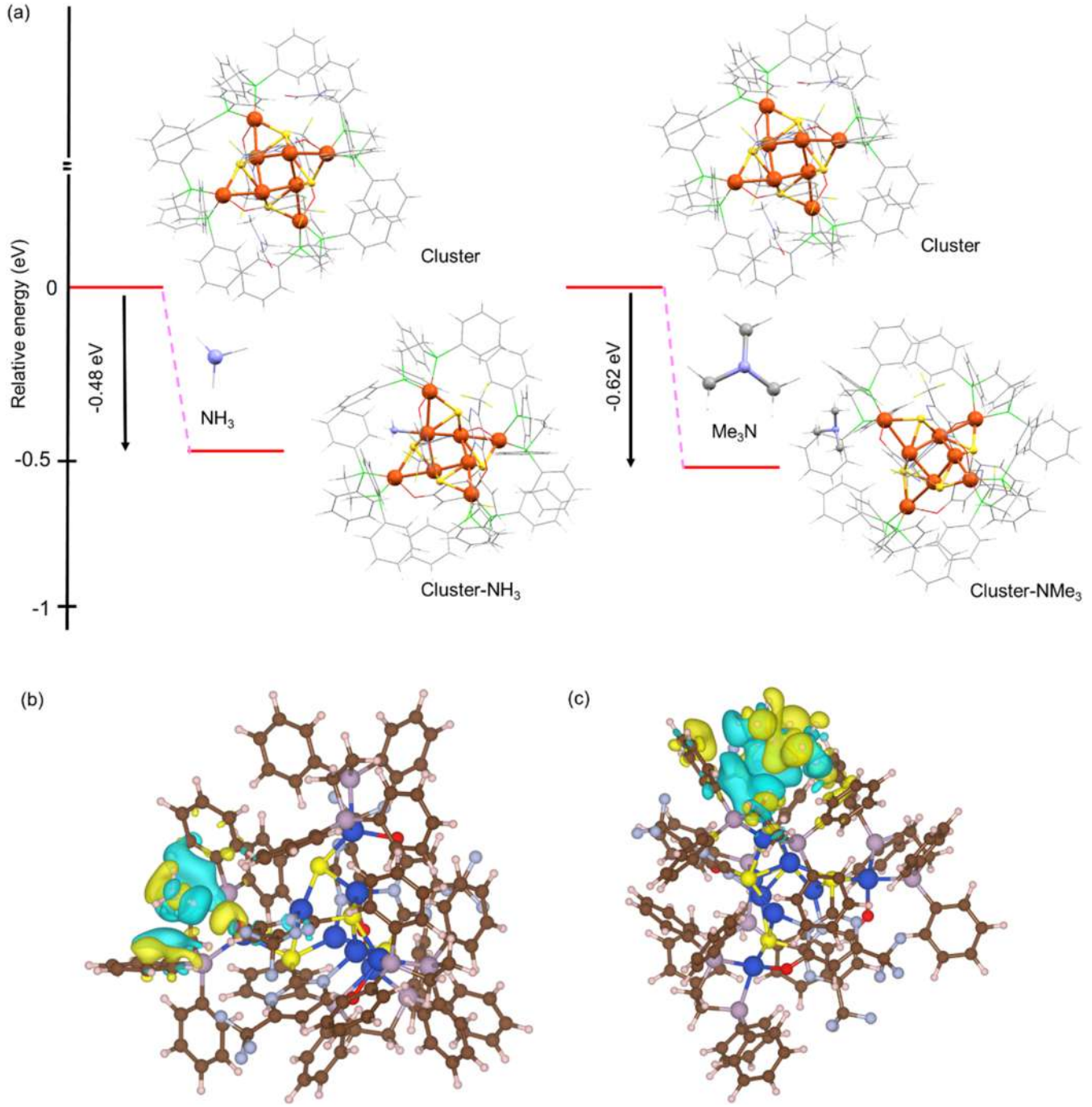


Figure 6. (a) Energetics of the binding of amines (NH_3 and NMe_3) to cluster as revealed by DFT calculation. (b, c) Charge density difference (CDD) due to adsorption on a cluster by NH_3 and NMe_3, respectively. Atomic color code: orange/blue = Cu, yellow = S, gray= C, red = O, light gray = F, gray with white background = P, and light magenta = H. The yellow and cyan electron density isosurfaces are plotted at a value of 0.00015 lel $Å^{-3}$.

photoluminescence lifetime decay profile shows that the as-synthesized luminescent spheroids are phosphorescent, and their lifetime increases with the amount (50−80 vol %) of water. Such luminescent spheroids were explored exclusively for rapid sensing of volatile amines (NH_3 and Me_3N) with ultralow detection limits of 0.001 and 0.002 ppm, respectively. In conclusion, this work introduces a novel cluster-assembled spheroid featuring a distinctive Cu_8 core structure that exhibits "turn-off" luminescence and fast sensing for volatile amines. This systematic study will help expand interest in such materials.

EXPERIMENTAL SECTION

Materials and Chemicals. Copper iodide (CuI), 1,2-bis-(diphenylphosphino)ethane (DPPE), sodium borohydride ($NaBH_4$, 98%), and 4-hydroxy-6-(trifluoromethyl) pyrimidine-2-thiol (TFMPT-H_2) were purchased from Sigma-Aldrich. Potassium bromide (KBr, IR grade) was obtained from Sigma-Aldrich. Milli-Q water was used for purification. High-performance liquid chromatography (HPLC)-grade acetonitrile (ACN), methanol (MeOH), *N,N*-dimethylformamide (DMF), amines (ammonia/25% aqueous, trimethyl amine/30% aqueous, diethyl amine, dimethyl amine, triethyl amine, and ethylene diamine), alcohols (methanol, ethanol, *n*-

https://doi.org/10.1021/acs.inorgchem.5c01082
Inorg. Chem. 2025, 64, 11001−11011

propanol, *n*-butanol, *t*-butanol, tetrahydrofuran, and dimethyl sulfoxide), acids (2-chloropropanoic acid and acetic acid), and nitro compound (2-nitrotoluene) were purchased from Rankem and Finar chemicals. All of the reagents and solvents were used without further purification.

Characterization Techniques. A PerkinElmer Lambda 365 UV−vis spectrometer with a bandpass filter of 1 nm was used to record the absorption spectra of the cluster in solution. The mass of nanoclusters (NCs) was measured in a Waters Synapt G2Si high-definition mass spectrometer. The following conditions, a flow rate of 15 μL/min, a capillary voltage of 2.95 kV, a source temperature of 100 °C, and a desolvation temperature of 150 °C with a gas flow rate of 400 L/h, were applied for ionization of NCs. The photoluminescence (PL) spectra of spheroidal assemblies were recorded using a Jobin Yvon Nanolog fluorescence spectrometer with a bandpass of 3 nm for excitation and emission. The lifetime of luminescent assemblies was measured using the HORIBA DeltaFlex time-correlated single-photon counting (TCSPC) spectrometer equipped with the detector HORIBA PPD-850 (HORIBA Delta Diode 405 nm laser). Fourier transform infrared spectroscopy was recorded using a PerkinElmer FT-IR JASCO-4100 spectrometer (4 mg of sample in 20 mg of dry KBr). X-ray photoelectron spectroscopy (XPS) of NCs was recorded using an ESCA Probe TPD spectrometer of Omicron Nanotechnology, equipped with a polychromatic Mg Kα X-ray source ($h\nu$ = 1253.6 eV). The binding energy of different elements was calibrated for C 1s (285.0 eV). Single-crystal X-ray diffraction (SC-XRD) data of single crystals were collected using a Bruker D8 VENTURE instrument equipped with a Cu Kα radiation source (1.54 Å) and a PHOTON II detector. The structure was solved by SHELXT-2018 and refined by full-matrix least-squares techniques using the SHELXL-2018 software package incorporated in the WinGX system version v2018.3. For molecular-level DFT calculations, the Gaussian 09 D.01 program was used. Powder X-ray diffraction data of microcrystalline solids was collected using a D8 Advance Bruker instrument with Cu Kα X-ray source of 1.54 Å. Thermogravimetric (TG) analysis, derivative thermogravimetry (DTG), and differential scanning calorimetry (DSC) measurements of microcrystals were recorded (25−1000 °C, N_2 gas flow of 20 mL/min.) using a NETZSCH STA 449 F3 Jupiter instrument equipped with Proteus-6.1.0 software. An optical microscope of LEICA equipped with LAS V4.8 software was used to view the single crystals of NCs at different magnifications and polarization angles. Field emission scanning electron microscopy (FESEM) images of single crystals and their energy-dispersive X-ray spectroscopy analysis were performed with a Verios G4 UC, FEI instrument. Crystals and aggregates were drop cast on the substrate (TEM grid) and dried at room temperature. The sample was then sputter-coated with gold (Au) to produce better-quality images. For transmission electron microscopy (TEM), a Talos F200i instrument operated at 300 kV was used.

Synthesis of $[Cu_{18}H_{16}(DPPE)_6]^{2+}$. Cu_{18} nanocluster was synthesized following the procedure available in the literature.[33] For one set of reactions, 95 mg of CuI and 120 mg of DPPE were mixed in 13 mL of ACN, and then the metal ion was reduced with 180 mg of dry $NaBH_4$. After 3.5 h of stirring, an orange precipitate was formed. The residue was washed multiple times with ACN and MeOH. Finally, the cluster was dissolved in DCM and used for further studies.

Synthesis of Cu_8 NC. Cu_8 nanocluster was synthesized following the LEIST method using Cu_{18} nanocluster as the precursor. Freshly prepared Cu_{18} NC was dissolved in 4 mL of DMF and then reacted with 15 mg of 4-hydroxy-6-(trifluoromethyl) pyrimidine-2-thiol (TFMPT-H_2) in 1 mL of DMF. After 4 h, the reaction mixture becomes the transparent solution. The as-synthesized cluster was kept for crystallization at room temperature. After 10 days, sheet-like single crystals were grown. The yield of Cu_8 NC is around 70% with respect to the Cu precursor.

Formation of Luminescent Aggregates. To the freshly prepared Cu_8 cluster in the DMF solution, different volume percentage of water was added. After 50% volume fraction of water, luminescence starts appearing in solution due to the formation of cluster-assembled spheroidal assemblies, as revealed by field emission scanning electron microscopy (FESEM) and dynamic light scattering (DLS) study.

Volatile Amine Compound Sensing. The freshly prepared luminescent aggregates were drop cast on a strip and dried in an oven (50 °C for 10 min). These strips were exposed to a gaseous amine environment. For practical applicability, food spoilage (fish and chicken) was monitored. The experimental setup is mentioned in the Supporting Information.

Computational Details. For molecular-level DFT calculations, the Gaussian 09 D.01 program has been used.[41a] The Becke's three-parameter hybrid exchange functional and Lee−Yang−Parr's (B3LYP) correlation functional with Pople's 6−31G* basis set were used for nonmetal elements along with LANL2DZ-ECP (effective core potential) for Cu atoms, respectively.[41f−i] For all of the calculations, an implicit solvation model based on density (SMD) has been adopted for *N*,*N*-dimethylformamide solvent (ε = 37.219) to mimic the experimental conditions.[41j] In the TDDFT calculations, 500 singlet-to-singlet excitation energies were considered. The Kohn−Sham orbital analysis has been performed using Multiwfn.[41k]

The Vienna Ab initio Simulation Package (VASP) was employed for periodic boundary condition-based calculations with generalized gradient approximation of Perdew−Burke−Ernzerhof (PBE) functional.[41l,m] The projector augmented wave (PAW) method was used to treat ion−electron interactions.[41n−p] The ionic relaxations were carried out using a conjugate gradient algorithm with convergence criteria of 10^{-4} eV and 0.02 eV $Å^{-1}$ for minimum energy and force, respectively. Owing to the large size of the unit cells of the compounds, the Brillouin zone was sampled at the γ point (1 × 1 × 1). The charge density differences (CDD) (ρ_{CDD}) have been calculated following eq 1 and plotted using visualization for electronic and structural analysis (VESTA) software.[41q]

$$\rho_{CDD} = \rho^{total} - \sum_i \rho_i^{fragments} \quad (1)$$

where ρ^{total} is the total charge density of Cu_8NC with adsorbates and $\rho_i^{fragments}$ is the charge density of the individual fragments.

■ ASSOCIATED CONTENT

Supporting Information

The Supporting Information is available free of charge at https://pubs.acs.org/doi/10.1021/acs.inorgchem.5c01082.

Photographs of experimental setup; crystal structure parameters; UV−vis; FESEM; XPS; FTIR; electronic transitions involving HOMO−LUMO; PL and lifetime data; TG and DTG; and associated figures (PDF)

Accession Codes

Deposition Number 2429176 contains the supplementary crystallographic data for this paper. These data can be obtained free of charge via the joint Cambridge Crystallographic Data Centre (CCDC) and Fachinformationszentrum Karlsruhe Access Structures service.

■ AUTHOR INFORMATION

Corresponding Authors

Biswarup Pathak − *Department of Chemistry, Indian Institute of Technology Indore, Indore 453552, India;* orcid.org/0000-0002-9972-9947; Email: biswarup@iiti.ac.in

Kumaran Nair Valsala Devi Adarsh − *Department of Physics, Indian Institute of Science Education and Research Bhopal, Bhopal 462066, India;* orcid.org/0000-0002-6337-6545; Email: adarsh@iiserb.ac.in

Thalappil Pradeep − *DST Unit of Nanoscience (DST UNS) and Thematic Unit of Excellence (TUE), Department of Chemistry, Indian Institute of Technology Madras, Chennai*

600036, India; orcid.org/0000-0003-3174-534X; Email: pradeep@iitm.ac.in

Authors

Subrata Duary − *DST Unit of Nanoscience (DST UNS) and Thematic Unit of Excellence (TUE), Department of Chemistry, Indian Institute of Technology Madras, Chennai 600036, India*

Arijit Jana − *DST Unit of Nanoscience (DST UNS) and Thematic Unit of Excellence (TUE), Department of Chemistry, Indian Institute of Technology Madras, Chennai 600036, India*

Amitabha Das − *Department of Chemistry, Indian Institute of Technology Indore, Indore 453552, India;* orcid.org/0000-0002-5000-4451

Ankit Sharma − *Department of Physics, Indian Institute of Science Education and Research Bhopal, Bhopal 462066, India*

Complete contact information is available at: https://pubs.acs.org/10.1021/acs.inorgchem.5c01082

Author Contributions

S.D. carried out the synthesis, crystallization, and the majority of the experimental studies. A.J. contributed to the design of the sensing experiments and participated in writing the manuscript. A.D. conducted the theoretical calculations, while B.P. gave insights into the theoretical data. A.S. measured the photoluminescence (PL) lifetime of the aggregates, and K.N.V.D.A. participated in discussions on the lifetime data. S.D. prepared the first draft of the manuscript and all authors contributed to finalize it. T.P. supervised the work and finalized the manuscript.

Notes

The authors declare no competing financial interest.

■ ACKNOWLEDGMENTS

S.D. acknowledges the Prime Minister's Research Fellowship (PMRF) from the Government of India (GoI). S.D. thanks the Sophisticated Analytical Instrument Facility, Indian Institute of Technology Madras (SAIF-IITM), for the single-crystal XRD and thermogravimetric (TG) measurements. A.J. acknowledges the financial support from IIT Madras. A.D. thanks GoI for a UGC fellowship. K.N.V.D.A. gratefully acknowledges the Science and Engineering Research Board (Project No. 5 CRG/2023/003013) and the Department of Science & Technology (Project No. DST/NM/TUE/QM-8/2019 342(G)/1). A.S. gratefully acknowledges the UGC for financial support with award No. 1379/(CSIR-UGC NET DECEMBER 2018). T.P. acknowledges funding from the Centre of Excellence (CoE) on Molecular Materials and Functions from the Institute of Eminence scheme of IIT Madras. He thanks the Science and Engineering Research Board (SERB), India, for funding through a research grant (SPR/2021/000439) and a JC Bose Fellowship.

■ REFERENCES

(1) Chakraborty, I.; Pradeep, T. Atomically precise clusters of noble metals: emerging link between atoms and nanoparticles. *Chem. Rev.* **2017**, *117* (12), 8208−8271.

(2) Luo, Z.; Castleman, A. W., Jr; Khanna, S. N. Reactivity of metal clusters. *Chem. Rev.* **2016**, *116* (23), 14456−14492.

(3) (a) Duary, S.; Jana, A.; Das, A.; Acharya, S.; Kini, A. R.; Roy, J.; Poonia, A. K.; Patel, D. K.; Yadav, V.; Antharjanam, P. S.; Pathak, B.; et al. Milling-Induced "Turn-off" Luminescence in Copper Nanoclusters. *Inorg. Chem.* **2024**, *63*, 18727−18737. (b) Jana, A.; Jash, M.; Dar, W. A.; Roy, J.; Chakraborty, P.; Paramasivam, G.; Lebedkin, S.; Kirakci, K.; Manna, S.; Antharjanam, S.; Machacek, J.; et al. Carborane-thiol protected copper nanoclusters: stimuli-responsive materials with tunable phosphorescence. *Chem. Sci.* **2023**, *14* (6), 1613−1626.

(4) (a) Chiang, C. H.; Tzeng, Y. W.; Yang, C. I.; Nakano, M.; Wan, W. L.; Lai, L. L.; Lee, G. H. The synthesis of three new Cu_5, Cu_8 and Cu_{12} clusters via the use of a semi-flexible aminotriazine-based bis-methylpyridine ligand. *Dalton Trans.* **2017**, *46* (4), 1237−1248. (b) Zhang, C.; Wang, Z.; Si, W. D.; Chu, H.; Zhou, L.; Li, T.; Huang, X. Q.; Gao, Z. Y.; Azam, M.; Tung, C. H.; Cui, P.; Sun, D. Dynamic and transformable Cu_{12} cluster-based CH··· π-stacked porous supramolecular frameworks. *Nat. Commun.* **2023**, *14* (1), No. 6413.

(5) Jana, A.; Duary, S.; Das, A.; Kini, A. R.; Acharya, S.; Macháček, J.; Pathak, B.; Base, T.; Pradeep, T. Multicolor Photoluminescence of Cu_{14} Cluster Modulated by Surface Ligands. *Chem. Sci.* **2024**, *15* (34), 13741−13752.

(6) Nematulloev, S.; Huang, R. W.; Yin, J.; Shkurenko, A.; Dong, C.; Ghosh, A.; Alamer, B.; Naphade, R.; Hedhili, M. N.; Maity, P.; Eddaoudi, M.; Mohammed, O. F.; Bakr, O. M. $[Cu_{15}(PPh_3)_6(PET)_{13}]^{2+}$: a copper nanocluster with crystallization enhanced photoluminescence. *Small* **2021**, *17* (27), No. 2006839.

(7) (a) Han, B. L.; Liu, Z.; Feng, L.; Wang, Z.; Gupta, R. K.; Aikens, C. M.; Tung, C. H.; Sun, D. Polymorphism in atomically precise Cu_{23} nanocluster incorporating tetrahedral [Cu4] 0 kernel. *J. Am. Chem. Soc.* **2020**, *142* (12), 5834−5841. (b) Nguyen, T. A. D.; Jones, Z. R.; Goldsmith, B. R.; Buratto, W. R.; Wu, G.; Scott, S. L.; Hayton, T. W. A Cu_{25} nanocluster with partial Cu (0) character. *J. Am. Chem. Soc.* **2015**, *137* (41), 13319−13324.

(8) Ghosh, A.; Huang, R. W.; Alamer, B.; Abou-Hamad, E.; Hedhili, M. N.; Mohammed, O. F.; Bakr, O. M. $[Cu_{61}(StBu)_{26}S_6Cl_6H_{14}]^+$: A Core−Shell Superatom Nanocluster with a Quasi-$J_{36}Cu_{19}$ Core and an "18-Crown-6" Metal-Sulfide-like Stabilizing Belt. *ACS Mater. Lett.* **2019**, *1* (3), 297−302.

(9) Huang, R. W.; Yin, J.; Dong, C.; Ghosh, A.; Alhilaly, M. J.; Dong, X.; Hedhili, M. N.; Abou-Hamad, E.; Alamer, B.; Nematulloev, S.; Han, Y.; et al. $[Cu_{81}(PhS)_{46}(t\ BuNH_2)_{10}(H)_{32}]^{3+}$ reveals the coexistence of large planar cores and hemispherical shells in high-nuclearity copper nanoclusters. *J. Am. Chem. Soc.* **2020**, *142* (19), 8696−8705.

(10) Fu, M. L.; Issac, I.; Fenske, D.; Fuhr, O. Metal-Rich Copper Chalcogenide Clusters at the Border Between Molecule and Bulk Phase: The Structures of $[Cu_{93}Se_{42}(SeC_6H_4SMe)_9(PPh_3)_{18}]$, $[Cu_{96}Se_{45}(SeC_6H_4SMe)_6(PPh_3)_{18}]$, and $[Cu_{136}S_{56}(SCH_2C_4H_3O)_{24}(dpppt)_{10}]$. *Angew. Chem., Int. Ed.* **2010**, *49* (38), 6899−6903.

(11) Ford, P. C.; Cariati, E.; Bourassa, J. Photoluminescence Properties of Multinuclear Copper (I) Compounds. *Chem. Rev.* **1999**, *99*, 3625−3647.

(12) Liu, X.; Astruc, D. Atomically precise copper nanoclusters and their applications. *Coord. Chem. Rev.* **2018**, *359*, 112−126.

(13) Qing, T.; Zhang, K.; Qing, Z.; Wang, X.; Long, C.; Zhang, P.; Hu, H.; Feng, B. Recent progress in copper nanocluster-based fluorescent probing: a review. *Microchim. Acta* **2019**, *186*, No. 670.

(14) Das, N. K.; Mukherjee, S. Size-controlled atomically precise copper nanoclusters: Synthetic protocols, spectroscopic properties and applications. *Phys. Sci. Rev.* **2018**, *3* (11), No. 20170081.

(15) Sharma, S.; Das, S.; Kaushik, K.; Yadav, A.; Patra, A.; Nandi, C. K. Unveiling the Long-Lived Emission of Copper Nanoclusters Embedded in a Protein Scaffold. *J. Phys. Chem. Lett.* **2023**, *14* (40), 8979−8987.

(16) Lin, Y.; Charchar, P.; Christofferson, A. J.; Thomas, M. R.; Todorova, N.; Mazo, M. M.; Chen, Q.; Doutch, J.; Richardson, R.; Yarovsky, I.; Stevens, M. M. Surface dynamics and ligand−core interactions of quantum sized photoluminescent gold nanoclusters. *J. Am. Chem. Soc.* **2018**, *140* (51), 18217−18226 2018.

(17) Wu, Z.; Du, Y.; Liu, J.; Yao, Q.; Chen, T.; Cao, Y.; Zhang, H.; Xie, J. Aurophilic Interactions in the Self-Assembly of Gold Nanoclusters into Nanoribbons with Enhanced Luminescence. *Angew. Chem., Int. Ed.* **2019**, *58*, 8139−8144.
(18) Chakraborty, S.; Bain, D.; Maity, S.; Kolay, S.; Patra, A. Controlling Aggregation-Induced Emission in Bimetallic Gold−Copper Nanoclusters via Surface Motif Engineering. *J. Phys. Chem. C* **2022**, *126*, 2896−2904.
(19) Wang, S.; Li, Q.; Kang, X.; Zhu, M. Customizing the structure, composition, and properties of alloy nanoclusters by metal exchange. *Acc. Chem. Res.* **2018**, *51* (11), 2784−2792.
(20) Huang, J. H.; Liu, L. Y.; Wang, Z. Y.; Zang, S. Q.; Mak, T. C. Modular Cocrystallization of Customized Carboranylthiolate-Protected Copper Nanoclusters via Host−Guest Interactions. *ACS Nano* **2022**, *16* (11), 18789−18794.
(21) Chakraborty, P.; Nag, A.; Sugi, K. S.; Ahuja, T.; Varghese, B.; Pradeep, T. Crystallization of a supramolecular coassembly of an atomically precise nanoparticle with a crown ether. *ACS Mater. Lett.* **2019**, *1* (5), 534−540.
(22) Kolay, S.; Bain, D.; Maity, S.; Devi, A.; Patra, A.; Antoine, R. Self-Assembled Metal Nanoclusters: Driving Forces and Structural Correlation with Optical Properties. *Nanomaterials* **2022**, *12*, No. 544.
(23) Rival, J. V.; Mymoona, P.; Lakshmi, K. M.; Nonappa; Pradeep, T.; Shibu, E. S. Self-Assembly of Precision Noble Metal Nanoclusters: Hierarchical Structural Complexity, Colloidal Superstructures, and Applications. *Small* **2021**, *17*, No. 2005718.
(24) Bera, D.; Goswami, N. Driving Forces and Routes for Aggregation-Induced Emission-Based Highly Luminescent Metal Nanocluster Assembly. *J. Phys. Chem. Lett.* **2021**, *12*, 9033−9046.
(25) Wu, Z.; Yao, Q.; Zang, S.; Xie, J. Directed Self-Assembly of Ultrasmall Metal Nanoclusters. *ACS Mater. Lett.* **2019**, *1*, 237−248.
(26) (a) Wu, Z.; Liu, J.; Gao, Y.; Liu, H.; Li, T.; Zou, H.; Wang, Z.; Zhang, K.; Wang, Y.; Zhang, H.; Yang, B. Assembly-Induced Enhancement of Cu Nanoclusters Luminescence with Mechanochromic Property. *J. Am. Chem. Soc.* **2015**, *137*, 12906−12913. (b) Deng, C. L.; Han, B. L.; Liu, Z. Y.; Pan, Z. H.; He, J.; Li, Y. L.; Yang, Z. L.; Luo, G. G.; Tung, C. H.; Sun, D.; Zheng, L. S. Hierarchical homochiral assembly of polyhedral cage-type nanoclusters. *CCS Chem.* **2024**, *6* (10), 2537−2548.
(27) Kumar, J. S.; Jana, A.; Raman, J.; Veera, H. M.; Kini, A. R.; Roy, J.; Jana, S. K.; Thomas, T.; Pradeep, T. Cysteine-Protected Antibacterial Spheroids of Atomically Precise Copper Clusters for Direct and Affordable Arsenic Detection from Drinking Water. *Environ. Sci. Technol. Lett.* **2024**, *11* (8), 831−837.
(28) Nag, A.; Chakraborty, P.; Thacharon, A.; Paramasivam, G.; Mondal, B.; Bodiuzzaman, M.; Pradeep, T. Atomically precise noble metal cluster-assembled superstructures in water: luminescence enhancement and sensing. *J. Phys. Chem. C* **2020**, *124* (40), 22298−22303.
(29) Nasrollahpour, H.; Sánchez, B. J.; Sillanpää, M.; Moradi, R. Metal nanoclusters in point-of-care sensing and biosensing applications. *ACS Appl. Nano Mater.* **2023**, *6* (14), 12609−12672.
(30) Budianto, A.; Pratiwi, A. G.; Ningsih, S. A.; Kusdarini, E. Reduction of Ammonia Nitrogen and Chemical Oxygen Demand of Fertilizer Industry Liquid Waste by Coconut Shell Activated Carbon in Batch and Continuous Systems. *J. Ecol. Eng.* **2023**, *24* (7), 156−164, DOI: 10.12911/22998993/164759.
(31) Jang, J. K. Amines as occupational hazards for visual disturbance. *Ind. Health* **2016**, *54* (2), 101−115.
(32) Grant, M. J.; Wolfe, K. M.; Harding, C. R.; Welch, G. C. Biogenic amine sensors using organic π-conjugated materials as active sensing components and their commercialization potential. *J. Mater. Chem. C* **2023**, *11* (29), 9749−9767.
(33) Li, J.; Ma, H. Z.; Reid, G. E.; Edwards, A. J.; Hong, Y.; White, J. M.; Mulder, R. J.; O'Hair, R. A. Synthesis and X-Ray Crystallographic Characterization of Frustum-Shaped Ligated $[Cu_{18}H_{16}(DPPE)_6]^{2+}$ and $[Cu_{16}H_{14}(DPPA)_6]^{2+}$ Nanoclusters and Studies on Their H_2 Evolution Reactions. *Chem. - Eur. J.* **2018**, *24* (9), 2070−2074.
(34) Das, A. K.; Biswas, S.; Wani, V. S.; Nair, A. S.; Pathak, B.; Mandal, S. $[Cu_{18}H_3(S\text{-}Adm)_{12}(PPh_3)_4Cl_2]$: fusion of Platonic and Johnson solids through a Cu (0) center and its photophysical properties. *Chem. Sci.* **2022**, *13* (25), 7616−7625.
(35) Wang, Y. M.; Lin, X. C.; Mo, K. M.; Xie, M.; Huang, Y. L.; Ning, G. H.; Li, D. An Atomically Precise Pyrazolate-Protected Copper Nanocluster Exhibiting Exceptional Stability and Catalytic Activity. *Angew. Chem., Int. Ed.* **2023**, *62* (9), No. 202218369.
(36) Liao, P. K.; Sarkar, B.; Chang, H. W.; Wang, J. C.; Liu, C. W. Facile entrapment of a hydride inside the tetracapped tetrahedral Cu_8^I cage inscribed in a S_{12} icosahedral framework. *Inorg. Chem.* **2009**, *48* (9), 4089−4097.
(37) Liu, L. J.; Wang, Z. Y.; Wang, Z. Y.; Wang, R.; Zang, S. Q.; Mak, T. C. Mediating CO_2 electroreduction activity and selectivity over atomically precise copper clusters. *Angew. Chem.* **2022**, *134* (35), No. 202205626.
(38) Sun, P. P.; Han, B. L.; Li, H. G.; Zhang, C. K.; Xin, X.; Dou, J. M.; Gao, Z. Y.; Sun, D. Real-Time Fluorescent Monitoring of Kinetically Controlled Supramolecular Self-Assembly of Atom-Precise Cu_8 Nanocluster. *Angew. Chem.* **2022**, *134* (20), No. 202200180.
(39) Xu, Y.; Dong, Q. G.; Dong, J. P.; Zhang, H.; Li, B.; Wang, R.; Zang, S. Q. Assembly of copper-clusters into a framework: enhancing the structural stability and photocatalytic HER performance. *Chem. Commun.* **2023**, *59* (21), 3067−3070.
(40) Li, H.; Wang, T.; Han, J.; Xu, Y.; Kang, X.; Li, X.; Zhu, M. Fluorescence resonance energy transfer in atomically precise metal nanoclusters by cocrystallization-induced spatial confinement. *Nat. Commun.* **2024**, *15* (1), No. 5351.
(41) (a) Frisch, M. J.; Trucks, G. W.; Schlegel, H. B.; Scuseria, G. E.; Robb, M. A.; Cheeseman, J. R.; Scalmani, G.; Barone, V.; Mennucci, B.; Petersson, G. A.et al. *Gaussian 09, Revision B.01*; Gaussian Inc.: Wallingford, CT, 2009. (b) Mandal, S. C.; Rawat, K. S.; Nandi, S.; Pathak, B. Theoretical insights into CO_2 hydrogenation to methanol by a Mn−PNP complex. *Catal. Sci. Technol.* **2019**, *9* (8), 1867−1878. (c) Becke, A. D. Density-functional thermochemistry. I. The effect of the exchange-only gradient correction. *J. Chem. Phys.* **1992**, *96* (3), 2155−2160. (d) Becke, A. D. Density-functional thermochemistry. IV. A new dynamical correlation functional and implications for exact-exchange mixing. *J. Chem. Phys.* **1996**, *104* (3), 1040−1046. (e) Krishnan, R. B. J. S.; Binkley, J. S.; Seeger, R.; Pople, J. A. Self-consistent molecular orbital methods. XX. A basis set for correlated wave functions. *J. Chem. Phys.* **1980**, *72* (1), 650−654. (f) Becke, A. Density-functional exchange-energy approximation with correct asymptotic behavior. *Phys. Rev. A* **1988**, *38*, No. 3098. (g) Becke, A. D. A new mixing of Hartree-Fock and local density-functional theories. *J. Chem. Phys.* **1993**, *98* (2), 1372−1377. (h) Hehre, W. J.; Ditchfield, R.; Pople, J. A. Self—consistent molecular orbital methods. XII. Further extensions of Gaussian—type basis sets for use in molecular orbital studies of organic molecules. *J. Chem. Phys.* **1972**, *56* (5), 2257−2261. (i) Hariharan, P. C.; Pople, J. A. The influence of polarization functions on molecular orbital hydrogenation energies. *Theor. Chim. Acta* **1973**, *28* (3), 213−222. (j) Marenich, A. V.; Cramer, C. J.; Truhlar, D. G. Universal solvation model based on solute electron density and on a continuum model of the solvent defined by the bulk dielectric constant and atomic surface tensions. *J. Phys. Chem. B* **2009**, *113* (18), 6378−6396. (k) Lu, T.; Chen, F. Multiwfn: A multifunctional wavefunction analyzer. *J. Comput. Chem.* **2012**, *33* (5), 580−592. (l) Perdew, J. P.; Burke, K.; Ernzerhof, M. Generalized gradient approximation made simple. *Phys. Rev. Lett.* **1996**, *77* (18), No. 3865. (m) Adamo, C.; Barone, V. Toward reliable density functional methods without adjustable parameters: The PBE0 model. *J. Chem. Phys.* **1999**, *110* (13), 6158−6170. (n) Mortensen, J. J.; Hansen, L. B.; Jacobsen, K. W. Real-space grid implementation of the projector augmented wave method. *Phys. Rev. B* **2005**, *71* (3), No. 035109. (o) Enkovaara, J.; Rostgaard, C.; Mortensen, J. J.; Chen, J.; Dułak, M.; Ferrighi, L.; Gavnholt, J.; Glinsvad, C.; Haikola, V.; Hansen, H. A.; Kristoffersen, H. H.; et al. Electronic structure calculations with GPAW: a real-space implementation of the projectoraugmented-wave method. *J. Phys.: Condens. Matter* **2010**,

22 (25), No. 253202. (p) Blöchl, P. E. Projector augmented-wave method. *Phys. Rev. B* **1994**, *50* (24), No. 17953. (q) Momma, K.; Izumi, F. VESTA: a three-dimensional visualization system for electronic and structural analysis. *J. Appl. Crystallogr.* **2008**, *41* (3), 653−658.
(42) Kresse, G.; Furthmüller, J. Efficient iterative schemes for ab initio total-energy calculations using a plane-wave basis set. *Phys. Rev. B* **1996**, *54* (16), No. 11169.
(43) (a) Shen, H.; Xu, J.; Fu, Z.; Wei, X.; Kang, X.; Shi, W.; Zhu, M. Photoluminescence Quenching of Hydrophobic Ag_{29} Nanoclusters Caused by Molecular Decoupling during Aqueous Phase Transfer and Emission Recovery through Supramolecular Recoupling. *Angew. Chem., Int. Ed.* **2024**, *63* (12), No. 202317995. (b) Bhattacharyya, A.; Tiwari, V.; Karmakar, T. Electrostatic-driven self-assembly of Janus-like monolayer-protected metal nanoclusters. *J. Phys. Chem. Lett.* **2024**, *15* (3), 687−692.
(44) Jülicher, F.; Lipowsky, R. Domain-induced Budding of Vesicles. *Phys. Rev. Lett.* **1993**, *70*, No. 2964.
(45) Zhou, Y.; Zeng, H. C. Simultaneous Synthesis and Assembly of Noble Metal Nanoclusters with Variable Micellar Templates. *J. Am. Chem. Soc.* **2014**, *136*, 13805−13817.
(46) Jash, M.; Jana, A.; Poonia, A. K.; Khatun, E.; Chakraborty, P.; Nagar, A.; Ahuja, T.; Adarsh, K. V.; Pradeep, T. Phosphine-Protected Atomically Precise Silver−Gold Alloy Nanoclusters and Their Luminescent Superstructures. *Chem. Mater.* **2023**, *35* (1), 313−326.
(47) Ai, L.; Liu, Z.; Zhou, D.; Liu, J.; Zou, H.; Wu, Z.; Liu, Y.; Zhang, H.; Yang, B. Copper inter-nanoclusters distance-modulated chromism of self-assembly induced emission. *Nanoscale* **2017**, *9* (47), 18845−18854.
(48) Andre, R. S.; Mercante, L. A.; Facure, M. H.; Sanfelice, R. C.; Fugikawa-Santos, L.; Swager, T. M.; Correa, D. S. Recent progress in amine gas sensors for food quality monitoring: novel architectures for sensing materials and systems. *ACS Sens.* **2022**, *7* (8), 2104−2131.
(49) (a) Das, G.; Garai, B.; Prakasam, T.; Benyettou, F.; Varghese, S.; Sharma, S. K.; Gándara, F.; Pasricha, R.; Baias, M.; Jagannathan, R.; Saleh, N. I.; et al. Fluorescence turn on amine detection in a cationic covalent organic framework. *Nat. Commun.* **2022**, *13* (1), No. 3904. (b) D, B.; Dey, D.; Varsha, T. L.; Salfeena, C. T. F.; Panda, M. K.; Somappa, S. B. Rapid visual detection of amines by pyrylium salts for food spoilage taggant. *ACS Appl. Bio Mater.* **2020**, *3* (2), 772−778. (c) Jia, R.; Tian, W.; Bai, H.; Zhang, J.; Wang, S.; Zhang, J. Amine-responsive cellulose-based ratiometric fluorescent materials for real-time and visual detection of shrimp and crab freshness. *Nat. Commun.* **2019**, *10* (1), No. 795. (d) Dalapati, S.; Jin, E.; Addicoat, M.; Heine, T.; Jiang, D. Highly emissive covalent organic frameworks. *J. Am. Chem. Soc.* **2016**, *138* (18), 5797−5800.


CAS BIOFINDER DISCOVERY PLATFORM™
BRIDGE BIOLOGY AND CHEMISTRY FOR FASTER ANSWERS
Analyze target relationships, compound effects, and disease pathways
Explore the platform
CAS
A division of the American Chemical Society

Supporting Information

Solvent-Modulated Luminescent Spheroidal Assemblies of Cu_8 Nanocluster for Volatile Amine Sensing

Subrata Duary,[a] Arijit Jana,[a] Amitabha Das,[b] Ankit Sharma,[c] Biswarup Pathak,*[b] Kumaran Nair Valsala Devi Adarsh,*[c] and Thalappil Pradeep*[a]

Authors affiliations

[a] DST Unit of Nanoscience (DST UNS) and Thematic Unit of Excellence (TUE), Department of Chemistry, Indian Institute of Technology Madras, Chennai – 600036, India.

*E-mail: pradeep@iitm.ac.in

[b] Department of Chemistry, Indian Institute of Technology Indore, Indore 453552, India.

*E-mail: biswarup@iiti.ac.in

[c] Department of Physics, Indian Institute of Science Education and Research Bhopal, Bhopal 462066, India.

*E-mail: adarsh@iiserb.ac.in

Table of contents

Items	Descriptions	Page No
	Experimental set up for amine sensing emphasizing foodstuffs (fish and chicken) spoilage monitoring	S3
Table S1	Crystal data and structure refinement of $[Cu_8(TFMPT)_4(DPPE)_4]$	S3
Table S2	Atomic coordinates and equivalent isotropic displacement parameters for Cu_8 NC	S4-S9
Figure S1	Essential characterization of $[Cu_{18}H_{16}(DPPE)_6]^{2+}$ nanoclusters	S9
Figure S2	FESEM images and EDS elemental spectrum of Cu_8	S10
Figure S3	Comparative structures of Cu_8 clusters reported in literature	S10
Figure S4	Metal clusters per unit cell and bond distances	S11
Figure S5	UV-vis. spectra of cluster	S11

Figure S6	Collision energy-dependent fragmentation of fragmented species	S12
Figure S7	XPS spectra of Cu_8	S12
Figure S8	ORTEP structure	S13
Figure S9	FTIR spectra	S13
Figure S10	DFT optimized structure of cluster and electronic transitions showing MOs involved	S14
Figure S11	Photograph of vials with 80% volume fraction of different polar protic solvents under UV	S14
Figure S12	DLS measurement of cluster aggregates	S14
Figure S13	HRSEM of cluster aggregates at different vol% water	S15
Figure S14	TEM images of spheroidal assembly	S15
Figure S15	TCSPC of aggregates at different vol% water	S15
Figure S16	pH-induced luminescence switching	S16
Figure S17	Oxygen sensing through PL measurement	S16
Figure S18	Stability of luminescent spheroids through PL study	S17
Figure S19	Effect of heating on PL intensity of luminescent spheroids	S17
Figure S20	Sensing of volatile amines	S18
Figure S21	Rate of PL intensity change upon amines (NH_3 and Me_3N) exposure	S18
Figure S22	Limit of detection (LoD) curve of NH_3 and Me_3N	S19
Figure S23	UV-vis spectra of cluster-assembled spheroids after sensing experiment	S19
Figure S24	Powder X-ray diffraction spectra of Cu_8	S20
Figure S25	Thermogravimetry (TG) and derivative thermogravimetry (DTG) plot of Cu_8	S20
	References	

Experimental set up for visual detection of volatile amine sensing, emphasizing on foodstuffs (fish and chicken) spoilage monitoring.

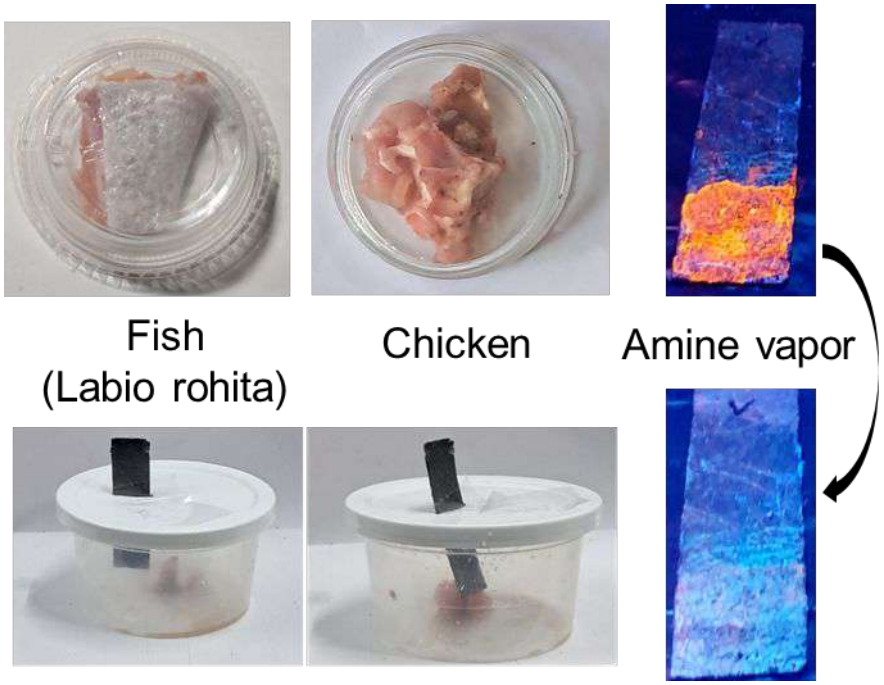


Table S1. Crystal data and structure refinement for Cu_8 NC.

Identification code	Cu_8 SM	
Empirical formula	$C_{130}\ H_{114}\ Cu_8\ F_{12}\ N_{10}\ O_6\ P_8\ S_4$	
Formula weight	3024.63	
Temperature	200(2) K	
Wavelength	1.54178 Å	
Crystal system	Triclinic	
Space group	P -1	
Unit cell dimensions	a = 16.7932(9) Å	a= 94.644(2)°.
	b = 16.9244(9) Å	b= 97.173(2)°.
	c = 26.2178(14) Å	g = 116.938(2)°.
Volume	6510.8(6) $Å^3$	
Z	2	
Density (calculated)	1.543 Mg/m^3	
Absorption coefficient	3.562 mm^{-1}	
F(000)	3072	
Crystal size	0.181 x 0.132 x 0.032 mm^3	
Theta range for data collection	1.719 to 68.482°.	
Index ranges	-20<=h<=20, -20<=k<=20, -30<=l<=31	

Reflections collected	226915
Independent reflections	23900 [R(int) = 0.0825]
Completeness to theta = 67.679°	99.9 %
Absorption correction	Semi-empirical from equivalents
Max. and min. transmission	0.6695 and 0.4908
Refinement method	Full-matrix least-squares on F^2
Data / restraints / parameters	23900 / 31 / 1604
Goodness-of-fit on F^2	1.059
Final R indices [I>2sigma(I)]	R1 = 0.0534, wR2 = 0.1376
R indices (all data)	R1 = 0.0728, wR2 = 0.1594
Extinction coefficient	0.00067(5)
Largest diff. peak and hole	0.518 and -0.562 e.$Å^{-3}$

Table S2. Atomic coordinates (x 10^4) and equivalent isotropic displacement parameters ($Å^2$x 10^3) for Cu_8NC. U(eq) is defined as one third of the trace of the orthogonalized U^{ij} tensor.

	x	y	z	U(eq)
Cu(1)	5878(1)	4273(1)	7592(1)	57(1)
Cu(2)	5981(1)	3032(1)	8074(1)	57(1)
Cu(3)	6734(1)	3089(1)	7270(1)	57(1)
Cu(4)	5088(1)	2802(1)	6942(1)	58(1)
Cu(5)	6737(1)	5751(1)	8369(1)	61(1)
Cu(6)	6148(1)	1602(1)	8493(1)	63(1)
Cu(7)	7364(1)	3120(1)	6358(1)	63(1)
Cu(8)	3327(1)	2642(1)	6689(1)	66(1)
C(1)	7239(3)	3328(3)	4960(2)	71(1)
C(2)	6759(5)	3802(5)	5006(3)	107(2)
C(3)	6354(6)	3969(6)	4566(3)	131(3)
C(4)	6409(5)	3656(6)	4083(3)	117(2)
C(5)	6910(5)	3218(4)	4028(2)	99(2)
C(6)	7321(4)	3050(4)	4465(2)	83(1)
C(7)	8955(3)	3658(3)	5526(2)	71(1)
C(8)	9478(4)	4491(4)	5819(2)	90(2)

C(9)	10392(4)	4983(5)	5798(3)	105(2)
C(10)	10788(4)	4640(5)	5495(3)	103(2)
C(11)	10299(4)	3811(5)	5205(3)	106(2)
C(12)	9380(4)	3317(4)	5218(2)	90(2)
C(13)	7399(3)	1890(3)	5372(2)	71(1)
C(14)	7683(3)	1534(3)	5837(2)	72(1)
C(15)	6058(3)	782(3)	6241(2)	71(1)
C(16)	5358(4)	969(4)	6117(3)	94(2)
C(17)	4479(4)	296(5)	5948(3)	114(2)
C(18)	4286(5)	-569(5)	5918(3)	105(2)
C(19)	4980(5)	-783(4)	6040(3)	115(2)
C(20)	5874(4)	-102(4)	6207(3)	102(2)
C(21)	7895(3)	1548(3)	6925(2)	69(1)
C(22)	7602(4)	846(4)	7209(2)	87(2)
C(23)	8213(5)	764(5)	7575(3)	106(2)
C(24)	9107(4)	1377(5)	7676(2)	99(2)
C(25)	9400(4)	2091(4)	7419(2)	90(2)
C(26)	8801(4)	2187(4)	7045(2)	80(1)
C(27)	6233(3)	-547(3)	8139(2)	72(1)
C(28)	5652(4)	-765(3)	7675(2)	81(1)
C(29)	5558(5)	-1438(4)	7296(3)	103(2)
C(30)	6060(5)	-1883(4)	7383(3)	108(2)
C(31)	6624(5)	-1686(4)	7836(3)	104(2)
C(32)	6734(4)	-1018(4)	8221(2)	88(2)
C(33)	5700(3)	-327(3)	9097(2)	72(1)
C(34)	4891(5)	-366(5)	9156(3)	120(3)
C(35)	4376(6)	-907(7)	9484(4)	168(4)
C(36)	4697(6)	-1362(5)	9777(4)	133(3)
C(37)	5489(6)	-1336(4)	9725(3)	109(2)
C(38)	5994(5)	-828(4)	9385(2)	92(2)
C(39)	7509(3)	876(3)	8953(2)	73(1)
C(40)	7704(3)	1637(3)	9372(2)	74(1)
C(41)	7302(3)	3047(3)	9713(2)	68(1)
C(42)	6828(4)	3525(4)	9676(2)	93(2)
C(43)	6766(5)	3992(6)	10114(3)	120(2)
C(44)	7164(5)	3965(5)	10594(3)	115(2)
C(45)	7630(5)	3489(5)	10644(2)	101(2)
C(46)	7708(4)	3043(4)	10207(2)	86(2)

C(47)	8429(3)	3309(3)	8954(2)	60(1)
C(48)	8649(4)	3140(4)	8480(2)	75(1)
C(49)	9457(4)	3755(4)	8348(2)	83(1)
C(50)	10035(4)	4528(4)	8677(2)	84(1)
C(51)	9807(4)	4703(4)	9142(2)	83(1)
C(52)	9014(3)	4105(3)	9282(2)	74(1)
C(53)	8417(3)	8067(3)	8753(2)	73(1)
C(54)	8770(4)	7991(4)	8312(2)	93(2)
C(55)	9310(4)	8737(6)	8109(3)	116(2)
C(56)	9497(5)	9573(6)	8352(4)	137(3)
C(57)	9164(5)	9664(5)	8788(4)	127(3)
C(58)	8619(4)	8911(4)	8988(3)	98(2)
C(59)	8331(3)	7010(3)	9568(2)	67(1)
C(60)	8572(4)	7609(4)	10024(2)	81(1)
C(61)	9089(4)	7553(4)	10464(2)	92(2)
C(62)	9369(5)	6918(5)	10448(3)	107(2)
C(63)	9147(6)	6334(5)	10000(3)	130(3)
C(64)	8627(5)	6374(4)	9563(2)	102(2)
C(65)	6812(3)	7310(3)	9201(2)	67(1)
C(66)	6008(3)	6449(3)	9276(2)	67(1)
C(67)	4782(3)	6066(3)	8303(2)	64(1)
C(68)	4645(4)	6767(4)	8501(2)	85(2)
C(69)	4106(4)	7043(4)	8199(3)	102(2)
C(70)	3683(4)	6608(4)	7702(3)	96(2)
C(71)	3805(5)	5907(5)	7507(2)	103(2)
C(72)	4358(4)	5649(4)	7801(2)	85(2)
C(73)	4685(3)	4676(3)	8903(2)	63(1)
C(74)	3790(3)	4475(4)	8908(2)	88(2)
C(75)	3242(4)	3747(5)	9130(3)	107(2)
C(76)	3571(4)	3212(4)	9339(2)	91(2)
C(77)	4444(4)	3402(4)	9332(2)	91(2)
C(78)	4997(4)	4121(4)	9112(2)	81(1)
C(79)	3487(4)	2642(3)	5371(2)	80(1)
C(80)	2843(4)	2441(4)	4929(2)	97(2)
C(81)	2803(6)	1909(6)	4491(3)	127(3)
C(82)	3381(9)	1578(7)	4486(3)	164(4)
C(83)	4026(9)	1750(8)	4913(4)	190(5)
C(84)	4062(6)	2284(6)	5358(3)	130(3)

C(85)	4519(3)	4393(3)	5999(2)	71(1)
C(86)	4698(4)	4996(4)	6439(2)	87(2)
C(87)	5384(5)	5855(4)	6502(3)	113(2)
C(88)	5908(5)	6118(5)	6133(4)	125(3)
C(89)	5768(5)	5520(6)	5703(3)	117(2)
C(90)	5070(4)	4642(4)	5629(2)	87(2)
C(91)	2586(4)	3537(4)	5847(2)	80(1)
C(92)	1724(3)	2735(4)	5924(2)	80(1)
C(93)	1208(5)	3753(5)	6780(3)	98(2)
C(94)	1087(5)	4362(5)	7096(3)	115(2)
C(95)	1395(5)	4523(5)	7609(3)	109(2)
C(96)	1838(4)	4077(5)	7827(3)	108(2)
C(97)	1991(4)	3487(4)	7513(2)	90(2)
C(98)	1677(3)	3315(4)	6981(2)	76(1)
C(99)	880(4)	1423(4)	6577(2)	81(1)
C(100)	998(5)	756(5)	6771(3)	129(3)
C(101)	259(6)	-78(6)	6776(4)	155(4)
C(102)	-593(5)	-221(6)	6584(3)	128(3)
C(103)	-717(5)	429(5)	6382(4)	130(3)
C(104)	8(4)	1256(5)	6377(3)	109(2)
C(105)	4880(3)	1164(3)	7352(2)	57(1)
C(106)	3586(3)	-109(3)	7315(2)	79(1)
C(107)	3098(3)	174(3)	7005(2)	77(1)
C(108)	3554(3)	1034(3)	6856(2)	64(1)
C(109)	3132(4)	-1007(5)	7493(4)	128(3)
C(110)	4046(3)	2599(3)	7903(2)	56(1)
C(111)	4434(3)	1782(3)	8475(2)	62(1)
C(112)	3501(3)	1328(3)	8513(2)	74(1)
C(113)	2928(3)	1572(3)	8243(2)	72(1)
C(114)	1941(4)	1123(5)	8277(3)	101(2)
C(115)	6793(3)	4666(3)	6685(2)	56(1)
C(116)	7100(3)	5927(3)	7276(2)	59(1)
C(117)	7758(3)	6444(3)	6985(2)	66(1)
C(118)	7864(3)	6011(3)	6562(2)	67(1)
C(119)	8555(4)	6518(4)	6236(3)	90(2)
C(120)	7954(3)	4779(3)	7987(2)	56(1)
C(121)	8578(3)	4477(3)	7291(2)	58(1)
C(122)	9373(3)	5292(3)	7495(2)	67(1)

C(123)	9378(3)	5771(3)	7934(2)	66(1)
C(124)	10221(4)	6638(4)	8172(3)	90(2)
O(1)	8504(2)	4001(2)	6876(1)	69(1)
O(2)	6947(2)	6262(2)	7675(1)	69(1)
O(3)	5012(2)	1596(2)	8716(1)	72(1)
O(4)	3151(2)	1356(2)	6572(1)	74(1)
S(1)	7004(1)	4480(1)	8308(1)	55(1)
S(2)	6065(1)	1821(1)	7610(1)	56(1)
S(3)	4375(1)	3402(1)	7469(1)	57(1)
S(4)	6198(1)	3485(1)	6492(1)	56(1)
P(1)	7745(1)	3092(1)	5546(1)	64(1)
P(2)	7201(1)	1727(1)	6401(1)	64(1)
P(3)	6309(1)	329(1)	8626(1)	65(1)
P(4)	7382(1)	2471(1)	9120(1)	62(1)
P(5)	7666(1)	7036(1)	8971(1)	62(1)
P(6)	5484(1)	5658(1)	8664(1)	59(1)
P(7)	3562(1)	3296(1)	5969(1)	67(1)
P(8)	1879(1)	2501(1)	6594(1)	72(1)
N(1)	8678(2)	5557(2)	8190(1)	63(1)
N(2)	7873(2)	4218(2)	7566(1)	54(1)
N(3)	6625(2)	5019(2)	7112(1)	55(1)
N(4)	7398(2)	5118(2)	6395(1)	63(1)
N(5)	4483(3)	364(2)	7497(2)	71(1)
N(6)	4476(2)	1519(2)	7043(1)	57(1)
N(7)	4691(2)	2447(2)	8169(1)	57(1)
N(8)	3173(2)	2200(3)	7925(2)	66(1)
F(1)	8902(4)	7385(3)	6360(2)	176(2)
F(2)	8202(4)	6346(4)	5742(2)	164(2)
F(3)	9211(3)	6325(3)	6257(2)	154(2)
F(4)	1504(3)	376(4)	7972(3)	204(3)
F(5)	1786(3)	910(5)	8732(2)	190(3)
F(6)	1518(3)	1556(4)	8163(3)	185(3)
F(7)	3395(4)	-1568(3)	7270(3)	203(3)
F(8)	2266(3)	-1424(3)	7349(3)	199(3)
F(9)	3353(4)	-1003(4)	7969(3)	216(4)
F(10)	10963(2)	6659(3)	8060(2)	152(2)
F(11)	10362(3)	6760(3)	8684(2)	156(2)
F(12)	10191(3)	7332(2)	8032(2)	156(2)

C(125)	1912(8)	-1054(7)	9055(5)	193(5)
C(126)	747(8)	-1182(12)	9510(6)	263(9)
C(127)	2161(10)	159(7)	9670(4)	195(6)
N(9)	1609(6)	-651(5)	9453(3)	140(3)
O(5)	2136(5)	679(5)	9940(3)	187(3)
O(6)	1704(11)	-1468(6)	5775(5)	276(6)
N(10)	1120(6)	-649(6)	5476(3)	159(3)
C(129)	1395(11)	273(9)	5383(7)	346(12)
C(128)	1861(10)	-760(10)	5676(6)	250(8)
C(130)	215(9)	-1277(10)	5337(7)	289(9)

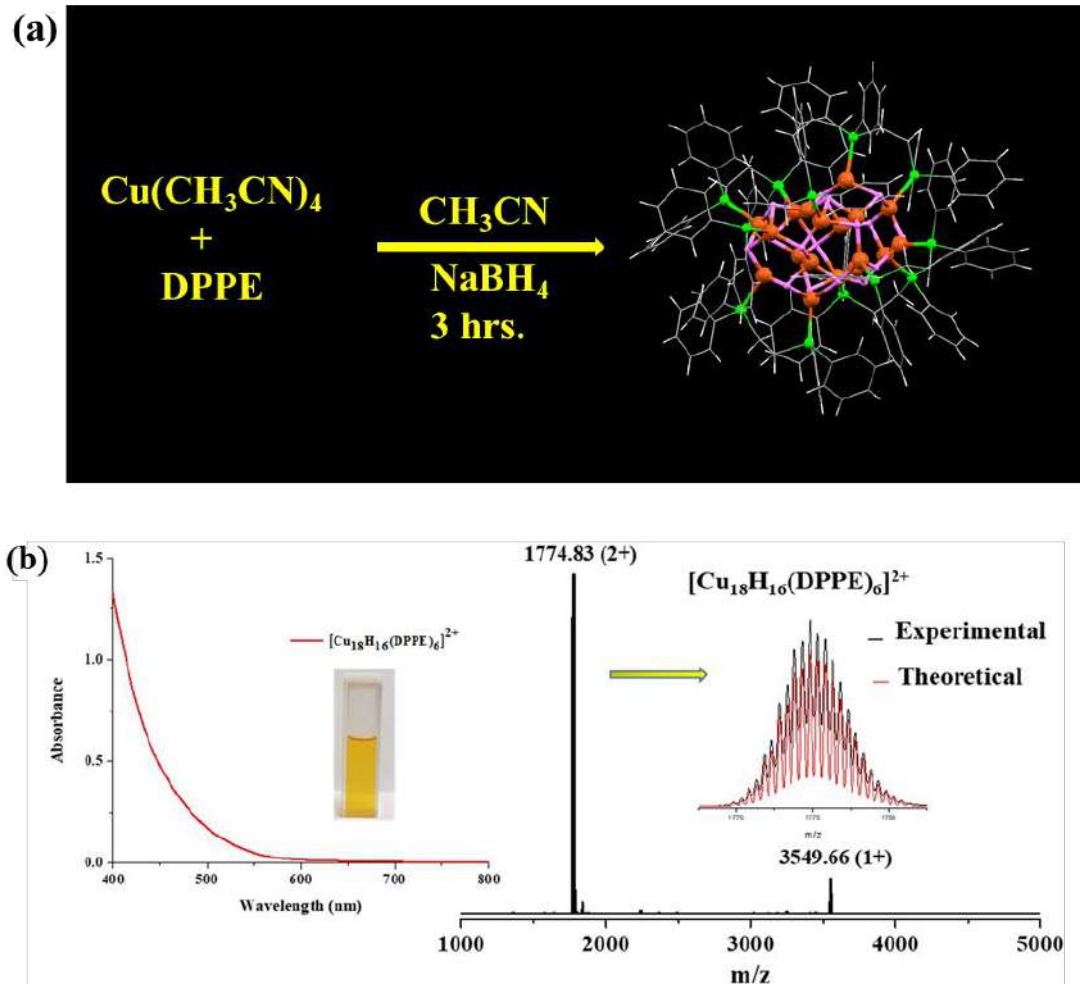
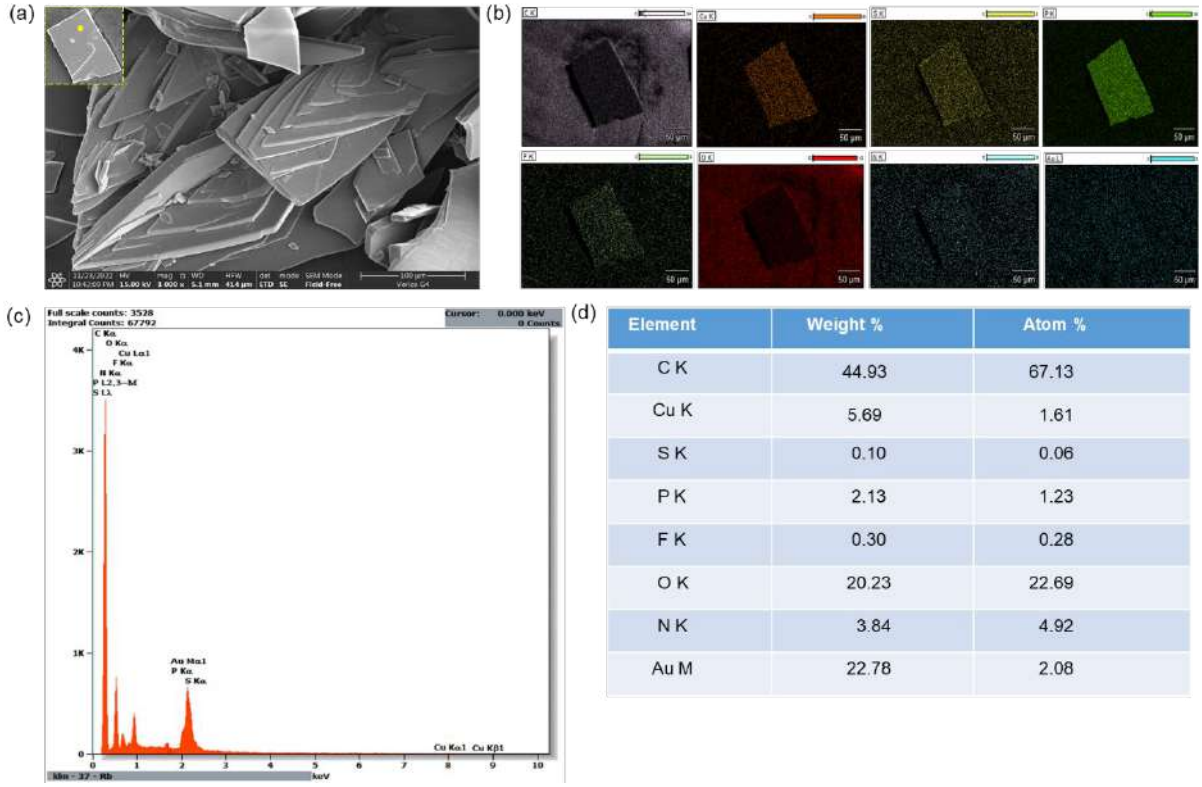


Figure S1. (a) Scheme for synthesis of Cu_{18} NC. (b) UV-vis. and ESI MS spectra of as synthesized Cu_{18} NC Atomic color code: orange=Cu, yellow=S, green=P, grey=C, red=O, blue=N, F= light green and white/magenta=H.



Element	Weight %	Atom %
C K	44.93	67.13
Cu K	5.69	1.61
S K	0.10	0.06
P K	2.13	1.23
F K	0.30	0.28
O K	20.23	22.69
N K	3.84	4.92
Au M	22.78	2.08

Figure S2. (a) FESEM images of agglomerated sheets of single crystals. (b) EDS mapping of each elements. (c) EDS spectra. (d) Weight and atomic percentage of elements from FESEM analysis.

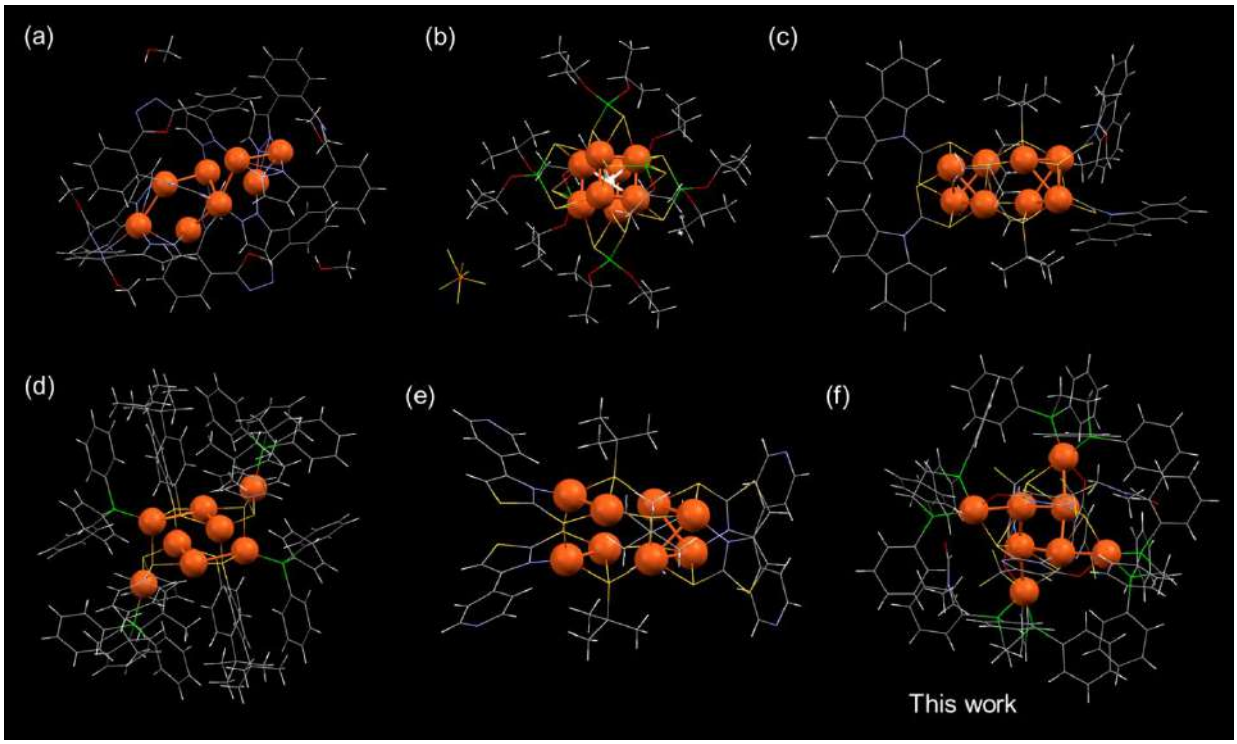


Figure S3. A comparison between single crystal structure of reported Cu_8 clusters, such as (a) puckered core [1] (b) cubic structure [2] (c) two fused tetrahedron [3], (d) bi-capped octahedral, [4] (e) one tetrahedral stapled by two Cu_2 unit [5] along with tetrahedral Cu_4 unit and (f) tetra capped distorted square planner structure. Atomic color code: orange=Cu, yellow=S, green=P, grey=C, red=O, blue=N, F= light green and white=H.

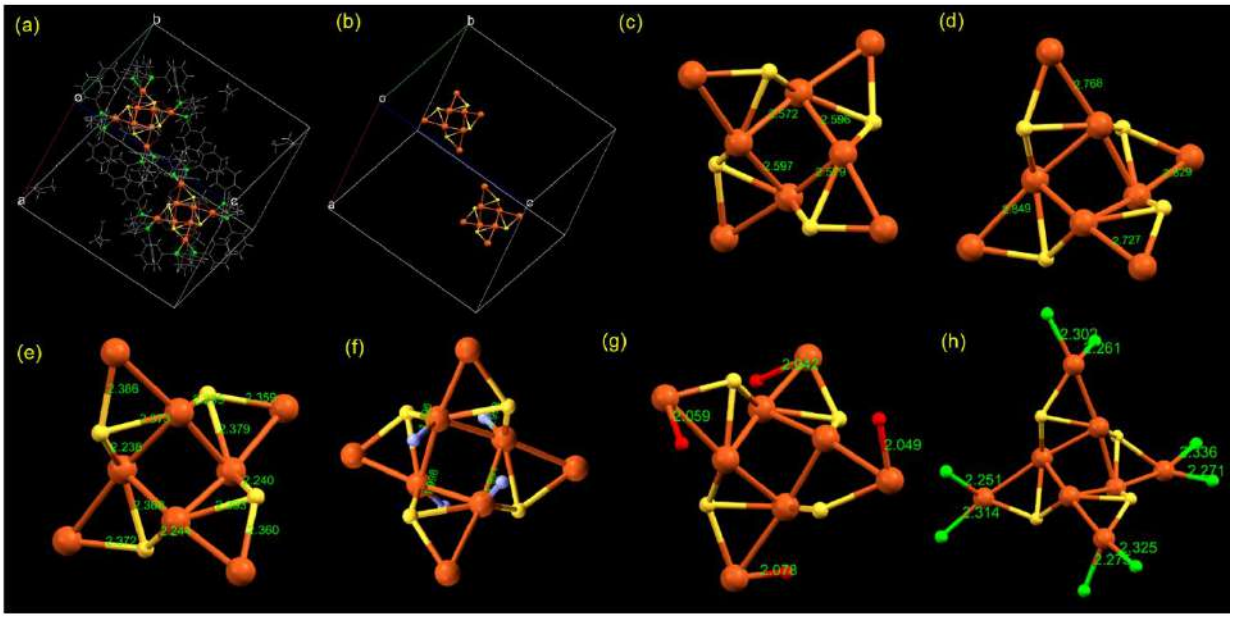


Figure S4. (a,b) Complete structure and core of clusters per unit cell. (c,d,e,f,g,h) bond distances of inner Cu-Cu, outer Cu-Cu, Cu-S, Cu-N, Cu-O and Cu-P respectively. Atomic color code: orange=Cu, yellow=S, green=P, grey=C, red=O, blue=N, F= light green and white=H.

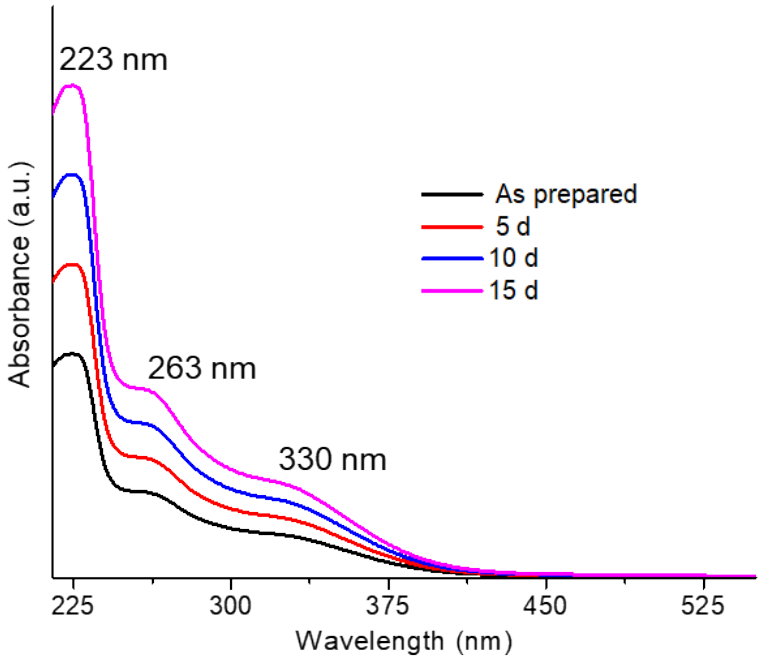


Figure S5. UV-vis. spectra of Cu_8 NC dissolved in acetonitrile indicating stability up to 15 days.

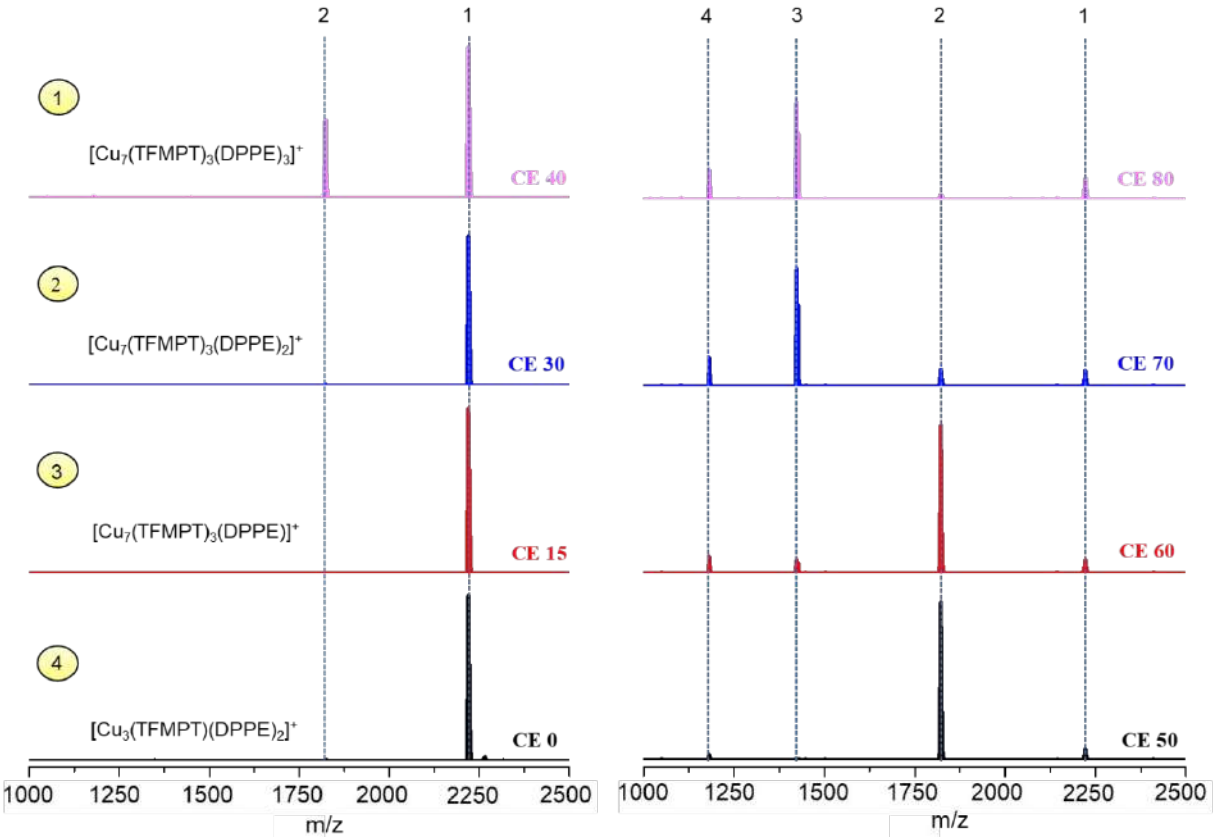


Figure S6. Collision energy dependent fragmentation of fragmented species. Inset shows molecular formula.

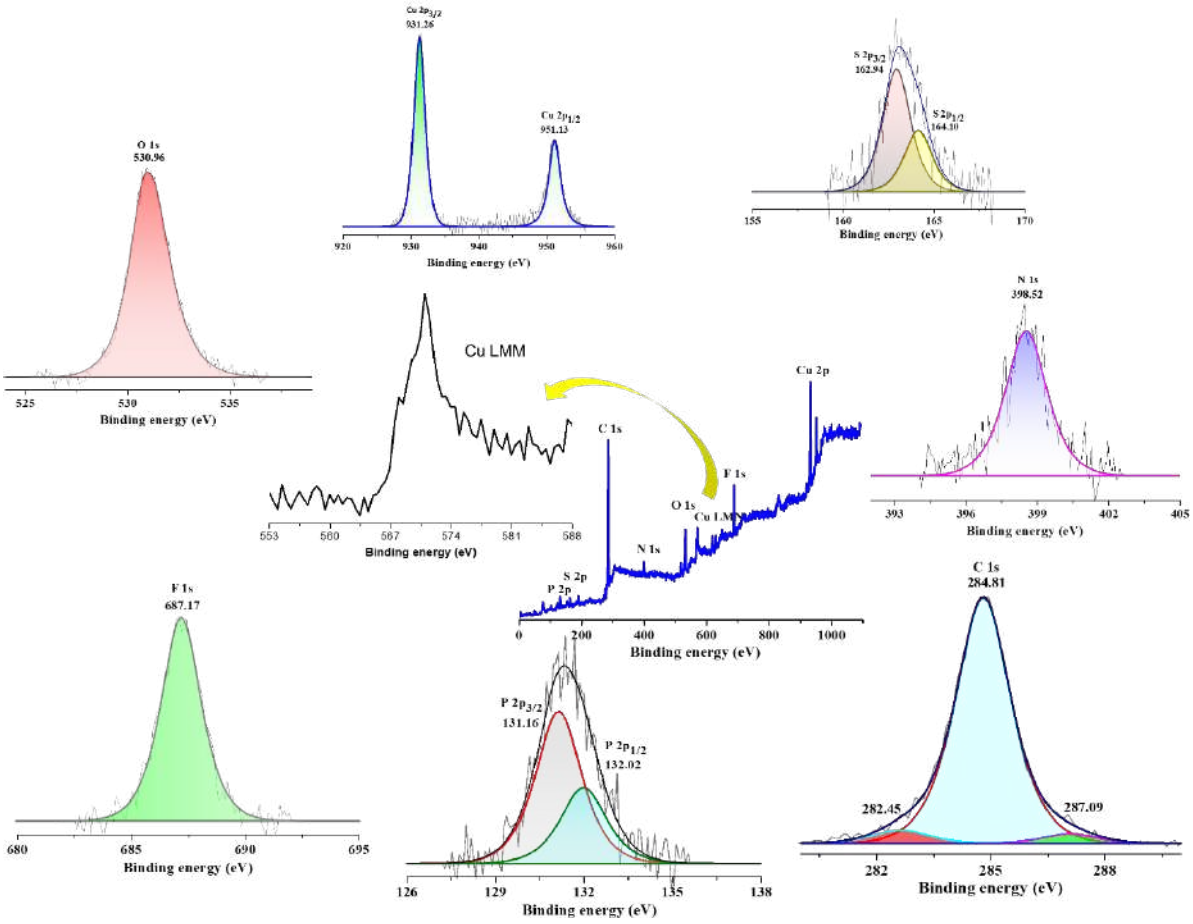


Figure S7. XPS survey spectra of singe crystals showing presence of respective elements. Expanded peak fittings of spectral region for each elements are shown. Inset shows Cu LMM auger spectral region.

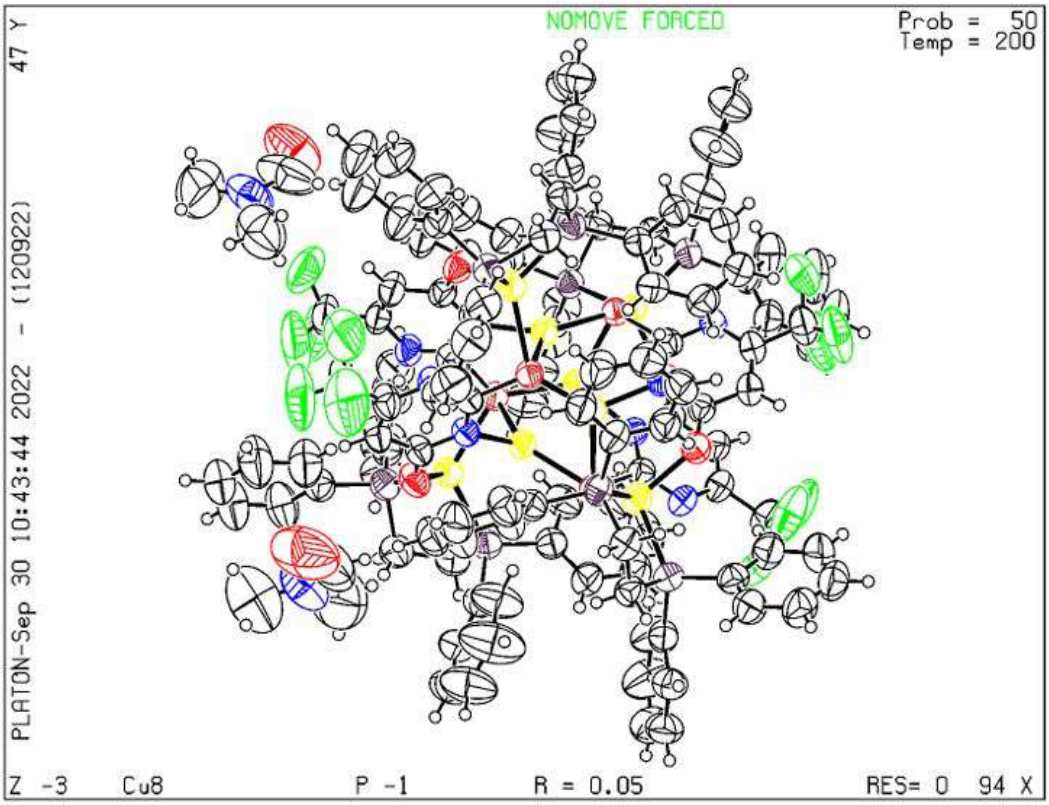


Figure S8. ORTEP structure of Cu_8 nanocluster with 50% thermal ellipsoid parameters.

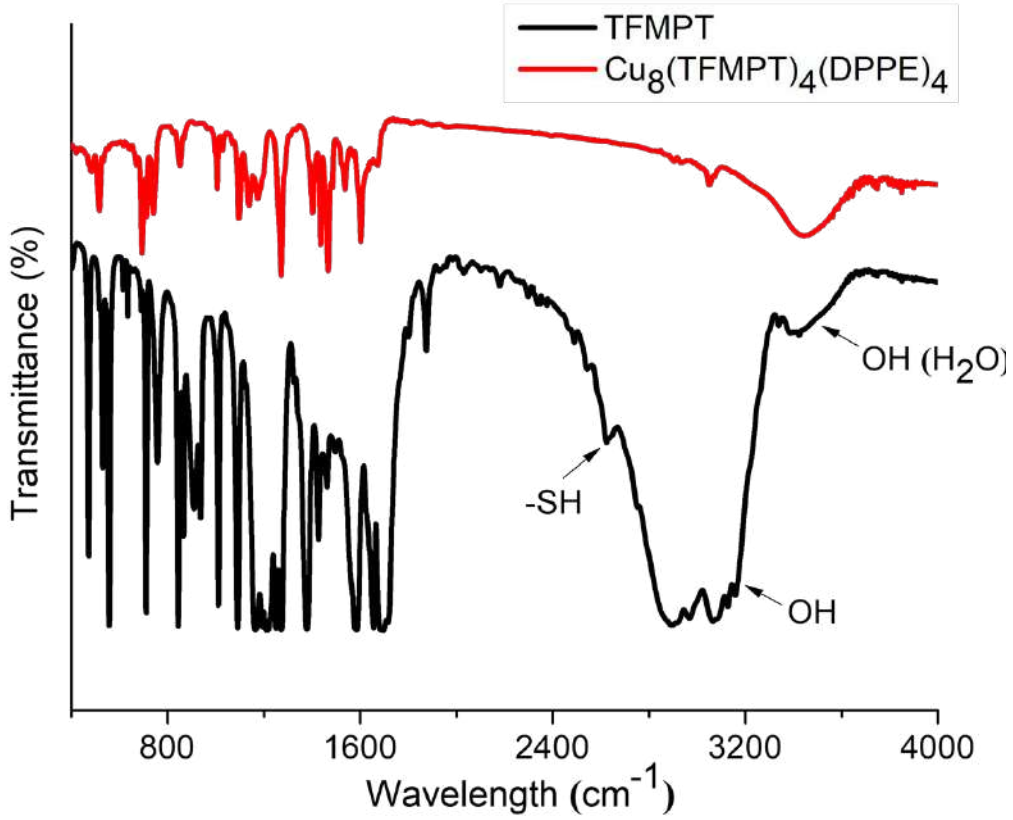


Figure S9. FTIR spectrum of Cu_8 NC in compared to the free ligand. Stretching vibrations are mentioned here.

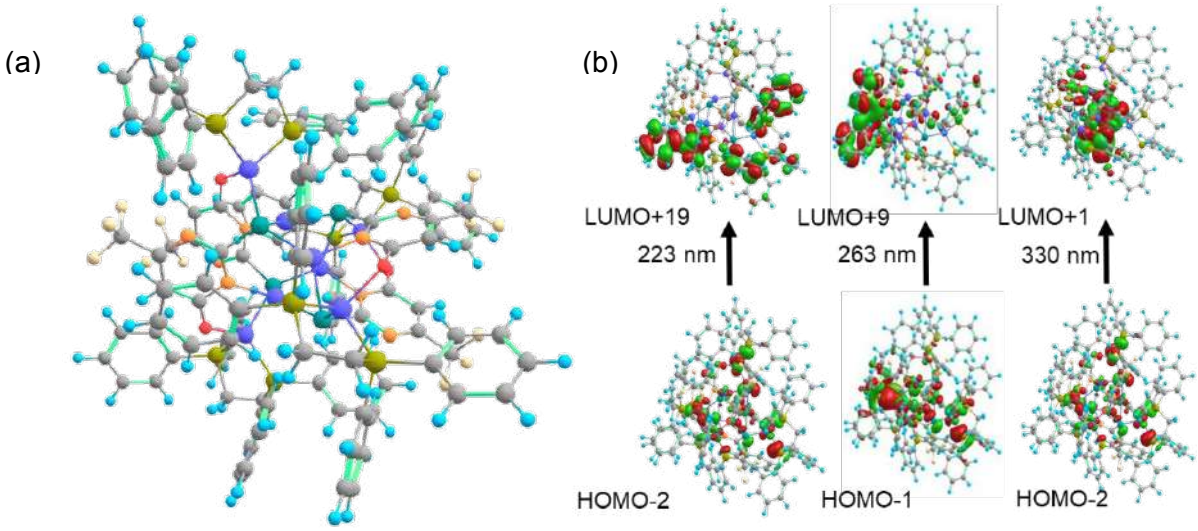


Figure S10. (a) DFT optimized structure of Cu_8. (b) Atomic color code: blue=Cu, green=S, grey=C,yellow=P, red=O, peaceful blue=N and bright blue=H.

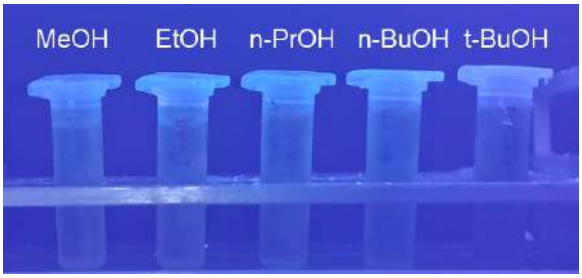


Figure S11. Volume fraction (80%) of polar protic solvents under UV light (365 nm) showing no emission from mixture.

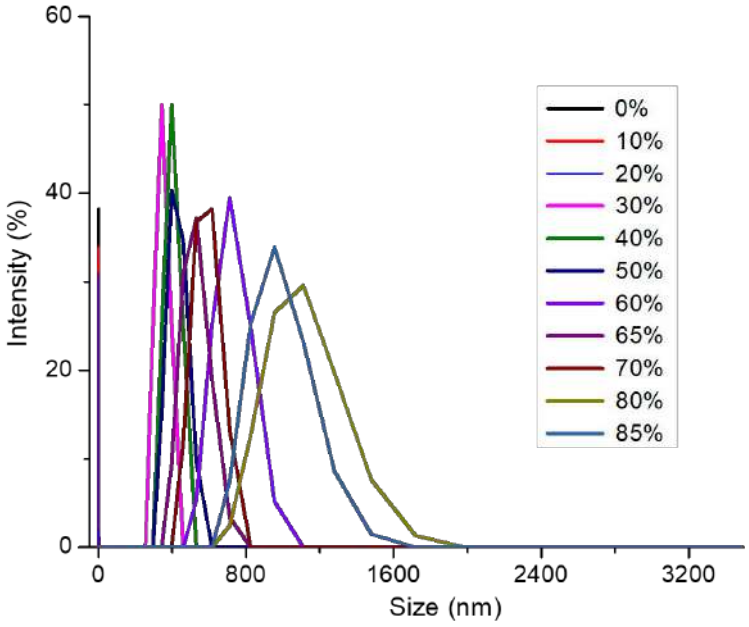


Figure S12. Dynamic Light Scattering (DLS) data of aggregated luminescent clusters with different vol% of water.

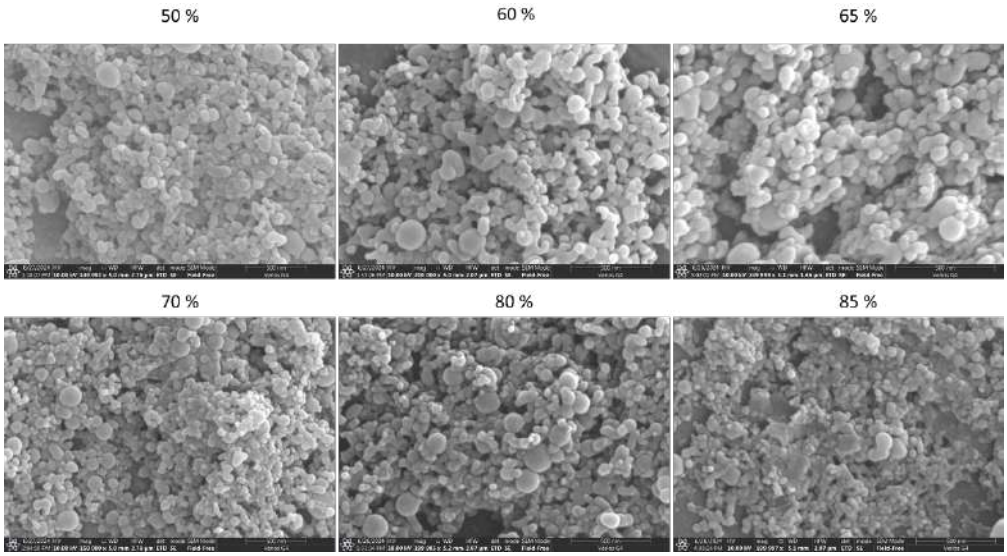


Figure S13. HRSEM images of clusters assembled spheroids at different vol% of water.

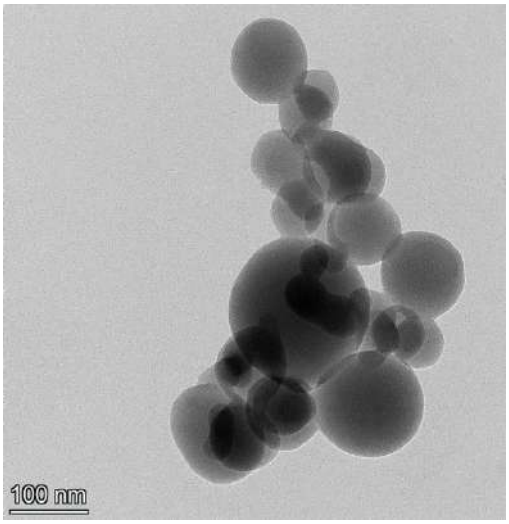


Figure S14. Transmission electron microscopy (TEM) image of spheroids (80% volume fraction of water) under 300 kV.

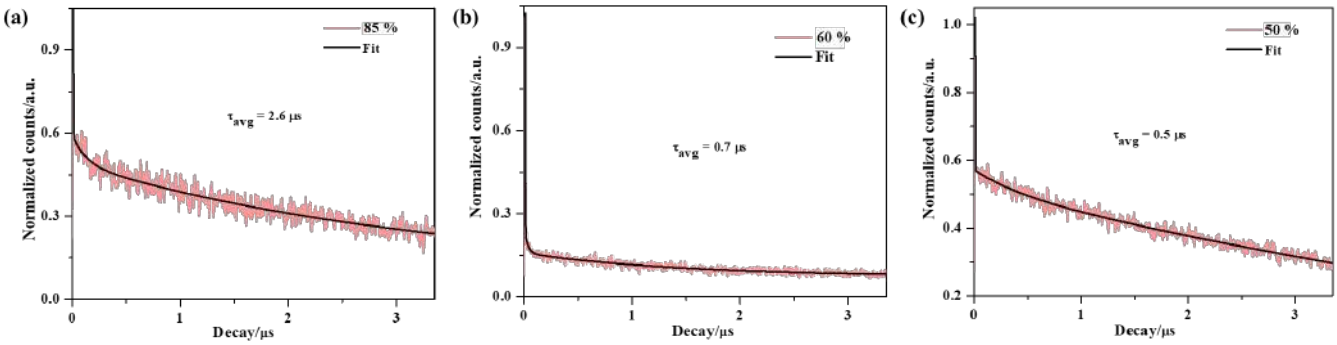


Figure S15. Lifetime decay profile of luminescent aggregates at different vol% of water (a) 85%, (b) 60% and (c) 50%. A deconvolution fit including the Instrument Response Function (IRF) of the laser diode (405 nm) was performed.

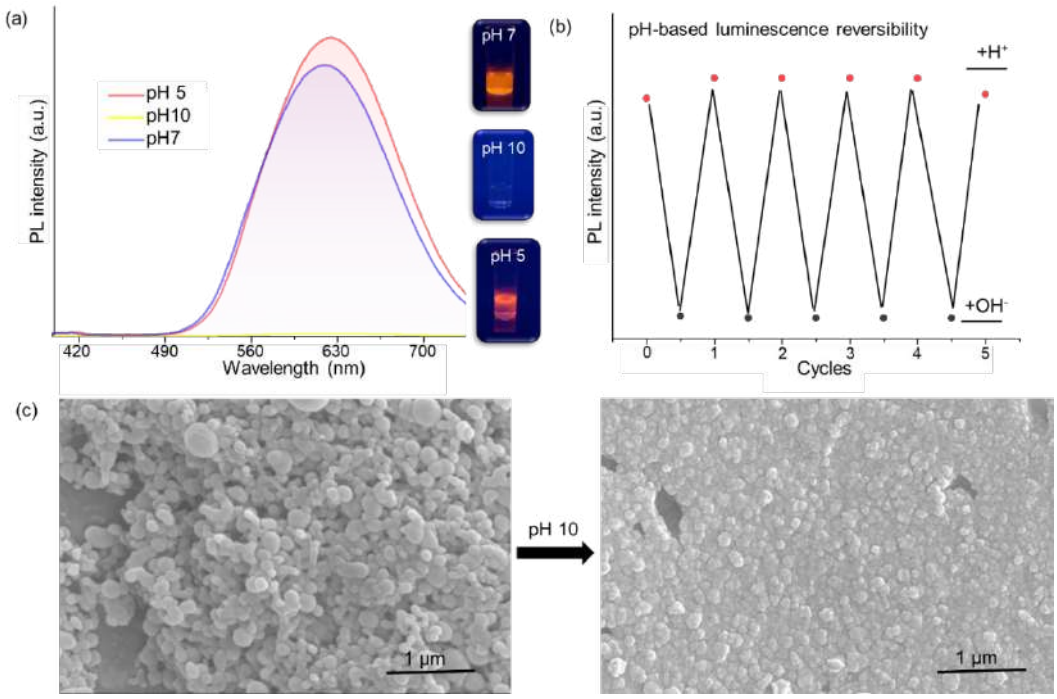


Figure S16. (a) pH-induced luminescence intensity change. (b) pH-based luminescence switching. (c) Surface morphology of spheroids upon change in pH from neutral to pH 10.

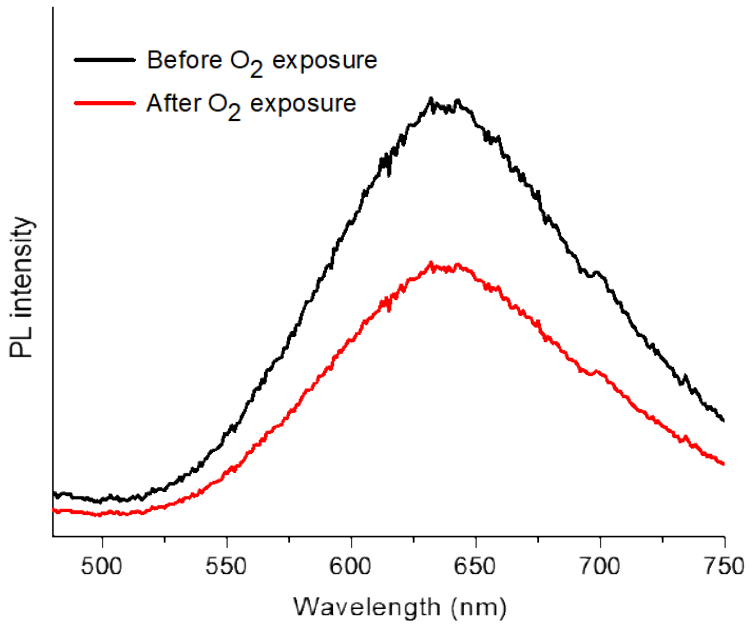


Figure S17. Comparative PL spectra of luminescent aggregates before and after oxygen exposure (Excitation at 365nm).

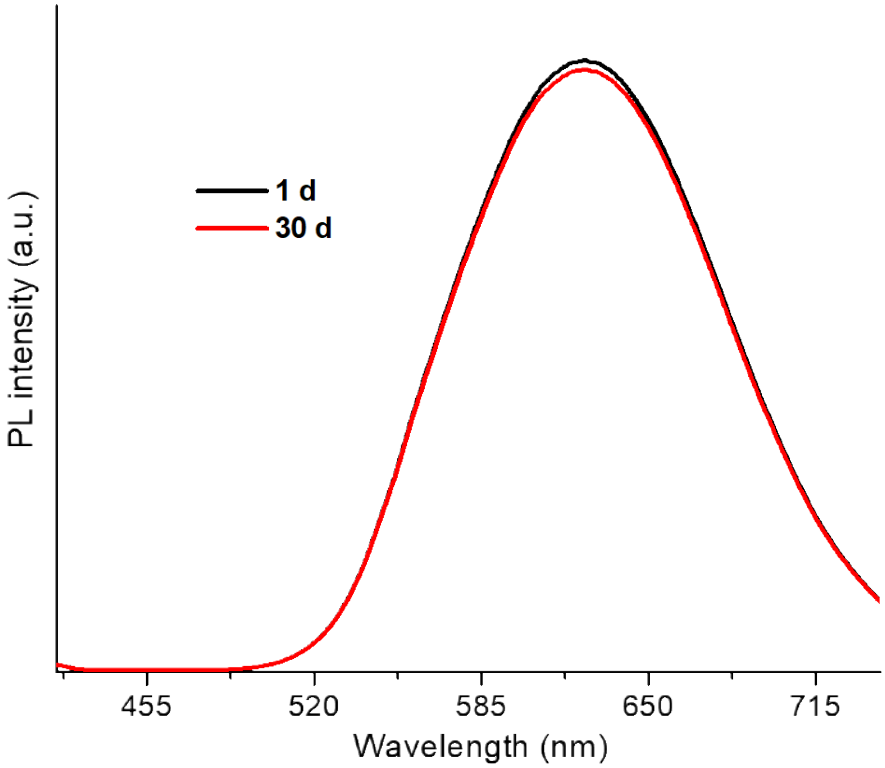


Figure S18. PL spectra for stability of luminescent aggregates, showed its ambient stability after 30 days (Excitation at 365 nm).

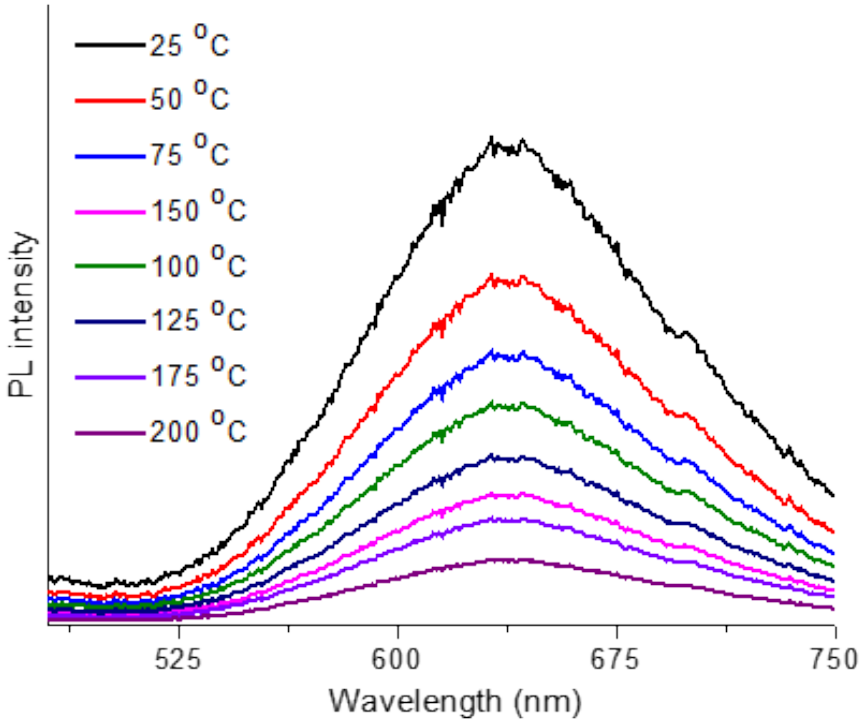


Figure S19. PL spectra of luminescent aggregates upon heating at different temperatures (Excitation at 365 nm and emission at 625 nm).

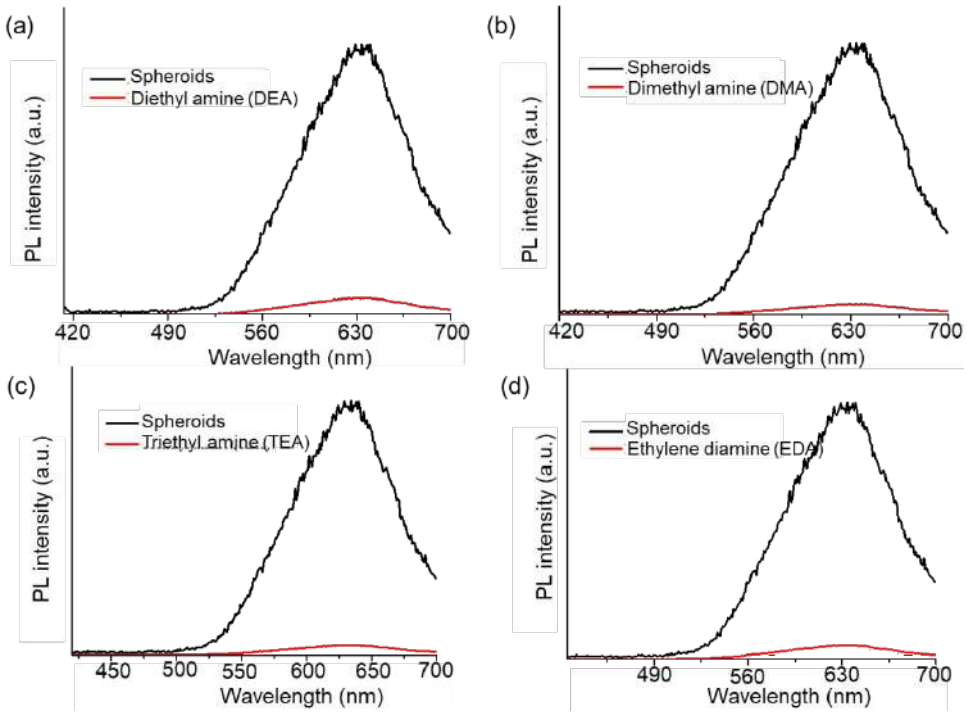


Figure S20. Comparative PL spectra of luminescent aggregates of Cu_8 clusters before and after the exposure to amine vapors (Excitation at 365 nm). Exposure time 12 mins.

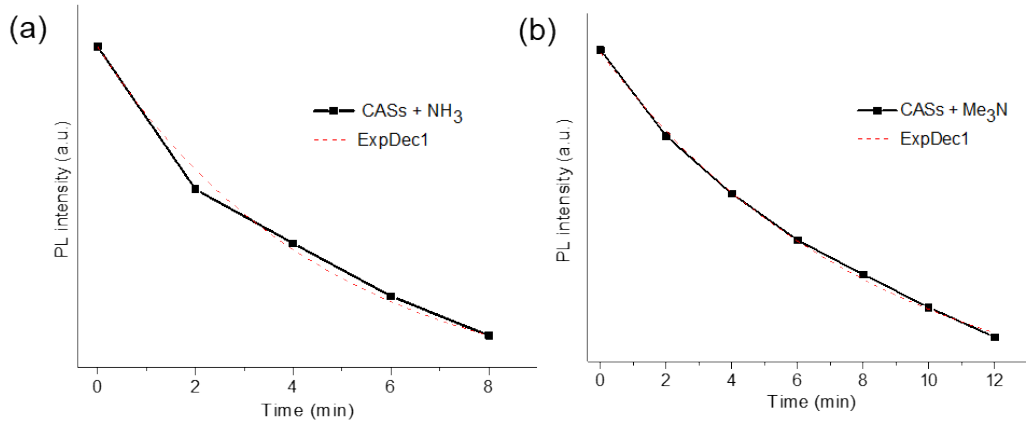


Figure S21. PL intensity change with time for (a) NH_3 and (b) NMe_3 respectively.

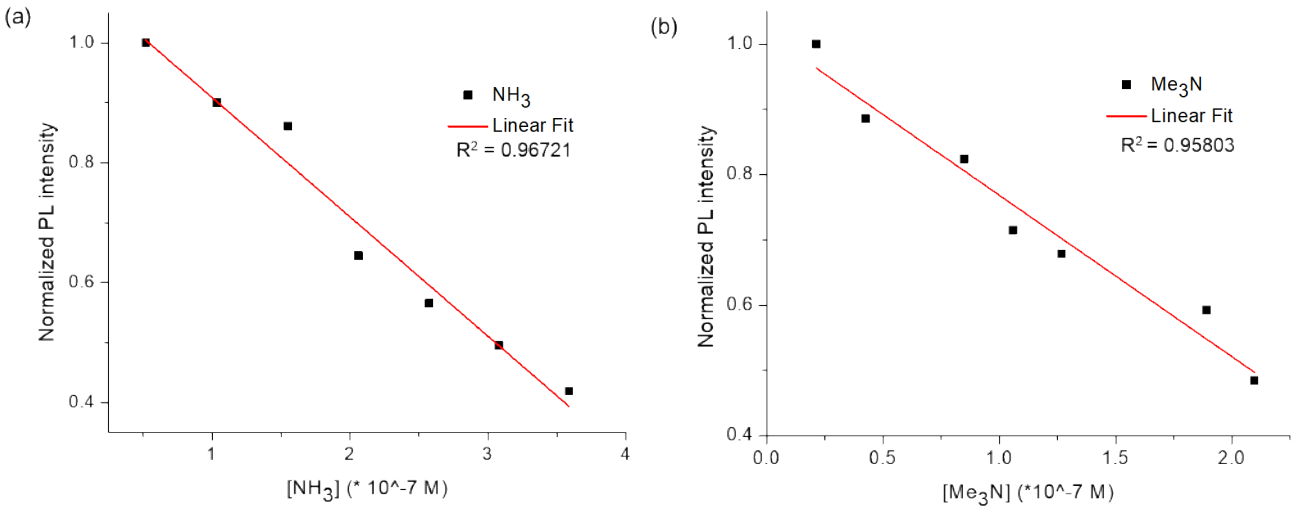


Figure S22. PL intensity change with concentration upon addition of (a) liquid NH_3 and (b) liquid NMe_3 to suspended aggregates in water respectively.

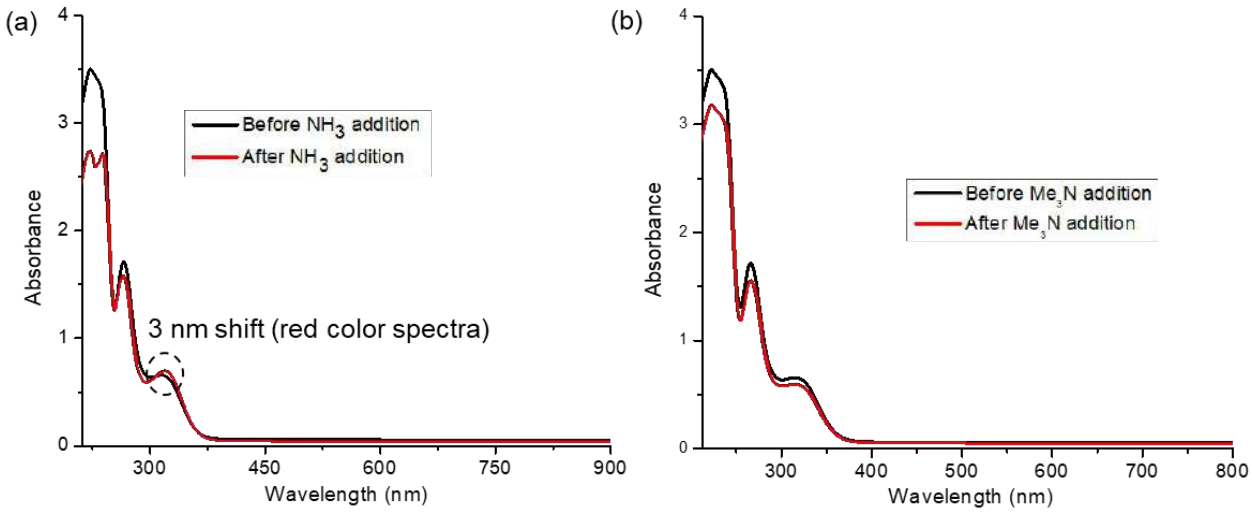


Figure 23. Stability check of cluster through UV-vis spectroscopy. (a) absorption spectra of solution before and after adding NH_3 to cluster-assembled luminescent aggregates. (b) absorption spectra of solution before and after adding Me_3N to cluster-assembled luminescent aggregates.

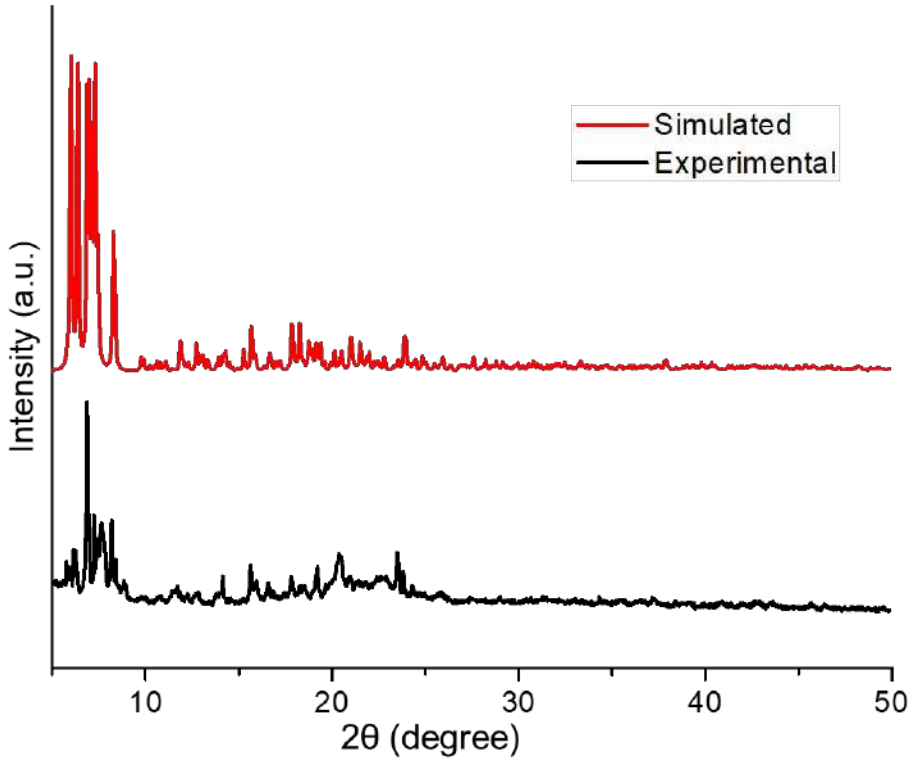


Figure S24. Comparative powder x-ray diffraction pattern of solid Cu_8 NC.

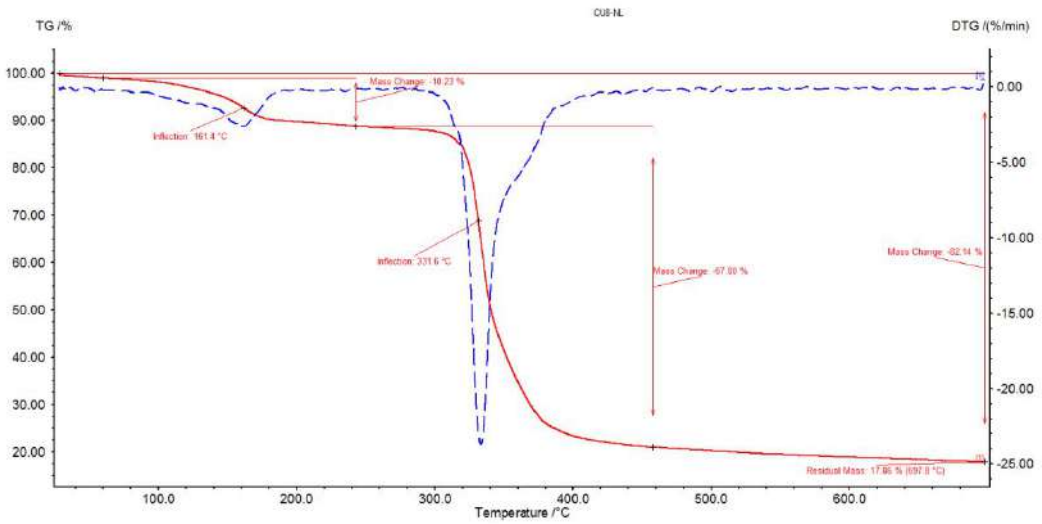


Figure S25. Thermogravimetry (TG) and derivative thermogravimetry (DTG) spectra of Cu_8 NC. Initial mass loss is possibly due to the evaporation of solvent molecules.

References

(1) Wang, Y.M.; Lin, X.C.; Mo, K.M.; Xie, M.; Huang, Y.L.; Ning, G.H.; Li, D. An Atomically Precise Pyrazolate-Protected Copper Nanocluster Exhibiting Exceptional Stability and Catalytic Activity. *Angew. Chem. Int. Ed.* **2023**, *62*(9), 202218369.

(2) Liao, P.K.; Sarkar, B.; Chang, H.W.; Wang, J.C.; Liu, C.W. Facile entrapment of a hydride inside the tetracapped tetrahedral Cu^{I}_{8} cage inscribed in a S_{12} icosahedral framework. *Inorg. Chem.* **2009**, *48*(9), 4089-4097.

(3) Liu, L.J.; Wang, Z.Y.; Wang, Z.Y.; Wang, R.; Zang, S.Q.; Mak, T.C. Mediating CO_2 electroreduction activity and selectivity over atomically precise copper clusters. *Angew. Chem.* **2022**, *134*(35), 202205626.

(4) Sun, P.P.; Han, B.L.; Li, H.G.; Zhang, C.K.; Xin, X.; Dou, J.M.; Gao, Z.Y.; Sun, D. Real-Time Fluorescent Monitoring of Kinetically Controlled Supramolecular Self-Assembly of Atom-Precise Cu_8 Nanocluster. *Angew. Chem.* **2022**, *134*(20), 202200180.

(5) Xu, Y.; Dong, Q.G.; Dong, J.P.; Zhang, H.; Li, B.; Wang, R.; Zang, S.Q. Assembly of copper-clusters into a framework: enhancing the structural stability and photocatalytic HER performance. *Chem. Commun.* **2023**, *59*(21), 3067-3070.

ACS Sustainable Chemistry & Engineering

pubs.acs.org/journal/ascecg

Research Article

Accelerated Synthesis of Pyrazoles Mediated by Water Microdroplets

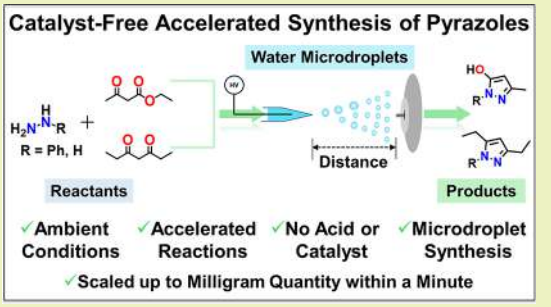
Manish Jana,[▽] Keerthana Unni,[▽] Thalappil Pradeep,* and R. Graham Cooks*

Cite This: *ACS Sustainable Chem. Eng.* 2025, 13, 7645−7654

Read Online

ACCESS | Metrics & More | Article Recommendations | Supporting Information

ABSTRACT: Microdroplets containing water in the presence of an electric field can generate superacids/superbases at the gas−liquid interface, and this unique property drives organic reactions within milliseconds in the absence of any catalyst under ambient conditions. Considering the importance of pyrazoles in organic/inorganic synthesis, in the food industry as well as in medicinal chemistry, we introduce an environmentally friendly approach to the synthesis of pyrazoles and their derivatives in water microdroplets. While the previously reported methods require the use of either a metal catalyst or acid along with organic solvents for long duration experiments at elevated temperatures, our microdroplet-based method offers a fast (typically on the millisecond time scale), green (water as solvent), and efficient alternative for the synthesis of pyrazoles. Studies with organic solvents showed that some water is essential for the formation of substituted pyrazoles. Additionally, spray distance effects suggest that the reaction proceeds via an interfacial mechanism. Based on these results, we propose that (a) the surfaces of the aqueous microdroplets are extremely dry and (b) the inherent acidity of the microdroplet surfaces catalyzes this dehydration reaction. We synthesized eight different substituted pyrazoles by using microdroplets with moderate to excellent conversion ratios (ion yields). This reaction proceeded in a scaled-up version at a rate of 0.81 mg/min. The final products were characterized by ^{1}H NMR and MS/MS experiments.



KEYWORDS: *Pyrazole Synthesis, Microdroplets, Sustainable, Scalable, Catalyst-Free*

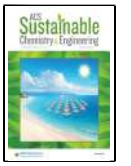
Downloaded via INDIAN INST OF TECH MADRAS on December 29, 2025 at 03:12:25 (UTC).
See https://pubs.acs.org/sharingguidelines for options on how to legitimately share published articles.

INTRODUCTION

Microdroplets are known to be important in advancing diverse chemistry through accelerated reactions occurring at the solution/air interface.[1−11] Although chemical derivatization[12,13] and fragmentation[14] have long been known to occur in microdroplets, the recognition that they accelerate chemical reactions came with experiments in which short reaction times were imposed[15] or products were collected.[16] Reactions in microdroplets occur with reaction times being reduced from days and hours to minutes and seconds while avoiding harsh reaction conditions including high temperatures, use of organic solvents, and phase transfer catalysts.[15,17−20] The enhanced rates of reactions in microdroplets are attributed to several factors, chiefly (a) partial solvation,[21] (b) the high interfacial electrical field,[22−28] (c) ordered molecular orientation,[29] (d) confinement of reagents,[30−34] and (e) extremes of pH.[8,35−37] These are all not independent factors; for example, the pH gradient at the interface is produced by the high electric field, and this generates highly active super acidic and basic species.[38−45] These properties of microdroplets mean that they can be utilized as an alternative to conventional catalysts during specific organic syntheses. Studies have also shown that the dielectric layer at the surface of water microdroplets generates water radical cations that in turn give free hydroxy radicals and hydronium ions.[46−48] Even trace amounts of water in organic solvents can help in reaction acceleration, e.g., benzimidazole formation (reaction between aromatic diamines and simple carboxylic acids),[49] and reaction of amines with carbon dioxide.[50] Reactions in microdroplets typically give the same products as the corresponding bulk phase reactions, although they may follow different pathways. For example, in the case of benzimidazole formation, the reaction is believed to occur through protonation of simple acids at the water interface, followed by nucleophilic attack at carbon and then elimination of a water molecule.[49] The reaction of amines with carbon dioxide occurs through protonation of carbon dioxide at the air−water interface.[50]

Recently, microdroplet reactions have been scaled up using arrays of sprayers[16] and solvent recycling systems[51] to achieve product formation at the gram per hour scale. Hence, microdroplet chemistry can no longer be considered exclusively as a small-scale synthesis technique. This chemistry has been used to study inter alia the following reaction types:

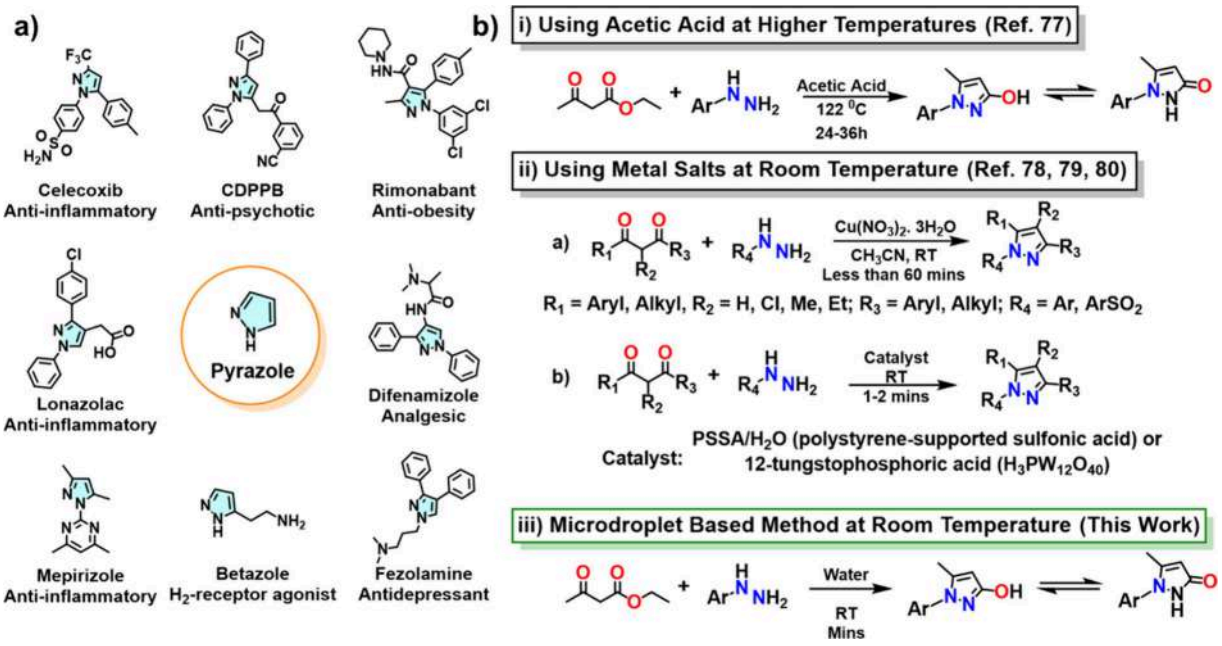
Received: April 2, 2025
Revised: April 29, 2025
Accepted: April 30, 2025
Published: May 9, 2025



ACS Publications

© 2025 American Chemical Society

Scheme 1. (a) Pyrazole Containing Drugs Available Commercially;[69] (b) Synthetic Methods Used to Produce Pyrazoles[77−80]



addition,[52,53] elimination,[21] biphasic,[17−19] redox,[4,54,55] and multicomponent reactions.[56−59]

Pyrazoles are important organic motifs which have gained significant attention due to their presence in bioactive drugs,[60] cosmetic dyes,[61] agrochemicals,[62] UV stabilizers[63] and functional materials.[64] Substituted pyrazoles have also been used as ligands in inorganic and organometallic chemistry.[65−68] Pyrazole-containing medicines have been marketed to alleviate or treat diseases ranging from bacterial infections to cancer and neurologic disorders, and they are listed as one of the highly used ring systems for small molecule drugs by the Food and Drug Administration (FDA) (Scheme 1a).[69]

Pyrazole itself was first synthesized by German chemist Hans von Pechmann in 1898 by reacting acetylene with diazomethane.[70] Over the last few decades, many other methods have been developed for the synthesis of pyrazoles and substituted pyrazoles.[71−74] Common methods include the cyclization of hydrazine with various electrophiles, including 1,3-dicarbonyl compounds, α,β-unsaturated carbonyl compounds, and dihalides, in the presence of an acid (Knorr-Pyrazole Synthesis).[75] A microdroplet-based green thiocyanation of pyrazoles was reported in 2023 by Cheng and co-workers.[76] However, the synthesis of starting material (substituted pyrazolone) requires the use of acetic acid as a solvent and the reaction conditions include reflux at 122 °C for 24 to 36 h (Scheme 1b).[77] A mild and acid-free condensation of 1,3-diketones with substituted hydrazine to generate pyrazole was reported by Wang and co-workers.[78] The optimal reaction conditions were obtained by using copper(II) nitrate as the catalyst, providing the cyclo-condensation products at room temperature in less than 60 min (Scheme 1b). A polystyrene supported sulfonic acid[79] or 12 tungsten phosphoric acid ($H_3PW_{12}O_{40}$)[80] has also been used as a catalyst for the synthesis of pyrazoles at room temperature (Scheme 1b). Several microwave assisted methods have also been reported.[81,82] Considering the importance of pyrazole in organic synthesis and the drug industry, it is desirable to develop a catalyst free, minute-scale method for high-efficiency pyrazole synthesis in a green solvent. Here, we report just such a microdroplet-based technique for the catalyst-free synthesis of pyrazoles/substituted pyrazoles using water as a green solvent.

EXPERIMENTAL SECTION

General Information. Ethyl acetoacetate (**1a**), heptane 3,5-dione (**1b**), phenyl hydrazine (**2a**), and hydrazine monohydrate (**2b**) were purchased from Sigma-Aldrich (St. Louis, MO). 2-Acetylcyclohexanone (**1c**), 1,3-diphenyl-1,3-propanedione (**1d**), and 2-chloro-6-hydrazineylpyridine (**2c**) were purchased from TCI America. HPLC-grade water was obtained from Fisher Scientific (Hampton, NH). MeOH (HPLC grade, water 0.1% maximum), IPA (HPLC grade, water 0.20% maximum), and ACN (LC/MS grade, water 0.1% maximum) used in this study were purchased from Fisher Scientific. Anhydrous ethanol were purchased from Decon Laboratories, Inc. The solvents and chemicals in this study were used as received without further purification. Borosilicate glass capillaries for nano-electrospray ionization mass spectrometry (nESI-MS) analysis (dimensions of 1.5 mm O.D., 0.86 mm i.d., and 10 cm length) were acquired from Sutter Instruments (Novato, CA).

All samples were analyzed by nESI coupled with a Finnigan LTQ linear ion trap mass spectrometer (ThermoFisher Scientific, San Jose, CA). In each case, a 5 μm internal diameter nESI emitter was prepared by using a P-97 Micropipette Puller (Novato, CA) and placed within a stainless-steel electrode. Positive 2 kV spray voltage was applied, and spray distances between the sprayer tip and MS inlet were varied from 3 to 50 mm during various experiments. For the conversion ratio determination, the distance was fixed at 20 mm for all experiments. Other instrumental parameters were MS inlet temperature of 250 °C, capillary voltage of 30 V, and tube lens of 65 V. Tandem mass spectrometry (MS/MS) was used for structural characterization of specific precursor ions. ^{1}H NMR spectra were recorded using a Bruker NEO300 spectrometer equipped with a 5 mm BBFO Z-gradient probe.

Scale up Experiment. A mixture of 200 mM each of 1,3-diketone and hydrazine was taken up in a glass syringe (final concentration = 100 mM). The reaction mixture was sprayed using a 150 μm capillary (Molex Polymicro) (i.d. = 150 μm and o.d. = 353 μm) at a rate of 50 μL min^{-1} using a syringe pump (Harvard Apparatus, PHD 2000, Infuse/Withdraw). It was nebulized using nitrogen gas at 120 psi, and a positive potential of 3 kV was applied to the syringe. Since phenyl

https://doi.org/10.1021/acssuschemeng.5c03026
ACS Sustainable Chem. Eng. 2025, 13, 7645−7654

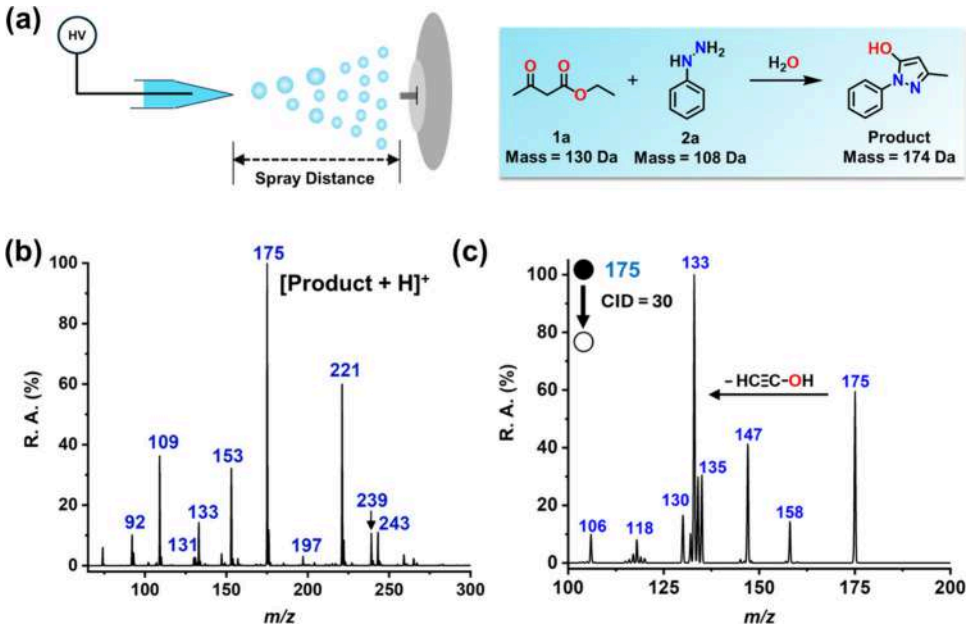


Figure 1. (a) Overview of the microdroplet-based synthesis of pyrazoles, including one representative reaction between ethyl acetoacetate (**1a**) and phenyl hydrazine (**2a**). (b) Mass spectrum of the reaction mixture showing the product ion peak at *m*/*z* 175. (c) Ion structure validation using the MS/MS experiment for *m*/*z* 175.

Table 1. Synthesis of Pyrazoles and Substituted Pyrazoles Using Different Substrates in Microdroplets and Their Conversion Ratios Calculated from the Mass Spectra[a]

Entry No.	1,3- Diketone	Hydrazine	Product	Conversion Ratio[b]	Characterization (MS/MS, Proposed Mechanism with Intermediates and NMR)
1.	1a	2a		47%	Figures S2 and S5
2.	1b	2a		82%	Figures S6, S7, S8, S9 and S10
3.	1c	2a		75%	Figures S11, S13 and S14
4.	1a	NH_2NH_2 2b		2% (**)	Figures S15, S16, S17
5.	1b	NH_2NH_2 2b		90%	Figures S18, S19 and S20
6.	1c	NH_2NH_2 2b		95%	Figures S21, S22 and S23
7.	1d	NH_2NH_2 2b		41%	Figures S24, S25 and S26
8.	1c	2c		15%	Figure S27, S28 (No NMR)

[a]The sprayer was kept 2 cm from the mass spectrometer inlet. [b]Conversion (measure of product yield) was calculated as ion intensity of product over the sum of product, intermediates, and reactant intensities.

https://doi.org/10.1021/acssuschemeng.5c03026
ACS Sustainable Chem. Eng. 2025, 13, 7645−7654

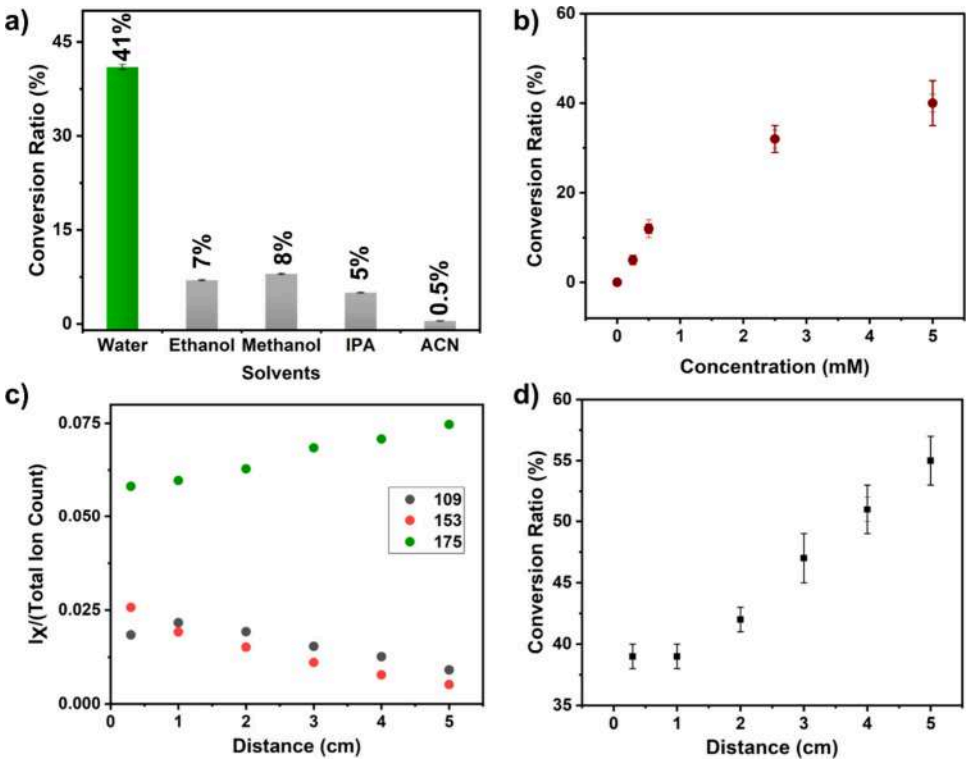


Figure 2. (a) Reaction conversion, defined as ion intensity ratio $I_P/(I_P + I_R + I_{Int})$, in various solvents ($H_2O$, EtOH, MeOH, IPA, and ACN microdroplets). The error bars correspond to the standard deviation of three separate experiments using microdroplets, and the distance of the sprayer was kept 2 cm from the mass spectrometer inlet. (b) Change in conversion ratio with concentration of the reactants. (c) Change in the ion intensity ratio for reactants and product with distance (concentration of the solution = 5 mM, I_X = ion intensities at m/z of 109, 153, and 175, TIC = Total ion count). (d) Change in conversion ratio upon changing the distance between the sprayer and the inlet of the mass spectrometer.

hydrazine and some of the diketones are air sensitive, nitrogen was used for nebulization during the product collection. In the case of hydrazine hydrate (as reagent), air was used at 120 psi to nebulize the solution. The sprayed product (3 mL) was collected for 1 h in a Pyrex bottle and subsequently analyzed using ^{1}H NMR without further purification or chromatographic separation. Schematic representation of the collection setup is shown in Supporting Information, Figure S1.

RESULTS AND DISCUSSION

Figure 1a presents a detailed overview of the microdroplet-based strategy and the reaction studied in this work. An equimolar solution of ethyl acetoacetate (**1a**; 10 mM) and phenyl hydrazine (**2a**; 10 mM) in water was introduced into a nESI capillary, and a spray voltage of +2 kV was applied to generate charged droplets. These droplets were then directed toward the vacuum system of a linear ion trap mass spectrometer. The mass spectrum of the crude reaction mixture, recorded in positive ion mode within milliseconds of introduction, exhibits a product peak at m/z 175 corresponding to the protonated substituted pyrazole, Figure 1b. Additionally, it shows the peaks of precursor ions, specifically phenyl hydrazine and ethyl acetoacetate, in their protonated and sodiated forms at m/z 131 and 153, respectively (Figure 1b). The peak at m/z 221 corresponds to the Schiff base product formed upon reaction between the carbonyl group of ethyl acetoacetate (**1a**) and the amine group of phenyl hydrazine (**2a**).

To validate the ion structure as well as confirm the absence of any covalent bond, tandem mass spectrometry was performed for m/z 175 (Figure 1c). The MS/MS spectrum of 175 (Figure 1c) shows the loss of CO (neutral loss of 28) as well as $^{\bullet}$OH (neutral loss of 17). Also, the diagnostic cross-ring fragment at m/z 133 shows a loss of HC≡C−OH (neutral loss of 42) (Figure 1c), which further confirms the formation of the phenyl substituted pyrazole/pyrazolone molecule. The versatility of this microdroplet-based synthetic approach was validated upon successful synthesis of eight substituted pyrazoles using various reagents (1,3-diketones and hydrazines) and analyzed using tandem mass spectrometry. This method highlights the efficiency and adaptability of microdroplets in organic synthesis.

To eliminate contributions of bulk reactions to the observed microdroplet experiments, we mixed equimolar concentrations of starting reagents (1,3-diketone and hydrazine hydrate) for NMR. The mixture was allowed to stand for 10 min before ^{1}H NMR analysis. Additionally, equimolar ratios of the reagents were sprayed and collected directly for ^{1}H NMR analysis. The schematic representation of the spray setup is given in Figure S1. While the bulk reaction showed no evidence of pyrazole product formation in the ^{1}H NMR spectrum (Figure S17a), the sprayed sample clearly indicated product formation (Figure S17b). This observation further validates the fast formation of pyrazoles in microdroplets containing water without the use of any catalyst under ambient conditions.

Conversion Ratio Calculation. The microdroplet reactions were monitored online by using a linear ion trap mass spectrometer. Conversion ratios were calculated from the ion intensities of the reactants and products using the following eq 1:

$$\text{Conversion Ratio} = \frac{I_P}{I_P + I_R + I_{INT}} \times 100\% \quad (1)$$

https://doi.org/10.1021/acssuschemeng.5c03026
ACS Sustainable Chem. Eng. 2025, 13, 7645−7654

where I_p, I_R, and I_{INT} are the total ion intensity of the products, reactants, and intermediates (respectively) formed during the reaction. Since the ionization efficiencies of the reactants and products might differ, the conversion ratios determined from the mass spectrum might not give accurate concentrations, but it can give an approximate estimation of the product formation during microdroplet reactions. Note that this is the strictest form of the conversion ratio; alternative forms, in which intermediates are also considered, are discussed in Section 1.2 of Supporting Information. The conversion ratio for each reaction is given in Table 1.

Solvent Effect. Conventional pyrazole synthesis requires use of glacial acetic acid as a solvent at higher temperatures (120−130 °C).[77] To understand the effect of solvent, we conducted the droplet reaction using five different solvents, namely, water, ethanol, methanol, isopropanol, and acetonitrile (Figure 2a). The results from the solvent study clearly indicate that the reaction is most efficient in water. Almost no product was observed when ACN was used as a solvent. In the case of anhydrous EtOH/MeOH (HPLC grade, water 0.1% maximum), although it shows formation of product in the microdroplet, the conversion ratio was very poor for this particular substrate (ethyl acetoacetate and phenyl hydrazine). From solvent studies, we conclude that water is essential to produce the interfacial superacidic/superbasic reagents for this reaction.

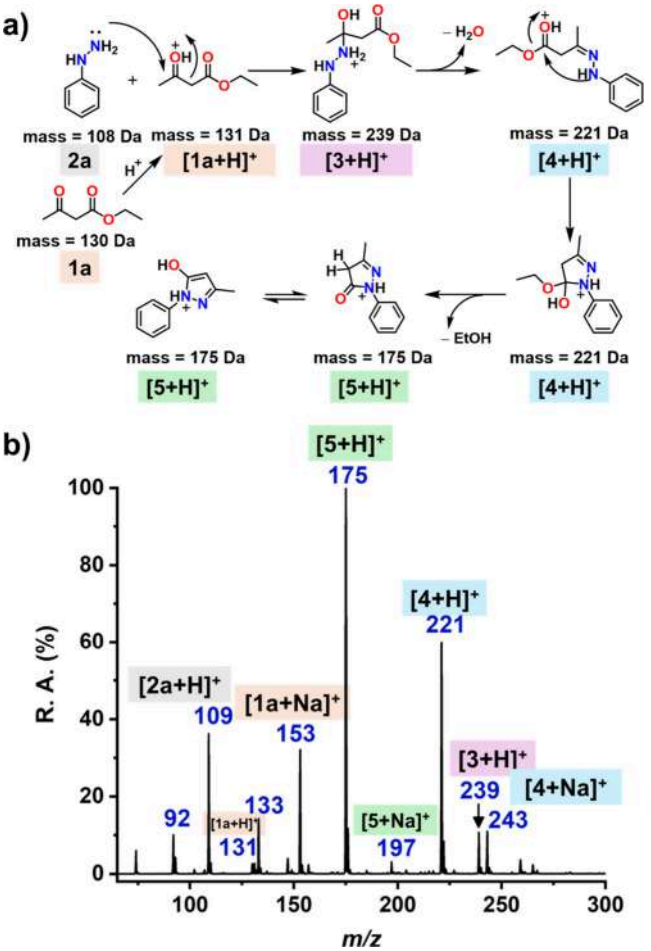
As befits a bimolecular reaction, the concentrations of the starting reagents play a significant role in the extent of formation of the product. The conversion of the starting reagents to the final product with respect to concentration is shown in Figure 2b. Lower concentrations of the starting reagents show less conversion to the product.

Distance Effect for the Microdroplet Reaction. A remarkable distance effect was observed during formation of pyrazole in water microdroplets which supports the hypothesis of the reaction at the surface of the droplet.[1] While increasing the distance from the mass spectrometer inlet to the sprayer from 3 to 50 mm, we observed a decrease in the fractional ratio of ion intensities of the protonated and sodiated reactant ions, while that of product ions increased (Figure S3). The observed distance effect suggests that this transformation occurs in the charged microdroplets generated by nESI. Increasing distances from the inlet of the mass spectrometer to the sprayer resulted in more Coulombic fission of the solvents (H_2O) to generate smaller droplets, and hence, surface-to-volume ratios increased. Although the longer reaction times associated with droplet flight times may also contribute to the relative increase in the ratio of product ion intensity. These changes resulted in a net large increase in conversion ratio intensity and gave higher conversions of reagents to the final product.

Figure 2c shows the change in the ratio of ion intensity by total ion count for reactants and product with increasing distance. By changing the distance (inlet of the mass spectrometer to the sprayer), the conversion ratio changes from 39% to 55% as shown in Figure 2d.

Proposed Reaction Mechanism. The conventional pyrazole synthesis occurs in the presence of acid at high temperatures (120−130 °C).[77] Based on conventional synthesis procedures, acid is necessary to catalyze the reaction. It has been known since 2011 that the acidity of the microdroplet surface is much higher than that of the bulk.[15,37,83] Recent studies on chemical reactions in microdroplets containing water reveal the presence of water radical cation and anion pairs at and near the gas−liquid interface which can spontaneously dissociate into hydronium/proton (H_3O^+) and hydroxide (OH^-) ions.[4,48] Consistent with a number of other examples from the literature,[8,35−37,49,50] we suggest that the very high proton concentration at the surface of a droplet containing water will protonate ethyl acetoacetate (**1a**) in competition with the phenyl hydrazine (**2a**) to create the electrophilic carbon. (The extremely strong acidic nature of the microdroplet surface results in a leveling of differences in basicity, as explained earlier.[49]) This electrophilic carbon center is then subjected to nucleophilic attack by the lone electron pair of the amine group of phenyl hydrazine to generate intermediate species ($[\mathbf{3} + H]^+$). (We also observed protonated ethyl acetoacetate ($[\mathbf{1a} + H]^{+}$) and phenyl hydrazine ($[\mathbf{2a} + H]^+$) in the mass spectrum (Scheme 2).) Subsequent loss of water results in the formation of a Schiff base intermediate ($[\mathbf{4} + H]^+$ and $[\mathbf{4} + Na]^+$ in Scheme 2). In the next step, another intramolecular nucleophilic attack occurs at the carbon atom of the ester group by the lone pair of the −NH group of phenyl hydrazine (**2a**) to form a five-membered cyclic intermediate ($[\mathbf{4} + H]^+$ in Scheme 2). Finally,

Scheme 2. (a) Proposed Mechanism for the Formation of Pyrazole/Pyrazolone in Water Microdroplet; (b) Mass Spectrum in the Positive Mode, Showing the Conversion of Reactants to the Product along with Reaction Intermediates[a]



[a]Note that both reagents are equally readily protonated by the superacid, but the reaction proceeds from ester protonation.

https://doi.org/10.1021/acssuschemeng.5c03026
ACS Sustainable Chem. Eng. 2025, 13, 7645−7654

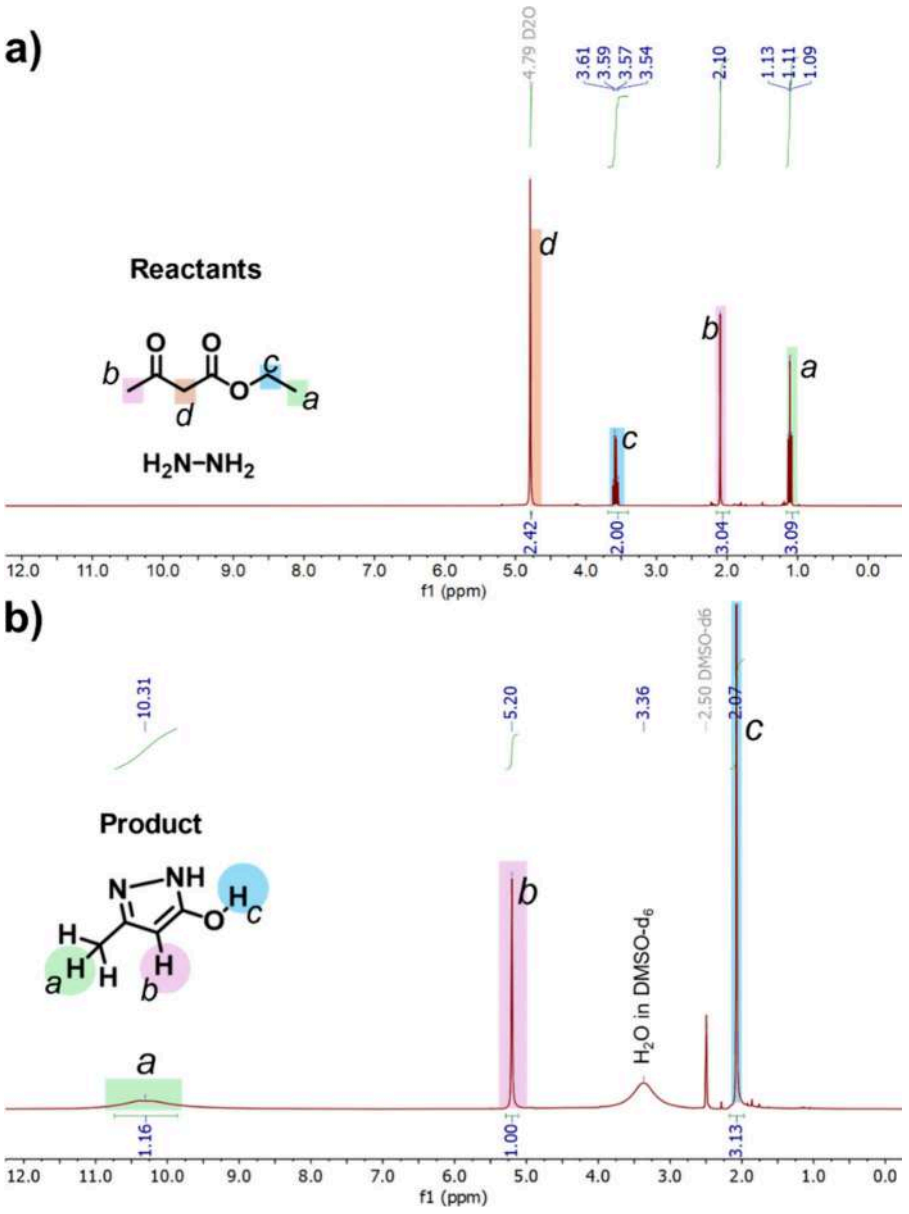


Figure 3. ^{1}H NMR of a mixture of ethyl acetoacetate (**1a**) and hydrazine monohydrate (**2b**): (a) prior to reaction in D_2O (indicating no product formation) and (b) after reaction in water microdroplets (demonstrating the formation of the pyrazole product and ^{1}H NMR is recorded in DMSO-d_6).

elimination of EtOH leads to pyrazole/pyrazolone (tautomer) as the final product. The reaction mechanism along with the products detected in the mass spectrum is shown in Scheme 2. The presence of pyrazole/pyrazolone is indistinguishable in the mass spectrometer as they show the same mass/charge ratio (m/z 175). The MS/MS spectrum of m/z 175 shows that this ion can lose both CO (neutral loss of 28) and hydroxide ($^{\bullet}$OH) (neutral loss of 17) groups. These two losses give us confidence in the fact that ion m/z 175 includes two tautomeric forms, as illustrated in Scheme 2a.

Instead of water, if we perform the reaction in an ethanol/water mixture, according to Le Châtelier's principle,[84] the elimination of the EtOH group is highly disfavored and the Schiff base (m/z 221) is found to be the major peak in the mass spectrum as shown in Figure S4.

From these results we deduce the following:

(i) Because acid catalyzed formation of pyrazole is well-known, we suggest that the exceptional acidity of the microdroplet surface can catalyze the reaction on the milli- or microsecond time scale without addition of external acid.

(ii) Since the dehydration reaction is occurring in water, it confirms the fact that the surface of the microdroplets containing water is dry (only partially solvated), as previously claimed.[4]

Substrate Scope. Considering the excellent conversion ratio for the microdroplet-based pyrazole synthesis (high conversions and minute time scale reactions in water without the addition of any external acid at room temperature), we set out to investigate the applicability of this method for other substrates. We have used four types of 1,3-diketones, namely, ethyl acetoacetate (**1a**), heptane 3,5-dione (**1b**), 2-acetylcyclohexanone (**1c**), and 1,3-diphenyl-1,3-propanedione (**1d**),

https://doi.org/10.1021/acssuschemeng.5c03026
ACS Sustainable Chem. Eng. 2025, 13, 7645−7654

and three different types of hydrazine, namely, phenyl hydrazine (**2a**), hydrazine monohydrate (**2b**), and 2-chloro-6-hydrazineylpyridine (**2c**). A total of eight reactions were conducted in microdroplets and initially analyzed by a mass spectrometer. The reactants, products, and the conversion ratios are provided in Table 1. Most of the reactions can be performed in water. For entry 3, the reaction was carried out in an ethanol/water mixture (80:20). When ethanol was used as the solvent (which contains some water), the product was observed in the mass spectrometry (MS) experiment, but the relative intensities of the intermediates were higher (Figure S12a). This resulted in a lower conversion ratio of the product (i.e., lower ion yield). However, when 20% water was added to the ethanol solution, the relative intensities of the intermediates decreased, leading to a higher conversion ratio of the product (Figure S12b).

In the case of entry 4, even though it shows only 2% conversion in the droplet-based reaction, it has been sprayed and collected for NMR analysis. The details of reaction 4 are provided in the Supporting Information (Section 5). Due to very poor solubility of 1,3-diphenyl-1,3-propanedione (**1d**) in water (entry 7), the reaction is performed in EtOH whereas hydrazine hydrate provided the water necessary for the reaction.

Scale up the Pyrazole Formation in Microdroplets. A mixture of 200 mM each of ethyl acetoacetate (**1a**) and hydrazine monohydrate (**2b**) was taken up in a glass syringe. The reaction mixture was sprayed using a 150 μm capillary (i.d. = 150 μm and o.d. = 353 μm) at a rate of 50 μL min^{-1} with a syringe pump. It was nebulized using air at 120 psi, and a positive potential of 3 kV was applied to the syringe. The sprayed product (3 mL) was collected for 1 h in a Pyrex bottle and subsequently analyzed using ^{1}H NMR without further purification or chromatographic separation. The ^{1}H NMR spectrum of the reagents after mixing (bulk reaction) and after spraying (microdroplet reaction) are shown in Figure 3.

The maximum rate of product formation (for entry 2) is found to be ∼0.81 mg min^{-1} using a single sprayer. A schematic representation of the collection setup is provided in the Supporting Information (Figure S1).

Sustainability of the Microdroplet-Based Method. Within the chemical and pharmaceutical industries, the fundamental goals in chemical process development include reduction of resource consumption and waste generation, along with the avoidance of hazardous chemicals and organic and chlorinated solvents, and the minimization of reaction temperature as well as time. Achieving these objectives not only lowers production costs but also enhances the safety of the process. Our microdroplet-based method of pyrazole formation in water leverages the unique acidity at the microdroplet interface to drive reactions within milliseconds, offering a rapid and scalable alternative to traditional long-duration methods. We have also compared the EcoScale[85] of this method with previously reported approaches. The EcoScale, which assesses a wide range of organic chemistry conditions and techniques, is calculated by deducting applicable penalty points from a maximum score of 100. The detailed calculations are provided in the Supporting Information. Our microdroplet-based method is found to be greener than other reported methods, as it eliminates the need for workup procedures, organic and halogenated solvents, high temperatures, and metal catalysts (for the reaction between heptane 3,5-dione (**1b**) and phenyl hydrazine (**2a**), the Ecoscale value was found to be 71 to be compared with a value of 51; see the SI). Since this method does not involve any catalysts or organic solvents (with only water and ethanol as side products), we did not assess its potential environmental impact using Life Cycle Assessment (LCA). Although at this moment the pyrazole product can be generated in milligram quantity within a minute, further research on optimizing and exploring the scalability to gram quantities would elevate the method for broader industrial adoption.

CONCLUSION

This report presents a green method for the synthesis of pyrazoles in electrically charged water microdroplets by using the reaction of 1,3-diketones with hydrazine and substituted hydrazine. Online mass spectrometric monitoring facilitates detection of the reaction intermediates and provides an overview of the reaction mechanism. Distance effects during the reaction suggest that the dehydration reaction occurs at the droplet interface; it is accelerated by a large factor over the corresponding reaction in the bulk. This further supports the previously reported fact that the surface of the microdroplets, although aqueous to begin with, must be extremely dry to facilitate the dehydration reaction. Studies of this reaction using various solvents indicate that water is necessary to create the superacidic/superbasic reagents to carry out the reaction. This reaction is further explored in terms of the substrate scope, concentration effects, and droplet flight distance. It can be scaled up to ca. 1 mg in a minute.

ASSOCIATED CONTENT

Supporting Information

The Supporting Information is available free of charge at https://pubs.acs.org/doi/10.1021/acssuschemeng.5c03026.

Additional experimental details, MS/MS experimental data, and NMR spectra of the products along with Ecoscale Data (PDF)

AUTHOR INFORMATION

Corresponding Authors

R. Graham Cooks − *Department of Chemistry, Purdue University, West Lafayette, Indiana 47907, United States;* orcid.org/0000-0002-9581-9603; Email: cooks@purdue.edu

Thalappil Pradeep − *DST Unit of Nanoscience (DST UNS) and Thematic Unit of Excellence (TUE), Department of Chemistry, Indian Institute of Technology Madras, Chennai 600036, India;* orcid.org/0000-0003-3174-534X; Email: pradeep@iitm.ac.in

Authors

Manish Jana − *Department of Chemistry, Purdue University, West Lafayette, Indiana 47907, United States*

Keerthana Unni − *DST Unit of Nanoscience (DST UNS) and Thematic Unit of Excellence (TUE), Department of Chemistry, Indian Institute of Technology Madras, Chennai 600036, India; Department of Chemistry, Purdue University, West Lafayette, Indiana 47907, United States*

Complete contact information is available at: https://pubs.acs.org/10.1021/acssuschemeng.5c03026

Author Contributions

$^{\nabla}$M.J. and K.U. contributed equally to this work.

Notes

The authors declare no competing financial interest.

■ ACKNOWLEDGMENTS

We acknowledge the financial support from the Multi-University Research Initiative of the Air Force Office of Scientific Research (FA9550-21-1-0170) via Stanford University (subaward 62741613-204669) and NCATS through the ASPIRE Reduction-to-Practice Challenge and the UG3 grant TR004139. R.G.C. and T.P. acknowledge funding from the Centre of Excellence on Molecular Materials and Functions under the Institution of Eminence scheme of IIT Madras. K.U. thanks IIT Madras and acknowledges a visiting doctoral fellowship from the Science and Engineering Research Board of India.

■ REFERENCES

(1) Yan, X.; Bain, R. M.; Cooks, R. G. Organic Reactions in Microdroplets: Reaction Acceleration Revealed by Mass Spectrometry. *Angew. Chem., Int. Ed.* **2016**, *55* (42), 12960−12972.
(2) Cooks, R. G.; Yan, X. Mass Spectrometry for Synthesis and Analysis. *Annual Review of Analytical Chemistry* **2018**, *11* (1), 1−28.
(3) Wei, Z.; Li, Y.; Cooks, R. G.; Yan, X. Accelerated Reaction Kinetics in Microdroplets: Overview and Recent Developments. *Annu. Rev. Phys. Chem.* **2020**, *71* (1), 31−51.
(4) Qiu, L.; Cooks, R. G. Spontaneous Oxidation in Aqueous Microdroplets: Water Radical Cation as Primary Oxidizing Agent. *Angew. Chem., Int. Ed.* **2024**, *63* (17), No. e202400118.
(5) Sarkar, D.; Mahitha, M. K.; Som, A.; Li, A.; Wleklinski, M.; Cooks, R. G.; Pradeep, T. Metallic Nanobrushes Made Using Ambient Droplet Sprays. *Adv. Mater.* **2016**, *28* (11), 2223−2228.
(6) Spoorthi, B. K.; Debnath, K.; Basuri, P.; Nagar, A.; Waghmare, U. V.; Pradeep, T. Spontaneous Weathering of Natural Minerals in Charged Water Microdroplets Forms Nanomaterials. *Science* **2024**, *384* (6699), 1012−1017.
(7) Banerjee, S.; Zare, R. N. Syntheses of Isoquinoline and Substituted Quinolines in Charged Microdroplets. *Angew. Chem., Int. Ed.* **2015**, *54* (49), 14795−14799.
(8) Lee, J. K.; Samanta, D.; Nam, H. G.; Zare, R. N. Micrometer-Sized Water Droplets Induce Spontaneous Reduction. *J. Am. Chem. Soc.* **2019**, *141* (27), 10585−10589.
(9) Song, X.; Basheer, C.; Zare, R. N. Making Ammonia from Nitrogen and Water Microdroplets. *Proc. Natl. Acad. Sci. U. S. A.* **2023**, *120* (16), No. e2301206120.
(10) Nam, I.; Lee, J. K.; Nam, H. G.; Zare, R. N. Abiotic Production of Sugar Phosphates and Uridine Ribonucleoside in Aqueous Microdroplets. *Proc. Natl. Acad. Sci. U. S. A.* **2017**, *114* (47), 12396−12400.
(11) Beattie, J. K.; Djerdjev, A. M. The Pristine Oil/Water Interface: Surfactant-Free Hydroxide-Charged Emulsions. *Angew. Chem., Int. Ed.* **2004**, *43* (27), 3568−3571.
(12) Cotte-Rodríguez, I.; Takáts, Z.; Talaty, N.; Chen, H.; Cooks, R. G. Desorption Electrospray Ionization of Explosives on Surfaces: Sensitivity and Selectivity Enhancement by Reactive Desorption Electrospray Ionization. *Anal. Chem.* **2005**, *77* (21), 6755−6764.
(13) Espy, R. D.; Wleklinski, M.; Yan, X.; Cooks, R. G. Beyond the Flask: Reactions on the Fly in Ambient Mass Spectrometry. *TrAC Trends in Analytical Chemistry* **2014**, *57*, 135−146.
(14) Banerjee, S.; Prakash, H.; Mazumdar, S. Evidence of Molecular Fragmentation inside the Charged Droplets Produced by Electrospray Process. *J. Am. Soc. Mass Spectrom.* **2011**, *22* (10), 1.
(15) Girod, M.; Moyano, E.; Campbell, D. I.; Cooks, R. G. Accelerated Bimolecular Reactions in Microdroplets Studied by Desorption Electrospray Ionization Mass Spectrometry. *Chem. Sci.* **2011**, *2* (3), 501−510.
(16) Müller, T.; Badu-Tawiah, A.; Cooks, R. G. Accelerated Carbon−Carbon Bond-Forming Reactions in Preparative Electrospray. *Angew. Chem., Int. Ed.* **2012**, *51* (47), 11832−11835.
(17) Yan, X.; Cheng, H.; Zare, R. N. Two-Phase Reactions in Microdroplets without the Use of Phase-Transfer Catalysts. *Angew. Chem., Int. Ed.* **2017**, *56* (13), 3562−3565.
(18) Zhu, X.; Zhang, W.; Lin, Q.; Ye, M.; Xue, L.; Liu, J.; Wang, Y.; Cheng, H. Direct Microdroplet Synthesis of Carboxylic Acids from Alcohols by Preparative Paper Spray Ionization without Phase Transfer Catalysts. *ACS Sustainable Chem. Eng.* **2019**, *7* (7), 6486−6491.
(19) Zhang, X.; Su, R.; Li, J.; Huang, L.; Yang, W.; Chingin, K.; Balabin, R.; Wang, J.; Zhang, X.; Zhu, W.; Huang, K.; Feng, S.; Chen, H. Efficient Catalyst-Free N_2 Fixation by Water Radical Cations under Ambient Conditions. *Nat. Commun.* **2024**, *15* (1), 1535.
(20) Lai, Y.-H.; Sathyamoorthi, S.; Bain, R. M.; Zare, R. N. Microdroplets Accelerate Ring Opening of Epoxides. *J. Am. Soc. Mass Spectrom.* **2018**, *29* (5), 1036−1043.
(21) Qiu, L.; Wei, Z.; Nie, H.; Cooks, R. G. Reaction Acceleration Promoted by Partial Solvation at the Gas/Solution Interface. *ChemPlusChem.* **2021**, *86* (10), 1362−1365.
(22) Song, Z.; Liang, C.; Gong, K.; Zhao, S.; Yuan, X.; Zhang, X.; Xie, J. Harnessing the High Interfacial Electric Fields on Water Microdroplets to Accelerate Menshutkin Reactions. *J. Am. Chem. Soc.* **2023**, *145* (48), 26003−26008.
(23) Zhu, C.; Pham, L. N.; Yuan, X.; Ouyang, H.; Coote, M. L.; Zhang, X. High Electric Fields on Water Microdroplets Catalyze Spontaneous and Fast Reactions in Halogen-Bond Complexes. *J. Am. Chem. Soc.* **2023**, *145* (39), 21207−21212.
(24) Chamberlayne, C. F.; Zare, R. N. Simple Model for the Electric Field and Spatial Distribution of Ions in a Microdroplet. *J. Chem. Phys.* **2020**, *152* (18), 184702.
(25) Xiong, H.; Lee, J. K.; Zare, R. N.; Min, W. Strong Electric Field Observed at the Interface of Aqueous Microdroplets. *J. Phys. Chem. Lett.* **2020**, *11* (17), 7423−7428.
(26) Hao, H.; Leven, I.; Head-Gordon, T. Can Electric Fields Drive Chemistry for an Aqueous Microdroplet? *Nat. Commun.* **2022**, *13* (1), 280.
(27) Xia, Y.; Xu, J.; Li, J.; Chen, B.; Dai, Y.; Zare, R. N. Visualization of the Charging of Water Droplets Sprayed into Air. *J. Phys. Chem. A* **2024**, *128* (28), 5684−5690.
(28) LaCour, R. A.; Heindel, J. P.; Zhao, R.; Head-Gordon, T. The Role of Interfaces and Charge for Chemical Reactivity in Microdroplets. *J. Am. Chem. Soc.* **2025**, *147* (8), 6299−6317.
(29) Nandy, A.; Kumar, A.; Mondal, S.; Koner, D.; Banerjee, S. Spontaneous Generation of Aryl Carbocations from Phenols in Aqueous Microdroplets: Aromatic SN1 Reactions at the Air-Water Interface. *J. Am. Chem. Soc.* **2023**, *145* (29), 15674−15679.
(30) Li, K.; Gong, K.; Liu, J.; Ohnoutek, L.; Ao, J.; Liu, Y.; Chen, X.; Xu, G.; Ruan, X.; Cheng, H.; Han, J.; Sui, G.; Ji, M.; Valev, V. K.; Zhang, L. Significantly Accelerated Photochemical and Photocatalytic Reactions in Microdroplets. *Cell Rep. Phys. Sci.* **2022**, *3* (6), 100917.
(31) Feng, C.; Zhang, L. Microdroplet Assisted Hollow ZnCdS@ PDA Nanocages' Synergistic Confinement Effect for Promoting Photocatalytic H2O2 Production. *Mater. Horiz.* **2024**, *11* (6), 1515−1527.
(32) Wilson, K. R.; Prophet, A. M. Chemical Kinetics in Microdroplets. *Annu. Rev. Phys. Chem.* **2024**, *75* (1), 185−208.
(33) Lee, J. K.; Banerjee, S.; Nam, H. G.; Zare, R. N. Acceleration of Reaction in Charged Microdroplets. *Q. Rev. Biophys.* **2015**, *48* (4), 437−444.
(34) Gong, K.; Nandy, A.; Song, Z.; Li, Q.-S.; Hassanali, A.; Cassone, G.; Banerjee, S.; Xie, J. Revisiting the Enhanced Chemical Reactivity in Water Microdroplets: The Case of a Diels-Alder Reaction. *J. Am. Chem. Soc.* **2024**, *146* (46), 31585−31596.
(35) Banerjee, S. On the Stability of Carbocation in Water Microdroplets. *Int. J. Mass Spectrom.* **2023**, *486*, 117024.

(36) Colussi, A. J.; Enami, S.; Ishizuka, S. Hydronium Ion Acidity Above and Below the Interface of Aqueous Microdroplets. *ACS Earth Space Chem.* **2021**, *5* (9), 2341−2346.
(37) Li, M.; Kan, Y.; Su, H.; Pöschl, U.; Parekh, S. H.; Bonn, M.; Cheng, Y. Spatial Homogeneity of pH in Aerosol Microdroplets. *Chem.* **2023**, *9* (4), 1036−1046.
(38) Li, K.; Gong, K.; Liu, J.; Ohnoutek, L.; Ao, J.; Liu, Y.; Chen, X.; Xu, G.; Ruan, X.; Cheng, H.; Han, J.; Sui, G.; Ji, M.; Valev, V. K.; Zhang, L. Significantly Accelerated Photochemical and Photocatalytic Reactions in Microdroplets. *Cell Rep. Phys. Sci.* **2022**, *3* (6), 100917.
(39) Gao, D.; Jin, F.; Lee, J. K.; Zare, R. N. Aqueous Microdroplets Containing Only Ketones or Aldehydes Undergo Dakin and Baeyer-Villiger Reactions. *Chemical Science* **2019**, *10* (48), 10974−10978.
(40) Wang, M.; Gao, X.-F.; Su, R.; He, P.; Cheng, Y.-Y.; Li, K.; Mi, D.; Zhang, X.; Zhang, X.; Chen, H.; Cooks, R. G. Abundant Production of Reactive Water Radical Cations under Ambient Conditions. *CCS Chemistry* **2022**, *4* (4), 1224−1231.
(41) Qiu, L.; Psimos, M. D.; Cooks, R. G. Spontaneous Oxidation of Aromatic Sulfones to Sulfonic Acids in Microdroplets. *J. Am. Soc. Mass Spectrom.* **2022**, *33* (8), 1362−1367.
(42) Gong, C.; Li, D.; Li, X.; Zhang, D.; Xing, D.; Zhao, L.; Yuan, X.; Zhang, X. Spontaneous Reduction-Induced Degradation of Viologen Compounds in Water Microdroplets and Its Inhibition by Host-Guest Complexation. *J. Am. Chem. Soc.* **2022**, *144* (8), 3510−3516.
(43) Lee, J. K.; Walker, K. L.; Han, H. S.; Kang, J.; Prinz, F. B.; Waymouth, R. M.; Nam, H. G.; Zare, R. N. Spontaneous Generation of Hydrogen Peroxide from Aqueous Microdroplets. *Proc. Natl. Acad. Sci. U. S. A.* **2019**, *116* (39), 19294−19298.
(44) Kumar, A.; Mondal, S.; Banerjee, S. Aqueous Microdroplets Capture Elusive Carbocations. *J. Am. Chem. Soc.* **2021**, *143* (6), 2459−2463.
(45) Kumar, A.; Mondal, S.; Banerjee, S. Efficient Desorption and Capture of Reactive Carbocations from Positively Charged Glass Surface Bombarded with High-Speed Water Microdroplets. *J. Phys. Chem. C* **2023**, *127* (14), 6662−6669.
(46) Qiu, L.; Cooks, R. G. Simultaneous and Spontaneous Oxidation and Reduction in Microdroplets by the Water Radical Cation/Anion Pair. *Angew. Chem., Int. Ed.* **2022**, *61* (41), No. e202210765.
(47) Ben-Amotz, D. Electric Buzz in a Glass of Pure Water. *Science* **2022**, *376* (6595), 800−801.
(48) Heindel, J. P.; LaCour, R. A.; Head-Gordon, T. The Role of Charge in Microdroplet Redox Chemistry. *Nat. Commun.* **2024**, *15* (1), 3670.
(49) Basuri, P.; Gonzalez, L. E.; Morato, N. M.; Pradeep, T.; Cooks, R. G. Accelerated Microdroplet Synthesis of Benzimidazoles by Nucleophilic Addition to Protonated Carboxylic Acids. *Chemical Science* **2020**, *11* (47), 12686−12694.
(50) Huang, K.-H.; Wei, Z.; Cooks, R. G. Accelerated Reactions of Amines with Carbon Dioxide Driven by Superacid at the Microdroplet Interface. *Chem. Sci.* **2021**, *12* (6), 2242−2250.
(51) Nie, H.; Wei, Z.; Qiu, L.; Chen, X.; Holden, D. T.; Cooks, R. G. High-Yield Gram-Scale Organic Synthesis Using Accelerated Microdroplet/Thin Film Reactions with Solvent Recycling. *Chem. Sci.* **2020**, *11* (9), 2356−2361.
(52) Ghosh, J.; Mendoza, J.; Cooks, R. G. Accelerated and Concerted Aza-Michael Addition and SuFEx Reaction in Microdroplets in Unitary and High-Throughput Formats. *Angew. Chem., Int. Ed.* **2022**, *61* (50), No. e202214090.
(53) Bain, R. M.; Sathyamoorthi, S.; Zare, R. N. "On-Droplet" Chemistry: The Cycloaddition of Diethyl Azodicarboxylate and Quadricyclane. *Angew. Chem., Int. Ed.* **2017**, *56* (47), 15083−15087.
(54) Qiu, L.; Morato, N. M.; Huang, K.-H.; Cooks, R. G. Spontaneous Water Radical Cation Oxidation at Double Bonds in Microdroplets. *Front. Chem.* **2022**, *10*, 1.
(55) Jin, S.; Chen, H.; Yuan, X.; Xing, D.; Wang, R.; Zhao, L.; Zhang, D.; Gong, C.; Zhu, C.; Gao, X.; Chen, Y.; Zhang, X. The Spontaneous Electron-Mediated Redox Processes on Sprayed Water Microdroplets. *JACS Au* **2023**, *3* (6), 1563−1571.
(56) Grooms, A. J.; Marcelo, I. M.; Huttner, R. T.; Badu-Tawiah, A. K. Programmable Plasma-Microdroplet Cascade Reactions for Multicomponent Systems. *J. Am. Chem. Soc.* **2024**, *146* (44), 30068−30077.
(57) Jin, X.; Wu, Y.; Sun, J.; Liu, J.; Cheng, H. Catalyst-Free Three-Component Petasis Reactions Accelerated in Microdroplets: Reaction Optimization and Senstive Detection by Mass Spectrometry. *Analysis & Sensing* **2023**, *3* (6), No. e202300031.
(58) Jin, X.; Wu, Y.; Dai, C.; Sun, J.; Ye, M.; Liu, J.; Cheng, H. Catalyst-Free Accelerated Three-Component Synthesis of Betti Bases in Microdroplets. *ChemPlusChem.* **2023**, *88* (2), No. e202200206.
(59) Grooms, A. J.; Huttner, R. T.; Stockwell, M.; Tadese, L.; Marcelo, I. M.; Kass, A.; Badu-Tawiah, A. K. Programmable C-N Bond Formation through Radical-Mediated Chemistry in Plasma-Microdroplet Fusion. *Angew. Chem.* **2025**, *137* (4), No. e202413122.
(60) Baren, M. H.; Ibrahim, S. A.; Al-Rooqi, M. M.; Ahmed, S. A.; El-Gamil, M. M.; Hekal, H. A. A New Class of Anticancer Activity with Computational Studies for a Novel Bioactive Aminophosphonates Based on Pyrazole Moiety. *Sci. Rep* **2023**, *13* (1), 14680.
(61) Sofan, M.; El-Taweel, F.; Abdel-Rahman, A.; Salman, H.; Negm, E. Synthesis of Novel Azo Pyrazole Disperse Dyes for Dyeing and Antibacterial Finishing of PET Fabric under Supercritical Carbon Dioxide. *Sci. Rep* **2024**, *14* (1), 1121.
(62) Giornal, F.; Pazenok, S.; Rodefeld, L.; Lui, N.; Vors, J.-P.; Leroux, F. R. Synthesis of Diversely Fluorinated Pyrazoles as Novel Active Agrochemical Ingredients. *J. Fluorine Chem.* **2013**, *152*, 2−11.
(63) Catalan, J.; Fabero, F.; Claramunt, R. M.; Santa Maria, M. D.; Foces-Foces, M. de la C.; Hernandez Cano, F.; Martinez-Ripoll, M.; Elguero, J.; Sastre, R. New Ultraviolet Stabilizers: 3- and 5-(2'-Hydroxyphenyl)Pyrazoles. *J. Am. Chem. Soc.* **1992**, *114* (13), 5039−5048.
(64) Ríos, M.-C.; Portilla, J. Recent Advances in Synthesis and Properties of Pyrazoles. *Chemistry* **2022**, *4* (3), 940−968.
(65) Estevan, F.; Hirva, P.; Ofori, A.; Sanaú, M.; Špec, T.; Úbeda, M. Pyrazole and Pyrazolate as Ligands in the Synthesis and Stabilization of New Palladium(II) and (III) Compounds. *Inorg. Chem.* **2016**, *55* (5), 2101−2113.
(66) Viciano-Chumillas, M.; Tanase, S.; de Jongh, L. J.; Reedijk, J. Coordination Versatility of Pyrazole-Based Ligands towards High-Nuclearity Transition-Metal and Rare-Earth Clusters. *Eur. J. Inorg. Chem.* **2010**, *2010* (22), 3403−3418.
(67) Smith, R. A.; Kulmaczewski, R.; Halcrow, M. A. Ligand-Directed Metalation of a Gold Pyrazolate Cluster. *Inorg. Chem.* **2023**, *62* (24), 9300−9305.
(68) Chang, Y.; Xie, C.; Liu, H.; Huang, S.; Wang, P.; Qin, W.; Yan, H. Organocatalytic Atroposelective Construction of Axially Chiral N, N- and N, S-1,2-Azoles through Novel Ring Formation Approach. *Nat. Commun.* **2022**, *13* (1), 1933.
(69) Li, G.; Cheng, Y.; Han, C.; Song, C.; Huang, N.; Du, Y. Pyrazole-Containing Pharmaceuticals: Target, Pharmacological Activity, and Their SAR Studies. *RSC Med. Chem.* **2022**, *13* (11), 1300−1321.
(70) von Pechmann, H. Pyrazol Aus Acetylen Und Diazomethan. *Berichte der deutschen chemischen Gesellschaft* **1898**, *31* (3), 2950−2951.
(71) Aziz, H.; Zahoor, A. F.; Shahzadi, I.; Irfan, A. Recent Synthetic Methodologies Towards the Synthesis of Pyrazoles. *Polycyclic Aromatic Compounds* **2021**, *41* (4), 698−720.
(72) Marković, V.; Joksović, M. D. "On Water" Synthesis of N-Unsubstituted Pyrazoles: Semicarbazide Hydrochloride as an Alternative to Hydrazine for Preparation of Pyrazole-3-Carboxylate Derivatives and 3,5-Disubstituted Pyrazoles. *Green Chem.* **2015**, *17* (2), 842−847.
(73) Ali, H. M.; El-Ossaily, Y. A.; Metwally, S. A.; Althobaiti, I. O.; Altaleb, H. A.; Naffea, Y. A.; Tolba, M. S. Catalytic and Multicomponent Reactions for Green Synthesis of Some Pyrazolone Compounds and Evaluation as Antimicrobial Agents. *ACS Omega* **2022**, *7* (33), 29142−29152.

(74) Vuluga, D.; Legros, J.; Crousse, B.; Bonnet-Delpon, D. Synthesis of Pyrazoles through Catalyst-Free Cycloaddition of Diazo Compounds to Alkynes. *Green Chem.* **2009**, *11* (2), 156−159.
(75) Knorr, L. Einwirkung von Acetessigester Auf Phenylhydrazin. *Berichte der deutschen chemischen Gesellschaft* **1883**, *16* (2), 2597−2599.
(76) Xue, L.; Zheng, B.; Sun, J.; Liu, J.; Cheng, H. Water Microdroplet Chemistry for Accelerating Green Thiocyanation and Discovering Water-Controlled Divergence. *ACS Sustainable Chem. Eng.* **2023**, *11* (34), 12780−12789.
(77) Kumar, V.; Chang, C.-K.; Tan, K.-P.; Jung, Y.-S.; Chen, S.-H.; Cheng, Y.-S. E.; Liang, P.-H. Identification, Synthesis, and Evaluation of New Neuraminidase Inhibitors. *Org. Lett.* **2014**, *16* (19), 5060−5063.
(78) Wang, H.; Sun, X.; Zhang, S.; Liu, G.; Wang, C.; Zhu, L.; Zhang, H. Efficient Copper-Catalyzed Synthesis of Substituted Pyrazoles at Room Temperature. *Synlett* **2018**, *29*, 2689−2692.
(79) Polshettiwar, V.; Varma, R. S. Greener and Rapid Access to Bio-Active Heterocycles: Room Temperature Synthesis of Pyrazoles and Diazepines in Aqueous Medium. *Tetrahedron Lett.* **2008**, *49* (2), 397−400.
(80) Zhang, D.; Ren, L.; Liu, A.; Li, W.; Liu, Y.; Gu, Q. One-Pot Solvent-Free Synthesis of 1,3,5-Trisubstituted 1H-Pyrazoles Catalyzed by H3[PW12O40]/SiO2 under Microwave Irradiation. *Monatsh. Chem.* **2022**, *153* (3), 257−266.
(81) Desai, N. C.; Bhatt, K.; Monapara, J.; Pandit, U.; Khedkar, V. M. Conventional and Microwave-Assisted Synthesis, Antitubercular Activity, and Molecular Docking Studies of Pyrazole and Oxadiazole Hybrids. *ACS Omega* **2021**, *6* (42), 28270−28284.
(82) Du, K.; Xia, C.; Wei, M.; Chen, X.; Zhang, P. Microwave-Assisted Rapid Synthesis of Sugar-Based Pyrazole Derivatives with Anticancer Activity in Water. *RSC Adv.* **2016**, *6* (71), 66803−66806.
(83) Wei, H.; Vejerano, E. P.; Leng, W.; Huang, Q.; Willner, M. R.; Marr, L. C.; Vikesland, P. J. Aerosol Microdroplets Exhibit a Stable pH Gradient. *Proc. Natl. Acad. Sci. U. S. A.* **2018**, *115* (28), 7272−7277.
(84) Melott, A. L. Le Châtelier's Principle. *J. Chem. Educ.* **1968**, *45* (6), A519.
(85) Van Aken, K.; Strekowski, L.; Patiny, L. EcoScale, a Semi-Quantitative Tool to Select an Organic Preparation Based on Economical and Ecological Parameters. *Beilstein J. Org. Chem.* **2006**, *2* (1), 3.

Supporting Information

Accelerated Synthesis of Pyrazoles Mediated by Water Microdroplets

Manish Jana[†a], Keerthana Unni[†b, a], Prof. Thalappil Pradeep*[b], Prof. R. Graham Cooks*[a]

[a] *Department of Chemistry, Purdue University, West Lafayette, Indiana 47907*

[b] *DST unit of Nanoscience (DST UNS) and Thematic unit of Excellence (TUE), Department of Chemistry, Indian Institute of Technology Madras, Chennai 600036, India.*

Email: cooks@purdue.edu, pradeep@iitm.ac.in

([†] These authors have contributed equally to this work)

Total number of pages: 23 (S1-S23)

Total number of figures: 28 (figure S1-S28)

Table of Contents

1. Additional Experimental Details.....S4

1.1. Collection Setup for Scale up Experiment……...……..S4

1.2. Conversion Ratio Calculation……S4

2. Microdroplet reaction of ethyl acetoacetate (1a) and phenyl hydrazine (2a) …….S5-S6

2.1. MS/MS characterization data of the product …….S5

2.2. Distance effect during the reaction between ethyl acetoacetate and phenyl hydrazine…..S5

2.3. Mass spectra for reaction between ethyl acetoacetate and phenyl hydrazine in EtOH…..S6

2.4. ^{1}H NMR spectra of the Pyrazole product……..….S6

3. Reaction between heptane 3,5-dione (1b) and phenyl hydrazine (2a)…….…….S7-S9

3.1. Mass spectra of reaction products in H_2O microdroplets…….……..……S7

3.2. Mass spectra of the reaction products in EtOH microdroplets…… .S8

3.3. MS/MS Characterization……...S8

3.4. Proposed reaction mechanism and the intermediates in the mass spectrum……..…S9

3.5. ^{1}H NMR spectra of the pyrazole product……..S9

4. Reaction between 2-acetylcyclohexanone (1c) and phenyl hydrazine (2a)……...S10-S11

4.1. Mass spectrum & MS/MS of reaction products in water microdroplets …….S10

4.2. Effect of using water during the reaction……..S10

4.3. Proposed reaction mechanism and the intermediates in the mass spectrum……...…S11

4.4. ^{1}H NMR Characterization……... ……..……..S11

5. Reaction between ethyl acetoacetate (1a) and hydrazine hydrate (2b)…….S12-S14

5.1. Mass spectrum & MS/MS of reaction products in water microdroplets ……S12

5.2. Proposed reaction mechanism and the intermediates in the mass spectrum……..…S13

5.3. ^{1}H NMR characterization……S14

6. Reaction between heptane 3,5-dione (1b) and hydrazine hydrate (2b)……S15-S16

6.1. Mass spectrum & MS/MS of reaction products in water microdroplets….……S15

6.2. Proposed reaction mechanism and the intermediates isolated in the mass spectra……..S15

6.3. ^{1}H NMR characterization……S16

7. Reaction between 2-acetylcyclohexanone (1c) and hydrazine hydrate (2b)…….S16-S17

7.1. Mass spectrum & MS/MS of reaction products in water microdroplets ……..……..S16

7.2. Proposed reaction mechanism and the intermediates in the mass spectrum……...…S17

7.3. ^{1}H NMR characterization……S17

8. Reaction of 1,3-diphenyl-1,3-propanedione (1d) and hydrazine hydrate (2b).…S18-S19

8.1. Mass spectrum & MS/MS of reaction products in water microdroplet……S18

8.2. Proposed reaction mechanism and the intermediates in the mass spectrum……...…S18

8.3. ^{1}H NMR characterization ……...…….S19

9. Reaction of 2-acetylcyclohexanone (1c) and 2-chloro-6-hydrazineylpyridine (2c)….S19-S20

9.1. Mass spectrum & MS/MS of reaction products in EtOH/Water (50:50) microdroplets. S19

9.2. Proposed reaction mechanism and the intermediates in the mass spectrum……..…S20

10. Ecoscale data……...…S20-S23

1. Additional Experimental Details

1.1. Collection Setup for Scale Up Experiment:

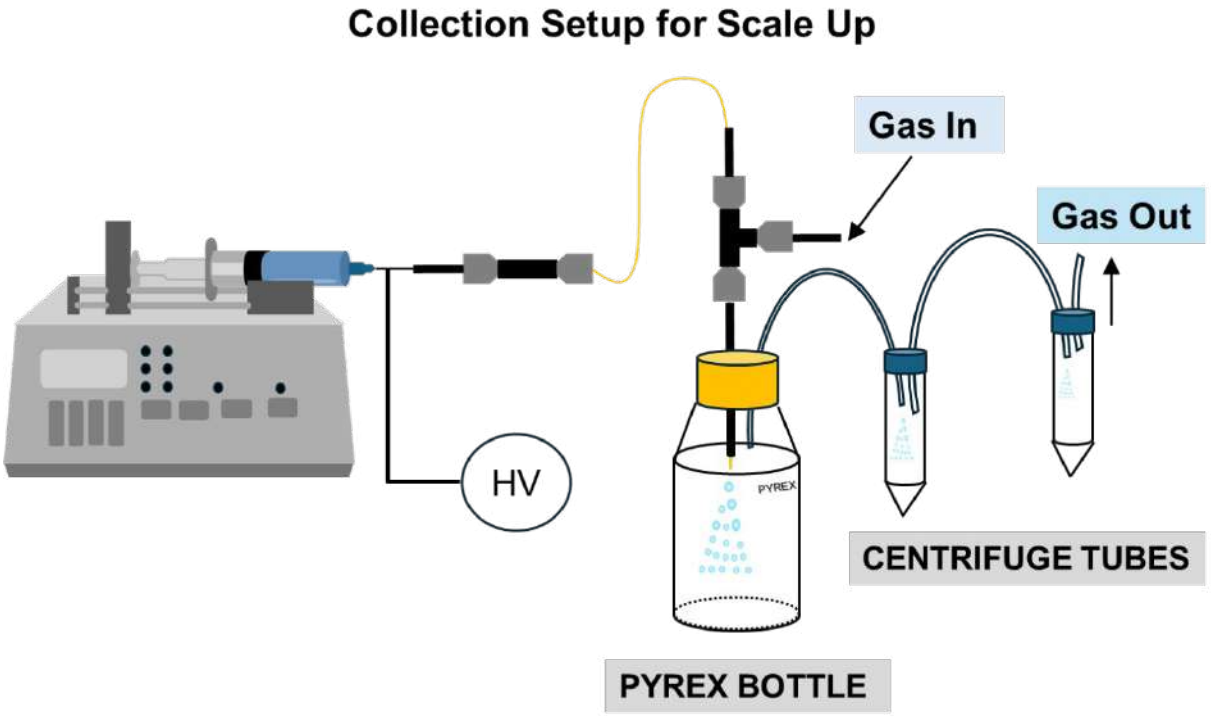


Figure S1. Schematic representation of the collection setup for scale up experiments.

1.2. Conversion Ratio Calculation.

Conversion ratios from a mass spectrum can be determined using the ion intensities of reactants, intermediates, and products, based on any of the following equations:

$$\text{Conversion Ratio} = \frac{I_P}{I_P + I_R + I_{INT}} * 100\ \% \quad \text{---------- (1)}$$

$$\text{Conversion Ratio} = \frac{I_P}{I_P + I_R} * 100\ \% \quad \text{---------- (2)}$$

$$\text{Conversion Ratio} = \frac{I_P + I_{INT}}{I_P + I_R + I_{INT}} * 100\ \% \quad \text{---------- (3)}$$

Where I_p, I_R and I_{INT} are the total ion intensity of the products, reactants and intermediates (respectively) formed during the reaction. In our case, we have used the first equation to determine the conversion ratio during the microdroplet reactions. This method represents the most stringent approach to calculating the conversion ratio, as it accounts for the ion intensity of the intermediates.

2. Microdroplet reaction of ethyl acetoacetate (1a) and phenyl hydrazine (2a).

2.1. MS/MS analysis of the product.

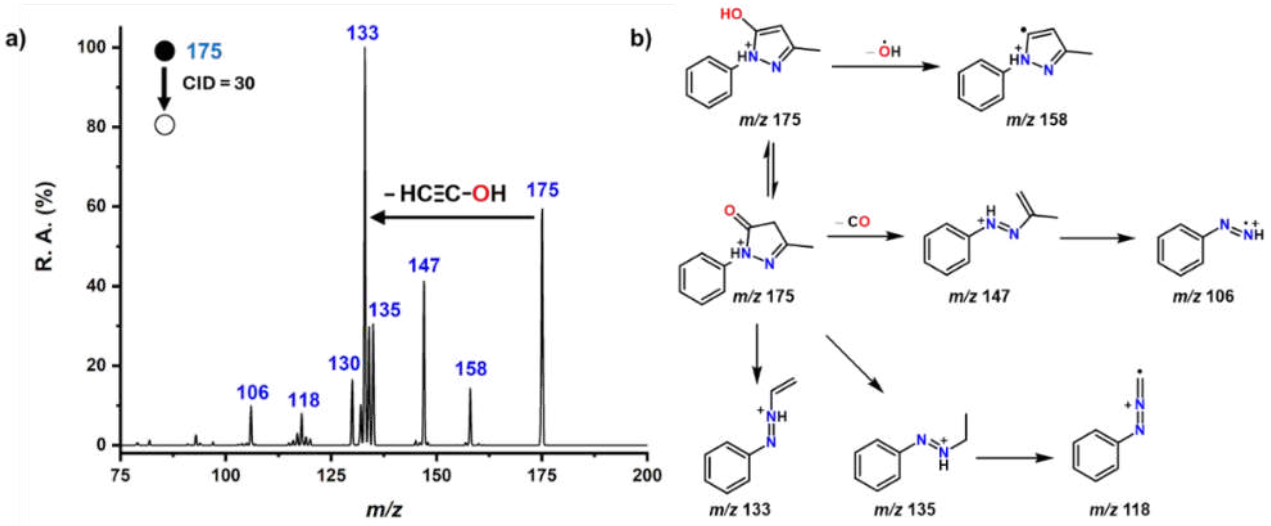


Figure S2. (a) MS/MS spectrum of product peak at *m/z* 175, (b) ChemDraw depiction of the rationalized MS/MS fragmentations.

2.2. Distance effect during the reaction between ethyl acetoacetate (1a) and phenyl hydrazine (2a).

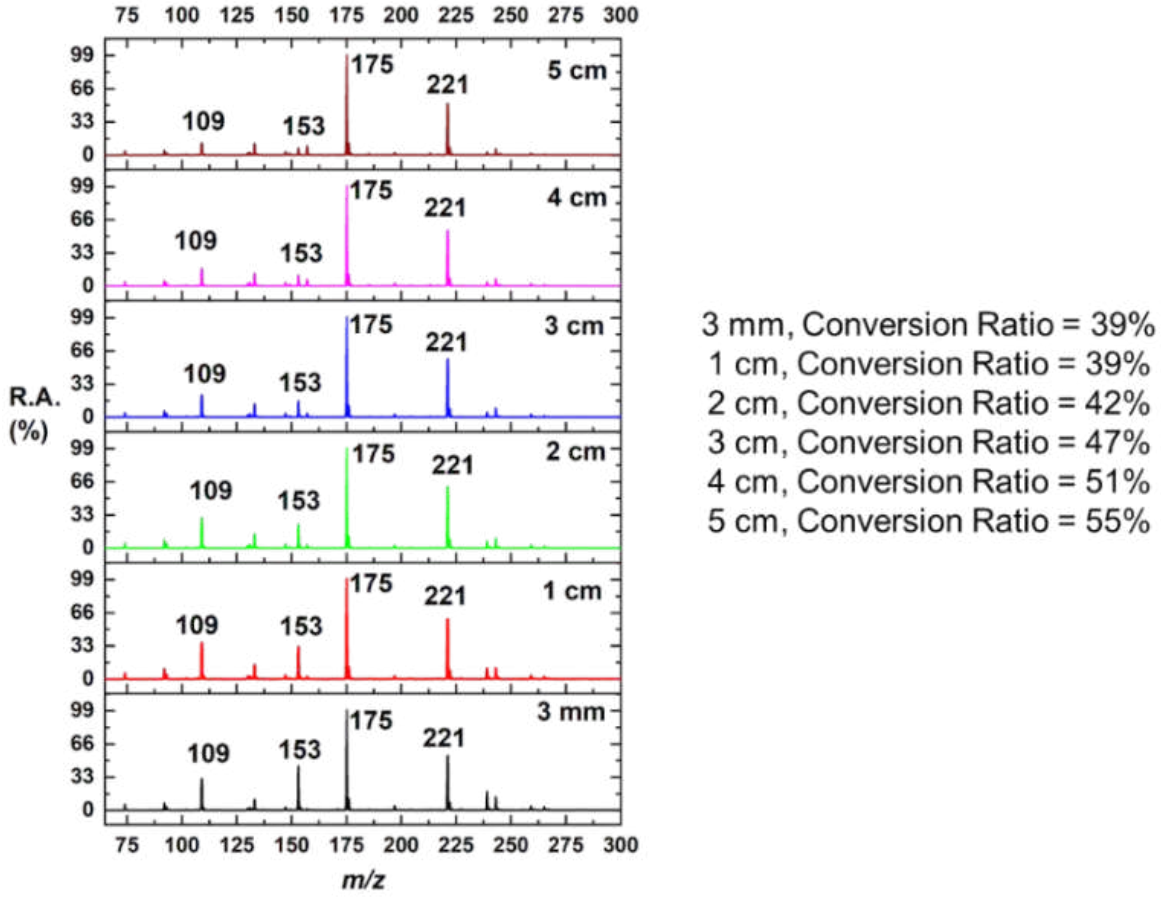


Figure S3. Distance effect during the reaction between ethyl acetoacetate and phenyl hydrazine showing greater conversion of the reactants to the final product at a distance of 5 cm.

2.3. Mass spectra for reaction between ethyl acetoacetate (1a) and phenyl hydrazine (2a) in EtOH.

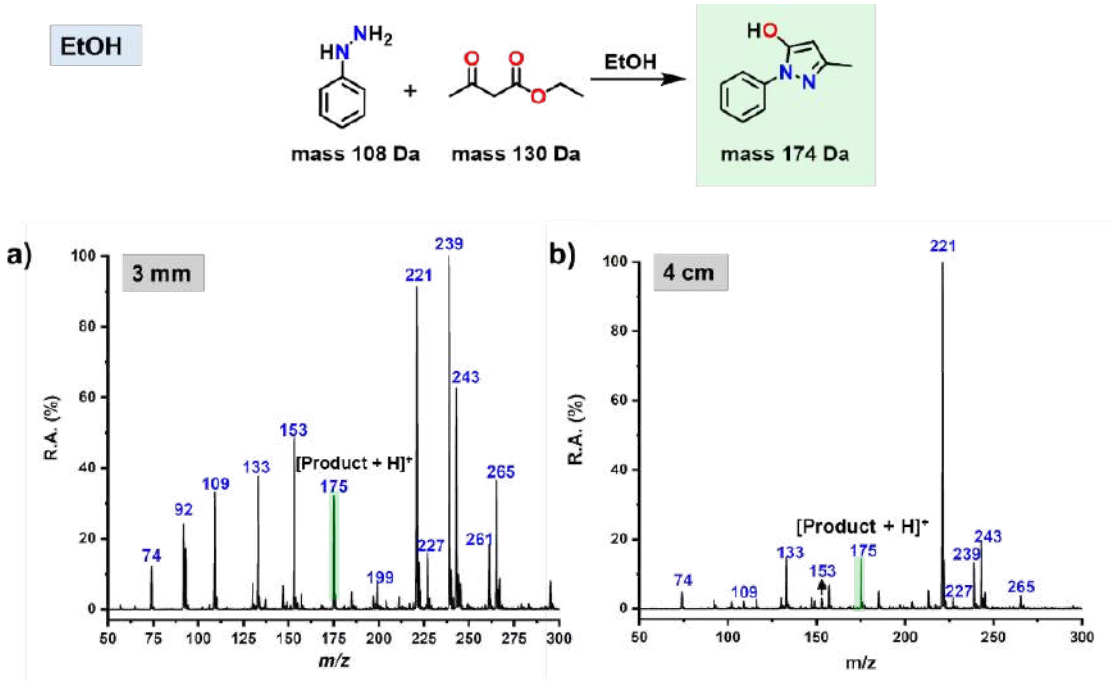


Figure S4. Mass spectra for the reaction between ethyl acetoacetate and phenyl hydrazine in EtOH a) at 3 mm distance, b) at 4 cm distance with increasing distance, the Schiff base product is found to be most abundant in the mass spectra.

2.4. ^{1}H NMR spectrum of the Pyrazole product

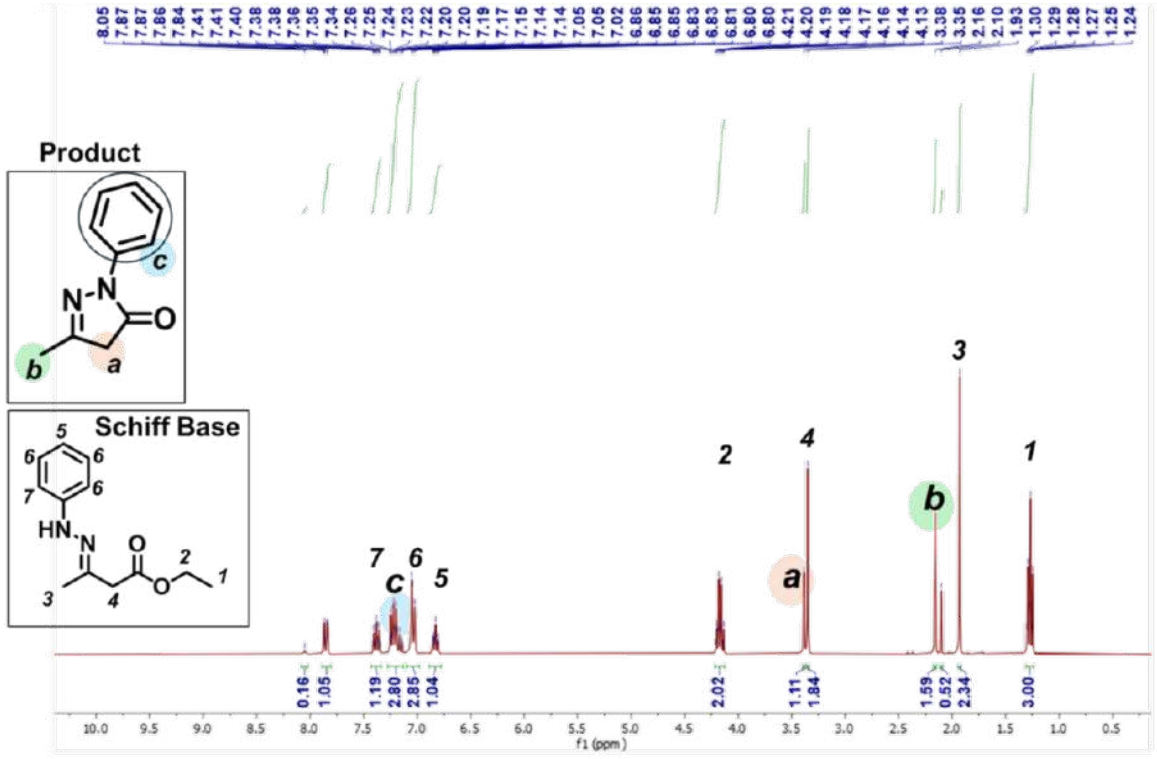


Figure S5. ^{1}H NMR spectrum (300 MHz, $CDCl_3$) for the sprayed sample. The Schiff base product is also observed in the NMR experiment. No efforts were made to separate the mixture using chromatographic techniques. From the integration value the pyrazole product was found to be 50% of the Schiff base product.

3. Reaction between heptane 3,5-dione (1b) and phenyl hydrazine (2a).

3.1. Mass spectra of the reaction between heptane 3,5-dione (1b) and phenyl hydrazine (2a) in H_2O microdroplets.

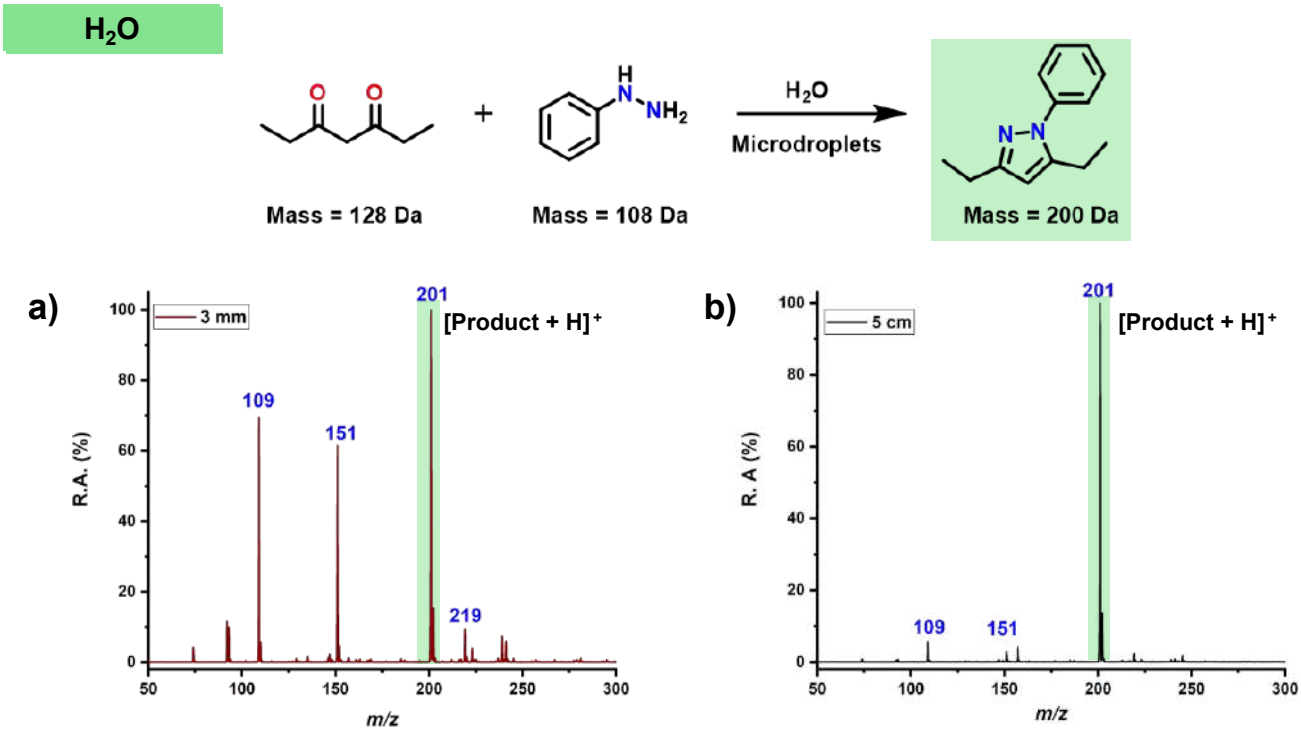


Figure S6. Mass spectra of the reaction between heptane 3, 5-dione and phenyl hydrazine in water microdroplets a) at 3 mm and b) at 5 mm distance. The reaction shows greater conversion to product upon increasing distance of the sprayer from the inlet of the mass spectrometer.

3.2. Mass spectra of the reaction between heptane 3,5-dione (1b) and phenyl hydrazine (2a) in EtOH microdroplets.

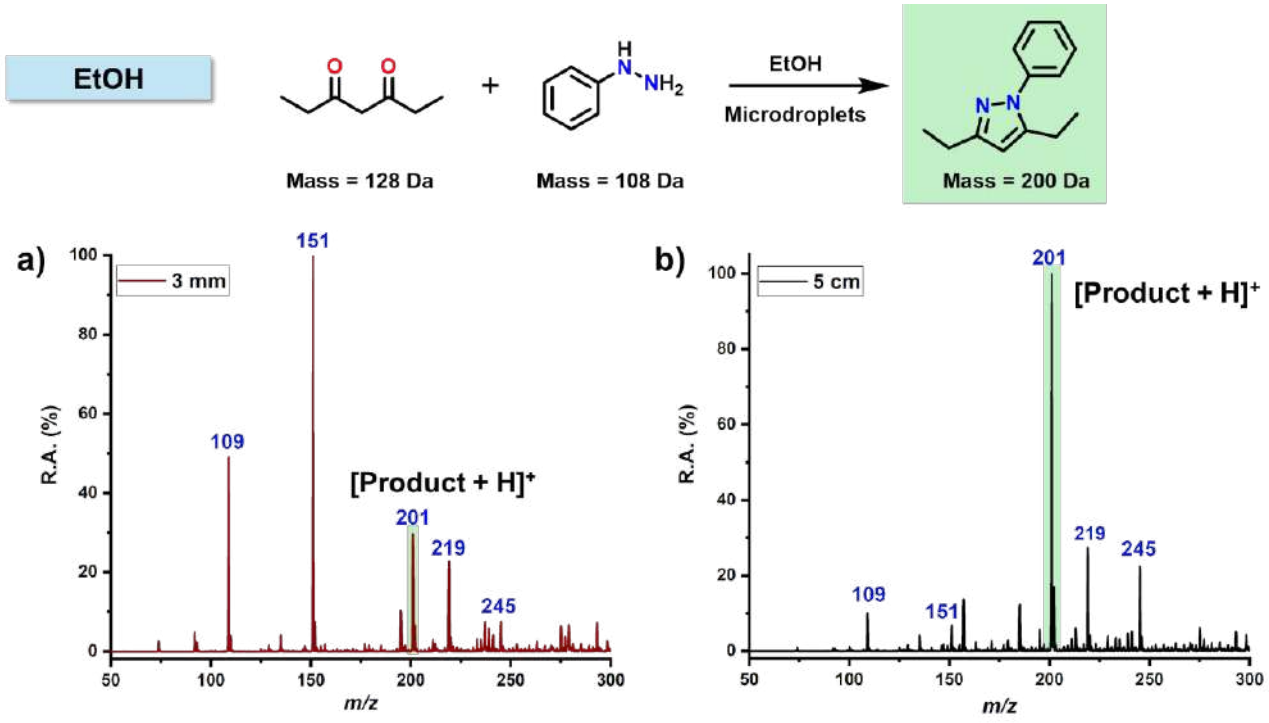


Figure S7. Mass spectra of the reaction between heptane 3,5-dione (1b) and phenyl hydrazine (2a) in ethanol microdroplets (a) at 3 mm and b) 5 cm distance. The reaction shows greater conversion to product upon increasing distance of the sprayer from the inlet of the mass spectrometer.

3.3. MS/MS Characterization.

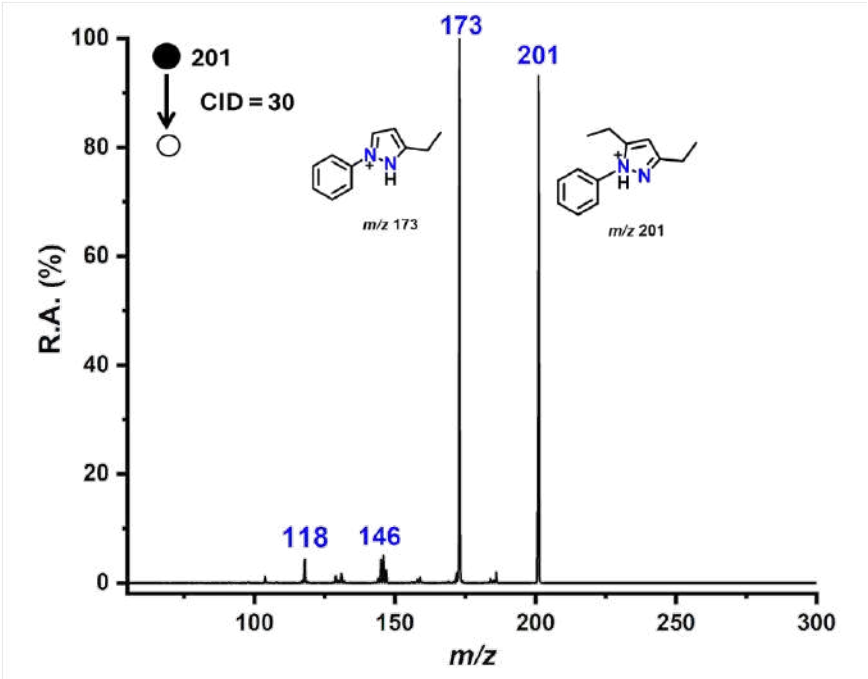


Figure S8. MS/MS spectrum for the product peak at *m/z* 201 and rationalized structures.

3.4. Proposed reaction mechanism and the intermediates in the mass spectrum.

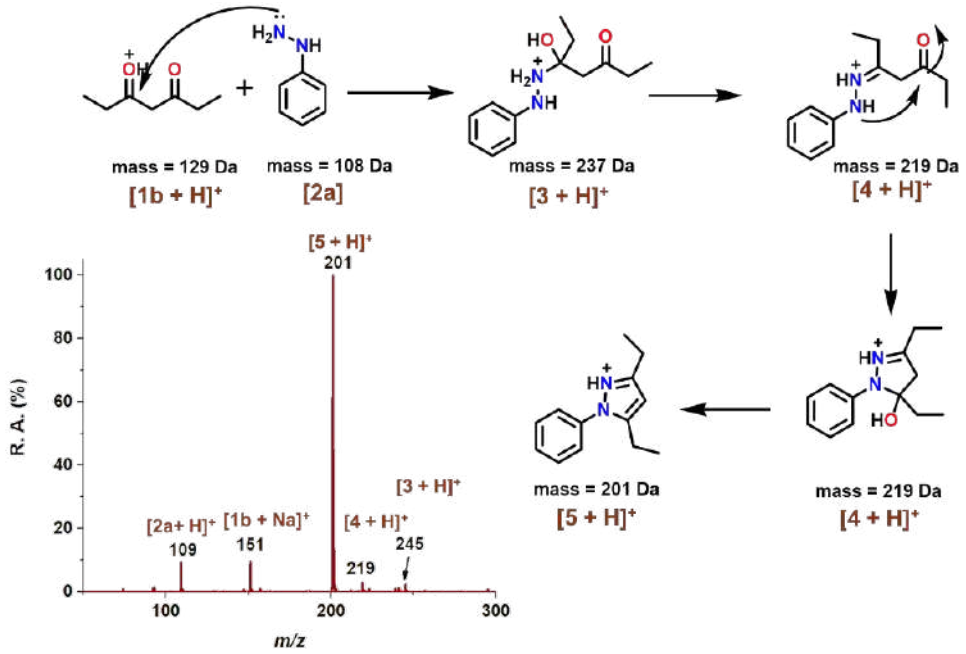


Figure S9. Proposed reaction mechanism and the intermediates and products as determined from the mass spectrum for the reaction between heptane 3,5-dione (1b) and phenyl hydrazine (2a).

3.5. ^{1}H NMR spectrum of the pyrazole product.

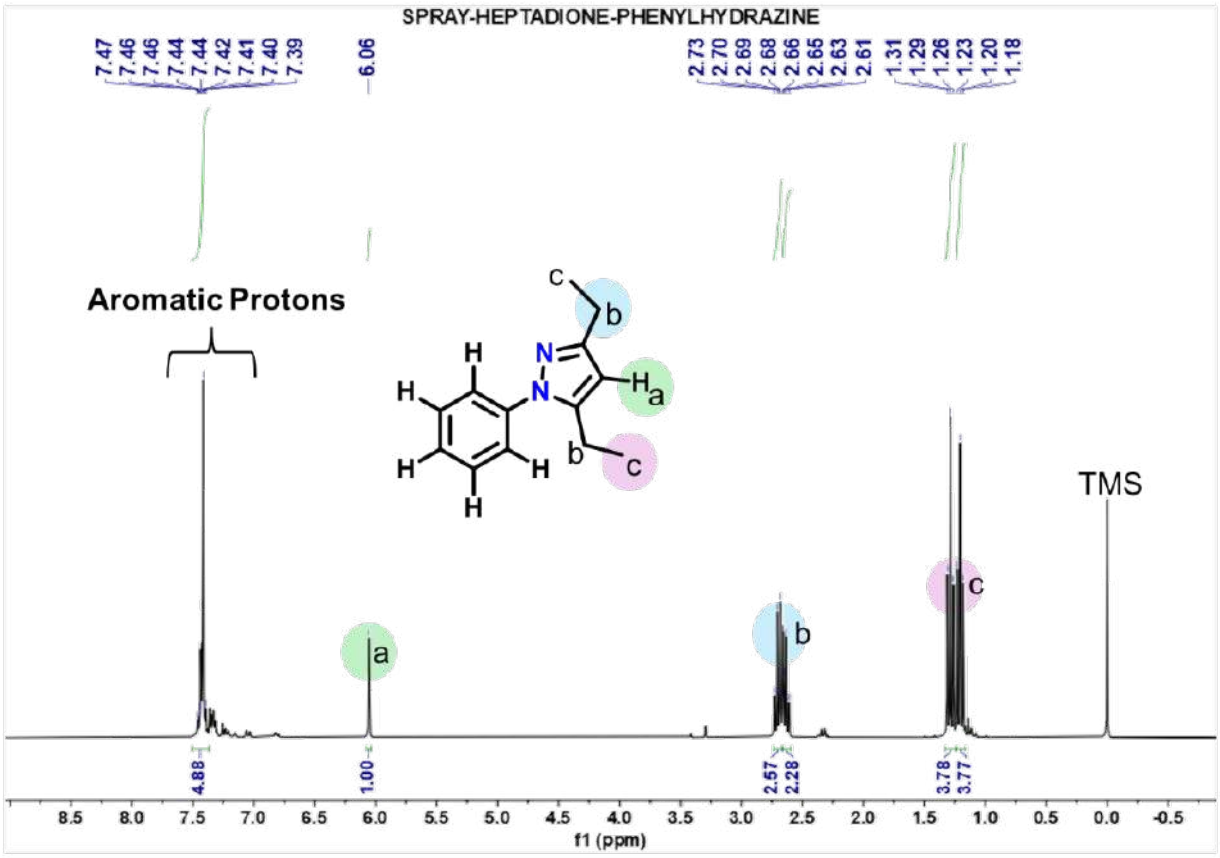


Figure S10. ^{1}H NMR (300 MHz, $CDCl_3$) of the pyrazole product formed in the reaction between heptane 3,5-dione (1b) and phenyl hydrazine (2a) in microdroplets.

4. Reaction between 2-acetylcyclohexanone (1c) and phenyl hydrazine (2a).

4.1. Mass spectrum of the reaction in ethanol/water (80:20 v/v) microdroplets and MS/MS analysis of the resulting product.

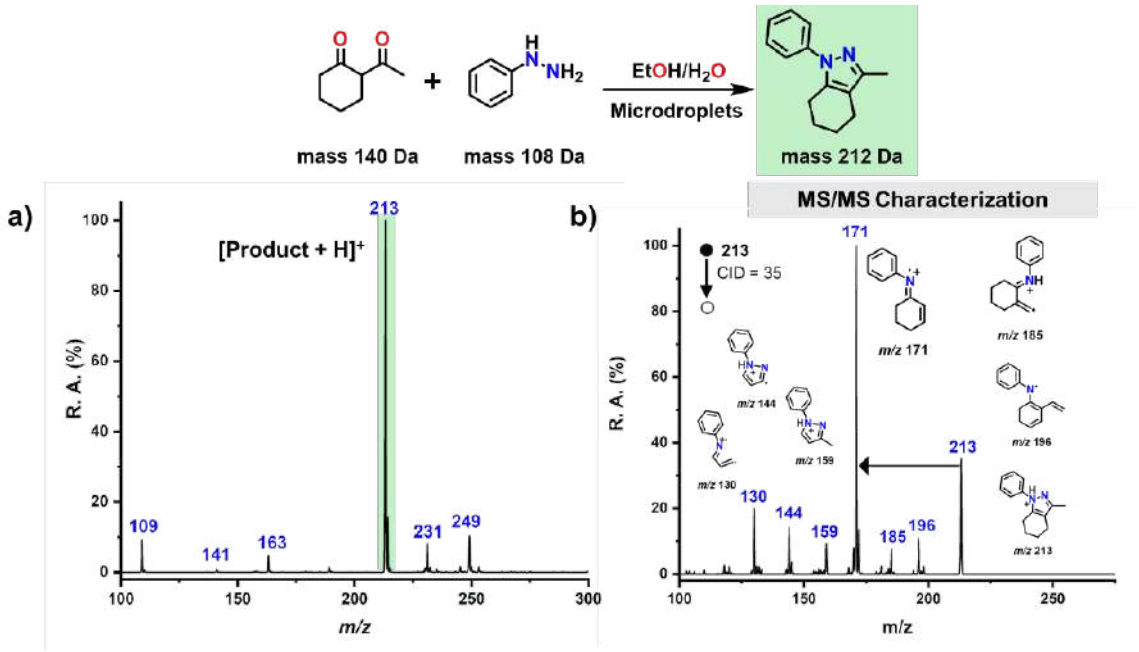


Figure S11. (a) Reaction between 2-acetylcyclohexanone (1c) and phenyl hydrazine (2a) in ethanol/water (80:20 v/v) microdroplets monitored online using a mass spectrometer. The distance of the sprayer was kept 20 mm away from the inlet of the mass spectrometer. (b) MS/MS characterization of the pyrazole product showing cross ring fragmentation as the most abundant peak in the mass spectrum. The corresponding MS/MS fragmentations are rationalized in the figure.

4.2. Effect of using water during the reaction

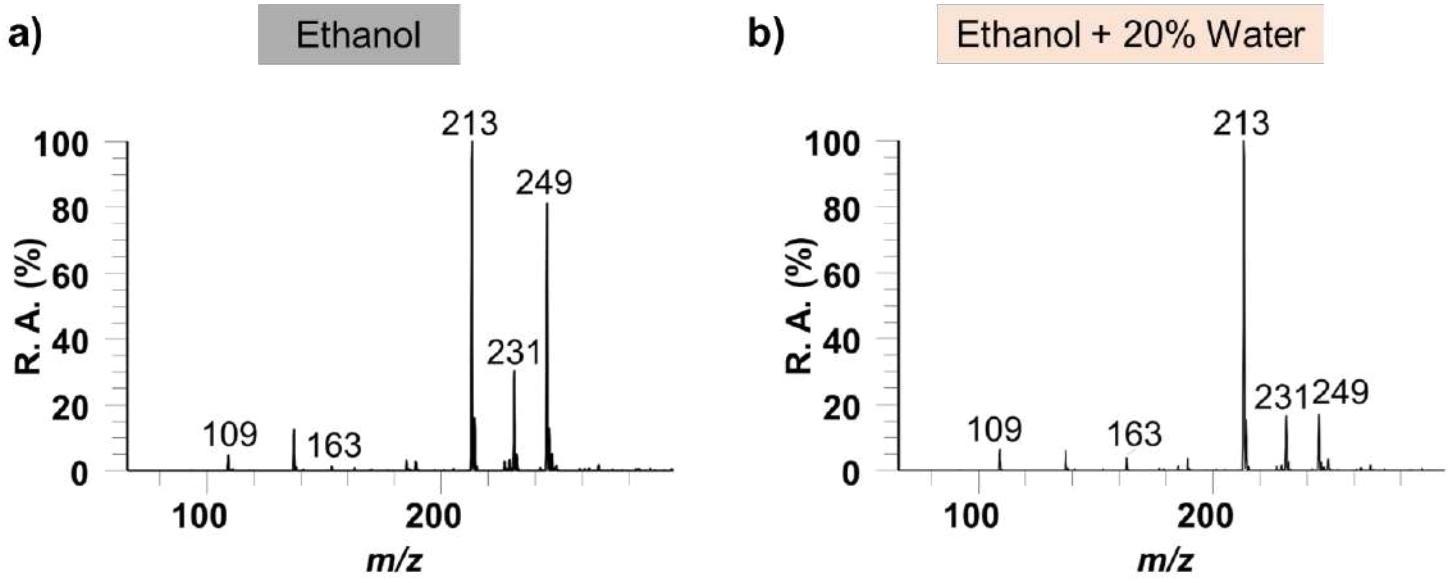


Figure S12. Reaction between 2-acetylcyclohexanone (1c) and phenyl hydrazine (2a) in (a) ethanol and (b) ethanol/water (80:20 v/v) mixture monitored online using a mass spectrometer.

4.3. Proposed reaction mechanism and the intermediates in the mass spectrum.

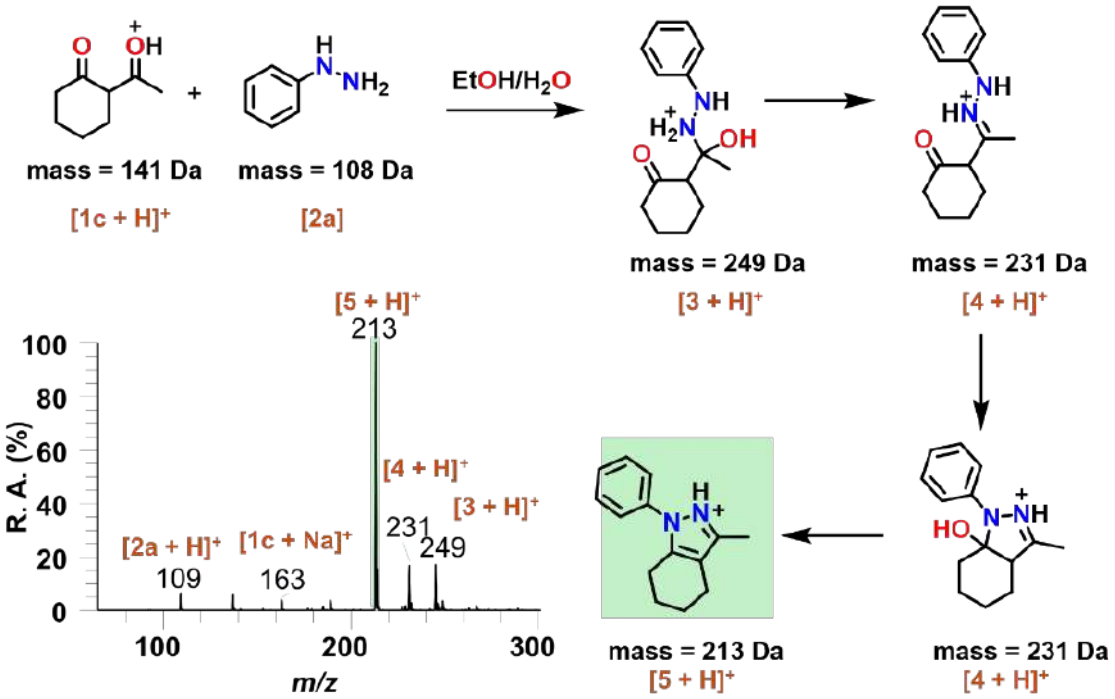


Figure S13. Proposed reaction mechanism and the intermediates and products as determined from the mass spectrum for the reaction between 2-acetylcyclohexanone (1c) and phenyl hydrazine (2a).

4.4. ^{1}H NMR spectrum of the pyrazole product.

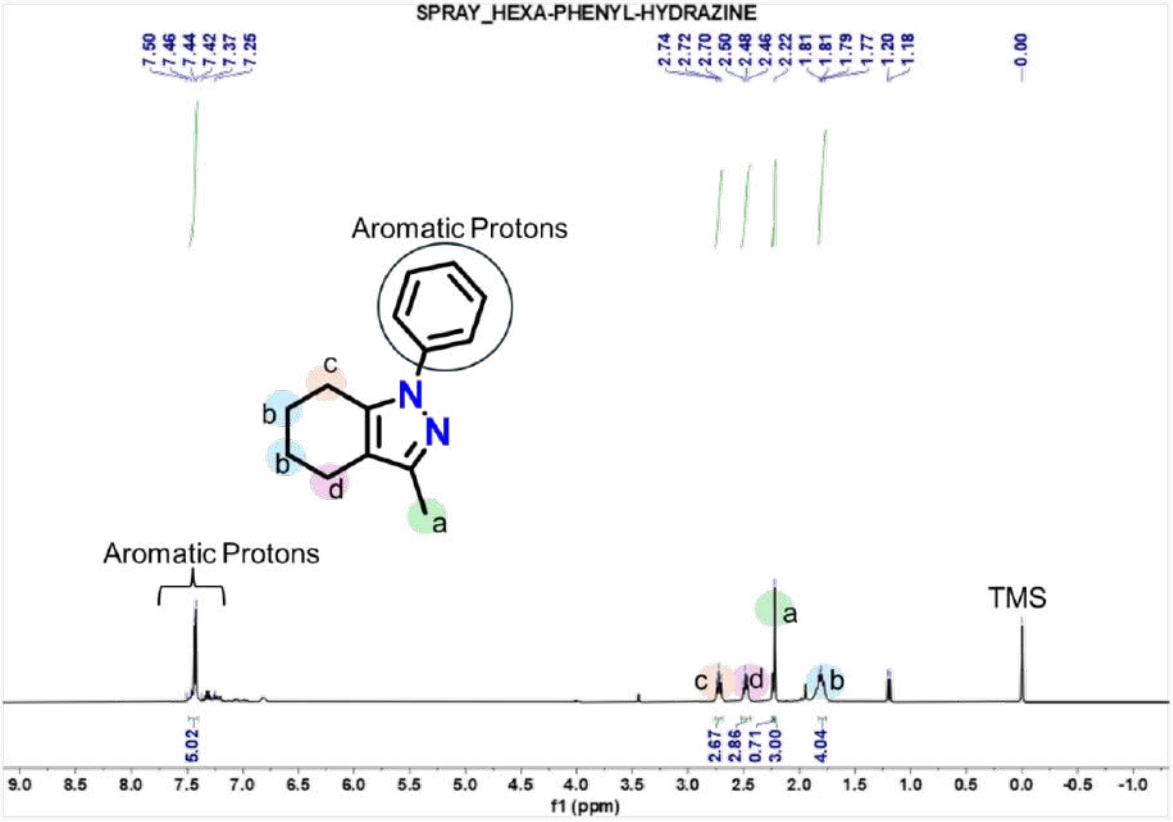


Figure S14. ^{1}H NMR(300 MHz, $CDCl_3$) of the pyrazole product after reaction between 2-acetylcyclohexanone (1c) and phenyl hydrazine (2a).

5. Reaction between ethyl acetoacetate (1a) and hydrazine hydrate (2b).

Although mass spectrum during this reaction showed only 2% conversion, the reagents were sprayed and collected for NMR analysis. From the ^{1}H NMR it has been found that there are no starting reagents present in the final product. The reduced conversion ratio (from the mass spectrum) might be due to

1. Low ionization efficiency of the pyrazole product as compared to other reaction intermediates.
2. The reaction might be a combination of microdroplet and thin film reaction.

5.1. Mass spectrum & MS/MS of reaction products in water microdroplets.

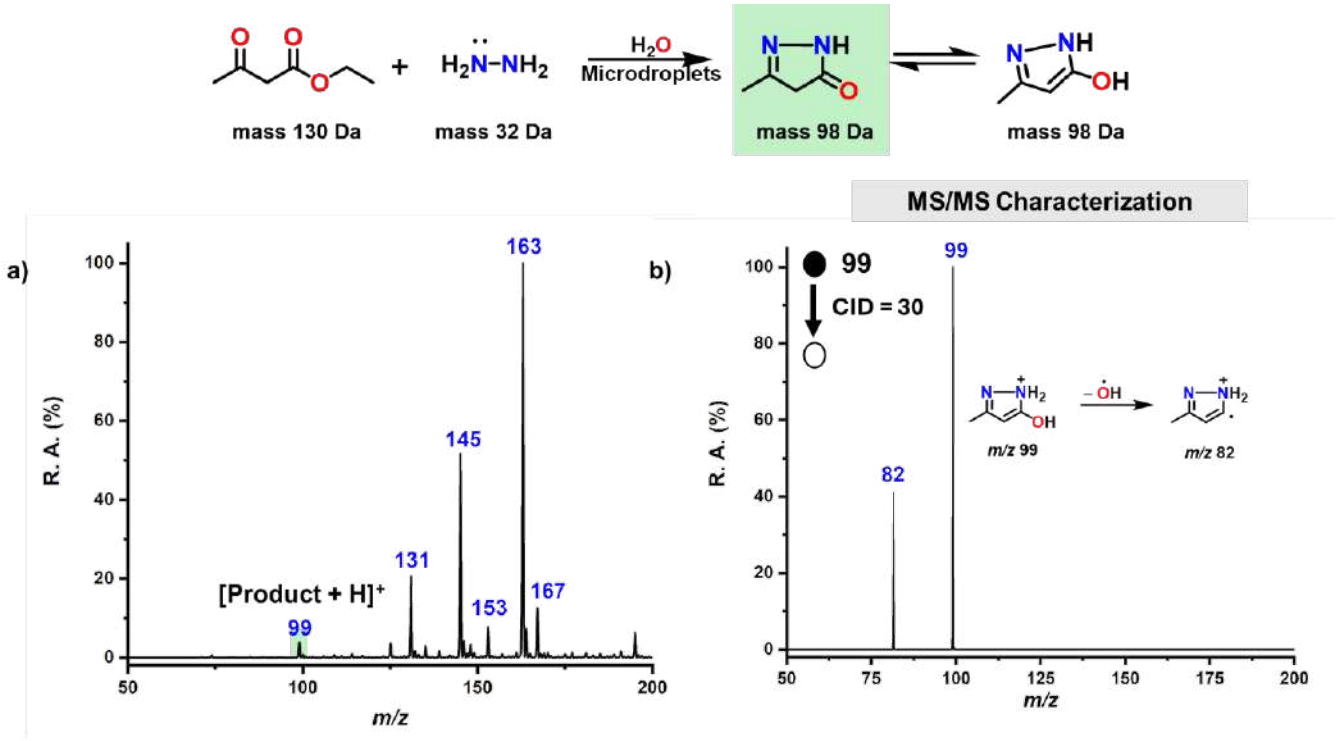


Figure S15. (a) Reaction between ethyl acetoacetate (1a) and hydrazine hydrate (2b) in water microdroplets monitored online using a mass spectrometer. The distance of the sprayer was kept 20 mm away from the inlet of the mass spectrometer. (b) MS/MS characterization of the pyrazole product. The corresponding MS/MS fragmentations are rationalized in the figure.

5.2. Proposed reaction mechanism and the intermediates in the mass spectrum.

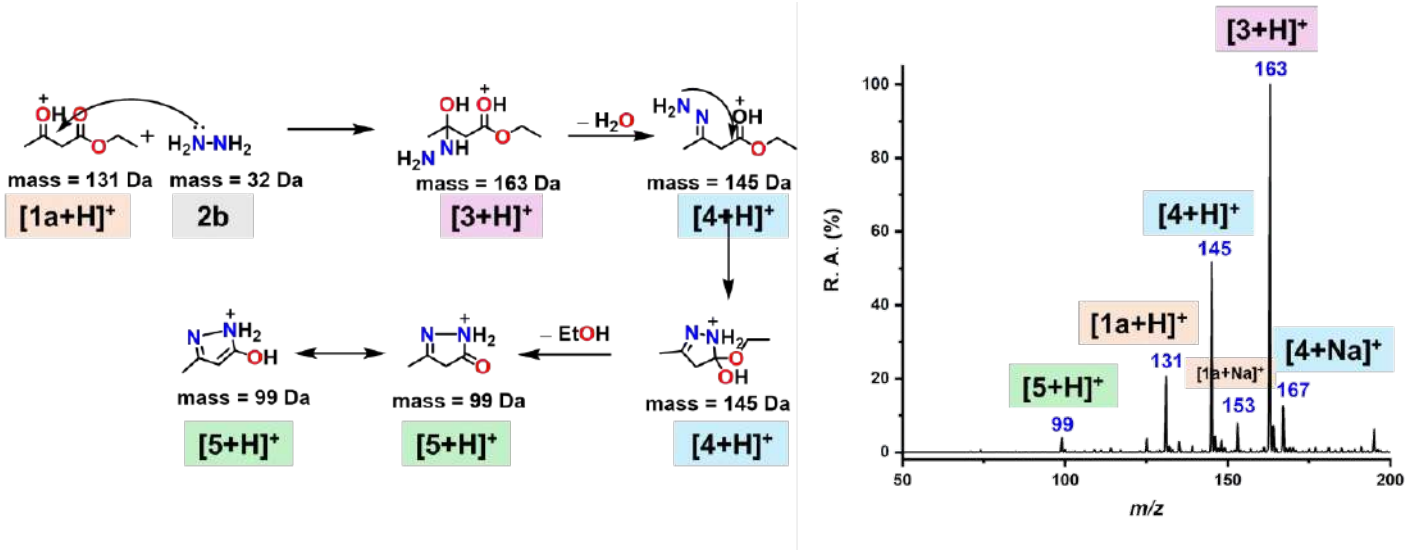


Figure S16. Proposed reaction mechanism and the intermediates and products as determined from the mass spectrum for the reaction between ethyl acetoacetate (1a) and hydrazine hydrate (2b).

5.3. ^{1}H NMR characterization.

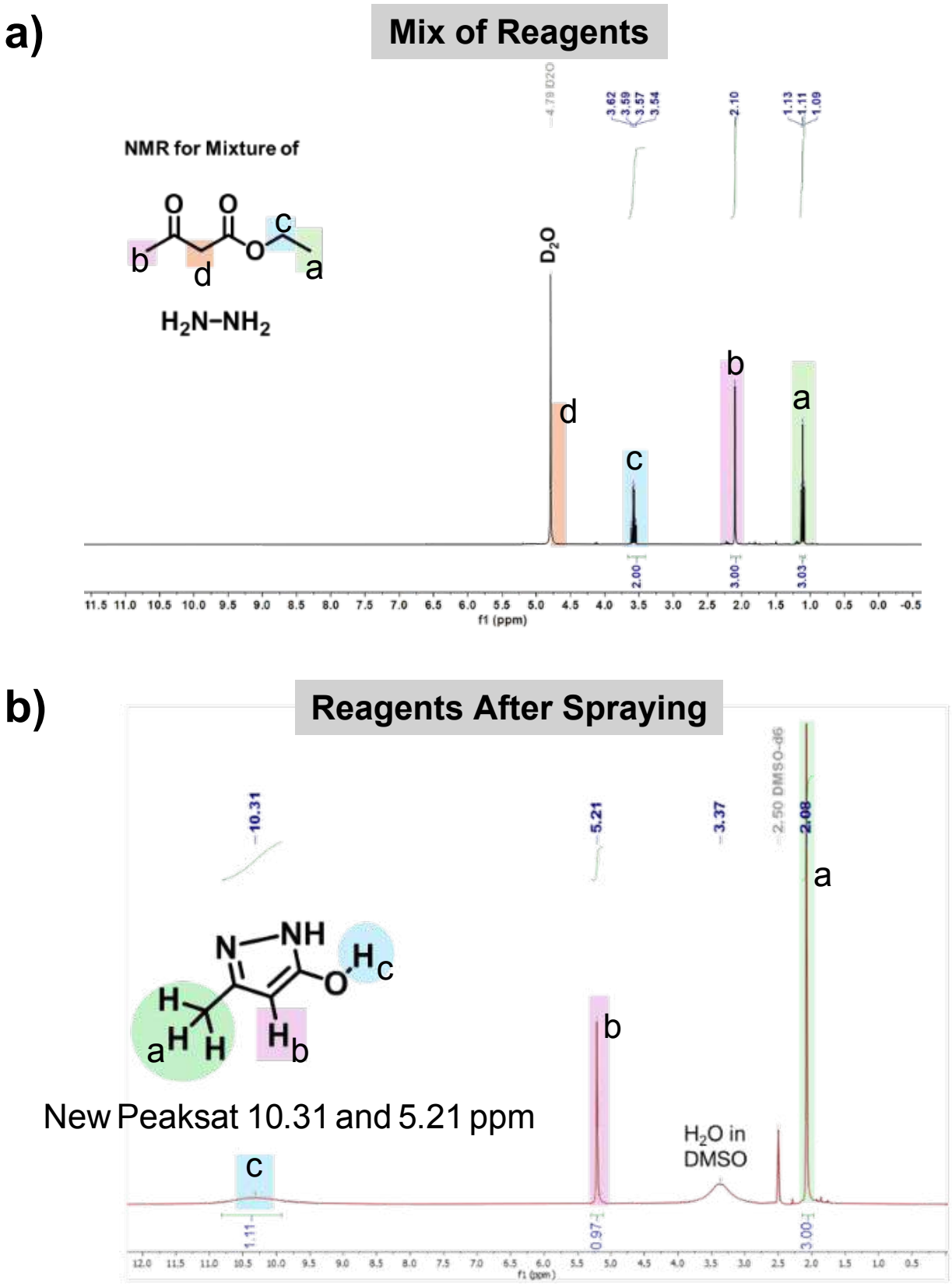


Figure S17. (a) ^{1}H NMR (300 MHz, D_2O) for the mixture of ethyl acetoacetate (1a) and hydrazine hydrate (2b) showing peaks for the starting reagents. (b) ^{1}H NMR (300 MHz, DMSO-d_6) of the product formed as the result of the reaction between ethyl acetoacetate (1a) and hydrazine hydrate (2b) in microdroplets.

6. Reaction between heptane 3,5-dione (1b) and hydrazine hydrate (2b).

6.1. Mass spectrum & MS/MS of reaction products in water microdroplets

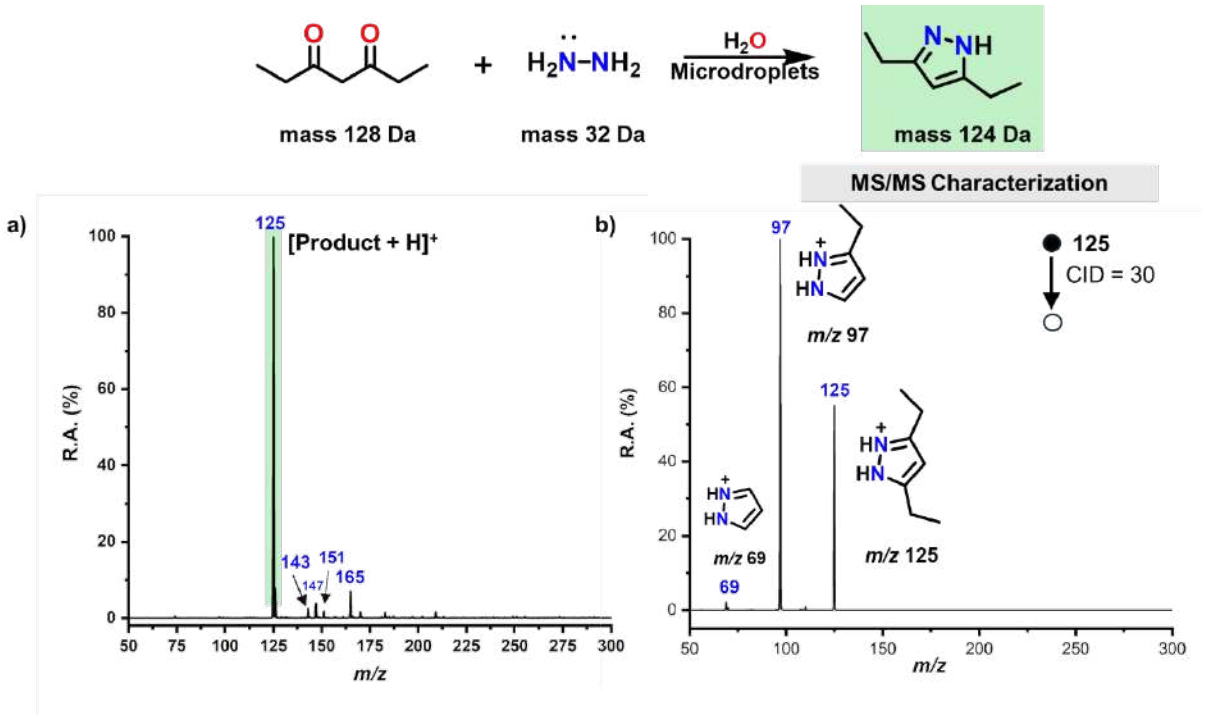


Figure S18. (a) Reaction between heptane 3,5-dione (1b) and hydrazine hydrate (2b) in water microdroplets monitored online using a mass spectrometer. The distance of the sprayer was kept 20 mm away from the inlet of the mass spectrometer. (b) MS/MS spectrum for the product peak at *m/z* 125. The corresponding MS/MS fragmentations are rationalized in the figure.

6.2. Proposed reaction mechanism and the intermediates in the mass spectrum.

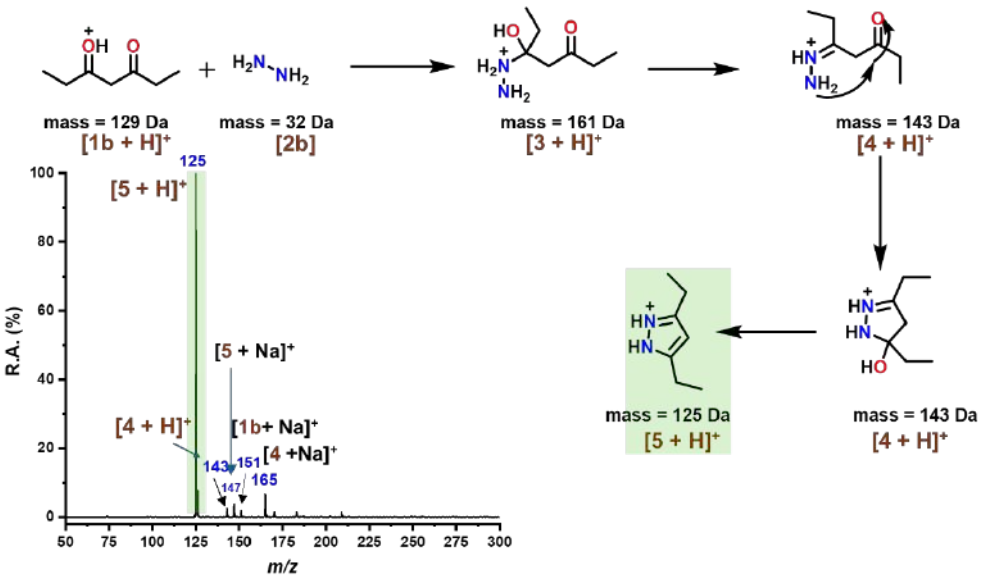


Figure S19. Proposed reaction mechanism and the intermediates and products as determined from the mass spectrum for the reaction between heptane 3,5-dione (1b) and hydrazine hydrate (2b) in water microdroplets.

6.3. ^{1}H NMR characterization of the product

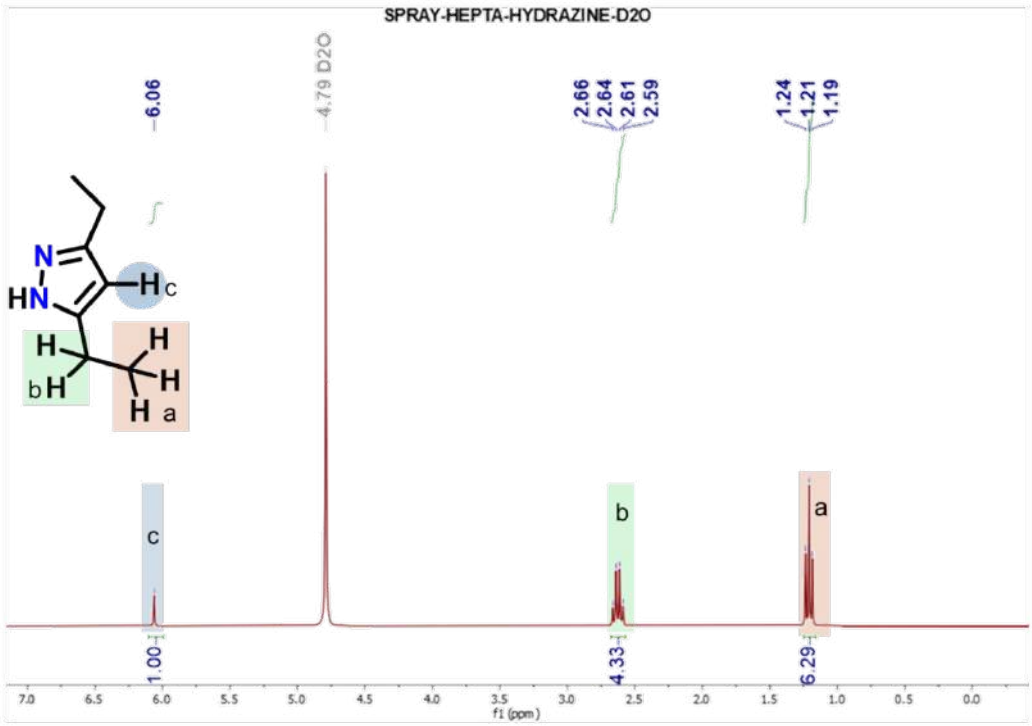


Figure S20. ^{1}H NMR (300 MHz, D_2O) of the product for the reaction between heptane 3,5-dione (1b) and hydrazine hydrate (2b) in water microdroplets.

7. Reaction between 2-acetylcyclohexanone (1c) and hydrazine hydrate (2b).

7.1. Mass spectrum & MS/MS of reaction products in water microdroplets.

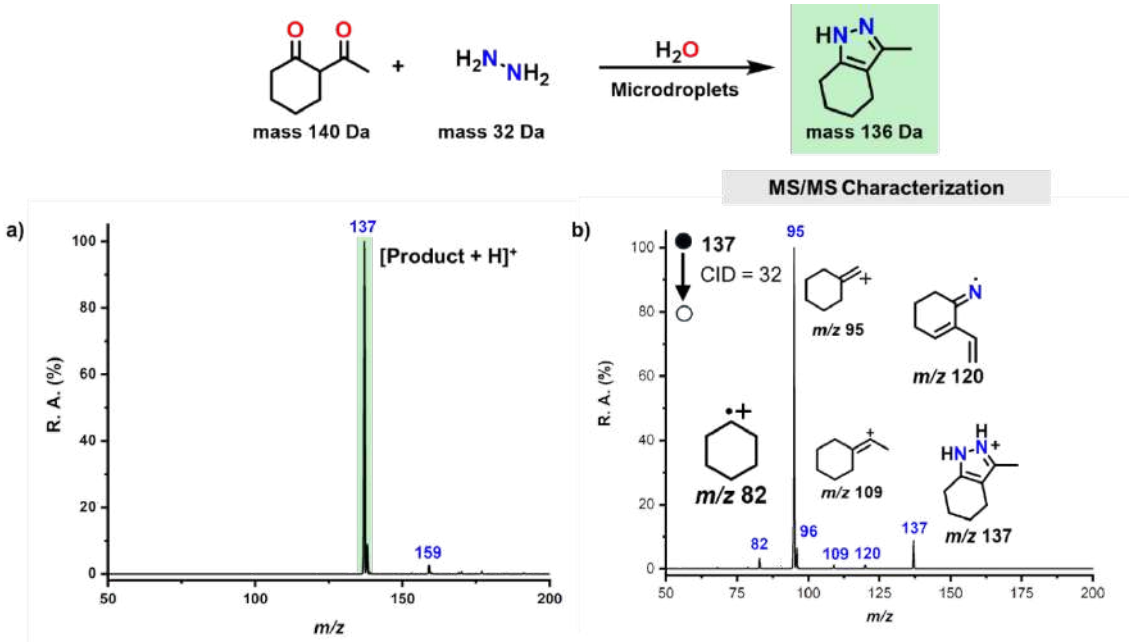


Figure S21. (a) Mass spectrum for the reaction between 2-acetylcyclohexanone (1c) and hydrazine hydrate (2b) in water microdroplets. The distance of the sprayer was kept 20 mm away from the inlet of the mass spectrometer. (b) MS/MS spectrum for the product peak at *m/z* 137. The corresponding MS/MS fragmentations are rationalized in the figure.

7.2. Proposed reaction mechanism and the intermediates in the mass spectrum.

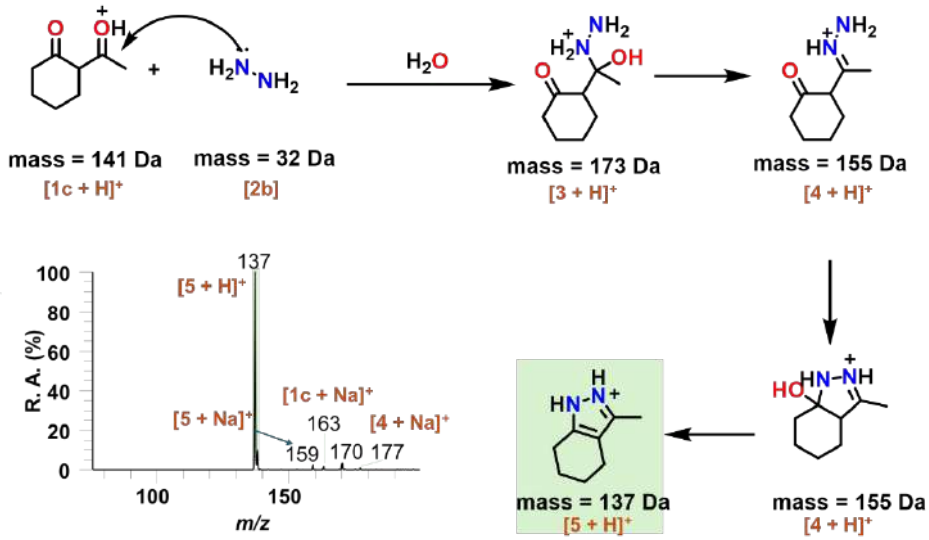


Figure S22. Proposed reaction mechanism and the intermediates and products as determined from the mass spectrum for the reaction between 2-acetylcyclohexanone (1c) and hydrazine hydrate (2b) in water microdroplets.

7.3. ^{1}H NMR characterization of the pyrazole product.

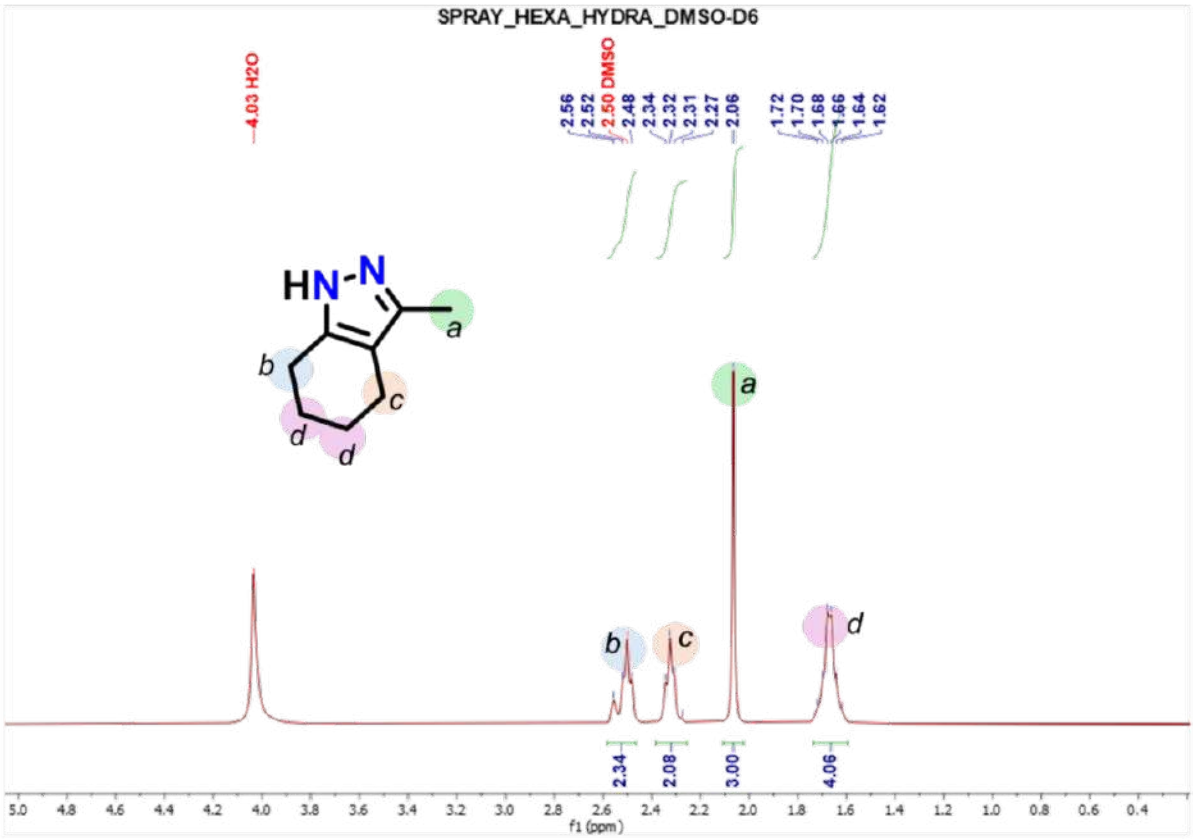


Figure S23. ^{1}H NMR (300 MHz, D_2O) of the product for the reaction between 2-acetylcyclohexanone (1c) and hydrazine hydrate (2b) in water microdroplets.

8. Reaction between 1,3-diphenyl-1,3-propanedione (1d) and hydrazine hydrate (2b).

8.1. Mass spectrum & MS/MS of reaction products in water microdroplet**.**

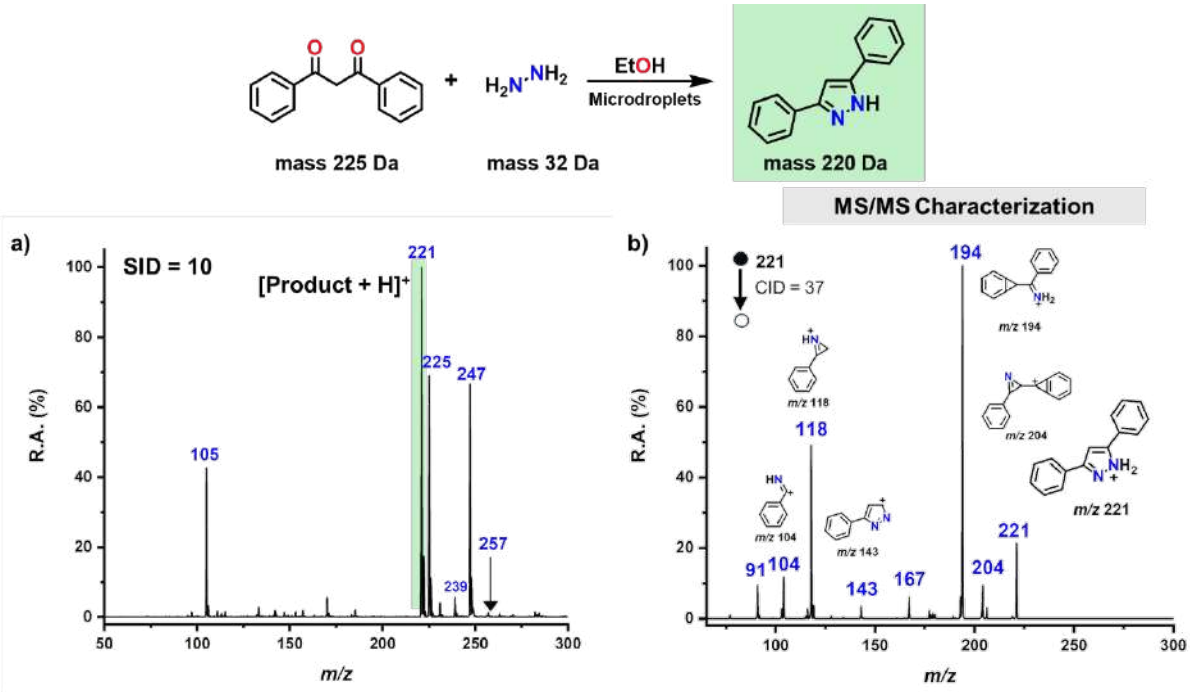


Figure S24. (a) Mass spectrum of the reaction between 1,3-diphenyl-1,3-propanedione (1d) and hydrazine hydrate (2b) in ethanol. The distance of the sprayer was kept 20 mm away from the inlet of the mass spectrometer. (b) MS/MS spectrum for the product peak at *m/z* 137. The corresponding MS/MS fragmentations are rationalized in the figure.

8.2. Proposed reaction mechanism and the intermediates in the mass spectrum.

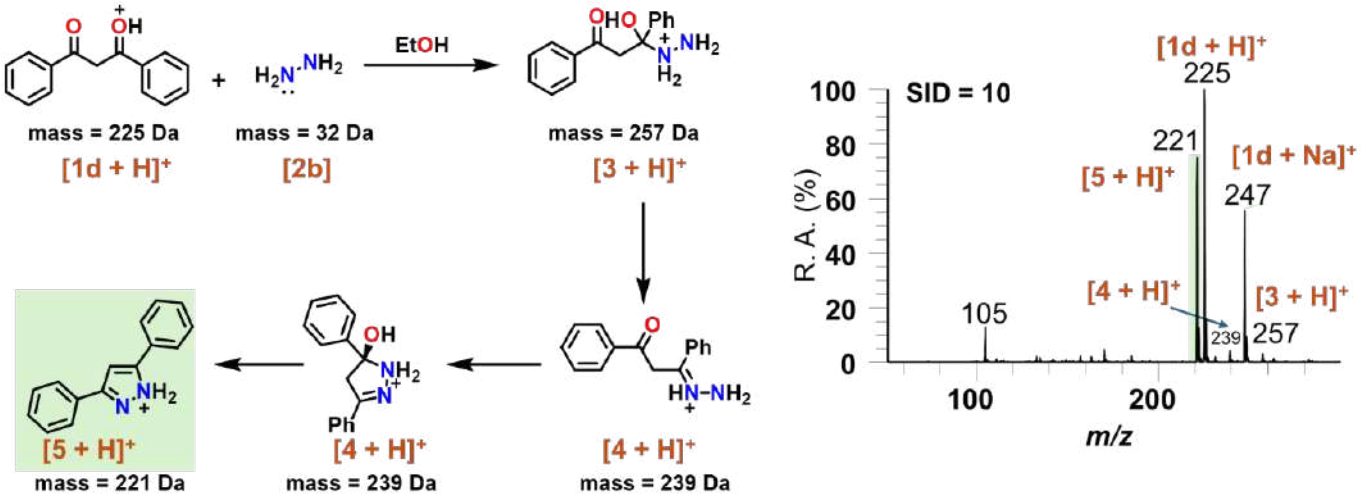


Figure S25. Proposed reaction mechanism and the intermediates and products as determined from the mass spectrum for the reaction between 1,3-diphenyl-1,3-propanedione (1d) and hydrazine hydrate (2b) in ethanol microdroplets.

8.3. ^{1}H NMR characterization of the product.

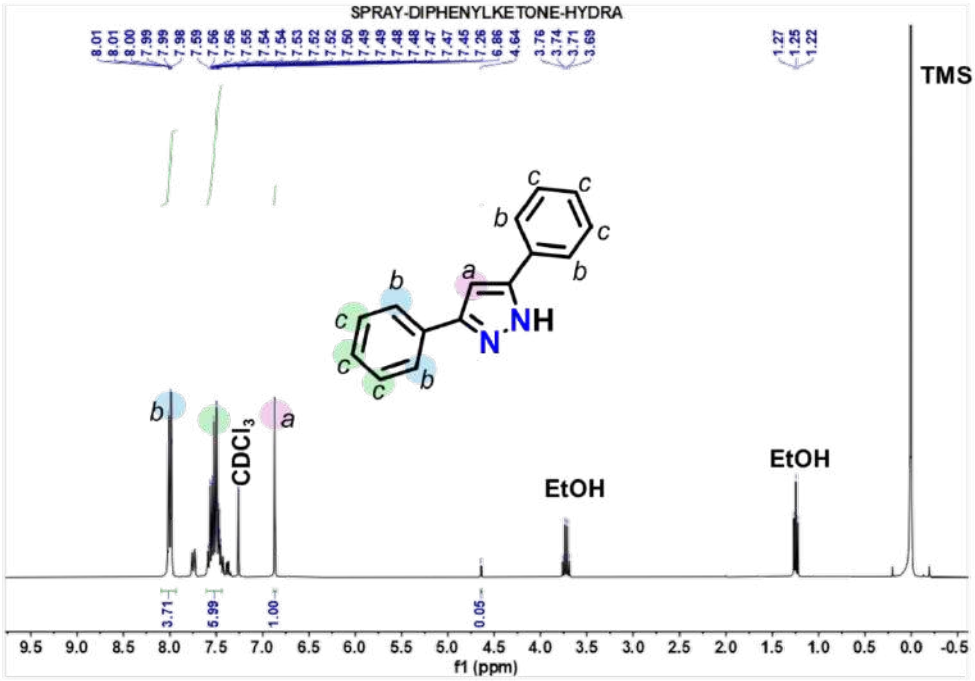


Figure S26. ^{1}H NMR (300 MHz, $CDCl_3$) of the product for the reaction between 1,3-diphenyl-1,3-propanedione (1d) and hydrazine hydrate (2b) in ethanol microdroplets.

9. Reaction between 2-acetylcyclohexanone (1c) and 2-chloro-6-hydrazineylpyridine (2c).

9.1. Mass spectrum & MS/MS of reaction products in EtOH/Water (50:50) microdroplets**.**

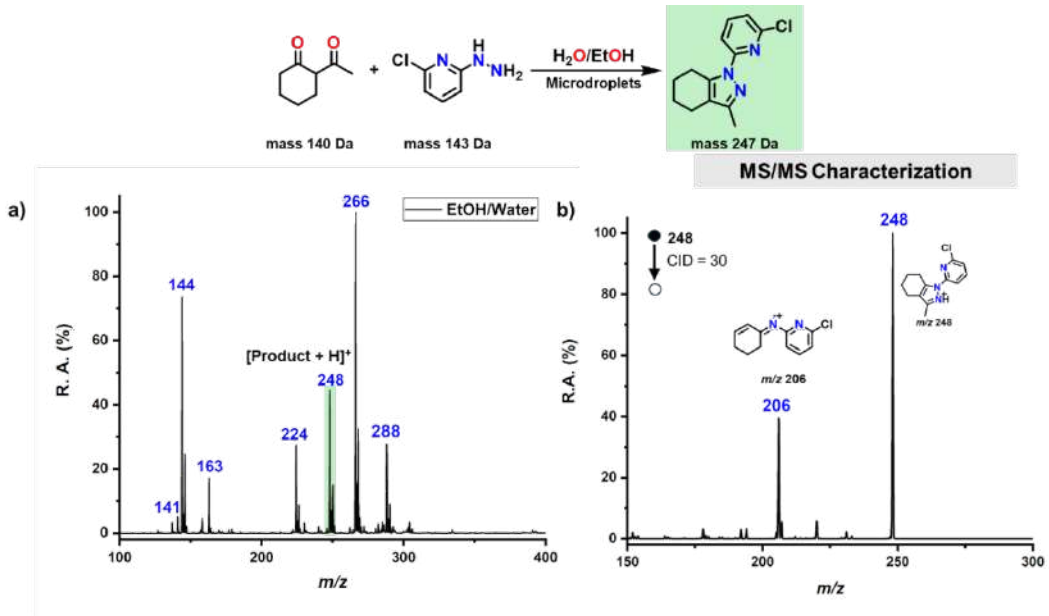


Figure S27. (a) Mass spectrum for the reaction between 2-acetylcyclohexanone (1c) and 2-chloro-6-hydrazineylpyridine (2c) in ethanol/water microdroplets. The distance of the sprayer was kept 20 mm away from the inlet of the mass spectrometer. (b) MS/MS spectrum of product peak at *m/z* 248. The corresponding MS/MS fragmentations are rationalized in the figure.

9.2. Proposed reaction mechanism and the intermediates in the mass spectrum.

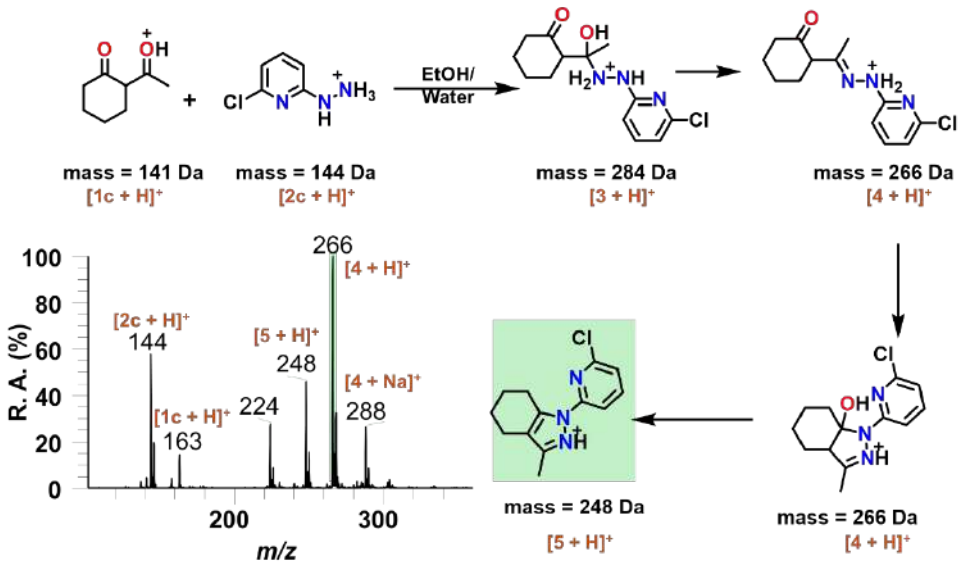
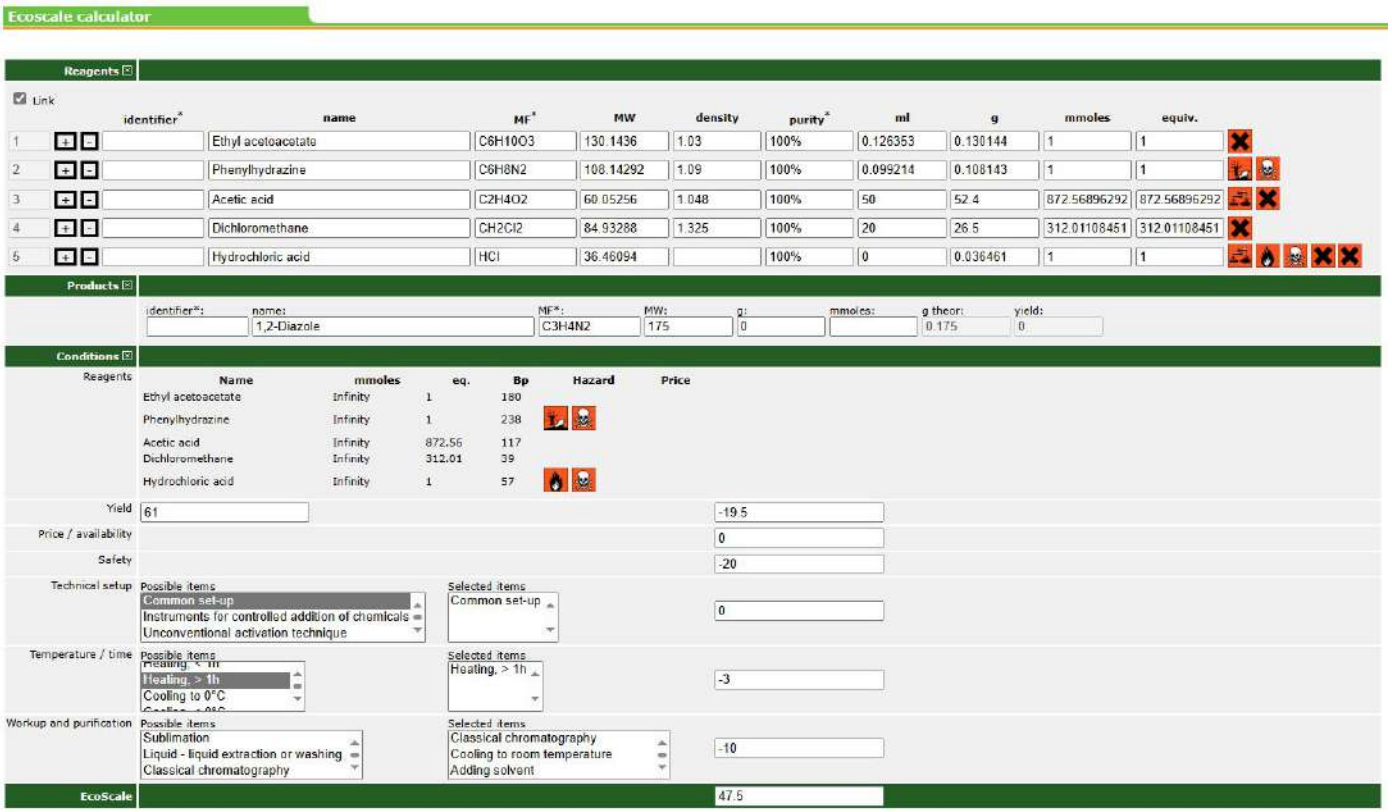


Figure S28. Proposed reaction mechanism and the intermediates and products as determined from the mass spectrum for the reaction between 2-acetylcyclohexanone (1c) and 2-chloro-6-hydrazineylpyridine (2c) in ethanol/water microdroplets.

10. Ecoscale Data:

Reference: *Org. Lett.* **2014**, *16* (19), 5060–5063 **(Ecoscale value = 47.5)**



Reference: *Synlett* **2018**, *29*, 2689–2692 **(Ecoscale value = 51)**

Ecoscale calculator

Reagents

Link

	identifier*	name	MF*	MW	density	purity*	ml	g	mmoles	equiv.
1		Ethyl acetoacetate	C6H10O3	130.1436	1.03	100%	0.063177	0.065072	0.5	1
2		Phenylhydrazine	C6H8N2	108.14292	1.09	100%	0.099214	0.108143	1	2
3		Acetonitrile	CH3CN	41.05252	0.781	100%	2	1.562	38.048821363	76.097642726
4		Copper nitrate basic	Cu(NO3)2 . 3Cu(	480.23784		100%	0	0.048024	0.1	0.2

Products

identifier*:	name:	MF*:	MW:	g:	mmoles:	g theor:	yield:
	1,2-Diazole	C3H4N2	175	0		1.200595	4

Conditions

Reagents

Name	mmoles	eq.	Bp	Hazard	Price
Ethyl acetoacetate	Infinity	1	180		
Phenylhydrazine	Infinity	2	238		
Acetonitrile	Infinity	76.09	81		
Copper nitrate basic	Infinity	0.2			

Yield	80	-10
Price / availability		-5
Safety		-20
Technical setup	Possible items: Common set-up; Instruments for controlled addition of chemicals; Unconventional activation technique — Selected items: Common set-up	0
Temperature / time	Possible items: Room temperature, < 1h; Room temperature, < 24h; Heating, < 1h — Selected items: Room temperature, < 24h	-1
Workup and purification	Possible items: Sublimation; Liquid - liquid extraction or washing; Classical chromatography — Selected items: Classical chromatography; Removal of solvent with bp < 150°C; Liquid - liquid extraction or washing	-13
EcoScale		51

Reference: *Tetrahedron Letters* **2008**, *49* (2), 397–400 **(Ecoscale value = 48)**

Ecoscale calculator

Reagents

Link

	identifier*	name	MF*	MW	density	purity*	ml	g	mmoles	equiv.
1		3,5-Heptanedione	C7H12O2	128.17108	0.945	100%	0.135631	0.128171	1	1
2		Phenylhydrazine	C6H8N2	108.14292	1.09	100%	0.109135	0.118957	1.1	1.1
3		Water	H2O	18.01528	1	100%	5	5	277.54217530	277.54217530
4		Sulfonic acids, C6-12 alkane and C6-12 alkar				100%	0	0	0.1	0.1
5		Ethyl acetate	C4H8O2	88.10632	0.902	100%	20	18.04	204.75262160	204.75262160
6		Sodium bicarbonate	CHNaO3	84.00691		100%	0	5	59.518913384	59.518913384
7		n-Hexane	C6H14	86.17716	0.659	100%	5	3.295	38.235188999	38.235188999

Products

identifier*:	name:	MF*:	MW:	g:	mmoles:	g theor:	yield:
	1,2-Diazole	C3H4N2	200	0		0.2	0

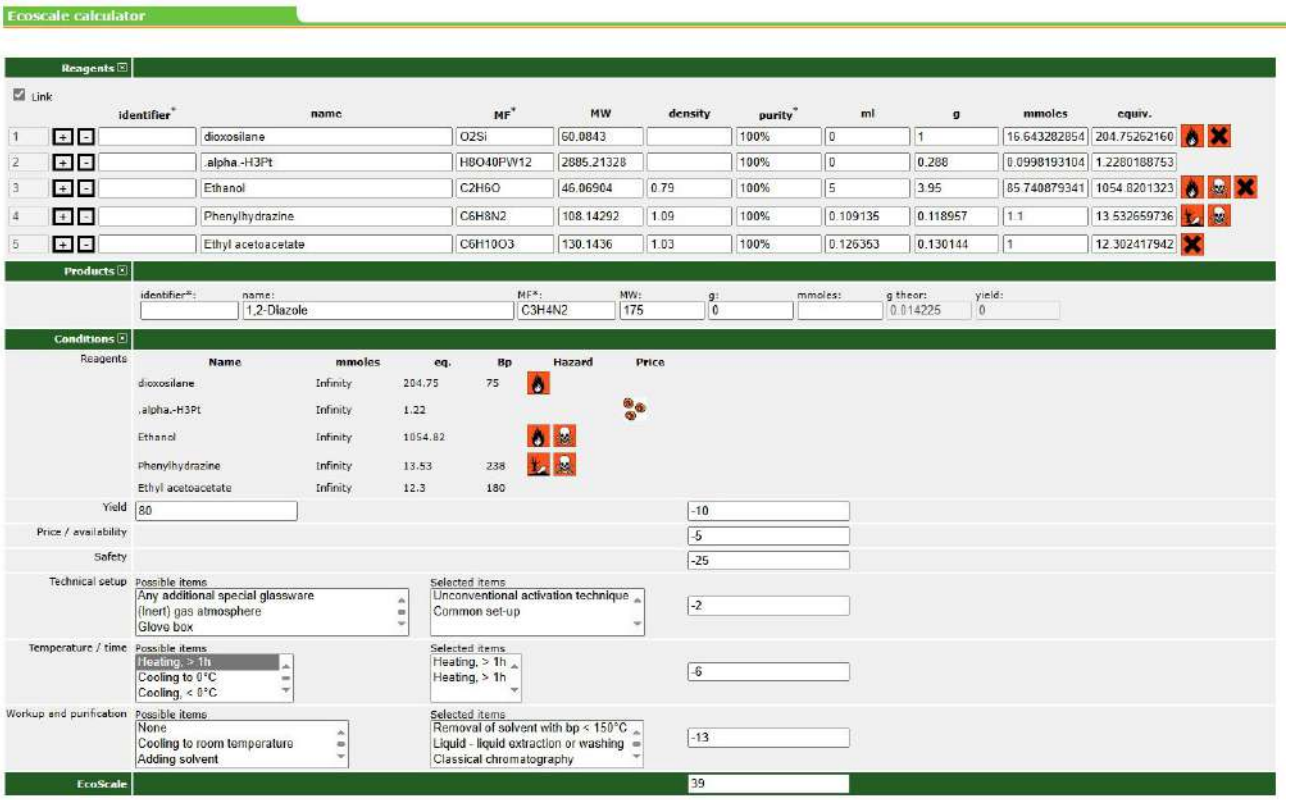
Conditions

Reagents

Name	mmoles	eq.	Bp	Hazard	Price
3,5-Heptanedione	Infinity	1	NaN		
Phenylhydrazine	Infinity	1.1	238		
Water	Infinity	277.54			
Sulfonic acids, C6-12 alkane and C6-12 alkane hydroxy and C6-12 alkene hydroxy, sodium salts	Infinity	0.1			
Ethyl acetate	Infinity	204.75	75		
Sodium bicarbonate	Infinity	59.51			
n-Hexane	Infinity	38.23	69		

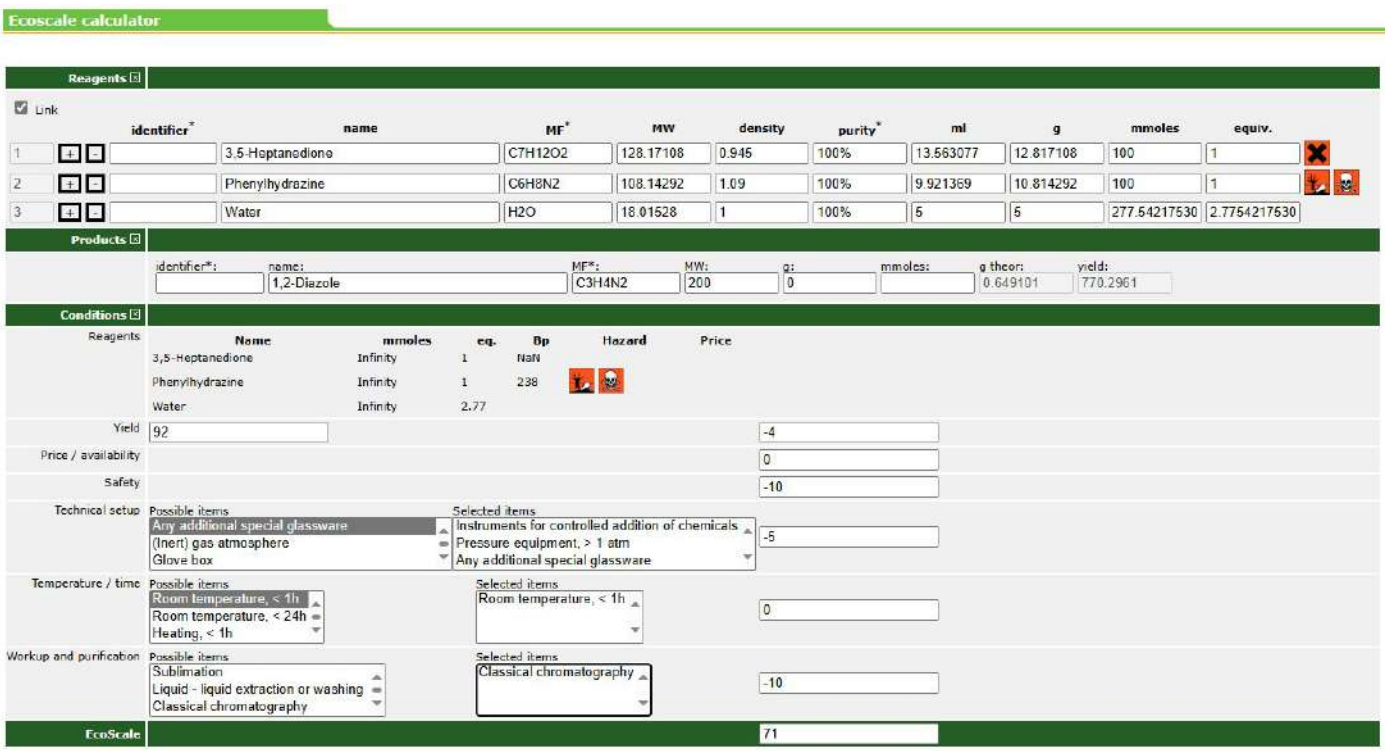
Yield	92	-4
Price / availability		-5
Safety		-30
Technical setup	Possible items: Common set-up; Instruments for controlled addition of chemicals; Unconventional activation technique — Selected items: Common set-up	0
Temperature / time	Possible items: Room temperature, < 1h; Room temperature, < 24h; Heating, < 1h — Selected items: Room temperature, < 1h	0
Workup and purification	Possible items: None; Cooling to room temperature; Adding solvent — Selected items: Removal of solvent with bp < 150°C; Liquid - liquid extraction or washing; Classical chromatography	-13
EcoScale		48

Reference: *Monatsh Chem* **2022**, *153* (3), 257–266 **(Ecoscale value = 39)**

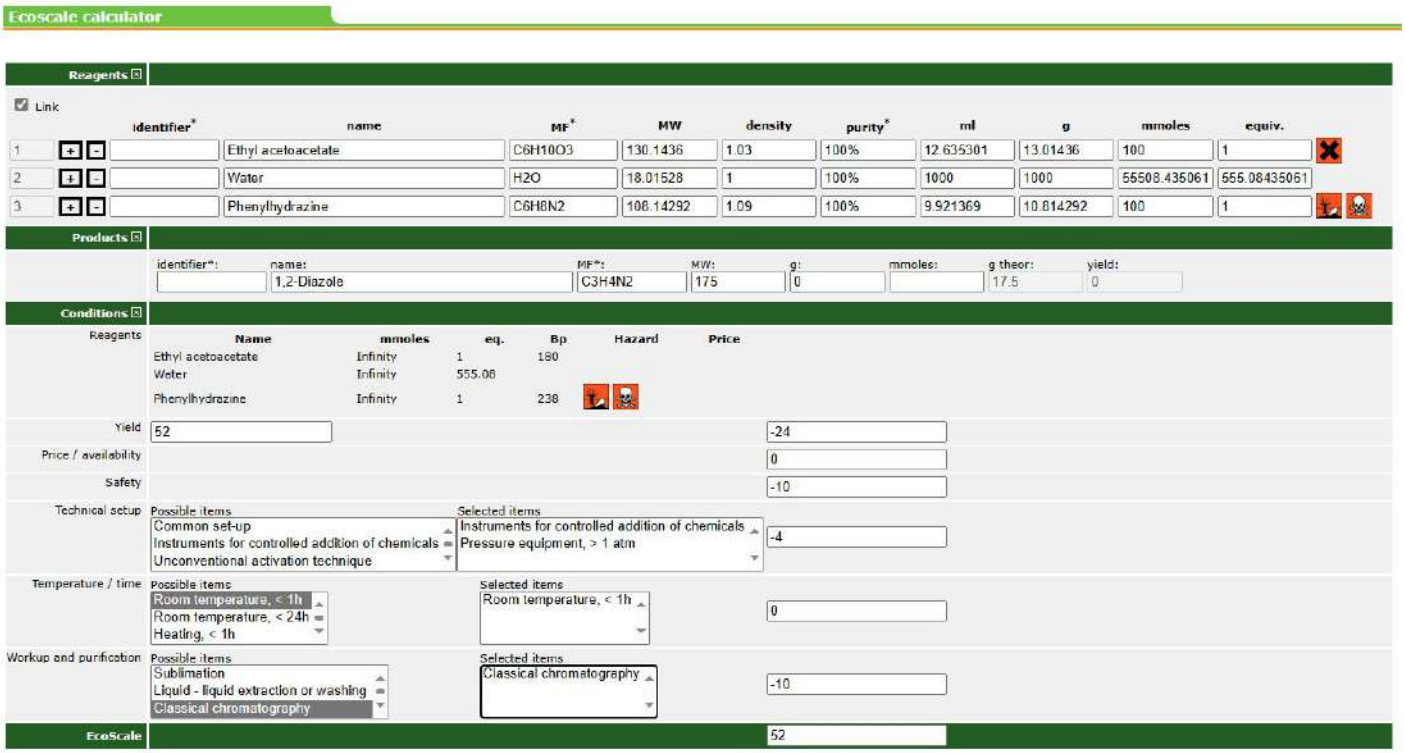


Reference: This Work (Microdroplet Based Method)

For reaction between heptane 3,5-dione (1b) and phenyl hydrazine (2a) **(Ecoscale value = 71)**



For reaction between ethyl acetoacetate (1a) and phenyl hydrazine (2a) **(Ecoscale value = 52)**



THE JOURNAL OF PHYSICAL CHEMISTRY LETTERS
A JOURNAL OF THE AMERICAN CHEMICAL SOCIETY

pubs.acs.org/JPCL Letter

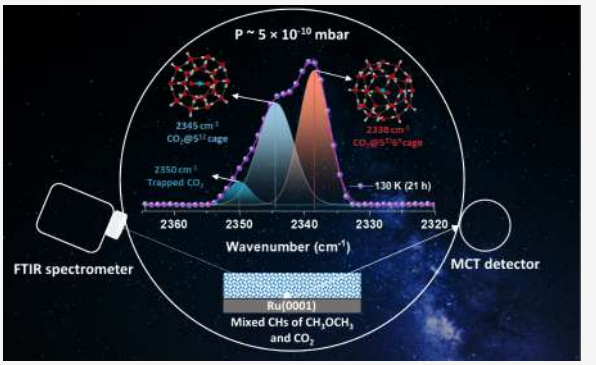
Dissociation and Reformation of CO_2 Clathrate Hydrate Cages in Amorphous Ice Thin Film under Ultrahigh Vacuum

Bijesh K. Malla, Soham Chowdhury, Gaurav Vishwakarma, Rajnish Kumar,* and Thalappil Pradeep*

Cite This: J. Phys. Chem. Lett. 2025, 16, 4982−4989 Read Online

ACCESS | Metrics & More | Article Recommendations | Supporting Information

ABSTRACT: The formation of clathrate hydrates (CHs) within amorphous ice holds significant astrochemical importance. CO_2 typically forms structure I (sI) CH under vacuum, upon nucleation from an amorphous water-CO_2 ice mixture. This study presents the first report of structure II (sII) CO_2 CH, where CO_2 occupies large cages in the presence of dimethyl ether (DME) or tetrahydrofuran (THF) under ultrahigh vacuum (UHV) conditions. Mixed CHs of DME-CO_2 were prepared by sequential vapor phase deposition of CO_2:water mixture over DME at 10 K and thermally annealing this mixed ice film to 130 K. During the formation of large cages of sII CH of DME, partial dissociation of the preformed small cage of sI of CO_2 CH occurs along with the formation of new large cages of sII CO_2 CH. Similar results were observed for THF-CO_2 mixed CHs. Additionally, mixed CHs of THF-DME-CO_2 formed sII hydrates when annealed at 130 K. Prolonged annealing (37 h) at 130 K led to the dissociation of mixed CHs, releasing CO_2 and DME and increasing the THF CH fraction. These observations highlight the greater stability of THF CH compared with those of CO_2 and DME under identical conditions. These findings enhance our understanding of the structural dynamics and formation mechanisms of mixed CHs under simulated interstellar conditions.



Downloaded via INDIAN INST OF TECH MADRAS on December 29, 2025 at 03:12:47 (UTC).
See https://pubs.acs.org/sharingguidelines for options on how to legitimately share published articles.

Formation of clathrate hydrates (CHs) under laboratory interstellar conditions of temperature (~10−100 K) and pressure (~10^{-10} mbar) is now well-known,[1,2] and these studies have been performed mostly with two components (a hydrate-forming guest molecule and water).[3−6] Although the original report used reflection absorption infrared spectroscopy (RAIRS),[2] the formation has also been confirmed recently by reflection high energy electron diffraction (RHEED).[7] The CHs manifest as host−guest complexes, with water molecules as the host, generating diverse cage structures to encage guest molecules such as CH_4, C_2H_6, C_3H_8, CO_2, N_2, and O_2, among others.[8−10] They typically exhibit three distinct crystalline structures, known as structure I (sI, cubic $Pm\bar{3}n$), structure II (sII, cubic $Fd\bar{3}m$), and structure H (sH, hexagonal $P6/mmm$).[11,12] These CHs were previously thought to form only under high-pressure circumstances.[13,14] Blake et al.'s study in 1991 demonstrated that CO_2 CH can form under high vacuum (10^{-6}−10^{-7} Torr) conditions too, using infrared spectroscopy and selected area electron diffraction.[15] The period of 1900−2000 witnessed extensive investigations in vacuum in the range of 10^{-6} to 10^{-8} Torr and temperatures near 80 to 150 K.[16−21] Ghosh et al. showed that CH_4 and CO_2 CH form even at 30 and 10 K, respectively, under ultrahigh vacuum (UHV, 5 × 10^{-10} mbar) conditions, where condensed molecules desorb at much lower temperatures than in high vacuum (~10^{-6} Torr).[2] There were questions that arose regarding the formation of these hydrates in unusual thermodynamic conditions, as highlighted by Choukroun et al.,[22] and they were addressed by Ghosh et al.[23] Subsequent investigations explored various CHs within UHV under cryogenic conditions.[5,6,24,25] The existence of CHs in UHV has also been shown by electron diffraction, as mentioned earlier.[7] A recent study has also demonstrated the possibility of formation of CO_2 CH at 10 K under UHV.[1] More than 300 atomic, ionic, and molecular species have been detected to date in the interstellar medium (ISM). Under such conditions, these molecules exist in the solid state or in the gas phase.[26] These condensed molecular matrices hold a wide spectrum of molecules together with water, which raises the possibility of formation of mixed and complex CHs.[27]

Typically, CO_2 and such small molecules usually form stable sI CH with 100% occupancy of the large $5^{12}6^2$ cages, and up to 70% occupancy of the small 5^{12} cages, under high-pressure conditions.[28−34] Additionally, the formation of sI CH of CO_2 has also been observed under cryogenic conditions in high vacuum.[1,2,24,35] In the presence of larger guest molecules such

Received: February 7, 2025
Revised: May 6, 2025
Accepted: May 7, 2025
Published: May 12, 2025



© 2025 American Chemical Society

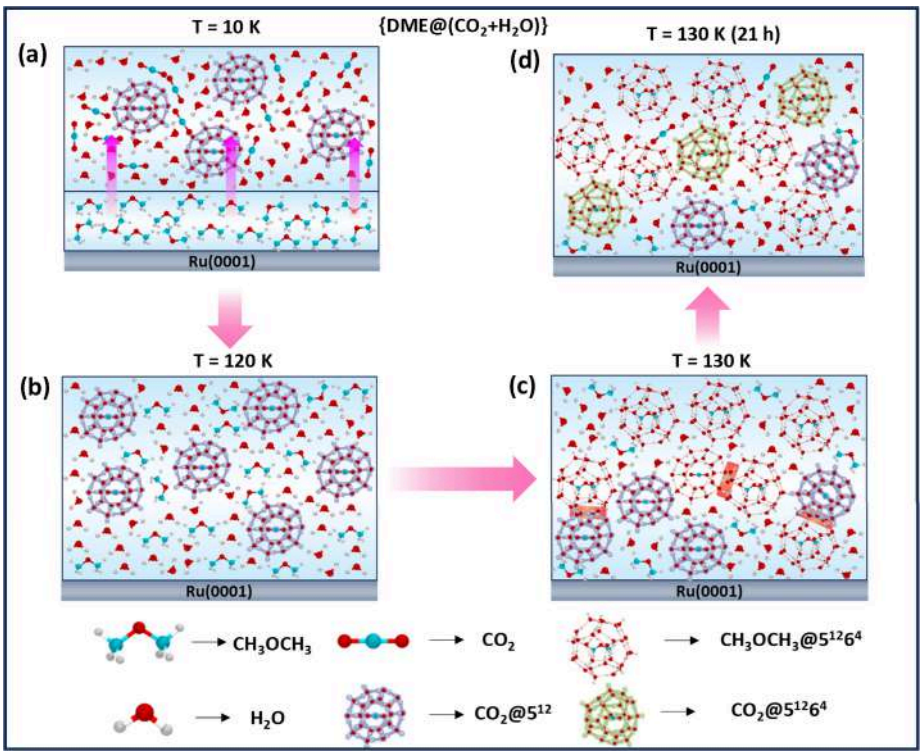


Figure 1. Schematic diagram for the reconstruction of large cages of sII CO_2 CH in the presence of DME molecules. The sequence involves the stepwise deposition of 150 ML of DME followed by 150 ML of a CO_2 + H_2O (1:10) ice mixture under conditions of 10 K (a), followed by thermal annealing to 120 K (b), 130 K (c), and a subsequent state after 21 h at 130 K (d). Small red rectangles in panel c demonstrate the interaction of large cages ($5^{12}6^4$) of DME with small cages (5^{12}) of CO_2.

as THF and cyclopentane, CO_2 mixed hydrates form classical sII CHs, where the larger guest molecules occupy the large $5^{12}6^4$ cages, and CO_2 occupies the small cages of sII, in both high-pressure and vacuum conditions.[21,36,37] Under high-pressure conditions, CO_2 can exist in $5^{12}6^4$ cages in presense of 1,3-dioxolane.[38,39] However, there is no report of its occupancy in large cages of sII mixed hydrates in UHV, with larger guest molecules capable of forming sII CHs. Additionally, the formation of mixed CHs of CO_2 with various guest molecules under UHV remains unexplored.

In this work, we have carried out an experiment taking two large guest molecules, DME and THF, separately, along with CO_2, in the form of an amorphous solid at 10 K, and subjected the mixture to anneal at 130 K. Both DME and THF have good solubility in water, and individually they are known to form classical sII hydrates in high-pressure as well as UHV conditions.[25,40−43] While CO_2[44] and DME[45] are confirmed constituents of the ISM, THF is yet to be detected there. The identification of structurally related ethers such as propylene oxide[46] and ethylene oxide,[47] however, suggests that THF could become observable with continued advancements in astrochemical detection techniques. In this work, we have studied the structural transition of CO_2 CH, when the CO_2+water mixture is sequentially deposited with THF or DME (abbreviated to THF/DME subsequently). It was observed that in the presence of THF/DME upon annealing, CO_2 moves from the small cages (in sI) and helps nucleate the sII hydrate, where it also occupies the large cages along with THF/DME. During this study, the formation of mixed CHs of CO_2, DME, and THF was also observed when both the large guest molecules were sequentially deposited along with CO_2 and water. All the experiments were carried out using a custom-built UHV instrument,[48,49] described in the Supporting Information (SI). Details of the experimental protocols and sample preparation are also presented in the SI.

The first set of experiments were performed with codeposited CO_2 and water vapor at a ratio of 1:10, on a Ru(0001) substrate, subsequently annealed to 120 K, and we observed the same results as reported previously.[2] In Figure S1, at 10 K, the two peaks at 2354 and 2346 cm^{-1} represent the pure CO_2 clusters in amorphous ice and CO_2 occupying the small cages of sI CH, respectively.[14] Typically, pure 100 ML of CO_2 ice at 10 K shows a RAIRS peak at 2381 cm^{-1} due to the LO mode of the C=O antisymmetric stretching region, where lowering the thickness leads to the redshift.[24,50,51]

The peak at 2346 cm^{-1}, however, arises from CO_2 interacting with or being trapped within the H_2O ice matrix, without contributions from LO or transverse optical (TO) coupling.[51] According to literature,[3,15,17,21,52] the 2346 cm^{-1} peak is assigned to the small cages of sI clathrate hydrates, although there was a debate regarding this assignment.[22] In our study, the 2346 cm^{-1} feature is attributed to the small cage of the sI CH of CO_2. This is in agreement with the fact that after 120 K, only one peak at 2346 cm^{-1} is seen. We then annealed the same mixture at 130 K for 6 h and observed a 2 cm^{-1} peak shift to 2344 cm^{-1} and a decrease in the peak intensity, which were attributed to partial dissociation of the small cage of sI, followed by desorption of CO_2 from the ice matrix. This suggests the metastable nature of sI CH of CO_2 at 130 K. It is noteworthy that our RAIR resolution is 2 cm^{-1}, a factor that is important for the observed peak position.

Subsequently, mixed CHs of DME and CO_2 were created by thermally annealing DME, water, and CO_2 ice mixtures at 130 K for tens of hours (Figure 1). First, 150 ML of DME vapor

https://doi.org/10.1021/acs.jpclett.5c00393
J. Phys. Chem. Lett. 2025, 16, 4982−4989

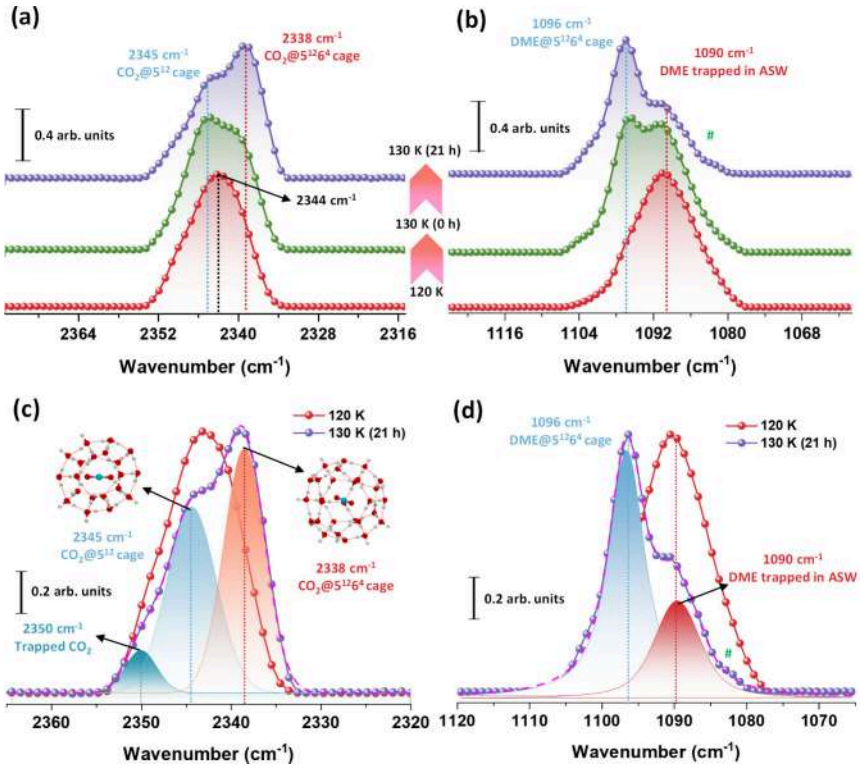


Figure 2. RAIR spectra of CO_2 and DME mixed binary CH. Temperature and time-dependent normalized RAIR spectra of DME (150 ML) @(CO_2+H_2O) (1:10) (150 ML) mixed ice in (a) C=O antisymmetric stretching region for CO_2 and (b) C−O antisymmetric stretching region for DME. A comparison of normalized spectra of same ice in (c) C=O antisymmetric stretching region for CO_2, (d) C−O antisymmetric stretching region for DME at 120 and 130 K (after annealing for 21 h). The spectrum labeled as 130 K (21 h) was deconvoluted to three components, shown in panel c in blue (2345 cm^{-1}), red (2338 cm^{-1}), and cyan blue (2350 cm^{-1}). In panel d, blue (1096 cm^{-1}) and red (1090 cm^{-1}) shades. The peak labeled as # in the spectrum at 130 K and 21 h is attributed to a very tiny amount of DME dilutes. Images depicting CO_2 molecules confined within 5^{12}, $5^{12}6^4$ CH cages and DME molecules within $5^{12}6^4$ CH cages are presented alongside their corresponding peak profiles.

was deposited on Ru(0001) substrate at 10 K. On it, 150 ML of water and CO_2 (10:1, together) were codeposited (illustrated in Figure 1a). The RAIR spectra of CO_2 and DME in the C=O and C−O antisymmetric stretching regions, respectively, are shown in Figure S2. In Figure S2a, the peak at 2346 cm^{-1} corresponds to CO_2 occupying the small cages of the sI clathrate structure, while the peak at 2354 cm^{-1} is due to CO_2 trapped within the pores of amorphous solid water (ASW). The sI CH of CO_2 is typically characterized by Fermi dyad peaks in Raman spectroscopy.[37,38,53−55] However, these features are weakly active in IR spectroscopy due to symmetry-imposed selection rules. Kumar et al.[55] presented a comparative study of sI and sII CO_2 CHs using both Raman and IR spectroscopy. In their work, the Fermi dyad peaks were used for identification in the Raman spectra, while the CO_2 antisymmetric stretch was employed in the IR spectra. Their assignments show good agreement with the present IR data. In Figure S2b, the peak at 1098 cm^{-1} is due to amorphous DME at 10 K. When the system was thermally annealed, DME gradually diffused into the ice matrix, resulting in a mixed system comprising DME, water, and CO_2. This diffusion was accompanied by a red shift in the peak position from 1098 cm^{-1} to 1090 cm^{-1} at 120 K, indicative of hydrogen bonding interactions between water and DME (illustrated in Figure 1b).[25] Here, it is worth noting that both the guest molecules are mobile at this temperature as CO_2 and DME desorb near 90 K, in their pure state in UHV, which is 30 K lower. Continuing the annealing process to 120 K, the peak associated with uncaged CO_2 (2354 cm^{-1}) disappeared completely, while the peak related to caged CO_2 (2344 cm^{-1}) remained, shifting slightly by 2 cm^{-1} from the original position (Figure S2a).

Figure 2a,b shows the normalized RAIR spectra at 120 K, 130 K (0 h), and 130 K (21 h) in the C=O and C−O antisymmetric regions of CO_2 and DME, respectively, in the narrow window of 120−130 K, "while the spectra in the whole temperature range" are given in Figure S2. The peak at 2344 cm^{-1} in the C=O antisymmetric stretching region (Figure 2a) at 120 K is attributed to the CO_2 encaged in small cages of sI CH. In Figure 2b, the peak at 1090 cm^{-1} in C−O antisymmetric region is attributed to the DME trapped in amorphous solid water (ASW), where DME is hydrogen bonded to ASW.[25] Upon further annealing to 130 K, a new peak arose at 2338 cm^{-1}, and the peak at 2344 cm^{-1} got blue-shifted slightly to 2345 cm^{-1}. After 21 h of annealing, the peak at 2338 cm^{-1} exhibited a significant increase in intensity relative to the peak at 2345 cm^{-1}. The new peak at 2338 cm^{-1} can be attributed to large cages of either sI or sII structure, as it does not correspond to any other interaction in pure CO_2 or CO_2−water. Simultaneously, in Figure 2b at 130 K, a new peak arose at 1096 cm^{-1}, which is attributed to DME encaged in the large cages of sII. In our previous study,[25] we extensively discussed the formation of sII CH of DME, wherein DME selectively occupies the large cages. This assignment was supported by both IR spectroscopy and density functional theory calculations. Beyond the well-established cubic sII, Udachin et al. reported that under high-pressure conditions, DME can also occupy three different cage types in a 1:1:1 ratio

https://doi.org/10.1021/acs.jpclett.5c00393
J. Phys. Chem. Lett. 2025, 16, 4982−4989

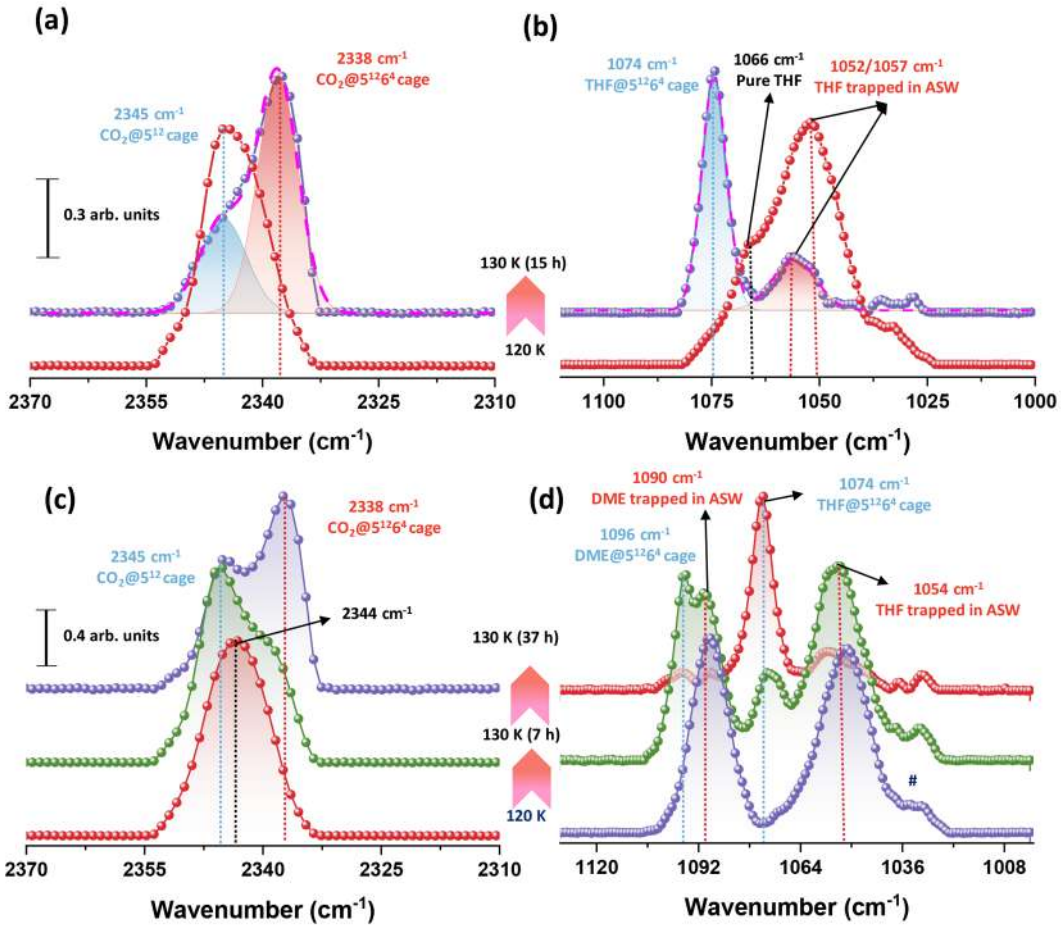


Figure 3. RAIR spectra of the mixed CHs. Temperature- and time-dependent normalized RAIR spectra of THF@(CO_2+H_2O) (50 ML @(20 ML + 180 ML)) mixed ice in (a) C=O antisymmetric stretching region for CO_2, (b) C−O antisymmetric stretching region for THF. Temperature- and time-dependent normalized RAIR spectra of THF@DME@(CO_2+H_2O) (50 ML@50 ML @(20 ML + 180 ML)) mixed ice in (c) C=O antisymmetric stretching region for CO_2 and (d) C−O antisymmetric stretching region for THF and DME.

($5^{12}6^3$:$5^{12}6^2$:$4^2$$5^8$$6^1$), forming a tetragonal clathrate hydrate structure.[56] However, in our current IR measurements, we observed only a single distinct new vibrational feature that is assigned to the occupation of the large cages in the sII hydrate. Further annealing led to the desorption of ASW-trapped DME, with decrease in the 1090 cm^{-1} peak intensity. During this process, the reordering of water molecules occurred, and the RAIR spectra in the O−H stretching region got sharper (Figure S3). Fleyfel et al.[21] demonstrated that the peak at 2338 cm^{-1} corresponded to the large cages of sI CO_2 CH at 135 K in the presence of pure CO_2. However, they also established that when THF was present, CO_2 occupied small cages exclusively while THF occupied large cages of sII CH. Similar findings were reported by Buch et al.[57] in the case where the guest was DME. It is worth noting that in both these studies, CHs were prepared from crystalline ice, whereas in this study, CHs were prepared from an amorphous ice mixture. Additionally, there was no significant shift in the spectrum for the occupancy of large cages of both sI and sII.[58] Our previous research had indicated the instability of the $5^{12}6^2$ cage in the presence of THF molecules in sI CH. Thus, the emergence of the 2338 cm^{-1} peak in the present work is attributed to the large cages of sII CH. We note that although the peak at 2345 cm^{-1} is attributed to the small cages, whether it originates from sI, sII, or both structures cannot be distinguished. In the case of sII clathrate hydrates of DME, where the small cages are empty, CO_2 can also occupy the small cages of the sII structure. Figure 2c,d shows the deconvoluted spectra of CO_2 and DME at 130 K after 21 h, along with the reference spectra at 120 K. It was found that, after 21 h at 130 K, 49% of the CO_2 occupied the newly formed large cages of sII, 45% resided in small cages, and 6% remained trapped in water ice. Similarly, 69% of DME was confined within the large cages of sII, while the remaining 31% was retained in water ice.

To strengthen our claim on the formation of large cages of sII CH of CO_2 and the dynamics of the cages at low temperatures, we used THF as another guest molecule which is known to form stable sII CH. A similar experimental procedure was carried out, where 50 ML of THF was deposited below 250 ML of a CO_2 + water mixture in 1:10 ratio, at 10 K. It was annealed to 130 K and held there for 15 h. At 10 K, THF stayed in an amorphous form (shown in Figure S4), and when annealed to 120 K, a mixed system of CO_2−THF−water was formed. Figure 3a,b shows normalized RAIR spectra of mixed CHs of THF and CO_2 at 120 and 130 K (after 15 h) in the C=O and C−O asymmetric stretching regions, respectively. In Figure 3a, at 120 K, the peak at 2345 cm^{-1} represents CO_2 in small cages of sI, and at 130 K, after 15 h of annealing, the new peak at 2338 cm^{-1} indicates the large cages of sII CH occurs.

https://doi.org/10.1021/acs.jpclett.5c00393
J. Phys. Chem. Lett. 2025, 16, 4982−4989

In Figure 3b, the formation of THF CH is shown. At 120 K, the peak at 1052 cm^{-1} represents the ASW-trapped THF, whereas the peak at 1066 cm^{-1} represents pure amorphous THF. After 15 h at 130 K, a new peak at 1074 cm^{-1} appeared, which showed the formation of large cages of sII hydrate, where THF occupies only the large cages.[42]

Here, the transformation mechanism mirrors that of the DME-CO_2 binary CHs. This transformation of sI to sII CH, where part of the large cages is occupied by CO_2 along with DME/THF, is attributed to better mobility of CO_2 compared to that of DME/THF (in the water matrix) at the annealing temperature. The presence of UHV, and a temperature of 130 K, which is very close to the glass transition temperature (136 K)[59,60] of water ice, creates a favorable environment for the formation, dissociation, and transformation of CHs.[61] At this temperature, most molecules adopt a metastable CH state.[6,25,62] At 130 K, pure CO_2 CH slowly dissociates, and the CO_2 formed is highly mobile compared to DME/THF. In the presence of DME/THF CH, the fraction of molecules coming out from small cages of sI CO_2 CH may nucleate other CHs along with free DME/THF molecules. These free molecules may also participate in the growth of the already nucleated sII hydrate. To explore the importance of intermolecular motion, the prepared DME@CO_2-water ice was kept at 115 K for 25 h where we observed no changes in the C=O stretching region of CO_2 other than a tiny intensity decrease. In the C−O antisymmetric stretching region of DME, a very weak hump was observed at 1096 cm^{-1}, indicating the presence of a minor fraction of sII DME CH (Figure S5). This indicates that no major change occurs in the CO_2 CH when the molecules are not mobile. Our previous study[25,42] showed that DME/THF occupies the large cages of sII CH at 130 K in both the codeposited and sequentially vapor-deposited DME/THF−water ice mixture. So, it is concluded that at 130 K, when DME/THF starts to form sII CH, it breaks the small cage of CO_2 CH and induces the formation of large cages (illustrated in Figure 1c,d). It is worth noting that Figure 1 does not depict the actual physical nucleation process of CHs but rather provides a pictorial representation of the molecules and CH cages.

To study the relative stability of each CH cage in multicomponent CHs, we have taken four-component systems (DME−CO_2−THF−water), created mixed CHs of three guest molecules, and observed the stability of individual CHs in the mixed system. First, 50 ML of THF was deposited on the Ru(0001) substrate, followed by 50 ML of DME, then 200 ML water−CO_2 were codeposited at a 10:1 ratio, at 10 K. Then, the whole system was annealed to 130 K, which created a mixed system of THF−DME−CO_2−water. Then, waiting at the same temperature for 37 h led to the formation, dissociation, desorption, and transformation events simultaneously. Figure 3c,d shows the RAIR spectra of CO_2, DME, and THF in C=O and C−O antisymmetric stretching regions. In Figure 3c, the evolution of CO_2 CH with respect to the temperature and time is shown. At 120 K, the peak at 2344 cm^{-1} represents the CO_2 trapped within 5^{12} cages of sI. Upon annealing at 130 K for 7 h, a new peak emerges at 2338 cm^{-1} (CO_2 trapped in the $5^{12}6^4$ cage). Subsequently, after 42 h, the intensity of the 2338 cm^{-1} peak increases relative to the 2345 cm^{-1} peak. In Figure 3d, the evolution of DME and THF is shown. At 120 K, DME and THF remained in the amorphous form within the ice matrix. After 7 h at 130 K, DME and THF form CH, which is indicated by the increase in the peak intensity at 1096 cm^{-1} and 1074 cm^{-1}, respectively. However, after 37 h, most of the DME desorbs from the matrix, including from the CH cages. This is a very complex system in which all three guest molecules in the same system transform simultaneously. We conclude that THF forms stable crystalline CH inside an amorphous matrix at 130 K,[42] where CO_2 and DME form metastable structures of CH.

We plotted the intensity of the peaks assigned to different molecules encaged in different CH systems versus time in Figure 4 (intensities of different peaks are derived from Figure S6) to better understand the relative stability of CHs. Here, it is worth noting that the assigned peak intensity for each cage is not the individual peak intensity but the overlapped peak intensity with other peaks. These peak intensities can help us understand the relative formation and dissociation of each CH. During thermal annealing for 37 h, the intensity of the peak at 1074 cm^{-1}, representing THF encaged within sII large cages, rises. Concurrently, the intensities of peaks assigned to small (2345 cm^{-1}) and large (2338 cm^{-1}) cages of CO_2 and large cages of DME (1096 cm^{-1}) decrease.

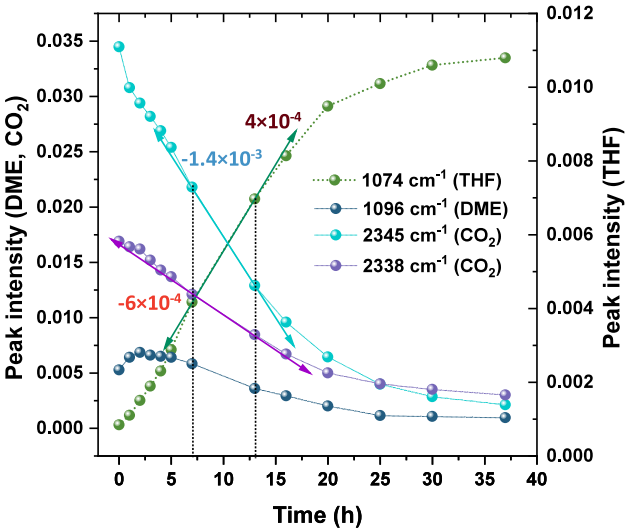


Figure 4. Time-dependent evolution of specific CH in mixed CH at 130 K. Intensity of the peak 1074 cm^{-1} (large cages of THF), 1096 cm^{-1} (large cages of DME), 2345 cm^{-1} (small cage of CO_2), and 2338 cm^{-1} (large cages of CO_2).

During the initial 2 h, increase in the 1096 cm^{-1} peak signifies increase in the formation of DME CH. However, shortly thereafter, it begins to dissociate. Here, the CO_2 transformation is largely dependent on THF, as THF CH is thermodynamically more stable. From the initial time to 20 h, the curves for CO_2 and THF show a linear change. Afterward, we observe saturation in their formation and dissociation. Considering this linear character, we calculated slopes for all three curves between 7 and 13 h; they showed a negative slope for the large cages (6×10^{-4}), less than for the small cages (1.4×10^{-3}), indicating that the fraction of the molecules coming from small cages create large cages, with some of them desorbing from the ice matrix. As we noted earlier, the 2338 cm^{-1} peak is overlapped with the peak at 2346 cm^{-1} and the peak intensity does not directly indicate the percentage of CO_2 in large cages. However, the reduced slope refers to the transformation from small cages to large cages.

https://doi.org/10.1021/acs.jpclett.5c00393
J. Phys. Chem. Lett. 2025, 16, 4982−4989

The nucleation of sII CHs of DME/THF is facile in amorphous ice under UHV conditions at 130 K. At this temperature, all guest molecules exhibit sufficient mobility, as the desorption temperatures of CO_2 and DME are below 100 K, while that of THF is approximately 130 K. Studies report that the glass transition temperature of water lies between 130 and 140 K, enabling water mobility in this range.[59,60,63,64] Previous research showed that metastable CHs dissociated at elevated temperatures, leading to the formation of hexagonal or cubic ice, when the guest molecules have desorption temperatures below 120 K.[3,6,25,62] Additionally, RAIRS studies indicate that nucleation does not occur uniformly across the ice film. The O−H stretching region exhibits partial ordering rather than the sharp, well-defined bands characteristic of fully crystallized ice. Jacobson's theoretical work highlights the importance of amorphous nucleation pathways, favoring intermediate metastable CH formation.[65] Notably, the metastable sII crystal polymorph tends to grow preferentially over the stable sI structure.[66] In this study, all transformations occurred in an amorphous ice environment, promoting the formation of metastable CHs. This environment particularly favors the formation of larger sII cages for CO_2. Overall, the stability and formation of CHs are closely linked to the desorption temperatures of guest molecules, which directly influence their intermolecular motion within the ice matrix. Although this study investigates the formation of large cages of CO_2 clathrate hydrates in the presence of DME, THF, or their mixture under UHV and cryogenic conditions, diffraction studies are necessary to fully resolve the exact structural transitions involved.

In conclusion, we present the first experimental evidence of the formation of large cages of sII CO_2 CH within an amorphous ice matrix in UHV under cryogenic conditions. While CO_2 typically stabilizes within small cages of sI at lower temperatures when it is in the pure form, the introduction of DME and THF promotes the formation of large cages. This phenomenon arises from the facile sII CH formation of DME and THF at 130 K, facilitating the nucleation and occupancy of CO_2 in the large sII cages. The metastable nature of sI CH at this temperature contributes to this intricate process. In the case of mixed CHs, where all three guest molecules are present, prolonged annealing led to an increase in the THF CH fraction over time, resulting in the breaking of most of the large cages of DME and the small cages of CO_2 and the release of DME and CO_2 from the matrix. Interestingly, CO_2 remains in significant quantities within the matrix, predominantly within the larger cages. This study explored the possibility of mixed hydrates in multicomponent interstellar ice mimics, highlighting a dynamic interplay between cages that could influence the evolution of ISM chemistry.

■ ASSOCIATED CONTENT

Supporting Information

The Supporting Information is available free of charge at https://pubs.acs.org/doi/10.1021/acs.jpclett.5c00393.

Experimental section (including experimental setup, materials and reagents, sample preparation) and temperature and time-dependent RAIR spectra (PDF)

Transparent Peer Review report available (PDF)

■ AUTHOR INFORMATION

Corresponding Authors

Rajnish Kumar − *Department of Chemical Engineering, Indian Institute of Technology Madras, Chennai 600036, India; International Centre for Clean Water, IIT Madras Research Park, Chennai 600113, India;* orcid.org/0000-0002-4172-2638; Email: rajnish@iitm.ac.in

Thalappil Pradeep − *DST Unit of Nanoscience (DST UNS) and Thematic Unit of Excellence (TUE), Department of Chemistry, Indian Institute of Technology Madras, Chennai 600036, India; International Centre for Clean Water, IIT Madras Research Park, Chennai 600113, India;* orcid.org/0000-0003-3174-534X; Email: pradeep@iitm.ac.in

Authors

Bijesh K. Malla − *DST Unit of Nanoscience (DST UNS) and Thematic Unit of Excellence (TUE), Department of Chemistry, Indian Institute of Technology Madras, Chennai 600036, India*

Soham Chowdhury − *DST Unit of Nanoscience (DST UNS) and Thematic Unit of Excellence (TUE), Department of Chemistry, Indian Institute of Technology Madras, Chennai 600036, India*

Gaurav Vishwakarma − *DST Unit of Nanoscience (DST UNS) and Thematic Unit of Excellence (TUE), Department of Chemistry, Indian Institute of Technology Madras, Chennai 600036, India;* orcid.org/0009-0002-6076-3299

Complete contact information is available at: https://pubs.acs.org/10.1021/acs.jpclett.5c00393

Author Contributions

T.P. and B.K.M. designed the research. B.K.M. and S.C. have performed the experiments. T.P. and R.K. supervised its progress. B.K.M. analyzed the results. The first draft of the manuscript was written by B.K.M. The final version of the manuscript was prepared, including the contributions of all authors.

Notes

The authors declare no competing financial interest.

■ ACKNOWLEDGMENTS

We acknowledge the Science and Engineering Research Board (SERB), Department of Science and Technology (DST), and Government of India for research funding. T.P. acknowledges funding from the Centre of Excellence on Molecular Materials and Functions under the Institution of Eminence scheme of IIT Madras. B.K.M. thanks the Council of Scientific and Industrial Research (CSIR) for his research fellowship. G.V. and S.C. thank IITM for their research fellowship. T.P. acknowledges funding from a JC Bose Fellowship.

■ REFERENCES

(1) Tychengulova, A.; Katpayeva, K.; Shomshekova, S.; Ibragimova, S.; Golikov, O.; Yerezhep, D.; Sokolov, D.; Aldiyarov, A. Laboratory Studies of the Clathrate Hydrate Formation in the Carbon Dioxide-Water Mixtures at Interstellar Conditions. *ACS Omega* **2025**, *10* (1), 1237−1248.

(2) Ghosh, J.; Methikkalam, R. R. J.; Bhuin, R. G.; Ragupathy, G.; Choudhary, N.; Kumar, R.; Pradeep, T. Clathrate Hydrates in Interstellar Environment. *Proc. Natl. Acad. Sci. U. S. A.* **2019**, *116* (5), 1526−1531.

(3) Ghosh, J.; Vishwakarma, G.; Kumar, R.; Pradeep, T. Formation and Transformation of Clathrate Hydrates under Interstellar Conditions. *Acc. Chem. Res.* **2023**, *56* (16), 2241−2252.
(4) Ghosh, J.; Bhuin, R. G.; Vishwakarma, G.; Pradeep, T. Formation of Cubic Ice via Clathrate Hydrate, Prepared in Ultrahigh Vacuum under Cryogenic Conditions. *J. Phys. Chem. Lett.* **2020**, *11* (1), 26−32.
(5) Malla, B. K.; Vishwakarma, G.; Chowdhury, S.; Selvarajan, P.; Pradeep, T. Formation of Ethane Clathrate Hydrate in Ultrahigh Vacuum by Thermal Annealing. *J. Phys. Chem. C* **2022**, *126* (42), 17983−17989.
(6) Vishwakarma, G.; Malla, B. K.; Chowdhury, S.; Khandare, S. P.; Pradeep, T. Existence of Acetaldehyde Clathrate Hydrate and Its Dissociation Leading to Cubic Ice under Ultrahigh Vacuum and Cryogenic Conditions. *J. Phys. Chem. Lett.* **2023**, *14* (23), 5328−5334.
(7) Malla, B. K.; Yang, D.-S.; Pradeep, T. Growth of Clathrate Hydrates in Nanoscale Ice Films Observed Using Electron Diffraction and Infrared Spectroscopy. *J. Phys. Chem. Lett.* **2025**, *16* (1), 365−371.
(8) Sloan, E. D., Jr.; Koh, C. A.; Koh, C. A. *Clathrate Hydrates of Natural Gases*; CRC Press, 2007.
(9) Takeya, S.; Shimada, W.; Kamata, Y.; Ebinuma, T.; Uchida, T.; Nagao, J.; Narita, H. In Situ X-Ray Diffraction Measurements of the Self-Preservation Effect of CH4 Hydrate. *J. Phys. Chem. A* **2001**, *105* (42), 9756−9759.
(10) Yamamoto, K.; Misawa, T.; Ito, H.; Takeya, S.; Alavi, S.; Ohmura, R. Phase Equilibrium Conditions and Crystal Structure of Binary Hydrates Formed with 1-Methylpiperidine. *J. Phys. Chem. C* **2024**, *128* (3), 1312−1322.
(11) Ratcliffe, C. I. The Development of Clathrate Hydrate Science. *Energy Fuels* **2022**, *36* (18), 10412−10429.
(12) Thakre, N.; Jana, A. K. Physical and Molecular Insights to Clathrate Hydrate Thermodynamics. *Renew. Sustain. Energy Rev.* **2021**, *135*, 110150.
(13) Sloan, E. D. J.; Koh, C. A. Introduction: Clathrate Hydrates of Natural Gases. *Clathrate Hydrates Nat. Gases* **2008**, I−XXV.
(14) Davy, H., VIII On a Combination of Oxymuriatic Gas and Oxygene Gas. *Philos. Trans. R. Soc. London* **1811**, *101*, 155−162.
(15) Blake, D.; Allamandola, L.; Sandford, S.; Hudgins, D.; Freund, F. Clathrate Hydrate Formation in Amorphous Cometary Ice Analogs in Vacuo. *Science.* **1991**, *254* (5031), 548−551.
(16) Fleyfel, F.; Devlin, J. P. Infrared Spectra of Large Clusters Containing Small Ether Molecules: Liquid, Crystalline, and Clathrate-Hydrate Cluster Spectra. *J. Chem. Phys.* **1990**, *92* (1), 36−42.
(17) Fleyfel, F.; Devlin, J. P. FT-IR Spectra of 90 K Films of Simple, Mixed, and Double Clathrate Hydrates of Trimethylene Oxide, Methyl Chloride, Carbon Dioxide, Tetrahydrofuran, and Ethylene Oxide Containing Decoupled D2O. *J. Phys. Chem.* **1988**, *92* (3), 631−635.
(18) Williams, K. D.; Devlin, J. P. Formation and Spectra of Clathrate Hydrates of Methanol and Methanol-Ether Mixtures. *J. Mol. Struct.* **1997**, *416* (1−3), 277−286.
(19) Ritzhaupt, G.; Devlin, J. P. Infrared Spectra of Nitric and Hydrochloric Acid Hydrate Thin Films. *J. Phys. Chem.* **1991**, *95*, 90−95.
(20) Bertie, J. E.; Devlin, J. P. Infrared Spectroscopic Proof of the Formation of the Structure I Hydrate of Oxirane from Annealed Low-Temperature Condensate. *J. Chem. Phys.* **1983**, *78* (10), 6340−6341.
(21) Fleyfel, F.; Devlin, J. P. Carbon Dioxide Clathrate Hydrate Epitaxial Growth: Spectroscopic Evidence for Formation of the Simple Type-II CO2 Hydrate. *J. Phys. Chem.* **1991**, *95* (9), 3811−3815.
(22) Choukroun, M.; Vu, T. H.; Fayolle, E. C. No Compelling Evidence for Clathrate Hydrate Formation under Interstellar Medium Conditions over Laboratory Time Scales. *Proc. Natl. Acad. Sci. U. S. A.* **2019**, *116* (29), 14407−14408.
(23) Ghosh, J.; Methikkalam, R. R. J.; Bhuin, R. G.; Ragupathy, G.; Choudhary, N.; Kumar, R.; Pradeep, T. Reply to Choukroun et Al.: IR and TPD Data Suggest the Formation of Clathrate Hydrates in Laboratory Experiments Simulating ISM. *Proc. Natl. Acad. Sci. U. S. A.* **2019**, *116* (29), 14409−14410.
(24) Vishwakarma, G.; Malla, B. K.; Reddy, K. S. S. V. P.; Ghosh, J.; Chowdhury, S.; Yamijala, S. S. R. K. C.; Reddy, S. K.; Kumar, R.; Pradeep, T. Induced Migration of CO 2 from Hydrate Cages to Amorphous Solid Water under Ultrahigh Vacuum and Cryogenic Conditions. *J. Phys. Chem. Lett.* **2023**, *14* (11), 2823−2829.
(25) Malla, B. K.; Vishwakarma, G.; Chowdhury, S.; Nayak, S. K.; Yamijala, S. S. R. K. C.; Pradeep, T. Formation and Dissociation of Dimethyl Ether Clathrate Hydrate in Interstellar Ice Mimics. *J. Phys. Chem. C* **2024**, *128* (6), 2463−2470.
(26) Arumainayagam, C. R.; Garrod, R. T.; Boyer, M. C.; Hay, A. K.; Bao, S. T.; Campbell, J. S.; Wang, J.; Nowak, C. M.; Arumainayagam, M. R.; Hodge, P. J. Extraterrestrial Prebiotic Molecules: Photochemistry vs. Radiation Chemistry of Interstellar Ices. *Chem. Soc. Rev.* **2019**, *48* (8), 2293−2314.
(27) Luspay-Kuti, A.; Mousis, O.; Hässig, M.; Fuselier, S. A.; Lunine, J. I.; Marty, B.; Mandt, K. E.; Wurz, P.; Rubin, M. The Presence of Clathrates in Comet 67P/Churyumov-Gerasimenko. *Sci. Adv.* **2016**, *2* (4), No. e1501781.
(28) Takeya, S.; Fujihisa, H.; Alavi, S.; Ohmura, R. Thermally Induced Phase Transition of Cubic Structure II Hydrate: Crystal Structures of Tetrahydropyran-CO2 Binary Hydrate. *J. Phys. Chem. Lett.* **2023**, *14* (7), 1885−1891.
(29) Takeya, S.; Udachin, K. A.; Moudrakovski, I. L.; Susilo, R.; Ripmeester, J. A. Direct Space Methods for Powder X-Ray Diffraction for Guest-Host Materials: Applications to Cage Occupancies and Guest Distributions in Clathrate Hydrates. *J. Am. Chem. Soc.* **2010**, *132* (2), 524−531.
(30) Muromachi, S.; Takeya, S.; Alavi, S.; Ripmeester, J. A. Structural CO 2 Capture Preference of Semiclathrate Hydrate Formed with Tetra- n -Butylammonium Chloride. *CrystEngComm* **2022**, *24* (24), 4366−4371.
(31) Misawa, T.; Ishikawa, T.; Takeya, S.; Alavi, S.; Ohmura, R. Continuous Hydrate-Based CO2 Separation from H2 + CO2 Gas Mixture Using Cyclopentane as Co-Guest. *J. Ind. Eng. Chem.* **2023**, *121*, 228−234.
(32) Maruyama, M.; Takeya, S.; Yoneyama, A.; Ishikawa, T.; Misawa, T.; Nagayama, S.; Alavi, S.; Ohmura, R. Characterization of Clathrate Hydrates with CO2 + 1-Propanol or 2-Propanol: Implications for Flow Assurance, Refrigeration, Carbon Capture, and Skincare Applications. *J. Ind. Eng. Chem.* **2024**, *131*, 305−314.
(33) Sun, D.; Daraboina, N.; Ripmeester, J.; Englezos, P. Capture of CO_2 and Storage in Depleted Gas Reservoirs in Alberta as Gas Hydrate. In *Gas Injection for Disposal and Enhanced Recovery*; Wiley, 2014; Vol. *9781118938*, pp 305−310.
(34) Dadhich, R.; Babu, P.; Daraboina, N. Kinetic and Performance Assessment of Hydrate-Based Precombustion CO 2 Capture Using Dry Water. *Energy & Fuels.* **2024**, *38* (24), 23625−23632.
(35) Bauer, R. P. C.; Ravichandran, A.; Tse, J. S.; Appathurai, N.; King, G.; Moreno, B.; Desgreniers, S.; Sammynaiken, R. In Situ X-Ray Diffraction Study on Hydrate Formation at Low Temperature in a High Vacuum. *J. Phys. Chem. C* **2021**, *125* (48), 26892−26900.
(36) Babu, P.; Linga, P.; Kumar, R.; Englezos, P. A Review of the Hydrate Based Gas Separation (HBGS) Process for Carbon Dioxide Pre-Combustion Capture. *Energy* **2015**, *85*, 261−279.
(37) Chen, L.; Lu, H.; Ripmeester, J. A. Raman Spectroscopic Study of CO2 in Hydrate Cages. *Chem. Eng. Sci.* **2015**, *138*, 706−711.
(38) Yao, Y.; Yin, Z.; Kumar, R.; Gao, X.; Chen, D. Tuning Effect of DIOX on the Thermodynamics and Cage Occupancy of CH4/CO2 + DIOX Mixed Hydrates. *Chem. Eng. J.* **2024**, *482*, 148984.
(39) Yao, Y.; Yin, Z.; Niu, M.; Liu, X.; Zhang, J.; Chen, D. Evaluation of 1,3-Dioxolane in Promoting CO2 Hydrate Kinetics and Its Significance in Hydrate-Based CO2 Sequestration. *Chem. Eng. J.* **2023**, *451*, 138799.
(40) Boese, A. D.; Boese, R. Tetrahydrothiophene and Tetrahydrofuran, Computational and x-Ray Studies in the Crystalline Phase. *Cryst. Growth Des.* **2015**, *15* (3), 1073−1081.

https://doi.org/10.1021/acs.jpclett.5c00393
J. Phys. Chem. Lett. 2025, 16, 4982−4989

(41) Sargent, D. F.; Calvert, L. D. Crystallographic Data for Some New Type II Clathrate Hydrates. *J. Phys. Chem.* **1966**, *70* (8), 2689−2691.
(42) Ghosh, J.; Bhuin, R. G.; Ragupathy, G.; Pradeep, T. Spontaneous Formation of Tetrahydrofuran Hydrate in Ultrahigh Vacuum. *J. Phys. Chem. C* **2019**, *123* (26), 16300−16307.
(43) Gough, S. R.; Garg, S. K.; Ripmeester, J. A.; Davidson, D. W. Dielectric Relaxation and Nuclear Magnetic Resonance Studies of Two Clathrate Hydrates of Dimethyl Ether. *J. Phys. Chem.* **1977**, *81* (23), 2158−2163.
(44) D'Hendecourt, L. B.; Jourdain de Muizon, M.; D'Hendecourt, L. B.; Jourdain de Muizon, M. The Discovery of Interstellar Carbon Dioxide. *A&A* **1989**, *223*, L5−L8.
(45) Snyder, L. E.; Buhl, D.; Schwartz, P. R.; Clark, F. O.; Johnson, D. R.; Lovas, F. J.; Giguere, P. T. Radio Detection of Interstellar Dimethyl Ether. *Astrophys. J.* **1974**, *191*, L79.
(46) McGuire, B. A.; Carroll, P. B.; Loomis, R. A.; Finneran, I. A.; Jewell, P. R.; Remijan, A. J.; Blake, G. A. Discovery of the Interstellar Chiral Molecule Propylene Oxide (CH3CHCH2O). *Science.* **2016**, *352* (6292), 1449−1452.
(47) McGuire, B. A.; Carroll, P. B.; Loomis, R. A.; Finneran, I. A.; Jewell, P. R.; Remijan, A. J.; Blake, G. A. Detection of Interstellar Ethylene Oxide (c-C2H4O). *Science (80-.).* **2016**, *352* (6292), 1449−1452.
(48) Bag, S.; Bhuin, R. G.; Methikkalam, R. R. J.; Pradeep, T.; Kephart, L.; Walker, J.; Kuchta, K.; Martin, D.; Wei, J. Development of Ultralow Energy (1−10 EV) Ion Scattering Spectrometry Coupled with Reflection Absorption Infrared Spectroscopy and Temperature Programmed Desorption for the Investigation of Molecular Solids. *Rev. Sci. Instrum.* **2014**, *85* (1), 014103.
(49) Malla, B. K.; Vishwakarma, G.; Chowdhury, S.; Pradeep, T. Vacuum Ultraviolet Photolysis of Condensed Methyl Chloride in Interstellar Model Conditions and Trapping of Intermediates at Intergrain Interfaces. *J. Phys. Chem. C* **2023**, *127* (50), 24149−24157.
(50) Escribano, R. M.; Muñoz Caro, G. M.; Cruz-Diaz, G. A.; Rodríguez-Lazcano, Y.; Maté, B. Crystallization of CO 2 Ice and the Absence of Amorphous CO 2 Ice in Space. *Proc. Natl. Acad. Sci. U. S. A.* **2013**, *110* (32), 12899−12904.
(51) Edridge, J. L.; Freimann, K.; Burke, D. J.; Brown, W. A. Surface Science Investigations of the Role of CO 2 in Astrophysical Ices. *Philos. Trans. R. Soc. A Math. Phys. Eng. Sci.* **2013**, *371* (1994), 20110578.
(52) Hernandez, J.; Uras, N.; Devlin, J. P. Coated Ice Nanocrystals from Water-Adsorbate Vapor Mixtures: Formation of Ether - CO2 Clathrate Hydrate Nanocrystals at 120 K. *J. Phys. Chem. B* **1998**, *102* (23), 4526−4535.
(53) Zhou, X.; Zhou, J.; Chen, P.; Wen, H.; Zang, X.; Fan, S.; Liang, D. Spectral Analysis on the Raman Peaks of CH4, CO2, and N2 in the Hydrate Phase. *Energy Fuels* **2025**, *39* (3), 1579−1587.
(54) Jeenmuang, K.; Pornaroontham, P.; Fahed Qureshi, M.; Linga, P.; Rangsunvigit, P. Micro Kinetic Analysis of the CO2 Hydrate Formation and Dissociation with L-Tryptophan in Brine via High Pressure in Situ Raman Spectroscopy for CO2 Sequestration. *Chem. Eng. J.* **2024**, *479*, 147691.
(55) Kumar, R.; Lang, S.; Englezos, P.; Ripmeester, J. Application of the ATR-IR Spectroscopic Technique to the Characterization of Hydrates Formed by CO2, CO2/H2 and CO 2/H2/C3H8. *J. Phys. Chem. A* **2009**, *113* (22), 6308−6313.
(56) Udachin, K. A.; Ratcliffe, C. I.; Ripmeester, J. A. A Dense and Efficient Clathrate Hydrate Structure with Unusual Cages. *Angew. Chemie Int. Ed.* **2001**, *40* (7), 1303−1305.
(57) Buch, V.; Devlin, J. P.; Monreal, I. A.; Jagoda-Cwiklik, B.; Uras-Aytemiz, N.; Cwiklik, L. Clathrate Hydrates with Hydrogen-Bonding Guests. *Phys. Chem. Chem. Phys.* **2009**, *11* (44), 10245−10265.
(58) Truong-Lam, H. S.; Truong-Lam, H. S.; Seo, S. D.; Kim, S.; Seo, Y.; Lee, J. D. In Situ Raman Study of the Formation and Dissociation Kinetics of Methane and Methane/Propane Hydrates. *Energy Fuels* **2020**, *34* (5), 6288−6297.
(59) Kohl, I.; Bachmann, L.; Mayer, E.; Hallbrucker, A.; Loerting, T. Glass Transition in Hyperquenched Water? *Nat. 2005 4357041* **2005**, *435* (7041), No. E1.
(60) Souda, R. Glass Transition and Intermixing of Amorphous Water and Methanol. *Phys. Rev. Lett.* **2004**, *93* (23), 1−4.
(61) Gudipati, M. S.; Fleury, B.; Wagner, R.; Henderson, B. L.; Altwegg, K.; Rubin, M. Thermal Behavior of Astrophysical Amorphous Molecular Ices. *Faraday Discuss.* **2023**, *245* (0), 467−487.
(62) Ghosh, J.; Vishwakarma, G.; Das, S.; Pradeep, T. Facile Crystallization of Ice I h via Formaldehyde Hydrate in Ultrahigh Vacuum under Cryogenic Conditions. *J. Phys. Chem. C* **2021**, *125* (8), 4532−4539.
(63) Chonde, M.; Brindza, M.; Sadtchenko, V. Glass Transition in Pure and Doped Amorphous Solid Water: An Ultrafast Microcalorimetry Study. *J. Chem. Phys.* **2006**, *125* (9), 94501.
(64) Tsekouras, A. A.; Iedema, M. J.; Cowin, J. P. Amorphous Water-Ice Relaxations Measured with Soft-Landed Ions. *Phys. Rev. Lett.* **1998**, *80* (26), 5798−5801.
(65) Jacobson, L. C.; Hujo, W.; Molinero, V. Amorphous Precursors in the Nucleation of Clathrate Hydrates. *J. Am. Chem. Soc.* **2010**, *132* (33), 11806−11811.
(66) Jacobson, L. C.; Molinero, V. Can Amorphous Nuclei Grow Crystalline Clathrates? The Size and Crystallinity of Critical Clathrate Nuclei. *J. Am. Chem. Soc.* **2011**, *133* (16), 6458−6463.

https://doi.org/10.1021/acs.jpclett.5c00393
J. Phys. Chem. Lett. 2025, 16, 4982−4989

Dissociation and Reformation of CO_2 Clathrate Hydrate cages in Amorphous Ice Thin Film under Ultrahigh Vacuum

Bijesh K. Malla[1], Soham Chowdhury[1], Gaurav Vishwakarma[1], Rajnish Kumar[2,3], and Thalappil Pradeep[1,3*]*

[1]DST Unit of Nanoscience (DST UNS) and Thematic Unit of Excellence (TUE), Department of Chemistry, Indian Institute of Technology Madras, Chennai 600036, India.

[2]Department of Chemical Engineering, Indian Institute of Technology Madras, Chennai 600036, India.

[3]International Centre for Clean Water, IIT Madras Research Park, Chennai 600113, India.

Corresponding authors

*Email: pradeep@iitm.ac.in, rajnish@iitm.ac.in

This PDF file includes:

Experimental section (pages S2-S4)

Figure S1 to S6 (pages S5-S10)

Reference (pages S11)

Experimental Section

In this study, all experiments were carried out in an ultrahigh vacuum (UHV) instrument (with a base pressure of ~ 5×10^{-10} mbar), discussed in detail in our previous literature.[1,2] The apparatus comprises three ultra-high vacuum (UHV) chambers: ionization, octupole, and scattering. It is equipped with various analytical techniques, including reflection absorption infrared spectroscopy (RAIRs), low energy ion scattering (LEIS), temperature-programmed desorption (TPD) mass spectrometry, and Cs^+ ion-based secondary ion mass spectrometry (SIMS). A vacuum ultraviolet (VUV) lamp is also integrated into the setup. Six turbomolecular pumps are employed to create UHV, complemented by multiple oil-free diaphragm pumps. The chamber pressure is monitored through a Bayard-Alpert gauge, regulated by a MaxiGauge vacuum gauge controller (Pfeiffer, Model TPG 256 A). A highly polished Ru(0001) single crystal was used as the substrate to create thin ice films that was mounted on a copper holder. This assembly was connected to a helium cryostat (Cold Edge technology) capable of maintaining temperatures as low as 8 K. To heat the substrate to 1000 K, a resistive heater (25 Ω) under the control of a temperature controller (Lakeshore 336) was utilized. The temperature of the substrate was measured using a K-type thermocouple sensor with an accuracy of ±0.5 K. Repeated heating to 400 K before each vapor deposition ensured a clean surface suitable for the current study. It is worth noting that the surface has a negligible role in the current study, as our experiments were on multilayer ice films.

RAIRS and TPD-MS Setup

The RAIRS data was collected in the 4000−550 cm^{-1} range with a spectral resolution of 2 cm^{-1}, using a Bruker FT-IR spectrometer called Vertex 70. The ice sample was exposed to an incident angle of $80^0 \pm 7^0$ by focusing the IR beam through a ZnSe viewport. The reflected IR beam from the sample was detected by using a liquid N_2-cooled mercury cadmium telluride (MCT) detector. The IR beam outside the vacuum chamber was purged with dry N_2 to prevent absorption by atmospheric moisture. Each RAIR spectrum was obtained by averaging over 512 scans to improve the signal-to-noise ratio. An Extrel quadrupole mass spectrometer was used for TPD-MS in an out-of-sight configuration.

Materials and reagents

CO_2 gas (99.99%) was purchased from Indogas and used without further purification. Tetrahydrofuran (THF) (99.8%) was purchased from Thermo Fisher Scientific India Pvt. Ltd., and Millipore water (H_2O of 18.2 M Ω resistivity) was kept in a vacuum-sealed test tube and was further purified by several freeze-pump-thaw cycles. DME (99.9%, Sigma-Aldrich) was used without further purification.

Sample preparations

Thin ice films were prepared by vapor deposition of different molecules at 10 K on a Ru(0001) substrate. Two sample inlet lines were attached to the UHV chamber through high-precision all-metal leak valves. Out of two sample lines, one was used for CO_2/THF, and the other was used for H_2O/DME. These lines can be interchanged between each other. All the lines are connected to one rotary pump for cleaning purposes. When two molecules were used through a single line, we made sure that before filling each gas, sample lines were evacuated to a maximum pressure of 1×10^{-2} mbar. Further purity of each molecule was confirmed by the presence of their distinctive molecular ion peaks in the mass spectrum using a residual gas analyzer. The vapor deposition coverage was expressed in monolayers (ML), assuming that 1.33×10^{-6} mbar s = 1 ML, estimated to contain $\sim 1.1 \times 10^{15}$ molecules cm^{-2}, as followed in our earlier studies.[3,4]

CO_2+H_2O (300 ML) (1:10)

To prepare CO_2+water ice mixture thin film, the UHV chamber was backfilled to a total pressure of 5×10^{-7} mbar of CO_2 and water vapors for 10 min, with CO_2 pressure reaching 0.5×10^{-7} mbar and water pressure also maintained at 4.5×10^{-7} mbar approximately.

DME (150 ML) @ CO_2+H_2O (150 ML) (1:10)

To form DME (150 ML) @ CO_2+H_2O (150 ML) (1:10) layered ice, at first, 150 ML of DME was deposited on the substrate by backfilling DME vapors at a pressure of 5×10^{-7} mbar for 5 min. Subsequently, a waiting period ensued to allow the UHV chamber pressure to return to base pressure. Then, on the top of DME ice-thin film, 150 ML of CO_2 and H_2O vapors were codeposited at a ratio of 1:10. For this, UHV chamber was backfilled to a total pressure of 5×10^{-7} mbar for 5

min, with CO_2 reaching 0.5 × 10^{-7} mbar and water pressure also maintained at 4.5 × 10^{-7} mbar approximately.

THF (50 ML) @ CO_2+H_2O (250 ML) (1:10)

To form THF (50 ML) @ CO_2+H_2O (250 ML) (1:10) layered ice, 50 ML of THF was deposited on the substrate by backfilling THF vapors at a pressure of 5×10^{-7} mbar for 1 min 40 sec. Subsequently, a waiting period ensued to allow the UHV chamber pressure to return to 5×10^{-10} mbar. Then, on the top of the THF ice-thin film, 250 ML of CO_2 and H_2O were co-deposited at a ratio of 1:10. For this, again, we backfilled the UHV chamber to a total pressure of 5 × 10^{-7} mbar for 8 min 20 sec, with CO_2 reaching 0.5 × 10^{-7} mbar and water pressure also maintained at 4.5 × 10^{-7} mbar approximately.

THF (50 ML) @ DME (50 ML)@CO_2+H_2O (200 ML) (1:10)

For the formation of THF (50 ML) @ DME (50 ML)@CO_2+H_2O (200 ML) (1:10) layered ice, 50 ML of THF was deposited on the substrate by backfilling THF vapors at a pressure of 5×10^{-7} mbar for 1 min 40 sec. Subsequently, 50 ML of DME was deposited atop the THF layer by backfilling DME vapors at a pressure of 5×10^{-7} mbar for 1 min 40 sec. Then, on the top of DME, 200 ML of CO_2 and H_2O codeposited at a ratio of 1:10. For this, again we backfilled the UHV chamber to a total pressure of 5 × 10^{-7} mbar for 6 min 40 sec, with CO_2 reaching 0.5 × 10^{-7} mbar and water pressure also maintained at 4.5 × 10^{-7} mbar approximately.

Supporting Information 1:

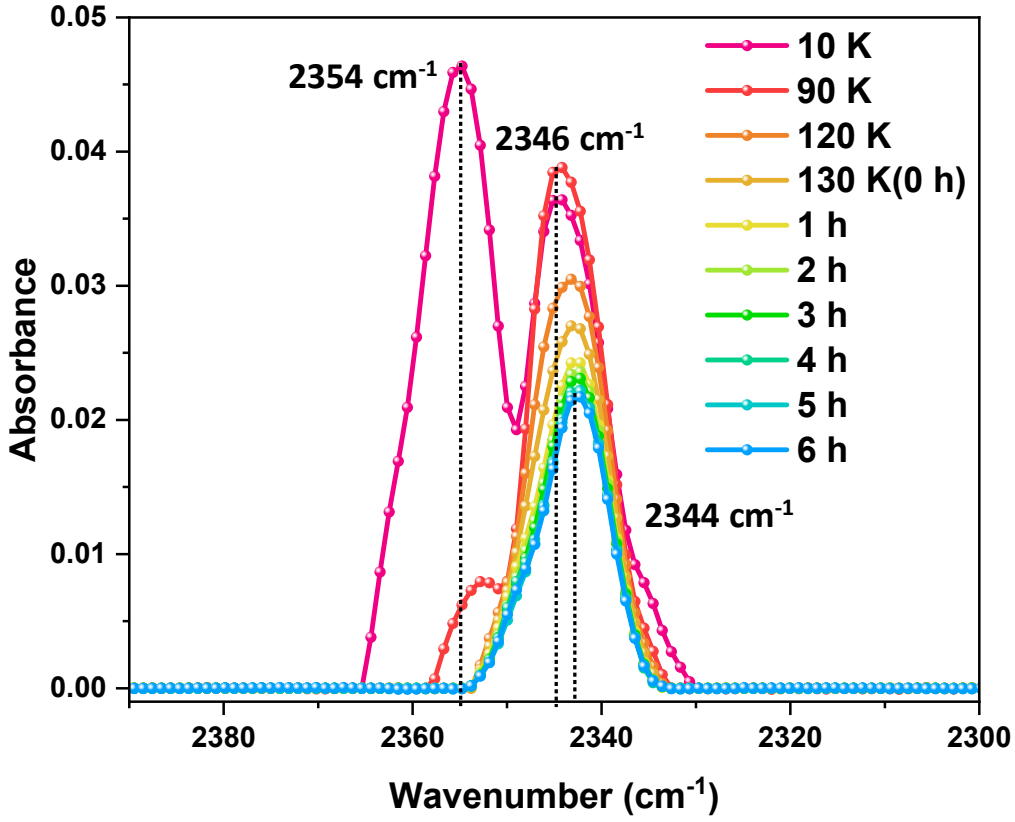


Figure S1. Temperature and time-dependent RAIR spectra of 300 ML of CO_2+H_2O (1:10) ice mixture. The ice sample was prepared by vapor deposition on Ru(0001) substrate at 10 K, then annealed to 130 K, and subsequently held at the same condition for 6 h.

Supporting Information 2:

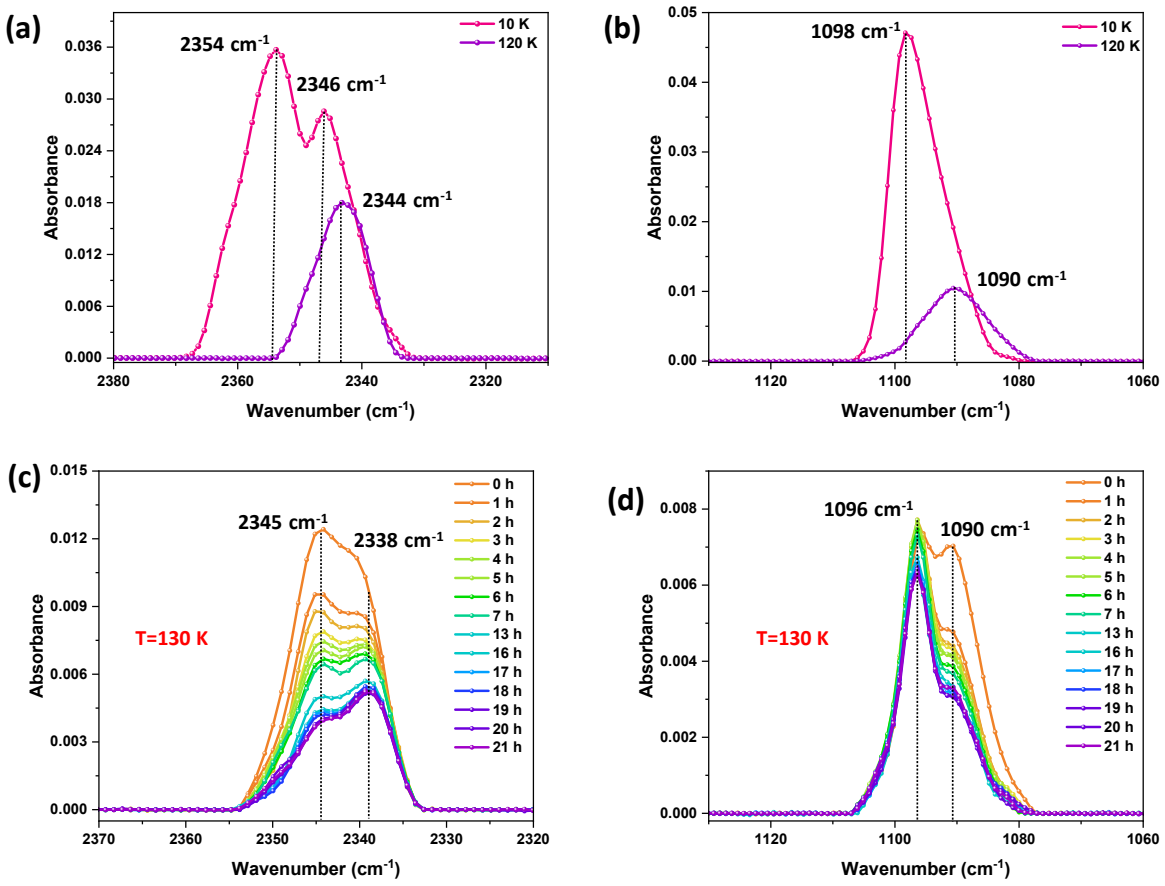


Figure S2. Temperature-dependent RAIR spectra of DME (150 ML)@(CO_2+H_2O) (1:10) (150 ML) mixed ice in (a) C=O antisymmetric stretching region for CO_2, (b) C-O antisymmetric stretching region for DME. Time-dependent RAIR spectra of DME (150 ML)@(CO_2+H_2O) (1:10) (150 ML) mixed ice at 130 K in (a) C=O antisymmetric stretching region for CO_2, (b) C-O antisymmetric stretching region for DME.

Supporting Information 3:

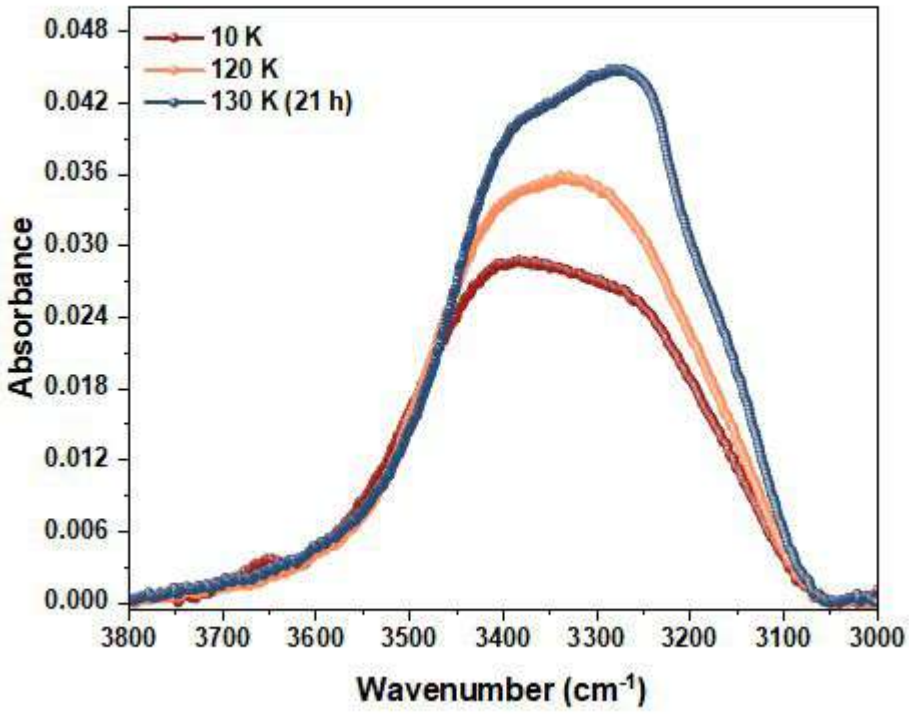


Figure S3. Time and temperature dependent RAIR spectra of DME (150 ML)@(CO_2+H_2O) (1:10) (150 ML) mixed ice in O-H stretching region.

Supporting Information 4:

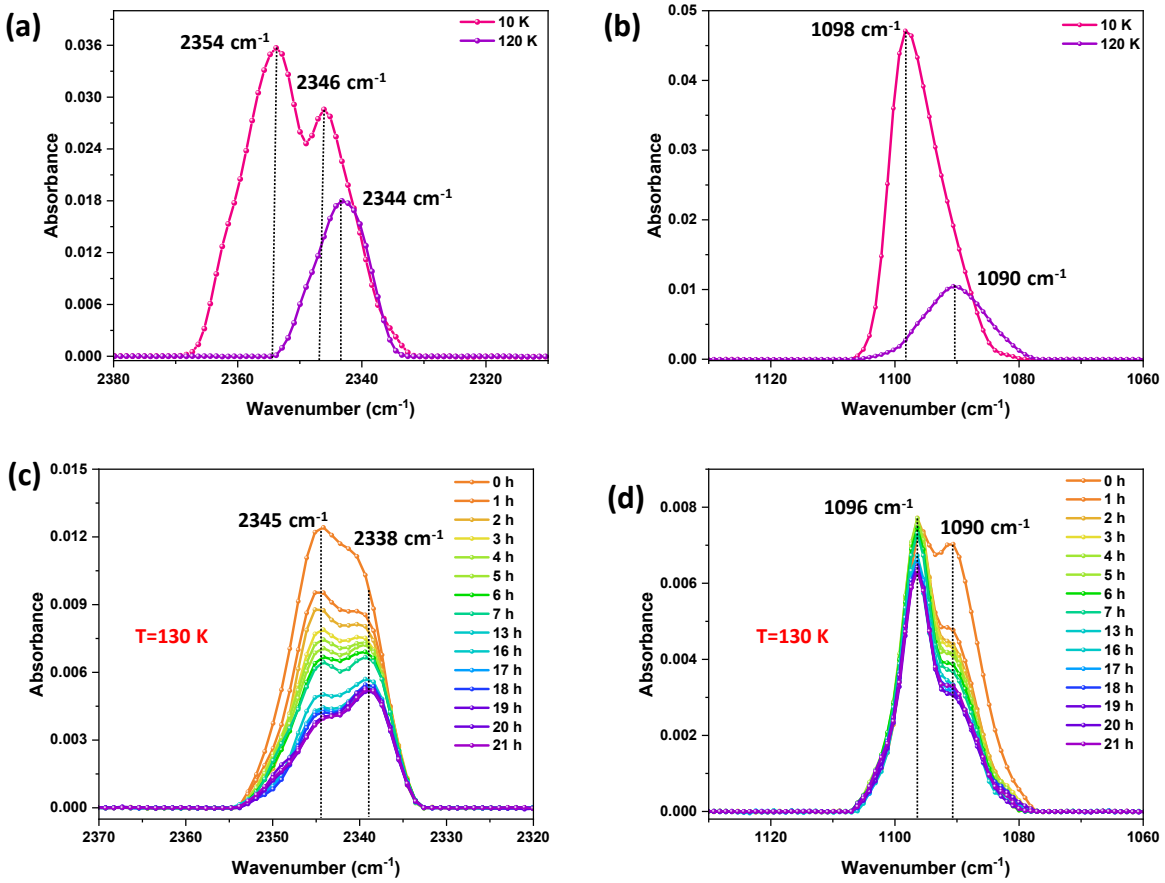


Figure S4. Temperature-dependent RAIR spectra of THF (50 ML)@(CO_2+H_2O) (1:10) (250 ML) mixed ice in (a) C=O antisymmetric stretching region for CO_2, (b) C-O antisymmetric stretching region for THF. Time-dependent RAIR spectra of THF (50 ML)@(CO_2+H_2O) (1:10) (250 ML) mixed ice at 130 K in (a) C=O antisymmetric stretching region for CO_2, (b) C-O antisymmetric stretching region for THF.

Supporting Information 5:

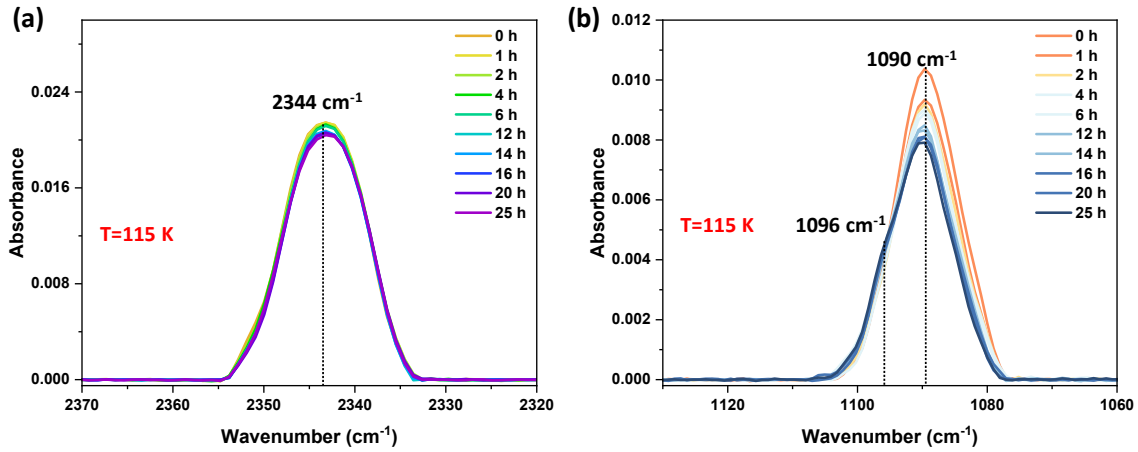


Figure S5: Time-dependent RAIR spectra of DME (150 ML)@(CO_2+H_2O) (1:10) (150 ML) mixed ice at 115 K in (a) C=O antisymmetric stretching region for CO_2, (b) C-O antisymmetric stretching region for DME.

Supporting Information 6:

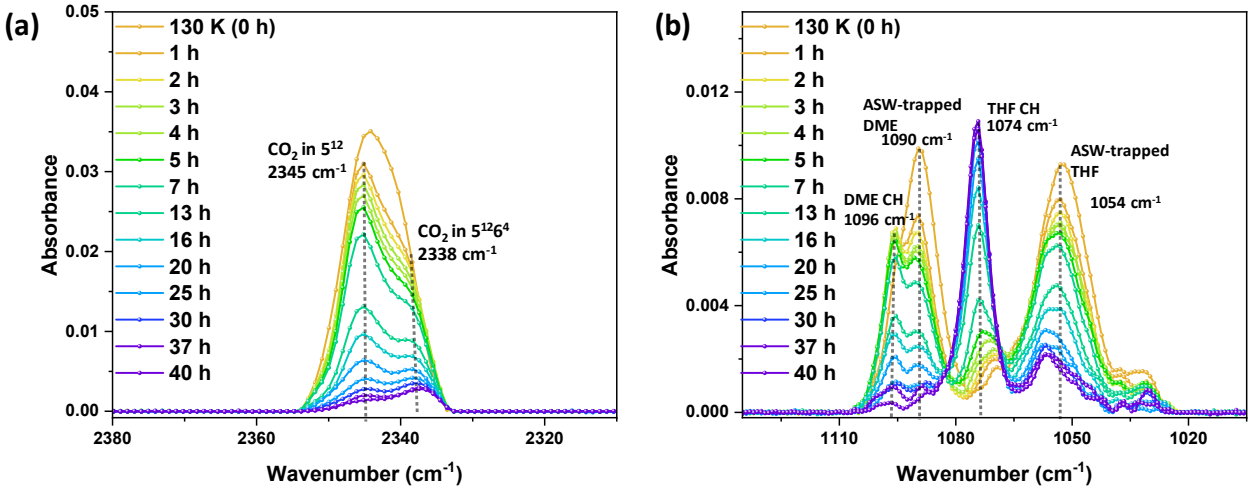


Figure S6. Time-dependent RAIR spectra of THF (50 ML)@DME (50 ML)@(CO_2+H_2O) (1:10) (100 ML) mixed ice in (a) C=O antisymmetric stretching region for CO_2, (b) C-O antisymmetric stretching region for THF and DME at 130 K.

References

(1) Bag, S.; Bhuin, R. G.; Methikkalam, R. R. J.; Pradeep, T.; Kephart, L.; Walker, J.; Kuchta, K.; Martin, D.; Wei, J. Development of Ultralow Energy (1-10 EV) Ion Scattering Spectrometry Coupled with Reflection Absorption Infrared Spectroscopy and Temperature Programmed Desorption for the Investigation of Molecular Solids. *Rev. Sci. Instrum.* **2014**, *85* (1), 1–7. https://doi.org/10.1063/1.4848895.

(2) Malla, B. K.; Vishwakarma, G.; Chowdhury, S.; Pradeep, T. Vacuum Ultraviolet Photolysis of Condensed Methyl Chloride in Interstellar Model Conditions and Trapping of Intermediates at Intergrain Interfaces. *J. Phys. Chem. C* **2023**, *127* (50), 24149–24157. https://doi.org/10.1021/acs.jpcc.3c05889.

(3) Kim, Y.; Moon, E.; Shin, S.; Kang, H. Acidic Water Monolayer on Ruthenium(0001). *Angew. Chemie* **2012**, *124* (51), 12978–12981. https://doi.org/10.1002/ange.201205756.

(4) Lee, D. H.; Kang, H. Acid-Promoted Crystallization of Amorphous Solid Water. *J. Phys. Chem. C* **2018**, *122* (42), 24164–24170. https://doi.org/10.1021/acs.jpcc.8b07858.

Check for updates

ADVANCED MATERIALS
www.advmat.de

Bimetallic Nanocluster-Based Light-Emitting Diodes With High External Quantum Efficiency and Saturated Red Emission

Jose V. Rival, Savita Chand, Arijit Jana, Nonappa, Vasudevanpillai Biju, Thalappil Pradeep, Pachaiyappan Rajamalli, and Edakkattuparambil Sidharth Shibu**

Dedicated to Professor Vijayamohanan K Pillai on the occasion of his 65th Birthday

Self-emissive atomically precise metal nanoclusters (NCs) are emerging as promising emissive layer material for next-generation light-emitting diodes (LEDs), thanks to their solid-state luminescence, well-defined structures, photo/thermal stability, low toxicity, and unique excited-state properties. However, achieving high external quantum efficiency (EQE) in solid-state NCs remains a formidable challenge. In this study, a highly stable bimetallic gold-copper NC forming $[Au_2Cu_6(Sadm)_6(DPPEO)_2]$ stabilized with 1-adamantanethiol (HSadm) and 1,2-bis(diphenylphosphino)ethane (DPPE) as the primary and secondary ligands, respectively is reported. Single-crystal X-ray diffraction and spectroscopic analyses suggest that the as-synthesized NC contains one phosphine bound to gold and the second phosphine has oxidized to phosphine oxide (P═O). The presence of such P═O moieties in the NC facilitated C—H···O interactions along with C—H···π and H···H interactions between ligands, promoting rapid crystallization. Due to the exceptional photo/thermal stability and enhanced solid-state photoluminescence quantum yield (PLQY), $[Au_2Cu_6(Sadm)_6(DPPEO)_2]$ NC is utilized to fabricate the NC-based LED (NC-LED) via the solution-processed technique, without using any additional host materials. The fabricated NC-LED shows a maximum brightness of 1246 cd m^{-2} and an EQE of 12.60% with a pure red emission ≈668 nm. This EQE value coupled with saturated pure red emission is the best among solution-processed and non-doped NC-LEDs, suggesting the enormous potential of the NCs for electro-optical devices.

1. Introduction

Self-emissive light-emitting diodes (LEDs) have received significant attention in recent years due to their reduced energy consumption, environmental compatibility, and cost-effectiveness compared to conventional cathode-ray tube (CRT) and liquid crystal display (LCD) technologies.[1,2] In the past few decades, organic (OLED), polymer (PLED), quantum dot (QLED), and emerging perovskite-based LEDs (PeLED) have been successfully developed using emissive organic molecules, polymers, inorganic nanocrystals, and organic/inorganic hybrid materials, respectively.[3–8] Though all these emissive materials offer unique advantages, they face challenges such as laborious, high-temperature, and multiple synthesis steps, minimal structural selection, resource sustainability, toxicity, the requirement of passivating agents, and instability under light, heat, and moisture.[9–11] In this context, atomically precise nanoclusters (NCs) have emerged as promising materials for simple and low-cost solution processing devices. This is attributed to their easy synthetic routes,

J. V. Rival, E. S. Shibu
Smart Materials Lab (SML)
Department of Nanoscience and Technology (DNST)
University of Calicut (UoC)
Thenhipalam, Kerala 673635, India
E-mail: shibu@uoc.ac.in

S. Chand, P. Rajamalli
Materials Research Centre
Indian Institute of Science
Bangalore 560012, India
E-mail: rajamalli@iisc.ac.in

A. Jana, T. Pradeep
Department of Chemistry
DST Unit of Nanoscience (DST UNS) and Thematic Unit of Excellence (TUE)
Indian Institute of Technology Madras
Chennai 600036, India

Nonappa
Faculty of Engineering and Natural Sciences
Tampere University
P.O. Box 541, Tampere FI-33101, Finland

V. Biju
Research Institute for Electronic Science
Hokkaido University
N20 W10, Sapporo, Hokkaido 001–0020, Japan

The ORCID identification number(s) for the author(s) of this article can be found under https://doi.org/10.1002/adma.202507893

DOI: 10.1002/adma.202507893

 © 2025 Wiley-VCH GmbH

low toxicity, well-defined crystal structure, unique excited state characteristics, photo/thermal stability, environmental compatibility, and solid-state photoluminescence (PL).[12–23] Although the external quantum efficiency (EQE) of NC-based LED (NC-LED) was initially below 0.1%,[24] a significant improvement has been made by combining them with various host materials.[18,25–31] However, the low PL quantum yield (PLQY), poor device compatibility due to the bulky ligands, and the need to incorporate additional host materials to achieve adequate conductivity continue limiting their applications in NC-LEDs.[32,33] Recent developments in metal core engineering, ligand engineering, self-assembly techniques, and advanced synthetic procedures significantly helped to overcome such issues.[34–44] The solid-state emitting NCs with improved PL properties have been recently developed using a combination of rigid ligands and multiple metal precursors.[45–47] Metal core/ligand engineering has reduced the PLQY gap between NCs and traditional luminescent materials by precisely controlling the core size, composition, and crystal structure.[48–57] However, developing an ideal blend of solid-state emitting NCs holding improved EQE is still in its infancy. To address this challenge, herein, we have designed and synthesized, highly stable and solid-state emitting gold-copper bimetallic NCs ($[Au_2Cu_6(Sadm)_6(DPPEO)_2]$) using 1-adamantanethiol (HSadm) and 1,2-bis(diphenylphosphino)ethane (DPPE) as the primary and secondary ligands, respectively. $[Au_2Cu_6(Sadm)_6(DPPEO)_2]$ NCs were readily crystallized compared to previously reported analog ($[Au_2Cu_6(Sadm)_6(TPP)_2]$; TPP: triphenylphosphine) NC.[58,59] The electrospray ionization mass spectrometry (ESI-MS) and single crystal X-ray diffraction (SC-XRD) data suggest that only one phosphine is bound to the gold. The second phosphine ligand is oxidized to phosphine oxide ($[Au_2Cu_6(Sadm)_6(DPPEO)_2]$), as confirmed by various spectroscopic analyses. Such electron-withdrawing P═O moieties are known to offer enhanced electron transport apart from their ability to form uniform thin films and resist chemical and oxidative stress.[60–62] Moreover, due to the exceptional thermal and photostability of solid-state emitting $[Au_2Cu_6(Sadm)_6(DPPEO)_2]$ NCs, we fabricated LEDs using this NC as an emitter. The solution-processed and non-doped NC-LEDs showed a maximum luminance of 1246 cd m^{-2} and EQE of 12.60%. The electroluminescence (EL) maximum of the device was ≈668 nm with a turn-on voltage of 3V. The International Commission on Illumination (CIE) chromaticity coordinates (0.70, 0.30) at the edge of the chromaticity diagram represent an extremely saturated pure red emission. These NCs with enhanced PL, better thermal/photostability, and high device performance are expected to offer new directions in designing and fabricating efficient and non-toxic NC-LEDs for future sustainable technology.

2. Results and Discussion

Figure 1a shows the chemical structure of ligands (HSadm and DPPE) and the photographs of the reaction mixture during various steps of NC synthesis. The synthesis of bimetallic gold-copper $[Au_2Cu_6(Sadm)_6(DPPEO)_2]$ NC was performed using a modified one-pot chemical reduction method reported previously for the synthesis of $[Au_2Cu_6(Sadm)_6(TPP)_2]$ NCs (see Experimental Section for the details).[58] The introduction of DPPE ligands instead of TPP helped to reduce the amount of gold precursor and improved the yield and synthetic purity of NC. Similar to $[Au_2Cu_6(Sadm)_6(TPP)_2]$ NC, the as-synthesized $[Au_2Cu_6(Sadm)_6(DPPEO)_2]$ NCs in a solution and powder show purple under visible light and exhibit strong red emission under UV light (Figure 1b). The absorption spectra of $[Au_2Cu_6(Sadm)_6(DPPEO)_2]$ (Figure 1d; d_1(i)) and $[Au_2Cu_6(Sadm)_6(TPP)_2]$ (Figure 1d; d_2(i)) NCs in toluene and dichloromethane (DCM), respectively, exhibit multiple absorption peaks at 325, 425, 515, and 592 nm (Figure 1d), with no observable shift in these regions.[63] The PL spectrum of $[Au_2Cu_6(Sadm)_6(DPPEO)_2]$ NCs (Figure $1d_1$; iii) displays two distinct emission maxima ≈675 and 798 nm when excited at 515 nm. In contrast, the PL spectrum of $[Au_2Cu_6(Sadm)_6(TPP)_2]$ NCs (Figure $1d_2$; iii) shows emission maxima ≈675 and 806 nm at the same excitation wavelength. Notably, the excitation spectra corresponding to emission ≈675 nm (ii) of both NCs (d_1 and d_2) closely resemble their respective absorption spectra (i), suggesting that the optical transitions are directly linked to the same electronic states, confirming a well-defined absorption-emission relationship in both systems. Similarly, the excitation spectra corresponding to the emissions ≈798 and 806 nm in the respective NCs also match with their absorbance spectra (Figure S1, Supporting Information). The ESI-MS spectra showed molecular ion peaks ≈m/z 2607.78 (e_1) and m/z 2303.52 (e_2) correspond to the parent molecular ions of $[Au_2Cu_6(Sadm)_6(DPPEO)_2]$ and $[Au_2Cu_6(Sadm)_6(TPP)_2]$ NCs (Figure 1e), in which both the experimental and simulated m/z values are in good agreement (inset in Figure 1e). The oxidation of one unbound phosphine group from each DPPE ligand, leading to the formation of a P═O bond, is evident from the observed m/z value. This result indicates that, during the synthesis of the NCs, only one phosphine group from each DPPE molecule directly coordinates with the Au center, while the second phosphine undergoes oxidation to form a phosphine oxide (P═O).

To further confirm the presence of bound ligands in the purified $[Au_2Cu_6(Sadm)_6(DPPEO)_2]$ NC, ^{1}H, and ^{31}P nuclear magnetic resonance (NMR) spectra were measured in $CDCl_3$ (Figures S2 and S3, Supporting Information). The ^{1}H chemical shifts at δ = 7.85–7.79, 7.69–7.63, 7.46–7.40, 7.38–7.32, 7.30–7.27, 2.95, and 2.69 ppm represent combined aromatic (-Ph) and aliphatic (-CH_2-CH_2-) chains of DPPEO ligand, and the peaks at 1.95–1.87 and 1.62–1.44 ppm represent adamantane moieties. The splitting and downfield shift of the broad aromatic peak ≈δ = 7.28 ppm, and the aliphatic triplet ≈2.06 ppm, in the ^{1}H NMR spectrum of the DPPE ligand confirm the conversion of unbound phosphine to the P═O bond. At the same time, the presence of two types of phosphines (bound and P═O) was observed in the ^{31}P NMR spectrum of NCs (Figure S3, Supporting Information). DPPE showed only a single peak at −12.5 ppm, while an apparent splitting and downfield shift (33.7 and 60.4 ppm) were observed in the case of NCs owing to the presence of anchored phosphine on the NC surface and free-standing phosphine bound to an electronegative oxygen atom. NCs were further characterized using transmission electron microscopy (TEM) imaging. Although the TEM images (Figure 1c) showed a nearly uniform size distribution, it is important to note that due to electron beam-induced fusion of $[Au_2Cu_6(Sadm)_6(DPPEO)_2]$ NCs, a few bigger particles were also observed during imaging. The X-ray photoelectron spectroscopy

© 2025 Wiley-VCH GmbH

15214095, 2025, 35, Downloaded from https://advanced.onlinelibrary.wiley.com/doi/10.1002/adma.202507893 by Central Library The Librarian, Wiley Online Library on [28/12/2025]. See the Terms and Conditions (https://onlinelibrary.wiley.com/terms-and-conditions) on Wiley Online Library for rules of use; OA articles are governed by the applicable Creative Commons License

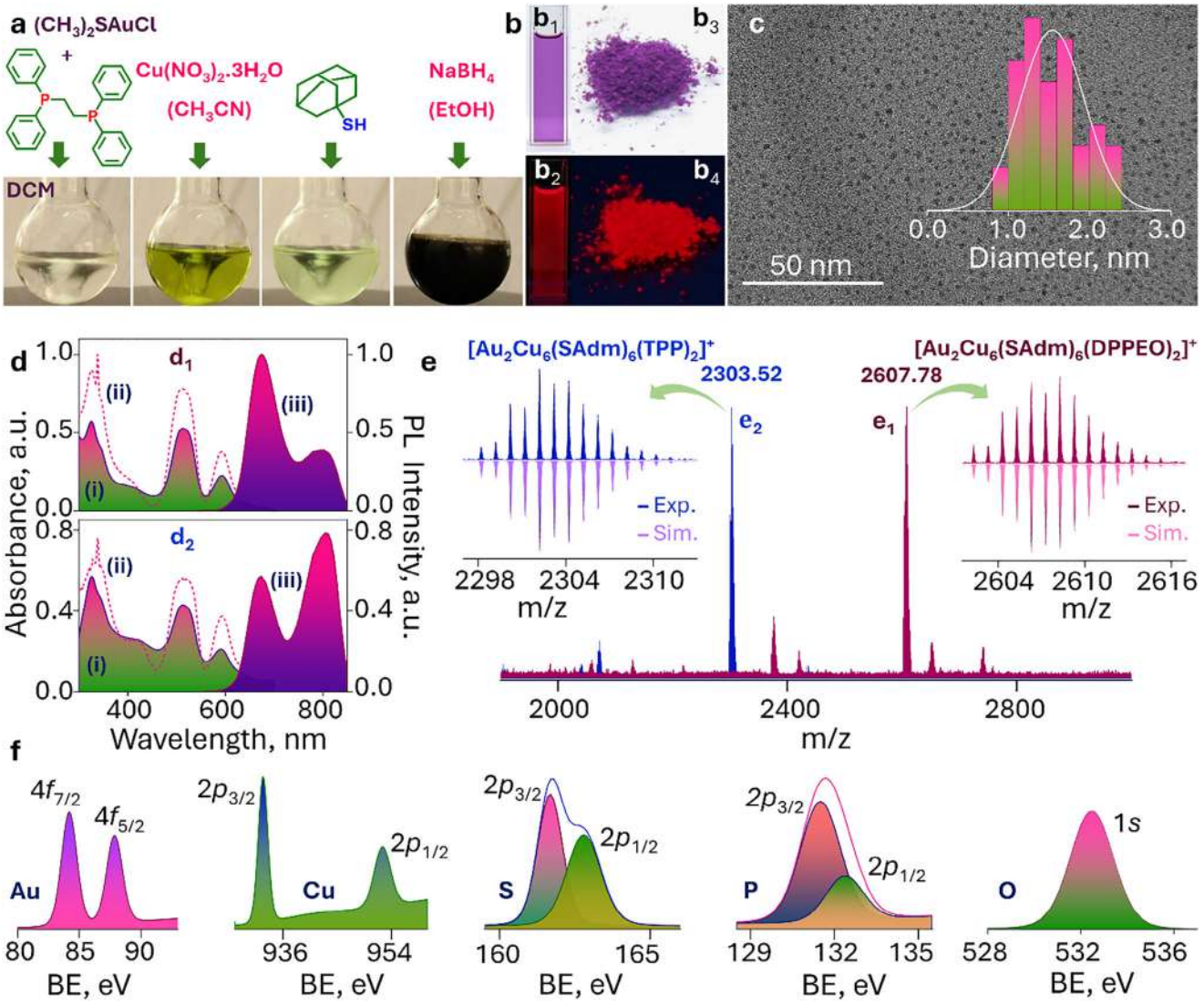


Figure 1. a) The photographs of reaction mixture showing different stages of $[Au_2Cu_6(Sadm)_6(DPPEO)_2]$ NC synthesis and the chemical structure of DPPE and HSadm ligands. b) Photographs of $[Au_2Cu_6(Sadm)_6(DPPEO)_2]$ NC solution (b_1 and b_2), and powder (b_3 and b_4) captured under visible (b_1 and b_3) and UV (b_2 and b_4) lights. c) TEM micrograph of NCs with size distribution in the inset. d) UV/Vis absorption (i), excitation (ii), and PL (iii) spectra of $[Au_2Cu_6(Sadm)_6(DPPEO)_2]$ NCs in toluene (d_1) and $[Au_2Cu_6(Sadm)_6(TPP)_2]$ NCs in DCM (d_2). e) The ESI-MS of (e_1) $[Au_2Cu_6(Sadm)_6(DPPEO)_2]$ and (e_2) $[Au_2Cu_6(Sadm)_6(TPP)_2]$ NCs. The inset shows the isotopic distribution of the experimental and simulated spectra. f) XPS spectral regions of $[Au_2Cu_6(Sadm)_6(DPPEO)_2]$ NCs, showing gold, copper, sulfur, phosphorus, and oxygen fingerprints.

(XPS) analysis revealed binding energy (BE) values of Au 4*f* and Cu 2*p* levels closely match with the previous report,[58] which showed the presence of zero valence state gold (84.2 and 87.9 eV for Au $4f_{7/2}$ and Au $4f_{5/2}$, respectively) and +1 valence state copper (952.5 and 932.7 eV for Cu $2p_{3/2}$ and Cu $2p_{1/2}$, respectively) (Figure 1f). The S 2*p* binding energy values (161.7 and 162.8 eV for S $2p_{3/2}$ and S $2p_{1/2}$, respectively) were consistent with thiolate binding, providing insights into the role of sulfur in the structure of NC. Further analysis unveiled P $2p_{3/2}$ and $2p_{1/2}$ peaks at 131.5 and 132.4 eV, respectively, along with an O 1*s* peak at 531.5 eV, confirming the presence of oxidized and bound DPPE within the NC. Though the two P atoms in each DPPE are different, it was difficult to differentiate them in XPS as the binding energies of Au-bound phosphine and P═O bonds are nearly identical.

Crystallization offers high-purity and quality single crystals for SC-XRD analysis to gain insight into molecular structure, packing, and inter-NC interactions. The solvent evaporation from the supersaturated toluene solution of $[Au_2Cu_6(Sadm)_6(DPPEO)_2]$ NC resulted in rod-like single crystals, which displayed red emission upon UV illumination (**Figure** 2a–c). The SC-XRD studies showed that the NCs crystallized in a triclinic crystal system with a *P-1* space group (cif file is provided). The core structure was found to be similar to that of earlier reported $[Au_2Cu_6(Sadm)_6(TPP)_2]$ NC (Figure 2d–f).[58] Figure 2d shows that the NC's central kernel consists of a benzenoid-like hexagonal planar copper (Cu_6) framework with an average intermetallic Cu—Cu distance of 2.67 Å. Two isolated gold atoms were capped on the top and bottom of the Cu_6, giving rise to a

© 2025 Wiley-VCH GmbH

15214095, 2025, 35, Downloaded from https://advanced.onlinelibrary.wiley.com/doi/10.1002/adma.202507893 by Central Library The Librarian, Wiley Online Library on [28/12/2025]. See the Terms and Conditions (https://onlinelibrary.wiley.com/terms-and-conditions) on Wiley Online Library for rules of use; OA articles are governed by the applicable Creative Commons License

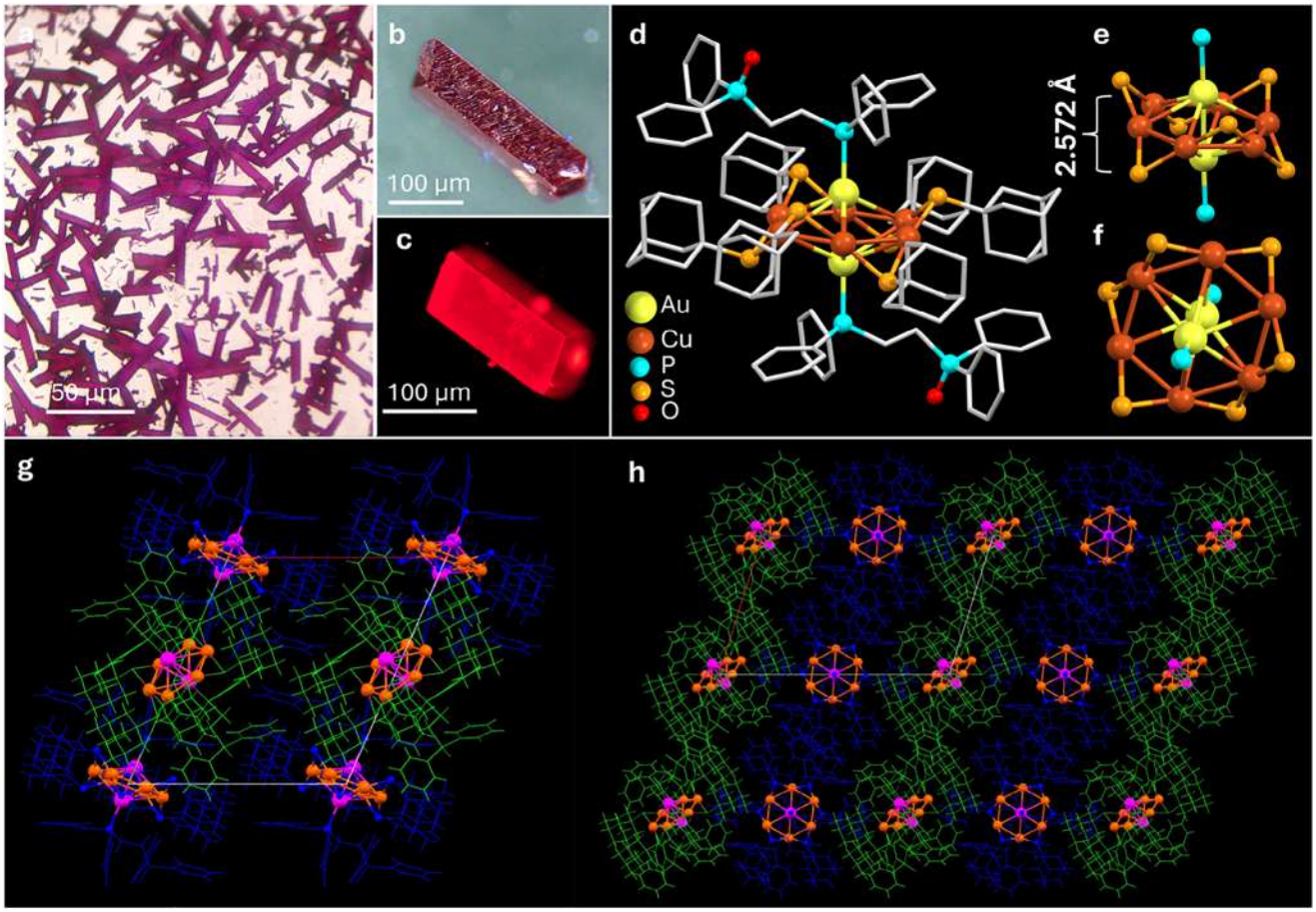


Figure 2. a) Large area optical microscopic image shows rod-like $[Au_2Cu_6(Sadm)_6(DPPEO)_2]$ crystals. The optical image under white light and fluorescence image under 435 nm excitation of a single-crystal are shown in Figures b and c, respectively. d) Crystal structure of $[Au_2Cu_6(Sadm)_6(DPPEO)_2]$ NC (hydrogen atoms omitted for clarity). e,f) The core of $[Au_2Cu_6(Sadm)_6(DPPEO)_2]$ NC, viewed from two perpendicular projections. g) Unit cell molecular packing of NCs. h) The extended supramolecular packing shows a slanted layer-like lamellar arrangement of $[Au_2Cu_6(Sadm)_6(DPPEO)_2]$ NCs.

hexagonal-bipyramidal geometry resembling the unidentified flying object (UFO)-like shape. The Cu-Au distance ranges from 2.8 to 3.0 Å, and the distance between two Au atoms is 2.572 Å. Six adamantane-thiolate is bonded with the hexagonal Cu_6, where each -Sadm is tied with the Cu—Cu edge of the hexagon through 'V-shaped' Cu—S—Cu motifs (Figure 2e). The average Cu-S distance is 2.1 Å and the Cu—S—Cu angle ranges from 73.87° to 76.03°. The overall arrangement of the six S atoms can be visualized as a chair-shaped S_6 unit, where alternative S atoms are placed up and down the hexagonal Cu_6 unit. 3D adamantane units are placed in the central body of the NC in a planar fashion, and they sterically protect the NCs. Furthermore, two secondary DPPEO ligands were independently anchored on each gold atom (Figure 2d), where one phosphine was connected with the Au atom having an Au—P bond distance of 2.34 Å, and another phosphine underwent oxidation to form a robust P═O bond. This P═O bond is recognized as an effective hydrogen bond acceptor and often forms strong hydrogen bonds, typically with polar donor groups such as hydroxyls or amines.[62] However, the absence of such strong hydrogen bonding donors in $[Au_2Cu_6(Sadm)_6(DPPEO)_2]$ NCs resulted in the C—H···O interactions between phosphine oxide and adamantane hydrogens. This facilitated the formation of NC dimers, which further extended into a zig-zag tape arrangement (Figure S4, Supporting Information). In addition to this, C—H···π and H···H interactions between the ligands also contributed to molecular packing, stabilizing crystal growth. The extended supramolecular packing reveals a slanted layer-like lamellar arrangement of NCs (Figure 2g,h). In comparison to the previously reported $[Au_2Cu_6(Sadm)_6(TPP)_2]$ NC,[64] the presence of phosphine oxide in $[Au_2Cu_6(Sadm)_6(DPPEO)_2]$ NCs induces a distinct orientation in alternating layers, driven by C—H···O interactions. The distance between two adjacent layers is 16.32 and 9.18 Å along a and b crystallographic directions, respectively.

To understand the emission mechanism of NC, we evaluated the optical absorption and PL behavior of $[Au_2Cu_6(Sadm)_6(DPPEO)_2]$ NC solution (toluene) under nitrogen and oxygen atmospheres. The PL intensity of the NC solution (both 675 nm and 798 nm emission bands) under nitrogen atmosphere increased (**Figure** 3a (i)) as compared to ambient conditions (Figure 3a (ii)). Nevertheless, the bubbling of oxygen gas caused a drop in the PL intensity (Figure 3a (iii)), indicating the involvement of the triplet state in $[Au_2Cu_6(Sadm)_6(DPPEO)_2]$ NC emission. At the same time, the UV/Vis absorption spectra of

© 2025 Wiley-VCH GmbH

15214095, 2025, 35, Downloaded from https://advanced.onlinelibrary.wiley.com/doi/10.1002/adma.202507893 by Central Library The Librarian, Wiley Online Library on [28/12/2025]. See the Terms and Conditions (https://onlinelibrary.wiley.com/terms-and-conditions) on Wiley Online Library for rules of use; OA articles are governed by the applicable Creative Commons License

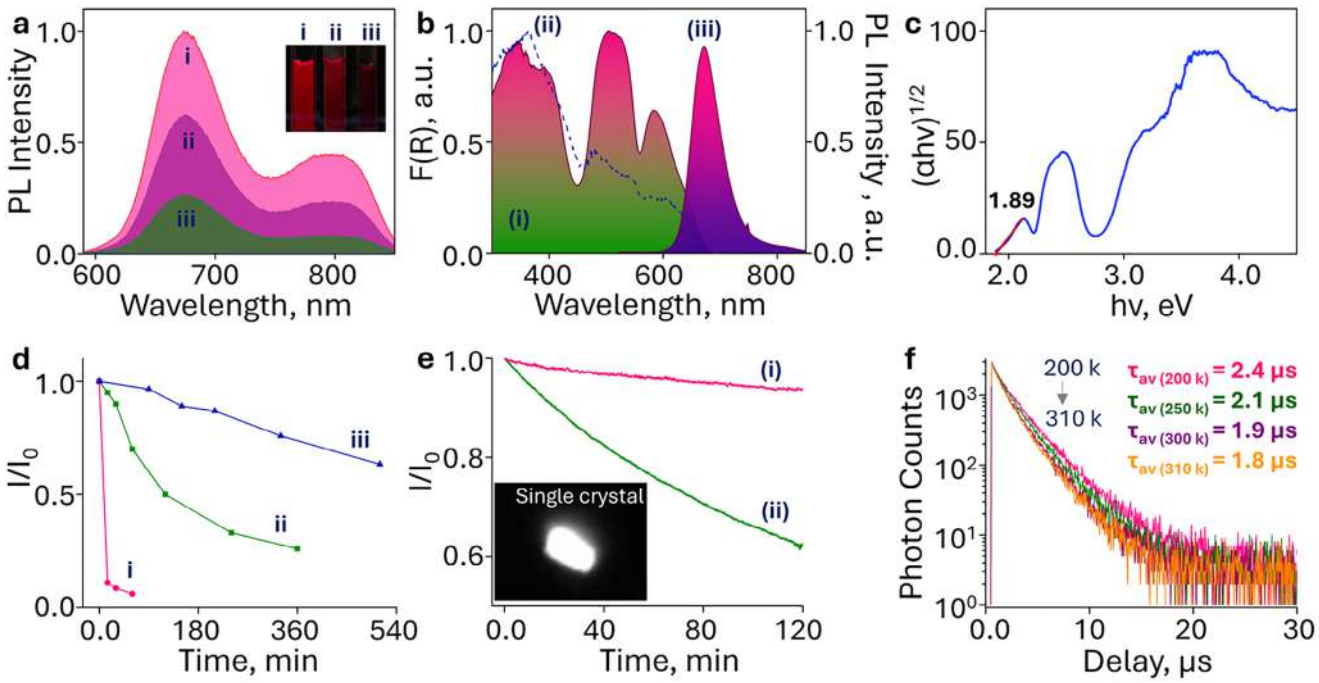


Figure 3. a) PL spectra of NC solution (≈50 μm) recorded under (i) argon, (ii) ambient, and (iii) oxygen atmospheres. The photographs of corresponding solutions are shown in the inset. b) Normalized solid-state absorption (i); converted from DRS using Kubelka-Munk function), excitation (ii) and PL spectra (iii) of $[Au_2Cu_6(Sadm)_6(DPPEO)_2]$ NC (under 325 nm excitation). c) Tauc plot of $[Au_2Cu_6(Sadm)_6(DPPEO)_2]$ NC. d) Plots of I/I_0 vs illumination time for (i) NC solution, and (ii and iii) NC film under (i and ii) ambient, and (iii) inert atmospheres. e) Plots of I/I_0 *vs* illumination time for a single NC crystal under (i) argon and (ii) oxygen/air atmospheres. The photograph of the single crystal is shown in the inset. f) Temperature-dependent PL decay profiles of $[Au_2Cu_6(Sadm)_6(DPPEO)_2]$ NC solid under inert atmosphere.

the NC solution (toluene) under argon and oxygen atmospheres showed unaltered optical absorption features (Figure S5, Supporting Information). A similar PL enhancement and quenching was also observed in $[Au_2Cu_6(Sadm)_6(TPP)_2]$ NC solution, when purged under nitrogen and oxygen gases, respectively (Figure S6, Supporting Information). The solid-state emission of NCs is an important property for their use in real-world devices. The solid-state diffuse reflectance spectrum (DRS) and PL spectrum of $[Au_2Cu_6(Sadm)_6(DPPEO)_2]$ NC solid (the reflectance spectrum has been converted to absorption spectrum using the Kubelka–Munk function) revealed that the absorbance features observed initially at 425, 515, and 594 nm in solution became broader and slightly blue shifted to 390, 510, and 584 nm, respectively. More importantly, the emission peak at 798 nm diminished drastically, while the 675 nm emission shifted slightly to 672 nm and remained prominent (Figure 3b). A similar trend was observed in the case of $[Au_2Cu_6(Sadm)_6(TPP)_2]$ NC (Figure S7, Supporting Information). The dominance of higher-energy emissive states (672 nm) in the solid-state likely arises due to the suppression of longer-wavelength emission, which is attributed to restricted molecular motions or the enhancement of non-radiative decay pathways. These observations suggest that the solid-state environment is crucial in activating a specific radiative channel, favoring a single dominant emission ≈672 nm. The optical bandgap of $[Au_2Cu_6(Sadm)_6(DPPEO)_2]$ NC solid is calculated from the Tauc plot and found to be 1.89 eV (Figure 3c). Electrochemical differential pulse voltammetry (DPV) was used to investigate the electrochemical band gap of the $[Au_2Cu_6(Sadm)_6(DPPEO)_2]$. As shown in Figure S8 (Supporting Information), the LUMO level is located at −3.05 eV with respect to the vacuum level (−1.93 V vs. Ag/Ag^+), and the HOMO level is located at ≈5.34 eV (+0.36 V vs. Ag/Ag^+), giving an electronic bandgap of ≈2.29 eV.

The photostability of NCs in both solution and solid-state (film) was examined by comparing their PL intensity before and after exposure to UV light (365 nm; low power) at different time intervals. A plot of I/I_0 (I_0 represents the PL intensity at $t = 0$) vs. illumination time shows better photostability for NC film under an argon atmosphere (Figure 3d (iii)) compared to the ambient condition (Figure 3d (ii)) or its solution under ambient condition (Figure 3d (i)). Though the NC solution photobleached within 60 min of illumination, the NC film withstood longer, as evident from the UV/Vis spectra recorded under UV light exposure (Figure S9a,b, Supporting Information). The intact optical absorption features of the NC film after UV exposure revealed the photostability of NC in the ensemble solid-state. The photostability of single crystals was also evaluated under different gaseous atmospheres. Before exposure to a high-power CW (continuous-wave) laser (512 nm), the single crystals placed inside a plastic petri dish were sealed and purged with argon gas using a syringe needle. The PL intensity trajectory of a single-crystal under an argon atmosphere showed stable photon counts (Figure 3e (i)). However, the crystals photobleached quickly when the argon was replaced with oxygen or air (Figure 3e (ii)). The photograph of a single crystal used for the experiment is shown in the inset of Figure 3e. The overall data suggest that the

© 2025 Wiley-VCH GmbH

15214095, 2025, 35, Downloaded from https://advanced.onlinelibrary.wiley.com/doi/10.1002/adma.202507893 by Central Library The Librarian, Wiley Online Library on [28/12/2025]. See the Terms and Conditions (https://onlinelibrary.wiley.com/terms-and-conditions) on Wiley Online Library for rules of use; OA articles are governed by the applicable Creative Commons License

photostability of NC is better when the crystals are stored under an inert atmosphere. The thermogravimetric analysis (TGA) revealed that the NC powder remained stable up to 200 °C (Figure S10, Supporting Information). We further investigated the decay profile of NC in detail. The average lifetime (τ_{av}) and PLQY of $[Au_2Cu_6(Sadm)_6(DPPEO)_2]$ NC solid (under vacuum) were found to be 1.9 µs (Figure S11, Supporting Information) and 62%, respectively. The long-excited state lifetime suggests that the triplet excitons are involved in the emission process. This excited state lifetime may be due to phosphorescent emission (triplet (T_1) to singlet (S_0)) or thermally activated delayed fluorescence (TADF) emission (T_1-S_1-S_0). To further confirm whether it is a phosphorescent emitter or TADF emitter, the temperature-dependent PL spectra (Figure S12, Supporting Information) and decay profiles (Figure 3f) were measured under vacuum by sandwiching the NC powder between two quartz plates. As shown in Figure S12 (Supporting Information) and Figure 3f, a temperature sweep between 310 to 200 K was carried out. The PL intensity and lifetime values (1.8 to 2.4 µs) were increased when the temperature decreased from 310 to 200 K. The increase in PL intensity and delayed lifetime is due to the decreased molecular vibrations at low temperatures, which decreases the non-radiative channels and results in efficient harvesting of the triplet state at low temperatures. Therefore, the increase in PL intensity with a decrease in temperature and delayed lifetime in microseconds shows that the emission comes mainly from the T_1 to the S_0 state. This confirms that $[Au_2Cu_6(Sadm)_6(DPPEO)_2]$ NC is a phosphorescent emitter and not the TADF emitter.[59]

Self-assembly approaches have been utilized to fabricate higher-order NC superstructures and alter the PLQY of luminescent NCs.[65,66] The self-assembly allows restricted intermolecular motions, reduces the rotational degree of freedom of the NC surface ligands, and prevents nonradiative relaxations, thereby amplifying the PL.[67] To explore the solid-state emission behavior and the impact of aggregation/assembly on the photophysical properties of NCs, we further examined the solvent-induced aggregation of $[Au_2Cu_6(Sadm)_6(DPPEO)_2]$ NC solution (tetrahydrofuran; THF) in the presence of a poor solvent such as H_2O. Remarkably, the purple-colored NC solution maintained its optical transparency even as the water volume fraction ($f_w = vol_{water}/vol_{THF+water}$) increased up to 50%. When the f_w increased from 50% to 90%, the solution turned cloudy with an enhancement in PL intensity (**Figure 4a**). To understand this phenomenon in detail, we analyzed the changes in PL intensity following the gradual addition of water (Figure 4b). Up to a 40% water fraction, no significant visual or PL changes were observed. However, at 50% f_w, the solution turned cloudy, accompanied by an increase in PL emission ≈675 nm and a slight reduction in the emission ≈800 nm. Notably, at 60% f_w, the lower-wavelength emission blue-shifted slightly to 672 nm and became dominant, while the higher-wavelength emission ≈800 nm has been completely suppressed. When the water content increased from 70% to 90%, the overall emission intensity was found to decrease compared to 60% f_w. These trends in PL spectra (Figure 4c) strongly suggest that the restricted molecular movement of ligands during the aggregation/assembly of NCs induces a specific emissive channel, favoring a single, dominant emission.

The TEM (Figure S13, Supporting Information) and field emission scanning electron microscopy (FESEM; Figure 4d) images of NC solutions at different f_w revealed spherical assemblies in all cases. However, the average diameter (size of the spheres) increased from 50% (≈140 nm) to 60% (≈250 nm) and then decreased systematically from 70% (≈150 nm) to 90% (≈70 nm). The results were in agreement with the dynamic light scattering (DLS) data (Figure S14, Supporting Information). Notably, the size of the spherical assemblies was found to be maximum when f_w is 60%, which is in good agreement with maximum intensity in the PL spectra (Figure 4b) and the scattering in the UV/Vis absorption spectra of NC solution at different f_w (Figure S15, Supporting Information). The atomic force microscopy (AFM) revealed the average thickness and diameter of a single sphere ≅ 200 and 250 nm, respectively (Figure S16, Supporting Information). The agreement in the size of the spherical assemblies in AFM, TEM, FESEM images, and DLS suggests the presence of spherical assemblies in the solution and not due to the possibility of evaporation-induced assemblies. The scanning transmission electron microscopy (STEM) image and elemental mapping revealed the presence of gold, copper, sulfur, phosphorus, and oxygen (Figure 4e; Figures S17 and S18, Supporting Information). To further understand the 3D internal structure of the assembly, TEM electron tomography (ET) reconstruction was performed (Figure 4f).[68] For 3D reconstruction, 2D TEM projections were collected by tilting the specimen between ± 70° with an increment angle of 2° (Figure S19, Supporting Information). The aligned tilt series suggests a spherical nature of the superstructure. The 3D reconstruction and cross-sectional views show the presence of densely packed NCs in the assembled spheres (Video S1, Supporting Information). The ET reconstruction data agree with AFM, FESEM, and TEM, as shown above. Importantly, a slight deformation is observed in all spherical particles due to strong adhesion to the carbon support film of the TEM grid.[69] The densely packed structure further suggests that the enhanced PL intensity is presumably due to the restricted rotation of ligands that reduces the non-emissive relaxation pathways.

To investigate the electroluminescence (EL) performance of $[Au_2Cu_6(Sadm)_6(DPPEO)_2]$ NCs, a non-doped device was fabricated with the following device architecture: Glass/ITO/PEDOT:PSS (40 nm)/PVK (30 nm)/$[Au_2Cu_6(Sadm)_6(DPPEO)_2]$ NCs (25 nm)/TPBi (50 nm)/Liq (2 nm)/Al (100 nm) (**Figure 5a**). The chemical structures of different layers used in the device fabrication is shown in Figure S20 (Supporting Information). The device performance characteristics are shown in Figure 5b–f and summarized in **Table 1** and Video S2 (Supporting Information). The EQE vs. luminance curve shows an EQE_{max} of 12.60% with a turn-on voltage of 3V. The J–V–L (current density vs voltage vs luminance) curve shows a maximum current density of 387 mA cm^{-2} and a maximum luminance of 1246 cd m^{-2}. The device shows the maximum current efficiency (CE_{max}) and power efficiency (PE_{max}) of 3.7 cd A^{-1} and 3.8 lm W^{-1}, respectively. The EL spectra show a maximum EL wavelength (λ_{EL}) of 668 nm with the CIE coordinates of (0.70 and 0.30), and FWHM (full-width half maximum) of 72 nm. The CIE coordinates of the $[Au_2Cu_6(Sadm)_6(DPPEO)_2]$ NCs-based device are located at the edge of the chromaticity diagram, which represents the most saturated red color light. The EL spectra of $[Au_2Cu_6(Sadm)_6(DPPEO)_2]$ NCs-based device were also taken at various voltages (5–10 V; Figure 5b), and no significant residual emission peak was observed. This indicates that the

© 2025 Wiley-VCH GmbH

15214095, 2025, 35, Downloaded from https://advanced.onlinelibrary.wiley.com/doi/10.1002/adma.202507893 by Central Library The Librarian, Wiley Online Library on [28/12/2025]. See the Terms and Conditions (https://onlinelibrary.wiley.com/terms-and-conditions) on Wiley Online Library for rules of use; OA articles are governed by the applicable Creative Commons License

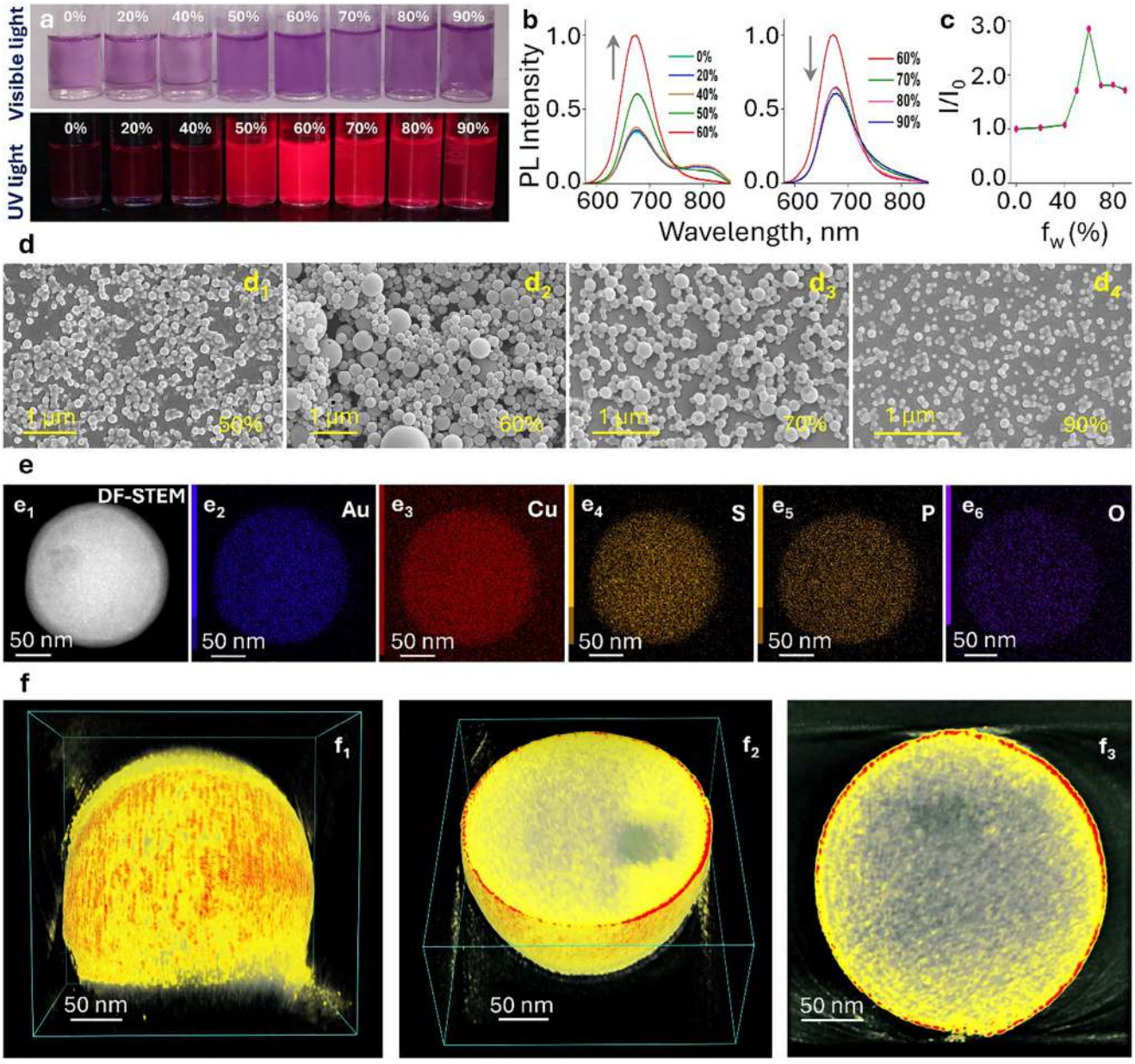


Figure 4. a) Photographs of NC solution (under visible and UV light) prepared in different f_w. The corresponding PL spectra are shown in Figure 4b. A Plot of I/I_0 vs f_w is shown in Figure 4c. d) FESEM images of NC assembly fabricated at (d_1) 50%, (d_2) 60%, (d_3) 70%, and (d_4) 90% f_w. (e_1) STEM image (60% f_w) and elemental maps of a single sphere showing (e_2) gold, (e_3) copper, (e_4) sulfur, (e_5) phosphorus, and (e_6) oxygen. (f_1) 3D reconstructed structure of the superstructures showing spherical assembly, and (f_2 and f_3) shows the cross-sectional view suggesting densely packed NCs.

fabricated $[Au_2Cu_6(Sadm)_6(DPPEO)_2]$ NCs-based device is very stable under different operating voltages, and the electron–hole recombination occurs within the emissive layer at different operating voltages. To evaluate the device's performance, the energy level alignment of the device was also analyzed (Figure S21, Supporting Information). The NC has a HOMO at ≈5.34 eV and LUMO at ≈3.05 eV (from DPV measurements), which suggests a reduced hole injection barrier (from PVK) and a moderate electron injection barrier (from TPBi). This energy alignment supports balanced carrier injection, reduced charge leakage, and efficient exciton confinement within the emissive layer. Compared to the previous reports, the exceptional device performance demonstrates that this is one of the first solution-processed non-doped NC-based devices holding high EQE and a deeply saturated red emission. As a control, we also fabricated the device with $[Au_2Cu_6(Sadm)_6(TPP)_2]$ NCs as an emissive layer in a similar device structure (Figure S22, Supporting Information). The EQE of $[Au_2Cu_6(Sadm)_6(TPP)_2]$ NC-based device was found to be only 3.24%, which is much less compared to $[Au_2Cu_6(Sadm)_6(DPPEO)_2]$ NC-based device (details are provided in Table 1). The performance comparison of $[Au_2Cu_6(Sadm)_6(DPPEO)_2]$ NC with previous reports is provided

© 2025 Wiley-VCH GmbH

15214095, 2025, 35, Downloaded from https://advanced.onlinelibrary.wiley.com/doi/10.1002/adma.202507893 by Central Library The Librarian, Wiley Online Library on [28/12/2025]. See the Terms and Conditions (https://onlinelibrary.wiley.com/terms-and-conditions) on Wiley Online Library for rules of use; OA articles are governed by the applicable Creative Commons License

15214095, 2025, 35, Downloaded from https://advanced.onlinelibrary.wiley.com/doi/10.1002/adma.202507893 by Central Library The Librarian, Wiley Online Library on [28/12/2025]. See the Terms and Conditions (https://onlinelibrary.wiley.com/terms-and-conditions) on Wiley Online Library for rules of use; OA articles are governed by the applicable Creative Commons License

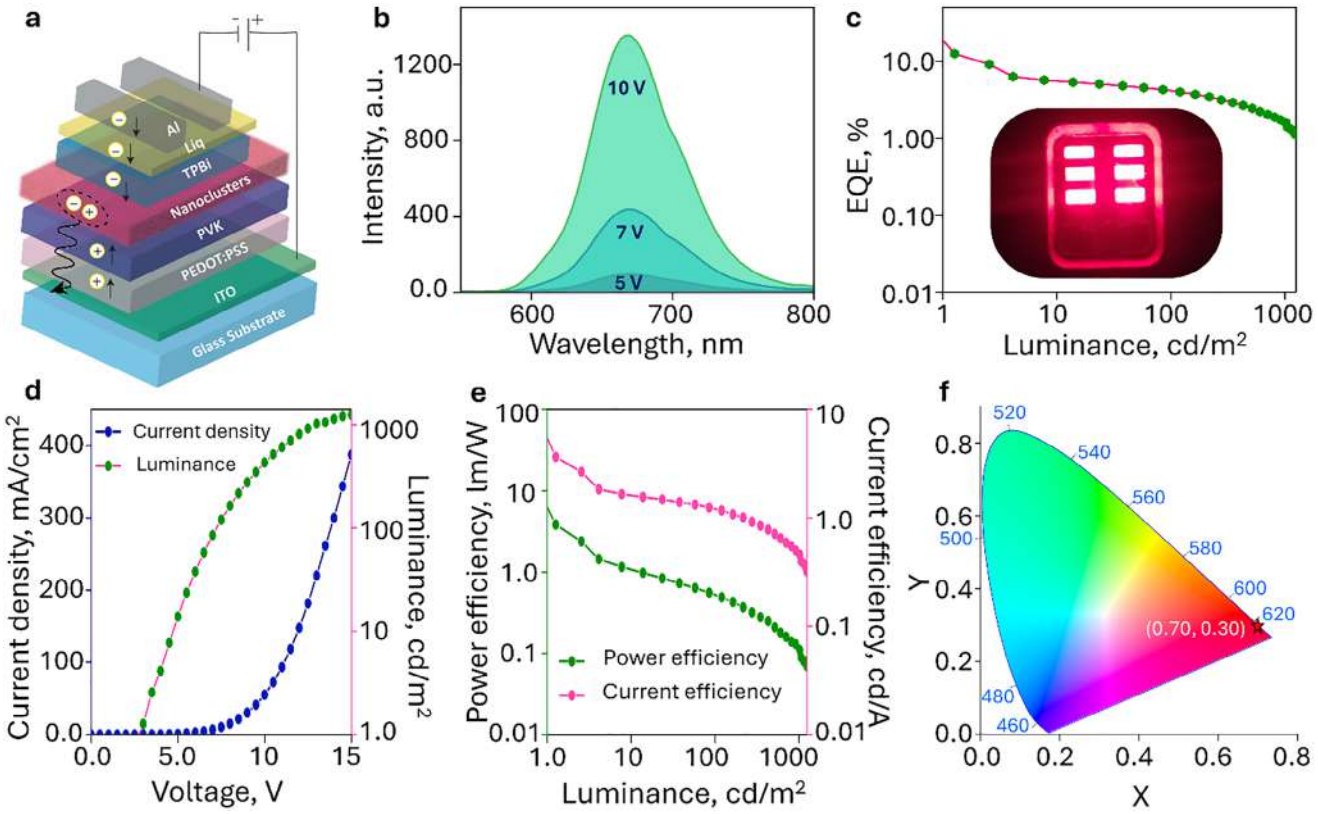


Figure 5. a) A schematic of the LED device. b) EL spectra of the device at 5, 7, and 10V. c) EQE vs luminance curve. The inset shows a photograph of the fabricated LED device. d) Current density–voltage–luminance (*J–V–L*) curves of the device. e) Power efficiency-luminance-current efficiency curves of the device. f) Chromaticity diagram of the device.

in the Table S1 (Supporting Information). The table shows that $[Au_2Cu_6(Sadm)_6(DPPEO)_2]$ NC performs the best in a solution-processed non-doped device with saturated red emission. This study not only demonstrates the high performance of the device but also looks into how ligand design can improve PLQY and overall performance. These NCs are expected to play an important role in developing next-generation LEDs.

3. Conclusion

In summary, we have successfully demonstrated the fabrication of NC-LED using the solid-state emitting $[Au_2Cu_6(Sadm)_6(DPPEO)_2]$ NCs. The gold-copper bimetallic NCs synthesized using the magical combination of HSadm and DPPE ligands showed rapid crystallization during solvent evaporation. These NCs showed exceptional photostability when their crystals/films were preserved under inert conditions. The NCs displayed solvent-induced aggregation behavior, resulting in spherical superstructures and self-assembly with enhanced PL. Multiple spectroscopic and microscopic techniques have been employed to study the assembly and morphology of superstructures. The average diameter of assembled superstructures was found to be at a maximum of 60% volume fraction, which was systematically reduced by increasing the volume fraction. DLS data were in good agreement with TEM and FESEM micrographs. HRTEM, ET reconstruction, AFM, and FESEM data revealed the presence of thickly packed NCs in the assembled superstructures. The restricted molecular movement of ligands during the aggregation/assembly of NCs helped to reduce the

Table 1. The summary of device characteristics.

Emitting layer	Turn-on Voltage [V] @ 1 cd m^{-2}	Current density [J_{max}] mA cm^{-2}	L_{max} [cd m^{-2}]	EQE_{max} [%]	CE_{max} [cd A^{-1}]	PE_{max} [lm W^{-1}]	$\lambda[EL]_{max}$ [nm]	CIE [x, y]	FWHM [nm]
$[Au_2Cu_6(Sadm)_6(DPPEO)_2]$	3.0	387.42 (@ 15 V)	1246 (@ 15 V)	12.60	3.70	3.80	668	(0.70, 0.30)	72.00
$[Au_2Cu_6(Sadm)_6(TPP)_2]$	5.8	54.55 (@ 15 V)	55.17 (@ 15 V)	3.24	2.31	1.21	666	(0.67, 0.31)	68.47

L_{max} = maximum luminance, EQE_{max} = maximum external quantum efficiency, CE_{max} = maximum current efficiency, PE_{max} = maximum power efficiency, $\lambda(EL)_{max}$ = electroluminescent maximum wavelength.

© 2025 Wiley-VCH GmbH

non-emissive relaxation pathways. Finally, the NC-LED has been fabricated using the solution-processed technique without using any additional host materials. The fabricated NC-LED showed a maximum brightness of 1246 cd m^{-2} and an EQE of 12.60% with a saturated pure red emission. This EQE value with saturated deep red emission is the best among solution-processed, non-doped NC-LED devices. The results presented in the work suggest the potential of NCs for the fabrication of sustainable, non-toxic, and efficient LEDs in the future.

4. Experimental Section

Reagents and Materials: All the chemicals and solvents are analytical grade and used without any further purification. Chloro(dimethylsulfide)gold(I) ($(CH_3)_2SAuCl$), copper (II) nitrate trihydrate ($Cu(NO_3)_2{\cdot}3H_2O$), 1-adamantanethiol (HSadm), and sodium borohydride ($NaBH_4$) were purchased from Sigma–Aldrich. 1,2-bis(diphenylphosphino)ethane (DPPE) and triphenylphosphine (TPP) were purchased from Tokyo Chemical Industry (TCI) Co. Ltd. Japan. Acetonitrile (ACN), dichloromethane (DCM), tetrahydrofuran (THF), toluene, ethanol, hexane, and chloroform-d ($CDCl_3$) were purchased from Sisco Research Laboratories (SRL). The different chemical layers used for the device fabrication were purchased commercially. Poly(3,4-ethylenedioxythiophene) polystyrene sulfonate (PEDOT: PSS) was purchased from Ossila Ltd. Polyvinyl carbazole (PVK) was purchased from Sigma–Aldrich. 2,2′,2″-(1,3,5-benzinetriyl)-tris(1-phenyl-1-H-benzimidazole) (TPBi) and lithium-8-hydroxyquinolinolate (Liq) were purchased from BLD Pharmatech (India) Pvt. Ltd. PEDOT: PSS and PVK were used as received, whereas TPBi and Liq were further purified by vacuum sublimation before the device fabrication.

Instrumentation: The ^1H and ^{31}P NMR measurements were carried out using Bruker, AVANCE III HD 400/500 MHz spectrometers. UV/Vis absorbance and DRS spectra were recorded in the JASCO-V-750 spectrophotometer. PL spectra were recorded using a PerkinElmer LS55 Spectrofluorimeter. Optical images of crystallized NCs were recorded using a Leica optical microscope. Absolute PLQY measurements and temperature-dependent PL lifetime of NC powder were carried out using an Edinburgh FLS 100 Fluorescence lifetime spectrometer (510 nm diode laser). The fluorescent image of the NC crystal was captured using an Olympus CKX53 inverted microscope (435 nm excitation). DLS measurements were performed in Zetasizer Nano S90 (Malvern). ESI-MS measurements were carried out on a Waters Synapt G2-Si high-definition mass spectrometer. DPV was performed using an Electrochem SAS OrigaLys electrochemical workstation at room-temperature. Measurements were carried out in a deaerated ACN/toluene mixture with tetrabutylammonium hexafluorophosphate as the supporting electrolyte. A glassy carbon electrode was used as the working electrode, with a Pt wire as the counter electrode and Ag/Ag^+ as the reference electrode. Ferrocene/ferrocenium (Fc/Fc^+) served as the internal standard, and all potential energy levels of a molecular orbital (MO) relative to vacuum level by E_{MO} (V, vs. NHE) = $-E_{MO}$ (eV, vs. Vacuum level) − 4.44.[57] HR-TEM images were recorded on a FEI Talos F200S (200 kV) TEM and JEOL 3010 (300 kV) TEM. A Jeol F200 STEM electron microscope operated at 200 keV was used for STEM images with EDS and elemental mapping and collecting data for 3D electron tomographic reconstruction. For tomographic reconstruction, 2D projections were collected between ± 70° with increment angles of 2°. The acquired raw 2D projections were first subjected to a series of pre-processing using the IMOD software package.[70,71] Coarse alignment was used to create the aligned file. The custom-made maximum entropy method (MEM) program was used for 3D reconstruction.[72,73] Chimera was used to produce colored images. FESEM analysis was performed with a Verios G4 UC, FEI instrument. The samples were sputter-coated with an Au/Pd mixture to produce better-quality images without charging. AFM images were captured using an Agilent Technologies 5500 series AFM/SPM microscope equipped with Pico View 1.14.1 software, and finally, images were processed using Gwyddion. XPS spectra were recorded using a Thermo Scientific ESCALAB 250Xi (XR6 Micro-focused Monochromator, Al Kα). SC-XRD data collection was performed using a Bruker D8 VENTURE single-crystal X-ray diffractometer. TGA was carried out using a TA Instrument Model SDT Q600. Silicon photodiode with Keithley 2450 source meter and Keithley 2100 multimeter were used to measure the current-voltage-luminescence (J-V-L) characteristics. The EL spectra were obtained using a Hitachi F-7100 fluorescence spectrophotometer.

Synthesis of $[Au_2Cu_6(Sadm)_6(TPP)_2]$ NCs: $[Au_2Cu_6(Sadm)_6(TPP)_2]$ NCs were synthesized using the previously reported protocol.[59]

Synthesis of $[Au_2Cu_6(Sadm)_6(DPPEO)_2]$ NCs: Briefly, $(CH_3)_2SAuCl$ (30 mg; 0.1 mmol) and DPPE (80 mg; 0.2 mmol) were dissolved in 10 mL DCM. In parallel, $Cu(II)NO_3{\cdot}3H_2O$ (50 mg; 0.2 mmol) was dissolved in 5 mL CH_3CN using ultrasonication. The addition of the freshly prepared copper salt solution into the stirring (≈1000 rpm) solution of gold/DPPE mixture prepared in DCM produced a greenish solution within 15 min of the reaction. The addition of HSadm (68 mg; 0.4 mmol) into the above-prepared greenish solution turned it colorless. To this colorless solution kept at 0 °C, $NaBH_4$ (40 mg (1 mmol) in 5 mL ethanol) was injected and stirred vigorously for another 20 h till a purple-colored precipitate was formed. The precipitate was washed independently with CH_3CN and hexane, extracted in DCM, and the final rotary evaporation produced a purple-colored NC powder. All the reactions were performed under dark conditions in an ambient atmosphere. The yield of the NC is 85% with respect to Cu.

Supporting Information

Supporting Information is available from the Wiley Online Library or from the author.

Acknowledgements

E.S.S. thanks SERB (Science and Engineering Research Board) and DST (Department of Science and Technology), India for the Ramanujan Fellowship (SB/S2/RJN-005/2017), Startup Research grant (SRG/2022/586), and Promotion of University Research and Scientific Excellence grant (SR/PURSE/2023/191). E.S.S. thanks Kerala State Council for Science - Environment (KSCSTE) for the SRS grant (123/2025/KSCSTE) and the University of Calicut for the seed money grant. E.S.S. and V.B. thank the Japan Society for the Promotion of Science (JSPS) and Hokkaido University for the JSPS-BRIDGE Fellowship program (BR230604). We thank Prof. Subi Jacob George, Miss Anju Ajayan, Dr. Saraswathi Chirakkara, and Miss Gayathri Govind V. (JNCASR, Bangalore) for temperature-dependent lifetime measurements. V. B. acknowledges a MEXT-JSPS Grant-in-Aid for Scientific Research (Kaken-hi 23H01781) and the Hokkaido University Photoexcitonix Program. We thank Dr. Reji Thomas (Farook College, Calicut) for the fluorescence imaging. J.V.R. thanks SERB and the University of Calicut for research fellowships. S.C. thanks the Ministry of Education (MoE), India, for the PMRF fellowship. The authors acknowledge the Research Council of Finland for project funding (352900), the Photonics Research and Innovation (PREIN) flagship, and the Tampere Microscopy Centre for imaging facilities. P.R. thanks the Indian Institute of Science (IISc) and SERB (SPG/2020/000107) for financial support.

Conflict of Interest

The authors declare no conflict of interest.

Data Availability Statement

The data that support the findings of this study are available from the corresponding author upon reasonable request.

© 2025 Wiley-VCH GmbH

15214095, 2025, 35, Downloaded from https://advanced.onlinelibrary.wiley.com/doi/10.1002/adma.202507893 by Central Library The Librarian, Wiley Online Library on [28/12/2025]. See the Terms and Conditions (https://onlinelibrary.wiley.com/terms-and-conditions) on Wiley Online Library for rules of use; OA articles are governed by the applicable Creative Commons License

Keywords

bimetallic nanocluster, light-emitting diodes, supramolecular assembly, phosphorescence, electroluminescence

Received: April 25, 2025
Published online: June 11, 2025

[1] Y. Shirasaki, G. J. Supran, M. G. Bawendi, V. Bulović, *Nat. Photonics* **2013**, *7*, 13.
[2] J. H. Burroughes, D. D. C. Bradley, A. R. Brown, R. N. Marks, K. Mackay, R. H. Friend, P. L. Burns, A. B. Holmes, *Nature* **1990**, *347*, 539.
[3] A. Zampetti, A. Minotto, F. Cacialli, *Adv. Funct. Mater.* **2019**, *29*, 1807623.
[4] B. Van der Zee, Y. Li, G.-J. A. H. Wetzelaer, P. W. M. Blom, *Adv. Mater.* **2022**, *34*, 2108887.
[5] L. Protesescu, S. Yakunin, M. I. Bodnarchuk, F. Krieg, R. Caputo, C. H. Hendon, R. X. Yang, A. Walsh, M. V. Kovalenko, *Nano Lett.* **2015**, *15*, 3692.
[6] S.-J. Zou, Y. Shen, F.-M. Xie, J.-D. Chen, Y.-Q. Li, J.-X. Tang, *Mater. Chem. Front.* **2020**, *4*, 788.
[7] E. Jang, H. Jang, *Chem. Rev.* **2023**, *123*, 4663.
[8] N. Wang, L. Cheng, R. Ge, S. Zhang, Y. Miao, W. Zou, C. Yi, Y. Sun, Y. Cao, R. Yang, Y. Wei, Q. Guo, Y. Ke, M. Yu, Y. Jin, Y. Liu, Q. Ding, D. Di, L. Yang, G. Xing, H. Tian, C. Jin, F. Gao, R. H. Friend, J. Wang, W. Huang, *Nat. Photonics* **2016**, *10*, 699.
[9] L. G. Franca, D. G. Bossanyi, J. Clark, P. L. Dos Santos, *ACS Appl. Opt. Mater.* **2024**, *2*, 2476.
[10] Z. Yang, M. Gao, W. Wu, X. Yang, X. W. Sun, J. Zhang, H.-C. Wang, R.-S. Liu, C.-Y. Han, H. Yang, W. Li, *Mater. Today* **2019**, *24*, 69.
[11] X. Zhao, J. D. A. Ng, R. H. Friend, Z.-K. Tan, *ACS Photonics* **2018**, *5*, 3866.
[12] H. Qian, M. Zhu, Z. Wu, R. Jin, *Acc. Chem. Res.* **2012**, *45*, 1470.
[13] I. Chakraborty, T. Pradeep, *Chem. Rev.* **2017**, *117*, 8208.
[14] R. Jin, C. Zeng, M. Zhou, Y. Chen, *Chem. Rev.* **2016**, *116*, 10346.
[15] K. Kwak, V. D. Thanthirige, K. Pyo, D. Lee, G. Ramakrishna, *J. Phys. Chem. Lett.* **2017**, *8*, 4898.
[16] L. G. AbdulHalim, M. S. Bootharaju, Q. Tang, S. Del Gobbo, R. G. AbdulHalim, M. Eddaoudi, D. Jiang, O. M. Bakr, *J. Am. Chem. Soc.* **2015**, *137*, 11970.
[17] J. V. Rival, P. Mymoona, R. Vinoth, A. M. V. Mohan, E. S. Shibu, *ACS Appl. Mater. Interfaces* **2021**, *13*, 10583.
[18] M. Xie, C. Han, Q. Liang, J. Zhang, G. Xie, H. Xu, *Sci. Adv.* **2019**, *5*, aav9857.
[19] N. Zhang, Y. Li, S. Han, Y. Wei, H. Hu, R. Huo, C. Duan, J. Zhang, C. Han, G. Xie, H. Xu, *Angew. Chem., Int. Ed.* **2023**, *62*, 202305018.
[20] H. Häkkinen, *Chem. Soc. Rev.* **2008**, *37*, 1847.
[21] T. Chen, S. Yang, J. Chai, Y. Song, J. Fan, B. Rao, H. Sheng, H. Yu, M. Zhu, *Sci. Adv.* **2017**, *3*, 1700956.
[22] Y. Negishi, K. Nobusada, T. Tsukuda, *J. Am. Chem. Soc.* **2005**, *127*, 5261.
[23] S. Knoppe, T. Bürgi, *Acc. Chem. Res.* **2014**, *47*, 1318.
[24] B. Niesen, B. P. Rand, *Adv. Mater.* **2014**, *26*, 1446.
[25] T.-W. Koh, A. M. Hiszpanski, M. Sezen, A. Naim, T. Galfsky, A. Trivedi, Y.-L. Loo, V. Menon, B. P. Rand, *Nanoscale* **2015**, *7*, 9140.
[26] L. Xu, J. Wang, X. Zhu, X. Zeng, Z. Chen, *Adv. Funct. Mater.* **2015**, *25*, 3033.
[27] L.-J. Xu, X. Zhang, J.-Y. Wang, Z.-N. Chen, *J. Mater. Chem. C* **2016**, *4*, 1787.
[28] N. Natarajan, L.-X. Shi, H. Xiao, J.-Y. Wang, L.-Y. Zhang, X. Zhang, Z.-N. Chen, *J. Mater. Chem. C* **2018**, *6*, 8966.
[29] N. Natarajan, L.-X. Shi, H. Xiao, J.-Y. Wang, L.-Y. Zhang, X. Zhang, Z.-N. Chen, *J. Mater. Chem. C* **2019**, *7*, 2604.
[30] Y.-Z. Huang, L.-X. Shi, J.-Y. Wang, H.-F. Su, Z.-N. Chen, *ACS Appl. Mater. Interfaces* **2020**, *12*, 57264.
[31] Z. Jiao, M. Yang, J.-Y. Wang, Y.-Z. Huang, P. Xie, Z.-N. Chen, *J. Mater. Chem. C* **2021**, *9*, 5528.
[32] T. Li, Z. Wang, Y. Zhang, Z. Wu, *Nanomaterials* **2022**, *12*, 3837.
[33] X. Zhang, H. Xu, *Angew. Chem., Int. Ed.* **2023**, *136*, 202317597.
[34] J. Lu, B. Shao, R.-W. Huang, L. Gutiérrez-Arzaluz, S. Chen, Z. Han, J. Yin, H. Zhu, S. Dayneko, M. N. Hedhili, X. Song, P. Yuan, C. Dong, R. Zhou, M. I. Saidaminov, S.-Q. Zang, O. F. Mohammed, O. M. Bakr, *J. Am. Chem. Soc.* **2024**, *146*, 4144.
[35] Y. Tian, W. Zheng, X. Zhang, Y. Wang, Y. Xiao, D. Yao, H. Zhang, *Nano Lett.* **2023**, *23*, 4423.
[36] X. Kang, Y. Li, M. Zhu, R. Jin, *Chem. Soc. Rev.* **2020**, *49*, 6443.
[37] X. Kang, M. Zhu, *Chem. Soc. Rev.* **2019**, *48*, 2422.
[38] J. V. Rival, P. Mymoona, K. M. Lakshmi, Nonappa, T. P, E. S. Shibu, *Small* **2021**, *17*, 2005718.
[39] M. Jash, A. Jana, A. K. Poonia, E. Khatun, P. Chakraborty, A. Nagar, T. Ahuja, K. V. Adarsh, T. Pradeep, *Chem. Mater.* **2023**, *35*, 313.
[40] S. Chakraborty, D. Bain, S. Maity, S. Kolay, A. Patra, *J. Phys. Chem. C* **2022**, *126*, 2896.
[41] J. V. Rival, Nonappa, E. S. S, *ACS Appl. Mater. Interfaces* **2020**, *12*, 14569.
[42] K. M. Lakshmi, J. V. Rival, P. Sreeraj, S. R. Nambiar, C. Jeyabharathi, Nonappa, E. S. S, *Small* **2023**, *19*, 2207119.
[43] Z. Xie, P. Sun, Z. Wang, H. Li, L. Yu, D. Sun, M. Chen, Y. Bi, X. Xin, J. Hao, *Angew. Chem., Int. Ed.* **2020**, *59*, 9922.
[44] A. K. Das, S. Biswas, S. S. Manna, B. Pathak, S. Mandal, *Chem. Sci.* **2022**, *13*, 8355.
[45] Y. Song, Y. Li, M. Zhou, X. Liu, H. Li, H. Wang, Y. Shen, M. Zhu, R. Jin, *Sci. Adv.* **2021**, *7*, abd2091.
[46] S.-S. Zhang, S. Havenridge, C. Zhang, Z. Wang, L. Feng, Z.-Y. Gao, C. M. Aikens, C.-H. Tung, D. Sun, *J. Am. Chem. Soc.* **2022**, *144*, 18305.
[47] A. Jana, M. Jash, W. A. Dar, J. Roy, P. Chakraborty, G. Paramasivam, S. Lebedkin, K. Kirakci, S. Manna, S. Antharjanam, J. Machacek, M. Kucerakova, S. Ghosh, K. Lang, M. M. Kappes, T. Base, T. Pradeep, *Chem. Sci.* **2023**, *14*, 1613.
[48] A. Jana, S. Duary, A. Das, A. R. Kini, S. Acharya, J. Machacek, B. Pathak, T. Base, T. Pradeep, *Chem. Sci.* **2024**, *15*, 13741.
[49] Z. Luo, X. Yuan, Y. Yu, Q. Zhang, D. T. Leong, J. Y. Lee, J. Xie, *J. Am. Chem. Soc.* **2012**, *134*, 16662.
[50] J. Xie, Y. Zheng, J. Y. Ying, *J. Am. Chem. Soc.* **2009**, *131*, 888.
[51] Y. Wang, Z. Liu, A. Mazumder, C. G. Gianopoulos, K. Kirschbaum, L. A. Peteanu, R. Jin, *J. Am. Chem. Soc.* **2023**, *145*, 26328.
[52] S. Takano, H. Hirai, T. Nakashima, T. Iwasa, T. Taketsugu, T. Tsukuda, *J. Am. Chem. Soc.* **2021**, *143*, 10560.
[53] M. Mitsui, D. Arima, Y. Kobayashi, E. Lee, Y. Niihori, *Adv. Opt. Mater.* **2022**, *10*, 2200864.
[54] X.-H. Ma, Y. Si, J.-H. Hu, X.-Y. Dong, G. Xie, F. Pan, Y.-L. Wei, S.-Q. Zang, Y. Zhao, *J. Am. Chem. Soc.* **2023**, *145*, 25874.
[55] Z. Liu, L. Luo, R. Jin, *Adv. Mater.* **2024**, *36*, 2309073.
[56] H. Lin, X. Song, O. J. H. Chai, Q. Yao, H. Yang, J. Xie, *Adv. Mater.* **2024**, *36*, 2401002.
[57] D. Arima, S. Hidaka, S. Yokomori, Y. Niihori, Y. Negishi, R. Oyaizu, T. Yoshinami, K. Kobayashi, M. Mitsui, *J. Am. Chem. Soc.* **2024**, *146*, 16630.
[58] X. Kang, S. Wang, Y. Song, S. Jin, G. Sun, H. Yu, M. Zhu, *Angew. Chem., Int. Ed.* **2016**, *55*, 3611.
[59] D. Arima, Y. Niihori, M. Mitsui, *J. Mater. Chem. C* **2022**, *10*, 4597.
[60] Y. Wei, W. Kan, J. Zhang, H. Xu, *Appl. Phys. Lett.* **2020**, *117*, 071901.

© 2025 Wiley-VCH GmbH

15214095, 2025, 35, Downloaded from https://advanced.onlinelibrary.wiley.com/doi/10.1002/adma.202507893 by Central Library The Librarian, Wiley Online Library on [28/12/2025]. See the Terms and Conditions (https://onlinelibrary.wiley.com/terms-and-conditions) on Wiley Online Library for rules of use; OA articles are governed by the applicable Creative Commons License

[61] C.-H. Lee, M.-C. Tang, W.-L. Cheung, S.-L. Lai, M.-Y. Chan, V. W.-W. Yam, *Chem. Sci.* **2018**, *9*, 6228.
[62] G. Mallesham, C. Swetha, S. Niveditha, M. E. Mohanty, N. J. Babu, A. Kumar, K. Bhanuprakash, V. J. Rao, *J. Mater. Chem. C* **2015**, *3*, 1208.
[63] X. Kang, X. Li, H. Yu, Y. Lv, G. Sun, Y. Li, S. Wang, M. Zhu, *RSC Adv.* **2017**, *7*, 28606.
[64] D. Zhang, P. Pan, X. Du, X. Kang, M. Zhu, *Nanoscale* **2024**, *16*, 11513.
[65] Nonappa, *Beilstein J. Nanotechnol.* **2020**, *11*, 533.
[66] N. Goswami, F. Lin, Y. Liu, D. T. Leong, J. Xie, *Chem. Mater.* **2016**, *28*, 4009.
[67] S. Chandra, Nonappa, G. B, A. Som, S. Zhou, J. Lahtinen, H. Jiang, J. V. I. Timonen, O. Ikkala, R. H. A. Ras, *Adv. Optical Mater.* **2019**, *7*, 1900620.
[68] Nonappa, *ACS Mater.* **2024**, *4*, 238.
[69] Nonappa, P. Engelhardt, *Imaging Microsc.* **2019**, *21*, 22.
[70] D. N. Mastronarde, *Microsc. Microanal. Microstruct.* **2003**, *9*, 1182.
[71] D. N. Mastronarde, *J. Struct. Biol.* **2005**, *152*, 36.
[72] P. Engelhardt, in *Electron Microscopy* (Ed: J. Kuo), Humana Press, Totowa, NJ, **2007**, pp. 365–385.
[73] P. Engelhardt, in *Encyclopedia of Analytical Chemistry* (Ed: R.A. Meyers), John Wiley & Sons, Ltd, Chichester, UK, **2006**, p. a1405.

© 2025 Wiley-VCH GmbH

15214095, 2025, 35, Downloaded from https://advanced.onlinelibrary.wiley.com/doi/10.1002/adma.202507893 by Central Library The Librarian, Wiley Online Library on [28/12/2025]. See the Terms and Conditions (https://onlinelibrary.wiley.com/terms-and-conditions) on Wiley Online Library for rules of use; OA articles are governed by the applicable Creative Commons License

ADVANCED MATERIALS

Supporting Information

for *Adv. Mater.*, DOI 10.1002/adma.202507893

Bimetallic Nanocluster-Based Light-Emitting Diodes With High External Quantum Efficiency and Saturated Red Emission

Jose V. Rival, Savita Chand, Arijit Jana, Nonappa, Vasudevanpillai Biju, Thalappil Pradeep, Pachaiyappan Rajamalli and Edakkattuparambil Sidharth Shibu**

Supporting Information

Bimetallic Nanocluster-based Light-Emitting Diodes with High External Quantum Efficiency and Saturated Red Emission

Jose V. Rival,[a] *Savita Chand,*[b] *Arijit Jana,*[c] *Nonappa,*[d] *Vasudevanpillai Biju,*[e] *Thalappil Pradeep,*[c] *Pachaiyappan Rajamalli,*[b]* *Edakkattuparambil Sidharth Shibu*[a]*

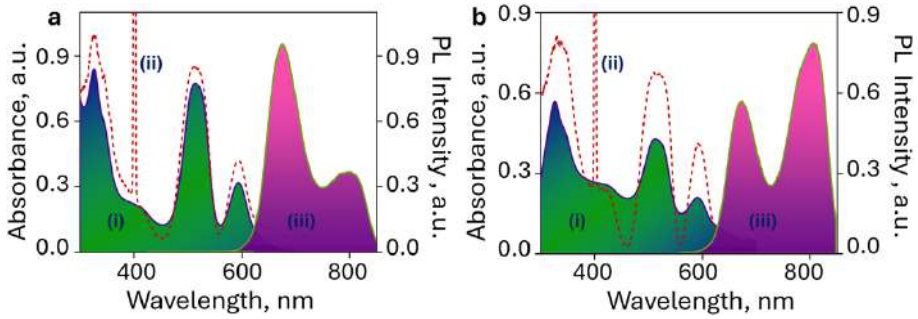


Figure S1. (i) UV/Vis absorption, (ii) excitation (corresponding to the emissions at 798 and 806 nm from $[Au_2Cu_6(Sadm)_6(DPPEO)_2]$ and $[Au_2Cu_6(Sadm)_6(TPP)_2]$ NCs, respectively) and PL (iii) spectra of (a) $[Au_2Cu_6(Sadm)_6(DPPEO)_2]$ and (b) $[Au_2Cu_6(Sadm)_6(TPP)_2]$ NCs.

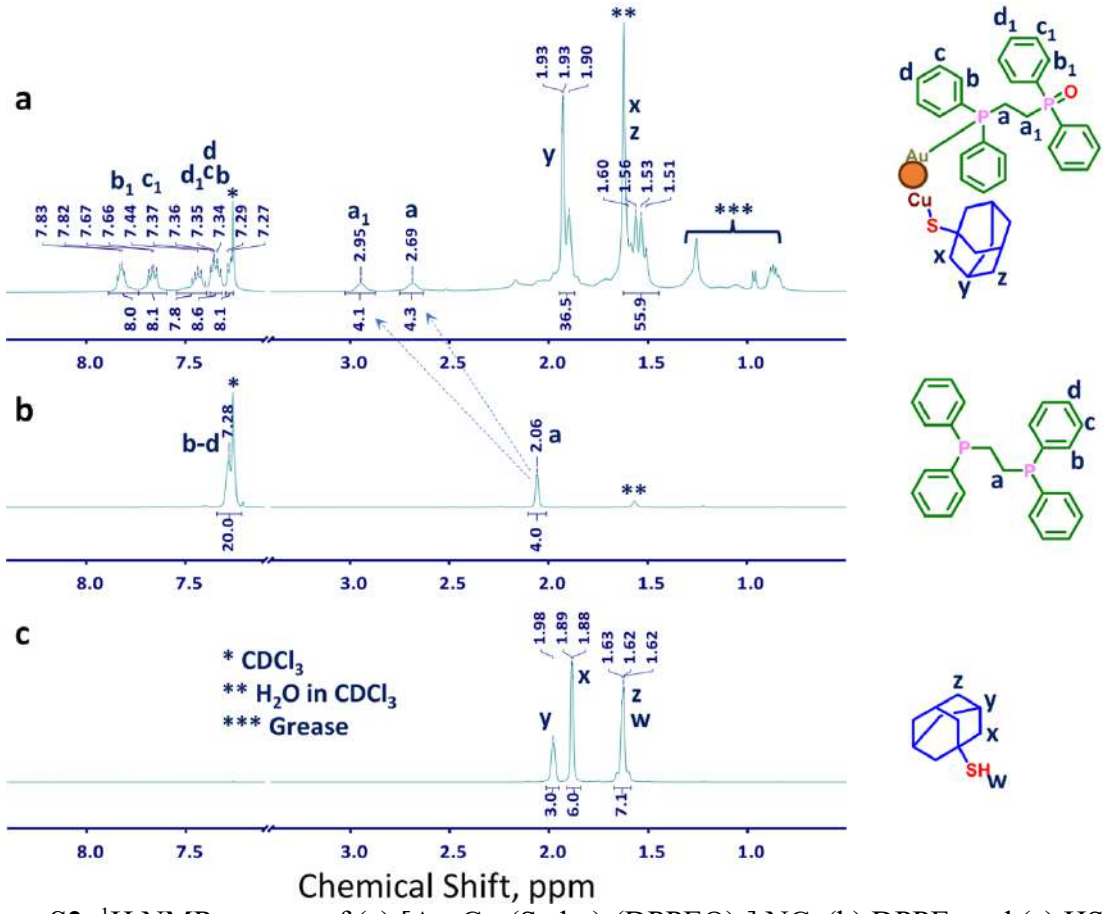


Figure S2. ^{1}H NMR spectra of (a) $[Au_2Cu_6(Sadm)_6(DPPEO)_2]$ NC, (b) DPPE, and (c) HSadm.

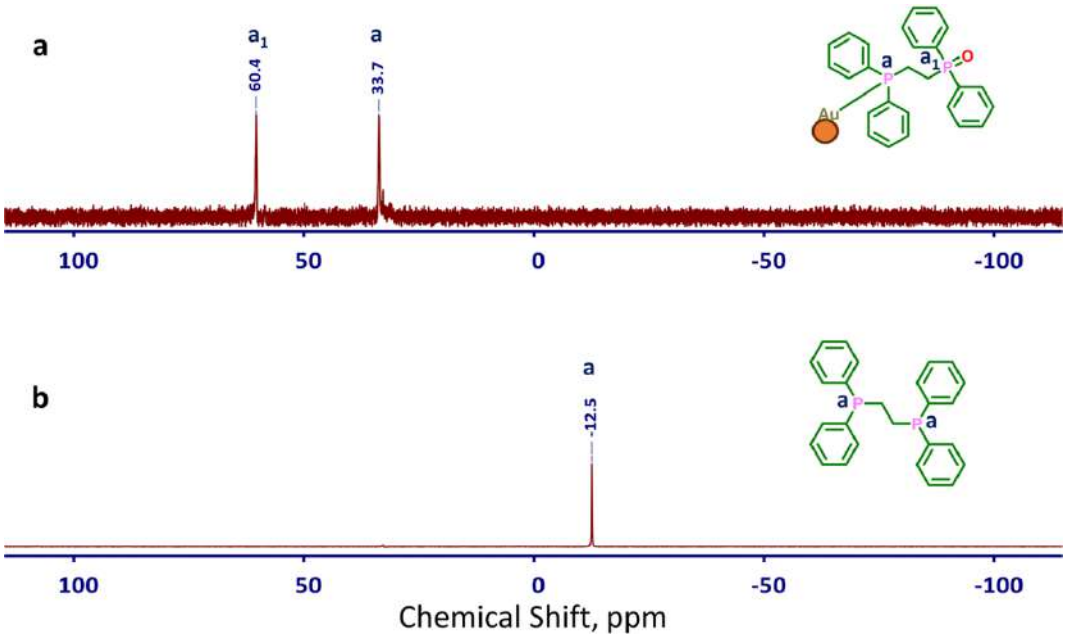


Figure S3. ^{31}P NMR spectra of (a) **[**$Au_2Cu_6(Sadm)_6(DPPEO)_2$] NC and (b) DPPE ligand in $CDCl_3$.

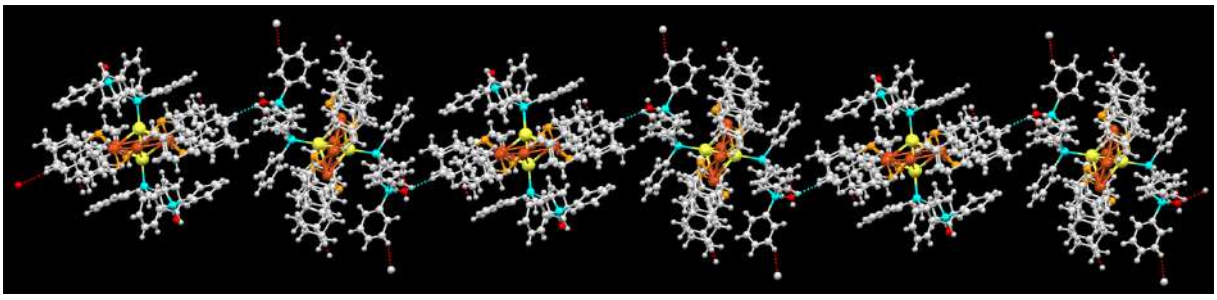


Figure S4. The C–H···O interactions between the neighboring NCs in the crystal resulted in a zig-zag tape arrangement of NCs.

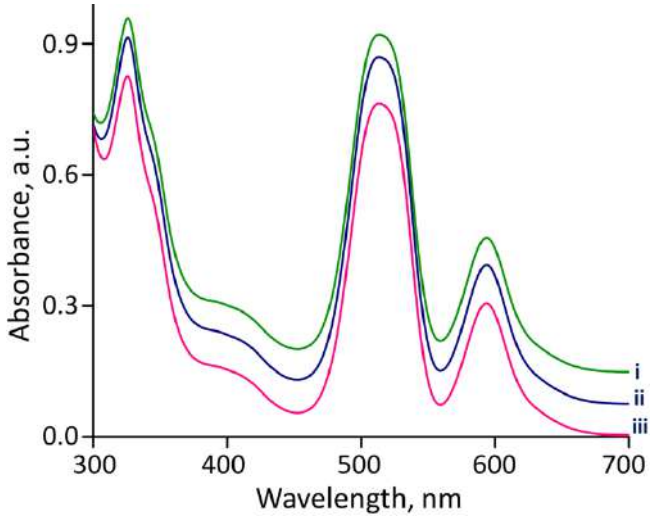


Figure S5. UV/Vis absorption spectra of NC solution recorded under (i) argon, (ii) ambient, and (iii) oxygen atmospheres (for clarity, spectra were vertically translated).

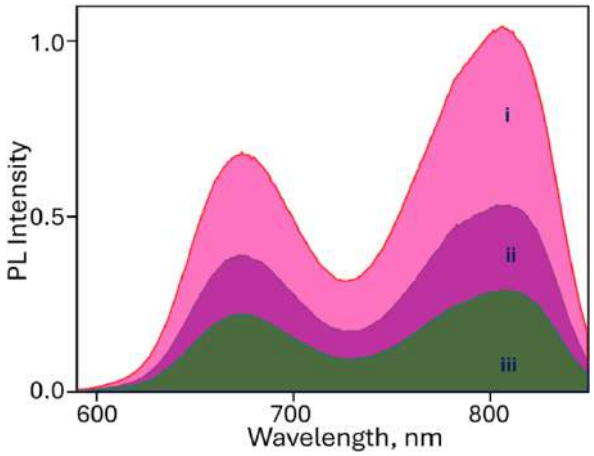


Figure S6. PL spectra of $[Au_2Cu_6(Sadm)_6(TPP)_2]$ NC solution NC solution recorded under (i) argon, (ii) ambient, and (iii) oxygen atmospheres.

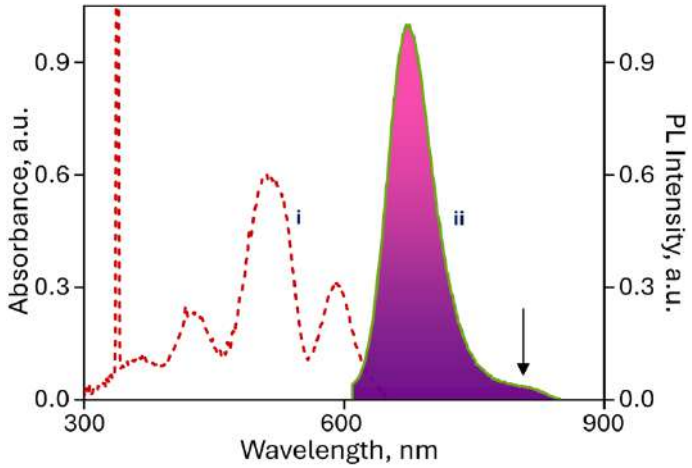


Figure S7. Excitation (i) and emission (ii) spectra of $[Au_2Cu_6(Sadm)_6(TPP)_2]$ NC.

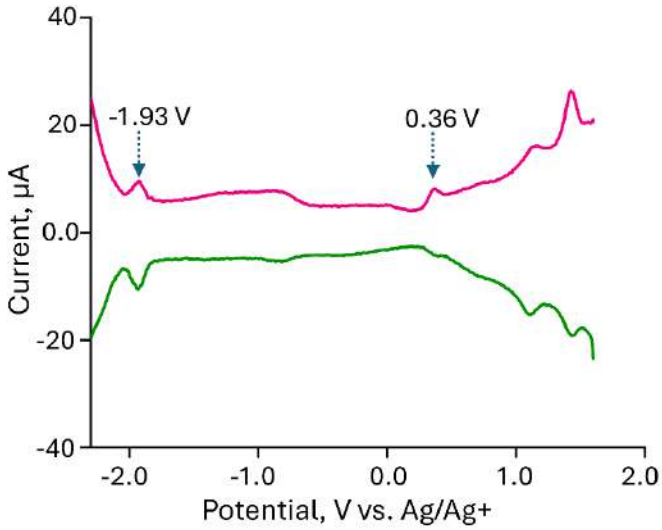


Figure S8. Differential pulse voltammetry (DPV) of $[Au_2Cu_6(Sadm)_6(DPPEO)_2]$ (20 µM) in acetonitrile/toluene mixture (1:1).

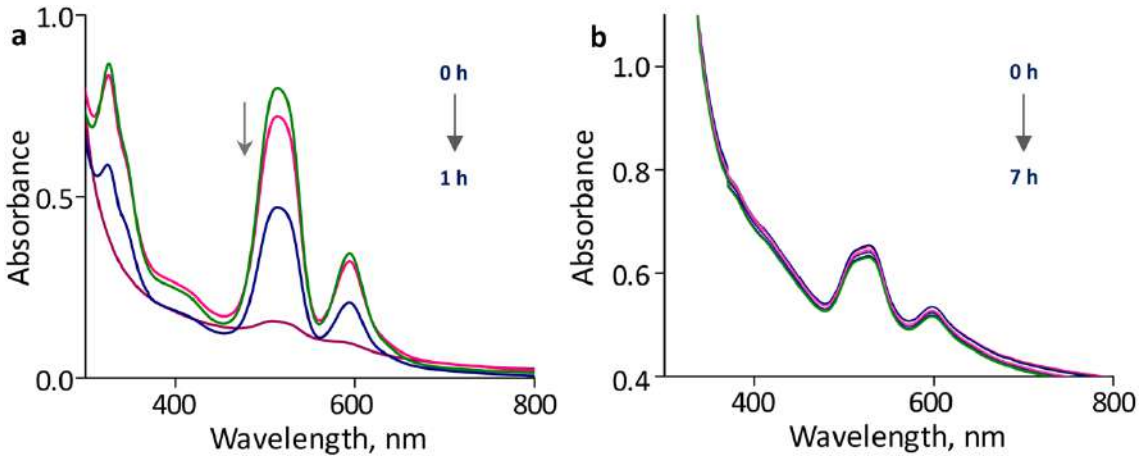


Figure S9. Temporal UV/Vis absorption spectra recorded from (a) NC solution and (b) NC film under UV illumination.

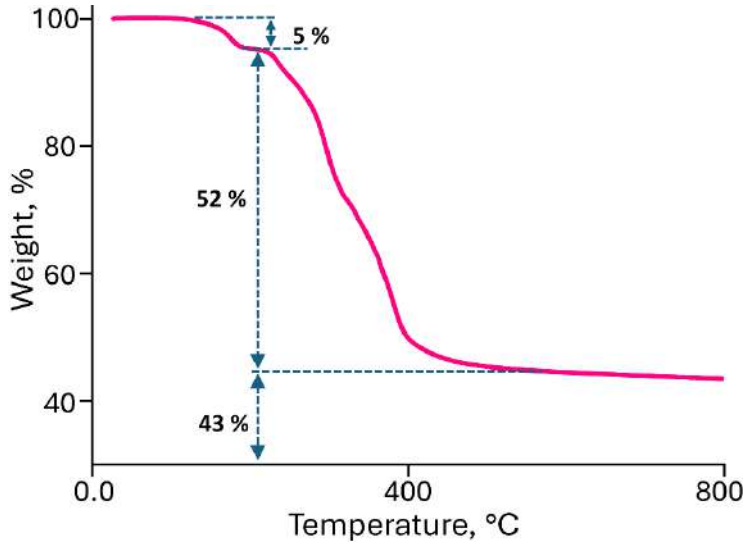


Figure S10. TGA curve of $[Au_2Cu_6(Sadm)_6(DPPEO)_2]$ NC.

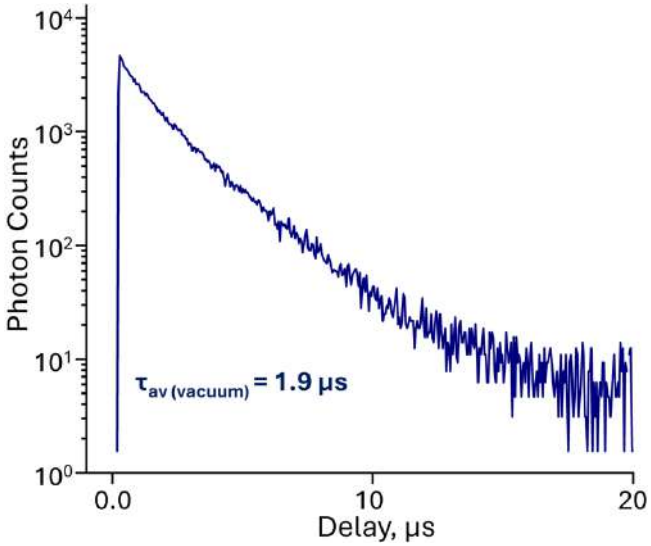


Figure S11. The PL decay profile of NC solid under vacuum.

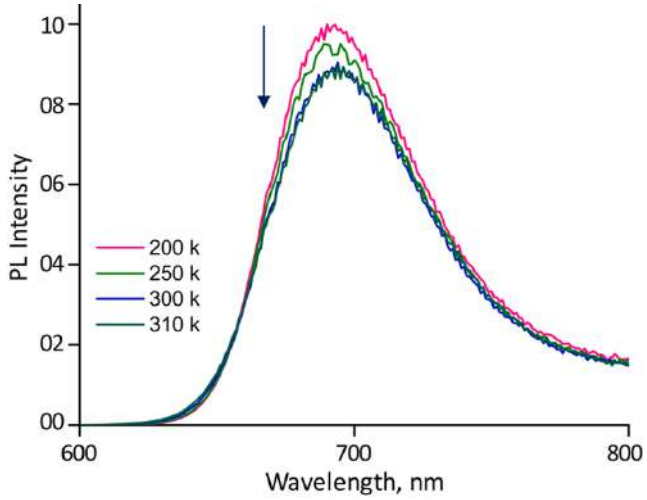


Figure S12. The temperature-dependent PL spectra recorded from NC solid.

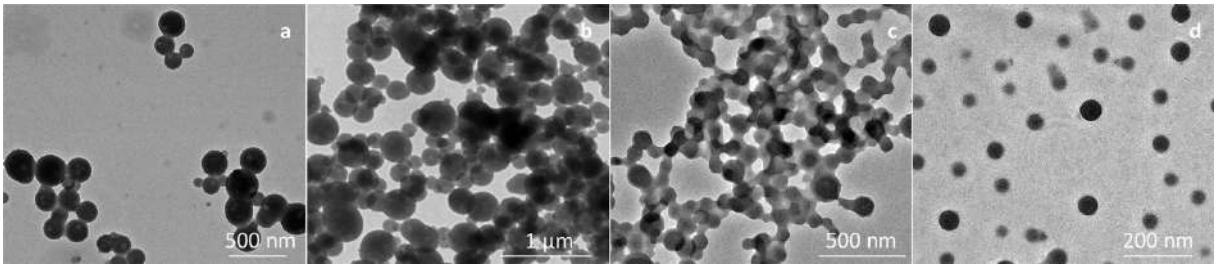


Figure S13. TEM micrographs of assembled-NCs at (a) 50%, (b) 60%, (c) 70%, and (d) 90% f_w.

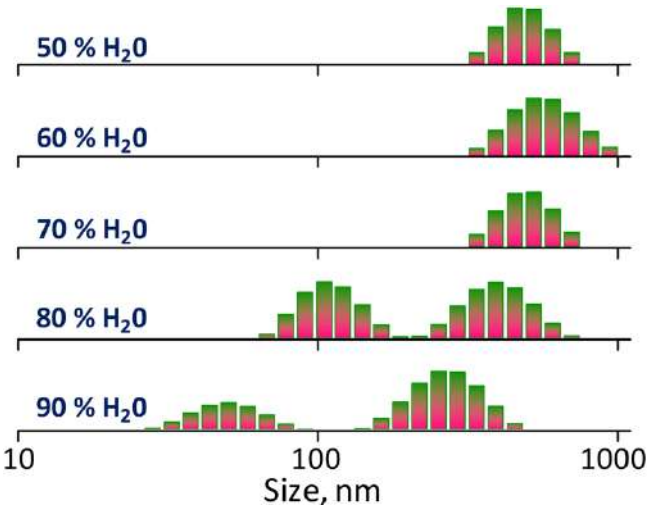


Figure S14. DLS spectra of $[Au_2Cu_6(Sadm)_6(DPPEO)_2]$ NCs in THF at different f_w.

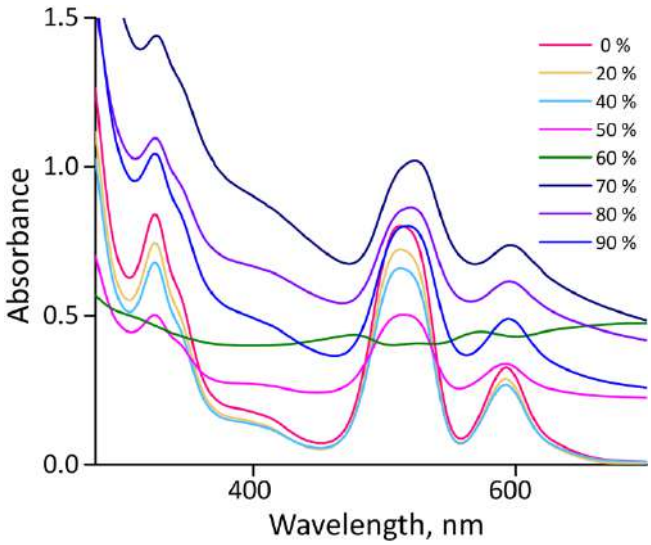


Figure S15. The UV/Vis absorption spectra of NC solution at different f_w.

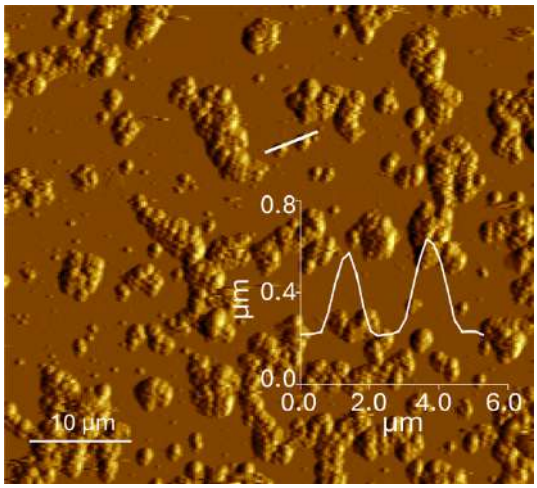


Figure S16. A large area AFM image of assembled-NCs (60% f_w). The height profile is shown in the inset.

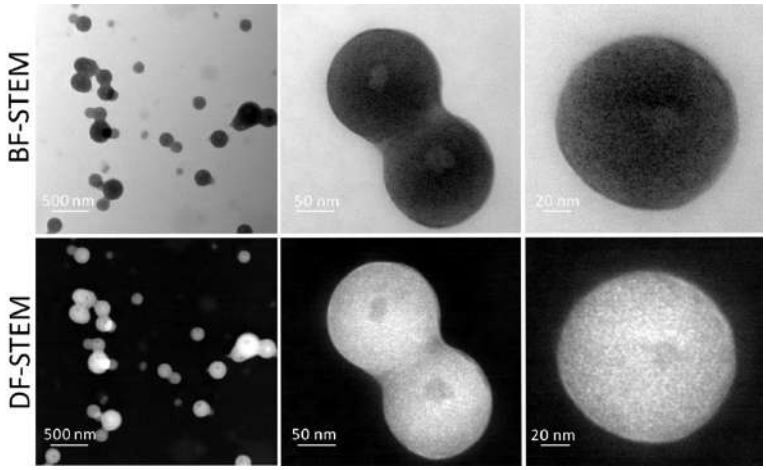


Figure S17. BF- and DF-STEM images show large area assembly, and assembled dimer and monomer.

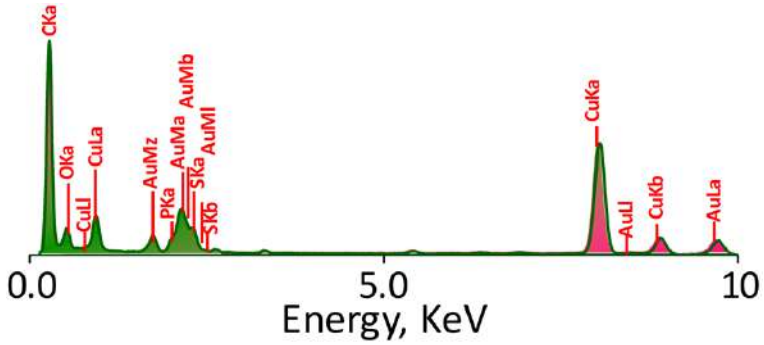


Figure S18. The EDS spectrum of assembled superstructures (f_w = 60%). Respective elements are labeled.

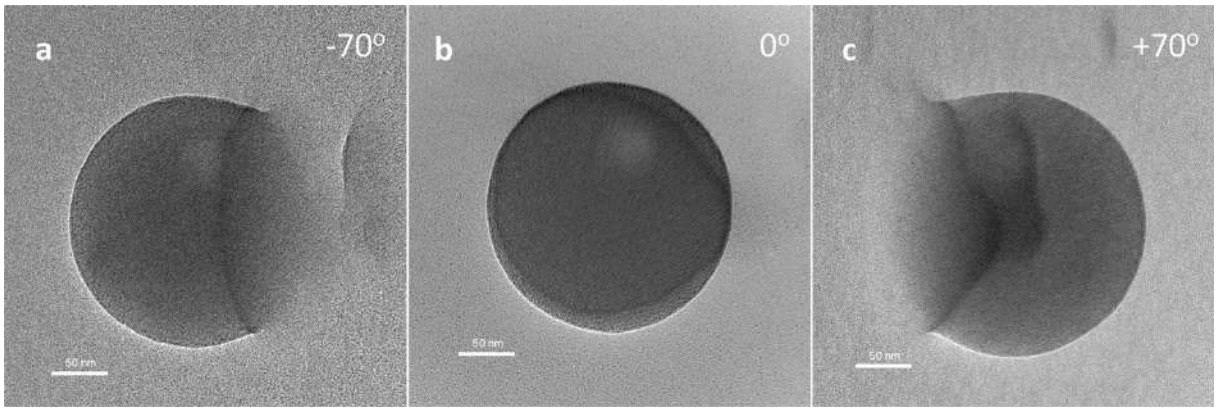


Figure S19. BF-TEM micrographs of $[Au_2Cu_6(Sadm)_6(DPPEO)_2]$ NC assembly (f_w = 60%) at different tilt angles.

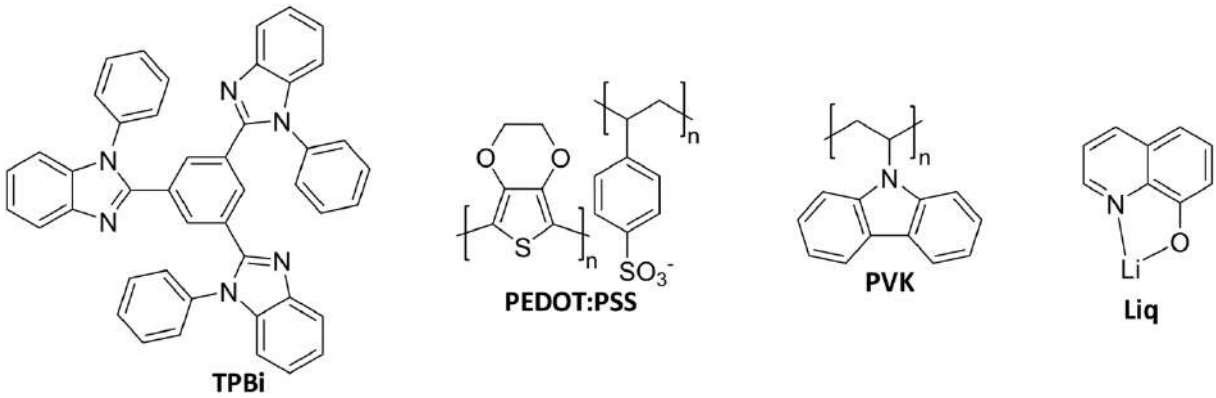


Figure S20. The chemical structure of different organic materials used for LED fabrication.

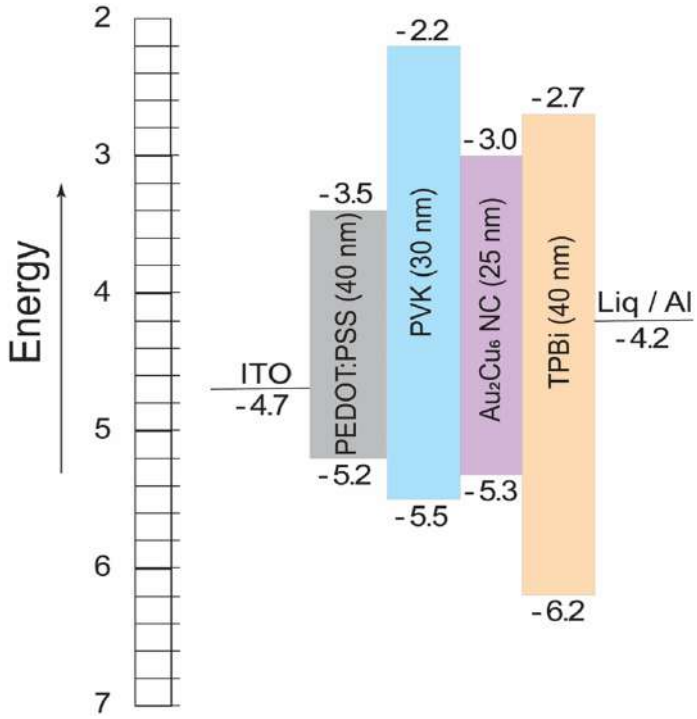


Figure S21. The energy level alignment in the device.

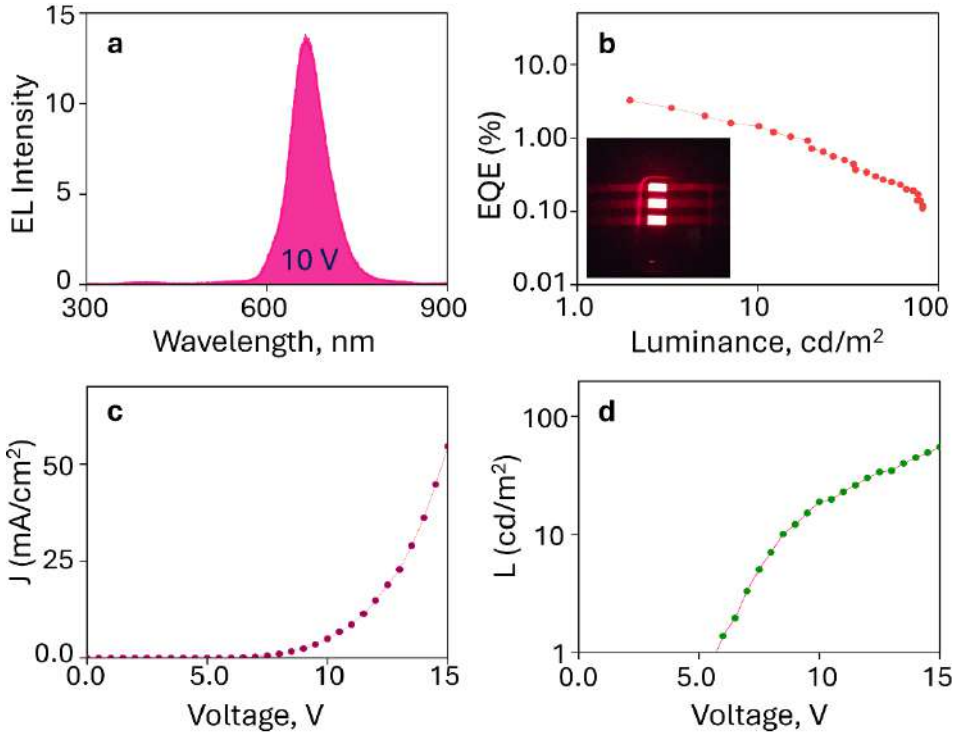


Figure S22. (a) EL spectra of $[Au_2Cu_6(Sadm)_6(TPP)_2]$ NC-based device at 10V. (b) EQE *vs* luminance curve. The inset shows a photograph of the fabricated LED device. (c) Current density-voltage curve of the device. (d) Luminance-voltage curve of the device.

Light emitting NC Layer	PLQY (%)	L_{max} (cd m^{-2})	Wavelength (nm)	EQE_{max} (%)	CIE Coordinates (x, y)	Ref.
Au_{25} or Ag_{25}	_	_	750	0.013	_	1
Au@GSH	15	40	625	0.12	(0.57– 0.59, 0.40 – 0.41)	2
Au@TOP	4.99	100	White light	0.08	(0.27,0.33)	3
$(Au_4L_4)_n/(Au_4D_4)_n$	41.4	_	503	1.5	_	4
TOAB/Arg/ATT@Au	73.4	1104	544	5.1	(0.31,0.65)	5
Au_4Ag_2	77.2	8804	539	7.0 (d)	_	6
Ag_6Cu	78	184	573	13.9 (d)	_	7
$PtAu_3$	90	1000	588	18.1 (d)	(0.33,0.61)	8
$PtAu_3$	90.1	6539	556	16.6 (d)	(0.30,0.61)	9
Au_3Ag	25	5211	440	2.06 (d)	(0.16,0.09)	10
Ag_8Au_{10}	77	14,859	567	15.7 (d)	(0.4714,0.5200)	11
Ag_3Cu_5	75	8554	585	14.7 (d)	(0.51,0.48)	12
R/S-Cu_2Au_2	94/ 89	2010/1670	564	36.5% (d) 23.5/20.8 (nd)	(0.395,0.572) (0.394,0.574)	13
$[Au_2Cu_6(Sadm)_6(DPPEO)_2]$	**62**	**1246**	**668**	**12.6 (nd)**	**(0.70,0.30)**	**Current Work**
$[Au_2Cu_6(Sadm)_6(TPP)_2]$	**17.8**	**55.17**	**666**	**3.24 (nd)**	**(0.67,0.31)**	**Current Work**
$[DBFDP]_2Cu_4I_4$	5	1500	White light	0.73 (d)	(0.37,0.45)	14
$[DtBCzDBFDP]_2Cu_4I_4$	65	7000	491	7.9 (d)	(0.22,0.43)	15
$[DPACDBFDP]_2Cu_4I_4$	81	4000	500	19.5 (d)	(0.21±0.1,0.45 ± 0.1)	16
$[TMeOPP]_4Cu_4I_4$	99	10710	550	15.6 (d)	(0.40±0.05, 0.53±0.04)	17
$Cu_2I_2[P\text{-}m\text{-}(Tol)_3]_2Pyrphos$	90	1426	560	19.1 (d)		18
$Cu_6I_6(ppda)_2$	36	_	564	0.31 (d)	(0.43,0.51)	19
$Cu_2I_2(BINAP)_2$	4.7	1200	515	0.54	_	20
$[DDMACDBFDP]_2Cu_4I_4$	99	5502	504	29.4 (d) 9.5 (nd)	(0.21,0.50)	21

Table S1. The comparison table shows the details of reported NCs in the device fabrication (d- doped and nd- non-doped).

References

[1] B. Niesen, B. P. Rand, *Adv. Mater.* **2014**, *26*, 1446.

[2] T.-W. Koh, A. M. Hiszpanski, M. Sezen, A. Naim, T. Galfsky, A. Trivedi, Y.-L. Loo, V. Menon, B. P. Rand, *Nanoscale* **2015**, *7*, 9140.

[3] Y.-C. Chao, K.-P. Cheng, C.-Y. Lin, Y.-L. Chang, Y.-Y. Ko, T.-Y. Hou, C.-Y. Huang, W. H. Chang, C.-A. J. Lin, *Sci. Rep.* **2018**, *8*, 8860.

[4] Z. Han, X. Zhao, P. Peng, S. Li, C. Zhang, M. Cao, K. Li, Z.-Y. Wang, S.-Q. Zang, *Nano Res.* **2020**, *13*, 3248.

[5] Y. Tian, W. Zheng, X. Zhang, Y. Wang, Y. Xiao, D. Yao, H. Zhang, *Nano Lett.* **2023**, *23*, 4423.

[6] L. Xu, J. Wang, X. Zhu, X. Zeng, Z. Chen, *Adv. Funct. Mater.* **2015**, *25*, 3033.

[7] L.-J. Xu, X. Zhang, J.-Y. Wang, Z.-N. Chen, *J. Mater. Chem. C* **2016**, *4*, 1787.

[8] N. Natarajan, L.-X. Shi, H. Xiao, J.-Y. Wang, L.-Y. Zhang, X. Zhang, Z.-N. Chen, *J. Mater. Chem. C* **2018**, *6*, 8966.

[9] N. Natarajan, L.-X. Shi, H. Xiao, J.-Y. Wang, L.-Y. Zhang, X. Zhang, Z.-N. Chen, *J. Mater. Chem. C* **2019**, *7*, 2604.

[10] J. Ni, C. Zhong, L. Li, M. Su, X. Wang, J. Sun, S. Chen, C. Duan, C. Han, H. Xu, *Angew. Chem. Int. Ed.* **2022**, *61*, e202213826.

[11] Y.-Z. Huang, L.-X. Shi, J.-Y. Wang, H.-F. Su, Z.-N. Chen, *ACS Appl. Mater. Interfaces* **2020**, *12*, 57264.

[12] Z. Jiao, M. Yang, J.-Y. Wang, Y.-Z. Huang, P. Xie, Z.-N. Chen, *J. Mater. Chem. C* **2021**, *9*, 5528.

[13] J. Lu, B. Shao, R.-W. Huang, L. Gutiérrez-Arzaluz, S. Chen, Z. Han, J. Yin, H. Zhu, S. Dayneko, M. N. Hedhili, X. Song, P. Yuan, C. Dong, R. Zhou, M. I. Saidaminov, S.-Q. Zang, O. F. Mohammed, O. M. Bakr, *J. Am. Chem. Soc.* **2024**, *146*, 4144.

[14] M. Xie, C. Han, J. Zhang, G. Xie, H. Xu, *Chem. Mater.* **2017**, *29*, 6606.

[15] M. Xie, C. Han, Q. Liang, J. Zhang, G. Xie, H. Xu, *Sci. Adv.* **2019**, *5*, eaav9857.

[16] N. Zhang, H. Hu, L. Qu, R. Huo, J. Zhang, C. Duan, Y. Meng, C. Han, H. Xu, *J. Am. Chem. Soc.* **2022**, *144*, 6551.

[17] Y. Li, S. Xu, X. Zhang, Y. Man, J. Zhang, G. Zhang, S. Chen, C. Duan, C. Han, H. Xu, *Angew. Chem. Int. Ed.* **2023**, 62, e202308410.

[18] J.-J. Wang, L.-Z. Feng, G. Shi, J.-N. Yang, Y.-D. Zhang, H. Xu, K.-H. Song, T. Chen, G. Zhang, X.-S. Zheng, F. Fan, Z. Xiao, H.-B. Yao, *Nat. Photon.* **2024**, *18*, 200.

[19] K. Xu, B.-L. Chen, R. Zhang, L. Liu, X.-X. Zhong, L. Wang, F.-Y. Li, G.-H. Li, K. A. Alamry, F.-B. Li, W.-Y. Wong, H.-M. Qin, *Dalton Trans.* **2020**, *49*, 5859.

[20] J.-J. Wang, H.-T. Zhou, J.-N. Yang, L.-Z. Feng, J.-S. Yao, K.-H. Song, M.-M. Zhou, S. Jin, G. Zhang, H.-B. Yao, *J. Am. Chem. Soc.* **2021**, *143*, 10860.

[21] N. Zhang, Y. Li, S. Han, Y. Wei, H. Hu, R. Huo, C. Duan, J. Zhang, C. Han, G. Xie, H. Xu, *Angew. Chem. Int. Ed.* **2023**, *62*, e202305018.

Chemical Science

ROYAL SOCIETY OF CHEMISTRY

EDGE ARTICLE

View Article Online
View Journal | View Issue

Check for updates

Cite this: *Chem. Sci.*, 2025, **16**, 14127

All publication charges for this article have been paid for by the Royal Society of Chemistry

Open Access Article. Published on 10 July 2025. Downloaded on 12/29/2025 3:13:31 AM. This article is licensed under a Creative Commons Attribution-NonCommercial 3.0 Unported Licence.

Cluster *versus* coordination: the chemistry of cyclopentadienyl titanium and vanadium complexes with B- and C-functionalized carborane-thiols, $[C_2B_{10}H_{12-n}(SH)_n]$ (n = 2 or 3)†

Subhash Bairagi, ‡[a] Deepak Kumar Patel, ‡[abc] Debipada Chatterjee,[a] Monika Kučeráková,[d] Jan Macháček,[c] Tomas Base, *[c] Thalappil Pradeep *[ab] and Sundargopal Ghosh *[a]

A series of B- and C-functionalized di- and trithiol chelating *o*-carborane ligands have been employed to explore the coordination chemistry with cyclopentadienyl titanium and vanadium complexes. Treatment of [Cp*TiCl$_3$] with [LiBH$_4$·THF], followed by thermolysis with a C-functionalized carborane-dithiol ligand [1,2-(SH)$_2$-1,2-$C_2B_{10}H_{10}$], yielded octacapped octahedral [(Cp*Ti)$_4${Ti(1,2-(S)$_2$-1,2-$C_2B_{10}H_{10}$)}$_2$(μ_3-S)$_6$(μ_3-O)$_2$] (**1**) and hexacapped trigonal bipyramidal [(Cp*Ti)$_4${Ti(1,2-(S)$_2$-1,2-$C_2B_{10}H_{10}$)}(μ_3-S)$_6$] (**2**) clusters. One of the driving forces of these reactions is the cleavage of C–S bonds of carborane-dithiols that resulted in sulfide ligands and subsequently generated clusters **1** and **2**. In contrast, a similar reaction with a B-functionalized carborane-dithiol [9,12-(SH)$_2$-1,2-$C_2B_{10}H_{10}$] led to B–B bond formation that yielded a κ^2-hydridoborato complex, [(Cp*Ti){κ^2-BH$_3$(9,12-(S)$_2$-1,2-$C_2B_{10}H_{10}$)}] (**3**). To the best of our knowledge, complex **3** is the first example of a carborane-dithiol functionalized hydridoborato complex. Interestingly, when the reactions of [Cp*TiCl$_3$] or [Cp$_2$TiCl$_2$] were carried out with a B-functionalized carborane-trithiol, [8,9,12-(SH)$_3$-1,2-$C_2B_{10}H_9$], they led to coordination complexes, [(Cp/Cp*Ti){8,9,12-(S)$_3$-1,2-$C_2B_{10}H_9$}] (Cp* (**4a**) and Cp (**4b**)). Similarly, when [(Cp*VCl$_2$)$_3$] was employed as a metal precursor, deboronation was observed at the icosahedral cage that resulted in a zwitterionic complex, [(Cp*V){1,5,6-(S)$_3$-*nido*-7,8-$C_2B_9H_9$}] (**5**). All the clusters have been characterized by NMR, IR, mass spectrometry, and X-ray diffraction analysis. Furthermore, the theoretical analyses provided valuable insights into the electronic structures of these unusual clusters.

Received 16th May 2025
Accepted 9th June 2025

DOI: 10.1039/d5sc03562g

rsc.li/chemical-science

Introduction

Since the inception of coordination chemistry from the work of Alfred Werner,[1] the field of inorganic chemistry has expanded into various branches, such as organometallics, polymers, bio-inorganics, and materials chemistry. Central to these developments and their comprehensive understanding is the specific design of ligands exhibiting specific geometry and enabling site-specific functionalization. These play a critical role in shaping the properties of metal complexes.[2] Ligand design not only influences the formation of new structures but also accelerates reaction rates, alters mechanisms, and fine-tunes the topology and functionality of metal–organic frameworks.[3] One of the biggest challenges in ligand design, which often involves modifying the chemical properties (such as electron-donating or withdrawing behaviour) as well as changing the steric requirements of ligands, is represented by modification of one whilst keeping the other identical.[4] In this regard, icosahedral carboranes represent a fascinating class of highly stable, boron-rich clusters that can be readily modified at various vertices through simple chemical reactions while preserving their steric demands.[5]

Despite significant progress in the coordination chemistry of carboranes, systematic investigation focusing on the effect of direct positional attachment of exo-substituents to carboranes has not been much explored.[5–7] This is surprising given that the distinct chemical reactivity of the CH and BH vertices in these clusters has been well established.[5] In this regard, Mirkin and

[a]*Department of Chemistry, Indian Institute of Technology Madras, Chennai 600036, India. E-mail: sghosh@iitm.ac.in*

[b]*DST Unit of Nanoscience (DST UNS) and Thematic Unit of Excellence (TUE), Department of Chemistry, Indian Institute of Technology Madras, Chennai 600036, India. E-mail: pradeep@iitm.ac.in*

[c]*Institute of Inorganic Chemistry, The Czech Academy of Science, 25068 Rez, Czech Republic. E-mail: tbase@iic.cas.cz*

[d]*Institute of Physics, The Czech Academy of Science, 182 21 Prague 8, Czech Republic*

† Electronic supplementary information (ESI) available. CCDC 2403346, 2451038, 2311787, 2358616, 2311786, and 2358617. For ESI and crystallographic data in CIF or other electronic format see DOI: https://doi.org/10.1039/d5sc03562g

‡ These authors contributed equally to this work.

© 2025 The Author(s). Published by the Royal Society of Chemistry

Open Access Article. Published on 10 July 2025. Downloaded on 12/29/2025 3:13:31 AM. This article is licensed under a Creative Commons Attribution-NonCommercial 3.0 Unported Licence.

Spokoyny showed that the coordination strength of a carborane-functionalized thioether to Pt(II) (complex **II**, Chart 1) can be significantly influenced by the positional attachment of the sulfur-containing moiety.[8] This means that icosahedral carboranes can function as strong electron withdrawing or donating ligands, a unique behaviour in coordination chemistry that could regulate ligand electronic properties.

Over several decades, the research on *o*-carborane derivatives has garnered significant attention due to their unique structures, fundamental properties, and potential applications in material synthesis, medicine, optics, and microelectronics.[7b,9,10] In this regard, the monometallic 16e half-sandwich *o*-carborane species **I**, such as, [Cp*M{1,2-$(E)_2$-1,2-$C_2B_{10}H_{10}$}] (M = Co, Rh, Ir; E = S, Se) have been well explored.[11,12] In these complexes, the thiolate ligands in the metalladithiolene ring [MS_2C_2] often modulate carbon-based substituent effects, allowing for the tuning of the steric and electronic properties of the compounds. These sterically congested, mononuclear coordination compounds serve as stable starting materials and have demonstrated rich reaction chemistries.[11–14] For instance, these complexes can undergo alkyne insertion into metal–chalcogen bonds, which can subsequently lead to B–H activation, the formation of metal–boron bonds, and the functionalization of the carborane cage at B(3)/B(6) positions.[12] Additionally, the construction of novel polycarborane molecular architecture using two or more [1,2-$(E)_2$-1,2-$C_2B_{10}H_{10}]^{2-}$ units has been reported.[15] One notable metalation product, [1-(σ-S)-2-(η^5-$C_5H_4CH(Ph)$)-1,2-$C_2B_{10}H_{10}$]Ti(NMe_2)$_2$, was synthesized, where the appended carborane-thiol unit functions as both a linking and η^1-bonding group.[16]

Jin group has nicely established the chemistry of bimetallic rhodium complexes utilizing the [1,2-$(E)_2$-1,2-$C_2B_{10}H_{10}]^{2-}$ ligand, such as [$(Cp^*Rh)_2${1,2-$(S)_2$-1,2-$C_2B_{10}H_{10}$}][17a] and [$(Cp'Rh)_2${1,2-$(E)_2$-1,2-$C_2B_{10}H_{10}$}][17b] (Cp′ = η^5-1,3-^{t}Bu$_2$$C_5H_3$). Subsequently, Jin and Herberhold demonstrated that type **I** complexes can serve as models for further transformations due to their quasi-aromaticity and electronic unsaturation.[7b,12c,17,18] These complexes are particularly useful for the synthesis of heterometallic clusters with metal–metal bonds, stabilized by carborane-dichalcogenolato ligands. Interestingly, Jin group reported the first trimetallic cluster [{Cp*Ir(1,2-$(Se)_2$-1,2-$C_2B_{10}H_{10}$)}$_2$Rh] (**V**), synthesized from the reaction of [Cp*Ir{1,2-$(Se)_2$-1,2-$C_2B_{10}H_{10}$}] with [RhCl(cod)$_2$].[19a] Using a similar method, they have prepared the tetrametallic clusters [{Cp*Ir(1,2-$(E)_2$-1,2-$C_2B_{10}H_9$)}$_2$$Rh_2$(cod)] (E = S or Se).[19b] It is noteworthy that 1,2-dithiol-*o*-carborane has been extensively used as a strong electron-withdrawing group in the construction of both mononuclear and multinuclear complexes. Furthermore, Mirkin and Spokoyny reported the first carborane-based pincer ligand family and the respective Pd complexes of these ligands (complex **III**).[7c] The structure represents a new class of compounds with a Pd–B σ-coordination bond pincer motif.

Although the chemistry of C-functionalized carborane-thiols are well established by several groups, the chemistry of B-functionalized carborane has not been explored much.[7c,8,20] Yan and co-workers reported a monometallic 16-electron half sandwich complex of cobalt containing a 9,12-dithiol-*o*-carborane ligand, [CpCo{9,12-$(S)_2$-1,2-$C_2B_{10}H_{10}$}], and demonstrated its utility in the synthesis of boron-fused 1,4-dithiin compounds.[20b] Furthermore, Yan and Bregadze synthesized a new B-functionalized 8,9,12-trithiol-*o*-carborane and used it as a strongly electron-donating ligand to construct an unusual, isolable trinuclear cobalt cluster **IV** with 51 cluster valence electrons.[20c] They also showed that boron-based substituents significantly influence the stability and reactivity of these trimeric cobalt clusters.

The chemistry of metallacarborane has progressed impressively from the isolation of small cages to 16-vertex clusters.[7a,21,22] Xie and co-workers recently isolated and structurally characterized the 16-vertex metallacarborane **VI** by reduction of a 15-vertex carborane [1,14-$(SiMe_3)_2$-1,14-$C_2B_{13}H_{13}$] with excess of sodium, followed by reaction with 0.5 equiv. [Ru(*p*-cym)Cl_2]$_2$.[22a] They have also developed the chemistry of metallacarboranes of early transition metals. Many metallacarboranes of group 4 were synthesized utilizing *closo*-12 or *nido*-11 vertex carboranes.[22b–d] These metallacarboranes exhibit reactivity with unsaturated organic substrates such as alkynes, alkyl nitriles, diaryl ketones, and carbodiimides, with reactions primarily occurring at the metal centers. In parallel, our group has also focused on transition metal–boron compounds with diverse structures and properties. These include higher-vertex metallaborane clusters,[23] electron-precise transition metal–boron complexes,[24] and metallachalcogenaboranes[25] containing group 4–9 metals. The synthetic methodologies to generate metallachalcogenaborane clusters involve treating chalcogens, diaryl dichalcogenides, or carbon disulfide with Cp*-based transition metal chlorides ([Cp*MCl_x]) in the presence of [$LiBH_4$·THF].[23–25] These synthetic strategies have enabled us to isolate complexes in which small borane fragments are stabilized within the coordination sphere of bimetallic or trimetallic frameworks. Inspired by these results, we have attempted to synthesize metallachalcogenaboranes using carborane-thiols as the chalcogen source. In this article, we have explored the

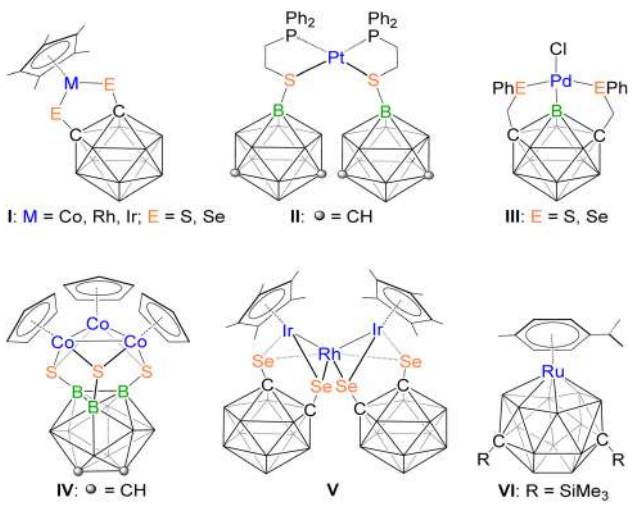


Chart 1 Various examples of functionalized-carborane-protected transition metal compounds.

© 2025 The Author(s). Published by the Royal Society of Chemistry

Open Access Article. Published on 10 July 2025. Downloaded on 12/29/2025 3:13:31 AM. This article is licensed under a Creative Commons Attribution-NonCommercial 3.0 Unported Licence.

chemistry of B- and C-functionalized *o*-carborane-thiol ligands with *in situ* generated intermediates, generated from the Cp*-based metal chlorides and [$LiBH_4$·THF]. These reactions led to the formation of clusters and coordination complexes featuring *o*-carborane-thiol ligands. We have further demonstrated how the C- or B-functionalized carboranethiol influences the formation of clusters or coordination complexes, respectively, without altering the steric properties of the ligands.

Results and discussion

Reactivity of [Cp*$TiCl_3$] with the C-functionalized carborane-dithiol [1,2-$(SH)_2$-1,2-$C_2B_{10}H_{10}$]

Reaction of [Cp*$TiCl_3$] with [$LiBH_4$·THF] at low temperature generated an unstable and sensitive intermediate, which, on treatment with [1,2-$(SH)_2$-1,2-$C_2B_{10}H_{10}$] at elevated temperature, led to the formation of an octacapped octahedral cluster [$(Cp^*Ti)_4${Ti(1,2-$(S)_2$-1,2-$C_2B_{10}H_{10}$)}$_2$(μ_3-S)$_6$(μ_3-O)$_2$] (**1**) and a hexacapped trigonal bipyramidal cluster [$(Cp^*Ti)_4${Ti(1,2-$(S)_2$-1,2-$C_2B_{10}H_{10}$)}(μ_3-S)$_6$] (**2**; Scheme 1). Note that this reaction also yielded other air and moisture sensitive products in low yields. The reaction mixture was separated using thin layer chromatography (TLC) on aluminium-supported silica gel plates. Although elution with hexane and dichloromethane solvent (50 : 50 v/v) allowed us to isolate **1** and **2** as brown solids, all of our attempts to isolate other species were unsuccessful. Detailed characterization of Ti-clusters **1** and **2** is discussed in the sections below.

1,2-Dithiol-*o*-carborane stabilized Ti_6-cluster, 1. Cluster **1** was isolated as a brown solid in 12% yield. The ^{1}H NMR spectrum of **1** showed three peaks at δ = 2.22, 2.25, and 2.28 ppm in a 1 : 1 : 2 ratio which corresponded to the Cp* protons. In addition, the ^{1}H{^{11}B} chemical shifts at δ = 2.52–2.98 ppm are attributed to the BH_t protons of the carborane ligand. The ^{11}B NMR spectrum of **1** displayed very broad resonances between δ = −13.0 and −1.0 ppm, consistent with the presence of the [1,2-$(S)_2$-1,2-$C_2B_{10}H_{10}$]$^{2-}$ ligand in cluster **1**. In the IR spectrum of **1**, an absorption band at 2580 cm^{-1} suggested the presence of B–H bonds. The mass spectrum of **1** exhibited a molecular-ion peak at *m*/*z* 1504.2403 ([M + K]$^+$). However, these spectroscopic data were not sufficient to identify the core geometry of **1**. A definitive structural explanation was achieved through single-crystal X-ray analysis of a suitable crystal of **1**, grown from an *n*-hexane/CH_2Cl_2 solution at −5 °C.

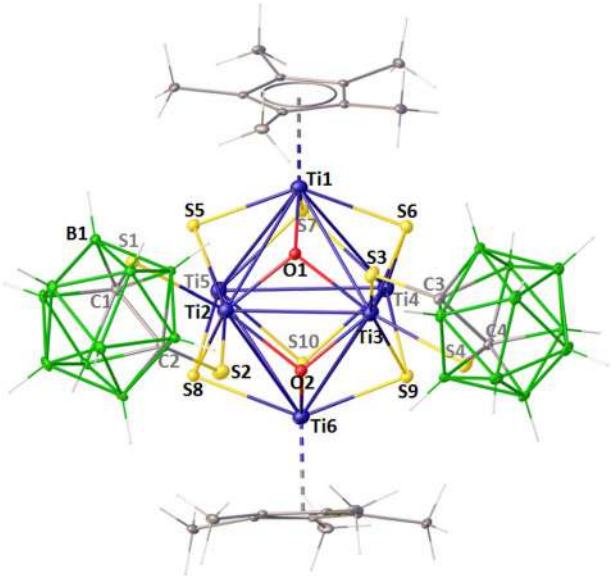
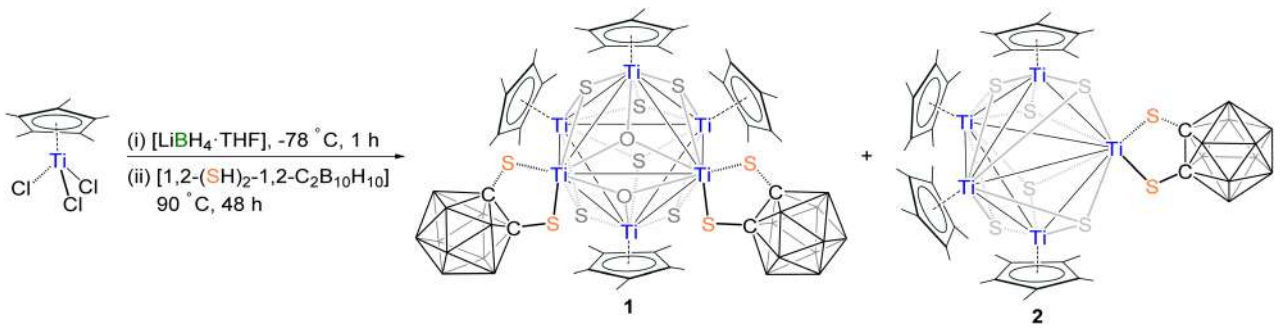


Fig. 1 Molecular structure and labelling diagram of **1**. Cp* ligands attached to Ti4 and Ti5 atoms are omitted for clarity. Selected bond lengths (Å) and bond angles (°): Ti···Ti 3.130–3.598, Ti1–S5 2.4274(12), Ti1–O1 1.919(2), Ti2–S5 2.4835(12), Ti2–S1 1.3963(13), C1–S1 1.785(4), B1–C1 1.703(7), Ti3–Ti2–Ti5 93.913, Ti1–S5–Ti2 82.52(4).

The solid-state X-ray structure of **1** revealed a distorted octahedral metallic framework consisting of six titanium atoms, where the eight triangular faces of the octahedron are capped by six triply bridging sulfur atoms and two triply bridging oxygen atoms, forming a distorted cube {S_6O_2} (Fig. 1). All the sulfur atoms in **1** must have originated from the de-thiolation of the ligand 1,2-dithiol-*o*-carborane, as this ligand is the only source of sulfur in the reaction. This agrees with previous studies, as the C–S bond is weaker than the B–S bond.[26] Furthermore, we believe that the trace amount of water bound to the silica gel led to the incorporation of oxygen that resulted in the formation of **1** during chromatographic work-up. Despite our best efforts, we were unable to isolate the unstable intermediate involved in this conversion. Although we are unable to provide any direct



Scheme 1 Synthesis of 1,2-dithiol-*o*-carborane protected Ti-clusters **1** and **2**.

© 2025 The Author(s). Published by the Royal Society of Chemistry

Open Access Article. Published on 10 July 2025. Downloaded on 12/29/2025 3:13:31 AM. This article is licensed under a Creative Commons Attribution-NonCommercial 3.0 Unported Licence.

evidence to support this, a similar phenomenon has previously been observed in transition metal boron complexes.[27] Interestingly, at two of six Ti atoms (Ti2 and Ti3), the Cp* ligand is replaced by the bidentate [1,2-(S)$_2$-1,2-$C_2B_{10}H_{10}$] ligand. To the best of our knowledge, cluster **1** is the first example of an [M_6] cluster containing a carborane ligand. The [$Ti_6S_6O_2$] core in **1** is isostructural with [Ti_6O_8] in [$Cp_6Ti_6O_8$].[28]

The coordination geometry around four Ti centers (Ti1, Ti4, Ti5, and Ti6) in **1** is square pyramidal, with the basal plane defined by μ_3-chalcogen atoms and the apex occupied by the Cp* ligand. The average displacement of titanium atoms from the basal plane is 0.951 Å, which is slightly higher compared to the reported complexes [$Cp_6Ti_6O_8$][28a] (0.762 Å) and [$Cp^*_6Ti_6S_8$][28b] (0.857 Å). The coordination geometry around the other two Ti centers (Ti2 and Ti3) is octahedral, with the equatorial plane defined by one μ_3-S, one μ_3-O, and two S atoms from one of the 1,2-dithiol-*o*-carborane ligands, while the axial positions are occupied by one μ_3-S and one μ_3-O ligand. The Ti–Ti bond distances in **1** range from 3.130 Å to 3.598 Å, which are comparable to those in [$Cp^*_6Ti_6S_8$] (av. 3.503 Å) and [$(CpTi)_5(\mu_3\text{-}S)_5(\mu_3\text{-}S_2)(\mu_4\text{-}O)$][28c] (3.207(3)–3.597(3) Å) but considerably longer than those in [$Cp_5Ti_5S_6$] (av. 3.156 Å).[28b,29] Furthermore, due to the replacement of Cp* by the 1,2-dithiol-*o*-carborane ligand, which reduces steric crowding at the titanium centers, the Ti2–Ti3 bond distance (3.130 Å) is significantly shorter compared to other Ti–Ti bond distances (3.230–3.598 Å). The average Ti–S–Ti bond angle in **1** is 89.68°, similar to the value observed in [$Cp^*_6Ti_6S_8$] (91.29°). The two 1,2-dithiol-*o*-carborane ligands attached to two equatorial titanium atoms are nearly coplanar with each other. Additionally, the Ti–S–C–C–S plane is not coplanar with the Ti_4 equatorial plane but is tilted by an average angle of 42.27°.

The cluster valence electron (CVE) count for an M_6 octahedral cluster is expected to have 86 valence electrons (VEs).[30] However, the total number of VEs available in **1** is 80 [9 (Cp*Ti) × 4 + 6 {Ti(1,2-(S)$_2$-1,2-$C_2B_{10}H_{10}$)} × 2 + 4 (μ_3-S) × 8]. For comparison, the clusters [$Cp_6Ti_6S_8$] and [$Cp_6Ti_6Cl_8$] possess 86 and 94 VEs, respectively. Therefore, while [$Cp_6Ti_6S_8$] and [$Cp_6Ti_6Cl_8$] are electronically saturated and hyper-electronic clusters, respectively, cluster **1** is hypo-electronic. On the other hand, if we consider **1** as an organometallic aggregate, one of the important aspects of this chemistry is the electronic configuration of [M_6X_8] (X = O, S, Cl) clusters. According to the inert gas formalism, clusters [$Cp_6M_6X_8$] (X = O, S, Cl) and **1** require 84 and 80 electrons, respectively.[28e,f] However, [$Cp_6Ti_6S_8$], [$Cp_6Ti_6Cl_8$], and **1** possess 86, 94, and 80 electrons, respectively. The number of electrons in excess of those required for Ti–Cp and Ti–X (X = O, S, Cl) bonding increases precisely with the formal number of Ti(III) d^1 ions present in each cluster: ten in [$Cp_6Ti_6Cl_8$], two in [$Cp_6Ti_6S_8$], and zero in **1**. Therefore, in terms of electronic configuration, cluster **1** is a new addition to these [M_6X_8] cluster series. Based on valence-bond arguments, Gillespie has suggested that the two excess electrons in [$Cp_6Ti_6S_8$] reside at the center of the octahedron.[31a] Mealli *et al.* have reported a qualitative molecular orbital (MO) analysis of such octahedral metal clusters.[31b] They have shown that the excess electron pair occupies the a_{1g} bonding MO, composed of metal d orbitals, resulting in 1/12 M–M bond order at each edge. In **1**, although, the a_{1g} remains unoccupied, there are other factors that cement the Ti_6 unit together, which include mixing of other orbitals and second-order perturbation effects. Notably, the electron count in clusters of the early transition metals can be as low as 80, and cluster **1** is an example of an 80 VE octahedral cluster.[31b] The MO calculations and presence of all Ti(+4) ions (resulting in zero VE) explain the diamagnetism of **1**, which is consistent with the intensity and low energy of the visible absorption; cluster **1** is brown.

Density functional theory (DFT) studies at the BP86/def2-SVP level were performed to understand the electronic structure and bonding situation in **1**. The optimized structural parameters are closely aligned with those obtained from X-ray crystallography. MO analysis of **1** revealed that the HOMO is predominantly localized on the p orbitals of the thiolato groups, with a minor contribution from the d orbitals of the Ti2 and Ti3 atoms (Fig. 2a). On the other hand, the LUMO is entirely localized on the d orbitals of the six Ti atoms (Fig. 2b). MO analysis further showed that the bonding of the Ti atoms (Ti2 and Ti3) with the thiolato groups of the 1,2-dithiol-*o*-carborane ligand involved substantial overlap of d orbitals of Ti with p orbitals of the sulfur atoms as observed in HOMO−13 (Fig. 2c). The coordination of the 1,2-dithiol-*o*-carborane ligand to the Ti atom through the thiolato groups was also depicted by a contour line diagram of the Laplacian of electron density drawn along the Ti2–S2–C1–C2–S1 ring (Fig. 2d). Additionally, the natural charge analysis revealed that the thiolato groups carry positive natural charges, while the μ_3-S atoms bear negative natural charges (Table S3†).

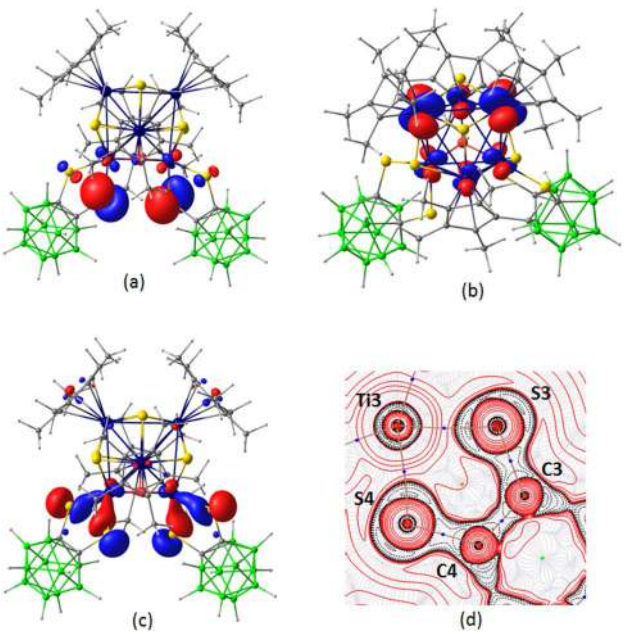


Fig. 2 (a) HOMO, (b) LUMO, and (c) HOMO−13 of **1** (isocontour values: ±0.045 [e bohr^{-3}]$^{1/2}$). (d) Contour-line diagram of the Laplacian of the electron density along the Ti3–S3–S4 plane in **1**.

© 2025 The Author(s). Published by the Royal Society of Chemistry

Open Access Article. Published on 10 July 2025. Downloaded on 12/29/2025 3:13:31 AM. This article is licensed under a Creative Commons Attribution-NonCommercial 3.0 Unported Licence.

1,2-Dithiol-*o*-carborane stabilized Ti_5-cluster, 2. Cluster **2** is isolated in the form of a brown solid in 18% yield. The ^{1}H NMR spectrum of **2** indicated the presence of two distinct Cp* environments, with resonances appearing at $\delta = 2.21$ and 2.23 ppm. In addition, the $^1H\{^{11}B\}$ chemical shifts at $\delta = 2.47$–3.04 ppm are attributed to the BH_t protons, which suggest the presence of the carborane ligand. This assessment was validated by the ^{13}C NMR spectrum. Furthermore, the presence of the carborane ligand was confirmed by the signals that appeared at $\delta = -12.4$ to -0.8 ppm in the ^{11}B NMR spectrum. The IR spectrum of complex **2** displayed peaks at 2589 cm^{-1}, attributed to the terminal B–H stretching frequencies of the carborane ligand. The mass spectrometric analysis showed the molecular ion peak at *m*/*z* 1291.1251 corresponding to the formula $[C_{45}H_{77}B_{10}S_8ONTi_5Na]$. Finally, in order to ascertain the solid-state structure of complex **2**, a single-crystal X-ray diffraction study was performed.

The solid-state X-ray diffraction study revealed the identity of **2** as $[(Cp^*Ti)_4\{Ti(1,2\text{-}(S)_2\text{-}1,2\text{-}C_2B_{10}H_{10})\}(\mu_3\text{-}S)_6]$, which showed that **2** contains sulfur atoms bridging the triangular faces of a distorted trigonal bipyramid of titanium (Fig. 3). The $[1,2\text{-}(S)_2\text{-}1,2\text{-}C_2B_{10}H_{10}]$ ligand replaced a Cp* ligand on one of the Ti atoms (Ti2) of the equatorial plane. The axial titanium (Ti1, Ti5) and one of the equatorial titanium centers (Ti2) have a coordination number of six. On the other hand, the titanium atoms (Ti3, Ti4) have a coordination number of seven. A crystallographic mirror plane lies in the vertical direction containing Ti1, Ti2, and Ti5 atoms. Cluster **2** represents another metal-sulfide cluster with a carborane ligand, which is isostructural with $[Cp_5Ti_5S_6]$.[29] The Ti–Ti bond distances (av. 3.274 Å) in **2** are shorter compared to those in cluster **1** (av. 3.384 Å) but are slightly longer than the Ti–Ti distance in $[Cp_5Ti_5S_6]$ (av. 3.156 Å).

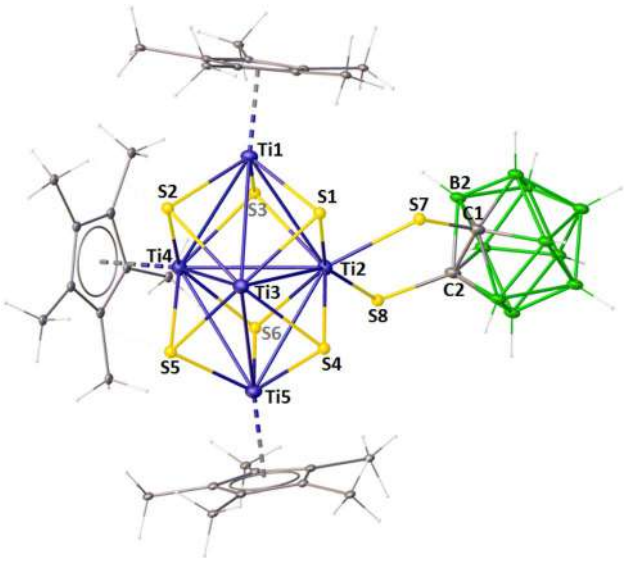


Fig. 3 Molecular structure and labelling diagram of **2**. The Cp* ligand attached to Ti3 atom is omitted for clarity. Selected bond lengths (Å) and bond angles (°): Ti···Ti 3.201–3.305, Ti1–S1 2.2839(17), Ti2–S1 1.5004(16), Ti2–S7 1.446(4), Ti3–S1 2.5089(17), C2–S8 1.782(9), Ti3–Ti2–Ti4 58.270, S7–Ti2–S8 81.09(12), Ti1–S1–Ti2 82.24(5).

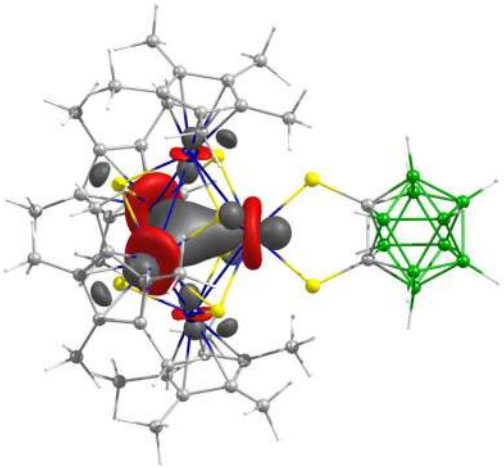


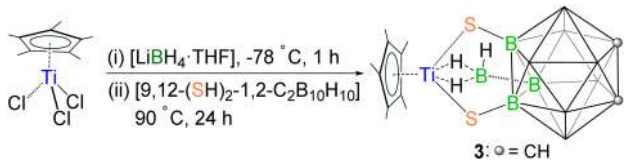
Fig. 4 HOMO of **2** showing 3c–2e equatorial trititanium interactions (isocontour values: ±0.045 [e bohr^{-3}]$^{1/2}$).

The Ti–S bond distances in **2** (av. 2.436 Å) are comparable to those in cluster **1** and $[Cp_5Ti_5S_6]$. Notably, the Ti3–Ti4 bond distance (3.201 Å), opposite to the Ti atom attached to the 1,2-dithiol-*o*-carborane ligand, is shorter than the other Ti– Ti bond distances (3.243–3.306 Å). The axial Ti–S distances (av. 2.290 Å) are significantly shorter than the equatorial Ti–S distances (av. 2.513 Å). The differing axial and equatorial Ti–S distances are due to the different formal oxidation states of the Ti atoms. The two axial Ti atoms adopt a +4 oxidation state, whereas among the equatorial Ti centers, two coordinated to Cp* are formally Ti(+3), while the remaining Ti, bound to the dithiol-*o*-carborane ligand, exhibits +4 oxidation state. In this regard, a 3c–2e bonding interaction was observed along the equatorial trititanium (Ti2–Ti3–Ti4) framework in the HOMO of **2** (Fig. 4). This kind of interaction in trimetallic frameworks has recently been well-studied due to their aromatic and magnetic properties.[32] Perhaps the most persuasive evidence for Ti–Ti interactions is the acute Ti–S–Ti angles, averaging 83.27°. Since the μ_3-sulfur bridge could hold the cluster together without any Ti–Ti interaction, one would expect that the Ti–S–Ti angles would approach the idealized tetrahedral angle without interaction. Therefore, the observed angles and distances indicate the presence of Ti–Ti interactions. The CVE count for an M_5 trigonal bipyramidal cluster is expected to be 72 VEs.[30] However, cluster **2** contains only 66 valence electrons, confirming that it is hypo-electronic.

The 1,2-dithiol-*o*-carborane ligand in **2** is attached to the equatorial Ti-atom in such an orientation that the Ti–S–C–C–S plane makes an angle of 43.28° with the Ti_3 equatorial plane. The incorporation of the 1,2-dithiol-*o*-carborane ligand has measurable effects on the bond lengths, angles, and overall geometry of the Ti-clusters **1** and **2**. The ligand appears to enhance structural stability by balancing electronic and steric factors, influencing both intra-cluster interactions and resistance to external perturbations. These findings suggest that carborane-based ligands are promising tools for stabilizing high-nuclearity metal-sulfide clusters with potential applications in catalysis and materials science.

© 2025 The Author(s). Published by the Royal Society of Chemistry

Open Access Article. Published on 10 July 2025. Downloaded on 12/29/2025 3:13:31 AM. This article is licensed under a Creative Commons Attribution-NonCommercial 3.0 Unported Licence.



Scheme 2 Synthesis of the 9,12-dithiol-*o*-carborane funcionalized hydridoborato complex of titanium, **3**.

Reactivity of [Cp*TiCl$_3$] with the B-functionalized carborane-dithiol [9,12-(SH)$_2$-1,2-C$_2$B$_{10}$H$_{10}$]

The successful isolation of clusters **1** and **2** interested us to investigate the role of ligand connectivity in cluster formation. Note that in these systems, the SH groups are influenced by the strong electron-donating effect of the carborane cage, causing them to act as weak acids.[33] The presence of these changes in B-functionalized carborane-dithiol is likely to modify the course of the reaction as compared to the C-functionalized ligand. As a result, we have explored the reactivity of B-functionalized carborane-dithiol [9,12-(SH)$_2$-1,2-C$_2$B$_{10}$H$_{10}$]. The low-temperature reaction of [Cp*TiCl$_3$] with [LiBH$_4$·THF] resulted in an unstable, sensitive intermediate, just like in the previous case, which on treatment with [9,12-(SH)$_2$-1,2-C$_2$B$_{10}$H$_{10}$] at elevated temperature yielded the yellow complex **3** with a relatively higher yield of 64% (Scheme 2). Unlike clusters **1** and **2**, the ^{1}H NMR spectrum of **3** displayed a single peak at δ = 2.24 ppm, which can be assigned to the chemically equivalent methyl protons of the Cp* ligand. Interestingly, the high-field region showed a broad resonance at $\delta = -0.86$ ppm that suggested the presence of the Ti–H–B proton. The ^{11}B{^{1}H} NMR showed six resonances at $\delta = -15.8$, -11.2, -10.1, -6.8, -3.1 and 8.4 ppm. The IR spectrum of **3** exhibits an absorption band at 2602 cm^{-1} that suggests the presence of terminal B–H$_t$ stretching vibrations originating from the 9,12-dithiol-*o*-carborane ligand. The ^{13}C NMR spectrum confirms the presence of Cp* (δ = 13.9 and 127.8 ppm) and 9,12-dithiol-*o*-carborane (δ = 44.3 ppm) ligands. Furthermore, the ESI-MS spectrum of **3** displayed a molecular ion peak at *m*/*z* 403.2129 with the typical isotopic distribution pattern corresponding to the [M+H]$^+$ fragment.

The single-crystal X-ray diffraction analysis of **3** revealed a structure that is completely different from that of **1** and **2**, a 9,12-dithiol-*o*-carborane-funcionalized κ^2-hydridoborato complex [(Cp*Ti){κ^2-BH$_3$(9,12-(S)$_2$-1,2-C$_2$B$_{10}$H$_{10}$)}] (Fig. 5). In complex **3**, one Cp* ligand and one {κ^2-BH$_3$(9,12-(S)$_2$-1,2-C$_2$B$_{10}$H$_{10}$)} ligand are coordinated to the central titanium atom opposite to each other. This 9,12-dithiol-*o*-carborane-funcionalized borate ligand is connected to the metal through four atoms: two are thiol substituents of the carborane cage, and two are hydrogens of the *exo*-BH$_3$ unit. Therefore, this structure can be described as a four-legged piano-stool geometry, where the coordination number around the titanium center is seven, assuming the Cp* ligand as three-coordinate. The structure possesses a σ-plane of symmetry through the plane containing [Ti1–B11–B1–B10–B9–B4] atoms. Unlike **1** and **2**, the metallacycle, [Ti1–S1–B2–B3–S2] in **3** is puckered at Ti caused by the newly formed Ti–dihydridoborato interaction, while the remaining four atoms [S1–B2–B3–S2] form an almost perfect plane. Consequently, the [TiS$_2$B$_2$] metallacycle in **3** is bent, and the titanium atom is out of the plane of the 9,12-dithiol-*o*-carborane ligand, with the dihedral angles between the planes defined by [Ti–S–S] and [S–B–B–S] being 66.29°. The Ti–S bond lengths in **3** (av. 2.327 Å) are shorter than those in clusters **1** (av. 2.47 Å) and **2** (av. 2.45 Å) but are in good agreement with the existing values in the literature for a wide variety of Ti–S σ-bonds.

One of the interesting features of complex **3** is the presence of the 9,12-dithiol-*o*-carborane functionalized hydridoborato ligand. The isolation of the Ti-hydridoborato unit suggests the formation of an intermediate [(Cp*Ti)(κ^2-BH$_4$){9,12-(S)$_2$-1,2-C$_2$B$_{10}$H$_{10}$}] followed by the formation of a new B–B bond *via* a dehydrocoupling reaction between one terminal hydrogen of (κ^2-BH$_4$) and one B(8)–H hydrogen from the [9,12-(SH)$_2$-1,2-C$_2$B$_{10}$H$_{10}$] ligand. The κ^2-coordinated BH$_3$R group exhibits a Ti···B distance of 2.259(4) in **3**, which is shorter than those for the κ^2-BH$_3$Me ligand in [(Cp*Ti)(κ^2-BH$_3$Me)(κ^3-BH$_3$Me)][32a] (2.377(2) Å), but longer than those in κ^3-hydridoborato ligands

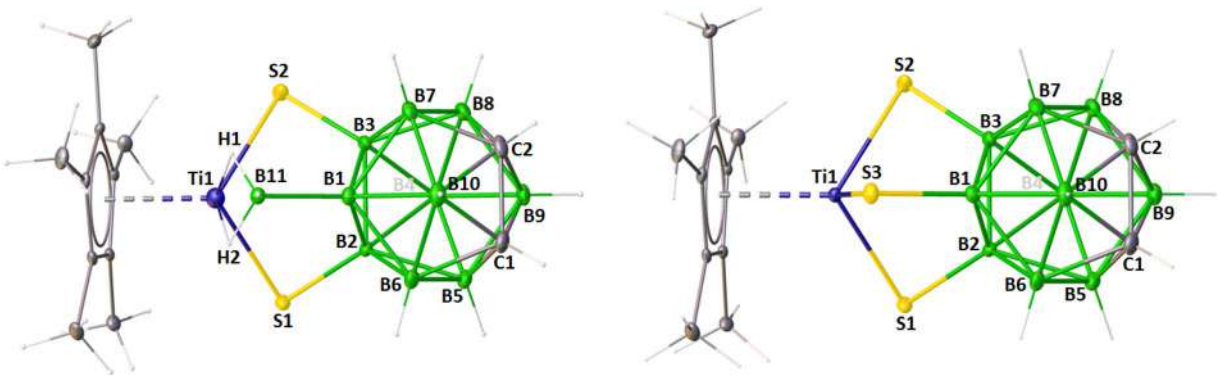


Fig. 5 Molecular structure and labelling diagram of **3** (left) and **4a** (right). Selected bond lengths (Å) and bond angles (°): **3**: Ti1–S1 2.3321(9), Ti1–S2 2.3214(9), Ti1···B11 2.259(4), Ti1–H1 2.00(3), Ti–H2 1.93(3), B11–H1 0.90(3), B11–H2 1.03(4), B1–B11 1.750(5), B2–S1 1.851(4), C1–C2 1.626(6), Ti1–S1–B2 81.17(11), B2–B1–B11 121.9(3). **4a**: Ti1–S1 2.3095(12), Ti1–S3 2.3231(12), B1–S3 1.849(5), B1–B2 1.829(5), C1–C2 1.635(7), C1–B10 1.713(7), Ti1–S1–B2 80.72(14).

© 2025 The Author(s). Published by the Royal Society of Chemistry

Open Access Article. Published on 10 July 2025. Downloaded on 12/29/2025 3:13:31 AM. This article is licensed under a Creative Commons Attribution-NonCommercial 3.0 Unported Licence.

in $[(Cp^*Ti)(\kappa^3\text{-}BH_4)(thf)_2](BPh_4)$[34a] (2.178(6) Å) and $[(CO)_4Ti(\kappa^3\text{-}BH_4)]$[34b] (2.158(7) Å). A qualitative electron counting scheme suggests **3** to be a 14 electron system ($(Cp^{*-}$ (6e) + $\{\kappa^2\text{-}BH_3(9,12\text{-}(S)_2\text{-}1,2\text{-}C_2B_{10}H_{10})\}^{3-}$ (6e)) + 2 Ti–H–B (2e)), and Ti^{4+} (0e), where Ti is in +4 oxidation state.

To get insight into the bonding scenario in dihydridoborate coordination, we have performed DFT calculations on **3**. The natural bond orbital (NBO) and MO analyses indicated the existence of strong 3c–2e bonding interactions along the Ti1–H–B11 units (Fig. 6a and S62d†). The Laplacian of electron density revealed the presence of BCP along the bond paths of Ti1–$H_{bridging}$ and B11–$H_{bridging}$, respectively (Fig. 6c). The bond paths appear to be curved inwards, confirming these interactions to be of 3c–2e type. Furthermore, an extended delocalized bonding interaction was observed in HOMO−6 that shed light on the coordination of the Ti-borate unit with the carborane cage through B1 boron (Fig. S62c†). In this regard, NBO analysis suggested the presence of a 2c–2e bond between B11–B1 (Fig. 6b), which was further supported by a BCP along the corresponding bond path in the electron density contour plot (Fig. 6d). Additionally, MO analysis illustrated the bonding of the two thiolato groups with the metal center aided by the overlap of the d orbital of Ti with p orbitals of S (Fig. S62b†).

Reactivity of $[Cp^*TiCl_3]$ and $[Cp_2TiCl_2]$ with the B-functionalized carborane-trithiol $[8,9,12\text{-}(SH)_3\text{-}1,2\text{-}C_2B_{10}H_9]$

To explore the coordination chemistry of carborane-thiol ligands, we have now explored the chemistry of the B-functionalized carborane-trithiol ligand $[8,9,12\text{-}(SH)_3\text{-}1,2\text{-}C_2B_{10}H_9]$ under similar reaction conditions. An unstable intermediate was formed through a low-temperature reaction of $[Cp^*TiCl_3]$ with $[LiBH_4\cdot THF]$, which on treatment with $[8,9,12\text{-}(SH)_3\text{-}1,2\text{-}C_2B_{10}H_9]$ yielded, $[(Cp^*Ti)\{8,9,12\text{-}(S)_3\text{-}1,2\text{-}C_2B_{10}H_9\}]$ (**4a**; Scheme 3). With an objective to isolate a trimetallic Ti_3 cluster, $[(Cp_2Ti)_3\{8,9,12\text{-}(S)_3\text{-}1,2\text{-}C_2B_{10}H_9\}_2]$, we carried out the reaction of the trithiol ligand with $[Cp_2TiCl_2]$. Unexpectedly, this led to the formation of $[(CpTi)\{8,9,12\text{-}(S)_3\text{-}1,2\text{-}C_2B_{10}H_9\}]$ (**4b**; Scheme 3), analogous to **4a**. Complexes **4a** and **4b** were isolated as pale-yellow solids in 72% and 57% yield, respectively. The ^1H NMR spectra of **4a** and **4b** showed single intense signals at δ = 2.24 and 6.65 ppm, corresponding to the Cp* and Cp ligands, respectively. The ^{13}C NMR spectra are consistent with one type of Cp* or Cp ligand.

Besides the Cp* or Cp signals, ^1H NMR spectra displayed additional peaks at $\delta = 3.49$ ppm for **4a** and $\delta = 3.59$ ppm for **4b** attributed to carborane-C*H* protons. The ^{13}C NMR peaks for **4a** and **4b** are also observed at $\delta = 39.7$ and 39.8 ppm, respectively, which confirmed the *C*H group of $[8,9,12\text{-}(SH)_3\text{-}1,2\text{-}C_2B_{10}H_9]$ ligand. The ^{11}B chemical shifts of the boron bonded to sulfur in **4a** and **4b** shifted to the downfield region compared to the free ligands, suggesting an electronic influence from the Cp*/CpTi-fragment on the carborane ligands. The IR spectra exhibited absorption bands at 2569 and 2605 cm^{-1} for **4a** and 2598 and 2623 cm^{-1} for **4b**, attributed to the terminal B–H stretches, respectively. Furthermore, the mass spectra of **4a** and **4b** showed molecular-ion peaks at m/z = 421.1511 and m/z = 723.1343, respectively, consistent with (M + H) and (2M + H). Finally, single-crystal X-ray diffraction analyses were conducted on suitable crystals of **4a** and **4b**.

As shown in Fig. 5 and S5,† the solid-state X-ray structures of **4a** and **4b** can be described as three-legged piano-stool geometry with a coordination number of six around the titanium center. In both the complexes, Cp*/Cp and $[8,9,12\text{-}(S)_3\text{-}1,2\text{-}C_2B_{10}H_9]$ ligands are coordinated to titanium atom in opposing positions. The dihedral angle between the Cp* plane and [B1–B2–B3] plane of the carborane cage is 1.05° (**4a**) and 0.91° (**4b**), which are closer to planar and less deviated as compared to **3** (2.15°). This may be due to the symmetrical nature of the $[8,9,12\text{-}(S)_3\text{-}1,2\text{-}C_2B_{10}H_9]$ ligand. In **4a** and **4b**, the three metalladithiolene $[TiS_2B_2]$ rings are formed to fix the monometallic Cp*Ti fragment into the carborane scaffold through three Ti–S bonds. The dihedral angle between $[B_2S_2]$ and $[TiS_2]$ in **4a** (av. 64.12°) and **4b** (64.86°) indicates that these metallacycles $[TiS_2B_2]$ are non-planar. The Ti–S bond lengths in **4a** (av. 2.313 Å) and **4b** (2.318 Å) are significantly shorter than in clusters **1** and **2** but are in good agreement with **3**. The overall structure possesses a σ-plane of symmetry, perpendicular to the C1–C2 bond and containing the [Ti1–S3–B1–B10–B9–B4] atoms. A qualitative electron counting scheme suggests **4a** and **4b** to be the 12 electron systems, where $Ti(d^0)$ is in +4 oxidation state.

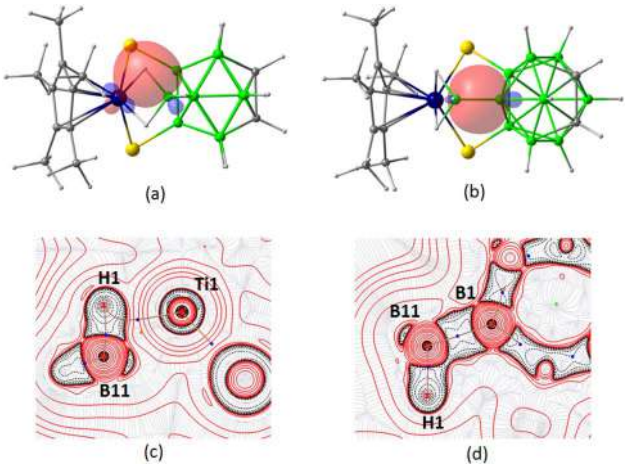
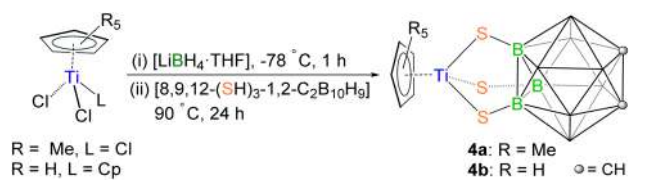


Fig. 6 Selected NBO of **3** showing (a) 3c–2e interaction of Ti1–H1–B11 and (b) 2c–2e interaction of B1–B11 (isocontour values: ±0.045 [e $bohr^{-3}]^{1/2}$). Contour-line diagram of the Laplacian of electron density along (c) Ti1–H1–B11 and (d) B1–B11–H1 planes in **3**.



Scheme 3 Synthesis of 8,9,12-trithiol-*o*-carborane protected Ti-thiolate complexes **4a** and **4b**.

© 2025 The Author(s). Published by the Royal Society of Chemistry

Open Access Article. Published on 10 July 2025. Downloaded on 12/29/2025 3:13:31 AM.
This article is licensed under a Creative Commons Attribution-NonCommercial 3.0 Unported Licence.

Reactivity of $[Cp^*VCl_2]_3$ with the B-functionalized carborane-trithiol $[8,9,12\text{-}(SH)_3\text{-}1,2\text{-}C_2B_{10}H_{10}]$

Intrigued by the formation of the BH_3-R group coordinated to Ti and relatively higher yields, we have done further experiments aimed at investigating the role of the metal in the formation of metal carborane-thiolate complexes. As a result, we have now changed the metal from Ti to V. The low-temperature reaction of $[Cp^*VCl_2]_3$ with $[LiBH_4\cdot THF]$ resulted in an unstable and sensitive intermediate, which on treatment with the $[8,9,12\text{-}(SH)_3\text{-}1,2\text{-}C_2B_{10}H_9]$ ligand at elevated temperature yielded a green solid **5** with a yield of 26% (Scheme 4). The ^1H and ^{13}C NMR spectra of **5** confirmed the presence of both Cp* and carborane ligands. Interestingly, an alluring signal at $\delta = -0.43$ ppm in the ^1H NMR spectrum suggests the formation of a B–H–B bridged bond. Unlike **4a** and **4b**, the ^{11}B NMR spectrum of **5** displayed five peaks at $\delta = -30.3, -25.8, -22.0, -6.4$, and -4.6 ppm, indicative of a different boron environment. The IR spectrum of **5** showed absorption bands at 2619 and 2683 cm^{-1} associated with terminal B–H stretches. To validate the spectroscopic data and elucidate the solid-state X-ray structure of **5**, the single-crystal X-ray diffraction analysis was carried out.

The molecular structure of **5**, shown in Fig. 7, revealed a six-coordinate vanadium atom, bonded to three S atoms from the *nido*-carborane ligand $[1,5,6\text{-}(S)_3\text{-}nido\text{-}7,8\text{-}C_2B_9H_9]$ and Cp* ligand, forming a three-legged piano-stool geometry. The C_2B_3 open face of the *nido*-carborane ligand is positioned opposite to the V–S coordination. The dihedral angle between the Cp* plane and the [B1–B2–B3] plane of the carborane cage measured 3.07°, indicating a near-planar orientation but with greater deviation compared to complexes **4a** and **4b**, likely due to the asymmetry of the *nido*-carborane ligand. The V–S bond lengths (2.213 Å) are typical and comparable with those observed in $[(^iPrCp)_2V_2S_4]$ (2.236 Å).[35] The C–C distance (1.555(8) Å) within the cup-shaped carborane cage is similar to the C–C bond lengths in *closo*-carborane cage complexes **4a** (1.629(3) Å) and **4b** (1.635(7) Å).

Interestingly, complex **5** can be considered as a zwitterionic complex, arising from the separation of the cationic metal fragment (Cp*V) and the *nido*-carborane anion, which was formed by deboronation of one of the B(3)/B(6) vertices.[36] The vanadium atom in **5** possesses 12 valence electrons, which accounts for the observed diamagnetism of the complex. During the reaction, the removal of a B(3)–H unit from the parent *closo*-carborane cage transformed it into a *nido*-carborane (C_2B_9) anion, with the anionic charge delocalized onto the pendant $[C_2B_3]$ ring and consequently, **5** became a zwitterion with the $[Cp^*V(\kappa^3\text{-}S,S,S)]^+$ fragment. Note that the conversion of *closo*-carboranes to *nido*-carboranes through deboronation is a well-known reaction, typically induced by nucleophilic attack.[11e,37] In this case, the employed borohydride anion (BH_4^-) can act as a nucleophile.[38] Additionally, deboronation reactions generally require higher energy.[5] Therefore, this transformation may be attributed to the combined effect of the nucleophile and the elevated temperature. In contrast to **4a** and **4b**, the isolation of **5** highlights the significant influence of both the ligand coordination and the metal center in directing the formation of transition-metal carborane-thiolate complexes.

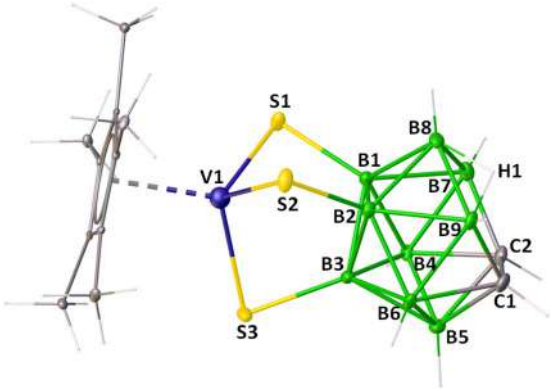
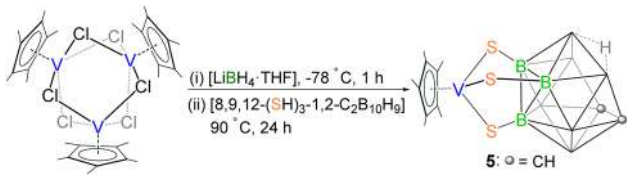


Fig. 7 Molecular structure and labelling diagram of **5**. Selected bond lengths (Å) and bond angles (°): V1–S1 2.2194(16), V1–S3 2.2099(15), B3–S3 1.859(6), B1–B8 1.780(9), C1–C2 1.555(8), C2–B7 1.596(8), B8-Hb 1.15(2), B9-Hb 1.16(2), V1–S1–B1 81.01(19), V1–S3–B3 79.42(17), B7–B8–B9 101.7(5), C1–C2–B7 114.3(5).



Scheme 4 Synthesis of 1,5,6-trithiol-*nido*-carborane protected V-thiolate complex **5**.

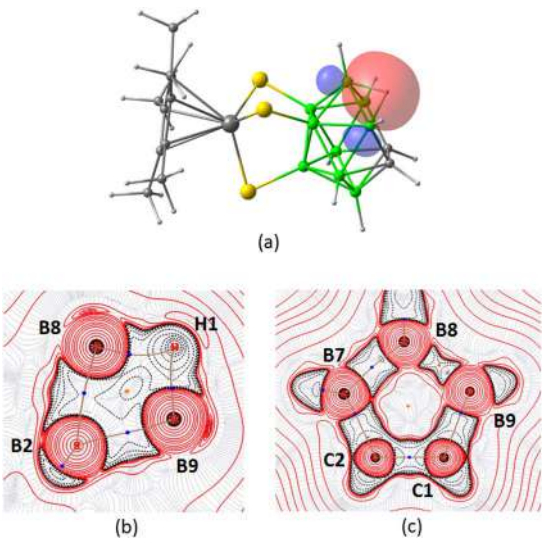
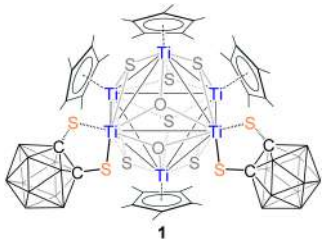
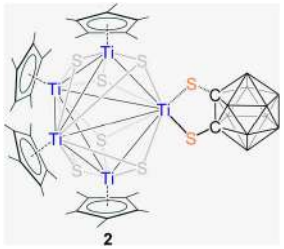
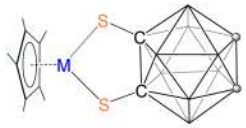
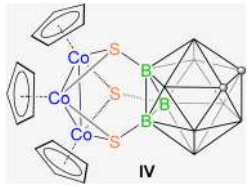
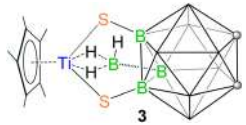
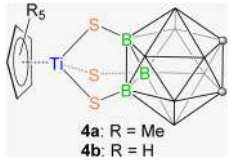


Fig. 8 (a) Selected NBO of **5** showing the 3c–2e interaction of B8–H1–B9 (isocontour values: ±0.045 [e $bohr^{-3}]^{1/2}$). Contour-line diagram of the Laplacian of the electron density along (b) B8–H1–B9 and (c) B7–B8–B9 planes in **5**.

© 2025 The Author(s). Published by the Royal Society of Chemistry

Open Access Article. Published on 10 July 2025. Downloaded on 12/29/2025 3:13:31 AM.
This article is licensed under a Creative Commons Attribution-NonCommercial 3.0 Unported Licence.

Table 1 Selected structural parameters, spectroscopic details, electron count, and oxidation state of the metal in **1–5**[a]

Complexes	Structural parameters			Spectroscopic details			
	$d_{av.M-S}$ (Å)	$\Theta_{av.S-M-S}$ (°)	$\Theta_{av.S-S\ vector}$ (°)	^{11}B NMR	IR	TEC	Oxidation state of M
 **1**	2.385	84.445	5.24	−13.0 to −1.0	2580	80	+4
 **2**	2.452	81.09	1.94	−12.4 to −0.8	2589	66	+3 and +4
 **I**: M = Co, Rh, Ir	2.125 (Co) (Rh)[b] 2.263 (Ir)	96.609 (Co) (Rh)[b] 92.69 (Ir)	3.00 (Co) (Rh)[b] 1.93 (Ir)	(Co)[b] −10.7 to −5.2 (Rh) (Ir)[b]	2554 (Co) 2590, 2561 (Rh) 2600, 2560 (Ir)	16	+3
 **IV**	2.203	97.983	11.91	−13.6 to 13.0	2601	51	+2
 **3**	2.327	101.497	66.29	−15.8 to 8.4	2602	14	+4
 **4a**: R = Me **4b**: R = H	2.313 (**4a**) 2.318 (**4b**)	103.555 (**4a**) 103.203 (**4b**)	64.12 (**4a**) 64.86 (**4b**)	−22.3 to 6.3 (**4a**) −22.2 to 7.1 (**4b**)	2605, 2569 (**4a**) 2623, 2598 (**4b**)	12	+4

© 2025 The Author(s). Published by the Royal Society of Chemistry

Open Access Article. Published on 10 July 2025. Downloaded on 12/29/2025 3:13:31 AM.
This article is licensed under a Creative Commons Attribution-NonCommercial 3.0 Unported Licence.

Table 1 (*Contd.*)

Complexes	Structural parameters			Spectroscopic details		TEC	Oxidation state of M
	$d_{av.M-S}$ (Å)	$\Theta_{av.S-M-S}$ (°)	$\Theta_{av.S-S\ vector}$ (°)	^{11}B NMR	IR		
5	2.213	106.293	67.94	−30.3 to −4.6	2683, 2619	14	+5

[a] ^{11}B NMR: range of ^{11}B chemical shifts; IR ($\bar{\upsilon}$ in cm^{-1}) corresponding to terminal B–H stretches of the carborane ring is shown; in $d_{av.M-S}$, $\Theta_{av.S-M-S}$, and $\Theta_{av.S-S\ vector}$ S atoms refer to the sulfur atoms attached to the carborane ligand only; $\Theta_{av.S-S\ vector}$ represents the angle between the planes of S–M–S and S–C/B–C/B–S. [b] Data not available.

The MO analysis of **4a** and **5** showed that the coordination of three thiolato groups with the metal in both the complexes involves similar bonding interactions of the metal d orbitals with the p orbitals of sulfur (Fig. S65 and S68†). The NBO analysis further revealed a 3c–2e interaction in **5**, involving bridging hydrogen (H1) and boron atoms B8 and B9 on the open face of the *nido*-carborane cage (Fig. 8a). This interaction was illustrated by the contour line diagram of Laplacian of electron density along the B8–H1–B9 unit (Fig. 8b). Additionally, a contour plot along the plane of the open face of the carborane cage showed the bonding situation within the five-membered ring (Fig. 8c).

Molecular structure, spectroscopic, and frontier molecular orbital analysis of 1–5

Having a series of carborane-thiol stabilized clusters and coordination complexes of titanium and vanadium, it became of interest to examine their structural and spectroscopic data (Table 1).[11b–d,20c] The Ti–$S_{carborane}$ bond lengths in **1** (av. 2.385 Å) and **2** (av. 2.452 Å) are significantly longer than those observed in **I** (Co: av. 2.125 Å and Ir: av. 2.263 Å). This difference can be attributed to π-type interactions in the latter, where electron donation from the sulfur pπ orbitals stabilizes the coordinatively unsaturated metal center, leading to shorter M–S bonds.[11b–d] In contrast, the longer Ti–S bond suggests the absence of these π-type interactions. Interestingly, the Ti–S bond lengths in **3–5** are shorter than those in **1** and **2**, likely due to different attachment sites of the thiol substituents of the carborane cage. While the S is attached to the more electropositive B rather than C, there is more electron donation from the S atoms to form a bond with the electron-deficient Ti atom, which makes the Ti–S bond stronger in **3**. Consequently, the Ti–S bond length decreased in **3–5** compared to **1** and **2**. The π-type interaction in complexes **I** makes the metallacycle, [M–S–C–C–S] planar. Although this π-type interaction is absent in **1** and **2**, the [Ti–S–C–C–S] rings in **1** and **2** are nearly planar, similar to **I**. However, unlike **1** and **2**, the [M–S–B–B–S] rings in **3–5** are puckered at the metal center resulting from the tridentate coordination of the ligand; the remaining four atoms [S–B–B–S] form an almost perfect plane. Thus, the [MS_2B_2] metallacycles in **3–5** are bent, and the metal atom is positioned out of the plane of the carborane ligand, with the dihedral angles between the planes defined by [M–S–S] and [S–B–B–S] being 64.12–66.29°.

On the other hand, in terms of spectroscopic data, if we look into the ^{11}B NMR spectra of the complexes **1–5**, the changes of ^{11}B chemical shifts in complexes **3** and **5** compared to free carborane-thiol ligands are significantly larger than those in **1**, **2**, **4a**, and **4b**, which is due to the B–B bond formation (in **3**) or deboronation of the carborane cage (in **5**). In the IR spectra, in addition to the terminal B–H stretches of the carborane ring, a distinct B–H stretch at 2489 cm^{-1} is observed in **3**, corresponding to the presence of an *exo*-BH_3 moiety. In UV-vis absorption spectra, the absorptions with λ > 300 nm (330–652 nm) primarily display two to three absorption bands, which can be assigned to charge transfer transitions (Fig. S54 and S55†).

© 2025 The Author(s). Published by the Royal Society of Chemistry

Open Access Article. Published on 10 July 2025. Downloaded on 12/29/2025 3:13:31 AM. This article is licensed under a Creative Commons Attribution-NonCommercial 3.0 Unported Licence.

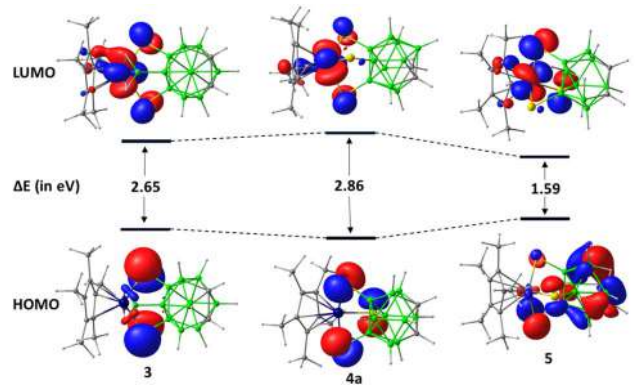


Fig. 9 Presentation of the energy levels, HOMO–LUMO gap, and orbital composition distribution of the HOMO and LUMO for **3**, **4a**, and **5** (isocontour values: ±0.045 [e bohr^{-3}]$^{1/2}$).

Time-dependent DFT studies indicate that the number of possible electronic transitions is higher in the hexa- and pentametallic clusters **1** and **2** than in the monometallic complexes **3–5** (Fig. S71–S82 and Tables S6–S11†). In complexes **1** and **2**, the low-intensity absorption bands near 365–490 nm can be assigned to intramolecular LMCT transitions, where electron density flows from the sulfur or carborane ring to the metal centers. In contrast, the absorption bands in the 330–388 nm region for complexes **3**, **4a**, and **4b** are mainly due to the electron density transfer from the Cp* ligand or sulfur atoms to the metal center. Notably, the absorption bands at 335 and 652 nm for **5** correspond to LMCT transition, where electron density flows from the carborane ring to the metal center. This is mainly due to the zwitterionic nature of the complex **5**, wherein the anionic charge is delocalized onto the pendant [C_2B_3] ring of the *nido*-carborane (C_2B_9). Furthermore, variation in the electronic configuration and oxidation state of metals across complexes in Table 1 is observed with the variation of the transition metal.

A comparative theoretical analysis of **3**, **4a**, and **5** was carried out. MO analysis revealed that **3** (2.65 eV) and **4a** (2.86 eV) have similar HOMO–LUMO gaps, both significantly larger than that of **5** (1.59 eV) (Fig. 9). The smaller HOMO–LUMO gap and energetically higher-lying HOMO of **5**, as compared to **3** and **4a**, suggest that **5** may exhibit a greater reactivity. Although the LUMOs of all three complexes are identical (localized on Ti or V center and two S atoms), the HOMOs feature different interactions. The HOMO of **4a** is completely localized on the p orbitals of the three sulfur atoms, while that of **3** has an additional small contribution from the borate boron (B11) center. In contrast, the HOMO of **5** is largely delocalized over the open [C_2B_3] face of the *nido*-carborane cage, along with little contribution from the p orbitals of sulfur atoms. This delocalization suggests the donating ability or reactive nature of the open face to generate a more stable *closo*-structure. Furthermore, it is evident that the thiolato groups in **3** and **4a** are more nucleophilic than those in **5**. This observation is also supported by natural population analysis that revealed negative natural charges on sulfur atoms of **3** and **4a** and positive charges on those of **5** (Table S3†).

Conclusions

In conclusion, we have demonstrated how the thiol functionalization site on carborane cages influences the formation of either cluster or coordination complexes when treated with cyclopentadienyl titanium and vanadium chlorides. The C-functionalized carborane-thiol, due to its lower C–S bond stability, resulted in the formation of penta- and hexa-metallic TiS clusters, whereas the B-functionalized variant, with its more stable B–S bond, gave rise to a coordination complex featuring an *exo*-BH_3 moiety. The formation of a new B–B bond in complex **3** offers strong evidence of metal-induced B–H activation. The B-functionalized di- and tri-thiol ligands are crucial in stabilizing the electron-deficient monometallic coordination complexes **3–5**. Interestingly, changing the metal from Ti to V facilitated the deboronation of the neutral *closo*-carborane, leading to the formation of 14-electron zwitterionic *nido*-**5**. This highlights the crucial role of ligand variation and emphasizes the significant impact of metal choice on the formation of transition metal–carborane thiolate coordination complexes. Our findings highlight the higher thermodynamic stability of B–S bonds over C–S bonds in carboranes, providing valuable insights into the nature of these bonding interactions. This work offers new opportunities for the strategic design of carborane-based complexes with specific properties, and potential applications in organometallic chemistry and materials science.

Data availability

The data supporting this article have been included as part of the ESI.† Crystallographic data have been deposited at the Cambridge Crystallographic Data Center under 2403346 (**1**), 2451038 (**2**), 2311787 (**3**), 2358616 (**4a**), 2311786 (**4b**), and 2358617 (**5**).

Author contributions

S. B., D. K. P., D. C., and J. M. executed the experimental synthesis, characterization, and data analysis. D. C. and S. B. carried out the theoretical calculations. M. K. carried out single-crystal X-ray diffraction data collection, structure refinement, and analysis. S. B. prepared the first draft of the manuscript and all authors contributed to the preparation of the manuscript. S. G., T. P., and T. B. supervised the project.

Conflicts of interest

There are no conflicts to declare.

Acknowledgements

S. G. thanks the support of the SERB, India, Grant No. CRG/2023/000189. T. B. acknowledges the support of the Ministry of Education, Youth, and Sports, Grant No. MSMT LTAIN 19152. T. P. thanks SERB for funding through Grant No. SPR/2021/000439 and a JC Bose Fellowship. We gratefully acknowledge

© 2025 The Author(s). Published by the Royal Society of Chemistry

Open Access Article. Published on 10 July 2025. Downloaded on 12/29/2025 3:13:31 AM. This article is licensed under a Creative Commons Attribution-NonCommercial 3.0 Unported Licence.

funding through the Center of Excellence (CoE) on Molecular Materials and Functions as part of the Institute of Eminence (IoE) scheme of IIT Madras. S. B. and D. C. thank IIT Madras, and D. K. P. thanks PMRF, Grant No. SB22230356CYPMRF008224 for fellowships. We thank Ms Swetashree Acharya for performing the ESI-MS experiment for complexes **1** and **2**. We also extend our gratitude to Dr B. Varghese and Dr Elias Jesu Packiam, IIT Madras, for Single Crystal X-ray diffraction data collection and structure refinement. We gratefully acknowledge DST-FIST, India, for HRMS and IIT Madras for providing computational facilities.

Notes and references

1 *Coordination Chemistry: A Century of Progress*, ed. G. B. Kauffman, American Chemical Society, Washington, DC, 1994, vol. 565.

2 (*a*) T. M. Trnka and R. H. Grubbs, *Acc. Chem. Res.*, 2001, **34**, 18–29; (*b*) B. Olenyuk, J. A. Whiteford, A. Fechtenkötter and P. J. Stang, *Nature*, 1999, **398**, 796–799.

3 (*a*) J. D. Atwood, M. J. Wovkulich and D. C. Sonnenberger, *Acc. Chem. Res.*, 1983, **16**, 350–355; (*b*) D. Zhao, D. J. Timmons, D. Yuan and H. Q. Zhou, *Acc. Chem. Res.*, 2011, **44**, 123–133.

4 (*a*) R. H. Crabtree, *The Organometallic Chemistry of the Transition Metals*, Wiley, 3rd edn, 2001; (*b*) O. Back, B. Donnadieu, P. Parameswaran, G. Frenking and G. Bertrand, *Nat. Chem.*, 2010, **2**, 369–373; (*c*) C. P. Casey, E. L. Paulsen, E. W. Beuttenmueller, B. R. Proft, L. M. Petrovich, B. A. Matter and D. R. Powell, *J. Am. Chem. Soc.*, 1997, **119**, 11817–11825.

5 R. N. Grimes, *Carboranes*, Elsevier, Oxford, 3rd edn, 2016.

6 (*a*) M. F. Hawthorne, J. I. Zink, J. M. Skelton, M. J. Bayer, C. Liu, E. Livshits, R. Baer and D. Neuhauser, *Science*, 2004, **303**, 1849–1851; (*b*) D. J. Crowther, N. C. Baenziger and R. F. Jordan, *J. Am. Chem. Soc.*, 1991, **113**, 1455–1457.

7 (*a*) A. K. Saxena and N. S. Hosmane, *Chem. Rev.*, 1993, **93**, 1081–1124; (*b*) G.-X. Jin, *Coord. Chem. Rev.*, 2004, **248**, 587–602; (*c*) A. M. Spokoyny, M. G. Reuter, C. L. Stern, M. A. Ratner, T. Seideman and C. A. Mirkin, *J. Am. Chem. Soc.*, 2009, **131**, 9482–9483; (*d*) J. L. Vlugt, *Angew. Chem., Int. Ed.*, 2010, **49**, 252–255.

8 A. M. Spokoyny, C. W. Machan, D. J. Clingerman, M. S. Rosen, M. J. Wiester, R. D. Kennedy, C. L. Stern, A. A. Sarjeant and C. A. Mirkin, *Nat. Chem.*, 2011, **3**, 590–596.

9 (*a*) J. Plesek, *Chem. Rev.*, 1992, **92**, 269–278; (*b*) A. S. Larsen, J. D. Holbrey, F. S. Tham and C. A. Reed, *J. Am. Chem. Soc.*, 2000, **122**, 7264–7272; (*c*) K. E. White, E. M. Avery, E. Cummings, Z. Hong, J. Langecker, A. Vetushka, M. Dušek, J. Macháček, J. Višnák, J. Endres, Z. Bastl, E. Mete, A. N. Alexandrova, T. Baše and P. S. Weiss, *Chem. Mater.*, 2024, **36**, 2085–2095.

10 (*a*) G. L. Moxham, T. M. Douglas, S. K. Brayshaw, G. Kociok-Köhn, J. P. Lowe and A. S. Weller, *Dalton Trans.*, 2006, 5492–5505; (*b*) *Comprehensive Organometallic Chemistry III*, ed. R. H. Crabtree and D. M. P. Mingos, Elsevier, Oxford, UK, 2007, vol. 3, pp. 175–264.

11 (*a*) M. Herberhold, G.-X. Jin, H. Yan, W. Milius and B. Wrackmeyer, *Eur. J. Inorg. Chem.*, 1999, 873–875; (*b*) M. Herberhold, G.-X. Jin, H. Yan, W. Milius and B. Wrackmeyer, *J. Organomet. Chem.*, 1999, **587**, 252–257; (*c*) D.-H. Kim, J. Ko, K. Park, S. Cho and S. O. Kang, *Organometallics*, 1999, **18**, 2738–2740; (*d*) J.-Y. Bae, Y.-I. Park, J. Ko, K.-I. Park, S.-I. Cho and S. O. Kang, *Inorg. Chim. Acta*, 1999, **289**, 141–148; (*e*) G.-X. Jin, *Coord. Chem. Rev.*, 2013, **257**, 2522–2535.

12 (*a*) M. Herberhold, H. Yan, W. Milius and B. Wrackmeyer, *Angew. Chem., Int. Ed.*, 1999, **38**, 3689–3691; (*b*) M. Herberhold, H. Yan, W. Milius and B. Wrackmeyer, *Chem.–Eur. J.*, 2002, **8**, 388–395; (*c*) Z.-J. Yaoa and W. Deng, *Coord. Chem. Rev.*, 2016, **309**, 21–35.

13 (*a*) M. Herberhold, H. Yan, W. Milius and B. Wrackmeyer, *Organometallics*, 2000, **19**, 4289–4294; (*b*) Q. Jiang, Z. Wang, Y. Li and H. Yan, *Chem. Commun.*, 2013, **49**, 5880–5882; (*c*) Z. Wang, H. Ye, Y. Li, Y. Li and H. Yan, *J. Am. Chem. Soc.*, 2013, **135**, 11289–11298.

14 (*a*) S. Liu, Y.-F. Han and G.-X. Jin, *Chem. Soc. Rev.*, 2007, **36**, 1543–1560; (*b*) G.-X. Jin, J.-Q. Wang, C. Zhang, L.-H. Weng and M. Herberhold, *Angew. Chem., Int. Ed.*, 2005, **44**, 259–262.

15 (*a*) J.-Q. Wang, C.-X. Ren and G.-X. Jin, *Chem. Commun.*, 2006, 162–164; (*b*) T. J. Wedge and M. F. Hawthorne, *Coord. Chem. Rev.*, 2003, **240**, 111–128; (*c*) D.-H. Wu, B.-H. Xu, Y.-Z. Li and H. Yan, *Organometallics*, 2007, **26**, 6300–6306.

16 J.-H. Wang, C. Zheng, J. A. Maguire and N. S. Hosmane, *Organometallics*, 2003, **22**, 4839–4841.

17 (*a*) S. Cai and G.-X. Jin, *Organometallics*, 2005, **24**, 5280–5286; (*b*) S. Cai, J. Wang and G.-X. Jin, *Organometallics*, 2005, **24**, 4226–4231.

18 (*a*) M. Herberhold, G.-X. Jin, H. Yan, W. Milius and B. Wrackmeyer, *J. Organomet. Chem.*, 1999, **587**, 252–257; (*b*) J. Q. Wang, C. X. Ren, L. H. Weng and G.-X. Jin, *Chem. Commun.*, 2006, 162–164.

19 (*a*) G.-X. Jin, J.-Q. Wang, Z. Zhang, L. H. Weng and M. Herberhold, *Angew. Chem., Int. Ed.*, 2005, **44**, 259–262; (*b*) G.-X. Jin and J.-Q. Wang, *Dalton Trans.*, 2006, 86–90.

20 (*a*) D. Olid, R. Núñez, C. Viñas and F. Teixidor, *Chem. Soc. Rev.*, 2013, **42**, 3318–3336; (*b*) X. Zhang, X. Zou and H. Yan, *Organometallics*, 2014, **33**, 2661–2666; (*c*) X. Zhang, X. Tang, J. Yang, Y. Li, H. Yan and V. I. Bregadze, *Organometallics*, 2013, **32**, 2014–2018.

21 (*a*) A. J. Mannix, X.-F. Zhou, B. Kiraly, J. D. Wood, D. Alducin, B. D. Myers, X. Liu, B. L. Fisher, U. Santiago, J. R. Guest, M. J. Yacaman, A. Ponce, A. R. Oganov, M. C. Hersam and N. P. Guisinger, *Science*, 2015, **350**, 1513–1516; (*b*) C. L. Tina, A. M. Spokoyny, C. She, O. K. Farha, C. A. Mirkin, T. J. Marks and J. T. Hupp, *J. Am. Chem. Soc.*, 2010, **132**, 4580–4582; (*c*) F. P. Olsen, R. C. Vasavada and M. F. Hawthorne, *J. Am. Chem. Soc.*, 1968, **95**, 3946–3951; (*d*) N. E. Miller and E. L. Muetterties, *J. Am. Chem. Soc.*, 1963, **85**, 3506.

22 (*a*) F. Zheng, T. H. Yui, J. Zhang and Z. Xie, *Nat. Chem.*, 2020, **11**, 5943–5947; (*b*) Z. Xie, *Coord. Chem. Rev.*, 2006, **250**, 259–

© 2025 The Author(s). Published by the Royal Society of Chemistry

Open Access Article. Published on 10 July 2025. Downloaded on 12/29/2025 3:13:31 AM. This article is licensed under a Creative Commons Attribution-NonCommercial 3.0 Unported Licence.

272; (*c*) L. Deng and Z. Xie, *Coord. Chem. Rev.*, 2007, **251**, 2452–2476; (*d*) Z. Qiu, S. Ren and Z. Xie, *Acc. Chem. Res.*, 2013, **44**, 299–309.

23 (*a*) S. Kar and S. Ghosh, Borane Polyhedra beyond Icosahedron, in *50th Anniversary of Electron Counting Paradigms for Polyhedral Molecules. Structure and Bonding*, ed. D. M. P. Mingos, Springer, Berlin, 2021, vol. 187, pp. 109–138; (*b*) S. Kar, A. N. Pradhan and S. Ghosh, in *Comprehensive Organometallic Chemistry IV*, ed. G. Parkin, K. Meyer and D. O'hare, Elsevier, Amsterdam, 2022, vol. 9, pp. 263–369; (*c*) S. Kar, S. Bairagi, J.-F. Halet and S. Ghosh, *Chem. Commun.*, 2023, **59**, 11676–11679.

24 (*a*) K. Saha, D. K. Roy, R. D. Dewhurst, S. Ghosh and H. Braunschweig, *Acc. Chem. Res.*, 2021, **54**, 1260–1273; (*b*) S. Kar, S. Bairagi, G. Joshi, E. D. Jemmis, H. Himmel and S. Ghosh, *Acc. Chem. Res.*, 2024, **57**, 2901–2914; (*c*) R. Bag, S. Bairagi, B. K. Rout and S. Ghosh, in *Encyclopedia of Inorganic and Bioinorganic Chemistry*, ed. R. Melen, Wiley, 2022; (*d*) S. Kar, S. Bairagi, A. Haridas, G. Joshi, E. D. Jemmis and S. Ghosh, *Angew. Chem., Int. Ed.*, 2022, **61**, e202208293.

25 (*a*) K. Pathak, C. Nandi and S. Ghosh, *Coord. Chem. Rev.*, 2022, **453**, 214303; (*b*) S. Bairagi, S. Giri, G. Joshi, E. D. Jemmis and S. Ghosh, *Angew. Chem., Int. Ed.*, 2025, **64**, e202417170; (*c*) S. Bairagi, D. Chatterjee, S. Giri and S. Ghosh, *Chem. Commun.*, 2025, **61**, 3696–3699.

26 T. Baše, J. Macháček, Z. Hájková, J. Langecker, J. D. Kennedy and M. J. Carr, *J. Organomet. Chem.*, 2015, **798**, 132–140.

27 (*a*) S. Gayen, F. Assanar, S. Shymal, D. P. Dorairaj and S. Ghosh, *Chem. Sci.*, 2024, **15**, 15913–15924; (*b*) D. K. Roy, B. Mondal, P. Shankhari, R. S. Anju, K. Geetharani, S. M. Mobin and S. Ghosh, *Inorg. Chem.*, 2013, **52**, 6705–6712; (*c*) E. J. Ditzel, X. L. R. Fontaine, H. Fowkes, N. N. Greenwood, J. D. Kennedy, P. MacKinnon, Z. Sisan and M. Thornton-Pett, *J. Chem. Soc., Chem. Commun.*, 1990, 1692–1694.

28 (*a*) J. C. Huffman, J. G. Stone, W. C. Krussel and K. G. Caulton, *J. Am. Chem. Soc.*, 1977, **99**, 5829–5831; (*b*) R. Gyepes, I. Císarová, J. Pinkas, J. Kubista, M. Horácek and K. Mach, *Eur. J. Inorg. Chem.*, 2013, **2013**, 3316–3322; (*c*) F. Bottomley and R. W. Day, *Can. J. Chem.*, 1992, **70**, 1250–1259; (*d*) D. E. Gindelberger, *Acta Crystallogr., Sect. C: Cryst. Struct. Commun.*, 1996, **52**, 2493–2495; (*e*) F. Bottomley and F. Grein, *Inorg. Chem.*, 1982, **21**, 4170–4178; (*f*) A. Roth, C. Floriani, A. Chiesi-Villa and C. Guastini, *J. Am. Chem. Soc.*, 1986, **108**, 6823–6825.

29 F. Bottomley, G. O. Egharevba and P. S. White, *J. Am. Chem. Soc.*, 1985, **107**, 4353–4354.

30 (*a*) K. Wade, *Inorg. Nucl. Chem. Lett.*, 1972, **8**, 559–562; (*b*) K. Wade, *Adv. Inorg. Chem. Radiochem.*, 1976, **18**, 1–66.

31 (*a*) R. Gillespie, *Chem. Soc. Rev.*, 1979, **8**, 315–352; (*b*) C. Mealli, J. A. Lopez, Y. Sun and M. J. Clahorda, *Inorg. Chim. Acta*, 1993, **213**, 199–212.

32 (*a*) X.-W. Li, W. T. Pennington and G. H. Robinson, *J. Am. Chem. Soc.*, 1995, **117**, 7578–7579; (*b*) J. T. Boronski, J. A. Seed, D. Hunger, A. W. Woodward, J. van Slageren, A. J. Wooles, L. S. Natrajan, N. Kaltsoyannis and S. T. Liddle, *Nature*, 2021, **598**, 72–75; (*c*) K. R. McClain, H. Kwon, K. Chakarawet, R. Nabi, J. G. C. Kragskow, N. F. Chilton, R. D. Britt, J. R. Long and B. G. Harvey, *J. Am. Chem. Soc.*, 2023, **145**, 8996–9002; (*d*) S. Kar, D. Chatterjee, J.-F. Halet and S. Ghosh, *Molecules*, 2022, **27**, 7473–7485.

33 J. C. Thomas, D. P. Goronzy, A. C. Serino, H. S. Auluck, O. R. Irving, E. Jimenez-Izal, J. M. Deirmenjian, J. Macháček, P. Sautet, A. N. Alexandrova, T. Baše and P. S. Weiss, *ACS Nano*, 2018, **12**, 2211–2221.

34 (*a*) A. C. Molina, E. Horno, J. Jover, A. P. -Redondo, C. Yélamos and R. Zapata, *Organometallics*, 2023, **42**, 1360–1372; (*b*) P. J. Fischer, V. G. Young Jr and J. E. Ellis, *Angew. Chem.*, 2000, **112**, 195–197.

35 C. M. Bolinger, T. B. Rauchfuss and A. L. Rheingold, *J. Am. Chem. Soc.*, 1983, **105**, 6321–6323.

36 X.-K. Huo, G. Su and G.-X. Jin, *Dalton Trans.*, 2010, **39**, 1954–1961.

37 (*a*) R. A. Wiesboeck and M. F. Hawthorne, *J. Am. Chem. Soc.*, 1964, **86**, 1642–1643; (*b*) M. A. Fox and K. Wade, *J. Organomet. Chem.*, 1999, **57**, 279–291; (*c*) Y. Taoda, T. Sawabe, Y. Endo, K. Yamaguchi, S. Fujii and H. Kagechika, *Chem. Commun.*, 2008, 2049–2051.

38 (*a*) H. C. Brown and S. Krishnamurthy, *J. Am. Chem. Soc.*, 1972, **94**, 7159–7161; (*b*) J. Clayden, N. Greeves and S. Warren, *Organic Chemistry*, Oxford University Press, Oxford, 2nd edn, 2012, pp. 125–140.

© 2025 The Author(s). Published by the Royal Society of Chemistry

Supplementary Information (SI) for Chemical Science.
This journal is © The Royal Society of Chemistry 2025

Supplementary Information

Cluster *versus* coordination: the chemistry of cyclopentadienyl titanium and vanadium complexes with B- and C-functionalized carborane-thiols, $[C_2B_{10}H_{12-n}(SH)_n]$ (n = 2 or 3)

Subhash Bairagi,[‡a] Deepak Kumar Patel,[‡a,b,c] Debipada Chatterjee,[a] Monika Kučeráková,[d] Jan Macháček,[c] Tomas Base,*[c] Thalappil Pradeep,*[a,b] and Sundargopal Ghosh*[a]

[a]Department of Chemistry, Indian Institute of Technology Madras, Chennai 600036, India, E-mail: sghosh@iitm.ac.in

[b]DST Unit of Nanoscience (DST UNS) and Thematic Unit of Excellence (TUE), Department of Chemistry, Indian Institute of Technology, Madras, Chennai 600036, India, Email: pradeep@iitm.ac.in

[c]Institute of Inorganic Chemistry, The Czech Academy of Science, 25068 Rez, Czech Republic, Email: tbase@iic.cas.cz

[d]Institute of Physics, The Czech Academy of Science, 182 21 Prague 8, Czech Republic.

[‡]These authors contributed equally to this work.

Table of contents

I Experimental Details

Scheme S1	Synthesis of **1** and **2**.	S6
Scheme S2	Synthesis of **3**.	S7
Scheme S3	Synthesis of **4a**.	S8
Scheme S4	Synthesis of **4b**.	S8
Scheme S5	Synthesis of **5**.	S9

I.1 UV-visible Studies S9

I.2 Supplementary Data

Figure S1	Molecular structure and labelling diagram of **1**.	S10
Figure S2	Molecular structure and labelling diagram of **2**.	S10
Figure S3	Molecular structure and labelling diagram of **3**.	S11
Figure S4	Molecular structure and labelling diagram of **4a**.	S11
Figure S5	Molecular structure and labelling diagram of **4b**.	S11
Figure S6	Molecular structure and labelling diagram of **5**.	S12

I.3 Spectroscopic Details

Figure S7	ESI-MS spectrum of **1**.	S12
Figure S8	$^{11}B\{^{1}H\}$ NMR spectrum of **1**.	S13
Figure S9	^{11}B NMR spectrum of **1**.	S13
Figure S10	^{1}H NMR spectrum of **1**.	S13
Figure S11	$^{1}H\{^{11}B\}$ NMR spectrum of **1**.	S14
Figure S12	Stacked ^{1}H (bottom) and $^{1}H\{^{11}B\}$ NMR (top) spectra of **1**.	S14
Figure S13	$^{13}C\{^{1}H\}$ NMR spectrum of **1**.	S14
Figure S14	IR spectrum of **1**.	S15
Figure S15	ESI-MS spectrum of **2**.	S15
Figure S16	$^{11}B\{^{1}H\}$ NMR spectrum of **2**.	S16
Figure S17	^{11}B NMR spectrum of **2**.	S16
Figure S18	^{1}H NMR spectrum of **2**.	S16
Figure S19	$^{1}H\{^{11}B\}$ NMR spectrum of **2**.	S17
Figure S20	Stacked ^{1}H (bottom) and $^{1}H\{^{11}B\}$ NMR (top) spectra of **2**.	S17
Figure S21	$^{13}C\{^{1}H\}$ NMR spectrum of **2**.	S17
Figure S22	IR spectrum of **2**.	S18
Figure S23	ESI-MS spectrum of **3**.	S18
Figure S24	$^{11}B\{^{1}H\}$ NMR spectrum of **3**.	S19
Figure S25	^{11}B NMR spectrum of **3**.	S19
Figure S26	^{1}H NMR spectrum of **3**.	S20
Figure S27	$^{1}H\{^{11}B\}$ NMR spectrum of **3**.	S20

Figure S28 Stacked ^{1}H (bottom) and $^{1}H\{^{11}B\}$ NMR (top) spectra of **3**. S21

Figure S29 $^{13}C\{^{1}H\}$ NMR spectrum of **3**. S21

Figure S30 IR spectrum of **3**. S22

Figure S31 ESI-MS spectrum of **4a**. S22

Figure S32 $^{11}B\{^{1}H\}$ NMR spectrum of **4a**. S23

Figure S33 ^{11}B NMR spectrum of **4a**. S23

Figure S34 ^{1}H NMR spectrum of **4a**. S24

Figure S35 $^{1}H\{^{11}B\}$ NMR spectrum of **4a**. S24

Figure S36 Stacked ^{1}H (bottom) and $^{1}H\{^{11}B\}$ NMR (top) spectra of **4a**. S25

Figure S37 $^{13}C\{^{1}H\}$ NMR spectrum of **4a**. S25

Figure S38 IR spectrum of **4a**. S26

Figure S39 ESI-MS spectrum of **4b**. S26

Figure S40 $^{11}B\{^{1}H\}$ NMR spectrum of **4b**. S27

Figure S41 ^{11}B NMR spectrum of **4b**. S27

Figure S42 ^{1}H NMR spectrum of **4b**. S28

Figure S43 $^{1}H\{^{11}B\}$ NMR spectrum of **4b**. S28

Figure S44 Stacked ^{1}H (bottom) and $^{1}H\{^{11}B\}$ NMR (top) spectra of **4b**. S29

Figure S45 $^{13}C\{^{1}H\}$ NMR spectrum of **4b**. S29

Figure S46 IR spectrum of **4b**. S30

Figure S47 $^{11}B\{^{1}H\}$ NMR spectrum of **5**. S30

Figure S48 ^{11}B NMR spectrum of **5**. S30

Figure S49 ^{1}H NMR spectrum of **5**. S31

Figure S50 $^{1}H\{^{11}B\}$ NMR spectrum of **5**. S31

Figure S51 Stacked ^{1}H (bottom) and $^{1}H\{^{11}B\}$ NMR (top) spectra of **5**. S32

Figure S52 $^{13}C\{^{1}H\}$ NMR spectrum of **5**. S32

Figure S53 IR spectrum of **5**. S32

Figure S54 Combined UV-vis spectra of **1** and **2** in CH_2Cl_2. S33

Figure S55 Combined UV-vis spectra of **3**-**5** in CH_2Cl_2. S33

I.4 X-ray Analysis Details S34

II Computational Details S34

Table S1 Selected geometrical parameters and Wiberg bond indices (WBI) of **1**-**5**. S35

Table S2 Selected experimental and Calculated bond angles of **1**-**5**. S36

Table S3 Calculated natural charges (q) and natural valence population (Pop) of **1**-**5**. S37

Table S4 Calculated HOMO–LUMO energy gap of **1**-**5**. S38

Table S5 Calculated ^{11}B chemical shifts for complexes **1**-**5**. S39

Figure S56 Selected molecular orbitals of **1**. S39

Figure S57 Selected NBO interactions of **1**. S40

Figure S58 Contour-line diagram of the Laplacian of the electron density of **1** in selected planes. S40

Figure S59 Selected molecular orbitals of **2**. S41

Figure S60 Selected NBO interactions of **2**. S41

Figure S61	Contour-line diagram of the Laplacian of the electron density of **2** in selected planes.	S42
Figure S62	Selected molecular orbitals of **3**.	S42
Figure S63	Selected NBO interactions of **3**.	S42
Figure S64	Contour-line diagram of the Laplacian of the electron density of **3** in selected planes.	S43
Figure S65	Selected molecular orbitals of **4a**.	S43
Figure S66	Selected NBO interactions of **4a**.	S44
Figure S67	Contour-line diagram of the Laplacian of the electron density of **4a** in selected planes.	S44
Figure S68	Selected molecular orbitals of **5**.	S45
Figure S69	Selected NBO interactions of **5**.	S45
Figure S70	Contour-line diagram of the Laplacian of the electron density of **5** in selected planes.	S45
Figure S71	Absorption spectrum of **1** computed at TD-DFT-PB86/Def2-SVP level of theory.	S46
Table S6	TD-DFT calculated energies (excitation energy (eV), λ_{calc} (nm)), oscillator strength (*f*), and main composition of the first UV−vis electronic excitations for **1**. Experimental absorption wavelengths (λ_{exp}, nm) of **1** are given for comparison.	S46
Figure S72	Selected molecular orbitals of **1** related to most intense electronic transitions.	S47
Figure S73	Absorption spectrum of **2** computed at TD-DFT-PB86/Def2-SVP level of theory.	S47
Table S7	TD-DFT calculated energies (excitation energy (eV), λ_{calc} (nm)), oscillator strength (*f*), and main composition of the first UV−vis electronic excitations for **2**. Experimental absorption wavelengths (λ_{exp}, nm) of **2** are given for comparison.	S48
Figure S74	Selected molecular orbitals of **2** related to most intense electronic transitions.	S48
Figure S75	Absorption spectrum of **3** computed at TD-DFT-PB86/Def2-SVP level of theory.	S49
Table S8	TD-DFT calculated energies (excitation energy (eV), λ_{calc} (nm)), oscillator strength (*f*), and main composition of the first UV−vis electronic excitations for **3**. Experimental absorption wavelengths (λ_{exp}, nm) of **3** are given for comparison.	S49
Figure S76	Selected molecular orbitals of **3** related to most intense electronic transitions.	S49
Figure S77	Absorption spectrum of **4a** computed at TD-DFT-PB86/Def2-SVP level of theory.	S50
Table S9	TD-DFT calculated energies (excitation energy (eV), λ_{calc} (nm)), oscillator strength (*f*), and main composition of the first UV−vis electronic excitations for **4a**. Experimental absorption wavelengths (λ_{exp}, nm) of **4a** are given for comparison.	S50
Figure S78	Selected molecular orbitals of **4a** related to most intense electronic transitions.	S50
Figure S79	Absorption spectrum of **4b** computed at TD-DFT-PB86/Def2-SVP level of theory.	S51
Table S10	TD-DFT calculated energies (excitation energy (eV), λ_{calc} (nm)), oscillator strength (*f*), and main composition of the first UV−vis electronic excitations for **4b**. Experimental absorption wavelengths (λ_{exp}, nm) of **4b** are given for comparison.	S51
Figure S80	Selected molecular orbitals of **4b** related to most intense electronic transitions.	S51
Figure S81	Absorption spectrum of **5** computed at TD-DFT-PB86/Def2-SVP level of theory.	S52
Table S11	TD-DFT calculated energies (excitation energy (eV), λ_{calc} (nm)), oscillator strength (*f*), and main composition of the first UV−vis electronic excitations for **5**. Experimental absorption wavelengths (λ_{exp}, nm) of **5** are given for comparison.	S52
Figure S82	Selected molecular orbitals of **5** related to most intense electronic transitions.	S53

III Cartesian Coordinates of all Optimized Structures

Figure S83 Optimized geometry of **1**. S54

Figure S84 Optimized geometry of **2**. S55

Figure S85 Optimized geometry of **3**. S57

Figure S86 Optimized geometry of **4a**. S58

Figure S87 Optimized geometry of **4b**. S59

Figure S88 Optimized geometry of **5**. S60

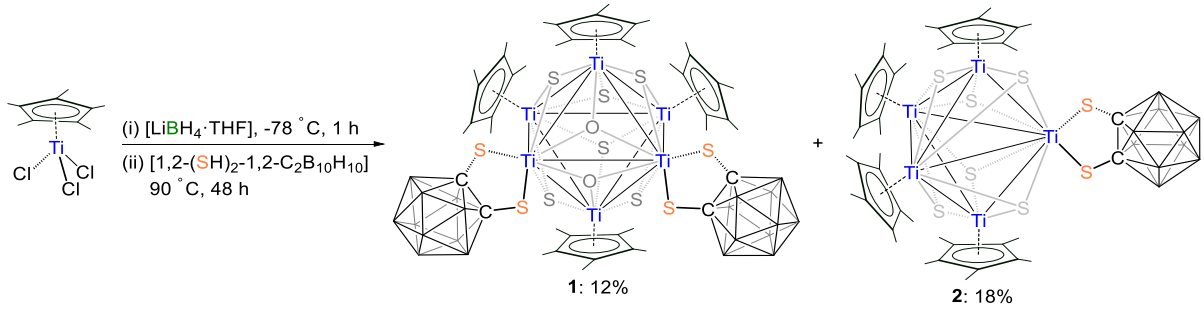
IV References S61

I Experimental Details

General Procedures and Instrumentation

All the manipulations were conducted under an Ar/N_2 atmosphere using standard Schlenk line techniques or in a glove box. Toluene, hexane, and THF solvents were distilled from purple solutions of benzophenone ketyl. Dichloromethane and $CDCl_3$ were distilled from calcium hydride before use. Metal precursors $[Cp^*TiCl_3]$[1], $[Cp^*VCl_2]_3$[2] and di/tri-thiol-*o*-carborane ligands $[1,2\text{-}(SH)_2\text{-}1,2\text{-}C_2B_{10}H_{10}]$[3], $[9,12\text{-}(SH)_2\text{-}1,2\text{-}C_2B_{10}H_{10}]$[4], and $[8,9,12\text{-}(SH)_3\text{-}1,2\text{-}C_2B_{10}H_9]$[5] were synthesized according to the literature methods while $LiBH_4$ (2.0 M in THF) and $[Cp_2TiCl_2]$ were used as received (Sigma Aldrich). Thin layer chromatography (TLC) was carried out on 250-μm diameter aluminum-supported silica gel TLC plates (MERCK TLC Plates) to separate the reaction mixtures. NMR spectra were recorded on a Bruker Avance III 500 MHz spectrometer. The residual solvent protons ($CDCl_3$, δ = 7.26 ppm) and carbon ($CDCl_3$, δ = 77.1 ppm) were employed as a reference for the ^1H and $^{13}C\{^1H\}$ NMR spectra, respectively. The ^{11}B decoupled ^1H spectrum was obtained with inverse gated decoupling (zgig) and power gated decoupling (zgpr) pulse sequences, respectively. $^{11}B\{^1H\}$ NMR spectra were processed with a backward linear prediction algorithm to eliminate the broad ^{11}B background signal of the NMR tube.[6] All pulse sequences are available in a commercial Bruker spectrometer. Electrospray mass (ESI-MS) spectrometric data were obtained on a Qtof Micro YA263 HRMS and 6545 Qtof LC/MS instrument. Infrared (IR) spectra were recorded on a JASCO FT/IR-1400 spectrometer. UV-vis spectra were recorded in dichloromethane on a Thermo Scientific (Evolution 300) UV-vis spectrometer.

Synthesis of 1 and 2: In a flame-dried Schlenk tube, $[(Cp^*TiCl_3]$ (0.100 g, 0.35 mmol) was suspended in 10 mL dry toluene and it was charged with lithium borohydride solution of 2.0 M in THF (0.6 mL, 1.2 mmol) dropwise at -78 °C and kept under constant stirring for 1 h. The red reaction mixture converted to dark green after 1 h. To this in situ-generated unstable dark green intermediate, one equivalent of $[1,2\text{-}(SH)_2\text{-}1,2\text{-}C_2B_{10}H_{10}]$ (0.038 g, 0.18 mmol) was added and kept at 90 °C for 48 h under stirring conditions. After the addition of $[1,2\text{-}(SH)_2\text{-}1,2\text{-}C_2B_{10}H_{10}]$, the mixture becomes brown and, after 48 h, changes to dark brown. After the completion of the reaction, the solvent was removed under vacuum. The residue was extracted with *n*-hexane /dichloromethane mixture (70:30 v/v) through a frit using 3 cm of celite. The filtrate was concentrated, and the residue was subjected to chromatographic workup on 250-μm diameter aluminium-supported silica gel TLC plates (MERCK TLC Plates). Note that we have done the chromatographic workup using TLC plates inside beakers, which were filled with Ar before and after filling them with properly distilled eluting solvents. Elution with a *n*-hexane/dichloromethane (50:50 v/v) mixture yielded brown **1** (0.010 g, 12%) and brown **2** (0.015 g, 18%).



Scheme S1. Synthesis of **1** and **2**.

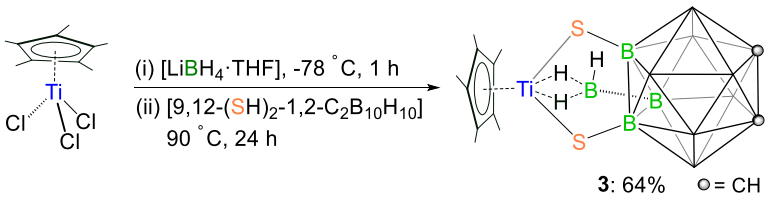
1: MS (ESI$^+$): *m/z* calculated for $[C_{44}H_{80}B_{20}S_{10}O_2Ti_6 + K]^+$: 1504.1911, found: 1504.2403; $^{11}B\{^1H\}$ NMR (160 MHz, $CDCl_3$, 22 °C): δ = -12.5 and -7.9 (vrey broad peak ranging from -11.0 to -1.0) ppm (br, 20B, *B*-H); ^{11}B NMR (160 MHz, $CDCl_3$, 22 °C): δ = -13.0 and -11.4 (d, $^1J_{B\text{-}H}$ = 209.0 Hz), -7.0 (vrey broad peak ranging from -10.0 to -1.0) ppm (br, 20B, *B*-H), ppm; ^1H NMR (500 MHz, $CDCl_3$, 22 °C): δ = 2.22 (s, 15H, 1Cp*), 2.25 (s, 15H, 1Cp*), 2.28 (s, 30H, 2Cp*) ppm; $^1H\{^{11}B\}$ NMR (500 MHz, $CDCl_3$, 22 °C): δ = 2.22 (s, 15H, 1Cp*), 2.25 (s, 15H, 1Cp*), 2.28 (s, 30H, 2Cp*), 2.52-2.98 (br, 20H, Carborane-B*H*) ppm; $^{13}C\{^1H\}$ NMR

(125 MHz, $CDCl_3$, 22 °C): δ = 14.7, 15.1, 15.3, and 15.5 ($4C_5\mathit{Me}_5$), 132.5, 132.9, and 133.6 ($4\mathit{C}_5Me_5$) ppm; IR (KBr, cm^{-1}): $\bar{\upsilon}$ = 2956, 2925, 2854, 2773, 2580 (B-H_t), 1740, 1643, 1459, 1262, 1088, 1024, 801, 699; UV-Vis (CH_2Cl_2): λ = 252, 375, 490 nm.

2: MS (ESI^+): *m/z* calculated for $[C_{42}H_{70}B_{10}S_8Ti_5 + CH_3OH + CH_3CN + Na]^+$: 1291.1833, found: 1291.1251; $^{11}B\{^1H\}$ NMR (160 MHz, $CDCl_3$, 22 °C): δ = -12.4, -9.8, -8.7, -8.4, -4.9, -3.7, -1.5, and -0.8 ppm (br, 10B, *B*-H); ^{11}B NMR (160 MHz, $CDCl_3$, 22 °C): δ = -12.8 and -11.4 (d, $^1J_{B\text{-}H}$ = 178 Hz), -10.4 (d, merged wih other peak), -9.0 and –7.9 (d, $^1J_{B\text{-}H}$ = 144 Hz), -5.3, -4.2 and -3.1 {(d, $^1J_{B\text{-}H}$ = 157 Hz) and (d, $^1J_{B\text{-}H}$ = 153 Hz)}, -2.1, -0.9 and -0.2 {(d, $^1J_{B\text{-}H}$ = 121 Hz) and (d, $^1J_{B\text{-}H}$ = 109 Hz)} ppm; ^1H NMR (500 MHz, $CDCl_3$, 22 °C): δ = 2.21 (s, 30H, 2Cp*), 2.23 (s, 30H, 2Cp*) ppm; $^1H\{^{11}B\}$ NMR (500 MHz, $CDCl_3$, 22 °C): δ = 2.21 (s, 30H, 2Cp*), 2.23 (s, 30H, 2Cp*), 2.47, 2.52 and 3.04 (br, 10H, Carborane-B*H*) ppm; $^{13}C\{^1H\}$ NMR (125 MHz, $CDCl_3$, 22 °C): δ = 14.3 ($2C_5\mathit{Me}_5$), 14.4 ($2C_5\mathit{Me}_5$), 68.1 (Carborane-*C*H), 132.2 ($2\mathit{C}_5Me_5$), 133.3 ($2\mathit{C}_5Me_5$) ppm; IR (KBr, cm^{-1}): $\bar{\upsilon}$ = 2961, 2925, 2854, 2800, 2589 (B-H_t), 1740, 1638, 1450, 1410, 1262, 1092, 1024, 867, 801, 692; UV-Vis (CH_2Cl_2): λ = 252, 365, 463 nm.

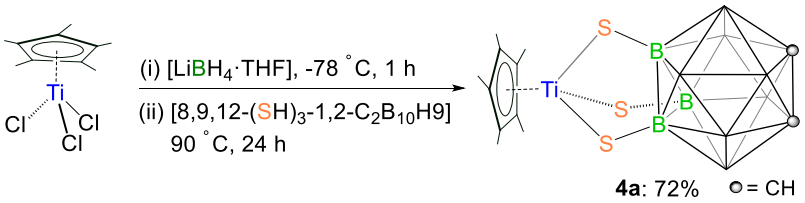
Synthesis of 3 and 4a: In a flame-dried Schlenk tube, $[(Cp^*TiCl_3]$ (0.100 g, 0.35 mmol) was suspended in 10 mL dry toluene and it was charged with lithium borohydride solution 2.0 M in THF (0.6 mL, 1.2 mmol) dropwise at -78 °C and kept under constant stirring for 1 h. The red reaction mixture converted to dark green after 1 h. To this in situ generated intermediate, one equivalent of $[9,12\text{-}(SH)_2\text{-}1,2\text{-}C_2B_{10}H_{10}]$ (0.073 g, 0.35 mmol) was added and kept at 90 °C for 24 h under stirring condition. After the addition of $[9,12\text{-}(SH)_2\text{-}1,2\text{-}C_2B_{10}H_{10}]$, the mixture becomes brown and, after 24 h, changes to yellow. After the completion of the reaction, the solvent was removed under vacuum. The residue was extracted with hexane/dichloromethane mixture (50:50 v/v) through a frit using 3 cm of celite. The filtrate was concentrated, and the residue was subjected to chromatographic workup on 250-µm diameter aluminium-supported silica gel TLC plates (MERCK TLC Plates). Elution with a hexane/dichloromethane (30:70 v/v) mixture yielded yellow **3** (0.089 g, 64%).

Under similar reaction conditions, treatment of the above-mentioned in situ generated intermediate with one equivalent of $[8,9,12\text{-}(SH)_3\text{-}1,2\text{-}C_2B_{10}H_9]$ (0.084 g, 0.35 mmol) yielded yellow solid **4a** (0.104 g, 72%).



Scheme S2. Synthesis of **3**.

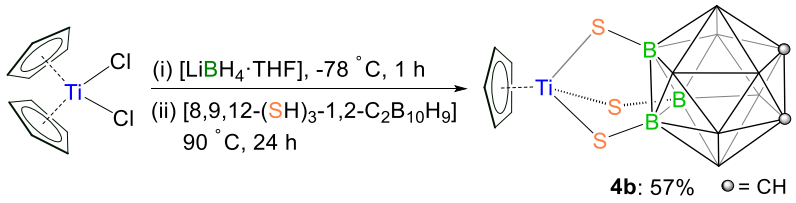
3: MS (ESI^+): *m/z* calculated for $[C_{12}H_{27}B_{11}S_2Ti + H]^+$: 403.2216, found: 403.2129; $^{11}B\{^1H\}$ NMR (160 MHz, $CDCl_3$, 22 °C): δ = -15.8 (br, 2B, *B*-H), -11.2 (br, 2B, *B*-H), -10.1 (br, 2B, *B*-H), -6.8 (br, 2B, *B*-H), -3.1 (br, 1B, BH_3), 8.4 (br, 2B, *B*-S) ppm; ^{11}B NMR (160 MHz, $CDCl_3$, 22 °C): δ = -16.5 and -15.2 (d, $^1J_{B\text{-}H}$ = 168 Hz, 2B, *B*-H), -11.8, -10.7 and -9.5 {(d, $^1J_{B\text{-}H}$ = 136 Hz, 2B, *B*-H) and (d, $^1J_{B\text{-}H}$ = 153 Hz, 2B, *B*-H)}, -6.8 (br, 2B, *B*-H), -3.2 (br, 1B, BH_3), 8.4 (br, 2B, *B*-S) ppm; ^1H NMR (500 MHz, $CDCl_3$, 22 °C): δ = -0.86 (br, 2H, Ti-*H*-B), 2.24 (s, 15H, 1Cp*), 2.58, 2.92 and 3.21 (br, 8H, Carborane-B*H*), 3.54 (br, 2H, Carborane-C*H*) ppm; $^1H\{^{11}B\}$ NMR (500 MHz, $CDCl_3$, 22 °C): δ = -0.87 (br, 2H, Ti-*H*-B), 2.24 (s, 15H, 1Cp*), 1.92, 2.43, 2.73 and 2.84 (br, 8H, Carborane-B*H*), 3.54 (br, 2H, Carborane-C*H*) ppm; $^{13}C\{^1H\}$ NMR (125 MHz, $CDCl_3$, 22 °C): δ = 13.9 ($C_5\mathit{Me}_5$), 44.3 (Carborane-*C*H), 127.8 (C_5Me_5) ppm; IR (KBr, cm^{-1}): $\bar{\upsilon}$ = 3060, 2954, 2923, 2852, 2738, 2602 (B-H_t), 2480 (B-H_t of *exo*-BH_3), 2117, (B-H_b),1707, 1459, 1259, 1094, 1021, 799; UV-Vis (CH_2Cl_2): λ = 238, 288, 336 nm.



Scheme S3. Synthesis of **4a**.

4a: MS (ESI$^+$): *m/z* calculated for $[C_{12}H_{24}B_{10}S_3Ti + H]^+$: 421.1608, found: 421.1511; $^{11}B\{^1H\}$ NMR (160 MHz, $CDCl_3$, 22 °C): δ = -22.3 (br, 1B, *B*-H), -16.4 (br, 2B, *B*-H), -12.5 (br, 2B, *B*-H), -11.3 (br, 2B, *B*-H), 1.3 (br, 1B, *B*-S), 6.3 (br, 2B, *B*-S) ppm; ^{11}B NMR (160 MHz, $CDCl_3$, 22 °C): δ = -23.1 and -21.9 (d, $^1J_{B\text{-}H}$ = 160 Hz, 1B, *B*-H), -17.1 and -15.8 (d, $^1J_{B\text{-}H}$ = 167 Hz, 2B, *B*-H), -13.4, -12.0 and -10.8 {(d, $^1J_{B\text{-}H}$ = 170 Hz, 2B, *B*-H) and (d, $^1J_{B\text{-}H}$ = 161 Hz, 2B, *B*-H)}, 1.3 (br, 1B, *B*-S), 6.3 (br, 2B, *B*-S) ppm; ^1H NMR (500 MHz, $CDCl_3$, 22 °C): δ = 2.24 (s, 15H, 1Cp*), 2.50, 2.97 and 3.29 (br, 8H, Carborane-B*H*), 3.49 (br, 2H, Carborane-C*H*) ppm; $^1H\{^{11}B\}$ NMR (500 MHz, $CDCl_3$, 22 °C): δ = 2.24 (s, 15H, 1Cp*), 2.03, 2.79 and 2.99 (br, 8H, Carborane-B*H*), 3.49 (br, 2H, Carborane-C*H*) ppm; $^{13}C\{^1H\}$ NMR (125 MHz, $CDCl_3$, 22 °C): δ = 13.8 (C_5Me_5), 39.7 (Carborane-*C*H), 127.7 (C_5Me_5) ppm; IR (KBr, cm^{-1}): $\bar{\upsilon}$ = 3072, 3033, 2995, 2918, 2850, 2605 (B-H_t), 2569 (B-H_t), 1636, 1425, 1085, 1021, 867, 799, 738; UV-Vis (CH_2Cl_2): λ = 230, 257, 289, 371 nm.

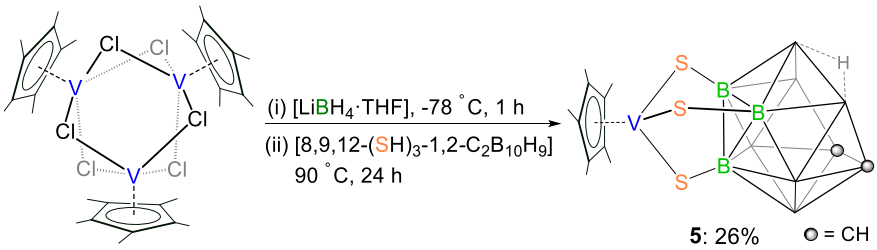
Synthesis of 4b: In a flame-dried Schlenk tube, $[(Cp_2TiCl_2]$ (0.100 g, 0.34 mmol) was suspended in 10 mL dry toluene and it was charged with lithium borohydride solution of 2.0 M in THF (0.6 mL, 1.2 mmol) dropwise at -78 °C and kept under constant stirring for 1 h. The red reaction mixture converted to dark blue after 1 h. To this in situ-generated unstable dark blue intermediate, one equivalent of $[8,9,12\text{-}(SH)_3\text{-}1,2\text{-}C_2B_{10}H_9]$ (0.084 g, 0.35 mmol) was added and kept at 90 °C for 24 h under stirring conditions. After the addition of $[8,9,12\text{-}(SH)_3\text{-}1,2\text{-}C_2B_{10}H_9]$, the mixture becomes brown and, after 24 h, changes to yellow. After the completion of the reaction, the solvent was removed under vacuum. The residue was extracted with *n*-hexane /dichloromethane mixture (50:50 v/v) through a frit using 3 cm of celite. The filtrate was concentrated, and the residue was subjected to chromatographic workup on 250-μm diameter aluminium-supported silica gel TLC plates (MERCK TLC Plates). Elution with a *n*-hexane /dichloromethane (30:70 v/v) mixture yielded yellow **4b** (0.080 g, 57%).



Scheme S4. Synthesis of **4b**.

4b: MS (ESI$^+$): *m/z* calculated for $[2(C_7H_{14}B_{10}S_3Ti) + H]^+$: 723.1394, found: 723.1343; $^{11}B\{^1H\}$ NMR (160 MHz, $CDCl_3$, 22 °C): δ = -22.2 (br, 1B, *B*-H), -16.6 (br, 2B, *B*-H), -11.8 (br, 2B, *B*-H), -10.7 (br, 2B, *B*-H), 2.1 (br, 1B, *B*-S), 7.1 (br, 2B, *B*-S) ppm; ^{11}B NMR (160 MHz, $CDCl_3$, 22 °C): δ = -23.0 and -21.6 (d, $^1J_{B\text{-}H}$ = 181 Hz, 1B, *B*-H), -17.4 and -16.1 (d, $^1J_{B\text{-}H}$ = 167 Hz, 2B, *B*-H), -12.4, -11.4 and -10.2 {(d, $^1J_{B\text{-}H}$ = 139 Hz, 2B, *B*-H) and (d, $^1J_{B\text{-}H}$ = 156 Hz, 2B, *B*-H)}, 2.1 (br, 1B, *B*-S), 7.1 (br, 2B, *B*-S) ppm; ^1H NMR (500 MHz, $CDCl_3$, 22 °C): δ = 2.55, 3.11 and 3.40 (br, 8H, Carborane-B*H*), 3.59 (br, 2H, Carborane-C*H*), 6.65 (s, 15H, 1Cp*) ppm; $^1H\{^{11}B\}$ NMR (500 MHz, $CDCl_3$, 22 °C): δ = 2.08, 2.92 and 3.13 (br, 8H, Carborane-B*H*), 3.59 (br, 2H, Carborane-C*H*), 6.65 (s, 15H, 1Cp*) ppm; $^{13}C\{^1H\}$ NMR (125 MHz, $CDCl_3$, 22 °C): δ = 39.8 (Carborane-*C*H), 114.0 (C_5H_5) ppm; IR (KBr, cm^{-1}): $\bar{\upsilon}$ = 3082, 3013, 2986, 2925, 2850, 2623 (B-H_t), 2598 (B-H_t), 1638, 1435, 1257, 1017, 872, 818, 741; UV-Vis (CH_2Cl_2): λ = 230, 256, 293, 330, 388 nm.

Synthesis of 5: In a flame-dried Schlenk tube, $[(Cp^*VCl_2)_3]$ (0.100 g, 0.13 mmol) was suspended in 10 mL dry toluene and it was charged with lithium borohydride solution 2.0 M in THF (0.5 mL, 1.0 mmol) dropwise at -78 °C through a syringe. Then, the reaction mixture was allowed to come to room temperature for over 1 h under stirring conditions, and no such drastic color change was observed in the brownish reaction mixture. After 1 h, three equivalents of $[8,9,12\text{-}(SH)_3\text{-}1,2\text{-}C_2B_{10}H_9]$ (0.093 g, 0.39 mmol) was added and kept at 90 °C for 24 h under stirring conditions. After 24 h, the mixture becomes brownish green. After the completion of the reaction, the solvent was removed under vacuum. The residue was extracted with hexane/dichloromethane mixture (70:30 v/v) through a frit using 3 cm of celite. The filtrate was concentrated, and the residue was subjected to chromatographic workup on 250-µm diameter aluminium-supported silica gel TLC plates (MERCK TLC Plates). Elution with a hexane/dichloromethane (50:50 v/v) mixture yielded green **5** (0.032 g, 26%).



Scheme S5. Synthesis of **5**.

5: $^{11}B\{^1H\}$ NMR (160 MHz, $CDCl_3$, 22 °C): δ = -30.3 (br, 2B, *B*-H), -25.8 (br, 2B, *B*-H), -22.0 (br, 1B, *B*-S), -6.4 (br, 2B, *B*-H), -4.6 (br, 2B, *B*-S) ppm; ^{11}B NMR (160 MHz, $CDCl_3$, 22 °C): δ = -30.8 and -29.8 (d, $^1J_{B\text{-}H}$ = 160 Hz, 2B, *B*-H), -26.3 and -25.1 (d, $^1J_{B\text{-}H}$ = 161 Hz, 2B, *B*-H), -21.9 (br, 1B, *B*-S), -7.0 and -5.8 (d, $^1J_{B\text{-}H}$ = 150 Hz, 2B, *B*-H), -4.6 (br, 2B, *B*-S) ppm; ^1H NMR (500 MHz, $CDCl_3$, 22 °C): δ = -0.43 (br, 1H, B-*H*-B), 2.28 (s, 15H, 1Cp*), 2.01, 2.52, 2.79, 3.10 and 3.39 (br, 7H, Carborane-B*H*) ppm; $^1H\{^{11}B\}$ NMR (500 MHz, $CDCl_3$, 22 °C): δ = -0.39 (br, 1H, B-*H*-B), 2.28 (s, 15H, 1Cp*), 2.01, 2.25, 2.95 and 3.49 (br, 7H, Carborane-B*H*) ppm; $^{13}C\{^1H\}$ NMR (125 MHz, $CDCl_3$, 22 °C): δ = 14.2 (C_5Me_5), 25.8 (Carborane-*C*H), 127.6 (C_5Me_5) ppm; IR (KBr, cm^{-1}): $\bar{\upsilon}$ = 3054, 2981, 2921, 2852, 2683 (B-H_t), 2619 (B-H_t), 1725, 1430, 1364, 1264, 1094, 1019, 897, 741; UV-Vis (CH_2Cl_2): λ = 230, 283, 335, 424, 591, 652 nm.

I.1 UV-visible Studies

In order to investigate the optical properties of these coloured clusters **1**-**5**, we have carried out UV-vis study in CH_2Cl_2 solution. The UV-vis absorption spectra of all the complexes were measured in the range of 200-800 nm in CH_2Cl_2 solution at 298 K (Figures S54-S55). All of them display the most intense peaks at higher energy regions 230-293 nm due to the π–π* transition of Cp* ligands, characteristic bands for most Cp* based metal complexes.[7] The absorptions with λ>300 nm exhibit mainly two to three absorption bands. These comparatively low energy bands, around 330-652 nm, have been assigned to the charge transfer bands.[8,9] Unlike other complexes, in complex **5**, relatively low energy absorption bands have been observed at 591 and 652 nm.[10]

To reproduce the UV-vis spectrum and get some idea about the electronic transitions, Time-Dependent DFT formalism was used. The studies show that the possible number of electronic transitions is more in hexa- and pentametallic clusters **1** and **2** compared to the monometallic complexes **3**-**5** (Figures S71, S73, S75, S77, S79, S81, and Tables S6-S11). The molecular orbitals of **1**-**5**, exhibiting the most intense electronic transitions, are shown in Figures S72, S74, S76, S78, S80, and S82. In complex **1** and **2**, the low-intensity absorption bands near 365-490 nm may be assigned as an intramolecular LMCT transition that correspond to electron density flow from the sulfur or carborane ring to the metal centers. The absorptions in 330-388 nm region for complexes **3**, **4a**, and **4b** are mainly due to the electron density flow from the Cp*

ligand or sulfur atoms to the metal center. In the contrary, the absorption bands at 335 and 652 nm for **5** are due to LMCT transition that correspond to electron density flow from the carborane ring to the metal center. This is mainly due to the zwitterionic nature of complex **5**, where the anionic charge delocalized onto the pendant [C_2B_3] ring of the *nido*-carborane (C_2B_9).

I.2 Supplementary Data

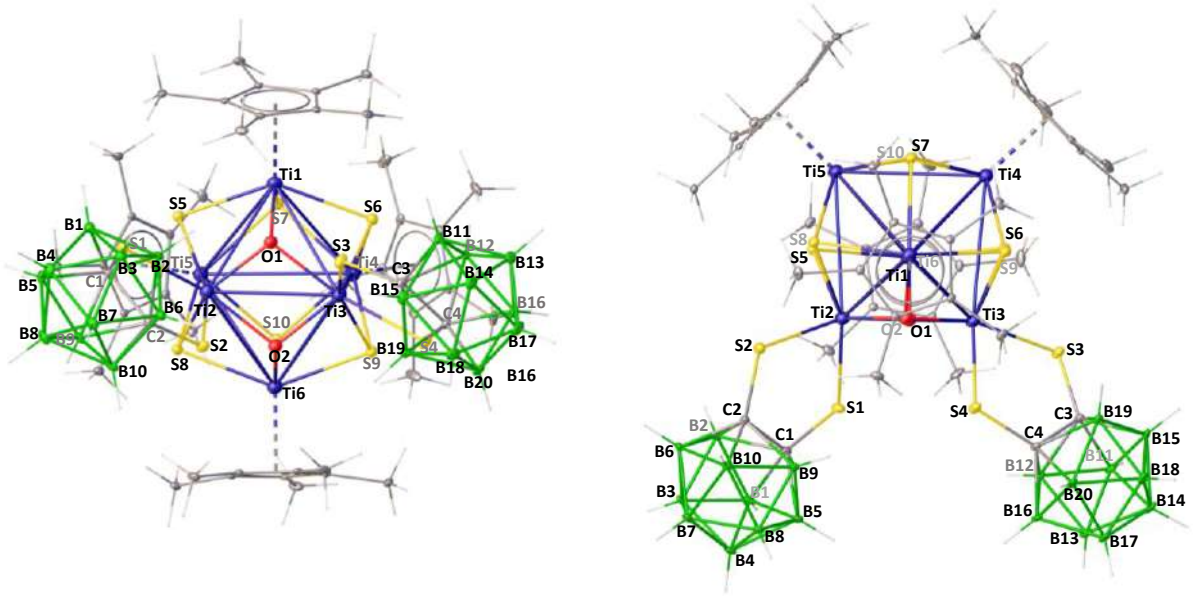


Figure S1. Molecular structure and labelling diagram of **1**. (left) side view; (right) top view. Selected bond lengths (Å) and bond angles (˚): Ti···Ti 3.130-3.598, Ti1-S5 2.4274(12), Ti1-O1 1.919(2), Ti2-S5 2.4835(12), Ti2-S1 1.3963(13), C1-S1 1.785(4), B1-C1 1.703(7), Ti3-Ti2-Ti5 93.913, Ti1-S5-Ti2 82.52(4).

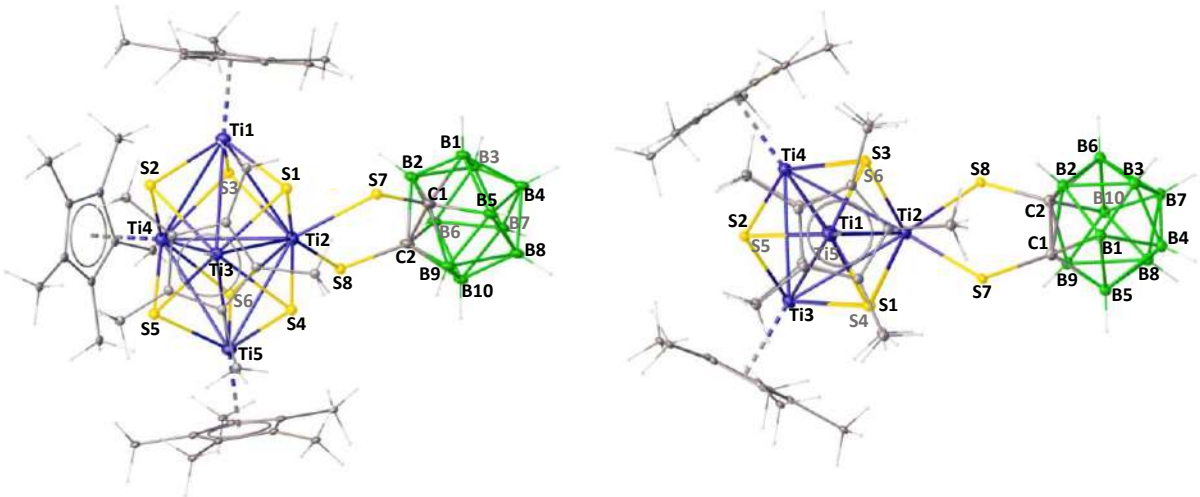


Figure S2. Molecular structure and labelling diagram of **2**. (left) side view; (right) top view. Selected bond lengths (Å) and bond angles (˚): Ti···Ti 3.201-3.305, Ti1-S1 2.2839(17), Ti2-S1 1.5004(16), Ti2-S7 1.446(4), Ti3-S1 2.5089(17), C2-S8 1.782(9), Ti3-Ti2-Ti4 58.270, S7-Ti2-S8 81.09(12), Ti1-S1-Ti2 82.24(5).

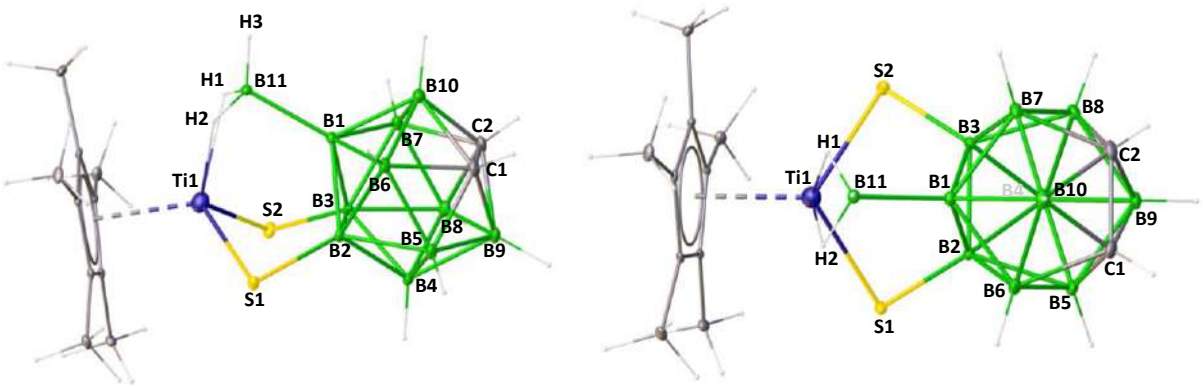


Figure S3. Molecular structure and labelling diagram of **3**. (left) side view; (right) top view. Selected bond lengths (Å) and bond angles (˚): Ti1-S1 2.3321(9), Ti1-S2 2.3214(9), Ti1···B11 2.259(4), Ti1-H1 2.00(3), Ti-H2 1.93(3), B11-H1 0.90(3), B11-H2 1.03(4), B1-B11 1.750(5), B2-S1 1.851(4) C1-C2 1.626(6), Ti1-S1-B2 81.17(11), B2-B1-B11 121.9(3).

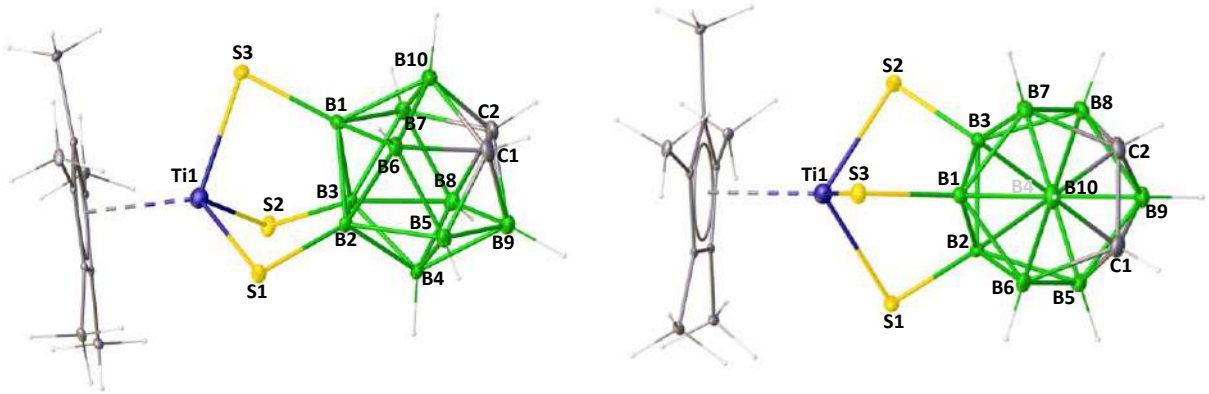


Figure S4. Molecular structure and labelling diagram of **4a**. (left) side view; (right) top view. Selected bond lengths (Å) and bond angles (˚): Ti1-S1 2.3095(12), Ti1-S3 2.3231(12), B1-S3 1.849(5), B1-B2 1.829(5), C1-C2 1.635(7), C1-B10 1.713(7), Ti1-S1-B2 80.72(14).

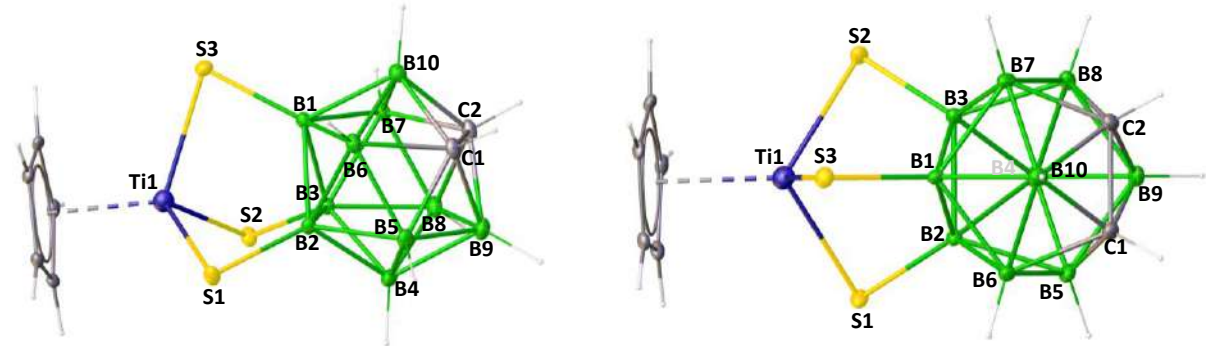


Figure S5. Molecular structure and labelling diagram of **4b**. (left) side view; (right) top view. Selected bond lengths (Å) and bond angles (˚): Ti1-S1 2.2992(7), Ti1-S3 2.3223(7), Ti1-S3 2.3182(7), B1-S3 1.843(3), B1-B2 1.835(3), C1-C2 1.629(3), C1-B10 1.711(4), Ti1-S1-B2 80.89(8).

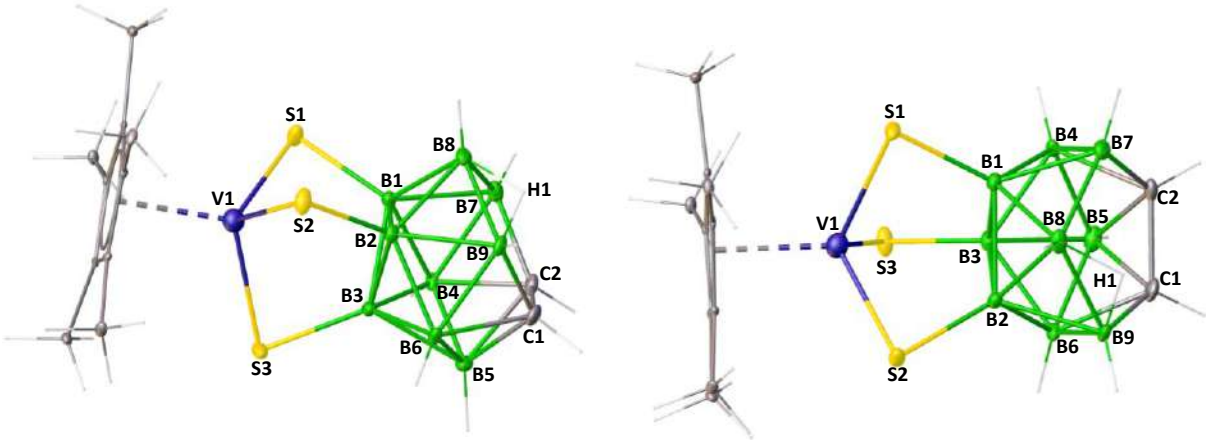


Figure S6. Molecular structure and labelling diagram of **5**. (left) side view; (right) top view. Selected bond lengths (Å) and bond angles (˚): V1-S1 2.2194(16), V1-S3 2.2099(15), B3-S3 1.859(6), B1-B8 1.780(9), C1-C2 1.555(8), C2-B7 1.596(8), B8-H_b 1.15(2), B9-H_b 1.16(2), V1-S1-B1 81.01(19), V1-S3-B3 79.42(17), B7-B8-B9 101.7(5), C1-C2-B7 114.3(5).

I.3 Spectroscopic Details

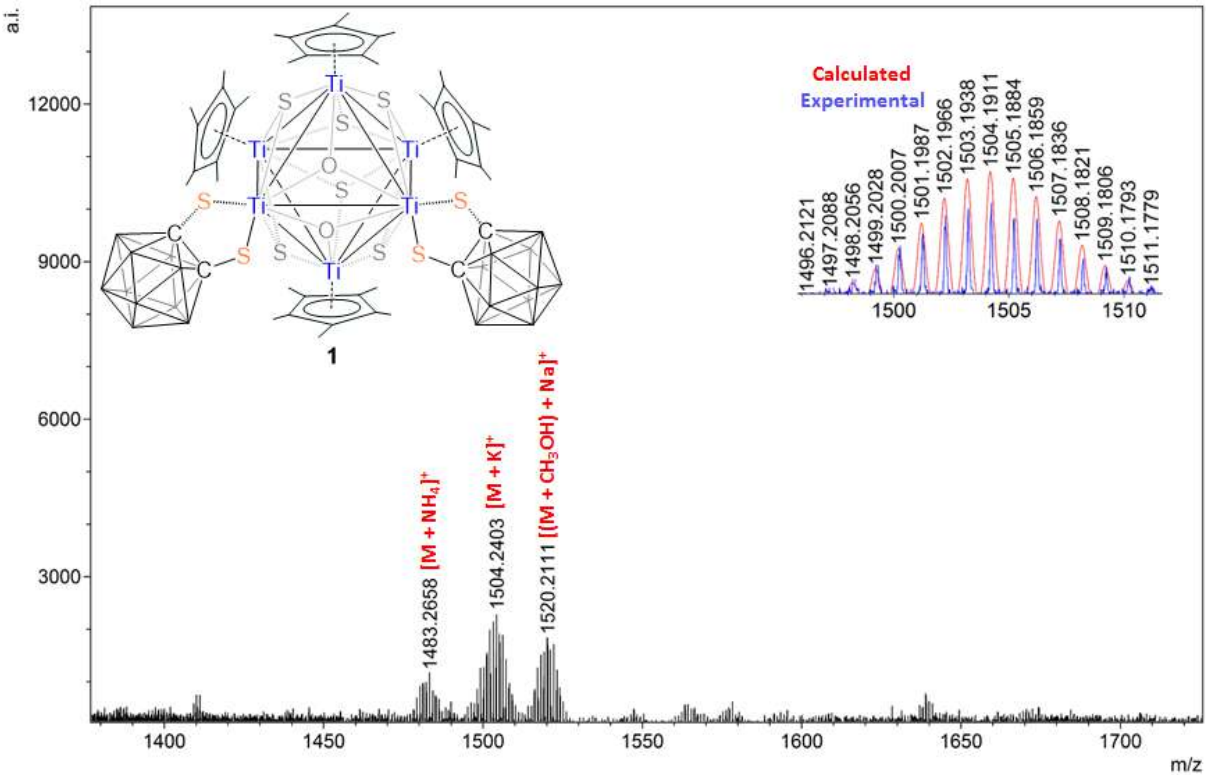


Figure S7. ESI-MS spectrum of **1**.

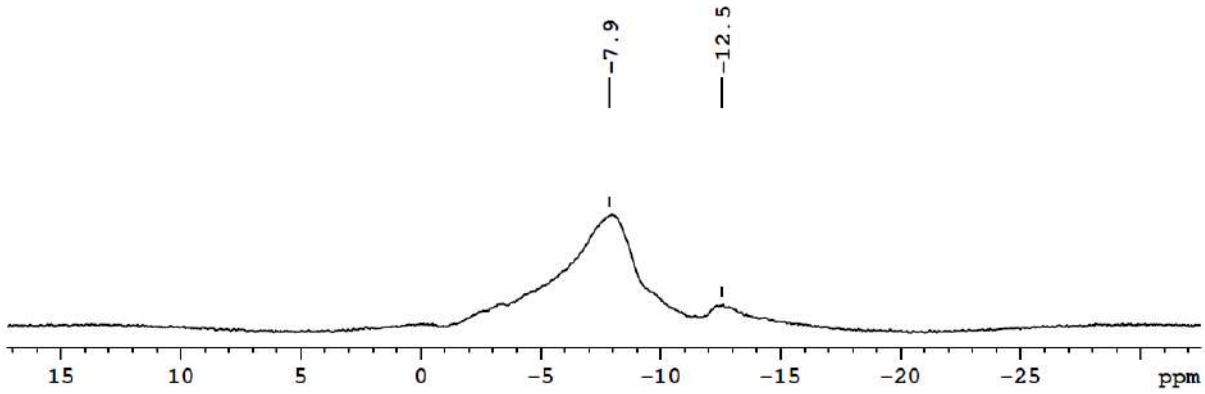


Figure S8. $^{11}B\{^{1}H\}$ NMR spectrum of **1** in $CDCl_3$. $^{11}B\{^{1}H\}$ NMR spectra were processed with a backward linear prediction algorithm to eliminate the broad ^{11}B background signal of the NMR tube.[6]

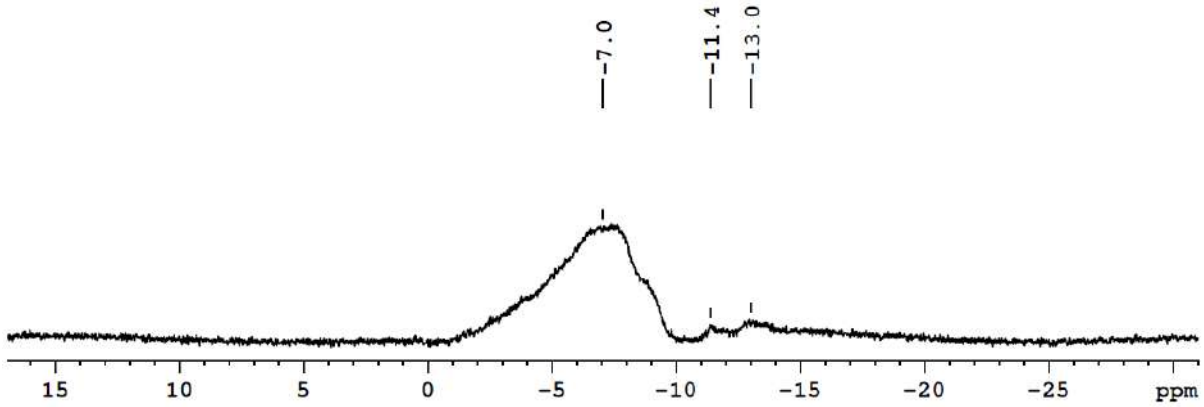


Figure S9. ^{11}B NMR spectrum of **1** in $CDCl_3$. $^{11}B\{^{1}H\}$ NMR spectra were processed with a backward linear prediction algorithm to eliminate the broad ^{11}B background signal of the NMR tube.[6]

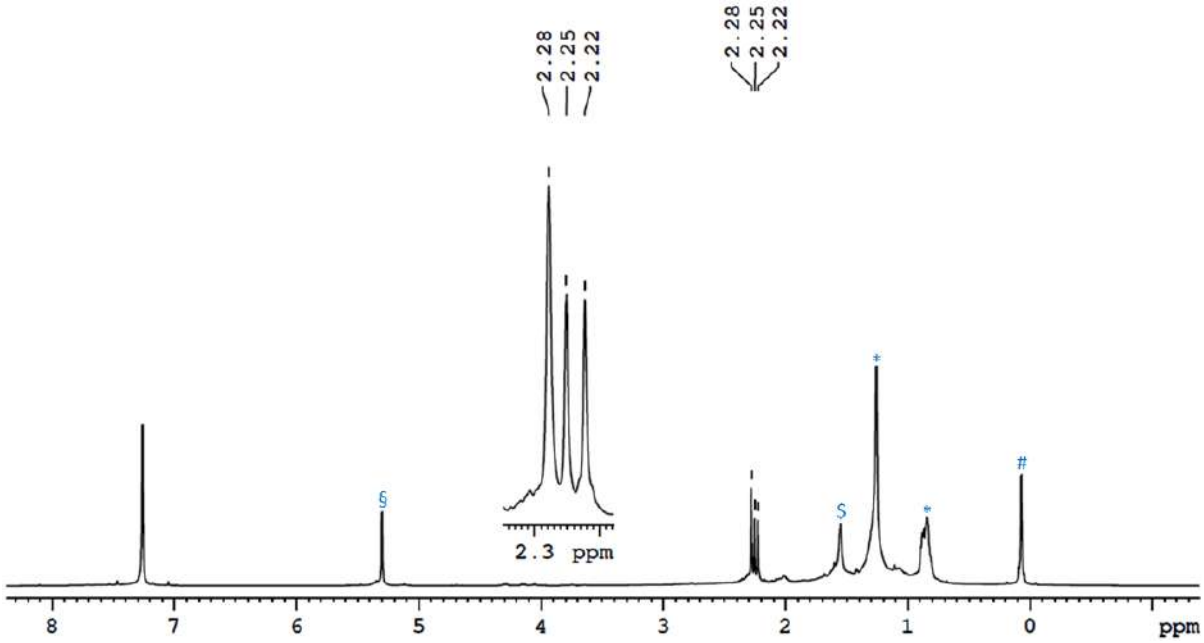


Figure S10. ^{1}H NMR spectrum of **1** in $CDCl_3$ (§Dichloromethane, $$H_2O$, *Grease, #Silicon grease).

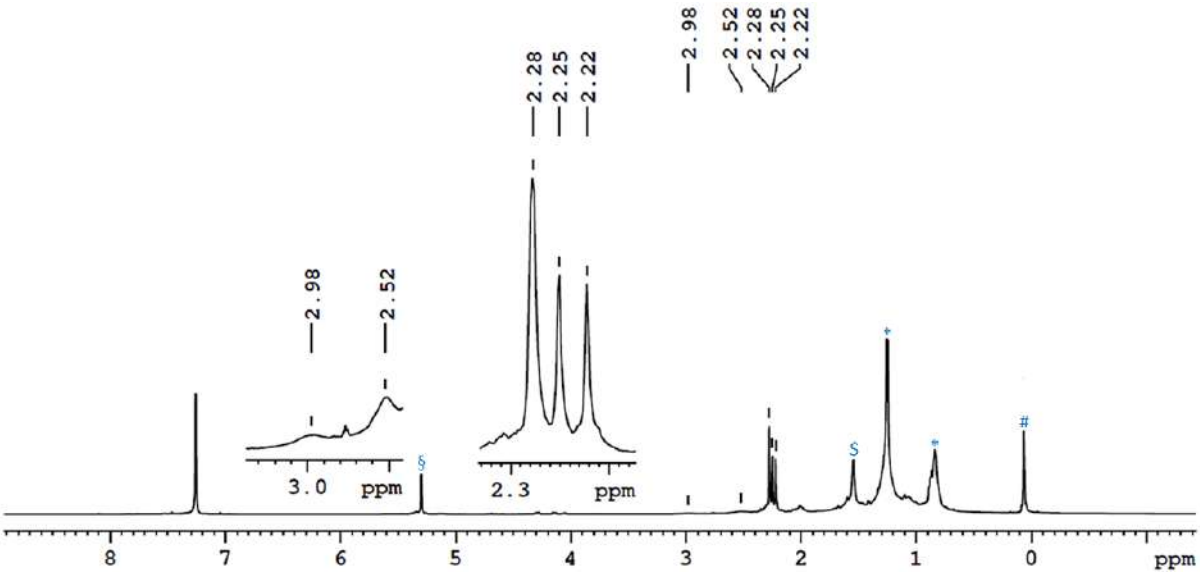


Figure S11. $^{1}H\{^{11}B\}$ NMR spectrum of **1** in $CDCl_3$ (§Dichloromethane, $$H_2O$, *Grease, #Silicon grease).

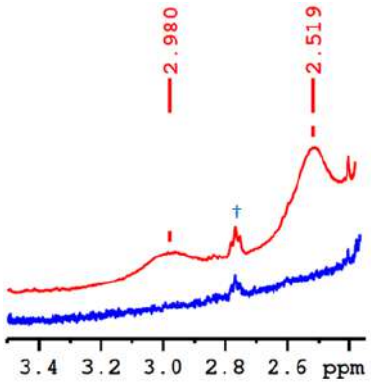


Figure S12. Stacked ^{1}H (bottom) and $^{1}H\{^{11}B\}$ NMR (top) spectra of **1** in $CDCl_3$ (†Inseparable impurity).

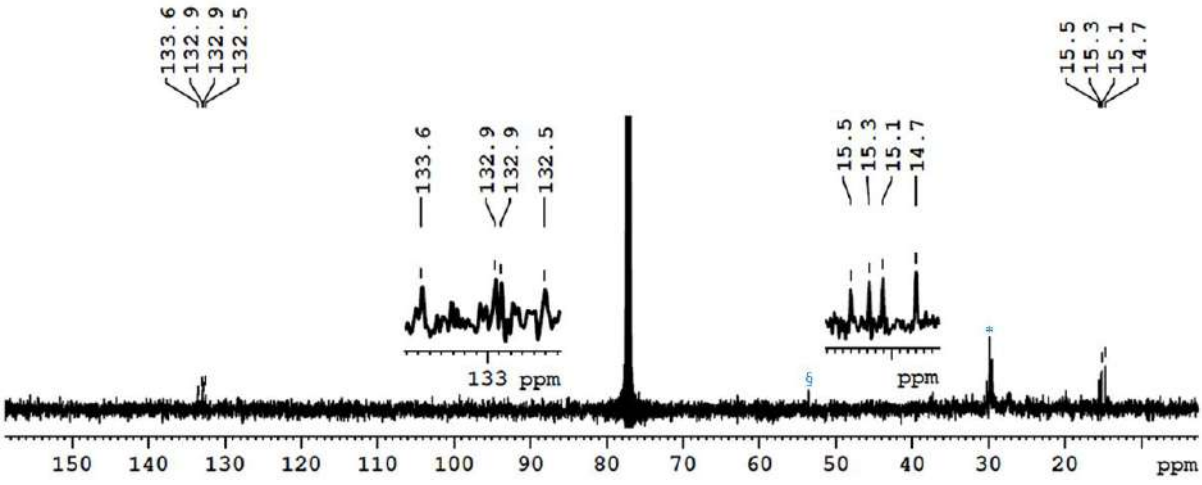


Figure S13. $^{13}C\{^{1}H\}$ NMR spectrum of **1** in $CDCl_3$ (§Dichloromethane, *Grease).

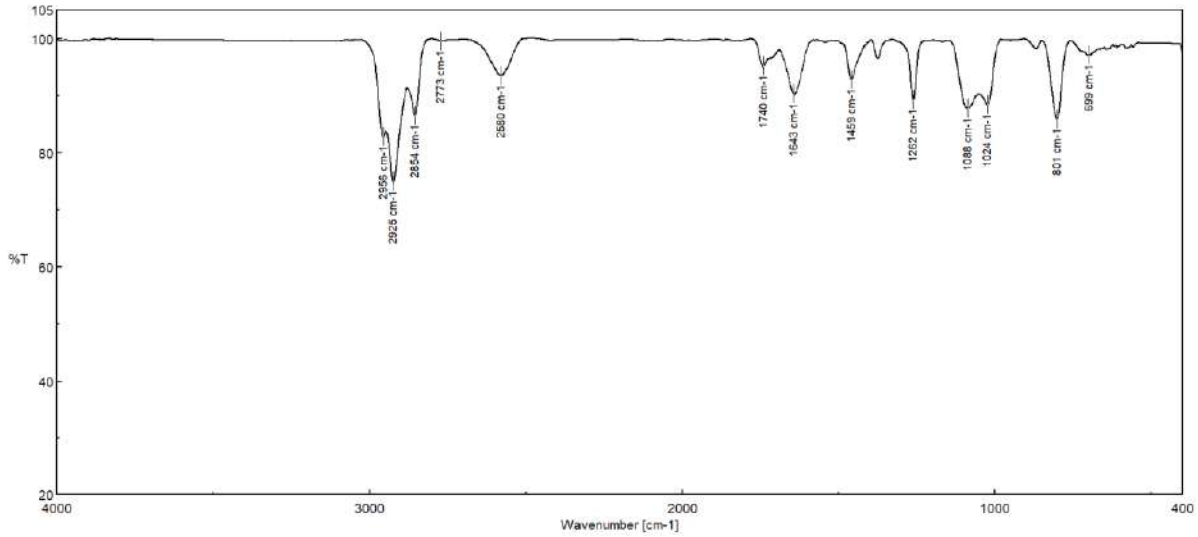


Figure S14. IR spectrum of **1**.

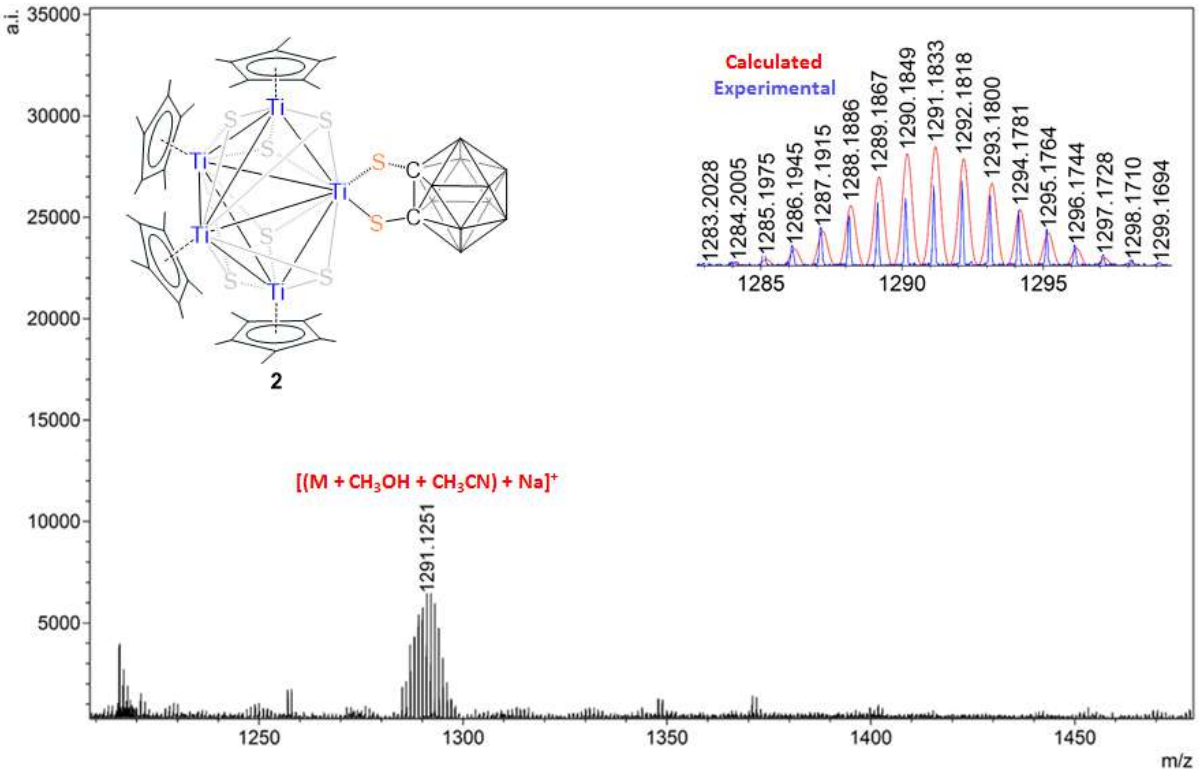


Figure S15. ESI-MS spectrum of **2**.

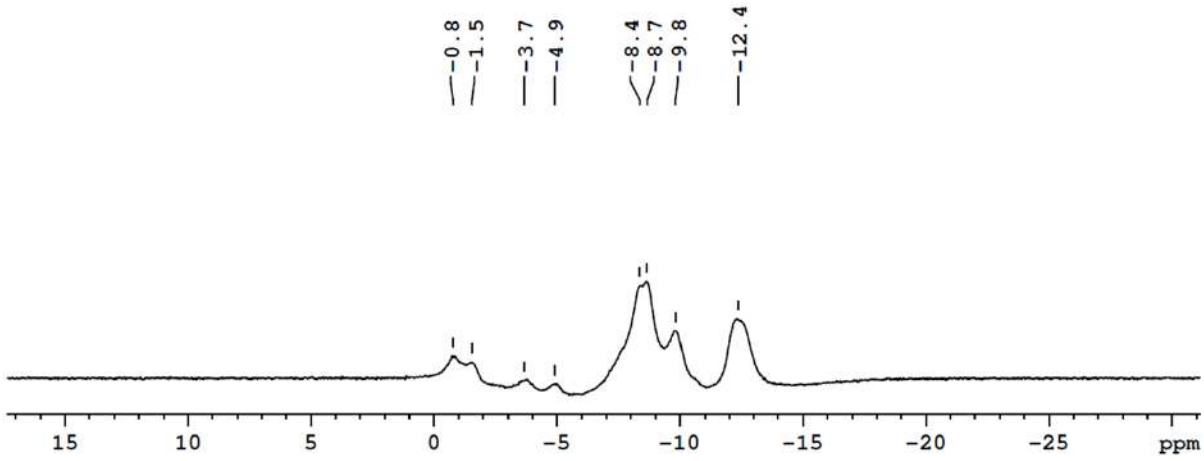


Figure S16. $^{11}B\{^{1}H\}$ NMR spectrum of **2** in $CDCl_3$. $^{11}B\{^{1}H\}$ NMR spectra were processed with a backward linear prediction algorithm to eliminate the broad ^{11}B background signal of the NMR tube.[6]

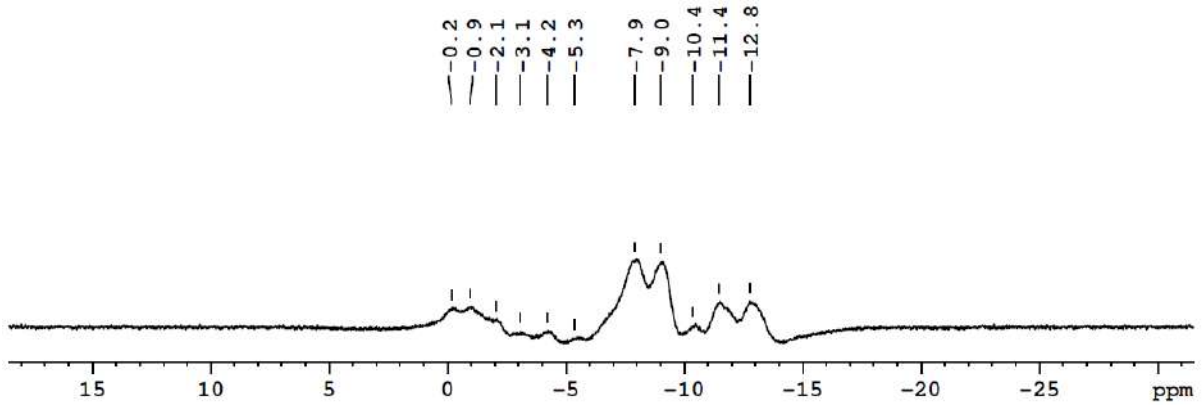


Figure S17. ^{11}B NMR spectrum of **2** in $CDCl_3$. $^{11}B\{^{1}H\}$ NMR spectra were processed with a backward linear prediction algorithm to eliminate the broad ^{11}B background signal of the NMR tube.[6]

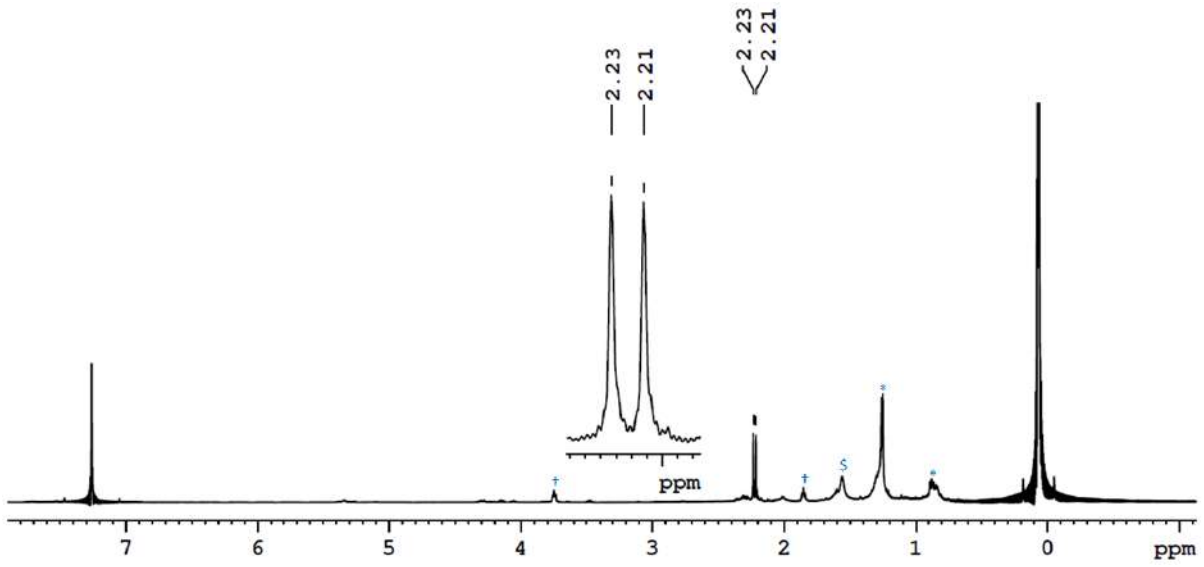


Figure S18. ^{1}H NMR spectrum of **2** in $CDCl_3$ (†Inseparable impurity, $\$H_2O$, *Grease, #Silicon grease).

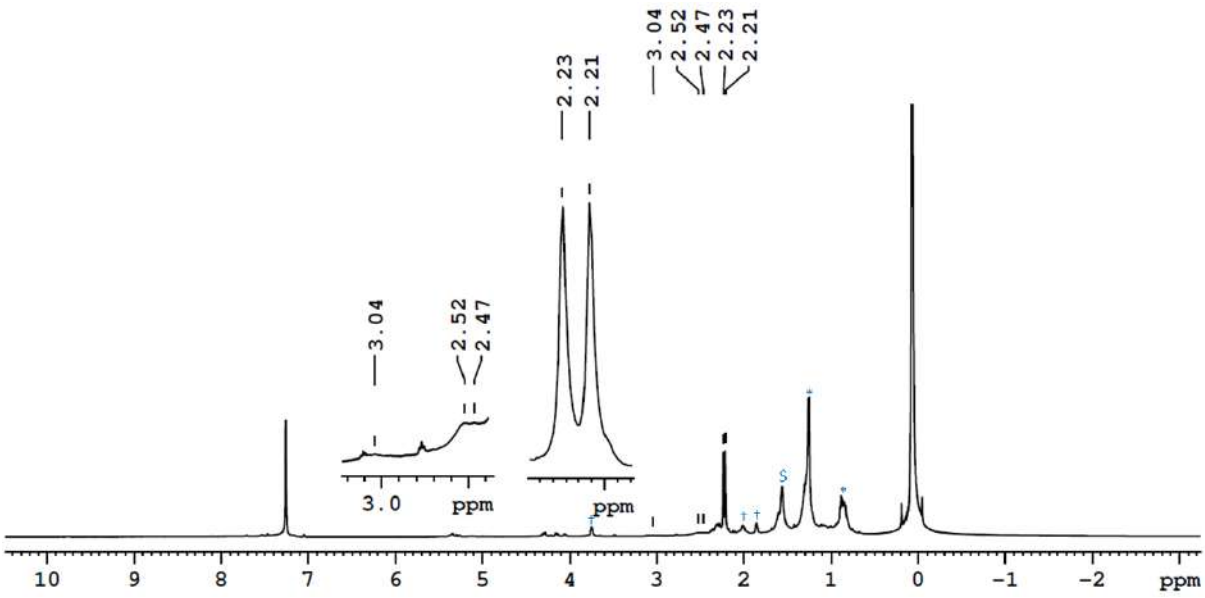


Figure S19. $^{1}H\{^{11}B\}$ NMR spectrum of **2** in $CDCl_3$ (†Inseparable impurity, $\dot{S}H_2O$, *Grease, #Silicon grease).

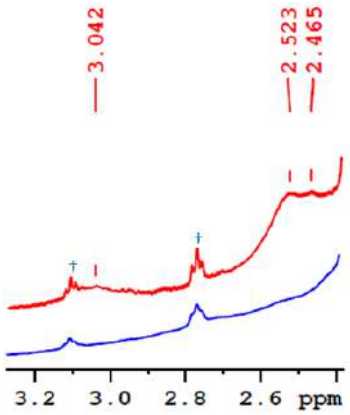


Figure S20. Stacked ^{1}H (bottom) and $^{1}H\{^{11}B\}$ NMR (top) spectra of **2** in $CDCl_3$ (†Inseparable impurity).

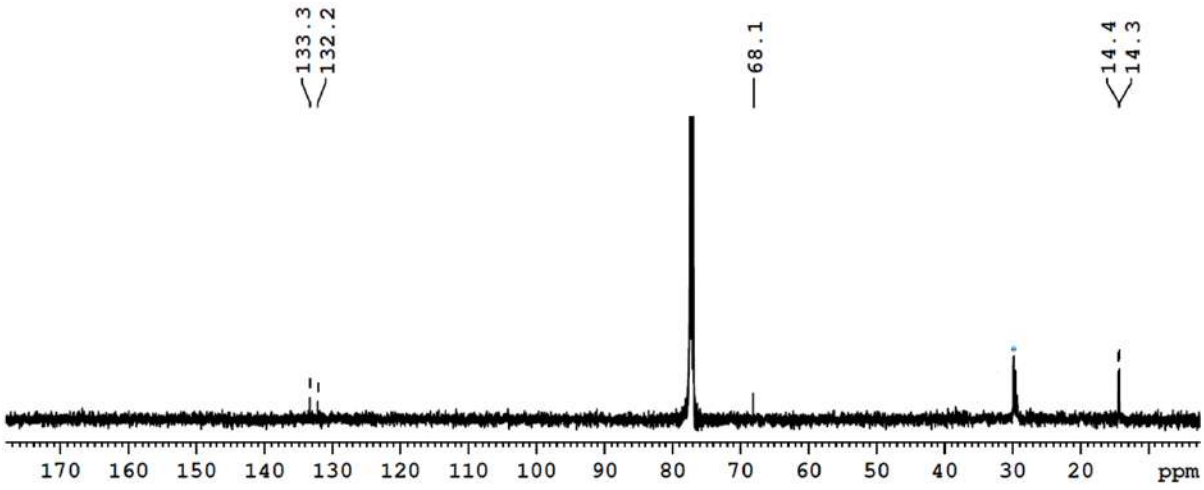


Figure S21. $^{13}C\{^{1}H\}$ NMR spectrum of **2** in $CDCl_3$ (*Grease).

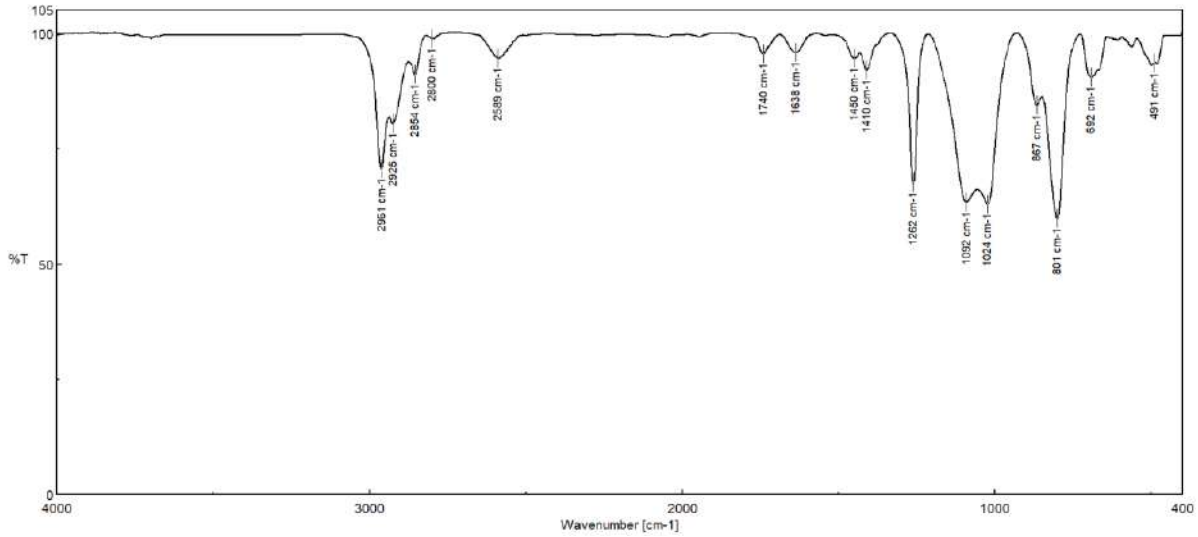


Figure S22. IR spectrum of **2**.

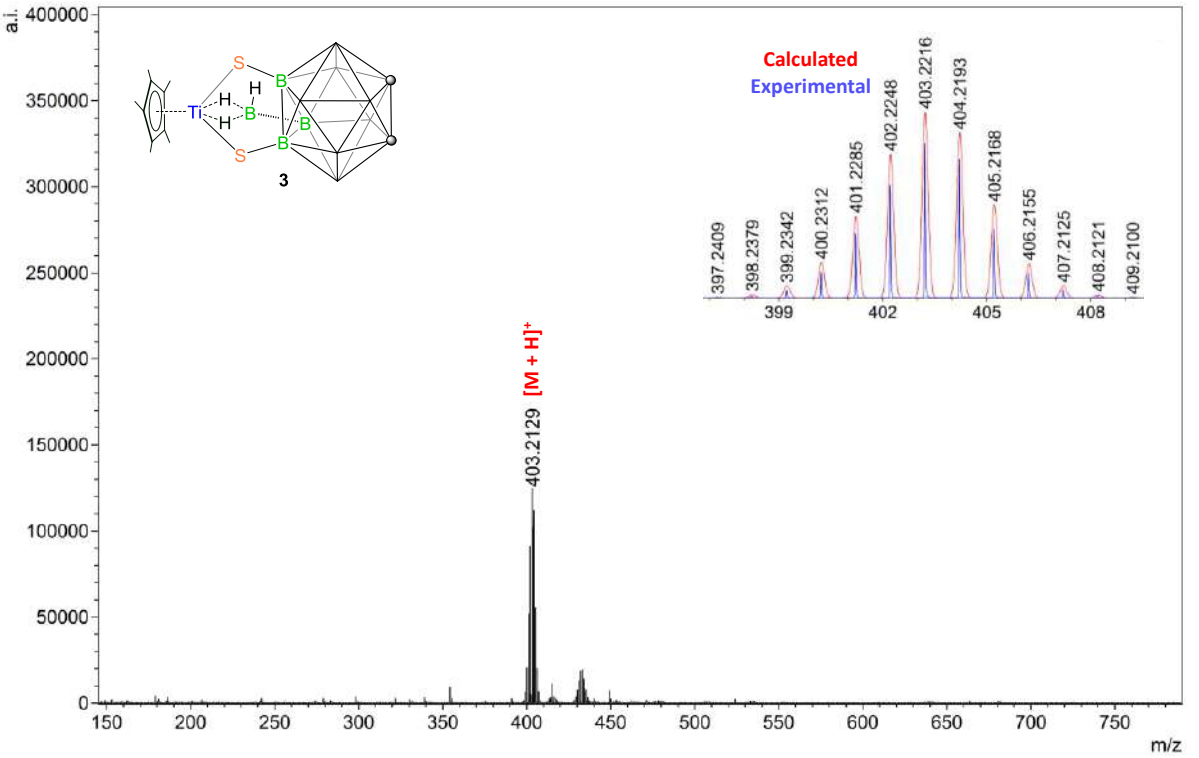


Figure S23. ESI-MS spectrum of **3**.

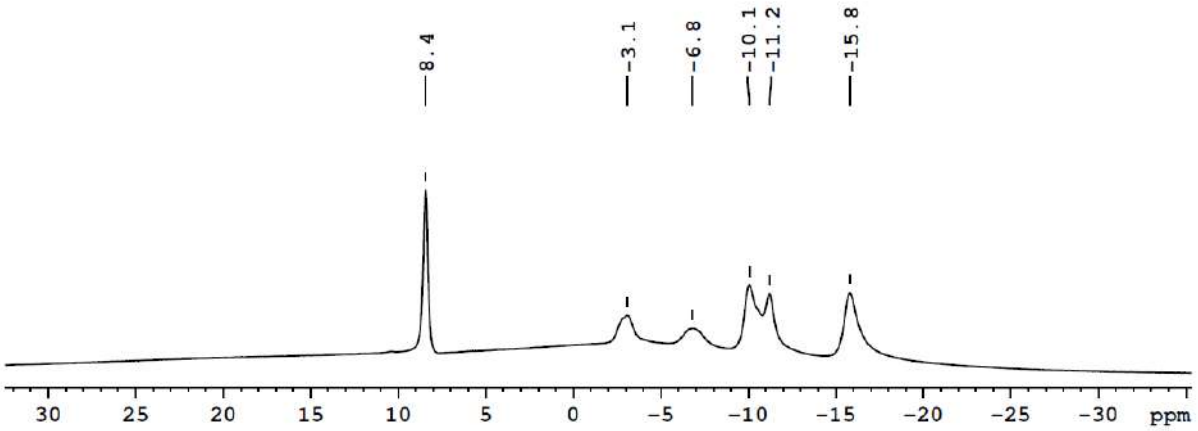


Figure S24. $^{11}B\{^{1}H\}$ NMR spectrum of **3** in $CDCl_3$.

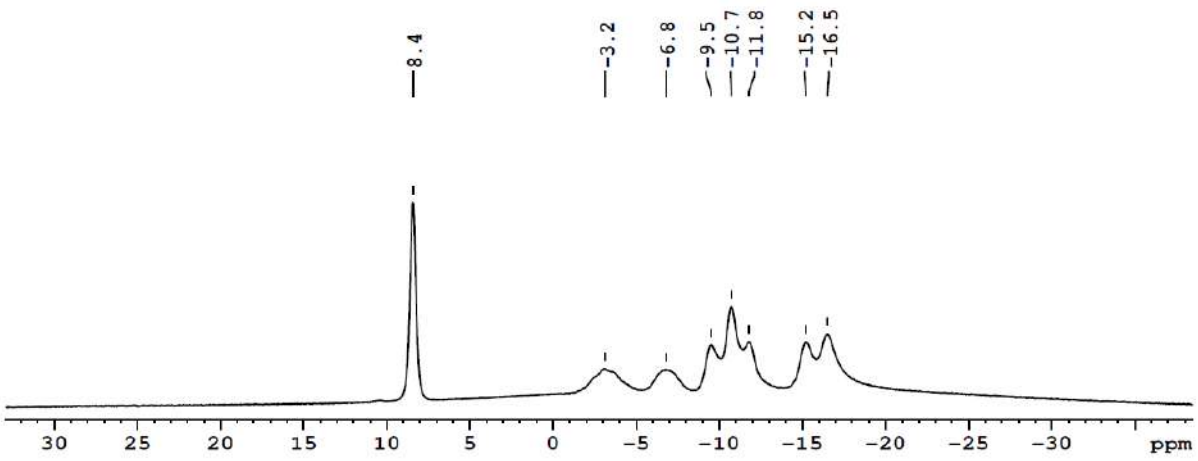


Figure S25. ^{11}B NMR spectrum of **3** in $CDCl_3$.

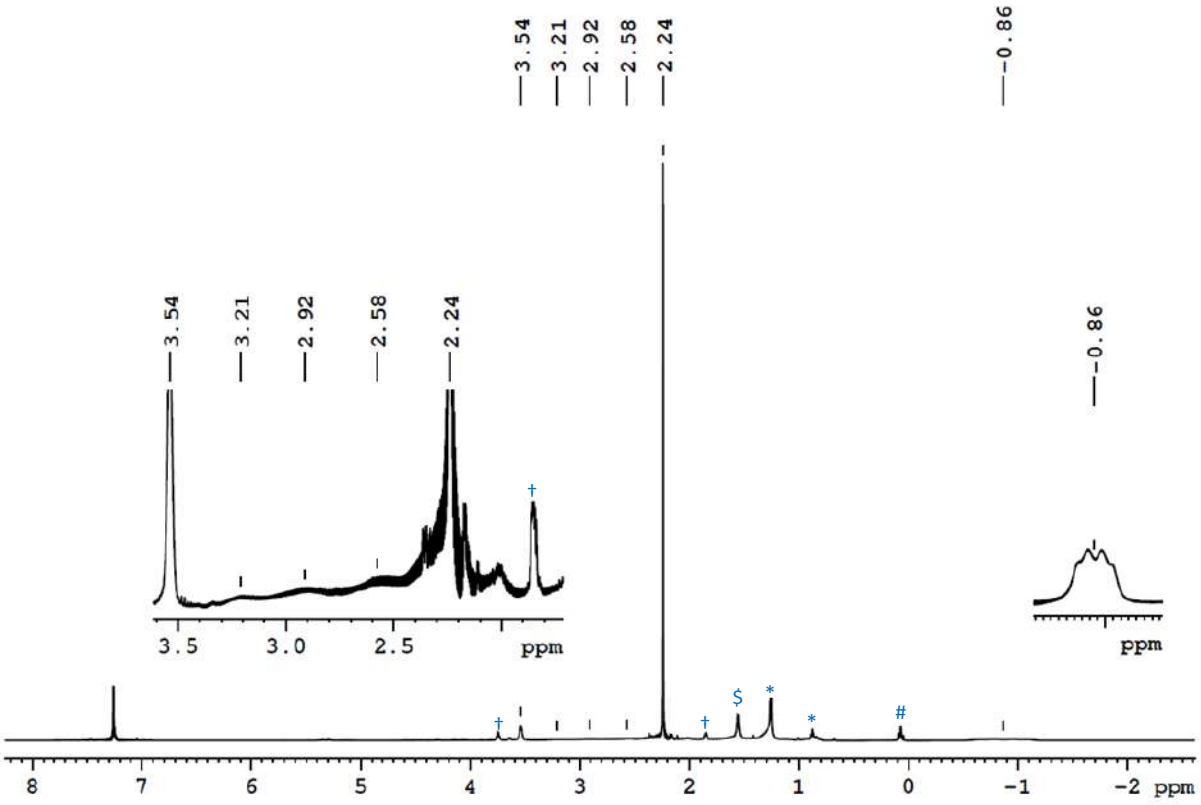


Figure S26. ^{1}H NMR spectrum of **3** in $CDCl_3$ (†Inseparable impurity, $$H_2O$, *Grease, #Silicon grease).

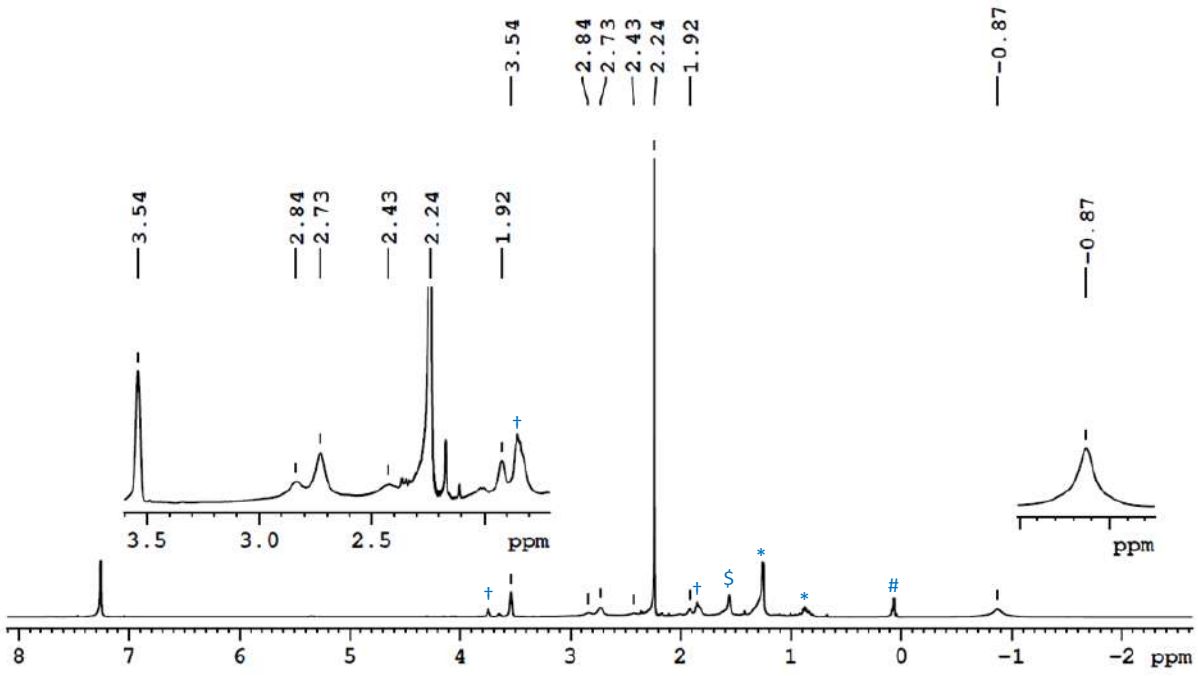


Figure S27. ^{1}H{^{11}B} NMR spectrum of **3** in $CDCl_3$ (†Inseparable impurity, $$H_2O$, *Grease, #Silicon grease).

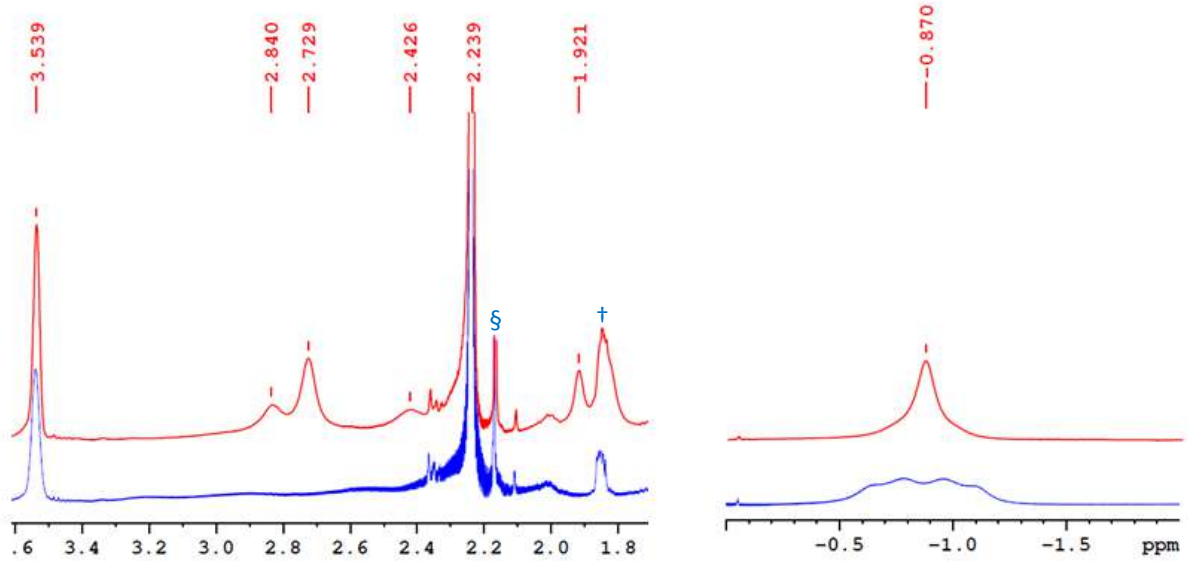


Figure S28. Stacked ^{1}H (bottom) and $^{1}H\{^{11}B\}$ NMR (top) spectra of **3** in $CDCl_3$ (§Acetone, †Inseparable impurity).

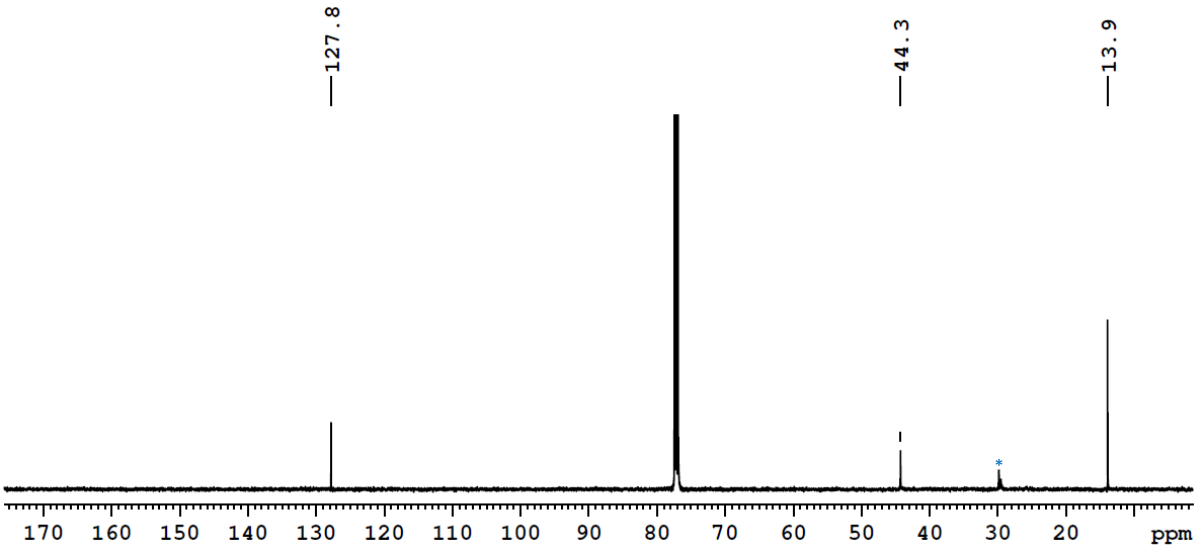


Figure S29. $^{13}C\{^{1}H\}$ NMR spectrum of **3** in $CDCl_3$ (*Grease).

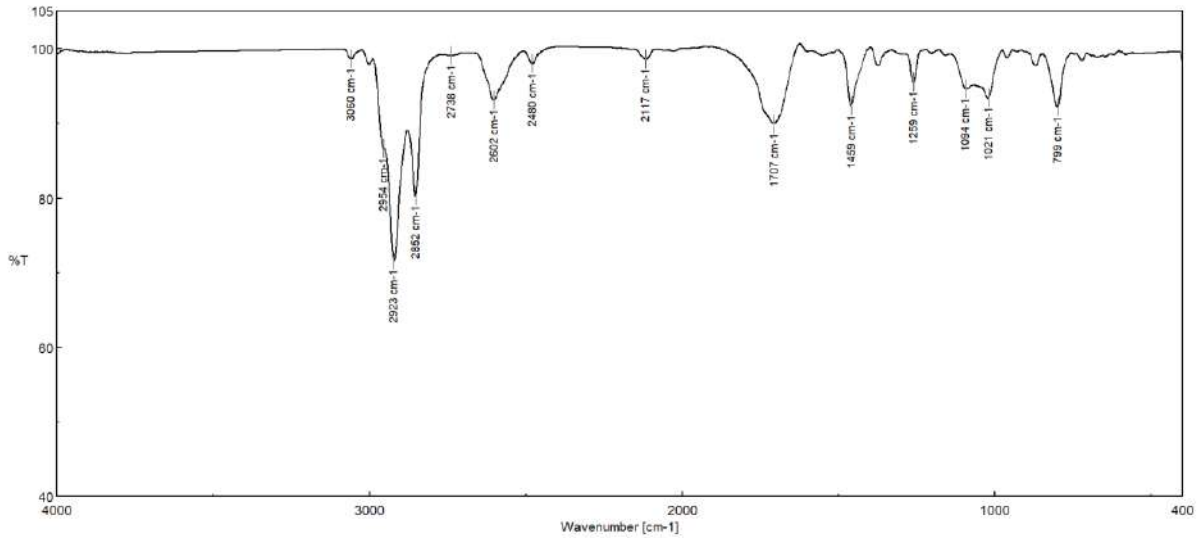


Figure S30. IR spectrum of **3**.

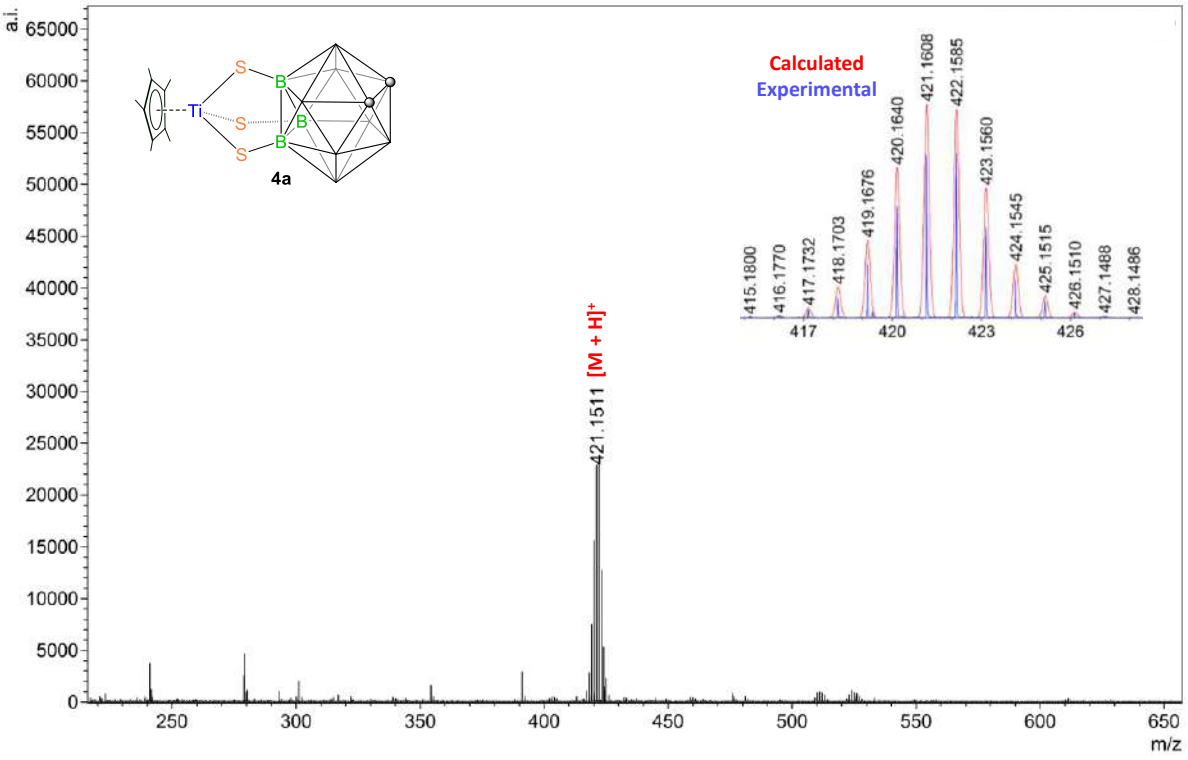


Figure S31. ESI-MS spectrum of **4a**.

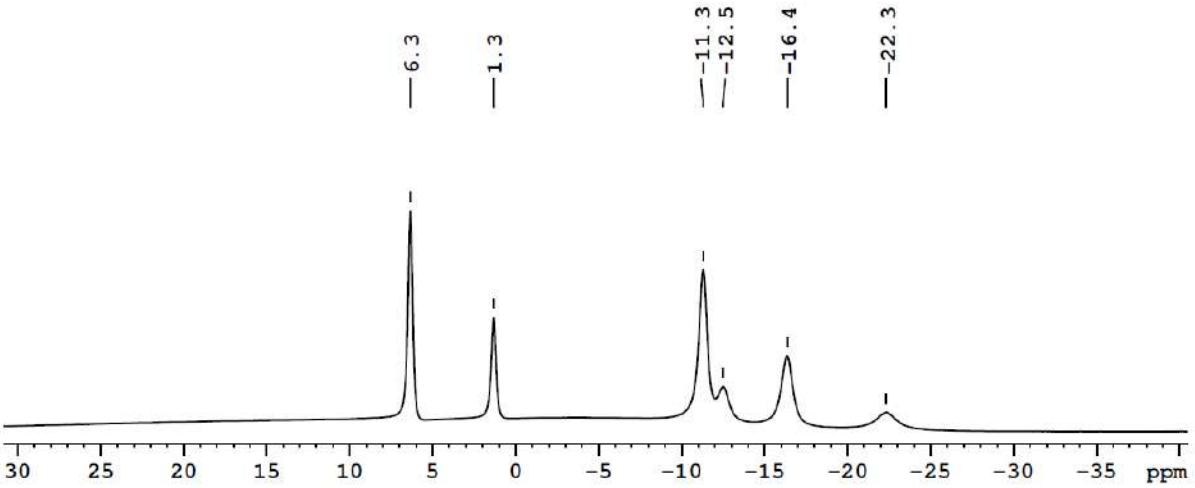


Figure S32. $^{11}B\{^{1}H\}$ NMR spectrum of **4a** in $CDCl_3$.

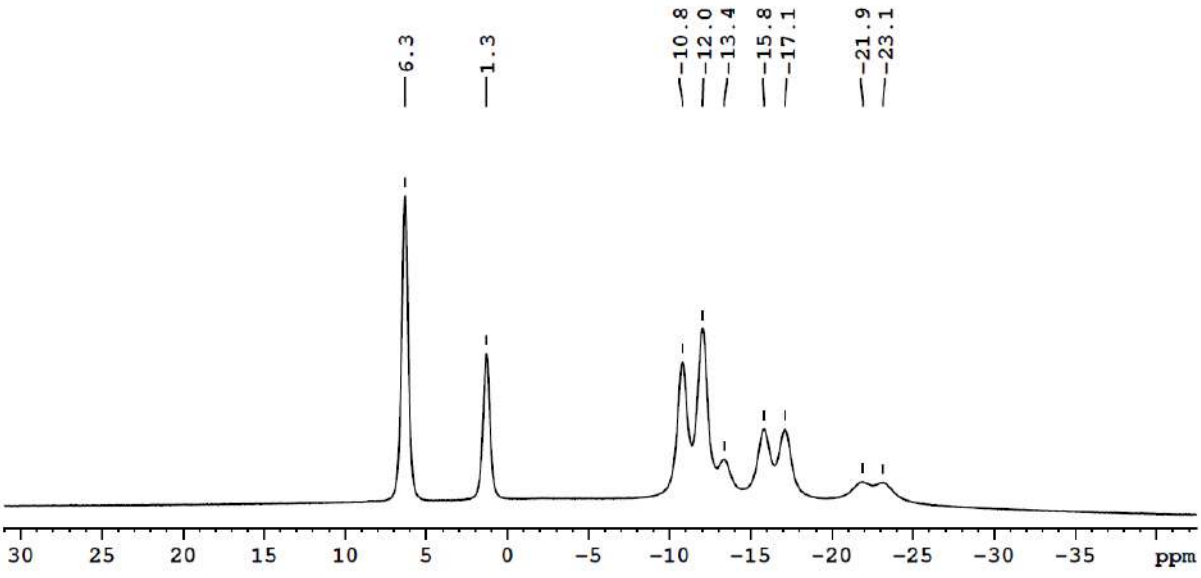


Figure S33. ^{11}B NMR spectrum of **4a** in $CDCl_3$.

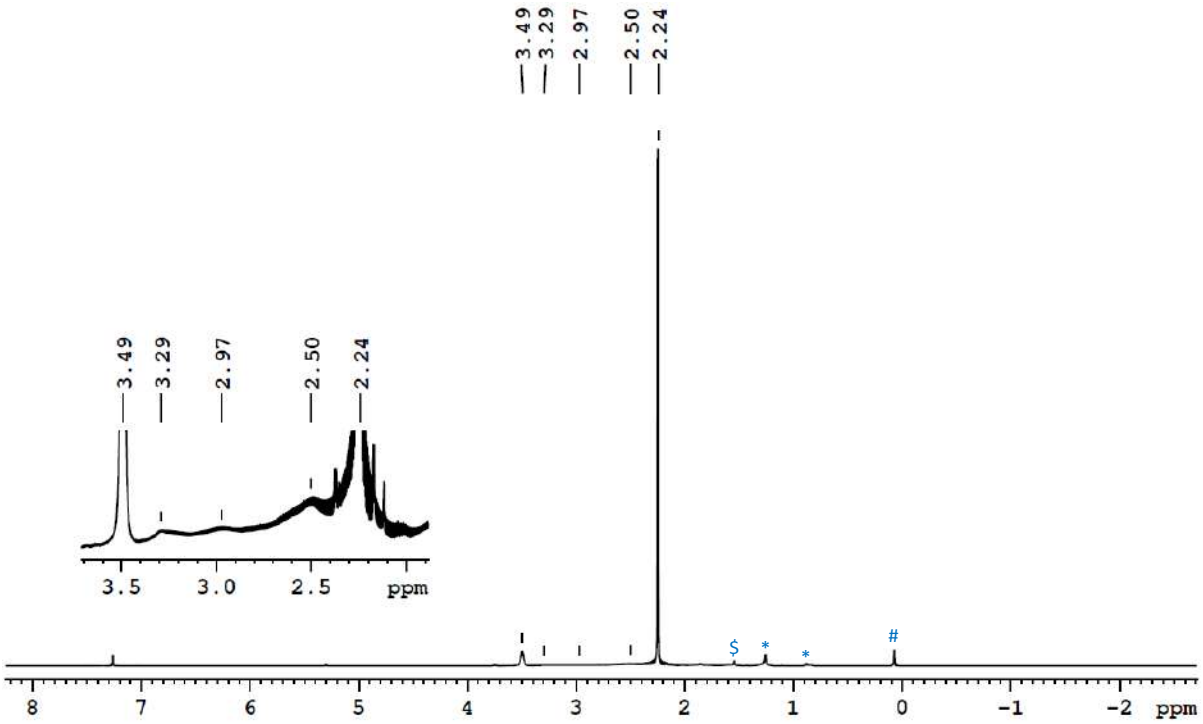


Figure S34. ^{1}H NMR spectrum of **4a** in $CDCl_3$ ($H_2O, *Grease, #Silicon grease).

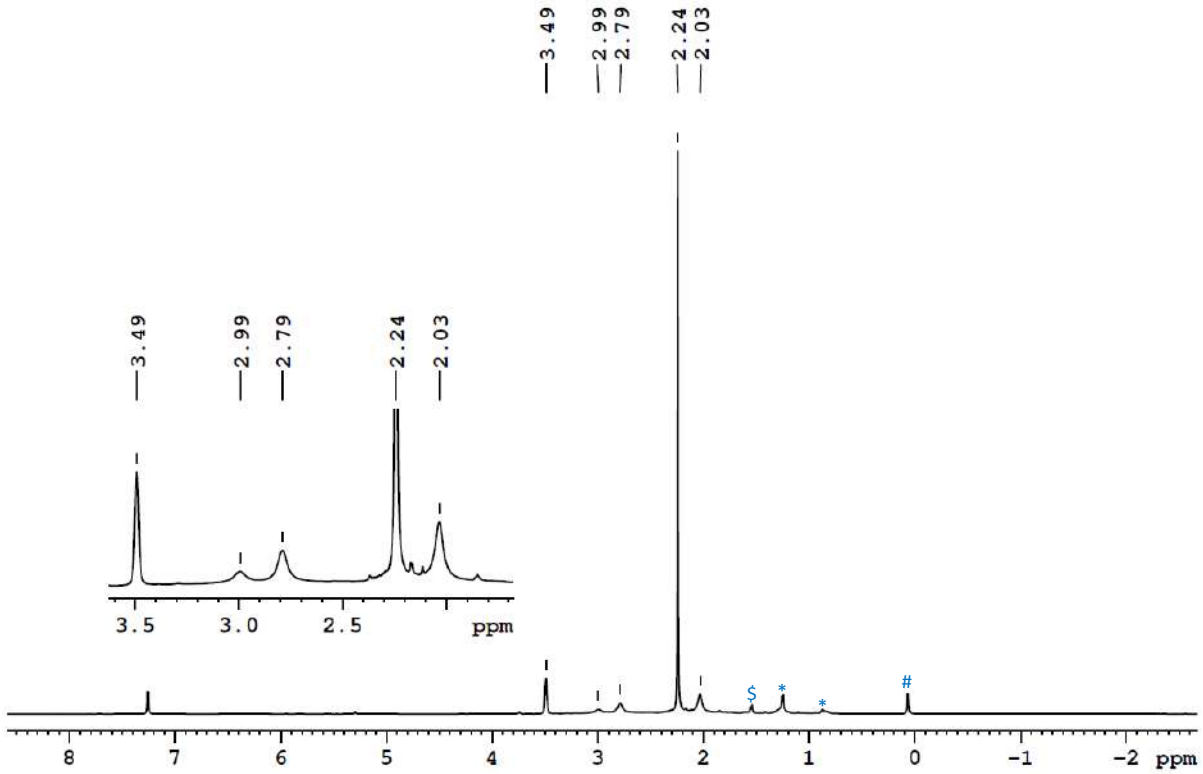


Figure S35. $^{1}H\{^{11}B\}$ NMR spectrum of **4a** in $CDCl_3$ ($H_2O, *Grease, #Silicon grease).

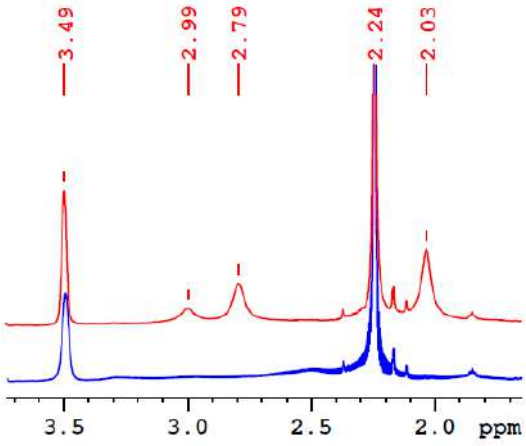


Figure S36. Stacked ^{1}H (bottom) and $^{1}H\{^{11}B\}$ NMR (top) spectra of **4a** in $CDCl_3$.

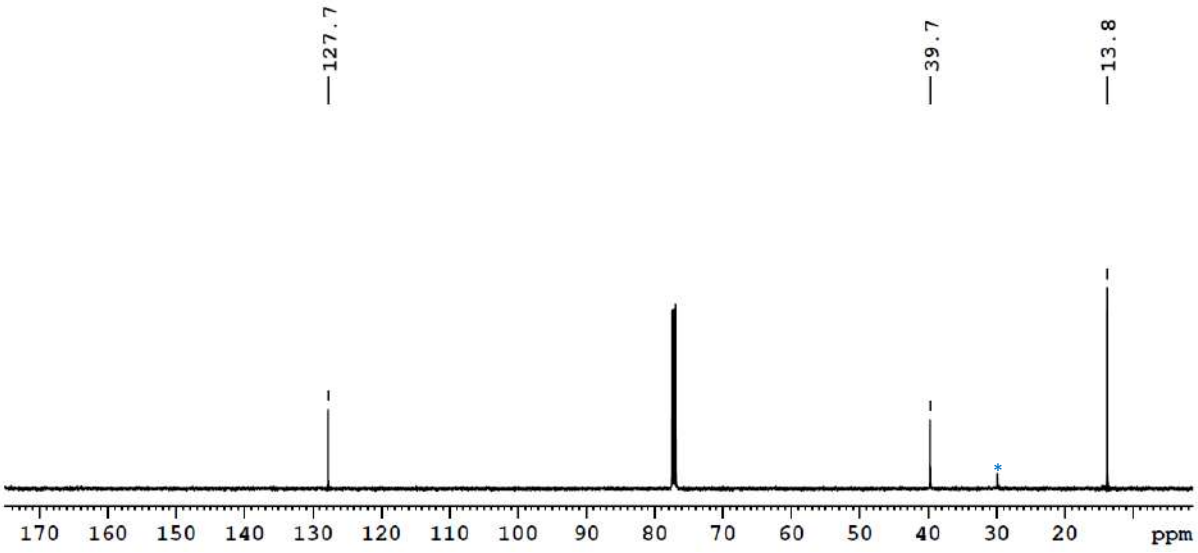


Figure S37. $^{13}C\{^{1}H\}$ NMR spectrum of **4a** in $CDCl_3$ (*Grease).

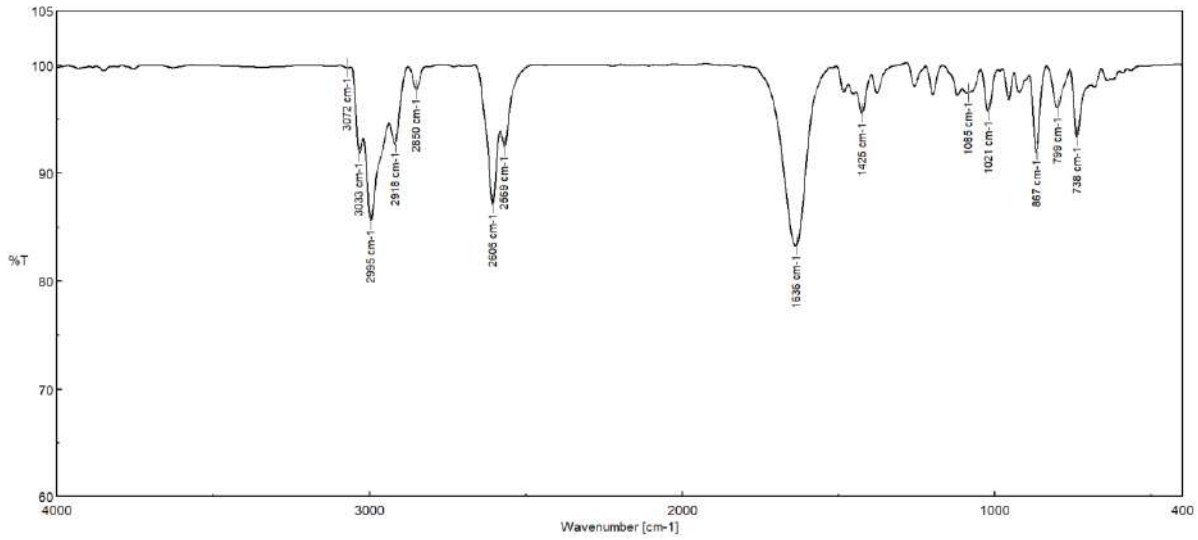


Figure S38. IR spectrum of **4a**.

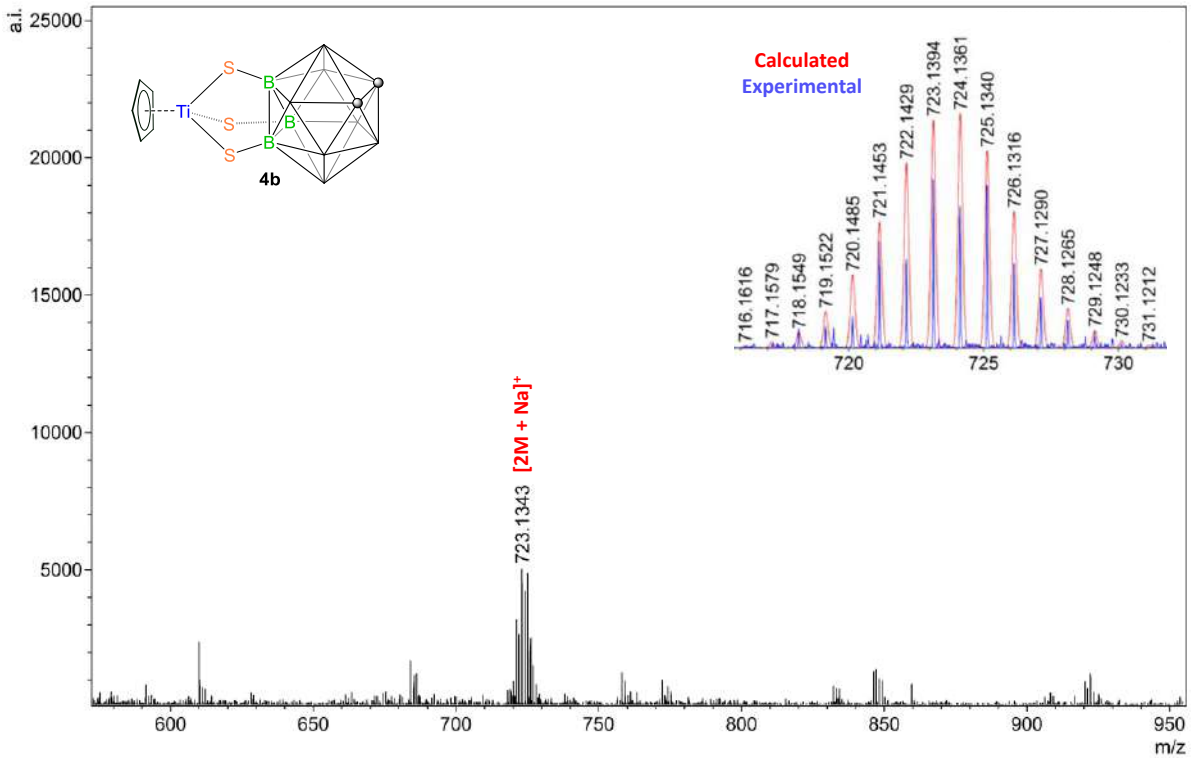


Figure S39. ESI-MS spectrum of **4b**.

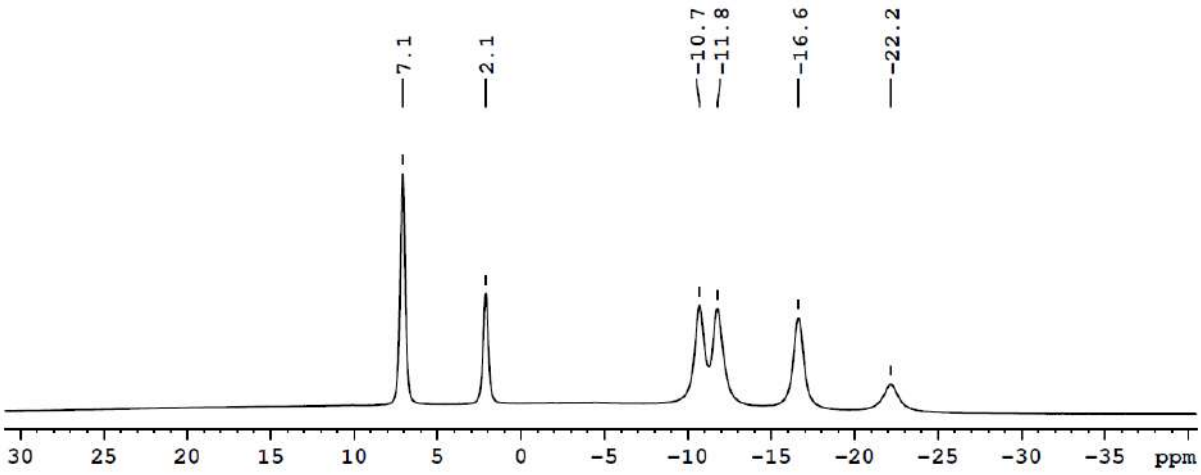


Figure S40. $^{11}B\{^{1}H\}$ NMR spectrum of **4b** in $CDCl_3$.

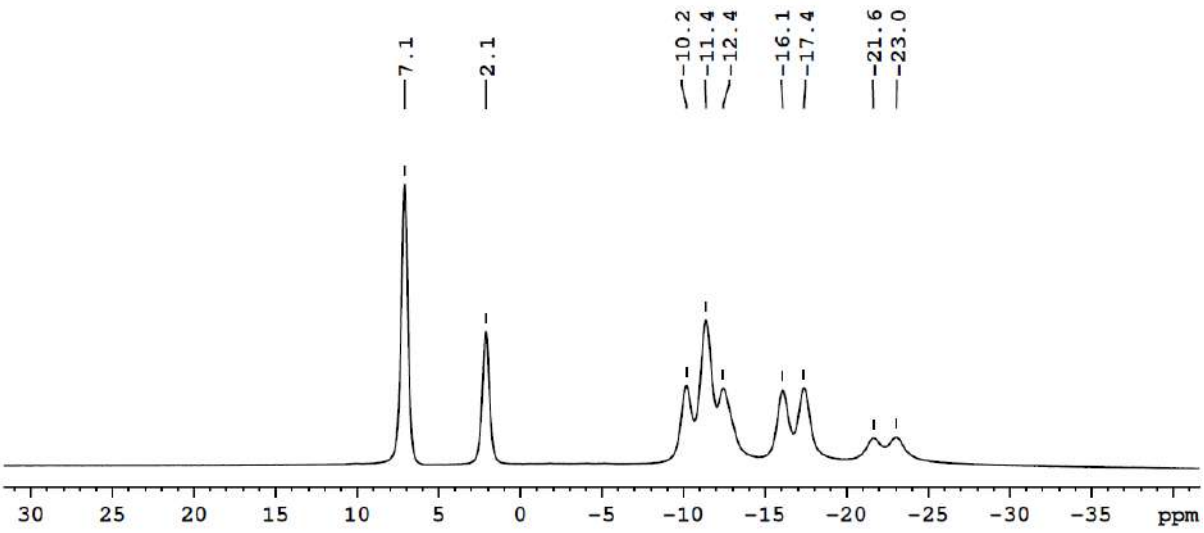


Figure S41. ^{11}B NMR spectrum of **4b** in $CDCl_3$.

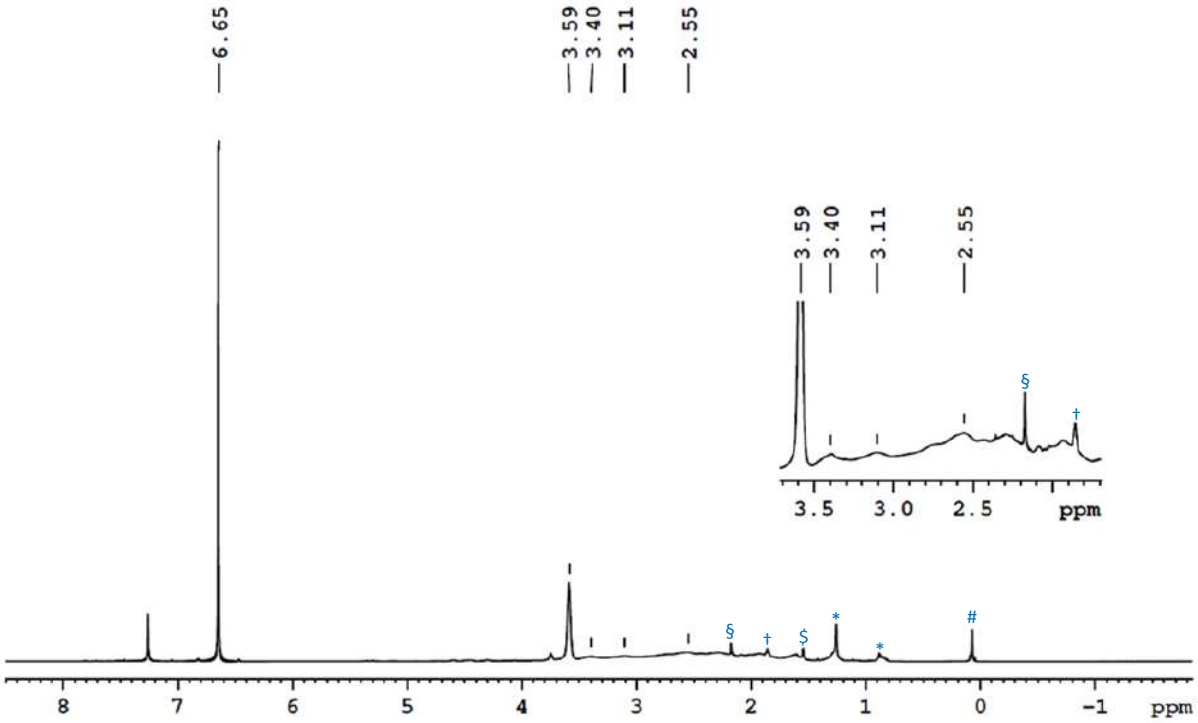


Figure S42. ^{1}H NMR spectrum of **4b** in $CDCl_3$ (§Acetone, †Inseparable impurity, $$H_2O$, *Grease, #Silicon grease).

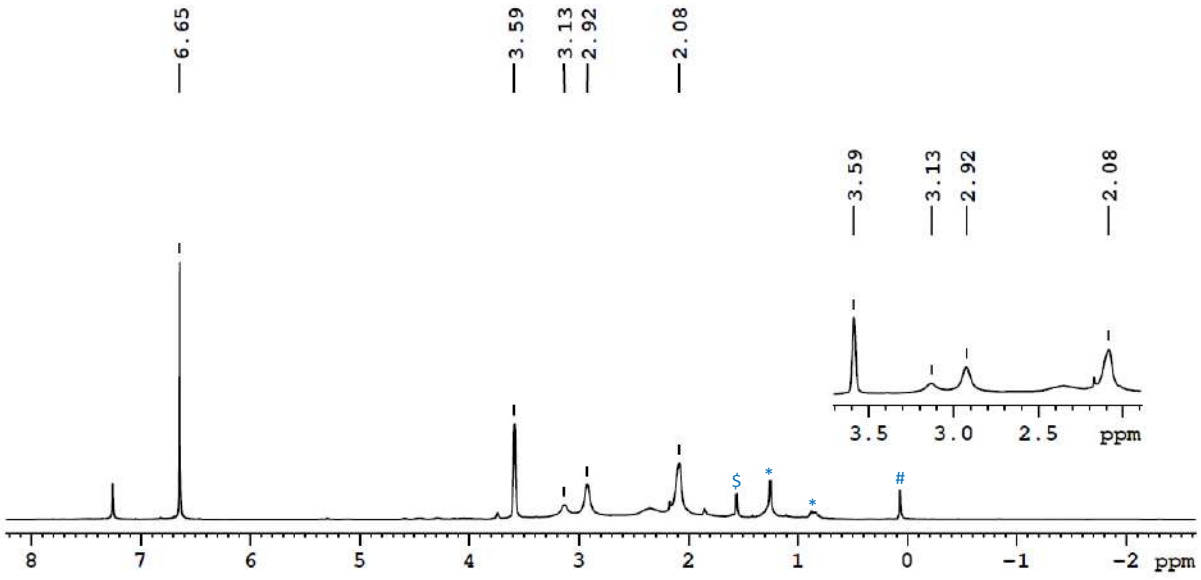


Figure S43. $^{1}H\{^{11}B\}$ NMR spectrum of **4b** in $CDCl_3$ ($$H_2O$, *Grease, #Silicon grease).

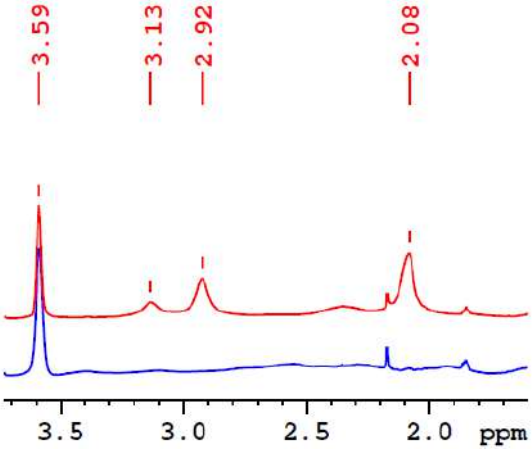


Figure S44. Stacked ^{1}H (bottom) and $^{1}H\{^{11}B\}$ NMR (top) spectra of **4b** in $CDCl_3$.

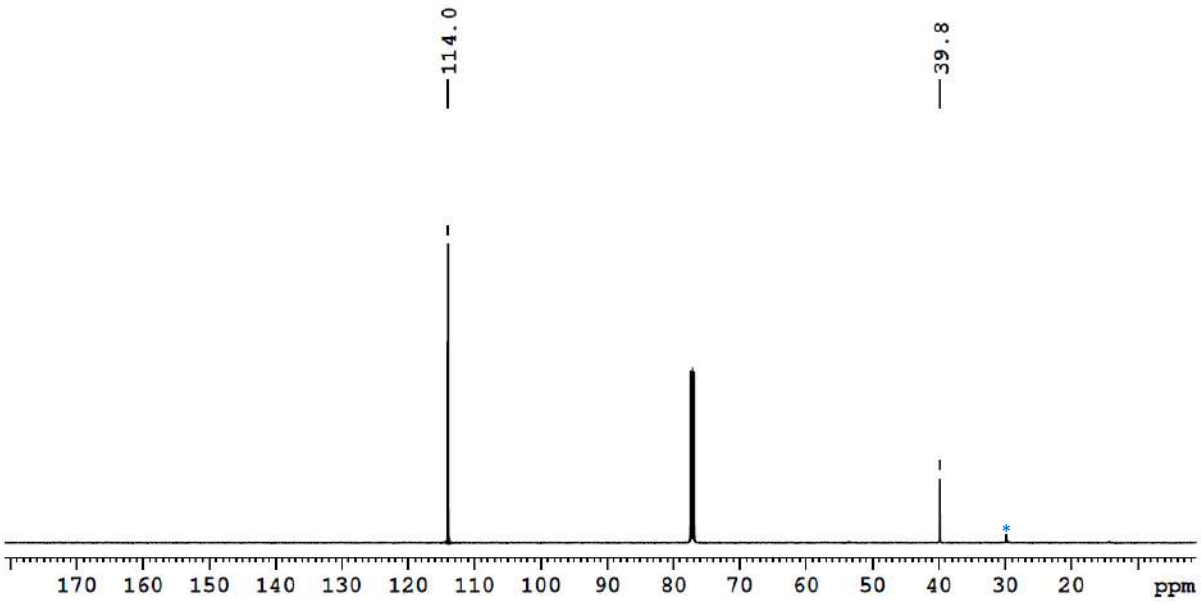


Figure S45. $^{13}C\{^{1}H\}$ NMR spectrum of **4b** in $CDCl_3$ (*Grease).

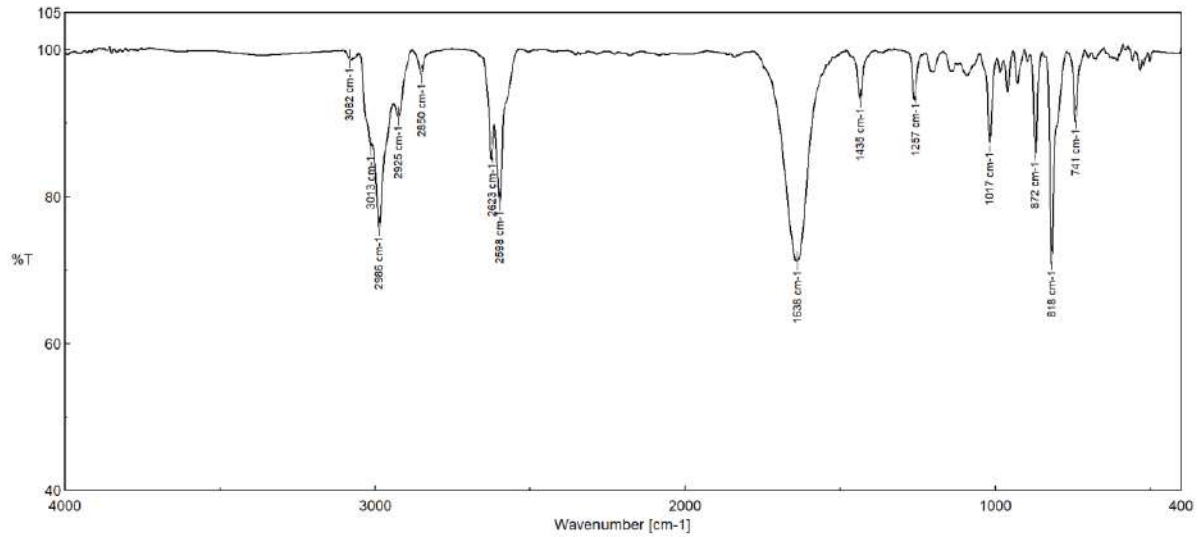


Figure S46. IR spectrum of **4b**.

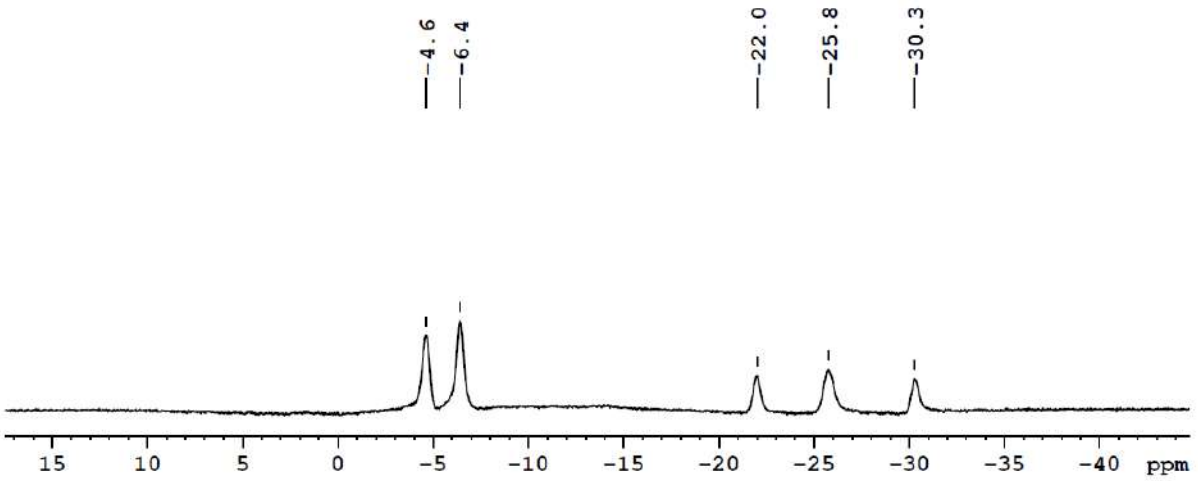


Figure S47. $^{11}B\{^{1}H\}$ NMR spectrum of **5** in $CDCl_3$.

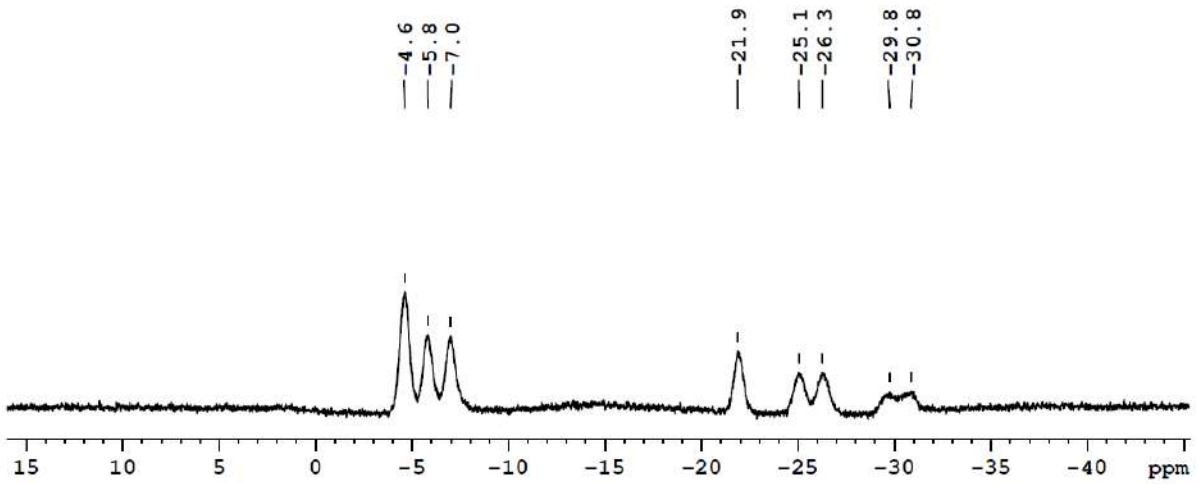


Figure S48. ^{11}B NMR spectrum of **5** in $CDCl_3$.

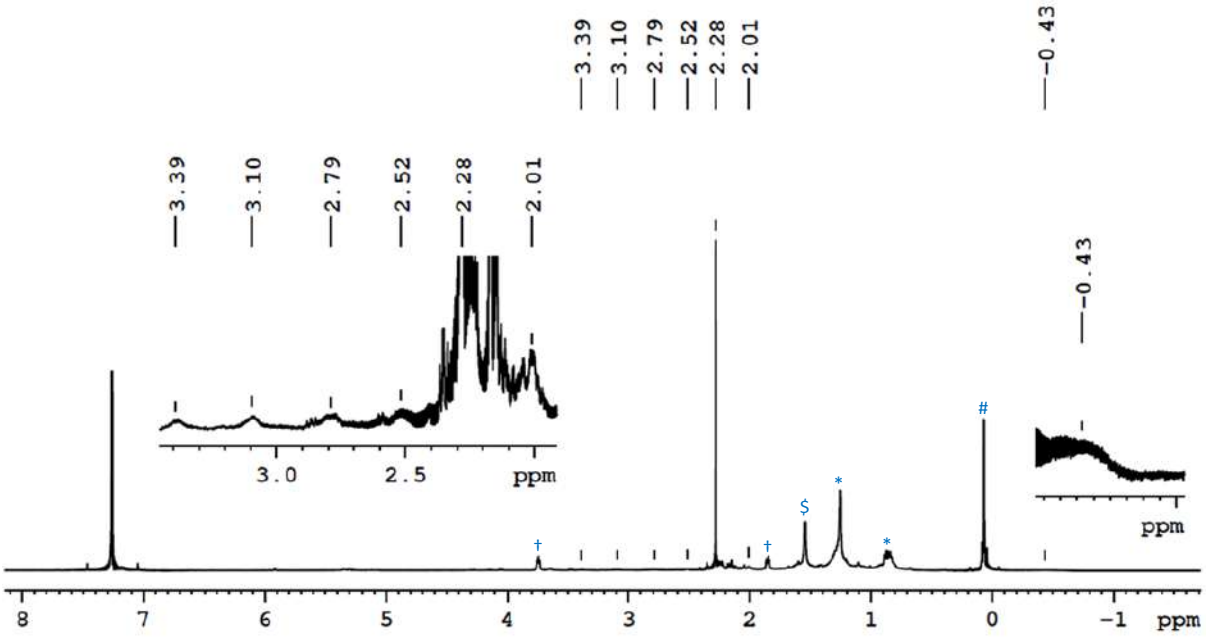


Figure S49. ^{1}H NMR spectrum of **5** in $CDCl_3$ (†Inseparable impurity, $$H_2O$, *Grease, #Silicon grease).

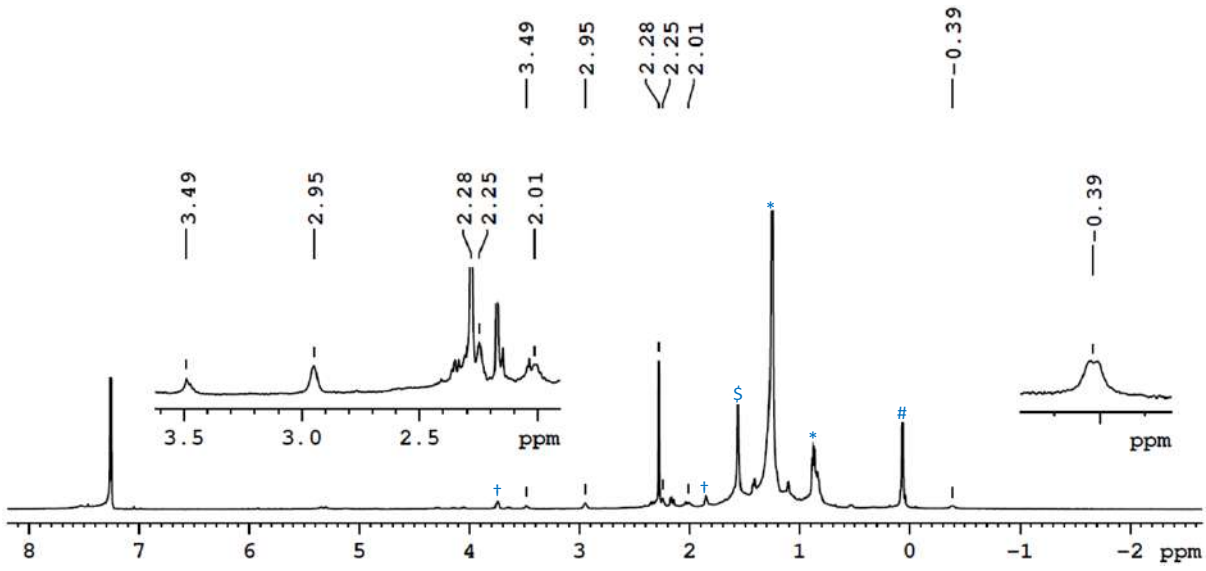


Figure S50. $^{1}H\{^{11}B\}$ NMR spectrum of **5** in $CDCl_3$ (†Inseparable impurity, $$H_2O$, *Grease, #Silicon grease).

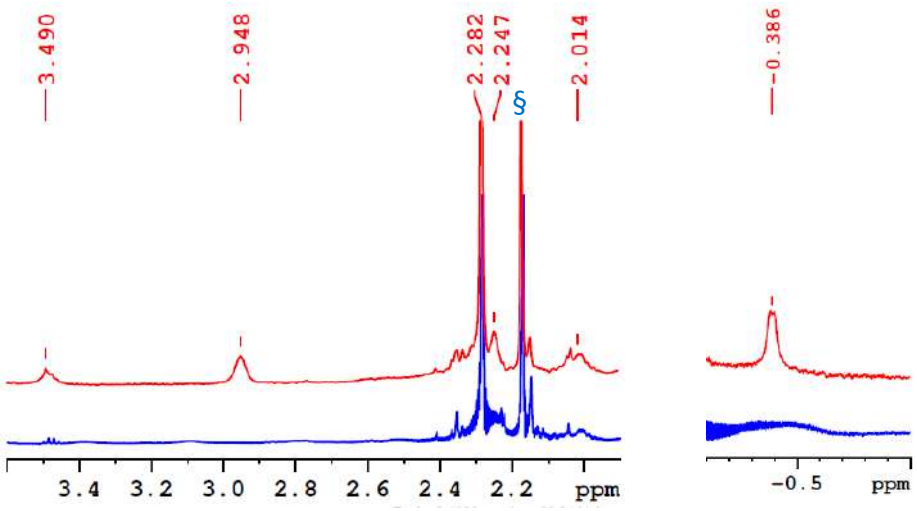


Figure S51. Stacked ^{1}H (bottom) and $^{1}H\{^{11}B\}$ NMR (top) spectra of **5** in $CDCl_3$ (§Acetone).

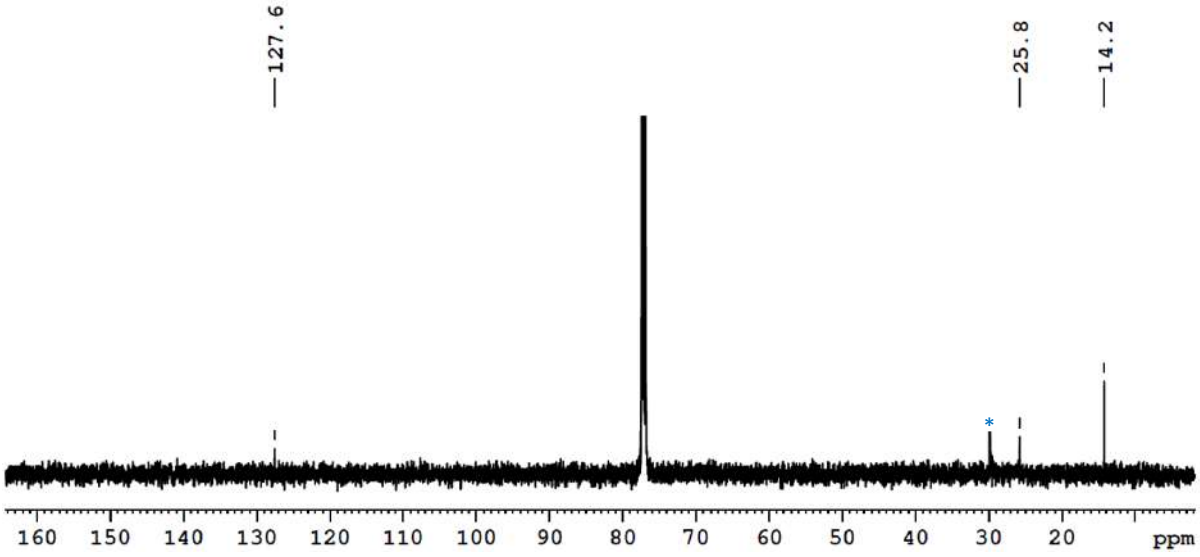


Figure S52. $^{13}C\{^{1}H\}$ NMR spectrum of **5** in $CDCl_3$ (*Grease).

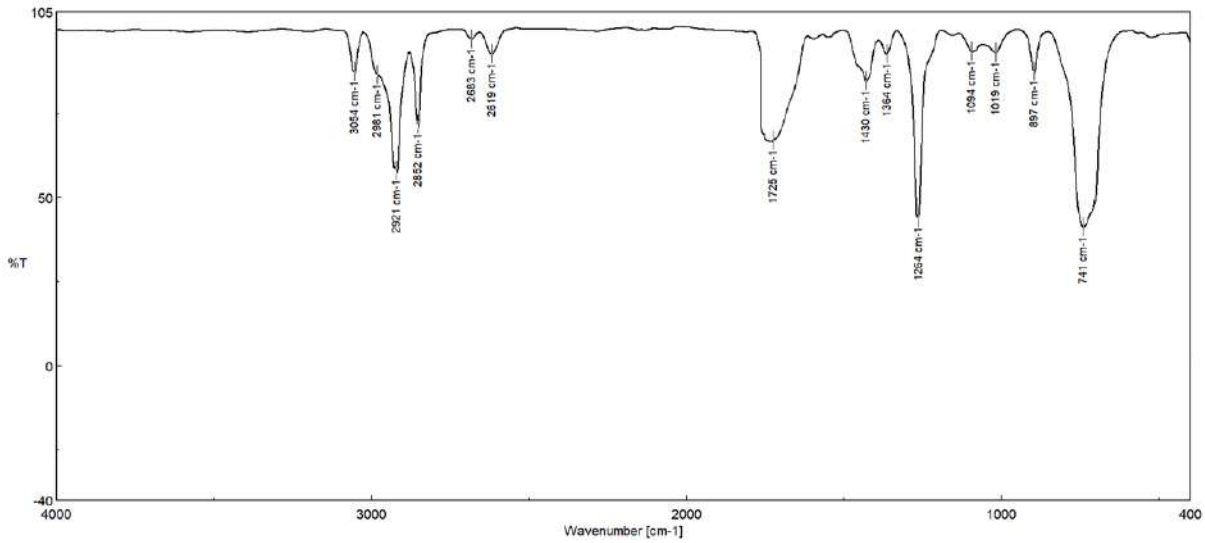


Figure S53. IR spectrum of **5**.

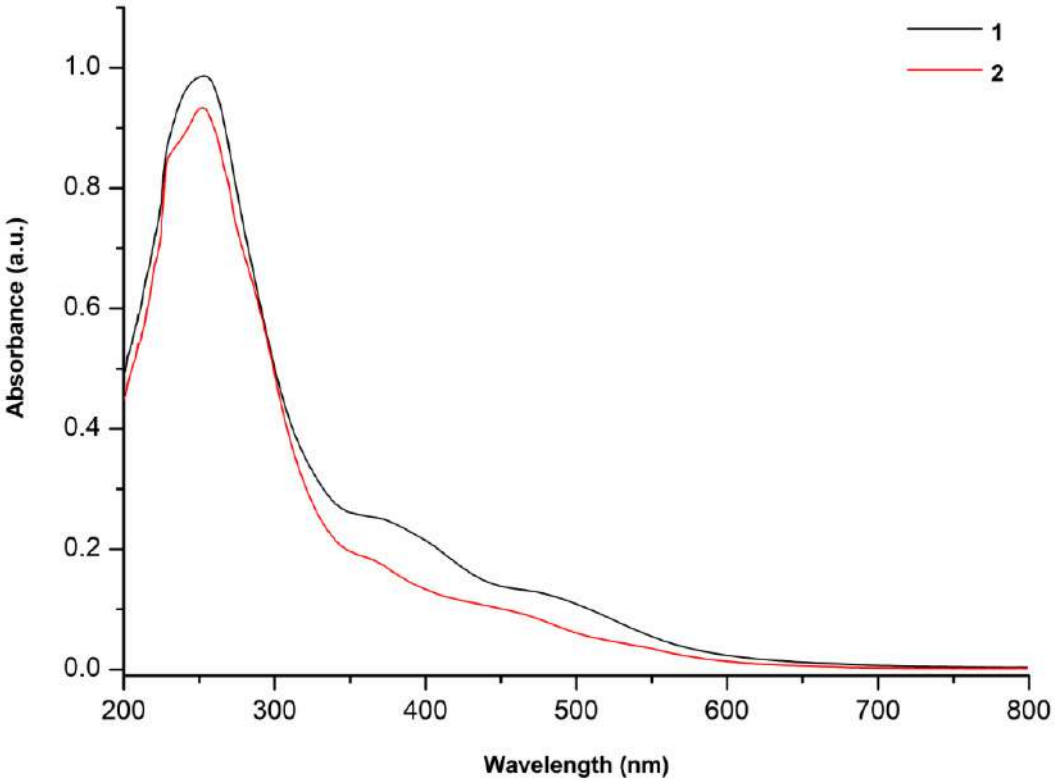


Figure S54. Combined UV-vis spectra of **1** and **2** in CH_2Cl_2.

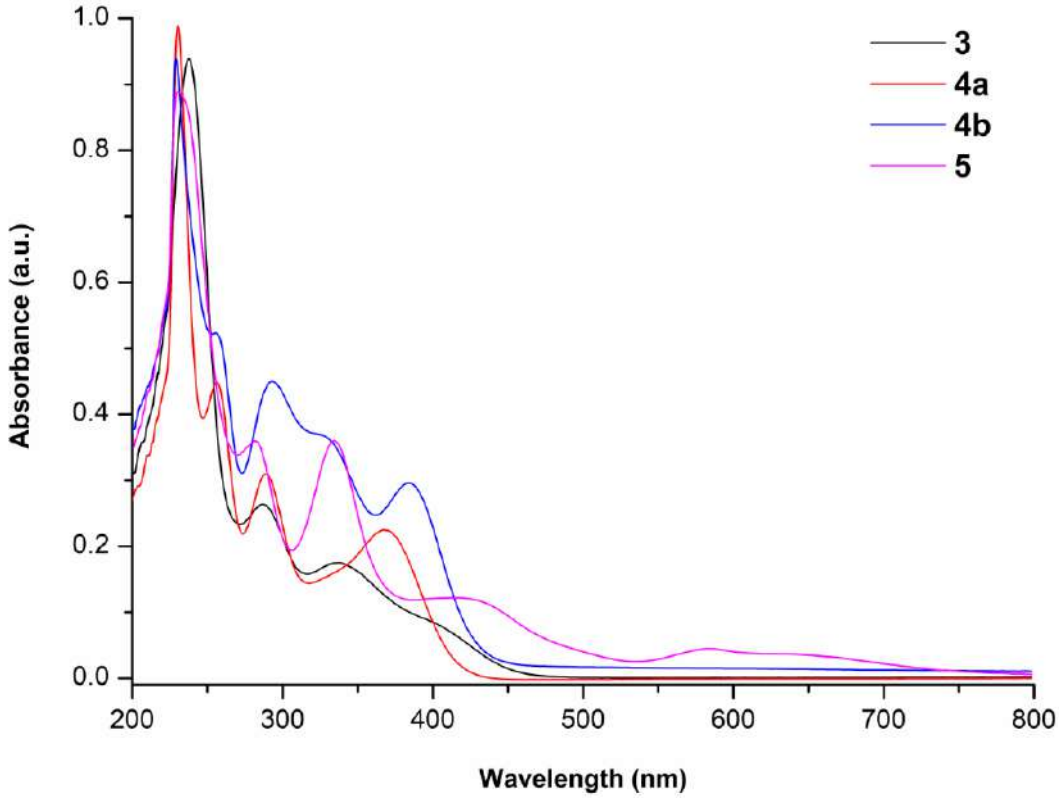


Figure S55. Combined UV-vis spectra of **3**-**5** in CH_2Cl_2.

I.4 *X-ray Analysis Details*

Suitable X-ray quality crystals of **1**-**5** were grown by slow diffusion of a hexane-dichloromethane solution at 5 ˚C. Crystal data of **1** and **2** were obtained and integrated using a Bruker V8 Venture diffractometer equipped with graphite monochromated MoKα (λ = 0.71073 Å) radiation at 300 K (for **1**) and 150 K (for **2**). Note that in **2**, all four Cp* ligands attached to the titanium centers, as well as both the C-S groups of the 1,2-dithiol-*o*-carborane ligand attached to Ti2 atom, exhibit disorder that was resolved into two positions. And crystal data of **3-5** were obtained and integrated using a Bruker APEX-II CCD diffractometer equipped with graphite monochromated MoKα (λ = 0.71073 Å) radiation at 296(2) K. The structures were solved using SIR92[11] and refined with SHELXT-2014/7, SHELXT-2018/3 and SHELXT-2019/3.[12] Using Olex2[13], the molecular structures were drawn. Crystallographic data has been deposited with the Cambridge Crystallographic Data Center as supplementary publication no CCDC - 2403346 (**1**), 2451038 (**2**), 2311787 (**3**), 2358616 (**4a**), 2311786 (**4b**), 2358617 (**5**). The data can be obtained free of charge from The Cambridge Crystallographic Data Centre via www.ccdc.cam.ac.uk/data_request/cif.

Crystal data for **1**: 2 ($C_{44}H_{80}B_{20}O_2S_{10}Ti_6$), M_r.= 2930.55, monoclinic, space group $P1_{21}/c1$, a = 13.4680(8) Å, b = 24.0416(15) Å, c = 22.5360(16) Å, α = 90°, β = 100.988(2)°, γ = 90°, V = 7163.2(8) Å^3, Z = 2, ρ_{calcd} = 0.962 g/cm^3, μ = 1.359 mm^{-1}, *F(000)* = 3008.0, R_1 = 0.0445, wR_2 = 0.1256, 14644 independent reflections [2θ ≤ 52.744°] and 759 parameters.

Crystal data for **2**: 2 ($C_{41.5}H_{65}B_5S_{7.5}Ti_5$), M_r.= 2195.86, monoclinic, space group $P1_{21}/n1$, a = 22.5923(5) Å, b = 21.4585(9) Å, c = 12.9948(10) Å, α = 90°, β = 96.7370(14)°, γ = 90°, V = 6256.3(6) Å^3, Z = 2, ρ_{calcd} = 1.166 g/cm^3, μ = 0.885 mm^{-1}, *F(000)* = 2276.0, R_1 = 0.0763, wR_2 = 0.2465, 12788 independent reflections [2θ ≤ 52.832°] and 666 parameters.

Crystal data for **3**: $C_{12}H_{27}B_{11}S_2Ti$, M_r.= 402.26, orthorhombic, space group *P*bca, a = 12.1687(9) Å, b = 12.8758(10) Å, c = 26.9268(18) Å, α = 90°, β = 90°, γ = 90°, V = 4218.9(5) Å^3, Z = 8, ρ_{calcd} = 1.267 g/cm^3, μ = 0.598 mm^{-1}, *F(000)* = 1664.0, R_1 = 0.0433, wR_2 = 0.1175 , 3705 independent reflections [2θ ≤ 49.994°] and 260 parameters.

Crystal data for **4a**: $C_{12}H_{24}B_{10}S_3Ti$, M_r.= 420.49, orthorhombic, space group *P*bca, a = 12.0927(5) Å, b = 12.8115(6) Å, c = 26.9444(9) Å, α = 90°, β = 90°, γ = 90°, V = 4174.4(3) Å^3, Z = 8, ρ_{calcd} = 1.331 g/cm^3, μ = 0.702 mm^{-1}, *F(000)* = 1712.0, R_1 = 0.0513 , wR_2 = 0.1205, 3677 independent reflections [2θ ≤ 50°] and 243 parameters.

Crystal data for **4b**: $C_7H_{14}B_{10}S_3Ti$, M_r.= 350.36, orthorhombic, space group *P*bca, a = 13.4518(6) Å, b = 12.5002(6) Å, c = 19.0272(11) Å, α = 90°, β = 90°, γ = 90°, V = 3199.4(3) Å^3, Z = 8, ρ_{calcd} = 1.455 g/cm^3, μ = 0.903 mm^{-1}, *F(000)* = 1408.0, R_1 = 0.0290, wR_2 = 0.0764, 2840 independent reflections [2θ ≤ 50.208°] and 244 parameters.

Crystal data for **5**: $C_{12}H_{24}B_9S_3V$, M_r.= 412.72, monoclinic, space group P_{21}/n, a = 10.449(2) Å, b = 14.2128(19) Å, c = 13.260(3) Å, α = 90°, β = 92.289(7)°, γ = 90°, V = 1967.6(6) Å^3, Z = 4, ρ_{calcd} = 1.393 g/cm^3, μ = 0.815 mm^{-1}, *F(000)* = 848.0, R_1 = 0.0565, wR_2 = 0.1322, 3337 independent reflections [2θ ≤ 50.078°] and 255 parameters.

II Computational Details

All molecules were fully optimized using the *Gaussian 16*[14] program employing the BP86 functional[15] in conjunction with a def2-SVP basis set from the EMSL Basis Set Exchange Library.[16] The model compounds were fully optimized in gaseous state (no solvent effect) starting from the X-ray crystallographic coordinates. Frequency calculations were performed at the same level of theory to verify the nature of the stationary states and the absence of any imaginary frequency to confirm that all structures represent minima on the potential energy hypersurface. Further, the gauge including atomic orbital (GIAO)[17-19] method was employed to compute the ^{11}B chemical shifts. The NMR chemical shifts were calculated using the hybrid Becke−Lee−Yang−Parr (B3LYP) functional[20] and the def2-SVP basis set on the BP86/def2-SVP optimized geometries. The ^{11}B NMR chemical shifts were calculated relative to B_2H_6 (B3LYP B shielding constant 84.05

ppm) and converted to the usual [$BF_3.OEt_2$] scale using the experimental δ (^{11}B) value of B_2H_6, 16.6 ppm.[21] Natural bonding analyses were performed with the natural bond orbital (NBO) partitioning scheme[22] as implemented in the Gaussian 16 suite of programs. Wiberg bond indexes (WBI)[23] were obtained from a natural bond orbital analysis. In order to understand the nature of bonding in the synthesized molecules in greater detail, the topological properties of the resultant electron density, ρ, obtained from the wave functions of all the optimized structures were analyzed with the quantum theory of atoms in molecules (QTAIM).[24] The QTAIM analysis was carried out utilizing the Multiwfn V.3.4 package[25,] whereas the wave functions were generated with Gaussian09 at the same level of theory as for geometry optimization. All the optimized structures and orbital graphics were generated using the Gaussview[26], and Chemcraft[27] visualization programs.

Table.S1. Selected geometrical parameters and Wiberg bond indices (WBI) of **1**-**5**.

1				**2**			
	Expt.	Cal.	WBI		Expt.	Cal.	WBI
Ti1···Ti2	3.250	3.308	0.077	Ti1···Ti2	3.244	3.210	0.199
Ti2···Ti3	3.110	3.162	0.064	Ti2···Ti3	3.272	3.300	0.288
Ti2-S1	2.386(9)	2.377	1.196	Ti1-S1	2.289(2)	2.297	1.101
Ti2-S2	2.407(10)	2.403	1.145	Ti2-S1	2.526(2)	2.465	0.773
Ti1-S5	2.472(6)	2.490	0.758	Ti2-S7	2.479(5)	2.399	1.137
Ti2-S5	2.396(5)	2.436	0.858	Ti2-S8	2.438(4)	2.399	1.137
Ti1-O1	1.952(12)	1.897	0.874	Ti4-S5	2.511(2)	2.515	0.710
Ti2-O1	2.044(12)	2.082	0.501	Ti5-S5	2.322(2)	2.329	1.036
C1-S1	1.798	1.800	0.962	C1-S7	1.754(16)	1.813	0.936
C2-S2	1.79(5)	1.812	0.938	C2-S8	1.906	1.813	0.936
C1-C2	1.58(6)	1.645	0.704	C1-C2	1.62(2)	1.644	0.705
C1-B1	1.72(8)	1.722	0.552	C1-B2	1.69(2)	1.723	0.552
B1-B2	1.734	1.780	0.430	B4-B8	1.810	1.794	0.526
3				**4a**			
	Expt.	Cal.	WBI		Expt.	Cal.	WBI
Ti1···B11	2.259(4)	2.240	0.591	Ti1-S1	2.3095(12)	2.326	1.192
Ti1-S1	2.3214(9)	2.341	1.194	Ti1-S2	2.3220(11)	2.327	1.192
Ti1-S2	2.3321(9)	2.341	1.192	Ti1-S3	2.3231(12)	2.332	1.667
B1-B11	1.750(5)	1.735	0.830	B1-S3	1.849(5)	1.851	1.081
B2-S1	1.851(4)	1.856	1.065	B2-S1	1.839(5)	1.855	1.073
B3-S2	1.843(4)	1.856	1.066	B3-S2	1.833(5)	1.855	1.074
B1-B2	1.811(5)	1.834	0.494	B1-B2	1.829(6)	1.853	0.474
C1-C2	1.626(6)	1.635	0.732	C1-C2	1.635(7)	1.646	0.716
C2-B10	1.720(6)	1.730	0.458	C2-B10	1.714(7)	1.721	0.466
B11-H3	0.98(4)	1.219	0.932				
B11-H2	1.03(4)	1.274	0.663				
Ti1-H2	1.93(3)	1.951	0.275				

4b				**5**			
	Expt.	Cal.	WBI		Expt.	Cal.	WBI
Ti1-S1	2.2992(7)	2.319	1.228	V1-S1	2.2194(16)	2.229	1.363
Ti1-S2	2.3182(7)	2.317	1.235	V1-S2	2.2088(18)	2.223	1.389
Ti1-S3	2.3223(7)	2.325	1.203	V1-S3	2.2099(15)	2.229	1.356
B1-S3	1.843(3)	1.851	1.080	B1-S1	1.860(6)	1.875	0.990
B2-S1	1.848(3)	1.855	1.073	B2-S2	1.860(6)	1.878	0.984
B3-S2	1.851(3)	1.856	1.070	B3-S3	1.859(6)	1.873	0.992
B1-B2	1.835(3)	1.855	0.472	B1-B2	1.837(9)	1.858	0.460
C1-C2	1.629(3)	1.646	0.716	B8-B9	1.850(11)	1.887	0.443
C2-B10	1.707(4)	1.720	0.467	B8-H1	1.15(2)	1.288	0.491
				C1-C2	1.555(8)	1.569	0.899
				C2-B5	1.695(8)	1.718	0.490

Table S2. Selected experimental and Calculated bond angles of **1**-**5**.

1			**2**		
	Expt.	Cal.		Expt.	Cal.
Ti1-Ti2-Ti3	60.57	59.96	Ti1-Ti2-Ti3	60.49	61.25
Ti2-Ti3-Ti4	93.95	93.85	Ti2-Ti3-Ti4	61.10	61.00
Ti1-S5-Ti2	83.73	84.36	Ti-S1-Ti2	84.56	84.70
Ti2-S5-Ti5	89.21	92.65	Ti2-S1-Ti3	82.00	82.24
Ti2-S1-C1	112.16	112.62	S7-Ti2-S8	81.50	84.67
C1-C2-S2	119.59	115.8	C2-S8-Ti2	114.55	111.73
Ti1-O1-Ti2	108.80	112.42	S8-C2-C1	117.20	115.94
S1-Ti2-S2	84.30	84.46	B6-C2-B9	117.90	113.67
S3-Ti2-S4	83.60	84.46			
Ti2-Ti3-S4	94.73	91.55			
3			**4a**		
	Expt.	Cal.		Expt.	Cal.
Ti1-S1-B2	81.17	80.62	Ti1-S1-B2	80.73	79.71
Ti-S2-B3	81.17	80.70	Ti1-S2-B3	80.58	79.71
S1-B2-B1	117.20	117.22	Ti1-S3-B1	80.50	79.30
B11-B1-B2	121.90	121.64	S1-B2-B1	119.10	118.83
C1-C2-B7	112.20	117.77	S3-B1-B2	119.50	120.19
			C1-C2-B7	112.0	111.75
4b			**5**		
	Expt.	Cal.		Expt.	Cal.
Ti1-S1-B2	80.89	79.44	V1-S1-B1	81.01	80.60
Ti1-S2-B3	80.48	79.45	V1-S2-B2	80.00	80.29

Ti1-S3-B1	80.33	79.02	V1-S3-B3	79.42	79.35
S1-B2-B1	118.25	118.63	S1-B1-B3	116.50	116.69
S3-B1-B2	119.54	119.96	S3-B3-B1	118.80	118.63
C1-C2-B7	111.96	111.77	C1-C2-B7	114.30	116.08

Table S3. Calculated natural charges (q) and natural valence population (Pop) of **1**-**5**.

1			**2**		
	q	Pop(val)		q	Pop(val)
Ti1	0.426	3.569	Ti1	0.159	3.840
Ti2	0.261	3.732	Ti2	-0.114	4.108
Ti3	0.261	3.732	Ti3	0.165	3.833
Ti4	0.205	3.790	Ti4	0.165	3.833
Ti5	0.205	3.790	Ti5	0.159	3.840
Ti6	0.426	3.569	S1	-0.025	6.015
S1	0.126	5.850	S2	-0.103	6.093
S2	0.074	5.903	S3	-0.003	5.991
S3	0.074	5.903	S4	-0.003	5.991
S4	0.126	5.850	S5	-0.103	6.093
S5	-0.088	6.078	S6	-0.025	6.015
S6	-0.078	6.068	S7	0.080	5.896
S7	-0.143	6.135	S8	0.080	5.896
S8	-0.078	6.068	C1	-0.580	4.555
S9	-0.088	6.078	C2	-0.580	4.555
S10	-0.143	6.134	B1	0.032	2.931
O1	-0.513	6.506	B2	0.037	2.923
O2	-0.513	6.506	B3	-0.155	3.126
C1	-0.585	4.560	B4	-0.174	3.145
C2	-0.582	4.557			
C3	-0.582	4.557			
C4	-0.585	4.560			
3			**4a**		
	q	Pop(val)		q	Pop(val)
Ti1	0.075	3.927	Ti1	0.128	3.871
S1	-0.069	6.058	S1	-0.080	6.068
S2	-0.071	6.059	S2	-0.082	6.070
C1	-0.610	4.590	S3	-0.092	6.080
C2	-0.610	4.590	C1	-0.614	4.594
B1	-0.228	3.188	C2	-0.614	4.594

B2	-0.074	3.021	B1	-0.113	3.058
B3	-0.073	3.020	B2	-0.092	3.037
B4	-0.170	3.135	B3	-0.092	3.037
B5	0.032	2.930	B4	-0.177	3.141
B6	0.033	2.928	B5	0.030	2.932
B7	0.033	2.928	B6	0.023	2.936
B8	0.032	2.931	B7	0.023	2.936
B9	0.194	2.767	B8	0.030	2.932
B10	0.228	2.730	B9	0.189	2.773
B11	-0.364	3.344	B10	0.208	2.751
4b			**5**		
	q	Pop(val)		q	Pop(val)
Ti1	0.051	3.946	V1	-0.137	5.139
S1	-0.046	6.035	S1	0.086	5.902
S2	-0.043	6.032	S2	0.083	5.903
S3	-0.057	6.046	S3	0.071	5.916
C1	-0.614	4.594	C1	-0.652	4.634
C2	-0.614	4.594	C2	-0.641	4.622
B1	-0.115	3.061	B1	-0.097	3.048
B2	-0.094	3.039	B2	-0.094	3.043
B3	-0.095	3.041	B3	-0.131	3.083
B4	-0.177	3.141	B4	-0.010	2.974
B5	0.031	2.931	B5	0.210	2.756
B6	0.023	2.936	B6	0.002	2.961
B7	0.023	2.936	B7	0.039	2.935
B8	0.031	2.931	B8	-0.303	3.274
B9	0.189	2.772	B9	0.030	2.944
B10	0.208	2.751			

Table S4. Calculated HOMO–LUMO energy gap of **1**-**5**.

	1	**2**	**3**	**4a**	**4b**	**5**
$\Delta E_{H\text{-}L}$ (eV)	1.300	0.386	2.646	2.857	2.783	1.558

Table S5. Calculated ^{11}B chemical shifts for complexes **1**-**5**.

Compounds	^{11}B NMR value (ppm)	
	Experimental	Theoretical
1[a]	-12.5 and -7.9 (vrey broad peak ranging from -11.0 to -1.0)	-17.6, -17.3, -17.1, -17.0, -15.6, -15.5, -14.0, -13.9, -10.8, -10.6
2[a]	-12.4, -9.8, -8.7, -8.4, -4.9, -3.7, -1.5, -0.8	-18.3,-17.7, -15.2, -13.7, -11.4
3	-15.8, -11.2, -10.1, -6.8, -3.1, 8.4	-25.9, -23.9, -23.8, -19.5, -18.7, -18.7, -18.4, -12.9, -10.0, 4.0, 4.3
4a	-22.3, -16.4, -12.5, -11.3, 1.3, 6.3	-31.9, -24.5, -24.3, -21.7, -19.7, -19.6, -18.6, -2.6, 2.0, 2.5
4b	-22.2, -16.6, -11.8, -10.7, 2.1, 7.1	-32.1, -24.8, -24.7, -21.5, -19.3, -19.0, -1.5, 2.6, 3.4
5	-30.3, -25.8, -22.0, -6.4, -4.6	-37.1, -35.5, -30.6, -27.0, -22.1, -17.5, -16.3, -9.6, -2.9

[a] For clusters **1** and **2**, each theoretical value corresponds to two boron atoms that are merged.

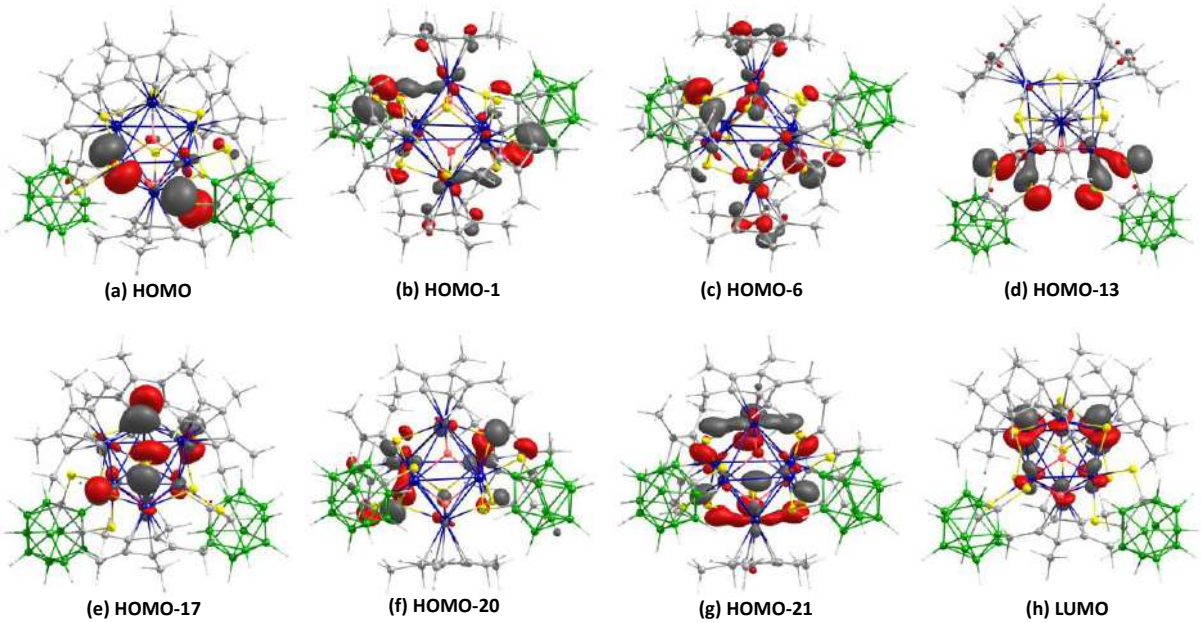


Figure S56. Selected molecular orbitals of **1** (isocontour values: ±0.045 [e.bohr^{-3}]$^{1/2}$).

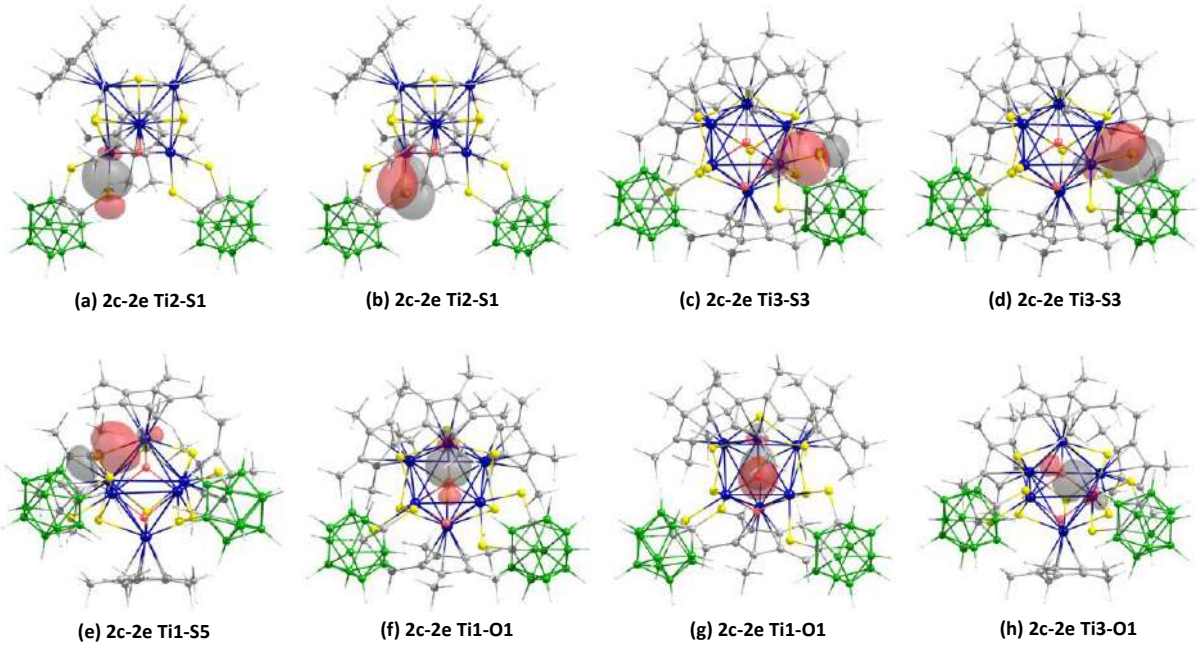


Figure S57. Selected NBO interactions of **1** (isocontour values: ±0.045 [e.bohr^{-3}]$^{1/2}$).

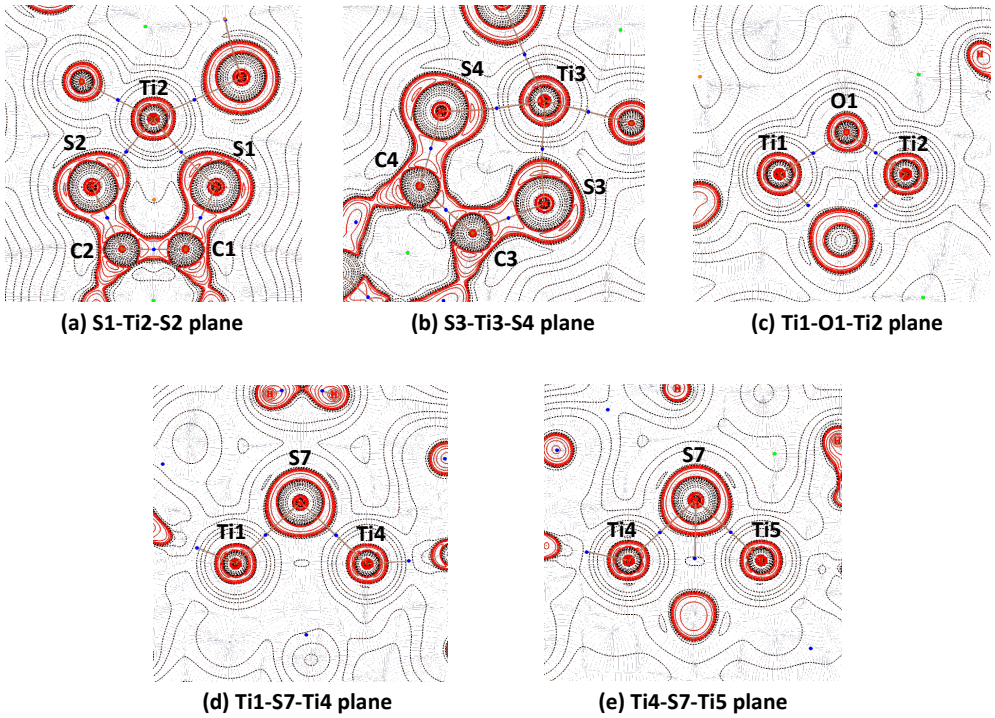


Figure S58. Contour-line diagram of the Laplacian of the electron density of **1** in selected planes. The solid brown lines are bond paths, whereas blue dots indicate the bond-critical points (BCP). Solid red lines indicate the areas of charge concentration ($\nabla^2\rho(r) < 0$), while dashed black lines show the areas of charge depletion ($\nabla^2\rho(r) > 0$).

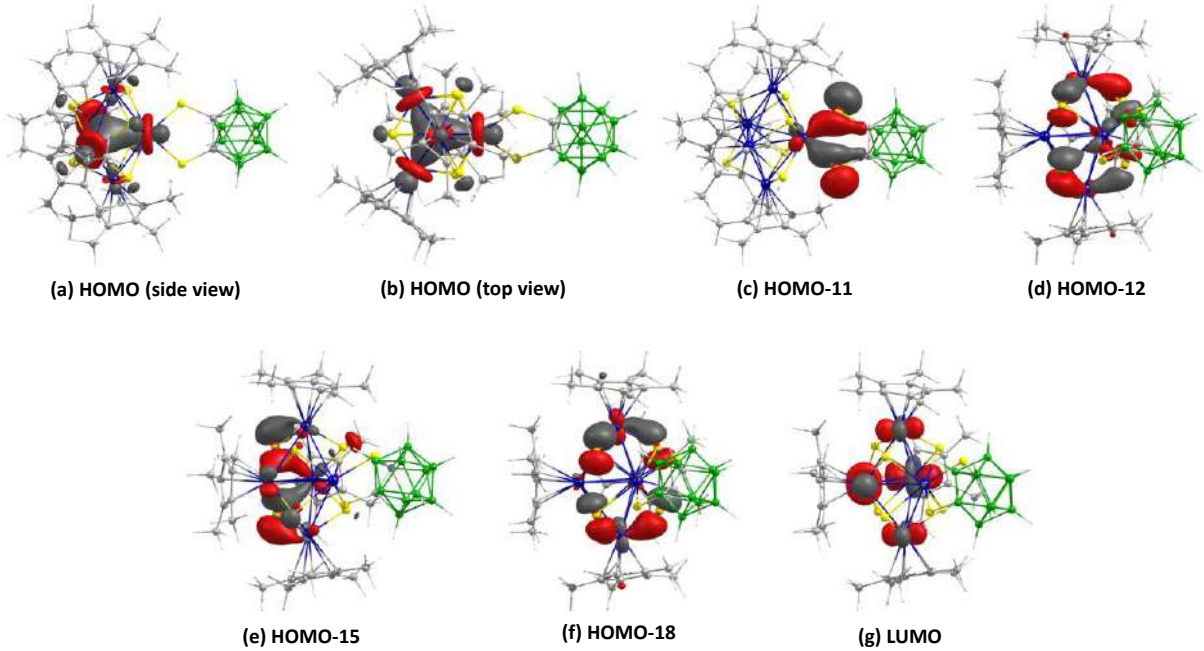


Figure S59. Selected molecular orbitals of **2** (isocontour values: ±0.045 [e.bohr^{-3}]$^{1/2}$).

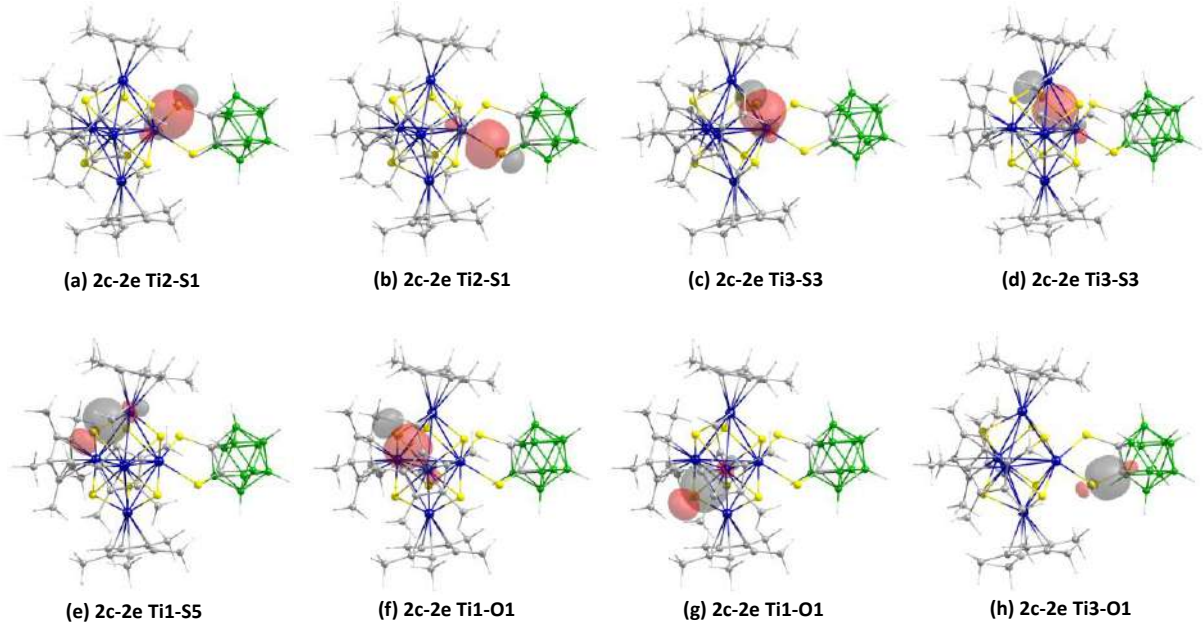
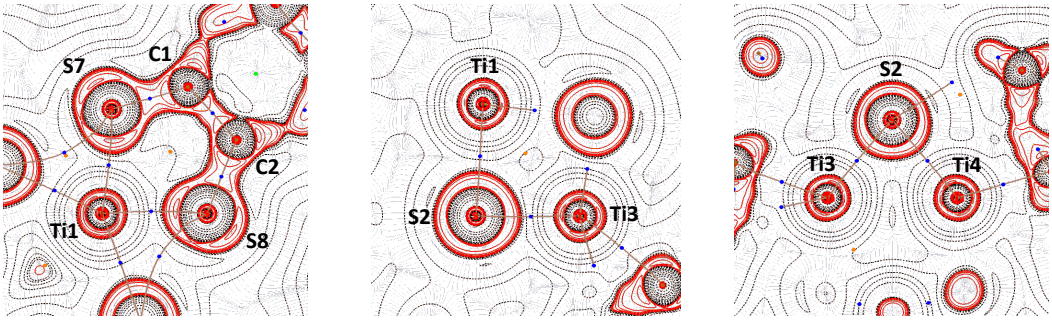
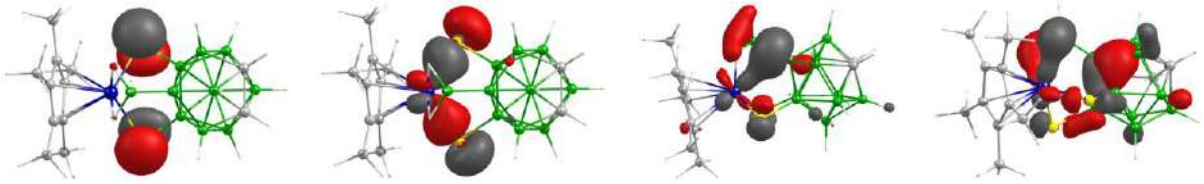


Figure S60. Selected NBO interactions of **2** (isocontour values: ±0.045 [e.bohr^{-3}]$^{1/2}$).

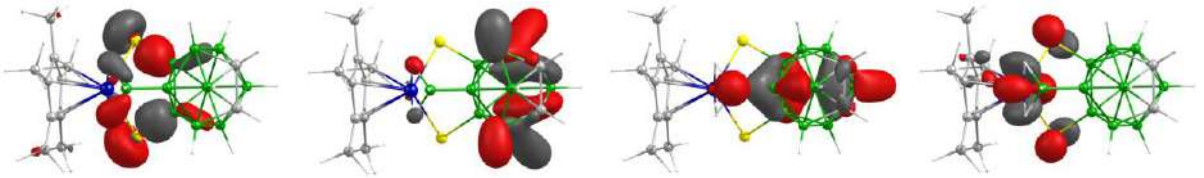


(a) S7-Ti1-S8 plane (b) Ti1-S2-Ti3 plane (c) Ti3-S2-Ti4 plane

Figure S61. Contour-line diagram of the Laplacian of the electron density of **2** in selected planes. The solid brown lines are bond paths, whereas blue dots indicate the bond-critical points (BCP). Solid red lines indicate the areas of charge concentration ($\nabla^2\rho(r) < 0$), while dashed black lines show the areas of charge depletion ($\nabla^2\rho(r) > 0$).

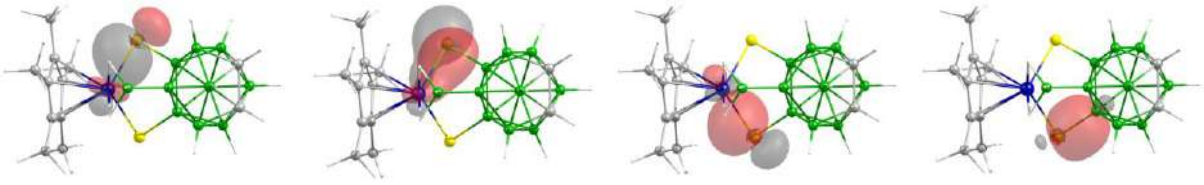


(a) HOMO (b) HOMO-5 (c) HOMO-6 (d) HOMO-8

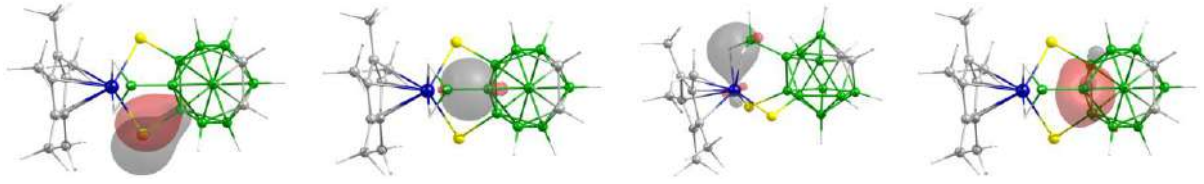


(e) HOMO-9 (f) HOMO-12 (g) HOMO-17 (h) LUMO

Figure S62. Selected molecular orbitals of **3** (isocontour values: ±0.045 [e.bohr^{-3}]$^{1/2}$).



(a) 2c-2e Ti1-S2 (b) 2c-2e Ti1-S2 (c) 2c-2e Ti1-S1 (d) 2c-2e B2-S1



(e) 2c-2e B2-S1 (f) 2c-2e B1-B1 (g) 3c-2e Ti1-H1-B11 (h) 3c-2e B1-B2-B3

Figure S63. Selected NBO interactions of **3** (isocontour values: ±0.045 [e.bohr^{-3}]$^{1/2}$).

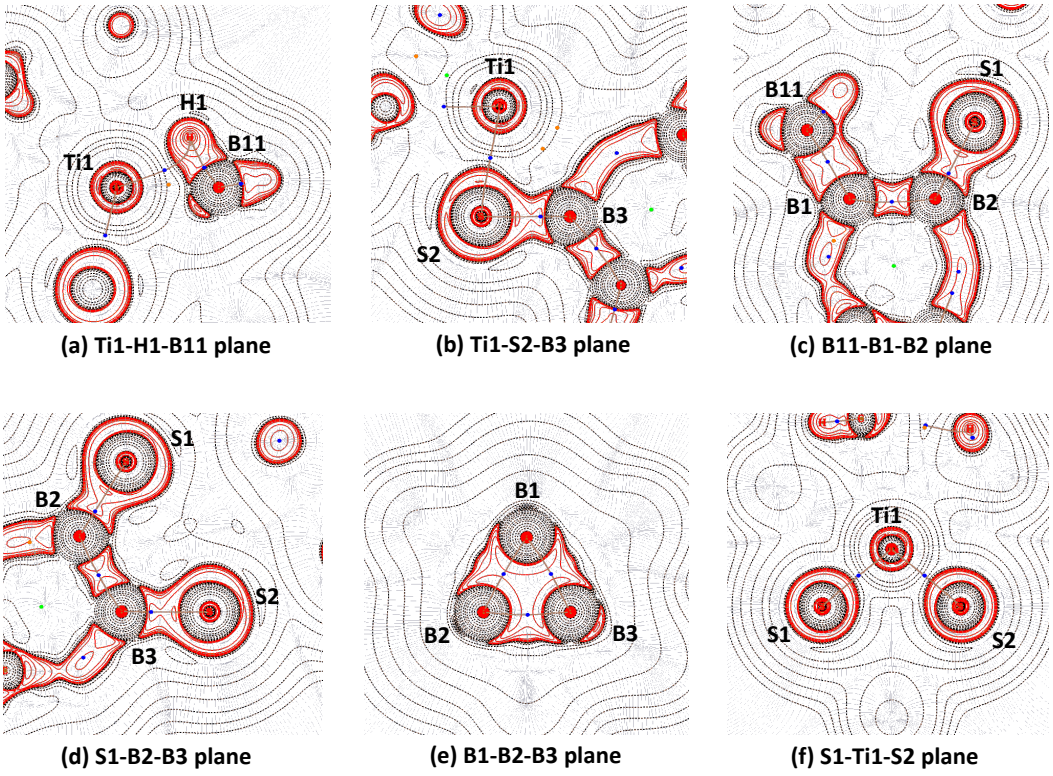


Figure S64. Contour-line diagram of the Laplacian of the electron density of **3** in selected planes. The solid brown lines are bond paths, whereas blue dots indicate the bond-critical points (BCP). Solid red lines indicate the areas of charge concentration ($\nabla^2\rho(r) < 0$), while dashed black lines show the areas of charge depletion ($\nabla^2\rho(r) > 0$).

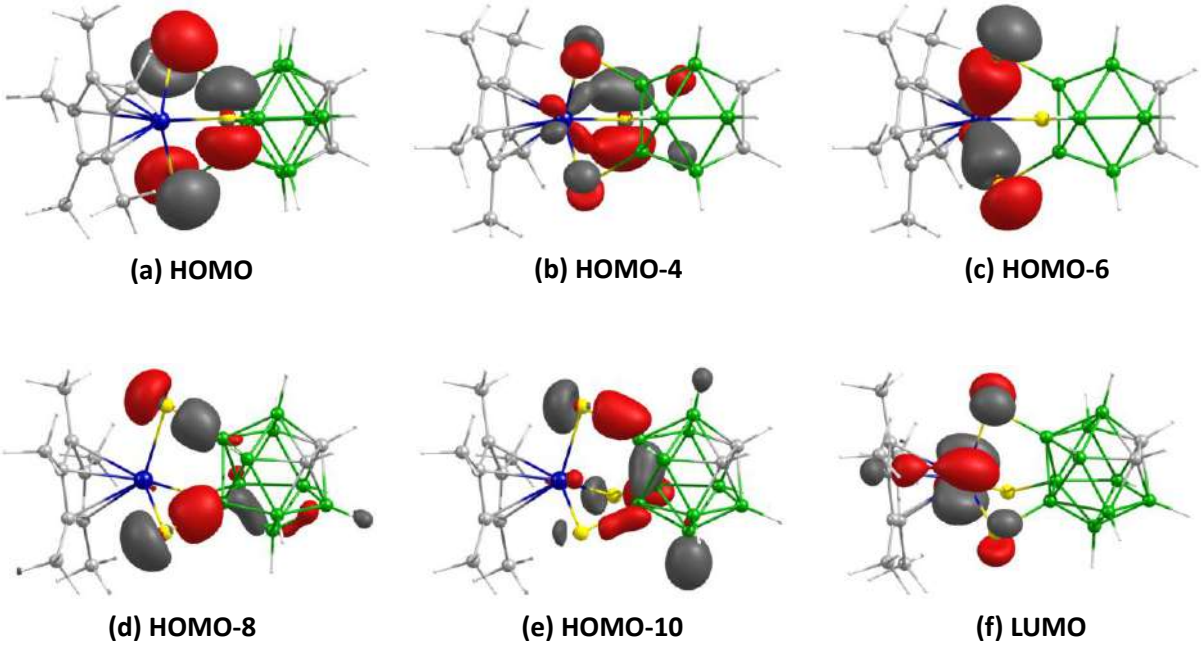


Figure S65. Selected molecular orbitals of **4a** (isocontour values: ±0.045 [e.bohr^{-3}]$^{1/2}$).

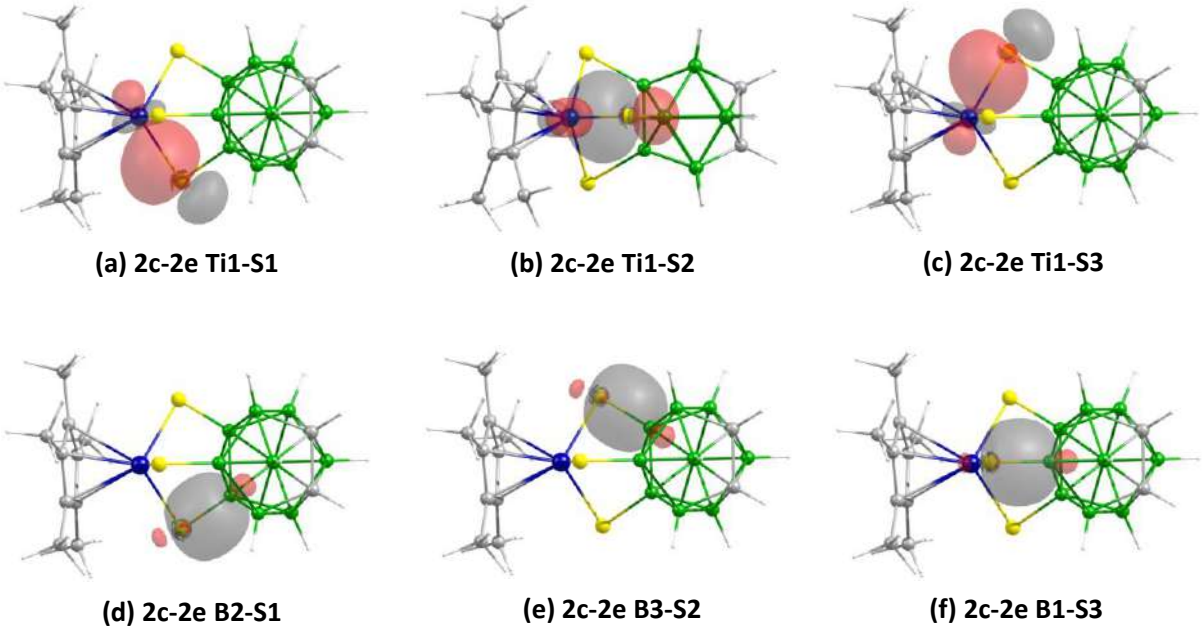


Figure S66. Selected NBO interactions of **4a** (isocontour values: ±0.045 [e.bohr^{-3}]$^{1/2}$).

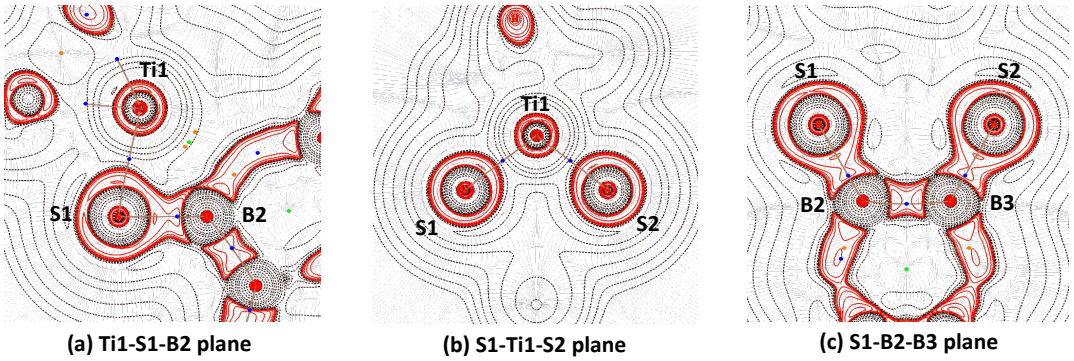


Figure S67. Contour-line diagram of the Laplacian of the electron density of **4a** in selected planes. The solid brown lines are bond paths, whereas blue dots indicate the bond-critical points (BCP). Solid red lines indicate the areas of charge concentration ($\nabla^2\rho(r) < 0$), while dashed black lines show the areas of charge depletion ($\nabla^2\rho(r) > 0$).

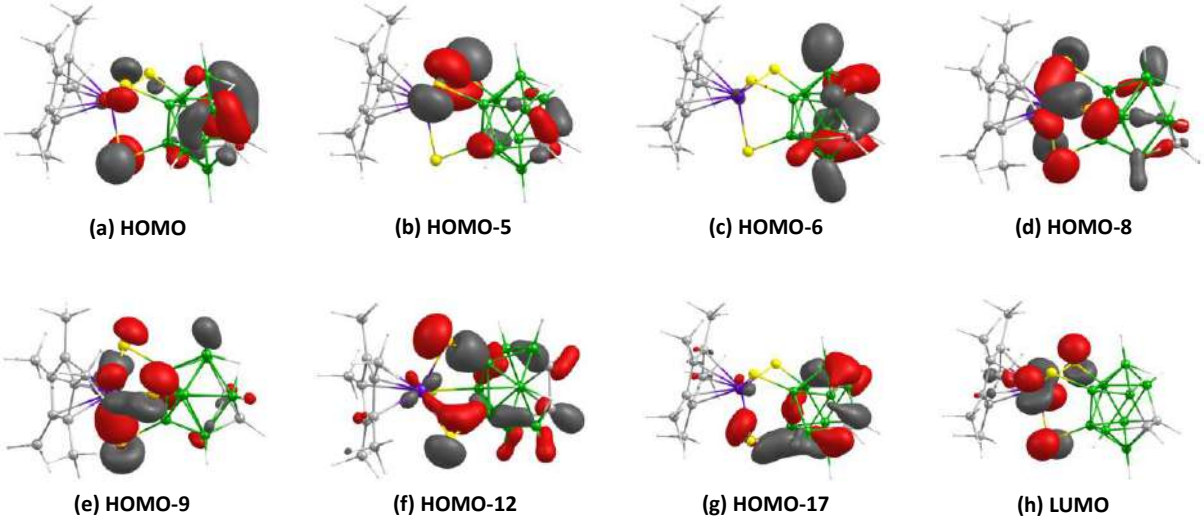


Figure S68. Selected molecular orbitals of **5** (isocontour values: ±0.045 [e.bohr^{-3}]$^{1/2}$).

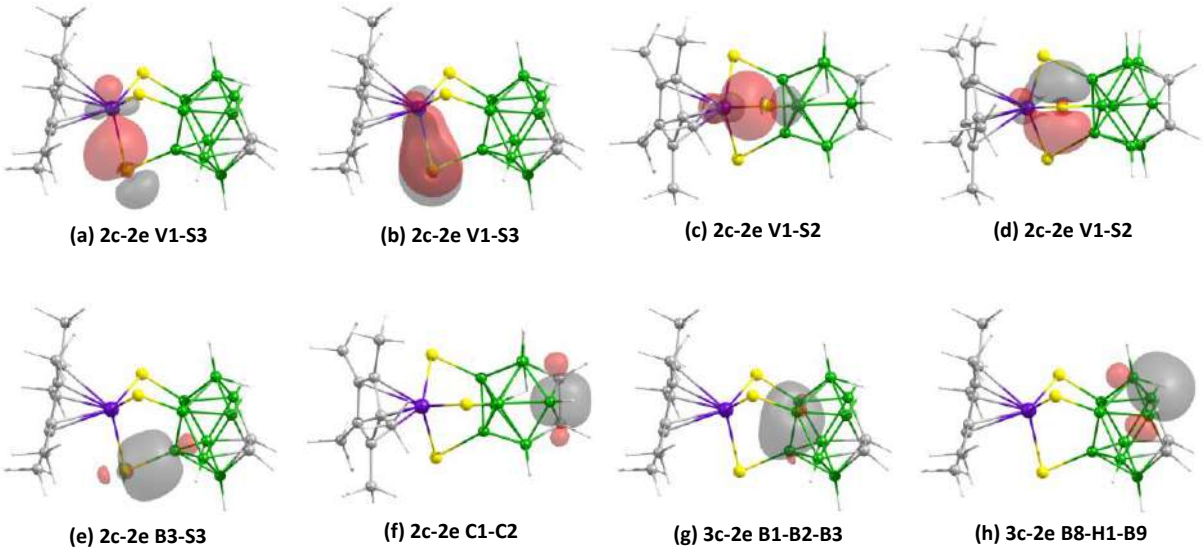


Figure S69. Selected NBO interactions of **5** (isocontour values: ±0.045 [e.bohr^{-3}]$^{1/2}$).

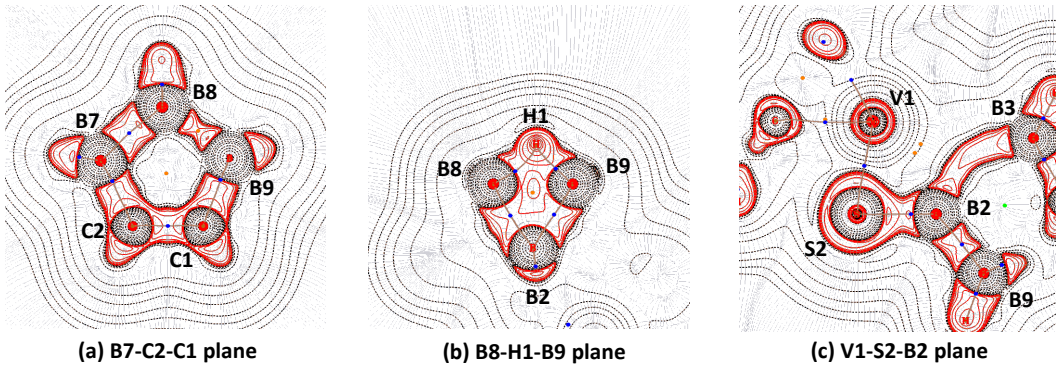


Figure S70. Contour-line diagram of the Laplacian of the electron density of **5** in selected planes. The solid brown lines are bond paths, whereas blue dots indicate the bond-critical points (BCP). Solid red lines indicate the areas of charge concentration ($\nabla^2\rho(r) < 0$), while dashed black lines show the areas of charge depletion ($\nabla^2\rho(r) > 0$).

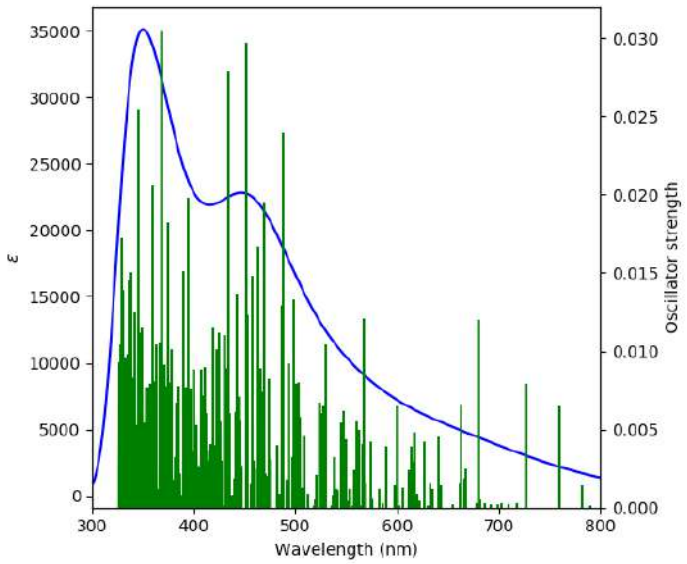


Figure S71. Absorption spectrum of **1** computed at TD-DFT- PB86/Def2-SVP level of theory (ε in $LM^{-1}cm^{-1}$).

Table S6. TD-DFT calculated energies (excitation energy (eV), λ_{calc} (nm)), oscillator strength (*f*), and main composition of the first UV−vis electronic excitations for **1**. Experimental absorption wavelengths (λ_{exp}, nm) of **1** are given for comparison.

No	Excitation Energy (eV)	Wavelength λ (nm)		Main electronic transition (% weight) [b]
		Calc. (*f*) [a]	Expt.	
1	1.822	680 (0.012)		HOMO-4→LUMO+1 (93)
2	2.184	568 (0.012)		HOMO-13→LUMO (34)
				HOMO-12→LUMO+1 (14)
				HOMO-10→LUMO+2 (28)
				HOMO→LUMO+6 (11)
3	2.487	499 (0.013)		HOMO-6→LUMO+6 (71)
4	2.544	487 (0.024)	490	HOMO-1→LUMO+8 (45)
				HOMO-8→LUMO+6 (22)
5	2.642	469 (0.020)		HOMO--18→LUMO (62)
6	2.747	451 (0.030)		HOMO-14→LUMO+5 (30)
				HOMO-4→LUMO+8 (14)
				HOMO-3→LUMO+9 (20)
7	2.853	435 (0.028)		HOMO-1→LUMO+10 (64)
8	3.359	369 (0.030)	375	HOMO-10→LUMO+11 (30)
				HOMO-5→LUMO+13 (22)
				HOMO-14→LUMO+9 (19)
9	3.448	360 (0.021)		HOMO-26→LUMO (27)
				HOMO-23→LUMO+3 (30)
				HOMO→LUMO+17 (15)
10	3.590	345 (0.025)		HOMO-14→LUMO+10 (41)
				HOMO-10→LUMO+14 (15)

[a]Oscillator strength greater than 0.010 and [b]Components with greater than 10% contribution shown.

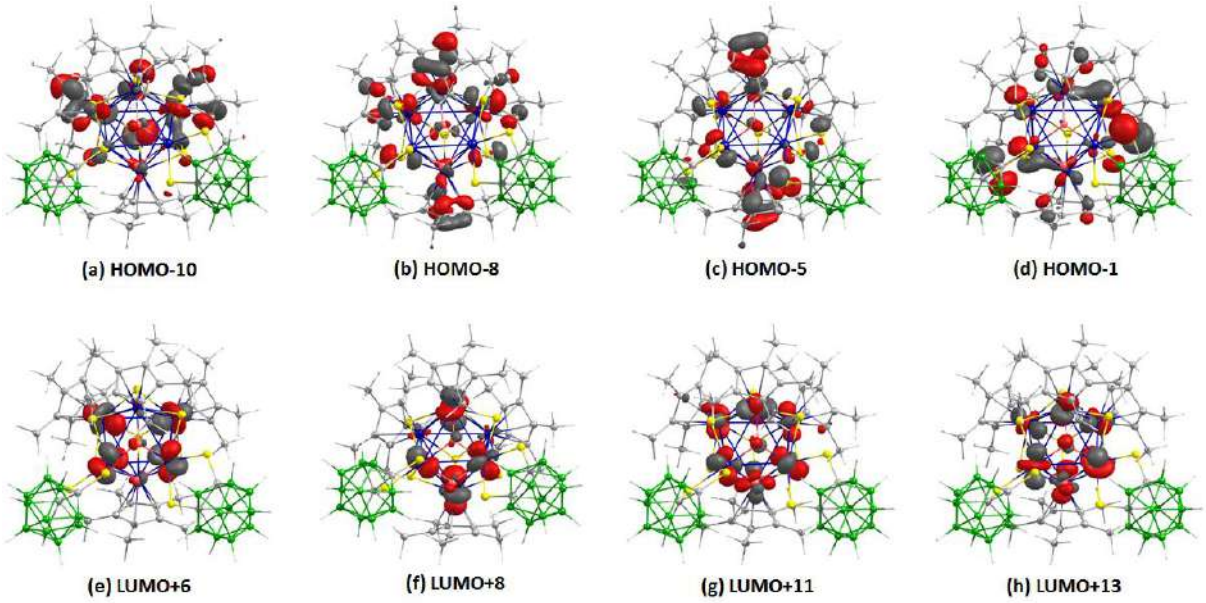


Figure S72. Selected molecular orbitals of **1** related to most intense electronic transitions [isocontour values: ±0.045 $(e/bohr^3)^{1/2}$].

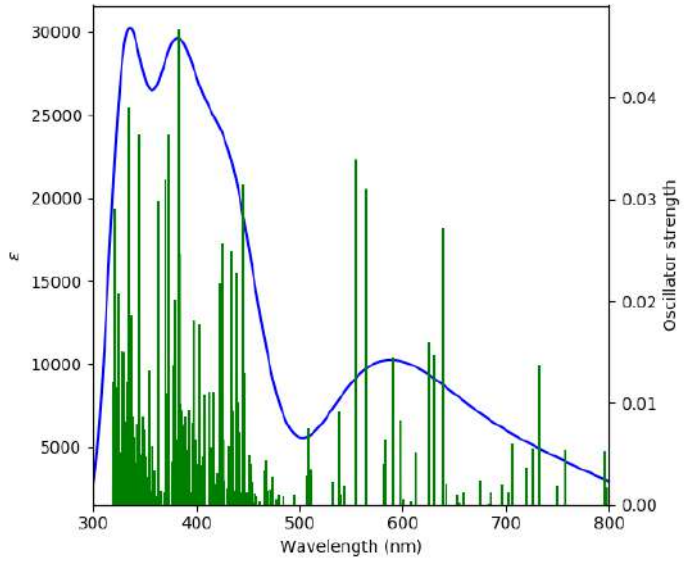


Figure S73. Absorption spectrum of **2** computed at TD-DFT-PB86/Def2-SVP level of theory (ε in $LM^{-1}cm^{-1}$).

Table S7. TD-DFT calculated energies (excitation energy (eV), λ_{calc} (nm)), oscillator strength (*f*), and main composition of the first UV−vis electronic excitations for **2**. Experimental absorption wavelengths (λ_{exp}, nm) of **2** are given for comparison.

No	Excitation Energy (eV)	Wavelength λ (nm)		Main electronic transition (% weight) [b]
		Calc. (*f*) [a]	Expt.	
1	1.693	733 (0.014)		HOMO-2→LUMO (91)
2	1.942	638 (0.027)		HOMO-6→LUMO+1(11)
				HOMO→LUMO+8 (67)
3	2.198	564 (0.031)		HOMO-9→LUMO+2 (15)
				HOMO-8→LUMO+2 (54)
4	2.240	554 (0.034)		HOMO→LUMO+10 (52)
				HOMO→LUMO+11 (16)
5	2.783	446 (0.032)	463	HOMO-5→LUMO+3 (41)
				HOMO→LUMO+18 (16)
				HOMO-1→LUMO+7 (12)
6	2.829	438 (0.023)		HOMO-7→LUMO+4 (12)
				HOMO-6→LUMO+3 (11)
				HOMO-5→LUMO+4 (22)
				HOMO-2→LUMO+7 (15)
7	2.856	434 (0.025)		HOMO-3→LUMO+6 (38)
				HOMO→LUMO+18 (12)
8	3.247	382 (0.047)		HOMO-17→LUMO+2 (10)
				HOMO-10→LUMO+6 (17)
				HOMO-1→LUMO+9 (23)
9	3.320	373 (0.036)	365	HOMO-20→LUMO+1 (77)
10	3.606	344 (0.036)		HOMO-3→LUMO+12 (64)

[a]Oscillator strength greater than 0.010 and [b]Components with greater than 10% contribution shown.

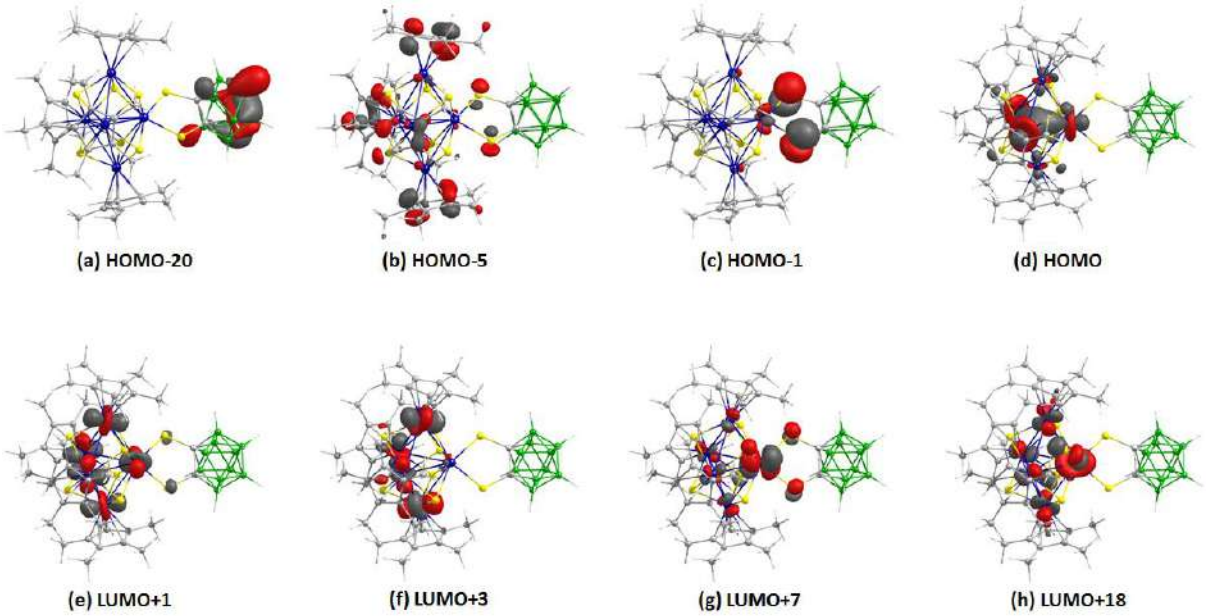


Figure S74. Selected molecular orbitals of **2** related to most intense electronic transitions [isocontour values: ±0.045 $(e/bohr^3)^{1/2}$].

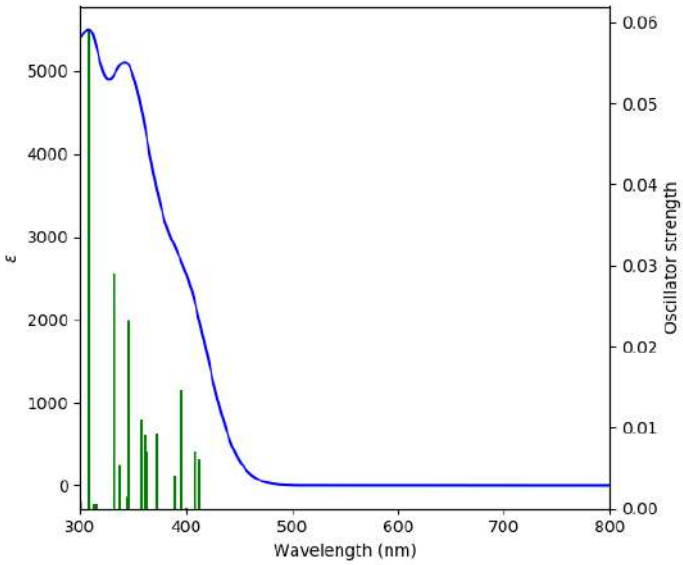


Figure S75. Absorption spectrum of **3** computed at TD-DFT-PB86/Def2-SVP level of theory (ε in $LM^{-1}cm^{-1}$).

Table S8. TD-DFT calculated energies (excitation energy (eV), λ_{calc} (nm)), oscillator strength (*f*), and main composition of the first UV−vis electronic excitations for **3**. Experimental absorption wavelengths (λ_{exp}, nm) of **3** are given for comparison.

No	Excitation Energy (eV)	Wavelength λ (nm)		Main electronic transition (% weight) [b]
		Calc. (*f*) [a]	Expt.	
1	3.131	396(0.015)		HOMO-2→LUMO (55)
				HOMO-1→LUMO+2 (11)
				HOMO→LUMO (18)
				HOMO→LUMO+1 (14)
2	3.467	358 (0.011)		HOMO-1→LUMO+2(82)
3	3.587	346 (0.023)		HOMO-2→LUMO+2 (91)
4	3.733	332 (0.029)	336	HOMO-4→LUMO (53)
				HOMO-3→LUMO (18)
10	4.011	309 (0.059)		HOMO-4→LUMO+1 (81)

[a]Oscillator strength greater than 0.010 and [b]Components with greater than 10% contribution shown.

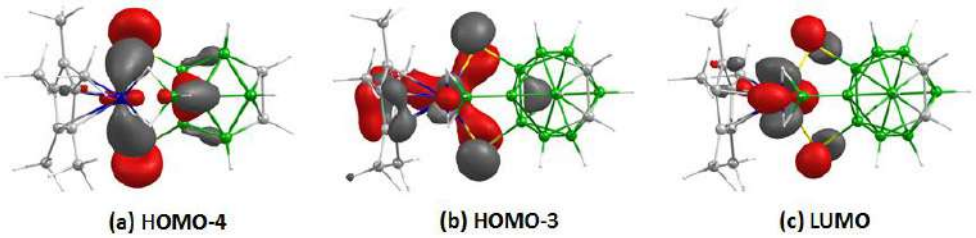


Figure S76. Selected molecular orbitals of **3** related to most intense electronic transitions [isocontour values: ±0.045 $(e/bohr^3)^{1/2}$].

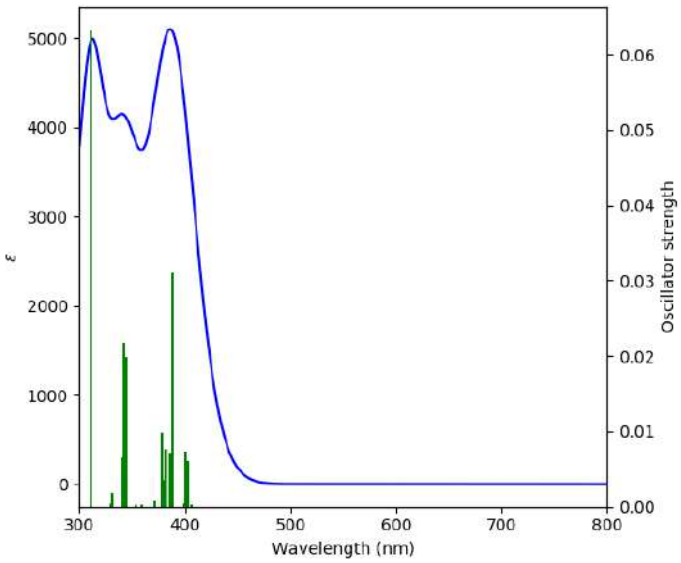


Figure S77. Absorption spectrum of **4a** computed at TD-DFT- PB86/Def2-SVP level of theory (ε in $LM^{-1}cm^{-1}$).

Table S9. TD-DFT calculated energies (excitation energy (eV), λ_{calc} (nm)), oscillator strength (*f*), and main composition of the first UV–vis electronic excitations for **4a**. Experimental absorption wavelengths (λ_{exp}, nm) of **4a** are given for comparison.

No	Excitation Energy (eV)	Wavelength λ (nm)		Main electronic transition (% weight) [b]
		Calc. (*f*) [a]	Expt.	
1	3.190	389 (0.031)	371	HOMO-1→LUMO+1 (62)
				HOMO-1→LUMO (18)
				HOMO-2→LUMO (11)
2	3.277	378 (0.010)		HOMO-2→LUMO (56)
				HOMO-2→LUMO+1 (24)
3	3.594	345 (0.020)		HOMO-4→LUMO (12)
				HOMO-3→LUMO+1 (61)
4	3.626	342 (0.022)		HOMO-4→LUMO (19)
				HOMO-4→LUMO+1 (25)
				HOMO-3→LUMO (30)
10	3.987	311 (0.063)		HOMO-5→LUMO+2 (82)

[a]Oscillator strength greater than 0.010 and [b]Components with greater than 10% contribution shown.

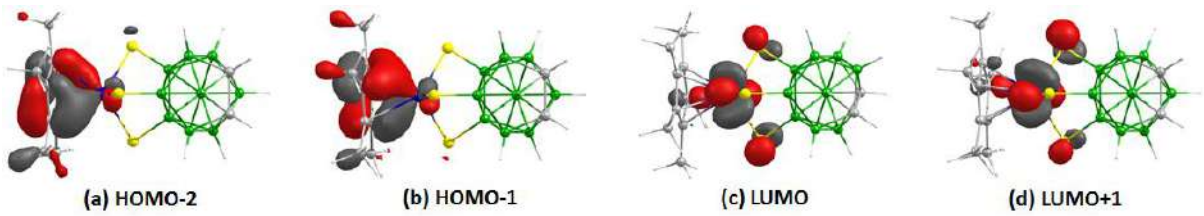


Figure S78. Selected molecular orbitals of **4a** related to most intense electronic transitions [isocontour values: ±0.045 $(e/bohr^3)^{1/2}$].

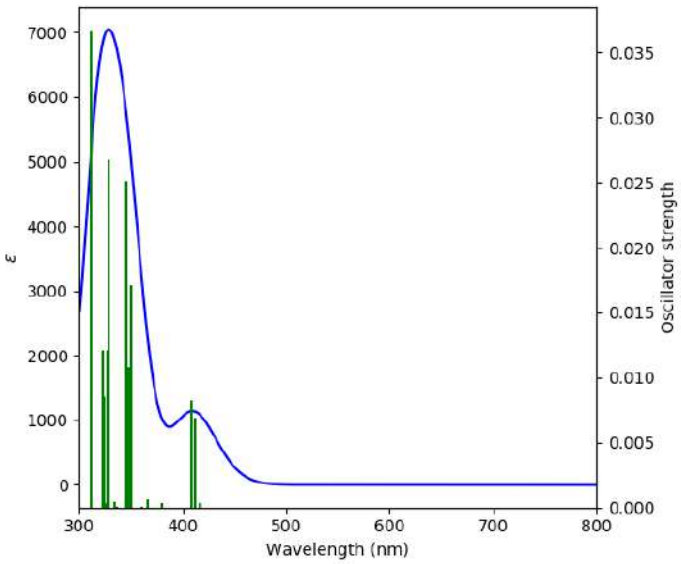


Figure S79. Absorption spectrum of **4b** computed at TD-DFT-PB86/Def2-SVP level of theory (ε in $LM^{-1}cm^{-1}$).

Table S10. TD-DFT calculated energies (excitation energy (eV), λ_{calc} (nm)), oscillator strength (*f*), and main composition of the first UV-vis electronic excitations for **4b**. Experimental absorption wavelengths (λ_{exp}, nm) of **4b** are given for comparison.

No	Excitation Energy (eV)	Wavelength λ (nm)		Main electronic transition (% weight) [b]
		Calc. (*f*) [a]	Expt.	
1	3.036	408 (0.008)	388	HOMO→LUMO+1 (76)
2	3.542	350 (0.017)		HOMO-1→LUMO (34)
				HOMO-1→LUMO+1 (37)
3	3.592	345 (0.025)		HOMO-2→LUMO+1 (37)
				HOMO-1→LUMO (21)
4	3.777	328 (0.027)	330	HOMO-5→LUMO (58)
				HOMO-4→LUMO (22)
10	3.983	311 (0.037)		HOMO-3→LUMO+2 (76)

[a]Oscillator strength greater than 0.010 and [b]Components with greater than 10% contribution shown.

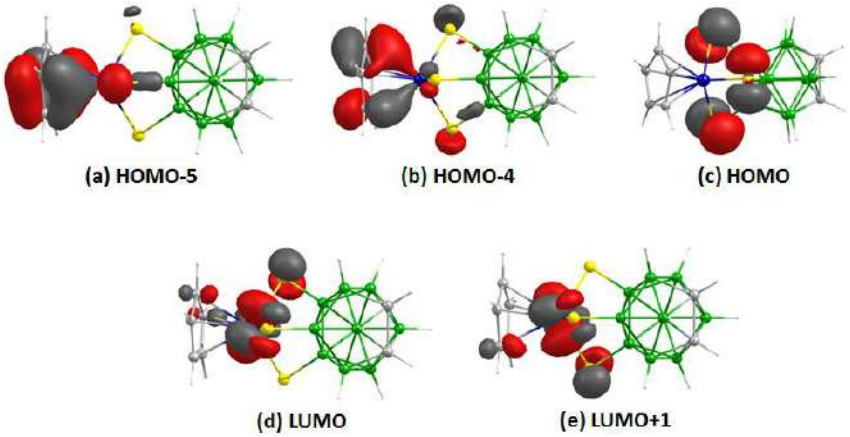


Figure S80. Selected molecular orbitals of **4b** related to most intense electronic transitions [isocontour values: ±0.045 $(e/bohr^3)^{1/2}$].

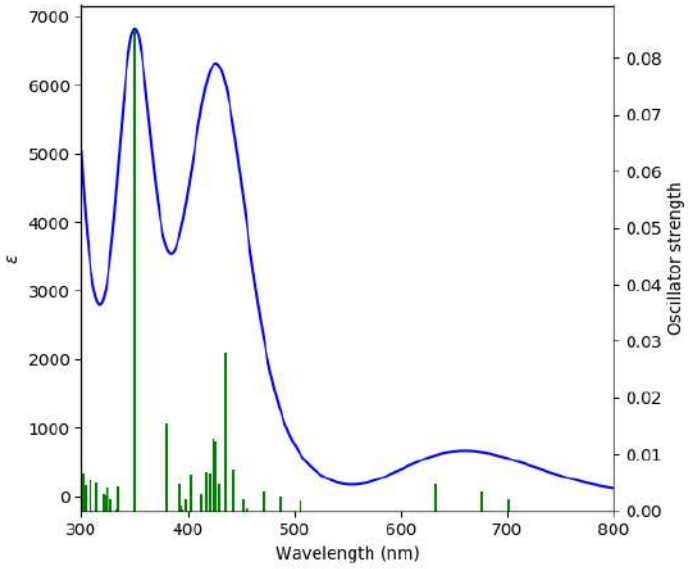


Figure S81. Absorption spectrum of **5** computed at TD-DFT-PB86/Def2-SVP level of theory (ε in $LM^{-1}cm^{-1}$).

Table S11. TD-DFT calculated energies (excitation energy (eV), λ_{calc} (nm)), oscillator strength (*f*), and main composition of the first UV−vis electronic excitations for **5**. Experimental absorption wavelengths (λ_{exp}, nm) of **5** are given for comparison.

No	Excitation Energy (eV)	Wavelength λ (nm)		Main electronic transition (% weight) [b]
		Calc. (*f*) [a]	Expt.	
1	1.960	632 (0.005)	591	HOMO→LUMO+2 (98)
2	2.847	435 (0.028)	424	HOMO-3→LUMO (65)
				HOMO-2→LUMO+2 (19)
3	2.922	424 (0.013)		HOMO-5→LUMO+1 (17)
				HOMO-2→LUMO (12)
				HOMO-2→LUMO+2 (16)
				HOMO-1→LUMO+1 (11)
4	3.262	380 (0.016)		HOMO-6→LUMO (11)
				HOMO-6→LUMO+1 (17)
				HOMO-5→LUMO+1 (13)
				HOMO-5→LUMO+2 (31)
10	3.538	350 (0.085)	335	HOMO-6→LUMO+2 (71)

[a]Oscillator strength greater than 0.010 and [b]Components with greater than 10% contribution shown.

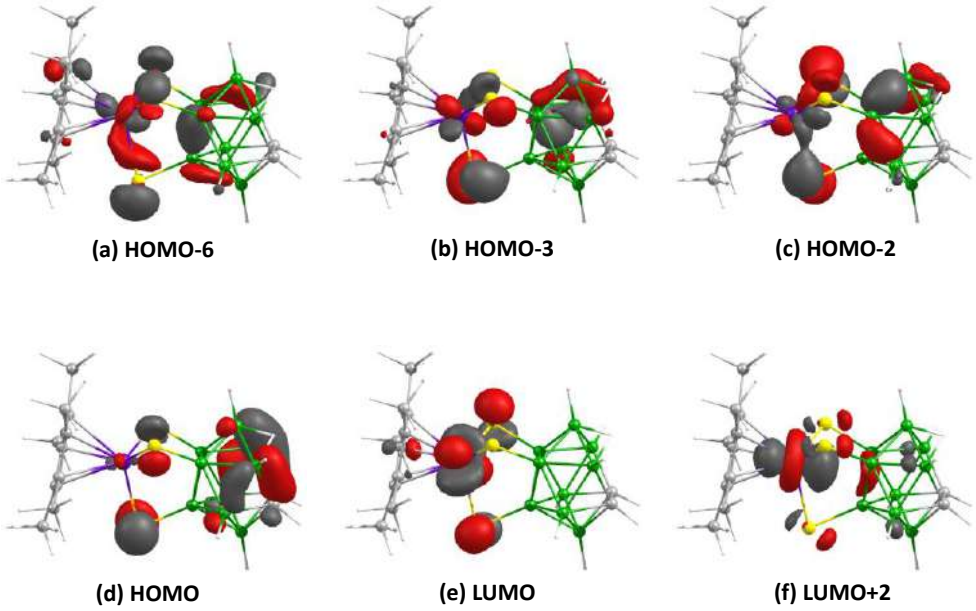


Figure S82. Selected molecular orbitals of **5** related to most intense electronic transitions [isocontour values: ±0.045 $(e/bohr^3)^{1/2}$].

III Cartesian Coordinates of all Optimized Structures

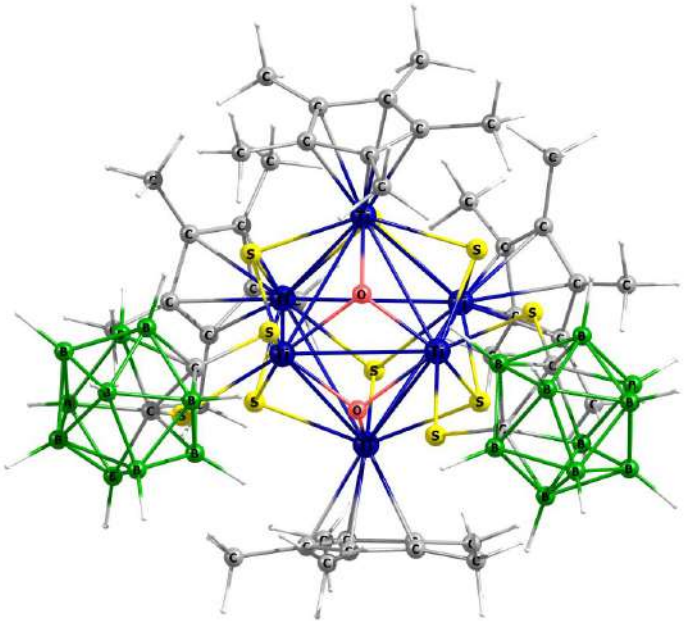


Figure S83. Optimized geometry of **1**.

Total energy = -11450.0995182 a.u.

Cartesian coordinates for the calculated structure **1** (in Å)

C	-4.154998000000	0.695467000000	-0.795999000000
C	-4.120077000000	-0.686347000000	-1.109673000000
C	-4.082435000000	-1.419629000000	0.109620000000
C	-4.107006000000	-0.480324000000	1.178105000000
C	-4.155338000000	0.821148000000	0.624317000000
C	-4.355795000000	1.797724000000	-1.776258000000
H	-3.966812000000	1.536234000000	-2.760352000000
H	-3.857089000000	2.712251000000	-1.457689000000
H	-5.425171000000	2.009436000000	-1.885314000000
C	-4.221809000000	-1.266772000000	-2.479732000000
H	-3.825751000000	-2.281645000000	-2.523542000000
H	-3.681703000000	-0.669042000000	-3.214985000000
H	-5.270461000000	-1.306585000000	-2.793258000000
C	-4.176418000000	-2.903858000000	0.241414000000
H	-5.224560000000	-3.220648000000	0.223189000000
H	-3.746290000000	-3.256343000000	1.179932000000
H	-3.668166000000	-3.421728000000	-0.573905000000
C	-4.194617000000	-0.785939000000	2.634508000000
H	-3.627998000000	-0.066586000000	3.228022000000
H	-3.821481000000	-1.782442000000	2.870178000000
H	-5.238381000000	-0.736251000000	2.964077000000
C	-4.386378000000	2.062469000000	1.414757000000
H	-5.338482000000	1.982773000000	1.950171000000
H	-4.432297000000	2.940709000000	0.774032000000
H	-3.598466000000	2.230955000000	2.151441000000
C	4.082601000000	-1.419608000000	-0.108120000000
C	4.119026000000	-0.685758000000	1.110895000000
C	4.154211000000	0.695894000000	0.796674000000
C	4.155833000000	0.821012000000	-0.623670000000
C	4.108242000000	-0.480778000000	-1.176944000000
C	4.176803000000	-2.903884000000	-0.239196000000
H	3.747922000000	-3.256748000000	-1.178147000000
H	3.667505000000	-3.421455000000	0.575660000000
H	5.224926000000	-3.220649000000	-0.219477000000
C	4.219570000000	-1.265637000000	2.481253000000
H	3.822666000000	-2.280164000000	2.525320000000
H	3.679533000000	-0.667088000000	3.215886000000
H	5.268031000000	-1.306134000000	2.795342000000
C	4.354267000000	1.798252000000	1.776946000000
H	5.423761000000	2.007531000000	1.889431000000
H	3.961335000000	1.538233000000	2.759867000000
H	3.858622000000	2.713699000000	1.456310000000
C	4.386920000000	2.062072000000	-1.414586000000
H	4.435537000000	2.940142000000	-0.773806000000
H	3.597608000000	2.231849000000	-2.149475000000
H	5.337697000000	1.981155000000	-1.952141000000
C	4.197065000000	-0.786828000000	-2.633193000000
H	3.823586000000	-1.783171000000	-2.869021000000
H	5.241172000000	-0.737810000000	-2.961791000000
H	3.631477000000	-0.067251000000	-3.227408000000
B	-0.840495000000	-1.454816000000	-1.782257000000
B	0.866019000000	-1.466005000000	-1.759395000000
B	0.009766000000	-0.158501000000	-0.960369000000
B	-0.866986000000	1.267685000000	-1.481020000000
H	-1.481276000000	1.283293000000	-2.510352000000
B	0.895944000000	1.266841000000	-1.461883000000
H	1.532432000000	1.280816000000	-2.479383000000
B	0.009411000000	2.675262000000	-0.882103000000
H	0.015908000000	3.701657000000	-1.488577000000
B	1.432248000000	2.088677000000	0.015274000000
H	2.369371000000	2.820916000000	0.025859000000
B	-0.009293000000	2.674557000000	0.882946000000

H	-0.015824000000	3.700455000000	1.490254000000
B	-1.432097000000	2.088623000000	-0.014903000000
H	-2.369258000000	2.820798000000	-0.025192000000
B	-0.895965000000	1.265612000000	1.461643000000
H	-1.532046000000	1.278885000000	2.479378000000
B	0.867103000000	1.266420000000	1.480789000000
H	1.480975000000	1.281369000000	2.510343000000
B	-0.009686000000	-0.159246000000	0.958899000000
B	-0.865967000000	-1.467517000000	1.756687000000
B	0.840578000000	-1.456298000000	1.779511000000
Ti	-2.073331000000	-0.217613000000	-0.019397000000
Ti	2.073347000000	-0.217797000000	0.017500000000
H	0.007627000000	-2.499697000000	-1.740664000000
H	1.332078000000	-1.395305000000	-2.853287000000
H	-1.276817000000	-1.377647000000	-2.887911000000
H	-1.699860000000	-1.893806000000	0.940081000000
H	1.703431000000	-1.880949000000	0.990367000000
H	1.276259000000	-1.380489000000	2.885494000000
H	-1.331476000000	-1.398084000000	2.850881000000
H	-0.007567000000	-2.501228000000	1.736391000000
H	-1.703076000000	-1.880288000000	-0.993273000000
H	1.699592000000	-1.893450000000	-0.943004000000

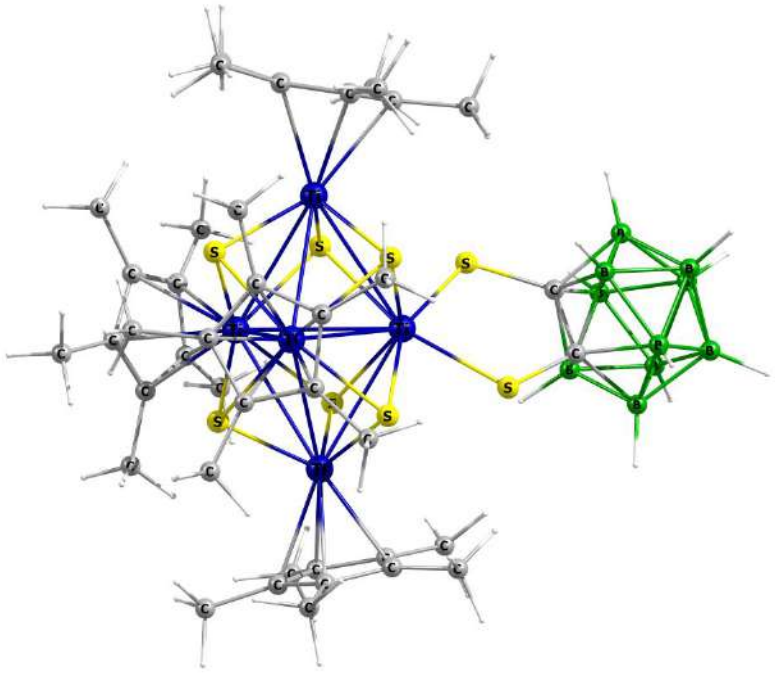


Figure S84. Optimized geometry of **2**

Total energy = -9323.13729863 a.u.

Cartesian coordinates for the calculated structure **2** (in Å)

Ti	-0.455801000	-2.673302000	-0.048789000
Ti	-0.455570000	2.673223000	0.049093000
Ti	-1.565800000	0.041743000	-1.599586000
Ti	-1.565940000	-0.041508000	1.599739000
Ti	1.320906000	-0.000009000	0.000169000
S	-2.554260000	-1.662620000	-0.037170000
S	-2.554220000	1.662927000	0.037102000
S	0.316926000	1.605048000	-1.803280000
S	0.474455000	1.482045000	1.778853000
S	0.316686000	-1.605051000	1.803472000
S	0.474574000	-1.482155000	-1.778398000
S	3.094097000	-1.183102000	1.100248000
C	4.724669000	-0.603477000	0.558874000
S	3.094088000	1.182882000	-1.100126000
B	6.058021000	-1.668267000	0.325689000
C	4.724688000	0.603247000	-0.558760000
B	5.186285000	0.989542000	1.071831000
B	6.059171000	-0.455882000	1.638961000
B	6.956305000	0.986396000	1.066950000
B	5.186265000	-0.989710000	-1.071709000
B	6.058029000	1.668031000	-0.325601000
B	6.956295000	-0.986635000	-1.066877000
B	7.506144000	-0.658788000	0.609030000
B	7.506158000	0.658551000	-0.608949000
B	6.059194000	0.455664000	-1.638885000
C	1.607142000	-4.638533000	2.021754000
C	0.666760000	-4.613479000	0.849766000
C	-0.747081000	-4.872046000	0.887018000
C	1.052718000	-4.492809000	-0.529279000
C	2.455651000	-4.327318000	-1.041366000
C	-1.236370000	-4.921050000	-0.465963000
C	-2.628796000	-5.339335000	-0.856681000
C	-0.086815000	-4.836907000	-2.839010000
C	-0.116922000	-4.699901000	-1.342131000
C	-1.535511000	-5.259452000	2.105660000
C	-3.222617000	2.607625000	3.275725000
C	-2.876787000	1.149018000	3.264731000
C	-3.708220000	0.107205000	2.730444000
C	-1.773870000	0.533042000	3.947803000
C	-0.758984000	1.222758000	4.816012000
C	-3.139984000	-1.154664000	3.111572000
C	-3.830522000	-2.478937000	2.960250000

C	-1.138257000	-1.897669000	4.636765000
C	-1.938772000	-0.894304000	3.855771000
C	-5.036184000	0.290505000	2.052086000
C	-3.830800000	2.478840000	-2.960481000
C	-3.140042000	1.154637000	-3.111554000
C	-1.938580000	0.894514000	-3.855521000
C	-3.708037000	-0.107329000	-2.730525000
C	-5.036179000	-0.291214000	-2.052683000
C	-1.773456000	-0.532784000	-3.947675000
C	-0.758313000	-1.222185000	-4.815831000
C	-3.222259000	-2.607569000	-3.275981000
C	-2.876291000	-1.148990000	-3.264683000
C	-1.138204000	1.898100000	-4.636377000
C	-2.628014000	5.339510000	0.858064000
C	-1.235918000	4.921014000	0.466427000
C	-0.747565000	4.872016000	-0.886892000
C	-0.115880000	4.699815000	1.341827000
C	-0.084853000	4.836772000	2.838685000
C	0.666312000	4.613453000	-0.850613000
C	1.605889000	4.638637000	-2.023247000
C	2.456482000	4.327390000	1.039357000
C	1.053218000	4.492789000	0.528161000
C	-1.536950000	5.259422000	-2.104901000
H	2.036081000	-5.658059000	2.146399000
H	2.449848000	-3.930638000	1.889973000
H	1.097936000	-4.370262000	2.968069000
H	2.953660000	-5.318727000	-1.132814000
H	2.475484000	-3.850017000	-2.040685000
H	3.069375000	-3.702571000	-0.362884000
H	-2.783353000	-6.420711000	-0.644914000
H	-3.407523000	-4.779182000	-0.299496000
H	-2.819777000	-5.187035000	-1.935702000
H	0.465070000	-5.758283000	-3.127931000
H	-1.102193000	-4.917692000	-3.273161000
H	0.429719000	-3.982118000	-3.322642000
H	-1.194449000	-4.726114000	3.015274000
H	-2.618730000	-5.071580000	1.978344000
H	-1.414204000	-6.347651000	2.308618000
H	-3.891522000	2.837266000	4.135707000
H	-2.322036000	3.240803000	3.379900000
H	-3.750500000	2.911721000	2.350968000
H	-1.078042000	1.182629000	5.882034000
H	0.240804000	0.749876000	4.749059000
H	-0.637246000	2.288887000	4.545854000
H	-4.711989000	-2.527263000	3.637822000
H	-4.196286000	-2.644566000	1.925805000
H	-3.164854000	-3.320353000	3.223788000
H	-1.543311000	-1.988290000	5.669898000
H	-1.170241000	-2.904684000	4.177622000
H	-0.072474000	-1.608221000	4.717593000
H	-5.857395000	0.314488000	2.803783000
H	-5.078161000	1.237709000	1.479028000
H	-5.253970000	-0.538324000	1.349760000
H	-4.713449000	2.526134000	-3.636564000
H	-3.165810000	3.320116000	-3.226179000
H	-4.194807000	2.645577000	-1.925577000
H	-5.856663000	-0.319763000	-2.805021000
H	-5.256466000	0.539585000	-1.353499000
H	-5.076544000	-1.236531000	-1.476362000
H	-1.076485000	-1.180637000	-5.882066000
H	-0.637591000	-2.288718000	-4.546819000
H	0.241756000	-0.750078000	-4.747568000
H	-3.891387000	-2.836863000	-4.135872000
H	-3.750010000	-2.911767000	-2.351171000
H	-2.321784000	-3.240850000	-3.380426000
H	-1.543941000	1.989651000	-5.669153000
H	-0.072595000	1.608277000	-4.718105000
H	-1.169394000	2.904792000	-4.176453000
H	-2.782270000	6.421070000	0.646982000
H	-3.407181000	4.779997000	0.300855000
H	-2.818572000	5.186692000	1.937085000
H	0.464783000	5.759616000	3.127256000
H	-1.100055000	4.914756000	3.273763000
H	0.434362000	3.983289000	3.321732000
H	2.034904000	5.658123000	-2.147916000
H	2.448580000	3.930575000	-1.892243000
H	1.095957000	4.370715000	-2.969267000
H	2.953939000	5.318965000	1.132011000
H	2.477063000	3.848713000	2.038015000
H	3.070261000	3.703920000	0.359764000
H	-1.416778000	6.347868000	-2.307238000
H	-1.195802000	4.726985000	-3.015006000
H	-2.619926000	5.070428000	-1.977200000
H	5.897480000	-2.836076000	0.582449000
H	8.518911000	-1.144345000	1.058003000
H	7.552035000	-1.701600000	-1.839160000
H	4.399032000	-1.602450000	-1.741410000
H	5.896922000	0.802319000	-2.782356000
H	8.518934000	1.144114000	-1.057896000
H	5.897494000	2.835843000	-0.582356000
H	7.552080000	1.701335000	1.839232000
H	4.398988000	1.602279000	1.741459000
H	5.896962000	-0.802554000	2.782436000

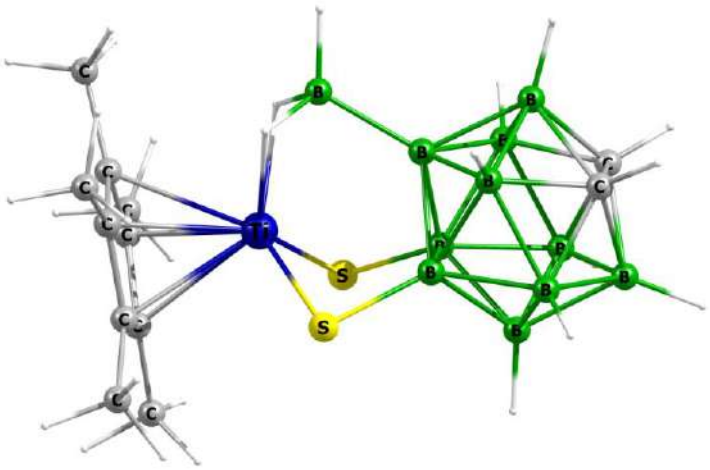


Figure S85. Optimized geometry of **3**.

Total energy = -2392.38887526 a.u.

Cartesian coordinates for the calculated structure **3** (in Å)

B	1.696365000	0.022743000	1.142592000
B	1.725486000	-0.924619000	-0.427423000
B	1.730880000	0.903474000	-0.466876000
B	2.785072000	-0.037990000	-1.599236000
H	2.608520000	-0.063061000	-2.792818000
B	3.407323000	-1.471618000	-0.714370000
H	3.779259000	-2.514869000	-1.189345000
B	2.746130000	-1.430511000	0.956749000
H	2.676656000	-2.452421000	1.592334000
B	2.754921000	1.460616000	0.895720000
H	2.691628000	2.508588000	1.488032000
B	3.416537000	1.427700000	-0.775351000
H	3.795012000	2.447684000	-1.293698000
B	4.426739000	-0.029397000	-0.948348000
H	5.502919000	-0.044099000	-1.486794000
B	3.350922000	0.031157000	1.777192000
H	3.776744000	0.053813000	2.902400000
C	-2.769945000	-0.983607000	-0.702180000
C	-2.724329000	0.383617000	-1.144334000
C	-2.810660000	1.230597000	0.017165000
C	-2.899108000	0.383711000	1.177578000
C	-2.860751000	-0.984378000	0.732661000
C	-2.879726000	-2.189332000	-1.591161000
H	-2.484521000	-3.102091000	-1.103465000
H	-2.325677000	-2.054735000	-2.540682000
H	-3.946597000	-2.379922000	-1.845575000
C	-2.700679000	0.828291000	-2.579960000
H	-2.046096000	0.179393000	-3.194974000
H	-2.327754000	1.865225000	-2.683781000
H	-3.723184000	0.789275000	-3.018254000
C	-2.918959000	2.730504000	0.016013000
H	-2.419266000	3.179269000	-0.864388000
H	-2.461986000	3.180284000	0.919605000
H	-3.987391000	3.041875000	-0.008010000
C	-3.121465000	0.840481000	2.593626000
H	-4.208168000	0.840194000	2.833782000
H	-2.745760000	1.868766000	2.760277000
H	-2.617826000	0.181051000	3.327795000
C	-3.001816000	-2.208187000	1.596889000
H	-2.727062000	-2.002863000	2.649821000
H	-2.360082000	-3.037852000	1.238810000
H	-4.053203000	-2.573198000	1.592012000
B	0.291164000	0.055667000	2.159855000
C	4.281372000	-0.814269000	0.588777000
C	4.286252000	0.820172000	0.554339000
H	5.195280000	-1.296238000	0.960143000
H	5.203145000	1.311854000	0.905262000
S	0.176372000	-1.831109000	-0.900946000
S	0.185129000	1.797596000	-0.971455000
Ti	-0.776264000	0.006924000	0.191560000
H	-0.433075000	1.041965000	1.802939000
H	0.438382000	0.096207000	3.369848000
H	-0.444938000	-0.941926000	1.863816000

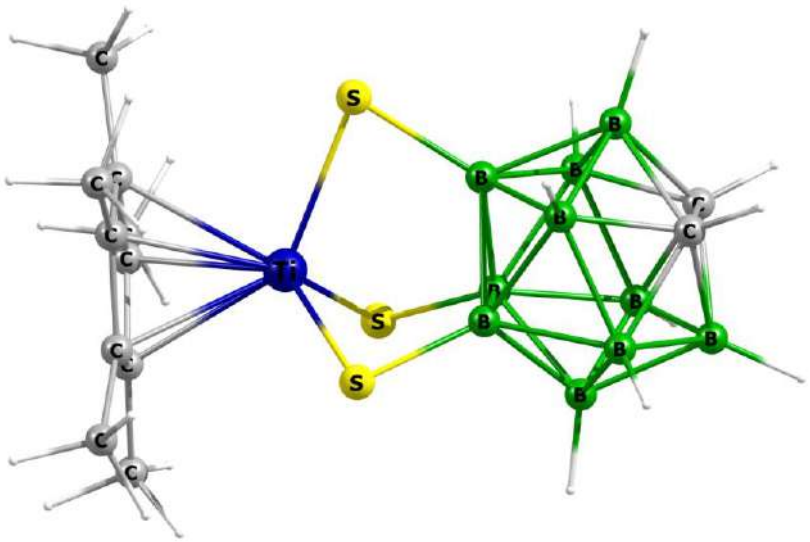


Figure S86. Optimized geometry of **4a**.

Total energy = -2763.92933711 a.u.

Cartesian coordinates for the calculated structure **4a** (in Å)

B	-0.344223000	2.566694000	1.659756000
B	-0.490019000	3.702710000	3.096798000
B	-1.684073000	2.297030000	2.913242000
B	-2.021931000	2.143685000	1.146067000
H	-2.389640000	1.145605000	0.581256000
B	-3.181268000	2.971558000	2.228351000
H	-4.327641000	2.638957000	2.375614000
B	-2.251030000	3.936303000	3.413638000
H	-2.781115000	4.212149000	4.459250000
B	-1.089971000	3.393587000	0.254030000
H	-0.836014000	3.230600000	-0.912378000
B	-0.151980000	4.354645000	1.440587000
H	0.905463000	4.857722000	1.149945000
B	-1.318619000	5.184099000	2.518741000
H	-1.227553000	6.298356000	2.967875000
B	-1.658331000	4.998113000	0.779835000
H	-1.878658000	5.914871000	0.032788000
C	2.379319000	1.171218000	5.506471000
C	2.852831000	0.569347000	4.287898000
C	2.017007000	-0.565078000	3.997650000
C	1.021308000	-0.660128000	5.033472000
C	1.240109000	0.418614000	5.959891000
C	3.053396000	2.287522000	6.254128000
H	3.556730000	2.999388000	5.570730000
H	2.336334000	2.867990000	6.867613000
H	3.826728000	1.877614000	6.941949000
C	4.060475000	1.015045000	3.510162000
H	4.152206000	2.119371000	3.494902000
H	4.992293000	0.608347000	3.963474000
H	4.021389000	0.672638000	2.458030000
C	2.210196000	-1.555564000	2.882567000
H	1.244239000	-1.944965000	2.504756000
H	2.745939000	-1.109868000	2.021848000
H	2.807881000	-2.426109000	3.235038000
C	0.025886000	-1.776578000	5.187354000
H	-0.863380000	-1.462022000	5.768304000
H	-0.333348000	-2.148766000	4.207825000
H	0.488252000	-2.635103000	5.724378000
C	0.455989000	0.688554000	7.214485000
H	-0.574062000	0.287693000	7.147252000
H	0.944728000	0.217664000	8.096831000
H	0.375022000	1.774896000	7.417655000
C	-2.840608000	4.642441000	1.993969000
C	-2.710713000	3.624942000	0.707072000
H	-3.717313000	5.303215000	2.004604000
H	-3.510643000	3.684623000	-0.042512000
S	-1.598998000	0.847000000	4.061359000
S	0.771423000	3.633456000	4.455478000
S	1.058783000	1.355620000	1.580394000
Ti	0.663601000	1.383696000	3.873280000

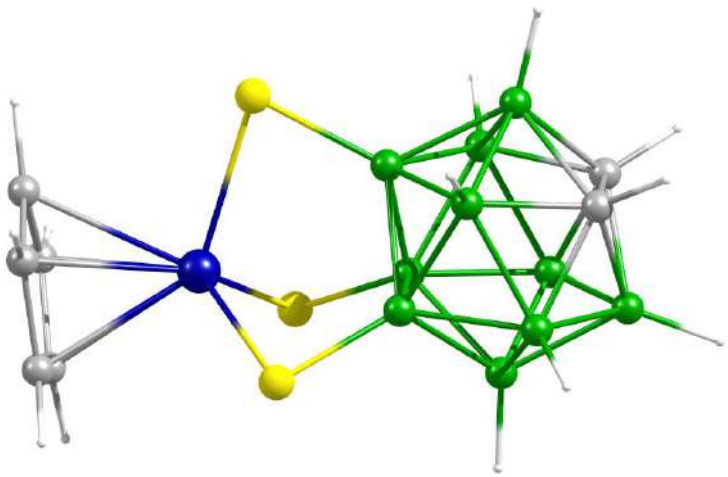


Figure S87. Optimized geometry of **4b**.

Total energy = -2567.49144199 a.u.

Cartesian coordinates for the calculated structure **4b** (in Å)

B	-1.678255000	-0.239887000	-1.037190000
B	-1.681743000	1.032449000	0.289303000
B	-1.672982000	-0.766535000	0.741238000
B	-2.717755000	-1.601678000	-0.471316000
H	-2.646266000	-2.761993000	-0.785066000
B	-3.345149000	-1.207348000	1.157903000
H	-3.767558000	-2.020631000	1.936379000
B	-2.725606000	0.406383000	1.621606000
H	-2.659866000	0.671337000	2.794350000
B	-3.362360000	-0.390829000	-1.632282000
H	-3.724360000	-0.745142000	-2.725143000
B	-2.734621000	1.224312000	-1.172559000
H	-2.541028000	2.083694000	-1.996737000
B	-3.369447000	1.614509000	0.457928000
H	-3.737258000	2.690205000	0.856043000
B	-4.381499000	0.760695000	-0.733688000
H	-5.452230000	1.154032000	-1.114831000
C	2.825256000	1.210804000	0.118518000
C	2.818381000	0.491423000	-1.114255000
C	2.819508000	-0.905091000	-0.811067000
C	2.825717000	-1.048116000	0.608923000
C	2.824262000	0.259577000	1.183798000
C	-4.250673000	0.235009000	0.911081000
C	-4.246308000	-0.904394000	-0.276466000
H	-5.170576000	0.314865000	1.505069000
H	-5.163698000	-1.497815000	-0.384478000
S	-0.155329000	-1.526647000	1.481234000
S	-0.154025000	2.036111000	0.606362000
S	-0.145392000	-0.504784000	-2.050576000
Ti	0.789383000	0.003746000	0.007279000
H	2.787193000	-1.723324000	-1.541294000
H	2.782511000	0.933148000	-2.118012000
H	2.813747000	-1.995920000	1.160785000
H	2.814099000	2.302087000	0.227460000
H	2.787129000	0.492391000	2.255748000

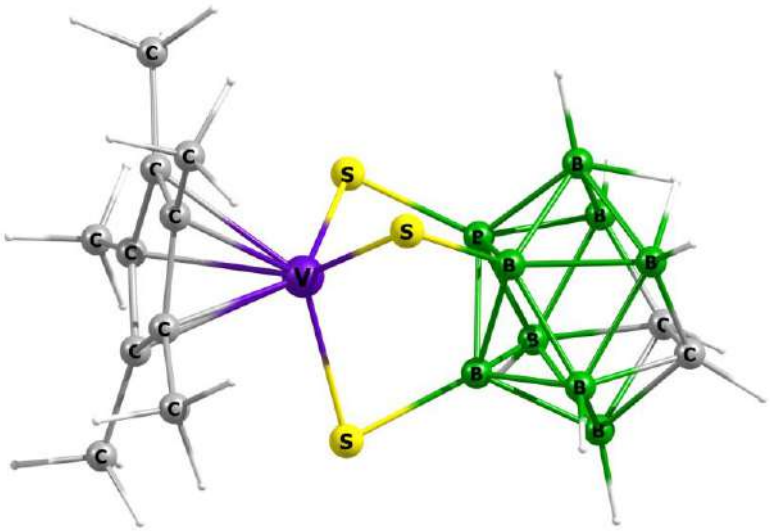


Figure S88. Optimized geometry of **5**.

Total energy = -2833.57027500 a.u.

Cartesian coordinates for the calculated structure **5** (in Å)

C	2.944491000	11.275983000	2.552201000
C	2.777411000	11.049482000	3.965247000
C	1.774457000	10.030017000	4.135852000
C	1.296686000	9.651752000	2.831474000
C	2.022073000	10.421229000	1.851514000
C	4.016793000	12.110883000	1.915498000
H	4.921635000	11.486409000	1.742968000
H	4.316805000	12.962504000	2.556610000
H	3.697572000	12.522230000	0.938542000
C	3.570396000	11.698852000	5.062345000
H	2.988453000	11.761446000	6.002008000
H	3.874319000	12.728031000	4.790025000
H	4.494422000	11.115305000	5.272437000
C	1.423511000	9.346008000	5.424437000
H	2.093262000	8.469955000	5.574224000
H	0.379135000	8.978736000	5.428314000
H	1.547482000	10.014580000	6.298414000
C	0.311356000	8.552857000	2.555504000
H	-0.167771000	8.666290000	1.564465000
H	-0.494328000	8.526070000	3.314760000
H	0.825912000	7.566193000	2.572479000
C	1.941927000	10.269330000	0.359850000
H	2.111785000	11.231932000	-0.160374000
H	0.956855000	9.883387000	0.035012000
H	2.718538000	9.553637000	0.008642000
C	-2.247574000	15.791850000	4.061346000
C	-2.565364000	15.568144000	2.540932000
B	-1.457954000	13.150904000	2.449921000
B	-0.180581000	14.336713000	3.029208000
B	-1.134883000	13.347569000	4.269163000
B	-2.792838000	13.075614000	3.633823000
B	-2.931862000	14.051152000	2.105520000
B	-1.314550000	14.746492000	1.702005000
H	-0.971988000	15.002341000	0.572273000
B	-0.944847000	15.947905000	2.970046000
H	-0.421808000	17.011419000	2.750611000
B	-0.775521000	15.077512000	4.519601000
H	-0.093478000	15.528139000	5.407979000
B	-2.431354000	14.415682000	4.912411000
S	-0.839792000	11.564067000	1.663873000
S	1.624610000	13.917159000	2.754003000
S	-0.193083000	11.979131000	5.146663000
V	0.786769000	11.889998000	3.153501000
H	-3.291631000	11.999130000	3.880875000
H	-3.665696000	13.797547000	1.175782000
H	-2.729811000	14.377685000	6.084553000
H	-2.513094000	16.765417000	4.498581000
H	-3.052754000	16.408973000	2.024494000
H	-3.524495000	14.000259000	4.154490000

References

1 G. H. Llinás, M. Mena, F. Palacios, P. Royo and R. Serrano, *J. Organomet. Chem.*, 1988, **340**, 37.

2 C. D. Abernethy, F. Bottomley and A. Decken, *Organometallics*, 1997, **16**, 1865.

3 A. R. Popescu, A. D. Musteti , A. Ferrer-Ugalde, C. Vinas , R. Nunez and F. Teixidor, *Chem.-Eur. J.*, 2012, **18**, 3174.

4 J. Plešek, Z. Janousek and S. Hermanek, *Collect. Czech. Chem. Commun.*, 1980, **45**, 1775.

5 X. Zhang, X. Tang, J. Yang, Y. Li, H. Yan and V. I. Bregadze, *Organometallics*, 2013, **32**, 2014.

6 *(a*) J. J. Led and H. Gesmar, *Chem. Rev.*, 1991, **91**, 1413; (*b*) L. Yang, R. Simionescu, A. Lough and H. Yan, *Dyes Pigm.* 2011, **91**, 264; (*c*) R. Weiss and R. N. Grimes, *J. Am. Chem. Soc.*, 1978, **100**, 1401.

7 P. Govindaswamy, Y. A. Mozharivskyj and M. R. Kollipara, *Polyhedron*, 2005, **24**, 1710.

8 *a*) C. E. Rao, S. K. Barik, K. Yuvaraj, K. Bakthavachalam, T. Roisnel, V. Dorcet, J.-F. Halet and S. Ghosh, *Eur. J. Inorg. Chem.*, 2016, 4913; *b*) A. Haridas, S. Kar, B. Raghavendra, T. Roisnel, V. Dorcet and S. Ghosh, *Organometallics*, 2020, **39**, 58.

9 S. Bairagi, S. Giri, G. Joshi, E. D. Jemmis and S. Ghosh, *Angew. Chem. Int. Ed.*, 2025, **64**, e202417170

10 S. Bairagi, A. N. Pradhan, M. Cordier, T. Roisnel and S. Ghosh, *Eur. J. Inorg. Chem.*, 2023, **26**, e202300060.

11 A. Altomare, G. Cascarano, C. Giacovazzo, A. Guagliardi, M. C. Burla, G. Polidori and M. Camalli, *J. Appl. Crystallogr*., 1994, **27**, 435.

12 *a*) G. M. Sheldrick, *Acta Cryst.*, 2015, **C71**, 3; *b*) L. J. Bourhis, O. V. Dolomanov, R. J. Gildea, J. A. K. Howard, H. Puschmann*, Acta Cryst.*, 2015, **A71**, 59.

13 O. V. Dolomanov, L. J. Bourhis, R. J. Gildea, J. A. K. Howard and H. Puschmann, *J. Appl. Cryst*., 2009, **42**, 339.

14 M. J. Frisch, G. W. Trucks, H. B. Schlegel, G. E. Scuseria, M. A. Robb, J. R. Cheeseman, G. Scalmani, V. Barone, B. Mennucci, G. A. Petersson, H. Nakatsuji, M. Caricato, X. Li, H. P. Hratchian, A. F. Izmaylov, J. Bloino, G. Zheng, J. L. Sonnenberg, M. Hada, M. Ehara, K. Toyota, R. Fukuda, J. Hasegawa, M. Ishida, T. Nakajima, Y. Honda, O. Kitao, H. Nakai, T. Vreven, J. A. Montgomery Jr., J. E. Peralta, F. Ogliaro, M. Bearpark, J. J. Heyd, E. Brothers, K. N. Kudin, V. N. Staroverov, R. Kobayashi, J. Normand, K. Raghavachari, A. Rendell, J. C. Burant, S. S. Iyengar, J. Tomasi, M. Cossi, N. Rega, J. M. Millam, M. Klene, J. E. Knox, J. B. Cross, V. Bakken, C. Adamo, J. Jaramillo, R. Gomperts, R. E. Stratmann, O. Yazyev, A. J. Austin, R. Cammi, C. Pomelli, J. W. Ochterski, R. L. Martin, K. Morokuma, V. G. Zakrzewski, G. A. Voth, P. Salvador, J. J. Dannenberg, S. Dapprich, A. D. Daniels, Ö. Farkas, J. B. Foresman, J. V. Ortiz, J. Cioslowski and D. J. Fox, *Gaussian 09, Revision C.01*, Gaussian, Inc., Wallingford, CT, 2010.

15 *a*) H. L. Schmider and A. D. Becke, *J. Chem. Phys.*, 1998, **108**, 9624; *b*) J. P. Perdew, *Phys. Rev. B: Condens. Matter Mater. Phys.*, 1986, **33**, 8822.

16 EMSL Basis Set Exchange Library. https://bse.pnl.gov/bse/portal

17 F. London, *J. Phys. Radium*., 1937, **8**, 397.

18 R. Ditchfield, *Mol. Phys.*, 1974, *27*, 789.

19 K. Wolinski, J. F. Hinton and P. Pulay, *J. Am. Chem. Soc.*, 1990, **112**, 8251.

20 *a*) A. D. Becke, *Phys. Rev. A.*, 1988, **38**, 3098; *b*) C. Lee, W. Yang and R. G. Parr, *Phys. Rev. B.*, 1988, **37**, 785; *c*) A. D. Becke, *J. Chem. Phys.*, 1993, **98**, 5648.

21 T. P. Onak, H. L. Landesman, R. E. Williams and I. Shapiro, *J. Phys.Chem.*, 1959, **63**, 1533.

22 *a*) E. D. Glendening, A. E. Reed, J. E. Carpenter and F. Weinhold, *NBO Program 3.1*, W. T. Madison, 1988; *b*) A. E. Reed, F. Weinhold and L. A. Curtiss, *Chem. Rev.*, 1988, **88**, 899; *c*) F. Weinhold and R. Landis, *Valency and bonding: A natural bond orbital donor-acceptor perspective;* Cambridge University Press: Cambridge, U.K, 2005.

23 K. Wiberg, *Tetrahedron*, 1968, **24**, 1083.

24 *a*) R. F. W. Bader, *Atoms in Molecules: A Quantum Theory*; Oxford University Press: Oxford, U. K., 1990; *b*) R. F. W. Bader, *J. Phys. Chem. A.*, 1998, **102**, 7314; *c*) R. F. W. Bader, *Chem. Rev.*, 1991, **91**, 893.

25 T. Lu, F. Chen, *J. Comput. Chem.*, 2012, **33**, 580.

26 I. I. Dennington, R. T. Keith, J. Millam, K. Eppinnett, W. L. Hovell and R. Gilliland, *GaussView, Version 3.09*; Semichem Inc.: Shawnee Mission, KS, 2003.

27 G. A. Zhurko, http://www.chemcraftprog.com.

ChemComm

COMMUNICATION

View Article Online
View Journal | View Issue

Check for updates

Cite this: *Chem. Commun.*, 2025, **61**, 10764

Received 7th May 2025,
Accepted 11th June 2025

DOI: 10.1039/d5cc02594j

rsc.li/chemcomm

Published on 11 June 2025. Downloaded on 12/29/2025 3:13:54 AM.

Mechanochromic luminescence in copper nanoclusters: resolving structural transitions through microcrystal electron diffraction†‡

Harshita Nagar, [ab] Subrata Duary,[ab] Vivek Yadav,[ab] Amoghavarsha Ramachandra Kini,[ab] Sudhadevi Antharjanam,[c] Tomas Base, *[d] Anirban Som, *[ab] Brent L. Nannenga *[e] and Thalappil Pradeep *[ab]

MicroED reveals insights into mechanochromic luminescence in copper nanoclusters, demonstrating structural transitions from crystalline to amorphous state upon grinding, with restoration of crystallinity following solvent exposure. Luminescence switching occurs due to reversible amorphization-recrystallization rather than chemical changes, providing critical design principles for such stimuli-responsive materials.

Noble metal nanoclusters (NCs) occupy a unique position between atomic and nanoparticle regimes of matter, exhibiting quantum-confined properties that depend critically on their precise atomic arrangements.[1,2] Accurate structural insight enables the building of structure–property relationships, identification of active sites for catalysis,[3] optimization of functionalities,[4] and doping of heteroatoms[5,6] for various applications in energy, medicine, and nanotechnology.[7–9] Detailed structural information also helps to understand stability, growth mechanisms, and ligand–cluster and cluster–cluster interactions, which are essential for tailoring the performance of NCs.[10] Among NCs, copper nanoclusters (Cu NCs) have emerged as useful materials due to their mechanochromic luminescence[11–13] and reversible emission changes upon mechanical grinding and solvent exposure, making them promising for sensing and *anti*-counterfeiting applications. Despite their emerging importance, the structural mechanisms underlying reversible luminescence remain poorly understood, primarily due to analytical limitations.

Conventional structural methods face significant challenges when investigating mechanochromic transitions. Single-crystal X-ray diffraction (SC-XRD), gold-standard for structure determination, fails when crystal size reduces to submicron dimensions after mechanical processing, while powder XRD provides limited atomic-level detail. This analytical gap has hindered mechanistic understanding of how grinding-induced structural changes correlate with altered luminescence properties, leaving fundamental questions about structural integrity and solvent interactions unresolved.

Microcrystal electron diffraction (MicroED) addresses these limitations by enabling atomic-resolution structure determination from submicron-sized crystals.[14] While used extensively for biomolecules[15] and previously applied to a single gold NC,[16] MicroED's potential for investigating mechanochromic phenomena in NCs remain unexplored. This technique is particularly suited for studying Cu NCs' complex behaviors given their distinctive coordination chemistry and cuprophilic interactions that fundamentally influence their photoluminescent properties.

Here, we demonstrate MicroED's capabilities through progressive investigation of three 4-atom Cu NC systems: first showcasing its accuracy through structural analysis of $Cu_4(MNA)_2(DPPE)_2$, then revealing solvent molecules in $Cu_4(m_9\text{-CBT})_4$ undetectable by SC-XRD, and finally providing direct structural evidence of the amorphization-recrystallization mechanism in mechanochromic $Cu_4(o_9\text{-CBT})_4$ (MNA, DPPE, o_9-CBT and m_9-CBT are 2-mercaptonicotonic acid, 1,2-bis-(diphenylphosphino) ethane, *ortho* carborane-9-thiol and *meta* carborane-9-thiol, respectively). Our findings establish that mechanical grinding disrupts long-range order without altering the structure of individual NCs, while solvent exposure facilitates recrystallization and restoration of luminescence, insights previously inaccessible through conventional techniques.

Previously reported by our group, these three Cu NCs serve as ideal candidates for MicroED investigations, exhibiting assembly-induced emission wherein their non-emissive solution behavior transforms to bright solid-state luminescence through molecular

[a] *DST Unit of Nanoscience (DST UNS) and Thematic Unit of Excellence (TUE), Department of Chemistry, Indian Institute of Technology, Madras, Chennai – 600036, India. E-mail: pradeep@iitm.ac.in, asomchem@gmail.com*
[b] *International Centre for Clean Water, Chennai-600113, India*
[c] *Sophisticated Analytical Instruments Facility (SAIF), Indian Institute of Technology, Madras, Chennai – 600036, India*
[d] *Department of Synthesis, Institute of Inorganic Chemistry, The Czech Academy of Science, 1001 Husinec-Rez, 25068, Czech Republic. E-mail: tbase@iic.acs.cz*
[e] *School of Engineering of Matter, Transport and Energy, Arizona State University, Tempe, Arizona, USA. E-mail: brent.nannenga@asu.edu*

† Dedicated to Prof. C. N. R. Rao, FRS on his 91st birthday.

‡ Electronic supplementary information (ESI) available. See DOI: https://doi.org/10.1039/d5cc02594j

This journal is © The Royal Society of Chemistry 2025

Published on 11 June 2025. Downloaded on 12/29/2025 3:13:54 AM.

ordering.[17,18] Their distinctive mechanochromic response provides a perfect platform for elucidating structure–property relationships at the nanoscale. The synthesis and crystallization protocols for these NCs are described in the Experimental section (ESI‡). These were fully characterized using UV-vis spectroscopy and ESI-MS (Fig. S1, ESI‡). For MicroED, microcrystals were deposited onto lacey carbon grids, clipped into autogrid-rings, and loaded into a Krios G4 Cryo-EM equipped with an X-FEG source operating at 300 kV (Fig. S2, ESI‡). Data were collected using EPU-D (ThermoFisher), with the overall procedure illustrated in Fig. S3 (ESI‡). An atlas preset at low magnification provided a global map, followed by a grid square preset to image a single region, then a search/auto eucentric preset to locate and center the crystals of interest, and finally a diffraction preset for the collection of continuous rotation electron diffraction data at a dose rate of 0.01 e^{-} $Å^{-2}$ s^{-1} using the smallest spot size (11) and a 1 s exposure, in nanoprobe mode. Samples were maintained at liquid nitrogen temperature, and diffraction data were recorded on a Ceta D CMOS camera and exported in SMV format. All diffraction datasets were indexed and integrated using XDS, scaled with XSCALE, and then converted to SHELX format through XDSCONV. Structures were subsequently solved with SHELXT and refined in SHELXL. Notably, the entire MicroED data collection and structure determination process required only a few hours, underscoring the rapid and efficient nature of this technique.

We first investigated $Cu_4(MNA)_2(DPPE)_2$ NC as a benchmark system to validate MicroED's capability for accurate structure determination of copper clusters. Microcrystals (Fig. 1A) suspended in DMF were deposited directly onto lacey carbon grids and analyzed using the continuous rotation methodology. Data collection from -50° to $+50^\circ$ in 1° increments at 1° s^{-1} achieved exceptional subatomic resolution (0.8 Å, Fig. 1B), comparable to high-quality SC-XRD data but from significantly smaller crystals. TEM images of the microcrystal at various tilt angles are shown in Fig. S4 (ESI‡).

The resulting structure revealed a Cu_4S_2 core formed by two Cu_2 units connected through bridging sulfur atoms (Fig. 1C). Each Cu_2 unit exhibited distinctive coordination environments: one copper center adopted tetrahedral coordination (μ_3-S, P, O, and Cu), while the other displayed pentacoordination (two μ_3-S, P, N, and Cu). This arrangement suggests cuprophilic interactions between copper centers. The DPPE ligands coordinated through phosphorus, while MNA was bound *via* nitrogen and oxygen atoms, creating a stable structural framework. Packing of the structure ($3 \times 3 \times 3$ along the *b*-axis) is shown in Fig. 1D and unit cell molecular packing along different axes are shown in Fig. S5 (ESI‡). Notably, all the geometric parameters determined through MicroED, including bond lengths, angles, and intermolecular distances matched well with the SC-XRD data (Table S1, ESI‡) validating MicroED's reliability for Cu NC characterization. These findings match perfectly with the SC-XRD structure (Fig. S6 ESI‡).

Building upon the successful structure determination of $Cu_4(MNA)_2(DPPE)_2$, we next examined $Cu_4(m_9\text{-CBT})_4$, where MicroED revealed critical structural insights beyond those accessible through conventional methods. Gently crushed crystals deposited on lacey carbon grids (Fig. 2A) were analyzed using MicroED with 1° continuous tilt increments over a -40° to $+40^\circ$ rotation range, achieving 0.9 Å resolution (Fig. 2B). The most significant finding was the detection of a disordered toluene (solvent) molecule within the unit cell (Fig. 2C), a critical structural feature not observed from SC-XRD (Fig. S7, ESI‡). This discovery necessitated reassignment of the space group from $P2_1/c$ (SC-XRD) to $P\bar{1}$ (MicroED), with corresponding adjustments to cell parameters (Table S2, ESI‡). MicroED-derived packing ($3 \times 3 \times 3$ along the *c*-axis) is shown in Fig. 2D and views along different axes are shown in (Fig. S8, ESI‡). The stronger interaction of electrons with matter makes MicroED particularly sensitive to lighter atoms and disordered structures, providing a more complete picture of the molecular environment within the crystal lattice. This finding highlights a

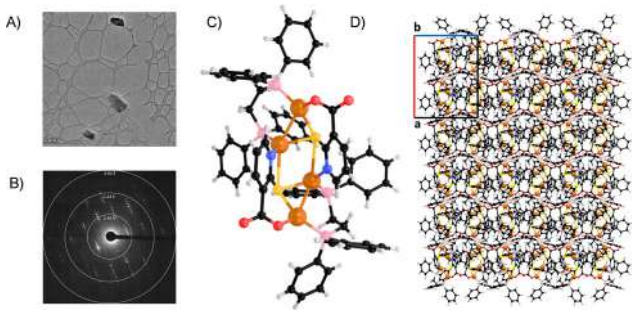


Fig. 1 MicroED enables subatomic resolution structure determination of $Cu_4(MNA)_2(DPPE)_2$. (A) TEM image of microcrystals on lacey carbon grids. (B) Initial diffraction frame showing high resolution reflections. (C) Resolved molecular structure revealing Cu_4S_2 core with distinct coordination environments. (D) $3 \times 3 \times 3$ crystal packing along *b*-axis. Color code: Cu (orange), S (yellow), O (red), N (blue), P (pink), C (black), H (white).

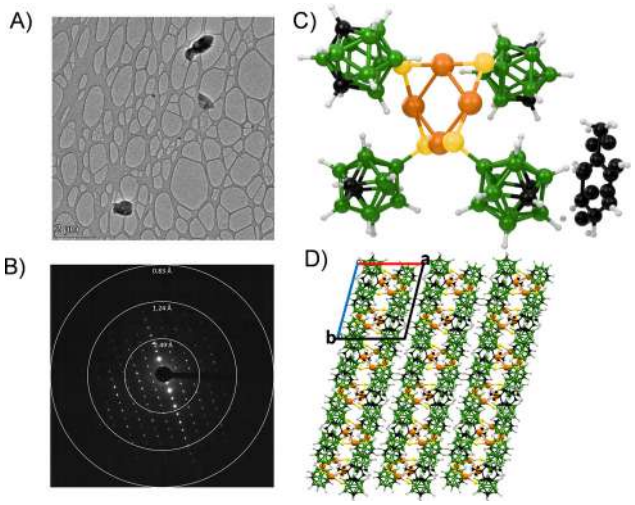


Fig. 2 MicroED reveals solvent inclusion in the $Cu_4(m_9\text{-CBT})_4$ structure. (A) TEM image of microcrystals. (B) Initial diffraction frames showing high-resolution data. (C) Resolved structure highlighting the disordered toluene molecule undetectable by SC-XRD. (D) $3 \times 3 \times 3$ crystal packing along *c*-axis. Color code: Cu (orange), S (yellow), B (green), C (black), H (white).

Published on 11 June 2025. Downloaded on 12/29/2025 3:13:54 AM.

distinctive advantage of MicroED: its capacity to resolve subtle structural features that might be missed by SC-XRD. It is important to note that geometric parameters observed through MicroED in the individual clusters were largely similar to that known from SC-XRD.

Previous studies on copper clusters have demonstrated that solvent molecules can modify intermolecular interactions and affect emission properties.[19] Perruchas *et al.* observed that changes in crystal packing and cuprophilic interactions directly influence luminescence behavior.[13] The ability to detect these previously invisible structural elements provides crucial insights into structure–property relationships in luminescent copper clusters.

This enhanced structural information proves valuable for understanding the factors that influence luminescence properties and mechanochromic behavior, which were explored further. The $Cu_4(o_9\text{-CBT})_4$ cluster exhibits a shift in emission from green to yellow upon mechanical grinding (~20 min), with restoration of the original emission following exposure to solvent vapor (DCM, ~30 min),[18] shown in Fig. 3A. Similar mechanochromic luminescence has been observed in various copper complexes, particularly copper iodide clusters with cubane geometry $[Cu_4I_4L_4]$.[13] However, the underlying structural mechanism has remained elusive due to the inability to obtain high-quality diffraction data from mechanically processed materials.

We conducted systematic MicroED analysis at three critical stages: before grinding, after grinding, and following solvent vapor exposure. The diffraction patterns clearly demonstrated: (i) well-defined crystallinity in the initial state, (ii) complete loss of diffraction following prolonged grinding, indicating amorphization, and (iii) restored crystallinity upon solvent vapor exposure (Fig. 3B). High-quality diffraction data enabled subatomic resolution (0.9 Å) structure determination (Fig. 3C) of the NC. Most remarkably, MicroED successfully resolved the structure from nanometer-sized regrown crystals after solvent exposure, confirming restoration of the original structural arrangement (Fig. 3E). The ground powder yielded no structure due to unresolvable diffraction (Fig. 3D).

This observation aligns with previous studies of copper iodide clusters, where mechanochromic properties have been attributed to distortions in crystal packing affecting cuprophilic interactions. As reported by Perruchas *et al.*, grinding-induced structural disorder can modify Cu–Cu interactions without altering the fundamental molecular structure, directly influencing emission properties.[20] The structural insights from our observations find strong theoretical support in the mechanochemical principles outlined by Yan *et al.* in their work on

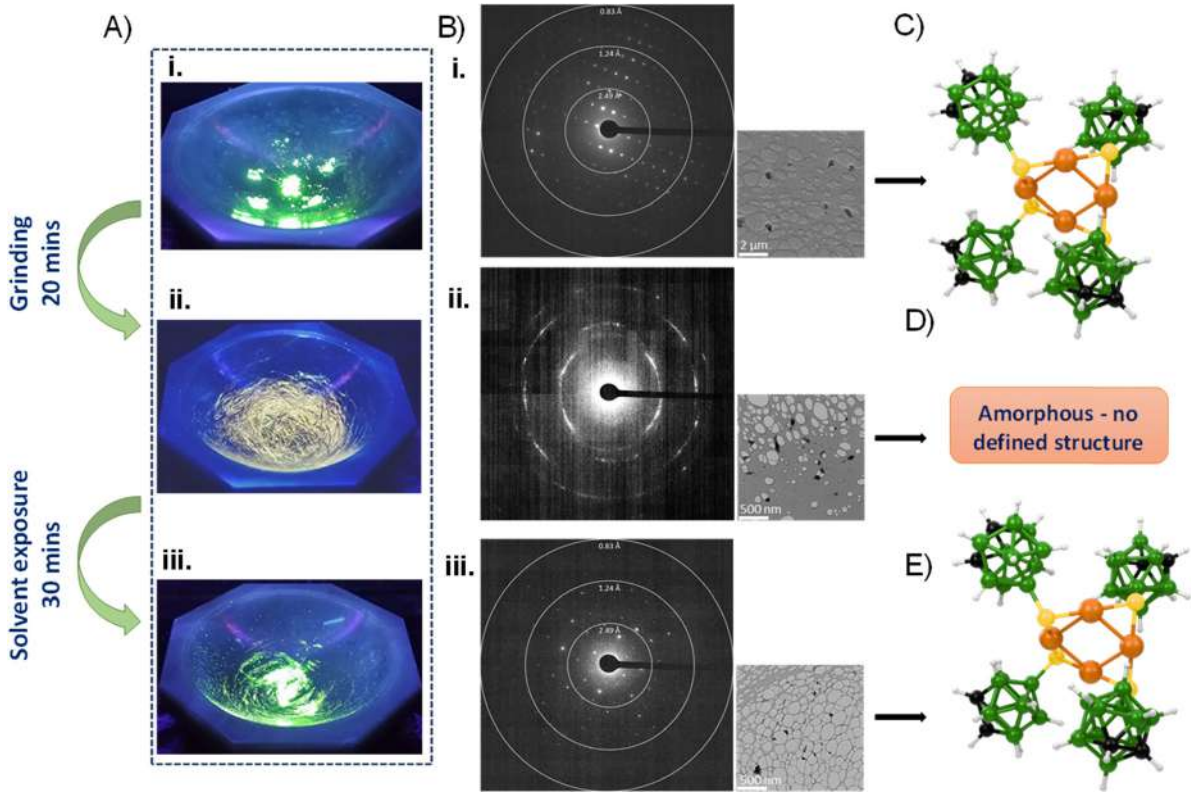


Fig. 3 MicroED directly visualizes the structural basis of mechanochromic luminescence in $Cu_4(o_9\text{-CBT})_4$. (A) Photographic images demonstrating reversible emission switching: (i) initial green emission, (ii) yellow emission after grinding (20 min), and (iii) restored green emission following DCM vapor exposure (30 min). (B) Corresponding diffraction patterns revealing: (i) initial crystallinity, (ii) complete amorphization after grinding, and (iii) restored crystallinity after solvent exposure. Crystallite sizes are visible in the inset TEM images. (C) MicroED structure from initial crystalline state. (D) Amorphous state with no resolvable structure after grinding. (E) Recovered structure from nanometer-sized recrystallized particles after solvent exposure, confirming structural restoration without molecular alteration.

This journal is © The Royal Society of Chemistry 2025

Published on 11 June 2025. Downloaded on 12/29/2025 3:13:54 AM.

sterically controlled reactions under hydrostatic pressure.[21] Their demonstration that isotropic compression induces anisotropic strain in metal–organic chalcogenides, particularly through ligand-mediated deformation of compressible Cu_4S_4 cores (Fig. S9, ESI‡) directly parallels our observation of amorphization-recrystallization cycles in $Cu_4(o_9\text{-CBT})_4$. They showed that rigid ligands (carboranes) act as ''molecular anvils'', transmitting stress to bend Cu–S–Cu bond angles. This aligns with our findings that grinding-induced loss of long-range order without Cu–S bond rupture drives luminescence switching, while solvent exposure enables structural recovery through ligand reorganization. Our direct structural evidence confirms that mechanochromic luminescence in $Cu_4(o_9\text{-CBT})_4$ arises from disruption of long-range order followed by recrystallization, rather than chemical transformation or degradation. Fig. S10 (ESI‡) displays unit cell packing of $Cu_4(o_9\text{-CBT})_4$ in both initial crystalline state and after solvent-induced recrystallization along various axes. Comparative analysis of geometric parameters like bond lengths, angles, and intermolecular distances, from structures before grinding and after solvent vapor exposure showed remarkable consistency (Table S3, ESI‡). This confirms that individual Cu NCs maintain their molecular integrity throughout the mechanochromic cycle, with changes occurring primarily in their arrangement and long-range order. The emission shift correlates directly with the loss of crystallinity, while recovery of the original emission coincides with recrystallization.

In conclusion, the ability to directly observe this relationship through MicroED analysis of submicron crystallites provides unprecedented insights into the structure–property relationship underlying mechanochromic behavior. Unlike previous studies that relied on indirect spectroscopic evidence or theoretical calculations, our approach provides direct structural confirmation of the mechanochromic mechanism. This represents a significant advancement in understanding stimuli-responsive luminescent materials and demonstrates MicroED's exceptional utility for studying mechanical transformations of functional materials.

H. N. acknowledges UGC, Government of India for her fellowship. MicroED data were acquired at the National Facility for Cryo-Electron Microscopy at IIT Madras, supported by the Anusandhan National Research Foundation (ANRF), Government of India. T. P. thanks ANRF for funding through the grant, SPR/2021/000439 and a J. C. Bose Fellowship. T. P. thanks the Centre of Excellence on Molecular Materials and Functions under the Institution of Eminence scheme of IIT Madras.

Conflicts of interest

There are no conflicts to declare.

Data availability

The data supporting this article have been included in the ESI.‡

Notes and references

1 I. Chakraborty and T. Pradeep, *Chem. Rev.*, 2017, **117**, 8208–8271.
2 R. Jin, C. Zeng, M. Zhou and Y. Chen, *Chem. Rev.*, 2016, **116**, 10346–10413.
3 Y. Du, H. Sheng, D. Astruc and M. Zhu, *Chem. Rev.*, 2020, **120**, 526–622.
4 Nonappa, *Chem. Commun.*, 2023, **59**, 13800–13819.
5 S. Hossain, Y. Niihori, L. V. Nair, B. Kumar, W. Kurashige and Y. Negishi, *Acc. Chem. Res.*, 2018, **51**, 3114–3124.
6 A. Ghosh, O. F. Mohammed and O. M. Bakr, *Acc. Chem. Res.*, 2018, **51**, 3094–3103.
7 M. F. Matus and H. Häkkinen, *Nat. Rev. Mater.*, 2023, **8**, 372–389.
8 K. S. Sugi, A. Maier and M. Scheele, *Chem. Commun.*, 2022, **58**, 6998–7017.
9 Y. Tao, M. Li, J. Ren and X. Qu, *Chem. Soc. Rev.*, 2015, **44**, 8636–8663.
10 K. R. Krishnadas, A. Ghosh, A. Baksi, I. Chakraborty, G. Natarajan and T. Pradeep, *J. Am. Chem. Soc.*, 2016, **138**, 140–148.
11 A. Baghdasaryan and T. Bürgi, *Nanoscale*, 2021, **13**, 6283–6340.
12 A. Ghosh, A. Sagadevan, K. Murugesan, S. A. F. Nastase, B. Maity, M. Bodiuzzaman, A. Shkurenko, M. N. Hedhili, J. Yin, O. F. Mohammed, M. Eddaoudi, L. Cavallo, M. Rueping and O. M. Bakr, *Mater. Horiz.*, 2024, **11**, 2494–2505.
13 Q. Benito, X. F. Le Goff, S. Maron, A. Fargues, A. Garcia, C. Martineau, F. Taulelle, S. Kahlal, T. Gacoin, J.-P. Boilot and S. Perruchas, *J. Am. Chem. Soc.*, 2014, **136**, 11311–11320.
14 B. L. Nannenga and T. Gonen, *Curr. Opin. Struct. Biol.*, 2014, **27**, 24–31.
15 X. Mu, C. Gillman, C. Nguyen and T. Gonen, *Annu. Rev. Biochem.*, 2021, **90**, 431–450.
16 S. Vergara, D. A. Lukes, M. W. Martynowycz, U. Santiago, G. Plascencia-Villa, S. C. Weiss, M. J. De La Cruz, D. M. Black, M. M. Alvarez, X. López-Lozano, C. O. Barnes, G. Lin, H.-C. Weissker, R. L. Whetten, T. Gonen, M. J. Yacaman and G. Calero, *J. Phys. Chem. Lett.*, 2017, **8**, 5523–5530.
17 S. Duary, A. Jana, A. Das, S. Acharya, A. R. Kini, J. Roy, A. K. Poonia, D. K. Patel, V. Yadav, P. K. S. Antharjanam, B. Pathak, A. Kumaran Nair Valsala Devi and T. Pradeep, *Inorg. Chem.*, 2024, **63**, 18727–18737.
18 A. Jana, M. Jash, W. Ahmed Dar, J. Roy, P. Chakraborty, G. Paramasivam, S. Lebedkin, K. Kirakci, S. Manna, S. Antharjanam, J. Machacek, M. Kucerakova, S. Ghosh, K. Lang, M. M. Kappes, T. Base and T. Pradeep, *Chem. Sci.*, 2023, **14**, 1613–1626.
19 A. Jana, S. Duary, A. Das, A. R. Kini, S. Acharya, J. Machacek, B. Pathak, T. Base and T. Pradeep, *Chem. Sci.*, 2024, **15**, 13741–13752.
20 S. Perruchas, X. F. Le Goff, S. Maron, I. Maurin, F. Guillen, A. Garcia, T. Gacoin and J.-P. Boilot, *J. Am. Chem. Soc.*, 2010, **132**, 10967–10969.
21 H. Yan, F. Yang, D. Pan, Y. Lin, J. N. Hohman, D. Solis-Ibarra, F. H. Li, J. E. P. Dahl, R. M. K. Carlson, B. A. Tkachenko, A. A. Fokin, P. R. Schreiner, G. Galli, W. L. Mao, Z.-X. Shen and N. A. Melosh, *Nature*, 2018, **554**, 505–510.

Supplementary Information (SI) for ChemComm.
This journal is © The Royal Society of Chemistry 2025

Supplementary Information

Mechanochromic Luminescence in Copper Nanoclusters: Resolving Structural Transitions through Microcrystal Electron Diffraction

*Harshita Nagar[ξ], Subrata Duary[ξ], Vivek Yadav[ξ], Amoghavarsha Ramachandra Kini[ξ], Sudhadevi Antharjanam[φ], Tomas Base[*ψ], Anirban Som[*ξ], Brent L. Nannenga[*€], and Thalappil Pradeep[*ξ]*

ξ DST Unit of Nanoscience (DST UNS) and Thematic Unit of Excellence (TUE), Department of Chemistry, Indian Institute of Technology, Madras, Chennai – 600036, International Centre for Clean Water, Chennai- 600113, India

€ School of Engineering of Matter, Transport and Energy, Arizona State University, Tempe, Arizona, United States

φ Sophisticated Analytical Instruments Facility (SAIF), Indian Institute of Technology, Madras, Chennai – 600036, India

ψ Department of Synthesis, Institute of Inorganic Chemistry, The Czech Academy of Science, 1001 Husinec-Rez, 25068, Czech Republic

* Email: pradeep@iitm.ac.in, brent.nannenga@asu.edu, asomchem@gmail.com, tbase@iic.acs.cz

Table of contents:

Sl No.	Contents	Page No.
1.	Experimental section	3
2.	Instrumentation	4
3.	Characterization	5
Fig S1.	UV–vis absorption spectra and ESI-MS of $Cu_4(MNA)_2(DPPE)_2$, $Cu_4(o_9\text{-CBT})_4$ and $Cu_4(m_9\text{-CBT})_4$	6
Fig S2.	MicroED sample preparation and data collection workflow	6
Fig S3.	MicroED data acquisition workflow	7
Fig S4.	TEM images (Images of crystal taken at different tilts from -50° to 50°)	7
Table S1.	Comparison of unit cell parameters, space group, bond lengths (Å), bond angles (°), and structure refinement details of $Cu_4(MNA)_2(DPPE)_2$ obtained from SC-XRD and MicroED	8
Fig S5.	Unit cell molecular packing of MicroED structure of	9

	$Cu_4(MNA)_2(DPPE)_2$	
Fig S6.	Single crystal X-ray structure of $Cu_4(MNA)_2(DPPE)_2$	9
Table S2.	Comparison of unit cell parameters, space group, bond lengths (Å), bond angles (°), and structure refinement details of $Cu_4(m_9\text{-}CBT)_4$ obtained from SC-XRD and MicroED	10
Fig S7.	Single crystal X-ray structure of $Cu_4(m_9\text{-}CBT)_4$	11
Fig S8.	Unit cell packing of MicroED structure of $Cu_4(m_9\text{-}CBT)_4$	11
Table S3.	Comparison of unit cell parameters, space group, bond lengths (Å), bond angles (°), and structure refinement details of $Cu_4(o_9\text{-}CBT)_4$ obtained from SC-XRD and MicroED in the initial crystalline state and after restoration of crystallinity upon solvent vapor exposure	12
Fig S9.	Single crystal X-ray structure of $Cu_4(o_9\text{-}CBT)_4$	13
Fig S10.	Unit cell packing of MicroED structure of $Cu_4(o_9\text{-}CBT)_4$	13
Table S4.	Crystallographic information of $Cu_4(MNA)_2(DPPE)_2$	14
Table S5.	Crystallographic information of $Cu_4(o_9\text{-}CBT)_4$	15
Table S6.	Crystallographic information of $Cu_4(m_9\text{-}CBT)_4$	16
Table S7.	Atomic coordinates of $Cu_4(MNA)_2(DPPE)_2$ crystal	17
Table S8.	Atomic coordinates of $Cu_4(o_9\text{-}CBT)_4$ crystal in initial state (before grinding)	20
Table S9.	Atomic coordinates of $Cu_4(o_9\text{-}CBT)_4$ crystal after solvent vapor exposure	21
Table S10.	Atomic coordinates of $Cu_4(m_9\text{-}CBT)_4$ crystal	22
	References	24

1. Experimental section

Chemicals

Copper iodide (CuI), 1,2-bis-diphenylphosphino ethane (DPPE), 2-mercaptonicotonic acid (MNA), and sodium borohydride ($NaBH_4$) were purchased from Aldrich Chemicals. ortho-carborane-9-thiol (o_9-CBT), and meta-carborane-9-thiol (m_9-CBT) were synthesized according to the reported procedure[1,2]. Solvents used were acetonitrile, methanol, acetone, toluene, dichloromethane, N,N-dimethylformamide, and n-hexane purchased from Rankem and Finar India.

Nanoclusters synthesis

All three Cu_4 nanoclusters were synthesized using previously reported method[3,4] with modifications where the LEIST method in $[Cu_{18}H_{16}(DPPE)]^{2+}$ nanocluster was used.

Synthesis of Cu_{18} NC – Cu_{18} NC was synthesized using a previously available procedure[5]. 95 mg of CuI with 120 mg DPPE was added in 15 ml acetonitrile. Then reduction is carried out using 180 mg of reducing agent i.e., $NaBH_4$. After 4 hrs of stirring, an orange colour precipitate was obtained which was cleaned three times using methanol and acetonitrile then Cu_{18} was extracted in DCM.

a) **Synthesis of $Cu_4(MNA)_2(DPPE)_2$ NC** - The Cu_4 nanoclusters were synthesized through Ligand Exchange-Induced Structural Transformation (LEIST) method using Cu_{18} as the precursor. Approximately 35 mg of purified Cu_{18}, dissolved in 4 mL of dichloromethane (DCM), was reacted with 15 mg of 2-mercaptonicotinic acid in 1 mL of dimethylformamide (DMF). The initial reaction mixture appeared transparent and reddish. After 45 minutes, the solution turned yellowish, indicating the progression of reaction, and then the reaction was stopped.

b) **Synthesis of $Cu_4(o_9$-CBT)$_4$ NC** – This cluster was formed using the above synthesized Cu_{18} NC using (LEIST) where 50 mg Cu_{18} in DCM was mixed with 35 mg ortho carborane-9-thiol ligand and kept for stirring at room temperature. After 3 hrs, the solution, initially yellow in color forms white precipitates. These white precipitates shows green emission under 365 nm UV lamp. The reaction was allowed to continue for 5 hrs until completion. The resulting microcrystalline white precipitates were thoroughly washed with methanol and DCM to remove any excess unreacted ligands. These white precipitates were soluble in acetone and further purified through crystallization.

c) **Synthesis of $Cu_4(m_9\text{-CBT})_4$ NC –** $Cu_4(m\text{-CBT})_4$ NC was formed using the same procedure used for $Cu_4(o\text{-CBT})_4$ NC but this time ligand used was meta carborane – 9 -thiol. The as formed cluster was soluble in DCM. The reaction solvents were removed using rotavapor, and the solid white product that formed showed a green luminescence under a 365 nm UV lamp.

Crystallization

$Cu_4(MNA)_2(DPPE)_2$ was crystallized through hexane vapor diffusion, resulting in a crude yellow solution at 4 °C[3].

$Cu_4(o_9\text{-CBT})_4$ – acetone solution of $Cu_4(o_9\text{-CBT})_4$ was mixed with equal amount of dichloromethane and kept for crystallization at 4°C. Large hexagonal crystals formed after a week[4].

$Cu_4(m_9\text{-CBT})_4$ – dichloromethane solution of $Cu_4(m_9\text{-CBT})_4$ was mixed with equal amount of toluene and kept for crystallization at 4°C. Large parallelepiped crystals formed after a week[4].

2. Instrumentation

UV-vis spectroscopy

UV-vis absorption spectra were recorded over a wavelength range of 1100–200 nm using a Perkin Elmer Lambda 365 UV-vis spectrometer equipped with a 1 nm bandpass filter. The spectra were acquired at a scan rate of 100 nm/min.

Mass spectrometry

Mass spectra of these three nanoclusters were obtained using a Waters Synapt G2Si HDMS instrument. For $Cu_4(MNA)_2(DPPE)_2$ NC, conditions used were capillary voltage - 3kV, flow rate – 20 µL/min, source temperature – 100° C, desolvation temperature – 150° C and gas flow rate – 400 L/h. In case of $Cu_4(o_9\text{-CBT})_4$ and $Cu_4(m_9\text{-CBT})_4$, formic acid and cesium acetate respectively were used as ionization enhancer. Conditions used were capillary voltage – 3kV, cone voltage – 0kV, source temperature – 50° C, desolvation temperature – 90° C and gas flow rate – 300L/h.

TEM

TEM imaging of the microcrystals was performed on a ThermoScientific Krios G4 transmission electron microscope operated at an accelerating voltage of 300 kV. Samples were

prepared by depositing microcrystals onto lacey carbon grids. Images were acquired using a Ceta D CMOS camera under low electron dose conditions (spot size 8) to minimize beam-induced damage and preserve structural integrity. This approach ensured high-contrast visualization of the microcrystalline morphology while maintaining sample quality for subsequent MicroED data collection.

3. Characterization

UV-vis. absorption spectra - The UV-vis optical absorption spectrum of $Cu_4(MNA)_2(DPPE)_2$ NC in acetonitrile displays distinct peaks at 297 nm and 380 nm. Also, the UV-vis optical absorption spectra of $Cu_4(o_9\text{-CBT})_4$ and $Cu_4(m_9\text{-CBT})_4$ in acetonitrile exhibit single absorption bands at 281 nm and 279 nm, respectively.

Mass spectrometry - The $Cu_4(MNA)_2(DPPE)_2$ NC was ionized in positive ion mode, exhibiting a characteristic peak at m/z 1357.95 (1+), corresponding to $[Cu_4(MNA)_2(DPPE)_2]^+$. The experimental isotopic distribution matches the theoretical isotopic distribution (inset left). Additional, prominent mass peaks observed at m/z 1380.90 (1+), 1396.94 (1+), and 1434.92 (1+), denoted as i, ii, and iii, respectively, are attributed to sodium and potassium species attached to the molecular ion of the cluster. When $Cu_4(o_9\text{-CBT})_4$ and $Cu_4(m_9\text{-CBT})_4$ were characterized by ESI-MS, no characteristic peaks were detected from the as-prepared samples in either positive or negative ion modes, indicating that the clusters are neutral. However, in the presence of formic acid, $Cu_4(o_9\text{-CBT})_4$ exhibited a characteristic peak at m/z 956.7, suggesting that protonation facilitated the ionization of the cluster. Similarly, in the presence of cesium acetate, $Cu_4(m_9\text{-CBT})_4$ displayed a peak at m/z 1088.26, corresponding to the Cs+ attached peak of the cluster. The experimental isotopic distributions of both clusters matched well with the calculated distributions (inset right).

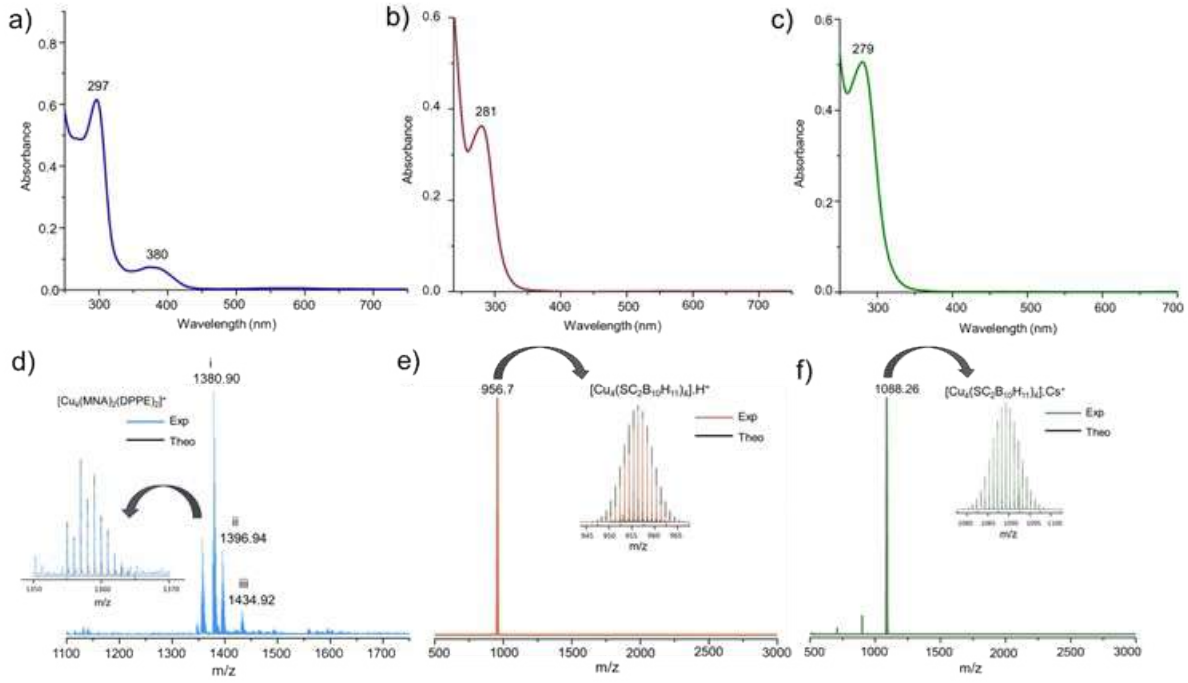


Fig S1 UV-vis absorption spectra of (a) $Cu_4(MNA)_2(DPPE)_2$, (b) $Cu_4(o_9\text{-CBT})_4$ and (c) $Cu_4(m_9\text{-CBT})_4$. ESI-MS spectra validate molecular integrity of (d) $Cu_4(MNA)_2(DPPE)_2$, (e) Cu_4(o9-CBT)$_4$ (formic acid as ionization enhancer), and (f) Cu_4(m9-CBT)$_4$ (caesium acetate as ionization enhancer). Insets: Experimental isotopic distributions align with theoretical predictions.

4. MicroED sample preparation and data collection workflow

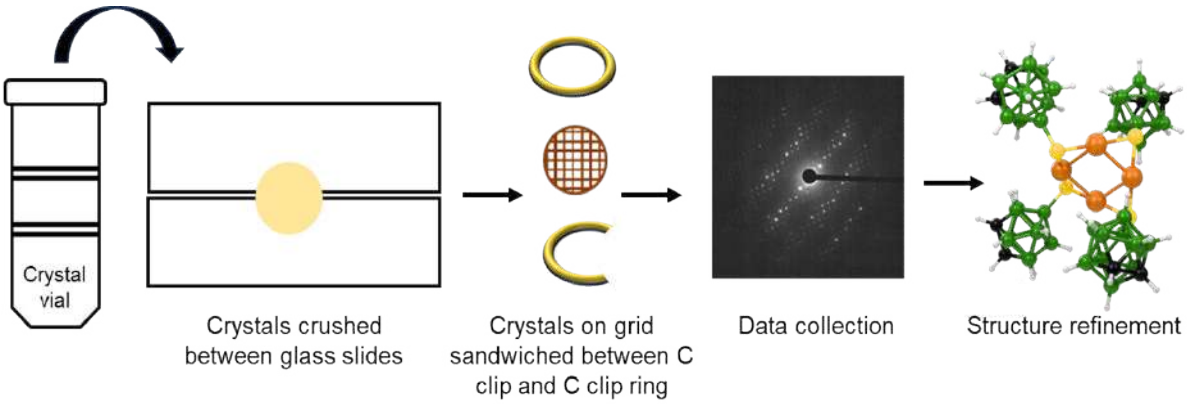


Fig. S2 Schematic workflow for MicroED structure determination: (1) Microcrystals are gently crushed to produce smaller crystallites; (2) these are deposited onto a lacey carbon TEM grid; (3) the grid is clipped and mounted in the cryo-EM; (4) electron diffraction data are collected from suitable crystallites; (5) data are processed and refined to yield the final atomic structure.

5. MicroED data acquisition workflow

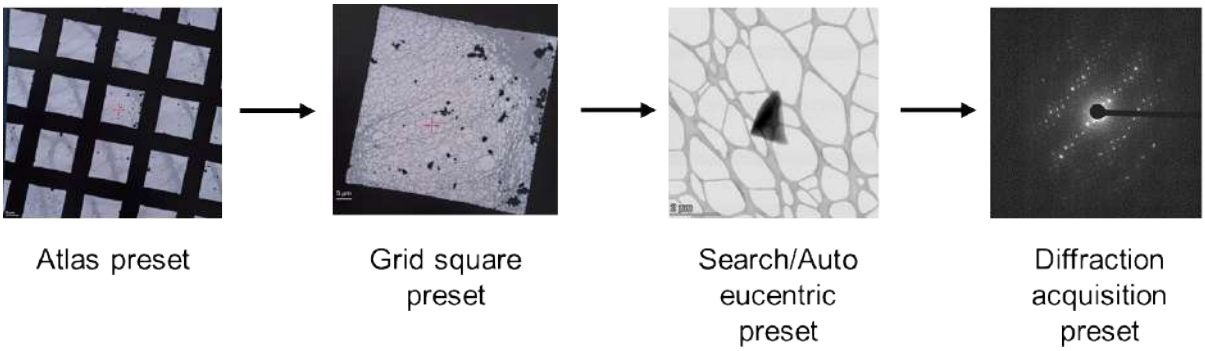


Fig. S3 Schematic workflow for continuous rotation MicroED data collection: Atlas preset (low-mag overview) → Grid square alignment → Auto-eucentric crystal centering → Diffraction preset for data acquisition, enabling atomic-resolution structure determination.

6. TEM tilt-series images

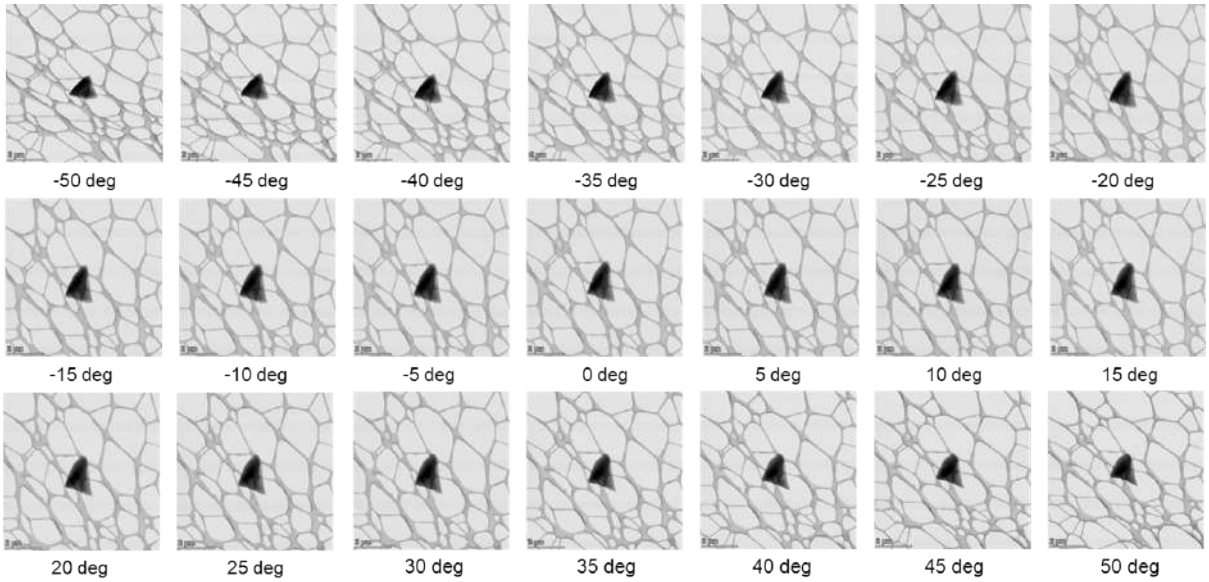


Fig. S4. Representative images of a $Cu_4(MNA)_2(DPPE)_2$ microcrystal captured at tilt angles from -50° to +50°.

Table S1. Structural comparison of $Cu_4(MNA)_2(DPPE)_2$ determined by SC-XRD and MicroED

$Cu_4(MNA)_2(DPPE)_2$		
	SC-XRD	**MicroED**
Unit cell	a=19.2367(15) Å b=21.2522(17) Å c=14.6063(11) Å α = 90° β = 90° γ = 90°	a = 18.910(4) Å b = 21.160(4) Å c = 14.440(3) Å α = 90.0° β = 90.0° γ = 90.0°
Space group	$Pna2_1$	$Pna2_1$
R1	0.0345	0.1372
wR2	0.0726	0.3296
GooF	1.077	0.866
Cu-Cu bond length	2.816Å, 2.759Å	2.743Å, 2.729Å
Cu-S bond length	2.836Å, 2.295Å, 2.249 Å, 2.937Å, 2.337 Å,2.211 Å	2.822Å, 2.280Å, 2.227 Å, 2.917Å, 2.325Å, 2.208 Å
Opposite S distance	4.161Å	4.128Å
Cu-S-Cu bond angle	74.64°, 76.59° 143.32°, 140.28° 71.89°,73.34°	72.32°, 73.98° 143.06°, 139.42° 73.60°,74.98°
Cu-P bond length	2.170Å, 2.221Å 2.212Å, 2.181Å	2.160Å, 2.209Å 2.205Å, 2.193Å
Cu-N bond length	2.016Å, 2.026Å	2.011Å, 2.037Å

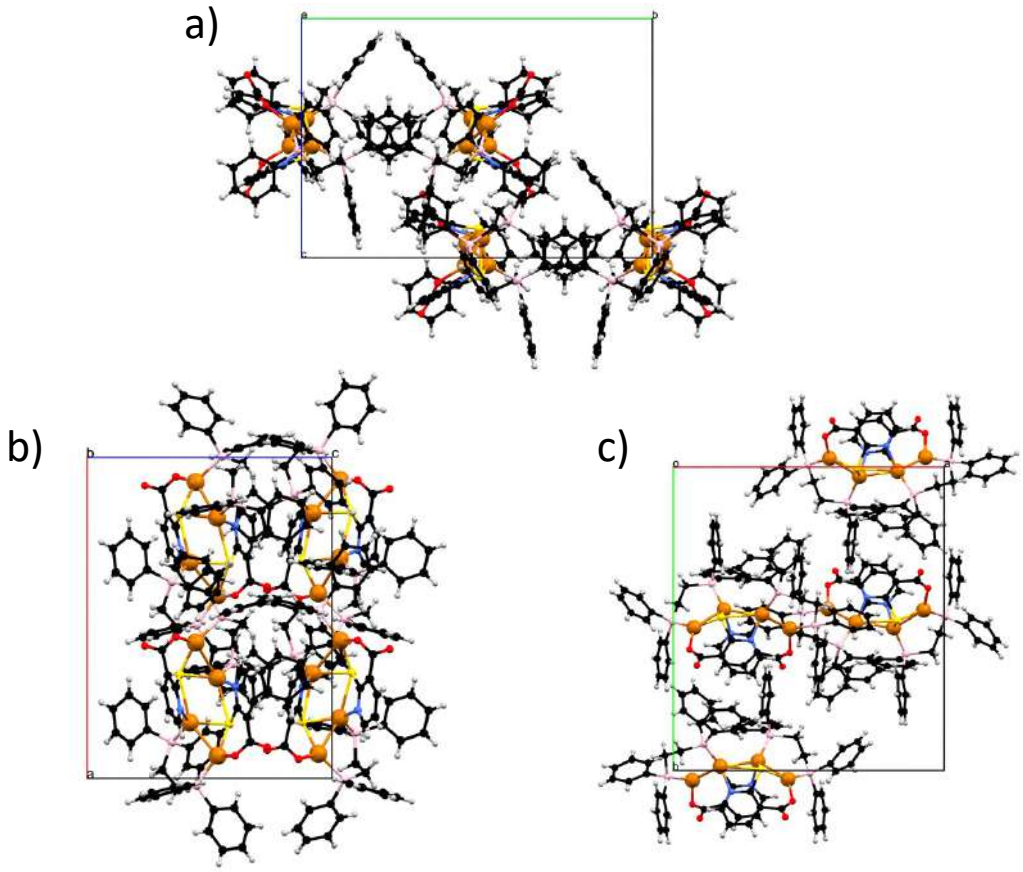


Fig. S5 Unit cell packing of $Cu_4(MNA)_2(DPPE)_2$ determined by MicroED along (a) *a*-axis, (b) *b*-axis, and (c) *c*-axis. Color code: Cu (orange), S (yellow), O (red), N (blue), P (pink), C (black), H (white).

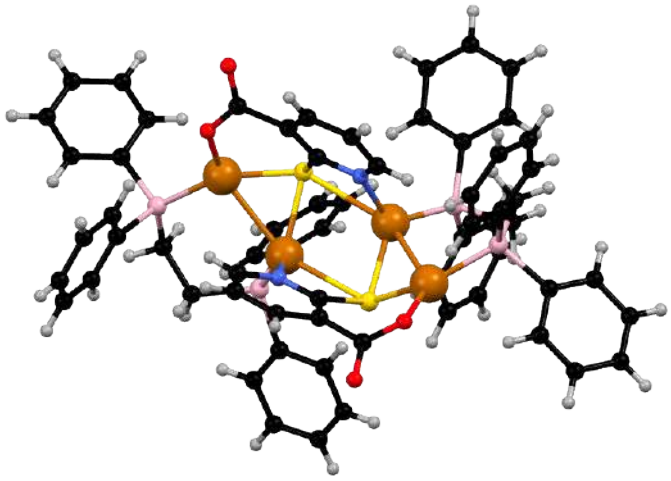


Fig. S6 Single-crystal X-ray structure of $Cu_4(MNA)_2(DPPE)_2$, illustrating the atomic arrangement and ligand coordination. Color code: Cu (orange), S (yellow), O (red), N (blue), P (pink), C (black), H (white).

Table S2. Structural comparison of $Cu_4(m_9\text{-CBT})_4$ determined by SC-XRD and MicroED.

$Cu_4(m_9\text{-CBT})_4$		
	SC-XRD	**MicroED**
Unit cell	a = 11.3989(7) Å b = 11.9482(7) Å c = 32.3144(19) Å α = 90° β = 91.213(2)° γ = 90°	a = 12.250(2) Å b = 13.320(3) Å c = 16.050(3) Å α = 97.18(3)° β = 110.76(3)° γ = 99.99(3)°
Space group	$P2_1/c$	P -1
R1	0.0986	0.1720
wR2	0.1819	0.4196
GooF	1.116	1.522
Cu-Cu bond length	2.682Å, 2.705Å 2.779Å, 2.692Å	2.673Å, 2.775Å 2.719Å, 2.725Å
Cu-Cu-Cu bond angle	89.91°, 89.75° 88.17°, 92.11°	89.72°, 89.83° 89.22°, 91.24°
Cu-S-Cu bond angle	76.48°, 77.29° 80.20°, 76.62°	79.59°, 76.55° 78.20°, 78.01°
Opposite S distance	5.415Å, 5.495Å	5.604Å, 5.463Å
Carborane B-S distance	1.86Å, 1.86Å 1.87Å, 1.91Å	1.86Å, 1.86Å, 1.86Å, 1.90Å

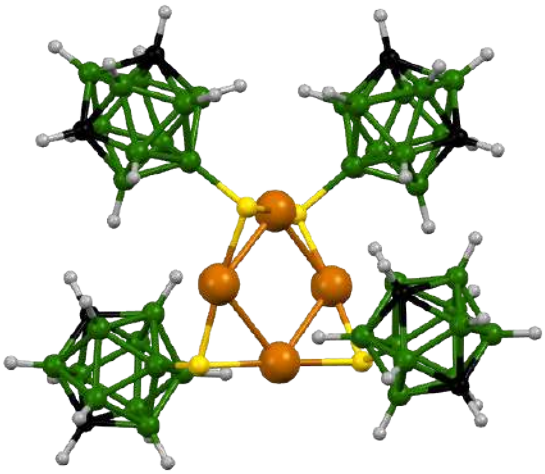


Fig. S7. Single-crystal X-ray structure of $Cu_4(m_9\text{-CBT})_4$, highlighting the square planar Cu_4 core and ligand coordination (toluene undetected in SC-XRD analysis). Color code: Cu (orange), S (yellow), B (green), C (black), H (white).

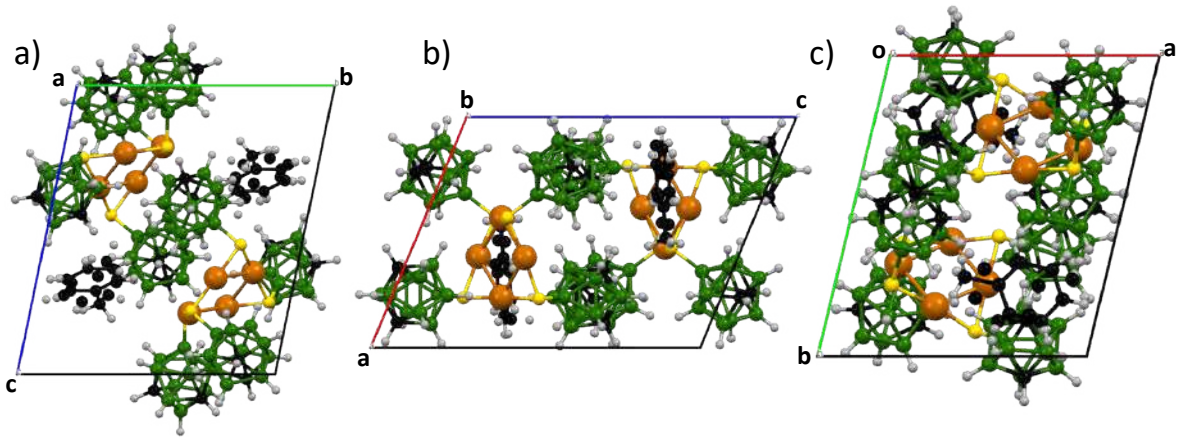


Fig. S8. MicroED-determined unit cell packing of $Cu_4(m_9\text{-CBT})_4$ along (a) *a*-axis, (b) *b*-axis, and (c) *c*-axis. Color code: Cu (orange), S (yellow), B (green), C (black), H (white).

Table S3. Structural comparison of $Cu_4(o_9\text{-CBT})_4$ determined by SC-XRD and MicroED

	$Cu_4(o_9\text{-CBT})_4$		
	SC-XRD	**MicroED**	**MicroED after solvent vapor exposure**
Unit cell	a = 11.434(6) Å b = 11.434(6) Å c = 29.439(16) Å α = 90° β = 90° γ = 120°	a = 11.310(2) Å b = 11.310(2) Å c = 29.080(6) Å α = 90.0° β = 90.0° γ = 120.0°	a = 11.300(2) Å b = 11.300(2) Å c = 29.050(6) Å α= 90.0° β= 90.0° γ = 120.0°
Space group	$P3_121$	$P\,3_22\,1$	$P\,3_22\,1$
R1	0.0513	0.1278	0.1271
wR2	0.1266	0.3409	0.3295
GooF	1.121	1.070	1.142
Cu-Cu bond length	2.684Å, 2.684Å 2.728Å, 2.728Å	2.686Å, 2.686Å 2.662Å, 2.662Å	2.667Å, 2.667Å 2.698Å, 2.698Å
Cu-Cu-Cu bond angle	87.29°, 93.58° 85.54°, 93.58°	85.48°, 94.04° 86.44°, 94.04°	85.42°, 93.95°, 86.67°, 93.95°
Cu-S-Cu bond angle	76.58°, 78.13° 78.13°, 76.58°	76.99°, 76.99° 75.78°, 75.78°	76.37°,76.37° 78.08°, 78.08°
Opposite S distance	5.540Å, 5.540Å	5.542Å,5.542Å	5.503Å, 5.503Å
Carborane B-S distance	1.88Å, 1.88Å 1.89Å, 1.89Å	1.85Å, 1.85Å 1.88Å, 1.88Å	1.86Å, 1.86Å 1.85Å, 1.85Å

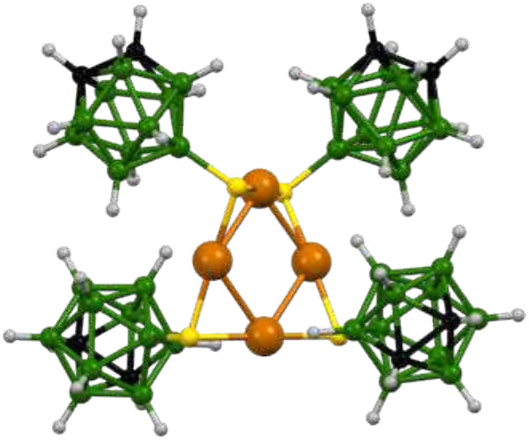


Fig. S9. Single crystal X-ray structure of $Cu_4(o_9\text{-CBT})_4$. Color code: Cu (orange), S (yellow), B (green), C (black), H (white).

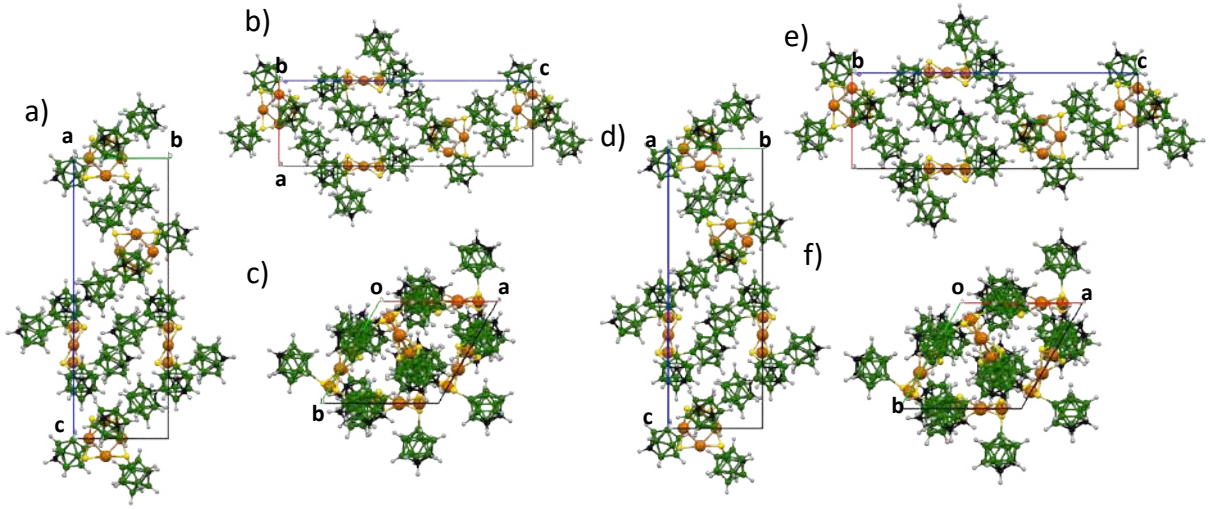


Fig. S10. MicroED analysis of $Cu_4(o_9\text{-CBT})_4$ unit cell packing. (a–c) Initial crystalline state and (d–f) post-solvent recrystallization viewed along *a*-, *b*-, and *c*-axes, respectively. Identical packing arrangements confirm structural restoration. Color code: Cu (orange), S (yellow), B (green), C (black), H (white).

Table S4. MicroED and SC-XRD - crystal data and structure refinement for $Cu_4(MNA)_2(DPPE)_2$

	MicroED	*SC-XRD
Empirical formula	C64 H54 Cu4 N2 O4 P4 S2	C64 H54 Cu4 N2 O4 P4 S2
Formula weight	1357.25	1357.25
Temperature	77(2) K	173(2) K
Crystal system	Orthorhombic	Orthorhombic
Space group	P n a 2_1	P n a 2_1
a (Å°)	18.910(4) Å	19.2367(15) Å
b (Å°)	21.160(4) Å	21.2522(17) Å
c (Å°)	14.440(3) Å	14.6063(11) Å
α (°)	90°	90°
β (°)	90°	90°
γ (°)	90°	90°
V (Å°)^3	5778(2) Å^3	5971.4(8) Å^3
Z	4	4
Density (cal. Mg/m^3)	1.560 Mg/m3	1.510 Mg/m3
Absorption coefficient	0.000 mm-1	1.632 mm-1
F(000)	1024	2768
Theta range for data collection	0.053 to 0.705°	3.064 to 28.301°
Index ranges	-23<=h<=23, -26<=k<=26, -18<=l<=18	-25<=h<=25, -28<=k<=28, -19<=l<=19
Reflections collected	46512	283464
Independent reflections	11692 [R(int) = 0.1825]	14836 [R(int) = 0.0908]
Completeness to theta	99.8 %	99.7 %
Extinction coefficient	1487(102)	n/a
Data / restraints / parameters	11692 / 733 / 722	14836 / 1 / 722
Goodness-of-fit on F^2	0.866	1.077
Final R indices [I>2sigma(I)]	R1 = 0.1372, wR2 = 0.3296	R1 = 0.0345, wR2 = 0.0726
R indices (all data)	R1 = 0.1587, wR2 = 0.3492	R1 = 0.0470, wR2 = 0.0783
Largest diff. peak and hole	0.264 and -0.186 e.Å^{-3}	0.770 and -0.391 e.Å^{-3}
CCDC No.	2391649	2339995

Table S5. MicroED and SC-XRD - crystal data and structure refinement for $Cu_4(o_9\text{-CBT})_4$

	MicroED	MicroED after solvent vapor exposure	*SC-XRD
Empirical formula	C8 H44 B40 Cu4 S4	C8 H44 B40 Cu4 S4	C8 H44 B40 Cu4 S4
Formula weight	955.23	955.23	955.23
Temperature	77(2) K	77(2) K	296(2) K
Crystal system	Trigonal	Trigonal	Trigonal
Space group	P 3_2 2 1	P 3_2 2 1	P 3_1 2 1
a (Å°)	11.310(2) Å	11.300(2) Å	11.4344(6) Å
b (Å°)	11.310(2) Å	11.300(2) Å	11.4344(6) Å
c (Å°)	29.080(6)	29.050(6) Å	29.4398(16) Å
α (°)	90.00	90.00	90.00
β (°)	90.00	90.00	90.00
γ (°)	120.00	120.00	120.00
V (Å°)^3	3221.4(13) Å^3	3212.4(13) Å^3	3333.4(4) Å^3
Z	3	3	3
Density (cal. Mg/m^3)	1.477 Mg/m^3	1.481 Mg/m^3	1.428 Mg/m^3
Absorption coefficient	0.000 mm^{-1}	0.000 mm^{-1}	2.091 mm^{-1}
F(000)	594	594	1416
Theta range for data collection	0.058 to 0.627°	0.058 to 0.628°	2.922 to 26.057°
Index ranges	-9<=h<=10, -12<=k<=12, -32<=l<=32	-12<=h<=12, -12<=k<=12, -32<=l<=32	-14<=h<=13, -14<=k<=14, -36<=l<=36
Reflections collected	7717	19119	64165
Independent reflections	3080 [R(int) = 0.1500]	3088 [R(int) = 0.2564]	4384 [R(int) = 0.0563]
Completeness to theta	99.7 %	99.6 %	99.6 %
Extinction coefficient	505(72)	656(55)	n/a
Data / restraints / parameters	3080 / 584 / 255	3088 / 956 / 255	4384/0/255
Goodness-of-fit on F^2	1.070	1.142	1.121
Final R indices [I>2sigma(I)]	R1 = 0.1278, wR2 = 0.3409	R1 = 0.1271, wR2 = 0.3295	R1 = 0.0513, wR2 = 0.1266
R indices (all data)	R1 = 0.1890, wR2 = 0.3780	R1 = 0.1751, wR2 = 0.3598	R1 = 0.0570, wR2 = 0.1305
Largest diff. peak and hole	0.172 and -0.158 e.Å^{-3}	0.187 and -0.150 e.Å^{-3}	1.205 and -0.613 e.Å^{-3}
CCDC No.	2391700	2443461	2192348

Table S6. MicroED and SC-XRD - crystal data and structure refinement for $Cu_4(m_9\text{-CBT})_4$

	MicroED	*SC-XRD
Empirical formula	C15 H52 B40 Cu4 S4	C15 H52 B40 Cu4 S4
Formula weight	1047.37	955.23
Temperature	77	296(2)
Crystal system	Triclinic	Monoclinic
Space group	P -1	$P2_1/c$
a (Å°)	12.250(2) Å	11.3989(7) Å
b (Å°)	13.320(3) Å	11.9482(7) Å
c (Å°)	16.050(3) Å	32.3144(19) Å
α (°)	97.18(3)°	90°
β (°)	110.76(3)°	91.213(2)°
γ (°)	99.99(3)°	90°
V (Å°)^3	2361.7(9) Å^3	4400.1(5) Å^3
Z	2	4
Density (cal. Mg/m^3)	1.473 Mg/m3	1.442 Mg/m3
Absorption coefficient	0.000 mm-1	2.112 mm-1
F(000)	440	1888
Theta range for data collection	0.038 to 0.626°	3.044 to 23.439°
Index ranges	-13<=h<=13, -14<=k<=14, -17<=l<=17	-12<=h<=12, -13<=k<=13, -36<=l<=36
Reflections collected	23335	54022
Independent reflections	6189 [R(int) = 0.2364]	6415 [R(int) = 0.1819]
Completeness to theta	91.2 %	99.2 %
Extinction coefficient	3093(18)	n/a
Data / restraints / parameters	6189 / 1542 / 657	6415/298/505
Goodness-of-fit on F^2	1.522	1.116
Final R indices [I>2sigma(I)]	R1 = 0.1720, wR2 = 0.4196	R1 = 0.0986, wR2 = 0.1819
R indices (all data)	R1 = 0.2457, wR2 = 0.4590	R1 = 0.1808, wR2 = 0.2141
Largest diff. peak and hole	0.344 and -0.234 e.Å^{-3}	0.484 and -0.429 e.Å^{-3}
CCDC No.	2391697	2192353

Table S7. Atomic coordinates (x 10^4) and equivalent isotropic displacement parameters (Å^{2}x 10^3) for **MicroED structure of $Cu_4(MNA)_2(DPPE)_2$**. U(eq) is defined as one third of the trace of the orthogonalized U^{ij} tensor.

	x	y	z	U(eq)
Cu(1)	4299(2)	5325(3)	5331(3)	29(1)
Cu(2)	3268(2)	4866(2)	4193(3)	24(1)
Cu(3)	1873(2)	4700(2)	5306(3)	24(1)
Cu(4)	763(2)	5287(3)	4434(3)	27(1)
C(1)	3865(7)	6286(8)	6661(11)	25(3)
C(2)	3094(7)	6107(8)	6526(10)	22(3)
C(3)	2606(7)	6551(8)	6820(11)	29(3)
C(4)	1916(8)	6484(9)	6744(12)	36(4)
C(5)	1685(7)	5916(8)	6317(12)	32(4)
C(6)	2812(7)	5536(7)	6137(10)	23(3)
C(7)	1003(8)	6265(9)	3060(11)	31(4)
C(8)	1792(7)	6221(8)	3295(12)	30(3)
C(9)	2211(8)	6764(8)	3151(13)	36(4)
C(10)	2924(9)	6786(9)	3366(15)	49(5)
C(11)	3215(7)	6275(8)	3700(10)	27(3)
C(12)	2154(7)	5703(7)	3617(10)	22(3)
C(13)	5364(9)	5864(8)	3731(11)	31(3)
C(14)	5242(8)	6469(8)	4109(11)	34(4)
C(15)	5281(10)	6972(9)	3553(11)	40(4)
C(16)	5462(8)	6956(8)	2635(11)	31(3)
C(17)	5610(9)	6346(8)	2288(11)	32(3)
C(18)	5556(9)	5823(9)	2798(11)	36(4)
C(19)	5987(7)	5118(8)	5170(11)	28(3)
C(20)	6648(7)	5372(9)	4966(14)	38(4)
C(21)	7243(8)	5282(9)	5528(12)	41(4)
C(22)	7160(10)	4909(11)	6338(15)	53(5)
C(23)	6527(9)	4643(9)	6570(11)	40(4)
C(24)	5928(10)	4755(9)	6001(12)	40(4)
C(25)	5308(7)	4505(8)	3722(10)	27(3)
C(26)	4738(7)	4371(7)	3065(10)	23(3)
C(27)	4038(6)	3453(7)	4170(10)	21(3)

C(28)	4624(8)	3037(8)	4084(13)	40(4)
C(29)	4666(9)	2499(10)	4622(12)	43(5)
C(30)	4199(8)	2368(8)	5304(12)	38(4)
C(31)	3619(7)	2768(8)	5412(11)	31(3)
C(32)	3548(8)	3315(8)	4858(10)	31(4)
C(33)	3495(8)	3728(7)	2454(9)	21(3)
C(34)	3909(8)	3407(9)	1786(11)	36(4)
C(35)	3581(9)	3028(9)	1184(12)	41(4)
C(36)	2836(9)	2986(8)	1068(12)	39(4)
C(37)	2415(8)	3320(9)	1722(12)	35(4)
C(38)	2765(8)	3685(8)	2366(11)	32(4)
C(39)	1548(8)	3090(7)	5375(10)	27(3)
C(40)	1715(9)	3109(9)	4436(12)	40(4)
C(41)	1700(10)	2516(10)	3955(13)	51(5)
C(42)	1586(9)	1944(9)	4402(11)	39(4)
C(43)	1473(8)	1937(9)	5303(11)	35(3)
C(44)	1424(10)	2500(8)	5820(11)	41(4)
C(45)	1663(8)	3667(9)	7102(10)	29(3)
C(46)	2386(9)	3671(10)	7320(13)	42(5)
C(47)	2585(10)	3552(9)	8219(11)	38(4)
C(48)	2109(10)	3435(10)	8941(14)	48(5)
C(49)	1407(10)	3438(9)	8733(12)	44(4)
C(50)	1170(8)	3542(8)	7796(10)	28(3)
C(51)	450(7)	3904(7)	5953(10)	22(3)
C(52)	175(7)	4515(8)	6356(10)	25(3)
C(53)	-807(9)	4779(9)	4943(12)	39(4)
C(54)	-1234(6)	4290(7)	5319(12)	28(3)
C(55)	-1804(7)	4058(9)	4826(12)	34(4)
C(56)	-1932(9)	4298(9)	3953(11)	39(4)
C(57)	-1566(9)	4805(10)	3605(13)	47(5)
C(58)	-992(7)	5028(8)	4078(10)	27(3)
C(59)	-291(7)	5778(7)	6145(10)	22(3)
C(60)	-460(10)	5784(10)	7073(12)	45(4)
C(61)	-592(12)	6310(11)	7611(12)	53(5)
C(62)	-517(9)	6882(10)	7161(12)	42(4)
C(63)	-301(8)	6928(9)	6234(12)	37(4)
C(64)	-174(10)	6396(8)	5702(12)	41(4)
N(1)	2124(6)	5488(7)	6046(9)	23(2)

N(2)	2863(6)	5704(6)	3807(8)	19(2)
O(1)	4297(6)	6114(7)	6042(10)	32(3)
O(2)	4025(6)	6579(7)	7341(9)	31(3)
O(3)	596(6)	6015(8)	3627(10)	40(4)
O(4)	870(7)	6541(7)	2351(9)	32(3)
S(1)	3300(3)	4890(4)	5802(5)	22(2)
S(2)	1761(4)	4951(4)	3778(5)	25(2)
P(1)	5224(4)	5204(4)	4472(6)	26(2)
P(2)	-33(4)	5085(4)	5497(5)	23(2)
P(3)	3869(4)	4123(4)	3463(5)	22(2)
P(4)	1423(4)	3839(4)	5934(5)	25(2)

Table S8. Atomic coordinates (x 10^4) and equivalent isotropic displacement parameters (Å^{2}x 10^3) for **MicroED structure of Cu_4(o_9-CBT)$_4$ before grinding** U(eq) is defined as one third of the trace of the orthogonalized U^{ij} tensor.

	x	y	z	U(eq)
Cu(1)	10078(6)	6686(7)	3960(2)	39(1)
Cu(2)	10000	4932(8)	3333	41(2)
Cu(3)	10000	8391(8)	3333	37(2)
C(1)	8337(19)	1409(19)	4982(5)	48(4)
C(2)	9160(20)	1240(20)	4533(6)	58(4)
C(3)	4160(20)	5330(20)	3811(6)	65(4)
C(4)	4900(20)	6840(20)	4056(7)	73(5)
B(1)	10060(19)	4010(20)	4337(6)	35(4)
B(2)	9130(20)	2310(20)	4111(6)	43(4)
B(3)	10580(20)	2790(20)	4457(7)	57(4)
B(4)	10000(20)	2090(20)	5013(7)	61(5)
B(5)	10580(20)	3790(20)	4898(6)	57(4)
B(6)	9170(20)	2930(20)	5252(6)	59(5)
B(7)	7810(20)	2510(20)	4885(5)	42(4)
B(8)	9230(20)	4100(20)	4829(6)	50(4)
B(9)	8280(20)	3100(20)	4355(6)	38(4)
B(10)	7690(20)	1420(20)	4462(6)	41(4)
B(11)	7400(20)	7020(20)	3940(6)	40(4)
B(12)	6660(20)	6740(20)	3394(6)	46(4)
B(13)	6390(20)	7770(30)	3800(7)	61(4)
B(14)	6300(30)	7090(30)	4347(7)	63(5)
B(15)	6390(20)	5600(20)	4275(6)	43(4)
B(16)	6560(20)	5350(20)	3679(5)	40(4)
B(17)	4860(20)	4390(20)	3945(6)	50(4)
B(18)	4750(20)	5490(30)	4348(8)	64(5)
B(19)	5080(30)	6690(30)	3501(7)	66(5)
B(20)	5080(30)	5140(30)	3386(7)	61(5)
S(1)	11130(9)	5517(10)	3970(3)	43(2)
S(2)	9294(9)	8060(9)	4038(2)	42(2)

Table S9. Atomic coordinates (x 10^4) and equivalent isotropic displacement parameters ($Å^2$x 10^3) for **MicroED structure of Cu_4(o_9-CBT)$_4$ after solvent vapour exposure**. U(eq) is defined as one third of the trace of the orthogonalized U^{ij} tensor.

	x	y	z	U(eq)
Cu(1)	8394(6)	10000	6667	37(2)
Cu(2)	6671(6)	10063(5)	6037(2)	45(1)
Cu(3)	4923(7)	10000	6667	44(2)
B(1)	7009(18)	7408(16)	6066(7)	40(3)
B(2)	5526(17)	6353(17)	5715(7)	44(4)
B(3)	5334(18)	6503(17)	6319(7)	43(3)
B(4)	6761(17)	6665(17)	6614(7)	41(3)
B(5)	7856(18)	6499(18)	6224(7)	47(4)
B(6)	7078(19)	6318(19)	5664(8)	51(4)
B(7)	5531(18)	4790(18)	5638(8)	54(4)
B(8)	4457(19)	4918(17)	6051(7)	45(4)
B(9)	5135(19)	5071(18)	6606(7)	48(4)
B(10)	6678(18)	5135(17)	6530(8)	51(4)
B(11)	4005(17)	10101(17)	5657(7)	41(3)
B(12)	3850(19)	10632(19)	5109(7)	55(4)
B(13)	2707(18)	10490(20)	5572(7)	53(4)
B(14)	2298(18)	9100(19)	5899(8)	51(4)
B(15)	3102(15)	8280(17)	5637(6)	40(3)
B(16)	2454(19)	7794(19)	5100(7)	49(4)
B(17)	1377(17)	7661(18)	5540(7)	46(4)
B(18)	2070(20)	10010(20)	5011(8)	66(4)
B(19)	2840(20)	9160(20)	4756(8)	60(4)
B(20)	4039(19)	9180(20)	5163(7)	51(4)
C(1)	5324(16)	4110(14)	6188(7)	54(4)
C(2)	6841(17)	4858(17)	5957(7)	64(4)
C(3)	1364(17)	8321(17)	5022(7)	55(4)
C(4)	1204(17)	9114(17)	5483(7)	58(4)
S(1)	8023(7)	9283(6)	5963(3)	37(2)
S(2)	5509(8)	11119(8)	6033(3)	49(2)

Table S10. Atomic coordinates (x 10^4) and equivalent isotropic displacement parameters ($Å^2$x 10^3) for **MicroED structure of Cu_4(*m*$_9$-CBT)$_4$**. U(eq) is defined as one third of the trace of the orthogonalized U^{ij} tensor.

	x	y	z	U(eq)
Cu(1)	5633(3)	7585(4)	7663(2)	46(1)
Cu(2)	3957(3)	6191(3)	7887(2)	41(1)
Cu(3)	3917(3)	8333(3)	6471(2)	43(1)
Cu(4)	2180(3)	6921(4)	6666(2)	46(1)
B(1)	6692(11)	6271(12)	9095(8)	43(3)
B(2)	7350(14)	7469(14)	9778(9)	72(3)
B(3)	8254(11)	6703(15)	9456(9)	71(3)
B(4)	7693(12)	5443(14)	9496(8)	57(3)
B(5)	6480(12)	5378(14)	9831(9)	53(3)
B(6)	6280(13)	6704(15)	9996(9)	66(3)
B(7)	8817(15)	7425(17)	10573(10)	80(3)
B(8)	8980(12)	6189(17)	10407(10)	79(4)
B(9)	6976(12)	6066(14)	10906(9)	66(3)
B(10)	8540(13)	6638(15)	11268(9)	69(3)
B(11)	2295(10)	7425(12)	8616(8)	38(2)
B(12)	1032(10)	7949(12)	8478(8)	46(3)
B(13)	2271(11)	8663(12)	8338(8)	49(3)
B(14)	3581(10)	8529(13)	9187(9)	51(3)
B(15)	3103(11)	7623(13)	9814(8)	55(3)
B(16)	1529(11)	7299(13)	9343(8)	48(3)
B(17)	1510(11)	9322(12)	8930(8)	48(3)
B(18)	3088(12)	9605(15)	9394(9)	59(3)
B(19)	2300(13)	8218(13)	10349(9)	60(3)
B(20)	2285(12)	9496(13)	10083(9)	58(3)
B(21)	2184(10)	6431(11)	4766(7)	35(2)
B(22)	2190(11)	5220(11)	5087(9)	44(3)
B(23)	933(10)	5415(12)	4201(9)	45(3)
B(24)	1413(12)	4310(14)	4056(9)	52(3)
B(25)	2989(12)	4638(13)	4529(9)	56(3)
B(26)	3451(10)	5896(12)	4949(9)	48(3)
B(27)	3004(11)	6529(13)	4046(8)	46(2)
B(28)	1427(11)	6253(12)	3577(8)	46(3)

B(29)	2153(11)	4361(13)	3310(9)	51(3)
B(30)	2207(12)	5640(13)	3055(9)	57(3)
B(31)	6642(10)	9426(12)	6881(8)	46(3)
B(32)	7251(13)	8408(16)	6457(9)	66(3)
B(33)	8202(12)	9423(15)	7377(9)	68(4)
B(34)	7729(11)	10607(14)	7131(9)	57(3)
B(35)	6464(11)	10236(14)	6115(9)	55(3)
B(36)	6192(12)	8966(14)	5704(9)	61(3)
B(37)	8668(13)	8972(16)	6494(11)	75(4)
B(38)	8948(12)	10346(15)	6909(9)	68(3)
B(39)	6975(12)	9765(14)	5273(9)	61(3)
B(40)	8484(12)	9849(13)	5753(9)	56(3)
C(1)	7607(13)	7347(13)	10844(8)	72(3)
C(2)	7831(10)	5438(12)	10569(7)	57(3)
C(3)	1101(9)	8444(11)	9520(7)	49(3)
C(4)	3475(10)	8946(13)	10184(7)	65(3)
C(5)	3356(10)	5409(12)	3920(8)	57(3)
C(6)	1040(10)	4934(11)	3217(8)	53(3)
C(7)	7436(11)	8785(12)	5524(8)	60(3)
C(8)	7870(10)	10682(12)	6164(8)	54(2)
S(1)	5666(4)	6017(5)	7865(3)	44(2)
S(2)	2165(4)	6231(5)	7816(3)	41(1)
S(3)	2116(4)	7628(5)	5509(3)	39(1)
S(4)	5637(4)	9169(5)	7507(3)	44(1)
C(9)	6099(10)	7614(16)	2890(11)	67(5)
C(10)	6703(15)	6885(13)	3264(14)	67(6)
C(11)	7951(15)	7129(14)	3647(12)	74(6)
C(12)	8595(10)	8102(16)	3657(12)	75(6)
C(13)	7990(15)	8831(13)	3283(15)	72(5)
C(14)	6742(15)	8587(15)	2899(13)	69(5)
C(15)	4757(15)	7360(20)	2428(16)	68(6)
C(9')	7573(13)	7651(17)	3393(12)	48(5)
C(10')	6530(17)	6889(14)	3177(16)	55(7)
C(11')	5415(13)	7096(15)	2738(15)	63(6)
C(12')	5344(13)	8064(17)	2515(11)	45(5)
C(13')	6388(17)	8826(14)	2731(16)	62(6)
C(14')	7502(14)	8620(15)	3170(15)	54(6)
C(15')	8775(19)	7440(30)	3901(18)	56(7)

References:

1 J. Plešek and S. Heřmánek, *Collect. Czechoslov. Chem. Commun.*, 1981, **46**, 687–692.
2 J. Plešek, Z. Janoušek and S. Heřmánek, *Collect. Czechoslov. Chem. Commun.*, 1978, **43**, 1332–1338.
3 S. Duary, A. Jana, A. Das, S. Acharya, A. R. Kini, J. Roy, A. K. Poonia, D. K. Patel, V. Yadav, P. K. S. Antharjanam, B. Pathak, A. Kumaran Nair Valsala Devi and T. Pradeep, *Inorg. Chem.*, 2024, **63**, 18727–18737.
4 A. Jana, M. Jash, W. Ahmed Dar, J. Roy, P. Chakraborty, G. Paramasivam, S. Lebedkin, K. Kirakci, S. Manna, S. Antharjanam, J. Machacek, M. Kucerakova, S. Ghosh, K. Lang, M. M. Kappes, T. Base and T. Pradeep, *Chem. Sci.*, 2023, **14**, 1613–1626.
5 J. Li, H. Z. Ma, G. E. Reid, A. J. Edwards, Y. Hong, J. M. White, R. J. Mulder and R. A. J. O'Hair, *Chem. Weinh. Bergstr. Ger.*, 2018, **24**, 2070–2074.

ACS APPLIED NANO MATERIALS

www.acsanm.org Article

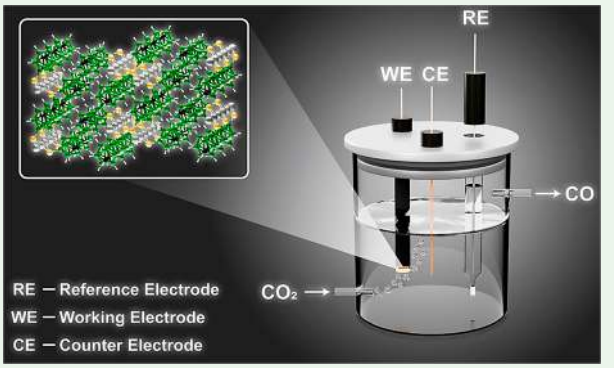
A Silver-Chalcogenide Nanomaterial Enveloped with a Carborane-Thiolate Shell for the Electroreduction of CO_2 to CO

Arijit Jana, Zhengyuan Li, Amoghavarsha Ramachandra Kini, Vivek Yadav, Akhil S. Nair, Astrid Campos Mata, Jingjie Wu, Jan Macháček, Tomas Base,* Biswarup Pathak,* Soumyabrata Roy,* and Thalappil Pradeep*

Cite This: *ACS Appl. Nano Mater.* 2025, 8, 13754−13762 Read Online

ACCESS | Metrics & More | Article Recommendations | Supporting Information

ABSTRACT: Electrocatalytic CO_2 reduction using atomically precise nanomaterials has garnered significant research interest, owing to their controllable molecular structures. Here, we have synthesized an electrocatalyst composed of single crystals having a one-dimensional assembly of silver atoms bridged by sulfur atoms of *meta*-carborane-9-thiolates. The molecular structure of the framework was further characterized through high-resolution ESI-MS, which exhibited silver- and carborane-thiolate-containing ions originating from the fragmentation of the framework. This thermally stable solid acted as an efficient catalyst for the electrocatalytic conversion of CO_2 to CO with a Faradaic efficiency of 85 ± 3%. In situ Raman studies provided experimental verification of binding of CO_2 to the framework. First-principles density functional theory calculations confirmed the feasible adsorption of CO_2 with the Ag chains, highlighting its favorable interaction with the catalyst. Furthermore, free energy calculations revealed the rate-determining step of the conversion process to be the formation of *COOH. This study presents an efficient electrocatalyst featuring a one-dimensional silver-chalcogenide framework.



KEYWORDS: *silver-chalcogenide, decarboxylation, solvothermal synthesis, one-dimensional solid, carborane-thiol, CO_2 electroreduction*

INTRODUCTION

The increase in atmospheric CO_2 levels has significantly contributed to global warming, leading to various environmental and societal challenges. Therefore, finding effective methods for CO_2 capture and utilization has become a global priority.[1,2] Techniques such as electrochemical,[3] thermochemical,[4] photochemical,[5] and biochemical catalytic reduction[6] of CO_2 offer promising pathways for converting CO_2 into valuable chemicals and fuels. Among these methods, electrocatalytic CO_2 reduction has gained considerable attention due to its wide range of possible products, the use of water as a key reagent, and its compatibility with renewable electricity sources.[7] Researchers have explored various nano- and microscale materials as catalysts for electrochemical CO_2 reduction, including single-atom catalysts,[8] nanoparticles,[9] nanoclusters,[10] metal−organic frameworks,[11] intermetallic compounds,[12] transition metal dichalcogenides,[13] and perovskites.[14] These materials serve as effective and durable catalysts in the conversion process. Significant efforts have been made to enhance catalyst performance by carefully controlling their size, shape, and composition, which allows for the fine-tuning of their electronic structures.[15−18] Additionally, the choice of solvent and electrolyte type affects catalytic efficiency by influencing CO_2 desolvation and mass transport to the electrodes.[19,20] All these advancements aim to improve overall reaction efficiency and selectivity by designing active catalysts, thereby contributing to the development of effective CO_2 reduction technologies.[21−23]

Atomically precise silver nanomaterials, particularly ligand-protected nanoclusters,[24] nanoparticles,[25] nanowires,[26] nanorings,[27] nanocubes,[28] nanoprisms,[29] and nanocomposites[30] are emerging as active catalysts for electrochemical reduction reactions. Compared to bulk silver metal, nanostructural features like exposed metal atoms, high index facets, and nanoscale pores have enhanced selective CO_2 reduction by promoting active sites that favor specific reactions.[31] In CO_2 electroreduction, a majority of silver-based nanosystems can favor the formation of carbon monoxide (CO) as an end product, thus highlighting the importance of tailoring catalyst design.[32] CO, a key component of syngas, has significant

Received: April 4, 2025
Revised: June 18, 2025
Accepted: June 19, 2025
Published: July 1, 2025



Downloaded via INDIAN INST OF TECH MADRAS on December 29, 2025 at 03:14:14 (UTC).
See https://pubs.acs.org/sharingguidelines for options on how to legitimately share published articles.

ACS Publications © 2025 American Chemical Society

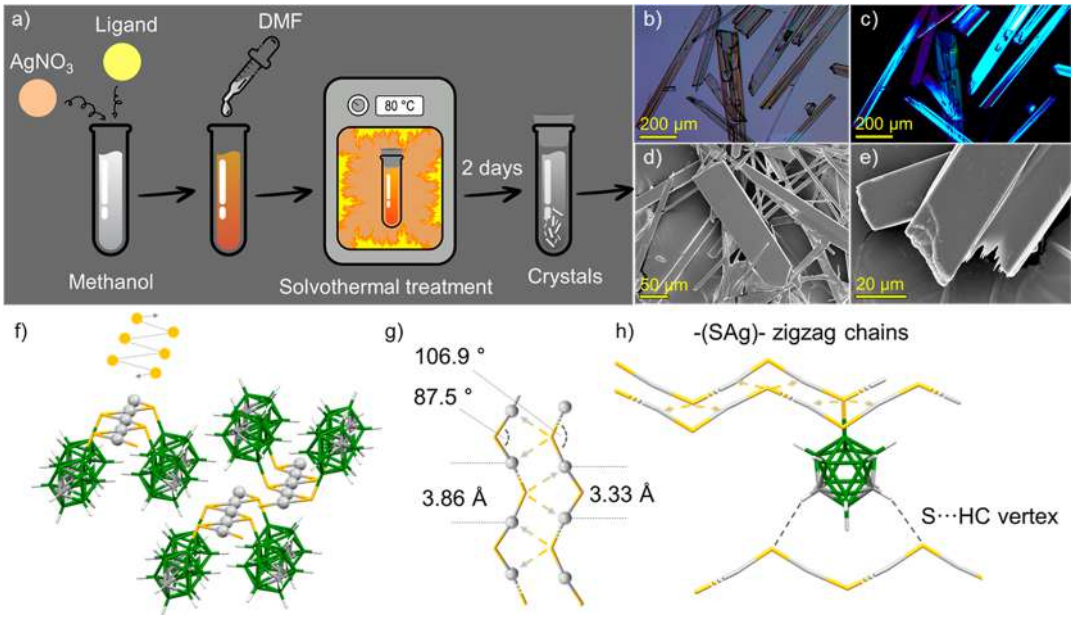


Figure 1. (a) Schematic representation of the synthesis of the Ag-CBT framework in DMF/methanol (3:1, v/v) solvent mixture using a decarboxylation-solvothermal synthesis. Optical micrographs of the as-synthesized microcrystals (b) without polarization and (c) with polarization. FESEM micrographs of the crystals at (d) lower and (e) higher resolution. (f) A small segment of the single-crystal supramolecular framework shows a linear arrangement of Ag atoms within a zigzag-shaped −(SAg)− chain. (g) A top view of two adjacent chains with the depiction of short contact S···Ag interactions pairing them together into a double-chain. (h) Interactions between sulfur atoms of one double-chain and positively charged carborane CH vertices from another, causing two double chains to pack into the 3D framework as depicted in (f). Color code: metallic gray = Ag, yellow = S, green = boron, gray = carbon, and white = hydrogen.

applications in producing synthetic fuels and chemical feedstock via the Fischer−Tropsch process and in the metal processing industry.[19] Specific structural types of silver-based nanocatalysts generate hydrogen gas as a side product along with CO during electrocatalysis of CO_2.[33,34] Therefore, achieving precise structural control is essential to fully harness the potential of nanostructured catalysts for the quantitative production of CO. From this perspective, monolayer-protected silver chalcogenides can offer a new category of precise nanomaterials with tremendous potential as selective CO_2 to the CO electrocatalyst.

Monolayer-protected metal chalcogenides typically consist of a layer of metal atoms or a metal-chalcogenide framework coated with thiol or selenol ligands. These systems can be based on both noble metals, such as gold (Au), silver (Ag), and copper (Cu)[35,36] as well as non-noble metals like lead (Pb), iron (Fe), and tin (Sn).[37,38] Many of these materials exhibit a range of optical activities, characterized by their sharply defined multicolor emissions, in-plane anisotropic electron transport,[39,40] strong exciton stability, and significant electron−phonon coupling.[41,42] A monolayer of surface ligands is crucial for controlling the atomic packing and dimensional growth of these systems. One notable ligand, carborane-thiols, is built from a 12-vertex icosahedral heteroborane cluster, known for its unique geometry, three-dimensional aromaticity, and redox properties.[43−46] This cage-like molecule, along with its metal-containing derivatives, such as complexes,[47,48] clusters,[49−52] and metal−organic frameworks,[53,54] holds significant interest due to its wide-ranging applications in chemistry, biology, and materials science.[55−57] In contrast to these materials, carborane-thiolated silver chalcogenides are rarely mentioned in the literature as active electrocatalysts. As a result, this work focuses on the electroreduction of CO_2 utilizing a carborane-thiolated silver-chalcogenide framework (abbreviated as Ag-CBT).

RESULTS AND DISCUSSION

The Ag-CBT framework was synthesized in 85% yield using a solvothermal process. This process involved mixing silver nitrate ($AgNO_3$) with 1-carboxy-9-thiol-1,7-carborane (referred to as M_9-COOH) in a solvent mixture of dimethylformamide (DMF) and methanol (MeOH) at a volume ratio of 3:1. Figure 1a presents a schematic representation of the synthesis, and the detailed procedure can be found in the Experimental Section. Within 48 h of the solvothermal treatment (at 80 °C), rod-shaped single crystals were formed inside the hydrothermal container. Optical microscopic images of the yellow crystals, exhibiting defined optical polarization, are shown in Figure 1b,c. Scanning electron micrographs (see Figure 1d,e) further confirmed the rod-like shape of the crystals, which had smooth surfaces. Elemental analysis via Energy Dispersive Spectroscopy (EDS) revealed the presence of silver (Ag), sulfur (S), carbon (C), and boron (B) within the crystals (illustrated in Figure S1), consistent with their nominal composition.

Single-crystal X-ray diffraction analysis demonstrated that this framework crystallized in the monoclinic crystal system with the space group $P2_1/m$. The crystallographic refinement and structural parameters of the framework are shown in Tables S1−S4. To investigate the specific role of the M_9-COOH ligand in the synthesis of the Ag-CBT framework, we conducted a reference hydrothermal reaction using 9-thiol-1,7-carborane, referred to as M_9, which is a noncarboxylated derivative of M_9-COOH. This reaction resulted in the formation of hair-like solids, as shown in Figure S2. The powder X-ray diffraction pattern of these solids differed from that of the crystalline Ag-CBT framework, indicating that a

https://doi.org/10.1021/acsanm.5c01918
ACS Appl. Nano Mater. 2025, 8, 13754−13762

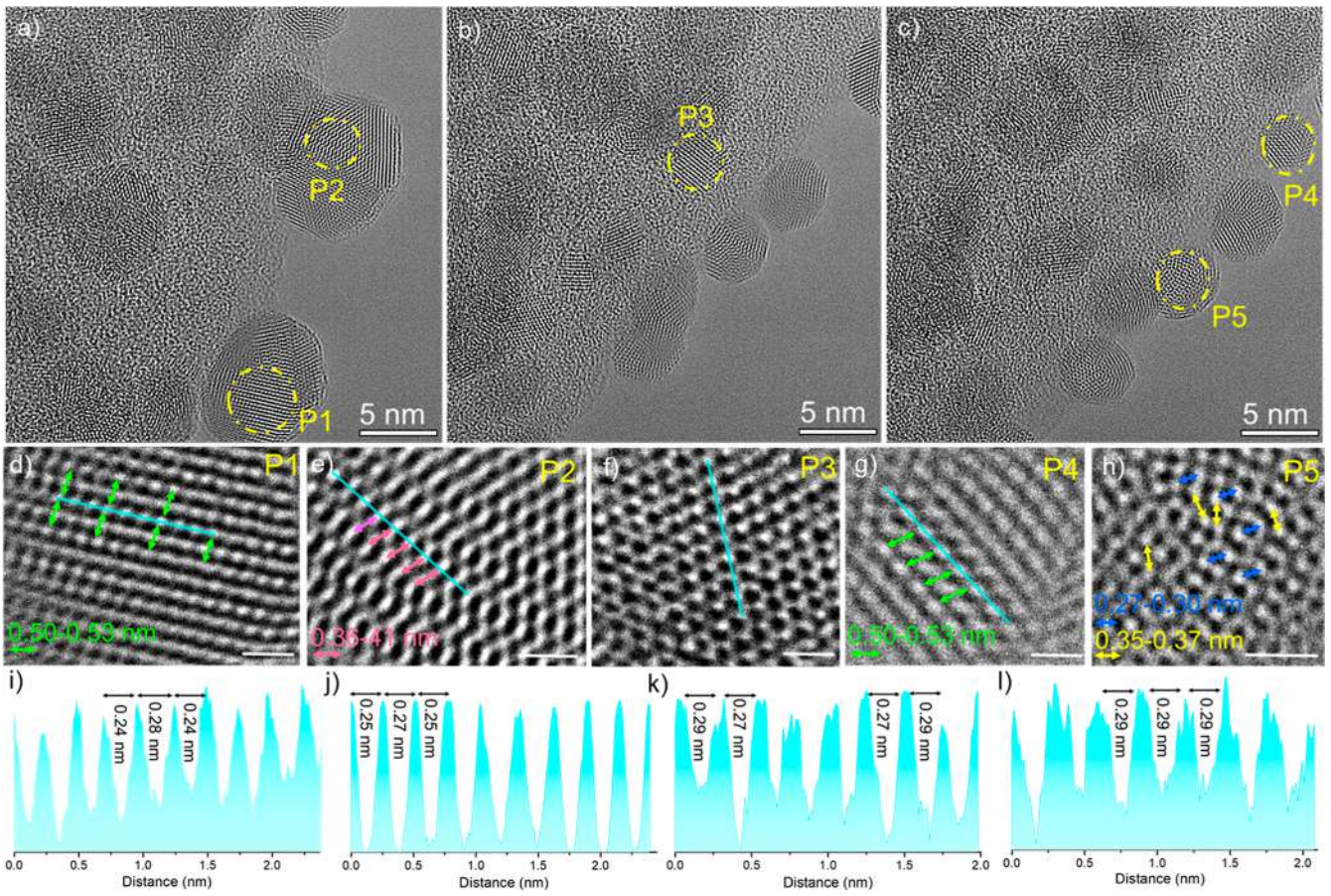


Figure 2. (a–c) Atomic resolution STEM images of three selected regions of the Ag-CBT crystallites. (d–h) Expanded view of the selected regions (marked as P1 to P5) showed linear assembly of Ag atoms in the framework (scale bar, 1 nm). Atomic density distribution in light blue marked lines of (i) P1, (j) P2, (k) P3, and (l) P4 regions.

different compound was formed by using the M_9 ligand (see Figure S3).

The supramolecular organization in single crystals of the Ag-CBT framework showed extended packing, primarily driven by interactions between silver and sulfur atoms (Figure 1f). These atoms formed zigzag −(SAg)− chains, with an interatomic distance of 4.79 Å between adjacent sulfur atoms. This arrangement was similar to the zigzag −(SH) chain reported for the supramolecular packing of the *para*-carborane cluster, which is an analogue of *para*-mercaptobenzoic acid.[58] Notably, in the −(SAg)− chain, half of the sulfur atoms participated in additional short-contact interactions with silver atoms from an adjacent −(SAg)− chain, resulting in the formation of a double-chain structure (Figure 1f,g). Meanwhile, the other half of the sulfur atoms engaged in short-contact interactions with positively charged hydrogen atoms from carborane C−H vertices in another double chain, thus linking the double chains into a three-dimensional supramolecular framework.

In this array, the angles between the Ag−S−Ag units alternated in one chain, measuring 106.9° and 87.53°. The corresponding Ag···Ag distances also alternated, with values of 3.86 and 3.33 Å, while the Ag−S distances were approximately 2.4 Å. The longer Ag···Ag distances suggested a weak argentophilic interaction, similar to what had been observed in other organo-thiolated silver-chalcogenide frameworks.[59−61] A more detailed analysis revealed that the two layers of these indefinite chains interlocked, forming an interesting U-shaped interlocking mechanism, as illustrated in Figure S4. In each interlocked unit, the Ag···Ag distance between the two complementary chains measured 13.50 Å, while the distance to the nearest adjacent Ag chain was 5.35 Å (Figure S5). The primary forces that held these chains together included short intralayer B−H···H−B interactions (ranging from 2.32 to 2.39 Å), as well as interlayer B−H···B (2.97−3.0 Å) and B···B (3.81 Å) van der Waals interactions, all derived from the carborane surroundings (see Figure S6). Additionally, we observed metal-centered interactions: Ag···S (3.16 Å), Ag···H−B (2.83 Å), and Ag···B (3.66 Å) between two neighboring chains also contributed to their extended packing (see Figure S7).

The phase purity of the solids synthesized through hydrothermal methods was confirmed by using powder X-ray diffraction (PXRD). The PXRD patterns displayed exact matching of various reflexes that corresponded to the simulated patterns derived from the single-crystal X-ray diffraction (SCXRD) data (see Figure S8).

Scanning transmission electron microscopy (STEM) investigations revealed a layered arrangement of silver atoms. Low-resolution STEM images indicated the formation of spherical crystallites at the outer periphery of the microcrystals (refer to Figure S9). At higher resolutions, we observed a chain of Ag atoms along the edges of the crystallites (Figure 2a−c). Upon closer examination, we identified a linear arrangement of silver (Ag) atoms in the P1, P2, P3, and P4 regions, as illustrated in Figure 2d−g. Similar arrangements were observed in various other locations. The interatomic distances between these Ag atoms ranged from 0.24 to 0.29 nm, as shown in the atomic

https://doi.org/10.1021/acsanm.5c01918
ACS Appl. Nano Mater. 2025, 8, 13754−13762

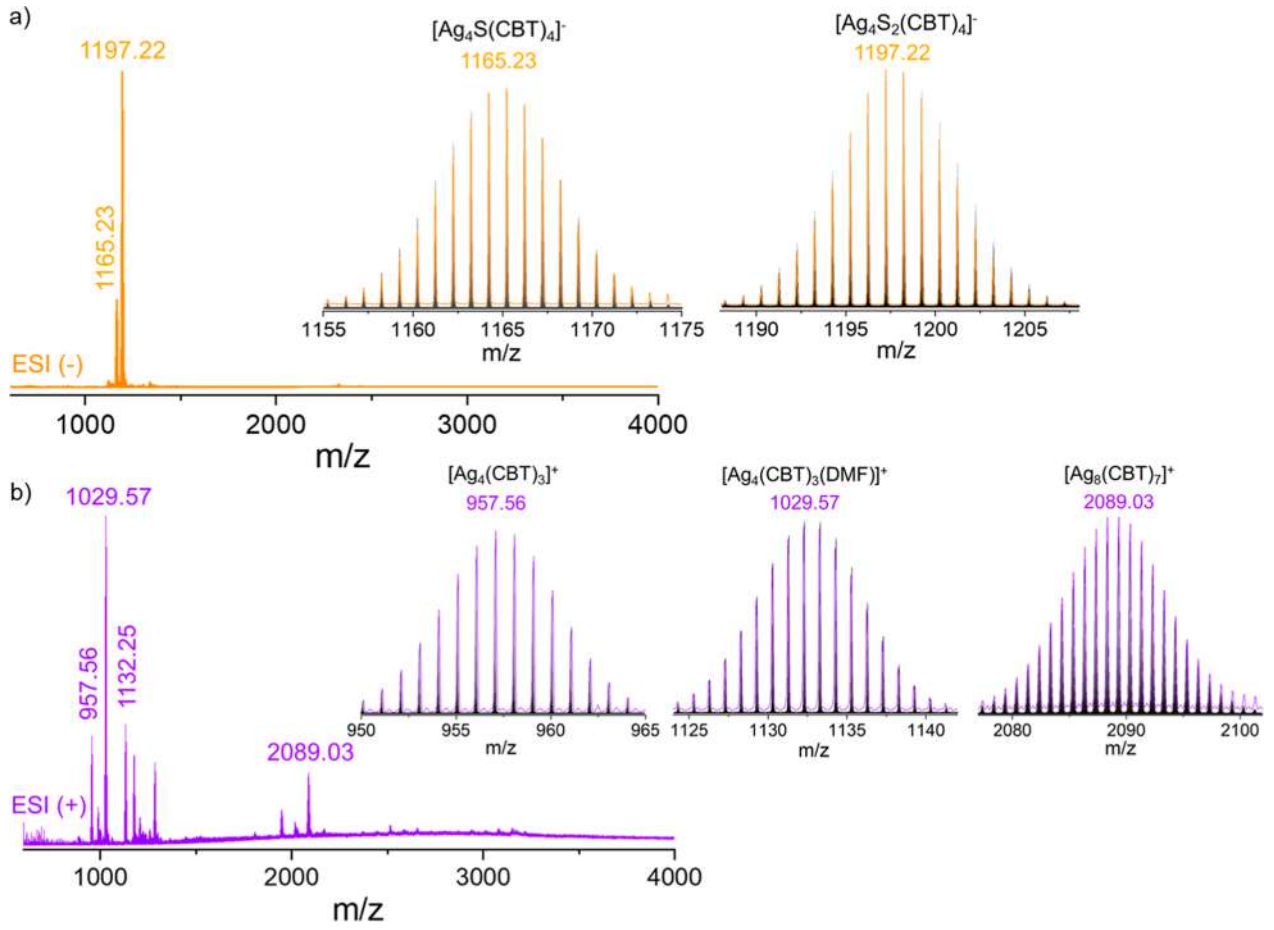


Figure 3. (a) Full range ESI-mass spectrum of the Ag-CBT framework in the negative-ion mode obtained after extraction of the molecular species in DMF. Inset shows the exact matching of the isotopic distribution of the respective fragments. (b) Positive-ion mode ESI-MS spectrum of the Ag-CBT framework. Inset shows the exact matching of the isotopic distribution of the species formed after fragmentation of the framework.

density distribution plots in Figure 2i–l. The slight variation in these distances may be attributed to damage caused by electron beam irradiation and the effects of mechanical exfoliation during sample preparation. Additionally, a random distribution of Ag atoms was also observed in the P5 region (illustrated in Figure 2h), with interatomic distances ranging from 0.27 to 0.30 nm and 0.35 to 0.37 nm. The interatomic distances of 0.35–0.37 nm closely match with the Ag···Ag distances of the framework. Further analysis revealed cross-diagonal distances of 0.50 to 0.53 nm for these Ag layers (P1 and P4 region), which correlated with the interlayer spacing of two nearest adjacent chains, obtained from SCXRD (shown in Figure S5). SCXRD and STEM analyses independently confirmed the unidirectional chain-like assembly of silver atoms within the framework.

The molecular composition of the Ag-CBT framework was analyzed using high-resolution electrospray ionization mass spectrometry (ESI-MS) with a Waters Synapt G2Si mass spectrometer (further details can be found in the Supporting Information). A small portion of the microcrystalline sample was ground in a mortar and then extracted with DMF through centrifugation after 20 min of ultrasonication. In the negative-ion mode ESI-MS, two prominent peaks were observed at m/z = 1165.23 and 1197.22, both with a charge state of 1-. These peaks corresponded to the molecular compositions of $[Ag_4S(CBT)_4]^-$ and $[Ag_4S_2(CBT)_4]^-$, respectively (as shown in Figure 3a).

In contrast, the positive-ion mode ESI-MS (Figure 3b) revealed several peaks with strong intensities, each exhibiting a monocationic charge state at m/z 957.56, 1029.57, and 1132.25. These peaks were identified as $[Ag_4(CBT)_3]^+$, $[Ag_4(CBT)_3(DMF)]^+$, and $[Ag_4(CBT)_4]^+$, respectively. Moreover, a significant peak at m/z 2089.03 (with a charge state of 1+) corresponded to the composition $[Ag_8(CBT)_7]^+$, which resulted from the combination of $[Ag_4(CBT)_3]$ and $[Ag_4(CBT)_4]$ fragments. All of these characteristic peaks correlated well with the one-dimensional framework structure.

The FT-IR and Raman spectroscopic measurements further confirmed the presence of carborane as surface envelopes within the Ag-CBT framework. The FT-IR spectrum of the Ag-CBT framework revealeds vibrational peaks at 3022 and 2599 cm^{-1}, corresponding to the C–H and B–H vibrational bands of the carboranes (see Figure S10). Additionally, we identified vibrational peaks at 1717 cm^{-1} (C═O stretching), 1286 cm^{-1} (C–O stretching), and 2878 cm^{-1} (O–H stretching) in the M_9-COOH ligand, which were absent in the Ag-CBT framework, thereby confirming the decarboxylation of the M_9-COOH ligand. The detection of the icosahedral $-C_2B_{10}H_{11}$ cage breathing vibrational mode at 725 cm^{-1} further supported the presence of carboranes within the Ag-CBT framework. Raman spectroscopic measurements revealed similar observations. The B–H spectral band of the M_9-COOH ligand, which initially exhibited three features at 2611, 2646, and 2672 cm^{-1}, was reduced to a single band centered at

https://doi.org/10.1021/acsanm.5c01918
ACS Appl. Nano Mater. 2025, 8, 13754–13762

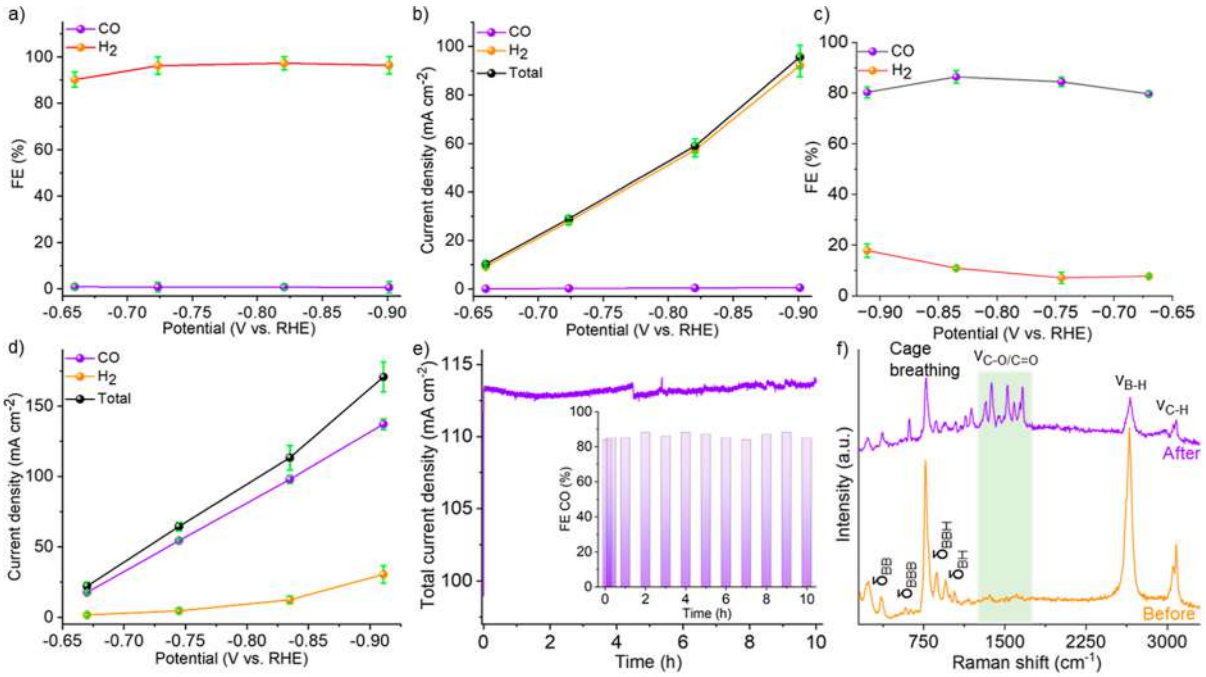


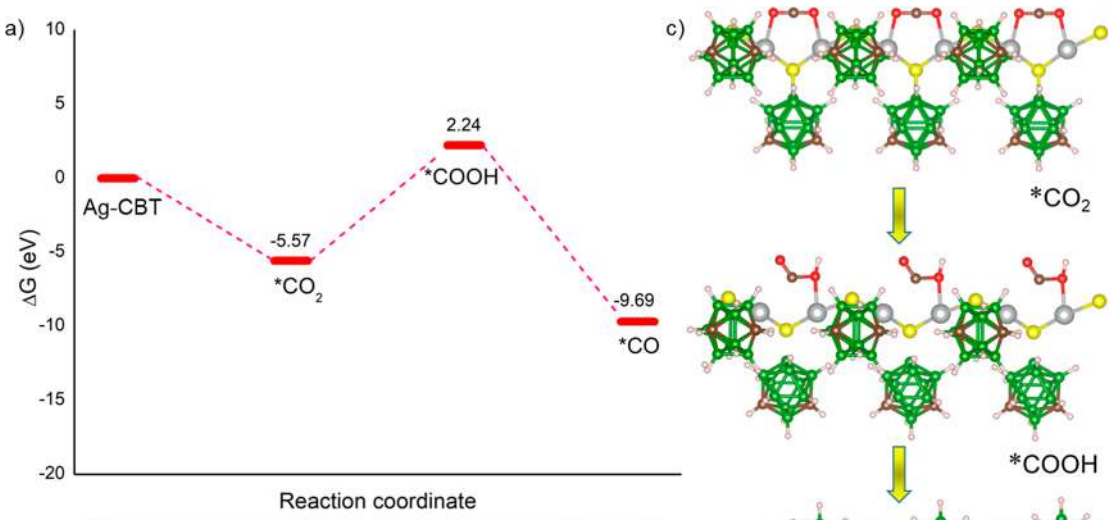
Figure 4. Electrochemical CO_2 reduction reaction using the Ag-CBT framework. (a) Faradaic efficiency and (b) current density of the electrode loaded with the Ag-CBT framework under an argon atmosphere. (c) Faradaic efficiency and (d) current density of the electrode at different potential under a CO_2 atmosphere. (e) Stability of the electrode during the electrocatalytic process. Inset shows time-dependent FE variation of the synthesized CO product using the same electrode. (f) Comparative Raman spectra of the catalyst-loaded electrode before (orange trace) and after (violet trace) CO_2 exposure. Peaks of interest are highlighted here.

2645 cm^{-1} in five different single crystals of the Ag-CBT framework (see Figures S11 and S12). Similarly, the C−H spectral band at 3079 cm^{-1} for the M_9-COOH ligand shifted to 3046 and 3082 cm^{-1} in the Ag-CBT framework. Additionally, three prominent bands at 1290, 1443, and 1682 cm^{-1}, associated with the −COOH group, were absent in the Ag-CBT framework, further indicating that decarboxylation had occurred. To investigate the band gap and associated electronic properties, we measured the solid-state absorption spectrum of the crystalline Ag-CBT sample. The absorption spectrum revealed two distinct bands: a broad, high-energy band ranging from 3.7 to 6.0 eV and a relatively weak, low-energy band between 1.8 and 3.5 eV (see Figure S13). By extrapolating the absorption band edge, we determined the framework's band gaps to be 1.74 and 3.75 eV. The presence of a multiband gap in these materials could facilitate the related electron transfer processes involved in electrocatalytic conversion. Additionally, thermogravimetric analysis (TGA) demonstrated robust thermal stability for the Ag-CBT framework solids, withstanding thermal decomposition initiating at approximately 300 °C (Figure S14). This thermal stability was significantly higher than that of carborane-thiol-protected silver clusters, which exhibited thermal stability between 150 and 200 °C.[62,63]

These framework solids were used as active catalysts to investigate electrocatalytic CO_2 reduction reactions. Initially, we conducted electrocatalysis using a Ag-CBT-loaded gas diffusion electrode in a flow cell. The product analysis revealed that hydrogen (H_2) was the sole product formed in an argon (Ar) atmosphere, achieving a Faradaic efficiency of approximately 90 ± 3% (see Figure 4a,b). Notably, no carbon monoxide (CO) was detected across a wide range of negative potentials (−0.65 to −0.9 V), indicating that CO generation was not possible from the decomposition of the Ag-CBT framework. When supplying CO_2 gas as the feedstock, the Ag-CBT framework maintained stable Faradaic efficiencies for CO production above 80% throughout the entire range of applied potentials studied (see Figure 4c). It may be noted that microcrystalline Ag-CBT framework, characterized by their porous void spaces having 6.5% volume of the unit cell, was suitable for the CO_2 adsorption and subsequent catalytic process (see Figure S15). The maximum Faradaic efficiency for CO reached 86%, with a corresponding partial current density of 98 mA/cm^2 at −0.83 V versus a reversible hydrogen electrode (RHE) (see Figure 4d). The CO partial current density was further increased to 137 mA/cm^2 at −0.91 V vs RHE, while maintaining a Faradaic efficiency of 80% for CO. The Ag-CBT framework was able to retain a steady current density of approximately 113 mA/cm^2 at −0.83 V vs RHE, with consistent CO Faradaic efficiencies of around 86% over a span of 10 h (see Figure 4e). The CO_2 electroreduction measurements conducted at three different pH levels (3, 7.8, and 14) showed that the Faradaic efficiencies for carbon monoxide (CO) were 84.9%, 87.1%, and 86.1% at pH = 3, 7.8, and 14, respectively. In contrast, the Faradaic efficiency for hydrogen was consistently ∼10% across all pH conditions (as shown in Figure S16). These results suggest that the catalyst maintains a robust performance across a wide range of pH levels. A comparison between various silver nanomaterials along with our Ag-CBT framework is shown in Table S5.

A comparative Raman spectroscopic analysis (Figure 4f) revealed that CO_2 was stabilized on the silver-chalcogenide lattice. After CO_2 bubbling, the catalyst-loaded electrode showed five new prominent peaks at 1326, 1371, 1521, 1589, and 1663 cm^{-1}. Note that these features were absent in the parent framework, as mentioned before. While we could not assign the bands to specific binding sites, these vibrational bands corresponded to the symmetric and asymmetric vibrational modes of adsorbed CO_2 and carboxylate anions

https://doi.org/10.1021/acsanm.5c01918
ACS Appl. Nano Mater. 2025, 8, 13754−13762



b)

Intermediate	Adsorption energy (eV)
*CO	-7.76
$*CO_2$	-5.57
*COOH	-1.50

Figure 5. DFT calculation of electrochemical CO_2 reduction using the Ag-CBT framework. (a) Free energy diagram of CO_2ER associated with the various intermediate species formed during this conversion. (b) Adsorption efficiencies of different activated species. (c) Schematic representation of the reaction intermediates of CO_2 electroreduction over the one-dimensional framework of the catalyst. Color code: metallic gray: Ag, yellow: S, brown: C, red: O, green: B, and faint pink: H.

on the Ag-CBT framework.[64] Our previous investigation had demonstrated that the binding of adsorbed CO_2 and carboxylate anions significantly influenced the position and intensity of the vibrational bands.[65] Raman spectrum of the M_9-COOH ligand showed the −COOH vibrational bands at 1290, 1443, and 1682 cm^{-1} (Figure S15). Comparative Raman spectra of the Ag-CBT loaded electrode before and after CO_2 exposure with that of pure M_9-COOH suggested that the one-dimensional silver framework is important for CO_2 uptake rather than the carborane cages. Previous studies have also indicated that silver (Ag) centers in various silver complexes, clusters, and nanoparticles can effectively catalyze organic carboxylation reactions by adsorbing CO_2 onto the Ag atoms.[66−68]

Density functional theory (DFT) calculations were conducted to investigate the potential of the Ag-CBT framework as a catalyst for the electrochemical reduction of CO_2. We focused on a reduction pathway involving the formation of COOH, which we identified as the primary rate-determining step in the conversion process. Energetics of the electrochemical reaction were analyzed using the computational hydrogen electrode (CHE) model (see the Supporting Information for details).[69] The reaction energy profile and adsorption configurations of the intermediates are displayed in Figure 5. The results showed that the Ag-CBT framework allows for thermodynamically favorable adsorption of all the involved intermediates: $*CO_2$, *COOH, and *CO. Both *CO and $*CO_2$ exhibited relatively strong adsorption with adsorption energies of −7.76 eV and −5.57 eV, respectively, due to their binding in a bridging configuration. In contrast, *COOH bound to the Ag-CBT framework through a single O atom, resulting in a weaker interaction. This difference in bonding strength made the formation of *COOH the rate-limiting step in the reaction pathway. The subsequent step, involving the dissociation of *COOH to produce *CO, was favored because *CO bound strongly to the Ag-CBT framework. Although the mechanism considered here includes only a limited number of intermediates, the favorable adsorption configurations for the two key intermediates, $*CO_2$ and *CO, suggested that the Ag-CBT framework could serve as a viable catalyst for a broader range of reaction pathways, ultimately leading to the production of other valuable chemicals from the electroreduction of CO_2.

■ CONCLUSION

In summary, we have developed and characterized a silver-chalcogenide framework featuring a −(SAg)− double chain structure, which is protected by *meta*-carborane-9-thiolate as surface envelopes. This framework was utilized for the electrocatalytic CO_2 reduction. Single-crystal X-ray diffraction (SCXRD) and high-resolution transmission electron microscopy studies confirmed the one-dimensional linear arrangement of silver atoms within the framework. Mass spectrometric analysis revealed that the fragmented species was originating from the framework in the solution. These thermally stable, atomically precise nanomaterials demonstrated efficient CO_2 adsorption and subsequent electroreduction of CO_2 to CO, achieving a Faradaic efficiency of approximately 85% across a wide pH range. Raman spectroscopy highlighted the binding affinity of CO_2 for the 1D silver-chalcogenide framework. Additionally, density functional theory calculations suggested that the Ag···Ag chains enhanced the CO_2 adsorption and facilitated the electroreduction process. This work showcased the synthesis and structural characterization of a robust

https://doi.org/10.1021/acsanm.5c01918
ACS Appl. Nano Mater. 2025, 8, 13754−13762

carborane-thiolate-appended silver-chalcogenide framework with a high capacity for CO_2 electroreduction. It illustrated the potential for diverse electrocatalytic processes using a semiconducting metal-chalcogenide framework, which was stabilized by thermally robust materials and encased in three-dimensional carborane molecular cages.

■ ASSOCIATED CONTENT

Supporting Information

The Supporting Information is available free of charge at https://pubs.acs.org/doi/10.1021/acsanm.5c01918.

Experimental section, instrumentation, computational details, crystallographic information files, and associated spectroscopic and microscopic characterization (PDF)

CIF files for the crystal data of Ag-CBT (CIF)

■ AUTHOR INFORMATION

Corresponding Authors

Tomas Base − *Department of Syntheses, Institute of Inorganic Chemistry, The Czech Academy of Science, Rez 25068, Czech Republic;* orcid.org/0000-0003-2533-8705; Email: tbase@iic.cas.cz

Biswarup Pathak − *Department of Chemistry, Indian Institute of Technology Indore, Indore 453552, India;* orcid.org/0000-0002-9972-9947; Email: biswarup@iiti.ac.in

Soumyabrata Roy − *Department of Materials Science and Nanoengineering, Rice University, Houston, Texas 77005, United States; Department of Sustainable Energy Engineering, Indian Institute of Technology Kanpur, Kanpur, Uttar Pradesh 208016, India*; Email: soumyar@iitk.ac.in

Thalappil Pradeep − *DST Unit of Nanoscience (DST UNS) and Thematic Unit of Excellence (TUE), Department of Chemistry, Indian Institute of Technology Madras, Chennai 600036, India;* orcid.org/0000-0003-3174-534X; Email: pradeep@iitm.ac.in

Authors

Arijit Jana − *DST Unit of Nanoscience (DST UNS) and Thematic Unit of Excellence (TUE), Department of Chemistry, Indian Institute of Technology Madras, Chennai 600036, India*

Zhengyuan Li − *Department of Chemical and Environmental Engineering, University of Cincinnati, Cincinnati, Ohio 45221, United States*

Amoghavarsha Ramachandra Kini − *DST Unit of Nanoscience (DST UNS) and Thematic Unit of Excellence (TUE), Department of Chemistry, Indian Institute of Technology Madras, Chennai 600036, India;* orcid.org/0009-0003-6863-7729

Vivek Yadav − *DST Unit of Nanoscience (DST UNS) and Thematic Unit of Excellence (TUE), Department of Chemistry, Indian Institute of Technology Madras, Chennai 600036, India*

Akhil S. Nair − *Department of Chemistry, Indian Institute of Technology Indore, Indore 453552, India;* orcid.org/0000-0001-5723-3970

Astrid Campos Mata − *Department of Materials Science and Nanoengineering, Rice University, Houston, Texas 77005, United States;* orcid.org/0000-0002-2138-562X

Jingjie Wu − *Department of Chemical and Environmental Engineering, University of Cincinnati, Cincinnati, Ohio 45221, United States*

Jan Macháček − *Department of Syntheses, Institute of Inorganic Chemistry, The Czech Academy of Science, Rez 25068, Czech Republic;* orcid.org/0000-0003-4723-0789

Complete contact information is available at: https://pubs.acs.org/10.1021/acsanm.5c01918

Author Contributions

A.J., A.R.K., and V.Y.: Synthesis, crystallization, and associated characterization of the Ag-CBT framework. Z.L., J.W., and S.R.: Electrocatalytic CO_2 reduction experiments. A.C.M.: STEM measurement. A.S.N. and B.P.: Quantum chemical calculations. J.M. and T.B.: Synthesis and characterization of the carborane derivatives. The first draft of the manuscript is written by A.J. and all authors contributed to finalize the manuscript. T.P. supervised the project and finalized the manuscript.

Notes

The authors declare no competing financial interest.

■ ACKNOWLEDGMENTS

We acknowledge the support of the Science and Engineering Research Board (SERB), Department of Science and Technology (DST), and Government of India. T.P. acknowledges funding from the Centre of Excellence on Molecular Materials and Functions under the Institution of Eminence scheme of IIT Madras. T.P. thanks the Science and Engineering Research Board (SERB), India, for funding through the SPR/2021/000439 research grant. We thank the Sophisticated Analytical Instruments Facility, IIT Madras, and Sudhadevi Antharjanam for the SC-XRD measurements. A.J. thanks IITM for his research fellowship. S.R. acknowledges funding from the Chandrakanta Kesavan Centre for Energy Policy and Climate Solutions, IIT Kanpur (Project No.: DORA/2021136H) and IIT Kanpur research grant IITK/SEE/2024098. A.R.K. thanks the Council of Scientific and Industrial Research (CSIR) for his research fellowship.

■ ABBREVIATIONS

ESI-MS, electrospray ionization mass spectrometry; DFT, density functional theory; EDS, energy dispersive spectroscopy; PXRD, powder X-ray diffraction; SCXRD, single crystal X-ray diffraction; STEM, scanning transmission electron microscopy; TGA, thermogravimetric analysis; CO_2, carbon dioxide; CO, carbon monoxide; ER, electroreduction; CHE, computational hydrogen electrode; DMF, dimethylformamide

■ REFERENCES

(1) Mac Dowell, N.; Fennell, P. S.; Shah, N.; Maitland, G. C. The Role of CO_2 Capture and Utilization in Mitigating Climate Change. *Nat. Clim. Chang.* **2017**, *7* (4), 243−249.

(2) Wei, Y. M.; Kang, J. N.; Liu, L. C.; Li, Q.; Wang, P. T.; Hou, J. J.; Liang, Q. M.; Liao, H.; Huang, S. F.; Yu, B. A Proposed Global Layout of Carbon Capture and Storage in Line with a 2 °C Climate Target. *Nat. Clim. Chang.* **2021**, *11* (2), 112−118.

(3) Nitopi, S.; Bertheussen, E.; Scott, S. B.; Liu, X.; Engstfeld, A. K.; Horch, S.; Seger, B.; Stephens, I. E. L.; Chan, K.; Hahn, C.; Nørskov, J. K.; Jaramillo, T. F.; Chorkendorff, I. Progress and Perspectives of Electrochemical CO_2 Reduction on Copper in Aqueous Electrolyte. *Chem. Rev.* **2019**, *119* (12), 7610−7672.

(4) Roy, S.; Cherevotan, A.; Peter, S. C. Thermochemical CO_2 Hydrogenation to Single Carbon Products: Scientific and Technological Challenges. *ACS Energy Lett.* **2018**, *3* (8), 1938−1966.

(5) Li, X.; Yu, J.; Jaroniec, M.; Chen, X. Cocatalysts for Selective Photoreduction of CO_2 into Solar Fuels. *Chem. Rev.* **2019**, *119* (6), 3962−4179.
(6) Appel, A. M.; Bercaw, J. E.; Bocarsly, A. B.; Dobbek, H.; Dubois, D. L.; Dupuis, M.; Ferry, J. G.; Fujita, E.; Hille, R.; Kenis, P. J. A.; Kerfeld, C. A.; Morris, R. H.; Peden, C. H. F.; Portis, A. R.; Ragsdale, S. W.; Rauchfuss, T. B.; Reek, J. N. H.; Seefeldt, L. C.; Thauer, R. K.; Waldrop, G. L. Frontiers, Opportunities, and Challenges in Biochemical and Chemical Catalysis of CO_2 Fixation. *Chem. Rev.* **2013**, *113* (8), 6621−6658.
(7) Costentin, C.; Robert, M.; Savéant, J. M. Catalysis of the Electrochemical Reduction of Carbon Dioxide. *Chem. Soc. Rev.* **2013**, *42* (6), 2423−2436.
(8) Roy, S.; Li, Z.; Chen, Z.; Mata, A. C.; Kumar, P.; Sarma, S. C.; Teixeira, I. F.; Silva, I. F.; Gao, G.; Tarakina, N. V.; Kibria, M. G.; Singh, C. V.; Wu, J.; Ajayan, P. M. Cooperative Copper Single-Atom Catalyst in 2D Carbon Nitride for Enhanced CO_2 Electrolysis to Methane. *Adv. Mater.* **2024**, *36* (13), 1−13.
(9) Gu, J.; Héroguel, F.; Luterbacher, J.; Hu, X. Densely Packed, Ultra Small SnO Nanoparticles for Enhanced Activity and Selectivity in Electrochemical CO_2 Reduction. *Angew. Chem., Int. Ed.* **2018**, *57* (11), 2943−2947.
(10) Kawawaki, T.; Okada, T.; Hirayama, D.; Negishi, Y. Atomically Precise Metal Nanoclusters as Catalysts for Electrocatalytic CO_2 Reduction. *Green Chem.* **2024**, *26* (1), 122−163.
(11) Song, B.; Liang, Y.; Zhou, Y.; Zhang, L.; Li, H.; Zhu, N. X.; Tang, B. Z.; Zhao, D.; Liu, B. CO_2-Based Stable Porous Metal-Organic Frameworks for CO_2 Utilization. *J. Am. Chem. Soc.* **2024**, *146* (21), 14835−14843.
(12) Wang, J.; Zou, J.; Hu, X.; Ning, S.; Wang, X.; Kang, X.; Chen, S. Heterostructured Intermetallic CuSn Catalysts: High Performance towards the Electrochemical Reduction of CO_2 to Formate. *J. Mater. Chem. A* **2019**, *7* (48), 27514−27521.
(13) Asadi, M.; Kim, K.; Liu, C.; Addepalli, A. V.; Abbasi, P.; Yasaei, P.; Phillips, P.; Behranginia, A.; Cerrato, J. M.; Haasch, R.; Zapol, P.; Kumar, B.; Klie, R. F.; Abiade, J.; Curtiss, L. A.; Salehi-Khojin, A. Nanostructured Transition Metal Dichalcogenide Electrocatalysts for CO_2 Reduction in Ionic Liquid. *Science* **2016**, *353* (6298), 467−470.
(14) Singh, M.; Nama, J.; Paul, T.; Makani, N. H.; Sahoo, A.; Sharma, S.; Banerjee, R. Photoelectrochemically Induced CO_2 Reduction Using Halide-Tunable Lead-Free Perovskites. *ACS Appl. Energy Mater.* **2023**, *6* (6), 3566−3578.
(15) Nabil, S. K.; Roy, S.; Algozeeb, W. A.; Al-Attas, T.; Bari, M. A. a.; Zeraati, A. S.; Kannimuthu, K.; Demingos, P. G.; Rao, A.; Tran, T. N.; Wu, X.; Bollini, P.; Lin, H.; Singh, C. V.; Tour, J. M.; Ajayan, P. M.; Kibria, M. G. Bifunctional Gas Diffusion Electrode Enables In Situ Separation and Conversion of CO_2 to Ethylene from Dilute Stream. *Adv. Mater.* **2023**, *35* (24), 2300389.
(16) Li, Z.; Zhang, T.; Raj, J.; Roy, S.; Wu, J. Revisiting Reaction Kinetics of CO Electroreduction to C_2^+ Products in a Flow Electrolyzer. *Energy Fuels* **2023**, *37* (11), 7904−7910.
(17) Chawla, G.; Sarma, S. C.; Raj, J.; Bagchi, D.; Riyaz, M.; Roy, S.; Mishra, V.; Goud, D.; Peter, S. C. Lattice Charge Tuning-Driven Multi-Carbon Products from Carbon Dioxide. *ACS Sustain. Chem. Eng.* **2024**, *12* (26), 9787−9794.
(18) Dutta, N.; Bagchi, D.; Chawla, G.; Peter, S. C. A Guideline to Determine Faradaic Efficiency in Electrochemical CO_2 Reduction. *ACS Energy Lett.* **2024**, *9* (1), 323−328.
(19) Al-Attas, T.; Nabil, S. K.; Zeraati, A. S.; Shiran, H. S.; Alkayyali, T.; Zargartalebi, M.; Tran, T.; Marei, N. N.; Al Bari, M. A.; Lin, H.; Roy, S.; Ajayan, P. M.; Sinton, D.; Shimizu, G.; Kibria, M. G. Permselective MOF-Based Gas Diffusion Electrode for Direct Conversion of CO_2 from Quasi Flue Gas. *ACS Energy Lett.* **2023**, *8* (1), 107−115.
(20) Marcandalli, G.; Monteiro, M. C. O.; Goyal, A.; Koper, M. T. M. Electrolyte Effects on CO_2 Electrochemical Reduction to CO. *Acc. Chem. Res.* **2022**, *55* (14), 1900−1911.
(21) O'Brien, C. P.; Miao, R. K.; Shayesteh Zeraati, A.; Lee, G.; Sargent, E. H.; Sinton, D. CO_2 Electrolyzers. *Chem. Rev.* **2024**, *124* (7), 3648−3693.
(22) Belsa, B.; Xia, L.; García de Arquer, F. P. CO_2 Electrolysis Technologies: Bridging the Gap toward Scale-up and Commercialization. *ACS Energy Lett.* **2024**, *9* (9), 4293−4305.
(23) Weekes, D. M.; Salvatore, D. A.; Reyes, A.; Huang, A.; Berlinguette, C. P. Electrolytic CO_2 Reduction in a Flow Cell. *Acc. Chem. Res.* **2018**, *51* (4), 910−918.
(24) Seong, H.; Choi, M.; Park, S.; Kim, H. W.; Kim, J.; Kim, W.; Yoo, J. S.; Lee, D. Promoting CO_2-to-CO Electroreduction via the Active-Site Engineering of Atomically Precise Silver Nanoclusters. *ACS Energy Lett.* **2022**, *7* (12), 4177−4184.
(25) Kim, C.; Jeon, H. S.; Eom, T.; Jee, M. S.; Kim, H.; Friend, C. M.; Min, B. K.; Hwang, Y. J. Achieving Selective and Efficient Electrocatalytic Activity for CO_2 Reduction Using Immobilized Silver Nanoparticles. *J. Am. Chem. Soc.* **2015**, *137* (43), 13844−13850.
(26) Liu, S.; Wang, X. Z.; Tao, H.; Li, T.; Liu, Q.; Xu, Z.; Fu, X. Z.; Luo, J. L. Ultrathin 5-Fold Twinned Sub-25 Nm Silver Nanowires Enable Highly Selective Electroreduction of CO_2 to CO. *Nano Energy* **2018**, *45*, 456−462.
(27) Pan, Y.; Paschoalino, W. J.; Bayram, S. S.; Blum, A. S.; Mauzeroll, J. Biosynthesized Silver Nanorings as a Highly Efficient and Selective Electrocatalysts for CO_2 Reduction. *Nanoscale* **2019**, *11* (40), 18595−18603.
(28) Liu, S.; Sun, C.; Xiao, J.; Luo, J. L. Unraveling Structure Sensitivity in CO_2 Electroreduction to Near-Unity CO on Silver Nanocubes. *ACS Catal.* **2020**, *10* (5), 3158−3163.
(29) Qi, K.; Zhang, Y.; Li, J.; Charmette, C.; Ramonda, M.; Cui, X.; Wang, Y.; Zhang, Y.; Wu, H.; Wang, W.; Zhang, X.; Voiry, D. Enhancing the CO_2-to-CO Conversion from 2D Silver Nanoprisms via Superstructure Assembly. *ACS Nano* **2021**, *15* (4), 7682−7693.
(30) Ma, S.; Luo, R.; Gold, J. I.; Yu, A. Z.; Kim, B.; Kenis, P. J. A. Carbon Nanotube Containing Ag Catalyst Layers for Efficient and Selective Reduction of Carbon Dioxide. *J. Mater. Chem. A* **2016**, *4* (22), 8573−8578.
(31) Li, S.; Chen, W.; Dong, X.; Zhu, C.; Chen, A.; Song, Y.; Li, G.; Wei, W.; Sun, Y. Hierarchical Micro/Nanostructured Silver Hollow Fiber Boosts Electroreduction of Carbon Dioxide. *Nat. Commun.* **2022**, *13* (1), 3080.
(32) Kim, C.; Eom, T.; Jee, M. S.; Jung, H.; Kim, H.; Min, B. K.; Hwang, Y. J. Insight into Electrochemical CO_2 Reduction on Surface-Molecule-Mediated Ag Nanoparticles. *ACS Catal.* **2017**, *7* (1), 779−785.
(33) Deng, X.; Alfonso, D.; Nguyen-Phan, T. D.; Kauffman, D. R. Resolving the Size-Dependent Transition between CO_2 Reduction Reaction and H_2 Evolution Reaction Selectivity in Sub-5 Nm Silver Nanoparticle Electrocatalysts. *ACS Catal.* **2022**, *12* (10), 5921−5929.
(34) Deng, X.; Alfonso, D.; Nguyen-Phan, T. D.; Kauffman, D. R. Breaking the Limit of Size-Dependent CO_2RR Selectivity in Silver Nanoparticle Electrocatalysts through Electronic Metal-Carbon Interactions. *ACS Catal.* **2023**, *13* (23), 15301−15309.
(35) Yan, H.; Hohman, J. N.; Li, F. H.; Jia, C.; Solis-Ibarra, D.; Wu, B.; Dahl, J. E. P.; Carlson, R. M. K.; Tkachenko, B. A.; Fokin, A. A.; Schreiner, P. R.; Vailionis, A.; Kim, T. R.; Devereaux, T. P.; Shen, Z. X.; Melosh, N. A. Hybrid Metal-Organic Chalcogenide Nanowires with Electrically Conductive Inorganic Core through Diamondoid-Directed Assembly. *Nat. Mater.* **2017**, *16* (3), 349−355.
(36) Sun, P.; Xie, M.; Zhang, L.-M.; Liu, J.-X.; Wu, J.; Li, D.-S.; Yuan, S.-F.; Wu, T.; Li, D. Ultrastable Anti-Acid Shield in Layered Silver Coordination Polymers. *Angew. Chem., Int. Ed.* **2022**, *61* (44), No. e202209971.
(37) Yang, H.; Mandal, S.; Lee, Y. H.; Park, J. Y.; Zhao, H.; Yuan, C.; Huang, L.; Chen, M.; Dou, L. Dimensionality Engineering of Lead Organic Chalcogenide Semiconductors. *J. Am. Chem. Soc.* **2023**, *145* (44), 23963−23971.
(38) Krebs, B.; Henkel, G. Transition-Metal Thiolates: From Molecular Fragments of Sulfidic Solids to Models for Active Centers in Biomolecules. *Angew. Chem., Int. Ed.* **1991**, *30*, 769−788.

(39) Paritmongkol, W.; Lee, W. S.; Shcherbakov-Wu, W.; Ha, S. K.; Sakurada, T.; Oh, S. J.; Tisdale, W. A. Morphological Control of 2D Hybrid Organic-Inorganic Semiconductor AgSePh. *ACS Nano* **2022**, *16* (2), 2054−2065.
(40) Paritmongkol, W.; Sakurada, T.; Lee, W. S.; Wan, R.; Müller, P.; Tisdale, W. A. Size and Quality Enhancement of 2D Semiconducting Metal-Organic Chalcogenolates by Amine Addition. *J. Am. Chem. Soc.* **2021**, *143* (48), 20256−20263.
(41) Lee, W. S.; Cho, Y.; Powers, E. R.; Paritmongkol, W.; Sakurada, T.; Kulik, H. J.; Tisdale, W. A. Light Emission in 2D Silver Phenylchalcogenolates. *ACS Nano* **2022**, *16* (12), 20318−20328.
(42) Hernandez Oendra, A. C.; Aspect, M. A.; Jaeggi, J. L.; Baumann, J.; Lightner, C. R.; Pun, A. B.; Norris, D. J. Tunable Synthesis of Metal-Organic Chalcogenide Semiconductor Nanocrystals. *Chem. Mater.* **2023**, *35* (21), 9390−9398.
(43) Mingos, M. P. In *50th Anniversary of Electron Counting Paradigms for Polyhedral Molecules*; Mingos, M. P., Ed.; Springer, 2021.
(44) Poater, J.; Escayola, S.; Poater, A.; Teixidor, F.; Ottosson, H.; Viñas, C.; Solà, M. Single-Not Double-3D-Aromaticity in an Oxidized Closo Icosahedral Dodecaiodo-Dodecaborate Cluster. *J. Am. Chem. Soc.* **2023**, *145* (41), 22527−22538.
(45) Fisher, S. P.; Tomich, A. W.; Lovera, S. O.; Kleinsasser, J. F.; Guo, J.; Asay, M. J.; Nelson, H. M.; Lavallo, V. Nonclassical Applications of Closo-Carborane Anions: From Main Group Chemistry and Catalysis to Energy Storage. *Chem. Rev.* **2019**, *119* (14), 8262−8290.
(46) Núñez, R.; Tarre's, M.; Ferrer-Ugalde, A.; De Biani, F. F.; Teixidor, F. Electrochemistry and Photoluminescence of Icosahedral Carboranes, Boranes, Metallacarboranes, and Their Derivatives. *Chem. Rev.* **2016**, *116* (23), 14307−14378.
(47) Kirlikovali, K. O.; Axtell, J. C.; Gonzalez, A.; Phung, A. C.; Khan, S. I.; Spokoyny, A. M. Luminescent Metal Complexes Featuring Photophysically Innocent Boron Cluster Ligands. *Chem. Sci.* **2016**, *7* (8), 5132−5138.
(48) Hablot, D.; Ziessel, R.; Alamiry, M. A. H.; Bahraidah, E.; Harriman, A. Nanomechanical Properties of Molecular-Scale Bridges as Visualised by Intramolecular Electronic Energy Transfer. *Chem. Sci.* **2013**, *4* (1), 444−453.
(49) Yadav, V.; Jana, A.; Acharya, S.; Malola, S.; Nagar, H.; Sharma, A.; Kini, A. R.; Antharjanam, S.; Machacek, J.; Adarsh, K. N. V. D.; Base, T.; Häkkinen, H.; Pradeep, T. Site-Specific Substitution in Atomically Precise Carboranethiol-Protected Nanoclusters and Concomitant Changes in Electronic Properties. *Nat. Commun.* **2025**, *16* (1), 1197.
(50) Jana, A.; Jash, M.; Dar, W. A.; Roy, J.; Chakraborty, P.; Paramasivam, G.; Lebedkin, S.; Kirakci, K.; Manna, S.; Antharjanam, S.; Machacek, J.; Kucerakova, M.; Ghosh, S.; Lang, K.; Kappes, M. M.; Base, T.; Pradeep, T. Carborane-Thiol Protected Copper Nanoclusters: Stimuli-Responsive Materials with Tunable Phosphorescence. *Chem. Sci.* **2023**, *14* (6), 1613−1626.
(51) Kini, A. R.; Debta, S.; Jana, A.; Aparna, C.; Yadav, V.; Kusiak, N.; Base, T.; Waghmare, U. V.; Ghosh, P.; Pradeep, T. Nanomechanical Investigations of Crystals of Copper Nanocluster Isomorphs: Enhanced Hardness of the Low-Density Analogue. *Chem. Mater.* **2025**, *37*, 1284−1296.
(52) Jana, A.; Spoorthi, B. K.; Nair, A. S.; Nagar, A.; Pathak, B.; Base, T.; Pradeep, T. A. Luminescent Cu_4 Cluster Film Grown by Electrospray Deposition: A Nitroaromatic Vapour Sensor. *Nanoscale* **2023**, *15* (18), 8141−8147.
(53) Huang, J. H.; Si, Y.; Dong, X. Y.; Wang, Z. Y.; Liu, L. Y.; Zang, S. Q.; Mak, T. C. W. Symmetry Breaking of Atomically Precise Fullerene-like Metal Nanoclusters. *J. Am. Chem. Soc.* **2021**, *143* (32), 12439−12444.
(54) Jana, A.; Duary, S.; Das, A.; Kini, A. R.; Acharya, S.; Machacek, J.; Pathak, B.; Base, T.; Pradeep, T. Multicolor Photoluminescence of Cu_{14} Clusters Modulated Using Surface Ligands. *Chem. Sci.* **2024**, *15* (34), 13741−13752.
(55) Kennedy, R. D.; Krungleviciute, V.; Clingerman, D. J.; Mondloch, J. E.; Peng, Y.; Wilmer, C. E.; Sarjeant, A. A.; Snurr, R. Q.; Hupp, J. T.; Yildirim, T.; Farha, O. K.; Mirkin, C. A. Carborane-Based Metal-Organic Framework with High Methane and Hydrogen Storage Capacities. *Chem. Mater.* **2013**, *25* (17), 3539−3543.
(56) Bae, Y. S.; Farha, O. K.; Spokoyny, A. M.; Mirkin, C. A.; Hupp, J. T.; Snurr, R. Q. Carborane-Based Metal-Organic Frameworks as Highly Selective Sorbents for CO_2 over Methane. *Chem. Commun.* **2008**, *0* (35), 4135−4137.
(57) Idrees, K. B.; Kirlikovali, K. O.; Setter, C.; Xie, H.; Brand, H.; Lal, B.; Sha, F.; Smoljan, C. S.; Wang, X.; Islamoglu, T.; Macreadie, L. K.; Farha, O. K. Robust Carborane-Based Metal-Organic Frameworks for Hexane Separation. *J. Am. Chem. Soc.* **2023**, *145* (43), 23433−23441.
(58) Thomas, J. C.; Boldog, I.; Auluck, H. S.; Bereciartua, P. J.; Dušek, M.; Macháček, J.; Bastl, Z.; Weiss, P. S.; Baše, T. Self-Assembled p-Carborane Analogue of p-Mercaptobenzoic Acid on Au{111. *Chem. Mater.* **2015**, *27* (15), 5425−5435.
(59) Veselska, O.; Demessence, A. d^{10} Coinage Metal Organic Chalcogenolates: From Oligomers to Coordination Polymers. *Coord. Chem. Rev.* **2018**, *355*, 240−270.
(60) Wang, G.-E.; Luo, S.; Di, T.; Fu, Z.; Xu, G. Layered Organic Metal Chalcogenides (OMCs): From Bulk to Two-Dimensional Materials. *Angew. Chem., Int. Ed.* **2022**, *61* (27), No. e202203151.
(61) Schriber, E. A.; Paley, D. W.; Bolotovsky, R.; Rosenberg, D. J.; Sierra, R. G.; Aquila, A.; Mendez, D.; Poitevin, F.; Blaschke, J. P.; Bhowmick, A.; Kelly, R. P.; Hunter, M.; Hayes, B.; Popple, D. C.; Yeung, M.; Pareja-Rivera, C.; Lisova, S.; Tono, K.; Sugahara, M.; Owada, S.; Kuykendall, T.; Yao, K.; Schuck, P. J.; Solis-Ibarra, D.; Sauter, N. K.; Brewster, A. S.; Hohman, J. N. Chemical Crystallography by Serial Femtosecond X-Ray Diffraction. *Nature* **2022**, *601* (7893), 360−365.
(62) Jana, A.; Jash, M.; Poonia, A. K.; Paramasivam, G.; Islam, M. R.; Chakraborty, P.; Antharjanam, S.; Machacek, J.; Ghosh, S.; Adarsh, K. N. V. D.; Base, T.; Pradeep, T. Light-Activated Intercluster Conversion of an Atomically Precise Silver Nanocluster. *ACS Nano* **2021**, *15* (10), 15781−15793.
(63) Jana, A.; Unnikrishnan, P. M.; Poonia, A. K.; Roy, J.; Jash, M.; Paramasivam, G.; Machacek, J.; Adarsh, K. N. V. D.; Base, T.; Pradeep, T. Carboranethiol-Protected Propeller-Shaped Photoresponsive Silver Nanomolecule. *Inorg. Chem.* **2022**, *61* (23), 8593−8603.
(64) Hadjiivanov, K. I.; Panayotov, D. A.; Mihaylov, M. Y.; Ivanova, E. Z.; Chakarova, K. K.; Andonova, S. M.; Drenchev, N. L. Power of Infrared and Raman Spectroscopies to Characterize Metal-Organic Frameworks and Investigate Their Interaction with Guest Molecules. *Chem. Rev.* **2021**, *121* (3), 1286−1424.
(65) Ahuja, T.; Chaudhari, K.; Paramasivam, G.; Ragupathy, G.; Mohanty, J. S.; Pradeep, T. Toward Vibrational Tomography of Citrate on Dynamically Changing Individual Silver Nanoparticles. *J. Phys. Chem. C* **2021**, *125* (6), 3553−3566.
(66) Sekine, K.; Yamada, T. Silver-Catalyzed Carboxylation. *Chem. Soc. Rev.* **2016**, *45* (16), 4524−4532.
(67) Liu, Y.; Chai, X.; Cai, X.; Chen, M.; Jin, R.; Ding, W.; Zhu, Y. Central Doping of a Foreign Atom into the Silver Cluster for Catalytic Conversion of CO_2 toward C−C Bond Formation. *Angew. Chem., Int. Ed.* **2018**, *57* (31), 9775−9779.
(68) Yu, D.; Tan, M. X.; Zhang, Y. Carboxylation of Terminal Alkynes with Carbon Dioxide Catalyzed by Poly (N-Heterocyclic Carbene)-Supported Silver Nanoparticles. *Adv. Synth. Catal.* **2012**, *354*, 969−974.
(69) Nørskov, J. K.; Rossmeisl, J.; Logadottir, A.; Lindqvist, L.; Kitchin, J. R.; Bligaard, T.; Jónsson, H. Origin of the Overpotential for Oxygen Reduction at a Fuel-Cell Cathode. *J. Phys. Chem. B* **2004**, *108* (46), 17886−17892.

Supporting Information

A Silver-chalcogenide Nanomaterial Enveloped with a Carborane-thiolate Shell for the Electroreduction of CO_2 to CO

Arijit Jana[1], Zhengyuan Li[2], Amoghavarsha Ramachandra Kini[1], Vivek Yadav[1], Akhil S. Nair[3], Astrid Campos Mata[4], Jingjie Wu[2], Jan Macháček[5], Tomas Base[5], Biswarup Pathak[3*], Soumyabrata Roy[4,6*], Thalappil Pradeep[1*]*

[1]DST Unit of Nanoscience (DST UNS) and Thematic Unit of Excellence (TUE), Department of Chemistry, Indian Institute of Technology, Madras, Chennai – 600036, India

[2]Department of Chemical and Environmental Engineering, University of Cincinnati, Cincinnati, OH 45221, USA

[3]Department of Chemistry, Indian Institute of Technology Indore, Indore 453552, India

[4]Department of Materials Science and Nanoengineering, Rice University, Houston, TX 77005 USA

[5]Department of Syntheses, Institute of Inorganic Chemistry, The Czech Academy of Science, 1001 Husinec-Rez, 25068, Czech Republic

[6]Department of Sustainable Energy Engineering, Indian Institute of Technology Kanpur, Kanpur, Uttar Pradesh 208016, India

Email: pradeep@iitm.ac.in, soumyar@iitk.ac.in, biswarup@iiti.ac.in, tbase@iic.cas.cz

Table of Content:

Sl. No	Items	Page no
	Experimental section	S-3, S-4
	Instrumentation	S-5, S-6
	Computational details	S-7
Figure S1.	The EDS spectral profile and elemental mapping of a Ag-CBT crystal	S-7
Table S1.	Crystal data and structure refinement for Ag-CBT framework	S-8
Table S2.	Atomic coordinates and equivalent isotropic displacement parameters for Ag-CBT framework	S-9
Table S3.	Anisotropic displacement parameters for Ag-CBT framework	S-10
Table S4.	Hydrogen coordinates and isotropic displacement parameters for Ag-CBT framework	S-11
Figure S2.	Optical micrographs of the hair-like solids formed from the hydrothermal reaction of $AgNO_3$ and M_9 ligand	S-12
Figure S3.	Powder X-ray diffraction pattern of the hair like solids obtained after the hydrothermal reaction of $AgNO_3$ and M_9 ligand	S-13
Figure S4.	The (3×3×3) extended packing of the Ag-CBT framework	S-13
Figure S5.	An extended packing structure of the Ag-CBT solid along the a-axis	S-14
Figure S6.	Carborane-centered short contact intermolecular interactions observed in Ag-CBT framework	S-14
Figure S7.	Metal-centered short contact intermolecular interactions observed in Ag-CBT framework	S-15
Figure S8.	Experimental and simulated PXRD spectra of the Ag-CBT framework	S-16
Figure S9.	Low-resolution STEM micrographs of a rod-shaped Ag-CBT crystals	S-17
Figure S10.	Comparative FT-IR spectra of M_9-COOH ligand and Ag-CBT framework	S-18
Figure S11.	Raman spectroscopic data of Ag-CBT framework	S-19
Figure S12.	Raman spectroscopic data of M_9-COOH ligand	S-20
Figure S13.	Solid-state UV-vis absorption spectrum of the Ag-CBT framework	S-21
Figure S14.	Thermogravimetric and differential thermal analysis plot of microcrystalline Ag-CBT framework	S-21
Figure S15.	Void spaces present in the Ag-CBT framework	S-22
Figure S16.	Variation in the Faradic efficiency of the Ag-CBT loaded electrode measured under three different pH conditions	S-22
Table S5.	Comparison between various silver-based catalysts used for CO_2 electroreduction	S-23, S-24
Figure S17.	Comparison of simulated and experimental powder X-ray diffraction patterns for various synthetic products obtained from the solvothermal reaction of $AgNO_3$ and M_9-COOH at temperatures	S-25
	References	S-26, S-27

Experimental section

Chemicals used

Silver nitrate ($AgNO_3$) was purchased from Rankem Chemicals. The M_9-COOH ligand was synthesized following our earlier report, using *meta*-carborane 9-thiol derivative.[1] Solvent grade dichloromethane, dimethylformamide, and methanol were purchased from Rankem chemicals and Finar, India. All chemicals were used as such without further purification.

Synthesis of Ag-CBT framework solid

The Ag-CBT framework was synthesized using a modified solvothermal method. Initially, 25 mg (24.52 mM) of $AgNO_3$ was dissolved in 1.5 ml of methanol under ultrasonic conditions. Then, 35 mg of M_9-COOH (26.51 mM) was added after being dissolved in 4.5 ml of DMF. A few drops of trimethylamine were introduced to the mixture. After stirring for one hour, the resulting transparent solution was transferred to a hydrothermal container with a Teflon-lined inner chamber. The mixture underwent hydrothermal treatment at 80 °C for 48 hours. After this period, it was allowed to cool slowly to room temperature. Colorless rod-shaped crystals were observed at the bottom of the Teflon cylinder and were collected through centrifugation. These crystals were washed with methanol (3 × 5 ml) and subsequently used for further studies. The yield of the Ag-CBT framework was determined to be 85 % based on the amount of silver precursor used.

To investigate the effect of temperature during the solvothermal synthesis, we conducted experiments across a range of temperatures from 60 °C to 150 °C. At 60 °C, no crystalline solids were formed after 48 hours of heating. Reactions conducted between 80 °C and 120 °C produced white microcrystalline solids, while reactions at 150 °C resulted in black precipitates. Comparative powder X-ray diffraction analysis showed that maintaining temperatures between 80 °C and 100 °C for 48 to 72 hours led to the formation of phase-pure Ag-CBT solids (shown in Figure S17).

Preparation of gas diffusion electrode

Sample-loaded catalyst inks were prepared using the air-brush method. First, microcrystalline powder of Ag-CBT solid was dispersed in isopropanol containing 5 wt% Nafion solution and the mixture was sonicated for 20 min. Afterward, the catalyst ink was air-brushed onto a gas diffusion layer (GDL, Sigracet 35BC, Fuel Cell Store) to create a gas diffusion electrode (GDE). The prepared GDE was dried at 80 °C under vacuum for 30 min. The catalyst loading for cathode

electrodes was kept at ≈ 0.5 mg cm^{-2}. The loading was calculated by weighing the GDL before and after coating catalyst layer.

Electrochemical CO_2 reduction measurements

A specially designed flow cell was used to evaluate CO_2 electroreduction under ambient conditions. In this setup, a catalyst-loaded gas diffusion electrode (GDE) served as the cathode, while nickel foam was used as the anode, with a 1 M KOH solution as the electrolyte. An FAA-3-PK-75 anion exchange membrane (from Fuel Cell Store) separated the cathodic and anodic compartments. The electrolyte was delivered using syringe pumps (New Era Pump Systems Inc.) at flow rates of 1.5 mL/min to the cathode and 2.0 mL/min to the anode. A CO_2 gas flow of 50 sccm was maintained at the cathode using an Alicat Scientific mass flow controller. A Gamry Interface 1010E potentiostat was employed to apply a constant voltage to the flow cell and measure the resulting current from the catalyst. The cathode potential was continuously monitored relative to an Ag/AgCl (3 M KCl) reference electrode by a multimeter (Fluke Store). The potentials were adjusted to the RHE scale using the following equation: $E_{RHE} = E_{Ag/AgCl} + 0.209\ V + 0.0591 \times pH$. Because of rapid dynamic evolutions of local environments,[2] the resistance (R) between the cathode and reference electrode was immediately measured using potentiostatic electrochemical impedance spectroscopy (EIS) after each electrolysis, and then the ohmic drop (iR) was manually compensated. The R was measured to be 3.1-3.3 Ω.

Product analysis

An online gas chromatograph (GC, SRI Instruments Multiple Gas) equipped with a flame ionization detector (FID) and a thermal conductivity detector (TCD) was used to analyze the gas products at each applied potential. The Faradaic efficiency (FE) for gas products was calculated using: $FE\ (\%) = zFxV \times 100\% / j_{total}$, where j_{total} is total current density; V is molar flow rate of outlet CO_2; x is the molar fraction of product with respect to CO_2 as determined by GC; F is Faraday constant; z is the number of electrons involved to form the target product. Argon gas was supplied at a rate of 10 sccm to the outlet gas stream of the flow cell before it was directed to the GC, enabling accurate determination of the actual CO_2 flow rate after electrolysis. Standard deviations were calculated from measurements taken on three separate electrodes.

Instrumentation

Optical microscopy

Optical microscopic images of crystals were collected in transmission mode using a LEICA optical microscope equipped with LAS V4.8 software. The polarization of the crystal was measured using an optical polarizer.

Scanning electron microscopy (SEM)

Scanning electron microscopic images are measured using a Verios G4 UC, Thermo Scientific field emission scanning electron microscope (FESEM). After transferring the sample on a carbon tape, gold sputtering was performed to increase the conductivity of the sample. All the images were collected in high vacuum at an operating voltage of 10-15 kV. Energy dispersive analysis of X-ray (EDAX) was performed using the same instrument.

Scanning transmission electron microscopy (STEM)

Morphology characterization and single atom imaging of the framework was performed using FEI Titan Themis3 STEM equipped with a field emission gun operating at 200kV. For STEM observations, a suspension of the sample in ethanol was sonicated for 15 min and then drop-casted to a Cu grid with a lacey carbon support and dried for 5 min. The “beam shower” procedure was performed for 30 mins to reduce hydrocarbon contamination during subsequent imaging at high magnification.

UV-vis absorption spectroscopy

The UV-vis absorption spectrum was measured at room temperature in reflectance mode using an Agilent Cary 5000 UV-Vis-NIR spectrophotometer equipped with a 6-inch integrating sphere. The microcrystalline samples were dispersed in NVH immersion oil, crushed between two quartz plates, and the resulting thin layer was used for measurement.

Mass spectrometry

The mass spectrum of Ag-CBT framework solid was measured using Waters Synapt G2Si HDMS instrument. The instrument was equipped with an electrospray ionization source, step wave ion transfer optics, a quadrupole mass filter, and time of flight detector. Each mass spectrum was recorded both in positive and negative ion-modes. An optimized condition of flow rate 25-30 µl/min, capillary voltage 2.5-3 kV, cone voltage 0 kV, spray current 100-125 nA, source

temperature 70-100 °C and desolation temperature 90-120 °C with gas flow rate of 300 L/h were used for the measurements.

Infrared spectroscopy

Perkin Elmer Fourier Transform Infrared spectrometer (FT-IR) was used to measure the vibrational spectra of the Ag-CBT framework. Thin pallet was made by compressing a fine mixture of dry KBr with a small amount of microcrystalline sample.

Raman spectroscopy

Raman spectra were recorded using a CRM-Alpha 300S, WI Tec GmbH confocal Raman microscope, equipped with 532 nm frequency doubled Nd:YAG laser and 632 nm Helium Neon laser. Laser beam was focused to the sample using an objective lense having 20x magnification. The dispersed light from the sample was collected by a Peltier cooled CCD detector.

Powder X-ray diffraction

Powder XRD measurements were performed using a Bruker D8 Advance instrument equipped with a Cu Kα X-Ray source (hν = 8047.8 eV). The microcrystalline sample was prepared as a thin layer on a glass slide for the measurements.

Thermogravimetric analysis

Thermogravimetric measurements in the temperature range of 25 to 800 °C were performed using a NETZSCH STA 449 F3 Jupiter instrument equipped with Proteus-6.1.0 software. Around 1.5 mg of crystalline sample was loaded into an alumina crucible for the measurement. Nitrogen and argon were used as purge gases during the measurement with a thermal flow rate of 10 °C/min.

Crystallographic details

Single crystal X-ray diffraction (SC-XRD) of a good quality single crystal was performed using a Bruker D8 VENTURE single crystal X-ray diffractometer equipped with graphite monochromatic Mo Kα (λ = 0.71073 Å) radiation and a PHOTON 100 CMOS detector. The data collection was performed at 283 K. The automatic cell determination routine, with 24 frames at two different orientations of the detector was employed to collect reflections for unit cell determination. Further, intensity dates for structure determination were collected through an optimized strategy which gave an average 4-fold redundancy. The program APEX3-SAINT (Bruker, 2016) was used for integrating the frames, followed by a multi-scan absorption correction using the program SADABS

(Bruker, 2016). The structure was solved by SHELXT-2014 (Sheldrick, 2014) and refined by full-matrix least squares techniques using SHELXL-2018, (Sheldrick, 2018) software package. Hydrogens on all carbon and boron atoms were fixed at calculated positions and refined as riding model with C-H or B-H = 1.10 Å, $U_{iso}(H) = 1.2U_{eq}$ (C or B).

Computational details

The DFT calculations are carried out using Vienna Ab-Initio Simulation Package (VASP) with generalized gradient approximation (GGA) of Perdew–Burke–Ernzerhof (PBE) functional.[3,4] Projector augmented wave (PAW) method is used for treating ion electron interactions.[5] The ionic relaxations have been carried out using a conjugate gradient algorithm with convergence criteria of 10^{-4} eV for minimum energy and 0.05 eVÅ^{-1} for Hellmann-Feynman forces on atoms. The Brillouin zone was sampled at the Gamma point (1×1×1). To study the energetics of CO_2 electrochemical reduction, we have used computational hydrogen electrode (CHE) model.[6]

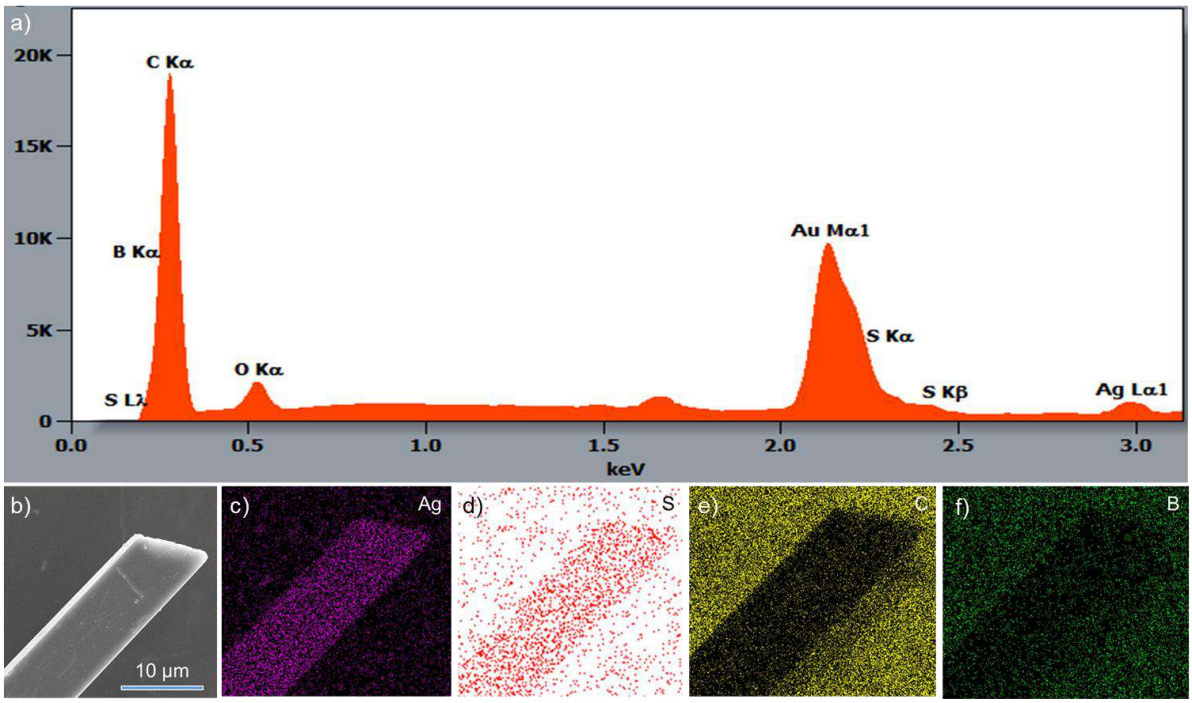


Figure S1. a) The EDS spectral profile of Ag-CBT crystal. b) FESEM micrograph of a single crystal used for elemental mapping. c-f) Elemental maps of the respective elements present in the crystal. The Au content is due to the gold sputtering on the crystal.

Table S1. Crystal data and structure refinement for Ag-CBT framework.

Identification code	Ag-CBT	
CCDC	2431392	
Empirical formula	$C_2H_{11}AgB_{10}S$	
Formula weight	283.14	
Temperature	200(2) K	
Wavelength	0.71073 Å	
Crystal system	Monoclinic	
Space group	P 21/m	
Unit cell dimensions	a = 9.2333(15) Å	α= 90°.
	b = 7.1911(10) Å	β= 97.372(6)°.
	c = 15.961(3) Å	γ = 90°.
Volume	1051.0(3) $Å^3$	
Z	4	
Density (calculated)	1.789 Mg/m^3	
Absorption coefficient	2.051 mm^{-1}	
F(000)	544	
Crystal size	0.200 x 0.150 x 0.100 mm^3	
Theta range for data collection	2.709 to 30.047°.	
Index ranges	-12<=h<=12, -10<=k<=10, -22<=l<=22	
Reflections collected	35235	
Independent reflections	3262 [R(int) = 0.0471]	
Completeness to theta = 25.242°	99.5 %	
Absorption correction	Semi-empirical from equivalents	
Max. and min. transmission	0.7460 and 0.6476	
Refinement method	Full-matrix least-squares on F^2	
Data / restraints / parameters	3262 / 64 / 148	
Goodness-of-fit on F^2	1.054	
Final R indices [I>2sigma(I)]	R1 = 0.0422, wR2 = 0.0897	
R indices (all data)	R1 = 0.0485, wR2 = 0.0935	
Extinction coefficient	n/a	
Largest diff. peak and hole	1.895 and -1.645 e.$Å^{-3}$	

Table S2. Atomic coordinates ($\times 10^4$) and equivalent isotropic displacement parameters ($Å^2 \times 10^3$) for Ag-CBT framework. U(eq) is defined as one third of the trace of the orthogonalized U^{ij} tensor.

	x	y	z	U(eq)
Ag(1)	3697(1)	4816(1)	8912(1)	35(1)
S(1)	2091(1)	2500	8211(1)	21(1)
S(2)	5041(1)	7500	9469(1)	22(1)
B(1)	2491(5)	2500	7094(3)	21(1)
B(2)	1416(8)	3704(13)	6268(3)	80(3)
B(3)	1562(9)	2500	5366(4)	61(2)
B(4)	3255(8)	2500	5068(4)	39(1)
B(5)	4219(8)	3665(11)	5874(3)	74(2)
B(6)	4270(8)	2500	6823(4)	67(3)
B(7)	3175(11)	545(8)	6613(3)	76(2)
B(8)	6691(5)	7500	8903(3)	19(1)
B(9)	6660(8)	7500	7786(4)	70(3)
B(10)	7286(6)	9447(8)	8379(5)	65(2)
B(11)	8203(6)	8711(14)	7529(4)	88(3)
B(12)	9773(7)	7500	7948(4)	38(1)
B(13)	9832(7)	7500	9055(5)	50(2)
B(14)	8296(5)	8701(10)	9313(4)	58(2)
C(1)	2531(12)	4420(9)	5523(4)	98(2)
C(2)	9138(5)	9265(7)	8462(4)	60(1)

Table S3. Anisotropic displacement parameters ($Å^2 \times 10^3$) for Ag-CBT framework. The anisotropic displacement factor exponent takes the form: $-2p^2[h^2 a^{*2} U^{11} + ... + 2 h k a^* b^* U^{12}]$

	U^{11}	U^{22}	U^{33}	U^{23}	U^{13}	U^{12}
Ag(1)	28(1)	41(1)	36(1)	-15(1)	11(1)	-13(1)
S(1)	19(1)	23(1)	20(1)	0	4(1)	0
S(2)	21(1)	22(1)	23(1)	0	3(1)	0
B(1)	19(2)	22(2)	20(2)	0	1(2)	0
B(2)	82(4)	135(7)	24(2)	16(3)	6(2)	77(5)
B(3)	35(3)	128(8)	17(3)	0	-4(2)	0
B(4)	46(4)	49(4)	21(3)	0	3(2)	0
B(5)	101(4)	101(5)	21(2)	-6(3)	15(2)	-74(4)
B(6)	24(3)	158(9)	21(3)	0	4(2)	0
B(7)	174(8)	29(3)	30(2)	4(2)	35(4)	35(3)
B(8)	19(2)	18(2)	19(2)	0	-1(2)	0
B(9)	22(3)	166(9)	21(3)	0	-1(2)	0
B(10)	43(3)	35(3)	126(5)	46(3)	43(3)	17(2)
B(11)	39(3)	165(8)	63(3)	73(4)	21(2)	23(4)
B(12)	28(3)	52(4)	36(3)	0	12(2)	0
B(13)	20(3)	95(6)	33(3)	0	-2(2)	0
B(14)	26(2)	90(4)	60(3)	-53(3)	14(2)	-25(2)
C(1)	209(7)	54(3)	38(3)	19(3)	37(4)	40(4)
C(2)	41(2)	27(2)	119(4)	-3(2)	42(3)	-10(2)

Table S4. Hydrogen coordinates ($\times 10^4$) and isotropic displacement parameters ($Å^2 \times 10^3$) for Ag-CBT framework.

	x	y	z	U(eq)
H(2)	431	4518	6390	96
H(3)	609	2500	4856	73
H(4)	3533	2500	4405	46
H(5)	5191	4495	5741	88
H(6)	5245	2500	7319	81
H(7)	3398	-783	6973	91
H(9)	5602	7500	7355	84
H(10)	6659	10783	8351	78
H(11)	8176	9552	6936	106
H(12)	10793	7500	7637	46
H(13)	10896	7500	9480	60
H(14)	8346	9538	9908	70
H(1)	2180(60)	5480(60)	5150(30)	72
H(2C)	9610(60)	10390(50)	8340(40)	72

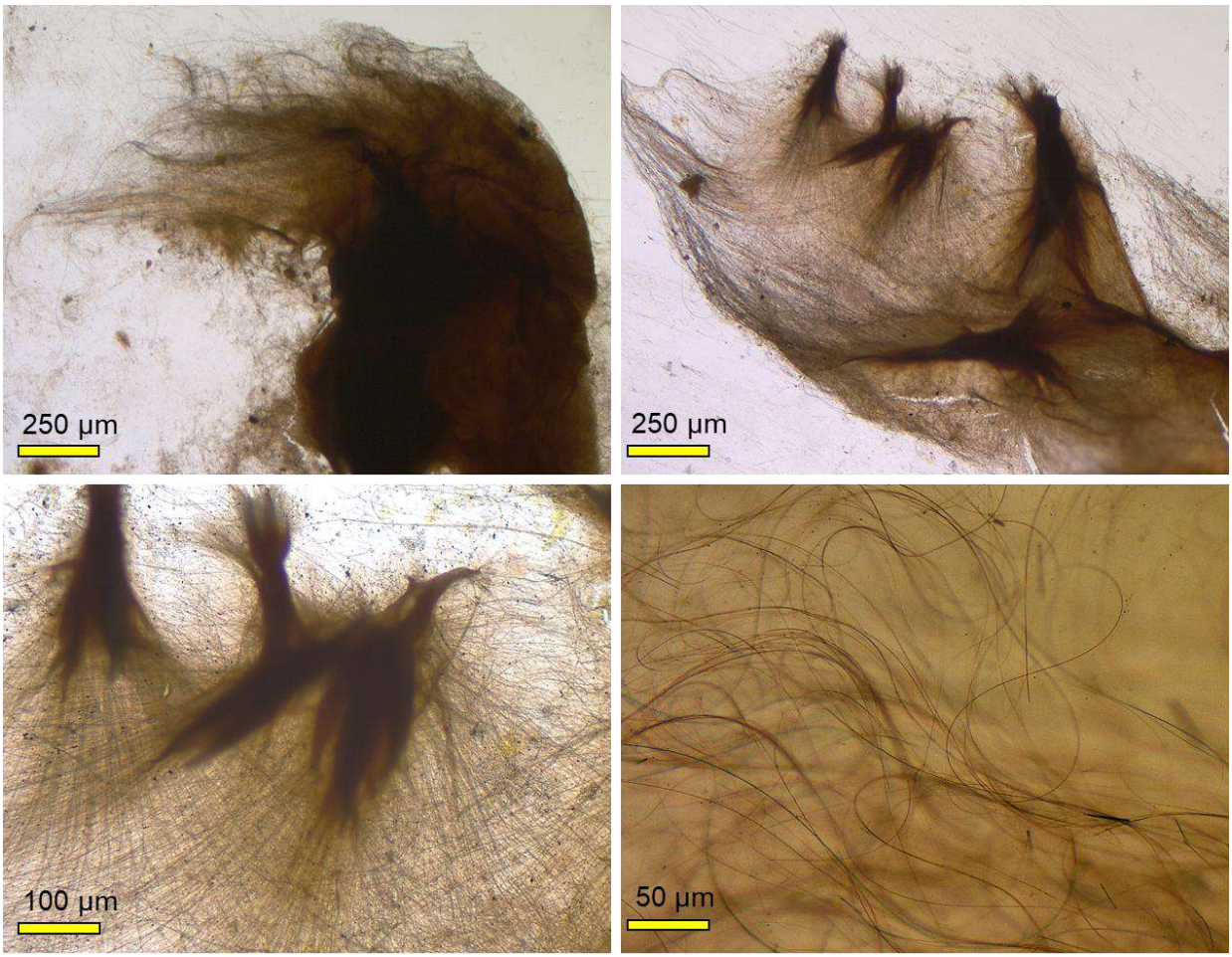


Figure S2. Optical micrographs of the hair-like solids formed from the hydrothermal reaction of $AgNO_3$ and M_9 ligand, captured at varying magnifications.

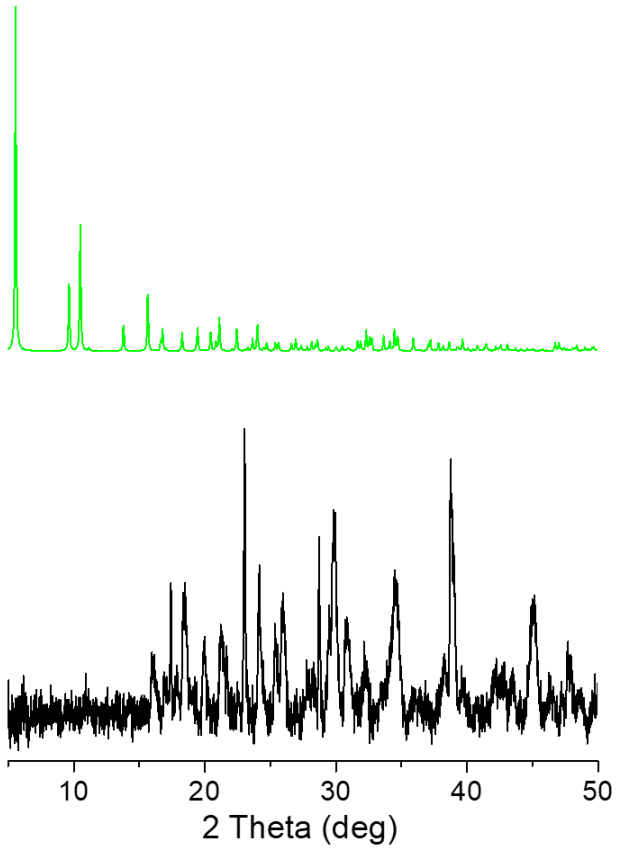


Figure S3. Powder X-ray diffraction pattern of the hair like solids (black trace) obtained after the 48 hours hydrothermal reaction of $AgNO_3$ and M_9 ligand. A comparative simulated diffraction pattern (green trace) of Ag-CBT is also shown here.

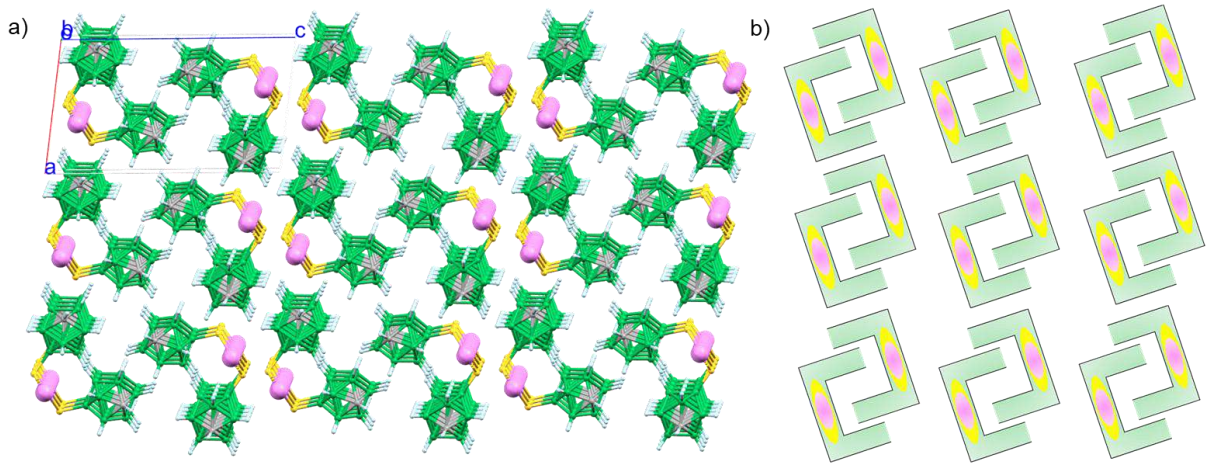


Figure S4. a) The (3×3×3) extended packing of the Ag-CBT framework reveals two one-dimensional U-shaped interlocking layers. Color code: pink =Ag, yellow = S, green = B, grey = C, light blue = H. b) Schematic representation of the interlocking.

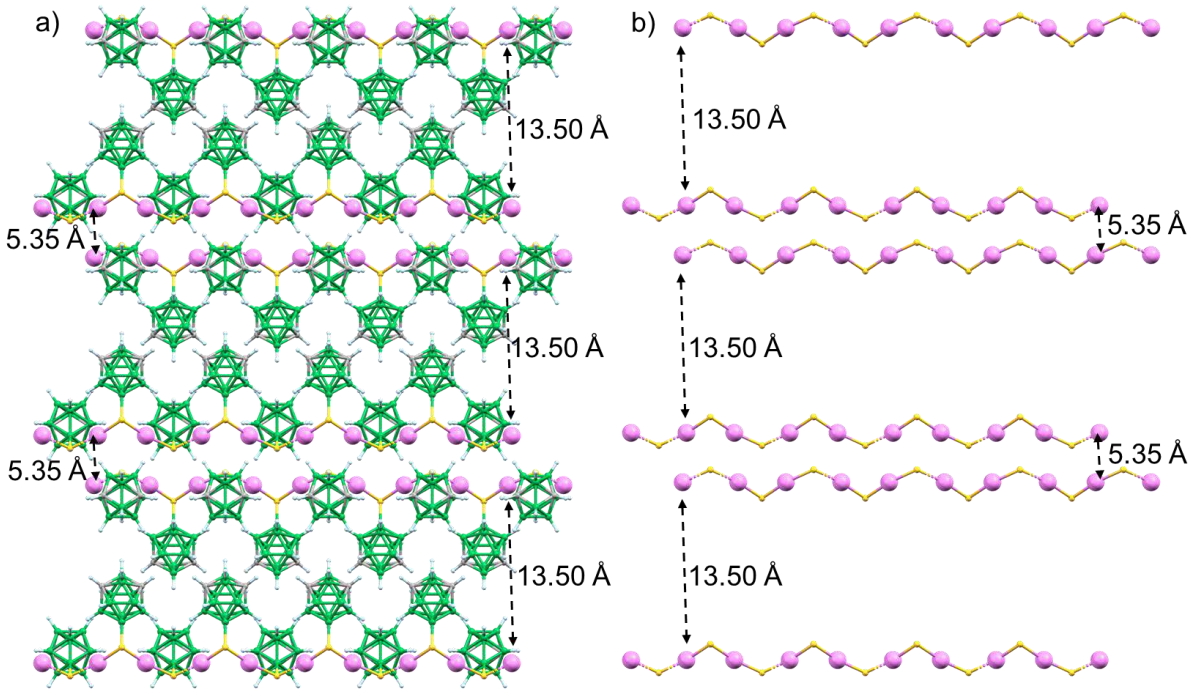


Figure S5. a) An extended packing structure of the Ag-CBT solid along the a-axis, featuring notable Ag···Ag distances. b) The same framework without carboranes.

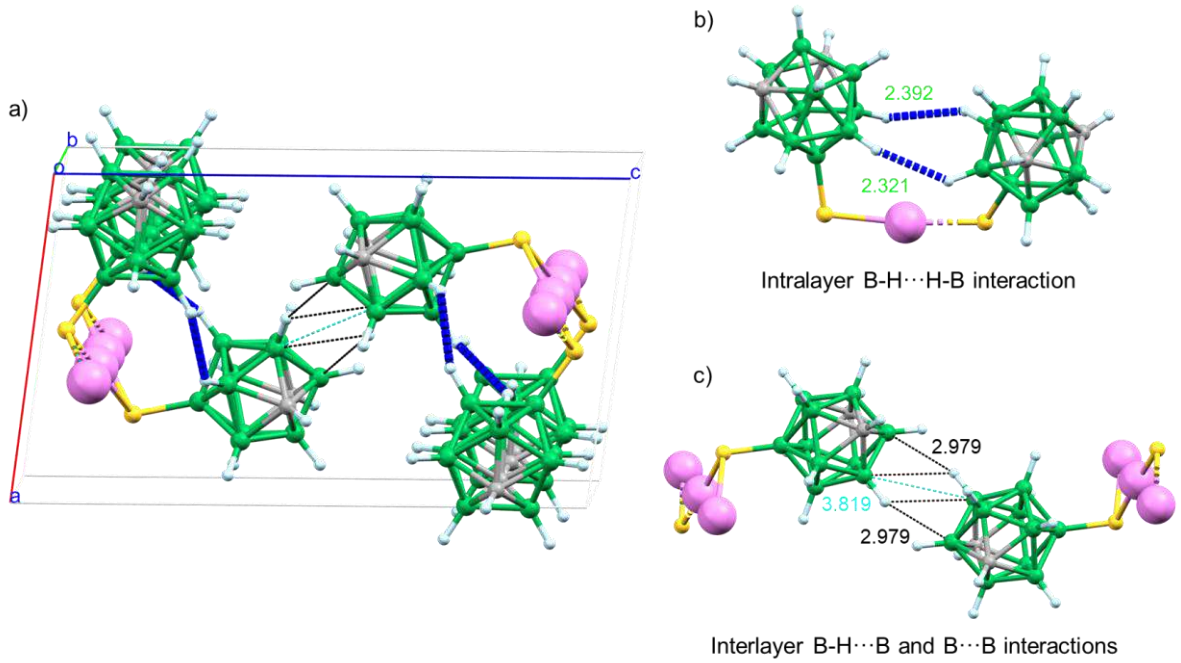


Figure S6. a) Carborane-centered short-contact intermolecular interactions were observed between the two layers. Expanded view of b) intralayer B-H···H-B interactions, and c) interlayer B-H···B and B···B interactions.

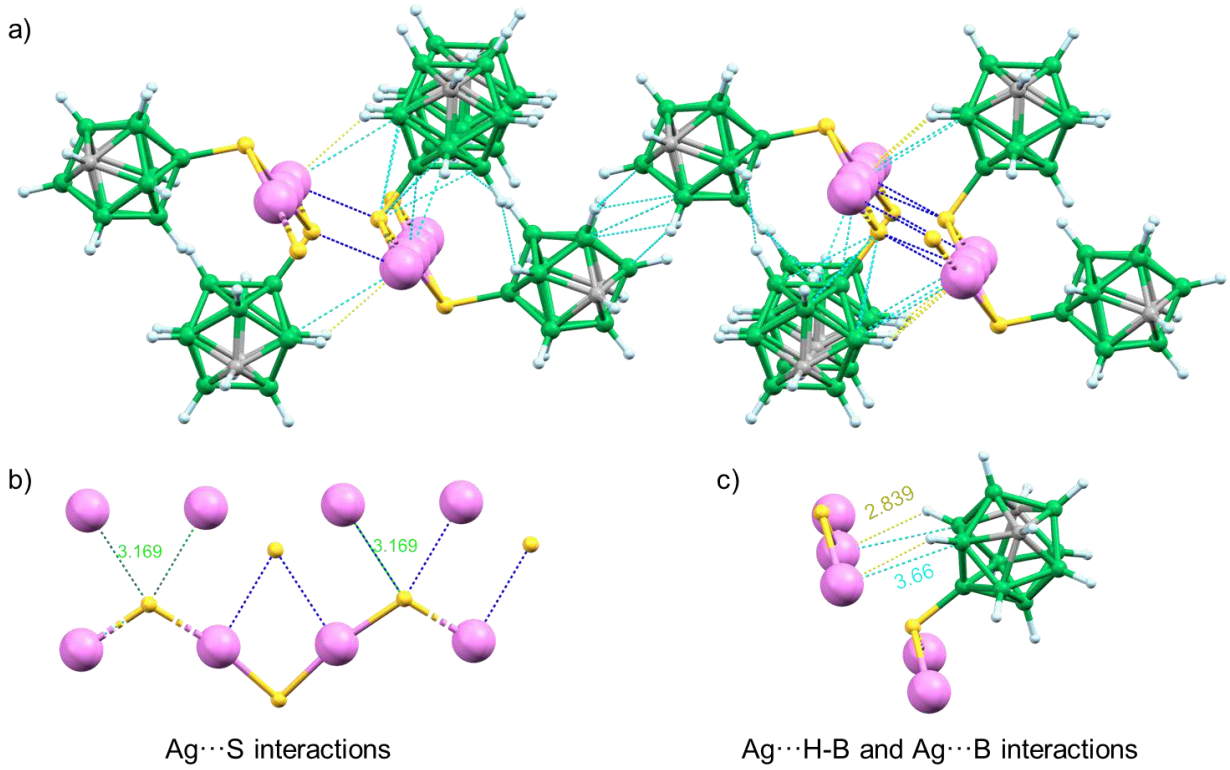


Figure S7. a) Metal-centered short contact intermolecular interactions observed in Ag-CBT framework solids. Expanded view of b) Ag···S interactions, and c) B-H···Ag and Ag···B interactions.

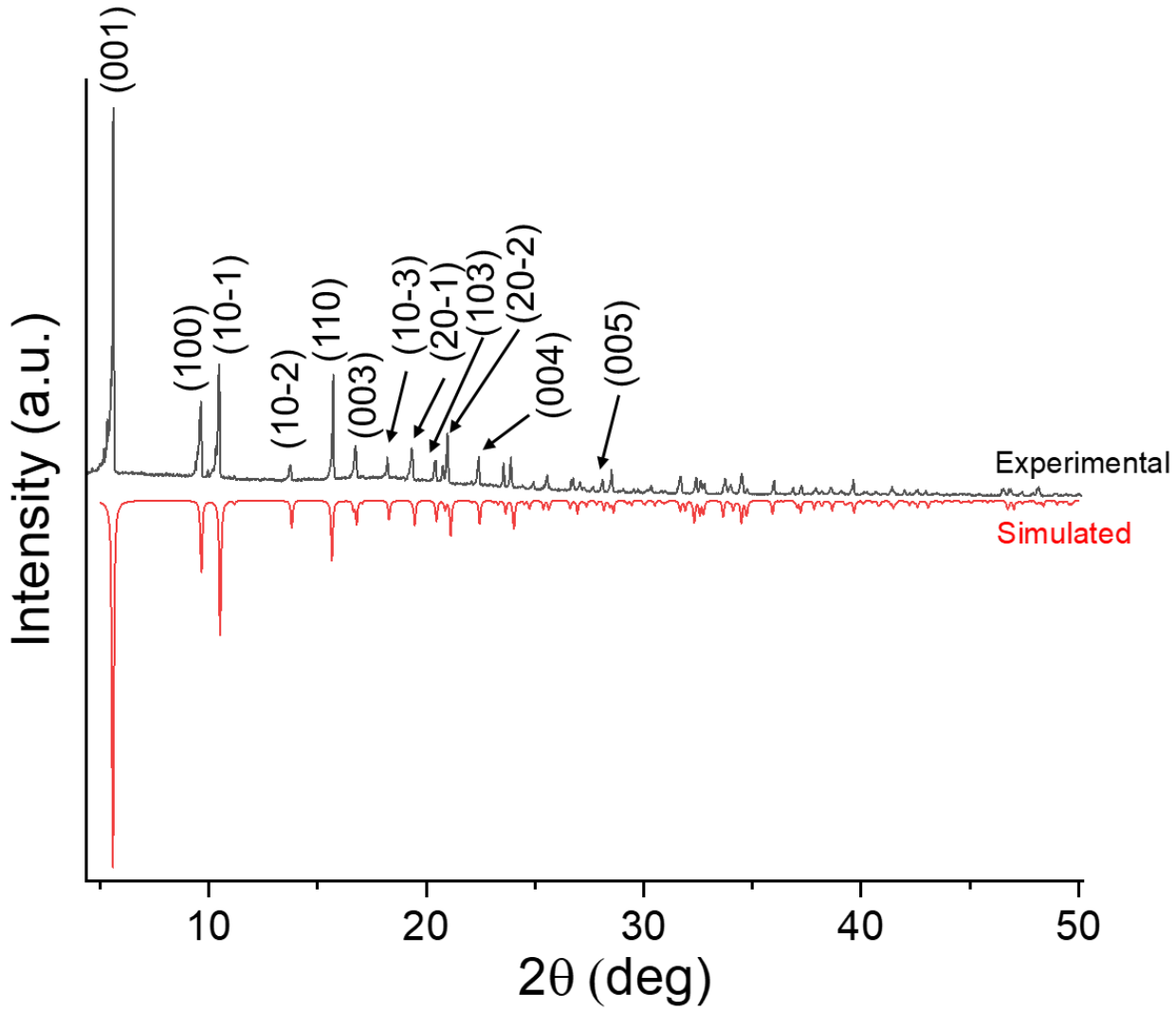


Figure S8. The experimental PXRD spectrum of the Ag-CBT framework compared with the simulated spectrum obtained from SCXRD data. Peaks of interest in the lower region are assigned here.

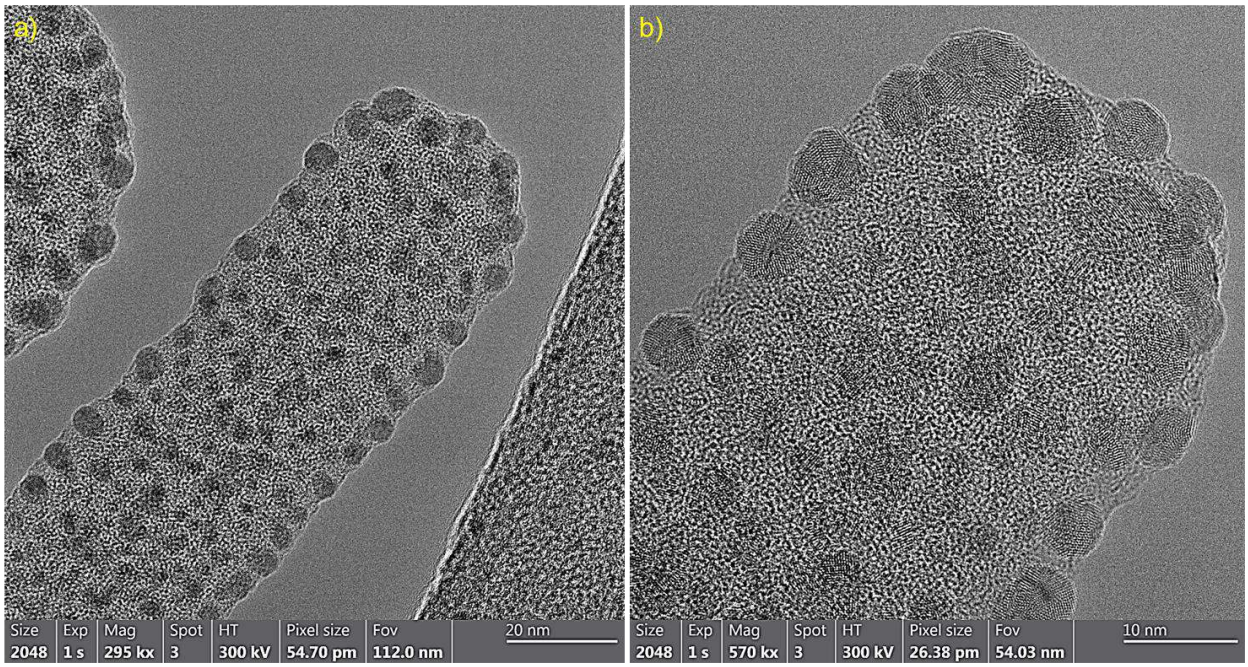


Figure S9. Low-resolution STEM micrographs of a rod-shaped Ag-CBT crystal under different magnification. The micrographs revealed the emergence of atom-resolved crystalline domains under electron beam irradiation.

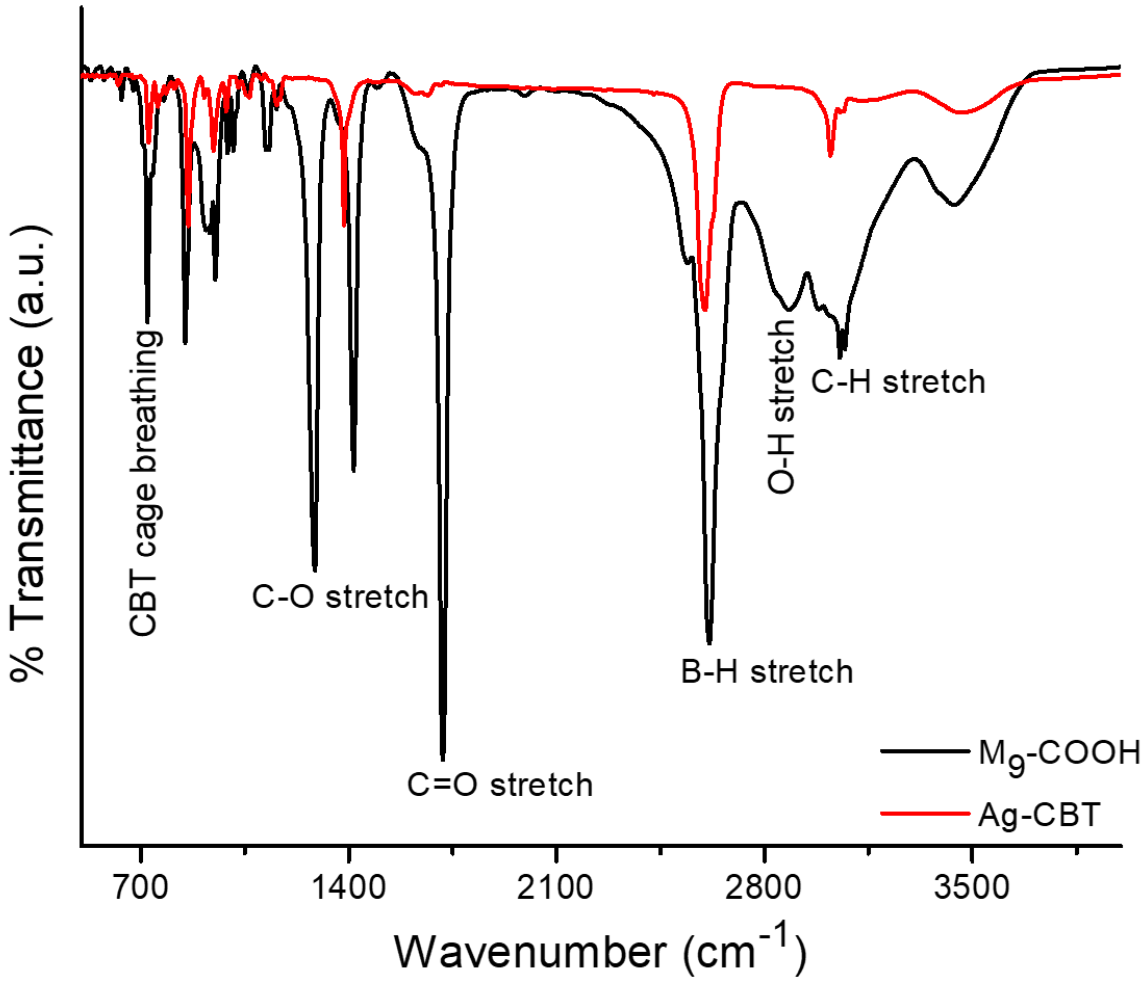


Figure S10. Comparative FT-IR spectra of M_9-COOH ligand and Ag-CBT framework solids. The decarboxylation of M_9-COOH in the Ag-CBT framework was evidenced by the disappearance of the 1717 cm^{-1} (C=O stretching), 1286 cm^{-1} (C-O stretching), and 2878 cm^{-1} (O-H stretching) bands. The broad vibrational band observed at ~3500 cm^{-1} is likely due to solvated water molecules.

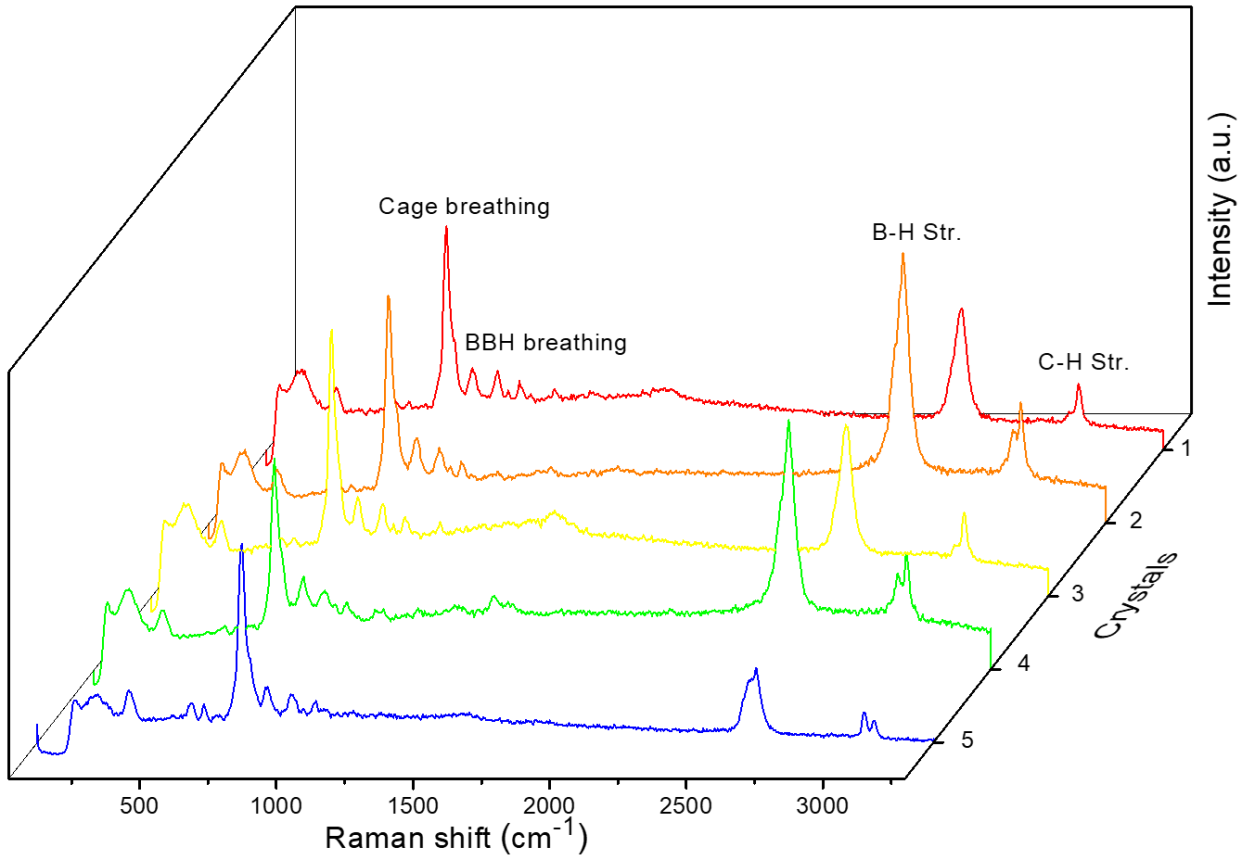


Figure S11. Raman spectroscopic data of Ag-CBT framework were collected, with each spectrum obtained from an individual crystal. The laser excitation used was 532 nm.

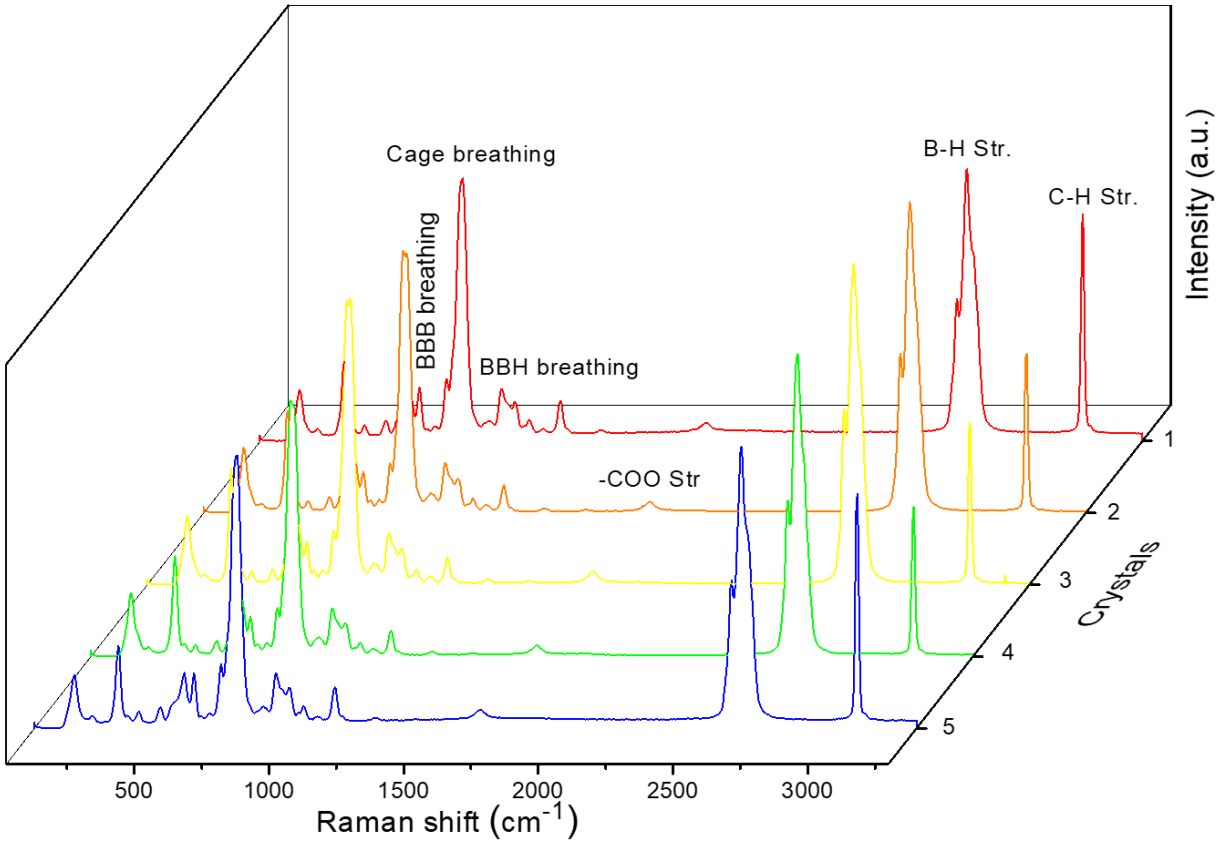


Figure S12. Raman spectroscopic data of M_9-COOH ligand. Each spectrum was collected from an individual single crystal. The laser excitation used was 532 nm.

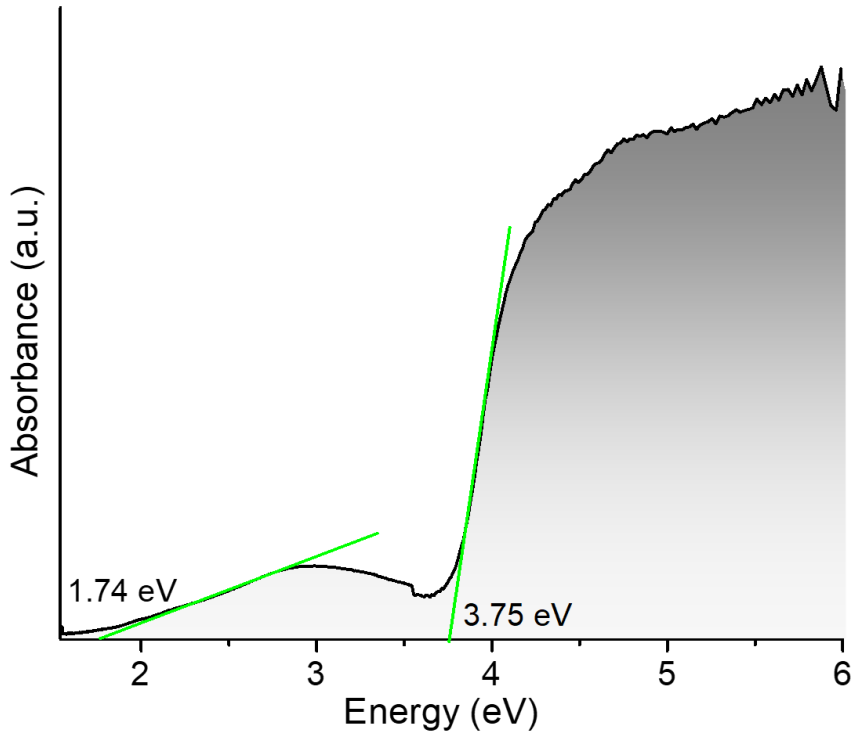


Figure S13. Solid-state UV-vis absorption spectrum of the Ag-CBT framework indicating two optical band gaps of 1.74 and 3.75 eV.

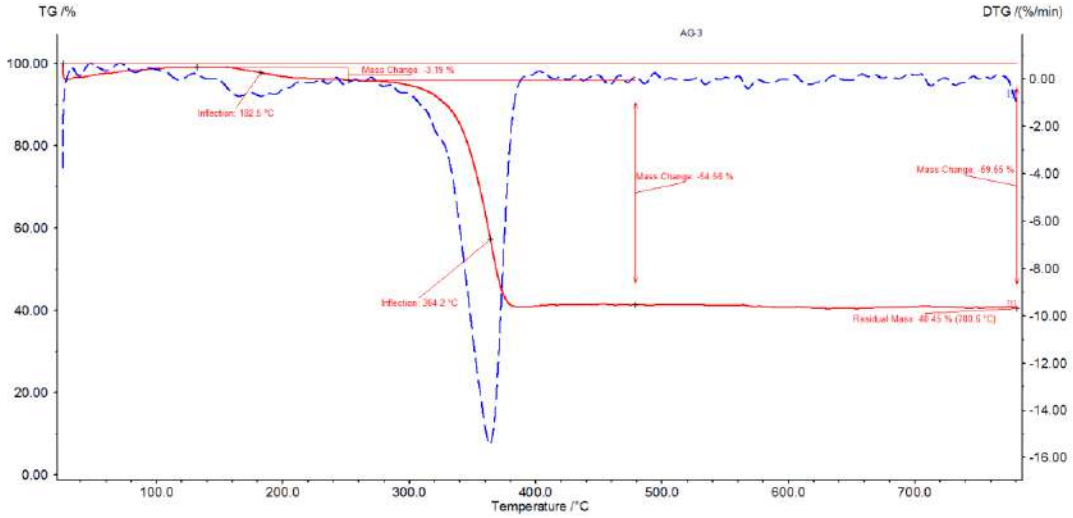


Figure S14. Thermogravimetric and differential thermal analysis plot of microcrystalline Ag-CBT chalcogenide framework. Minor variation (3.19 %) of the mass at 182.5 °C is due to the losses of adsorbed solvent molecules. The decomposition of the framework began at ~300 °C, with maximum mass loss observed at 364 °C.

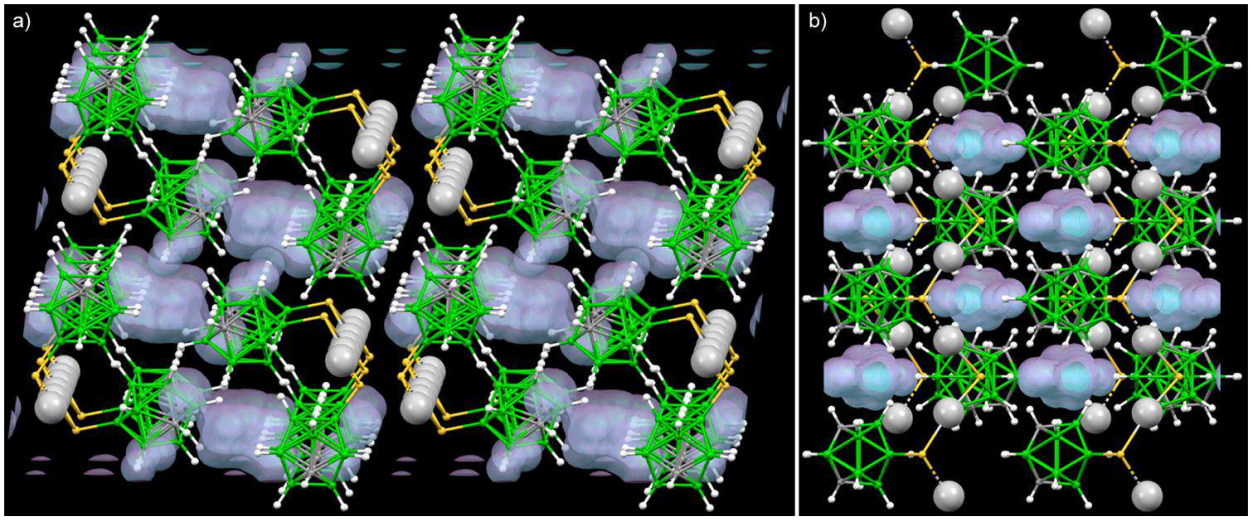


Figure S15. Void spaces present in the (2 × 2 × 2) lattices of the Ag-CBT chalcogenide framework. Voids are calculated using a grid spacing of 0.2 Å and radius of the probe as 0.75 Å. Such voids are present in the 6.5 % volume of the unit cell of the lattice.

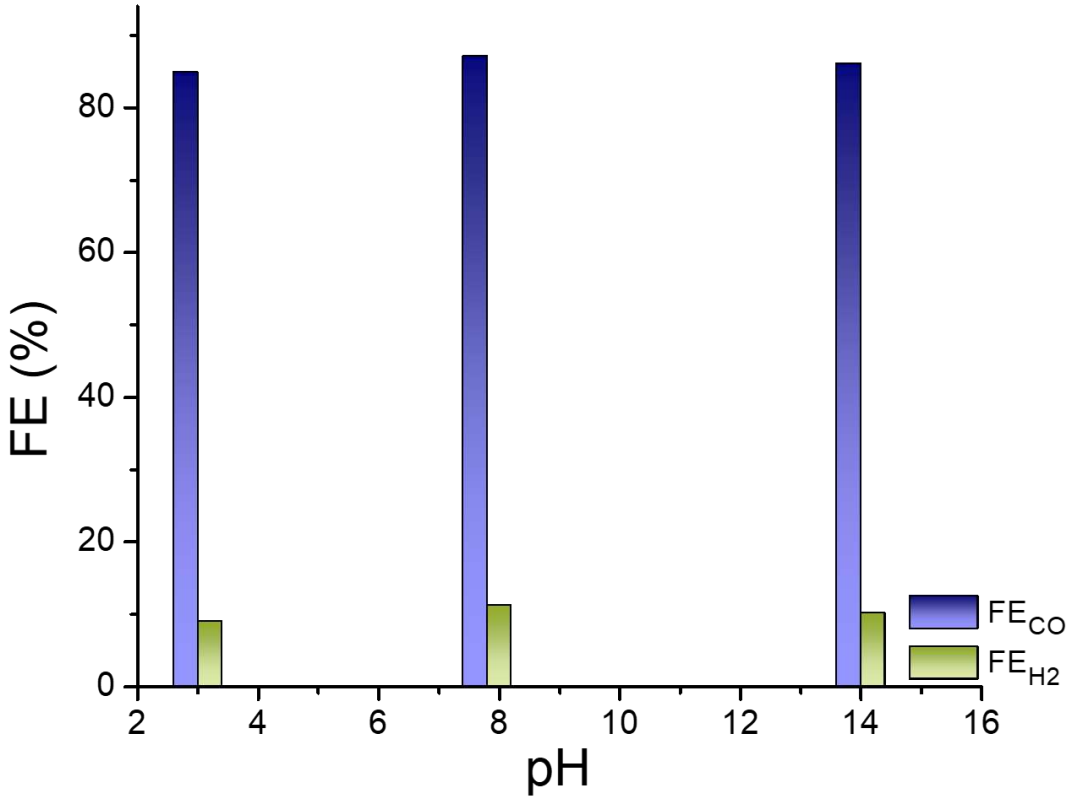


Figure S16. Variation in the Faradic efficiency of the Ag-CBT loaded electrode measured under three different pH conditions.

Table S5. Comparison between various silver based catalysts used for CO_2 electroreduction.

Sl. No	Catalyst	Max FE_{CO} (%) / Max j_{CO} (mA cm^{-2})	E_0 for FE_{CO} (max) (V vs RHE)	Cell setup	Electrolyte	Reference
1.	Ag foil	70.5	−0.75	Two-compartment electrochemical cell	0.5 M $KHCO_3$	7
2.	3 nm Ag nanoparticles	76.8	−0.75	Two-compartment electrochemical cell	0.5 M $KHCO_3$	7
3.	5 nm Ag nanoparticles	84.4	−0.75	Two-compartment electrochemical cell	0.5 M $KHCO_3$	7
4.	Ligand free Cubic Ag nanoparticle	62.7/ 0.1	-0.80	H-cell	0.5 M $KHCO_3$	8
5.	Ligand free octahedral Ag nanoparticle	48.1/ 0.08	-0.80	H-cell	0.5 M $KHCO_3$	8
6.	Nanoporous monolithic Ag nanoparticle	92/ 30	-0.70	H-cell	0.5 M $KHCO_3$	9

7.	Triangular Ag nanoplates	96.8	-0.746	H-cell	0.5 M $KHCO_3$	10
8.	Ag Nanocubes	99	-0.856	Flow-cell	0.1 M KHCO3	11
9.	Ag_{25} cluster	80/ 94	-0.65 V	Flow shell	1 M KOH	12
10.	$ClAg_{14}$ (C≡C $^{t}Bu)_{12}$ Nanocluster	80 /285	-0.65 V	Flow shell	0.5 M KOH	12
11.	Ag-CBT chalcogenide framework solid	86 /98	-0.83	Flow shell	1 M KOH	This work

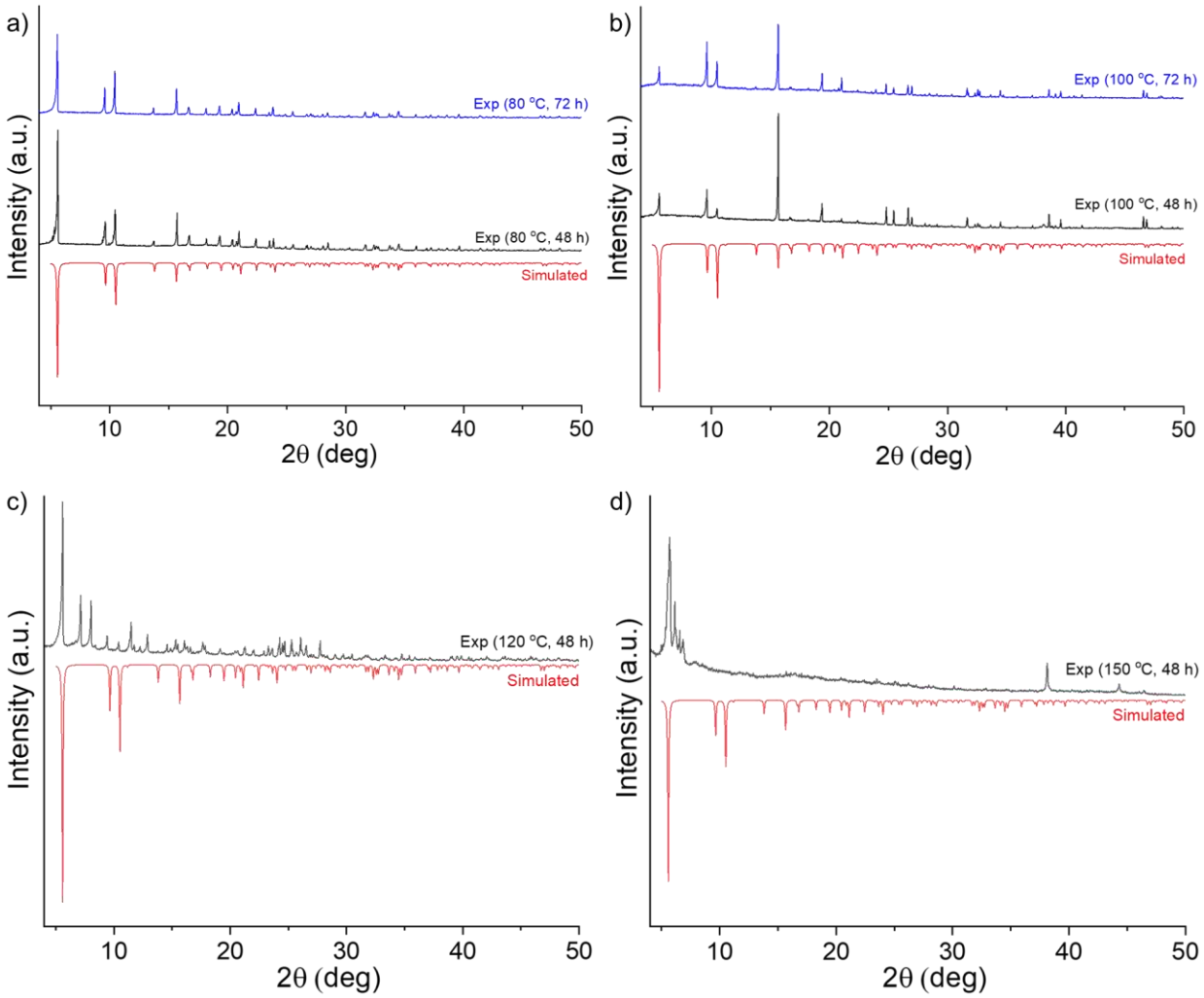


Figure S17. Comparison of simulated and experimental powder X-ray diffraction patterns for various synthetic products obtained from the solvothermal reaction of $AgNO_3$ and M_9-COOH at temperatures of a) 80 °C, b) 100 °C, c) 120 °C, and d) 150 °C.

References:

(1) Goronzy, D. P.; Staněk, J.; Avery, E.; Guo, H.; Bastl, Z.; Dušek, M.; Gallup, N. M.; Gün, S.; Kučeráková, M.; Levandowski, B. J.; Macháček, J.; Šícha, V.; Thomas, J. C.; Yavuz, A.; Houk, K. N.; Danlşman, M. F.; Mete, E.; Alexandrova, A. N.; Baše, T.; Weiss, P. S. Influence of Terminal Carboxyl Groups on the Structure and Reactivity of Functionalized M-Carboranethiolate Self-Assembled Monolayers. *Chem. Mater.* **2020**, *32* (15), 6800–6809.

(2) Liu, K.; Smith, W. A.; Burdyny, T. Introductory Guide to Assembling and Operating Gas Diffusion Electrodes for Electrochemical CO_2 Reduction. *ACS Energy Lett.* **2019**, *4* (3), 639–643.

(3) Kresse, G.; Hafner, J. Ab Initio Molecular-Dynamics Simulation of the Liquid-Metalamorphous- Semiconductor Transition in Germanium. *Phys. Rev. B* **1994**, *49* (20), 14251–14269.

(4) Perdew, J. P.; Chevary, J. A.; Vosko, S. H.; Jackson, K. A.; Pederson, M. R.; Singh, D. J.; Fiolhais, C. Atoms, Molecules, Solids, and Surfaces: Applications of the Generalized Gradient Approximation for Exchange and Correlation. *Phys. Rev. B* **1992**, *48* (11), 6673–6687.

(5) Kresse, G.; Joubert, D. From Ultrasoft Pseudopotentials to the Projector Augmented-Wave Method. *Phys. Rev. B - Condens. Matter Mater. Phys.* **1999**, *59* (3), 1758–1775.

(6) Nørskov, J. K.; Rossmeisl, J.; Logadottir, A.; Lindqvist, L.; Kitchin, J. R.; Bligaard, T.; Jónsson, H. Origin of the Overpotential for Oxygen Reduction at a Fuel-Cell Cathode. *J. Phys. Chem. B* **2004**, *108* (46), 17886–17892.

(7) Kim, C.; Jeon, H. S.; Eom, T.; Jee, M. S.; Kim, H.; Friend, C. M.; Min, B. K.; Hwang, Y. J. Achieving Selective and Efficient Electrocatalytic Activity for CO_2 Reduction Using Immobilized Silver Nanoparticles. *J. Am. Chem. Soc.* **2015**, *137* (43), 13844–13850.

(8) Yang, M.; Zhang, J.; Cao, Y.; Wu, M.; Qian, K.; Zhang, Z.; Liu, H.; Wang, J.; Chen, W.; Weixin, H. Facet Sensitivity of Capping Ligand-Free Ag Crystals in CO_2 Electrochemical Reduction to CO. *ChemCatChem* **2018**, *10*, 5128–5134.

(9) Lu, Q.; Rosen, J.; Zhou, Y.; Hutchings, G. S.; Kimmel, Y. C.; Chen, J. G.; Jiao, F. A Selective and Efficient Electrocatalyst for Carbon Dioxide Reduction. *Nat. Commun.*

2014, *5* (3242), 1–6.

(10) Liu, S.; Tao, H.; Zeng, L.; Liu, Q.; Xu, Z.; Liu, Q.; Luo, J. L. Shape-Dependent Electrocatalytic Reduction of CO_2 to CO on Triangular Silver Nanoplates. *J. Am. Chem. Soc.* **2017**, *139* (6), 2160–2163.

(11) Liu, S.; Sun, C.; Xiao, J.; Luo, J. L. Unraveling Structure Sensitivity in CO_2 Electroreduction to Near-Unity CO on Silver Nanocubes. *ACS Catal.* **2020**, *10* (5), 3158–3163.

(12) Seong, H.; Chang, K.; Sun, F.; Lee, S.; Han, S. M.; Kim, Y.; Choi, C. H.; Tang, Q.; Lee, D. $ClAg_{14}(C{\equiv}C^tBu)_{12}$ Nanoclusters as Efficient and Selective Electrocatalysts Toward Industrially Relevant CO_2 Conversion. *Adv. Sci.* **2024**, *11* (2306089), 1–13.

THE JOURNAL OF PHYSICAL CHEMISTRY LETTERS
A JOURNAL OF THE AMERICAN CHEMICAL SOCIETY

pubs.acs.org/JPCL

Letter

Charging of Ligand-Protected Gold Nanoparticles in Electrospray Ionization: Probing Ligand Bond Strength by Charge Detection Mass Spectrometry

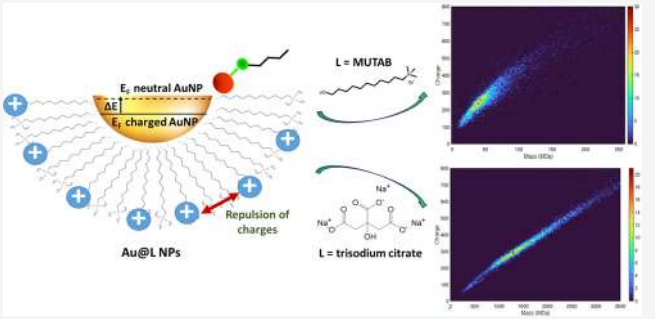
B. S. Sooraj, Sylvain Maclot, Anagha Jose, Clothilde Comby-Zerbino, Tessa Reinert, Keerthana Unni, Rodolphe Antoine,* and Thalappil Pradeep*

Cite This: *J. Phys. Chem. Lett.* 2025, 16, 7004−7011

Read Online

ACCESS | Metrics & More | Article Recommendations | Supporting Information

ABSTRACT: The ionization of large, megadalton (MDa) and gigadalton (GDa), nanoparticles leading to their mass spectrometric analysis has been an interesting challenge in the past decades. In this work, the charging behavior of 20 nm sized gold nanoparticles (AuNPs) protected with 11-mercaptoundecyl-*N*,*N*,*N*-trimethylammonium bromide (MUTAB) ligands of ∼50 MDa was studied by using Charge Detection Mass Spectrometry (CDMS) interfaced with electrospray ionization. The findings indicate that these nanoparticles can achieve a charging state higher than the Rayleigh limit for a 20 nm solvent droplet. However, citrate-protected 60 nm sized AuNPs of ∼1.3 GDa charge only ∼0.45 times the Rayleigh limit, under identical electrospray conditions. The higher efficiency of charging in Au−MUTAB nanoparticles may be correlated to the higher ligand binding energy of the gold−sulfur interface compared to the gold−citrate interface. This work showcases the impact of ligand selection on the electrostatic behavior, stability, and charging of nanoparticles in electrospray ionization mass spectrometric applications.



Ligand-protected metal nanoparticles are a class of materials well-known for their diverse applications.[1−7] Understanding the composition of these materials is crucial for tuning their properties.[8] However, nanoparticles have an intrinsic size dispersion leading to high heterogeneity in both mass and charge, which prevents their analysis by conventional mass spectrometry techniques.[9] Indeed, as heterogeneity is very high, resulting m/z spectra are highly congested and do not provide useful information.[10] Single-ion MS methods[11] overcome these limitations by directly measuring the mass for each individual ion. In the past decade, charge detection mass spectrometry (CDMS), a single-ion MS method, has evolved as an alternative technique for weighing heterogeneous samples[12] with masses in the megadalton (MDa) range.[13] CDMS (and related orbitrap-based CDMS) combines mass spectrometry (MS) with (direct or indirect) charge detection to measure the charge and m/z ratio of individual particles.[14,15] Further, all the individual nanoparticle measurements are compiled into histograms to obtain the charge and mass distribution of the sample.[16] Werts et al. first demonstrated the importance of CDMS in a low mass resolution mode for the determination of the size distribution and composition of gold nanoparticles, where the mass can be directly translated to particle size, if the density and shape of the particle are known.[17] Advancements in CDMS instrumentation further demonstrated its application in characterizing assemblies of larger nanoparticles, providing insights into their shape, surface properties, etc.[18−20]

In the past, charging of nanoparticles through electrospray ionization (ESI) has been a topic of significant interest.[21,22] In ESI, highly charged droplets are generated from solutions, followed by solvent evaporation and droplet fission, leading to particles (or analytes) carrying multiple charges.[23] In ESI, the maximum charge a liquid droplet could accommodate without undergoing Coulombic fission is driven by the Rayleigh limit.[24] This limit originates from the competition between the bulk electrostatic repulsion and the interfacial surface tension. Beyond this limit, the droplet becomes unstable and splits into smaller droplets with lower charges. The Rayleigh limit serves as a benchmark for assessing the charging capacity of charged analytes transferred into the gas phase by the electrospray process.[25] The charging phenomenon is dependent on various factors, such as the size and shape of the analyte and instrumental settings, etc. In the past decade, several studies

Received: April 9, 2025
Revised: June 24, 2025
Accepted: June 26, 2025
Published: June 30, 2025



Downloaded via INDIAN INST OF TECH MADRAS on December 29, 2025 at 03:14:32 (UTC).
See https://pubs.acs.org/sharingguidelines for options on how to legitimately share published articles.

© 2025 American Chemical Society

were reported on increasing charging of analytes in ESI. The commonly used strategies include, changing solvent composition, pH, addition of supercharging agents, etc.[26,27] However, for nanoparticles, these strategies were limited to polymeric nanoparticles[21] and such efforts were not very successful in achieving high charging for ligand-protected metal nanoparticles.

In this work, we utilize ligand engineering as a strategy to achieve a high charging capability of gold nanoparticles. The limit of charge detection has drastically improved from ∼350 e (elementary charges) in the first generation of CDMS instrument[28] to ∼70 e in the present CDMS instrument which uses cool field-effect transistor (coolFET) based detection.[29] Here, we have performed the CDMS analysis of a 20 nm sized gold nanoparticle protected with a cationic thiol ligand, i.e., (11-mercaptoundecyl)-*N*,*N*,*N*-trimethylammonium bromide (MUTAB). These results were compared with that of a 60 nm citrate-protected Au nanoparticle to demonstrate the role of the MUTAB ligand in the charging. The MUTAB ligand provides electrostatic stabilization and enhances the charge-carrying capacity of the nanoparticles, boosting the charging capabilities of the NPs. The higher efficiency of MUTAB in enhancing nanoparticle charging may be correlated to the strength of the thiol-gold binding (leaving the ammonium group free), which is stronger than gold−citrate interaction. A simple model is derived to evaluate the ligand binding strength of gold nanoparticles by charge and mass (or size) measurements through CDMS.

The 20 nm sized Au−MUTAB nanoparticles were synthesized using a reported procedure.[30] The size distribution of the nanoparticle was studied by transmission electron microscopy (TEM), and the images were collected at a lower beam intensity to reduce beam-induced aggregation, as shown in Figure 1c. The images showed that the Au−MUTAB nanoparticles are spherical in shape. The diameter distribution of the particles ranged from 10 to 30 nm, where most of the particles were close to 20 nm in diameter. These nanoparticles were subjected to CDMS analysis, and we obtained a spectrum (Figure 1a) showing the peak maximum at 50 MDa. We have translated the mass obtained from CDMS to the size of the particle by considering their density and shape. The obtained size from these calculations was 20 nm, which corresponds to the mass of 50 MDa for a spherical gold particle with a density of 19.3 g/cm^3 (Figure 1b). This was further verified by using dynamic light scattering (DLS) measurements, as shown in Figure 1d. The measurements were performed using water as the solvent medium. The size distribution showed a similar size range of 10 to 30 nm, which showed a maximum at 20 nm.

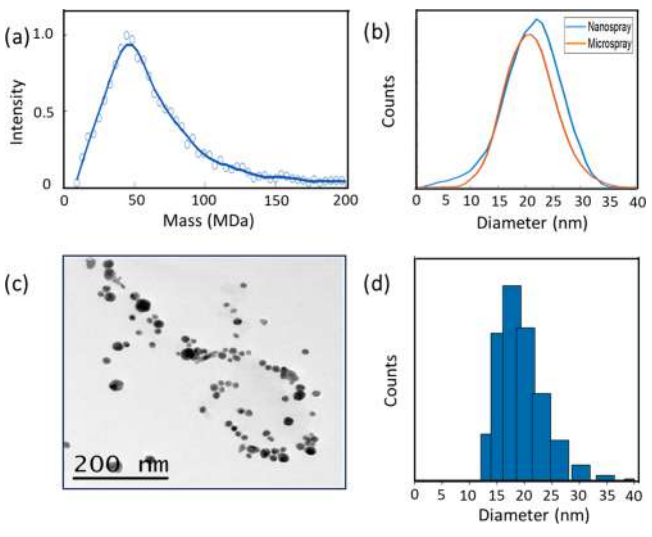


Figure 1. (a) Mass distribution of Au−MUTAB nanoparticles obtained from CDMS analysis; (b) size distribution estimated from the CDMS data obtained under two different spray conditions; (c) TEM image of Au−MUTAB nanoparticles; and (d) size distribution of Au−MUTAB nanoparticles obtained from DLS measurements.

The CDMS analysis of the Au−MUTAB nanoparticles was conducted under two different ionization conditions, i.e., nanospray and macrospray. Both of these techniques primarily differ in terms of the scale of the spray, the ionization technique, and the sample volumes that they handle. The samples used for the measurements were diluted in a water/methanol (1:1) mixture to a concentration of 50 μM (in terms of elemental gold concentration). Figure S1 shows the data obtained from the CDMS analysis under both spray conditions. Figure S1a shows the mass versus charge data obtained for the sample under nanospray ionization conditions. Each point in the graph represents the measurement of a single ion. The streak extends from 100 e (elementary charges) to around 450 e. Figure S1b shows the typical mass distribution from CDMS, with a broad peak centered at 50 MDa. Figure S1c shows the charge distribution for each ion observed in the analysis, which shows a broad peak centered around 250 e due to the main peak of 50 MDa in mass distribution. The broad distribution in the mass distribution accounts to the polydispersity in the sample which is evident from their TEM and DLS measurements. The mass versus charge data obtained for the sample under macrospray ionization conditions are shown in Figure S1d. Here the streak extends from 100 e to around 500 e. Figure S1e shows a similar mass distribution, with a broad peak centered at 50 MDa that is more intense than the nanospray results. Figure S1f shows the charge distribution having a more intense peak centered at around 250 e only.

The data obtained from both nanospray and macrospray conditions were compared, as shown in Figure S2, to better understand the data. The mass distribution plot (Figure S2a) illustrates that in both cases the peaks are centered at 50 MDa. But for macrospray, the intensity of the peak at 50 MDa is more than in nanospray. This hints that, in macrospray, the analyzed sample has a greater number of species with 50 MDa mass, which can be due to the larger volume of the sample used. In the case of nanospray, we can observe more intense peaks in the higher mass region above 100 MDa. This slight increase in the intensity might be due to the formation of aggregated dimers. The particle size estimation from CDMS also shows similar results in both spray conditions (Figure S2b), which further supports the precision of our results.

The maximum charge deposited on a spherical ion can be predicted from the Rayleigh charge limit for a water droplet with the same diameter as the analyte. The charge corresponding to the Rayleigh limit, Z_R, is given by $eZ_R = 8\pi(\varepsilon_0\gamma R^3)^{1/2}$ where R is the droplet radius, γ is the surface tension of droplets (72 nN/m), and ε_0 is the permittivity of the surrounding media.[31] The theoretically calculated Rayleigh limit is illustrated in Figure 2a, where the dotted line indicates the limiting charge at the corresponding size distribution. To further understand this, we plotted the histogram of the fraction of the Rayleigh limit in the sample (Figure 2b). The

https://doi.org/10.1021/acs.jpclett.5c01075
J. Phys. Chem. Lett. 2025, 16, 7004−7011

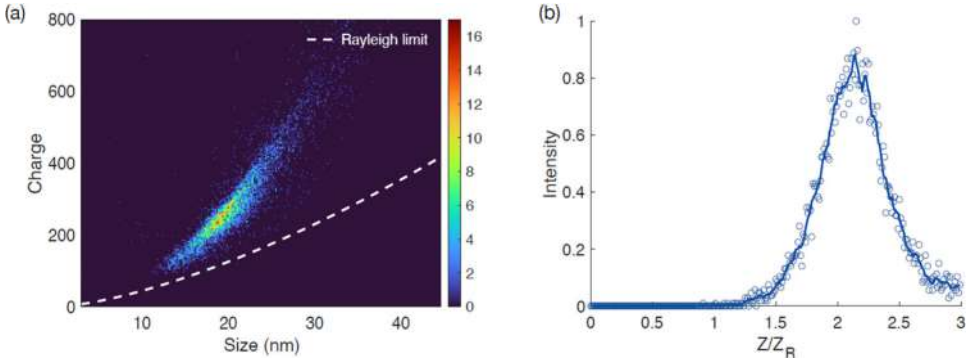


Figure 2. (a) Charge vs size plot of Au−MUTAB nanoparticles. The dotted curve shows the calculated Rayleigh limit. (b) Plots of the fraction of the Rayleigh limit (z/z_R) for Au−MUTAB nanoparticles.

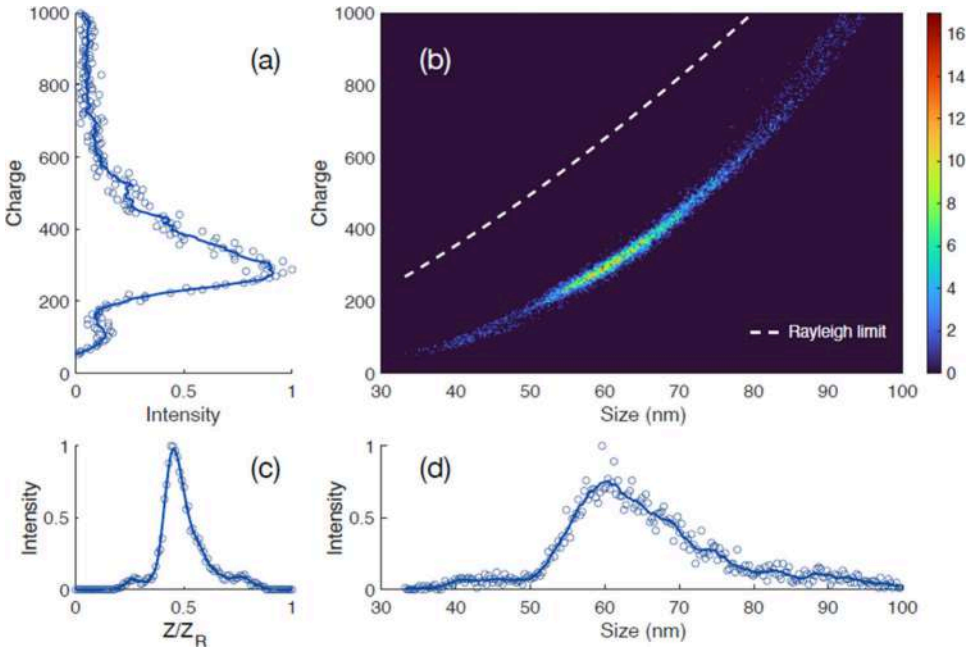


Figure 3. CDMS plots of a 60 nm sized Au−citrate nanoparticles showing the (a) charge distribution, (b) charge vs size plot, and (d) size distribution. The dotted curve in panel (b) shows the Rayleigh limit. (c) Plots of the fraction of the Rayleigh limit (z/z_R) for Au−citrate nanoparticles.

histogram shows that Z/Z_R ratio is centered around 2.1. It was already observed that ions from nanoparticles in the megadalton range were charged higher than the Rayleigh limit,[18,32] demonstrating that the charging capability of nanoparticles cannot be necessarily driven by the charging of a water droplet with the same diameter as the analyte, which makes sense since nanoparticles may have different morphology, charging nature and origin as water droplets (they can be coated by ligands with permanent charges as it is the case in this study). The fact that MUTAB-capped AuNPs (20 nm size) have charging exceeding the Rayleigh limit means that the charging of electrosprayed NPs is not driven by the charging of a water droplet with the same diameter as the analyte. The charging capability is, in fact, driven by the stability of capping ligands on the NP surface, possessing permanent charges.

To understand the role of MUTAB ligands on the charging behavior of nanoparticles, we have also studied 60 nm sized gold nanoparticles protected with a citrate ligand. The size distribution of the particles obtained from TEM is shown in Figure S3. The size of the particles ranged from 40 to 80 nm, and centered at 60 nm. The data obtained from the CDMS analysis of 60 nm sized Au−citrate nanoparticles are shown in Figure 3. The mass distribution shows a broad peak ranging from 700 to 2500 MDa, centered around 1300 MDa (Figure S4). The corresponding charge analysis shows a peak centered at 300e, with a broad distribution from 200 to 600e (Figure 3a). The charging capacity of the Au−citrate nanoparticle was compared with the Rayleigh limit of a 60 nm sized 1:1 water:methanol droplet, as illustrated in Figure 3b. The dotted lines imply that the charging capacity of the nanoparticle is much less than the limiting charges. A histogram of the fraction of Rayleigh limit in the sample was plotted (Figure 3c), which inferred that the Z/Z_R is centered around 0.45, with the maximum charge reaching ∼70−80% of that corresponding to the Rayleigh limit, confirming their low charging capacity.

The spray conditions under negative ion mode using the standard pressurized electrospray inlet were much more difficult to reproduce and maintain than those under positive ion mode. Hence, the charging studies for both gold nanoparticles (AuNPs) were done in the positive ion mode.

https://doi.org/10.1021/acs.jpclett.5c01075
J. Phys. Chem. Lett. 2025, 16, 7004−7011

Table 1. Summary of the Findings for Citrate-Capped and MUTAB-Capped Gold Nanoparticles by CDMS and DLS Analysis, Leading to the Estimation of the Binding Energy, $E_{L\text{-}Au}$

Type of nanoparticles	Z	R (nm)	N	U (eV)	$E_{L\text{-}Au}$ (eV) Present work	$E_{L\text{-}Au}$ (eV) Literature
MUTAB- capped gold nanoparticles	250	10	6280	6590	1.05	1.7 (Au−S)[33]
Citrate-capped gold nanoparticles	270	19	6280−35343[a]	2907	0.06−0.36[a]	0.09 (Au−O_{COOH})[34]
	297	25	8050−47300[a]	3200	0.09−0.51[a]	
	358	35	12315−69272[a]	3290	0.05−0.27[a]	

[a]The range of $E_{L\text{-}Au}$ is due to the uncertainty in estimating "N", which in turn is due to the uncertainty in estimating the area per ligand.

Our results confirm that the MUTAB ligand plays a crucial role in increasing the charge-carrying capacity of the ligand-protected AuNPs. The long alkyl chain of MUTAB contributes to steric stabilization, preventing nanoparticle aggregation and maintaining colloidal stability even under high-charge conditions. However, the citrate-capped AuNPs only achieve charge states much lower than the Rayleigh limit due to limited surface charge density and weaker electrostatic stabilization. Hence, the nature of the protecting ligand is crucial in developing methodologies for charging a nanoparticle under electrospray ionization. To understand whether there is a role for the negative charge of citrate ligands in the lower charging behavior of Au−citrate nanoparticles, we analyzed different sizes of citrate-capped AuNPs with 40, 60, and 80 nm diameters. The size distribution of these particles obtained from DLS measurements is shown in Figure S5. The charge and mass data obtained from CDMS are shown in Figure S6. The average charge increases from 270e to 297e to 358e for 40, 60, and 80 nm diameter particles, respectively. For 80 nm AuNPs, we succeeded in measuring the ESI-CDMS in both positive and negative ionization modes (Figure S7). However, in negative mode, we observed that the particles appear to carry slightly higher charges than in positive mode (Figure S7e,f). The reason for this difference is that in the negative ionization mode, the source is prone to discharges, and it leads to two effects: (i) ion efficiency in ESI negative mode was severely reduced (by at least 1 order of magnitude), and (ii) unstable spray conditions may lead to incomplete desolvation and/or fragmentation (leading to broader mass and charge distribution). To better understand this, we have made a 2D plot of charge vs mass distribution for 80 nm AuNPs in both modes (Figure S7a,b). While comparing the charging for the same mass (expected for 80 nm AuNPs, e.g., ∼3.11 GDa), we find that the charges are similar in both positive and negative modes of ionization. Hence, the charge distributions in both modes are similar, suggesting that charging capability is not driven by the charge state of the ligands in nanoparticles.

To better appreciate this issue, we aim to develop a simple model to link the charging capability of ligand-protected gold NPs with energetic considerations and particularly the ligand-gold binding properties. Let us assume that citrate- and MUTAB-capped gold nanoparticles are uniformly charged spheres. In these nanoparticles, we have a distribution of charges specified by a charge density, $\rho = Q/V$ (with $Q = Ze$ total charge and V is the volume of the sphere of radius R) and corresponding total electrostatic energy (where the sum of the energies of all possible pairs of charges to be replaced by an integral).

The total energy of a particle, expressed in terms of the total charge of the sphere is

$$U = \frac{3}{5}\frac{Q^2}{4\pi\epsilon_0 R} \tag{1}$$

The isopotential (R, Z) map of the electrostatic energy U (in eV) for a nanoparticle of charge Z and radius R is given in Figure S8.

In 1882, Lord Rayleigh theoretically estimated the maximum charge Q_R a liquid droplet could carry; it is known as the Rayleigh limit, above which a charged, incompressible spherical droplet of radius R and surface tension γ becomes unstable:

$$Q_R = 8\pi\sqrt{\varepsilon_0\gamma R^3} \tag{2}$$

This criterion was particularly powerful to model electrospray processes (e.g., charged residue model (CRM) where Rayleigh-charged nanodroplets that contain a single analyte evaporate to dryness). In particular, the observed agreement between the charges on the proteins and the charges on water droplets of the same size at the Rayleigh limit was attributed because of the multiply charged proteins being formed by CRM.

Let us assume now that for citrate- and MUTAB-protected gold nanoparticles, the limiting factor to charge them by electrospray process is given by the balance between the Coulomb repulsion energy (U) and the Ligand binding energy (E_{lb}) of the capping ligands to the gold surface, assuming that the charges reside on the ligands. Then the limit for charging will be given by

$$U = E_{lb} \tag{3}$$

The total ligand binding energy (E_{lb}) is a product of the number of ligands (N) and the binding energy of each ligand bound to the gold surface ($E_{L\text{-}Au}$), such that $E_{lb} = N \times E_{L\text{-}Au}$. By knowing the values of N, R, and Q, it is possible to estimate the binding energy $E_{L\text{-}Au}$ as

$$E_{L-Au} = \frac{3}{5}\frac{Q^2}{4\pi\epsilon_0 RN} \tag{4}$$

The values of Z and R are estimated from the present CDMS analysis and DLS measurements, respectively. The value of N is calculated knowing the surface coverage of ligands (∼5/nm^2 for thiolates[35] and 0.8−4.5/nm^2 for citrate[36−38]) on the sphere. The estimated $E_{L\text{-}Au}$ energies from the CDMS analysis (see Table 1) are in fair agreement with binding energies reported in the literature for thiolates and citrates. One can argue that the charging capability of gas-phase monolayer-protected metal particles generated by electrospray is driven by the binding energy of ligands, and therefore, charge detection mass spectrometry might be a pertinent probe of the ligand binding strength. The assumption here is that the ligands desorb as integrated units (-SR for MUTAB), although other bond dissociations can also occur. This channel (-SR loss) is most common in nanoparticles, although they dimerize to form RS-SR, R-S-R, and other units during thermal desorption.

https://doi.org/10.1021/acs.jpclett.5c01075
J. Phys. Chem. Lett. 2025, 16, 7004−7011

Usually, in most modeling studies, the ligands are modeled as enveloping uniformly the surface of nanoparticles, assumed as a perfect sphere.[36] In our crude electrostatic model, we assume that MUTAB- and citrate-capped gold nanoparticles are uniformly charged spheres. The energy of such an arrangement can be calculated using classical electrostatics and is shown in eq 1. The effective charge of a nanoparticle can be deduced from zeta-potential measurements.[22] The data obtained from zeta-potential and size measurements of all of the nanoparticles are presented in Table S1. With zeta potentials of 17.6 and −35 mV, the total charge in solution is respectively 20e and 112e for 20 nm MUTAB−AuNPs and 60 nm citrate−AuNPs. However, the charging capacity extracted by zeta measurements cannot be directly compared with gas-phase measurements since zeta potential is the potential difference between the surface of a solid particle and the surrounding liquid in which the particles are dispersed.

The ionization energy of a neutral metallic NP in a vacuum is higher than the corresponding work function of the bulk metal. Hence, electrons in neutral metallic NPs are at a Fermi level lower than that in the bulk metal. In a vacuum, the ionization energy of a neutral AuNP lies somewhere between that of a gold atom, 9.2 eV, and the work function of bulk gold metal, which is approximately 5.3 eV. When the NP is charged due to the presence of adsorbed ionic species or ligands, the difference between these ionization energies under neutral and charged conditions is related to the excess charge on the NP. The excess charge in the nanoparticle is directly related to the outer potential. Hence, when citrate molecules adsorb onto the AuNP, the surface potential of the AuNP changes, leading to the alteration of local Fermi energy levels of the metal nanoparticle, as was modeled by Girault and coworkers.[39] For instance, a surface atom carrying a nucleophilic molecule acquires a small positive charge, and the interior of the colloidal particles receives a corresponding negative charge. The Fermi potential at equilibrium is shifted to a more negative value.[40] Therefore, the charging energy is related to the Fermi energy. However, in our crude electrostatic model, we simplified the gold NP as a uniformly charged sphere, and the charge of the sphere is given by the number of ligands with permanent charges. A schematic representation of these concepts and correlations regarding ligand bond strength (brought by the gold−sulfur interface), charging energy (brought by the repulsion of charged ligands), and modification of the Fermi level of a gold NP due to chemisorption of thiolated ligands is shown in Scheme S1.

The composition of the highly charged Au−MUTAB nanoparticles was tentatively assigned using details in the literature on the surface coverage of ligands on a gold surface. The number of MUTAB ligands on a 20 nm sized spherical particle is estimated to be 6280, and the corresponding number of Au atoms was calculated as 246000, for a 50 MDa particle. The obtained composition of $Au_{\sim 246000}L_{\sim 6280}$ was further verified by elemental analysis, using high-resolution scanning electron microscopy (HRSEM) coupled with energy dispersive X-ray spectroscopy (EDS), as shown in Figure S9. The ratio of the number percentages of Au and S atoms is in good agreement with the assigned composition. Dass et al. had previously reported a methodology to estimate the number of metal atoms and ligands using mathematical modeling, which is termed as the nanoscaling law.[41] These reports show that for nanoparticles protected with linear chain alkyl thiol ligand, the number of Au atoms (N) and ligands (L) follows a mathematical relation, $L = 1.82N^{2/3}$. The 2/3 scaling reflects the surface area to volume ratio of the Platonic solids.[42,43] This suggests that as the size of the nanomolecule increases, the surface area to volume ratio decreases proportionally to the power of 2/3. This is because the volume scales with the cube of the linear size, while the surface area scales with the square. A log−log plot of the number of ligands vs gold atoms in linear alkyl chain thiol-protected gold nanoparticles is shown in Figure 4. Here, we have compared the tentatively assigned

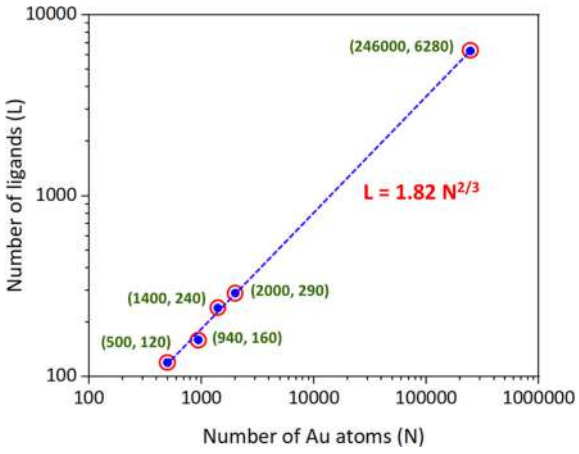


Figure 4. Log−log plot of the number of ligands vs gold atoms in linear alkyl chain thiol-protected gold nanoparticles (Au_nL_m). The composition (m, n) of previously reported nanoparticles is compared with the tentatively assigned composition of Au−MUTAB nanoparticles (246000, 6280).

composition of Au−MUTAB nanoparticles with some known nanoparticles. The larger-sized nanoparticles whose composition is determined to date are $Au_{\sim 2000}L_{\sim 290}$,[44] $Au_{\sim 1400}L_{\sim 240}$,[45] $Au_{\sim 940}L_{\sim 160}$,[46] and $Au_{\sim 500}L_{\sim 120}$.[47] Figure 4 shows that the assigned composition of $Au_{\sim 246000}L_{\sim 6280}$ for the Au−MUTAB nanoparticle agrees with the nanoscaling law, $L = 1.82N^{2/3}$. The linear relation between the points suggests that even at the megadalton mass regime the nanoscaling law is valid and enables the assignment of the composition of nanoparticles.

Our work confirms the role of ligand selection in the design of nanoparticles for applications involving charging in mass spectrometric analysis. Robust patterning is essential for the fabrication of nanoparticle-based devices. Charging of particles is crucial for placing nanoparticles accurately via Coulomb interactions on a charged substrate. In this work, playing with the ligand−gold interface strength (by using thiolates) and permanently charged ligands (trimethylammonium group) leads to high charging in Au−MUTAB gold nanoparticles. Even though the charging efficiency of nanoparticles is enhanced using the MUTAB ligand, it is still challenging to achieve sufficient charging in particles smaller than 20 nm. Future research should focus on ligand selection in nanoparticle design to overcome this limitation. In our proposed electrostatic model, we simplified the gold nanoparticle to a uniformly charged sphere. However, our model is similar to the Rayleigh limit calculations, but instead of equilibrating the electrostatic energy with the surface tension of droplets, here, we equilibrate the electrostatic energy with the total binding energy of charged ligands.

In conclusion, the charging behavior of 20 nm sized gold nanoparticles protected with MUTAB ligands was studied by

https://doi.org/10.1021/acs.jpclett.5c01075
J. Phys. Chem. Lett. 2025, 16, 7004−7011

using charge detection mass spectrometry (CDMS) interfaced with electrospray ionization. The findings indicate that these nanoparticles can achieve a charging state higher than the theoretical Rayleigh limit for a 20 nm solvent droplet. This charging capability of MUTAB-protected 20 nm particles strongly contrasts with the charging capability of 60 nm citrate-protected AuNPs, which reached only 0.45 times the theoretical limit for similar-sized solvent droplets under similar electrospray conditions. The higher efficiency of MUTAB in enhancing nanoparticle charging may be correlated to the higher ligand binding energy of the gold−sulfur interface as compared with the gold−citrate interface. The estimated binding energies from the CDMS analysis are in fair agreement with the binding energies reported in the literature for thiolate- and citrate-capped gold nanoparticles. One can argue that the charging capability of gas-phase monolayer-protected metal particles generated by electrospray is driven by the ligand binding energy, and therefore, CDMS might be a pertinent probe for determining the ligand binding strength of isolated nanoparticles.

EXPERIMENTAL SECTION

Charge Detection Mass Spectrometry Analysis. MS experiments were performed on the custom-built charge-sensing mass spectrometer coupled with a nanospray source; a 50 μM concentration of Au−MUTAB in water/methanol (50/50 v/v) mixture was used for the measurements. The CDMS instrument was described in detail earlier.[48,49] The mass spectrometer, operating in the positive mode was equipped with a customized Macrospray (Analytica of Branford)[48] and Nanospray (nESI) Flex Ion Source (Thermo Fisher Scientific).[29] Electrosprayed ions were guided up to the terminal vacuum chamber, which contained the charge detection device (CDD), working in a single-pass mode.[28,50] The CDD consisted of a conductive tube collinear to the ion beam and connected to a junction field-effect transistor (JFET). The collected signal was amplified by a low-noise charge-sensitive preamplifier (Amptek A250CF CoolFET) and then shaped and differentiated. The signal was recorded with a waveform digitizer card. The data were transferred to a desktop computer, where they were analyzed with an in-house developed program. Calibration in charge was performed using a test capacitor that allowed a known amount of charge to be pulsed onto the pick-up tube. An ionic train device, composed of multipole radiofrequency (RF) ion guides, permitted the transfer of ions (in the optimal 100−100,000 m/z window of transmission) through the capillary interface of the nanoelectrospray ionization source to the charge detection device. The nanospray ionization was customized to fit the entrance of the CDMS instrument. The ion source consisted of a housing with a manual XYZ-manipulator and fittings, a Direct Junction adaptor for online analysis, and a camera setup including one LCD monitor. Electrospray Fused Silica PicoTips (with ∼30 μm tip inner diameter) were used and changed for each sample analysis.

ASSOCIATED CONTENT

Supporting Information

The Supporting Information is available free of charge at https://pubs.acs.org/doi/10.1021/acs.jpclett.5c01075.

Experimental section, complete information on the CDMS mass and charge plots, TEM images, DLS data, and isopotential map, HRSEM-EDS elemental analysis, and other data (PDF)

AUTHOR INFORMATION

Corresponding Authors

Rodolphe Antoine − *Institut Lumière Matière, University of Lyon, Université Claude Bernard Lyon 1, CNRS, Lyon F-69622, France*; Email: rodolphe.antoine@univ-lyon1.fr

Thalappil Pradeep − *Department of Chemistry, DST Unit of Nanoscience (DST UNS) and Thematic Unit of Excellence (TUE), Indian Institute of Technology Madras, Chennai 600036, India; International Centre for Clean Water, Chennai, Tamil Nadu 600113, India;* orcid.org/0000-0003-3174-534X; Email: pradeep@iitm.ac.in

Authors

B. S. Sooraj − *Department of Chemistry, DST Unit of Nanoscience (DST UNS) and Thematic Unit of Excellence (TUE), Indian Institute of Technology Madras, Chennai 600036, India;* orcid.org/0000-0002-6963-6491

Sylvain Maclot − *Institut Lumière Matière, University of Lyon, Université Claude Bernard Lyon 1, CNRS, Lyon F-69622, France;* orcid.org/0000-0001-5587-7182

Anagha Jose − *Department of Chemistry, DST Unit of Nanoscience (DST UNS) and Thematic Unit of Excellence (TUE), Indian Institute of Technology Madras, Chennai 600036, India*

Clothilde Comby-Zerbino − *Institut Lumière Matière, University of Lyon, Université Claude Bernard Lyon 1, CNRS, Lyon F-69622, France*

Tessa Reinert − *Institut Lumière Matière, University of Lyon, Université Claude Bernard Lyon 1, CNRS, Lyon F-69622, France;* orcid.org/0009-0005-7434-8450

Keerthana Unni − *Department of Chemistry, DST Unit of Nanoscience (DST UNS) and Thematic Unit of Excellence (TUE), Indian Institute of Technology Madras, Chennai 600036, India*

Complete contact information is available at: https://pubs.acs.org/10.1021/acs.jpclett.5c01075

Author Contributions

B.S.S. performed the synthesis, characterization, and other experimental studies. S.M. and T.R. performed the charge detection mass spectrometry studies. A.J. performed the synthesis and characterization studies of nanoparticles. C.C.Z. performed the DLS measurements. K.U. performed the elemental analysis of the samples. B.S.S. wrote the first draft with inputs from R.A. T.P. and R.A. conceptualized the work, discussed the results, and edited the final version of the manuscript. All authors have approved the final version of the manuscript.

Notes

The authors declare no competing financial interest.

ACKNOWLEDGMENTS

B.S.S. thanks the Council of Scientific & Industrial Research (CSIR) for the Shyama Prasad Mukherjee (SPM) fellowship. S.M. is grateful for the postdoc fellowship of the Horizon 2020 Research and Innovation program under grant #964553 (project ARIADNE-Vibe). A.J. thanks the Ministry of Human Resources and Development (MHRD) for the Prime Minister's Research Fellowship (PMRF). K.U. thanks the

University Grants Commission (UGC) for the research fellowship. T.P. thanks the Science and Engineering Research Board (SERB), India, for funding through the research grant, SPR/2021/000439 and through a JC Bose Fellowship. T.P. also acknowledges funding from the Centre of Excellence on Molecular Materials and Functions under the Institution of Eminence scheme of IIT Madras. We acknowledge Indo-French Centre for the Promotion of Advanced Research (IFCPAR/CEFIPRA) for funding through the workshop on metal nanoclusters and their self-assembly initiating this collaborative work. R.A. thanks French National Centre for Scientific Research (CNRS) for funding through International Emerging Actions between France and India. R.A. acknowledges Agence Nationale de la Recherche (projects MANBAMM, ANR-21-CE29-0020, nanoGOLD, ANR-22-CE29-0022 and MOONSTONE, ANR-22-CE42-0031), the European Horizon 2020 research and innovation program's projects #964553 (ARIADNE-Vibe) and HORIZON-EIC-2022-PATHFINDEROPEN-01 #101099058 (Virusong) for support. The authors would like to thank Fabien Rossetti (iLM) for the DLS measurements.

DEDICATION

Dedicated to Prof. R. Graham Cooks on the occasion of his 84th birthday.

REFERENCES

(1) Barbalinardo, M.; Ori, G.; Lungaro, L.; Caio, G.; Migliori, A.; Gentili, D. Direct Cationization of Citrate-Coated Gold and Silver Nanoparticles. *J. Phys. Chem. C* **2024**, *128* (38), 16220−16226.

(2) Heuer-Jungemann, A.; Feliu, N.; Bakaimi, I.; Hamaly, M.; Alkilany, A.; Chakraborty, I.; Masood, A.; Casula, M. F.; Kostopoulou, A.; Oh, E.; Susumu, K.; Stewart, M. H.; Medintz, I. L.; Stratakis, E.; Parak, W. J.; Kanaras, A. G. The Role of Ligands in the Chemical Synthesis and Applications of Inorganic Nanoparticles. *Chem. Rev.* **2019**, *119* (8), 4819−4880.

(3) Daniel, M.-C.; Astruc, D. Gold Nanoparticles: Assembly, Supramolecular Chemistry, Quantum-Size-Related Properties, and Applications toward Biology, Catalysis, and Nanotechnology. *Chem. Rev.* **2004**, *104* (1), 293−346.

(4) Ishida, Y.; Suzuki, J.; Akita, I.; Yonezawa, T. Ultrarapid Cationization of Gold Nanoparticles via a Single-Step Ligand Exchange Reaction. *Langmuir* **2018**, *34* (36), 10668−10672.

(5) Tsunoyama, H.; Sakurai, H.; Ichikuni, N.; Negishi, Y.; Tsukuda, T. Colloidal Gold Nanoparticles as Catalyst for Carbon-Carbon Bond Formation: Application to Aerobic Homocoupling of Phenylboronic Acid in Water. *Langmuir* **2004**, *20* (26), 11293−11296.

(6) Alloway, D. M.; Graham, A. L.; Yang, X.; Mudalige, A.; Colorado, R.; Wysocki, V. H.; Pemberton, J. E.; Lee, T. R.; Wysocki, R. J.; Armstrong, N. R. Tuning the Effective Work Function of Gold and Silver Using ω-Functionalized Alkanethiols: Varying Surface Composition through Dilution and Choice of Terminal Groups. *J. Phys. Chem. C* **2009**, *113* (47), 20328−20334.

(7) Baer, D. R.; Engelhard, M. H.; Johnson, G. E.; Laskin, J.; Lai, J.; Mueller, K.; Munusamy, P.; Thevuthasan, S.; Wang, H.; Washton, N.; Elder, A.; Baisch, B. L.; Karakoti, A.; Kuchibhatla, S. V. N. T.; Moon, D. Surface Characterization of Nanomaterials and Nanoparticles: Important Needs and Challenging Opportunities. *J. Vac. Sci. Technol. A* **2013**, *31* (5), 50820.

(8) Jose, A.; Walker, J. N.; Khatun, M.; Malola, S.; Sooraj, B. S.; Häkkinen, H.; Brodbelt, J. S.; Pradeep, T. Ultraviolet Photoactivation Perturbs the Metal-Ligand Interface of Atomically Precise Nanoclusters. *Chem. Commun.* **2025**, *61* (35), 6482−6485.

(9) Bustos, A. R. M.; Encinar, J. R.; Sanz-Medel, A. Mass Spectrometry for the Characterisation of Nanoparticles. *Anal. Bioanal. Chem.* **2013**, *405* (17), 5637−5643.

(10) Comby-Zerbino, C.; Dagany, X.; Chirot, F.; Dugourd, P.; Antoine, R. The Emergence of Mass Spectrometry for Characterizing Nanomaterials. Atomically Precise Nanoclusters and Beyond. *Mater. Adv.* **2021**, *2* (15), 4896−4913.

(11) Lai, S.-H.; Maclot, S.; Antoine, R.; Masselon, C. D. Advances in Single Particle Mass Analysis. *Mass Spectrom. Rev.* **2024**, 1−20.

(12) Jarrold, M. F. Single-Ion Mass Spectrometry for Heterogeneous and High Molecular Weight Samples. *J. Am. Chem. Soc.* **2024**, *146* (9), 5749−5758.

(13) Doussineau, T.; Désert, A.; Lambert, O.; Taveau, J. C.; Lansalot, M.; Dugourd, P.; Bourgeat-Lami, E.; Ravaine, S.; Duguet, E.; Antoine, R. Charge Detection Mass Spectrometry for the Characterization of Mass and Surface Area of Composite Nanoparticles. *J. Phys. Chem. C* **2015**, *119* (20), 10844−10849.

(14) Keifer, D. Z.; Shinholt, D. L.; Jarrold, M. F. Charge Detection Mass Spectrometry with Almost Perfect Charge Accuracy. *Anal. Chem.* **2015**, *87* (20), 10330−10337.

(15) Kafader, J. O.; Melani, R. D.; Durbin, K. R.; Ikwuagwu, B.; Early, B. P.; Fellers, R. T.; Beu, S. C.; Zabrouskov, V.; Makarov, A. A.; Maze, J. T.; Shinholt, D. L.; Yip, P. F.; Tullman-Ercek, D.; Senko, M. W.; Compton, P. D.; Kelleher, N. L. Multiplexed Mass Spectrometry of Individual Ions Improves Measurement of Proteoforms and Their Complexes. *Nat. Methods* **2020**, *17* (4), 391−394.

(16) Doussineau, T.; Bao, C. Y.; Antoine, R.; Dugourd, P.; Zhang, W.; D'Agosto, F.; Charleux, B. Direct Molar Mass Determination of Self-Assembled Amphiphilic Block Copolymer Nanoobjects Using Electrospray-Charge Detection Mass Spectrometry. *ACS Macro Lett.* **2012**, *1* (3), 414−417.

(17) Loumaigne, M.; Midelet, C.; Doussineau, T.; Dugourd, P.; Antoine, R.; Stamboul, M.; Débarre, A.; Werts, M. H. V. Optical Extinction and Scattering Cross Sections of Plasmonic Nanoparticle Dimers in Aqueous Suspension. *Nanoscale* **2016**, *8* (12), 6555−6570.

(18) Harper, C. C.; Miller, Z. M.; McPartlan, M. S.; Jordan, J. S.; Pedder, R. E.; Williams, E. R. Accurate Sizing of Nanoparticles Using a High-Throughput Charge Detection Mass Spectrometer without Energy Selection. *ACS Nano* **2023**, *17* (8), 7765−7774.

(19) Harper, C. C.; Jordan, J. S.; Papanu, S.; Williams, E. R. Characterization of Mass, Diameter, Density, and Surface Properties of Colloidal Nanoparticles Enabled by Charge Detection Mass Spectrometry. *ACS Nano* **2024**, *18* (27), 17806−17814.

(20) Miller, L. M.; Young, T. W.; Wang, Y.; Draper, B. E.; Ye, X.; Jacobson, S. C.; Jarrold, M. F. Complementary Nanoparticle Characterization by Resistive-Pulse Sensing, Electron Microscopy, and Charge Detection Mass Spectrometry. *Anal. Chem.* **2024**, *96* (35), 14239−14247.

(21) Doussineau, T.; Santacreu, M.; Antoine, R.; Dugourd, P.; Zhang, W.; Chaduc, I.; Lansalot, M.; D'Agosto, F.; Charleux, B. The Charging of Micellar Nanoparticles in Electrospray Ionization. *ChemPhysChem* **2013**, *14* (3), 603−609.

(22) Ouadah, N.; Doussineau, T.; Hamada, T.; Dugourd, P.; Bordes, C.; Antoine, R. Correlation between the Charge of Polymer Particles in Solution and in the Gas Phase Investigated by Zeta-Potential Measurements and Electrospray Ionization Mass Spectrometry. *Langmuir* **2013**, *29* (46), 14074−14081.

(23) Suh, J.; Han, B.; Okuyama, K.; Choi, M. Highly Charging of Nanoparticles through Electrospray of Nanoparticle Suspension. *J. Colloid Interface Sci.* **2005**, *287* (1), 135−140.

(24) Konermann, L. A Simple Model for the Disintegration of Highly Charged Solvent Droplets during Electrospray Ionization. *J. Am. Soc. Mass Spectrom.* **2009**, *20* (3), 496−506.

(25) Konermann, L.; Ahadi, E.; Rodriguez, A. D.; Vahidi, S. Unraveling the Mechanism of Electrospray Ionization. *Anal. Chem.* **2013**, *85* (1), 2−9.

(26) Going, C. C.; Xia, Z.; Williams, E. R. New Supercharging Reagents Produce Highly Charged Protein Ions in Native Mass Spectrometry. *Analyst* **2015**, *140* (21), 7184−7194.

(27) Miladinović, S. M.; Fornelli, L.; Lu, Y.; Piech, K. M.; Girault, H. H.; Tsybin, Y. O. In-Spray Supercharging of Peptides and Proteins in

Electrospray Ionization Mass Spectrometry. *Anal. Chem.* **2012**, *84* (11), 4647−4651.
(28) Antoine, R. Weighing Synthetic Polymers of Ultra-High Molar Mass and Polymeric Nanomaterials: What Can We Learn from Charge Detection Mass Spectrometry? *Rapid Commun. Mass Spectrom.* **2020**, *34* (S2), No. e8539.
(29) Tsirkou, A.; Kaczorowski, F.; Verdurand, M.; Raffoul, R.; Pansieri, J.; Quadrio, I.; Chauveau, F.; Antoine, R. Charge Detection Mass Spectrometry on Human-Amplified Fibrils from Different Synucleinopathies. *Chem. Commun.* **2022**, *58* (51), 7192−7195.
(30) Shen, C.; Xue, Y.; Li, Y.; Wei, M.; Wen, M.; Zhang, L.; Shang, L. Kinetically Regulated One-Pot Synthesis of Cationic Gold Nanoparticles and Their Size-Dependent Antibacterial Mechanism. *J. Mater. Sci. Technol.* **2023**, *162*, 145−156.
(31) Rayleigh, L. On the Equilibrium of Liquid Conducting Masses Charged with Electricity. *Philos. Mag.* **1882**, *14* (87), 184−186.
(32) Elliott, A. G.; Merenbloom, S. I.; Chakrabarty, S.; Williams, E. R. Single Particle Analyzer of Mass: A Charge Detection Mass Spectrometer with a Multi-Detector Electrostatic Ion Trap. *Int. J. Mass Spectrom.* **2017**, *414*, 45−55.
(33) Nuzzo, R. G.; Zegarski, B. R.; Dubois, L. H. Fundamental Studies of the Chemisorption of Organosulfur Compounds on Gold (111). Implications for Molecular Self-Assembly on Gold Surfaces. *J. Am. Chem. Soc.* **1987**, *109* (3), 733−740.
(34) Chen, F.; Li, X.; Hihath, J.; Huang, Z.; Tao, N. Effect of Anchoring Groups on Single-Molecule Conductance: Comparative Study of Thiol-, Amine-, and Carboxylic-Acid-Terminated Molecules. *J. Am. Chem. Soc.* **2006**, *128* (49), 15874−15881.
(35) Hinterwirth, H.; Kappel, S.; Waitz, T.; Prohaska, T.; Lindner, W.; Lämmerhofer, M. Quantifying Thiol Ligand Density of Self-Assembled Monolayers on Gold Nanoparticles by Inductively Coupled Plasma-Mass Spectrometry. *ACS Nano* **2013**, *7* (2), 1129−1136.
(36) Franco-Ulloa, S.; Tatulli, G.; Bore, S. L.; Moglianetti, M.; Pompa, P. P.; Cascella, M.; De Vivo, M. Dispersion State Phase Diagram of Citrate-Coated Metallic Nanoparticles in Saline Solutions. *Nat. Commun.* **2020**, *11* (1), 5422.
(37) Chong, G.; Hernandez, R. Adsorption Dynamics and Structure of Polycations on Citrate-Coated Gold Nanoparticles. *J. Phys. Chem. C* **2018**, *122* (34), 19962−19969.
(38) Lin, Y.; Pan, G. B.; Su, G. J.; Fang, X. H.; Wan, L. J.; Bai, C. L. Study of Citrate Adsorbed on the Au(111) Surface by Scanning Probe Microscopy. *Langmuir* **2003**, *19* (24), 10000−10003.
(39) Scanlon, M. D.; Peljo, P.; Méndez, M. A.; Smirnov, E.; Girault, H. H. Charging and Discharging at the Nanoscale: Fermi Level Equilibration of Metallic Nanoparticles. *Chem. Sci.* **2015**, *6* (5), 2705−2720.
(40) Henglein, A. Physicochemical Properties of Small Metal Particles in Solution: "Microelectrode" Reactions, Chemisorption, Composite Metal Particles, and the Atom-to-Metal Transition. *J. Phys. Chem.* **1993**, *97* (21), 5457−5471.
(41) Dass, A. Nano-Scaling Law: Geometric Foundation of Thiolated Gold Nanomolecules. *Nanoscale* **2012**, *4* (7), 2260−2263.
(42) Otto, H. H. Ratio of In-Sphere Volume to Polyhedron Volume of the Great Pyramid Compared to Selected Convex Polyhedral Solids. *J. Appl. Math. Phys.* **2021**, *09* (01), 41−56.
(43) Boulanger, N.; Buisseret, F.; Dierick, F.; White, O. The Two-Thirds Power Law Derived from an Higher-Derivative Action. *Physics* **2024**, *6* (4), 1251−1263.
(44) Vergara, S.; Santiago, U.; Kumara, C.; Alducin, D.; Whetten, R. L.; Jose Yacaman, M.; Dass, A.; Ponce, A. Synthesis, Mass Spectrometry, and Atomic Structural Analysis of $Au_{\sim 2000}(SR)_{\sim 290}$ Nanoparticles. *J. Phys. Chem. C* **2018**, *122* (46), 26733−26738.
(45) Kumara, C.; Hoque, M. M.; Zuo, X.; Cullen, D. A.; Whetten, R. L.; Dass, A. Isolation of a 300 KDa, $Au_{\sim 1400}$ Gold Compound, the Standard 3.6 Nm Capstone to a Series of Plasmonic Nanocrystals Protected by Aliphatic-like Thiolates. *J. Phys. Chem. Lett.* **2018**, *9* (23), 6825−6832.
(46) Kumara, C.; Zuo, X.; Cullen, D. A.; Dass, A. Faradaurate-940: Synthesis, Mass Spectrometry, Electron Microscopy, High-Energy X-Ray Diffraction, and X-Ray Scattering Study of $Au_{\sim 940 \pm 20}(SR)_{\sim 160 \pm 4}$ Nanocrystals. *ACS Nano* **2014**, *8* (6), 6431−6439.
(47) Kumara, C.; Zuo, X.; Ilavsky, J.; Chapman, K. W.; Cullen, D. A.; Dass, A. Super-Stable, Highly Monodisperse Plasmonic Faradaurate-500 Nanocrystals with 500 Gold Atoms: $Au_{\sim 500}(SR)_{\sim 120}$. *J. Am. Chem. Soc.* **2014**, *136* (20), 7410−7417.
(48) Doussineau, T.; Kerleroux, M.; Dagany, X.; Clavier, C.; Barbaire, M.; Maurelli, J.; Antoine, R.; Dugourd, P. Charging Megadalton Poly(Ethylene Oxide)s by Electrospray Ionization. A Charge Detection Mass Spectrometry Study. *Rapid Commun. Mass Spectrom.* **2011**, *25* (5), 617−623.
(49) Doussineau, T.; Yu Bao, C.; Clavier, C.; Dagany, X.; Kerleroux, M.; Antoine, R.; Dugourd, P. Infrared Multiphoton Dissociation Tandem Charge Detection-Mass Spectrometry of Single Megadalton Electrosprayed Ions. *Rev. Sci. Instrum.* **2011**, *82* (8), No. 084104.
(50) Keifer, D. Z.; Pierson, E. E.; Jarrold, M. F. Charge Detection Mass Spectrometry: Weighing Heavier Things. *Analyst* **2017**, *142* (10), 1654−1671.

https://doi.org/10.1021/acs.jpclett.5c01075
J. Phys. Chem. Lett. 2025, 16, 7004−7011

Supporting Information

Charging of Ligand Protected Gold Nanoparticles in Electrospray Ionization: Probing Ligand Bond Strength by Charge Detection Mass Spectrometry

*B. S. Sooraj,[a] Sylvain Maclot,[b] Anagha Jose,[a] Clothilde Comby-Zerbino,[b] Tessa Reinert,[b] Keerthana Unni,[a] Rodolphe Antoine,[*b] and Thalappil Pradeep[*a,c]*

[a]Department of Chemistry, DST Unit of Nanoscience (DST UNS) and Thematic Unit of Excellence (TUE), Indian Institute of Technology Madras, Chennai 600036, India. E-mail: *pradeep@iitm.ac.in*

[b]Institut Lumière Matière, University of Lyon, Université Claude Bernard Lyon 1, CNRS, Lyon F-69622, France. Email: *rodolphe.antoine@univ-lyon1.fr*

[c]International Centre for Clean Water, Chennai, Tamil Nadu 600113, India.

Table of contents

Title	Description	Page no
1.	Experimental section	2
2.	Instrumentation	3
Figure S1	CDMS charge and mass plots obtained under nanospray and macrospray ionization conditions	5
Figure S2	Comparison plot of mass and size under nanospray and macrospray ionization conditions	5
Figure S3	TEM image and histogram of 60 nm sized Au-citrate nanoparticles obtained in the solid state	6
Figure S4	Mass distribution of 60 nm sized citrate-protected gold particles	6
Table S1	The size and zeta potential values of AuNPs obtained from DLS measurements	6
Figure S5	DLS size distribution of all gold nanoparticles in water dispersion	7
Figure S6	ESI-CDMS measurements on the positive mode of different-sized Au-citrate nanoparticles	7
Figure S7	ESI-CDMS measurements in positive and negative modes of the 80 nm sized Au-citrate nanoparticles	8
Figure S8	Iso-potential map of the electrostatic energy for nanoparticle of charge Z and Radius R	8
Scheme S1	Illustration of the concepts and correlations regarding ligand bond strength, charging energy, and Fermi potential	9
Figure S9	Elemental analysis of Au-MUTAB nanoparticle using HRSEM-EDS	9

1. Experimental section

Materials. All the materials were commercially available. (11-mercaptoundecyl)-N,N,N-trimethylammonium bromide (MUTAB), and Gold (III) chloride trihydrate ($HAuCl_4 \cdot 3H_2O$)

were purchased from Sigma Aldrich. Methanol and Water were purchased from J. T. Baker. All chemicals and solvents were used as such without further purification.

Synthesis of Au-MUTAB nanoparticles

Initially, MUTAB (40 mM, 150 μL) was first dissolved in water (1.8 mL) at 30 °C, and kept for stirring at 1500 rpm. Then $HAuCl_4.3H_2O$ (50 mM, 40 μL) was slowly added dropwise to the solution, and the reaction was continued for 24 hours in dark conditions. Finally, the resultant solution was centrifuged at 14000 rpm for 5 min, and the precipitate was collected. This centrifugation step was repeated three times for extreme purification of the product. The obtained precipitate, which is the Au-MUTAB nanoparticle, was purple in color and re-dispersed in water for further analysis.

40, 60, 80 nm Au nanoparticles

Gold nanoparticles, stabilized suspension in citrate buffer, were purchased from Sigma-Aldrich (Refs. 741981, 742015, and 742023). The stock solutions were directly diluted in the water/methanol (1:1) mixture.

2. Instrumentation

Inst Perkin Elmer Lambda 25 UV-vis spectrometer was used to record the UV-vis spectra of the nanoparticles. Absorption spectra were typically measured in the range of 300-1100 nm with a bandpass filter of 1 nm. Dynamic light scattering (DLS) measurements was done using a Malvern Zetasizer ZSP instrument equipped with a 633 nm (He-Ne) laser. Transmission electron microscopy was performed using a JEOL 3010, 300 kV instrument at an accelerating voltage of 200 kV. The accelerating voltage was kept low to reduce beam induced damage. Samples were prepared by drop casting the solution on a carbon-coated copper grid and dried under ambient conditions.

Charge calibration procedure in CDMS

Calibration of charge was performed using a test capacitor that allows a known amount of charge to be pulsed onto the pick-up tube. The test tube pulses are generated with a shaping-pulse generator so that the time-dependent signal response can be determined as well. An ion with 300 charges generates a ~49 mV peak-to-peak pulse (82 µV/e^-). The charge of a particle is then directly deduced from this calibration and from the average value of the voltage intensity of the pulses generated by the particle on the detector. Also, the rms noise with the present set-up is equivalent to ~10e^-. The mass-to-charge m/z ratio of an ion is determined from the time-of-flight (time delay between the positive and negative pulses that correspond to the entrance and exit of ions from the detector tube).

To further improve the calibration, we used polystyrene microspheres (54 nm, 120 nm, 200 nm supplied by ABCR and 320 nm supplied by Sigma-Aldrich) as external calibrants. Such polystyrene microspheres cover the mass range of gold nanoparticles investigated in this work, have low dispersion, and have been found to be softly and efficiently transfer in the gas phase by ESI. The average masses obtained from the mass distribution of the polystyrene microsphere ions measured by CD-MS using the internal calibration were plotted against their calculated mass (the average volumes of polystyrenes were converted into molecular mass assuming perfectly spherical nanoobjects and a homogeneous density of 1.05). A linear fit through the measured mass values was used for the external calibration.

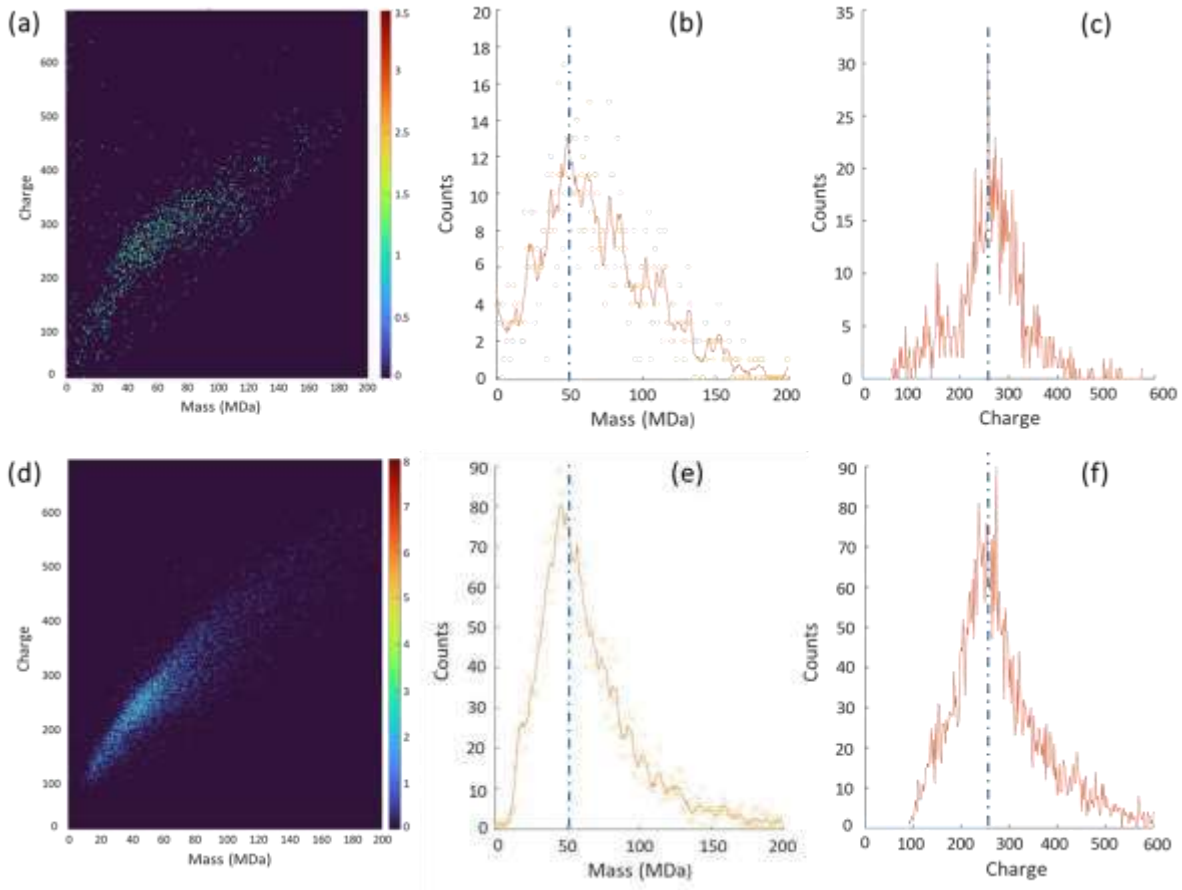


Figure S1. The charge versus mass plot obtained in CDMS under two different ionization conditions of (**a**) nanospray and (**d**) macrospray; The mass plot obtained from (**b**) nanospray and (**e**) macrospray; The charge plot obtained from (**c**) nanospray and (**f**) macrospray. (Dotted lines indicate the maximum value).

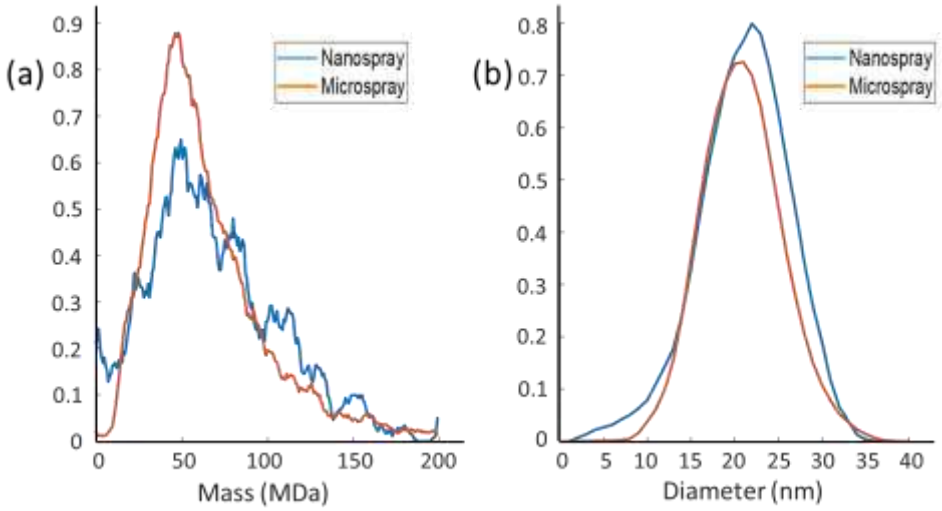


Figure S2. The comparison of the results obtained at nanospray and macrospray ionization conditions shown by their (**a**) mass distribution; (**b**) estimated size from mass plots.

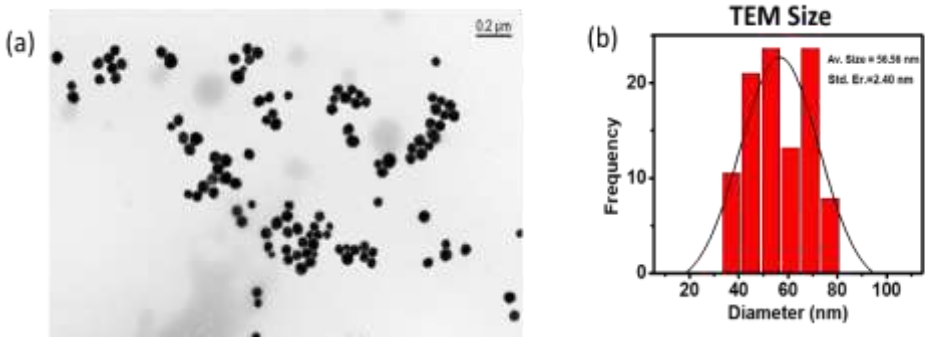


Figure S3. (**a**) TEM image and (**b**) histogram of Au-citrate nanoparticle (60 nm), obtained in the solid state.

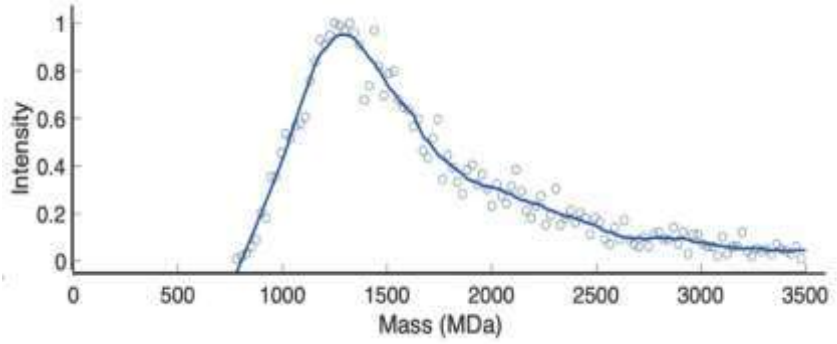


Figure S4. The mass distribution obtained from the CDMS analysis of 60 nm sized Au-citrate nanoparticles.

Table S1. The size and zeta potential values of all the AuNPs obtained from DLS measurements.

Nanoparticles	**Size in nm (DLS)**	**Zeta-potential (mV)**
MUTAB-capped gold nanoparticles	20	+17.6
Citrate-capped gold nanoparticles, SIGMA – 40 nm	38	-35.0
Citrate-capped gold nanoparticles, SIGMA – 60 nm	50	-36.2
Citrate-capped gold nanoparticles, SIGMA – 80 nm	70	-38.0

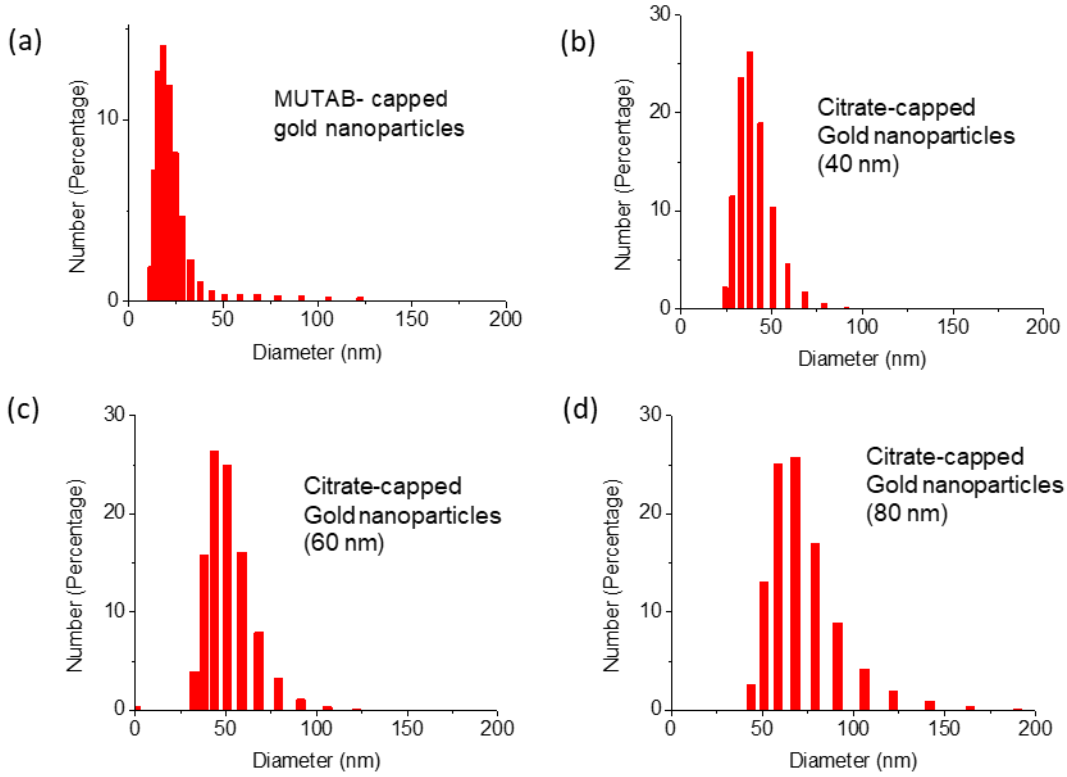


Figure S5. The size distribution obtained from DLS measurements for all the different-sized gold nanoparticles in water dispersion.

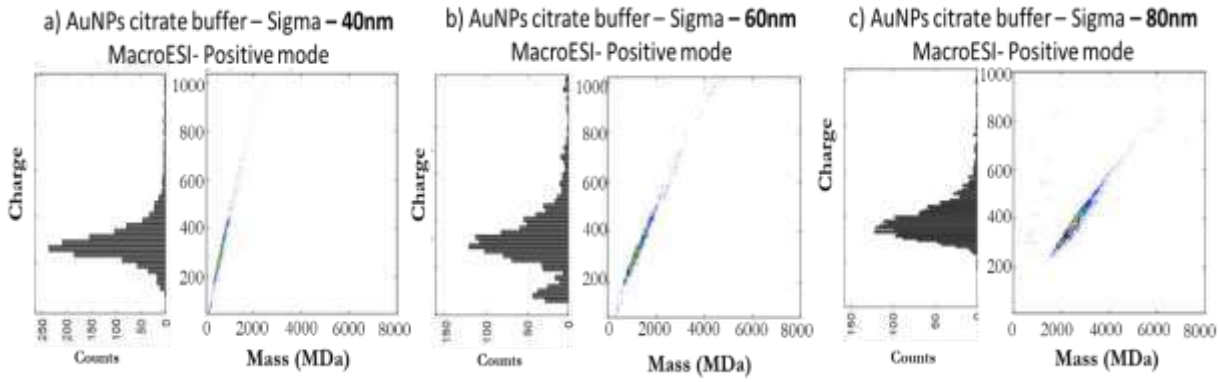


Figure S6. ESI-CDMS measurements on positive mode of different-sized Au-citrate NPs, (**a**) 40 nm; (**b**) 60 nm; (**c**) 80 nm.

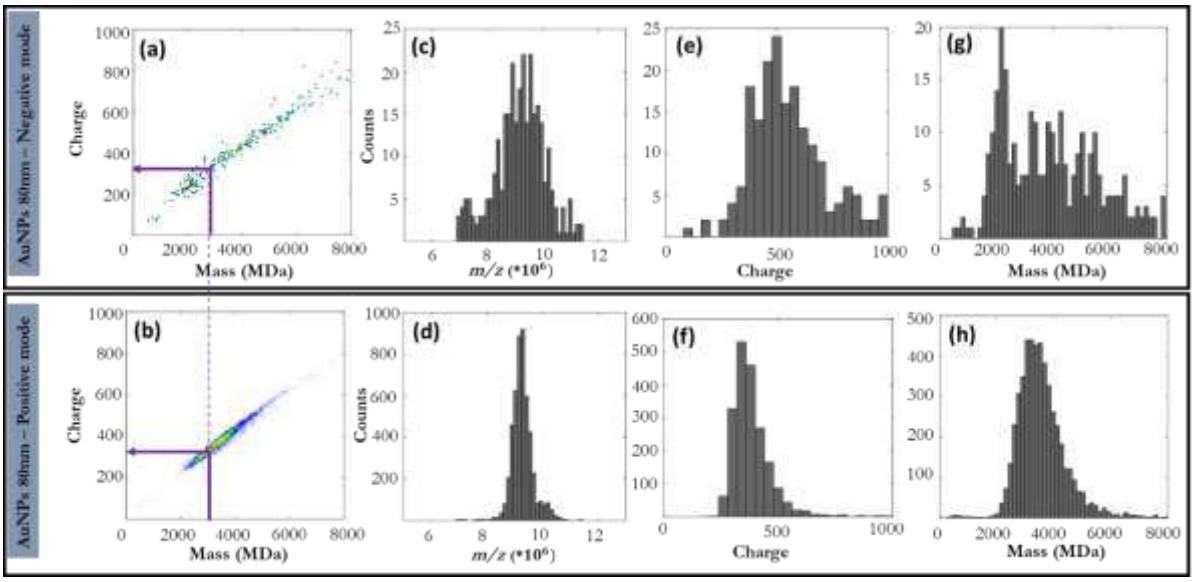


Figure S7. The data obtained for positive and negative ESI modes of the 80 nm sized Au-citrate NPs; (**a,b**) 2D plot, (**c,d**) distributions of *m/z*, (**e,f**) charge distribution, (**g,h**) mass distribution. The purple arrow on the 2D plot shows the charging for the expected mass of 80 nm AuNPs, e.g., ~ 3.11 GDa.

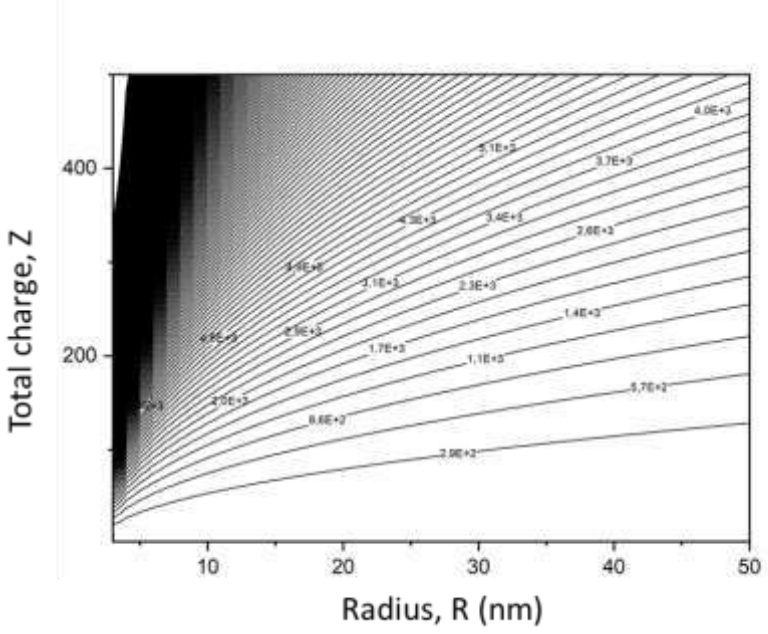
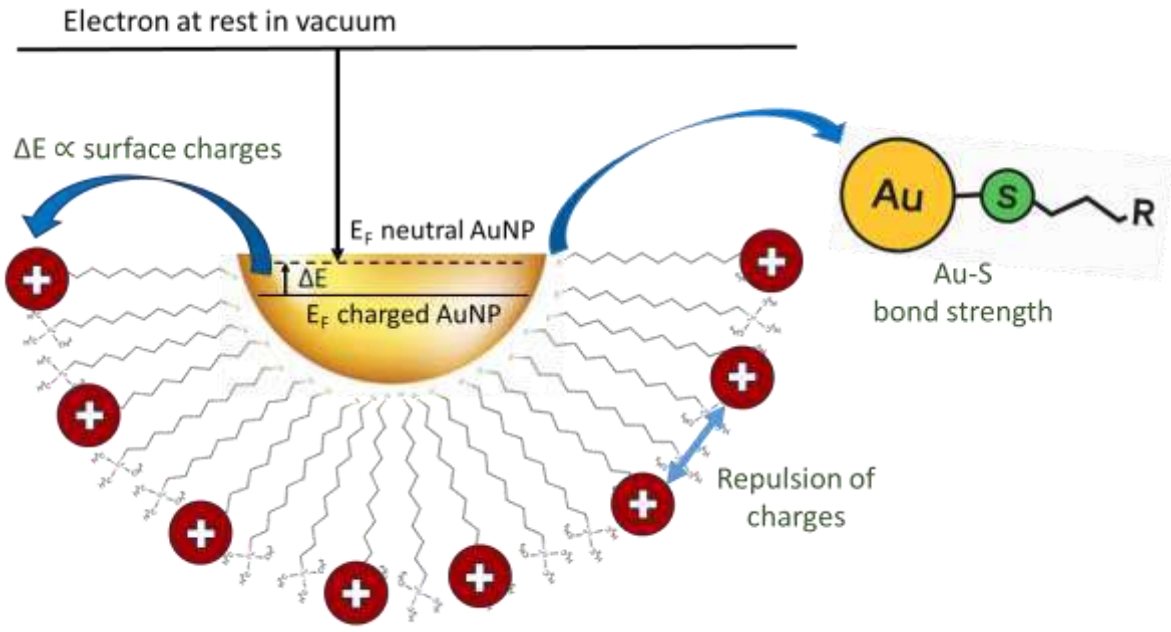
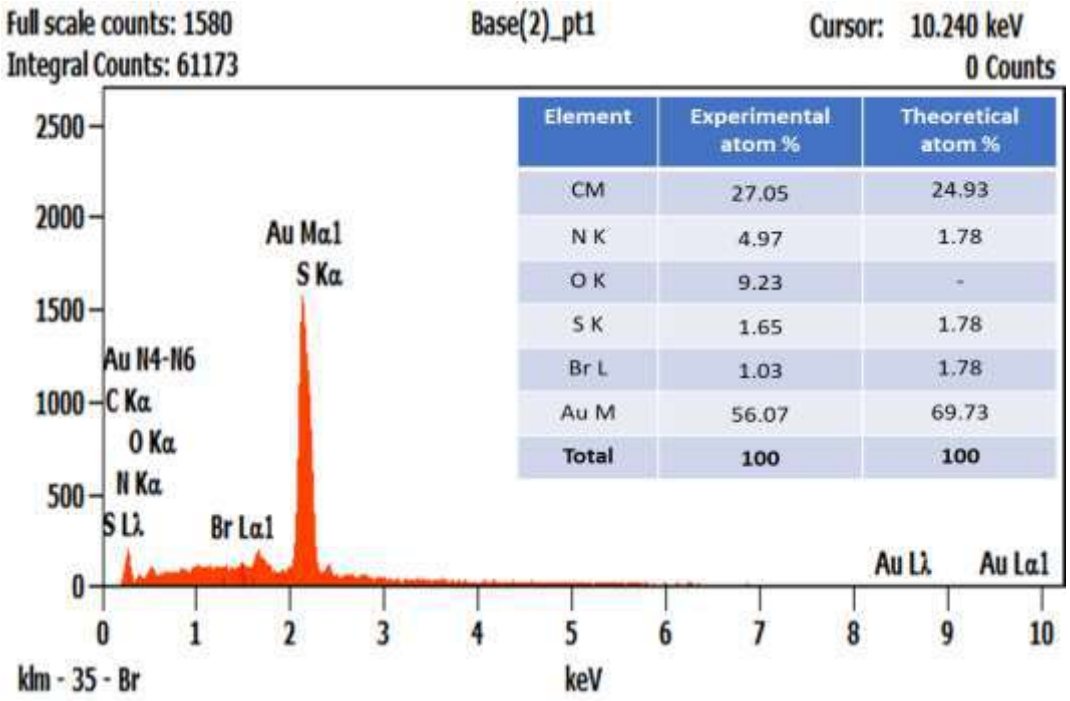


Figure S8. Iso-potentials (R, Z = Q/e) map of the electrostatic energy U (in eV) for a nanoparticle of charge Z and radius R.



Scheme S1. Illustration of the concepts and correlations regarding ligand bond strength (brought by the gold-sulfur interface), charging energy (brought by the repulsion of charged ligands), and modification of the Fermi level of a gold NP due to chemisorption of thiolated ligands.



Element	Experimental atom %	Theoretical atom %
CM	27.05	24.93
N K	4.97	1.78
O K	9.23	-
S K	1.65	1.78
Br L	1.03	1.78
Au M	56.07	69.73
Total	**100**	**100**

Figure S9. The percentage of elemental composition in 20 nm sized Au-MUTAB nanoparticles obtained from HRSEM-EDS. The theoretical percentage is calculated considering that the composition is $Au_{246000}(MUTAB)_{6280}$ (where, MUTAB = $C_{14}H_{32}NBrS$).

ACS Sustainable Chemistry & Engineering

pubs.acs.org/journal/ascecg

Research Article

Enhanced U(VI) Removal from Groundwater Using Amide-Functionalized Biopolymer-Based Adsorbent for a Practical Solution

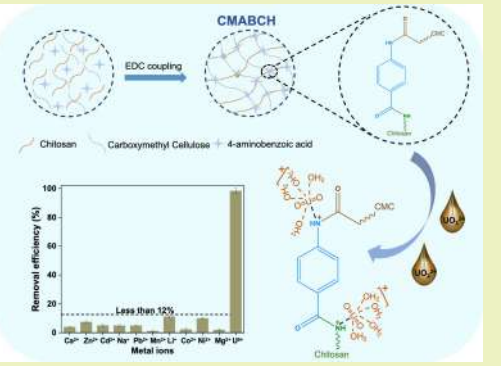
Sonali Seth, Md Rabiul Islam, Tanmayaa Nayak, Amoghavarsha Ramachandra Kini, Sujan Manna, Bijesh K. Malla, Ankit Nagar, and Thalappil Pradeep*

Cite This: *ACS Sustainable Chem. Eng.* 2025, 13, 10918−10929

Read Online

ACCESS | Metrics & More | Article Recommendations | Supporting Information

ABSTRACT: Uranium (U(VI)) contamination poses a serious threat to groundwater, which is the primary source of drinking water in many regions across the world. Removal of the predominant UO_2^{2+} species present in environmental water samples at affordable cost in resource-limited settings is challenging, particularly in the presence of competing ions. In this work, we introduced a sustainable approach for developing a biopolymer-based carboxymethyl cellulose (CMC)-chitosan (CH) adsorbent, free of metals, for selective removal of U(VI) from water. Amide functionalities, which serve as active sites for U(VI) capture, have been introduced by cross-linking CMC and CH with 4-aminobenzoic acid via 1-ethyl-3-(3-(dimethylamino)propyl)-carbodiimide (EDC) coupling. The adsorbent demonstrated excellent U(VI) removal efficiency in the presence of counterions such as transition metals, alkaline earth metals, and pentavalent vanadium (V(V)), which interfere strongly with many adsorbents. The composite showed 99.5% removal efficiency when tested on a field water sample containing 102 μg/L of U(VI). Mechanistic insights into U(VI) adsorption on the composite were obtained through infrared spectroscopy and X-ray photoelectron spectroscopy, which revealed that nitrogen in the amide functionalities facilitates interaction with U(VI). Raman measurements were performed to understand the speciation of U(VI) in solution at pH 7, which confirmed no change in the charge state of uranium in solution upon interaction with the composite. The adsorbed U(VI) can be easily removed by 10 mM HCl (10 mL) within 90 min of reaction, and the adsorbent can be reused. The adsorbent maintained a removal efficiency of more than 92% over three reactivation cycles. Cost of the composite was estimated to be around $10 for treating 1 KL of contaminated water at a U(VI) concentration of 1000 μg/L. However, as *N*-hydroxysuccinimide and EDC reagents, used for the synthesis, are contributing more than >90% of the overall cost, further optimization or substitution of these reagents by industrial chemicals will ensure economic viability of the process.



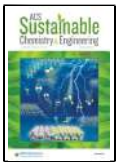
KEYWORDS: *Uranium, Adsorption, Biopolymers, Amide functionalities, Sustainability metrics*

Downloaded via INDIAN INST OF TECH MADRAS on December 29, 2025 at 03:14:49 (UTC).
See https://pubs.acs.org/sharingguidelines for options on how to legitimately share published articles.

INTRODUCTION

U(VI), a naturally occurring radionuclide, widely distributed in the earth's crust with an average concentration of around 2.7 mg/L, is found in various sources including rocks, minerals, groundwater, and seawater; in the latter it is at 3.3 μg/L.[1,2] Despite its crucial role in nuclear power generation and as a carbon-free energy source, it poses significant radiological and toxicological effects.[3] Although geogenic sources are the primary contributors of uranium in groundwater,[4] human activities such as mining, production and use of phosphate fertilizers, and nuclear power plant operations significantly contribute to its release into the environment.[4] Human exposure to uranium occurs through food, drinking water and dermal contact, causing adverse health effects, including nephrotoxicity and reproductive toxicity.[3,5] Uranium concentrations in the High Planes and Central Valley aquifers of the United States have been reported to reach 180 times the World Health Organization's (WHO) permissible limit of 30 μg/L.[6] In India, where 85% of rural drinking water supplies rely on groundwater, uranium contamination exceeds the WHO's limit in 18 states.[7−9] In groundwater systems, uranium predominantly exists in two oxidation states: U(IV) (as UO_2) and U(VI) (as UO_2^{2+}). U(IV) is sparingly soluble (~10^{-6} mol/kg), largely immobile, and typically precipitates under reducing conditions as insoluble minerals or complexes. In contrast, U(VI) is highly soluble, mobile, and environmentally toxic. A study by Patnaik et al. reported that elevated concentrations of U(VI) in the groundwater of Punjab are primarily attributed to the weathering of the Siwalik

Received: April 3, 2025
Revised: June 28, 2025
Accepted: July 1, 2025
Published: July 8, 2025



ACS Publications

© 2025 American Chemical Society

mountains. Meanwhile, U(IV) tends to accumulate at the redox fronts within the paleo-channels of the Siwalik formations.[10] Furthermore, the presence of nitrates in groundwater can oxidize U(IV) to U(VI), enhancing its dissolution.[4] Depending on the availability of counterions, U(IV) can form stable, soluble complexes, thereby increasing its mobility and leaching potential in groundwater systems. U(IV) minerals readily convert to dissolved U(VI) species under oxidizing conditions.[6] U(VI) can also complex with other ions like carbonates, phosphates and humic substances (HS) present in water.[11,12] HS can interfere with and affect U(VI) adsorption. Liu et al. demonstrated that HS can mobilize U(VI) under reducing conditions.[13] Similarly, A. Krepelova et al. investigated the adsorption of U(VI) on kaolinite in the presence and absence of HS. Their study showed that pH plays a significant role in U(VI) sorption; at neutral pH, the formation of uranyl-humate complexes inhibits U(VI) adsorption onto kaolinite.[14] However, A. Kumar et al. have shown that carbonates exert a stronger influence on U(VI) sorption as compared to HS in the pH range 3.5−9.5.[15]

There are several methods for removing U(VI) from water, including membrane filtration,[16] electrocoagulation,[17] ion exchange,[18] and biological methods.[19] These methods are expensive and are effective only when the concentration of pollutants is high.[20] Among all the techniques, U(VI) removal via adsorption is the most cost-effective and efficient technique. Adsorption of contaminants onto a solid surface is a simple and well-known technology for heavy metal removal from water.[21] A variety of adsorbents, including zeolites,[22] biosorbents,[23] activated carbon,[24] carbon nanotubes,[25] clays,[26] metal oxides,[27] and metal−organic frameworks (MOFs),[28] have been reported for U(VI) removal from water.

In the following, we briefly review the literature on the use of biopolymer-based materials for U(VI) removal. Biopolymers like chitosan (CH) and cellulose, known for their biocompatibility, nontoxic character and multiple active sites, have been widely used for heavy metal remediation.[29] They have reactive functional groups in their matrix like hydroxyls (−OH), carboxylic acid (−COOH) and amine ($-NH_2$) that can be easily tuned to interact with heavy metals including U(VI).[30] CH, a naturally abundant biopolymer with $-NH_2$ groups, is a potential candidate for heavy metal removal from water.[31,32] However, it has poor chemical and mechanical stability in aqueous solutions,[33] rendering its usage. To overcome this limitation, it is crucial to develop novel adsorbents with improved stability and enhanced affinity for U(VI). Cross-linking of biopolymers is one such approach to enhance the stability of the adsorbents.[34] Moreover, cross-linking of biopolymers by introducing specific functionalities that serve as active sites enhances the heavy metal removal efficiency.[35] Carboxymethyl cellulose (CMC), an anionic derivative of cellulose having ether functionalities ($-O-CH_2COONa$), is particularly known for its ease of modification, and it provides active sites for cross-linking with other polymers.[36,37] Manzoor et al. demonstrated the cross-linking of CMC with CH using ethylenediaminetetraacetic acid (EDTA) for copper (Cu) removal from wastewater.[38] However, the preparation of the adsorbent requires *p*-toluene sulfonic acid (*p*-TSA), which is toxic,[39] and the reaction needs high temperatures. Similarly, Wang et al. modified CH using 3-indoleacetic acid in *p*-TSA for U(VI) removal from water, and the reaction needed elevated temperatures.[30] These methods are unsustainable due to reliance on high temperatures and organic solvents for adsorbent preparation. It is known that functional groups like phosphates,[12] imines,[40] amines,[41] carboxyls,[42] and amidoximes[43] form stable complexes with U(VI) and can be integrated into biopolymers to enhance their adsorption capacity as well as mechanical and chemical stability. It is also possible to introduce amide functionalities into biopolymers for enhanced U(VI) removal efficiency. Galindo et al. investigated the cosorption of uranyl and phosphates and the formation of uranyl phosphates on alumina surface at pH 3 through IR spectroscopy, highlighting the role of phosphates in enhancing uranyl adsorption on the surface of alumina.[44] Kushwaha et al. explored the adsorption of U(VI) on palm-shell-based adsorbent to understand the role of −COOH functionality in reducing U(VI) to U(V) and U(IV) through XPS, Extended X-ray Absorption Fine Structure (EXFAS) and IR spectroscopy.[45]

Several methods have been reported for the introduction of amide functionalities. For example, Wang et al. introduced amide groups to CH in the presence of *p*-TSA at 60 °C.[46] Additionally, Sabatini et al. have described approaches for amide bond formation focusing on sustainability and efficiency.[47] Various coupling agents, such as thionyl chloride, oxalyl chloride, and carbodiimide-based reagents like EDC and dicyclohexylcarbodiimide (DCC), are commonly used for amide bond synthesis. The choice of solvent and reaction temperature also significantly influences the efficiency and outcome of these reactions.

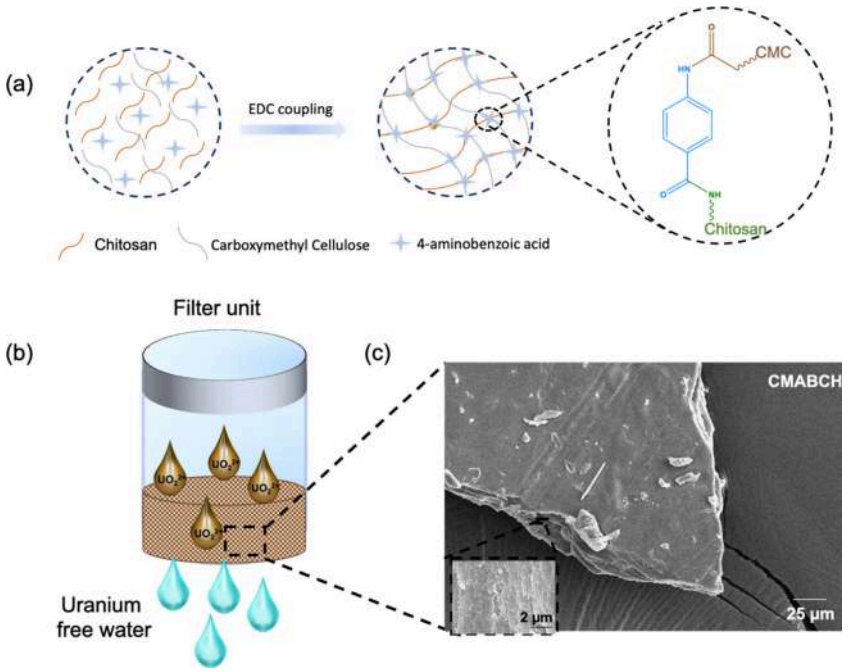
In this research, CMC and CH were chosen as precursors due to their abundance, nontoxicity, biocompatibility, active functional groups, low cost and ease of modification. A novel adsorbent (CMABCH) was developed by cross-linking CMC and CH with 4-aminobenzoic acid (PABA) to introduce amide functionalities through EDC coupling (details in materials and methods). EDC/NHS was selected due to its water solubility and compatibility with our reaction conditions, as many alternatives are water-insoluble. This method utilized the facile coupling of $-NH_2$ and −COOH to introduce amide functionalities in aqueous media.[48] Our work focused on elucidating the role of amide functionalities in enhancing U(VI) adsorption, with insights obtained through IR spectroscopy and Raman spectroscopy. Along with it, the mechanism of interaction of U(VI) with CMABCH was elucidated by XPS. Batch adsorption studies were conducted to examine the adsorption capacity of CMABCH, which demonstrated excellent adsorption capacity for U(VI) over a broad range of pH and in the presence of competing ions. Furthermore, CMABCH demonstrated excellent adsorption capacity over three reactivation cycles, highlighting its reusability and robustness. Real-field groundwater samples, containing U(VI) were collected from a well in Shamshabad village, Fazilka, Punjab State, India to evaluate the performance of the adsorbent, and we found a removal efficiency of 99.5% by CMABCH in the real-field sample.

EXPERIMENTAL SECTION

Materials. CMC and CH were purchased from Avantor Performance Materials India Ltd. and Pelican Biotech & Chemicals Laboratories Pvt. Ltd. (India), respectively. PABA was purchased from Merck Chemicals Pvt. Ltd. (India). EDC and NHS were purchased from Spectrochem Pvt. Ltd. (India). Uranyl nitrate ($UO_2(NO_3)_2.6H_2O$) was procured from Thomas Baker (Chemicals) Ltd. (India). Analytical-grade chemicals were utilized without additional purification. Porous filters were purchased from local

https://doi.org/10.1021/acssuschemeng.5c03058
ACS Sustainable Chem. Eng. 2025, 13, 10918−10929

Scheme 1. (a) Schematic of the Synthesis of CMABCH through EDC Coupling Using Water as the Solvent.[a] (b) Schematic Illustration of the Use of CMABCH Filter for U(VI) Removal from Water. (c) HRSEM Image of Granular CMABCH Used for U(VI) Removal[b]



[a]The active sites of CMABCH convert U(VI) to U(IV), enhancing the adsorption capacity. [b]Inset shows an expanded HRSEM image of the selected region with a scale bar of 2 μm.

suppliers and deionized water (DI) was used throughout the experiments unless otherwise specified.

Synthesis of CMC−CH Adsorbent (CMABCH). A simple approach was employed to synthesize CMABCH. Initially, 2 g of CMC was dissolved in 100 mL of water and stirred for 30 min to achieve a uniform dispersion. Subsequently, 0.5 g each of EDC and NHS were added to the CMC solution, and the reaction mixture was stirred for 24 h. Following this, 2 g of PABA was introduced to the reaction mixture and stirred for an additional 12 h, facilitating the linkage of PABA to CMC via EDC coupling. To this reaction mixture, another 0.5 g of EDC and 0.5 g of NHS were added and the solution was stirred for another 24 h. Subsequently, 2 g of CH solution in 100 mL of 1% HCl was added to the mixture and incubated for 12 h. The resulting precipitate (CMABCH) was washed thoroughly with water and dried at 60 °C. Finally, the dried material was mechanically ground and sieved with a 200-μm sieve to obtain a granular powder. The composite was insoluble in water and the yield of the composite was about 4.2 g. The synthesis was performed under ambient conditions using water as the solvent, making the process greener and more sustainable. EDC and NHS were used as catalysts to facilitate amide bond formation. The dual functional groups of PABA ($-NH_2$ and $-COOH$) enabled it to function as a chelating ligand,[49] effectively cross-linking CMC and CH and facilitating amide bond formation as shown in Scheme 1a. The high-resolution scanning electron microscopy (HRSEM) image of CMABCH demonstrated granular and rough surface, making it suitable for its use in water purification cartridge as shown in Scheme 1b and 1c. Brunauer−Emmett−Teller (BET) surface area measurement was performed to analyze the structural framework of CMABCH, revealing a surface area of 20.6 m^2/g with an average pore size of 2.44 nm, making it a mesoporous material as shown in Figure S1.

Batch Adsorption Studies. U(VI) removal efficiency of the composite was checked by adding 30 mg of CMABCH to 10 mL of U(VI) spiked water at a concentration of 1000 μg/L. Water samples were collected at regular time intervals to determine the leftover U(VI) concentration. This was measured using Inductively Coupled Plasma Mass Spectrometry (ICP-MS) after acidifying the samples with 5% HNO_3. The maximum uptake capacity of U(VI) was calculated using eq 2 in Supporting Information.

pH Effect. pH-dependent studies were conducted to investigate the effect of pH on the adsorption of U(VI) on CMABCH. 30 mg of CMABCH was added to U(VI) spiked (1000 μg/L) DI water (10 mL), and pH was adjusted using 1 M NaOH/1 M HCl. After 2 h of reaction, the water samples were collected and analyzed by ICP-MS.

Interfering Ions. To evaluate the selectivity of CMABCH toward U(VI), an adsorption experiment was conducted with 10 mL water solution spiked with 1000 μg/L multimetal ions containing cadmium (Cd^{2+}), lead (Pb^{2+}), zinc (Zn^{2+}), manganese (Mn^{2+}), lithium (Li^{+}), nickel (Ni^{2+}), cobalt (Co^{2+}), sodium (Na^{+}), calcium (Ca^{2+}), magnesium (Mg^{2+}), and U^{6+}. Thirty mg CMABCH was added to the solution to check its selectivity for U(VI). Also, Since V(V) have properties similar to U(VI) and competes for active adsorption sites, batch adsorption study was carried out with 10 mL water spiked with almost equal concentrations (1000 μg/L) of U(VI) and V(V). Thirty mg of CMABCH was added to the solution to check the performance of CMABCH in the presence of V(V). Water sample was collected after 2 h, and ICP-MS analysis was performed. Further studies were performed to analyze the effect of common anions on U(VI) removal. A multianion mixture (10 mL) containing 1000 μg/L each of fluoride(F^-), chloride(Cl^-), bromide (Br^-), nitrate (NO_3^-), nitrite (NO_2^-), sulfates (SO_4^{2-}), and phosphates (PO_4^{3-}) was spiked with 1000 μg/L of U(VI) (10 mL) and ICP-MS analysis was done after 2h treatment with 30 mg of CMABCH.

Instrumentation. IR spectra were recorded using a PerkinElmer FT-IR spectrometer, keeping spectrometer resolution at 4 cm^{-1}. HRSEM images and Energy Dispersive X-ray Spectroscopy (EDS) mapping were carried out on a Thermo Scientific Verios G4 UC SEM. XPS measurements were performed with an Omicron Nanotechnology ESCA Probe TPD spectrometer, utilizing a Mg Kα X-ray source ($h\nu$ = 1253.6 eV). A constant analyzer energy of 20 eV was applied for the measurements, and binding energies were calibrated with respect to the C 1s peak at 284.8 eV. Residual U(VI) concentration was analyzed using a PerkinElmer NexION 300X ICP-MS. Thermogravimetric analysis (TGA) was performed with a TA

https://doi.org/10.1021/acssuschemeng.5c03058
ACS Sustainable Chem. Eng. 2025, 13, 10918−10929

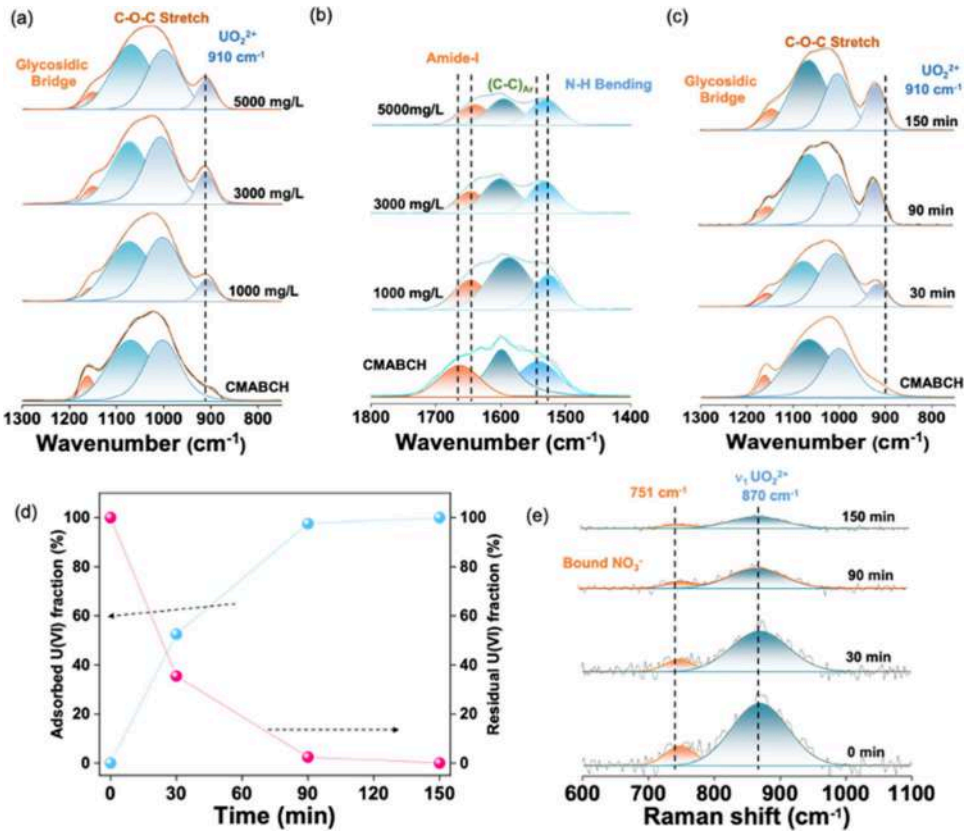


Figure 1. FTIR studies of CMABCH before and after U(VI) adsorption. Deconvoluted concentration-dependent IR spectra, before and after U(VI) adsorption (m-50 mg, V-10 mL, pH-7): (a) in the U(VI) antisymmetric region and (b) in the amide I and amide II regions. Deconvoluted time-dependent IR spectra ($U(VI)_o$-5000 mg/L, m-50 mg, V-10 mL, pH-7), (c) before and after U(VI) adsorption in the U(VI) antisymmetric region. (d) Adsorbed U(VI) fraction (%) in CMABCH and residual U(VI) fraction (%) in water, as a function of time. (e) Raman spectra of residual UO_2^{2+} species in solution after treatment with CMABCH at regular time intervals ($U(VI)_o$ - 5000 mg/L, m-50 mg, V-10 mL, pH-7).

Instruments Q500 Thermogravimetric Analyzer. The analysis was carried out under air and nitrogen atmospheres, covering a temperature range from room temperature to 900 °C, with a scan rate of 5 °C/min. Raman spectra were obtained using a CRM 200 micro Raman spectrometer of WiTec GmbH (Germany). The substrate was mounted on a sample stage of a confocal Raman spectrometer with 633 nm laser excitation. The treated water samples were taken on a glass substrate and analyzed keeping the laser and other parameters the same. BET surface area measurement was done using Micromeritics ASAP 2020 by degassing the sample at 120 °C for 12 h. Zeta potential studies were done using a Malvern Zetasizer Nano ZSP.

RESULTS AND DISCUSSION

Characterization of CMABCH, before and after U(VI) Adsorption. The IR spectra of CMABCH and its precursors, i.e., CMC, PABA, and CH were recorded to confirm the synthesis of CMABCH as shown in Figure S2. For CMABCH, a peak at 1598 cm^{-1}, corresponding to C−C aromatic stretching, confirmed the successful cross-linking of PABA to CMC and CH.[50,51] Additionally, shoulder peaks at 1660 cm^{-1} (amide-I) and 1540 cm^{-1} (amide-II) confirmed the amide bond formation.[52,53] A broad peak at 1000−1070 cm^{-1}, along with a shoulder peak at 1160 cm^{-1}, attributed to C−O−C stretching of glucopyranose ring,[54,55] further supported the cross-linking and formation of CMABCH. IR spectra depict the changes in the active sites of CMABCH on treatment with U(VI) solutions ranging from 1000 mg/L to 5000 mg/L, to determine the U(VI) adsorption mechanism at equilibrium. Figures 1a and 1b present the deconvoluted concentration-dependent IR of CMABCH, before and after U(VI) adsorption, in the regions corresponding to UO_2^{2+} antisymmetric stretch and amide band region, while the parent IR spectra of CMABCH, before and after U(VI) adsorption, are presented in Figure S3. The characteristic antisymmetric vibration of UO_2^{2+} at 940 cm^{-1} (as shown in Figure S4)[43] was red-shifted to 910 cm^{-1} upon U(VI) binding to CMABCH (as shown in Figure 1a), with increased intensity at higher U(VI) concentrations indicating high adsorption capacity of CMABCH. It is worth noting that the shift in the amide-I peak occurs from 1660 cm^{-1} to 1640 cm^{-1}, and the amide-II peak shifts from 1540 cm^{-1} to 1530 cm^{-1}, along with reduction in −N-H band intensity with higher U(VI) concentrations suggests nitrogen interaction and complexation with U(VI), confirming the role of nitrogen of amide functionalities as active sites in U(VI) binding, shown in Figure 1b. The reaction mechanism is represented by eq 1.

$$\text{-C-CO-NH-} + [UO_2(H_2O)_5]^{2+} \rightarrow \text{C-(CO)-N}\cdots UO_2(H_2O)_4]^+ + H^+ \quad (1)$$

Further analysis included monitoring the IR spectra of CMABCH, before and after U(VI) adsorption at regular time intervals as shown in Figure S5. The deconvoluted time-dependent IR spectra in the region of UO_2^{2+} antisymmetric stretch are shown in Figure 1c, indicating that active sites on CMABCH reached saturation within 90 min, beyond which no

https://doi.org/10.1021/acssuschemeng.5c03058
ACS Sustainable Chem. Eng. 2025, 13, 10918−10929

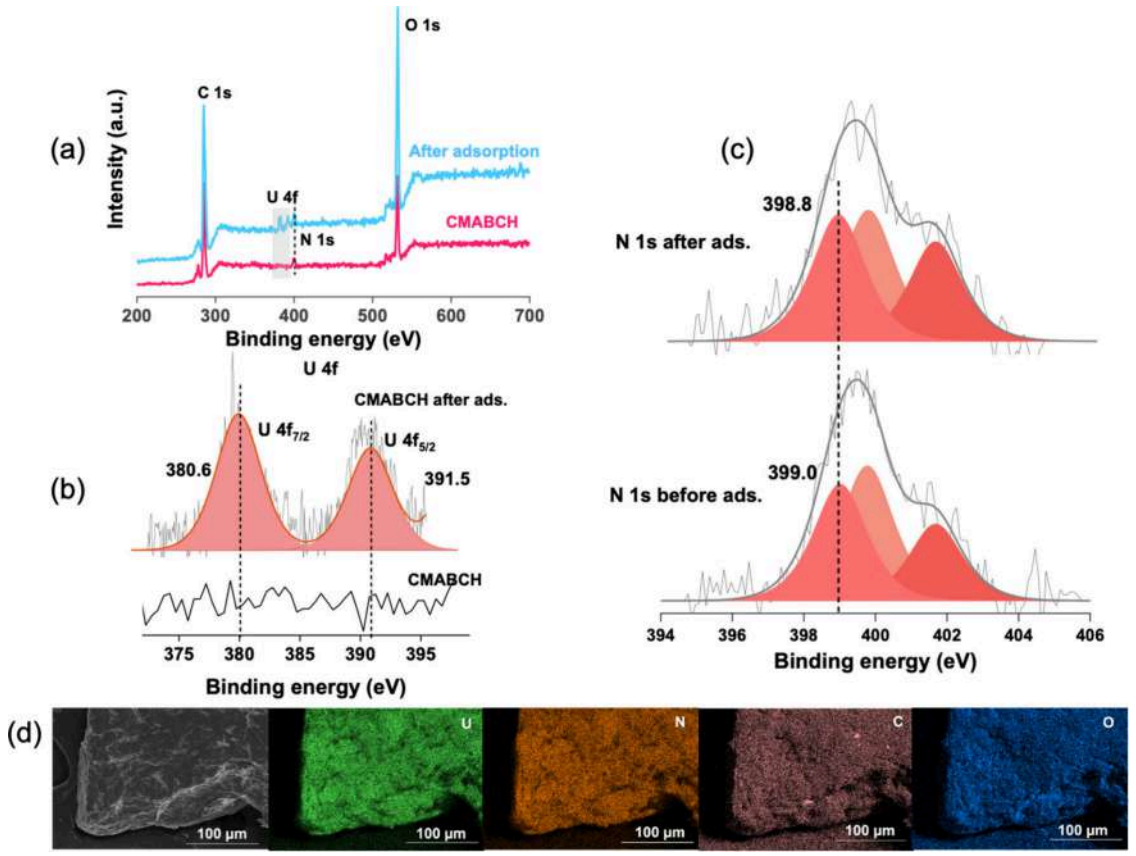


Figure 2. XPS survey spectra of (a) CMABCH before and after U(VI) adsorption.(b) U 4f regions of CMABCH, before and after U(VI) adsorption ($U(VI)_o$- 5000 mg/L, m-50 mg, V-10 mL, pH-7). (c) Deconvoluted XPS spectra of N 1s region before and after U(VI) adsorption. (d) HRSEM of CMABCH after U(VI) adsorption and corresponding EDS elemental mapping of U, N, C, and O ($U(VI)_o$ - 5000 mg/L, m-50 mg, V-10 mL, pH-7).

significant adsorption was observed. To quantify the availability of U(VI) adsorption in relation to the availability of active sites, the peak area at 914 cm^{-1} was used to estimate the fraction of U(VI) adsorbed with respect to the availability of active sites with time. The fraction (%) of U(VI) adsorbed was calculated using eq S1a (Supporting Information)[56] and compared with residual U(VI) fractions determined from ICP-MS data (Supporting Information, eq S1b). This strongly suggests that the active sites were fully occupied within 90 min, as all the amide functionalities were engaged in binding with U(VI). Additionally, Raman spectroscopic studies were performed at room temperature to understand the species of U(VI) in water over time at pH 7. The standard aqueous U(VI) solution (5000 mg/L, Figure 1e) showed two characteristic peaks at 870 cm^{-1} and 751 cm^{-1}, corresponding to UO_2^{2+} symmetric stretching and bound NO_3^- of $UO_2(NO_3)_2^0$, respectively.[57] Over time, the peak intensity of the U(VI) species in solution decreased, suggesting no change in U(VI) species in solution upon interaction with CMABCH, as shown in Figure 1e. Raman spectroscopy is particularly informative on the speciation of uranium in solution.

XPS provided further insights into U(VI) interaction with CMABCH. The survey spectra revealed C 1s, N 1s, and O 1s peaks, with additional peaks appearing after U(VI) adsorption due to U 4f, as shown in Figure 2a. Peaks for adsorbed U(VI) were detected at 380.6 eV (U $4f_{7/2}$) and 391.5 eV (U $4f_{5/2}$), with a 2 eV shift compared to standard UO_2^{2+}, suggesting a partial reduction of U(VI) to U(IV),[45] as presented in Figure 2b and Table 1. To further investigate the U(VI) adsorption process on CMABCH, deconvoluted XPS spectra before and after U(VI) adsorption were compared and the deconvoluted N 1s peaks were observed at 399.0 eV (R−N−H-C═O), 399.7 eV (N−C═O), and 401.3 eV ($-NH_3^+$), with a post adsorption major shift of C−N−H-C═O bond to 398.8 eV,

Table 1. Binding Energies (eV) of C 1s, O 1s, N 1s, and U 4f before and after U(VI) Adsorption onto CMABCH

Valence states	Samples	Binding energy (eV) before U(VI) adsorption	Binding energy (eV) after U(VI) adsorption	Reference
C 1s	C−C, C−N	284.7	284.7	53
	C−O, C−OH, C−N−C═O	286.3	286.4	53
	N−C═O	288.0	288.1	55
O 1s	C−O	530.4	530.5	30
	Aromatic C═O	531.7	531.8	58
N 1s	-C-NH−CO-	399.0	398.7	59
	N−C═O	399.7	399.6	60
	$-NH_3^+$	401.3	401.3	53
U 4f	U(VI) $4f_{7/2}$	382.8		39
	U(VI) $4f_{5/2}$	393.6		43
	U(IV) $4f_{7/2}$		380.6	61
	U(IV) $4f_{5/2}$		391.5	61

https://doi.org/10.1021/acssuschemeng.5c03058
ACS Sustainable Chem. Eng. 2025, 13, 10918−10929

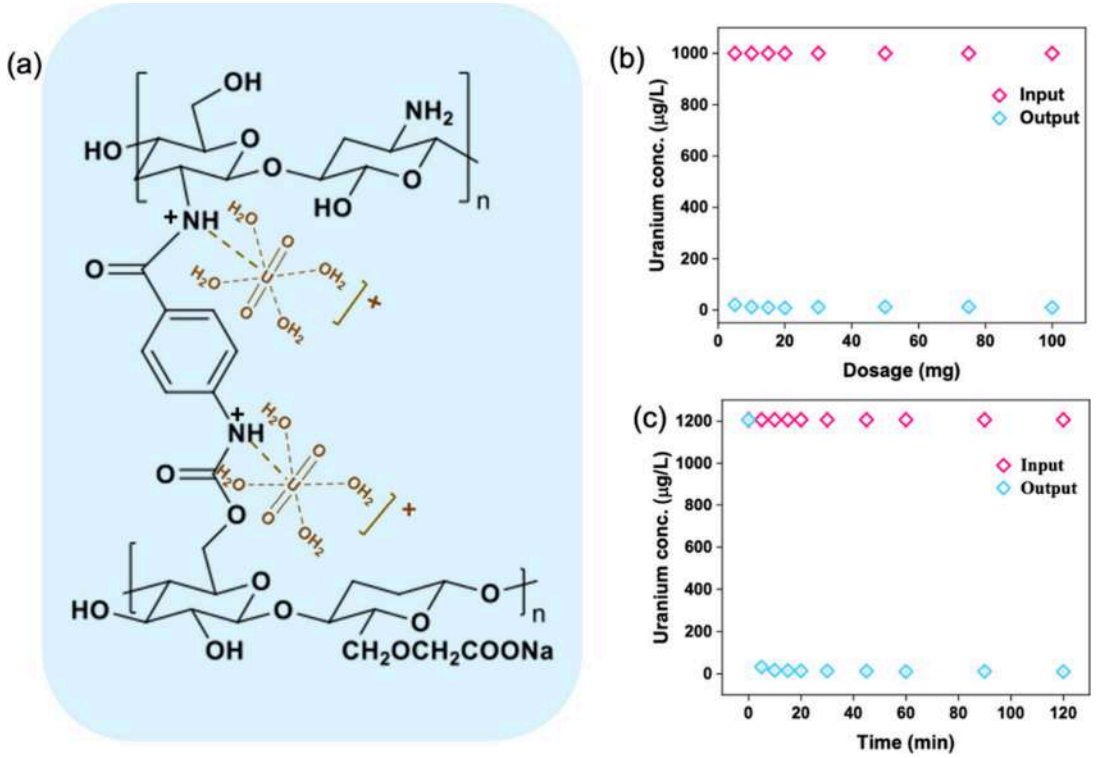


Figure 3. (a) Possible adsorption mechanism of U(VI) onto amide active sites of CMABCH. (b) Concentrations as a function of dosage of CMABCH.(Conditions- $U(VI)_o$-1000 μg/L, V-10 mL, pH-7). (c) U(VI) concentration as a function of contact time. (Conditions- $U(VI)_o$-1000 μg/L, m-30 mg,V-10 mL, pH-7).

indicating the interaction of nitrogen with U(VI) as shown in Figure 2c. The deconvoluted C 1s spectra (Figure S5) showed peaks for −C-C and −C-N bonds (284.7 eV), C−O, C−OH, and C−N−C═O bonds (286.3 eV), and N−C═O bonds (288.0 eV) with no significant change after U(VI) adsorption. Similarly, no notable shift in binding energies of O 1s was observed, as shown in Figure S6 and Table 1. These findings suggest that the nitrogen atoms in amide groups serve as the active sites for U(VI) immobilization on CMABCH, facilitating charge transfer and contributing to the reduction of U(VI) to U(IV),[55] consistent with the IR studies. Based on the observations from IR and XPS, the proposed mechanism involves the amide functionalities providing active sites for U(VI) binding and chelation. Upon adsorption of U(VI) onto the surface of CMABCH, the lone pair electrons on the nitrogen atoms facilitate charge transfer to U(VI), leading to its partial reduction to U(IV). This charge transfer alters the electronic environment surrounding U(VI), as evidenced by the shift in N 1s binding energy from 399.0 to 398.8 eV and U 4f shift to 380.6 and 391.5 eV, confirming U(VI) binding and reductive adsorption on the CMABCH surface, indicating that the reduction step plays an essential role in the adsorption process.

The surface morphology of CMABCH was examined before and after U(VI) adsorption using HRSEM. The HRSEM image of granular CMABCH, along with its corresponding elemental mapping, is provided in Figure S7. The high carbon and oxygen content were coming from the polymer backbone, and the nitrogen was coming from amide functionalities. No changes in the morphology of CMABCH were observed after exposure to a concentrated U(VI) solution and U(VI) was homogeneously adsorbed on the surface of CMABCH and the corresponding elemental mapping is shown in Figure 2d. This confirms the successful adsorption of U(VI) onto CMABCH. Figure S8 shows powder XRD patterns of the precursors CMC,[62] PABA,[63] CH,[64] CMABCH, and CMABCH after U(VI) adsorption. In the case of CMABCH, the diffraction patterns display a peak at 15.5° along with a broad hump between 16° and 30°, originating from its precursors, which confirms the amorphous−crystalline nature of CMABCH. Following U(VI) adsorption, only a broad peak is observed, indicating the amorphous nature of CMABCH and the disappearance of distinct crystallinity peaks as a result of the adsorption process.

The studies have shown the interactions of nitrogen, phosphonate and oxygen functional groups with U(VI).[9,65] Based on our studies, we can interpret the probable binding of U(VI) with the nitrogen of amide functionalities, dependent on the availability of amide sites, supported by IR and XPS studies, as shown in Figure 3a.

Control studies were conducted with CMC which removed 100−200 μg/L of U(VI) from 1000 μg/L U(VI) spiked water, suggesting that it could be used as a platform for U(VI) adsorption. Thermal stability of CMABCH was analyzed by TGA. Analysis was performed under nitrogen and air atmosphere within the temperature range from room temperature to 900 °C at the heating rate of 5 °C min^{-1} as shown in Figure S9. It is known that CMC and CH start decomposing at 250 and 175 °C, respectively,[30,38] while PABA degrades within the temperature range of 200−300 °C.[66] In the case of CMABCH, a three-step degradation was observed. Around 8% weight loss was due to the adsorbed water molecules below 120 °C. CMABCH exhibited thermal stability until 235 °C. A significant mass loss of 45% occurred in the temperature range of 238 to 400 °C, due to the decomposition of organic molecules into low molecular weight organic compounds.[67]

https://doi.org/10.1021/acssuschemeng.5c03058
ACS Sustainable Chem. Eng. 2025, 13, 10918−10929

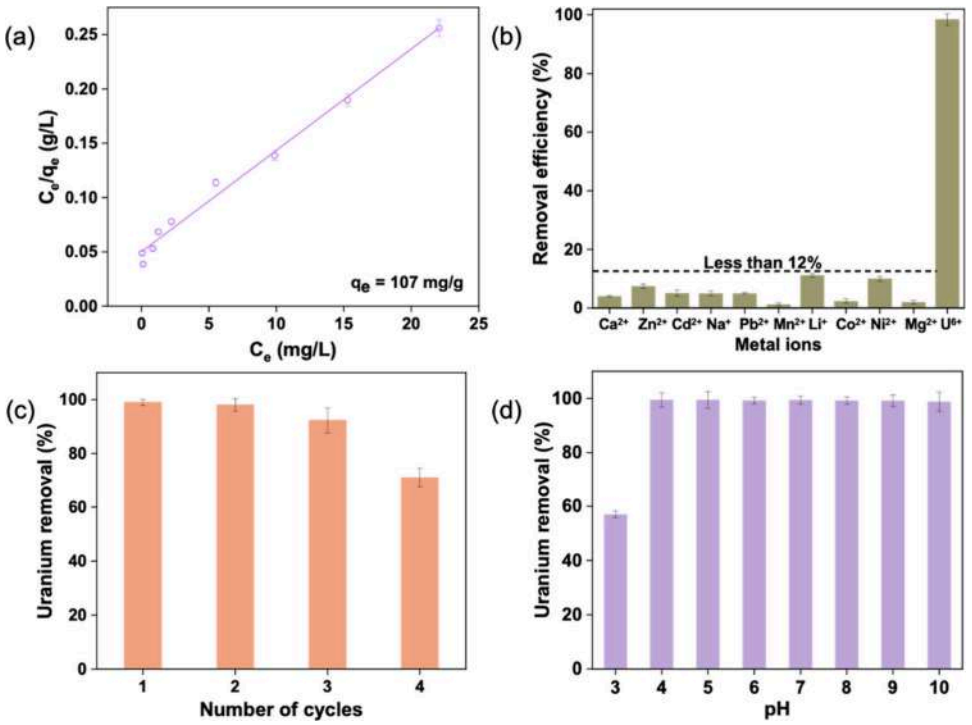


Figure 4. (a) Langmuir adsorption isotherm of CMABCH (m-5 mg, V-10 mL, pH-7). (b) Selective U(VI) capture from 10-ions mixture solution (M_o and $U(VI)_o$-1000 μg/L, m-30 mg, V-10 mL, pH-7). (c) Batch adsorption studies for adsorption−desorption cycles of U(VI) on CMABCH ($U(VI)_o$-1000 μg/L, m-30 mg, V-10 mL, pH-7). (d) Batch adsorption studies of CMABCH as a function of pH ($U(VI)_o$-1000 μg/L, m-30 mg, V-10 mL).

The final degradation of CMABCH, from 400 to 600 °C, was attributed to the complete degradation of CMABCH to CO_2 and H_2O.[68] We infer that the cross-linking of CH and CMC enhanced the thermal stability of the composite as compared to their pristine forms.

Batch Studies of U(VI) Adsorption on CMABCH. Figure 3 illustrates the performance of CMABCH for U(VI) adsorption, derived from batch studies. Ten mL of 1000 μg/L U(VI) spiked water was treated with CMABCH and its performance was evaluated. Different dosages of CMABCH ranging from 2 mg to 100 mg were checked and we found that less than 30 mg of CMABCH was enough to reduce the concentration of U(VI) below 10 μg/L within 2 h, as shown in Figure 3b. CMABCH also exhibited faster uptake kinetics as shown in Figure 3c. CMABCH showed high capacity to rapidly reduce the concentration of U(VI) below 10 μg/L, dependent on the number of active sites available for U(VI) adsorption. To analyze the kinetics data of U(VI) adsorption onto CMABCH, Ho's pseudo-second-order model was applied. The linear form of the equation used is presented in eq S3 (Supporting Information). The plot of t/q_e versus time gave a linear fit for U(VI) adsorption, as shown in Figure S10, with a correlation coefficient of 1 indicating that chemical adsorption[69] is the primary mechanism for U(VI) removal. Furthermore, it also suggests that the rate determination step is influenced by the availability of active adsorption sites[20] and the involvement of amide functionalities in U(VI) adsorption, as supported by the IR and XPS analysis discussed in Figures 1 and 2.

The maximum U(VI) uptake capacity of CMABCH was evaluated by introducing it into U(VI) spiked water, with U(VI) concentrations ranging from 1 to 100 mg/L at neutral pH. The Langmuir isotherm model was used to understand the influence of equilibrium concentration on the adsorption capacity of CMABCH. This model assumes that adsorption occurs at discrete, homogeneous sites on the adsorbent surface, forming a monolayer at equilibrium with no lateral interaction between adsorbed molecules. A plot of C_e/q_e versus C_e resulted in a linear fit using the eq S4 (Supporting Information), consistent with the Langmuir model. The adsorption isotherm gave the maximum adsorption capacity (q_{max}) of 107 mg/g for CMABCH, with a strong correlation coefficient of 0.99 as shown in Figure 4a. This confirms monolayer adsorption, which is also in agreement with Freundlich isotherm (Figure S11) having less R^2 value and n value greater than unity, confirming chemical adsorption (Table 2).[70]

Table 2. Parameters of the Adsorption Isotherm Models for U(VI) Adsorption

Langmuir model		Freundlich model		
q_{max} (mg/g)	R^2	K_F ($mg^{1-n}\cdot L^n/g$)	n	R^2
107	0.99	10.54	2.07	0.95

The performance of CMABCH was assessed for its selectivity toward U(VI) in the presence of competing metal ions at neutral pH. A selectivity study was conducted using a mixed solution containing 1000 μg/L (10 mL) Cd^{2+}, Pb^{2+}, Zn^{2+}, Mn^{2+}, Li^+, Ni^{2+}, Co^{2+}, Na^+, Ca^{2+}, Mg^{2+}, and U^{6+} as shown in Figure 4b. Figure 4b presents the removal efficiencies of individual ions by CMABCH within the mixture. CMABCH exhibited complete removal of U^{6+}, while the removal efficiencies for the other metal ions were below 12%, demonstrating exceptional selectivity for U(VI) over the coexisting ions in the same mixture. Since V(V) is the major

https://doi.org/10.1021/acssuschemeng.5c03058
ACS Sustainable Chem. Eng. 2025, 13, 10918−10929

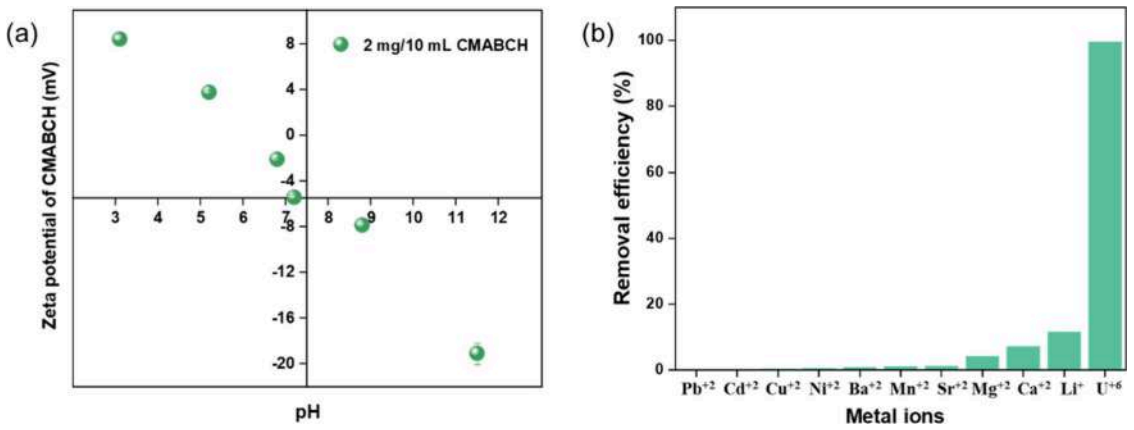


Figure 5. (a) Zeta potential vs pH (pH window 3−11) for CMABCH in water (2 mg in 10 mL). (b) U(VI) removal efficiency of CMABCH of groundwater containing 102 μg/L U(VI) and other coexisting ions. (m-30 mg, V-10 mL).

Table 3. Comparison of Adsorption Capacities of Other Cellulose/CH-Based Reported Materials for U(VI)

S.no.	Adsorbents	Uptake capacity (mg/g)	Optimum pH	Time (min)	Reusability	Reference
1	Deacetylated chitosan	17.44	3.5	1440	3	75
2	Chitosan modified phosphate rock	8.06	2.5	300	-	76
3	Chitosan bentonite composite	49.09	8	60	6	77
4	Hyper cross-linked polymer	46.74	8	70	4	78
5	Functionalized natural cellulose fibres	16.0	-	240	-	79
6	CMABCH	107	neutral	120	3	This work

competitor during U(VI) extraction from seawater, CMABCH performance was evaluated for U(VI) in the presence of V(V) and it was observed that CMABCH removed 99% U(VI) and only 30% V(V), as shown in Figure S12. This selectivity is attributed to the preferential interaction of V(V) with imide-dioxime groups.[71,72] Superior selectivity for U(VI) over other ions is due to the strong interaction of U(VI) with nitrogen atoms in the amide functionalities within CMABCH. These studies align well with IR and XPS analysis, further confirming the affinity of CMABCH for U(VI). Additionally, to assess the adsorption capacity of CMABCH in the presence of common anions, a multianion water mixture containing 1000 μg/L each of F^-, Cl^-, Br^-, NO_3^-, NO_2^-, SO_4^{2-}, and PO_4^{3-} was spiked with 1000 μg/L of U(VI) (10 mL). Under these conditions, CMABCH also achieved a U(VI) removal efficiency of 98%. The reusability of CMABCH was evaluated across multiple cycles as shown in Figure 4c. The adsorbent was recovered by centrifugation to minimize material loss, and the adsorbed U(VI) was effectively desorbed using 10 mM HCl (10 mL) within 90 min, and the composite retained a removal efficiency of 70% after three consecutive cycles. Comparative testing of various eluents (Table S1) showed low desorption efficiencies, while higher concentrations of HCl damaged the CMABCH structure and reduced its adsorption performance. In contrast, mild 10 mM HCl (10 mL) treatment efficiently desorbed UO_2^{2+} without compromising the functional groups of CMABCH, as confirmed by post-treatment IR analysis (Figure S13). Notably, the amide functionalities were retained for consecutive adsorption−desorption first cycle. However, after the third cycle, the composite exhibited a reduction in U(VI) removal efficiency to 70%, accompanied by damage to the amide functionalities, as evidenced in Figure S13. This deterioration is likely due to cumulative HCl exposure, which appears to degrade amide groups beyond the third cycle. Additionally, the appearance of a peak at 910 cm^{-1} in the IR spectrum suggests the presence of residual adsorbed U(VI), contributing to the decreased efficiency observed after three cycles. Note that U(VI) removal efficiency was evaluated over a wide pH range (pH 3−10), as illustrated in Figure 4d. The composite demonstrated excellent U(VI) removal efficiency between pH 4 and 10, with reduced efficiency at pH 3. The decline at lower pH is likely due to the protonation of amide functionalities[73] and competitive adsorption of H^+ ions, which interferes with UO_2^{2+} adsorption, reducing U(VI) removal efficiency. These observations align with the reusability of CMABCH, as the adsorbed U(VI) could be desorbed using 10 mM HCl. Changes in the pH not only affect the surface charge of the adsorbent but also influence the U(VI) speciation.[33]

Zeta potential studies were conducted to examine the surface charge of CMABCH to understand the preference of U(VI) adsorption. The zeta potential shifted from +8 mV at pH 3 to −20 mV at pH 12, as shown in Figure 5a. As the pH changed from acidic to neutral media, zeta potential shifted from positive to negative indicating reduced protonation of amide functionalities. At neutral pH, CMABCH acquired negative surface charge, enhancing the electrostatic attraction between the adsorbent and the UO_2^{2+}, thereby improving the removal efficiency. However, at very high pH beyond 10, CMABCH became highly negatively charged, leading to repulsions between CMABCH and the uranium species and decreasing the U(VI) removal efficiency.[74] To gain insights into U(VI) removal efficiency of CMABCH in real field samples, groundwater samples were collected from a well in Shamshabad village, Fazilka, Punjab. The water samples had a high concentration of U(VI), i.e. 102 μg/L, with other chemical characteristics as shown in Table S2. The field water exhibited high alkalinity, approximately 240 mg/L, elevated concentrations of SO_4^{2-} and Cl^-, while the PO_4^{3-} concentration was negligible, remaining below the detection limit. The adsorbent demonstrated a remarkable removal capacity,

https://doi.org/10.1021/acssuschemeng.5c03058
ACS Sustainable Chem. Eng. 2025, 13, 10918−10929

achieving 99.5% U(VI) removal. It effectively reduced U(VI) concentration to levels within the permissible limit set by WHO, even in the presence of coexisting ions as shown in Figure 5b.

The U(VI) adsorption capacity of CMABCH was compared with the existing composites and CMABCH showed higher U(VI) removal efficiency as shown in Table 3.

Aspects of Sustainability. The extent of "greenness" of this technology was assessed through mass-based sustainability parameters, with the formulas mentioned in the Supporting Information (eqs S7−S10).

Raw Materials. CMC and CH were used majorly because of their nontoxicity, renewable and biodegradable nature, with water being used as the solvent. The mass intensity (excluding water) came out to be 1.9, while water intensity was 47.6. The mass intensity could be further reduced to 1 by minimizing composite loss during filtration and washing. The reaction mass efficiency was determined to be 52.5%.

Resulting Emissions. The synthesis of the composite avoided the use of toxic harmful solvents. The E factor (environmental factor) was calculated to be 0.8 (without solvent recovery), indicating minimum emissions. NHS and EDC were removed through washing. The spent adsorbent may be processed similar to other such adsorbents following an evaluation of toxicity characteristic leaching procedure (TCLP), causing negligible environmental impact.[31] U(VI) was desorbed using 10 mM HCl (10 mL), and the acidic effluent generated during this process can be subsequently neutralized with NaOH and $CaCO_3$. Specifically, 0.4 g of NaOH and 0.5 g of $CaCO_3$ are sufficient to treat 1000 mL of 10 mM HCl solution.[80]

Economic Analysis. A cost analysis of the composite revealed that the composite can give uranium-free water at an approximate cost of $10/1000L. This cost, based on the cost of laboratory reagents, equipment use and labor, can be reduced by optimizing or substituting NHS/EDC with industrial raw materials, improving economic viability of the technology. According to the commercially available raw materials, the cost of CMC, CH and PABA (per kg) is around $10 whereas the cost of EDC/NHS (per kg) is approximately $50 which contributes to the total cost in the synthesis of CMABCH. Various alternative coupling agents are available for amide bond synthesis. For instance, Elschner et al. reported the synthesis of cellulose carbamate using phenyl chloroformate.[81] However, this reaction was carried out in organic solvents, under inert conditions, and at elevated temperatures. Such processes tend to be highly energy-intensive and generate significant amounts of secondary waste. Similarly, Wang et al. modified and introduced amide functionalities with the help of chloroformate at high temperatures.[82] While less expensive reagents such as oxalyl chloride or chloroformates could be considered for industrial-scale applications, their successful implementation would require substantial optimization of reaction conditions, including solvent systems and temperature controls, to achieve efficient and sustainable processes. A thorough techno-economic and process optimization study would be essential before considering the alternatives for industrial-scale optimization. However, a cost reduction by an order of magnitude is expected considering the cost of alternate reagents.

CONCLUSIONS

In this work, we present an eco-friendly method to cross-link CMC and CH by incorporating amide functionalities for efficient U(VI) removal from water. The removal mechanism involves the initial coordination of U(VI) ions with the nitrogen atoms of amide functionalities, followed by charge transfer and subsequent reduction to U(IV) as confirmed by IR and XPS. HRSEM analysis confirmed that the surface morphology remained the same after saturation with uranium. The adsorption capacity of CMABCH reached 107 mg/g, determined from the Langmuir adsorption model, which is superior as compared to other reported cellulose/chitosan materials. The adsorbent exhibited excellent U(VI) removal efficiency in the presence of other counterions, and the composite could be easily recovered and reused, giving a high U(VI) removal efficiency of more than 92% over three reactivation cycles. Its efficiency in removing U(VI) from groundwater in Punjab state, India, in the presence of many competing ions, highlights its potential as an excellent composite for drinking water decontamination.

ASSOCIATED CONTENT

Supporting Information

The Supporting Information is available free of charge at https://pubs.acs.org/doi/10.1021/acssuschemeng.5c03058.

Equations used in the main text; BET surface area plots (a) N_2 adsorption−desorption plot. (b) Pore size distribution; IR spectra of CMABCH and its precursors i.e., CMC, 4-PABA, and CH; IR spectra of CMABCH, before and after treatment with various concentrations of U(VI); IR spectra of standard $(UO_2(NO_3)_2.6H_2O)$; IR spectra of CMABCH, before and after U(VI) adsorption, at regular time intervals; Deconvoluted XPS spectra of (a) C 1s and (b) O 1s regions before and after U(VI) adsorption (bottom to top); HRSEM image of CMABCH and its corresponding elemental mapping; Powder XRD of CMABCH, its precursors i.e. CMC, PABA and CH and CMABCH after U(VI) adsorption; TGA of CMABCH in air and nitrogen atmospheres from room temperature to 900 °C at a scan rate of 5 °C min^{-1}; Ho's pseudo-second-order kinetic plot for the adsorption of U(VI) onto CMABCH; Freundlich isotherm plot for the adsorption of U(VI) on CMABCH; Removal efficiency of CMABCH when U(VI) and V(V) coexist; Desorption efficiencies by various eluents; FTIR of CMABCH after adsorption−desorption cycles; Chemical parameters for the groundwater sample from the well in Shamshabad village, Fazilka, Punjab, India (PDF)

AUTHOR INFORMATION

Corresponding Author

Thalappil Pradeep − *DST Unit of Nanoscience (DST UNS) and Thematic Unit of Excellence (TUE), Department of Chemistry, Indian Institute of Technology Madras, Chennai 600036, India; International Centre for Clean Water, IIT Madras Research Park, Chennai 600113, India;* orcid.org/0000-0003-3174-534X; Email: pradeep@iitm.ac.in

Authors

Sonali Seth − *DST Unit of Nanoscience (DST UNS) and Thematic Unit of Excellence (TUE), Department of Chemistry, Indian Institute of Technology Madras, Chennai 600036, India*

Md Rabiul Islam − *DST Unit of Nanoscience (DST UNS) and Thematic Unit of Excellence (TUE), Department of Chemistry, Indian Institute of Technology Madras, Chennai 600036, India;* orcid.org/0000-0001-6454-4013

Tanmayaa Nayak − *DST Unit of Nanoscience (DST UNS) and Thematic Unit of Excellence (TUE), Department of Chemistry, Indian Institute of Technology Madras, Chennai 600036, India*

Amoghavarsha Ramachandra Kini − *DST Unit of Nanoscience (DST UNS) and Thematic Unit of Excellence (TUE), Department of Chemistry, Indian Institute of Technology Madras, Chennai 600036, India;* orcid.org/0009-0003-6863-7729

Sujan Manna − *DST Unit of Nanoscience (DST UNS) and Thematic Unit of Excellence (TUE), Department of Chemistry, Indian Institute of Technology Madras, Chennai 600036, India*

Bijesh K. Malla − *DST Unit of Nanoscience (DST UNS) and Thematic Unit of Excellence (TUE), Department of Chemistry, Indian Institute of Technology Madras, Chennai 600036, India*

Ankit Nagar − *DST Unit of Nanoscience (DST UNS) and Thematic Unit of Excellence (TUE), Department of Chemistry, Indian Institute of Technology Madras, Chennai 600036, India*

Complete contact information is available at: https://pubs.acs.org/10.1021/acssuschemeng.5c03058

Notes

The authors declare no competing financial interest.

■ ACKNOWLEDGMENTS

The authors thank the Sophisticated Analytical Instrumental Facility (SAIF) IIT Madras for TGA measurements and the Department of Chemistry, IIT Madras. T.P. acknowledges financial support from the Ministry of Mines (MOM), India (SP21221094CYMOMI002505), funding from SERB SUPRA (Grant SPR/2021/000439), and the Centre of Excellence on Molecular Materials and Functions under the Institution of Eminence scheme of IIT Madras. S.S. thanks the Ministry of Human Resource Development, Prime Minister's Research Fellowship, Government of India. The authors also thank the Department of Science and Technology, Government of India, for supporting our research program on nanomaterials.

■ REFERENCES

(1) Smedley, P. L.; Kinniburgh, D. G. Uranium in Natural Waters and the Environment: Distribution, Speciation and Impact. *Appl. Geochem.* **2023**, *148*, No. 105534.

(2) Daniel, R.; Tripathi, D.; Singh, S.; Sharma, N.; Yuvraaj, A.; Katyal, D.; Kumar, V. Uranium: Occurrence, Distribution across India and Its Potential Health Effects. *J. Radioanal. Nucl. Chem.* **2022**, *331* (7), 2805−2815.

(3) Ma, M.; Wang, R.; Xu, L.; Xu, M.; Liu, S. Emerging Health Risks and Underlying Toxicological Mechanisms of Uranium Contamination: Lessons from the Past Two Decades. *Environ. Int.* **2020**, *145*, No. 106107.

(4) Balaram, V.; Rani, A.; Rathore, D. P. S. Uranium in Groundwater in Parts of India and World: A Comprehensive Review of Sources, Impact to the Environment and Human Health, Analytical Techniques, and Mitigation Technologies. *Geosystems Geoenvironment* **2022**, *1* (2), No. 100043.

(5) Zhang, L.; Chu, J.; Xia, B.; Xiong, Z.; Zhang, S.; Tang, W. Health Effects of Particulate Uranium Exposure. *Toxics* **2022**, *10* (10), 575.

(6) Nolan, J.; Weber, K. A. Natural Uranium Contamination in Major U.S. Aquifers Linked to Nitrate. *Environ. Sci. Technol. Lett.* **2015**, *2* (8), 215−220.

(7) Verma, M.; Loganathan, V. A. Hydrogeochemical Constraints on Uranium Contamination of Groundwater for Drinking Water Supplies and Associated Health Risks. *Groundw. Sustain. Dev.* **2023**, *23*, No. 100973.

(8) Bala, R.; Karanveer; Das, D. Occurrence and Behaviour of Uranium in the Groundwater and Potential Health Risk Associated in Semi-Arid Region of Punjab, India. *Groundw. Sustain. Dev.* **2022**, *17*, No. 100731.

(9) Nayak, T.; Mukherjee, S.; Kini, A. R.; Islam, M. R.; Nagar, A.; Seth, S.; Pradeep, T. Cellulose-Derived Nanomaterials for Affordable and Rapid Remediation of Uranium in Water. *ACS Sustain. Chem. Eng.* **2025**, *13* (4), 1838−1850.

(10) Patnaik, R.; Lahiri, S.; Chahar, V.; Naskar, N.; Sharma, P. K.; Avhad, D. K.; Bassan, M. K. T.; Knolle, F.; Schnug, E.; Srivastava, A. Study of Uranium Mobilization from Himalayan Siwaliks to the Malwa Region of Punjab State in India. *J. Radioanal. Nucl. Chem.* **2016**, *308* (3), 913−918.

(11) Kopylova, Y.; Guseva, N.; Shestakova, A.; Khvaschevskaya, A.; Arakchaa, K. Uranium and Thorium Behavior in Groundwater of the Natural Spa Area "Choygan Mineral Water" (East Tuva). *IOP Conf. Ser. Earth Environ. Sci.* **2015**, *27*, No. 012034.

(12) Lehtonen, J.; Hassinen, J.; Kumar, A. A.; Johansson, L.-S.; Mäenpää, R.; Pahimanolis, N.; Pradeep, T.; Ikkala, O.; Rojas, O. J. Phosphorylated Cellulose Nanofibers Exhibit Exceptional Capacity for Uranium Capture. *Cellulose* **2020**, *27* (18), 10719−10732.

(13) Luo, W.; Gu, B. Dissolution and Mobilization of Uranium in a Reduced Sediment by Natural Humic Substances under Anaerobic Conditions. *Environ. Sci. Technol.* **2009**, *43* (1), 152−156.

(14) Křepelová, A.; Sachs, S.; Bernhard, G. Uranium(VI) Sorption onto Kaolinite in the Presence and Absence of Humic Acid. *Radiochim. Acta* **2006**, *94* (12), 825−833.

(15) Kumar, A.; Rout, S.; Mishra, M. K.; Karpe, R.; Ravi, P. M.; Tripathi, R. M. Impact of Particle Size, Temperature and Humic Acid on Sorption of Uranium in Agricultural Soils of Punjab. *SpringerPlus* **2015**, *4* (1), 262.

(16) Shen, J.; Schäfer, A. Removal of Fluoride and Uranium by Nanofiltration and Reverse Osmosis: A Review. *Chemosphere* **2014**, *117*, 679−691.

(17) Choi, A. E. S.; Futalan, C. C. M.; Yee, J.-J. Fuzzy Optimization for the Removal of Uranium from Mine Water Using Batch Electrocoagulation: A Case Study. *Nucl. Eng. Technol.* **2020**, *52* (7), 1471−1480.

(18) Zhou, S.; Dong, F.; Qin, Y. High Efficiency Uranium(VI) Removal from Wastewater by Strong Alkaline Ion Exchange Fiber: Effect and Characteristic. *Polymers* **2023**, *15* (2), 279.

(19) Chowdhury, A. A.; Basak, N.; Islam, E. Removal of Uranium from Water Using Biofilm of Uranium Sensitive Methylobacterium Sp. *J. Hazard. Mater. Adv.* **2023**, *10*, No. 100296.

(20) Mukherjee, S.; Kumar, A. A.; Sudhakar, C.; Kumar, R.; Ahuja, T.; Mondal, B.; Srikrishnarka, P.; Philip, L.; Pradeep, T. Sustainable and Affordable Composites Built Using Microstructures Performing Better than Nanostructures for Arsenic Removal. *ACS Sustain. Chem. Eng.* **2019**, *7* (3), 3222−3233.

(21) Qasem, N. A. A.; Mohammed, R. H.; Lawal, D. U. Removal of Heavy Metal Ions from Wastewater: A Comprehensive and Critical Review. *Npj Clean Water* **2021**, *4* (1), 36.

(22) Camacho, L. M.; Deng, S.; Parra, R. R. Uranium Removal from Groundwater by Natural Clinoptilolite Zeolite: Effects of pH and

Initial Feed Concentration. *J. Hazard. Mater.* **2010**, *175* (1−3), 393−398.
(23) Embaby, M. A.; Haggag, E. A.; El-Sheikh, A. S.; Marrez, D. A. Biosorption of Uranium from Aqueous Solution by Green Microalga Chlorella Sorokiniana. *Environ. Sci. Pollut. Res.* **2022**, *29* (38), 58388−58404.
(24) Aslani, C. K.; Amik, O. Active Carbon/PAN Composite Adsorbent for Uranium Removal: Modeling Adsorption Isotherm Data, Thermodynamic and Kinetic Studies. *Appl. Radiat. Isot.* **2021**, *168*, No. 109474.
(25) Zhuang, S.; Wang, J. Poly Amidoxime Functionalized Carbon Nanotube as an Efficient Adsorbent for Removal of Uranium from Aqueous Solution. *J. Mol. Liq.* **2020**, *319*, No. 114288.
(26) Zahran, F.; El-Maghrabi, H. H.; Hussein, G.; Abdelmaged, S. M. Fabrication of Bentonite Based Nanocomposite as a Novel Low Cost Adsorbent for Uranium Ion Removal. *Environ. Nanotechnol. Monit. Manag.* **2019**, *11*, No. 100205.
(27) Yu, Z.; Li, Q.; Liao, J.; Zhang, Y.; Zhang, L.; Zhu, W. Efficient Removal of Uranium (VI) by Nano-Manganese Oxide Materials: A Synthetic Experimental and Mechanism Studies. *J. Alloys Compd.* **2021**, *868*, No. 159069.
(28) Song, Y.; Li, H.; Shan, T.; Yang, P.; Li, S.; Liu, Z.; Liu, C.; Shen, C. MOF-Implanted Poly (Acrylamide-Co-Acrylic Acid)/Chitosan Organic Hydrogel for Uranium Extraction from Seawater. *Carbohydr. Polym.* **2023**, *302*, No. 120377.
(29) Nasrollahzadeh, M.; Sajjadi, M.; Iravani, S.; Varma, R. S. Starch, Cellulose, Pectin, Gum, Alginate, Chitin and Chitosan Derived (Nano)Materials for Sustainable Water Treatment: A Review. *Carbohydr. Polym.* **2021**, *251*, No. 116986.
(30) Wang, Y.; Ai, Y.; Liu, X.; Chen, B.; Zhang, Y. Indole-Functionalized Cross-Linked Chitosan for Effective Uptake of Uranium(vi) from Aqueous Solution. *Polym. Chem.* **2022**, *13* (12), 1751−1762.
(31) Kumar, A. A.; Som, A.; Longo, P.; Sudhakar, C.; Bhuin, R. G.; Gupta, S. S.; Anshup; Sankar, M. U.; Chaudhary, A.; Kumar, R.; Pradeep, T. Confined Metastable 2-Line Ferrihydrite for Affordable Point-of-Use Arsenic-Free Drinking Water. *Adv. Mater.* **2017**, *29* (7), No. 1604260.
(32) Zhuang, S.; Zhu, K.; Wang, J. Fibrous Chitosan/Cellulose Composite as an Efficient Adsorbent for Co(II) Removal. *J. Clean. Prod.* **2021**, *285*, No. 124911.
(33) Dai, Z.; Sun, Y.; Zhang, H.; Ding, D.; Li, L. Rational Synthesis of Polyamidoxime/Polydopamine-Decorated Graphene Oxide Composites for Efficient Uranium(VI) Removal from Mine Radioactive Wastewater. *Ind. Eng. Chem. Res.* **2019**, *58* (41), 19280−19291.
(34) Wang, J.; Zhuang, S. Removal of Various Pollutants from Water and Wastewater by Modified Chitosan Adsorbents. *Crit. Rev. Environ. Sci. Technol.* **2017**, *47* (23), 2331−2386.
(35) Khalil, T. E.; Abdel-Salam, A. H.; Mohamed, L. A.; El-Meligy, E.; El-Dissouky, A. Crosslinked Modified Chitosan Biopolymer for Enhanced Removal of Toxic Cr(VI) from Aqueous Solution. *Int. J. Biol. Macromol.* **2023**, *234*, No. 123719.
(36) Allouss, D.; Essamlali, Y.; Chakir, A.; Khadhar, S.; Zahouily, M. Effective Removal of Cu(II) from Aqueous Solution over Graphene Oxide Encapsulated Carboxymethylcellulose-Alginate Hydrogel Microspheres: Towards Real Wastewater Treatment Plants. *Environ. Sci. Pollut. Res.* **2020**, *27* (7), 7476−7492.
(37) Pettignano, A.; Charlot, A.; Fleury, E. Solvent-Free Synthesis of Amidated Carboxymethyl Cellulose Derivatives: Effect on the Thermal Properties. *Polymers* **2019**, *11* (7), 1227.
(38) Manzoor, K.; Ahmad, M.; Ahmad, S.; Ikram, S. Synthesis, Characterization, Kinetics, and Thermodynamics of EDTA-Modified Chitosan-Carboxymethyl Cellulose as Cu(II) Ion Adsorbent. *ACS Omega* **2019**, *4* (17), 17425−17437.
(39) Hamilton, G. S. *P*-Toluenesulfonic Acid. In *Encyclopedia of Reagents for Organic Synthesis*; John Wiley & Sons, Ltd: Chichester, UK, 2001; p rt134. DOI: 10.1002/047084289X.rt134.
(40) Mollick, S.; Saurabh, S.; More, Y. D.; Fajal, S.; Shirolkar, M. M.; Mandal, W.; Ghosh, S. K. Benchmark Uranium Extraction from Seawater Using an Ionic Macroporous Metal−Organic Framework. *Energy Environ. Sci.* **2022**, *15* (8), 3462−3469.
(41) Wang, C.; Huang, D.; He, F.; Jin, T.; Huang, B.; Xu, J.; Qian, Y. Efficient Removal of Uranium(VI) from Aqueous Solutions by Triethylenetetramine-Functionalized Single-Walled Carbon Nanohorns. *ACS Omega* **2020**, *5* (43), 27789−27799.
(42) Priya, S.; Ilaiyaraja, P.; Priyadarshini, N.; Subalekha, N. Effective Removal of Uranium (VI) Using Magnetic Acid Functionalized Fe3O4@TiO2 Nanocomposite from Aqueous Solutions. *Process Saf. Environ. Prot.* **2023**, *178*, 480−493.
(43) Sun, Q.; Aguila, B.; Perman, J.; Ivanov, A. S.; Bryantsev, V. S.; Earl, L. D.; Abney, C. W.; Wojtas, L.; Ma, S. Bio-Inspired Nano-Traps for Uranium Extraction from Seawater and Recovery from Nuclear Waste. *Nat. Commun.* **2018**, *9* (1), 1644.
(44) Galindo, C.; Nero, M. D.; Barillon, R.; Halter, E.; Made, B. Mechanisms of Uranyl and Phosphate (Co)Sorption: Complexation and Precipitation at α-Al2O3 Surfaces. *J. Colloid Interface Sci.* **2010**, *347* (2), 282−289.
(45) Kushwaha, S.; Sreedhar, B.; Padmaja, P. XPS, EXAFS, and FTIR As Tools To Probe the Unexpected Adsorption-Coupled Reduction of U(VI) to U(V) and U(IV) on *Borassus Flabellifer* -Based Adsorbents. *Langmuir* **2012**, *28* (46), 16038−16048.
(46) Wang, Y.; Ai, Y.; Liu, X.; Chen, B.; Zhang, Y. Indole-Functionalized Cross-Linked Chitosan for Effective Uptake of Uranium(vi) from Aqueous Solution. *Polym. Chem.* **2022**, *13* (12), 1751−1762.
(47) Sabatini, M. T.; Boulton, L. T.; Sneddon, H. F.; Sheppard, T. D. A Green Chemistry Perspective on Catalytic Amide Bond Formation. *Nat. Catal.* **2019**, *2* (1), 10−17.
(48) Nakajima, N.; Ikada, Y. Mechanism of Amide Formation by Carbodiimide for Bioconjugation in Aqueous Media. *Bioconjugate Chem.* **1995**, *6* (1), 123−130.
(49) Noorian, S. A.; Hemmatinejad, N.; Navarro, J. A. R. Ligand Modified Cellulose Fabrics as Support of Zinc Oxide Nanoparticles for UV Protection and Antimicrobial Activities. *Int. J. Biol. Macromol.* **2020**, *154*, 1215−1226.
(50) Zhang, X.; Zhang, L.; Wang, Q.; Xin, Q.; Xiong, Y.; Wang, H. Selective, Rapid Extraction of Uranium from Aqueous Solution by Porous Chitosan−Phosphorylated Chitosan−Amidoxime Macroporous Resin Composite and Differential Charge Calculation. *Int. J. Biol. Macromol.* **2023**, *253*, No. 126661.
(51) Samsonowicz, M.; Hrynaszkiewicz, T.; Świsłocka, R.; Regulska, E.; Lewandowski, W. Experimental and Theoretical IR, Raman, NMR Spectra of 2-, 3- and 4-Aminobenzoic Acids. *J. Mol. Struct.* **2005**, *744*−*747*, 345−352.
(52) Verma, S.; Dutta, R. K. Development of Cysteine Amide Reduced Graphene Oxide (CARGO) Nano-Adsorbents for Enhanced Uranyl Ions Removal from Aqueous Medium. *J. Environ. Chem. Eng.* **2017**, *5* (5), 4547−4558.
(53) Cai, Y.; Chen, L.; Yang, S.; Xu, L.; Qin, H.; Liu, Z.; Chen, L.; Wang, X.; Wang, S. Rational Synthesis of Novel Phosphorylated Chitosan-Carboxymethyl Cellulose Composite for Highly Effective Decontamination of U(VI). *ACS Sustain. Chem. Eng.* **2019**, *7* (5), 5393−5403.
(54) D'Orsi, R.; Canale, V. C.; Cancelliere, R.; Hassan Omar, O.; Mazzuca, C.; Micheli, L.; Operamolla, A. Tailoring the Chemical Structure of Cellulose Nanocrystals by Amine Functionalization. *Eur. J. Org. Chem.* **2023**, *26* (11), No. e202201457.
(55) Kushwaha, S.; Mane, M.; Ravindranathan, S.; Das, A. Polymer Nanorings with Uranium Specific Clefts for Selective Recovery of Uranium from Acidic Effluents via Reductive Adsorption. *ACS Sens.* **2020**, *5* (10), 3254−3263.
(56) Malla, B. K.; Vishwakarma, G.; Chowdhury, S.; Nayak, S. K.; Yamijala, S. S. R. K. C.; Pradeep, T. Formation and Dissociation of Dimethyl Ether Clathrate Hydrate in Interstellar Ice Mimics. *J. Phys. Chem. C* **2024**, *128* (6), 2463−2470.
(57) Lu, G.; Forbes, T. Z.; Haes, A. J. Evaluating Best Practices in Raman Spectral Analysis for Uranium Speciation and Relative

Abundance in Aqueous Solutions. *Anal. Chem.* **2016**, *88* (1), 773−780.
(58) Sánchez, C.; Bustos, C.; Alvarado, F.; Schott, E.; Gatica, N.; Bernede, J.-C. Synthesis, Characterization and Properties of Polymers Containing Simultaneously the Imine and Amide Moieties. *E-Polym.* **2007**, *7* (1). DOI: 10.1515/epoly.2007.7.1.434.
(59) Du, W.-Q.; Fu, T.; Li, X.-L.; Li, Y.; Deng, C.; Wang, X.-L.; Wang, Y.-Z. High-Performance Biobased Polyesters with High Gas Barrier, Glass Transition Temperature, and Tensile Strength Enabled by Hydrogen Bonds and Flexible Segments. *ACS Sustain. Chem. Eng.* **2022**, *10* (43), 14240−14247.
(60) Dutta, R. K.; Shaida, Md. A.; Singla, K.; Das, D. Highly Efficient Adsorptive Removal of Uranyl Ions by a Novel Graphene Oxide Reduced by Adenosine 5′-Monophosphate (RGO-AMP). *J. Mater. Chem. A* **2019**, *7* (2), 664−678.
(61) Cai, Y.; Wu, C.; Liu, Z.; Zhang, L.; Chen, L.; Wang, J.; Wang, X.; Yang, S.; Wang, S. Fabrication of a Phosphorylated Graphene Oxide−Chitosan Composite for Highly Effective and Selective Capture of U(vi). *Environ. Sci. Nano* **2017**, *4* (9), 1876−1886.
(62) Badry, R.; El-Nahass, M. M.; Nada, N.; Elhaes, H.; Ibrahim, M. A. Structural and UV-Blocking Properties of Carboxymethyl Cellulose Sodium/CuO Nanocomposite Films. *Sci. Rep.* **2023**, *13* (1), 1123.
(63) Sun, L.; Hu, K.; Jin, S.; Lu, Y.; Xu, C.; Liu, B.; Wang, D.; Xia, G. Single-Crystal and Molecular Structures of Five Hydrogen-Bonding Supramolecular Salts Based on 4-Aminobenzoic Acid, 2-Aminobenzoic Acid and Acidic Components. *J. Mol. Struct.* **2019**, *1178*, 229−241.
(64) Abomosallam, M.; Elalfy, M.; Zheng, Z.; Nagata, K.; Suzuki, M. Adsorption Kinetics and Thermodynamics of Toxic Metal Ions onto Chitosan Nanoparticles Extracted from Shrimp Shells. *Nanotechnol. Environ. Eng.* **2022**, *7* (1), 35−47.
(65) Husnain, S. M.; Kim, H. J.; Um, W.; Chang, Y.-Y.; Chang, Y.-S. Superparamagnetic Adsorbent Based on Phosphonate Grafted Mesoporous Carbon for Uranium Removal. *Ind. Eng. Chem. Res.* **2017**, *56* (35), 9821−9830.
(66) Gómez, N.; Silva, G.; Wilhelm, H.; Wypych, F. Zn2Al Layered Double Hydroxides Intercalated with Nitrate and P-Aminobenzoate as Ultraviolet Protective Agents in Low-Density Polyethylene Nanocomposites and Natural Insulating Oils. *J. Braz. Chem. Soc.* **2020**, DOI: 10.21577/0103-5053.20190262.
(67) Jin, H.-X.; Xu, H.; Wang, N.; Yang, L.-Y.; Wang, Y.-G.; Yu, D.; Ouyang, X.-K. Fabrication of Carboxymethylcellulose/Metal-Organic Framework Beads for Removal of Pb(II) from Aqueous Solution. *Materials* **2019**, *12* (6), 942.
(68) Poornachandhra, C.; Jayabalakrishnan, R. M.; Prasanthrajan, M.; Balasubramanian, G.; Lakshmanan, A.; Selvakumar, S.; John, J. E. Cellulose-Based Hydrogel for Adsorptive Removal of Cationic Dyes from Aqueous Solution: Isotherms and Kinetics. *RSC Adv.* **2023**, *13* (7), 4757−4774.
(69) Wang, Y.; Lin, Z.; Zhu, J.; Liu, J.; Yu, J.; Liu, Q.; Chen, R.; Li, Y.; Wang, J. Enhancing Adsorption Performance and Selectivity for Uranium by Constructing Biaxial Adsorption Sites on Eco-Friendly Bamboo Strips. *Sep. Purif. Technol.* **2023**, *315*, No. 123727.
(70) Meng, F.; Yuan, G.; Larson, S. L.; Ballard, J. H.; White, J. R.; Arslan, Z.; Han, F. X. Kinetics and Thermodynamics of Uranium (VI) Adsorption onto Humic Acid Derived from Leonardite. *Int. J. Environ. Res. Public. Health* **2019**, *16* (9), 1552.
(71) Ivanov, A. S.; Leggett, C. J.; Parker, B. F.; Zhang, Z.; Arnold, J.; Dai, S.; Abney, C. W.; Bryantsev, V. S.; Rao, L. Origin of the Unusually Strong and Selective Binding of Vanadium by Polyamidoximes in Seawater. *Nat. Commun.* **2017**, *8* (1), 1560.
(72) Zhang, Y.; Wang, Y.; Dong, Z.; Wang, Y.; Liu, Y.; Cao, X.; Zhang, Z.; Xu, C.; Wang, N.; Liu, Y. Boosting Uranium Extraction from Seawater by Micro-Redox Reactors Anchored in a Seaweed-like Adsorbent. *Nat. Commun.* **2024**, *15* (1), 9124.
(73) Emre, D.; Zorer, Ö. S.; Bilici, A.; Budak, E.; Yilmaz, S.; Kilic, N. C.; Sogut, E. G. Adsorption of Uranium (VI) from Aqueous Solutions Using Boron Nitride/Polyindole Composite Adsorbent. *J. Appl. Polym. Sci.* **2024**, *141* (4), No. e54856.
(74) Zhao, M.; Tesfay Reda, A.; Zhang, D. Reduced Graphene Oxide/ZIF-67 Aerogel Composite Material for Uranium Adsorption in Aqueous Solutions. *ACS Omega* **2020**, *5* (14), 8012−8022.
(75) Szlachta, M.; Neitola, R.; Peräniemi, S.; Vepsäläinen, J. Effective Separation of Uranium from Mine Process Effluents Using Chitosan as a Recyclable Natural Adsorbent. *Sep. Purif. Technol.* **2020**, *253*, No. 117493.
(76) Sun, Z.; Chen, D.; Chen, B.; Kong, L.; Su, M. Enhanced Uranium(VI) Adsorption by Chitosan Modified Phosphate Rock. *Colloids Surf. Physicochem. Eng. Asp.* **2018**, *547*, 141−147.
(77) Anirudhan, T. S.; Lekshmi, G. S.; Shainy, F. Synthesis and Characterization of Amidoxime Modified Chitosan/Bentonite Composite for the Adsorptive Removal and Recovery of Uranium from Seawater. *J. Colloid Interface Sci.* **2019**, *534*, 248−261.
(78) Bai, J.; Ma, X.; Yan, H.; Zhu, J.; Wang, K.; Wang, J. A Novel Functional Porous Organic Polymer for the Removal of Uranium from Wastewater. *Microporous Mesoporous Mater.* **2020**, *306*, No. 110441.
(79) Tellería-Narvaez, A.; Talavera-Ramos, W.; Santos, L. D.; Arias, J.; Kinbaum, A.; Luca, V. Functionalized Natural Cellulose Fibres for the Recovery of Uranium from Seawater. *RSC Adv.* **2020**, *10* (11), 6654−6657.
(80) Busca, G. Bases and Basic Materials in Industrial and Environmental Chemistry: A Review of Commercial Processes. *Ind. Eng. Chem. Res.* **2009**, *48* (14), 6486−6511.
(81) Elschner, T.; Lüdecke, C.; Kalden, D.; Roth, M.; Löffler, B.; Jandt, K. D.; Heinze, T. Zwitterionic Cellulose Carbamate with Regioselective Substitution Pattern: A Coating Material Possessing Antimicrobial Activity. *Macromol. Biosci.* **2016**, *16* (4), 522−534.
(82) Wang, L.; Liu, X.; Tan, W.; Li, Q.; Guo, Z.; Zhang, J. Preparation and Antioxidant Activity of Novel Chitosan Oligosaccharide Quinolinyl Urea Derivatives. *Carbohydr. Res.* **2022**, *521*, No. 108678.



Supporting Information

Enhanced U(VI) Removal from Groundwater Using Amide-Functionalised Biopolymer-Based Adsorbent for a Practical Solution

Sonali Seth[1], Md Rabiul Islam[1], Tanmayaa Nayak[1], Amoghavarsha Ramachandra Kini[1], Sujan Manna[1], Bijesh K. Malla[1], Ankit Nagar[1] and Thalappil Pradeep[1,2*]

[1]DST Unit of Nanoscience (DST UNS) and Thematic Unit of Excellence (TUE), Department of Chemistry, Indian Institute of Technology Madras Chennai 600036, India.

[2]International Centre for Clean Water, IIT Madras Research Park, Chennai 600113, India.

[*]E-mail: pradeep@iitm.ac.in

Tel.: +91-44 2257 4208; Fax: +91-44 2257 0545/0509

Supporting information content

Total number of pages: 19

Total number of figures: 12

Total number of tables: 2

Total number of equations: 9

Table of Contents

Supporting items	Title	Page No.
Equations used	Equations used in main text	S3-S4
Figure S1	BET surface area plots (a) N_2 adsorption-desorption plot. (b) Pore size distribution.	S5
Figure S2	IR spectra of CMABCH and its precursors i.e., CMC, PABA, and CH.	S6
Figure S3	IR spectra of CMABCH, before and after treatment with various concentrations of U(VI).	S7
Figure S4	IR spectra of standard ($UO_2(NO_3)_2.6H_2O$).	S8
Figure S5	IR spectra of CMABCH, before and after U(VI) adsorption, at regular time intervals.	S9
Figure S6	Deconvoluted XPS spectra of (a) C 1s and (b) O 1s regions before and after U(VI) adsorption (bottom to top).	S10
Figure S7	HRSEM image of CMCBACH and its corresponding elemental mapping.	S11
Figure S8	Powder XRD of CMABCH, its precursors i.e. CMC, PABA and CH and CMABCH after U(VI) adsorption.	S12
Figure S9	TGA of CMABCH in air and nitrogen atmospheres from room temperature to 900 °C at a scan rate of 5°C min^{-1}.	S13
Figure S10	Ho's pseudo-second-order kinetic plot for the adsorption of U(VI) onto CMABCH.	S14
Figure S11	Freundlich isotherm plot for the adsorption of U(VI) on CMABCH.	S15
Figure S12	Removal efficiency of CMABCH when U(VI) and V(V) coexist.	S16
Table S1	Desorption efficiencies by various eluents	S17
Figure S13	FTIR of CMABCH after adsorption-desorption cycles	S18
Table S2	Chemical parameters for the groundwater sample from the well in Shamshabad village, Fazilka, Punjab, India	S19

Equation (1): The fraction (%) of U(VI) adsorbed by CMABCH at different time intervals were calculated from IR spectra using the equation below

1a $$x(t) = \frac{\Delta A(1)}{\Delta A(2)} \times 100$$

where x(t) is the fraction of U(VI) adsorbed at time t, ΔA(1) is the difference between adsorption at specific time t and one at time 0 and ΔA(2) is the corresponding value for the difference between adsorption at time 0 and completely adsorbed U(VI). Similarly, residual U(VI) fraction in water is calculated by firstly measuring the leftover concentration of U(VI) in water through ICP-MS and then the fraction of residual U(VI) was calculated using the equation below

1b $$y(t) = (1 - \frac{\Delta A(1)}{\Delta A(2)}) \times 100$$

where y(t) is the residual fraction of U(VI) at time t, ΔA(1) is the difference between adsorption at specific time t and one at time 0 and ΔA(2) is the corresponding value for the difference between adsorption at time 0 and completely adsorbed U(VI).

Equation (2): The maximum uptake capacity (q_e) of U(VI) was determined by the equation below

$$\text{Uptake } (q_e) = \frac{(C_o - C_e)V}{m}$$

where q_e is the amount of U(VI) ions adsorbed per gram of adsorbent (mg/g) at equilibrium concentration, C_e is the equilibrium concentration of U(VI) in the bulk solution (mg/L), C_o is the initial U(VI) concentration (mg/L), V is the volume of solution (L) and m is the mass of adsorbent (g).

Equation (3): Ho's pseudo-second-order equation is described as

$$\frac{t}{q_e} = \frac{1}{k_2 q_e^2} + \frac{1}{q_e} t$$

where q_e is the amount of U(VI) ions adsorbed per gram of adsorbent (mg/g), k_2 (g/mg/min) is the pseudo-second-order rate constant.

Equation (4): The linear form of Langmuir equation used

$$\frac{C_e}{q_e} = \frac{C_e}{q_{max}} + \frac{1}{bq_{max}}$$

where q_e is the amount of U(VI) ions adsorbed per gram of adsorbent (mg/g), C_e is the equilibrium concentration of U(VI) in the bulk solution (mg/L), q_{max} is the maximum surface density at monolayer coverage and b is the Langmuir adsorption constant (L/mg) related to the free energy of adsorption and $1/q_{max}$ and $1/bq_{max}$ are Langmuir constants.

Equation (5): Freundlich adsorption isotherm model was applied and the linear form of the equation used was

$$\log(q_e) = \log k_f + \frac{1}{n}\log(C_e)$$

where q_e is the amount of U(VI) ions adsorbed per gram of adsorbent (mg/g), C_e is the equilibrium concentration of U(VI) in the bulk solution (mg/L), k_f (mg/g) is the multilayer adsorption capacity and n is the empirical parameter connected with intensity of adsorption.

Equation (6): Mass intensity =

$$\frac{\text{mass of all products used excluding water}}{\text{mass of product}} \text{ kg/kg product}$$

Equation (7): Water intensity (W_p) =

$$\frac{\text{mass of all water used}}{\text{mass of product}} \text{ kg/kg product}$$

Equation (8): Reaction mass efficiency (RME) =

$$\frac{\text{mass of product}}{\text{mass of all reactants}} \times 100\%$$

Equation (9): E factor =

$$\frac{[\text{Kg(raw materials)} - \text{Kg(desired product)}]}{\text{Kg(total product including water)}}$$

Supporting Information 1

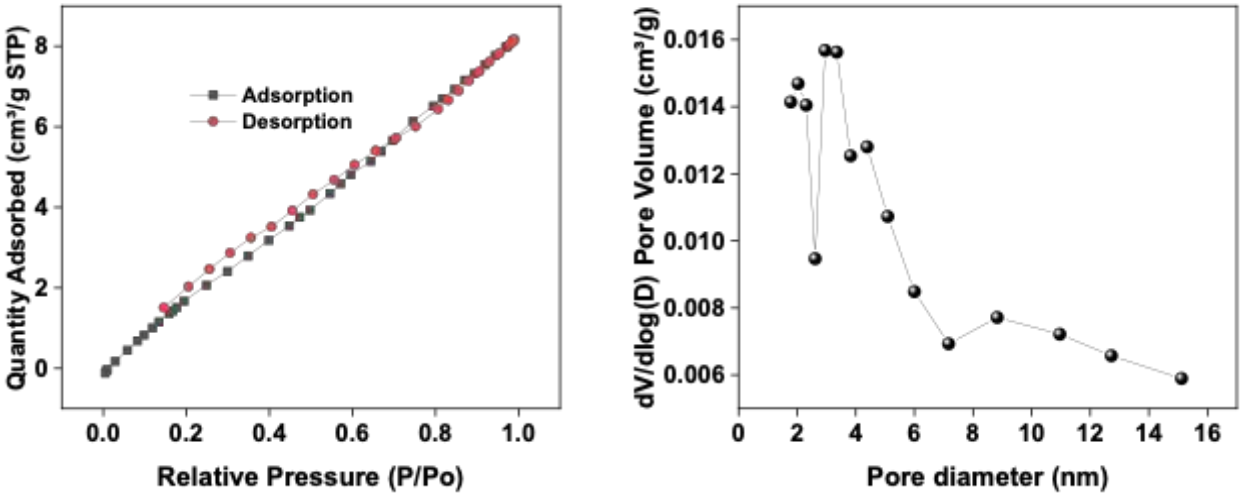


Figure S1. BET surface area (a) N_2 adsorption-desorption plot. (b) Pore size distribution.

Supporting Information 2

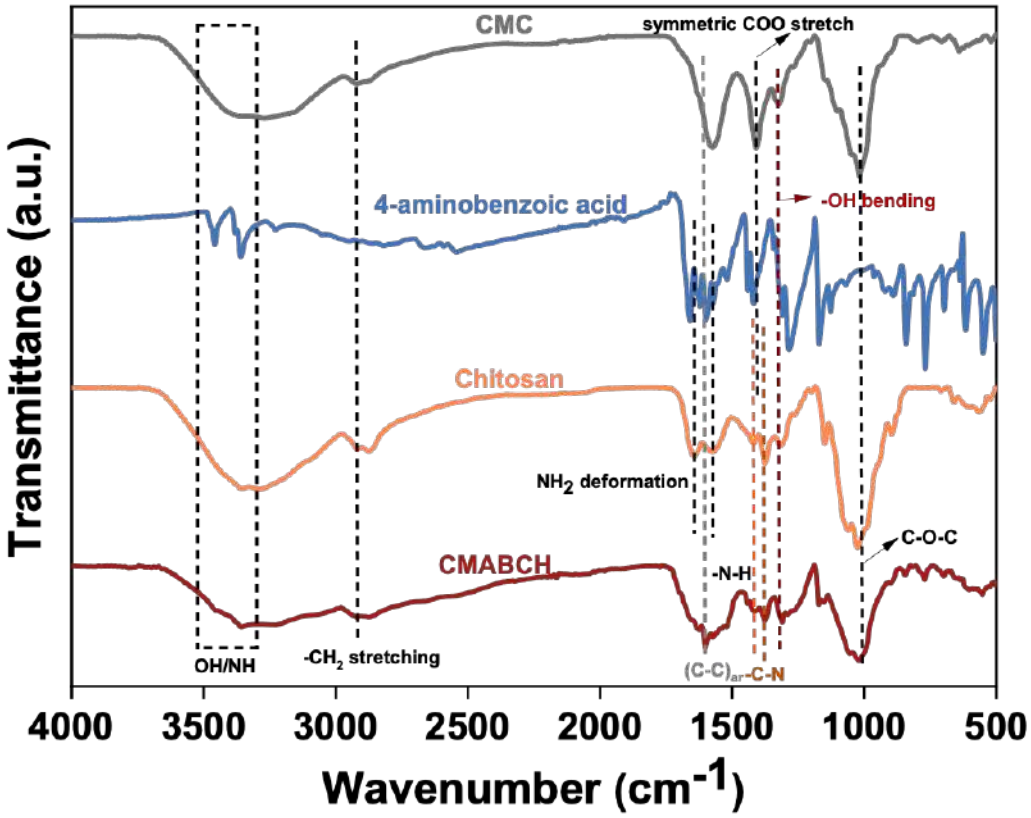


Figure S2. IR spectra of CMABCH and its precursors i.e., CMC, PABA, and CH.

Supporting Information 3

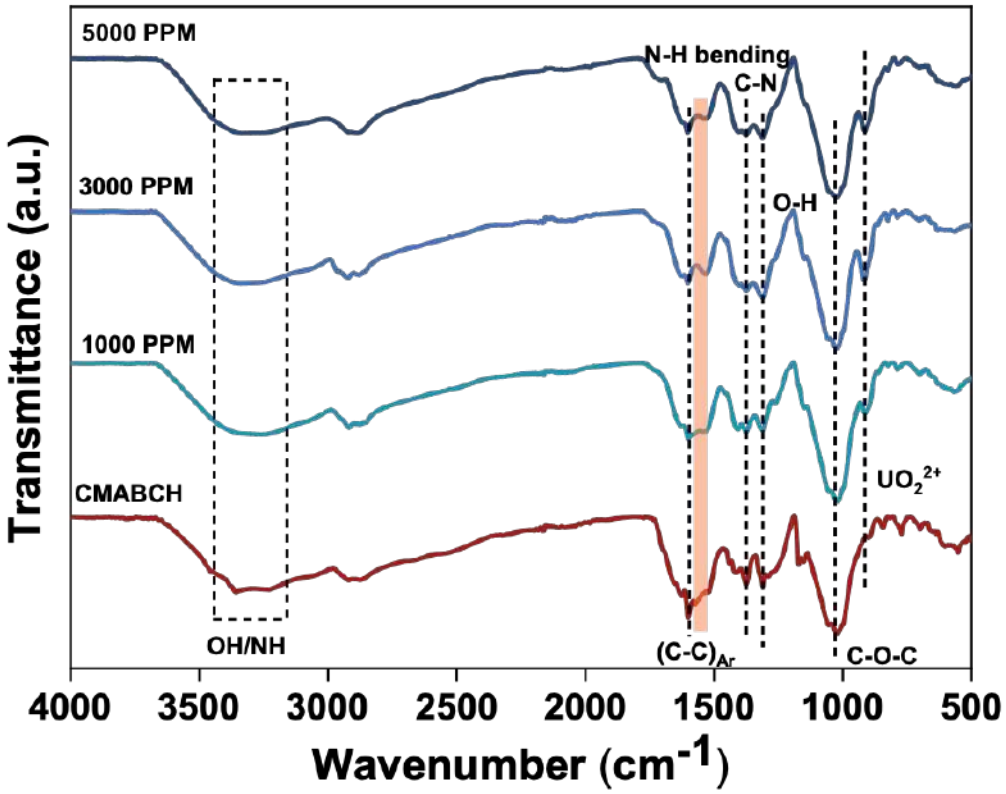


Figure S3. IR spectra of CMABCH, before and after treatment with various concentrations of U(VI) (m-50 mg, V-10 mL, pH-7).

Supporting Information 4

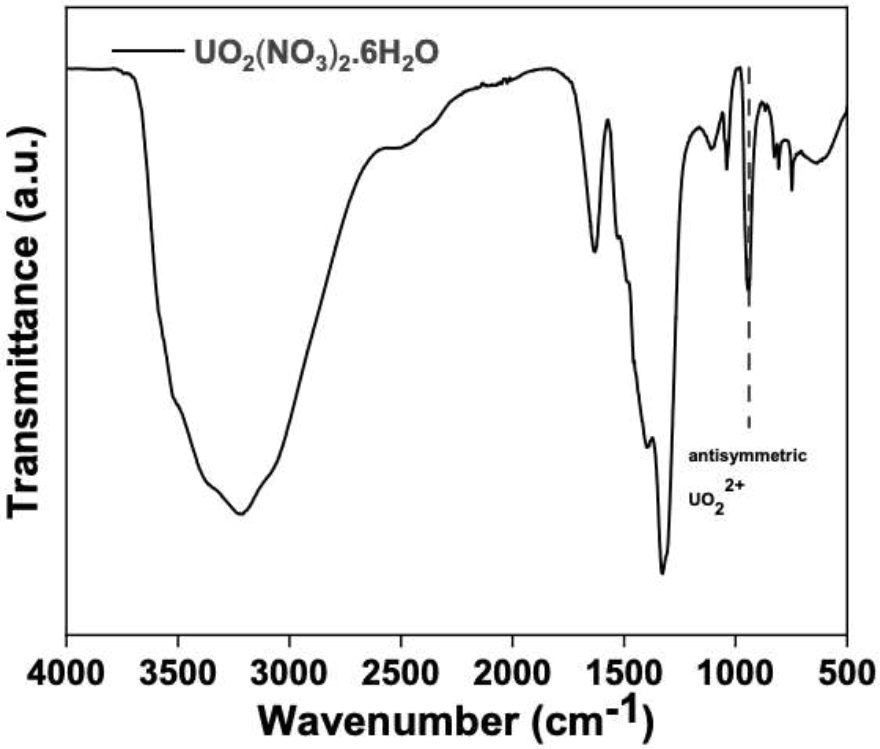


Figure S4. IR spectra of standard ($UO_2(NO_3)_2.6H_2O$).

Supporting Information 5

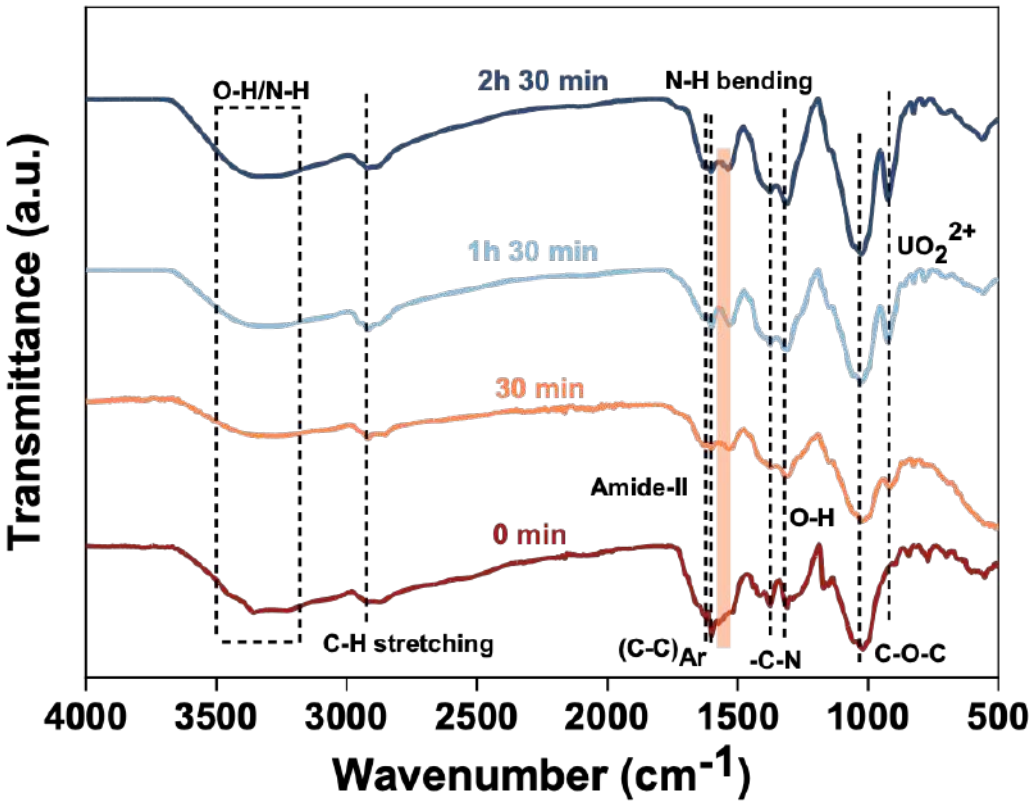


Figure S3. IR spectra of CMABCH, before and after U(VI) adsorption, at regular time intervals ($U(VI)_o$- 5000 mg/L, m- 50 mg, V-10 mL, pH-7).

Supporting Information 6

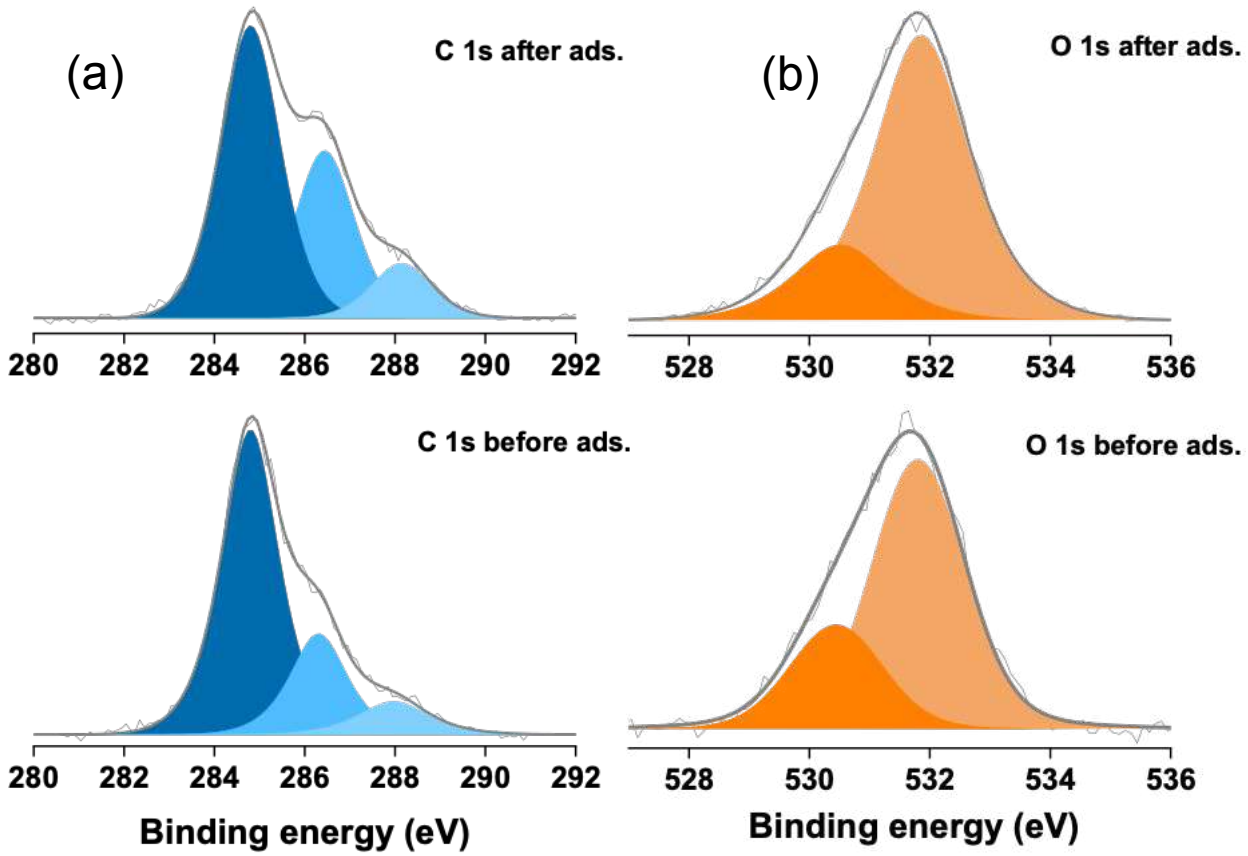


Figure S6. Deconvoluted XPS spectra of (a) C 1s and (b) O 1s regions of CMCBACH, before and after U(VI) adsorption (bottom to top). ($U(VI)_o$-5000 mg/L, m-50 mg, V-10 mL, pH-7).

Supporting Information 7

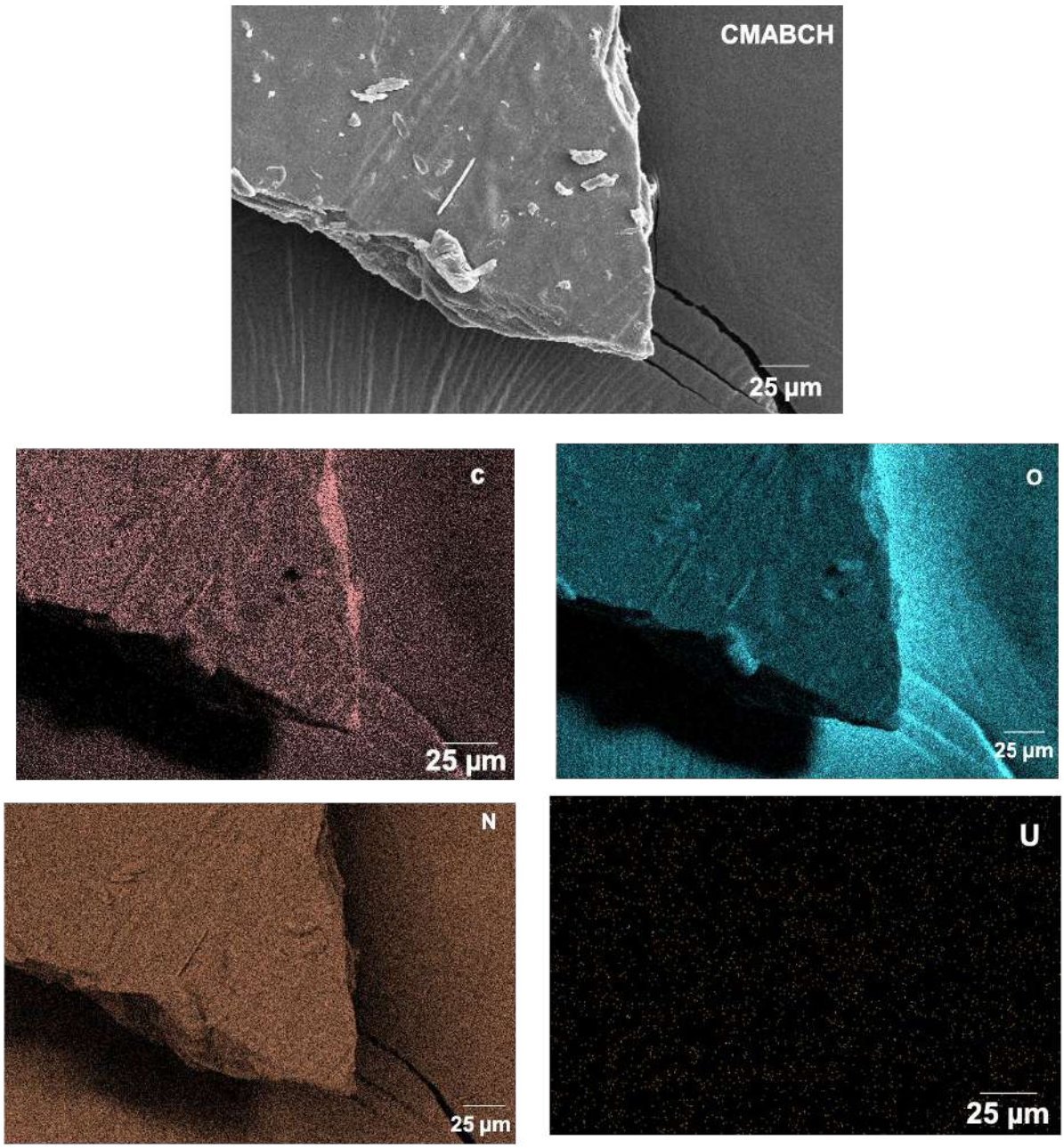


Figure S7. HRSEM image of CMABCH and its corresponding elemental mapping ($U(VI)_o$-5000 mg/L, m-50 mg, V-10 mL, pH-7).

Supporting Information 8

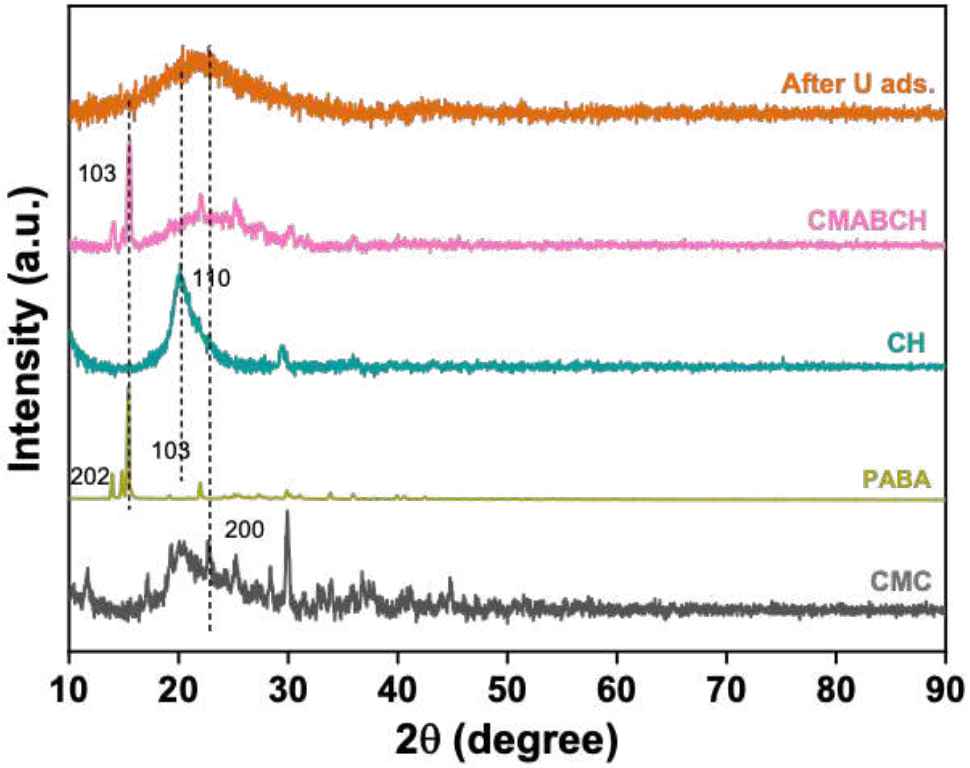
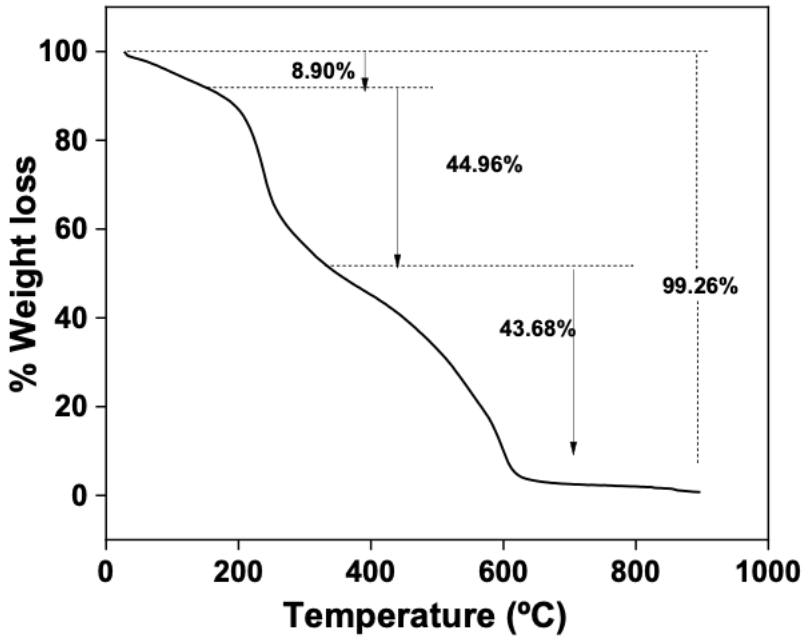


Figure S8. Powder XRD of CMABCH and its precursors, i.e. CMC, PABA and CH, and CMABCH after U(VI) adsorption ($U(VI)_o$-5000 mg/L, m-50 mg, V-10 mL, pH-7).

Supporting Information 9

TGA in air



TGA in nitrogen

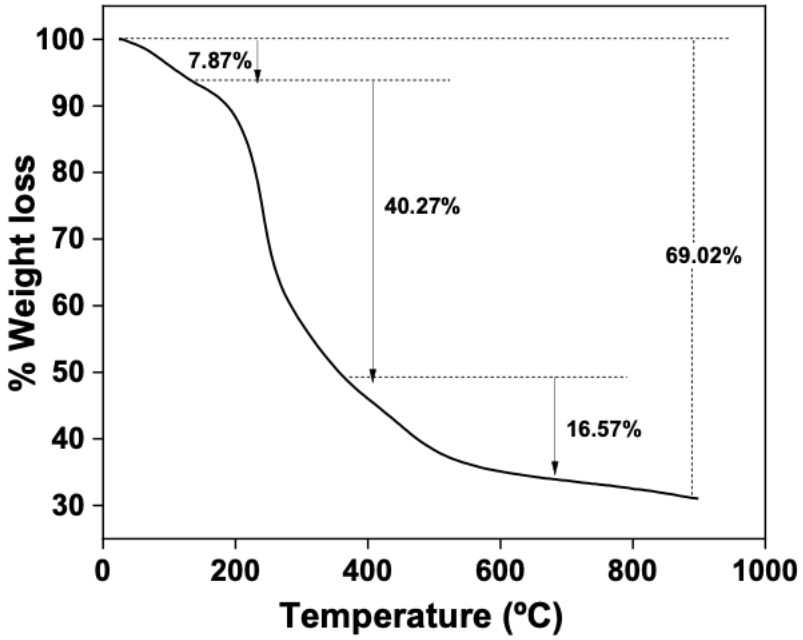


Figure S9. TGA of CMABCH in air and nitrogen atmospheres from room temperature to 900 °C at a scan rate of 5°C min^{-1}.

Supporting Information 10

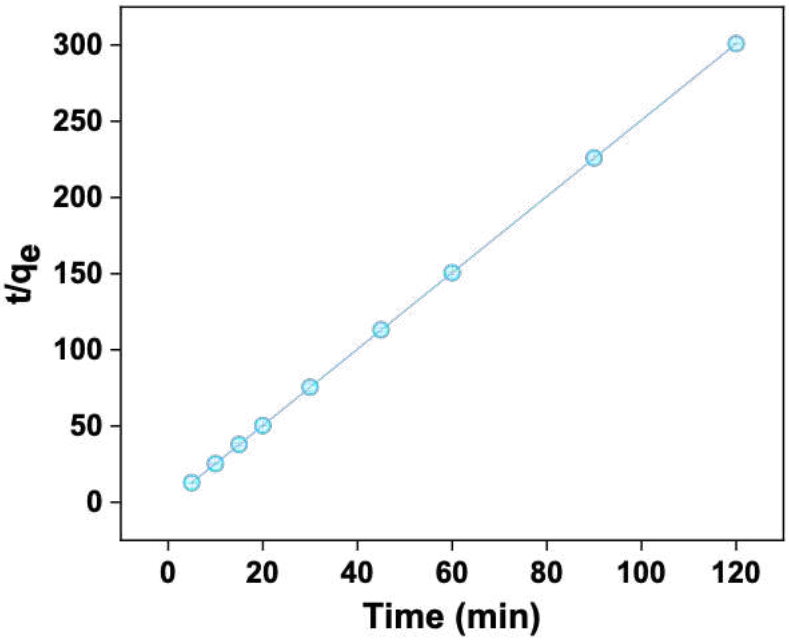


Figure S10. Ho's pseudo-second-order kinetic plot for the adsorption of U(VI) onto CMABCH, using eq S3.

Supporting Information 11

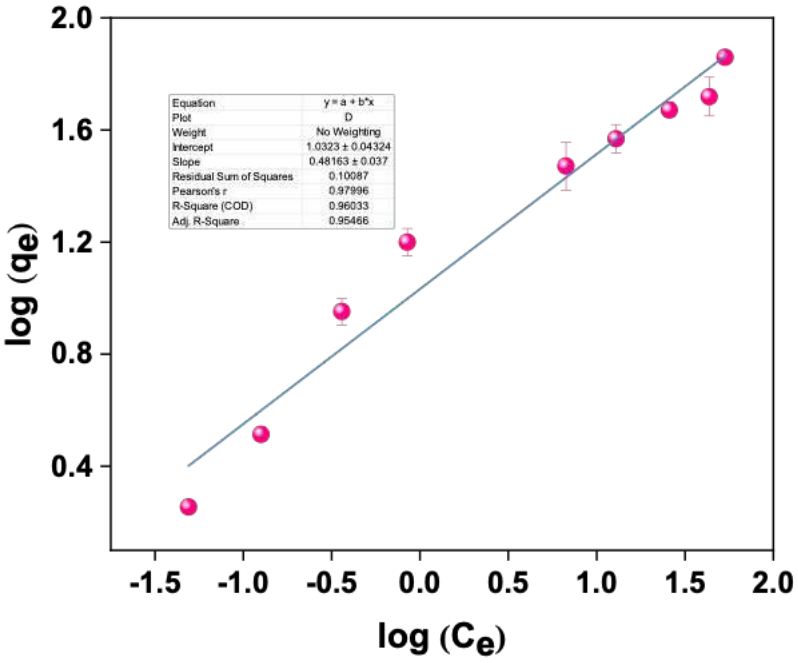


Figure S11. Freundlich isotherm plot for the adsorption of U(VI) on CMABCH using eq S5.

Supporting Information 12

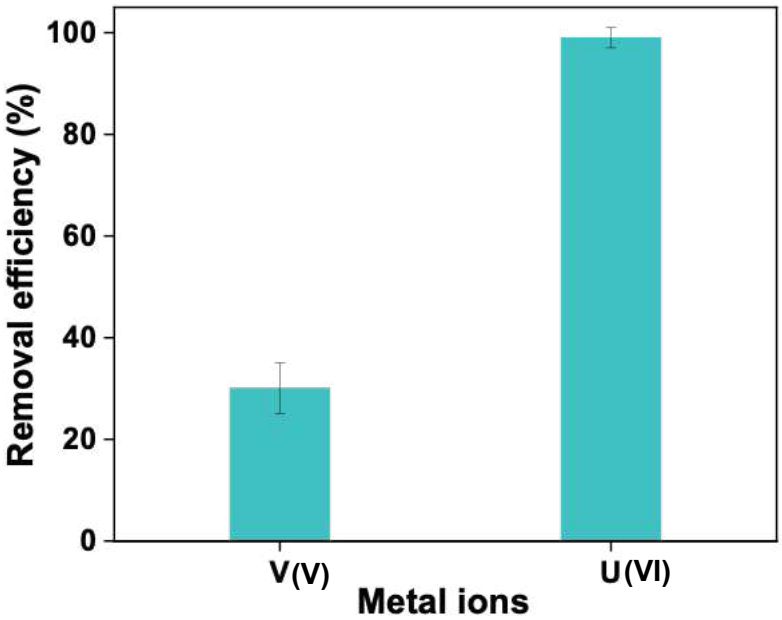


Figure S12. Removal efficiency of CMABCH when U(VI) and V(V) coexist U(VI)-1000 μg/L, V(V)-1000 μg/L, m-30 mg, V-10 mL, pH-7).

Supporting Information 13

Table S1: Desorption efficiency by various eluents

Eluents	Desorption efficiency (%)	Time (min)
HCl (100 mM)	**65**	**180**
HCl (50 mM)	**98.2**	**90**
HCl (10 mM)	**98.0**	**90**
Na_2CO_3 (100 mM)	**40**	**180**

Supporting Information 14

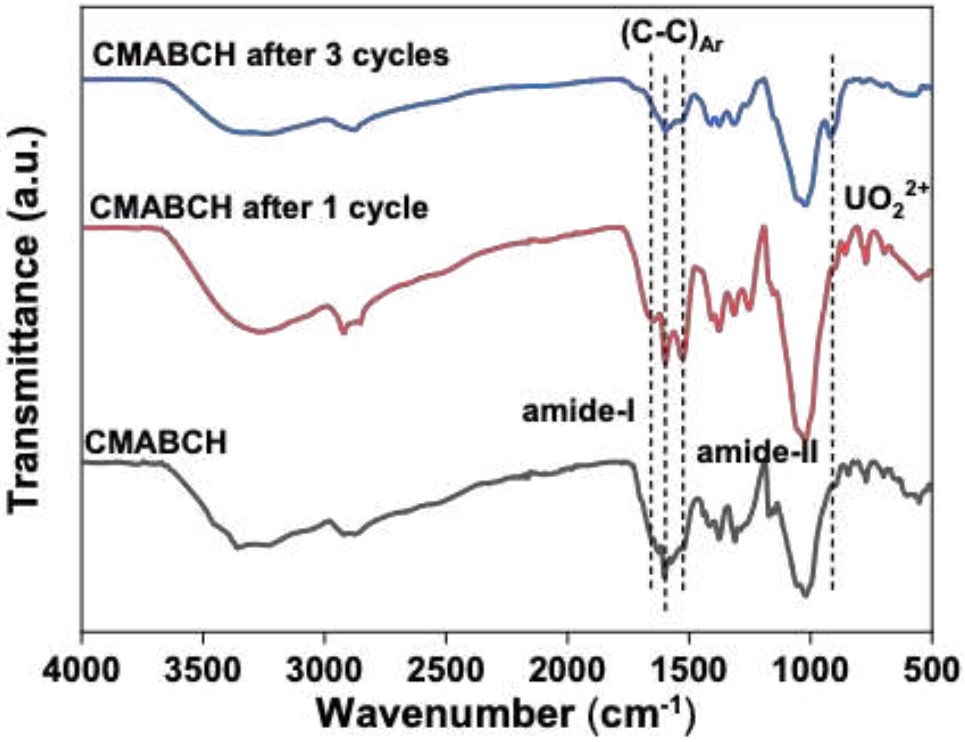


Figure S13. FTIR of CMABCH after adsorption-desorption cycles.

Table S2: Chemical parameters for the groundwater sample from the well in Shamshabad village, Fazilka, Punjab, India.

Parameter	Groundwater sample
TDS	663.5 mg/L
EC	2750 µS/cm
Turbidity	3.37 NTU
pH	8.5
Total alkalinity	240 mg/L
Mg^{2+}	16.72 mg/L
Ca^{2+}	6.45 mg/L
Li^{+}	4.76 mg/L
Ba^{2+}	0.043 mg/L
Sr^{2+}	0.504 mg/L
Mn^{2+}	0.417 mg/L
Pb^{2+}	0.0004 mg/L
Cd^{2+}	0.0001 mg/L
Ni^{2+}	0.0008 mg/L
U(VI)	0.102 mg/L
F^{-}	0.547 mg/L
Cl^{-}	134.6 mg/L
Br^{-}	0.684 mg/L
NO_3^{-}	0.709 mg/L
SO_4^{2-}	275.1 mg/L
PO_4^{3-}	Below detection limit

ChemComm

COMMUNICATION

View Article Online
View Journal | View Issue

Published on 01 August 2025. Downloaded by Indian Institute of Technology Chennai on 12/29/2025 3:15:06 AM.

Check for updates

Cite this: *Chem. Commun.*, 2025, **61**, 15846

Received 24th May 2025,
Accepted 25th July 2025

DOI: 10.1039/d5cc02952j

rsc.li/chemcomm

From micro-to-nano in charged water microdroplets: unveiling steps in the weathering of minerals†

Anubhav Mahapatra,[a] Anirban Som,[a] B. K. Spoorthi,[a] Depanjan Sarkar[ac] and Thalappil Pradeep *[abc]

The recent discovery of the rapid conversion of micron-sized common minerals to nanoparticles in charged water microdroplets has attracted significant attention. Here, we studied this micro-to-nano transition as a function of applied electric potential and tip-to-substrate distance using high-resolution transmission electron microscopy (HRTEM). Our observations revealed that the fragmentation progresses through distinct stages, from larger particles to flower-like intermediates and finally to nanoparticles. The results suggested the need for a critical droplet size to initiate the disintegration process, with Coulomb explosion playing a significant role in particle scission. Our results provide new insights for the efficient green synthesis of nanomaterials.

Nanoparticles of common minerals have garnered significant attention from the scientific community due to their distinct physicochemical properties compared to their bulk counterparts. These attributes have driven their applications in agriculture, where engineered nanoparticles (*e.g.*, ZnO, SiO_2) enhance soil fertility and crop yield.[1,2] However, conventional nanoparticle synthesis methods often involve harsh chemicals and extreme conditions, raising sustainability concerns. These processes generate harmful byproducts, consume excessive energy, and limit scalability – key barriers for the development of green nanotechnology.[3]

Charged water microdroplets have emerged as a sustainable alternative for accelerating chemical reactions, acting as highly efficient microreactors that can speed up processes by orders of magnitude. Water is the most sustainable reaction medium. While water droplets have long been considered important in various environmental contexts,[4] their unique properties and reactivity have captured significant scientific attention only recently. In the laboratory, these microdroplets can be generated using electrospray, which stands out among related techniques for its ability to produce charged droplets with extreme interfacial electric fields (up to $\sim 10^9$ V m^{-1}). These intense fields promote the separation of hydronium and hydroxide ions, concentrate reactants at the droplet air–water interface,[5,6] and accelerate solvent evaporation, creating a dynamic environment that dramatically enhances reaction rates and enables the rapid formation of functional nanomaterials. Beyond accelerating organic reactions,[7,8] this can cause unusual phenomena to happen, like chemical reactions in the surrounding gas induced by luminescence.[9] Apart from this, charged microdroplets have also shown immense promise in fabricating a variety of nanomaterials.[10] Our research group has demonstrated the creation of structures ranging from zero-dimensional nanoparticles to three-dimensional nanopyramids, as well as large-area microstructures, all under ambient conditions and directly from salt precursors without the need for any external reagents.[11,12] This approach not only streamlines synthesis, but also enhances sustainability. Notably, we found that, in addition to forming nanomaterials from dissolved ions, charged water microdroplets can even fragment hard mineral microparticles such as quartz, reducing them to nanoparticles—a surprising and powerful capability that further expands the potential of this technique.[13,14] Ever since this discovery, there has been growing interest in understanding the mechanism behind this rapid transformation. While studies have also reported the conversion of nanosheets to nanoparticles in similar conditions,[15] the field has moved beyond simply observing these conversions to probing the underlying process. This was supported by density functional theory (DFT) calculations. The presence of various reactive species such as $OH^{\bullet}$, $H_2O^{+\bullet}$, H_2O_2, and others in droplets was speculated in the literature.[6] One recent investigation at the interface of oil droplets using Raman spectroscopy has focused on elucidating the structure and orientation of water molecules and the results have shown that oil–water emulsion interfaces exhibit reduced water structural order

[a] *DST Unit of Nanoscience (DST UNS) & Thematic Unit of Excellence (TUE), Department of Chemistry, Indian Institute of Technology Madras (IITM), Chennai 600036, India. E-mail: pradeep@iitm.ac.in*
[b] *International Centre for Clean Water, 2nd Floor, B-Block, IIT Madras Research Park, Kanagam Road, Taramani, Chennai 600113, India*
[c] *Centre of Excellence on Molecular Materials and Functions, Department of Chemistry, Indian Institute of Technology Madras, Chennai – 600036, India*

† Dedicated to Prof. Robert Graham Cooks on his 84th birthday.

This journal is © The Royal Society of Chemistry 2025

Published on 01 August 2025. Downloaded by Indian Institute of Technology Chennai on 12/29/2025 3:15:06 AM.

and weaker hydrogen bonding. This is evidenced by a $\sim$95 cm^{-1} redshift of the free O–H stretch compared to planar interfaces.[16] The involvement of protons in the process leading to silicate species among the fragmented products was confirmed by mass spectrometric measurements. From all of these, a tentative mechanism was drawn, but a key question remained as to whether the mineral underwent fragmentation within the water droplet itself and got deposited on the substrate as nanoparticles. In the present work, we demonstrate a systematic investigation of the fragmentation process; we observed distinct stages in the disintegration of micron-sized mineral particles within charged microdroplets. Notably, during the intermediate stage of fragmentation, we captured unique flower-like structures, providing visual evidence of the ongoing breakdown. These intermediate forms were crucial in demonstrating that mineral fragmentation occurs within the droplets during their flight, rather than after deposition. Our findings also confirm that the applied electrical potential is the most fundamental and decisive factor influencing the outcome of the process. The experiment involved generating charged water microdroplets using electrospray, as described previously and detailed in the SI, with an important modification. Specifically, we collected the deposited products at an applied potential of 3.5 kV and varying distances (L) from the electrospray tip, as shown in Fig. 1A and detailed in Fig. S1, SI, while maintaining all other experimental conditions constant. For these experiments, quartz particles (5–10 μm) were suspended in ultrahigh-purity water (18 MΩ Milli-Q) at a concentration of 0.2 mg mL^{-1} and electrosprayed at a flow rate of approximately 0.1 mL $hour^{-1}$. The suspension was subjected to electrospray at varied collection distances to capture different stages of particle fragmentation. Optical images of the bulk micron-sized quartz powder and high-resolution SEM images are shown in Fig. 1B and 1C, respectively. The electrospray was directed onto a TEM grid for product collection and subsequent imaging. By collecting samples at various tip-to-substrate distances, specifically at 1.5, 2.0, and 2.5 cm, as schematically demonstrated in Fig. 1A, we observed significant variation in the fate of the micron-sized particles. At the shortest distance (1.5 cm), TEM images (Fig. 1D) revealed that the particles largely remained intact as larger aggregates. As the distance increased to 2.0 cm, partial fragmentation was observed, with distinctive flower-like intermediate structures captured in the TEM images (Fig. 1E). When the distance was further increased to 2.5 cm, complete fragmentation occurred, resulting in monodisperse nanoparticles as shown in Fig. 1F.

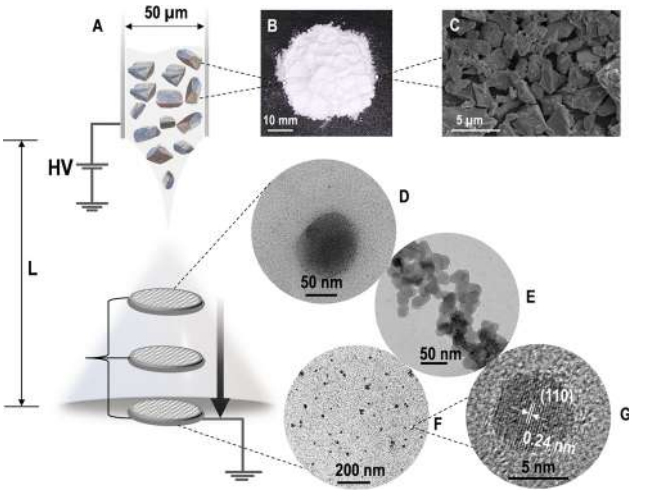


Fig. 1 The disintegration process of natural quartz particles in charged water microdroplets. Schematic diagram showing the different components of the home-built electrospray set-up with (A) a fused silica capillary of inner diameter 50 μm, (B) an optical image of the ground quartz powder, and (C) field emission scanning electron microscopy (FESEM) of the separated quartz particles revealing the size range of 5 to 10 μm. Transmission electron microscopic (TEM) images of these particles after electrospray deposition at an applied potential of 3.5 kV, with varying tip-to-substrate distances of (D) 1.5 cm, (E) 2.0 cm, and (F) 2.5 cm, demonstrating different stages of fragmentation. (G) High-resolution TEM (HRTEM) image showing the (110) plane of quartz.

All these experiments described here were performed under identical conditions except varying the tip-to-substrate distance. As evident from the data, the flight time of the microdroplets has a great impact on the weathering process. High-resolution TEM (HRTEM) images, presented in Fig. 1G and Fig. S2, SI, confirmed the identity of these nanoparticles as quartz, based on the lattice spacing of 0.24 nm, which corresponds to the (110) plane of quartz.

A detailed study was performed in which aqueous suspensions of quartz (0.2 mg mL^{-1}) were electrosprayed, and the resultant charged microdroplets were collected at varying tip-to-substrate distances under fixed applied potentials. This experiment was repeated across a range of potentials (3.0–4.5 kV). A systematic series of TEM images is summarized in Fig. 2. At 3 kV, no particle disintegration was observed as reported previously. At 3 kV, at a tip-to-substrate distance of 1.5 cm, the particles remained largely intact. However, at 2.0 cm, flower-like intermediate structures were captured in the TEM images, indicating ongoing fragmentation, while complete disintegration into nanoparticles was achieved at 2.5 cm. A similar trend was observed at 3.5 kV. When the potential was increased to 4 kV, fragmentation was initiated even at the shorter distance of 1.5 cm, and monodisperse nanoparticles were formed at 2.0 and 2.5 cm. At 4.5 kV, complete disintegration was observed at 1.5 cm, demonstrating that higher potentials and longer distances facilitate efficient fragmentation. A distinct boundary (marked by a red dotted line in Fig. 2) was established to delineate the threshold for effective disintegration, emphasizing the critical role of smaller, highly charged droplets in particle scission. At lower potentials and shorter distances, flower-like intermediates were identified, suggesting a stepwise cleavage process within the micron-sized particles, during flight. The control experiments with neutral droplets are detailed in Fig. S5 and section S4, SI to rule out other factors dominating fragmentation.

A similar set of observations was made when ruby (0.2 mg mL^{-1}) was subjected to the same electrospray conditions, with all other experimental parameters kept constant, and the results are presented in Fig. 3. FESEM images of ruby before electrospray are

Published on 01 August 2025. Downloaded by Indian Institute of Technology Chennai on 12/29/2025 3:15:06 AM.

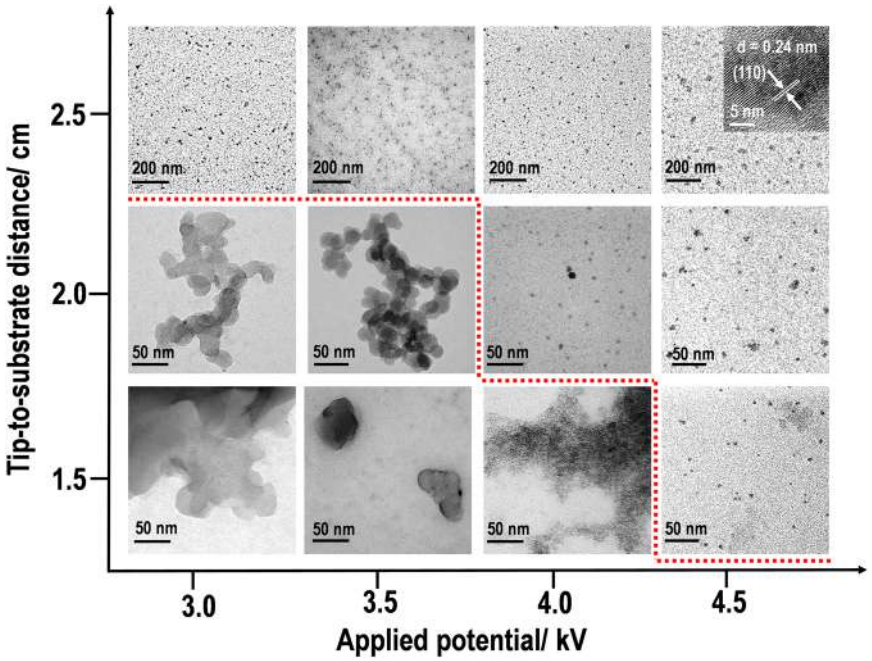


Fig. 2 TEM images showing the disintegration pathway of quartz particles as a function of applied potential (in kV) and tip-to-substrate distance (in cm). The applied potential was varied from 3 to 4.5 kV and tip-to-substrate distance was varied from 1.5 to 2.5 cm. The potential and distance values for an experiment are indicated at the centre of the corresponding TEM images. The dotted line differentiates the relatively big particles of quartz from the nanoparticles. An HRTEM image of one particle showing the (110) plane of quartz is placed as an inset.

shown in Fig. S3, SI. At a lower potential of 3 kV, fragmentation of ruby particles was observed only at a tip-to-substrate distance of 2.5 cm. When the potential was increased to 4.0 kV, flower-like intermediate structures were captured at 2.0 cm, and complete disintegration into nanoparticles was achieved at 2.5 cm. However, even at 5 kV, fragmentation was not complete at shorter distances, indicating that ruby requires higher potential due to its greater hardness and mechanical strength for the complete disintegration of ruby compared to quartz. This difference may be attributed to the higher elastic modulus and Mohs hardness of ruby ($\geq$9) relative to quartz ($\geq$7).[17] A detailed explanation is provided in S5, SI. The effect is particularly evident at a distance of 1.5 cm and potential of 5 kV, where ruby particles remain larger and do not fully fragment, in contrast to the behaviour observed for quartz. Nanoparticle formation was observed at 2.5 cm under all tested conditions, underscoring the importance of smaller droplets with a higher surface-to-volume ratio in facilitating the process. From the TEM images, it can be speculated that ruby exhibits more gradual fragmentation than quartz, which may be attributed to its higher hardness. HRTEM images, presented in Fig. 3 and Fig. S4, SI, reveal a lattice spacing of 0.23 nm, corresponding to the (110) plane of ruby. The size distribution of the nanoparticles along with the EDS analysis of flower-like intermediate species of quartz and ruby are shown in Fig. S6–S8, SI.

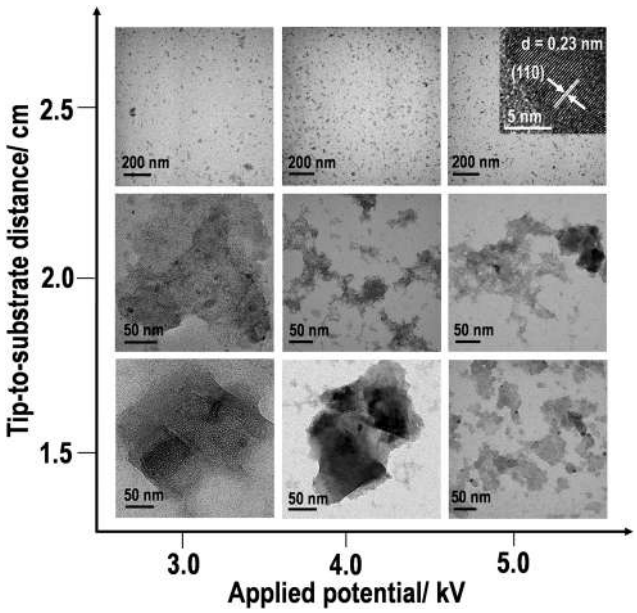


Fig. 3 TEM images showing the disintegration pathway of ruby particles into nanoparticles as a function of applied potential (in kV) and tip-to-substrate distance (in cm). The applied potential varies from 3 to 5.0 kV and the tip-to-substrate distance varies from 1.5 to 2.5 cm. The indicated potential and distance values are placed at the centre of the TEM images. An HRTEM image of one particle showing the (110) plane of ruby is placed as an inset.

To further investigate the dependence of mineral disintegration on the electric field, an experiment was conducted using quartz particles while maintaining a constant electric field strength of E = 3 kV cm^{-1}. This was achieved by keeping the ratio of applied potential to tip-to-substrate distance constant across all trials. The results, presented in Fig. 4, show that while the electric field was held steady, the applied potential along with tip-to-substrate distance are clearly the critical parameters influencing the fragmentation process.

This journal is © The Royal Society of Chemistry 2025

Published on 01 August 2025. Downloaded by Indian Institute of Technology Chennai on 12/29/2025 3:15:06 AM.

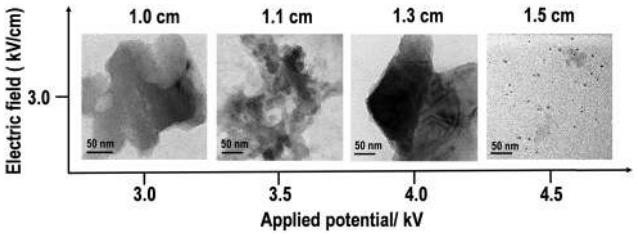


Fig. 4 TEM images showing the particle size of quartz collected at varied conditions of potential and tip-to-substrate distance to maintain the constant electric field of 3 kV cm^{-1}.

It was observed that a minimum tip-to-substrate distance of 1.5 cm was necessary for the disintegration of quartz to occur within the charged water microdroplets. These findings emphasize that, although both electric field strength and distance are important, the absolute value of the applied potential plays a decisive role in enabling mineral fragmentation under these conditions. Collectively, these results indicate that mineral disintegration within charged water microdroplets is strongly influenced by both applied potential and droplet dynamics. At high potentials and optimal tip-to-substrate distances, charged droplets will reach the Rayleigh limit, leading to Coulomb explosion of the droplets along with particle fragmentation. Alternatively, or in parallel, the buildup of intense electric fields during the Coulomb explosion can generate highly charged regions that, in turn, facilitate the formation of reactive species (*e.g.*, hydroxyl radicals or protons) which can induce mineral fragmentation. Both pathways may contribute to the observed disintegration process. Incomplete disintegration at lower potentials or shorter distances suggests that a threshold in droplet size and charge must be surpassed for nanoparticle formation. Overall, the findings suggest that electrical, mechanical and chemical effects within the shrinking charged droplets are important for efficient mineral fragmentation and nanoparticle synthesis.

In conclusion, we established that the key factor in determining particle scission in charged water microdroplets is the applied potential and flight distance. Disintegration occurs within the droplets. This outcome establishes the significance of a critical size for a droplet in inducing disintegration. This can be a way forward in deciding the optimal parameters to synthesize nanoparticles of any material in charged water microdroplets. Observing flower-like intermediates within the droplets at the critical size will be important in establishing the finer details of the events involved. In future, detailed computational and statistical studies will be needed to assess the degree of fragmentation and its underlying mechanism.

The authors thank the Anusandhan National Research Foundation (ANRF), Department of Science and Technology (DST), University Grant Commission (UGC), Government of India and Centre of Excellence on Molecular Materials and Functions under the Institution of Eminence Scheme of IIT Madras for generous funding and supporting our research on nanomaterials. TEM measurements were collected at the ANRF National Facility for Cryo-Electron Microscopy at IIT Madras.

Conflicts of interest

There are no conflicts to declare.

Data availability

The data supporting this article are included in the main article and its SI. No additional data have been deposited in external repositories.

Supplementary information is available. See DOI: **https://doi.org/10.1039/d5cc02952j**.

Notes and references

1 L. V. Subbaiah, T. N. V. K. V. Prasad, T. G. Krishna, P. Sudhakar, B. R. Reddy and T. Pradeep, *J. Agric. Food Chem.*, 2016, **64**, 3778–3788.
2 Z. Kang, J. Lu, S. Zheng, X. Hu, L. Wang, L. Jiang, Y. Zheng, L. Lv, J. L. Gardea-Torresdey, J. C. White and L. Zhao, *ACS Nano*, 2025, **19**, 3752–3763.
3 D. G. Gomes, J. C. Pieretti, C. N. Lange, B. D. M. Santana, B. L. Batista, P. S. Parreira, C. Zucareli, A. B. Seabra and H. C. Oliveira, *ACS Appl. Nano Mater.*, 2024, **7**, 20058–20070.
4 X. Jia, J. Wu and F. Wang, *JACS Au*, 2024, **4**, 4141–4147.
5 H. Wei, E. P. Vejerano, W. Leng, Q. Huang, M. R. Willner, L. C. Marr and P. J. Vikesland, *Proc. Natl. Acad. Sci. U. S. A.*, 2018, **115**, 7272–7277.
6 J. Zhou, Q. Wang, G. Cheng, W. Shen, R. N. Zare and X. Sun, *J. Am. Chem. Soc.*, 2025, **147**, 10916–10924.
7 Y. Wu, J. Li, J. Sun, Y. Wang, J. Liu and H. Cheng, *J. Org. Chem.*, 2024, **89**, 18493–18503.
8 K. Naveen, V. S. Rawat, R. Verma and E. Gnanamani, *Chem. Commun.*, 2024, **60**, 13263–13266.
9 Y. Meng, Y. Xia, J. Xu and R. N. Zare, *Sci. Adv.*, 2025, **11**, eadt8979.
10 Z. Wei, Y. Li, R. G. Cooks and X. Yan, *Annu. Rev. Phys. Chem.*, 2020, **71**, 31–51.
11 A. Jana, S. K. Jana, D. Sarkar, T. Ahuja, P. Basuri, B. Mondal, S. Bose, J. Ghosh and T. Pradeep, *J. Mater. Chem. A*, 2019, **7**, 6387–6394.
12 D. Sarkar, M. K. Mahitha, A. Som, A. Li, M. Wleklinski, R. G. Cooks and T. Pradeep, *Adv. Mater.*, 2016, **28**, 2223–2228.
13 B. K. Spoorthi, K. Debnath, P. Basuri, A. Nagar, U. V. Waghmare and T. Pradeep, *Science*, 2024, **384**, 1012–1017.
14 R. G. Cooks and D. T. Holden, *Science*, 2024, **384**, 958–959.
15 B. K. Spoorthi, A. R. Chowdhuri, B. Mondal, S. Manna, A. Mahapatra, A. R. Kini and T. Pradeep, *Chem. Commun.*, 2025, **61**, 5577–5580.
16 L. Shi, R. A. LaCour, N. Qian, J. P. Heindel, X. Lang, R. Zhao, T. Head-Gordon and W. Min, *Nature*, 2025, **640**, 87–93.
17 S. Ruppi, A. Larsson and A. Flink, *Thin Solid Films*, 2008, **516**, 5959–5966.

Supplementary Information (SI) for ChemComm.
This journal is © The Royal Society of Chemistry 2025

Electronic Supplementary Information

From micro-to-nano in charged water microdroplets: Unveiling steps in the weathering of minerals †

Anubhav Mahapatra,[a] Anirban Som,[a] B. K. Spoorthi,[a] Depanjan Sarkar,[a c] and Thalappil Pradeep *[a b c]

[a.]DST Unit of Nanoscience (DST UNS) & Thematic Unit of Excellence (TUE), Department of Chemistry, Indian Institute of Technology Madras (IITM), Chennai - 600036, India.

[b.]International Centre for Clean Water, 2nd Floor, B-Block, IIT Madras Research Park, Kanagam Road, Taramani, Chennai - 600113, India.

[c.]Centre of Excellence on Molecular Materials and Functions, Department of Chemistry, Indian Institute of Technology Madras, Chennai – 600036, India.

Table of contents

Name	Description	Page No.
S1	Materials	S3
S2	Electrospray deposition experiments	S3
S3	Characterization	S3
S4	Nebulization of quartz and ruby suspension	S3
S5	Mechanical factors influencing the fragmentation of mineral particles	S4
Fig. S1	Photograph of the device used for electrospraying. A TEM grid was kept on the substrate below the tip of the capillary at different tip-to-substrate distances. The spray plume was illuminated by a green laser.	S5
Fig. S2	High-resolution transmission electron microscopic (HRTEM) images showing the plane (110) of quartz in A) disintegrated intermediate species and B) nanoparticle	S5

Fig. S3	**Field emission scanning electron microscopic (FESEM) images of ruby particles before electrospray at different scale bar A) 10 µm and B) 5 µm**	**S6**
Fig. S4	**High-resolution transmission electron microscopic (HRTEM) images showing the plane (110) of ruby in A) disintegrated intermediate species and B) nanoparticle**	**S6**
Fig. S5	**TEM images showing bigger aggregates of A) quartz and B) ruby upon nebulization with N_2 at a pressure of 50 psi**	**S7**
Fig. S6	**Particle size distribution of nanoparticles of A) quartz and B) ruby**	**S7**
Fig. S7	**Flower-like intermediate species of quartz A) TEM image; B) HAADF image of the magnified portion of the image; EDS elemental mapping showing the presence of C) Silicon and D) Oxygen**	**S8**
Fig. S8	**Flower-like intermediate species of ruby A) TEM image; B) HAADF image of the magnified portion of the image; EDS elemental mapping showing the presence of C) Aluminium; D) Chromium; and E) Oxygen**	**S8**

S1. Materials:

River sand and natural ruby samples were procured from a local marketplace and used without further purification. The samples were mechanically ground using mortar and pestle to obtain fine powders. Ultrapure milli-Q water (18.5 MΩ·cm at 25 °C) was employed throughout the experimental procedures. The resulting ground materials were then dispersed in milli-Q water to form particle suspensions. These suspensions were subjected to ultrasonication using an ultrasonic bath having specifications 40 kHz, 100 W for 10 minutes to enhance dispersion and break up agglomerates. Subsequently, the suspensions were centrifuged with Remi RM-03 Plus for 1 minute to achieve preliminary size separation, allowing the removal of larger particulates and enrichment of finer and mid ranged micro-particles.

S2. Electrospray deposition experiments:

A custom-built electrospray setup as shown in Fig. 1 was used to generate microdroplets. The use of gastight Hamilton syringe (0.5 mL) with 22 gauge (inner diameter of 413 µm) needle was connected with 50 µm inner diameter fused silica capillary via union connector. The syringe needle was connected with the high voltage power supply and the carbon coated copper TEM grid with 300 mesh was kept on the plate collector and it was grounded. The stepper motor with 400 steps per rotation was used to control the flow rate of the suspension precisely. The deposition experiments were conducted in ambient conditions of 25 °C and relative humidity of 50-60 % for 1 hour. Polyimide coated fused silica capillary was procured from Polymicro Technologies™, Molex, USA and the other components like union connector, PEEK tubing, ferrules were purchased from IDEX Health & Science, USA.

S3. Characterization:

Thermo Fisher Scientific Verios G4 UC high-resolution field emission scanning electron microscope (FESEM) at an accelerating voltage of 10 kV with emission current of 0.10 nA was used to image the micro-sized particles of quartz and ruby. A thin layer of gold ~ 0.2 nm was sputtered on the sample kept on aluminium substrate by use of Quorum Q150T S plus to make it conductive and necessary for FESEM imaging. Glow discharge was used for carbon coated copper TEM grids to remove unnecessary impurities and make the surface more hydrophilic by Quorum GloQube Plus and Thermofischer Talos™ F200i transmission electron microscope (TEM) was used at an accelerating voltage of 200 kV to image the nanoscale particles of quartz and ruby.

S4. Nebulization of quartz and ruby suspension:

Suspensions of quartz and ruby (0.2 mg/mL) were prepared according to the method detailed in Section S1. These were separately loaded into a Hamilton syringe and dispensed through a polyimide-coated fused silica capillary (50 µm inner diameter) using a syringe pump. Nitrogen gas (N_2) at 50 psi was used to nebulize the suspension and generate microdroplets. No applied potential was used, ensuring that the generated droplets remained largely uncharged. The capillary was directed into a 100 mL round-bottom flask to collect the products over 30 minutes, after which the collected materials were redispersed in ultrapure water. 20 µL aliquot

of the collected suspensions were drop-cast onto carbon-coated TEM grids and allowed to dry. As shown in the TEM images in Fig. S5, the disintegration of mineral particles into nanoparticles was not feasible with neutral microdroplets, which resulted in the formation of larger aggregates of particles.

S5: Mechanical factors influencing the fragmentation of mineral particles:

The distinct fragmentation behaviors of minerals in charged water microdroplets can be attributed to their hardness and elastic moduli. Ruby, characterized by strong Al–O bonds and dense atomic packing, has a high elastic modulus (~ 400 GPa) and high hardness. In contrast, quartz exhibits a lower elastic modulus (~117 GPa).[1,2] These properties hinder slippage of lattice planes in ruby, delaying initiation of fragmentation compared to quartz. Consequently, the combined influence of high hardness, elevated elastic modulus, and concentrated charges at the droplet interface necessitates higher potentials for the fragmentation of ruby.

Supplementary figures:

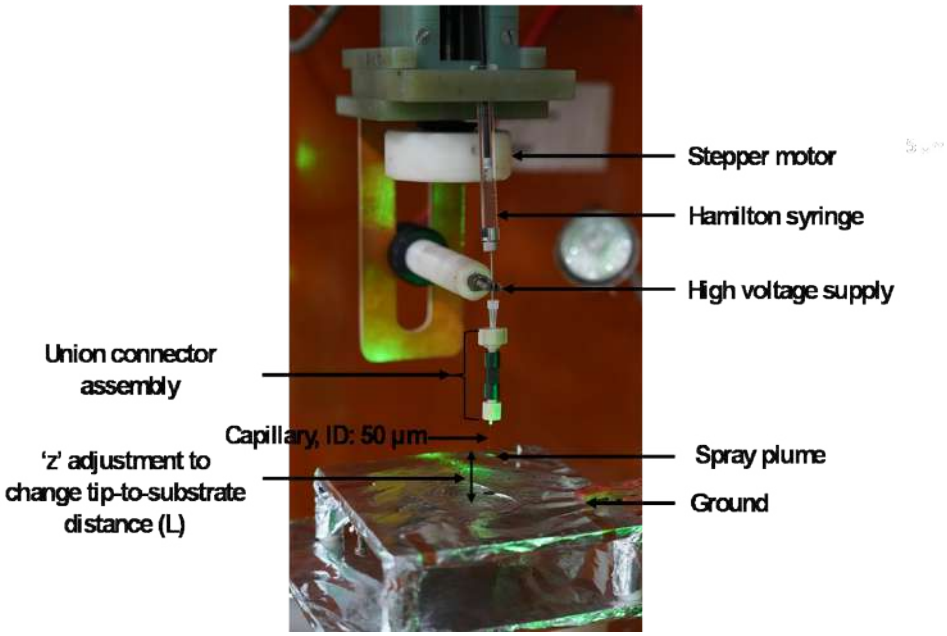


Fig. S1: Photograph of the device used for electrospraying. A TEM grid was kept on the substrate below the tip of the capillary at different tip-to-substrate distances. The spray plume was illuminated by a green laser.

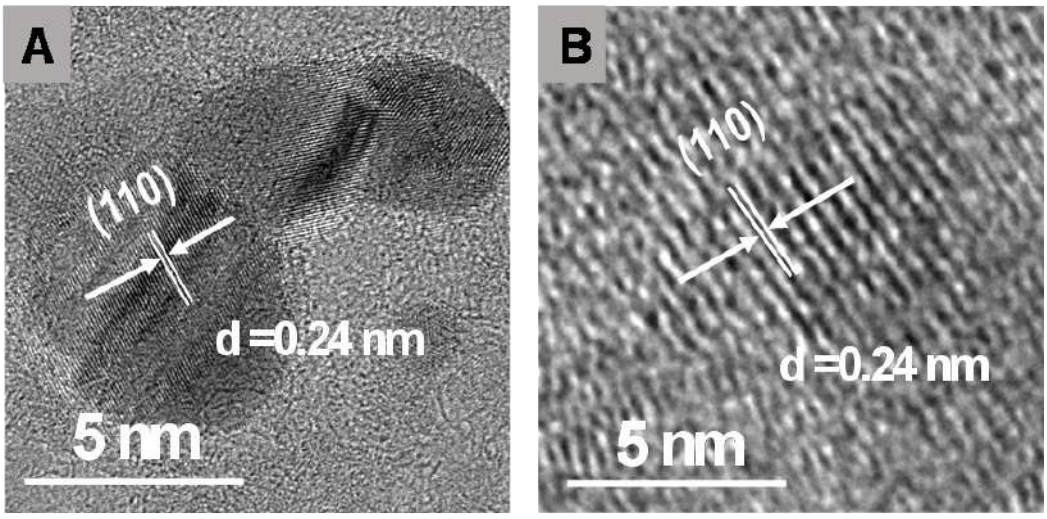


Fig. S2: High-resolution transmission electron microscopic (HRTEM) images showing the plane (110) of quartz in **A)** disintegrated intermediate species and **B)** nanoparticle.

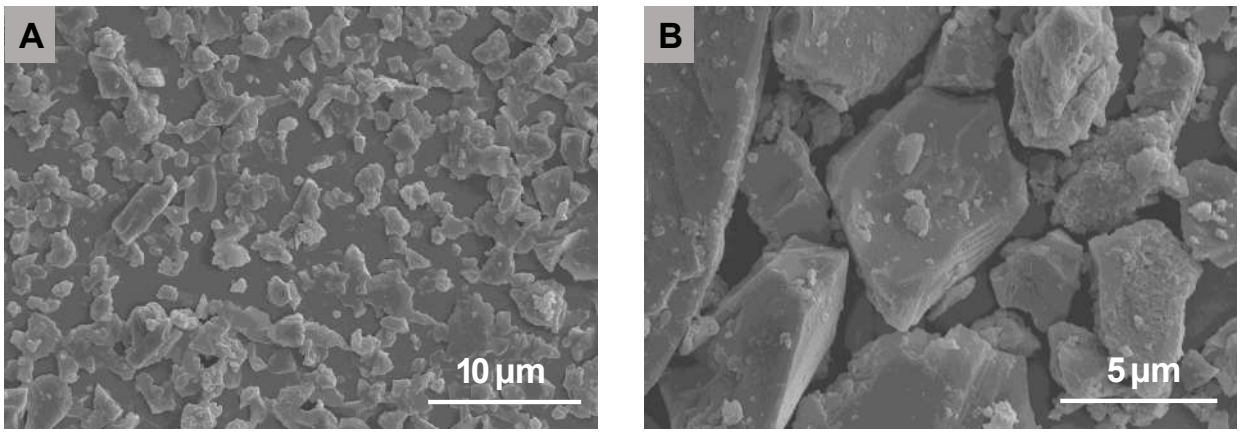


Fig. S3: Field emission scanning electron microscopic (FESEM) images of ruby particles before electrospray at different scale bar **A)** 10 µm and **B)** 5 µm**.**

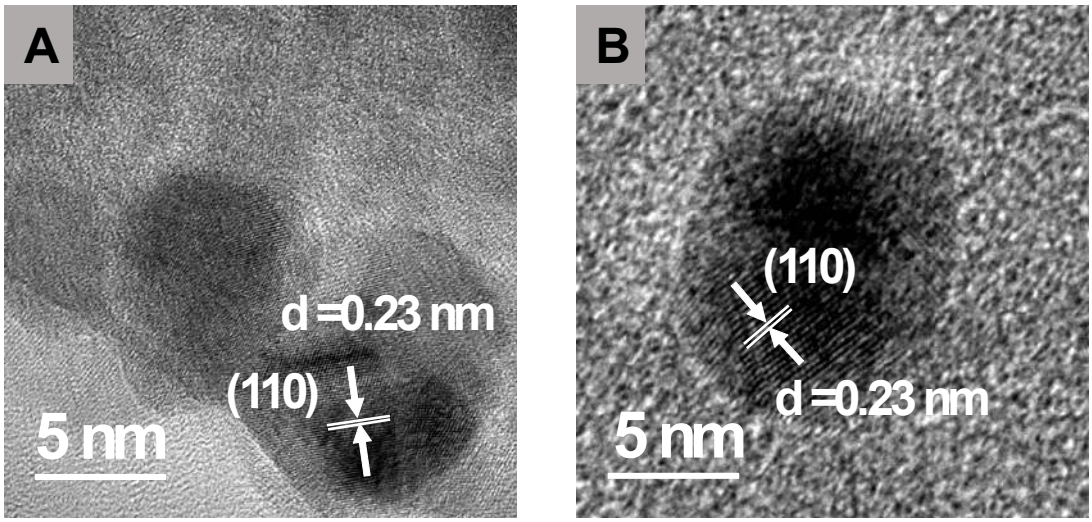


Fig. S4: High-resolution transmission electron microscopic (HRTEM) images showing the plane (110) of ruby in **A)** disintegrated intermediate species and **B)** nanoparticle.

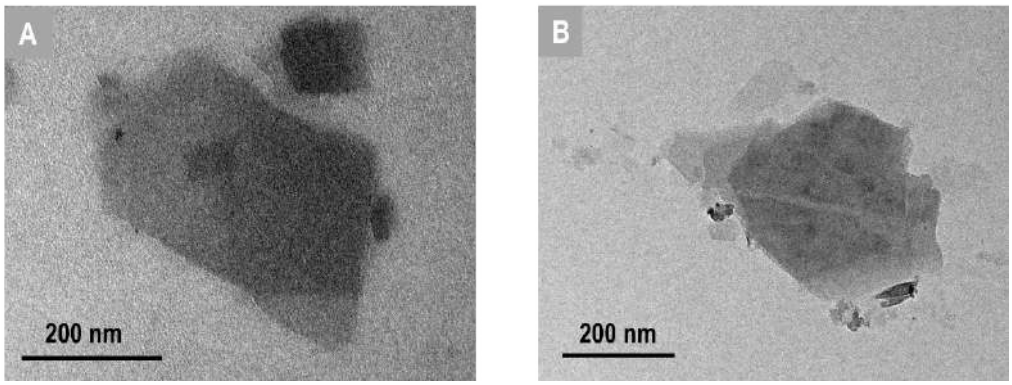


Fig. S5: TEM images showing bigger aggregates of **A)** quartz and **B)** ruby upon nebulization with N_2 at a pressure of 50 psi.

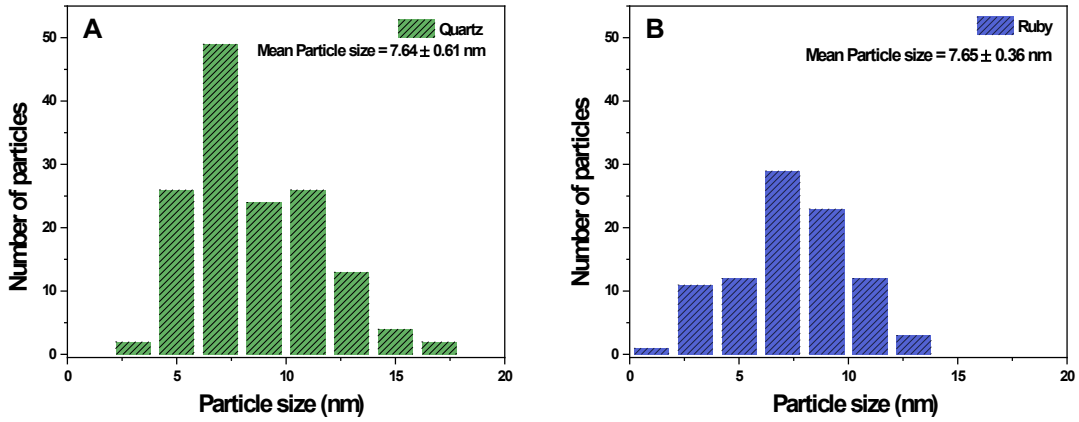


Fig. S6: Particle size distribution of nanoparticles of **A)** quartz and **B)** ruby.

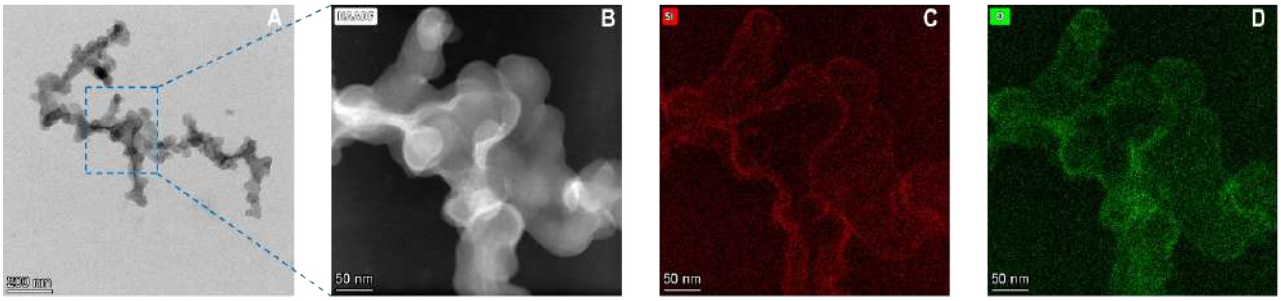


Fig. S7: Flower-like intermediate species of quartz **A)** TEM image; **B)** HAADF image of the magnified portion of the image; EDS elemental mapping showing the presence of **C)** Silicon and **D)** Oxygen.

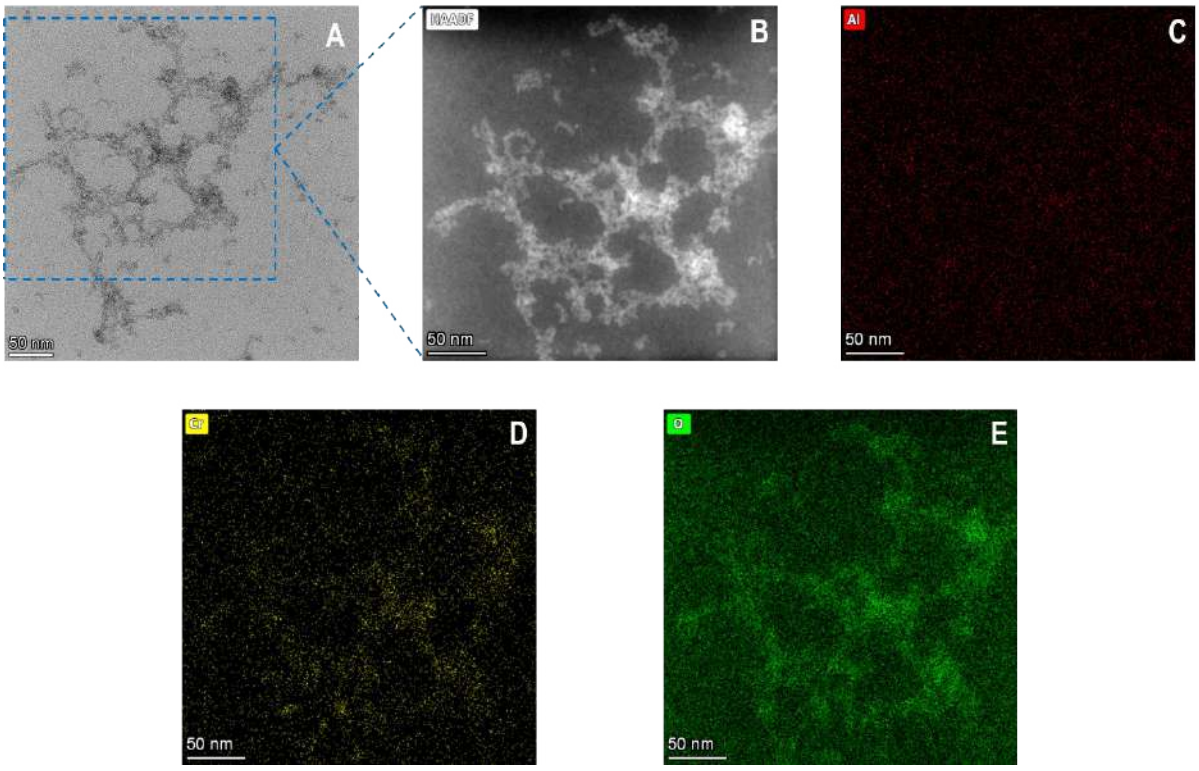


Fig. S8: Flower-like intermediate species of ruby **A)** TEM image; **B)** HAADF image of the magnified portion of the image; EDS elemental mapping showing the presence of **C)** Aluminium; **D)** Chromium; and **E)** Oxygen.

References:

1 L. Zhang, F. Jiao, W. Qin and Q. Wei, *ACS Omega*, 2023, **8**, 43644–43650.

2 S. Ruppi, A. Larsson and A. Flink, *Thin Solid Films*, 2008, **516**, 5959–5966.

Coordination Chemistry Reviews 548 (2026) 217186

Contents lists available at ScienceDirect

Coordination Chemistry Reviews

journal homepage: www.elsevier.com/locate/ccr

Recent advances in the recycling of precious metals using sustainable chemistry

Abhijit Nag [a,b,c,*], Ahsanulhaq Qurashi [b,*], Carole A. Morrison [c,*], Kasper Moth-Poulsen [a,d,e,*], Thalappil Pradeep [f,*], Jason B. Love [c,*]

[a] Department of Chemical Engineering, Universitat Politècnica de Catalunya, EEBE, Eduard Maristany 10-14, Barcelona 08019, Spain
[b] Department of Chemistry, CeCaS, Khalifa University of Science and Technology, Abu Dhabi, P.O. Box 127788, United Arab Emirates
[c] EaStCHEM School of Chemistry, University of Edinburgh, Edinburgh, EH93FJ, UK
[d] The Institute of Materials Science of Barcelona, ICMAB-CSIC, Bellaterra, 08193 Barcelona, Spain
[e] Catalan Institution for Research & Advanced Studies, ICREA Pg. Llu'ıs Companys, 23, Barcelona, Spain
[f] DST Unit of Nanoscience and Thematic Unit of Excellence, Department of Chemistry, Indian Institute of Technology Madras, Chennai 600036, India.

ARTICLE INFO

Keywords:
Dissolution
Precious metal recovery
Selective separation
Sustainable chemistry
Electronic waste recycling

ABSTRACT

Precious metals (PMs) such as silver, gold, palladium, platinum, and rhodium are used not just in traditional industries like jewelry, but also in modern electronics, medicine, catalysis and others. Their scarcity, as well as the environmental impact of current extraction procedures that frequently include harmful compounds such as cyanide and mercury, provide substantial global issues. With a growing interest in sustainable chemistry, researchers are developing eco-benign ways to extract PMs from secondary sources, like electronic waste, spent catalysts which frequently have greater PM concentrations. This review presents a contemporary analysis of PM recovery with focus on underexplored and emergent avenues, such as bio-based leaching, mechanochemistry, photocatalysis, ionic liquids and deep eutectic solvents, and computationally driven ligand design, in addition to reviewing conventional procedures. Sustainability criteria including toxicity, energy use, recyclability, and life-cycle assessment (LCA) are prioritized. Comparative tables and cross-cutting studies reveal which techniques are industrially scalable, which are still in proof-of-concept stage, and where knowledge gaps persist. This review gives a unique perspective on chemical innovation and sustainability evaluation, complementing existing surveys and providing actionable information for academics and industries seeking greener PM recovery.

1. Introduction

The increasing strain on earth's ecological systems has focused emphasis on how we manage finite natural resources, especially precious metals (PMs). These elements are critical to supporting both renewable energy technologies and the establishment of digital infrastructure, making them vital to a low-carbon economy and modern communication networks. However, their limited global supply, along with the environmental cost of extraction and unequal geographic distribution, puts at risk the viability of these developments. As we strive for a cleaner and more connected society, the capacity to protect PMs through sustainable recovery methods becomes increasingly important. Using secondary sources, such industrial by-products and end-of-life electronics, is a viable way to lessen reliance on primary mining and promote a circular economy while staying within the safe operating parameters of our planet.

PMs include gold (Au), silver (Ag), and the platinum group metals (PGMs - Pt, Pd, Rh, Ru, Ir, and Os). PMs not only have value in jewelry and investment but also have extensive applications in modern electronics, medicine, and chemical catalysis. As representative PMs, Au and Ag have long been important components of national monetary systems, and have served as symbols of wealth for thousands of years. Similarly, it is widely known that the catalytic effect of Pd is required to produce gasoline from petroleum during the cracking and processing. [1] Pt, Pd, and Rh catalysts are necessary for gasoline-burning vehicles to remove NOx gases from their exhaust emissions. [2] CO_2 emissions arising from the combustion of fossil fuel resources has a significant greenhouse effect that results in anthropogenic global warming. PM catalysts can be used to transform CO_2 into carbon raw materials with significant added value. [3]

* Corresponding authors.
E-mail addresses: abhijit.nag@upc.edu (A. Nag), kasper.moth-poulsen@upc.edu (K. Moth-Poulsen).

https://doi.org/10.1016/j.ccr.2025.217186
Received 3 July 2025; Accepted 11 September 2025
Available online 23 September 2025
0010-8545/© 2025 The Authors. Published by Elsevier B.V. This is an open access article under the CC BY license (http://creativecommons.org/licenses/by/4.0/).

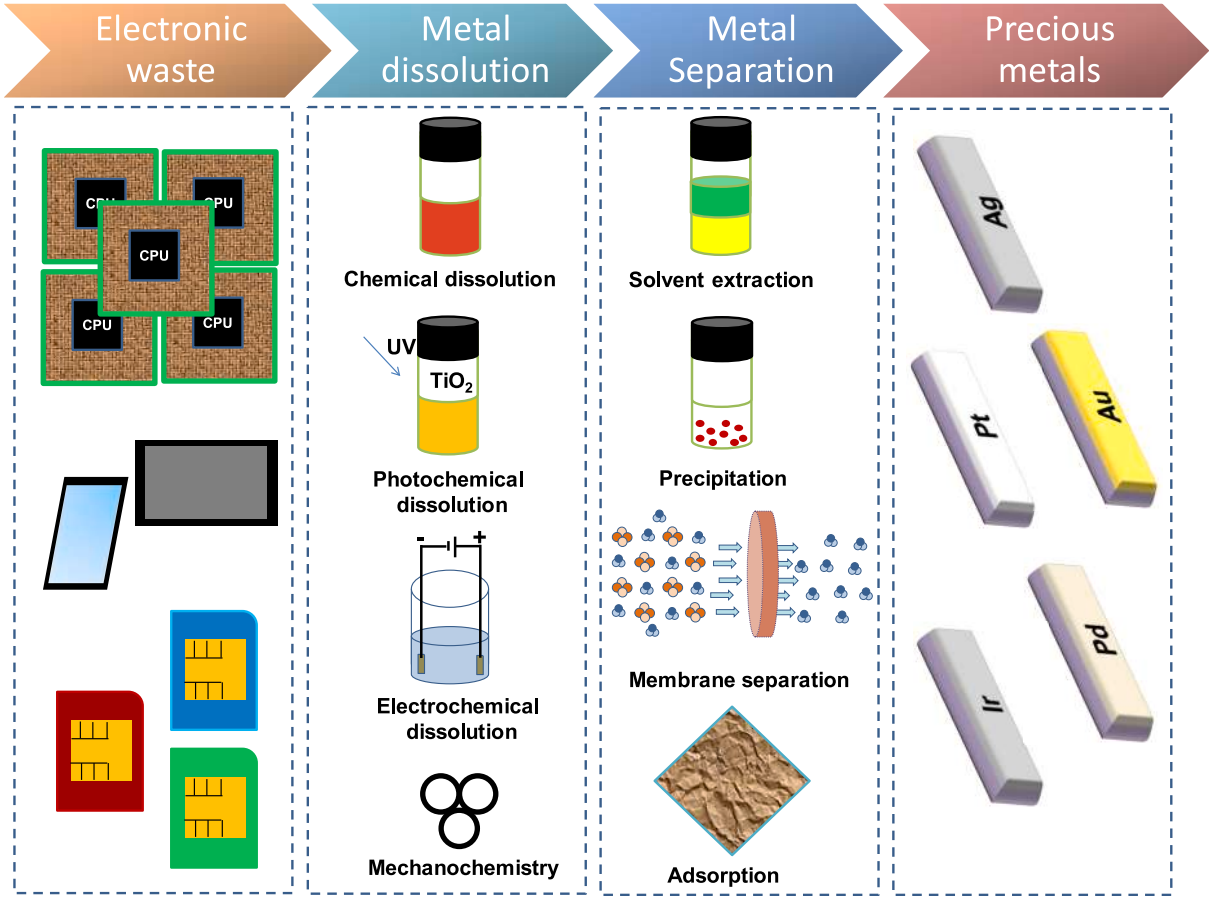
The monetary value of PMs also stems from their low abundance in their ores, although more recently secondary sources such as nanomaterials and electronic waste (e-waste) have attracted attention due to the higher concentrations found in these resources. [4–6] E-waste and spent catalysts are the most common secondary sources of PMs. The catalytic converter in an automobile is made of a porous ceramic material that is coated with PMs, such as Rh, Pd, and Pt. The PM content in used electrical equipment, car exhaust catalysts, electroplated objects, and industrial catalysts is high and, as a result, the strategy of recovering PMs from secondary resources has gained increased attention.

The markets for high-efficiency small storage devices, photovoltaics, medical diagnostics, imaging, and other gold-based nanotechnology applications are expected to grow dramatically. [7] According to estimates, the global market value of gold nanoparticles (AuNPs) was $1.34 billion in 2014. [8] By 2022, the market for gold-based nanotechnologies was expected to increase rapidly, with an estimated 20,000 kg/yr of gold used in the nanotechnology industry. [8] The World Gold Council estimates that about 190,000 tons of gold have been extracted from mines worldwide, with almost two-thirds of that amount having been extracted since 1950. [9] But, according to the distribution of known resources, worldwide gold reserves were only projected to be about 53,000 tons in 2020, despite the enormous amount that had previously been collected. [6] PGM minerals have a much lower global annual output than gold. COVID-19 had a significant impact on global demand for PGMs in 2020. [6] Furthermore, the increased adoption of alternative energy-powered vehicles is likely to drive up demand for PGMs even further in the coming years. According to the World Platinum Investment Council (WPIC), there will be a growing need for PGMs as a result of increased manufacturing of both heavy-duty and lightweight automobiles.

PMs can be extracted and recycled by leaching them from ore or secondary sources, separating the targeted PM ions from the multimetal leachate, and isolating or reducing the separated PM ions to their elemental form or metal compounds (Scheme 1). Each of these stages is associated with considerable energy use, global warming potential, and severe environmental pollution. [10] Current industrial gold extraction procedures (over 90 %) typically use highly toxic sodium cyanide to leach gold in the form of the soluble coordination complex, $NaAu(CN)_2$. [11] In more informal and artisanal practices, highly toxic mercury is used to alloy with gold and is the world's largest source of mercury pollution. [12] Alternative approaches to current procedures, which rely on selective precipitation, extraction, or adsorption of Au from leach solutions, are being actively investigated, but recovery of gold from ores, as well as e-waste, has both technological and environmental challenges. The discovery of environmentally friendly and economically feasible methods for recycling e-waste would give global circular economy aspirations a boost, and thus inspire increased research efforts. [5]

Over the last decade, various reviews have examined green leaching reagents, solvent extraction (SX), precipitation, and adsorption techniques for PM recovery. [5,6,13–16] However, the majority of these studies primarily catalogue existing chemistries rather than offering a unified framework for sustainability evaluation or covering emergent and underexplored methods. For example, recent advances in mechanochemistry, photocatalytic dissolution, microbial leaching, and bio-derived ligands have received little attention, despite their potential to minimize hazardous chemical inputs and energy demands. Similarly, computational chemistry and machine learning (ML) are increasingly directing the design of selective ligands, although their involvement in PM recovery is limited.

The present review fills these gaps by conducting a thorough and



Scheme 1. Schematic presentation of various PM recovery methods.

critical examination of both conventional and new recovery approaches within the context of sustainable chemistry. We also prioritize comparative study of toxicity, recyclability, energy consumption, and scalability across various techniques, which are supported by summary tables and LCA considerations. Unlike previous reviews, which primarily describe methods in isolation, our analysis emphasizes cross-cutting insights that inform practical adoption, as well as identifying future research directions required to translate laboratory discoveries into industrially viable, and environmentally responsible technologies.

2. Dissolution of PMs

In this part, we first describe the key techniques (old and recent) used to dissolve PMs, followed by a discussion of current breakthroughs, mechanism, problems, and prospects for developing greener and more selective dissolution processes.

2.1. Cyanide method

One of the most important steps in the recovery of PMs is leaching, which is underpinned by chemistry at the interface. The cyanide method is one of the main leaching technologies used for gold because of its cost-effectiveness, high recovery rate, and 100 years of technological maturity. [6] In this method, Au and Ag are treated with alkali metal cyanide in an aqueous solution. There are many theories to explain the mechanism of this process, including Bodlander's hydrogen peroxide theory, Elsner's oxygen theory, and Boonstra's corrosion theory. [17,18] At the initial stage, in order to form $[Au(CN)_2]^-$, Au is oxidized to Au^+, and forms a soluble complex with CN^- (eq. 1). Meanwhile, dissolved O_2 in the solution is reduced and reacts with H_2O to produce H_2O_2 and OH^-. The essential ingredient in this extraction process, cyanide, is toxic and its use in several cases resulted in environmental disasters. Cyanide combines with carbon dioxide to form hydrocyanic acid (HCN), a very poisonous chemical that, when inhaled, can paralyze the respiratory system and be lethal. Furthermore, traditional cyanidation is renowned for its low efficiency in leaching PGMs. However, pressure or high-temperature cyanidation can alleviate this constraint. [19]

$$4Au + 8NaCN + 2H_2O_2 \rightarrow 4NaAuCN_2 + 4NaOH \quad (1)$$

2.2. Cyanide-free dissolution

The use of aqua regia (1:3 mixture of concentrated HNO_3 and HCl) is another highly used method for the dissolution of PMs from e-waste. [6] Pd can be dissolved using HNO_3, H_2SO_4, or aqua regia. Au and Pt, on the other hand, can only be dissolved in aqua regia. Meanwhile, Os, Ru, Rh, and Ir are insoluble in aqua regia and other acids. Silver, on the other hand, does not dissolve in aqua regia because it forms insoluble silver chloride (AgCl). Dissolution of Au, Pt, and Pd in aqua regia results in the generation of chloridometalate complexes like $HAuCl_4$, H_2PtCl_6, and H_2PdCl_4, respectively (eqs. 2, 3, and 4). The major challenge with this dissolution method is the release the highly toxic gases NO and NO_2.

$$Au + 4HCl + HNO_3 \rightarrow HAuCl_4 + 2H_2O + NO\uparrow \quad (2)$$

$$3Pd + 12HCl + 2HNO_3 \rightarrow 3H_2PdCl_4 + 4H_2O + 2NO\uparrow \quad (3)$$

$$3Pt + 18HCl + 4HNO_3 \rightarrow 3H_2PtCl_6 + 8H_2O + 4NO\uparrow \quad (4)$$

More environmentally benign methods of dissolving PMs have been developed as awareness of the negative health and environmental effects of the cyanide leach and aqua regia methods mentioned above have become better appreciated. [6] Thiourea, thiosulfate, KI-I_2, and electrochemical methods have been developed to dissolve Au and Ag. Thiourea is a reductive ligand that can form stable complexes with a diverse variety of metal ions in solution. As a result, a small amount of oxidant is required to aid the dissolution of Au and Ag. [20] Thiourea possesses unbound electron pairs on its nitrogen and sulfur atoms, allowing it to adsorb on the gold surface. As a result, this interaction reduces the redox potential of gold, allowing for its dissolution under milder reaction conditions. Thiourea, however, is unstable in alkaline solutions and readily breaks down into cyanamide and sulfide. [13] Consequently, the thiourea leaching process has higher costs than cyanidation but with lower toxicity. [6] Thiosulfate can also dissolve Au under alkaline conditions, [21] forming a stable complex after the reaction with Au, to form $[Au(S_2O_3)_2]^-_3$. [22]

The stability of Au complexes generated with different anions varies, influencing the complexation process and, as a result, the leaching efficiency. [23] Au-anion complexes are stable in the following order: $CN^- > I^- > Br^- > Cl^- > NCS^- > NCO^-$. The gold-iodine complex is the second most stable, following the gold-cyanide complex. The electronegativity and oxidizing power of the halogen elements decreases down the periodic table grouping, making heavier halogens less effective as oxidants. Consequently, iodination (the process of generating the iodide ion by combining iodine (I_2) and potassium iodide) is a frequently used technique for Au leaching. [24] It has various benefits, such as being relatively non-toxic, having good leaching capabilities while remaining relatively stable. In addition to the classical methods of PMs dissolution, electrochemical dissolution techniques have received interest in recent applications. However, because of the complicated equipment requirements, they have not yet received much practical use. [25]

2.3. Recent developments in dissolution of PMs

2.3.1. Mild dissolution processes

Challenges of the above-mentioned extraction technologies typically include lengthy dissolution cycles, high reagent and energy consumption, complicated operational procedures, and significant environmental pollution. [6] In order to address these challenges and make PMs dissolution more practical, more environmental benign and economically feasible leaching techniques are currently receiving significant research interest.

In this context, Lin et al. demonstrated that PMs like Au and Pd can be dissolved with high leaching rates under favorable conditions using straightforward mixtures of thionyl chloride ($SOCl_2$) and some organic solvents/reagents such as *N*,*N*-dimethylformamide (DMF), pyridine (Py), and imidazole (Fig. 1). [26] This mixture of organic solvents and reagents has been referred to as 'Organic Aqua Regia'. Modifying the content of organic solvents enabled the selective dissolution of certain PMs, including Au and Pd from a mixture of Pt, Au, and Pd, and Au from a mixture of Au and Pd; this latter example comprises dissolving Au in a $SOCl_2$/DMF solution, followed by the dissolution of Pd in a $SOCl_2$/Py mixture. Organic aqua regia represents a novel strategy to selectively dissolving PMs, with specific advantages over traditional inorganic procedures. However, $SOCl_2$ is a volatile liquid with a powerful, irritating odour, and pyridine has a distinctly unpleasant smell. Furthermore, the toxicity of these reagents raises significant health and environmental concerns, and the need for substantial post-reaction processing complicates and extends the procedure. Serpe et al. showed that the mixture of tetraethylthiuram disulfide (Et_4TDS) and I_2 in acetone has the ability to dissolve Au and form valuable metal complexes, with the stoichiometry of these complexes depending on the composition of the mixture. [27] Under mild conditions, these mixtures also uniformly and selectively removed the Au layer from thin-layered $Si/SiO_2/Ti/Au$ structures. In an alternative study, with the use of Py and N-bromosuccinimide (NBS), Yang et al. created a novel chemical process with mild reaction conditions and a significantly reduced environmental impact. With this process, Au from e-waste and ore can be directly dissolved into water to produce Au(III) complexes. [28] At ambient conditions and a neutral pH, the process yielded about 90 % Au dissolution using an NBS/Py etchant. According to the reaction mechanism (Fig. 1B), Au(0) is initially oxidized by NBS in step 1 resulting in the conversion of Au(0) to Au(III) as $AuBr^-_4$. In step 2, the Au(III) species

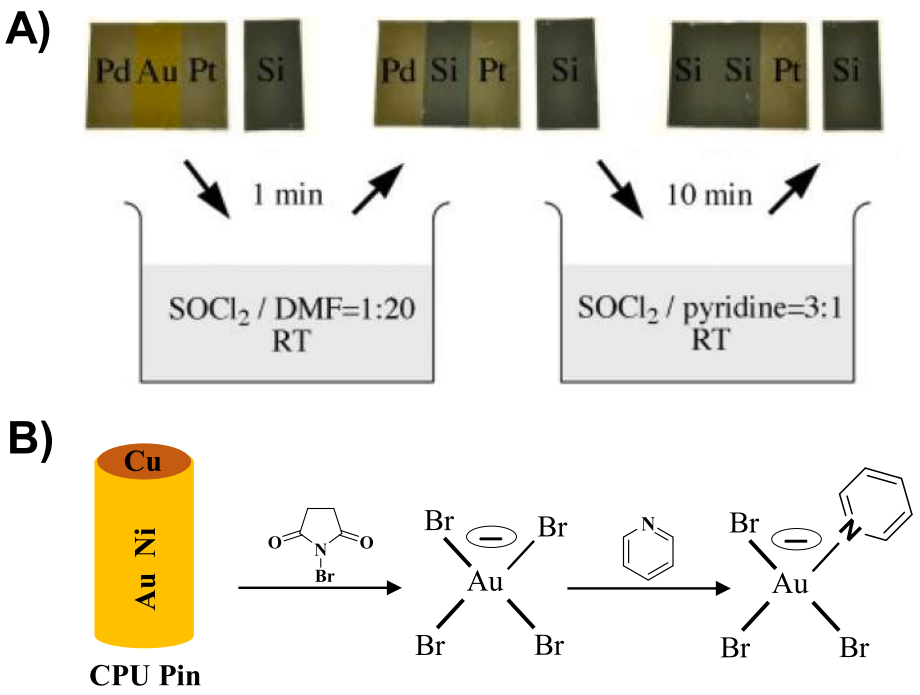


Fig. 1. A) A schematic representation of an effective and selective leaching of Pd, Au and Pt. Pd and Au were leached sequentially in $SOCl_2$/py and $SOCl_2$/DMF, respectively from a Si substrate. The photographs in the top row depict the Pd/Au/Pt layer on a Si substrate during the selective leaching method. (Adopted from ref. 26, Copyright 2010 Wiley.) **B)** Dissolution of Au from CPU pin using *N*-bromosuccinimide/pyridine mixture in water. (Reproduced from ref. 28, Copyright 2017 Wiley.)

($AuBr_4^-$) coordinates with pyridine (Py) ligands to produce the (Py) $AuBr_3$ complex with a binding constant ranging from 10^5 to 10^6 M. The dissolution of Au and PGMs was examined in highly concentrated solutions of hydrated $AlCl_3$ and $Al(NO_3)_3$ salts by Forte et al. [29] The research was motivated by a 1973 paper by Sare et al. in which it was noted that boiling aqua regia does not dissolve PMs as quickly as concentrated solutions of $AlCl_3 6H_2O$ and $Al(NO_3)_3 9H_2O$. [30] Using similar methods, 95 % of Pd was leached in 15 min at 80 °C from used automotive catalysts, whereas Pt required longer times, and 20 % Rh dissolution was achieved. The same procedure permitted the dissolution of Au from waste-electronic wiring in 24 h. While aluminium salt solutions are substantially less hazardous and safer to handle than aqua regia, they are not reusable or recyclable. The dissolution of various PMs using various reagents in different solvents and their toxicity is presented in Table 1.

Baksi et al. showed that Ag has a very strong chemical affinity for carbohydrates, allowing it to dissolve directly from the metallic state into an aqueous solution. [31] The inclusion of common ions considerably increased the method's efficiency, offering a new perspective on extractive metallurgy. An analysis of calorimetric data shows that the route is thermodynamically desirable. Continuous Ag extraction causes the surface to corrode, and as a result, microscopic roughness was seen (Fig. 2A). Studies have shown that the release of Ag occurs in two stages, with the formation of Ag ions at the metal surface followed by their binding with glucose. Using mass spectrometry, the resultant Ag-G complexes have been determined (Fig. 2B). The process was further extended with the use of glutathione in combination with glucose, which resulted in a 45 times enhancement in the dissolution process. [32]

Repo et al. described an effective approach for dissolving Au(0) that employed solutions of DMF containing pyridine-4-thiol (4-PSH) as a reactive ligand and hydrogen peroxide as an oxidizing agent (Fig. 3A). [33] The process of dissolving metallic Au involved a number of fundamental steps, including isomerizing the 4-PSH to pyridine-4-thione (4-PS), coordination with Au(0), and oxidizing the Au(0) thione species to Au(I). The final product from the dissolution is an Au(I) complex with

Table 1
Dissolution of PMs in various solvents with indicated toxicity.*

Entry	Solvent	Reagents	Targeted PM	Toxicity of the reagent & solvent	Ref.
1	Py, DMF, and imidazole	$SOCl_2$	Au and Pd	High	26
2	Acetone	Et_4TDS and I_2	Au	Low	27
3	Py	NBS	Au	Moderate	28
4	Water	$Al(NO_3)_3$ and $AlCl_3$	Au, Pt, Pd and Rh	Low	29
5	Water	Glucose	Ag	Low	31
6	DMF	4-PSH and H_2O_2	Au	Moderate	33
7	Ethanol	Catalytic amount of I_2, 2-MBI and H_2O_2	Au	Low	34
8	Acetonitrile and dichloromethane	TiO_2 photocatalyst	Au, Ag, Pt, Pd, Ru, Rh, and Ir	Moderate	41
9	Acetonitrile	Ph_3PCl_2 or $(COCl)_2$ and H_2O_2	Au, Pd, Pt and Cu	Moderate	10
10	Ethanol	CH_3COBr or CH_3COCl and H_2O_2	Au and Cu	Low	35
11	Tributyldecylphosphonium trihalide ionic liquids as solvent and reagent		Au, Cu and Pd	Low	49
12	Deep eutectic solvents		Au, Ag and Cu	Low	55

* Toxicity levels were assigned based on reported risks using PubChem and MSDS. We categorize chemicals as low (usually safe/biodegradable, e.g., water, ethanol), moderate (some dangers, managed with normal safety, e.g., thiourea, acetonitrile), and high (poisonous, carcinogenic, or persistent, e.g., cyanide, aqua regia, $SOCl_2$).

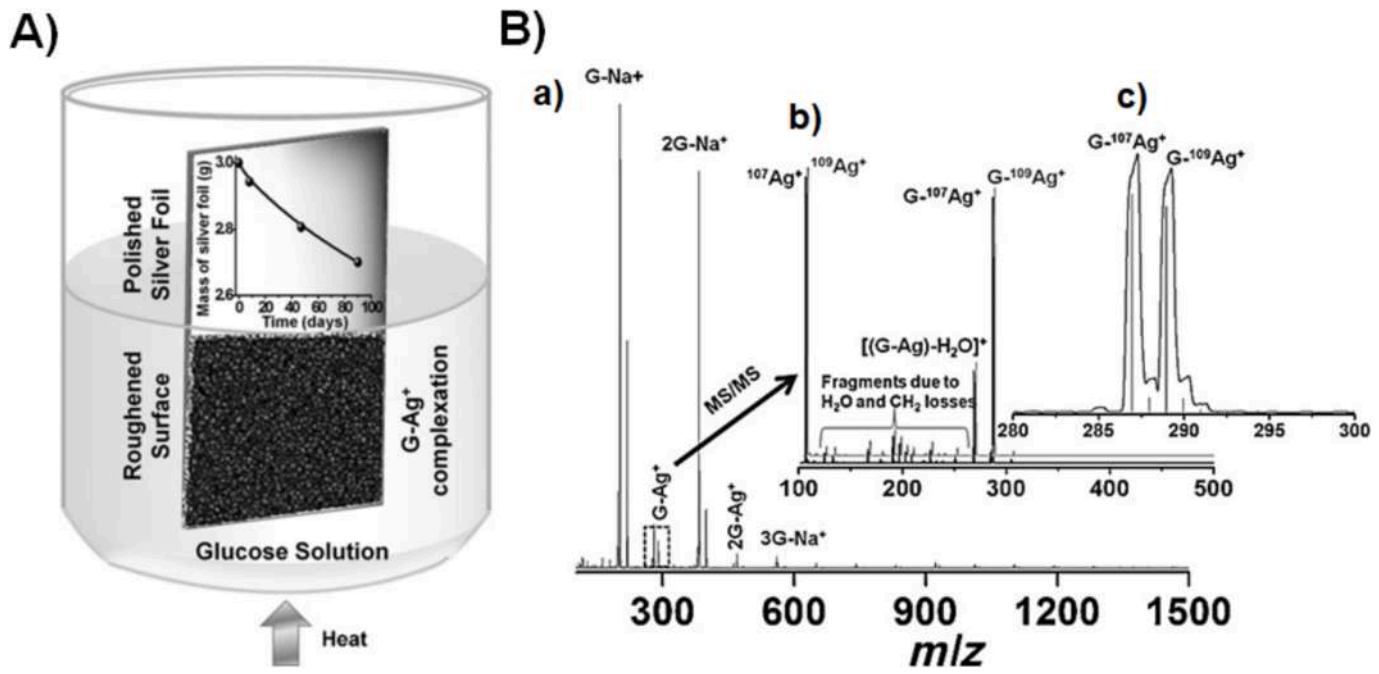


Fig. 2. A) Ag extraction by glucose (G) is depicted schematically (not to scale). After being partially immersed in a glucose solution at 70 °C, a silver foil piece gradually turned black in the immersed area. B) a) ESI MS analysis of G-Ag complexes. b) MS/MS of G-Ag^{+} indicating the loss of one G to yield Ag^{+}. c) Isotopic distribution of G-Ag^{+} complex. (Adopted from ref. 31, Copyright 2016 Wiley.)

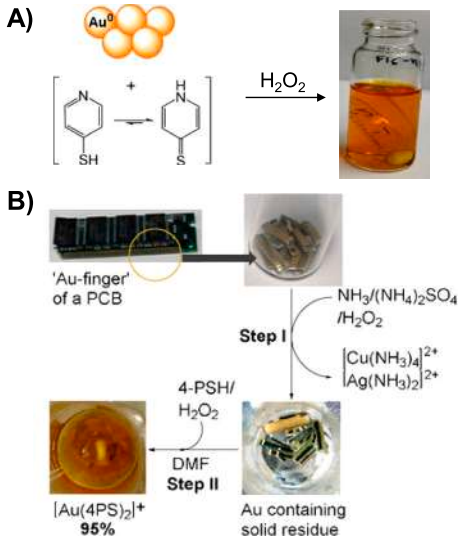


Fig. 3. A) A schematic representation of an efficient and selective dissolution of Au using 4-PSH and H_2O_2. **B)** Au dissolution in PCB samples Step I: Cu and Ag extraction with $NH_3/(NH4)_2SO_4/H_2O_2$. Step II: Quantitative Au dissolution in 30 min using the 4-PSH/H_2O_2 method. (Adopted from ref. 33, Copyright 2018 Wiley.)

two 4-PS ligands and a SO_4^{2-} counterion. The ligand was essential because it promoted oxidation and formed a stable complex with enhanced solubility. The authors were able to recover Au from printed circuit boards (PCBs) (Fig. 3B). PCBs only have 0.25 wt% of Au (and 0.008 wt% of Ag) compared with 23.4 wt% of Cu. Due to the higher Cu content than Au in this case, direct 4-PSH leaching of Au is not practical. To dissolve Cu and Ag and not gold, the authors therefore first treated the sample with $NH_3/(NH_4)_2SO_4$ and H_2O_2. Following filtration and immersion of the residue in a DMF solution of 4-PSH/H_2O_2, a significant 95 % yield of dissolved Au was recorded in 30 min. In another study from the same group, gold was dissolved quantitatively in ethanol using a catalytic amount of iodine and 2-mercaptobenzimidazole (2-MBI) as a ligand. [34] In terms of its mechanism, Au dissolved when I_2 oxidized Au (0) to create a $[AuI_2]^-$ species. This species then went through a series of ligand-exchange reactions to create a stable bis-MBI Au(I) complex. Free iodide was oxidized by H_2O_2 and then regenerated I_2 for the catalytic cycle. A reductant ($NaBH_4$) was added to the reaction mixture to quantitatively precipitate Au and partially regenerate the ligand (41 %).

Love et al. developed a new process for the dissolution of PMs in organic solvents rapidly by combining triphenylphosphine dichloride or oxalyl chloride with hydrogen peroxide, resulting in metal chloride salts. [10] At room temperature, almost complete dissolution of metallic Au, Cu and Pd occurred in minutes. Dissolution of Pt was achieved, though at a slower rate, with the chlorinating oxidant alone, but was slowed by the addition of hydrogen peroxide. Fig. 4A shows the CPU images before and after the leaching process. The leachate solution (Fig. 4B) extracted from electronic CPUs, the retaining of Au(III) chloride salt in the organic phase made it easier for it to be selectively separated from Ni and Cu. About 95 % pure gold was achieved by this process from CPUs (Fig. 4C and D).

Following this work, the same group discovered that the rapid dissolution of Au was possible using the mixtures of acetyl halides and hydrogen peroxide at room temperature in environmentally benign alcohols like ethanol, 1-butanol and 1-octanol. [35] Through the in-situ generation of halogens, both procedures quantitatively dissolve Au to create Au(III) halometalates. Compared with acetyl chloride, the dissolution rate with acetyl bromide is faster (within minutes). Significantly, following the recycling of the alcohol, this dissolution technique can be connected to a selective precipitation approach for the full extraction of Au from mixed-metal solutions. Based on these findings, this leaching process may be used in the future to purify gold from ores, used catalysts and electronic and nano waste.

2.3.2. *Photocatalytic dissolution*

Photocatalytic technology is an environmentally friendly solution that has enormous potential in the energy and environmental sectors, since light is a chemical-free reagent, that is becoming cheaper to employ due to the greatly improved efficiency of light-generating

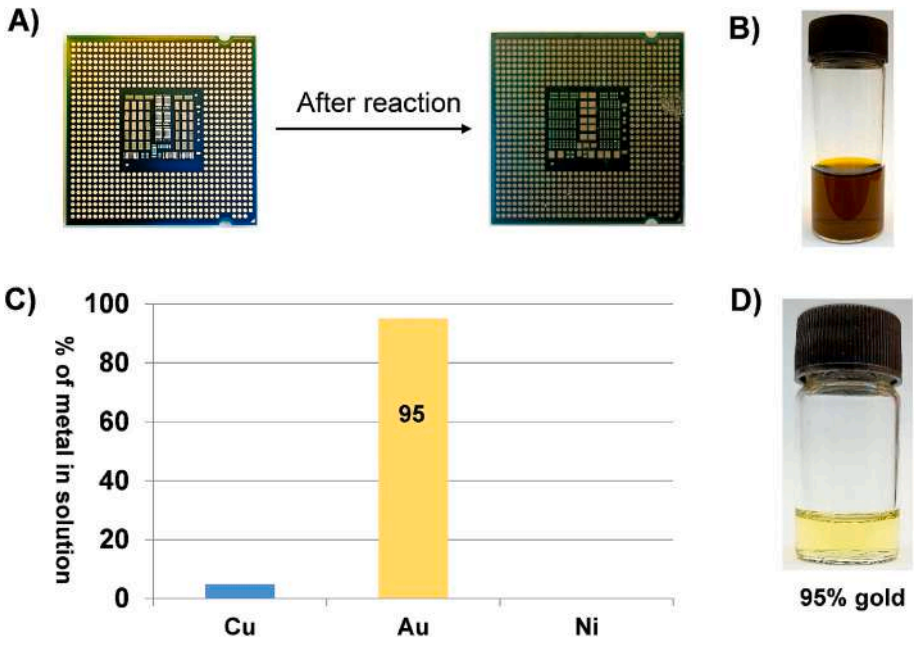


Fig. 4. **A)** Photographs of CPU before and after the leaching process. **B)** Leachate solution obtained from the CPU. **C)** ICP-OES data of Au solution after the separation process. **D)** 95 % pure Au solution after separation. (Adopted from ref. 10, Copyright 2022 Wiley.)

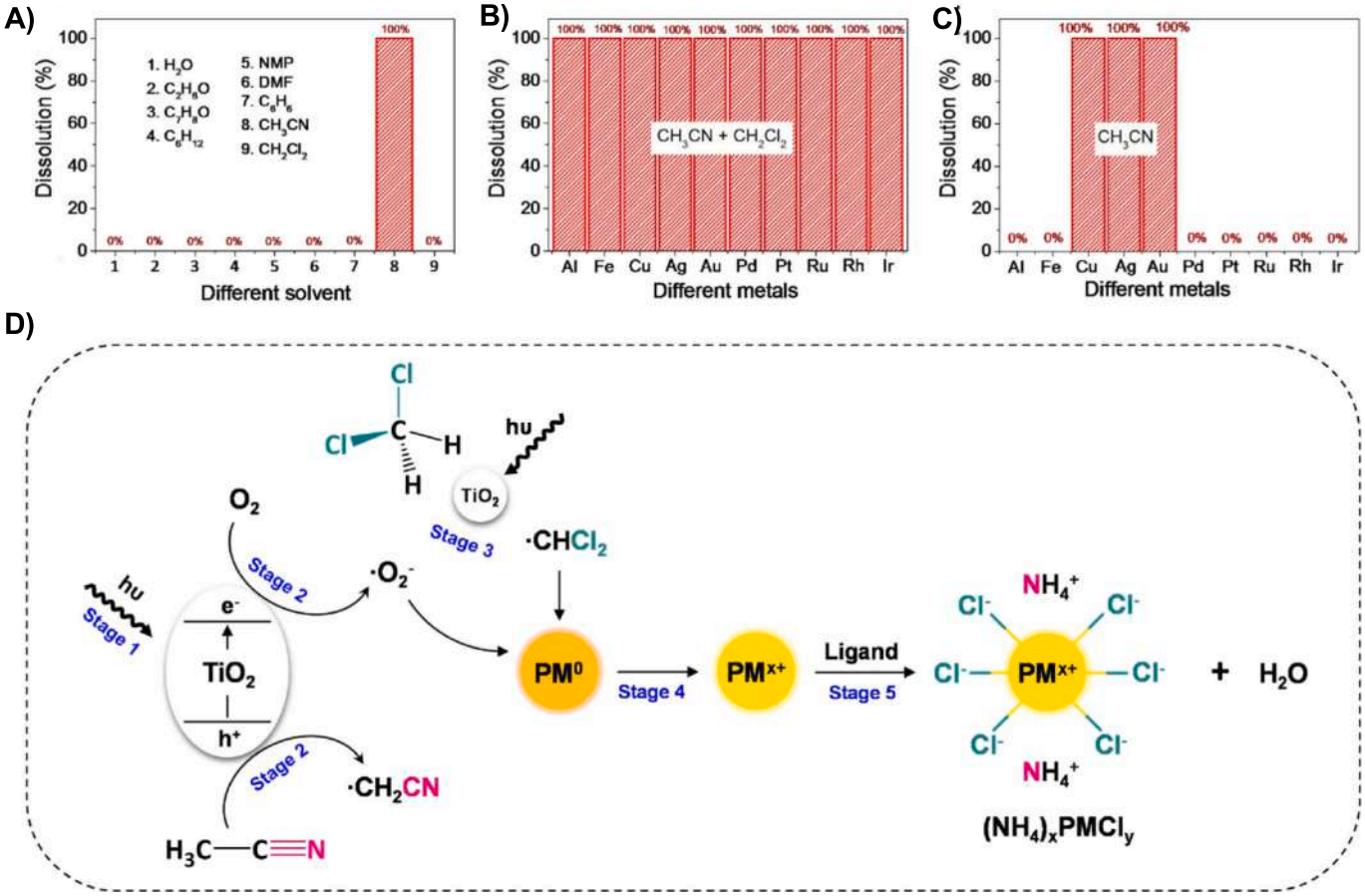


Fig. 5. **A)** The leaching of Au in different organic solvents in percentage. **B)** The leaching of Fe, Al, Ag, Cu, Au, Pt, Pd, Rh, Ru, and Ir in the mixture of DCM and MeCN using a photocatalyst. **C)** The leaching rate of Fe, Al, Ag, Cu, Au, Pt, Pd, Rh, Ru, and Ir in MeCN using a photocatalyst. **D)** A presentation of the mechanism of dissolution procedure using a photocatalyst. (Adopted from ref. 6, Copyright 2021 Elsevier Publishing Group.)

devices. Examples include light emitting diodes (LEDs), with white LEDs displaying a power-to-light conversion efficiency of around 40 %, which is significantly higher than the 2–5 % efficiency of traditional incandescent light bulbs. [36] Light stimulation of catalysts produces photogenerated electrons and vacancies, resulting in active species that include hydroxyl and superoxide radicals. These reactive entities can undergo oxidation-reduction processes with PMs, providing a novel technique for their dissolution. [37–40]

Bian et al. described a photocatalytic process for the selective leaching of seven PMs, including Ag, Pt, Au, Pd, Ru, Ir, and Rh from ternary automotive catalysts, ores, and scrap circuit boards (Fig. 5A, B and C). [41] Strong acids, bases, or toxic cyanide were not used for the entire process; instead, ultraviolet (UV) light and photocatalysts like titanium dioxide were employed for the dissolution of these PMs. Over 99 % of the necessary elements from waste sources could be dissolved, allowing for the recovery of PMs with purity (≥98 %) through a simple reduction procedure. Unfortunately, the breakdown of organic solvents is required for the dissolving process. Acetonitrile (MeCN) and dichloromethane (DCM) were converted into highly reactive organic radicals via photocatalysis, which facilitated in the dissolution of PMs as their corresponding chloridometalate complexes. Selective recovery of Au from e-waste was achieved using this method. The mechanism of the overall process is shown in Fig. 5D. Stage 1 of the process begins with UV light excitation of TiO_2, which produces holes and electrons. The photogenerated holes interact with MeCN in mixed solution to produce $CHCN^{\bullet}$ radicals, while the photogenerated electrons interact with O_2 to generate $O_2^{\bullet-}$ (stage 2). DCM breaks down into oxidizing $CH_2Cl^{\bullet}$ (stage 3), while the oxidation of PM(0) to PM^{x+} (stage 4) and the formation of $(NH4)_xPMCl_y$ were accomplished by these active species in tandem (stage 5).

The successful photocatalytic dissolution of Pd and Au was also achieved in water by the same group. [42] In order to create intermediate active substances to oxidize and dissolve Pd and Au by photocatalysis, bromine and iodine ions were utilized as reactants. Electron paramagnetic resonance (EPR) spectroscopy was utilized to exemplify the crucial role that the intermediate radical active substances play.

2.3.3. *Mild dissolution in ionic liquids and deep eutectic solvents*

Unfortunately, the use of organic solvents presents many environmental concerns related to toxicity, volatility and global warming, and impacts on the overall LCA of the dissolution process. [43,44] In an attempt to overcome these challenges, ionic liquids (ILs) have been explored as alternatives to conventional organic solvents. [45–47] The applicability of ILs in oxidative metal dissolution have mainly focused on alkyl phosphonium, alkylammonium, and alkyl methylimidazolium cations combined with halogen or sulfur-based anions. [45] An IL can act as oxidizing agents without the need for an added oxidant when the anionic component is a trihalogen ion. For example, the phosphonium trichloride room-temperature IL [P444,14][Cl_3] was utilized in the dissolution of the noble metals Au and Pt, base metals Fe, Cu, In, Zn, Ga, Sb, Ge, and Ta, the rare-earth metals Sm and Dy, and the alloys GaAs and InAs. [48] Another representative trihalide IL, [P444,10][Br_3] was tested for the oxidative dissolution of the noble metals Au, Pd, Pt, and Rh as well as the base metals Fe, Cu, Sb, Co, Zn, In, Ga, Bi, Ge, and Sn. [49] In this latter case, all metals were successfully dissolved except Pt and Rh which were described as being “more noble” than Au and Pd. The polyhalide IL [Hmim][Br_2I] was found to leach Cu, Au, and Ag foils at 40°-50 °C, although dissolution yields were below 50 %. [50] Room temperature ILs with polypseudohalide anions were formed on mixing BrCN with [$NBuEt_2Me$][Br] IL. [51] The resulting IL was found to dissolve Au overnight at 60 °C to form Au(I) and Au(III) cyanido as well as bromidocyanido species. Alternatively, ILs can be exploited solely as solvents in metal dissolution with the addition of an oxidizing agent and additional ligands. Several studies were undertaken to investigate the leaching of Au from ores, primarily using imidazolium cation ILs with varying anions. [52–54] Using [Bmim][HSO_4] with thiourea as the complexing agent and $Fe_2(SO_4)_3$ as the oxidizing agent, [52] highly selective leaching for Au (86 %) and Ag (60 %) as thiourea complexes were achieved. The efficacy of dissolution on variation of the anion, such as $CH_3SO_3^-$, BF_4^-, $N(CN)_2^-$, Cl^- and $[HSO_4]^-$, was studied with the outcome being that ILs with the $[HSO_4]^-$ anion performed best. This suggested that the solubility of the resulting complexes and the capacity of the IL to ion-pair with the metal cation are important factors. [53]. The poor performance of the IL [Bmim][Cl] was thought to be due to the insolubility of the Fe-based oxidant in the IL, while H_2O_2 was deemed unsuitable as it would oxidize the thiourea, requiring the need for alternative oxidants to be explored. [54] In this case, the optimum system was found to be [Bmim][Cl]/NaI/$[HSO_5]^-$ which leached up to 85 % Au from gold ore. More recently, a novel method for providing greater selectivity of dissolution was discovered utilizing biomass-derived ionic liquids and the green oxidant H_2O_2 to dissolve single metals from Cu, Ag, and Au combinations. [55] Magdalena et al. studied the leaching of Cu from e-waste with hydrogen sulfate ionic liquids in presence of H_2O_2. [56]

Deep eutectic solvents [13,57,58] (DESs), consisting of hydrogen bond (HB) donors (such as amides and organic acids) and acceptors (such as organic alcohols and choline chloride), have emerged as sustainable substitutes for conventional solvents. These solvents enable extraction of PMs through their unique coordination properties, proton transfer mechanisms, and oxidative potentials. Acidic DESs possess strong proton activity, and can efficiently break metallic bonds to forming metal-ligand complexes, thereby enhancing metal dissolution. The protonation process releases protons which diffuse into the solvent, further facilitating metal extraction. In contrast, non-acidic DESs exhibit lower proton activity, thereby limiting their dissolution efficiency, resulting in metal extraction being primarily reliant on coordination interactions. Enhancing the oxidative strength and coordination capacity of DESs remain crucial for optimizing their ability to dissolve PMs effectively. DESs have been found to be successful at dissolving and extracting metals, such as Au oxidation, sulfide processing, rare earth carbonates, and treating electric arc furnace and flue dusts. [59–65] Rivera et al. developed a DES with $CaCl_2{\cdot}6H_2O$ as the HB acceptor and ethylene glycol as the donor. [66] $FeCl_3$ and $CuCl_2$ acted as redox catalysts, allowing for selective Cu extraction from PCBs. Au and Ni were retrieved using simple filtration. The low-viscosity solvent system (40 mPa·s) greatly increased the Cu dissolution rate. $FeCl_3$ and $CuCl_2$ enhanced the leaching process due to their high solubility and rapid electron exchange. Rivera et al. used this DES system to investigate the effect of ultrasound-assisted catalytic dissolution of metals from PCBs. [67] Ultrasonic-induced density fluctuations (UIDF) assisted cavity formation by improving mass transfer efficiency and facilitating metal dissolution through random reaction zones. The results showed that high-power ultrasound greatly boosted the dissolution rate for Cu, by ca. 10,000 times compared with standard approaches. [66] Ultrasound triggers both physical and chemical processes, including loss of protective surface layers, resulting in better mass transfer, exposure of new reactive sites, and the formation of free radicals, all of which boosted the recovery of Au from PCBs. Furthermore, localized UIDF aided in the creation of cavities, boosting mass transfer efficiency and aiding the flow of reactants and dissolved compounds, with cavities varying in size and position. Recently, Repo et al. revealed a new method for sequentially dissolving single metals from Cu, Ag, and Au combinations with biomass-derived ionic solvents and green oxidants. [55] Cu was dissolved selectively in the presence of Ag and Au using a mixture of choline chloride, urea, and H_2O_2, followed by Ag dissolution in lactic acid/H_2O_2. Finally, the metallic Au, which is not soluble in either of the preceding solutions, is dissolved in choline chloride/urea/oxone. The metals were then collected from dissolutions in a simple and quantitative manner, while the solvents were recycled and re-used. The feasibility of this method was displayed by recovering metals from PCBs, Au fingers, and solar panels.

2.3.4. Dissolution using mechanochemistry

Mechanochemistry is an excellent complement to typical liquid-phase reactions and has proven to be important in enabling various kinds of chemistry by fully eliminating the need for expensive, toxic, and combustible solvents, so reducing the environmental burden. [68] In order to create complex molecules and nanostructured materials, mechanochemistry uses mechanical energy to promote chemical and physical transformations. It also promotes the dispersion and recombination of multiphase components and uses highly reactive surfaces to speed up reaction rates and efficiencies. Mechanochemistry generally involves solid-solid interfacial reactions. Tomislav et al. used mechanochemistry to convert PMs into water-soluble halide complexes or metal-organic catalysts at room temperature without the use of solvents (Fig. 6a). [68] With a focus on Pd and Au, this study showed that the mild oxidant oxone and halide salts ($(NH_4Cl$, KCl) worked together to activate PMs pellets, powder, or wire without the use of any harsh reagents or solvents (Fig. 6b-e). The method is much easier, cleaner, and safer than traditional methods for transforming metals into complexes. In an alternative study, a novel method for extracting Au from anode slime was developed by Shufeng et al. using in situ oxidative chlorine generated by a mechanochemistry approach. [69] Au in anode slime was efficiently converted into water-soluble $AuCl_3$ by dry ball milling the mixed anode slime with $KMnO_4$ and NH_4Cl, and then separated from solids by simple water leaching.

2.3.5. Electrochemical dissolution

Electrochemical dissolution is significantly advancing PM leaching. This technique uses electric currents to oxidize PMs at the anode, allowing them to shift into an ionic form in solution. PMs dissolve by cyclic potential shifts between oxidation and reduction. However, increasing the surface free energy in PM nano particles promotes Ostwald ripening, substantially lowering the efficiency of dissolution. [70] Surface-modifying agents can successfully address these issues, by e.g. preventing dissolved Pt from recrystallizing under reducing conditions while still allowing for improved dissolution during oxidation. The results showed that PMs that used this process dissolved at twice the rate of those without it. This dynamic surface regulation provides a viable technique for electrochemical PM leaching.

Song et al. established a novel method for dissolving PMs using the oxidation potential differences between Cu^{2+} halides and PMs. [71] Electrochemical dissolution tests showed that substituting sulfate with bromide ions increased the Cu^{2+}/Cu^{+} redox potential from 0.4 V to 0.75 V. This study found that altering ligand types and concentrations enabled Cu^{2+} and Fe^{3+} to selectively dissolve metals. Gold corroded efficiently in Cu^{2+}/Fe^{3+}-Br^{-}, while Pd dissolved quickly in Cu^{2+}/Fe^{3+}-Cl^{-}. Dissolution rates improved with optimum oxidant and halide levels. Electrodeposition resulted in nearly full PM recovery at the cathode and regenerated Cu^{2+}/Fe^{3+} at the anode.

2.3.6. Bio-based dissolution

In addition to conventional chemical processes, bio-based strategies have gained popularity as ecologically friendly and sustainable alternatives to PM recovery. One well-known example is bio-cyanidation, in which cyanogenic bacteria, such as *Bacillus megaterium*, generate cyanide in situ to leach gold, achieving recovery levels of over 87 % from certain low-grade sources, which is comparable to typical chemical cyanidation. [72] Reviews of biogenic lixiviants emphasize the use of cyanogenic bacteria such as *Chromobacterium violaceum*, *Pseudomonas aeruginosa*, and Micrococcus spp., as well as microbial synthesis of iodine species and amino acids, in gold extraction. [73]

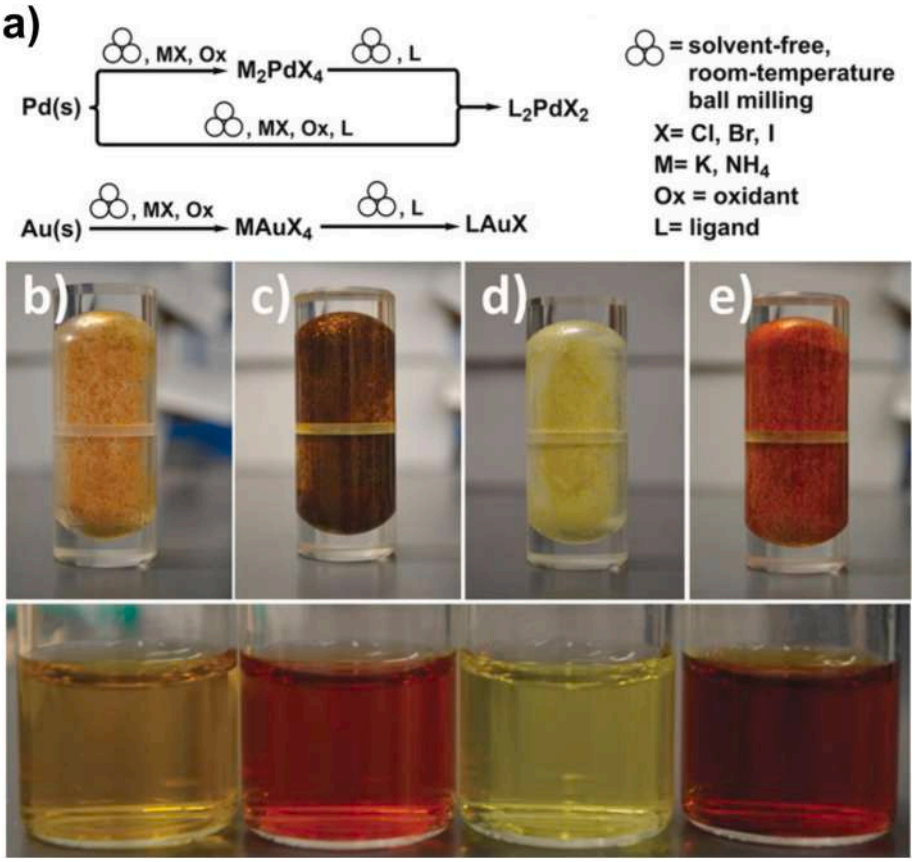


Fig. 6. a) A schematic representation of the formation of Pd and Au complexes using a mechanochemistry approach. Formation of Pd and Au complexes a using mechanochemistry approach presented in milling jars and dissolved in H_2O: **b)** $(NH_4)_2PdCl_4$, **c)** $(NH_4)_2PdBr_4$, **d)** NH_4AuCl_4 and **e)** NH_4AuBr_4. (Adopted from ref. 68, Copyright 2018 Wiley.)

Another environmentally benign option is through fungal and heterotrophic microbial leaching, in which species like Aspergillus niger and Penicillium spp. release organic acids such as citric, oxalic, and gluconic acids that act as natural chelating agents. These acids effectively dissolve metals, sometimes mobilizing more than 90 % of the target elements. [74] Bioleaching electronic waste with fungi yielded high concentrations of citric (up to ~152 mM), tartaric, oxalic, and gluconic acids, as well as significant yields of metals such as Zn, Cu, and Ni. [75] Broader studies have also shown the importance of fungal-produced citric acid in selectively dissolving PGMs and rare earth metals from residues and industrial waste. [76]

These microbial and biogenic ligand-based approaches adhere to green chemistry principles by reducing hazardous chemical input, and waste creation, and allowing for selective and potentially scalable recovery procedures. While these approaches are still in their early stages when compared with known hydrometallurgical procedures, they offer a fascinating and developing frontier in PM recovery, and so ought to be included alongside traditional techniques in any comprehensive consideration of green PM recovery.

Sustainable dissolution strategies for PMs can be generally classified based on their current level of maturity. Thiourea- and thiosulfate-based systems are among the most established and effective techniques and, while not without obstacles, they have consistently performed as greener alternatives to cyanide. Biogenic ligand-assisted leaching, mechanochemistry-assisted dissolution, mild dissolution and DESs systems, on the other hand, are intriguing but still emerging technologies that need to be validated under practical circumstances. Enhancing selectivity, increasing reaction kinetics, and demonstrating scalability remain critical issues for these techniques, as does the need for complete LCA to determine their genuine sustainability credentials. Section 6 of this review provides a more in-depth analysis of these strategies and their future possibilities.

3. Integration of computational approaches in metal extraction

Recent breakthroughs in computational chemistry are increasingly being used to predict metal-ligand interactions and lead the development of selective, environmentally benign extraction technology. For example, density functional theory (DFT) and related quantum-chemical methods have been used to design ligand extractants, calculate stability constants and elucidate bonding characteristics in chlorido complexes of Au(III), Pd(II), and Pt(II) in aqueous media, providing quantitative thermodynamic insights that guide leachant selection and optimization. [77] Furthermore, DFT has been utilized to study ligand interactions in gold leaching systems by looking at orbital interactions, electron back-donation, and energy decomposition in distinct Au-ligand complexes. [78]

Beyond static quantum-chemical modeling, molecular simulations such as enhanced-sampling molecular dynamics (e.g., metadynamics) are being used to characterize the conformational free-energy landscapes of extractants in solution. These methods illustrate how ligand flexibility and solvation effects affect the capacity of extractants to adopt metal-binding conformations, a key but often neglected aspect of ligand performance. [79]

Furthermore, ML models are gaining popularity for predicting metal-ligand stability constants. Notably, techniques that combine ML with ligand design tools (e.g., LOGKPREDICT coupled with HostDesigner) allow for rapid screening and ranking of ligands based on projected binding affinity and selectivity, which speeds up discovery procedures in hydrometallurgical applications. [80]

Taken together, computational tools such as DFT, molecular dynamics, and ML-assisted prediction provide a valuable supplement to experimental investigations by allowing for rational design of selective ligands and green solvents with less reliance on trial-and-error. Even this brief mention highlights the potential for modeling studies to facilitate the transition towards more sustainable PM recovery.

4. Separation methods

This section outlines the key strategies employed for separating PMs after dissolution, including precipitation, adsorption, and solvent extraction, with a focus on their mechanism, efficiency, selectivity, and environmental impact. Various separation methods are summarised in Table 2.

4.1. Precipitation and encapsulation

Precipitation is a crucial technique for recovering PMs due to its selective recovery, high purity control, efficiency, scalability, environmental considerations, and versatility. It allows for the selective removal of specific metals from a solution, ensuring purity and efficiency. Precipitation methods can be tailored to produce high-purity solids, making them essential for industries with exacting standards. These methods are also scalable, suitable for both small-scale refining operations and large-scale industrial applications. As precipitation methods often negate, or at least minimize, the need for organic solvents, they are more environmentally benign than the traditional biphasic solvent extraction approaches.

Stoddart et al. identified that $KAuBr_4$ and α-cyclodextrin (α-CD) form a host-guest complex $\{[K(H_2O)_6][AuBr_4](\alpha\text{-CD})_2\}_n$ in solution. This complex precipitated as needle-like crystals, generating a superstructure in which the α-CD nanochannels were filled alternately by $[K(H_2O)_6]^+$ and $[AuBr_4]^-$ ion pairs. These ion pairs were kept in place within the channels by a series of preorganised HBs (Fig. 7 Aa). [81] The formation and co-precipitation of $\{[K(H_2O)_6][AuBr_4](\alpha\text{-CD})_2\}_n$ indicated that the self-assembly process was governed by an optimal structural match between the stereoelectronic characteristics of $[K(H_2O)_6]^+$, $[AuBr_4]^-$, and α-CD, enabling their precise interaction and organization within the superstructure (Fig. 7A b-d). The axial [Au − Br···H − O] and equatorial [Au − Br···H − C] HBs induced second-sphere coordination, directing the formation of {[K(H2O)6][AuBr4](α-CD)2}n and its rapid precipitation. These interactions were critical to the structural assembly and stability of the complex. Starting with Au-bearing materials and mixtures of square planar anions ($[PtX_4]^{2-}$, $[AuX_4]^-$, and $[PdX_4]^{2-}$, X = Cl, Br), this particular precipitation method recognized a theme for the selective isolation of Au in the form of $KAuBr_4$. According to life-cycle analysis, this approach has the potential to significantly mitigate the environmental risks connected with Au nanoparticle production. [8] After this initial finding, more research showed that mixing β-cyclodextrin (β-CD) with small molecule additives, such as dibutylcarbitol (DBC), produced almost complete precipitation of the metalate, surpassing 99 % [Fig. 7B]. [82] The same group achieved another Au recovery protocol based on rapid complexation of $[AuX_4]^-$ (X = Cl/Br) and cucurbit [6]uril (CB [6]) (Fig. 7 Ca). [83] Mixing CB [6] with $MAuX_4$ (X = Br/Cl, M = H/K) in aqueous solution resulted in the formation of yellow or brown precipitates. The presence of weak [O=C···X-Au] ion-dipole interactions and [C-H···X-Au] HBs contributed to this outcome (Fig. 7C(b)). Under optimal conditions, the efficiency of the precipitation process reached 99.2 %. The same group reported on the simultaneous co-crystallization and co-precipitation of $[PtCl_6]^{2-}$ dianions and CB [6], which was based on the selective recognition of these dianions via non-covalent bonding interactions on the outer surface of CB [6]. [84] Weak [C-H···Cl-Pt] and [O=C···Cl-Pt] interactions drove the selective $[PtCl_6]^{2-}$ dianion recognition. CB [6] was found to selectively isolate $[PtCl_6]^{2-}$ dianions from a mixture containing $[PdCl_4]^{2-}$, $[PtCl_6]^{2-}$, and $[RhCl_6]^{3-}$. In a separate study, two macrocyclic tetralactam receptors have been demonstrated by Smith et al. to be capable of selectively encapsulating anionic, square-planar bromide and chloride complexes of Pd (II), Pt (II), and Au (III). [85] The prearranged structure of both receptors was intended to complement their PM guests. The receptors offered a variety of arene-electron donors that interacted with the electropositive metal and HB donors that interacted with the surrounding electronegative ligands, rather than coordinating directly with

Table 2
Separation of PMs using various mechanisms with toxicity.*

Entry	Reagents	Targeted PMs	Mechanism	Toxicity of the reagent	Ref.
1	α-cyclodextrin	Au	Supramolecular recognition	Low	69
2	Cucurbit[6]uril	Au	Supramolecular recognition	Low	71
3	Cucurbit[6]uril	Pt	Supramolecular recognition	Low	72
4	Tetralactam receptors	Au, Pd, and Pt	Supramolecular recognition	Low	73
5	Niacin	Au	Electrostatic attraction and supramolecular interactions	Low	74
6	Simple tertiary diamide	Au, and Pt	Electrostatic attraction and supramolecular interactions	Low	75
7	Triamidoarene	La	Electrostatic attraction and supramolecular interactions	Low	76
8	Triphenylphosphine oxide	Au	Electrostatic attraction and supramolecular interactions	Low	77
9	Fe-BTC/PpPDA MOF	Au	Adsorption	Low	86
10	3D bio-MOF of L-methionine	Au	Adsorption	Low	87
11	COP-180	Au	Adsorption	Low	88
12	Porphyrin-phenazine-based polymers	Au	Adsorption	Low	89
13	rGO	Au	Adsorption	Low	91
14	Polymeric membranes comprised of the UiO-66 series	Pd and Pt	Adsorption	Low	92
15	Peralkylated pillar[5]arenes	Ag	Adsorption	Low	94
16	Pyridine-based porous organic polymers	Pd	Adsorption	Low	95

* Toxicity levels were assigned based on reported risks using PubChem and MSDS. We categorize chemicals as low (usually safe/biodegradable, e.g., water, ethanol), moderate (some dangers, managed with normal safety, e.g., thiourea, acetonitrile), and high (poisonous, carcinogenic, or persistent, e.g., cyanide, aqua regia, $SOCl_2$).

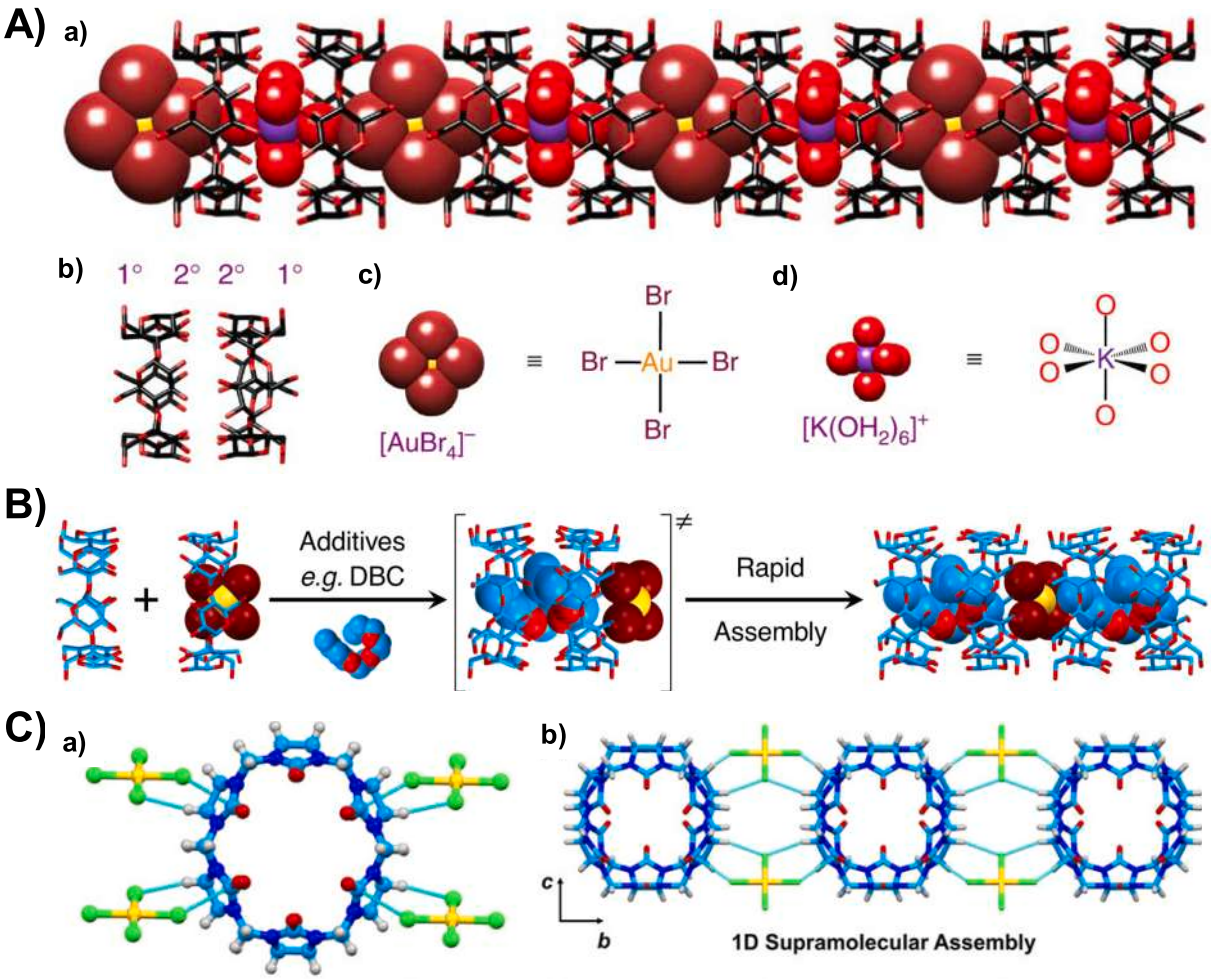


Fig. 7. A) a) A schematic presentation of a 1D structure extending along the c-axis in which the α-CD (**b**) tori form a continuous channel occupied by alternating $[AuBr_4]^-$ (**c**) and $[K(H_2O)_6]^+$ (**d**) ions. C, O, Br, Au, and K stand for black, red, brown, yellow, and purple, respectively (Adopted from ref. 81, Copyright 2013 Nature Publishing Group.) B) Graphical representation of the process of additive-induced precipitation of $[AuBr_4]^-$ anion using DBC additives to the β-CD. (Adopted from ref. 82, Copyright 2023 Nature Publishing Group.) **C)a)** The single crystal XRD structure of $HAuCl_4$ and CB [6] adduct. Interactions of CB [6] with four $[AuCl_4]^-$ anions via ion-dipole interactions and [C-H···Cl-Au] HB interactions. **b)** Assembly of a 1-D structure extending along the b axis, with two parallelly aligned $[AuCl_4]^-$ anions connecting adjacent CB [6] molecules. Cl, H, N, C, O, and Au stand for green, grey, blue, pale blue, red, and yellow, respectively. (Adopted from ref. 83, Copyright 2020 American Chemical Society.) (For interpretation of the references to colour in this figure legend, the reader is referred to the web version of this article.)

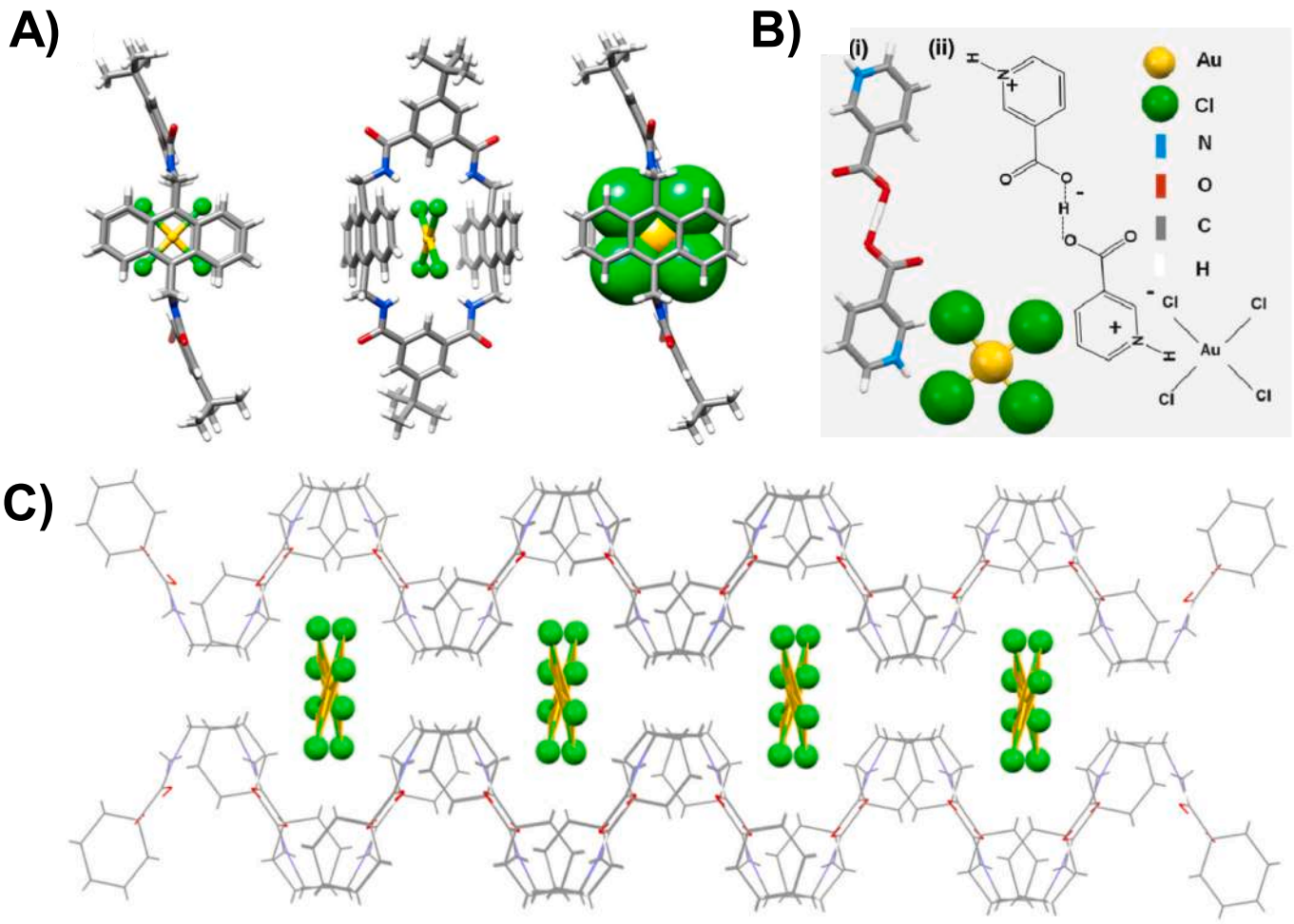


Fig. 8. A) Single crystal XRD structure of macrocyclic tetralactam receptors and $[AuCl_4]^-$. H, C, O, Cl, and Au stand for white, grey, red, green, and yellow, respectively. (Adopted from ref. 85, Copyright 2018 American Chemical Society.) **B) i)** Single crystal XRD and **ii)** ChemDraw structure of niacin and $[AuCl_4]^-$. (Reproduced from ref. 86, Copyright 2021 American Chemical Society.) **C)** Single crystal XRD structure of simple diamide and $[AuCl_4]^-$. H, C, O, Cl, and Au stand for white, grey, red, green, and yellow, respectively. (Adopted from ref. 87, Copyright 2021 Nature Publishing Group.) (For interpretation of the references to colour in this figure legend, the reader is referred to the web version of this article.)

the metal centre. The encapsulation of $[AuCl_4]^-$ within the ligand was validated by single crystal X-ray diffraction (SCXRD), demonstrating a unique method of supramolecular recognition (Fig. 8A).

By creating compounds with the biomolecule niacin, Pradeep et al. were able to precipitate aqueous $HAuCl_4$, resulting in the overall formula [2Niacin + H][$AuCl_4$], which was a very economical and environmentally benign approach for recovering gold (Fig. 8B). [86] This precipitation is selective for Au^{3+} in the presence of Ni^{2+}, Cu^{2+}, and Zn^{2+}, as well as alkaline earth (Mg^{2+}/Ca^{2+}) and alkali (Na^+/K^+) ions that are commonly found in metal waste streams. With further support from spectroscopic analysis, SCXRD investigations demonstrated that supramolecular interactions and electrostatic attraction were the driving forces behind the co-precipitation. This method made it possible to recover roughly 97 % of gold from e-waste that contained Au, Cu, and Ni in just two minutes. A simple tertiary diamide was shown by Love et al. to precipitate Au selectively from an acidic aqueous solution comprising 29 metals. [87] SCXRD showed the precipitate comprised an infinite chain of diamide cations interspersed with $[AuCl_4]^-$ (Fig. 8C). For [HL][$AuCl_4$] (L = diamide ligand), the methyl and phenyl substituents within the ribbon-like structure of the protonated diamides provide rhombohedral clefts that hosted the $AuCl_4^-$ guest through noncovalent interactions. When exposed to water, the precipitate released gold, allowing the ligand to be reused. At 2 M HCl, the diamide displayed excellent selectivity for gold, whereas gold, iron, tin, and platinum were completely precipitated at 6 M HCl, suggesting that this single variable could be used to regulate the selectivity of metal precipitation.

Recently, Love et al. reported a novel technique for the selective recycling of copper and gold which mitigated the need for organic solvents commonly used in solvent extraction procedures (Fig. 9 A and C). [88] The compound $[(TPPO)_4(H_5O_2)][AuCl_4]$ (9Bi) (designated **1**, where TPPO = triphenylphosphine oxide), was used to selectively extract gold from a multi-metal solution (containing Fe(III), Cu(II), Zn (II), Ni(II), Pd(II) and Pt(IV)) in HCl. Iron, zinc, and gold could be precipitated under controlled conditions by adjusting the acid concentration. Susequently, 2,3-pyrazinedicarboxylic acid (2,3-PDCA) was used to preferentially precipitate copper as the polymeric coordination compound $[Cu(2,3\text{-}PDCA\text{-}H)_2]n \cdot 2n(H_2O)$ (9Bii). Combining these two precipitation techniques allowed for the extraction of 99.5 % Au and 98.5 % Cu from an end-of-life computer processing unit. These precipitation methods show promise for future industrial applications in purifying Au and Cu from e-waste due to their high selectivity, convenience of use, and ability to recycle and reuse the precipitants.

4.2. Adsorption

Adsorption is a crucial method for recovering PMs due to its high selectivity, efficiency, economic viability, and environmental benefits. [89–94] It can capture target metals from complex mixtures or low-

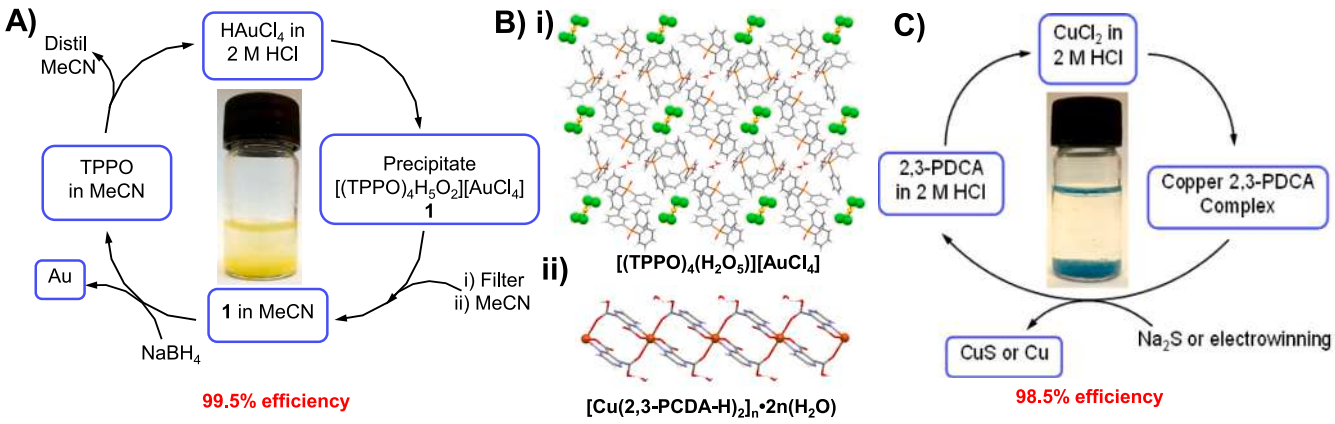


Fig. 9. **A)** Gold recycling using TPPO in 2 M HCl, followed by reduction of the Au(III) complex with $NaBH_4$ to generate Au(0) and recycling TPPO. **B) i)** SCXRD of **1** showing two pockets in which $H_5O_2^+$ and $AuCl_4^-$ reside, colour codes: P, Cl, green; orange; O, red; C, grey; Au, yellow; and H, white. **ii)** Crystal structure of [Cu(2,3-PCDA-H)$_2$]n•2n(H_2O). **C)** Recycling of Cu from 2 M HCl using 2,3-PDCA. (Reproduced from ref. 88, Copyright 2023 Wiley.) (For interpretation of the references to colour in this figure legend, the reader is referred to the web version of this article.)

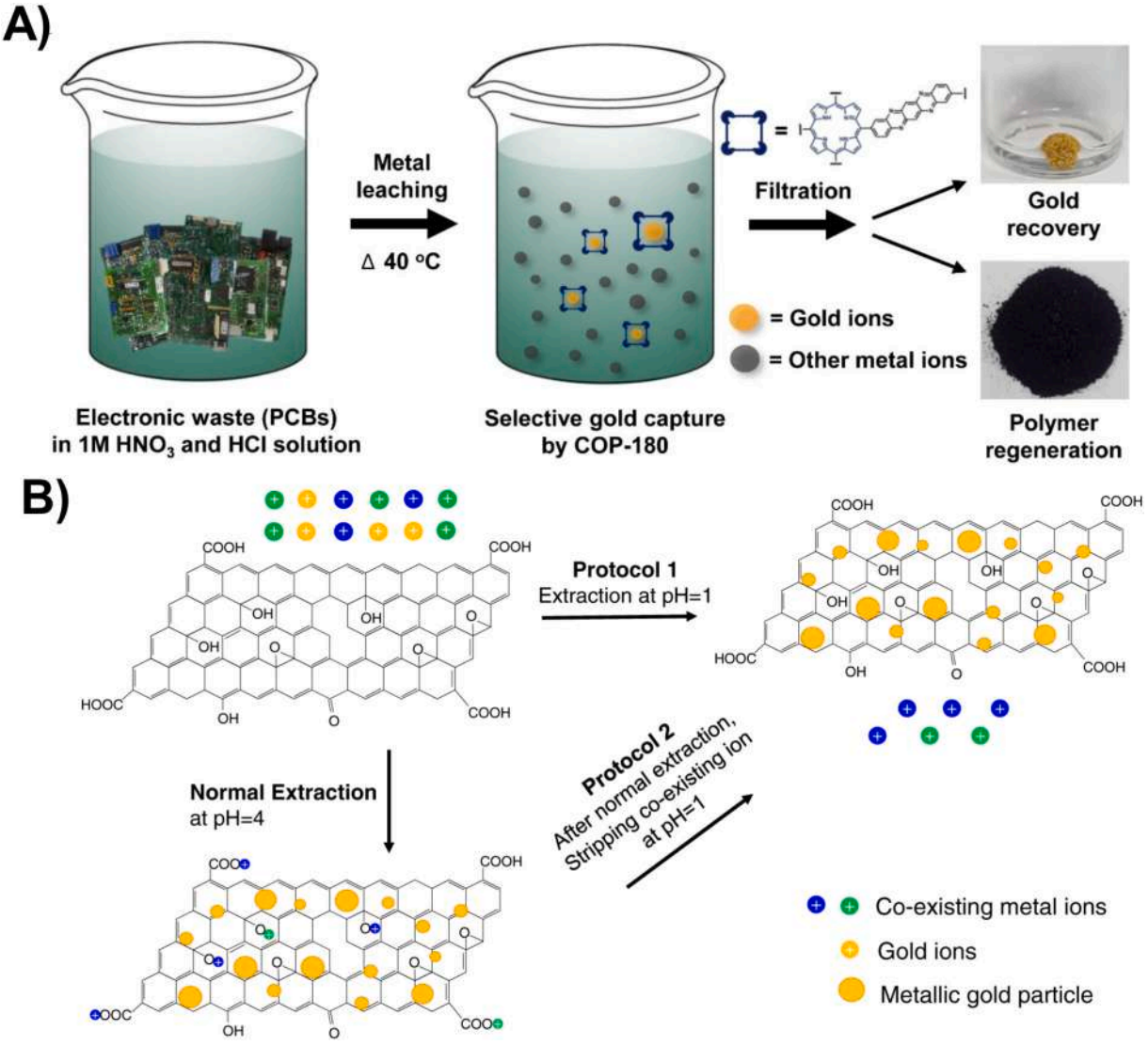


Fig. 10. **A)** Recovery of gold using COP-180 from PCBs. The gold was >99.6 % pure. (Adopted from ref. 99, Copyright 2020 National Academy of Sciences.) **B)** A schematic representation showing two additional protocols to enhance selectivity by modifying pH conditions. Co-existing ions are either prevented from adsorption (protocol 1) or removed later after Au reductive adsorption (protocol 2). (Adopted from ref. 102, Copyright 2022 Nature Publishing Group.) (For interpretation of the references to colour in this figure legend, the reader is referred to the web version of this article.)

concentration solutions, making it ideal for diluted sources like mine tailings or industrial wastewater. Many adsorption technologies can operate at ambient temperatures and pressures, so reducing operational costs. They are also more environmentally benign than traditional extraction methods, reducing the need for harsh chemicals. Adsorption techniques can be adapted to various scales and applications, making it suitable for various scenarios. Adsorption is the most common technology used in processes involving solid-liquid interfaces. [95]

Adsorption of $[Au(CN)_2]^-$ on activated carbon is a simple and cost-effective approach The technique benefits from the use of large activated carbon particles, which can be easily separated from the leach liquor via screening or filtration. [96]. Queen et al. reported a design blueprint for several highly porous composites comprising a metal-organic framework (MOF) template and redox-active polymeric building block. Fe-BTC/PpPDA [(BTC = 1,3,5-benzenetricarboxylate), (PpPDA = poly(para-phenylenediamine))] is one such MOF composite that has been shown to rapidly extract trace amounts of gold from a variety of complex water mixtures, including fresh water, wastewater, and seawater, as well as solutions used to leach gold from e-waste and sewage sludge ash. [97] The material had a remarkable removal capacity of 934 mg Au/g of composite, and it extracted Au at rates as little as 2 min from these complex mixtures. The composite efficiently concentrated Au to 23.9 K purity, and is highly cyclable. In another study, a new chiral 3D bio-MOF with functional channels derived from L-methionine was sensibly synthesized by Marta et al. [98] Au exhibits a strong attraction to sulfur-containing compounds, and the flexible thioether groups present in the channels enable the selective recovery of Au (III) and Au(I) species. This high selectivity continues even in the presence of other metal ions commonly present in e-waste, confirming efficient Au recovery. Alternatively, Hong et al. presented a porous polymer containing porphyrins (COP-180) that selectively captured PMs from e-waste leached solution (Fig. 10A). [99] The nanoporous polymer was produced in two steps using low-cost monomers and without the need of expensive catalysts, making it suitable for scalable production without compromising functionality. This reductive capture method recovered Au at ten times the theoretical maximum, with a record of 1.62 g/g. The adsorbed PMs on the porous polymer can be quickly desorbed and recycled for repeated batches because 99 % of the uptake occurred in the first 30 min. According to DFT calculations, energetically advantageous multinuclear-Au binding improved adsorption as clusters, resulting in rapid capture, while Pt capture still primarily occurred at single porphyrin sites. The same group reported Au and other PM recovery using a family of porphyrin-phenazine-based polymers from e-waste. [100] The performance of these adsorbents was shown to be affected by the pH of the solution and the illumination conditions, with the maximum capacity of 1.354 g/g being attained under nonstop UV exposure at acidic pH. Similarly, a 2D acridine-based COF was developed to detect and trap gold selectively and efficiently. [101] Li et al. recently devised a technique using reduced graphene oxide (rGO) to enable the selective extraction of Au ions at ultrahigh capacity, extracting more than 1000 mg of Au per gram of rGO at a concentration of 1 ppm. [102] The excellent gold extraction performance of rGO is due to its graphene domains and oxidized areas. The graphene domains actively reduce Au ions to metallic Au, whilst the oxidized regions boost rGO dispersibility, allowing for more effective adsorption and reduction of Au ions at graphene domains. Au can be selectively recovered by controlling the protonation of the oxidized portions of rGO, preventing contamination from the 14 other elements commonly found in e-waste. These findings were used to establish the scalability and cost-effectiveness of recycling Au from real-world e-waste via rGO membranes in a continuous flow-through process. A schematic representation is shown in Fig. 10B where two additional protocols were used to enhance selectivity by modifying pH conditions.

A collection of polymeric fibrous membranes comprising the UiO-66 series was synthesized, and the compatibilities between MOF and polymer were examined by Liu et al. [103] These membranes were tested for their abilities to adsorb and desorb Pt(IV) and Pd(II) from a strongly acidic medium. Strong π–π interactions between MOF NP and polyurethane (PU) with a high configuration of energy were responsible for the high chemical stability and strong acid resistance of polyurethane (PU)/UiO-66-NH_2. The effectiveness of these MOF membranes was established in both gravity-driven and continuous-flow systems, with outstanding recycling selectivity and performance. The membranes showed excellent adsorption/desorption performance, with no nanofiber breakage or aggregation, as well as no MOF NP leakage. The use of zero-valent iron nanoparticles on a large scale for gold enrichment and recovery from industrial wastewater was achieved by Zhang et al. [104] In these materials, a metallic iron core is surrounded by a thin layer of iron oxides/hydroxides in the core-shell structure of iron nanoparticles. The two nanocomponents work synergistically to separate, enrich, and stabilize metal ions such as Au, Ag, Ni, and Cu. Only a small amount of iron nanoparticles were required for the recovery of metals due to their advantages of small size, large surface area, and high reactivity.

Hua et al. were the first to present the metal ion-pair recognition using a pillarene. [105] Three peralkylated pillar[5]arenes (Fig. 11A) formed complexes with CF_3COOAg. X-ray crystallography of single crystals revealed that CF_3COOAg generated a unique dinuclear silver motif that intruded into the pillar[5]arene cavity within these structures (Fig. 11B). Multiple O···H–C and F···H–C HBs arise between the counterion and the pillar[5]arene host, in addition to π…Ag interactions, which were crucial in stabilizing and preserving the integrity of the host-guest complexes. Furthermore, through Ag ion-pair recognition, perethylated pillar[5]arene (EtP_5) acts as a solid absorbent capable of efficiently absorbing CF_3COOAg from solution (Fig. 11C), indicating its potential utility in precious metal recycling. Ma et al. demonstrated the adsorption of Pd using pyridine-based porous organic polymers (POPs). [106] POPs were created strategically; with the nitrogen site in the pyridine monomer acting as a Lewis base to enable coordination with Pd. This study investigated the effects of introducing an amino group and how positional variation affects the entire system for Pd capturing. Incorporating the amino group enhanced the nucleophilicity of the pyridine binding site, resulting in improved kinetics, excellent selectivity, optimal absorption capacity, and better chemical stability. Furthermore, placing the amino group at the ortho site aided in the formation of a more robust Pd complex, as evidenced by X-ray photoelectron spectroscopy and SCXRD. A schematic representation is shown in Fig. 11D where selective recovery of Pd was shown using pyridine-based POPs.

Researchers are motivated to develop biosorption technology because of its high repeatability and low sludge production, which helps to prevent the release of secondary pollutants. Various studies showed that PM ions can be selectively adsorbed by a variety of proteins. [107] Histidine-containing proteins, for example, interact specifically with Pd^{2+} and Au^{3+}. Consequently, Au^{3+} and Pd^{2+} can be successfully extracted from PM refining solutions using protein-rich biomass. According to Dodson's review, the selective extraction of PMs can be enhanced by surface and biochelate modification, or the choice of particular parent biomass. [108] A recent study investigated protein amyloid nanofibrils (AF) generated from whey, a by-product of the dairy industry, as a new adsorbent for gold recovery from e-waste. [109]

4.3. Solvent extraction

SX is an important method for recovering precious metals because of its selectivity, efficiency, adaptability, scalability, and environmental benefits. It can successfully separate metals such as Au, Ag, Pd, and Pt from complicated mixes or low-concentration solutions, increasing recovery yields while reducing losses. SX can withstand a variety of conditions, temperatures, and pressures, making it appropriate for both small-scale and large-scale mining projects. It also enables the selective removal of metals from loaded organic phases, improving recovery efficiency and lowering reagent use. SX can be environmentally benign,

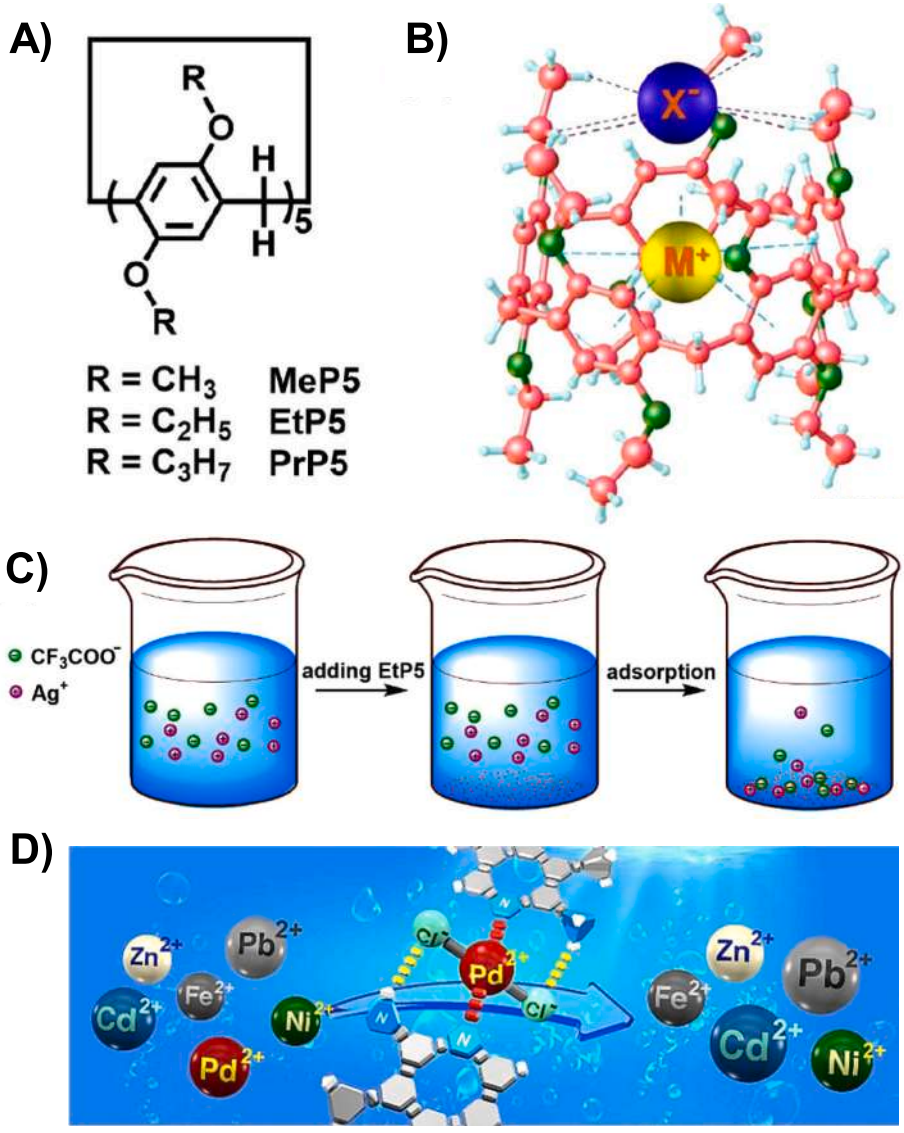


Fig. 11. A) Molecular formula of various peralkylated pillar[5]arenes used. **B)** The proposed structure of metal ion-pair recognition based on EtP_5. **C)** A schematic representation of adsorption of CF_3COOAg using treated EtP_5 powders in methanol by ion-pair recognition. (Reproduced from ref. 105, Copyright 2019 American Chemical Society.) **D)** A schematic representation of Pd^{2+} selectivity over other common ions using pyridine-based POPs. (Reproduced from ref. 106, Copyright 2020 Wiley.)

using fewer chemicals and producing less waste than other techniques. It works particularly well for digesting complicated ores and residues.

The effectiveness of the SX process is dependent on the efficiency and selectivity of the extracting ligand, and on achieving complete phase separation. Selectivity is engineered by utilizing coordination and supramolecular chemistry concepts, with customized ligands designed to bind selectively to target metal ions based on their charge, size, shape, and solvent interactions. [110–113] In commercial applications, solvents like dibutyl carbitol (DBC), methyl isobutyl ketone (MIBK), and 2-ethyl hexanol (2-EH) are routinely used to extract the halometalate $[AuCl_4]^-$ from gold ore halide leach solutions. Organic amides have been studied extensively as reagents for gold recovery by SX. Tertiary amides like DOAA (*N*,*N*-di-*n*-octylacetamide) and DOLA (*N*,*N*-di-*n*-octyllauramide) exhibit good selectivity for gold compared with base metals like Fe, Cu, Ni, and Zn and other PMs like Pt, Pd, and Rh. [114] In these instances, thiourea is required for the back extraction of gold, which could affect mass balance by forming some precipitation. The selective separation of gold as $[AuCl_4]^-$ from a mixed-metal solution obtained from HCl-leached PCBs was presented more recently using the simple primary amide 3,5,5-trimethylhexanamide (L1). [115] Protonation of L1 is crucial for selective gold extraction because it produces the neutral, hydrophobic complex assembly $[H(L1)_2][AuCl_4]$ that is stabilised via HBs and electrostatic interactions (Fig. 12A).

At 2.0 M HCl, this method extracted around 80 % of the gold from a complex mixture of metals, whereas the extraction of other metals such as Fe, Cu, and Zn, which are frequently found in PCBs, was low. One of the primary benefits of this approach is that the extractant concentration is low (0.1 M), and $[AuCl_4]^-$ can be transported into a pure aqueous solution using only water, which varies greatly from standard Au extractants like DBC and MIBK. According to further research, the analogous secondary (N-3,5,5-tetramethylhexanamide) and tertiary (N, N-3,5,5-pentamethylhexanamide) amides display better gold extraction capabilities when applied to single-metal solutions (Fig. 12B). [116] However, when used on mixed-metal solutions made from e-waste, these techniques showed low extraction efficiency, forming viscous third phases comprising Fe, Cu, and Sn. that did. More polar organic solvents inhibited the formation of third phases but lowered the selectivity for gold,. This study further underlined the significance of the

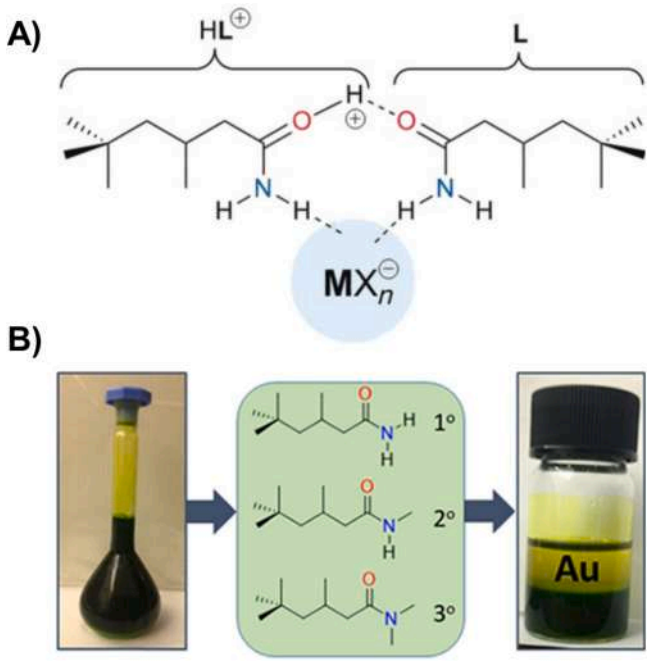


Fig. 12. A) Structure of the $[AuCl_4]^-$ and L1 for gold extraction. The presence of HBs and electrostatic interactions are shown between $H(L1)_2^+$ and $[AuCl_4]^-$ from MD calculations. (Adopted from ref. 115, Copyright 2016 Wiley.) **B)** Separating $[AuCl_4]^-$ using a primary, secondary, and tertiary amide. (Adopted from ref. 116, Copyright 2019 American Chemical Society.) (For interpretation of the references to colour in this figure legend, the reader is referred to the web version of this article.)

ability of the amide group to transfer a stabilize the proton in the organic phase as $H(L)_2^+$ (where L = amide) and showed that water plays an insignificant role in the formation organic phase assembly.

Recently, ILs are becoming promising candidates for the extraction of PMs from e-waste using a SX process. The hydrophobic ILs [Bmim][PF_6], [Bmim][Tf_2N], and Cyphos 101 were used as alternative extractants for Ag and Au from an aqua regia e-waste leach solution and were highly effective, with Au extraction efficiency exceeding 90 %. [117] Recovery of Ag in [Bmim][PF_6] and Cyphos 101 was greater than 93 %, whereas no recovery was seen in [Bmim][Tf_2N]. Recovery of Cu ranged between 60 % in [Bmim][PF_6] and 99 % in Cyphos 101. Unfortunately, the mechanism of the process was not explored in detail. Several ILs containing bis(trifluoromethanesulfonyl)imide (Tf_2N^-) or halide anions and cations 1-octylpyridinium, 1-methyl-1-octylpyrrolidinium or 1-octyl-3-methylimidazolium, were used to extract tetrachloroaurate or tetrabromoaurate anions from acidic media. By combining Au complexes in aqueous solutions with water-soluble halide ILs, the extraction f Au anionic species from aqueous solutions was first investigated. A liquid phase or a solid precipitate, similar to a hydrophobic IL with tetrahaloaurate anions, was produced as a result of this process. [118] The liquid-liquid extraction of anionic Au complexes with hydrophobic ILs was further investigated. Gold was successfully recovered from aqueous solutions regardless of pH or type of IL used. The extraction procedure involved an anion exchange, with Tf_2N^- (Y) anions replacing the Au complex (eq. 5). The IL is written as Cat^+Y^-.

$$Cat^+Y^- + KAuX_4 + HNO_3 \rightarrow [Cat][AuX_4] + K^+Y^- \quad (5)$$

Various reports by the same group described IL-based methods for separating PM complexes. [119–122] In the first step, Au was extracted from water using the hydrophobic IL 1,2-dimethyl-3-octylimidazolium bis(trifluoromethylsulfonyl)imide. Pt was subsequently extracted from a solution in KSCN by employing 1-methyl-3-octylimidazolium bis(trifluoromethylsulfonyl)imide. [123]

4.4. Other methods

Electrochemical recovery transports metal ions to electrodes, where they deposit without the need for additional redox agents. [124] Electrodeposition, electrodialysis, electrocoagulation, and electrosorption are the four most used electrochemical recovery procedures. [125–127]

Liu et al. established a sustainable electrodeposition technique for selectively recovering Ag—Pd alloy from polymetallic e-waste leachates containing Cu, Ni, Ag, Bi, and Pd. [128] The viability of this strategy was determined using linear sweep voltammetry. Controlling the applied voltage resulted in a high-purity Ag—Pd alloy with recovery of both metals over 97 after 5 h from 0.5 mol/L HNO_3 at 0.35 V. A chronoamperometry study demonstrated that Ag—Pd electrodeposition occurred in a 3D instantaneous nucleation and growth model, consistent with Scharifker-Hills theory, and resulted in a solid solution. Halli et al. used electrochemical principles to extract metals from complex solutions on pyrolyzed carbon using the electrodeposition-redox replacement technique. [129] The Pt/Ni deposition ratio on the pyrolyzed carbon electrode reached around 900 in the improved synthetic Ni electrolyte with 60 g L^{-1} Ni and 20 ppm Pt. This novel approach produced outstanding recovery results. According to Korolev et al., this method for selective PM extraction involved electrodepositing nonferrous metal ions with a steady current, which then interacted with PM ions in solution, reducing them to their elemental state under open-circuit conditions. [130] The redox replacement step between electrodeposition cycles allowed for the effective recovery of PMs in this procedure. Cotty et al. developed an electrochemical redox-based approach that used a polyvinylferrocene (PVF) electrode to selectively extract and concentrate Au from simulated mining ores and e-waste. [131] The PVF electrosorbent was highly selective for $[Au(CN)_2]^-$, with a 20:1 selectivity ratio over other ions such as Ag, Cu, Ni, and Fe. The $[Au(CN)_2]^-$ ion transferred charge to the ferrocene binding site, resulting in selective binding and oxidation. The electrochemical properties of the ferrocene sites enabled the recovery of approximately 99 % of the Au in just five minutes, yielding a product purity of 88.4 %. The PVF recovery technique was evaluated for cost-efficiency and performance, using just 15 kJ g^{-1} Au, which is less than 1/75 of the energy required by standard activated carbon-in-pulp methods. An asymmetric electrochemical method was developed to recover Au and Cu from CPU leached solutions. [131] Polyaniline (PANI) was electropolymerized on carbon cloth (CC), resulting in electrostatic interaction, complexation, and reduction characteristics. Even when competing metal ions were present, the CC/PANI anode selectively removed Au. In this case, $[AuCl_4]^-$ dissolved in acid was attracted to the anode and spontaneously reduced to Au. Cu was simultaneously deposited on the CC electrode in the cathode chamber. This unique technique recovers both Au and Cu, offering vital insights into the simultaneous extraction of numerous precious metals.

A recent study demonstrated the effective use of a polymer inclusion membrane (PIM) incorporating aminocarbonylmethylglycine as an extractant to efficiently isolate Au from an e-waste leached solution. [132] Here, gold is transported from the leach solution to an aqueous strip solution containing thiourea via the extractant-embedded PIM, avoiding the need for an organic solvent in the traditional SX method.

In terms of development, precipitation and adsorption technologies are among the most established and effective approaches, providing great selectivity while having a low environmental impact. SX is still important and flexible in the industrial sector, but its reliance on organic solvents and phase separation issues necessitates the use of greener solvents such as ILs and PIM. Newer techniques, such as supramolecular host-guest encapsulation, bio-inspired adsorption, and electrochemical separation, show great promise in terms of selectivity and energy efficiency, but they need to be tested on bigger scales. Additional research should focus on fine-tuning selectivity in complex leachates, enhancing the long-term stability of adsorbents and membranes, assuring scalability, and conducting LCA to validate sustainability claims. Section 6 provides a broader comparative examination of various strategies.

5. LCA study for PM recovery

Despite being advertised as sustainable and selective, precipitation-based PM recovery technologies are rarely analysed by systematic LCA. Where such assessments exist, they clearly indicate the environmental benefits of recycling secondary sources over primary mining. Conventional gold mining emits 16 t CO_2 eq per kg due to low ore grade and cyanide leaching. [133] Recovery from high-value waste by hydrometallurgical techniques like aqua regia results in significantly lower emissions of only 0.058 t CO_2 eq per kg of Au. [133] Pt manufacturing produces 13,500 kg CO_2 eq per kg, whereas recycling reduces this to 694 kg CO_2 eq per kg, a reduction of more than 95 %. [134] LCA studies for Pd estimate that mining and refining emit around 3880 kg CO_2 eq per kg of Pd, [135] but recovery from spent catalysts reduces this burden from 9670 to 1962 kg CO_2 eq per kg Pd, resulting in an 80 % reduction. [136]

Recycling, despite its high chemical and energy requirements, can cut CO_2 emissions by one to two orders of magnitude compared with mining. However, most studies using recovery methods such as precipitation, SX, and adsorption solely report on recovery efficiency and selectivity, without taking into account broader environmental factors. To make these methods a truly sustainable separation approach, future research should include LCA that determines CO_2-equivalent emissions, cumulative energy demand, waste generation, and reagent biodegradability. These assessments will enable the methods to be benchmarked against mining and alternative recycling technologies, as well as giving strong proof of their environmental benefits. In recycling, the process must not generate waste that itself becomes unmanageable (new metrics are proposed in this context). [137]

6. Discussions on comparative assessment of PM recovery technologies

The trade-offs between scalability, sustainability, and efficiency are highlighted by the comparative study of PM recovery systems (Table 3). Because of their high selectivity and throughput, respectively, traditional methods like pyrometallurgy and conventional hydrometallurgy are still used extensively. However, they are less desirable in the context of sustainable chemistry because to their high energy consumption, toxic reagents (such as cyanide and aqua regia), and the production of hazardous by-products.

Mechanochemistry and biometallurgy, on the other hand, appear to be more environmentally benign alternatives with low energy requirements and emissions. While promising technologies, their slow kinetics, restricted scalability, and lack of industrial adoption currently limit their widespread application. Similarly, adsorption and precipitation are environmentally acceptable, low-energy options with good metal selectivity, but also have potential scalability issues when applied to complex waste streams.

Thiosulfate and thiourea leaching are greener alternatives to cyanide-based hydrometallurgy, with lower toxicity and controlled effluents. However, reagent instability and low economic success prevent broad adoption. Mild solvents such as DES and ILs, are gaining popularity due to their versatility, recyclability, and low environmental effect. However, high costs and difficulties in synthesis/recycling remain important barriers.

Emerging approaches like photochemical and electrochemical leaching provide selective recovery pathways. Photochemical approaches have low reagent toxicity but are limited by solvent volatility, whereas electrochemical processes enable direct electrodeposition of

Table 3
Comparative assessment of PM recovery technologies.

Method	Applicability / Feedstock	Targeted Metals	Energy Requirement	Reagent Toxicity	Waste / By-products	Remarks	Key References
Pyrometallurgy	Broad (ores, e-waste, catalysts)	Au, Ag, Pt, Pd, Rh	Very high (furnaces, smelting)	High (risk of dioxins & halides from plastics)	Slag with residual metals & flue gases	High throughput, not sustainable	[138,139]
Mechanochemistry	Composites, powders	Au, Pd, etc.	Low-moderate	Low	Minimal emissions	Slow, Not scalable, emerging, sustainable	[68,69]
Conventional hydrometallurgy (cyanide, aqua regia, halogens)	Ores, e-waste, jewelry scrap	Au, Ag, Pt, Pd, Rh	Moderate-high	High (CN^-, HNO_3, Cl_2)	Wastewater, toxic residues	High selectivity & yield, not sustainable	[6]
Thiosulfate & thiourea leaching	Gold & silver-rich feeds	Au, Ag	Moderate	Low	Less toxic effluents	Greener cyanide alternatives, limited adoption	[6]
Mild solvents dissolution (DES, ILs, etc.)	Catalysts, e-waste, mixed wastes	Ag, Au, Pd, Pt	Moderate	Low	Mostly recyclable, low gaseous emissions	Eco-friendly, tunable, costly, synthesis & recycling issues	[48,49 and 55]
Photochemical leaching	*E*-waste, catalysts	Au, Pt, Pd	Low-moderate (UV/visible source)	Low	Catalyst residues	Selective but issue with the organic solvent volatility	[41]
Electrochemical leaching	E-waste, catalysts	Au, Pt, Pd, Rh	Moderate (electricity-driven)	Low	Spent electrolytes (recyclable)	Enables direct electrodeposition	[71]
Biometallurgy (microbial, biosorbents, plants)	Low-grade ores, wastewaters	Au, Ag, Pt, Pd	Low-moderate	Low	Biodegradable residues	Cheap, sustainable, slow kinetics	[72–75]
Precipitation	E-waste, catalysts	Au, Ag, Pt, Pd	Low	Low	Ligand recyclable	Cheap, eco-friendly, not scalable for all methods	[82–88]
Adsorption (Carbon, Resins, MOFs, Biomass)	Leachates, dilute waste streams	Au, Ag, Pt, Pd	Very low	Low	Adsorbent regeneration waste	High selectivity, renewable adsorbents emerging	[100–106]
Membrane & ion exchange	Dilute leachates, wastewater	Au, Pt, Pd	Low-moderate	Low	Concentrated brines; fouling	Good separation, but fouling issues	[132]
Solvent extraction	E-waste, catalysts	Au, Ag, Pt, Pd	Low-moderate	Moderate (organic solvent)	Recyclable	High selectivity, less greener	[114–116]

*Energy requirements are grouped according to reported process demands: Low for near-ambient conditions (<150 °C, atmospheric pressure). Moderate for moderate heating/pressurization (150–400 °C); High for energy-intensive operations (> 400 °C or high-pressure procedures). [140] Toxicity levels were assigned based on reported risks using PubChem and MSDS. We categorize chemicals as low (usually safe/biodegradable, e.g., water, ethanol), moderate (some dangers, managed with normal safety, e.g., thiourea, acetonitrile), and high (poisonous, carcinogenic, or persistent, e.g., cyanide, aqua regia, $SOCl_2$). [141,142]

PMs, although energy consumption and electrolyte management must be tuned.

Membrane and ion exchange techniques can effectively separate PMs from dilute leachates with low toxicity and moderate energy needs. However, membrane fouling and concentrated brine production present operational issues. Similarly, solvent extraction remains a strong technology with great selectivity, but its reliance on hazardous organic solvents undermines its sustainability.

Overall, the Table 3 demonstrates a paradigm shift from traditional, high-impact methods to sustainable, low-toxicity solutions. While no single method emerges as universally desirable, future research should prioritize hybrid approaches that consider efficiency, selectivity, and the environment, as well as the ability to scale up promising sustainable technologies like mechanochemistry, biometallurgy, precipitation and mild solvent systems.

7. Conclusion and future perspectives

PM recovery is transitioning from old hydrometallurgical techniques to more sustainable chemistries. Established techniques, such as oxidative leaching, pyrometallurgy and conventional hydrometallurgy and SX, continue to be prevalent in the industry, but their reliance on hazardous reagents and large energy inputs restricts their sustainability. Emerging techniques, such as bio-based dissolution, DESs and mild dissolution, mechanochemistry, photocatalysis, supramolecular separations and precipitations, provide more environmentally benign options, although challenges with kinetics, selectivity, and scale-up remain.

A thorough evaluation of these techniques finds that IL-based separation, supramolecular recognition, and adsorption materials have good selectivity, while bioleaching and mechanochemistry have low chemical inputs and energy needs; however, none of these approaches meet all of the conditions for industrial feasibility. This emphasizes the importance of hybrid process designs that integrate the benefits of many methods.

Future progress will be determined by three factors: (i) the systematic integration of LCA, eco-toxicity, and energy metrics into method evaluation, (ii) the use of computational chemistry and machine learning to design selective ligands and predict process viability, and (iii) the advancement of techno-economic analysis and pilot-scale demonstrations to connect laboratory advances with industrial adoption.

Unlike previous surveys, this review offers a unique perspective by combining current and new ideas within a sustainability framework. It focuses not only on chemical advances, but also on the metrics and strategy required to transform PM recovery into scalable, ecologically acceptable solutions that correspond with circular economy and net zero objectives.

Declaration of competing interest

The authors declare the following financial interests/personal relationships which may be considered as potential competing interests: Kasper Moth-Poulsen reports financial support was provided by European Research Council. Kasper Moth-Poulsen reports a relationship with European Research Council that includes: funding grants. Abhijit Nag reports a relationship with European Commission Marie Sklodowska-Curie Actions that includes: funding grants. If there are other authors, they declare that they have no known competing financial interests or personal relationships that could have appeared to influence the work reported in this paper.

Acknowledgements

A.N. and K.M.P. acknowledges the Marie Skłodowska-Curie Actions–European Commission post-doctoral grant (REWCHEM, Grant agreement ID: 101152892) and Sustain-a-Print project (Grant agreement ID: 101070556) from European Commission for research funding. K.M.P. acknowledges funding from the European Research Council (ERC) and the Catalan Institution for Research and Advanced Studies (ICREA). A.N. and A.Q. would like to express their gratitude for the support received from AMCC and chemistry department at Khalifa University of Science and Technology. A.N., C.A.M., and J.B.L would like to acknowledge the support received from the EPSRC-GCRF (grant number EP/T020504/1) and the University of Edinburgh. T.P. acknowledges funding from the Centre of Excellence (CoE) on Molecular Materials and Functions under the Institution of Eminence scheme of IIT Madras.

Data availability

Data will be made available on request.

References

[1] X.-F. Jiang, H. Huang, Y.-F. Chai, T.L. Lohr, S.-Y. Yu, W. Lai, Y.-J. Pan, M. Delferro, T.J. Marks, Nat. Chem. 9 (2017) 188–193.
[2] H.B. Trinh, J.-C. Lee, Y.-J. Suh, J. Lee, Waste Manag. 114 (2020) 148–165.
[3] C. Dong, C. Lian, S. Hu, Z. Deng, J. Gong, M. Li, H. Liu, M. Xing, J. Zhang, Nat. Commun. 9 (2018) 1252.
[4] M.D. Rao, K.K. Singh, C.A. Morrison, J.B. Love, Sep. Purif. Technol. 263 (2021) 118400.
[5] A. Zupanc, J. Install, M. Jereb, T. Repo, Angew. Chem. Int. Ed. 62 (2023) e202214453.
[6] Y. Chen, Q. Qiao, J. Cao, H. Li, Z. Bian, Joule 5 (2021) 3097–3115.
[7] M.C. Roco, C.A. Mirkin, M.C. Hersam, J. Nanopart. Res. 13 (2011) 897–919.
[8] P. Pati, S. McGinnis, P.J. Vikesland, Environ. Sci, Nano 3 (2016) 1133–1143.
[9] C. Ince, J. Clean. Prod. 238 (2019) 117871.
[10] A. Nag, C.A. Morrison, J.B. Love, ChemSusChem 15 (2022) e202201285.
[11] B. Kenzhaliyev, T. Surkova, A. Koizhanova, D. Yessimova, L. Amanzholova, Z. Dosymbayeva, Inorganics 11 (2023) 461.
[12] L.J. Esdaile, J.M. Chalker, Chem. Eur. J. 24 (2018) 6905–6916.
[13] Y. Wei, W. Zhang, J. Gao, Green Chem. 26 (2024) 5684–5707.
[14] A. Serpe, 11 - green chemistry for precious metals recovery from WEEE**this chapter is dedicated to Prof. Paola Deplano on the occasion of her retirement, in: F. Vegliò, I. Birloaga (Eds.), Waste Electrical and Electronic Equipment Recycling, Woodhead Publishing, 2018, pp. 271–332.
[15] Z. Zuhra, M. Haris Khan, S. Ali, M. Ahmad, Z. Zhaowei, Chem. Eng. J. 500 (2024) 157105.
[16] J. Xia, A. Ghahreman, Sci. Total Environ. 916 (2024) 170154.
[17] A. Birich, S. Stopic, B. Friedrich, Sci. Rep. 9 (2019) 7191.
[18] A.L. Suherman, G. Zampardi, S. Kuss, E.E.L. Tanner, H.M.A. Amin, N.P. Young, R. G. Compton, Phys. Chem. Chem. Phys. 20 (2018) 28300–28307.
[19] J. Chen, K. Huang, Hydrometallurgy 82 (2006) 164–171.
[20] H. Lee, E. Molstad, B. Mishra, JOM 70 (2018) 1616–1621.
[21] D. Burdinski, M.H. Blees, Chem. Mater. 19 (2007) 3933–3944.
[22] J. Son, Y. Hong, C.T. Yavuz, J.-I. Han, Ind. Eng. Chem. Res. 59 (2020) 8086–8092.
[23] C.J. Liang, J.Y. Li, Sep. Purif. Technol. 54 (2019) 1055–1066.
[24] S. Sun, M. Gao, G. Lei, H. Zou, J. Ma, C. Huang, Nano Res 9 (2016) 1125–1134.
[25] P.P. Lopes, D. Tripkovic, P.F.B.D. Martins, D. Strmcnik, E.A. Ticianelli, V. R. Stamenkovic, N.M. Markovic, J. Electroanal. Chem. 819 (2018) 123–129.
[26] W. Lin, R.-W. Zhang, S.-S. Jang, C.-P. Wong, J.-I. Hong, Angew. Chem. Int. Ed. 49 (2010) 7929–7932.
[27] A. Serpe, L. Marchiò, F. Artizzu, M.L. Mercuri, P. Deplano, Eur. J. Chem. 19 (2013) 10111–10114.
[28] C. Yue, H. Sun, W.-J. Liu, B. Guan, X. Deng, X. Zhang, P. Yang, Angew. Chem. Int. Ed. 56 (2017) 9331–9335.
[29] F. Forte, S. Riaño, K. Binnemans, Chem. Commun. 56 (2020) 8230–8232.
[30] E.J. Sare, C.T. Moynihan, C.A. Angell, J. Phys. Chem. 77 (1973) 1869–1876.
[31] A. Baksi, M. Gandi, S. Chaudhari, S. Bag, S.S. Gupta, T. Pradeep, Angew. Chem. Int. Ed. 55 (2016) 7777–7781.
[32] A. Nag, A. Baksi, K.C. Krishnapriya, S.S. Gupta, B. Mondal, P. Chakraborty, T. Pradeep, Eur. J. Inorg. Chem. 2017 (2017) 3072–3079.
[33] M. Räisänen, E. Heliövaara, F.A. Al-Qaisi, M. Muuronen, A. Eronen, H. Liljeqvist, M. Nieger, M. Kemell, K. Moslova, J. Hämäläinen, K. Lagerblom, T. Repo, Angew. Chem. Int. Ed. 57 (2018) 17104–17109.
[34] A. Zupanc, E. Heliövaara, K. Moslova, A. Eronen, M. Kemell, Č. Podlipnik, M. Jereb, T. Repo, Angew. Chem. Int. Ed. 61 (2022) e202117587.
[35] A. Nag, C.A. Morrison, J.B. Love, ChemSusChem 17 (2024) e202301695.
[36] J.Y. Tsao, H.D. Saunders, J.R. Creighton, M.E. Coltrin, J.A. Simmons, J. Phys. D. Appl. Phys. 43 (2010) 354001.
[37] Y. Chen, H. He, S. Xu, Z. Zou, W. Hua, Z. Bian, H. Li, Y. Yue, Green Chem. 25 (2023) 7518–7523.
[38] P. Chen, Y. Liang, B. Yang, F. Jia, S. Song, A.C.S. Sustain, Chem. Eng. 8 (2020) 3673–3680.
[39] M. Muscetta, R. Andreozzi, R. Marotta, I. Di Somma, J. Environ. Chem. Eng. 9 (2021) 106523.

[40] R. Wang, Y. Shangguan, X. Feng, X. Gu, W. Dai, S. Yang, H. Tang, J. Liang, Y. Tian, D. Yang, H. Chen, Nano Lett. 23 (2023) 2219–2227.
[41] Y. Chen, M. Xu, J. Wen, Y. Wan, Q. Zhao, X. Cao, Y. Ding, Z.L. Wang, H. Li, Z. Bian, Nat. Sustain. 4 (2021) 618–626.
[42] J. Cao, Y. Chen, H. Shang, X. Chen, Q. Qiao, H. Li, Z. Bian, ACS ES&T Eng. 2 (2022) 1445–1453.
[43] D.R. Joshi, N. Adhikari, J. Pharm. Res. Int. 28 (2019) 1–18.
[44] X. Zhou, X. Zhou, C. Wang, H. Zhou, Chemosphere 313 (2023) 137489.
[45] J. He, J. Yang, S.M. Tariq, C. Duan, Y. Zhao, J. Clean. Prod. 256 (2020) 120368.
[46] J. Bailey, E.L. Byrne, P. Goodrich, P. Kavanagh, M. Swadźba-Kwaśny, Green Chem. 26 (2024) 1092–1131.
[47] D. Hinchcliffe, A. Dodd, A. Schmidt, P. Nockemann, 2.29 - coordination chemistry in ionic liquids: A review, in: E.C. Constable, G. Parkin, L. Que Jr. (Eds.), Comprehensive Coordination Chemistry III, Elsevier, Oxford, 2021, pp. 557–589.
[48] X. Li, A. Van den Bossche, T. Vander Hoogerstraete, K. Binnemans, Chem. Commun. 54 (2018) 475–478.
[49] A. Van den Bossche, E. De Witte, W. Dehaen, K. Binnemans, Green Chem. 20 (2018) 3327–3338.
[50] B. May, M. Lexow, N. Taccardi, H.-P. Steinrück, F. Maier, ChemistryOpen 8 (2019) 15–22.
[51] B. Schmidt, B. Schröder, K. Sonnenberg, S. Steinhauer, S. Riedel, Angew. Chem. Int. Ed. 58 (2019) 10340–10344.
[52] J.A. Whitehead, G.A. Lawrance, A. McCluskey, Green Chem. 6 (2004) 313–315.
[53] J.A. Whitehead, J. Zhang, N. Pereira, A. McCluskey, G.A. Lawrance, Hydrometallurgy 88 (2007) 109–120.
[54] J.A. Whitehead, J. Zhang, A. McCluskey, G.A. Lawrance, Hydrometallurgy 98 (2009) 276–280.
[55] A. Zupanc, J. Install, T. Weckman, M.M. Melander, M.J. Heikkilä, M. Kemell, K. Honkala, T. Repo, Angew. Chem. Int. Ed. 63 (2024) e202407147.
[56] S. Wstawski, M. Emmons-Burzyńska, M. Rzelewska-Piekut, A. Skrzypczak, M. Regel-Rosocka, Hydrometallurgy 205 (2021) 105730.
[57] Z. Yuan, H. Liu, W.F. Yong, Q. She, J. Esteban, Green Chem. 24 (2022) 1895–1929.
[58] S. Anggara, F. Bevan, R.C. Harris, J.M. Hartley, G. Frisch, G.R.T. Jenkin, A. P. Abbott, Green Chem. 21 (2019) 6502–6512.
[59] A.P. Abbott, G. Frisch, J. Hartley, K.S. Ryder, Green Chem. 13 (2011) 471–481.
[60] G.R.T. Jenkin, A.Z.M. Al-Bassam, R.C. Harris, A.P. Abbott, D.J. Smith, D. A. Holwell, R.J. Chapman, C.J. Stanley, Miner. Eng. 87 (2016) 18–24.
[61] A.P. Abbott, F. Bevan, M. Baeuerle, R.C. Harris, G.R.T. Jenkin, Electrochem. Commun. 76 (2017) 20–23.
[62] A.P. Abbott, A.Z.M. Al-Bassam, A. Goddard, R.C. Harris, G.R.T. Jenkin, F. J. Nisbet, M. Wieland, Green Chem. 19 (2017) 2225–2233.
[63] A. Entezari-Zarandi, F. Larachi, J. Rare Earths 37 (2019) 528–533.
[64] A.P. Abbott, J. Collins, I. Dalrymple, R.C. Harris, R. Mistry, F. Qiu, J. Scheirer, W. R. Wise, Aust. J. Chem. 62 (2009) 341–347.
[65] P. Zürner, G. Frisch, A.C.S. Sustain, Chem. Eng. 7 (2019) 5300–5308.
[66] R. Marin Rivera, G. Zante, J.M. Hartley, K.S. Ryder, A.P. Abbott, Green Chem. 24 (2022) 3023–3034.
[67] R. Marin Rivera, C.E. Elgar, B. Jacobson, A. Feeney, P. Prentice, K. Ryder, A. P. Abbott, RSC Sustain. 2 (2024) 403–415.
[68] J.-L. Do, D. Tan, T. Friščić, Angew. Chem. Int. Ed. 57 (2018) 2667–2671.
[69] L. Xiao, Y. Wang, Z. Sun, P. Qian, P. Han, B. Yu, S. Ye, A.C.S. Sustain, Chem. Eng. 7 (2019) 11415–11425.
[70] R. Sharma, S.B. Simonsen, P. Morgen, S.M. Andersen, Electrochim. Acta 321 (2019) 134662.
[71] Q. Song, H. Sun, L. Zhang, Z. Xu, J. Hazard. Mater. 420 (2021) 126568.
[72] F. Faraji, J. Wang, H. Mahandra, A. Ghahreman, A.C.S. Sustain, Chem. Eng. 9 (2021) 236–245.
[73] E. Jorjani, H. Askari Sabzkoohi, Curr. Res. Biotechnol. 4 (2022) 10–20.
[74] A. Pathak, L. Morrison, M.G. Healy, Bioresour. Technol. 229 (2017) 211–221.
[75] S. Ilyas, J.-C. Lee, Min. Metall. Explor. 30 (2013) 151–156.
[76] W.-Q. Zhuang, J.P. Fitts, C.M. Ajo-Franklin, S. Maes, L. Alvarez-Cohen, T. Hennebel, Curr. Opin. Biotechnol. 33 (2015) 327–335.
[77] A.I. Petrov, J. Mol. Model. 28 (2022) 391.
[78] N. Zhang, J. Kou, C. Sun, Molecules 28 (2023) 1508.
[79] X. Wang, M.J. Servis, J. Phys. Chem. B 128 (2024) 263–272.
[80] F. Zahariev, T. Ash, E. Karunaratne, E. Stender, M.S. Gordon, T.L. Windus, M. Pérez García, J. Chem. Phys. 160 (2024).
[81] Z. Liu, M. Frasconi, J. Lei, Z.J. Brown, Z. Zhu, D. Cao, J. Iehl, G. Liu, A. C. Fahrenbach, Y.Y. Botros, O.K. Farha, J.T. Hupp, C.A. Mirkin, J. Fraser Stoddart, Nat. Commun. 4 (2013) 1855.
[82] H. Wu, Y. Wang, C. Tang, L.O. Jones, B. Song, X.-Y. Chen, L. Zhang, Y. Wu, C. L. Stern, G.C. Schatz, W. Liu, J.F. Stoddart, Nat. Commun. 14 (2023) 1284.
[83] H. Wu, L.O. Jones, Y. Wang, D. Shen, Z. Liu, L. Zhang, K. Cai, Y. Jiao, C.L. Stern, G.C. Schatz, J.F. Stoddart, A.C.S. Appl, Mater. Interfaces 12 (2020) 38768–38777.
[84] H. Wu, Y. Wang, L.O. Jones, W. Liu, L. Zhang, B. Song, X.-Y. Chen, C.L. Stern, G. C. Schatz, J.F. Stoddart, Angew. Chem. Int. Ed. 60 (2021) 17587–17594.
[85] W. Liu, A.G. Oliver, B.D. Smith, J. Am. Chem. Soc. 140 (2018) 6810–6813.
[86] A. Nag, M.R. Islam, T. Pradeep, A.C.S. Sustain, Chem. Eng. 9 (2021) 2129–2135.
[87] L.M.M. Kinsman, B.T. Ngwenya, C.A. Morrison, J.B. Love, Nat. Commun. 12 (2021) 6258.
[88] A. Nag, M.K. Singh, C.A. Morrison, J.B. Love, Angew. Chem. Int. Ed. 62 (2023) e202308356.
[89] T. Xue, T. He, L. Peng, O.A. Syzgantseva, R. Li, C. Liu, D.T. Sun, G. Xu, R. Qiu, Y. Wang, S. Yang, J. Li, J.-R. Li, W.L. Queen, Sci. Adv. 9 (2023) eadg4923.
[90] J. Kolařík, A. Bakandritsos, Z. Bad'ura, R. Lo, G. Zoppellaro, Š. Kment, A. Naldoni, Y. Zhang, M. Petr, O. Tomanec, J. Filip, M. Otyepka, P. Hobza, R. Zbořil, ACS Nano 15 (2021) 3349–3358.
[91] J. Guo, X. Fan, Y. Li, S. Yu, Y. Zhang, L. Wang, X. Ren, J. Hazard. Mater. 415 (2021) 125617.
[92] S. Zhang, S. Ning, H. Liu, X. Wang, Y. Wei, X. Yin, Sep. Purif. Technol. 258 (2021) 117670.
[93] M. Peydayesh, E. Boschi, F. Donat, R. Mezzenga, Adv. Mater. 36 (2024) 2310642.
[94] S. Daliran, M. Ghazagh-Miri, A.R. Oveisi, M. Khajeh, S. Navalón, M. Âlvaro, M. Ghaffari-Moghaddam, H. Samareh Delarami, H. García, ACS Appl. Mater. Interfaces 12 (2020) 25221–25232.
[95] N. Das, Hydrometallurgy 103 (2010) 180–189.
[96] M.D. Rao, K.K. Singh, C.A. Morrison, J.B. Love, RSC Adv. 10 (2020) 4300–4309.
[97] D.T. Sun, N. Gasilova, S. Yang, E. Oveisi, W.L. Queen, J. Am. Chem. Soc. 140 (2018) 16697–16703.
[98] M. Mon, J. Ferrando-Soria, T. Grancha, F.R. Fortea-Pérez, J. Gascon, A. Leyva-Pérez, D. Armentano, E. Pardo, J. Am. Chem. Soc. 138 (2016) 7864–7867.
[99] Y. Hong, D. Thirion, S. Subramanian, M. Yoo, H. Choi, H.Y. Kim, J.F. Stoddart, C. T. Yavuz, Proc. Natl. Acad. Sci. USA 117 (2020) 16174–16180.
[100] T.S. Nguyen, Y. Hong, N.A. Dogan, C.T. Yavuz, Chem. Mater. 32 (2020) 5343–5349.
[101] D. Mei, B. Yan, Angew. Chem. Int. Ed. 63 (2024) e202402205.
[102] F. Li, J. Zhu, P. Sun, M. Zhang, Z. Li, D. Xu, X. Gong, X. Zou, A.K. Geim, Y. Su, H.-M. Cheng, Nat. Commun. 13 (2022) 4472.
[103] Y. Liu, S. Lin, Y. Liu, A.K. Sarkar, J.K. Bediako, H.Y. Kim, Y.-S. Yun, Small 15 (2019) 1805242.
[104] L. Ling, X.-Y. Huang, W.-X. Zhang, Adv. Mater. 30 (2018) 1705703.
[105] B. Hua, L. Shao, Z. Zhang, J. Liu, F. Huang, J. Am. Chem. Soc. 141 (2019) 15008–15012.
[106] B. Aguila, Q. Sun, H.C. Cassady, C. Shan, Z. Liang, A.M. Al-Enizic, A. Nafadyc, J. T. Wright, R.W. Meulenberg, S. Ma, Angew. Chem. Int. Ed. 59 (2020) 19618–19622.
[107] T. Maruyama, H. Matsushita, Y. Shimada, I. Kamata, S. Sonokawa, N. Kamiya, M. Goto, Environ. Sci. Technol. 41 (2007) 1359–1364.
[108] J.R. Dodson, H.L. Parker, A. Muñoz García, A. Hicken, K. Asemave, T.J. Farmer, H. He, J.H. Clark, A.J. Hunt, Green Chem. 17 (2015) 1951–1965.
[109] M. Peydayesh, E. Boschi, F. Donat, R. Mezzenga, Adv. Mater. 36 (2024) 2310642.
[110] I. Carson, K.J. MacRuary, E.D. Doidge, R.J. Ellis, R.A. Grant, R.J. Gordon, J. B. Love, C.A. Morrison, G.S. Nichol, P.A. Tasker, A.M. Wilson, Inorg. Chem. 54 (2015) 8685–8692.
[111] J.R. Turkington, V. Cocalia, K. Kendall, C.A. Morrison, P. Richardson, T. Sassi, P. A. Tasker, P.J. Bailey, K.C. Sole, Inorg. Chem. 51 (2012) 12805–12819.
[112] A.M. Wilson, P.J. Bailey, P.A. Tasker, J.R. Turkington, R.A. Grant, J.B. Love, Chem. Soc. Rev. 43 (2014) 123–134.
[113] R.M. Izatt, S.R. Izatt, R.L. Bruening, N.E. Izatt, B.A. Moyer, Chem. Soc. Rev. 43 (2014) 2451–2475.
[114] H. Narita, M. Tanaka, K. Morisaku, T. Abe, Hydrometallurgy 81 (2006) 153–158.
[115] E.D. Doidge, I. Carson, P.A. Tasker, R.J. Ellis, C.A. Morrison, J.B. Love, Angew. Chem. Int. Ed. 55 (2016) 12436–12439.
[116] E.D. Doidge, L.M.M. Kinsman, Y. Ji, I. Carson, A.J. Duffy, I.A. Kordas, E. Shao, P. A. Tasker, B.T. Ngwenya, C.A. Morrison, J.B. Love, A.C.S. Sustain, Chem. Eng. 7 (2019) 15019–15029.
[117] M. Masilela, S. Ndlovu, J. Environ. Chem. Eng. 7 (2019) 102810.
[118] N. Papaiconomou, G. Vite, N. Goujon, J.-M. Lévêque, I. Billard, Green Chem. 14 (2012) 2050–2056.
[119] N. Schaeffer, J.H.F. Conceição, M.A.R. Martins, M.C. Neves, G. Pérez-Sánchez, J. R.B. Gomes, N. Papaiconomou, J.A.P. Coutinho, Green Chem. 22 (2020) 2810–2820.
[120] N. Schaeffer, M. Gras, H. Passos, V. Mogilireddy, C.M.N. Mendonça, E. Pereira, E. Chainet, I. Billard, J.A.P. Coutinho, N. Papaiconomou, A.C.S. Sustain, Chem. Eng. 7 (2019) 1769–1777.
[121] S. Génand-Pinaz, N. Papaiconomou, J.-M. Leveque, Green Chem. 15 (2013) 2493–2501.
[122] M. Gras, N. Papaiconomou, N. Schaeffer, E. Chainet, F. Tedjar, J.A.P. Coutinho, I. Billard, Angew. Chem. Int. Ed. 57 (2018) 1563–1566.
[123] N. Papaiconomou, S. Génand-Pinaz, J.-M. Leveque, S. Guittonneau, Dalton Trans. 42 (2013) 1979–1982.
[124] L.A. Diaz, T.E. Lister, Waste Manag. 74 (2018) 384–392.
[125] R. Li, K. Xiang, Z. Peng, Y. Zou, S. Wang, Adv. Energy Mater. 11 (2021) 2102292.
[126] I. Ali, V. Shrivastava, J. Environ. Manag. 294 (2021) 112926.
[127] K. Kim, R. Candeago, G. Rim, D. Raymond, A.-H.A. Park, X. Su, iScience 24 (2021).
[128] Y. Liu, Q. Song, L. Zhang, Z. Xu, Sep. Purif. Technol. 280 (2022) 118944.
[129] P. Halli, J.J. Heikkinen, H. Elomaa, B.P. Wilson, V. Jokinen, K. Yliniemi, S. Franssila, M. Lundström, A.C.S. Sustain, Chem. Eng. 6 (2018) 14631–14640.
[130] I. Korolev, S. Spathariotis, K. Yliniemi, B.P. Wilson, A.P. Abbott, M. Lundström, Green Chem. 22 (2020) 3615–3625.
[131] S.R. Cotty, N. Kim, X. Su, A.C.S. Sustain, Chem. Eng. 11 (2023) 3975–3986.
[132] F. Kubota, R. Kono, W. Yoshida, M. Sharaf, S.D. Kolev, M. Goto, Sep. Purif. Technol. 214 (2019) 156–161.
[133] B. Fritz, C. Aichele, M. Schmidt, Int. J. Life Cycle Assess. 25 (2020) 1930–1941.
[134] H. Hwang, T. Kweon, H. Kang, Y. Hwang, Sustainability 16 (2024) 80.
[135] S. McCarthy, D.C. Braddock, J.D.E.T. Wilton-Ely, Coord. Chem. Rev. 442 (2021) 213925.
[136] K.-Y. Shin, S.-Y. Lee, H.-Y. Kang, Resour. Recycl. 30 (2021) 47–54.

[137] T. Pradeep, M.K.C. Tam, D.J. Carrier, J. Chen, B.J. Hwang, M. Meier, B. Subramaniam, R.S. Brower, P. Licence, ACS Sustain. Chem. Eng. 13 (2025) 14675–14676.
[138] K. Nakajima, O. Takeda, T. Miki, K. Matsubae, S. Nakamura, T. Nagasaka, Environ. Sci. Technol. 44 (2010) 5594–5600.
[139] M. Benson, C.R. Bennett, J.E. Harry, M.K. Patel, M. Cross, Resources, Conservation and Recycling 31 (2000) 1–7.
[140] IEA, Renewable Energy for Industry, 2017. IEA, Paris https://www.iea.org/reports/renewable-energy-for-industry, Licence: CC BY 4.0.
[141] National Center for Biotechnology Information (NCBI), PubChem Database. https://pubchem.ncbi.nlm.nih.gov.
[142] Sigma-Aldrich, Safety Data Sheets. https://www.sigmaaldrich.com/safety-center.html.

ACS NANO

www.acsnano.org

ARTICLE

$[Ag_{62}S_{12}(CBT)_{32}]^{4+}$: A 2.2 nm Two-Electron Superatomic Carborane-Thiolated Silver Nanocluster Exhibiting Multilayer Charge Separation

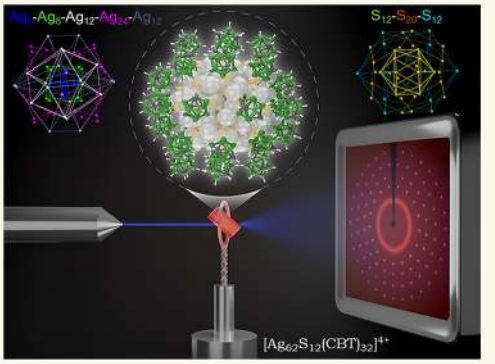
Arijit Jana, Vivek Yadav, Monika Kučeráková, Sami Malola, Amoghavarsha Ramachandra Kini, Swetashree Acharya, Ajay K. Poonia, Jan Macháček, Kumaran Nair Valsala Devi Adarsh,* Hannu Häkkinen,* Tomas Base,* and Thalappil Pradeep*

Cite This: *ACS Nano* 2025, 19, 35015−35026

Read Online

ACCESS | Metrics & More | Article Recommendations | Supporting Information

ABSTRACT: Investigating large metal nanoclusters decorated with three-dimensional molecular cages, with complete structural characterization, is challenging; however, their detailed understanding is important to study electronic confinement and associated properties. We have structurally resolved a nearly spherical 2.2 nm silver cluster with the molecular composition $[Ag_{62}S_{12}(CBT)_{32}]^{4+}$, altogether having 842 atoms, solely protected with *meta*-carborane-thiolates (CBTs). This is the largest nanocluster with carborane-based molecular cages reported so far. Abscission of the cluster reveals that it has a face-centered-cubic Ag_{14} inner core encapsulated with 12 sulfides, which is further surrounded by an outer scaffold of $Ag_{48}-S_{32}$ shell, protected with 32 *meta*-carboranes. The silver-sulfide skeleton of the nanocluster showed an assembly of multilayered polyhedra, having a mixture of Platonic and Archimedean solids. High-resolution mass spectrometric analyses and other spectroscopic studies further confirmed the molecular composition. This nanocluster exhibits characteristic molecular multiband optical absorption features along with a weak near-infrared (NIR) emission band. Ultrafast femtosecond transient absorption studies revealed stable photoexcited states linked to interlayer electron mobility between the neutral Ag_{14} core and the positively charged Ag_{48} shell, which are surrounded by negatively charged sulfide (S_{12} and S_{32}) layers. Computational analysis shows that this cluster behaves as a two-electron superatom with a band gap of 1.77 eV, which is associated with the energy difference between the 1S symmetric and 1P nonsymmetric states. Successful structural characterization and associated optical properties of the nanocluster suggested that other larger metal nanoclusters encapsulated by three-dimensional molecular cages may be suitable for single-particle photonic and optoelectronic applications.



KEYWORDS: *silver nanoclusters, carboranes, polyhedral nests, superatoms, optical properties, multilayer charge separation*

INTRODUCTION

Monolayer-protected metal clusters or nanoclusters of 1 to 3 nm core diameter have emerged as an interesting class of precise nanomaterials bridging the gap between single atoms (as in the form of molecular complexes) and traditional nanoparticles.[1−3] These nanoscale objects exhibit molecule-like discrete energy levels leading to characteristic optical and electrochemical properties.[4,5] Specific electronic structure with transitions within these confined energy levels also results in phenomena such as electrochemiluminescence,[6] photoluminescence,[7] and size-dependent electronic conductivity.[8] They have diverse uses in fields such as solar cells,[9] biomedicine,[10] sensing,[11,12] radiosensitization,[13] catalysis,[14,15] laser printing,[16] and photothermal applications.[17,18] Among the various metal clusters, those composed of noble metals, such as gold, silver, and copper, are particularly prominent due to their ease of

Received: July 15, 2025
Revised: September 16, 2025
Accepted: September 18, 2025
Published: September 26, 2025



Downloaded via INDIAN INST OF TECH MADRAS on December 29, 2025 at 03:16:13 (UTC).
See https://pubs.acs.org/sharingguidelines for options on how to legitimately share published articles.

© 2025 American Chemical Society

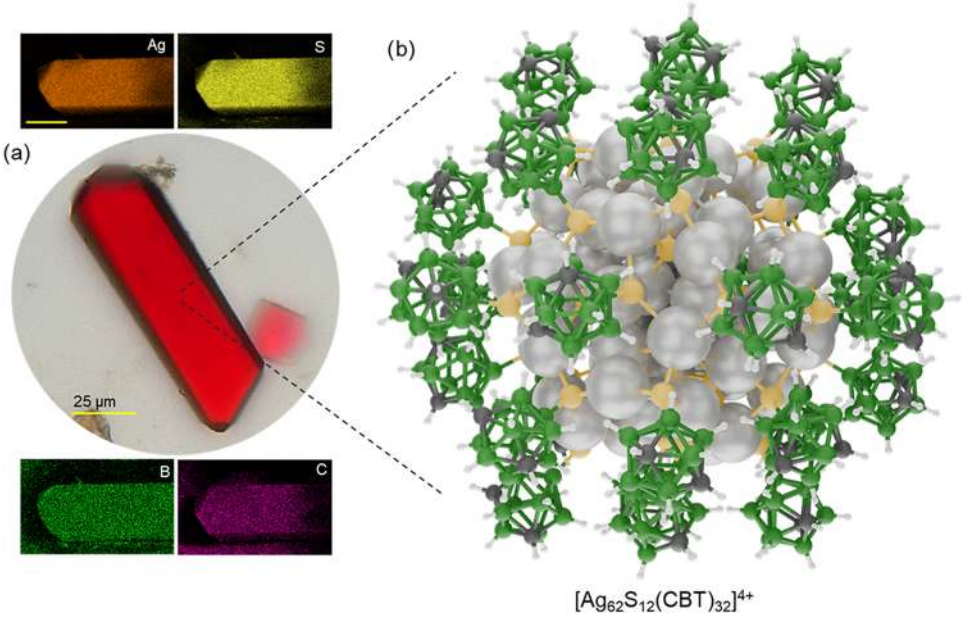


Figure 1. (a) Optical micrograph of a cuboidal single crystal of the $[Ag_{62}S_{12}(CBT)_{32}]^{4+}$ nanocluster. The inset shows the EDS elemental mapping of the crystal, having the elements Ag, S, B, and C in it (scale bar 25 μm). (b) Complete molecular structure of the $[Ag_{62}S_{12}(CBT)_{32}]^{4+}$ cluster. Color codes: metallic gray = silver, yellow = sulfur, green = boron, gray = carbon, and white = hydrogen.

synthesis, stability, structural characteristics, and drastic changes induced by atomic-level modifications.[1−3] Sometimes, in addition to structures consisting of metal cores and thiolate-anchored outer ligands, the clusters exhibit more complicated inner compositions with chalcogen atoms (S, Se, and Te) forming a multilayer structure with metal cores, metal sulfide interlayers, and ligand structures.[19,20] Some of these structurally resolved silver chalcogenide clusters are $[Ag_{14}S(SC_6H_4NCS)_{12}(PPh_3)_8]$,[21] $[Ag_{115}S_{34}(SCH_2C_6H_4{}^tBu)_{47}(dpph)_6]$,[22] $[Ag_{70}S_{20}(SPh)_{28}(dppm)_{10}]$,[23] $[Ag_{262}S_{100}(S^tBu)_{62}(dppb)_6]$,[23] $[Ag_{154}Se_{77}(dppxy)_{18}]$,[24] $[Ag_{320}(S^tBu)_{60}S_{130}(dppp)_{12}]$,[24] $[Ag_{352}S_{128}(S^tC_5H_{11})_{96}]$,[24] and $[Ag_{490}S_{188}(S^tC_5H_{11})_{114}]$.[24] Most of these clusters were synthesized through reduction using silylated metal chalcogenide sources. Embedding chalcogen atoms in the cluster framework, as well as heterometal doping in them, has been reported to enhance structural stability and boost the electron mobility within the framework. As a result, enhanced emission characteristics and efficient photoelectric responses were observed in these nanomaterials.[25,26]

Among the various silver nanoclusters, those of specific dimensions exhibit distinct electronic properties. For example, silver nanoclusters with the nuclearity between 4 and 50 atoms show multiband optical absorption features, while those in the nuclearity range from 51 to 120 exhibit a continuous transition to the plasmonic regime, and nuclearity beyond 150 is plasmonic.[27] Although the second category of materials is interesting for size−property correlations, only a handful of such clusters have been structurally resolved to date. In monolayer-protected silver clusters, organic molecules such as thiols,[28−34] phosphines,[35] alkynes,[36,37] carbenes,[38] dithiophosphates,[39] amides,[40] deoxyribonucleic acids,[41] thiacalixarenes,[42,43] and carboxylates[44] are used as protective ligands, and they play crucial roles in controlling the nuclearity and electronic properties of the clusters. These ligands also bring structural stability to these nanoentities through interfacial charge transfer between the metal core and the ligand shell. Structure-specific properties can also be tuned by chemical modifications of the ligands. Among the various thiols, carborane-thiol cage molecules emerged as an interesting class of ligands with robust thermal and chemical stability and three-dimensional aromaticity dispersed around the icosahedral C_2B_{10} cage.[45−47] In combination, metal nanoclusters protected by carboranethiols have been reported to possess greater stability and chemical functionalities, as well. In addition, they show tunable luminescence,[48,49] catalytic activity,[50,51] sensing capability,[52] nanomechanical properties,[53] and they are also promising as high-energy hypergolic materials.[54,55] Compared to conventional organic thiols, carboranethiols have most often resulted in silver clusters with lower nuclearity, such as $[Ag_{14}(C_2B_{10}H_{10}S_2)_6(CH_3CN)_8]$,[56] $[Ag_{14}(C_2B_{10}H_{10}S_2)_6(C_5H_5N)_8]$,[56] $[Ag_{14}(C_2B_{10}H_{10}S_2)_6(C_6H_7N)_8]$,[56] $[Ag_{14}(C_2B_{10}H_{10}S_2)_6(PPh_3)_6]$,[57] $[Ag_{17}I_3S(C_2B_{10}H_{10}S_2)_6(CH_3CN)_{11}]$,[58] $[Ag_{17}(C_2B_{10}H_{11}S)_{12}]$,[59] $[Ag_{21}(C_2B_{10}H_{11}S)_{12}(PPh_3)_2]$,[60] $[Ag_{30}(C_2B_{10}H_9S_3)_8(C_{25}H_{22}P_2)_6]$,[61] and $[Ag_{33}(C_2B_{10}H_{10}S_2)_{12}]$.[62] The 3D architecture and associated steric demands of the cage ligands make the formation of large metal clusters challenging. In this regard, we report here a breakthrough in the preparation of a large silver/silver chalcogenide cluster, comprising 62 silver atoms, 12 sulfides, and a surface envelope consisting of 32 *meta*-carborane-thiolate ligands, altogether having 842 atoms.

RESULTS AND DISCUSSION

Synthesis and Structural Details. The $[Ag_{62}S_{12}(CBT)_{32}]^{4+}$ (abbreviated as Ag_{62}) nanocluster was synthesized through dimethylformamide/methanol (DMF/MeOH, 2:1 by volume) assisted thermochemical reduction of silver nitrate in the presence of the M_9-COOH precursor (where M_9-COOH is *meta*-carborane-9-thiol-12-carboxylic acid). In brief, solvothermal treatment (75 ± 3 °C for 15 h)

https://doi.org/10.1021/acsnano.5c11836
ACS Nano 2025, 19, 35015−35026

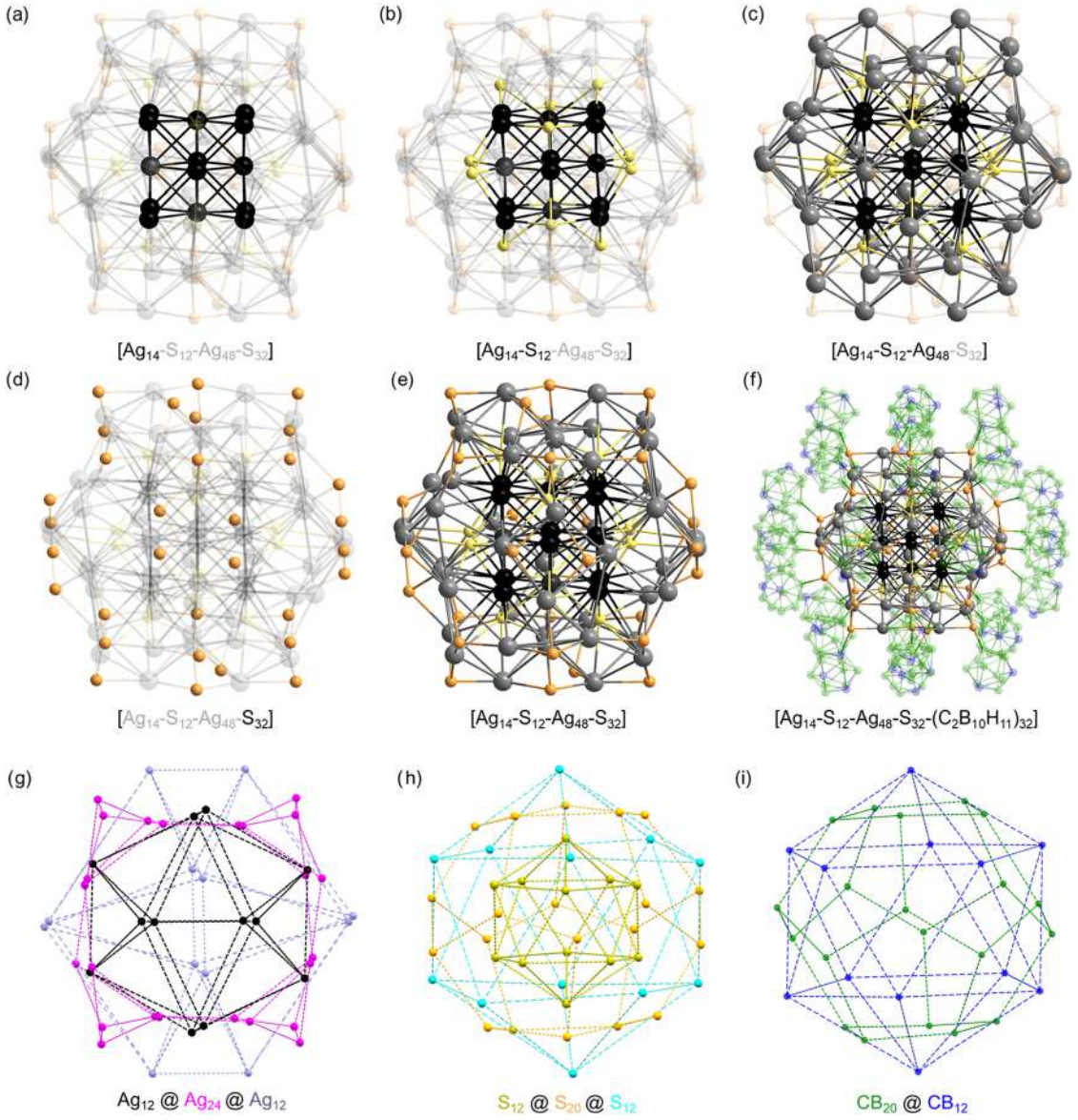


Figure 2. Structural anatomy of the $[Ag_{62}S_{12}(CBT)_{32}]^{4+}$ cluster. (a) The innermost Ag_6 octahedron, surrounded by eight capping Ag atoms, resulted in an Ag_{14} geometry. (b) Ag_{14} is surrounded by 12 interstitial sulfides, resulting in the Ag_{14}−S_{12} structure. (c) Ag_{14}−S_{12} is further protected by the Ag_{48} shell. (d) Arrangement of the 32 sulfur atoms connected with the carboranes. (e) The total silver-sulfide skeleton of the cluster. (f) Complete structural skeleton of the cluster along with carborane ligands. Hydrogen atoms are removed for clarity. Color code: black and gray = silver, yellow and orange = sulfur, green = boron, and blue = carbon. Alignment of multilayer symmetry element in the structural skeleton outside the fcc-Ag_{14}: (g) the outer Ag_{48} shell can be viewed as an icosahedron (Ag_{12}), a truncated cube (Ag_{24}), and a distorted icosahedron (Ag_{12}). (h) The 12 interstitial sulfides and outer 32 thiolate sulfur atoms can be viewed as an inner icosahedron (S_{12}), dodecahedron (S_{20}), and outer icosahedron (S_{12}). (i) The centroids of 32 carboranes can be visualized as an interpenetration dodecahedron (CB_{20}) and an icosahedron (CB_{12}).

of an equimolar mixture of $AgNO_3$ and M_9-COOH in DMF/MeOH placed in a hydrothermal bomb or closed glass container resulted in the red-colored Ag_{62} cluster. Time-dependent growth of the cluster, monitored by UV−vis absorption spectroscopy, is shown in Figure S1 (more synthetic details are provided in the Experimental Section). To understand the specific role of the M_9-COOH ligand, a similar solvothermal synthesis was performed using the *meta*-carborane 9-thiol (M_9) ligand. However, this reaction did not result in any distinct features of Ag_{62} clusters (shown in Figure S2). It may be noted that we have synthesized and purified the M_9-COOH ligand according to our earlier report.[63] To further assess the purity of the compound, we conducted mass spectrometry, Infrared (IR) spectroscopy, and Raman analysis (see Figures S3 and S4). These investigations confirm the presence of the −COOH group attached to the carborane cage. Most of the silver clusters have been synthesized either from silver-thiolate precursors using chemical reducing agents like sodium borohydride, sodium cyanoborohydride, or borane-amine complexes, or through ligand exchange reactions starting from pre-existing clusters under either low-temperature or ambient conditions.[64−66] However, the formation of the Ag_{62} cluster using thermal decarboxylation of Ag-M_9-COOH thiolates reported here differs from the usual methods. To investigate the decarboxylation of the M_9-COOH ligand during thermal treatment, we conducted a comparative

https://doi.org/10.1021/acsnano.5c11836
ACS Nano 2025, 19, 35015−35026

$^{11}B\{^{1}H\}$ NMR analysis of the M_9-COOH ligand before and after thermal treatment at 55 °C. The NMR spectra (shown in Figure S5) clearly demonstrate the decarboxylation of the M_9-COOH ligand that occurred during thermal treatment. We have also tried the direct reduction of $AgNO_3$ and M_9 precursors using $NaBH_4$ and $NaBH_3CN$ as reducing agents (shown in Figures S6 and S7). However, these methods did not result in the desired Ag_{62} cluster.

It shows the synthesis without any of the conventional reducing agents and occurs at a relatively higher temperature. Despite numerous challenges in crystallization, single crystals were successfully grown with a yield of ∼75% from the saturated solution of the cluster in the DMF/MeOH (1:1, by volume) mixture. An optical micrograph of a typical red-colored single crystal is shown in Figure 1a. The inset of Figure S1 shows many such crystals. Energy-dispersive spectroscopy (EDS) elemental mapping of different single crystals revealed the presence of the respective elements, as shown in the inset of Figure 1a. The atomic percentages of silver, sulfur, and the combined elements of boron and carbon in the crystal are approximately 8.60%, 6.49%, and 55.37%, respectively, which closely align with the nominal stoichiometry of the cluster. Additionally, nitrogen and oxygen, associated with the nitrate (NO_3^-) counterions, are also detected in the crystal (shown in Figure S8).

Single-crystal X-ray diffraction showed that the cluster crystallizes in a monoclinic crystal system with the space group $P2_1/n$ (additional crystallographic details are summarized in Table S1). The complete molecular structure of the cluster consists of 62 silver atoms, 12 sulfides, and 32 *meta*-carborane-thiolates filling up the surface (shown in Figure 1b). The inner sulfur atoms in the structure of $[Ag_{62}S_{12}(CBT)_{32}]^{4+}$ come from M_9-COOH itself, as no other sulfur source was used in the synthesis. Similar thiol dissociative processes giving sulfur are known in the cluster literature.[20] Complete set of crystallographic data, including structural refinement, is in the Supporting Information. Detailed analysis of the silver/silver-sulfide skeleton of the cluster can be visualized as an $Ag_{14}-S_{12}$ inner core encapsulated by a shell of $Ag_{48}-S_{32}$. Formation of the molecular skeleton of the cluster (shown in Figure 2a–2f) starts with a face-centered cubic (fcc) Ag_{14} inner core, in which the average Ag–Ag distance of 2.87 Å indicates a strong Ag–Ag interaction as in bulk silver (see Figure 2a). This Ag_{14} core can be described as an Ag_6 octahedron surrounded by eight Ag atoms in a cubic fashion, forming Ag_6-Ag_8 geometry. The Ag_{14} core is further enclosed by 12 sulfides, each exhibiting triple coordination (μ_3) with the Ag_{14} framework, and Ag–S bond distance ranging between 2.49 and 2.63 Å (see Figures 2b and S3). More precisely, two of the Ag–S bonds are connected to the outer Ag_8 cube, while the third Ag–S bond is connected to the inner Ag_6 octahedron (see Figure S9). Structural expansion of the framework upon considering the $Ag_{14}-S_{12}$ core and the $Ag_{48}-S_{32}$ shell revealed that among the 12 inner sulfides, two exhibit μ_7 coordination, two adopt μ_8 coordination, and the remaining eight display μ_6 coordination with Ag atoms (see Figure S10).

The outer framework beyond the $Ag_{14}-S_{12}$ of the cluster comprises an encapsulating $Ag_{48}-S_{32}$ silver-sulfide shell (shown in Figure 2c,d). The complete silver-sulfide skeleton is further surrounded by 32 *meta*-carboranes (Figure 2e,2f). Structural analysis of the $Ag_{48}-S_{32}$ shell reveals an $Ag_{32}S_{12}$ ring, further enclosed by subunits of three distinct types: Ag_2S_4, Ag_2S_4, and Ag_4S_2 (see Figure S11). Two units of each subunit type are arranged in opposite positions of the $Ag_{32}S_{12}$ envelope. Each of these outer Ag atoms forms μ_3, μ_4, and μ_5 intermetallic coordination with an Ag–Ag distance of 3.02 to 3.81 Å (shown in Figures S11 and S12).

Symmetry Analysis and Solid-State Packing. We conducted an analysis of the symmetry elements present in the multilayer skeleton of the cluster. The inner skeleton of the cluster is composed of fcc Ag_{14} (Figure 2a), and the outer Ag_{48} skeleton is composed of three layers. The innermost layer of 12 Ag atoms forms a regular icosahedron (Ih) with Ag_{12} (Schläfli symbol (3,5)). The next layer is formed by an Archimedean solid, which is a truncated cube with Ag_{24} units (Schläfli symbol t{4,3}). This is followed by a distorted Ag_{12} icosahedron (Schläfli symbol (3,5)). Notably, each of the two corners of the inner and outer icosahedra is cross-linked with each of the octagonal faces of the truncated cube (see Figures 2g and S13). Next, we analyzed the sulfur atoms, which include 12 inner sulfides and 32 outer thiolated S atoms. The sulfides form an inner S_{12} icosahedron (Ih) (Schläfli symbol (3,5)), and the outer 32 thiolated S atoms create an S_{20} dodecahedron (Ih) (Schläfli symbol (5,3)). This is followed by another S_{12} icosahedron (Ih) (Schläfli symbol (3,5)), which is larger in size (see Figures 2h and S14). These two icosahedra are stacked on top of each other, with the corners of each one pointing toward the centroid of each pentagonal face of the S_{20} dodecahedron.

More careful analysis reveals that all of the carborane cages are arranged in two ways, where the first group of ligands was surrounded by five nearby carboranes and the other category of carboranes was surrounded by six carboranes. We have observed that out of 32 carboranes, 12 result in pentagonal surface cavities, while 20 exhibit hexagonal surface cavities (see Figure S15). A more detailed analysis of the symmetry arrangement of all of the carborane centroids shows that they form an interpenetrating CB_{20} dodecahedron (Ih), as well as a CB_{12} icosahedron (Ih), which correlates with hexagonal and pentagonal surface envelopes (see Figures 2i and S16). All of the carborane-thiolate ligands adopt μ_3-coordination modes with Ag–S distances within the range of 2.39–3.00 Å (see Figure S17). Due to the structural complexity, some disorder has been observed in the outer sulfur atoms (as depicted in Figure S18). The unit cell packing comprises six clusters, with four molecules aligned along the center of the *b*-axis and two positioned along the center of the *ac* plane, resulting in an overall packing density (Z) of 2 (see Figure S19).

The three-dimensional extended supramolecular packing of the cluster molecules reveals lamellar packing of clusters (see Figure S20), which enables intermolecular B–H···B, B–H···H–C, B···H–C, and C–H···B interactions between the clusters via their carborane ligands (see Figure S21). These interactions are prominent between the large clusters, as each cluster molecule features 32 carborane molecules on its surface. The electrostatic potential map of a *meta*-carborane-9-thiol molecule exhibits dipole–dipole and electrostatic interactions between C–H and H–B of carboranes that constitute the surface shell in the Ag_{62} cluster, which is also correlated with our previously reported studies (see Figure S22).[63,67,68] Residual electron density maps were observed in the extended lattice, attributed to the presence of solvent molecules and counterions (see Figure S23). We note that this is the largest atomically precise metal cluster reported to date, featuring carborane-based ligands on its surface. Table S2 presents a detailed summary of all of the structurally resolved carborane-

https://doi.org/10.1021/acsnano.5c11836
ACS Nano 2025, 19, 35015–35026

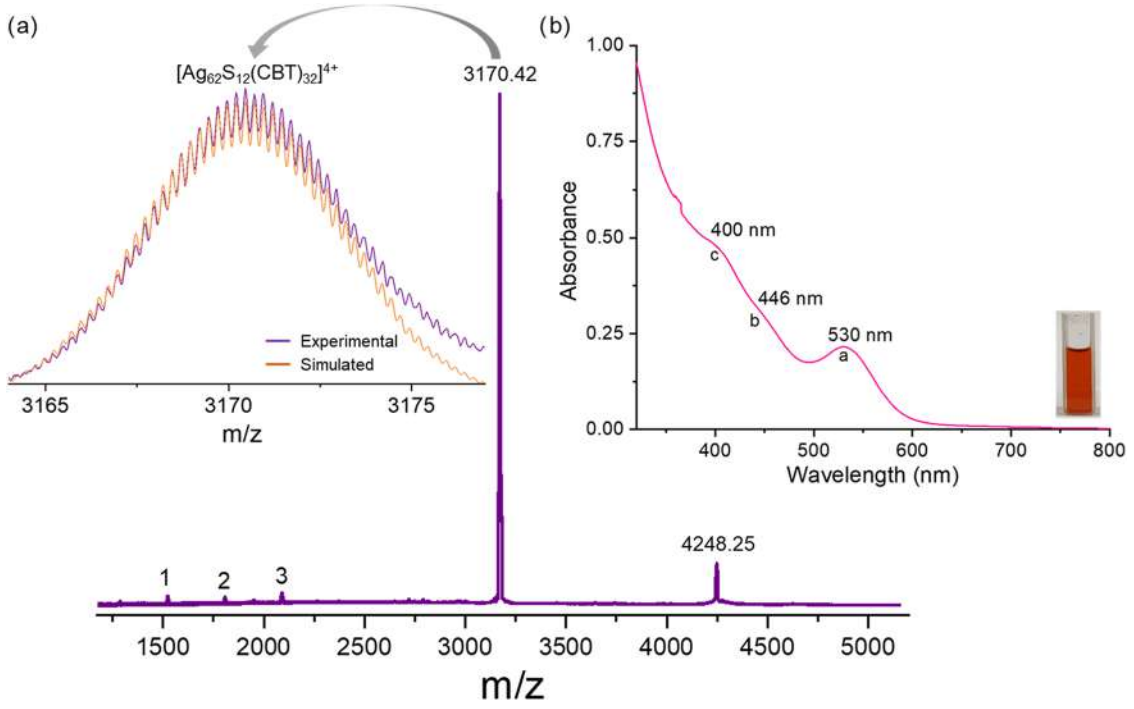


Figure 3. (a) Positive-ion mode ESI-MS spectrum of the cluster. The prominent peak at m/z 3170.42 with a charge state of 4+ confirmed the composition as $[Ag_{62}S_{12}(CBT)_{32}]^{4+}$. Another minor peak at m/z 4248.25 (charge state of 3+) is assigned as the $[Ag_{62}S_{12}(CBT)_{32}\cdot(MeO)\cdot(MeOH)]^{3+}$ species. Other peaks marked as 1 (m/z 1523.60), 2 (m/z 1806.60), and 3 (m/z 2089.61) are assigned to the formation of species $[Ag_6(CBT)_5]^+$, $[Ag_7(CBT)_6]^+$, and $[Ag_8(CBT)_7]^+$, respectively. The left inset shows an exact matching of the isotopic distributions of the high-resolution experimental spectrum with the simulated one, with a spacing of m/z 0.25. (b) UV−vis absorption spectrum of the Ag_{62} cluster in DMF, with peaks marked. The inset shows a photograph of the cluster solution in DMF.

thiolated and carborane-alkynylated metal clusters reported so far.

Mass Spectrometry and Spectroscopic Characterization. High-resolution mass spectrometry (instrumentation and sample preparation provided in the Supporting Information) was performed to further investigate the molecular cluster, gain additional independent insights into its composition, and examine its ionic character. The positive-ion mode electrospray ionization (ESI) mass spectrum shows a prominent peak at m/z = 3170.42 (Figure 3a). The m/z difference between two successive peaks is 0.25, indicating that the cluster carries a charge of 4+. Thus, the total molecular mass of 12681.68 is assigned to the composition $[Ag_{62}S_{12}(CBT)_{32}]^{4+}$ with the experimental isotopic distribution pattern (purple trace) matching well with the simulated one (orange trace) (inset of Figure 3a). Another minor peak at m/z 4248.25 shows the 3+ charge state assigned with the composition $[Ag_{62}S_{12}(CBT)_{32}\cdot(MeO)\cdot(MeOH)]^{3+}$, and it indicates solvation of the parent cluster with methanol and methoxide. Collision energy (CE)-dependent MS-MS fragmentation analysis was performed on the m/z 3170.42 peak (shown in Figure S24).

Upon sequential increase of the CE from 0 to 40 eV, a prominent peak corresponding to m/z 3126.58 with a 4+ charge state was formed because of one CBT ($C_2B_{10}H_{11}S$) loss from the parent cluster. Further increase of the CE to 50 eV led to the appearance of another peak, at m/z 3082.75, with a 4+ charge state, due to the loss of two CBT ligands from the parent cluster. Another prominent peak that appeared at m/z 2957.93 with a 4+ charge state is assigned to the composition $[Ag_{59}S_{12}(CBT)_{29}]^{4+}$. Two other peaks of lower intensity at m/z 2913.92 and 2887.07 (at CE 50 eV) are assigned to $[Ag_{59}S_{12}(CBT)_{28}]^{4+}$ and $[Ag_{58}S_{12}(CBT)_{28}]^{4+}$, respectively. With increasing CE to 60 eV, another peak appeared at m/z 2745.44 (with 4+ charge state), assigned to $[Ag_{56}S_{12}(CBT)_{26}]^{4+}$. The specific mass losses of 849.96 correspond to $[Ag_3(CBT)_3]$ fragments, which correspond to the structural motifs observed on the surface of the cluster (as resolved through SC XRD). We did not observe any specific fragments characteristic of the losses of silver-sulfide moieties, which clearly suggested stronger binding of the interstitial sulfides. Mass spectrometry analysis of the DMF solution, after dissolving selected single crystals, also confirmed the presence of nitrate (NO_3^-) counterions in the crystal structure (see Figure S25). These counterions are hidden inside the lattice and contribute to unresolved residual electron density around the cluster in the single-crystal XRD analysis (see Figure S23).

High-resolution transmission electron microscopic (HRTEM) investigation of a selected microcrystal shows the presence of small particles uniform in size with an average diameter of 1.4 ± 0.1 nm (see Figure S26). The drop-cast cluster solution displayed a similar distribution of particles in the lower magnification TEM analysis (see Figure S27). However, at higher magnifications with increased beam exposure, we observed beam-induced aggregation and a corresponding size expansion. The original size of ∼1.4 nm matches the molecular dimensions of the metal-sulfide skeleton of the cluster, as measured using data from SC XRD analysis (Figure S28). Additional characterization of the cluster was performed using X-ray photoelectron spectroscopy (XPS) and infrared spectroscopy. The XPS survey scan of freshly prepared microcrystals confirms the presence of Ag (368.2 and 374.1 eV), S (161.3 and 162.9 eV), B (189.8 eV), and C (285.0 eV) elements, corresponding to their character-

https://doi.org/10.1021/acsnano.5c11836
ACS Nano 2025, 19, 35015−35026

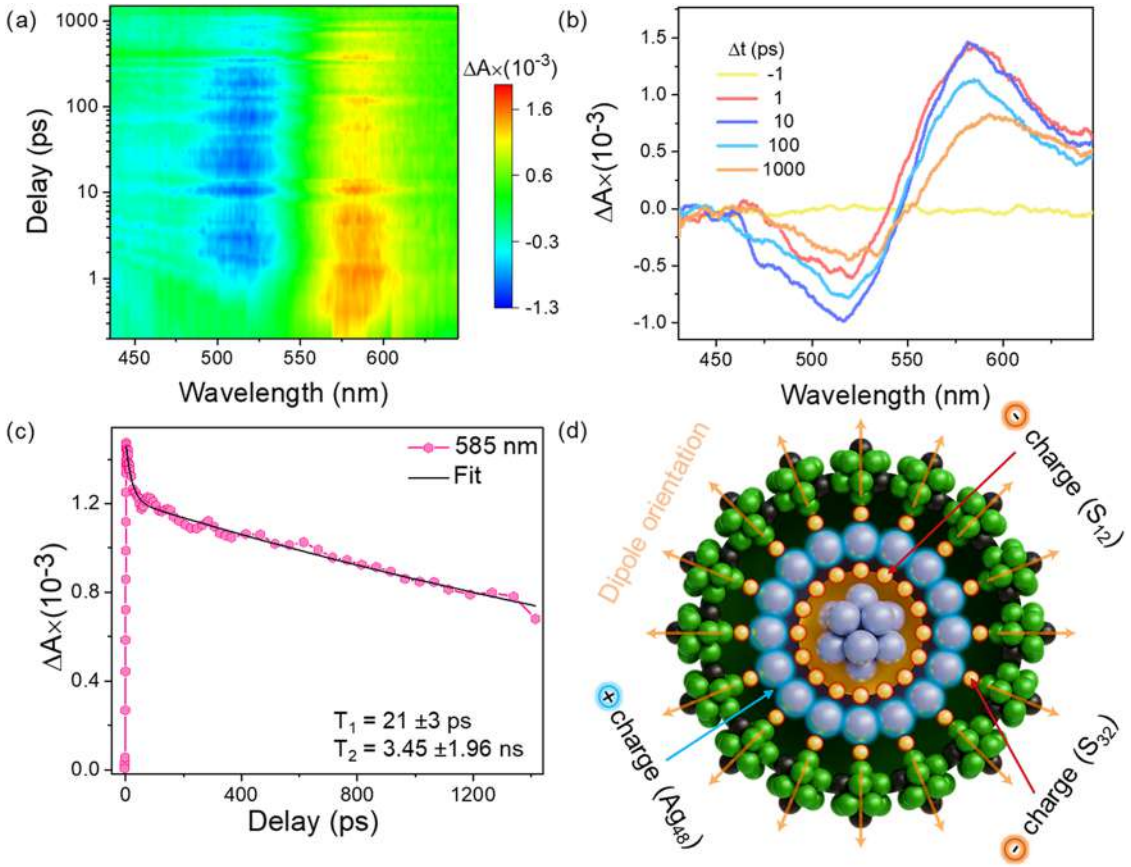


Figure 4. (a) Pseudo color map of femtosecond-TA for the Ag_{62} cluster in DMF solution by a pump excitation of 400 nm and fluence of 200 $\mu J \cdot cm^{-2}$. (b) Selected TA spectral profile as a function of time delay. (c) Kinetic decay traces for a 585 nm ESA signal. (d) A schematic representation of the multilayer charge separation within the cluster.

istic features (see Figure S29). The binding energy (BE) values of Ag $3d_{5/2}$ and $3d_{3/2}$ are consistent with those of the mixed metallic Ag(0) and Ag(1+) oxidation states. A detailed spectral scan of the S 2p region revealed two types of sulfur (1:3 ratio) in the cluster: inner sulfide with binding energies at 161.63 and 162.81 eV for S $2p_{3/2}$ and $2p_{1/2}$, and thiolate sulfide (from CBT) with binding energies at 162.99 and 164.17 eV for S $2p_{3/2}$ and $2p_{1/2}$, respectively (see Figure S30). Additionally, two peaks were observed at 401.5 eV (N 1s) and 531.9 eV (O 1s), corresponding to nitrogen and oxygen, respectively, originating from nitrate counterions in the crystal (Figure S29). Infrared (IR) spectroscopy further confirmed changes in the ligand shell associated with the decarboxylation of the starting ligand, M_9-COOH, during the solvothermal reaction. The IR spectrum of the Ag_{62} cluster exhibits characteristic bands at 2602 and 3042 cm^{-1}, corresponding to B−H and C−H stretching vibrations, similar to those observed in the spectra of M_9 or M_9-COOH molecules (see Figure S31). Additionally, carborane cage breathing and B−B bending vibrational modes were detected at 860 and 724 cm^{-1}, respectively. Weakly resolved, low-intensity bands associated with B−B and B−C bending vibrations were observed, likely due to the presence of electron-dense silver atoms near the carborane in the cluster. An important feature is the absence of C−O (1287 cm^{-1}), O−H (1417 cm^{-1}), and C═O (1713 cm^{-1}) bands, which are characteristic of M_9-COOH. Their absence in the spectrum of the Ag_{62} cluster clearly confirms the decarboxylation process during solvothermal synthesis. In conjunction with other methods, IR characterization confirms the presence of decarboxylated *meta*-carborane-thiolate as a surface envelope of the metal cluster. Metal-catalyzed thermal decarboxylation of carborane acids has been reported in previous studies.[69,70] The presence of the 1383 cm^{-1} vibrational band (antisymmetric N−O stretching band) further confirms the nitrate as counterions in the crystals. So, the composition of the compound is $[Ag_{62}S_{12}(CBT)_{32}](NO_3)_4$.

Optical Properties. The optical absorption spectrum of the Ag_{62} nanocluster (measured in DMF solution) exhibits one prominent absorption band centered at 530 nm (2.34 eV) along with two shoulder bands at 446 nm (2.78 eV) and 400 nm (3.1 eV) (Figure 3b). The characteristic optical absorption bands representing molecule-like discrete electronic energy levels suggest a transition from a molecular regime to a bulk metallic regime. UV−visible absorption spectra recorded at specific intervals over a period of half a year, using the same solution, showed no spectral changes, indicating remarkable stability of the nanocluster (see Figure S32), especially in comparison to a cluster of similar nuclearity protected by conventional organothiolate (*i.e.*, 2,4-dimethylbenzenethiolate) ligands.[71]

Ultrafast femtosecond transient absorption (fs-TA) studies were performed to understand the excited-state dynamics of the Ag_{62} nanocluster. In the measurement, the Ag_{62} nanocluster was excited using 120 fs pump pulses centered at 400 nm (3.1 eV). The resulting excited-state dynamics were investigated using time-delayed probe pulses. The color plot of obtained TA and spectral cross sections at selected time-delays with pump fluence of 200 $\mu J/cm^2$ is plotted in Figure 4a,b.

https://doi.org/10.1021/acsnano.5c11836
ACS Nano 2025, 19, 35015−35026

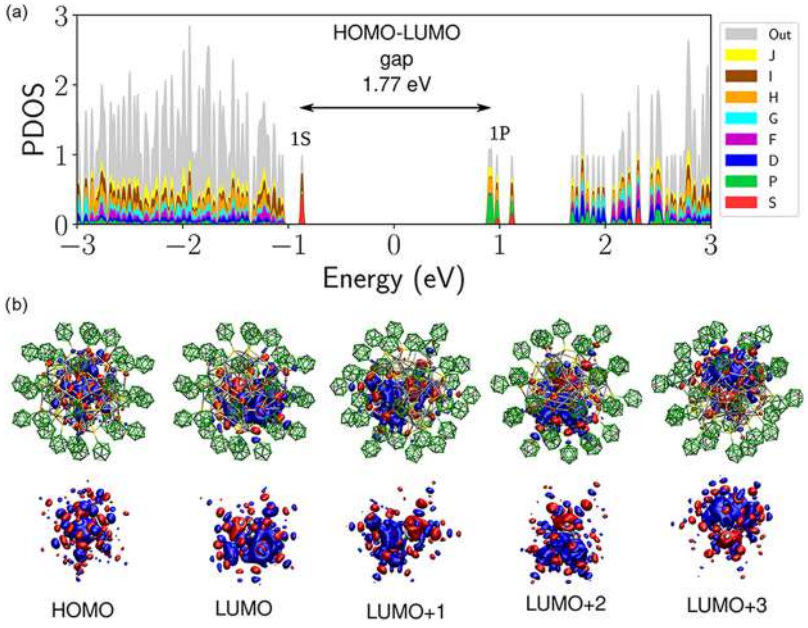


Figure 5. (a) Projected density of electron states to spherical harmonics functions centered at the center of the mass of the cluster. (b) The frontier molecular orbitals visualized with and without the full atomic structure from HOMO to LUMO+3 states.

From these figures, we see that the main TA features are ground state photobleaching (GSPB) in the regime of 515 nm, and excited state absorption (ESA) starts from 550 nm. The GSPB is located in the regime, where we observed a primary optical absorption band centered at 530 nm (see Figure 3b), and it represents the filling of closely spaced electronic excited states by the pump excitation. Further, the ESA arises from the transition of initially photoexcited states to higher excited states. We also see that ESA grows quickly while GSPB grows relatively slowly in the TA map (Figure 4a). To get more insight into these features for a longer time scale, we have plotted the time evolution profiles of TA for both GSPB and ESA in Figures S33 and 4c. These figures reveal a fast decay of excited states with a lifetime of 760 ± 23 ps for 515 nm GSPB. In contrast, the 585 nm ESA band exhibited a fast component with a lifetime of 21 ± 3 ps and stable excited states with a lifetime of 3.45 ± 1.96 ns. We also investigated the TA features at different pump fluences of 100 and 200 $\mu J \cdot cm^{-2}$ (shown in Figure S34). From this comparison, we see a small increase (ΔA of 0.2×10^{-3}) for the GSPB signal and a relatively large increase (ΔA of 0.6×10^{-3}) for the ESA signal upon increasing the pump fluence from 100 to 200 $\mu J \cdot cm^{-2}$.

The decay time of the excited states remains unaffected by the pump fluence of 100 $\mu J \cdot cm^{-2}$ (as shown in Figure S35). This result of invariant lifetime is as per the molecular nature of Ag_{62}, where relaxation of the excited states does not change as a function of the pump fluence.[72] An insight into such distinct behavior indicates multilayer charge separation within the molecule. A comprehensive analysis of the cluster indicates that the silver-sulfide structure, specifically $Ag_{62}S_{12}S_{32}$, has a charge state of 4+ as observed from the mass spectrometry analysis depicted in Figure 3a. Considering the electronegativity difference between silver and sulfur, along with the strong metallic bonding in the inner Ag_{14} core, the structure of $[Ag_{62}S_{12}S_{32}]^{4+}$ can be understood as comprising four distinct layers. At the center is a charge-neutral Ag_{14} core, surrounded by a S_{12} ring that carries −12 charges. Outside of this, there is a positively charged Ag_{48} layer with +48 charges, followed by an outer S_{32} layer that has −32 charges, as schematically illustrated in Figure 4d. This core−shell architecture of the cluster suggests a distinct photophysical mechanism for excited-state dynamics after pump excitation. Initially, photoexcitation creates excited states dominantly localized on the outer S_{32} shell. This immediate population of shells causes the prompt rise of the ESA signal. Subsequently, these electrons move from the outer shell toward the inner Ag_{14} core in an interlayer charge transfer event. This charge transfer process is experimentally observed in the form of a time-delayed appearance of the GSPB signal. Finally, these electrons dispersed on the core and shell relax back to the ground state through two different pathways with distinct time scales of ∼760 ps and 3.45 ns. Excited-state dynamics influenced by the electronic perturbation from secondary metal atom dopants was also observed in gold nanoclusters.[73] Further, our suggested mechanism is supported by computational investigation of the Ag_{62} cluster that reveals that the absorption peak around 530 nm arises from the core part of the cluster (see below). As a result, the electron mobility of excited states within this charged multilayer can give rise to stable ESA and GSPB features in the cluster.

The Ag_{62} cluster did not exhibit any strong visible luminescence in either solution or in the solid state when exposed to 365 nm UV light (see inset of Figure S36). PL excitation measurement showed two excitation bands centered at 505 nm (2.45 eV) and 433 nm (2.86 eV) for the cluster, which are close to the absorption bands of the cluster (see Figure S36a). The cluster showed a weak NIR emission band centered at around 988 nm (1.25 eV) upon photoexcitation by 500 nm (2.48 eV) (shown in Figure S36b). Intermetallic charge transfer across charged multilayers rather than metal to ligand (ML) or ligand to metal (LM) charge transfer may contribute to the observed weak NIR emission, distinguishing it from the red-emitting Ag_{62} clusters encapsulated by *tert*-butyl thiolate ligands.[74,75]

Computational Insights. Computational modeling of the Ag_{62} nanocluster was performed with density functional theory

https://doi.org/10.1021/acsnano.5c11836
ACS Nano 2025, 19, 35015−35026

(DFT) using GPAW (see details of methods in the Supporting Information file). The initial structure, as obtained from the single-crystal X-ray diffraction analysis, was optimized using a real-space grid and Perdew–Burke–Ernzerhof functional, after which further analysis of electronic and optical properties was done using the GLLB-SC functional. At first, the electron states were projected with respect to spherical harmonic functions centered at the center of the mass of the cluster. This analysis reveals the superatom state symmetries that are delocalized in the inner metal core of the cluster.[76]

It is noted that the $[Ag_{62}S_{12}(CBT)_{32}]^{4+}$ cluster has a valence electron count of 2. This is calculated using the formula ($Nv_A - M - Z$), where Nv_A represents the total valence electrons of the metal atoms, M is the total electrons of electron-withdrawing ligands, and Z denotes the charge of the cluster.[76] In this case, the calculation is as follows: $[62 - (12 \times 2) - 32 - 4 = 2]$. The DFT results in Figure 5a show a clear change from 1S symmetric states to 1P nonsymmetric states when going over the HOMO–LUMO gap (1.77 eV), which indicates that the system could be characterized as a two-electron superatom system. These delocalized superatom states are present mostly on the inner $Ag_{14}S_{12}$ part (as is visualized in Figure 5b), which indicates this part as the two-electron superatom "nucleus". The visualized 1P states are non-symmetric with respect to the center of the cluster and reflect the underlying symmetry of the inner $Ag_{14}S_{12}$ part (the S_{12} shell has an icosahedral symmetry).

Next, we calculated the optical absorption spectrum using the linear response time-dependent density functional theory (Figure 6). The estimated optical gap of ~700 nm is rather close to the measured gap of ~630 nm. The absorption spectrum has three main features in very good agreement with the experimental results. The overall shape of the calculated spectrum and the positions of the main features at 547, 448, and 398 nm coincide well with the measured spectrum. The two shortest wavelength bands (398 and 448 nm) are almost precisely at the same positions as the measured peaks (400 and 446 nm, respectively). The 547 nm peak has a shoulder around 617 nm, while the measured peak at 530 nm has a single maximum.

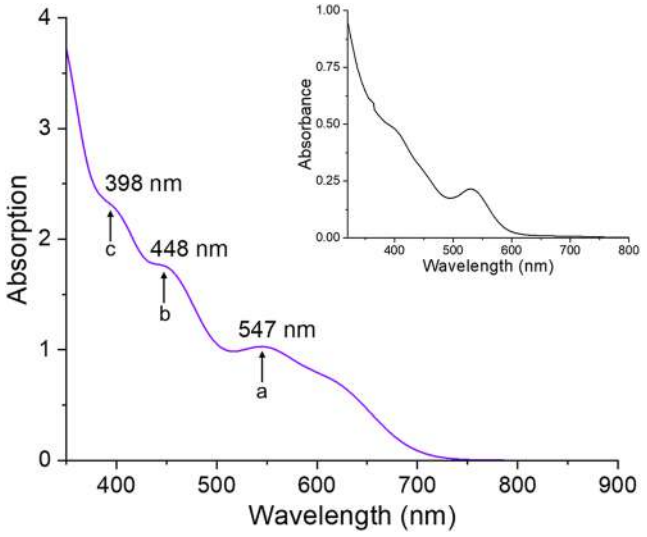


Figure 6. Calculated optical absorption spectrum of the Ag_{62} cluster (in purple) as compared to the experimental spectrum shown in the inset. The main features are labeled with arrows.

Origin of the absorption bands was analyzed using time-dependent density functional perturbation theory and dipole transition contribution maps (DTCM). The DTCM shows the most important strengthening and screening contributions in a contour plot for each band as decomposed to the transitions between occupied and unoccupied Kohn–Sham states. The analysis was done here for all three main bands and the longest wavelength shoulder. All of the DTCM plots are shown in Figure S37. Analysis of the shoulder feature at 617 nm in Figure S37a confirms the optical activity of the 1S to 1P transitions over the HOMO–LUMO gap. The first main peak still has a weak contribution from 1S to 1P transitions, but the main contribution is already from the states between −1.0 eV and −1.5 eV to 1P states. Based on the analysis, there is no optical activity from the 1S to LUMO+3 state, which can therefore be separated from the 1P states seen at LUMO, LUMO+1, and LUMO+2. For the two shorter wavelength peaks (547 and 448 nm), the main contributions are from lower energy occupied states between −1.0 eV and −2.0 eV to 1P states, while the shortest wavelength peak (398 nm) does not have contributions from 1S or 1P states.

CONCLUSIONS

In summary, we have synthesized a large silver/silver-sulfide nanocluster of composition $[Ag_{62}S_{12}(CBT)_{32}]^{4+}$. This nanocluster, protected by *meta*-carborane-thiolates (CBTs), was prepared by a solvothermal process, starting from the metal precursor, $AgNO_3$, and ligand, M_9-COOH (where M_9-COOH is *meta*-carborane-9-thiol-12-carboxylic acid), which undergoes thermochemical decarboxylation. Structural anatomy reveals that this highly symmetrical nanocluster has an interesting multilayer structural arrangement, starting with a fcc Ag_{14} inner kernel, encapsulated by 12 sulfide atoms, followed by a layer of $[Ag_{48}(CBT)_{32}]$ shell. Symmetry analysis of the nanocluster shows that there are five layers of silver atoms, beginning from the center of the molecule: octahedron, cube, icosahedron, truncated cube, and distorted icosahedron; containing 6, 8, 12, 24, and 12 Ag atoms, respectively. The sulfur atoms form three layers: an icosahedron, a dodecahedron, and another icosahedron, consisting of 12, 20, and 12 sulfur atoms, respectively. The overall structural organization (composed of a mixture of Platonic and Archimedean solids) can be considered as a cluster-over-cluster structure, with a silver/silver-sulfide kernel encapsulated by three-dimensional carborane ligands. This is the largest metal nanocluster reported to date, modified with carborane ligands. This cluster exhibits a characteristic optical absorption feature with multiple optical absorption bands. The cluster emits weakly in the NIR region and the excited electrons move across the charged multilayer silver-sulfide skeleton of the cluster. DFT calculations show that the cluster is a two-electron superatomic system having a band gap of 1.77 eV with the lowest-energy optical transitions of 1S to 1P superatomic character. This finding showed the way for further structure–property investigations of large metal clusters decorated with various types of molecular cluster cages.

EXPERIMENTAL SECTION

Chemicals Used. Silver nitrate ($AgNO_3$) was purchased from Rankem Chemicals. *Meta*-carborane-9-thiol-12-carboxylic acid (M_9-COOH) was synthesized following our previous report.[63] Crystalline

https://doi.org/10.1021/acsnano.5c11836
ACS Nano 2025, 19, 35015–35026

M_9-COOH ligands (98.9% purity) were used for the thermochemical synthesis of the Ag_{62} cluster. High-performance liquid chromatography (HPLC)-grade solvents, including dichloromethane, chloroform, *N*,*N*-dimethylformamide, acetonitrile, and methanol (99.5%), were sourced from Rankem Chemicals and Finar, India. All of the chemicals were commercially available and used as such without further purification.

Synthesis of M_9-COOH Ligand. 2 g of portion (11.33 mmol) of *meta*-carborane-9-thiol was dissolved in 100 mL of dry and freshly distilled diethyl ether under inert conditions of argon, and the flask with the reaction mixture was cooled to −78 °C using an acetone bath with dry ice. *n*-Butyllithium (10.0 mL, 24.6 mmol) was added dropwise via a septum over a period of 20 min, which resulted in a precipitate of a white solid. The mixture was further stirred for another hour before an excess of dry ice was added to it, and the mixture was then left at room temperature to warm up slowly under an argon atmosphere. Distilled water (200 mL) was added, the mixture was shaken, and the ether fraction was separated. The aqueous solution was acidified with 30 mL of aqueous solution of hydrochloric acid (∼15%), and a white solid precipitated immediately. The mixture was extracted using diethyl ether (5 × 50 mL), and the collected ether fractions were dried by standing over anhydrous $MgSO_4$. The crude product was purified by sublimation (80 °C) to yield (∼40%) the white microcrystalline product, which was used further for the synthesis of the Ag_{62} nanocluster.

Thermochemical Synthesis of the Ag_{62} Nanocluster. The Ag_{62} cluster was synthesized by following a solvothermal synthetic method. In brief, 20 mg (0.12 mM) of $AgNO_3$ was dissolved in 2 mL of methanol upon stirring. After 20 min, 3 mL of DMF was mixed with the solution, followed by a dropwise addition of 25 mg (0.11 mM) of M_9-COOH ligand (dissolved in 1 mL of DMF). After 1 h of additional stirring at room temperature, the transparent mixture was then transferred either to a closed glass bottle or a Teflon-lined hydrothermal bomb and placed in a preheated oven (75 ± 3 °C) for 15 h. A red-colored solution was formed in the container during the thermal process. After the treatment, the solution was gradually cooled to room temperature (25 °C). The red solution was centrifuged and left to crystallize at room temperature in a dark environment. Red crystals were formed at room temperature after one month of crystallization from a DMF/methanol (1:1 v/v) saturated solution. The yield of the Ag_{62} crystals was ∼75% based on $AgNO_3$. The crystalline samples were redissolved in DMF for further analysis.

ASSOCIATED CONTENT

Supporting Information

The Supporting Information is available free of charge at https://pubs.acs.org/doi/10.1021/acsnano.5c11836.

Experimental section, instrumentation, computational details, X-ray crystallographic details, and additional experimental and computational results (PDF)

M40 new file (PDF)

M50 new file (PDF)

Accession Codes

Single-crystal X-ray diffraction data of Ag_{62} (CCDC 2374547). This data can be obtained free of charge via www.ccdc.cam.ac.uk/ data_request/cif.

AUTHOR INFORMATION

Corresponding Authors

Kumaran Nair Valsala Devi Adarsh − *Department of Physics, Indian Institute of Science Education and Research Bhopal, Bhopal 462066, India;* orcid.org/0000-0002-6337-6545; Email: adarsh@iiserb.ac.in

Hannu Häkkinen − *Departments of Physics and Chemistry, Nanoscience Center, University of Jyväskylä, FI 40014 Jyväskylä, Finland;* orcid.org/0000-0002-8558-5436; Email: hannu.j.hakkinen@jyu.fi

Tomas Base − *Department of Syntheses, Institute of Inorganic Chemistry, The Czech Academy of Sciences, 250 68 Husinec-Řež, Czech Republic;* orcid.org/0000-0003-2533-8705; Email: tbase@iic.cas.cz

Thalappil Pradeep − *DST Unit of Nanoscience (DST UNS) and Thematic Unit of Excellence (TUE), Department of Chemistry, Indian Institute of Technology, Madras, Chennai 600036, India;* orcid.org/0000-0003-3174-534X; Email: pradeep@iitm.ac.in

Authors

Arijit Jana − *DST Unit of Nanoscience (DST UNS) and Thematic Unit of Excellence (TUE), Department of Chemistry, Indian Institute of Technology, Madras, Chennai 600036, India;* orcid.org/0000-0002-5676-0688

Vivek Yadav − *DST Unit of Nanoscience (DST UNS) and Thematic Unit of Excellence (TUE), Department of Chemistry, Indian Institute of Technology, Madras, Chennai 600036, India;* orcid.org/0009-0004-0244-0541

Monika Kučeráková − *Department of Structure Analysis, Institute of Physics, The Czech Academy of Sciences, Prague 8 182 21, Czech Republic;* orcid.org/0000-0002-1177-9238

Sami Malola − *Departments of Physics and Chemistry, Nanoscience Center, University of Jyväskylä, FI 40014 Jyväskylä, Finland*

Amoghavarsha Ramachandra Kini − *DST Unit of Nanoscience (DST UNS) and Thematic Unit of Excellence (TUE), Department of Chemistry, Indian Institute of Technology, Madras, Chennai 600036, India;* orcid.org/0009-0003-6863-7729

Swetashree Acharya − *DST Unit of Nanoscience (DST UNS) and Thematic Unit of Excellence (TUE), Department of Chemistry, Indian Institute of Technology, Madras, Chennai 600036, India*

Ajay K. Poonia − *Department of Physics, Indian Institute of Science Education and Research Bhopal, Bhopal 462066, India*

Jan Macháček − *Department of Syntheses, Institute of Inorganic Chemistry, The Czech Academy of Sciences, 250 68 Husinec-Řež, Czech Republic;* orcid.org/0000-0003-4723-0789

Complete contact information is available at: https://pubs.acs.org/10.1021/acsnano.5c11836

Notes

The authors declare no competing financial interest.

ACKNOWLEDGMENTS

A.J. acknowledges an institute research fellowship from IIT Madras. V.Y. and S.A. acknowledge Prime Minister's Research Fellowships (PMRF) from the Government of India (GoI). A.R.K. thanks the GoI for a CSIR fellowship. K.N.V.D.A. gratefully acknowledges funding from the Science and Engineering Research Board (project no. CRG/2019/002808) and Department of Science and Technology (FIST) project for the Department of Physics, IISER Bhopal (PSI-195/2014) and DST/NM/TUE/QM-8/2019(G)/1). T.B. and J.M. thank the support of the Ministry of Education, Youth and Sports of the Czech Republic (grant no. LTAIN19152, Program Inter-Excellence, subprogram Inter-

Action, and the project e-INFRA CZ, ID: 90254, providing computational resources), and the Czech Academy of Sciences (project Mobility Plus DAAD 25-07). The computational work at the University of Jyväskylä was supported by the grant from the Research Council of Finland. The computations were performed at the Finnish National Supercomputing Center CSC. T.P. thanks funding from the Center of Excellence (CoE) on Molecular Materials and Functions under the Institute of Eminence (IoE) scheme of IIT Madras, Science and Engineering Research Board (SERB), India, for funding through the SPR/2021/000439 research grant and a JC Bose Fellowship.

ABBREVIATIONS

CBT, *meta*-carborane-thiolate; NIR, near-infrared; DMF, dimethylformamide; M_9-COOH, *meta*-carborane-9-thiol-12-carboxylic acid; M_9, *meta*-carborane-9-thiol; EDS, energy-dispersive spectroscopy; fcc, face-centered cubic; Ih, icosahedron; Oh, octahedron; ESI, electrospray ionization; CE, collision energy; XRD, X-ray diffraction; HRTEM, high-resolution transmission electron microscope; XPS, X-ray photoelectron spectroscopy; BE, binding energy; IR, infrared; fs-TA, femtosecond transient absorption; GSPB, ground state photobleach; ESA, excited state absorption; DFT, density functional theory; HOMO, highest occupied molecular orbital; LUMO, lowest unoccupied molecular orbital; DTCM, dipole transition contribution map.

REFERENCES

(1) Jin, R.; Zeng, C.; Zhou, M.; Chen, Y. Atomically Precise Colloidal Metal Nanoclusters and Nanoparticles: Fundamentals and Opportunities. *Chem. Rev.* **2016**, *116*, 10346−10413.

(2) Chakraborty, I.; Pradeep, T. Atomically Precise Clusters of Noble Metals: Emerging Link between Atoms and Nanoparticles. *Chem. Rev.* **2017**, *117* (12), 8208−8271.

(3) Luo, X. M.; Li, Y. K.; Dong, X. Y.; Zang, S. Q. Platonic and Archimedean Solids in Discrete Metal-Containing Clusters. *Chem. Soc. Rev.* **2023**, *52* (1), 383−444.

(4) Deng, G.; Malola, S.; Yuan, P.; Liu, X.; Teo, B. K.; Häkkinen, H.; Zheng, N. Enhanced Surface Ligands Reactivity of Metal Clusters by Bulky Ligands for Controlling Optical and Chiral Properties. *Angew. Chem., Int. Ed.* **2021**, *60* (23), 12897−12903.

(5) Reato, M.; Dainese, T.; Antonello, S.; Maran, F. Electron Transfer in Films of Atomically Precise Gold Nanoclusters. *Chem. Mater.* **2021**, *33* (11), 4177−4187.

(6) Díez, I.; Pusa, M.; Kulmala, S.; Jiang, H.; Walther, A.; Goldmann, A. S.; Müller, A. H. E.; Ikkala, O.; Ras, R. H. A. Color Tunability and Electrochemiluminescence of Silver Nanoclusters. *Angew. Chem., Int. Ed.* **2009**, *48* (12), 2122−2125.

(7) Kang, X.; Zhu, M. Tailoring the Photoluminescence of Atomically Precise Nanoclusters. *Chem. Soc. Rev.* **2019**, *48* (8), 2422−2457.

(8) Feng, A.; Hou, S.; Yan, J.; Wu, Q.; Tang, Y.; Yang, Y.; Shi, J.; Xiao, Z. Y.; Lambert, C. J.; Zheng, N.; Hong, W. Conductance Growth of Single-Cluster Junctions with Increasing Sizes. *J. Am. Chem. Soc.* **2022**, *144* (34), 15680−15688.

(9) Abbas, M. A.; Kamat, P. V.; Bang, J. H. Thiolated Gold Nanoclusters for Light Energy Conversion. *ACS Energy Lett.* **2018**, *3* (4), 840−854.

(10) Luo, Z.; Zheng, K.; Xie, J. Engineering Ultrasmall Water-Soluble Gold and Silver Nanoclusters for Biomedical Applications. *Chem. Commun.* **2014**, *50* (40), 5143−5155.

(11) Jose, A.; Jana, A.; Gupte, T.; Nair, A. S.; Unni, K.; Nagar, A.; Kini, A. R.; Spoorthi, B. K.; Jana, S. K.; Pathak, B.; Pradeep, T. Vertically Aligned Nanoplates of Atomically Precise Co_6S_8 Cluster for Practical Arsenic Sensing. *ACS Mater. Lett.* **2023**, *5* (3), 893−899.

(12) Kumar, J. S.; Jana, A.; Raman, J.; Veera, H. M.; Kini, A. R.; Roy, J.; Jana, S. K.; Thomas, T.; Pradeep, T. Cysteine-Protected Antibacterial Spheroids of Atomically Precise Copper Clusters for Direct and Affordable Arsenic Detection from Drinking Water. *Environ. Sci. Technol. Lett.* **2024**, *11* (8), 831−837.

(13) Hua, Y.; Huang, J. H.; Shao, Z. H.; Luo, X. M.; Wang, Z. Y.; Liu, J. Q.; Zhao, X.; Chen, X.; Zang, S. Q. Composition-Dependent Enzyme Mimicking Activity and Radiosensitizing Effect of Bimetallic Clusters to Modulate Tumor Hypoxia for Enhanced Cancer Therapy. *Adv. Mater.* **2022**, *34*, No. 2203734.

(14) Qin, L.; Sun, F.; Gong, Z.; Ma, G.; Chen, Y.; Tang, Q.; Qiao, L.; Wang, R.; Liu, Z. Q.; Tang, Z. Electrochemical NO_3^- Reduction Catalyzed by Atomically Precise $Ag_{30}Pd_4$ Bimetallic Nanocluster: Synergistic Catalysis or Tandem Catalysis? *ACS Nano* **2023**, *17* (13), 12747−12758.

(15) Du, Y.; Sheng, H.; Astruc, D.; Zhu, M. Atomically Precise Noble Metal Nanoclusters as Efficient Catalysts: A Bridge between Structure and Properties. *Chem. Rev.* **2020**, *120* (2), 526−622.

(16) Kunwar, P.; Hassinen, J.; Bautista, G.; Ras, R. H. A.; Toivonen, J. Direct Laser Writing of Photostable Fluorescent Silver Nanoclusters in Polymer Films. *ACS Nano* **2014**, *8* (11), 11165−11171.

(17) Wang, Z.; Alkan, F.; Aikens, C. M.; Kurmoo, M.; Zhang, Z. Y.; Song, K. P.; Tung, C. H.; Sun, D. An Ultrastable 155-Nuclei Silver Nanocluster Protected by Thiacalix[4]Arene and Cyclohexanethiol for Photothermal Conversion. *Angew. Chem., Int. Ed.* **2022**, *61*, No. e202206742.

(18) Wang, Z.; Li, L.; Feng, L.; Gao, Z.; Tung, C.; Zheng, L.; Sun, D. Solvent-Controlled Condensation of $[Mo_2O_5(PTC4A)_2]^{6-}$ Metalloligand in Stepwise Assembly of Hexagonal and Rectangular Ag_{18} Nanoclusters. *Angew. Chem.* **2022**, *134* (20), No. e202200823, DOI: 10.1002/ange.202200823.

(19) Fuhr, O.; Dehnen, S.; Fenske, D. Chalcogenide Clusters of Copper and Silver from Silylated Chalcogenide Sources. *Chem. Soc. Rev.* **2013**, *42* (4), 1871−1906.

(20) Su, Y. M.; Wang, Z.; Tung, C. H.; Sun, D.; Schein, S. Keplerate Ag_{192} Cluster with 6 Silver and 14 Chalcogenide Octahedral and Tetrahedral Shells. *J. Am. Chem. Soc.* **2021**, *143* (33), 13235−13244.

(21) Langer, R.; Breitung, B.; Wünsche, L.; Fenske, D.; Fuhr, O. Functionalised Silver Chalcogenide Clusters. *Z. Anorg. Allg. Chem.* **2011**, *637* (7−8), 995−1006.

(22) Bestgen, S.; Fuhr, O.; Breitung, B.; Kiran Chakravadhanula, V. S.; Guthausen, G.; Hennrich, F.; Yu, W.; Kappes, M. M.; Roesky, P. W.; Fenske, D. $[Ag_{115}S_{34}(SCH_2C_6H_4{}^tBu)_{47}(Dpph)_6]$: Synthesis, Crystal Structure and NMR Investigations of a Soluble Silver Chalcogenide Nanocluster. *Chem. Sci.* **2017**, *8* (3), 2235−2240.

(23) Fenske, D.; Persau, C.; Dehnen, S.; Anson, C. E. Synthesen Und Kristallstrukturanalysen Der Ag-S-Cluster $[Ag_{70}S_{20}(SPh)_{28}(Dppm)_{10}](CF_3CO_2)_2$ and $[Ag_{262}S_{100}(S^tBu)_{62}(Dppb)_6]$. *Angew. Chem.* **2004**, *116* (3), 309−313.

(24) Anson, C. E.; Eichöfer, A.; Issac, I.; Fenske, D.; Fuhr, O.; Sevillano, P.; Persau, C.; Stalke, D.; Zhang, J. Synthesis and Crystal Structures of the Ligand-Stabilized Silver Chalcogenide Clusters $[Ag_{154}Se_{77}(Dppxy)_{18}]$, $[Ag_{320}(S^tBu)_{60}S_{130}(Dppp)_{12}]$, $[Ag_{352}S_{128}(S^tC_5H_{11})_{96}]$, and $[Ag_{490}S_{188}(S^tC_5H_{11})_{114}]$. *Angew. Chem., Int. Ed.* **2008**, *47* (7), 1326−1331.

(25) Zhang, S. S.; Havenridge, S.; Zhang, C.; Wang, Z.; Feng, L.; Gao, Z. Y.; Aikens, C. M.; Tung, C. H.; Sun, D. Sulfide Boosting Near-Unity Photoluminescence Quantum Yield of Silver Nanocluster. *J. Am. Chem. Soc.* **2022**, *144* (40), 18305−18314.

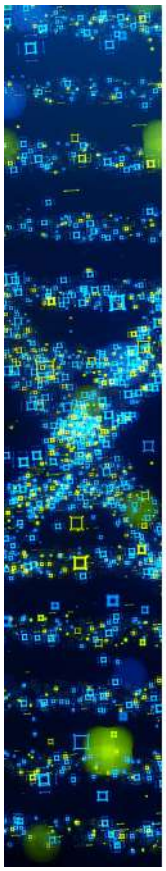
(26) Wu, T.; Zhang, Q.; Hou, Y.; Wang, L.; Mao, C.; Zheng, S. T.; Bu, X.; Feng, P. Monocopper Doping in Cd-In-S Supertetrahedral Nanocluster via Two-Step Strategy and Enhanced Photoelectric Response. *J. Am. Chem. Soc.* **2013**, *135* (28), 10250−10253.

(27) Song, Y.; Lambright, K.; Zhou, M.; Kirschbaum, K.; Xiang, J.; Xia, A.; Zhu, M.; Jin, R. Large-Scale Synthesis, Crystal Structure, and Optical Properties of the $Ag_{146}Br_2(SR)_{80}$ Nanocluster. *ACS Nano* **2018**, *12* (9), 9318−9325.

(28) Desireddy, A.; Conn, B. E.; Guo, J.; Yoon, B.; Barnett, R. N.; Monahan, B. M.; Kirschbaum, K.; Griffith, W. P.; Whetten, R. L.;

Landman, U.; Bigioni, T. P. Ultrastable Silver Nanoparticles. *Nature* **2013**, *501* (7467), 399−402.
(29) Joshi, C. P.; Bootharaju, M. S.; Alhilaly, M. J.; Bakr, O. M. $[Ag_{25}(SR)_{18}]$-: The "Golden" Silver Nanoparticle. *J. Am. Chem. Soc.* **2015**, *137* (36), 11578−11581.
(30) Yang, H.; Wang, Y.; Huang, H.; Gell, L.; Lehtovaara, L.; Malola, S.; Häkkinen, H.; Zheng, N. All-Thiol-Stabilized Ag_{44} and $Au_{12}Ag_{32}$ Nanoparticles with Single-Crystal Structures. *Nat. Commun.* **2013**, *4*, No. 2422.
(31) Yang, H.; Wang, Y.; Chen, X.; Zhao, X.; Gu, L.; Huang, H.; Yan, J.; Xu, C.; Li, G.; Wu, J.; Edwards, A. J.; Dittrich, B.; Tang, Z.; Wang, D.; Lehtovaara, L.; Häkkinen, H.; Zheng, N. Plasmonic Twinned Silver Nanoparticles with Molecular Precision. *Nat. Commun.* **2016**, *7*, No. 12809.
(32) Ren, L.; Yuan, P.; Su, H.; Malola, S.; Lin, S.; Tang, Z.; Teo, B. K.; Häkkinen, H.; Zheng, L.; Zheng, N. Bulky Surface Ligands Promote Surface Reactivities of $[Ag_{141}X_{12}(S\text{-}Adm)_{40}]^{3+}$ (X = Cl, Br, I) Nanoclusters: Models for Multiple-Twinned Nanoparticles. *J. Am. Chem. Soc.* **2017**, *139* (38), 13288−13291.
(33) Zhou, Q.; Kaappa, S.; Malola, S.; Lu, H.; Guan, D.; Li, Y.; Wang, H.; Xie, Z.; Ma, Z.; Häkkinen, H.; Zheng, N.; Yang, X.; Zheng, L. Real-Space Imaging with Pattern Recognition of a Ligand-Protected Ag_{374} Nanocluster at Sub-Molecular Resolution. *Nat. Commun.* **2018**, *9*, No. 2948.
(34) Bootharaju, M. S.; Lee, S.; Deng, G.; Malola, S.; Baek, W.; Häkkinen, H.; Zheng, N.; Hyeon, T. $Ag_{44}(EBT)_{26}(TPP)_4$ Nanoclusters With Tailored Molecular and Electronic Structure. *Angew. Chem.* **2021**, *133* (16), 9120−9126.
(35) Bootharaju, M. S.; Dey, R.; Gevers, L. E.; Hedhili, M. N.; Basset, J. M.; Bakr, O. M. A New Class of Atomically Precise, Hydride-Rich Silver Nanoclusters Co-Protected by Phosphines. *J. Am. Chem. Soc.* **2016**, *138* (42), 13770−13773.
(36) Lei, Z.; Wan, X.-K.; Yuan, S.-F.; Guan, Z.-J.; Wang, Q.-M. Alkynyl Approach toward the Protection of Metal Nanoclusters. *Acc. Chem. Res.* **2018**, *51* (10), 2465−2474.
(37) Qu, M.; Li, H.; Xie, L. H.; Yan, S. T.; Li, J. R.; Wang, J. H.; Wei, C. Y.; Wu, Y. W.; Zhang, X. M. Bidentate Phosphine-Assisted Synthesis of an All-Alkynyl-Protected Ag_{74} Nanocluster. *J. Am. Chem. Soc.* **2017**, *139* (36), 12346−12349.
(38) Najafabadi, B. K.; Corrigan, J. F. N-Heterocyclic Carbene Stabilized Ag-P Nanoclusters. *Chem. Commun.* **2015**, *51* (4), 665−667.
(39) Dhayal, R. S.; Liao, J.-H.; Liu, Y.-C.; Chiang, M.-H.; Kahlal, S.; Saillard, J.-Y.; Liu, C. W. $[Ag_{21}\{S_2P(O^iPr)_2\}_{12}]^+$: An Eight-Electron Superatom. *Angew. Chem.* **2015**, *127*, 3773−3777.
(40) Yuan, S. F.; Xu, C. Q.; Liu, W. Di.; Zhang, J. X.; Li, J.; Wang, Q. M. Rod-Shaped Silver Supercluster Unveiling Strong Electron Coupling between Substituent Icosahedral Units. *J. Am. Chem. Soc.* **2021**, *143* (31), 12261−12267.
(41) Cerretani, C.; Kanazawa, H.; Vosch, T.; Kondo, J. Crystal Structure of a NIR-Emitting DNA-Stabilized Ag_{16} Nanocluster. *Angew. Chem.* **2019**, *131* (48), 17313−17317.
(42) Guan, Z. J.; Zeng, J. L.; Nan, Z. A.; Wan, X. K.; Lin, Y. M.; Wang, Q. M. Thiacalix[4]Arene: New Protection for Metal Nanoclusters. *Sci. Adv.* **2016**, *2* (8), No. e1600323.
(43) Wang, Z.; Su, H. F.; Gong, Y. W.; Qu, Q. P.; Bi, Y. F.; Tung, C. H.; Sun, D.; Zheng, L. S. A Hierarchically Assembled 88-Nuclei Silver-Thiacalix[4]Arene Nanocluster. *Nat. Commun.* **2020**, *11*, No. 308.
(44) Liu, K.-G.; Gao, X.-M.; Liu, T.; Hu, M.-L.; Jiang, D. All-Carboxylate-Protected Superatomic Silver Nanocluster with an Unprecedented Rhombohedral Ag_8 Core. *J. Am. Chem. Soc.* **2020**, *142* (40), 16905−16909.
(45) Poater, J.; Viñas, C.; Bennour, I.; Escayola, S.; Solà, M.; Teixidor, F. Too Persistent to Give Up: Aromaticity in Boron Clusters Survives Radical Structural Changes. *J. Am. Chem. Soc.* **2020**, *142* (20), 9396−9407.
(46) Núñez, R.; Tarrés, M.; Ferrer-Ugalde, A.; De Biani, F. F.; Teixidor, F. Electrochemistry and Photoluminescence of Icosahedral Carboranes, Boranes, Metallacarboranes, and Their Derivatives. *Chem. Rev.* **2016**, *116* (23), 14307−14378.
(47) Fister, T. T.; Vila, F. D.; Seidler, G. T.; Svec, L.; Linehan, J. C.; Cross, J. O. Local Electronic Structure of Dicarba-Closo-Dodecarboranes $C_2B_{10}H_{12}$. *J. Am. Chem. Soc.* **2008**, *130* (3), 925−932.
(48) Jana, A.; Jash, M.; Dar, W. A.; Roy, J.; Chakraborty, P.; Paramasivam, G.; Lebedkin, S.; Kirakci, K.; Manna, S.; Antharjanam, S.; Machacek, J.; Kucerakova, M.; Ghosh, S.; Lang, K.; Kappes, M. M.; Base, T.; Pradeep, T. Carborane-Thiol Protected Copper Nanoclusters: Stimuli-Responsive Materials with Tunable Phosphorescence. *Chem. Sci.* **2023**, *14* (6), 1613−1626.
(49) Jana, A.; Duary, S.; Das, A.; Kini, A. R.; Acharya, S.; Machacek, J.; Pathak, B.; Base, T.; Pradeep, T. Multicolor Photoluminescence of Cu_{14} Clusters Modulated Using Surface Ligands. *Chem. Sci.* **2024**, *15* (34), 13741−13752.
(50) Wang, J.; Cai, J.; Ren, K. X.; Liu, L.; Zheng, S. J.; Wang, Z. Y.; Zang, S. Q. Stepwise Structural Evolution toward Robust Carboranealkynyl-Protected Copper Nanocluster Catalysts for Nitrate Electroreduction. *Sci. Adv.* **2024**, *10* (18), No. eadn7556.
(51) Wang, J.; Xu, F.; Wang, Z.-Y.; Zang, S.-Q.; Mak, T. C. W. Ligand-Shell Engineering of a Au_{28} Nanocluster Boosts Electrocatalytic CO_2 Reduction. *Angew. Chem., Int. Ed.* **2022**, *61*, No. e202207492.
(52) Jana, A.; Spoorthi, B. K.; Nair, A. S.; Nagar, A.; Pathak, B.; Base, T.; Pradeep, T. A Luminescent Cu_4 Cluster Film Grown by Electrospray Deposition: A Nitroaromatic Vapour Sensor. *Nanoscale* **2023**, *15*, 8141−8147.
(53) Kini, A. R.; Debta, S.; Jana, A.; Aparna, C.; Yadav, V.; Kusiak, N.; Base, T.; Waghmare, U. V.; Ghosh, P.; Pradeep, T. Nanomechanical Investigations of Crystals of Copper Nanocluster Isomorphs: Enhanced Hardness of the Low-Density Analogue. *Chem. Mater.* **2025**, *37* (3), 1284−1296.
(54) Wang, Q. Y.; Wang, J.; Wang, S.; Wang, Z. Y.; Cao, M.; He, C. L.; Yang, J. Q.; Zang, S. Q.; Mak, T. C. W. O-Carborane-Based and Atomically Precise Metal Clusters as Hypergolic Materials. *J. Am. Chem. Soc.* **2020**, *142* (28), 12010−12014.
(55) Huang, J. H.; Ji, A. Q.; Wang, Z. Y.; Wang, Q. Y.; Zang, S. Q. Boosting 2000-Fold Hypergolic Ignition Rate of Carborane by Substitutes Migration in Metal Clusters. *Adv. Sci.* **2024**, *11*, No. 2401861.
(56) Wang, Z. Y.; Wang, M. Q.; Li, Y. L.; Luo, P.; Jia, T. T.; Huang, R. W.; Zang, S. Q.; Mak, T. C. W. Atomically Precise Site-Specific Tailoring and Directional Assembly of Superatomic Silver Nanoclusters. *J. Am. Chem. Soc.* **2018**, *140* (3), 1069−1076.
(57) Jana, A.; Jash, M.; Poonia, A. K.; Paramasivam, G.; Islam, M. R.; Chakraborty, P.; Antharjanam, S.; Machacek, J.; Ghosh, S.; Adarsh, K. N. V. D.; Base, T.; Pradeep, T. Light-Activated Intercluster Conversion of an Atomically Precise Silver Nanocluster. *ACS Nano* **2021**, *15* (10), 15781−15793.
(58) Li, Y. L.; Wang, Z. Y.; Ma, X. H.; Luo, P.; Du, C. X.; Zang, S. Q. Distinct Photophysical Properties in Atom-Precise Silver and Copper Nanocluster Analogues. *Nanoscale* **2019**, *11* (12), 5151−5157.
(59) Yadav, V.; Jana, A.; Acharya, S.; Malola, S.; Nagar, H.; Sharma, A.; Kini, A. R.; Antharjanam, S.; Machacek, J.; Nair, K.; Devi, V.; Base, T.; Häkkinen, H.; Pradeep, T. Site-Specific Substitution in Atomically Precise Carboranethiol-Protected Nanoclusters and Concomitant Changes in Electronic Properties. *Nat. Commun.* **2025**, *16*, No. 1197.
(60) Jana, A.; Unnikrishnan, P. M.; Poonia, A. K.; Roy, J.; Jash, M.; Paramasivam, G.; Machacek, J.; Adarsh, K. N. V. D.; Base, T.; Pradeep, T. Carboranethiol-Protected Propeller-Shaped Photoresponsive Silver Nanomolecule. *Inorg. Chem.* **2022**, *61* (23), 8593−8603.
(61) Huang, J. H.; Wang, Z. Y.; Zang, S. Q.; Mak, T. C. W. Spontaneous Resolution of Chiral Multi-Thiolate-Protected Ag_{30} Nanoclusters. *ACS Cent. Sci.* **2020**, *6* (11), 1971−1976.
(62) Huang, J. H.; Si, Y.; Dong, X. Y.; Wang, Z. Y.; Liu, L. Y.; Zang, S. Q.; Mak, T. C. W. Symmetry Breaking of Atomically Precise Fullerene-like Metal Nanoclusters. *J. Am. Chem. Soc.* **2021**, *143* (32), 12439−12444.

(63) Goronzy, D. P.; Staněk, J.; Avery, E.; Guo, H.; Bastl, Z.; Dušek, M.; Gallup, N. M.; Gün, S.; Kučeráková, M.; Levandowski, B. J.; Macháček, J.; Šícha, V.; Thomas, J. C.; Yavuz, A.; Houk, K. N.; Danlşman, M. F.; Mete, E.; Alexandrova, A. N.; Baše, T.; Weiss, P. S. Influence of Terminal Carboxyl Groups on the Structure and Reactivity of Functionalized M-Carboranethiolate Self-Assembled Monolayers. *Chem. Mater.* **2020**, *32* (15), 6800−6809.
(64) Xie, Y. P.; Shen, Y. L.; Duan, G. X.; Han, J.; Zhang, L. P.; Lu, X. Silver Nanoclusters: Synthesis, Structures and Photoluminescence. *Mater. Chem. Front.* **2020**, *4* (8), 2205−2222.
(65) Bhattarai, B.; Zaker, Y.; Atnagulov, A.; Yoon, B.; Landman, U.; Bigioni, T. P. Chemistry and Structure of Silver Molecular Nanoparticles. *Acc. Chem. Res.* **2018**, *51* (12), 3104−3113.
(66) Bootharaju, M. S.; Burlakov, V. M.; Besong, T. M. D.; Joshi, C. P.; Abdulhalim, L. G.; Black, D. M.; Whetten, R. L.; Goriely, A.; Bakr, O. M. Reversible Size Control of Silver Nanoclusters via Ligand-Exchange. *Chem. Mater.* **2015**, *27* (12), 4289−4297.
(67) White, K. E.; Avery, E. M.; Cummings, E.; Hong, Z.; Langecker, J.; Vetushka, A.; Dušek, M.; Macháček, J.; Višnák, J.; Endres, J.; Bastl, Z.; Mete, E.; Alexandrova, A. N.; Baše, T.; Weiss, P. S. Competing Intermolecular and Molecule-Surface Interactions: Dipole-Dipole-Driven Patterns in Mixed Carborane Self-Assembled Monolayers. *Chem. Mater.* **2024**, *36* (4), 2085−2095.
(68) Baše, T.; Macháček, J.; Hájková, Z.; Langecker, J.; Kennedy, J. D.; Carr, M. J. Thermal Isomerizations of Monothiolated Carboranes $(HS)C_2B_{10}H_{11}$ and the Solid-State Investigation of 9-(HS)-1,2-$C_2B_{10}H_{11}$ and 9-(HS)-1,7-$C_2B_{10}H_{11}$. *J. Organomet. Chem.* **2015**, *798*, 132−140.
(69) Lee, K.; Harper, J. L.; Kim, T. H.; Chan Noh, H.; Kim, D.; Cheong, P. H.-Y.; Lee, P. H. Regiodivergent Metal-Catalyzed B(4)- and C(1)-Selenylation of o-Carboranes. *Chem. Sci.* **2023**, *14* (3), 643−649.
(70) Quan, Y.; Xie, Z. Controlled Functionalization of o-Carborane via Transition Metal Catalyzed B-H Activation. *Chem. Soc. Rev.* **2019**, *48*, 3660−3673.
(71) Alhilaly, M. J.; Bootharaju, M. S.; Joshi, C. P.; Besong, T. M.; Emwas, A. H.; Juarez-Mosqueda, R.; Kaappa, S.; Malola, S.; Adil, K.; Shkurenko, A.; Häkkinen, H.; Eddaoudi, M.; Bakr, O. M. $[Ag_{67}(SPhMe_2)_{32}(PPh_3)_8]^{3+}$: Synthesis, Total Structure, and Optical Properties of a Large Box-Shaped Silver Nanocluster. *J. Am. Chem. Soc.* **2016**, *138* (44), 14727−14732.
(72) Wang, J. Q.; Shi, S.; He, R. L.; Yuan, S. F.; Yang, G. Y.; Liang, G. J.; Wang, Q. M. Total Structure Determination of the Largest Alkynyl-Protected Fcc Gold Nanocluster Au_{110} and the Study on Its Ultrafast Excited-State Dynamics. *J. Am. Chem. Soc.* **2020**, *142* (42), 18086−18092.
(73) Wang, X.; Zhong, Y.; Li, T.; Wang, K.; Dong, W.; Lu, M.; Zhang, Y.; Wu, Z.; Tang, A.; Bai, X. Sequential Addition of Cations Increases Photoluminescence Quantum Yield of Metal Nanoclusters near Unity. *Nat. Commun.* **2025**, *16*, No. 587.
(74) Li, G.; Lei, Z.; Wang, Q. Luminescent Molecular Ag-S Nanocluster $[Ag_{62}S_{13}(S^tBu)_{32}](BF_4)_4$. *J. Am. Chem. Soc.* **2010**, *132*, 17678−17679.
(75) Jin, S.; Wang, S.; Song, Y.; Zhou, M.; Zhong, J.; Zhang, J.; Xia, A.; Pei, Y.; Chen, M.; Li, P.; Zhu, M. Crystal Structure and Optical Properties of the $[Ag_{62}S_{12}(S^tBu)_{32}]^{2+}$ Nanocluster with a Complete Face-Centered Cubic Kernel. *J. Am. Chem. Soc.* **2014**, *136*, 15559−15565.
(76) Walter, M.; Akola, J.; Lopez-Acevedo, O.; Jadzinsky, P. D.; Calero, G.; Ackerson, C. J.; Whetten, R. L.; Grönbeck, H.; Häkkinen, H. A Unified View of Ligand-Protected Gold Clusters as Superatom Complexes. *Proc. Natl. Acad. Sci. U.S.A.* **2008**, *105* (27), 9157−9162.


CAS BIOFINDER DISCOVERY PLATFORM™
STOP DIGGING THROUGH DATA —START MAKING DISCOVERIES
CAS BioFinder helps you find the right biological insights in seconds
Start your search
CAS
A division of the American Chemical Society

Supporting Information

$[Ag_{62}S_{12}(CBT)_{32}]^{4+}$: A 2.2 nm Two-Electron Superatomic Carborane-Thiolated Silver Nanocluster Exhibiting Multilayer Charge Separation

Arijit Jana,[a] Vivek Yadav,[a] Monika Kučeráková,[b] Sami Malola,[c] Amoghavarsha Ramachandra Kini,[a] Swetashree Acharya,[a] Ajay K. Poonia,[d] Jan Macháček,[e] Kumaran Nair Valsala Devi Adarsh,*[d] Hannu Häkkinen,*[c] Tomas Base,*[e] and Thalappil Pradeep*[a]

[a] DST Unit of Nanoscience (DST UNS) and Thematic Unit of Excellence (TUE), Department of Chemistry, Indian Institute of Technology, Madras, Chennai – 600036, India

[b] Department of Structure Analysis, Institute of Physics, The Czech Academy of Sciences, Na Slovance 2, 182 21 Prague 8, Czech Republic

[c] Departments of Physics and Chemistry, Nanoscience Center, University of Jyväskylä, FI 40014 Jyväskylä, Finland

[d] Department of Physics, Indian Institute of Science Education and Research Bhopal, Bhopal – 462066, India

[e] Department of Syntheses, Institute of Inorganic Chemistry, The Czech Academy of Sciences, 250 68 Husinec-Řež, č.p. 1001, Czech Republic

* Email: *pradeep@iitm.ac.in, tbase@iic.cas.cz, hannu.j.hakkinen@jyu.fi, adarsh@iiserb.ac.in*

Table of content:

Sl. no	Description	Page no
	Instrumentation	4-6
Table S1	Crystallographic parameters and refinement data for Ag_{62} nanocluster	7, 8
	Theoretical calculation	9
Figure S1	The comparative UV-vis absorption spectra of the M_9-COOH ligand and intermediate species formed during the synthesis of Ag_{62} nanocluster	9
Figure S2	The UV-vis absorption spectrum and MS data of the synthesized product obtained from the solvothermal reaction of $AgNO_3$ and M_9 ligand	10
Figure S3	The negative ion mode ESI-mass spectrum of the M_9-COOH ligand	11
Figure S4	Comparative IR and Raman spectra of different samples of M_9-COOH ligands	12
Figure S5	The comparative $^{11}B\{^1H\}$ NMR spectra of the M_9-COOH ligand before and after thermal treatment at 55 °C	13
Figure S6	Synthetic details of direct reduction of $AgNO_3$ and M_9 precursors using $NaBH_4$	14
Figure S7	Synthetic details of the direct reduction of $AgNO_3$ and M_9 precursors using $NaBH_3CN$	15
Figure S8	The EDS spectra measured from three different single crystals of Ag_{62} nanocluster along with atomic weight % of respective elements	16
Figure S9	The Ag_{14}-S_{12} inner skeleton of the Ag_{62} cluster with marked Ag–S distances	16
Figure S10	Various types of silver-sulfide bonding of twelve inner sulfide atoms present in the Ag_{62} cluster	17
Figure S11	Sequential fragmentation of outer $[Ag_{48}S_{32}]$ skeleton of the Ag_{62} cluster	18
Figure S12	The outer $[Ag_{48}S_{32}]$ skeleton of the Ag_{62} cluster with and without thiolated S atoms	18
Figure S13	An independent view of three different symmetry elements in the outer Ag_{48} skeleton	19
Figure S14	An independent view of three symmetry elements in the inner S_{12} and outer S_{32} skeletons	20
Figure S15	Various types of carborane arrangement in the Ag_{62} nanocluster	21
Figure S16	An independent view of the two types of symmetry present in the centroids of 32 carboranes	22
Figure S17	Silver-sulfide bonding of the outer thiolated S atoms connected with carborane ligands	23
Figure S18	Disorder of S atoms in the outer silver sulfide skeleton of the Ag_{62} nanocluster	23
Figure S19	Unit cell molecular packing of the Ag_{62} nanocluster	24
Figure S20	Extended supramolecular packing of the Ag_{62} nanocluster	25
Figure S21	Various types of intermolecular interactions present in the crystal lattice	25
Figure S22	Molecular electrostatic potential mapped on an isosurface of the electron density for *meta*-carborane-9-thiol ligand	26

Figure S23	Residual electron density maps of the solvent molecules or counter ions present in the crystal lattice of Ag_{62} cluster	27
Table S2	A summary of the structurally resolved carborane thiol- and alkynyl-protected metal (gold, silver, copper and alloy) nanoclusters	28-30
Figure S24	Collision energy dependent MS-MS fragmentation pattern of the peak at m/z 3170.42	31
Figure S25	The negative ion mode ESI-MS spectra of two distinct set of Ag_{62} crystals reveal the presence of nitrate as counter ions	32
Figure S26	High resolution TEM micrograph of a cuboidal Ag_{62} crystal	33
Figure S27	TEM images obtained from the drop-cast solution of Ag_{62} clusters	34
Figure S28	The Ag_{62} nanocluster size was analyzed by measuring distances between carborane–carborane and silver–sulfur	34
Figure S29	The XPS spectrum of Ag_{62} crystals	35
Figure S30	The XPS spectral fitting of the S 2p region of Ag_{62} nanocluster	35
Figure S31	Comparative FT-IR spectra of M_9, M_9-COOH and Ag_{62} nanocluster	36
Figure S32	Time-dependent UV-vis absorption spectra of the Ag_{62} nanocluster manifested its stability	37
Figure S33	Kinetic decay traces for 515 nm GSPB under 400 nm pump excitation and fluence of 200 $\mu J.cm^{-2}$	37
Figure S34	Pump fluence dependent comparative decay kinetics of GSPB and ESA peaks	38
Figure S35	TA spectral profile of the Ag_{62} nanocluster in DMF solution under a pump excitation of 400 nm and a fluence of 100 $\mu J.cm^{-2}$	39
Figure S36	PL excitation and emission spectra of Ag_{62} nanocluster	40
Figure S37	Dipole transition contribution map (DTCM) of the selected absorption peaks of the Ag_{62} nanocluster obtained from theoretical calculations	41
	References	42-44

Instrumentation

Optical microscopy: Optical microscopic images of the crystals were collected in transmission mode using a LEICA optical microscope equipped with LAS V4.8 software.

Scanning Electron microscopy: Scanning electron microscopic (SEM) images are recorded using Verios G4 UC, Thermo Scientific field emission scanning electron microscope (FESEM). After transferring the crystal on a carbon tape, gold sputtering (2 min) was performed to increase the conductivity. FESEM images were collected in high vacuum at an operating voltage of 10-15 kV.

UV-vis absorption spectroscopy: UV-vis absorption spectra were measured in transmission mode using Perkin Elmer Lambda 365 UV-vis spectrometer using a bandpass filter of 1 nm. **Photoluminescence spectroscopy:** Photoluminescence spectra were measured using a Jobin Yvon Nanolog fluorescence spectrometer using a slit width of 3 nm and a resolution bandwidth of 5 nm. The Nanolog instrument has a 450 W xenon-arc lamp source, double monochromator with kinetic gratings, associated reflective optics, and CCD detector. Cluster were dissolved in DMF (2.5 ml) was placed in a 1 cm quartz cuvette to measure the spectrum.

Mass spectrometry: Mass spectra of the cluster was measured using Waters Synapt G2Si HDMS instrument. The instrument is equipped with an electrospray ionization source, mass selected ion trap, ion mobility cells, and time of flight mass analyzer. An optimized operating conditions such as flow rate 20 μL/min, capillary voltage 2.5 kV, cone voltage 20 V, source offset 10 V, desolvation gas flow 400 L/min and source temperature 80-100 °C were used for the measurements. Collision-induced dissociation (CID) studies were performed upon colliding the selected molecular ion with argon gas inside the trap cell of the instrument. Gradually increasing the collision energy (CE 0 to 70 for Ag_{62}) leads to the fragmentation of the species. All the measurements used low concentration (~ 1 μg/ml) of cluster sample.

Infrared spectroscopy: FT-IR spectra were measured using a JASCO-4100 FT-IR spectrometer after preparing potassium bromide (KBr) pallets of the respective samples.

NMR Spectroscopy: The $^{11}B\{^{1}H\}$ NMR spectra were obtained using a 600 MHz JEOL ECZ600R/M3 spectrometer. The compound was dissolved in a 2:1 mixture of DMF and deuterated methanol for NMR measurement, utilizing the automatic boron reference mode.

Raman spectroscopy: Raman spectra of M_9-COOH ligand were recorded using a CRM-Alpha 300S, WITec GmbH confocal Raman microscope, equipped with 532 nm frequency doubled Nd:YAG laser having an output power of 650 μW. This instrument was equipped with a Peltier cooled charge-coupled detector system.

X-ray Photoelectron Spectroscopy: XPS data were measured using an ESCA probe TPD equipped with a polychromatic Mg Kα X-ray source ($h\nu$ = 1253.6 eV). The binding energy of the spectral regions of different elements was calibrated with respect to C 1s (285.0 eV).

Femtosecond transient absorption studies: The femtosecond TA measurements were performed using an ultrafast short laser pulse (pulse width 120 fs) centered at 800 nm. The pulse was generated by spectra physics Maitai oscillator with a few hundred nJ energy. The output beam was sent to Ti: sapphire optical amplifier to produce high energy pulses (pulse energy 4 mJ, width 120 fs, repetition rate 1 kHz). The output beam is further split into two parts: the first high-energy beam produces the second harmonic using β-barium borate crystal. The obtained 400 nm pulses are used to excite the sample with an intensity of 250 μJ/cm^2. The second part of the beam was used to generate the white light continuum probe pulses (450-800 nm) by CaF_2 crystal. The computer-controlled motion controller creates the delay between pump and probe pulses. The absorbance changes in the probe beam are due to the pump being calculated using the equation-

$$\Delta A = \log [(s)/I_0(s)] — [I_{ex}(r)/I_0(r)]$$

Where, r and s correspond to the reference and sample, I_{ex} and I_o are transmitted intensities of probe pulse after excitation and in the ground state, respectively. The intensity of the transmitted pulse is measured with the help of MS 2004.

Single crystal X-ray Diffraction: Single-crystal diffraction data were collected on a Rigaku OD Supernova diffractometer using an Atlas S2 CCD detector and mirror collimated Mo-Kα (λ = 0.71073 Å) from a micro-focused sealed X-ray tube. The sample was cooled to 95 K during the measurement. Integration of the CCD images, absorption correction and scaling were performed by software CrysAlisPro. Crystal structures were solved by charge flipping with program SUPERFLIP and refined with the JANA2020 program package by full-matrix least-squares technique on F^2.[1,2] Hydrogen atoms were not visible in difference Fourier maps and were added from geometry. As per common practice hydrogen atoms attached to borons were kept in ideal

positions during the refinement with B-H distance 1.00 Å. The isotropic atomic displacement parameters of hydrogen atoms were evaluated as 1.2Ueq of the parent atom.

All non-solvent and non-hydrogen atoms were refined harmonically. All hydrogen atoms were kept in the geometrically correct positions with the B–H distance of 1 Å. The isotropic atomic displacement parameters of hydrogen atoms were evaluated as $1.2*U_{eq}$ of the parent boron atom. Atoms Ag16 – Ag31 are disordered in two positions (labelled as "a" and "b"). For two atoms of silver (Ag31 and Ag29), a third position (labelled as "c") was observed in the difference Fourier maps. Similarly, five surface sulfur atoms (S19 - S23) were also observed as disordered in two positions (labelled as "a" and "b").

The disorder of carborane cages is modelled using rigid body approaches, where the 12-vertex carboranyl ($C_2B_{10}H_{11}$) cages were modeled as all boron $B_{12}H_{11}$ cages in 21 positions, some of which had partial occupancy. Distinguishing two carbon and 10 boron atoms in each cage was not possibly due to their negligible 1e difference and numerous disorders. All atoms in the vertices were nevertheless clearly visible in the difference Fourier map. There is a residual electron density near some Ag and B atoms, which could refer to even more complicated disorder. However, its modeling is not possible from current data.

Atoms of the solvent molecules (DMF) cannot be clearly distinguished in the electron density maps. Only oxygen atoms are depicted as they match the strongest maxima of the difference Fourier.

Table S1. Crystallographic parameters and refinement data for Ag_{62} nanocluster.

	Ag_{62} – at 95K
CCDC	**2374547**
Empirical formula	$Ag_{62}B_{320}C_{64}H_{352}S_{44}$
Diffractometer	four-cycle diffractometer Cryostream, AtlasS2, Rigaku OD Supernova
M_r /g mol^{-1}	12681.67 (formula weight)
T/K	95
Wavelength / Å	0.71073
Crystal system	Monoclinic
Space group	$P2_1/n$
a/Å	24.3524 (4)
b/Å	35.5608 (5)
c/Å	26.0322 (4)
α/deg	90
β/deg	91.0215 (14)
γ/deg	90
V/Å^3	22540.1 (6)
Z	2

	Ag_{62} – at 95K
Calc. density/g cm^{-3}	1.904
μ mm^{-1}	2.86
F(000)	12100
Crystal size /mm^3	0.19 × 0.09 × 0.08
θ range /°	2.3–26.6°
Index ranges /*hkl*	-33-33, -46-48, -28-32
Reflections collected (R_{int})	0.109
Independent reflections	55437
Completeness /% to θ /°	98, 27.61
Absorption correction	Multi-scan
Max. and min. transmission	Tmin = 1.9, Tmax = 29.7
Data / restraints / constraints / parameters	55437/1/395/632
Goodness-of-fit on F^2	2.28
*R*1, *wR*2 [I>3σ(I)]	0.1474, 0.2800
*R*1, *wR*2 (all data)	0.3006, 0.3202
Largest diff. peak and hole, e$Å^{-3}$	5.83, −4.15

Theoretical calculation

Theoretical calculations were done using density functional theory (DFT) as implemented in software GPAW.[3,4] We used real space grid with 0.2 Å grid spacing and Perdew-Ernzerhof-Burke (PBE) exchange correlation functional in structure optimization that was done for the crystal structure.[5] Structure was optimized until the forces acting on atoms were below 0.05 eV/Å. After structure optimization the further analysis was done using GLLB-sc xc-functional.[6] Density of states was projected to spherical harmonics functions centered at the center of the mass of the cluster.[7] Optical absorption spectra were calculated using linear response time dependent density functional theory (LR-TDDFT) using PBE xc-functional as a LR-TDDFT kernel.[3,8] Origin of the peaks of the absorption spectra were analysed using dipole transition contribution maps which is showing the strengthening and screening contributions to total transition dipole moment as decomposed to Kohn-Sham basis.[9]

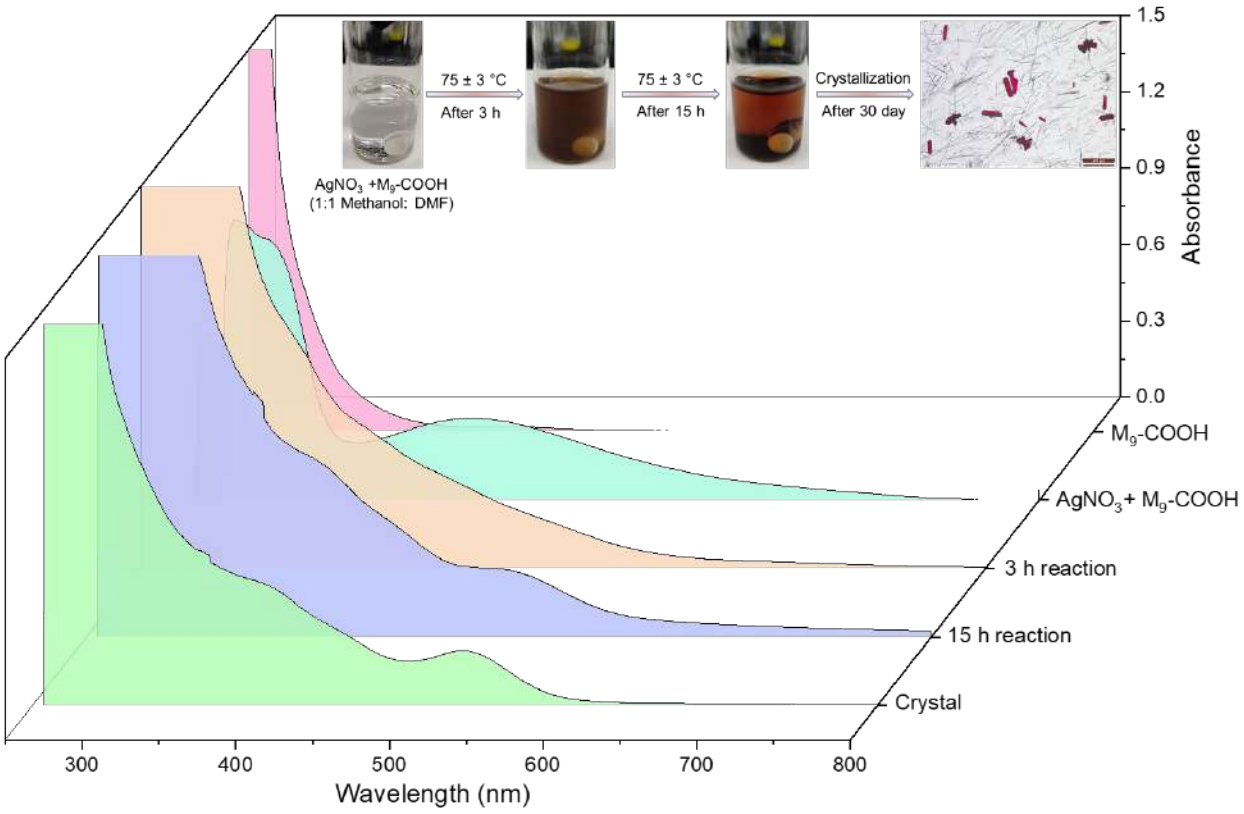


Figure S1. The comparative UV-vis absorption spectra of the M_9-COOH ligand and intermediate species formed during the synthesis of Ag_{62} nanocluster. Inset shows the photographs capturing the reaction vial at different stages throughout the synthesis process. An optical micrograph displays rod-shaped Ag_{62} crystals.

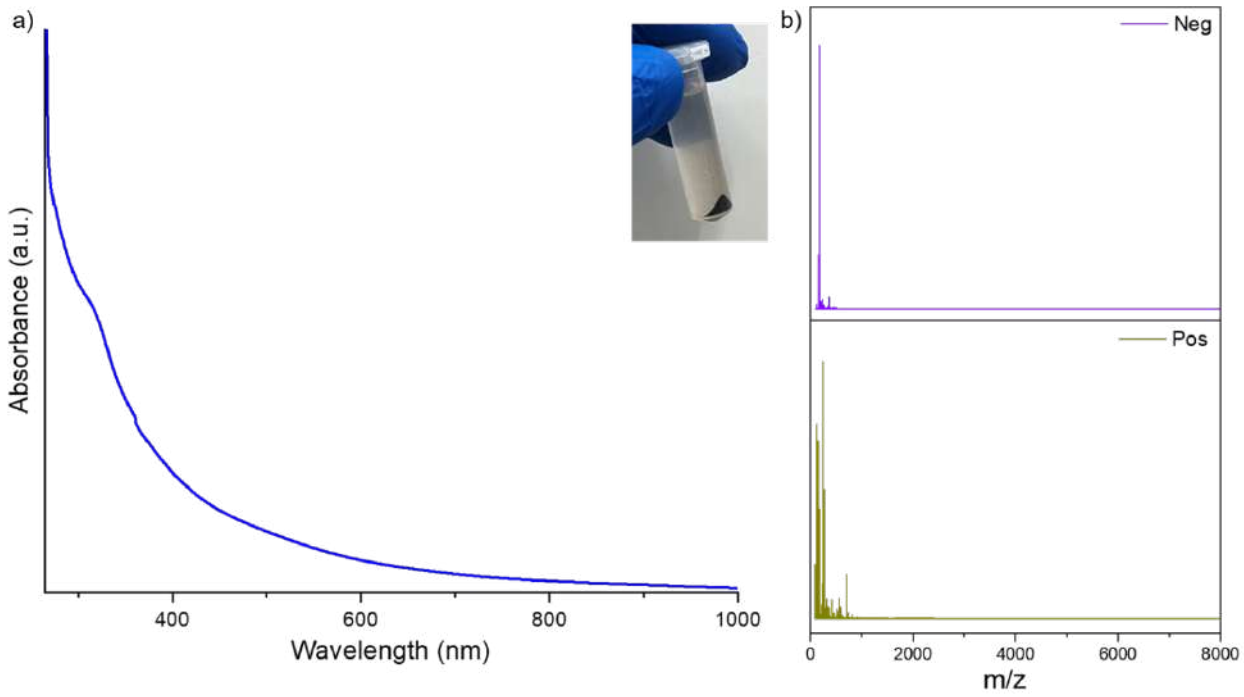


Figure S2. a) The UV-vis absorption spectrum of the synthesized product obtained from the solvothermal reaction of $AgNO_3$ and M_9 ligand. Inset shows the photograph of the crude product. b) The comparative ESI-MS spectra of the same reaction product revealed an absence of distinct features.

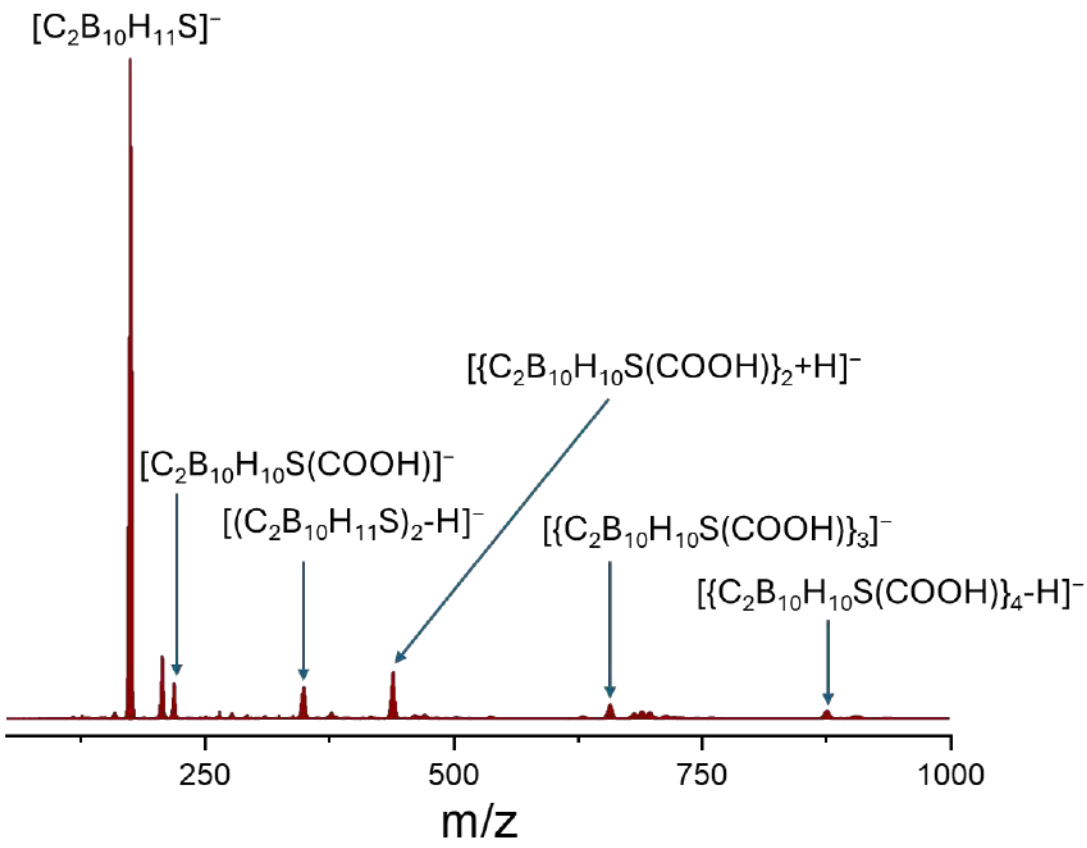


Figure S3. The negative ion mode ESI-mass spectrum of the M_9-COOH ligand was obtained by dissolving it in a solution of dichloromethane and methanol (1:1 v/v). The spectrum revealed a molecular ion peak at m/z 219.17, along with peaks indicating di (m/z 439.31), tri (m/z 658.41), and tetrameric (m/z 875.61) polymerization of the M_9-COOH. This polymerization is primarily attributed to hydrogen bonding of the -COOH groups and disulfide linkages.

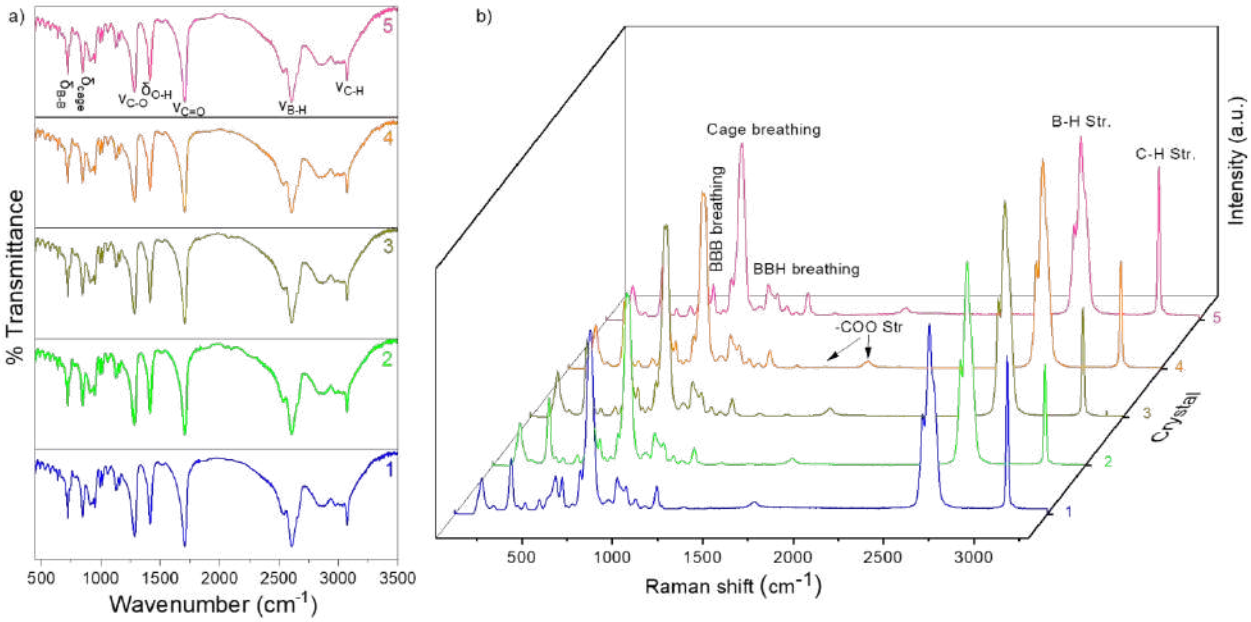


Figure S4. Comparative a) IR and b) Raman spectra of five different samples of M_9-COOH ligands show the presence of an acid group associated with the carborane cage in the ligand.

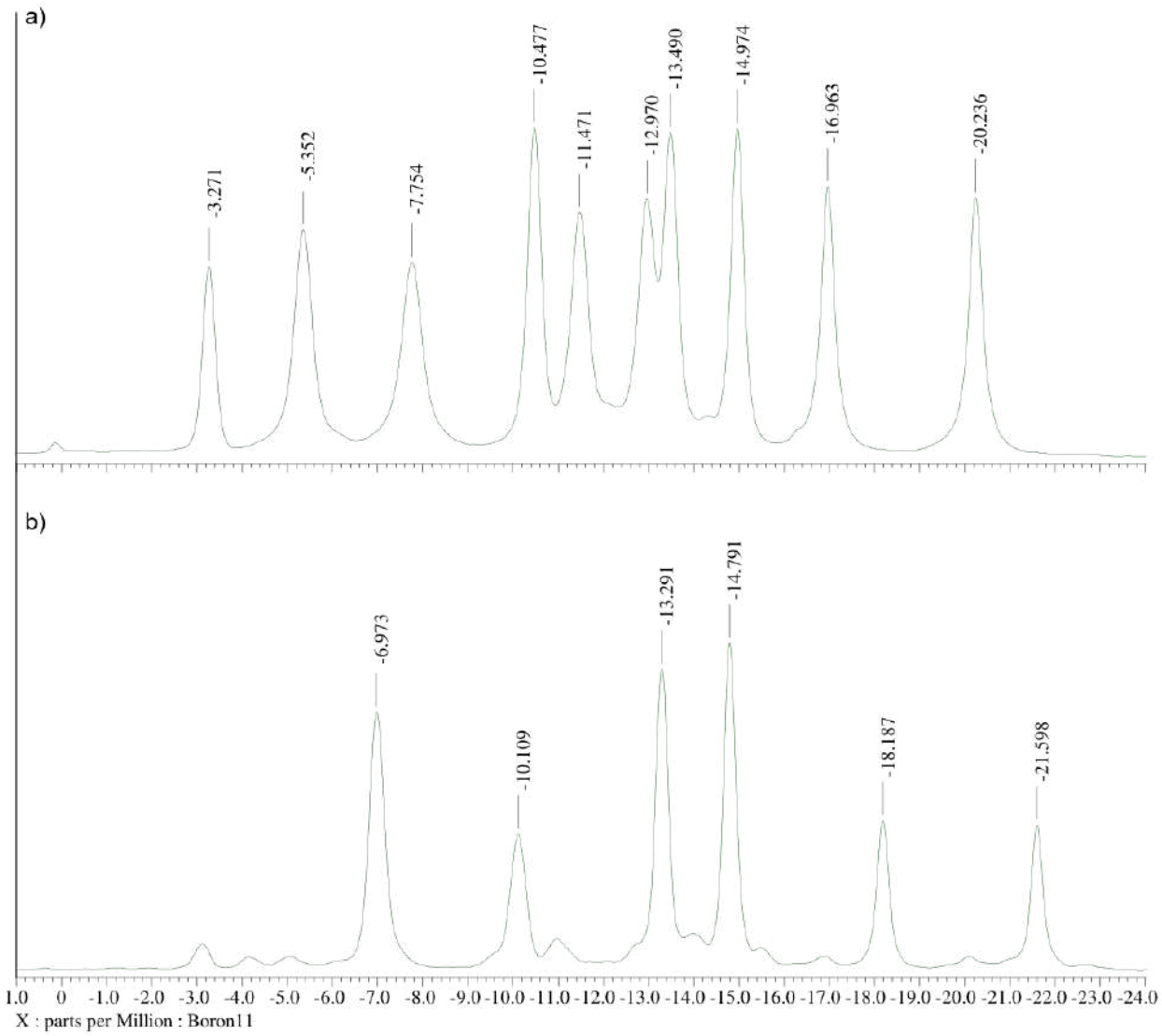


Figure S5. The comparative $^{11}B\{^{1}H\}$ NMR spectra of the M_9-COOH ligand (dissolved in 2:1 DMF: deuterated methanol) are presented as follows: a) before thermal treatment and b) after thermal treatment at 55 °C.

The ^{11}B NMR peaks of M_9-COOH before treatment appear at the following chemical shift values: -3.271, -5.352, -7.754, -10.477, -11.471, -12.970, -13.490, -14.974, -16.963, and -20.236 ppm, all in a 1:1:1:1:1:1:1:1:1:1 ratio. After thermal treatment, these peaks shift to -3.08, -6.973, -10.109, -13.291, -14.791, -18.187, and -21.598 (in 1:2:1:2:2:1:1 ratio), indicating a clear decarboxylation of the ligand as a result of the thermal treatment.

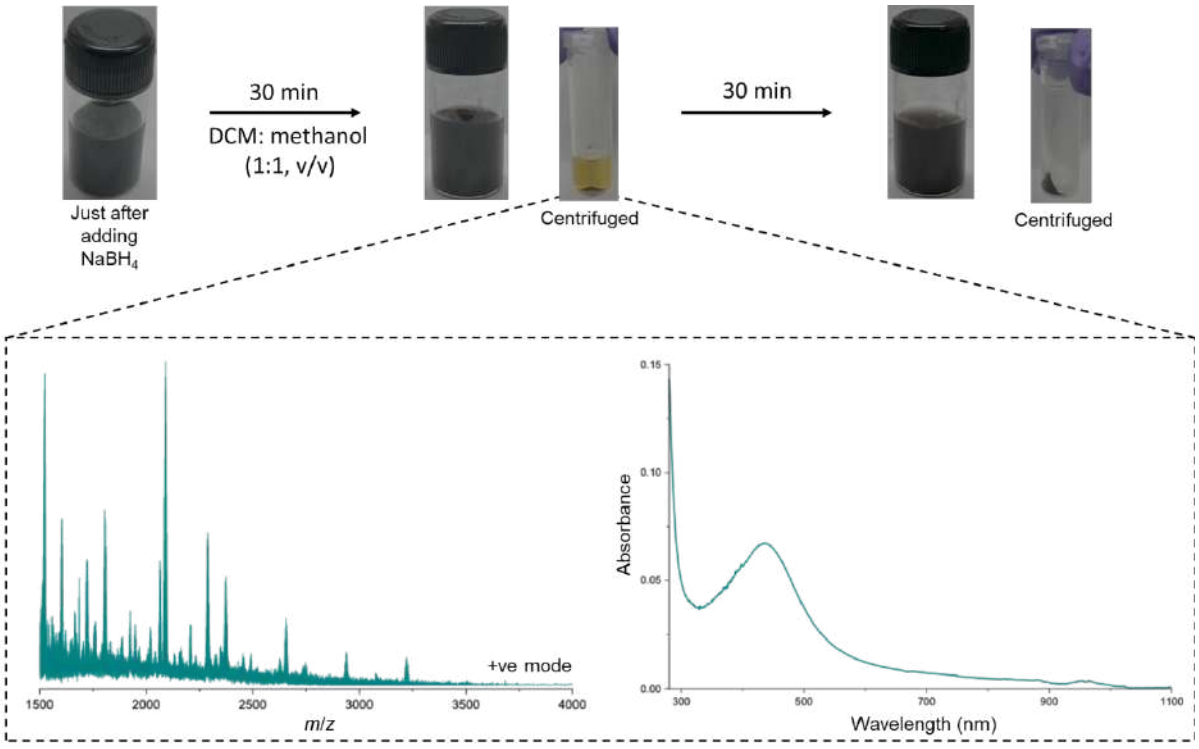


Figure S6. Photographs capturing the different stages of the direct reduction process of $AgNO_3$ and M_9 precursors, utilizing $NaBH_4$ as reducing agent. The inset features the positive ion mode ESI mass spectrum and UV-vis absorption spectrum of a slightly orange solution that formed after 30 minutes of reaction.

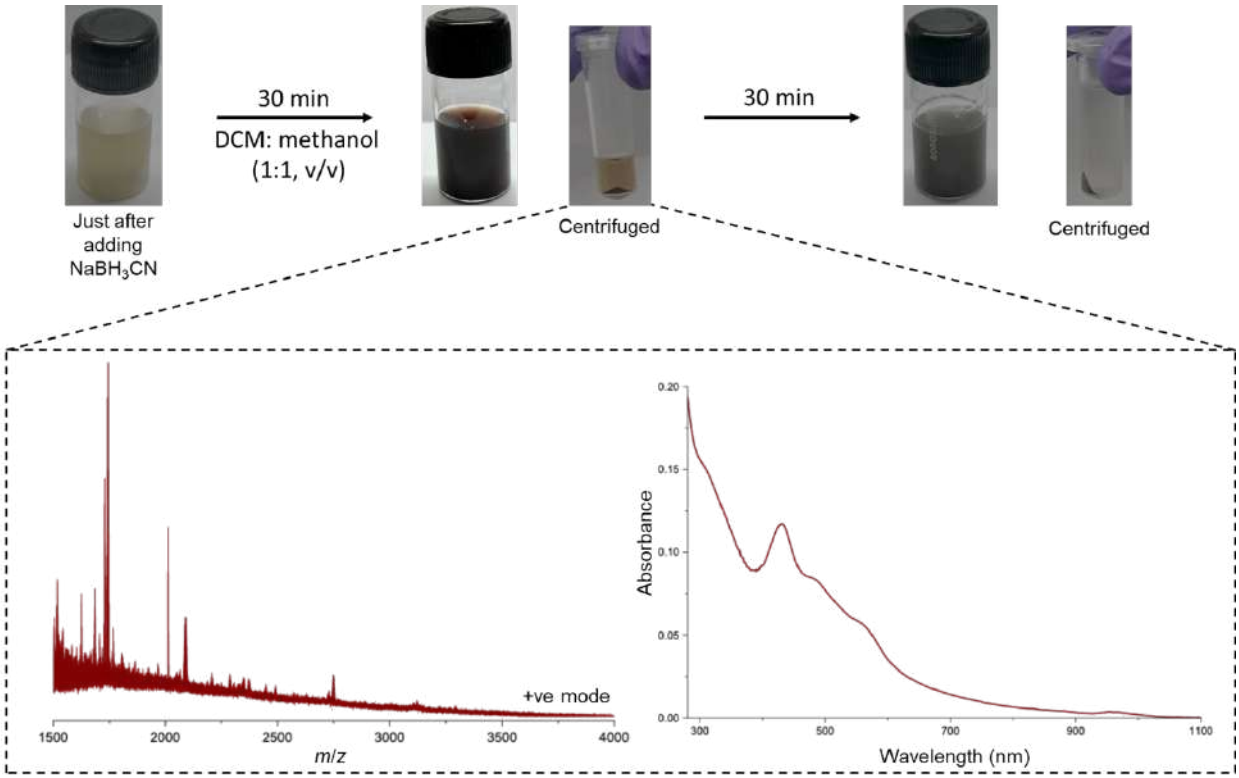
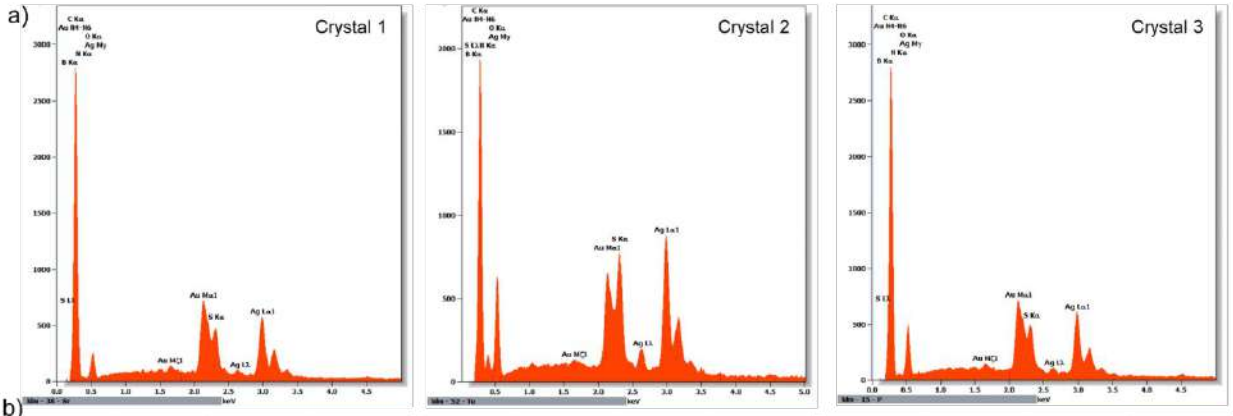


Figure S7. Photographs capturing the different stages of the direct reduction process of $AgNO_3$ and M_9 precursors, utilizing $NaBH_3CN$ as reducing agent. The inset features the positive ion mode ESI mass spectrum and the UV-vis absorption spectrum of a slightly orange solution that formed after 30 minutes of reaction.

a)



b)

Element			
	Net Counts	Weight %	Atom %
B K	330	5.92	7.05
C K	16365	26.04	45.17
N K	352	6.74	7.33
O K	3981	15.29	19.13
S K	8903	6.12	6.62
Ag L	8161	22.88	8.37
Au L	1245	17.01	6.33
		100.00	100.00

Element			
	Net Counts	Weight %	Atom %
B K	389	6.15	7.62
C K	17992	28.81	47.16
N K	339	2.99	4.85
O K	2973	9.29	19.11
S K	5097	3.98	6.33
Ag L	8505	21.86	8.72
Au L	1721	26.92	6.21
		100.00	100.00

Element			
	Net Counts	Weight %	Atom %
B K	360	5.68	6.81
C K	17164	25.17	48.50
N K	345	4.50	5.48
O K	2488	8.90	17.15
S K	4807	7.28	6.49
Ag L	8386	23.52	8.60
Au L	1592	24.95	6.97
		100.00	100.00

Figure S8. a) The EDS spectra measured from three different single crystals of Ag_{62} nanocluster. b) The content of the elements present in the crystals are shown here. The Au content is due the effect of gold sputtering onto the crystal.

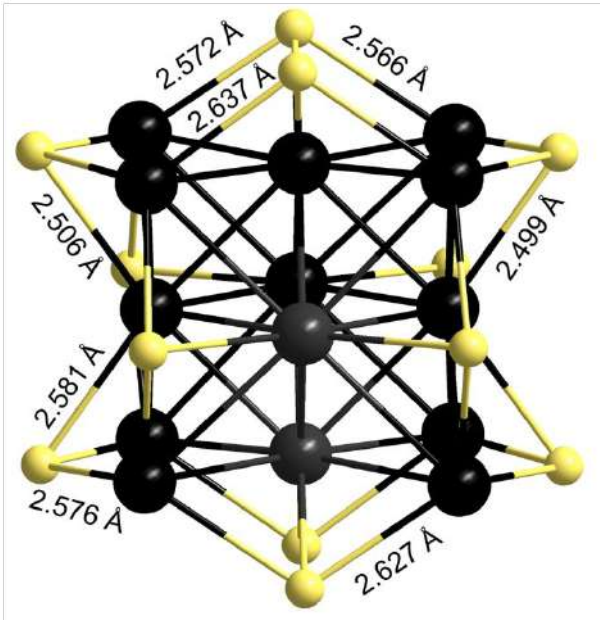


Figure S9. The Ag_{14}-S_{12} inner skeleton of the Ag_{62} nanocluster with marked Ag–S distances. Color code as, black: Ag, yellow = S.

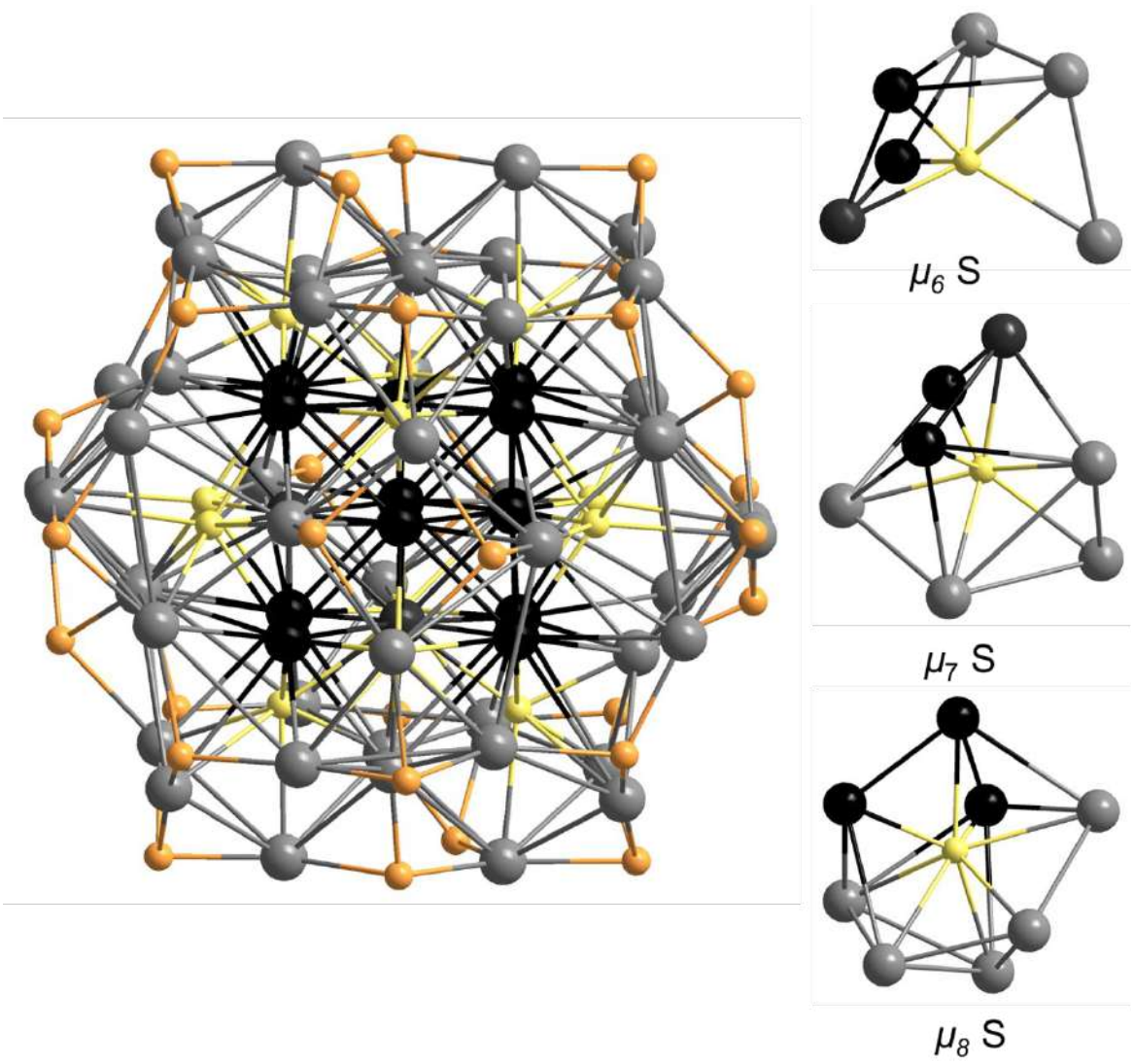


Figure S10. Various types of silver-sulfide bonding of twelve inner sulfide atoms present in the Ag_{62} nanocluster.

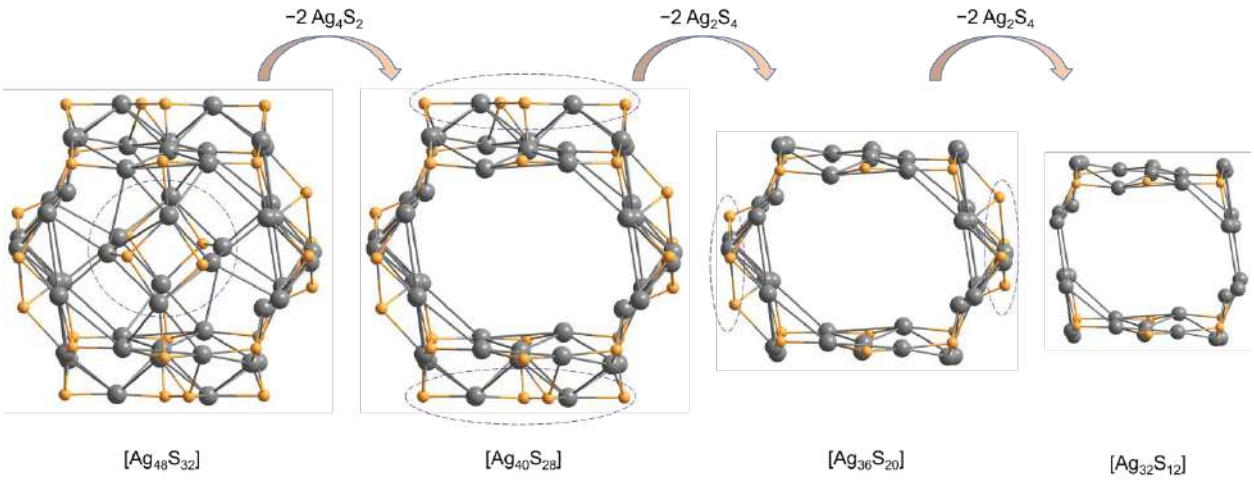


Figure S11. Sequential fragmentation of outer $[Ag_{48}S_{32}]$ skeleton of the Ag_{62} nanocluster.

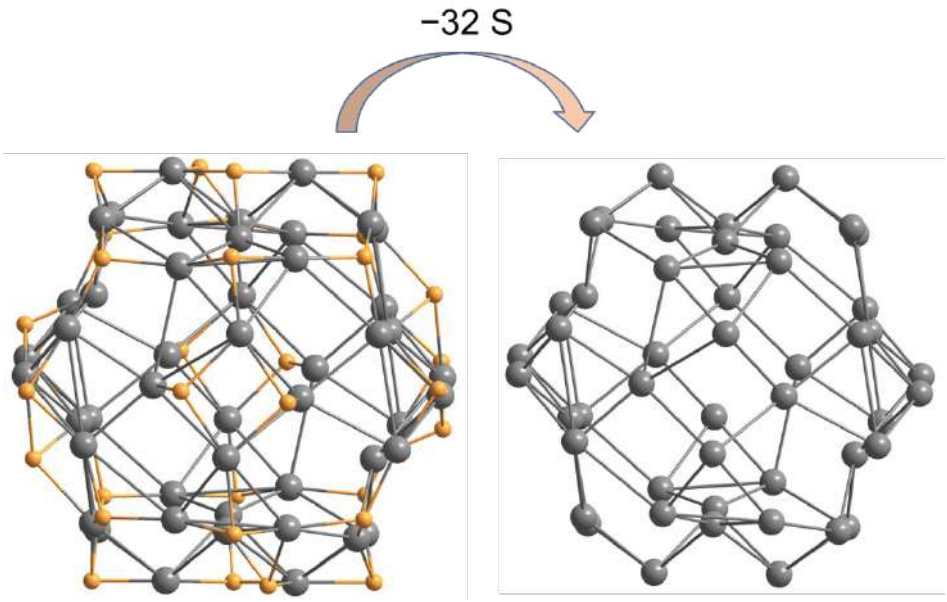


Figure S12. The outer $[Ag_{48}S_{32}]$ skeleton of the Ag_{62} nanocluster with and without thiolated S atoms.

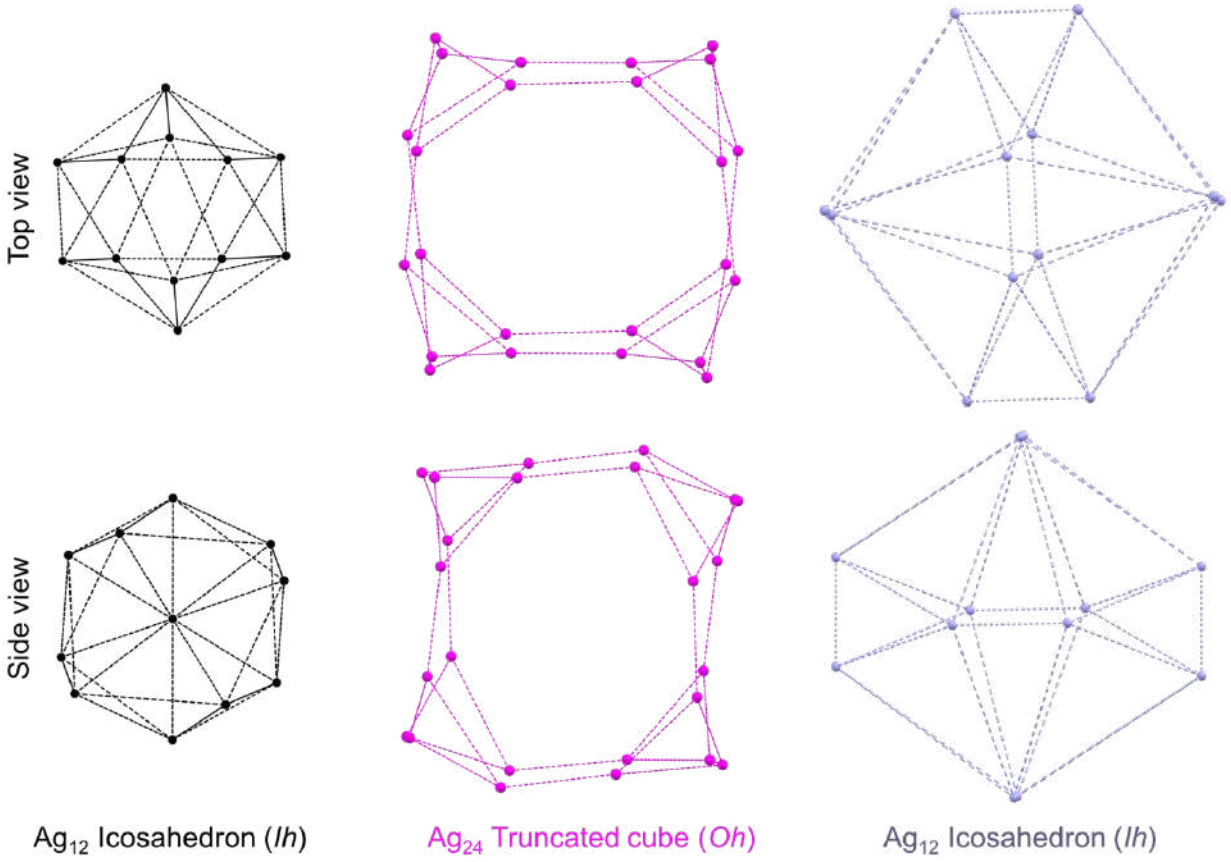


Figure S13. An independent view of three different symmetry elements in the outer Ag_{48} skeleton. All of these atoms are Ag.

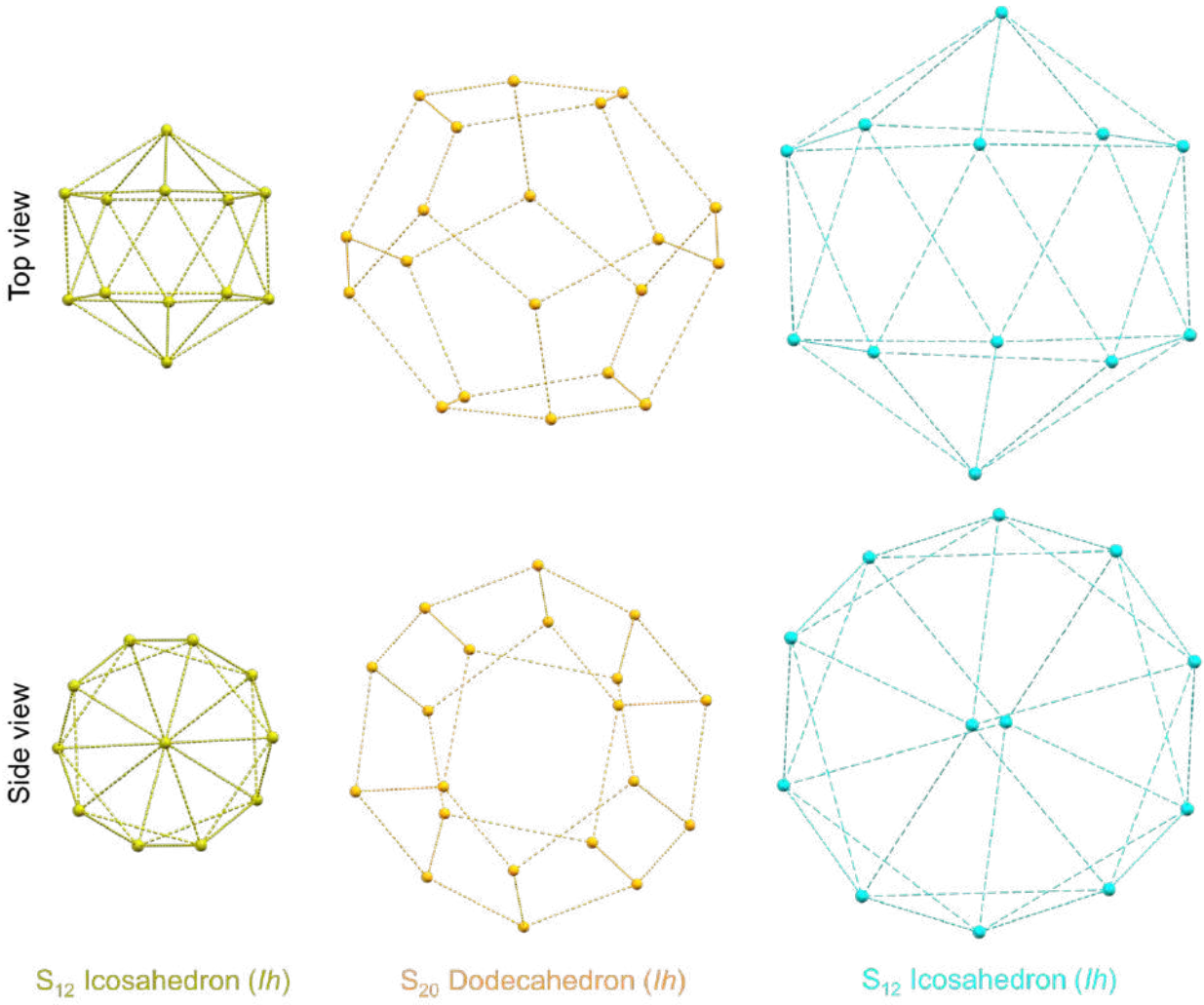


Figure S14. An independent view of three symmetry elements in the inner S_{12} and outer S_{32} (S_{20} and S_{12}) skeletons. All of these atoms are S.

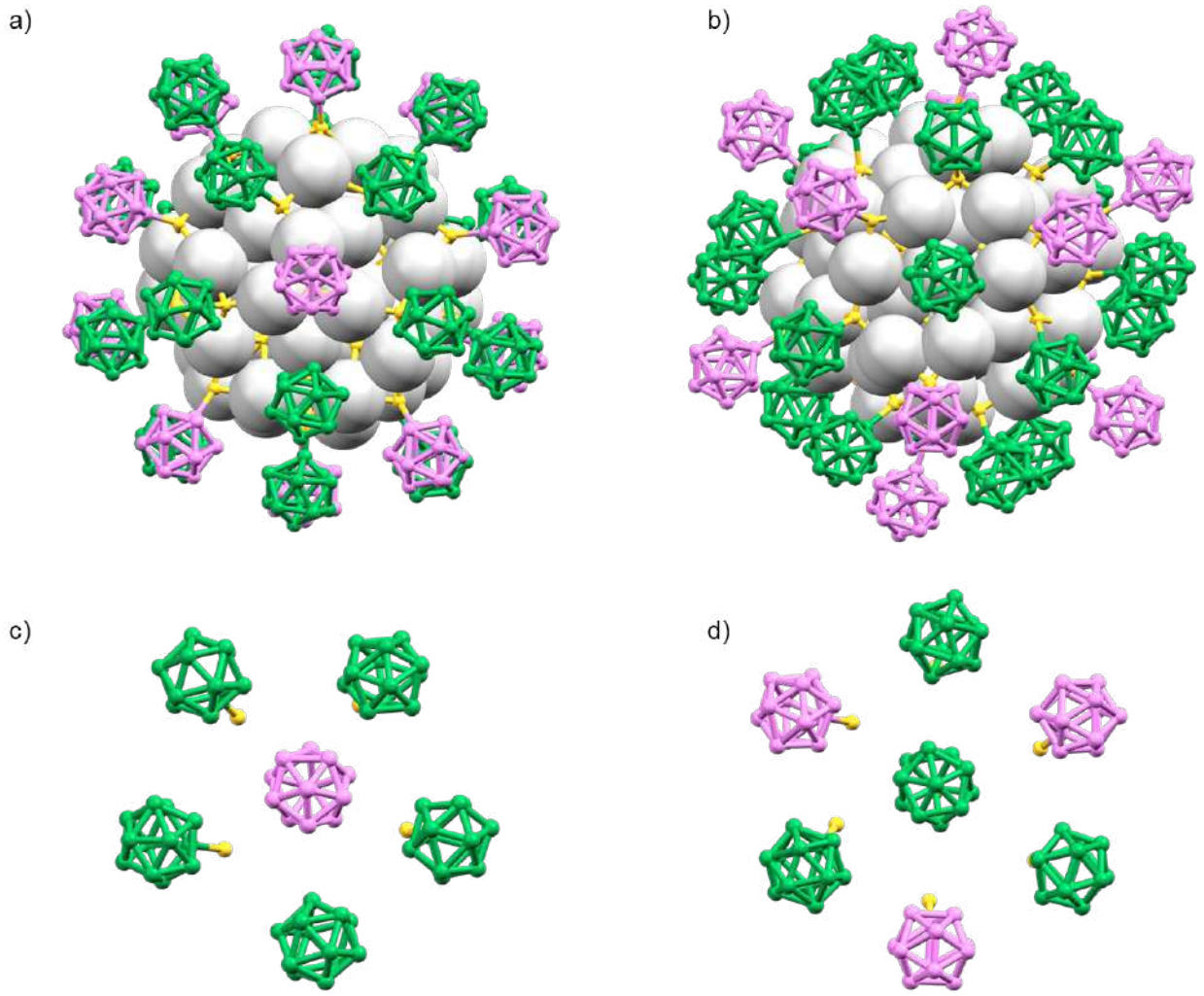


Figure S15. a) Distribution of carboranes (pink in color) encircled by five additional nearby carboranes. b) Distribution of carboranes (green in color) encircled by six additional nearby carboranes. Hydrogen atoms are removed for clarity. c and d) Corresponding pentagonal and hexagonal assembly of carboranes. Silver atoms are omitted for clarity.

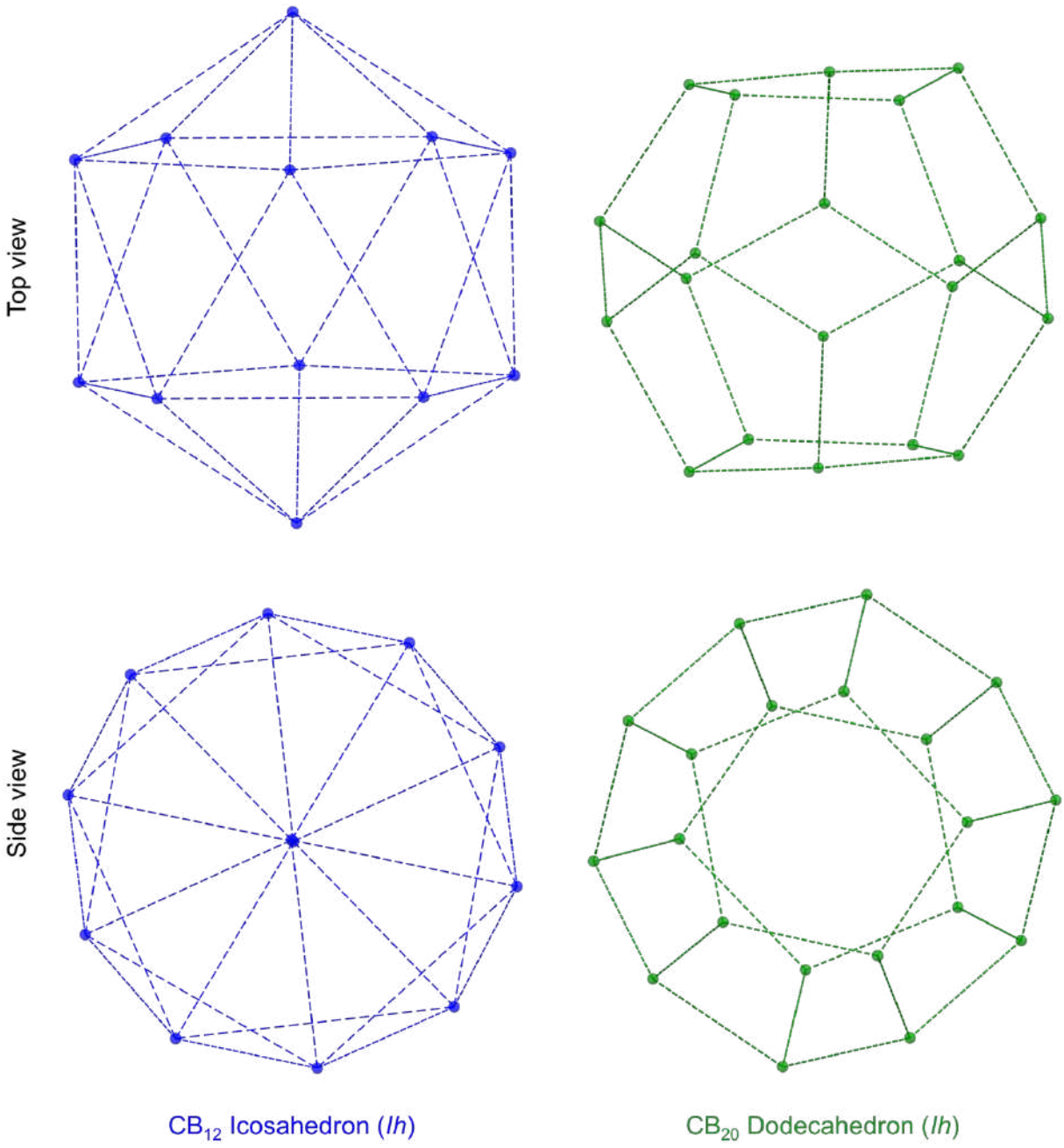


Figure S16. An independent view of the two types of symmetry present in the centroids of 32 carboranes. All of these points are the centroids of each carborane.

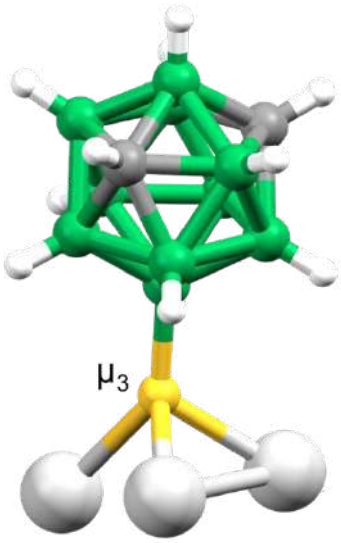


Figure S17. Silver-sulfide bonding of the outer thiolated S atoms connected with carborane ligands.

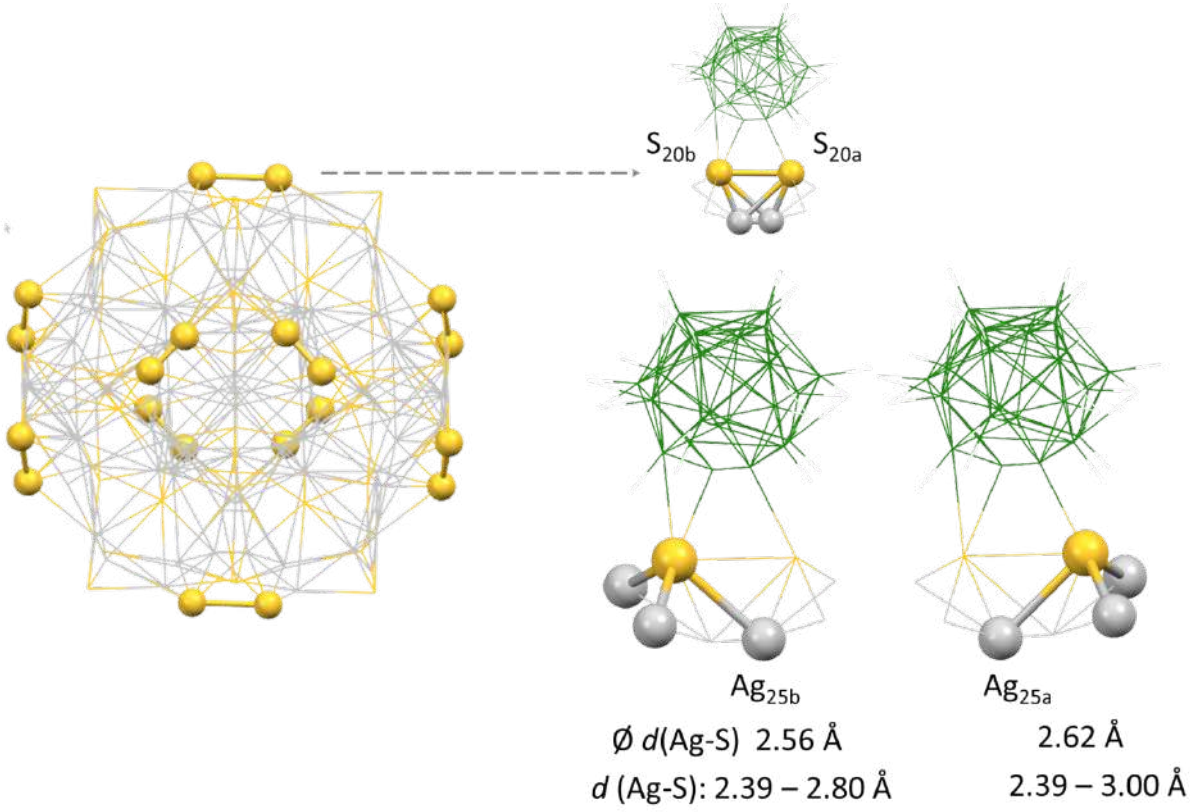


Figure S18. Disorder of S atoms in the outer silver sulfide skeleton of the Ag_{62} nanocluster.

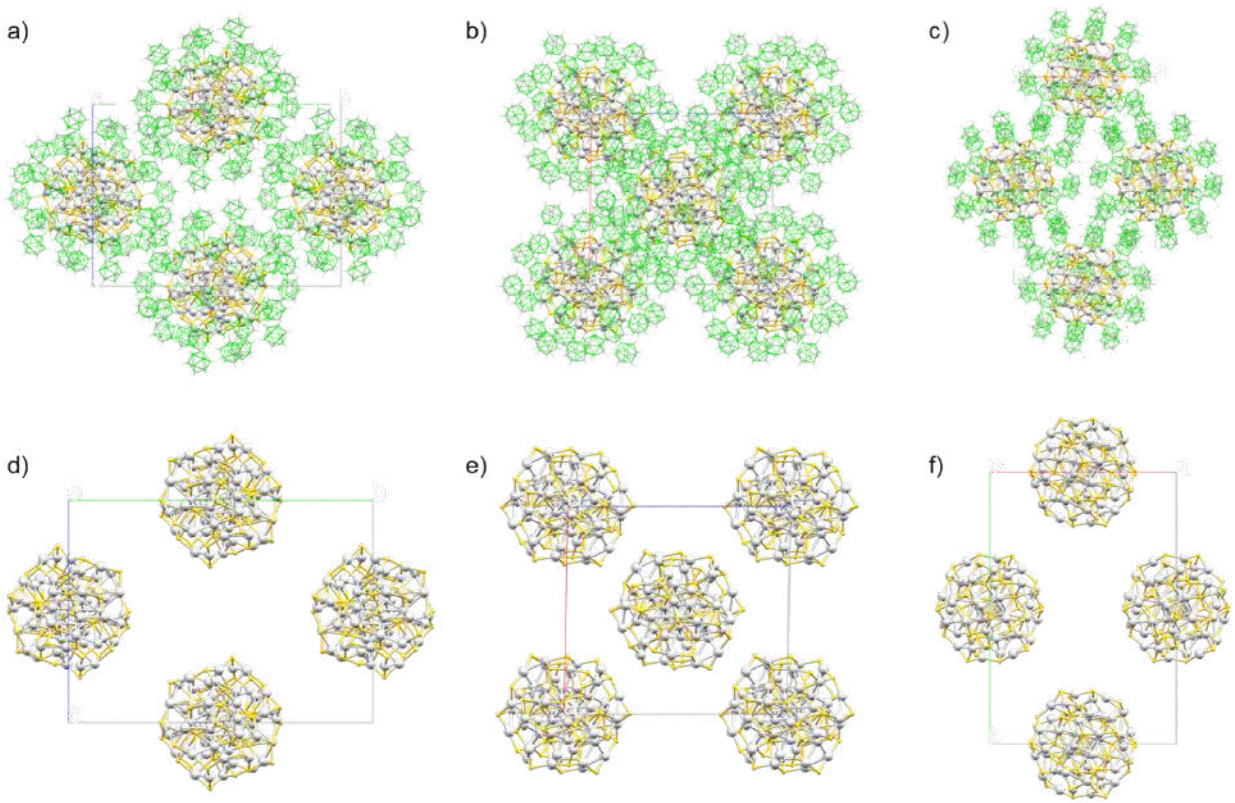


Figure S19. Unit cell molecular packing of the Ag_{62} nanocluster along a) a, b) b, and c) c crystallographic axis. Unit cell packing of the silver-sulfide skeleton along d) a, e) b, and f) c crystallographic axis.

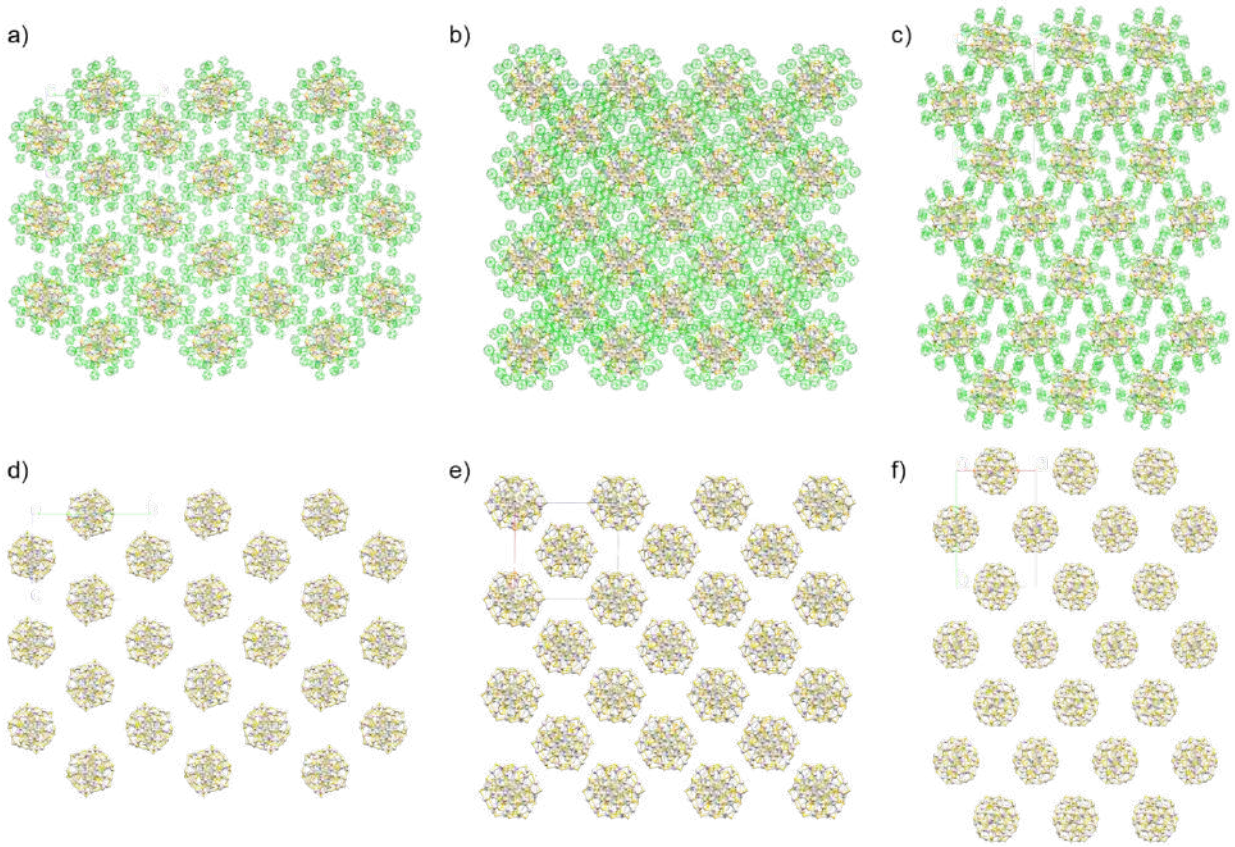


Figure S20. Extended (3×3×3) supramolecular packing of the Ag_{62} nanocluster along a) a, b) b, and c) c crystallographic axis. The packing of the silver sulfide skeleton along d) a, e) b, and f) c crystallographic axis.

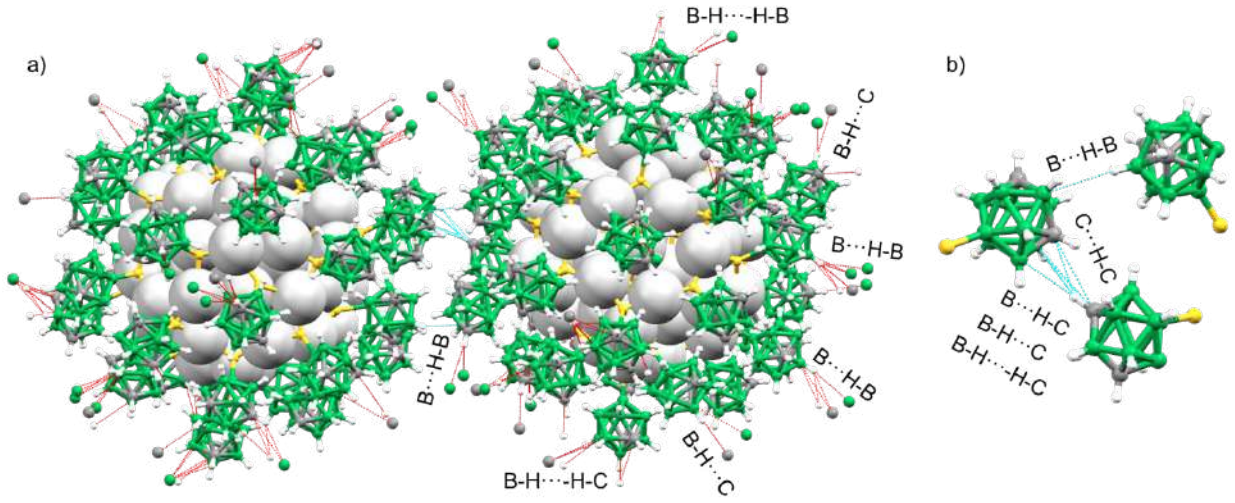


Figure S21. a) Various types of intermolecular interactions present in the crystal lattice. b) Expanded view of carborane centered interactions responsible for supramolecular packing of the clusters.

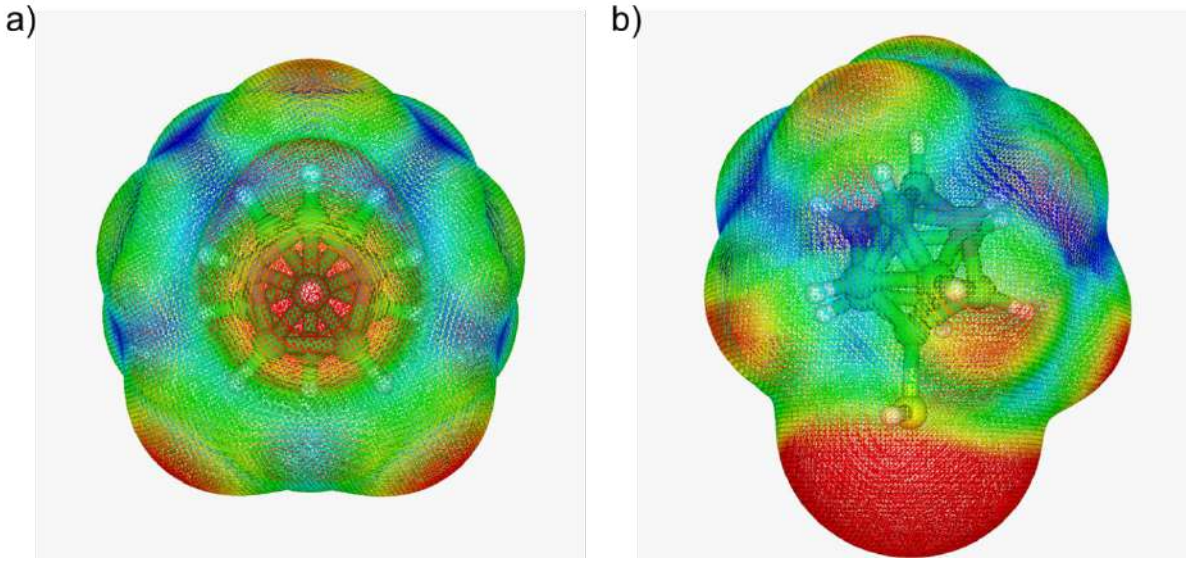


Figure S22. Molecular electrostatic potential mapped on an isosurface of the electron density for *meta*-carborane-9-thiol ligand. a: top view, b: side view.

The molecular electrostatic potential mapped on an isosurface of the electron density offers valuable insight into the nature of intermolecular interactions and, by extension, the arrangement between the carborane shells of the $[Ag_{62}S_{12}(CBT)_{32}]^{4+}$ clusters. This figure shows a single molecule of the CBT-H ligand from two perspectives. The top view illustrates how the molecule is oriented toward the outer environment while the side view highlights interactions between neighboring carborane molecules within the ligand shell of metal cluster. Regions in red represent areas of lowest electrostatic potential. In addition to sulfur atoms (which are buried beneath the carborane units on the metal cluster surface), B–H vertices also appear red which corresponds with their hydridic character ($B–H^{\delta-}$), whereas hydrogen atoms bonded to carbon atoms are positively charged ($C–H^{\delta+}$).

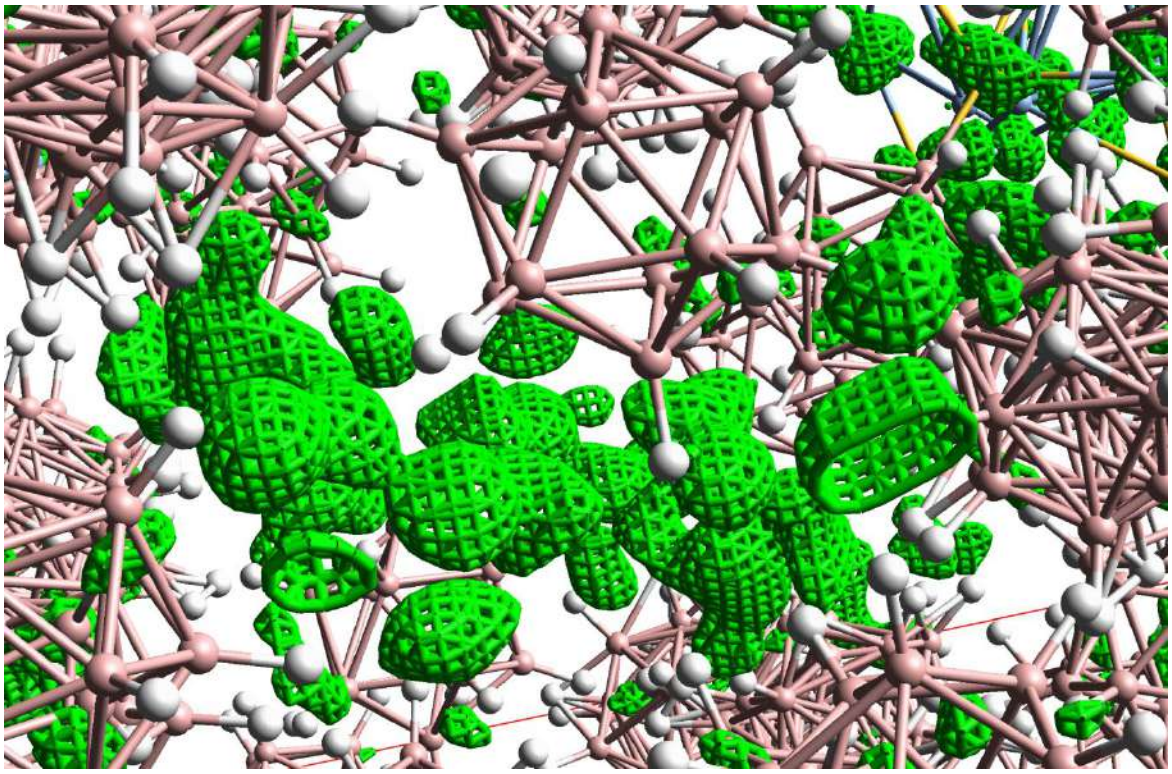


Figure S23. Residual electron density maps of the solvent molecules or counter ions present in the crystal lattice of Ag_{62} nanocluster.

Table S2. A summary of the structurally resolved carborane thiol- and alkynyl-protected metal (gold, silver, copper and alloy) nanoclusters.

Sl. No	Composition	Ligand used	Crystal system (space group)	Core @ shell structure	Ref
1.	$[Ag_{14}(C_2B_{10}H_{10}S_2)_6(CH_3CN)_8]$	*ortho*-carborane 1, 2-dithiol	Triclinic (*P*-1)	Ag_6 octahedron @ Ag_8 cube	10
2.	$[Ag_{14}(C_2B_{10}H_{10}S_2)_6(pyridine)_8]$	*ortho*-carborane 1, 2-dithiol	Tetragonal (*I*4/*m*)	Ag_6 octahedron @ Ag_8 cube	10
3.	$[Ag_{14}(C_2B_{10}H_{10}S_2)_6(methyl\text{-}pyridine)_8]$	*ortho*-carborane 1, 2-dithiol	Orthorhombic (*Pbca*)	Ag_6 octahedron @ Ag_8 cube	10
4.	$[Ag_{14}(C_2B_{10}H_{10}S_2)_6(PPh_3)_6]$	*ortho*-carborane 1, 2-dithiol	Triclinic (*P*-1)	Ag_8 @ Ag_6 isolated	11
5.	$[Ag_{14}(C_4B_{10}H_{11})_{12}(CH_3CN)_2]$	9-alkynyl *ortho*-carborane	Monoclinic (*C*2/*c*)	Ag_8 cube @ Ag_6 octahedron	12
6.	$[Cu_6Ag_8(C_4B_{10}H_{11})_{12}(CH_3CN)_2]$	9-alkynyl *ortho*-carborane	Cubic ($Im\bar{3}$)	Ag_8 cube @ Cu_6 octahedron	12
7.	$[Cu_{14}(C_2B_{10}H_{10}S_2)_6(CH_3CN)_8]$	*ortho*-carborane 1, 2-dithiol	Cubic ($Fm\bar{3}m$)	Cu_6 octahedron @ Cu_8 cube	13
8.	$[Cu_{14}(S_2C_2B_{10}H_{10})_6(DMF)_6O_2]$	*ortho*-carborane 9, 12-dithiol	Trigonal (*R*-3:*H*)	Cu_6 octahedron @ Cu_8 cube	14
9.	$[Cu_{16}(C_2B_{10}H_{10}S_2)_8]$	*ortho*-carborane 9, 12-dithiol	Monoclinic ($P2_1/n$)	Cu_{12} drum with 4 capping Cu	15
10.	$[Cu_{14}(C_2B_{10}H_{10}S_2)_6(CH_3CN)_6]$ and $[Cu_{16}(C_2B_{10}H_{10}S_2)_8]$ cocrystal	*ortho*-carborane 9, 12-dithiol	Tetragonal ($P42_12$)	-	16
11.	$[Ag_{17}I_3S(C_2B_{10}H_{10}S_2)_6(CH_3CN)_{11}]$	*ortho*-carborane 1, 2-dithiol	Hexagonal ($P6_3/m$)	Ag_6S central triangular prism @ Ag_{11} isolated	17
12.	$[Cu_{17}I_3S(C_2B_{10}H_{10}S_2)_6(CH_3CN)_{11}]$	*ortho*-carborane 1, 2-dithiol	Hexagonal ($P6_3$/m)	Cu_6S central triangular prism @ Cu_{11} isolated	17
13.	$[Ag_{21}(C_2B_{10}H_{11}S)_{12}(PPh_3)_2]$	*meta*-carborane 9-thiol	Cubic ($Pa\bar{3}$)	Ag_{13} central icosahedral @ Ag_6-Ag_2 motifs	18
14.	$[Au_{23}(C_4B_{10}H_{11})_9(tht)_6]$	9-alkynyl *ortho*-carborane	Monoclinic ($P2_1/n$)	Au_{17} kernel and three $[Au_2(C_4B_{10}H_{11})_3]$ motifs	19
15.	$[Au_{28}(C_4B_{10}H_{11})_{12}(tht)_8]$	9-alkynyl *ortho*-carborane	Triclinic (*P*-1)	Au_4 tetrahedron and truncated Au_{24} tetrahedron	19

16.	$[Au_{28}(C_2B_{10}H_{11}S)_{12}(tht)_4Cl_4]$	*ortho*-carborane 1-thiol	Tetragonal ($P2_1c$)	Au_{12} kernel and two saddle-shaped Au_8 motifs	20
17.	$[Ag_{30}(C_2B_{10}H_9S_3)_8DPPM_6]$	*ortho*-carborane 8, 9, 12 trithiol	Trigonal ($P31c$)	Triangular Ag_3 surrounded by crown like Ag_{27} motifs	21
18.	$[Ag_{33}(C_2B_{10}H_{10}S_2)_{12}]$	*ortho*-carborane 9, 12-dithiol	Trigonal (R-3)	Ag_{13} central icosahedral @ Ag_{20} dodecahedron	22
19.	$[Ag_{13}Ag_{14}Cu_6(C_2B_{10}H_{10}S_2)_{12}(CH_3CN)_2]$	*ortho*-carborane 9, 12-dithiol	Orthorhombic ($P2_12_12_1$)	Ag_{13} central icosahedral @ $Ag_{14}Cu_6$ distorted dodecahedron	22
20.	$[Ag_{13}Cu_{20}((C_2B_{10}H_{10}S_2)_{12}]$	*ortho*-carborane 9, 12-dithiol	Cubic ($Im\bar{3}$)	Ag_{13} central icosahedral @ Cu_{20} dodecahedron	22
21.	$[Cu_4(SC_2B_{10}H_{11})_4]$	*ortho*-carborane 9-thiol	Trigonal ($P3_121$)	Cu_4 square planner	23
22.	$[Cu_4(SC_2B_{10}H_{11})_4]$	*meta*-carborane 9-thiol	Monoclinic ($P2_1/c$)	Cu_4 square planner	23
23.	$[Cu_4I_3(SC_2B_{10}H_{11})_4]$	*ortho*-carborane 12-iodo 9-thiol	Tetragonal ($P4_32_12$)	Cu_4 square planner	23
24.	$[Cu_{20}(C_4B_{10}H_{11})_{16}(OC_3H_6)_2]$	9-alkynyl *ortho*-carborane	Monoclinic ($P2_1/c$)	Two fused Pentagonal bipyramids @ two Cu_3 triangles	24
25.	$[Cu_{14}(C_4B_{10}H_{11})_{10}(OC_3H_6)_6]$	9-alkynyl *ortho*-carborane	Triclinic (P-1)	Two shared pentagonal bipyramids @ two capping Cu atoms	24
26.	$[Cu_{13}(C_4B_{10}H_{11})_{10}(PPh_3)_2(CH_3CN)_2]$	9-alkynyl *ortho*-carborane	Triclinic (P-1)	Pentagonl pyramid shared with a pentagonal bipyramid @ two capping Cu atoms	24
27.	$[Cu_{26}(C_4B_{10}H_{11})_{16}(C_2B_9H_{10}C_2)_2(PPh_3)_2(CH_3CN)_4]$	9-alkynyl *ortho*-carborane	Triclinic (P-1)	Dimer of Cu_{13}	24
28.	$[Ag_{17}(SC_2B_{10}H_{11})_{12}]$	*ortho*-carborane-1-thiol	Orthorhombic ($Pbcn$)	Central icosahedral Ag_{13}@ four	25

				capping Ag atoms	
29.	$[AuAg_{16}(SC_2B_{10}H_{11})_{12}]$	*ortho*-carborane-1-thiol	Trigonal (*R*-3)	Central icosahedral $AuAg_{12}$@ four capping Ag atoms	25
30.	$[Ag_{13}Cu_4(SC_2B_{10}H_{11})_{12}]$	*ortho*-carborane-1-thiol	Triclinic (*P*-1)	Central icosahedral Ag_{13}@ four capping Cu atoms	25
31.	$[AuAg_{12}Cu_4(SC_2B_{10}H_{11})_{12}]$	*ortho*-carborane-1-thiol	Cubic ($Fd\bar{3}$)	Central icosahedral $AuAg_{12}$@ four capping Cu atoms	25
28.	**$[Ag_{62}S_{12}(SC_2B_{10}H_{11})_{32}]$**	***meta*-carborane-9-thiol 12-carboxilic acid**	**Monoclinic ($P2_1/n$)**	**$Ag_{14}S_{12}$ core @ $Ag_{48}(CBT)_{32}$ shell**	**This work**

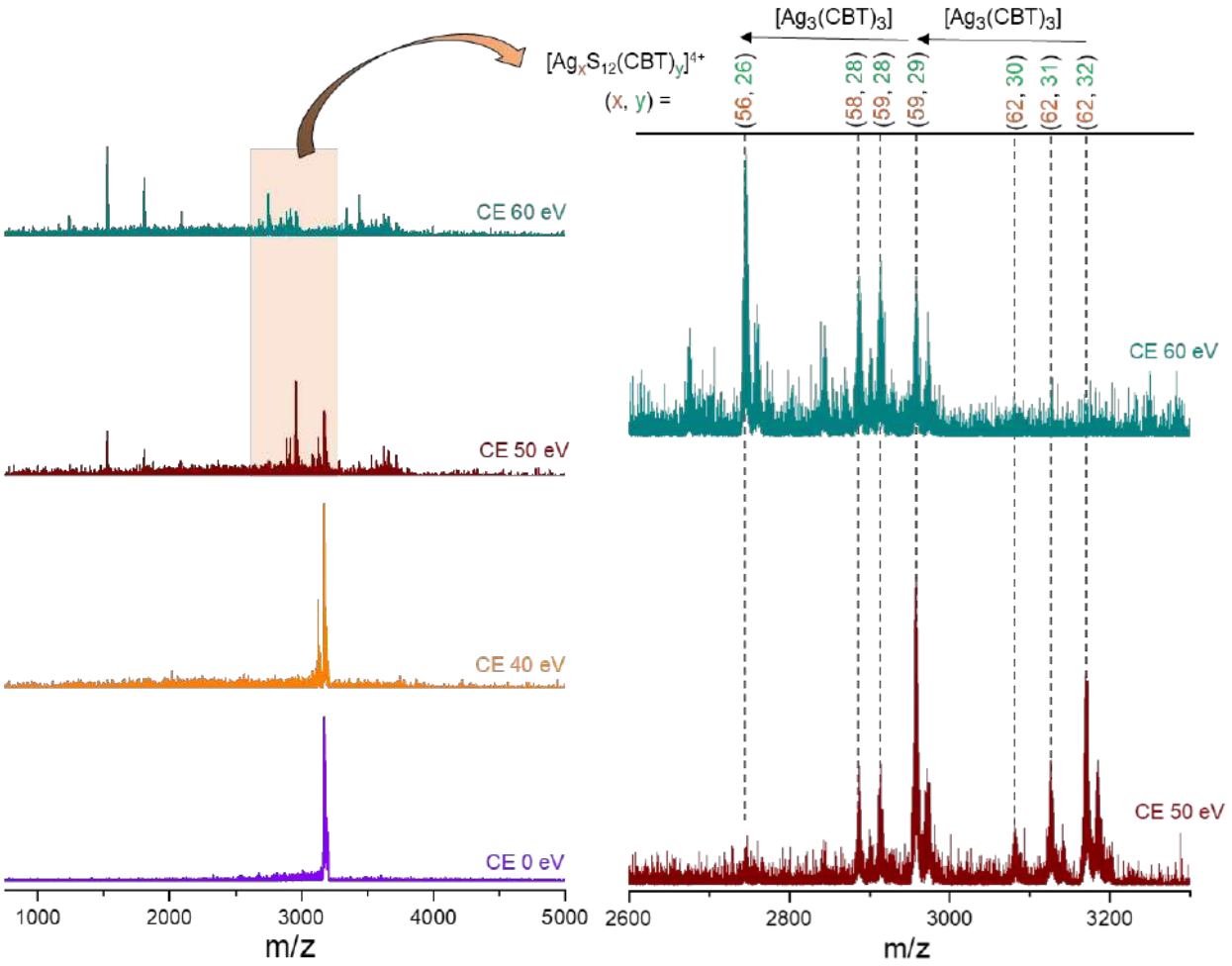


Figure S24. Collision energy dependent MS-MS fragmentation pattern upon selectin the primary peak at m/z 3170.42 having a charge state of 4+. Inset shows the expanded view of the highlighted region of the fragmentation spectra. Assignment of the molecular composition of the respective fragments are shown here. The weak ion intensity and broad isotopic distribution of the fragmented peaks [(62, 31), (62, 30), (59, 28) and (58, 28)] allowing for the possibility of additional proton attachment with them for balancing the 4+ charge state.

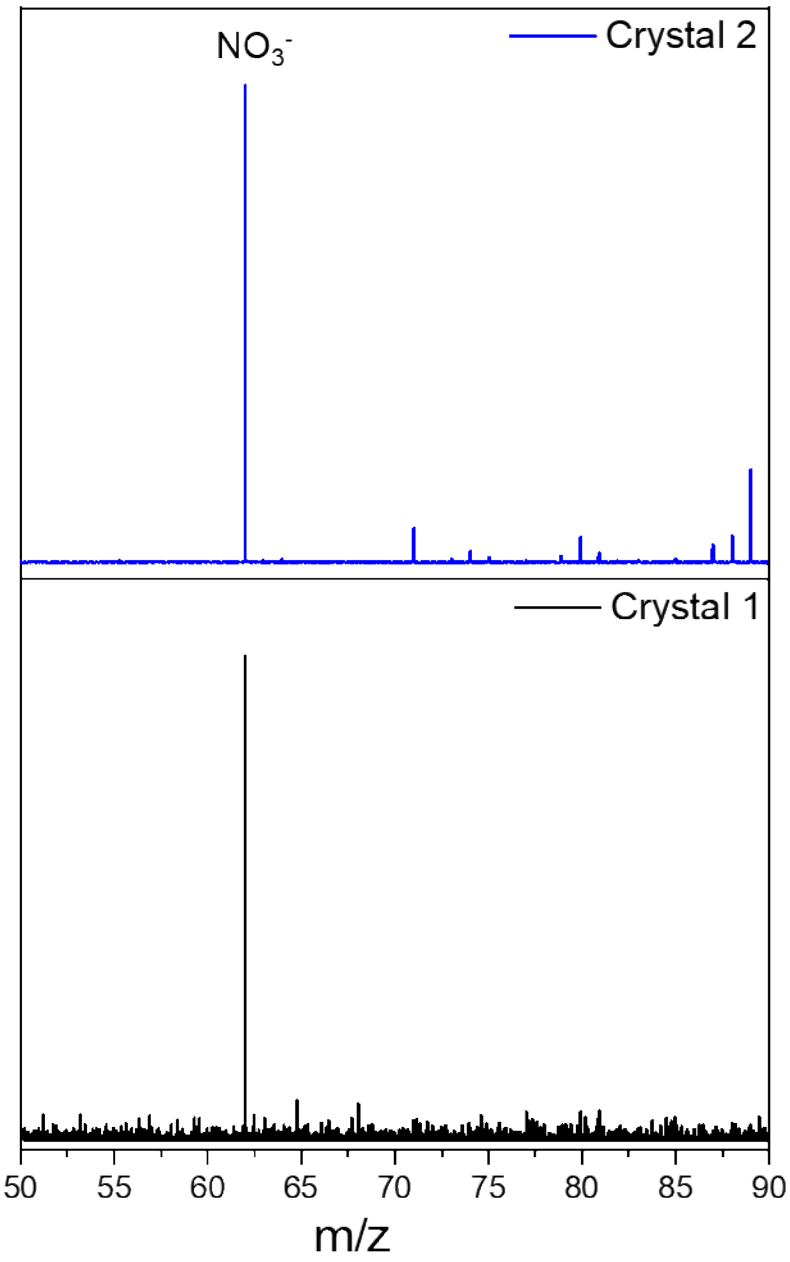


Figure S25. The negative ion mode ESI-MS spectra of two distinct set of Ag_{62} crystals reveal the presence of nitrate as counter ions.

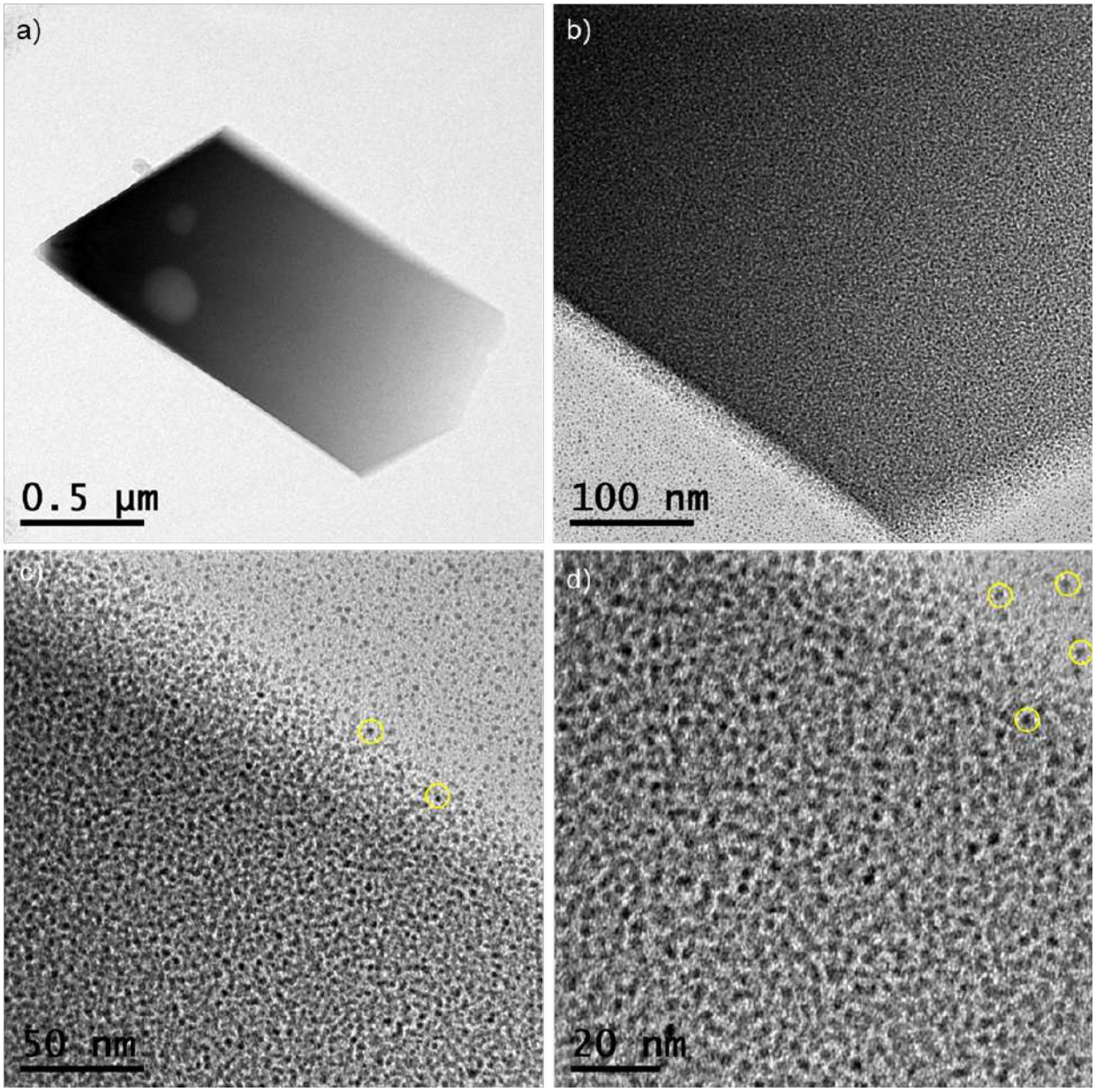


Figure S26. a) High resolution TEM micrograph of a cuboidal Ag_{62} crystal. b-d) Progressive magnification of an ultrathin edge of the crystal reveals the presence of uniform particles with an average diameter of 1.4±0.1 nm.

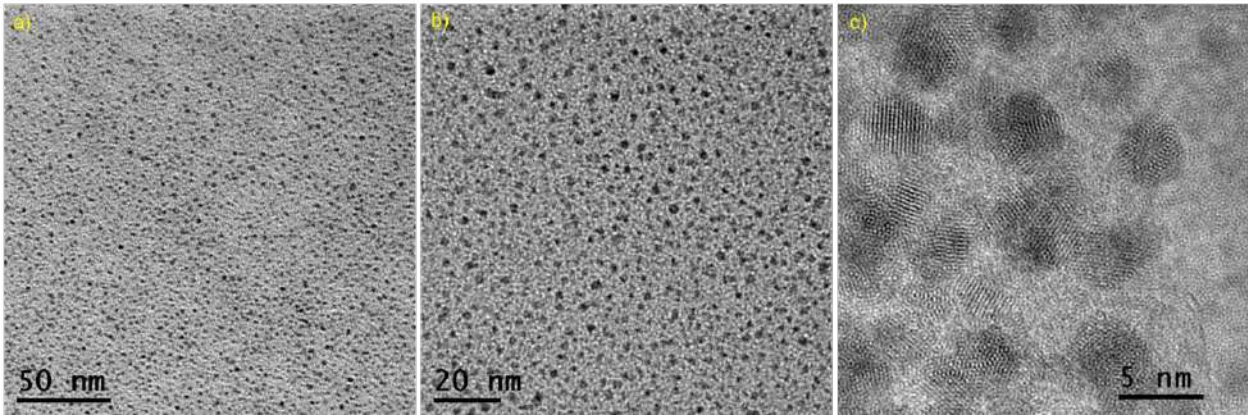


Figure S27. TEM images obtained from the drop-cast solution of Ag_{62} clusters at various magnifications show beam-induced aggregation and a corresponding size increase of the nanocluster particles.

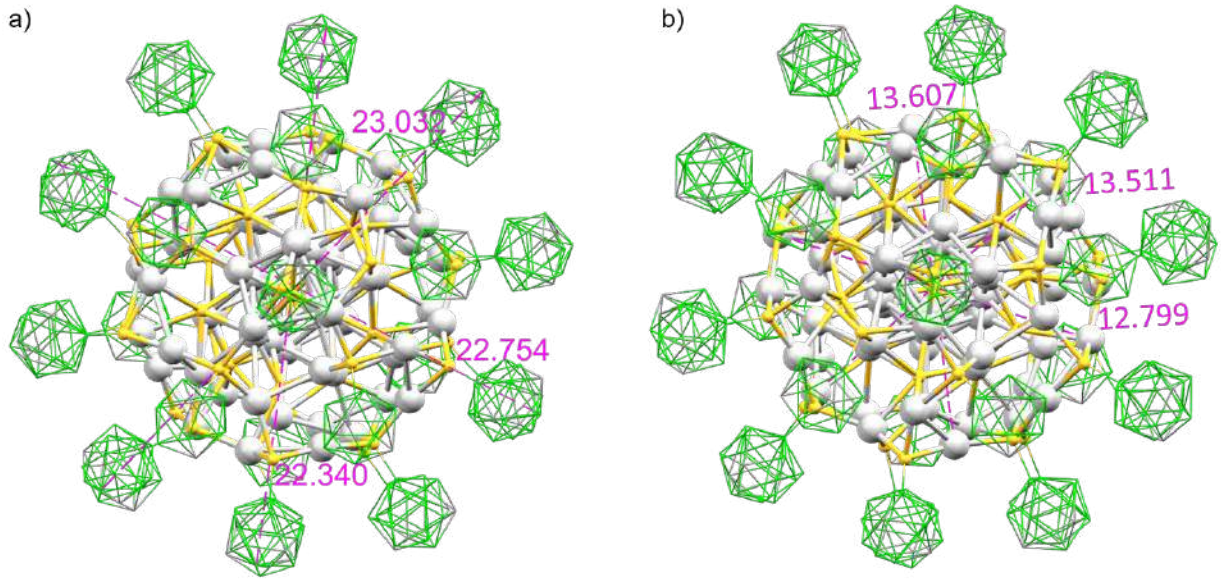


Figure S28. a) Marked distances (in Å) between the two antipodal carborane units of the cluster. b) Interatomic distances of oppositely arranged Ag atoms of the Ag–S kernel region of the cluster. Hydrogen atoms are removed for clarity.

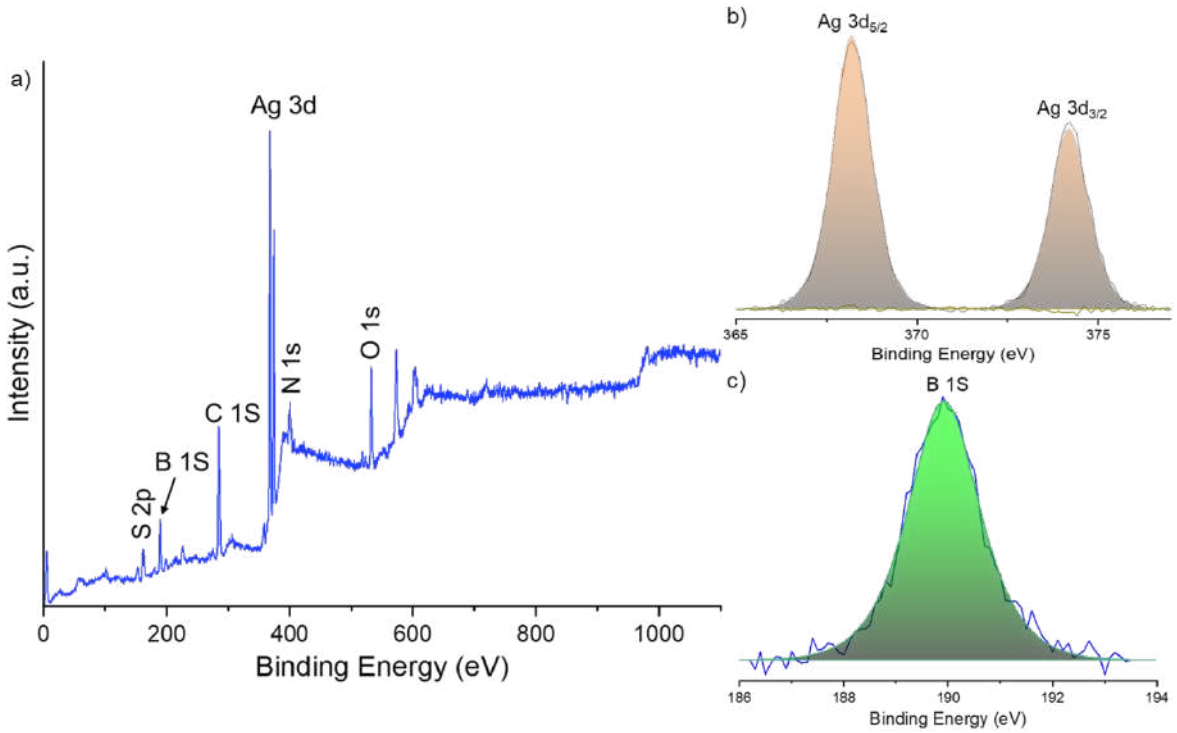


Figure S29. a) The XPS survey spectrum of Ag_{62} crystals. Selected spectral scan of b) Ag 3d and d) B 1s region of the Ag_{62} nanocluster.

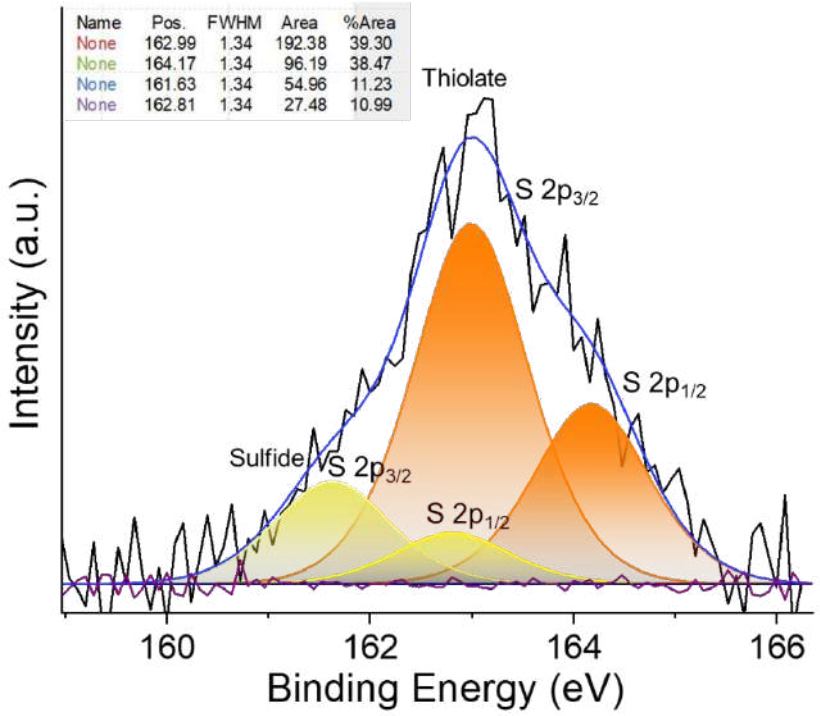


Figure S30. The XPS spectral fitting of the S 2p region of Ag_{62} nanocluster, obtained from few single crystals. Relative percentage of two types of S are shown in the inset.

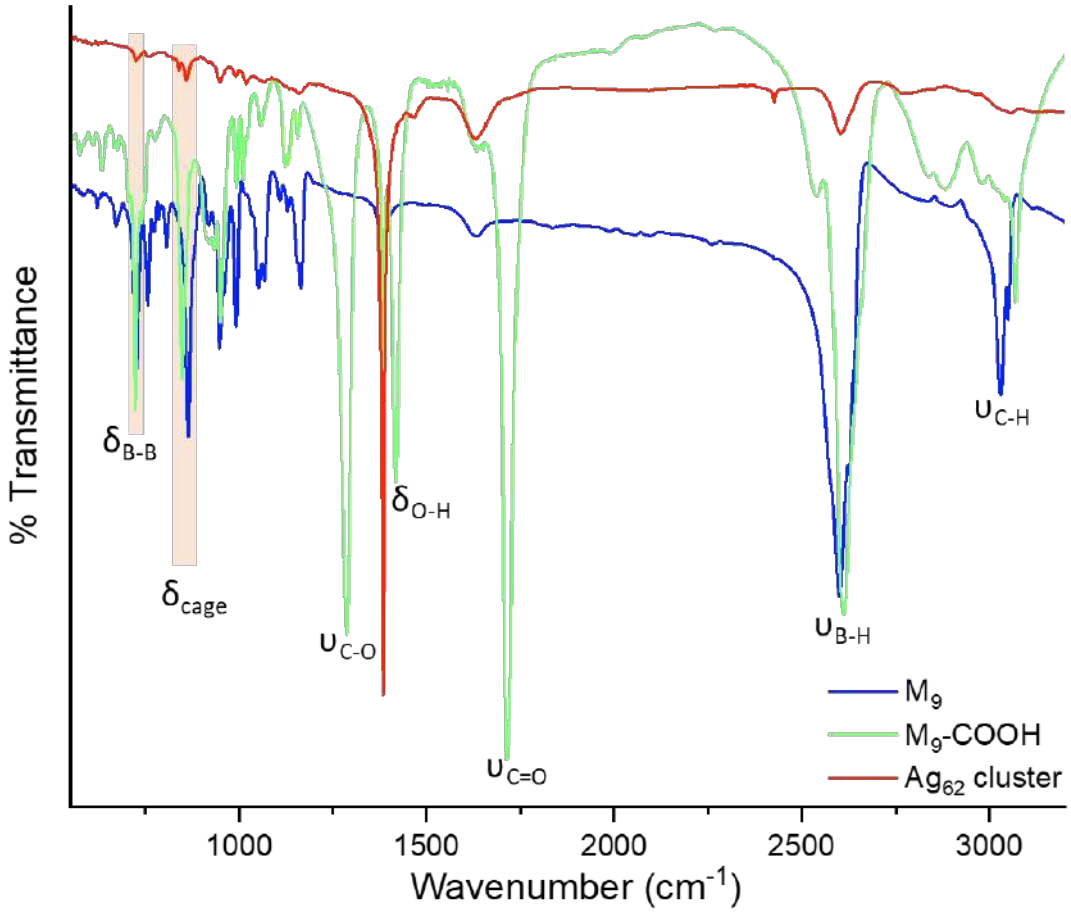


Figure S31. Comparative FT-IR spectra of M_9, M_9-COOH and Ag_{62} nanocluster. A considerable reduction in the intensity of the vibrational band was noted for the Ag_{62} nanocluster. The strong band at 1383 cm^{-1} is due to antisymmetric N–O stretching band of NO_3^- counter ions.

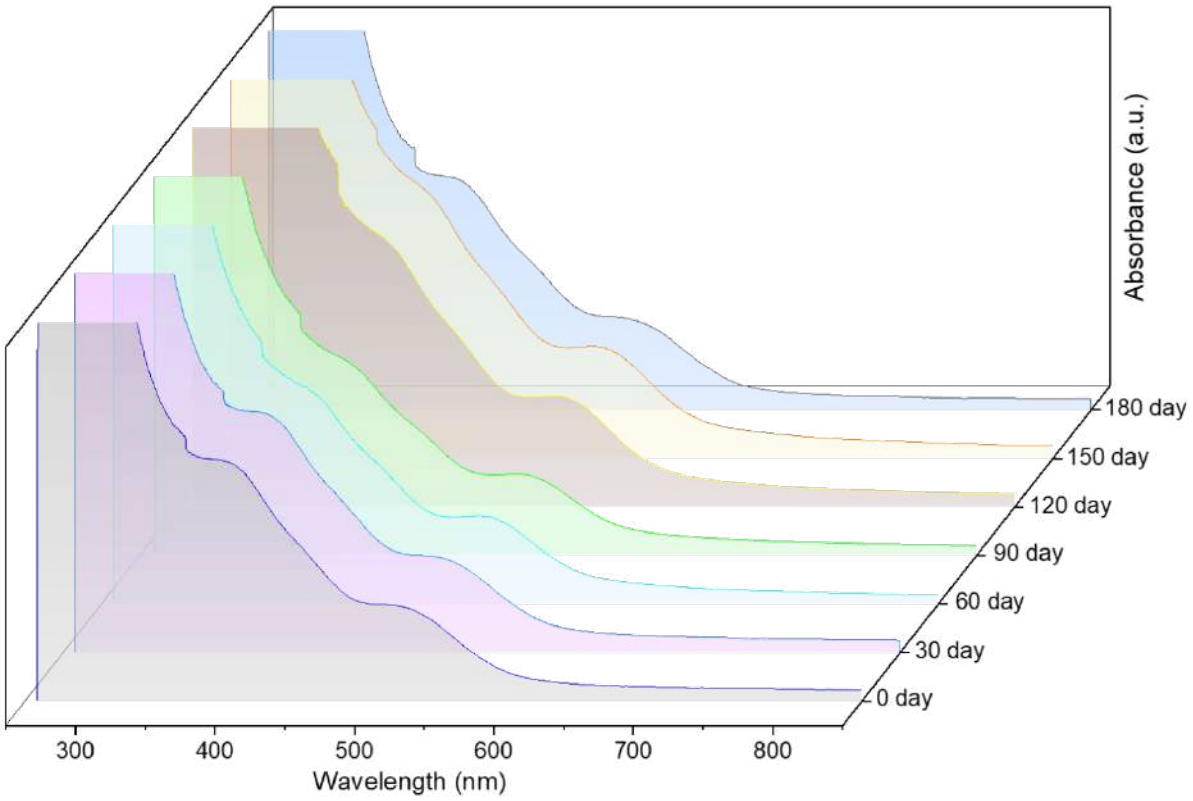


Figure S32. Time-dependent UV-vis absorption spectra of the Ag_{62} nanocluster manifested the cluster remains stable for more than 180 days under ambient condition.

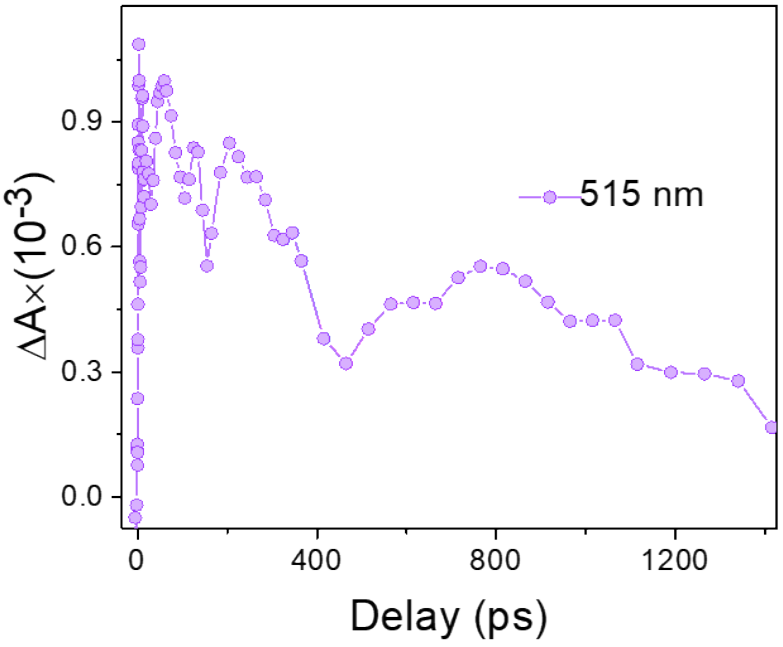


Figure S33. Kinetic decay traces for 515 nm GSPB under 400 nm pump excitation and fluence of 200 $\mu J.cm^{-2}$.

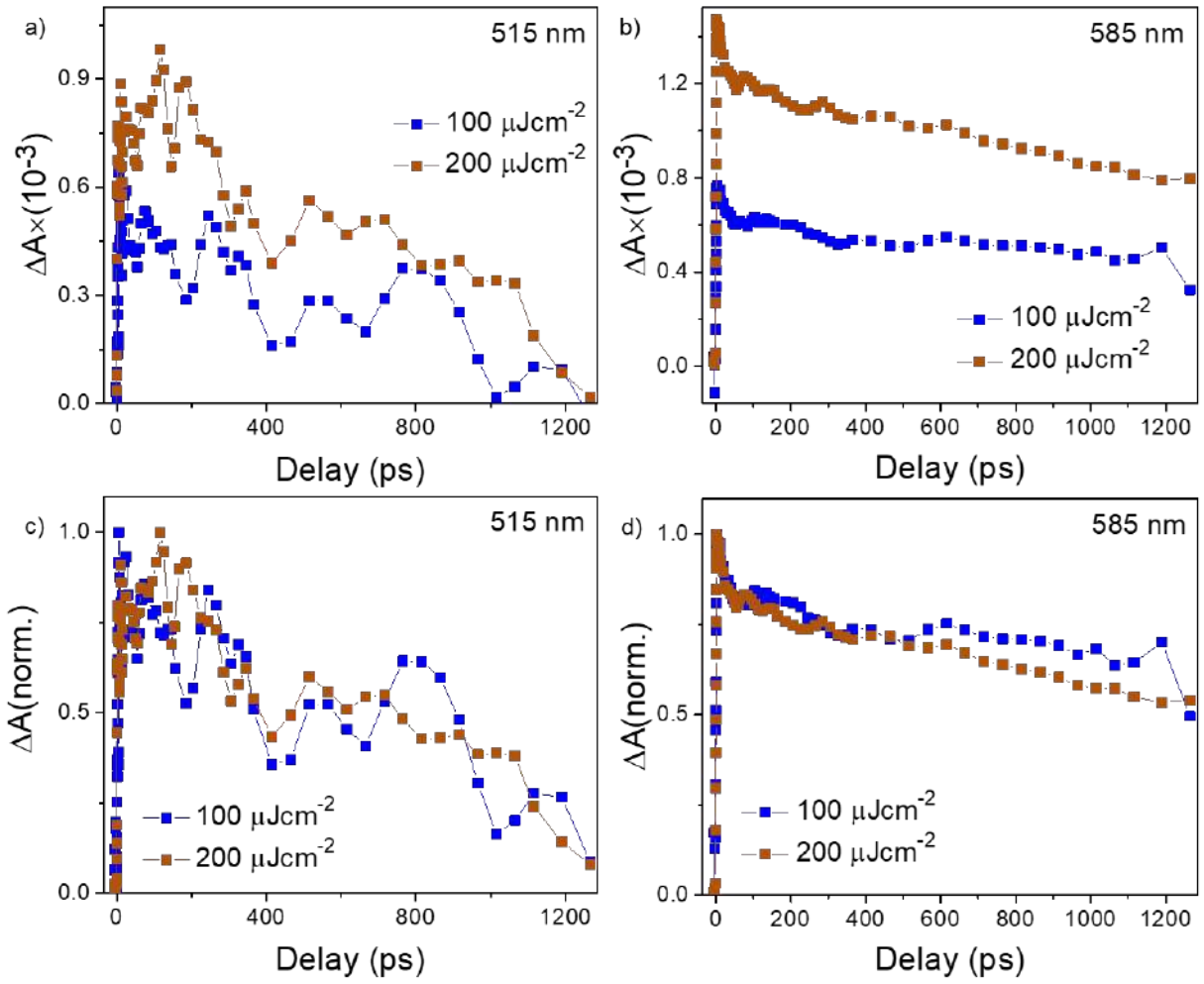


Figure S34. Pump fluence dependent comparative decay kinetics of a) 515 nm GSPB and b) 585 nm ESA peak with absolute intensity. Normalized decay kinetics for c) 515 nm GSPB and d) 585 nm ESA feature.

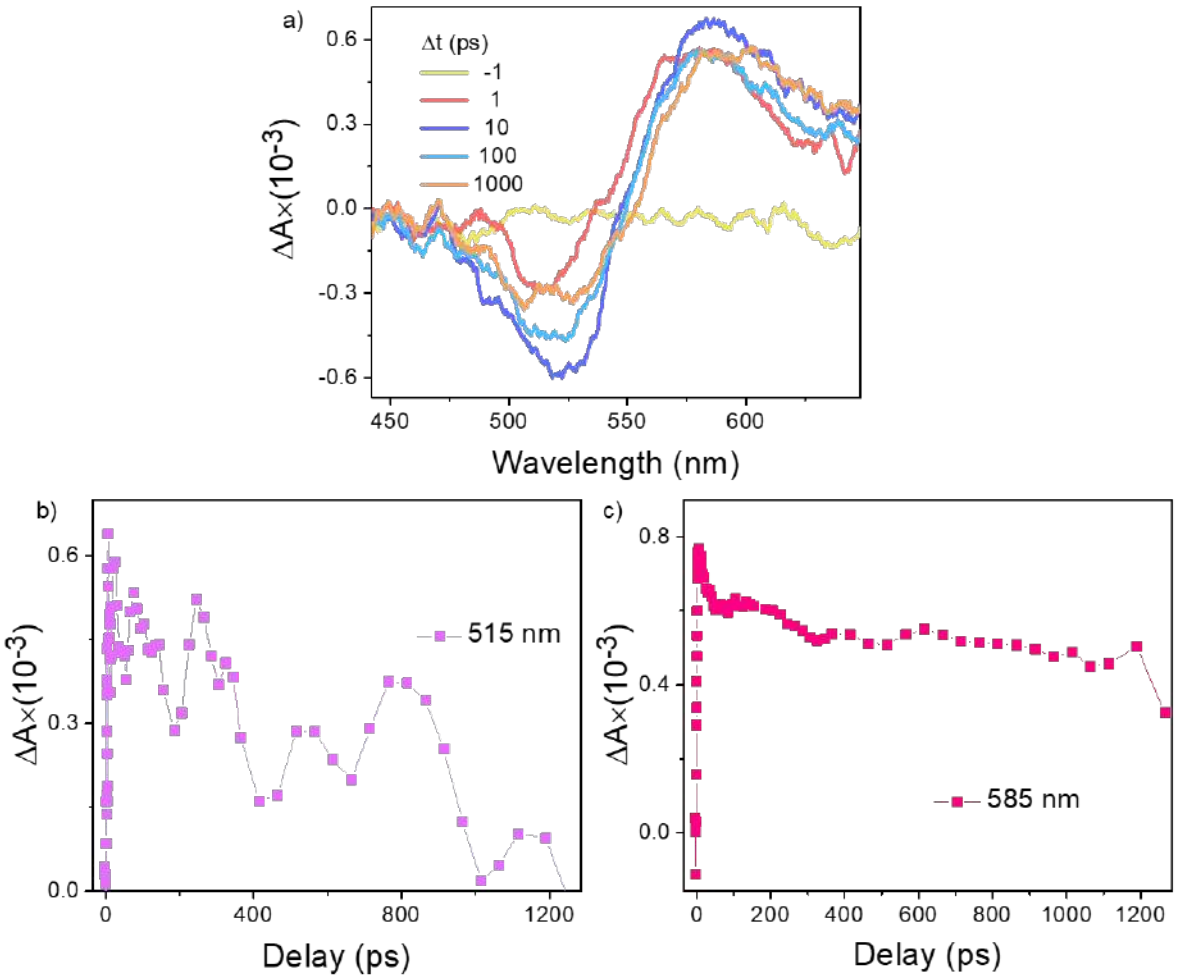


Figure S35. a) TA spectral profile of the Ag_{62} nanocluster in DMF solution under a pump excitation of 400 nm and a fluence of 100 μJ.cm^{-2} during different time evolution intervals. Kinetic decay traces of b) 515 nm GSPB and c) 585 nm ESA spectral regions.

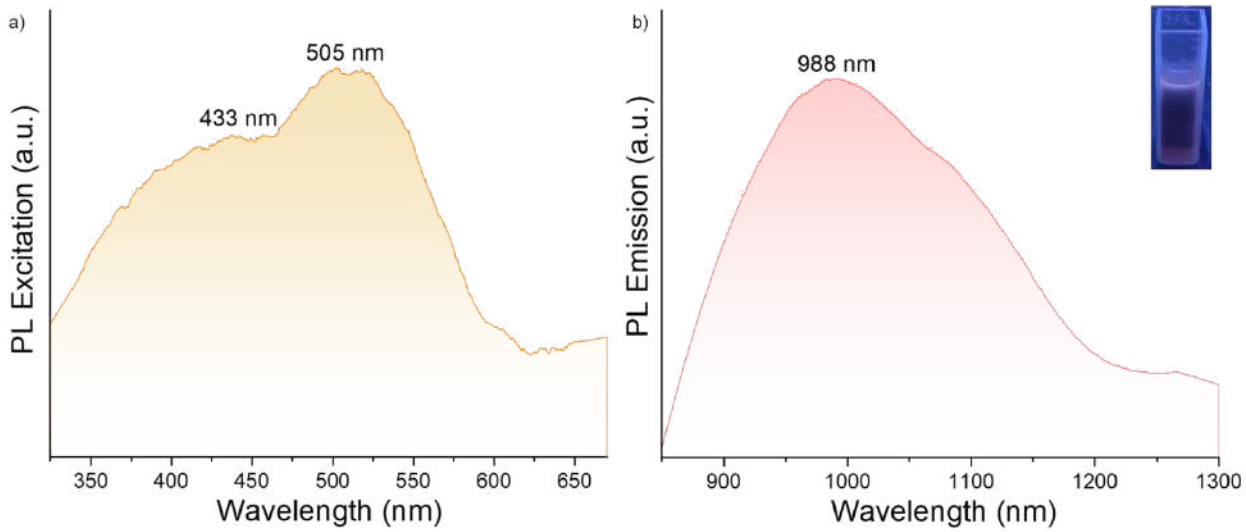


Figure S36. PL a) excitation and b) emission spectra of the Ag_{62} cluster (in DMF solution) showed a weak NIR emission band center at 988 nm having an excitation band at 505 nm and 433 nm. Inset shows the photograph of the cluster solution under 365 nm UV lamp.

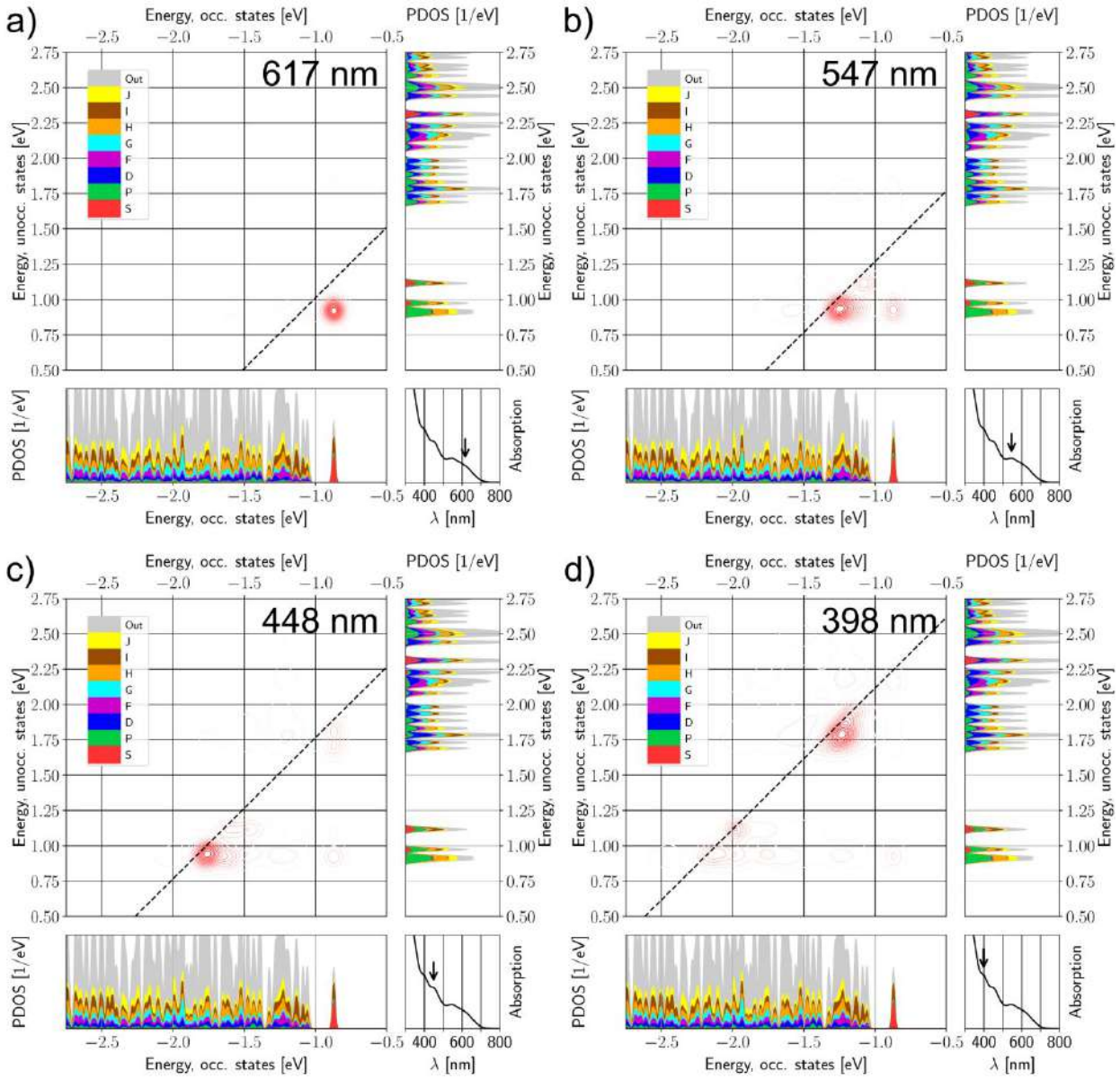


Figure S37. Dipole transition contribution map (DTCM) of the selected absorption peaks in panel. Upper left plot of each panel in a-d) shows the strengthening and screening contributions in red and blue contours respectively. Lower left and upper right plots show the projected density of states of the occupied and unoccupied Kohn-Sham states with respect to spherical harmonics functions. Lower right plot of each subfigure shows the absorption spectrum and the arrow labels the analysed feature. Different colors denote different angular momenta of the superatom state characteristics.

References:

(1) Palatinus, L.; Chapuis, G. SUPERFLIP - A Computer Program for the Solution of Crystal Structures by Charge Flipping in Arbitrary Dimensions. *J. Appl. Crystallogr.* **2007**, *40* (4), 786–790.

(2) Petříček, V.; Palatinus, L.; Plášil, J.; Dušek, M. JANA 2020 - a New Version of the Crystallographic Computing System JANA. *Zeitschrift fur Krist. - Cryst. Mater.* **2023**, *238* (7–8), 271–282.

(3) Mortensen, J. J.; Larsen, A. H.; Kuisma, M.; Ivanov, A. V.; Taghizadeh, A.; Peterson, A.; Haldar, A.; Dohn, A. O.; Schäfer, C.; Jónsson, E. Ö.; Hermes, E. D.; Nilsson, F. A.; Kastlunger, G.; Levi, G.; Jónsson, H.; Häkkinen, H.; Fojt, J.; Kangsabanik, J.; Sødequist, J.; Lehtomäki, J.; Heske, J.; Enkovaara, J.; Winther, K. T.; Dulak, M.; Melander, M. M.; Ovesen, M.; Louhivuori, M.; Walter, M.; Gjerding, M.; Lopez-Acevedo, O.; Erhart, P.; Warmbier, R.; Würdemann, R.; Kaappa, S.; Latini, S.; Boland, T. M.; Bligaard, T.; Skovhus, T.; Susi, T.; Maxson, T.; Rossi, T.; Chen, X.; Schmerwitz, Y. L. A.; Schiøtz, J.; Olsen, T.; Jacobsen, K. W.; Thygesen, K. S. GPAW: An Open Python Package for Electronic Structure Calculations. *J. Chem. Phys.* **2024**, *160* (9).

(4) Enkovaara, J.; Rostgaard, C.; Mortensen, J. J.; Chen, J.; Dułak, M.; Ferrighi, L.; Gavnholt, J.; Glinsvad, C.; Haikola, V.; Hansen, H. A.; Kristoffersen, H. H.; Kuisma, M.; Larsen, A. H.; Lehtovaara, L.; Ljungberg, M.; Lopez-Acevedo, O.; Moses, P. G.; Ojanen, J.; Olsen, T.; Petzold, V.; Romero, N. A.; Stausholm-Møller, J.; Strange, M.; Tritsaris, G. A.; Vanin, M.; Walter, M.; Hammer, B.; Häkkinen, H.; Madsen, G. K. H.; Nieminen, R. M.; Nørskov, J. K.; Puska, M.; Rantala, T. T.; Schiøtz, J.; Thygesen, K. S.; Jacobsen, K. W. Electronic Structure Calculations with GPAW: A Real-Space Implementation of the Projector Augmented-Wave Method. *J. Phys. Condens. Matter* **2010**, *22* (25).

(5) Perdew, J. P.; Burke, K.; Ernzerhof, M. Generalized Gradient Approximation Made Simple. *Phys. Rev. Lett.* **1996**, *77* (18), 3865–3868.

(6) Kuisma, M.; Ojanen, J.; Enkovaara, J.; Rantala, T. T. Kohn-Sham Potential with Discontinuity for Band Gap Materials. *Phys. Rev. B - Condens. Matter Mater. Phys.* **2010**, *82* (115106), 1–7.

(7) Walter, M.; Akola, J.; Lopez-Acevedo, O.; Jadzinsky, P. D.; Calero, G.; Ackerson, C. J.; Whetten, R. L.; Grönbeck, H.; Häkkinen, H. A Unified View of Ligand-Protected Gold Clusters as Superatom Complexes. *Proc. Natl. Acad. Sci. U. S. A.* **2008**, *105* (27), 9157–9162.

(8) Walter, M.; Häkkinen, H.; Lehtovaara, L.; Puska, M.; Enkovaara, J.; Rostgaard, C.; Mortensen, J. J. Time-Dependent Density-Functional Theory in the Projector Augmented-Wave Method. *J. Chem. Phys.* **2008**, *128* (244101), 1–10.

(9) Malola, S.; Lehtovaara, L.; Enkovaara, J.; Häkkinen, H. Birth of the Localized Surface Plasmon Resonance in Monolayer-Protected Gold Nanoclusters. *ACS Nano* **2013**, *7* (11), 10263–10270.

(10) Wang, Z. Y.; Wang, M. Q.; Li, Y. L.; Luo, P.; Jia, T. T.; Huang, R. W.; Zang, S. Q.; Mak, T. C. W. Atomically Precise Site-Specific Tailoring and Directional Assembly of

Superatomic Silver Nanoclusters. *J. Am. Chem. Soc.* **2018**, *140* (3), 1069–1076.

(11) Jana, A.; Jash, M.; Poonia, A. K.; Paramasivam, G.; Islam, M. R.; Chakraborty, P.; Antharjanam, S.; Machacek, J.; Ghosh, S.; Adarsh, K. N. V. D.; Base, T.; Pradeep, T. Light-Activated Intercluster Conversion of an Atomically Precise Silver Nanocluster. *ACS Nano* **2021**, *15* (10), 15781–15793.

(12) Wang, Q. Y.; Wang, J.; Wang, S.; Wang, Z. Y.; Cao, M.; He, C. L.; Yang, J. Q.; Zang, S. Q.; Mak, T. C. W. O-Carborane-Based and Atomically Precise Metal Clusters as Hypergolic Materials. *J. Am. Chem. Soc.* **2020**, *142* (28), 12010–12014.

(13) Li, Y. L.; Wang, J.; Luo, P.; Ma, X. H.; Dong, X. Y.; Wang, Z. Y.; Du, C. X.; Zang, S. Q.; Mak, T. C. W. Cu_{14} Cluster with Partial Cu(0) Character: Difference in Electronic Structure from Isostructural Silver Analog. *Adv. Sci.* **2019**, *6* (1900833), 1–6.

(14) Jana, A.; Duary, S.; Das, A.; Kini, A. R.; Acharya, S.; Machacek, J.; Pathak, B.; Base, T.; Pradeep, T. Multicolor Photoluminescence of Cu_{14} Clusters Modulated Using Surface Ligands. *Chem. Sci.* **2024**, *15* (34), 13741–13752.

(15) Huang, J. H.; Liu, Y. J.; Si, Y.; Cui, Y.; Dong, X. Y.; Zang, S. Q. Carborane-Cluster-Wrapped Copper Cluster with Cyclodextrin-like Cavities for Chiral Recognition. *J. Am. Chem. Soc.* **2024**, *146* (24), 16729–16736.

(16) Huang, J. H.; Liu, L. Y.; Wang, Z. Y.; Zang, S. Q.; Mak, T. C. W. Modular Cocrystallization of Customized Carboranylthiolate-Protected Copper Nanoclusters via Host-Guest Interactions. *ACS Nano* **2022**, *16* (11), 18789–18794.

(17) Li, Y. L.; Wang, Z. Y.; Ma, X. H.; Luo, P.; Du, C. X.; Zang, S. Q. Distinct Photophysical Properties in Atom-Precise Silver and Copper Nanocluster Analogues. *Nanoscale* **2019**, *11* (12), 5151–5157.

(18) Jana, A.; Unnikrishnan, P. M.; Poonia, A. K.; Roy, J.; Jash, M.; Paramasivam, G.; Machacek, J.; Adarsh, K. N. V. D.; Base, T.; Pradeep, T. Carboranethiol-Protected Propeller-Shaped Photoresponsive Silver Nanomolecule. *Inorg. Chem.* **2022**, *61* (23), 8593–8603.

(19) Wang, J.; Wang, Z. Y.; Li, S. J.; Zang, S. Q.; Mak, T. C. W. Carboranealkynyl-Protected Gold Nanoclusters: Size Conversion and UV/Vis–NIR Optical Properties. *Angew. Chemie - Int. Ed.* **2021**, *60* (11), 5959–5964.

(20) Wang, J.; Xu, F.; Wang, Z. Y.; Zang, S. Q.; Mak, T. C. W. Ligand-Shell Engineering of a Au_{28} Nanocluster Boosts Electrocatalytic CO_2 Reduction. *Angew. Chemie - Int. Ed.* **2022**, *61* (32), 1–6.

(21) Huang, J. H.; Wang, Z. Y.; Zang, S. Q.; Mak, T. C. W. Spontaneous Resolution of Chiral Multi-Thiolate-Protected Ag_{30} Nanoclusters. *ACS Cent. Sci.* **2020**, *6* (11), 1971–1976.

(22) Huang, J. H.; Si, Y.; Dong, X. Y.; Wang, Z. Y.; Liu, L. Y.; Zang, S. Q.; Mak, T. C. W. Symmetry Breaking of Atomically Precise Fullerene-like Metal Nanoclusters. *J. Am. Chem. Soc.* **2021**, *143* (32), 12439–12444.

(23) Jana, A.; Jash, M.; Dar, W. A.; Roy, J.; Chakraborty, P.; Paramasivam, G.; Lebedkin, S.;

Kirakci, K.; Manna, S.; Antharjanam, S.; Machacek, J.; Kucerakova, M.; Ghosh, S.; Lang, K.; Kappes, M. M.; Base, T.; Pradeep, T. Carborane-Thiol Protected Copper Nanoclusters: Stimuli-Responsive Materials with Tunable Phosphorescence. *Chem. Sci.* **2022**, *14* (6), 1613–1626.

(24) Wang, J.; Cai, J.; Ren, K. X.; Liu, L.; Zheng, S. J.; Wang, Z. Y.; Zang, S. Q. Stepwise Structural Evolution toward Robust Carboranealkynyl-Protected Copper Nanocluster Catalysts for Nitrate Electroreduction. *Sci. Adv.* **2024**, *10* (18), 1–8.

(25) Yadav, V.; Jana, A.; Acharya, S.; Malola, S.; Nagar, H.; Sharma, A.; Kini, A. R.; Antharjanam, S.; Machacek, J.; Nair, K.; Devi, V.; Base, T.; Häkkinen, H.; Pradeep, T. Site-Specific Substitution in Atomically Precise Carboranethiol-Protected Nanoclusters and Concomitant Changes in Electronic Properties. *Nat. Commun.* **2025**, *16* (1197), 1–13.

Nanoscale

REVIEW

View Article Online
View Journal

Published on 27 October 2025. Downloaded by Indian Institute of Technology Chennai on 12/29/2025 3:17:01 AM.

Check for updates

Cite this: DOI: 10.1039/d5nr03845f

Precision at the nanoscale: an 'ionic' view of composition, structure and properties

Anagha Jose, [a] B. S. Sooraj [a] and Thalappil Pradeep *[a,b]

The study of matter at the nanoscale has traditionally relied on electron microscopy and optical spectroscopy to relate particle size with emerging properties. Mass spectrometry (MS), although a century-old analytical technique, has emerged in recent decades as a central tool for investigating atomically precise clusters (APCs). The introduction of soft ionisation methods, such as electrospray ionisation (ESI) and matrix-assisted laser desorption/ionisation (MALDI), has enabled the detailed analysis of cluster composition, fragmentation pathways, and structural features of APCs. The integration of ion mobility spectrometry with MS has further allowed direct correlations among their molecular formula, structure, and stability. At the same time, new developments such as charge-detection MS, ultraviolet photodissociation, and mass photometry have expanded the analytical range to larger and more complex systems. Beyond fundamental characterisation, MS is increasingly being applied to probe intrinsic properties such as ionisation potentials and support material applications through cluster deposition and related approaches. This review highlights the expanding role of MS in APC research and the impact of mass spectrometry-based techniques in materials science.

Received 11th September 2025,
Accepted 26th October 2025

DOI: 10.1039/d5nr03845f

rsc.li/nanoscale

1. Introduction

As John Fenn stated in his Nobel lecture, "Electrospray: Wings for Molecular Elephants",[1] the technique has evolved, 'from flames to flying elephants.' What once seemed an improbable task, namely, transferring large biomolecules such as proteins and polymers into their gaseous phase, became possible through electrospray ionisation, a development that transformed modern mass spectrometry. This development has great consequence to cluster science as well.

The origin of mass spectrometry dates to the early 20th century, when Sir J. J. Thomson constructed the first mass spectrograph,[2,3] then referred to as a "parabola spectrograph", to measure the mass-to-charge (m/z) ratio of gaseous ions. His

[a]DST Unit of Nanoscience (DST UNS) & Thematic Unit of Excellence (TUE), Department of Chemistry, Indian Institute of Technology Madras (IITM), Chennai 600036, India. E-mail: pradeep@iitm.ac.in
[b]International Centre for Clean Water, 2nd Floor, B-Block, IIT Madras Research Park, Kanagam Road, Taramani, Chennai 600113, India



Anagha Jose

Anagha Jose received her BSc from the University of Calicut and M.Sc. from Cochin University of Science and Technology (CUSAT). She is currently a PhD scholar at the Indian Institute of Technology Madras (IITM) under the guidance of Prof. Thalappil Pradeep. She has been awarded the Prime Minister's Research Fellowship (PMRF). Her research interests include mass spectrometry of nanoclusters and nanoparticles, as well as the applications of atomically precise metal clusters.



B. S. Sooraj

B. S. Sooraj received a BS-MS Dual Degree from the Indian Institute of Science Education and Research Bhopal (IISERB) in 2019. He is currently a PhD scholar at the Indian Institute of Technology Madras (IITM) under the guidance of Prof. Thalappil Pradeep. He is a recipient of the prestigious Shyama Prasad Mukherjee (SPM) Fellowship. His research interests include atomically precise metal clusters, mass spectrometry of megadalton clusters and nanoparticles, and CryoEM-based single-particle reconstruction of nanoparticles.

Published on 27 October 2025. Downloaded by Indian Institute of Technology Chennai on 12/29/2025 3:17:01 AM.

pioneering work not only led to the development of MS as an analytical technique but also provided the first evidence of isotopes. Francis W. Aston further expanded this observation and discovered isotopes in elements, for which he was awarded the Nobel Prize in Chemistry in 1922.[4] In the early decades, MS was widely used in organic chemistry, primarily for the analysis of small molecules. Ionisation methods such as electron impact (EI) and electric discharge were well-suited for volatile and thermally stable compounds. As this field evolved, the utility of MS expanded to include more complex analytes such as sugars, alkaloids, and peptides.[5] The development of hyphenated techniques, especially gas chromatography-mass spectrometry (GC–MS), significantly enhanced the ability to resolve and identify components in complex mixtures, establishing MS as an inevitable tool in analytical chemistry.[6,7]

However, the expansion of MS into the realm of biomolecular analysis posed new challenges due to the fragility and high mass of proteins and nucleic acids. To address this, high-resolution double-focusing mass spectrometers were developed, as demonstrated by Todd, McGilvery, and Baldwin.[8] These instruments enabled more accurate *m*/*z* measurements and facilitated early tandem MS (also designated as MS/MS) experiments for structural elucidation. However, the lack of efficient and non-destructive ionisation methods limited the analysis of large biomolecules.



Thalappil Pradeep

Thalappil Pradeep is an Institute Professor and Deepak Parekh Institute Chair Professor at the Indian Institute of Technology Madras (IITM), Chennai, India. His research interests are in molecular and nanoscale materials. He has authored 600 scientific papers, 10 books, 100+ Indian and 29 US/PCT patents, co-founded 7 start-ups and founded the International Centre for Clean Water (https://iccw.world). He is involved in the development of affordable technologies for drinking water purification. His pesticide removal technology has reached >10 million people. His arsenic removal technology, approved for national implementation, is delivering arsenic-free water to >1.4 million people every day. He is a recipient of the Shanti Swaroop Bhatnagar Prize, The World Academy of Sciences (TWAS) prize, Padma Shri, Nikkei Asia Prize, Prince Sultan Bin Abdulaziz International Prize for Water, VinFuture Prize and ENI award. He is a Fellow of all the science and engineering academies of India, TWAS, American Association for the Advancement of Science, African Academy of Sciences, US National Academy of Engineering and Academia Europaea. He has received the Lifetime Achievement Research Award of IITM and Distinguished Alumnus Award of Indian Institute of Science. As part of philanthropy, he supports a school in his village where 500 students are enrolled.

A major paradigm shift occurred in the late 1980s with the introduction of soft ionisation techniques, notably electrospray ionisation (ESI)[9] and matrix-assisted laser desorption ionisation (MALDI).[10,11] These techniques enabled the ionisation of large, fragile molecules under mild conditions, preserving their molecular integrity and allowing their introduction into the gas phase for mass analysis.[12] These breakthroughs had a profound impact, particularly in proteomics and macromolecular research, and their significance was recognised with the 2002 Nobel Prize in Chemistry awarded to John Fenn for electrospray ionisation (ESI) and Koichi Tanaka for soft laser desorption.[13] These historical milestones reflect the continuous innovation in mass spectrometry that has expanded its analytical capabilities from elemental and isotopic analysis to the structural and compositional characterisation of large and complex molecular assemblies.

Atomically precise clusters (APCs), composed of tens to thousands of metal atoms stabilised by ligands and with core sizes below 3 nm, bridge the gap between atoms and bulk. Their closely spaced electronic orbitals give rise to multiple electronic transitions, photoluminescence, chirality, conductivity, and magnetism, distinguishing them from bulk metals.[14–17] Over 700 atomically precise clusters with nuclearities ranging from 2 to 2000 atoms have been reported,[18] with more than 350 being structurally characterised by crystallography,[19] including metals such as Au, Ag, Pt, and Cu, as well as their alloys. Conventional characterisation methods, such as transmission electron microscopy (TEM), scanning electron microscopy (SEM), X-ray diffraction (XRD), and dynamic light scattering (DLS), often lack the resolution to fully capture the precise size and composition of these clusters.[20] However, MS offers capabilities that surpass conventional techniques, which make it an indispensable analytical tool in the analysis of APCs. Although electron microscopy and optical methods primarily provide information on morphology and size-dependent properties, MS enables the direct and accurate determination of cluster composition, isotopic distribution, charge states, and ligand architecture at the molecular level. It enables in-depth analysis of both bare and ligand-protected NCs, helping to understand their reactivity, transformation pathways, and gas-phase structures. MS/MS involves the analysis of mass-selected ions, which provides further insights into their structural features and fragmentation behaviour. Additionally, ion mobility mass spectrometry (IM-MS) enables the exploration of structural isomerism and conformational changes in the gas phase. Emerging techniques, including charge detection mass spectrometry (CDMS) and mass photometry (MP), are expanding the capabilities of MS by enabling single-particle sensitivity and accurate mass measurements for large, heterogeneous, or weakly ionising NCs.[21]

With the advancement of mass spectrometric (MS) instrumentation, recent developments have significantly expanded the analytical window in terms of accessible mass range, resolution and detection limit. Techniques such as Fourier transform ion cyclotron resonance (FT-ICR)[22,23] and Orbitrap mass spectrometry[24,25] now achieve resolutions above

This journal is © The Royal Society of Chemistry 2025

Published on 27 October 2025. Downloaded by Indian Institute of Technology Chennai on 12/29/2025 3:17:01 AM.

1 000 000 and 500 000, respectively, with sub-femtomole sensitivity, enabling the accurate characterisation of molecules from small ions to multi-megadalton assemblies. Time-of-flight (TOF) and quadrupole-TOF (Q-TOF) analysers provide rapid acquisition and high-throughput analysis with resolutions approaching 100 000, making them valuable for complex biological and chemical systems.[26,27] CDMS and Orbitrap-CDMS extend measurements to the megadalton and gigadalton scales by directly determining the charge and mass of single ions with near unit-charge accuracy.[28,29] Mass photometry complements these approaches by offering label-free, single-particle mass analysis in solutions across the 30 kDa–10 MDa range.[30] Collectively, these developments provide powerful and versatile tools for high-resolution and high-sensitivity analysis in chemistry, biology, and materials science.

In addition to structural and compositional analysis, MS has enabled the real-time monitoring of cluster growth, ligand exchange, redox behaviour, and intermediate species during synthesis. The resemblance of NCs to biomolecules in terms of mass range and surface ligand environment makes ESI-MS particularly suited to their analysis, such as protein characterisation. Furthermore, the ability of MS to resolve complex mixtures and detect species with varying charge states expands its utility to very large NCs and even small nanoparticles with emerging surface plasmon resonance (*e.g.*, $Au_{279}(TBBT)_{84}$ and $Ag_{146}Br_2(TIBT)_{80}$).[31,32] Complementary to MS, mass photometry enables the label-free, solution-phase quantification of the aggregation states and supramolecular assemblies of atomically precise clusters at the single-particle level.[33]

Collectively, advancements in MS instrumentation and methodologies have firmly established both ESI and MALDI as indispensable platforms for the molecular-level characterisation of metal NCs.[34,35] They provide accurate data that is in strong agreement with the crystallographically and theoretically predicted structures, and thereby play a crucial role in the rational design of nanocluster-based materials. The field of mass spectrometry of APCs has expanded significantly over the years, with the research output now exceeding 700 publications (Fig. 1), indicating the rapidly growing interest and suggesting a surge in research efforts in this direction soon.

Mass spectrometry (MS), along with its advanced and hyphenated variants, has become a cornerstone in the characterisation of nanoclusters, providing unparalleled insights into their composition, structure, and dynamics.[35–38] In this review, we discuss the recent advances in MS-based approaches for studying atomically precise nanoclusters (APCs), with a focus on four key aspects including composition,[39] structure,[40] properties,[41] and applications[42,43] (Fig. 2).

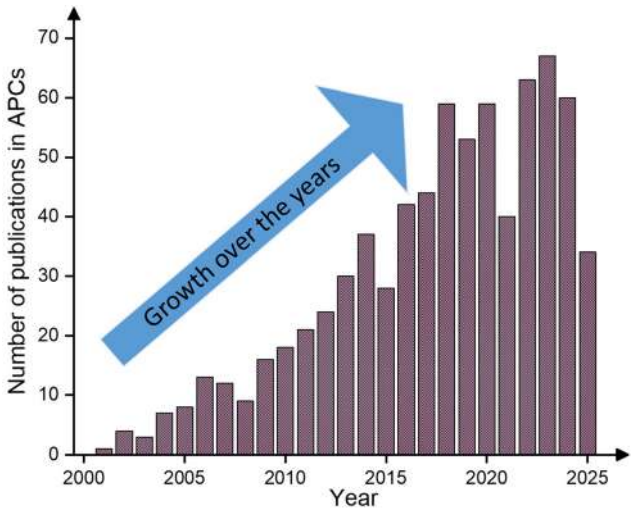


Fig. 1 Number of papers published each year on nanoclusters and mass spectrometry (collected from Web of Science using the keywords "nanoclusters", "metal clusters", "mass spectrometry" and "mass"). The data were collected up to July 31, 2025.

2. Mass spectrometry: the gateway to nanoparticle characterisation

2.1. Composition of clusters

Since the 1980s, advancements in ionisation sources such as supersonic expansion and laser desorption ionisation (LDI) have established MS as a critical technique for characterising gas-phase metal clusters,[44,45] fullerenes,[46] and semiconductor clusters.[47,48] In 1994, Brust *et al.* made a breakthrough in the synthesis of thiol-protected gold nanoparticles (<3 nm),[49] which enabled the preparation of monodisperse, atomically precise nanoclusters, leading to extensive research in this area.

MS has rapidly emerged as an indispensable tool for determining the composition of noble metal nanoclusters, particularly gold (Au), silver (Ag), and platinum (Pt) nanoclusters. The early work by Murray and Whetten employed LDI-MS to analyse thiolate-protected gold nanoclusters, which initiated the use of MS in cluster science.[50–52] However, LDI, being a relatively harsh ionisation method, often caused fragmentation, limiting its utility for accurate molecular composition analysis. This challenge led to the adoption of softer ionisation techniques such as matrix-assisted laser desorption ionisation (MALDI) and electrospray ionisation (ESI), which allowed the detection of intact ligand-protected clusters. ESI-MS, in particular, has proven highly effective due to its gentle ionisation process, enabling the high-resolution detection of intact molecular ions, accurate charge-state determination, and precise elemental composition, which is crucial for structural elucidation. A notable example includes the identification of a 10.4 kDa glutathione-protected gold cluster, initially reported as $Au_{28}(SG)_{16}$ by Schaaff *et al.* in 1998 using MALDI and ESI-MS,[53] and later reassigned as $Au_{25}(SG)_{18}$ by Negishi *et al.* in 2005.[54] These advances have significantly deepened the molecular-level understanding of the structure and composition of gold nanoclusters.[55]

At present, ESI-MS and MALDI-MS have become predominant analytical tools to precisely characterise the composition of ligand-protected metal nanoclusters. Numerous atomically precise gold NCs, including $[Au_{24}(SAdm)_{16}]$ (Fig. 3a),[56]

Published on 27 October 2025. Downloaded by Indian Institute of Technology Chennai on 12/29/2025 3:17:01 AM.

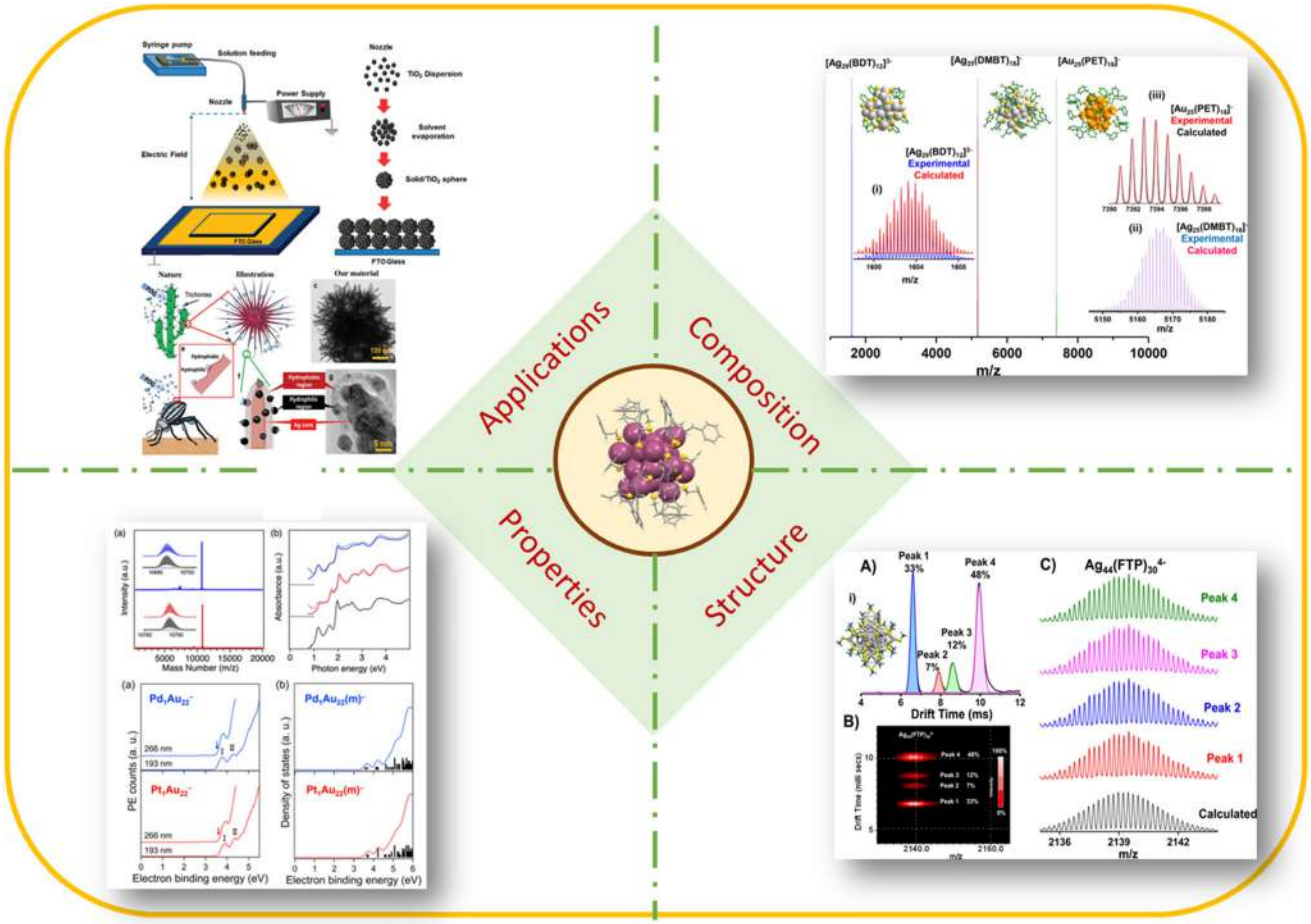


Fig. 2 Schematic depicting the role of mass spectrometry in atomically precise clusters (APCs), enabling a detailed understanding of their composition, structure, properties, and applications. Images under composition are adapted with permission from ref. 39. Copyright 2018, the American Chemical Society. Images under structure are adapted from ref. 40. Copyright 2017, the American Chemical Society. Images under properties are adapted from ref. 41. Copyright 2022, the American Chemical Society. Images under applications are adapted from ref. 42 and 43. Copyright 2011, the American Chemical Society and Copyright 2018, John Wiley and Sons, respectively.

$[Au_{25}(PET)_{18}]$,[57,58] and $[Au_{32}(SC_2H_4Ph)_{24}]$ (Fig. 3b),[59] have been successfully characterised by ESI-MS, where the experimentally observed charge states and molecular weights closely match the crystallographic data, validating the cluster formulae with atomic-level accuracy. Although silver nanoclusters present analytical challenges due to their dual isotopes (^{107}Ag and ^{109}Ag) and lower stability, these issues have been effectively addressed by ESI-MS. The broader isotopic envelopes observed (*e.g.*, $Ag_{25}(DMBT)_{18}$)[60] allow clear differentiation from their gold counterparts. ESI-MS has precisely identified nanoclusters such as $[Ag_{141}X_{12}(S\text{-}Adm)_{40}]$[61] and $Ag_{67}(SPhMe_2)_{32}(PPh_3)_8$ (Fig. 3c),[62] confirming both their 3+ charge state and molecular formula, in excellent agreement with their crystal structures. To improve the ionisation efficiency, especially for clusters with low intrinsic ionizability, ionisation enhancers such as caesium acetate (CsOAc)[63,64] are utilised, facilitating the formation of intact molecular ions. MALDI-MS, enhanced with optimised matrices such as DCTB (*trans*-2-[3-(4-*tert*-butylphenyl)-2-methyl-2-propenylidene] malononitrile), is widely used to analyse larger nanoclusters (*e.g.*, $Au_{133}(SPh\text{-}^tBu)_{52}$ and $Au_{329}(SCH_2CH_2Ph)_{84}$),[65–67] often yielding intact molecular ion peaks with minimal fragmentation. MS has been extended beyond noble metals to non-noble metal clusters, heterometallic nanoclusters, and other ligand types. These clusters include metals such as Fe, Co, Ni, Cu, and Ir, as well as ligands such as hydrides, carboranes, carbenes, phosphines, and alkynyls. For example, $[Ag_{18}H_{16}(TPP)_{10}]$, $[Ag_{25}H_{22}(DPPE)_8]$,[68] $Ag_{40}(C_2B_{10}H_{10}S_2)_{12}(PPh_3)_8$,[69] $Ag_{61}(dpa)_{27}(SbF_6)_4$,[70] $Ag_{74}(C{\equiv}CPh)_{44}$,[71] $[Au_{13}(NHC)_5Cl_2]Cl_3$,[72] $[Au_{20}(dppp_3)_4]Cl_4$,[73] $Au_{22}(C{\equiv}CPh)_{18}$,[74] $Au_{110}(C{\equiv}CC_3H_6Ph)_{48}$,[75] $Cu_{18}(PET)_{16}(PPh_3)_4Cl$,[76] $Cu_{33}H_{18}(Medpf)_{12}$,[77] $Cu_{75}(S\text{-}Adm)_{32}$,[78] $Pd_{21}(SCH_2CH_2Ph)_{18}$,[79] $Pt_8(C_2H_2O_2S)_8$,[80] $[Fe_{55}H_{46}(PtBu_3)_{12}]$[81] and $[Ir_9(PET)_6]$.[82]

ESI-MS confirmed the molecular composition and the fact that $Au_{44}(2,4\text{-}DMBT)_{26}$ was charge-neutral prior to ionisation by identifying the $[Au_{44}(2,4\text{-}DMBT)_{26} + 2Cs]^{2+}$ ion at m/z 6250.3. The observed 2+ charge state, arising from the addition of Cs^+, supported the neutral nature of the cluster, in agreement with X-ray crystallography and XPS data.[83] In bimetallic

This journal is © The Royal Society of Chemistry 2025

Published on 27 October 2025. Downloaded by Indian Institute of Technology Chennai on 12/29/2025 3:17:01 AM.

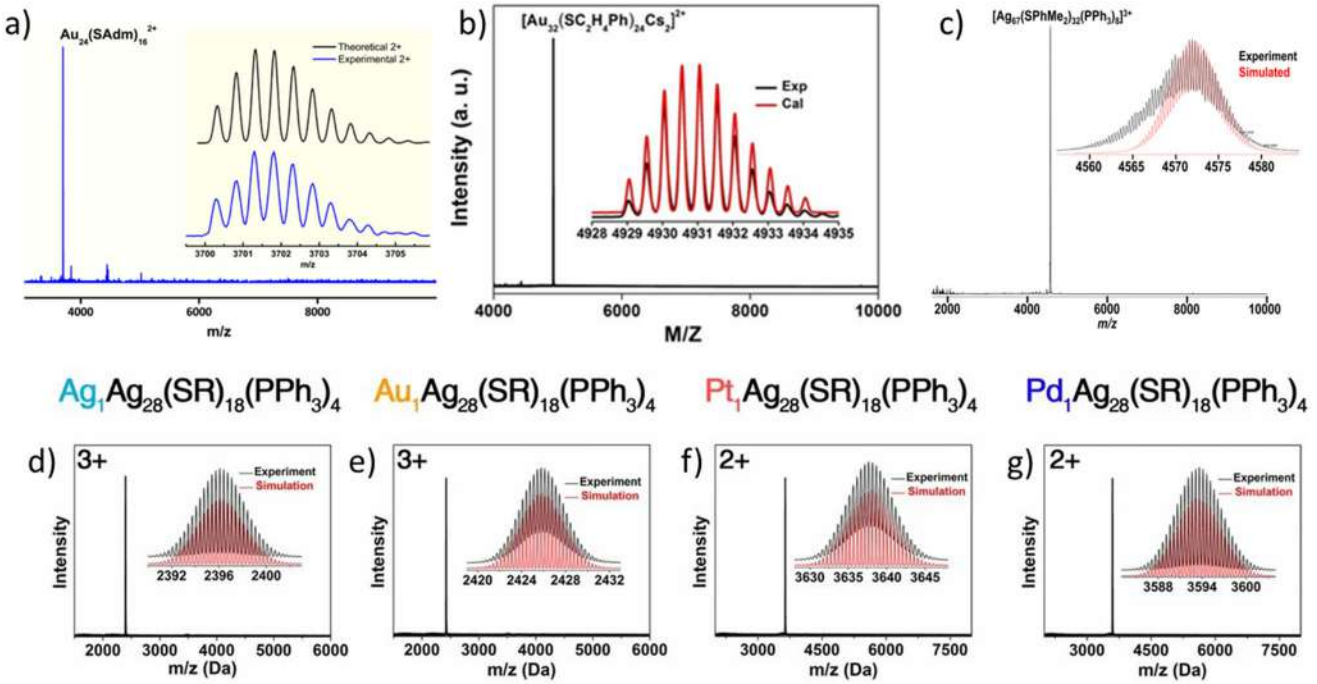


Fig. 3 ESI-MS of (a) $Au_{24}(SAdm)_{16}$, (b) $Au_{32}(SC_2H_4Ph)_{24}$, (c) $Ag_{67}(SPhMe_2)_{32}(PPh_3)_2$, (d) $Ag_1Ag_{28}(SR)_{18}(PPh_3)_4$, (e) $Au_1Ag_{28}(SR)_{18}(PPh_3)_4$, (f) $Pt_1Ag_{28}(SR)_{18}(PPh_3)_4$, and (g) $Pd_1Ag_{28}(SR)_{18}(PPh_3)_4$. Simulated and experimental isotopic distributions are shown in the inset. Reproduced with permission from (a) ref. 56, (b) ref. 59, (c) ref. 62, (d) ref. 85, (e) ref. 85, (f) ref. 85 and (g) ref. 85. Copyright 2014, the American Chemical Society. Copyright 2021, John Wiley and Sons. Copyright 2016, the American Chemical Society. Copyright 2019, National Academy of Sciences.

systems, such as the $Au_{27}Cd_1(SAdm)_{14}(DPPF)Cl$ nanocluster, both ESI-MS and MALDI-MS played complementary roles, where ESI-MS determined the precise molecular formula, while MALDI-MS helped identify surface ligands, supporting the structural data obtained from single-crystal X-ray diffraction.[84] Kang *et al.* constructed a comprehensive library of 21 atomically precise M_{29} nanoclusters, ranging from monometallic to tetrametallic compositions, using a novel $M_{29}(S\text{-}Adm)_{18}(PPh_3)_4$ template. ESI-MS was pivotal in confirming the exact compositions and uniformity of these clusters, revealing single, intense peaks for each species (Fig. 3d–g). The charge states were identified as 3+ for Ag_{29} and Au_1Ag_{28}, and 2+ for Pt_1Ag_{28} and Pd_1Ag_{28}, which helped to establish their electronic configurations.[85] Zhu and coworkers utilised ESI-MS to confirm the atomic precision in the site-specific doping of $Au_{25}(SR)_{18}$ clusters, resolving single-atom substitutions and tracking the doping reversibility.[86] Similarly, Bootharaju *et al.* employed ESI-MS to verify single-atom gold doping in $[Ag_{24}Au(SR)_{18}]$ clusters.[87] Soldan *et al.* quantified the gold doping levels in $Ag_{29}(BDT)_{12}(TPP)_4$, detecting up to five Au dopants (with minor populations of six and seven) through characteristic *m*/*z* shifts of 30 per substitution.[88]

Overall, MS, particularly ESI-MS, is a critical technique for confirming the composition, charge, stoichiometry, and atomic-level doping of metal nanoclusters. It offers an unparalleled molecular-level understanding that complements crystallographic and spectroscopic methods.

2.2. Mass spectrometric insights into ligand-induced transformation

MALDI-MS and ESI-MS have been extensively used in elucidating the mechanistic details of ligand exchange-induced structural transformation (LEIST) in atomically precise nanoclusters by providing molecular-level insights into both the intermediate and final species.[89]

Amala Dass and coworkers monitored the time-dependent core transformation in $Au_{144}(SCH_2CH_2Ph)_{60}$ using MALDI-MS. In the initial 2 h, they identified a new peak for $Au_{133}(SPh\text{-}t\text{Bu})_{52}$, and further they detected subsequent species such as $Au_{102}(SPh\text{-}t\text{Bu})_{44}$ and $Au_{279}(SPh\text{-}t\text{Bu})_{84}$ (Fig. 4a). However, due to its greater fragmentation, MALDI-MS failed to detect key intermediates such as $Au_{191}(SPh\text{-}t\text{Bu})_{66}$. This limitation was overcome by ESI-MS, which through softer ionisation, successfully identified $Au_{191}(SPh\text{-}t\text{Bu})_{66}$ *via* its +2 and +3 charge states and Cs^+ adducts (Fig. 4b). ESI-MS further confirmed the disappearance of Au_{133} at 14 h, indicating its full conversion, and revealed the presence of intermediate-sized clusters (Au_{98-104}) that were not seen clearly by MALDI-MS. ESI-MS confirmed the purity of $Au_{144}(PET)_{60}$ and detected trace amounts of larger polydisperse species at later stages, suggesting cluster growth beyond Au_{279}.[90] Similarly, ESI-MS and optical spectroscopy were used to monitor the ligand-induced transformation of $Au_{38}(PET)_{24}$ to $Au_{36}(TBBT)_{24}$ (Fig. 4c). The reaction proceeds through four stages, *i.e.* ligand exchange, structural distortion,

Published on 27 October 2025. Downloaded by Indian Institute of Technology Chennai on 12/29/2025 3:17:01 AM.

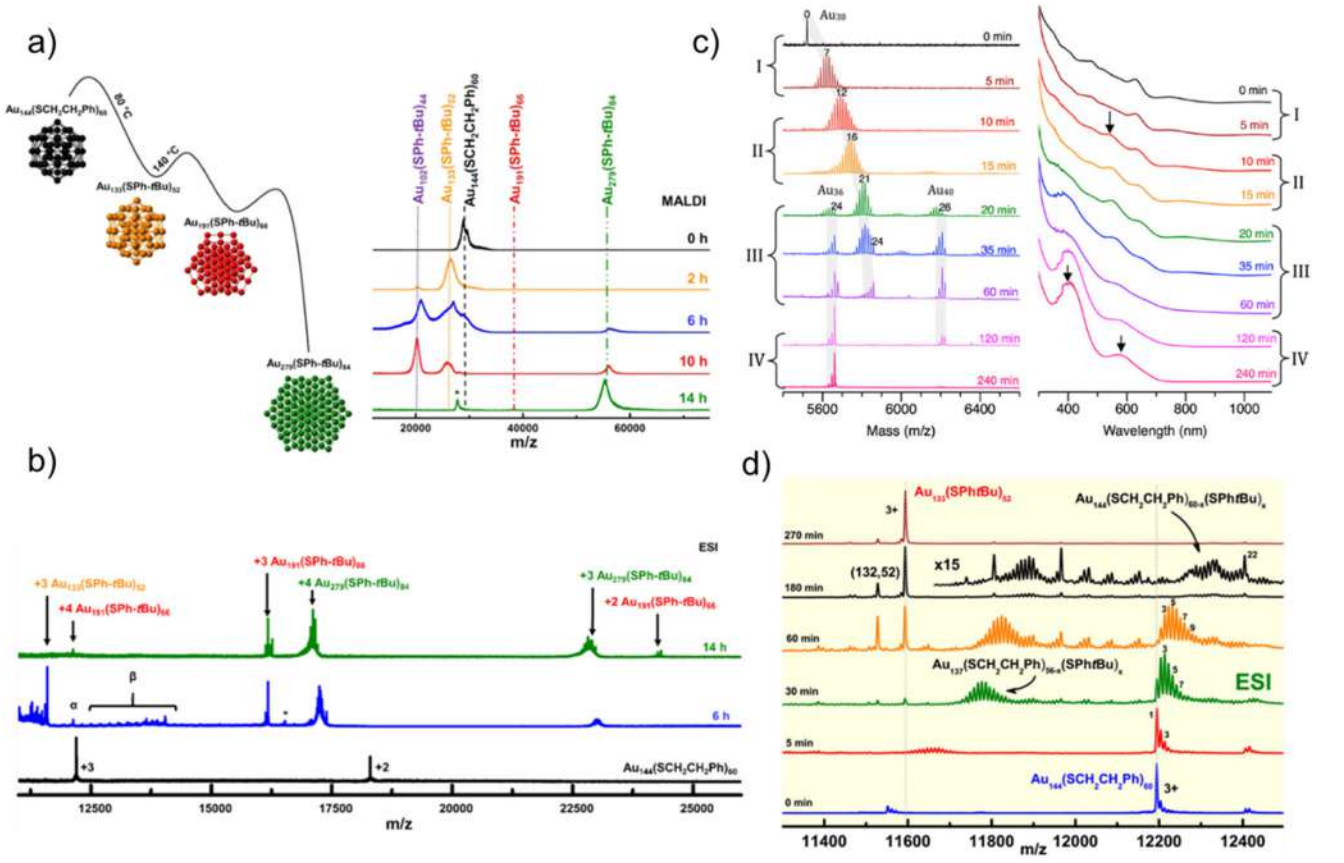


Fig. 4 (a) Schematic of the transformation of $Au_{144}(SCH_2CH_2Ph)_{60}$, and MALDI-MS of the starting $Au_{144}(SCH_2CH_2Ph)_{60}$ and its transformation to Au_{133}(SPh-*t*Bu)$_{52}$, Au_{191}(SPh-*t*Bu)$_{66}$, and Au_{279}(SPh-*t*Bu)$_{84}$ upon reacting with 4-*tert*-butylbenzenethiol ligand at ~140 °C for 14 h. (b) ESI-MS of the starting $Au_{144}(SCH_2CH_2Ph)_{60}$ at 0 h and its transformation to Au_{133}(SPh-*t*Bu)$_{52}$, Au_{191}(SPh-*t*Bu)$_{66}$, and Au_{279}(SPh-*t*Bu)$_{84}$ upon reacting with 4-*tert*-butylbenzenethiol ligand at ~140 °C for 14 h. (c) Time-dependent ESI-MS of the transformation reaction of Au_{38} to Au_{36} and corresponding UV–vis spectra of different times in parallel with ESI-MS. (d) Core size conversion of $Au_{144}(SCH_2CH_2Ph)_{60}$ to Au_{133}(SPh-*t*Bu)$_{52}$ by ESI-MS. Adapted from (a) ref. 90, (b) ref. 90, (c) ref. 91 and (d) ref. 93. Copyright 2021, the American Chemical Society. Copyright 2013, the American Chemical Society. Copyright 2015, the American Chemical Society.

disproportionation to Au_{36} and Au_{40}, and size focusing that yields $Au_{36}(TBBT)_{24}$ in ~90% yield.[91] Liu *et al.* successfully developed a synthetic protocol combining ligand exchange and size focusing. MALDI-MS revealed broad initial polydispersity centred around $m/z \sim 25\,000$, while the final product was confirmed as a single, well-defined $Au_{99}(SPh)_{42}$ nanocluster at $m/z \sim 24\,000$.[92] Nimmala *et al.* describe the ligand-induced transformation of $Au_{144}(SCH_2CH_2Ph)_{60}$ into Au_{133}(SPh-*t*Bu)$_{52}$ upon treatment with excess *tert*-butylbenzenethiol. ESI-MS precisely characterised the molecular compositions of both the starting and product clusters, capturing mixed-ligand intermediates such as $Au_{144}(SCH_2CH_2Ph)_{60-x}$(SPh-*t*Bu)$_x$. The core-size conversion begins after ~22 ligand substitutions, with $Au_{144}(SCH_2CH_2Ph)_{38}$(SPh-*t*Bu)$_{22}$ showing enhanced stability. The detailed time-dependent mass spectral data (Fig. 4d) further revealed a stepwise evolution through intermediate-sized clusters (*e.g.*, Au_{137}–Au_{139}) with varying ligand compositions, providing mechanistic insights into the ligand-exchange-induced structural rearrangements.[93]

Collectively, MALDI-MS and ESI-MS facilitated a comprehensive understanding of the ligand-induced core transformations of clusters and the identification of intermediate species and final products, thereby providing insights into the mechanisms.

2.3. Atomic-scale insights into high-nuclearity nanoclusters

In 2014, Kumara *et al.* reported the synthesis and precise characterization of 'Faradaurate-500' ($Au_{500}(SR)_{120}$), a highly stable and monodisperse plasmonic gold nanocrystal with a diameter of approximately 2.4 nm, using ESI-MS and MALDI (Fig. 5a). Through analysis of multiply charged ions and ligand exchange experiments, they determined its molecular mass (115 kDa) and ligand number (120), achieving atomic-level compositional control rarely attained at this size.[94] Building on this, Dass and coworkers synthesised a larger gold thiolate cluster, 'Faradaurate-940'($Au_{940}(SR)_{160}$), the largest cluster characterised by ESI-MS to date. They combined ESI-MS and MALDI-MS to determine its molecular mass,

Published on 27 October 2025. Downloaded by Indian Institute of Technology Chennai on 12/29/2025 3:17:01 AM.

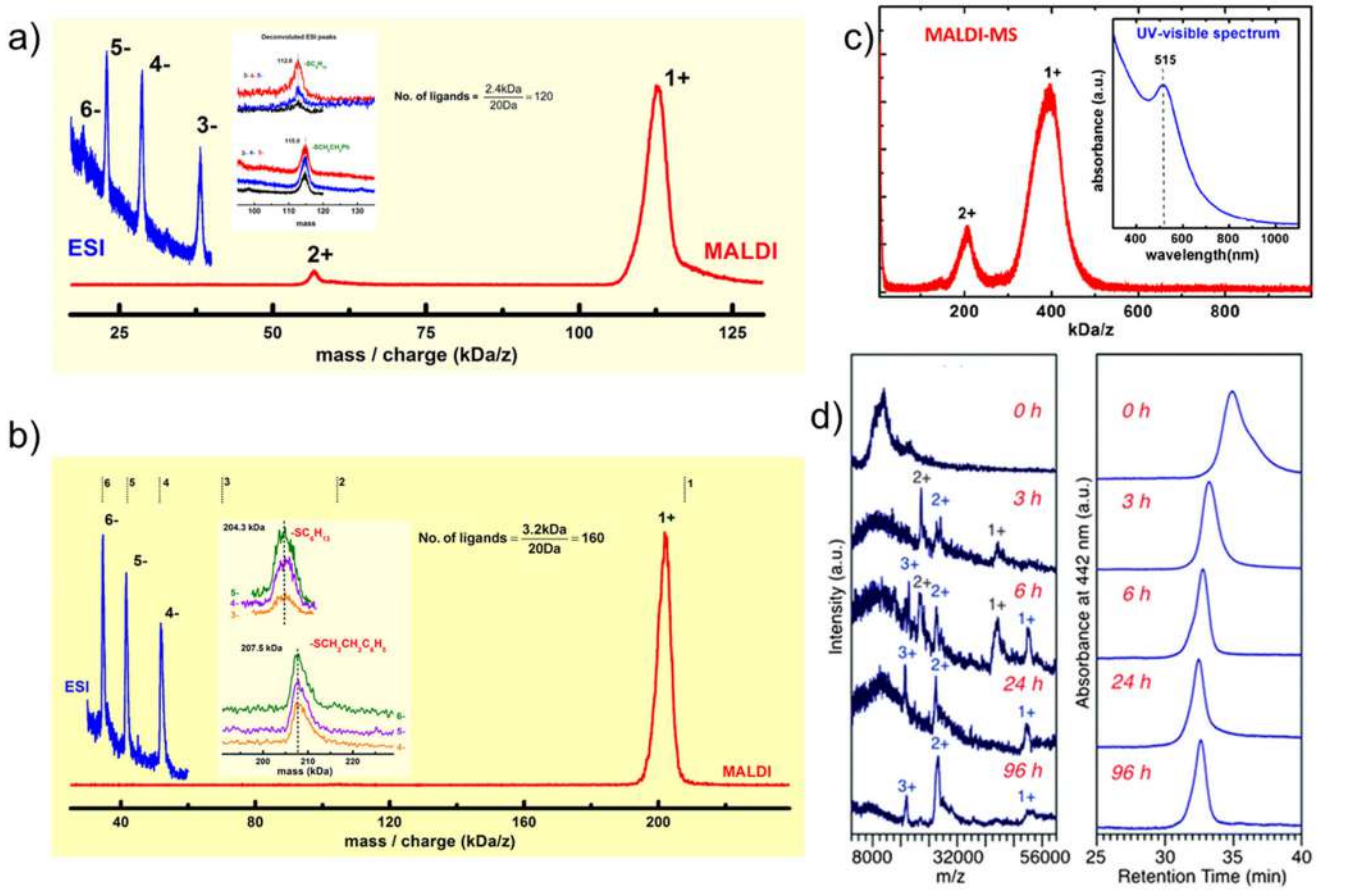


Fig. 5 (a) MALDI (red) and ESI (blue) mass spectra of $Au_{\sim 500 \pm 10}(SCH_2CH_2Ph)_{\sim 120 \pm 3}$. MALDI-MS shows 1+ and 2+ ions, while ESI MS yields 3–, 4–, 5–, and 6– ions. (b) MALDI (red) and ESI (blue) mass spectra of $Au_{940 \pm 20}(SR)_{160 \pm 4}$. (c) MALDI-MS and UV–visible spectrum (inset) of $Au_{\sim 2000}(SR)_{\sim 290}$. (d) Positive-ion ESI mass spectra and GPC chromatograms of $Ag_{\sim 280}(SBB)_{\sim 120}$. Adapted from (a) ref. 94, (b) ref. 95, (c) ref. 97 and (d) ref. 98. Copyright 2014, the American Chemical Society. Copyright 2014, the American Chemical Society. Copyright 2018, the American Chemical Society. Copyright 2011, The Royal Society of Chemistry.

which is 207.5 kDa, and confirmed the ligand count (160) by comparing nanoclusters synthesised with two different thiols, hexanethiol and phenylethanethiol. The gold atom number (~940 ± 20) was back-calculated from the total mass, while MALDI-MS verified the sample purity (Fig. 5b).[95] Kumara *et al.* reported the synthesis and characterisation of ~300 kDa and ~400 kDa Au-hexanethiolate nanoparticles with compositions of approximately $Au_{1385}(SR)_{240}$ and $Au_{2000}(SR)_{290}$, respectively. MALDI-MS enabled compositional assignment, revealing peaks at 288 kDa and 394 kDa.[96] Vergara *et al.* characterised $Au_{\sim 2000}(SC_6H_{13})_{\sim 290}$ nanoparticles using MALDI-MS, which detected molecular ions at ~394 kDa (1+) and ~200 kDa (2+), confirming a gold core of approximately 2000 atoms and ~290 ligands (Fig. 5c). These studies showed the development in the synthesis and mass spectrometric characterisation of gold nanocrystals from ~500 to ~2000 atoms, demonstrating how ESI-MS and MALDI-MS serve as complementary, high-precision techniques for atomic-level compositional analysis and structural elucidation across progressively larger nanocrystal sizes.[97] Mass spectrometry provided insights into the formation, composition, and stability of silver clusters protected by 4-(*tert*-butyl) benzyl mercaptan (BBSH). Positive-ion ESI-MS tracked the evolution of the cluster over time, initially showing broad peaks (~10–15 kDa), which shifted to defined clusters at 43.5 kDa after 3 h, and finally to stable 51.8 kDa clusters by 24 h, with no signs of etching (Fig. 5d). LDI-MS revealed that the 51.8 kDa cluster lost ~18 kDa upon laser-induced cleavage of C–S bonds, corresponding to the loss of approximately 120 BBS ligands, leading to an estimated formula of $Ag_{280}(BBS)_{120}$. Similarly, the 43.5 kDa intermediate was assigned as $Ag_{223}(BBS)_{108}$.[98]

2.4. Nanocluster chemistry unveiled: inter-cluster reactions

Inter-cluster reactions involve the exchange of metal atoms and/or ligands between two atomically precise clusters, leading to the formation of alloy clusters, mixed ligand clusters, cluster polymers and new clusters. These reactions occur spontaneously under ambient conditions, revealing that nanoclusters are dynamic, chemically active entities.[99] These reactions were first demonstrated by Krishnadas *et al.* using ESI-MS to observe the real-time metal (Au–Ag) and ligand (PET–FTP) exchange between $[Au_{25}(SR)_{18}]$ and $[Ag_{44}(SR)_{30}]$ clus-

Published on 27 October 2025. Downloaded by Indian Institute of Technology Chennai on 12/29/2025 3:17:01 AM.

ters, revealing the formation of alloys with mass shifts of 89 and 99 Da.[100] Building on this, Pradeep and coworkers showed that mixing of $[Ag_{25}(SR)_{18}]$ and $[Au_{25}(SR)_{18}]$ leads to the formation of bimetallic nanoclusters, with ESI-MS capturing a short-lived dimer intermediate, $[Ag_{25}Au_{25}(SR)_{536}]^{2-}$, which enabled atomic exchange (Fig. 6a).[101] Subsequently, Neumaier *et al.* developed a kinetic model based on the reaction between $[Ag_{25}(DMBT)_{18}]$ and $[Au_{25}(PET)_{18}]$, showing that inter-cluster exchange occurs through three steps, as follows: (i) formation of a dimer, (ii) internal exchange of metal atoms, and (iii) breakdown into alloyed monomers.[102] Recently, Sooraj *et al.* showed that solid-state grinding of $[Au_{25}(PET)_{18}]$ with $[Ag_{25}(DMBT)_{18}]$ led to the rapid formation of polymer species, including dimers, trimers, and higher oligomers (Fig. 6b).

The rate of reaction appeared to be faster in the solid state compared to the solution phase. Control experiments showed that metal exchange between clusters is the driving factor for polymerisation. The polymer species were stabilised by weak interactions such as van der Waals forces, aurophilicity, C–H···π and π–π stacking.[103] Isotopic labelling studies using

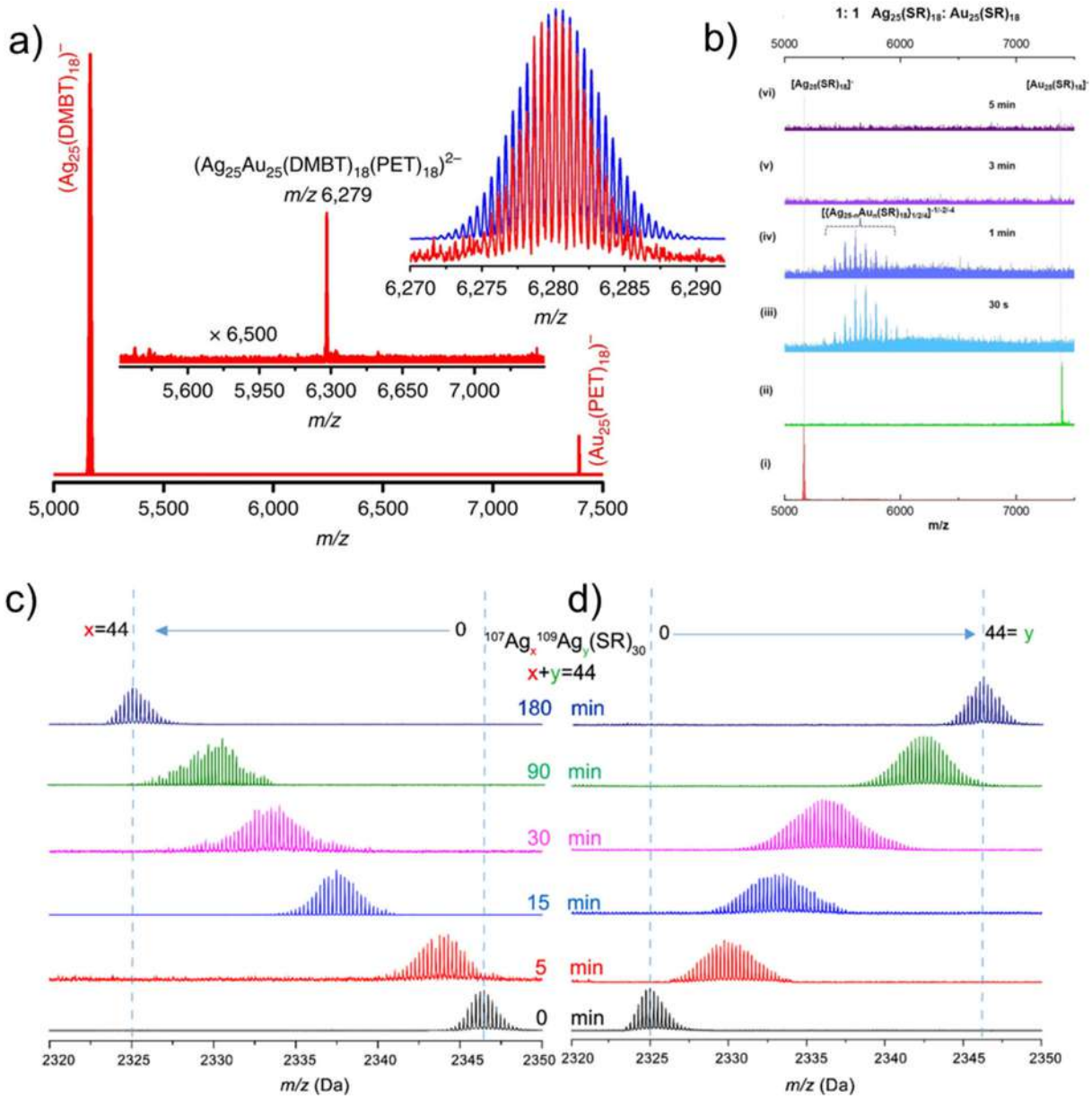


Fig. 6 (a) ESI-MS of the mixture of $Ag_{25}(DMBT)_{18}$(I) and $Au_{25}(PET)_{18}$(II), showing a feature due to the dianionic adduct, $(Ag_{25}Au_{25}(DMBT)_{18}(PET)_{18})^{2-}$ formed between I and II. (b) ESI-MS of $Ag_{25}(SR)_{18}$ and $Au_{25}(SR)_{18}$, and the time-dependent MS of the of $Ag_{25}(SR)_{18}$: $Au_{25}(SR)_{18}$ (ratio 1 : 1) produced monomers, dimers, and tetramers of the exchanged species. (c) Time-dependent ESI-MS results of the conversion from $^{109}Ag_{44}(SR)_{30}$ to $^{107}Ag_{44}(SR)_{30}$. (d) Time-dependent ESI-MS results of the conversion from $^{107}Ag_{44}(SR)_{30}$ to $^{109}Ag_{44}(SR)_{30}$. Reproduced with permission from (a) ref. 101, (b) ref. 103, (c) ref. 105 and (d) ref. 105. Copyright 2016, Springer Nature Group. Copyright 2024 and 2021, the American Chemical Society.

Published on 27 October 2025. Downloaded by Indian Institute of Technology Chennai on 12/29/2025 3:17:01 AM.

$[^{107}Ag_{25}(DMBT)_{18}]^-$ and $[^{109}Ag_{25}(DMBT)_{18}]^-$ showed that all 25 silver atoms could be exchanged within a minute.[104] Tang *et al.* showed that more rigid clusters such as $Ag_{29}(BDT)_{12}(TPP)_4$ exchanged atoms much more slowly, proving that flexibility plays a key role in reactivity. Their study showed that all the silver atoms in $Ag_{44}(SR)_{30}$ can dynamically exchange with Ag(I)-thiolate *via* an entropy-driven, isotopic metal exchange process, occurring first in the shell, and then in the kernel. Time-dependent ESI-MS showed complete, reversible conversion between ^{107}Ag and ^{109}Ag clusters over time (Fig. 6c and d), respectively.[105] In a related study, Suyama *et al.* found that spontaneous electron transfer (not atom exchange) occurred between two $PtAu_{24}$ clusters, protected with different alkanethiol ligands. The longer alkyl chains stabilised the dimer intermediates, which facilitated electron transfer between the clusters. These dimers were directly observed by ESI-MS, and their stability was found to increase with an increase in alkyl chain length.[106]

In a recent study by Acharya *et al.*, they reported that very stable dimers were formed between $[Ag_{29}(BDT)_{12}]^{3-}$ and $[Mag_{24}(DMBT)_{18}]^-$ (M = Ag, Au, Pd, or Pt), which remained intact for up to 48 h in solution due to the strong Ag–S bonds and non-covalent interactions at the interface. Altogether, these studies prove that nanoclusters are not fixed structures but can dynamically transform through inter-cluster interactions. ESI-MS plays a central role in understanding the products and intermediates, monitoring the real-time kinetics, and elucidating the mechanism of inter-cluster reactions.[107]

3. Mass spectrometry and structure

Ion mobility spectrometry (IM-MS) and tandem mass spectrometry (MS/MS) techniques such as collision-induced dissociation (CID), surface-induced dissociation (SID), and ultraviolet photodissociation (UVPD) are powerful approaches for probing the structure and fragmentation of metal nanoclusters. CID and SID induce fragmentation through energetic collisions, while UVPD uses light to activate ions, each revealing distinct dissociation pathways. IMS adds an additional dimension by separating ions based on their shape and size, enabling detailed insight into nanocluster conformations and fragmentation dynamics in the gas phase.

3.1. Unravelling the dissociation pathways of APCs in the gas phase

Collision-induced dissociation is a widely used MS/MS technique that enables the detailed study of the structure and stability of gas-phase ions by inducing fragmentation through collisions with inert gases such as helium, nitrogen, and argon. By accelerating mass-selected ions and causing them to collide with neutral gas molecules, CID converts kinetic energy into internal energy, leading to controlled bond cleavage within the ion. Fields-Zinna *et al.* applied CID MS/MS to a thiolate-protected gold nanocluster, $Na_xAu_{25}(SC_2H_4Ph)_{18-y}(S(C_2H_4O)_5CH_3)_y$, revealing that fragmentation predominantly involves the loss of the Au_2L_3 semi-ring motifs that bridge the Au_{13} core. The major fragment ions detected include $[Na_2AuL_2]^+$, $[Na_2Au_2L_3]^+$, $[NaAu_3L_3]^+$, and $[NaAu_4L_4]^+$, with no intermediates containing Au_5–Au_{17}, indicating that the Au_{13} core remained intact under the CID conditions.[108] Dass and coworkers reported the first complete structural and fragmentation analysis of an $Au_{25}(SR)_{18}$ nanocluster using IM-MS and CID MS/MS. This study revealed that the major fragments of $Au_{25}(SR)_{18}^{\mp}$ were $Au_{21}(SR)_{14}^{\mp}$ and $Au_{17}(SR)_{10}^{\mp}$ formed due to the successive loss of neutral $Au_4(SR)_4$ fragments.[109] Black *et al.* utilised in-source CID MS to analyse larger gold NCs such as $Au_{144}(SR)_{60}$ and $Au_{130}(SR)_{50}$, observing that triply charged (3+) ions undergo more efficient fragmentation (~80%) due to coulombic repulsion and higher energy absorption. Their fragmentation patterns involve characteristic neutral loss of disulfide ligands $(SR)_2$ and hydrocarbon units, with core-specific gold-containing fragments such as $Au_4(SR)_4$ for Au_{144} and $Au_3(SR)_2$ for Au_{130}, reflecting the differences in cluster core dissociation.[110] Chakraborty *et al.* demonstrated that $[Ag_{29}(S_2R)_{12}]^{3-}$, $[Ag_{25}(SR)_{18}]^-$, and $[Ag_{44}(SR)_{30}]^{4-}$ exhibit distinct dissociation pathways and gas-phase stabilities, which are correlated with their geometric and electronic structures. $[Ag_{29}(S_2R)_{12}]^{3-}$ undergoes stepwise cleavage into $[Ag_{24}(S_2R)_9]^{2-}$ and $[Ag_5(S_2R)_3]^-$, while $[Ag_{44}(SR)_{30}]^{4-}$ fragments into $[Ag(SR)_2]^-$ and $[Ag_2(SR)_3]^-$, retaining their closed-shell configurations. $[Ag_{25}(SR)_{18}]^-$ differs from its gold analogue by losing neutral $Ag_3(SR)_3$ units. This study found that the gas-phase stability trends (Ag_{29} > Ag_{25} > Ag_{44}) are correlated with the solution-phase behaviour.[111] Yao *et al.* revealed the atomic-level mechanism of isoelectronic size conversion from $[Au_{23}(SR)_{16}]$ to $[Au_{25}(SR)_{18}]$ *via* a surface-motif-exchange (SME)-induced core transformation from cuboctahedral to icosahedral Au_{13}. The isoelectronic size-conversion of Au_{23} nanoclusters proceeds according to the following definitive reaction: $[Au_{23}(SR)_{16}]^- + 2[Au_2(SR')_3]^- \rightarrow [Au_{25}(SR)_{12}(SR')_6]^- + 2[Au(SR)_2]^-$. ESI-MS was central in tracking the real-time reaction kinetics, showing a simultaneous decrease in $[Au_{23}(SR)_{16}]^-$ and increase in $[Au_{25}(SR)_{18}]^-$ peak intensities, as shown in Fig. 7a. The MS/MS spectra of $[Au_{23}(SR)_{16}]^-$ (Fig. 7b) undergoes sequential loss of $[Au(SR)_2]^-$, $[Au_2(SR)]^-$ and $[Au_{25}(SR)_{18}]^-$ (Fig. 7c) and shows the dominant dissociation of $[Au_2(SR)]^-$, with an increase in the collision energy. The fragmentation pathways of $[Au_{23}(SR)_{16}]^-$ and $[Au_{25}(SR)_{18}]^-$ are shown in Fig. 7d and e, respectively. Based on the definitive equation and according to MS/MS analysis, they constructed an SME-induced symmetry-breaking core structure transformation mechanism for the isoelectronic size-conversion reaction.[112] Xie and coworkers studied the molecular-level oxidative etching mechanism of water-soluble $[Au_{25}(SR)_{18}]$ nanoclusters using time-dependent ESI-MS and MS/MS. They identified over 20 intermediate species and revealed a two-stage process, as follows: (i) rapid decomposition into smaller clusters and Au(I)-SR complexes; (ii) followed by isoelectronic recombination into larger clusters (*e.g.*, $[Au_{24}SR_{20}]^0$) or ligand-rich clusters. MS/MS revealed size-dependent fragmentation patterns and verified the evolution of the surface motifs from $[Au_4SR_4]$ in $[Au_{18}SR_{14}]^0$ to $[Au_6SR_6]$

Published on 27 October 2025. Downloaded by Indian Institute of Technology Chennai on 12/29/2025 3:17:01 AM.

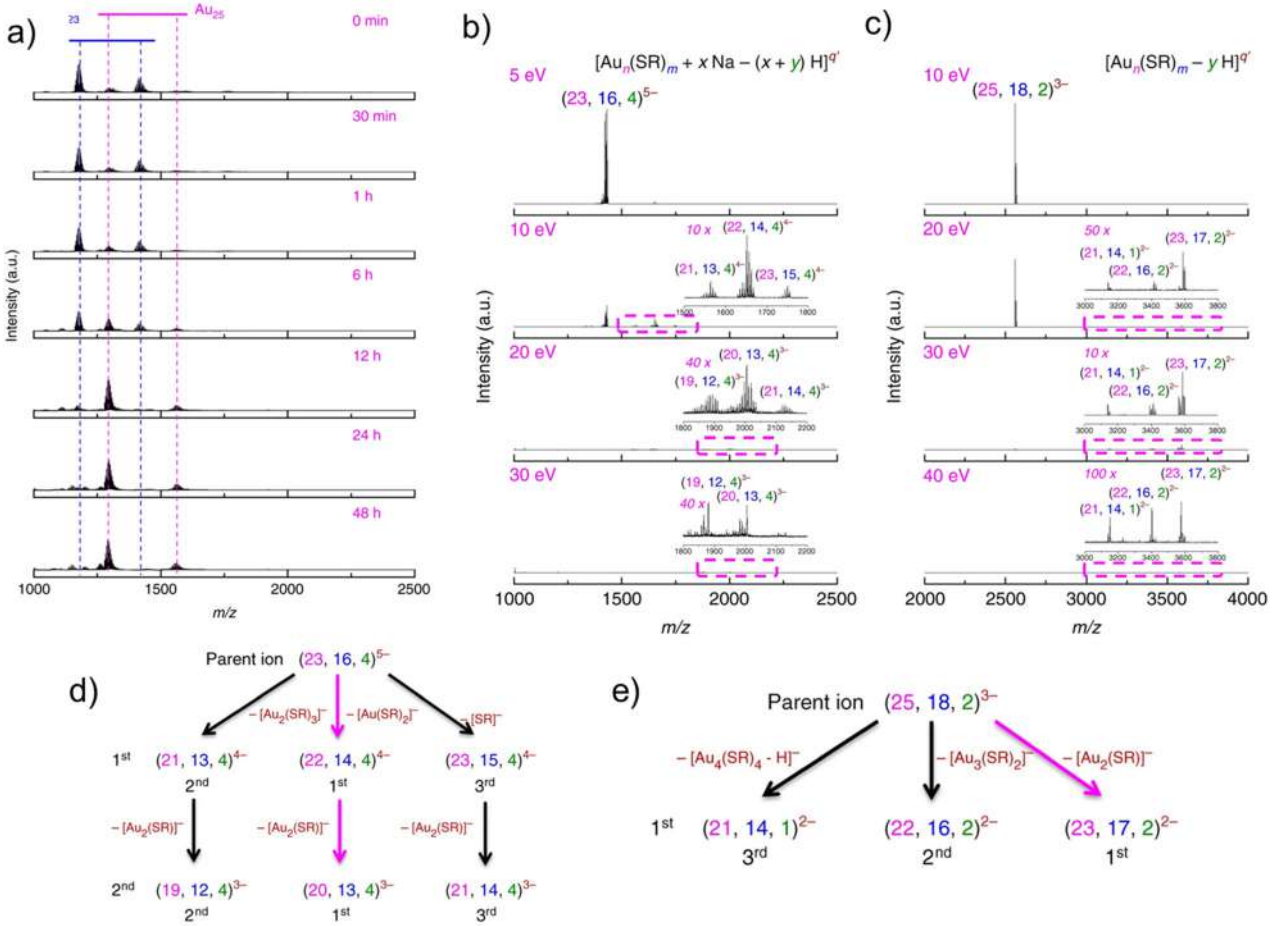


Fig. 7 (a) ESI-MS of the isoelectronic size conversion from $[Au_{23}(SR)_{16}]^-$ to $[Au_{25}(SR)_{18}]^-$ in water. Structural relation between Au_{23} and Au_{25} nanoclusters. (b, c) Tandem mass spectra and (d, e) fragmentation pathways of $[Au_{23}(SR)_{16}]^-$ and $[Au_{25}(SR)_{18}]^-$. Adapted from (a)–(e) ref. 112. Copyright 2018, Springer Nature Group.

in $[Au_{24}SR_{20}]^0$. MS/MS also revealed that larger clusters fragmented more extensively at the same collision energy, with the onset fragmentation energies generally decreasing with size, except for $[Au_{24}SR_{20}]^0$.[113] Surface-induced dissociation (SID) is a powerful ion activation technique, wherein mass-selected ions collide with functionalized surfaces (*e.g.*, alkanethiol-protected gold), enabling precise probing of the fragmentation energetics and kinetics. Unlike CID, SID offers finer control over the collision energy, allowing quantitative determination of the threshold dissociation energies, activation entropies, and microcanonical rate constants. Johnson *et al.* used SID to demonstrate that the $[Au_8(TPP)_6]^{2+}$ cluster exhibits greater stability toward dissociation compared to $[Au_7(TPP)_6]^{2+}$, $[Au_8(TPP)_7]^{2+}$, and $[Au_9(TPP)_7]^{2+}$.[114] Further, Baksi *et al.* studied $Ag_{11}(SG)_7^-$ and showed that SID induced greater fragmentation and charge stripping compared to CID.[115] MS/MS investigations have proven indispensable for understanding the fragmentation pathways, core–ligand interactions, structural integrity, and dynamic transformations in APCs. These mass spectrometric studies complement crystallographic and spectroscopic techniques by providing molecular-level insights.

3.2. UVPD

Ultraviolet photodissociation (UVPD) mass spectrometry uses high-energy UV photons, typically from a pulsed laser at 193 nm (also 213 or 266 nm are used), to excite ions to electronically excited states, inducing extensive and specific fragmentation. This technique provides deeper structural insights than conventional methods such as collision-induced dissociation (CID) or electron-based methods such as electron capture dissociation (ECD) and electron transfer dissociation (ETD).[116] Its applications extend across proteomics, including peptide sequencing and PTM localisation, top-down protein analysis, native mass spectrometry of protein complexes, as well as lipidomics, nucleic acid characterisation, and glycomics. In APCs, CID and SID produce limited fragments, whereas UVPD generates extensive, detailed fragmentation, enabling deeper structural analysis.

Black *et al.* performed the structural analysis of $Au_{25}(pMBA)_{18}$ and $Au_{36}(pMBA)_{24}$ clusters using UVPD, which enabled the systematic cleavage of ligand staples (Au–S and C–S bonds) without disrupting the gold core. At higher laser

Published on 27 October 2025. Downloaded by Indian Institute of Technology Chennai on 12/29/2025 3:17:01 AM.

doses, UVPD triggered monomer evaporation, generating Au_4–Au_{20} bare gold cluster ions from $Au_{25}(pMBA)_{18}$, thereby permitting the accurate determination of the ligand and gold atom counts.[117] Li and coworkers utilised UVPD to study the size dependence of gold clusters in catalytic applications. The $Au_{144}(PET)_{60}$ cluster was fragmented by UVPD at 193 nm to generate size-selected Au_nS_m clusters (n = 12–122), and their acetylene adsorption was monitored by ESI-MS, revealing a clear size-dependent hierarchy in C_2H_2 binding. Further, they extended this study to a smaller Au_{25} cluster and showed that acetylene binding occurs up to ~11 molecules per cluster. These studies demonstrate that smaller clusters have significantly stronger acetylene adsorption, highlighting the distinct electronic effects that govern catalytic activity in acetylene hydrochlorination.[118,119] Jose *et al.* showed that UV photoactivation resulted in unique dissociation pathways in APCs such as $[Ag_{29}(BDT)_{12}]^{3-}$ and $[PtAg_{24}(DMBT)_{18}]^{2-}$, primarily *via* electron photodetachment. UVPD leads to single ligand losses, perturbing the metal–ligand interface, with dissociation characteristics different from that in collision-based methods.[120] The study by Li and coworkers provided direct experimental evidence for the photon energy-dependent photoreaction pathways of an $[Au_{25}(PPh_3)_{10}(SC_2H_4Ph)_5Cl_2]^{2+}$ (Au_{25}) cluster and correlated these pathways with its photocatalytic performance on TiO_2 (P25). Using photodissociation mass spectrometry (PD-MS), it was found that visible light (455 nm) induces the selective loss of the PPh_3 and PPh_3AuCl ligands, while preserving the Au_{25} core (Fig. 8a–c), exposing the active sites and enabling high catalytic activity. In contrast, UV light (193 nm) causes complete decomposition into small $[Au_nS_m]^+$ fragments, leading to a reduced performance due to cluster destabilisation. Fig. 8d and e show the mass spectrum of Au_{25} under ultraviolet light (193 nm).[121] Collectively, these studies establish UVPD as a powerful technique for understanding complex nanostructures and linking their fragmentation behaviour to functional and catalytic properties with high specificity and precision.

3.3. Ion mobility–mass spectrometry (IM-MS)

Ion mobility–mass spectrometry (IM–MS) is a powerful analytical technique that separates gas-phase ions based on their size, shape, and charge by measuring their drift through a buffer gas under an electric field.[122,123] Since its early development in the 1960s and integration with ESI and MALDI,[124] IM–MS has evolved through innovations such as drift tube ion mobility spectrometry (DTIMS), travelling wave ion mobility spectrometry (TWIMS), and trapped ion mobility spectrometry (TIMS), a key tool for resolving isomers and probing gas-phase structures in fields such as structural biology, nanochemistry, and materials science. DTIMS is the most common method for the structural analysis of nanoclusters, where ions drift through a uniform electric field against a counter-flowing buffer gas. It enables direct, calibration-free calculation of collision cross sections (CCS) using the Mason–Schamp equation, making it ideal for early structural characterisation and a reference for other IMS techniques. The Mason–Schamp equation states that the mobility of an ion (K) is inversely proportional to its collision cross section (Ω), meaning that smaller, more compact ions move faster under an electric field than larger or more extended ions. Mathematically, it is expressed as follows:

$$\Omega = \frac{3Ze}{16NK}\sqrt{\frac{2\pi}{\mu k_B T}}$$

where Z is the charge of the ion, e is the elementary charge, N is the number of gas molecules, μ is the reduced mass of the ion–gas pair, k_B is the Boltzmann constant, T is the gas temperature, and Ω is the ion–neutral collision cross section.[125] TWIMS uses a stacked ring ion guide with RF and transient DC voltages to generate travelling waves that propel ions through a buffer gas, separating them by mobility. Higher-mobility ions are carried by the wave, whereas lower-mobility ions roll over it, taking longer to traverse the mobility cell. Although direct CCS calculation is not possible due to the dynamic field, CCS can be determined after calibration using standards with known values.[126] TIMS is a recent innovation that traps ions by counterbalancing a buffer gas flow with a spatially varying electric field, holding them at defined positions based on their mobility, and sequentially releasing them as the electric field is reduced. This design offers high sensitivity, resolution, and improved duty cycle through synchronised accumulation and analysis. TIMS requires calibration of CCS and is widely used in structural biology and multi-omics.[127,128] The structural information obtained from ion mobility spectrometry arises from the experimentally determined CCS, which reflects the average area of an ion as it collides with the buffer gas. Compact ions with smaller surface areas exhibit lower CCS values and move faster, whereas extended structures show larger CCS values and drift more slowly. The reduced mass term in the Mason–Schamp equation accounts only for the momentum exchange between the ion and gas molecules and does not contain any structural information. Thus, the shape or conformation is inferred indirectly from the CCS, which represents the dynamic interaction of the molecule with its environment rather than its exact atomic arrangement. When the measured CCS values are combined with molecular modelling or dynamic simulations, one can identify the most probable conformation and estimate the overall structural form. Modern ion mobility instruments employing drift-tube, trapped, and travelling-wave systems routinely achieve resolving powers of 200–400, while the extended-path or cyclic systems can reach up to about 700 after nearly 100 passes. These advances allow the separation of closely related conformers and intermediate states in proteins, peptides, and nanoclusters. However, current IM–MS methods provide qualitative information on molecular compactness and topology, and accurate atomic-scale structure determination still requires complementary spectroscopic or computational validation.[129,130]

IM-MS has emerged as a powerful hyphenated technique for understanding the structural complexity of atomically precise metal nanoclusters in the gas phase. In silver nano-

Published on 27 October 2025. Downloaded by Indian Institute of Technology Chennai on 12/29/2025 3:17:01 AM.

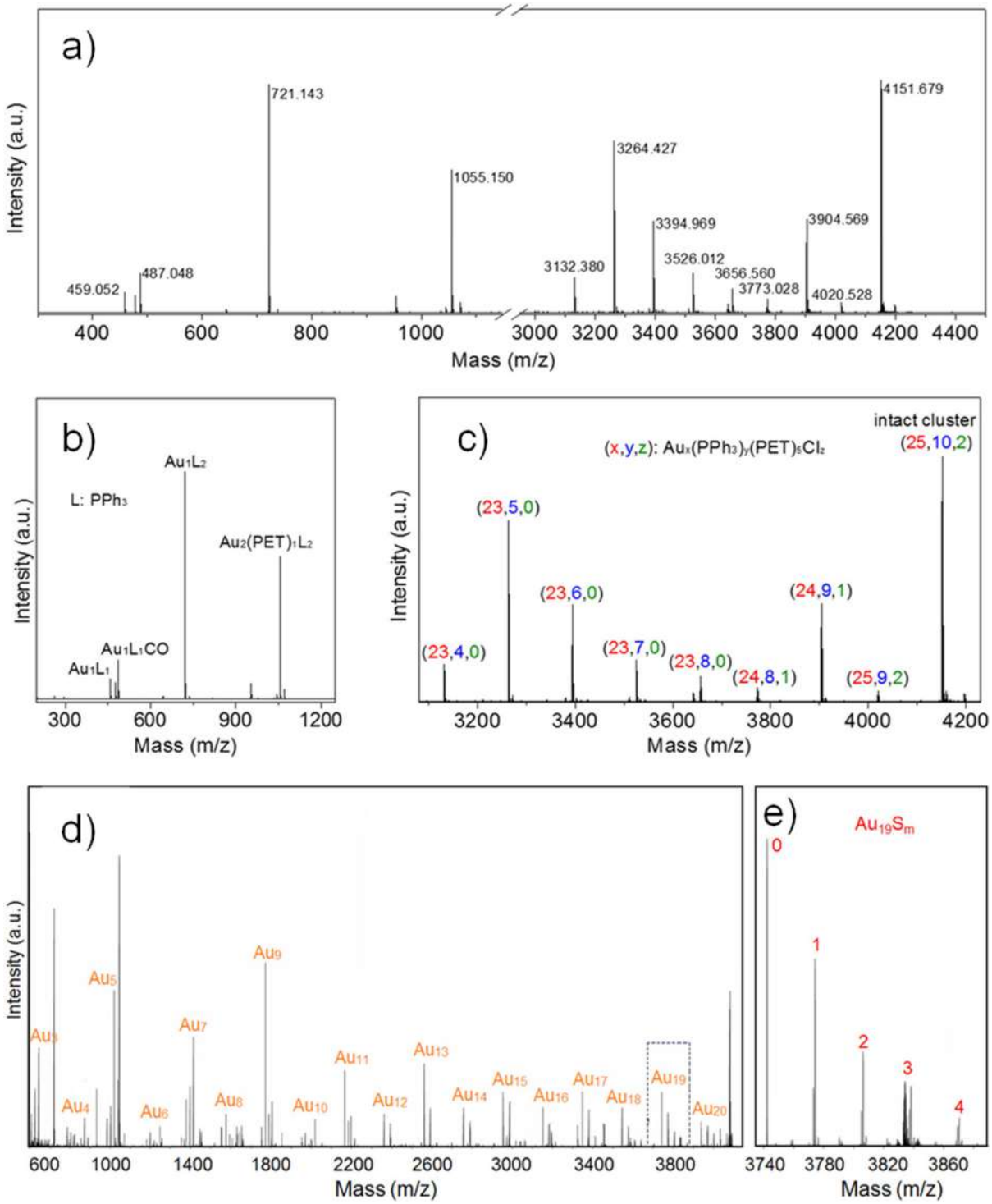


Fig. 8 Photodissociation of Au_{25} at 455 nm. (a) Wide-range photodissociation MS (in positive mode). (b) and (c) Enlarged views of panel a and assignment of the photofragments, respectively. (d) Wide-range photodissociation MS (in positive mode) spectrum of Au_{25} at 193 nm. (e) Extracted region of the $Au_{19}S_m$ (m = 0–4) species. Adapted from (a)–(e) ref. 121. Copyright 2023, the American Chemical Society.

clusters, IM-MS gave insights into gas-phase isomers, which are inaccessible through conventional mass spectrometry or crystallography. These isomers, although identical in mass, exhibited distinct drift times and CCS values, indicating significant differences in their three-dimensional structures. Baksi *et al.* reported the first experimental evidence for gas-phase dimers, trimers, and tetramers of $Au_{25}(PET)_{18}$ clusters using IM-MS, with their distinct drift times and CCS values

Published on 27 October 2025. Downloaded by Indian Institute of Technology Chennai on 12/29/2025 3:17:01 AM.

confirming their existence. The monomer appeared at 12.7 ms (CCS = 297.8 Å^2), the dimer at 10.8 ms (CCS = 453.4 Å^2), and the trimer at 8.3 ms (CCS = 668.3 Å^2), indicating an increase in their size and structural complexity. The formation of these aggregates was shown to be highly sensitive to the experimental conditions; increasing the He gas flow and lowering the cone voltage promoted their aggregation, while higher voltages led to their dissociation, reflecting the fragile, noncovalent nature of these gas-phase polymers.[131] Pradeep and coworkers used IM-MS to demonstrate the presence of gas-phase isomers, with $Ag_{44}(SR)_{30}$ exhibiting multiple isomers in its 3^- and 4^- charge states, while $Ag_{29}(BDT)_{12}$ showed two isomers in its common 3^- charge state. Density functional theory calculations indicated that this isomerism originates from the variations in ligand orientations and staple rearrangements, leading to differences in the overall geometry. In contrast, no isomeric species were observed for $Au_{25}(SR)_{18}$ or $Ag_{25}(SR)_{18}$, underscoring the role of ligand chemistry and charge state in governing structural diversity.[40] Kalenius *et al.* provided the first experimental evidence for a gas-phase topological isomer of the well-studied $Au_{25}(SR)_{18}$ cluster in both anionic and cationic forms. This isomer, energetically close and topologically connected to the known ground-state structure, arises *via* a collective rotation of the icosahedral Au_{13} core without breaking any Au–S bonds. The measured collision cross sections closely match theoretical predictions, and the relative abundance of the isomeric structures can be controlled by in-source activation, demonstrating that interconversion between isomers is feasible in the gas phase.[132] Zeng *et al.* demonstrated how ligand exchange can influence the structural and optical properties of atomically precise silver. Partially replacing the 1,3-benzene-dithiol (BDT) ligands with dihydrolipoic acid (DHLA) in $Ag_{29}(BDT)_{12}$ led to a 44-fold increase in its photoluminescence quantum yield. High-resolution electrospray ionisation mass spectrometry (HRESI-MS) confirmed the successful ligand exchange (Fig. 9a), with species containing up to six substituted ligands $[Ag_{29}(BDT)_{12-x}(DHLA)_x]^{3-}$ (x = 0–6). The CCS value increased from 480 to 583 Å^2 for x = 0–6 DHLA substitutions (Fig. 9b), which was consistent with DFT predictions and correlated with the increase in rigidity and reduced nonradiative decay.[133] Chakraborty *et al.* used trapped ion mobility spectrometry (TIMS-MS) together with density functional theory (DFT) to investigate the fragmentation dynamics of $[Ag_{29}L_{12}]^{3-}$ clusters. This study showed that the cluster mainly dissociates by gradually losing $[Ag_5L_3]^-$ units, which leads to fragments such as $[Ag_{24}L_9]^{2-}$ and $[Ag_{19}L_6]^-$. The experimental collision cross sections showed excellent agreement with DFT predictions, enabling the reliable structural assignment of these fragments. The larger $[Ag_{24}L_9]^{2-}$ and $[Ag_{19}L_6]^-$ fragments retain compact superatom-like core-staple structures, indicating that kinetic control governs dissociation rather than thermodynamic stability.[134] In another example of structural transformation, Baski *et al.* used TIMS to investigate alloy formation in $Ag_{29}(BDT)_{12}(PPh_3)_4$ nanoclusters through intercluster reactions with $Cu_{12}S_6(DPPPT)_4$. This study showed that up to 14 Ag atoms could be replaced by Cu atoms, corresponding to nearly 50% exchange, without disrupting the overall cluster structure. TIMS measurements revealed a linear decrease in the collision cross section (CCS) with an increase in Ag/Cu exchange (Fig. 9c), indicating a gradual size contraction. DFT-based CCS simulations confirmed that the exchanged atoms are predominantly confined to the cluster surface, while the core remains intact.[135] Roy *et al.* examined the interaction of $[Ag_{29}(L)_{12}]^{3-}$ nanoclusters with a secondary ligand (L′) using ion mobility mass spectrometry (IM-MS) supported by spectroscopy and DFT. IM-MS confirmed the formation of $[Ag_{29}(L)_{12}]L'_n{}^{3-}$ adducts (n = 1–4), with distinct mass separations (~m/z 116 per ligand). A systematic increase in collision cross-sections (CCSs) was observed as more L′ ligands attached, directly evidencing the progressive structural expansion of the nanocluster. The IM-MS data correlated closely with DFT models, validating the structural assignments. Fig. 9d clearly shows this trend, with mobilograms shifting to higher CCS values for each additional ligand, highlighting the sequential and specific nature of L′ binding.[136] These studies highlight the role of IM-MS in revealing the dynamic, structural behaviour of ligand-protected metal nanoclusters, establishing it as an essential tool for probing isomerism, aggregation, ligand interactions, and compositional tuning at the atomic scale.

The cyclic ion mobility–mass spectrometry (cIM-MS) system is a significant advancement over conventional IM-MS, built on a Waters SYNAPT G2-Si platform with a 98 cm closed-loop travelling-wave (TW) ion mobility separator. Its racetrack-like geometry allows ions to traverse the mobility cell multiple times, increasing the resolving power with the square root of the number of passes from approximately 78 in a single pass to approximately 750 after 100 passes, providing "dial-up" mobility resolution. This instrument features a flexible electrode array and software-controlled optics, enabling multifunction experiments such as mobility selection, ion storage, activation, and IMS^n, while maintaining high ion transmission. Fig. 10a schematically represents the instrument layout, highlighting the cIM device orthogonal to the main ion path, integration with quadrupole and TOF analysers, and associated ion guides and chambers. This design extends the IM-MS capabilities to the high-resolution, multifunctional structural analysis of molecular species.[137] Its applications include the separation of isomeric pentasaccharides[138] and conformational studies of ubiquitin ions,[139] showcasing its ability to probe complex gas-phase structures.

Kappes and coworkers demonstrated the power of multipass cIM-MS in resolving subtle structural changes during the thermal decomposition of $[Pt_{17}(CO)_{12}(PPh_3)_8]^{2+}$ clusters. Gas-phase CID coupled with cIM-MS resolved distinct isomeric fragments after CO desorption, with CCS differences of less than 1%, indicating CO loss from nonequivalent sites. Fig. 10b shows that sequential CO loss from $[Pt_{17}(CO)_{12}(PPh_3)_8]^{2+}$ produces multiple structural isomers, as revealed by the distinct ion mobility peaks. (0,0) shows that the intact parent ion $[Pt_{17}(CO)_{12}(PPh_3)_8]^{2+}$ has a single, well-defined structure with no isomeric forms. Upon sequential CO loss ((1,0) to (3,0)), the

Published on 27 October 2025. Downloaded by Indian Institute of Technology Chennai on 12/29/2025 3:17:01 AM.

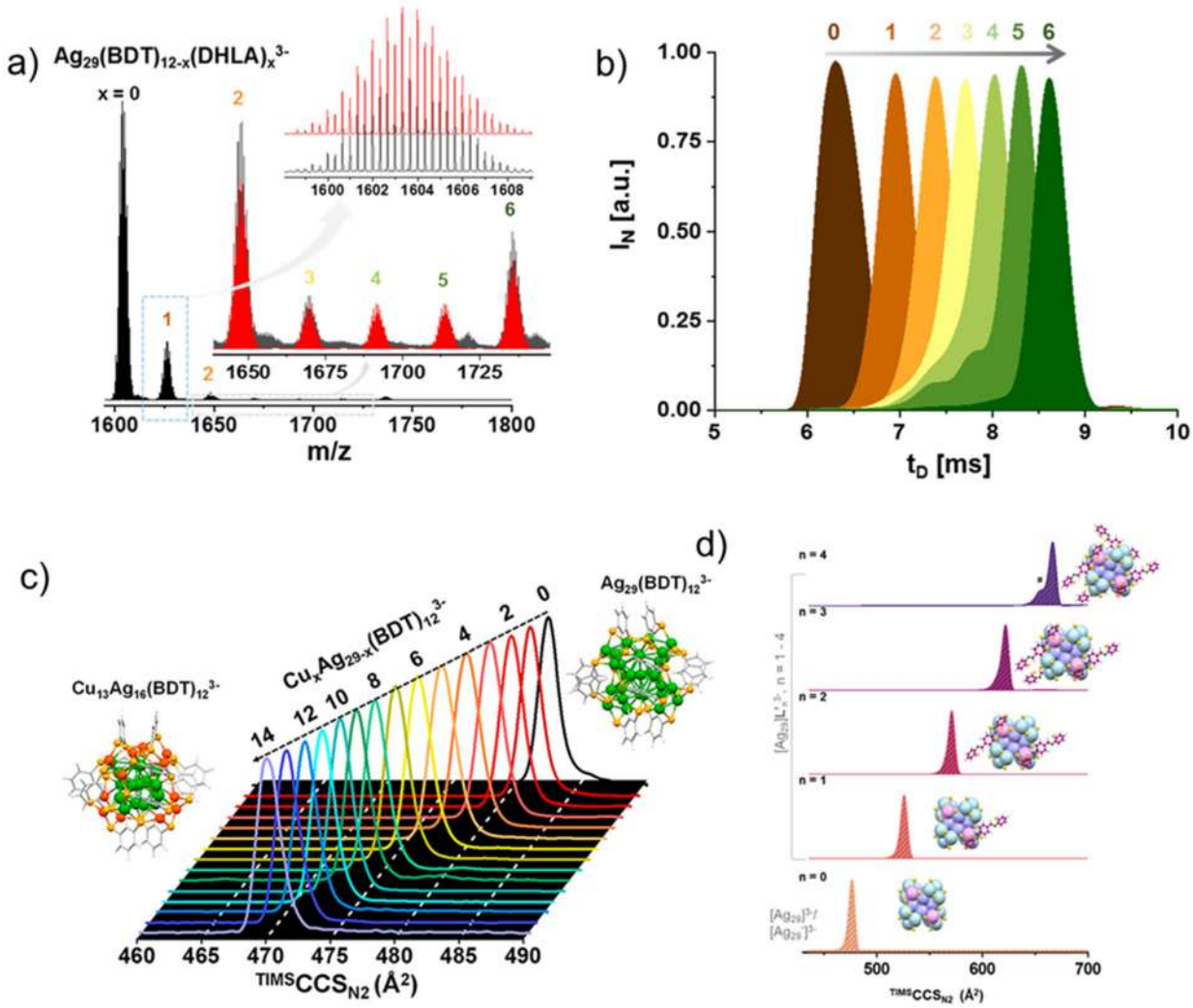


Fig. 9 (a) ESI MS of an $Ag_{29}(BDT)_{12-x}(DHLA)_x$ NC solution showing a maximum of six ligands exchanged. An expanded view (black trace) is presented in the inset with the corresponding calculated spectra (red trace). A further expanded view of the MS spectrum of $Ag_{29}(BDT)_{12-x}(DHLA)_x^{3-}$ with x = 1, which resolves the isotopologue distribution and shows an exact match with the calculated spectrum. (b) Drift time profile of $Ag_{29}(BDT)_{12-x}(DHLA)_x^{3-}$ measured in IM mode, showing an increase in the size of the ligand exchanged NCs. (c) Extracted ion mobilograms, that is, ion intensity *versus* CCS, determined for $Cu_xAg_{29-x}(BDT)_{12}^{3-}$ (x = 0–14) by TIMS-TOFMS. (d) Mobilograms of individual $[Ag_{29}]L'_n{}^{3-}$ (n = 0–4) ions showing an increase in CCS with an increase in the number of L′-adducts to $[Ag_{29}]^{3-}$ NCs. Reproduced with permission from (a) ref. 133, (b) ref. 133, (c) ref. 135 and (d) ref. 136. Copyright 2021, 2020 and 2025, the American Chemical Society.

ion mobility spectra reveal multiple peaks, indicating the emergence of different isomeric structures. Fig. 10c presents the overall trend in CCS *versus* m/z for the fragment ions, showing an initial linear decrease in size as CO and benzene are lost, followed by a steeper decline when higher-energy pathways, such as phenyl and H_2 elimination, generate a more compact and reorganised cluster framework. DFT calculations validated the observed fragment geometries. The Pt_{17} core remains robust throughout, demonstrating its stability.[140]

Similarly, Hennrich *et al.* used cIM-MS to study the superatom dianions $[Mau_{24}(C{\equiv}CR)_{18}]^{2-}$ (M = Ni, Pd, and Pt), achieving the precise separation of three structurally analogous clusters based on minor CCS variations (Ni: 721.5 Å^2, Pd: 723.3 Å^2, and Pt: 724.9 Å^2) after 50 passes. The high resolving power enabled direct correlation with both the crystallographic data and DFT models, confirming that the gas-phase geometries closely mirrored their solid-state analogues. Interestingly, the Ni-centred cluster exhibited energy-dependent isomerisation under collision-induced activation, producing a larger, previously unobserved structural form, while its Pd and Pt analogues remained conformationally stable. This demonstrates the ability of cIM-MS not only to resolve minute structural differences but also to capture dynamic isomerisation phenomena.[141]

cIM-MS opens new avenues for exploring the structural and dynamic behaviour of metal nanoclusters and complex molecular assemblies. Future research can utilize its ultra-high resolution and multi-pass capabilities to resolve subtle iso-

This journal is © The Royal Society of Chemistry 2025

Published on 27 October 2025. Downloaded by Indian Institute of Technology Chennai on 12/29/2025 3:17:01 AM.

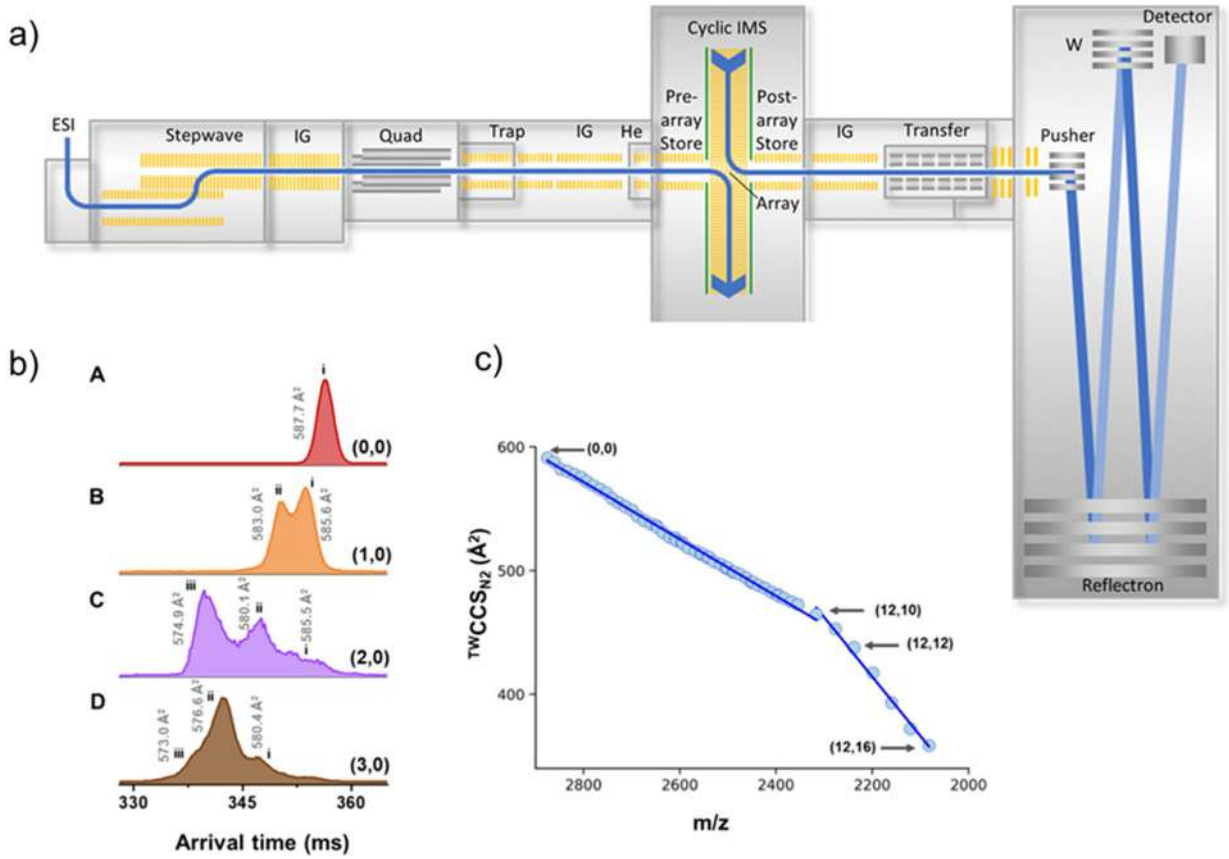


Fig. 10 (a) Schematic showing the Q-cIM-ToF instrument. (b) Arrival time distributions recorded after 10 separation passes using cyclic ion mobility spectrometry (cIMS): (A) (0,0), (B) (1,0), (C) (2,0), and (D) (3,0) ions. The $^{TW}CCS_{N2}$ values of the isomers of these species are indicated. These are mean values based on three different measurements. The standard error of the mean is within ±0.3 Å^2. (c) Plot of experimental $^{TW}CCS_{N2}$ values (blue dots; lines are meant to guide the eye) obtained from (lower resolution) single pass measurements for the full range of (*m*,*n*) fragment ions as a function of their *m*/*z* values. Adapted from (a) ref. 137, (b) ref. 140 and (c) ref. 140. Copyright 2019 and 2025, the American Chemical Society, respectively.

meric differences, monitor real-time conformational changes, and map detailed fragmentation pathways.

4. Expanding properties

The electronic properties of APCs are often studied in solution; however, solvent and counterion effects can distort the results. Thus, to overcome these limitations and understand the exact electronic structure, gas-phase techniques such as anion photoelectron spectroscopy (PES) are employed. PES directly measures fundamental parameters such as the HOMO–LUMO gap and electron affinity of mass-selected cluster anions in a vacuum, eliminating solvation and ion-pairing effects.[142] Mass selection is a critical component of PES measurements, given that it isolates specific cluster ions and prevents spectral overlap or interference. Enhancements such as increased ion beam intensity and reduced laser fluence improve the measurement precision by minimising multiphoton artefacts. This allows the accurate determination of the electron binding energies, detachment dynamics, and superatomic orbital structures, revealing the core electronic features of nanoclusters. Multiple studies demonstrated the strength of mass-selected PES in uncovering the intrinsic behaviour of nanoclusters. Hirata *et al.* reported the first PES of $[Au_{25}(SC_{12}H_{25})_{18}]^-$, confirming its superatomic $(1S)^2(1P)^6$ electronic configuration and revealing an adiabatic electron affinity (AEA) of 2.2 eV, which is significantly lower than theoretical predictions. This highlighted the discrepancies between theory and experiment in modelling these clusters.[143] Similarly, Hamouda *et al.* investigated $[Au_{25}(SG)_{18} - 6H]^{7-}$, a highly charged glutathione-protected cluster, and showed that its gas-phase optical absorption closely matches its solution-phase spectrum. This indicated that the core electronic structure remains stable across environments, with photodetachment occurring *via* tunnelling through a Coulomb barrier rather than fragmentation.[144] Tasaka *et al.* studied a silver cluster $[Ag_{44}(SC_6H_3F_2)_{30}]^{4-}$ and inferred that the cluster possesses unique stability despite its negative electron affinity. Electron loss was suppressed due to its strong repulsive Coulomb barrier, and fragmentation occurred preferentially through ligand–metal bond dissociation. PES, coupled with DFT and tunnelling models, elucidated the detachment mechanism and confirmed an 18-electron superatom struc-

Published on 27 October 2025. Downloaded by Indian Institute of Technology Chennai on 12/29/2025 3:17:01 AM.

ture.[145] Ito *et al.* made some refinements in the PES measurements and studied ligand-protected M_{13} clusters. They identified that the previously known electron affinity values of M_{13} clusters were underestimated due to multiphoton effects. Owing to the improved ion intensity and reduced laser fluence, they measured more accurate AEA values, validating the theoretical models.[146]

Doping and ligand modifications were shown to modulate the electron affinities without altering the overall superatomic electronic framework. Kim *et al.* studied the PES of doped superatoms such as $[XAg_{24}(SR)_{18}]^-$ (X = Ag and Au) and $[YAg_{24}(SR)_{18}]^{2-}$ (Y = Pd and Pt). They observed that doping with Pd and Pt significantly shifted the superatomic orbital energies and reduced AEAs, which was attributed to the changes in the core charge and Coulomb interactions. However, despite these energy shifts, the orbital ordering and HOMO–LUMO gaps remained consistent.[147] Further, Ito *et al.* tested the supervalence bond (SVB) model for bi-icosahedral gold clusters, specifically the Au_{23} core in $Au_{38}(PET)_{24}$. Neutral precursors, $[M_1Au_{37}(PET)_{24}]^0$ (M = Pd and Pt), which are isoelectronic and structurally similar to $Au_{38}(PET)_{24}$, were synthesised and chemically reduced to form $[M_1Au_{37}(PET)_{24}]^-$ anions. The gas-phase anion (PES) of these mass-selected clusters revealed spectral features consistent with the superatomic orbital interactions predicted by the SVB model, providing direct experimental support for the bonding framework.[41] Akazawa *et al.* investigated the intrinsic electronic structure of the gold nanocluster $[Au_{38}(PET)_{24}]^0$ by measuring its HOMO–LUMO gap using gas-phase PES on the MALDI-generated $[Au_{38}(PET)_{24}]^-$ anion. In their custom-built experimental setup (Fig. 11a), they integrated a MALDI source for ion generation, a time-of-flight mass spectrometer for mass selection, and a magnetic-bottle photoelectron spectrometer for electron kinetic energy analysis. This setup enabled stable generation and precise measurement of cluster anions in vacuum. The MALDI MS measurements confirmed the presence of an intact $[Au_{38}(PET)_{24}]^-$ cluster and its fragmentation products (Fig. 11b). Fig. 11c presents the photoelectron spectra recorded at 266 nm and 213 nm, revealing the key spectral features attributed to electron detachment from the singly occupied molecular orbital (SOMO) and HOMO orbitals. Analysis of these spectra yields a direct gas-phase HOMO–LUMO gap of 0.78 ± 0.06 eV, which is smaller than the previously reported solution-phase values. This discrepancy was attributed to the structural changes upon reduction, notably the elongation of the Au_{23} core due to the occupation of an antibonding orbital.[148] Recently, Tsukuda and coworkers used anion photoelectron spectroscopy and DFT to investigate how deprotonation of $[Au_{25}(pMBA)_{18-n}H^+]^{(n+1)-}$ affects the electronic structure of its Au_{13} (8e) core.[149]

Overall, gas-phase PES, in combination with high-resolution mass spectrometry and theoretical modelling, offers a robust and solvent-free platform for investigating the fundamental electronic structure of nanoclusters. It provides precise information on the superatomic orbitals, electron detachment processes, and the effects of structural and compositional modifications, thereby broadening our understanding on the superatom behaviour of nanoclusters.

5. Additional advances

5.1. CDMS

Charge detection mass spectrometry (CDMS) is a powerful analytical technique designed to overcome the limitations of traditional MS to analyse very large and heterogeneous nanomaterials, such as megadalton-sized nanoparticles, self-assembled nanoclusters, and virus assemblies. Conventional MS struggles to characterise these samples due to the overlapping charge states, broad mass distributions, and extremely high mass-to-charge (m/z) ratios, which reduce the detection efficiency and resolution.[150]

CDMS directly measures both the charge (z) and m/z of individual ions independently, enabling precise mass determination without assumptions about charge states. The instrument detects the image charge induced when ions pass through a conductive cylinder, combined with ion velocity and energy measurements, to calculate absolute mass. Since the initial coupling of CDMS with electrospray ionisation by Fuerstenau and Benner in 1995, CDMS has evolved significantly, especially through advances such as electrostatic linear ion traps (ELIT), which allow repeated single-ion measurements and improved charge resolution.

This technique excels at characterising large, heterogeneous biological assemblies, nanoparticles, and polymer assemblies, providing insights into their mass distribution spanning from the megadalton to gigadalton range. For example, studies on ligand-protected gold nanoclusters and their zinc-induced aggregates revealed broad mass distributions (~75 MDa to >1 GDa), highlighting the ability of CDMS to analyse complex hierarchical nanomaterials with sub-30 nm dimensions. CDMS has also been successfully applied to synthetic polymer nanoobjects. Doussineau *et al.* developed a setup combining two charge detection devices (CDDs) with infrared multiphoton dissociation (IRMPD) to perform MS/MS on single megadalton ions, such as 7 MDa polyethylene oxide and 31.5 MDa lambda phage DNA. This single-ion MS/MS approach enabled ion trapping and repeated irradiation, allowing detailed, ensemble-free analysis of fragmentation dynamics in large molecules.[151] Charleux and coworkers reported the first direct molar mass and mass distribution measurements of self-assembled amphiphilic block copolymer nano-objects without model-based assumptions, revealing their narrow mass distributions and charges approaching Rayleigh limits.[152] Advancements in instrumentation have further expanded the capabilities of CDMS. William's group developed the single particle analyser of mass and mobility (SPAMM), integrating CDMS with tandem MS (MS^n) and ion mobility measurements on individual ions up to 8 MDa. SPAMM tracks the ion kinetic energy, fragmentation through multiple stages, and ion mobility differences, revealing the dynamic behaviour, structural

This journal is © The Royal Society of Chemistry 2025

Published on 27 October 2025. Downloaded by Indian Institute of Technology Chennai on 12/29/2025 3:17:01 AM.

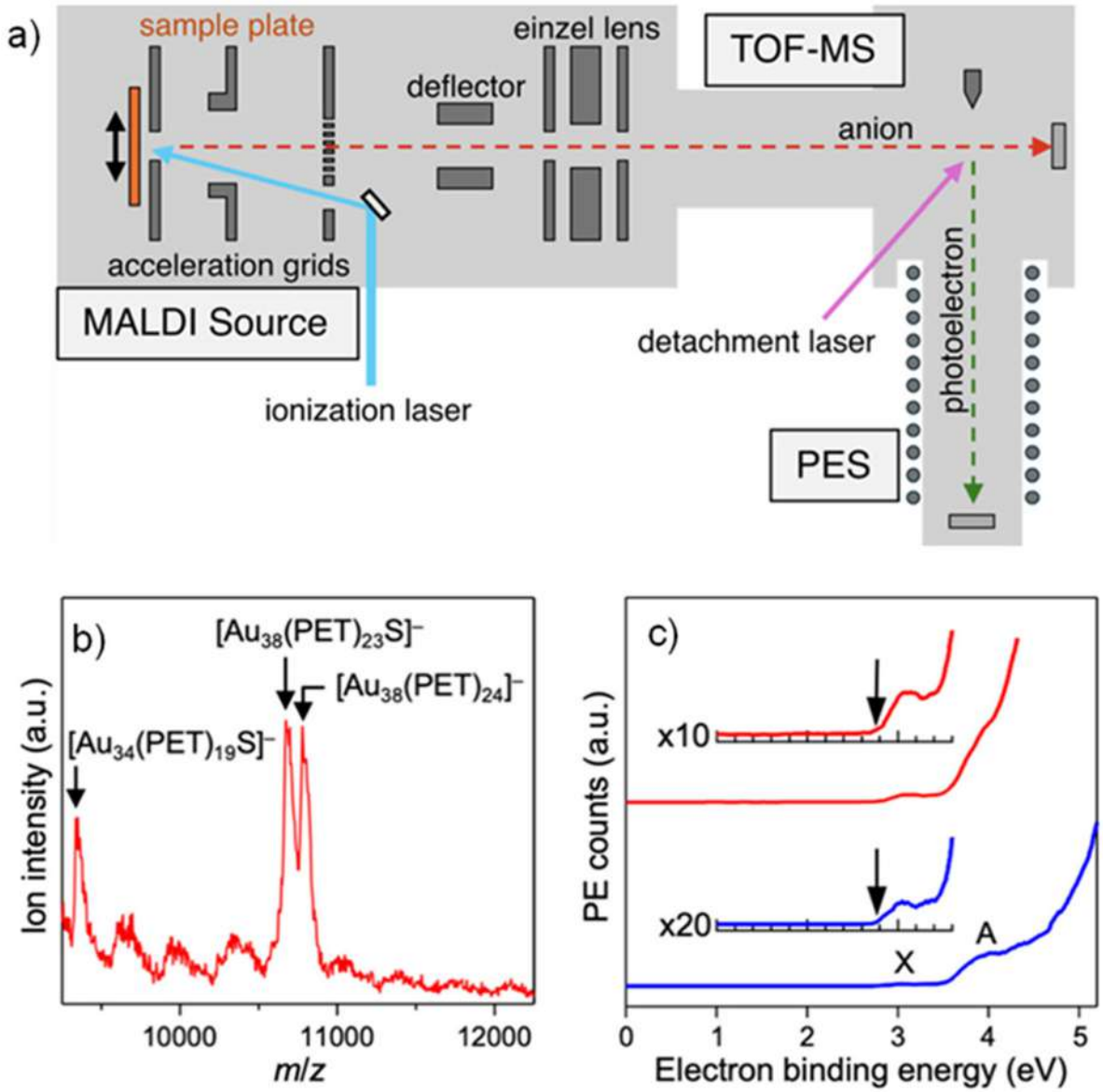


Fig. 11 (a) Schematic of the experimental apparatus. (b) Negative-mode MALDI mass spectrum of $[Au_{38}(PET)_{24}]^-$. (c) PE spectra of $[Au_{38}(PET)_{24}]^-$ recorded with a 266 nm laser (red) and 213 nm laser (blue). Reproduced with permission from (a)–(c) ref. 148. Copyright 2025, the American Chemical Society.

heterogeneity, and fragmentation pathways in large polymer ions. This represents a major leap in analysing large, complex ions with integrated mass, charge, and mobility data.[153] Elliott *et al.* demonstrated that CDMS can simultaneously determine the mass and collisional cross-section of multiply charged protein ions by analysing frequency shifts during ion trapping. This provides structural information, along with accurate mass measurements, which is crucial for large heterogeneous proteins that are difficult to study using conventional methods.[154] Todd *et al.* achieved a significant improvement in the resolution of CDMS through dynamic charge calibration and enhanced electrostatic linear ion trap design, attaining charge uncertainties below 0.2 elementary charges and m/z resolving power near 330. This enabled the resolution of highly heterogeneous viral assemblies and the tracking of intermediate species with unprecedented precision, which solidifies CDMS as a powerful tool to analyse complex biomolecular systems.[155]

Harper *et al.* demonstrated that CDMS can rapidly measure the mass and charge of thousands of individual ~100 nm nanoparticles with sub-nanometer diameter resolution and about 1% mass uncertainty. Unlike TEM, CDMS offers faster analysis, high throughput, and sensitivity to surface chemistry, distinguishing nanoparticle populations based on charge differences even when their masses are similar. This positions CDMS as a powerful complementary tool for nanoparticle

Published on 27 October 2025. Downloaded by Indian Institute of Technology Chennai on 12/29/2025 3:17:01 AM.

density determination, surface analysis, and quality control.[156] Orbitrap-based CDMS has also advanced considerably in the past decade. The Heck group demonstrated that multi-megadalton ions remain remarkably stable in the Orbitrap analyser, surviving extended gas-phase collisions mostly *via* solvent loss. Using a frequency-chasing method to correct transient frequency drifts, they achieved mass resolutions up to 100 000 and sub-10 ppm accuracy for large particles such as viral capsids.[157,158]

The Jarrold group demonstrated CDMS and Orbitrap-based individual ion mass spectrometry (I2MS) as breakthrough techniques for analysing large, heterogeneous biomolecules such as viruses, gene therapy vectors, and vaccines. CDMS uses an electrostatic linear ion trap (ELIT) for repeated ion detection, achieving sub-charge-unit resolution and high throughput (>100 ions per s).[159] Sooraj *et al.* investigated the charging behaviour of ligand-protected gold nanoparticles using CDMS coupled with ESI. They compared the charging behaviour of 20 nm Au-MUTAB (50 MDa) and 60 nm Au-citrate NPs (1.3 GDa). The results showed that Au-MUTAB achieved a charging state higher than the Rayleigh limit for a 20 nm water droplet ($z/z_R \approx 2.1$) (Fig. 12a). However, Au-citrate NPs could achieve only a charging of ~0.45 times the Rayleigh limit, under identical conditions (Fig. 12b). This study correlated charging capacity under ESI with the ligand–gold binding energy, estimating 1.05 eV for Au-MUTAB and 0.09 eV for Au-citrate. This work demonstrated the ability of CDMS to quantitatively probe the ligand binding strength and confirmed its utility in analysing large nanoparticles with complex interfaces and high heterogeneity.[160]

Charge detection mass spectrometry (CDMS) has achieved significant progress in the accuracy of charge detection, advancing from early systems limited by electronic noise to modern instruments capable of unit charge resolution.[161,162] Improvements such as random trapping mode, cryogenically cooled junction field-effect transistor (JFET),[162] extended trapping times, and dynamic calibration have reduced the charge uncertainty to below 0.2 e. Meanwhile, feedback-free charge-sensitive amplifiers now permit the detection of singly charged ions with high precision.[163] Orbitrap-based CDMS typically achieves a charge accuracy of 1–3*e*, whereas custom instruments demonstrate sub-charge resolution.[164,165] However, despite these advances, CDMS faces experimental challenges in ionizing and analysing large particles, where low ionization yields, nonvolatile buffers, and insulating ligands impede efficient charge transfer and desolvation.[166] Buffer exchange in volatile, ESI-compatible solvents can compromise the integrity of nanoparticles, and the single-ion detection mode inherently limits the throughput. Emerging solutions such as multiplexed detection and improved ion-optical designs aim to enhance the sensitivity and accommodate complex, heterogeneous nanosystems. With the availability of commercial CDMS instruments with high resolution, studies on NCs will reach new heights.

5.2. Mass photometry

Mass photometry (MP) is a label-free optical technique that enables the direct measurement of the molecular mass of individual particles in solution by detecting their interferometric scattering (iSCAT) signal upon landing on a surface. It relies on the proportionality between scattering contrast and molecular mass, allowing rapid and quantitative analysis under native conditions. The interferometric contrast, arising from the interference between scattered and reflected light at the glass–buffer interface, scales linearly with mass and is calibrated using known standards. Accurate conversion requires calibration in the same buffer as the sample, given that small refractive-index mismatches can introduce errors. Solvent-related interference, seen as baseline noise or contrast instability, can arise from impurities, buffer composition, temperature shifts, or surface contamination. These effects are minimized by filtering (0.22 μm) the buffer, maintaining a moderate ionic strength (≥10 mM), reducing the glycerol and detergent levels, and equilibrating the samples and optics to room temperature. Under these optimized conditions, MP provides a stable and reproducible linear relationship between scattering contrast

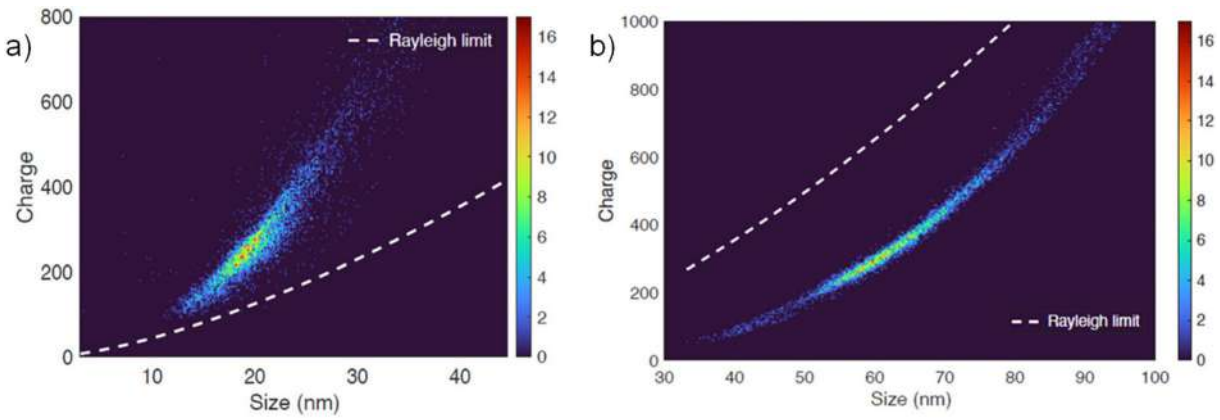


Fig. 12 (a) Charge *vs.* size plot of Au-MUTAB nanoparticles. (b) Charge *vs.* size plot of Au–citrate nanoparticles. Adapted from ref. 160. Copyright 2025, the American Chemical Society.

Published on 27 October 2025. Downloaded by Indian Institute of Technology Chennai on 12/29/2025 3:17:01 AM.

and molecular mass, enabling precise single-particle mass measurements in complex environments.[167]

Taylor *et al.* established iSCAT microscopy as a highly sensitive platform for detecting unlabeled biomolecules, smaller nanoparticles (~2 nm), and proteins (~50–65 kDa), with nanometer spatial and sub-millisecond temporal resolution. This study emphasised the linear response of iSCAT with particle volume and its utility in tracking viruses and proteins in real-time, without photobleaching or labelling.[168] Building on this, Melo *et al.* developed an optimised iSCAT setup with ratiometric imaging to accurately measure gold nanoparticles (<20 nm) in solution. They demonstrated the high-throughput, real-time classification of thousands of particles per minute, and revealed diffusion-limited deposition behaviour, where larger particles reached the surface earlier due to their slower diffusion. The obtained particle size distribution was in good agreement with the TEM results, validating the accuracy of this method. The application of MP has recently been extended beyond biological samples to nanoclusters.[169] Roy *et al.* extended MP to study the solvent-induced aggregation of atomically precise silver–gold alloy nanoclusters, $[Ag_{11-x}Au_x(DPPB)_5Cl_5O_2]^{2+}$ (Fig. 13a). Using β-amylase and thyroglobulin standards, they calibrated MP in the range of 50–660 kDa (r^2 = 0.9999, ~5% error). Fig. 13b shows the instrumental setup and mechanism of MP. In the experiment, initially, NC aggregates are dispersed in a solvent mixture and land on a non-coated glass surface. Upon landing, each particle causes a localised reduction in reflected light intensity due to interferometric scattering. These events are captured optically as dark spots, and the scattering contrast is quantitatively linked to mass using calibration curves. The schematic shows the flow from solution to detection, *i.e.*, nanoclusters aggregate in the solvent, deposition on the glass surface, and optical detection *via* a high numerical aperture objective lens through immersion oil. MP revealed that the average mass increased from 65 to 103 kDa with an increase in the solvent polarity, corresponding to aggregation numbers of 13 to 50 nanoclusters (Fig. 13c). Time-resolved MP measurements captured the real-time aggregation dynamics, which correlated well with the cryo-EM and room-temperature TEM results, confirming the growth and hollow-sphere morphology of the aggregates.[33]

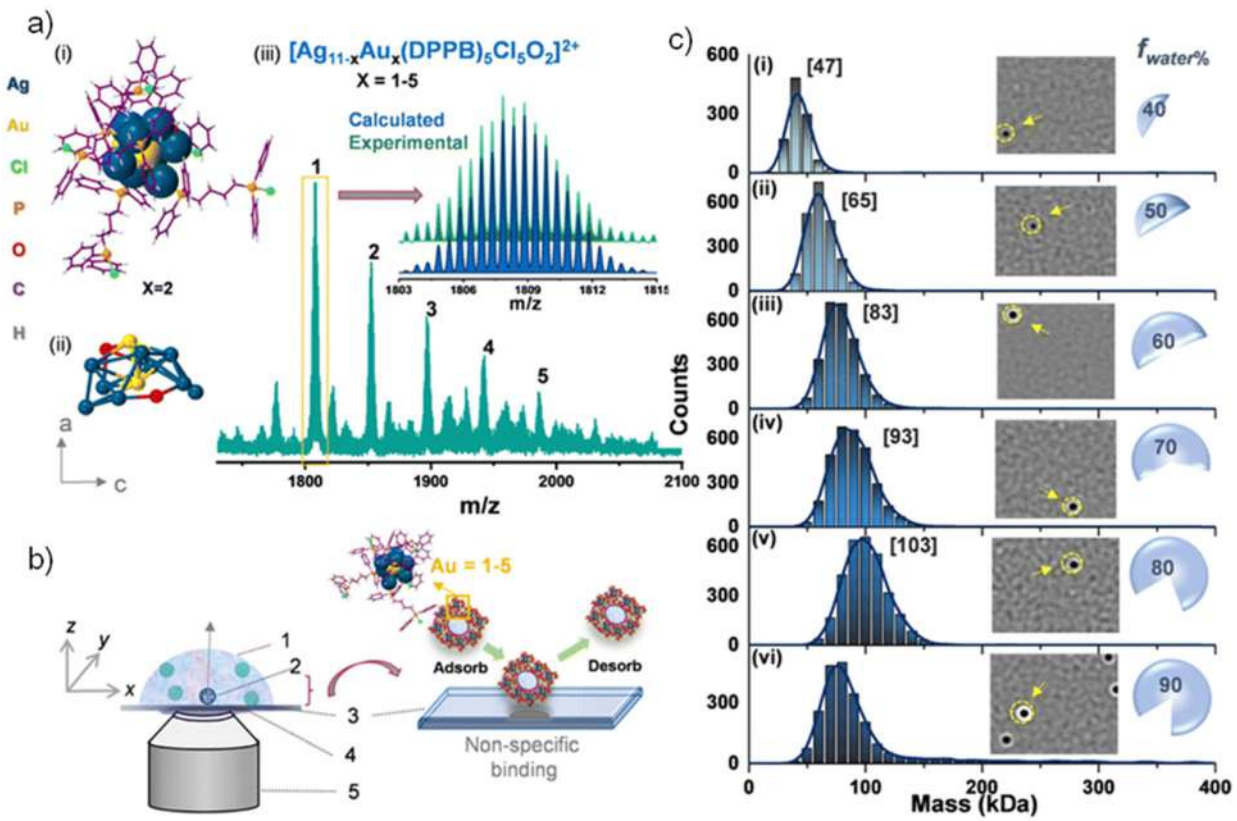


Fig. 13 (a) (i) Calculated structure (x = 2), (ii) metal, $Ag_{11-x}Au_x$core (x = 2), and (iii) ESI MS of $[Ag_{11-x}Au_x(DPPB)_5Cl_5O_2]^{2+}$ (x = 1–5) nanoclusters. In the inset, calculated isotopic distribution is stacked with the experimental one. (b) Concept and experimental implementation of MP. Parts in the graphic representation: (1) solvent mixture (sol mix) containing nanoclusters; (2) nanocluster aggregates in solution; (3) glass surface; (4) immersion oil; and (5) objective lens. Single-particle landing event on a non-coated cover slide is shown on the right. (c) Stacked plot of the MP histogram of various-sized nanoaggregates with the counts of particle landing events and varying solvent composition. Adapted from ref. 33. Copyright 2024, The Royal Society of Chemistry.

Published on 27 October 2025. Downloaded by Indian Institute of Technology Chennai on 12/29/2025 3:17:01 AM.

6. Non-noble metal nanoclusters

The study of non-noble metal nanoclusters, particularly those derived from first-row transition metals such as cobalt (Co), iron (Fe), and nickel (Ni), has significantly broadened the scope of atomically precise materials beyond the traditional gold and silver systems. These clusters exhibit diverse electronic, magnetic, and catalytic properties.[170–172] MS has emerged as an indispensable technique, providing insights into their composition, stability, and growth mechanisms. The composition of the well-known cobalt sulfide superatom $[Co_6S_8L_6]^+$ (L = ligand) was established through high-resolution mass spectrometric analysis. ESI-MS confirmed the precise size and monodispersity of neutral nickel nanoclusters such as $Ni_4(PET)_8$ and $Ni_6(PET)_{12}$, sometimes requiring the addition of agents such as cesium acetate (CsOAc) to facilitate ionization, yielding species such as $[Ni_6(PET)_{12} + Cs]^+$.[173] MS plays a key role in understanding the atom-by-atom substitution and redox behavior in non-noble metal nanoclusters. Gholipour-Ranjbar *et al.* demonstrated the incorporation of up to six Fe atoms into the cobalt sulfide core of $[Co_{6-x}Fe_xS_8L_6]^+$ clusters, whereas Ni substitution yielded only the singly substituted species $[Co_5NiS_8L_6]^+$, reflecting distinct substitution energetics. MS further revealed the pronounced redox sensitivity of Fe-doped clusters, which readily oxidized in solution to generate abundant doubly charged species $[Co_{6-x}Fe_xS_8L_6]^{2+}$ (particularly for $x \geq 4$), highlighting their higher oxidation propensity compared to their Ni- or Co-only analogues.[174] Beyond composition, CID studies gave important information about the bonding and gas-phase stability of these clusters. CID analysis of $[Co_5MS_8L_6]^+$ clusters (M = Mn, Fe, Co, and Ni) revealed that sequential ligand loss is the dominant pathway, which competes with the unusual loss of ligand sulfide (LS). Fe-substituted clusters, such as $[Co_5FeS_8L_6]^+$, demonstrated substantially reduced stability towards the first ligand loss compared to their Ni- or Co-analogs, characterised by lower collision energies needed for 50% fragmentation ($CID_{50\%}$), indicating weaker metal–ligand bonds.[175] Li *et al.* utilized ESI-MS and IM–MS to elucidate the composition and structure of a nickel chalcogenide nanocluster, $[Ni_3S_3H(PEt_3)_5]^+$, unlike the M_6S_8 frameworks typically formed from Co or Fe precursors. The observed *m/z* 863.1792 peak and isotopic pattern validated its composition (Fig. 14a), while deuteration studies showed that hydrogen is incorporated during synthesis. IM–MS analysis, supported by theoretical CCS calculations, confirmed a planar Ni_3S_3 core and the absence of isomers.[176] ESI-MS played a central role in confirming the composition and charge states of the open-shell nanocluster $[Ni_{30}S_{16}(PEt_3)_{11}]$, revealing peaks corresponding to its mono- and di-cationic species at *m/z* 3572.43 and 1786.20, respectively. In situ ESI-MS monitoring further elucidated its formation pathway through smaller intermediates, such as $[Ni_8S_5(PEt_3)_7]^+$, $[Ni_{20}S_{12}(PEt_3)_7]^+$, $[Ni_{21}S_{14}(PEt_3)_7]^+$, $[Ni_{21}S_{14}(PEt_3)_8]^+$, $[Ni_{23}S_{14}(PEt_3)_9]^+$ and $[Ni_{26}S_{14}(PEt_3)_{10}]^+$, establishing the sequential cluster growth mechanism leading to the final Ni_{30} species.[177] Higaki *et al.* recently reported a 55-atom iron cluster, which has been characterized *via* ESI-MS, confirming the dicationic formula $[Fe_{55}H_{46}(PtBu_3)_{12}]^{2+}$ (Fig. 14b). Deuterium labeling coupled with ESI-MS further traced the H/D exchange pathways, revealing extensive hydrogen mobility across the cluster surface and ligand framework during synthesis, while the final species remained exchange-inactive.[178]

These studies highlight how advances in MS have transformed the understanding of non-noble metal nanoclusters, providing atomic-level insights into their composition, substitution behavior, structural motifs, and hydride dynamics.

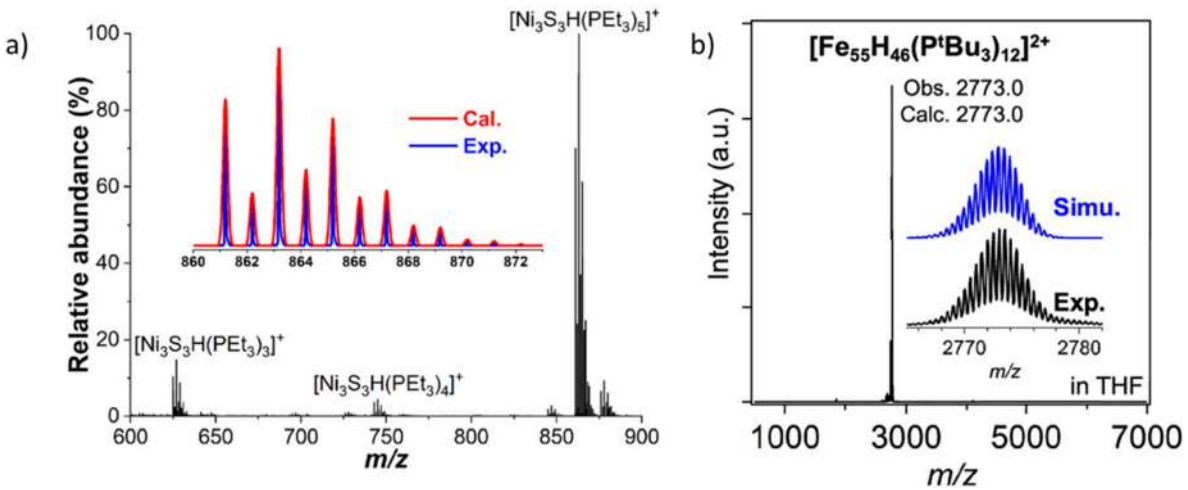


Fig. 14 (a) Representative positive-mode ESI mass spectrum of cationic Pet_3-ligated nickel sulfide NCs. The inset shows the experimental isotopic pattern (blue) of $[Ni_3S_3H(PEt_3)_5]^+$ overlaid with the calculated pattern (red). (b) Positive-mode ESI mass spectra of Fe_{55} in THF. Insets show the observed and simulated isotope patterns of the major peaks. Adapted from (a) ref. 176 and (b) ref. 178. Copyright 2025, John Wiley and Sons. Copyright 2025, the American Chemical Society.

Published on 27 October 2025. Downloaded by Indian Institute of Technology Chennai on 12/29/2025 3:17:01 AM.

7. Materials and applications of ESI

ESI-MS, traditionally an analytical technique, has undergone a significant transformation into a powerful preparative method for materials synthesis, through techniques such as electrospray deposition (ESD) and ion soft landing (SL). These approaches enable precise control over composition, morphology, thickness, and surface patterning, without the need for additives, ligands, or reducing agents.[179–181] ESD is a simple, ambient method that deposits charged microdroplets onto substrates, where solvated ions nucleate into nanostructures.[182] It supports the fabrication of diverse materials, including nanoparticles,[183] nanowires,[184] nanosheets,[185] nanobrushes,[186] nanoclusters,[187] and onion-like carbons.[188] ESD was employed to directly deposit hierarchically structured TiO_2 spheres onto FTO substrates, serving as efficient photoelectrodes in dye-sensitised solar cells.[42] In another example, ESD enabled the fabrication of hydrophilic–hydrophobic patterned silver nanowire "nanobrushes" that mimic natural water-harvesting systems and achieved record efficiencies in atmospheric moisture collection.[43] Using a home-built nano-electrospray source (Fig. 15a), Jose *et al.* deposited charged microdroplets of a Co_6S_8 cluster solution onto ultrapure water, forming a transparent thin film of vertically aligned nanoplates (Fig. 1b) (~200 nm thick and ~600 nm edge length). The nanoplates of Co_6S_8 cluster formed *via* electrospray deposition provide a high surface area, catalytically active film enabling the sensitive and selective electrochemical detection of As^{3+} in water.[189] Jana *et al.* fabricated a porous, luminescent Cu_4@ICBT film *via* ambient electrospray deposition (ESD) that selectively and reversibly senses nitroaromatic vapours.[190]

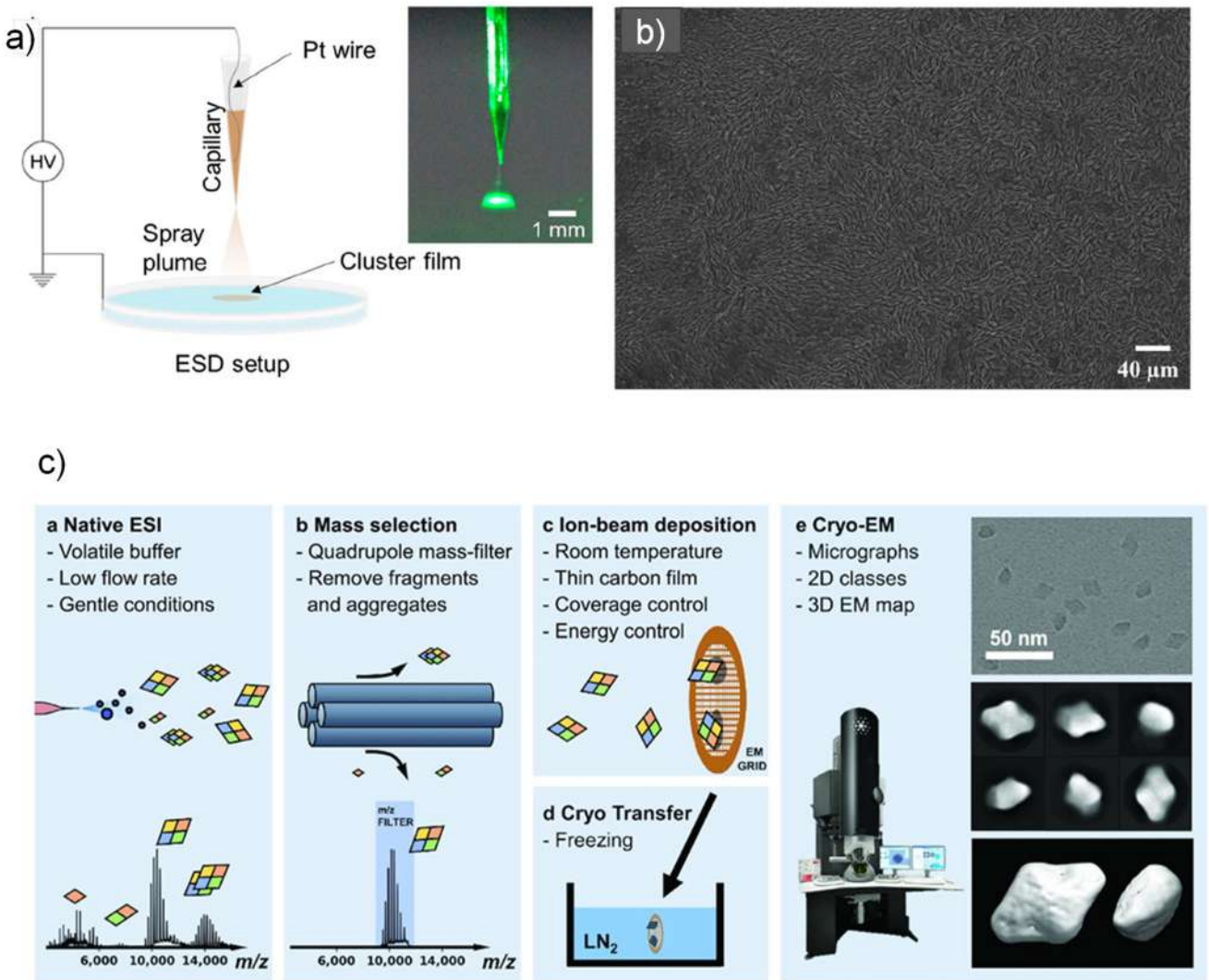


Fig. 15 (a) Schematic of our home-built electrospray setup. The inset shows a photographic image of the nanospray plume generated from the tip of the capillary. The plume is visualized using a green laser, which scatters from it. (b) Large-area FESEM micrographs of the vertically aligned nanoplates. (c) Schematic of mass-selective cryo-EM sample preparation using the native ES-IBD workflow. Adapted from (a)–(b) ref. 189 and (c) ref. 198. Copyright 2023, the American Chemical Society. Copyright 2022, National Academy of Sciences.

Published on 27 October 2025. Downloaded by Indian Institute of Technology Chennai on 12/29/2025 3:17:01 AM.

SL is a mass-selective technique that deposits intact polyatomic ions onto surfaces at low kinetic energies (~10 eV), preserving their molecular structure and charge state. It enables contamination-free fabrication due to the absence of counterions and allows precise control over surface composition and functionality.[191,192] SL has been used to prepare atomically defined metal clusters (*e.g.*, Ni_n, Pt_n, and Au_n) for catalytic CO oxidation,[193] designing redox-active electrode–electrolyte interfaces with polyoxometalates,[194] and fabricating protein microarrays[195] with retained biological activity.[196] Johnson *et al.* demonstrate that soft landing of mass-selected ions enables the preparation of clean, high-coverage, monodisperse Au_{11} clusters on surfaces, overcoming the limitations of solution synthesis and facilitating precise structural analysis by TEM/STEM.[197] A notable extension is native electrospray ion-beam deposition (native ES-IBD), which enables the solvent-free, mass-selected deposition of folded proteins for cryo-EM. A schematic representation of mass-selective cryo-EM sample preparation using the native ES-IBD workflow is shown in Fig. 15c. It avoids ice formation and contamination, yielding homogeneous, structurally intact samples suitable for 3D reconstruction, bridging mass spectrometry and structural biology.[198]

ESD and SL extend electrospray ionisation into material synthesis by enabling the controlled deposition of ions or charged droplets onto surfaces. SL allows mass and charge-selected species to be precisely immobilised, ideal for chemically defined interfaces, while ESD enables the ambient, ligand-free fabrication of diverse nanostructures (*e.g.*, nanoparticles, nanosheets, and nanobrushes) with tunable morphology and functionality, which are applicable in catalysis, sensing, and bioimaging.

8. MS-guided insights into catalysis

Mass spectrometry has developed rapidly in recent years and has established itself as a central technique in nanoscience for characterising materials at the atomic level. Nanocluster chemistry demands a precise understanding of the composition, structure, and electronic properties of APCs, which makes mass spectrometry a primary tool for their characterisation. In several aspects of nanoclusters, MS provides greater insights than the established methods, such as electron microscopy and optical spectroscopy. It allows high-resolution mass analysis and helps understand their growth mechanisms, reaction kinetics, fragmentation pathways, and structure–property relationships. These aspects are key to designing new functional nanomaterials. MS-based insights into cluster composition and ligand dynamics also help identify active sites and correlate structural features with catalytic, optical, and electronic behaviour, advancing the rational design of functional materials.

Recent studies show that mass spectrometry not only helps in characterising nanoclusters but also provides direct understanding of their catalytic behaviour. In situ and real-time mass spectrometric studies allow the detection of short-lived intermediates and reaction products formed during catalysis.[199] These observations help identify the active sites and the role of supports or ligands in promoting specific reaction steps. For example, real-time MS tracking of photocatalytic degradation on g-C_3N_4 and TiO_2 revealed their distinct oxidative pathways under visible and UV light, while Pd-based systems showed surface-specific dehydrogenation behaviour, clarifying the active roles of metal sites and supports.[200] Similarly, deep-learning-enabled single-particle mass spectrometry now quantifies the reaction products from individual nanoparticles, linking their surface structure to catalytic turnover with unprecedented precision.[201] Together, these developments establish MS as a predictive tool for correlating atomic-scale composition and ligand dynamics with macroscopic properties such as activity, selectivity, and stability. This approach also extends to other fields such as photonics and nanoelectronics, where MS-based insights are being used to design materials with improved optical, electronic, and chemical properties.

9. Current limitations and challenges

Although mass spectrometry has emerged as a powerful technique for studying atomically precise nanoclusters, several challenges continue to restrict its wider application. The ionisation efficiency of large or weakly charged clusters remains low, leading to signal suppression and incomplete detection, while maintaining the integrity of fragile species during soft ionisation remains a persistent concern. Techniques such as ESI and MALDI, though gentle, can still induce partial fragmentation or ligand loss, complicating structural interpretation. Its quantitative accuracy is further affected by overlapping charge states, adduct formation, and matrix-dependent effects. Instrumental limitations also pose constraints; the transmission efficiency of large ions is often low, and the resolving power of most analysers decreases significantly at higher mass ranges, limiting the precise characterisation of high-nuclearity clusters and assemblies.

Ion mobility–mass spectrometry (IM–MS) provides valuable insights into molecular compactness and conformational states through the experimentally determined CCS, but it also has limitations. The CCS reflects an averaged measure of ion–gas interactions and does not directly describe atomic-level structures. Consequently, reliable interpretation requires correlation with molecular modelling or dynamics simulations. Although modern drift-tube, trapped, and travelling-wave instruments typically achieve resolving powers of 200–400, and cyclic designs may extend this to about 700, both their mass range and resolution remain insufficient for large and heterogeneous nanoclusters.

Overcoming these limitations will require improved intact ionisation methods, higher transmission efficiency, and ultra-high-resolution instruments capable of maintaining precision at extended mass ranges. The continued integration of IM–MS

This journal is © The Royal Society of Chemistry 2025

Published on 27 October 2025. Downloaded by Indian Institute of Technology Chennai on 12/29/2025 3:17:01 AM.

with spectroscopic and theoretical approaches will be essential for achieving accurate structural determination, reliable structure–property correlations, and a predictive understanding of nanocluster behavior across different environments.

10. Conclusions and future perspectives

Recent advances in mass spectrometry have positioned it as a central analytical method in nanoscience for characterising materials at the atomic level. Nanocluster chemistry demands a precise understanding of the composition, structure, and electronic properties, which makes mass spectrometry a primary tool for the characterisation of APCs. In several aspects of nanoclusters, MS provides greater insights than the established methods, such as electron microscopy and optical spectroscopy. It allows high-resolution mass analysis and helps understand the growth mechanisms, reaction kinetics, fragmentation pathways, and structure–property relationships. These aspects are key to designing new functional nanomaterials. MS-based insights into cluster composition and ligand dynamics also help identify active sites and correlate structural features with catalytic, optical, and electronic behaviour, advancing the rational design of functional materials. A summary of APCs characterized by MS to date is provided in Table 1.

Recent advancements in instrumentation have greatly expanded the scope of mass spectrometry. Charge detection MS methods now allow the measurement of charge and mass-to-charge ratio of single ions, facilitating the study of bigger systems such as protein assemblies, viral particles, and nanoparticles, which was previously not possible. Mass photometry, a non-destructive and label-free method for measuring molecular mass in solution, has also emerged as a powerful approach to investigate molecular interactions, including protein and nanocluster binding and aggregation, with high accuracy at the level of single entities. Nano-electro-mechanical sensor-based MS (NEMS-MS), which directly measures the inertial mass of particles without relying on charge states, represents a powerful emerging approach for materials research. Its nanoscale dimensions provide exceptional miniaturisation potential, making it attractive for the characterisation of nanoclusters and heterogeneous materials at the single-particle level.[21]

While this review focused on characterizing ions, they can also serve as precursors for creating materials that lead to various applications. The examples presented in Section 7 also point to an "ionic path" for cluster-based materials. The application of mass spectrometry has tremendously expanded from mass analysis to materials processing. Soft ionisation and deposition methods such as electrospray ionisation, electrospray deposition, and soft landing make it possible to transfer intact molecular ions or clusters onto substrates under gentle conditions. These techniques enable the assembly of thin films and nanostructures with controlled properties, which can be useful in sensing, catalysis, and nanoelectronics. Given that these methods operate under mild and tunable conditions, they are particularly suitable for preserving fragile systems during their synthesis and characterisation. The electrospray-deposited clusters and cluster superstructures could be characterised using cryogenic electron microscopy (cryo-EM) and microcrystal electron diffraction (microED). These advances could integrate MS with structural techniques, opening a new dimension in this area.

The progress in ion activation and spectroscopic methods has further improved the structural analysis of nanoclusters. Advanced techniques such as ion mobility spectrometry, tandem mass spectrometry, and ultraviolet photodissociation allow the elucidation of isomeric structures, dissociation pathways, and core–shell structure arrangements. Advancements in multidimensional MS, particularly two-dimensional tandem MS, enable the rapid and high-throughput screening of complex mixtures, and these inputs can be extended to other systems to accelerate the discovery and optimisation of nanoclusters, alloys, and hybrid materials.[202] Laser-based action spectroscopy,[203] when used along with ion mobility, enables the study of excited states and weak intermolecular interactions. Recent developments, such as cyclic ion mobility, allow recirculation of ions for enhanced resolution, making it possible to distinguish nearly identical species.[204]

Future developments in this field lie in the integration of mass spectrometry with other complementary characterisation techniques. Approaches that combine MS with electron microscopy,[205] infrared, Raman,[206] UV–vis and photoelectron spectroscopy,[207] *etc*. could derive correlations among composition, morphology, structure, and electronic properties. These multifaceted approaches could unveil the relationship between structure and functions in nanoscale materials. Ultrahigh-resolution mass spectrometry imaging, widely applied for mapping biomolecules in biological samples,[208,209] can be extended to materials research to probe the dopants, interfaces, and nanoscale defects in heterogeneous solids with molecular precision. Native-state approaches, such as matrix-landing MS,[210] expand the scope of intact nanoclusters or supramolecular assemblies to be transferred directly from the gas phase onto surfaces for electron microscopy imaging or device integration.

In parallel, theoretical and computational approaches are also advancing rapidly. Machine-learned interatomic potentials, such as the Atomic Cluster Expansion (ACE) model developed by McCandler *et al.*, are enabling long-timescale molecular dynamics simulations with near-DFT (density functional theory) accuracy and much greater efficiency. These models offer valuable insights into ligand exchange, reactive isomerism, and structural rearrangements in nanoclusters, which align with experimental observations. A growing direction in this field is the integration of mass spectrometry with theoretical modelling, where MS data are combined with DFT and other computational methods to predict stable geometries, electronic structures, and fragmentation pathways. The combination of experiment and simulation could provide a better understanding of the gas-phase chemistry and aggregation-

Published on 27 October 2025. Downloaded by Indian Institute of Technology Chennai on 12/29/2025 3:17:01 AM.

Table 1 Summary of atomically precise nanoclusters characterised by mass spectrometry thus far (as of July 31, 2025, using Web of Science using "nanoclusters", "metal clusters", "mass spectrometry" and "mass" as keywords). Unprotected or naked clusters are not included. The list is alphabetical and in ascending order of nuclearity of clusters. Alloy clusters, listed separately, are arranged in ascending order of total nuclearity. For each nuclearity, alphabetical order is followed

Core	Ligands	Composition	Counter ions	Ionization	Fragmentation/ion-mobility/mass selected PES	Ref.
Ag_2	1,1-Bis(diphenylphosphino)methane	$Ag_2(dppm)_2(AcO)_2$		ESI-MS		213
Ag_6	Oligonucleotide dC_{12}	$(Ag^+)_6\ dC_{12}^{10-}$		ESI-MS		214
Ag_6	Diisopropyldithiophosphate, 1,1-bis (diphenylphosphino)methane	$[Ag_6\{S_2P(O^iPr)_2\}_4(dppm)_2]$		ESI-MS		215
Ag_6	1,1-Bis(diphenylphosphino)methane	$Ag_6(dppm)_4(AcO)_3$	OAc^-	ESI-MS		213
Ag_7	2,3-Dimercaptosuccinic acid	$Ag_7(DMSA)_4$		ESI-MS		216
Ag_7	Mercaptosuccinic acid	$Ag_7(H2MSA)_7$		MALDI-MS		217
Ag_8	Mercaptosuccinic acid	$Ag_8(H2MSA)_8$		MALDI-MS		217
Ag_8	(3,5-Dimethyl-4-(phenyldiazenyl)-1*H*-pyrazole), (bis(diphenylphosphino)methane), isopropylbenzenethiol	$[Ag_8(iPrPhS)_5(dppm)_3(azopz)_2]\cdot ClO_4$	ClO_4^-	ESI-MS		218
Ag_8	Bisimidazole	$Ag_8K_2L_4(CO_3)_2(PF_6)_6$		ESI-MS		219
Ag_9	Iodide	Ag_9I_2		ESI-MS		220
Ag_9	Mercaptosuccinic acid	$Ag_9(H_2MSA)_7$		ESI-MS		221
Ag_9	1,2-Benzenedithiolate	$[Ag_9(1,2\text{-}BDT)_6]^{3-}$		ESI-MS		222
Ag_{9-15}	Glutathione	$Ag_{9-15}(SR)_{5-10}$		ESI-MS		223
Ag_{10}	Diisopropyldithiophosphate	$[Ag_{10}\{S_2P(OiPr)_2\}_8]$		ESI-MS		224
Ag_{11}	Glutathione	$[Ag_{11}(SG)_7]$		ESI-MS	MS/MS (SID), ion mobility	225 and 226
Ag_{11}	Deoxyribonucleic acid	$Ag_{11}(DNA)_2$		ESI-MS		227
Ag_{12}	*tert*-Butylthiol, trifluoroacetate	$Ag_{12}(TBT)_6(TFA)_6(pyz)_6]\cdot 2CH_3CN$ $Ag_{12}S_2(TBT)_8(TFA)_4(bpy)_8]\cdot bpy$		ESI-MS		228
Ag_{14}	3,4-Difluoro-benzenethiol, triphenylphosphine	$Ag_{14}(SC_6H_3F_2)_{12}(PPh_3)_8$		ESI-MS		229
Ag_{15}	Bovine serum albumin	Ag_{15}@BSA		MALDI-MS		230
Ag_{15}	1,6-Bis(diphenylphosphino)hexane	$[Ag_{15}H_{13}(DPPH)_5]$		ESI-MS	MS/MS (CID)	231
Ag_{15}	Glutathione	$Ag_{15}(SG)_{11}$		ESI-MS		232
Ag_{16}	*tert*-Butyl thiol, trifluoroacetate	$[Ag_{16}(TBT)_8(TFA)_7(CH_3CN)_3Cl]$		ESI-MS		233
Ag_{16}	Deoxyribonucleic acid	$Ag_{16}Cl_2(DNA)_2$		ESI-MS		234
Ag_{16}	Deoxyribonucleic acid	$Ag_{16}Cl_2(DNA)_2$		ESI-MS	MS/MS (CID), ion mobility	235
Ag_{17}	Deoxyribonucleic acid	$Ag_{17}(DNA)_2$		ESI-MS		236
Ag_{17}	*tert*-Butyl thiol, trifluoroacetate	$[Ag_{17}(TBT)_8(TFA)_7(CH_3CN)_3Cl]$		ESI-MS		233
Ag_{17}	1-((Naphthalen-4-yl)ethyl)prop-2-yn-1-amine	$[Ag_{17}(NYA)_{12}]^{3+}$		ESI-MS		237
Ag_{17}	*ortho*-Carboranethiol	$[Ag_{17}(o1\text{-}CBT)_{12}]^{3-}$		ESI-MS	MS/MS (CID)	238
Ag_{18}	Deoxyribonucleic acid	$Ag_{18}(DNA)_2$		ESI-MS		239
Ag_{18}	Triphenylphosphine	$[Ag_{18}H_{16}(TPP)_{10}]^{2+}$		ESI-MS		240
Ag_{19}	1,2-Bis(diphenylphosphino)methane, phenylacetylene	$[Ag_{19}(dppm)_3(PhC{\equiv}C)_{14}](SbF_6)_3$	SbF_6^-	ESI-MS		241
Ag_{20}	Dithiophosphonate	$[Ag_{20}[S_2P(OiPr)_2]_{12}]$		ESI-MS		242
Ag_{21}	Dithiophosphonate, 4-methoxythiophenol	$[Ag_{21}\{S_2P(OR)(p\text{-}C_6H_4OCH_3)\}_{12}]PF_6$	PF_6^-	ESI-MS		243
Ag_{21}	Dithiophosphonate	$[Ag_{21}[S_2P(OiPr)_2]_{12}]^+$		ESI-MS		244
Ag_{21}	4-*tert*-Butylthiacalix[4]arene	$[Ag_{21}(H_2BTCA)_3(O_2PPh_2)_6]SbF_6$	SbF_6^-	ESI-MS		245
Ag_{21}	Deoxyribonucleic acid	$Ag_{21}(DNA)_3$		ESI-MS		246
Ag_{21}	1-Ethynyl-3,5-dimethoxybenzene	$[Ag_{21}(C{\equiv}CC_6H_3\text{-}3,5\text{-}R_2)_6\text{-}(O_2PPh_2)_{10}]SbF_6$	SbF_6^-	ESI-MS		245
Ag_{21}	4-Formylphenylethyne	$[Ag_{21}(Ph_2PO_2)_{10}(p\text{-}CHOPhC{\equiv}C)_6]SbF_6$	SbF_6^-	ESI-MS		247

This journal is © The Royal Society of Chemistry 2025

Published on 27 October 2025. Downloaded by Indian Institute of Technology Chennai on 12/29/2025 3:17:01 AM.

Table 1 *(Contd.)*

Core	Ligands	Composition	Counter ions	Ionization	Fragmentation/ion-mobility/mass selected PES	Ref.
Ag_{21}	9-SH *meta*-carboranethiol, triphenylphosphine	$[Ag_{21}(MCT)_{12}(TPP)_2]$		ESI-MS	MS/MS (CID)	248
Ag_{22}	1,2-Bis(diphenylphosphino)ethane, 2,5-dimethylbenzenethiol	$Ag_{22}(dppe)_4(2,5\text{-}DMBT)_{12}Cl_4]^{2+}$		ESI-MS		249
Ag_{24}	*tert*-Butylthiol, proline	$Ag_{24}(S^tBu)_{10}(L/D\text{-}proline)_8(NO_3)_4(H_2O)$		ESI-MS		250
Ag_{25}	2,4-Dimethylbenzenethiol	$Ag_{25}(DMBT)_{18}$		ESI-MS	MS/MS (CID)	60 and 111
Ag_{25}	1,2-Bis(diphenylphosphino)ethane	$[Ag_{25}H_{22}(DPPE)_8]^{3+}$		ESI-MS		240
Ag_{26}	Tris(4-fluorophenyl)phosphine	$[Ag_{26}H_{22}(TFPP)_{13}]^{2+}$		ESI-MS		240
Ag_{27}	1,4-Bis(diphenylphosphino)butane	$[Ag_{27}H_{22}(DPPB)_7]^{3+}$		ESI-MS	MS/MS (CID)	231
Ag_{28}	Deoxyribonucleic acid	$Ag_{28}(DNA)_2$		ESI-MS		251
Ag_{29}	1,3-Benzenedithiol, triphenylphosphine	$Ag_{29}(BDT)_{12}(TPP)_4$		ESI-MS	MS/MS (CID)	111 and 252
Ag_{29}	1,3-Benzenedithiol, fullerene	$[Ag_{29}(BDT)_{12}(C_{60})_n]^{3-}$		ESI-MS	MS/MS (CID), ion mobility	253
Ag_{29}	1,3-Benzenedithiol, triphenylphosphine	$Ag_{29}(BDT)_{12}(TPP)_4$		ESI-MS	MS/MS (UVPD)	120
Ag_{29}	Dihydrolipoic acid, 1,3-benzenedithiol	$Ag_{29}(BDT)_{12-x}(DHLA)_x$		ESI-MS		133
Ag_{29}	1,3-Benzenedithiol, 1,2-bis (diphenylphosphino) ethane	$Ag_{29}(BDT)_{12}(dppe)_4$		ESI-MS		254
Ag_{29}	Lipoic acid	$Ag_{29}(LA)_{19}$		ESI-MS	MS/MS (CID), ion mobility	255
Ag_{29}	1,3-Benzenedithiol, 2,2′-[1,4-phenylenebis (methylidynenitrilo)]bis[benzenethiol]	$[Ag_{29}(L)_{12}]L'_4$		ESI-MS	Ion mobility	136
Ag_{30}	Captopril	$Ag_{30}(Capt)_{18}$		ESI-MS		256
Ag_{31}	Glutathione	$Ag_{31}(SG)_{19}$		ESI-MS		232
Ag_{31}	6-(Dibutylamino)-1,3,5-triazine-2,4-dithiol	$Ag_{31}(TRZ)_{10}$		ESI-MS		257
Ag_{31}	Glutathione	$Ag_{31}(SG)_{19}$		ESI-MS		258
Ag_{32}	Glutathione	$Ag_{32}(SG)_{19}$		ESI-MS		259
Ag_{32}	*N*-(2-Mercaptopropionyl)glycine	$Ag_{32}(MPG)_{19}$		ESI-MS, MALDI-MS		260
Ag_{33}	4-*tert*-Butylthiacalix[4]arene, cyclohexanethiol	$Ag_{33}(TC_4A)_4(CyS)_{10}$		ESI-MS		261
Ag_{34}	3,3-Dimethyl-1-butyne	$Ag_{34}(^tBuC{\equiv}C)_{24}(CH_3COO)_2$	CH_3COO^-	ESI-MS		262
Ag_{34}	4-*tert*-Butylbenzyl mercaptan	$Ag_{34}S_3SBB_{20}(CF_3COO)_6^{2+}$		ESI-MS		263
Ag_{35}	3,3-Dimethyl-1-butyne, 4-*tert*-butylthiacalix[4] arene	$[Ag_{35}(H_2L)_2(L)(C{\equiv}CBut)_{16}]^{3+}$		ESI-MS		264
Ag_{37}	Trifluoroacetate, *tert*-butylbenzenethiol	$[Ag_{37}S_4(SC_6H_4{}^tBu)_{24}(CF_3COO)_6(H_2O)_{12}]^-$		ESI-MS		265
Ag_{39}	Pentafluorobenzenethiol, triphenylphosphine	$[Ag_{39}(PFBT)_{24}(TPP)_8]^{2-}$		ESI-MS		266
Ag_{40}	1,7-Bis(mercapto)-*m*-carborane, triphenylphosphine	$Ag_{40}(C_2B_{10}H_{10}S_2)_{12}(PPh_3)_8$		ESI-MS		69
Ag_{40}	2,4-Dimethylbenzenethiol	$[Ag_{40}(2,4\text{-}DMBT)_{24}(PPh_3)_8]$		ESI-MS		267
Ag_{40}	Dimethylbenzenethiol, triphenylphosphine	$[Ag_{40}(SPhMe_2)_{24}(PPh_3)_8](NO_3)_2$		ESI-MS	MS/MS (CID)	268
Ag_{42}	*o*-Carborane-1,2-dithiol, triphenylphosphine	$[Ag_{42}(CBDT)_{15}(TPP)_4]^{2-}$		ESI-MS	MS/MS (CID)	269
Ag_{42}	6-(Dibutylamino)-1,3,5-triazine-2,4-dithiol	$Ag_{42}(TRZ)_{13}$		ESI-MS	MS/MS (CID)	257
Ag_{42}	4-*tert*-Butylthiacalix[4]arene	$Ag_{42}(MoO_3\text{-}TC4A)_6(EtS)_{14}(CH_3CN)_5Cl$		ESI-MS		270
Ag_{44}	4-*tert*-Butylthiacalix[4]arene	$Ag_{44}(BTCA)_6$		ESI-MS		271
Ag_{44}	5-Mercapto-2-nitrobenzoic acid	$[Ag_{44}(MNBA)_{30}]^{4-}$		ESI-MS		272
Ag_{44}	4-Mercaptobenzoic acid	$Na_4Ag_{44}(MBA)_{30}$		ESI-MS		273
Ag_{44}	2-Ethylbenzenethiolate, triphenylphosphine	$Ag_{44}(EBT)_{26}(TPP)_4$		MALDI-MS		274

Published on 27 October 2025. Downloaded by Indian Institute of Technology Chennai on 12/29/2025 3:17:01 AM.

Table 1 *(Contd.)*

Core	Ligands	Composition	Counter ions	Ionization	Fragmentation/ion-mobility/mass selected PES	Ref.
Ag_{44}	Benzeneselenol	$[Ag_{44}(SePh)_{30}]^{4-}$		ESI-MS		275
Ag_{44}	Benzeneselenol	$[Ag_{44}(SePh)_{30}]^{4-}$		MALDI-MS		276
Ag_{44}	4-Mercaptobenzoic acid	$M_4Ag_{44}(MBA)_{30}$		ESI-MS		277
Ag_{44}	3,4-Difluorobenzenethiolate	$[Ag_{44}(SC_6H_3F_2)_{30}]^{4-}$		ESI-MS	Mass-selected PES	145
Ag_{44}	4-Fluorothiophenol	$Ag_{44}(4\text{-FTP})_{30}$		ESI-MS	MS/MS (CID), ion mobility	40, 111 and 278
Ag_{46}	2,4-Dimethylbenzenethiol, triphenylphosphine	$[Ag_{46}(SPhMe_2)_{24}(PPh_3)_8](NO_3)_2$		ESI-MS		268
Ag_{47}	3,3-Dimethyl-1-butyne, L-/D-valine, L-/D-isoleucine	$[Ag_{47}L_{12}(C{\equiv}C^tBu)_{16}]BF_4$	BF_4^-	ESI-MS		279
Ag_{48}	3,3-Dimethyl-1-butyne	$[Ag_{48}(C{\equiv}CtBu)_{20}(CrO_4)_7]$	CrO_4^-	ESI-MS		280
Ag_{48}	1-Adamantanethiol, cyclohexanethiol	$Ag_{48}Cl_{14}(S\text{-}Adm)_{26}(S\text{-}c\text{-}C_6H_{11})_4$		ESI-MS		281
Ag_{50}	1,3-Bis(diphenylphosphino) propane, 1-adamantanethiol	$Ag_{50}Cl_{16}(S\text{-}Adm)_{28}(dppp)_2$		ESI-MS		250
Ag_{50}	1,1-Bis(diphenylphosphino) methane	$Ag_{50}(dppm)_6(SR)_{30}$		ESI-MS		282
Ag_{52}	Isopropylmercaptan	$Ag_{52}(^iPrS)_{25}(CF_3COO)_{16}(H_2O)_3(CH_3OH)_2]$		ESI-MS		283
Ag_{52}	*N*,*N*′-Di(5-fluoro-2-pyridinyl)formamidine	$[Ag_{52}(5\text{-}F\text{-}dpf)_{16}Cl_4](SbF_6)_2$	SbF_6^-	ESI-MS		284
Ag_{53}	*N*,*N*′-Di(5-methyl-2-pyridinyl)formamidine	$[Ag_{53}(5\text{-}Me\text{-}dpf)_{18}](NO_3)_5$	NO_3^-	ESI-MS		284
Ag_{54}	4-*tert*-Butylthiacalix[4]arene, cyclohexanethiol	$Ag_{54}(TC_4A)_6(CyS)_{11}(OAc)_4(CH_3CN)_2Cl$	Cl^-	ESI-MS		261
Ag_{55}	4-*tert*-Butylbenzylthiol, phenylethanethiol	$Ag_{55}(SR)_{31}$		ESI-MS, MALDI-MS		285
Ag_{58}	Trifluoroacetic acid, isopropylthiophenol	$Ag_{58}(^iPrC_6H_4S)_{40}(CF_3COO)_6(H_2O)_{10}$		ESI-MS		286
Ag_{59}	2,5-Dichlorobenzenethiol	$[Ag_{59}(2,5\text{-}DCBT)_{32}]^{3-}$		ESI-MS		287
Ag_{60}	*tert*-Butylthiol	$[Ag_{60}(^tBuS)_{20}(o\text{-}CH_3OPhCOO)_{16}(H_2O)_4(Cl)_2]$	Cl^-	ESI-MS		288
Ag_{61}	Dipyridylamine	$Ag_{61}(dpa)_{27}(SbF_6)_4$	SbF_6^-	ESI-MS		70
Ag_{67}	2,4-Dimethylbenzenethiol, triphenylphosphine	$[Ag_{67}(SPhMe_2)_{32}(PPh_3)_8]^{3+}$		ESI-MS		62
Ag_{68}	4-*tert*-Butylbenzylmercaptan	$Ag_{68}(SBB)_{34}$		MALDI-MS		289
Ag_{71}	1,1-Bis-(diphenylphosphino)methane, *tert*-butylthiol	$[Ag_{71}(S\text{-}Bu)_{31}(dppm)](SbF_6)_2$	SbF_6^-	ESI-MS		290
Ag_{74}	Phenylacetylene	$Ag_{74}(C{\equiv}CPh)_{44}$		ESI-MS		71
Ag_{74}	2-Methylphenylacetylene	$Ag_{74}(2\text{-}CH_3C_6H_4C{\equiv}C)_{44}$		ESI-MS		291
Ag_{75}	Glutathione	$Ag_{75}(SG)_{40}$		ESI-MS		292
Ag_{78}	1,1-Bis-(diphenylphosphino)methane	$[Ag_{78}(^iPrPhS)_{30}(dppm)_{10}Cl_{10}]^{4+}$	Cl^-	ESI-MS		293
Ag_{86}	2-Methylphenylacetylene	$Ag_{86}(2\text{-}CH_3C_6H_4C{\equiv}C)_{50}$		ESI-MS		291
Ag_{88}	4-*tert*-Butylthiacalix[4]arene	$Ag_{88}(TC4A)_8(EtS)_{32}(OAc)_8(CH_3CN)$		ESI-MS		294
Ag_{93}	4-Methoxyphenylacetylene	$Ag_{93}(PPh_3)_6(C{\equiv}CR)_{50}$		ESI-MS		295
Ag_{98}	2-Methylphenylacetylene	$Ag_{98}(2\text{-}CH_3C_6H_4C{\equiv}C)_{52}$		ESI-MS		291
Ag_{110}	2-Fluorothiophenol, triphenylphosphine	$Ag_{110}(SPhF)_{48}(PPh_3)_{12}$		MALDI-MS		296
Ag_{112}	3,5-Trifluoromethylphenylacetylene	$[Ag_{112}Cl_6(3,5\text{-}(CF_3)_2PhC{\equiv}C)_{51}]^{3-}$		ESI-MS		297
Ag_{123}	*tert*-Butyl thiol	$[Ag_{123}S_{35}(S^tBu)_{50}]$		MALDI-MS		298
Ag_{136}	4-*tert*-Butylbenzenethiol	$[Ag_{136}(SR)_{64}Cl_3Ag_{0.45}]^-$		ESI-MS		299
Ag_{140}	4-*tert*-Butylbenzylmercaptan	$Ag_{140}BBT_{53}$		MALDI-MS		300
Ag_{141}	Adamantanethiol	$[Ag_{141}X_2(S\text{-}Adm)_{40}]^{3+}$		ESI-MS		61
Ag_{146}	4-Isopropylbenzenethiolate	$Ag_{146}Br_2(SR)_{80}$		ESI-MS		32
Ag_{152}	Phenylethanethiol	$Ag_{152}(SCH_2CH_2Ph)_{60}$		MALDI-MS		301
Ag_{154}	1,4-Bis-(diphenylphosphanylmethyl)benzene	$[Ag_{154}Se_{77}(Dppxy)_{18}]$		MALDI-MS		302

Published on 27 October 2025. Downloaded by Indian Institute of Technology Chennai on 12/29/2025 3:17:01 AM.

Table 1 *(Contd.)*

Core	Ligands	Composition	Counter ions	Ionization	Fragmentation/ion-mobility/mass selected PES	Ref.
Ag_{213}	Adamantanethiol	$Ag_{213}(Adm\text{-}S)_{44}Cl_{33}$		ESI-MS		303
Ag_{280}	4-*tert*-Butylbenzylmercaptan	$Ag_{280}(SBB)_{120}$		ESI-MS		53
Ag_{320}	1,1-Bis(diphenylphosphino)propane, *tert*-butyl thiol	$[Ag_{320}S_{130}(S^tBu)_{60}(dppp)_{12}]$		MALDI-MS		302
Ag_{344}	*tert*-Butyl thiol	$[Ag_{344}S_{124}(S^tBu)_{96}]$		MALDI-MS		298
Ag_{352}	*tert*-Butyl thiol	$[Ag_{352}S_{128}(StC_5H_{11})]$		MALDI-MS		302
Ag_{374}	4-*tert*-Butylbenzenethiol	$[Ag_{374}(SR)_{113}Br_2Cl_2]$		ESI-MS		299
Ag_{490}	*tert*-Butyl thiol	$[Ag_{490}S_{188}(S^tC_5H_{11})_{114}]$		MALDI-MS		302
Au_5	Triphenylphosphine	$Au_5(PPh_3)_5]^+$		ESI-MS		304
Au_6	1,3-Bis(diphenylphosphino) propane	$[Au_6(dppp)_4]^{2+}$		ESI-MS		305
Au_6	Polyethylene glycol, biotin	$Au_6(S\text{-}PEG_{70}\text{-biotin})_6$		ESI-MS		306
Au_7	Polyethylene glycol, biotin	$Au_7(S\text{-}PEG_{70}\text{-biotin})_7$		ESI-MS		306
Au_9	Dibenzimidazolium salt	$[Au_9(NHC)_4Br]Br_2$	Br^-	ESI-MS		307
Au_9	2,6-Bis(1-(diphenylphosphaneyl)ethyl)pyridine	$Au_9(PNP)_6$		ESI-MS		308
Au_{10}	Mercaptosuccinic acid	$Au_{10}(MSA)_6$		MALDI-MS		309
Au_{10}	*tert*-Butylbenzenethiol	$Au_{10}(TBBT)_{10}$		MALDI-MS		310
Au_{10}	Polyethylene glycol	$Au_{10}(S\text{-}PEG_{12}\text{-}CO_2H)_{10}$		ESI-MS		306
Au_{10}	Dibenzimidazolium salt	$[Au_{10}(NHC)_4Br_2](O_2CCF_3)_2$		ESI-MS		307
Au_{10}	Polyethylene glycol, biotin	$Au_{10}(S\text{-}PEG_{70}\text{-biotin})_{10}$		ESI-MS		306
Au_{10}	1,3-Di(2,4,6-trimethylbenzyl)benzimidazolium halide	$[Au_{10}(MesCH_2Bimy)_6X_3]$		ESI-MS		311
Au_{11}	3-Mercaptopropionic acid	$Au_{11}(SCH_2CH_2COOH)_7(TOA)_7$	TOA^+	ESI-MS		312
Au_{11}	1,3-Bis(diphenylphosphino)propane	$[Au_{11}(dppp)_5]^{3+}$		ESI-MS		305
Au_{11}	DPEphos	$[Au_{11}(DPEphos)_4Cl_2]Cl$	Cl^-	ESI-MS		313
Au_{11}	Polyethylene glycol	$Au_{11}(SPEG_{12}\text{-}CO_2H)_{11}$		ESI-MS		306
Au_{11}	Xantphos	$[Au_{11}(Xantphos)_4Cl_2]Cl$	Cl^-	ESI-MS		313
Au_{11}	Diphosphine	$[Au_{11}(DP)_4L_2]^+$		ESI-MS		314
Au_{11}	Triphenylphosphine (X = chloride or phenylacetylene)	$[Au_{11}(PPh_3)_8X_2]^+$		ESI-MS	MS/MS (CID)	315
Au_{12}	Polyethylene glycol	$Au_{12}(S\text{-}PEG_{12}\text{-}CO_2H)_{12\text{–}14}$		ESI-MS		306
Au_{13}	1,2-Bis(diphenylphosphino)ethane	$[Au_{13}(dppe)_5Cl_2]Cl_3$	Cl^-	ESI-MS		316
Au_{13}	1,3-Bisubstituted benzimidazolium chloride	$[Au_{13}(NHC)_{10}Cl_2]^{3+}$		ESI-MS		317
Au_{13}	1,3-Disubstituted benzimidazolium chloride	$[Au_{13}(NHC)_5Cl_2]Cl_3$	Cl^-	ESI-MS		72
Au_{14}	1,3-Bis(diphenylphosphinopropane)	$Au_{14}(dppp)_5I_4$	Cl^-	ESI-MS		318
Au_{15}	Glutathione	$Au_{15}(SG)_{13}$		ESI-MS		54
Au_{15}	Glutathione, cyclodextrin	Au_{15}@CD		ESI-MS		319
Au_{15}	Glutathione	$Au_{15}(SG)_{13}$		ESI-MS		320
Au_{16}	1-Adamantanethiol	$Au_{16}(S\text{-}Adm)_{12}$		ESI-MS		321
Au_{18}	Glutathione	$Au_{18}(SG)_{14}$		ESI-MS		322
Au_{18}	Glutathione, Thiol-17mer	$Au_{18}(SG)_{13}$-17mer		ESI-MS		323
Au_{18}	Glutathione	$Au_{18}(SG)_{14}$		ESI-MS		324
Au_{18}	Cyclohexanethiol	$Au_{18}(SC_6H_{11})_{14}$		ESI-MS		325
Au_{18}	2,4,6-Triisopropylbenzylmercaptan	$Au_{18}S_2\text{-}(STipb)_{12}$		ESI-MS		326
Au_{18}	3-Mercaptopropionic acid	$Au_{18}(SC_2H_4CO_2H)_{14}$		MALDI-MS		327
Au_{19}	*N*,*N*-Bis(diphenylphosphino)amine, phenylacetylene	$[Au_{19}(PhC{\equiv}C)_9(Hdppa)_3](SbF_6)_2$	SbF_6^-	ESI-MS		328
Au_{19}	Phenylethanethiol	$Au_{19}(SC_2H_4Ph)_{13}$		ESI-MS		329
Au_{20}	4-Pyridinethanethiol	$Au_{20}(4\text{-}PyET)_{14}CN$		MALDI-MS		330

This journal is © The Royal Society of Chemistry 2025

Published on 27 October 2025. Downloaded by Indian Institute of Technology Chennai on 12/29/2025 3:17:01 AM.

Table 1 *(Contd.)*

Core	Ligands	Composition	Counter ions	Ionization	Fragmentation/ion-mobility/mass selected PES	Ref.
Au_{20}	1-Adamantanethiol, diphenyl-2-pyridylphosphine	$Au_{20}(AdmS)_{14}(PhPy_2P)$		ESI-MS		331
Au_{20}	Triphenylphosphine	$[Au_{20}(PPh_3)_4]$		ESI-MS		332
Au_{20}	Tris(2-(diphenylphosphino) ethyl)phosphine	$[Au_{20}(dppp_3)_4]Cl_4$	Cl^-	ESI-MS		73
Au_{21}	1-Adamantanethiol, tris(4-fluorophenyl) phosphine	$Au_{21}(AdmS)_{13}S(F_3Ph_3P)$		ESI-MS		331
Au_{21}	3-Methylbenzenethiol, *N*,*N*-bis (diphenylphosphino)amine	$Au_{21}(m\text{-MBT})_{12}(Hdppa)_2$		ESI-MS		333
Au_{22}	Cysteinyl-lysyl-cysteine	$Au_{22}(Lys–Cys–Lys)_{16}$		ESI-MS		334
Au_{22}	Glutathione, porphyrin	$Au_{22}[(SG)_{15}(SAOPPTH_2)_2]$		MALDI-MS		335
Au_{22}	1,8-Bis-(diphenylphosphino)octane	$Au_{22}(L)_6$		ESI-MS		336
Au_{22}	Glutathione, boric acid	$Au_{22}(SG)_{18}$		MALDI-MS		337
Au_{22}	Glutathione	$Au_{22}(SG)_{18}$		ESI-MS		338
Au_{22}	3-Ethynylthiophene, phenylacetylene, 3-ethynyltoluene, 3-ethynylanisole	$Au_{22}(C{\equiv}CPh)_{18}$		MALDI-MS		74
Au_{22}	Dimethylaminobenzenethiol	$Au_{22}(DMAT)_{15}H$		ESI-MS		339
Au_{22}	1,2-Bis-(diphenylphosphino)ethane, triphenylphosphine, hydride	$Au_{22}H_3(dppe)_3(PPh_3)_8$		ESI-MS		340
Au_{22}	Bis(2-diphenylphosphino)ethyl ether, hydride	$Au_{22}H_3(dppee)_7$		ESI-MS	Ion mobility	341
Au_{23}	Cyclohexanethiol	$[Au_{23}(SC_6H_{11})_{16}]^-$		MALDI-MS		342
Au_{23}	Glutathione	$Au_{23}(SG)_{18}$		MALDI-MS		343
Au_{23}	Cyclohexanethiol	$[Au_{23}(SC_6H_{11})_{16}]^-$		ESI-MS		344
Au_{23}	3,3-Dimethyl-1-butyne	$Au_{23}(C{\equiv}C^tBu)_{15}$		MALDI-MS		345
Au_{23}	Phenylethanethiol, 4-*tert*-butylbenzenethiol	$Au_{23}(SPh^tBu)_{17}$		ESI-MS, MALDI-MS		346
Au_{24}	Phenylethanethiol, triphenylphosphine	$[Au_{24}(PPh_3)_{10}(SC_2H_4Ph)_5X_2]^+$		ESI-MS		347
Au_{24}	Benzene selenol	$Au_{24}(SePh)_{20}$		ESI-MS		348
Au_{24}	Adamantanethiol	$Au_{24}(SAdm)_{16}$		ESI-MS		56
Au_{24}	Polyvinyl 2-pyrrolidone (PVP)	$Au_{24}Cl_x$ (x = 0–3)		MALDI-MS		349
Au_{25}	Glutathione	$Au_{25}(SG)_{18}$		ESI-MS		350
Au_{25}	Triphenylphosphine, alkanethiol	$[Au_{25}(PPh_3)_{10}(SC_nH_{2n+1})_5Cl_2]^{2+}$	Cl^-	ESI-MS		351
Au_{25}	Hexanethiol	$Au_{25}(SC_6H_{13})_{18}$		ESI-MS		352
Au_{25}	Glutathione	$Au_{25}(SG)_{18}$		ESI-MS		353
Au_{25}	Glutathione	$Au_{25}(SG)_{18}$		ESI-MS		354
Au_{25}	Phenylethanethiol	$Au_{25}(SCH_2CH_2Ph)_{18}^-$		ESI-MS		355
Au_{25}	Phenylethanethiol	$Au_{25}(SCH_2CH_2Ph)_{18}$		ESI-MS		356
Au_{25}	Glutathione	$Au_{25}(SG)_{18}$		MALDI-MS		357
Au_{25}	Phenylethanethiol	$Au_{25}(SCH_2CH_2Ph)_{18}$		ESI-MS		358
Au_{25}	Glutathione	$[Au_{25}(SG)_{18} - 6H]^{7-}$		ESI-MS	MS/MS (CID), action spectroscopy	144
Au_{25}	Phenylethanethiol	$[Au_{25}(SCH_2CH_2Ph)_{18}]$-		ESI-MS	MS/MS (CID), ion mobility	109
Au_{25}	Phenylethanethiol	$[Au_{25}(SCH_2CH_2Ph)_{18}]$-		MALDI-MS, FAB-MS		359 and 360
Au_{25}	Dioctyl diselenide	$Au_{25}(SeC_8H_{17})_{18}$		ESI-MS		361
Au_{25}	Dodecanethiol	$Au_{25}(SC_{12}H_{25})_{18}$		MALDI-MS		362
Au_{25}	Ethanethiol	$Au_{25}(SC_2H_5)_{18}$		MALDI-MS		363

Published on 27 October 2025. Downloaded by Indian Institute of Technology Chennai on 12/29/2025 3:17:01 AM.

Table 1 *(Contd.)*

Core	Ligands	Composition	Counter ions	Ionization	Fragmentation/ion-mobility/mass selected PES	Ref.
Au_{25}	*para*-Mercaptobenzoic acid	$Au_{25}(pMBA)_{18}$		ESI-MS	MS/MS (CID), MS/MS (UVPD)	117
Au_{25}	Cysteine	$Au_{25}(Cys)_{18}$		ESI-MS		364
Au_{25}	Glutathione	$Au_{25}(SG)_{18}$		MALDI-MS		365
Au_{25}	Glutathione	$Au_{25}(SG)_{18}$		ESI-MS		366
Au_{25}	4-Mercapto-*n*-butoxycalix[4]arene	$[Au_{25}(Calix\text{-}4S)_{18}]$		ESI-MS		367
Au_{25}	Butanethiol	$Au_{25}(BT)_{18}$		MALDI-MS		368
Au_{25}	6-Mercaptohexanoic acid	$Au_{25}(MHA)_{18}$		ESI-MS		369
Au_{25}	2-Methacryloyloxyethyl, phosphorylcholine	$Au_{25}(MPC)_{18}$		ESI-MS		370
Au_{25}	4-*tert*-Butylbenzyl mercaptan	$Au_{25}(SBB)_{18}$		ESI-MS, MALDI-MS		371
Au_{25}	Phenylethanethiol	$[Au_{25}(PET)_{18}(O_2)_n]^-$		ESI-MS		372
Au_{25}	(*R*)-5,5′,6,6′,7,7′,8,8′-Octafluoro-[1,1′-binaphthalene]-2,2′-dithiol	$Au_{25}(R\text{-}BINAS)_{18}$		MALDI-MS		373
Au_{25}	2-Phenylethanethiol, triphenylphosphine	$Au_{25}(PPh_3)_{10}(SC_2H_4Ph)_5Cl_2$	Cl^-	ESI-MS	MS/MS (UVPD)	121
Au_{25}	(1*R*,1′*R*)-6,6′-(1,4-Phenylene)di-1,1′-binaphthyl-2,2′-dithiol	$Au_{25}(PET)_{14}(BINAS)_2$		MALDI-MS		374
Au_{25}	4-Mercaptobenzoic acid, arginylglycylaspartic acid	$Au_{25}(pMBA)_{18-x}(cRGD)_x$		ESI-MS		375
Au_{25}	Diphenyl-2-pyridylphosphine, *N*,*N*-diethyldithiocarbamate	$Au_{25}(DETC)_5(DPPY)_{10}Cl_2$	Cl^-	ESI-MS		376
Au_{25}	Cysteine	$Au_{25}(Cys)_{18}$		ESI-MS		377
Au_{25}	4-Mercaptobenzoic acid, Thiol-17mer	$Au_{25}(pMBA)_{(18-n)}17mer_{(n)}$		ESI-MS		323
Au_{26}	1,3-Diisopropylimidazole, *N*,*N*′-di(3,4-dimethyl-phenyl)formamidine	$Au_{26}(3,4\text{-}Me_2\text{-}Phform)_9(^iPr_2\text{-}imy)_3(Me_2S)$		ESI-MS		378
Au_{28}	Glutathione	$Au_{28}(SG)_{14}$		ESI-MS		379
Au_{28}	Glutathione	$Au_{28}(SG)_{14}$		MALDI-MS		53
Au_{28}	4-Methylbenzenethiol, *N*,*N*-bis(diphenylphosphino)amine	$Au_{28}(p\text{-}MBT)_{14}(Hdppa)_3$		ESI-MS		333
Au_{28}	2-Phenylpropane-1-thiol	$Au_{28}(PPT)_{21}$		ESI-MS		380
Au_{28}	4-*tert*-Butylphenylacetylene	$Au_{28}(^tBuC_6H_4C{\equiv}C)_{20}$		ESI-MS		381
Au_{28}	*N*,*N*′-Diphenylformamidinate	$[Au_{28}(Ph\text{-}form)_{12}](OTf)_2$		ESI-MS		382
Au_{28}	9-HC≡C-*closo*-1,2-$C_2B_{10}H_{11}$, tetrahydrothiophene	$[Au_{28}(C_4B_{10}H_{11})_{12}(tht)_8]^{3+}$		ESI-MS		383
Au_{28}	*tert*-Butylbenzenethiol	$Au_{28}(SCH_2Ph\text{-}^tBu)_{22}$		ESI-MS		384
Au_{29}	Glutathione	$Au_{29}(SG)_{18}$		ESI-MS		385
Au_{30}	Adamantanethiol	$Au_{30}(SAd)_{18}$		MALDI-MS		386
Au_{30}	*tert*-Butyl thiol	$Au_{30}(S\text{-}^tC_4H_9)_{18}$		ESI-MS, MALDI-MS		387
Au_{30}	*tert*-Butyl thiol	$Au_{30}S(S\text{-}^tC_4H_9)_{18}$		ESI-MS		388
Au_{34}	Phenylacetylene, triphenylphosphine	$Au_{34}(PhC{\equiv}C)_{14}(Ph_3P)_6$		ESI-MS		389
Au_{36}	Thiophenol	$Au_{36}(SPh)_{23}$		MALDI-MS		390
Au_{36}	4-*tert*-Butylbenzenethiol	$Au_{36}(SPh\text{-}^tBu)_{24}$		ESI-MS		391
Au_{36}	*para*-Mercaptobenzoic acid	$Au_{36}(pMBA)_{24}$		ESI-MS	MS/MS (CID), MS/MS (UVPD)	117
Au_{36}	Naphthalenethiol	$Au_{36}(NT)_{24}$		MALDI-MS		392
Au_{36}	4-Methylthiophenol	$Au_{36}(MTP)_{24}$		ESI-MS		393
Au_{36}	Phenylacetylene	$Au_{36}(C{\equiv}CPh)_{24}$		MALDI-MS		394
Au_{37}	4-*tert*-Butylbenzenethiol, triphenylphosphine	$Au_{37}(TBBT)_{21}(TPP)_2$		ESI-MS		395

This journal is © The Royal Society of Chemistry 2025

Published on 27 October 2025. Downloaded by Indian Institute of Technology Chennai on 12/29/2025 3:17:01 AM.

Table 1 *(Contd.)*

Core	Ligands	Composition	Counter ions	Ionization	Fragmentation/ion-mobility/mass selected PES	Ref.
Au_{38}	Alkanethiol	$Au_{38}(SR)_{24}$		ESI-MS		396
Au_{38}	Alkanethiol	$Au_{38}(SR)_{24}$		MALDI-MS		397
Au_{38}	Dodecanethiol	$Au_{38}(SC_{12}H_{25})_{24}$		ESI-MS, MALDI-MS		398
Au_{38}	2-Phenylethanethiol	$Au_{38}(SCH_2CH_2Ph)_{24}$		MALDI-MS		399
Au_{38}	2-Phenylethanethiol	$Au_{38}(SCH_2CH_2Ph)_{24}$		MALDI-MS		400
Au_{38}	2-Phenylethanethiol	$Au_{38}(SCH_2CH_2Ph)_{24}$		MALDI-MS		401
Au_{38}	2-Phenylethanethiol	$Au_{38}(SCH_2CH_2Ph)_{24}$		MALDI-MS		402
Au_{38}	Hexanethiol	$Au_{38}(SC_6H_{13})_{24}$		MALDI-MS		403
Au_{38}	Hexanethiol	$Au_{38}(SC_6H_{13})_{24}$		MALDI-MS		404
Au_{38}	Dodecanethiol	$Au_{38}(SC_{12}H_{25})_{24}$		MALDI-MS		405
Au_{40}	2-Phenylethanethiol	$Au_{40}(SCH_2CH_2Ph)_{24}$		MALDI-MS		406
Au_{40}	2-Phenylethanethiol	$Au_{40}(SCH_2CH_2Ph)_{24}$		MALDI-MS		407
Au_{40}	2-Phenylethanethiol	$Au_{40}(SCH_2CH_2Ph)_{24}$		MALDI-MS		399
Au_{40}	2-Phenylethanethiol	$Au_{40}(SCH_2CH_2Ph)_{24}$		MALDI-MS		401
Au_{40}	4-*tert*-Butylbenzenethiol, 1,2-bis (diphenylphosphine)benzene	$Au_{40}(TBBT)_{24}$(dppbe)		ESI-MS		408
Au_{41}		$Au_{41}(S\text{-}Eind)_{12}$		MALDI-MS		409
Au_{42}	4-*tert*-Butylbenzenelthiol	$Au_{42}(Ph^tBu)_{26}$		ESI-MS		410
Au_{42}	5-Trifluoropyridyl-2-amine, triphenylphosphine	$Au_{42}(Ph_3P)_{10}(5\text{-}CF_3\text{-}Hpa)_8$		ESI-MS		411
Au_{42}	2-(Trifluoromethyl)phenylacetylene	$Au_{42}(C{\equiv}CC_6H_4\text{-}2\text{-}CF_3)_{22}$		MALDI-MS		412
Au_{43}	Phenylacetylene	$Au_{43}L_{22}$		MALDI-MS		413
Au_{44}	4-*tert*-Butylbenzenelthiol	$Au_{44}(TBBT)_{28}$		ESI-MS		408
Au_{44}	2,4-Dimethylbenzenethiol	$Au_{44}(2,4\text{-}DMBT)_{26}$		ESI-MS		83
Au_{44}	Phenylacetylene	$Au_{44}(C{\equiv}CPh)_{28}$		MALDI-MS		394
Au_{49}	2,4-Dimethylbenzenethiol	$Au_{49}(2,4\text{-}DMBT)_{27}$		ESI-MS		414
Au_{50}	3-(Trifluoromethyl)phenylacetylene	$Au_{50}(C{\equiv}CC_6H_4\text{-}3\text{-}F)_{26}$		MALDI-MS		412
Au_{54}	Phenylacetylene	$Au_{54}(C{\equiv}CPh)_{26}$		MALDI-MS		415
Au_{54}	Phenylacetylene	$Au_{54}(C{\equiv}CPh)_{26}$		MALDI-MS		413
Au_{55}	Octadecanethiol	$Au_{55}(SC_{18})_{32}$		MALDI-MS		416
Au_{55}	Octadecanethiol	$Au_{55}(SC_{18})_{32}$		MALDI-MS		417
Au_{55}	Phenylethanethiol	$Au_{55}(SCH_2CH_2Ph)_{31}$		ESI-MS		418
Au_{55}	4-Methylbenzenethiolate, triphenylphosphine	$[Au_{55}(p\text{-}MBT)_{24}(Ph_3P)_6](SbF_6)_3$	SbF_6^-	ESI-MS		419
Au_{60}	Triphenylphosphine, benzeneselenol	$[Au_{60}Se_2(Ph_3P)_{10}(SeR)_{15}]^+$		MALDI-MS		420
Au_{64}	Cyclohexanethiol	$Au_{64}(S\text{-}c\text{-}C_6H_{11})_{32}$		ESI-MS, MALDI-MS		421
Au_{65}	Cyclohexanethiol	$Au_{65}(SCy)_{30}$		MALDI-MS		386
Au_{67}	Hexanethiol	$Au_{67}(SR)_{35}$		MALDI-MS		422
Au_{67}	3-Mercaptopropionsulfonic acid	$Au_{67}(MPSA)_{35}$		ESI-MS		423
Au_{68}	Phenylethanethiol	$Au_{68}(SCH_2CH_2Ph)_{34}$		MALDI-MS		424
Au_{75}	Hexanethiol	$Au_{75}(SC_6H_{13})_{40}$		MALDI-MS		425
Au_{76}	4-(2-Mercaptoethyl)benzoic acid	$Au_{76}(4\text{-}MEBA)_{44}$		ESI-MS		426
Au_{78}	4-*tert*-Butylbenzenelthiol	$Au_{78}(TBBT)_{40}$		ESI-MS		427
Au_{82}	3-Mercaptopropionsulfonic acid	$Au_{82}(MPSA)_{44}$		ESI-MS		376
Au_{92}	4-*tert*-Butylbenzenelthiol	$Au_{92}(TBBT)_{44}$		ESI-MS		428
Au_{92}	4-*tert*-Butylbenzenelthiol	$Au_{92}(TBBT)_{44}$		ESI-MS		429
Au_{99}	2,4-Difluorophenylacetylene	$Au_{99}(C{\equiv}CC_6H_3\text{-}2,4\text{-}F_2)_{40}$		MALDI-MS		430

Published on 27 October 2025. Downloaded by Indian Institute of Technology Chennai on 12/29/2025 3:17:01 AM.

Table 1 *(Contd.)*

Core	Ligands	Composition	Counter ions	Ionization	Fragmentation/ion-mobility/mass selected PES	Ref.
Au_{99}	Thiophenol	$Au_{99}(SPh)_{42}$		ESI-MS, MALDI-MS		431
Au_{100}	Naphthalenethiol	$Au_{100}(Napt)_{42}$		ESI-MS, MALDI-MS		432
Au_{102}	4-Mercaptobenzoic acid	$Au_{102}(pMBA)_{44}$		ESI-MS, MALDI-MS		433
Au_{102}	4-Mercaptobenzoic acid	$Au_{102}(pMBA)_{44}$		ESI-MS		434
Au_{102}	Thiophenol	$Au_{102}(SPh)_{44}$		ESI-MS, MALDI-MS		435
Au_{102}	Isopropyl benzenethiol	$Au_{102}(IPBT)_{44}$		ESI-MS, MALDI-MS		433
$Au_{102-104}$	4-*tert*-Butylbenzenelthiol	$Au_{102-104}(TBBT)_{44-46}$		ESI-MS, MALDI-MS		436
Au_{103}	Naphthalenethiol	$Au_{103}S_2(S\text{-}Nap)_{41}$		ESI-MS		437
$Au_{103-105}$	Phenylethanethiol	$Au_{103-105}(CH_2CH_2Ph)_{45-46}$		ESI-MS		438
Au_{106}	3,5-Bis(trifluoromethyl)phenylacetylene	$[Au_{106}L_{40}Cl_{12}][HNEt_3]_4$		ESI-MS		439
Au_{110}	4-(Trifluoromethyl)phenylacetylene	$[Au_{110}(4\text{-}CF_3C_6H_4C{\equiv}C)_{48}]\ [HNEt_3]_2$	$HNEt_3^+$	ESI-MS		440
Au_{110}	Phenylpentyne	$Au_{110}(C{\equiv}CC_3H_6Ph)_{48}$		ESI-MS		75
Au_{126}	4-*tert*-Butylbenzenethiol	$Au_{126}I_4(TBBT)_4$		ESI-MS		441
Au_{127}	4-*tert*-Butylbenzenethiol	$Au_{127}I_4(TBBT)_4$		ESI-MS		441
Au_{130}	4-Bromothiophenol	$Au_{130}(SPh\text{-}Br)_{50}$		MALDI-MS		442
Au_{130}	Dodecanethiol	$Au_{130}(SC_{12}H_{25})_{50}$		ESI-MS, MALDI-MS		443
Au_{130}	2-Flurophenylacetylene	$Au_{130}(C{\equiv}CR)_{50}$		MALDI-MS		444
Au_{130}	Dodecanethiol	$Au_{130}(SR)_{50}$		ESI-MS		445
Au_{130}	Phenylethanethiol	$Au_{130}(SR)_{50}$		MS/MS (CID)		110
Au_{133}	4-*tert*-Butylbenzenethiol	$Au_{133}(TBBT)_{52}$		ESI-MS, MALDI-MS		65
Au_{133}	4-*tert*-Butylbenzenethiol	$Au_{133}(TBBT)_{52}$		ESI-MS		66
Au_{137}	Dodecanethiol	$Au_{137}(SC_{12}H_{25})_{56}$		MALDI-MS		446
Au_{137}	Phenylethanethiol, hexanethiol	$Au_{137}(SR)_{56}$		ESI-MS		447
Au_{138}	2,4-Dimethylbenzenethiol	$Au_{138}(SR)_{48}$		ESI-MS		448
$Au_{144-146}$	Butanethiol, hexanethiol, octanethiol	$Au_{144-146}(SR)_{50-60}$		LDI-MS		449
Au_{144}	2-Flurophenylacetylene	$Au_{144}(2\text{-}FC_6H_4C{\equiv}C)_{60}$		MALDI-MS		450
Au_{144}	2-Phenylethanethiol, hexanethiol, butanethiol	$Au_{144}(SR)_{60}$		ESI-MS, MALDI-MS		451
Au_{144}	Phenylacetylene	$Au_{144}(PhC{\equiv}C)_{60}$		ESI-MS		452
Au_{145}	Butanethiol, pentanethiol	$Au_{145}(SR)_{60}X$ (X = Br, Cl)	X^-	ESI-MS		453
Au_{146}	4-Mercaptobenzoic acid	$Au_{146}(pMBA)_{57}$		ESI-MS		454
Au_{156}	4-(Trifluoromethyl)phenylacetylene	$Au_{156}(4\text{-}CF_3C_6H_4C{\equiv}C)_{60}$		ESI-MS		455
Au_{187}	Dodecanethiol	$Au_{187}(SC_{12}H_{25})_{68}$		ESI-MS, MALDI-MS		445
Au_{191}	4-*tert*-Butylbenzenethiol	$Au_{191}(TBBT)_{66}$		ESI-MS		456
Au_{246}	4-Methylbenzenethiol	$Au_{246}(pMBT)_{80}$		ESI-MS, MALDI-MS		457
Au_{329}	Phenylethanethiol	$Au_{329}(SCH_2CH_2Ph)_{84}$		ESI-MS, MALDI-MS		458
Au_{333}	Phenylethanethiol	$Au_{333}(SR)_{79}$		ESI-MS, MALDI-MS		64

This journal is © The Royal Society of Chemistry 2025

Published on 27 October 2025. Downloaded by Indian Institute of Technology Chennai on 12/29/2025 3:17:01 AM.

Table 1 *(Contd.)*

Core	Ligands	Composition	Counter ions	Ionization	Fragmentation/ion-mobility/mass selected PES	Ref.
Au_{333}	Hexanethiol	$Au_{333}(SR)_{79}$		MALDI-MS		459
$Au_{\sim500}$	Phenylethanethiol, hexanethiol	$Au_{\sim500}(SR)_{\sim120}$		ESI-MS, MALDI-MS		94
$Au_{\sim940}$	Phenylethanethiol, hexanethiol	$Au_{\sim940\pm20}(SR)_{\sim160\pm4}$		ESI-MS, MALDI-MS		95
$Au_{\sim1400}$	Phenylethanethiol, hexanethiol	$Au_{\sim1400}(SR)_{\sim240}$		MALDI-MS		96
$Au_{\sim2000}$	Phenylethanethiol, hexanethiol	$Au_{\sim2000}(SR)_{\sim290}$		MALDI-MS		97
Cu_4	2-Mercaptobenzimidazole	$Cu_4(C_7H_5N_2S)_4$		ESI-MS	IM-MS	460
Cu_4	1,2-Bis(diphenylphosphino)ethane, 2-mercaptonicotinic acid	$[Cu_4(MNA)_2(DPPE)_2]$		MS/MS (CID)		461
Cu_6	2-Mercaptonicotinic acid	$[Cu_6(MNA)_6]$		MS/MS (CID)		461
Cu_6	2-Mercaptobenzoxazole	$Cu_6(SR)_6$		ESI-MS		462
Cu_6	Glutathione	$Cu_6(GS)_2$		MALDI-MS		463
Cu_6	Triphenylphosphine, benzeneselenol	$[Cu_6(SePh)_6(PPh_3)_3(4,4'\text{-bpy})]$		ESI-MS		464
Cu_6	Dithiophosphinate	$Cu_6[\mu_3\text{-}S_2P(OEt)_2]_6$		ESI-MS		465
Cu_6	2-Mercaptobenzimidazole	$Cu_6H(C_7H_5N_2S)_6$		IM-MS		463
Cu_6	Diphenylethylphosphine, benzenetellurol	$[Cu_6(TePh)_6(PEtPh_2)_5]$		ESI-MS		466
Cu_7	4-Chlorothiophenol, triphenylphosphine	$Cu_7L_4(PPh_3)_3$		ESI-MS		467
Cu_8	4-Hydroxy-6-(trifluoromethyl) pyrimidine-2-thiol, 1,2-bis(diphenylphosphino)ethane	$[Cu_8(TFMPT)_4(DPPE)_4]$		ESI-MS		468
Cu_8	4-Aminobenzenethiol, triphenylphosphine	$Cu_8(m\text{-ABT})_8\text{-}[P(PhPF)_3]_4$		ESI-MS		469
Cu_8	4-Methylbenzenethiol, triphenylphosphine	$Cu_8(p\text{-MBT})_8(PPh_3)_4$		ESI-MS		469
Cu_8	4-*tert*Butylbenzenethiol, triphenylphosphine	$Cu_8(TBBT)_8(PPh_3)_4$		ESI-MS		469
Cu_8	Triphenylphosphine	$[Cu_8Te_4(PPh_3)_7]$		ESI-MS		470
Cu_{11}	*N*,*N*′-Di(5-trifluoromethyl-2-pyridyl) formamidinate, hydride	$Cu_{11}H_3(Tf\text{-}dpf)_6(OAc)_2$	OAc^-	ESI-MS		471
Cu_{11}	4-Chlorothiophenol, triphenylphosphine	$Cu_{11}L_5(PPh_3)_3$		ESI-MS		467
Cu_{12}	*N*,*N*′-Di(5-trifluoromethyl-2-pyridyl) formamidinate, hydride	$[Cu_{12}H_3(Tfdpf)_6(OAc)_2]$	OAc^-	ESI-MS		471
Cu_{12}	1,8-Bis(diphenylphosphino)octane	$Cu_{12}S_6(dppo)_4$		MALDI-MS		472
Cu_{12}	Triethylphosphine, benzenetellurol	$[Cu_{12}Te_3(TePh)_6(PEt_3)_6]$		ESI-MS		473
Cu_{12}	Triethylphosphine	$[Cu_{12}S_6(PEt_3)_8]$		ESI-MS		474
Cu_{14}	*o*-9,12-Carboranedithiol	$[Cu_{14}(S_2C_2B_{10}H_{10})_6]$		ESI-MS	MS/MS (CID)	475
Cu_{14}	1,3-Dimercaptopropane, triphenylphosphine	$[Cu_{14}(DMP)_6(PPh_3)H]$		ESI-MS		476
Cu_{14}	Isopropylthiol, triphenylphosphine	$[Cu_{14}(iPrS)_3(PPh_3)_8H_{10}]$		ESI-MS		477
Cu_{14}	Glutathione	$Cu_{14}(SG)_{12}$		ESI-MS		478
Cu_{15}	2-Phenylethanethiol, triphenylphosphine	$[Cu_{15}(PPh_3)_6(PET)_{13}]^{2+}$		ESI-MS		479
Cu_{15}	2-Phenylethanethiol, triphenylphosphine	$[Cu_{15}(PhCH_2CH_2S)_{13}(PPh_3)_6][BF_4]_2$	BF_4^-	ESI-MS		480
Cu_{16}	1,2-Bis-(diphenylphosphino)ethane, dimercaptomaleonitrile	$[Cu_{16}(Se)_6(DPPE)_4(MNT)_2]$		ESI-MS		481
Cu_{18}	2-Phenylethanethiol, triphenylphosphine	$Cu_{18}(PET)_{16}(PPh_3)_4Cl$	Cl^-	ESI-MS		76
Cu_{18}	2-Phenylethanethiol, triphenylphosphine	$[Cu_{18}H(PhCH_2CH_2S)_{14}(PPh_3)_6Cl_3]$		ESI-MS		480
Cu_{20}	Triphenylphosphine	$[Cu_{20}S_{10}(PPh_3)_8]$		ESI-MS		474
Cu_{20}	*N*,*N*′-Di(5-trifluoromethyl-2-pyridyl) formamidinate, hydride	$[Cu_{20}H_8(Tf\text{-}dpf)_{10}]\cdot(BF_4)_2$	BF_4^-	ESI-MS		482
Cu_{23}	4-Toluenethiol, triphenylphosphine	$Cu_{23}H_4(SC_7H_7)_{18}(PPh_3)_6$		ESI-MS		483
Cu_{23}	Triphenylphosphine	$[Cu_{23}(PhSe)_{16}(Ph_3P)_8(H)_6]\cdot BF_4$	BF_4^-	ESI-MS		484
Cu_{25}	Triphenylphosphine	$[Cu_{25}H_{22}(PPh_3)_{12}]Cl$	Cl^-	ESI-MS		485

Published on 27 October 2025. Downloaded by Indian Institute of Technology Chennai on 12/29/2025 3:17:01 AM.

Table 1 *(Contd.)*

Core	Ligands	Composition	Counter ions	Ionization	Fragmentation/ion-mobility/mass selected PES	Ref.
Cu_{26}	Dimercaptomaleonitrile, 1,2-bis-(diphenylphosphino)ethane	$Cu_{26}(Se)_{12}(DPPE)_6$		ESI-MS		481
Cu_{27}	Dithiocarbamate, hydride	$Cu_{27}H_{15}\{S_2CNnBu_2\}_{12}$		ESI-MS		486
Cu_{31}	1,2-Bis(diphenylphosphino)ethane, 4-Methoxyphenylacetylene	$Cu_{31}(4\text{-MeO-PhC}{\equiv}C)_{21}(dppe)_3$		ESI-MS		487
Cu_{32}	2-Phenylethanethiol	$Cu_{32}(PET)_{24}H_8Cl_2$	Cl^-	ESI-MS		488
Cu_{32}	Phenylethanethiol, hydride	$[Cu_{32}(PET)_{24}H_8Cl_2](PPh_4)_2$	PPh_4^+	ESI-MS		489
Cu_{33}	*N*,*N*′-Di(5-methyl-2-pyridinyl)formamidine, hydride	$Cu_{33}H_{18}(Medpf)_{12}$, $Cu_{33}H_{16}(Medpf)_{12}Cl_2$		ESI-MS		77
Cu_{32-34}	Phenylethanethiol, hydride	$[Cu_{32}(PET)_{24}H_8Cl_2](PPh_4)_2$	PPh_4^+	ESI-MS		490
Cu_{36}	2-(2-(Diphenylphosphaneyl)-phenethyl) quinoline, 1-adamantanethiol	$Cu_{36}L_7(S\text{-Adm})_3(OAc)$	OAc^-	ESI-MS		491
Cu_{38}	Phenylphosphinic acid, 1-ethynyl-1-cyclohexanol	$Cu_{38}(C_2)_4(HOchxC{\equiv}C)_{22}(PhHPO_2)_2(PhPO_3)_2(CH_3OH)$		ESI-MS		492
Cu_{41}	2-Fluorothiophenol, triphenylphosphine, hydride	$Cu_{41}Cl_2(2\text{-F-}C_6H_4S)_{12}(CF_3COO)_6(PPh_3)_6H_{19}$		ESI-MS		493
Cu_{47}	Benzene selenol, triphenylphosphine, hydride	$Cu_{47}(PhSe)_{15}(PPh_3)_5(CF_3COO)_{12}H_{12}$		ESI-MS		494
Cu_{50}	4-Fluorothiophenol, triphenylphosphine, hydride	$Cu_{50}(CF_3COO)_{10}(4\text{-F-PhS})_{20}(PPh_3)_6H_2$		ESI-MS		495
Cu_{50}	Diphenylethylphosphine, TePh	$[Cu_{50}Te_{17}(TePh)_{20}(PEtPh_2)_8]$		ESI-MS		466
Cu_{54}	2-Methyl-2-propanethiol	$Cu_{54}XCl_{12}(^tBuS)_{20}(NO_3)_{12}$		ESI-MS		487
Cu_{61}	4-*tert*-Butylbenzenethiol	$Cu_{61}(StBu)_{26}S_6Cl_6H_{14}$		ESI-MS		496
Cu_{75}	Adamantanethiol	$Cu_{75}(S\text{-Adm})_{32}$		ESI-MS		78
Cu_{81}	4-*tert*-Butylbenzenethiol	$[Cu_{81}(PhS)_{46}(^tBuNH_2)_{10}(H)_{32}]^{3+}$		ESI-MS		497
Cu_{93}	Triphenylphosphine	$[Cu_{93}Se_{42}(SeC_6H_4SMe)_9(PPh_3)_{18}]$		MALDI-MS		498
Cu_{96}	Triphenylphosphine	$[Cu_{96}Se_{45}(SeC_6H_4SMe)_6(PPh_3)_{18}]$		MALDI-MS		498
Cu_{136}	1,5-Bis-(diphenylphosphino)pentane	$[Cu_{136}S_{56}(SCH_2C_4H_3O)_{24}(Dpppt)_{10}]$		MALDI-MS		498
Ir_9	Phenylethanethiol	$Ir_9(PET)_6$		MALDI-MS		82
Ir_{50}	Phenylacetylene	$Ir_{50}(PA)_{25}$		ESI-MS		499
Pd_7	Ketimide	$Pd_7(N{=}C^tBu_2)_6$		ESI-MS		500
Pd_8	Adamantanethiol, triphenylphosphine	$Pd_8(PPh)_2PPh_3(S\text{-Adm})_6$		ESI-MS		501
Pd_{21}	Phenylethanethiol	$Pd_{21}(SCH_2CH_2Ph)_{18}$		ESI-MS		79
Pd_{38}	Phenylethanethiol	$Pd_{38}(SCH_2CH_2Ph)_{21}S_2$		ESI-MS		79
Pt_6	Triphenylphosphine	$Pt_6(PPh_3)_4Cl_5$		ESI-MS		502
Pt_6	Glutathione	$Pt_6(SG)_6$		ESI-MS		502
Pt_8	PAMAM-OH dendrimer	$Pt_8(C_2H_2O_2S)_8$		ESI-MS		80
Pt_{17}	Triphenylphosphine	$Pt_{17}(CO)_{12}(PPh_3)_8$		ESI-MS, MALDI-MS		503
Pt_{17}	Triphenylphosphine	$Pt_{17}(CO)_{12}(PPh_3)_8$		ESI-MS	Cyclic ion mobility, MS/MS (CID)	140
Pt_{23}	2,6-Dimethylphenyl isocyanide	$Pt_{23}(XylNC)_{20}(CO)_5Cl_2$		ESI-MS		504
Au_2Ni_3	Phenylethanethiol	$Au_2Ni_3(SEtPh)_8$		ESI-MS		505
Ag_4Ni_2	Dimercaptosuccinic acid	$Ag_4Ni_2(DMSA)_4$		ESI-MS		506
Au_4Cu_2	3-Mercaptopropionic acid	$Au_4Cu_2(MPA)_5$		ESI-MS		507
Au_4Ni_2	Phenylethanethiol	$Au_4Ni_2(SEtPh)_8$		ESI-MS		508
Au_4Ni_2	Phenylethanethiol	$Au_4Ni_2(SEtPh)_8$		Paper spray MS		509
Au_4Pd_2	Phenylethanethiol	$Au_4Pd_2(PET)_8$		ESI-MS		510
Au_4Pd_2	Phenylethanethiol	$Au_4Pd_2(PET)_8$		MALDI-MS		511

This journal is © The Royal Society of Chemistry 2025

Published on 27 October 2025. Downloaded by Indian Institute of Technology Chennai on 12/29/2025 3:17:01 AM.

Table 1 *(Contd.)*

Core	Ligands	Composition	Counter ions	Ionization	Fragmentation/ion-mobility/mass selected PES	Ref.
Au_4Pt_2	Phenylethanethiol	$Au_4Pt_2(PET)_8$		MALDI-MS		512
Au_3Ag_5	Mercaptosuccinic acid	$Au_3Ag_5(MSA)_3$		ESI-MS		513
Au_4Cu_4	1,1-Bis(diphenylphosphino)methane, adamantanethiol	$[Au_4Cu_4(Dppm)_2(SAdm)_5]Br$	Br^-	ESI-MS		514
Au_6Ag_2	2-(Diphenylphosphino)-5-pyridinecarboxaldehyde	$[Au_6Ag_2(C)(L1)_6](BF_4)_4$	BF_4^-	ESI-MS		515
Au_4Ag_5	1,1-Bis(diphenylphosphino)methane, adamantanethiol	$[Au_4Ag_5(dppm)_2(SAdm)_6]^+$		ESI-MS		516
Au_4Cu_5	1,1-Bis(diphenylphosphino)methane, cyclohexanethiol	$[Au_4Cu_5(C_6H_{11}S)_6(dppm)_2](BPh_4)$	BPh_4^-	ESI-MS		514
$PdAu_8$	Triphenylphosphine	$PdAu_8(PPh_3)_8$		ESI-MS	Ion mobility	517
$PdAu_9$	Triphenylphosphine	$PdAu_9(PPh_3)_8(CN)$	CN^-	ESI-MS		518
$PtAg_9$	Tris(4-fluorophenyl)phosphine	$PtAg_9[P(Ph–F)_3]_7Cl_3$	Cl^-	ESI-MS		519
Au_8Ag_3	Triphenylphosphine	$Au_8Ag_3(PPh_3)_7Cl_3$	Cl^-	ESI-MS		520
$AuCu_{11}$	Phenylacetylene, diisopropyldithiophosphate	$AuCu_{11}(H)\{S_2P(OiPr)_2\}_6(C{\equiv}CPh)_3$		ESI-MS		521
Ag_7Au_6	Mercaptosuccinic acid	$Ag_7Au_6(H_2MSA)$		ESI-MS		522
$PtAg_{12}$	2,4-Bimethylbenzenethiol, 1,1-bis (diphenylphosphino) methane	$PtAg_{12}(dppm)_5(SPhMe_2)_2$		ESI-MS		523
Au_9M_4 (M = Ag, Cu)	Diphenylmethylphosphine	$[Au_9M_4Cl_4(PMePh_2)_8][C_2B_9H_{12}]{\cdot}CH_2Cl_2$		ESI-MS		524
$CoAu_{12}$	1,1-Bis(diphenylphosphino)methane	$CoAu_{12}(dppm)_6$		ESI-MS		525
$Ag_{14-x}Cu_x$	Fluorothiophenol	$Ag_{14-x}Cu_x(SPhF_5)_{12}(P(Ph\text{-}m\text{-}OMe)_3)_4$		ESI-MS		526
$PdAg_{13}$	Diisopropyldithiophosphate	$Pd(H)Ag_{13}(S)\{S_2P(O^iPr)_2\}_{10}$		ESI-MS		527
$Ag_{14}M$ (M = Pd/Pt)	1,3-Bis(diphenylphosphino)propane	$([M_1Ag_{14}(DPPP)_6Cl_4](OTf)_2$	OTf^-	ESI-MS		528
Au_7Ag_8	1,10-Bis-(diphenylphosphino)ferrocene, proline	$Au_7Ag_8(dppf)_3$(L-/D-proline)$_6$		ESI-MS		529
$CdAu_{14}$	*tert*-Butylthiol	$CdAu_{14}(S^tBu)_{12}$		ESI-MS		321
Au_7Ag_9	1,1′-Bis(diphenylphosphino)ferrocene	$[Au_7Ag_9(dppf)_3(CF_3CO_2)_7BF_4]_n$	BF_4^-	ESI-MS		530
$Ag_{13}Cu_4$	*m*-Carborane-1,7-dithiol	$Ag_{13}Cu_4(CBDT)_{12}$		ESI-MS		531
$AuAg_{12}Cu_4$	*o*-Carboranethiol	$AuAg_{12}Cu_4(o1\text{-}CBT)_{12}$		ESI-MS		238
Au_7Cu_{10}	Adamantanethiol, disphenyl-2-pyridylphosphine	$Au_7Cu_{10}(1\text{-}Adm)_3(PPh_2Py)_6Cl_3$		ESI-MS		532
$Au_{13}Cu_4$	4-Mercaptobenzoic acid	$Au_{13}Cu_4(pMBA)_{12}$		ESI-MS		533
$Au_{16}Ag$	Adamantanethiol	$[Au_{16}Ag(S\text{-}Adm)_{13}]$		ESI-MS		534
Pt_2Ag_{15}	Adamantanethiol, bis(2-diphenyphosphinophenyl)ether	$Pt_2Ag_{15}(SAdm)_4(DPPOE)_4H$		ESI-MS		535
$Au_{15}Ag_3$	2,4-Dimethylbenzenethiol	$Au_{15}Ag_3(SPhMe_2)_{14}$		ESI-MS		536
$Au_{17}M_2$ (M = Pd, Pt)	Diethylphenylphosphine	$M_2Au_{17}(depp)_{10}Cl_7$		ESI-MS		537
$AuAg_{19}$[Editor37]	*O*,*O*-Diisopropyl dithiophosphate	$[AuAg_{19}\{S_2P(O^nPr)_2\}_{12}]$		ESI-MS		538
$Au_{18}Cd_2$	4-Methylbenzenethiol, triphenylphosphine	$Au_{18}Cd_2(p\text{-}MBT)_{14}(PPh_3)_2$		ESI-MS		539
Cu_3Ag_{17}	Diisopropyldithiophosphate	$Cu_3Ag_{17}\{S_2P(O^nPr)_2\}_{12}$		ESI-MS		540
Au_9Ag_{12}	1,1-Bis(diphenylphosphino)methane, adamantanethiol, 4-*tert*-butylmercaptan	$[Au_9Ag_{12}(SR)_4(dppm)_6X_6]^{3+}$		ESI-MS		541
$Au_{21-x}Ag_x$	*tert*-Butylthiol	$Au_{21-x}Ag_x(SR)_{15}$ (x = 4–8)		ESI-MS		542
$Au_{21-x}Cu_x$	*tert*-Butylthiol	$Au_{21-x}Cu_x(SR)_{15}$ (x = 0–5)		ESI-MS		542
$Au_{16}Cu_6$	*tert*-Butylphenylacetylene	$Au_{16}Cu_6(^tBuPhC{\equiv}C)_{18}$		ESI-MS		543
$Au_{19}Cd_3$	3,5-Dimethylbenzenethiol	$Au_{19}Cd_3(3,5\text{-}DMBT)_{18}$		ESI-MS		544
$Au_{22-x}Cu_x$	*tert*-Butylphenylacetylene	$Au_{22-x}Cu_x(^tBuC_6H_4C{\equiv}C)_{18}$		ESI-MS		545
$AuAg_{22}$	Adamantanethiol	$[AuAg_{22}(S\text{-}Adm)_{12}]^{3+}$		ESI-MS		546

Published on 27 October 2025. Downloaded by Indian Institute of Technology Chennai on 12/29/2025 3:17:01 AM.

Table 1 *(Contd.)*

Core	Ligands	Composition	Counter ions	Ionization	Fragmentation/ion-mobility/mass selected PES	Ref.
$Au_{23-x}Ag_x$	Adamantanethiol	$Au_{23-x}Ag_x(S\text{-}Adm)_{16}$		MALDI-MS		547
$Au_{24-x}Ag_x$	*tert*-Butylbenzylmercaptan	$Au_{24-x}Ag_x(TBBM)_{20}$		ESI-MS		548
$Au_{25-x}Ag_x$	Phenylethanethiol	$[Au_{25-x}Ag_x(PET)_{18}]$		ESI-MS		549
Ag_5Au_{20}	Captopril	$Ag_5Au_{20}(Capt)_{18}$		ESI-MS		550
Ag_6Au_{19}	Triphenylphosphine	$[Ag_6Au_{19}(MeOPhS)_{17}(PPh_3)_6]^{2+}$		ESI-MS		551
$Ag_{13}Au_{12}$	Triphenylphosphine, phenylethanethiol	$[Ag_{13}Au_{12}(PPh_3)_{10}(SR)_5Cl_2]^{2+}$		ESI-MS		552
$Ag_{23}Pd_2$	Triphenylphosphine	$[Ag_{23}Pd_2(PPh_3)_{10}Cl_7]$		ESI-MS		553
$Ag_{23}Pt_2$	Triphenylphosphine	$[Pt_2Ag_{23}Cl_7(PPh_3)_{10}]$		ESI-MS		554
$Ag_{24}Au$	1,1-Bis(diphenylphosphino)methane	$[AuAg_{24}(dppm)_3(SR)_{17}]^{2+}$		ESI-MS		555
$Ag_{24}Au$	6-Mercaptohexanoic acid	$AuAg_{24}(MHA)_{18}$		ESI-MS		556
$Ag_{24}Au$	2,4-Dimethylbenzenethiol	$[Ag_{24}Au(DMBT)_{18}]$-		ESI-MS		87
$Ag_{24}M$ (M = Pd/Pt)	2,4-Dichlorobenzenethiol	$[Ag_{24}M(SR)_{18}](PPh_4)_2$	PPh_4^-	ESI-MS		557
$Ag_{24}M$ (M = Pt)	2,4-Dimethylbenzenethiol	$[Ag_{24}Pt(DMBT)_{18}]$-		ESI-MS	MS/MS (UVPD)	120
$Au_{24}M$ (M = Cd/Hg)	Phenylethanethiol	$Au_{24}M(SC_2H_4Ph)_{18}$		ESI-MS, MALDI-MS		86
$Au_{24}Pd$	3,5-Bis(trifluoromethyl)phenylacetylene	$PdAu_{24}(PA)_{18}$		ESI-MS		558
$Au_{24}Pd$	2-Phenylethanethiol	$[Au_{24}Pd(PET)_{18}]^-$		ESI-MS		559
$Au_{24}Pt$	*tert*-Butylbenzenethiol, thiodithiol	$[Au_{24}Pt(TBBT)_{12}(TDT)_3]$		ESI-MS		560
$Au_{24}Pt$	2-Phenylethanethiol	$[Au_{24}Pt(PET)_{18}]^-$		MALDI-MS		561
$Au_{24}Pt$	Alkanethiol	$[Au_{24}Pt(SC_n)_{18}]^-$		ESI-MS	Mass selected PES	207
$Au_{24}M$ (M = Pt, Pd)	3,5-Bis(trifluoromethyl)phenylacetylene	$[MAu_{24}(C{\equiv}CR)_{18}]^{2-}$		ESI-MS	MS/MS (CID)	562
$Au_{24-x}Ag_xM_1$ (M = Cd/Hg)	Phenylethanethiol	$Ag_xAu_{24-x}M_1(SR)_{18}$		ESI-MS		563
$Au_{24-x-y}Ag_xCu_yPd$	1-Dodecanethiol	$Au_{24-x-y}Ag_xCu_yPd(SC_{12}H_{25})_{18}$		MALDI-MS		564
$Au_{25-x}Cu_x$	2-Phenylethanethiol	$[Au_{25-x}Cu_x(PET)_{18}]$		MALDI-MS		565
$Ag_{18}Cu_8$	*tert*-Butylphenylacetylene, 1,3-bis (diphenylphosphino)propane	$Ag_{18}Cu_8(dppp)_4(^tBu\text{-}C_6H_4C{\equiv}C)_{22}$		ESI-MS		566
$Au_{24}Cd_2$	1-Adamantanethiol, 1,3-bis (diphenylphosphino)propane	$Au_{24}Cd_2(SAdm)_{12}(dppp)_2Cl_2$	Cl^-	ESI-MS		567
$Au_{25}Cd$	4-Methylbenzenethiol, triphenylphosphine	$Au_{25}Cd(p\text{-}MBT)_{17}(PPh_3)_2$		ESI-MS		539
Ag_2Au_{25}	Phenylethanethiol	$Ag_2Au_{25}(SR)_{18}$		MALDI-MS		568
$Ag_{15}Cu_{12}$	Cyclohexanethiol	$Ag_{15}Cu_{12}(S\text{-}c\text{-}C_6H_{11})_{18}(CH_3COO)_3$		ESI-MS		569
Au_4Ag_{23}	1,1′-Bis(diphenylphosphino)ferrocene, *tert*-butylalkynyl	$[Au_4Ag_{23}(^tBuC{\equiv}C)_{10}Cl_7(dppf)_4]^{2+}$		ESI-MS		570
$Au_{26}Pd$	2-Phenylethanethiol	$Au_{26}Pd(SPh^tBu)_{20}$		ESI-MS		346
$Au_{27}Cd$	1,1′-Bis(diphenylphosphino)ferrocene, adamantanethiol	$Au_{27}Cd(SAdm)_{14}(DPPF)Cl$	Cl^-	ESI-MS, MALDI-MS		84
$Ag_{16}Au_{13}$	3-Bromoprop-1-yne, hydroxybenzonitrile	$[Au_{13}Ag_{16}(C_{10}H_6NO)_{24}]^{3-}$		ESI-MS		571
$Ag_{17}Au_{12}$	1,3-Benzenedithiol, triphenylphosphine	$Au_{12}Ag_{17}(BDT)_{12}(PPh_3)_4$		ESI-MS		572
$Ag_{17}Cu_{12}$	1,3-Benznedithiol, triphenylphosphine	$Ag_{17}Cu_{12}(SR)_{12}(PPh_3)_4$		ESI-MS		573
$Ag_{25}Cu_4$	1,4-Bis(diphenylphosphine)butane, phenylacetylene	$Ag_{25}Cu_4Cl_6(dppb)_6(PhC{\equiv}C)_{12}$		ESI-MS		574
$Ag_{25}Cu_4$	Phenylacetylene, triphenylphosphine	$[Ag_{25}Cu_4H_8Br_6(C{\equiv}CPh)_{12}(PPh_3)_{12}]^{3+}$		ESI-MS		575
$Ag_{28}Hg$	1,3-Benzenedithiol	$Ag_{28}Hg(BDT)_{12}$		ESI-MS		576
MAg_{28} (M = Ni, Pd)	1,3-Benznedithiol, triphenylphosphine	$MAg_{28}(BDT)_{12}(PPh_3)_4$		ESI-MS		572
$Ag_{28-x}Au_xM$ (M = Ni/Pd/Pt)	1,3-Benzenedithiol, triphenylphosphine	$MAu_xAg_{28-x}(BDT)_{12}(PPh_3)_4$		MALDI-MS		577
$PtAg_{12}Cu_{12}Au_4$	Adamantanethiol, triphenylphosphine	$PtAg_{12}Cu_{12}Au_4(S\text{-}Adm)_{18}(PPh_3)_4$		ESI-MS		85
$Au_{24}Cu_6$	4-*tert*-Butylbenzenethiol	$Au_{24}Cu_6(TBBT)_{22}$		ESI-MS		578

This journal is © The Royal Society of Chemistry 2025

Published on 27 October 2025. Downloaded by Indian Institute of Technology Chennai on 12/29/2025 3:17:01 AM.

Table 1 *(Contd.)*

Core	Ligands	Composition	Counter ions	Ionization	Fragmentation/ion-mobility/mass selected PES	Ref.
$Cu_{28}Ag_4$	Phenylethanethiol, triphenylphosphine	$[Ag_4Cu_{28}H_6(PET)_{16}\text{-}Cl_8(PPh_3)_8]$		ESI-MS		579
$Ag_{20}Cu_{12}$	2,4-Dimethylbenzenethiol, 1,1-bis (diphenylphosphino) methane	$[Ag_{20}Cu_{12}(SR)_{14}(dppm)_6Br_8]^{2+}$		ESI-MS		580
$Cu_{20}Ag_{13}$	Phenylethanethiol, triphenylphosphine	$Ag_{13}Cu_{20}(PPh_3)_4(PET)_{24}]$		ESI-MS		581
$Au_{25}Cu_8$	Adamantanethiol, triphenylphosphine	$Au_{25}Cu_8(S\text{-}Adm)_{19}(PPh_3)_5$		MALDI-MS		582
$Ag_{22}Cu_{12}$	3,5-Bis(trifluoromethyl)phenylacetylene	$Ag_{22}Cu_{12}(C{\equiv}CR)_{28}$		ESI-MS		583
$Au_{34}Rh$	Polyvinyl-2-pyrrolidone (PVP)	$Au_{34}RhCl^-$		MALDI-MS		584
$Au_{36-x}Ag_x$	*tert*-Butylbenzenethiol	$Au_{36-x}Ag_x(SPh\text{-}^tBu)_{24}$		ESI-MS		585
$Au_{38-x}Ag_x$	2-Phenylethanethiol	$Ag_xAu_{38-x}(SR)_{24}$		MALDI-MS		586
$Au_{36}Pd_2$	2-Phenylethanethiol	$Au_{36}Pd_2(SC_2H_4Ph)_{24}$		MALDI-MS		400
$Ag_{28}Cu_{12}$	2,4-Dichlorobenzenethiol	$[Ag_{28}Cu_{12}(SR)_{24}]^{4-}$		ESI-MS		587
$Ag_{32}Au_{12}$	Fluorobenzenethiol	$[Ag_{32}Au_{12}(SR)_{30}]^{4-}$		ESI-MS		588
$Ag_{32}Cd_{12}$	Benzene selenol	$[Ag_{32}Cd_{12}(SePh)_{36}]$		MALDI-MS		589
$Ag_{32}Cu_{12}$	Tris(4-methoxyphenyl)phosphine, adamantanethiol	$[Ag_{32}Cu_{12}(CH_3COO)_{12}(SAdm)_{12}(P(CH_3OPh)_3)_4]$		ESI-MS		590
$Ag_{44-x}Au_x$	Fluorothiophenol	$Ag_{44-x}Au_x(FTP)_{26}$		ESI-MS	MS/MS (CID)	591
$Au_{24+x}Ag_{20-x}$	4-*tert*-Butylbenzenethiol	$Au_{24+x}Ag_{20-x}(SPh^tBu)_{26}$		ESI-MS		592
$Au_{44-x}Ag_x$	4-Trifluoromethylthiophenol	$Au_{44-x}Ag_x(SR)_{30}$		ESI-MS		593
$Au_{41}Cd_6$	Phenylmethanethiol	$Au_{41}Cd_6S_2(SCH_2Ph)_{33}$		ESI-MS		594
$Cu_{47-x}Ag_x$	Benzene selenol, triphenylphosphine	$[(CuAg)_{47}(PhSe)_{18}(PPh_3)_6(CF_3COO)_{12}H_6]$		ESI-MS		494
$Au_{19}Cu_{30}$	3-Ethynylthiophene, ethynylbenzene	$[Au_{19}Cu_{30}(C{\equiv}CR)_{22}(Ph_3P)_6Cl_2]$		ESI-MS		595
$Ag_{20}Au_{12}Cu$	Pentafluorobenzenethiol	$Au_{12}Ag_{20}Cu_{18}(PFBT)_{36}$		ESI-MS		596
$Ag_{50-x}Au_x$	*tert*-Butylbenzylmercaptan, 1,1-bis (diphenylphosphino)methane	$Au_xAg_{50-x}(dppm)_6(SR)_{30}$		ESI-MS		282
$Au_{12}Ag_{20}Cu_{18}$	Pentafluorobenzenethiol	$Au_{12}Ag_{20}Cu_{18}(PFBT)_{36}$		ESI-MS		596
$Cu_{32}Au_{18}$	4-Methoxythiophenol	$[Au_{18}Cu_{32}(SR\text{–}O)_{36}]$		ESI-MS		597
$Ag_{53-x}M$	2,4-Dimethylbenzenethiol, 1,3-benzenedithiol	$MAg_{53-x}(BDT)_{12}(DMBT)_{18-y}$		ESI-MS	MS/MS (CID)	107
$Ag_{42}Cu_{12}$	3,5-Bis(trifluoromethyl)phenylacetylene	$Ag_{42}Cu_{12}(C{\equiv}CR)_{36}$		ESI-MS		583
$Cu_{56}Au$	Adamantanethiol	$[AuCu_{56}S_{12}(SAdm)_{20}(O_3SAdm)_{12}]$		MALDI-MS		598
$Ag_{43}Au_{16}$	2,4-Dichlorobenzenethiol	$[Au_{16}Ag_{43}H_{12}(SPhCl_2)_{34}]^{5-}$		ESI-MS		599
$Au_{34}Ag_{28}$	Phenylacetylene	$Au_{34}Ag_{28}(PhC{\equiv}C)_{34}$		ESI-MS		600
$Au_{43}Ag_{38}$	Dodecanethiol	$Au_{43}Ag_{38}(C_{12}H_{13})_{36}Cl$		ESI-MS		601
$Au_{57}Ag_{53}$	Phenylacetylene	$[Au_{57}Ag_{53}(PhC{\equiv}C)_{40}Br_{12}]$		MALDI-MS		602
$Au_{80}Ag_{30}$	Phenylacetylene	$[Au_{80}Ag_{30}(PhC{\equiv}C)_{42}Cl_9]Cl$		MALDI-MS		603
$Au_{52}Cu_{72}$	4-Methylthiophenol	$Au_{52}Cu_{72}(SPh)_{55}$		ESI-MS		604
$Au_{130-x}Ag_x$	4-*tert*-Butylbenzenethiol	$Au_{130-x}Ag_x(SR)_{55}$		MALDI-MS		605
$Au_{74}Ag_{60}$	Phenylacetylene	$[Au_{74}Ag_{60}(PhC{\equiv}C)_{40}Br_{12}]$		MALDI-MS		606
$Au_{137-x}M_x$ (M = Ag, Pd)	2-Phenylethanethiol	$Au_{137-x}M_x(SR)_{60}$		ESI-MS		447
$Au_{78}Ag_{66}$	Phenylacetylene	$[Au_{78}Ag_{66}(PhC{\equiv}C)_{48}Cl_8]$		MALDI-MS		606
$Au_{144-x}Ag_x$	2-Phenylethanethiol	$Au_{144-x}Ag_x(SR)_{60}$		ESI-MS, MALDI-MS		607
$Au_{144-x}Cu_x$	2-Phenylethanethiol	$Au_{144-x}Ag_x(SR)_{60}$		ESI-MS, MALDI-MS		608
$Au_{144-x}Ag_x$	Hexanethiol	$Au_{144-x}Cu_x(SR)_{60}$		ESI-MS, MALDI-MS		609
$Au_{144-x}Pd_x$	2-Phenylethanethiol	$Au_{144-x}Pd_x(SR)_{60}$		ESI-MS, MALDI-MS		610
$Au_{329-x}Ag_x$	2-Phenylethanethiol	$Au_{329-x}Ag_x(SR)_{84}$		ESI-MS, MALDI-MS		611

Published on 27 October 2025. Downloaded by Indian Institute of Technology Chennai on 12/29/2025 3:17:01 AM.

induced properties of nanoclusters.[211] Finally, incorporating MS into closed-loop smart synthesis frameworks driven by artificial intelligence and automation, will enable real-time feedback between synthesis and property assessment, thereby accelerating the rational design of materials with tailored catalytic, optical, and electronic properties.[212] The integration of real-time MS analysis with computational modelling and machine learning will enable the design of clusters with targeted composition, stability, and functionality, transforming MS into a predictive tool for materials discovery.

To conclude, the scope of mass spectrometry has significantly expanded from an analytical tool. Currently, it occupies a central position across various disciplines, including materials science, nanotechnology, and biochemistry. With its broad capabilities, ranging from synthesis and soft landing to high-resolution structural studies and integration with computation, it redefines the design and investigation of materials at the atomic scale. Continued advancements in the field of mass spectrometry will establish it as a foundational tool for developing next-generation functional nanomaterials.

Author contributions

T. P. conceived the idea and initiated the project. A. J. drafted the manuscript and prepared the figures. B. S. S. compiled the list of clusters. All authors reviewed and approved the final version of the manuscript.

Conflicts of interest

There are no conflicts to declare.

Data availability

All the data supporting this review article have been included in the main article itself.

Acknowledgements

A. J. acknowledges the MHRD for the PMRF grant. B. S. S. thanks the Council of Scientific & Industrial Research (CSIR) for the Shyama Prasad Mukherjee (SPM) research fellowship. T. P. thanks the SERB, India, for funding through the research grant, SPR/2021/000439, and through the JC Bose Fellowship. T. P. also acknowledges funding from the Centre of Excellence (CoE) on Molecular Materials and Functions through the Institute of Eminence Scheme, IIT Madras.

References

1 J. B. Fenn, *Angew. Chem., Int. Ed.*, 2003, **42**, 3871–3894.
2 J. M. Thomas, *Angew. Chem., Int. Ed.*, 2006, **45**, 6797–6800.
3 J. J. Thomson, *London, Edinburgh Dublin Philos. Mag. J. Sci.*, 1912, **23**, 449–457.
4 F. W. Aston, *Isotopes*, Edward Arnold & Company, London, 1922, p. 252.
5 F. W. McLafferty, *Annu. Rev. Anal. Chem.*, 2011, **4**, 1–22.
6 R. S. Gohlke, *Anal. Chem.*, 1959, **31**, 535–541.
7 R. S. Gohlke and F. W. McLafferty, *J. Am. Soc. Mass Spectrom.*, 1993, **4**, 367–371.
8 F. W. Mclafferty, P. J. Todd, D. C. Mcgilvery and M. A. Baldwin, *J. Am. Chem. Soc.*, 1980, **102**, 3360–3363.
9 J. B. Fenn, M. Mann, C. K. Meng, S. F. Wong and C. M. Whitehouse, *Science*, 1989, **246**, 64–71.
10 M. Karas, D. Bachmann, U. Bahr and F. Hillenkamp, *Int. J. Mass Spectrom. Ion Processes*, 1987, **78**, 53–68.
11 K. Tanaka, H. Waki, Y. Ido, S. Akita, Y. Yoshida, T. Yoshida and T. Matsuo, *Rapid Commun. Mass Spectrom.*, 1988, **2**, 151–153.
12 R. J. Wenzel, U. Matter, L. Schultheis and R. Zenobi, *Anal. Chem.*, 2005, **77**, 4329–4337.
13 K. Tanaka, *Angew. Chem., Int. Ed.*, 2003, **42**, 3860–3870.
14 X. Kang and M. Zhu, *Chem. Soc. Rev.*, 2019, **48**, 2422–2457.
15 I. Chakraborty and T. Pradeep, *Chem. Rev.*, 2017, **117**, 8208–8271.
16 R. Jin, C. Zeng, M. Zhou and Y. Chen, *Chem. Rev.*, 2016, **116**, 10346–10413.
17 K. S. Sugi, A. P. Sandra, N. Nonappa, D. Ghosh, J. S. Mohanty, M. Paulthangam Kannan, B. S. Sooraj, P. Srikrishnarka, J. Roy, W. A. Dar and T. Pradeep, *Nanoscale*, 2023, **15**, 11927–11934.
18 T. Pradeep, *Atomically precise metal clusters*, Elsevier, 1st edn, 2023.
19 A. Pihlajamäki, S. Malola and H. Häkkinen, ChemRxiv, 2024.
20 B. H. Kim, M. J. Hackett, J. Park and T. Hyeon, *Chem. Mater.*, 2014, **26**, 59–71.
21 S.-H. Lai, S. Maclot, R. Antoine and C. D. Masselon, *Mass Spectrom. Rev.*, 2025, **44**, 850–869.
22 R. D. Smith, *J. Am. Soc. Mass Spectrom.*, 2023, **34**, 803–812.
23 R. Chen, X. Cheng, D. W. Mitchell, S. A. Hofstadler, Q. Wu, A. L. Rockwood, M. G. Sherman and R. D. Smith, *Anal. Chem.*, 1995, **67**, 1159–1163.
24 A. Makarov, *Anal. Chem.*, 2000, **72**, 1156–1162.
25 R. A. Zubarev and A. Makarov, *Anal. Chem.*, 2013, **85**, 5288–5296.
26 U. Bahr, U. Röhling, C. Lautz, K. Strupat, M. Schürenberg and F. Hillenkamp, *Int. J. Mass Spectrom. Ion Processes*, 1996, **153**, 9–21.
27 H. C. Chang, *Annu. Rev. Anal. Chem.*, 2009, **2**, 169–185.
28 M. F. Jarrold, *Chem. Rev.*, 2022, **122**, 7415–7441.
29 T. P. Wörner, J. Snijder, A. Bennett, M. Agbandje-McKenna, A. A. Makarov and A. J. R. Heck, *Nat. Methods*, 2020, **17**, 395–398.
30 G. Young, N. Hundt, D. Cole, A. Fineberg, J. Andrecka, A. Tyler, A. Olerinyova, A. Ansari, E. G. Marklund, M. P. Collier, S. A. Chandler, O. Tkachenko, J. Allen,

Published on 27 October 2025. Downloaded by Indian Institute of Technology Chennai on 12/29/2025 3:17:01 AM.

M. Crispin, N. Billington, Y. Takagi, J. R. Sellers, C. Eichmann, P. Selenko, L. Frey, R. Riek, M. R. Galpin, W. B. Struwe, J. L. P. Benesch and P. Kukura, *Science*, 2018, **360**, 423–427.
31 N. A. Sakthivel, S. Theivendran, V. Ganeshraj, A. G. Oliver and A. Dass, *J. Am. Chem. Soc.*, 2017, **139**, 15450–15459.
32 Y. Song, K. Lambright, M. Zhou, K. Kirschbaum, J. Xiang, A. Xia, M. Zhu and R. Jin, *ACS Nano*, 2018, **12**, 9318–9325.
33 J. Roy, I. Marathe, V. Wysocki and T. Pradeep, *Chem. Commun.*, 2024, **60**, 6655–6658.
34 T. Chen, Q. Yao, R. R. Nasaruddin and J. Xie, *Angew. Chem.*, 2019, **131**, 12093–12103.
35 Y. Lu and W. Chen, *Anal. Chem.*, 2015, **87**, 10659–10667.
36 C. Comby-Zerbino, X. Dagany, F. Chirot, P. Dugourd, R. Antoine and R. Antoine, *Mater. Adv.*, 2021, **2**, 4896–4913.
37 P. Chakraborty and T. Pradeep, *NPG Asia Mater.*, 2019, **11**, 48.
38 K. M. Harkness, D. E. Cliffel and J. A. McLean, *Analyst*, 2010, **135**, 868–874.
39 A. Baksi, P. Chakraborty, A. Nag, D. Ghosh, S. Bhat and T. Pradeep, *Anal. Chem.*, 2018, **90**, 11351–11357.
40 A. Baksi, A. Ghosh, S. K. Mudedla, P. Chakraborty, S. Bhat, B. Mondal, K. R. Krishnadas, V. Subramanian and T. Pradeep, *J. Phys. Chem. C*, 2017, **121**, 13421–13427.
41 E. Ito, S. Ito, S. Takano, T. Nakamura and T. Tsukuda, *AuJACS*, 2022, **2**, 2627–2634.
42 D. Hwang, H. Lee, S. Y. Jang, S. M. Jo, D. Kim, Y. Seo and D. Y. Kim, *ACS Appl. Mater. Interfaces*, 2011, **3**, 2719–2725.
43 D. Sarkar, A. Mahapatra, A. Som, R. Kumar, A. Nagar, A. Baidya and T. Pradeep, *Adv. Mater. Interfaces*, 2018, **5**, 1800667.
44 M. Broyer, *Phys. Scr., T*, 1989, **26**, 84–89.
45 W. D. Knight, K. Clemenger, W. A. De Heer, W. A. Saunders, M. Y. Chou and M. L. Cohen, *Phys. Rev. Lett.*, 1984, **52**, 2141–2143.
46 H. W. Kroto, J. R. Heath, S. C. O'Brien, R. F. Curl and R. E. Smalley, *Nature*, 1985, **318**, 162–163.
47 E. A. Rohlfing, D. M. Cox and A. Kaldor, *J. Chem. Phys.*, 1984, **81**, 3322–3330.
48 L. A. Bloomfield, M. E. Geusic, R. R. Freeman and W. L. Brown, *Chem. Phys. Lett.*, 1985, **121**, 33–37.
49 M. Brust, M. Walker, D. Bethell, D. J. Schiffrin and R. Whyman, *J. Chem. Soc., Chem. Commun.*, 1994, **7**, 801–802.
50 R. L. Whetten, J. T. Khoury, M. M. Alvarez, S. Murthy, I. Vezmar, Z. L. Wang, P. W. Stephens, C. L. Cleveland, W. D. Luedtke and U. Landman, *Adv. Mater.*, 1996, **8**, 428–433.
51 A. C. Templeton, W. P. Wuelfing and R. W. Murray, *Acc. Chem. Res.*, 2000, **33**, 27–36.
52 J. F. Hicks, A. C. Templeton, S. Chen, K. M. Sheran, R. Jasti, R. W. Murray, J. Debord and T. G. Schaaff, *Anal. Chem.*, 1999, **71**, 3703–3711.
53 T. Gregory Schaaff, G. Knight, M. N. Shafigullin, R. F. Borkman and R. L. Whetten, *J. Phys. Chem. B*, 1998, **102**, 10645–10646.
54 Y. Negishi, K. Nobusada and T. Tsukuda, *J. Am. Chem. Soc.*, 2005, **127**, 5261–5270.
55 N. K. Chaki, Y. Negishi, H. Tsunoyama, Y. Shichibu and T. Tsukuda, *J. Am. Chem. Soc.*, 2008, **130**, 8608–8610.
56 D. Crasto, G. Barcaro, M. Stener, L. Sementa, A. Fortunelli and A. Dass, *J. Am. Chem. Soc.*, 2014, **136**, 14933–14940.
57 M. W. Heaven, A. Dass, P. S. White, K. M. Holt and R. W. Murray, *J. Am. Chem. Soc.*, 2008, **130**, 3754–3755.
58 M. Zhu, C. M. Aikens, F. J. Hollander, G. C. Schatz and R. Jin, *J. Am. Chem. Soc.*, 2008, **130**, 5883–5885.
59 Z. Gan, N. Xia, N. Yan, S. Zhuang, J. Dong, Y. Zhao, S. Jiang, Q. Tao and Z. Wu, *Angew. Chem., Int. Ed.*, 2021, **60**, 12253–12257.
60 C. P. Joshi, M. S. Bootharaju, M. J. Alhilaly and O. M. Bakr, *J. Am. Chem. Soc.*, 2015, **137**, 11578–11581.
61 L. Ren, P. Yuan, H. Su, S. Malola, S. Lin, Z. Tang, B. K. Teo, H. Häkkinen, L. Zheng and N. Zheng, *J. Am. Chem. Soc.*, 2017, **139**, 13288–13291.
62 M. J. Alhilaly, M. S. Bootharaju, C. P. Joshi, T. M. Besong, A. H. Emwas, R. Juarez-Mosqueda, S. Kaappa, S. Malola, K. Adil, A. Shkurenko, H. Häkkinen, M. Eddaoudi and O. M. Bakr, *J. Am. Chem. Soc.*, 2016, **138**, 14727–14732.
63 Z. Gan, J. Chen, J. Wang, C. Wang, M. B. Li, C. Yao, S. Zhuang, A. Xu, L. Li and Z. Wu, *Nat. Commun.*, 2017, **8**, 14739.
64 H. Qian, Y. Zhu and R. Jin, *Proc. Natl. Acad. Sci. U. S. A.*, 2012, **109**, 696–700.
65 A. Dass, S. Theivendran, P. R. Nimmala, C. Kumara, V. R. Jupally, A. Fortunelli, L. Sementa, G. Barcaro, X. Zuo and B. C. Noll, *J. Am. Chem. Soc.*, 2015, **137**, 4610–4613.
66 C. Zeng, Y. Chen, K. Kirschbaum, K. Appavoo, M. Y. Sfeir and R. Jin, *Sci. Adv.*, 2015, **1**, e1500045.
67 C. Kumara and A. Dass, *Anal. Chem.*, 2014, **86**, 4227–4232.
68 A. Ghosh, M. Bodiuzzaman, A. Nag, M. Jash, A. Baksi and T. Pradeep, *ACS Nano*, 2017, **11**, 11145–11151.
69 J. H. Huang, Y. Cui, P. Luo, Z. Y. Wang and S. Q. Zang, *Adv. Sci.*, 2025, **12**, e01186.
70 S. F. Yuan, C. Q. Xu, W. Di Liu, J. X. Zhang, J. Li and Q. M. Wang, *J. Am. Chem. Soc.*, 2021, **143**, 12261–12267.
71 M. Qu, H. Li, L. H. Xie, S. T. Yan, J. R. Li, J. H. Wang, C. Y. Wei, Y. W. Wu and X. M. Zhang, *J. Am. Chem. Soc.*, 2017, **139**, 12346–12349.
72 H. Yi, K. M. Osten, T. I. Levchenko, A. J. Veinot, Y. Aramaki, T. Ooi, M. Nambo and C. M. Crudden, *Chem. Sci.*, 2021, **12**, 10436–10440.
73 J. Chen, Q. F. Zhang, P. G. Williard and L. S. Wang, *Inorg. Chem.*, 2014, **53**, 3932–3934.
74 S. Ito, S. Takano and T. Tsukuda, *J. Phys. Chem. Lett.*, 2019, **10**, 6892–6896.
75 F. Hu, G. Yang, Z. C. Long, W. Q. Shi, G. J. Liang, J. Q. Wang and Q. M. Wang, *Small*, 2025, **21**, e2502106.
76 X. Gong, C. Zheng, D. Zuo, S. Li, W. H. Fang and H. Shen, *Dalton Trans.*, 2025, **54**, 9368–9375.
77 B. Zhang, X. Tan, Z.-H. Zhang, C.-Y. Liu, F. Hu, H.-S. Hu, C. Chen and Q.-M. Wang, *CCS Chem.*, 2025, 1–8.

This journal is © The Royal Society of Chemistry 2025

Published on 27 October 2025. Downloaded by Indian Institute of Technology Chennai on 12/29/2025 3:17:01 AM.

78 J. Tang, C. Liu, C. Zhu, K. Sun, H. Wang, W. Yin, C. Xu, Y. Li, W. Wang, L. Wang, R. Wu, C. Liu and J. Huang, *Nanoscale*, 2023, **15**, 2843–2848.
79 S. K. Eswaramoorthy and A. Dass, *J. Phys. Chem. C*, 2022, **126**, 444–450.
80 S.-I. Tanaka, K. Aoki, A. Muratsugu, H. Ishitobi, T. Jin and Y. Inouye, *Opt. Mater. Express*, 2013, **3**, 157.
81 T. Higaki, K. Tanaka, H. Izu, S. Oishi, K. Kawamoto, M. Tada, W. M. C. Sameera, R. Takahata, T. Teranishi, S. Kikkawa, S. Yamazoe, T. Shiga, M. Nihei, T. Kato, R. E. Cramer, Z. Zhang, K. Meyer and Y. Ohki, *J. Am. Chem. Soc.*, 2025, **147**, 3215–3222.
82 S. Bhat, I. Chakraborty, T. A. Maark, A. Mitra, G. De and T. Pradeep, *RSC Adv.*, 2016, **6**, 26679–26688.
83 L. Liao, S. Zhuang, C. Yao, N. Yan, J. Chen, C. Wang, N. Xia, X. Liu, M. B. Li, L. Li, X. Bao and Z. Wu, *J. Am. Chem. Soc.*, 2016, **138**, 10425–10428.
84 L. Xu, Q. Li, T. Li, J. Chai, S. Yang and M. Zhu, *Inorg. Chem. Front.*, 2021, **8**, 4820–4827.
85 X. Kang, X. Wei, S. Jin, Q. Yuan, X. Luan, Y. Pei, S. Wang, M. Zhu and R. Jin, *Proc. Natl. Acad. Sci. U. S. A.*, 2019, **116**, 18834–18840.
86 S. Wang, Y. Song, S. Jin, X. Liu, J. Zhang, Y. Pei, X. Meng, M. Chen, P. Li and M. Zhu, *J. Am. Chem. Soc.*, 2015, **137**, 4018–4021.
87 M. S. Bootharaju, C. P. Joshi, M. R. Parida, O. F. Mohammed and O. M. Bakr, *Angew. Chem.*, 2016, **128**, 934–938.
88 G. Soldan, M. A. Aljuhani, M. S. Bootharaju, L. G. AbdulHalim, M. R. Parida, A. Emwas, O. F. Mohammed and O. M. Bakr, *Angew. Chem.*, 2016, **128**, 5843–5847.
89 C. Zeng, Y. Chen, A. Das and R. Jin, *J. Phys. Chem. Lett.*, 2015, **6**, 2976–2986.
90 K. H. Wijesinghe, N. A. Sakthivel, L. Sementa, B. Yoon, A. Fortunelli, U. Landman and A. Dass, *J. Phys. Chem. C*, 2021, **125**, 20488–20502.
91 C. Zeng, C. Liu, Y. Pei and R. Jin, *ACS Nano*, 2013, **7**, 6138–6145.
92 C. Liu, J. Lin, Y. Shi and G. Li, *Nanoscale*, 2015, **7**, 5987–5990.
93 P. R. Nimmala, S. Theivendran, G. Barcaro, L. Sementa, C. Kumara, V. R. Jupally, E. Apra, M. Stener, A. Fortunelli and A. Dass, *J. Phys. Chem. Lett.*, 2015, **6**, 2134–2139.
94 C. Kumara, X. Zuo, J. Ilavsky, K. W. Chapman, D. A. Cullen and A. Dass, *J. Am. Chem. Soc.*, 2014, **136**, 7410–7417.
95 C. Kumara, X. Zuo, D. A. Cullen and A. Dass, *ACS Nano*, 2014, **8**, 6431–6439.
96 C. Kumara, M. M. Hoque, X. Zuo, D. A. Cullen, R. L. Whetten and A. Dass, *J. Phys. Chem. Lett.*, 2018, **9**, 6825–6832.
97 S. Vergara, U. Santiago, C. Kumara, D. Alducin, R. L. Whetten, M. Jose Yacaman, A. Dass and A. Ponce, *J. Phys. Chem. C*, 2018, **122**, 26733–26738.
98 Y. Negishi, R. Arai, Y. Niihori and T. Tsukuda, *Chem. Commun.*, 2011, **47**, 5693–5695.
99 P. Bose, K. Kumaranchira Ramankutty, P. Chakraborty, E. Khatun and T. Pradeep, *Nanoscale*, 2024, **16**, 1446–1470.
100 K. R. Krishnadas, A. Ghosh, A. Baksi, I. Chakraborty, G. Natarajan and T. Pradeep, *J. Am. Chem. Soc.*, 2016, **138**, 140–148.
101 K. R. Krishnadas, A. Baksi, A. Ghosh, G. Natarajan and T. Pradeep, *Nat. Commun.*, 2016, **7**, 13447.
102 M. Neumaier, A. Baksi, P. Weis, E. K. Schneider, P. Chakraborty, H. Hahn, T. Pradeep and M. M. Kappes, *J. Am. Chem. Soc.*, 2021, **143**, 6969–6980.
103 B. S. Sooraj, J. Roy, M. Mukherjee, A. Jose and T. Pradeep, *Langmuir*, 2024, **40**, 15244–15251.
104 P. Chakraborty, A. Nag, G. Natarajan, N. Bandyopadhyay, G. Paramasivam, M. K. Panwar, J. Chakrabarti and T. Pradeep, *Sci. Adv.*, 2019, **5**, eaau7555.
105 L. Tang, X. Kang, X. Wang, X. Zhang, X. Yuan and S. Wang, *Inorg. Chem.*, 2021, **60**, 3037–3045.
106 M. Suyama, S. Takano and T. Tsukuda, *J. Am. Chem. Soc.*, 2023, **145**, 3361–3368.
107 S. Acharya, J. Roy, D. Roy, B. Pathak and T. Pradeep, *J. Phys. Chem. C*, 2025, **129**, 5840–5850.
108 C. A. Fields-Zinna, J. S. Sampson, M. C. Crowe, J. B. Tracy, J. F. Parker, A. M. DeNey, D. C. Muddiman and R. W. Murray, *J. Am. Chem. Soc.*, 2009, **131**, 13844–13851.
109 L. A. Angel, L. T. Majors, A. C. Dharmaratne and A. Dass, *ACS Nano*, 2010, **4**, 4691–4700.
110 D. M. Black, N. Bhattarai, R. L. Whetten and S. B. H. Bach, *J. Phys. Chem. A*, 2014, **118**, 10679–10687.
111 P. Chakraborty, A. Baksi, E. Khatun, A. Nag, A. Ghosh and T. Pradeep, *J. Phys. Chem. C*, 2017, **121**, 10971–10981.
112 Q. Yao, V. Fung, C. Sun, S. Huang, T. Chen, D.-E. Jiang, J. Y. Lee and J. Xie, *Nat. Commun.*, 2018, **9**, 1979.
113 Y. Cao, T. Liu, T. Chen, B. Zhang, D. en Jiang and J. Xie, *Nat. Commun.*, 2021, **12**, 3212.
114 G. E. Johnson, T. Priest and J. Laskin, *Chem. Sci.*, 2014, **5**, 3275–3286.
115 A. Baksi, S. R. Harvey, G. Natarajan, V. H. Wysocki and T. Pradeep, *Chem. Commun.*, 2016, **52**, 3805–3808.
116 J. S. Brodbelt, L. J. Morrison and I. Santos, *Chem. Rev.*, 2020, **120**, 3328–3380.
117 D. M. Black, C. M. Crittenden, J. S. Brodbelt and R. L. Whetten, *J. Phys. Chem. Lett.*, 2017, **8**, 1283–1289.
118 Y. Zhang, X. Gu, Z. Li, P. Sanwal, Y. X. Miao and G. Li, *J. Phys. Chem. Lett.*, 2025, **16**, 2314–2319.
119 Y. Zhang, X. Gu, F. K. Busari, S. Barkaoui, Z. K. Han, A. Baiker, Z. Zhao and G. Li, *Nano Res.*, 2024, **17**, 9594–9600.
120 A. Jose, J. N. Walker, M. Khatun, S. Malola, B. S. Sooraj, H. Häkkinen, J. S. Brodbelt and T. Pradeep, *Chem. Commun.*, 2025, **61**, 6482–6485.
121 J. Zhang, H. D. Wang, Y. Zhang, Z. Li, D. Yang, D. H. Zhang, T. Tsukuda and G. Li, *J. Phys. Chem. Lett.*, 2023, **14**, 4179–4184.
122 H. H. Hill Jr., W. F. Siems, R. H. St Louis and D. G. McMinn, *Anal. Chem.*, 1990, **62**, 1201A–1209A.

Published on 27 October 2025. Downloaded by Indian Institute of Technology Chennai on 12/29/2025 3:17:01 AM.

123 A. B. Kanu, P. Dwivedi, M. Tam, L. Matz and H. H. Hill Jr., *J. Mass Spectrom.*, 2008, **43**, 1–22.
124 G. A. Eiceman, *Crit. Rev. Anal. Chem.*, 1991, **22**, 471–490.
125 J. N. Dodds and E. S. Baker, *J. Am. Soc. Mass Spectrom.*, 2019, **30**, 2185–2195.
126 A. A. Shvartsburg and R. D. Smith, *Anal. Chem.*, 2008, **80**, 9689–9699.
127 F. Lanucara, S. W. Holman, C. J. Gray and C. E. Eyers, *Nat. Chem.*, 2014, **6**, 281–294.
128 K. Michelmann, J. A. Silveira, M. E. Ridgeway and M. A. Park, *J. Am. Soc. Mass Spectrom.*, 2014, **26**, 14–24.
129 E. Christofi and P. Barran, *Chem. Rev.*, 2023, **123**, 2902–2949.
130 J. N. Dodds and E. S. Baker, *J. Am. Soc. Mass Spectrom.*, 2019, **30**, 2185–2195.
131 A. Baksi, P. Chakraborty, S. Bhat, G. Natarajan and T. Pradeep, *Chem. Commun.*, 2016, **52**, 8397–8400.
132 E. Kalenius, S. Malola, M. F. Matus, R. Kazan, T. Bürgi and H. Häkkinen, *J. Am. Chem. Soc.*, 2021, **143**, 1273–1277.
133 Y. Zeng, S. Havenridge, M. Gharib, A. Baksi, K. L. D. M. Weerawardene, A. R. Ziefuß, C. Strelow, C. Rehbock, A. Mews, S. Barcikowski, M. M. Kappes, W. J. Parak, C. M. Aikens and I. Chakraborty, *J. Am. Chem. Soc.*, 2021, **143**, 9405–9414.
134 P. Chakraborty, S. Malola, M. Neumaier, P. Weis, H. Häkkinen and M. M. Kappes, *Angew. Chem., Int. Ed.*, 2023, **62**, e202305836.
135 A. Baksi, E. K. Schneider, P. Weis, I. Chakraborty, O. Fuhr, S. Lebedkin, W. J. Parak and M. M. Kappes, *ACS Nano*, 2020, **14**, 15064–15070.
136 J. Roy, A. Das, A. Jana, P. Chakraborty, M. Neumaier, H. Hahn, B. Pathak, M. M. Kappes and T. Pradeep, *ACS Nano*, 2025, **19**, 5727–5738.
137 K. Giles, J. Ujma, J. Wildgoose, S. Pringle, K. Richardson, D. Langridge and M. Green, *Anal. Chem.*, 2019, **91**, 8564–8573.
138 J. Ujma, D. Ropartz, K. Giles, K. Richardson, D. Langridge, J. Wildgoose, M. Green and S. Pringle, *J. Am. Soc. Mass Spectrom.*, 2019, **30**, 1028–1037.
139 S. I. Merenbloom, S. L. Koeniger, B. C. Bohrer, S. J. Valentine and D. E. Clemmer, *Anal. Chem.*, 2008, **80**, 1918–1927.
140 P. Chakraborty, M. Neumaier, J. Seibel, N. Da Roit, A. Böttcher, C. Schmitt, D. Wang, C. Kübel, S. Behrens and M. M. Kappes, *ACS Nano*, 2025, **19**, 3624–3634.
141 F. Hennrich, S. Ito, P. Weis, M. Neumaier, S. Takano, T. Tsukuda and M. M. Kappes, *Phys. Chem. Chem. Phys.*, 2024, **26**, 8408–8418.
142 L.-M. Wang and L.-S. Wang, *Nanoscale*, 2012, **4**, 4038–4053.
143 K. Hirata, K. Yamashita, S. Muramatsu, S. Takano, K. Ohshimo, T. Azuma, R. Nakanishi, T. Nagata, S. Yamazoe, K. Koyasu and T. Tsukuda, *Nanoscale*, 2017, **9**, 13409–13412.
144 R. Hamouda, B. Bellina, F. Bertorelle, I. Compagnon, R. Antoine, M. Broyer, D. Rayane and P. Dugourd, *J. Phys. Chem. Lett.*, 2010, **1**, 3189–3194.
145 Y. Tasaka, K. Nakamura, S. Malola, K. Hirata, K. Kim, K. Koyasu, H. Häkkinen and T. Tsukuda, *J. Phys. Chem. Lett.*, 2020, **11**, 3069–3074.
146 S. Ito, Y. Tasaka, K. Nakamura, Y. Fujiwara, K. Hirata, K. Koyasu and T. Tsukuda, *J. Phys. Chem. Lett.*, 2022, **13**, 5049–5055.
147 K. Kim, K. Hirata, K. Nakamura, H. Kitazawa, S. Hayashi, K. Koyasu and T. Tsukuda, *Angew. Chem.*, 2019, **131**, 11763–11767.
148 K. Akazawa, S. Ito, Y. Hamasaki, K. Koyasu and T. Tsukuda, *J. Phys. Chem. A*, 2025, **129**, 6043–6048.
149 S. Ito, Y. Fujiwara, T. Mohr, S. Masuda, K. Koyasu, M. Kappes and T. Tsukuda, *J. Phys. Chem. Lett.*, 2025, 8531–8535.
150 D. Z. Keifer, E. E. Pierson and M. F. Jarrold, *Analyst*, 2017, **142**, 1654–1671.
151 T. Doussineau, C. Y. Bao, C. Clavier, X. Dagany, M. Kerleroux, R. Antoine and P. Dugourd, *Rev. Sci. Instrum.*, 2011, **82**, 084104.
152 T. Doussineau, C. Y. Bao, R. Antoine, P. Dugourd, W. Zhang, F. D'Agosto and B. Charleux, *ACS Macro Lett.*, 2012, **1**, 414–417.
153 A. G. Elliott, C. C. Harper, H. W. Lin and E. R. Williams, *Analyst*, 2017, **142**, 2760–2769.
154 A. G. Elliott, C. C. Harper, H. W. Lin, A. C. Susa, Z. Xia and E. R. Williams, *Anal. Chem.*, 2017, **89**, 7701–7708.
155 A. R. Todd, L. F. Barnes, K. Young, A. Zlotnick and M. F. Jarrold, *Anal. Chem.*, 2020, **92**, 11357–11364.
156 C. C. Harper, J. S. Jordan, S. Papanu and E. R. Williams, *ACS Nano*, 2024, **18**, 17806–17814.
157 T. P. Wörner, K. Aizikov, J. Snijder, K. L. Fort, A. A. Makarov and A. J. R. Heck, *Nat. Chem.*, 2022, **14**, 515–522.
158 M. A. Zenaidee and J. A. Loo, *Nat. Chem.*, 2022, **14**, 482–483.
159 M. F. Jarrold, *J. Am. Chem. Soc.*, 2024, **146**, 5749–5758.
160 B. S. Sooraj, S. Maclot, A. Jose, C. Comby-Zerbino, T. Reinert, K. Unni, R. Antoine and T. Pradeep, *J. Phys. Chem. Lett.*, 2025, **16**, 7004–7011.
161 Z. M. Miller, C. C. Harper, H. Lee, A. J. Bischoff, M. B. Francis, D. V. Schaffer and E. R. Williams, *J. Am. Soc. Mass Spectrom.*, 2022, **33**, 2129–2137.
162 D. Z. Keifer, D. L. Shinholt and M. F. Jarrold, *Anal. Chem.*, 2015, **87**, 10330–10337.
163 A. R. Todd, A. W. Alexander and M. F. Jarrold, *J. Am. Soc. Mass Spectrom.*, 2020, **31**, 146–154.
164 J. O. Kafader, R. D. Melani, K. R. Durbin, B. Ikwuagwu, B. P. Early, R. T. Fellers, S. C. Beu, V. Zabrouskov, A. A. Makarov, J. T. Maze, D. L. Shinholt, P. F. Yip, D. Tullman-Ercek, M. W. Senko, P. D. Compton and N. L. Kelleher, *Nat. Methods*, 2020, **17**, 391–394.
165 T. P. Wörner, J. Snijder, A. Bennett, M. Agbandje-McKenna, A. A. Makarov and A. J. R. Heck, *Nat. Methods*, 2020, **17**, 395–398.
166 A. C. Susa, Z. Xia and E. R. Williams, *Angew. Chem.*, 2017, **129**, 8020–8023.

This journal is © The Royal Society of Chemistry 2025

Published on 27 October 2025. Downloaded by Indian Institute of Technology Chennai on 12/29/2025 3:17:01 AM.

167 D. Wu and G. Piszczek, *Eur. Biophys. J.*, 2021, **50**, 403–409.
168 R. W. Taylor and V. Sandoghdar, *Nano Lett.*, 2019, **19**, 4827–4835.
169 L. Melo, A. Hui, M. Kowal, E. Boateng, Z. Poursorkh, E. Rocheron, J. Wong, A. Christy and E. Grant, *J. Phys. Chem. B*, 2021, **125**, 12466–12475.
170 A. Pinkard, A. M. Champsaur and X. Roy, *Acc. Chem. Res.*, 2018, **51**, 919–929.
171 C. H. Lee, L. Liu, C. Bejger, A. Turkiewicz, T. Goko, C. J. Arguello, B. A. Frandsen, S. C. Cheung, T. Medina, T. J. S. Munsie, R. D'Ortenzio, G. M. Luke, T. Besara, R. A. Lalancette, T. Siegrist, P. W. Stephens, A. C. Crowther, L. E. Brus, Y. Matsuo, E. Nakamura, Y. J. Uemura, P. Kim, C. Nuckolls, M. L. Steigerwald and X. Roy, *J. Am. Chem. Soc.*, 2014, **136**, 16926–16931.
172 A. Turkiewicz, D. W. Paley, T. Besara, G. Elbaz, A. Pinkard, T. Siegrist and X. Roy, *J. Am. Chem. Soc.*, 2014, **136**, 15873–15876.
173 K. S. Joya, L. Sinatra, L. G. Abdulhalim, C. P. Joshi, M. N. Hedhili, O. M. Bakr and I. Hussain, *Nanoscale*, 2016, **8**, 9695–9703.
174 H. Gholipour-Ranjbar, H. Fang, J. Guan, D. Peters, A. Seifert, P. Jena and J. Laskin, *Small*, 2021, **17**, e2002927.
175 H. Gholipour-Ranjbar, Deepika, P. Jena and J. Laskin, *Commun. Chem.*, 2022, **5**, 130.
176 X. Li, X. Wu, N. Dilley, H. Gholipour-Ranjbar, S. Lee, D. Zemlyanov, H. Fang, P. Jena and J. Laskin, *Small*, 2025, **21**, e2500070.
177 A. J. Touchton, G. Wu and T. W. Hayton, *Chem. Sci.*, 2022, **13**, 5171–5175.
178 T. Higaki, K. Tanaka, H. Izu, S. Oishi, K. Kawamoto, M. Tada, W. M. C. Sameera, R. Takahata, T. Teranishi, S. Kikkawa, S. Yamazoe, T. Shiga, M. Nihei, T. Kato, R. E. Cramer, Z. Zhang, K. Meyer and Y. Ohki, *J. Am. Chem. Soc.*, 2025, **147**, 3215–3222.
179 S. Rauschenbach, M. Ternes, L. Harnau and K. Kern, *Annu. Rev. Anal. Chem.*, 2016, **9**, 473–498.
180 H. J. Räder, A. Rouhanipour, A. M. Talarico, V. Palermo, P. Samorì and K. Müllen, *Nat. Mater.*, 2006, **5**, 276–280.
181 B. Gologan, Z. Takáts, J. Alvarez, J. M. Wiseman, N. Talaty, Z. Ouyang and R. G. Cooks, *J. Am. Soc. Mass Spectrom.*, 2004, **15**, 1874–1884.
182 T. He and J. V. Jokerst, *Biomater. Sci.*, 2020, **8**, 5555–5573.
183 A. Li, Q. Luo, S. J. Park and R. G. Cooks, *Angew. Chem., Int. Ed.*, 2014, **53**, 3147–3150.
184 J. K. Lee, D. Samanta, H. G. Nam and R. N. Zare, *Nat. Commun.*, 2018, **9**, 1562.
185 D. Sarkar, R. Singh, A. Som, C. K. Manju, M. A. Ganayee, R. Adhikari and T. Pradeep, *J. Phys. Chem. C*, 2018, **122**, 17777–17783.
186 D. Sarkar, M. K. Mahitha, A. Som, A. Li, M. Wleklinski, R. G. Cooks and T. Pradeep, *Adv. Mater.*, 2016, **28**, 2223–2228.
187 S. Bose, A. Chatterjee, S. K. Jenifer, B. Mondal, P. Srikrishnarka, D. Ghosh, A. R. Chowdhuri, M. P. Kannan, S. V. Elchuri and T. Pradeep, *ACS Sustainable Chem. Eng.*, 2021, **9**, 4554–4563.
188 D. Satyabola, T. Ahuja, S. Bose, B. Mondal, P. Srikrishnarka, M. P. Kannan, B. K. Spoorthi and T. Pradeep, *J. Phys. Chem. C*, 2021, **125**, 10998–11006.
189 A. Jose, A. Jana, T. Gupte, A. S. Nair, K. Unni, A. Nagar, A. R. Kini, B. K. Spoorthi, S. K. Jana, B. Pathak and T. Pradeep, *ACS Mater. Lett.*, 2023, **5**, 893–899.
190 A. Jana, B. K. Spoorthi, A. S. Nair, A. Nagar, B. Pathak, T. Base and T. Pradeep, *Nanoscale*, 2023, **15**, 8141–8147.
191 G. E. Johnson, Q. Hu and J. Laskin, *Annu. Rev. Anal. Chem.*, 2011, **4**, 83–104.
192 B. Gologan, J. R. Green, J. Alvarez, J. Laskin and R. G. Cooks, *Phys. Chem. Chem. Phys.*, 2005, **7**, 1490–1500.
193 U. Heiz, A. Sanchez, S. Abbet and W.-D. Schneider, *Chem. Phys.*, 2000, **262**, 189–200.
194 V. Prabhakaran, B. L. Mehdi, J. J. Ditto, M. H. Engelhard, B. Wang, K. D. D. Gunaratne, D. C. Johnson, N. D. Browning, G. E. Johnson and J. Laskin, *Nat. Commun.*, 2016, **7**, 11399.
195 Z. Ouyang, Z. Takáts, T. A. Blake, B. Gologan, A. J. Guymon, J. M. Wiseman, J. C. Oliver, V. J. Davisson and R. G. Cooks, *Science*, 2003, **301**, 1351–1354.
196 P. Fremdling, T. K. Esser, B. Saha, A. A. Makarov, K. L. Fort, M. Reinhardt-Szyba, J. Gault and S. Rauschenbach, *ACS Nano*, 2022, **16**, 14443–14455.
197 G. E. Johnson, C. Wang, T. Priest and J. Laskin, *Anal. Chem.*, 2011, **83**, 8069–8072.
198 T. K. Esser, J. Böhning, P. Fremdling, M. T. Agasid, A. Costin, K. Fort, A. Konijnenberg, J. D. Gilbert, A. Bahm, A. Makarov, C. V. Robinson, J. L. P. Benesch, L. Baker, T. A. M. Bharat, J. Gault and S. Rauschenbach, *PNAS Nexus*, 2022, **1**, gac153.
199 J. Lyu, J. Qian, Z. Yang and J. Xie, *Nanoscale Horiz.*, 2025, **10**, 2304–2339.
200 Q. Tang, C. Cui, H. Ying, Q. Zeng, Y. Li, Z. Shi, S. C. Lin, B. Weng, Z. Zhou, F. Qi and L. S. Zheng, *Anal. Chem.*, 2025, **97**, 18404–18414.
201 H. Klein Moberg, G. Abbondanza, I. Nedrygailov, D. Albinsson, J. Fritzsche and C. Langhammer, *Nat. Commun.*, 2025, **16**, 7203.
202 T. C. Sams, S. E. Ying, M. Q. Edwards, E. T. Dziekonski and R. G. Cooks, *Analysis Sensing*, 2024, **5**, e202400103.
203 R. Hamouda, B. Bellina, F. Bertorelle, I. Compagnon, R. Antoine, M. Broyer, D. Rayane and P. Dugourd, *J. Phys. Chem. Lett.*, 2010, **1**, 3189–3194.
204 S. J. P. Marlton and A. J. Trevitt, *Chem. Commun.*, 2022, **58**, 9451–9467.
205 M. S. Westphall, K. W. Lee, A. Z. Salome, J. M. Lodge, T. Grant and J. J. Coon, *Nat. Commun.*, 2022, **13**, 2276.
206 P. W. Fedick, N. M. Morato, F. Pu and R. G. Cooks, *Int. J. Mass Spectrom.*, 2020, **452**, 116326.
207 Y. Tasaka, M. Suyama, S. Ito, K. Koyasu, M. Kappes, F. Maran and T. Tsukuda, *Angew. Chem., Int. Ed.*, 2024, **63**, e202408335.

Published on 27 October 2025. Downloaded by Indian Institute of Technology Chennai on 12/29/2025 3:17:01 AM.

208 A. Mathew, F. Giskes, A. Lekkas, J. F. Greisch, G. B. Eijkel, I. G. M. Anthony, K. Fort, A. J. R. Heck, D. Papanastasiou, A. A. Makarov, S. R. Ellis and R. M. A. Heeren, *J. Am. Soc. Mass Spectrom.*, 2023, **34**, 1359–1371.
209 K. Chughtai and R. M. A. Heeren, *Chem. Rev.*, 2010, **110**, 3237–3277.
210 A. Z. Salome, K. W. Lee, T. Grant, M. S. Westphall and J. J. Coon, *Anal. Chem.*, 2022, **94**, 17616–17624.
211 C. A. McCandler, A. Pihlajamäki, S. Malola, H. Häkkinen and K. A. Persson, *ACS Nano*, 2024, **18**, 19014–19023.
212 Z. Yang, A. Shi, R. Zhang, Z. Ji, J. Li, J. Lyu, J. Qian, T. Chen, X. Wang, F. You and J. Xie, *ACS Nano*, 2024, **18**, 27138–27166.
213 H. Xiang, Y. Wang, X. Xu, C. Ruan, K. Wang, W. Cheng, M. Zhou, X. Liu and C. Yao, *J. Am. Chem. Soc.*, 2024, **146**, 28572–28579.
214 K. Koszinowski and K. Ballweg, *Chem. – Eur. J.*, 2010, **16**, 3285–3290.
215 Y. M. Tseng, J. H. Liao, T. H. Chiu, H. Liang, S. Kahlal, J. Y. Saillard and C. W. Liu, *Inorg. Chem.*, 2023, **62**, 3866–3874.
216 Z. Wu, E. Lanni, W. Chen, M. E. Bier, D. Ly and R. Jin, *J. Am. Chem. Soc.*, 2009, **131**, 16672–16674.
217 T. Udaya Bhaskara Rao and T. Pradeep, *Angew. Chem., Int. Ed.*, 2010, **49**, 3925–3929.
218 Y. M. Tseng, J. H. Liao, T. H. Chiu, H. Liang, S. Kahlal, J. Y. Saillard and C. W. Liu, *Inorg. Chem.*, 2023, **62**, 3866–3874.
219 L. Y. Sun, F. Wang, Y. Shui, T. Yang and Y. F. Han, *Angew. Chem., Int. Ed.*, 2025, **64**, e202510845.
220 H. Wu, M. Yang, B. Huang, W. Gan and Z. Luo, *Sci. China: Chem.*, 2022, **65**, 1594–1600.
221 T. U. B. Rao, B. Nataraju and T. Pradeep, *J. Am. Chem. Soc.*, 2010, **132**, 16304–16307.
222 B. J. Alamer, M. S. Bootharaju, S. M. Kozlov, Z. Cao, A. Shkurenko, S. Nematulloev, P. Maity, O. F. Mohammed, M. Eddaoudi, L. Cavallo, J. M. Basset and O. M. Bakr, *Inorg. Chem.*, 2021, **60**, 4306–4312.
223 K. Zheng, X. Yuan and J. Xie, *Chem. Commun.*, 2017, **53**, 9697–9700.
224 W. J. Yen, J. H. Liao, T. H. Chiu, J. Y. Chen, Y. J. Chen, S. Kahlal, J. Y. Saillard and C. W. Liu, *Nanoscale*, 2024, **16**, 7011–7018.
225 A. Baksi, M. S. Bootharaju, X. Chen, H. Häkkinen and T. Pradeep, *J. Phys. Chem. C*, 2014, **118**, 21722–21729.
226 A. Baksi, S. R. Harvey, G. Natarajan, V. H. Wysocki and T. Pradeep, *Chem. Commun.*, 2016, **52**, 3805–3808.
227 V. Rück, V. A. Neacșu, M. B. Liisberg, C. B. Mollerup, P. H. Ju, T. Vosch, J. Kondo and C. Cerretani, *Adv. Opt. Mater.*, 2023, **12**, 2301928.
228 W. A. Dar, A. Jana, K. S. Sugi, G. Paramasivam, M. Bodiuzzaman, E. Khatun, A. Som, A. Mahendranath, A. Chakraborty and T. Pradeep, *Chem. Mater.*, 2022, **34**, 4703–4711.
229 H. Yang, J. Lei, B. Wu, Y. Wang, M. Zhou, A. Xia, L. Zheng and N. Zheng, *Chem. Commun.*, 2013, **49**, 300–302.
230 A. Mathew, P. R. Sajanlal and T. Pradeep, *J. Mater. Chem.*, 2011, **21**, 11205–11212.
231 M. Jash, E. Khatun, P. Chakraborty, C. Sudhakar and T. Pradeep, *J. Phys. Chem. C*, 2020, **124**, 20569–20577.
232 F. Bertorelle, R. Hamouda, D. Rayane, M. Broyer, R. Antoine, P. Dugourd, L. Gell, A. Kulesza, R. Mitrić and V. Bonačić-Koutecký, *Nanoscale*, 2013, **5**, 5637–5643.
233 W. A. Dar, M. Bodiuzzaman, D. Ghosh, G. Paramasivam, E. Khatun, K. S. Sugi and T. Pradeep, *ACS Nano*, 2019, **13**, 13365–13373.
234 A. Gonzàlez-Rosell, S. Malola, R. Guha, N. R. Arevalos, M. F. Matus, M. E. Goulet, E. Haapaniemi, B. B. Katz, T. Vosch, J. Kondo, H. Häkkinen and S. M. Copp, *J. Am. Chem. Soc.*, 2023, **145**, 10721–10729.
235 R. Guha, S. Malola, M. Rafik, M. Khatun, A. Gonzàlez-Rosell, H. Häkkinen and S. M. Copp, *Nanoscale*, 2024, **16**, 20596–20607.
236 A. Gonzàlez-Rosell, V. Rück, M. B. Liisberg, C. Cerretani, V. R. M. Nielsen, T. Vosch and S. M. Copp, *Adv. Opt. Mater.*, 2025, **13**, 2402752.
237 M. M. Zhang, X. Y. Dong, Z. Y. Wang, X. M. Luo, J. H. Huang, S. Q. Zang and T. C. W. Mak, *J. Am. Chem. Soc.*, 2021, **143**, 6048–6053.
238 V. Yadav, A. Jana, S. Acharya, S. Malola, H. Nagar, A. Sharma, A. R. Kini, S. Antharjanam, J. Machacek, K. N. V. D. Adarsh, T. Base, H. Häkkinen and T. Pradeep, *Nat. Commun.*, 2025, **16**, 1197.
239 V. Rück, M. B. Liisberg, C. B. Mollerup, Y. He, J. Chen, C. Cerretani and T. Vosch, *Angew. Chem., Int. Ed.*, 2023, **62**, e202309760.
240 M. S. Bootharaju, R. Dey, L. E. Gevers, M. N. Hedhili, J. M. Basset and O. M. Bakr, *J. Am. Chem. Soc.*, 2016, **138**, 13770–13773.
241 S. F. Yuan, P. Li, Q. Tang, X. K. Wan, Z. A. Nan, D. E. Jiang and Q. M. Wang, *Nanoscale*, 2017, **9**, 11405–11409.
242 R. S. Dhayal, Y. R. Lin, J. H. Liao, Y. J. Chen, Y. C. Liu, M. H. Chiang, S. Kahlal, J. Y. Saillard and C. W. Liu, *Chem. – Eur. J.*, 2016, **22**, 9943–9947.
243 P. Kumar, S. Khirid, D. K. Jangid, C. S. Nishad, P. Chauhan, P. Kumari, S. Meena, S. K. Bose, A. Kumar, B. Banerjee and R. S. Dhayal, *Inorg. Chem.*, 2024, **63**, 13724–13737.
244 R. S. Dhayal, J. H. Liao, Y. C. Liu, M. H. Chiang, S. Kahlal, J. Y. Saillard and C. W. Liu, *Angew. Chem., Int. Ed.*, 2015, **54**, 3702–3706.
245 Z. J. Guan, R. L. He, S. F. Yuan, J. J. Li, F. Hu, C. Y. Liu and Q. M. Wang, *Angew. Chem., Int. Ed.*, 2022, **61**, e202116965.
246 R. Guha, A. Gonzàlez-Rosell, M. Rafik, N. Arevalos, B. B. Katz and S. M. Copp, *Chem. Sci.*, 2023, **14**, 11340–11350.
247 R. L. He, F. Hu, Z. J. Guan and Q. M. Wang, *Angew. Chem., Int. Ed.*, 2024, **63**, e202410827.
248 A. Jana, P. M. Unnikrishnan, A. K. Poonia, J. Roy, M. Jash, G. Paramasivam, J. Machacek, K. N. V. D. Adarsh, T. Base and T. Pradeep, *Inorg. Chem.*, 2022, **61**, 8593–8603.

Published on 27 October 2025. Downloaded by Indian Institute of Technology Chennai on 12/29/2025 3:17:01 AM.

249 E. Khatun, M. Bodiuzzaman, K. S. Sugi, P. Chakraborty, G. Paramasivam, W. A. Dar, T. Ahuja, S. Antharjanam and T. Pradeep, *ACS Nano*, 2019, **13**, 5753–5759.
250 S. Li, X. Y. Dong, K. S. Qi, S. Q. Zang and T. C. W. Mak, *J. Am. Chem. Soc.*, 2021, **143**, 20574–20578.
251 G. Romolini, H. Kanazawa, C. B. Mollerup, M. B. Liisberg, S. W. Lind, Z. Huang, C. Cerretani, J. Kondo and T. Vosch, *Small Struct.*, 2025, **6**, 2500022.
252 L. G. AbdulHalim, M. S. Bootharaju, Q. Tang, S. Del Gobbo, R. G. AbdulHalim, M. Eddaoudi, D. E. Jiang and O. M. Bakr, *J. Am. Chem. Soc.*, 2015, **137**, 11970–11975.
253 P. Chakraborty, A. Nag, G. Paramasivam, G. Natarajan and T. Pradeep, *ACS Nano*, 2018, **12**, 2415–2425.
254 E. Khatun, A. Ghosh, P. Chakraborty, P. Singh, M. Bodiuzzaman, P. Ganesan, G. Nataranjan, J. Ghosh, S. K. Pal and T. Pradeep, *Nanoscale*, 2018, **10**, 20033–20042.
255 M. Van Der Linden, A. Barendregt, A. J. Van Bunningen, P. T. K. Chin, D. Thies-Weesie, F. M. F. De Groot and A. Meijerink, *Nanoscale*, 2016, **8**, 19901–19909.
256 N. Xia, J. Yang and Z. Wu, *Nanoscale*, 2015, **7**, 10013–10020.
257 A. Jana, W. A. Dar, S. K. Jana, A. K. Poonia, V. Yadav, J. Roy, S. Chandra, K. N. V. D. Adarsh, R. H. A. Ras and T. Pradeep, *Chem. Mater.*, 2023, **35**, 7020–7031.
258 H. Yuan, M. Theresa, D. Bain, H. Fakhouri, K. Sreekanth, A. Ravi, S. Thomas, N. Kalarikkal, R. Antoine and E. K. Radhakrishnan, *Inorg. Chem. Commun.*, 2024, **159**, 111799.
259 J. Guo, S. Kumar, M. Bolan, A. Desireddy, T. P. Bigioni and W. P. Griffith, *Anal. Chem.*, 2012, **84**, 5304–5308.
260 T. Udayabhaskararao, M. S. Bootharaju and T. Pradeep, *Nanoscale*, 2013, **5**, 9404–9411.
261 Z. Wang, Y. Wang, T. Y. Xu, L. Li, C. M. Aikens, Z. Y. Gao, M. Azam, C. H. Tung and D. Sun, *Angew. Chem., Int. Ed.*, 2024, **63**, e202403464.
262 B. Wu, X. X. Li, S. T. Zheng and J. Xie, *Chem. Commun.*, 2023, **59**, 2927–2930.
263 C. K. Manju, D. Ghosh, M. Bodiuzzaman and T. Pradeep, *Dalton Trans.*, 2019, **48**, 8664–8670.
264 Z. J. Guan, J. L. Zeng, Z. A. Nan, X. K. Wan, Y. M. Lin and Q. M. Wang, *Sci. Adv.*, 2016, **2**, e1600323.
265 X. Y. Li, H. F. Su, K. Yu, Y. Z. Tan, X. P. Wang, Y. Q. Zhao, D. Sun and L. S. Zheng, *Nanoscale*, 2015, **7**, 8284–8288.
266 X. H. Ma, Y. Si, L. L. Luo, Z. Y. Wang, S. Q. Zang and T. C. W. Mak, *ACS Nano*, 2022, **16**, 5507–5514.
267 J. Chai, S. Yang, Y. Lv, T. Chen, S. Wang, H. Yu and M. Zhu, *J. Am. Chem. Soc.*, 2018, **140**, 15582–15585.
268 M. Bodiuzzaman, A. Ghosh, K. S. Sugi, A. Nag, E. Khatun, B. Varghese, G. Paramasivam, S. Antharjanam, G. Natarajan and T. Pradeep, *Angew. Chem.*, 2019, **131**, 195–200.
269 A. Jana, M. Jash, A. K. Poonia, G. Paramasivam, M. R. Islam, P. Chakraborty, S. Antharjanam, J. Machacek, S. Ghosh, K. N. V. D. Adarsh, T. Base and T. Pradeep, *ACS Nano*, 2021, **15**, 15781–15793.
270 Z. Wang, H. F. Su, L. P. Zhang, J. M. Dou, C. H. Tung, D. Sun and L. Zheng, *ACS Nano*, 2022, **16**, 4500–4507.
271 L. M. Zheng, W. Q. Shi, F. Hu, Z. J. Guan and Q. M. Wang, *J. Am. Chem. Soc.*, 2024, **146**, 25101–25107.
272 L. G. Abdulhalim, S. Ashraf, K. Katsiev, A. R. Kirmani, N. Kothalawala, D. H. Anjum, S. Abbas, A. Amassian, F. Stellacci, A. Dass, I. Hussain and O. M. Bakr, *J. Mater. Chem. A*, 2013, **1**, 10148–10154.
273 A. Desireddy, B. E. Conn, J. Guo, B. Yoon, R. N. Barnett, B. M. Monahan, K. Kirschbaum, W. P. Griffith, R. L. Whetten, U. Landman and T. P. Bigioni, *Nature*, 2013, **501**, 399–402.
274 M. S. Bootharaju, S. Lee, G. Deng, S. Malola, W. Baek, H. Häkkinen, N. Zheng and T. Hyeon, *Angew. Chem., Int. Ed.*, 2021, **60**, 9038–9044.
275 I. Chakraborty, W. Kurashige, K. Kanehira, L. Gell, H. Häkkinen, Y. Negishi and T. Pradeep, *J. Phys. Chem. Lett.*, 2013, **4**, 3351–3355.
276 I. Chakraborty and T. Pradeep, *Nanoscale*, 2014, **6**, 14190–14194.
277 B. E. Conn, A. Desireddy, A. Atnagulov, S. Wickramasinghe, B. Bhattarai, B. Yoon, R. N. Barnett, Y. Abdollahian, Y. W. Kim, W. P. Griffith, S. R. J. Oliver, U. Landman and T. P. Bigioni, *J. Phys. Chem. C*, 2015, **119**, 11238–11249.
278 M. S. Bootharaju, V. M. Burlakov, T. M. D. Besong, C. P. Joshi, L. G. Abdulhalim, D. M. Black, R. L. Whetten, A. Goriely and O. M. Bakr, *Chem. Mater.*, 2015, **27**, 4289–4297.
279 W. Di Liu, J. Q. Wang, S. F. Yuan, X. Chen and Q. M. Wang, *Angew. Chem., Int. Ed.*, 2021, **60**, 11430–11435.
280 S. S. Zhang, F. Alkan, H. F. Su, C. M. Aikens, C. H. Tung and D. Sun, *J. Am. Chem. Soc.*, 2019, **141**, 4460–4467.
281 X. Wei, H. Shen, C. Xu, H. Li, S. Jin, X. Kang and M. Zhu, *Inorg. Chem.*, 2021, **60**, 5931–5936.
282 W. Du, S. Jin, L. Xiong, M. Chen, J. Zhang, X. Zou, Y. Pei, S. Wang and M. Zhu, *J. Am. Chem. Soc.*, 2017, **139**, 1618–1624.
283 Z. Wang, Y. J. Zhu, Y. Z. Li, G. L. Zhuang, K. P. Song, Z. Y. Gao, J. M. Dou, M. Kurmoo, C. H. Tung and D. Sun, *Nat. Commun.*, 2022, **13**, 1802.
284 F. Hu, H. W. Luyang, R. L. He, Z. J. Guan, S. F. Yuan and Q. M. Wang, *J. Am. Chem. Soc.*, 2022, **144**, 19365–19371.
285 I. Chakraborty, S. Mahata, A. Mitra, G. De and T. Pradeep, *Dalton Trans.*, 2014, **43**, 17904–17907.
286 Z. Wang, M. D. Li, J. Y. Shi, H. F. Su, J. W. Liu, L. Feng, Z. Y. Gao, Q. W. Xue, C. H. Tung, D. Sun and L. S. Zheng, *CCS Chem.*, 2022, **4**, 1788–1795.
287 E. Khatun, A. Ghosh, D. Ghosh, P. Chakraborty, A. Nag, B. Mondal, S. Chennu and T. Pradeep, *Nanoscale*, 2017, **9**, 8240–8248.
288 Y. M. Su, X. Y. Li, Z. Wang, Z. Y. Gao, X. Q. Huang, C. H. Tung and D. Sun, *J. Chem. Phys.*, 2021, **155**, 234303.
289 A. Ghosh and T. Pradeep, *Eur. J. Inorg. Chem.*, 2014, **2014**, 5271–5275.

Published on 27 October 2025. Downloaded by Indian Institute of Technology Chennai on 12/29/2025 3:17:01 AM.

290 M. Zhou, Y. Bao, S. Jin, S. Wen, S. Chen and M. Zhu, *Chem. Commun.*, 2021, **57**, 10383–10386.
291 L. M. Zheng, Z. C. Long, F. Hu, J. Chan, W. Q. Shi, B. Zhang, Z. Wang and Q. M. Wang, *Angew. Chem., Int. Ed.*, 2025, **64**, e202506971.
292 I. Chakraborty, T. Udayabhaskararao and T. Pradeep, *Chem. Commun.*, 2012, **48**, 6788–6790.
293 W. J. Zhang, Z. Liu, K. P. Song, C. M. Aikens, S. S. Zhang, Z. Wang, C. H. Tung and D. Sun, *Angew. Chem., Int. Ed.*, 2021, **60**, 4231–4237.
294 Z. Wang, H. F. Su, Y. W. Gong, Q. P. Qu, Y. F. Bi, C. H. Tung, D. Sun and L. S. Zheng, *Nat. Commun.*, 2020, **11**, 308.
295 F. Hu, R. L. He, Z. J. Guan, C. Y. Liu and Q. M. Wang, *Angew. Chem., Int. Ed.*, 2023, **62**, e202304134.
296 M. Qu, F. Q. Zhang, G. L. Zhang, M. M. Qiao, L. X. Zhao, S. L. Li, M. Walter and X. M. Zhang, *Angew. Chem., Int. Ed.*, 2024, **63**, e202318390.
297 F. Hu, J. Li, Z. Guan, S. Yuan and Q. Wang, *Angew. Chem.*, 2020, **132**, 5350–5353.
298 D. Fenske, C. E. Anson, A. Eichhöfer, O. Fuhr, A. Ingendoh, C. Persau and C. Richert, *Angew. Chem., Int. Ed.*, 2005, **44**, 5242–5246.
299 H. Yang, Y. Wang, X. Chen, X. Zhao, L. Gu, H. Huang, J. Yan, C. Xu, G. Li, J. Wu, A. J. Edwards, B. Dittrich, Z. Tang, D. Wang, L. Lehtovaara, H. Häkkinen and N. Zheng, *Nat. Commun.*, 2016, **7**, 12809.
300 M. R. Branham, A. D. Douglas, A. J. Mills, J. B. Tracy, P. S. White and R. W. Murray, *Langmuir*, 2006, **22**, 11376–11383.
301 I. Chakraborty, A. Govindarajan, J. Erusappan, A. Ghosh, T. Pradeep, B. Yoon, R. L. Whetten and U. Landman, *Nano Lett.*, 2012, **12**, 5861–5866.
302 C. E. Anson, A. Eichöfer, I. Issac, D. Fenske, O. Fuhr, P. Sevillano, C. Persau, D. Stalke and J. Zhang, *Angew. Chem., Int. Ed.*, 2008, **47**, 1326–1331.
303 C. G. Shi, J. H. Jia, Y. Jia, G. Li and M. L. Tong, *CCS Chem.*, 2023, **5**, 1154–1162.
304 M. A. Hewitt, H. Hernández and G. E. Johnson, *J. Am. Soc. Mass Spectrom.*, 2021, **32**, 237–246.
305 X. Ren, J. Fu, X. Lin, X. Fu, J. Yan, R. Wu, C. Liu and J. Huang, *Dalton Trans.*, 2018, **47**, 7487–7491.
306 L. Moreaud, J. Prasad, S. Mazères, C. Marcelot, C. Comby-Zerbino, R. Antoine, O. Heintz and E. Dujardin, *J. Mater. Chem. C*, 2022, **10**, 2263–2270.
307 R. W. Y. Man, H. Yi, S. Malola, S. Takano, T. Tsukuda, H. Häkkinen, M. Nambo and C. M. Crudden, *J. Am. Chem. Soc.*, 2022, **144**, 2056–2061.
308 C. L. Lin, X. Lei, Y. Zhang, H. Wang, H. Li, Y. Zhao, S. Zhang, W. Fan, W. W. Xu and M. B. Li, *Nano Lett.*, 2025, **25**, 11374–11381.
309 N. Rashi, A. Devi and A. Patra, *J. Phys. Chem. C*, 2025, **129**, 12633–12640.
310 L. D. Plath, H. Abroshan, C. Zeng, H. J. Kim, R. Jin and M. E. Bier, *J. Am. Soc. Mass Spectrom.*, 2022, **33**, 521–529.
311 P. A. Lummis, K. M. Osten, T. I. Levchenko, M. Sabooni Asre Hazer, S. Malola, B. Owens-Baird, A. J. Veinot, E. L. Albright, G. Schatte, S. Takano, K. Kovnir, K. G. Stamplecoskie, T. Tsukuda, H. Häkkinen, M. Nambo and C. M. Crudden, *JACS Au*, 2022, **2**, 875–885.
312 Z. Wang, W. Cai and J. Sui, *ChemPhysChem*, 2009, **10**, 2012–2015.
313 T. H. Huang, F. Z. Zhao, Q. L. Hu, Q. Liu, T. C. Wu, D. Zheng, T. Kang, L. C. Gui and J. Chen, *Inorg. Chem.*, 2020, **59**, 16027–16034.
314 N. Shinjo, S. Takano and T. Tsukuda, *Bull. Korean Chem. Soc.*, 2021, **42**, 1265–1268.
315 R. Tomihara, K. Hirata, H. Yamamoto, S. Takano, K. Koyasu and T. Tsukuda, *ACS Omega*, 2018, **3**, 6237–6242.
316 Y. Shichibu, K. Suzuki and K. Konishi, *Nanoscale*, 2012, **4**, 4125–4129.
317 M. R. Narouz, S. Takano, P. A. Lummis, T. I. Levchenko, A. Nazemi, S. Kaappa, S. Malola, G. Yousefalizadeh, L. A. Calhoun, K. G. Stamplecoskie, H. Häkkinen, T. Tsukuda and C. M. Crudden, *J. Am. Chem. Soc.*, 2019, **141**, 14997–15002.
318 H. Zhao, Q. You, W. Zhu, J. Li, H. Deng, M. B. Li, Y. Zhao and Z. Wu, *Small*, 2023, **19**, e2207936.
319 E. S. Shibu and T. Pradeep, *Chem. Mater.*, 2011, **23**, 989–999.
320 G. F. Combes, H. Fakhouri, C. Moulin, M. Girod, F. Bertorelle, S. Basu, R. Ladouce, M. P. Bakulić, Ž. S. Maršić, I. Russier-Antoine, P. F. Brevet, P. Dugourd, A. Krisko, K. Trajković, M. Radman, V. Bonačić-Koutecký and R. Antoine, *Commun. Chem.*, 2021, **4**, 69.
321 S. Yang, S. Chen, L. Xiong, C. Liu, H. Yu, S. Wang, N. L. Rosi, Y. Pei and M. Zhu, *J. Am. Chem. Soc.*, 2018, **140**, 10988–10994.
322 Q. Yao, Y. Yu, X. Yuan, Y. Yu, J. Xie and J. Y. Lee, *Small*, 2013, **9**, 2696–2701.
323 A. Alhalabi, C. Saint-Pierre, E. Boeri-Erba, P. H. Elchinger, H. Kaur, D. Gasparutto and X. Le Guével, *Nanoscale*, 2025, **17**, 12775–12785.
324 A. Ghosh, T. Udayabhaskararao and T. Pradeep, *J. Phys. Chem. Lett.*, 2012, **3**, 1997–2002.
325 S. Chen, S. Wang, J. Zhong, Y. Song, J. Zhang, H. Sheng, Y. Pei and M. Zhu, *Angew. Chem., Int. Ed.*, 2015, **54**, 3145–3149.
326 T. Shigeta, S. Takano and T. Tsukuda, *Angew. Chem., Int. Ed.*, 2022, **61**, e202113275.
327 R. Itteboina, U. Di. Madhuri, P. Ghosal, M. Kannan, T. K. Sau, T. Tsukuda and S. Bhardwaj, *J. Phys. Chem. A*, 2018, **122**, 1228–1234.
328 X. K. Wan, Q. Tang, S. F. Yuan, D. E. Jiang and Q. M. Wang, *J. Am. Chem. Soc.*, 2015, **137**, 652–655.
329 Z. Wu, M. A. MacDonald, J. Chen, P. Zhang and R. Jin, *J. Am. Chem. Soc.*, 2011, **133**, 9670–9673.
330 L. Wang, K. Koyasu and T. Tsukuda, *J. Cluster Sci.*, 2025, **36**, 139.
331 S. Wang, C. Han, X. Chen, Y. Xiang, Q. Li, J. Chai, S. Yang, Y. Du, Q. Luo and M. Zhu, *ACS Nano*, 2025, **19**, 25334–25341.

Published on 27 October 2025. Downloaded by Indian Institute of Technology Chennai on 12/29/2025 3:17:01 AM.

332 Q. F. Zhang, X. Chen and L. S. Wang, *Acc. Chem. Res.*, 2018, **51**, 2159–2168.
333 X. K. Wan, X. S. Han, Z. J. Guan, W. Q. Shi, J. J. Li and Q. M. Wang, *Nat. Commun.*, 2024, **15**, 7214.
334 P. Aminfar, T. Ferguson, E. Steele, E. M. MacNeil, M. F. Matus, S. Malola, H. Häkkinen, P. N. Duchesne, H. P. Loock and K. G. Stamplecoskie, *Nanoscale*, 2023, **16**, 205–211.
335 E. S. Shibu, B. Radha, P. K. Verma, P. Bhyrappa, G. U. Kulkarni, S. K. Pal and T. Pradeep, *ACS Appl. Mater. Interfaces*, 2009, **1**, 2199–2210.
336 J. Chen, Q. F. Zhang, T. A. Bonaccorso, P. G. Williard and L. S. Wang, *J. Am. Chem. Soc.*, 2014, **136**, 92–95.
337 H. Heo, S. Cho, Y. Kim, S. Ahn, J. H. Mok, H. Lee and D. Lee, *Nanoscale*, 2024, **16**, 20147–20154.
338 Y. Yu, Z. Luo, D. M. Chevrier, D. T. Leong, P. Zhang, D. E. Jiang and J. Xie, *J. Am. Chem. Soc.*, 2014, **136**, 1246–1249.
339 Q. Li, Y. Tan, B. Huang, S. Yang, J. Chai, X. Wang, Y. Pei and M. Zhu, *J. Am. Chem. Soc.*, 2023, **145**, 15859–15868.
340 Z. H. Gao, K. Wei, T. Wu, J. Dong, D. E. Jiang, S. Sun and L. S. Wang, *J. Am. Chem. Soc.*, 2022, **144**, 5258–5262.
341 J. Dong, P. Weis, V. Wani, M. M. Kappes and L. S. Wang, *J. Phys. Chem. Lett.*, 2025, **16**, 4975–4981.
342 S. Gratious, E. N. Nahan, R. Jin and S. Mandal, *Acc. Mater. Res.*, 2024, **5**, 1291–1302.
343 M. A. H. Muhammed, P. K. Verma, S. K. Pal, R. C. A. Kumar, S. Paul, R. V. Omkumar and P. Thalappil, *Chem. – Eur. J.*, 2009, **15**, 10110–10120.
344 A. Das, T. Li, K. Nobusada, C. Zeng, N. L. Rosi and R. Jin, *J. Am. Chem. Soc.*, 2013, **135**, 18264–18267.
345 Z. J. Guan, F. Hu, J. J. Li, Z. R. Wen, Y. M. Lin and Q. M. Wang, *J. Am. Chem. Soc.*, 2020, **142**, 2995–3001.
346 Y. Negishi, H. Horihata, A. Ebina, S. Miyajima, M. Nakamoto, A. Ikeda, T. Kawawaki and S. Hossain, *Chem. Sci.*, 2022, **13**, 5546–5556.
347 A. Das, T. Li, K. Nobusada, Q. Zeng, N. L. Rosi and R. Jin, *J. Am. Chem. Soc.*, 2012, **134**, 20286–20289.
348 Y. Song, S. Wang, J. Zhang, X. Kang, S. Chen, P. Li, H. Sheng and M. Zhu, *J. Am. Chem. Soc.*, 2014, **136**, 2963–2965.
349 S. Hasegawa, S. Takano, K. Harano and T. Tsukuda, *JACS Au*, 2021, **1**, 660–668.
350 Y. Shichibu, Y. Negishi, T. Tsukuda and T. Teranishi, *J. Am. Chem. Soc.*, 2005, **127**, 13464–13465.
351 Y. Shichibu, Y. Negishi, T. Watanabe, N. K. Chaki, H. Kawaguchi and T. Tsukuda, *J. Phys. Chem. C*, 2020, **111**, 7845–7847.
352 Y. Negishi, N. K. Chaki, Y. Shichibu, R. L. Whetten and T. Tsukuda, *J. Am. Chem. Soc.*, 2007, **129**, 11322–11323.
353 M. A. Habeeb Muhammed, A. K. Shaw, S. K. Pal and T. Pradeep, *J. Phys. Chem. C*, 2008, **112**, 14324–14330.
354 M. A. Habeeb Muhammed, S. Ramesh, S. S. Sinha, S. K. Pal and T. Pradeep, *Nano Res.*, 2008, **1**, 333–340.
355 M. Zhu, W. T. Eckenhoff, T. Pintauer and R. Jin, *J. Phys. Chem. C*, 2008, **112**, 14221–14224.
356 M. Zhu, E. Lanni, N. Garg, M. E. Bier and R. Jin, *J. Am. Chem. Soc.*, 2008, **130**, 1138–1139.
357 M. A. H. Muhammed and T. Pradeep, *J. Cluster Sci.*, 2009, **20**, 365–373.
358 A. C. Dharmaratne, T. Krick and A. Dass, *J. Am. Chem. Soc.*, 2009, **131**, 13604–13605.
359 V. R. Jupally, R. Kota, E. Van Dornshuld, D. L. Mattern, G. S. Tschumper, D. E. Jiang and A. Dass, *J. Am. Chem. Soc.*, 2011, **133**, 20258–20266.
360 A. Dass, G. R. Dubay, C. A. Fields-Zinna and R. W. Murray, *Anal. Chem.*, 2008, **80**, 6845–6849.
361 Y. Negishi, W. Kurashige and U. Kamimura, *Langmuir*, 2011, **27**, 12289–12292.
362 S. Xie, H. Tsunoyama, W. Kurashige, Y. Negishi and T. Tsukuda, *ACS Catal.*, 2012, **2**, 1519–1523.
363 T. Dainese, S. Antonello, J. A. Gascón, F. Pan, N. V. Perera, M. Ruzzi, A. Venzo, A. Zoleo, K. Rissanen and F. Maran, *ACS Nano*, 2014, **8**, 3904–3912.
364 Y. Yu, Z. Luo, Y. Yu, J. Y. Lee and J. Xie, *ACS Nano*, 2012, **6**, 7920–7927.
365 Z. Wu, J. Chen and R. Jin, *Adv. Funct. Mater.*, 2011, **21**, 177–183.
366 C. E. Angevine, A. E. Chavis, N. Kothalawala, A. Dass and J. E. Reiner, *Anal. Chem.*, 2014, **86**, 11077–11085.
367 J. Hassinen, P. Pulkkinen, E. Kalenius, T. Pradeep, H. Tenhu, H. Häkkinen and R. H. A. Ras, *J. Phys. Chem. Lett.*, 2014, **5**, 585–589.
368 A. Ghosh, J. Hassinen, P. Pulkkinen, H. Tenhu, R. H. A. Ras and T. Pradeep, *Anal. Chem.*, 2014, **86**, 12185–12190.
369 Q. Yao, X. Yuan, Y. Yu, Y. Yu, J. Xie and J. Y. Lee, *J. Am. Chem. Soc.*, 2015, **137**, 2128–2136.
370 J. Yoshimoto, A. Sangsuwan, I. Osaka, K. Yamashita, Y. Iwasaki, M. Inada, R. Arakawa and H. Kawasaki, *J. Phys. Chem. C*, 2015, **119**, 14319–14325.
371 A. Mathew, E. Varghese, S. Choudhury, S. K. Pal and T. Pradeep, *Nanoscale*, 2015, **7**, 14305–14315.
372 S. Bhat, R. P. Narayanan, A. Baksi, P. Chakraborty, G. Paramasivam, R. R. J. Methikkalam, A. Nag, G. Natarajan and T. Pradeep, *J. Phys. Chem. C*, 2018, **122**, 19455–19462.
373 Y. Wang and T. Bürgi, *Nanoscale*, 2022, **14**, 2456–2464.
374 M. Swierczewski, F. Cousin, E. Banach, A. Rosspeintner, L. M. Lawson Daku, A. Ziarati, R. Kazan, G. Jeschke, R. Azoulay, L. T. Lee and T. Bürgi, *Angew. Chem., Int. Ed.*, 2023, **62**, e202215746.
375 X. Luo, J. Kong, H. Xiao, D. Sang, K. He, M. Zhou and J. Liu, *Angew. Chem., Int. Ed.*, 2024, **63**, e202404129.
376 J. Sen Yang, Y. J. Zhao, X. M. Li, X. Y. Dong, Y. B. Si, L. Y. Xiao, J. H. Hu, Z. Yu and S. Q. Zang, *Angew. Chem., Int. Ed.*, 2024, **63**, e202318030.
377 C. Zhou, M. Wang, Q. Yao, Y. Zhou, C. Hou, J. Xia, Z. Wang, J. Chen and J. Xie, *Aggregate*, 2023, **5**, e401.
378 Y. Y. Dong, C. Y. Liu, W. Q. Shi, Z. J. Guan and Q. M. Wang, *Angew. Chem., Int. Ed.*, 2025, **64**, e202420314.

Published on 27 October 2025. Downloaded by Indian Institute of Technology Chennai on 12/29/2025 3:17:01 AM.

379 T. Gregory Schaaff and R. L. Whetten, *J. Phys. Chem. B*, 2000, **104**, 2630–2641.
380 Y. Wang, B. Nieto-Ortega and T. Bürgi, *Chem. Commun.*, 2019, **55**, 14914–14917.
381 W. Q. Shi, L. Zeng, Z. C. Long, Z. J. Guan, X. S. Han, F. Hu, M. Zhou and Q. M. Wang, *J. Phys. Chem. Lett.*, 2025, **16**, 2204–2211.
382 S. F. Yuan, R. L. He, X. S. Han, J. Q. Wang, Z. J. Guan and Q. M. Wang, *Angew. Chem., Int. Ed.*, 2021, **60**, 14345–14349.
383 J. Wang, Z. Y. Wang, S. J. Li, S. Q. Zang and T. C. W. Mak, *Angew. Chem., Int. Ed.*, 2021, **60**, 5959–5964.
384 J. Dong, Z. Gan, W. Gu, Q. You, Y. Zhao, J. Zha, J. Li, H. Deng, N. Yan and Z. Wu, *Angew. Chem., Int. Ed.*, 2021, **60**, 17932–17936.
385 Y. Yu, Q. Yao, K. Cheng, X. Yuan, Z. Luo and J. Xie, *Part. Part. Syst. Charact.*, 2014, **31**, 652–656.
386 P. J. Krommenhoek, J. Wang, N. Hentz, A. C. Johnston-Peck, K. A. Kozek, G. Kalyuzhny and J. B. Tracy, *ACS Nano*, 2012, **6**, 4903–4911.
387 D. Crasto and A. Dass, *J. Phys. Chem. C*, 2013, **117**, 22094–22097.
388 D. Crasto, S. Malola, G. Brosofsky, A. Dass and H. Häkkinen, *J. Am. Chem. Soc.*, 2014, **136**, 5000–5005.
389 X. K. Wan, T. T. Liu, N. L. Li, Q. Dai, J. Wei and Q. M. Wang, *ACS Nano*, 2025, **19**, 11371–11380.
390 P. R. Nimmala and A. Dass, *J. Am. Chem. Soc.*, 2011, **133**, 9175–9177.
391 C. Zeng, H. Qian, T. Li, G. Li, N. L. Rosi, B. Yoon, R. N. Barnett, R. L. Whetten, U. Landman and R. Jin, *Angew. Chem., Int. Ed.*, 2012, **51**, 13114–13118.
392 M. Sakamoto, Y. Mizuhata, W. Ota, T. Konishi, H. Tahara, K. Kamada and T. Sato, *J. Am. Chem. Soc.*, 2025, **147**, 23451–23457.
393 Y. Y. Lin, Z. A. Nan, Z. Lei and Q. M. Wang, *Nanoscale*, 2025, **17**, 8724–8730.
394 X. Wan, Z. Guan and Q. Wang, *Angew. Chem.*, 2017, **129**, 11652–11655.
395 Y. Tan, K. Li, J. Xu, Q. Li, S. Yang, J. Chai, Y. Pei, D. Jia and M. Zhu, *Nanoscale*, 2024, **16**, 15663–15669.
396 J. Kim, K. Lema, M. Ukaigwe and D. Lee, *Langmuir*, 2007, **23**, 7853–7858.
397 D. Stellwagen, A. Weber, G. L. Bovenkamp, R. Jin, J. H. Bitter and C. S. S. R. Kumar, *RSC Adv.*, 2012, **2**, 2276–2283.
398 H. Qian, M. Zhu, U. N. Andersen and R. Jin, *J. Phys. Chem. A*, 2009, **113**, 4281–4284.
399 S. Knoppe, A. C. Dharmaratne, E. Schreiner, A. Dass and T. Bürgi, *J. Am. Chem. Soc.*, 2010, **132**, 16783–16789.
400 Y. Negishi, K. Igarashi, K. Munakata, W. Ohgake and K. Nobusada, *Chem. Commun.*, 2012, **48**, 660–662.
401 S. Knoppe, J. Boudon, I. Dolamic, A. Dass and T. Bürgi, *Anal. Chem.*, 2011, **83**, 5056–5061.
402 H. Qian, Y. Zhu and R. Jin, *ACS Nano*, 2009, **3**, 3795–3803.
403 O. Toikkanen, S. Carlsson, A. Dass, G. Rönnholm, N. Kalkkinen and B. M. Quinn, *J. Phys. Chem. Lett.*, 2010, **1**, 32–37.
404 O. Toikkanen, V. Ruiz, G. Rönnholm, N. Kalkkinen, P. Liljeroth and B. M. Quinn, *J. Am. Chem. Soc.*, 2008, **130**, 11049–11055.
405 S. Gaur, J. T. Miller, D. Stellwagen, A. Sanampudi, C. S. S. R. Kumar and J. J. Spivey, *Phys. Chem. Chem. Phys.*, 2012, **14**, 1627–1634.
406 H. Qian, Y. Zhu and R. Jin, *J. Am. Chem. Soc.*, 2010, **132**, 4583–4585.
407 S. Knoppe, I. Dolamic, A. Dass and T. Bürgi, *Angew. Chem., Int. Ed.*, 2012, **51**, 7589–7591.
408 J. Li, Z. Wang, J. Ye, Q. Li, S. Yang, J. Chai and M. Zhu, *Chem. Commun.*, 2025, **61**, 5146–5149.
409 J. I. Nishigaki, R. Tsunoyama, H. Tsunoyama, N. Ichikuni, S. Yamazoe, Y. Negishi, M. Ito, T. Matsuo, K. Tamao and T. Tsukuda, *J. Am. Chem. Soc.*, 2012, **134**, 14295–14297.
410 S. Zhuang, L. Liao, J. Yuan, N. Xia, Y. Zhao, C. Wang, Z. Gan, N. Yan, L. He, J. Li, H. Deng, Z. Guan, J. Yang and Z. Wu, *Angew. Chem.*, 2019, **131**, 4558–4562.
411 H. W. Luyang, C. Q. Xu, S. F. Yuan, J. Li and Q. M. Wang, *Angew. Chem., Int. Ed.*, 2025, **64**, e202417904.
412 Z. J. Guan, F. Hu, J. J. Li, Z. R. Liu and Q. M. Wang, *Nanoscale*, 2020, **12**, 13346–13350.
413 P. Maity, H. Tsunoyama, M. Yamauchi, S. Xie and T. Tsukuda, *J. Am. Chem. Soc.*, 2011, **133**, 20123–20125.
414 L. Liao, S. Zhuang, P. Wang, Y. Xu, N. Yan, H. Dong, C. Wang, Y. Zhao, N. Xia, J. Li, H. Deng, Y. Pei, S. Tian and Z. Wu, *Angew. Chem.*, 2017, **129**, 12818–12822.
415 P. Maity, T. Wakabayashi, N. Ichikuni, H. Tsunoyama, S. Xie, M. Yamauchi and T. Tsukuda, *Chem. Commun.*, 2012, **48**, 6085–6087.
416 H. Tsunoyama, Y. Negishi and T. Tsukuda, *J. Am. Chem. Soc.*, 2006, **128**, 6036–6037.
417 R. Tsunoyama, H. Tsunoyama, P. Pannopard, J. Limtrakul and T. Tsukuda, *J. Phys. Chem. C*, 2010, **114**, 16004–16009.
418 H. Qian and R. Jin, *Chem. Commun.*, 2011, **47**, 11462–11464.
419 X. K. Wan, J. Q. Wang and Q. M. Wang, *Angew. Chem., Int. Ed.*, 2021, **60**, 20748–20753.
420 Y. Song, F. Fu, J. Zhang, J. Chai, X. Kang, P. Li, S. Li, H. Zhou and M. Zhu, *Angew. Chem.*, 2015, **127**, 8550–8554.
421 C. Zeng, Y. Chen, G. Li and R. Jin, *Chem. Mater.*, 2014, **26**, 2635–2641.
422 P. R. Nimmala, B. Yoon, R. L. Whetten, U. Landman and A. Dass, *J. Phys. Chem. A*, 2013, **117**, 504–517.
423 O. J. H. Chai and J. Xie, *J. Phys. Chem. Lett.*, 2024, **15**, 5137–5142.
424 A. Dass, *J. Am. Chem. Soc.*, 2009, **131**, 11666–11667.
425 R. Balasubramanian, R. Guo, A. J. Mills and R. W. Murray, *J. Am. Chem. Soc.*, 2005, **127**, 8126–8132.
426 S. Takano, S. Yamazoe, K. Koyasu and T. Tsukuda, *J. Am. Chem. Soc.*, 2015, **137**, 7027–7030.
427 W. Wang, D. Chen, V. Fung, S. Zhuang, Y. Zhou, C. Wang, G. Bian, Y. Zhao, N. Xia, J. Li, H. Deng, L. Liao, J. Yang, D. en Jiang and Z. Wu, *Angew. Chem., Int. Ed.*, 2025, **64**, e202410109.

Published on 27 October 2025. Downloaded by Indian Institute of Technology Chennai on 12/29/2025 3:17:01 AM.

428 L. Liao, J. Chen, C. Wang, S. Zhuang, N. Yan, C. Yao, N. Xia, L. Li, X. Bao and Z. Wu, *Chem. Commun.*, 2016, **52**, 12036–12039.
429 C. Zeng, C. Liu, Y. Chen, N. L. Rosi and R. Jin, *J. Am. Chem. Soc.*, 2016, **138**, 8710–8713.
430 J. J. Li, Z. Liu, Z. J. Guan, X. S. Han, W. Q. Shi and Q. M. Wang, *J. Am. Chem. Soc.*, 2022, **144**, 690–694.
431 P. R. Nimmala and A. Dass, *J. Am. Chem. Soc.*, 2014, **136**, 17016–17023.
432 X. Du, T. Higaki, H. Ma, X. Zhang, G. Wang, H. Wang and R. Jin, *Nanoscale*, 2025, **17**, 14408–14414.
433 Y. Levi-Kalisman, P. D. Jadzinsky, N. Kalisman, H. Tsunoyama, T. Tsukuda, D. A. Bushnell and R. D. Kornberg, *J. Am. Chem. Soc.*, 2011, **133**, 2976–2982.
434 D. M. Black, M. M. Alvarez, F. Yan, W. P. Griffith, G. Plascencia-Villa, S. B. H. Bach and R. L. Whetten, *J. Phys. Chem. C*, 2017, **121**, 10851–10857.
435 Y. Chen, J. Wang, C. Liu, Z. Li and G. Li, *Nanoscale*, 2016, **8**, 10059–10065.
436 N. A. Sakthivel, L. Sementa, B. Yoon, U. Landman, A. Fortunelli and A. Dass, *J. Phys. Chem. C*, 2020, **124**, 1655–1666.
437 T. Higaki, C. Liu, M. Zhou, T. Y. Luo, N. L. Rosi and R. Jin, *J. Am. Chem. Soc.*, 2017, **139**, 9994–10001.
438 A. Dass, P. R. Nimmala, V. R. Jupally and N. Kothalawala, *Nanoscale*, 2013, **5**, 12082–12085.
439 J. J. Li, Z. J. Guan, S. F. Yuan, F. Hu and Q. M. Wang, *Angew. Chem., Int. Ed.*, 2021, **60**, 6699–6703.
440 J. Q. Wang, S. Shi, R. L. He, S. F. Yuan, G. Y. Yang, G. J. Liang and Q. M. Wang, *J. Am. Chem. Soc.*, 2020, **142**, 18086–18092.
441 G. Bian, D. Chen, Y. Chen, W. Zhang, L. Fang, Q. You, R. Wang, W. Gu, Y. Zhou, N. Yan, S. Zhuang, S. Ji, M. Zhou, C. Wang, L. Liao, Q. Tang, J. Yang and Z. Wu, *Sci. Adv.*, 2025, **11**, eadu1996.
442 X. Ren, X. Fu, X. Lin, C. Liu, J. Huang and J. Yan, *Chem. Res. Chin. Univ.*, 2018, **34**, 719–722.
443 Y. Negishi, C. Sakamoto, T. Ohyama and T. Tsukuda, *J. Phys. Chem. Lett.*, 2012, **3**, 1624–1628.
444 Z. Lei, P. Zhao, Z. J. Guan, Z. A. Nan, M. Ehara and Q. M. Wang, *Chem. – Eur. J.*, 2024, **30**, e202401094.
445 X. Du, X. Zhang, H. Ma, M. Zhou, T. Higaki, G. Wang, H. Wang and R. Jin, *ChemElectroChem*, 2024, **11**, e202300528.
446 Y. Negishi, T. Nakazaki, S. Malola, S. Takano, Y. Niihori, W. Kurashige, S. Yamazoe, T. Tsukuda and H. Häkkinen, *J. Am. Chem. Soc.*, 2015, **137**, 1206–1212.
447 V. R. Jupally, A. C. Dharmaratne, D. Crasto, A. J. Huckaba, C. Kumara, P. R. Nimmala, N. Kothalawala, J. H. Delcamp and A. Dass, *Chem. Commun.*, 2014, **50**, 9895–9898.
448 L. J. Liu, F. Alkan, S. Zhuang, D. Liu, T. Nawaz, J. Guo, X. Luo and J. He, *Nat. Commun.*, 2023, **14**, 2397.
449 T. G. Schaaff, M. N. Shafigullin, J. T. Khoury, I. Vezmar and R. L. Whetten, *J. Phys. Chem. B*, 2001, **105**, 8785–8796.
450 Z. Lei, J. Li, X. Wan, W. Zhang and Q. Wang, *Angew. Chem.*, 2018, **130**, 8775–8779.
451 H. Qian and R. Jin, *Chem. Mater.*, 2011, **23**, 2209–2217.
452 X. Ma, Z. Tang, L. Qin, J. Peng, L. Li and S. Chen, *Nanoscale*, 2020, **12**, 2980–2986.
453 T. Dainese, S. Antonello, S. Bonacchi, D. Morales-Martinez, A. Venzo, D. M. Black, M. Mozammel Hoque, R. L. Whetten and F. Maran, *Nanoscale*, 2021, **13**, 15394–15402.
454 S. Vergara, D. A. Lukes, M. W. Martynowycz, U. Santiago, G. Plascencia-Villa, S. C. Weiss, M. J. De La Cruz, D. M. Black, M. M. Alvarez, X. López-Lozano, C. O. Barnes, G. Lin, H. C. Weissker, R. L. Whetten, T. Gonen, M. J. Yacaman and G. Calero, *J. Phys. Chem. Lett.*, 2017, **8**, 5523–5530.
455 F. Hu, Z. J. Guan, G. Yang, J. Q. Wang, J. J. Li, S. F. Yuan, G. J. Liang and Q. M. Wang, *J. Am. Chem. Soc.*, 2021, **143**, 17059–17067.
456 N. A. Sakthivel, M. Shabaninezhad, L. Sementa, B. Yoon, M. Stener, R. L. Whetten, G. Ramakrishna, A. Fortunelli, U. Landman and A. Dass, *J. Am. Chem. Soc.*, 2020, **142**, 15799–15814.
457 M. Zhou, C. Zeng, Y. Song, J. W. Padelford, G. Wang, M. Y. Sfeir, T. Higaki and R. Jin, *Angew. Chem.*, 2017, **129**, 16475–16479.
458 C. Kumara, X. Zuo, J. Ilavsky, D. Cullen and A. Dass, *J. Phys. Chem. C*, 2015, **119**, 11260–11266.
459 K. Kwak, V. D. Thanthirige, K. Pyo, D. Lee and G. Ramakrishna, *J. Phys. Chem. Lett.*, 2017, **8**, 4898–4905.
460 L. Zhang, R. Guo, C. Fang, D. Kong, D. Lv and X. Sun, *J. Phys. Chem. A*, 2025, **129**, 4892–4902.
461 S. Duary, A. Jana, A. Das, S. Acharya, A. R. Kini, J. Roy, A. K. Poonia, D. K. Patel, V. Yadav, P. K. S. Antharjanam, B. Pathak, A. Kumaran Nair Valsala Devi and T. Pradeep, *Inorg. Chem.*, 2024, **63**, 18727–18737.
462 X. H. Gao, S. J. He, C. M. Zhang, C. Du, X. Chen, W. Xing, S. L. Chen, A. Clayborne and W. Chen, *Adv. Sci.*, 2016, **3**, 1600126.
463 B. Mondal, K. Basu, R. Jana, P. Mondal, B. Hansda, A. Datta and A. Banerjee, *ACS Appl. Nano Mater.*, 2022, **5**, 7932–7943.
464 M. L. Fu, D. Fenske, B. Weinert and O. Fuhr, *Eur. J. Inorg. Chem.*, 2010, **2010**, 1098–1102.
465 A. Avdeef and J. P. Fackler Jr., *Inorg. Chem.*, 1978, **8**, 2182–2187.
466 J. F. Corrigan and D. Fenske, *Angew. Chem., Int. Ed. Engl.*, 1997, **36**, 1981–1983.
467 R. Gupta, S. Agrawal, S. Rai, J. Sarkar, S. Kumari, D. Shil and S. Mukherjee, *ACS Appl. Opt. Mater.*, 2024, **2**, 1880–1890.
468 S. Duary, A. Jana, A. Das, A. Sharma, B. Pathak, K. N. V. D. Adarsh and T. Pradeep, *Inorg. Chem.*, 2025, **64**, 11001–11011.
469 M. Chang, Y. Xu, Y. Lv, H. Yu, H. Li, X. Kang and M. Zhu, *Chem. Commun.*, 2025, **61**, 11215–11218.
470 A. Eichhöfer, J. F. Corrigan, D. Fenske and E. Tröster, *Z. Anorg. Allg. Chem.*, 2000, **626**, 338–348.
471 C. Y. Liu, S. F. Yuan, S. Wang, Z. J. Guan, D. en Jiang and Q. M. Wang, *Nat. Commun.*, 2022, **13**, 2082.

Published on 27 October 2025. Downloaded by Indian Institute of Technology Chennai on 12/29/2025 3:17:01 AM.

472 M. J. Trenerry and G. A. Bailey, *Nanoscale*, 2024, **16**, 16048–16057.
473 M. W. DeGroot, M. W. Cockburn, M. S. Workentin and J. F. Corrigan, *Inorg. Chem.*, 2001, **40**, 4678–4685.
474 S. Dehnen, A. Schäfer, D. Fenske and R. Ahlrichs, *Angew. Chem., Int. Ed. Engl.*, 1994, **33**, 746–749.
475 A. Jana, S. Duary, A. Das, A. R. Kini, S. Acharya, J. Machacek, B. Pathak, T. Base and T. Pradeep, *Chem. Sci.*, 2024, **15**, 13741–13752.
476 J. Zhu, R. Zhao, H. Shen, C. Zhu, M. Zhou, X. Kang and M. Zhu, *Aggregate*, 2024, **6**, e720.
477 A. K. Das, S. Hegde, T. J. Woods, V. S. Wani and M. P. Backlund, *Nano Lett.*, 2025, **25**, 7491–7498.
478 M. Oyebanji, L. Chen, R. Qian, M. Tu, Q. Zhang, X. Yang, H. Yu and M. Zhu, *Anal. Methods*, 2024, **16**, 6688–6695.
479 S. Nematulloev, R. W. Huang, J. Yin, A. Shkurenko, C. Dong, A. Ghosh, B. Alamer, R. Naphade, M. N. Hedhili, P. Maity, M. Eddaoudi, O. F. Mohammed and O. M. Bakr, *Small*, 2021, **17**, e2006839.
480 A. Nag, A. M. Butt, M. Y. Yang, P. B. Managutti, B. M. Pirzada, M. I. H. Mohideen, A. L. Abdelhady, M. A. Haija, S. Mohamed, B. V. Merinov, W. A. Goddard and A. Qurashi, *ACS Mater. Lett.*, 2025, **7**, 442–449.
481 C. Zhang, W. D. Si, Z. Wang, A. Dinesh, Z. Y. Gao, C. H. Tung and D. Sun, *J. Am. Chem. Soc.*, 2024, **146**, 10767–10775.
482 C. Y. Liu, T. Y. Liu, Z. J. Guan, S. Wang, Y. Y. Dong, F. Hu, D. E. Jiang and Q. M. Wang, *CCS Chem.*, 2024, **6**, 1581–1590.
483 S. Biswas, Y. Shingyouchi, M. Kamiyama, M. Ogami, H. Song, B. Li, S. Wang, T. Kawawaki, D. E. Jiang and Y. Negishi, *J. Am. Chem. Soc.*, 2025, **147**, 23733–23742.
484 R. W. Huang, J. Yin, C. Dong, P. Maity, M. N. Hedhili, S. Nematulloev, B. Alamer, A. Ghosh, O. F. Mohammed and O. M. Bakr, *ACS Mater. Lett.*, 2021, **3**, 90–99.
485 T. A. D. Nguyen, Z. R. Jones, B. R. Goldsmith, W. R. Buratto, G. Wu, S. L. Scott and T. W. Hayton, *J. Am. Chem. Soc.*, 2015, **137**, 13319–13324.
486 R. P. B. Silalahi, J. H. Liao, Y. F. Tseng, T. H. Chiu, S. Kahlal, J. Y. Saillard and C. W. Liu, *Dalton Trans.*, 2023, **52**, 2106–2114.
487 X. Sun, B. Yan, X. Gong, Q. Xu, Q. Guo and H. Shen, *Chem. – Eur. J.*, 2024, **30**, e202400527.
488 S. Zheng, D. H. Si, H. Guo, Q. J. Wu, H. J. Zhu, Y. B. Huang and R. Cao, *ACS Nano*, 2025, **19**, 24130–24139.
489 S. Lee, M. S. Bootharaju, G. Deng, S. Malola, W. Baek, H. Häkkinen, N. Zheng and T. Hyeon, *J. Am. Chem. Soc.*, 2020, **142**, 13974–13981.
490 S. Maity, D. Bain and A. Patra, *J. Phys. Chem. C*, 2019, **123**, 2506–2515.
491 H. Wang, C. L. Lin, E. Fan, H. T. Yin, S. Zhang, Y. Zhao, M. B. Li and Z. Wu, *ACS Nano*, 2025, **19**, 25295–25303.
492 H. Zhao, C. Zhang, B. L. Han, P. Mahato, C. Z. Yang, P. X. Yu, Z. Wang, C. H. Tung and D. Sun, *Nano Lett.*, 2025, **25**, 9132–9138.
493 J. Sun, X. Tang, X. Yan, W. Jing, Z. Xie, H. Wang, Chaolumen, J. He and H. Shen, *Next Mater.*, 2024, **3**, 100091.
494 J. Sun, J. Liu, H. F. Su, S. Li, X. Tang, Z. Xie, Z. Xu, W. Jiang, J. Wei, X. Gong, A. He, S. Wang, D. E. Jiang, N. Zheng and H. Shen, *Chem. Sci.*, 2025, **16**, 6392–6401.
495 J. Sun, X. Tang, Z. H. Liu, Z. Xie, B. Yan, R. Yin, C. Chaolumen, J. Zhang, W. Fang, J. Wei and H. Shen, *ACS Mater. Lett.*, 2024, **6**, 281–289.
496 A. Ghosh, R. W. Huang, B. Alamer, E. Abou-Hamad, M. N. Hedhili, O. F. Mohammed and O. M. Bakr, *ACS Mater. Lett.*, 2019, **1**, 297–302.
497 R. W. Huang, J. Yin, C. Dong, A. Ghosh, M. J. Alhilaly, X. Dong, M. N. Hedhili, E. Abou-Hamad, B. Alamer, S. Nematulloev, Y. Han, O. F. Mohammed and O. M. Bakr, *J. Am. Chem. Soc.*, 2020, **142**, 8696–8705.
498 M. L. Fu, I. Issac, D. Fenske and O. Fuhr, *Angew. Chem., Int. Ed.*, 2010, **49**, 6899–6903.
499 H. Yamamoto, P. Maity, R. Takahata, S. Yamazoe, K. Koyasu, W. Kurashige, Y. Negishi and T. Tsukuda, *J. Phys. Chem. C*, 2017, **121**, 10936–10941.
500 A. W. Cook, P. Hrobárik, P. L. Damon, G. Wu and T. W. Hayton, *Inorg. Chem.*, 2020, **59**, 1471–1480.
501 Q. You, X. L. Jiang, W. Fan, Y. S. Cui, Y. Zhao, S. Zhuang, W. Gu, L. Liao, C. Q. Xu, J. Li and Z. Wu, *Angew. Chem., Int. Ed.*, 2024, **63**, e202313491.
502 X. Wang, L. Zhao, X. Li, Y. Liu, Y. Wang, Q. Yao, J. Xie, Q. Xue, Z. Yan, X. Yuan and W. Xing, *Nat. Commun.*, 2022, **13**, 1–10.
503 K. Oiwa, K. Ikeda, R. Kurosaki, K. Sato, N. Nishi, H. Tachibana, M. A. Haque, T. Kawawaki, K. Iida and Y. Negishi, *J. Mater. Chem. A*, 2025, **13**, 12124–12132.
504 R. Wang, D. Chen, L. Fang, W. Fan, Q. You, G. Bian, Y. Zhou, W. Gu, C. Wang, L. Bai, J. Li, H. Deng, L. Liao, J. Yang and Z. Wu, *Angew. Chem., Int. Ed.*, 2024, **63**, e202402565.
505 H. Seong, Y. Jo, V. Efremov, Y. Kim, S. Park, S. M. Han, K. Chang, J. Park, W. Choi, W. Kim, C. H. Choi, J. S. Yoo and D. Lee, *J. Am. Chem. Soc.*, 2023, **145**, 2152–2160.
506 S. R. Biltek, S. Mandal, A. Sen, A. C. Reber, A. F. Pedicini and S. N. Khanna, *J. Am. Chem. Soc.*, 2013, **135**, 26–29.
507 A. Devi, H. Seksaria, D. Bain, S. Kolay, N. Rashi, A. De Sarkar and A. Patra, *Phys. Chem. Chem. Phys.*, 2023, **25**, 9513–9521.
508 H. Seong, Y. Jo, V. Efremov, Y. Kim, S. Park, S. M. Han, K. Chang, J. Park, W. Choi, W. Kim, C. H. Choi, J. S. Yoo and D. Lee, *J. Am. Chem. Soc.*, 2023, **145**, 2152–2160.
509 Y. Yun, K. Zhu, Z.-Y. Wei, T. Guo, S. Lin, T. Li, L. Li, X. Sun, S.-X. Hu, H. Sheng and M. Zhu, *Appl. Catal., B*, 2025, **368**, 125121.
510 Y. K. Lv, Y. Han, K. Wang, W. Y. Sun, C. X. Du, R. W. Huang, P. Peng and S. Q. Zang, *ACS Nano*, 2024, **18**, 32186–32195.
511 J. Chen, L. Liu, X. Liu, L. Liao, S. Zhuang, S. Zhou, J. Yang and Z. Wu, *Chem. – Eur. J.*, 2017, **23**, 18187–18192.

Published on 27 October 2025. Downloaded by Indian Institute of Technology Chennai on 12/29/2025 3:17:01 AM.

512 S. Hossain, Y. Imai, Y. Motohashi, Z. Chen, D. Suzuki, T. Suzuki, Y. Kataoka, M. Hirata, T. Ono, W. Kurashige, T. Kawawaki, T. Yamamoto and Y. Negishi, *Mater. Horiz.*, 2020, **7**, 796–803.
513 L. Chen, Y. Du, Y. Lv, D. Fan, J. Wu, L. Wu, M. Cui, H. Yu and M. Zhu, *Nano Res.*, 2023, **16**, 7770–7776.
514 M. Zhou, S. Jin, X. Wei, Q. Yuan, S. Wang, Y. Du and M. Zhu, *J. Phys. Chem. C*, 2020, **124**, 7531–7538.
515 Y. Yang, S. Guo, Q. Zhang, Z.-J. Guan and Q.-M. Wang, *Angew. Chem., Int. Ed.*, 2024, **63**, e202404798.
516 S. Jin, W. Liu, D. Hu, X. Zou, X. Kang, W. Du, S. Chen, S. Wei, S. Wang and M. Zhu, *Chem. – Eur. J.*, 2018, **24**, 3712–3715.
517 K. Hirata, P. Chakraborty, A. Nag, S. Takano, K. Koyasu, T. Pradeep and T. Tsukuda, *J. Phys. Chem. C*, 2018, **122**, 23123–23128.
518 T. Imagawa, S. Ito, F. Hennrich, M. Neumaier, P. Weis, K. Koyasu, M. M. Kappes and T. Tsukuda, *J. Chem. Phys.*, 2024, **161**, 024303.
519 W. Sun, S. Jin, W. Du, X. Kang, A. Chen, S. Wang, H. Sheng and M. Zhu, *Eur. J. Inorg. Chem.*, 2020, **2020**, 590–594.
520 Z. Qin, D. Zhao, L. Zhao, Q. Xiao, T. Wu, J. Zhang, C. Wan and G. Li, *Nanoscale Adv.*, 2019, **1**, 2529–2536.
521 R. P. B. Silalahi, S. Kahlal, J. Y. Saillard and C. W. Liu, *Molecules*, 2024, **29**, 4427.
522 T. Udayabhaskararao, Y. Sun, N. Goswami, S. K. Pal, K. Balasubramanian and T. Pradeep, *Angew. Chem., Int. Ed.*, 2012, **51**, 2155–2159.
523 X. Kang and M. Zhu, *Chem. Soc. Rev.*, 2019, **48**, 2422–2457.
524 R. C. B. Copley and D. M. P. Mingos, *J. Chem. Soc., Dalton Trans.*, 1996, **4**, 491–500.
525 H. Liu, K. Li, F. Li, Y. Zhao, W. Fan, Y. Pei and M.-B. Li, *Chin. Chem. Lett.*, 2025, 111230.
526 A. Ma, Y. Ren, Y. Zuo, J. Zhao, S. Zhang, X. Ma and S. Wang, *Chem. Commun.*, 2025, **61**, 10772–10775.
527 Y. R. Ni, R. T. Pangal, M. N. Pillay, T. H. Chiu, S. Kahlal, J. Y. Saillard and C. W. Liu, *Molecules*, 2025, **30**, 404.
528 B. Yin, J. Kong, M. Guo, J. Kong, Q. You, M. Zhou and Z. Luo, *Small*, 2025, **21**, e2504958.
529 J. Q. Wang, R. L. He, W. Di Liu, Q. Y. Feng, Y. E. Zhang, C. Y. Liu, J. X. Ge and Q. M. Wang, *J. Am. Chem. Soc.*, 2023, **145**, 12255–12263.
530 Z. R. Wen, Z. J. Guan, Y. Zhang, Y. M. Lin and Q. M. Wang, *Chem. Commun.*, 2019, **55**, 12992–12995.
531 J. H. Huang, H. Zhang, Z. Y. Wang, J. H. Hu, J. Li, J. Cai and S. Q. Zang, *J. Am. Chem. Soc.*, 2025, **147**, 16593–16601.
532 W. Zhang, T. Xu, J. Kong, Y. Li, X. Zhou, J. Zhang, Q. Zhang, Y. Song, Y. Luo and M. Zhou, *Chem. Sci.*, 2025, **16**, 8910–8921.
533 M. Kim, S. Park, M. Kim, S. Kim, J. Seo and S. S. Park, *Nano Lett.*, 2025, **25**, 9110–9117.
534 X. Kang, L. Xiong, S. Wang, Y. Pei and M. Zhu, *Inorg. Chem.*, 2018, **57**, 335–342.
535 Y. Feng, Y. Lv, X. Wei, H. Yu, X. Kang and M. Zhu, *J. Phys. Chem. Lett.*, 2024, **15**, 8910–8916.
536 X. Kang, C. Silalai, Y. Lv, G. Sun, S. Chen, H. Yu, F. Xu and M. Zhu, *Eur. J. Inorg. Chem.*, 2017, **10**, 1414–1419.
537 R. Saito, K. Isozaki, Y. Mizuhata and M. Nakamura, *J. Am. Chem. Soc.*, 2024, **146**, 20930–20936.
538 Y. R. Lin, P. V. V. N. Kishore, J. H. Liao, S. Kahlal, Y. C. Liu, M. H. Chiang, J. Y. Saillard and C. W. Liu, *Nanoscale*, 2018, **10**, 6855–6860.
539 Y. Zhou, W. Gu, R. Wang, W. Zhu, Z. Hu, W. Fei, S. Zhuang, J. Li, H. Deng, N. Xia, J. He and Z. Wu, *Nano Lett.*, 2024, **24**, 2226–2233.
540 W. J. Yen, J. H. Liao, T. H. Chiu, Y. S. Wen and C. W. Liu, *Inorg. Chem.*, 2022, **61**, 6695–6700.
541 S. Jin, F. Xu, W. Du, X. Kang, S. Chen, J. Zhang, X. Li, D. Hu, S. Wang and M. Zhu, *Inorg. Chem.*, 2018, **57**, 5114–5119.
542 S. Yang, J. Chai, Y. Song, J. Fan, T. Chen, S. Wang, H. Yu, X. Li and M. Zhu, *J. Am. Chem. Soc.*, 2017, **139**, 5668–5671.
543 W.-Q. Shi, L. Zeng, R.-L. He, X.-S. Han, Z.-J. Guan, M. Zhou and Q.-M. Wang, *Science*, 2024, **383**, 326–330.
544 W. Liu, H. Wang, X. Zhang, Q. Li, J. Chai, S. Yang and M. Zhu, *Small Methods*, 2025, **9**, e2500044.
545 W. W. Jia, Y. Dai, L. L. Zeng, Z. C. Long, W. Q. Shi, M. Zhou, J. Qiao and Q. M. Wang, *Angew. Chem., Int. Ed.*, 2025, **64**, e202508578.
546 S. Chen, W. Du, C. Qin, D. Liu, L. Tang, Y. Liu, S. Wang and M. Zhu, *Angew. Chem.*, 2020, **132**, 7612–7617.
547 C. Liu, X. Ren, F. Lin, X. Fu, X. Lin, T. Li, K. Sun and J. Huang, *Angew. Chem.*, 2019, **131**, 11457–11461.
548 Q. Li, M. G. Taylor, K. Kirschbaum, K. J. Lambright, X. Zhu, G. Mpourmpakis and R. Jin, *J. Colloid Interface Sci.*, 2017, **505**, 1202–1207.
549 C. Kumara, C. M. Aikens and A. Dass, *J. Phys. Chem. Lett.*, 2014, **5**, 461–466.
550 N. Xia and Z. Wu, *J. Mater. Chem. C*, 2016, **4**, 4125–4128.
551 W. Q. Shi, Z. J. Guan, J. J. Li, X. S. Han and Q. M. Wang, *Chem. Sci.*, 2022, **13**, 5148–5154.
552 S. Wang, X. Meng, A. Das, T. Li, Y. Song, T. Cao, X. Zhu, M. Zhu and R. Jin, *Angew. Chem., Int. Ed.*, 2014, **53**, 2376–2380.
553 S. Hossain, S. Miyajima, T. Iwasa, R. Kaneko, T. Sekine, A. Ikeda, T. Kawawaki, T. Taketsugu and Y. Negishi, *J. Chem. Phys.*, 2021, **155**, 024302.
554 M. S. Bootharaju, S. M. Kozlov, Z. Cao, M. Harb, N. Maity, A. Shkurenko, M. R. Parida, M. N. Hedhili, M. Eddaoudi, O. F. Mohammed, O. M. Bakr, L. Cavallo and J. M. Basset, *J. Am. Chem. Soc.*, 2017, **139**, 1053–1056.
555 Y. Li, M. Zhou, S. Jin, L. Xiong, Q. Yuan, W. Du, Y. Pei, S. Wang and M. Zhu, *Chem. Commun.*, 2019, **55**, 6457–6460.
556 K. Zheng, V. Fung, X. Yuan, D. E. Jiang and J. Xie, *J. Am. Chem. Soc.*, 2019, **141**, 18977–18983.
557 J. Yan, H. Su, H. Yang, S. Malola, S. Lin, H. Häkkinen and N. Zheng, *J. Am. Chem. Soc.*, 2015, **137**, 11880–11883.

Published on 27 October 2025. Downloaded by Indian Institute of Technology Chennai on 12/29/2025 3:17:01 AM.

558 S. Ito, K. Hirano, K. Koyasu, X. K. Wan, Q. M. Wang and T. Tsukuda, *J. Phys. Chem. Lett.*, 2024, **15**, 11060–11066.
559 C. A. Fields-Zinna, M. C. Crowe, A. Dass, J. E. F. Weaver and R. W. Murray, *Langmuir*, 2009, **25**, 7704–7710.
560 M. Sera, S. Hossain, S. Yoshikawa, K. Takemae, A. Ikeda, T. Tanaka, T. Kosaka, Y. Niihori, T. Kawawaki and Y. Negishi, *J. Am. Chem. Soc.*, 2024, **146**, 29684–29693.
561 S. Tian, L. Liao, J. Yuan, C. Yao, J. Chen, J. Yang and Z. Wu, *Chem. Commun.*, 2016, **52**, 9873–9876.
562 S. Ito, K. Koyasu, S. Takano and T. Tsukuda, *J. Phys. Chem. C*, 2020, **124**, 19119–19125.
563 S. Yang, S. Wang, S. Jin, S. Chen, H. Sheng and M. Zhu, *Nanoscale*, 2015, **7**, 10005–10007.
564 S. Sharma, S. Yamazoe, T. Ono, W. Kurashige, Y. Niihori, K. Nobusada, T. Tsukuda and Y. Negishi, *Dalton Trans.*, 2016, **45**, 18064–18068.
565 Y. Negishi, K. Munakata, W. Ohgake and K. Nobusada, *J. Phys. Chem. Lett.*, 2012, **3**, 2209–2214.
566 X. Sun, X. Tang, Y. L. Gao, Y. Zhao, Q. Wu, D. Cao and H. Shen, *Nanoscale*, 2022, **15**, 2316–2322.
567 J. Zhou, T. Li, Q. Li, P. Zheng, S. Yang, J. Chai and M. Zhu, *Inorg. Chem.*, 2022, **61**, 6493–6499.
568 Y. Li, M. Chen, S. Wang and M. Zhu, *Nanomaterials*, 2018, **8**, 1070.
569 Z. Lin, T. Zhang, C. Fang, S. Jin, C. Xu, D. Hu and M. Zhu, *Dalton Trans.*, 2022, **52**, 971–976.
570 Y. Du, Z. J. Guan, Z. R. Wen, Y. M. Lin and Q. M. Wang, *Chem. – Eur. J.*, 2018, **24**, 16029–16035.
571 Z. Qin, S. Sharma, C. qing Wan, S. Malola, W. wu Xu, H. Häkkinen and G. Li, *Angew. Chem., Int. Ed.*, 2021, **60**, 970–975.
572 E. Khatun, P. Chakraborty, B. R. Jacob, G. Paramasivam, M. Bodiuzzaman, W. A. Dar and T. Pradeep, *Chem. Mater.*, 2020, **32**, 611–619.
573 X. Kang, H. Abroshan, S. Wang and M. Zhu, *Inorg. Chem.*, 2019, **58**, 11000–11009.
574 S. F. Yuan, Z. J. Guan and Q. M. Wang, *J. Am. Chem. Soc.*, 2022, **144**, 11405–11412.
575 K. Mikami, S. Hui, K. Kubo, S. Kume and T. Mizuta, *Dalton Trans.*, 2021, **50**, 5659–5665.
576 P. Chakraborty, S. Malola, P. Weis, M. Neumaier, E. K. Schneider, H. Häkkinen and M. M. Kappes, *J. Phys. Chem. Lett.*, 2023, **14**, 11659–11664.
577 S. Hossain, Y. Imai, Y. Motohashi, Z. Chen, D. Suzuki, T. Suzuki, Y. Kataoka, M. Hirata, T. Ono, W. Kurashige, T. Kawawaki, T. Yamamoto and Y. Negishi, *Mater. Horiz.*, 2020, **7**, 796–803.
578 J. Chai, S. Yang, Y. Lv, H. Chong, H. Yu and M. Zhu, *Angew. Chem.*, 2019, **131**, 15818–15821.
579 A. Nag, A. M. Butt, M. Y. Yang, P. B. Managutti, B. M. Pirzada, M. I. H. Mohideen, A. L. Abdelhady, M. Abu Haija, S. Mohamed, B. V. Merinov, W. A. GoddardIII and A. Qurashi, *Mater. Horiz.*, 2025, **12**, 5252–5258.
580 X. Zou, S. Jin, S. Wang, M. Zhu and R. Jin, *Nano Futures*, 2018, **2**, 045004.
581 Y. Yao, W. Hao, J. Tang, K. Kirschbaum, C. G. Gianopoulos, A. Ren, L. Ma, L. Zheng, H. Li and Q. Li, *Angew. Chem., Int. Ed.*, 2024, **63**, e202407214.
582 F. Xuemei, X. Zuoyi, Y. Qianyu, L. Zhonghai, L. Yixuan, Z. Qiang and L. Songgang, *Russ. J. Inorg. Chem.*, 2024, **69**, 207–214.
583 F. Hu, Z.-J. Guan, S.-F. Yuan and Q.-M. Wang, *Chem. – Asian J.*, 2023, **18**, e202300605.
584 S. Hasegawa, S. Takano, S. Yamazoe and T. Tsukuda, *Chem. Commun.*, 2018, **54**, 5915–5918.
585 S. Theivendran, L. Chang, A. Mukherjee, L. Sementa, M. Stener, A. Fortunelli and A. Dass, *J. Phys. Chem. C*, 2018, **122**, 4524–4531.
586 C. Kumara, K. J. Gagnon and A. Dass, *J. Phys. Chem. Lett.*, 2015, **6**, 1223–1228.
587 J. Yan, H. Su, H. Yang, C. Hu, S. Malola, S. Lin, B. K. Teo, H. Häkkinen and N. Zheng, *J. Am. Chem. Soc.*, 2016, **138**, 12751–12754.
588 K. R. Krishnadas, A. Baksi, A. Ghosh, G. Natarajan and T. Pradeep, *ACS Nano*, 2017, **11**, 6015–6023.
589 M. S. Bootharaju, H. Chang, G. Deng, S. Malola, W. Baek, H. Häkkinen, N. Zheng and T. Hyeon, *J. Am. Chem. Soc.*, 2019, **141**, 8422–8425.
590 J. Chai, S. Yang, T. Chen, Q. Li, S. Wang and M. Zhu, *Inorg. Chem.*, 2021, **60**, 9050–9056.
591 H. Ansari, N. Bharadwaj, G. Pramanik, I. Chakraborty, B. Pathak and A. Baksi, *Small*, 2025, **21**, e2502758.
592 J. Han, H. Li, H. Shen, Y. Xu, X. Zou, X. Kang and M. Zhu, *Precis. Chem.*, 2023, **1**, 139–145.
593 H. F. Su, H. Deng, L. S. Zheng and B. K. Teo, *Inorg. Chem.*, 2025, **64**, 10478–10487.
594 Z. Liu, X. Meng, W. Gu, J. Zha, N. Yan, Q. You, N. Xia, H. Wang and Z. Wu, *Acta Phys.-Chim. Sin.*, 2023, **39**, 2212064.
595 X. K. Wan, X. L. Cheng, Q. Tang, Y. Z. Han, G. Hu, D. E. Jiang and Q. M. Wang, *J. Am. Chem. Soc.*, 2017, **139**, 9451–9454.
596 X. H. Ma, J. T. Jia, P. Luo, Z. Y. Wang, S. Q. Zang and T. C. W. Mak, *Nano Res.*, 2022, **15**, 5569–5574.
597 L. Tang, B. Wang, R. Wang and S. Wang, *Nanoscale*, 2023, **15**, 1602–1608.
598 S. Gratious, B. Li, D. Mondal, A. Kumar, D. A. Varghese, J. Thomas, D. E. Jiang, V. Kamble and S. Mandal, *Chem. Sci.*, 2025, **16**, 11849–11857.
599 X. Wei, X. Kang, T. Duan, H. Li, S. Wang, Y. Pei and M. Zhu, *Inorg. Chem.*, 2021, **60**, 11640–11647.
600 Y. Wang, X. K. Wan, L. Ren, H. Su, G. Li, S. Malola, S. Lin, Z. Tang, H. Häkkinen, B. K. Teo, Q. M. Wang and N. Zheng, *J. Am. Chem. Soc.*, 2016, **138**, 3278–3281.
601 J. Xu, L. Xiong, X. Cai, S. Tang, A. Tang, X. Liu, Y. Pei and Y. Zhu, *Chem. Sci.*, 2022, **13**, 2778–2782.
602 Z. Guan, J. Zeng, S. Yuan, F. Hu, Y. Lin and Q. Wang, *Angew. Chem.*, 2018, **130**, 5805–5809.
603 J. L. Zeng, Z. J. Guan, Y. Du, Z. A. Nan, Y. M. Lin and Q. M. Wang, *J. Am. Chem. Soc.*, 2016, **138**, 7848–7851.

This journal is © The Royal Society of Chemistry 2025

Published on 27 October 2025. Downloaded by Indian Institute of Technology Chennai on 12/29/2025 3:17:01 AM.

604 X. Li, P. Fang, X. Li, S. Ajmal, X. Zhou, Z. Sun, Y. Song, M. Zhu and P. Li, *Eur. J. Inorg. Chem.*, 2024, **27**, e202300657.
605 T. Higaki, C. Liu, D. J. Morris, G. He, T. Y. Luo, M. Y. Sfeir, P. Zhang, N. L. Rosi and R. Jin, *Angew. Chem., Int. Ed.*, 2019, **58**, 18798–18802.
606 X. Yuan, S. Malola, G. Deng, F. Chen, H. Häkkinen, B. K. Teo, L. Zheng and N. Zheng, *Inorg. Chem.*, 2021, **60**, 3529–3533.
607 C. Kumara and A. Dass, *Nanoscale*, 2011, **3**, 3064–3067.
608 X. Du, H. Ma, X. Zhang, M. Zhou, Z. Liu, H. Wang, G. Wang and R. Jin, *Nano Res.*, 2022, **15**, 8573–8578.
609 A. C. Dharmaratne and A. Dass, *Chem. Commun.*, 2014, **50**, 1722–1724.
610 N. Kothalawala, C. Kumara, R. Ferrando and A. Dass, *Chem. Commun.*, 2013, **49**, 10850–10852.
611 C. Kumara, X. Zuo, D. A. Cullen and A. Dass, *J. Phys. Chem. Lett.*, 2015, **6**, 3320–3326.

Check for updates

RESEARCH ARTICLE

Rising Stars

NANO · MICRO small

www.small-journal.com

CO_2 Electroreduction to CO Over Silver Nanoclusters: The Impact of Nuclearity on Synergistic Activity Modulation

*Parvathy Jayan, Arijit Jana, Zhengyuan Li, Rahul Kumar Sharma, Vivek Yadav, Astrid Campos Mata, Ming-Hsuan Li, Ali Shayesteh Zeraati, Tomas Base, Sung-Fu Hung, Jingjie Wu, Biswarup Pathak, Thalappil Pradeep, and Soumyabrata Roy**

Electrochemical reduction of CO_2 (eCO_2R) powered by renewable energy holds the potential to produce sustainable platform chemicals and decarbonize the hard-to-abate sectors. Herein, the structure-activity correlation of atomically precise silver nanoclusters (NCs) in eCO_2R to carbon monoxide (CO) is studied, elucidating the effect of the nuclearity of metal core and the electronic nature of the ligands. Electrocatalytic studies on Ag NCs, $[Ag_{21}(MCT)_{12}(TPP)_2]^+$, $[Ag_{31}(TRZ)_{10}]^{2-}$, $[Ag_{42}(CBDT)_{15}(TPP)_4]^{2-}$ (shortly, Ag_{21}, Ag_{31}, and Ag_{42}, respectively), reveal that the CO Faradaic efficiency (FE_{CO}) increases while the $FE_{CO(max)}$ (the maximum FE_{CO}) moves to higher positive potentials upon decreasing the nuclearity of these Ag NCs, almost in a quantitative correlation. Notably, every ≈ten Ag atoms variation in the cluster shifts the potentials for $FE_{CO(max)}$ and maximum partial current density, $j_{CO(max)}$ by ≈70 and ≈80 mV, respectively. The smallest nanocluster, Ag_{21}, achieved a near-unity $FE_{CO(max)}$ of 99.6% at −0.59 V vs RHE, and a competitive eCO_2R-to-CO rate, producing a $j_{CO(max)}$ of 148 mA cm^{-2} at −0.7 V vs RHE. First principle calculations reveal that decreasing the atomicity in Ag NCs reduces the activation energy barriers for the $2e^-$ reduction pathway due to the modulation of surface charge distribution and the electronic density of states of the active Ag sites.

1. Introduction

Renewable energy (RE) powered electrochemical CO_2 reduction reaction (eCO_2R) offers a promising approach to transform greenhouse gases like CO_2 into valuable products that can close the artificial carbon cycle and store intermittent RE in chemical bonds (C—C, C—H, and C—O bonds).[1–4] ECO_2R offer significant advantages over other chemical conversion routes, due to its ambient operational conditions, adaptability to renewable energy infrastructure, and the wide product scope comprising C_1—C_3 hydrocarbons, oxygenates, and key commodity chemicals.[5–11] Among these, CO is a promising eCO_2R product having low thermodynamic potential requirements (−0.1 V vs reversible hydrogen electrode [RHE]), fast kinetics, and ubiquitous applications in the chemical (use as syngas in Fischer-Tropsch process), fertilizer, biorefineries, and metal/steel processing sectors.[12–18]

P. Jayan, S. Roy
Department of Sustainable Energy Engineering
Indian Institute of Technology Kanpur
Uttar Pradesh 208016, India
E-mail: soumyar@iitk.ac.in

A. Jana, V. Yadav, T. Pradeep
Department of Science and Technology (DST)
Unit of Nanoscience and Thematic Unit of Excellence
Department of Chemistry
Indian Institute of Technology (IIT) Madras
Chennai 600036, India

Z. Li, J. Wu
Department of Chemical and Environmental Engineering
University of Cincinnati
Cincinnati, OH 45221, USA

R. K. Sharma, B. Pathak
Department of Chemistry
Indian Institute of Technology
Indore, Madhya Pradesh 453552, India

A. C. Mata
Department of Materials Science and Nanoengineering
Rice University
Houston, TX 77005, USA

M.-H. Li, S.-F. Hung
Department of Applied Chemistry and Centre for Emergent Functional Matter Science
National Yang Ming Chiao Tung University
Hsinchu 300, Taiwan

A. Shayesteh Zeraati
Acceleration Consortium
University of Toronto
80 St. George St., Toronto, ON M5S 3H6, Canada

T. Base
Department of Syntheses
Institute of Inorganic Chemistry
The Czech Academy of Sciences
250 68 Husinec-Rez, Prague 25068, Czech Republic

The ORCID identification number(s) for the author(s) of this article can be found under https://doi.org/10.1002/smll.202505305

DOI: 10.1002/smll.202505305

© 2025 Wiley-VCH GmbH

Coinage metals viz. Cu, Ag, and Au have shown tremendous potential in eCO_2R due to their partially filled d orbitals, which can favorably interact and overlap with the 2p orbitals of carbon to activate CO_2.[19,20] Among these, Cu easily stabilizes the CO intermediate, leading to the formation of higher hydrocarbon and multi-electron (beyond $2e^-$) reduced products.[21] Ag and Au, on the other hand, are highly selective for the production of CO due to the weak binding and easy desorption of CO.[22–25] Ag is considered more viable due to its cost benefits over Au and has demonstrated its eCO_2R-to-CO potential in various nanoengineered forms.[26–29] CO, a 2-electron reduced eCO_2R product, usually forms via a proton-coupled electron transfer process ($CO_2 + 2H^+ + 2e^- \rightarrow CO + H_2O$), involving activated *COOH as a key intermediate. CO_2 gets adsorbed and activated as $*CO_2^-$ intermediate, which on subsequent hydrogenation forms C-bound *COOH, which is further reduced and eventually desorbs as CO.[30,31] Activation of CO_2 and formation of *COOH can both be rate-limiting steps on Ag/Au catalysts.[32,33]

Various nanoengineering levers, such as morphology, size, doping/alloying, superstructural assembly, surface modifications, and nano-structuring, have started pushing the boundaries of eCO_2R-to-CO production on Ag catalysts.[34–38] However, achieving near-unity selectivity of eCO_2R-to-CO at competitive current densities is challenging, due to high overpotential needed for CO_2 activation and competing hydrogen evolution reaction in aqueous electrolytes.[33] Moreover, the heterogeneity and dynamic nature of these nanostructures and inconclusive active site configuration impede the development of meaningful and reliable structure-activity correlations.

To that end, ligand (monolayer) stabilized atomically precise metal nanoclusters (MNCs), typically consisting of 4–500 metal atoms with well-defined structures, are an ideal platform for tuning eCO_2R activity at the molecular level and elucidating the tunable interface of heterogeneous catalysis.[39–44] These molecular materials comprising coinage metals are steadily emerging as a unique class of catalysts owing to their high surface area-to-volume ratio, distinct electronic properties, and metal-ligand interactions.[45,46] Such features can improve the performance by activating reactant molecules on the undercoordinated and charge-modulated surface active sites, steering the pathways and energetics of the redox processes.[47–49] Further, the quantum confinement effect in MNCs can alter the band gap, which can resonate with the activation energy barriers of the intermediate species.[50,51] Engineering approaches on Au and Ag NCs are extensively exploring these features to fine-tune and boost their eCO_2R-to-CO activity.[52–56]

For example, in one of the early pioneering studies on thiol-protected Au NC involving $[Au_{25}(SC_2H_4Ph)_{18}]^-$, Kauffman et al. achieved 100% Faradaic efficiency (FE) for CO, although the rates were low even at higher potentials.[57] Alkynyl-protected $[Ag_{15}(C{\equiv}C\text{-}tBu)_{12}]$ was shown to demonstrate $FE_{CO(max)}$ of 95.0% at −0.6 V.[58] Kim et al. compared the relative performance of the thiolate-protected Ag/Au-MNCs comprising $[Au_{25}(SR)_{18}]$, $[Ag_{25}(SR)_{18}]$, and $[AuAg_{12}@Au_{12}(SR)_{18}]$ NCs, which exhibited an industrially relevant current density of 200 mA cm^{-2}.[59] Various factors such as ligand effects,[60] size and morphology of clusters,[61] doping and alloying,[62,63] and polymerization[64] have been studied to probe their influence on eCO_2R activity. Nuclearity of MNCs is a unique modulation tool in this regard, not only because of the conventional surface area effect, but also, the resultant surface charge tunability of the active metal sites on the outer motifs and the ligament. Very few studies have critically examined this aspect while also controlling the performance of NCs for CO production. Seong et al., conducted an activity comparison on Au_{25}, Au_{38}, and Au_{144} model catalysts, although their study primarily focused on the identification of active sites after de-thiolation, where contrary to the conventional trend, the activity order was found to increase with the size.[65] Li et al. studied the comparative activity of Au NCs with different sizes (1–2.5 nm regime) to find out a higher surface-to-volume ratio in smaller size NCs leads to a higher eCO_2R-CO activity.[66] Zhou et al. mapped out three distinct size-dependent states (metallic [>2.3 nm], transition regime [2.3–1.7 nm], and non-metallic or excitonic states [<1.7 nm]) for thiolate-protected Au_{25}, Au_{38}, Au_{144}, Au_{333}, $Au_{\approx 520}$ and $Au_{\approx 940}$ clusters and showed its impact on electrocatalytic CO and alcohol oxidation.[67] Despite these studies, a clear gap exist in the elucidation of lucid structure-activity rationales on the influence of the nuclearity of Ag-NCs and the ligands on eCO_2R-to-CO performance outcomes.

To bridge that, herein, we report the comparative electrocatalytic efficiency of three atomically precise silver nanoclusters, i.e., $[Ag_{21}(MCT)_{12}(TPP)_2]^+$, $[Ag_{31}(TRZ)_{10}]^{2-}$ and $[Ag_{42}(CBDT)_{15}(TPP)_4]^{2-}$ (abbreviated as Ag_{21}, Ag_{31}, and Ag_{42}, respectively), demonstrating highly selective eCO_2R-to-CO activity at competitive rates under low overpotentials.[68–70] The Ag_{21} and Ag_{42} clusters are bound by carborane-thiolate cages, viz. *meta*-carborane-9-thiol (MCT-H), and *ortho*-carborane-1,2-dithiol ($CBDT\text{-}H_2$), respectively. The Ag_{31} cluster comprises TRZ ligand shell (where $TRZ\text{-}H_2$ is 6-(dibutylamino)-1,3,5-triazine-2,4-dithiol). The study also attempts at elucidating the relative influence of nuclearity and ligand modulation on the catalytic behaviour of Ag NCs for eCO_2R. To that end, we explored two reported nanoclusters, $[Ag_{22}(dppe)_4(2,5\text{-}DMBT)_{12}Cl_4]^{2+}$ (abbreviated as Ag_{22}) and $(PPh_4)_4[Ag_{44}(SPhF_2)_{30}]$ (abbreviated as Ag_{44}), to carry out control experiments with NCs having comparable nuclearity (Ag_{21} & Ag_{22} NC and Ag_{42} & Ag_{44} NC) but different ligands (carborane-thiol and benzene-thiol).[71,72] Ligands can modulate the electronic density of the metal core through inductive and delocalization effects and also impact the structural properties, accessibility of active sites, and surface hydrophobicity. Consequently, nanoclusters with comparable nuclearity can display similar baseline activity, although their selectivity and efficiency may vary depending on the nature of the protecting ligands.

Ag_{21} NC achieved a near-unity $FE_{CO(max)}$ of 99.6% at a low potential of −0.59 V vs RHE and a maximum partial current density for CO ($j_{CO(max)}$) of 148 mA cm^{-2} at −0.7 V vs RHE. In contrast, the larger Ag_{31} and Ag_{42} NCs exhibited slightly lower FE_{COmax} of 97% and 95%, respectively. Interestingly, the potentials for $FE_{CO(max)}$ and $j_{CO(max)}$ were observed to shift by ≈70 and ≈80 mV respectively for every ≈ten Ag atoms in the NC. Several spectroscopic techniques were explored to probe the relative electronic and chemical properties of the Ag NCs. Quantum chemical studies simulated the adsorption of intermediates *COOH and *CO at different catalytic sites of Ag_{21} and Ag_{42} corroborating the better performance of Ag_{21} from the thermodynamic standpoint. The enhanced overlap between the Ag (5d) and C (2p) states and increased charge delocalization are primarily responsible for

© 2025 Wiley-VCH GmbH

16136829, 0, Downloaded from https://onlinelibrary.wiley.com/doi/10.1002/smll.202505305 by Central Library The Librarian, Wiley Online Library on [28/12/2025]. See the Terms and Conditions (https://onlinelibrary.wiley.com/terms-and-conditions) on Wiley Online Library for rules of use; OA articles are governed by the applicable Creative Commons License

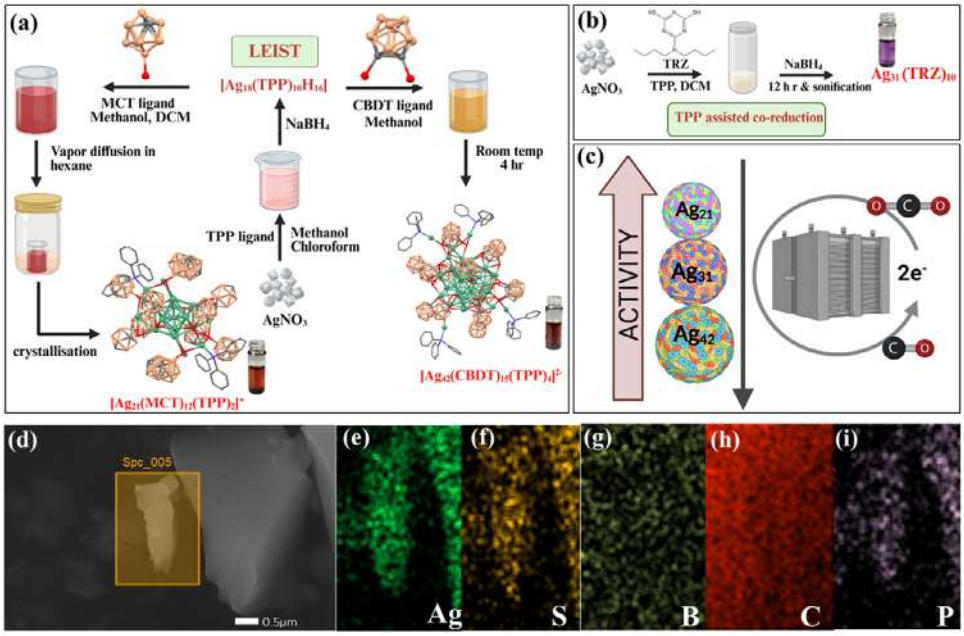


Figure 1. Schematic illustration of the synthesis of $[Ag_{21}(MCT)_{12}(TPP)_2]^+$ and $[Ag_{42}(CBDT)_{15}(TPP)_4]^{2-}$ using LEIST reaction starting from Ag_{18} NC. b) Synthesis Scheme of the TPP-assisted co-reduction method for synthesizing $[Ag_{31}(TRZ)_{10}]^{2-}$ cluster. c) Schematic of the relative performance of three Ag NCs for eCO_2R. d) SEM image of microcrystalline Ag_{21} NC before loading on the GDE (Scale Bar is 0.5 μm). e–i) EDS elemental mapping of the selected region showing the presence of Ag, S, B, C, and P elements.

the activity enhancement on Ag_{21}. This would allow for greater charge transfer from Ag to the C atoms of *COOH, leading to stronger intermediate binding and a lower overpotential on Ag_{21}.

2. Results and Discussion

2.1. Synthesis and Characterization of Ag Nanoclusters

Three distinct Ag NCs, with varying nuclearity of the Ag core (about ten Ag atoms each), are chosen for examination of their eCO_2R performance. The thermal and ambient stable Ag NCs, Ag_{21}, Ag_{31}, and Ag_{42} were synthesized according to our earlier report.[68–70] $[Ag_{21}(MCT)_{12}(TPP)_2]^+$, and $[Ag_{42}(CBDT)_{15}(TPP)_4]^{2-}$ are coprotected by carborane-thiolate (MCT or CBDT) and TPP ligands, which are synthesized from TPP and hydride-protected $[Ag_{18}(TPP)_{10}H_{16}]$ cluster, using ligand exchange-induced size or structure transformation (LEIST) method (where TPP is triphenylphosphine) (**Figure 1a**). Nanoclusters having carborane (featuring an icosahedral C_2B_{10} cage) or TRZ-based ligands, rarely explored for catalytic applications so far, are expected to impart remarkable chemical resistance and unique electronic properties boosting eCO_2R performance.[73,74]

$[Ag_{31}(TRZ)_{10}]^{2-}$ cluster was synthesized through a single-step, TPP-assisted co-reduction reaction of silver, TRZ-dithiolate, and TPP precursors using sodium borohydride as a reducing agent (Figure 1b). TRZ is a six-membered aromatic heterocycle with three nitrogen atoms at positions 1, 3, and 5. The hexagonal triazine ring is less electron-dense than benzene due to the electron-withdrawing capacity of the three nitrogens. A detailed synthesis procedure of the Ag NCs can be found in the experimental section. The gas diffusion electrodes (GDE) were prepared via spray coating of the purified Ag NC powders, to carry out eCO_2R in a flow cell setup. Figure 1c illustrates the effect of the decreasing nuclearity/size of Ag NCs on the catalytic activity. Field-emission scanning electron microscopy (FE-SEM) of Ag_{21}, before electrode loading, displayed microcrystallites having nanoplatelet-like morphology (Figure 1d). Elemental mapping via energy dispersive spectroscopy (EDS) showed the presence of Ag in addition to S, B, C, and P elements with nominal stoichiometry (Figure 1e–i). The mass and atomic percentage of each element are shown in the EDS spectra in Figure S1 (Supporting Information).

Molecular characterization of the clusters were conducted through UV–vis absorption spectroscopy and high-resolution mass spectrometric studies. UV–vis spectrum exhibited multiple absorption bands for the NCs associated with the size confinement and discrete electronic energy levels. Four characteristic peaks were observed for the Ag_{21} in DCM solution at 305, 355, 396, and 494 nm, along with a broad peak at 697 nm (**Figure 2a**). Ag_{31} NC exhibits absorption peaks at 402, 525, and 593 nm, respectively, and the Ag_{42} cluster shows two absorption peaks at 571 and 456 nm (Figure 2b,c). Photographic images of all three cluster solution are shown in Figure S2 (Supporting Information). The specific absorption peak patterns from UV–Vis spectra match well with our earlier reports confirming the chemical purity of the clusters (Figure S3, Supporting Information).[68–72] Time-dependent UV–vis measurements showed stability of these clusters up to 2 months at ambient conditions. The molecular compositions of Ag NCs in solution were investigated using high-resolution electrospray ionization mass spectrometry (ESI-MS). The ESI-MS of the Ag_{21} cluster in positive-ion mode show a prominent peak at m/z 4893.24 in mono positive charge state. The molecular composition of the cluster is assigned as $[Ag_{21}(MCT)_{12}(TPP)_2]^+$, and the isotopic distribution of the experimental peak matches the simulated pattern well. Two additional

© 2025 Wiley-VCH GmbH

16136829, 0, Downloaded from https://onlinelibrary.wiley.com/doi/10.1002/smll.202505305 by Central Library The Librarian, Wiley Online Library on [28/12/2025]. See the Terms and Conditions (https://onlinelibrary.wiley.com/terms-and-conditions) on Wiley Online Library for rules of use; OA articles are governed by the applicable Creative Commons License

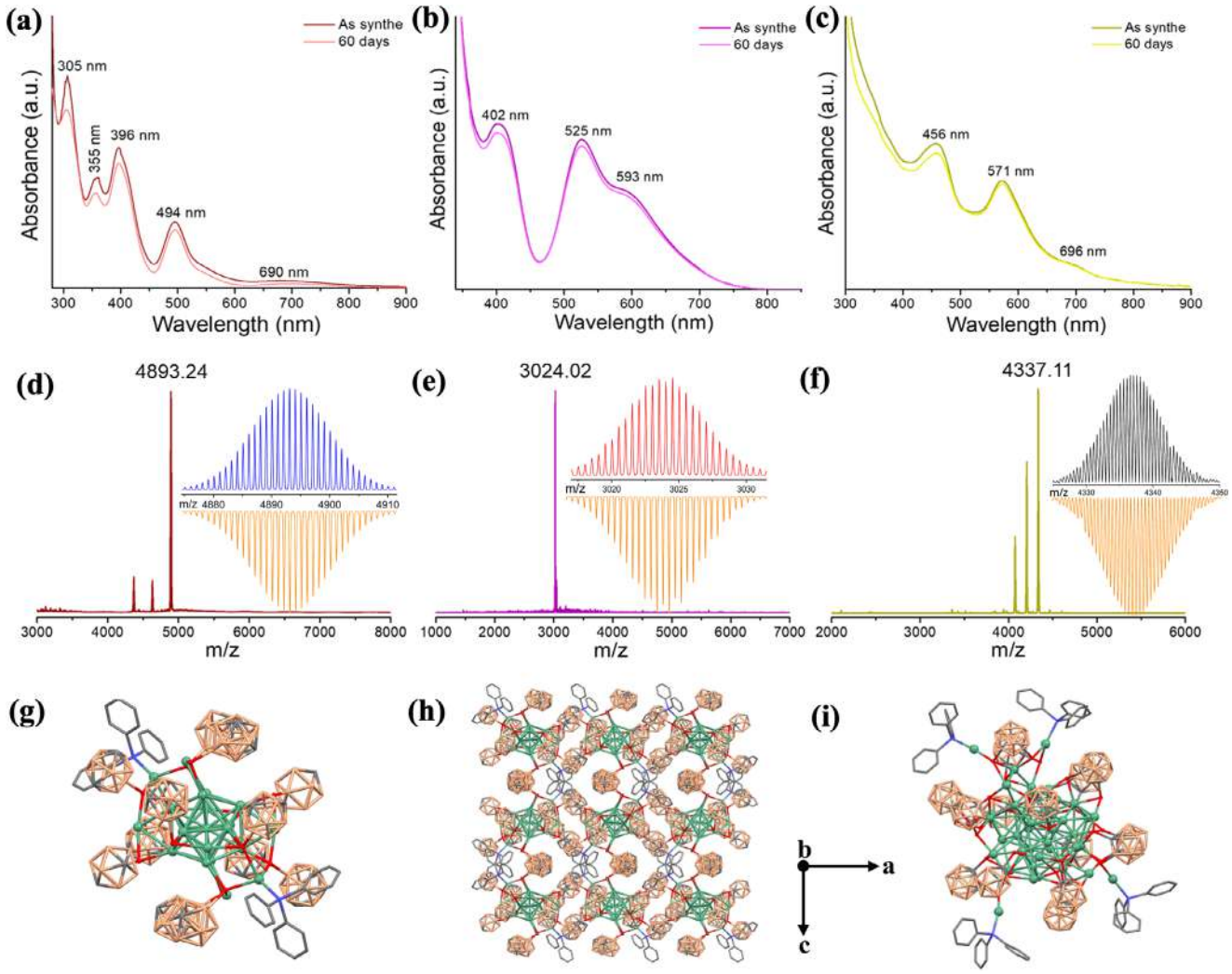


Figure 2. Characterization of Ag NCs. UV–vis absorption spectra of a) Ag_{21}, b) Ag_{31}, and c) Ag_{42} clusters before loading on the GDE, showing long-term stability at ambient condition, d–f) High-resolution mass spectrometric data of the catalyst materials, with inset showing the comparison of respective experimental and simulated spectra, g) single crystal molecular structure of Ag_{21} NC, h) Fully packed structure of Ag_{21}NC, i) DFT optimized structure of Ag_{42}. All the structures are along the direction of the b axis. Color legend - dark green: silver, red: sulfur, blue: phosphorus, light orange: boron. gray: carbon. The SCXRD structural data of Ag_{21} and the DFT optimized structure of Ag_{42} have been used from reported literature.[68,70]

minor peaks at m/z 4630.5 and m/z 4368.35 indicate sequential losses of TPP from the parent cluster (Figure 2d). The ESI-mass spectrum of the Ag_{31} in negative-ion mode indicates a prominent peak at m/z 3024.02 (Figure 2e). A peak-to-peak spacing of 0.5 for m/z 3024.02 confirms the presence of the dianionic state. In the case of the Ag_{42} nanocluster, a prominent peak was observed at m/z 4337.11, with an isotopic peak-to-peak separation of 0.5, indicative of a dianionic charge state. Additionally, two less intense peaks appear at m/z values of 4205.67 and 4074.21, which corresponded to the removal of TPP ligands from the parent cluster (Figure 2f). The Ag_{22} NC exhibit a peak at m/z 2877.39 having 2^+ charge state, in good agreement with the simulated spectra, as shown in Figure S4 (Supporting Information). Negative ion mode ESI-MS of Ag_{44} exhibits a prominent peak at m/z 2853.29 corresponding to the 3^- charge state, along with a minor peak at 2140.20 corresponding to the 4^- charge state of Ag_{44} cluster. Single-crystal structure of Ag_{21} NC showed that it has a central icosahedral Ag_{13} core and a shell of eight silver atoms, while the DFT-optimized structure of Ag_{42} has a larger Ag_{28} core and a shell of 14 silver atoms (Figure 2g–i; Figure S5, Supporting Information). Thiolates are bound to the cluster through Ag-S bonds, while Ag-P linkages coordinate with phosphines.

Transmission electron microscopy (TEM) analysis shows the nanosized structures of Ag_{21}, $Ag_{31,}$ and Ag_{42}, with particle sizes ranging from 1.5 to 3 nm (**Figure** 3a–c and Figure S6 (Supporting Information)). The overall size of the NC (including the ligand) falls well within the NC size regime. The presence of Ag and other elements in Ag_{21} NC can be observed in Figure S7 (Supporting Information), showing the elemental mapping in HAADF-STEM (High-Angle Annular Dark Field Scanning Transmission Electron Microscopy). The IR spectra of Ag_{21} and the free MCT ligand were measured and compared (Figure 3d). The presence of carborane was confirmed from the appearance of C—B and B—B vibrational peaks at 1050 and 866 cm^{-1}, respectively.

© 2025 Wiley-VCH GmbH

16136829, 0, Downloaded from https://onlinelibrary.wiley.com/doi/10.1002/smll.202505305 by Central Library The Librarian, Wiley Online Library on [28/12/2025]. See the Terms and Conditions (https://onlinelibrary.wiley.com/terms-and-conditions) on Wiley Online Library for rules of use; OA articles are governed by the applicable Creative Commons License

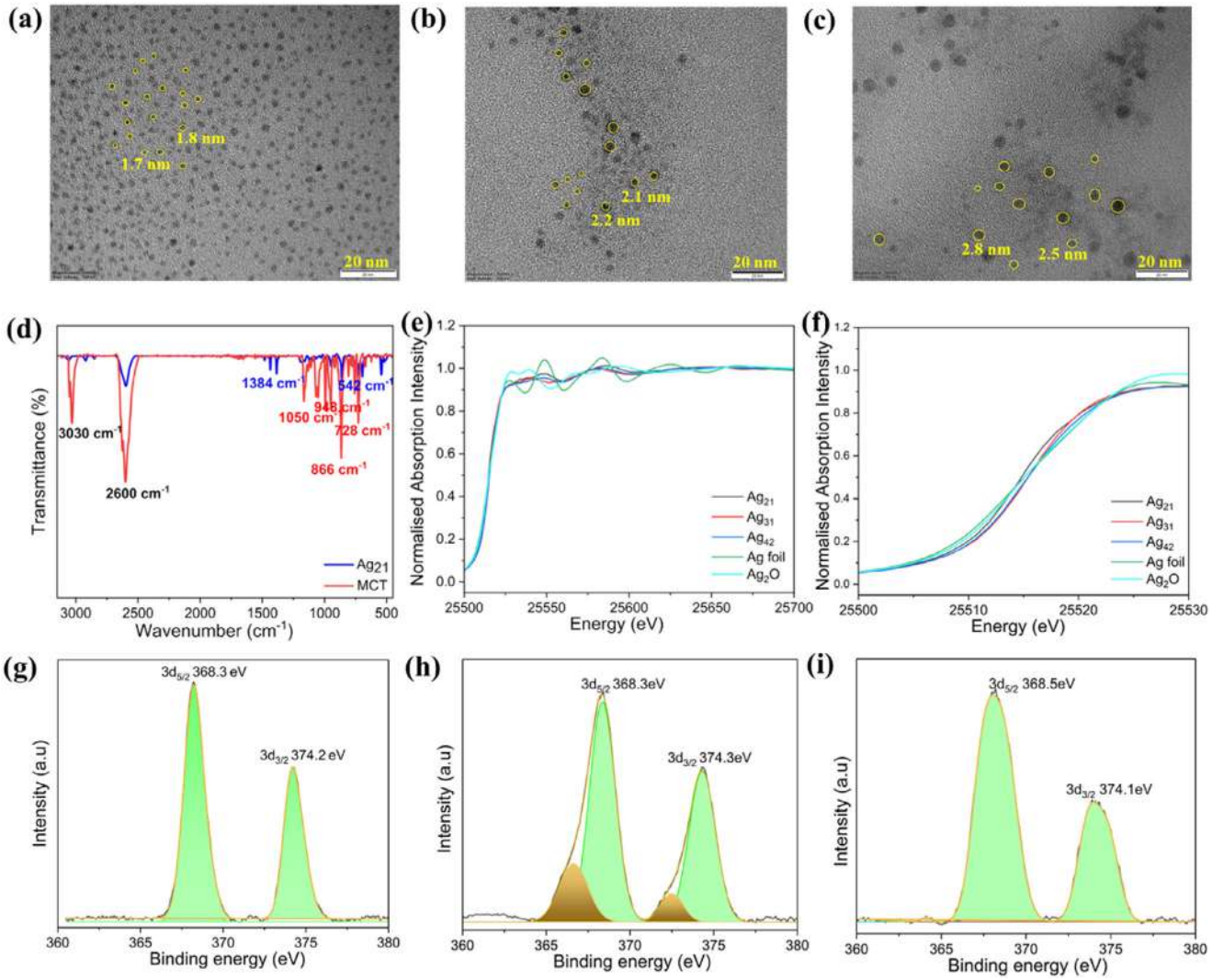


Figure 3. TEM images showing ultrasmall particle distribution for the clusters of a) Ag_{21} b) Ag_{31} c) Ag_{42}. d) Full range FTIR spectra of Ag_{21} NC and MCT ligand, e,f) XANES spectra of Ag_{21}, Ag_{31} and Ag_{42} catalysts with reference samples (Ag foil and Ag_2O) at Ag-K edge indicating intermediate oxidation states, g–i) selected area HR-XPS spectra of Ag 3d region of Ag_{21}, Ag_{31}, Ag_{42}, respectively.

Another band observed at 1384 cm^{-1} corresponds to the stretching frequency of the N—O bond of NO_3^- counterions. Likewise, measurements and comparisons of the FT-IR spectra of Ag_{42} and free CBDT ligands are shown in Figure S8b (Supporting Information). For Ag_{31}, peaks at 743 and 1543 cm^{-1} are consistent with C—S stretching from the thiol and the C═N stretching, respectively, which are constituents of the TRZ ligand (Figure S8a, Supporting Information). The electronic states analyzed through X-ray Absorption Near Edge Structure (XANES) (Figure 3e–f) suggest mixed oxidation state of the Ag atoms in the Ag NCs. This can be attributed to the different charge distribution on the Ag atoms arising from their distinct chemical environments at the core and surface of the clusters. This is further supported by the Bader charge analysis conducted through theoretical calculations (Tables S4 and S5, Supporting Information).

Further XPS analysis was conducted on Ag NCs to investigate the elemental and chemical composition of the clusters. All the clusters exhibited peaks corresponding to Ag $3d_{5/2}$ and Ag $3d_{3/2}$. Ag_{21} showed an Ag $3d_{5/2}$ peak at 368.2 eV and Ag $3d_{3/2}$ peak at 374.3 eV, indicating the presence of mostly metallic silver (Ag (0)) (Figure 3g). In addition to Ag, XPS also revealed the elements present in the MCT and TPP ligand. The intense peaks observed in the XPS survey spectra of Ag_{21} NC at 189.7 and 284.8 eV, confirmed the presence of B and C (Figure S9a, Supporting Information), respectively, in the carborane ring. The deconvoluted C 1s and B 1s are shown in Figure S9b,c (Supporting Information). The sulfur in carborane thiolate shows peaks at 164.2 eV for S $2p_{3/2}$ and 162.4 eV for S $2p_{1/2}$ (Figure S9d, Supporting Information). Similarly, P 2p spectra show peaks at 129.3 and 130.2 eV, corresponding to the P $2p_{1/2}$ and P $2p_{3/2}$, respectively, corresponding to the phosphorus in the TPP ligand (Figure S9e, Supporting Information). For Ag_{31} NC, apart from Ag (Figure 3h), N 1s and S 2p were observed in the XPS survey scan at peak positions of 399.5 and 164.5 eV, arising from the TRZ ligand (Figure S10a, Supporting Information). From the C1s spectra, the peak due to the C═N bond in TRZ is visible at

© 2025 Wiley-VCH GmbH

16136829, 0, Downloaded from https://onlinelibrary.wiley.com/doi/10.1002/smll.202505305 by Central Library The Librarian, Wiley Online Library on [28/12/2025]. See the Terms and Conditions (https://onlinelibrary.wiley.com/terms-and-conditions) on Wiley Online Library for rules of use; OA articles are governed by the applicable Creative Commons License

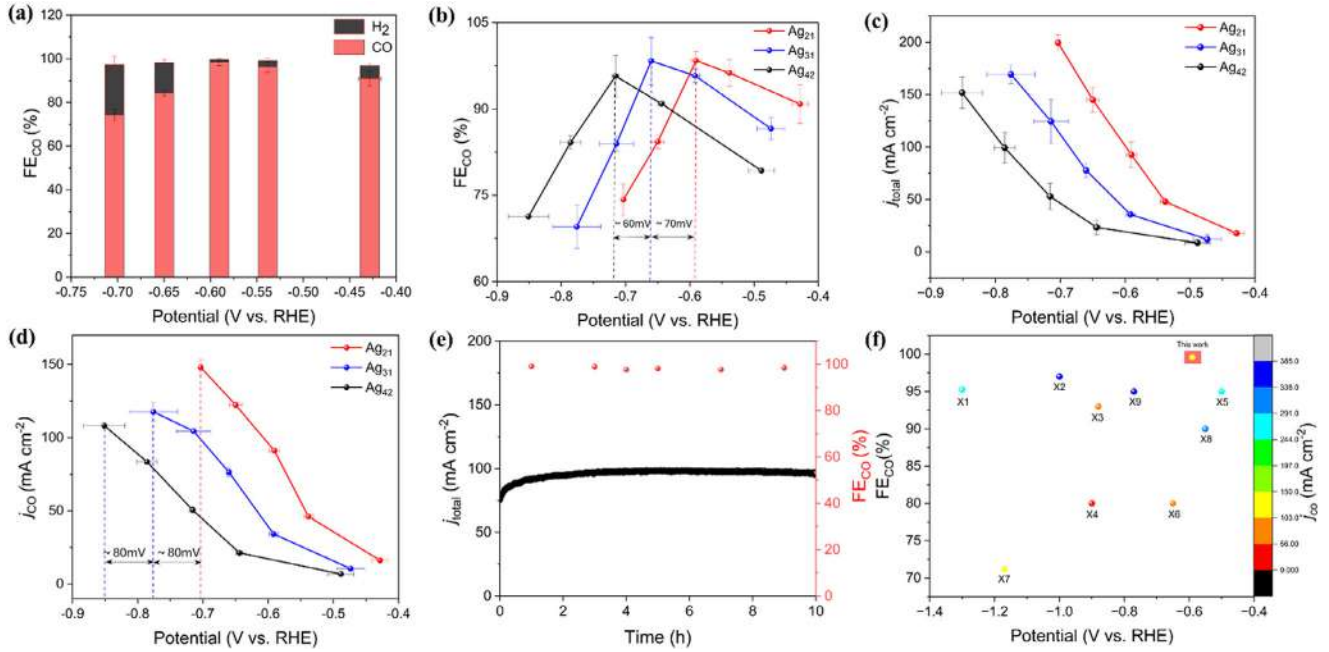


Figure 4. eCO_2R performance of Ag NCs in 1 M KOH in an alkaline flow cell. a) FE (%) of products with varying potential for Ag_{21}, b) FE (%) of CO with varying potential for all the clusters c) total current density across the potential range for $Ag_{21}$the three Ag NCs, d) partial current density for CO (j_{CO}) across the potential range for all the clusters, e) Electrocatalytic stability plot of Ag_{21} measured at a constant voltage of −0.59 V vs RHE, f) FE_{CO} vs potential plots illustrating comparison between various reported Ag-based catalysts (primarily nanoclusters) and Ag_{21} for eCO_2R-to-CO, in flow cell systems. The entries for the plot has been provided in Table S2 (Supporting Information).

peak position 286.5 eV (Figure S10b, Supporting Information). The peaks at 399.6 and 401.2 eV in the N1s spectra, correspond to C—N and C=N bonds in TRZ ligands (Figure S10c, Supporting Information). Similarly, the XPS spectra of Ag_{42} NC, showed the presence of Ag (Figure 3i) and other elements present in the ligands (Figure S11, Supporting Information).

2.2. Electrochemical Performance of Ag Nanoclusters

The electrocatalytic CO_2 reduction performance of the Ag clusters (Ag_{21}, Ag_{31}, and Ag_{42}) was evaluated in a flow cell with a 1 M KOH electrolyte in the potential range of −0.4 to −0.9 V vs RHE. For all three nanoclusters, CO is the primary product generated upon electrochemical CO_2 reduction, with H_2 as a minor byproduct. With minimal HER side reaction, the $FE_{CO(max)}$ for Ag_{21}-loaded GDE turned out to be 99.6% at −0.59 V (vs RHE) (**Figure 4a**). As the nuclearity of the clusters increased, the $FE_{CO(max)}$ gradually declined; the highest nuclearity cluster, Ag_{42}, exhibited the lowest $FE_{CO(max)}$, 95%, at a more negative potential of −0.71 V vs RHE, and the Ag_{31} NC-loaded GDE achieved $FE_{CO(max)}$ 97% at ≈−0.67 V vs RHE (Figure 4b; Figure S12, Supporting Information). To understand the relative effect of nuclearity and ligand contributions on the eCO_2R performance, we further examined Ag_{21} and Ag_{22} nanoclusters, which possess nearly identical nuclearity but are stabilized by different ligands. Ag_{22} exhibited a $FE_{CO(max)}$ of 96.2% at −0.6 V (j_{CO} = 78 mA cm^{-2}), which is slightly lower than that of Ag_{21} under similar conditions (Figure S13a,b, Supporting Information). The comparable nuclearity of these two clusters minimizes size-dependent influences, thereby allowing a direct assessment of ligand and associated effects. The slightly higher performance of Ag_{21} ($FE_{CO(max)}$ is 99.6 at −0.59 V vs RHE, j_{CO} is 91 mA cm^{-2}) is attributed to the carborane-thiol ligands, which impart both electronic modulation through charge delocalization and redistribution of surface electron density, as well as may have other structural and physico-chemical effects such as reduced steric hindrance, enhanced site accessibility, and different surface hydrophobicity. Together, these factors can promote more efficient CO_2 activity compared to the benzene-thiol-protected Ag_{22}. However, broadly speaking, the nuclearity of the clusters was found to have a more dominant effect on the overall performance of the clusters. Extending this analysis to higher nuclearity systems, Ag_{44} achieved a $FE_{CO(max)}$ of 90.2% at −0.74 V, which is lower than that of Ag_{42} at −0.71 V ($FE_{CO(max)}$ of 95%) (Figure S14a,b, Supporting Information). This trend again highlights the superior performance of carborane-based (CBDT) ligands relative to benzenethiol-based (SPhF) ligands in steering CO_2 electroreduction, underscoring the influence of ligand-modulated structural and electronic effects in dictating nanocluster reactivity. Interestingly, we note that while the value of $FE_{CO(max)}$ varies, the potential for $FE_{CO(max)}$ matches closely for clusters with similar nuclearity (Ag_{21}/Ag_{22} and Ag_{42}/Ag_{44}).

The total current density also followed the similar trend of $FE_{CO(max)}$, with Ag_{21} reaching 200 mA cm^{-2} at −0.7 V vs RHE, outperforming Ag_{31} and Ag_{42} which reached 169.2 and 151 mA cm^{-2} at more negative potentials of −0.77 V vs RHE and −0.85 V vs RHE, respectively (Figure 4c). The Ag_{21}-loaded GDE exhibited the highest partial current densities for CO (j_{CO}), reaching 148 mA cm^{-2} at −0.7 V vs RHE, whereas Ag_{31} and Ag_{42} exhibited

© 2025 Wiley-VCH GmbH

16136829, 0, Downloaded from https://onlinelibrary.wiley.com/doi/10.1002/smll.202505305 by Central Library The Librarian, Wiley Online Library on [28/12/2025]. See the Terms and Conditions (https://onlinelibrary.wiley.com/terms-and-conditions) on Wiley Online Library for rules of use; OA articles are governed by the applicable Creative Commons License

117 mA cm^{-1} at −0.77 V vs RHE and 108 mA cm^{-1} at −0.85 V vs RHE (Figure 4d). Comparative studies show that Ag_{22} exhibits a $j_{CO(max)}$ of 130 mA cm^{-2} and a j_{max} (maximum total current density) of 187 mA cm^{-2} at −0.71 V, respectively (Figure S13c,d, Supporting Information), which are slightly lower than those of Ag_{21}. Similarly, Ag_{44} delivered a lower activity than Ag_{42} with a $j_{CO(max)}$ of 82.75 mA cm^{-2} and a j_{max} of 141.65 mA cm^{-2} at a higher potential of −0.88 V (Figure S14c,d, Supporting Information).

The electrocatalytic stability of Ag_{21} was investigated in a flow cell at −0.59 V vs RHE. For up to 10 h, the CO selectivity remained steady at about FE_{CO} of 99% (Figure 4e). We also extended the stability test at the same potential for over 50 h and observed that both the total current density (j_{total}) and FE_{CO} remained largely stable (Figure S15, Supporting Information). However, the performance was occasionally disturbed by systemic issues such as flooding of the gas diffusion layer (GDL) due to salt deposition, which hinder CO_2 transport, diminishing the activity. This issue was mitigated through periodic washing of the GDL with water. The Ag_{21} exhibited a TOF of 0.36 s^{-1} at the potential −0.7 V vs RHE, where j_{CO} was found to be maximum. Further, to assess the catalyst stability, structural and chemical integrity were examined through XPS analysis (Figures S16–S18, Supporting Information). Pre- and post-electroreduction XPS spectra revealed that Ag_{21} and Ag_{31} retained their chemical and electronic states, indicating robust cluster stability. The presence of minor satellite peaks in the Ag 3d XPS spectra after electrocatalysis may arise from negligible Ag-O formation due to adsorbed KOH electrolyte on the surface. EXAFS (Extended X-ray Absorption Fine Structure) analysis (Figures S19 and S20 and Table S1, Supporting Information) confirmed the presence of Ag–S bonds in both Ag_{21} and Ag_{42} after the reaction, further supporting the structural integrity and stability of these nanoclusters during CO_2 electroreduction.

2.3. Mechanistic Understanding of eCO_2R Activity from DFT Studies

Density functional theory (DFT) was employed to study the CO_2 to *CO mechanism over Ag_{21} and Ag_{42} clusters using the Vienna ab initio simulation package (VASP)[75] with the Perdew–Burke–Ernzerhof (PBE)[76] functional under generalized gradient approximation (GGA).[77] *Computational Details* in Supporting Information provide the detailed information. To circumvent the computational cost, a single molecular unit of Ag_{21} and Ag_{42} was modelled and considered for further calculations. The DFT-optimized geometries, in terms of their metal and ligand arrangement, are shown in **Figure 5**a,b, respectively. The negative E_{Int} (interaction energy) of Ag_{21} and Ag_{42} complexes represent the thermodynamic stability of these clusters under the electrocatalytic condition of eCO_2R due to stabilization effect of the carborane-thiol ligands (Table S3, Supporting Information). Interestingly, Bader charge analysis reveals distinct charge distributions across different regions of the Ag clusters, suggesting varying oxidation states of Ag atoms in the staple motifs and core regions, as tabulated in Tables S4 and S5 (Supporting Information). To compare their activity, adsorption of *COOH and *CO (asterisk symbol (*) denotes the adsorbed species) was simulated at different heterogeneous sites, as represented in Figures S21 and S22 (Supporting Information), and the most stable optimized configurations were selected for further analysis. The higher number of local minima in Ag_{21} clusters indicates greater surface accessibility for intermediate binding, in contrast to the sterically hindered Ag_{42} clusters with limited exposed active sites. In the most stable geometries, the *COOH and intermediates preferentially bind to the one-fold top positions of Ag atoms that are bridged between two S atoms, indicating that the exposed Ag atoms on the surface act as the active sites for the eCO_2R activity in these clusters. Notably, the carbon atoms of these intermediates on Ag_{21} clusters exhibit a higher charge density (i.e., are less positively charged) compared to those on Ag_{42} clusters (Figure S23, Supporting Information). This increased electron density likely enhances the activation of the initial intermediates, accounting for the higher catalytic activity of Ag_{21} clusters.

Using the computational hydrogen electrode (CHE) model,[78] we calculated the thermodynamic Gibbs free energy (ΔG) associated with the CO_2 to *CO formation, following the adsorbate-evolution mechanism (AEM) via a concerted proton-electron transfer (CPET) pathway (Figure 5c). The lower ΔG values of 0.42 eV observed for Ag_{21}, in comparison to 1.21 eV for Ag_{42}, suggest that the smaller Ag_{21} clusters exhibit superior catalytic activity for eCO_2R, which can be attributed to its size-dependent surface charge density and electronic structure. Due to their smaller size, the Ag_{21} cluster exhibits a large number of undercoordinated surface atoms, leading to greater charge localization and a more negatively charged surface (Figure 5d). This increased surface charge facilitates stronger electrostatic interactions with the CO_2 molecule, stabilizing the adsorption and subsequent activation of the molecule during the CPET step. To further examine the effect of cluster size and ligand environment on catalytic performance, we compared the eCO_2R activity of Ag_{21}, Ag_{42}, and Ag_{44} clusters, where Ag_{44} was studied with different ligands, and heterogeneous sites were investigated for stable adsorption positions (Figure S24, Supporting Information). The higher ΔG value of Ag_{44} (1.29 eV), relative to Ag_{21} (0.42 eV) and Ag_{42} (1.21 eV) indicates its lower eCO_2R activity (Figure S25, Supporting Information).

The electronic structure analysis reveals that in Ag_{21}, there is an enhanced orbital overlap between Ag (5d) and C (2p) states within the −2 to −4 eV range (Figure 5e; Figure S26, Supporting Information). This stronger orbital interaction facilitates more efficient charge transfer from the Ag surface to the adsorbed *COOH intermediate, thereby enhancing its stabilization and lowering the energy barrier for its formation. In contrast, the larger Ag_{42} clusters, with more bulk-like features and lower surface charge density per active site, exhibit weaker site CO_2 interactions and less efficient charge transfer, leading to higher ΔG values. In addition to the orbital overlap between Ag (5d) and C (2p) orbitals, we observed a strong overlap between the frontier orbitals of Ag (5d) and S (3p) orbitals, highlighting their strong interactions in Ag_{21} and Ag_{42} clusters, as represented in Figures S27 and S28 (Supporting Information). Such strong interaction between Ag and P atoms contributes to the enhanced stability of these clusters under eCO_2R conditions. Thus, the superior CO_2 reduction activity of Ag_{21} is intrinsically linked to the synergistic effects of cluster size, surface charge accumulation, and site-specific electronic interactions, together modulating the reaction

© 2025 Wiley-VCH GmbH

16136829, 0, Downloaded from https://onlinelibrary.wiley.com/doi/10.1002/smll.202505305 by Central Library The Librarian, Wiley Online Library on [28/12/2025]. See the Terms and Conditions (https://onlinelibrary.wiley.com/terms-and-conditions) on Wiley Online Library for rules of use; OA articles are governed by the applicable Creative Commons License

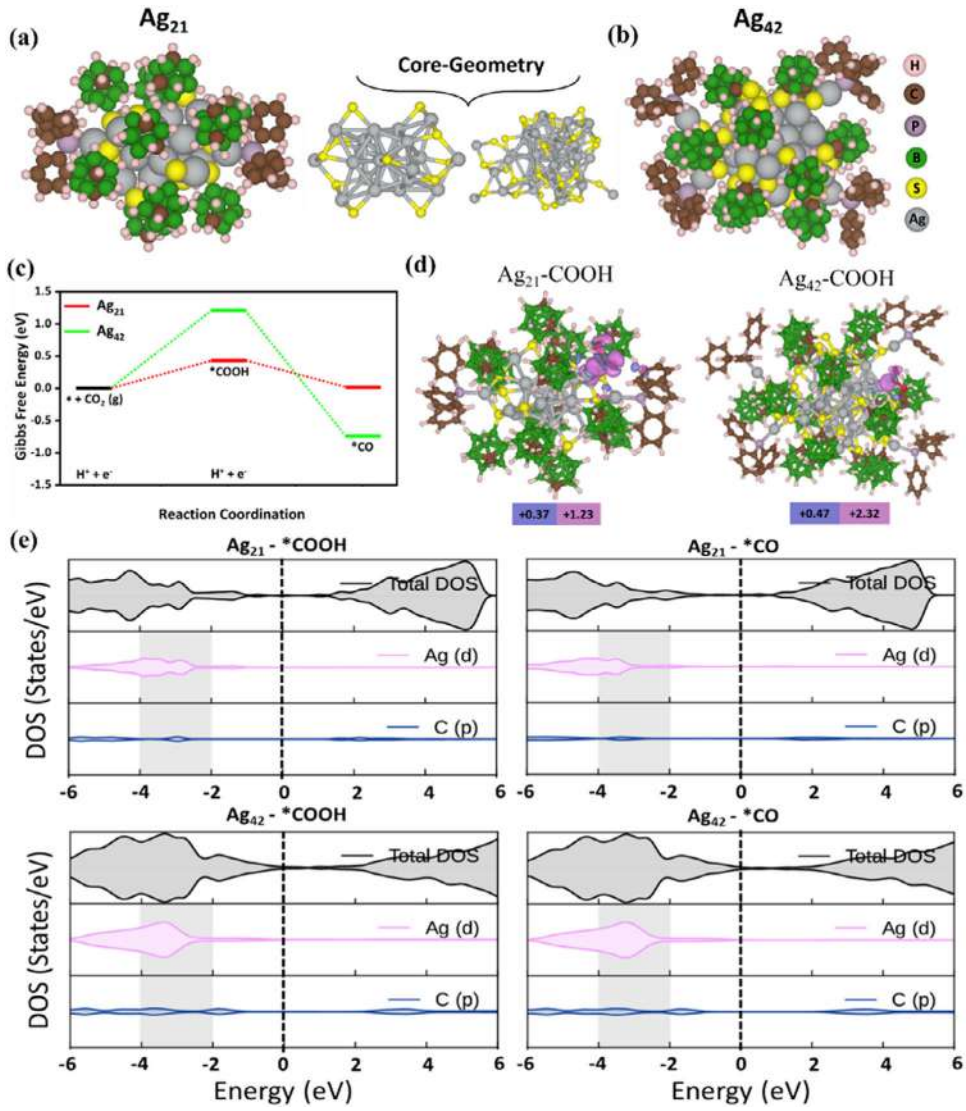


Figure 5. Optimized geometries of a) Ag_{21} and b) Ag_{42} clusters, with multiple heterogeneous active sites for intermediate adsorption represented in Figures S22 and S23 (Supporting Information). c) Gibbs free energy diagram of Ag_{21} and Ag_{42} clusters, with the black solid horizontal line denoting the neutral surface reference. d) Charge density difference (CDD) plots at an isosurface of 0.002 eV $Å^{-3}$, where pink and green regions indicate charge accumulation and depletion, respectively. Numeric values represent charge transfer (in |e| units) derived from Bader charge analysis on Ag and C atoms. e) Subplots for total and partial density of states (DOS) for Ag (5d) and C (2p) states, with the Fermi-level set at 0.00 eV. Note that total and partial DOS analysis for pristine, *COOH, and *CO-adsorbed Ag_{21} and Ag_{42} clusters are provided in Figure S25 (Supporting Information).

energy profile by enhancing the stabilization of key reaction intermediates.

3. Conclusion

To summarize, this study provides an account of the comparative eCO_2R-to-CO activity of three Ag nanoclusters with varying nuclearity of ≈ten Ag atoms between them. The order of activity and $FE_{CO(max)}$ (selectivity) is found to follow the trend of decreasing metal cluster atomicity/size. Ag_{21}, being the smallest nanocluster, demonstrates excellent performance in electrochemical reduction of CO_2 to CO, achieving a near-unity $FE_{CO(max)}$ of 99.6% at a low applied potential of −0.59 V vs RHE, indicating exceptional selectivity with minimal parasitic reactions. The j_{max} of 200 mA cm^{-2} underscores its ability to drive CO_2 conversion at high rates. Interestingly, an increase of ten Ag atoms across the clusters was found to shift the $FE_{CO(max)}$ and $j_{CO(max)}$ potentials (for CO production) by 70 and 80 mV, respectively, showcasing a semi-quantitative correlation. The enhanced activity can be attributed to the distinct structural and electronic features of the Ag_{21} cluster. Its small size ensures a high surface-to-volume ratio and a relatively larger fraction of low-coordination Ag atoms, both of which contribute to an increased density of active sites. Moreover, the Ag_{21} cluster displays favorable electronic interactions that facilitate the CO_2 reduction reaction. Specifically, the overlap between the Ag 5d orbitals and the C 2p orbitals of CO_2 and key reaction intermediates, such as *COOH and *CO, leads to enhanced adsorption and activation of reactant molecules and

© 2025 Wiley-VCH GmbH

16136829, 0, Downloaded from https://onlinelibrary.wiley.com/doi/10.1002/smll.202505305 by Central Library The Librarian, Wiley Online Library on [28/12/2025]. See the Terms and Conditions (https://onlinelibrary.wiley.com/terms-and-conditions) on Wiley Online Library for rules of use; OA articles are governed by the applicable Creative Commons License

intermediates. The delocalization of electronic charge across the cluster further supports efficient electron transfer and stabilizes the reaction intermediates, thereby lowering the activation energy barrier and improving the overall reaction kinetics. Together, these factors establish Ag_{21} as an efficient catalyst for CO_2 electroreduction, with its performance closely tied to its unique atomic configuration and frontier orbital characteristics. Interestingly, control experiments in this case, reveal a more dominant effect of nuclearity in dictating the baseline activity of Ag nanoclusters, while ligands impart subtle yet significant contributions that fine-tune selectivity and activity. Such enhancements, arising from electronic modulation and structural accessibility provided by the ligand shell, underscore the importance of ligand engineering in steering eCO_2R performance beyond nuclearity alone. Fundamentally, this study attempts to elucidate some new structure-activity insights in metal nanocluster-driven CO_2 electroreduction that can find broader applications in establishing materials design rationales in this field.

4. Experimental Section

Chemicals Used: Silver nitrate was bought from Rankem Chemicals. Triphenylphosphine, 2,5-dimethylbenzenethiol, 3,4-difluorobenzenethiol, tetraphenylphosphonium chloride, tetraphenylphosphonium bromide, 1,2-bis(diphenylphosphino)ethane, and sodium borohydride (98%) were purchased from Aldrich and Sigma–Aldrich Chemicals. The *meta*-carborane 9-thiol and *ortho*-carborane-1, 2-dithiol were synthesized using carborane derivatives, bought from *Katchem s.r.o*. (Czech Republic). The TRZ-H_2 ligand was acquired from TCI America. Chloroform ($CHCl_3$), *n*-hexane, *N,N*-dimethylformamide (DMF), solvent grade dichloromethane (DCM), trimethylamine, and methanol (99.5%) were acquired from Rankem Chemicals and Finar, India. All the chemicals were commercially available and used as such without any further purification.

Synthesis of Ag_{21} and Ag_{42} Nanoclusters: The Ag_{21} and Ag_{42} clusters were synthesized through a LEIST reaction starting from the $[Ag_{18}(TPP)_{10}H_{16}]$ cluster, following the earlier reports.[68,70] The precursor $[Ag_{18}(TPP)_{10}H_{16}]$ was synthesized through a single-step reduction of $AgNO_3$ (20 mg) and TPP (70–75 mg) mixture in methanol-chloroform (1:2 v/v) solution, under constant stirring at room temperature. Later, sodium borohydride (6.5 mg) solution dissolved in 1 mL of Milli-Q water was added to the prior mixture. After 3–3.5 h, the reduction reaction results in the dark green solution, which indicates the formation of the desired nanocluster.

The Ag_{21} was synthesized via LEIST reaction between $[Ag_{18}(TPP)_{10}H_{16}]$ and MCT-H. ≈10 mg of the Ag_{18} precursor nanocluster was dissolved in 5 mL of methanol and mixed with 8 mg of MCT-H. The solution gradually changed from yellowish to dark red within 10 min of the thiol addition. After 12 h of stirring, a red precipitate formed, which was isolated by centrifugation, and it was isolated through repeated washing with methanol and cold water. The resulting Ag_{21} cluster (synthetic yield of 60%), obtained as a red powder, was used for further studies.

The Ag_{42} cluster was synthesized using a similar LEIST protocol. In this reaction, 4.2 mg of CBDT-H_2 dissolved in methanol was added to a methanolic solution of the Ag_{18} nanocluster (≈10 mg). The mixture was stirred thoroughly, initially forming a white precipitate, which gradually transformed into a brownish solid after 5 h of continuous stirring, indicating the formation of the Ag_{42} cluster. The brown product (yield of 65%) was collected and purified by multiple washings with methanol prior to further studies.

Synthesis of Ag_{31} Nanocluster: The synthesis was carried out via a TPP-assisted co-reduction of $AgNO_3$ and TRZ-H_2, following the previously reported procedure.[69] Briefly, 20 mg of $AgNO_3$ was dissolved in 5 mL of methanol and mixed with 25 mg of TRZ-H_2 dissolved in 9 mL of DCM. Subsequently, 45 mg of TPP was added to the mixture. After 20 min of stirring, the resulting solution was reduced by adding 12 mg of $NaBH_4$ dissolved in 1 mL of ice-cold water. The reaction was allowed to proceed for 6 h, ultimately yielding a purple-colored Ag_{31} cluster. The dark violet solid (synthetic yield of 75%) was isolated by repeated washings with methanol and hexane and was used for further studies.

Synthesis of Ag_{22} Nanocluster: In a typical one-pot synthesis reported previously, $AgNO_3$ (20 mg) was dissolved in MeOH/DCM (5/9 mL, v/v), followed by the addition of 2,5-DMBT (10 µL) and DPPE (10 mg).[71] After stirring for 15–20 min, $NaBH_4$ (20 mg) in 1 mL ice-cold water) was added dropwise, changing the solution color from yellow to dark brown. 15 mg of PPh_4Cl and a few drops of triethylamine were then introduced, and the reaction was stirred for 12 h under ice-cold conditions. The product was isolated by washing, solvent evaporation, and MeOH extraction, yielding purified nanoclusters soluble in a wide range of organic solvents. Dried powder obtained from a methanol solution was used for further studies.

Synthesis of Ag_{44} Nanocluster: 20 mg of $AgNO_3$ was dissolved in DCM/MeOH (10/5 mL, v/v), followed by the addition of 3,4-difluorobenzenethiol (10 µL) and PPh_4Br (15 mg) at 0 °C. After 20 min, $NaBH_4$ (40–45 mg) and a few drops of triethylamine were introduced, and the reaction was aged for 12 h at 0 °C. The organic phase was washed, and powder of $(PPh_4)_4[Ag_{44}(SC_6H_3F_2)_{30}]$ was obtained upon drying the DCM solution of the cluster.[72]

Gas-Diffusion Electrode Preparation: The catalyst ink was prepared by dispersing 4 mg of samples in 3 mL of isopropanol and 6 µL of Nafion solution (5% wt.). The prepared solution was sonicated for 30 min. The obtained solution, which was the catalyst ink, was coated on the gas diffusion layer (Sigracet 35BC GDL) using the airbrush method to generate a gas diffusion electrode (GDE). The GDE was then dried at 130 °C for 1 h inside a vacuum oven. The loading was calculated by precisely weighing the GDL before and after applying the catalyst via airbrushing. Catalyst loading was optimized within the range of 0.2–1 mg cm^{-2}, with 0.5 mg cm^{-2} being selected for the eCO_2R tests.

Electrochemical Reduction of CO_2 and Product Analysis: Electrochemical measurements were conducted under dark conditions to minimize the photosensitive behavior of silver clusters. All CO_2 electrochemical reduction tests were performed using a Gamry Interface 1010E potentiostat under the chronoamperometric mode, which applies a constant voltage to a customized flow cell. A 1 M KOH electrolyte was used in the flow cell setup, with Ni foam as the anode and an anion exchange membrane FAA-3-PK-75 as the separator. Utilizing a mass flow controller (Alicat Scientific), a CO_2 gas flow of 50 sccm (standard cubic centimeters per minute) was controlled at the cathode. The electrolyte was supplied to the cell using syringe pumps (New Era Pump Systems Inc.), with flow rates set at 1.0 mL min^{-1} for the cathode and 2.0 mL min^{-1} for the anode. The reference electrode used was Ag/AgCl (3 M KCl), which was utilized for determining cathodic potential. All potentials were referenced to the RHE scale using the following conversion equation:

$$E_{RHE} = E_{Ag/AgCl} + 0.209\,V + 0.0591 \times pH \quad (1)$$

For product monitoring and gas analysis, an online gas chromatograph (GC, SRI Multiple Gas #5) equipped with a flame ionization detector and thermal conductivity detectors was utilized. To measure the actual CO_2 flow rate at the outlet of the flow cell, an argon gas stream at 10 sccm was mixed with the outlet gas stream from the flow cell before being directed to the GC in a closed loop.

Faradaic Efficiency Calculation:

$$FE\,(\%) = \frac{zF \times V \times 100\%}{j_{total}} \quad (2)$$

where z is the number of electrons required to form the target product, F is the Faraday constant (964850), x represents the molar fraction of the product relative to CO_2 (determined from GC analysis), V is the molar flow rate of CO_2 at the outlet, and j_{total} is the total current density.

© 2025 Wiley-VCH GmbH

16136829, 0, Downloaded from https://onlinelibrary.wiley.com/doi/10.1002/smll.202505305 by Central Library The Librarian, Wiley Online Library on [28/12/2025]. See the Terms and Conditions (https://onlinelibrary.wiley.com/terms-and-conditions) on Wiley Online Library for rules of use; OA articles are governed by the applicable Creative Commons License

Turnover Frequency Calculation (TOF):

$$TOF = (j/N/F) / \left(m/M_{Ag}\right) \quad (3)$$

where j is the partial current for CO production at a specific potential, N is the number of electrons transferred to generate one molecule of CO, which is 2, and F is the Faraday constant (96485 C mol^{-1}). m represents the mass of Ag active sites in the electrode, calculated as $m_{cat} \times \omega$ where m_{cat} is the mass of catalyst loaded onto the electrode on GDL and ω is the Ag content in the catalyst (wt.%). Finally, M_{Ag} is the atomic mass of Ag (107.86 g mol^{-1}).

Supporting Information

Supporting Information is available from the Wiley Online Library or from the author.

Acknowledgements

P.J. and A.J. contributed equally to this work. S.R. acknowledges research support from IIT Kanpur (Project 2024098) and the Chandrakanta Kesavan Centre for Energy Policy and Climate Solutions at IIT Kanpur (Project 2021136H). P.J. acknowledges the IIT Kanpur Institute fellowship (2024). The authors thank Shared Equipment Authority of Rice University and central facilities of IIT Kanpur for infrastructure access. T.P. gratefully acknowledges financial support from the Centre of Excellence on Molecular Materials and Functions under the Institution of Eminence program of IIT Madras. T.P. and T.B. acknowledge joint funding from Department of Science and Technology (DST), India and the Ministry of Education, Youth and Sports (MEYS) at Czech Republic's for bilateral initiatives (DST/INT/Czech/P-16/2020; LTAIN19152). T.P. also acknowledges the Science and Engineering Research Board (SERB), India, for the research grant SPR/2021/000439. Additionally, the authors acknowledge BioRender for offering resources to create graphical schemes (Created in BioRender. Jayan, P. (2025) https://BioRender.com/00xbqi).

Conflict of Interest

The authors declare no conflict of interest.

Data Availability Statement

The additional data and analysis has been provided in the supporting information. Data available from the authors upon reasonable request.

Keywords

carborane-thiol, CO, electrochemical CO_2 reduction, faradaic efficiency, silver nanoclusters

Received: April 30, 2025
Revised: October 26, 2025
Published online:

[1] D. Bagchi, S. Roy, S. Ch. Sarma, S. C. Peter, *Adv. Funct. Mater.* **2022**, *32*, 2209023.
[2] S. Roy, Z. Li, Z. Chen, A. C. Mata, P. Kumar, S. Ch. Sarma, I. F. Teixeira, I. F. Silva, G. Gao, N. V. Tarakina, M. G. Kibria, C. V. Singh, J. Wu, P. M. Ajayan, *Adv. Mater.* **2024**, *36*, 2300713.
[3] O. S. Bushuyev, P. De Luna, C. T. Dinh, L. Tao, G. Saur, J. Van De Lagemaat, S. O. Kelley, E. H. Sargent, *Joule* **2018**, *2*, 825.
[4] S. Nitopi, E. Bertheussen, S. B. Scott, X. Liu, A. K. Engstfeld, S. Horch, B. Seger, I. E. L. Stephens, K. Chan, C. Hahn, J. K. Nørskov, T. F. Jaramillo, I. Chorkendorff, *Chem. Rev.* **2019**, *119*, 7610.
[5] A. Al-Mamoori, A. Krishnamurthy, A. A. Rownaghi, F. Rezaei, *Energy Tech.* **2017**, *5*, 834.
[6] T. Wilberforce, A. G. Olabi, E. T. Sayed, K. Elsaid, M. A. Abdelkareem, *Sci. Total Environ.* **2021**, *761*, 143203.
[7] B. Dziejarski, R. Krzyżyńska, K. Andersson, *Fuel* **2023**, *342*, 127776.
[8] H. Shin, K. U. Hansen, F. Jiao, *Nat. Sustain.* **2021**, *4*, 911.
[9] H.-R. Molly Jhong, S. Ma, P. J. Kenis, *Curr. Opin. Chem. Eng.* **2013**, *2*, 191.
[10] L. Chi, Y. Zhang, Z. Niu, X. Zhang, Y. Li, T. Zhang, S. Sun, P. Lu, K. Tang, M. Gao, *Angew. Chem. Int. Ed.* **2025**, *64*, 202503539.
[11] Z.-Z. Niu, L.-P. Chi, Z.-Z. Wu, P.-P. Yang, M.-H. Fan, M.-R. Gao, *NSO* **2023**, *2*, 20220044.
[12] J. Hense, M. Bachmann, L. Polte, N. Von Der Aßen, A. Jupke, *Chem. Ing. Tech.* **2022**, *94*, 1524.
[13] B. Molitor, H. Richter, M. E. Martin, R. O. Jensen, A. Juminaga, C. Mihalcea, L. T. Angenent, *Bioresour. Technol.* **2016**, *215*, 386.
[14] Y. H. Chan, S. N. F. Syed Abdul Rahman, H. M. Lahuri, A. Khalid, *Environ. Pollut.* **2021**, *278*, 116843.
[15] C. George, in *Kirk-Othmer Encyclopedia of Chemical Technology* (Ed.: K. Othmer), Wiley, New York **2001**.
[16] S. Mahajan, S. Jagtap, *Appl. Mater. Today* **2020**, *18*, 100483.
[17] T. P. Araújo, A. Shah, C. Mondelli, J. A. Stewart, D. Curulla Ferré, J. Pérez-Ramírez, *Appl. Catal., B* **2021**, *285*, 119878.
[18] Z. Li, X. Li, R. Wang, A. C. Mata, C. S. Gerke, S. Xiang, A. Mathur, L. Zhang, D.-Z. Lin, T. Li, K. N. Jayarapu, A. Liu, L. Gupta, A. I. Frenkel, V. S. Thoi, P. M. Ajayan, S. Roy, Y. Liu, Y. Liu, *Nat. Commun.* **2025**, *16*, 3206.
[19] D. Roy, A. Pal, T. Pal, *RSC Adv.* **2022**, *12*, 12116.
[20] C. McManus, J. Hicks, X. Cui, L. Zhao, G. Frenking, J. M. Goicoechea, S. Aldridge, *Chem. Sci.* **2021**, *12*, 13458.
[21] G. Zhang, L. Li, Z.-J. Zhao, T. Wang, J. Gong, *Acc. Mater. Res.* **2023**, *4*, 212.
[22] S. Zhao, R. Jin, R. Jin, *ACS Energy Lett.* **2018**, *3*, 452.
[23] M. Z. Iqbal, S. Imteyaz, C. Ghanty, S. Sarkar, *J. Indust. Eng. Chem.* **2022**, *113*, 15.
[24] D. L. T. Nguyen, H. H. Do, M. T. Nguyen, D.-V. N. Vo, V.-H. Nguyen, C. C. Nguyen, S. Y. Kim, Q. V. Le, *Chem. Eng. Sci.* **2021**, *234*, 116403.
[25] Q. Chen, P. Tsiakaras, P. Shen, *Catalysts* **2022**, *12*, 1348.
[26] K. Qi, Y. Zhang, J. Li, C. Charmette, M. Ramonda, X. Cui, Y. Wang, Y. Zhang, H. Wu, W. Wang, X. Zhang, D. Voiry, *ACS Nano* **2021**, *15*, 7682.
[27] R. Wang, H. Haspel, A. Pustovarenko, A. Dikhtiarenko, A. Russkikh, G. Shterk, D. Osadchii, S. Ould-Chikh, M. Ma, W. A. Smith, K. Takanabe, F. Kapteijn, J. Gascon, *ACS Energy Lett.* **2019**, *4*, 2024.
[28] S. Liu, H. Tao, L. Zeng, Q. Liu, Z. Xu, Q. Liu, J.-L. Luo, *J. Am. Chem. Soc.* **2017**, *139*, 2160.
[29] C. Tricella, M. Muhyuddin, R. Nisticò, S. Tosoni, C. Santoro, *Curr. Opin. Electrochem.* **2025**, *51*, 101696.
[30] Y. Y. Birdja, E. Pérez-Gallent, M. C. Figueiredo, A. J. Göttle, F. Calle-Vallejo, M. T. M. Koper, *Nat. Energy* **2019**, *4*, 732.
[31] S. Jin, Z. Hao, K. Zhang, Z. Yan, J. Chen, *Angew. Chem.* **2021**, *133*, 20795.
[32] M. R. Singh, J. D. Goodpaster, A. Z. Weber, M. Head-Gordon, A. T. Bell, *Proc. Natl. Acad. Sci. USA* **2017**, *114*, E8812.
[33] S. Jin, Z. Hao, K. Zhang, Z. Yan, J. Chen, *Angew. Chem.* **2021**, *133*, 20795.
[34] L. Zeng, J. Shi, H. Chen, C. Lin, *Energies* **2021**, *14*, 2840.
[35] X. Deng, D. Alfonso, T.-D. Nguyen-Phan, D. R. Kauffman, *ACS Catal.* **2022**, *12*, 5921.

© 2025 Wiley-VCH GmbH

16136829, 0, Downloaded from https://onlinelibrary.wiley.com/doi/10.1002/smll.202505305 by Central Library The Librarian, Wiley Online Library on [28/12/2025]. See the Terms and Conditions (https://onlinelibrary.wiley.com/terms-and-conditions) on Wiley Online Library for rules of use; OA articles are governed by the applicable Creative Commons License

[36] X. Zou, A. Li, C. Ma, Z. Gao, B. Zhou, L. Zhu, Z. Huang, *Chem. Eng. J.* **2023**, *468*, 143606.
[37] J. Zeng, W. Zhang, Y. Yang, D. Li, X. Yu, Q. Gao, *ACS Appl. Mater. Interfaces* **2019**, *11*, 33074.
[38] L. Zeng, J. Shi, H. Chen, C. Lin, *Energies* **2021**, *14*, 2840.
[39] I. Chakraborty, T. Pradeep, *Chem. Rev.* **2017**, *117*, 8208.
[40] T. Kawawaki, T. Okada, D. Hirayama, Y. Negishi, *Green Chem.* **2024**, *26*, 122.
[41] Y. Du, H. Sheng, D. Astruc, M. Zhu, *Chem. Rev.* **2020**, *120*, 526.
[42] R. Jin, G. Li, S. Sharma, Y. Li, X. Du, *Chem. Rev.* **2021**, *121*, 567.
[43] M. Neumaier, A. Baksi, P. Weis, E. K. Schneider, P. Chakraborty, H. Hahn, T. Pradeep, M. M. Kappes, *J. Am. Chem. Soc.* **2021**, *143*, 6969.
[44] S. Li, A. V. Nagarajan, Y. Li, D. R. Kauffman, G. Mpourmpakis, R. Jin, *Nanoscale* **2021**, *13*, 2333.
[45] M. F. Matus, H. Häkkinen, *Nat. Rev. Mater.* **2023**, *8*, 372.
[46] S. Li, A. V. Nagarajan, D. R. Alfonso, M. Sun, D. R. Kauffman, G. Mpourmpakis, R. Jin, *Angew. Chem. Int. Ed.* **2021**, *60*, 6351.
[47] F. Lü, H. Bao, Y. Mi, Y. Liu, J. Sun, X. Peng, Y. Qiu, L. Zhuo, X. Liu, J. Luo, *Sustain. Energy Fuels* **2020**, *4*, 1012.
[48] K. Kwak, D. Lee, *Acc. Chem. Res.* **2019**, *52*, 12.
[49] Y. Du, H. Sheng, D. Astruc, M. Zhu, *Chem. Rev.* **2020**, *120*, 526.
[50] H. Qian, M. Zhu, Z. Wu, R. Jin, *Acc. Chem. Res.* **2012**, *45*, 1470.
[51] J. Zhao, A. Ziarati, T. Bürgi, *Angew. Chem. Int. Ed.* **2025**, *137*, 202504320.
[52] D. Yang, J. Wang, Q. Wang, Z. Yuan, Y. Dai, C. Zhou, X. Wan, Q. Zhang, Y. Yang, *ACS Nano* **2022**, *16*, 15681.
[53] V. K. Kulkarni, B. N. Khiarak, S. Takano, S. Malola, E. L. Albright, T. I. Levchenko, M. D. Aloisio, C.-T. Dinh, T. Tsukuda, H. Häkkinen, C. M. Crudden, *J. Am. Chem. Soc.* **2022**, *144*, 9000.
[54] Z.-H. Gao, K. Wei, T. Wu, J. Dong, D. Jiang, S. Sun, L.-S. Wang, *J. Am. Chem. Soc.* **2022**, *144*, 5258.
[55] S. Yuan, R. He, X. Han, J. Wang, Z. Guan, Q. Wang, *Angew. Chem. Int. Ed.* **2021**, *60*, 14345.
[56] V. Yadav, A. Jana, S. Acharya, S. Malola, H. Nagar, A. Sharma, A. R. Kini, S. Antharjanam, J. Machacek, K. N. V. D. Adarsh, T. Base, H. Häkkinen, T. Pradeep, *Nat. Commun.* **2025**, *16*, 1197.
[57] D. R. Kauffman, D. Alfonso, C. Matranga, H. Qian, R. Jin, *J. Am. Chem. Soc.* **2012**, *134*, 10237.
[58] L. Qin, F. Sun, X. Ma, G. Ma, Y. Tang, L. Wang, Q. Tang, R. Jin, Z. Tang, *Angew. Chem. Int. Ed.* **2021**, *60*, 26136.
[59] H. Seong, M. Choi, S. Park, H. Kim, J. Kim, W. Kim, J. S. Yoo, D. Lee, *ACS Energy Lett.* **2022**, *7*, 4177.
[60] J. F. Parker, K. A. Kacprzak, O. Lopez-Acevedo, H. Häkkinen, R. W. Murray, *J. Phys. Chem. C* **2010**, *114*, 8276.
[61] S. Zhao, N. Austin, M. Li, Y. Song, S. D. House, S. Bernhard, J. C. Yang, G. Mpourmpakis, R. Jin, *ACS Catal.* **2018**, *8*, 4996.
[62] G. Deng, H. Yun, M. S. Bootharaju, F. Sun, K. Lee, X. Liu, S. Yoo, Q. Tang, Y. J. Hwang, T. Hyeon, *J. Am. Chem. Soc.* **2023**, *145*, 27407.
[63] R. Guo, R. W. Murray, *J. Am. Chem. Soc.* **2005**, *127*, 12140.
[64] Y.-M. Wang, F.-Q. Yan, Q.-Y. Wang, C.-X. Du, L.-Y. Wang, B. Li, S. Wang, S.-Q. Zang, *Nat. Commun.* **2024**, *15*, 1843.
[65] H. Seong, V. Efremov, G. Park, H. Kim, J. S. Yoo, D. Lee, *Angew. Chem. Int. Ed.* **2021**, *60*, 14563.
[66] S. Li, A. V. Nagarajan, X. Du, Y. Li, Z. Liu, D. R. Kauffman, G. Mpourmpakis, R. Jin, *Angew. Chem. Int. Ed.* **2022**, *61*, 202211771.
[67] M. Zhou, C. Zeng, Y. Chen, S. Zhao, M. Y. Sfeir, M. Zhu, R. Jin, *Nat. Commun.* **2016**, *7*, 13240.
[68] A. Jana, P. M. Unnikrishnan, A. K. Poonia, J. Roy, M. Jash, G. Paramasivam, J. Machacek, K. N. V. D. Adarsh, T. Base, T. Pradeep, *Inorg. Chem.* **2022**, *61*, 8593.
[69] A. Jana, W. A. Dar, S. K. Jana, A. K. Poonia, V. Yadav, J. Roy, S. Chandra, K. N. V. D. Adarsh, R. H. A. Ras, T. Pradeep, *Chem. Mater.* **2023**, *35*, 7020.
[70] A. Jana, M. Jash, A. K. Poonia, G. Paramasivam, M. R. Islam, P. Chakraborty, S. Antharjanam, J. Machacek, S. Ghosh, K. N. V. D. Adarsh, T. Base, T. Pradeep, *ACS Nano* **2021**, *15*, 15781.
[71] E. Khatun, M. Bodiuzzaman, K. S. Sugi, P. Chakraborty, G. Paramasivam, W. A. Dar, T. Ahuja, S. Antharjanam, T. Pradeep, *ACS Nano* **2019**, *13*, 5753.
[72] H. Yang, Y. Wang, H. Huang, L. Gell, L. Lehtovaara, S. Malola, H. Häkkinen, N. Zheng, *Nat. Commun.* **2013**, *4*, 2422.
[73] H. Y. V. Ching, X. Wang, M. He, N. P. Holland, R. Guillot, C. Slim, S. Griveau, H. C. Bertrand, C. Policar, F. Bedioui, M. Fontecave, *Inorg. Chem.* **2017**, *56*, 2966.
[74] A. Lashgari, C. K. Williams, J. L. Glover, Y. Wu, J. Chai, J. Jimmy Jiang, *Chem. A Eur. J.* **2020**, *26*, 16774.
[75] G. Kresse, J. Hafner, *Phys. Rev. B* **1994**, *49*, 14251.
[76] J. P. Perdew, J. A. Chevary, S. H. Vosko, K. A. Jackson, M. R. Pederson, D. J. Singh, C. Fiolhais, *Phys. Rev. B* **1992**, *46*, 6671.
[77] G. Kresse, D. Joubert, *Phys. Rev. B* **1999**, *59*, 1758.
[78] J. K. Nørskov, J. Rossmeisl, A. Logadottir, L. Lindqvist, J. R. Kitchin, T. Bligaard, H. Jónsson, *J. Phys. Chem. B* **2004**, *108*, 17886.

© 2025 Wiley-VCH GmbH

16136829, 0, Downloaded from https://onlinelibrary.wiley.com/doi/10.1002/smll.202505305 by Central Library The Librarian, Wiley Online Library on [28/12/2025]. See the Terms and Conditions (https://onlinelibrary.wiley.com/terms-and-conditions) on Wiley Online Library for rules of use; OA articles are governed by the applicable Creative Commons License

Supplementary Information

CO_2 Electroreduction to CO over Silver Nanoclusters: The Impact of Nuclearity on Synergistic Activity Modulation

Parvathy Jayan[1#], Arijit Jana[2#], Zhengyuan Li[3], Rahul Kumar Sharma[4], Vivek Yadav[2],Astrid Campos Mata[5], Ming-Husan Li[6], Ali Shayesteh Zeraati[7], Tomas Base[8], Sung-Fu Hung[6], Jingjie Wu[3], Biswarup Pathak[4], Thalappil Pradeep[2], Soumyabrata Roy*[1,5]

[1]Department of Sustainable Energy Engineering, Indian Institute of Technology Kanpur, Uttar Pradesh, India

[2]Department of Science and Technology (DST) Unit of Nanoscience and Thematic Unit of Excellence, Department of Chemistry, Indian Institute of Technology (IIT) Madras, Chennai, India

[3]Department of Chemical Engineering, University of Cincinnati, Cincinnati, OH 45221, USA

[4]Department of Chemistry, Indian Institute of Technology, Indore, Madhya Pradesh. India

[5]Department of Materials Science and Nanoengineering, Rice University, Houston, Texas 77005, USA

[6]Department of Applied Chemistry and Centre for Emergent Functional Matter Science, National Yang Ming Chiao Tung University, Hsinchu 300, Taiwan.

[7]Acceleration Consortium, University of Toronto, 80 St. George St., Toronto, ON M5S 3H6, Canada

[8]Department of Syntheses, Institute of Inorganic Chemistry, The Czech Academy of Sciences, 1001 Husinec-Rez, 25068, Czech Republic.

[#] These authors contributed equally: Parvathy Jayan, Arijit Jana

Email: soumyar@iitk.ac.in (Soumyabrata Roy)

Index

1. **Instrumental details and characterization** S4
2. **Computational Detail** S5
3. **Figures**

Figure S1. SEM-EDS images of Ag_{21} NC and EDS spectra S6

Figure S2. Photographic images of UV-visible samples of AgNCs in cuvettes S6

Figure S3. UV-vis absorption spectra of (a) Ag_{22}, (b) Ag_{44} before loading the GDL S6

Figure S4. HR-MS spectra of Ag_{22} and Ag_{44} NCs S7

Figure S5. Single-crystal images of Ag_{21} NC and Ag_{42} NC S7

Figure S6. TEM image of Ag NCs S8

Figure S7. HAADF elemental mapping of Ag_{21} NC S8

Figure S8. FTIR Spectra of Ag_{31} and Ag_{42} S9

Figure S9. HR-Elemental XPS scans and peak fitting of Ag_{21} NC catalysts S9

Figure S10. HR-Elemental XPS scans and peak fitting of Ag_{31} NC catalysts S10

Figure S11. HR-Elemental XPS scans and peak fitting of Ag_{42} NC catalysts S10

Figure S12. Faradaic Efficiency (FE) of CO for Ag_{31}NC and Ag_{42} NC S11

Figure S13. Electrochemical performance of Ag_{22} in comparison with Ag_{21} S11

Figure S14. Electrochemical performance of Ag_{42} in comparison with Ag_{44} S12

Figure S15. Long-term stability data of Ag_{21} S12

Figure S16. Pre- and post-electrochemical XPS peak fitting of Ag_{21}NC catalyst-coated electrode. S13

Figure S17. Pre- and post-electrochemical XPS peak fitting of Ag_{31}NC catalyst-coated electrode. S13

Figure S18. Pre- and post-electrochemical XPS peak fitting of Ag_{42}NC catalyst-coated electrode. S14

Figure S19. EXAFS spectra of Ag K edge for the AgNCs post eCO_2R S14

Figure S20. EXAFS fitting result of AgNCs at R space after eCO_2R S15

Figure S21. Heterogeneous Active Sites Investigated for *CO and *COOH adsorption on the Ag_{21} cluster. S15

Figure S22. Heterogeneous Active Sites Investigated for *CO and *COOH adsorption on the Ag_{42} cluster. S16

Figure S23. CDD plots on intermediate *COOH and CO on Ag_{21} and Ag_{42} S16

Figure S24. Heterogeneous Active Sites Investigated for *CO, and *COOH adsorption on the Ag_{44} cluster S17

Figure S25. Gibbs free energy diagram of Ag_{21}, Ag_{42}, and Ag_{44} clusters S17

Figure S26. Total and partial DOS analysis for *COOH and *CO-adsorbed Ag_{21} and Ag_{42} clusters S18

Figure S27. Subplots for total and partial density of states (DOS) for *COOH, and *CO-adsorbed on Ag_{42}. S28

Figure S28. Subplots for total and partial density of states (DOS) for *COOH, and *CO-adsorbed on Ag_{21}. S19

4. Tables

Table S1. EXAFS fitting parameters of Ag NC catalyst S19

Table S2. Comparison of eCO_2R performance (FE_{CO} vs potential) between Ag_{21} and recent catalysts. S20

Table S3. Interaction energies E_{int} of Ag_{21} and Ag_{42} with MCT/CBDT and TPP ligands in eV units S21

Table S4. Bader charge on different Ag atoms in Ag_{21} clusters S21

Table S5. Bader charge on different Ag atoms in Ag_{21} clusters S22

5. References S23

1. Instrumental details and characterization

UV-vis absorption spectra of clusters were recorded using a Perkin Elmer Lambda-1050 UV–Vis-NIR spectrophotometer. The electrospray ionization mass spectra (ESI-MS) of nanoclusters (NCs) were acquired on a Waters Synapt G2Si HDMS instrument. ESI-MS instrumental parameters were maintained with the following values: capillary voltage, 2-3 kV; source temperature, 80-100 °C; flow rate, 15-20 μL/min; cone voltage, 20 V. Ag_{21} and Ag_{42} spectra were recorded in positive ion mode, whereas Ag_{31} was recorded in negative mode. Fourier-transform infrared (FTIR) spectrum was collected from KBr pellets in the range of 3000 - 500 cm^{-1} with a JASCO-4100 FT-IR spectrometer. For the spectral measurement, microcrystalline samples were positioned on top of the diamond crystal. For understanding the morphological features of silver clusters, scanning electron microscopy (SEM) and high-resolution transmission electron microscopy (HR-TEM) have been performed on the AgNCs samples. For imaging of the clusters, SEM, JSM-6500F, JEOL, has been used. Using a field emission gun running at 200kV, the Talos F200X, JEOL, and JSM-2010F were utilized to acquire the cluster images. A cold-field emission gun and a high-angle silicon drift energy dispersive X-ray (EDX) detector for elemental mapping were incorporated with this 80 kV device.

A JEOL-3010, 300 kV device was used to measure transmission electron microscopy (TEM). The images were taken using a Gatan 794 multiscan CCD camera. For XPS (X-ray photoelectron spectroscopy) characterization studies, PHI Quantera XPS and 1486.68 eV Al Kα X-ray source were used. The shift in the binding energy due to the buildup of charges from insulating samples (mainly from organic ligands) is corrected by the carbon 1s correction. C1s, S2p, N1s, O1s, Ag3d, P2p, and B1s signals of the three different clusters were deconvoluted and fitted using the Fityk software and the Gaussian-Lorentzian function. To study and investigate the local oxidation state and coordination number to which each of the Ag atoms is bonded, XAS (X-ray Absorption Spectroscopy) was conducted at the BL01C1 beamline of TLS, NSRRC. Ag K-edge measurements (25,514 eV) were conducted in fluorescence mode. The XAS results were processed using Athena software, with normalization to the incident beam intensity. Beam energy calibration was performed at the first inflection point of the Ag absorption edge using an Ag foil as a reference.

2. Computational Details

The first principle spin-polarized calculations were performed using the Vienna *ab initio* simulation package (VASP).[1,2] The Generalized Gradient approximation with Perdew-Burke-Ernzerhof (GGA-PBE) was employed to describe the exchange-correlations functionals and the Projector Augmented Wave (PAW) was utilized to describe the ion core and valence electron interactions.[3,4] The cutoff energy for the plane-wave basis sets was set to 470 eV and a conjugate-gradient algorithm with an energy convergence criterion of 10^{-4} and Hellman-Feynman force convergence criteria of < 0.02 eVÅ^{-1} was utilized during structural optimizations. Gaussian smearing of 0.2 eV and the DFT-D3 method were used to correctly define the van der Waals interactions.[5] All the spin-polarized calculations were performed for all the oxygen-adsorbed intermediates and molecular species. The Gibbs free energies of elementary steps during the CO_2RR were calculated using the computational hydrogen electrode (CHE) model proposed by Nørskov and co-workers by using the following equation:[6]

$$\Delta G = \Delta E + \Delta ZPE + T\Delta S - eU \quad \textbf{(S1)}$$

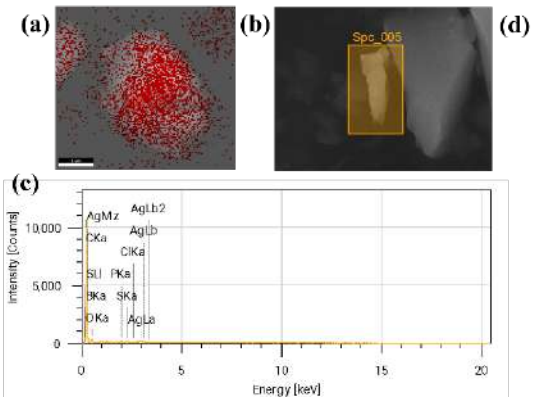
where ΔE is the total energy change in the reaction, ΔZPE is the change in the zero-point energy, T is 300 K temperature, ΔS is the entropy change, U is the electrode potential referenced to the standard hydrogen electrode, and *e* is the transferred electronic charge. The ZPE and entropies were calculated from harmonic oscillator approximation using the following formula:

$$ZPE = \sum_i \frac{1}{2} h\nu_i \quad \textbf{(S2)}$$

$$S_v = R \sum \frac{\hbar\nu_i}{k_B T\left(\exp\left(\frac{\hbar\nu_i}{kT}-1\right)\right)} - \ln\left(1-\exp\left(\frac{\hbar\nu_i}{kT}\right)\right) \quad \textbf{(S3)}$$

where h is the Planck constant, S_v is the vibrational entropy, R is the gas constant, k_B is the Boltzmann constant, ν_i is the frequency of the i_{th} vibrational mode and $\hbar = h/2\pi$. The single molecular unit cell Ag_{21} and Ag_{42} were optimized in 30 × 35 × 35 Å^3, to minimize the interactions between periodic images. The Γ-centered (1×1×1) k-point grids were considered for the sampling of the Brillouin zone considering the large size of the box. A higher (3 × 3 × 3) k-mesh was used to calculate the density of states (DOS). Bader atomic charges were determined using the Henkelman code with the near-grid algorithm refine edge method.[7,8] All of the isosurface values for the charge density difference analysis were set to be 0.002 eV Å^{-3}, where pink and blue colors gradients represent charge depletion and accumulation regions, respectively.

3. Figures



(d)

Element	Line	Mass%	Atom%
B	K	6.27±0.04	7.26±0.05
C	K	83.24±0.19	86.79±0.20
O	K	6.63±0.15	5.19±0.12
P	K	0.52±0.02	0.21±0.01
S	K	0.44±0.02	0.17±0.01
Ag	L	2.90±0.08	0.37±0.01
Total		100.00	100.00
Spc_005		Fitting ratio 0.0114	

Figure S1. (a, b) SEM-EDS images of Ag_{21} NC (c) EDS spectra of Ag_{21} NC, d) All the elements present in Ag_{21} and its corresponding mass percentage and atomic percentage



Figure S2. Photographic images of UV-visible samples of a) Ag_{21}, b) Ag_{31}, c) Ag_{42}

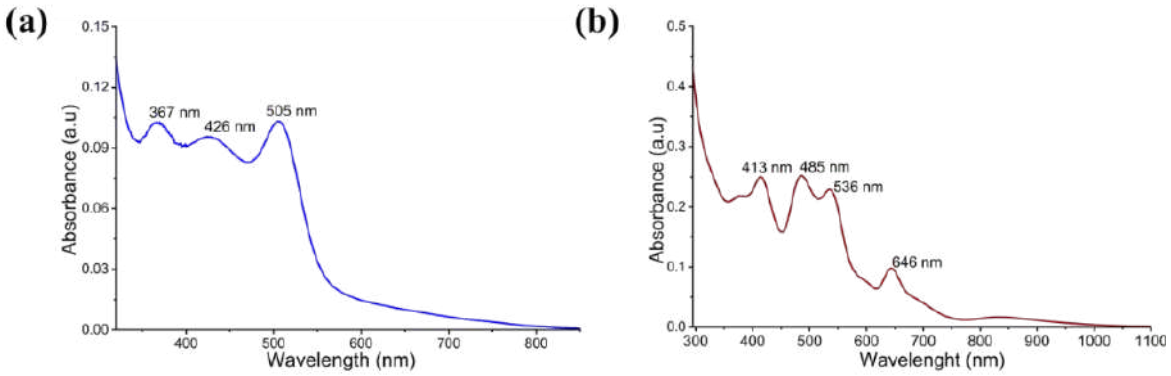


Figure S3. UV-vis absorption spectra of (a) Ag_{22}, (b) Ag_{44} before loading the GDE

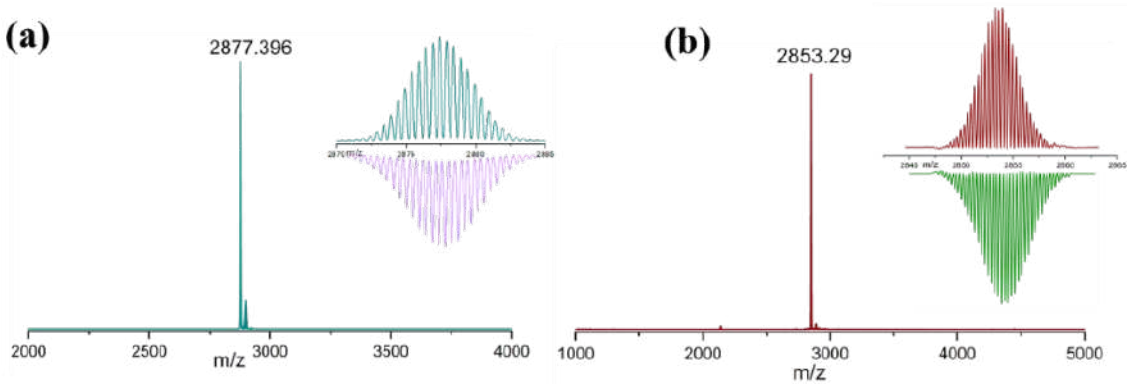


Figure S4. High-resolution mass spectrometric data of the catalyst materials before GDE loading, with inset showing the comparison of respective experimental and simulated spectra, (a) Ag_{22} (b) Ag_{44}

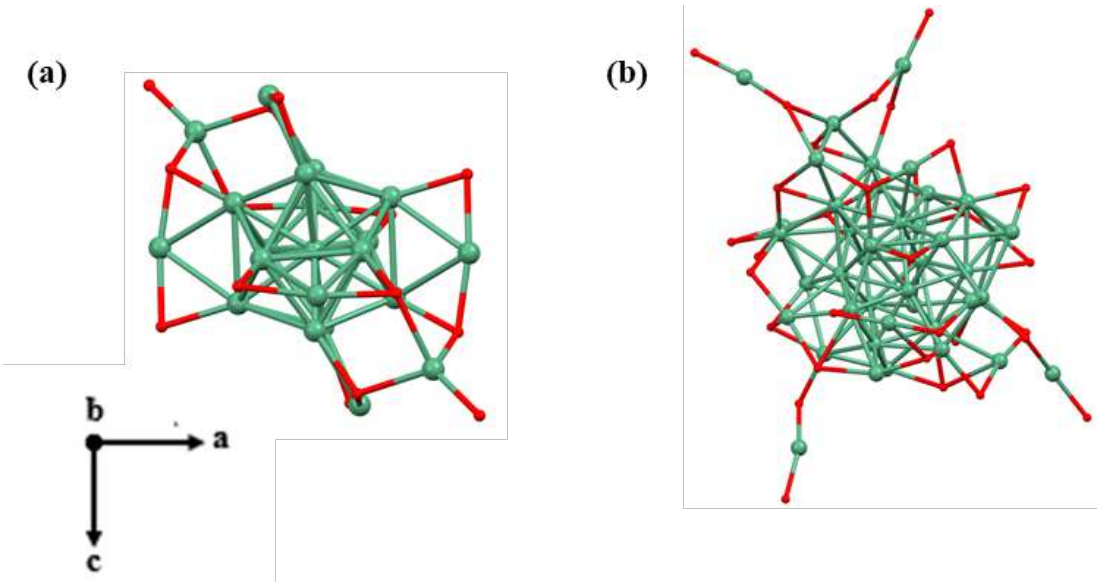


Figure S5. The metal core structure of (a) Ag_{21} NC (from SCXRD) (b) Ag_{42} NC (DFT optimized structure). Both structures are aligned in the direction of the b-axis. Colour code - Dark green: silver, Red: sulfur.

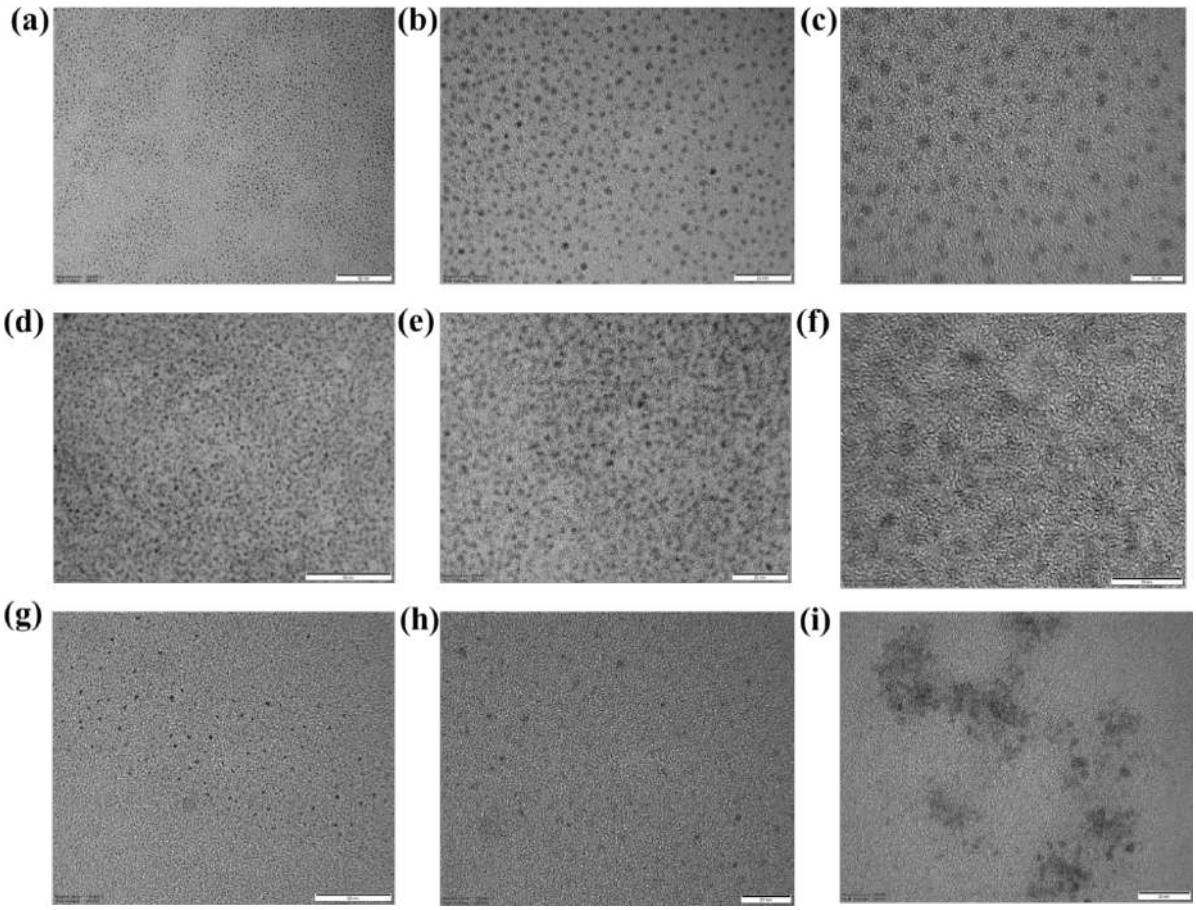


Figure S6. TEM images of Ag NCs (a-c) Ag_{21}, (d-f) Ag_{31}, (g-i) Ag_{42}

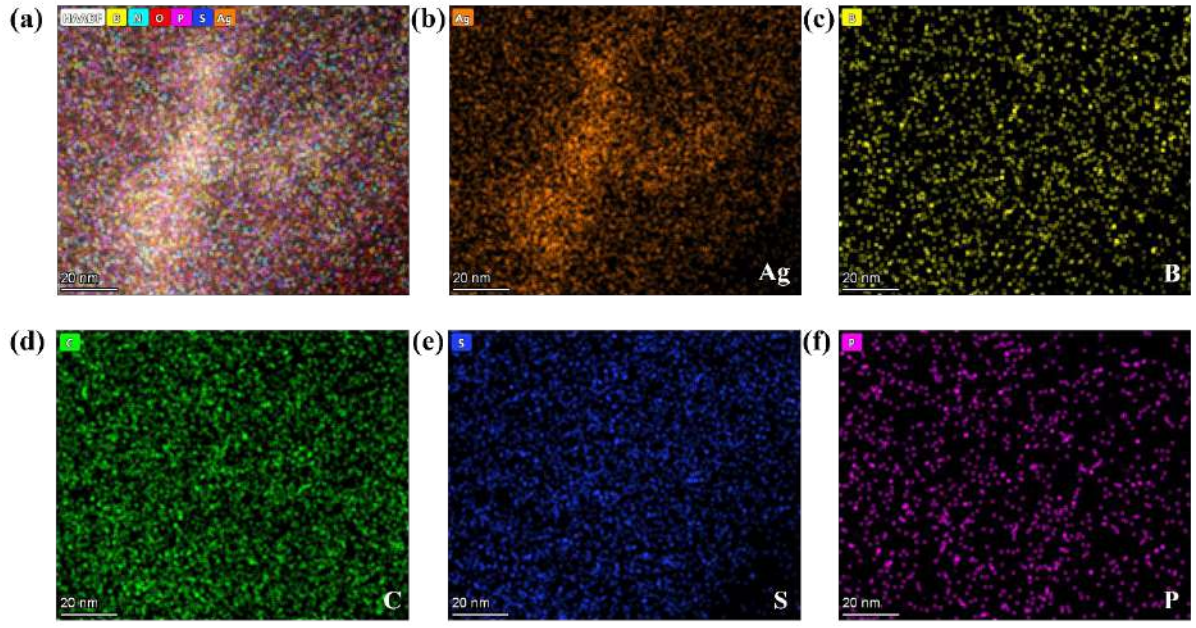


Figure S7. HAADF STEM elemental mapping of Ag_{21} NC

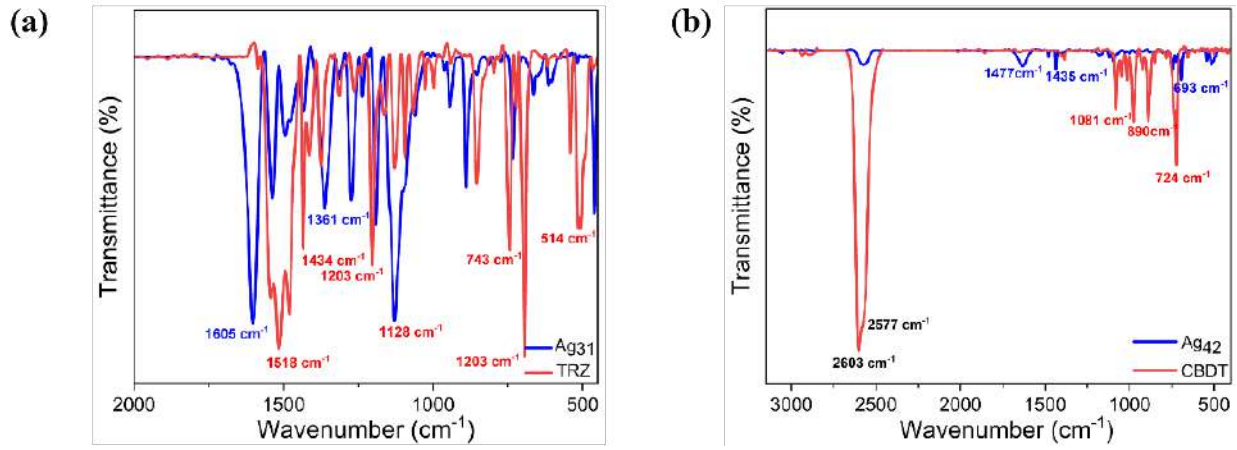


Figure S8. FTIR Spectra of (a) Ag_{31} and TRZ, (b) Ag_{42} and CBDT

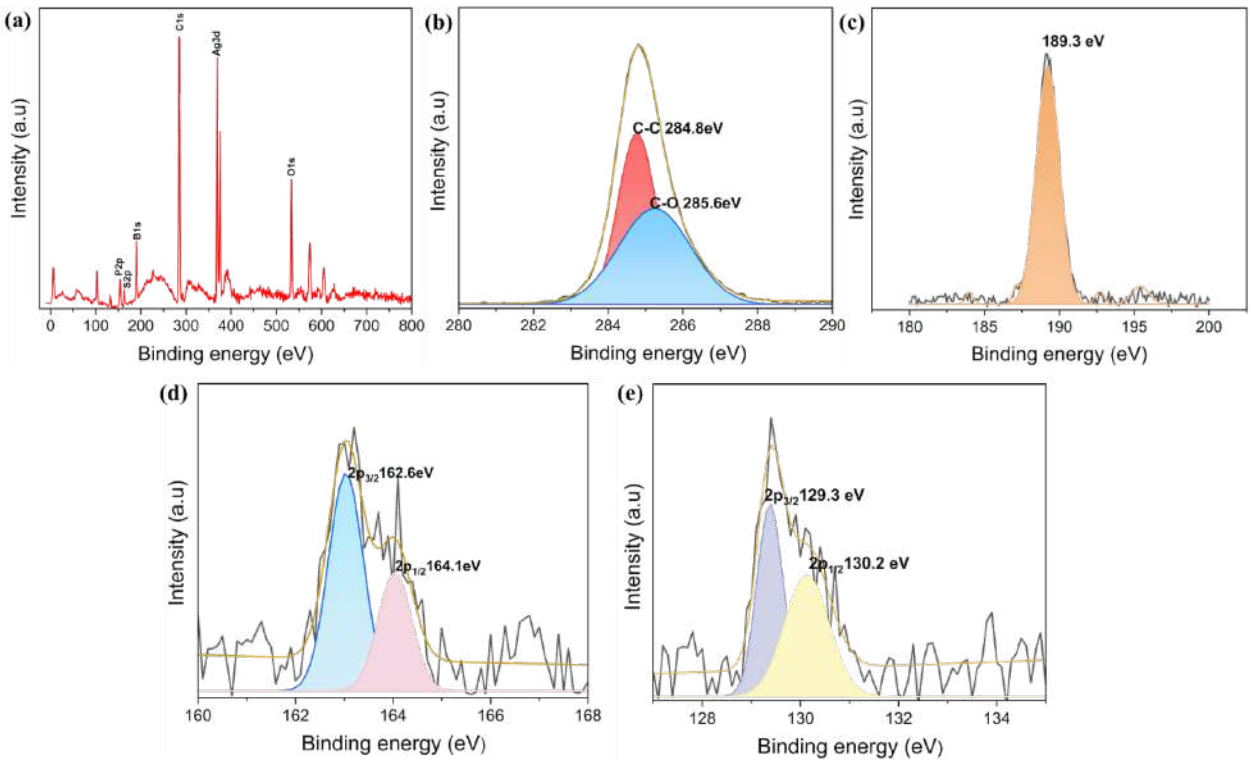


Figure S9. HR-Elemental XPS scans and peak fitting of Ag_{21} NC catalysts. (a) Full scan survey XPS (b) C1s, (c) B1s (d) S2p e) P2p

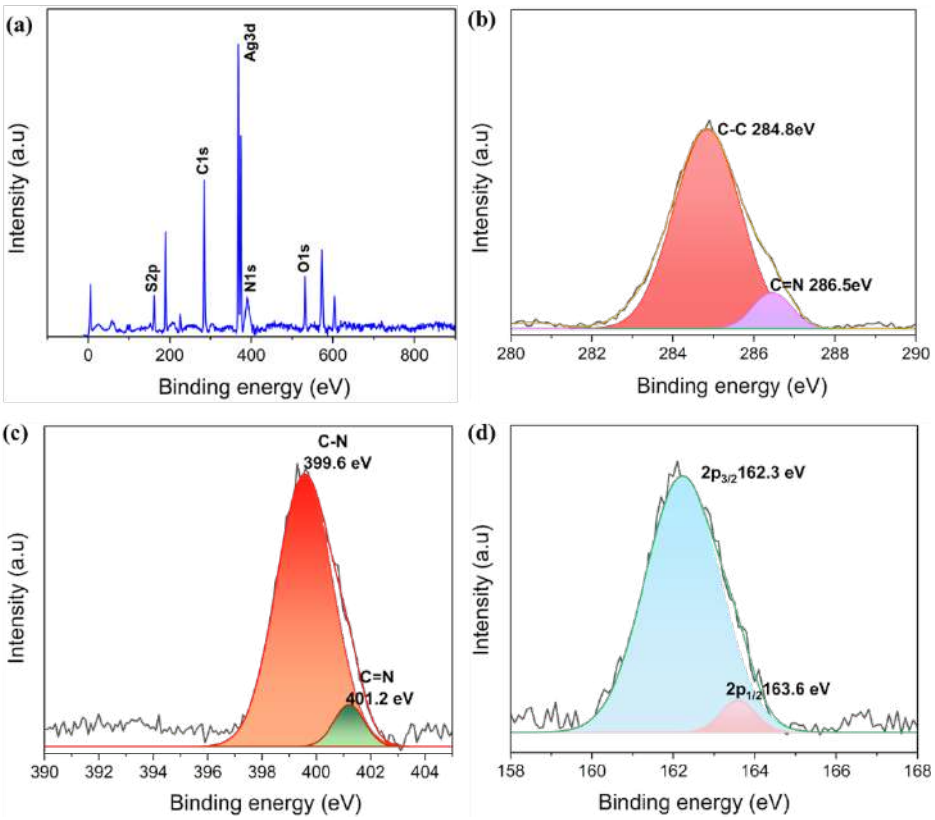


Figure S10. HR-Elemental XPS scans and peak fitting of Ag_{31} NC catalysts. (a) Full scan survey XPS b) C1s (c) N 1s, (d) S 2p

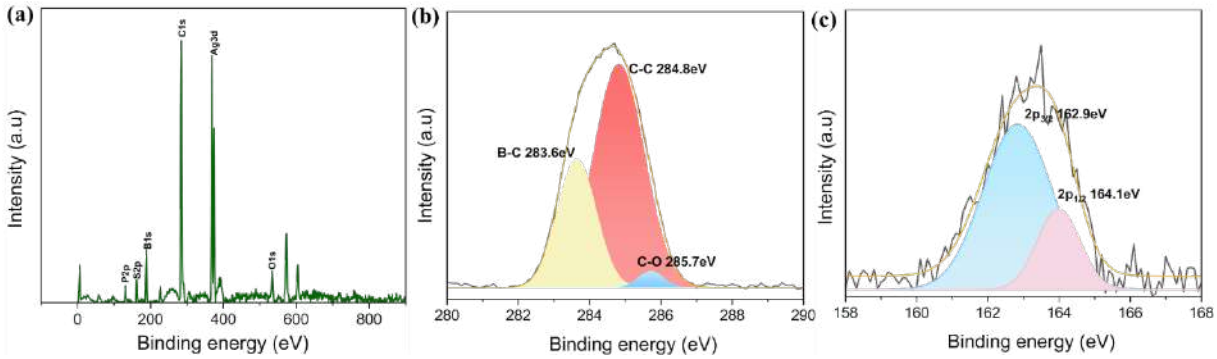


Figure S11. HR-Elemental XPS scans and peak fitting of Ag_{42} NC catalysts. (a) Full scan survey XPS (b) C 1s (c) S 2p

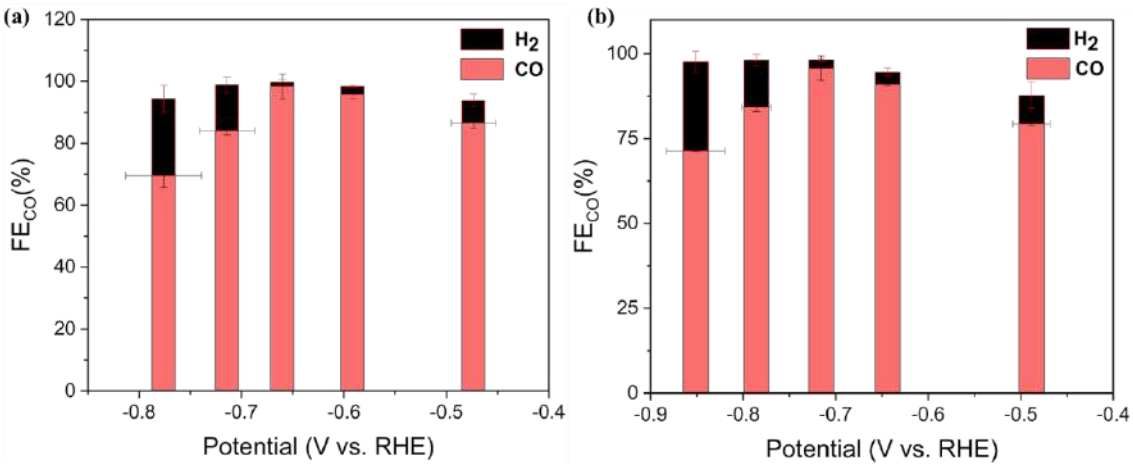


Figure S12. eCO_2R performance of Ag NCs in 1 M KOH in an alkaline flow cell. FE (%) of CO vs potential for (a) Ag_{31} NC (b) Ag_{42} NC

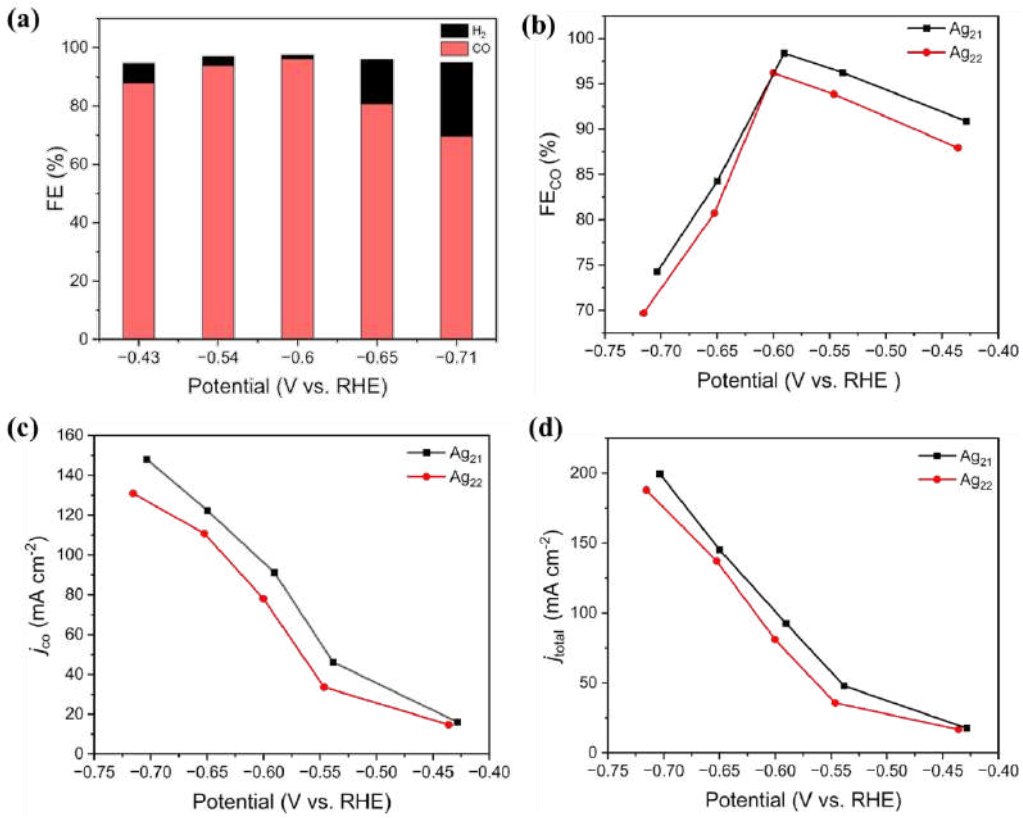


Figure S13. eCO_2R performance of Ag_{22} in 1 M KOH in an alkaline flow cell. (a) FE (%) of products with varying potential, (b) FE (%) of CO with varying potential in comparison with Ag_{21} (c) partial current density for CO across the potential range in comparison with Ag_{21} (d) (d) total current density across the potential range in comparison with Ag_{21}

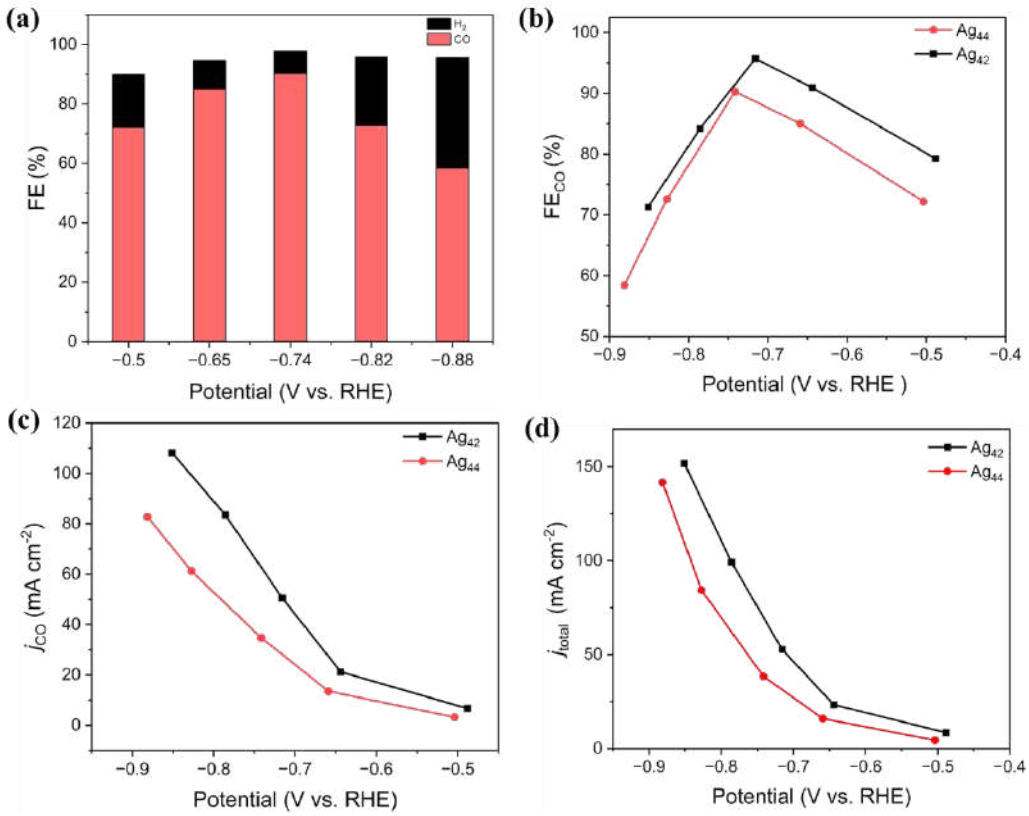


Figure S14. eCO_2R performance of Ag_{44} in 1 M KOH in an alkaline flow cell. (a) FE (%) of products with varying potential, (b) FE (%) of CO with varying potential in comparison with Ag_{42} (c) partial current density for CO across the potential range in comparison with Ag_{42} d) (d) total current density across the potential range in comparison with Ag_{42}

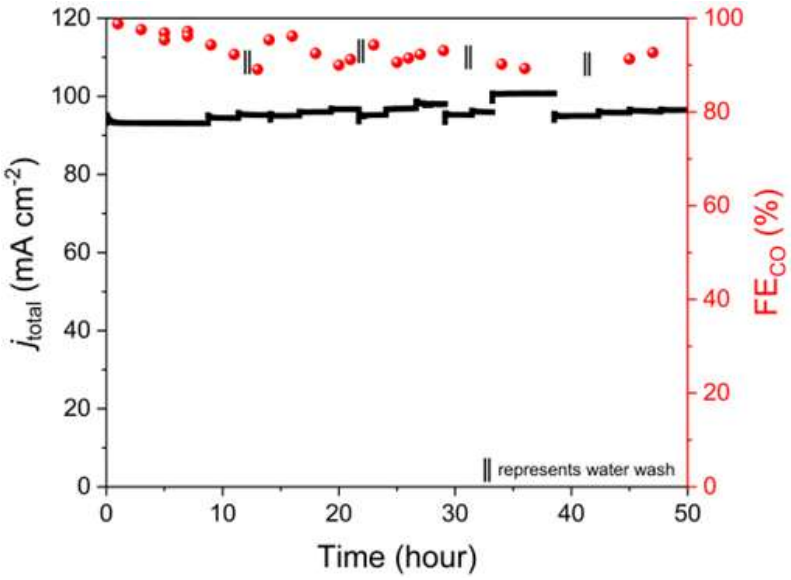


Figure S15. (e) Electrocatalytic Stability plot of Ag_{21} measured at a constant voltage of 0.59V vs RHE for 50 hours

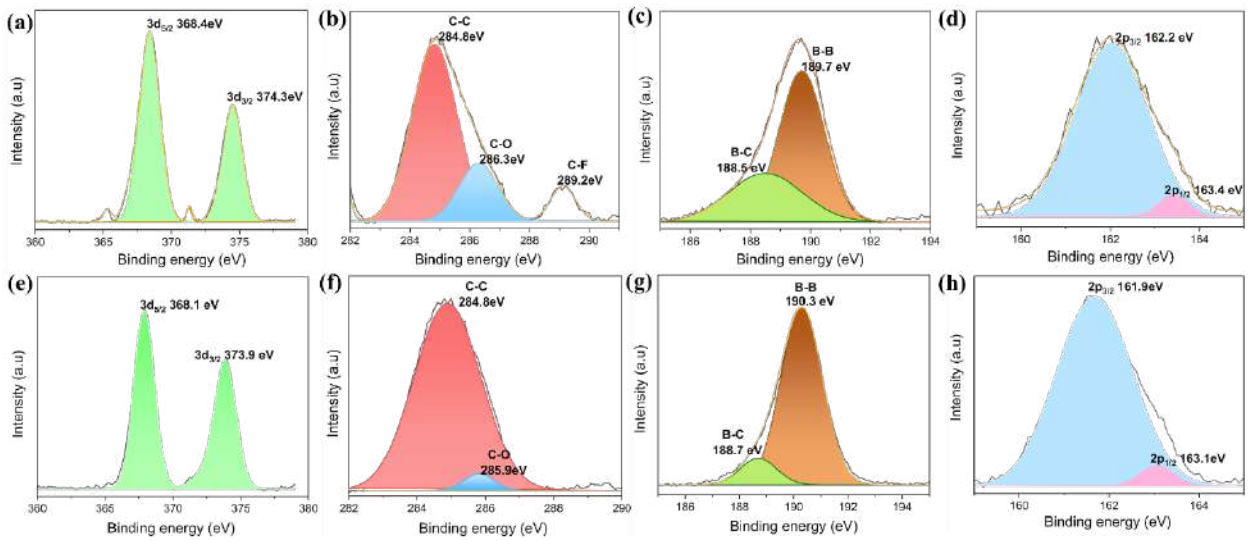


Figure S16. Pre- and post-electrochemical XPS peak fitting of Ag_{21} NC catalyst-coated electrode. (a, e) Ag3d, (b, f) C1s, (c, g) B1s, and (d, h) S2p respectively

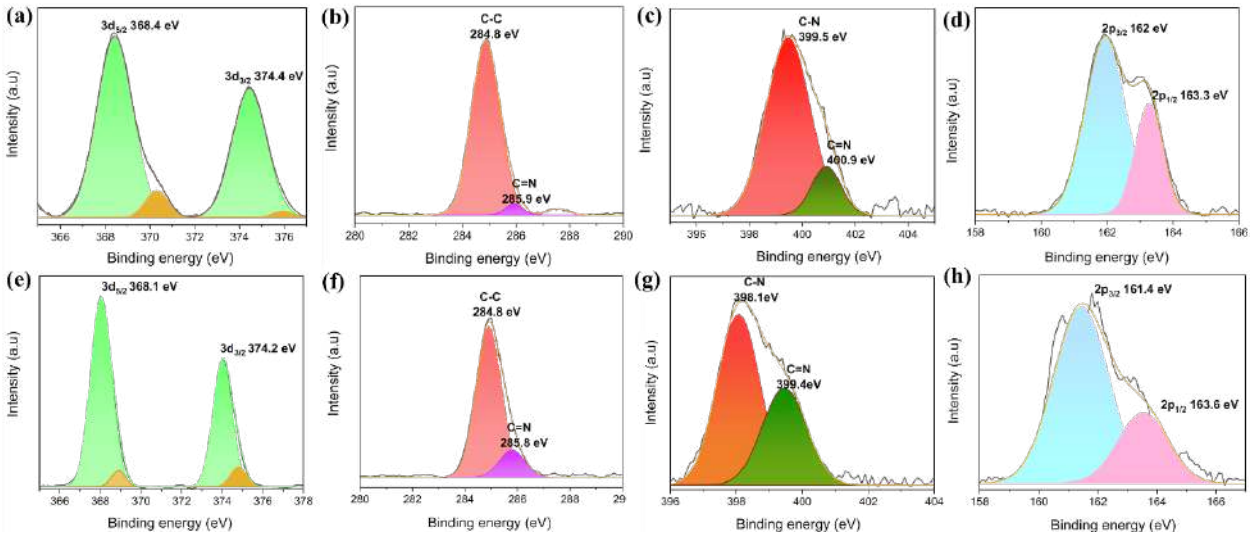


Figure S17. Pre- and post-electrochemical XPS peak fitting of Ag_{31} NC catalyst-coated electrode. (a, e) Ag3d, (b, f) C1s, (c, g) N 1s, and (d, h) S 2p.

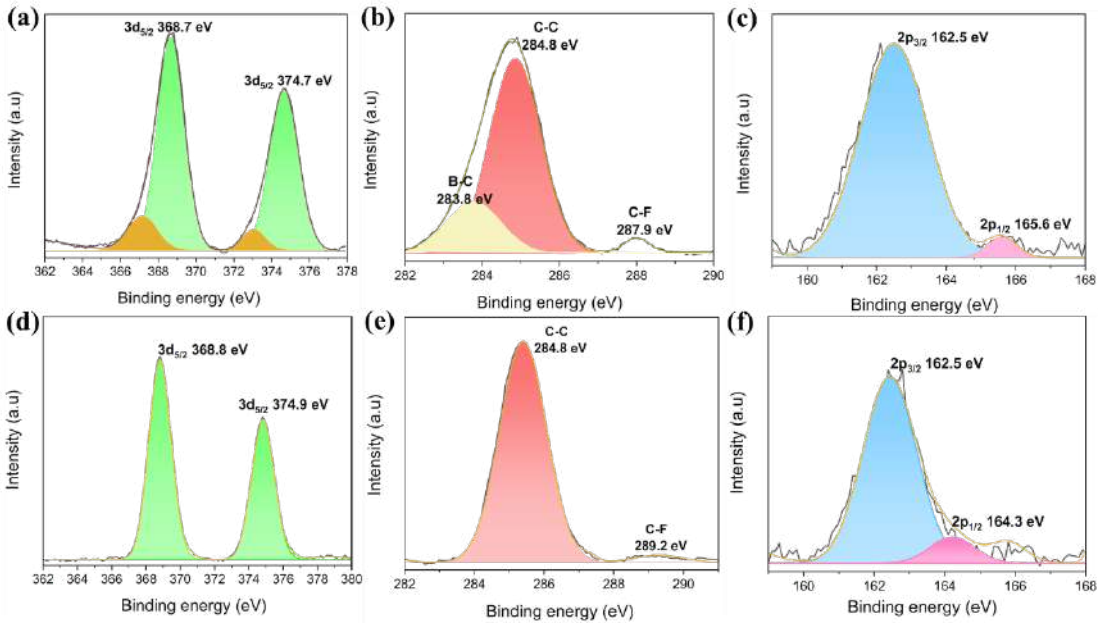


Figure S18. Pre- and post-electrochemical XPS peak fitting of Ag_{42} NC catalyst-coated electrode. (a, d) Ag3d, (b, e) C1s, (c, f) S 2p.

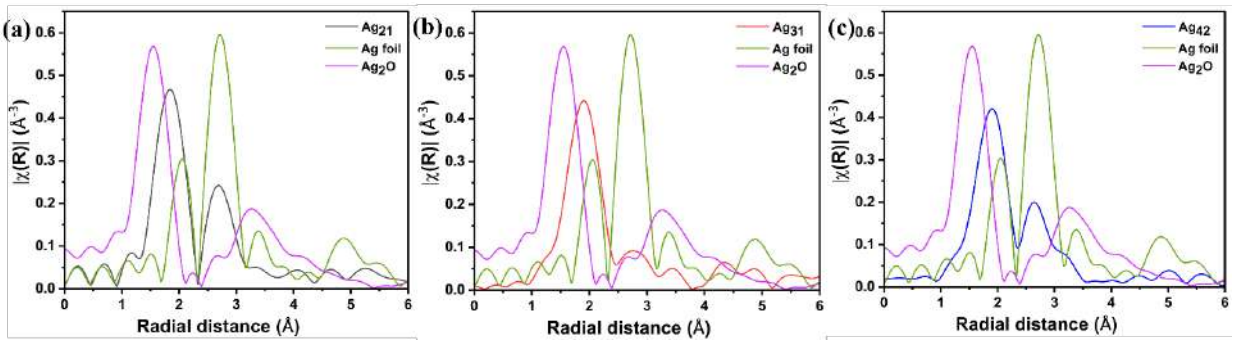


Figure S19. EXAFS spectra of Ag K edge for the AgNCs post eCO_2R

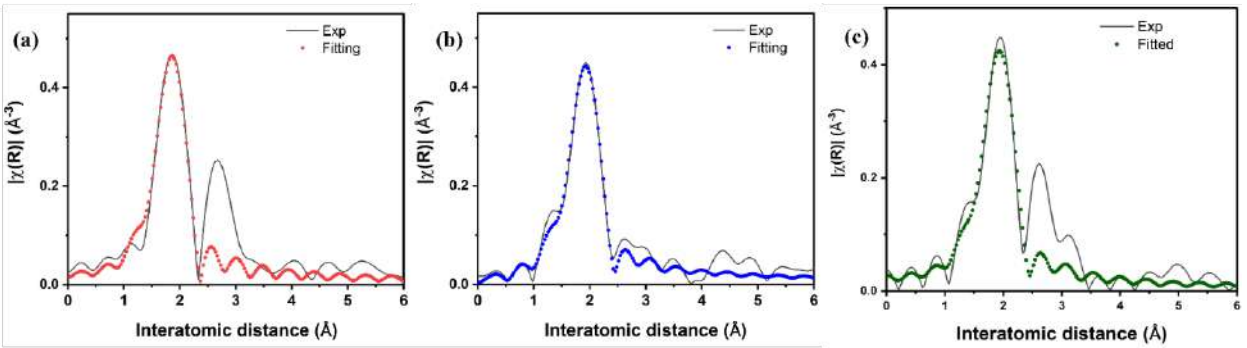


Figure S20. EXAFS fitting result of (a) Ag_{21} NC (b) Ag_{31} NC (c) Ag_{42} NC at R space post eCO_2R

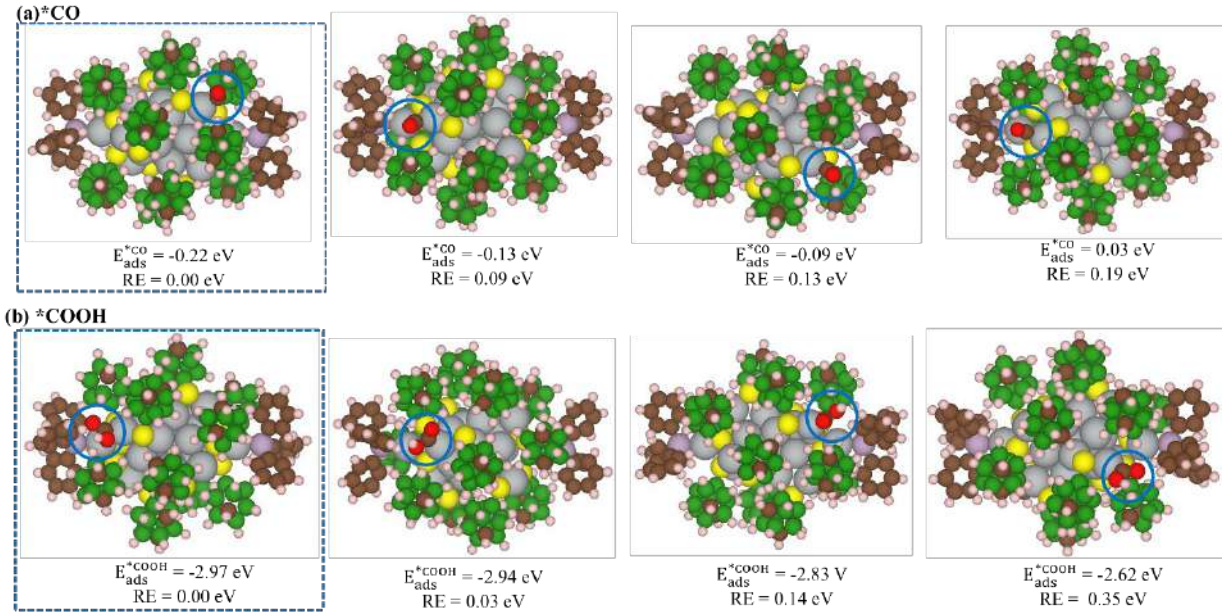


Figure S21. Heterogeneous Active Sites Investigated for **(a)** *CO, and **(b)** *COOH adsorption on the Ag_{21} cluster, with E_{Ads}^{*COOH} representing adsorption energy in eV. The most stable configurations are highlighted with blue boxes.

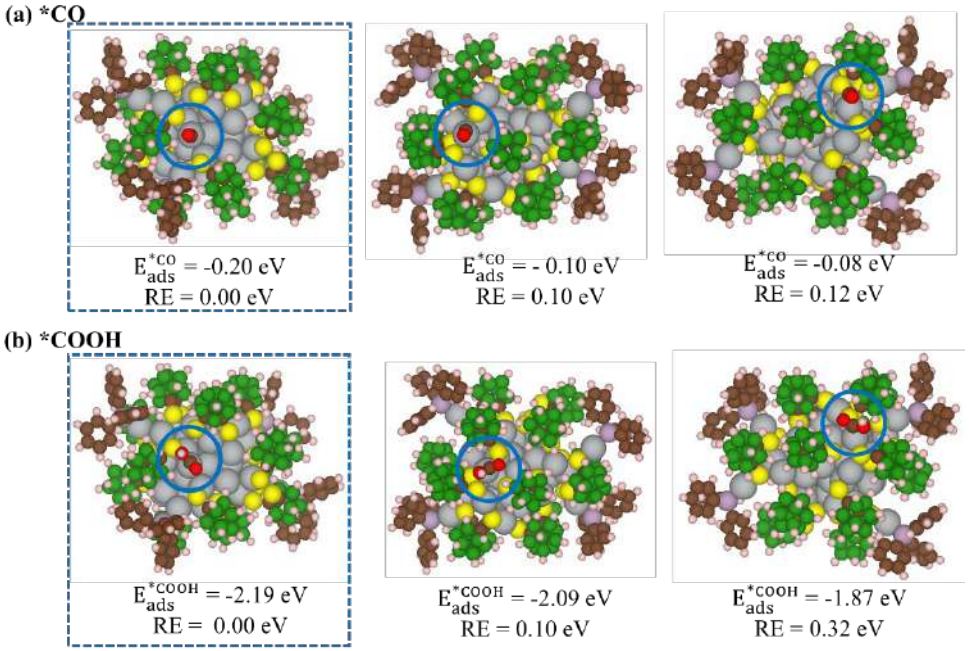


Figure S22. Heterogeneous Active Sites Investigated for **(a)** *CO, and **(b)** *COOH adsorption on the Ag_{42} cluster, with E_{Ads}^{*COOH} representing adsorption energy in eV. The most stable configurations are highlighted with blue boxes.

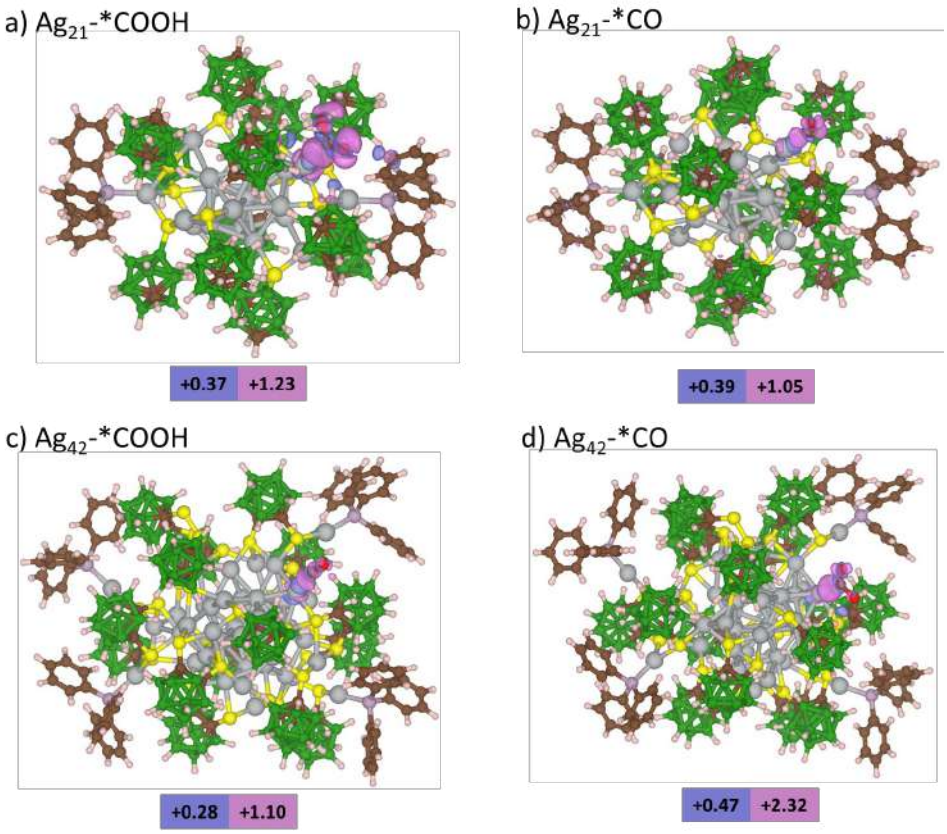


Figure S23: Charge density difference (CDD) plots at an isosurface of 0.002 eV/Å^3, where pink and green regions indicate charge accumulation and depletion, respectively. Numeric values represent charge transfer (in |e| units) derived from Bader charge analysis on Ag and C atom.

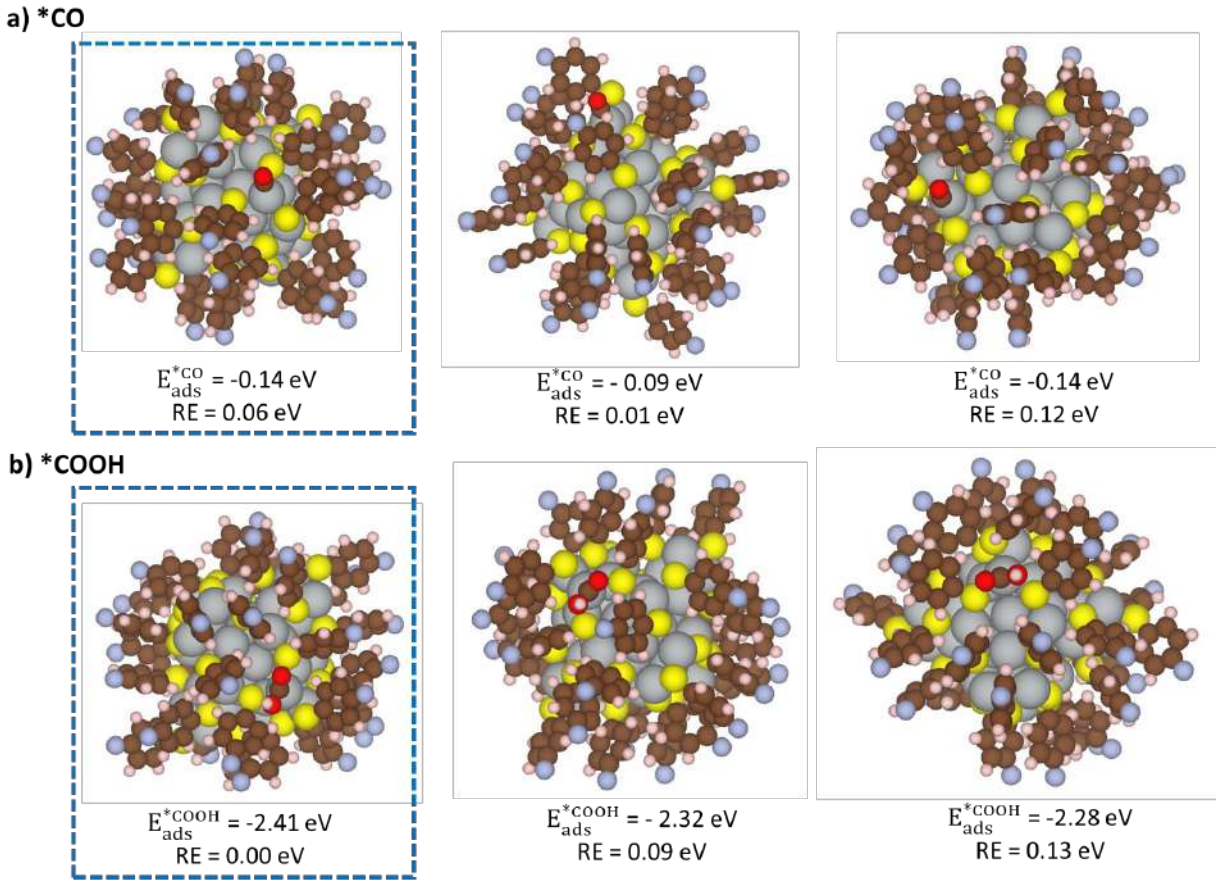


Figure S24. Heterogeneous Active Sites Investigated for **(a)** *CO, and **(b)** *COOH adsorption on the Ag_{44} cluster, with E_{Ads}^{*COOH} representing adsorption energy in eV. The most stable configurations are highlighted with blue boxes. The relative energies (RE) are referenced against the most stable geometries, marked as RE = 0.00 eV.

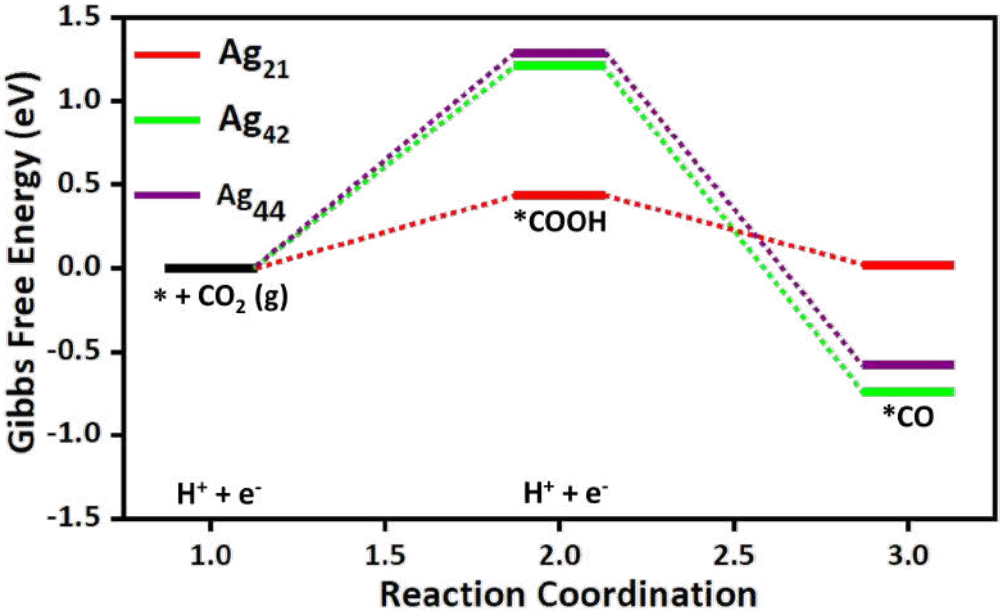


Figure S25. Gibbs free energy diagram of Ag_{21}, Ag_{42}, and Ag_{44} clusters, with the black solid horizontal line denoting the neutral surface reference.

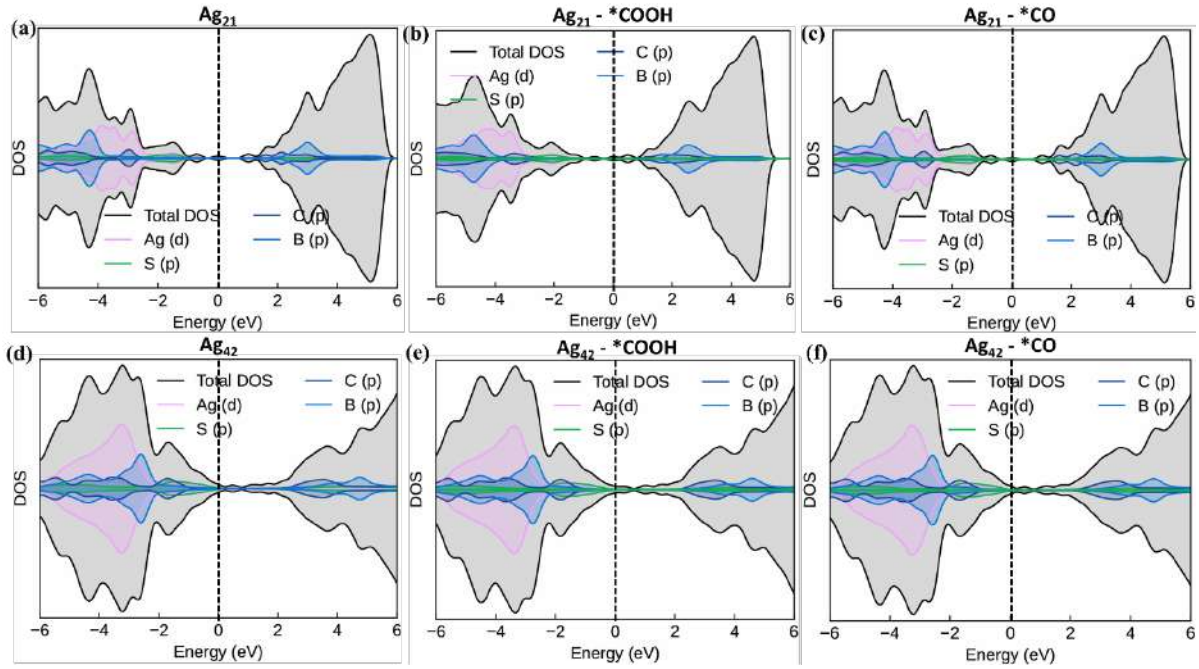


Figure S26. Total and partial DOS analysis for pristine, *COOH, and *CO-adsorbed Ag_{21} and Ag_{42} clusters, with the Fermi-level set at 0.00 eV.

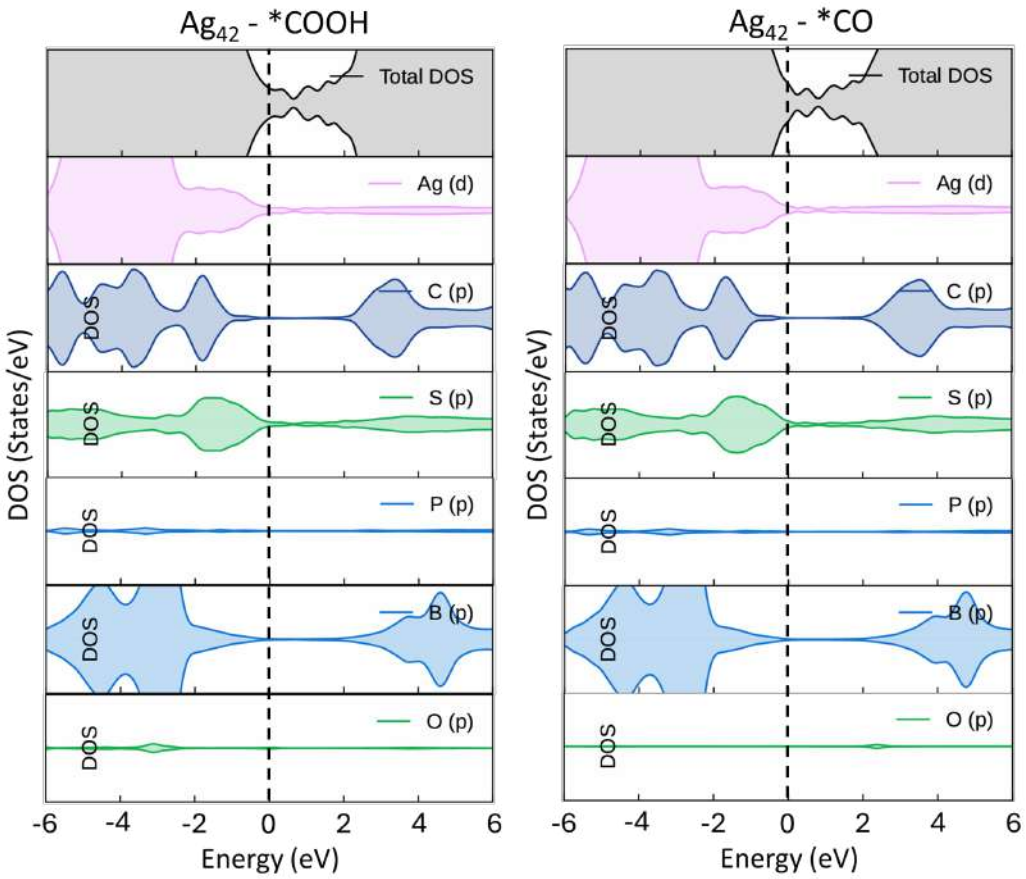


Figure S27. Subplots for total and partial density of states (DOS) for Ag(5d), C(p), S(p), P(p), B(p), and O(p), respectively, with the Fermi-level set at 0.00 eV for **(a)** *COOH, and **(b)** *CO-adsorbed on Ag_{42}.

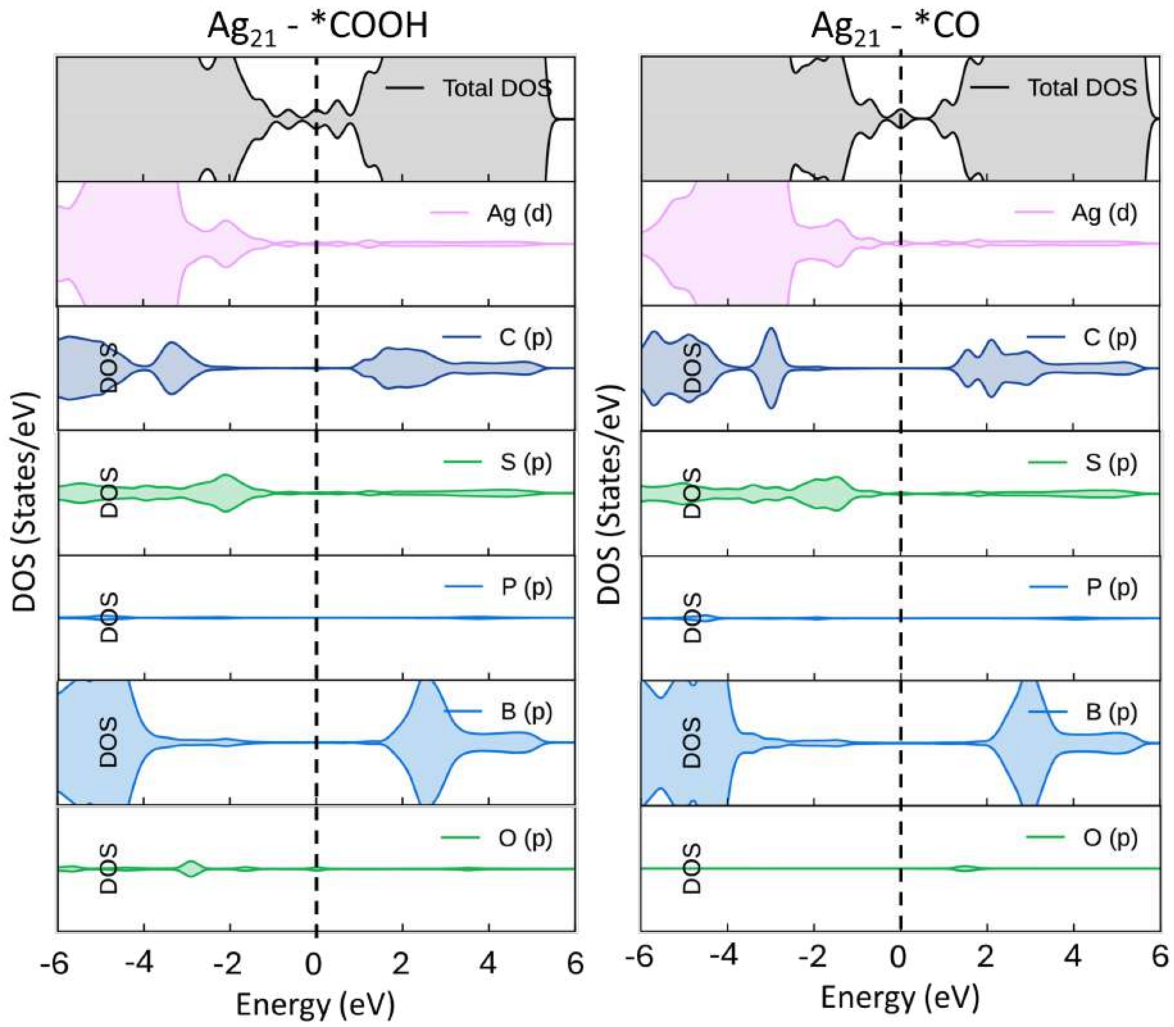


Figure S28. Subplots for total and partial density of states (DOS) for Ag(5d), C(p), S(p), P(p), B(p), and O(p), respectively, with the Fermi-level set at 0.00 eV for **(a)** *COOH, and **(b)** *CO-adsorbed on Ag_{21}.

4. Tables

Table S1. EXAFS fitting parameters of Ag NC catalysts.

	path	N	R	dE	DW	R factor
Ag_{21}	Ag-S	0.9 ± 0.1	2.40 ± 0.02	-0.7 ± 0.5	0.007	0.0048
Ag_{31}-before	Ag-S	1.1 ± 0.1	2.47 ± 0.02	-1.0 ± 0.4	0.009	0.0025
Ag_{31}-after	Ag-S	1.5 ± 0.3	2.46 ± 0.04	-3.2 ± 0.6	0.008	0.0081
Ag_{41}	Ag-S	1.0 ± 0.3	2.46 ± 0.07	3.4 ± 0.9	0.009	0.0106

Table S2: Comparison between Ag_{21} and the most advanced Ag-based catalysts (mostly reported clusters) for eCO_2R in terms of maximum partial current density (j_{CO}) and maximum Faradaic efficiency for CO (FE_{CO})

	Catalyst	Max FE_{CO} (%)	E_0 for max FE_{CO} (V vs. RHE)	Max j_{CO} (mA cm^{-2})	Cell setup	Electrolyte	Reference
	$[Ag_{21}(MCT)_{12}(TPP)_2]^+$	99.6	-0.59	148	Flow cell	1 M KOH	This work
X1	$Ag_{19}Cu_2(C \equiv CAr^F)_{12}(PPh_3)_6Cl_6$	95.26	-1.3	257.2	NA	1 M KOH	Nanoscale.2024;16(36):16952-7.[9]
X2	Ag-CP	>96	-1.0	385	Flow cell	0.1 M $KHCO_3$	ACS Energy Lett. 2019, 4, 8, 2024–2031[10]
X3	NiAD/AgNPs@CN	>90	-0.88	79.7	Flow cell	0.1 M $KHCO_3$	Applied Catalysis B: Environment and Energy. 2024 Jul 15;349:123886[11]
X4	Ag-Zn-ZIF-8 (10% Ag, 90% Zn)	80	-0.9	9	Flow cell	0.1 M $KHCO_3$	Catalysts. 2023 May 10;13(5):867.[12]
X5	$ClAg_{14}$ $(C \equiv CBu)_{12}$	95	-0.5	285	Flow cell	1 M KOH	Advanced Science. 2024 Mar;11(10):2306089.[13]
X6	$Ag_{25}(SPhMe_2)_{18}$	80	~-0.65	94	Flow cell	1 M KOH	Advanced Science. 2024 Mar;11(10):2306089.[13]
X7	$Ag_{12}Cu_7(4^tBuPhC{\equiv}C)_{14}(Dpppe)_3Cl_3(SbF_6)_2$	71.2	-1.17 V	117.9	Flow cell	1 M KOH	ACS Cent. Sci. 2025, 11, 8, 1428–1437[14]
X8	Ag@C NPs	90	-0.55	300	Flow cell	1M KOH	Cell Reports Physical Science. 2022 Jul 20;3(7)[15]
X9	Ag/MWNC	>95	-0.77	338	Flow cell	1 M KOH	Journal of Materials Chemistry A. 2016;4(22):8573-8[16]
X10	$Ag_{15}(C{\equiv}C{-}CH_3)^+$	~96	2V (Ag/AgCl)	92	Flow cell	1 M NaCl	J. Am. Chem. Soc. 2025, 147, 3, 2699–2713[17]
X11	$AuAg_{24}(IPBT)_{18}$	90	-3.6 (Cell Voltage)	200	MEA cell	0.5 M $KHCO_3$	J Am Chem Soc. 2025 Apr 16;147(15):12546-12554.[18]
X12	$[Ag_{15}Cu_6(C{\equiv}CR)_{18}(DPPE)_2]^-$	90.6	-3.75 (Cell Voltage)	40	MEA cell	0.1 M $KHCO_3$	J. Am. Chem. Soc. 2023, 145, 6, 3401–3407[19]
X13	5 nm Ag/C	79.20	~-0.75	8	H- cell	0.5 M $KHCO_3$	J. Am. Chem. Soc. 2015, 137, 43, 13844–13850[20]
X14	$Ag_{15}(C{=}C\text{-}tBu)_{12}^+$	95	-0.6	~21	H-cell	0.5 M $KHCO_3$	Angewandte Chemie International Edition. 2021 Dec 6;60(50):26136-41.[21]
X15	$[Ag_{15}Cu_6(C{\equiv}CR)_{18}(DPPE)_2]^-$	91	-0.81	~18	H-cell	0.1 M $KHCO_3$	J. Am. Chem. Soc. 2023, 145, 6, 3401–3407[19]
X16	$(AuAg)_{44}(C_{10}H_9)_{28}$	98	-0.8	~18	H-cell	0.5 M $KHCO_3$	Chem. Eur. J. 2022, 28, e202201262[22]
X17	$AuAg_{24}(IPBT)_{18}$	70	-0.6	-24.1	H-cell	0.5 M $KHCO_3$	J. Am. Chem. Soc. 2025, 147, 15, 12546–12554[18]
X18	$PtAg_{24}(IPBT)_{18}$	30	لِي□	-5.8	H-cell	0.5 M $KHCO_3$	J. Am. Chem. Soc. 2025, 147, 15, 12546–12554[18]
X19	Ag_1/MnO_2	95.7	- c0.85	3.4	H-cell	0.5 M $KHCO_3$	Angew. Chem. Int. Ed. 2021, 60, 6170 – 6176[23]
X20	2D Ag Superstructures	92.5	-0.8	6.82	H-cell	0.1 M $KHCO_3$	ACS Nano 2021, 15, 4, 7682–7693[24]
X21	Nanoporous Ag	92	-0.7	36	H-cell	0.5 M $KHCO_3$	Nat. Commun. 5, 1-6 (2014)[25]
X22	Ag foil	70.5	-0.8	7	H-cell	0.5 M $KHCO_3$	J. Am. Chem. Soc. 137, 13844-13850 (2015)[20]

Table S3. Interaction energies (E_{Int}) of Ag_{21} and Ag_{42} with MCT/CBDT and TPP ligands in eV units. The equation used to calculate the E_{Int} follows:

$$E_{Int} = \frac{E_{Complex} - [\, n_1 * E_{L_1} + n_2 * E_{L_2} \,]}{N}$$

where $E_{Complex}$, E_{L_1}, E_{L_2} represent the total electronic energies of Ag complex, MCT/CBDT, and TPP, respectively. And n_1, n_2 and N represents the number of MCT/CBDT, TPP, and the total number of ligands in the Ag complexes.

Cluster	$E_{Complex}$(eV)	E_{L_1}(eV)	E_{L_2}(eV)	n_1	n_2	N	E_{Int} (eV)
Ag_{21}	-2088.40	-124.72	-222.31	12	2	14	-10.54
Ag_{42}	-2971.57	-117.82	-222.36	15	4	19	-16.57

Table S4. Bader charge on different Ag atoms in Ag_{21} clusters, with its core geometry represented below.

Atom	Charge	Atom	Charge	Atom	Charge
Ag1	0.31	**Ag8**	0.13	**Ag15**	0.10
Ag2	0.31	**Ag9**	0.13	**Ag16**	0.10
Ag3	0.32	**Ag10**	0.13	**Ag17**	0.10
Ag4	0.32	**Ag11**	0.13	**Ag18**	0.10
Ag5	0.32	**Ag12**	0.13	**Ag19**	0.10
Ag6	0.32	**Ag13**	0.01	**Ag20**	0.32
Ag7	0.13	**Ag14**	0.10	**Ag21**	0.32

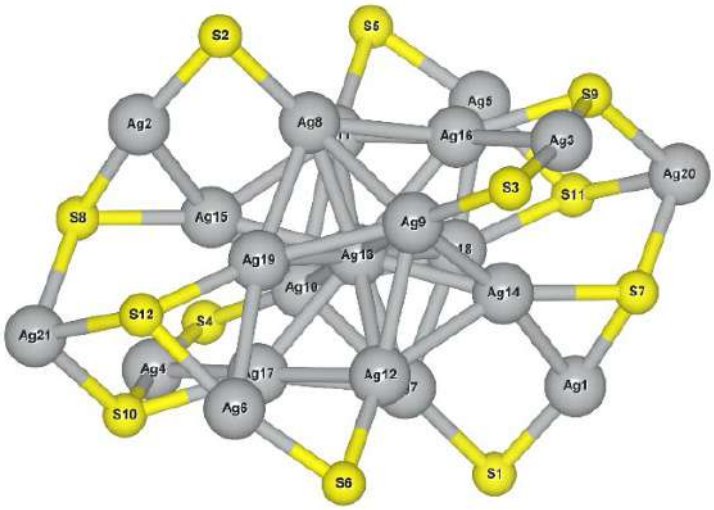
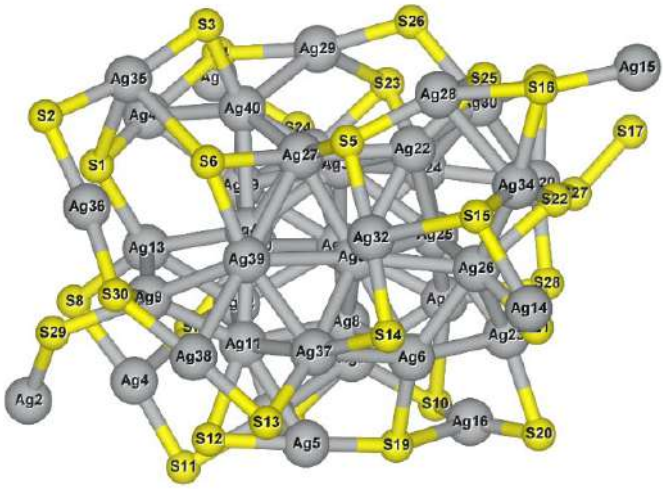


Table S5. Bader charge on different Ag atoms in Ag_{42} clusters, with its core geometry represented below.

Atom	Charge	Atom	Charge	Atom	Charge
Ag1	0.28	**Ag15**	0.30	**Ag29**	0.36
Ag2	0.27	**Ag16**	0.35	**Ag30**	0.31
Ag3	0.19	**Ag17**	0.18	**Ag31**	0.06
Ag4	0.32	**Ag18**	0.18	**Ag32**	0.35
Ag5	0.33	**Ag19**	0.03	**Ag33**	0.00
Ag6	0.18	**Ag20**	0.32	**Ag34**	0.34
Ag7	0.26	**Ag21**	0.01	**Ag35**	0.38
Ag8	0.08	**Ag22**	0.17	**Ag36**	0.38
Ag9	0.21	**Ag23**	0.29	**Ag37**	0.18
Ag10	0.22	**Ag24**	0.12	**Ag38**	0.35
Ag11	0.11	**Ag25**	0.02	**Ag39**	0.15
Ag12	0.12	**Ag26**	0.15	**Ag40**	0.17
Ag13	0.20	**Ag27**	0.18	**Ag41**	0.03
Ag14	0.32	**Ag28**	0.43	**Ag42**	0.36



References

[1] G. Kresse, D. Joubert, *Phys. Rev. B* **1999**, *59*, 1758.

[2] G. Kresse, J. Furthmüller, *Phys. Rev. B* **1996**, *54*, 11169.

[3] J. P. Perdew, K. Burke, M. Ernzerhof, *Phys. Rev. Lett.* **1996**, *77*, 3865.

[4] J. P. Perdew, J. A. Chevary, S. H. Vosko, K. A. Jackson, M. R. Pederson, D. J. Singh, C. Fiolhais, *Phys. Rev. B* **1992**, *46*, 6671.

[5] S. Grimme, J. Antony, S. Ehrlich, H. Krieg, *J. Chem. Phys.* **2010**, *132*, 154104.

[6] J. K. Nørskov, J. Rossmeisl, A. Logadottir, L. Lindqvist, J. R. Kitchin, T. Bligaard, H. Jónsson, *J. Phys. Chem. B* **2004**, *108*, 17886.

[7] W. Tang, E. Sanville, G. Henkelman, *J. Phys. Condens. Matter* **2009**, *21*, 084204.

[8] G. Henkelman, A. Arnaldsson, H. Jónsson, *Comput. Mater. Sci.* **2006**, *36*, 354.

[9] X. Zhu, P. Zhu, X. Cong, G. Ma, Q. Tang, L. Wang, Z. Tang, *Nanoscale* **2024**, *16*, 16952.

[10] R. Wang, H. Haspel, A. Pustovarenko, A. Dikhtiarenko, A. Russkikh, G. Shterk, D. Osadchii, S. Ould-Chikh, M. Ma, W. A. Smith, K. Takanabe, F. Kapteijn, J. Gascon, *ACS Energy Lett.* **2019**, *4*, 2024.

[11] Z. Zhao, L. Lin, Y. Ni, L. Jin, L. Feng, Y. Wang, Y. Wei, J. Zhang, J. Chen, *Appl. Catal. B Environ. Energy* **2024**, *349*, 123886.

[12] M. Usman, M. H. Suliman, *Catalysts* **2023**, *13*, 867.

[13] H. Seong, K. Chang, F. Sun, S. Lee, S. M. Han, Y. Kim, C. H. Choi, Q. Tang, D. Lee, *Adv. Sci.* **2024**, *11*, 2306089.

[14] Y.-X. Wang, J. Li, F.-Q. Zhang, Z. Qi, F. Zhang, X.-M. Zhang, *ACS Cent. Sci.* **2025**, *11*, 1428.

[15] J. Zhang, T. H. M. Pham, Y. Ko, M. Li, S. Yang, C. D. Koolen, L. Zhong, W. Luo, A. Züttel, *Cell Rep. Phys. Sci.* **2022**, *3*, 100949.

[16] S. Ma, R. Luo, J. I. Gold, A. Z. Yu, B. Kim, P. J. A. Kenis, *J. Mater. Chem. A* **2016**, *4*, 8573.

[17] Y. Chen, X. Zhou, X. Liu, Z. Tang, L. Wang, Q. Tang, *J. Am. Chem. Soc.* **2025**, *147*, 2699.

[18] S. Yoo, D. Kim, G. Deng, Y. Chen, K. Lee, S. Yoo, X. Liu, Q. Tang, Y. J. Hwang, T. Hyeon, M. S. Bootharaju, *J. Am. Chem. Soc.* **2025**, *147*, 12546.

[19] G. Deng, J. Kim, M. S. Bootharaju, F. Sun, K. Lee, Q. Tang, Y. J. Hwang, T. Hyeon, *J. Am. Chem. Soc.* **2023**, *145*, 3401.

[20] C. Kim, H. S. Jeon, T. Eom, M. S. Jee, H. Kim, C. M. Friend, B. K. Min, Y. J. Hwang, *J. Am. Chem. Soc.* **2015**, *137*, 13844.

[21] L. Qin, F. Sun, X. Ma, G. Ma, Y. Tang, L. Wang, Q. Tang, R. Jin, Z. Tang, *Angew. Chem. Int. Ed.* **2021**, *60*, 26136.

[22] S. Tang, J. Xu, X. Liu, Y. Zhu, *Chem. – Eur. J.* **2022**, *28*, e202201262.

[23] N. Zhang, X. Zhang, L. Tao, P. Jiang, C. Ye, R. Lin, Z. Huang, A. Li, D. Pang, H. Yan, Y. Wang, P. Xu, S. An, Q. Zhang, L. Liu, S. Du, X. Han, D. Wang, Y. Li, *Angew. Chem. Int. Ed.* **2021**, *60*, 6170.

[24] K. Qi, Y. Zhang, J. Li, C. Charmette, M. Ramonda, X. Cui, Y. Wang, Y. Zhang, H. Wu, W. Wang, X. Zhang, D. Voiry, *ACS Nano* **2021**, *15*, 7682.

[25] Q. Lu, J. Rosen, Y. Zhou, G. S. Hutchings, Y. C. Kimmel, J. G. Chen, F. Jiao, *Nat. Commun.* **2014**, *5*, 3242.

ACS APPLIED NANO MATERIALS

www.acsanm.org Article

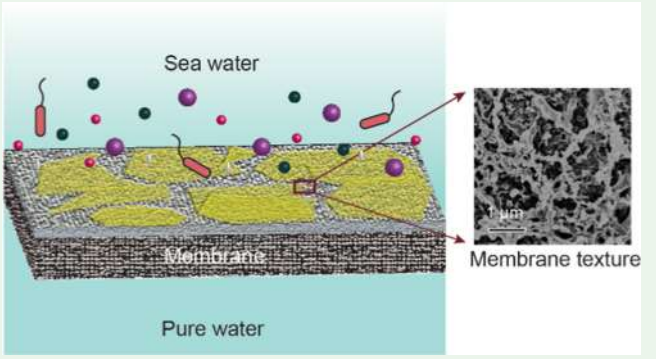
A Holey 2D MoS_2-Based Membrane with Mo-Rich Edges for Water Desalination

Biswajit Mondal, Sudhin Rathnakumaran, Amrita Chakraborty, Pragin Chettiyankandy, Pillalamarri Srikrishnarka, Md Rabiul Islam, Jenifer Shantha Kumar, Ramesh Kumar, Sandeep Bose, Sooraj Kunnikuruvan,* and Thalappil Pradeep*

Cite This: *ACS Appl. Nano Mater.* 2025, 8, 23814–23823 Read Online

ACCESS | Metrics & More | Article Recommendations | Supporting Information

ABSTRACT: Developing thin-film composite membranes that simultaneously exhibit high water permeability and ion rejection (IR) remains a persistent challenge in desalination research. Here, we report the fabrication of polyamide (PA) membranes embedded with holey molybdenum disulfide nanosheets via controlled interfacial polymerization. The introduction of nanoscale Mo-rich pores within MoS_2 provides low-friction water transport channels, while maintaining effective ion exclusion. Systematic optimization of interfacial polymerization conditions—specifically monomer contact time of 60 s each and nanosheet loading of 0.01 wt % resulted in an optimal water flux (WF) of ∼96 L m^{-2} h^{-1} and IR of ∼99.4%, outperforming both pristine PA and nonporous MoS_2-based membranes. Molecular dynamics simulations revealed that water molecules align preferentially along hydrophilic Mo-edge sites, forming ordered, high-density transport channels responsible for the observed flux enhancement. Together, the experimental and computational results establish holey MoS_2-embedded PA membranes as a promising platform for next-generation nanofiltration and desalination technologies.



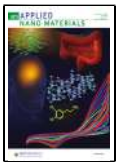
KEYWORDS: *Mo-rich holey MoS_2, ambient electrospray deposition, interfacial polymerization, membrane, desalination of water*

1. INTRODUCTION

Although water covers 75% of the surface of the Earth, producing fresh water is one of the most pressing global challenges of the 21st century. This crisis is exacerbated by rapid population growth, escalating industrial and agricultural demands, contamination of existing water resources, and the impacts of unprecedented climate change.[1−5] Since over 97.5% of Earth's water is contained in the oceans, desalination of seawater and brackish sources becomes indispensable to meet the growing demand for fresh water.[1] Among various desalination techniques, membrane-based separation techniques such as reverse osmosis (RO) has emerged as the most efficient and widely adopted method to produce clean water from seawater, brackish water, and various sources of wastewater. RO is favored due to its low energy consumption, modular operation, minimal use of chemical additives, and technological simplicity compared with conventional distillation-based approaches.[2,6] Although most of the available commercial membranes are composed of polysulfone (psf) and polyamide, alternative materials such as zeolite-based membranes and mesoporous ceramics have also been explored.[6,7] Despite their widespread applications, conventional polymeric nanofiltration membranes face several challenges including poor thermal stability, high sensitivity to acidic, basic, or organic solvent media, high energy requirement, lower WF, and low fouling resistance.[8,9] On the other hand, ceramic membranes, while offering excellent chemical and mechanical stability, are prohibitively expensive for large-scale implementation, and zeolite-based materials often suffer from inherently low permeation rates despite their structural advantages.[10,11]

To overcome these limitations, scientists have focused on exploring alternative materials and architectures. In recent years, two-dimensional (2D) materials have emerged as a compelling platform for the next-generation membranes for separation. Their atomically thin structure, precise nanocapillary channels between layers, and the possibility of engineered nanopores make them promising in the membrane technology due to high flux and high rejection.[12−14]

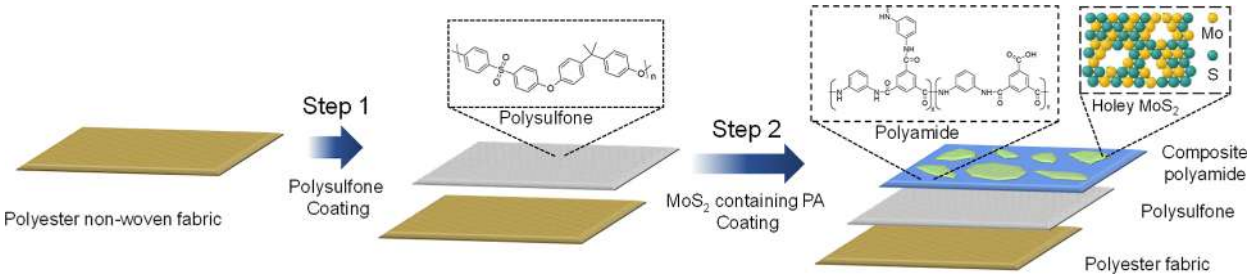
Received: November 16, 2025
Revised: November 23, 2025
Accepted: November 24, 2025
Published: December 2, 2025



Downloaded via INDIAN INST OF TECH MADRAS on December 29, 2025 at 03:19:55 (UTC).
See https://pubs.acs.org/sharingguidelines for options on how to legitimately share published articles.

© 2025 American Chemical Society

Scheme 1. Fabrication Process of the Membrane Used in This Study



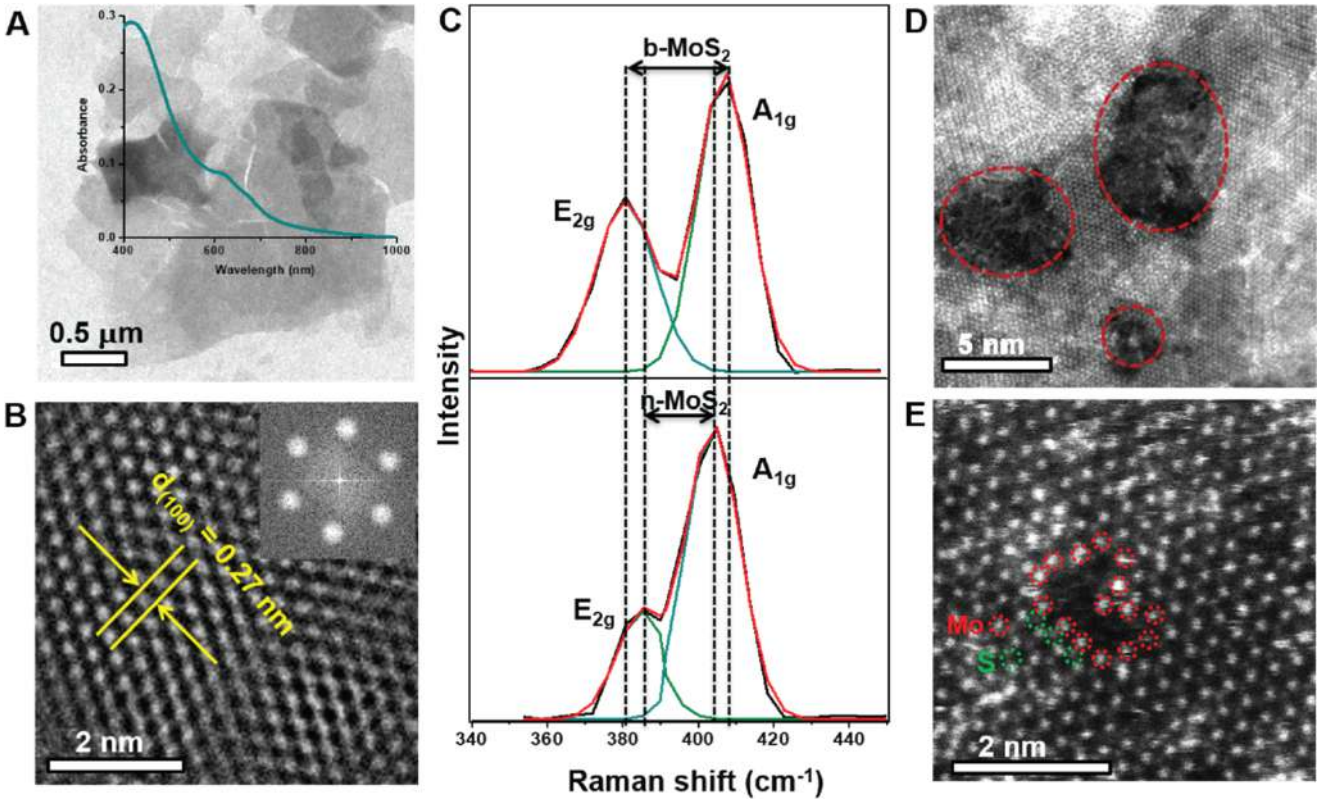


Figure 1. (A) TEM image of the as-synthesized MoS_2 NSs. The inset shows the corresponding UV/vis absorption spectrum. (B) HRTEM image of a MoS_2 NS and the corresponding fast Fourier transform pattern shown in the inset of (B). (C) Raman spectra collected from the MoS_2 NSs (n-MoS_2) and bulk MoS_2 (b-MoS_2). (D) Scanning transmission electron microscopy (STEM) image of a holey MoS_2 NS collected after electrospray of Ag^+ ions, and (E) HAADF STEM of the same showing a Mo-enriched edge. Red circles in image (E) denote Mo, and the green circles represent S.

Continuous water channels form either through intrinsic interlayer spacings or deliberately perforated nanopores, enabling control over molecular and ionic transport via steric, electrostatic, and interfacial interactions. Among 2D materials, MoS_2 nanosheets (NSs) are found superior over other 2D materials in the membrane technology due to their excellent mechanical properties, tunable surface chemistry, high fouling resistance, and stability in the aqueous environments.[15−18] Unlike oxidized graphene derivatives, the absence of oxygenated functional groups in MoS_2 provides reduced resistance for the transport of water molecules and resists swelling in aqueous media[15,19] Existing reports demonstrate that the MoS_2-based membrane has a promising separation efficiency and excellent WF, precisely 2−5 times higher than the GO-based membranes under similar experimental conditions.[20] MoS_2-based RO membranes show enhanced IR performance due to the presence of negative charge on MoS_2 NSs, which repel the ions of salt. Furthermore, exfoliated MoS_2 NSs give rise to increased hydrophilicity on the membrane's surface. High negative charge and hydrophilic sites provided by Mo/S atoms of MoS_2 NSs can effectively change the physicochemical properties of the membrane such as roughness, electrostatic charge, and hydrophilicity, which influence IR, water permeation rate, and membrane fouling.[21] The layered structure of MoS_2 permits the formation of nanocapillary channels when stacked and the potential to introduce nanopores offers a route to improve both flux and rejection.[22,23]

Molecular dynamics (MD) studies have been used to study ion/water permeation through nanoporous MoS_2 membranes. In a seminal study, Heiranian et al. demonstrated that single-layer MoS_2 NSs containing nanopores show enhanced water permeation rate compared to graphene nanopores under the same conditions.[24] The nanopores decorated with Mo atoms

https://doi.org/10.1021/acsanm.5c05244
ACS Appl. Nano Mater. 2025, 8, 23814−23823

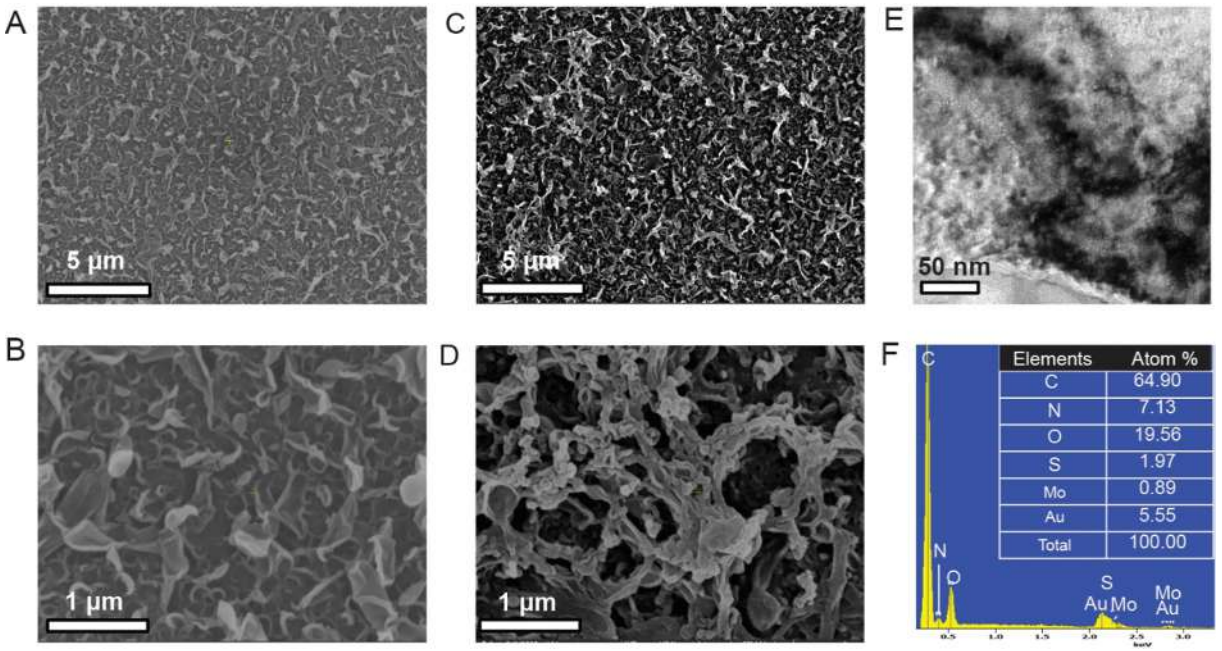


Figure 2. FESEM images of blank membrane (A,B) and the membrane containing 0.01 wt % holey MoS_2 (C,D) at different magnifications after gold sputtering. (E) TEM image of the holey MoS_2-based membrane. EDS elemental analysis of the corresponding membrane is shown in (F).

show the highest flux due to the higher density and velocity of water inside the Mo-pores.[24] MD and first-principles simulations have since revealed how variations in edge chemistry, pore size, ion−pore interactions, hydration, and applied pressure affect desalination efficiency.[25−29] Recent MD studies have shown that Mo-rich edges promote water restructuring and reduce energy barriers which facilitate water transport.[24] Meanwhile, comparative theoretical study has revealed that MoS_2 nanopores outperform graphene-based analogues under some conditions.[24,30]

Despite significant progress, the experimental realization of scalable, defect-controlled, nanopore-engineered MoS_2 remains highly challenging. Existing demonstrations are often confined to small membrane areas or depend on costly, high-precision fabrication methods—such as electron-beam sculpting, ion-beam drilling, or focused ion beam processing—that lack scalability.[31−33] Although vacuum filtration and chemical vapor deposition approaches have been used to produce MoS_2 thin films and laminar membranes,[20,34] control over pore chemistry and antifouling behavior remains limited. Consequently, there is a pressing need for a scalable and cost-effective MoS_2-based RO membrane that combines engineered nanopores with high flux, selectivity, and fouling resistance.

In this work, we combine our experimental membrane fabrication with corroborative MD simulations to dissect the roles of pore chemistry and nanosheets architecture in water/ion transport. We demonstrated a facial, ambient, solution-based home-grown method for Mo-rich, holey MoS_2 nanosheets and their integration into the polyamide membranes. Specifically, a copolymerization method was used to fabricate the membrane, where holey MoS_2 NSs were added during the polymerization process to increase the performance of the membrane (schematic 1). We systematically tuned the nanosheet loading, monomer contact time, and pore chemistry and correlated these parameters with desalination performance and fouling resistance. Benchmarking against control membranes, we demonstrate that holey-MoS_2-based membranes exhibit superior performance. This work advances the practical realization of high-performance 2D-material membranes by coupling scalable synthesis with mechanistic insights into pore effects and surface interaction.

2. RESULTS AND DISCUSSION

2.1. Characterization of MoS_2 and Holey MoS_2 NSs. MoS_2 NSs were first synthesized using a standard chemical exfoliation method.[35,36] Figure 1 summarizes the essential characterization data of as-synthesized NSs. Transmission electron microscopy (TEM) and HRTEM images of the as-synthesized NSs are shown in Figure 1A,B, respectively. Their structural integrity was further assessed using Raman spectroscopy. The characteristic E_2g and A_1g vibrational modes of 2D MoS_2 were clearly observed, and the reduced peak separation between these modes for MoS_2 NSs (n-MoS_2) indicates the successful exfoliation of bulk MoS_2 (b-MoS_2) to its nanoscale form (Figure 1C).[37,38] Mo-rich holey MoS_2 NSs were subsequently prepared using a facile, cost-effective, ambient, solution-based method developed in our group.[39] In this process, Ag^+ ions were electrosprayed on an aqueous suspension of chemically synthesized MoS_2 NSs. During deposition, Ag^+ ions react with the NSs to form Ag_2S, leaving behind Mo-enriched nanopores within the sheets (Figure 1D,E).[39,40] In Figure 1E, Mo and S atoms are highlighted with red and green dotted circles, respectively. UV/vis absorption spectrum and Raman spectroscopic data show no significant deviation from those of pristine MoS_2 NSs, confirming that the introduction of nanopores does not alter the intrinsic electronic structure of the material.

2.2. Characterization of Membranes. After the fabrication of membranes (discussed in the Experimental Section), they were characterized using various microscopic and spectroscopic techniques. Surface morphology and roughness of the membranes were observed with field emission scanning electron microscopy (FESEM) (Figure 2A−D) after gold sputtering. The incorporation of holey MoS_2 nanosheets

https://doi.org/10.1021/acsanm.5c05244
ACS Appl. Nano Mater. 2025, 8, 23814−23823

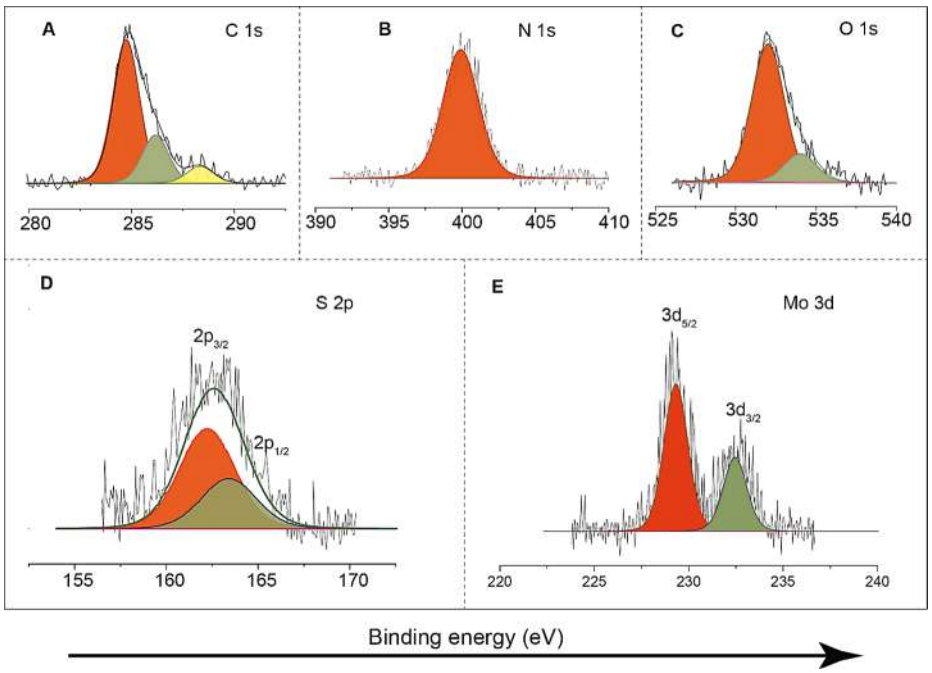


Figure 3. XPS of the membrane containing 0.01 wt % of holey MoS_2. (A–E) XPS in the C 1s, N 1s, O 1s, S 2p, and Mo 3d regions, respectively.

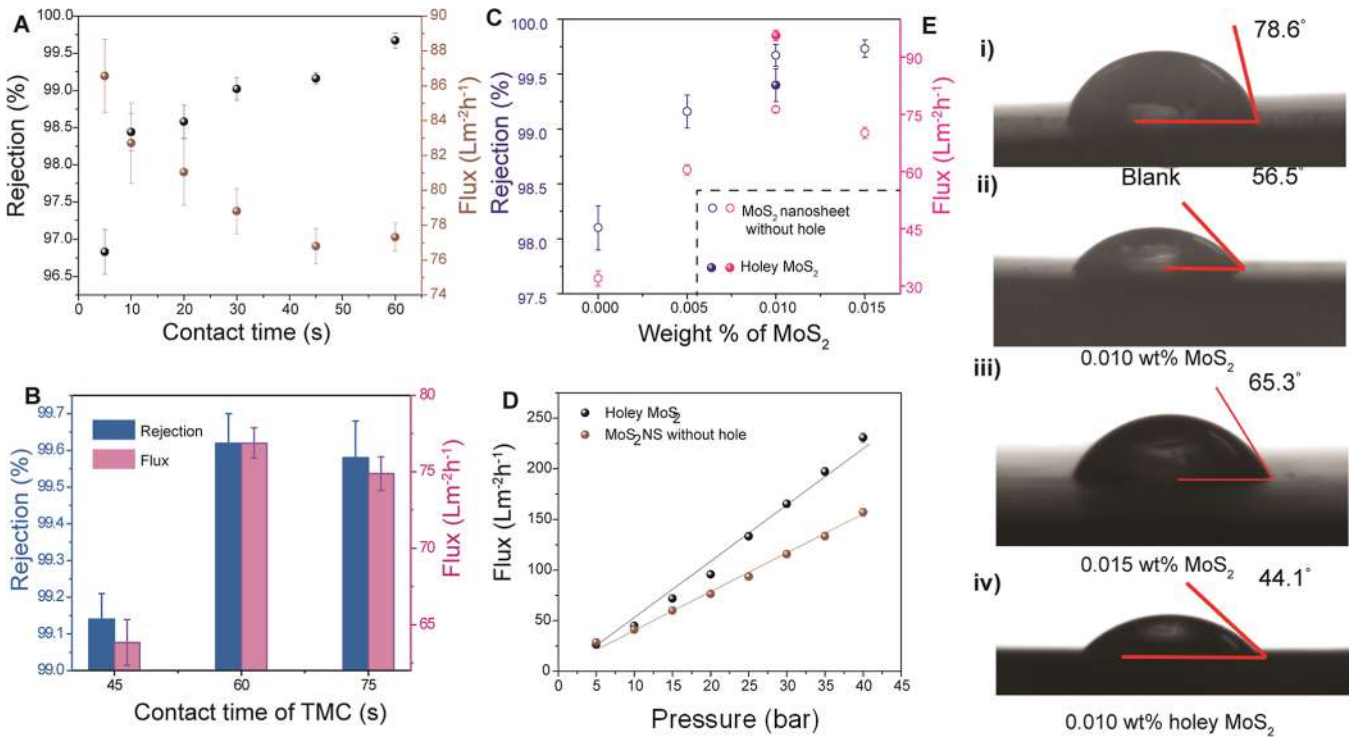


Figure 4. (A) Change in flux and rejection (%) with the change in contact time, and (B) effect of permeation rate and rejection performance with variation of contact time of TMC solution. (C) MoS_2 concentration-dependent rejection performance and water permeation rate, and (D) variation of flux as a function of pressure. (E) Water contact angle on blank membrane (i), membranes containing different amounts of MoS_2 (ii,iii), and holey MoS_2-based membrane (iv). (A–C) contain two *Y* axes (rejection and flux).

(NSs) induced a noticeable change in surface texture—from a distinctly leaf-like morphology in the blank polyamide membrane (without MoS_2 NSs, abbreviated hereafter as bM, Figure 2A,B) to less leaf-like and more nodular structure for the membrane containing 0.01 wt % of holey MoS_2 NSs, abbreviated hereafter as 0.01 wt % $hMoS_2M$ (Figure 2C,D). Among the prepared membranes, the 0.01 wt % $hMoS_2M$ exhibited the best performance and was therefore selected for detailed TEM analysis (Figure 2E). The surface morphology of holey MoS_2-based membranes (abbreviated hereafter as $hMoS_2M$) and those incorporating nonporous MoS_2 NSs (abbreviated hereafter as MoS_2M) were found to be comparable when equivalent nanosheet loadings were used (Figure S1). The presence of MoS_2 NS on the membrane

https://doi.org/10.1021/acsanm.5c05244
ACS Appl. Nano Mater. 2025, 8, 23814−23823

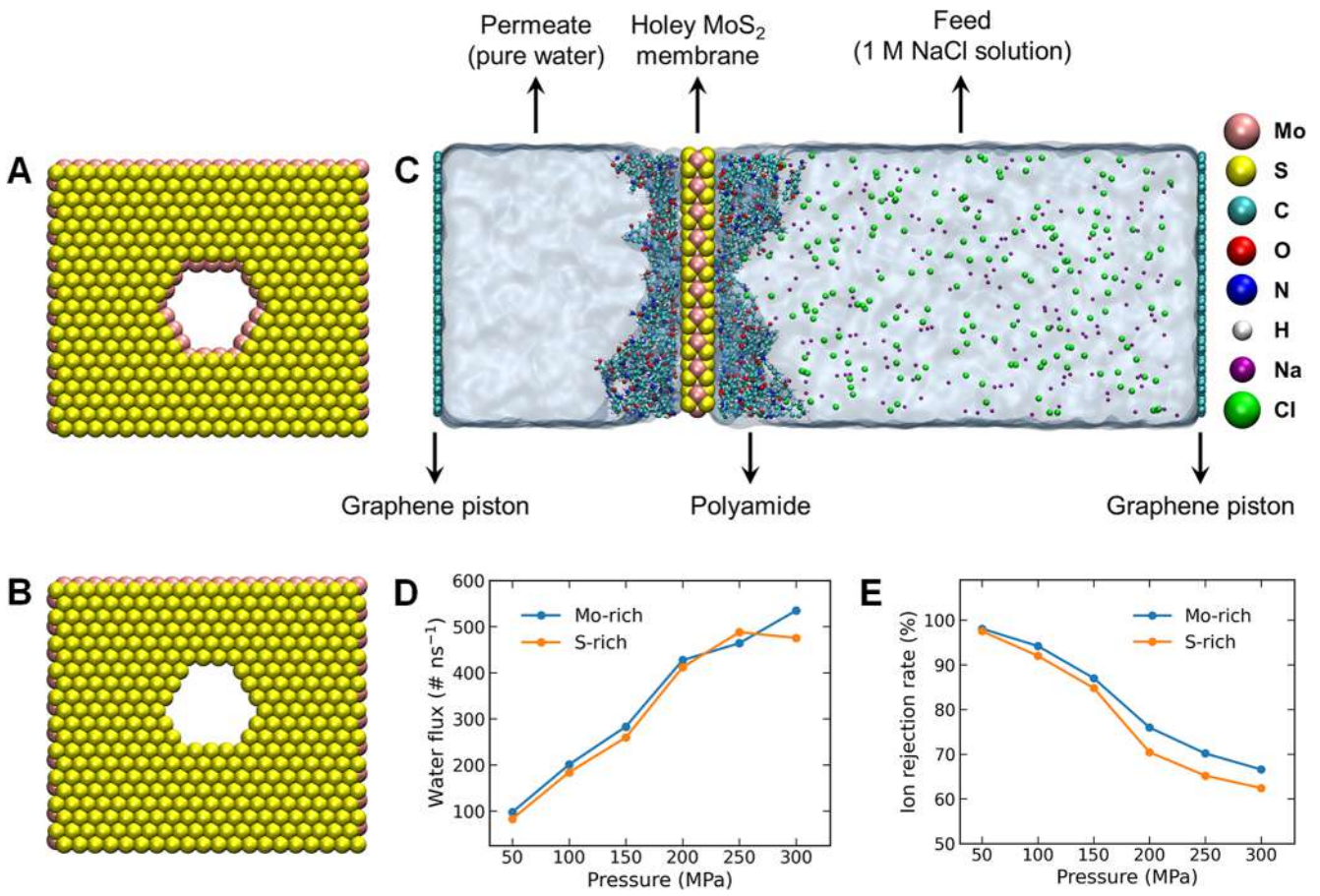


Figure 5. $hMoS_2$NSs with (A) Mo-rich and (B) S-rich pores used in MD simulations. (C) Side view of the representative MD setup showing feed (1 M NaCl), permeate (pure water), $hMoS_2$NS, PA, and graphene pistons. (D) WF and (E) IR rates at different applied pressures for the Mo-rich and S-rich $hMoS_2$Ms.

surface was confirmed by energy-dispersive spectroscopy (EDS) analysis in TEM (Figure 2F). At higher loadings, MoS_2 NSs tended to aggregate owing to their high surface energy in the nonpolar organic solvent (Figure S2).

X-ray photoelectron spectroscopy (XPS) was performed to further analyze the surface composition and chemical states. Spectra in the C 1s, O 1s, N 1s, S 2p, and Mo 3d regions are presented in Figure 3. The Mo 3d region shows two peaks at 229.3 and 232.4 eV corresponding to $3d_{5/2}$ and $3d_{3/2}$, respectively (Figure 3E). The two peaks at 161.6 and 162.9 eV correspond to $2p_{3/2}$ and $2p_{1/2}$ of S^{2-} of MoS_2 (Figure 3D), which confirms that there is no chemical change in holey MoS_2 NS after the fabrication of the membrane. The sensitivity of XPS even at such a low loading suggests the existence of $hMoS_2$ on the surface of the membrane.

The FT-IR spectrum of $hMoS_2$M (Figure S3) displays all the characteristic peaks of polyamide. The broad band between 3200 and 3500 cm^{-1} arises from N−H and O−H stretching vibrations. Peaks at 1660, 1580, and 1150 cm^{-1} are attributed to C═O stretching, aromatic C═C stretching, and C−N stretching, respectively. The bands at 1543 and 832 cm^{-1} correspond to N−H bending and aromatic C−H bending modes. Additionally, a weak peak around 460 cm^{-1} is assigned to Mo−S stretching, further confirming the incorporation of MoS_2 NSs within the membrane structure.

2.3. Performance of Membranes. The desalination performance of the fabricated membranes was systematically evaluated using a laboratory-scale RO setup (Figure S4). The influence of interfacial polymerization parameters—specifically, the contact time between the aqueous *m*-phenylenediamine (MPD) solution and the 1,3,5-benzenetricarbonyl trichloride (TMC) solution in hexane—and MoS_2 NS loadings were quantitatively analyzed in terms of WF and IR.

The contact time between the two monomer phases determines the thickness and cross-linking density of the polyamide (PA) layer, which in turn control both flux and rejection. The variation in WF and IR performance was measured as a function of contact time of both MPD solution and TMC solution (Figure 4A). An optimal balance between WF and IR was achieved when the contact time for each monomer was set to 60 s. Shorter exposure times resulted in a thinner, loosely cross-linked PA layer that permitted partial ion leakage, thereby lowering IR. In another set of experiments, the contact time of TMC solution was varied (45, 60, and 75 s); while maintaining MPD exposure at 60 s, a similar trend was observed (Figure 4B). Increasing TMC exposure to 60 s yielded the maximum WF and IR, whereas prolonged contact (75 s) reduced flux, likely due to excessive cross-linking and reduced pore connectivity. These observations confirm that the interfacial polymerization conditions govern the morphology and permeability of the selective layer.

The effect of MoS_2 NS loadings on the membrane performance was next investigated by varying the nanosheet concentration from 0 to 0.015 wt % in the polymerization mixture (Figure 4C). Compared to the blank membrane, MoS_2 NS loadings significantly enhanced water permeability, reach-

https://doi.org/10.1021/acsanm.5c05244
ACS Appl. Nano Mater. 2025, 8, 23814−23823

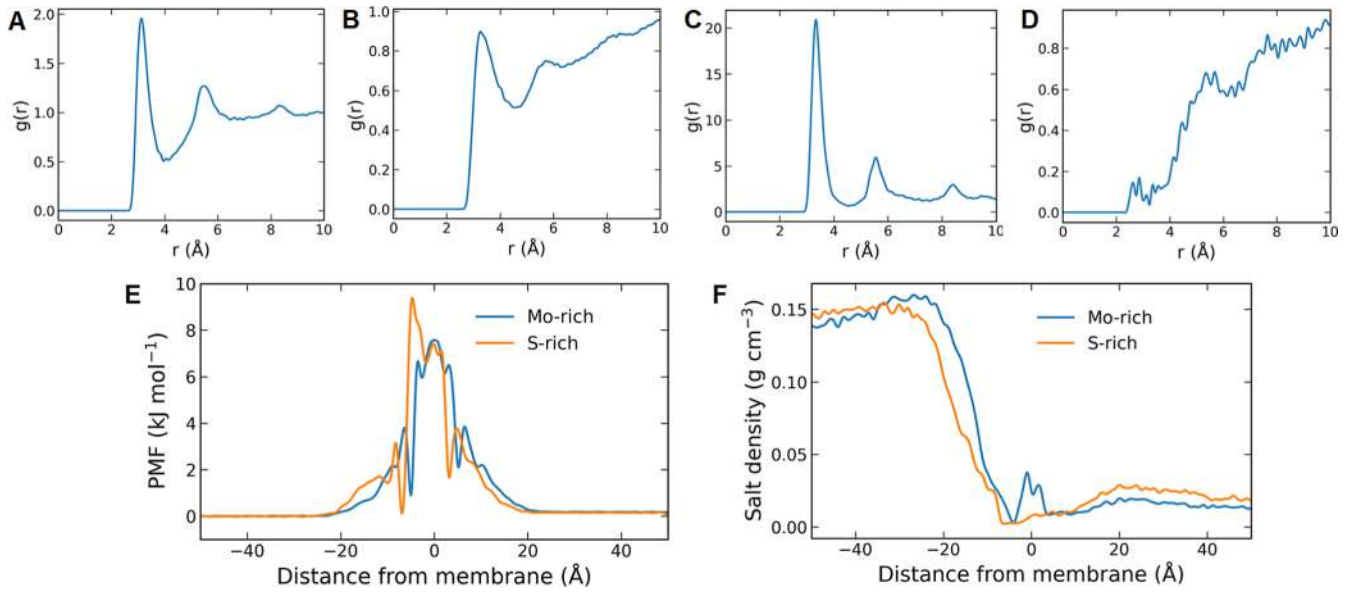


Figure 6. RDF plots between (A) pore Mo atoms of Mo-rich $hMoS_2M$ and O atoms of water, (B) pore S atoms of S-rich $hMoS_2M$ and O atoms of water, (C) pore Mo atoms of Mo-rich $hMoS_2M$ and salt ions, and (D) pore S atoms of S-rich $hMoS_2M$ and salt ions, computed from RO simulations at 200 MPa. (E) 1-D PMF profiles of water molecules, and (F) salt ion density profiles along the *Z*-direction, computed from RO simulations at 200 MPa.

ing a maximum at 0.01 wt % MoS_2. This improvement is attributed to the formation of additional nanocapillary channels and increased hydrophilicity imparted by the exposed Mo−S surface sites. However, further loading led to a decline in flux—possibly due to nanosheet agglomeration within the PA matrix that increased transport resistance. Simultaneously, the IR improved with increasing MoS_2 content, driven by stronger electrostatic repulsion between negatively charged MoS_2 surfaces and anionic species in saline feed, as well as by a denser polymer network induced by nanosheet−polymer interactions. Overall, 0.01 wt % MoS_2M exhibited the best trade-off between flux and rejection. Further enhancement was achieved by introducing Mo-rich nanopores (2−8 nm) within the nanosheets. The holey MoS_2 membrane ($hMoS_2M$) at 0.01 wt % loading achieved a WF of ∼96 L m^{-2} h^{-1}—*a* ∼ 26% increase compared to the nonholey MoS_2 membrane under identical testing conditions. Simultaneously, salt rejection of ∼99.4% indicates that nanopore introduction does not compromise selectivity. This improvement can be rationalized by the unique water structuring as supported by MD simulations. The hydrophilic Mo sites at the pore edges attract and orient water molecules, creating low-friction transport channels that facilitate rapid and efficient water flow without compromising ion selectivity.

Water fluxes through the membranes as a function of externally applied pressure are presented in Figure 4D. To assess the relative performance, $hMoS_2M$ was compared with the MoS_2M, which had already demonstrated promising water permeation characteristics. Across the entire pressure range tested, $hMoS_2M$ consistently exhibited higher WF than MoS_2M. The WF increased linearly with applied pressure, indicating stable membrane integrity and consistent transport behavior, while the IR remained nearly constant throughout the tested pressure range (Figure S5).

The higher water permeation rate observed for 0.01 wt % $hMoS_2M$ compared to the other membranes (MoS_2M and bM) can be explained in terms of its altered surface morphology and roughness, which together change surface hydrophilicity. Figure 4E shows the variation in water contact angles on different membranes. A significant decrease in contact angle for 0.01 wt % $hMoS_2M$ compared to the bM indicates enhanced surface wettability upon incorporation of nanoporous MoS_2 NSs. To further examine how MoS_2 nanosheets influence the physicochemical properties of the membrane, a series of membranes was fabricated with varying MoS_2 loadings, and their water contact angles were measured (Figure 4E(i−iii)). As the MoS_2 concentration increased up to 0.01 wt %, the contact angle progressively decreased due to the greater exposure of polar Mo−S sites at the surface. However, at higher loadings, the contact angle increased again, likely due to nanosheet aggregation and the intrinsically lower hydrophilicity of MoS_2 compared with the polyamide matrix.

2.4. MD Simulations. To scrutinize the effect of Mo-rich and S-rich pores on the RO performance of the $hMoS_2Ms$, classical MD simulations were performed. Hexagonal nanopores were introduced into MoS_2 NSs to create the holey MoS_2 NSs ($hMoS_2NSs$) with either Mo-rich or S-rich pore edges (Figure 5A,B). The lateral dimensions of the NSs were 6.21 nm × 5.47 nm, and nanopores with a diameter of about 2 nm were used in the RO simulations. The RO setup (Figure 5C) includes a 1 M NaCl solution in the feed layer and pure water in the permeate layer. In the initial structure, the feed layer (11.2 nm) consists of 10,075 water molecules, 181 Na^+ ions, and 181 Cl^- ions, while the permeate layer (5.6 nm) consists of 4671 water molecules. MD simulations were performed using the LAMMPS software package,[41] and visualization and analyses were carried out using the Visual Molecular Dynamics (VMD) program.[42] Information on the force field parameters and additional simulation details can be found in the "Computational details" section of the Supporting Information.

The performances of Mo-rich and S-rich $hMoS_2Ms$ were compared in terms of the computed WF and IR. Furthermore, the local environment and interfacial interactions were

https://doi.org/10.1021/acsanm.5c05244
ACS Appl. Nano Mater. 2025, 8, 23814−23823

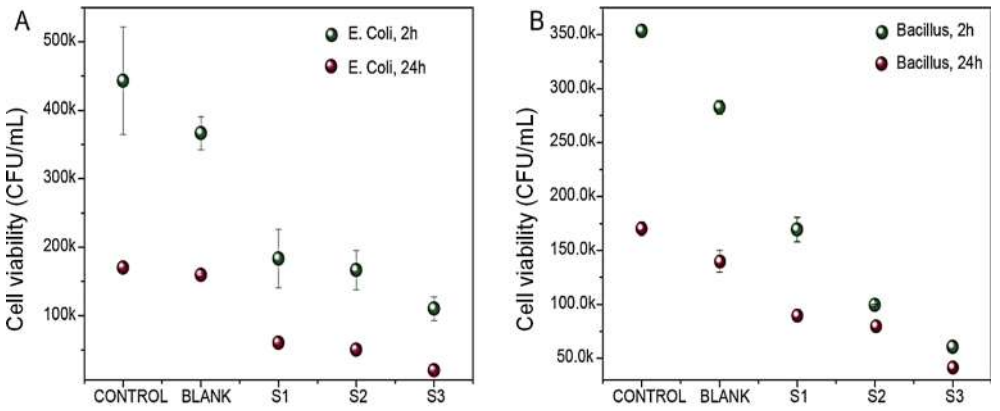


Figure 7. Antifouling experiment with *E. coli* (A) and *B. subtilis* (B) where incubation times are 2 and 24 h. Labels S1, S2, and S3 refer to the loading of MoS_2 (see the text).

analyzed to gain insights into the structural and chemical features contributing to their RO effectiveness. The RO simulations indicate that the equilibrated membrane structures (Figure S9) had a nonuniform thickness varying from 20 to 40 Å. The PA oligomers showed strong affinity toward the $hMoS_2$NSs but were not found inside the nanopore region. The S atoms of the $hMoS_2$NSs and the H atoms of the PA oligomers had the closest interaction distance of about 2.5 Å. During the RO simulations, the number of filtered water molecules increased linearly with time (Figure S10), indicating that the system has attained the stationary state. The WF and IR rates were calculated using the equations below

$$\mathrm{WF} = \frac{N_{\mathrm{water}}}{t}$$

where N_{water} is the number of permeated water molecules and t is the simulation time in ns.

$$\mathrm{IR}\ (\%) = \frac{N_{\mathrm{ion}} - N_{\mathrm{ion}}^{\mathrm{P}}}{N_{\mathrm{ion}}} \times 100$$

where N_{ion} is the total number of ions in the feed, and $N_{\mathrm{ion}}^{\mathrm{P}}$ is the number of ions that permeated through the membrane. The WF (Figure 5D) was comparable for the membranes, with the Mo-rich $hMoS_2M$ exhibiting slightly higher flux at most of the applied pressures and a significantly higher flux at 300 MPa. The IR (Figure 5E) was consistently superior for the Mo-rich $hMoS_2M$ across all applied pressures, and the difference became more pronounced at higher pressures.

The radial distribution function (RDF) plots[43] were computed between the O atoms of water molecules and atoms along the internal pore edges (Mo atoms for Mo-rich $hMoS_2M$ and S atoms for S-rich $hMoS_2M$). The first coordination shells of the pore Mo and pore S atoms were found to be centered around 3.1 Å and 3.2 Å, respectively (Figure 6A,B). A higher $g(r)$ for Mo−O corresponding to the first coordination shell indicates a higher probability of finding the water molecules near the pore edges in the case of Mo-rich $hMoS_2M$ (Figure S11). This localized water density at the pore region of the Mo-rich $hMoS_2M$ could be responsible for its slightly enhanced water permeability, which is consistent with the computed water fluxes (Figure 5D).

The RDF plots between the pore atoms and salt ions show a prominent peak in the Mo-salt ion RDF (Figure 6C) for the Mo-rich $hMoS_2M$ at r = 3.3 Å, whereas the corresponding $g(r)$ for S-salt ion (Figure 6D) for the S-rich $hMoS_2M$ was found to be weak. This peak in the Mo-salt RDF can be attributed to the strong interactions between the Mo atoms and Cl^- ions (Figure S12A). The comparatively lower $g(r)$ for the first coordination shell of S-salt ion interactions is in line with the weak S−Cl^- interactions (Figure S12B). The sustained Mo−Cl^- interactions (Figure S13) and the repulsive Mo−Na^+ ions interactions could be responsible for the enhanced IR observed for Mo-rich $hMoS_2M$. The RDF plots between water O atoms and the O atoms of the PA (Figure S14A) showed no significant differences, though slightly higher $g(r)$ values were observed for the S-rich $hMoS_2M$. In contrast, RDF plots between water O atoms and the N atoms of the PA (Figure S14B) showed slightly stronger interactions in the Mo-rich $hMoS_2M$ as compared to S-rich $hMoS_2M$. A similar trend was observed for salt ions, i.e., the O atoms in S-rich $hMoS_2M$ had slightly stronger interactions with the ions compared to the O atoms in Mo-rich $hMoS_2M$ (Figure S14C), while the N atoms in Mo-rich $hMoS_2M$ exhibited slightly stronger interactions with salt ions compared to those of S-rich $hMoS_2M$ (Figure S14D).

To complement the structural insights from RDF analysis and to assess the barriers for water transport, potential of mean force (PMF) profiles were computed to compare the permeability of $hMoS_2$Ms. The one-dimensional PMF for water molecules along the Z-direction (Figure 6E) from the center of the membrane was computed, perpendicular to the NS surface, using the relation below

$$\mathrm{F}(r) = -RT\ln \rho(r)$$

where R is the gas constant, T is the temperature, and $\rho(r)$ is the density of water at a distance r from the membrane.[44]

The 1-D PMF computed from RO simulations at 200 MPa indicates a comparable free-energy barrier for S-rich $hMoS_2M$ (9 kJ mol^{-1}) and Mo-rich $hMoS_2M$ (8 kJ mol^{-1}). This is in line with the comparable WF observed for Mo-rich and S-rich $hMoS_2$Ms (Figure 5D) at 200 MPa. Furthermore, the analysis of salt ion density profiles along the Z-direction (Figure 6F) indicates a noticeably lower ion density in the permeate region for the Mo-rich $hMoS_2M$ as compared to the S-rich $hMoS_2M$. This is in line with its higher IR rates observed in the RO simulations (Figure 5E). Distinct salt ion density peaks were observed at the pore region of the Mo-rich $hMoS_2$NS. This can be ascribed to stronger interactions between the ions and the Mo atoms at the edges of the pore, thereby reducing ion permeation.

https://doi.org/10.1021/acsanm.5c05244
ACS Appl. Nano Mater. 2025, 8, 23814−23823

To investigate the effect of the MoS_2 NSs on the filtration properties of $hMoS_2Ms$, an independent simulation involving bM, composed solely of PA oligomers (Figure S15), was performed. To model bM, 12 PA oligomers were used, ensuring a thickness comparable to the $hMoS_2Ms$. Here, four C atoms from each oligomer were fixed during the RO simulations to keep the center of mass of bM fixed in the *Z*-direction, and the simulations were performed at 100 MPa. The RO simulation showed an IR of 89.2% and a WF of 353 # ns^{-1} for bM, compared to 94.2% and 201 # ns^{-1} for the Mo-rich $hMoS_2M$. This shows that the MoS_2 NS plays a significant role in enhancing salt IR as the rejection rate is considerably lower in the absence of the NS. The higher WF in the bM can be attributed to the modeled concentration (200.32 wt %) of MoS_2 NSs in the $hMoS_2M$, which is much higher than the optimal value of 0.01 wt % used in our experiments.

2.5. Antifouling Properties of Membranes. Fouling of membranes by microorganisms is the major limiting factor in the membrane technology, resulting in a decrease in membrane selectivity and water permeation rate, an increase in energy consumption, and a decrease in membrane lifetime. Although pretreatment of feedwater can reduce the number of microorganisms but cannot remove the bacterial cells completely, which colonize and form biofilms on the membrane surface resulting in blockage of nanocapillaries present in the membrane. Therefore, it is very important to address this problem. Foulants are less likely to adhere to the MoS_2 NS surfaces due to the extremely low friction.[45] Besides, in our previous report, we demonstrated that holey MoS_2 NS exhibits excellent antibacterial property.[39] Therefore, antifouling properties of both MoS_2M and $hMoS_2M$ were tested with both Gram-positive (*Bacillus subtillis*) (Figure 7A) and Gram-negative (Escherichia coli) (Figure 7B) bacteria. The bacterial cells were incubated (2 and 24 h) with 1 cm × 1 cm pieces of the membranes, and the number of live cells after incubation was counted by plating the cells on nutrient agar plates. In comparison to a bM, $hMoS_2M$ shows the highest reduction in the bacteria count, and the antifouling efficiency increases with the amount of loading of MoS_2 (S1 = 0.01 wt % of MoS_2; S2 = 0.015 wt % of MoS_2; and S3 = 0.01 wt % of holey MoS_2).

3. CONCLUSION

In summary, we have successfully designed and fabricated holey MoS_2-incorporated thin-film composite membranes that demonstrate a synergistic improvement in water permeability and IR. The performance enhancement arises from three cooperative effects: (i) optimized interfacial polymerization conditions (60 s/60 s) that ensure uniform, defect-free PA layer formation; (ii) MoS_2 nanosheet incorporation (0.01 wt %) that increases surface hydrophilicity and introduces additional nanocapillary pathways; and (iii) nanoscale pores within MoS_2 that promote fast, directional water transport while preserving charge-based ion exclusion. The best-performing membrane achieved a WF of ∼96 L m^{-2} h^{-1} and NaCl rejection of ∼99.4%, confirming the potential of holey MoS_2 as a structural and functional modifier for high-performance RO membranes. MD simulations further support the experimental observations by elucidating how Mo-rich pore edges facilitate low-friction water flow through selective membrane−water interactions. Stabilizing Mo−Cl^- interactions and repulsive Mo−Na^+ interactions could be responsible for the superior IR in the case of Mo-rich $hMoS_2M$. The lower IR exhibited by bM in MD simulation highlights the critical role of MoS_2 NSs in enhancing membrane performance for effective RO filtration. Antifouling properties of the membrane were also tested with both Gram-positive and Gram-negative bacteria, and it was observed that holey MoS_2-based membranes show excellent antifouling properties due to their very low friction and fascinating disinfection property. This study not only provides a scalable route for engineering defect-tolerant, high-flux membranes but also delivers a mechanistic understanding of transport in 2D-material-assisted PA layers. The combined experimental−computational framework presented here offers valuable design principles for developing next-generation nanocomposite membranes tailored for sustainable desalination and water purification.

■ ASSOCIATED CONTENT

Supporting Information

The Supporting Information is available free of charge at https://pubs.acs.org/doi/10.1021/acsanm.5c05244.

Details of chemicals used; synthesis of MoS_2 NS; preparation of Mo-rich holey MoS_2 NS; fabrication of membranes; FESEM images of $hMoS_2M$, MoS_2M, and 0.015 wt % $hMoS_2M$; photograph of the setup used; pressure-dependent IR performance; computational details; structure of PA monomers and oligomers; simulation boxes; various RDF plots; MD snapshots of pore regions; and equilibrated membrane structures (PDF)

■ AUTHOR INFORMATION

Corresponding Authors

Sooraj Kunnikuruvan − *Department of Chemistry and Centre for Atomistic Modelling and Materials Design & Centre for Molecular Materials and Functions, Indian Institute of Technology Madras, Chennai 600036, India;* orcid.org/0000-0002-6734-4786; Email: soorajk@iitm.ac.in

Thalappil Pradeep − *DST Unit of Nanoscience (DST UNS) and Thematic Unit of Excellence (TUE), Department of Chemistry, Indian Institute of Technology Madras, Chennai 600036, India;* orcid.org/0000-0003-3174-534X; Email: pradeep@iitm.ac.in

Authors

Biswajit Mondal − *DST Unit of Nanoscience (DST UNS) and Thematic Unit of Excellence (TUE), Department of Chemistry, Indian Institute of Technology Madras, Chennai 600036, India*

Sudhin Rathnakumaran − *Department of Chemistry, Indian Institute of Technology Madras, Chennai 600036, India*

Amrita Chakraborty − *DST Unit of Nanoscience (DST UNS) and Thematic Unit of Excellence (TUE), Department of Chemistry, Indian Institute of Technology Madras, Chennai 600036, India; Department of Chemistry, BITS Pilani Hyderabad Campus, Telangana 500078, India*

Pragin Chettiyankandy − *Department of Chemistry, Indian Institute of Technology Madras, Chennai 600036, India*

Pillalamarri Srikrishnarka − *DST Unit of Nanoscience (DST UNS) and Thematic Unit of Excellence (TUE), Department of Chemistry, Indian Institute of Technology Madras, Chennai 600036, India;* orcid.org/0000-0001-5187-6879

Md Rabiul Islam − *DST Unit of Nanoscience (DST UNS) and Thematic Unit of Excellence (TUE), Department of*

Chemistry, Indian Institute of Technology Madras, Chennai 600036, India; orcid.org/0000-0001-6454-4013

Jenifer Shantha Kumar − *DST Unit of Nanoscience (DST UNS) and Thematic Unit of Excellence (TUE), Department of Chemistry, Indian Institute of Technology Madras, Chennai 600036, India;* orcid.org/0009-0003-7502-7005

Ramesh Kumar − *DST Unit of Nanoscience (DST UNS) and Thematic Unit of Excellence (TUE), Department of Chemistry, Indian Institute of Technology Madras, Chennai 600036, India*

Sandeep Bose − *DST Unit of Nanoscience (DST UNS) and Thematic Unit of Excellence (TUE), Department of Chemistry, Indian Institute of Technology Madras, Chennai 600036, India;* orcid.org/0000-0002-3471-5392

Complete contact information is available at: https://pubs.acs.org/10.1021/acsanm.5c05244

Author Contributions

B.M. planned and designed the whole project. He synthesized MoS_2 NS and characterized MoS_2 and holey MoS_2 NS. He fabricated the membranes and tested the performance of the membranes. He wrote the first draft of the manuscript. A.C. conducted the Raman spectroscopic measurements and contributed to the production of figures and the manuscript. S.R. and P.C. carried out the computational studies under the supervision of S.K. P.S. measured the contact angles and did the FESEM imaging of the membranes. R.I. and R.K. helped to fabricate and to test the membranes, and J.S.K. carried out antifouling measurements. S.B. helped to prepare holey MoS_2 NS. T.P. suggested the problem, supervised the project, and finalized the manuscript.

Notes

The authors declare no competing financial interest.

■ ACKNOWLEDGMENTS

We thank the Department of Science and Technology, Government of India for constantly supporting our research program on nanomaterials. B.M., P.K., and J.S.K. thank IIT Madras, and A.C. and R.I. thank the CSIR, Govt. of India for their research fellowships. S.K. thanks Anusandhan National Research Foundation (ANRF), India, for the funding through the Core Research Grant (CRG/2022/003771). S.R. thanks the Department of Science and Technology, Government of India, for the INSPIRE fellowship. P.C. thanks the Centre for Atomistic Modelling and Materials Design (CAMMD) Centre of Excellence, IIT Madras, for the postdoctoral fellowship through the IoE scheme. S.K., S.R., and P.C. thank CAMMD and IIT Madras for the HPC facilities. T.P. thanks funding from the Centre of Excellence (CoE) on Molecular Materials and Functions under the Institute of Eminence (IoE) scheme of IIT Madras, Science and Engineering Research Board (SERB), India, for funding through the SPR/2021/000439 research grant and a JC Bose Fellowship.

■ ABBREVIATIONS

NS, nanosheet; FESEM, field emission scanning electron microscopy; TEM, transmission electron microscopy; bM, blank membrane; hMoS_2M, holey MoS_2-based membrane; MoS_2M, MoS_2-based (without holes) membrane; EDS, energy-dispersive spectroscopy; WF, water flux; IR, ion rejection

■ REFERENCES

(1) Shannon, M. A.; Bohn, P. W.; Elimelech, M.; Georgiadis, J. G.; Mariñas, B. J.; Mayes, A. M. Science and Technology for Water Purification in the Coming Decades. *Nature* **2008**, *452* (7185), 301−310.

(2) Elimelech, M.; Phillip, W. A. The Future of Seawater Desalination: Energy, Technology, and the Environment. *Science* **2011**, *333* (6043), 712.

(3) Nagar, A.; Pradeep, T. Clean Water through Nanotechnology: Needs, Gaps, and Fulfillment. *ACS Nano* **2020**, *14* (6), 6420−6435.

(4) Henthorne, L.; Boysen, B. State-of-the-Art of Reverse Osmosis Desalination Pretreatment. *Desalination* **2015**, *356*, 129−139.

(5) UNESCO *Water and Climate Change*; United Nations Educational, Scientific and Cultural Organization: Paris, 2020; S. and C. O., Ed..

(6) Pendergast, M. M.; Hoek, E. M. V. A Review of Water Treatment Membrane Nanotechnologies. *Energy Environ. Sci.* **2011**, *4* (6), 1946−1971.

(7) Werber, J. R.; Osuji, C. O.; Elimelech, M. Materials for Next-Generation Desalination and Water Purification Membranes. *Nat. Rev. Mater.* **2016**, *1* (5), 16018.

(8) Wei, W.; Xiangli, F.; Jin, W.; Xu, N. Solvent Resistant Nanofiltration Membranes. *Prog. Chem.* **2007**, *19*, 1592−1597.

(9) Van der Bruggen, B.; Mänttäri, M.; Nyström, M. Drawbacks of Applying Nanofiltration and How to Avoid Them: A Review. *Sep. Purif. Technol.* **2008**, *63* (2), 251−263.

(10) Condom, S.; Larbot, A.; Alami Younssi, S.; Persin, M. Use of Ultra- and Nanofiltration Ceramic Membranes for Desalination. *Desalination* **2004**, *168*, 207−213.

(11) Zhu, B.; Myat, D. T.; Shin, J.-W.; Na, Y.-H.; Moon, I.-S.; Connor, G.; Maeda, S.; Morris, G.; Gray, S.; Duke, M. Application of Robust MFI-Type Zeolite Membrane for Desalination of Saline Wastewater. *J. Membr. Sci.* **2015**, *475*, 167−174.

(12) Sun, P.; Wang, K.; Zhu, H. Recent Developments in Graphene-Based Membranes: Structure, Mass-Transport Mechanism and Potential Applications. *Adv. Mater.* **2016**, *28* (12), 2287−2310.

(13) Liu, G.; Jin, W.; Xu, N. Two-Dimensional-Material Membranes: A New Family of High-Performance Separation Membranes. *Angew. Chem., Int. Ed.* **2016**, *55* (43), 13384−13397.

(14) Zhao, Y.; Xie, Y.; Liu, Z.; Wang, X.; Chai, Y.; Yan, F. Two-Dimensional Material Membranes: An Emerging Platform for Controllable Mass Transport Applications. *Small* **2014**, *10* (22), 4521−4542.

(15) Deng, M.; Kwac, K.; Li, M.; Jung, Y.; Park, H. G. Stability, Molecular Sieving, and Ion Diffusion Selectivity of a Lamellar Membrane from Two-Dimensional Molybdenum Disulfide. *Nano Lett.* **2017**, *17* (4), 2342−2348.

(16) Sri Abirami Saraswathi, M. S.; Rana, D.; Vijayakumar, P.; Alwarappan, S.; Nagendran, A. Tailored PVDF Nanocomposite Membranes Using Exfoliated MoS2 Nanosheets for Improved Permeation and Antifouling Performance. *New J. Chem.* **2017**, *41* (23), 14315−14324.

(17) Azamat, J.; Khataee, A.; Sadikoglu, F. Computational Study on the Efficiency of MoS2Membrane for Removing Arsenic from Contaminated Water. *J. Mol. Liq.* **2018**, *249*, 110−116.

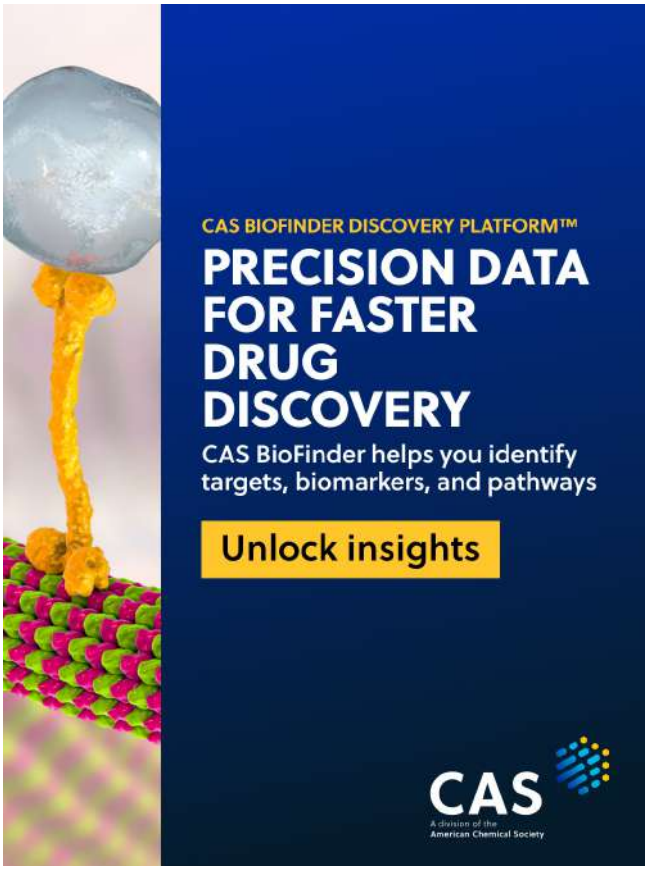
(18) Zhou, J.; Qin, Z.; Lu, Y.; Li, X.; An, Q.; Ji, S.; Wang, N.; Guo, H. MoS2/Polyelectrolytes Hybrid Nanofiltration (NF) Membranes with Enhanced Permselectivity. *J. Taiwan Inst. Chem. Eng.* **2018**, *84*, 196−202.

(19) Hirunpinyopas, W.; Prestat, E.; Iamprasertkun, P.; Bissett, M. A.; Dryfe, R. A. W. Potential Dependent Ionic Sieving through Functionalized Laminar MoS2Membranes. *2d Mater.* **2020**, *7* (1), 015030.

(20) Sun, L.; Huang, H.; Peng, X. Laminar MoS2Membranes for Molecule Separation. *Chem. Commun.* **2013**, *49* (91), 10718−10720.

(21) Kang, G.; Cao, Y. Development of Antifouling Reverse Osmosis Membranes for Water Treatment: A Review. *Water Res.* **2012**, *46* (3), 584−600.

(22) Wu, B.; Song, Z.; Xiang, Y.; Sun, H.; Yao, H.; Chen, J. Desalination Performance of MoS2Membranes with Different Single-Pore Sizes: A Molecular Dynamics Simulation Study. *ACS Omega* **2024**, *9* (21), 22851−22857.
(23) Dillenburg, R.F.; Abal, J. P. K.; Barbosa, M. C. Computational Investigation on Water and Ion Transport in MoS2 Nanoporous Membranes: Implications for Water Desalination. *ACS Appl. Nano Mater.* **2023**, *6* (6), 4465−4476.
(24) Heiranian, M.; Farimani, A. B.; Aluru, N. R. Water Desalination with a Single-Layer MoS2 Nanopore. *Nat. Commun.* **2015**, *6* (1), 8616.
(25) Opetubo, O.; Kitalu, R.; Oviroh, P.; Oyinbo, S.; Imoisili, P.; Jen, T.-C. A Mini-Review on MoS2Membrane for Water Desalination: Recent Development and Challenges. *Nanotechnol. Rev.* **2023**, *12*, 20220563.
(26) Nawal, N.; Nizam, R.; Das, P.; Morshed, M. M. Desalination Performance of Nano Porous Mos2Membrane on Different Salts of Saline Water: A Molecular Dynamics Study. *arXiv* **2023**, arXiv.2310.05729.
(27) Kleinubing Abal, J. P.; Barbosa, M. C. Molecular Fluid Flow in MoS2 Nanoporous Membranes and Hydrodynamics Interactions. *J. Chem. Phys.* **2021**, *154* (13), 134506.
(28) Barati Farimani, O.; Cao, Z.; Barati Farimani, A. Fast Water Desalination with a Graphene−MoS2 Nanoporous Heterostructure. *ACS Appl. Mater. Interfaces* **2024**, *16* (22), 29355−29363.
(29) Levita, G.; Restuccia, P.; Righi, M. C. Graphene and MoS2 Interacting with Water: A Comparison by Ab Initio Calculations. *Carbon* **2016**, *107*, 878−884.
(30) Song, Z.; Niu, Y.; Yang, J.; Chen, L.; Chen, J. Comparison of Water Desalination Performance of Porous Graphene and MoS2 Nanosheets. *RSC Adv.* **2022**, *12* (42), 27641−27647.
(31) Feng, J.; Liu, K.; Graf, M.; Lihter, M.; Bulushev, R. D.; Dumcenco, D.; Alexander, D. T. L.; Krasnozhon, D.; Vuletic, T.; Kis, A.; Radenovic, A. Electrochemical Reaction in Single Layer MoS2: Nanopores Opened Atom by Atom. *Nano Lett.* **2015**, *15* (5), 3431−3438.
(32) He, Y.; Tsutsui, M.; Zhou, Y.; Miao, X.-S. Solid-State Nanopore Systems: From Materials to Applications. *NPG Asia Mater.* **2021**, *13* (1), 48.
(33) Hoenig, E.; Han, Y.; Xu, K.; Li, J.; Wang, M.; Liu, C. In Situ Generation of (Sub) Nanometer Pores in MoS2Membranes for Ion-Selective Transport. *Nat. Commun.* **2024**, *15* (1), 7911.
(34) Hirunpinyopas, W.; Prestat, E.; Worrall, S. D.; Haigh, S. J.; Dryfe, R. A. W.; Bissett, M. A. Desalination and Nanofiltration through Functionalized Laminar MoS2Membranes. *ACS Nano* **2017**, *11* (11), 11082−11090.
(35) Dines, M. B. Lithium Intercalation via N-Butyllithium of the Layered Transition Metal Dichalcogenides. *Mater. Res. Bull.* **1975**, *10* (4), 287−291.
(36) Zeng, Z.; Yin, Z.; Huang, X.; Li, H.; He, Q.; Lu, G.; Boey, F.; Zhang, H. Single-Layer Semiconducting Nanosheets: High-Yield Preparation and Device Fabrication. *Angew. Chem., Int. Ed.* **2011**, *50* (47), 11093−11097.
(37) Lee, C.; Yan, H.; Brus, L. E.; Heinz, T. F.; Hone, J.; Ryu, S. Anomalous Lattice Vibrations of Single- and Few-Layer MoS2. *ACS Nano* **2010**, *4* (5), 2695−2700.
(38) Mak, K. F.; Lee, C.; Hone, J.; Shan, J.; Heinz, T. F. Atomically Thin ${\mathrm{MoS}}_{2}$: A New Direct-Gap Semiconductor. *Phys. Rev. Lett.* **2010**, *105* (13), 136805.
(39) Sarkar, D.; Mondal, B.; Som, A.; Ravindran, S. J.; Jana, S. K.; Manju, C. K.; Pradeep, T. Holey MoS2 Nanosheets with Photocatalytic Metal Rich Edges by Ambient Electrospray Deposition for Solar Water Disinfection. *Global chall.* **2018**, *2* (12), 1800052.
(40) Mondal, B.; Som, A.; Chakraborty, I.; Baksi, A.; Sarkar, D.; Pradeep, T. Unusual Reactivity of MoS2 Nanosheets. *Nanoscale* **2016**, *8* (19), 10282−10290.
(41) Thompson, A. P.; Aktulga, H. M.; Berger, R.; Bolintineanu, D. S.; Brown, W. M.; Crozier, P. S.; in 't Veld, P. J.; Kohlmeyer, A.; Moore, S. G.; Nguyen, T. D.; Shan, R.; Stevens, M. J.; Tranchida, J.; Trott, C.; Plimpton, S. J. LAMMPS - a Flexible Simulation Tool for Particle-Based Materials Modeling at the Atomic, Meso, and Continuum Scales. *Comput. Phys. Commun.* **2022**, *271*, 108171.
(42) Humphrey, W.; Dalke, A.; Schulten, K. VMD: Visual Molecular Dynamics. *J. Mol. Graphics* **1996**, *14* (1), 33−38.
(43) Levine, B. G.; Stone, J. E.; Kohlmeyer, A. Fast Analysis of Molecular Dynamics Trajectories with Graphics Processing Units—Radial Distribution Function Histogramming. *J. Comput. Phys.* **2011**, *230* (9), 3556−3569.
(44) Giorgino, T. Computing 1-D Atomic Densities in Macromolecular Simulations: The Density Profile Tool for VMD. *Comput. Phys. Commun.* **2014**, *185* (1), 317−322.
(45) Alam, I.; Guiney, L. M.; Hersam, M. C.; Chowdhury, I. Antifouling Properties of Two-Dimensional Molybdenum Disulfide and Graphene Oxide. *Environ. Sci.:Nano* **2018**, *5* (7), 1628−1639.



Supporting Information

A Holey 2D MoS_2-based Membrane with Mo-rich Edges for Water Desalination

Biswajit Mondal[1], Sudhin Rathnakumaran[2], Amrita Chakraborty[1,4], Pragin Chettiyankandy[2], Pillalamarri Srikrishnarka[1], Md Rabiul Islam[1], Jenifer Shantha Kumar[1], Ramesh Kumar[1], Sandeep Bose[1], Sooraj Kunnikuruvan[2,3] and Thalappil Pradeep[1]**

[1]DST Unit of Nanoscience (DST UNS) and Thematic Unit of Excellence (TUE), Department of Chemistry, Indian Institute of Technology Madras, Chennai – 600036, India.

[2]Department of Chemistry, Indian Institute of Technology Madras, Chennai – 600036, India

[3]Centre for Atomistic Modelling and Materials Design & Centre for Molecular Materials and Functions, Indian Institute of Technology Madras, Chennai – 600036, India

[4]Department of Chemistry, BITS Pilani Hyderabad Campus, Telangana 500078, India

*E-mail: pradeep@iitm.ac.in

soorajk@iitm.ac.in

Table of contents

Number	Description	Page No.
	Experimental section	2
S1	FESEM images of $hMoS_2M$ and MoS_2M	4
S2	FESEM images of 0.015 wt% $hMoS_2M$	4
S3	FT-IR spectrum of $hMoS_2M$	5
S4	Photograph of the set-up	5

S5	Pressure-dependent ion rejection performance	6
	Computational details	6
S6	Structure of the PA oligomer	7
S7	Structure of the PA monomer	8
Table S1	Calculated ESP charges for atoms of the PA monomer	8
S8	Periodic simulation boxes	10
S9	Equilibrated membrane structures	11
S10	Plot of number of filtered water molecules vs simulation time	11
S11	Snapshots showing the pore regions and water molecules	12
S12	RDF plots of the pore atoms and Na^+/Cl^- ions	12
S13	Snapshots showing the Mo-rich pore region and Cl^- ions	13
S14	RDF plots of the PA atoms and water/salt ions	13
S15	Side and top views of the equilibrated bM structure	14
	References	14

EXPERIMENTAL SECTION

Chemicals: All the commercially available chemicals were used without further purification. Silver acetate (AgOAc), molybdenum disulfide (MoS_2), 1.6 M n-butyllithium in hexane, camphorsulfonic acid, sodium lauryl sulfate (SLS), and 1,3,5-Benzenetricarbonyl trichloride (TMC) were purchased from Sigma Aldrich, India. All the solvents hexane and N-Methyl-2-pyrrolidone were used without further purification.

Synthesis of MoS_2 NS: MoS_2 NSs were synthesized using the chemical exfoliation method from bulk MoS_2 powder. In the typical synthesis, 300 mg of MoS_2 powder was taken in a round bottom flask, under argon atmosphere, and 3 mL of 1.6 M n-butyllithium was added. The resulting solution was stirred for 2 days under the same inert conditions. Then the resulting

lithium-intercalated product was washed repeatedly with hexane, to remove excess n-butyllithium. Then, it was centrifuged to collect cleaned lithium-intercalated product and 100 mL of distilled water was added to it. The product was sonicated in a bath sonicator for 1 h to get exfoliated MoS_2 NS. This aqueous dispersion of MoS_2 NSs was centrifuged at a speed of 18000 rpm to remove un-exfoliated MoS_2. The quality of the synthesized MoS_2 NSs was checked using electron microscopy, UV-Vis, and Raman spectroscopy.

Preparation of Mo-rich holey MoS_2 NS: For electrospray deposition of Ag^+ ions, a home-built nanoelectrospray ionization (nESI) source was used. The nESI source was made by pulling a borosilicate glass capillary (0.86 mm ID and 1.5 mm OD) into two, using a micropipette puller (Sutter Instruments, U.S.A.). Each tip, after pulling, was checked using an optical microscope to ensure the size and quality of the cut. Tips with an opening of 10-15 µm were used for the electrospray deposition of Ag^+ ions. 10 mM aqueous solution of AgOAc was filled in the nESI tips using a microinjector pipette tip and Pt wire was inserted into the solution, making an electrode for high voltage connection. For electrospray deposition on MoS_2 NSs, an aqueous suspension of MoS_2 NS was taken in an Eppendorf vial and the Ag^+ ions were guided towards it. The aqueous MoS_2 suspension was grounded through a picoammeter using a copper strip. The pore size is primarily governed by the deposition time. We attempted to control the pore size by varying the deposition duration; however, for a fixed deposition time, no significant variation in pore size was observed. The sizes of the nanopores were further checked using transmission electron microscope.

Fabrication of membranes: Membranes were fabricated using an easy and cost-effective co-polymerization method. In the first step, a solution of polysulfone (psf) in NMP was coated on a polyester non-woven fabric and immediately, it was dipped into water. Then, a mixture of solutions of holey MoS_2 NS, MPD, SLS, and camphorsulfonic acid was added to psf-coated polyester non-woven fabric. Then the solution was carefully drained off after a certain time. A solution of TMC in hexane was added and kept in contact for a certain time. The solution was

drained off and then the membrane was dried inside an oven at 60 ^{o}C. The concentration of all the reagents and the contact time of both solutions were optimized.

Test of performance of the membranes: The performance of the membranes was tested using RO membrane test skid. All the experiments were done at a pressure of 20 bar (except "pressure dependent flux" experiment) and the TDS of feed water was 2000 ppm. The pressure-dependent experiments were done in the pressure range of 5 bar to 40 bar. Photograph of test skid is shown in Figure S3.

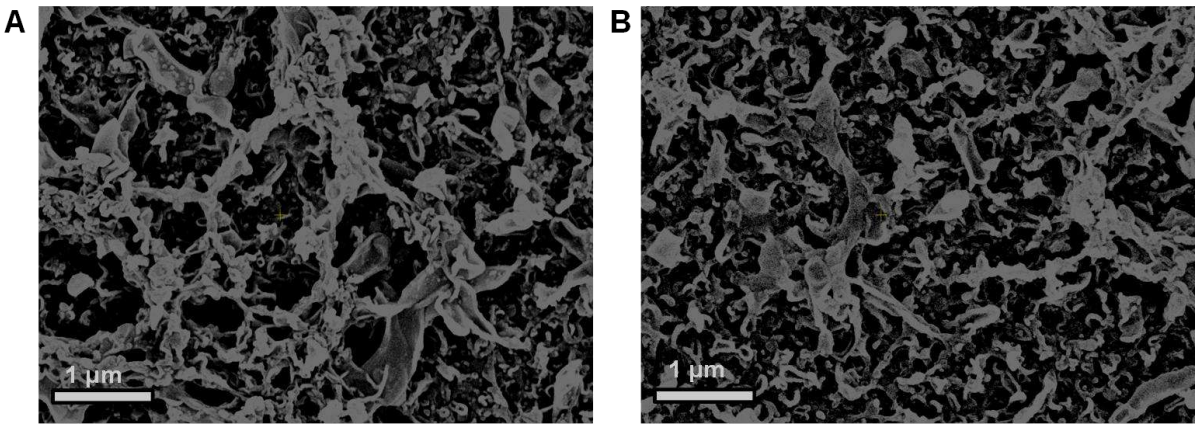


Figure S1. FESEM images of hMoS_2M (A) and MoS_2M (B).

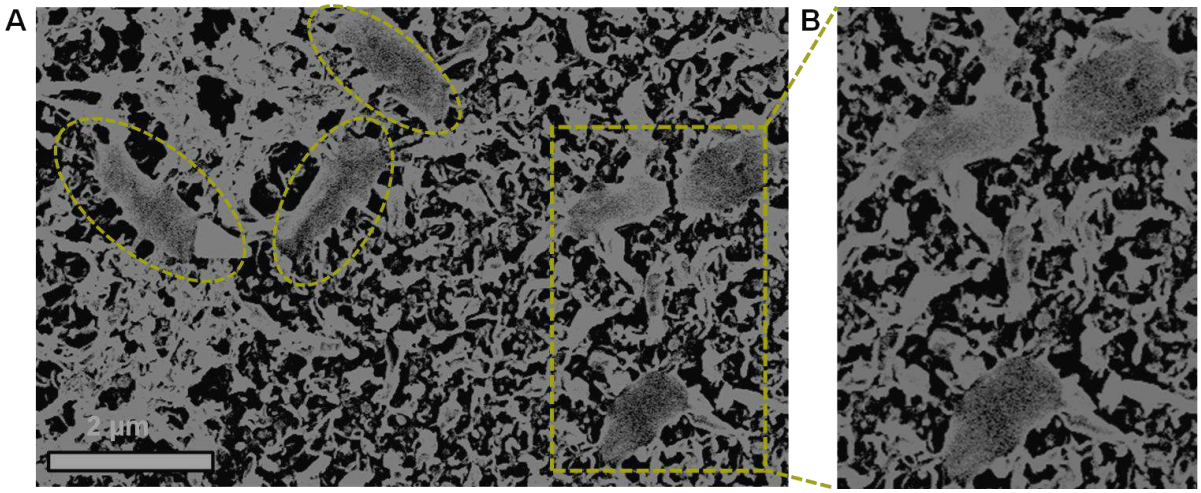


Figure S2. FESEM images of 0.015 wt% hMoS_2M showing agglomeration of MoS_2 NSs.

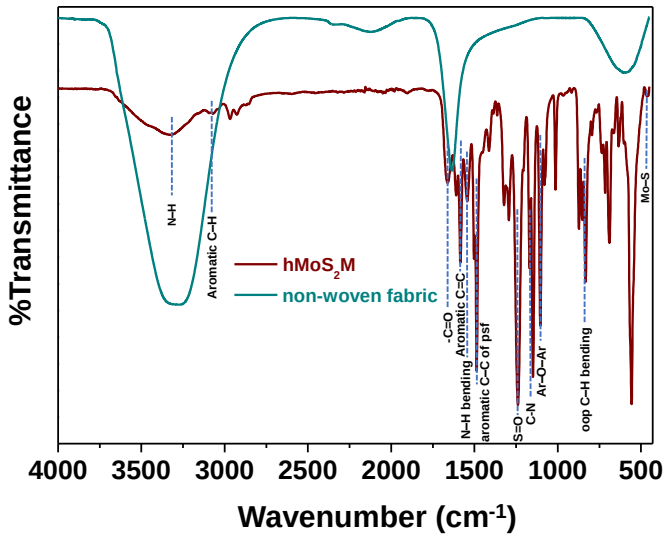


Figure S3. The FT-IR spectrum of hMoS$_2$M confirms the presence of all characteristic peaks associated with PA and MoS$_2$.

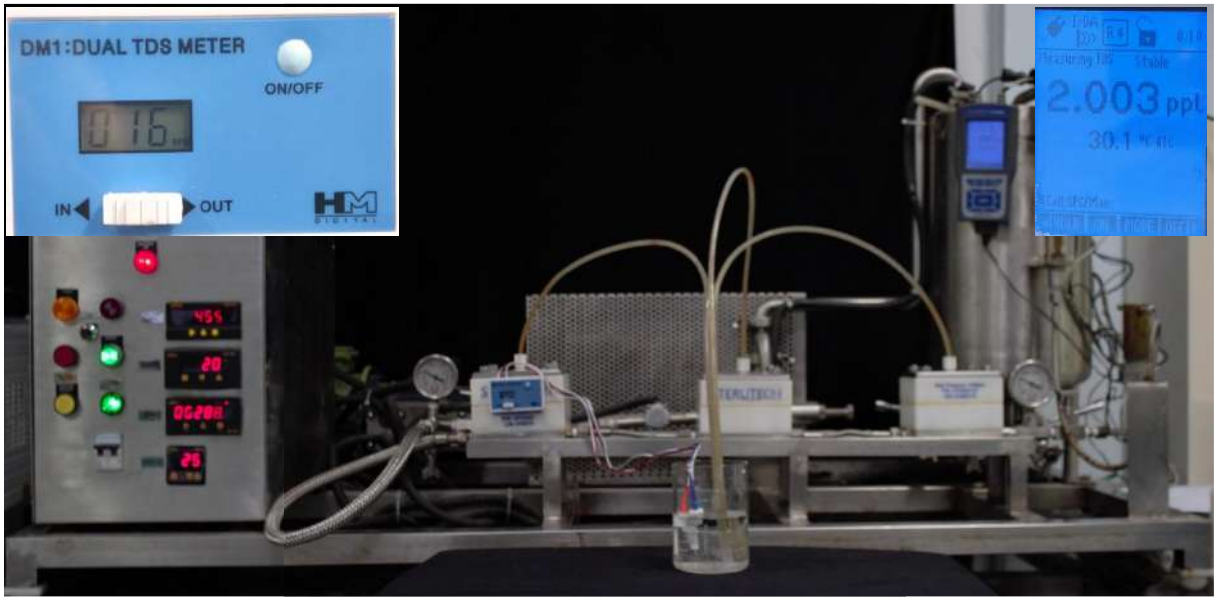


Figure S4. Photograph of the set-up used to test the performance of the membranes.

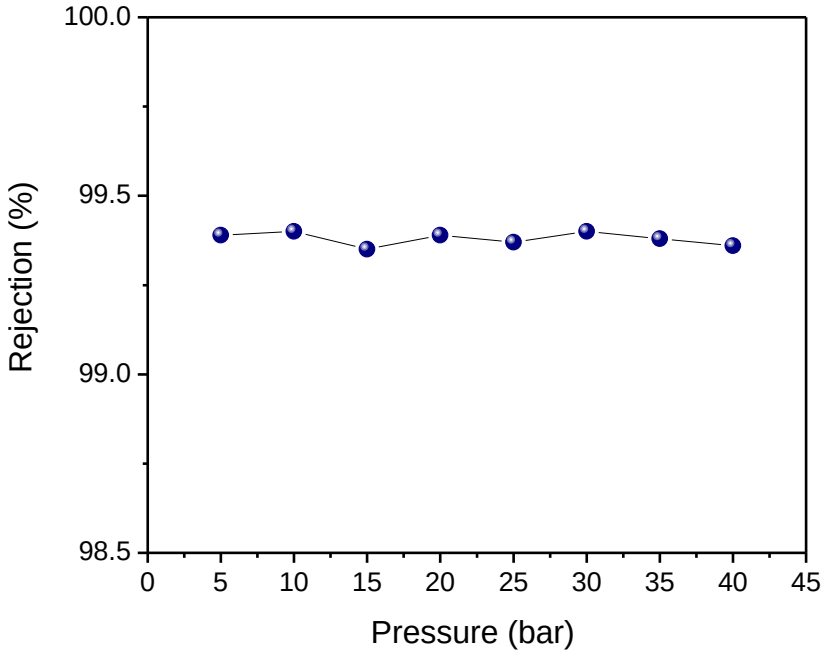


Figure S5. Pressure-dependent ion rejection performance of holey MoS_2-based membrane.

Computational details:

The MoS_2 NSs were constructed using the CHARMM-GUI Nanomaterial Modeler.[1] The PA oligomer structure (Figure S5) was prepared based on a previous study,[2] which reports a degree of crosslinking (DC) of about 71%. The cross-linked PA oligomer was formed via condensation between 11 MPD and 10 TMC monomers. To build the membrane models for MD simulations, five such PA oligomers were placed on either side of the hMoS_2NSs in a sandwiched configuration. This initial molecular arrangement was generated using PACKMOL.[3] At both ends of the system, graphene pistons were placed. Periodic boundary conditions (PBC) were applied, and a vacuum layer of 10 nm was added in the Z-direction to avoid interactions between the periodic images.

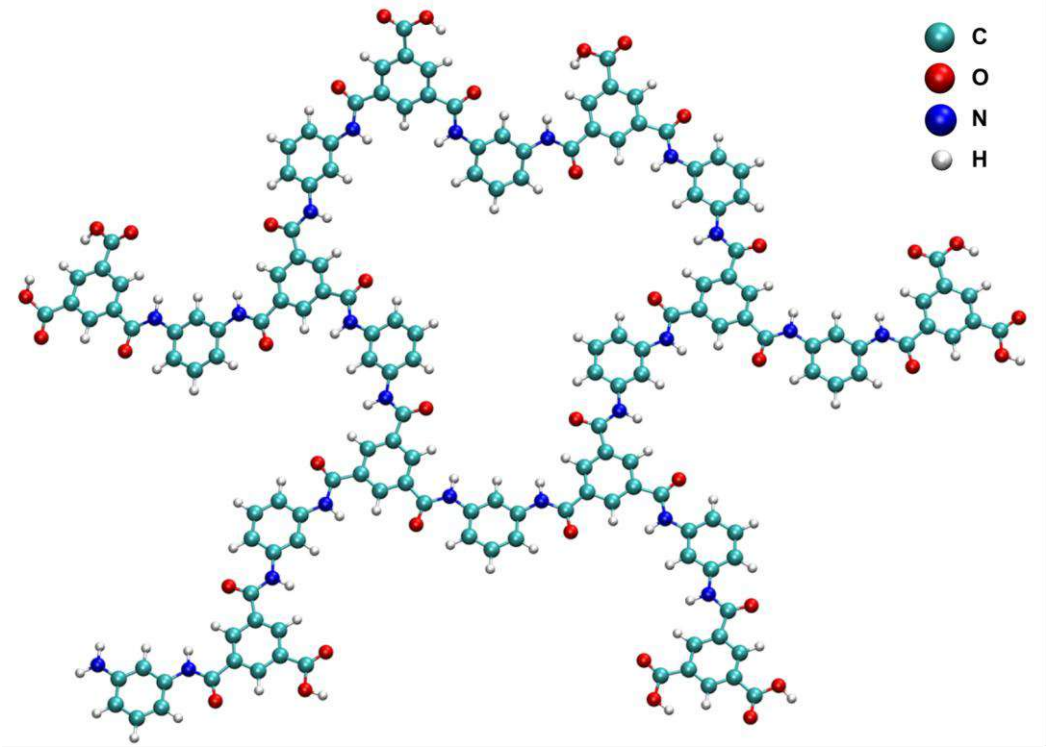


Figure S6: Optimized structure of the PA oligomer used in the MD simulations.

The TIP3P water model was used here,[4] and the SHAKE algorithm with a tolerance of 0.0001 was employed to constrain bond lengths and angles of water molecules.[5] The Lennard-Jones (LJ) parameters for Mo, S, Na, and Cl were adopted from a previous study.[6] The Mo and S atoms were assigned atomic charges of +0.5 and -0.25, respectively.[7] The PA oligomers were described using the DREIDING force field,[8] with atomic charges derived from electrostatic potential (ESP) charges calculated on the monomer unit (Figure S6 and Table S1) using the Gaussian 16 suite of programs at the B3LYP/6-311++G(d,p) level of theory.[9] All the other LJ parameters for the pairwise interactions were computed using the Lorentz-Berthelot mixing rules. A cutoff distance of 12 Å was used for both LJ and Coulombic interactions. Long-range Coulombic interactions were treated using the particle-particle particle-mesh (PPPM) method implemented in LAMMPS, with a relative root-mean-square (RMS) error of 0.0001 in the forces.

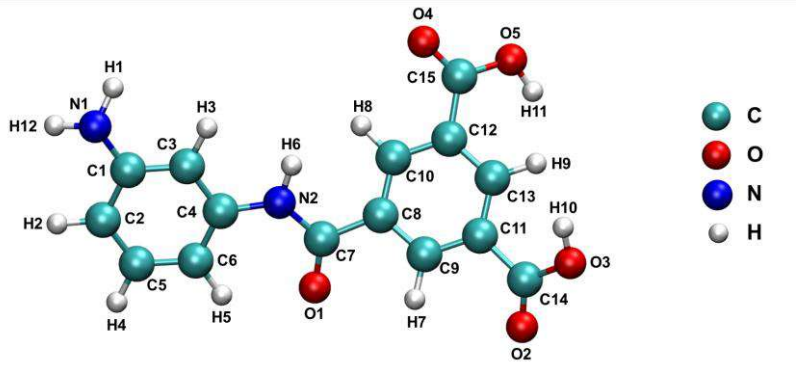


Figure S7: Optimized structure of the PA monomer used for the ESP charge calculations.

Table S1: Calculated ESP charges for atoms of the PA monomer. Atom labels are consistent with Figure S7.

Atom	ESP charge (*e*)
C1	0.4
C2	-0.33
C3	-0.53
C4	-0.1
C5	0.59
C6	-0.36
C7	0.7
C8	-0.07
C9	-0.03
C10	-0.03
C11	-0.19
C12	-0.19
C13	-0.08
C14	0.74

C15	0.74
H1	0.33
H2	0.18
H3	0.23
H4	0.15
H5	0.2
H6	0.3
H7	0.12
H8	0.12
H9	0.11
H10	0.4
H11	0.4
H12	0.33
N1	-0.75
N2	-0.73
O1	-0.51
O2	-0.48
O3	-0.58
O4	-0.48
O5	-0.58

Initially, energy minimization was performed on the RO setup, setting the relative energy tolerance to 10^{-8} and force tolerance to 10^{-10} kcal mol^{-1} $Å^{-1}$. The graphene pistons were constrained in the XY-plane, while the $hMoS_2NSs$ were fixed in all three spatial dimensions. Following minimization, NPT and NVT equilibrations were performed at a temperature of 300

K and a pressure of 1 atm for 1 ns. RO simulations were then carried out on the equilibrated setup under the NVT ensemble at 300 K for 10 ns at each applied pressure. During the NVT equilibration and RO simulations, the pistons were subjected to the required amount of pressure (p) using forces applied in the Z-direction, calculated as:

$$F = \frac{pA}{N}$$

where F is the force per atom, A is the surface area of the piston, and N is the number of C atoms in the piston. For the NVT equilibration runs, the pistons were maintained at a pressure of p = 1 atm. During the RO simulations, pressures of p = 50 to 300 MPa with an interval of 50 MPa were applied to the piston on the feed side, while the piston on the permeate side was kept at p = 1 atm. A time step of 1 fs was used in all these simulations. The equilibrated RO setups within the periodic simulation boxes are shown in Figure S7.

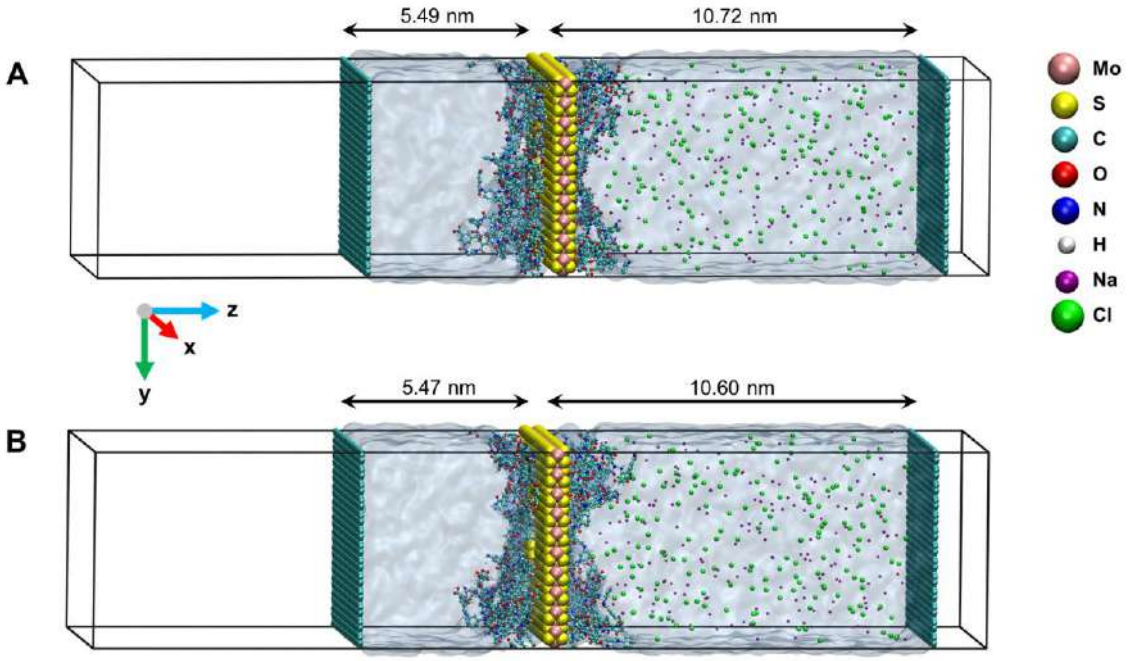


Figure S8. Periodic simulation boxes used in the RO simulations showing the feed and permeate layer sizes for the (A) Mo-rich and (B) S-rich hMoS_2Ms.

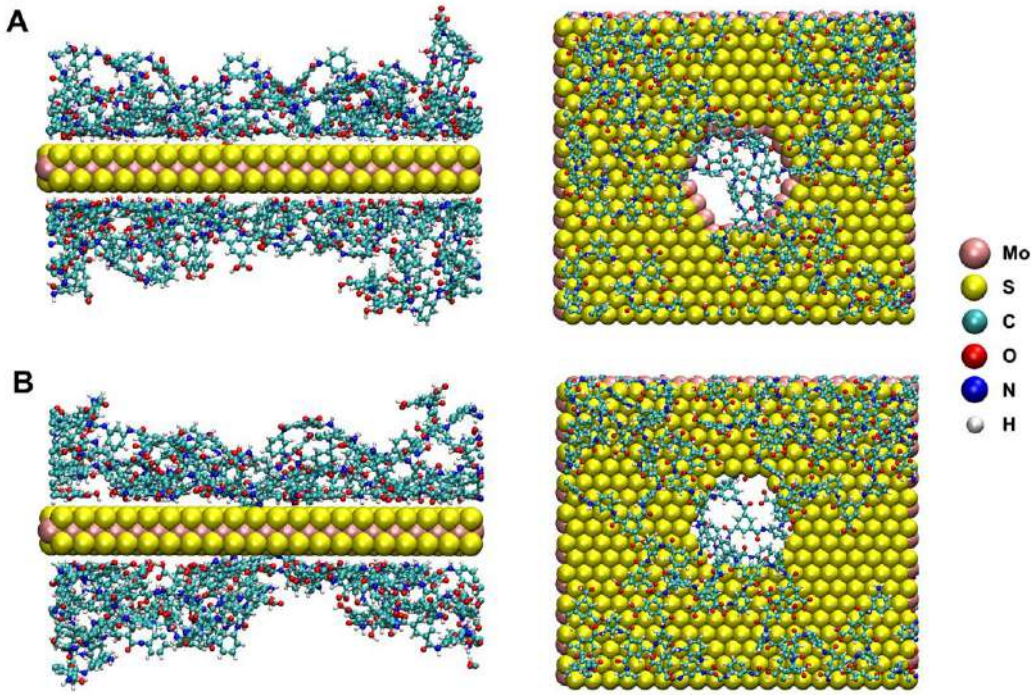


Figure S9. Equilibrated membrane structures (side and top views) of (A) Mo-rich and (B) S-rich $hMoS_2Ms$.

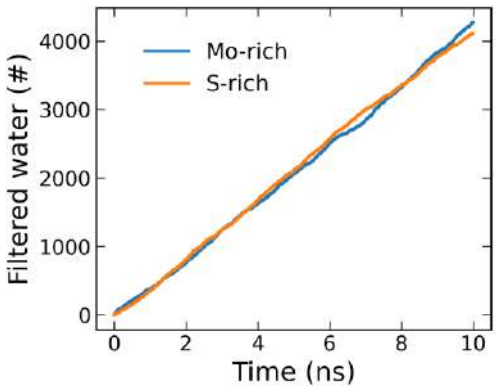


Figure S10: Number of filtered water molecules as a function of simulation time for the Mo-rich and S-rich $hMoS_2Ms$ at an applied pressure of 200 MPa.

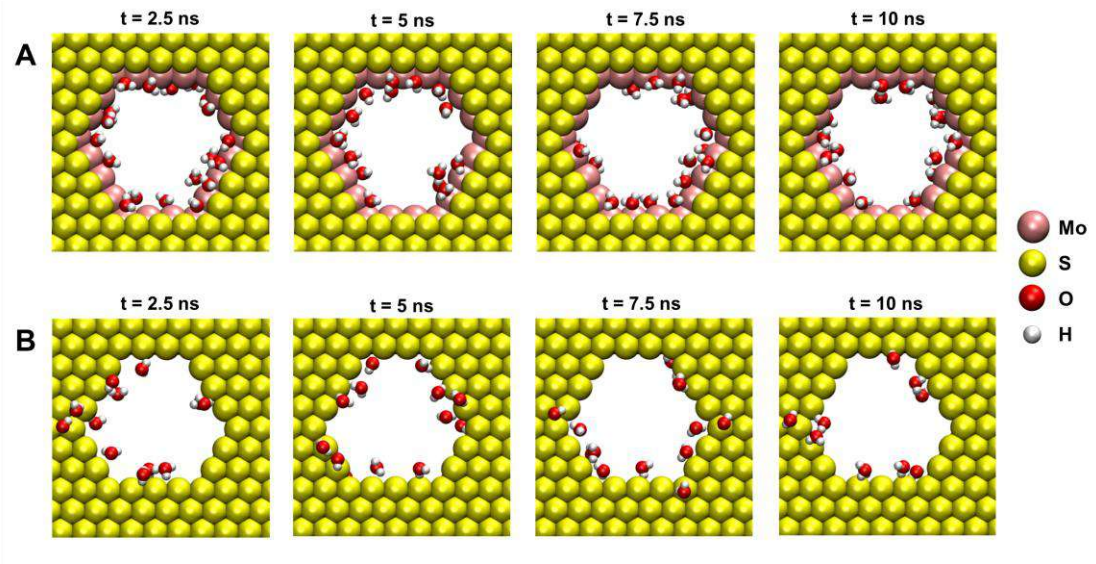


Figure S11. Snapshots showing the pore region and water molecules within 3.3 Å of the pore atoms for (A) Mo-rich hMoS_2M and (B) S-rich hMoS_2M from RO simulations performed at 200 MPa.

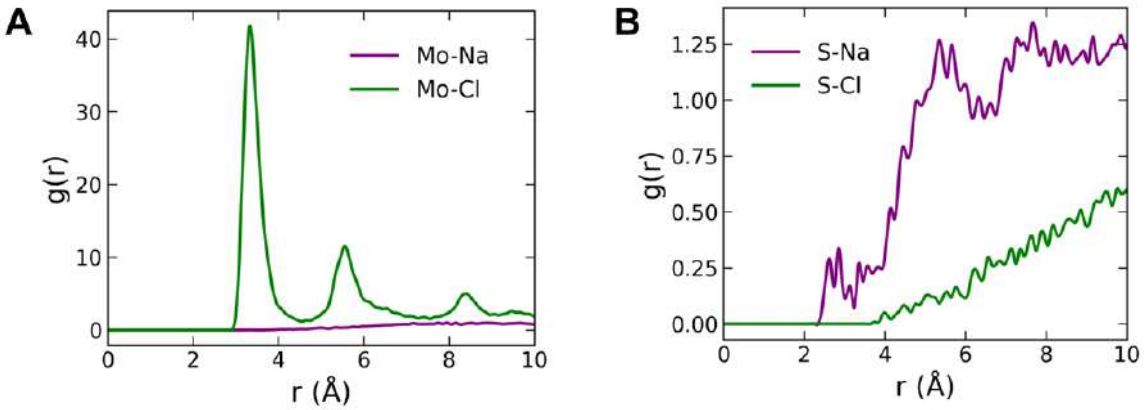


Figure S12. RDF plots between (A) salt ions and Mo atoms, and (B) salt ions and S atoms for the Mo-rich and S-rich hMoS_2Ms, computed from RO simulations at 200 MPa.

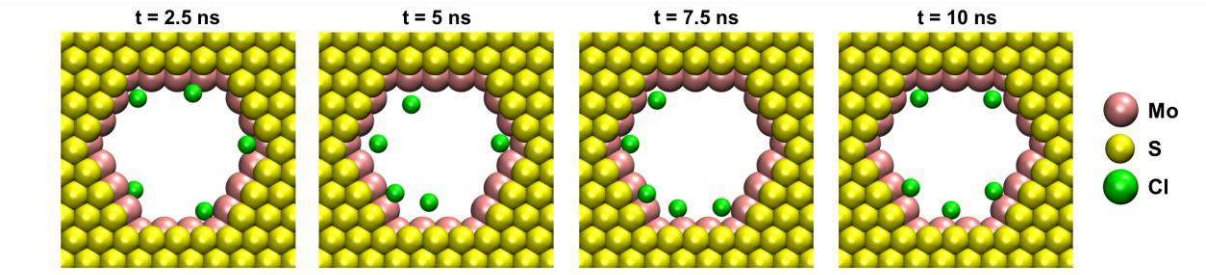


Figure S13. Snapshots showing the pore region and Cl^- ions within 4 Å of the pore Mo atoms for Mo-rich hMoS_2M from RO simulation performed at 200 MPa.

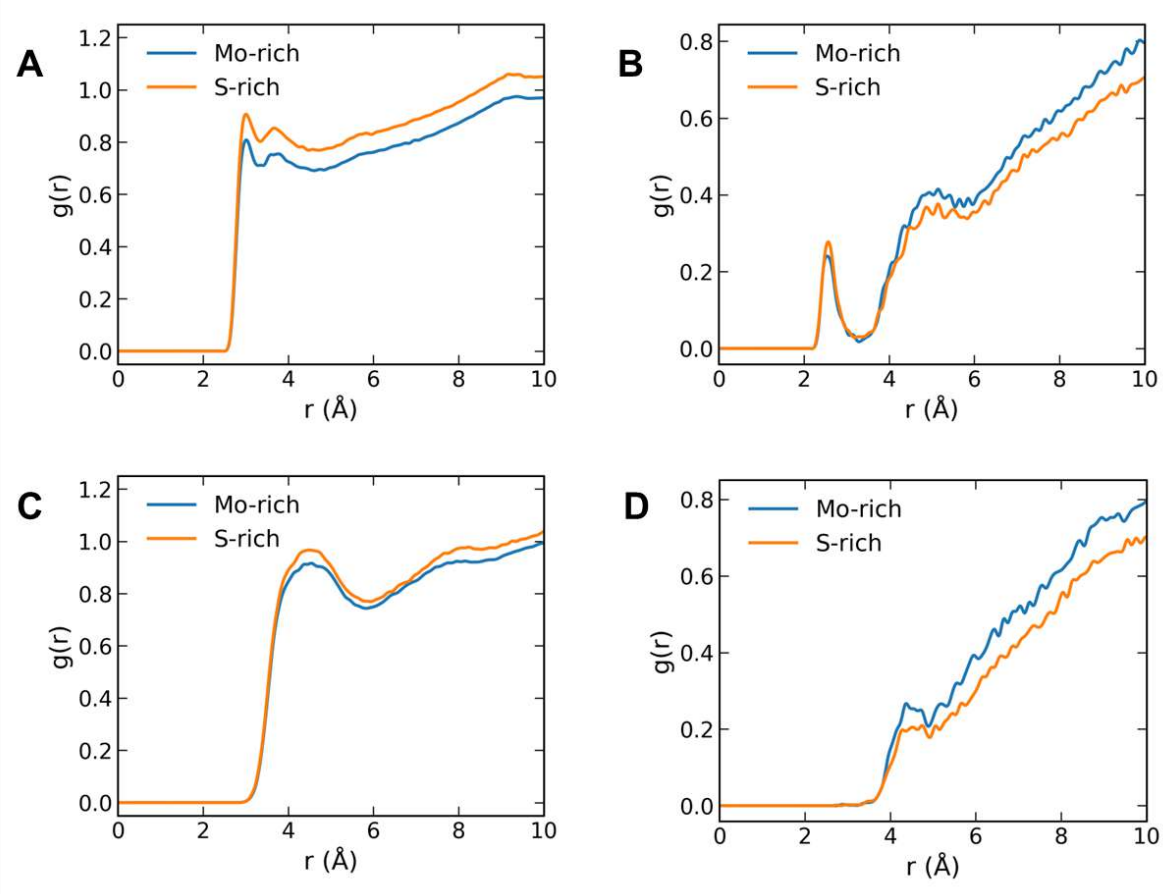


Figure S14. RDF plots between (A) O of PA and O of water, (B) N of PA and O of water, (C) O of PA and salt ions, and (D) N of PA and salt ions, for the Mo-rich and S-rich hMoS_2Ms, computed from RO simulations at 200 MPa.

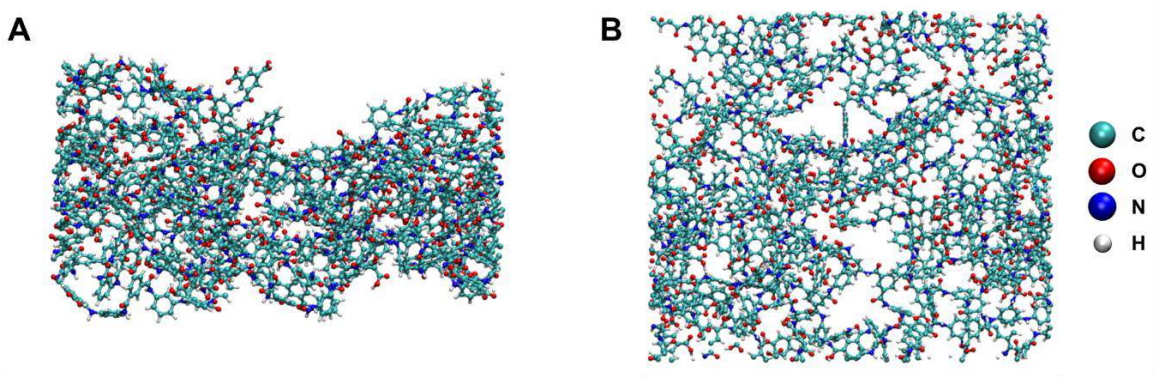


Figure S15. (A) Side and (B) top views of the equilibrated bM structure composed solely of PA oligomers.

Computational data and code availability:

The LAMMPS input and data files used for the MD simulations in this work are available at:

https://drive.google.com/drive/folders/1DZeFyLgIpvCdsc9hmNEi0Ab6TFPKMO1Y

References

(1) Choi, Y. K.; Kern, N. R.; Kim, S.; Kanhaiya, K.; Afshar, Y.; Jeon, S. H.; Jo, S.; Brooks, B. R.; Lee, J.; Tadmor, E. B.; Heinz, H.; Im, W. CHARMM-GUI Nanomaterial Modeler for Modeling and Simulation of Nanomaterial Systems. *J Chem Theory Comput* **2022**, *18* (1), 479–493. https://doi.org/10.1021/acs.jctc.1c00996.

(2) Yoshioka, T.; Kotaka, K.; Nakagawa, K.; Shintani, T.; Wu, H.-C.; Matsuyama, H.; Fujimura, Y.; Kawakatsu, T. Molecular Dynamics Simulation Study of Polyamide Membrane Structures and RO/FO Water Permeation Properties. *Membranes (Basel)* **2018**, *8* (4), 127. https://doi.org/10.3390/membranes8040127.

(3) Martínez, L.; Andrade, R.; Birgin, E. G.; Martínez, J. M. PACKMOL: A Package for Building Initial Configurations for Molecular Dynamics Simulations. *J Comput Chem* **2009**, *30* (13), 2157–2164. https://doi.org/10.1002/jcc.21224.

4) Price, D. J.; Brooks, C. L. A Modified TIP3P Water Potential for Simulation with Ewald Summation. *J Chem Phys* **2004**, *121* (20), 10096–10103. https://doi.org/10.1063/1.1808117.

(5) Andersen, H. C. Rattle: A "Velocity" Version of the Shake Algorithm for Molecular Dynamics Calculations. *J Comput Phys* **1983**, *52* (1), 24–34. https://doi.org/10.1016/0021-9991(83)90014-1.

(6) Wu, B.; Song, Z.; Xiang, Y.; Sun, H.; Yao, H.; Chen, J. Desalination Performance of MoS_2 Membranes with Different Single-Pore Sizes: A Molecular Dynamics Simulation Study. *ACS Omega* **2024**, *9* (21), 22851–22857. https://doi.org/10.1021/acsomega.4c01208.

(7) Sresht, V.; Govind Rajan, A.; Bordes, E.; Strano, M. S.; Pádua, A. A. H.; Blankschtein, D. Quantitative Modeling of MoS_2–Solvent Interfaces: Predicting Contact Angles and Exfoliation Performance Using Molecular Dynamics. *The Journal of Physical Chemistry C* **2017**, *121* (16), 9022–9031. https://doi.org/10.1021/acs.jpcc.7b00484.

(8) Mayo, S. L.; Olafson, B. D.; Goddard, W. A. DREIDING: A Generic Force Field for Molecular Simulations. *J Phys Chem* **1990**, *94* (26), 8897–8909. https://doi.org/10.1021/j100389a010.

(9) Frisch, M. J.; Trucks, G. W.; Schlegel, H. B.; Scuseria, G. E.; Robb, M. A.; Cheeseman, J. R.; Scalmani, G.; Barone, V.; Petersson, G. A.; Nakatsuji, H.; Li, X.; Caricato, M.; Marenich, A. V; Bloino, J.; Janesko, B. G.; Gomperts, R.; Mennucci, B.; Hratchian, H. P.; Ortiz, J. V; Izmaylov, A. F.; Sonnenberg, J. L.; Williams-Young, D.; Ding, F.; Lipparini, F.; Egidi, F.; Goings, J.; Peng, B.; Petrone, A.; Henderson, T.; Ranasinghe, D.; Zakrzewski, V. G.; Gao, J.; Rega, N.; Zheng, G.; Liang, W.; Hada, M.; Ehara, M.; Toyota, K.; Fukuda, R.; Hasegawa, J.; Ishida, M.; Nakajima, T.; Honda, Y.; Kitao, O.; Nakai, H.; Vreven, T.; Throssell, K.; Montgomery Jr., J. A.; Peralta, J. E.; Ogliaro, F.; Bearpark, M. J.; Heyd, J. J.; Brothers, E. N.; Kudin, K. N.; Staroverov, V. N.; Keith, T. A.; Kobayashi, R.; Normand, J.; Raghavachari, K.; Rendell, A. P.; Burant, J. C.; Iyengar, S. S.; Tomasi, J.; Cossi, M.; Millam, J. M.; Klene, M.; Adamo, C.; Cammi, R.; Ochterski, J. W.; Martin, R. L.; Morokuma, K.; Farkas, O.; Foresman, J. B.; Fox, D. J. Gaussian 16, Revision C.01. 2016.

THE JOURNAL OF PHYSICAL CHEMISTRY LETTERS
A JOURNAL OF THE AMERICAN CHEMICAL SOCIETY

pubs.acs.org/JPCL Letter

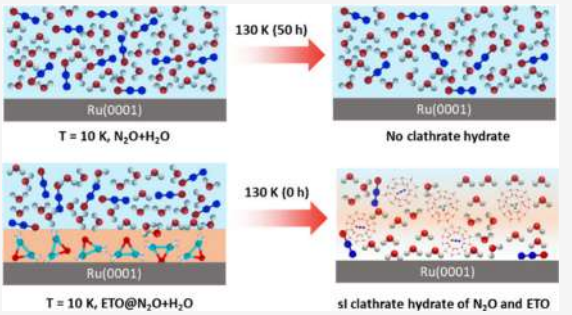
Secondary Guest-Driven Nucleation of N_2O Clathrate Hydrate in Amorphous Ice Mixture under Ultrahigh Vacuum

Bijesh K. Malla,[‡] Soham Chowdhury,[‡] Samir Kumar Nayak, Sofia Sara Baji, Teena J Mathew, Rabin Rajan J Methikkalam, Sharma S. R. K. C. Yamijala,* Rajnish Kumar,* and Thalappil Pradeep*

Cite This: *J. Phys. Chem. Lett.* 2025, 16, 12720−12727 Read Online

ACCESS | Metrics & More | Article Recommendations | Supporting Information

ABSTRACT: We report the first observation of nitrous oxide (N_2O) clathrate hydrate (CH) under ultrahigh vacuum (UHV) conditions using infrared spectroscopy. While nucleation of CHs from water and guest molecules either spontaneously or in the presence of promoters is well-established under high-pressure conditions, their occurrence under cryogenic UHV remains less understood, particularly in multiguest systems. In this study, binary and ternary ice mixtures of N_2O, ethylene oxide (ETO), dimethyl ether (DME), tetrahydrofuran (THF), and H_2O were investigated via thermal annealing at 130 K. The binary N_2O−H_2O system showed no signs of hydrate formation after 50 h of annealing, whereas the addition of ETO, DME, or THF led to immediate CH formation under identical conditions. This demonstrates a clear promoter-assisted heterogeneous nucleation mechanism. In situ reflection absorption infrared (RAIR) spectroscopy confirms that ETO facilitates the formation of structure I hydrates, incorporating both ETO and N_2O in the cages, while DME and THF promote larger-cage CHs. Density functional theory calculations support experimental RAIR results, which predict stronger host−guest interactions and blue shifts for small cages and weaker shifts for large cages. These findings offer new mechanistic insights into multiguest hydrate nucleation and establish N_2O CH formation under UHV as a relevant process in cryogenic and astrochemical environments.



Downloaded via INDIAN INST OF TECH MADRAS on December 29, 2025 at 03:20:12 (UTC).
See https://pubs.acs.org/sharingguidelines for options on how to legitimately share published articles.

Nitrous oxide (N_2O) is a potent greenhouse gas with a global warming potential approximately 300 times greater than that of carbon dioxide (CO_2) over a 100-year time scale.[1] Beyond its climatic impact, N_2O contributes to stratospheric ozone depletion through photodissociation.[2] According to the U.S. Environmental Protection Agency (EPA), anthropogenic sources accounted for about 5% of total greenhouse gas emissions in the United States in 2013.[3] Interestingly, N_2O is not confined to Earth; it has also been detected in interstellar regions such as Orion KL and Sagittarius B2, indicating that nitrogen−oxygen bond formation occurs under extreme conditions of the interstellar medium (ISM).[4,5] Recent observations from the James Webb Space Telescope (JWST) suggest the presence of condensed-phase N_2O in protostellar environments, further underscoring its astrochemical relevance.[6]

Considering the presence of N_2O in terrestrial and astrophysical environments, understanding its potential for physical trapping and chemical transformation in icy matrices is of significant interest. One mechanism by which volatile molecules such as N_2O may be sequestered is through clathrate hydrates (CHs). CHs are crystalline solids made of hydrogen-bonded water molecules that form polyhedral cages that encapsulate guest species such as CH_4, CO_2, ethane, etc.[7,8] These structures, which typically adopt structure I (sI), structure II (sII), or structure H (sH), naturally form under high-pressure and low-temperature conditions found in deep ocean sediments and planetary ices.[9,10] CHs are believed to play a major role in cometary outgassing events. The observed outgassing patterns in the Northern Hemisphere suggest that comet 67P's nucleus contains a combination of crystalline ice, CHs, and other ices, contradicting the hypothesis that its volatiles were primarily trapped in an amorphous ice phase.[11] Recent laboratory experiments have demonstrated that CHs can also form under UHV and cryogenic conditions, broadening the potential relevance of CHs to astrophysical ices.[12−14] For instance, thin-film clathrates of THF have been successfully synthesized and structurally confirmed via electron diffraction.[15]

Despite growing evidence for clathrate formation under nontraditional conditions, the fundamental process of nucleation remains poorly understood. Classical nucleation theory (CNT) suggests that hydrate formation begins once a critical cluster of host and guest molecules is formed.[16] In

Received: September 8, 2025
Revised: November 18, 2025
Accepted: November 24, 2025
Published: December 5, 2025



© 2025 American Chemical Society

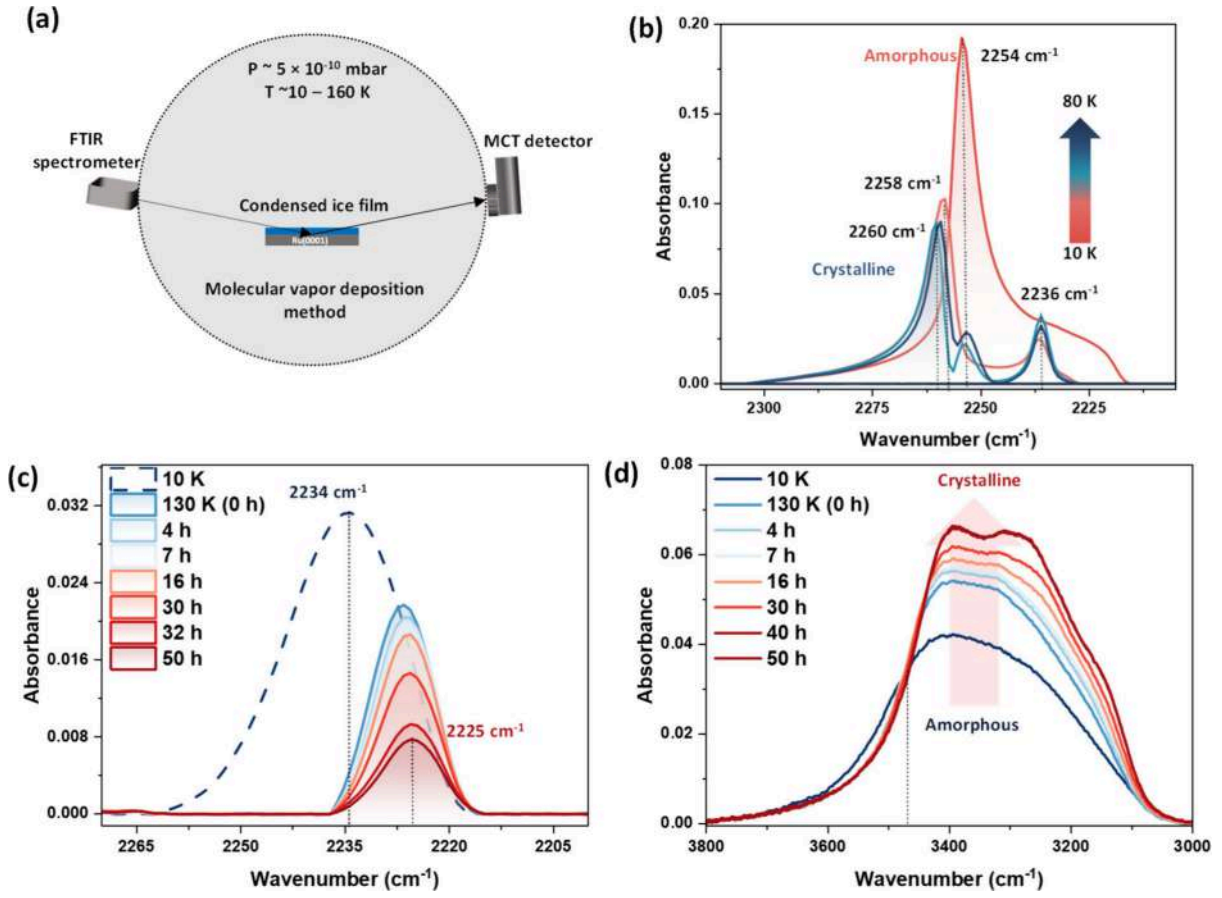


Figure 1. (a) A simplified schematic of the UHV instrument used for this work. (b) Temperature-dependent RAIR spectra of 150 ML of N_2O ice in the N−N−O asymmetric stretching region. Temperature- and time-dependent RAIR spectra of 300 ML of N_2O + H_2O ice in the N−N−O asymmetric stretching region (c) and in the O−H stretching region (d).

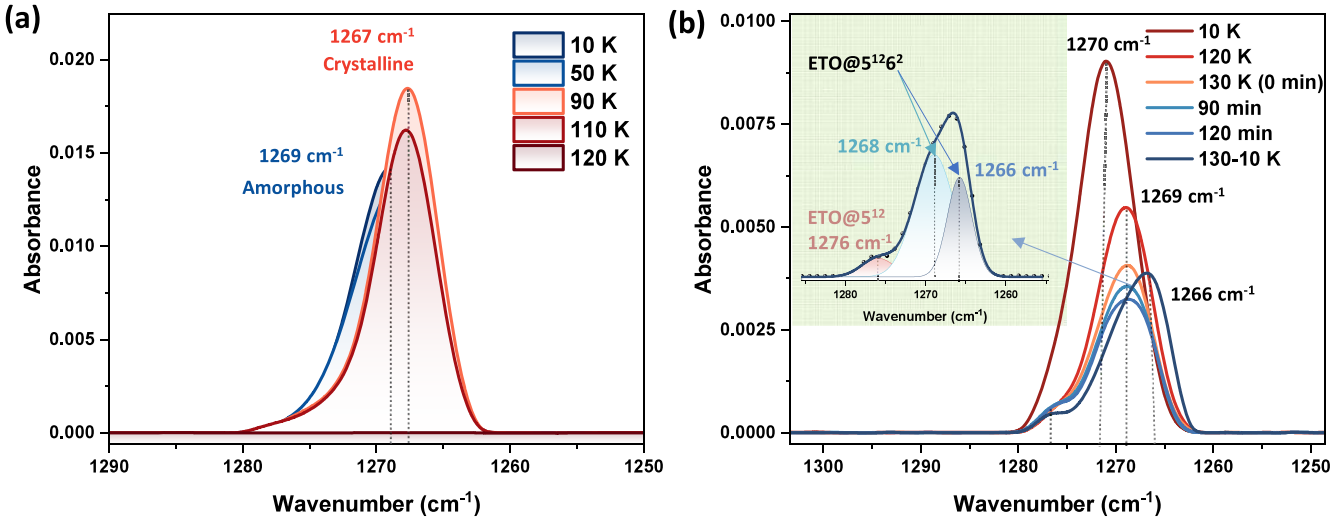


Figure 2. (a) Temperature-dependent RAIR spectra of ETO ice in the ring-breathing region. (b) RAIR spectra of ETO + H_2O ice in the ring-breathing region. The spectrum, acquired after annealing at 130 K for 2 h and subsequently cooling to 10 K, is deconvoluted into three distinct peaks located at 1276 cm^{-1} (red), 1268 cm^{-1} (sky blue), and 1266 cm^{-1} (blue).

contrast, simulations propose a two-step mechanism involving the formation of an amorphous precursor that later crystallizes into a stable hydrate structure.[17,18] Our prior work using amorphous mixtures of water and various guest molecules under UHV revealed that most CHs formed under these conditions are metastable,[19] often reverting to cubic or hexagonal ice.[20−22] Among the systems tested, only tetrahydrofuran (THF, C_4H_8O) consistently formed stable CHs, and these findings were attributed primarily to homogeneous nucleation processes.[15,23]

Building upon these observations, we turned our attention to N_2O, a known sI clathrate former under high-pressure

https://doi.org/10.1021/acs.jpclett.5c02778
J. Phys. Chem. Lett. 2025, 16, 12720−12727

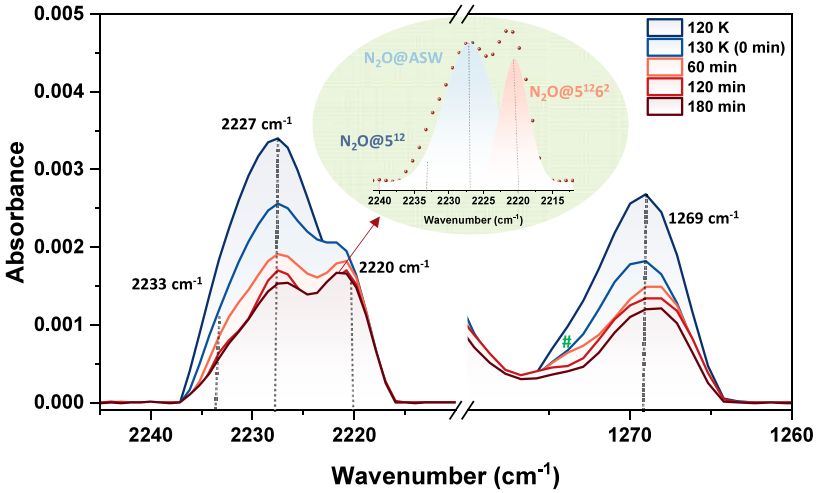


Figure 3. RAIR spectra of ETO@N_2O + H_2O showing the N−N−O asymmetric stretching region of N_2O and the ring-breathing mode of ETO. After 180 min, the N−N−O stretching band is deconvoluted into three components, with peaks centered at 2233 cm^{-1} (deep blue), 2227 cm^{-1} (light blue), and 2220 cm^{-1} (red). The peak labeled as # in the spectra in the ring breathing mode is attributed to the ETO occupied in the small cage.

Table 1. Calculated Infrared Frequencies of N_2O and ETO in the N−N−O Asymmetric Stretching Region and the Ring-Breathing Region

System	N_2O	$N_2O@5^{12}$	$N_2O@5^{12}6^2$	$N_2O@5^{12}6^4$
Frequency (cm^{-1})	2267.93	2286.69	2272.89	2269.74
System	**ETO**	**ETO@5^{12}**	**ETO@$5^{12}6^2$**	**ETO@$5^{12}6^4$**
Frequency (cm^{-1})	1257.19	1272.19	1262.70	1259.17

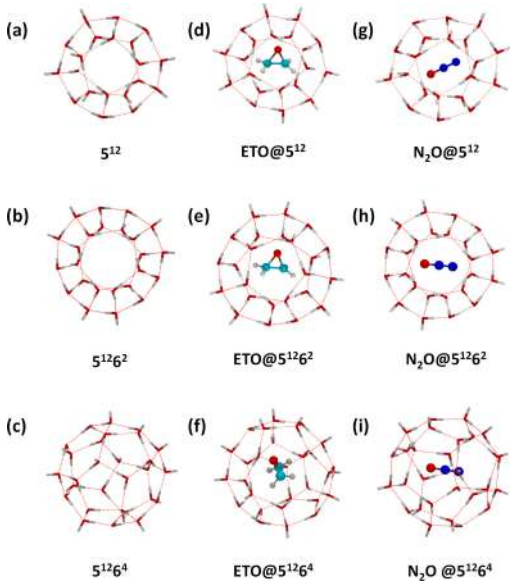


Figure 4. Optimized geometries of (a−c) empty 5^{12}, $5^{12}6^2$, and $5^{12}6^4$ CH cages; (d−f) ETO inside the 5^{12}, $5^{12}6^2$, and $5^{12}6^4$ CH cages; (g−i) nitrous oxide encaged in the 5^{12}, $5^{12}6^2$, and $5^{12}6^4$ CH cages.

conditions, as supported by X-ray diffraction and Raman data.[24−26] We aimed to investigate whether N_2O could form CHs from amorphous N_2O−H_2O ice mixtures under UHV and cryogenic conditions, which more closely resemble interstellar ice environments.[6] Surprisingly, N_2O alone failed to nucleate a clathrate phase in contrast to other guest molecules. To address this, we introduced ethylene oxide (ETO/C_2H_4O), a molecule previously shown to nucleate sI CHs under vacuum conditions, as a coguest.[27−29] Remarkably, as ETO initiated CH formation, N_2O got incorporated into the clathrate lattice, suggesting a conucleation mechanism or surface-mediated heterogeneous nucleation. This mechanism is further supported by additional experiments involving other known hydrate formers such as THF and dimethyl ether (DME/C_2H_6O).

This work presents the first IR spectroscopic evidence of the existence of N_2O CH under UHV conditions. The ability of N_2O to form mixed CHs with ETO extends the known range of CH-forming systems and offers important implications for astrochemistry. In particular, such mixed ices could serve as precursors for complex organic molecules, including amino acids and nucleobases, when exposed to ionizing radiation in space.[30] This study provides new insights into the physical chemistry of clathrate nucleation and potential pathways for molecular evolution in icy astrophysical environments.

All experiments were conducted using a custom-built ultrahigh vacuum (UHV) chamber, as described in detail in our previous study (Figure 1a).[31] Thin ice films of N_2O, H_2O, ETO, DME, and THF were prepared by background vapor deposition. The ice thickness was estimated based on the ion gauge sensitivity factor, deposition time, and background pressure. Quantum chemical calculations for free and encapsulated N_2O and ETO were performed using the B3LYP[32] functional with the 6-311++G(d,p)[33] basis set. Additional methodological details are provided in the Supporting Information.

At the outset, 150 ML of N_2O ice were deposited on a Ru(0001) substrate at 10 K. Figure 1b and Figure S1 present the temperature-dependent RAIR spectra of the deposited N_2O ice in the N−N−O asymmetric and symmetric stretching region. At 10 K, a sharp peak at 2254 cm^{-1} and a broad feature in the lower wavenumber region (2245−2215 cm^{-1}) were observed, indicating that the N_2O ice is in an amorphous state. Since N_2O is structurally similar to CO_2, it exhibits two distinct peaks for the ν_3 stretching mode, corresponding to the transverse optical (TO) and longitudinal optical (LO) modes. The higher wavenumber feature (2254 cm^{-1}) corresponds to the LO mode, while the lower wavenumber broad peak

https://doi.org/10.1021/acs.jpclett.5c02778
J. Phys. Chem. Lett. 2025, 16, 12720−12727

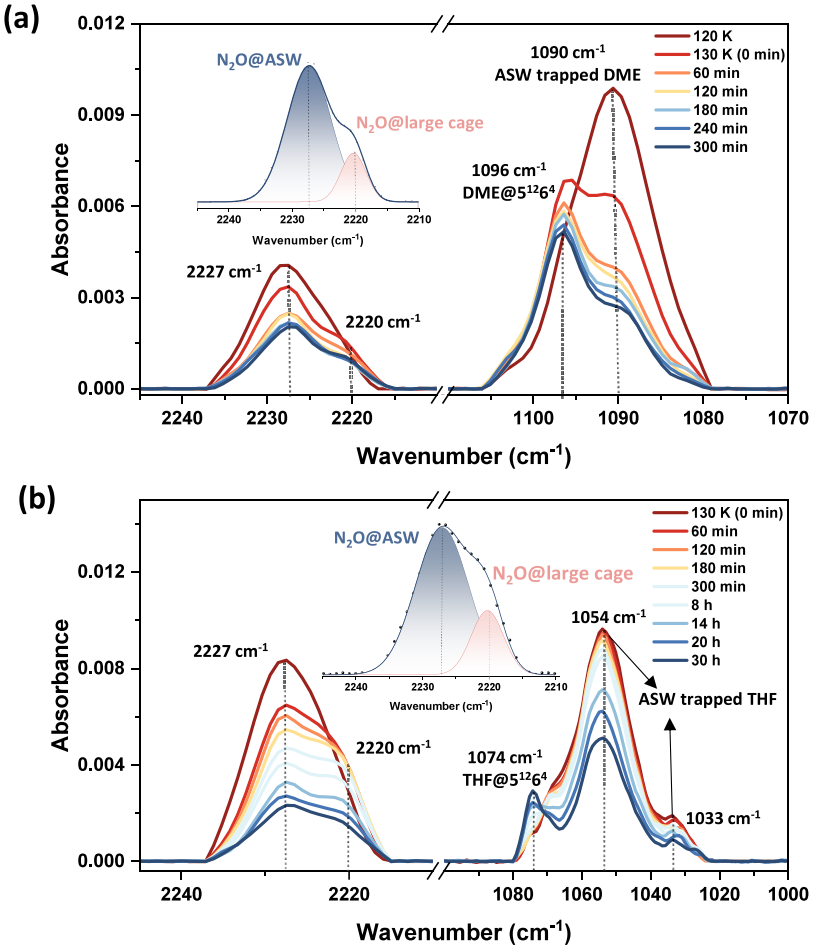


Figure 5. (a) RAIR spectra of DME@N_2O + H_2O in the N−N−O asymmetric stretching region of N_2O and the C−O−C asymmetric stretching region of DME. After 300 min, the N−N−O stretching band is deconvoluted into two components, centered at 2227 cm^{-1} (highlighted in deep blue) and 2220 cm^{-1} (highlighted in red). (b) RAIR spectra of THF@N_2O + H_2O in the N−N−O asymmetric stretching region of N_2O and the C−O asymmetric stretching region of THF. Similarly, the spectrum after 300 min shows the N−N−O stretching band resolved into two components at 2227 cm^{-1} (deep blue) and 2220 cm^{-1} (red).

represents the TO mode.[34−37] The RAIRS measurement was performed at a grazing incidence angle of 82.75°,[31] which enhances the contribution from the LO mode, thus explaining the higher intensity of the 2254 cm^{-1} peak. We note that the experiments were performed on a Ru metal surface, where the surface dipole selection rule suppresses the TO mode, thereby making the LO mode more prominent.[38] Consistent with this substrate dependence, Cassidy et al.[39] reported two distinct infrared spectra for the N−N−O asymmetric stretch of N_2O on silica versus Cu: the silica support retains TO activity, whereas the metallic Cu surface, subject to the same selection rule as Ru, leads to an LO-dominated profile.[39]

Upon annealing the N_2O ice to its desorption temperature (~80 K), the amorphous ice undergoes crystallization, likely forming cubic crystalline ice in two stages.[40,41] During this process, the 2254 cm^{-1} peak splits into two components (2258 and 2254 cm^{-1}), and its intensity decreases. The broad peak also sharpens, evolving into a distinct peak at 2236 cm^{-1}. This decrease in intensity is attributed to dipole alignment during crystallization, which reduces the dipole moment fluctuations and hence the infrared absorption. Similar behavior has been previously reported using various spectroscopic techniques.[42,43] In the symmetric stretching region (Figure S1), a broad peak at 1296 cm^{-1} indicates the amorphous phase and a sharp peak at 1299 cm^{-1} indicates the crystalline phase. We note here that 150 ML of N_2O ice RAIR spectra are also given in our earlier paper,[44] Supporting Information, but a detailed analysis of spectral features has not been done.

To investigate the formation of N_2O CH, 300 ML of a N_2O:H_2O ice mixture in a 1:5 ratio was codeposited and thermally annealed to 130 K, where it was held for 50 h. During the initial warming from 10 to 130 K, a red shift was observed, accompanied by a decrease in the peak intensity of the N−N−O asymmetric stretch (Figure 1c, Figure S2), which is attributed to the desorption of N_2O from the ice matrix. Upon annealing at 130 K, the band intensity decreases with no further frequency change, indicating no new interaction, only a declining N_2O/H_2O ratio. Thus, once the frequency stabilizes, the number of H_2O molecules coordinated to N_2O appears to be constant. Additionally, in the symmetric stretching region, the same trend was observed, where we only saw a decrease in the peak position at 1299 cm^{-1} (Figure S3). We note here that the available data do not allow us to distinguish specific N_2O−H_2O conformations, so we refrain from making a conformer assignment. Additional temperature-dependent experiments with 1:10 and 1:20 of N_2O:H_2O (Figure S4) ratios showed similar behavior, peak red-shifting and decreasing intensity, likely due to enhanced hydrogen bonding between the N_2O

https://doi.org/10.1021/acs.jpclett.5c02778
J. Phys. Chem. Lett. 2025, 16, 12720−12727

and surrounding water molecules.[35] Unlike our earlier work, N_2O does not exhibit facile homogeneous nucleation of CHs. In the O−H stretching region (Figure 1d), sharpening of the peaks was observed, consistent with the formation of crystalline water ice.[45] At low N_2O concentrations in H_2O ice, the O−H stretching region is only weakly perturbed. Increasing the mixing ratio to 1:1 (N_2O:H_2O) produces a prominent dangling O−H feature at 3652 cm^{-1} (Figure S5). A weaker hump at 3491 cm^{-1} is also observed, attributable to N_2O−H_2O interactions, although its specific origin remains unclear. Upon warming to 100 K, both peaks vanish, indicating compaction of the ice matrix and reduced N_2O content. These experiments show that N_2O CH does not form spontaneously from an N_2O−H_2O ice mixture under UHV conditions. Consequently, we focused on the formation of sI ETO CH, which was later used as a promoter for N_2O CH formation.

To begin, pure ETO ice was investigated under UHV conditions. Figure 2a shows the temperature-dependent RAIR spectra of ETO in the ring-breathing region (ν_3). At 10 K, vapor-deposited ETO formed an amorphous ice, evident from a broad peak centered at 1269 cm^{-1}. Upon annealing to 90 K, crystallization occurred, as indicated by the emergence of a sharp peak at 1267 cm^{-1}.[46] In the CH_2 bending region, the initially broad band sharpens and resolves into two peaks at 1466 and 1460 cm^{-1} (Figure S6a). Upon further warming to 120 K, ETO completely desorbs from the surface.

To study the formation of ETO CH, approximately 300 ML of ETO−H_2O (1:5) vapor mixture was codeposited and annealed to 130 K (Figure 2b). It is well-established that ETO forms sI CH under both high-pressure and vacuum conditions, and its characteristic RAIR spectra are also well-documented.[47−52] In particular, the ring-breathing mode of ETO in sI CHs typically exhibits a doublet with a 2 cm^{-1} splitting, attributed to ETO molecules occupying large cages in two distinct orientations.[48] A smaller hump, ∼13 cm^{-1} blue-shifted from the main peak, has been assigned to ETO trapped in smaller cages.[48] Although this splitting is not always fully resolved at elevated temperatures, it becomes clearer at lower temperatures due to reduced thermal broadening.[48,51]

In our experiment, after annealing to 130 K, we observed a broadened peak with a small shoulder at around 1276 cm^{-1} (Figure 2b), suggesting the formation of clathrate structures. Upon cooling the sample back down to 10 K, a clearer spectral splitting emerged with increased peak intensity, indicative of more ordered structural arrangements. Deconvolution of the spectrum revealed two sharp peaks at 1268 cm^{-1} and 1266 cm^{-1}, along with a smaller intensity feature at 1276 cm^{-1} (Figure 2b). This splitting is possible due to the different orientation of ETO inside sI large cages.[47] The peak positions are consistent with those in earlier reports. Bertie and Othen[48] observed features at 1268 and 1270 cm^{-1}, while Fleyfel and Devlin[47] reported 1266 and 1268 cm^{-1} for ETO in a $5^{12}6^2$ cage. Taken together, these observations suggest the facile formation of ETO CH from the amorphous ice mixture at 130 K. In the CH_2 bending region (Figure S6b), no definitive changes were observed due to very low intensity. Concurrently, crystallization of amorphous solid water (ASW) was evident, as indicated by the sharpening of features in the O−H stretching region (Figure S7). While ETO CH formation under vacuum has been previously reported,[48,53] its formation from in ASW under UHV conditions has not been demonstrated. One motivation for studying ETO CH in this manner is to examine whether the surface of ETO CH can facilitate the nucleation of N_2O CH.

In the first attempt, we failed to create N_2O CH by thermal annealing the N_2O−H_2O ice mixture. Later, we took a N_2O−H_2O ice mixture on top of ETO ice and, through thermal annealing, created a mixture of ETO−N_2O−H_2O ice at 130 K (Figure 3). When ETO started to form sI CH, a clear splitting was observed in the N−N−O asymmetric stretching region. The peak at 2227 cm^{-1} was split to make a new peak at 2220 cm^{-1}, and a small hump was observed at 2233 cm^{-1}. The peak intensity at 2233 cm^{-1} decreases relatively slowly (and remains nearly constant over 120−180 min), compared to the peak intensity of 2227 cm^{-1} (Figure 3). This behavior indicates two N_2O populations, with the persistent component stabilized in well-defined sites consistent with N_2O trapped in CH cages, whereas the faster-decreasing band reflects more weakly bound ASW-trapped N_2O that desorbs. The area under the two peaks (at 2233 cm^{-1} and 2220 cm^{-1}) gave a ratio of 1:4.5, which is close to the population distribution in the small and large cages of sI CH. In the symmetric stretching region (Figure S8) two new peaks were observed at 1282 and 1292 cm^{-1}. It is worth noting that peak deconvolution can not be done for symmetric stretch due to a poor signal-to-noise ratio. Additionally, in the ring-breathing mode of ETO, a broadened peak at 1269 cm^{-1} and a small hump at 1276 cm^{-1} (Figure 3) were observed, consistent with previous observations of pure ETO sI CH.[48] A Raman spectroscopic study reported by Yang et al.[54] shows the difference between the large cage and small cage peak is 13 cm^{-1} (for asymmetric stretch) and 8 cm^{-1} (for symmetric stretch), respectively, which closely match with the current IR study. This proves the formation of sI N_2O CH in the presence of ETO CH.

The nucleation behavior of CH from N_2O is notably complex. In the absence of ETO, prolonged thermal annealing over several hours failed to induce CH formation; instead, the ASW began to crystallize. This observation clearly indicates that the homogeneous nucleation of CH from an amorphous N_2O:H_2O ice mixture is not feasible without the presence of a third component. However, once the sI CH formation of ETO commenced in the ETO−N_2O−H_2O ice mixture, CH formation from N_2O was also observed. Two possible nucleation pathways can be considered: (i) simultaneous nucleation of ETO and N_2O hydrates due to their homogeneous distribution in the ice matrix, or (ii) heterogeneous nucleation of N_2O hydrate on the surface of the preformed ETO hydrate. Given the limited experimental technique, it remains challenging to distinguish between these mechanisms or to rule out the possibility that both are occurring concurrently.

To support the IR results, we carried outgas-phase DFT calculations for N_2O and ETO in sI and sII CH cages. The optimized geometries of the empty 5^{12}, $5^{12}6^2$, and $5^{12}6^4$ CH cages, as well as those containing ETO and N_2O, are shown in Figure 4. The vibrational frequencies of the isolated ethylene oxide and nitrous oxide molecules, along with their frequencies when confined within the three different cages, are shown in Table 1. Free N_2O exhibits an asymmetric stretch at 2267.93 cm^{-1}, consistent with a prior report,[55] and ETO shows ring breathing mode at 1257.19 cm^{-1}. When these molecules are confined within the smaller 5^{12} CH cage, they exhibit blue shifts of 18.76 cm^{-1} and 15 cm^{-1} for N_2O and ETO, respectively. However, when placed inside the comparatively larger $5^{12}6^2$ and $5^{12}6^4$ CH cages, the N_2O molecule shows

https://doi.org/10.1021/acs.jpclett.5c02778
J. Phys. Chem. Lett. 2025, 16, 12720−12727

lower blue shifts of 4.96 cm^{-1} and 1.81 cm^{-1}, while the ETO molecule exhibits blue shifts of 5.51 cm^{-1} and 1.98 cm^{-1}, respectively. The molecules exhibit a stronger blue shift when confined within smaller cages due to steric restrictions that distort molecular bonds and elevate vibrational frequencies. In contrast, larger cages provide greater spatial freedom and structural flexibility, minimizing steric effects and resulting in only slight changes in vibrational modes.[56] It is important to note that no chemical bond formation was observed between the water molecules of the CH cages and guest molecules (N_2O and ETO). Though we observed distortion of the CH cages, we did not observe cage breakage while guest molecules were confined in them. Hydrogen bonding between the oxygen and hydrogen molecules forming the CH cages and weak interaction between the cage and guest molecules provide the stability to molecule-confined CH cages.[57]

To further prove the heterogeneous nucleation of N_2O CH in amorphous ice, we have used two stable sII CH former molecules, DME and THF (Figure 5).[58] Both of the molecules are known to form sII large cage CH in UHV under cryogenic conditions. We deposited sequentially THF/DME and H_2O + N_2O ice mixture at 10 K and annealed the sample at 130 K for a few hours. Figure 5 shows IR spectra of DME@H_2O+N_2O (Figure 5a) and THF@H_2O+N_2O (Figure 5b) ice mixture in the N−N−O and C−O asymmetric stretch. Previous studies showed that THF and DME form sII CH where the $5^{12}6^4$ cage is occupied by the THF and DME with a distinct assigned IR peak 1074 cm^{-1} and 1096 cm^{-1}.[22,53,59] The peaks at 1090 cm^{-1} and 1033/1054 cm^{-1} are attributed to DME and THF molecules trapped within ASW. In this system, during the formation of THF/DME CHs in the N−N−O asymmetric stretching region a new peak arises at 2220 cm^{-1}, which can be assigned to the large cages. Interestingly, we have not observed any peak around 2233 cm^{-1}, which indicates the absence of small cages. Here, it is difficult to assign whether this assignment occurs due to the large cages of sI or sII. It is worth noting that N_2O is not going to preexisting vacant small cages created by THF/DME. These additional experiments demonstrate that, without any incubation time at 130 K, N_2O can spontaneously form a CH only in the presence of supporting guest molecules such as ETO, DME, or THF, which facilitate nucleation.

In conclusion, we have demonstrated the formation of N_2O and ETO CHs under UHV and cryogenic conditions. While the formation of ETO CHs in high vacuum was previously reported by the Devlin group,[28,58] to the best of our knowledge, this is the first report of ETO CH formation under such conditions. Notably, we also present the first IR spectra of N_2O CHs. A key conclusion from this study is that homogeneous nucleation of N_2O CH does not occur readily from an amorphous N_2O−H_2O ice mixture, even upon annealing to 130 K. However, when codeposited with a secondary guest molecule known to spontaneously form clathrates, such as ETO, DME, or THF, N_2O readily forms CHs upon annealing. In the presence of ETO, N_2O forms sI CHs, while in the presence of DME or THF, N_2O appears to occupy larger cages; however, due to limited spectroscopic evidence, we could not conclusively assign these to either sI or sII CHs. To support our experimental observations, DFT calculations were performed for free and encaged N_2O and ETO molecules within 5^{12}, $5^{12}6^2$, and $5^{12}6^4$ cages. The calculated IR spectra indicate that molecules confined in smaller cages experience greater steric hindrance, resulting in larger blue shifts compared to those in larger cages.

■ ASSOCIATED CONTENT

Supporting Information

The Supporting Information is available free of charge at https://pubs.acs.org/doi/10.1021/acs.jpclett.5c02778.

Experimental section (including experimental setup, materials and reagents, and sample preparation) and temperature and time-dependent RAIR spectra (PDF)

Transparent Peer Review report available (PDF)

■ AUTHOR INFORMATION

Corresponding Authors

Sharma S. R. K. C. Yamijala − *Department of Chemistry, Indian Institute of Technology Madras, Chennai 600036, India;* orcid.org/0000-0003-1773-9226; Email: yamijala@iitm.ac.in

Rajnish Kumar − *International Centre for Clean Water, IIT Madras Research Park, Chennai 600113, India; Department of Chemical Engineering and School of Sustainability, Indian Institute of Technology Madras, Chennai 600036, India;* orcid.org/0000-0002-4172-2638; Email: rajnish@iitm.ac.in

Thalappil Pradeep − *DST Unit of Nanoscience (DST UNS) and Thematic Unit of Excellence (TUE), Department of Chemistry, Indian Institute of Technology Madras, Chennai 600036, India; International Centre for Clean Water, IIT Madras Research Park, Chennai 600113, India;* orcid.org/0000-0003-3174-534X; Email: pradeep@iitm.ac.in

Authors

Bijesh K. Malla − *DST Unit of Nanoscience (DST UNS) and Thematic Unit of Excellence (TUE), Department of Chemistry, Indian Institute of Technology Madras, Chennai 600036, India; Department of Chemical Engineering, Indian Institute of Technology Madras, Chennai 600036, India;* orcid.org/0009-0005-1148-0884

Soham Chowdhury − *DST Unit of Nanoscience (DST UNS) and Thematic Unit of Excellence (TUE), Department of Chemistry, Indian Institute of Technology Madras, Chennai 600036, India*

Samir Kumar Nayak − *Department of Chemistry, Indian Institute of Technology Madras, Chennai 600036, India*

Sofia Sara Baji − *Department of Chemistry, Mar Ivanios College, Thiruvananthapuram, Kerala 695015, India*

Teena J Mathew − *Department of Chemistry, Mar Ivanios College, Thiruvananthapuram, Kerala 695015, India*

Rabin Rajan J Methikkalam − *Department of Chemistry, Mar Ivanios College, Thiruvananthapuram, Kerala 695015, India*

Complete contact information is available at: https://pubs.acs.org/10.1021/acs.jpclett.5c02778

Author Contributions

‡B.K.M. and S.C. contributed equally. B.K.M. designed the experiments. B.K.M., S.C., S.S.B., and T.J.M. performed the experiments. B.K.M. and S.C. analyzed the results. T.P. and R.K. supervised the progress. S.K.N. and S.S.R.K.C.Y. performed the quantum chemical calculations. B.K.M. wrote the first draft of the manuscript. The final version of the manuscript was prepared with the contributions of all authors.

Notes

The authors declare no competing financial interest.

■ ACKNOWLEDGMENTS

We acknowledge the Science and Engineering Research Board (SERB), Department of Science and Technology (DST), and Government of India for research funding. T.P. acknowledges funding from the Centre of Excellence (CoE) on Molecular Materials and Functions under the Institution of Eminence scheme of IIT Madras. S.S.R.K.C.Y. acknowledges the financial support of IIT Madras through the MPHASIS faculty fellowship and its new faculty support grants NFSG (IP2021/0972CY/NFSC008973), NFIG (RF2021/0577CY/NFIG008973), and Anusandhan National Research Foundation (ANRF). S.C. thanks IITM for their research fellowship. S.K.N. thanks the Prime Minister's Research Fellowship (PMRF) for his research fellowship.

■ REFERENCES

(1) Griffis, T. J.; Chen, Z.; Baker, J. M.; Wood, J. D.; Millet, D. B.; Lee, X.; Venterea, R. T.; Turner, P. A. Nitrous Oxide Emissions Are Enhanced in a Warmer and Wetter World. *Proc. Natl. Acad. Sci. U. S. A.* **2017**, *114* (45), 12081−12085.

(2) Portmann, R. W.; Daniel, J. S.; Ravishankara, A. R. Stratospheric Ozone Depletion Due to Nitrous Oxide: Influences of Other Gases. *Philos. Trans. R. Soc. B Biol. Sci.* **2012**, *367* (1593), 1256−1264.

(3) *Climate Change 2022 - Mitigation of Climate Change*; Intergovernmental Panel on Climate Change (IPCC), Ed.; Cambridge University Press, 2023.

(4) Ziurys, L. M.; Apponi, A. J.; Hollis, J. M.; Snyder, L. E. Detection of Interstellar N_2O: A New Molecule Containing an N-O Bond. *Astrophys. J.* **1994**, *436*, L181.

(5) Halfen, D. T.; Apponi, A. J.; Ziurys, L. M. Evaluating the N/O Chemical Network: The Distribution of N_2O and NO in the Sagittarius B2 Complex. *Astrophys. J.* **2001**, *561* (1), 244−253.

(6) Nazari, P.; Rocha, W. R. M.; Rubinstein, A. E.; Slavicinska, K.; Rachid, M. G.; Van Dishoeck, E. F.; Megeath, S. T.; Gutermuth, R.; Tyagi, H.; Brunken, N.; et al. Hunting for Complex Cyanides in Protostellar Ices with the JWST - A Tentative Detection of CH3CN and C2H5CN. *Astron. Astrophys.* **2024**, *686*, A71.

(7) Sloan, E. D., Jr.; Koh, C. A.; Koh, C. A. *Clathrate Hydrates of Natural Gases*; CRC Press, 2007.

(8) Sloan, E. D. Fundamental Principles and Applications of Natural Gas Hydrates. *Nature.*; Nature Publishing Group November 20, 2003; pp 353−359.

(9) Sloan, E. D. J.; Koh, C. A. Hydrates in the Earth. *Clathrate Hydrates of Natural Gases* **2007**, *20074156*, 537−642.

(10) Sloan, E. D. J.; Koh, C. A. Introduction: Clathrate Hydrates of Natural Gases. *Clathrate Hydrates Nat. Gases* **2008**, I−XXV.

(11) Luspay-Kuti, A.; Mousis, O.; Hässig, M.; Fuselier, S. A.; Lunine, J. I.; Marty, B.; Mandt, K. E.; Wurz, P.; Rubin, M. The Presence of Clathrates in Comet 67P/Churyumov-Gerasimenko. *Sci. Adv.* **2016**, *2* (4), No. e1501781.

(12) Ghosh, J.; Vishwakarma, G.; Kumar, R.; Pradeep, T. Formation and Transformation of Clathrate Hydrates under Interstellar Conditions. *Acc. Chem. Res.* **2023**, *56* (16), 2241−2252.

(13) Malla, B. K.; Vishwakarma, G.; Chowdhury, S.; Selvarajan, P.; Pradeep, T. Formation of Ethane Clathrate Hydrate in Ultrahigh Vacuum by Thermal Annealing. *J. Phys. Chem. C* **2022**, *126* (42), 17983−17989.

(14) Tychengulova, A.; Katpayeva, K.; Shomshekova, S.; Ibragimova, S.; Golikov, O.; Yerezhep, D.; Sokolov, D.; Aldiyarov, A. Laboratory Studies of the Clathrate Hydrate Formation in the Carbon Dioxide-Water Mixtures at Interstellar Conditions. *ACS Omega* **2025**, *10* (1), 1237−1248.

(15) Malla, B. K.; Yang, D.-S.; Pradeep, T. Growth of Clathrate Hydrates in Nanoscale Ice Films Observed Using Electron Diffraction and Infrared Spectroscopy. *J. Phys. Chem. Lett.* **2025**, *16* (1), 365−371.

(16) Khurana, M.; Yin, Z.; Linga, P. A Review of Clathrate Hydrate Nucleation. *ACS Sustain. Chem. Eng.* **2017**, *5* (12), 11176−11203.

(17) Guo, G.-J.; Zhang, Z. Open Questions on Methane Hydrate Nucleation. *Commun. Chem.* **2021**, *4* (1), 102.

(18) Jacobson, L. C.; Molinero, V. Can Amorphous Nuclei Grow Crystalline Clathrates? The Size and Crystallinity of Critical Clathrate Nuclei. *J. Am. Chem. Soc.* **2011**, *133* (16), 6458−6463.

(19) Malla, B. K.; Chowdhury, S.; Vishwakarma, G.; Kumar, R.; Pradeep, T. Dissociation and Reformation of CO2 Clathrate Hydrate Cages in Amorphous Ice Thin Film under Ultrahigh Vacuum. *J. Phys. Chem. Lett.* **2025**, *16* (20), 4982−4989.

(20) Chowdhury, S.; Malla, B. K.; Vishwakarma, G.; Nyayban, A.; Pradeep, T. Composition-Dependent Formation and Dissociation of Structure I and Structure II Clathrate Hydrates of Trimethylene Oxide in Ultrahigh Vacuum. *J. Phys. Chem. C* **2025**, *129* (19), 8937−8945.

(21) Vishwakarma, G.; Malla, B. K.; Chowdhury, S.; Khandare, S. P.; Pradeep, T. Existence of Acetaldehyde Clathrate Hydrate and Its Dissociation Leading to Cubic Ice under Ultrahigh Vacuum and Cryogenic Conditions. *J. Phys. Chem. Lett.* **2023**, *14* (23), 5328−5334.

(22) Malla, B. K.; Vishwakarma, G.; Chowdhury, S.; Nayak, S. K.; Yamijala, S. S. R. K. C.; Pradeep, T. Formation and Dissociation of Dimethyl Ether Clathrate Hydrate in Interstellar Ice Mimics. *J. Phys. Chem. C* **2024**, *128* (6), 2463−2470.

(23) Ghosh, J.; Bhuin, R. G.; Ragupathy, G.; Pradeep, T. Spontaneous Formation of Tetrahydrofuran Hydrate in Ultrahigh Vacuum. *J. Phys. Chem. C* **2019**, *123* (26), 16300−16307.

(24) Sugahara, T.; Kawazoe, A.; Sugahara, K.; Ohgaki, K. High-Pressure Phase Equilibrium and Raman Spectroscopic Studies on the Nitrous Oxide Hydrate System. *J. Chem. Eng. Data* **2009**, *54* (8), 2301−2303.

(25) Takeya, S.; Hachikubo, A. Crystal Structure and Guest Distribution of N2O Hydrate Determined by Powder X-Ray Diffraction Measurements. *Cryst. Growth Des.* **2022**, *22* (2), 1345−1351.

(26) Sun, N.; Li, Y.; Qiu, N.; Du, S. Ab Initio Studies of Structural and Mechanical Properties of NH 3, NO, and N 2 O Hydrates. *ACS Omega* **2023**, *8* (24), 22018−22025.

(27) Tse, J. S.; McKinnon, W. R.; Marchi, M. Thermal Expansion of Structure I Ethylene Oxide Hydrate. *J. Phys. Chem.* **1987**, *91* (15), 4188−4193.

(28) Maşlakcı, Z.; Devlin, J. P.; Uras-Aytemiz, N. H-Bonding Behavior of Ethylene Oxide within the Clathrate Hydrates Revisited: Experiment and Theory. *Chem. Phys. Lett.* **2020**, *754* (May), 137728.

(29) Bauer, R. P. C.; Ravichandran, A.; Tse, J. S.; Appathurai, N.; King, G.; Moreno, B.; Desgreniers, S.; Sammynaiken, R. In Situ X-Ray Diffraction Study on Hydrate Formation at Low Temperature in a High Vacuum. *J. Phys. Chem. C* **2021**, *125* (48), 26892−26900.

(30) Zang, X.; Ueno, Y.; Kitadai, N. Photochemical Synthesis of Ammonia and Amino Acids from Nitrous Oxide. *Astrobiology* **2022**, *22* (4), 387−398.

(31) Bag, S.; Bhuin, R. G.; Methikkalam, R. R. J.; Pradeep, T.; Kephart, L.; Walker, J.; Kuchta, K.; Martin, D.; Wei, J. Development of Ultralow Energy (1−10 EV) Ion Scattering Spectrometry Coupled with Reflection Absorption Infrared Spectroscopy and Temperature Programmed Desorption for the Investigation of Molecular Solids. *Rev. Sci. Instrum.* **2014**, *85* (1), 014103.

(32) Becke, A. D. Density-functional Thermochemistry. III. The Role of Exact Exchange. *J. Chem. Phys.* **1993**, *98* (7), 5648−5652.

(33) Krishnan, R.; Binkley, J. S.; Seeger, R.; Pople, J. A. Self-consistent Molecular Orbital Methods. XX. A Basis Set for Correlated Wave Functions. *J. Chem. Phys.* **1980**, *72* (1), 650−654.

(34) Laane, J.; Ohlsen, J. R. Characterization of Nitrogen Oxides by Vibrational Spectroscopy. *Prog. Inorg. Chem.* **1980**, *27*, 465−513.

(35) Gimmler, G.; Havenith, M. High-Resolution IR Spectroscopy of the N2O-H2O and N_2O-D_2O van Der Waals Complexes. *J. Mol. Spectrosc.* **2002**, *216* (2), 315−321.

(36) Kumi, G.; Malyk, S.; Hawkins, S.; Reisler, H.; Wittig, C. Amorphous Solid Water Films: Transport and Guest-Host Interactions with CO_2 and N_2O Dopants. *J. Phys. Chem. A* **2006**, *110* (6), 2097−2105.
(37) Hudson, R. L.; Loeffler, M. J.; Gerakines, P. A. Infrared Spectra and Band Strengths of Amorphous and Crystalline N2O. *J. Chem. Phys.* **2017**, *146* (2), 24304.
(38) Elisabetta Palumbo, M.; Baratta, G. A.; Collings, M. P.; McCoustra, M. R. S. The Profile of the 2140 Cm^{-1} Solid CO Band on Different Substrates. *Phys. Chem. Chem. Phys.* **2006**, *8* (2), 279−284.
(39) Cassidy, A.; Jørgensen, M. R. V.; Rosu-Finsen, A.; Lasne, J.; Jørgensen, J. H.; Glavic, A.; Lauter, V.; Iversen, B. B.; McCoustra, M. R. S.; Field, D. Dipole-Oriented Molecular Solids Can Undergo a Phase Change and Still Maintain Electrical Polarization. *J. Phys. Chem. C* **2016**, *120* (42), 24130−24136.
(40) Cardini, G.; Signorini, G. F.; Salvi, P. R.; Righini, R. Molecular Dynamics and Head-Tail Disorder in the Raman Spectrum of Crystalline N2O. *Chem. Phys. Lett.* **1987**, *142* (6), 570−574.
(41) Mills, R. L.; Olinger, B.; Cromer, D. T.; LeSar, R. Crystal Structures of N2O to 12 GPa by X-ray Diffraction. *J. Chem. Phys.* **1991**, *95* (7), 5392−5398.
(42) Balog, R.; Cicman, P.; Jones, N. C.; Field, D. Spontaneous Dipole Alignment in Films of N_2O. *Phys. Rev. Lett.* **2009**, *102* (7), 073003.
(43) Mifsud, D. V.; Hailey, P. A.; Herczku, P.; Sulik, B.; Juhász, Z.; Kovács, S. T. S.; Kaňuchová, Z.; Ioppolo, S.; McCullough, R. W.; Paripás, B.; Mason, N. J. Comparative Electron Irradiations of Amorphous and Crystalline Astrophysical Ice Analogues. *Phys. Chem. Chem. Phys.* **2022**, *24* (18), 10974−10984.
(44) Malla, B. K.; Chowdhury, S.; Paliwal, D.; K. M, H.; Vishwakarma, G.; Methikkalam, R. R. J.; Pradeep, T. Simulated Interstellar Photolysis of N_2O Ice: Selectivity in Photoproducts. *J. Phys. Chem. C* **2025**, *129* (2), 1120−1128.
(45) Smith, R. S.; Matthiesen, J.; Knox, J.; Kay, B. D. Crystallization Kinetics and Excess Free Energy of H_2O and D_2O Nanoscale Films of Amorphous Solid Water. *J. Phys. Chem. A* **2011**, *115* (23), 5908−5917.
(46) Hudson, R. L.; Gerakines, P. A.; Yarnall, Y. Y. Infrared Spectra and Optical Constants of Astronomical Ices: V. Cyclopropane and Ethylene Oxide. *Icarus* **2023**, *396*, 115499.
(47) Fleyfel, F.; Devlin, J. P. FT-IR Spectra of 90 K Films of Simple, Mixed, and Double Clathrate Hydrates of Trimethylene Oxide, Methyl Chloride, Carbon Dioxide, Tetrahydrofuran, and Ethylene Oxide Containing Decoupled D_2O. *J. Phys. Chem.* **1988**, *92* (3), 631−635.
(48) Bertie, J. E.; Othen, D. A. The Infrared Spectrum of Ethylene Oxide Clathrate Hydrate at 100°K between 4000 and 360 Cm^{-1}. *Can. J. Chem.* **1973**, *51* (8), 1159−1168.
(49) Yang, X.; Du, S.; Hao, Y.; Xu, J. Molecular Dynamics Simulation of Promoting Nucleation of CO 2 Hydrate by Ethylene Oxide and Tetrahydrofuran. *IOP Conf. Ser. Earth Environ. Sci.* **2021**, *675* (1), 012183.
(50) Fleyfel, F.; Devlin, J. P. Carbon Dioxide Clathrate Hydrate Epitaxial Growth: Spectroscopic Evidence for Formation of the Simple Type-II CO_2 Hydrate. *J. Phys. Chem.* **1991**, *95* (9), 3811−3815.
(51) Cwiklik, L.; Devlin, J. P. Hindering of Rotational Motion of Guest Molecules in the Type I Clathrate Hydrate. *Chem. Phys. Lett.* **2010**, *494* (4−6), 206−212.
(52) Williams, K. D.; Devlin, J. P. Formation and Spectra of Clathrate Hydrates of Methanol and Methanol-Ether Mixtures. *J. Mol. Struct.* **1997**, *416* (1−3), 277−286.
(53) Richardson, H. H.; Wooldridge, P. J.; Devlin, J. P. FT-IR Spectra of Vacuum Deposited Clathrate Hydrates of Oxirane H_2S, THF, and Ethane. *J. Chem. Phys.* **1985**, *83* (9), 4387.
(54) Yang, Y.; Shin, D.; Choi, S.; Lee, J. W.; Cha, M.; Kim, D.; Yoon, J. H. Cage Occupancy and Stability of N_2O-Encaged Structure i and II Clathrate Hydrates. *Energy Fuels* **2016**, *30* (11), 9628−9634.
(55) Zúñiga, J.; Bastida, A.; Requena, A. Theoretical Calculations of Vibrational Frequencies and Rotational Constants of the N_2O Isotopomers. *J. Mol. Spectrosc.* **2003**, *217* (1), 43−58.
(56) Ramamurthy, A.; Baburao, G.; Jahnavi, A.; Ragupathy, G. Encapsulation of Greenhouse Gases in Clathrate Hydrates with Insights into Structure, Energetics, Chemical Interactions, and Environmental Implications. *Sci. Rep.* **2025**, *15* (1), 24090.
(57) Ramya, K. R.; Pavan Kumar, G. V.; Venkatnathan, A. Raman Spectra of Vibrational and Librational Modes in Methane Clathrate Hydrates Using Density Functional Theory. *J. Chem. Phys.* **2012**, *136* (17), 174305.
(58) Buch, V.; Devlin, J. P.; Monreal, I. A.; Jagoda-Cwiklik, B.; Uras-Aytemiz, N.; Cwiklik, L. Clathrate Hydrates with Hydrogen-Bonding Guests. *Phys. Chem. Chem. Phys.* **2009**, *11* (44), 10245−10265.
(59) Peeters, Z.; Rodgers, S. D.; Charnley, S. B.; Schriver-Mazzuoli, L.; Schriver, A.; Keane, J. V.; Ehrenfreund, P. Astrophysics Astrochemistry of Dimethyl Ether. *A&A* **2006**, *445*, 197−204.

https://doi.org/10.1021/acs.jpclett.5c02778
J. Phys. Chem. Lett. 2025, 16, 12720−12727

Supporting Information

Secondary Guest–Driven Nucleation of N_2O Clathrate Hydrate in Amorphous Ice Mixture under Ultrahigh Vacuum

Bijesh K. Malla,[1,5‡], Soham Chowdhury[1‡], Samir Kumar Nayak[3], Sofia Sara Baji[4], Teena J Mathew[4], Rabin Rajan J Methikkalam[4], Sharma S. R. K. C. Yamijala[3], Rajnish Kumar[2,5,6*] and Thalappil Pradeep[1,2*]*

[1]DST Unit of Nanoscience (DST UNS) and Thematic Unit of Excellence (TUE), Department of Chemistry, Indian Institute of Technology Madras, Chennai 600036, India,

[2]International Centre for Clean Water, IIT Madras Research Park, Chennai 600113, India

[3]Department of Chemistry, Indian Institute of Technology Madras, Chennai 600036, India

[4]Department of Chemistry, Mar Ivanios College, Thiruvananthapuram, Kerala 695015, India

[5]Department of Chemical Engineering, Indian Institute of Technology Madras, Chennai 600036, India

[6]School of Sustainability, Indian Institute of Technology Madras, Chennai 600036, India

Corresponding authors

***Email:** pradeep@iitm.ac.in, rajnish@iitm.ac.in, yamijala@iitm.ac.in

Instrumentation

All the experiments were conducted in an ultrahigh vacuum chamber described in detail elsewhere.[S1] The vacuum chamber is equipped with reflection absorption infrared spectroscopy (RAIRS), temperature-programmed desorption (TPD) mass spectrometry, secondary ion mass spectrometry (SIMS), low energy ion scattering (LEIS) mass spectrometry, and a VUV deuterium continuum. The base pressure of the chamber was ~5×10^{-10} mbar and it was maintained by seven oil-free turbomolecular pumps backed by two scroll pumps (Pfeiffer vacuum). Vacuum was monitored by a Bayard-Alpert (BA) gauge (PBR 260, Pfeiffer Vacuum) and controlled by a MaxiGauge controller (Pfeiffer, Model TPG 256 A).

A Ru(0001) single crystal surface (1.5 cm diameter and 1 mm thick) was used as the substrate to grow the thin ice films. The substrate was mounted on a copper holder and connected to the cold tip of the closed-cycle He cryostat (Coldedge Technologies). The substrate temperature could be varied by a resistive heater (25 Ω) from 8-1000 K, and measured with a K-type thermocouple and a platinum sensor with a temperature accuracy/uncertainty of 0.5 K. Temperature (ramping) was controlled and monitored with a temperature controller, Lakeshore, Model 336. Before each experiment, the Ru(0001) was heated to 400 K repeatedly to ensure cleanliness. It is worth noting that the substrate has no effect in this study due to the multilayer deposition.

Material and Sample Preparation

Millipore water (H_2O of 18.2 MΩ resistivity) was taken in a vacuum-sealed test tube (with a glass-to-metal seal) and was further purified by several freeze–pump–thaw cycles. N_2O (99.9 %, Chemix), ETO (49.5%, 50 % N_2 gas, Vinayaka gas), DME (99.9%, Sigma-Aldrich) gas were used without further purification. 50 % N_2 in ETO gas is confirmed by residual gas analyzer mass spectrum during deposition. This N_2 sublime completely at 40 K, and TPD confirms that only ETO is present in the experimental temperature window (above 120 K).

Thin films of the N_2O-H_2O mixture were created at 10 K by backfilling the vacuum chamber at a total pressure of ~5×10^{-7} mbar for few minutes. Different ratios of N_2O and H_2O (1:5, 1:10, and 1:20) were prepared at 10 K by keeping the total pressure constant and varying the inlet pressure of N_2O and water vapors accordingly. For quantification purposes, we considered that 1.33×10^{-6} mbar exposure for one second, equated to 1 monolayer (ML), was estimated to contain

approximately 1.1×10^{15} molecules cm^{-2}, assuming the ion gauge sensitivity factor of H_2O and N_2O is ~1.0.[S2,S3] The BA gauge sensitivity factors for DME, ETO, and THF are approximately 3–4. Since ETO was introduced as a 50:50 mixture with N_2, we did not determine the exact ML coverage for ETO, DME, or THF. For ternary systems (ETO@N_2O+H_2O, DME@N_2O+H_2O, and THF@N_2O+H_2O), the total deposition time was fixed at 10 minutes. In these cases, the first component (ETO, DME, or THF) was deposited for 200 seconds at 5×10^{-7} mbar, followed by co-deposition of N_2O and H_2O for 400 seconds, using inlet pressures of 1×10^{-7} mbar for N_2O and 4×10^{-7} mbar for H_2O.

For temperature and time-dependent experiments, the as-prepared thin films at 10 K were annealed at a rate of 2 $K \cdot min^{-1}$ to the set temperatures. After maintaining the ice samples at a particular temperature, they were examined by RAIRS.

Computational Details

We employed the Gaussian 16[S4] suite of programs for all quantum chemical calculations. Initially, the geometries of the individual molecules, N_2O, ETO and three distinct CH cages (5^{12}, $5^{12}6^2$, and $5^{12}6^4$ were optimized using the B3LYP[S5] functional in conjunction with the 6-311++G(d,p)[S6] basis set. Subsequently, ETO and N_2O were encapsulated within the clathrate hydrate cages, and the resulting host-guest complexes were subjected to full geometry optimization and frequency calculations at the same level of theory. The calculated vibrational frequencies were scaled by a factor of 0.9679.[S7] Table S1 (Supporting Information 9) lists the calculated frequencies for N_2O and ETO before and after applying the scaling factor. The absence of imaginary frequencies in all optimized structures confirms that true minima were located on the potential energy surface.

Supporting information 1

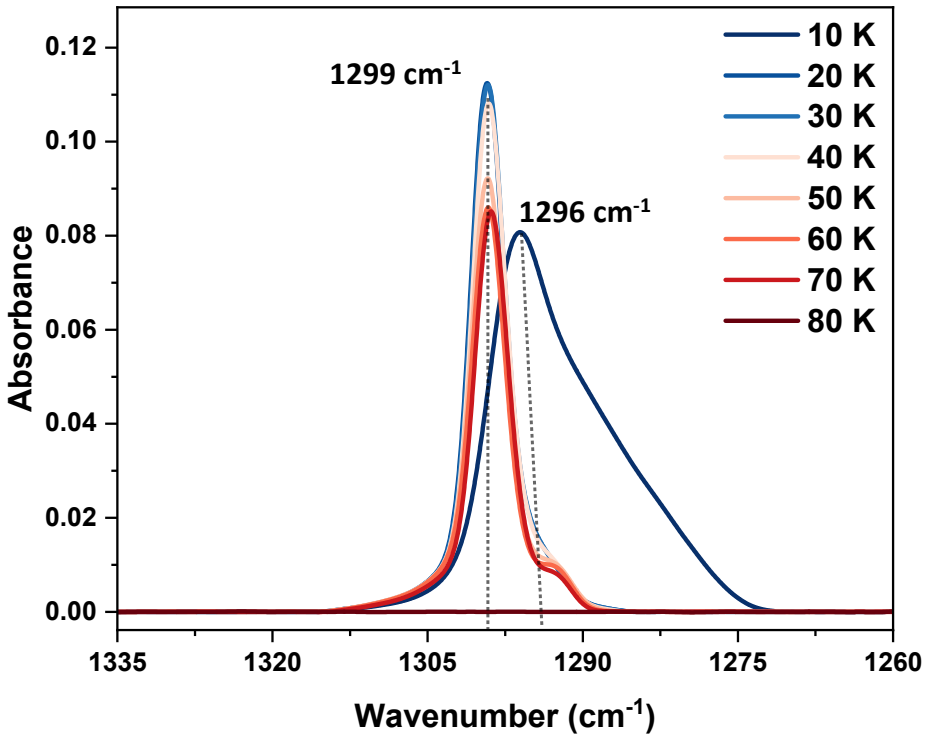


Figure S1. Temperature-dependent RAIR spectra of pure 150 ML N_2O ice in the N–N–O symmetric stretching region.

Supporting information 2

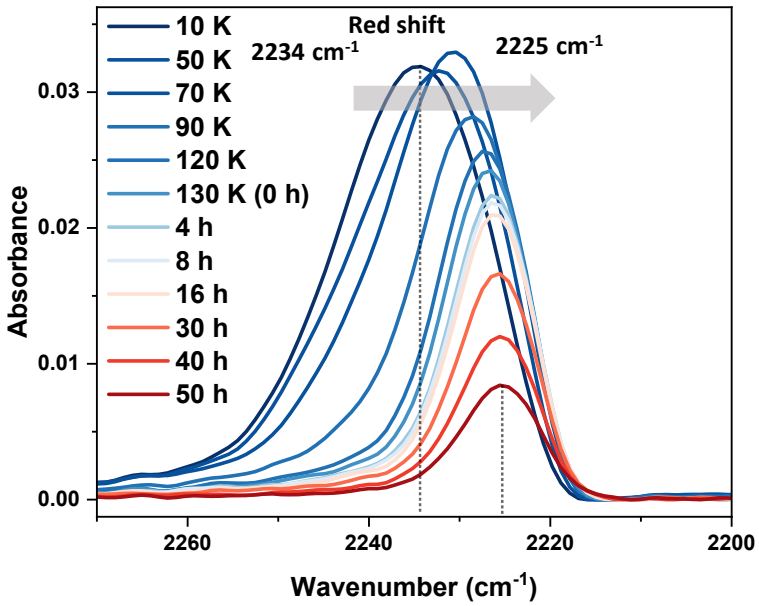


Figure S2. Temperature dependent RAIR spectra of 150 ML of N2O ice in N-N-O asymmetric stretching region.

Supporting information 3

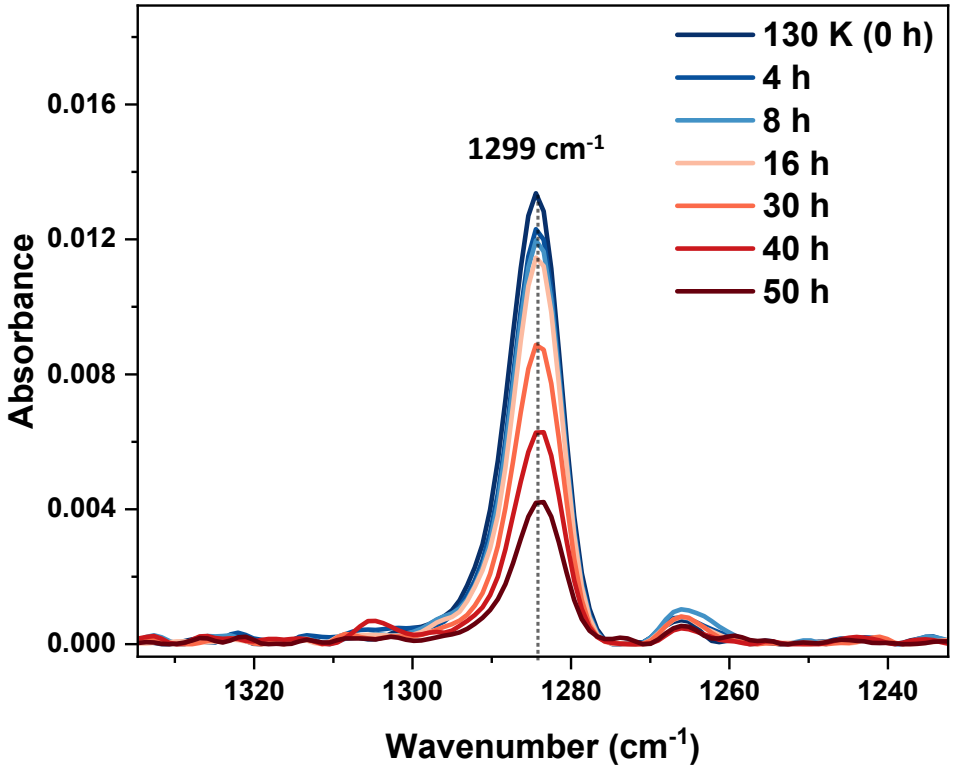


Figure S3. Time-dependent RAIR spectra of a 300 ML N_2O + H_2O ice mixture, showing the N–N–O symmetric stretching region

Supporting information 4

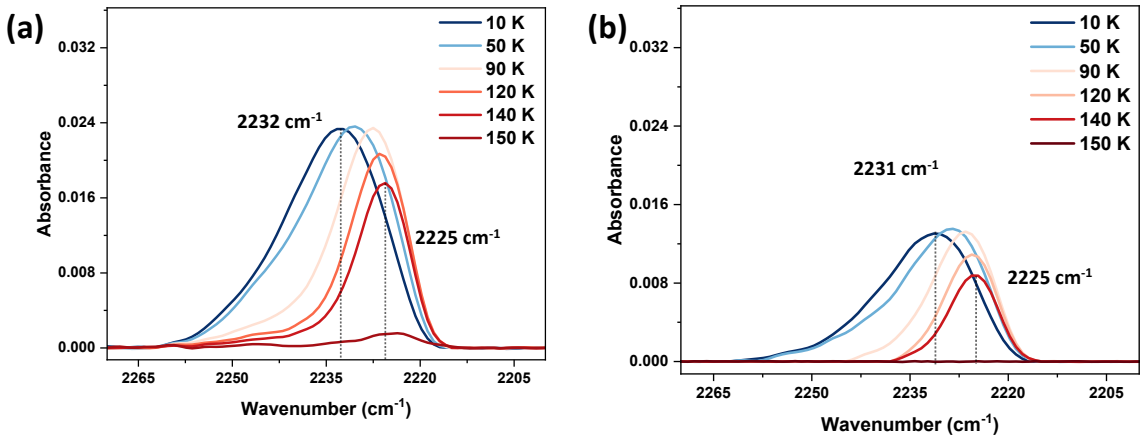


Figure S4. Temperature-dependent RAIR spectra of a 300 ML N_2O + H_2O ice mixture, showing the N–N–O asymmetric stretching region. Figure (a) corresponds to a 1:10 N_2O:H_2O ratio, and figure (b) to a 1:20 ratio.

Supporting information 5

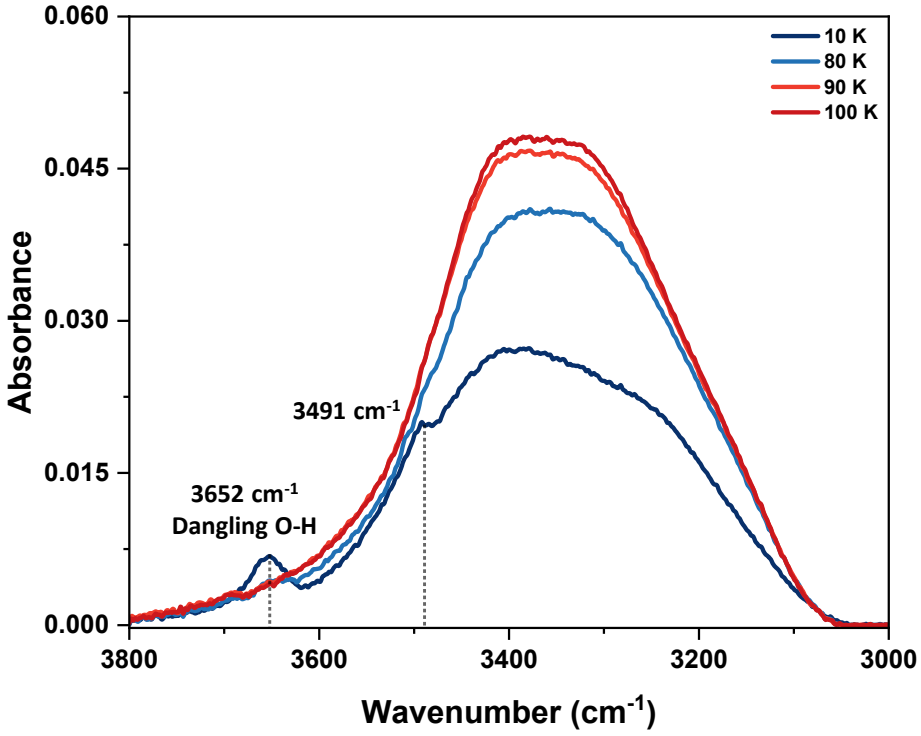


Figure S5. Temperature-dependent RAIR spectra of 300 ML of N_2O-H_2O (1:1) ice mixture in O-H stretching region.

Supporting information 6

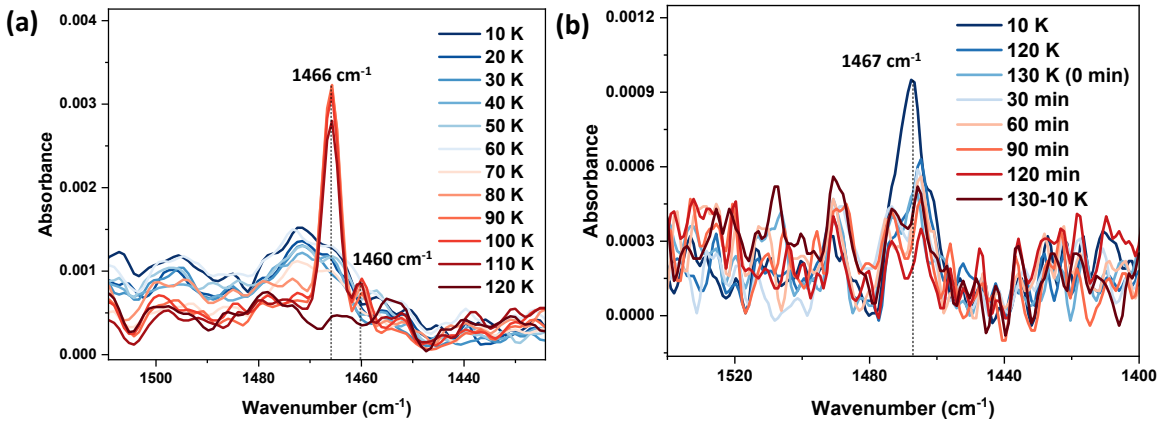


Figure S6. (a) RAIR spectra of pure ETO ice (a) and ETO+H_2O ice mixture (b) in CH_2 bending region.

Supporting information 7

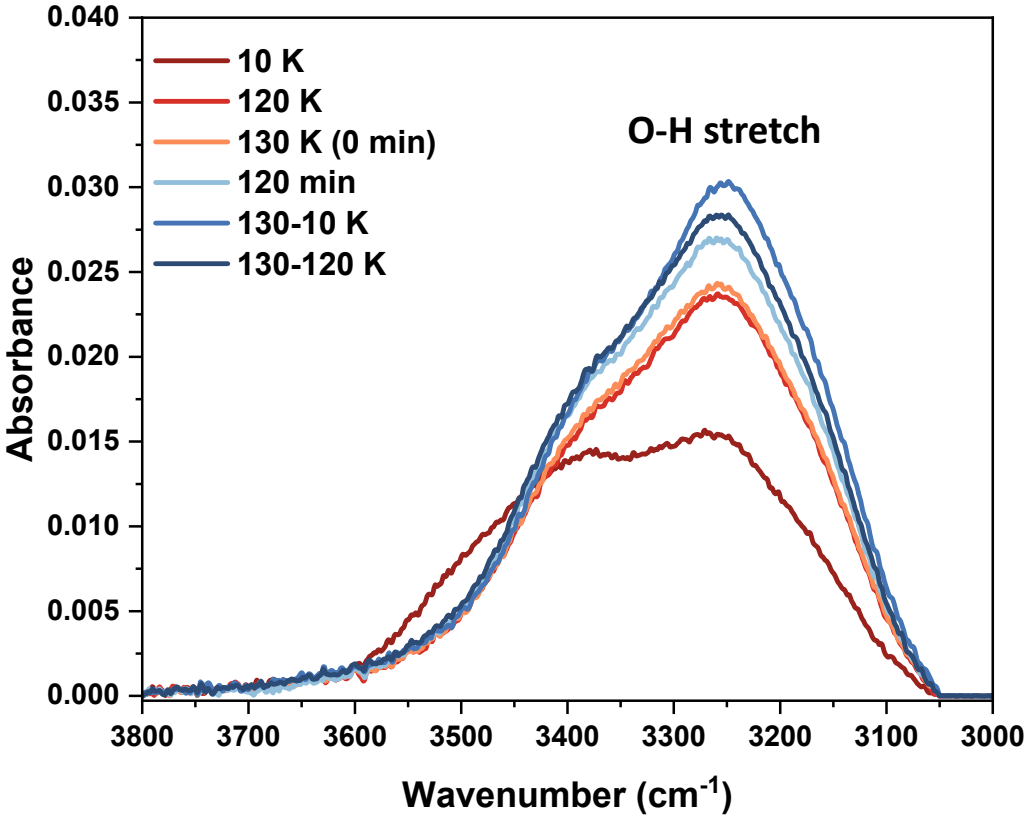


Figure S7. RAIR spectra of ETO + H_2O ice in the O-H stretching region.

Supporting information 8

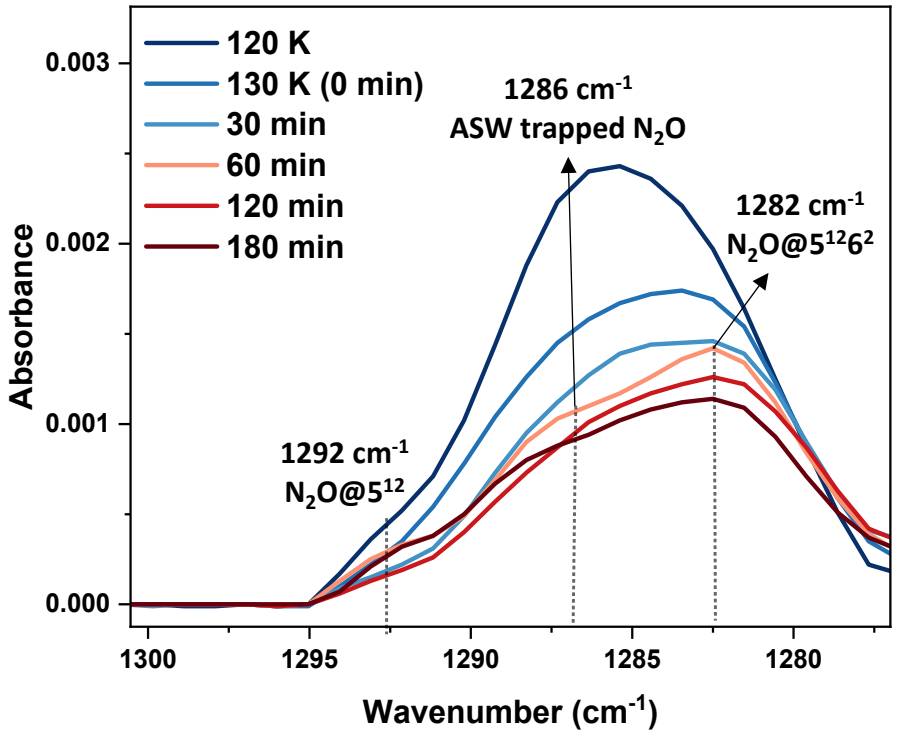


Figure S8. RAIR spectra of ETO@N_2O + H_2O in the N–N–O symmetric stretching region of N_2O.

Supporting information 9

Table S1. Before and after multiplication of scaling factor to calculated frequency.

System	Frequency (Unscaled)	Frequency (Scaled)	System	Frequency (Unscaled)	Frequency (Scaled)
N_2O	2343.15	2267.93	ETO	1298.88	1257.19
$5^{12}@N_2O$	2362.53	2286.69	5^{12}@ETO	1314.38	1272.19
$5^{12}6^2@N_2O$	2348.27	2272.89	$5^{12}6^2$@ETO	1304.58	1262.70
$5^{12}6^4@N_2O$	2345.02	2269.74	$5^{12}6^4$@ETO	1300.93	1259.17

References

(S1) Bag, S.; Bhuin, R. G.; Methikkalam, R. R. J.; Pradeep, T.; Kephart, L.; Walker, J.; Kuchta, K.; Martin, D.; Wei, J. Development of Ultralow Energy (1–10 EV) Ion Scattering Spectrometry Coupled with Reflection Absorption Infrared Spectroscopy and Temperature Programmed Desorption for the Investigation of Molecular Solids. *Rev. Sci. Instrum.* **2014**, *85* (1), 1–7. https://doi.org/10.1063/1.4848895.

(S2) Bartmess, J. E.; Georgiadis, R. M. Empirical Methods for Determination of Ionization Gauge Relative Sensitivities for Different Gases. *Vacuum* **1983**, *33* (3), 149–153. https://doi.org/10.1016/0042-207X(83)90004-0.

(S3) Malla, B. K.; Chowdhury, S.; Paliwal, D.; K. M., H.; Vishwakarma, G.; Methikkalam, R. R. J.; Pradeep, T. Simulated Interstellar Photolysis of N 2 O Ice: Selectivity in Photoproducts. *J. Phys. Chem. C* **2025**, *129* (2), 1120–1128. https://doi.org/10.1021/acs.jpcc.4c06624.

(S4) Gaussian 16, Revision C. 01, M. J. Frisch, G. W. Trucks, H. B. Schlegel, G. E. Scuseria, M. A. Robb, J. R. Cheeseman, G. Scalmani, V. Barone, G. A. Petersson, H. Nakatsuji, X. Li, M. Caricato, A. V. Marenich, J. Bloino, B. G. Janesko, R. Gomperts, B. Mennucci, H. P. Hratchian, J. V. Ortiz, A. F. Izmaylov, J. L. Sonnenberg, D. Williams-Young, F. Ding, F. Lipparini, F. Egidi, J. Goings, B. Peng, A. Petrone, T. Henderson, D. Ranasinghe, V. G. Zakrzewski, J. Gao, N. Rega, G. Zheng, W. Liang, M. Hada, M. Ehara, K. Toyota, R. Fukuda, J. Hasegawa, M. Ishida, T. Nakajima, Y. Honda, O. Kitao, H. Nakai, T. Vreven, K. Throssell, J. A. Montgomery, J. E. Peralta, F. Ogliaro, M. J. Bearpark, J. J. Heyd, E. N. Brothers, K. N. Kudin, V. N. Staroverov, T. A. Keith, R. Kobayashi, J. Normand, K. Raghavachari, A. P. Rendell, J. C. Burant, S. S. Iyengar, J. Tomasi, M. Cossi, J. M. Millam, M. Klene, C. Adamo, R. Cammi, J. W. Ochterski, R. L. Martin, K. Morokuma, O. Farkas, J. B. Foresman, and D. J. Fox, Gaussian, Inc. , Wallingford CT, 2016. Gaussian16.

(S5) Becke, A. D. Density-Functional Thermochemistry. III. The Role of Exact Exchange. J. Chem. Phys. 1993, 98 (7), 5648–5652.

(S6) Krishnan, R.; Binkley, J. S.; Seeger, R.; Pople, J. A. Self-Consistent Molecular Orbital Methods. XX. A Basis Set for Correlated Wave Functions. J. Chem. Phys. 1980, 72 (1), 650–654.

(S7) Andersson, M. P.; Uvdal, P. New Scale Factors for Harmonic Vibrational Frequencies Using the B3LYP Density Functional Method with the Triple-Zeta Basis Set 6-311+G(d,p). J Phys Chem A 2005, 109 (12), 2937–2941.

ACS Sustainable Chemistry & Engineering

pubs.acs.org/journal/ascecg

Perspective

Microdroplet Mechanochemistry

Thalappil Pradeep*

Cite This: https://doi.org/10.1021/acssuschemeng.5c12102

Read Online

ACCESS | Metrics & More | Article Recommendations

ABSTRACT: Water, mother of all fluids, long considered passive, is now shown to be highly active in the form of droplets, where chemical reactions requiring intense stimuli, happen rapidly. Discoveries from our lab in the recent past have shown that hard, common minerals such as quartz and ruby disintegrate spontaneously to form nanoparticles in charged water microdroplets. This occurs due to a combination of intense electric fields, reactive chemical species and mechanical forces in the droplets, acting in concert on the minerals. Subsequent studies have shown that this is a generic process occurring in a variety of materials. This evolving field of microdroplet mechanochemistry presents a low energy, reagent-free and ambient method for water-based transformations of materials. As the process occurs in milliseconds rather than the millennia conventionally associated with mineral disintegration, it effectively compresses geological time scales. The possibilities of such a process as a new method of materials discovery and green manufacture is outlined here. This positions water as a green factory making materials sustainably.



KEYWORDS: *microdroplet chemistry, mechanochemistry, mass spectrometry, materials, environmental science, catalysis, multiscale modeling, sustainable chemistry*

Downloaded via INDIAN INST OF TECH MADRAS on January 5, 2026 at 07:27:34 (UTC).
See https://pubs.acs.org/sharingguidelines for options on how to legitimately share published articles.

INTRODUCTION

When Water Becomes Active. Water dissolves, disperses and solvates matter but rarely constructs it directly. A medium that is typically a silent observer is now beginning to be very active at small scale, in the size regime of microdroplets. At the interface of charged, levitating, sprayed, and evaporating microdroplets, large electric fields[1,2] in the range of 10^8 V m^{-1} are reported. Consequently, reactive chemical species and mechanical stresses are observed and they collectively make the confined droplet to a microreactor, figuratively a dynamo. Our discovery[3] of disintegration of common minerals to nanoparticles extends the microdroplet chemistry[4−6] to the solid state, unveiling a new field of science−microdroplet mechanochemistry.

Microdroplet Mechanochemistry (MDMC) is defined as the "*transformation of materials within charged or confined liquids by coupled electrical, mechanical and chemical effects*". The curved surfaces of droplets experience strong electric fields, chemical gradients arising from reactive species such as protons and intense transient mechanical stresses such as those arising from Coulomb fission, inducing lattice reconstruction, fracture and associated effects in the materials. Unlike conventional mechanochemistry driven by external stimuli, MDMC occurs due to the energy inherent in the system and occurs under ambient conditions. The process represents a unique electro-mechanochemical regime where solvent−most efficiently water itself−acts as an agent of materials synthesis and transformation.

Discovery and Implications. When rocks break in milliseconds: In our initial work, quartz, ruby and synthetic alumina particles of 5−10 μm were dispersed in water sprayed to make charged droplets.[3] The products were collected a few cm away from the spray showed uniform nanocrystalline particles of ∼5−10 nm in diameter exhibiting specific crystallographic planes. From the distance traveled and estimated number of charges, for accelerating droplets of finite size, we estimate the time taken for spray deposition as ∼30 ms. As the particles disintegrate, transient structures such as "flower-like" intermediates were seen. High resolution transmission electron microscopy (TEM) coupled with powder X-ray diffraction (XRD) confirmed that the minerals disintegrated to form nanoparticles. Computations suggested that the intense electric fields and the chemical species, especially protons are involved in the process. The electric fields polarize the bonds and the protons help in the breakage of the particles. Other chemical

Received: November 8, 2025
Revised: December 17, 2025
Accepted: December 22, 2025
Published: December 25, 2025

ACS Publications © 2025 American Chemical Society

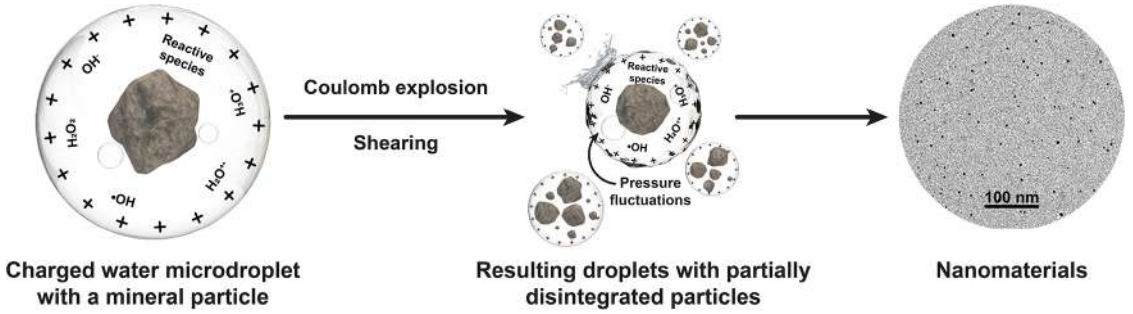


Figure 1. A schematic representation of one form of *Microdroplet Mechanochemistry* where materials transform within charged or confined aqueous microdroplets through coupled electrical, mechanical, and chemical effects. The charges shown may be due to different species. Species other than $OH^{\bullet}$, $H_2O^{+\bullet}$, H_3O^{+}, OH^{-}, etc., can also be present depending on the ingredients in the droplet. The case shown is that of water. The TEM image shown was adapted from ref 3, Spoorthi et al., Science, DOI: 10.1126/science.adl3364 [2024], AAAS.

species such as $H_2O^{+\bullet}$ and $OH^{\bullet}$ might also be involved. These species reduce the barrier for slip or fracture. The transient mechanical stresses produced during the Coulomb fission of the droplets might be the trigger to cause the disintegration and further facilitated by the reactive chemical species. The observed phenomenon for fracture is labeled as "proton-induced slip". On the whole, these processes constitute a field-driven, proton-assisted lattice breakdown—a unique coupling of electrostatic and mechanical forces in the confinement of droplets. Microdroplet Mechanochemistry leading to the disintegration of minerals is represented schematically in Figure 1.

Mechanistic Framework. Microdroplet mechanochemistry integrates three otherwise independent stimuli for transformation: (i) electrostatic fields concentrated by curvature, (ii) proton mediated processes at hydrated interfaces, and (iii) mechanical impulses from Coulomb fission, or physical events. These act cooperatively, enabling reactions inaccessible in bulk liquids or classical mills. The interface clearly represents a distinct phase of reactivity[7]—a transient "electro-mechano-chemical state" of matter. Subsequently, it was shown that graphene and MoS_2 also disintegrate in charged water microdroplets making corresponding nanoparticles.[8] Disintegration occurs as the droplets fly through air and the process could be visualized systematically.[9]

Connecting to Sustainability and Green Chemistry. Microdroplet mechanochemistry aligns naturally with the core principles of green chemistry;[10] (i) waste prevention (no auxiliary reagents), (ii) safer solvents (water), (iii) energy efficiency (ambient conditions), and (iv) inherently benign design (minimal waste). It enables (v) rapid, high-yield transformations (atom economy), using (vi) abundant minerals (renewable raw materials), without external energy inputs and facilitates (vii) circularity (recycling) of the medium. Other aspects of green chemistry may also be considered. The process parallels events in nature—such as those in aerosols and clouds—and therefore offers a direct connection between the planet's material cycling and manufacturing processes. For industrial adoption of this technology, cost of manufacture by microdroplet mechanochemistry must be comparable to conventional processes. In view of the benefits outlined above, the cost of manufacture is expected to be lower although production at scale is needed to make realistic cost calculations.

Natural Nanofactory. Aerosols are everywhere in Nature. Such particles carry charges[11] due to triboelectricity due to atmospheric friction as well as dissolved ions and they have been long implicated in interface chemistry. Droplets are known to have potential differences. Due to the diversity of processes by which such droplets can be produced such as sea spray, fog, and rain, events such as the ones demonstrated in our work may have been important in early-Earth chemistry such as weathering of rocks, formation of colloidal minerals and associated chemistry making early molecules.[7] From this perspective, every raindrop can be viewed as a nanofactory of minerals.

Interfacial Chemistry. Microdroplets can contain nanobubbles composed of dissolved gases, which possess reactive interfaces. Changing solubility of gases in charged confined media may lead to such phenomena. These bubbles can be visualized exhibiting unusual phenomena.[12] Electric fields at such interfaces due to the presence of surfactants and physical effects of shape and concentration gradients can induce reactivity, leading to transient chemical species. The observed MDMC may be initiated by a combination of reactive species (originating from micro/nano bubbles or otherwise), just as radical initiators start certain polymerization reactions. Electric fields of $(5-9) \times 10^7$ V cm^{-1} have been observed at the interface oil droplets of 250 μm diameter in water.[13]

Origins. Right after the discovery of molecular reactions in organic and aqueous environments,[4−6] nanoparticles of gold were synthesized using microdroplets.[14] Controlled deposition of such nanoparticles gave functional and patterned Raman active surfaces.[15] Controlling electric fields on depositing particles created nanowires from nanoparticles.[16] Such nanowire structures, created over cm^2 areas, harvest water efficiently.[17] Zare and colleagues too made gold nanoparticles.[18] Later, it was found that large, polydisperse, monolayer-protected silver nanoparticles anneal to form smaller, monodisperse analogues within ambient microdroplets.[19] This demonstrates the capacity of droplets to reorganize matter, breaking and making hundreds of chemical bonds. Together, these findings established a continuum—from droplet-assisted synthesis to restructuring. This prompted us to explore the possibility of transforming macroscopic materials with extended chemical bonds, as in a piece of rock, by electro-mechanochemical transformation in a charged droplet. That culminated in positioning microdroplet mechanochemistry as a sustainable route to the creation of materials. While many of the observed processes still need deeper investigations to understand better, it is beyond doubt that droplets can break and make chemical bonds from molecular to macroscopic length scales.

Green Nanomanufacturing. MDMC can be harnessed for green nanomanufacturing. The only consumables needed are solvents—and water is preferred—which can be recycled. The power requirement is minimum as processes occur under ambient conditions. The applied electrical potentials are in the

https://doi.org/10.1021/acssuschemeng.5c12102
ACS Sustainable Chem. Eng. XXXX, XXX, XXX−XXX

range of kV, but currents are low. Types of products and their properties, such as size and shape, can be controlled by the experimental parameters such as potential, spray distance, concentration of the reagents and composition of solvents. Conducting experiments with multinozzle electrospray and continuous spray with repeated cycling can increase conversion yields.[20] Because droplets disintegrate in air and deposit nanoparticles directly onto substrates, the process functions as a room-temperature nanoparticle sprayer—an ambient, scalable route to catalysts, coatings, and sensors. Renewable sources may be used for electrical power.

Comparison with Conventional Mechanochemistry. Conventional mechanochemistry uses macroscopic grinding, friction, or compression to drive reactions in the solid state, generally at significant energy cost.[21] In contrast, microdroplet mechanochemistry operates through intrinsic electro-mechanochemical coupling at ambient conditions, performing reactions without external mechanical energy input. Besides, unlike conventional mechanochemistry where forces operate from outside, MDMC operates from within as electro-mechanochemical coupling occurs at this length scale, within the droplet.

Next Steps. The materials formed have active surfaces and naturally, they are sites for new catalysis. The droplets can contain reagents which can be transformed at these surfaces using the transient ingredients in the droplets. Stimuli such as photons can provide additional incentives for such processes. As chemical reactions can also occur in microdroplets, MDMC can also make new solids like solvothermal synthesis, although at unprecedently shorter time scales.

Impact on Other Disciplines. Potential impacts of MDMC span various fields, including: atmospheric chemistry (aerosol reactivity and cloud nucleation), environmental remediation (defect-rich, in situ-born nanoparticles for catalysis), planetary science (charged ice−regolith interactions), and sustainability education (a new paradigm of water as an architect of matter). Many of these implications are presented in Figure 2. In the following, we dwell on some of these aspects.

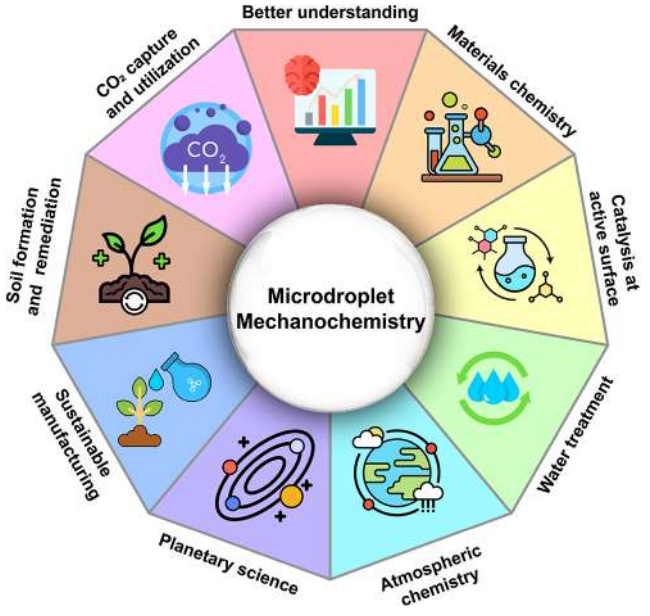


Figure 2. Expansion of the phenomenon of MDMC and implications to other areas.

Atmospheric Chemistry and Cloud Nucleation. Charged water microdroplets are ubiquitous in sea spray and clouds, yet their application as active chemical reactors remains underexplored. Laboratory observations[3] of spontaneous mineral disintegration in such environments suggest similar pathways for making silicates, metal oxides, clays, etc., analogous to those detected in the atmosphere. MDMC therefore provides a unified framework to examine chemo-mechano-electro-driven processes that may underlie atmospheric processes, complementing studies of interfacial oxidation in atmospheric aerosols.

Environmental Remediation and Catalysis. Surfaces of nanoparticles formed by MDMC can possess high catalytic activity. Spraying contaminated water through charged nozzles could generate active nanocatalysts for in situ degradation of dyes, nitrates, or emerging pollutants such as perfluorinated alkyl substances (PFAS). Analogous field-driven reduction of CO_2 to formate and nitrogen fixation in aqueous microdroplets illustrate the feasibility of such reagent-free remediation processes through interfacial electrochemistry.[22,23] Triboelectric degradation of poly(trifluoroethylene) (PTFE) in water occurs when PTFE-covered magnetic pellets are stirred in bulk water.[24] PFAS degradation has been demonstrated by microdroplet chemistry.[25] Active radicals and other species in conjunction with nanomaterials could offer a method for water treatment. Such processes along with traditional water treatment materials such as aluminates, silicates and phosphates (e.g., $NaAlO_2$, $CaSiO_3$) may be advantageous as no unknown substance is then introduced in the treatment process. Besides MDMC, microdroplet chemistry in other forms can also help in environmental remediation. For example, Mo-rich holes can be created in MoS_2 nanosheets by electrospray, which can make H_2O_2 from water upon light exposure, leading to water disinfection.[26] Nanowires formed by microdroplet chemistry can be used for water harvesting, as noted before.[17]

Planetary and Geochemical Contexts. Evolution of the planet, soil formation, dissolution of minerals, chemical synthesis or relevance to life, etc., are important to consider in the context of MDMC. Triboelectrification of droplets can lead to MDMC of entrapped particles and molecules. Field-assisted mineral transformation or redox chemistry may occur at ice surfaces and at cryogenic temperatures of relevance to other planets or outer space, paralleling liquid droplet-driven fragmentation in the laboratory. These considerations extend MDMC to space, although in the solid state, where similar forces may sculpt surfaces and prebiotic materials.

Educational Perspective. MDMC represents sustainability in action—chemistry without external energy or waste. Demonstrations of mineral-to-nanoparticle conversion under ambient conditions provide a compelling tool for teaching interfacial phenomena, green chemistry, and materials transformation. An MDMC experiment in the classroom may be an important way to demonstrate sustainable synthesis of nanomaterials.

Multi-Scale Modeling Opportunities. A challenge or an opportunity in MMDC is that the relevant physics spans multiple orders of magnitude, from Å-scale solvation structures to tens-of-micrometer hydrodynamic deformations and from femtosecond bond dynamics to millisecond droplet lifetimes. It is clear that no single modeling approach can capture this range currently. At the molecular level, reactive MD, QM/MM, and machine-learned potentials can reveal how constituent species experience partial desolvation, interfacial orientation, field fluctuations, evaporation-driven compression within charged

https://doi.org/10.1021/acssuschemeng.5c12102
ACS Sustainable Chem. Eng. XXXX, XXX, XXX−XXX

droplets as well as their Coulombic fission. Such simulations are ideally suited to quantify the relative contributions of electric fields, confinement, ion partitioning, and mechanical stresses to bond activation. However, such simulations will require realistic inputs such as evolving local concentrations, which in turn demand microkinetic descriptions and field-dependent elementary reaction rates that must be determined self-consistently.

At mesoscopic and continuum scales, coarse-grained MD, dissipative particle dynamics (DPD), and electrohydrodynamic models can describe evaporation kinetics, hydrodynamic shear, droplet oscillations, charge redistribution, and Rayleigh instabilities—the boundary conditions actually experienced by molecules. A long-term goal is the development of a coupled multiscale framework in which continuum electromechanics provides time-resolved surface charge, curvature, evaporation rate, and stress fields, while atomistic simulations model chemistry under these evolving conditions, allowing feedback between chemical events and droplet mechanics. Such an integrated approach would enable predictive modeling of reaction acceleration, selective bond activation, nanoparticle nucleation, and even triboelectrically charged nebulized droplets, which may operate under distinct mechanochemical regimes.

Developing this hierarchy of models is central to establishing microdroplet mechanochemistry as a quantitative, designable platform for chemical and materials discovery. Such models are especially valuable in regimes that are experimentally inaccessible—allowing one to predict, for example, whether ultrafast field spikes during droplet deformation can transiently lower activation barriers, how concentration and desolvation profiles evolve in droplets below optical diffraction limit, or whether triboelectrically charged nanodroplets reach charge−density or curvature thresholds capable of initiating chemistry. Ultimately, such predictions must help explain experimental realities.

Although classical electrohydrodynamics of droplets such as Taylor cones, the leaky-dielectric model, charge relaxation, and Rayleigh instabilities, is well developed in certain parameter regimes, these frameworks describe systems that are closer to equilibrium than those encountered in MDMC. In microdroplet regime, several interfacial processes occur simultaneously, creating a regime where electric fields, hydrodynamic flow, reactive transport, and mechanical stresses are coupled and evolving dynamically. The resulting electro-reacto-hydrodynamics of curved, deforming, and chemically active droplet interfaces is largely unexplored, and defining its governing principles represents a major open challenge - and a rewarding opportunity - for the field.

Critical Overview. Although the observed phenomena have been reproduced across laboratories, there have not been consensus on the origin of reaction acceleration in microdroplets. In particular, questions have been raised about the extent to which electric fields contribute relative to other factors such as concentration, phase behavior, and confinement. Early interpretations of microdroplet reactivity often invoked extraordinarily strong interfacial electric fields,[1] estimated at 10^7-10^8 V·cm^{-1} (equivalent to roughly 0.01−0.1 V·Å^{-1}), as inferred from Stark-shift measurements.

Reactive-force-field simulations of curved interfaces predicted average surface field strengths of ∼16 MV/cm, which when projected onto free surface O−H bonds can reach an order of magnitude larger.[27] Measured fields of $(5-9) \times 10^7$ V cm^{-1} at oil−water interfaces,[13] mentioned earlier in the text may arise from anisotropic hydrogen bonding and charge asymmetry. At the same time, quantum many-body analyses report that interfacial electric fields at the pristine air−water interface are systematically ∼10% weaker[28] than in bulk, reflecting density depletion rather than amplification, and *ab initio* molecular dynamics simulations on a model Diels−Alder (DA) reaction show that interfacial electric fields fluctuate between −0.1 and +0.1 V·Å^{-1} but average to only ∼0.007 V·Å^{-1}, a magnitude far too small to meaningfully influence the reaction barrier.[29] Even a perfectly oriented external field of 0.1 V·Å^{-1} lowers this barrier by only ∼2−3 kcal·mol^{-1} (ref 29), understandable for a nonpolar/nonionic intermediate of a DA reaction. Complementary SFG studies[30] report no persistent macroscopic fields at pristine air−water interfaces. Xie and colleagues suggest that many earlier "giant-field" interpretations conflate rapidly fluctuating microscopic fields—present in all hydrogen-bonded liquids—with sustained macroscopic electrostatic forces capable of catalysis.[29] These findings, together with the broader framework of electric-field-mediated catalysis,[31] indicate that although strong fields may occur at certain chemically structured interfaces, pristine air−water and neutral microdroplet interfaces do not typically exhibit anomalously large, catalytically dominant fields.

In the present Perspective, however, *Microdroplet Mechanochemistry* is introduced based on observations of materials transformations occurring within charged microdroplets generated by electrospray, an environment different from that of neutral interfaces.[32−34] Electrosprayed droplets inherently possess net charge, exhibit surface charge segregation, and undergo evaporation, shape oscillation, Coulombic deformation, and Rayleigh fission, which are well-documented.[32−36] These processes generate intrinsic interfacial electric fields, steep charge-density gradients, and intense pressure fluctuations absent in macroscopic liquids. It is within this highly nonequilibrium environment, characterized by partial desolvation, transient confinement, hydrodynamic shear, evaporation-driven compression, and charge-induced interfacial restructuring, that chemical reactions and materials transformations occur.[37,3] Thus, the "mechanochemistry" in Microdroplet Mechanochemistry arises not from macroscopic grinding but from the synergistic action of confinement, charge, interfacial fields, and dynamic mechanical stresses unique to charged electrospray droplets.[33−37] Moreover, at sufficiently high liquid flow rates, nebulization without electrospray can itself generate substantial triboelectric charging, creating transient interfacial fields and stresses that may also contribute to Microdroplet Mechanochemistry.[11] Overall neutral droplets too may possess transient fields due to dynamic fluctuations at the nanometer length enhancing chemical reactions.

Currently, the most important limitation of the area is processing at scale. The synthesis of nanoscale materials using MDMC is limited to milligrams per hour in published literature (2024) and processing at tens of grams per day is happening now. Scale-up to kilograms is essential for detailed investigations and adoption of the method to other materials of industrial value. Processing in water suggests potential applications of such materials in agriculture, water treatment, construction industry, CO_2 sequestration, cosmetics, personal care products, paints, detergents and many others, although capacity to make materials at hundreds of tons at affordable cost is essential for industrial adoption. At that scale, the green chemistry advantages will begin to drive many industries to adopt MDMC in the production workflow, with consequent benefits to Sustainable Development Goals. The science of MDMC will be understood

https://doi.org/10.1021/acssuschemeng.5c12102
ACS Sustainable Chem. Eng. XXXX, XXX, XXX−XXX

better with a combined electro-mechanochemical approach with inputs from time-resolved examination of droplets with nanosecond or better resolution. The phenomena occurring in the droplets such as luminescence, formation of reactive species, propagation of shock waves during droplet fission, etc., need examination. These provide crucial insights leading to accurate modeling of the process.

Future Directions. For a mature discipline of microdroplet chemistry in general, and MDMC in particular, in which processes can occur with predictive outcomes so that engineering and technology development become possible, we need to (i) establish international partnerships and shared resources; (ii) develop in situ diagnostics for droplets in flight with good time resolution; (iii) test scaling laws linking droplet size, charge and experimental parameters with material hardness, and nanomaterial yield; (iv) Advance modeling spanning multiple scales, including (a) electronic and atomistic methods to capture field–reactivity coupling at curved, charged interfaces, (b) mesoscale electrohydrodynamics to describe evaporation, deformation, and reactive flow, and (c) upscaling frameworks that connect MDMC principles to atmospheric, environmental, and geological processes; (v) quantify the relevance of observed phenomena to atmospheric processes using experiments in controlled environments; and finally (vi) engineer continuous droplet reactors at scale for circular materials chemistry so that industrial applications become possible.

The subject of MDMC presents a new possibility of conducting chemistry without external energy. The process unites chemical, electrical and mechanical forces to transform or make materials fast with reduced impact on the environment. An expansion of the area will lead to greater collaborations between chemistry, physics, biology, geoscience, and sustainability science. In the years ahead, I see the establishment of factories where materials are made in droplets sustainably with new application areas being evolved.

While the discussion has focused on water as a Newtonian fluid, the principles of MDMC extend naturally to complex fluids. Polymer and biopolymer solutions, surfactant-rich mixtures, ionic liquids, and colloidal or nanoparticle suspensions are important to consider. In them, viscoelasticity, microphase separation, interfacial structuring, and long relaxation times may couple nonlinearly with charge transport, evaporation, and interfacial fields, creating mechanochemical pathways distinct from those in simple aqueous droplets. For example, understanding how chain entanglement, micellar dynamics, or colloidal assembly respond to droplet deformation, fission, and interfacial charging represents an unexplored frontier. Obviously, MDMC in complex fluids is a rich direction for discovering new reactivity, emergent materials, and nonequilibrium structures that are inaccessible in bulk phases. Although some experiments have been performed, work in this area is at infancy.

CONCLUSIONS

Microdroplet chemistry in general and microdroplet mechanochemistry in particular, transform our understanding of both water and matter, blurring boundaries between electrical, mechanical, and chemical forces at small scales. In fact, the emergence of the area is a unification of these disciplines to address sustainability. In Green Chemistry terms, it is a zero-carbon, zero-waste pathway to materials chemistry. Every droplet becomes a reminder that this chemistry is already happening around us—in clouds, in rain, and now, in the laboratory.

AUTHOR INFORMATION

Corresponding Author

Thalappil Pradeep − *DST Unit of Nanoscience and Thematic Unit of Excellence, Department of Chemistry, Indian Institute of Technology Madras, Chennai 600 036, India; International Centre for Clean Water, Chennai 600113, India;* orcid.org/0000-0003-3174-534X; Email: pradeep@iitm.ac.in

Complete contact information is available at: https://pubs.acs.org/10.1021/acssuschemeng.5c12102

Author Contributions

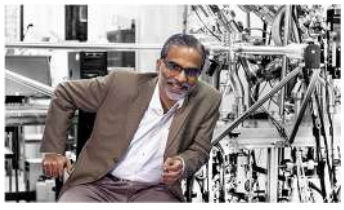
T.P. conceived the idea and wrote the manuscript.

Notes

We emphasize that the process described is not mechanochemistry in the conventional sense of stress- or strain-driven chemistry in the solid state, but rather an electric-field-dominated regime in which mechanical effects are themselves field-induced and the mechanical component is not externally applied but emerges from the electrostatic forces and Coulomb instabilities in charged droplets. As microdroplets are often formed by electrospray, electrical charges are already part of the droplets. Even for microdroplets formed by other means such as nebulization or cavitation, charges exist on their surfaces. The reactive chemical species in droplets exist largely due to the large electric field. Although chemo-electro-mechano effects are acting in unison at this length scale, we propose to call the area as Microdroplet Mechanochemistry. Adding prefixes (such as electro-, chemo-, physico- to mechanochemistry) can dilute the conceptual beauty and may risk the growth of the field to be inclusive with other stimuli.

The author declares no competing financial interest.

Biography



Thalappil Pradeep is an Institute Professor and Deepak Parekh Institute Chair Professor at the Indian Institute of Technology Madras (IITM), Chennai, India. His research interests are in molecular and nanoscale materials. He has authored 600 scientific papers, 10 books, 100+ Indian and 29 US/PCT patents, cofounded 7 start-ups and founded the International Centre for Clean Water (https://iccw.world). He is involved in the development of affordable technologies for drinking water purification. His pesticide removal technology has reached >10 million people. His arsenic removal technology, approved for national implementation, is delivering arsenic free water to >1.4 million people every day. He is a recipient of recognitions including the Shanti Swaroop Bhatnagar Prize, The World Academy of Sciences (TWAS) prize, Padma Shri, Vigyan Shri, Nikkei Asia Prize, Prince Sultan Bin Abdulaziz International Prize for Water, VinFuture Prize and ENI award. He is a Fellow of all the science and engineering academies of India, TWAS, American Association for the Advancement of Science, African Academy of Sciences, US National Academy of Engineering and Academia Europaea. He has received the *Lifetime Achievement Research Award* of IITM and *Distinguished Alumnus Award* of Indian

Institute of Science. As part of philanthropy, he supports a school in his village where 500 students are on rolls.

■ ACKNOWLEDGMENTS

T.P. thanks all his co-workers for their contributions at various stages of the microdroplet work which have led to the conclusions reported here. He acknowledges financial support from the Centre of Excellence (CoE) on Molecular Materials and Functions, established under the Institution of Eminence (IoE) scheme of IIT Madras and the Department of Science and Technology, Government of India, for sustained funding. He also acknowledges funding through a JC Bose Fellowship.

■ REFERENCES

(1) Xiong, H.; Lee, J. K.; Zare, R. N.; Min, W. Strong Electric Field Observed at the Interface of Aqueous Microdroplets. *J. Phys. Chem. Lett.* **2020**, *11*, 7423−7428.
(2) Liu, Y.; Ge, Q.; Wang, T.; Chen, J.; Chan, C. K.; Zhang, L.; et al. Strong Electric Field Force at the Air/Water Interface Drives Fast Sulfate Production in the Atmosphere. *Chem* **2024**, *10*, 330−351.
(3) Spoorthi, B. K.; Debnath, K.; Basuri, P.; Nagar, A.; Waghmare, U. V.; Pradeep, T. Spontaneous Weathering of Natural Minerals in Charged Water Microdroplets Forms Nanomaterials. *Science* **2024**, *384*, 1012−1017.
(4) Müller, T.; Badu-Tawaiah, A.; Cooks, R. G. Accelerated Carbon-Carbon Bond-Forming Reactions in Preparative Electrospray. *Angew. Chem., Int. Ed.* **2012**, *51*, 11832−11835.
(5) Wei, Z.; Li, Y.; Cooks, R. G.; Yan, X. Accelerated Reaction Kinetics in Microdroplets: Overview and Recent Developments. *Annu. Rev. Phys. Chem.* **2020**, *71*, 31−51.
(6) Lee, J. K.; Banerjee, S.; Nam, H. G.; Zare, R. N. Acceleration of Reaction in Charged Microdroplets. *Q. Rev. Biophys.* **2015**, *48*, 437−444.
(7) Cooks, R. G.; Holden, D. T. Breaking Down Microdroplet Chemistry. *Science* **2024**, *384*, 958−959.
(8) Spoorthi, B. K.; Chowdhuri, A. R.; Mondal, B.; Manna, S.; Mahapatra, A.; Kini, A. R.; Pradeep, T. Nanosheet-to-Nanoparticle Transformation in Charged Water Microdroplets: A Pathway for 2D to 0D Materials. *Chem. Commun.* **2025**, *61*, 5577−5580.
(9) Mahapatra, A.; Som, A.; Spoorthi, B. K.; Sarkar, D.; Pradeep, T. From Micro-to-Nano in Charged Water Microdroplets: Unveiling Steps in the Weathering of Minerals. *Chem. Commun.* **2025**, *61*, 15846−15849.
(10) Anastas, P. T.; Warner, J. C. *Green Chemistry: Theory and Practice*; Oxford University Press: New York, 1998.
(11) Xia, Y.; Xu, J.; Li, J.; Chen, B.; Dai, Y.; Zare, R. N. Visualization of the Charging of Water Droplets Sprayed into Air. *J. Phys. Chem. A* **2024**, *128*, 5684−5690.
(12) Basuri, P.; Chakraborty, A.; Ahuja, T.; Mondal, B.; Kumar, J. S.; Pradeep, T. Spatial Reorganization of Analytes in Charged Aqueous Microdroplets. *Chem. Sci.* **2022**, *13*, 13321−13329.
(13) Shi, L.; LaCour, R. A.; Qian, N.; Heindel, J. P.; Lang, X.; Zhao, R.; Head-Gordon, T.; Min, W. Water Structure and Electric Fields at the Interface of Oil Droplets. *Nature* **2025**, *640*, 87−93.
(14) Li, A.; Luo, Q.; Park, S.-J.; Cooks, R. G. Synthesis and Catalytic Reactions of Nanoparticles Formed by Electrospray Ionization of Coinage Metals. *Angew. Chem., Int. Ed.* **2014**, *53*, 3147−3150.
(15) Li, A.; Baird, Z.; Bag, S.; Sarkar, D.; Prabhath, A.; Pradeep, T.; Cooks, R. G. Using Ambient Ion Beams to Write Nanostructured Patterns for Surface Enhanced Raman Spectroscopy. *Angew. Chem., Int. Ed.* **2014**, *53*, 12528−12531.
(16) Sarkar, D.; Mahitha, M. K.; Som, A.; Li, A.; Wleklinski, M.; Cooks, R. G.; Pradeep, T. Metallic Nanobrushes Made Using Ambient Droplet Sprays. *Adv. Mater.* **2016**, *28*, 2223−2228.
(17) Sarkar, D.; Mahapatra, A.; Som, A.; Kumar, R.; Nagar, A.; Baidya, A.; Pradeep, T. Patterned Nanobrush Nature Mimics with Unprecedented Water-Harvesting Efficiency. *Adv. Mater. Interfaces* **2018**, *5*, No. 1800667.
(18) Lee, J. K.; Samanta, D.; Nam, H. G.; Zare, R. N. Spontaneous Formation of Gold Nanostructures in Aqueous Microdroplets. *Nat. Commun.* **2018**, *9*, No. 1562.
(19) Chowdhuri, A. R.; Spoorthi, B. K.; Mondal, B.; Bose, P.; Bose, S.; Pradeep, T. Ambient Microdroplet Annealing of Nanoparticles. *Chem. Sci.* **2021**, *12*, 6370−6377.
(20) Nie, H.; Wei, Z.; Qiu, L.; Chen, X.; Holden, D. T.; Cooks, R. G. High-yield Gram-scale Organic Synthesis Using Accelerated Microdroplet/thin Film Reactions With Solvent Recycling. *Chem. Sci.* **2020**, *11*, 2356−2361.
(21) Dong, L.; Li, L.; Chen, H.; Cao, Y.; Lei, H. Mechanochemistry: Fundamental Principles and Applications. *Adv. Sci.* **2025**, *12*, No. 2403949.
(22) Mehrgardi, M. A.; Mofidfar, M.; Li, L.; Chamberlayne, C. F.; Lynch, S. R.; Zare, R. N. Catalyst-Free Transformation of Carbon Dioxide to Small Organic Compounds in Water Microdroplets Nebulized by Different Gases. *Adv. Sci.* **2024**, *11*, No. 2406785.
(23) Song, X.; Basheer, C.; Zare, R. N. Making Ammonia from Nitrogen and Water Microdroplets. *Proc. Natl. Acad. Sci. U.S.A.* **2023**, *120*, No. e2301206120.
(24) Nag, A.; Baksi, A.; Ghosh, J.; Kumar, V.; Bag, S.; Mondal, B.; Ahuja, T.; Pradeep, T. Tribochemical Degradation of Polytetrafluoroethylene in Water and Generation of Nanoplastics. *ACS Sustainable Chem. Eng.* **2019**, *7*, 17554−17558.
(25) Xia, D.; Zhang, H.; Ju, Y.; Xie, H.-B.; Su, L.; Ma, F.; Jiang, J.; Chen, J.; Francisco, J. S. Spontaneous Degradation of the "Forever Chemicals" Perfluoroalkyl and Polyfluoroalkyl Substances (PFASs) on Water Droplet Surfaces. *J. Am. Chem. Soc.* **2024**, *146*, 11266−11271.
(26) Sarkar, D.; Mondal, B.; Som, A.; Ravindran, S. J.; Jana, S. J.; Manju, C. K.; Pradeep, T. Holey MoS_2 Nanosheets with Photocatalytic Metal Rich Edges by Ambient Electrospray Deposition for Solar Water Disinfection. *Global Challenges* **2018**, *2*, No. 1800052.
(27) Hao, H.; Leven, I.; Head-Gordon, T. Can electric fields drive chemistry for an aqueous microdroplet? *Nat. Commun.* **2022**, *13*, No. 280.
(28) Cassone, G.; Amante, S.Reconceiving Catalysis at Air-Water Interfaces: Interfacial Electric Fields Are Milder Than Bulk Fields. *ChemRxiv* 2025 DOI: 10.26434/chemrxiv-2025-rnpmd.
(29) Gong, K.; Nandy, A.; Song, Z.; Li, Q.-S.; Hassanali, A.; Cassone, G.; Banerjee, S.; Xie, J. Revisiting the Enhanced Chemical Reactivity in Water Microdroplets: The Case of a Diels-Alder Reaction. *J. Am. Chem. Soc.* **2024**, *146*, 31585−31596.
(30) Shirley, J. C.; Ng, Z. X.; Chiang, K.-Y.; Nagata, Y.; Litman, Y.; Hazrah, A. S.; Bonn, M. Reevaluating Anomalous Electric Fields at the Air−Water Interface: A Surface-Specific Spectroscopic Survey. *J. Am. Chem. Soc.* **2025**, *147*, 46163−46173.
(31) Shaik, S.; Danovich, D.; Joy, J.; Wang, Z.; Stuyver, T. Electric-Field Mediated Chemistry: Uncovering and Exploiting the Potential of (Oriented) Electric Fields to Exert Chemical Catalysis and Reaction Control. *J. Am. Chem. Soc.* **2020**, *142*, 12551−12562.
(32) Fenn, J. B.; Mann, M.; Meng, C. K.; Wong, S. F.; Whitehouse, C. M. Electrospray Ionization for Mass Spectrometry of Large Biomolecules. *Science* **1989**, *246*, 64−71.
(33) Iribarne, J. V.; Thomson, B. A. On the Evaporation of Small Ions from Charged Droplets. *J. Chem. Phys.* **1976**, *64*, 2287−2294.
(34) De La Mora, J. F.; Loscertales, I. G. The Current Emitted by Highly Conducting Taylor Cones. *J. Fluid Mech.* **1994**, *260*, 155−184.
(35) Rayleigh, L. On the Equilibrium of Liquid Conducting Masses Charged with Electricity. *London, Edinburgh Dublin Philos. Mag. J. Sci.* **1882**, *14*, 184−186.
(36) de la Mora, J. F. The Fluid Dynamics of Taylor Cones. *Annu. Rev. Fluid Mech.* **2007**, *39*, 217−243.
(37) Girod, M.; Moyano, E.; Campbell, D. I.; Cooks, R. G. Accelerated bimolecular reactions in microdroplets studied by desorption electrospray ionization mass spectrometry. *Chem. Sci.* **2011**, *2*, 501−510.

Publications from other groups

Check for updates

RESEARCH ARTICLE

NANO · MICRO small
www.small-journal.com

Enhancement of Photoluminescence Quantum Yield of Silver Clusters by Heavy Atom Effect

Aoi Akiyama, Sakiat Hossain, Yoshiki Niihori, Kazutaka Oiwa, Jayoti Roy, Tokuhisa Kawawaki, Thalappil Pradeep, and Yuichi Negishi**

Many ligand-protected metal clusters exhibit phosphorescence at room temperature. However, strategies for improving their phosphorescence quantum yield, a critical parameter of performance, remain poorly developed. In contrast, fluorescent dyes are commonly modified by introducing heavy atoms, such as iodine (I), to enhance intersystem crossing in the excited state, thereby harnessing the heavy atom effect to increase phosphorescence efficiency. In this study, a pair of ligand-protected silver (Ag) clusters is successfully synthesized with internal cavities encapsulating anions (X^{z-}), namely sulfide ions (S^{2-}) or iodide ions (I^-), which significantly differ in atomic number each other. Single-crystal X-ray diffraction and nuclear magnetic resonance spectroscopy revealed that the resulting Ag clusters are composed of $X@Ag_{54}S_{20}(thiolate)_{20}(sulfonate)_m$, where (X, *m*) = (S, 12) or (I, 11). X-ray photoelectron spectroscopy revealed that the Ag atoms in these compounds exhibit a mixed-valence state. Furthermore, experiments on their photoluminescence revealed that a heavy central anion induced an internal heavy-atom effect similar to that observed in organic fluorescent dyes. As a result, the phosphorescence quantum yield became 16 times higher when S^{2-} is replaced by I^- as the central atom.

1. Introduction

Progress in nanotechnology is facilitated by the development of precise synthesis methods and the detailed characterization of fine and sophisticated nanomaterials. Ligand-protected metal clusters, a representative group of nanomaterials, have been the focus of numerous studies, resulting in the establishment of precise synthesis methods and the elucidation of their properties through synergistic experimental and theoretical investigations.[1] Among these, ligand-protected metal clusters composed of noble metal elements, such as gold (Au), silver (Ag), and copper (Cu), exhibit unique properties according to the number of constituent atoms and dopant elements, including photoluminescence (PL),[2] magnetic properties,[3] and catalytic activity.[4] These characteristics have attracted significant attention in both fundamental research and practical applications.[5] Recently, studies have also been conducted on clusters with complex structures arising from combinations of noble metal elements and main group elements.[6] Among these, Ag–sulfur (Ag—S) based clusters are metal clusters with cavities[7] capable of encapsulating various anions,[8] and recent efforts have focused on altering the encapsulated anionic species to modulate the physicochemical properties of these clusters.[7b,9]

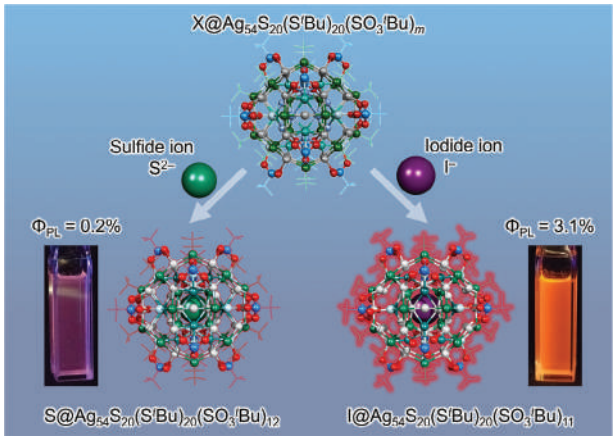
Ligand-protected metal clusters often exhibit PL.[10] Recent experimental studies have shown that phosphorescence originates in the excited triplet state.[11] Therefore, enhancing the population of the excited triplet state of metal clusters is crucial for their application as room-temperature phosphorescent materials and triplet sensitizers.[12] Generally, transition from the excited singlet state (S_n) to the excited triplet state (T_m) is spin-forbidden, resulting in a zero transition-moment. However, studies on organic fluorescent dyes have shown that introducing heavy atoms, such as iodine (I), into the fluorophore enhances spin-orbit coupling (the internal heavy-atom effect), which increases the rate constant for intersystem crossing (ISC) from S_n to T_m, thereby improving the efficiency of phosphorescence.[13] Similarly, encapsulating a heavy atom into Ag—S clusters may enhance the phosphorescence quantum yield. However, to date, there are limited reports on the internal heavy-atom effect of ligand-protected metal clusters.[14]

A. Akiyama, K. Oiwa, T. Kawawaki
Department of Chemistry
Graduate School of Science
Tokyo University of Science
1–3 Kagurazaka, Shinjuku-ku, Tokyo 162–8601, Japan
S. Hossain, Y. Niihori, Y. Negishi
Research Institute for Science & Technology
Tokyo University of Science
1–3 Kagurazaka, Shinjuku-ku, Tokyo 162–8601, Japan
E-mail: niihori@rs.tus.ac.jp; yuichi.negishi.a8@tohoku.ac.jp
J. Roy, T. Pradeep
DST Unit of Nanoscience (DST UNS) and Thematic Unit of Excellence (TUE)
Department of Chemistry
Indian Institute of Technology
Madras, Chennai 600036, India
Y. Negishi
Institute of Multidisciplinary Research for Advanced Materials
Tohoku University
2–1–1 Katahira, Aoba-ku, Sendai 980–8577, Japan

The ORCID identification number(s) for the author(s) of this article can be found under https://doi.org/10.1002/smll.202500700

© 2025 The Author(s). Small published by Wiley-VCH GmbH. This is an open access article under the terms of the Creative Commons Attribution License, which permits use, distribution and reproduction in any medium, provided the original work is properly cited.

DOI: 10.1002/smll.202500700



Scheme 1. Enhancement of phosphorescence quantum yield by encapsulating S^{2-} or I^- anions inside the central cavity of the $Ag_{54}S_{20}(S^tBu)_{20}(SO_3{}^tBu)_m$ framework.

In this study, we successfully synthesized ligand-protected Ag—S clusters with central cavities encapsulating anions X^{z-}, where $X^{z-} = S^{2-}$ (sulfide) or I^- (iodide), which significantly differ in atomic number each other (**Scheme 1**). Single-crystal X-ray diffraction (SC-XRD) and proton nuclear magnetic resonance (^{1}H NMR) spectroscopy revealed that the resulting Ag clusters were composed of $X@Ag_{54}S_{20}$(thiolate)$_{20}$(sulfonate)$_m$, where (X, m) = (S, 12) or (I, 11) **(X@Ag54)**. Furthermore, a comparison of the optical properties of the obtained pair of **X@Ag54** (X = S or I) demonstrated that an internal heavy-atom effect occurred in these Ag–S clusters, similar to that in organic fluorescent dyes. Accordingly, the phosphorescence quantum yield was 16 times higher when S^{2-} was replaced by I^- as the encapsulated atom (Scheme 1).

2. Results and Discussion

2.1. Synthesis

For the synthesis of **S@Ag54**, 48.6 mg (0.22 mmol) of silver trifluoroacetate (Ag(TFA)) and 10.6 mg (0.044 mmol) of copper(II) nitrate trihydrate ($Cu(NO_3)_2{\bullet}3H_2O$) were dissolved in 4 mL of a mixture of acetone and acetonitrile (50/50 vol%). Then, 15 µL (0.13 mmol) of *tert*-butanethiol (^{t}BuSH) was added to this solution, and the resulting mixture was transferred into a glass tube (Figure S1A, Supporting Information). A cap with a small hole (Figure S1B, Supporting Information) was placed on the glass tube, and the tube was left undisturbed under a LED for light irradiation to promote copper-catalyzed thiol oxidation (Figure S1C, Supporting Information). Orange crude crystals of **S@Ag54** were obtained after ≈1 week (Figure S2Aa, Supporting Information). The crude crystals were dissolved in chloroform, and hexane was slowly added to the upper layer. The solution was left to stand for one month, resulting in the formation of single crystals of **S@Ag54** (Figure S2Ba, Supporting Information).

I@Ag54 was synthesized in the same manner as **S@Ag54**, except 20 mg (0.054 mmol) of tetrabutylammonium iodide (TBAI), as well as ^{t}BuSH, was added to the acetone/acetonitrile mixture of Ag(TFA)/$Cu(NO_3)_2$. Red-orange crude crystals of **I@Ag54** were obtained after ≈2 weeks (Figure S2Ab, Supporting Information). The crude crystals were dissolved in chloroform, and hexane was slowly added to the upper layer. The solution was left to stand for one month, resulting in the formation of single crystals of **I@Ag54** (Figure S2Bb, Supporting Information).

2.2. Chemical Composition

S@Ag54 and **I@Ag54** were crystallized in space groups of *Fm*−3 and *Pa*−3, respectively (Table S1, Supporting Information), and their geometric structures were determined using SC-XRD (**Figure 1A,B**). According to these geometric structures, the chemical compositions of **S@Ag54** and **I@Ag54** were $X@Ag_{54}S_{20}(S^tBu)_{20}(SO_3{}^tBu)_m$ (X = S and I; S^tBu = *tert*-butanethiolate; $SO_3{}^tBu$ = *tert*-butyl sulfonate) (hereafter, **X@Ag54**). Although the number of S^tBu and $SO_3{}^tBu$ ligands for both **S@Ag54** and **I@Ag54** were estimated by SCXRD to be 20 and 12, respectively, **S@Ag54** and **I@Ag54** may have different ligand numbers because S and I have different families on the periodic table. Therefore, an attempt was made to estimate the number of ligands in **I@Ag54** through ^{1}H NMR analysis. In the ^{1}H NMR spectra of **S@Ag54** and **I@Ag54** (**Figure 2**), the two peaks at 1.63 and 1.38 ppm can be attributed to the protons of S^tBu and $SO_3{}^tBu$, respectively.[6b,h] The integral values of these peaks revealed that **S@Ag54** contained 20 S^tBu and 12 $SO_3{}^tBu$ ligands, while **I@Ag54** contained 20 S^tBu and 11 $SO_3{}^tBu$ ligands. These results indicated that the chemical compositions of **S@Ag54** and **I@Ag54** were $S@Ag_{54}S_{20}(S^tBu)_{20}(SO_3{}^tBu)_{12}$ and $I@Ag_{54}S_{20}(S^tBu)_{20}(SO_3{}^tBu)_{11}$, respectively (Figure 1).

The above chemical compositions indicate that there is a difference in the number of $SO_3{}^tBu$ ligand between **S@Ag54** and **I@Ag54**. Ligand-protected metal clusters are generally formed when the total number of valence electrons is even.[6g,15] In this study, the geometrical structure obtained by SC-XRD and electrospray ionization (ESI) mass spectrum at the low mass region showed that TFA^-, which could be a counter ion, was not observed for either **S@Ag54** or **I@Ag54**, suggesting that these clusters were neutral. In this case, because $S@Ag_{54}S_{20}(S^tBu)_{20}(SO_3{}^tBu)_{12}$ has an even number of valence electrons, **I@Ag54** with the same ligand combination ($I@Ag_{54}S_{20}(S^tBu)_{20}(SO_3{}^tBu)_{12}$) should have an odd number of valence electrons. Therefore, it can be considered that **I@Ag54** was formed with one fewer $SO_3{}^tBu$ ligand than **S@Ag54** to prevent destabilization due to the odd number of valence electrons.

To gain a deeper understanding of the chemical composition, we also acquired ESI mass spectra of the products. The ESI-mass spectra of both **S@Ag54** and **I@Ag54** contained multiple peaks attributed to ions in which AgS or ligands were adsorbed or desorbed from the clusters[16] (e.g., **I@Ag54** + 2 AgS) (Figure S3 and Tables S2 and S3, Supporting Information). These results confirmed that the estimation of the above chemical compositions is correct for both **X@Ag54**.

2.3. Geometric Structure

The geometric structures of **X@Ag54** clusters were similar each other, with both containing an $X@\{Ag_{12}S_8\}$ core

 © 2025 The Author(s). Small published by Wiley-VCH GmbH

16136829, 2025, 25, Downloaded from https://onlinelibrary.wiley.com/doi/10.1002/smll.202500700 by Central Library The Librarian, Wiley Online Library on [04/01/2026]. See the Terms and Conditions (https://onlinelibrary.wiley.com/terms-and-conditions) on Wiley Online Library for rules of use; OA articles are governed by the applicable Creative Commons License

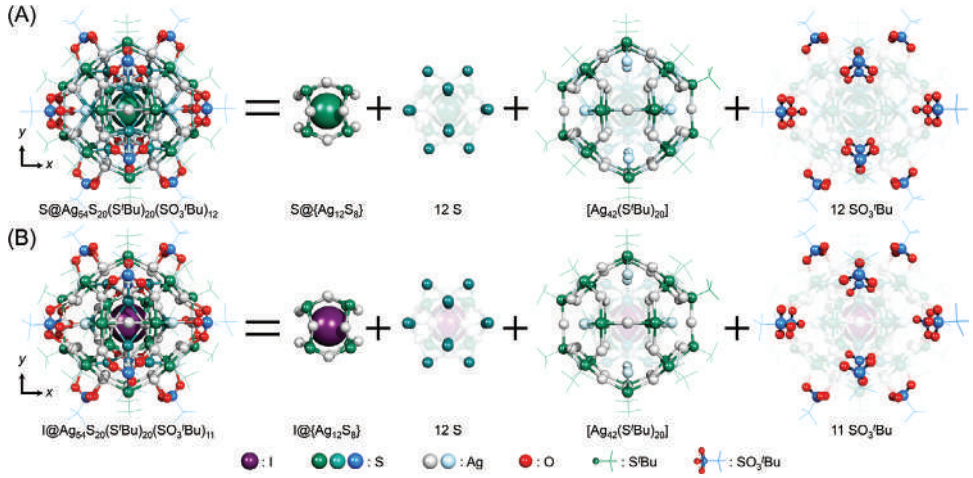


Figure 1. Geometric structures of A) **S@Ag54** and B) **I@Ag54**. The distances between the central atoms (S or I) and the nearest Ag atoms in **S@Ag54** and **I@Ag54** are 3.19 and 3.27 Å, respectively (Figure S5, Supporting Information). Considering the ionic radius, **S@Ag54** can be considered to have no bond between S and the Ag atoms of core. However, this distance is shorter than the total value of van der Waals radius of S and Ag atoms. Therefore, it can be considered that a weak bond exists also in the core of **S@Ag54**.

(Figure 1A,B). In this core, the central anion X (S^{2-} or I^-) was surrounded by 12 Ag atoms, forming an icosahedron (point group I_h) (Figure S4, Supporting Information), with 8 S atoms in a cubic arrangement surrounding this core. On the surface of the X@{$Ag_{12}S_8$} core, 12 S atoms formed an intermediate layer (highlighted in yellow, Figure S4A, Supporting Information), which was connected to outer $Ag_{42}(S^tBu)_{20}$. The 12 S atoms of the intermediate layer were bonded to 12 Ag atoms of $Ag_{42}(S^tBu)_{20}$ (X@{$Ag_{12}S_8$}S_{12}[$Ag_{42}(S^tBu)_{20}$]) (highlighted in blue, Figure S4A, Supporting Information). On the surface of X@{$Ag_{12}S_8$}S_{12}[$Ag_{42}(S^tBu)_{20}$], the S atoms of S(^{t}Bu) were arranged in a regular icosahedral structure with two coordination modes: μ_3-S(^{t}Bu) and μ_4-S(^{t}Bu) (Figure S4B,C, Supporting Information). The m $SO_3{}^tBu$ ligands were coordinated with 12 Ag atoms of $Ag_{42}(S^tBu)_{20}$ (highlighted in blue, Figure S4A, Supporting Information), which were bonded to the S atoms of the intermediate layer, as well as 2 Ag atoms of remaining $Ag_{30}(S^tBu)_{20}$ (highlighted in red, Figure S4A, Supporting Information) in the coordination mode of μ_3-$O_3S(^tBu)$-κ^3O, O′, O″ (Figure S4D, Supporting Information). Owing to this structure, **X@Ag54** can be described as X@{$Ag_{12}S_8$}S_{12}[$Ag_{42}(S^tBu)_{20}$$(SO_3{}^tBu)_m$].

In these structures, both the X@{$Ag_{12}S_{20}$} part and surrounding $Ag_{42}(S^tBu)_{20}(SO_3{}^tBu)_m$ shell exhibit the same T_h symmetry. However, as mentioned earlier, **I@Ag54** has one fewer $SO_3{}^tBu$ ligand than **S@Ag54**. The SC-XRD results suggest that a $SO_3{}^tBu$ ligand is missing from a random site, rather than a specific site, in **I@Ag54**. Therefore, in **I@Ag54**, the 12 coordination sites are randomly occupied by 11 $SO_3{}^tBu$ ligands, leading to the formation of multiple structural isomers and accordingly, disorder in the geometric structure of **I@Ag54**.

These geometric structures of **X@Ag54** are similar to those of previously reported clusters, such as $S@Ag_{40.13}Cu_{13.87}S_{18}(S^tBu)_{20}(SO_3{}^tBu)_{12}$ and $S@Cu_{54}S_{12}O_6(S^tBu)_{20}(SO_3{}^tBu)_{12}$.[6h,i] In the two previously reported clusters, the $M_{42}(S^tBu)_{20}(SO_3{}^tBu)_{12}$ (M = Ag or Cu) shell, which has T_h symmetry, also covers the core. However, there are two major differences between these two previously reported clusters and **X@Ag54**: 1) in the previously reported clusters, Ag and Cu, or only Cu, are included as metals, whereas in **X@Ag54**, only Ag is present as the metal of the clusters; 2) the previously reported clusters have two fewer chalcogenide ions (S^{2-} or O^{2-}) other than the central ion (18 chalcogenide ions) than **X@Ag54** (20 sulfide ions). As a result, the diameter of the cavity of the $M_{12}S_8$ core of **X@Ag54** (≈5.04 and 5.13 Å for **S@Ag54** and **I@Ag54**, respectively; Figures S4E and S5, Supporting Information), is greater than that of the two previously reported clusters (4.94 and 4.88 Å).[6b–i,17] For this reason, both S^{2-} (ionic radius = 1.84 Å) and I^- (ionic radius = 2.20 Å),[18] were stably encapsulated inside the {$M_{12}S_8$} core of **X@Ag54**.

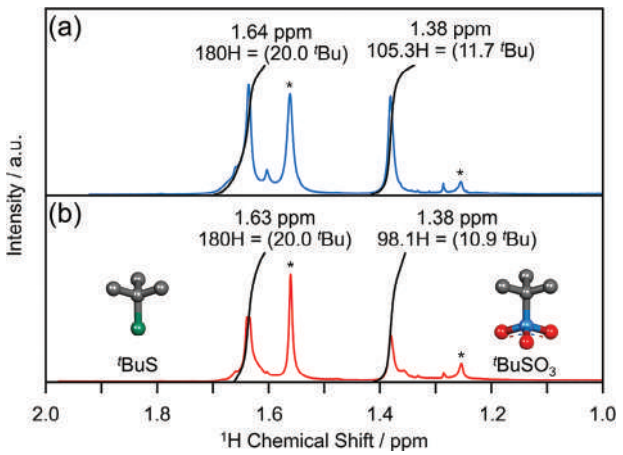


Figure 2. ^{1}H NMR spectra of a) **S@Ag54** and b) **I@Ag54** in $CDCl_3$. The asterisks (*) mark the peaks attributed to impurities, such as water (1.56 ppm) or alkanes/grease (1.25 ppm).

© 2025 The Author(s). Small published by Wiley-VCH GmbH

16136829, 2025, 25, Downloaded from https://onlinelibrary.wiley.com/doi/10.1002/smll.202500700 by Central Library The Librarian, Wiley Online Library on [04/01/2026]. See the Terms and Conditions (https://onlinelibrary.wiley.com/terms-and-conditions) on Wiley Online Library for rules of use; OA articles are governed by the applicable Creative Commons License

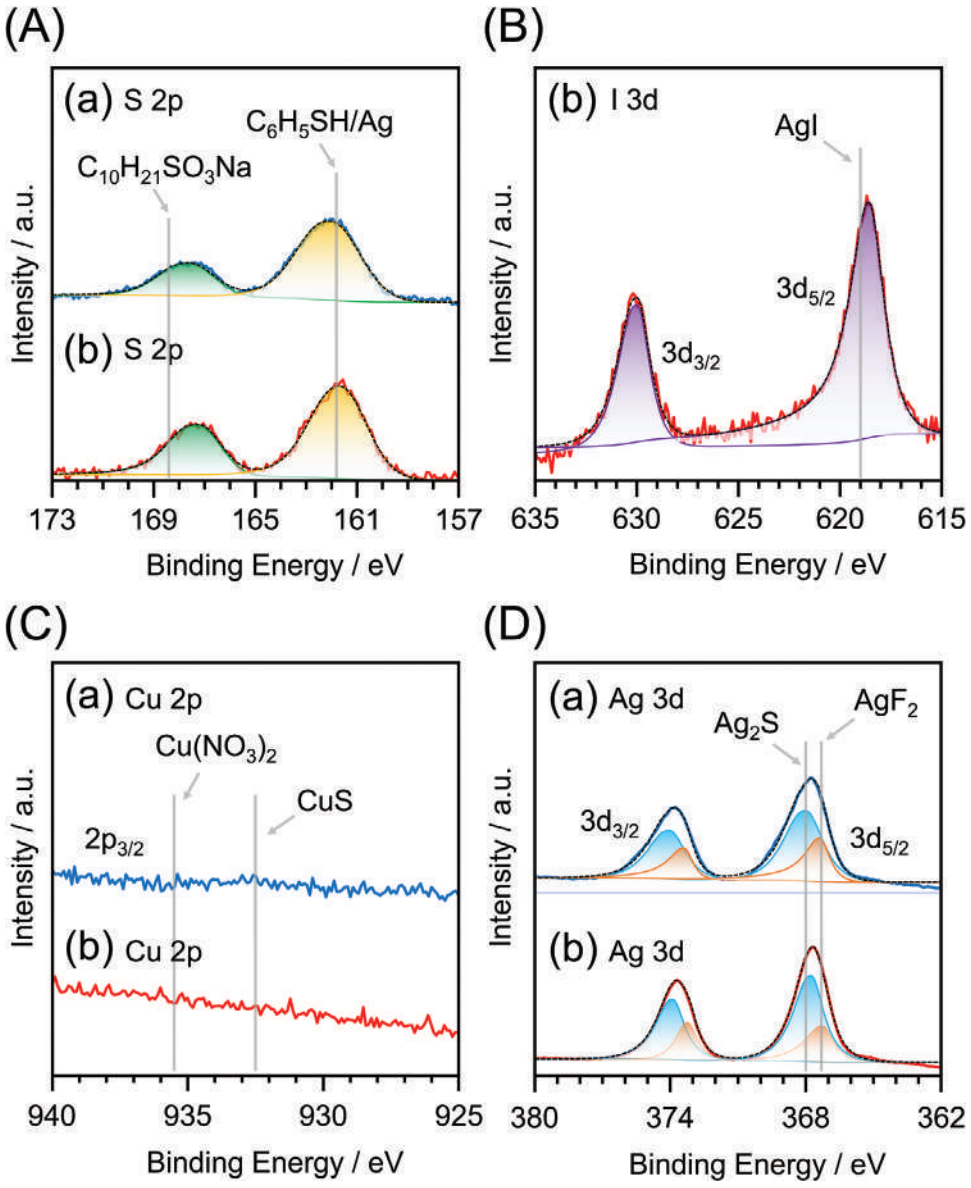


Figure 3. X-ray photoelectron spectra of A) S 2p, B) I 3d, C) Cu 2p, D) and Ag 3d for (a) **S@Ag54** and (b) **I@Ag54**. Different colors of fitting curves in spectra correspond to different oxidation states. In (A), the peaks on the low binding energy side (yellow) are attributed to sulfide S^{2-} or thiolate $^{t}BuS^{-}$, and the peaks on the high binding energy side (green) are attributed to S derived from sulfonate $^{t}BuSO_3^{-}$. Spectrum (B) indicates that the charge state of I is similar to that of I^{-}. Spectrum (C) indicates that **X@Ag54** does not include Cu. In (D), the peaks ≈368 and 374 eV are attributed to Ag $3d_{5/2}$ and Ag $3d_{3/2}$, respectively. These spectra indicated that the oxidation state of Ag in **X@Ag54** was similar to that of Ag_2S and AgF_2.

2.4. Formation Mechanism

X@Ag54 contains 20 S atoms. These S atoms are considered to be produced through the reaction between Ag—S^{t}Bu and Ag^{+}: this reaction produces Ag_2S.[6a] In this study, although only ^{t}BuSH was added as the ligand during the synthesis, in situ produced $SO_3{}^{t}Bu$ was also included as a ligand in **X@Ag54**, as confirmed by SC-XRD (Figure 1), ^{1}H NMR (Figure 2), and ESI-mass spectroscopy (Figure S3, Supporting Information), in addition to X-ray photoelectron spectroscopy (XPS) (**Figure 3**; Figures S6, and S7, Supporting Information) and Fourier-transform infrared (FT-IR) absorption spectroscopy (Figure S8, Supporting Information), of the products. The catalytic oxidation of thiols by Cu^{2+} (Scheme S1, Supporting Information) is responsible for the formation of these $SO_3{}^{t}Bu$ ligands.[6h,i] In this reaction, Cu^{2+} coordinates with RSH, which reduces Cu (Cu^{+}) and generates the thiyl radical (RS•).[19] RS• reacts with oxygen molecular (O_2) and unreacted RSH in the system to produce RSO_3H (Figure S9, Supporting Information). After coordinating with RSH, Cu^{+} is oxidized to Cu^{2+} by O_2, returning to its original state. As these reactions proceed, $SO_3{}^{t}Bu$ is formed in the reaction solvent and coordinates with the metal cluster (Scheme S1, Supporting Information). In these reactions, the coordination and reduction of Cu^{2+} and formation of RSO_3H from RS• proceed with rate

© 2025 The Author(s). Small published by Wiley-VCH GmbH

16136829, 2025, 25, Downloaded from https://onlinelibrary.wiley.com/doi/10.1002/smll.202500700 by Central Library The Librarian, Wiley Online Library on [04/01/2026]. See the Terms and Conditions (https://onlinelibrary.wiley.com/terms-and-conditions) on Wiley Online Library for rules of use; OA articles are governed by the applicable Creative Commons License

constants of $\approx 10^{8-10}$ $M^{-1}s^{-1}$,[19] which is very fast. Moreover, these reactions are faster than the oxidation of Cu^+ to Cu^{2+} by O_2, which becomes the rate-limiting step. Indeed, when $Cu(NO_3)_2$ and ^{t}BuSH were mixed, the blue color of the solution immediately disappeared owing to the reduction of Cu^{2+} to colorless Cu^+, whereas this blue color took 2 days to reappear as Cu^+ reverted to Cu^{2+} (Figure S10Ba, Supporting Information). However, when Ag^+ coexisted with Cu^{2+} and ^{t}BuSH, the recovery of Cu^{2+} from Cu^+ occurred more rapidly (Figure S10, Supporting Information), with the disappearance of ^{t}BuSH confirmed by electron spin resonance (ESR) spectroscopy of the reaction solution. These results demonstrate that the presence of Ag^+ accelerates the rate-limiting step of RSH oxidation by Cu^{2+}, thereby accelerating the formation of RSO_3H.

Zhu et al. have reported the synthesis of $S@Ag_{40.13}Cu_{13.87}S_{18}(S^tBu)_{20}(SO_3{}^tBu)_{12}$ containing both Ag and Cu as metals under reaction conditions similar to those used in our study.[6h] However, in our study, **X@Ag54**, which contains only Ag as the metal, was synthesized (Figure 3C). In our study, unlike the research by Zhu et al., we did not add the reducing reagents, such as borane amine complexes,[6h] into the reaction solvent. Moreover, compared to their study, we significantly reduced the amount of Cu^{2+} catalyst relative to Ag^+ (1.260 vs 0.198 atom %). These factors likely contributed to the successful synthesis of **X@Ag54** with only Ag as the metal, which enabled the encapsulation of I^-.

2.5. Oxidation State of Ag

The core of **X@Ag54** consisted of only Ag and S and formed a central cavity, as observed in previously reported $[S@Ag_{50}S_{12}(S^tBu)_{20}](TFA)_4$.[6c] In the previously reported cluster, all the Ag atoms are in the +1 oxidation state, giving rise to a single sharp peak in both the Ag $3d_{3/2}$ and $3d_{5/2}$ regions of its XPS spectrum. In contrast, broad peaks were observed in the Ag $3d_{5/2}$ and $3d_{3/2}$ regions of the XPS spectra of **X@Ag54** (Figure 3D). These peaks were fitted with two functions, and the position of the peak on the high-energy side was close to the position of the peak corresponding to Ag_2S or AgF_2 (Figure 3D; Figure S6 and Table S4, Supporting Information).[20] These observations indicates that Ag in **X@Ag54** is in a mixed-valence state, rather than the single-valence state of Ag in $[S@Ag_{50}S_{12}(S^tBu)_{20}](TFA)_4$.[6c] In fact, there have been several reports on Ag existing in mixed-valence states.[20,21] Furthermore, Cu atoms in Cu–chalcogen clusters with geometric structures similar to those of **X@Ag54**, such as $[S@Cu_{54}S_{12}O_6(S^tBu)_{20}(SO_3{}^tBu)_{12}]$ and $[Cu_{50}S_{12}(S^tBu)_{20}(TFA)_{12}]$, also exist in a mixed-valence state of Cu^I and Cu^{II}.[6b,i,22] Unlike $[S@Ag_{50}S_{12}(S^tBu)_{20}](TFA)_4$, **X@Ag54** contained two types of ligands (S^tBu and $SO_3{}^tBu$), and this can be considered to cause the mixed-valence state of Ag. As discussed in the (Section S3.1, Supporting Information), when **X@Ag54** has neutral charge and is 0-electron system, the mixed-valence states of Ag in **S@Ag54** and **I@Ag54** can be estimated to be $S@Ag^I{}_{34}Ag^{II}{}_{20}$ and $I@Ag^I{}_{36}Ag^{II}{}_{18}$, respectively. In this composition, the ratio of AgI: AgII is 62.9:37.1 and 66.7:33.3 for **S@Ag54** and **I@Ag54**, respectively. Figure 3D shows that the ratio of Ag^I: Ag^{II} is 63.7:36.3 and 65.8:34.2 for **S@Ag54** and **I@Ag54**, respectively. In this way, the results of Ag 3d XPS will reproduce the expected mixed-valence states of Ag for **S@Ag54** and **I@Ag54**.

2.6. Stability

To apply the clusters as materials, information on their stability is crucial. Therefore, the stability of **X@Ag54** against the following three factors was investigated: 1) degradation in solution, 2) heat-induced dissociation, and 3) collision-induced dissociation (CID).

Stability against degradation in solution was evaluated by heating **X@Ag54** in toluene and tracking changes in its ultraviolet–visible (UV–vis) absorption spectrum. The results showed that 1) the stabilities of both clusters are similar, and 2) the absorption spectra of both samples in toluene can remain unchanged over 20 h of heating at 60 °C (**Figure** 4Aa,Ab; Figure S11, Supporting Information). The half-life of both clusters under these degradation conditions was estimated to be ≈200 h (Table S5, Supporting Information).

Stability against heat-induced dissociation was evaluated using thermogravimetric analysis (TGA). Both clusters underwent three stages of weight loss (Figure 4Ba,Bb; Figure S12, Supporting Information). According to the weight of the ligands and their functional groups, the weight loss at ≈115 °C is attributed to the removal of $SO_3{}^tBu$ ligands (theoretical loss = 16.6% for **S@Ag54** and 15.3% for **I@Ag54**), while the weight loss at ≈140 °C is attributed to the removal of ^{t}Bu groups from S^tBu ligands (theoretical loss = 11.5% for **S@Ag54** and 11.6% for **I@Ag54**). The final weight loss at ≈170 °C is interpreted as the removal of sulfur (theoretical loss = 6.46% for **S@Ag54** and 6.49% for **I@Ag54**). The slow weight loss at subsequent temperatures can be attributed to the desorption of sulfur or X from the remaining $X@Ag_{54}S_{20}$. The dissociation energies of $Ag—SO_3{}^tBu$ and $AgS—{}^tBu$, calculated using density functional theory (DFT), were 54.2 and 57.4 kcal mol^{-1}, respectively (Table S6, Supporting Information). This should be the reason why thermal dissociation occurred in the order. Each weight-loss also occurred at a similar temperature. These results indicates that the stability of both clusters against thermal dissociation is similar to each other.

Stability against CID was investigated in a vacuum.[23] Specifically, **X@Ag54** was introduced into an ESI-mass spectrometer, where it collided with argon (Ar) to undergo CID. The stability of each cluster was examined by evaluating the chemical composition and ion intensity of the generated fragment ions. Mass spectra were obtained following the collision of $[\mathbf{S@Ag54} + SO_3{}^tBu]^{2+}$ and $[\mathbf{I@Ag54} + SO_3{}^tBu + 2AgS]^{2+}$ with Ar at different collision energies (**Figure** 5A,B; Table S9, Supporting Information). The parent ions of **X@Ag54** dissociated as the collision energy increased. The main dissociation patterns corresponded to the radical cleavage of $Ag—O_3S^tBu$ and $S—{}^tBu$ (Figure 5C). These dissociation patterns closely resembled those observed in the TGA curves. Furthermore, these dissociation reactions of both clusters occurred at similar collision energies (Figures S13 and S14 and Tables S7 and S8, Supporting Information), indicating that the stability of both clusters against CID was also similar to each other.

In these experiments, detachment of surface ligands was the first step of degradation. It can be considered that since the difference in the kinds of the central anions (X) do not significantly

© 2025 The Author(s). Small published by Wiley-VCH GmbH

16136829, 2025, 25, Downloaded from https://onlinelibrary.wiley.com/doi/10.1002/smll.202500700 by Central Library The Librarian, Wiley Online Library on [04/01/2026]. See the Terms and Conditions (https://onlinelibrary.wiley.com/terms-and-conditions) on Wiley Online Library for rules of use; OA articles are governed by the applicable Creative Commons License

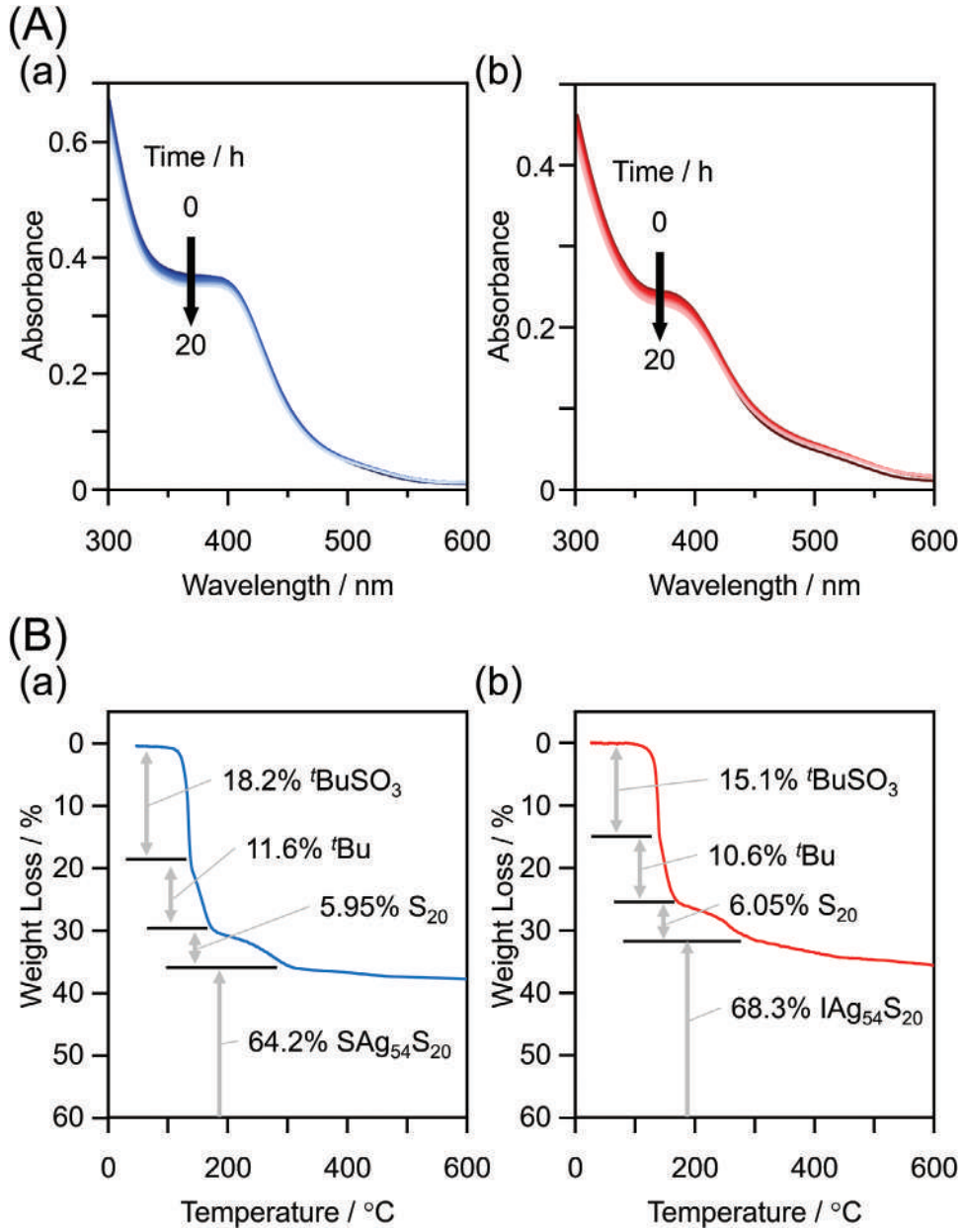


Figure 4. Stability of **X@Ag54**. A) Time evolution of the absorption spectrum of toluene solutions of (a) **S@Ag54** and (b) **I@Ag54** at 60 °C. B) TGA curves of (a) **S@Ag54** and (b) **I@Ag54**.

affect the binding energy between surface Ag and the ligands, the two **X@Ag54** clusters showed similar stability against the three factors tested in the above experiments.

2.7. Photoluminescence

Figure 6A shows the PL spectra of **X@Ag54** in toluene under an Ar atmosphere. To obtain strong PL, the excitation wavelength was set to 405 nm. Both cluster solutions exhibited a broad PL peak at ≈610 nm (Figure S15, Supporting Information). Recent studies have shown that the PL of metal clusters consisting of a large number of metal atoms entails photoexcitation to generate a dark excited singlet state, which subsequently undergoes intersystem crossing (ISC) to a bright excited triplet state, resulting in phosphorescence.[10e,11,12c,24] Because **X@Ag54** also comprised a large number of metal atoms, the observed emission of **X@Ag54** is likely phosphorescence. In fact, the estimated radiative lifetime of **X@Ag54** was on the order of tens to hundreds of microseconds (**Table 1**), which is significantly longer than that of fluorescent materials (≤1 µs).[25]

The photoluminescence quantum yield (Φ_{PL}) of **X@Ag54** was evaluated using a relative method,[26] revealing that the Φ_{PL} of

© 2025 The Author(s). Small published by Wiley-VCH GmbH

16136829, 2025, 25, Downloaded from https://onlinelibrary.wiley.com/doi/10.1002/smll.202500700 by Central Library The Librarian, Wiley Online Library on [04/01/2026]. See the Terms and Conditions (https://onlinelibrary.wiley.com/terms-and-conditions) on Wiley Online Library for rules of use; OA articles are governed by the applicable Creative Commons License

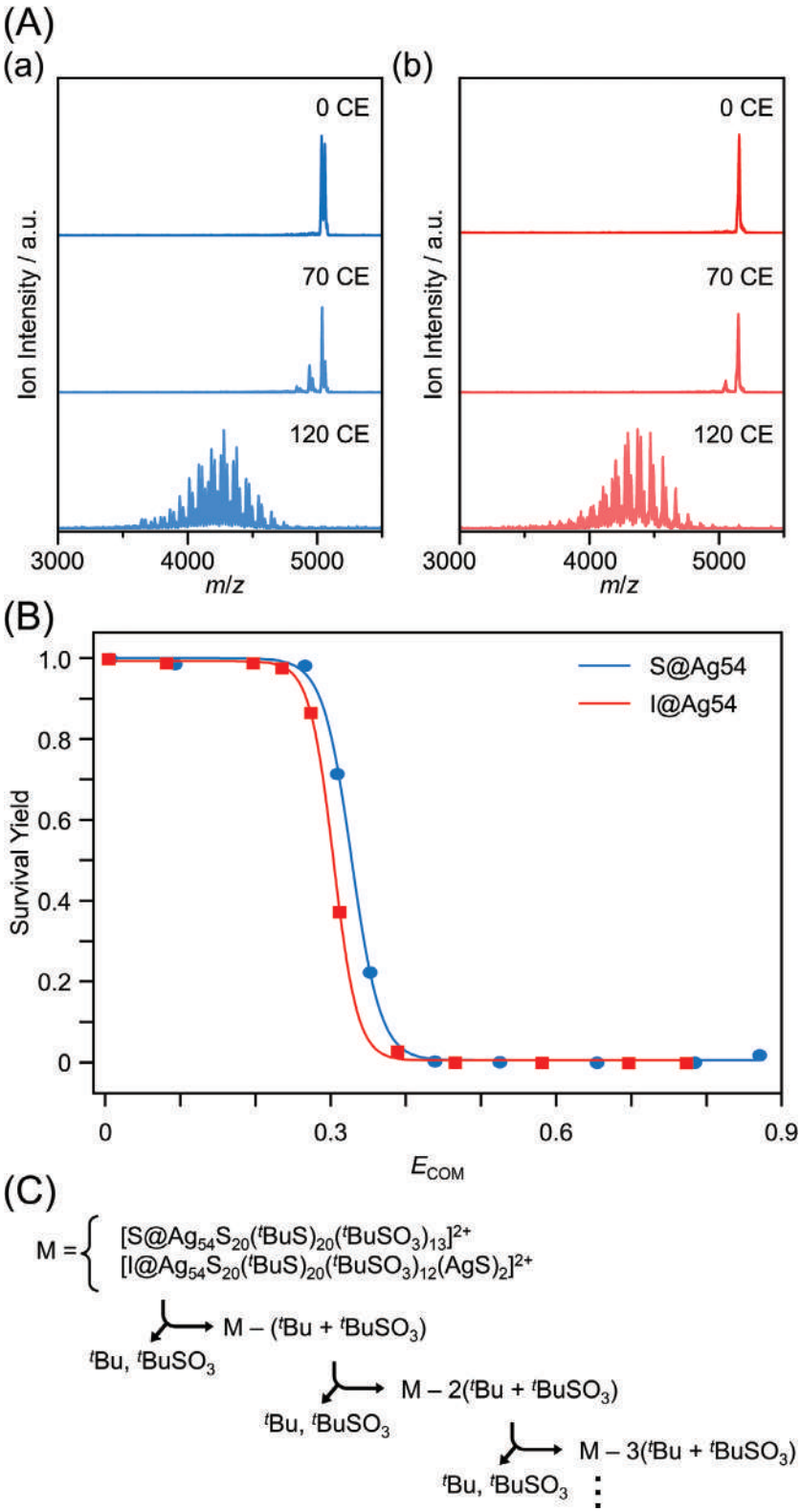


Figure 5. A) CID-mass spectra of (a) **S@Ag54** and (b) **I@Ag54** as a function of collision energy. CE indicates the collision energy. B) Survival yield obtained from CID profiles of **X@Ag54** (Figure 5A). Details for calculating the survival yield are provided in the (Section S1.8, Supporting Information). C) CID process of **X@Ag54**.

© 2025 The Author(s). Small published by Wiley-VCH GmbH

16136829, 2025, 25, Downloaded from https://onlinelibrary.wiley.com/doi/10.1002/smll.202500700 by Central Library The Librarian, Wiley Online Library on [04/01/2026]. See the Terms and Conditions (https://onlinelibrary.wiley.com/terms-and-conditions) on Wiley Online Library for rules of use; OA articles are governed by the applicable Creative Commons License

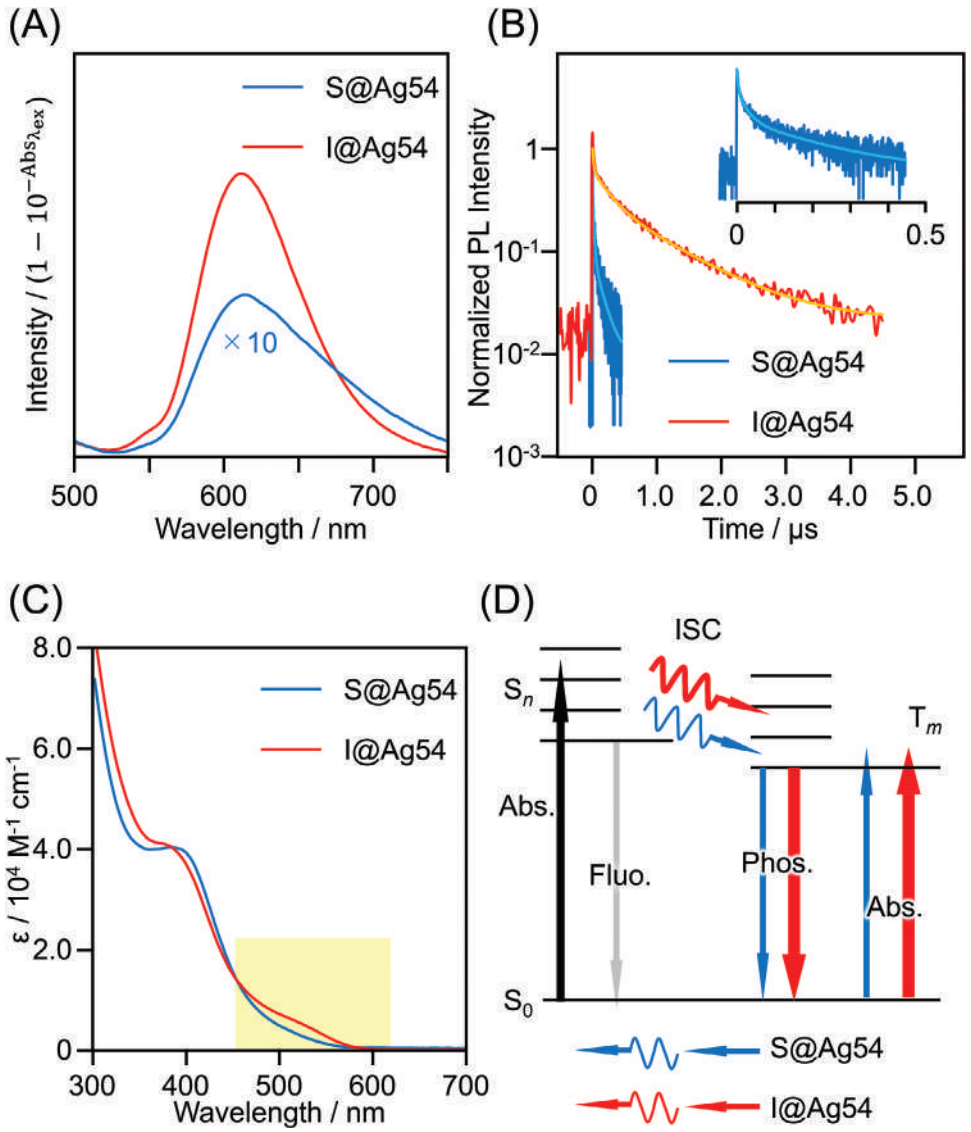


Figure 6. A) PL spectra of deuterated toluene solutions of **X@Ag54**. The excitation wavelength was fixed at 405 nm. The vertical axis is the PL intensity divided by the transmittance of the sample at the excitation light wavelength. B) PL decay curves of deuterated toluene solutions of **X@Ag54**. Excitation wavelength of pulse laser was fixed at 405 nm. C) UV–vis absorption spectra of toluene solutions of **S@Ag54** and **I@Ag54**. ϵ represents the molar absorption coefficient. The yellow part highlights the absorption assignable to S—T transition. D) Predicted scheme of the relaxation and absorption for **X@Ag54**.

I@Ag54 was ≈16 times greater than that of **S@Ag54** (Table 1). Because there was no significant difference in the symmetry of the geometries of the two **X@Ag54** clusters, the difference in Φ_{PL} did not arise from symmetry breaking.[27]

Table 1. Photoluminescence properties of **X@Ag54**.

Sample	Φ_{PL} [a]	τ_{PL} [ns] [b]	k_r [s^{-1}] [c]	k_{nr} [s^{-1}] [d]	τ_r [μs] [e]
S@Ag54	2.0×10^{-4}	106.2	1.9×10^3	9.4×10^6	530
I@Ag54	3.1×10^{-2}	652.9	4.8×10^4	1.5×10^6	21

[a] PL quantum yield; [b] averaged PL lifetime; [c] radiative rate constant; [d] nonradiative rate constant; [e] radiative lifetime (reciprocal of k_r).

However, 1) the two **X@Ag54** clusters differs in the type of anion present in their internal cavities, and 2) Φ_{PL} increases with increasing atomic number of encapsulated anion. Introducing heavy halogens (heavy atoms) into aromatic dyes, such as acene-based compounds, enhances ISC from the excited singlet to the excited triplet state owing to the heavy atom effect, which increases the radiative rate constant (k_r) and, consequently, Φ_{PL}.[28] In the present system, a similar effect likely occurred for **I@Ag54** to exhibit photoluminescence with high Φ_{PL}.

To confirm the presence of an internal heavy-atom effect, the PL decay curves of **X@Ag54** in deuterated toluene were evaluated using the time-correlated single-photon counting method (Figure 6B). The obtained decay curves were fitted with multiple exponential decays to determine the average

© 2025 The Author(s). Small published by Wiley-VCH GmbH

16136829, 2025, 25, Downloaded from https://onlinelibrary.wiley.com/doi/10.1002/smll.202500700 by Central Library The Librarian, Wiley Online Library on [04/01/2026]. See the Terms and Conditions (https://onlinelibrary.wiley.com/terms-and-conditions) on Wiley Online Library for rules of use; OA articles are governed by the applicable Creative Commons License

photoluminescence lifetimes (τ_{PL}) of **S@Ag54** and **I@Ag54**, which were 106.2 and 652.9 ns, respectively (Table 1; Table S10, Supporting Information). From this fitting, the radiative rate constants (k_r) of **S@Ag54** and **I@Ag54** were estimated to be 1.9×10^3 and 4.8×10^4 s^{-1}, respectively (Table 1). Therefore, when X changed from S^{2-} to I^-, k_r increased by ≈25 times. This trend is similar to the enhancement of phosphorescent parameters through the heavy atom effect in conventional fluorescent dyes. Therefore, it can be interpreted that replacing S^{2-} with heavier I^- as X in **X@Ag54** accelerated ISC via the heavy atom effect,[29] which increases the population of the bright triplet state and k_r, thereby improving the Φ_{PL} of **X@Ag54**.

The non-radiative rate constant (k_{nr}) of **I@Ag54** was ≈1/6 of that of **S@Ag54** (Table 1). Because I^- has a larger ionic radius than S^{2-}, it fills a greater volume of the cavity than S^{2-}, and thus **I@Ag54** seems to have a more rigid framework than **S@Ag54**. In addition, the bond enthalpies of Ag—I and Ag—S bonds are 234 and 217 kJ mol^{-1}, respectively, indicating that the Ag—I bond has a slightly higher bond energy than the Ag—S bond.[30] These factors seems to accelerate the vibrational relaxation of **I@Ag54** compared with that of **S@Ag54**, thereby reducing the non-radiative rate constant of **I@Ag54** to ≈1/6 of that of **S@Ag54**.

2.8. Optical Absorption

Finally, we discuss about the optical absorption of **S@Ag54** and **I@Ag54** (Figure 6C). Both spectra exhibited shoulder-like absorptions ≈400 and 550 nm, and their overall optical absorption spectra were quite similar to each other. However, upon closer inspection, the spectrum of **I@Ag54** contained a more distinct shoulder-like peak at ≈500 nm compared with the spectrum of **S@Ag54**. The heavy atom effect increases the oscillator strength of the spin-forbidden transition from the ground state to the triplet excited state ($S_0 \rightarrow T_1$), leading to the S—T absorption peak in the absorption spectrum.[31] In fact, in the optical absorption spectrum of some ligand-protected metal clusters, the absorption peak attributable to S—T transition appears with a relatively high oscillator strength at a slightly longer wavelength than the peak attributed to $S_0 \rightarrow S_n$ transition.[11] Therefore, we predict that the shoulder peak at ≈500 nm in the optical absorption spectrum of **X@Ag54** is derived from S—T absorption, which is promoted by the heavy atom effect (Figure 6D). The assignment of these optical absorption peaks is expected to be clarified through DFT calculations[32] in future studies.

3. Conclusion

In this study, we successfully synthesized a pair of **X@Ag54** clusters (X = S or I) protected by two types of ligands, thiolate and sulfonate, by adding Ag^+ and a catalytic amount of Cu^{2+} to the reaction system. No significant difference was observed between the two **X@Ag54** clusters (X = S or I) in terms of geometric structure and stability against degradation. However, notable differences were observed in their PL and optical absorption. We concluded that the differences in their optical properties are derived from the heavy atom effect. This effect enhances the oscillator strength of transitions from the spin-forbidden excited singlet state to the triplet excited state, as well as transitions from the ground singlet state to the triplet excited state. This study clearly demonstrated that incorporating heavy atoms into Ag—S clusters significantly enhances their phosphorescence quantum yield, similar to organic fluorescent dyes. These findings are expected to provide clear design guidelines for developing metal clusters as room-temperature phosphorescent materials and triplet sensitizers.

Supporting Information

Supporting Information is available from the Wiley Online Library or from the author.

Acknowledgements

The authors thank Dr. Tatsuo Nakagawa and Toshiaki Suzuki (UNISOKU Co., Ltd.) for the measurements of PL decay curves. The authors also thank Dr. Sourav Biswas for valuable comments on the valence electron model of **X@Ag54** and Ms. Mana Nakamoto for helping with the experiments. The computation was performed using the Research Center for Computational Science, Okazaki, Japan (Project: 24-IMS-C282). This research was financially supported by the Japan Society for the Promotion of Science (JSPS) KAKENHI (grant nos. 22K04858, 22K19012, 23KK0098, and 23H00289), Yazaki Memorial Foundation for Science and Technology, and The Sumitomo Foundation.

Conflict of Interest

The authors declare no conflict of interest.

Data Availability Statement

The data that support the findings of this study are available from the corresponding author upon reasonable request.

Keywords

anion templating, heavy atom effect, ligand-protected clusters, phosphorescence, precise synthesis

Received: January 17, 2025
Revised: February 21, 2025
Published online: March 3, 2025

[1] a) M. Sera, S. Hossain, S. Yoshikawa, K. Takemae, A. Ikeda, T. Tanaka, T. Kosaka, Y. Niihori, T. Kawawaki, Y. Negishi, *J. Am. Chem. Soc.* **2024**, *146*, 29684; b) T. Kawawaki, Y. Mitomi, N. Nishi, R. Kurosaki, K. Oiwa, T. Tanaka, H. Hirase, S. Miyajima, Y. Niihori, D. J. Osborn, T. Koitaya, G. F. Metha, T. Yokoyama, K. Iida, Y. Negishi, *Nanoscale* **2023**, *15*, 7272; c) H. Qian, M. Zhu, Z. Wu, R. Jin, *Acc. Chem. Res.* **2012**, *45*, 1470; d) Y. Negishi, H. Horihata, A. Ebina, S. Miyajima, M. Nakamoto, A. Ikeda, T. Kawawaki, S. Hossain, *Chem. Sci.* **2022**, *13*, 5546; e) S. Li, N.-N. Li, X.-Y. Dong, S.-Q. Zang, T. C. W. Mak, *Chem. Rev.* **2024**, *124*, 7262.
[2] a) Y. Zhong, J. Zhang, T. Li, W. Xu, Q. Yao, M. Lu, X. Bai, Z. Wu, J. Xie, Y. Zhang, *Nat. Commun.* **2023**, *14*, 658; b) S. Takano, H. Hirai,

 © 2025 The Author(s). Small published by Wiley-VCH GmbH

16136829, 2025, 25, Downloaded from https://onlinelibrary.wiley.com/doi/10.1002/smll.202500700 by Central Library The Librarian, Wiley Online Library on [04/01/2026]. See the Terms and Conditions (https://onlinelibrary.wiley.com/terms-and-conditions) on Wiley Online Library for rules of use; OA articles are governed by the applicable Creative Commons License

T. Nakashima, T. Iwasa, T. Taketsugu, T. Tsukuda, *J. Am. Chem. Soc.* **2021**, *143*, 10560; c) W. Ishii, Y. Okayasu, Y. Kobayashi, R. Tanaka, S. Katao, Y. Nishikawa, T. Kawai, T. Nakashima, *J. Am. Chem. Soc.* **2023**, *145*, 11236; d) D. A. Buschmann, H. Hirai, T. Tsukuda, *Inorg. Chem. Front.* **2024**, *11*, 6694; e) H. Liu, G. Hong, Z. Luo, J. Chen, J. Chang, M. Gong, H. He, J. Yang, X. Yuan, L. Li, X. Mu, J. Wang, W. Mi, J. Luo, J. Xie, X.-D. Zhang, *Adv. Mater.* **2019**, *31*, 1901015.

[3] a) M. Agrachev, S. Antonello, T. Dainese, J. A. Gascón, F. Pan, K. Rissanen, M. Ruzzi, A. Venzo, A. Zoleo, F. Maran, *Chem. Sci.* **2016**, *7*, 6910; b) M. Zhu, C. M. Aikens, M. P. Hendrich, R. Gupta, H. Qian, G. C. Schatz, R. Jin, *J. Am. Chem. Soc.* **2009**, *131*, 2490.

[4] a) E. L. Albright, T. I. Levchenko, V. K. Kulkarni, A. I. Sullivan, J. F. DeJesus, S. Malola, S. Takano, M. Nambo, K. Stamplecoskie, H. Häkkinen, T. Tsukuda, C. M. Crudden, *J. Am. Chem. Soc.* **2024**, *146*, 5759; b) M. Brust, M. Walker, D. Bethell, D. J. Schiffrin, R. Whyman, *J. Chem. Soc., Chem. Commun.* **1994**, 801; c) K. Sakamoto, S. Masuda, S. Takano, T. Tsukuda, *ACS Catal.* **2023**, *13*, 3263; d) A. V. Artem'ev, C. W. Liu, *Chem. Commun.* **2023**, *59*, 7182.

[5] a) S. Li, D. Alfonso, A. V. Nagarajan, S. D. House, J. C. Yang, D. R. Kauffman, G. Mpourmpakis, R. Jin, *ACS Catal.* **2020**, *10*, 12011; b) P. D. Jadzinsky, G. Calero, C. J. Ackerson, D. A. Bushnell, R. D. Kornberg, *Science* **2007**, *318*, 430; c) S. Knoppe, T. Bürgi, *Acc. Chem. Res.* **2014**, *47*, 1318; d) Y. Negishi, K. Nobusada, T. Tsukuda, *J. Am. Chem. Soc.* **2005**, *127*, 5261; e) S.-F. Yuan, C.-Q. Xu, W.-D. Liu, J.-X. Zhang, J. Li, Q.-M. Wang, *J. Am. Chem. Soc.* **2021**, *143*, 12261.

[6] a) Z.-A. Nan, Y. Xiao, X.-Y. Liu, T. Wang, X.-L. Cheng, Y. Yang, Z. Lei, Q.-M. Wang, *Chem. Commun.* **2019**, *55*, 6771; b) C. Xu, Y. Jin, H. Fang, H. Zheng, J. C. Carozza, Y. Pan, P.-J. Wei, Z. Zhang, Z. Wei, Z. Zhou, H. Han, *J. Am. Chem. Soc.* **2023**, *145*, 25673; c) S. Biswas, A. K. Das, A. C. Reber, S. Biswas, S. Bhandary, V. B. Kamble, S. N. Khanna, S. Mandal, *Nano Lett.* **2022**, *22*, 3721; d) Z.-A. Nan, Y. Wang, Z.-X. Chen, S.-F. Yuan, Z.-Q. Tian, Q.-M. Wang, *Commun. Chem.* **2018**, *1*, 99; e) D. Sun, H. Wang, H.-F. Lu, S.-Y. Feng, Z.-W. Zhang, G.-X. Sun, D.-F. Sun, *Dalton Trans.* **2013**, *42*, 6281; f) S. Jin, S. Wang, Y. Song, M. Zhou, J. Zhong, J. Zhang, A. Xia, Y. Pei, M. Chen, P. Li, M. Zhu, *J. Am. Chem. Soc.* **2014**, *136*, 15559; g) G. Li, Z. Lei, Q.-M. Wang, *J. Am. Chem. Soc.* **2010**, *132*, 17678; h) S. Yang, J. Chai, H. Chong, Y. Song, H. Yu, M. Zhu, *Chem. Commun.* **2018**, *54*, 4314; i) L.-J. Liu, J.-W. Zhang, M. Asad, Z.-Y. Wang, S.-Q. Zang, T. C. W. Mak, *Chem. Commun.* **2021**, *57*, 5586; j) F. Ma, K. A. Abboud, C. Zeng, *Nat. Synth.* **2023**, *2*, 949.

[7] a) J.-W. Liu, L. Feng, H.-F. Su, Z. Wang, Q.-Q. Zhao, X.-P. Wang, C.-H. Tung, D. Sun, L.-S. Zheng, *J. Am. Chem. Soc.* **2018**, *140*, 1600; b) L.-P. Cheng, Z. Wang, Q.-Y. Wu, H.-F. Su, T. Peng, G.-G. Luo, Y.-A. Li, D. Sun, L.-S. Zheng, *Chem. Commun.* **2018**, *54*, 2361.

[8] a) Z. Wang, H.-F. Su, X.-P. Wang, Q.-Q. Zhao, C.-H. Tung, D. Sun, L.-S. Zheng, *Chem. Eur. J.* **2018**, *24*, 1640; b) C. W. Liu, H.-W. Chang, P.-K. Liao, C.-S. Fang, J.-Y. Saillard, S. Kahlal, *J. Cluster Sci.* **2011**, *22*, 381; c) Y. Horita, M. Ishimi, Y. Negishi, *Sci. Technol. Adv. Mater.* **2023**, *24*, 2203832.

[9] a) J.-H. Liao, C. Latouche, B. Li, S. Kahlal, J.-Y. Saillard, C. W. Liu, *Inorg. Chem.* **2014**, *53*, 2260; b) Y. Horita, S. Hossain, M. Ishimi, P. Zhao, M. Sera, T. Kawawaki, S. Takano, Y. Niihori, T. Nakamura, T. Tsukuda, M. Ehara, Y. Negishi, *J. Am. Chem. Soc.* **2023**, *145*, 23533.

[10] a) H. Hirai, S. Takano, T. Nakashima, T. Iwasa, T. Taketsugu, T. Tsukuda, *Angew. Chem., Int. Ed.* **2022**, *61*, 202207290; b) X. Kang, M. Zhou, S. Wang, S. Jin, G. Sun, M. Zhu, R. Jin, *Chem. Sci.* **2017**, *8*, 2581; c) J.-S. Yang, Z. Han, X.-Y. Dong, P. Luo, H.-L. Mo, S.-Q. Zang, *Angew. Chem., Int. Ed.* **2020**, *59*, 11898; d) M. Hesari, Z. Ding, *J. Am. Chem. Soc.* **2021**, *143*, 19474; e) Y.-J. Kong, J.-H. Hu, X.-Y. Dong, Y. Si, Z.-Y. Wang, X.-M. Luo, H.-R. Li, Z. Chen, S.-Q. Zang, T. C. W. Mak, *J. Am. Chem. Soc.* **2022**, *144*, 19739.

[11] M. Mitsui, Y. Wada, R. Kishii, D. Arima, Y. Niihori, *Nanoscale* **2022**, *14*, 7974.

[12] a) W.-M. He, Z. Zhou, Z. Han, S. Li, Z. Zhou, L.-F. Ma, S.-Q. Zang, *Angew. Chem., Int. Ed.* **2021**, *60*, 8505; b) Y. Niihori, T. Kosaka, Y. Negishi, *Mater. Horiz.* **2024**, *11*, 2304; c) D. Arima, M. Mitsui, *J. Am. Chem. Soc.* **2023**, *145*, 6994; d) W.-D. Si, C. Zhang, M. Zhou, W.-D. Tian, Z. Wang, Q. Hu, K.-P. Song, L. Feng, X.-Q. Huang, Z.-Y. Gao, C.-H. Tung, D. Sun, *Sci. Adv.* **2023**, *9*, eadg3587.

[13] a) A. Rodriguez-Serrano, V. Rai-Constapel, M. C. Daza, M. Doerr, C. M. Marian, *Phys. Chem. Chem. Phys.* **2015**, *17*, 11350; b) Y. He, J. Wang, Q. Li, S. Qu, C. Zhou, C. Yin, H. Ma, H. Shi, Z. Meng, Z. An, *Adv. Opt. Mater.* **2023**, *11*, 2201641.

[14] H. Hirai, S. Takano, S. Masuda, T. Tsukuda, *ChemElectroChem* **2024**, *11*, 202300669.

[15] M. Walter, J. Akola, O. Lopez-Acevedo, P. D. Jadzinsky, G. Calero, C. J. Ackerson, R. L. Whetten, H. Grönbeck, H. Häkkinen, *Proc. Natl. Acad. Sci.* **2008**, *105*, 9157.

[16] a) R. K. Gupta, L. Li, Z. Wang, B.-L. Han, Z.-Y. Gao, C.-H. Tung, D. Sun, *Chem. Sci.* **2023**, *14*, 1138; b) C. Zhu, J. Xin, J. Li, H. Li, X. Kang, Y. Pei, M. Zhu, *Angew. Chem., Int. Ed.* **2022**, *61*, 202205947.

[17] X. Sun, B. Yan, X. Gong, Q. Xu, Q. Guo, H. Shen, *Chem. Eur. J.* **2024**, *30*, 202400527.

[18] R. D. Shannon, *Acta Crystallogr., Sect. A* **1976**, *A32*, 751.

[19] a) R. C. Smith, V. D. Reed, W. E. Hill, *Phosphorus, Sulfur Silicon Relat. Elem.* **1994**, *90*, 147; b) G. Saez, P. J. Thornalley, H. A. O. Hill, R. Hems, J. V. Bannister, *Biochim. Biophys. Acta Gen. Subj.* **1982**, *719*, 24.

[20] a) K. Yonesato, S. Yamazoe, D. Yokogawa, K. Yamaguchi, K. Suzuki, *Angew. Chem., Int. Ed.* **2021**, *60*, 16994; b) N. Haraguchi, T. Okunaga, Y. Shimoyama, N. Ogiwara, S. Kikkawa, S. Yamazoe, M. Inada, T. Tachikawa, S. Uchida, *Eur. J. Inorg. Chem.* **2021**, *2021*, 1531; c) H.-H. Wang, J. Wei, F. Bigdeli, F. Rouhani, H.-F. Su, L.-X. Wang, S. Kahlal, J.-F. Halet, J.-Y. Saillard, A. Morsali, K.-G. Liu, *Nanoscale* **2023**, *15*, 8245.

[21] a) E. Nag, S. Battuluri, K. Chandra Mondal, S. Roy, *Chem. Eur. J.* **2022**, *28*, 202202324; b) Y. Jin, C. Zhang, X.-Y. Dong, S.-Q. Zang, T. C. W. Mak, *Chem. Soc. Rev.* **2021**, *50*, 2297; c) X.-Y. Wang, W. Meng, H.-P. Xie, D.-N. Song, M.-H. Du, J.-X. Chen, P. Braunstein, J.-P. Lang, *Inorg. Chem.* **2024**, *63*, 13014.

[22] D.-N. Yu, Z.-X. Yao, F. Bigdeli, X.-M. Gao, X. Cheng, J.-Z. Li, J.-W. Zhang, W. Wang, Z.-J. Guan, Y. Bu, K.-G. Liu, A. Morsali, *Inorg. Chem.* **2023**, *62*, 401.

[23] a) J. Roy, P. Chakraborty, G. Paramasivam, G. Natarajan, T. Pradeep, *Phys. Chem. Chem. Phys.* **2022**, *24*, 2332; b) Y. Fujiwara, S. Ito, K. Koyasu, T. Tsukuda, *J. Phys. Chem. A* **2024**, *128*, 3119; c) S. Ito, K. Koyasu, S. Takano, T. Tsukuda, *J. Phys. Chem. C* **2020**, *124*, 19119; d) R. Tomihara, K. Hirata, H. Yamamoto, S. Takano, K. Koyasu, T. Tsukuda, *ACS Omega* **2018**, *3*, 6237.

[24] a) Y. Niihori, Y. Wada, M. Mitsui, *Angew. Chem., Int. Ed.* **2021**, *60*, 2822; b) M. Mitsui, D. Arima, Y. Kobayashi, E. Lee, Y. Niihori, *Adv. Opt. Mater.* **2022**, *10*, 2200864; c) M. Mitsui, D. Arima, A. Uchida, K. Yoshida, Y. Arai, K. Kawasaki, Y. Niihori, *J. Phys. Chem. Lett.* **2022**, *13*, 9272; d) K. Yoshida, D. Arima, M. Mitsui, *J. Phys. Chem. Lett.* **2023**, *14*, 10967; e) M. Mitsui, A. Uchida, *Nanoscale* **2024**, *16*, 3053; f) M. Mitsui, Y. Miyoshi, D. Arima, *Nanoscale* **2024**, *16*, 14757.

[25] N. J. Turro, V. Ramamurthy, J. C. Scaiano, *Principles of Molecular Photochemistry: An Introduction*, University Science Books, California **2009**.

[26] V. Bernard, M. Berberan-Santos, *Molecular fluorescence: principles and applications*, 2nd ed., Wiley-VCH, Singapore **2013**.

[27] E. Khatun, A. Ghosh, P. Chakraborty, P. Singh, M. Bodiuzzaman, P. Ganesan, G. Nataranjan, J. Ghosh, S. K. Pal, T. Pradeep, *Nanoscale* **2018**, *10*, 20033.

[28] a) V. Bernard, M. Berberan-Santos, *Molecular fluorescence: principles and applications*, 2nd ed., Wiley-VCH, Singapore **2012**; b) V. R. N. J. Turro, J. C. Scaiano, *Modern Molecular Photochemistry of Organic Molecules*, Wiley-VCH, Singapore **2011**.

© 2025 The Author(s). Small published by Wiley-VCH GmbH

16136829, 2025, 25, Downloaded from https://onlinelibrary.wiley.com/doi/10.1002/smll.202500700 by Central Library The Librarian, Wiley Online Library on [04/01/2026]. See the Terms and Conditions (https://onlinelibrary.wiley.com/terms-and-conditions) on Wiley Online Library for rules of use; OA articles are governed by the applicable Creative Commons License

[29] a) N. N. Greenwood, A. Earnshaw, *Chemistry of the Elements*, 2nd ed., Butterworth-Heinemann, Oxford **1997**; b) W. C. Martin, *J. Res. Natl. Bur. Stand., Sect. A* **1971**, *75*, 109.

[30] Y.-R. Luo, *Comprehensive Handbook of Chemical Bond Energies*, 1st ed., CRC Press, Boca Raton **2007**.

[31] M. Nakajima, S. Nagasawa, K. Matsumoto, T. Kuribara, A. Muranaka, M. Uchiyama, T. Nemoto, *Angew. Chem., Int. Ed.* **2020**, *59*, 6847.

[32] a) B. D. Peter, W. Pei, G. N. Andrew, S. Zhou, Z. Luo, *Nanoscale* **2024**, *16*, 8090; b) K. Maghrebi, I. Chantrenne, S. Messaoudi, T. Frauenheim, A. Fihey, C. R. Lien-Medrano, *J. Phys. Chem. C* **2023**, *127*, 19675; c) K. Li, P. Wang, Y. Pei, *J. Phys. Chem. Lett.* **2024**, *15*, 9216; d) E. L. Albright, S. Malola, S. I. Jacob, H. Yi, S. Takano, K. Mimura, T. Tsukuda, H. Häkkinen, M. Nambo, C. M. Crudden, *Chem. Mater.* **2024**, *36*, 1279; e) S. Havenridge, C. M. Aikens, *J. Phys. Chem. A* **2023**, *127*, 9932; f) T. Okada, T. Kawawaki, K. Takemae, S. Tomihari, T. Kosaka, Y. Niihori, Y. Negishi, *J. Phys. Chem. Lett.* **2024**, *15*, 1539.

© 2025 The Author(s). Small published by Wiley-VCH GmbH

16136829, 2025, 25, Downloaded from https://onlinelibrary.wiley.com/doi/10.1002/smll.202500700 by Central Library The Librarian, Wiley Online Library on [04/01/2026]. See the Terms and Conditions (https://onlinelibrary.wiley.com/terms-and-conditions) on Wiley Online Library for rules of use; OA articles are governed by the applicable Creative Commons License

NANO · MICRO
small

Supporting Information

for *Small*, DOI 10.1002/smll.202500700

Enhancement of Photoluminescence Quantum Yield of Silver Clusters by Heavy Atom Effect

Aoi Akiyama, Sakiat Hossain, Yoshiki Niihori, Kazutaka Oiwa, Jayoti Roy, Tokuhisa Kawawaki, Thalappil Pradeep and Yuichi Negishi**

Supporting Information

Enhancement of Photoluminescence Quantum Yield of Silver Clusters by Heavy Atom Effect

Aoi Akiyama, Sakiat Hossain, Yoshiki Niihori, Kazutaka Oiwa, Jayoti Roy, Tokuhisa Kawawaki, Thalappil Pradeep, and Yuichi Negishi**

Table of Contents

S1. Experimental····· Page 3

S2. Calculation····· Page 6

S3. Discussion····· Page 7

S4. Additional Scheme····· Page 8

S5. Additional Tables····· Page 9

S6. Additional Figures····· Page 15

S7. References····· Page 25

S1 Experimental

S1.1 Chemicals

All chemicals were obtained commercially and were used without further purification. Silver(I) trifluoroacetate (Ag(TFA)), copper(II) nitrate trihydrate ($Cu(NO_3)_2 \cdot 3H_2O$) were from FUJIFILM Wako Pure Chemical Co. *tert*-Butyl mercaptan (^{t}BuSH), tetrabutylammonium iodide (TBAI), coumarin 153 were from Tokyo Chemical Industry Co. Acetonitrile, acetone, toluene, and chloroform-d_1 ($CDCl_3$) were from Kanto Chemical Co., Inc.

S1.2 Detail of Synthesis

The glass tube used for synthesis and crystal growth was made by MARUEMU CO., INC. (part number: STC-4), with an outer diameter of 10 mm and a height of 75 mm **(Figure S1A)**. The cap made of polyethylene at the top has a single hole with a diameter of 0.8 mm **(Figure S1B)**. The raw material solution was poured into the glass tube and capped with the holed cap. At this time, the solution was confirmed to be light blue in color and free of the smell of ^{t}BuSH. A white LED (PENDY.LD, UW-SP19) was placed 13 cm above the top of the glass tube and the LED light was continuously irradiated until orange crystals were formed **(Figure S1C)**. When a similar synthesis experiment was conducted in a closed system, sulfonate formation and cluster formation did not occur due to the lack of oxygen inflow.

After approximately two weeks, the orange crystals were collected and dissolved in chloroform. To this solution, *n*-hexane was slowly poured to prepare a single crystal for X-ray diffraction **(Figure S2B)**.

S1.3 Single Crystal X-ray Diffraction and Crystallographic Data

The single crystal X-ray diffraction (SC-XRD) data were collected using a Bruker D8 QUEST diffractometer equipped with a fine-focus sealed X-ray tube producing multi-layer mirror-monochromated Mo-Kα radiation (λ = 0.71073 Å). The crystal was kept at −173(2) °C during data collection. The structure was solved by APEX4 program. Final refinement was performed by SHELXL-2018/3 using the Olex 2 platform. The crystallographic data were summarized in **Table S1**.

S1.4 X-ray Photoelectron Spectroscopy

X-ray photoelectron spectroscopy (XPS) was performed using JEOL's JPS-9010MC. The sample was placed on an indium plate, irradiated with Mg-Kα (1253.6 eV) radiation under reduced pressure of ~2×10^{-8} Torr, and the photoelectron spectra were measured. After measurement, the spectra were corrected using reference values for In $3d_{5/2}$ (443.8 eV) [1]. The Sherwood functions were used for the fitting curves **(Figure 3, S6, S7 and Table S4)**.

S1.5 Fourier Transform Infrared Absorption Spectroscopy

Fourier transform infrared (FT-IR) absorption spectra were recorded using a JASCO FT/IR-4600 spectrometer. X@Ag54 sample was dissolved in chloroform and deposited onto a diamond prism, followed by solvent evaporation. The spectrum of the prepared sample was then measured in the range of 400 to 4000 cm^{-1}. The results of IR spectra are depicted in **Figure S8**.

S1.6 Electrospray Ionization Mass Spectrometry

For the infusion analysis by electrospray ionization mass spectrometry (ESI-MS), we used MicroToF, Bruker and otofControl system. **X@Ag54** was dissolved in chloroform containing methanol and electrospray ionization mass spectrometry was attempted in positive ion mode. The spray voltage was set to 6000 V, the desolvation temperature to 200 °C, and the flow rate to 200 µL/h. However, multiple peaks were observed in both X@Ag54 clusters, and the nondestructive peaks attributed to $X@Ag_{54}S_{20}(S^tBu)_{20}(SO_3{}^tBu)_m$ (X, m) = (S, 12), (I, 11)

obtained by single crystal X-ray diffraction and ^{1}H NMR were not observed **(Figure S3 and Table S2, S3)**.

S1.7 Thermal Gravitational Analysis

Thermogravimetric (TG) curves and differential thermal analysis (DTA) of the samples were measured using Bruker, TG-DTA 2010SA. Before measurement, the samples were heated at 60 °C and dried under vacuum condition for 10 hours. Measurements were performed under nitrogen flow conditions at 50 mL/min and a temperature increase rate of 7 °C/min from room temperature to 800°C.

S1.8 Collision Induced Dissociation and Their Analysis

ESI-MS studies were performed using a Waters Synapt G2-Si high-definition mass spectrometer (HDMS). All mass spectrometric measurements were performed in the positive ion mode. For ESI-MS studies, **X@Ag54** nanocluster was dissolved in a solvent mixture of chloroform : methanol (1 : 1). During ESI, the capillary voltage, sampling cone, and source offset were kept at 3.2 kV, 10V, and 0 V, respectively, to obtain a well resolved mass spectrum of the **X@Ag54** nanocluster. The source temperature and desolvation temperature were maintained at 100 °C and 150 °C, respectively. Desolvation gas flow and cone gas flow were set to 400 and 10 L h^{-1}, respectively. In the Synapt G2-Si instrument, the mass-selected ions pass through trap, ion mobility and transfer cells before entering the time-of-flight analyzer. The collision induced dissociation (CID) of isolated ion can be performed at trap and transfer cells after isolating the ion using quadrupole mass filter. In our experiments, we carried out CID in both trap and transfer cells, while the IMS cell was kept off. No extra voltages were applied in the IMS cell to avoid additional fragmentation of the ions. The trap and transfer cells were filled with inert Ar gas. In trap, the collision energy (CE) was varied between 0 and 200 V. Further increase of CE was attained by increasing the voltages in the transfer cells. As the IMS cell did not contribute any effect on the applied collision voltages, the total CE is considered as the sum of the trap and transfer CEs (in V).[2] The results are summarized in **Figure S13**, **S14** and **Table S7**, **S8**.

From the CID mass spectrum at each collision energy (E_{CE}), the survival yield (*SY*) of the parent ion was calculated using the following formula.

$$SY = \frac{I_P}{\sum I_F + I_P} \qquad \textbf{(Equation S1)}$$

E_{CE} was converted to center-of-mass kinetic energy using the following equations, where m_{Ar} and m_P are the mass number of the colliding gas (Ar) and parent ion, respectively.

$$E_{COM} = \frac{m_{Ar}}{m_{Ar} + m_P} E_{CE}. \qquad \textbf{(Equation S2)}$$

The CE dependence of *SY* of the parent ion was fitted by the following sigmoid function **(Figure 5B)**.

$$SY = \frac{1}{1 + \exp\left(\frac{E_{COM} - E_{50}}{c}\right)}. \qquad \textbf{(Equation S3)}$$

, where E_{COM} is the collision energy, c is the curvature in the sigmoid curve, and E_{50} is the collision energy when *SY* is 50% **(Table S9)**.

S1.9 Kinetic Analysis of Decomposition of X@Ag54 in Solution

X@Ag54 was dissolved in toluene and the time evolution of absorbance was monitored **(Figure S11)**. To perform a reaction rate analysis, a decay process according to a first-order rate equation was considered. However, **X@Ag54** was stable and did not decay significantly after 20 hours. Therefore, we attempted to analyze the kinetics near t = 0 by Taylor

expansion of the analytical solution of the first-order differential rate equation. The analytical solution obtained from the first-order differential velocity equation is expressed as follows.

$$[\mathrm{M}]_t = [\mathrm{M}]_0 \exp(-kt). \qquad \textbf{(Equation S4)}$$

, where M represents **X@Ag54** and $[\mathrm{M}]_t$ is the concentration of M at time *t*. *k* is the rate constants for the assumed first-order decays. If we perform a Taylor expansion of this analytical solution near $t = 0$ and omit the terms after the second order, we obtain following relation.

$$[\mathrm{M}]_t = [\mathrm{M}]_0 \sum_{i=0}^{\infty} \frac{(-kt)^i}{i!} \approx [\mathrm{M}]_0(1 - kt). \qquad \textbf{(Equation S5)}$$

Since concentration is proportional to absorbance, the above equation can be rewritten as follows.

$$A_t \approx -A_0 kt + A_0. \qquad \textbf{(Equation S6)}$$

The unknown parameters A_0 and k were estimated using the least squares method, with the above equation serving as the fitting function for **Figure S11**. The fitting results were described in **Table S5**.

S1.10 Photoluminescence Spectroscopy and Their Analysis

First, **X@Ag54** was dissolved in toluene and the solution was poured into quartz cuvette with optical length of 1.0 cm. Oxygen molecules in the solution were removed from the solution by bubbling argon containing saturated toluene vapor. The emission spectra of sample ($I_{\mathrm{X}}(\lambda_{\mathrm{em}})$) were measured under deoxygenated conditions by irradiation of 405 nm excitation light using JASCO's FP-6300 and the absorbance $A(\lambda_{\mathrm{ex}})$ at the excitation wavelength was measured by JASCO's V-770. The emission spectra (F_{norm}) **(Figure 6C)** normalized by absorptance was obtained using the following equation:

$$F_{\mathrm{norm}}(\lambda_{\mathrm{em}}) = \frac{I_{\mathrm{X}}(\lambda_{\mathrm{em}})}{1 - 10^{-A(\lambda_{\mathrm{ex}})}}. \qquad \textbf{(Equation S7)}$$

The photoluminescence quantum yield (PLQY, Φ_{PL}) of **X@Ag54** was determined by the relative method[3] using coumarin 153 ($\Phi_{\mathrm{std}} = 0.544$ in deaerated ethanol)[4] as a standard sample. The obtained values were substituted into the following formula to evaluate the relative spectral quantum yield of the unknown sample X.

$$\Phi_{\mathrm{PL,X}} = \frac{1 - 10^{-A_{\mathrm{std}}(\lambda_{\mathrm{ex}})}}{1 - 10^{-A_{\mathrm{X}}(\lambda_{\mathrm{ex}})}} \cdot \frac{\int I_{\mathrm{X}}(\lambda_{\mathrm{em}})\mathrm{d}\lambda_{\mathrm{em}}}{\int I_{\mathrm{std}}(\lambda_{\mathrm{em}})\mathrm{d}\lambda_{\mathrm{em}}} \cdot \left(\frac{n_{\mathrm{X}}}{n_{\mathrm{std}}}\right)^2 \cdot \Phi_{\mathrm{std}}. \qquad \text{(Equation S8)}$$

, where λ_{ex} and λ_{em} are the excitation and emission wavelengths, respectively, *n* is the refractive index of the solvent ($n_{\mathrm{toluene}} = 1.496$, $n_{\mathrm{ethanol}} = 1.361$). The integration of PL spectrum represents the area of PL spectrum.

S1.11 Photoluminescence Lifetime

Time-correlated single photon counting measurement was conducted by using UNISOKU's Pico-TAS. **X@Ag54** was dissolved in toluene and the solution was degassed by bubbling with argon containing saturated toluene vapor. A 405 nm pulse laser as the excitation source was used to evaluate the PL decay curve of **X@Ag54 (Figure 6B)**. The PL decay curve $I_{\mathrm{PL}}(t)$ was fitted by the least-squares method using the following multiple exponential function:

$$I_{\mathrm{PL}}(t) = \sum_{i=1}^{3} A_i \exp\left(-\frac{t}{\tau_i}\right) + B. \qquad \text{(Equation S9)}$$

, where *A* is the amplitude (pre-exponential factor), *B* is the background, and τ is the emission lifetime. The fractional amplitude α and fractional population *f* were calculated as follows:

$$\alpha_i = \frac{A_i}{\sum_{j=1}^{3} A_j}, \qquad f_i = \frac{\alpha_i \tau_i}{\sum_{j=1}^{3} \alpha_j \tau_j}. \qquad \text{(Equation S10)}$$

The lifetime of **X@Ag54** was evaluated as the average PL lifetime based on the number of emitted photons using the following formula:

$$\tau_{\mathrm{PL}} = \sum_{i=1}^{3} f_i \tau_j \qquad \textbf{(Equation S11)}$$

The fitting results were shown in **Table S10**.

S1.12 Radiative and Non-radiative Rate Constant

The radiative and non-radiative rate constant (k_r and k_{nr}, respectively) were estimated by the following equations.

$$k_{\mathrm{r}} = \frac{\Phi_{\mathrm{PL}}}{\tau_{\mathrm{PL}}}, \qquad k_{\mathrm{nr}} = \frac{1 - \Phi_{\mathrm{PL}}}{\tau_{\mathrm{PL}}}. \qquad \text{(Equation S12)}$$

The radiative lifetime (τ_r) is a reciprocal of k_r as follows.

$$\tau_{\mathrm{r}} = \frac{1}{k_{\mathrm{r}}}. \qquad \text{(Equation S13)}$$

S1.13 Electron Spin Resonance Spectroscopy

We conducted X-band electron spin resonance (ESR) measurements to monitor the oxidation of thiols to sulfonates catalyzed by Cu and the promotion of thiol oxidation by the addition of Ag. $Cu(NO_3)_2{\cdot}3H_2O$ 8.0 mg was dissolved in 3 mL of an acetone/acetonitrile (50v%/50v%) mixture, followed by the addition of 3.5 mg of Ag(TFA) or none. This solution was transferred to a reaction tube **(Figure S1A)**, where 11 μL of ^{t}BuSH was added to initiate the reaction. At designated reaction times, aliquots of the reaction solution were collected into ESR tubes, and ESR spectra were recorded at room temperature. An EMX-nano spectrometer (Bruker, Boston, MA, USA) was used for the ESR measurements.

S2. Calculation

Density functional theory (DFT) calculations with the program Gaussian 16 (ES64L-G16, RevB.01) [5] were performed to investigate the dissociation energies at Ag−O and AgS−O_3S^tBu of the **X@Ag54** surface. B3LYP was used for the functional, with LanL2DZ (for Ag) [6] and 6-31G(d,p) (for H, C, O, and S) [7] basis sets. For Ag atoms, effective core potential was adapted. To simplify the system, only the Ag−O_3S^tBu and AgS−^{t}Bu binding units were optimized instead of the full structure of X@Ag54. In this system, we didn't consider basis set superposition error (BSSE), since these Ag−O and S−C bonds are strong covalent bonds. The Ag−O and S−C binding energies in Ag−O_3S^tBu and AgS−^{t}Bu, respectively, were then calculated by subtracting the energy of the optimized structure of each fragment from the total electronic energy of each unit. The total electronic energies of each unit and fragment are summarized in **Table S6**. As the results, we obtained following dissociation energy ΔE.

$$\mathrm{Ag} - \mathrm{O_3}S^{\mathrm{t}}\mathrm{Bu} \;\rightarrow\; \mathrm{Ag}\cdot + \cdot \mathrm{O_3S^tBu}, \qquad \Delta E = 54.21 \text{ kcal mol}^{-1}$$

$$\mathrm{AgS} - {}^{\mathrm{t}}\mathrm{Bu} \;\rightarrow\; \mathrm{AgS}\cdot + \cdot {}^{\mathrm{t}}\mathrm{Bu}, \qquad \Delta E = 57.38 \text{ kcal mol}^{-1}$$

S3. Discussion

S3.1 Mixed-valence state

Here we consider the valence state of silver atoms in X@Ag54. In the case of **X@Ag54** ($X@Ag_{54}S_{20}(S^tBu)_{20}(SO_3{}^tBu)_m$), the contribution of the number of donor electrons from the ligand, sulfide, and X anion to the molecule can be calculated as $x + m + 60$ {(x, m) = (2, 12) and (1, 11) for X = S and I, respectively}, since X, S, S^tBu, and $SO_3{}^tBu$ can donate x, 2, 1, and 1 electrons, respectively.

Let y be the average oxidation number per Ag atom; then, the following equation holds: $54y = x + m + 60$. Solving this equation for y, the averaged oxidation number of Ag atom in S@Ag54 and I@Ag54 are calculated to be $+1.37$ and $+1.33$, respectively.

On the other hand, if the number of Ag^{II} atoms among the 54 Ag atoms is n, the number of Ag^{I} atoms can be $54 - n$, so the number of accepted electrons can be $2n + (54 - n)$ electrons. When **X@Ag54** has neutral charge and is 0-electron system, these numbers of donated and accepted electrons balance out and we obtain the equation $2n + (54 - n) = x + m + 60$. Solving the equation for n, the mixed-valence states of Ag in **S@Ag54** and **I@Ag54** can be $\mathbf{S@Ag^{I}_{34}Ag^{II}_{20}}$ and $\mathbf{I@Ag^{I}_{36}Ag^{II}_{18}}$, respectively.

S3.2 Heavy Atom Effect

The ISC rate constant k_{ISC} can be expressed as Fermi's golden rule by adapting first-order perturbation theory to the Schrödinger equation of time evolution as follows. [8]

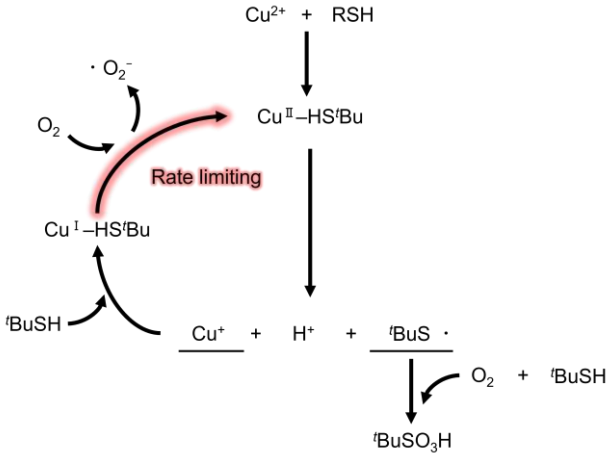
$$k_{\mathrm{ISC}} \propto \frac{\left\langle \Psi_{\mathrm{T}_m} \middle| \hat{H}_{\mathrm{SOC}} \middle| \Psi_{\mathrm{S}_n} \right\rangle^2}{{\Delta E_{\mathrm{ST}}}^2}. \qquad \textbf{(Equation S14)}$$

, where Ψ is the wave function and k_{ISC} is proportional to the square of the matrix elements from the singlet (S_n) and triplet (T_m) wave functions and the spin-orbit coupling Hamiltonian (H_{SOC}). ΔE_{ST} is energy difference between singlet and triplet state. H_{SOC} is also expressed as the inner product of the proportionality constant ζ, the orbital angular momentum operator $\hat{\boldsymbol{l}}$, and the spin angular momentum operator $\hat{\boldsymbol{s}}$, as follows.

$$\hat{H}_{\mathrm{SOC}} = \zeta \sum_i \hat{l}_i \cdot \hat{s}_i. \qquad \textbf{(Equation S15)}$$

Based on the experimental results, the absorption and emission spectra of **S@Ag54** and **I@Ag54** did not change significantly, so the ΔE_{ST} of **Equation S14** should not change significantly. If the electronic states involved in ISC were unchanged between **S@Ag54** and **I@Ag54**, the rate of change of k_{ISC} from S ($\zeta = 2.88 \times 10^2$ cm^{-1}) to I ($\zeta = 4.96 \times 10^3$ cm^{-1})[9] would be 297 times the ratio of ζ squared, but since this value is one order of magnitude different from the ratio of k_r (25 times), the inclusion of S or I would cause a change in the electronic states involved in ISC, and consequently the matrix element values may also change. In addition to the structure optimization of the ground state of **X@Ag54** and the vertical transition calculation, the structure optimization of the excited singlet and triplet states is also necessary to clarify these excitation and relaxation processes in detail, but at present no appropriate theory-based calculation method has been established.

S4. Additional Scheme



Scheme S1. Oxidation of thiol by Cu catalyst.

S5. Additional Tables

Table S1. Crystal data and structure refinement

	S@Ag54	**I@Ag54**
CCDC No.	2407225	2407226
Empirical formula	$C_{128}H_{288}Ag_{54}O_{36}S_{53}$	$C_{128}H_{282}Ag_{54}IO_{36}S_{52}$
Formula weight	9927.75	10016.39
Temperature / K	100.15	100.15
Crystal system	cubic	cubic
Space group	*Fm*−3	*Pa*−3
a / Å	32.1653(17)	29.8732(8)
b / Å	32.1653(17)	29.8732(8)
c / Å	32.1653(17)	29.8732(8)
α / °	90	90
β / °	90	90
γ / °	90	90
Volume / Å^3	33278(5)	26659(2)
Z	4	4
ρ_{calc} / g·cm^{-3}	1.982	2.496
μ / mm^{-1}	3.462	4.430
F(000)	18920.0	19044.0
Crystal size / mm^3	0.2 × 0.2 × 0.2	0.2 × 0.2 × 0.2
Radiation (wavelength)	Mo Kα (λ = 0.71073)	Mo Kα (λ = 0.71073)
2Θ range for data collection / °	4.2 to 41.64	3.34 to 35.984
Index ranges	-28 ≤ *h* ≤ 32, -23 ≤ *k* ≤ 32, -32 ≤ *l* ≤ 30	-25 ≤ *h* ≤ 25, -25 ≤ *k* ≤ 19, -20 ≤ *l* ≤ 25
Reflections collected	12516	136245
Independent reflections	1564 [R_{int} = 0.0949, R_{sigma} = 0.0427]	7824 [R_{int} = 0.0953, R_{sigma} = 0.0180]
Data/restraints/parameters	1564/181/139	7824/223/393
Goodness-of-fit on F_2	1.026	1.073
Final R indexes [I >= 2σ (I)]	R_1 = 0.0788, $_wR_2$ = 0.1785	R_1 = 0.1058, $_wR_2$ = 0.5874
Final *R* indexes [all data]	R_1 = 0.1049, $_wR_2$ = 0.2002	R_1 = 0.1053, $_wR_2$ = 0.2138
Largest diff. peak/hole / e Å^{-3}	2.42/-2.13	6.41/-3.43

Table S2. Assignment of peaks in ESI mass spectrum of **S@Ag54 (Figure S3A)**

Peak	Assignment [a]	Exp. *m/z* [b]	Cal. *m/z* [b]
a	S@Ag54 – S^{t}Bu + SO$_3$^{t}Bu + AgS	5057.7	5058.2
b	S@Ag54 + SO$_3$^{t}Bu	5032.2	5032.2
c	S@Ag54 + AgS + ^{t}Bu – Ag	5008.4	5008.2
d	S@Ag54 + AgS + 2 ^{t}Bu – 2 Ag	4983.0	4983.3

[a] S@Ag54 = SAg$_{54}$S$_{20}$(S^{t}Bu)$_{20}$(SO$_3$^{t}Bu)$_{12}$; [b] *m/z* giving maximum ion intensity.

Table S3. Assignment of peaks in ESI mass spectrum of **I@Ag54** (**Figure S3B**)

Peak	Assignment [a]	Exp. *m/z* [b]	Cal. *m/z* [b]
a	I@Ag54 + 2 AgS	5151.3	5151.1
b	I@Ag54 + 2 AgS + S^{t}Bu – SO$_3$^{t}Bu	5127.5	5127.1
c	I@Ag54 + 2 AgS + S^{t}Bu – SO$_3$^{t}Bu + ^{t}Bu – Ag	5102.0	5102.2
d	I@Ag54 + 2 AgS + 2 S^{t}Bu – 2 SO$_3$^{t}Bu + ^{t}Bu – Ag	5077.9	5078.2

[a] I@Ag54 = IAg$_{54}$S$_{20}$(S^{t}Bu)$_{20}$(SO$_3$^{t}Bu)$_{11}$; [b] *m/z* giving maximum ion intensity.

Table S4. Fitting result of X-ray photoelectron spectra of **X@Ag54** (**Figure 3**)

Sample	Assignment	Energy / eV	FWHM / eV [a]	Ratio [b]
S@Ag54	Ag 3d$_{5/2}$	367.404	0.501096	23.7850
		368.001	0.854979	43.7911
	Ag 3d$_{3/2}$	373.418	0.430232	12.5033
		374.052	0.786515	19.9206
	S 2p$_{3/2}$ (Ag$_2$S or AgS^{t}Bu)	161.998	1.3118	78.3707
	S 2p (SO$_3$^{t}Bu)	167.575	1.14173	21.6293
I@Ag54	Ag 3d$_{5/2}$	367.223	0.544069	22.5915
		367.734	0.643328	47.1520
	Ag 3d$_{3/2}$	373.201	0.456266	11.5903
		373.880	0.603143	18.6661
	S 2p (Ag$_2$S or AgS^{t}Bu)	161.675	1.221	65.7059
	S 2p (SO$_3$^{t}Bu)	167.248	1.03238	34.2941
	I 3d$_{5/2}$	618.586	0.879174	72.5754
	I 3d$_{3/2}$	629.974	0.720445	27.4246

[a] Full width of half maxima; [b] Area ratio in one element.

Table S5. First-order kinetic analysis of decomposition of **X@Ag54** in toluene (60 °C) (**Figure S11**)

Sample	A_0 [a]	k / 10^{-3} h^{-1} [b]	$\tau_{1/2}$ / h (/ d) [c]
S@Ag54	0.3689	2.86	242 (10.1)
I@Ag54	0.2438	3.75	185 (7.70)

[a] Initial absorbance; [b] First-order rate constant; [c] Half-life.

Table S6. Total electron energy (E) of optimized binding units and fragments[a]

Binding unit (E / Hartree)	Fragment 1 (E / Hartree)	Fragment 2 (E / Hartree)
Ag−O_3S^tBu (−927.4464)	Ag· (−145.7587)	·O_3S^tBu (−781.6013)
AgS−^{t}Bu (−701.8360)	AgS· (−543.9336)	·^{t}Bu (−157.8110)

[a] B3LYP/LanL2DZ(Ag),6-31G(d,p)(H,C,O,S).

Table S7. Assignment of peaks in CID mass spectra of **S@Ag54** (**Figure S13**)

Assignment [a]		Exp. *m/z* [b]	Cal. *m/z* [b]
{S@Ag54 − S^{t}Bu + AgS + SO$_3$^{t}Bu}		5057.7	5058.2
{S@Ag54 + SO$_3$^{t}Bu}		5034.2	5032.2
{S@Ag54 − S^{t}Bu + AgS + SO$_3$^{t}Bu}	− 1 ^{t}Bu − 1 SO$_3$^{t}Bu	4960.7	4961.1
{S@Ag54 + SO$_3$^{t}Bu}	− 1 ^{t}Bu − 1 SO$_3$^{t}Bu	4937.1	4935.2
{S@Ag54 − S^{t}Bu + AgS + SO$_3$^{t}Bu}	− 2 ^{t}Bu − 2 SO$_3$^{t}Bu	4863.7	4863.1
{S@Ag54 + SO$_3$^{t}Bu}	− 2 ^{t}Bu − 2 SO$_3$^{t}Bu	4840.2	4838.1
{S@Ag54 − S^{t}Bu + AgS + SO$_3$^{t}Bu}	− 3 ^{t}Bu − 3 SO$_3$^{t}Bu	4766.6	4766.0
{S@Ag54 + SO$_3$^{t}Bu}	− 3 ^{t}Bu − 3 SO$_3$^{t}Bu	4743.0	4741.1
{S@Ag54 − S^{t}Bu + AgS + SO$_3$^{t}Bu}	− 4 ^{t}Bu − 4 SO$_3$^{t}Bu	4669.5	4669.0
{S@Ag54 + SO$_3$^{t}Bu}	− 4 ^{t}Bu − 4 SO$_3$^{t}Bu	4645.3	4644.0
{S@Ag54 − S^{t}Bu + AgS + SO$_3$^{t}Bu}	− 5 ^{t}Bu − 5 SO$_3$^{t}Bu	4572.4	4571.9
{S@Ag54 + SO$_3$^{t}Bu}	− 5 ^{t}Bu − 5 SO$_3$^{t}Bu	4548.5	4547.0
{S@Ag54 − S^{t}Bu + AgS + SO$_3$^{t}Bu}	− 6 ^{t}Bu − 6 SO$_3$^{t}Bu	4475.5	4474.9
{S@Ag54 + SO$_3$^{t}Bu}	− 6 ^{t}Bu − 6 SO$_3$^{t}Bu	4451.5	4449.9
{S@Ag54 − S^{t}Bu + AgS + SO$_3$^{t}Bu}	− 7 ^{t}Bu − 7 SO$_3$^{t}Bu	4478.5	4377.8
{S@Ag54 + SO$_3$^{t}Bu}	− 7 ^{t}Bu − 7 SO$_3$^{t}Bu	4354.5	4352.9
{S@Ag54 − S^{t}Bu + AgS + SO$_3$^{t}Bu}	− 8 ^{t}Bu − 8 SO$_3$^{t}Bu	4281.5	4280.8
{S@Ag54 + SO$_3$^{t}Bu}	− 8 ^{t}Bu − 8 SO$_3$^{t}Bu	4257.5	4254.8
{S@Ag54 − S^{t}Bu + AgS + SO$_3$^{t}Bu}	− 9 ^{t}Bu − 9 SO$_3$^{t}Bu	4184.5	4183.7
{S@Ag54 + SO$_3$^{t}Bu}	− 9 ^{t}Bu − 9 SO$_3$^{t}Bu	4169.4	4157.8
{S@Ag54 − S^{t}Bu + AgS + SO$_3$^{t}Bu}	− 10 ^{t}Bu − 10 SO$_3$^{t}Bu	4087.3	4086.7
{S@Ag54 + SO$_3$^{t}Bu}	− 10 ^{t}Bu − 10 SO$_3$^{t}Bu	4062.3	4060.7
{S@Ag54 − S^{t}Bu + AgS + SO$_3$^{t}Bu}	− 11 ^{t}Bu − 11 SO$_3$^{t}Bu	3988.2	3989.6
{S@Ag54 + SO$_3$^{t}Bu}	− 11 ^{t}Bu − 11 SO$_3$^{t}Bu	3965.4	3963.7
{S@Ag54 − S^{t}Bu + AgS + SO$_3$^{t}Bu}	− 12 ^{t}Bu − 12 SO$_3$^{t}Bu	3892.6	3891.6
{S@Ag54 + SO$_3$^{t}Bu}	− 12 ^{t}Bu − 12 SO$_3$^{t}Bu	3867.2	3866.7

[a] S@Ag54 = SAg$_{54}$S$_{20}$(S^{t}Bu)$_{20}$(SO$_3$^{t}Bu)$_{12}$; [b] *m/z* giving maximum ion intensity.

Table S8. Assignment of peaks in CID mass spectra of **I@Ag54** (**Figure S14**)

Assignment [a]		Exp. *m/z* [b]	Cal. *m/z* [b]
{I@Ag54 + 2 AgS + $SO_3{}^t$Bu}		5151.0	5151.1
{I@Ag54 + 2 AgS + $SO_3{}^t$Bu}	− 1 ^{t}Bu − 1 $SO_3{}^t$Bu	5054.3	5054.0
{I@Ag54 + 2 AgS + $SO_3{}^t$Bu}	− 2 ^{t}Bu − 2 $SO_3{}^t$Bu	4957.1	4957.0
{I@Ag54 + 2 AgS + $SO_3{}^t$Bu}	− 3 ^{t}Bu – 3 $SO_3{}^t$Bu	4859.9	4859.9
{I@Ag54 + 2 AgS + $SO_3{}^t$Bu}	− 4 ^{t}Bu – 4 $SO_3{}^t$Bu	4762.3	4762.9
{I@Ag54 + 2 AgS + $SO_3{}^t$Bu}	− 5 ^{t}Bu – 5 $SO_3{}^t$Bu	4665.2	4665.8
{I@Ag54 + 2 AgS + $SO_3{}^t$Bu}	− 6 ^{t}Bu – 6 $SO_3{}^t$Bu	4568.6	4568.8
{I@Ag54 + 2 AgS + $SO_3{}^t$Bu}	− 7 ^{t}Bu – 7 $SO_3{}^t$Bu	4471.8	4470.7
{I@Ag54 + 2 AgS + $SO_3{}^t$Bu}	− 8 ^{t}Bu – 8 $SO_3{}^t$Bu	4374.1	4373.7
{I@Ag54 + 2 AgS + $SO_3{}^t$Bu}	− 9 ^{t}Bu – 9 $SO_3{}^t$Bu	4276.8	4276.6
{I@Ag54 + 2 AgS + $SO_3{}^t$Bu}	− 10 ^{t}Bu – 10 $SO_3{}^t$Bu	4180.1	4179.6
{I@Ag54 + 2 AgS + $SO_3{}^t$Bu}	− 11 ^{t}Bu – 11 $SO_3{}^t$Bu	4083.3	4082.5

[a] I@Ag54 = $IAg_{54}S_{20}(S^tBu)_{20}(SO_3{}^tBu)_{11}$; [b] *m/z* giving maximum ion intensity.

Table S9. Fitting results of survival yield obtained from CID profiles (**Figure 5B**)

Sample	E_{50} / E_{COM}	c / E_{COM}
S@Ag54	0.29370	0.01766
I@Ag54	0.30071	0.01647

[a] Coefficient of determination for the fitting.

Table S10. Fitting results of the PL decay curves of X@Ag54 in deaerated toluene (**Figure 6B**)

Sample	τ / ns	α [a]	f [b]	τ_{PL} / ns [c] (χ^2) [d]
S@Ag54	3.1	0.628	0.088	106.2 (1.0535)
	20.6	0.278	0.260	
	154.1	0.934	0.653	
I@Ag54	16.3	0.464	0.029	652.9 (1.0069)
	217.1	0.320	0.267	
	844.8	0.216	0.704	

[a] Fractional amplitude; [b] Fractional population; [c] Photon-number-based averaged lifetime; [d] Chi-square value for the fitting.

S6. Additional Figures

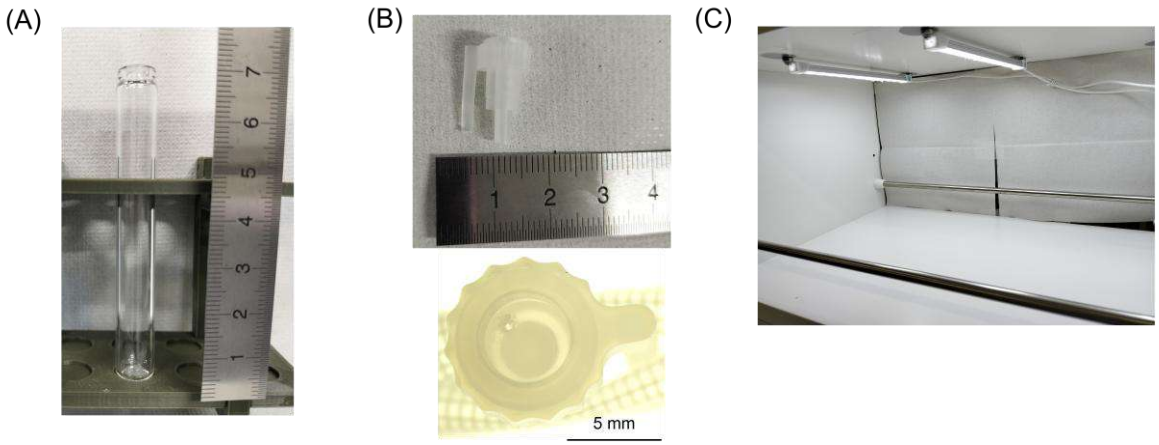


Figure S1. Photographs of (A) the tube for synthesis and crystal growth, (B) holed cap, and (C) light irradiation system.

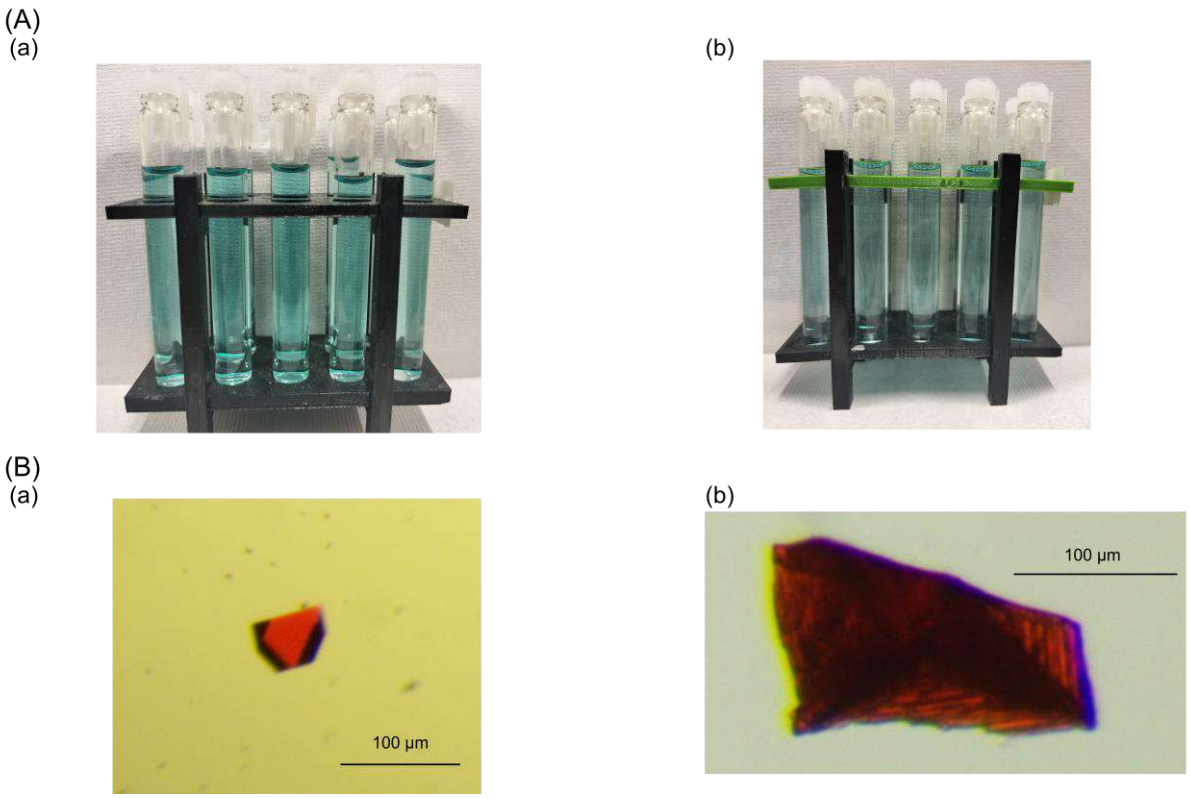


Figure S2. Photographs of (A) the reaction solution and (B) the single crystal for SC-XRD: (a) **S@Ag54** and (b) **I@Ag54**.

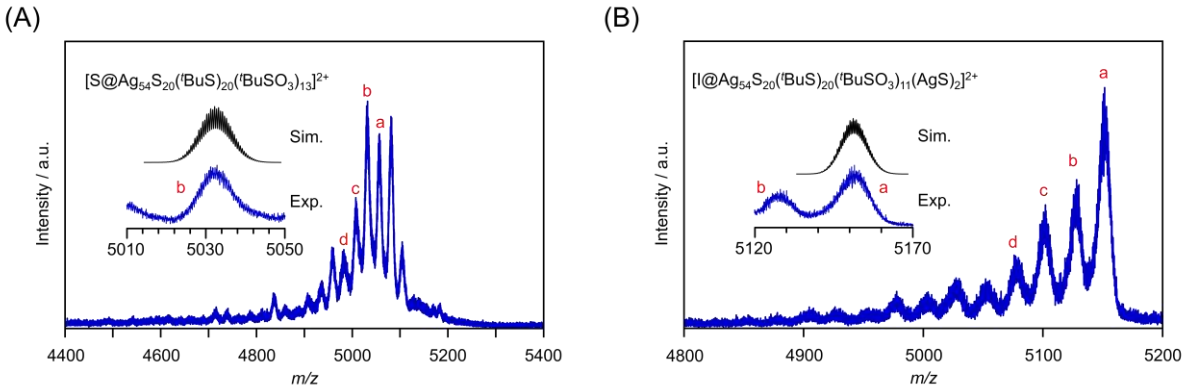


Figure S3. ESI-mass spectra of **X@Ag54** in the positive-ion mode. (A) **S@Ag54** and (B) **I@Ag54**. The assignment of each peak is summarized in **Table S2** (for **S@Ag54**) and **Table S3** (for **I@Ag54**).

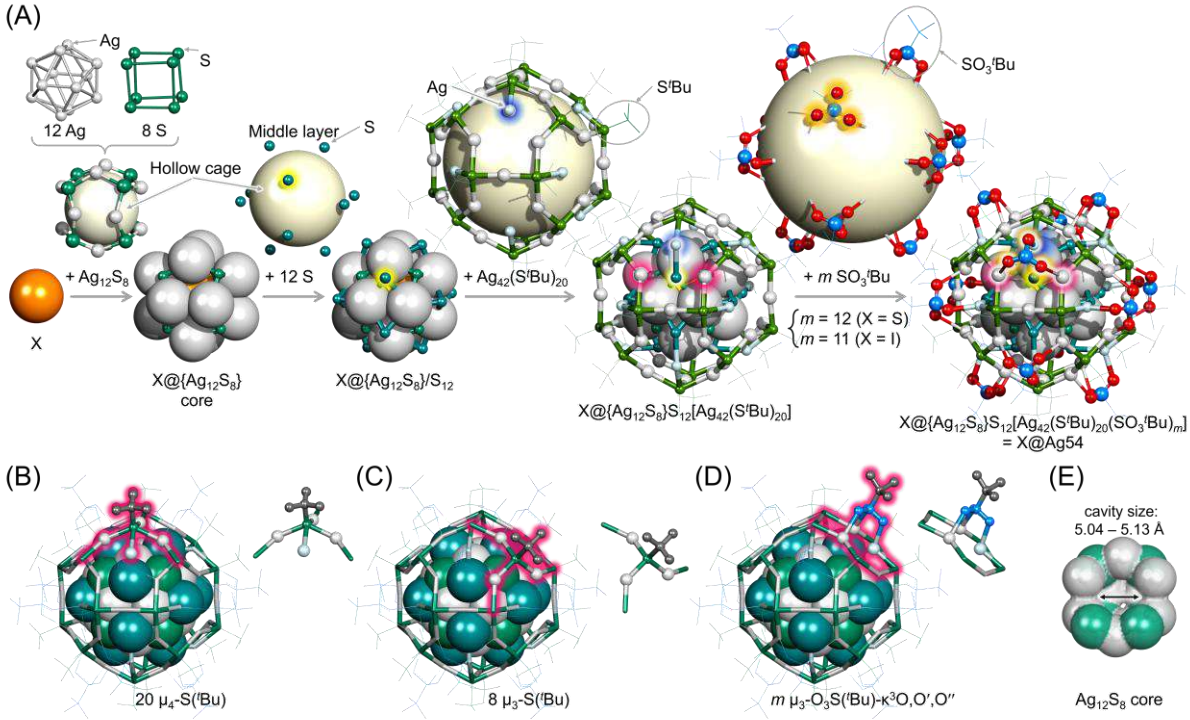


Figure S4. Details of the structure of **X@Ag54**. (A) Assembly of **X@Ag54**. (B) Structure of μ_4-S(^{t}Bu). (C) Structure of μ_3-S(^{t}Bu) (D) Structure of μ_3-$O_3S(^t$Bu)-κ^3O,O′,O″. (E) Cavity inside $Ag_{12}S_8$ core.

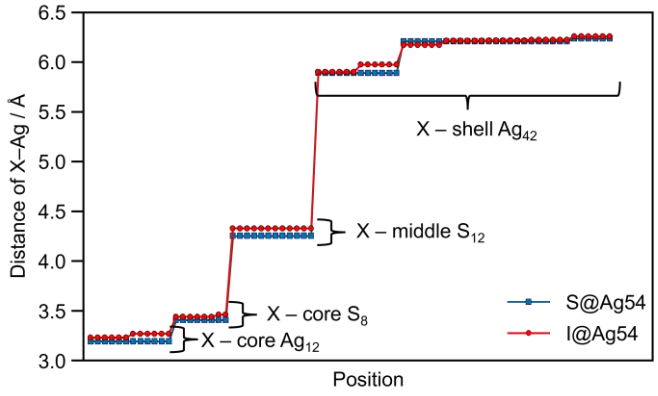


Figure S5. X−Y (Y = Ag, S) distance distribution in **X@Ag54**. The distances between the central atoms (S or I) and the nearest Ag atoms in **S@Ag54** and **I@Ag54** are 3.19 Å and 3.27 Å, respectively (**Figure S5**). Considering the ionic radius, **S@Ag54** can be considered to have no bond between S and the Ag atoms of core. However, this distance is shorter than the total value of van der Waals radius of S and Ag atoms. Therefore, it can be considered that a weak bond exists also in the core of **S@Ag54**.

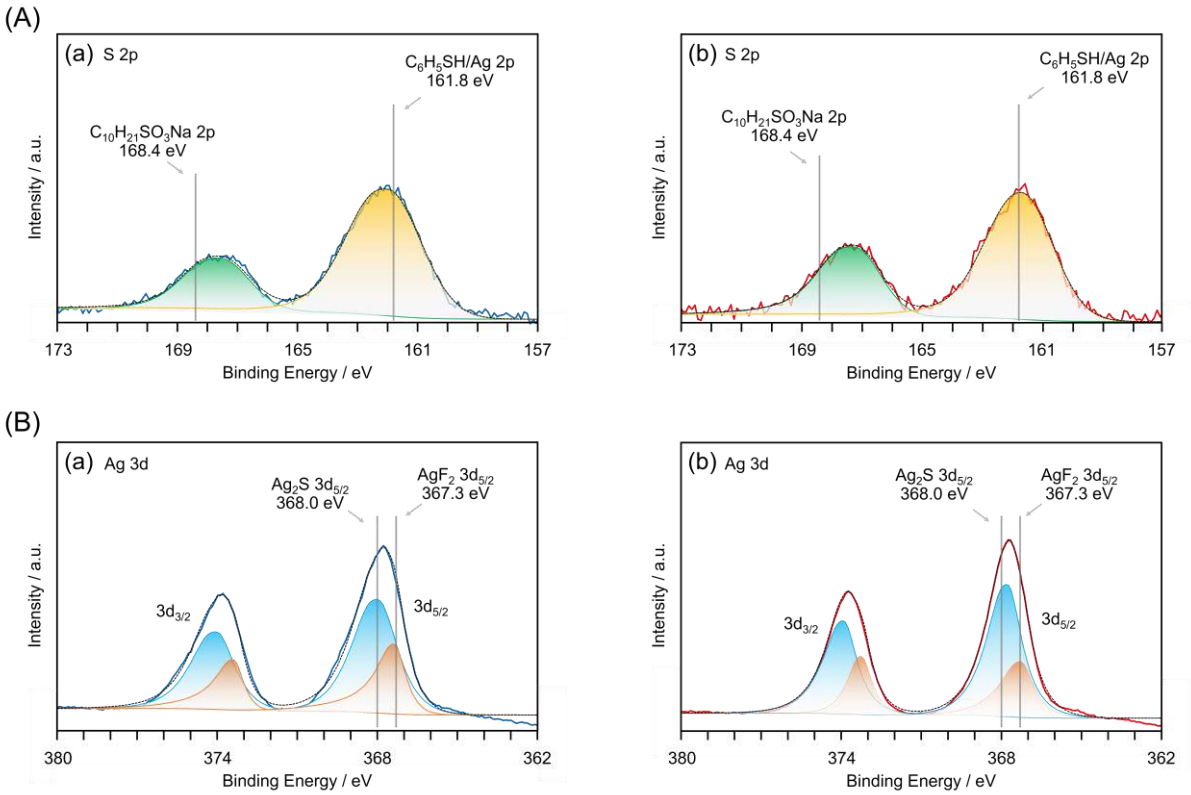


Figure S6. XPS spectra of (A) S 2p and (B) Ag 3d of (a) **S@Ag54** and (b) **I@Ag54**. The gray lines represent the values of binding energy from the references.[10] Figure (B) shows that the ratio of Ag^{I}:Ag^{II} is 63.7:36.3 and 65.8:34.2 for S@Ag54 and I@Ag54, respectively. As shown in Discussion of S3.1, when **X@Ag54** has neutral charge and is 0-electron system, the mixed-valence states of Ag in **S@Ag54** and **I@Ag54** can be estimated to be $S@Ag^{I}_{34}Ag^{II}_{20}$ and $I@Ag^{I}_{36}Ag^{II}_{18}$, respectively. In this composition, the ratio of Ag^{I} : Ag^{II} is 62.9 : 37.1 and 66.7 : 33.3 for S@Ag54 and I@Ag54, respectively. In this way, the results of Ag 3d XPS well reproduce the expected mixed-valence states of Ag for **S@Ag54** and **I@Ag54**.

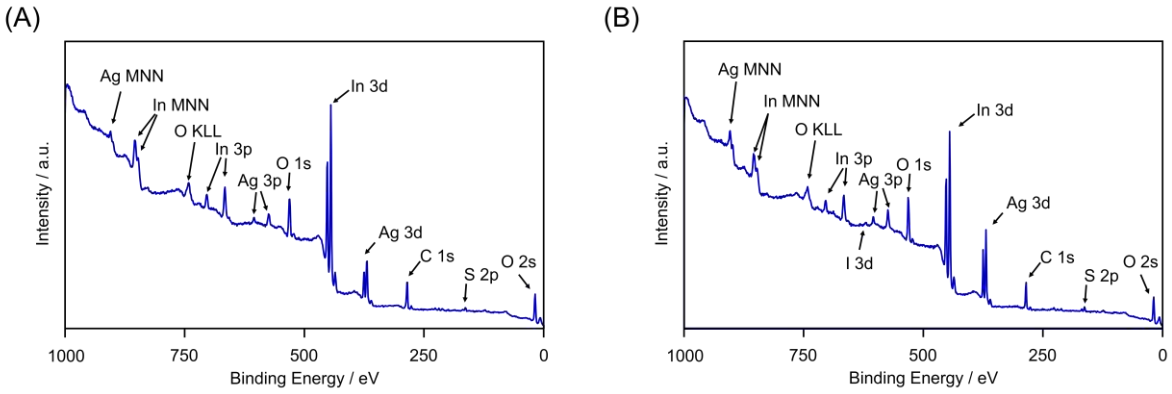


Figure S7. Wide-ranged X-ray photoelectron spectra of (A) **S@Ag54** and (B) **I@Ag54**. Indium was used as the substrate for calibration.

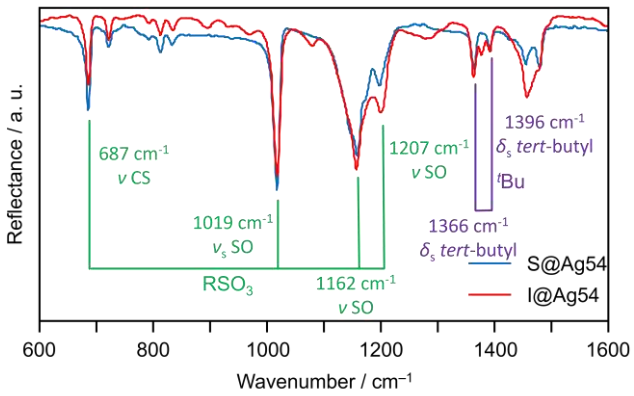


Figure S8. FT-IR absorption spectra of **X@Ag54**.

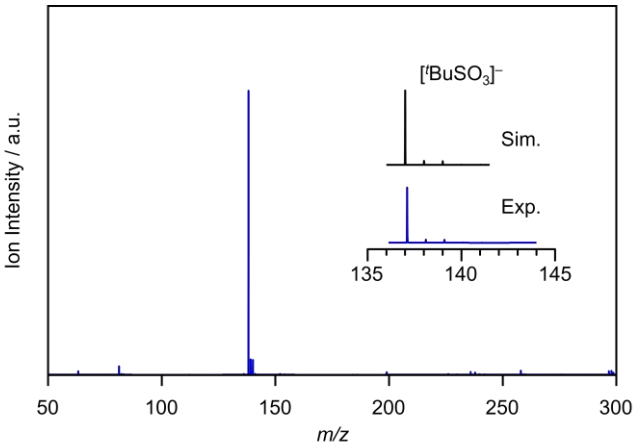


Figure S9. ESI-MS spectrum of $^{t}BuSO_3^-$ produced from the corresponding thiol and oxygen molecule in the presence of $Cu(NO_3)_2$ catalyst. The inset shows the comparison of the isotope pattern between experimental and simulation spectra. The product was obtained by adding $^{t}BuSH$ dropwise into a mixed acetonitrile-acetone solution of $Cu(NO_3)_2 \cdot 3H_2O$, followed by standing for two days in the reaction vessel. The resulting white precipitate was dissolved in methanol for the measurement.

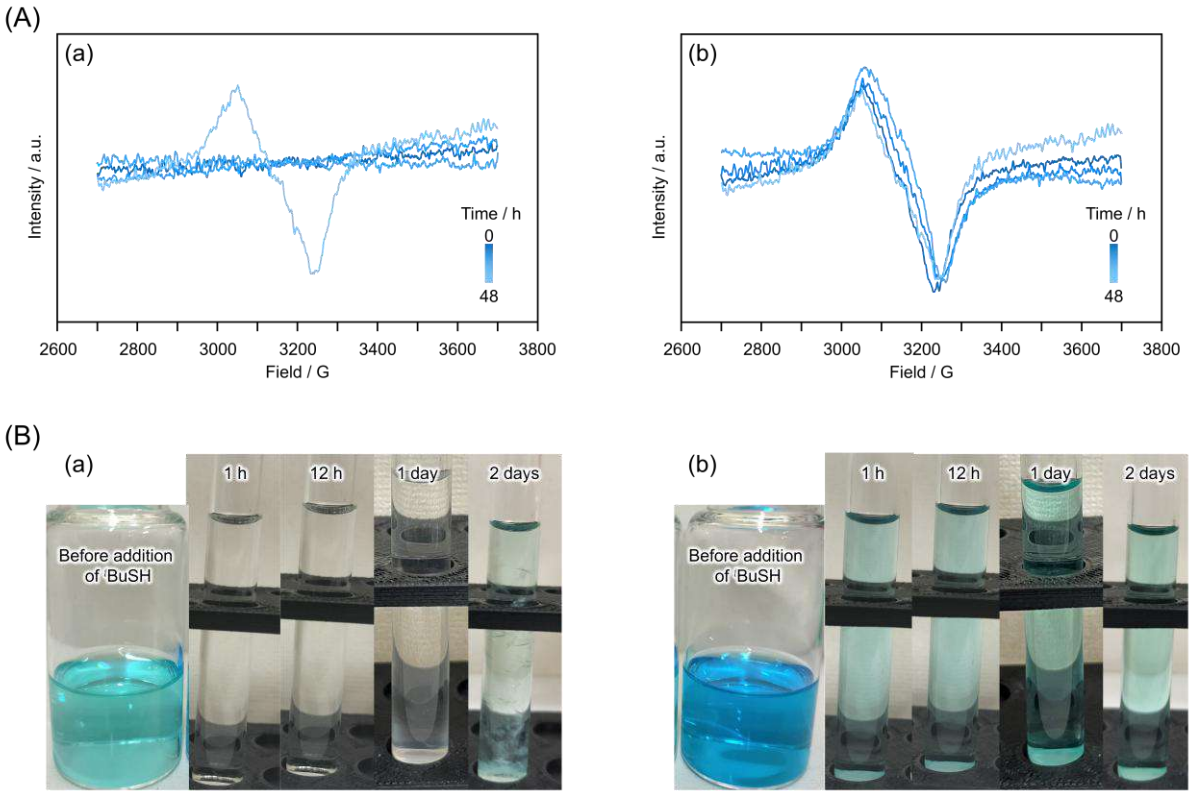


Figure S10. (A) ESR spectra and (B) photographs of reaction solution of (a) mixture of $Cu(NO_3)_2$ and ^{t}BuSH, and (b) mixture of $Cu(NO_3)_2$, ^{t}BuSH, and Ag(TFA) as a function of reaction time. These characteristic signals in ESR spectra originate from blue Cu^{2+} ($3d^9 4s^0$ electron configuration), while colorless Cu^+ ($3d^{10} 4s^0$ electron configuration) shows no ESR signal. In (a), the color of the solution suddenly changed from blue to colorless after the addition of thiol, indicating that the reduction of Cu^{2+} (Cu^{2+} (blue) → Cu^+ (colorless)) occurred. 2 days later, the solution turned blue and the ESR signal appeared. This indicates that the oxidation of Cu^+ (Cu^+ (colorless) → Cu^{2+} (blue)) is slowly occurring. On the other hand, in (b), the solution remained blue and the Cu^{2+} derived signal was observed from the early stage of the reaction. This suggests that the oxidation of Cu^+ was accelerated by the addition of Ag^+.

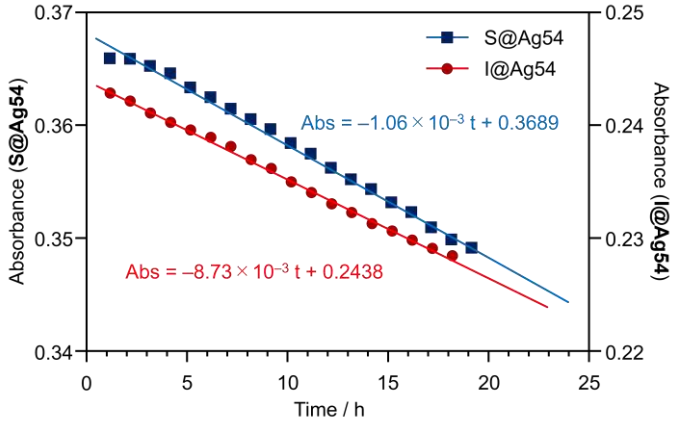


Figure S11. Time dependence of absorbance of **X@Ag54** in toluene (60 °C) at 370 nm.

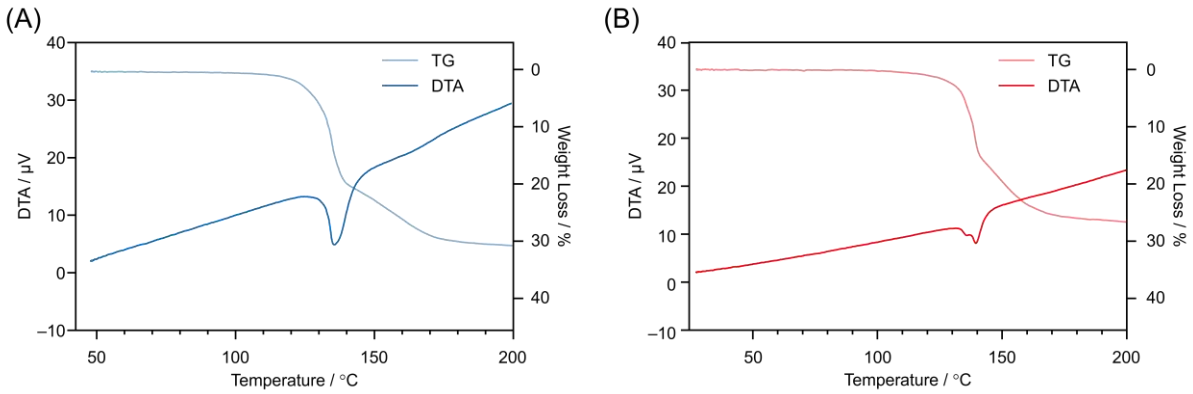


Figure S12. DTA curves of (A) **S@Ag54** and (B) **I@Ag54**. In these analyses, negative DTA peaks were observed at the temperatures corresponding to the dissociation of S–^{t}Bu and Ag–O_3S^tBu. This indicates that these dissociations are endothermic processes.

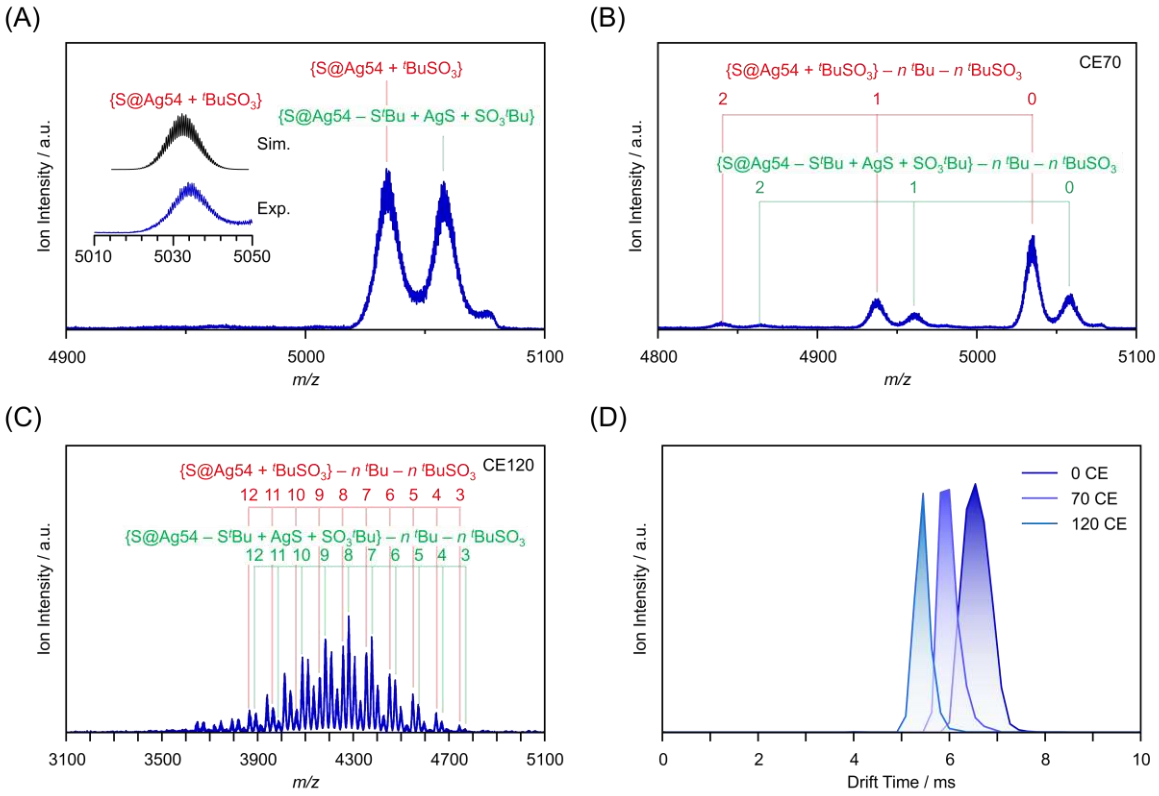


Figure S13. Positive-ion ESI-mass spectra of **S@Ag54** for CID. (A) Mass-selected molecular ion peak. (B) and (C) CID-MS spectra at collision energy (CE) of 70 and 120, respectively. In (A), since the *m*/*z*-difference between two main peaks were too close, both two-mother ions were analyzed by CID. (D) Ion-mobility spectra of **S@Ag54**. With the increase in CE, the ion mobility decreased. Based on a series of analyses (**Table S7**), the E_{50} values of **S@Ag54** and **I@Ag54** were evaluated as 74.2 CE and 78.9 CE, respectively, indicating that both **X@Ag54** possess similar stability against CID.

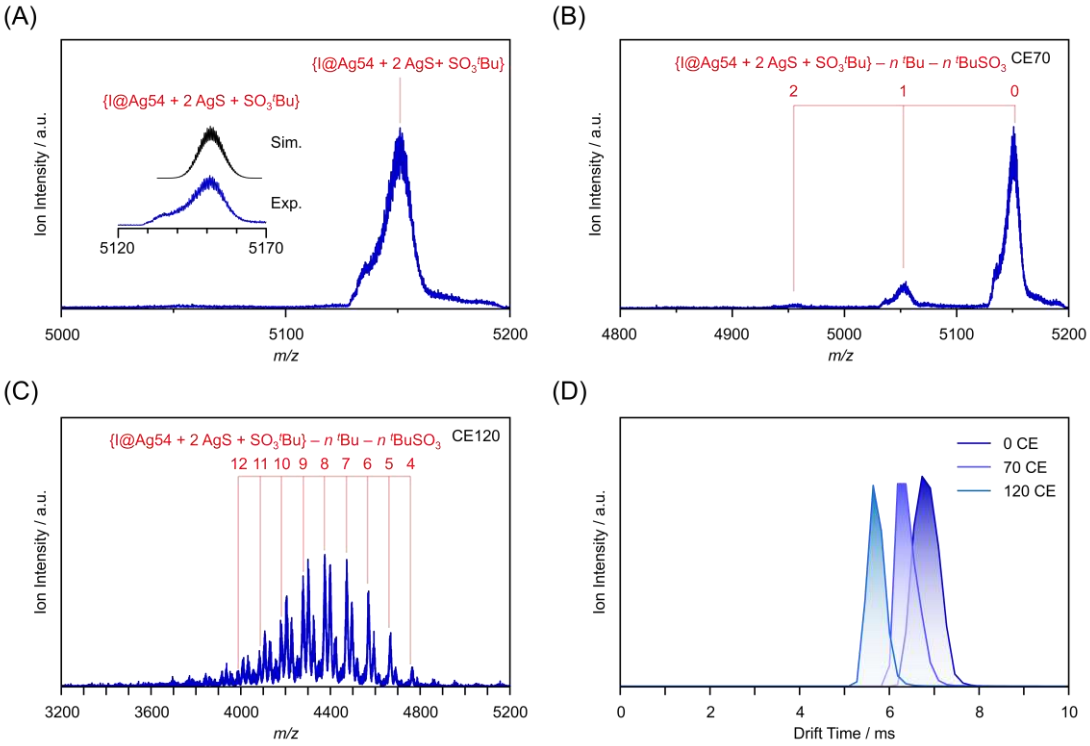


Figure S14. Positive-ion ESI-mass spectra of **I@Ag54** for CID. (A) Mass-selected molecular ion peak. (B), (C) CID-MS mass spectra at CE of 70 and 120, respectively. In (A), the isotope pattern was distorted because of mass-selection filter. (D) Ion-mobility spectra of **I@Ag54**. With the increase in CE, the ion mobility decreased. Based on a series of analyses (**Table S8**), the E_{50} values of **S@Ag54** and **I@Ag54** were evaluated as 74.2 CE and 78.9 CE, respectively, indicating that both **X@Ag54** possess similar stability against CID.

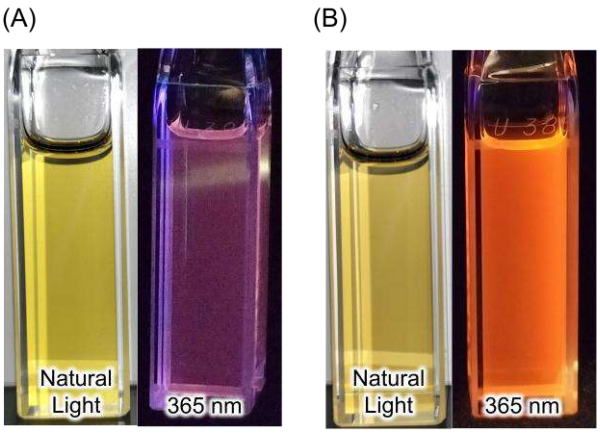


Figure S15. Photographs of solution of **X@Ag54** under natural light and 365 nm light. (A) **S@Ag54** and (B) **I@Ag54**. The emission spectra of **X@Ag54** at 365 nm excitation were also measured. Although the emission intensities were weaker than that otbained by 405 nm excitation, the emission spectrum showed the same feature as that otbained by 405 nm excitation.

S7. References

[1] A. Naumkin, A. Kraut-Vass, S. Gaarenstroom, C. Powell; **2023**; *NIST X-ray Photoelectron Spectroscopy Database*; 5.0; 10.18434/T4T88K.

[2] J. Roy, P. Chakraborty, G. Paramasivam, G. Natarajan, T. Pradeep, *Phys. Chem. Chem. Phys.* **2022**, *24*,2332.

[3] B. Valeur, M. Berberan-Santos, *Molecular Fluorescence: Principles and Applications*, 2nd ed., Wiley-VCH, Singapore, **2013**.

[4] K. Rurack, M. Spieles, *Anal. Chem.* **2011**, *83*,1232.

[5] M. J. Frisch, G. W. Trucks, H. B. Schlegel, G. E. Scuseria, M. A. Robb, J. R. Cheeseman, G. Scalmani, V. Barone, G. A. Petersson, H. Nakatsuji, X. Li, M. Caricato, A. V. Marenich, J. Bloino, B. G. Janesko, R. Gomperts, B. Mennucci, H. P. Hratchian, J. V. Ortiz, A. F. Izmaylov, J. L. Sonnenberg, Williams, F. Ding, F. Lipparini, F. Egidi, J. Goings, B. Peng, A. Petrone, T. Henderson, D. Ranasinghe, V. G. Zakrzewski, J. Gao, N. Rega, G. Zheng, W. Liang, M. Hada, M. Ehara, K. Toyota, R. Fukuda, J. Hasegawa, M. Ishida, T. Nakajima, Y. Honda, O. Kitao, H. Nakai, T. Vreven, K. Throssell, J. A. Montgomery Jr., J. E. Peralta, F. Ogliaro, M. J. Bearpark, J. J. Heyd, E. N. Brothers, K. N. Kudin, V. N. Staroverov, T. A. Keith, R. Kobayashi, J. Normand, K. Raghavachari, A. P. Rendell, J. C. Burant, S. S. Iyengar, J. Tomasi, M. Cossi, J. M. Millam, M. Klene, C. Adamo, R. Cammi, J. W. Ochterski, R. L. Martin, K. Morokuma, O. Farkas, J. B. Foresman, D. J. Fox, Gaussian 16 Rev. B.01, Program for the computational chemistry and electronic structure modeling, Gaussian, Inc., Wallingford (USA), **2016**

[6] P. J. Hay, W. R. Wadt, *J. Chem. Phys.* **1985**, *82*,299.

[7] M. M. Francl, W. J. Pietro, W. J. Hehre, J. S. Binkley, M. S. Gordon, D. J. DeFrees, J. A. Pople, *J. Chem. Phys.* **1982**, *77*,3654.

[8] N. J. Turro, V. Ramamurthy, J. C. Scaiano, *Modern Molecular Photochemistry of Organic Molecules*, Wiley-VCH, Singapore, **2011**.

[9] N. N. Greenwood, A. Earnshaw, *Chemistry of the Elements*, 2nd ed., Butterworth-Heinemann, Oxford, **1997**.

[10] a) M. Volmer, M. Stratmann, H. Viefhaus, *Surf. Interface Anal.* **1990**, *16*,278; b) L. J. Gerenser, K. E. Goppert-Berarducci, R. C. Baetzold, J. M. Pochan, *J. Chem. Phys.* **1991**, *95*,4641.

Biological Trace Element Research
https://doi.org/10.1007/s12011-025-04903-8

RESEARCH

Association of Urine Heavy Metals with Prevalence of Type 1 Diabetes and Poor Glycaemic Control

Samrat Ashok Vasudevan[1,2] · Srinidhi Narayani Seenivasan[1] · Avinash Kumar Raghupathy[3] · Dinakaran Vasudevan[1] · Parthasarathy Ayothi[1,4] · Tanmayaa Nayak[4] · Buvaneswari Gajendran[1] · Karthika Durairaj[1] · Divya Shree Sathish[1] · Srilaxmi Balaji[3] · Abisheak Kandasamy[3] · P. Amaravathy[1] · Sundaresan Mohanraj[3,5] · Shankar Dhandapani[6] · Thalappil Pradeep[4] · Krishnan Swaminathan[7] · Ganesan Velmurugan[1,5,8]

Received: 29 August 2025 / Accepted: 3 November 2025
© The Author(s), under exclusive licence to Springer Science+Business Media, LLC, part of Springer Nature 2025

Abstract
Emerging evidence suggests that endocrine-disrupting chemicals specifically heavy metals, may influence metabolic disorders including Type 1 Diabetes mellitus (T1DM). Poor glycaemic control is a key issue in management of T1DM. This cross-sectional study explores the association of toxic heavy metals with prevalence of T1DM and glycaemia. A total of 153 individuals with T1DM with mean age of 13 years and age- and sex matched 60 healthy controls from Coimbatore, South India were recruited. Clinical data including glycated haemoglobin and sociodemographic and environmental exposure data were collected. Urine samples were analysed for Copper (Cu), Zinc (Zn), Cadmium (Cd), Arsenic (As), Barium (Ba) and Lead (Pb), which are all known endocrine-disrupting chemicals. Urinary concentrations of all heavy metals were normalized to urine creatinine and expressed as *ug/mg creatinine. The levels of all analyzed metals* were significantly higher in T1DM compared to controls. Correlation analysis revealed the positive association between glycaemia and heavy metals. Arsenic and lead showed significant trend with T1D prevalence on comparison to control while zinc and cadmium showed significant trend with uncontrolled glycaemia. This study reveals the association of heavy metals exposure on the etiology and pathophysiology of T1DM. In addition, this study highlights the need of screening of urinary heavy metals as part of metabolic risk assessment and development of targeted therapies for heavy metal detoxification for achieving better glycaemia in T1DM.

Keywords Type 1 diabetes mellitus · Heavy metals · Endocrine-disrupting chemicals · Poor glycaemia · Uncontrolled diabetes · Glycated hemoglobulin

✉ Ganesan Velmurugan
vel@kmchrf.org

[1] Chemomicrobiomics Laboratory, Department of Biochemistry and Microbiology, KMCH Research Foundation, Coimbatore 641 014, Tamil Nadu, India

[2] School of Chemical and Biotechnology, SASTRA (Deemed to be University), Thanjavur 613 401, Tamil Nadu, India

[3] Cardio-Hepato-Renal and Metabolic Research Unit, Department of Biochemistry and Microbiology, KMCH Research Foundation, Coimbatore 641 014, Tamil Nadu, India

[4] DST Unit of Nanoscience and TUE, Department of Chemistry, Indian Institute of Technology Madras, Chennai 600 036, Tamil Nadu, India

[5] Central Research Laboratory, KMCH Institute of Health Sciences and Research, Coimbatore 641 014, Tamil Nadu, India

[6] Department of Endocrinology, Kovai Medical Centre and Hospital, Coimbatore 641 014, Tamil Nadu, India

[7] Department of Endocrinology, Madhuram Diabetes and Thyroid Centre, Coimbatore 641 048, Tamil Nadu, India

[8] Chemomicrobiomics Laboratory, Department of Biochemistry & Microbiology, KMCH Research Foundation, Coimbatore 641 014, Tamil Nadu, India

Published online: 15 November 2025

Introduction

Type 1 diabetes mellitus (T1DM) is a chronic metabolic disorder that occurs during childhood and adolescence, posing a significant social and economic burden on families and nations. Globally, it is estimated that T1DM accounts for approximately 5–10% of all diabetes cases [1] and in the general population, the global prevalence ranges between 0.8 and 4.6 per 1,000 individuals [2]. These data may not truly reflect the actual cases in low- and middle-income countries (LMICs) due to limited access to healthcare facilities and health awareness [3]. During the last decade, there has been a three- to five-fold increase in the incidence of T1DM in children, particularly in LMICs [4]. This sudden escalation of T1DM cannot be attributed merely to genetically related auto-immune factors [5]. The global prevalence of T1DM incidence coincides with a period where there has been tremendous increase in the production and release of endocrine-disrupting chemicals (EDCs) into the environment [6]. Studies have documented the association between T1DM incidence and exposure to different EDCs including persistent organic pollutants, bisphenol A, plasticizers, pesticides, disinfectants, and toxic heavy metals [5, 7]. Although data on the mode of action of EDCs on triggering T1DM are sparse, studies indicate these chemicals could cause impairment of pancreatic beta cells, directly contributing to insulin deficiency or modulation of immune cell functions that lead to immune system-mediated insulin deficiency [8]. Among the EDCs, heavy metals are unique as they are naturally occurring unlike other EDCs, which are man-made and some of them have essential functions in body physiology. Heavy metals such as zinc, nickel, selenium, and copper are essential elements and they become toxic at higher levels while other heavy metals like arsenic, cadmium, lead, are non-essential and toxic. Several studies have documented the association of heavy metals with type 2 diabetes mellitus (T2DM) prevalence across different regions of the world [9, 10]. In contrast to T2DM, very few studies have explored the role of toxic elements in T1DM. The levels of essential elements (selenium, zinc, magnesium, copper, nickel, manganese) are significantly lower in the blood of individuals with T1DM and are associated with increased oxidative stress markers [11, 12]. An interesting study revealed the detection of aluminium, mercury, and arsenic above detection limits in the cord blood of children who later developed T1DM, indicating gestational exposure to heavy metals could contribute to the etiology of T1DM [13]. Studies have unveiled the association of toxic heavy metals in drinking water with the prevalence of T1DM in Canada [14] and Poland [15]. Altogether, though studies reported the association of toxic metals with T1DM, no study has investigated their levels in the bodily fluids of individuals with T1DM.

In comparison with T2DM, the prevalence of poor glycaemic control is very high among individuals with T1DM. This situation is worse in LMICs, where the resources are limited and maintaining adequate glycaemic control is a huge challenge [16]. Different studies have documented nearly two-thirds prevalence of poor glycaemic control among individuals with T1DM are in LMICs [17–19]. A longitudinal study revealed the strong association of poor glycaemic control and increased cardiovascular mortality in individuals with T1DM [20]. Though sociodemographic factors, lack of awareness and resources are attributed to the poor glycaemic control, the etiology of uncontrolled glycaemia remains poorly understood. In recent years, studies have highlighted the possible association of heavy metals with prevalence of poor glycaemic control among T2DM patients [21, 22] Click or tap here to enter text. A three-year follow-up in individuals with T2DM reported the association between urine heavy metals (arsenic, lead, cadmium, nickel and tin) and faster increases in measures of glycaemia [23]. Despite the increased recognition of toxic heavy metals as contributors to metabolic diseases, their association with prevalence and progression of T1DM remains largely unexplored. Furthermore, no study has comprehensively assessed urinary heavy metal levels in individuals with T1DM and glycaemic control from LIMCs. Therefore, this study aims to understand the association of urine heavy metals with T1DM prevalence and poor glycaemic control in South Indian population.

Materials and Methods

Study Population

The study participants were part of the Microbiota-Environmental chemicals orchestration on type 1 diabetes (Micro-Eco-T1D) study. This cross-sectional study include 153 individuals with T1DM attending endocrinology clinics of Kovai Medical Center and Hospital and Madhuram Diabetic and Thyroid Centre, Coimbatore, Tamil Nadu India. T1DM patients with pregnancy, chronic diseases and other complications were excluded from the study. 60 Nos of age and sex matached healthy controls also included in the study. Complete blood anthropometry included glycated hemoglobulin was performed in the healthy controls and those with any self-reported chronic conditions and/on regular medications were excluded. All participants had established T1DM and are on insulin therapy. Individuals who were pregnant and had life-threatening illnesses, or underwent recent surgeries were excluded. Age- and sex- matched healthy controls

were also included in the study. The study protocol was approved by Institute Human Ethics Committee (Reference no: EC/AP/535/05/2017). Written informed consent was obtained from the parents or legal guardians of participants aged below 18 years and directly from participants aged above 18 years. Demographic details and disease history were collected from all participants using a standard questionnaire. Fasting blood and spot urine samples were collected and stored under appropriate conditions. The blood samples were processed for serum and plasma segregation as per standard protocols and stored at −80 °C.

Biochemical Measurements

Peripheral blood samples were collected separately in clot and EDTA tubes were immediately processed for serum and plasma separation respectively as per standard protocols. The plasma and serum were stored at −80° C deep freezer (Thermo Scientific™ TSX70086FA. The spot urine samples were collected and an aliquot is and stored at −80 °C in deep freezer) for further elemental analysis and creatinine analysis was performed immediately. Whole blood were analysed for Glycated haemoglobin (HbA_{1c}), which was measured using the D-10® Haemoglobin Testing System (Bio-Rad Laboratories, Hercules, CA, USA). Based on HbA_{1c} values, individuals with T1DM were categorized as controlled glycaemia [≤8.5% (69 mmol/mol)] or uncontrolled glycaemia [>8.5% (69 mmol/mol)]. Urine samples were analysed for spot creatinine using the Cobas® e 601 module of the Cobas 6000 analyser series (Roche Diagnostics, Germany).

Urine Heavy Metal Analysis

Urine samples were analysed for Copper (Cu), Zinc (Zn), Cadmium (Cd), Arsenic (As), Barium (Ba) and Lead (Pb) by Inductively coupled plasma mass spectrometry (ICP-MS) (NexION® 300X; PerkinElmer Inc.) as per standard protocols [9]. The ICP-MS (NexION 300X, PerkinElmer) was calibrated using multi-element standard solutions prepared from a certified stock standard [Multielement calibration standard 3 (No Hg); Catalogue No. HNO_3 (7697-37−2); Perkin Elmer Inc., USA]. Quantification was performed using a four-point calibration curve with a correlation coefficient (R^2) greater than 0.999. The limits of detection (LOD) and quantification (LOQ) for the elements were determined to be 0.01 ppb and 10 ppb, respectively. Method accuracy was assessed by analyzing a standard solution as a sample, yielding recovery values between 90% and 98%. Analytical precision was evaluated through triplicate measurements, with relative standard deviations (RSD) below 5%. Procedural blanks and spiked samples were routinely analyzed to maintain data quality and ensure reliability of the results. 200 µl urine sample was diluted with 1.8 mL diluent (5% nitric acid + 1.5% ethanol) and filtered through a 20 µm nylon-66 membrane filter. The filtrate was subjected to ICP-MS analysis. The concentrations of metals were normalised to urinary creatinine and expressed as µg/mg creatinine.

Statistical Analysis

All statistical analyses were conducted using SPSS Version 26.0 (IBM Corp., Armonk, NY, USA) and R programming language V 4.1.0 (R Core Team, 2021). Continuous variables were presented as mean ± standard error (SE), and categorical variables as counts and percentages. To minimize the influence of extreme outliers, urinary metal concentrations were subjected to winsorization at the 5th and 95th percentiles. Values below the 5th percentile were set to the 5th percentile value, and those above the 95th percentile were set to the 95th percentile value. Comparison between individuals with T1DM and healthy controls was done using the Mann-Whitney test for continuous variables and Pearson's chi square test for categorical variables. The dot and violin plots were generated using ggplot2, R-package [24]. Spearman's correlation coefficient was calculated between metals and HbA_{1c} values. Urine metal concentrations were categorised into quartiles based on the weighted sample distribution. The association between risk factors and disease outcomes was studied. For each metal, we used logistic regression to estimate odds ratios (ORs) and confidence intervals (CIs) levels for T1DM and glycaemic control by comparing each quartile with the lowest quartile. Our logistic regression models were fitted with appropriate degrees of adjustment. In each analysis, we also evaluated the significance of the differences of the average proportion of T1DM across the four quartiles of the model by a generalised maximum likelihood Wald $\chi 2$ test. Subsequently, we tested for linear trends across quartiles of urine metals by including the median of each quartile as a continuous variable in logistic regression models. Statistical significance was determined on the basis of two-sided p values of < 0.05.

Results

Participant Characteristics

A total of 213 individuals were enrolled in the study, including 153 participants with T1DM and 60 healthy controls. The healthy controls were age- and sex- matched. Sociodemographic and exposure characteristics are represented in Table 1. There has been relatively increased incidence of T1DM among the females (63.4%) in our study area. 79% of the T1DM population fell within the age group of 07–18

Table 1 Demographic characteristics of children with type 1 diabetes (T1DM) ($n=153$) and healthy controls ($n=60$)

		Control *n* (%)	T1DM *n* (%)	*p*-value
Sex	Male	28 (46.67%)	56 (36.60%)	0.213
	Female	32 (53.33%)	97 (63.40%)	
Age Group	< 6 yrs	13 (21.67%)	9 (5.88%)	0.005
	7–12 yrs	21 (35.00%)	65 (42.48%)	
	13–18 yrs	15 (25.00%)	56 (36.60%)	
	> 18 yrs	11 (18.33%)	23 (15.03%)	
Residence area	Urban	35 (58.33%)	58 (37.91%)	0.007
	Rural	25 (41.67%)	95 (62.09%)	
Presence of farmland near residence	Yes	32 (53.33%)	84 (54.90%)	0.836
	No	28 (46.67%)	69 (45.10%)	
Presence of industries near residence	Yes	13 (21.67%)	26 (17.00%)	0.436
	No	47 (78.33%)	127 (83.00%)	
Presence of farmland or industries near residence	Yes	34 (56.67%)	93 (60.00%)	0.542
	No	26 (43.33%)	60 (40.00%)	
Drinking Water Source	Ground water	9 (15.25%)	26 (14.44%)	0.356
	Piped river water	42 (71.19%)	92 (51.11%)	
	Processed water	9 (15.25%)	35 (19.44%)	

years indicating higher prevalence in these age groups. It is interesting to note that 62% of the T1DM population were from rural areas and living near farm lands or industries that could be potential sources of heavy metals. Only 19.44% of the population uses processed drinking water. The healthy controls were matched for all the demographic variables.

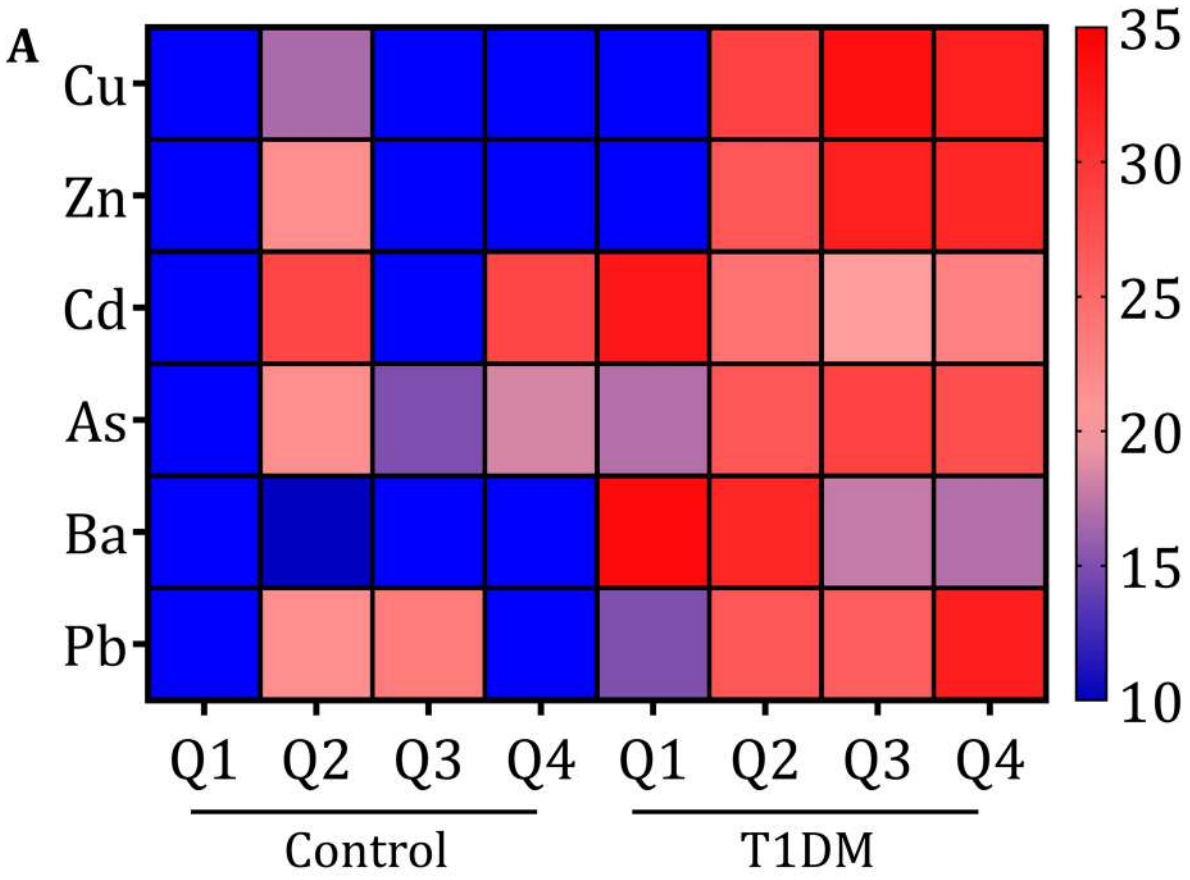
Association of Urine Heavy Metals with T1DM on Comparison to Healthy Controls

The levels of all the urine heavy metals analysed (Cu, Zn, Cd, As, Ba, Pb) are significantly higher in individuals with T1DM compared to controls (Fig. S1). Based on metal accumulation, the population was divided into quartiles and logistic regression analysis was performed between the quartiles, using the lowest quartile as reference group. More than 50% of healthy controls falls within the lowest quartiles for all heavy metals analysed while in case of T1DM, more than 50% of population fell within the highest quartiles (Fig. 1A and Supplementary Table S1). Urinary concentrations of all six metals showed statistically significant differences between T1DM and control participants ($p<0.001$; Fig. 1A and Supplementary Table S1). Copper and zinc were markedly elevated in the T1DM group, with 32.0% and 31.4% of participants falling in the highest quartile (Q4), respectively, compared to only 6.7% and 8.3% of controls. Conversely, the lowest quartile (Q1) for copper and zinc included 73.3% and 63.3% of controls, but only 5.9% and 9.8% of T1DM individuals, respectively. Cadmium also showed an increased distribution in T1DM, with 32.7% in Q1 compared to just 5% in controls. Arsenic concentrations were similarly higher in T1DM, with 56.2% occupying Q3 and Q4, compared to 33.3% of controls; only 17% of T1DM participants were in Q1 compared to 45% of controls. Urinary barium levels were 33.9% in Q1 compared to 1.7% of controls. Lead concentrations were higher in T1DM, with 58.2% of individuals in Q3 and Q4, while half of the control group clustered in Q1. Logistic regression was performed with adjusted models included age and sex as covariates, and quartile 1 (Q1) served as the reference group. T1DM participants were substantially overrepresented in the highest quartiles of copper and zinc. The odds of T1DM increased sharply across quartiles for both metals. Particularly, individuals with T1DM in Q4 had significantly higher odds of disease for copper (adjusted odds ratio = 0.020 vs. Q1; CI: 0.001–0.568), same trend was seen for zinc, where T1DM participants in Q4 had an OR of 0.035 ($p<0.025$ and 0.011, respectively). Arsenic showed a strong association with individuals in the highest quartile (Q4), which is found to be having 15.62-fold higher odds of developing T1DM compared to those in the lowest quartile (Q1) (95% CI: 1.952–101.25; $p<0.002$). A similar pattern was observed in lead (Pb) with T1DM participants in Q4 showing increased odds compared to those in lower quartiles ($p<0.016$). Altogether, upon logistic regression analysis, significant trends were obtained for the highest quartiles for Cu, Zn, As and Pb on comparing the odds ratio of T1DM with controls (Table 2).

Fig. 1 Distribution of urinary metal concentrations categorized across quartiles. (**A**) T1DM and Controls. (**B**) T1DM with controlled and uncontrolled glycaemic control

Heavy Metals and Glycaemic Control in T1DM

To assess the relationship between urinary metal concentrations and HbA_{1c} among individuals with T1DM, Spearman's rank correlation analysis was performed (Table 3). Significant positive correlations were found between HbA_{1c} and the urinary levels of zinc ($\rho=0.181$, $p=0.025$), lead ($\rho=0.185$, $p=0.022$), and barium ($\rho=0.174$, $p=0.032$). Though cadmium and arsenic also showed positive correlations with HbA_{1c}, they did not reach statistical significance. Participants were stratified by glycaemic control using an HbA_{1c} threshold of 8.5% [69 mmol/mol] (controlled ≤ 8.5% [69 mmol/mol]), uncontrolled > 8.5% [69 mmol/mol])), and metal concentrations were assessed across quartiles (Fig. 1B and Supplementary table S2). For copper, individuals with uncontrolled glycaemia were more frequently


A
Cu
Zn
Cd
As
Ba
Pb
Q1 Q2 Q3 Q4 Q1 Q2 Q3 Q4
Control
T1DM
35
30
25
20
15
10

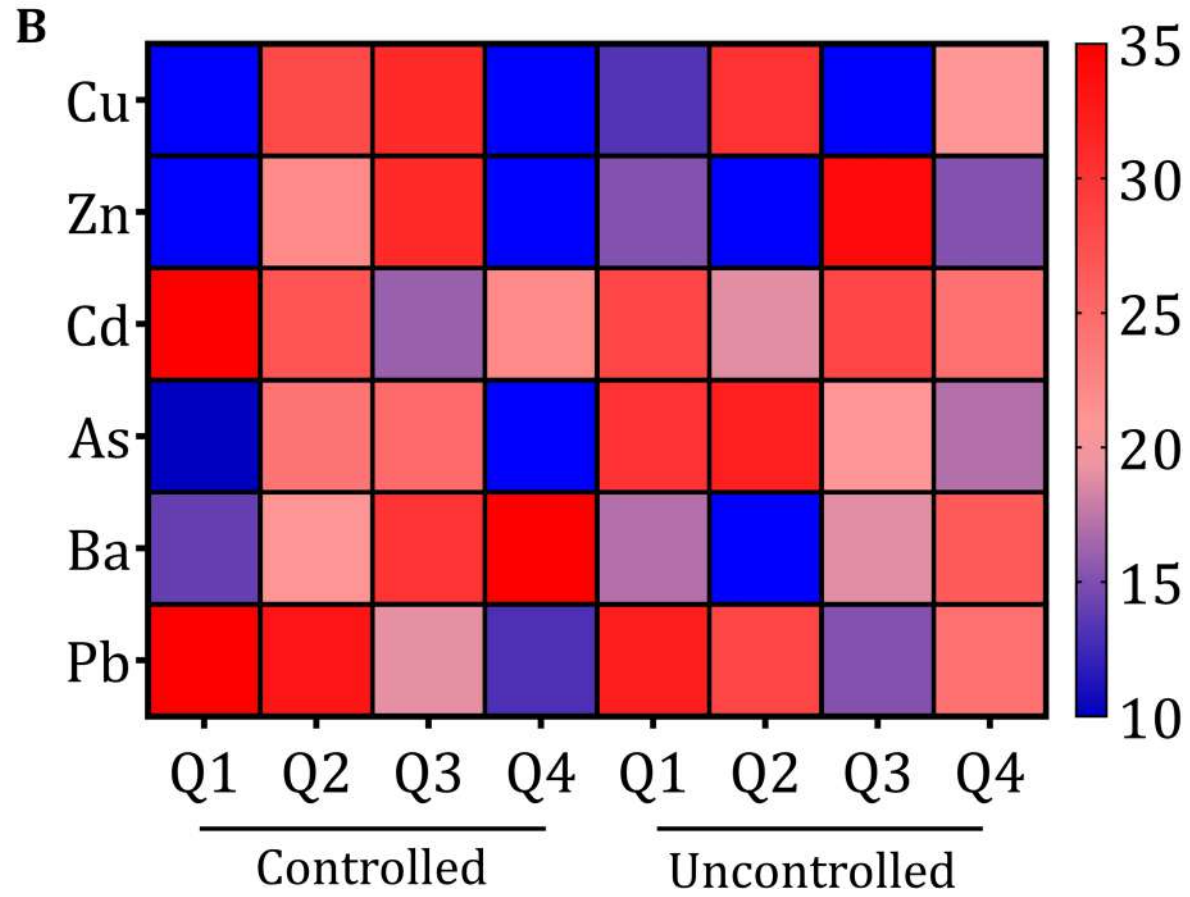

B
Cu
Zn
Cd
As
Ba
Pb
Q1 Q2 Q3 Q4 Q1 Q2 Q3 Q4
Controlled
Uncontrolled
35
30
25
20
15
10

Table 2 Binomial logistic regression analysis comparing the odds of having T1DM across increasing quartiles of urinary metal concentrations

Metal	Model	Q1	Q2	Q3	Q4	P_{trend}
Cu	Unadjusted	1	0.027 (0.003–0.266) **	0.013 (0.001–0.218) **	0.014 (0.001–0.258) **	**0.025**
	Model 1	1	0.030 (0.002–0.377) **	0.015 (0.001–0.327) **	0.019 (0.001–0.466) *	
	Model 2	1	0.042 (0.023–0.456)**	0.018 (0.001–0.235)*	0.020 (0.001–0.568)*	
Zn	Unadjusted	1	0.053 (0.006–0.464) **	0.008 (0.000–0.233) **	0.030 (0.001–1.186)	**0.011**
	Model 1	1	0.045 (0.004–0.504) **	0.006 (0.000–0.245) **	0.020 (0.000–1.451)	
	Model 2	1	0.012 (0.005–0.483) **	0.005 (0.001–0.315)*	0.035 (0.001–1.548)	
Cd	Unadjusted	1	5.923 (0.612–57)	0.573 (0.012–27.781)	10.227 (0.159–658.675)	**0.711**
	Model 1	1	6.338 (0.620–64)	0.882 (0.012–62.296)	8.586 (0.101–727.684)	
	Model 2	1	6.584 (1.025–41.0)	0.954 (0.012–34.523)	7.561 (0.201–523.0)	
As	Unadjusted	1	0.473 (0.012–18.328)	4.184 (0.326–53.752)	12.765 (1.012–161.053) *	**0.002**
	Model 1	1	0.813 (0.015–44.189)	4.006 (0.270–59.361)	17.879 (1.259–253.983) *	
	Model 2	1	1.023 (0.020–35.641)	4.521 (0.549–39.152)	15.625 (1.952–101.25)*	
Ba	Unadjusted	1	11.686 (0.207–659.437)	20.812 (0.261–1661.516)	72.213 (0.746–6993.940)	**0.262**
	Model 1	1	15.720 (0.198–1250.860)	38.262 (0.283–5167.881)	220.090 (1.081–44806) *	
	Model 2	1	18.112 (0.568–715.0)	28.353 (0.315–1654.0)	132.0 (1.284–1002)*	
Pb	Unadjusted	1	0.350 (0.026–4.633)	1.035 (0.016–66.445)	0.121 (0.001–22.661)	**0.016**
	Model 1	1	0.193 (0.011–3.388)	1.976 (0.022–179.931)	0.143 (0.001–40.095)	
	Model 2	1	0.254 (0.235–5.325)	1.890 (0.050–77.253)	0.152 (0.002–28.99)	

ORs and 95% CIs are shown for both unadjusted and adjusted models. Q1 (lowest quartile) is the reference group. Model 1 adjusted for age and sex while model 2 adjusted for age, sex, presence of industries and farmlands near residence and drinking water source

Table 3 Spearman's rank correlation coefficients between metals and HbA_{1c}

Variable	Spearman ρ (*p*-value)
Cu	0.098 (0.227)
Zn	0.181 (0.025) *
Cd	0.143 (0.078)
As	0.101 (0.213)
Ba	0.174 (0.032) *
Pb	0.185 (0.022) *
BMI	−0.114 (0.162)
No. of Hospitalizations	0.241 (0.003) **

Values represent Spearman's correlation coefficient (rho) between HbA_{1c} and each parameter. *$p<0.05$, **$p<0.01$, ***$p<0.001$

distributed in the lower quartiles. A greater proportion of uncontrolled participants were present in the first quartile (13.2%) and third quartile (35.8%), while only 20.8% fell into the highest quartile. In contrast, 38% of those with controlled glycaemia were in the highest quartile, indicating a statistically significant shift in distribution ($p=0.013$). Zinc showed a similar pattern in uncontrolled individuals more frequently found in the second (35.8%) and third (34.0%) quartiles, while the fourth quartile comprised only 15.1% of this group compared to 40.0% among those with controlled glycaemia. For arsenic, a higher proportion of uncontrolled individuals were found in the second (32.1%) and fourth (19.0%) quartiles, whereas it was 24.0% and 9.0% in controlled group. Urinary metal concentrations were associated with uncontrolled glycaemia ($HbA_{1c}\geq 8.5\%$ [69 mmol/mol])) among T1DM participants using binomial logistic regression. Lowest quartile (Q1) was considered the reference group and odds ratios (ORs) were calculated for both unadjusted and age- and sex-adjusted models (Fig. 2 and Supplementary table S3). In the adjusted model, urinary zinc levels were associated significantly with glycaemic control status (p trend = 0.015). For zinc, an odds ratio of 0.242 (95% CI: 0.060–0.983) for having uncontrolled glycaemia was observed in the highest quartile (Q4) compared to those in the lowest quartile. A significant association was also shown by cadmium levels, with increased odds of uncontrolled glycaemia (OR = 4.023, 95% CI: 0.991–12.361; p trend = 0.017) being exhibited by participants in the highest quartile (Q4). No statistically significant associations were found for copper, arsenic, barium, and lead in the adjusted models. However, the unadjusted model showed reduced odds in some quartiles (e.g., Q3 for arsenic), these associations were not sustained after adjustment for age and sex.

Discussion

Our study reports a comprehensive analysis of urinary trace element concentrations among T1DM participants and healthy controls, with a focus on their association with HbA_{1c}. In our cohort there was a slightly increased proportion of females compared to male T1DM participants though it is not statistically significant. This pattern is supported

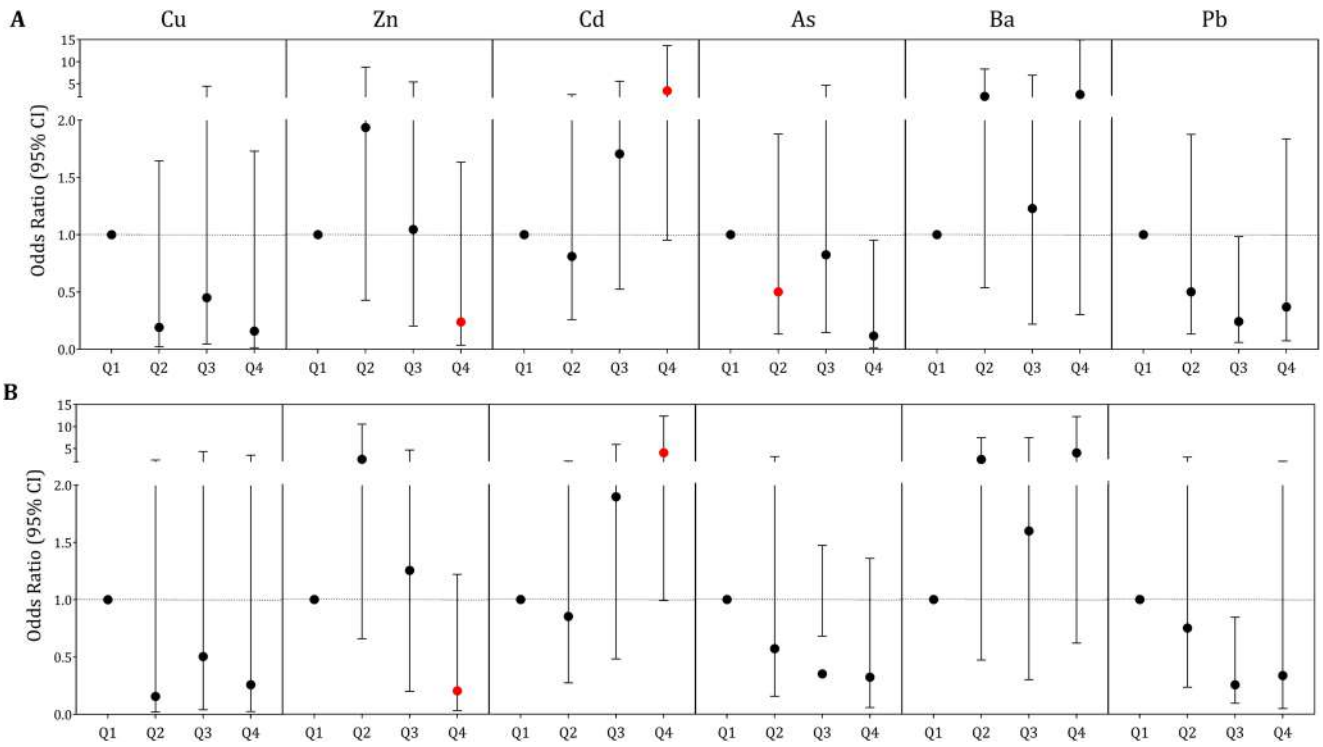


Fig. 2 Odds ratio (95% CI) for glycaemic control associated with the quartiles of heavy metals. The red colour indicates statistical significance. (**A**) Unadjusted model (**B**) Multivariate adjustment included age, sex, presence of industries and farmlands near residence and drinking water source

by recent literature, attributing to difference in the immune regulatory effects of genes on the X chromosome and sex-specific immune responses. There are also certain conditions like systemic lupus erythematosus (SLE), rheumatoid arthritis and multiple sclerosis where the presence of estrogen influences the degree of immune response [25, 26]. On the contrary other studies have reported equal or increased male population in their cohort [27, 28]. While this pattern in T1DM remains incompletely defined, further studies in sex-specific investigation in the South Asian population is required. Our results demonstrated differences in urinary metal levels across HbA_{1c}, with several trace elements, particularly zinc and cadmium showing significant associations with glycaemic outcomes. Copper (Cu) levels were found to be significantly elevated in T1DM participants, with a greater number of individuals classified into the higher urinary Cu quartiles, and this pattern was confirmed by regression analysis, which indicated a strong association between increased Cu excretion and T1DM status. Individuals with uncontrolled HbA_{1c} were found more in the highest Cu quartiles and although correlation and regression were not significant, the pattern reinforced the link between elevated Cu and poorer glycaemic control. These findings are consistent with the literature in which Cu dysregulation is linked to T1DM pathophysiology. β-cell function has been shown to be impaired by excess Cu through oxidative stress, disruption of Cu transporter activity, and activation of inflammatory pathways [29–31]. These mechanisms may underlie the observed association between elevated copper levels and poorer glycaemic control in our cohort. Zinc (Zn) plays an important role in synthesis of insulin [32] and acts as antioxidant [33], was considerably elevated in individuals T1DM, indicating increased renal Zn loss. Logistic regression model reveals higher Zn quartiles is associated with increased odds of T1DM. Additionally, individuals with T1DM with elevated Zn tend to have a controlled glycaemia, suggesting a complex interplay between insulin regulation, glycaemic control, and disease severity. These findings are similar with a condition called “hyperzincuria” reported in T1DM [34–36] Urinary Zn can also serve as biomarker for metabolic stress. Galvez-Fernandez et al. [36] further demonstrated that adequate zinc status is associated with better glycaemic outcomes in children with T1DM. The interplay between Zn and Cu was an interesting observation in our study. It is known that both these elements share common transporters and regulatory pathways, so any disruption can affect the homeostasis of these elements. Dinicolantonio et al. [37] emphasized that excessive copper can inhibit zinc

absorption and impair glycaemic control via altered redox signalling. In this study, the dysregulated zinc-copper axis was suggested by the inverse relationship between zinc and HbA_{1c}, in parallel with elevated Cu contributing to impaired β-cell function.

A more complex relationship was shown by cadmium (Cd), though it was not considered to be statistically significant among the different groups; a greater odds of uncontrolled glycaemia was observed in individuals with higher urinary Cd. This observation is similar to previous reports claiming its effect on insulin resistance [38], it also plays a role in oxidative stress and other metabolic pathway. Cd levels can serve as stress biomarker for pancreatic beta cell [39]. Hong et al. [40] showed that cadmium disrupts β-cell function by impairing mitochondrial pathways, reducing insulin secretion, and altering lipid metabolism. Wen et al. [41] reported that cadmium exposure elevates oxidative stress and inflammatory signalling, aggravating glycaemic instability. Buha et al. [38] further emphasized cadmium's ability to interfere with insulin sensitivity and impair pancreatic health even at low environmental levels. Arsenic (As) is known for its diabetogenic role and has been a public health concern. There was a strong and statistically significant association with T1DM with highest quartile urinary As being 18-fold increase in odds of T1DM, even after adjusting for possible confounders. Cameran et al. [42] reported that chronic arsenic exposure is associated with disruption of insulin signalling pathways and induction of oxidative stress, which contribute to pancreatic β-cell dysfunction. Arsenic's ability to impair glucose uptake and promote the production of inflammatory cytokines was demonstrated by Liu et al. [43]. While Pánico et al. [44] have shown that arsenic impacts endothelial and immune pathways involved in metabolic dysregulation. Additionally, extensive agricultural usage of arsenic-containing fertilizers has been reported, and arsenic occurs naturally as a contaminant in groundwater, often as a result of geogenic factors or anthropogenic activities such as mining. Prolonged exposure to arsenic-contaminated groundwater, which is a global issue, continues to pose substantial risks to public health due to the widespread reliance on these water sources for drinking and agriculture [45].

Barium (Ba) is a non-essential element with limited biological function. Ba levels were significantly elevated in T1DM cohort and showed a positive association with HbA_{1c}, pointing its role in glycaemic dysregulation. However, Evidence linking glucose dyshomeostasis is underreported [46]. Acute barium poisoning can lead to "hypokalemia" as it interferes ion channel as reported by Tao et al. [47]. Lead (Pb) is widely known for its versatility, but it is also known for its toxicity which, upon exposure, can inflict damage to pancreatic beta cell, promotes oxidative stress, and plays a major role in activation of immune system [48]. Elevated level of Pb was observed in T1DM population and positively correlated with glycaemic level, which is consistent with prior research that states exposure to Pb is associated with elevated blood glucose. Participants in the highest quartile of urinary lead has significantly increased odds of T1DM. These exposures stem from contaminated sources such as water, air, and cooking utensils and industrial residues in our environment [49–51]. In overall, the heavy metals can induce the pancreatic beta cell destruction through immune and non-autoimmune pathways mediated through reactive oxygen species and oxidative stress (Fig. 3).

This study has limitations, adjustment for urine concentration variability was achieved using creatinine; however, the long-term or cumulative exposure may not have been accurately reflected by spot urine sampling. While a more reliable estimate could have been provided by a 24-hour collection, this was not practically feasible in our paediatric T1DM outpatient setting. Additionally, more robust data could have been obtained if complementary analysis of blood and hair samples had been performed. The detailed information on the longitudinal history of exposure to environmental chemicals, metal speciation, and data on dietary intake were also limited.

Conclusion

Our study reveals significant associations between urinary metals and T1DM status in South Indian children. Elevated levels of heavy metals were linked to both disease risk and glycaemic control. Despite the limitations, this study provides important preliminary insights into the relationship between environmental metal exposure and glycaemic health in the T1DM cohort. Future studies should include prospective cohort designs and mechanistic approaches to determine pathways followed by interventions like dietary modification and chelation therapy for better glycaemic control among heavy metal-exposed T1DM population.

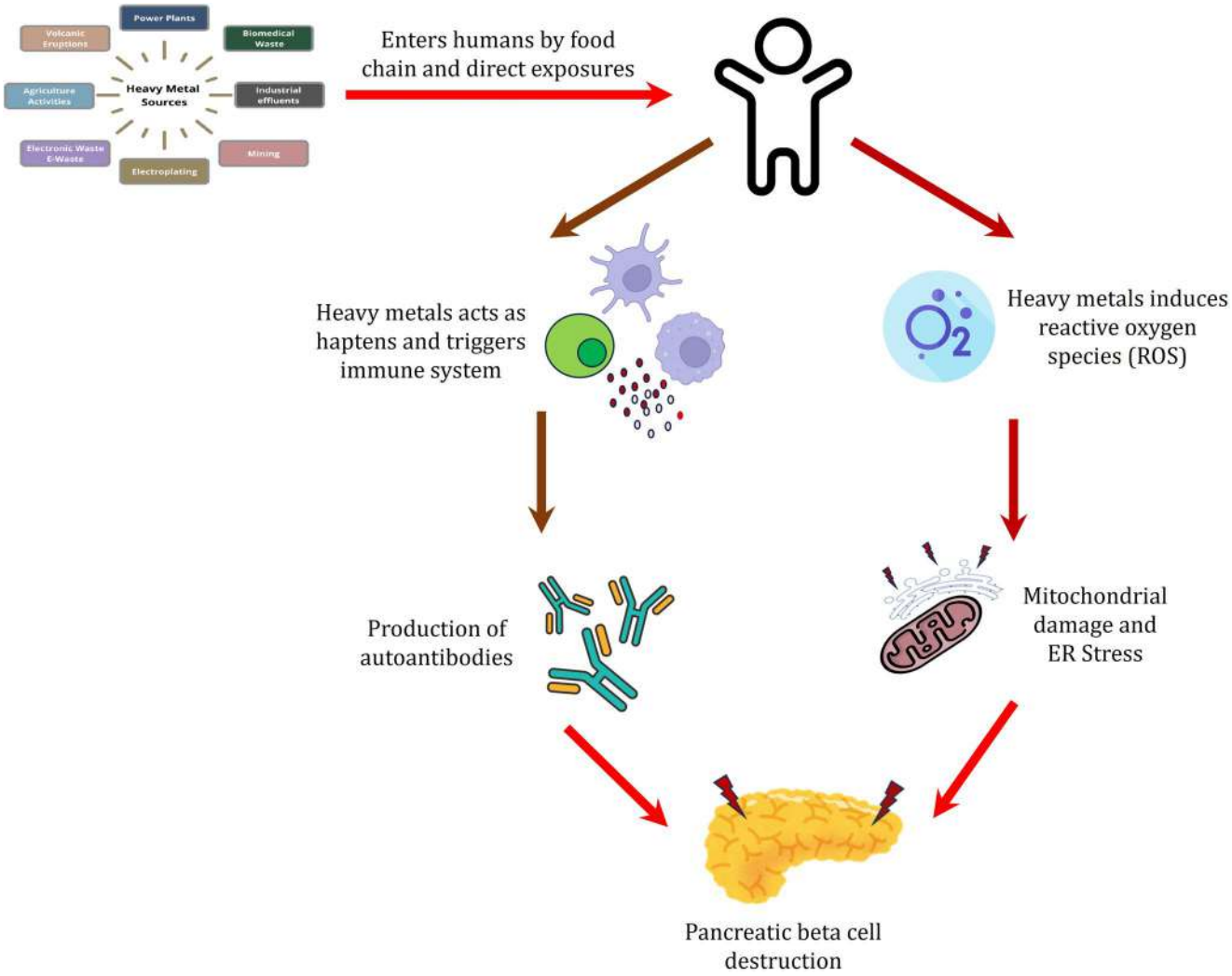


Fig. 3 Schematic illustration of heavy metals-induced beta-cell destruction through immune and non-immune pathway

Supplementary Information The online version contains supplementary material available at https://doi.org/10.1007/s12011-025-04903-8.

Acknowledgements We thank the children and their families who participated in this study. We gratefully acknowledge the clinical and nursing staff at Kovai Medical Centre and Hospital (KMCH) and Madhuram Diabetes and Thyroid Centre (MDTC) for their assistance in sample collection and participant coordination. We further express our gratitude to the Founding Trustees and the President of KMCH Research Foundation for the institutional support.

Author Contributions Samrat Ashok Vasudevan: Writing – original draft, Validation, Data collection & curation, Methodology, Investigation, Formal analysis. Srinidhi Narayani Seenivasan : Writing – review and editing, Formal analysis, Investigation, Data collection & curation. Avinash Kumar Raghupathy : Writing – review and editing, Formal analysis, Data collection & curation. Dinakaran Vasudevan : Investigation, Data collection & curation. Parthasarathy Ayothi: Investigation, Data collection & curation. Tanmayaa Nayak: Methodology, Investigation. Buvaneswari Gajendran: Data collection & curation. Karthika Durairaj : Data collection & curation. Divya Shree Sathish: Data collection & curation. Srilaxmi Balaji: Data collection & curation. Abisheak Kandasamy: Data collection & curation. Amaravathy P: Writing – review and editing, Formal analysis. Mohanraj Sundaresan: Writing – review and editing, Formal analysis, Data collection & curation, conceptualisation. Shankar Dhandapani: Data collection & curation, conceptualisation. Thalappil Pradeep: Investigation, funding acquisition, conceptualisation. Krishnan Swaminathan: Writing – review and editing, Funding acquisition, conceptualisation, supervision, Project administration. Velmurugan Ganesan: Writing – review and editing, Validation, Methodology, Investigation, Formal analysis, Data collection & curation, Funding acquisition, conceptualisation, supervision, Project administration.

Funding This work was supported by the Endocrine Society of Tamil Nadu (ESTN-2020 and ESTN-2022) and Research Society for the Study of Diabetes in India (RSSDI/HQ/Grants/2021/04).

Data Availability All raw data are available as supplementary materials.

Declarations

Ethics Approval and Consent to Participate The study was conducted in accordance with Declaration of Helsinki and approved by the Institu-

tional Human Ethics Committee (Reference no: EC/AP/535/05/2017) at Kovai Medical Centre and Hospital Limited (KMCH), Coimbatore, India. Informed consent was obtained from the parents or directly from participants aged 18 years and older.

Competing Interests The authors declare no competing interests.

References

1. IDF Diabetes Atlas (2025) 2025 | Global Diabetes Data & Insights n.d. https://diabetesatlas.org/resources/idf-diabetes-atlas-2025/
2. Ghojazadeh M, Mobasseri M, Azar FP, Lotfi A, Ghojazadeh M, Mobasseri M et al (2024) Prevalence and Incidence of Type 1 Diabetes in the World. Type 1 Diabetes - Causes, Symptoms, and Treatments [Working Title]. https://doi.org/10.5772/INTECHOPEN.1007015
3. Chan JCN, Lim LL, Wareham NJ, Shaw JE, Orchard TJ, Zhang P et al (2020) Lancet 396:2019–2082. https://doi.org/10.1016/S0140-6736(20)32374-6/ASSET/5FF393CC-06D4-4BDA-9BDF-BDEB60045960/MAIN.ASSETS/GR3.JPG. The Lancet Commission on diabetes: using data to transform diabetes care and patient lives
4. Kandemir N, Vuralli D, Ozon A, Gonc N, Ardicli D, Jalilova L et al (2024) Epidemiology of type 1 diabetes mellitus in children and adolescents: a 50-year, single-center experience. J Diabetes 16:e13562. https://doi.org/10.1111/1753-0407.13562
5. Rewers M, Ludvigsson J (2016) Environmental risk factors for type 1 diabetes. Lancet 387:2340–2348. https://doi.org/10.1016/S0140-6736(16)30507-4
6. Velmurugan G, Ramprasath T, Gilles M, Swaminathan K, Ramasamy S, Gut Microbiota (2017) Endocrine-Disrupting Chemicals, and the diabetes epidemic. Trends Endocrinol Metabolism 28:612–625. https://doi.org/10.1016/j.tem.2017.05.001
7. Bodin J, Stene LC, Nygaard UC (2015) Can exposure to environmental chemicals increase the risk of diabetes type 1 development? BioMed Res Int 2015:208947. https://doi.org/10.1155/2015/208947
8. Keskesiadou GN, Tsokkou S, Konstantinidis I, Georgaki MN, Sioga A, Papamitsou T et al (2024) Endocrine-Disrupting chemicals and the development of diabetes mellitus type 1: A 5-Year systematic review. Int J Mol Sci 25:10111. https://doi.org/10.3390/IJMS251810111
9. Velmurugan G, Swaminathan K, Veerasekar G, Purnell JQ, Mohanraj S, Dhivakar M et al (2018) Metals in urine in relation to the prevalence of pre-diabetes, diabetes and atherosclerosis in rural India. Occup Environ Med 75:661–667. https://doi.org/10.1136/OEMED-2018-104996
10. Briffa J, Sinagra E, Blundell R (2020) Heavy metal pollution in the environment and their toxicological effects on humans. Heliyon 6:e04691. https://doi.org/10.1016/J.HELIYON.2020.E04691
11. Forte G, Bocca B, Peruzzu A, Tolu F, Asara Y, Farace C et al (2013) Blood metals concentration in type 1 and type 2 diabetics. Biol Trace Elem Res 156:79–90. https://doi.org/10.1007/S12011-013-9858-6
12. Alghobashy AA, Alkholy UM, Talat MA, Abdalmonem N, Zaki A, Ahmed IA et al (2018) Trace elements and oxidative stress in children with type 1 diabetes mellitus. Diabetes Metabolic Syndrome Obes 11:85–92. https://doi.org/10.2147/DMSO.S157348
13. Ludvigsson J, Andersson-White P, Guerrero-Bosagna C (2019) Toxic metals in cord blood and later development of type 1 diabetes. Pediatr Dimens 4. https://doi.org/10.15761/PD.1000186. 10.15761/PD.1000186
14. Chafe R, Aslanov R, Sarkar A, Gregory P, Comeau A, Newhook LA (2018) Association of type 1 diabetes and concentrations of drinking water components in Newfoundland and Labrador, Canada. BMJ Open Diabetes Res Care. https://doi.org/10.1136/BMJDRC-2017-000466
15. Zorena K, Michalska M, Bartoszewicz M, Wąż P, Krawczyk S, Beń-Skowronek I et al (2024) The presence of heavy metals in drinking water and its possible impact on the development of type 1 diabetes in children. Water. https://doi.org/10.3390/W16213083
16. Ali L, Alhassan M (2024) Challenges in achieving adequate glycemic control among children with type 1 diabetes mellitus in a resource-limited setting: a cross-sectional study from Sudan. Diabetes Res Clin Pract. https://doi.org/10.1016/j.diabres.2024.111113
17. Huo L, Deng W, Shaw JE, Magliano DJ, Zhang P, McGuire HC et al (2020) Factors associated with glycemic control in type 1 diabetes patients in China: a cross-sectional study. J Diabetes Investig 11:1575–1582. https://doi.org/10.1111/JDI.13282
18. Habteyohans BD, Hailu BS, Meseret F, Mohammed A, Berhanu Y, Alemu A et al (2023) Poor glycemic control and its associated factors among children with type 1 diabetes mellitus in Harar, Eastern Ethiopia: a cross-sectional study. BMC Endocr Disord. https://doi.org/10.1186/S12902-023-01453-9
19. Najem S, Majaliwa ES, Ramaiya K, Swai ABM, Jasem D, Ludvigsson J (2020) Glycemic control and complications of type 1 diabetes among children in Tanzania. J Clin Transl Endocrinol 23:100245. https://doi.org/10.1016/J.JCTE.2020.100245
20. Lind M, Svensson A-M, Kosiborod M, Gudbjörnsdottir S, Pivodic A, Wedel H et al (2014) Glycemic control and excess mortality in type 1 diabetes. N Engl J Med 371:1972–1982. https://doi.org/10.1056/NEJMOA1408214/SUPPL_FILE
21. Zhu J, Hu S, Wang S, Zhang Y, Zhu Q, Zhang M et al (2023) Association between metal mixture exposure and abnormal glucose metabolism in multiple mixture exposure models: evidence from NHANES 2015–2016. Curr Res Toxicol 5:100141. https://doi.org/10.1016/J.CRTOX.2023.100141
22. Adokwe JB, Pouyfung P, Kuraeiad S, Wongrith P, Inchai P, Yimthiang S et al (2025) Concurrent lead and cadmium exposure among diabetics: A Case-Control study of Socio-Demographic and consumption behaviors. Nutrients 17:710. https://doi.org/10.3390/NU17040710/S1
23. Weiss MC, Sun J, Jackson BP, Turyk ME, Wang L, Brown EL et al (2024) Accelerated longitudinal glycemic changes in relation to urinary toxic/essential metals and metal mixtures among Mexican Americans living in Starr County, Texas. Diabetes Care 47:1908–1915. https://doi.org/10.2337/DC24-0646
24. Wickham H (2016) ggplot2. https://doi.org/10.1007/978-3-319-24277-4
25. Fairweather D, Frisancho-Kiss S, Rose NR (2008) Sex differences in autoimmune disease from a pathological perspective. Am J Pathol 173:600. https://doi.org/10.2353/AJPATH.2008.071008
26. Feng Z, Liao M, Zhang L (2024) Sex differences in disease: sex chromosome and immunity. J Transl Med 22:1150. https://doi.org/10.1186/S12967-024-05990-2
27. Barkai L, Kiss Z, Rokszin G, Abonyi-Tóth Z, Jermendy G, Wittmann I et al (2019) Changes in the incidence and prevalence of type 1 and type 2 diabetes among 2 million children and adolescents in Hungary between 2001 and 2016 - a nationwide population-based study. Arch Med Sci 16:34–41. https://doi.org/10.5114/AOMS.2019.88406
28. Wandell P, Carlsson A (2013) Time trends and gender differences in incidence and prevalence of type 1 diabetes in Sweden. Curr Diabetes Rev 9:342–349. https://doi.org/10.2174/15733998113099990064
29. Jia D, Liu L, Liu W, Li J, Jiang X, Xin Y (2024) Copper metabolism and its role in diabetic complications: a review. Pharmacol Res 206:107264. https://doi.org/10.1016/J.PHRS.2024.107264
30. Cui X, Wang Y, Liu H, Shi M, Wang J, Wang Y (2022) The molecular mechanisms of defective copper metabolism in diabetic cardiomyopathy. Oxid Med Cell Longev 2022:5418376. https://doi.org/10.1155/2022/5418376

31. Chen X, Cai Q, Liang R, Zhang D, Liu X, Zhang M et al (2023) Copper homeostasis and copper-induced cell death in the pathogenesis of cardiovascular disease and therapeutic strategies. Cell Death Dis 14(2):2. https://doi.org/10.1038/s41419-023-05639-w
32. Nakamura A, Kido T, Seki Y, Suka M (2024) Zinc deficiency affects insulin secretion and alters insulin-regulated metabolic signaling in rats. J Trace Elem Med Biol 83:127375. https://doi.org/10.1016/J.JTEMB.2023.127375
33. Costa MI, Sarmento-Ribeiro AB, Gonçalves AC (2023) Zinc: from biological functions to therapeutic potential. Int J Mol Sci. https://doi.org/10.3390/ijms24054822
34. Bandeira VdaS, Pires LV, Hashimoto LL, de Alencar LL, Almondes KGS, Lottenberg SA et al (2017) Association of reduced zinc status with poor glycemic control in individuals with type 2 diabetes mellitus. J Trace Elem Med Biol 44:132–136. https://doi.org/10.1016/J.JTEMB.2017.07.004
35. Fukunaka A, Fujitani Y (2018) Role of zinc homeostasis in the pathogenesis of diabetes and obesity. Int J Mol Sci. https://doi.org/10.3390/IJMS19020476
36. Galvez-Fernandez M, Powers M, Grau-Perez M, Domingo-Relloso A, Lolacono N, Goessler W et al (2022) Urinary zinc and incident type 2 diabetes: prospective evidence from the strong heart study. Diabetes Care 45:2561–2569. https://doi.org/10.2337/DC22-1152
37. Dinicolantonio JJ, Mangan D, O'Keefe JH (2018) Copper deficiency may be a leading cause of ischaemic heart disease. Open Heart. https://doi.org/10.1136/OPENHRT-2018-000784
38. Buha A, Dukić-Ćosić D, Ćurčić M, Bulat Z, Antonijević B, Moulis JM et al (2020) Emerging links between cadmium exposure and insulin resistance: Human, Animal, and cell study data. Toxics 8:63. https://doi.org/10.3390/TOXICS8030063
39. Hong H, Xu J, He H, Wang X, Yang L, Deng P et al (2022) Cadmium perturbed metabolomic signature in pancreatic beta cells correlates with disturbed metabolite profile in human urine. Environ Int 161:107139. https://doi.org/10.1016/J.ENVINT.2022.107139
40. Hong H, Xu J, He H, Wang X, Yang L, Deng P et al (2022) Cadmium perturbed metabolomic signature in pancreatic beta cells correlates with disturbed metabolite profile in human urine. Environ Int. https://doi.org/10.1016/j.envint.2022.107139
41. Wen S, Xu M, Zhang W, Song R, Zou H, Gu J et al (2023) Cadmium induces mitochondrial dysfunction via SIRT1 suppression-mediated oxidative stress in neuronal cells. Environ Toxicol 38:743–753. https://doi.org/10.1002/TOX.23724
42. Carmean CM, Seino S (2019) Braving the element: pancreatic β-cell dysfunction and adaptation in response to arsenic exposure. Front Endocrinol (Lausanne) 10:344. https://doi.org/10.3389/FENDO.2019.00344
43. Liu Y, Wang W, Liang B, Zou Z, Zhang A (2025) NLRP3 inflammasome activation and disruption of IRS-1/PI3K/AKT signaling: potential mechanisms of arsenic-induced pancreatic beta cells dysfunction in rats. Ecotoxicol Environ Saf 289:117504. https://doi.org/10.1016/J.ECOENV.2024.117504
44. Pánico P, Velasco M, Salazar AM, Picones A, Ortiz-Huidobro RI, Guerrero-Palomo G et al (2022) Is arsenic exposure a risk factor for metabolic syndrome? A review of the potential mechanisms. Front Endocrinol (Lausanne) 13:878280. https://doi.org/10.3389/FENDO.2022.878280
45. Hashem MA, Rahman MA, Hasan M, Momen MA, Lamia QF, Sahen MS et al (2024) Effect of agricultural fertilizers on arsenic leaching from sediment under aerobic conditions. Case Stud Chem Environ Eng 10:100794. https://doi.org/10.1016/J.CSCEE.2024.100794
46. Kravchenko J, Darrah TH, Miller RK, Lyerly HK, Vengosh A (2014) A review of the health impacts of barium from natural and anthropogenic exposure. Environ Geochem Health 36:797–814. https://doi.org/10.1007/S10653-014-9622-7
47. Tao H, Man Y, Shi X, Zhu J, Pan H, Qin Q et al (2016) Inconceivable hypokalemia: a case report of acute severe barium chloride poisoning. Case Rep Med 2016:2743134. https://doi.org/10.1155/2016/2743134
48. Collin MS, Venkatraman SK, Vijayakumar N, Kanimozhi V, Arbaaz SM, Stacey RGS et al (2022) Bioaccumulation of lead (Pb) and its effects on human: a review. J Hazard Mater Adv 7:100094. https://doi.org/10.1016/J.HAZADV.2022.100094
49. Leff T, Stemmer P, Tyrrell J, Jog R (2018) Diabetes and exposure to environmental lead (Pb). Toxics. https://doi.org/10.3390/TOXICS6030054
50. Mahmoud R, Farh F, Atwa HA, Khafagy AA, Mohammed MA (2024) Assessment of Mercury, lead and cadmium levels among children with type 1 diabetes in Suez Canal region: review Article. Egypt J Hosp Med 97:3738–3743. https://doi.org/10.21608/EJHM.2024.388695
51. Fellows KM, Samy S, Whittaker SG ARTICLE evaluating metal cookware as a source of lead exposure n.d. https://doi.org/10.1038/s41370-024-00686-7

Publisher's Note Springer Nature remains neutral with regard to jurisdictional claims in published maps and institutional affiliations.

Springer Nature or its licensor (e.g. a society or other partner) holds exclusive rights to this article under a publishing agreement with the author(s) or other rightsholder(s); author self-archiving of the accepted manuscript version of this article is solely governed by the terms of such publishing agreement and applicable law.

Supplementary Data:

Association of urine heavy metals with prevalence of type 1 diabetes and poor glycaemic control

Samrat Ashok Vasudevan[1,2], Srinidhi Narayani Seenivasan[1], Avinash Kumar Raghupathy[3], Dinakaran Vasudevan[1], Parthasarathy Ayothi[1,4], Tanmayaa Nayak[4], Buvaneswari Gajendran[1], Karthika Durairaj[1], Divya Shree Sathish[1], Srilaxmi Balaji[3], Abisheak Kandasamy[3], Amaravathy P[1], Sundaresan Mohanraj[3,5], Shankar Dhandapani[6], Thalappil Pradeep[4], Krishnan Swaminathan[7], Ganesan Velmurugan [1,5]*

Table S1. Distribution of urinary metal concentrations categorized by quartiles among T1DM participants and controls.

Variable		Control	T1DM	p-values
Cu	Q1	44 (73.33%)	9 (5.88%)	<0.001
	Q2	10 (16.67%)	44 (28.76%)	
	Q3	2 (3.33%)	51 (33.33%)	
	Q4	4 (6.67%)	49 (32.03%)	
Zn	Q1	38 (63.33%)	15 (9.80%)	<0.001
	Q2	13 (21.67%)	41 (26.80%)	
	Q3	4 (6.67%)	49 (32.03%)	
	Q4	5 (8.33%)	48 (31.37%)	
Cd	Q1	3 (5.00%)	50 (32.68%)	<0.001
	Q2	17 (28.33%)	37 (24.18%)	
	Q3	23 (38.33%)	31 (20.26%)	
	Q4	17 (28.33%)	35 (22.88%)	
As	Q1	27 (45.00%)	26 (16.99%)	<0.001
	Q2	13 (21.67%)	41 (26.80%)	
	Q3	9 (15.00%)	44 (28.76%)	
	Q4	11 (18.33%)	42 (27.45%)	
Ba	Q1	1 (1.67%)	52 (33.99%)	<0.001
	Q2	6 (10.00%)	48 (31.37%)	
	Q3	26 (43.33%)	27 (17.65%)	
	Q4	27 (45.00%)	26 (16.99%)	
Pb	Q1	30 (50.00%)	23 (15.03%)	<0.001
	Q2	13 (21.67%)	41 (26.80%)	
	Q3	14 (23.33%)	40 (26.14%)	
	Q4	3 (5.00%)	49 (32.03%)	

Note: Data are presented as frequency and percentage within each quartile. Differences between groups were tested using the Kruskal–Wallish test; p values < 0.05 were considered statistically significant.

Table S2: Distribution of Urinary Metal Quartiles among T1DM Participants by Glycaemic Control (HbA_{1c} < 8.5% vs. ≥ 8.5%).

Variable		Controlled	Uncontrolled	p-values
Cu	Q1	3 (3.0%)	7 (13.2%)	0.013
	Q2	28 (28.0%)	16 (30.2%)	
	Q3	31 (31.0%)	19 (35.8%)	
	Q4	38 (38.0%)	11 (20.8%)	
Zn	Q1	7 (7.0%)	8 (15.1%)	0.008
	Q2	22 (22.0%)	19 (35.8%)	
	Q3	31 (31.0%)	18 (34.0%)	
	Q4	40 (40.0%)	8 (15.1%)	
Cd	Q1	35 (35.0%)	15 (28.3%)	0.25
	Q2	27 (27.0%)	10 (18.9%)	
	Q3	16 (16.0%)	15 (28.3%)	
	Q4	22 (22.0%)	13 (24.5%)	
As	Q1	10 (10.0%)	16 (30.2%)	0.001
	Q2	24 (24.0%)	17 (32.1%)	
	Q3	25 (25.0%)	11 (20.8%)	
	Q4	41 (41.0%)	9 (17.0%)	
Ba	Q1	14 (14.0%)	9 (17.0%)	0.099
	Q2	21 (21.0%)	20 (37.7%)	
	Q3	30 (30.0%)	10 (18.9%)	
	Q4	35 (35.0%)	14 (26.4%)	
Pb	Q1	35 (35.0%)	17 (32.1%)	0.342
	Q2	33 (33.0%)	15 (28.3%)	
	Q3	19 (19.0%)	8 (15.1%)	
	Q4	13 (13.0%)	13 (24.5%)	

Note: Data are presented as frequency and percentage per quartile. p values are from Kruskal–Wallish tests. Pearson and Spearman correlation coefficients (ρ) are also shown for associations between individual elements and HbA_{1c}. *p ≤ 0.05, **p < 0.01

Table S3. Binomial Logistic Regression Analysis of Uncontrolled glycaemia by Urinary Metal Quartiles in T1DM

Metal	Model	Controlled vs Uncontrolled				P_{trend}
		Q1	Q2	Q3	Q4	
Cu	Unadjusted	1	0.191 (0.022–1.644)	0.450 (0.046–4.426)	0.158 (0.014–1.729)	0.310
	Model 1	1	0.227 (0.024–2.111)	0.570 (0.052–6.236)	0.231 (0.018–2.911)	
	Model 2	1	0.156 (0.02 – 2.412)	0.504 (0.04 – 4.345)	0.285 (0.025 – 3.511)	
Zn	Unadjusted	1	1.935 (0.428–8.745)	1.045 (0.203–5.390)	0.238 (0.035–1.632)	**0.015***
	Model 1	1	2.041 (0.428–9.727)	0.824 (0.146–4.644)	**0.116 (0.014–0.952)** *	
	Model 2		2.555 (0.658 – 10.54)	1.254 (0.198 – 4.654)	**0.203 (0.031 – 1.22)***	
As	Unadjusted	1	0.501 (0.133–1.878)	**0.242 (0.060–0.983)** *	0.369 (0.074–1.835)	0.317
	Model 1	1	0.621 (0.133–2.893)	0.256 (0.053–1.247)	0.294 (0.045–1.929)	
	Model 2	1	0.571 (0.156 – 3.156)	0.351 (0.68 – 1.472)	0.322 (0.058 – 1.359)	
Cd	Unadjusted	1	0.810 (0.259–2.534)	1.704 (0.524–5.543)	**3.655 (0.981–13.621)** *	**0.017***
	Model 1	1	0.788 (0.244–2.541)	1.772 (0.516–6.087)	**3.843 (1.008–14.655)** *	
	Model 2		0.852 (0.273 – 2.149)	1.896 (0.482 – 5.910)	**4.023 (0.991 – 12.361)**	
Ba	Unadjusted	1	2.112 (0.537–8.314)	1.228 (0.219–6.901)	2.524 (0.302–21.054)	0.860
	Model 1	1	2.303 (0.563–9.425)	1.495 (0.248–9.018)	3.805 (0.411–35.178)	
	Model 2		2.503 (0.472 – 7.453)	1.589 (0.301- 7.49)	4.015 (0.620 – 14.95)	
Pb	Unadjusted	1	0.501 (0.133–1.878)	0.242 (0.060–0.983)	0.369 (0.074–1.835)	0.232
	Model 1	1	0.621 (0.133–2.893)	0.256 (0.053–1.247)	0.294 (0.045–1.929)	
	Model 2		0.751 (0.235 – 3.055)	0.256 (0.095 – 0.845)	0.336 (0.049 – 2.112)	

Note: ORs and 95% CIs are shown for both unadjusted and adjusted models. Q1 (lowest quartile) is the reference group. Model 1 adjusted for age and sex while model 2 adjusted for age, sex, presence of industries and farmlands near residence and drinking water source.

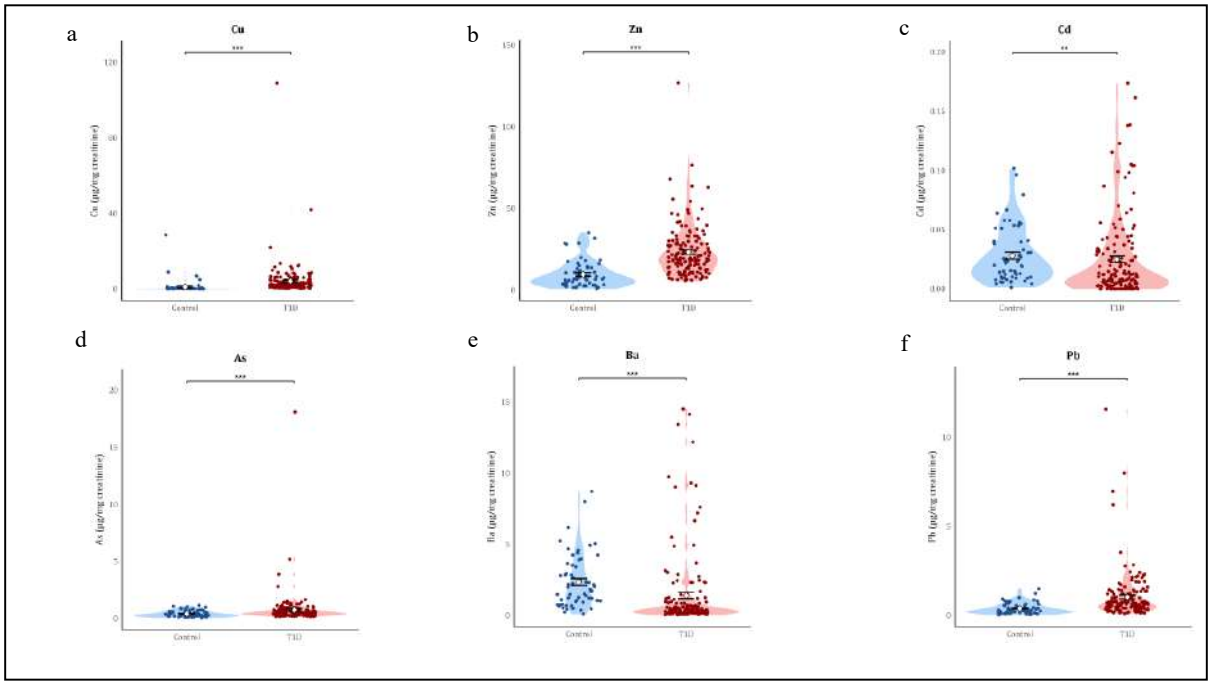


Figure S1. Urinary elemental concentrations in children with Type 1 Diabetes (T1D) and healthy controls. (a–f) Violin and dot plots showing urinary concentrations (µg/mg creatinine) of Cu, Zn, Cd, As, Ba and Pb in T1D patients (n = 153) and healthy controls (n = 60). Data are presented as mean ± standard error (SE). White diamonds represent group means; error bars indicate SE. Group comparisons were performed using the Wilcoxon rank-sum test. ***p < 0.0005, **p < 0.005, *p < 0.05.

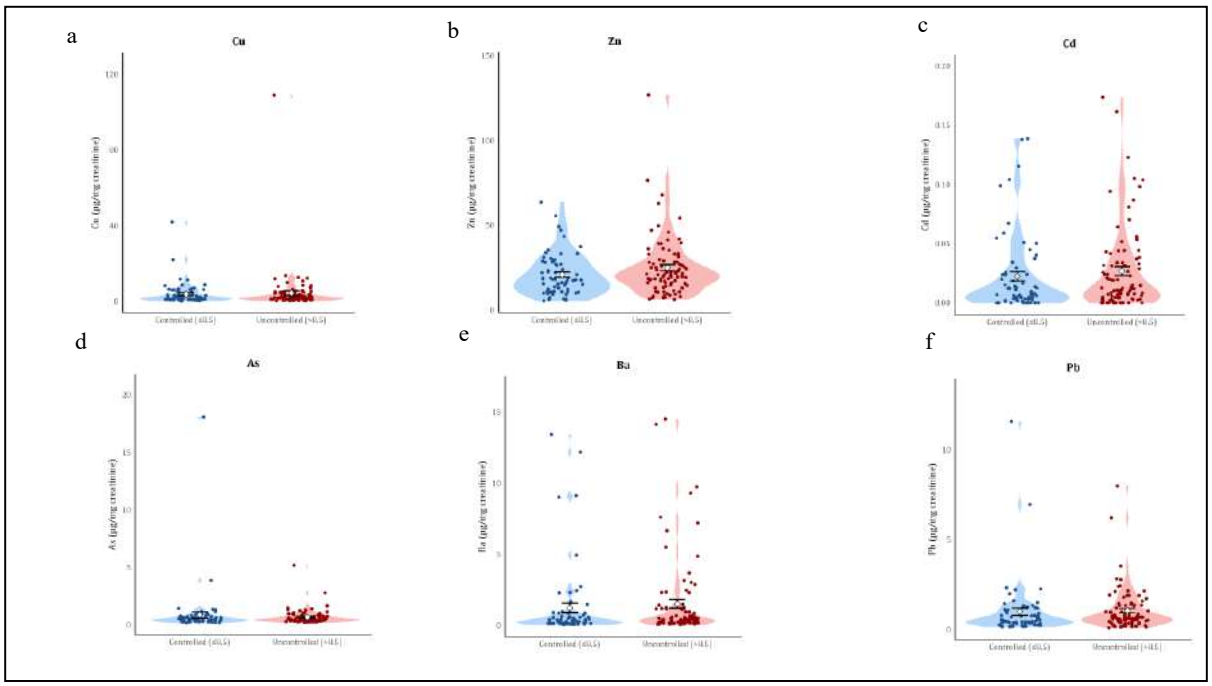


Figure S2 Urinary elemental concentrations in children with controlled and uncontrolled Type 1 Diabetes (T1D). (a–f) Violin and dot plots showing concentrations (µg/mg creatinine) of Cu, Zn, Cd, As, Ba and Pb in children with controlled glycaemia (HbA1c ≤ 8.5%; n = 61) and uncontrolled glycaemia (HbA1c > 8.5%; n = 92). Data are represented as mean ± SE. White diamonds denote group means, and black error bars show SE. Wilcoxon rank-sum test was used for group comparisons. *p < 0.05, **p < 0.005, ***p < 0.0005.

Chemical Science

ROYAL SOCIETY OF CHEMISTRY

EDGE ARTICLE

View Article Online
View Journal

Check for updates

Cite this: DOI: 10.1039/d5sc06346a

All publication charges for this article have been paid for by the Royal Society of Chemistry

Open Access Article. Published on 15 December 2025. Downloaded on 1/5/2026 7:13:20 AM.
This article is licensed under a Creative Commons Attribution-NonCommercial 3.0 Unported Licence.

Cooperative borane activation by tuning hemilability of different Os-κ^2-*N*,*Se*-chelated complexes

Faneesha Assanar, Sourav Gayen, Deepak Kumar Patel, Thalappil Pradeep * and Sundargopal Ghosh *

In an effort to investigate the cooperative activation of boranes, we have designed Os(III) based paramagnetic mono- and bis-κ^2-1,3-*N*,*Se*-chelated complexes, $[Os(PPh_3)_2(\kappa^2\text{-}N,Se\text{-}L)Cl_2]$, **1** and $[Os(PPh_3)(\kappa^2\text{-}N,Se\text{-}L)_2(L')]$, **2–3** (L = C_5H_4NSe; **2**: L′ = Cl and **3**: L′ = κ^1-*Se*-L). These complexes were synthesised by the thermolysis of $[Os(PPh_3)_3Cl_2]$ with the potassium salt of 2-selenopyridine, which also afforded a diamagnetic species, $[Os(PPh_3)_2(\kappa^2\text{-}N,Se\text{-}L)_2]$, **4**. A comprehensive study utilizing EPR spectroscopy, DFT calculations, and both photochemical and electrochemical analyses has elucidated the distinctive electronic characteristics of these complexes. To probe the electronic influence on hemilability, the OsNCSe osmaheterocycle-based paramagnetic complexes featuring a hard Os(III) centre and a soft Se donor were studied for B–H activation, highlighting synergistic hemilability and metal–ligand cooperativity. Treatment of **2** with $[BH_3{\cdot}SMe_2]$ yielded the Os(dihydridoborate)(octatrihydridoborate) complex, $[Os(PPh_3)(\kappa^3\text{-}H,H,N\text{-}BH_3L)(\kappa^2\text{-}H,Se\text{-}B_3H_7L)]$ (**5**) *via* ring opening of both Os–Se and Os–N bonds and the Os–borallyl complex, $[(PPh_3)(H)_2Os(\eta^5\text{-}B_3H_5L_2)]$ (**6**) through cleavage of the Os–N bonds. To further assess steric effects on cooperative borane activation, **2** was treated with the bulky aryl-substituted borane BH_2R (R = $(CF_3)_2C_6H_3$), which afforded $[(PPh_3)Os\{\kappa^3\text{-}H,Se,Se'\text{-}(NHRBSeBHRN)(SeC_5H_4)_2\}]$, **7** *via* dual Os–N bond cleavage and insertion of two BHR units followed by B–Se bond formation. Interestingly, we have isolated a unique vertex-fused metallaborane cluster, **8** from the reaction of **6** with an excess of borane. In stark contrast, the diamagnetic bis-κ^2-1,3-*N*,*Se*-chelated complex $[Os(PPh_3)_2(\kappa^2\text{-}N,Se\text{-}L)_2]$, **4** exhibited no tendency to activate sterically demanding boranes. However, using an electronically distinct ligand framework in $[Os(PPh_3)_2(\kappa^2\text{-}N,S\text{-}C_7H_4NS_2)_2]$ ($\mathbf{4^{mbz}}$), we observed notable B–H activation patterns of BHR_2 that led to the isolation of the Os(σ-borate) complex, $[Os(PPh_3)_2(\kappa^2\text{-}N,S\text{-}C_7H_4NS_2)(\kappa^3\text{-}H,S,S'\text{-}HBR_2(C_7H_4NS_2))]$ (**11**), where the steric hindrance from the aryl substituents prevented dual-site activation. The bonding insights of these activated species were investigated on the basis of DFT calculations.

Received 19th August 2025
Accepted 26th November 2025

DOI: 10.1039/d5sc06346a

rsc.li/chemical-science

Introduction

Metal–ligand cooperativity (MLC) has experienced immense growth over the past few decades as a powerful mechanistic strategy in the field of bond activation and catalysis. It serves as an alternative to conventional catalysis due to the synergistic interaction between the metal and ligand, which plays a crucial role in facilitating both bond breaking and bond formation processes.[1–3] In particular, MLC has been widely investigated in the activation of various E–H (E = H, B, C, N, O or Si) bonds[4–10] and has subsequently been employed in a range of catalytic reactions.[11–13] In the context of MLC, several strategies have been developed to promote the E–H bond activation process: (a) utilizing a combination of a Lewis acidic metal and a Lewis basic ligand that cooperatively cleave the E–H bond in a synergistic fashion;[4,5] (b) employing the inverse arrangement, where Lewis acidic ligands abstract electrons from the donor site of the substrate, with the metal acting as a Lewis base to cooperatively facilitate bond activation;[6,7] (c) using complexes containing aromatic chelating ligand frameworks, which can undergo dearomatization through deprotonation to provide a reactive site for cooperative bond activation;[8,9] (d) incorporating redox non-innocent ligands[10] that either directly mediate the bond activation process or act as electron reservoirs within the catalytic cycle.

In the context of type (a), the predominant class of Lewis basic ligands are typically found in a multidentate framework. Notably, metal complexes featuring hemilabile 1,3-chelating homo and hetero bidentate ligands have garnered significant interest in small molecule activation, as a key attribute of these ligands is their ability to provide coordinative unsaturation at

Department of Chemistry, Indian Institute of Technology Madras, Chennai 600036, India. E-mail: sghosh@iitm.ac.in; pradeep@iitm.ac.in

© 2025 The Author(s). Published by the Royal Society of Chemistry

Open Access Article. Published on 15 December 2025. Downloaded on 1/5/2026 7:13:20 AM.
This article is licensed under a Creative Commons Attribution-NonCommercial 3.0 Unported Licence.

the metal centre. For instance, Yamaguchi proposed an Ir(III) complex (**I**),[14] featuring a κ^2-*N*,*O*-pyridionate ligand as an intermediate species in the oxidant-free catalytic oxidation of alcohols.[14a] Subsequently, Rauchfuss demonstrated that complex **I** functioned as a more efficient catalyst in the same context.[14b] Schafer and Love developed group-9 phosphoramidate complexes with different ancillary ligands (**II** and **III**, Chart 1), which promote B–H and C–H activation processes.[15] These complexes were subsequently utilized in catalytic chemoselective hydroboration of aldehydes and anti-Markovnikov *O*-phosphoramidation of alkynes. Interestingly, a proton responsive bifunctional ruthenium complex, **IV** promoted the facile E–H bond activation in H_2 and HBPin across the Ru–O bond.[16] Beyond traditional hemilabile ligands, Gessner and co-workers designed a ruthenium-based 1,3-chelated complex (**V**) with a carbene ligating centre, where substrate activation induces a transition between a carbene and an alkyl ligand without complete cleavage of the M=C bond.[5a]

In the course of our recent studies, we have synthesized a group of early- and late-transition metal-based mono- and bis-κ^2-1,3-*N*,*S*-chelated complexes and investigated their role in the cooperative activation of E–H (E = B, C or Si) bonds in small molecules.[17–19] The hemilability of four-membered metallaheterocycles, arising from the coexistence of hard (N) and soft (S) donor sites within polydentate ligands, was pivotal in facilitating E–H bond activation. For instance, we have developed Ru- and Os-based bis-κ^2-1,3-*N*,*S*-chelated species featuring non-innocent ligands (**VI**, Chart 1), which upon activation of the simplest borane, $[BH_3{\cdot}SMe_2]$, resulted in the formation of unique σ-borate complexes.[17b,c] However, in the field of MLC, the influence of concerted modulation of electronic properties in both metal and ligand scaffolds remains uncharted. In pursuit of this objective, we have designed different osmaheterocycles by fine-tuning the hardness of both the metal and ligand components. In this study, we synthesised a series of κ^2-*N*,*Se*-chelated Os(III) complexes such as $[Os(PPh_3)_2(\kappa^2\text{-}N,Se\text{-}C_5H_4NSe)Cl_2]$ (**1**), $[Os(PPh_3)(\kappa^2\text{-}N,Se\text{-}C_5H_4NSe)_2Cl]$ (**2**) and $[Os(PPh_3)(\kappa^2\text{-}N,Se\text{-}C_5H_4NSe)_2(\kappa^1\text{-}Se\text{-}C_5H_4NSe)]$ (**3**), and engaged them in the cooperative activation of boranes. The perturbed hemilability of the OsNCSe heterocycle led to the cleavage of the Os–N and Os–Se bonds, which facilitated the cooperative activation of free borane. Furthermore, a comparative study was conducted to evaluate the impact of steric and electronic factors by employing both substituted and unsubstituted hydroborane reagents in the cooperative activation process. The activation of sterically encumbered boranes enabled the successful isolation of unique Os–(σ-borate) complexes, utilizing a series of both paramagnetic and diamagnetic Os–*N*,*E*-chelated complexes (E = S or Se).

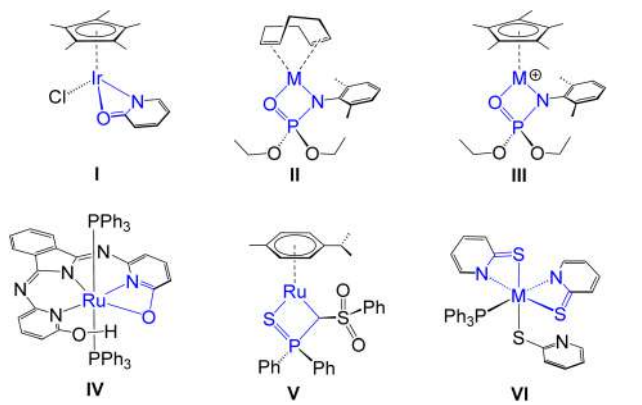


Chart 1 Various TM complexes featuring 1,3-chelated hemilabile ligands (M = Rh and Ir for II and III; M = Ru and Os for VI).

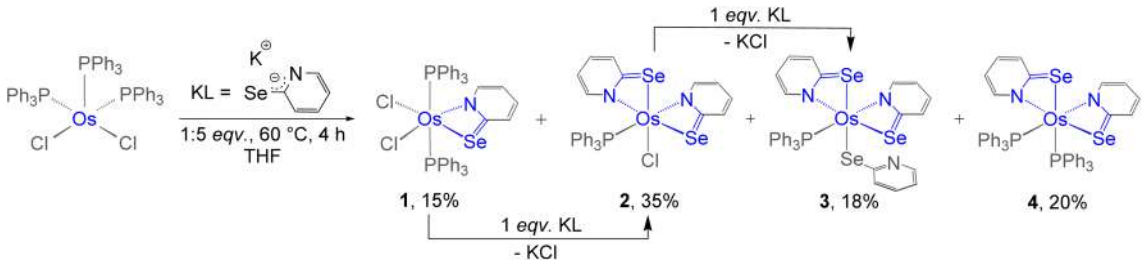
Results and discussion

Recently, we successfully synthesised Cp* based κ^2-*N*,*Se*-chelated group-6 complexes from the reaction of $[Cp^*M(CO)_3Cl]$ (M = Mo, W) and $[K^+L^-]$ (L = C_5H_4NSe).[19] With the objective of synthesizing chelated osmium complexes containing a heavier chalcogen atom, we performed the thermolysis of $[Os(PPh_3)_3Cl_2]$, with excess [KL] at 60 °C. The reaction yielded complexes **1**, **2**, **3** and **4** which were further isolated in their purest forms by chromatographic techniques (Scheme 1). The complexes were characterized by different spectroscopic methods, mass spectrometry and X-ray diffraction studies. The ^1H NMR spectra for complexes **1**, **2**, and **3** showed several broad resonance peaks in the upfield region, while the $^{31}P\{^1H\}$ NMR spectra did not reveal any noteworthy signals. In contrast, the ^1H NMR spectrum of **4** displayed aromatic signals within the chemical shift range of δ = 8.00–6.25 ppm. Furthermore, species **4** exhibited a single resonance peak at $\delta = -6.3$ ppm in the $^{31}P\{^1H\}$ NMR spectrum. This detailed analysis suggested that complexes **1**, **2**, and **3** exhibit paramagnetic behavior, whereas complex **4** appears to be diamagnetic in nature. Mass spectrometric analysis of **1**, **2**, **3**, and **4** indicated that their respective molecular formulae are $[Os(PPh_3)_2(L)Cl_2]$, $[Os(PPh_3)(L)_2Cl]$, $[Os(PPh_3)(L)_3]$, and $[Os(PPh_3)_2(L)_2]$. However, a clear assignment could not be done until the single-crystal X-ray diffraction analysis of these species was carried out.

As illustrated in Fig. 1 (left), the molecular structure of complex **1** can be classified as a mono-κ^2-*N*,*Se*-chelated complex of Os(III), represented as $[Os(PPh_3)_2(\kappa^2\text{-}N,Se\text{-}L)Cl_2]$. The molecule exhibited approximately C_s symmetry, with the σ-plane containing the bidentate ligand and two chlorine atoms. On the other hand, the solid-state structure of complex **2** was identified as a bis-κ^2-*N*,*Se*-chelated Os(III) complex, where the osmium centre is coordinated to two bidentate selenopyridinyl ligands, one chloride, and one PPh_3 ligand (Fig. 1, middle). The Os–Cl bond lengths and the bite angles of the osmaheterocycles in complexes **1** and **2** are comparable. The mono-κ^2-*N*,*Se*-chelated complex **1** was formed through the release of one PPh_3 ligand from $[Os(PPh_3)_3Cl_2]$, followed by the coordination of a selenopyridinyl ligand (Scheme 1). The subsequent dissociation of another PPh_3 ligand from complex **1** and the binding of an additional unit of ligand (L) with concomitant elimination of KCl afforded complex **2**. Although we were unable to obtain any suitable crystals for the XRD analysis of **3**, it can be identified as $[Os(PPh_3)(\kappa^2\text{-}N,Se\text{-}L)_2(\kappa^1\text{-}Se\text{-}L)]$ based on mass spectrometry and preliminary spectroscopic data.[17c] The primary distinction between complexes **2** and **3** stems from the substitution of the

© 2025 The Author(s). Published by the Royal Society of Chemistry

Open Access Article. Published on 15 December 2025. Downloaded on 1/5/2026 7:13:20 AM.
This article is licensed under a Creative Commons Attribution-NonCommercial 3.0 Unported Licence.



Scheme 1 Syntheses of Os(II) and Os(III)–*N*,*Se*-chelated complexes, 1–4.

chloride ligand with a non-innocent ligand. The formation of complex **3** can be rationalized by the monodentate coordination of the selenopyridinyl ligand subsequent to the elimination of KCl. The X-ray diffraction analysis of a suitable orange crystal of complex **4** revealed an octahedral geometry around the Os centre, which includes two κ^2-1,3-*N*,*Se*-chelated rings and two triphenylphosphine ligands (Fig. 1, right). This complex was formed by the dissociation of one PPh_3 ligand from $[Os(PPh_3)_3Cl_2]$, followed by coordination of two selenopyridinyl ligands with concurrent KCl elimination.

To verify the monophasic nature of complexes **1** and **2**, powder X-ray diffraction (PXRD) patterns were compared with those simulated from their single-crystal X-ray diffraction (SCXRD) data. The powder XRD patterns of both complexes showed reasonable agreement with the simulated patterns based on their single-crystal structures, confirming the homogeneity of the bulk samples (Fig. S6 and S9). However, a few unidentified low-intensity reflections were observed in both cases, which do not significantly affect the overall bulk phase purity. These results support that the synthesized complexes are largely monophasic and homogeneous.

The paramagnetic properties of complexes **1**, **2** and **3** were examined using electron paramagnetic resonance (EPR) spectroscopy at both room temperature and low temperature. While the room temperature EPR spectra of these species in CH_2Cl_2 (**1** and **2**) and toluene (**3**) solution were inconclusive, the X-band frozen glass EPR spectra provided valuable insights. As shown in Fig. 2(a) and (c), the EPR spectra of complexes **1** and **2** exhibited a rhombic pattern with three distinct *g* values. For both complexes, the g_z values (**1**: 2.724; **2**: 2.851) and g_y values (**1**: 2.227; **2**: 2.052) were clearly resolved, whereas the g_x signal appeared broadened and was observed over a range of 1.2–1.7. The line broadening and reduced spectral resolution of these EPR signals are attributed to the pronounced spin–orbit coupling observed in heavy transition metals such as osmium. Furthermore, density functional theory (DFT) calculations revealed that the Mulliken spin density of the unpaired electron in **1** and **2** is predominantly localized on the Os atom (**1**: +0.87; **2**: +0.71) (Fig. 2(b) and (d)). Notably, a substantial spin density was also detected on the Cl atom in **2**, which suggests that coupling with the chloride ligand may have contributed to the observed broadening of the EPR signal. To complement these findings, an Evans NMR study was carried out to determine the solution-state magnetic susceptibility. The experimentally determined magnetic moments (μ_{exp}) of **1** (1.68 μB) and **2** (1.80 μB) are in good agreement with the theoretically expected value (1.73 μB). This indicated that both complexes exhibit a low-spin Os(III) ($5d^5$) electronic configuration, consistent with previously

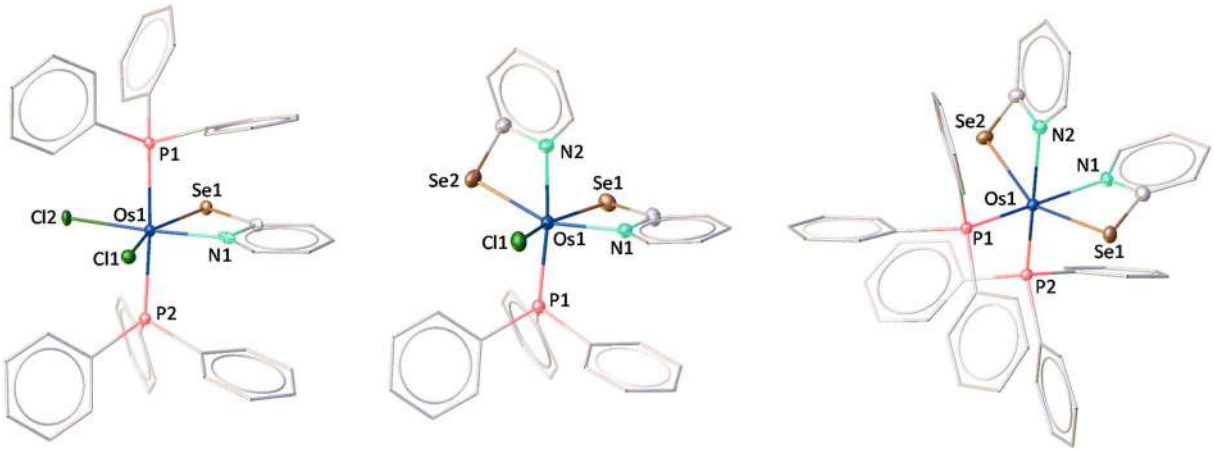


Fig. 1 Molecular structure and labelling diagram of **1** (left), **2** (middle) and **4** (right). Selected bond lengths (Å) and bond angles (°) of **1**: Os1–N1 2.093(4), Os1–Se1 2.5518(6), Os1–Cl1 2.3672(13), Os1–Cl2 2.3840(13), Se1–Os1–N1 68.31(13); **2**: Os1–N1 2.110(3), Os1–N2 2.098(2), Os1–Se1 2.4510(3), Os1–Se2 2.5351(4), Os1–Cl1 2.3676(8), Se1–Os1–N1 70.16(7), Se2–Os1–N2 68.56(7); **4**: Os1–N1 2.154(8), Os1–Se1 2.5494(11), Se1–Os1–N1 68.3(2), and Se2–Os1–N2 68.1(2) (aromatic hydrogens are not shown for better clarity).

© 2025 The Author(s). Published by the Royal Society of Chemistry

Open Access Article. Published on 15 December 2025. Downloaded on 1/5/2026 7:13:20 AM.
This article is licensed under a Creative Commons Attribution-NonCommercial 3.0 Unported Licence.

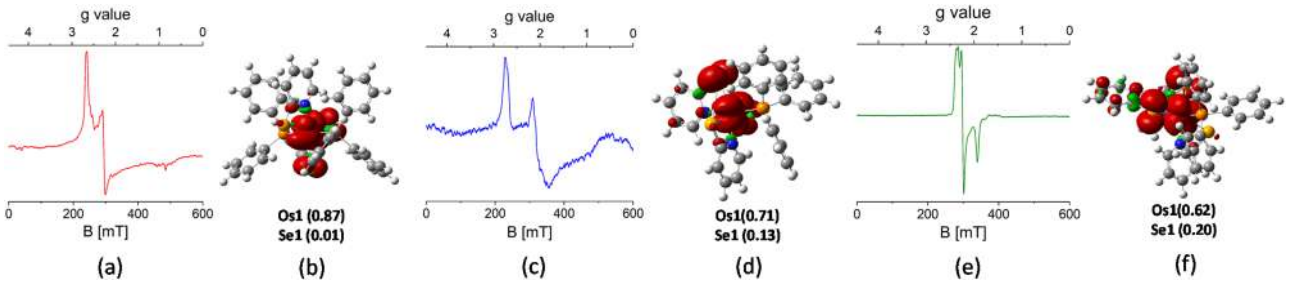


Fig. 2 EPR spectra of **1** (a), **2** (c) and **3** (e); spin density plots of **1** (b), **2** (d) and **3** (f).

reported Os(III) systems.[20] Furthermore, the EPR spectrum of **3** exhibited a rhombic pattern with a relatively lower g_z value (2.324) compared to **1** and **2** (Fig. 2(e)). In this context, spin density analysis revealed a significant accumulation of spin density on the Se atom of κ^2-*Se*-L, accompanied by a decrease in spin density on the metal atom (Fig. 2(f)). Thus, complex **3** can be described as a superposition of two resonating forms: $[(L^-)Os^{III}]$ and $[(L^{\bullet})Os^{II}]$, similar to $[M(PPh_3)(\kappa^2\text{-}N,S\text{-}C_5H_4NS)_2(\kappa^1\text{-}S\text{-}C_5H_4NS)]$ (M = Ru, Os).[17b,c] Due to the pronounced spin–orbit coupling in predominantly metal-centred spin systems like **1** and **2**, a higher degree of anisotropy was observed in comparison to **3**.

Owing to the distinct ligand environments around the Os(III) centre in these paramagnetic complexes, we were interested in exploring their redox properties. Redox potentials were measured by cyclic voltammetry, with all values referenced to the Fc^+/Fc couple, as summarized in Table S1. The cyclic voltammograms of complexes **1** and **2** revealed two quasi-reversible redox processes each (**1**: $E_{1/2} = -0.727$ V and 0.737 V; **2**: $E_{1/2} = -0.850$ V and 0.621 V), well-separated within the electrochemical window (Fig. 3(a) and (b)). The cathodic and anodic waves are attributed to the Os^{III}/Os^{II} reduction and Os^{III}/Os^{IV} oxidation processes, respectively. Similar redox behaviour and assignments have been reported for other Os(III) complexes.[21,22] Furthermore, the cyclic voltammogram of complex **3** yielded three quasi-reversible redox processes where signals at $E_{1/2} = -0.948$ V and 1.123 V correspond to the Os^{III}/Os^{II} and Os^{IV}/Os^{III} couples, respectively (Table S1). In addition to this, another quasi-reversible wave at 0.148 V is associated with a redox event centred on the dangling heterocyclic ligand, assigned to the $Os^{II}(L^{\bullet})/Os^{III}(L^-)$ redox couple. This behaviour closely resembles that observed in redox non-innocent ligand-based Ru and Os complexes, $[M(PPh_3)(\kappa^2\text{-}N,S\text{-}L')_2(\kappa^1\text{-}S\text{-}L')]$ (M = Ru, Os; L′ = C_5H_4NS, $C_7H_4NS_2$) which was recently reported by our group.[17b,c] Furthermore, the cyclic voltammogram of the diamagnetic κ^2-*N*,*Se* chelated complex, **4** exhibited characteristic redox events associated with the Os(III)/Os(II) and Os(IV)/Os(III) couples, which is consistent with the electrochemical behaviour observed for its sulfur analogue.[17c]

With an objective to gain more insightful information about the electronic transitions and structural characteristics of these Os–*N*,*Se* chelated complexes, UV-vis absorption spectroscopy was performed on complexes **1**, **2**, **3** and **4** in CH_2Cl_2. All these complexes exhibited intense absorption in the UV region and a notably distinct absorption pattern in the visible region. The strong absorption in the high-energy region appeared due to the π–π* transitions in ligand moieties. In addition, relatively weaker bands observed in the 300–400 nm range for both Os(II) and Os(III) species were ascribed to ligand-to-metal charge transfer (LMCT) transitions (Fig. 3(d) and S15). Notably, the paramagnetic Os(III)–*N*,*Se* chelated complexes exhibited broad absorptions extending into the lower-energy visible region, which can be assigned to the $d(Os^{III}) \rightarrow \pi^*$(ligand) metal-to-ligand charge transfer (MLCT). The introduction of an additional κ^2-*N*,*Se*-L ligand in complex **2** caused a hypsochromic shift of this peak compared to complex **1**. Furthermore, a bathochromic shift in the lower-energy absorption band was observed when going from complex **2** to **3**, attributed to the presence of a different monodentate anionic ligand. Time-dependent DFT (TD-DFT) analysis shows that the transitions calculated at longer wavelengths for these complexes correspond to specific electronic excitations (Table S2). In complex **3**,

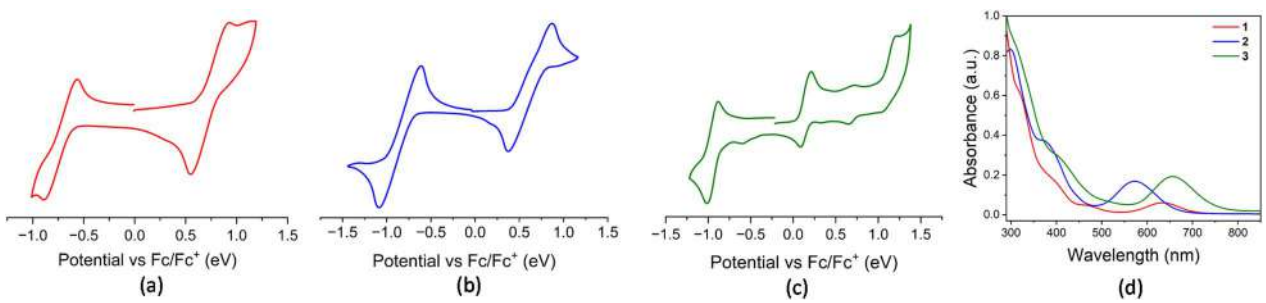


Fig. 3 Cyclic voltammograms of **1** (a), **2** (b) and **3** (c) collected at 100 mV s^{-1}; (d) combined UV-vis spectra of **1**, **2** and **3**.

© 2025 The Author(s). Published by the Royal Society of Chemistry

Open Access Article. Published on 15 December 2025. Downloaded on 1/5/2026 7:13:20 AM. This article is licensed under a Creative Commons Attribution-NonCommercial 3.0 Unported Licence.

the transition at longer wavelength mainly arises from the excitations from β-HOMO−1 to β-LUMO, while in complex **2**, analogous transitions from β-HOMO−2 and β-HOMO−3 to β-LUMO are observed in a relatively higher energy region.

It is worth noting that **2** can be regarded as electronically analogous to the [(L$^-$)Os^{III}] tautomer of **VI^{Os}** (*vide supra*, Chart 1) 17c due to the absence of a non-innocent ligand. As a result, the osmium centre in **2** exhibits enhanced hardness associated with its higher oxidation state, while the sulfur atom in the osma-heterocycle of **VI^{Os}** is replaced by a relatively softer selenium atom in **2**. To examine the hemilability of the OsNCSe heterocycle in **2**, its reactivity with free borane was investigated under various conditions. Thermolysis of **2** with four equivalents of [$BH_3{\cdot}SMe_2$] at 60 °C changed its colour from deep green to orange and yielded **5** and **6** along with some air and moisture sensitive products (Scheme 2). The $^{31}P\{^1H\}$ NMR spectrum of **5** displayed a singlet at δ = 27.9 ppm which suggested the retention of the PPh_3 unit. The appearance of four chemical shifts at δ = 59.9, 14.2, 4.6 and −15.2 ppm in the $^{11}B\{^1H\}$ NMR spectrum was attributed to the presence of four different boron environments. In addition to the aromatic region peaks, the room temperature ^1H NMR spectrum of **5** unveiled three types of broad signals at δ = −11.66, −11.61 and −7.65 ppm in the upfield region. Additionally, mass spectrometry revealed isotopic distribution patterns at *m*/*z* 818.0868, consistent with the molecular formula [$C_{28}H_{31}PN_2Se_2B_4Os$]. However, a comprehensive understanding could not be achieved until single-crystal X-ray diffraction analysis of complex **5** was performed.

The X-ray diffraction study of **5** was carried out on an orange crystal obtained from the slow evaporation of hexane layered CH_2Cl_2 solution. As illustrated in Fig. 4, the osmium centre is coordinated to a substituted octatrihydridoborate unit, B_3H_7L, where its interaction with the metal fragment appears to differ from that observed in conventional TM–octatrihydridoborate complexes.[23,24] Interestingly, the B2 atom is coordinated to osmium through an Os–H–B interaction, while a selenopyridinyl group bridges between Os1 and B1. The Os1–B1 bond length is shorter than that of Os1–B2, likely due to a secondary interaction mediated by the selenopyridinyl unit. In this context, the broad shielded ^1H chemical shifts at δ = −7.65 ppm can be attributed to the presence of the Os–H–B unit. However, a definitive upfield signal characteristic of a B–H–B unit was not observed in the room-temperature ^1H NMR spectrum. To probe this further, variable-temperature (VT) ^1H NMR studies were performed. Upon lowering the temperature, two broad upfield

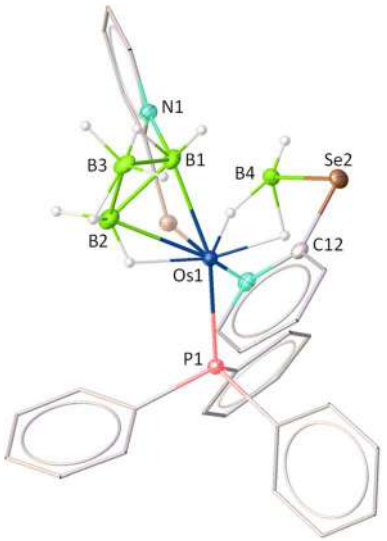
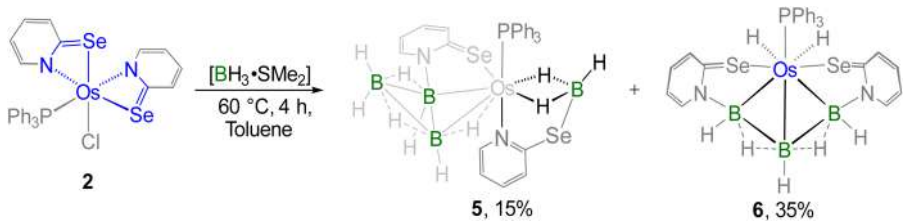


Fig. 4 Molecular structure and labelling diagram of **5**. Selected bond lengths (Å) of **5**: Os1–B1 2.223(8), Os1–B2 2.306(8), Os1–B4 2.056(8), Os1–N2 2.132(5); B1–B2 1.758(12), B2–B3 1.771(13), B3–B1 1.862(12), and Se2–B4 2.001(8) (aromatic hydrogens are not shown for better clarity).

resonances at δ = −0.39 and −2.64 ppm emerged, which can be attributed to two distinct B–H–B units. These findings indicate rapid exchange between the B–H–B and terminal B–H protons at room temperature. Note that a similar dynamic behaviour has also been reported for rhodatetraborane dihydride, [Rh(η^2-B_3H_8)(H)$_2$(PPh_3)$_2$].[24a]

On the other hand, the remaining coordination sites in complex **5** were occupied by one PPh_3 ligand and a chelating ligand, $[H_3BL]^-$ in a κ^3-*H*,*H*,*N* bonding mode, leading to the formation of an Os–dihydridoborate moiety. The formation of this Os–dihydridoborate entity is proposed to result from the insertion of BH_3 into the Os–Se bond of the κ^2-*N*,*Se*-chelated ring in complex **5**. The Os1–B4 separation aligns well with that observed in the Os–dihydridoborate complex, [Os(PPh_3)(κ^2-*N*,*S*-C_5H_4NS){κ^3-*H*,*H*,*S*-$H_3BO(C_5H_4NS)$}],[17c] but it is significantly shorter than the bond lengths typically found in TM–(σ-borane/borate) species.[25,26] The bond separations of B4–Se2 and C12–Se2 are consistent with the typical ranges for B–Se and C–Se single bonds, respectively.[27] Thus, complex **5** can be designated as an Os(dihydridoborate)(octatrihydridoborate) species, with the formulation [Os(PPh_3)(κ^3-*H*,*H*,*N*-BH_3L){κ^2-*H*,*Se*-B_3H_7L)}]. The formation of **5** likely proceeds *via* two concurrent steps: (i)



Scheme 2 Cooperative borane activation utilizing Os(III)–*N*,*Se*-chelated complex **2**.

© 2025 The Author(s). Published by the Royal Society of Chemistry

Open Access Article. Published on 15 December 2025. Downloaded on 1/5/2026 7:13:20 AM. This article is licensed under a Creative Commons Attribution-NonCommercial 3.0 Unported Licence.

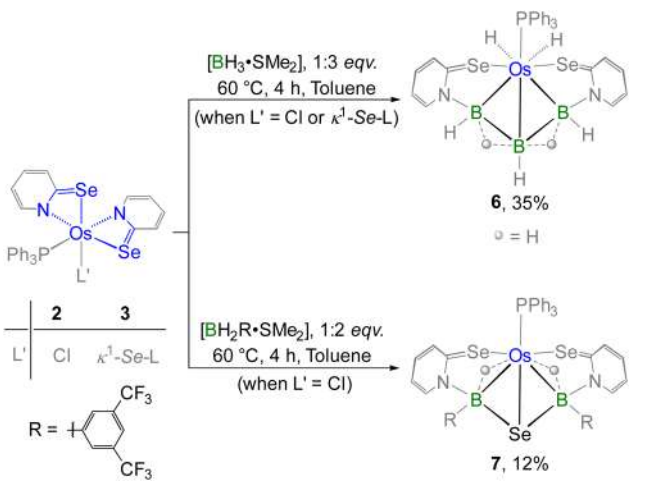
the insertion of a preformed triborane fragment into the Os–N bond, resulting in the formation of the Os–octahydridotriborate unit, and (ii) the cooperative activation of two B–H bonds from BH_3 through the cleavage of the Os–Se bond in another hemilabile OsNCSe metallacycle, which eventually furnishes the Os(dihydridoborate) unit. It is worth noting that this process constitutes a rare example of cooperative activation of borane in which both types of M–E bonds (E = N, Se) in hemilabile metallaheterocycle undergo cleavage.

Furthermore, complex **6** was obtained as a yellow crystalline solid after chromatographic separation. Notably, **6** could also be isolated in improved yield when $[BH_3{\cdot}SMe_2]$ was treated with the non-innocent ligand based Os–*N*,*Se*-chelated complex, **3** (Scheme 3). The $^{11}B\{^1H\}$ NMR spectrum of **6** displayed two distinct resonance signals at δ = 17.0 and −39.0 ppm, indicating the existence of two different boron environments. Furthermore, single phosphorus and selenium environments were identified by the singlet resonance at δ = 16.1 ppm in the $^{31}P\{^1H\}$ NMR spectrum and at δ = 234.8 ppm in the ^{77}Se NMR spectrum, respectively. In the upfield region of the ^1H NMR spectrum of **6**, two non-equivalent hydride signals were detected at δ = −13.40 and −1.41 ppm, which presumably arise due to the presence of M–H and B–H–B protons, respectively. The ESI-MS data of **6** exhibited an isotopic pattern at *m*/*z* 805.0319 that aligns with the molecular formula $[C_{28}H_{15}PN_2Se_2B_3Os]$. Although spectroscopic data in combination with mass spectrometry indicated the formation of an osmium borallyl species, structural confirmation was obtained by X-ray diffraction analysis of **6**. The molecular structure of **6** reveals an Os–borallyl complex characterized by a primary η^3-borallyl coordination of the $[B_3H_5L_2]^{2-}$ fragment, along with secondary interactions involving the selenidopyridinyl selenium atom (Fig. S1). The spectroscopic and structural characteristics of **6** are consistent with those of a recently reported Os–borallyl complex, $[(PPh_3)(H)_2Os(\eta^5\text{-}B_3H_5(C_5H_4NS)_2)]$.[28] Similar to the analogous complex, the presence of two hydride ligands in **6** was confirmed by the sharp upfield resonance signal at δ = −13.40 ppm in the ^1H NMR spectrum. The formation of **6** can be attributed to the insertion of the triborane unit facilitated by the ring opening of two osma-heterocycles.

As part of our ongoing research, we have studied the unconventional dual-site activation of both free and bulky boranes by the redox-active species, $\mathbf{VI^{Ru}}$. (*vide supra*, Chart 1).[17b] Strikingly, the activation of free boranes led to the formation of $[Ru(PPh_3)\{\kappa^3\text{-}H,S,S'\text{-}(NH_2BSBH_2N)(S_2C_7H_4)_2\}]$, while a unique Ru-bis(dihydridoborate) complex was obtained from the cooperative activation of BH_2Mes (Mes = $(CH_3)_3C_6H_3$).[17b] To investigate the influence of steric and electronic characteristics of substituted aryl groups of boranes on the cooperative activation process, we carried out reactions of complexes **2** and **3** with $[BH_2R{\cdot}SMe_2]$ and $[BHR_2{\cdot}SMe_2]$ (R = $(CF_3)_2C_6H_3$) (Scheme 3). Thermolysis of **2** with two equivalents of $[BH_2R{\cdot}SMe_2]$ generated **7** in 12% yield along with a few air-sensitive products, whereas complex **3** underwent decomposition under the same reaction conditions. The $^{31}P\{^1H\}$ NMR spectrum of **7** revealed a sharp singlet at δ = 22.3 ppm which suggested the retention of the PPh_3 group. Similar to the $^{31}P\{^1H\}$ NMR spectrum, a single resonance was observed at δ = 27.8 ppm in the $^{11}B\{^1H\}$ NMR spectrum and at δ = −62.2 ppm in the $^{19}F\{^1H\}$ NMR spectrum. This suggested the presence of a highly symmetric geometry with chemically equivalent phosphorus, boron, and fluorine environments. Furthermore, the ^1H NMR spectrum of **7** showed a broad upfield resonance at δ = −9.72 ppm, likely arising from the presence of an Os–H–B unit. Notably, no characteristic broad resonance corresponding to a terminal B–H proton was observed in the ^1H NMR spectrum. However, the precise structure of **7** remained unresolved until solid-state X-ray diffraction analysis was performed on orange, needle-like crystals grown from a CH_2Cl_2 : hexane mixture at −5 °C.

As depicted in Fig. 5, complex **7** adopts a symmetrical core geometry featuring a mirror plane passing through the Se3–Os1–P1 fragment, which allows us to classify the molecule under C_s point group. The molecular structure of **7** consists of two five-membered {OsBNCSe} osmacycles fused *via* a single {OsB_2Se} butterfly unit, where osmium and selenium were positioned at the hinge tips and boron atoms were located at the wing tips. Although we were unable to find any proper mechanistic evidence, we believe that the Se atom in the butterfly core is presumably generated from the C–Se bond cleavage of the selenopyridinyl moiety. Interestingly, complex **7** can be viewed as a tetraborane derivative, exhibiting structural and electronic resemblance with the Os–borallyl species, **6** and $[(PPh_3)(H)_2Os(\eta^5\text{-}B_3H_5(C_5H_4NS)_2)]$.[28] The average Os–B distance (2.263 Å) is elongated in comparison to the average Ru–B bond length of the analogous species, $[(PPh_3)Ru\{\kappa^3\text{-}H,S,S'\text{-}(NH_2BSBH_2N)(S_2C_7H_4)_2\}]$,[17b] yet it aligns well with the typical distances observed in osmium-based σ-borane/borate species.[29] Moreover, the average B–Se distance of 2.103 Å is slightly higher than that found in typical borane–selenate species.[27] The formation of **7** can be described by the insertion of two BHR units *via* ring opening of both the Os–N bonds and subsequent formation of B–Se bonds.

TM–borallyl complexes and their analogues are often unreactive due to the strong bonding between the borallyl entity



Scheme 3 Cooperative activation of free and substituted boranes utilizing paramagnetic Os(III)–*N*,*Se*-chelated species, **2–3**.

© 2025 The Author(s). Published by the Royal Society of Chemistry

Open Access Article. Published on 15 December 2025. Downloaded on 1/5/2026 7:13:20 AM. This article is licensed under a Creative Commons Attribution-NonCommercial 3.0 Unported Licence.

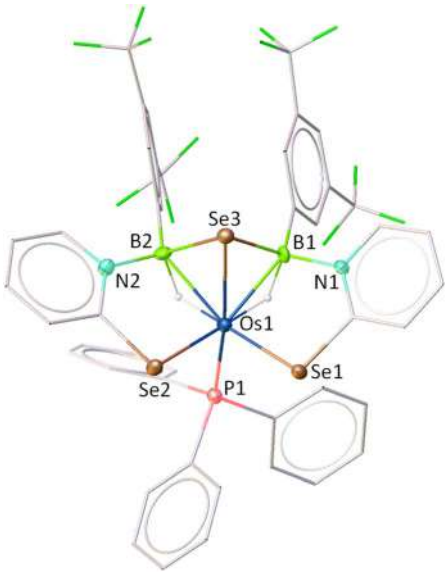
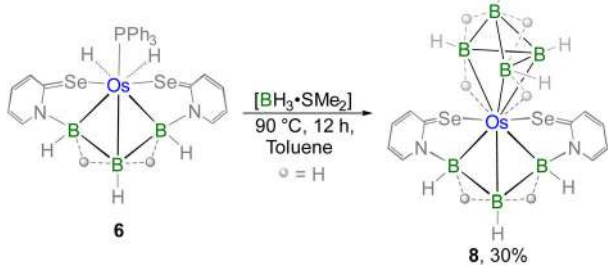


Fig. 5 Molecular structure and labelling diagram of **7**. Selected bond lengths (Å) and bond angles (°) of **7**: Os1–Se1 2.4771(7), Os1–Se2 2.4705(7), Os1–Se3 2.5612(7), Os1–B1 2.289(7), Os1–B2 2.237(7), B1–Se3 2.113(7); B2–Se3 2.093(7) (aromatic hydrogens are not shown for better clarity).

and the metal centre. Additionally, these complexes typically feature strongly π-acidic or π-basic ligands, which further restrict their reactivity.[28,30] However, in the case of complex **6**, the osmium centre is coordinated to two hydride ligands and one PPh_3 ligand which are relatively labile. To examine their lability, we performed prolonged thermolysis of **6** with an excess of $[BH_3{\cdot}SMe_2]$ that yielded complex **8** in moderate yield (Scheme 4). The $^{31}P\{^1H\}$ NMR analysis of **8** revealed no resonance peaks, indicating the loss of the PPh_3 unit from **6**. The ^1H NMR spectrum of **8** at room temperature displayed broad resonance signals in the upfield region at $\delta = -9.83, -4.19, -2.79, -1.44, -1.29$ and -0.54 ppm. These broad signals are due to the presence of either M–H–B or B–H–B protons. Additionally, in the ^1H NMR spectrum, multiple sets of broad signals were observed in the range of $\delta = 3.74$–2.66 ppm that correspond to terminal B–H protons while the $^{11}B\{^1H\}$ NMR spectrum shows peaks at $\delta = 12.2, 10.4, 8.9, -2.6, -7.2, -10.3, -11.5, -21.3, -22.4$, and -28.1 ppm. The mass spectrometric data revealed an isotopic distribution pattern at m/z 593.0291. The comprehensive spectroscopic analysis suggests a highly asymmetrical nature of the complex. However, a definitive structure could not be established until X-ray diffraction analysis was conducted.

The X-ray diffraction study was carried out on a suitable yellow crystal obtained from the slow evaporation of a 9/1 DCM/hexane solution of **8** at −4 °C. The solid-state X-ray diffraction study of **8** revealed an unusual geometry surrounding the osmium centre (Fig. 6). One part of the structure can be described as an Os–borallyl entity, wherein the triborane ligand $[B_3H_5(C_5H_4NSe)_2]^{2-}$ coordinates to the osmium centre in an η^3-fashion. The other part of the molecule resembles a pentaborane derivative, where the osmium atom occupies one of the vertices in the basal plane of a square pyramidal geometry. The core geometry of **8** can be best described as a fusion of a butterfly $\{OsB_3\}$ unit with a square pyramidal $\{OsB_4\}$ unit, with the osmium centre serving as the common vertex. The B–B and Os–B bond lengths in **8** fall within the range reported for metallaborane clusters.[31,32] Notably, the average B–B bond length in the tetraborane analogue(1.83 Å) is slightly longer as compared to that of the pentaborane analogue (1.73 Å). However, the Os–B bond lengths in the osmatetraborane unit are comparatively longer than those in the osmatriborane unit. The formation of **8** probably proceeds *via* a two-step pathway: initial dissociation of PPh_3 from complex **6**, followed by the formation of $\{OsB_4H_8\}$ *via* monoborane pyrolysis.[32,33] Notably, a careful assessment of the crystallographic data revealed the presence of two different isomeric forms of **8** (Fig. S2 and S3). The primary distinction between these isomers lies in the relative orientation of the square-pyramidal $\{OsB_4\}$ unit with respect to the butterfly $\{OsB_3\}$ one. The co-existence of these isomers in solution accounts for the complexity observed in the ^1H and ^{11}B NMR spectra (Fig. S36–S40). Similar instances of isomeric co-existence have also been well observed in TM-complexes and metallaborane clusters.[34]

Notably, both complexes **6** and **8** feature a borallyl entity stabilized by heterocyclic ligand assisted secondary interactions involving the selenopyridinyl selenium atom. However, the



Scheme 4 Pyrolysis of Os–borallyl species $[(PPh_3)(H)_2Os(\eta^5\text{-}B_3H_5(\text{-}C_5H_4NSe)_2)]$, **6** with excess borane.

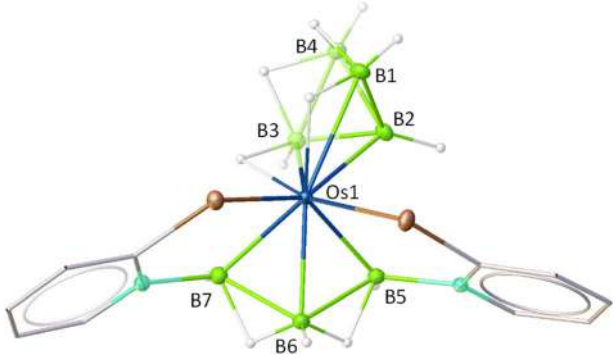


Fig. 6 Molecular structure and labelling diagram of **8**. Selected bond lengths (Å) of **8**: Os1–B1 2.416(3), Os1–B2 2.210(3), Os1–B3 2.268(3), B1–B2 1.713(4), and B1–B4 1.788(4) (aromatic hydrogens are not shown for better clarity).

© 2025 The Author(s). Published by the Royal Society of Chemistry

Open Access Article. Published on 15 December 2025. Downloaded on 1/5/2026 7:13:20 AM.
This article is licensed under a Creative Commons Attribution-NonCommercial 3.0 Unported Licence.

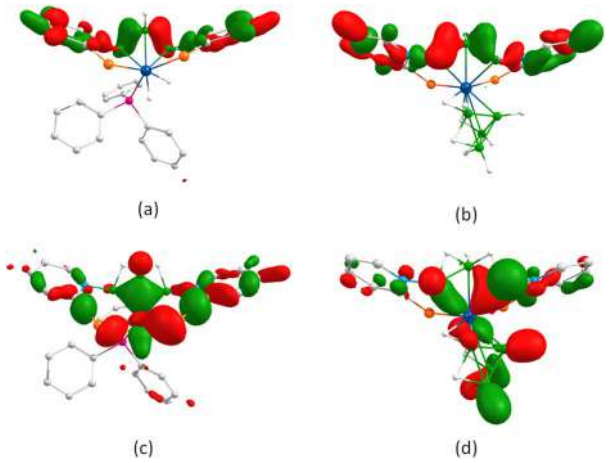
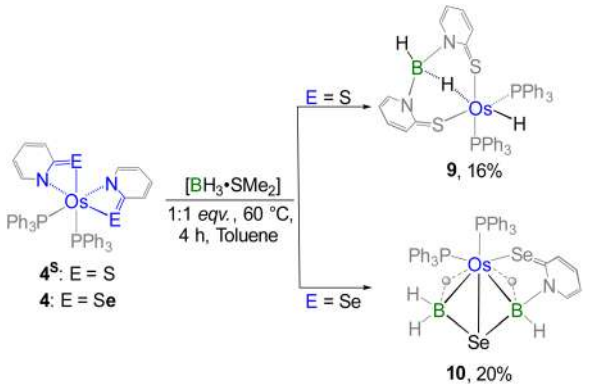


Fig. 7 (a) HOMO−37 of **6** (b) HOMO−26 of **8**; (c) HOMO−27 of **6**; (d) HOMO−14 of **8** (isovalue 0.004 [e per bohr^3]$^{1/2}$).



Scheme 5 Cooperative activation of free borane utilizing diamagnetic Os(II)–*N*,*E*-chelated complexes (E = S, Se).

bonding characterstics of other counterparts differ significantly from each other. To understand how this variation influences the bonding mode of the borallyl entity, we conducted DFT calculations. Molecular orbital (MO) analysis revealed that HOMO−37 of **6** exhibits extended bonding interaction across the triborane fragment (Fig. 7(a)), similar to the related complex $[(PPh_3)(H)_2Os(\eta^5\text{-}B_3H_5(C_5H_4NS)_2)]$.[28] Similarly, HOMO−26 of **8** displays a comparable interaction but with enhanced energy stabilization (Fig. 7(b)). The bonding interaction between osmium and the triborane unit is particularly pronounced in HOMO−27 of **6** (Fig. 7(c)) and HOMO−14 of **8** (Fig. 7(d)), with greater stabilization observed in the case of **6**. This highlights the increased stability of the osmium borallyl framework in the presence of the PPh_3 counterpart. This observation is also consistent with the lower charge accumulation on the wing-tip boron atoms of the borallyl unit in species **6**. Moreover, HOMO−21 and HOMO−25 of **8** indicate the presence of substantial multi-centred bonding interactions within the $\{OsB_4\}$ square pyramidal core.

Furthermore, we shifted our attention to the diamagnetic bis-κ^2-*N*,*Se*-chelated species **4**, which is analogous to recently reported $[Os(PPh_3)_2(\kappa^2\text{-}N,S\text{-}C_5H_4NS)_2]$, $\mathbf{4^S}$.[17c] Notably, complex $\mathbf{4^S}$ undergoes cooperative borane activation, where two inequivalent B–H activation events led to the formation of an Os(σ-borate)hydride species, **9** (Scheme 5).[17c] The primary difference between complexes **4** and $\mathbf{4^S}$ lies in the identity of their chalcogen atoms. Additionally, complex **4** is distinct from complexes **2** and **3** due to the different oxidation state of the osmium centre. To evaluate the impact of these electronic factors on metal–ligand cooperativity (MLC), complex **4** was subjected to the cooperative activation of both free and substituted borane. Treatment of **4** with one equivalent of $[BH_3\cdot SMe_2]$ led to the formation of complex **10** (Scheme 5). Interestingly, the ^{11}B NMR spectrum of **10** displayed two signals at δ = 0.6 and −21.0 ppm, indicating the presence of two inequivalent boron environments. Likewise, the upfield region of the ^{1}H NMR spectrum exhibited two broad signals at δ = −14.14 and −11.17 ppm, corresponding to two distinct Os–H–B units. Following the reaction, the appearance of two well-separated $^{31}P\{^1H\}$ NMR signals implied the emergence of an asymmetric phosphorus environment. Nonetheless, a detailed interpretation remained elusive until single-crystal X-ray diffraction analysis of complex **10** was conducted.

As depicted in Fig. 8, the molecular structure of complex **10** reveals an octahedral geometry around the osmium centre, in which two PPh_3 ligands, two bridging hydride ligands, and two selenium atoms are each positioned *cis* to one another. Similar to complex **7**, complex **10** also contains a butterfly-shaped $\{OsB_2Se\}$ core and can thus be classified as a tetraborane derivative. The dihedral angle across the butterfly-shaped core in complex **10** (103.8°) is considerably smaller than that observed in the analogous complex **7** (112.2°) and the Os–borallyl species **6** (111.7°). This difference may be attributed to the presence of two inequivalent tetracoordinate borate moieties in complex **10**, wherein one of the boron centres (B2) lacks coordination to a selenopyridinyl unit. Furthermore, the Os–Se and average B–Se bond distances are comparable in both complexes **7** and **10**. Notably, the average Os–B bond length in complex **10** (2.376 Å) is significantly longer than that in complex **7** (2.263 Å),

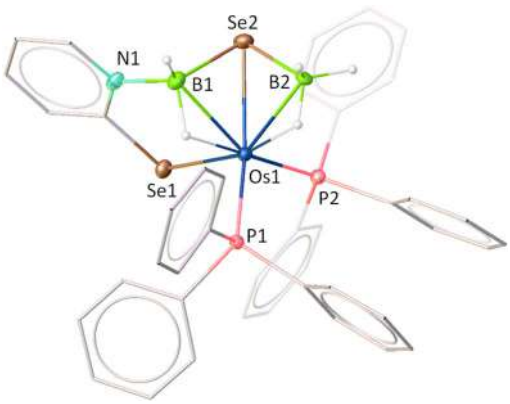


Fig. 8 Molecular structure and labelling diagram of **10**. Selected bond lengths (Å) of **10**: Os1–Se1 2.4950(5), Os1–Se2 2.529(2), Os1–B1 2.375(6), Os1–B2 2.380(5), B1–Se2 2.053(7); B2–Se2 2.078(6) (aromatic hydrogens and carbons are not shown for better clarity).

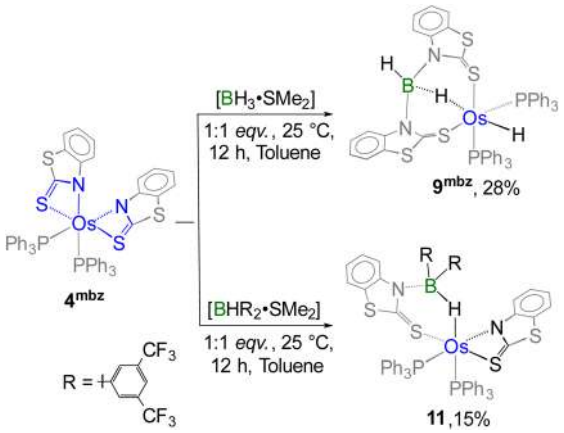
© 2025 The Author(s). Published by the Royal Society of Chemistry

Open Access Article. Published on 15 December 2025. Downloaded on 1/5/2026 7:13:20 AM. This article is licensed under a Creative Commons Attribution-NonCommercial 3.0 Unported Licence.

likely due to the presence of electron-withdrawing substituents in complex **7**.

The presence of the {OsB_2Se} butterfly core with distinct ligand environments in both **7** and **10** prompted us to explore their bonding scenario. Molecular orbital (MO) analysis demonstrates that the HOMOs in both complexes are predominantly localized on the osmium centre and the selenium atom within the selenopyridinyl ring, whereas the LUMOs exhibit π-orbital delocalization across the pyridinyl ring. Importantly, the HOMO–LUMO energy gaps ($\Delta E_{HOMO-LUMO}$) are nearly identical for both complexes. Similarly, variations in ligand environments do not significantly influence the interaction between the osmium atom and the free selenium atom, as reflected by their similar bond distances and Wiberg bond index (WBI) values (Table S2). Natural bonding orbital (NBO) analysis further revealed the presence of three-centre two-electron (3c–2e) bonding interactions along the Os–H–B moieties (Fig. 9). In complex **7**, the two boron atoms exhibit comparable natural charges, whereas in complex **10**, the B1 atom shows higher charge accumulation than B2. This suggests that B1 possesses a more pronounced borate character, likely due to differences in its electronic environment.

On the other hand, complex **4** underwent decomposition when reacted with substituted boranes, [$BH_2R{\cdot}SMe_2$] and [$BHR_2{\cdot}SMe_2$]. To facilitate the cooperative activation of bulkier aryl-substituted boranes, we employed an alternative diamagnetic bis-κ^2-*N*,*S*-chelated species, [$Os(PPh_3)_2(\kappa^2\text{-}N,S\text{-}C_7H_4NS_2)_2$] (**4^{mbz}**) in which the heterocyclic ligands impart a distinct electronic environment compared to its analogous species. Similar to the case of **4^{S}**, the cooperative B–H activation of free borane utilizing **4^{mbz}** resulted in the formation of the Os(σ-borate) hydride species, **9^{mbz}**.[17c] Building on this finding, the reaction of **4^{mbz}** with one equivalent of [$BHR_2{\cdot}SMe_2$] at room temperature afforded complex **11** (Scheme 6). In contrast, reaction with [$BH_2R{\cdot}SMe_2$] generated air and moisture-sensitive products in low yield. Complex **11** was isolated in 15% yield after chromatographic separation and further characterized by multinuclear spectroscopy, mass spectrometry and solid-state X-ray diffraction. The $^{11}B\{^1H\}$ NMR spectrum revealed a resonance peak at δ = 2.2 ppm that suggested the presence of a tetracoordinated boron atom in a single environment. Furthermore, the ^1H NMR spectrum of **11** exhibited a broad signal in the shielded region at $\delta = -5.51$ ppm, which appeared relatively downfield compared to that in **10**. The observed chemical shift is presumably due to the electron-withdrawing effect of the aryl substituents attached to boron. Notably, the appearance of two separate sharp signals in the $^{31}P\{^1H\}$ NMR spectrum implies that **4^{mbz}** experiences a reduction in symmetry following the reaction. Although the spectroscopic data suggested a probable activation of the B–H bond of BHR_2, a detailed understanding of the structural characteristics of **11** could only be obtained through solid-state X-ray diffraction analysis.



Scheme 6 Cooperative activation of free and substituted boranes utilizing diamagnetic Os(II)–*N*,*S*-chelated complex **4^{mbz}**.

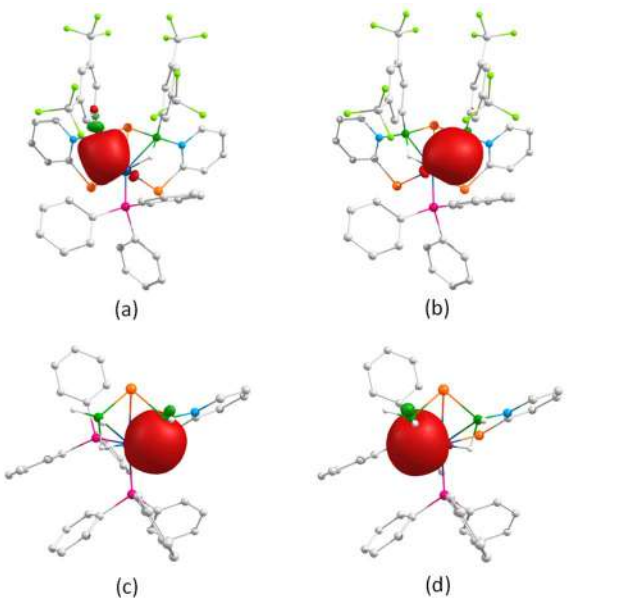


Fig. 9 3c–2e bonding interaction along the Os–H–B unit of **7** (a and b) and **10** (c and d) (isovalue 0.004 [e per bohr^3]$^{1/2}$).

As shown in Fig. 10, complex **11** can be identified as a κ^2-*N*,*S*-chelated Os(σ-borate) complex which can be formulated as [$Os(PPh_3)_2(\kappa^2\text{-}N,S\text{-}C_7H_4NS_2)(\kappa^3\text{-}H,S,S'\text{-}HBR_2(C_7H_4NS_2))$]. The molecular structure of **11** exhibited a distorted octahedral geometry around the osmium centre with the retention of two PPh_3 units and one OsNCS metallacycle from **4^{mbz}**. Additionally, the formation of a nonplanar six-membered osma-heterocycle (OsHBNCS) can be attributed to the hemilabile ring opening of an Os–N bond, followed by the capture of a B–H bond of BHR_2. The Os–B separation in complex **11** is considerably larger than that found in reported Os(σ-borane) complexes[29] as well as other σ-borate complexes of group-8 TM.[17,25a] It is noteworthy that one of the osma-heterocycles (OsNCS) remained intact after the reaction, and its bite angle is comparable to that of other OsNCS metallacycles.[17c] However, we believe that the steric hindrance caused by the two aryl groups on the boron atom prevented the B–H activation of the second BHR_2 unit. Indeed, this can be considered as one of the rarest examples of cooperative activation involving a sterically demanding disubstituted borane.

© 2025 The Author(s). Published by the Royal Society of Chemistry

Open Access Article. Published on 15 December 2025. Downloaded on 1/5/2026 7:13:20 AM.
This article is licensed under a Creative Commons Attribution-NonCommercial 3.0 Unported Licence.

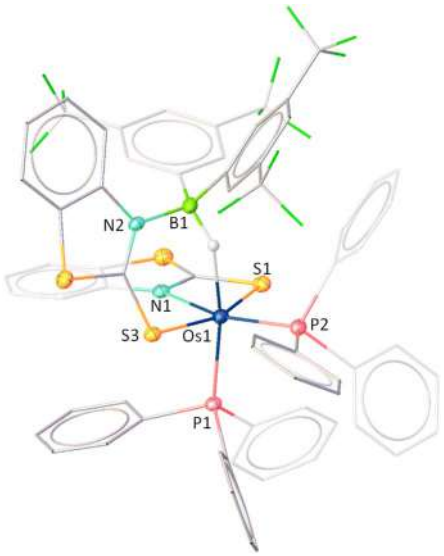


Fig. 10 Molecular structure and labelling diagram of **11**. Selected bond lengths (Å) and bond angles (°) of **11**: Os1–S1 2.441(3), Os1–S3 2.339(3), Os1–P1 2.309(3), Os1–P2 2.314(3), Os1–B1 3.001, and N1–Os1–S1 67.3(2) (aromatic hydrogens are not shown for better clarity).

DFT calculations offered valuable insights into the energetics of the cooperative B–H activation of BR_2H as well as the bonding nature in complex **11**. The observed negative Gibbs free energy change ($\Delta G = -12.6$ kcal mol^{-1}) for this reaction indicates that the sterically hindered borane activation by $\mathbf{4^{mbz}}$ is thermodynamically favourable. Molecular orbital (MO) analysis revealed that HOMO is primarily localized on the metal centre and the mercaptobenzothiazolyl sulphur atoms, while the LUMO is mainly delocalized over the aryl substituents of boron with only marginal involvement of the metal centre. A notable HOMO–LUMO energy gap of 3.379 eV was identified for **11**. Natural bonding orbital (NBO) analysis further confirmed a strong donor–acceptor interaction between the σ(B–H) orbital and the Os centre in **11** (Fig. 11, left). Second-order perturbation theory estimated a substantial stabilization energy of 43.9 kcal mol^{-1}, emphasizing the strength of this interaction. Additionally, the σ-borate unit in **11** was found to exhibit bond critical points (BCPs) along the Os–H and B–H bonds (Fig. 11, right).

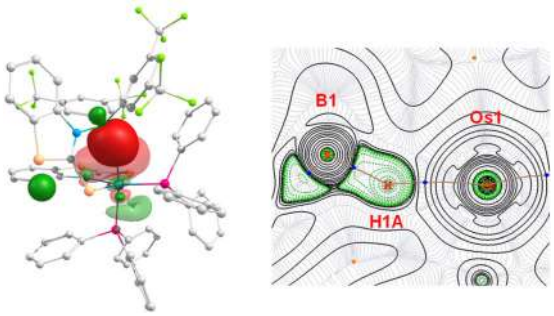


Fig. 11 Donor–acceptor interaction among the σ(B–H) orbital and Os centre in **11** (left); contour-line diagram of the Laplacian of the electron density along Os–H–B planes in **11** (right).

Conclusions

In this study, we have developed various Os(III)-based 1,3-*N*,*Se*-chelated complexes as model systems for investigating metal–ligand cooperativity. By systematically tuning the electronic characteristics of both the metal and the ligand frameworks, we modulated the hemilability of osma-heterocycle motifs. The modes of electron localization within these paramagnetic species were thoroughly characterized using spectroscopic, electrochemical, and photophysical techniques. To evaluate the impact of these tailored electronic characteristics, we investigated the cooperative activation of free borane. The cooperative activation of free borane employing the bis-1,3-*N*,*Se*-chelated Os(III) complex (**2**) resulted in the formation of a unique Os(dihydridoborate)(octatrihydridoborate) complex. This transformation proceeds *via* cleavage of both the Os–Se and Os–N bonds of two different metallacycles. In contrast, when employing complex **3**, the activation was dominated by selective Os–N bond cleavage, highlighting the sensitivity of the cooperative activation pathway to the electronic environment of the complex. We further examined the distinct activation pattern of sterically hindered boranes using various paramagnetic and diamagnetic bis-1,3-*N*,*E*-chelated complexes (E = S, Se). The mono- and di-substituted hydroboranes led to the formation of Os(σ-borate) species through cooperative B–H bond activation. Interestingly, with a sterically demanding di-aryl substituted borane, only one metallacycle unit underwent activation, while the second osma-heterocycle remained intact, presumably due to steric hindrance of aryl substituents. This study provides valuable insights into metal–ligand cooperativity and opens the way for the development of unique transition metal–boron complexes with potential applications in catalysis.

Author contributions

F. Assanar and S. Gayen have executed the experimental synthesis, characterization and analysis of the data. S. Gayen has performed the theoretical calculations. D. K. Patel has performed the X-ray diffraction analysis. All authors have contributed to the preparation of the manuscript. S. Ghosh and T. Pradeep have supervised the project.

Conflicts of interest

There are no conflicts to declare.

Data availability

The data supporting this article have been included as part of the supplementary information (SI). Supplementary information is available. See DOI: https://doi.org/10.1039/d5sc06346a.

CCDC 2481059 (**1**), 2481057 (**2**), 2466501 (**4**), 2481058 (**5**), 2466499 (**6**) 2466503 (**7**), 2466500 (**8**), 2472949 (**10**) and 2472945 (**11**) contain the supplementary crystallographic data for this paper.[35a–i]

© 2025 The Author(s). Published by the Royal Society of Chemistry

Open Access Article. Published on 15 December 2025. Downloaded on 1/5/2026 7:13:20 AM. This article is licensed under a Creative Commons Attribution-NonCommercial 3.0 Unported Licence.

Acknowledgements

S. Ghosh acknowledges the support of the SERB, India, Grant No. CRG/2023/000189. T. Pradeep thanks SERB for funding through Grant No. SPR/2021/000439 and the JC Bose Fellowship. We thankfully acknowledge the support from the CoE on Molecular Materials and Functions under the IoE scheme, IIT Madras for the single crystal XRD facility. F. A. thanks UGC, S. G. thanks CSIR and D. K. P. thanks PMRF (Grant No. SB22230356CYPMRF008224) for research fellowships. The computational facility of IIT Madras is gratefully acknowledged.

Notes and references

1 (*a*) R. Peters, *Cooperative Catalysis*, Wiley-VCH, Weinheim, 2015; (*b*) J. Khusnutdinova and D. Milstein, *Angew. Chem., Int. Ed.*, 2015, **54**, 12236; (*c*) L. Buchwald and D. Milstein, *Ligand Design in Metal Chemistry: Reactivity and Catalysis*, John Wiley & Sons, 2016.

2 (*a*) S. Schneider, J. Meiners and B. Askevold, *Eur. J. Inorg. Chem.*, 2012, 412–429; (*b*) B. Chatterjee, W. C. Chang, S. Jena and C. Werle, *ACS Catal.*, 2020, **10**(23), 14024–14055; (*c*) V. K. K. Praneeth, M. R. Ringenberg and T. R. Ward, *Angew. Chem., Int. Ed.*, 2012, **51**, 10228–10234.

3 (*a*) O. R. Luca and R. H. Crabtree, *Chem. Soc. Rev.*, 2013, **42**, 1440–1459; (*b*) J. I. van der Vlugt and J. N. H. Reek, *Angew. Chem., Int. Ed.*, 2009, **48**, 8832–8846; (*c*) M. Stradiotto and R. J. Lundgren, *Ligand Design in Metal Chemistry*, Wiley Online Library, 2016.

4 (*a*) M. Bassetti, *Eur. J. Inorg. Chem.*, 2006, 4473–4482; (*b*) P. O. Lagaditis, P. E. Sues, J. F. Sonnenberg, K. Y. Wan, A. J. Lough and R. H. Morris, *J. Am. Chem. Soc.*, 2014, **136**(4), 1367–1380; (*c*) F. Forster and M. Oestreich, *Metal–Ligand Cooperative Si–H Bond Activation in Organosilicon Chemistry–Novel Approaches and Reactions*, ed. T. Hiyama and M. Oestreich, Wiley-VCH, Weinheim, 2019, pp. 115–130; (*d*) L. Omann, C. D. F. Konigs, H. F. T. Klare and M. Oestreich, *Acc. Chem. Res.*, 2017, **50**(5), 1258–1269; (*e*) S. P. Cronin, J. M. Strain, M. S. Mashuta, J. M. Spurgeon, R. M. Buchanan and C. A. Grapperhaus, *Inorg. Chem.*, 2020, **59**(7), 4835–4841.

5 (*a*) K.-S. Feichtner and V. H. Gessner, *Chem. Commun.*, 2018, **54**, 6540–6553; (*b*) C. C. Comanescu and V. M. Iluc, *Chem. Commun.*, 2016, **52**, 9048–9051; (*c*) Q. Liang, H. A. G. Mayerstein and D. Song, *Organometallics*, 2023, **42**(9), 816–824; (*d*) T. Higashi, S. Kusumoto and K. Nozaki, *Chem. Rev.*, 2019, **119**(8), 10393–10402; (*e*) S. Zhang, X. Zhai, Y. Song, L. Feng, C. H. Tung and W. Wang, *Organometallics*, 2021, **40**(11), 1692–1698; (*f*) M. G. Cameo, A. Urriolabeitia, E. Barrenas, V. Passarelli, J. J. Pérez-Torrente, A. D. Giuseppe, V. Polo and R. Castarlenas, *ACS Catal.*, 2021, **11**(12), 7553–7567; (*g*) B. Español-Sánchez, J. Moradell, M. Galiana-Cameo, E. Barrenas, J. J. Pérez-Torrente, V. Passarelli and R. Castarlenas, *Angew. Chem., Int. Ed.*, 2025, **64**, e202507424.

6 (*a*) G. R. Owen, *Chem. Soc. Rev.*, 2012, **41**, 3535–3546; (*b*) G. Bouhadir and D. Bourissou, *Chem. Soc. Rev.*, 2016, **45**, 1065–1079; (*c*) J. A. Zurakowski, B. Stadler, M. W. Drover and M. R. Crimmin, *Angew. Chem., Int. Ed.*, 2025, **64**, e202512684.

7 (*a*) W. H. Harman and J. C. Peters, *J. Am. Chem. Soc.*, 2012, **134**(11), 5080–5082; (*b*) A. M. Poitras, S. E. Knight, M. W. Bezpalko, B. M. Foxman and C. M. Thomas, *Angew. Chem., Int. Ed.*, 2018, **57**(6), 1497–1500; (*c*) W. H. Harman, T. P. Lin and J. C. Peters, *Angew. Chem., Int. Ed.*, 2014, **53**(4), 1081–1086.

8 (*a*) C. Gunanathan and D. Milstein, *Acc. Chem. Res.*, 2011, **44**(8), 588–602; (*b*) R. H. Morris, *Acc. Chem. Res.*, 2015, **48**(5), 1494–1502; (*c*) M. Rauch, S. Kar, A. Kumar, L. Avram, L. J. W. Shimon and D. Milstein, *J. Am. Chem. Soc.*, 2020, **142**(34), 14513–14521; (*d*) Y. Liang, J. Luo, Y. D. Posner and D. Milstein, *J. Am. Chem. Soc.*, 2023, **145**(16), 9164–9175.

9 (*a*) H. Li, M. Fan and Q. Liu, *J. Am. Chem. Soc.*, 2024, **146**(39), 26649–26656; (*b*) J. J. Gair, Y. Qiu, R. L. Khade, N. H. Chan, A. S. Filatov, Y. Zhang and J. C. Lewis, *Organometallics*, 2019, **38**(7), 1407–1412; (*c*) H. Li, T. P. Goncalves, D. Lupp and K. W. Huang, *ACS Catal.*, 2019, **9**(3), 1619–1629.

10 (*a*) V. Lyaskovskyy and B. d. Bruin, *ACS Catal.*, 2012, **2**(2), 270–279; (*b*) D. L. Broere, R. Plessius and J. I. V. Vlugt, *Chem. Soc. Rev.*, 2015, **44**, 6886–6915; (*c*) O. R. Luca and R. H. Crabtree, *Chem. Soc. Rev.*, 2013, **42**, 1440–1459.

11 (*a*) C. Erken, A. Kaithal, S. Sen, T. Weyhermuller, M. Holscher, C. Werle and W. Leitner, *Nat. Commun.*, 2018, **9**, 4521; (*b*) B. Wang, C. Rong, M. Lei, S. Liu and F. D. Proft, *Inorg. Chem.*, 2023, **62**(19), 7366–7375; (*c*) H. Song, K. Ye, P. Geng, X. Han, R. Liao, C.-H. Tung and W. Wang, *ACS Catal.*, 2017, **7**(11), 7709–7717; (*d*) M. Pang, C. Wu, X. Zhuang, F. Zhang, M. Su, Q. Tong, C.-H. Tung and W. Wang, *Organometallics*, 2018, **37**(9), 1462–1467; (*e*) X. Zhai, M. Pang, L. Feng, J. Jia, C. H. Tung and W. Wang, *Chem. Sci.*, 2021, **12**, 2885–2889.

12 (*a*) M. R. Elsby and R. T. Baker, *Chem. Commun.*, 2019, **55**, 13574–13577; (*b*) M. A. Nesbit, D. L. Suess and J. C. Peters, *Organometallics*, 2015, **34**(19), 4741–4752; (*c*) S. N. MacMillan, W. H. Harman and J. C. Peters, *Chem. Sci.*, 2014, **5**, 590–597; (*d*) S. Lau, D. Gasperini and R. L. Webster, *Angew. Chem., Int. Ed.*, 2021, **60**, 14272–14294; (*e*) L. A. Grose and D. Willcox, *Chem. Commun.*, 2023, **59**, 7427–7430.

13 (*a*) J. F. C. Perez, F. L. Kirlin, E. F. Reynolds, C. E. A. Jarczyk, B. T. Joseph, J. M. Keith and A. R. Chianese, *ACS Catal.*, 2024, **14**(21), 16497–16507; (*b*) P. O. Lagaditis, P. E. Sues, J. F. Sonnenberg, K. Y. Wan, A. J. Lough and R. H. Morris, *J. Am. Chem. Soc.*, 2014, **136**(4), 1367–1380; (*c*) S. Werkmeister, K. Junge, B. Wendt, E. Alberico, H. Jiao, W. Baumann, H. Junge, F. Gallou and M. Beller, *Angew. Chem., Int. Ed.*, 2014, **53**(33), 8722–8726; (*d*) B. L. Ramirez and C. C. Lu, *J. Am. Chem. Soc.*, 2020, **142**, 5396–5407; (*e*) M. Hasenbeck, T. Müller and U. Gellrich, *Catal. Sci. Technol.*, 2019, **9**, 2438–2444.

14 (*a*) K. Fujita, N. Tanino and R. Yamaguchi, *Org. Lett.*, 2007, **9**(1), 109–111; (*b*) A. M. Royer, T. B. Rauchfuss and D. L. Gray, *Organometallics*, 2010, **29**, 6763–6768.

15 (*a*) M. W. Drover, L. L. Schafer and J. A. Love, *Angew. Chem., Int. Ed.*, 2016, **55**(9), 3181–3186; (*b*) M. W. Drover, J. A. Love

© 2025 The Author(s). Published by the Royal Society of Chemistry

Open Access Article. Published on 15 December 2025. Downloaded on 1/5/2026 7:13:20 AM. This article is licensed under a Creative Commons Attribution-NonCommercial 3.0 Unported Licence.

and L. L. Schafer, *J. Am. Chem. Soc.*, 2016, **138**(27), 8396–8399; (*c*) N. M. Leeb, M. W. Drover, J. A. Love and L. L. Schafer, *Organometallics*, 2018, **37**(24), 4630–4638.

16 J. B. Geri and N. K. Szymczak, *J. Am. Chem. Soc.*, 2015, **137**(40), 12808–12814.

17 (*a*) Md. Zafar, R. Ramalakshmi, A. Ahmad, P. K. S. Antharjanam, S. Bontemps, S. S. Etienne and S. Ghosh, *Inorg. Chem.*, 2021, **60**(2), 1183–1194; (*b*) M. Zafar, A. Ahmad, S. Saha, R. Rongala, T. Roisnel and S. Ghosh, *Chem. Sci.*, 2022, **13**, 8567–8575; (*c*) S. Gayen, F. Assanar, S. Shyamal, D. P. Dorairaj and S. Ghosh, *Chem. Sci.*, 2024, **15**, 15913–15924.

18 (*a*) M. Zafar, R. Ramalakshmi, K. Pathak, A. Ahmad, T. Roisnel and S. Ghosh, *Chem. Eur J.*, 2019, **25**, 13537–13546; (*b*) A. Ahmad, S. Saha, M. Zafar, T. Roisnel, P. Ghosh and S. Ghosh, *Eur. J. Org Chem.*, 2023, **989**, e202201283.

19 (*a*) S. Saha, A. Haridas, F. Assanar, C. Bansal, P. K. S. Antharjanam and S. Ghosh, *Dalton Trans.*, 2022, **51**, 4806–4813; (*b*) S. Saha, F. Assanar, A. Ahmad, A. Bains, S. Nagendran and S. Ghosh, *Organometallics*, 2024, **43**(7), 718–725.

20 (*a*) R. E. DeSimone, *J. Am. Chem. Soc.*, 1973, **95**(19), 6238–6244; (*b*) P. Singh, B. Sarkar, M. Sieger, M. Niemeyer, J. Fiedler, S. Zalis and W. Kaim, *Inorg. Chem.*, 2006, **45**(12), 4602–4609.

21 (*a*) P.-S. Kuhn, G. E. Buchel, K. K. Jovanovic, L. Filipovic, S. Radulovic, P. Rapta and V. B. Arion, *Inorg. Chem.*, 2014, **53**, 11130–11139; (*b*) F. Chen, G.-F. Wang, Y.-Z. Li, X.-T. Chen and Z.-L. Xue, *Inorg. Chem. Commun.*, 2012, **21**, 88–91.

22 K. W. Given, S. H. Wheeler, B. S. Jick, L. J. Maheu and L. H. Pignolet, *Inorg. Chem.*, 1979, **18**, 1261–1266.

23 (*a*) N. N. Greenwood, J. D. Kennedy, M. T. Pett and J. D. Woollins, *J. Chem. Soc., Dalton Trans.*, 1985, 2397–2406; (*b*) M. Bown, X. L. R. Fontaine, N. N. Greenwood, P. MacKinnon, J. D. Kennedy and M. T. Pett, *J. Chem. Soc., Dalton Trans.*, 1987, 2781–2787.

24 (*a*) F. Diaw-Ndiaye, P. J. S. Miguel, R. Rodríguez and R. Macías, *Molecules*, 2023, **28**(18), 6462; (*b*) A. Ahmad, S. Saha, M. Zafar, M. Cordier and S. Ghosh, *Eur. J. Inorg. Chem.*, 2023, **26**, e202300196.

25 (*a*) K. Saha, D. K. Roy, R. D. Dewhurst, S. Ghosh and H. Braunschweig, *Acc. Chem. Res.*, 2021, **54**, 1260–1273; (*b*) K. Saha, R. Ramalakshmi, S. Gomosta, K. Pathak, V. Dorcet, T. Roisnel, J.-F. Halet and S. Ghosh, *Chem. Eur J.*, 2017, **23**, 9812–9820; (*c*) S. Gayen, S. Shyamal, S. Mohapatra, P. K. S. Antharjanam and S. Ghosh, *Chem. Eur J.*, 2024, **30**, e202302362; (*d*) M. R. St.-J. Foreman, A. F. Hill, G. R. Owen, A. J. P. White and D. J. Williams, *Organometallics*, 2003, **22**, 4446–4450.

26 (*a*) C. Lenczyk, D. K. Roy, J. Nitsch, K. Radacki, F. Rauch, R. D. Dewhurst, F. M. Bickelhaupt, T. B. Marder and H. Braunschweig, *Chem. Eur J.*, 2019, **25**, 13566–13571; (*b*) R. N. Perutz, S. S. Etienne and A. S. Weller, *Angew. Chem., Int. Ed.*, 2021, **60**, 2–24; (*c*) C. N. Muhoro, X. He and J. F. Hartwig, *J. Am. Chem. Soc.*, 1999, **121**(21), 5033–5046.

27 (*a*) D. Auerhammer, M. Arrowsmith, R. D. Dewhurst, T. Kupfer, J. Bohnke and H. Braunschweig, *Chem. Sci.*, 2018, **9**, 2252–2260; (*b*) A. Ahmad, S. Gayen, S. Mishra, Z. Afsan, S. Bontemps and S. Ghosh, *Inorg. Chem.*, 2024, **63**(7), 3376–3382.

28 S. Gayen, S. Shyamal, F. Assanar and S. Ghosh, *Organometallics*, 2024, **43**(22), 2935–2943.

29 (*a*) M. L. Buil, J. J. F. Cardo, M. A. Esteruelas, I. Fernandez and E. Onate, *Organometallics*, 2015, **34**(3), 547–550; (*b*) J. C. Babon, M. A. Esteruelas, I. Fernandez, A. M. Lopez and E. Onate, *Inorg. Chem.*, 2018, **57**(8), 4482–4491; (*c*) N. Arnold, S. Mozo, U. Paul, U. Radius and H. Braunschweig, *Organometallics*, 2015, **34**(24), 5709–5715.

30 X. Lei, M. Shang and T. P. Fehlner, *Organometallics*, 1998, **17**(8), 1558–1563.

31 (*a*) S. Shyamal, D. Chatterjee, K. Kar and S. Ghosh, *Inorg. Chem.*, 2024, **63**(46), 21838–21848; (*b*) K. Kar, S. Kar and S. Ghosh, *Chem. Sci.*, 2024, **15**, 4179–4186.

32 (*a*) S. K. Bose, K. Geetharani, B. Varghese and S. Ghosh, *Inorg. Chem.*, 2010, **49**(14), 6375–6377; (*b*) K. Geetharani, B. S. Krishnamoorthy, S. Kahlal, S. M. Mobin, J.-F. Halet and S. Ghosh, *Inorg. Chem.*, 2012, **51**(19), 10176–10184; (*c*) R. Borthakur, K. Saha, S. Kar and S. Ghosh, *Coord. Chem. Rev.*, 2019, **399**, 213021; (*d*) S. Kar, A. N. Pradhan and S. Ghosh, *Coord. Chem. Rev.*, 2021, **436**, 213796.

33 (*a*) S. Ghosh, B. C. Noll and T. P. Fehlner, *Dalton Trans.*, 2008, 371–378; (*b*) S. Sahoo, R. S. Dhayal, B. Varghese and S. Ghosh, *Organometallics*, 2009, **28**(5), 1586–1589; (*c*) S. Ghosh, B. C. Noll and T. P. Fehlner, *Angew. Chem., Int. Ed.*, 2005, **44**(19), 2916–2918; (*d*) R. S. Anju, D. K. Roy, K. Geetharani, B. Mondal, B. Varghese and S. Ghosh, *Dalton Trans.*, 2013, **42**, 12828–12831.

34 (*a*) J. R. Shapley, J. T. Park, M. R. Churchill, C. Bueno and H. J. Wasserman, *J. Am. Chem. Soc.*, 1981, **103**, 7385–7387; (*b*) U. Kölle, J. Kossakowski, N. Klaff, L. Wesemann, U. Englert and G. E. Herberich, *Angew. Chem., Int. Ed.*, 1991, **30**, 690–691; (*c*) S. Ghosh, X. Lei, C. L. Cahill and T. P. Fehlner, *Angew. Chem., Int. Ed.*, 2000, **39**, 2900–2902.

35 (*a*) CCDC 2481059: Experimental Crystal Structure Determination, 2025, DOI: 10.5517/ccdc.csd.cc2p8r5x.; (*b*) CCDC 2481057: Experimental Crystal Structure Determination, 2025, DOI: 10.5517/ccdc.csd.cc2p8r3v; (*c*) CCDC 2466501: Experimental Crystal Structure Determination, 2025, DOI: 10.5517/ccdc.csd.cc2nslkm; (*d*) CCDC 2481058: Experimental Crystal Structure Determination, 2025, DOI: 10.5517/ccdc.csd.cc2p8r4w; (*e*) CCDC 2466499: Experimental Crystal Structure Determination, 2025, DOI: 10.5517/ccdc.csd.cc2nslhk; (*f*) CCDC 2466503: Experimental Crystal Structure Determination, 2025, DOI: 10.5517/ccdc.csd.cc2nslmp; (*g*) CCDC 2466500: Experimental Crystal Structure Determination, 2025, DOI: 10.5517/ccdc.csd.cc2nsljl; (*h*) CCDC 2472949: Experimental Crystal Structure Determination, 2025, DOI: 10.5517/ccdc.csd.cc2p09kl; (*i*) CCDC 2472945: Experimental Crystal Structure Determination, 2025, DOI: 10.5517/ccdc.csd.cc2p09fg.

© 2025 The Author(s). Published by the Royal Society of Chemistry

Supplementary Information (SI) for Chemical Science.
This journal is © The Royal Society of Chemistry 2025

SUPPLEMENTARY INFORMATION

Cooperative Borane Activation by Tuning Hemilability of Different Os-κ^2-*N,Se*-Chelated Complexes

Faneesha Assanar, Sourav Gayen, Deepak Kumar Patel, Thalappil Pradeep and Sundargopal Ghosh**

Department of Chemistry, Indian Institute of Technology Madras, Chennai 600036, India. Tel: +91 44- 22574230; E-mail: sghosh@iitm.ac.in

Table of Contents

I Supplementary Data

Table S1 g-values of **1-3** determined by EPR spectroscopy (X-band frozen glass EPR spectra) and redox Potentials of **1-3** determined by Cyclic Voltammetry. S5

Figure S1 Molecular structure and labelling diagram of **6**. S5

Figure S2 Molecular packing of isomers of **8** in unit cell along b-axis. S6

Figure S3 Two isomeric forms of **8**. S6

II Experimental Details

II.1 Synthesis and Characterizations S7 – S10

II.2 Spectroscopic Details

Figure S4 ESI-MS spectrum of **1** S11

Figure S5 Evans NMR spectrum of **1** S11

Figure S6 Powder X-ray diffraction (PXRD) patterns of **1** S11

Figure S7 ESI-MS spectrum of **2**. S12

Figure S8 Evans NMR spectrum of **2** S12

Figure S9 Powder X-ray diffraction (PXRD) patterns of **2** S12

Figure S10 ESI-MS spectrum of **3**. S13

Figure S11 ESI-MS spectrum of **4**. S13

Figure S12 ^{1}H NMR spectrum of **4** in $CDCl_3$. S14

Figure S13 $^{31}P\{^{1}H\}$ NMR spectrum of **4** in $CDCl_3$. S14

Figure S14 $^{13}C\{^{1}H\}$ NMR spectrum of **4** in $CDCl_3$. S15

Figure S15 Cyclic voltammetry and UV-Vis spectrum of **4**. S15

Figure S16 ESI-MS spectrum of **5**. S16

Figure S17 $^{11}B\{^{1}H\}$ NMR spectrum of **5** in C_6D_6. S16

Figure S18 ^{1}H NMR spectrum of **5** in C_6D_6. S17

Figure S19 ^{1}H VT-NMR spectra of **5** in toluene-D_8. S17

Figure S20 $^{31}P\{^{1}H\}$ NMR spectrum of **5** in C_6D_6. S18

Figure S21 $^{13}C\{^{1}H\}$ NMR spectrum of **5** in C_6D_6. S18

Figure S22 IR spectrum of **5**. S19

Figure S23 ESI-MS spectrum of **6**. S19

Figure S24 $^{11}B\{^{1}H\}$ NMR spectrum of **6** in $CDCl_3$. S19

Figure S25 ^{1}H NMR spectrum of **6** in $CDCl_3$. S20

Figure S26 $^{1}H(^{11}B)/^{11}B(^{1}H)$ HSQC spectrum of **6** in $CDCl_3$. S20

Figure S27 $^{31}P\{^{1}H\}$ NMR spectrum of **6** in $CDCl_3$. S21

Figure S28 ^{77}Se NMR spectrum of **6** in $CDCl_3$. S21

Figure S29	$^{13}C\{^{1}H\}$ NMR spectrum of **6** in $CDCl_3$.	S21
Figure S30	IR spectrum of **6**.	S22
Figure S31	$^{11}B\{^{1}H\}$ NMR spectrum of **7** in C_6D_6.	S22
Figure S32	^{1}H NMR spectrum of **7** in C_6D_6.	S23
Figure S33	$^{31}P\{^{1}H\}$ NMR spectrum of **7** in C_6D_6.	S23
Figure S34	$^{19}F\{^{1}H\}$ NMR spectrum of **7** in C_6D_6.	S24
Figure S35	IR spectrum of **7**.	S24
Figure S36	ESI-MS spectrum of **8**.	S25
Figure S37	$^{11}B\{^{1}H\}$ NMR spectrum of **8** in $CDCl_3$.	S25
Figure S38	^{1}H NMR spectrum of **8** in $CDCl_3$.	S26
Figure S39	Stacked ^{1}H (blue) and $^{1}H\{^{11}B\}$ (red) NMR spectrum of **8** in $CDCl_3$.	S27
Figure S40	$^{1}H(^{11}B)/^{11}B(^{1}H)$ HSQC spectrum of **8** in $CDCl_3$.	S27
Figure S41	^{77}Se NMR spectrum of **8** in $CDCl_3$.	S28
Figure S42	$^{13}C\{^{1}H\}$ NMR spectrum of **8** in $CDCl_3$.	S28
Figure S43	IR spectrum of **8**.	S29
Figure S44	ESI-MS spectrum of **10**.	S29
Figure S45	$^{11}B\{^{1}H\}$ NMR spectrum of **10** in C_6D_6.	S30
Figure S46	^{1}H NMR spectrum of **10** in C_6D_6.	S30
Figure S47	$^{31}P\{^{1}H\}$ NMR spectrum of **10** in C_6D_6.	S31
Figure S48	$^{13}C\{^{1}H\}$ NMR spectrum of **10** in C_6D_6.	S31
Figure S49	IR spectrum of **10**	S32
Figure S50	ESI-MS spectrum of **11**.	S32
Figure S51	$^{11}B\{^{1}H\}$ NMR spectrum of **11** in C_6D_6.	S33
Figure S52	^{1}H NMR spectrum of **11** in C_6D_6.	S33
Figure S53	$^{31}P\{^{1}H\}$ NMR spectrum of **11** in C_6D_6.	S34
Figure S54	$^{19}F\{^{1}H\}$ NMR spectrum of **11** in C_6D_6.	S34
Figure S55	IR spectrum of **11**.	S35

II.3 X-ray Analysis Details S36 – S37

III Computational Details S37

Table S2	Selected geometrical parameters and Wiberg Bond Indices (WBI) of **1, 2, 3, 6, 7, 8, 10** and **11**.	S38
Table S3	Calculated natural charge and HOMO-LUMO energy gap of **1, 2, 3, 6, 7, 8, 10** and **11**.	S39– S40
Table S4	TD-DFT calculated energies (excitation energy (cm^{-1}), λ_{calc} (nm)), oscillator strength (*f*), and main composition of the first UV−vis electronic excitations for **1**, **2** and **3**.	S38
Figure S56	Selected molecular orbitals of **1**.	S41
Figure S57	Selected molecular orbitals of **2**.	S41

Figure S58	Contour-line diagram of the Laplacian of electron density in the Os1-N1-Se1 (a) Os1-N2-Se2 (b) and Cl1-Os1-P1 (c) planes of **2**.	S42
Figure S59	ELF plot in the Os1-N1-Se1 (a) Os1-N2-Se2 (b) and Cl1-Os1-P1 (c) planes of **2**.	S42
Figure S60	Selected molecular orbitals of **3**.	S42
Figure S61	Contour-line diagram of the Laplacian of electron density in the Os1-N1-Se1 (a) Os1-N2-Se2 (b) and Se1-Os1-P1 (c) planes of **3**.	S43
Figure S62	ELF plot in the Os1-N1-Se1 (a) Os1-N2-Se2 (b) and Se1-Os1-P1 (c) planes of **3**.	S43
Figure S63	Selected molecular orbitals of **6**.	S43
Figure S64	Contour-line diagram of the Laplacian of electron density in the B1-B2-B3 (a), Os1-B1-B2 (b) and Se1-Os1-B1 (c) planes of **6**.	S44
Figure S65	ELF plot in the B1-B2-B3 (a), Os1-B1-B2 (b) and Se1-Os1-B1 (c) planes of **6**.	S44
Figure S66	Selected molecular orbitals of **7**.	S44
Figure S67	Contour-line diagram of the Laplacian of electron density in the B1-Se3-B2 (a), Os1-B1-B2 (b), Os1-H1A-B1 (c), Os1-Se3-B1 (b) and Os1-B1-Se1 (c) planes of **7**.	S45
Figure S68	ELF plot in the B1-Se3-B2 (a) and Os1-B1-B2 (b) planes of **7**.	S45
Figure S69	Selected molecular orbitals of **8**.	S46
Figure S70	Contour-line diagram of the Laplacian of electron density in the Os1-B5-B7 (a) B5-B6-B7 (b), Os1-B5-B6 (c) B1-B2-B4 (d), Os1-B1-B2 (e) and Os1-B1-B4-B3 (f) planes of **8**.	S46
Figure S71	ELF plot in the Os1-B5-B7 (a) B5-B6-B7 (b) and Os1-B1-B4-B3 (c) planes of **8**.	S47
Figure S72	Selected molecular orbitals of **10**.	S47
Figure S73	Contour-line diagram of the Laplacian of electron density in the B1-Se2-B2 (a) Os1-H1B-B1 (b) and Os1-H2C-B2-Se2 (c) planes of **10**.	S47
Figure S74	ELF plot in the B1-Se2-B2 (a) Os1-H1B-B1 (b) and Os1-H2C-B2-Se2 (c) planes of **10**.	S48
Figure S75	Selected molecular orbitals of **11**.	S48

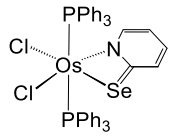
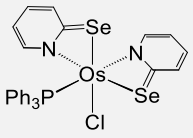
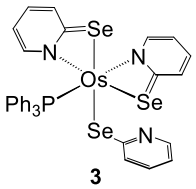
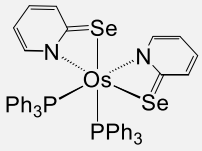
IV Cartesian Coordinates of all Optimized Structures

Figure S76	Optimized geometry of **1**.	S49 – S50
Figure S77	Optimized geometry of **2**.	S51
Figure S78	Optimized geometry of **3**.	S52
Figure S79	Optimized geometry of **6**.	S53
Figure S80	Optimized geometry of **7**.	S54 – S55
Figure S81	Optimized geometry of **8**.	S55 – S56
Figure S82	Optimized geometry of **10**.	S56 – S57
Figure S83	Optimized geometry of **11**.	S57 – S58

V References S59

I Supplementary Data

Table S1. g-values of **1-3** determined by EPR spectroscopy (X-band frozen glass EPR spectra) and redox Potentials of **1-4** determined by Cyclic Voltammetry.

Complexes	g-value	Redox Potentials		
		E^1,V	E^2,V	E^3,V
 **1**	g_z = 2.724 g_x = 2.227 g_y = 1.2-1.7	-0.892 (red) -0.562 (ox)	0.547(red) 0.927 (ox)	-
 **2**	g_z= 2.851 g_y= 2.052, g_x =1.4–1.7	-1.089 (red) -0.611 (ox)	0.371 (red) 0.871 (ox)	-
 **3**	g_z = 2.324 g_y= 2.200 g_x =1.928	-1.014 (red) -0.883 (ox)	0.085 (red) 0.211 (ox)	1.047 (red) 1.200 (ox)
 **4**	-	0.043 (red) 0.319 (ox)	0.960 (red) 1.368 (ox)	-

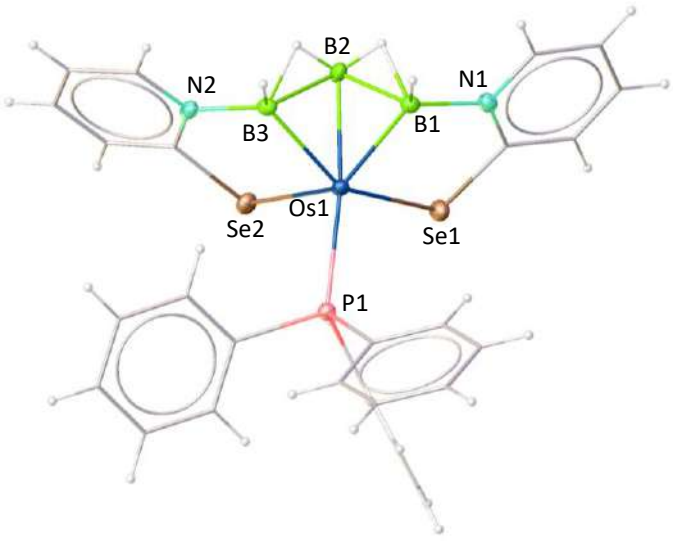


Figure S1. Molecular structure and labelling diagram of **6**. Selected bond lengths (Å) and bond angles (˚) of **6**: B1-B2 1.878(8), B2-B3 1.916(8) Os1-B1 2.133(7), B2-Os1 2.240(6), B3-Os1 2.157(6), B1-B2-B3 93.7(4).

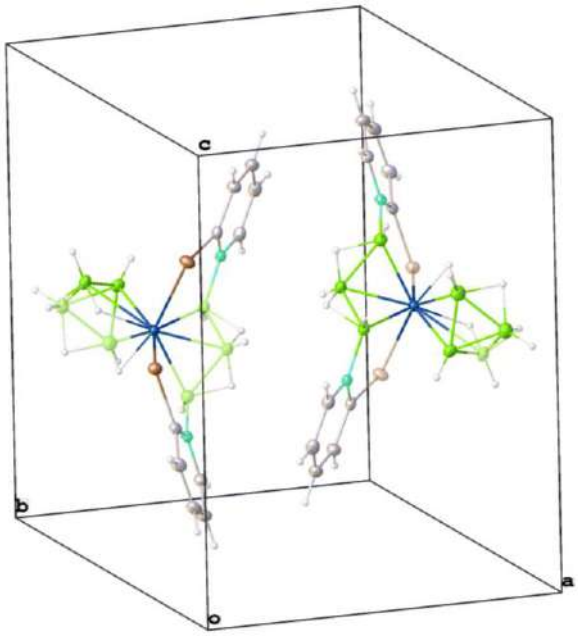


Figure S2. Molecular packing of isomers of **8** in unit cell along b-axis.

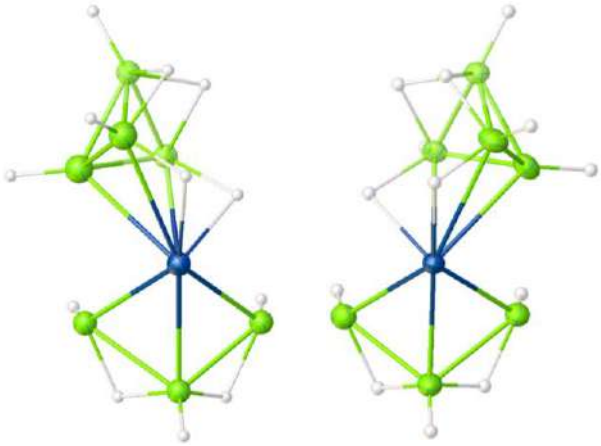


Figure S3. Two isomeric forms of **8**.

II Experimental Details

General Procedures and Instrumentation

All manipulations were carried out using standard Schlenk line and glove box techniques under inert atmosphere of dry argon. Solvents such as toluene, hexane and THF were distilled through Na/benzophenoneketyl and dichloromethane was dried over calcium hydride prior to use under argon. Chloroform-d was degassed by three freeze-thaw cycles, dried over calcium hydride for 12 h, and stored over 4 Å molecular sieves in a Young's ampoule under argon. $[Os(PPh_3)_3Cl_2]$, $[(3,5\text{-}(CF_3)_2C_6H_3)BH_2{\cdot}SMe_2]$ and $[(3,5\text{-}(CF_3)_2C_6H_3)_2BH{\cdot}SMe_2]$ were synthesized according to the reported literature procedure[1-3] and $[BH_3{\cdot}SMe_2]$ were obtained commercially (Sigma Aldrich) and used as received. The preparative TLC was performed with Merck 105554 TLC silica gel 60 F254 and thickness of layer 250 µm on aluminum sheets with 20x20 cm size. The external reference for the ^{11}B NMR spectroscopy, $[Bu_4N][(B_3H_8)]$ was synthesized according to the literature method.[4] The ^{1}H, $^{11}B\{^{1}H\}$, $^{19}F\{^{1}H\}$, $^{31}P\{^{1}H\}$, $^{13}C\{^{1}H\}$, and ^{77}Se NMR spectra were recorded on Bruker 400 and 500 MHz instruments. The residual solvent protons were used as reference (δ, ppm, C_6D_6; 7.16, $CDCl_3$; 7.26, C_7D_8; 7.09 ppm), while a sealed tube containing $[Bu_4N][(B_3H_8)]$ in C_6D_6 (δ_B, ppm, -30.07) was used as an external reference for $^{11}B\{^{1}H\}$ NMR spectra. ^{1}H decoupled $^{11}B\{^{1}H\}$ spectra of all complexes were processed with a backward linear prediction algorithm to remove the broad $^{11}B\{^{1}H\}$ background signal of the NMR tube.[5] ^{1}H NMR Evans measurements were performed at 25.8 °C on a 500 MHz spectrometer. A sealed capillary containing 2.0 mM $^{t}BuOH$ in $CDCl_3$ was placed inside an NMR tube containing only the sample solution (**1**: 12.127 mM, **2**: 12.453 mM in $CDCl_3$; no $^{t}BuOH$ added to the bulk), note that diamagnetic corrections were applied using Pascal constants.[6] EPR measurements were conducted using a JEOL model JES FA200 X-band (9.5 GHz) electron spin resonance spectrometer. Samples of the paramagnetic complexes were prepared in a dichloromethane (for **1** and **2**) or toluene (for **3**) solution, loaded into quartz capillary tubes, and analyzed at 77 K. Mass spectra were carried out using Qtof Micro YA263 HRMS instrument and Bruker MicroTOF-II mass spectrometer in ESI ionization mode. All cyclic voltammetry (CV) experiments were performed at room temperature using a Metrohm Autolab PGSTAT 204 potentiostat. A conventional three-electrode setup was employed, consisting of a 1 mm diameter glassy carbon disc as the working electrode, an Ag/AgCl reference electrode (3.0 M KCl, connected by a Vycor tip), and a platinum wire counter electrode. All potentials are referenced to the ferrocenium/ferrocene ($FeCp_2^{+/0}$) couple for measurements conducted in organic solvent. Cyclic voltammograms of complexes **1**, **2**, and **3** were recorded in dichloromethane containing 0.1 M $(nBu_4N)PF_6$) at a scan rate of 100 mV/s. UV-vis absorption spectra were gained from Jasco V-650 spectrometer. Infrared spectra were obtained on a Jasco FT/IR–1400 spectrometer.

II.1 Synthesis and Characterizations

Syntheses of 1, 2, 3 and 4: In a flame-dried Schlenk tube, $[Os(PPh_3)_3Cl_2]$, (0.600 g, 0.573 mmol) and K[L] (L = 2-selanopyridine, (0.562 g, 2.863 mmol) was taken in 1:5 stoichiometric ratio. After adding 30 mL of THF the reaction was thermalized for 4 h at 60 °C during which the colour of the mixture changed from green to brown. The solvent was removed using vacuum and the residue was extracted in hexane/CH_2Cl_2 (40:60 v/v) and passed through celite. The products were further isolated by performing chromatographic work-up using silica-gel TLC plates by eluting in 100% toluene. This enabled us to isolate pale green **1** (0.90 g, 15%, R_f= 0.6), blueish green **2** (0.210 g, 35%, R_f= 0.4), dark green **3** (0.110 g, 18%, R_f= 0.1) and orange **4** (0.120 g, 20%, R_f= 0.8).

Modified Syntheses of 1, 2 and 3: In a flame-dried Schlenk tube, $[Os(PPh_3)_3Cl_2]$ (0.600 g, 0.573 mmol) and K[L] (0.562 g, 2.863 mmol) were taken in a 1:5 molar ratio. To this, 30 mL of THF was added at –78 °C, and the reaction mixture was allowed to warm to room temperature and stirred for 12 h under an open-air atmosphere. The solution gradually changed to a greenish-brown color, affording complexes **1** (0.108 g, 18%), **2** (0.240 g, 40%), and **3** (0.110 g, 18%), along with trace amounts of **4**. Although the Os(III) complexes (**1**-**3**) formed in comparatively higher yields than the Os(II) complex **4**, the overall product yield was modest, with substantial decomposition observed under aerobic conditions relative to the reaction carried out under inert atmosphere.

Modified Syntheses of 1 and 2: In a flame-dried Schlenk tube, $[Os(PPh_3)_3Cl_2]$, (0.600 g, 0.573 mmol) and K[L] (0.562 g, 2.863 mmol) was taken in 1:5 ratio. 30 mL of CCl_4 solvent was added and it was further thermalized for 12 h at 60 °C. The colour of the reaction mixture changed from green to blueish green yielding **1** and **2** with an enhanced yield of 30% (0.180 g) and 65% (0.390 g) respectively with a trace amount of **3** and **4**.

Modified Syntheses of 3 and 4: In a flame-dried Schlenk tube, $[Os(PPh_3)_3Cl_2]$, (0.600 g, 0.573 mmol) and K[L] (0.562 g, 2.863 mmol) was taken in 1:5 stoichiometric ratio. 30 mL of THF solvent was added to it at -78 °C, after attaining room temperature the reaction was stirred for 4 h under inert atmosphere. The colour of the reaction mixture changed from green to orange yielding **3** and **4** with an enhanced yield of 30% (0.180 g) and 61% (0.365 g) respectively with a trace amount of **1** and **2**.

1: MS (ESI^+): *m/z* calculated for $[M+NH_4]^+$: 962.0648, found: 962.0597; ^1H NMR (500 MHz, $CDCl_3$, 22 °C): δ = 17.20 (br), 13.73 (br), 7.32 (br), 6.80 (br), 5.81 (br), 2.05 (br), -0.93 (br), -1.75 (br), -8.33 (br), -10.96 (br), -16.61 (br) ppm.

2: MS (ESI^+): *m/z* calculated for $[M]^+$: 802.9227, found: 802.9211; ^1H NMR (500 MHz, $CDCl_3$, 22 °C): δ = 26.54 (br), 10.41 (br), 6.82 (br), 6.66 (br), 5.65 (br), 5.48 (br), 3.42 (br), 2.53 (br), -2.50 (br), -13.33 (br), -21.34 (br) ppm.

3: MS (ESI^+): *m/z* calculated for $[M]^+$: 923.9056, found: 923.9076; ^1H NMR (500 MHz, $CDCl_3$, 22 °C): δ = 24.42 (br), 17.71 (br), 14.66 (br), 14.10 (br), 13.42 (br), 11.96 (br), 6.31 (br), 5.92 (br), -1.26 (br), -4.62 (br), -6.63 (br), -11.13 (br), -12.91 (br), -17.97 (br) ppm.

4: MS (ESI^+): *m/z* calculated for $[M]^+$: 1030.0461, found: 1030.0479; ^1H NMR (500 MHz, $CDCl_3$, 22 °C): δ = 7.93 (d, J = 5.5 Hz, 2H, L), 7.19 (t, J = 8.0 Hz, 12H, $Ar_{(ph)}$), 7.07 (t, J = 7.1 Hz, 6H, $Ar_{(ph)}$), 6.95 (t, J = 7.4 Hz, 12H, $Ar_{(ph)}$), 6.73 (t, J = 7.5 Hz, 2H, L), 6.36 (d, J = 7.9 Hz, 2H, L), 6.19 (t, J = 6.4 Hz, 2H, $Ar_{(ph)}$) ppm; $^{31}P\{^1H\}$ NMR (202 MHz, $CDCl_3$, 22 °C): δ = -6.3 (s, 2P) ppm; $^{13}C\{^1H\}$ NMR (100 MHz, $CDCl_3$, 22 °C): δ = 176.6 (s, C=Se), 148.1 (s, C-N), 138.9, 138.8, 138.5, 138.4, 134.5, 133.5, 130.3, 128.5, 127.2, 117.3 (s, C=C, $Ar_{(Ph/L)}$) ppm.

Syntheses of 5 and **6**: In a flame-dried Schlenk tube, $[OsCl(PPh_3)(\kappa^2\text{-}N,Se\text{-}L)_2]$, **2** (100 mg, 0.125 mmol) in 15 mL dry toluene was treated with stoichiometric amount of $[BH_3{\cdot}SMe_2]$ (0.1 mL, 0.498 mmol) was thermalized for 4 h at 60 °C. During course of the reaction the colour of the reaction changed from blueish green to orange. The volatile components were removed under vacuum and the remaining residue was extracted into hexane/CH_2Cl_2 (80:20 v/v) and passed through Celite. After removal of the solvent, the residue was subjected to chromatographic work-up by using TLC plates. Elution with

hexane/CH_2Cl_2 (60:40 v/v) mixture yielded red solid **5** (15 mg, 15%, Rf= 0.7) and orange solid **6** (35 mg, 35%, Rf= 0.3).

5: MS (ESI^+): *m/z* calculated for $[M-2H]^+$: 818.0568, found: 818.0868; $^{11}B\{^1H\}$ NMR (160 MHz, C_6D_6, 22 °C): δ = 59.9 (br, 1B), 14.2 (br, 1B), 4.6 (br, 1B), -15.2(br, 1B) ppm; ^1H NMR (500 MHz, C_6D_6, 22 °C): δ = 8.05 (d, J = 5.8 Hz, 1H, L), 7.82 (d, J = 8.2 Hz, 1H, L), 7.64 (d, J = 8.8 Hz, 1H, L), 7.62 (d, J = 8.6 Hz, 1H, L), 7.71-7.67, 7.58-6.91 (m, 15H, $Ar_{(Ph)}$), 6.25 (t, J = 7.2 Hz, 1H, L), 6.11 (t, J = 7.5 Hz, 1H, L), 5.80 (t, J = 6.5 Hz, 1H, L), 5.46 (t, J = 6.7 Hz, 1H, L), 4.47(br, B-H_t), 3.39(br, B-H_t), -7.65 (br, Os-*H*-B), -11.61 (d, 1H, Os-*H*-B), -11.66 (d, 1H, Os-*H*-B) ppm; $^{31}P\{^1H\}$ NMR (202 MHz, C_6D_6, 22 °C): δ = 27.9 (s, 1P) ppm; $^{13}C\{^1H\}$ NMR (100 MHz, C_6D_6, 22 °C): δ = 196.0 (s, C=Se), 179.0 (s, C-Se), 172.5, 159.1 (s, C-N), 149.7, 145.2, 144.4, 138.7, 137.0, 136.6, 134.8, 133.5, 132.4, 131.5, 130.6, 130.1, 128.7, 127.8, 125.6, 121.0, 116.5 (s, C=C, $Ar_{(Ph/L)}$) ppm ; IR (dicholoromethane, cm^{-1}): $\tilde{\nu}$ = 2507 (B-H), 2452 (B-H-B, Os-H-B), 1436 (C=Se).

6: MS (ESI^+): *m/z* calculated for $[M-H]^+$: 805.0311, found: 805.0319; $^{11}B\{^1H\}$ NMR (160 MHz, $CDCl_3$, 22 °C): δ = 17.0 (br, 1B), -39.0 (br, 2B) ppm; ^1H NMR (500 MHz, $CDCl_3$, 22 °C): δ = 8.40 (d, J = 5.8 Hz, 2H, L), 7.70 (d, J = 8.1 Hz, 2H, L), 7.34-7.21 (m, 15H, $Ar_{(ph)}$), 7.13 (t, J = 7.1 Hz, 2H, L), 6.84 (t, J = 6.3 Hz, 2H, L), 4.10 (br, 3H, B-H_t), −1.41 (br, 2H, B-*H*-B), −13.40 (d, 2H, Os-*H*) ppm; $^{31}P\{^1H\}$ NMR (202 MHz, $CDCl_3$, 22 °C): δ = 16.1 (s, 1P) ppm; ^{77}Se NMR (95 MHz, $CDCl_3$, 22 °C): δ = 234.8 (s, 2Se) ppm; $^{13}C\{^1H\}$ NMR (100 MHz, $CDCl_3$, 22 °C): δ = 175.8 (s, C=Se), 147.0 (s, C-N), 137.2, 136.8, 133.8, 133.7, 131.7, 129.4, 127.7, 127.6, 116.3 (s, C=C, $Ar_{(Ph/L)}$) ppm ; IR (dicholoromethane, cm^{-1}): $\tilde{\nu}$ = 2499 (B-H), 2431 (B-H-B), 1534 (C=Se).

Syntheses of 7: In a flame-dried Schlenk tube, $[OsCl(PPh_3)(\kappa^2\text{-}N,Se\text{-}L)_2]$ **2** (100 mg, 0.125 mmol) in 15 mL dry toluene was treated with stoichiometric amount of $[(3,5\text{-}(CF_3)_2C_6H_3)BH_2{\cdot}SMe_2]$ (71.8 mg, 0.249 mmol) and thermalized for 4 h at 60 °C. The volatile components were removed under vacuum and the remaining residue was extracted into hexane/CH_2Cl_2 (60:40 v/v) and passed through Celite. After removal of the solvent, the residue was subjected to chromatographic work-up by using TLC plates. Elution with hexane/CH_2Cl_2 (50:50 v/v) mixture yielded yellow solid **7** (12 mg, 12%, Rf= 0.4).

7: $^{11}B\{^1H\}$ NMR (160 MHz, C_6D_6, 22 °C): δ = 27.8 (br, 2B) ppm, ^1H NMR (500 MHz, C_6D_6, 22 °C): δ = 8.39-6.07 (m, 29H, H_{Ar}), -9.72 (t, 2H, Os-*H*-B) ppm; $^{31}P\{^1H\}$ NMR (202 MHz, C_6D_6, 22 °C): δ = 22.3 (s, 1P) ppm; ^{19}F NMR (470 MHz, C_6D_6, 22 °C): δ −62.2 (s, 6F) ppm; IR (n-Hexane, cm^{-1}): $\tilde{\nu}$ = 2360 (Os-H-B), 1454 (C=Se).

Syntheses of 8: In a flame-dried Schlenk tube, $[(PPh_3)(H)_2Os(\eta^5\text{-}B_3H_5(C_5H_4NSe)_2)]$ **6** (100 mg, 0.124 mmol) in 15 mL dry toluene was treated with excess $[BH_3{\cdot}SMe_2]$ (0.5 mL) and thermalized for 12 h at 90 °C. The colour of the mixture changed from orange to pale yellow. The volatile components were removed under vacuum and the remaining residue was extracted into hexane/CH_2Cl_2 (60:40 v/v) and passed through Celite. After removal of the solvent, the residue was subjected to chromatographic work-up by using TLC plates. Elution with hexane/CH_2Cl_2 (60:40 v/v) mixture yielded yellow solid **8** (30 mg, 30%, Rf = 0.5).

8: MS (ESI^+): *m/z* calculated for $[M]^+$: 593.0259, found: 593.0291; $^{11}B\{^1H\}$ NMR (160 MHz, $CDCl_3$, 22 °C): δ = 12.2 (br), 10.4 (br), 8.9 (br), -2.6(br), -7.2(br), -10.3(br), -11.5 (br), -21.3(br), 22.4 (br), -28.1(br) ppm; ^1H NMR (500 MHz, $CDCl_3$, 22 °C): δ 8.32 (t, J = 6.2 Hz, L), 7.86 (d, J = 8.4 Hz, L), 7.84 (d, J = 8.8 Hz, L), 7.63 (q, J = 5.3 Hz, L), 7.36 (t, J = 7.6 Hz, L), 7.23 (t, J = 7.1 Hz, L), 7.00 (t, J = 6.5 Hz, L), 6.87 (t, J =

6.4 Hz, L), 3.74 (br, B-H_t), 2.66 (br, B-H_t), -0.54(br, B-*H*-B), -1.29 (br, B-*H*-B), -1.44 (br, B-*H*-B), -2.79 (br, B-*H*-B) ppm, -4.19 (br, Os-*H*-B), -9.83 (br, Os-*H*-B) ppm; ^{77}Se NMR (95 MHz, $CDCl_3$, 22 °C): δ = 125.0 ppm (s, 2Se); $^{13}C\{^1H\}$ NMR (100 MHz, $CDCl_3$, 22 °C): δ = 174.7, 172.6 (s, C=Se), 147.2, 146.9 (s, C-N), 136.3–116.9 (s, C=C, $Ar_{(Ph/L)}$) ppm; IR (dicholoromethane, cm^{-1}): $\tilde{\nu}$ = 2541 (B-H), 2482 (B-H-B, Os-H-B), 1536 (C=Se).

Syntheses of 10: In a flame-dried Schlenk tube, $[Os(PPh_3)_2(\kappa^2\text{-}N,Se\text{-}(C_5H_4NSe))_2]$ **4** (500 mg, 0.485 mmol) in 15 mL dry toluene was treated with stoichiometric amount of $[BH_3{\cdot}SMe_2]$ (0.1 mL, 0.970 mmol) and thermalized for 4 h at 60 °C. The colour of the mixture changed from orange to red. The volatile components were removed under vacuum and the remaining residue was extracted into hexane/toluene (60:40 v/v) and passed through Celite. After removal of the solvent, the residue was subjected to chromatographic work-up by using TLC plates. Elution with hexane/CH_2Cl_2 (50:50 v/v) mixture yielded red solid **10** (20 mg, 20%, Rf = 0.6).

10: MS (ESI$^+$): *m/z* calculated for $[M]^+$: 978.0715, found: 978.0793; $^{11}B\{^1H\}$ NMR (160 MHz, C_6D_6, 22 °C): δ = 0.6 (br, 1B), -21.0 (br, 1B) ppm; ^{1}H NMR (500 MHz, C_6D_6, 22 °C): δ 7.58 (m, 1H, L), 7.51 (m, 6H, $Ar_{(ph)}$), 7.44 (t, J = 8.4 Hz, 7H, $Ar_{(ph)}$), 7.13 (d, J =7.4 Hz, 1H, L), 7.06-6.91 (m, 17H, $Ar_{(ph)}$), 6.05 (t, J = 7.5 Hz, 1H, L), 5.73 (t, J = 8.0 Hz, 1H, L), 2.90, 2.11 (br,B-H_t), -11.17 (br, 1H, Os-*H*-B), -14.14 (br,1H, Os-*H*-B) ppm; $^{31}P\{^1H\}$ NMR (202 MHz, C_6D_6, 22 °C): δ = 13.6 (d, 1P), 6.1 (s, 1P) ppm; $^{13}C\{^1H\}$ NMR (100 MHz, C_6D_6, 22 °C): δ = 175.9 (s, C=Se), 147.1 (s, C-N), 140.6, 140.2, 136.1, 135.7, 134.7, 134.6, 134.5, 134.4, 132.7, 132.1, 129.4, 129.2, 128.6, 127.7, 127.6, 127.5, 127.4, 125.7, 116.0(s, C=C, $Ar_{(Ph/L)}$) ppm; IR (n-hexane, cm^{-1}): $\tilde{\nu}$ = 2381 (B-H),2342 (Os-H-B) 1431 (C=Se).

Syntheses of 11: In a flame-dried Schlenk tube, $[Os(PPh_3)_2(\kappa^2\text{-}N,S\text{-}C_7H_4NS_2)_2]$ $\mathbf{4^{mbz}}$ (100 mg, 0.095 mmol) in 15 mL dry toluene was treated with stoichiometric amount of $[(3,5\text{-}(CF_3)_2C_6H_3)_2BH{\cdot}SMe_2]$ (47.75 mg, 0.095 mmol). The reaction was stirred at room temperature for 2hr. The volatile components were removed under vacuum and the remaining residue was extracted into hexane and passed through Celite. After removal of the solvent, the residue was subjected to chromatographic work-up by using TLC plates. Elution with hexane/CH_2Cl_2 (80:20 v/v) mixture yielded orange crystalline solid **11** (15 mg, 15%, Rf = 0.8).

11: MS (ESI$^+$): *m/z* calculated for $[M]^+$: 1486.1462, found: 1486.1342; $^{11}B\{^1H\}$ NMR (160 MHz, C_6D_6, 22 °C): δ = 2.2 (br, 1B) ppm; ^{1}H NMR (500 MHz, C_6D_6, 22 °C): δ = 8.97-6.14 (m, 44H, H_{Ar}), -5.51 (br,1H, Os-*H*-B) ppm; $^{31}P\{^1H\}$ NMR (202 MHz, C_6D_6, 22 °C): δ = -5.5 (s, 1P) ppm, δ = -16.8 (s, 1P) ppm; ^{19}F NMR (470 MHz, C_6D_6, 22 °C) : δ = -62.2 (s, 6F), -62.6 (s, 6F) ppm; IR (n-hexane, cm^{-1}): $\tilde{\nu}$ = 2360 (Os-H-B), 1356 (C=S).

II.2 Spectroscopic details

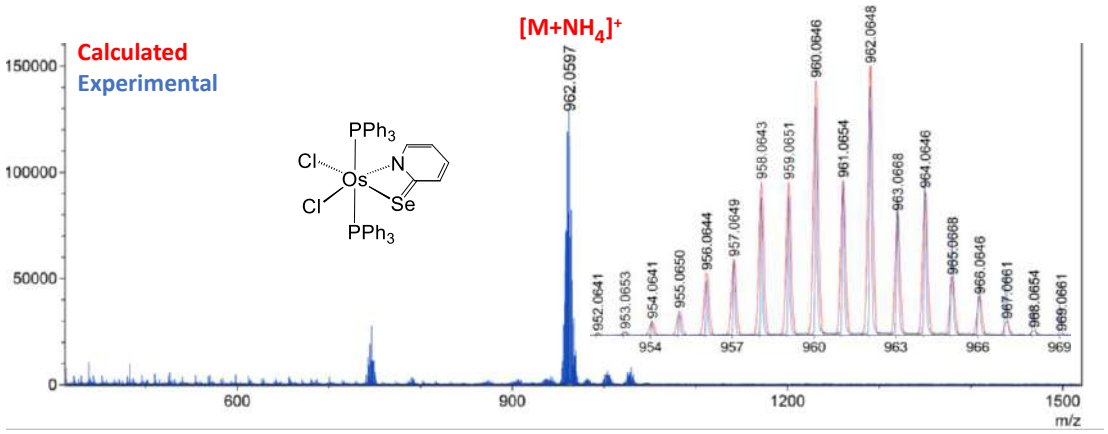


Figure S4. ESI-MS spectrum of **1**.

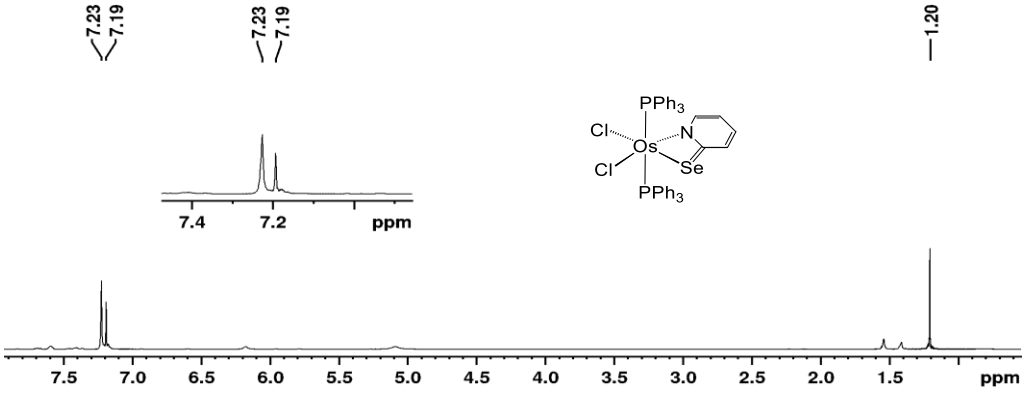


Figure S5. Evans NMR spectrum of **1**

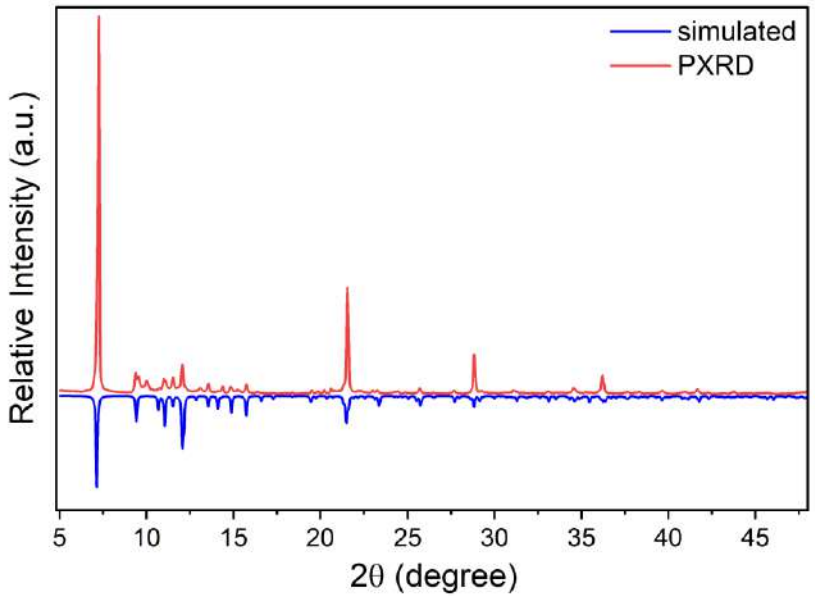


Figure S6. Comparison of powder X-ray diffraction (PXRD) patterns with the simulated patterns from single-crystal X-ray diffraction (SCXRD) for **1**.

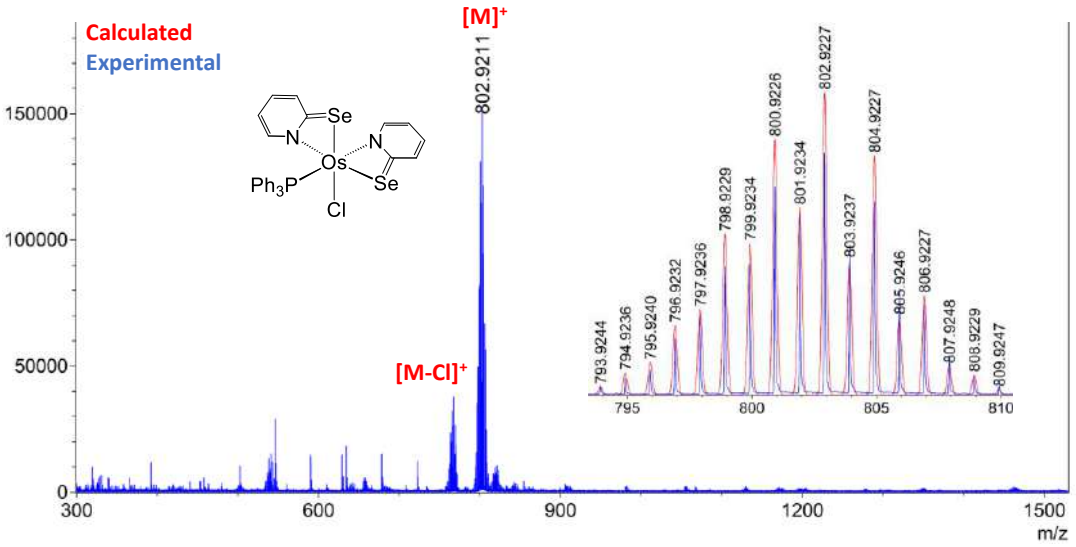


Figure S7. ESI-MS spectrum of **2**.

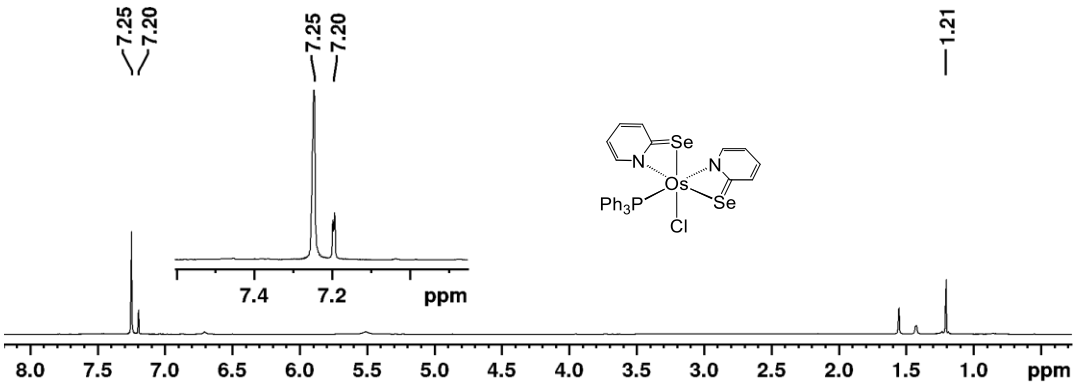


Figure S8. Evans NMR spectrum of **2**

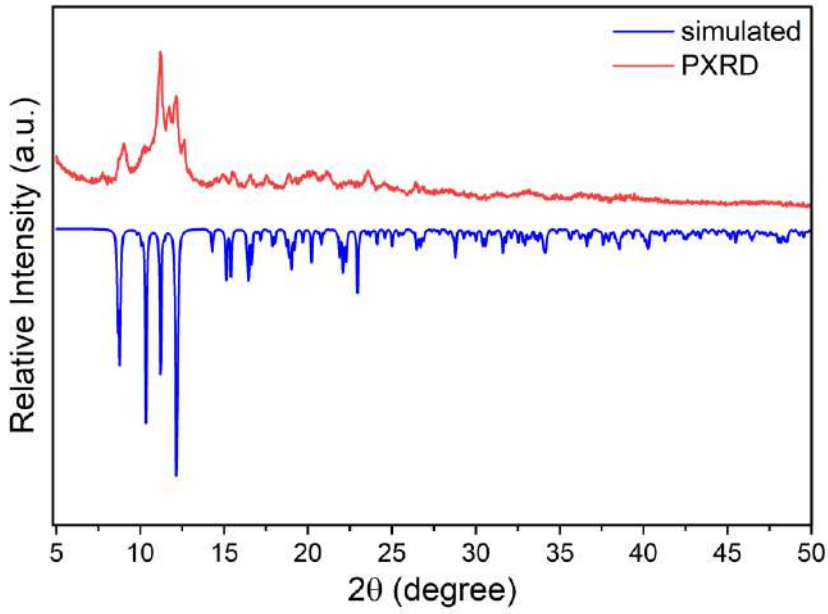


Figure S9. Comparison of powder X-ray diffraction (PXRD) patterns with the simulated patterns from single-crystal X-ray diffraction (SCXRD) for **2**.

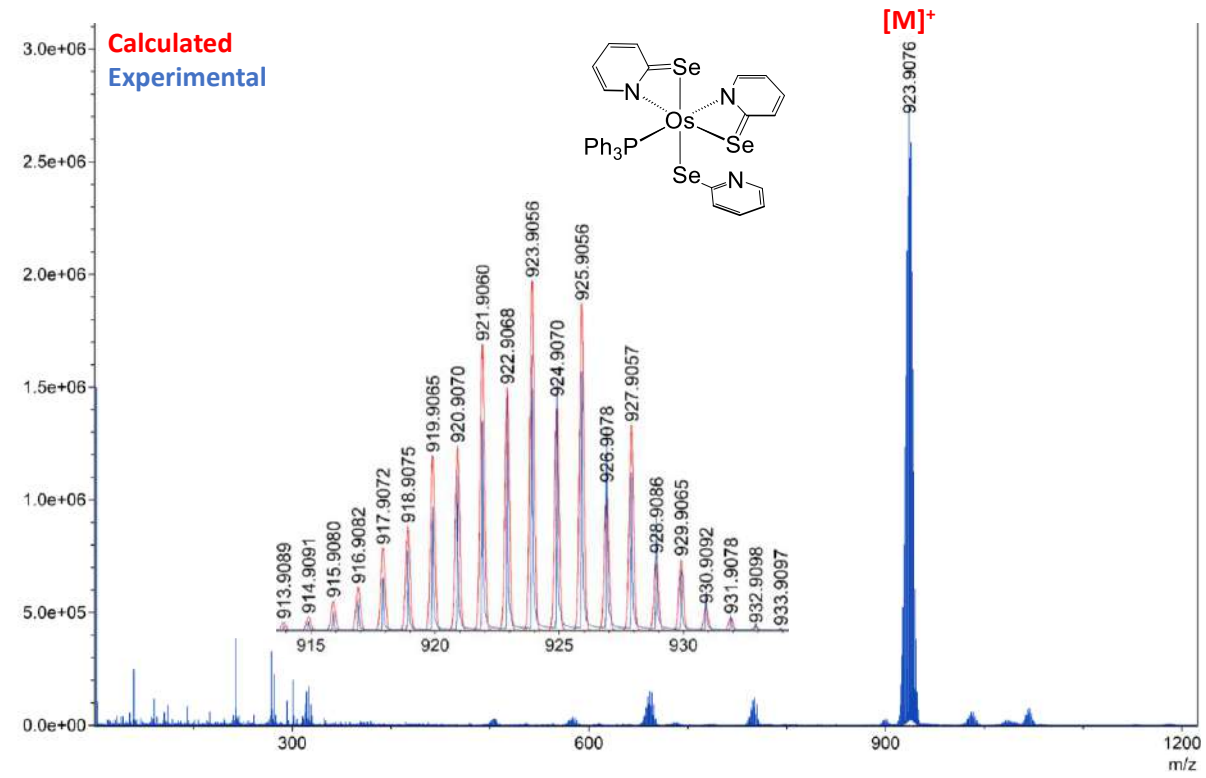


Figure S10. ESI-MS spectrum of **3**.

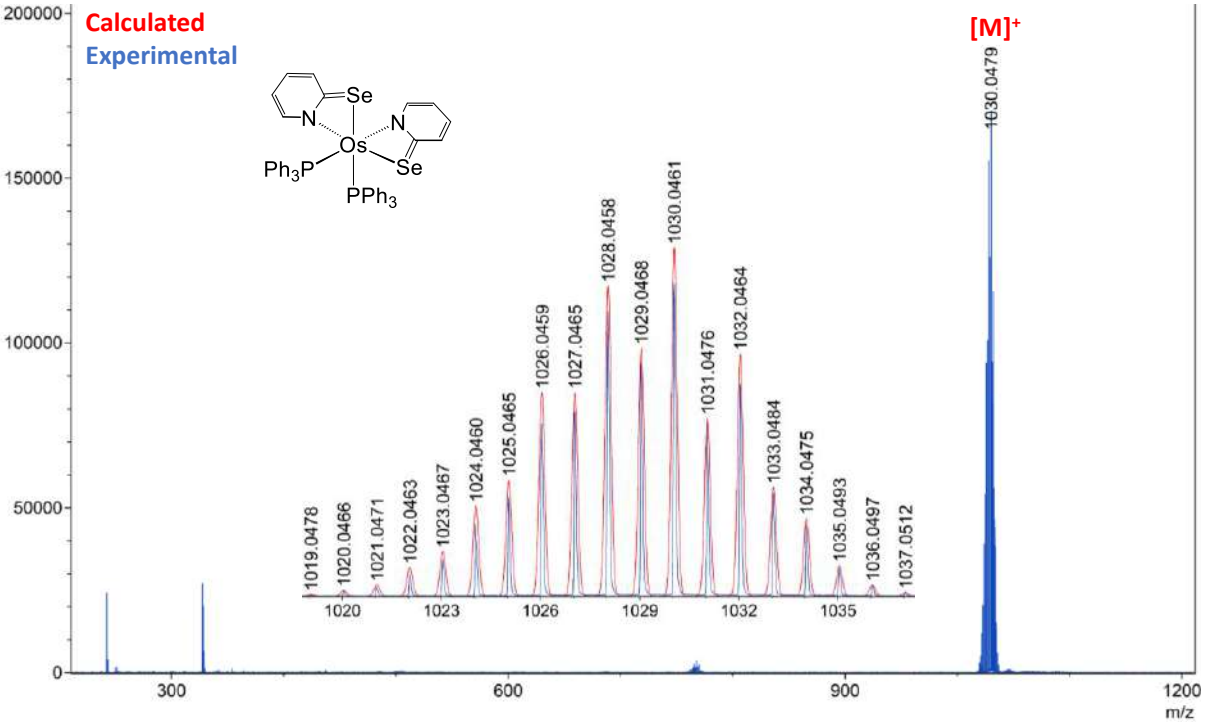


Figure S11. ESI-MS spectrum of **4**.

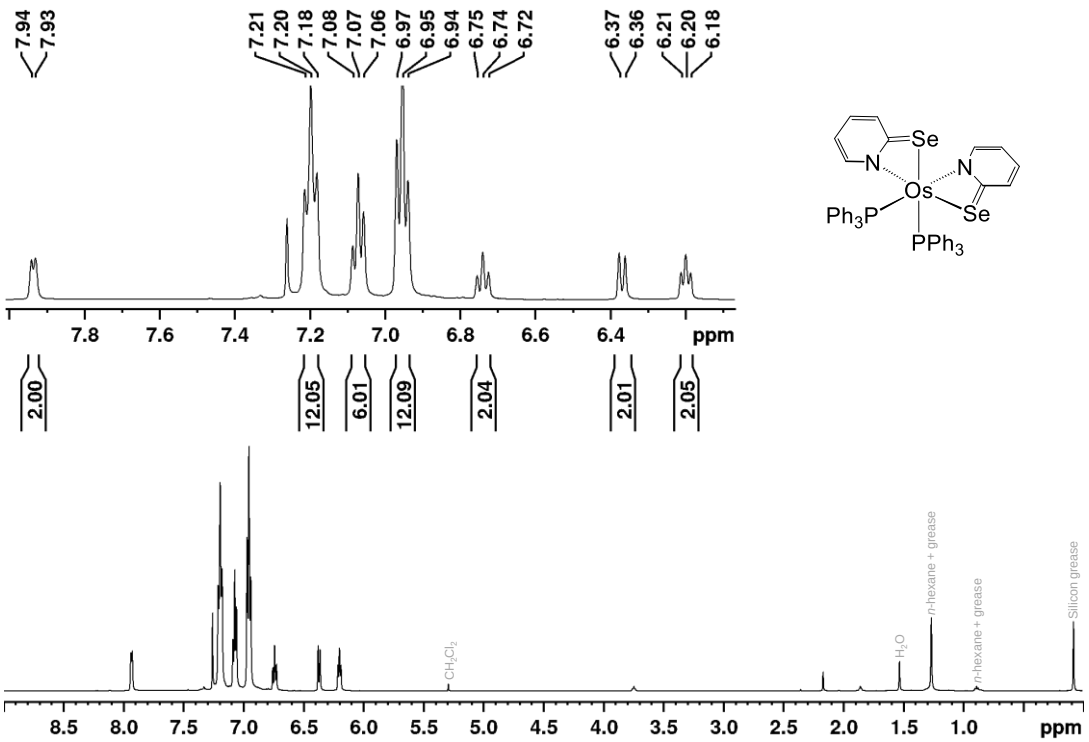


Figure S12. ^{1}H NMR spectrum of **4** in $CDCl_3$.

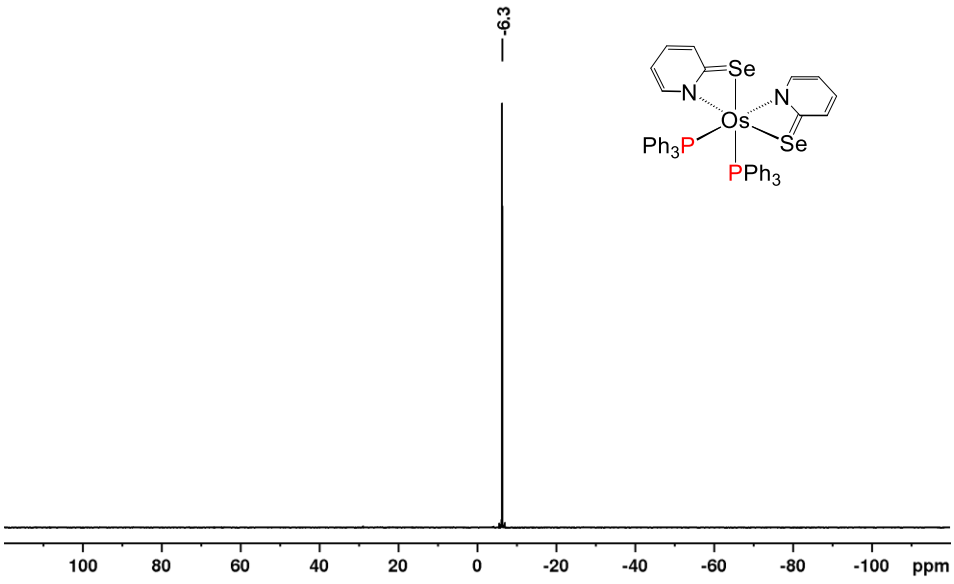


Figure S13. $^{31}P\{^{1}H\}$ NMR spectrum of **4** in $CDCl_3$.

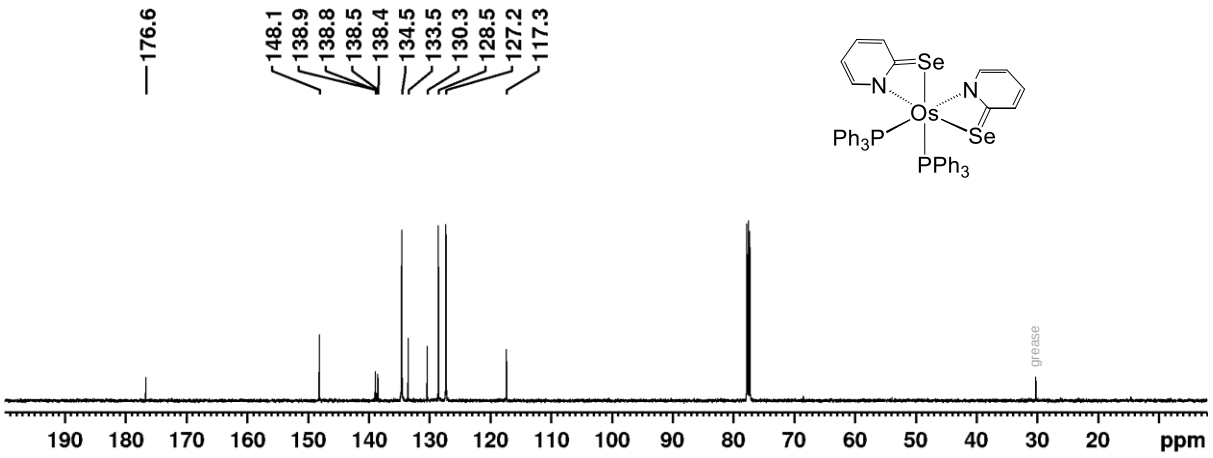
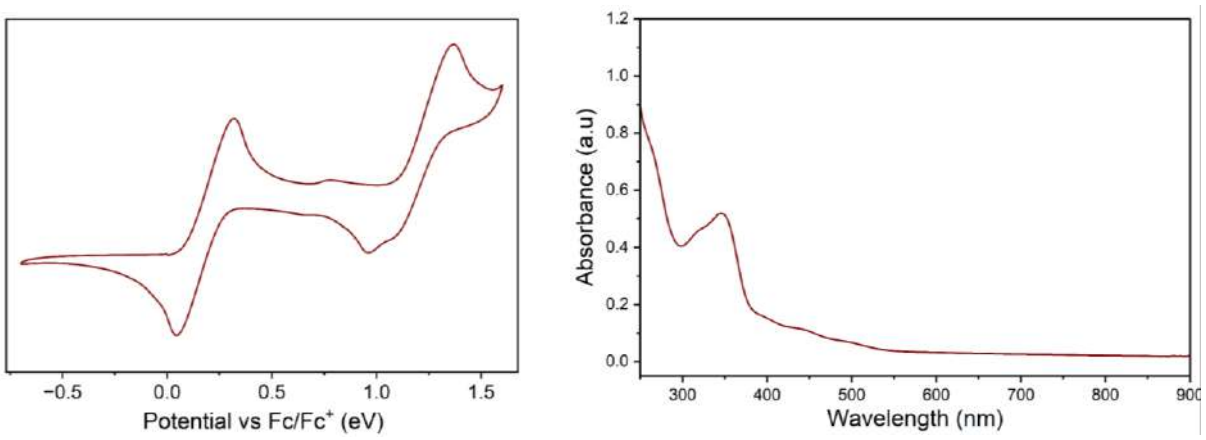


Figure S14. $^{13}C\{^{1}H\}$ NMR spectrum of **4** in $CDCl_3$.



(a) (b)

Figure S15. Cyclic voltammetry and UV-Vis spectrum of **4**.

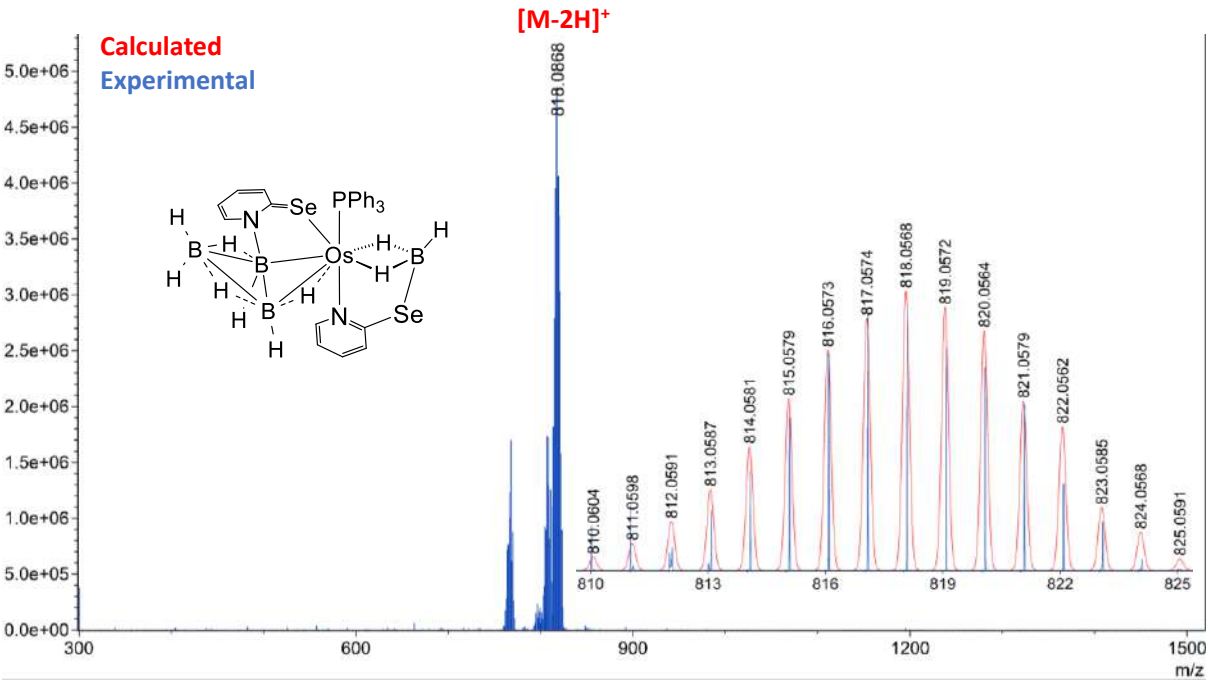


Figure S16. ESI-MS spectrum of **5**.

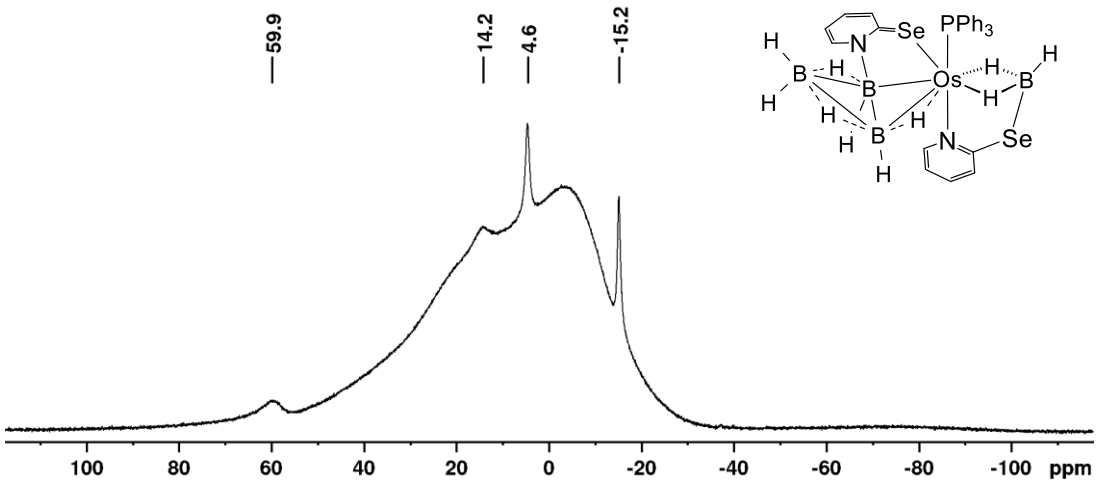


Figure S17. $^{11}B\{^{1}H\}$ NMR spectrum of **5** in C_6D_6.

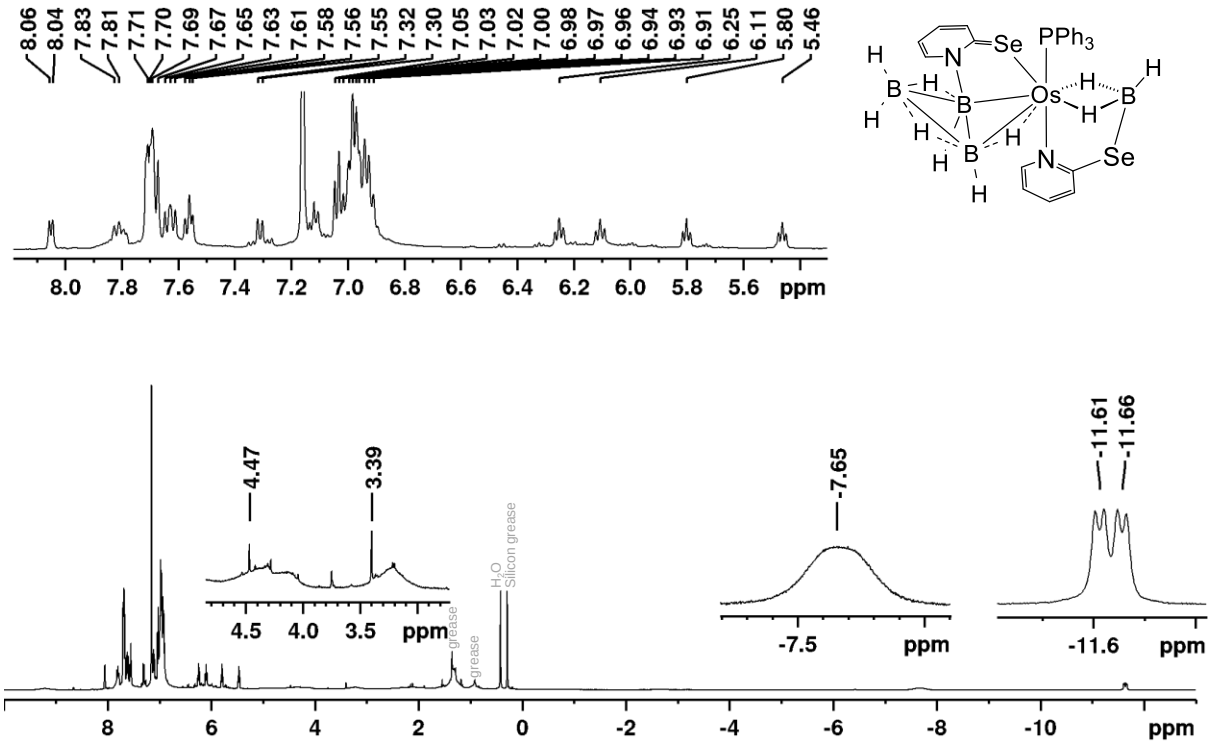


Figure S18. ^{1}H NMR spectrum of **5** in C_6D_6.

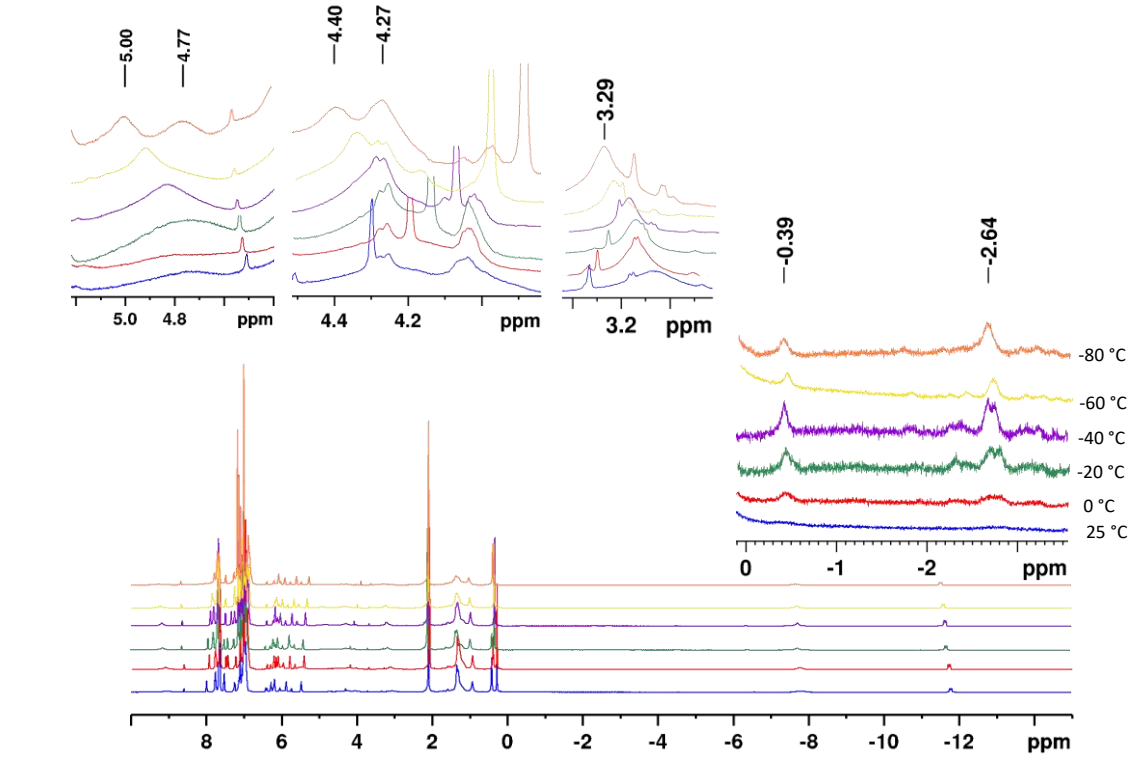


Figure S19. ^{1}H VT-NMR spectra of **5** in toluene-D_8.

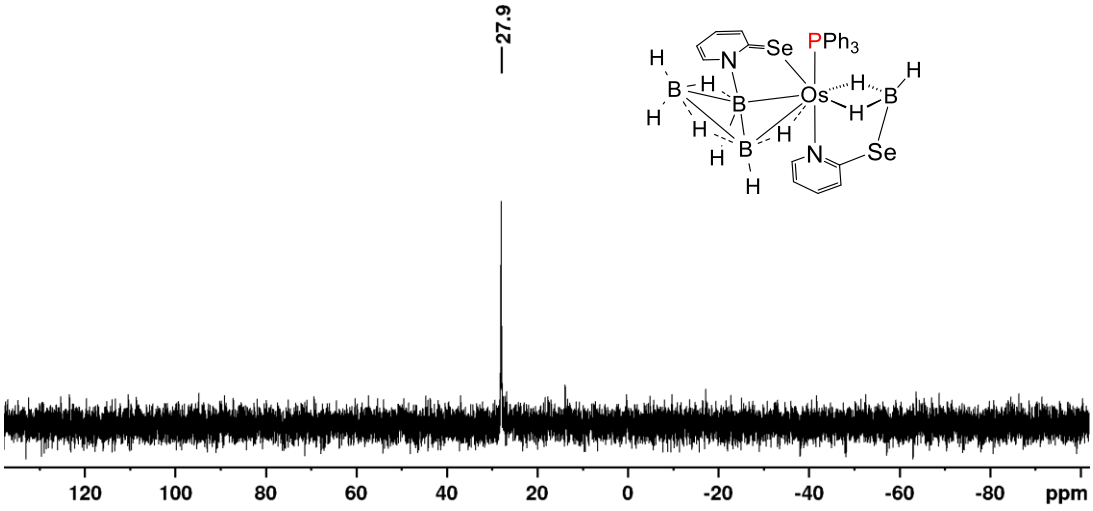


Figure S20. $^{31}P\{^{1}H\}$ NMR spectrum of **5** in C_6D_6.

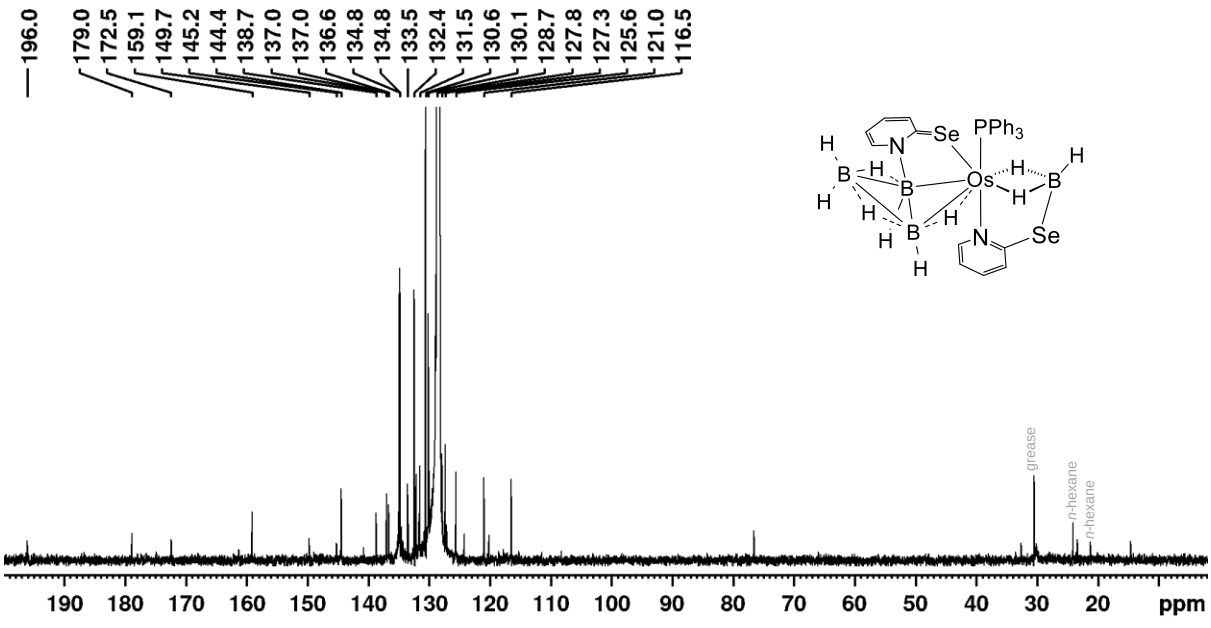


Figure S21. $^{13}C\{^{1}H\}$ NMR spectrum of **5** in C_6D_6.

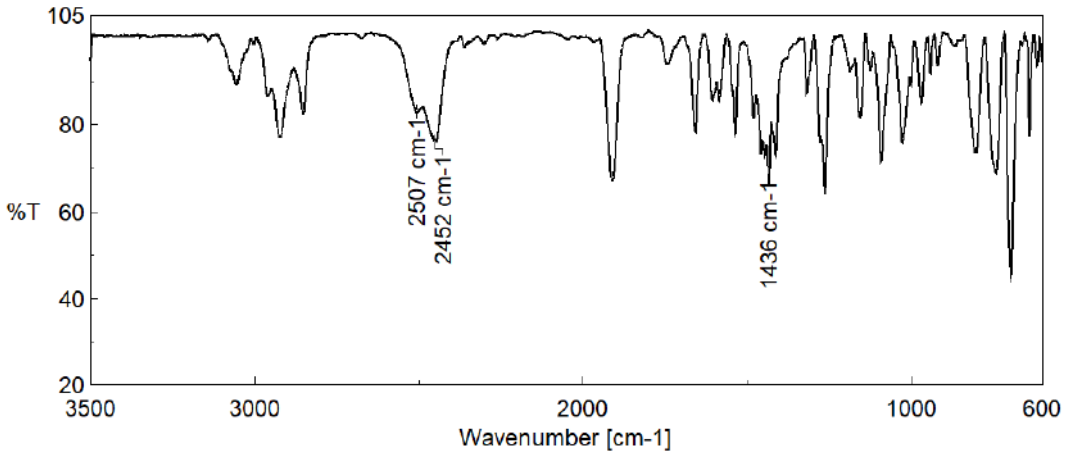


Figure S22. IR spectrum of **5**.

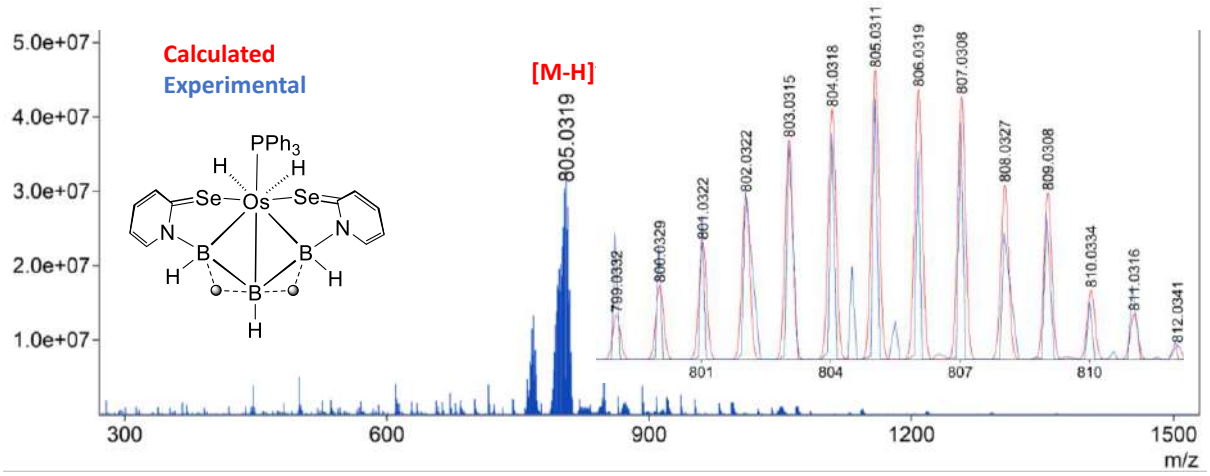


Figure S23. ESI-MS spectrum of **6**.

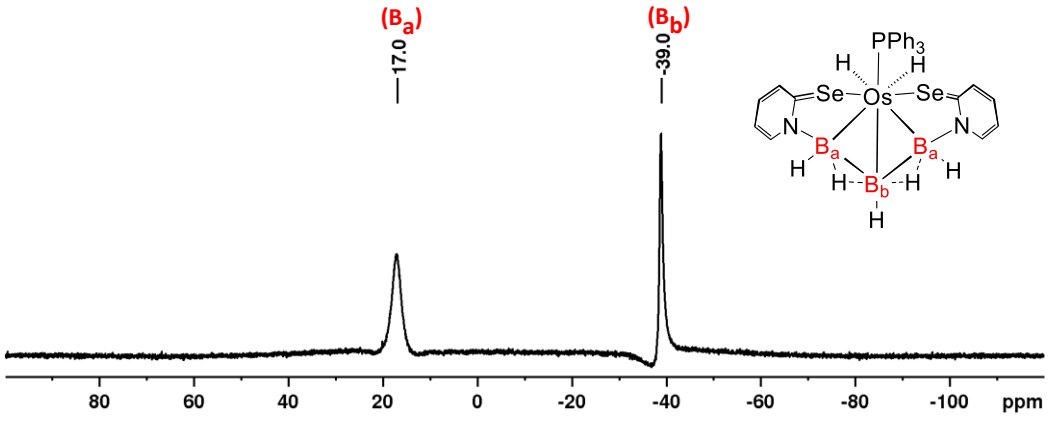


Figure S24. $^{11}B\{^{1}H\}$ NMR spectrum of **6** in $CDCl_3$.

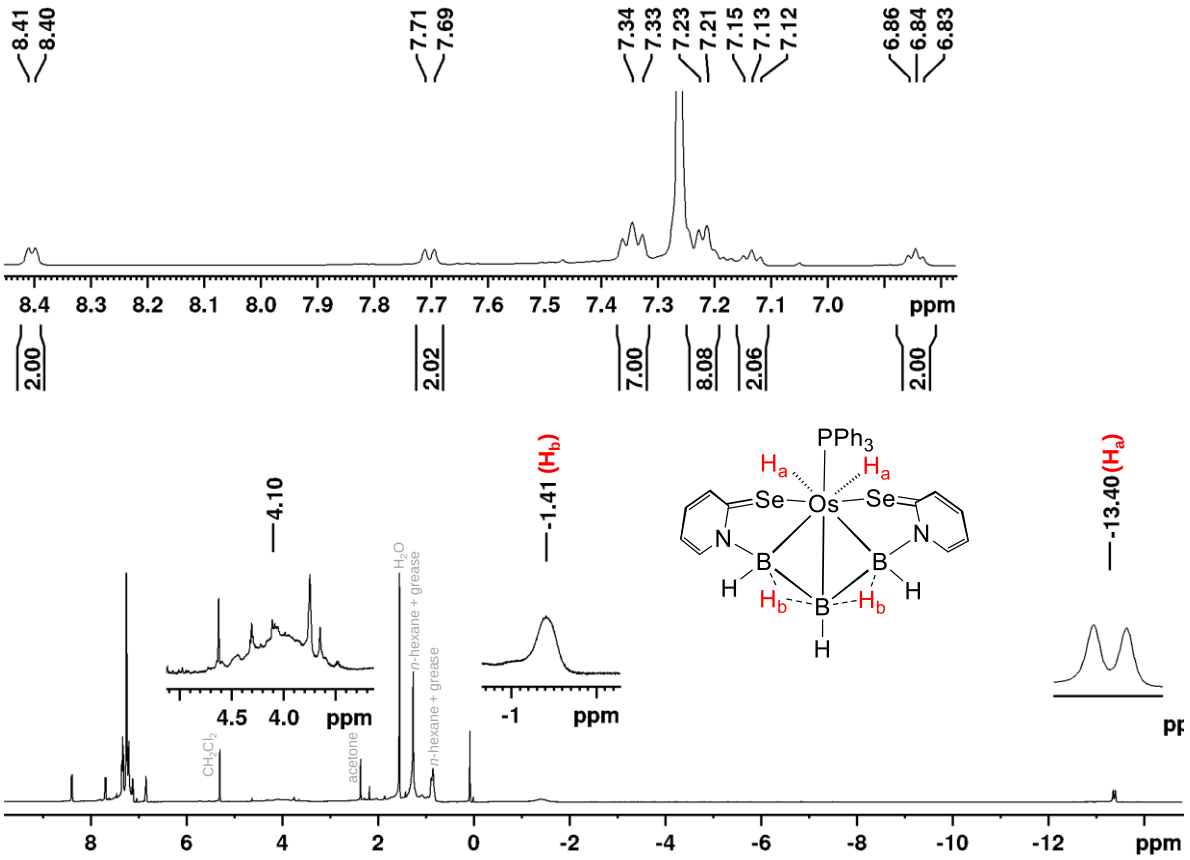


Figure S25. ^{1}H NMR spectrum of **6** in $CDCl_3$.

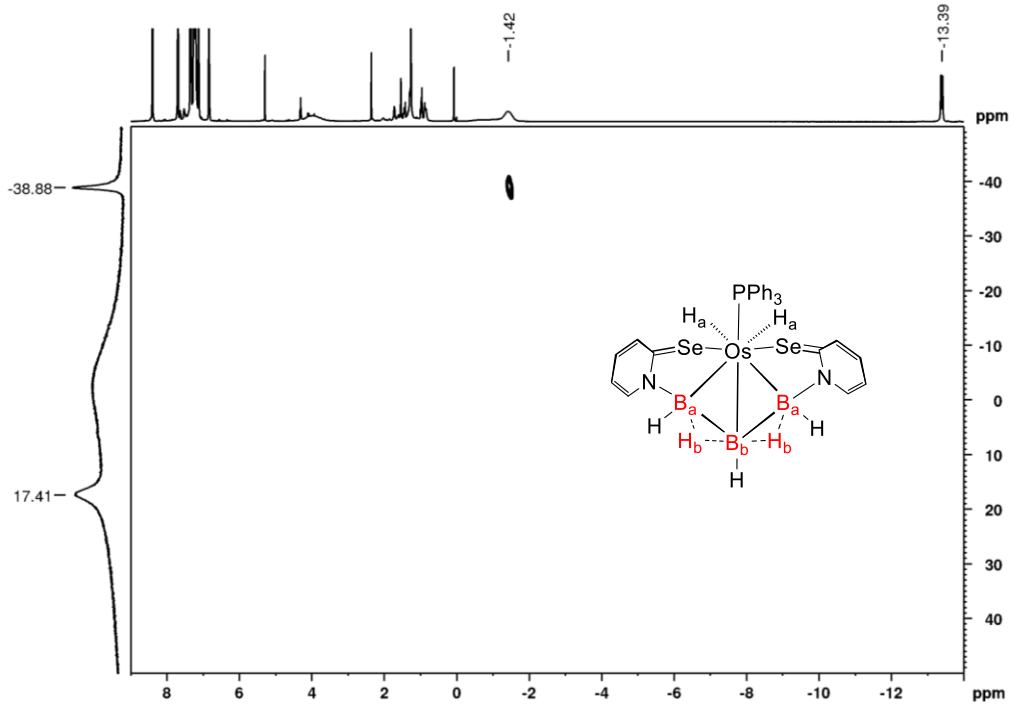


Figure S26. ^{1}H(^{11}B)/^{11}B(^{1}H) HSQC spectrum of **6** in $CDCl_3$.

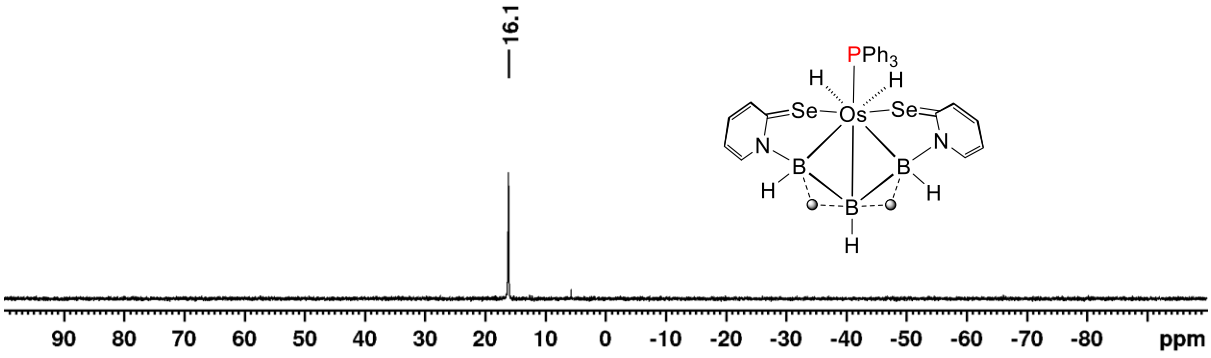


Figure S27. $^{31}P\{^{1}H\}$ NMR spectrum of **6** in $CDCl_3$.

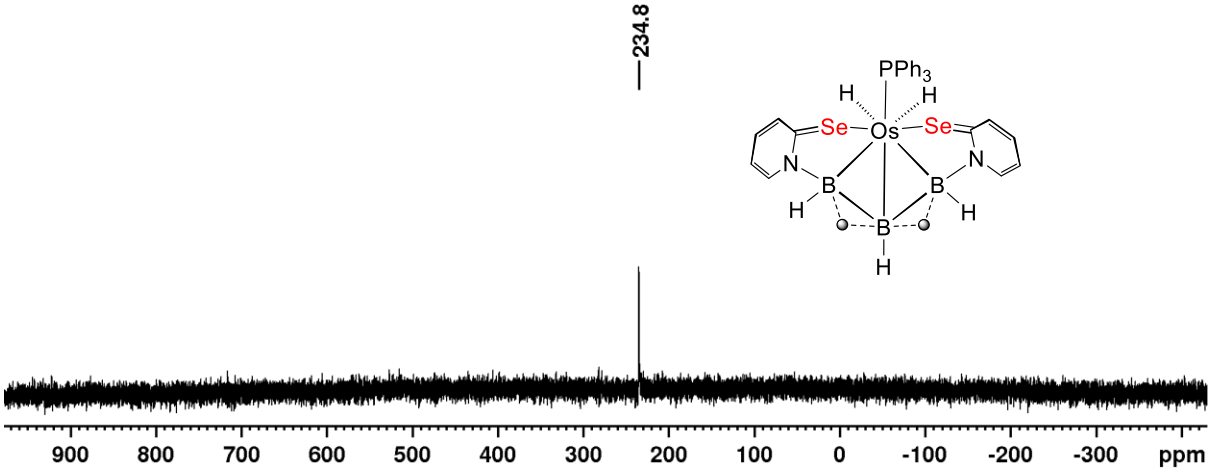


Figure S28. ^{77}Se NMR spectrum of **6** in $CDCl_3$.

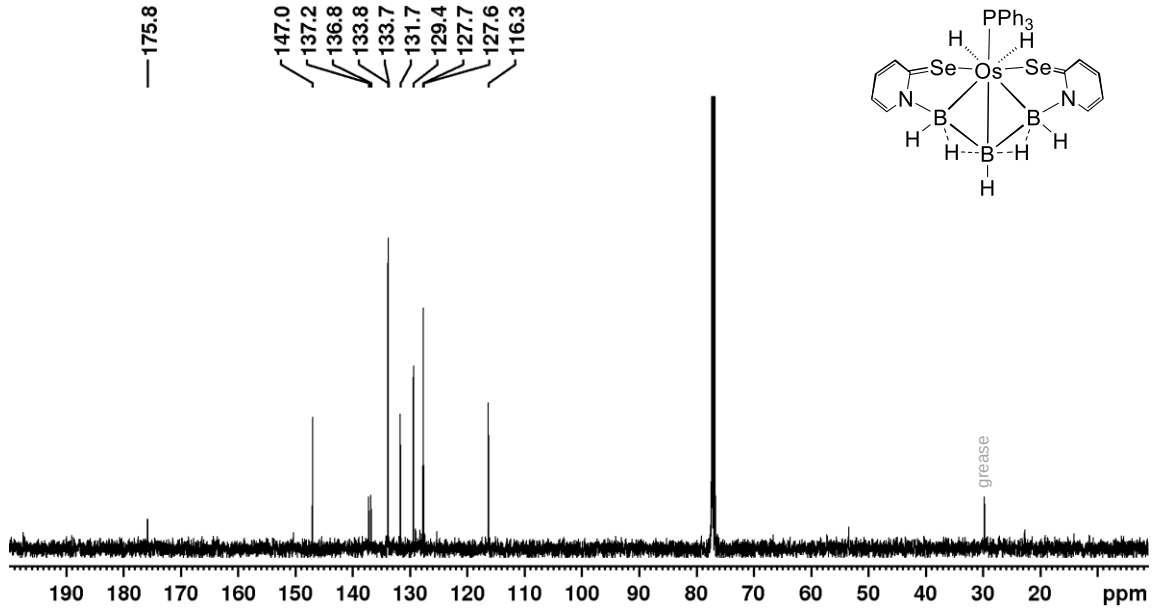


Figure S29. $^{13}C\{^{1}H\}$ NMR spectrum of **6** in $CDCl_3$.

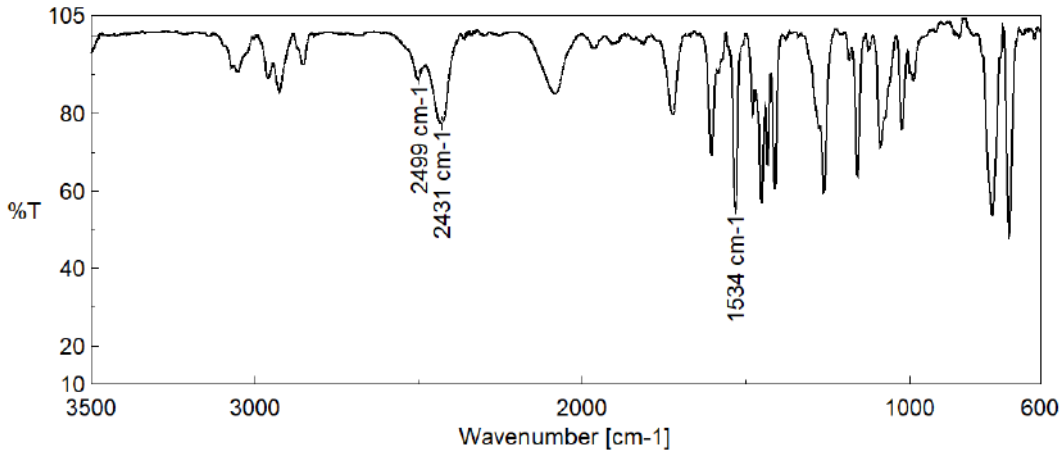


Figure S30. IR spectrum of **6**.

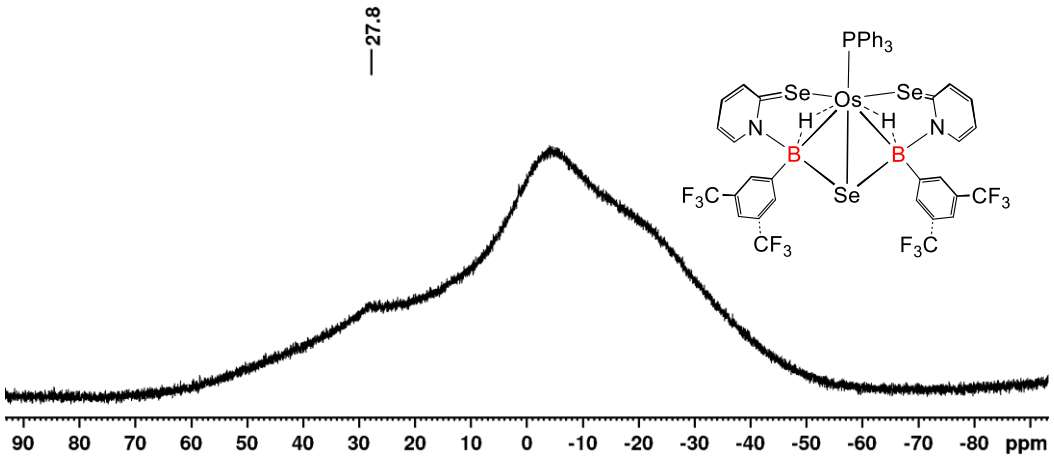


Figure S31. $^{11}B\{^{1}H\}$ NMR spectrum of **7** in C_6D_6.

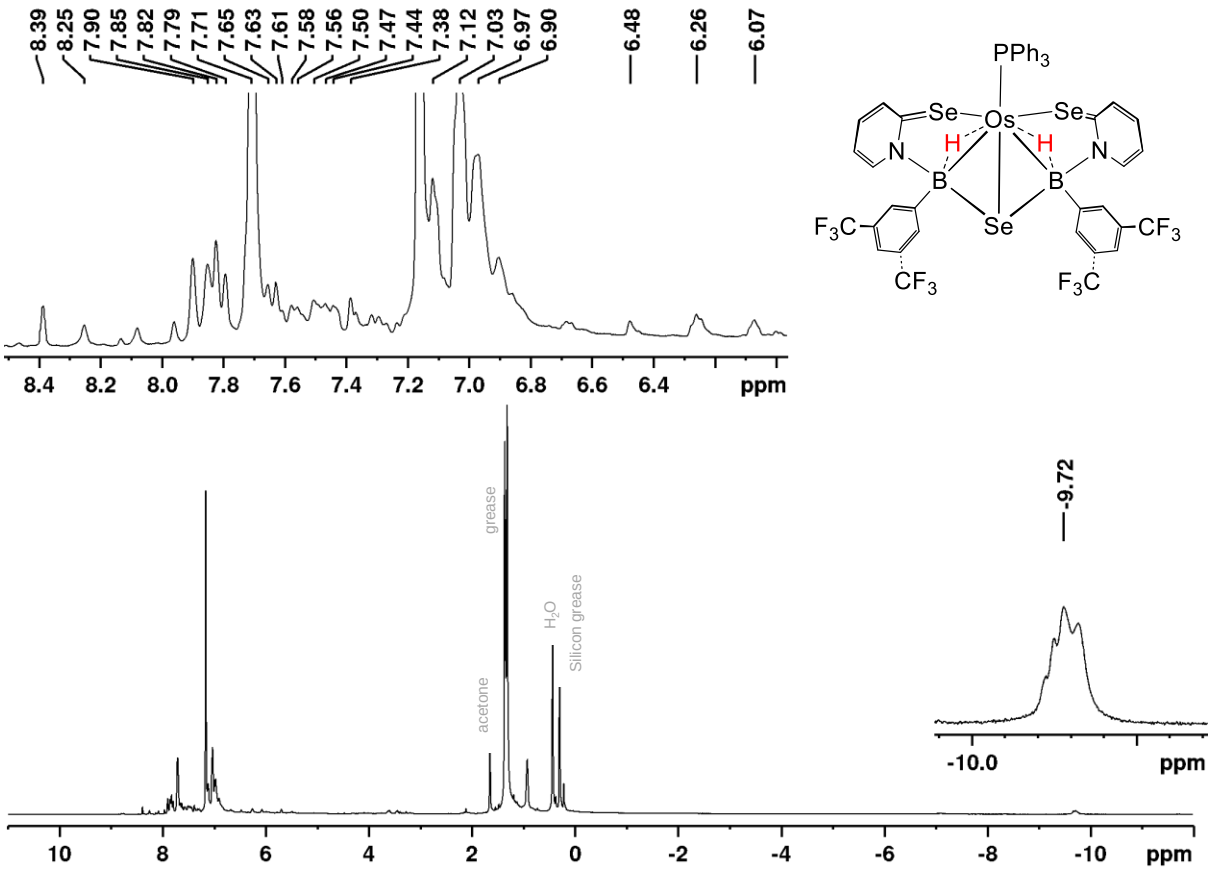


Figure S32. ^{1}H NMR spectrum of **7** in C_6D_6.

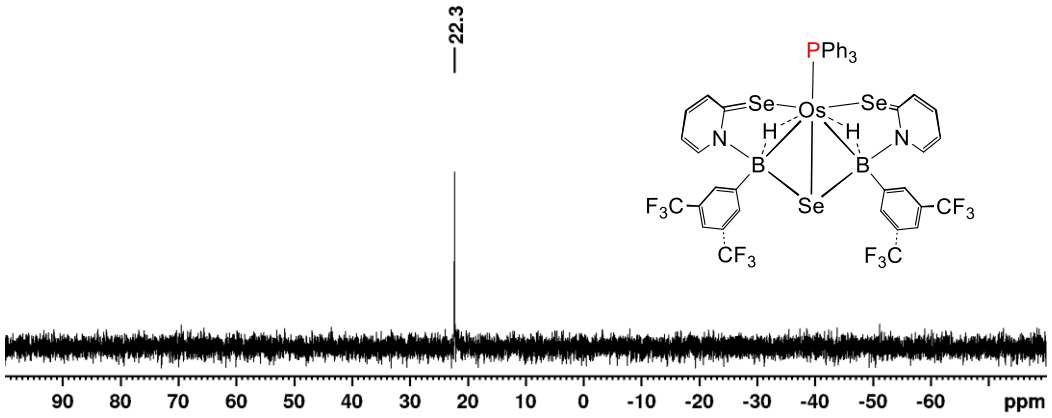


Figure S33. $^{31}P\{^{1}H\}$ NMR spectrum of **7** in C_6D_6.

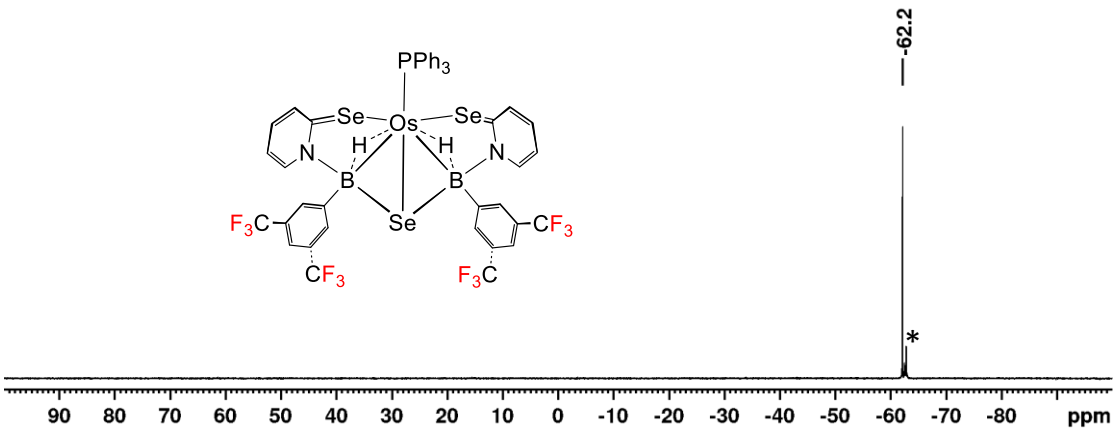


Figure S34. $^{19}F\{^{1}H\}$ NMR spectrum of **7** in C_6D_6. (* = inseparable impurity of BH_2R; R = $(CF_3)_2C_6H_3$)

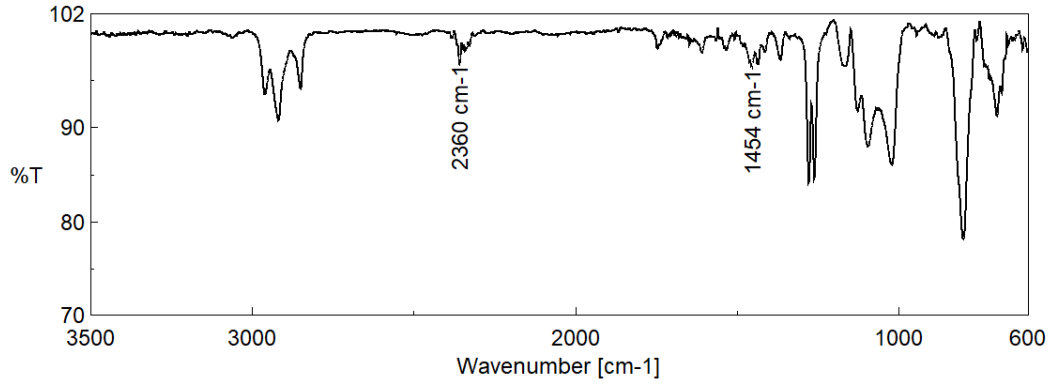


Figure S35. IR spectrum of **7**.

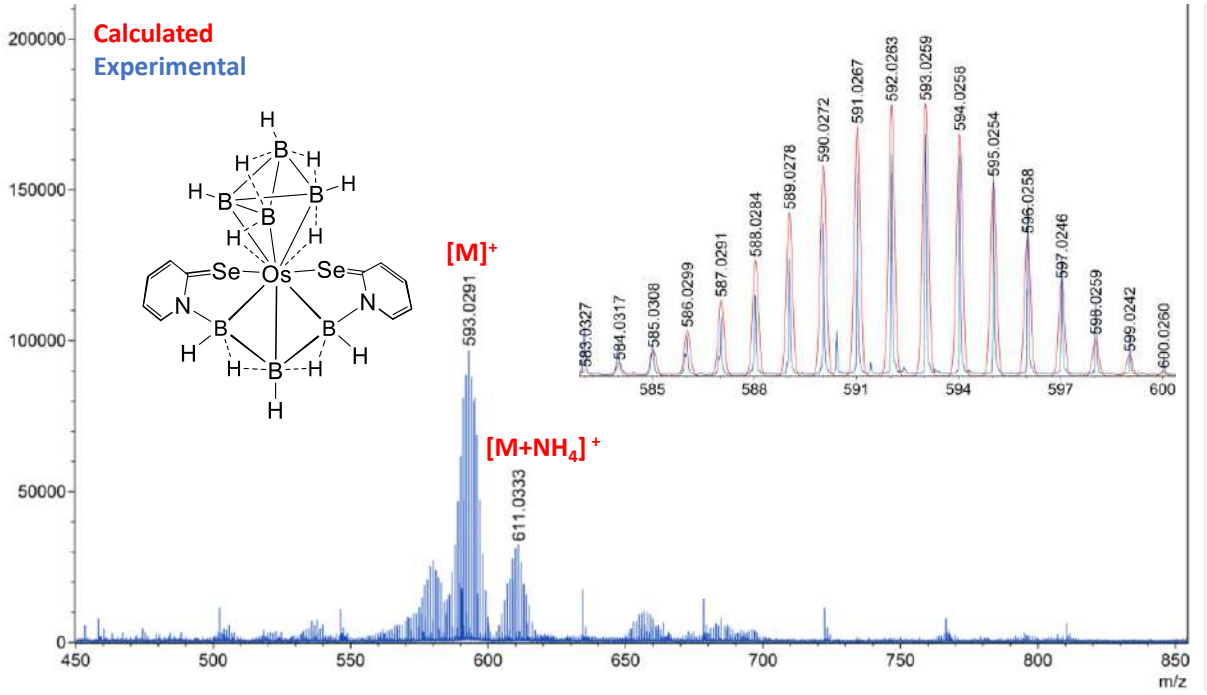


Figure S36. ESI-MS spectrum of **8**.

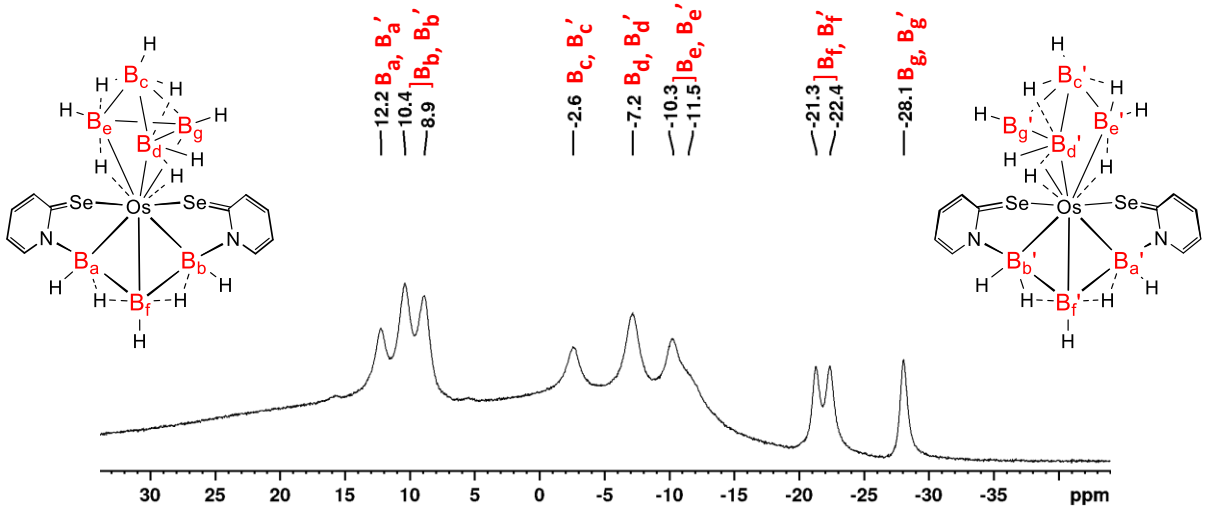


Figure S37. $^{11}B\{^{1}H\}$ NMR spectrum of **8** in $CDCl_3$.

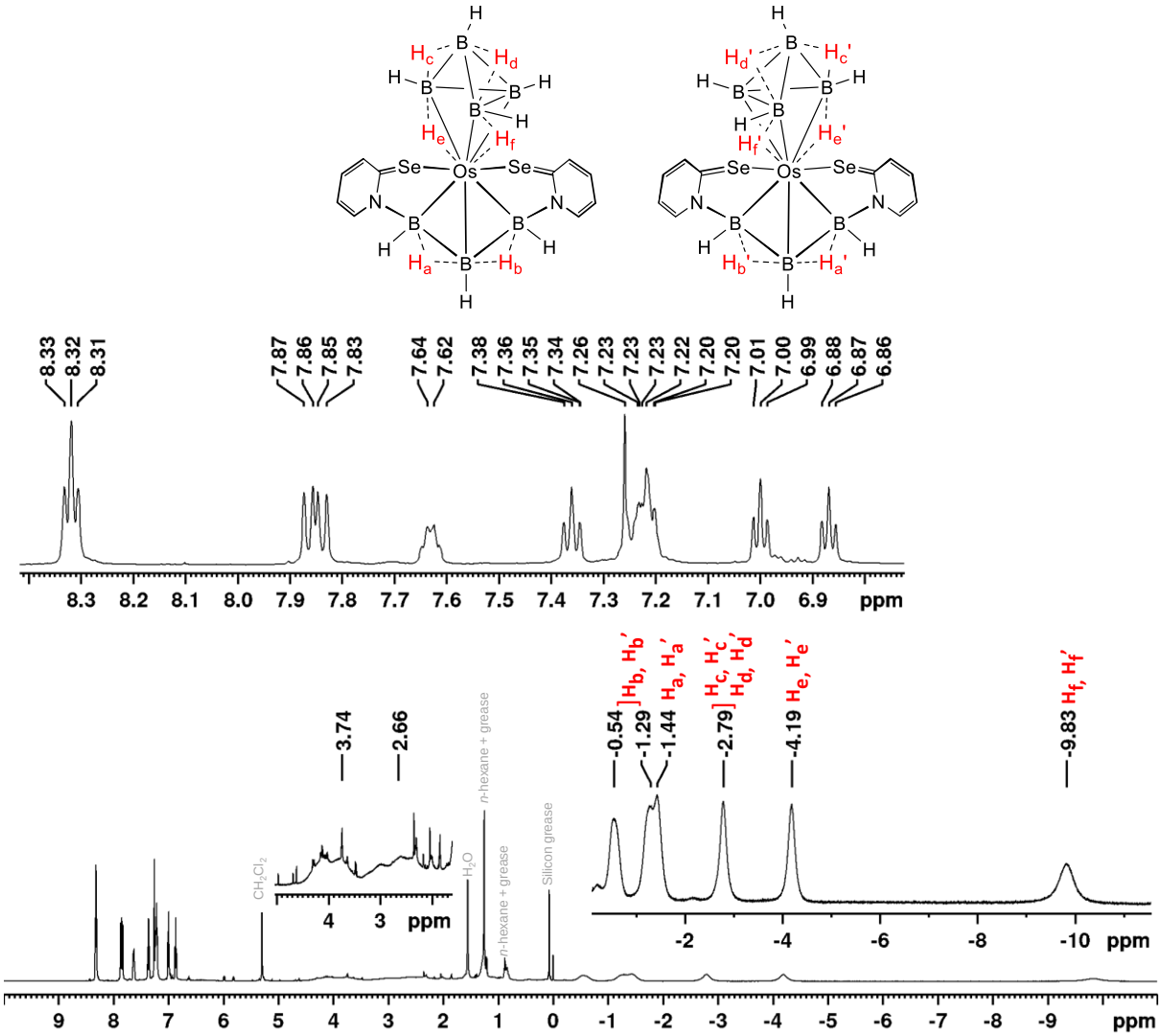


Figure S38. ^{1}H NMR spectrum of **8** in $CDCl_3$.

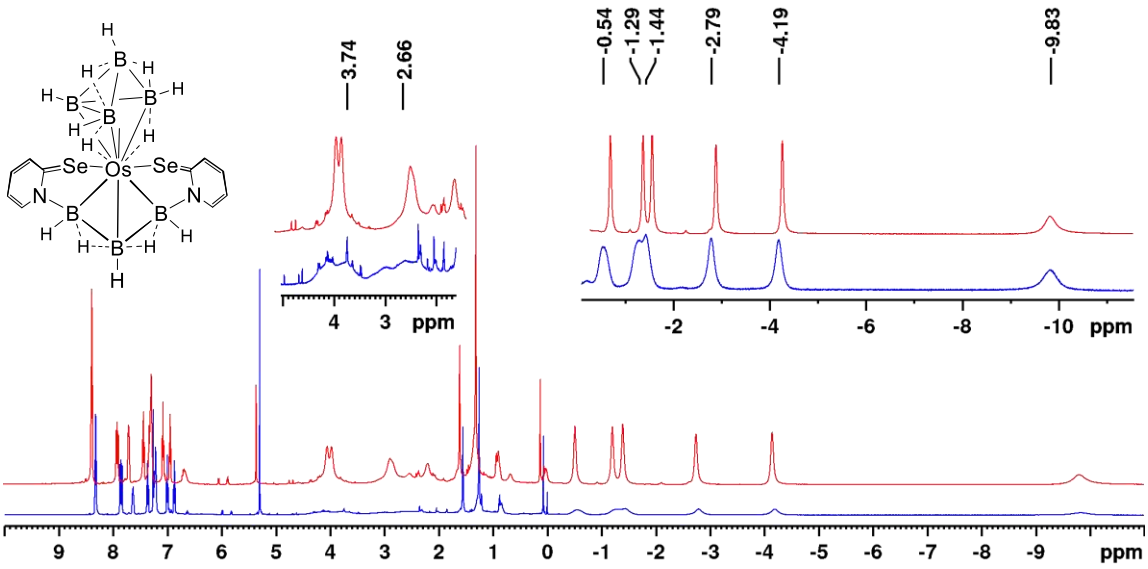


Figure S39. Stacked ^{1}H (blue) and $^{1}H\{^{11}B\}$ (red) NMR spectrum of **8** in $CDCl_3$.

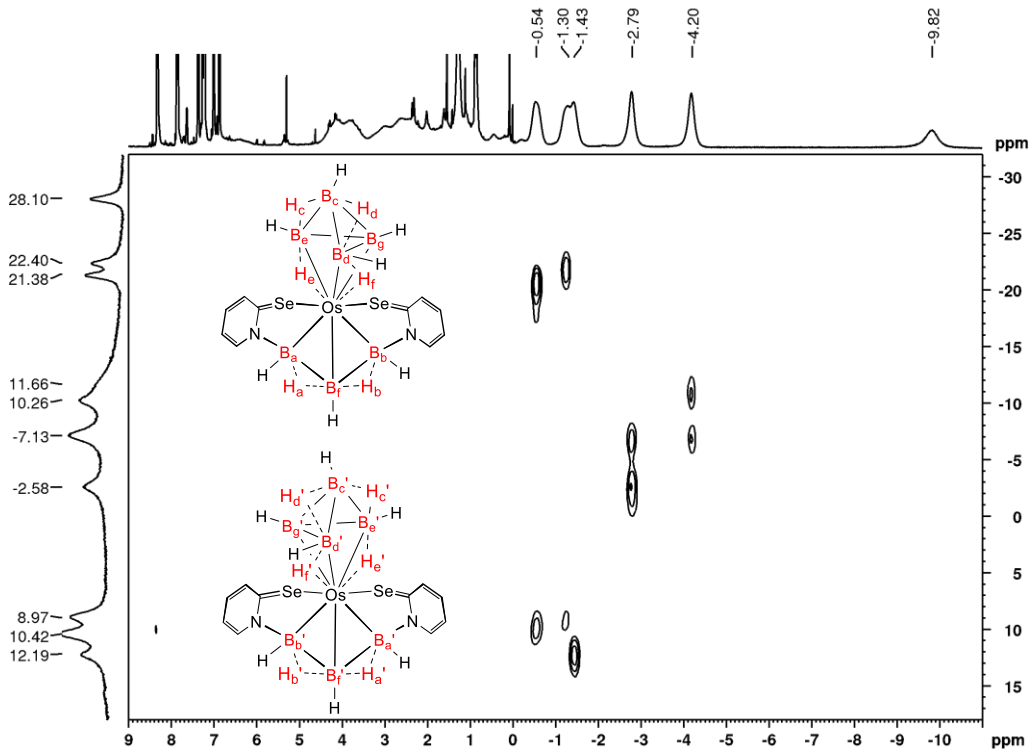


Figure S40. $^{1}H(^{11}B)/^{11}B(^{1}H)$ HSQC spectrum of **8** in $CDCl_3$.

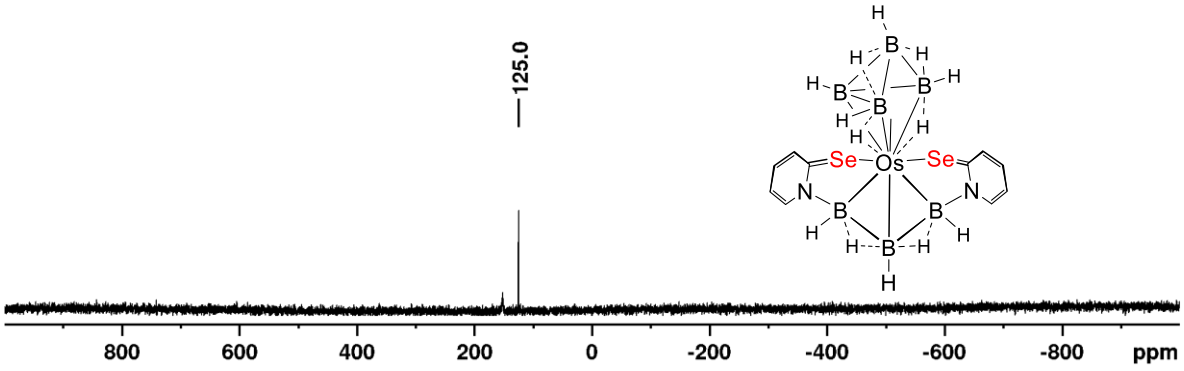


Figure S41. ^{77}Se NMR spectrum of **8** in $CDCl_3$.

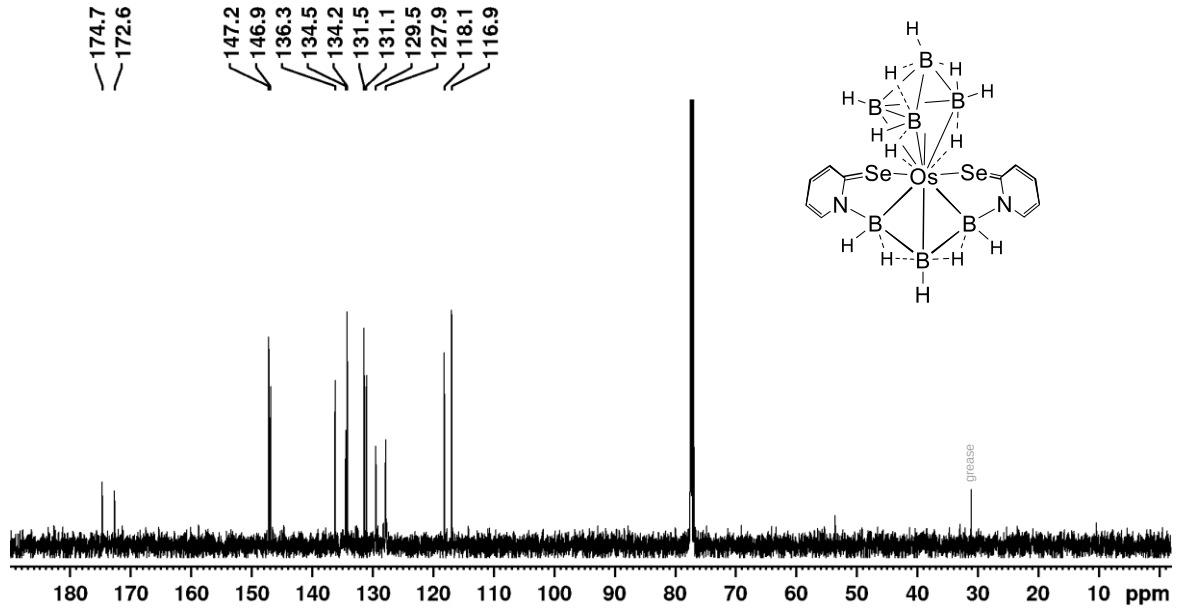


Figure S42. $^{13}C\{^1H\}$ NMR spectrum of **8** in $CDCl_3$.

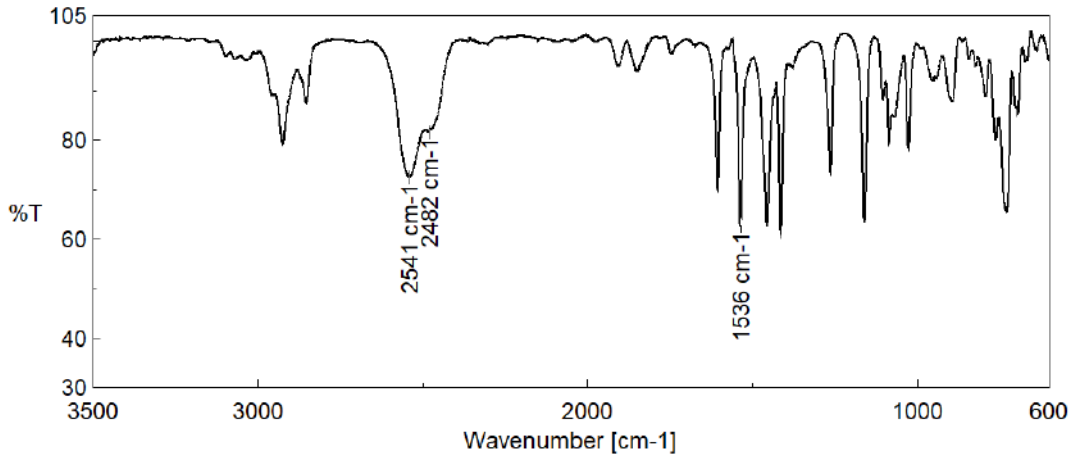


Figure S43. IR spectrum of **8**.

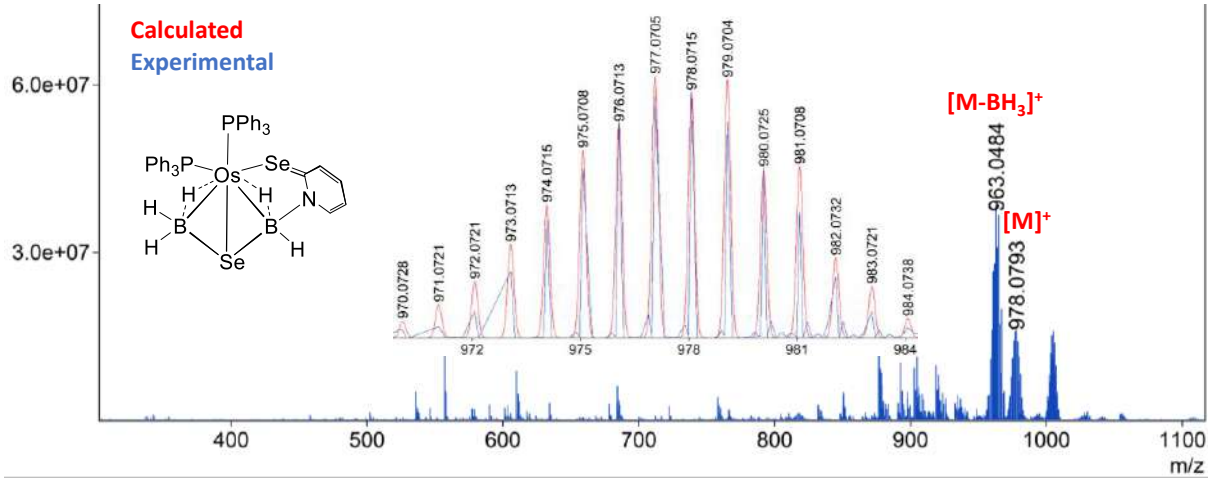


Figure S44. ESI-MS spectrum of **10**.

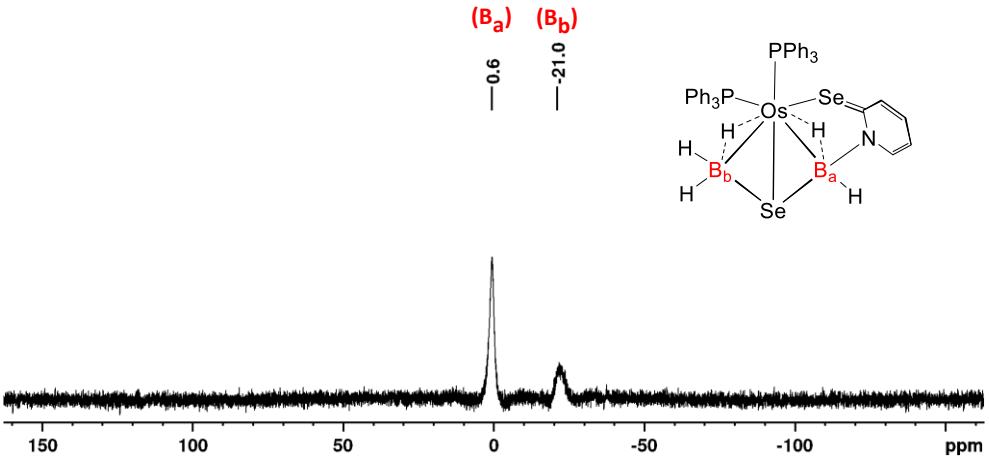


Figure S45. $^{11}B\{^{1}H\}$ NMR spectrum of **10** in C_6D_6.

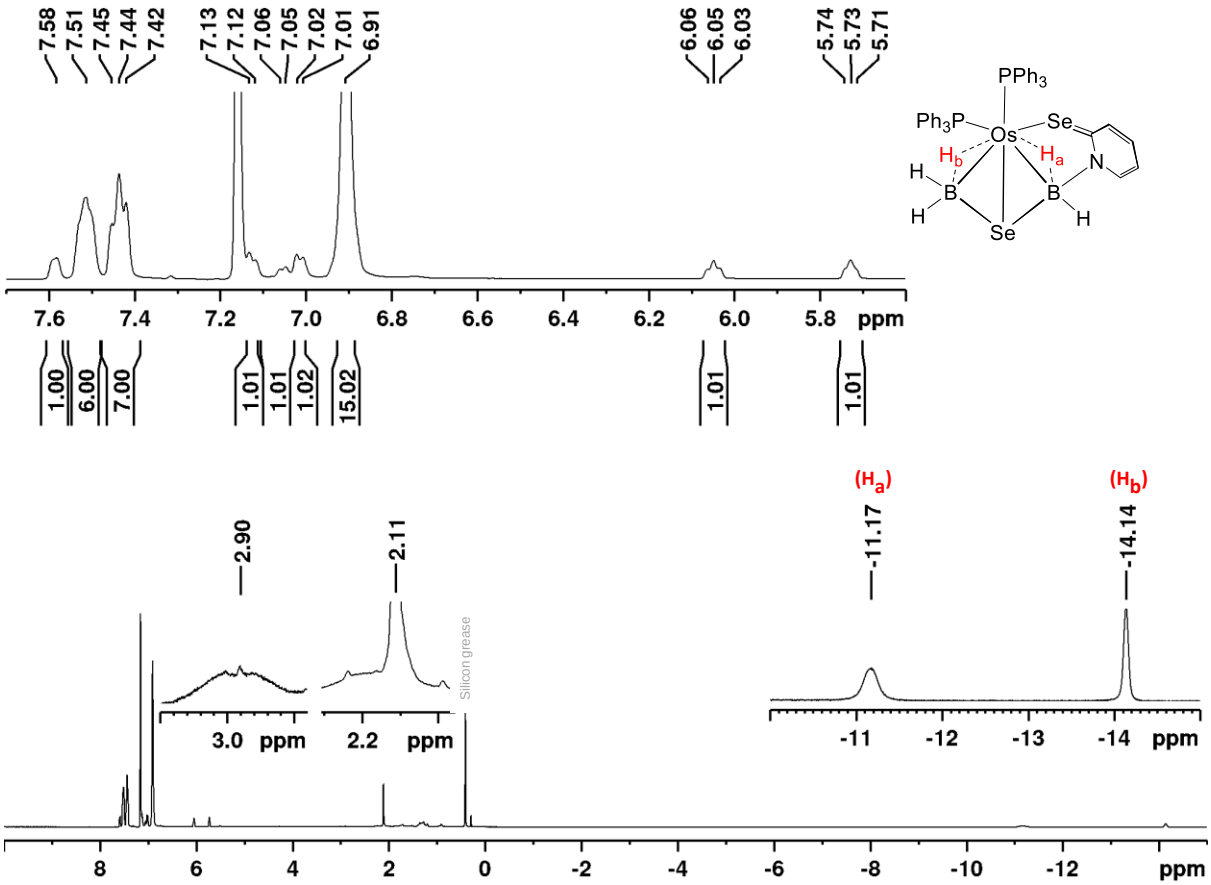


Figure S46. ^{1}H NMR spectrum of **10** in C_6D_6.

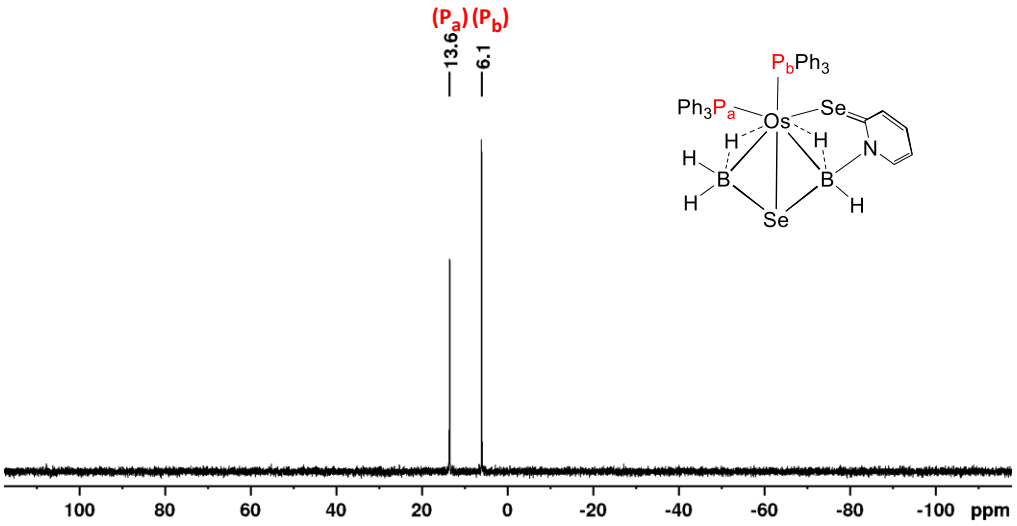


Figure S47. $^{31}P\{^{1}H\}$ NMR spectrum of **10** in C_6D_6.

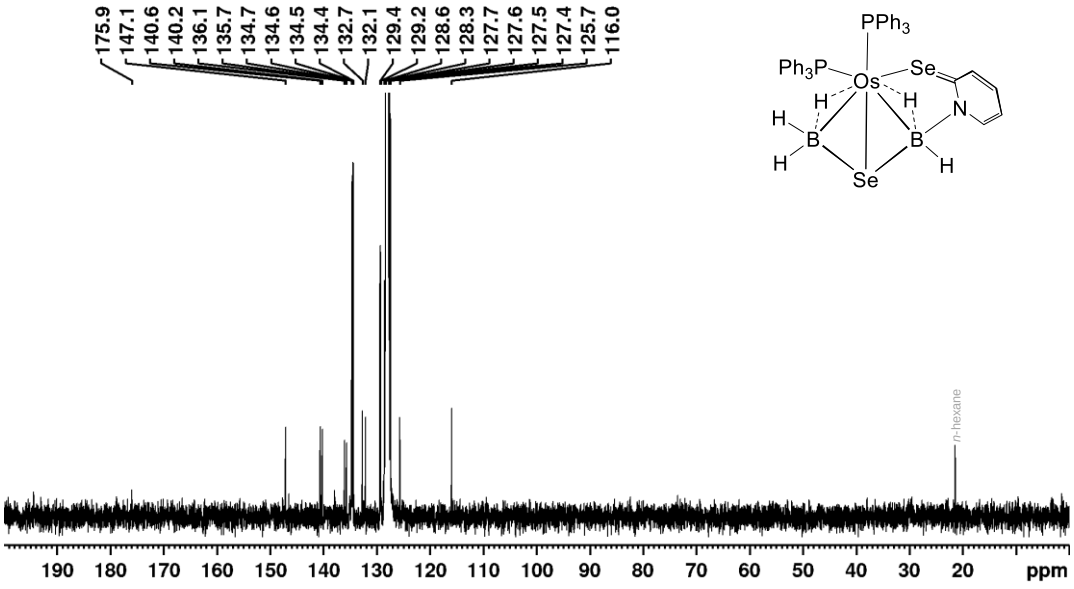


Figure S48. $^{13}C\{^{1}H\}$ NMR spectrum of **10** in C_6D_6.

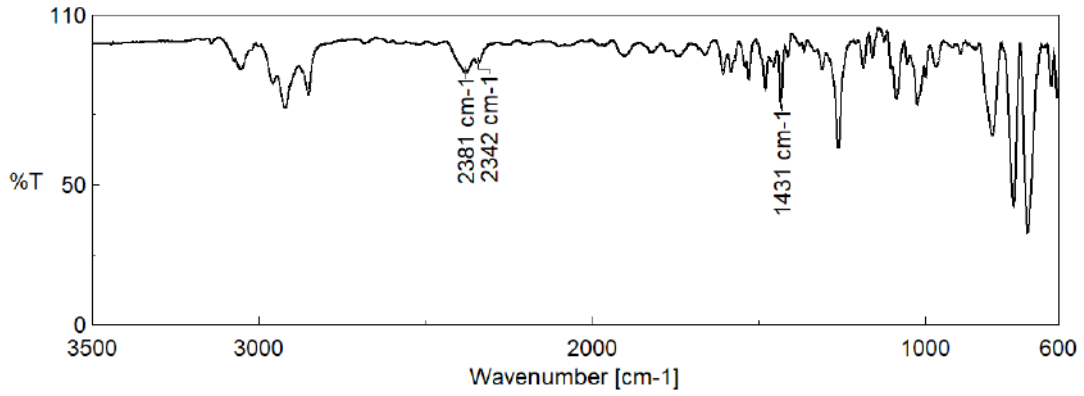


Figure S49. IR spectrum of **10**.

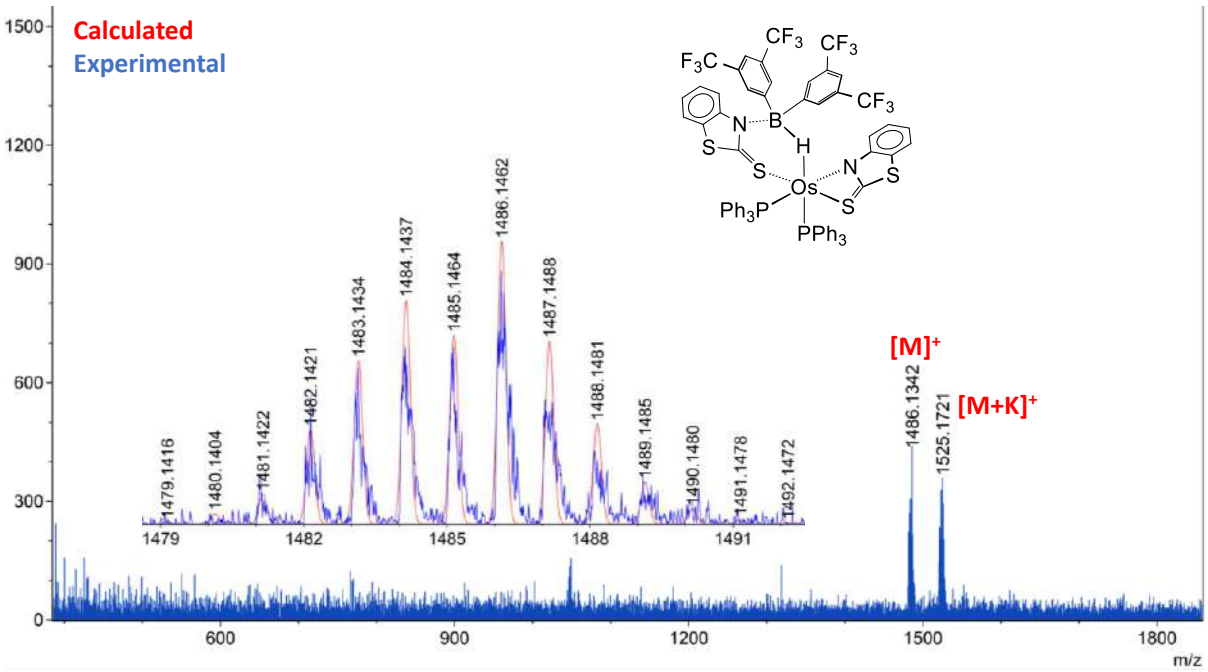


Figure S50. ESI-MS spectrum of **11**.

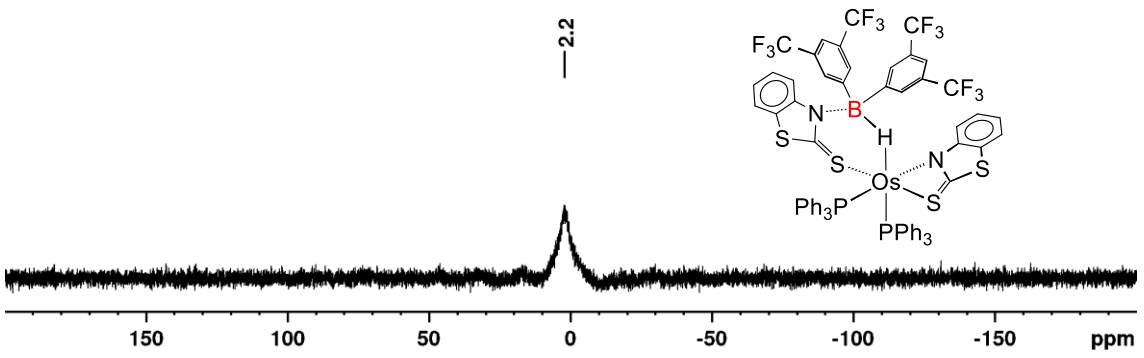


Figure S51. $^{11}B\{^{1}H\}$ NMR spectrum of **11** in C_6D_6.

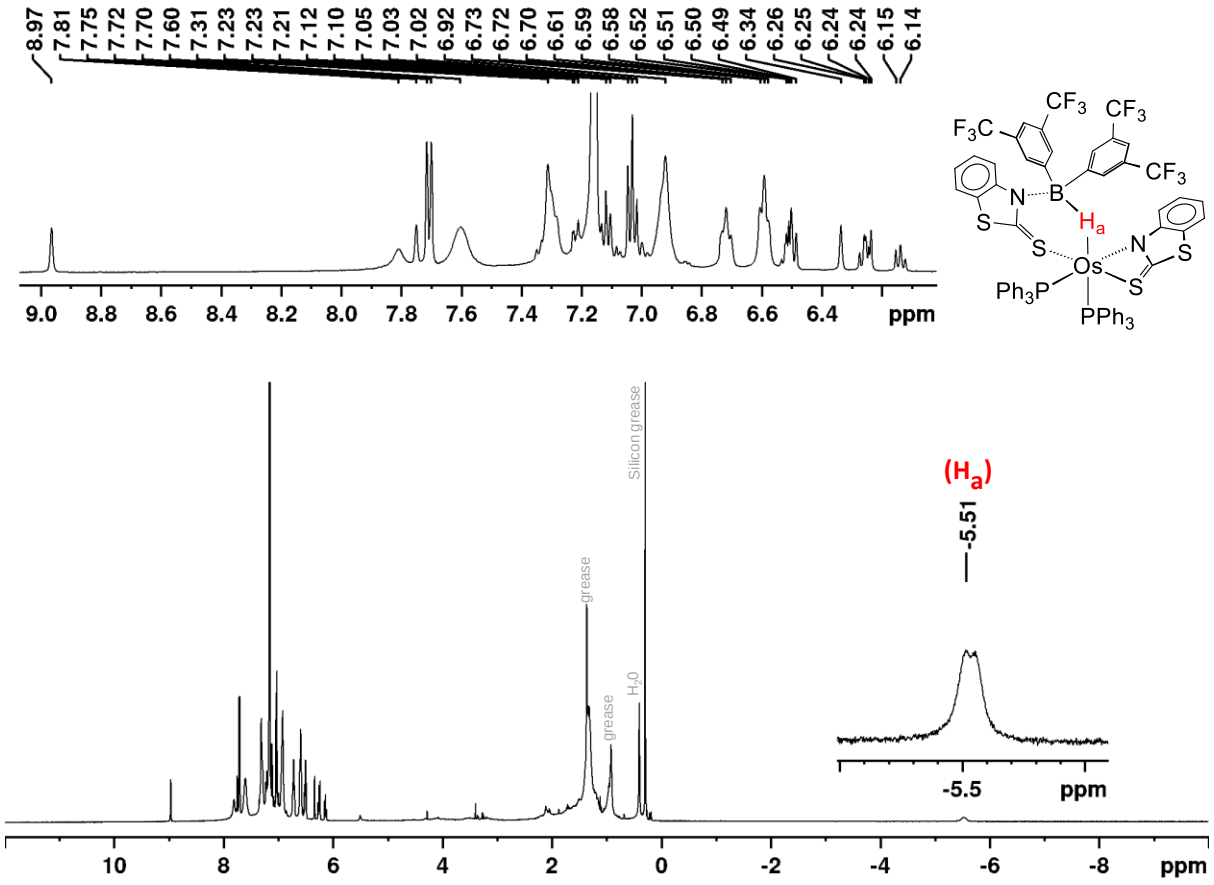


Figure S52. ^{1}H NMR spectrum of **11** in C_6D_6.

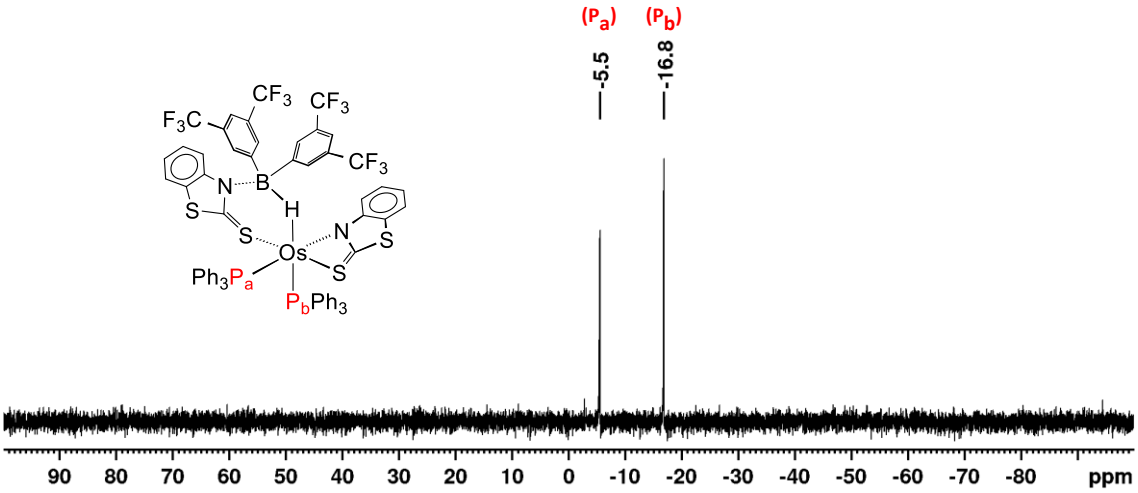


Figure S53. $^{31}P\{^{1}H\}$ NMR spectrum of **11** in C_6D_6.

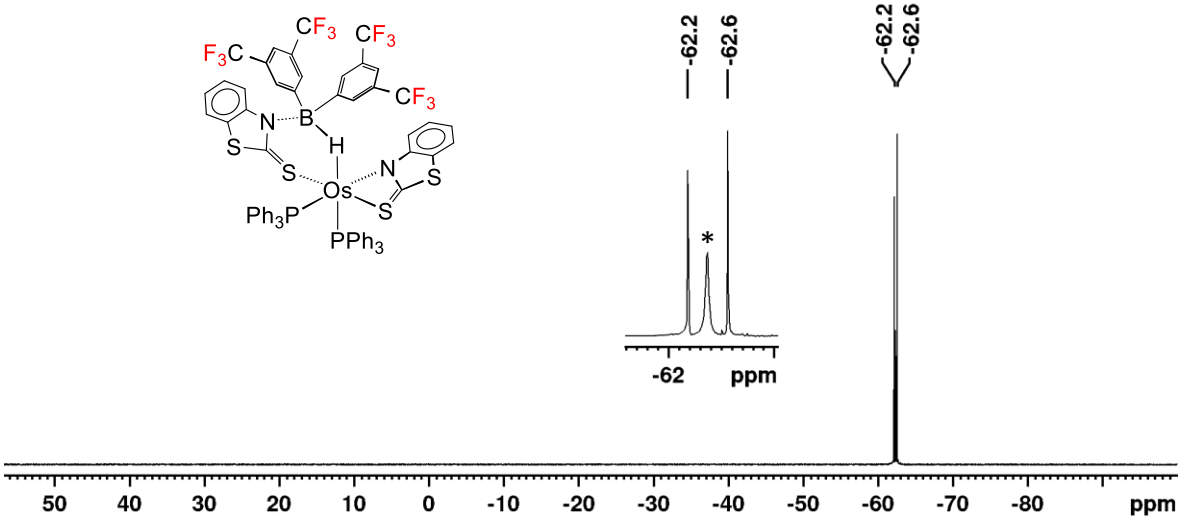


Figure S54. $^{19}F\{^{1}H\}$ NMR spectrum of **11** in C_6D_6.(* = inseparable impurity of BHR_2; R = $(CF_3)_2C_6H_3$)

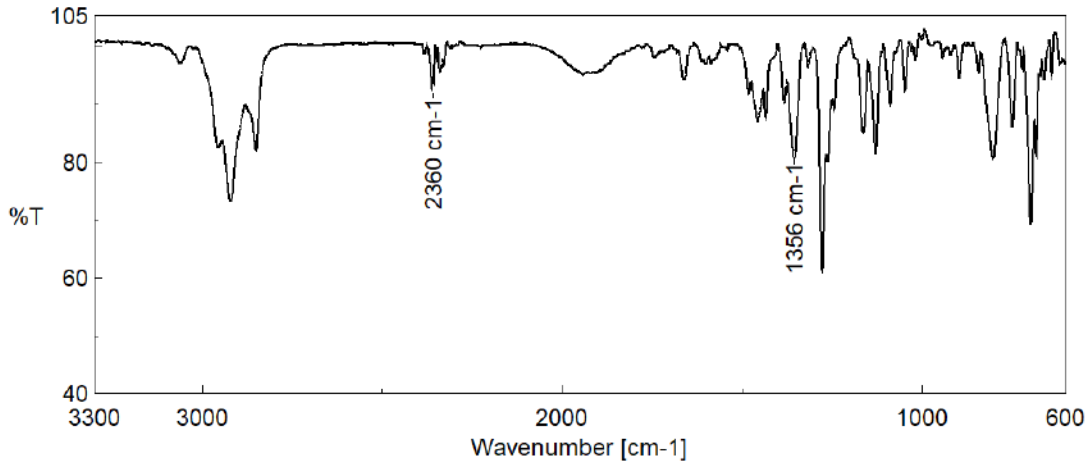


Figure S55. IR spectrum of **11**.

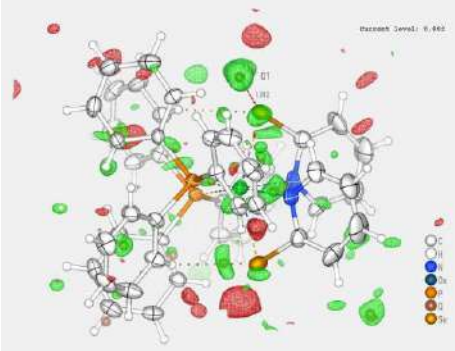
II.3 X-ray Analysis Details

Suitable X-ray quality crystals of complexes **1**, **2**, **4**, **5**, **6**, **7**, and **8** were obtained by slow diffusion of a hexane–CH_2Cl_2 solution at –4 °C, while crystals of complexes **10** and **11** were grown from hexane. Crystal data of **6** was obtained and integrated using a Bruker APEX-II CCD diffractometer with graphite monochromated Mo-Kα (λ = 0.71073 Å) radiation at 296(2) K. All other crystal data were obtained and integrated using a D8 VENTURE Bruker AXS diffractometer with PHOTON II detector with graphite monochromated Mo-Kα (λ = 0.71073 Å) radiation at 156(2) K for **1**, 200(2) K for **2**, 269(2) K for **4**, 150(2) K for **5**, 296(2) K for **6**, 150(2) K for **7**, 150(2) K for **8**, 301(2) K for **10**, 150(2) K for **11**. All the structures were solved using SHELXT-2018 and SHELXS-97[4] and refined using SHELXL−2018, SHELXL-2014 and SHELXL-2019.[7] Note that for compounds **6, 7** and **11** highly disordered lattice solvent molecules were removed using the SQUEEZE procedure in PLATON. Using Olex2 all the molecular structures were drawn.[8] Powder X-ray diffraction (XRD) patterns were recorded on a Bruker D8 Advanced Powder X-ray diffractometer using Cu Kα (*λ* = 1.5418 Å) radiation. The monophasic nature of each of the three compounds **1** and **2** was verified by comparing their powder XRD patterns with those simulated, using the MERCURY program,[9] on the basis of their single-crystal X-ray structures. Crystallographic data have been deposited with the Cambridge Crystallographic Data Center as supplementary publication no CCDC- 2481059 (**1**), 2481057 (**2**), 2466501 (**4**), 2481058 (**5**), 2466499 (**6**), 2466503 (**7**), 2466500 (**8**), 2472949 (**10**), 2472945 (**11**). These data can be obtained free of charge from The Cambridge Crystallographic Data Centre via www.ccdc.cam.ac.uk/data_request/cif.

Crystal data for **1***:* $C_{41}H_{34}Cl_2NOsP_2Se$, M_r= 942.69, monoclinic, space group $P2_1/n$, a = 9.5636(5) Å, b = 15.3610(8) Å, c = 25.2268(15) Å, α = 90 °, β = 100.93 °, γ = 90 °, V = 3638.8(3) Å^3, Z = 4, ρ_{calcd} = 1.721 g/cm^3, μ = 4.771 mm^{-1}, F(000) = 1844, R_1 = 0.0336, wR_2 = 0.0724, 7566 independent reflections [2θ ≤ 52.7 °] and 867 parameters.

Crystal data for **2***:*$C_{28}H_{23}ClN_2OsPSe_2$, M_r= 802.02 , monoclinic, space group $P2_1/n$, a = 12.1253(9) Å, b = 18.0329(10) Å, c = 12.3810(9) Å, α = 90 °, β = 91.515(3) °, γ = 90 °, V = 2706.2(3) Å^3, Z =4, ρ_{calcd} = 1.968 g/cm^3, μ = 7.580 mm^{-1}, F(000) = 1524, R_1 = 0.0228, wR_2 = 0.0517, 6722 independent reflections [2θ ≤ 56.6 °] and 316 parameters.

Crystal data for **4***:* $C_{46}H_{38}N_2OsP_2Se_2$, M_r= 1028.84, monoclinic, space group $P2_1/c$, a= 19.9615(18) Å, b = 17.6882(17) Å, c= 11.2486(11) Å, α = 90 °, β = 95.367(3) °, γ = 90 °, V= 3954.3(6) Å^3, Z= 4, ρ_{calcd} = 1.728 g/cm^3, μ = 5.182 mm^{-1}, F(000) = 2008, R_1 = 0.0729, wR_2 = 0.1605, 105792 independent reflections [2θ ≤ 52.88 °] and 480 parameters.



Note: The complex **4** was having non-merohedral twinning. The twin matrix is: (1 0 0.332; 0 -1 0; 0 0 -1) and program PLATON was used to generate the twin matrix and make HKLF5 format data. The

heaviest peak at 1.38 angstrom from Se1 (as shown in above image) measured 7.9 e/Å^3 and gave an A-level alert in the checkcif. After the twinning was resolved and HKLF5 data generated, the difference peaks have considerably reduced in height. But such techniques won't ideally clean the effects of non-merohedral twinning. Some effects of insufficient twin separation are still shown as elevated difference peaks.

Crystal data for **5***:* $C_{28}H_{33}B_4N_2OsPSe_2$, M_r= 819.89, orthorhombic, space group Pna21, a = 15.3411(5) Å, b = 9.6807(3) Å, c = 20.0705(5) Å, α = 90 °, β = 90 °, γ = 90 °, V = 2980.72(15) Å^3, Z = 4, ρ_{calcd} = 1.827 g/cm^3, μ = 6.795 mm^{-1}, F(000) =1576, R_1 = 0.0218, wR_2 = 0.0449, 5802 independent reflections [2θ ≤ 52.00 °] and 373 parameters.

Crystal data for **6***:* $C_{28}H_{28}B_3N_2OsPSe_2$,0.5[$CH_2Cl_2$], M_r= 846.604, triclinic, space group P-1, a = 11.1170(3) Å, b = 15.9224(5) Å, c = 17.8651(5) Å, α = 78.0360(1) °, β = 81.905(1) °, γ = 84.906 (1) °, V = 3056.97(15) Å^3, Z = 4, ρ_{calcd} = 1.839 g/cm^3, μ = 6.713 mm^{-1}, F(000) = 1618.9 , R_1 = 0.0282, wR_2 = 0.0712, 10760 independent reflections [2θ ≤ 50.00 °] and 707 parameters.

Crystal data for **7***:* $C_{44}H_{31}B_2F_{12}N_2OsPSe_3$, C_7H_8, M_r= 1387.51, monoclinic, space group $P2_1/n$, a = 10.8616(7) Å, b = 30.8022(19) Å, c = 14.9297(10) Å, α = 90 °, β = 97.324(2) °, γ = 90 °, V = 4954.1(6) Å^3, Z =4, ρ_{calcd} = 1.860 g/cm^3, μ = 4.895 mm^{-1}, F(000) = 2680.0, R_1 = 0.0506, wR_2 = 0. 0.1149, 12305 independent reflections [2θ ≤ 56.58 °] and 779 parameters.

Crystal data for **8***:* $C_{10}H_{21}B_7N_2OsSe_2$, M_r= 593.08 , monoclinic, space group $P2_1/c$, a = 12.7281(8) Å, b = 9.4036(6) Å, c = 15.1331(9) Å, α = 90 °, β = 101.480(2) °, γ = 90 °, V = 1775.04(19) Å^3, Z =4, ρ_{calcd} = 2.219 g/cm^3, μ =11.275 mm^{-1}, F(000) = 1096, R_1= 0.0136, wR_2 = 0.0333, 3628 independent reflections [2θ ≤ 52.7780 °] and 247 parameters.

Crystal data for **10***:* $C_{41}H_{39}B_2NOsP_2Se_2$,$C_7H_8$ M_r= 1069.58, monoclinic, space group $P2_1/n$, a = 11.0801(15) Å, b = 11.7542(12) Å, c = 34.230(4) Å, α = 90 °, β = 90.696(5) °, γ = 90 °, V = 4457.7(9) Å^3, Z =4, ρ_{calcd} = 1.594 g/cm^3, μ = 4.599 mm^{-1}, F(000) = 2104, R_1 = 0.0308, wR_2 = 0.0785, 9111 independent reflections [2θ ≤ 52.7760 °] and 512 parameters.

Crystal data for **11***:* $C_{66}H_{45}BF_{12}N_2OsP_2S_4$,0.5[$C_7H_8$], M_r= 1531.29, triclinic, space group P-1, a = 20.9226(9) Å, b = 24.4708(12) Å, c = 24.7349(12) Å, α = 73.662(2) °, β = 84.215(2) °, γ = 87.098(2) °, V = 12087.5(10) Å^3, Z =6, ρ_{calcd} = 1.262 g/cm^3, μ = 1.789 mm^{-1}, F(000) = 4578, R_1 = 0.0622, wR_2 = 0.1864, 42528 independent reflections [2θ ≤ 50.00 °] and 2745 parameters.

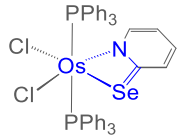
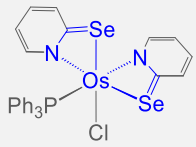
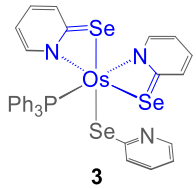
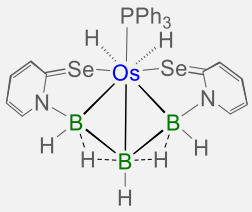
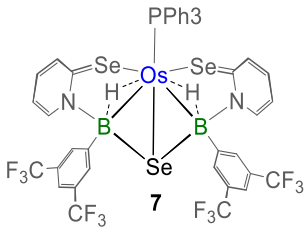
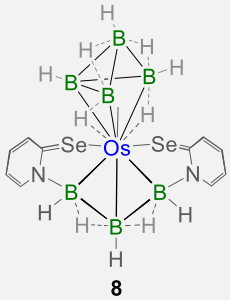
III Computational Details

All molecules were fully optimized with the Gaussian 16 program[10] using the gradient-corrected Becke–Lee–Yang–Parr (B3LYP) functional[11] in conjunction with the 6-31g(d)-LANL2DZ basis set from the EMSL Basis Set Exchange Library.[12] The model complexes were fully optimized starting from X-ray coordinates in the gaseous state (no solvent effect). Frequency calculations were carried out for the verification of the nature of the stationary state and to confirm the absence of any imaginary frequency which eventually confirmed the minima on the potential energy hypersurface for all structures. Furthermore, the gauge including atomic orbital (GIAO)[13] method was employed to compute the ^{11}B chemical shifts. Wiberg bond indices (WBI)[14] was generated from natural bond orbital analysis (NBO).[15] All the optimized geometries and orbital pictures were drawn by Chemcraft[16] visualization programs. Laplacian electronic distribution plots and Two-dimensional electron density and were generated using the Multiwfn package.[17]

Table S2. Selected geometrical parameters and Wiberg Bond Indices (WBI) of **1, 2, 3, 6, 7, 8, 10** and **11**.

1				**2**			
	Expt.	Cal.	WBI		Expt.	Cal.	WBI
Os1-N1	2.046(18)	2.118	0.559	Os1-N1	2.108(3)	2.105	0.593
Os1-Se1	2.5523(19)	2.663	0.781	Os1-N2	2.098(3)	2.135	0.531
Os1-Cl1	2.374(4)	2.404	0.820	Os1-Se1	2.4515(4)	2.533	0.943
Os1-Cl2	2.381(4)	2.428	0.788	Os1-Se2	2.5355(4)	2.642	0.804
Os1-P1	2.387(4)	2.493	0.699	Os1-Cl1	2.3681(9)	2.474	0.798
Os1-P2	2.385(5)	2.488	0.704	Os1-P1	2.2951(9)	2.443	0.784
3				**6**			
	Expt.	Cal.	WBI		Expt.	Cal.	WBI
Os1-N1	-	2.105	0.542	Os1-B1	2.132(7)	2.180	0.620
Os1-N2	-	2.147	0.528	Os1-B2	2.241(6)	2.256	0.477
Os1-Se1	-	2.559	0.899	Os1-B3	2.153(6)	2.221	0.605
Os1-Se2	-	2.680	0.733	B1-B2	1.877(8)	1.811	0.549
Os1-Se3	-	2.523	0.965	B2-B3	1.918(9)	1.848	0.512
Os1-P1	-	2.445	0.766	Os1-Se1	2.5263(5)	2.625	0.754
7				**8**			
	Expt.	Cal.	WBI		Expt.	Cal.	WBI
Os1-B1	2.234(7)	2.308	0.404	Os1-B1	2.416(3)	2.463	0.305
Os1-B2	2.289(7)	2.352	0.372	Os1-B2	2.210(3)	2.224	0.517
B1-Se3	2.093(7)	2.151	0.893	B1-B2	1.713(4)	1.721	0.710
B2-Se3	2.111(7)	2.154	0.881	Os1-B5	2.160(3)	2.165	0.576
Os1-Se1	2.4711(7)	2.548	0.815	Os1-B6	2.181(3)	2.201	0.520
Os1-Se2	2.5617(7)	2.551	0.809	Os1-B7	2.191(3)	2.221	0.503
Os1-Se3	2.5617(7)	2.633	0.579	B5-B6	1.860(4)	1.864	0.464
10				**11**			
	Expt.	Cal.	WBI		Expt.	Cal.	WBI
Os1-B1	2.374(5)	2.425	0.320	Os1-B1	3.001	3.104	0.129
Os1-B2	2.379(4)	2.478	0.318	Os1-S1	2.441(3)	2.508	0.667
B1-Se2	2.062(6)	2.080	0.950	Os1-N1	2.176(8)	2.220	0.432
B2-Se2	2.082(5)	2.087	0.949	Os1-S3	2.339(3)	2.410	0.707
Os1-Se1	2.4951(5)	2.591	0.786	Os1-P1	2.309(3)	2.373	0.833
Os1-Se2	2.5288(5)	2.620	0.652	Os1-P2	2.314(3)	2.394	0.818

Table S3. Calculated natural charge and HOMO-LUMO energy gap of **1, 2, 3, 6, 7, 8, 10** and **11**.

Complexes	Natural Charge (q)				ΔE_{H-L} (eV)
	q_{Os}	q_B	q_N	q_E (E=S, Se)	
 **1**	-0.570	-	-0.461	0.199	2.087
 **2**	-0.494	-	-0.434 (N1) -0.458 (N2)	0.286 (Se1) 0.199 (Se2)	2.060
 **3**	-0.706	-	-0.431 (N1) -0.456 (N2) -0.493 (N3)	0.253 (Se1) 0.174 (Se3) 0.245 (Se5)	2.088
 **6**	-1.831	0.290 (B1) -0.293 (B2) 0.316 (B3)	-0.573 (N1) -0.567 (N2)	0.334 (Se1) 0.364 (Se2)	3.159
 **7**	-1.523	0.419 (B1) 0.426 (B2)	-0.600 (N1) -0.594 (N2)	0.345 (Se1) 0.360 (Se2) 0.230 (Se3)	3.053
 **8**	-1.370	-0.211 (B1) -0.181 (B2) -0.043 (B3) -0.142 (B4) 0.387 (B5) -0.205 (B6) 0.321 (B7)	-0.564 (N1) -0.560 (N2)	0.388 (Se1) 0.328 (Se2)	3.343

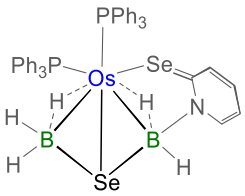
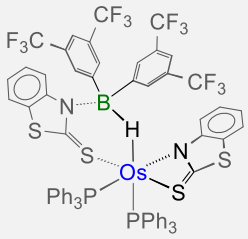
 **10**	-1.507	0.081 (B1) -0.262 (B2)	-0.562 (N1)	0.299 (Se1) 0.301 (Se2)	2.996
 **11**	-0.812	0.566	-0.529 (N1) -0.637 (N2)	0.088 (S1) 0.142 (S3)	3.379

Table S4. TD-DFT calculated energies (excitation energy (cm^{-1}), λ_{calc} (nm)), oscillator strength (*f*), and main composition of the first UV–vis electronic excitations for **1**, **2** and **3**.

Complex	No	Excitation Energy (cm^{-1})	Calc. Wavelength (nm) (*f*) [a]	Main electronic transition (% weight) [b]
1	1	14980	667 (0.030)	β-HOMO-2→ β-LUMO (79) β-HOMO→ β-LUMO (13)
	2	19804	504 (0.04)	β-HOMO-3→ β-LUMO (89)
2	1	16084	621 (0.052)	β-HOMO-3→ β-LUMO (66) β-HOMO-2→ β-LUMO (19)
	2	16316	612 (0.035)	β-HOMO-3→ β-LUMO (17) β-HOMO-2→ β-LUMO (76)
	3	23748	421 (0.012)	α-HOMO→ α-LUMO+1 (11) β-HOMO→ β-LUMO+1 (24) β-HOMO→ β-LUMO+2 (39)
3	1	14271	700 (0.052)	β-HOMO-1→ β-LUMO (91)
	2	19780	505 (0.037)	β-HOMO-5→ β-LUMO+2 (43) β-HOMO-4→ β-LUMO+2 (49)
	3	20130	496 (0.020)	β-HOMO-5→ β-LUMO+2 (49) β-HOMO-4→ β-LUMO+2 (32)

[a]Oscillator strength greater than 0.010 and [b]Components with greater than 10% contribution shown.

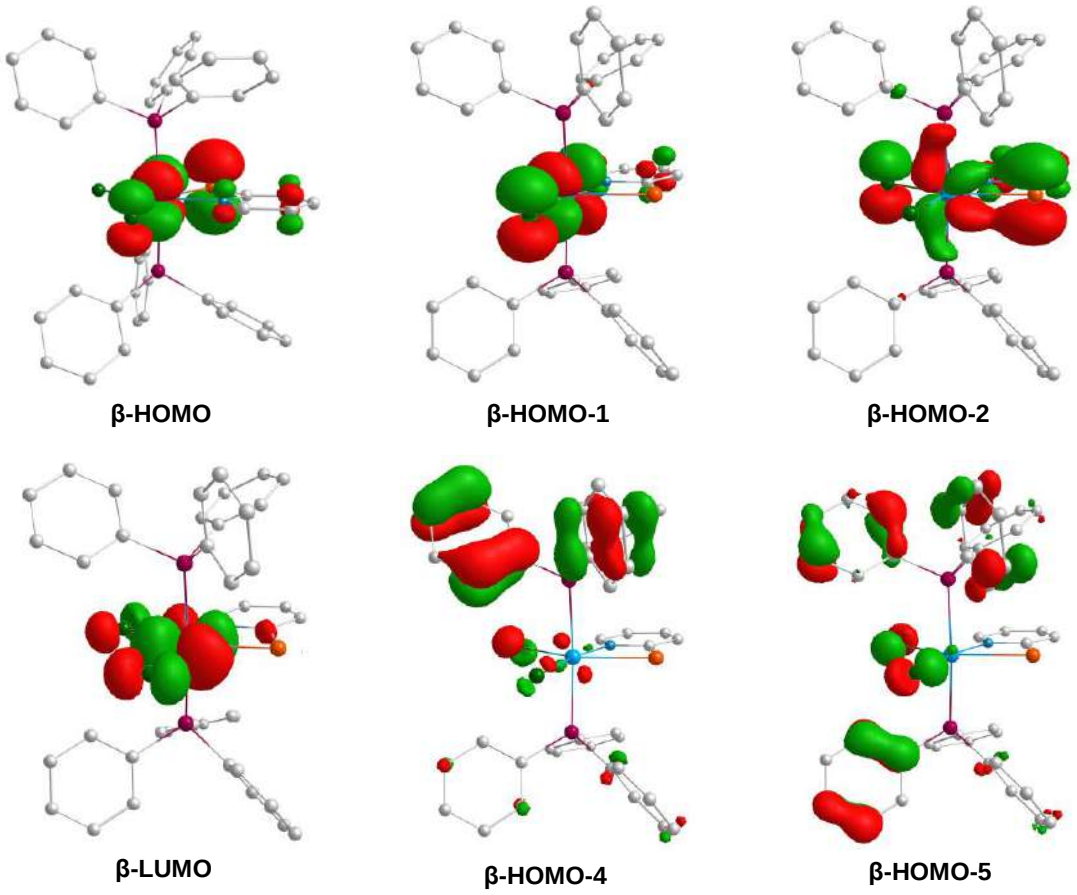


Figure S56. Selected molecular orbitals of **1** (isocontour values: ±0.043 [e.bohr^{-3}]$^{1/2}$).

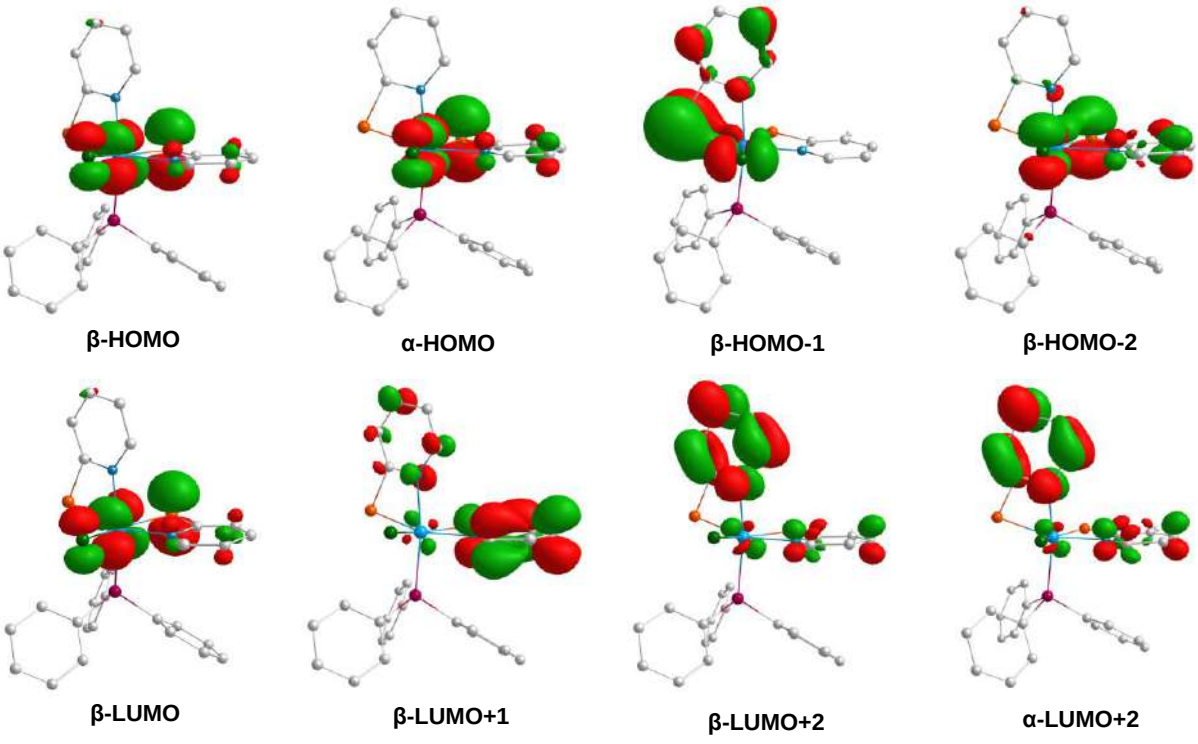


Figure S57. Selected molecular orbitals of **2** (isocontour values: ±0.043 [e.bohr^{-3}]$^{1/2}$).

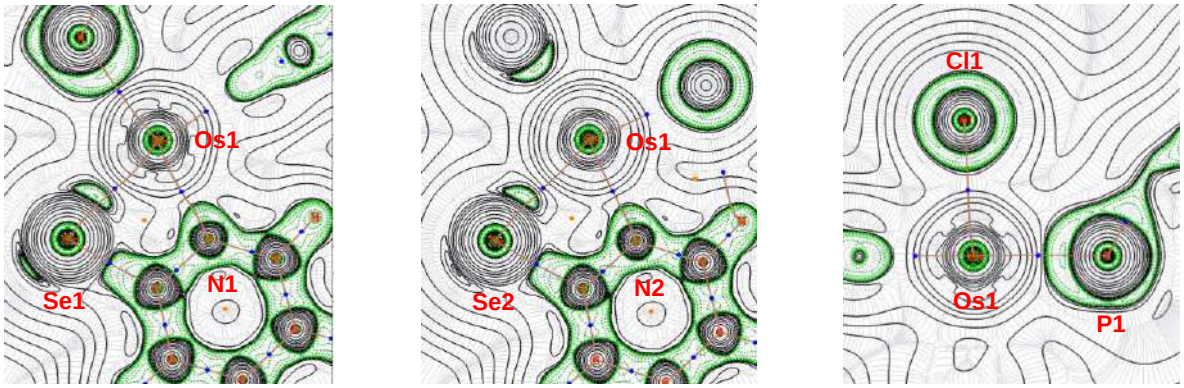


Figure S58. Contour-line diagram of the Laplacian of electron density in the Os1-N1-Se1 (a) Os1-N2-Se2 (b) and Cl1-Os1-P1 (c) planes of **2**. The solid brown lines are bond paths, while blue spheres indicate the bond critical points and orange sphere indicates ring critical points. Area of charge concentration [$\nabla^2\rho(r)<0$] are indicated by solid lines and area of charge depletion [$\nabla^2\rho(r)>0$] are shown by dashed lines.

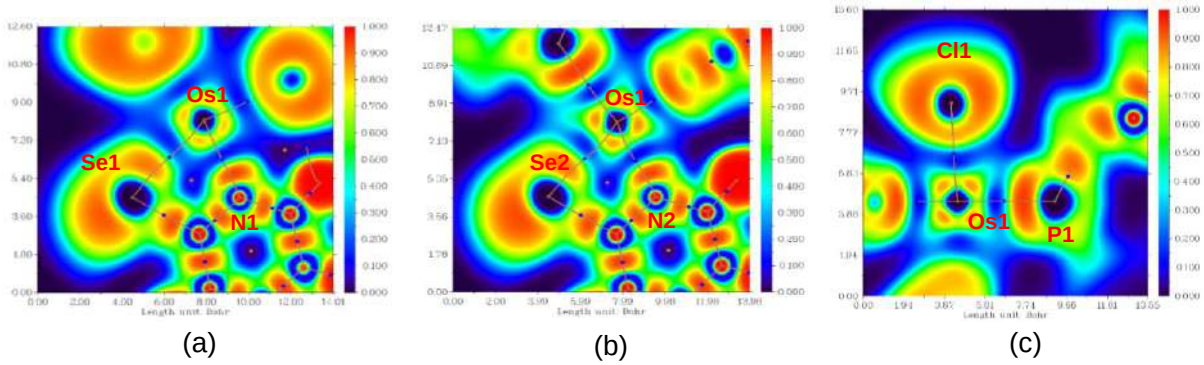


Figure S59. ELF plot in the Os1-N1-Se1 (a) Os1-N2-Se2 (b) and Cl1-Os1-P1 (c) planes of **2**.

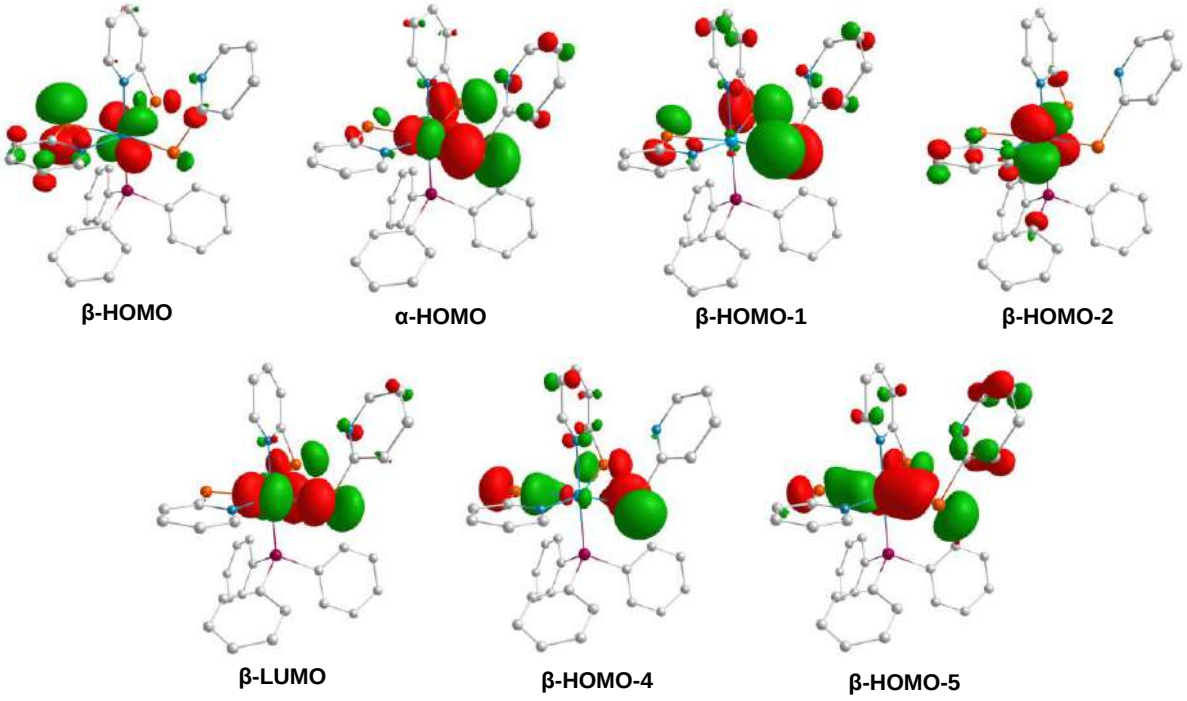
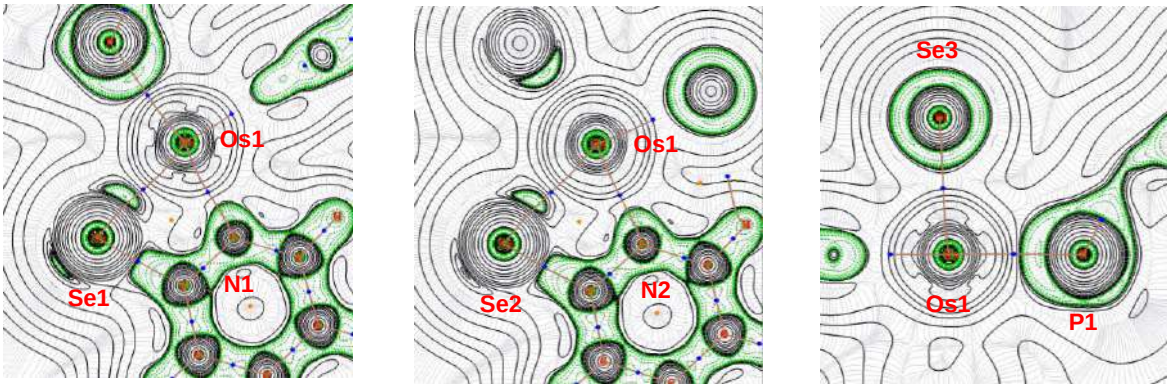
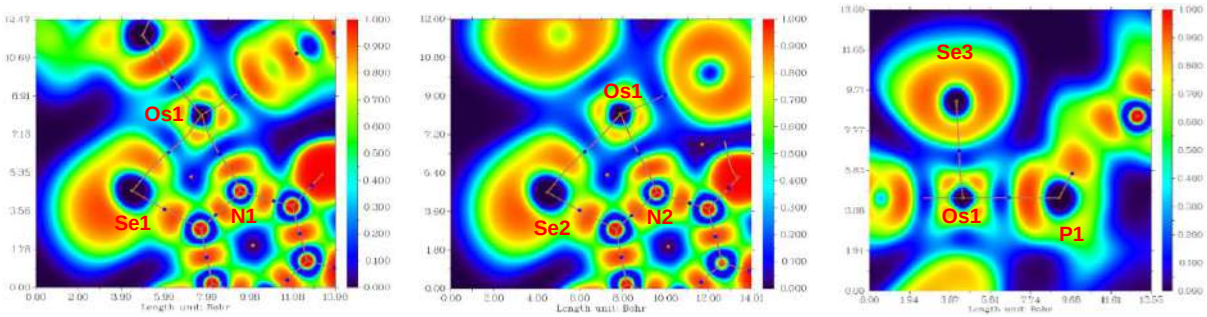


Figure S60. Selected molecular orbitals of **3** (isocontour values: ±0.043 [e.bohr^{-3}]$^{1/2}$).



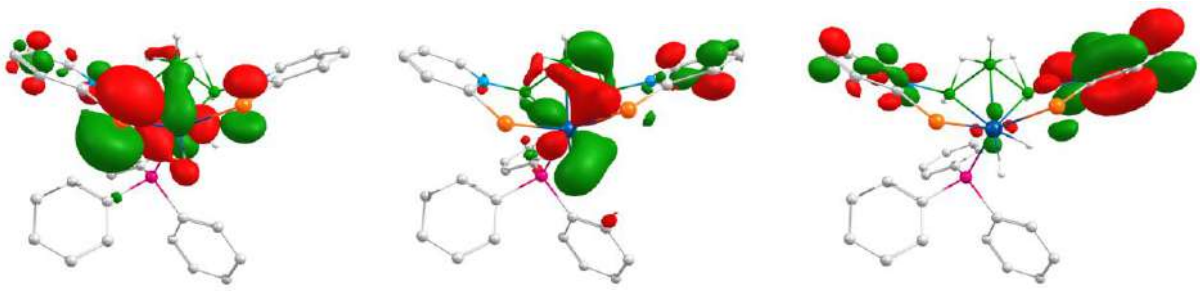
(a) (b) (c)

Figure S61. Contour-line diagram of the Laplacian of electron density in the Os1-N1-Se1 (a) Os1-N2-Se2 (b) and Se1-Os1-P1 (c) planes of **3**.



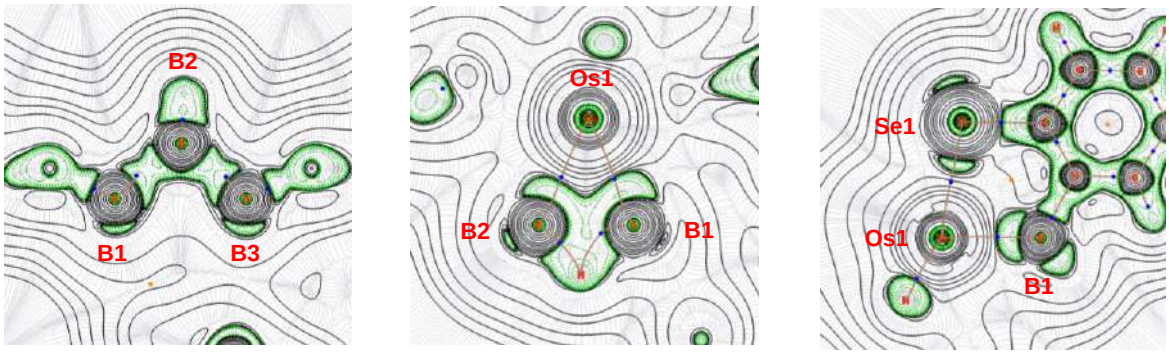
(a) (b) (c)

Figure S62. ELF plot in the Os1-N1-Se1 (a) Os1-N2-Se2 (b) and Se1-Os1-P1 (c) planes of **3**.



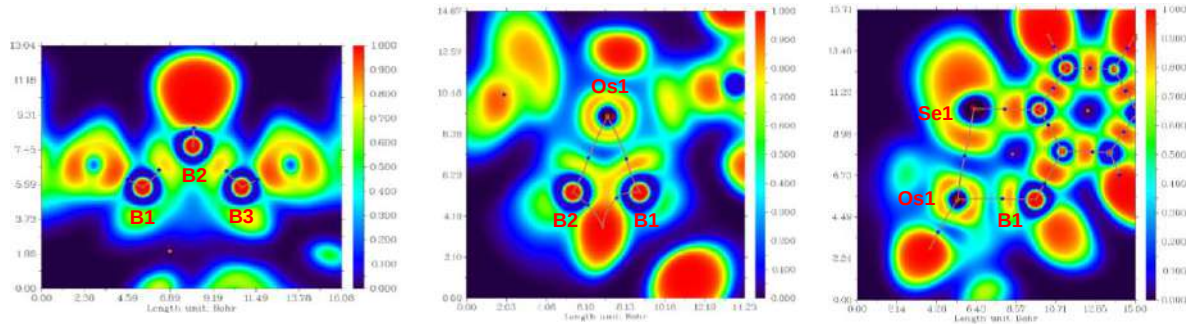
HOMO **HOMO-12** **LUMO**

Figure S63. Selected molecular orbitals of **6** (isocontour values: ±0.043 [e.bohr^{-3}]$^{1/2}$).



(a) (b) (c)

Figure S64. Contour-line diagram of the Laplacian of electron density in the B1-B2-B3 (a), Os1-B1-B2 (b) and Se1-Os1-B1 (c) planes of **6**.



(a) (b) (c)

Figure S65. ELF plot in the B1-B2-B3 (a), Os1-B1-B2 (b) and Se1-Os1-B1 (c) planes of **6**.

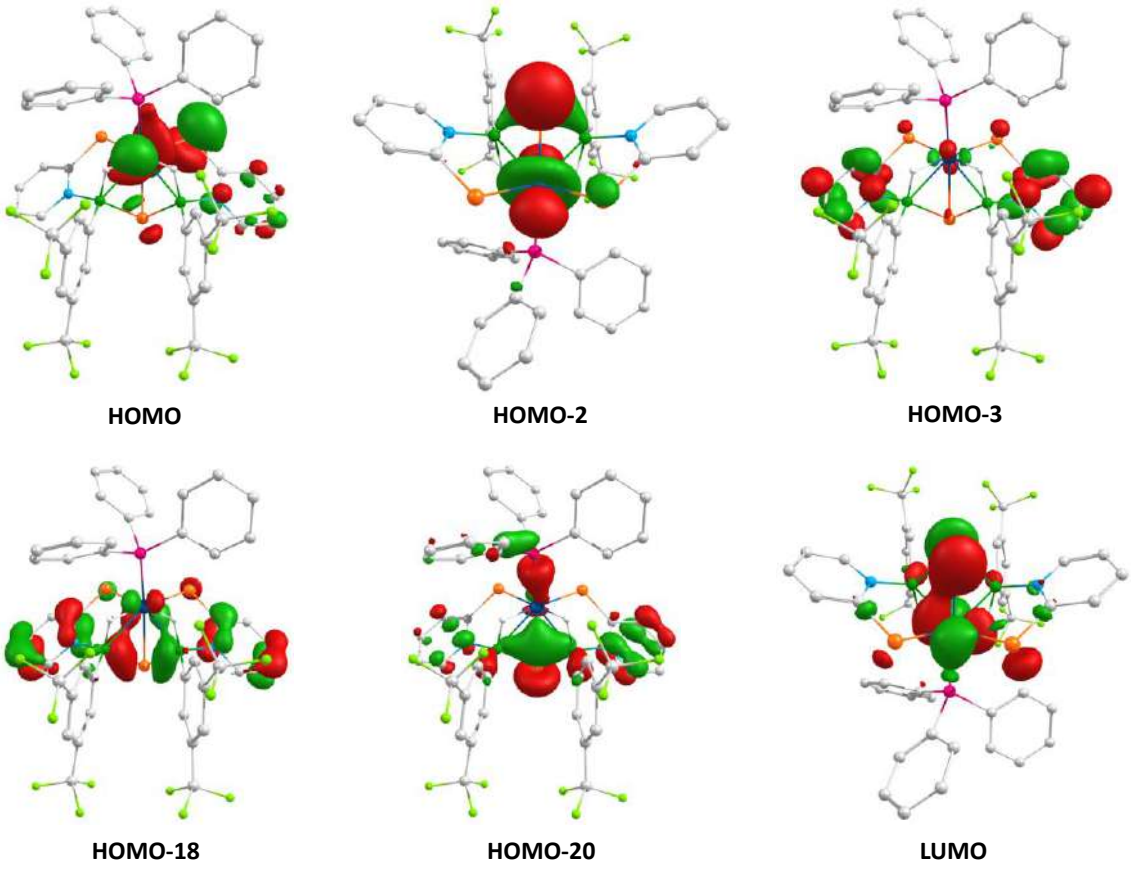


Figure S66. Selected molecular orbitals of **7** (isocontour values: ±0.043 [e.bohr^{-3}]$^{1/2}$).

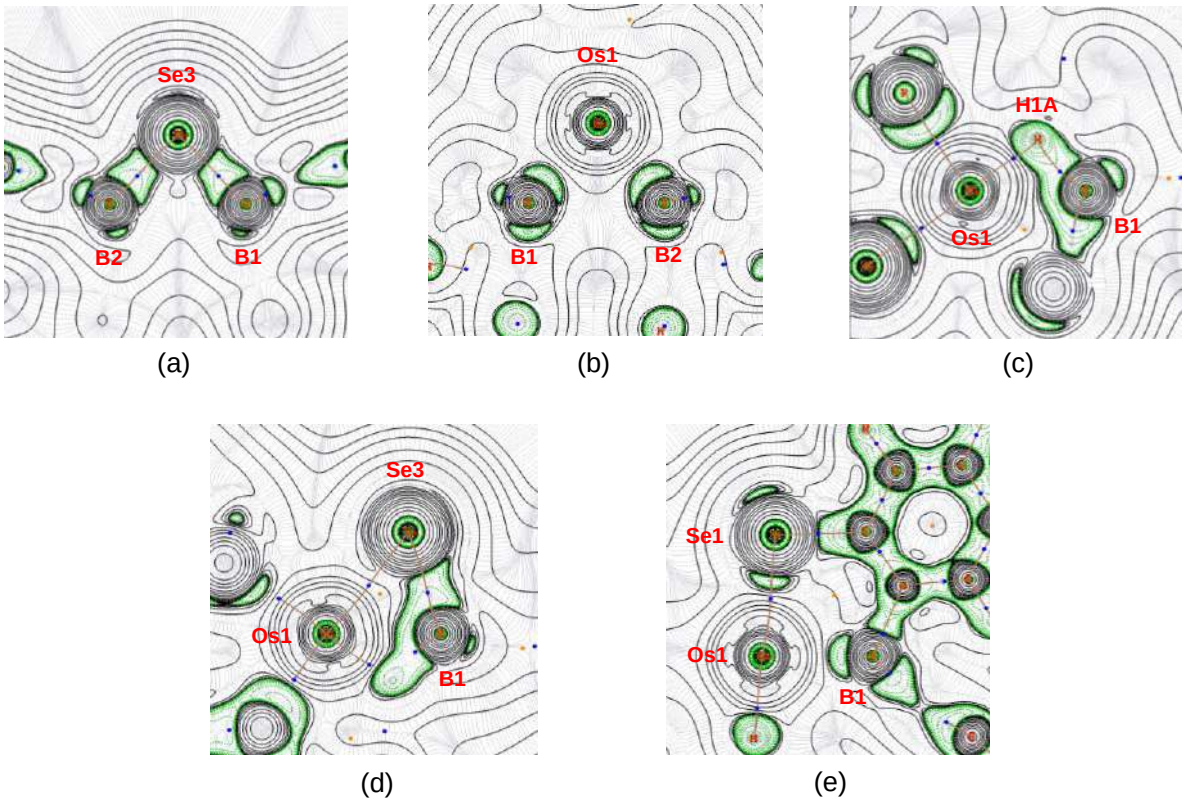


Figure S67. Contour-line diagram of the Laplacian of electron density in the B1-Se3-B2 (a), Os1-B1-B2 (b), Os1-H1A-B1 (c), Os1-Se3-B1 (b) and Os1-B1-Se1 (c) planes of **7**.

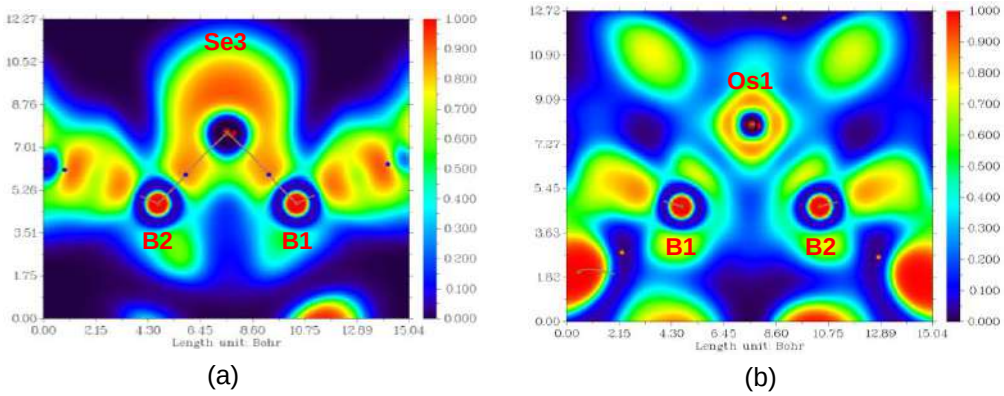


Figure S68. ELF plot in the B1-Se3-B2 (a) and Os1-B1-B2 (b) planes of **7**.

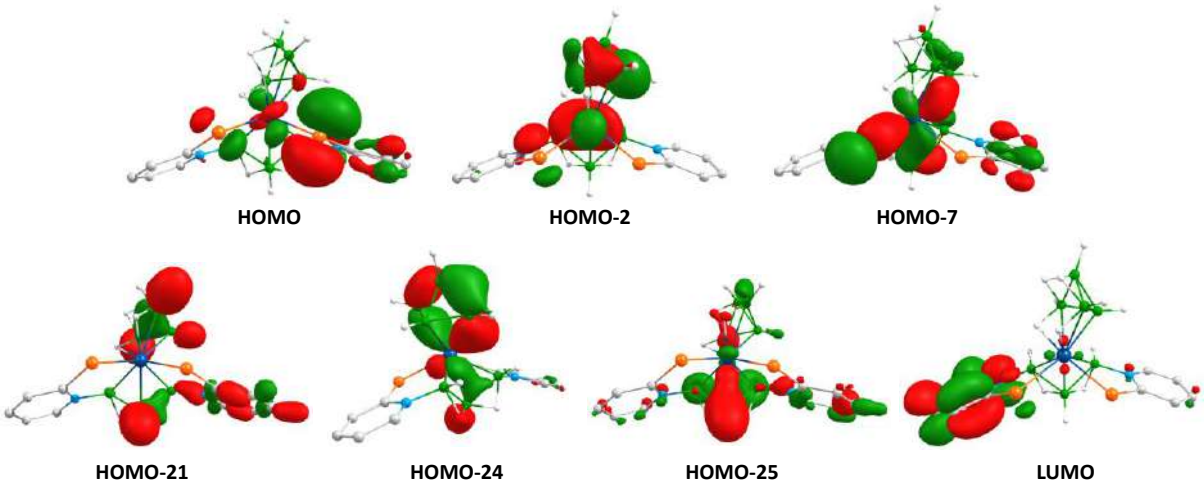


Figure S69. Selected molecular orbitals of **8** (isocontour values: ±0.043 [e.bohr^{-3}]$^{1/2}$).

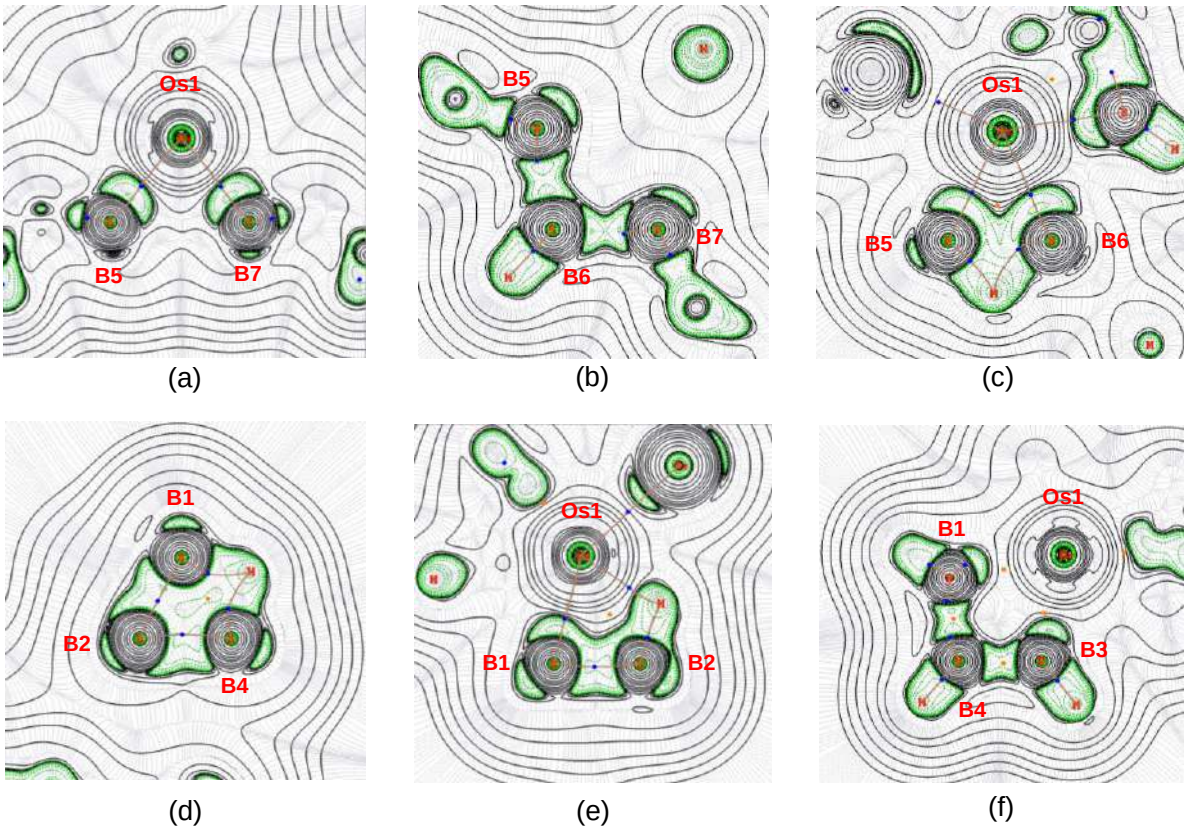


Figure S70. Contour-line diagram of the Laplacian of electron density in the Os1-B5-B7 (a) B5-B6-B7 (b), Os1-B5-B6 (c) B1-B2-B4 (d), Os1-B1-B2 (e) and Os1-B1-B4-B3 (f) planes of **8**.

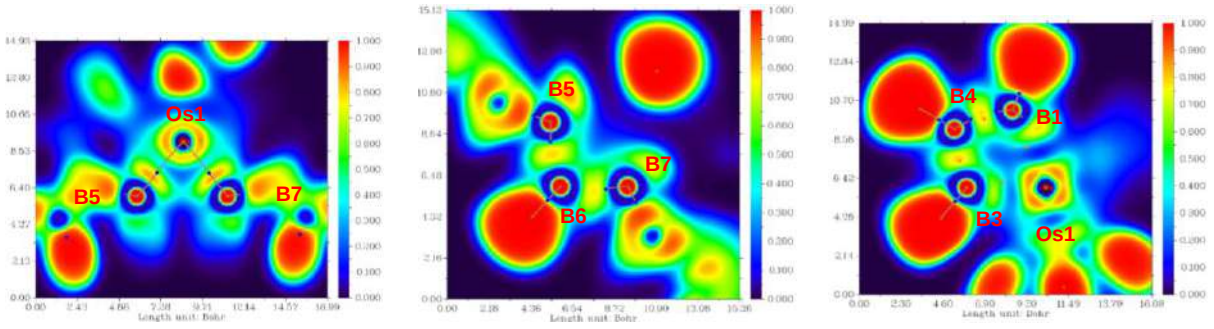


Figure S71. ELF plot in the Os1-B5-B7 (a) B5-B6-B7 (b) and Os1-B1-B4-B3 (c) planes of **8**.

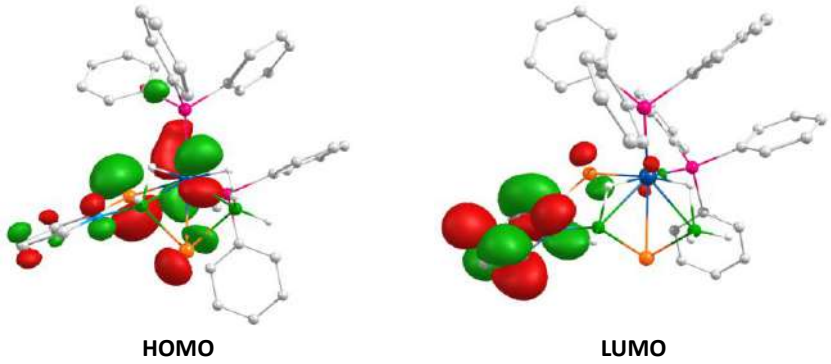


Figure S72. Selected molecular orbitals of **10** (isocontour values: ±0.043 [e.bohr^{-3}]$^{1/2}$).

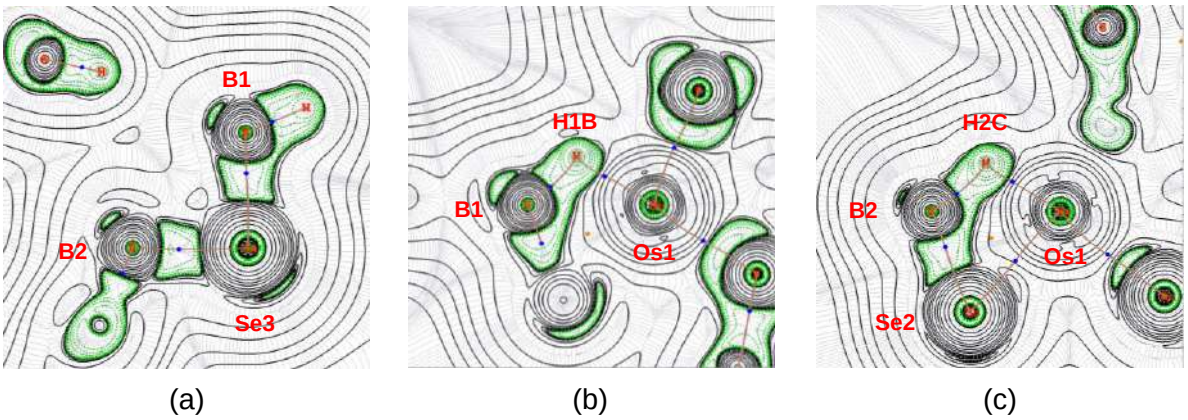


Figure S73. Contour-line diagram of the Laplacian of electron density in the B1-Se2-B2 (a) Os1-H1B-B1 (b) and Os1-H2C-B2-Se2 (c) planes of **10**.

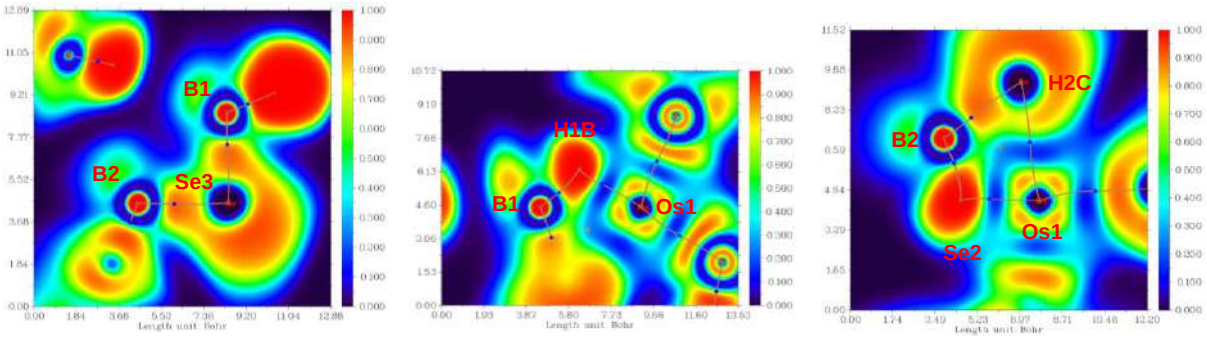


Figure S74. ELF plot in the B1-Se2-B2 (a) Os1-H1B-B1 (b) and Os1-H2C-B2-Se2 (c) planes of **10**.

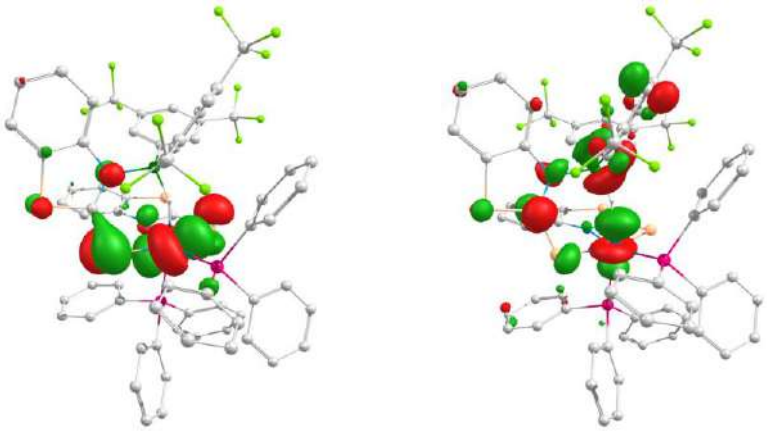


Figure S75. Selected molecular orbitals of **11** (isocontour values: ±0.043 [e.bohr^{-3}]$^{1/2}$).

IV Cartesian Coordinates of all Optimized Structures

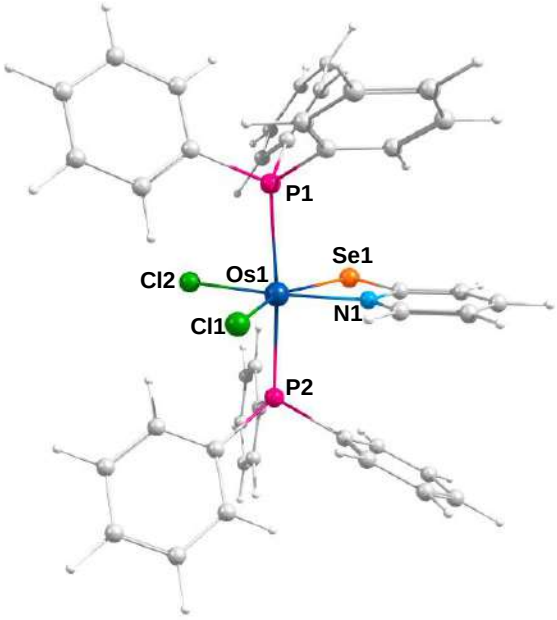


Figure S76. Optimized geometry of **1**.
Total energy = -2671.85535246 a.u.
Cartesian coordinates for the calculated structure **1** (in Å)

C	0.086480000	2.534786000	-1.647536000	H	-5.248327000	-2.237494000	4.643772000
C	-0.051734000	2.534429000	0.686067000	C	-3.294659000	1.330082000	-0.376959000
C	-0.070019000	3.928985000	0.721285000	C	-3.217205000	1.893094000	-1.655998000
N	0.015537000	1.855675000	-0.486607000	C	-3.922595000	2.043680000	0.646476000
P	-2.477917000	-0.333675000	-0.055024000	C	-3.787950000	3.137164000	-1.912624000
C	-3.249057000	-1.476023000	-1.351453000	H	-2.718878000	1.356032000	-2.454844000
C	-4.387747000	-1.123782000	-2.079271000	C	-4.484682000	3.294006000	0.388680000
C	-2.690868000	-2.745856000	-1.524895000	H	-3.976706000	1.627666000	1.644223000
C	-4.960375000	-2.029277000	-2.973231000	C	-4.426233000	3.839856000	-0.891243000
H	-4.837218000	-0.146757000	-1.958407000	H	-3.732099000	3.556992000	-2.910868000
C	-3.268719000	-3.648479000	-2.413468000	H	-4.971577000	3.836701000	1.191369000
H	-1.807414000	-3.030349000	-0.968346000	H	-4.872133000	4.807668000	-1.092110000
C	-4.402680000	-3.293455000	-3.142374000	Os	0.007441000	-0.218558000	-0.059174000
H	-5.842731000	-1.741392000	-3.534285000	C	0.073959000	3.918189000	-1.679073000
H	-2.825273000	-4.629894000	-2.539460000	C	-0.010517000	4.625975000	-0.476471000
H	-4.847297000	-3.997000000	-3.837504000	H	-0.131415000	4.436504000	1.675391000
C	-3.362054000	-0.949646000	1.499423000	H	-0.027059000	5.710105000	-0.476794000
C	-2.664380000	-1.237296000	2.671746000	H	0.131467000	4.428585000	-2.631474000
C	-4.748007000	-1.143405000	1.466615000	Se	-0.085989000	1.290935000	2.132828000
C	-3.343005000	-1.699164000	3.799969000	H	0.153646000	1.930591000	-2.541583000
H	-1.591980000	-1.125084000	2.702852000	Cl	-0.027352000	-0.677172000	-2.443251000
C	-5.425192000	-1.599573000	2.593987000	Cl	0.044954000	-2.445665000	0.844264000
H	-5.306148000	-0.946077000	0.559744000	P	2.498471000	-0.313677000	-0.055335000
C	-4.722761000	-1.877252000	3.766337000	C	3.329562000	-0.151502000	1.635277000
H	-2.785483000	-1.924146000	4.702196000	C	2.819855000	-0.920332000	2.686771000
H	-6.499130000	-1.743635000	2.552938000	C	4.456601000	0.642627000	1.854164000

C	3.428410000	-0.888356000	3.938072000
H	1.952551000	-1.548550000	2.525638000
C	5.059965000	0.678199000	3.112619000
H	4.877158000	1.232338000	1.050316000
C	4.547597000	-0.085659000	4.157075000
H	3.024199000	-1.490786000	4.743978000
H	5.933248000	1.301891000	3.269133000
H	5.017179000	-0.058628000	5.134067000
C	3.296061000	-1.910493000	-0.683167000
C	2.614183000	-2.760502000	-1.555266000
C	4.598238000	-2.235558000	-0.288093000
C	3.232149000	-3.916869000	-2.031324000
H	1.607641000	-2.523761000	-1.867413000
C	5.211514000	-3.391776000	-0.764514000
H	5.137409000	-1.595831000	0.398792000
C	4.529333000	-4.236015000	-1.639130000
H	2.689842000	-4.569540000	-2.706283000
H	6.219992000	-3.632736000	-0.446955000
H	5.004881000	-5.138477000	-2.007180000
C	3.329737000	1.004771000	-1.110662000
C	3.913374000	0.676941000	-2.336863000
C	3.315115000	2.342150000	-0.698929000
C	4.487532000	1.668933000	-3.131275000
H	3.924451000	-0.351254000	-2.674563000
C	3.899640000	3.329441000	-1.488492000
H	2.855399000	2.618576000	0.242560000
C	4.488501000	2.995551000	-2.707195000
H	4.936953000	1.399129000	-4.080454000
H	3.889683000	4.359922000	-1.151290000
H	4.942731000	3.764591000	-3.322043000

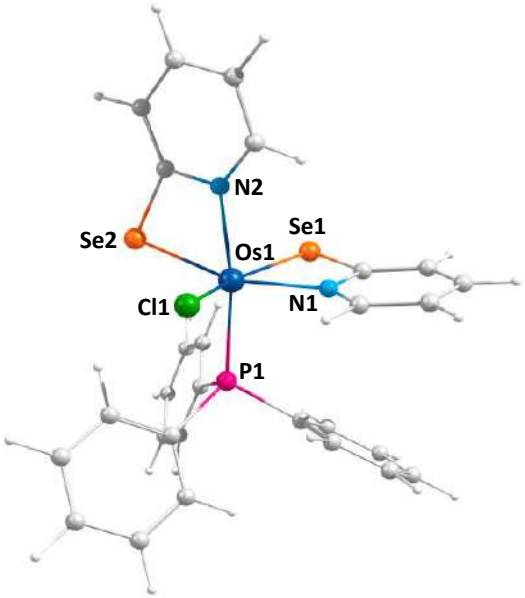


Figure S77. Optimized geometry of **2**.
Total energy = -1321.71260555 a.u.
Cartesian coordinates for the calculated structure **2** (in Å)

C	-3.205760000	1.672000000	0.080904000	H	3.047914000	-4.194166000	-1.832945000
C	-3.976137000	-0.375459000	-0.720562000	H	3.999754000	-3.482184000	2.293810000
C	-5.287093000	0.081510000	-0.713594000	H	4.056817000	-4.964839000	0.302556000
C	-0.890841000	-2.749260000	-1.619216000	C	2.463739000	1.081384000	-1.476029000
C	-1.100770000	-2.552331000	0.702638000	C	1.910040000	2.255320000	-1.993779000
C	-1.242788000	-3.933898000	0.843213000	C	3.684853000	0.622437000	-1.975721000
N	-0.919373000	-1.981422000	-0.513529000	C	2.574035000	2.963085000	-2.991925000
N	-2.959689000	0.404196000	-0.326758000	H	0.952159000	2.608982000	-1.635349000
P	1.561331000	0.222953000	-0.055291000	C	4.344395000	1.329367000	-2.981683000
Se	-1.498575000	2.465767000	0.538533000	H	4.129461000	-0.284900000	-1.587016000
C	2.267197000	1.171941000	1.424480000	C	3.791738000	2.502184000	-3.489708000
C	3.582486000	1.649461000	1.397310000	H	2.130043000	3.868804000	-3.389172000
C	1.487929000	1.401614000	2.559550000	H	5.289965000	0.960519000	-3.363732000
C	4.108774000	2.335129000	2.489163000	H	4.303388000	3.051054000	-4.272512000
H	4.199400000	1.498201000	0.520721000	Os	-0.873921000	0.134506000	-0.231939000
C	2.014799000	2.090286000	3.652534000	C	-1.033627000	-4.124859000	-1.547866000
H	0.467971000	1.048297000	2.593636000	C	-1.205373000	-4.724939000	-0.295283000
C	3.325818000	2.556904000	3.621453000	H	-1.383436000	-4.359169000	1.828573000
H	5.128817000	2.701047000	2.450756000	H	-1.314542000	-5.800593000	-0.213565000
H	1.393774000	2.262776000	4.524368000	H	-1.008904000	-4.713072000	-2.456088000
H	3.734354000	3.094689000	4.469796000	C	-4.490958000	2.198361000	0.114577000
C	2.420720000	-1.448136000	0.074781000	C	-5.545815000	1.385417000	-0.289767000
C	2.440242000	-2.293887000	-1.039850000	H	-4.649779000	3.216817000	0.444382000
C	2.981560000	-1.888847000	1.274939000	H	-6.560861000	1.765810000	-0.276990000
C	3.030728000	-3.552413000	-0.959058000	H	-6.085320000	-0.573419000	-1.037963000
H	2.006293000	-1.966185000	-1.977305000	H	-3.718231000	-1.374347000	-1.047565000
C	3.566214000	-3.152887000	1.356031000	Se	-1.177106000	-1.183256000	2.038235000
H	2.966476000	-1.249368000	2.148273000	H	-0.762919000	-2.218162000	-2.553786000
C	3.596596000	-3.985034000	0.239942000	Cl	-0.874953000	0.463832000	-2.684065000

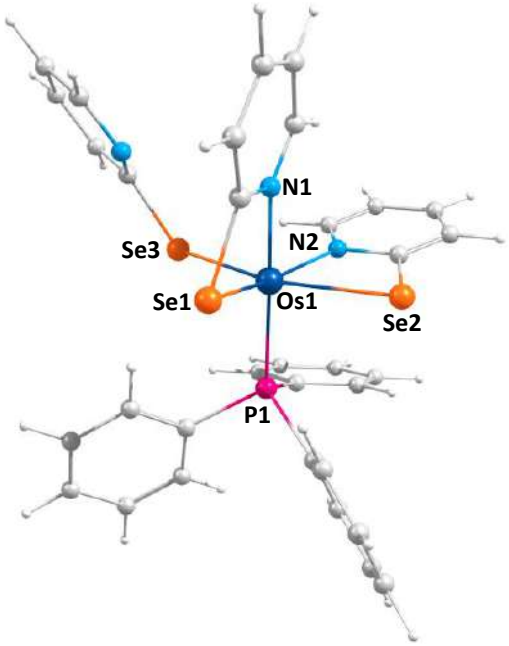


Figure S78. Optimized geometry of **3**.

Total energy = -1563.71855705 a.u.

Cartesian coordinates for the calculated structure **3** (in Å)

C	-3.207054000	1.683105000	1.206243000
C	-5.166496000	1.630842000	0.024381000
C	-5.880212000	2.253909000	1.041549000
C	-2.597724000	-0.729596000	-1.919978000
C	-3.104417000	-2.000052000	-0.034333000
C	-4.288667000	-2.438038000	-0.608013000
C	0.413890000	-2.907144000	0.835874000
C	-0.180595000	-1.658763000	2.721913000
C	0.046154000	-2.740127000	3.556099000
N	-0.006690000	-1.739200000	1.388529000
N	-2.277786000	-1.163844000	-0.677736000
N	-3.859379000	1.349189000	0.097096000
P	1.843208000	0.623964000	-0.046272000
Se	-1.269528000	1.403635000	1.354947000
Se	0.582548000	-2.716460000	-1.055340000
Se	-1.191151000	0.448533000	-2.505895000
C	2.675733000	0.268753000	1.605470000
C	2.553336000	1.164278000	2.671736000
C	3.314126000	-0.958344000	1.814541000
C	3.085228000	0.847881000	3.921495000
H	2.045477000	2.110804000	2.532152000
C	3.846672000	-1.270769000	3.063551000
H	3.398043000	-1.671847000	1.003348000
C	3.738070000	-0.366913000	4.119274000
H	2.988673000	1.554669000	4.738274000
H	4.345066000	-2.222605000	3.209920000
H	4.155899000	-0.609716000	5.089967000
C	3.129690000	0.091172000	-1.331478000
C	2.698114000	-0.221504000	-2.622002000
C	4.498627000	0.093516000	-1.052638000
C	3.622128000	-0.524901000	-3.619544000
H	1.640038000	-0.236255000	-2.850803000
C	5.422050000	-0.219852000	-2.049234000
H	4.855802000	0.330020000	-0.058374000
C	4.986218000	-0.528078000	-3.335907000
H	3.271325000	-0.766830000	-4.616552000
H	6.481386000	-0.220671000	-1.816916000
H	5.704474000	-0.770651000	-4.111140000
C	1.997522000	2.503405000	-0.229938000
C	0.945358000	3.236496000	-0.779620000
C	3.186085000	3.160694000	0.105565000
C	1.080039000	4.609048000	-0.991560000
H	0.017855000	2.742791000	-1.034996000
C	3.315713000	4.531946000	-0.097510000
H	4.015957000	2.610252000	0.531250000
C	2.261677000	5.259904000	-0.649506000
H	0.253841000	5.165362000	-1.419825000
H	4.240818000	5.029569000	0.171863000
H	2.363511000	6.327379000	-0.810869000
Os	-0.387010000	-0.363085000	-0.215601000
C	0.654546000	-4.036824000	1.624461000
C	0.469459000	-3.950373000	2.995073000
H	-0.517910000	-0.700897000	3.095165000
H	-0.104214000	-2.633505000	4.622526000
H	0.650509000	-4.814116000	3.625323000
H	0.979267000	-4.954154000	1.150052000
C	-3.837231000	2.309466000	2.295542000
C	-5.190638000	2.598154000	2.205540000
H	-5.660292000	1.341658000	-0.899502000
H	-6.937160000	2.461773000	0.926182000
H	-5.702202000	3.083434000	3.029928000
H	-3.268383000	2.561328000	3.182120000
C	-3.760267000	-1.137328000	-2.564013000
C	-4.618129000	-2.000922000	-1.892810000
H	-3.976998000	-0.778895000	-3.562055000
H	-5.533971000	-2.335981000	-2.366864000
H	-4.935403000	-3.109721000	-0.058449000
H	-2.797399000	-2.313505000	0.955249000

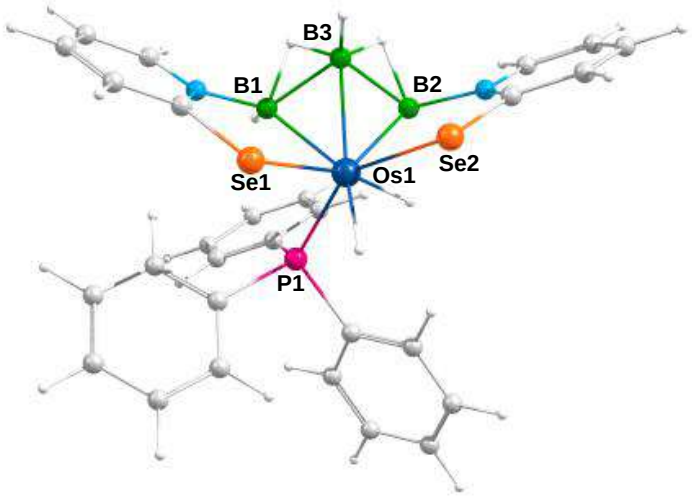


Figure S79. Optimized geometry of **6**.
Total energy = -1720.43700776 a.u.
Cartesian coordinates for the calculated structure **6** (in Å)

B	-0.260968000	-1.282977000	1.554953000
B	2.107100000	0.202869000	1.454588000
N	-1.115101000	-2.580552000	1.279550000
C	-1.788293000	-3.131756000	2.330726000
C	-2.497521000	-4.298133000	2.224451000
C	-2.527312000	-4.949086000	0.972585000
C	-1.865201000	-4.392224000	-0.093393000
C	-1.150662000	-3.178907000	0.053428000
N	3.624151000	0.386175000	1.072209000
C	4.452916000	0.963439000	1.988306000
C	5.800444000	1.099087000	1.784741000
C	6.344885000	0.615787000	0.577421000
C	5.515222000	0.041687000	-0.354732000
C	4.126286000	-0.069804000	-0.113358000
C	-2.674859000	0.522235000	-0.917052000
C	-3.431214000	-0.522344000	-0.369444000
C	-4.517856000	-1.054037000	-1.058363000
C	-4.855379000	-0.565814000	-2.319494000
C	-4.097124000	0.456614000	-2.883299000
C	-3.017208000	0.998386000	-2.187267000
C	-0.938002000	2.829007000	-0.825114000
C	0.148715000	3.116903000	-1.656756000
C	0.276373000	4.372419000	-2.252989000
C	-0.679888000	5.358646000	-2.030503000
C	-1.768167000	5.083371000	-1.203200000
C	-1.893913000	3.832603000	-0.605515000
C	-1.829806000	1.718330000	1.620021000
C	-3.184050000	1.723415000	1.969273000
C	-3.596979000	2.216040000	3.209095000
C	-2.664827000	2.719701000	4.111245000
C	-1.312908000	2.727886000	3.767021000
C	-0.900313000	2.229123000	2.535629000
B	1.529268000	-1.552346000	1.500025000
Os	0.713010000	-0.256841000	-0.157093000
P	-1.172085000	1.152401000	-0.028861000
H	-0.798570000	-0.651208000	2.412299000
H	1.853593000	0.949958000	2.352670000
H	2.246247000	-0.931869000	2.333665000
H	2.080549000	-2.553181000	1.184491000
H	0.697681000	-1.817994000	2.425407000
H	1.362574000	1.222894000	0.057402000
H	-3.176291000	-0.926174000	0.602337000
H	-2.440961000	1.793553000	-2.642634000
H	-4.343441000	0.838260000	-3.868022000
H	-5.697482000	-0.983824000	-2.859731000
H	-5.094647000	-1.856855000	-0.612412000
H	0.152714000	2.227186000	2.285841000
H	-0.577385000	3.120418000	4.460726000
H	-2.986740000	3.104845000	5.072455000
H	-4.651825000	2.209767000	3.461699000
H	-3.929368000	1.352752000	1.278002000
H	0.896003000	2.358061000	-1.840153000
H	1.128328000	4.573299000	-2.893238000
H	-0.579131000	6.333857000	-2.494084000
H	-2.519531000	5.843313000	-1.018658000
H	-2.743584000	3.643865000	0.038553000
H	-1.720174000	-2.577334000	3.257226000
H	-3.013865000	-4.697285000	3.086913000
H	-3.073781000	-5.877586000	0.851313000
H	-1.877930000	-4.860283000	-1.068873000
H	5.900946000	-0.328607000	-1.295525000
H	7.407769000	0.702248000	0.382227000
H	6.416241000	1.568394000	2.539876000
H	3.965505000	1.306890000	2.890410000
H	0.431626000	0.358790000	-1.676305000
Se	-0.291056000	-2.358136000	-1.397595000
Se	2.961554000	-0.802593000	-1.396017000

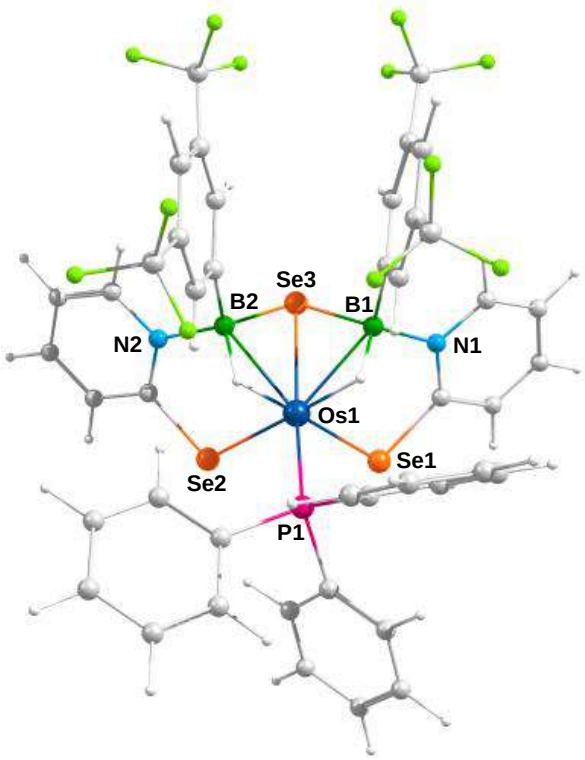


Figure S80. Optimized geometry of **7**.
Total energy = -3513.88669676 a.u.
Cartesian coordinates for the calculated structure **7** (in Å)

C	4.480716000	0.312858000	1.160999000
C	5.007463000	1.139911000	2.158042000
H	4.380603000	1.491246000	2.966549000
C	6.350195000	1.520636000	2.129325000
H	6.738657000	2.165203000	2.910205000
C	7.185804000	1.075762000	1.109709000
H	8.228295000	1.372855000	1.088146000
C	6.672710000	0.240341000	0.117796000
H	7.314954000	-0.119327000	-0.678355000
C	5.333727000	-0.136546000	0.143124000
H	4.958611000	-0.797666000	-0.628794000
C	-0.758201000	-3.070738000	-3.095165000
H	-1.758936000	-2.960089000	-2.712326000
C	-0.469542000	-4.015945000	-4.041041000
H	-1.259230000	-4.655496000	-4.411376000
C	0.855528000	-4.126517000	-4.501395000
H	1.123178000	-4.864559000	-5.248525000
C	1.805415000	-3.282203000	-3.984468000
H	2.836731000	-3.334443000	-4.307980000
C	1.470508000	-2.312912000	-3.012048000
C	2.975917000	-2.054531000	1.592208000
C	2.299887000	-3.086508000	0.938749000
H	1.627412000	-2.852854000	0.125877000
C	2.500434000	-4.417475000	1.305820000
H	1.965193000	-5.204012000	0.785903000
C	3.387090000	-4.733401000	2.330546000
H	3.543866000	-5.767181000	2.617233000
C	4.079791000	-3.712452000	2.981882000
H	4.779546000	-3.949141000	3.775607000
C	3.879798000	-2.385684000	2.613298000
H	4.434540000	-1.606319000	3.121957000
C	1.991918000	0.468144000	2.671513000
C	1.516249000	-0.305394000	3.734650000
H	1.582697000	-1.384992000	3.698505000
C	0.939888000	0.302878000	4.851428000
H	0.561051000	-0.313849000	5.658294000
C	0.840881000	1.688312000	4.924792000
H	0.390706000	2.158099000	5.791484000
C	1.307615000	2.469080000	3.866301000
H	1.226847000	3.549604000	3.910196000
C	1.867340000	1.864869000	2.744989000
H	2.210871000	2.481153000	1.921363000
C	1.472564000	3.595705000	-1.181882000
C	1.827517000	4.941866000	-1.429901000
H	2.854976000	5.146876000	-1.700757000
C	0.907000000	5.952795000	-1.323203000
H	1.191924000	6.980580000	-1.515697000
C	-0.408850000	5.627046000	-0.947719000
H	-1.174906000	6.381528000	-0.830581000
C	-0.721810000	4.313981000	-0.725795000
H	-1.717453000	4.031601000	-0.430958000
C	-1.654861000	-1.561415000	-0.774925000

C	-2.937397000	-1.376599000	-1.312275000
H	-3.051858000	-0.822593000	-2.236812000
C	-4.073978000	-1.885867000	-0.684593000
C	-3.971894000	-2.581938000	0.517765000
H	-4.855036000	-2.966319000	1.010663000
C	-2.711270000	-2.754436000	1.079311000
C	-1.575979000	-2.256268000	0.439985000
H	-0.612527000	-2.406271000	0.911901000
C	-1.754630000	1.723899000	0.100859000
C	-1.853966000	1.401728000	1.458641000
H	-0.962351000	1.132101000	2.013070000
C	-3.086423000	1.406435000	2.122609000
C	-4.251970000	1.761865000	1.456806000
H	-5.202394000	1.772496000	1.973059000
C	-4.173072000	2.086849000	0.102402000
C	-2.952507000	2.046716000	-0.562508000
H	-2.929647000	2.269958000	-1.622792000
C	-5.420680000	-1.752782000	-1.344702000
C	-2.563049000	-3.545284000	2.352283000
C	-3.135234000	1.061646000	3.587755000
C	-5.413811000	2.554162000	-0.611178000
B	-0.300950000	-1.101577000	-1.531243000
B	-0.329367000	1.783038000	-0.658873000
F	-1.513502000	-3.132377000	3.094702000
F	-2.356295000	-4.865653000	2.095124000
F	-3.662757000	-3.474285000	3.132458000
F	-5.687949000	-2.824637000	-2.140597000
F	-6.427675000	-1.681478000	-0.447783000
F	-5.503030000	-0.661271000	-2.133024000
F	-5.323396000	2.426376000	-1.950383000
F	-5.652401000	3.873152000	-0.364893000
F	-6.517951000	1.887641000	-0.211775000
F	-2.621536000	2.057690000	4.356431000
F	-2.420355000	-0.049897000	3.871358000
F	-4.394842000	0.846907000	4.026265000
N	0.176351000	-2.215856000	-2.571522000
N	0.177058000	3.285981000	-0.852237000
Os	1.428842000	0.224564000	-0.769786000
P	2.710179000	-0.273726000	1.131680000
Se	2.832695000	-1.179967000	-2.367489000
Se	2.828718000	2.291657000	-1.294637000
Se	-0.416060000	0.781475000	-2.564583000
H	0.461278000	1.174445000	0.283669000
H	0.537633000	-1.164455000	-0.400865000

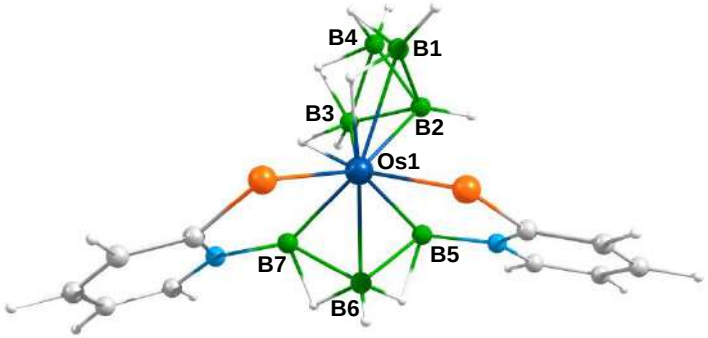


Figure S81. Optimized geometry of **8**.
Total energy = -786.983998268 a.u.
Cartesian coordinates for the calculated structure **8** (in Å)

C	-2.973832000	-0.978605000	-0.232252000
C	-4.225116000	-1.516674000	-0.597240000
H	-4.385887000	-1.790324000	-1.631740000
C	-5.221237000	-1.658938000	0.340902000
H	-6.187046000	-2.058336000	0.053192000
C	-4.981950000	-1.265890000	1.670963000
H	-5.744817000	-1.343221000	2.433542000
C	-3.743132000	-0.773594000	1.990802000
H	-3.481934000	-0.457376000	2.991049000
C	3.204902000	-0.657476000	-0.216862000
C	4.506636000	-1.086669000	-0.557808000
H	4.745651000	-1.217030000	-1.604932000
C	5.445640000	-1.311636000	0.420818000
H	6.446145000	-1.630880000	0.152254000
C	5.102549000	-1.109748000	1.772000000
H	5.816737000	-1.261005000	2.569804000
C	3.825608000	-0.708667000	2.063725000
H	3.487844000	-0.533622000	3.076129000
B	-0.873254000	2.609829000	-1.155361000
B	-1.494305000	2.257296000	0.410682000
B	-0.099139000	2.554382000	1.358447000
B	-0.679173000	3.742093000	0.206203000
B	-1.348443000	-0.138395000	1.549267000
B	0.091997000	-1.253958000	1.153698000
B	1.436655000	-0.116142000	1.555839000
N	-2.748502000	-0.646411000	1.069241000
N	2.885296000	-0.501704000	1.097970000
Os	0.005899000	0.653618000	0.057323000
Se	-1.613264000	-0.684123000	-1.506573000
Se	1.917709000	-0.273515000	-1.537722000
H	-0.095893000	3.680678000	-1.010240000
H	-1.469012000	2.772268000	-2.167340000
H	-2.625001000	2.189760000	0.756351000
H	0.062167000	2.677633000	2.524983000
H	-1.139902000	4.819917000	0.370931000
H	-1.438605000	0.352226000	2.630536000

H	0.157957000	-2.261544000	0.536275000	H	0.493511000	3.650821000	0.815492000
H	1.485106000	0.458618000	2.597880000	H	-0.825645000	-1.365704000	2.023970000
H	0.148321000	1.853083000	-1.374021000	H	0.987149000	-1.309565000	2.072571000
H	0.994055000	1.826991000	0.838152000				

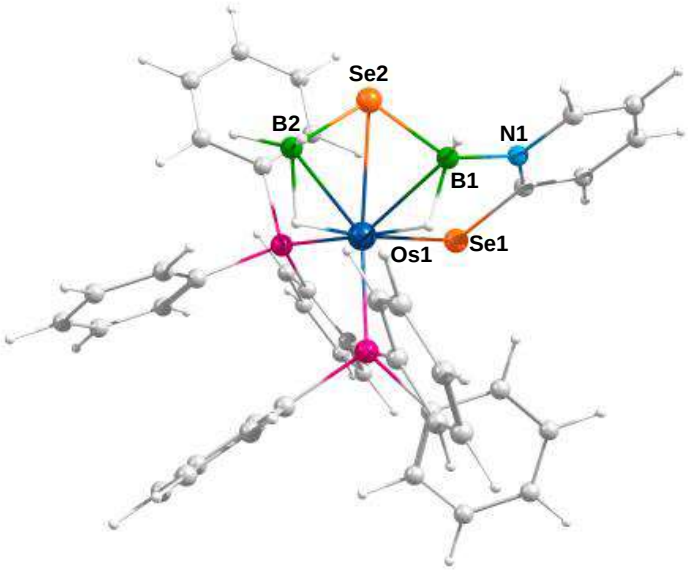


Figure S82. Optimized geometry of **10**.
Total energy = -2483.14378986 a.u.
Cartesian coordinates for the calculated structure **10** (in Å)

C	-2.322049000	-0.240695000	1.932503000	C	1.617664000	3.012143000	2.459680000
Os	0.275753000	-0.438662000	-0.594550000	C	3.272577000	2.250636000	4.050767000
Se	0.900422000	-1.762179000	1.544068000	C	-2.633474000	-3.030763000	0.165863000
Se	0.132883000	-2.624045000	-2.033804000	C	3.760430000	-3.519095000	-0.875573000
P	1.129126000	1.689596000	-0.072071000	C	-4.199753000	1.540863000	0.169911000
P	-1.992363000	-0.287655000	0.096717000	C	2.279433000	3.153082000	3.681289000
N	2.718838000	-2.750690000	-0.439482000	C	4.422540000	-4.400754000	-0.063591000
C	2.604387000	1.703543000	-2.504242000	C	-4.777858000	3.043041000	-1.632691000
C	-3.085135000	1.080323000	-0.543202000	C	4.009126000	-4.512602000	1.278001000
C	-2.982045000	-1.790202000	-0.386882000	C	-5.037182000	2.515457000	-0.369437000
C	-3.478221000	-0.805090000	2.491598000	C	-4.747660000	-2.887681000	-1.637105000
C	-1.410746000	0.388087000	2.787820000	C	-4.407804000	-4.110662000	-1.068143000
C	-2.808004000	-0.085093000	4.699849000	C	-3.347215000	-4.177754000	-0.163442000
C	-1.038995000	3.399218000	0.595813000	C	2.563148000	2.155571000	-1.179666000
C	-3.718612000	-0.726774000	3.861734000	C	1.930851000	1.958156000	1.593658000
C	2.306536000	-2.834706000	0.862298000	C	0.060398000	3.206030000	-0.252044000
C	3.636486000	2.093068000	-3.357634000	C	-3.670317000	2.594855000	-2.348323000
C	-4.041920000	-1.731858000	-1.295552000	C	-2.828583000	1.625705000	-1.806297000
C	-1.651435000	0.469885000	4.158767000	B	2.001775000	-1.874376000	-1.512465000
C	-1.833289000	4.537588000	0.492814000	B	-0.284318000	-0.811338000	-2.980341000
C	3.601700000	1.203567000	3.190355000	H	2.021743000	3.978867000	4.335567000
C	0.318947000	4.174919000	-1.229765000	H	3.789840000	2.363453000	4.997128000
C	-0.486551000	5.308003000	-1.343955000	H	4.377293000	0.496985000	3.464333000
C	2.933912000	1.056183000	1.978738000	H	3.203364000	0.239611000	1.322057000
C	2.967465000	-3.736671000	1.726681000	H	0.868276000	3.741793000	2.184084000
C	-1.559430000	5.498507000	-0.478402000	H	3.572738000	3.381387000	0.283939000
C	4.646724000	2.935798000	-2.900706000	H	5.396092000	4.049624000	-1.216329000
C	4.615503000	3.392616000	-1.584183000	H	5.452017000	3.233822000	-3.563117000
C	3.581136000	3.009805000	-0.732689000	H	3.647973000	1.730152000	-4.379411000

H	1.833352000	1.043299000	-2.876294000
H	1.154142000	4.056915000	-1.906630000
H	-0.266266000	6.043102000	-2.110363000
H	-2.181141000	6.382843000	-0.562911000
H	-2.674869000	4.663984000	1.164113000
H	-1.283998000	2.663163000	1.350198000
H	-1.972065000	1.288549000	-2.372335000
H	-3.453848000	3.001267000	-3.329904000
H	-5.431166000	3.799542000	-2.053363000
H	-5.893639000	2.859948000	0.200163000
H	-4.421079000	1.147524000	1.153288000
H	-1.797510000	-3.101183000	0.852341000
H	-3.066868000	-5.128178000	0.277194000
H	-4.958831000	-5.007128000	-1.330321000
H	-5.564080000	-2.824312000	-2.348105000
H	-4.326643000	-0.788816000	-1.743284000
H	2.629237000	-3.793744000	2.753065000
H	4.507819000	-5.200157000	1.951533000
H	5.240283000	-4.987120000	-0.459976000
H	4.019773000	-3.382426000	-1.915861000
H	-1.430098000	-0.756373000	-3.304824000
H	0.541590000	-0.540512000	-3.801730000
H	-0.114215000	0.276861000	-2.107356000
H	1.952060000	-0.624018000	-1.078772000
H	2.710798000	-1.713092000	-2.458023000
H	-0.491055000	0.796124000	2.390178000
H	-0.924863000	0.956068000	4.799988000
H	-2.994104000	-0.028831000	5.766664000
H	-4.616851000	-1.173600000	4.273741000
H	-4.191510000	-1.318684000	1.859184000

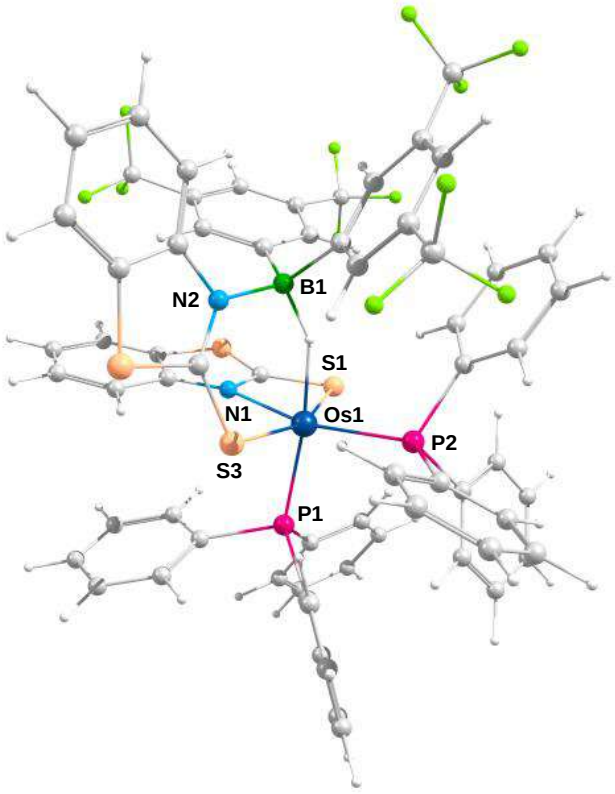


Figure S83. Optimized geometry of **11**.
Total energy = -6242.52235302 a.u.
Cartesian coordinates for the calculated structure **11** (in Å)

Os	1.181770000	0.122059000	0.018383000
S	0.891610000	-0.062501000	-2.366997000
S	1.067548000	1.136410000	2.309322000
S	-1.079806000	0.483902000	-4.477220000
S	0.379123000	4.167279000	1.815946000
N	-1.825963000	0.370095000	-1.987857000
N	0.727629000	2.295364000	0.037032000
C	0.723222000	2.512296000	1.341842000
C	0.343246000	3.562470000	-2.085885000
C	-3.494208000	3.414983000	2.068789000
C	2.554497000	-2.544594000	3.303669000
C	-0.583865000	-4.072047000	1.546458000
C	0.200822000	4.577682000	0.110135000
C	2.771400000	-2.532307000	1.919820000
C	-3.008249000	0.562792000	-2.744318000
C	-3.407741000	3.556824000	0.687035000
C	1.610426000	-3.580352000	-0.492189000
C	-1.594558000	-4.543576000	2.384099000
C	0.023737000	4.797593000	-2.635939000
C	3.601353000	3.383201000	-0.947394000
C	-0.733322000	0.265678000	-2.762830000
C	4.333640000	0.597167000	2.436413000

C	4.545498000	1.149925000	1.170288000
C	-2.425758000	1.331045000	0.451800000
C	-0.071345000	-2.777818000	1.699037000
C	-2.749950000	-1.306225000	-0.254484000
C	-3.020308000	2.240571000	2.644863000
C	-3.802158000	-1.467499000	0.654071000
C	-4.318497000	0.645077000	-2.260888000
C	3.796349000	4.472055000	-1.791718000
C	3.722208000	2.071398000	-1.426745000
C	-0.620855000	-1.964394000	2.700449000
C	3.599802000	-2.803983000	4.190600000
C	4.577698000	-0.644231000	-1.101116000
C	5.613747000	2.047413000	1.008351000
C	-2.530119000	-2.368816000	-1.146963000
C	4.040143000	-1.523267000	-2.047851000
C	4.067883000	-2.791934000	1.452849000
C	-1.622080000	-2.439602000	3.544683000
C	-0.112749000	5.816718000	-0.441797000
C	-2.869851000	2.540436000	-0.102950000
C	1.784934000	-5.733875000	-2.298928000
C	-0.204619000	5.917127000	-1.826529000
C	-2.109898000	-3.735560000	3.393088000
C	1.074415000	-3.484950000	-1.780338000
C	-2.788155000	0.661388000	-4.126603000
C	6.429307000	2.390283000	2.084317000
C	5.149973000	0.939310000	3.513150000
C	-3.828272000	0.857098000	-5.030764000
C	4.881207000	-3.062054000	3.712398000
C	4.849176000	-2.438382000	-2.720395000
C	6.196882000	1.840196000	3.343468000
C	1.160703000	-4.548851000	-2.677454000
C	-3.958400000	4.807728000	0.058249000
C	-5.360706000	0.838039000	-3.160985000
C	2.224415000	-4.786014000	-0.118767000
C	4.018541000	1.881759000	-2.781212000
C	-4.596786000	-2.616390000	0.666518000
C	-5.123949000	0.948177000	-4.534566000
C	-3.323686000	-3.512116000	-1.145411000
C	2.314199000	-5.848847000	-1.014640000
C	4.098027000	4.271276000	-3.137382000
C	5.109777000	-3.055531000	2.338045000
C	5.953836000	-0.710551000	-0.841240000
C	6.214374000	-2.494394000	-2.453516000
C	-4.371561000	-3.646880000	-0.236434000
C	4.201308000	2.973458000	-3.630002000
C	-2.498026000	1.221082000	1.850088000
C	6.762281000	-1.627252000	-1.509815000
H	-0.684312000	-0.184860000	-0.021626000
C	-3.045856000	-4.637653000	-2.103397000
C	-5.755524000	-2.701668000	1.622532000
C	-3.032899000	2.103278000	4.143111000
B	-1.892464000	0.076546000	-0.415198000
P	1.392401000	-2.162453000	0.705520000
P	3.483044000	0.624542000	-0.272796000
C	0.426254000	3.439486000	-0.695462000
F	-6.861039000	-2.080522000	1.132248000
F	-5.484691000	-2.116497000	2.810591000
F	-6.116733000	-3.979565000	1.881690000
F	-4.184606000	-5.213457000	-2.556923000
F	-2.322653000	-5.632371000	-1.524252000
F	-2.347165000	-4.235671000	-3.189290000
F	-3.010050000	0.811120000	4.544459000
F	-4.129162000	2.671061000	4.698344000
F	-1.959354000	2.704405000	4.717270000
F	-5.317432000	4.831006000	0.094957000
F	-3.546530000	5.927327000	0.705945000
F	-3.604367000	4.945327000	-1.235246000
H	2.982302000	-1.511481000	-2.263133000
H	4.403342000	-3.111734000	-3.443458000
H	6.844592000	-3.208878000	-2.971183000
H	7.823219000	-1.663577000	-1.287746000
H	6.403508000	-0.058222000	-0.105846000
H	3.527924000	-0.101827000	2.592014000
H	4.957772000	0.500621000	4.485373000
H	6.826775000	2.112241000	4.183195000
H	7.244821000	3.089247000	1.934776000
H	5.818001000	2.485884000	0.040994000
H	3.374850000	3.562756000	0.096167000
H	3.705004000	5.477490000	-1.396980000
H	4.249496000	5.119763000	-3.795197000
H	4.434824000	2.803142000	-4.675209000
H	4.125395000	0.883263000	-3.183682000
H	1.566587000	-2.369108000	3.705634000
H	3.402240000	-2.812881000	5.256892000
H	5.692040000	-3.270126000	4.401476000
H	6.101108000	-3.257347000	1.948151000
H	4.271017000	-2.807360000	0.391625000
H	2.630299000	-4.906568000	0.876617000
H	2.793678000	-6.770340000	-0.703219000
H	1.851585000	-6.563469000	-2.993870000
H	0.732722000	-4.448967000	-3.668335000
H	0.600881000	-2.566334000	-2.094935000
H	-1.976432000	-5.548316000	2.240756000
H	-2.891350000	-4.105514000	4.047109000
H	-2.023084000	-1.791491000	4.315783000
H	-0.264083000	-0.951681000	2.831972000
H	-0.203921000	-4.726621000	0.774983000
H	-4.996607000	-4.529934000	-0.237296000
H	-4.034316000	-0.680779000	1.359701000
H	-1.738439000	-2.296928000	-1.881315000
H	-3.916266000	4.200898000	2.682068000
H	-2.808359000	2.704326000	-1.169706000
H	-2.144230000	0.320984000	2.332739000
H	-4.527491000	0.558923000	-1.206155000
H	-6.374256000	0.901984000	-2.783696000
H	-5.951430000	1.099905000	-5.217136000
H	-3.631274000	0.931069000	-6.093371000
H	-0.043090000	4.895241000	-3.713305000
H	-0.459789000	6.868722000	-2.277445000
H	-0.292252000	6.677745000	0.190591000
H	0.551909000	2.710130000	-2.715782000

V References

1. G. Ferrando and K. G. Caulton, *Inorg. Chem.,* 1999, **38**, 4168–4170.
2. C. S. MacNeil, S-J. Hsiang and P. G. Hayes, *Chem. Commun., 2020,* **56***,* 12323—12326.
3. K. Samigullin, M. Bolte, H.-W. Lerner, and M. Wagner, *Organometallics,* 2014, **33**, 13, 3564–3569.
4. G. E. Ryschlewitsch, K. C. Nainan, S. R. Miller, L. J. Todd, W. J. Dewkett, M. Grace, H. Beall, M. F. Hawthorne and R. Leyden, *Inorg. Synth.,* 2007, **15**, 111-118.
5. (*a*) J. J. Led and H. Gesmar, *Chem. Rev.*, 1991, **91**, 1413−1426; (*b*) L. Yang, R. Simionescu, A. Lough and H. Yan, *Dyes Pigm*., 2011, **91**, 264−267; (*c*) R. Weiss and R. N. Grimes, *J. Am. Chem. Soc.*, 1978, **100**, 1401−1405.
6. (*a*) C.-G. Lin, M. Hutin, C. Busche, N. L. Bell, D.-L. Long and L. Cronin, *Dalton Trans*., 2021, **50**, 2350–2353; (*b*) D. F. Evans, *J. Chem. Soc.,* 1959, 2003.
7. G. M. Sheldrick, *Acta Crystallogr., Sect. C: Struct. Chem.* 2015, **C71**, 3 – 8.
8. O. V. Dolomanov, L. J. Bourhis, R. J. Gildea, J. A. K. Howard and H. Puschmann, *J. Appl. Crystallogr*., 2009, **42**, 339–341.
9. C. F. Macrae, P. R. Edgington, P. McCabe, E. Pidcock, G. P. Shields, R. Taylor, M. Towler and J. Van De Streek, *J. Appl. Crystallogr.,* 2006, **39**, 453-457.
10. M. J. Frisch, G. W. Trucks, H. B. Schlegel, G. E. Scuseria, M. A. Robb, J. R. Cheeseman, G. Scalmani, V. Barone, B. Mennucci, G. A. Petersson, H. Nakatsuji, M. Caricato, X. Li, H. P. Hratchian, A. F. Izmaylov, J. Bloino, G. Zheng, J. L. Sonnenberg, M. Hada, M. Ehara, K. Toyota, R. Fukuda, J. Hasegawa, M. Ishida, T. Nakajima, Y. Honda, O. Kitao, H. Nakai, T. Vreven, J. A. Montgomery, J. E. Peralta, F. Ogliaro, M. Bearpark, J. J. Heyd, E. Brothers, K. N. Kudin, V. N. Staroverov, T. Keith, R. Kobayashi, J. Normand, K. Raghavachari, A. Rendell, J. C. Burant, S. S. Iyengar, J. Tomasi, M. Cossi, N. Rega, J. M. Millam, M. Klene, J. E. Knox, J. B. Cross, V. Bakken, C. Adamo, J. Jaramillo, R. Gomperts, R. E. Stratmann, O. Yazyev, A. J. Austin, R. Cammi, C. Pomelli, J. W. Ochterski, R. L. Martin, K. Morokuma, V. G. Zakrzewski, G. A. Voth, P. Salvador, J. J. Dannenberg, S. Dapprich, A. D. Daniels, O. Farkas, J. B. Foresman, J. V. Ortiz, J. Cioslowski and D. J. Fox, *Gaussian16, Rev. B.01;* Gaussian, Inc., Wallingford CT, 2016.
11. C. Lee, W. Yang and R. G. Parr, *Phys*. *Rev*. *B,* 1988, **37**, 785–789.
12. EMSL Basis Set Exchange Library. https://bse.pnl.gov/bse/portal
13. F. London, *J. Phys. Radium*, 1937, **8**, 397–409; (*b*) R. Ditchfield, *Mol. Phys.*, 1974, **27**, 789 - 807; (*c*) K. Wolinski, J. F. Hinton and P. Pulay, *J. Am. Chem. Soc.*, 1990, **112**, 8251–8260.
14. K. Wiberg, *Tetrahedron,* 1968, **24**, 1083–1096.
15. E. D. Glendening, J. K. Badenhoop, A. E. Reed, J. E. Carpenter, J. A. Bohmann, C.M. Morales, C. R. Landis and F. Weinhold, *NBO Program 6.0*; Theoretical Chemistry Institute, University of Wisconsin: Madison, WI, USA, 2013.
16. Chemcraft-Graphical Software for Visualization of Quantum Chemistry Computations. Available online: https://www.chemcraftprog.com (accessed on 1 December 2021).
17. T. Lu and F. Chen, *J. Comput. Chem.* 2012, **33**, 580–592.

Editorial

ACS Sustainable Chemistry & Engineering

pubs.acs.org/journal/ascecg

Editorial

The ACS Sustainable Family—Complementary yet Distinct: Some Evolving Thoughts from the Editors' Desks

Cite This: *ACS Sustainable Chem. Eng.* 2025, 13, 14675−14676

Read Online

ACCESS | Metrics & More | Article Recommendations

Downloaded via INDIAN INST OF TECH MADRAS on January 5, 2026 at 07:24:33 (UTC).
See https://pubs.acs.org/sharingguidelines for options on how to legitimately share published articles.

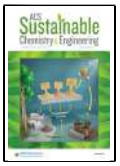
Sustainability has rapidly become a defining criterion for decision-making across science, industry, and government. It now shapes how policymakers, businesses, and consumers evaluate the viability of products, processes, and technologies. This is done not only to improve their performance but also to ensure sustained economic and environmental vitality. In 2013, the American Chemical Society (ACS) launched the journal *ACS Sustainable Chemistry & Engineering* (*ACS-SCE*) to convene and celebrate advances and discoveries in chemical processes and technologies that demonstrate the principles of green chemistry and green engineering. Thanks to the global research community, *ACS-SCE* has experienced rapid growth in stature and is now among the leading journals in the discipline, based on the increasing number of submissions from authors worldwide. During the past decade, the topics of waste recycling and circularity have become increasingly important in the context of sustainability. To provide more bandwidth for publishing work in these rapidly emerging areas, *ACS Sustainable Resource Management* (*ACS-SRM*) was launched in 2024. Together, these journals form a cohesive journal family that reflects ACS's commitment to sustainability from cutting-edge scientific, technological, and systems-based perspectives.

While both titles continue to rapidly grow in submissions, we are often challenged, as editors, to articulate how the two journals differ in scope and to clarify what attributes set these two journals apart. This editorial seeks to offer a clear comparison between *ACS-SCE* and *ACS-SRM*, helping authors determine the best venue for their work while underscoring the shared vision that unites both journals.

ACS-SCE continues to focus on the design of novel processes, technologies, and materials that minimize negative environmental impacts and maximize the efficiency of these activities. The key principles under consideration are (i) green chemistry and engineering that reduce hazardous compounds in chemical processes, (ii) circularity that produces products that can be reused, recycled or degraded by organisms, and (iii) efficiency of energy utilization and storage by focusing on advanced materials and low-energy manufacturing processes. A key motivation of *ACS-SCE* is thus to minimize the generation of toxic waste during chemical production, develop environmentally friendlier materials that produce less waste, and enhance industrial processes to reduce their ecological footprint. Examples of *ACS-SCE* principles include (i) life cycle assessment (LCA), which examines the environmental impact of extraction of raw materials, their use, and finally their disposal, (ii) the application of appropriate mass and/or intensity based metrics the at drive waste minimization thereby quantitatively leading to more effective and productive processes, (iii) the use of renewable feedstock instead of crude oil or coals, and (iv) intensification of chemical processes that minimize energy use or waste generation. Several editorials on these topics and others provide guidelines to authors on manuscript attributes that have the best chance of being published in *ACS-SCE*. Some of these editorials can be found in the repository of editorials as indicated in ref 1.

In contrast, ***ACS-SRM*** welcomes manuscripts that present novel approaches in managing natural resources (air, water, soil, minerals, and forests) and "wastes" (from food, textiles, agriculture, batteries, mining, energy-related elements, etc.) that preserve the environment and guarantee the long-term availability of these resources for sustaining human and ecological activities. *ACS-SRM* is dedicated to (i) resource efficiency by reducing wastes during resource extraction and consumption, (ii) protecting the environment through a controlled management of effluent discharge to air, water, and soil by utilizing technologies that minimize discharges, and (iii) developing strategic policy and governance guidelines that facilitate the proper implementation of regulations to ensure the sustainable use of our resources. The goal of *ACS-SRM* is to ensure the fulfillment of the United Nations Sustainable Development Goals (UNSDGs) in complementary ways to those addressed by *ACS-SCE*.[2−4] Examples of *ACS-SRM* content include (i) material flow analysis (MFA) of natural and waste resources as exemplified in a recent paper that describes the MFA of pesticides generated from the use of chemical fertilizers in Sri Lanka,[5] (ii) the conversion of biomass residues/wastes and industrial waste streams into functional materials that promote circular resource flows while mitigating carbon emissions, (iii) management of critical planetary resources such as air, water, and soil through remediation and pollution control using natural or waste streams of "biological" carbon, and (iv) promoting the recycling and reuse of consumer products such as building materials, textiles, and food, energy generation systems such as

Published: September 15, 2025



batteries, and mining wastes from the extraction of rare earth metals and critical minerals.

In summary, it should be recognized that both *ACS-SCE* and *ACS-SRM* showcase topics that are central to the achievement of the UNSDGs. *ACS-SCE* seeks to focus on the development of new principles and practices that spearhead the enhancement of sustainability. An *ACS-SRM* paper could use established techniques to address a new question or challenge associated with a resource or, indeed, the valorization of a waste. *ACS-SCE*, on the other hand, aims to showcase new techniques and insight at a fundamental level, which could result from the application of a resource-based question; however, clear novelty in the underpinning science and/or technology must be evident.

To further support this distinction, the ACS Sustainable Family of journals continues to promote the use of sustainability metrics, quantifiable indicators used to assess the environmental and economic impacts of technologies. In addition, *ACS-SRM* aims to promote the concept and development of metrics that meaningfully assess SUStainable MAnagement (SUSMA) of natural resources to better demonstrate benefits and challenges of processes reported in its pages. SUSMA metrics should be quantifiable parameters to ensure that management of waste does not lead to the generation of additional or unmanageable waste. For example, removal of contaminants from water, while essential for broader sustainability, should not lead to the generation of new or secondary wastes or toxicity that could be more problematic for the environment and become unmanageable.

As an editorial team, we recognize that current forms of sustainability metrics often fail to comprehensively evaluate the downstream impacts of a product, or "new waste", which may be associated with a technological intervention or treatment. *ACS-SRM* will focus its attention on the development and celebration of management technologies that demonstrate benefits and challenges that can be identified with the aid of suitable SUSMA metrics.

The SUSMA metrics are structured to evaluate key dimensions of sustainability, including but not limited to resource efficiency, circularity, environmental impact, societal and ethical impact, and management and resilience. Each technology or solution will be assessed using individual and composite scores, differentiating its suitability for a sustainable planet. To facilitate analysis, we envision an initial framework depicted in Figure 1. We understand that further dialogue and refinement are necessary to synthesize a universally acceptable framework for SUSMA metrics, and we aim to encourage such discourse in ACS-SRM.



Figure 1. Important components of proposed SUSMA metrics, with each metric being evaluated individually and weighted suitably to arrive at a cumulative score that may be used to quantify technologies for their appropriateness.

We hope that this editorial clarifies the key differences and complementarities of the two journals within the ACS Sustainable Family. We invite the research community to take advantage of these unique forums to submit their manuscripts. When warranted, the editors of these two journals will encourage authors to consider transfer offers within the ACS portfolio to ensure that their manuscript is being processed by the journal that best aligns with the scope of their work. The transfer process will be seamless and obviates the need to resubmit manuscripts. We truly appreciate the support of the global research community and welcome queries and feedback as always to serve you better.

Thalappil Pradeep, Associate Editor, *ACS Sustainable Resource Management* orcid.org/0000-0003-3174-534X

Michael K. C. Tam, Deputy Editor, *ACS Sustainable Resource Management* orcid.org/0000-0002-7603-5635

Danielle Julie Carrier, Executive Editor, *ACS Sustainable Resource Management* orcid.org/0000-0003-3322-4660

Jingwen Chen, Executive Editor, *ACS Sustainable Chemistry & Engineering* orcid.org/0000-0002-5756-3336

Bing Joe Hwang, Executive Editor, *ACS Sustainable Chemistry & Engineering* orcid.org/0000-0002-3873-2149

Michael Meier, Executive Editor, *ACS Sustainable Chemistry & Engineering* orcid.org/0000-0002-4448-5279

Bala Subramaniam, Executive Editor, *ACS Sustainable Chemistry & Engineering* orcid.org/0000-0001-5361-1954

Rowan S. Brower, Assistant Managing Editor, ACS Publications orcid.org/0000-0002-0324-9173

Peter Licence, Editor-in-Chief, *ACS Sustainable Chemistry & Engineering* orcid.org/0000-0003-2992-0153

AUTHOR INFORMATION

Complete contact information is available at: https://pubs.acs.org/10.1021/acssuschemeng.5c08629

Notes

Views expressed in this editorial are those of the authors and not necessarily the views of the ACS.

REFERENCES

(1) https://pubs.acs.org/action/doSearch?SeriesKey=ascecg&sortBy=Earliest&ContentItemType=editorial.

(2) Sustainable Development Goals: 17 Goals to Transform our World. https://www.un.org/en/exhibits/page/sdgs-17-goals-transform-world.

(3) Anastas, P.; et al. The Power of the United Nations Sustainable Development Goals in Sustainable Chemistry and Engineering Research. *ACS Sustainable Chem. Eng.* **2021**, *9* (24), 8015−8017.

(4) Tam, M. Welcome to ACS Sustainable Resource Management. *ACS Sustainable Resour. Manage.* **2024**, *1* (1), 1−3.

(5) Fein-Cole, M. J.; Esham, M.; Jayathilake, N.; Otoo, M.; Koliba, C.; Galford, G. L.; Porterfield, K. K.; Wijethunga, I. B.; Roy, E. D. Lessons from the Short-Lived 2021 Fertilizer Import Ban in Sri Lanka Based on Analysis of Nutrient Flows. *ACS Sustainable Resour. Manage.* **2024**, *1* (11), 2361−2371.

ACS Sustainable Resource Management

pubs.acs.org/acssrm

Editorial

The ACS Sustainable Family—Complementary yet Distinct: Some Evolving Thoughts from the Editors' Desks

Cite This: *ACS Sustainable Resour. Manage.* 2025, 2, 1618−1619

Read Online

ACCESS | Metrics & More | Article Recommendations

Downloaded via INDIAN INST OF TECH MADRAS on January 5, 2026 at 07:24:51 (UTC).
See https://pubs.acs.org/sharingguidelines for options on how to legitimately share published articles.

Sustainability has rapidly become a defining criterion for decision-making across science, industry, and government. It now shapes how policymakers, businesses, and consumers evaluate the viability of products, processes, and technologies. This is done not only to improve their performance but also to ensure sustained economic and environmental vitality. In 2013, the American Chemical Society (ACS) launched the journal *ACS Sustainable Chemistry & Engineering* (*ACS-SCE*) to convene and celebrate advances and discoveries in chemical processes and technologies that demonstrate the principles of green chemistry and green engineering. Thanks to the global research community, *ACS-SCE* has experienced rapid growth in stature and is now among the leading journals in the discipline, based on the increasing number of submissions from authors worldwide. During the past decade, the topics of waste recycling and circularity have become increasingly important in the context of sustainability. To provide more bandwidth for publishing work in these rapidly emerging areas, *ACS Sustainable Resource Management* (*ACS-SRM*) was launched in 2024. Together, these journals form a cohesive journal family that reflects ACS's commitment to sustainability from cutting-edge scientific, technological, and systems-based perspectives.

While both titles continue to rapidly grow in submissions, we are often challenged, as editors, to articulate how the two journals differ in scope and to clarify what attributes set these two journals apart. This editorial seeks to offer a clear comparison between *ACS-SCE* and *ACS-SRM*, helping authors determine the best venue for their work while underscoring the shared vision that unites both journals.

ACS-SCE continues to focus on the design of novel processes, technologies, and materials that minimize negative environmental impacts and maximize the efficiency of these activities. The key principles under consideration are (i) green chemistry and engineering that reduce hazardous compounds in chemical processes, (ii) circularity that produces products that can be reused, recycled or degraded by organisms, and (iii) efficiency of energy utilization and storage by focusing on advanced materials and low-energy manufacturing processes. A key motivation of *ACS-SCE* is thus to minimize the generation of toxic waste during chemical production, develop environmentally friendlier materials that produce less waste, and enhance industrial processes to reduce their ecological footprint. Examples of *ACS-SCE* principles include (i) life cycle assessment (LCA), which examines the environmental impact of extraction of raw materials, their use, and finally their disposal, (ii) the application of appropriate mass and/or intensity based metrics the at drive waste minimization thereby quantitatively leading to more effective and productive processes, (iii) the use of renewable feedstock instead of crude oil or coals, and (iv) intensification of chemical processes that minimize energy use or waste generation. Several editorials on these topics and others provide guidelines to authors on manuscript attributes that have the best chance of being published in *ACS-SCE*. Some of these editorials can be found in the repository of editorials as indicated in ref 1.

In contrast, ***ACS-SRM*** welcomes manuscripts that present novel approaches in managing natural resources (air, water, soil, minerals, and forests) and "wastes" (from food, textiles, agriculture, batteries, mining, energy-related elements, etc.) that preserve the environment and guarantee the long-term availability of these resources for sustaining human and ecological activities. *ACS-SRM* is dedicated to (i) resource efficiency by reducing wastes during resource extraction and consumption, (ii) protecting the environment through a controlled management of effluent discharge to air, water, and soil by utilizing technologies that minimize discharges, and (iii) developing strategic policy and governance guidelines that facilitate the proper implementation of regulations to ensure the sustainable use of our resources. The goal of *ACS-SRM* is to ensure the fulfillment of the United Nations Sustainable Development Goals (UNSDGs) in complementary ways to those addressed by *ACS-SCE*.[2−4] Examples of *ACS-SRM* content include (i) material flow analysis (MFA) of natural and waste resources as exemplified in a recent paper that describes the MFA of pesticides generated from the use of chemical fertilizers in Sri Lanka,[5] (ii) the conversion of biomass residues/wastes and industrial waste streams into functional materials that promote circular resource flows while mitigating carbon emissions, (iii) management of critical planetary resources such as air, water, and soil through remediation and pollution control using natural or waste streams of "biological" carbon, and (iv) promoting the recycling and reuse of consumer products such as building materials, textiles, and food, energy generation systems such as

Published: September 25, 2025



batteries, and mining wastes from the extraction of rare earth metals and critical minerals.

In summary, it should be recognized that both *ACS-SCE* and *ACS-SRM* showcase topics that are central to the achievement of the UNSDGs. *ACS-SCE* seeks to focus on the development of new principles and practices that spearhead the enhancement of sustainability. An *ACS-SRM* paper could use established techniques to address a new question or challenge associated with a resource or, indeed, the valorization of a waste. *ACS-SCE*, on the other hand, aims to showcase new techniques and insight at a fundamental level, which could result from the application of a resource-based question; however, clear novelty in the underpinning science and/or technology must be evident.

To further support this distinction, the ACS Sustainable Family of journals continues to promote the use of sustainability metrics, quantifiable indicators used to assess the environmental and economic impacts of technologies. In addition, *ACS-SRM* aims to promote the concept and development of metrics that meaningfully assess SUStainable MAnagement (SUSMA) of natural resources to better demonstrate benefits and challenges of processes reported in its pages. SUSMA metrics should be quantifiable parameters to ensure that management of waste does not lead to the generation of additional or unmanageable waste. For example, removal of contaminants from water, while essential for broader sustainability, should not lead to the generation of new or secondary wastes or toxicity that could be more problematic for the environment and become unmanageable.

As an editorial team, we recognize that current forms of sustainability metrics often fail to comprehensively evaluate the downstream impacts of a product, or "new waste", which may be associated with a technological intervention or treatment. *ACS-SRM* will focus its attention on the development and celebration of management technologies that demonstrate benefits and challenges that can be identified with the aid of suitable SUSMA metrics.

The SUSMA metrics are structured to evaluate key dimensions of sustainability, including but not limited to resource efficiency, circularity, environmental impact, societal and ethical impact, and management and resilience. Each technology or solution will be assessed using individual and composite scores, differentiating its suitability for a sustainable planet. To facilitate analysis, we envision an initial framework depicted in Figure 1. We understand that further dialogue and refinement are necessary to synthesize a universally acceptable framework for SUSMA metrics, and we aim to encourage such discourse in ACS-SRM.



Figure 1. Important components of proposed SUSMA metrics, with each metric being evaluated individually and weighted suitably to arrive at a cumulative score that may be used to quantify technologies for their appropriateness.

We hope that this editorial clarifies the key differences and complementarities of the two journals within the ACS Sustainable Family. We invite the research community to take advantage of these unique forums to submit their manuscripts. When warranted, the editors of these two journals will encourage authors to consider transfer offers within the ACS portfolio to ensure that their manuscript is being processed by the journal that best aligns with the scope of their work. The transfer process will be seamless and obviates the need to resubmit manuscripts. We truly appreciate the support of the global research community and welcome queries and feedback as always to serve you better.

Thalappil Pradeep, Associate Editor, *ACS Sustainable Resource Management* orcid.org/0000-0003-3174-534X

Michael K. C. Tam, Deputy Editor, *ACS Sustainable Resource Management* orcid.org/0000-0002-7603-5635

Danielle Julie Carrier, Executive Editor, *ACS Sustainable Resource Management* orcid.org/0000-0003-3322-4660

Jingwen Chen, Executive Editor, *ACS Sustainable Chemistry & Engineering* orcid.org/0000-0002-5756-3336

Bing Joe Hwang, Executive Editor, *ACS Sustainable Chemistry & Engineering* orcid.org/0000-0002-3873-2149

Michael Meier, Executive Editor, *ACS Sustainable Chemistry & Engineering* orcid.org/0000-0002-4448-5279

Bala Subramaniam, Executive Editor, *ACS Sustainable Chemistry & Engineering* orcid.org/0000-0001-5361-1954

Rowan S. Brower, Assistant Managing Editor, ACS Publications orcid.org/0000-0002-0324-9173

Peter Licence, Editor-in-Chief, *ACS Sustainable Chemistry & Engineering* orcid.org/0000-0003-2992-0153

AUTHOR INFORMATION

Complete contact information is available at: https://pubs.acs.org/10.1021/acssusresmgt.5c00410

Notes

Views expressed in this editorial are those of the authors and not necessarily the views of the ACS.

REFERENCES

(1) https://pubs.acs.org/action/doSearch?SeriesKey=ascecg&sortBy=Earliest&ContentItemType=editorial.

(2) Sustainable Development Goals: 17 Goals to Transform our World. https://www.un.org/en/exhibits/page/sdgs-17-goals-transform-world.

(3) Anastas, P.; et al. The Power of the United Nations Sustainable Development Goals in Sustainable Chemistry and Engineering Research. *ACS Sustainable Chem. Eng.* **2021**, *9* (24), 8015−8017.

(4) Tam, M. Welcome to ACS Sustainable Resource Management. *ACS Sustainable Resour. Manage.* **2024**, *1* (1), 1−3.

(5) Fein-Cole, M. J.; Esham, M.; Jayathilake, N.; Otoo, M.; Koliba, C.; Galford, G. L.; Porterfield, K. K.; Wijethunga, I. B.; Roy, E. D. Lessons from the Short-Lived 2021 Fertilizer Import Ban in Sri Lanka Based on Analysis of Nutrient Flows. *ACS Sustainable Resour. Manage.* **2024**, *1* (11), 2361−2371.

Patents

Indian patents (Granted)

1. Materials and methods for sustainable and affordable atmospheric water harvesting Thalappil Pradeep, Ankit Nagar, Sonali Seth, application no. 202241049229 dated 2022, issued as patent no. 564434, issued on March 28, 2025.

Indian patents applied

1. Nanocluster-catalyzed ambient C-F bond activation, Thalappil Pradeep, Vivek Yadav, Parveen Kumar, Meena Nemiwal, Tomas Base, application no. 202541089113 dated August 26, 2025.

2. Method and system for manufacturing nanosilica using microdroplets, Thalappil Pradeep, Depanjan Sarkar, Angad Mahesh Yadav, Mridula, Rajesh Chandresh Parikh, application no. 202541133057 dated December 29, 2025.

PCT applied

1. A method for making nanoparticles from natural minerals using high-pressure water jets, Thalappil Pradeep, B. K. Spoorthi, Anubhav Mahapatra, application no. WO2025248553 dated May 28, 2025

2. A method of efficient transformation of crystalline minerals to nanoparticles by salt containing microdroplets, Thalappil Pradeep, Jamshiya Sulthana P, Anubhav Mahapatra, B. K. Spoorthi, Depanjan Sarkar, application no. PCT/IN2025/052153 dated December 28, 2025.

News reports (selected)

3 IIT-Madras professors honoured with Rashtriya Vigyan Puraskar

Chennai, Oct 28: Three professors from the Indian Institute of Technology Madras (IITM) have been selected for 'Rashtriya Vigyan Puraskar 2025', considered India's highest recognition for outstanding contributions by scientists, technologists, and innovators.

The award is conferred under four categories — VigyanRatna (VR), Vigyan Shri (VS), VigyanYuva Shanti SwarupBhatnagar (VY-SSB) and Vigyan Team (VT) — stated a press release issued by IITM on Tuesday. Prof Thalappil Pradeep is being awarded a VS for his globally-recognised research in clean water technologies, advanced materials, and molecular clusters.

The award is conferred under four categories —VigyanRatna (VR), Vigyan Shri (VS), VigyanYuva Shanti SwarupBhatnagar (VY-SSB) and Vigyan Team (VT) — stated a press release issued by IIT-M on Tuesday. Professor Thalappil Pradeep was awarded a VS and the VY-SSB award conferred on Professor Mohanasankar Sivaprakasam and Professor Shweta Prem Agrawal

The VY-SSB award is being conferred on Prof Mohanasankar Sivaprakasam for developing affordable healthcare technologies, medical devices, high-resolution large scale human brain imaging technologies, and establishing globally recognised R&D centres in the health-tech area.

Prof Shweta Prem Agrawal from Department of Computer Science and Engineering is also being awarded VY-SSB for her pioneering research contributions in the field of cryptography.

Congratulating the three professors, Prof V Kamakoti, Director, IIT Madras, said it is a recognition of not only their individual brilliance, but of the spirit of innovation and dedication that defines IITM.

"Their achievements reaffirm IIT Madras's commitment to advancing science and technology for the nation's development, and serve as an inspiration to our entire academic community," he added. —*PTI*

ਪੰਜਾਬ ਯੂਨੀਵਰਸਿਟੀ 'ਚ 13 ਦਸੰਬਰ ਨੂੰ ਹੋਣ ਵਾਲੇ ਡਿਗਰੀ ਵੰਡ ਸਮਾਰੋਹ ਦੌਰਾਨ ਆਨਰੇਰੀ ਡਿਗਰੀ ਲਈ ਚੁਣੀਆਂ ਨਾਮੀ ਹਸਤੀਆਂ ਦਾ ਐਲਾਨ

ਸੁਪਰ ਕੰਪਿਊਟਰ ਤਿਆਰ ਕਰਨ ਵਾਲੇ ਡਾ.ਵਿਜੈ ਨੂੰ ਮਿਲੇਗੀ ਡਾਕਟਰ ਆਫ ਸਾਇੰਸ ਦੀ ਆਨਰੇਰੀ ਡਿਗਰੀ

ਚੰਡੀਗੜ੍ਹ, 10 ਦਸੰਬਰ (ਕੇਲਨਾ) : ਪੰਜਾਬ ਯੂਨੀਵਰਸਿਟੀ 'ਚ 13 ਦਸੰਬਰ ਨੂੰ ਹੋਣ ਵਾਲੇ ਡਿਗਰੀ ਵੰਡ ਸਮਾਰੋਹ ਦੌਰਾਨ ਮਹਾਰਾਸ਼ਟਰ ਦੇ ਡਾ ਵਿਜੇ ਪੀ. ਭਟਕਰ ਨੂੰ ਡਾਕਟਰ ਆਫ ਸਾਇੰਸ ਦੀ ਆਨਰੇਰੀ ਡਿਗਰੀ (ਆਨਰੇਰੀ ਕਾਜ਼ਾ) ਨਾਲ ਸਨਮਾਨਿਤ ਕੀਤਾ ਜਾਵੇਗਾ। ਉਹ ਨਾਲੰਦਾ ਯੂਨੀਵਰਸਿਟੀ ਦੇ ਉਪ ਕੁਲਪਤੀ ਹਨ, ਜਿਨ੍ਹਾਂ ਨੂੰ ਪਰਮ ਸੁਪਰ ਕੰਪਿਊਟਰ ਤਿਆਰ ਕਰਨ ਲਈ ਜਾਣਿਆ ਜਾਂਦਾ ਹੈ। ਉਨ੍ਹਾਂ ਨੂੰ ਦੇਸ਼ੀਆਣੀ ਵਿਗਿਆਨੀ 100, ਪਦਮ ਭੂਸ਼ਣ, ਪਦਮਸ਼੍ਰੀ, ਮਹਾਰਾਸ਼ਟਰ ਭੂਸ਼ਣ ਜਿਹੇ ਕਈ ਐਵਾਰਡਾਂ ਨਾਲ ਚੁੱਕਿਆ ਹੈ। ਉਹ ਨਾਮੀ ਭਾਰਤੀ ਕੰਪਿਊਟਰ ਵਿਗਿਆਨੀ, ਆਈ ਟੀ. ਲੀਡਰ ਤੇ ਸਿੱਖਿਆ ਸ਼ਾਸਤਰੀ ਹਨ। ਉਹ ਇਸ ਸਮੇਂ ਭਾਰਤ ਲਈ ਐਕਸਾਸਕੇਲ ਸੁਪਰ ਕੰਪਿਊਟਰ ਵਿਕਸਤ ਕਰਨ 'ਤੇ ਕੰਮ ਕਰ ਰਹੇ ਹਨ। ਉਹ ਵਿਗਿਆਨ ਭਾਰਤੀ ਸੰਸਥਾ ਦੇ ਚੇਅਰਮੈਨ ਹਨ। ਉਨ੍ਹਾਂ ਨੇ 1991 'ਚ ਪਹਿਲਾ ਭਾਰਤੀ ਸੁਪਰ ਕੰਪਿਊਟਰ ਪਰਮ 8000 ਤੇ 1998 'ਚ ਪਰਮ 10000 ਵਿਕਸਤ ਕੀਤਾ ਉਹ 12 ਤੋਂ ਜ਼ਿਆਦਾ ਕਿਤਾਬਾਂ, 80 ਤਕਨੀਕੀ ਤੇ ਖੋਜ ਪੱਤਰ ਦਾ ਲੇਖਣ ਤੇ ਸੰਪਾਦਨ ਕਰ ਚੁੱਕੇ ਹਨ।

ਅਮਿਤਾਭ ਘੋਸ਼ ਨੂੰ ਡਾਕਟਰ ਆਫ ਲਿਟਰੇਚਰ

ਭਾਰਤੀ-ਬੰਗਾਲੀ ਲੇਖਕ ਅਮਿਤਾਭ ਘੋਸ਼ ਨੂੰ ਡਾਕਟਰ ਆਫ ਲਿਟਰੇਚਰ ਦੀ ਹਾਨਰੇਰੀ ਕਾਜ਼ਾ ਡਿਗਰੀ ਨਾਲ ਸਨਮਾਨਿਤ ਕੀਤਾ ਜਾਵੇਗਾ। ਉਨ੍ਹਾਂ ਨੂੰ 2007 'ਚ ਪਦਮਸ਼੍ਰੀ ਤੇ 2018 'ਚ ਗਿਆਨਪੀਠ ਪੁਰਸਕਾਰ ਮਿਲ ਚੁੱਕਿਆ ਹੈ। ਉਨ੍ਹਾਂ ਨੇ ਕੋਮੀ ਪਛਣ, ਬਗਤੀਵਾਦ ਤੇ ਜਲਵਾਯੂ ਤਬਦੀਲੀ ਜਿਹੇ ਵਿਸ਼ਿਆਂ ਨੂੰ ਆਪਣੇ ਨਾਵਲਾਂ ਦਾ ਵਿਸ਼ਾ ਬਣਾਇਆ ਹੈ। ਉਹ 'ਦਿ ਸਰਕਲ ਆਫ ਰੀਜ਼ਨ', 'ਦਿ ਗਿੱਲੇ ਲਾਈਨਜ਼', 'ਦਿ ਗਲਾਸ ਪੈਲੇਸ' ਜਿਹੇ ਨਾਵਲਾਂ ਦੇ ਰਚੇਤਾ ਹਨ।

ਜਸਟਿਸ ਗੋਇਲ ਨੂੰ ਡਾਕਟਰ ਆਫ ਲਾਅ

ਜਸਟਿਸ ਆਦਰਸ਼ ਕੁਮਾਰ ਗੋਇਲ ਨੂੰ ਡਾਕਟਰ ਆਫ ਲਾਅ ਦੀ ਆਨਰੇਰੀ ਡਿਗਰੀ ਨਾਲ ਸਨਮਾਨਿਤ ਕੀਤਾ ਜਾਵੇਗਾ। ਉਹ ਸੁਪਰੀਮ ਕੋਰਟ ਦੇ ਸਾਬਕਾ ਜੱਜ ਰਹਿਣ ਤੋਂ ਇਲਾਵਾ ਨੈਸ਼ਨਲ ਗਰੀਨ ਟ੍ਰਿਬਿਊਨਲ ਦੇ ਚੇਅਰਮੈਨ ਵੀ ਰਹਿ ਚੁੱਕੇ ਹਨ।

ਡਾ.ਵੇਰੂ ਨੂੰ ਉਦਯੋਗ ਰਤਨ

ਦੇਸ਼ ਦੀਆਂ ਨਾਮੀ ਸਾਫਟਵੇਅਰ ਕੰਪਨੀਆਂ 'ਚੋਂ ਇਕ ਤੇ ਦੇਸ਼ ਦੀਆਂ ਸ਼ੁਰੂਆਤੀ ਬੁਟਸਟ੍ਰੈਪਡ ਯੂਨੀਕਾਰਨ ਕੰਪਨੀਆਂ 'ਚੋਂ ਇਕ ਜੋਹੋ ਕਾਰਪੋਰੇਸ਼ਨ ਦੇ ਸੰਸਥਾਪਕ ਡਾ ਸ਼ੀਧਰ ਵੇਂਧੂ ਨੂੰ ਤਕਨਾਲੋਜੀ ਦੇ ਖੇਤਰ 'ਚ ਉਨ੍ਹਾਂ ਦੇ ਯੋਗਦਾਨ ਤੇ ਚੋਟੀ ਸਫਲਤਾ ਰਾਹੀਂ ਪੇਂਡੂ ਭਾਰਤ 'ਚ ਸਾਫਟਵੇਅਰ ਵਿਕਾਸ ਦੇ ਵਿਕੇਂਦਰੀਕਰਨ 'ਚ ਉਨ੍ਹਾਂ ਦੀ ਭੂਮਿਕਾ ਲਈ ਉਦਯੋਗ ਰਤਨ ਨਾਲ ਸਨਮਾਨਿਤ ਕੀਤਾ ਜਾਵੇਗਾ। ਉਨ੍ਹਾਂ ਨੂੰ ਪਦਮਸ਼੍ਰੀ ਪੁਰਸਕਾਰ ਵੀ ਮਿਲ ਚੁੱਕਿਆ ਹੈ।

ਪ੍ਰੋ. ਪ੍ਰਦੀਪ ਨੂੰ ਵਿਗਿਆਨ ਰਤਨ

ਭਾਰਤੀ-ਬੰਗਾਲੀ ਵਿਗਿਆਨ ਰਤਨ ਪੁਰਸਕਾਰ ਉਘੇ ਭਾਰਤੀ ਰਸਾਇਣ ਸ਼ਾਸਤਰੀ ਪ੍ਰੋ. ਪ੍ਰਦੀਪ ਥਲੱਪਿਲ ਨੂੰ ਦਿੱਤਾ ਜਾਵੇਗਾ। ਉਹ ਆਈ. ਆਈ. ਟੀ. ਮਦਰਾਸ 'ਚ ਪ੍ਰੋਫੈਸਰ ਹਨ। ਉਨ੍ਹਾਂ ਨੂੰ ਪਦਮਸ਼੍ਰੀ ਪੁਰਸਕਾਰ ਨਾਲ ਸਨਮਾਨਿਤ ਕੀਤਾ ਜਾ ਚੁੱਕਿਆ ਹੈ। ਉਨ੍ਹਾਂ ਵੱਲੋਂ ਨੈਨੋਤੈਕਨਾਲੋਜੀ 'ਚ ਕੀਤੇ ਗਏ ਮਹੱਤਵਪੂਰਨ ਕੰਮਾਂ ਨਾਲ ਆਲਮੀ ਪੱਧਰ 'ਤੇ ਮਾਨਤਾ ਪ੍ਰਾਪਤ ਪੀਣ ਵਾਲੇ ਪਾਣੀ ਨੂੰ ਸ਼ੁੱਧ ਕਰਨ ਦੀਆਂ ਤਕਨੀਕਾਂ ਦਾ ਵਿਕਾਸ ਹੋਇਆ।

ਅਮਰਜੀਤ ਗਰੇਵਾਲ ਨੂੰ ਸਾਹਿਤ ਰਤਨ ਪੁਰਸਕਾਰ

ਅਮਰਜੀਤ ਸਿੰਘ ਗਰੇਵਾਲ ਨੂੰ ਸਾਹਿਤ ਰਤਨ ਪੁਰਸਕਾਰ ਲਈ ਚੁਣਿਆ ਗਿਆ ਹੈ। ਉਹ ਜ਼ਿਲ੍ਹਾ ਨੂਰਮਹਿਲ ਦੇ ਪਿੰਡ ਨਾਰੰਗਵਾਲ ਦੇ ਜੰਮਪਲ ਹਨ। ਉਨ੍ਹਾਂ ਨੇ ਪੰਜਾਬ ਦੀ ਵਿਰਾਸਤ ਤੇ ਫ਼ਲਸਫ਼ੇ ਨੂੰ ਚਿੰਤਨ ਦਾ ਆਧਾਰ ਬਣਾਇਆ। ਮਸਨੂਈ ਬੁੱਧੀ (ਆਰਟੀਫਿਸ਼ੀਅਲ ਇੰਟੈਲੀਜੈਂਸ) 'ਤੇ ਵੀ ਉਨ੍ਹਾਂ ਨੇ ਬੜਾ ਕੰਮ ਕੀਤਾ ਹੈ। 'ਚੁਪ ਦੌੜ', 'ਵਾਪਸੀ', 'ਸੋ ਦਰੁ' ਤੇ 'ਦੇਹੀ' ਉਨ੍ਹਾਂ ਦੇ ਚਰਚਿਤ ਨਾਟਕ ਰਹੇ। 'ਦੇਹੀ' ਉਨ੍ਹਾਂ ਦਾ ਮਸਨੂਈ ਬੁੱਧੀ ਬਾਰੇ ਭਾਰਤ ਦਾ ਪਹਿਲਾ ਨਾਟਕ ਹੈ, ਜਿਸ ਨੂੰ ਕਈ ਸਟੇਜਾਂ 'ਤੇ ਪੇਸ਼ ਕੀਤਾ ਜਾ ਚੁੱਕਿਆ ਹੈ। ਉਨ੍ਹਾਂ ਨੇ ਕਾਂਵਤਾ, ਨਾਟਕ ਤੇ ਆਲੋਚਨਾ 'ਤੇ ਮਹੱਤਵਪੂਰਨ ਕੰਮ ਕੀਤਾ ਹੈ।

ਸਾਬਕਾ ਉਪ ਕੁਲਪਤੀ ਨੂੰ ਡਾਕਟਰ ਆਫ ਸਾਇੰਸ

ਪੰਜਾਬ ਯੂਨੀਵਰਸਿਟੀ ਦੇ ਉਪ ਕੁਲਪਤੀ ਰਹੇ ਪ੍ਰੋ. ਕੇ.ਐਨ. ਪਾਠਕ ਨੂੰ ਪਦਾਰਥ ਭੌਤਿਕੀ 'ਚ ਉਨ੍ਹਾਂ ਦੇ ਯੋਗਦਾਨ ਤੇ ਯੂਨੀਵਰਸਿਟੀ 'ਚ ਪ੍ਰਮੁੱਖ ਕੇਂਦਰਾਂ ਦੀ ਸਥਾਪਨਾ 'ਚ ਉਨ੍ਹਾਂ ਦੀ ਅਗਵਾਈ ਲਈ ਡਾਕਟਰ ਆਫ ਸਾਇੰਸ ਦੀ ਆਨਰੇਰੀ ਡਿਗਰੀ ਨਾਲ ਸਨਮਾਨਿਤ ਕੀਤਾ ਜਾਵੇਗਾ। ਉਹ 2000 ਤੋਂ ਲੈ ਕੇ 2006 ਤੱਕ ਉਪ ਕੁਲਪਤੀ ਰਹੇ ਸਨ।

ਸਰਬਜੋਤ ਸਿੰਘ ਨੂੰ ਖੇਡ ਰਤਨ ਪੁਰਸਕਾਰ

ਯੂਨੀਵਰਸਿਟੀ ਦੇ ਸਾਬਕਾ ਵਿਦਿਆਰਥੀ ਤੇ ਓਲੰਪੀਅਨ ਸਰਬਜੋਤ ਸਿੰਘ ਨੂੰ 10 ਮੀਟਰ ਏਅਰ ਪਿਸਟਲ ਮੁਕਾਬਲੇ 'ਚ ਪ੍ਰਾਪਤੀਆਂ ਲਈ ਖੇਡ ਰਤਨ ਪੁਰਸਕਾਰ ਨਾਲ ਸਨਮਾਨਿਤ ਕੀਤਾ ਜਾਵੇਗਾ। ਉਨ੍ਹਾਂ ਨੇ ਵਿਸ਼ਵ ਚੈਂਪੀਅਨਸ਼ਿਪ, ਏਸ਼ੀਆਈ ਖੇਡਾਂ ਤੇ ਪੈਰਿਸ 2024 ਓਲੰਪਿਕ 'ਚ ਮੈਡਲ ਜਿੱਤੇ। ਉਹ ਡਾਵਾਂ ਹਰਿਆਣਾ ਨਾਲ ਸਬੰਧਤ ਹਨ ਪਰ ਉਨ੍ਹਾਂ ਨੇ ਆਪਣੀ ਪੜ੍ਹਾਈ ਚੰਡੀਗੜ੍ਹ 'ਚ ਹੀ ਕੀਤੀ। ਉਹ ਇੰਵੇ ਦੇ ਡੀ.ਏ.ਵੀ. ਕਾਲਜ ਮਗਰੋਂ ਪੰਜਾਬ ਯੂਨੀਵਰਸਿਟੀ 'ਚ ਵੀ ਪੜ੍ਹੇ।

दैनिक भास्कर चंडीगढ़ भास्कर 11-12-2025

पीयू की 73वीं कन्वोकेशन 13 को • ओलिंपिक मेडलिस्ट सरबजोत सिंह को खेल रत्न

डॉ. विजय भटकर, अमिताव घोष और जस्टिस एके गोयल को मिलेगी ऑनरिस कॉसा डिग्री

एजुकेशन रिपोर्टर | चंडीगढ़

पंजाब यूनिवर्सिटी की 73वीं कन्वोकेशन सेरेमनी के लिए ऑनरिस कॉसा डिग्री और पीयू रत्न अवॉर्ड्स की लिस्ट फाइनल हो गई है। भारत के उपराष्ट्रपति और पीयू के चांसलर सीपी राधाकृष्णन ने नामों को मंजूरी दे दी है। समारोह 13 दिसंबर को होगा, जिसकी अध्यक्षता पंजाब के राज्यपाल व यूटी के प्रशासक गुलाब चंद कटारिया करेंगे।

पीयू की वाइस चांसलर प्रो. रेनु विग ने तैयारियों की समीक्षा की और सभी कमेटियों को निर्देश दिए कि समारोह को यादगार बनाया जाए। इस बार जिन दिग्गज हस्तियों को ऑनरिस कॉसा मिलेगा, उनमें परम सुपरकंप्यूटर के पायनिर और आर्किटेक्ट डॉ. विजय पी. भटकर, प्रसिद्ध फिजिसिस्ट प्रो. केएन पाठक, सुप्रीम कोर्ट के पूर्व जज जस्टिस आदर्श कुमार गोयल और जिनानपीठ सम्मानित लेखक डॉ. अमिताव घोष शामिल हैं। वहीं पीयू रत्न अवॉर्ड्स में जोहो के फाउंडर डॉ. श्रीधर वेंबू को उद्योग रत्न, आईआईटी मद्रास के प्रो. प्रदीप थलप्पिल को विज्ञान रत्न, 10 एम एयर पिस्टल में ओलिंपिक मेडलिस्ट सरबजोत सिंह को खेल रत्न और राइटर-फिलॉस्फर अमरजीत ग्रेवाल को साहित्य रत्न शामिल हैं।

किसे कौन सा सम्मान मिलेगा...



-डॉ. विजय पी. भटकर
डॉक्टर ऑफ साइंस (ऑनरिस कॉसा)
सुपरकंप्यूटिंग, मल्टीलिंगुअल टेक्नोलॉजी में योगदान



-प्रो. केएन पाठक
ऑनरिस कॉसा, कंडेंस्ड मैटर फिजिक्स में रिसर्च और पीयू में प्रमुख सेंटर की स्थापना



-जस्टिस आदर्श कुमार गोयल, डॉक्टर ऑफ लॉज
संवैधानिक और पर्यावरणीय न्याय में योगदान



-डॉ. अमिताव घोष
डॉक्टर ऑफ लिटरेचर
साहित्य और वैश्विक मुद्दों पर लेखन के लिए

पीयू रत्न अवॉर्ड्स...



-डॉ. श्रीधर वेंबू
उद्योग रत्न



-प्रो. प्रदीप थलप्पिल
विज्ञान रत्न



-सरबजोत सिंह
खेल रत्न



-अमरजीत ग्रेवाल
साहित्य रत्न

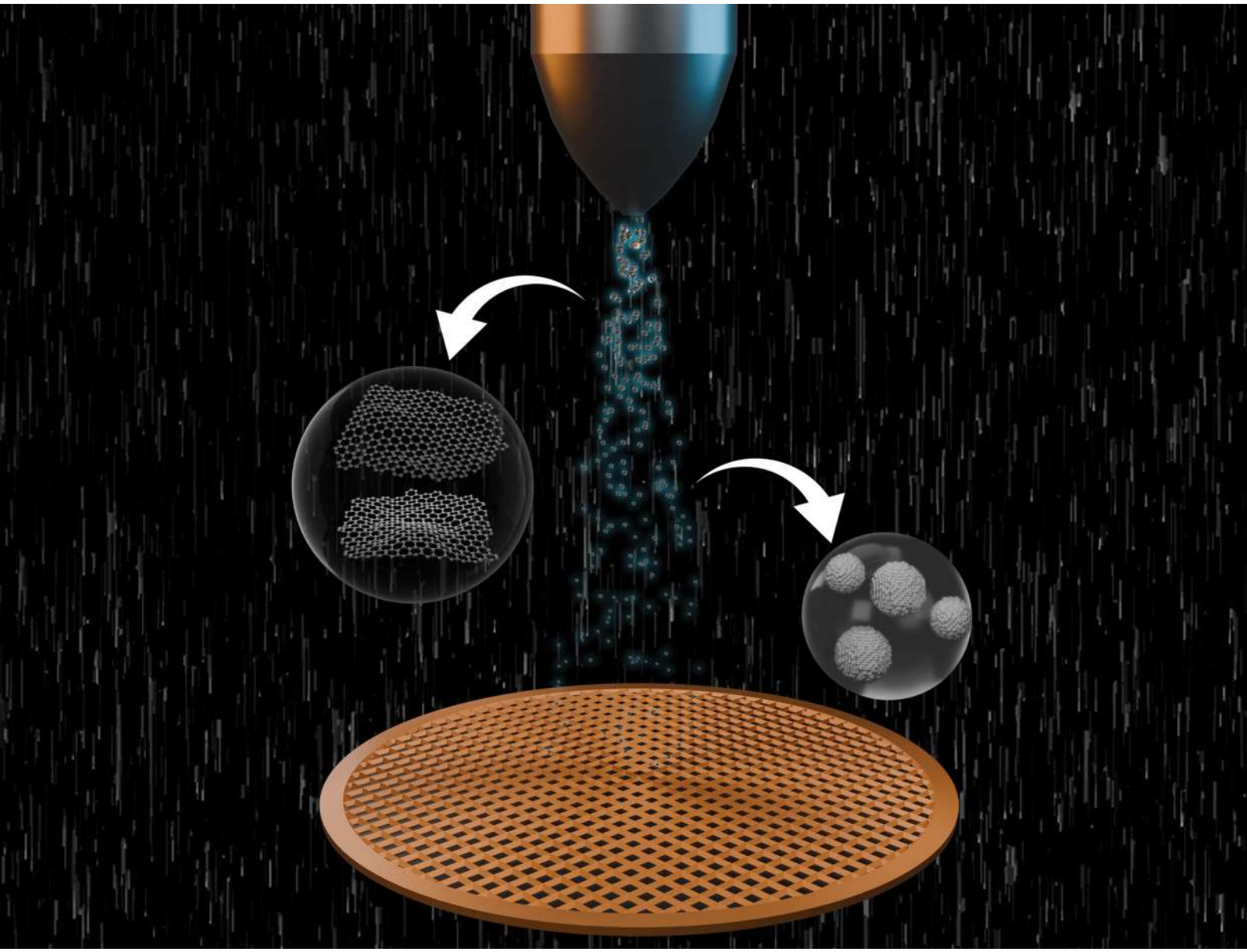
Cover arts

Volume 61
Number 30
18 April 2025
Pages 5529–5676

ChemComm

Chemical Communications

rsc.li/chemcomm



ISSN 1359-7345

ROYAL SOCIETY OF CHEMISTRY

COMMUNICATION

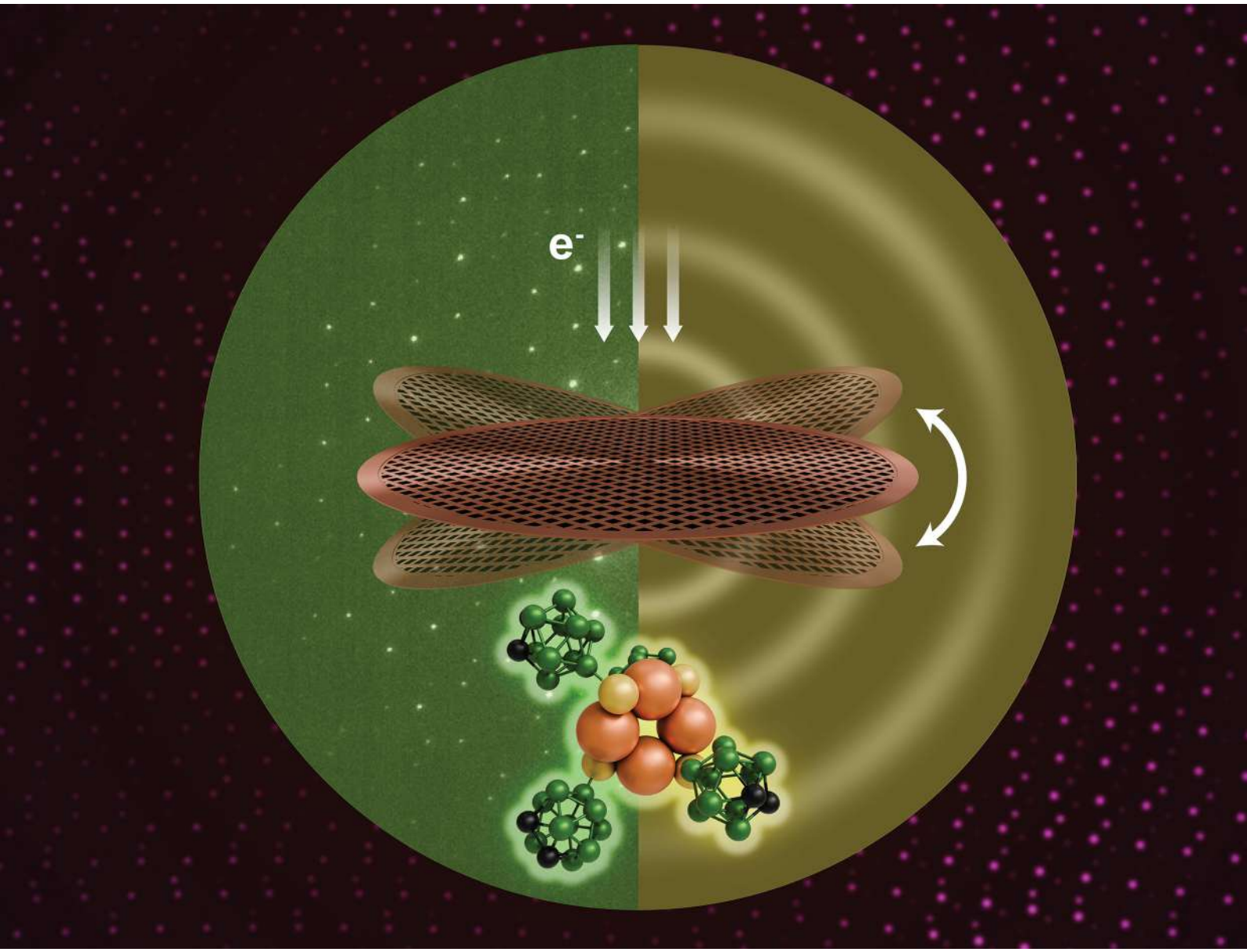
Thalappil Pradeep *et al.*
Nanosheet-to-nanoparticle transformation in charged water microdroplets: a pathway for 2D to 0D materials

Volume 61
Number 58
25 July 2025
Pages 10617–10866

ChemComm

Chemical Communications

rsc.li/chemcomm



ISSN 1359-7345

COMMUNICATION

Tomas Base, Anirban Som, Brent L. Nannenga, Thalappil Pradeep *et al.*
Mechanochromic luminescence in copper nanoclusters: resolving structural transitions through microcrystal electron diffraction

Pradeep Research Group



Acknowledgements

We thank our collaborators and students for their hard work. We are grateful to IIT Madras for its continuous support. Department of Science and Technology (DST), Government of India, Anusandhan National Research Foundation (ANRF), Science and Engineering Research Board (SERB), MRF Ltd., Government of Punjab, Eureka Forbes Ltd., National Investment and Infrastructure Fund Limited (NIIFL), Scheme for Promotion of Academic and Research Collaboration (SPARC) by GoI, Shanmugha Arts, Science, Technology & Research Academy (SASTRA), Rajiv Gandhi Centre for Biotechnology (RGCB), Vellore Institute of Technology, Indian Space Research Organization (ISRO), VA Tech Wabag Limited, Decision Point Pvt. Limited and Janpad Panchayat Kuwakonda are thanked for their generous funding.